

CLIMATE CHANGE & SUSTAINABLE DEVELOPMENT: NEW CHALLENGES OF THE CENTURY

T E X T B O O K



- *supported by*
- Visegrad Fund
-



- Visegrad Fund

• •



Petro Mohyla Black Sea National University, Ukraine



CLIMATE CHANGE & SUSTAINABLE DEVELOPMENT: NEW CHALLENGES OF THE CENTURY

TEXTBOOK

edited by
prof. Olena Mitryasova

- supported by
- Visegrad Fund

Mykolaiv – Lviv – 2022

UDC 502.131.1+551.58] = 111

Reviewers:

Oleg Aleksandrowicz, DSc, Professor, Head of the Department of Zoology and Animal Physiology, Institute of Biology and Earth Sciences, Pomeranian University in Slupsk, Poland;

Chad Staddon, Professor, Ph.D, FRGS, Associate Head of Department Geography & Environmental Management, University of the West of England, Director, International Water Security Network, United Kingdom;

Vasyli Retruk, DSc, Professor, Head of the Ecology, Chemistry, and Environmental Technologies Department, Vinnytsia National Technical University, Ukraine.

Approved for publication by the Academic Council of Petro Mohyla Black Sea National University, Ukraine (№3 14.04.2022)

Climate Change & Sustainable Development: New Challenges of the Century: Textbook / edited by prof. Olena Mitryasova. – Mykolaiv: PMBSNU, 2022. – 252 p.

Editor: prof. Olena Mitryasova

Climate Change & Sustainable Development: New Challenges of the Century: Textbook / edited by prof. Olena Mitryasova. – Lviv : PE "Publisher "BONA", 2022. – 252 p.

Editor: prof. Olena Mitryasova

ISBN 978-617-8097-01-1

The textbook is devoted to problems strategy of sustainable development as a road map of civilization; main components supporting the sustainable development of the planet; environmental ethics and economics as key instruments for sustainable development; inland waters: types, threats, challenges; water management: history; water purification; wastewater and sewage treatment; sustainable and environmental land management; green chemistry: principles, metrics and examples.

The book is written for students, postgraduate students, lecturers who are specialized and interested in the field of environmental research.

**Chapter I. – prof. Olena Mitryasova; Chapter II – assoc. prof. Pavel Nováček;
Chapter III. – prof. Piotr Koszelnik, Ph.D Małgorzata Kida; Chapter IV. – prof. Eva Chmielewská;
Chapter V. – Ph.D Lenka Bobušká; Chapter VI. – assoc. prof. Ruslan Mariychuk;
Chapter VII. – assoc. prof. Rita Bodáné-Kendrovics; prof. Zoltán Juvancz.**

The textbook prepared and funded under Visegrad Project.

This project was made possible though Grant #22110149 from International Visegrad Fund.

Publisher:

Petro Mohyla Black Sea National University, Ukraine
10, 68-Desantnykiv St., Mykolaiv, 54003, Ukraine
tel.: +380512765568
e-mail: rector@chdu.edu.ua; <http://www.chdu.edu.ua>

Publisher and Printed by: PE "Publisher "BONA", Phone: +38 (032) 234-04-12;
Certificate subject publishing DK №4275 from 06/03/2012.
Naukova St., Lviv, Ukraine, 79060

The authors of the sections are responsible for the reliability of the results.

The project is co-financed by the Governments of Czechia, Hungary, Poland and Slovakia through Visegrad Grant from International Visegrad Fund. The mission of the fund is to advance ideas for sustainable regional cooperation in Central Europe.

ISBN 978-617-8097-01-1

© Petro Mohyla Black Sea National University, Ukraine, 2022

All rights reserved. No part of this publication may be reproduced, stored in retrieval system or animated or transmitted in any form or by any means, electronic, mechanical, photocopying, recording or otherwise without the prior permission of the publisher.

About the authors



Olena MITRYASOVA - Professor, DSc, Professor of the Ecology Department of the Petro Mohyla Black Sea National University, Mykolaiv, Ukraine. Graduate with honors of the chemical faculty (diploma in organic chemistry) of the Mechnykov Odessa National University, Odessa, Ukraine. The author about 350 scientific works, including: 19 monographs and chapters of monographs, 14 textbooks on general chemistry, organic chemistry, history of chemistry, chemical ecology, environmental monitoring, water security for students. She has experience in coordinating international projects on internationalization of higher education and water security. Areas of research interests are: higher education; teaching methods; conceptual approaches, content, methods, forms, tools of environmental, natural and sustainable development education; water monitoring and security; problems of balanced nature management. She took part in 5 International projects, and in 3 she worked as a coordinator since from 2016. Prof. Olena Mitryasova is a coordinator of the Project the Grant #22110149 from Inretnational Visegrad Fund.



Pavel NOVÁČEK - Assoc. Professor of Environmental Studies at Palacký University in Olomouc, Faculty of Science. After graduating from the Palacký University (specialization „Environmental Protection“) he worked at the Institute of Landscape Ecology at the Slovak Academy of Sciences. In 1990 he returned to Palacký University in Olomouc. His work focuses on global environmental issues, sustainable development, and the study of foresight. He is founder of the study program „International Development Studies“. He earned his habilitation in 2005 at the Faculty of Science, of Constantine the Philosopher University in Nitra (Slovakia). Since 2007 he has been the head of the Department of Development Studies, at the Faculty of Science, Palacký University. Since 1998 ha has been a member of the Planning Committee of the Millennium Project (Washington, D.C.), and since 2008 Chairman of the Czech Association of the Club of Rome (until 2018). He has written a number of scholarly as well as popular book such as „Strategy for Sustainable Development“ (with Peter Mederly, 1996), „Crossroads of the Future“ (1999), „Quality of Life and Sustainable Development Indicators“ (with Peter Mederly and Jan Topercer), and „Sustainable Development“ (in 2011). These books are available at www.pavelnovacek.eu. Assoc. Prof. Pavel Nováček is a main expert of the partner's Palacký University in Olomouc in the Project the Grant #22110149 from Inretnational Visegrad Fund.



Eva CHMIELEWSKÁ - Professor, PhD., Eng. Obtained MSc. Diploma in Technical Chemistry at University of Applied Sciences (THC Merseburg) Germany; PhD. Degree of Inorganic Technology at Faculty of Chemical and Food Technology in Bratislava & Water Research Institute (Bratislava) in 1985, where she was employed over 10 years; in 1992–1994 worked as the Regional Director of US-Swiss Company Comco Martech, which provided remediation and environmental protection activities for the Central Europe Region; since 1994 she has been worked at the Faculty of Natural Sciences of Comenius University in Bratislava in the Environmental Section (Full Professor of Environmental Engineering since 2005). She published 25 monographs or Chapters of monographs (incl. in German and English), 6 text-books; over 110 papers in refereed scientific journals, 140 communications at scientific meetings, over 80 science popularizing articles and took a part or managed over 50 research projects. She guided nearly 60 students since 1985 by their various Diploma works (MSc., Bc., PhD). Prof. Eva Chmielewska is a main expert of the partner's Comenius University in the Project the Grant #22110149 from International Visegrad Fund.



Piotr KOSZELNIK – Professor, DSc, Present of the Rzeszów University of Technology, Poland. Professional background: 2010 – present: associate professor, Department of Environmental Engineering and Chemistry, Faculty of Civil and Environmental Engineering, Rzeszów University of Technology, Poland, 2010 – 2020 Head of the Department; 2012 – 2019 Dean of the Faculty; 2020- Present of the Rzeszów University of Technology, Poland. 1996-2010: doctoral and post-doctoral research scientist at the same institution. Educational background: 2009 – habilitation (D.Sc), environmental engineering. Warsaw University of Technology, Poland. 2003 – Ph.D., environmental engineering. Lublin University of Technology, Poland. 1996 – M. Sc., chemical technology. Rzeszów University of Technology, Poland. His main academic interests include environmental chemistry especially water chemistry, carbon and nitrogen cycling, stable isotopes, eutrophication, micropollutants in water, man-made lakes. Piotr Koszelnik is an author or co-author of 63 papers listed in the Scopus, four books and over 100 peer-reviewed publications. He took part in 11 projects – and in 3 he worked as a project manager. Prof. Piotr Koszelnik is a main expert of the partner's Rzeszów University of Technology, Poland in the Project the Grant #22110149 from International Visegrad Fund.



Małgorzata KIDA – Ph.D Eng. Professional background: 2019 – present: Assistant professor, Department of Environmental Engineering and Chemistry, Faculty of Civil and Environmental Engineering, Rzeszów University of Technology, Poland. 2013 – 2019: Research Associate, Department of Environmental Engineering and Chemistry, Rzeszów University of Technology, Poland. Educational background: 2019 – PhD., water and wastewater technology. Rzeszów University of Technology, Poland. 2013 – M.Sc., wastewater treatment and waste disposal. Rzeszów University of Technology, Poland. Her main scientific interest include the occurrence of micropollutants in the environment, methods of elimination of organic pollutants from various environmental samples, in particular in advanced oxidation processes. Author of 41 scientific publications, including 24 indexed in the Scopus. She participated in 8 research projects, including four as project manager. Dr. Małgorzata Kida - is a main expert of the partner's Rzeszów University of Technology, Poland in the Project the Grant #22110149 from Inretnational Visegrad Fund.



Lenka BOBUĽSKÁ – Ph.D, researcher and teacher of the Department of Ecology at University of Prešov in Prešov, Slovakia. She obtained MSc. degree in Ecology at Technical University in Zvolen and PhD. degree in Ecology at University of Prešov in Prešov. She worked as a postdoctoral researcher (2012-2013) at the Institute of Biogeochemistry and Pollutant Dynamics, ETH Zurich, Switzerland in Environmental Microbiology group. Since 2013 she has been working as a researcher and teacher at the Department of Ecology. She is an author of 2 university textbooks, 1 monograph chapter and over 45 scientific papers in soil ecology, microbial ecology and environmental impact assessment. She has participated on several national (KEGA, VEGA) and international projects (Interreg, Visegrad fund, Sciex). She has extensive experience in foreign scientific field works in Switzerland, Brazil, Poland, Romania. Her pedagogical activity is focused on the teaching of subjects Soil Science, Microbial Ecology, Environmental Education and Molecular Ecology. She has completed several foreign mobilities in Denmark, England, Romania, Spain, Brazil, Poland and Czechia. PhD Lenka Bobuľská is a main expert of the partner's University of Prešov in the Project the Grant #22110149 from Inretnational Visegrad Fund.



Ruslan MARIYCHUK - Dr. CSc., Associate Professor at the Department of Ecology, Faculty of Humanities and Natural Sciences, University of Prešov, Prešov, Slovakia. He has obtained MSc. Diploma in Faculty of Chemistry at the Uzhhorod State University (Uzhhorod, Ukraine) in 1994

in Inorganic Chemistry. PhD degree in Inorganic chemistry in 2000 at the Taras Shevchenko National University of Kyiv, Ukraine. From 2000 has worked as Assistant Professor at the Department of Ecology and Environment Protection, Faculty of Chemistry, Uzhhorod State University (Uzhhorod, Ukraine). Postdoctoral Studies on 2003-2007 at Departments of Inorganic chemistry, Regensburg University and Bayreuth University, Germany. From 2009, he obtained his Associate Professor diploma in Ecology and Environment Protection at Uzhhorod National University, Ukraine. From 2013 occupies the position of Associate Professor of the Department of Ecology at the Faculty of Humanities and Natural Sciences, University of Prešov, Slovakia. He has published more 200 scientific publications, including 50 papers in reputed journals, 3 handbooks and 3 patents. Research interests: green technologies, green chemistry, and nanomaterials. Assoc. Prof. Ruslan Mariychuk is a main expert of the partner's University of Prešov in the Project the Grant #22110149 from International Visegrad Fund.



Rita BODÁNÉ-KENDROVICS – Ph.D. She is the Vice Dean of the Rejtő Sándor Faculty of Light Industry and Environmental Engineering, and Director of the Environmental Engineering and Nature Sciences Institute, Óbuda University, Budapest, Hungary. M.Sc. thesis in the

Technical University of Budapest in mechanical engineering (1991), Ph.D in environmental sciences and education (2012), Municipal wastewater management special engineering course (2017). She works at Óbuda University in Rejtő Sándor Light Industry and Environmental Engineering Faculty as an associate professor. She teaches Water quality protection, Wastewater treatment technologies, Technical drawing. Her education skills cover theoretical lectures, laboratory practices, and fieldwork. She is an expert in water quality protection, treatment technologies, and project education. She is acting as vice dean of the Faculty. She is a member of the Hungarian Water Association and Hungarian Hydrological Society. Research experience in environmental education, project-work education, water quality protection, university lectures, 85 scientific publications.



Zoltán JUVANCZ – Emeritus Professor, Óbuda University, Budapest, Hungary. M.Sc. thesis in ELTE TTK in chemistry (1975), Ph.D. (1992), and D.Sc. in Hungarian Academy of Sciences (2003).

During his carrier, he made research in USA, Germany, Switzerland, and Sweden. He is an expert in analytical chemistry including chromatography, chiral separations and water chemistry, endocrine disruptive chemicals, pharmaceuticals in environments. He is a member of the EU expert board in environmental protection. His education skills cover theoretical lectures, laboratory practices, and field works. His scientific activities result in 220 publications (IF:103.81) with 1372 citations. He is a member of the Hungarian Chemical Society. His special interest is the selective degradation of enantiomer pairs in the environment. Prof. Zoltán Juvancz is a main expert of the partner's Óbuda University, Budapest, Hungary.

CONTENTS

Foreword	10
Chapter I. Main components supporting the sustainable development of the planet	13
§1.1. Scientific view of the Earth	16
§1.2. Systems that determine the stability of our planet	20
§1.3. Biodiversity as a major factor in the stability of the planet	24
§1.4. The water cycle as a factor in the stability of the biosphere	26
§1.5. Circulation of nutrients as a condition for the existence of the biosphere	30
§1.6. Acidification of the oceans	33
§1.7. Anthropogenic pollutants and the ozone layer	35
§1.8. The limits of sustainability of the planet and zero Carbon emission target	42
Chapter II. Environmental ethics and economics as key instruments for sustainable development	59
§2.1. Nowadays new challenges	60
§2.2. Cultural evolution	62
§2.3. Sustainable development – general background	64
§2.4. Value orientations	69
§2.5. Environmental economics	80
Chapter III. Inland waters: types, threats, challenges	94
§3.1. Inland water resources	95
§3.2. Hydrological and ecological characteristics of artificial water reservoirs.	98
§3.3. Large and small retention	101
§3.4. Types of artificial retention reservoirs	103
§3.5. Quality of inland waters	106
§3.6. The role of bottom sediments in the aquatic ecosystem	113
§3.7. Technological possibilities of removing organic pollutants from bottom sediments	118

Chapter IV. Water management: history; water purification; wastewater and sewage treatment	141
§4.1. History of water supply and sanitation	143
§4.2. Water purification	154
§4.3. Wastewater and sewage treatment	163
Chapter V. Sustainable and environmental land management	189
§5.1. Soil ecosystem: definition, composition and its functions	190
§5.2. Soil physical, chemical and biological properties	192
§5.3. Contamination in soil ecosystem: the sources of pollution, causes of contamination and the reducing of soil contamination	199
§5.4. Soil degradation: definition and what can involve	202
§5.5. Soil quality indicators of sustainable soil management	203
§5.6. General principles of sustainable land management	205
Chapter VI. Green Chemistry: Principles, Metrics, Examples	212
§6.1. Principles of green chemistry	213
§6.2. Green chemistry metrics: atom economy, E-factor, calculation waste prevention	215
§6.3. Green solutions in the chemical syntheses	224
Chapter VII. The Role of the Environmental Ethics and Project-Based Learning in the Education of Environmental Engineers	237
§7.1. Definition of environmental ethics and its trends	239
§7.2. Pedagogical methods of environmental education	241
§7.3. The strategy and methods of project-based education	243
§7.4. Evaluation of a project based environmental course	245

FOREWORD

Quality of life and sustainable development of society depends on the ability to join forces. Today the sustainable development concept is one of the main documents of development of the world and European countries, in particular the Visegrad countries. Among the great priorities of the movement of Ukraine to Europe, there are directives and regulations concerning sustainable development goals, namely the issue of climate change. Environmental management and climate change issues, environmental security and quality of natural resources, monitoring remain important, and the issue of adapting the national strategy for the future country's development to European policies is extremely relevant.

The problem is that in order to stop the worsening weather conditions by 2050, the increase in global temperature must be limited to about 1.5°C, in line with preindustrial levels. However, the world has already warmed to 1.2°C, thanks to the greenhouse gases that are released into the atmosphere, and the prospects for limiting further temperature increases over the next 30 years look distant. In fact, estimates based on current country pledges to cut emissions suggest that temperatures are likely to rise more than 2°C above pre-industrial levels by mid-century. In such a future, most of the planet is likely to suffer from drought; rainforests are at risk of extinction, and melting ice sheets will cause dangerous sea levels to rise and cause major changes in the behavior of ocean currents such as the Gulf Stream.

Environmental policy is a priority area of cooperation between Ukraine and the Visegrad. The innovative element is that Visegrad–Ukraine partners join efforts of academic and civil societies in the environmental field. Integration in the field may be achieved through the creation of a harmonized legal, regulatory, methodological, and organizational base that should meet the requirements of European and national environmental security. Actual new challenges are in implementing new Visegrad–Ukraine different methodologies into national practices aimed at goals of improving sustainable development. It is extremely important to improve the understanding of the content of European environmental activities in Ukraine.

Professionals are gathered to exchange practices and experiences in the field of climate change and sustainable development. The attractive and close collaboration of the partners provides discussion and reflection on Visegrad–Ukraine research partnership and study experience with regard to environmental management, eco-innovations. The content of the book has a strong impact on all students, young researchers, and also officials, and publicity through getting knowledge about actual environmental policy in the field of climate change and sustainable development in the EU.

The main thematic chapters of the textbook:

- ✓ Main components supporting the sustainable development of the planet;
- ✓ Environmental ethics and economics as key instruments for sustainable development;
- ✓ Inland waters: types, threats, challenges;
- ✓ Water management: history; water purification; wastewater and sewage treatment;
- ✓ Sustainable and environmental land management;
- ✓ Green chemistry: principles, metrics, examples;
- ✓ The role of the environmental ethics and project-based learning in the education of environmental engineers.

The book is co-financed by the Governments of Czechia, Hungary, Poland and Slovakia though Visegrad Grant from International Visegrad Fund. The mission of the fund is to advance ideas for sustainable regional cooperation in Central Europe.

There are chapters of scientists from Visegrad countries and Ukraine on the book's pages. The textbook is the result of the work of scientists, leading experts from universities:

Chapter I. – prof. Olena Mitryasova, Ecology Department of the Petro Mohyla Black Sea National University, Mykolaiv, Ukraine;

Chapter II. – assoc. prof. Pavel Nováček, the Environmental Studies Department, Faculty of Science Palacký University in Olomouc, Olomouc, Czech Republic;

Chapter III. – prof. Piotr Koszelnik, Ph.D Małgorzata Kida, the Department of Chemistry and Environmental Engineering, Rzeszow University of Technology, Rzeszow, Poland;

Chapter IV. – prof. Eva Chmielewská, the Faculty of Natural Sciences of Comenius University in Bratislava, Bratislava, Slovakia;

Chapter V. – Ph.D Lenka Bobušská, the Department of Ecology, Faculty of Humanities and Natural Sciences, University of Prešov, Prešov, Slovakia;

Chapter VI. – assoc. prof. Ruslan Mariychuk, the Department of Ecology, Faculty of Humanities and Natural Sciences, University of Prešov, Prešov, Slovakia;

Chapter VII. – assoc.prof. Rita Bodáné-Kendrovics; emeritus prof. Zoltán Juvancz, Department of Environmental Engineering, Óbuda University, Budapest, Hungary.

The content of the book does not cover all questions of climate change and sustainable development problems.

We express our sincere thanks to all the authors, who have presented the own, interesting chapters on the problems of climate change and sustainable development, contributing to this book was published.

In the future we hope that the content is on the pages of this edition will find creative affiliate cooperation through successful joint implementation of actual ideas, proposals, scientific and practical developments.

We would like to thank the International Visegrad Fund for supporting the publication of the book within the Grant #22110149.

Professor Olena Mitryasova

Mykolaiv, Ukraine,

March 2022

Chapter I

MAIN COMPONENTS SUPPORTING THE SUSTAINABLE DEVELOPMENT OF THE PLANET



In this section you will learn about

- ✓ Scientific view of the Earth.
- ✓ Systems that determine the stability of our planet.
- ✓ Biodiversity as a major factor in the stability of the planet.
- ✓ The water cycle as a factor in the stability of the biosphere.
- ✓ Circulation of nutrients as a condition for the existence of the biosphere.
- ✓ Anthropogenic pollutants.
- ✓ The ozone layer.
- ✓ The limits of sustainability of the planet.
- ✓ Zero Carbon emission target.



Key words:

the Holocene
the Anthropocene
Biome
Biodiversity
Water cycle
Nutrients

Desertification
Eutrophication
Dead zones
Anthropogenic pollutants
Aerosol
The ozone layer
Carbon neutrality
Circular (green) economy

Understandings of how our planet works are constantly changing. Since the appearance of the first people in ten years, the average temperature has reached 10°C. The temperature-stabilized only 10 thousand years ago. It was a stable interglacial period called the Holocene. The stability of the planet is due to the stable temperature of the Holocene. The sea level stabilized. Predictable seasons began to exist. Stability was very important, which made possible the rapid development of human civilization. The exponential growth of human pressure on the planet has allowed us to reach the limit at which our geological epoch, which has been called anthropogenic, has already formed.

The most alarming sign is the melting of glaciers. Since 1980, significant global warming has led to new much faster melting of glaciers around the world, leaving many extinct and many others in jeopardy. According to scientists, if the glaciers of Greenland melt, the sea level will increase by 7 m. The planetary climate limit is a warming of 1.5°C.

The stability of our planet depends not only on climate. Additional research by scientists has shown that there are four more boundaries in the planet's biosphere, namely: terrain; biodiversity; water cycle; nutrients.

Mankind continues to degrade tropical rainforests at a rate that threatens to cross critical ecological boundaries. It's not just tropical forests, all the trees on our planet play a role in maintaining their stability. The loss of 25% of the Earth's forest can lead to catastrophic consequences.

In just 50 years, humanity has wiped out 68% of the world's wildlife population. About 70% of crops depend on insect pollination. Deterioration of nature is not limited to insects. Today, only 30% of all birds on the planet are wild. Among all mammals on the planet, wild species make up only 4% by weight.

The next boundary of the biosphere is related to the circulation of water on the planet. It is determined that for 1 person per day requires about 3000 liters of freshwater, for drinking and personal hygiene requires 50 liters; for household needs a person uses about 100 liters per day and for industrial needs 150 liters. The remaining 2,500 liters are needed for food, ie for growing everything that a person eats. Every person on the planet uses about 1.5 million liters of water a year! By 2025, about 2.8 billion people from 48

countries will be short of water, and by 2050 the number of people who are constantly short of water will reach 7 billion.

The combination of climate change and increased nutrient consumption will lead to a decrease in ocean oxygen levels by an average of 3% –4% by 2100. Two main causes of deoxygenation are outlined: ocean warming from fossil fuel combustion and excessive algae growth (eutrophication). Ocean deoxygenation has a wide range of implications for marine biodiversity and the day-to-day functioning of ocean ecosystems.

According to forecasts, in the future the oceans will continue to absorb CO₂ and become more acidic. Estimates of future CO₂ levels show that by the end of the XXI century, the acidity of ocean surface waters can increase by almost 150%. This will lead to unprecedented pH levels in the oceans in 20 million years.

Aerosols are one of the most dangerous forms of pollutants that globally affect the state of the biosphere. 75% of aerosols are formed due to the combustion of fossil fuels. Aerosols can capture sunlight and scatter it. These particles can affect the climate, absorbing solar radiation and thus cause cooling of the planet. The cooling effect of aerosols masks 45% of the effects of global warming. Every year, about 7 million people die from air pollution. Life expectancy in large cities is reduced by an average of 3 years. However, scientists have not yet determined where the limit of air pollution passes, but it is estimated that 7 million deaths from air pollution are the limit for aerosols. Aerosols are dust, particles of smoke and ash from fires, fuel combustion, volcanic eruptions, pollen and plant spores, and others. On average, each square centimeter of the earth's surface contains about 10⁹ aerosol particles.

The question of the ozone screen, predicting its depletion and the consequences of this process affects the stability of the Earth's ecosystem and, above all, all living things on Earth.

Currently, scientists have defined a clear structure of planetary boundaries. There is strong evidence that humanity is at risk of climate change and biodiversity loss. There is a frequency of droughts, the number of fires on many continents, the negative impact on the Amazon rainforest, the acceleration of melting glaciers, the catastrophic state of coral reefs. Corals are a kind of indicator of the state of the environment, they fade when the water becomes too warm. Under conditions of global warming there is a mass extinction of corals. The effects of discoloration are 10 times greater than those of a large-scale tropical cyclone of the fifth category.

The planet will experience harsher and more devastating weather events over the next 30 years. To stop the deterioration of weather conditions by 2050, the increase in global temperature should be limited to about 1.5 ° C according to the pre-industrial level.

1.1. Scientific view of our planet.

Recent discoveries by scientists studying how our planet works are certainly important for all the inhabitants of the Earth. On the one hand, these discoveries are very disturbing, but on the other hand, they give us hope for the best and knowledge of how to fix everything.

Scientists say there are ways to overcome the global environmental crisis. It is not about the planet, but about humanity and the future of mankind. We still have a chance, we have a chance for a better future! And it's great that today we have such an opportunity (Fig. 1.1.)!

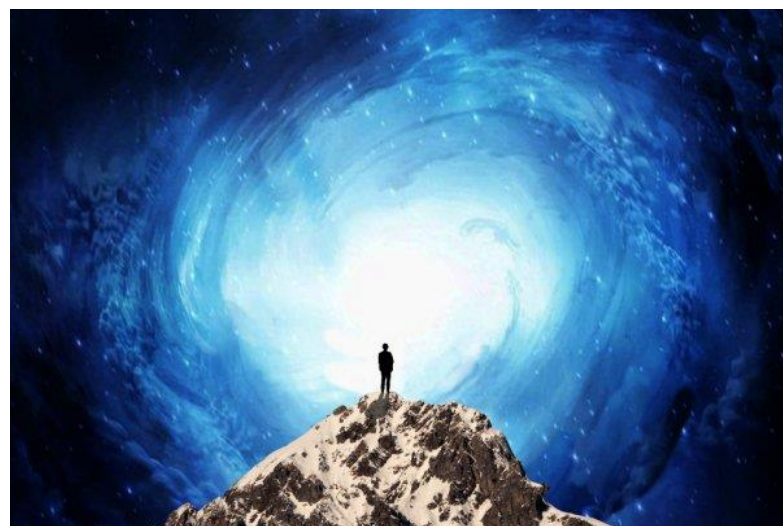


Fig. 1.1. Man and the Universe.

Understandings of how our planet functions are constantly changing. We now understand better than ever how the relationships in the environment are important to human survival. But biodiversity is shrinking and our climate is changing.

What factors support the stability of the planet Earth? It is thanks to science that we have become the first generation to learn what factors support the stability of the planet and what undermines its existence.

Thus, the graph of the state of ice objects shows how the temperature of our planet has changed over the past millennia (Fig. 1.2).

Since the appearance of the first people in ten years, the average temperature has reached 10°C. These were very difficult times. It should be noted that the temperature stabilized only 10 thousand years ago. It was a stable interglacial period. Geologists gave this period a special name – the **Holocene**.

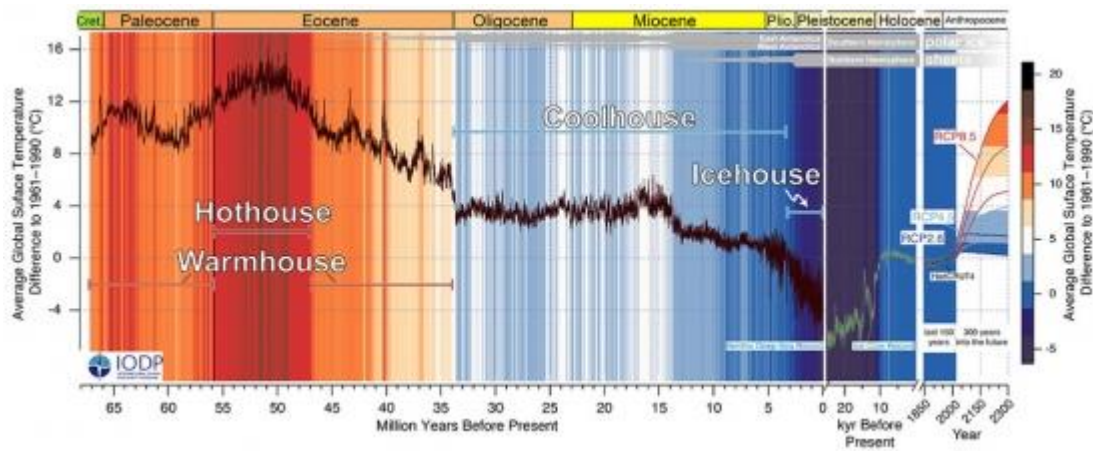


Fig. 1.2. The average global temperature for the last 66 million years.

The Holocene (from the Greek ὅλος – whole, whole; and the Greek Καίνος – new, recent) – a modern, latest epoch of the Quaternary period, which covers the postglacial period. It began 11,700 years ago and continues to this day. During this period, land and sea acquired modern contours, formed geographical areas, formed riverbeds and peatlands. The Holocene is an incredible phenomenon, a period during which the average global temperature varies within 1°C. Only 1°C! Due to this period, our planet has acquired the form it has today (Fig. 1.3).



Fig. 1.3. Thanks to the Holocene, our planet has acquired the appearance that it has now.

The stability of the planet is due to the stable temperature of the Holocene. The sea level stabilized. Predictable seasons began to exist. Stability was very important, which made possible the rapid development of human civilization. And humanity, without wasting time, took advantage of this. Intensive development of agricultural production began with the cultivation of such crops as rice, wheat, corn, sorghum,

and others. This interglacial period helped to reach the modern level of civilization. Thus, the Holocene is the only state on the planet that can support the modern form of life.

Since the beginning of human civilization, we have depended on the stable state of the planet, on its constant two ice sheets, the flow of rivers, forests, stable weather and a variety of life forms. Throughout the Holocene, a stable planet provided humanity with food, clean water, and clean air. But this period is behind us.

The exponential growth of human pressure on the planet has allowed us to reach the limit beyond which our geological epoch has already formed. Scientists have recently announced that the Holocene has ended and a new period has begun – **Anthropocene**.

Anthropocene – a geological era when the level of human activity plays a crucial role in the Earth's ecosystem. The term was introduced into scientific practice in the 1980s by ecologist Eugene Stormer, and was widely popularized by atmospheric chemist Paul Krutzen, a Nobel laureate in chemistry, who first used the term anthropocene in 2000. Since mid-2015, the term has been considered by special workers. groups of geological scientific societies.

Thus, humanity is now the main driving factor on the planet Earth (Fig. 1.4). We have turned half of the habitable areas into agricultural fields. We move more sediment and rocks than all-natural phenomena combined. We catch most of the fish in the ocean. Nine out of ten people breathe polluted air.



Fig. 1.4. Humanity is the main driving factor on the planet Earth.

What does the future of greenhouse gas emissions look like?

In fig. 1.5. presents some potential future scenarios of global greenhouse gas emissions (measured in gigatons of carbon dioxide equivalent) based on Climate Action Tracker data. There are five scenarios:

- Lack of climate policy: projected future emissions, if climate policy is not implemented, will lead to warming of 4.1–4.8° C by 2100 (compared to pre-industrial temperatures);
- Current climate policy: projected warming of 2.8–3.2° C by 2100 based on current climate policy;
- National promises: if all countries achieve their current goals and promises set out in the Paris Climate Agreement. It is estimated that the average warming by 2100 will be between 2.5 and 2.8° C. This will far exceed the overall goal of the Paris Agreement to keep warming "well below 2 ° C".
- 2 ° C consecutive: limit the average warming to 2° C by 2100. This would require a significant increase in the ambitions of current commitments under the Paris Agreement.
- 1.5 ° C consecutive: limit the average warming to 1.5° C by 2100. This requires a very urgent and rapid reduction in global greenhouse gas emissions.

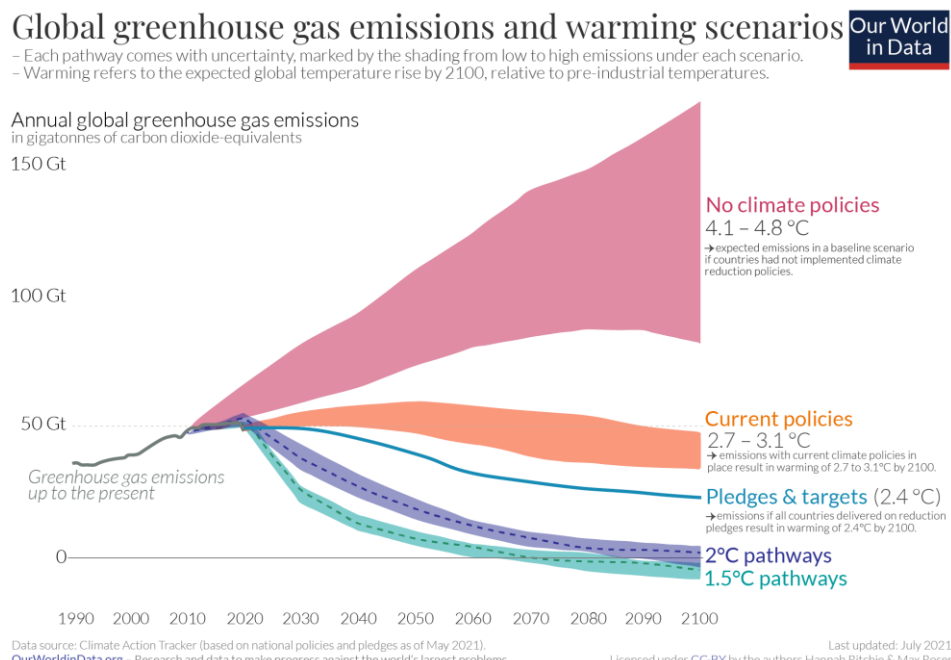


Fig. 1.5. Future greenhouse gas emissions scenarios.
(<https://ourworldindata.org/future-emissions>)

During the life of one person, we heated the Earth by more than 1°C. In just 50 years, humanity has changed the state of the Earth's ecosystem, which our planet has been for the last 10,000 years. Mankind risks destabilizing the entire planet.

Indeed, today's human civilization must seriously consider the risk of destabilizing the entire planet.

1.2. Systems that determine the stability of the Earth.

What systems determine the stability of our planet? These systems maintained the stable state of the planet throughout the Holocene. The more impact we have on Earth, the more likely it is that these systems will fail if we cross certain boundaries. This will be the collapse of the stability of the Earth on which we depend. Scientists are now working to find the point at which humanity will cause nonlinear changes in the planet's ecosystem.

If scientists can define planetary boundaries, will they be able to provide a roadmap, a plan for overcoming this global crisis?

The first limit is quite well defined. Now, when the temperature is higher than at the beginning of human civilization, there is a possibility that humanity has already crossed the Earth's climate.

The most alarming sign is the melting of glaciers (Fig. 1.6). Since 1980, significant global warming has led to a new much faster melting of glaciers around the world, leaving many of them extinct and the existence of many others under significant threat.

In certain parts of the Andes and the Himalayas, the disappearance of glaciers will have significant consequences for the supply of freshwater to the surrounding population and local ecosystems. The current rapid destruction of the Greenland and West Antarctic glacier glaciers, which began around 1985, could have the effect of rising ocean levels, affecting coastal areas around the world.



Fig. 1.6. View of the Whitchack Glacier in the Glacier Peak Wilderness in 1973 and 2006.

What we see in Fig. 1.5 does not yet destabilize the planet, but the presence of two ice masses in the Arctic and Antarctica is an important condition for the planet to remain stable. So, the melting of glaciers is an alarming signal of destabilization of our planet, as all the glaciers of the Earth are cooling it.

This cooling effect from the two Arctic and Antarctic massifs maintained the planet's stable temperature throughout the Holocene and reflected excess energy into space. This huge white surface of glaciers (Fig. 1.7) reflects 90-95% of the heat coming from the Sun. As these ice sheets begin to melt, they shrink in size, causing their edges to darken and absorb heat. The fact that liquid is formed on the surface of glaciers leads to the fact that glacial shields cease to cool themselves and begin to heat up. This is a critical point, the point when change begins to become irreversible and humanity loses control over processes or phenomena.



Fig. 1.7. The surface of glaciers reflects 90-95% of the heat coming from the Sun.

Snow that has accumulated in Greenland for thousands of years has formed a 3 km long ice dome. Due to the melting of the dome is lowered into warmer air, which accelerates this process. The more the glacier melts, the colder the climate must become to compensate for these changes, but the climate in Greenland is too warm right now. Today, this island has already crossed the border, through which 10 thousand m^3 of ice melts in one second. This is the average rate of melting, and it will continue to increase as the climate gets warmer.

Thus, scientists claim that Greenland is almost lost due to the irreversible climate change that is happening today. The danger of a critical point is that after crossing it, the process can be stopped. After a critical point, the planet may fall into a state of irreversibility, which will pose a complete threat to human existence.

According to scientists, if the glaciers of Greenland melt, the sea level will increase by 7 m. Rising sea levels threaten hundreds of coastal cities. After all, a stable sea level was very important for the development of civilizations. The Greenland Glaciers are not the only ones on our planet that maintain the stability of their temperature. There are also glaciers in Antarctica, which until recently were

considered a stable glacial system. But due to climate change, the area of Antarctic glaciers is also declining. The water formed by this melting flows into the ocean.

If West Antarctica melts completely, the sea level will rise by more than 5 m, and if the East, the sea level will rise by more than 50 m.

Everything in the Earth's ecosystem is interconnected. If one part of the system crosses a critical point, there is a high probability that other parts of the system will cross this limit. This is similar to the domino effect. Thus, if global warming continues, there is a high probability that Earth's systems will cross critical points.

Crossing critical points, we trigger irreversible changes. This means that our planet will turn into a sphere that will relieve stress by absorbing carbon dioxide and absorbing heat. Climate warming is due to the absorption of greenhouse gases. Long before the advent of human civilization, the concentration of carbon dioxide in the Earth's atmosphere precisely regulated the temperature on the planet. During the Holocene, the CO₂ concentration was relatively stable (Fig. 1.8).

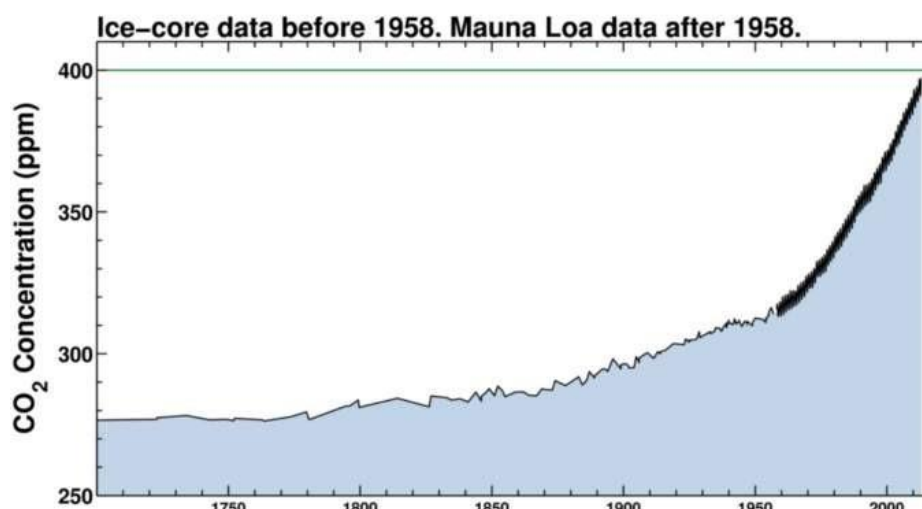


Рис. 1.8. Carbon dioxide concentration.

With the industrial revolution, everything changed. In 1988, we achieved emissions of 350 parts per million of carbon dioxide into the Earth's atmosphere. Then humanity crossed the critical line, causing rapid climate change. Therefore, at a concentration of CO₂ of 350 ppm in the atmosphere, the planet falls into the danger zone. This is the so-called first mess that humanity crossed more than 30 years ago.

We have now reached a point where the concentration of carbon dioxide in the atmosphere is 415 parts per million and we are already seeing the effects of being within the critical zone of climate change. Thus, the frequency of droughts and floods has significantly increased, ice melting has accelerated, permafrost has thawed, and the frequency of forest fires has increased.

Ahead is the second limit, and humanity is rapidly approaching the mark of 450 parts per million. The dangerous zone of planetary boundaries is marked by a range of uncertainty in science. Currently, scientists claim that this range is within 550 ppm. Thus, an area where the concentration of carbon dioxide is 550 parts per million and more is defined as a high-risk area, where irreversible critical points are quite probable and inevitable.

The planetary limit of the climate is warming by 1.50C. And the only way not to cross this line is to completely abandon mining for 30 years. This topic has now received a very wide discussion among scientific, governmental, and public circles.

The stability of our planet depends not only on climate.

Additional research by scientists has shown that there are four more boundaries in the planet's biosphere. The first is the terrain. Thus, the Earth's biome consists of three tropical forests, mixed forests, taiga, meadows, and swamps.

A **biome** is a large regional or subcontinental system. The classification of terrestrial ecosystems by biomes is based on vegetation types and the main unchanging physical characteristics of the landscape. The geographical distribution of biomes corresponds to the soil and climatic zones of the continents. They have existed for a long time and are sufficiently adapted to the specific physical and geographical conditions of the environment.

Secondly, it is biodiversity, all forms of life at all levels of biological organization.

Third is the water cycle.

Fourth, these are nutrients that are essential for the existence of the biosphere.

The first of the boundaries of the biosphere is the composition of the Earth's habitats. It is about how humanity is changing these habitats. We are fast approaching a critical point in one of the largest wildlife areas in the Amazon. After all, tropical forests play an important role in maintaining the stability of the planet. Vast areas of the Amazon were cleared for growing crops.

A large-scale scientific project has been underway since 1998, which has determined that a large area of tropical forests is experiencing drought. In the Amazon, the drought season usually lasts three months. Due to changes in global temperatures, plowing, the drought season has increased by 6 days every decade since the 1980s.

Due to the reduction of forest area, its ability to recycle water is reduced. If the dry season lasts more than four months, the trees in the jungle will die and be replaced by the savannah. This phenomenon is called **savannization**, or **desertification**.

Desertification is a phenomenon of reducing the natural resource potential of the territory below the conditional (permissible) level, which affects the degradation of vegetation, deterioration of biological productivity of lands, can lead to conditions similar to desert.

If deforestation exceeds 20–25% of their area, then with increasing global warming, there is a high probability that the process of savannization (desertification) will become irreversible. This will be possible for 50–60% of the Amazon area. As of now, about 20% of the Amazon rainforest has been lost.

The Amazon jungle is capable of absorbing up to 200 billion tons of carbon dioxide over the next 30 years, which is equivalent to the amount of CO₂ emitted into the atmosphere over the past 5 years. And this is a significant reason for decisive action to address the problems of declining rainforest and global warming.



Fig. 1.9. The Amazon jungle is capable of absorbing up to 200 billion tons of carbon dioxide over the next 30 years.

Mankind continues to reduce rainforests at a rate that threatens to cross critical levels. It's not just tropical forests, all the trees on our planet play a role in maintaining their stability. The loss of 25% of the Earth's forest can lead to catastrophic consequences.

1.3. Biodiversity as a major factor in the stability of the planet.

Reducing the forest area of the Earth causes the next important consequence - the reduction of biodiversity. Biodiversity itself is another important condition for the sustainability of the planet's existence. About 1 million species of plants and animals from 8 million are threatened with extinction. If this negative trend continues, it could lead to the sixth mass extinction of species.

In just 50 years, humanity has wiped out 68% of the world's wildlife population. The planet is at the epicenter of a crisis to reduce biodiversity. Due to the

tendency to reduce biodiversity, humanity will not be able to feed the entire planet, because for this the ecosystem must function properly. For example, in the United Kingdom in the 1990s, the complete extinction of jamals, which are the main pollinator of crops, was recognized.

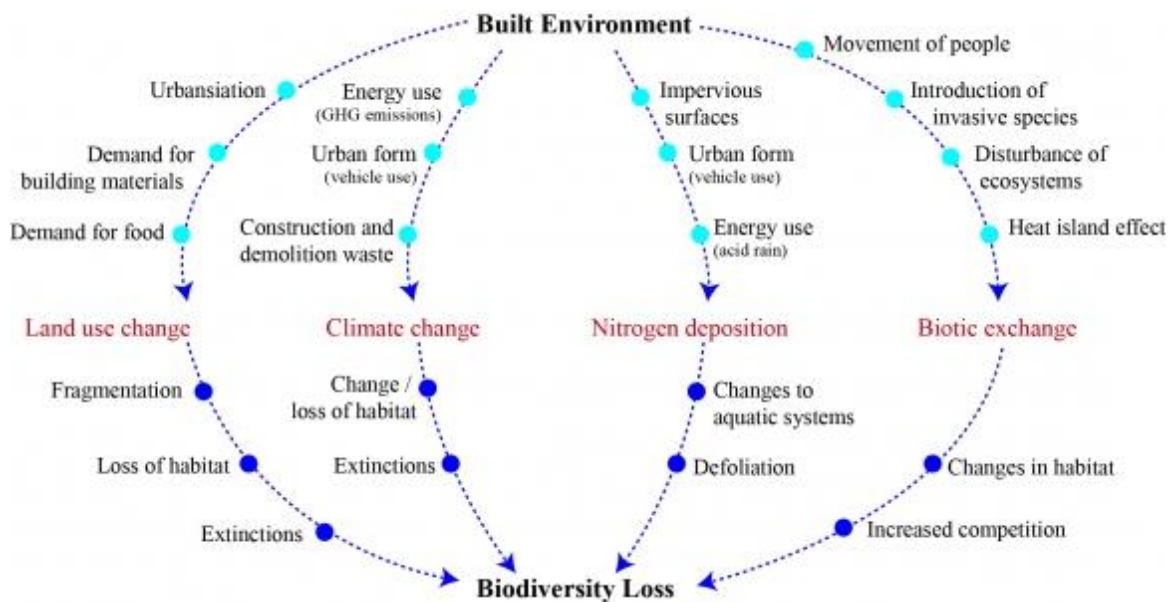


Fig. 1.10. Ecosystem services analysis in response to biodiversity loss.

About 70% of crops depend on insect pollination. However, due to the increase in sowing areas by monocultures, the insect population decreases sharply. Paradoxically, an increase in arable production capacity nullifies the foundations on which this industry is based. The harmonious existence of flora and fauna is a set of tools for the existence of human civilization.

Scientists have tried to calculate the benefits of insects that perform various functions in the Earth's ecosystem. However, their value cannot be calculated until the insects suddenly disappear.

Of course, the deterioration of nature is not limited to insects. Mankind has displaced wildlife, expanding agricultural land to most of the habitable Earth. Today, only 30% of all birds on the planet are wild. Among all mammals on the planet, wild species make up only 4% by weight.

What other part of the natural world can humanity lose? There are many critical points regarding the loss of biodiversity, because life is very difficult. The single boundary of an ecological catastrophe is difficult to determine due to the scarcity of nature itself, the relationships between the many natural components. However, today humanity is in the red zone, when species are disappearing and its

ecosystems are being destroyed.

At the beginning of the decade of 2022, it is time to set a strategic goal – zero losses of natural resources.

The value of global warming at 1.5°C will be zero loss of natural resources.

1.4. The water cycle as a factor in the stability of the biosphere.

The next boundary of the biosphere is related to the circulation of water on the planet. This is another fundamental factor on which humanity depends.

Thus, scientists have estimated that 1 person a day requires more than 3,000 liters of freshwater to survive. Does it seem like so much ?! After all, 50 liters are required for drinking and personal hygiene; for household needs a person uses about 100 liters per day, and for industrial needs 150 liters. The remaining 2,500 liters are needed for food, ie to express everything that a person eats.

Every person on the planet uses about 1.5 million liters of water a year!



Every product we buy, from t-shirts, bread to electrical appliances, requires water to produce.

For example, water footprint indicators for some products:

- ✓ tea – 90 liters of water per 1 teapot;
- ✓ wheat – 650 liters of water per 500 g;
- ✓ milk – 1000 liters of water per 1 liter;
- ✓ hamburger – 2500 liters of water per 1 hamburger (150 g of beef);
- ✓ beef – 4650 liters of water per 1 chop (300 g);
- ✓ 1 kg of chocolate – 24,000 liters of water;
- ✓ 1 kg of sugar – 1500 liters of water;
- ✓ 1 cup of coffee – 140 liters of water.

The water footprint covers three components:

- ✓ blue;
- ✓ green;
- ✓ gray.

The blue water footprint includes the amount of surface and groundwater

consumed during the production of goods or services.

Green water footprint is the amount of rainwater consumed in the production process, which is especially relevant for agricultural and forestry products.

Gray water footprint is an indicator of freshwater pollution that may be associated with production. It is defined as the amount of freshwater required to absorb the load of pollutants based on current environmental quality standards.

The comparison of the planet's population by continent with the percentage of water supply is given in Fig. 1.11.

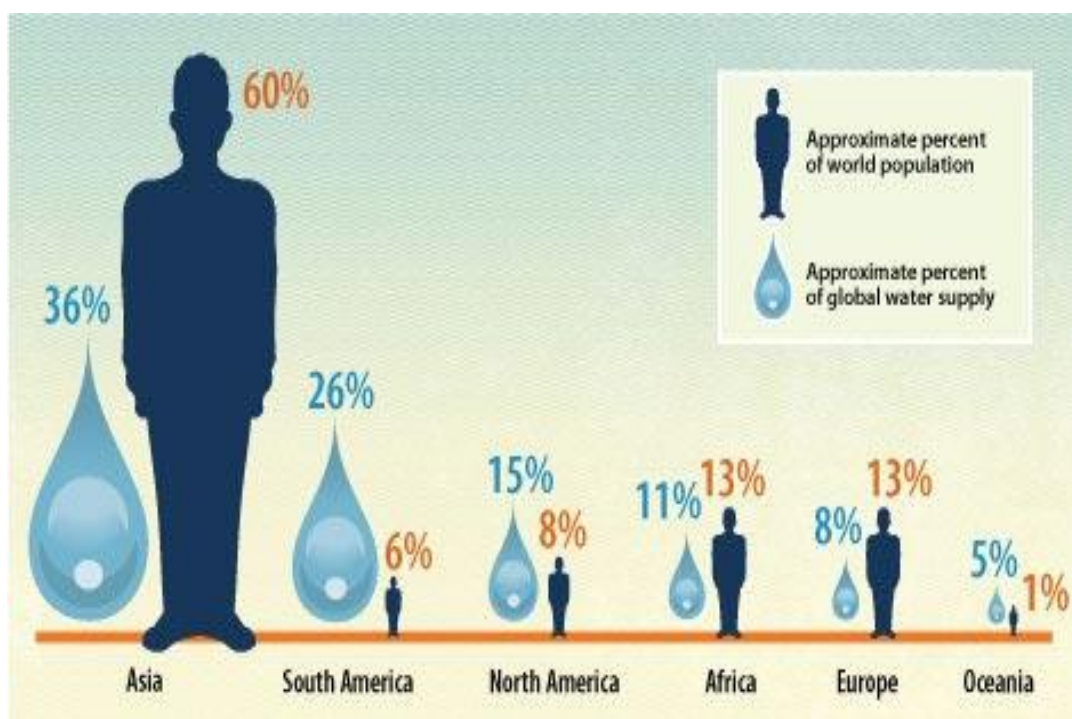


Fig. 1.11. Approximate percentage of the world's human population and approximate percentage of the world's water supply (water drop)

(<http://www.climateinfo.org.ua/content/chomu-slid-dbaty-pro-svii-vodnii-slid>)

The following countries have the largest water footprint: USA ($2.483 \text{ m}^3/\text{year}$); Greece ($2.389 \text{ m}^3/\text{year}$); Malaysia ($2.344 \text{ m}^3/\text{year}$); Italy ($2.322 \text{ m}^3/\text{year}$); Thailand ($2.223 \text{ m}^3/\text{year}$).

The countries that are most dependent on water imports include: Kuwait (87%); Malta (87%); The Netherlands (82%); Bahrain (80%); Belgium (80%).

The richest in renewable water resources: Brazil ($8233 \text{ km}^3/\text{year}$); Russia ($4507 \text{ km}^3/\text{year}$); USA ($3069 \text{ km}^3/\text{year}$); China ($2896 \text{ km}^3/\text{year}$); Indonesia ($2838 \text{ km}^3/\text{year}$).

By 2025, about 2.8 billion people from 48 countries will be experiencing water

shortages, and by 2050 the number of people who are constantly experiencing water shortages will reach 7 billion.

In Ukraine, the average water footprint is 1575 m³/year per capita, but the world average is 1240 m³/year per capita. In terms of water, Ukraine ranks 51st among the countries of the world. Thus, Ukraine has a fairly significant water footprint, but belongs to one of the low-water countries in Europe.

Pure water is a colorless transparent liquid, the density of which is at a temperature of 4°C, Max 1,00 g/cm³. Water has an abnormally high heat capacity of 4,17 J/(g •K).

The high dipole moment of water molecules (1,82 D) and the ability to form four hydrogen bonds: two – as the donor protons and two as acceptor protons, that is not only increases the ability of the water as the solvent, but also contribute to the formation of certain structures of water associates, as well as molecules of biopolymers in aqueous solutions.

A high dielectric water constant ($\epsilon=78,5$) promotes the opening of salts, acids, bases and their dissociation on ions. An ionic state of substances in the aquatic environment contributes to high speed flow of biochemical reactions.

At standard conditions about 30% of all the molecules of water are in the form of individual molecules, 70% included in the associates. 40% of them are stabilized associates with the structure that is «structured water» and 30% of them are random associates that do not have a specific structure.

Ordinary clean water is a complex dynamic system! On the state of equilibrium in the water environment influence: temperature; acoustic, magnetic and electric fields; ions H⁺ and OH⁻, which arise due to the dissociation of water; radicals, which are generated in the process of radiation exposure in the water.

To increase content of structured water may: melting ice (meltwater) with support for low temperature (below 10°C); long contact with the surface of insoluble in water minerals: apatite, calcite, quartz; shungit; silica; flint; clay and some others, which leads to the formation of spring water; dissolve in water of substances for ions or molecules which characterized positive hydration; effect of vibration and the different fields with certain characteristics: acoustic, magnetic, electric; effect of supercritical temperature and pressure.

Water with high content of «structured» water is useful for living organisms and therefore often referred to as «alive water». This water is better absorbed by organisms because without significant adjustment used for the hydration of tissues, proteins and other biological substratum.

The presence in water of various associates which have a different structure

and a different time of life, allows justifying yet another feature of water - structural-information memory. The ability to transition to different structural-information states is characteristically not only for clean water, but for water systems in living organisms.

There are positive and negative hydrations depending on the time of water molecules' life. Positive hydration characteristic for ions with a large charge and a small radius: Li^+ ; Na^+ ; Mg^{2+} ; Al^{3+} ; Fe^{3+} ; Cr^{3+} ; F^- ; Cl^- ; CO_3^{2-} ; HCO_3^- . A lifetime of water molecules in a hydration shell is larger than the "free" water. Ions with positive hydration contribute an increase in the solution of the «structured» water. Probably, ions Na^+ and Cl^- are concentrated in the intercellular fluid. Negative hydration is characteristic for ions with a low surface density charge: K^+ ; Cs^+ ; NH_4^+ ; I^- ; Br^- ; HPO_4^{2-} ; H_2PO_4^- ; NO_3^- ; ClO_3^- . These ions weakly attract water molecules and have in hydrate shell a thin dense structured layer and a big destructured layer. Probably, K^+ ; HPO_4^{2-} ; H_2PO_4^- ions are concentrated in the intracellular fluid, contributing to the increase in its destructured water.

The unique property is that the water is at the same time for all organisms are the substrate and metabolite.

The water on the way to the human body: absorb from air gases, volatile organic substances; extract organic and mineral substances from plants; dissolves the salt, minerals, organic compounds from soil; enriched by viruses, bacteria, fungi, algae and other aquatic and their metabolites; team up with metabolic water; is irradiatehaving by the electromagnetic fields; accumulate the possible information. Drinking water should have a «memory»: about diverse life that it created; about the myriad of living creatures that inhabit the surface water; about close contacts which water had with live and inert matter for natural conditions; but not about the «high-tech treatment» technology. Any chemical and/or physical-chemical treatment ("clearing") of natural water degrades its quality and moves away from the drinking water, destructured water. Drinking water has a «memory»: about diverse life that it created; about the myriad of living creatures that inhabit the surface water; about close contacts which water had with live and inert matter for natural conditions; about the «high-tech treatment» technology.

A human body 60% consists of water, of which 42% falls on the intracellular liquid, others on the intercellular fluid, which is divided into intravascular and intracellular liquid. Water is not only the environment, but also an active participant in the processes of life.

Factors such as land use, population growth, water pollution and climate change are harming on the quantitative and qualitative state of water resources almost all over the world. Climate change is a major global problem that threatens

the existence of both humanity and biodiversity on Earth. Since the beginning of the industrial revolution, the global temperature of the planet has increased by almost 1.5°C. Such slight warming is already leading to serious problems – the area of glaciers is decreasing, sea levels are rising, severe storms, tornadoes, heavy floods and droughts have become more frequent.

Among European countries, Ukraine ranks 17th in terms of water supply and 124th in the list of 181 countries in the world. On average, there is only 1 thousand m³ of local runoff per capita in Ukraine, however, in Canada this figure is 94.3 thousand m³, Russia – 31.0 thousand m³, the United States – 7.4 thousand m³, Germany – 1,9 thousand m³.

Provision of local water resources in some areas country differs almost 60 times: from 0.14 km³/year in the Kherson region, to 7.92 km³/year – in the Zakarpatska region. The least supplied water resources are Donbas, Kryvyi Rih, Crimea and southern regions Ukraine, where the largest consumers of water are concentrated.

There are different scenarios about the future of water resources. Thus, according to the National Meteorological Service of Great Britain in Central and Eastern Europe, including Ukraine, the flow of rivers in the middleXXI century will decrease by 50% in summer. According to the results of the assessment of possible changes in the water resources of Ukraine in the context of global warming during the XXI century (except for river basins within the Ukrainian Carpathians and Zakarpatska) there will be a reduction in water runoff by 25–50%. According to researchers, by the middle of this century there will be a significant reduction in water resources of the plains of Ukraine (up to 70% in the southeast), and the Ukrainian Carpathians will stabilize and even increase water resources.

By 2050, the semi-arid zone will expand to the north. In the period 2031–2050, the reduction of water resources in the south of Ukraine may reach 60–70%, and in the north – at least 30–40%.

The question is to determine the critical threshold of freshwater content, crossing which the system will collapse. The volume of river water currently in use is the reason for their drying up. In general, scientists estimate that freshwater reserves are still out of risk, but humanity is rapidly approaching the risk zone.

1.5. Circulation of nutrients as a condition for the existence of the biosphere.

The last limit of the biosphere is the circulation of nutrients. The main nutrients for plants are compounds of Nitrogen and Phosphorus. However, the consequences of increasing the use of these compounds as fertilizers lead to

disruption of the circulation of elements in the aquatic ecosystems of the planet.

For example, in the Baltic Sea, the biodiversity of predatory fish, including cod, has declined significantly in recent decades due to the removal of fertilizer residues from fields that then end up in the sea. Today, the Baltic Sea is the most polluted in the world, and there are many such examples.

The process of getting Nitrogen and Phosphorus compounds into water bodies, which leads to its gradual decrease in productivity and destruction, is called **eutrophication** (Fig. 1.12). This phenomenon is accompanied by intense flowering of blue-green algae, which leads to a significant reduction in the amount of soluble oxygen in the water. The amount of phosphorus compounds in the water body is increasing.

As a result of massive and unbalanced eutrophication, most of the flora and fauna of the reservoir can be destroyed, and the ecosystem of the reservoir - dramatically and catastrophically changed.



Fig. 1.12. Eutrophication of the reservoir.

- ✓ By 2100 the population of the Earth will increase by 50%. This will increase the amount of wastewater that enters the reservoirs. The current rate of population growth means that by 2100 eutrophication will increase 2-4 times.

- ✓ Increased storms and stormwater runoff will increase nutrient losses on land and into water bodies. This will promote the growth of algae, zooplankton and phytoplankton in the lakes, rivers and seas of the planet.

- ✓ Global warming will lead to water warming. Warm water will promote the rapid growth of algae. In addition, the melting of ice at the poles of the Earth will increase the area of water bodies, which will lead to an even greater increase in methane emissions.

The same, eutrophication, occurs in the ocean when dead zones form (Fig. 1.13). **Dead zones** are areas with low oxygen content. They are formed due to the ingress of nitrogen-phosphorus fertilizers from wastewater into the world's oceans.

Such sites already exist in several parts of the world. The eutrophication of the ocean was to be one of the causes of previous periods of mass extinction of living organisms. Today, such areas are spread over tens of thousands of square kilometers.

O₂ levels in the ocean have fallen by about 2% since the 1950s, and the amount of water completely depleted of oxygen has quadrupled since the 1960s. Sixty years ago, only 45 marine areas suffered from low oxygen levels, and in 2021 the number was over 700. About 50% of the oxygen loss in the upper ocean is the result of rising temperatures.

The combination of climate change and increased nutrient consumption will lead to a decrease in ocean oxygen levels by an average of 3% –4% by 2100. Researchers have named two main causes of deoxygenation: ocean warming from burning fossil fuels and excessive algae growth (eutrophication). Ocean deoxygenation has a wide range of implications for marine biodiversity and the day-to-day functioning of ocean ecosystems.

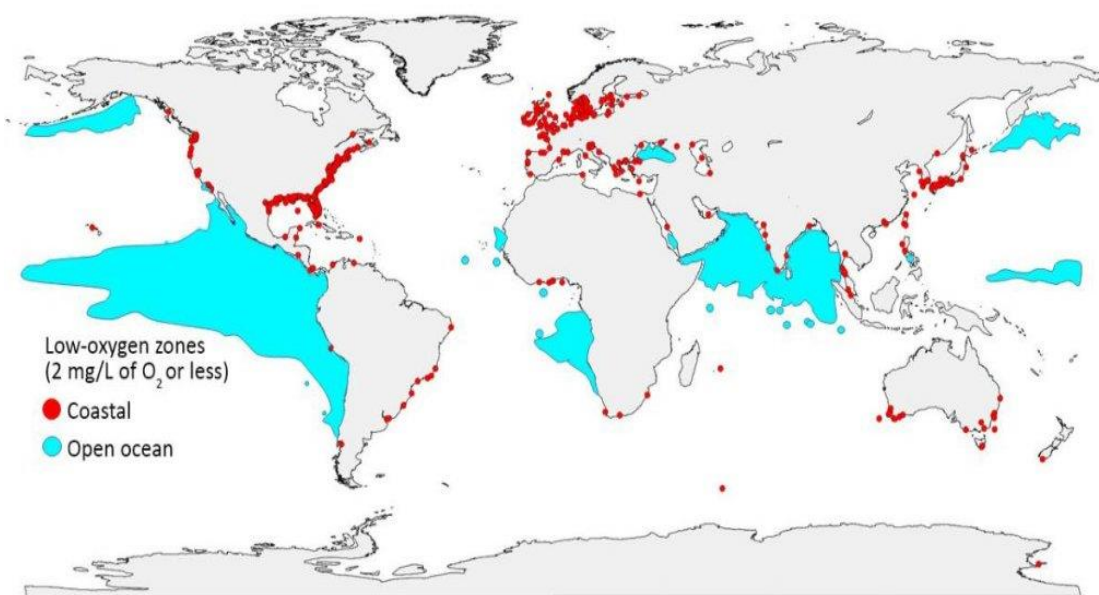


Fig. 1.13. The largest dead zones are found in the Gulfs of Mexico, Chesapeake, Black and Baltic Seas.

Declining oxygen levels in the ocean are one of the most serious environmental problems. If the temperature continues to rise, the ocean will continue to lose oxygen. So, humanity has already crossed the limit of nutrient consumption!

- ✓ Nutrients;
- ✓ Water;

- ✓ Forests;
- ✓ Biodiversity, and
- ✓ climate are the main components that supports the stability of our planet.

1.6. Acidification of the oceans.

When carbon dioxide is released into the atmosphere, about 2/3 of the amount of this gas enters the oceans. This phenomenon changes the chemical composition of the ocean, in particular the pH level. The result is a decrease in the acidity of the environment, it makes the pain sour. The chemistry of this process is as follows:



During the dissolution of carbon dioxide in water, carboxylic acid is formed. In recent decades, the acidity of the world's oceans has fallen by 26%. This process continues today.

Then the acid interacts with chemical compounds, carbonate ions, reducing their concentration. This affects various living organisms, especially those that require carbonate (CO_3^{2-}) to form the skeleton. Ocean acidification, changing chemical characteristics of seawater, affects growth, reproduction and metabolic processes of many marine organisms. Plants and animals whose shells are formed, in particular, of calcium carbonate are the most vulnerable, because lowering the pH leads to deterioration of calcification conditions. Low saturation with calcium carbonate (CaCO_3) its mineral components – aragonite and calcite – can adversely affect the rate of calcification of many marine species. A more acidic environments will harm the sea species such as mollusks, corals and some species of plankton. The shells and skeletons of these animals may become less dense or strong, and coral reefs are more vulnerable to damage by storms and slow down restoration.

Acidification can affect other physiological processes that affect, in particular, growth and survival in the early stages of life of organisms. In addition, acidification changes the behavior of living organisms. For example, it can affect the formation of shoals of fish due to their deterioration of sensory mechanisms, hearing, smell and sight.

Ocean acidification has different effects on different species. Increasing CO_2 concentrations in the ocean can have a positive effect on some species of algae and seaweed as it can increase the rate of their photosynthesis and growth. In any case, the acidification of the ocean changes food chains as a result affects ecosystems. These changes can intensify in combination with the effects of other new climate risks. So, for example, a decrease in oxygen levels in the ocean (state ocean deoxygenation) in some regions already affects marine flora and fauna. Moreover, all

these influences are amplified globally warming. Rising temperature in the ocean affects marine species and ecosystems, causes discoloration of corals and loss of space reproduction of marine fish and mammals (Fig. 1.14).

Ocean acidification affects all parts of the world's oceans, including coastal estuaries. Many economies depend on fish and shellfish. Food from the ocean is a major source of protein for people around the world.

Ocean acidification is a new global problem. According to forecasts, in the future the oceans will continue to absorb CO₂ and become more acidic. Estimates of future CO₂ levels show that by the end of the XXI century, the acidity of ocean surface waters can increase by almost 150%. This will lead to unprecedented pH levels in the oceans in 20 million years.

As the rate of ocean acidification increases, scientists, conservationists and politicians recognize the urgent need to strengthen the scientific basis for decision-making and action.

An effective policy to combat ocean acidification should encourage the rapid phasing out of fossil fuels, given its significant role in this problem.

Thus, the oxidation of the ocean, which leads to changes in the pH of the environment, can cause the mass extinction of certain species of flora and fauna, which was observed in the geological record. Therefore, increasing the amount of carbon dioxide in the atmosphere is a "game with fire" given the unpredictable future scenarios of the planet's ecosystem. While the planet is in a safe zone, in terms of ocean acidification, but risks becoming dangerous.

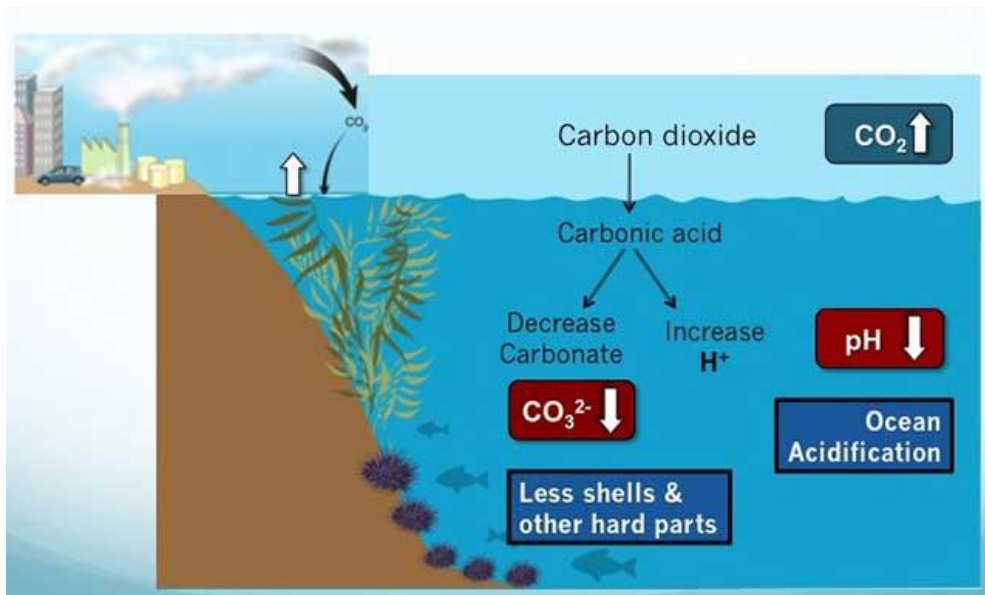


Fig. 1.14. The process of ocean acidification.

1.7. Anthropogenic pollutants and the ozone layer.

Although the Earth is a complex structure, only a few systems have been identified that support its stability.

One of them is the classification of anthropogenic pollutants. These are the so-called new compounds, which include nuclear waste, persistent organic pollutants. As well as heavy metals and microplastics. Human civilization is constantly creating new synthetic materials that can interact catastrophically with the environment. At present, it is impossible to determine the extent of these pollutants. So far, the cumulative effect of these pollutants has been little studied. However, most anthropogenic pollutants can cause global destabilization if left unchecked.

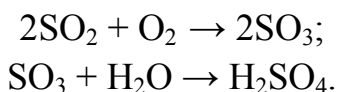
Currently, one of the forms of pollutants that globally affect the state of the biosphere is **aerosols**. These are dispersed systems consisting of fine solid or liquid particles (dispersed phase) and a dispersed gaseous medium (eg air). 75% of aerosols are formed due to the combustion of fossil fuels.

Aerosols can capture sunlight and scatter it. These particles can affect the climate, absorbing solar radiation and thus cause cooling of the planet. The cooling effect of aerosols masks 45% of the effects of global warming. Every year, about 7 million people die from air pollution. Life expectancy in large cities is reduced by an average of 3 years. However, scientists have not yet determined where the limit of air pollution passes, but it is estimated that 7 million deaths from air pollution are the limit for aerosols.

Aerosols are dust, particles of smoke and ash from fires, fuel combustion, volcanic eruptions, pollen and plant spores, and others. On average, each square centimeter of the earth's surface contains about 10⁹ aerosol particles.

The total level of man-made air pollution reaches about 1 billion tons of aerosols and gaseous emissions, as well as 300–5000 million tons of dust. This amount is still a small part of the total mass of the atmosphere. But the intensity of pollution is growing, and the bulk of pollutants are concentrated in the lower atmosphere and concentrated in areas of accumulation of industry and transport.

Sulfur (IV) oxide is emitted mainly by thermal power plants and chemical plants. Sulfur dioxide CO₂ is a colorless gas with a pungent odor. It is well soluble in water, thus forming sulfuric acid. A similar process occurs in the humid air. Sulfur(IV) oxide can oxidize in air, forming sulfuric acid according to the scheme:



Oxidation of SO₂ in SO₃ is facilitated by:

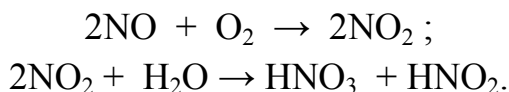
- oxides and salts of metals in the air in the form of dust, which play a role

catalysts;

- drops of water, fog;
- photons of solar radiation (photochemical oxidation).

Acid rain causes significant damage to the environment (Fig. 1.15).

Nitrogen oxides act similarly according to the scheme:



Precipitates that contain acids ("acid" rains) have a detrimental effect on the environment. For example, sulfur dioxide irritates the mucous membranes of the nose and eyes, causes coughing, sore throat, bronchitis. In large quantities, this gas is life threatening. It is environmentally dangerous for plants, especially fruit trees. Also, this gas can destroy works of art made of marble, cladding (marble turns into plaster). Forests suffer from "acid rain", defoliation is often carried out (artificial dropping of needles or leaves).

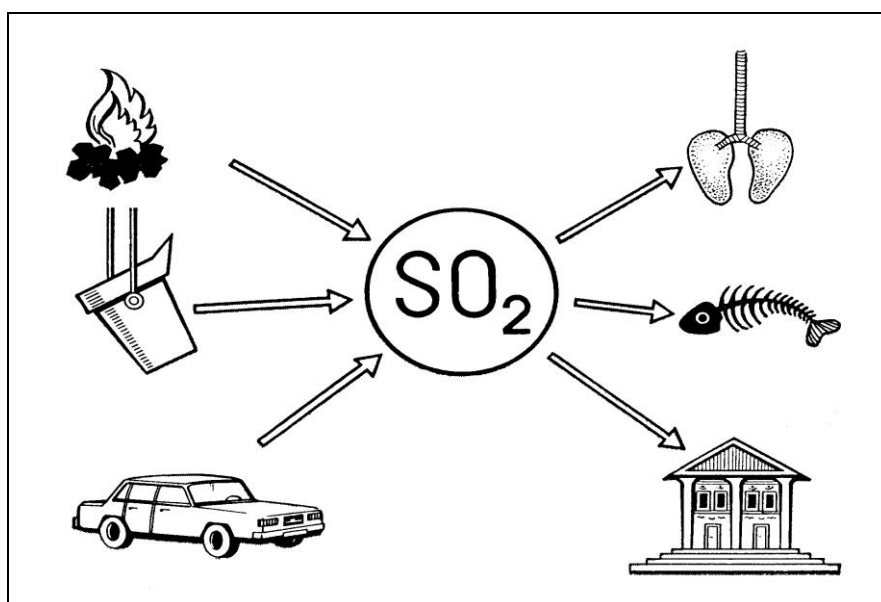


Fig. 1.15. Sources and harmful effects of sulfur dioxide on humans and the environment.

Sulfate aerosols in the stratosphere can scatter the sun's ultraviolet radiation, thus "helping" the ozone layer to absorb UV rays. This indicates the complexity of the interactions of different pollutants and the need to study the chemistry of the atmosphere in a single complex.

Nitrogen oxides can enter the atmosphere as a result of the activity of soil bacteria (mainly N_2O and NO). Human economic activity also makes a significant contribution to the emission of nitrogen oxides. In addition to participating in the formation of "acid rain", nitrogen oxides affect the formation of photochemical smog

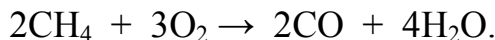
(a word derived from the English smog – smoke and fog – dust) – complex air pollution due to the concentration of air masses in large cities.

Car internal combustion engines are a major source of pollution. In addition to nitrogen oxides NO_x and ozone, in the photochemical smog there are:

- carbon(II) oxide CO (product of incomplete combustion of gasoline fuel);
- C_xH_y hydrocarbons;
- aldehydes and more complex organic compounds.

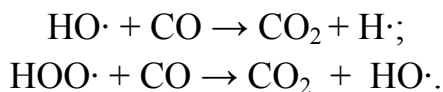
All this "bouquet" in wet weather is in the air of big cities. This phenomenon was often observed in London, Los Angeles, Buenos Aires, Sao Paulo, Rio de Janeiro, Mexico City, Ankara, Tokyo, Moscow, St. Petersburg, and in Ukraine - in the cities of Dnieper and Donbas (Zaporizhzhia, Dnieper, etc.). Photochemical smog is now more common. Unlike conventional smog, which is formed in low clouds and high humidity in cold weather, photochemicals are formed on clear, sunny days. They occur in a polluted atmosphere under the influence of solar radiation. This creates new substances that are more toxic than those that enter the atmosphere. This smog dramatically reduces the transparency of the air, irritating of the mucous membranes, nose and mouth, exacerbation of lung and allergic diseases. Vegetable and ornamental plants wither quickly. Smog causes corrosion of metals, cracking of paints, rubber products, damage to clothing, etc.

Atmospheric carbon(II) oxide is formed mainly (70%) naturally, mainly during incomplete oxidation of methane:



CO is also formed during the incomplete combustion of gasoline. A car emits up to 3 m³ of carbon monoxide per hour, and a truck emits up to 6 m³. The annual share of CO emissions from incomplete combustion of fuel, vehicles, thermal power plants is an additional 20-30%. But the concentration of carbon(II) oxide in the atmosphere increases slowly. This is because in nature there are processes that lead to the absorption of the latter. Binding of CO in the biosphere is carried out in the following ways:

- oxidation to CO₂ (partially and very slowly);
- absorption by soil organisms;
- dissolution in ocean waters;
- diffusion into the stratosphere and interaction there with more reactive molecules and atoms according to the scheme:



Carbon monoxide has a very harmful property for humans: it can specifically bind to hemoglobin Hb blood – a protein – a carrier of oxygen in the body, forming a

stable complex of carboxyhemoglobin HbCO. Carbon monoxide molecules compete with oxygen molecules for the right to bind to blood hemoglobin and are 210 times superior to oxygen!

The molecules of CO and O₂ are very similar in electronic structure, but CO has a greater than O₂ chemical affinity for the Fe²⁺ ion in hemoglobin.

Almost a small amount of CO can remove most of the hemoglobin from the blood, and the body receives less oxygen. For example, a person who inhales air with a CO content of only 0.1% for several hours absorbs it so much that most of the hemoglobin (60%) binds to the COHb complex (the same reduces the normal function of blood with O₂ transfer). This process is accompanied by tinnitus, dizziness, loss of consciousness. Smokers are subject to a similar action of CO. There is a direct relationship between smoking and the level of carboxyhemoglobin in the blood. The high content of CO in the atmosphere of megacities contributes to the growth of cardiovascular disease, because the heart is forced to distill in a more "hard" rhythm poisoned by carboxyhemoglobin blood.

Atmospheric pollutants also include solid suspended particles. The main sources of their entry into the atmosphere are metallurgical plants, construction industry, transport and others. The problem of these pollutants is extremely relevant. They can be allergic, carcinogenic (asbestos), cause respiratory diseases.

Due to air pollution, large industrial cities receive 15% less sunlight and 10% more precipitation in the form of rain, hail and snow.

There was a significant (by 25–30%) reduction in the yield of most crops by 2–3 km around the source of pollution. Some plant species respond to even small concentrations of pollutants. For example, conifers, walnuts, tobacco, clover are very sensitive to sulfur dioxide, and onions, strawberries, spruce and pine - to fluoride. Cases of mass death of cattle and poultry during smog have been noted. Bees are very sensitive to air pollution.

For a long time, the only way to solve air pollution problems was the ability of the atmosphere to self-clean. Mechanical particles and gases dispersed in the air, fell to the ground with rain and snow, and were neutralized by interacting with natural substances. However, the ability of the atmosphere to self-clean. The magnitude and speed of industrial, transport and domestic emissions far outweigh the natural possibilities for self-organization. Therefore, the processing of industrial waste, the installation of gas and dust treatment plants at all existing enterprises, the transition to waste-free technological processes, the improvement of internal combustion engines in cars and others are important.

One of the important measures to be taken for air purification is landscaping. The composition of harmful substances should be taken into account, because

different plants purify the air differently. Where the air is polluted with smoke, it is best to plant white acacia, mulberry, Canadian poplar, and where dust - elm. Horse chestnut cleans the air very well from vehicle emissions, and Karelian birch, sharp-leaved maple, weeping willow, etc. from gasoline and gas.

It is necessary to control the concentration of harmful substances in the air at the level of maximum permissible levels, ie those indicators at which these substances do not show toxic effects.

Atmospheric pollution is a global phenomenon. The atmosphere knows no borders and therefore requires the mobilization of people around the world to protect it from pollution.

Solar radiation, especially its short-wave ultraviolet part, is one of the strongest factors in the environment that determine the conditions for the development and existence of all living things on Earth. It is known that the biological activity of radiation is greater the shorter the wavelength. Therefore, UV radiation quanta have a particularly high radiological activity. Almost a small amount of radiation is enough to quickly destroy all living things on the earth's surface, but the atmosphere does not reliably protect the biosphere from UV radiation (Fig. 1.16).

The question of the ozone screen, predicting its depletion and the consequences of this process affects the stability of the Earth's ecosystem and, above all, all living things on Earth.

Ozone – translated from Greek fragrant. It is a gas whose molecule contains three atoms of Oxygen – O_3 (one of the forms of existence of Oxygen in the free state). Its smell can be felt after a thunderstorm, because in the lower atmosphere it is formed during lightning discharges, and in the stratosphere it is formed under the action of the Sun.

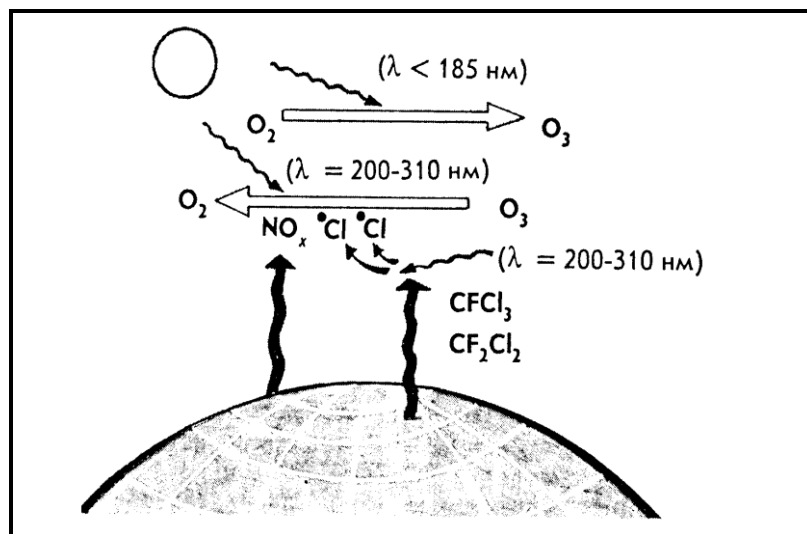


Fig. 1.16. Scheme of influence of fluorochlorocarbons and nitrogen oxides on the ozone layer.

Ozone in the atmosphere is very small - millionths of a percent. The largest amount of this gas at an altitude of 20–25 km – 0.001%. At this altitude, ozone forms a shell, which is called the ozone "screen" of the Earth. The thickness of this layer is only a few millimeters. In small quantities, ozone is very useful for living organisms. People experience a noticeable improvement in well-being when breathing "ozone" air after a thunderstorm. But when the amount of ozone increases significantly, there is an increase in human morbidity. A small decrease in the thickness of the ozone layer increases the likelihood of skin cancer. Reducing this layer twice would have disastrous consequences for the earth's funds.

The ozone problem consists of the following aspects.

1) This layer protects our planet from the harmful effects of ultraviolet radiation from the Sun. Small doses of such radiation are useful because they promote the formation in the human body of vitamins "D", which increase the body's resistance (immunity). However, significant doses of this radiation can kill living organisms, especially humans.

The ozone layer in the lower stratosphere absorbs significant amounts of the sun's ultraviolet radiation.

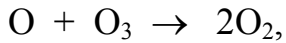
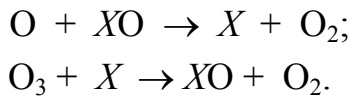
2) In recent decades, a zone with very low ozone concentrations over Antarctica has emerged and is expanding rapidly. This area was called the "ozone hole". There are many reasons for the depletion of the ozone layer. For example, nitrogen oxides pose a significant risk to the ozone layer. In the Northern Hemisphere, the amount of ozone decreased by 3–6%. After the major powers of the world agreed to end nuclear tests, this danger disappeared.

Ozone is also lost during the launch of artificial satellites of the Earth, because it forms a hole for several kilometers, which disappears very slowly.

Chlorine and its compounds are involved in the process of ozone depletion. Chlorine compounds, the sources of which are chemical plants, as well as the operation of household appliances, rise to the heights of the ozone layer. Freons (polyhydric chloro-, bromoorganic compounds such as: methylchloroform – CH_3Cl_3 , Freons-11 (CFCl_3), –12 (CF_2Cl_2), methyl bromide (CH_3Br), gallons – 1301 (CF_3Br) and 1211 (CF_2ClBr) are widely used. The latter are released into the atmosphere as sprays, solvents, refrigerants in refrigerators and air conditioners, and organically brominated substances are widely used for firefighting, military, and agricultural purposes, and have been banned since 1995, but are currently banned. no effective replacement was found.

In the lower atmosphere, chloro- and bromo-organic compounds remain inert. But under the action of solar radiation in the stratosphere, freons decompose and destroy ozone when they interact with ozone. The chemistry of ozone depletion in

catalytic cycles is as follows:



where X – catalyst ($-\text{OH}$, NO_x , Cl, Br, Me etc.).

The most common CFCs have a long "relaxation time" (the time of their "life" in the stratosphere, which is defined as the average time from entry into the atmosphere or the formation of a molecule to its photochemical destruction). For example, for CFCs-11, -12 it is 60 and 120 years, respectively. Thus, freons-11 and -12 almost after the cessation of their production and use will be present in the atmosphere for many decades. As for bromine atoms, their ozone-depleting properties are 10 times greater than chlorine atoms. In addition, if chlorine depletes ozone at an altitude of about 40 km, where its amount is relatively small, the maximum effect of bromine on ozone falls on the layer of 14-22 km, which is close to the ozone maximum. Scientists have determined that each chlorine atom destroys almost 100,000 ozone molecules.

As already noted, nitrogen oxides can also destroy ozone molecules. One of the sources of supply of nitrogen oxides to the atmosphere is agro-industrial production. In soils treated with nitrate fertilizers, anaerobic bacteria reduce nitrate ions to molecular nitrogen and nitrogen(I) oxide N_2O .

Cultivated soils seem to "breathe" this oxide, which enters the stratosphere and interacts with oxygen atoms according to the scheme:



It is known that nitrogen(II) oxide is a catalyst for the destruction of ozone molecules.

Thus, in a few decades, ozone has evolved from a little-known component of atmospheric air into gas, which has one of the main roles in ensuring life on Earth.

Among the chemical measures to restore the ozone layer, scientists suggest the following:

- increasing the photochemical source of ozone by excitation of molecular oxygen and the rate of its photolysis by laser radiation in the lower stratosphere;
- destruction of fluoro-, chlorocarbon molecules in the upper layers of the stratosphere during a gas discharge that occurs at the intersection of several strong microwave rays;
- reduction of the use of fluoro-, chlorocarbons and search for environmentally friendly substitutes.

Scientists who have studied the ozone layer have found that the amount of

ozone decreases by about 1% over a decade. But as early as 1985, there were unexpected reports of ozone depletion over Antarctica almost halving in seven years. This phenomenon has been studied by scientists from all countries exploring Antarctica. The greatest losses of ozone are observed at an altitude of 16.5 km, where it remains 3% of the normal amount.

Scientists around the world are trying to draw the attention of governments and industrialists to the protection of the ozone layer. They have proven not only the harmfulness of CFCs for the ozone layer, but also the use of solid fuels in rockets, and are seeking a ban on some ozone-depleting chemical technologies. In addition, there is an urgent need to reduce the use of nitrogen fertilizers and take measures to introduce more environmentally friendly tillage methods.

1.8. The limits of sustainability of the planet1 and zero Carbon emission target.

It is unbelievable that the warning of scientists could turn into political action. This is an example of the fact that humanity can still control the processes on the planet.

So, our planet has several boundaries, beyond which there are certain global environmental risks. There are problems –

- ozone layer;
- freshwater;
- ocean acidification;
- aerosol air pollution;
- climate;
- forests;
- nutrient intake;
- conservation of biodiversity.

So far, humanity is in a safe zone against the problems of the ozone layer, the acidification of the ocean and freshwater. The risks to air polluted by the new compounds are still unknown. However, humanity has already crossed dangerous zones of environmental risk in terms of climate, forests, nutrient supply and biodiversity conservation.

Currently, scientists have defined a clear structure of planetary boundaries. There is strong evidence that humanity is at risk of climate change and biodiversity loss. There is a frequency of droughts, the number of fires on many continents, the negative impact on the Amazon rainforest, the acceleration of melting glaciers, the

catastrophic state of coral reefs.

Corals are a kind of indicator of the state of the environment, they discolor when the water becomes too warm (Fig. 1.17). So, the Great Barrier Reef – the world's largest network of coral reefs is located off the coast of Australia. However, its area is rapidly declining: over the past three decades, the ecosystem has lost much of its coral. The reef is affected by several factors: tropical hurricanes; starfish that feed on polyps; rising water temperatures and ocean pollution. All this leads to discoloration of the corals, which is a sign that the colony is left by microscopic algae that live in their tissues. Such coral becomes vulnerable and soon dies (Fig. 1.18).

Under conditions of global warming there is a mass extinction of corals. The effects of discoloration are 10 times greater than those of a large-scale tropical cyclone of the fifth category.



Fig. 1.17. The Great Barrier Reef is the largest reef system in the world.

The reef system has already experienced several mass extinctions of coral, and in addition, it has adapted to changes in ocean levels. In particular, during ice ages, ocean levels and temperatures are at minimum levels (about 118 meters lower than now), and at this time the reef "crawled" to the outer limit of the shelf. But with the departure of ice and rising temperatures, corals began to move in the opposite direction, capturing areas that became comfortable for them. The fact is that rising ocean levels lead to an increase in the rate of formation of carbonate deposits, which degrades water quality, but the reef has learned to respond quickly to new conditions.

However, recent changes in global temperature significantly reduce the time intervals between mass extinctions of corals, which creates a risk of their

reproduction.

However, recent changes in global temperature significantly reduce the time intervals between mass extinctions of corals, which creates the danger of their reproduction. Today, half of the coral reef is dead. According to scientists, due to climate change and environmental pollution, 70–90% of coral reefs will disappear within the next 20 years, and completely coral reefs will disappear by 2100.



Fig. 1.18. Coral discoloration is caused by an increase in water temperature.

Today, the Great Barrier Reef is almost completely discolored and will become a coral graveyard soon. Mankind has crossed the critical precision of coral discoloration.

Thus, scientists are struggling to determine the effects of global warming over the next thirty years.

In 2020, Australia had a hell of a summer. Due to the record high temperature and months of drought, 20 million hectares of land were burned. Scientists estimate that 3 billion animals died or were displaced by the fires: 1.43 million mammals; 2.46 billion reptiles; 187 million birds; 51 million frogs. These are huge numbers that show the enormous consequences for the planet's ecosystem.

In 2021, abnormal heat was recorded in Canada and the Northwestern United States. The air temperature in the Canadian province of British Columbia reached a record 49.5°C , and in the States this year's heat has already been called "historic" (Fig. 1.19). Meteorologists have linked the extreme heat in Canada and the United States to the "thermal dome" effect due to high atmospheric pressure.

About 500 sudden deaths have been linked to abnormal heat in Canada, where temperatures in some regions have reached 49.5°C . However, the record

temperature for the country affected the animals. Scientists estimate that the heat in Canada has killed about a billion marine animals, including a huge number of mussels, mollusks and starfish.

On the coast, scientists have recorded temperatures above 50°C. Because of this, much marine life had no chance of surviving, they just boiled. Empty shells of animals covered the shore. Mass deaths of fish, oysters and other representatives of flora and fauna affected by abnormal heat have been recorded.

Such anomalies lead to significant changes in the ecosystem, because the same mussels and mollusks filter the water in the sea and, thanks to their work, other species of animals have a chance to live. And if mussels can rebuild their population in a few years, other marine life will need much more time.



Fig. 1.19. In 2021, abnormal heat was recorded in Canada.

In 2021, catastrophic floods killed 160 people in Germany, while more than 50 people died after floods swept through the Chinese province of Henan. At the same time, forest fires engulfed one of the coolest places in the world – Siberia.

Every year, factories, power plants and vehicles pump tens of billions of tons of carbon dioxide into the atmosphere, which absorbs solar radiation, which will further raise the global temperature.

Even if all greenhouse gas emissions are reduced to zero tomorrow, the carbon dioxide already in the atmosphere will remain there for decades and continue to heat the planet, drying out vegetation and allowing air to retain more moisture and then emit precipitation with sudden devastating effects.

Human society fears that this may become a new norm, but scientists predict

that the concept of the norm will not be.

It is very doubtful that humanity will quickly destroy its dependence on fossil fuels. At best, this goal can be achieved by 2050, a date set by world leaders to achieve zero greenhouse gas emissions.

In other words, the planet will experience harsher and more destructive weather events over the next 30 years. Floods, fires and storms, along with melting glaciers, rising sea levels, the disappearance of coral reefs and the spread of deserts, may be the norm. And this is the best that can be hoped for over the next three decades.

The problem, scientists say, is that to stop the deterioration of weather conditions by 2050, the rise in global temperature should be limited to about 1.5°C according to pre-industrial levels. However, the world has already warmed to 1.2°C, thanks to greenhouse gases emitted into the atmosphere, and the prospect of limiting further temperature rises over the next 30 years looks remote. Estimates based on countries' current promises to reduce emissions suggest that temperatures are likely to rise more than 2°C above pre-industrial levels by the middle of the century.

In such a future, most of the planet is likely to suffer from drought; tropical forests are at risk of extinction, and melting ice sheets will lead to dangerous sea levels and major changes in the behavior of ocean currents such as the Gulf Stream. In addition, the loss of ice cover will cause the oceans to absorb more solar radiation, while the melting of permafrost will lead to increased methane emissions. The inevitable temperature will rise even more.

This disappointing prospect is because politicians and business leaders for decades have failed to assess the risks associated with the massive impact of human activities on the planet, and have not begun to act in time to limit harm. As a result, the world may face a climate catastrophe, and there is little time left to resist the threat.

The prospects look very problematic. As demonstrated in the Naples talks, when the G20 energy and environment ministers, who together account for 85% of annual emissions, failed to agree on a full package of commitments to combat climate change.

In addition, rich and developing countries cannot agree on cost-sharing to combat global warming. This was one of the problems of the international climate negotiations on the eve of the Paris Agreement of 2015, which obliged the world to keep global warming below 1.5°C, but rich countries have not fulfilled these commitments.

Mankind has crossed the line of climate, causing droughts, fires, coral discoloration and other consequences. The decline of Nature was the main reason for

the large-scale destabilization of the planet, namely the COVID-19 pandemic. It has affected the lives of all mankind. Many were surprised that the WHO warned of this situation in advance. Indeed, human society continues to destroy nature, conducts very aggressive arable production, destroys large-scale forests. Added to this is the fact that most people live in highly polluted cities with a high population density. All these factors became the basis for the ideal scenario of the spread of a new virus.

New viruses emerge and spread among humans as nature's resilience declines. Transmission of diseases occurs only in certain species and under certain conditions, when humanity aggressively interferes with their habitat. As a result, human, animal health and environmental state are closely linked.

The COVID-19 pandemic, which has affected the entire world economy, has caused humanity to think about the future scenarios of society. The emergence of the COVID-19 virus was a warning that the planet's ecosystem is in danger, but humanity has also been able to change the vector of development towards a stable future.

Today, it is no longer a question of reducing economic growth along with reducing anthropogenic pressure. Mankind must build a new planetary model of development for its stability.

First of all, it is necessary to achieve zero carbon emissions and achieve the lowest possible stable temperature in the world. Of the energy used by mankind today, 34% of the world's energy comes from burning oil, 27% from coal, and 24% from natural gas. Nuclear energy, as well as hydroelectric power and other renewable sources, together now account for only 15%. The result of burning fossil fuels is the current industrial economy, and for the planet as a whole it is 9.5 billion tons of carbon annually, which is released from the ground into the atmosphere.

After the beginning of the industrial revolution, carbon dioxide emissions amounted to 2.400 billion tons. In order not to exceed the threshold of 1.5oC, we must emit 300 billion tons less. If humanity continues to emit 40 billion tons of CO₂ per year, it will reach a critical level in 7 years!

Currently, the Carbon cycle is unbalanced. In fig. 1.20 the schemes of Carbon flows in gigatons in the pre-industrial period, Holocene (A) are given. On the left is the biosphere; in the center – the atmosphere; on the right – the ocean; below – the geosphere.

Figure (B) shows the period of the early Anthropocene, modernity. 325 gigatons of carbon were taken from the geosphere, 240 of which were in the atmosphere. We can see how the exchange between the atmosphere and the oceans and the biosphere has increased accordingly.

The lower (C) figure shows the late Anthropocene, the desired "almost zero"

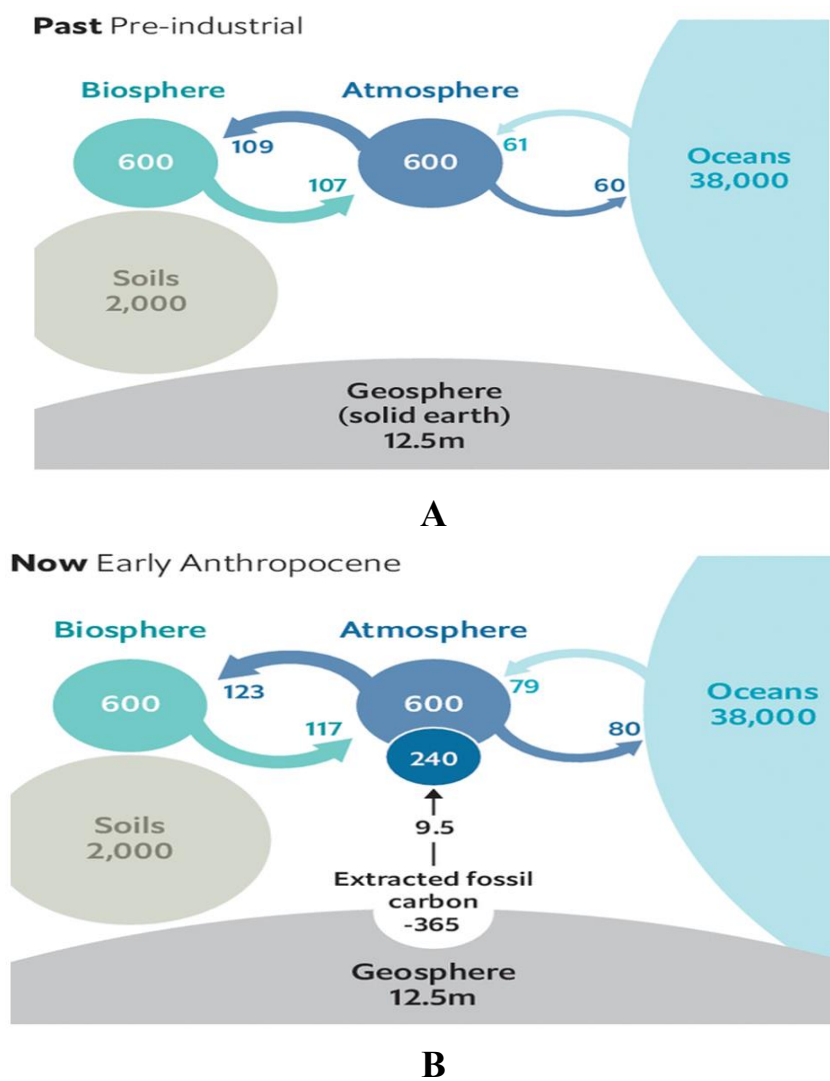
future. In particular, the means of "negative emissions" (ie, carbon sequestration due to anthropogenic activities):

- increased weathering (carbon binding in minerals);
- reproduction of forests;
- soil improvement.

However, all figures for the future model (Figure C) are unknown.

The current intensification of the Carbon cycle has side effects. Plants grow better. Thus, according to scientists, the level of photosynthesis on the planet is 3-7% higher than it was 30 years ago. Satellite images show that the Earth is turning green. This "carbon fertilizer" has improved the yields of some crops, as well as the growth of some forests and other ecosystems. This is not enough to compensate for the damage caused by climate change due to rising temperatures and changing rainy cycles.

However, increasing the amount of soluble carbon dioxide for the oceans means more acid. Even if fossil fuels do not heat the planet, the oxidation of the ocean is a change on a planetary scale.



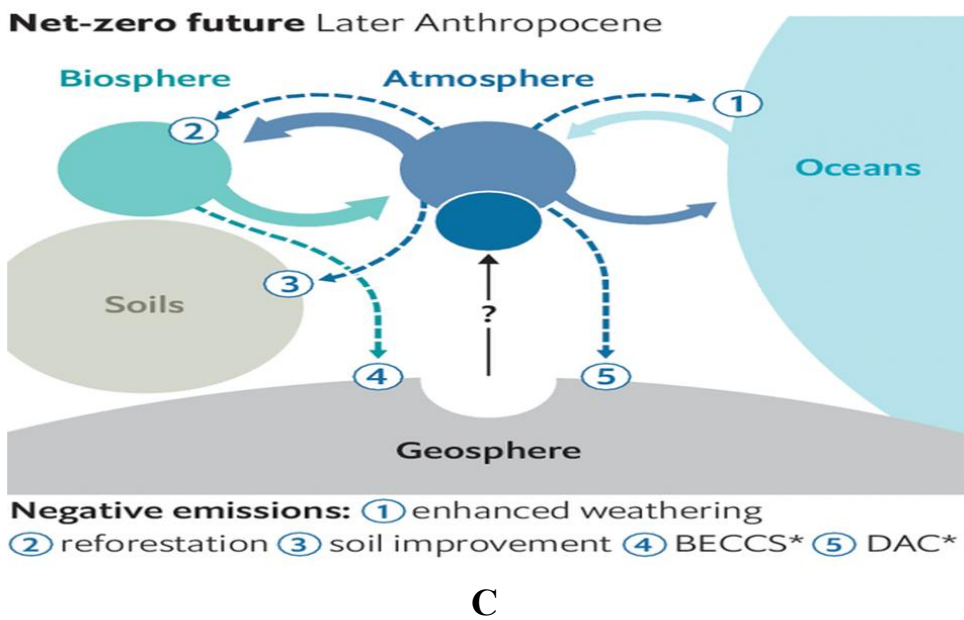


Fig. 1.20. Schemes of Carbon flows in gigatons in the pre-industrial period, in the early Anthropocene and late Anthropocene.

(<https://inlnk.ru/577ZBx>)

The 2015 Paris Agreement aims to halt rising levels of carbon dioxide in the atmosphere by burning fossil fuels by the middle of the 21st century.

However, the planet is undergoing erosion, during which silicates are bound to the surface, which binds carbon dioxide, eventually forming solid minerals, from which carbon is not released as easily as from coal or oil. Such "chemical weathering" is much slower than the ocean and biosphere uptake. According to geochemists, it will take a thousand years just to bring the level of carbon dioxide, which will occur after the end of the fossil fuel era, to the level of the mid-20th century.

Today, humanity is facing the problem of developing technologies for "negative emissions", ie the absorption of carbon, which will reduce CO₂ emissions.

Such forms of "negative emissions" exist. This is the cultivation of agricultural plants; reforestation and planting new ones; growing plants for combustion and electricity – while chemically binding CO₂ and accumulating it underground.

This approach is called "carbon capture and storage bioenergy" (BECCS). Next, there is the idea of capturing CO₂ from the atmosphere using chemical engineering, "direct capture from the air" (DAC).

So, if by 2060 the world refuses to use 90% of fossils compared to the current level, to balance the remaining 10% it is necessary to absorb about a billion tons of carbon per year. So far, Carbon absorption systems of this magnitude are barely able to absorb only one-thousandth of this amount. Ensuring the necessary absorption by

photosynthesis will require additional forest cover of large areas.

Mankind can avoid raising the global temperature by 2°C, even by 1.5°C, although this possibility is incredible and requires the efforts of all countries.

What is the greatest level of emission reductions that humanity can achieve?

Scientists have proved that if it is 6–7% per year, it will be reduced by 2 times in a decade. Reducing emissions 2 times every 10 years is an exponential rate of change. If everyone on our planet maintains this rate of emission reduction, we can give up fossil fuels in one generation (about 30 years).

The abandonment of fossil fuels could return humanity to a safe zone for climate change. This will significantly reduce air pollution, ocean acidification, and reduce the pressure on biodiversity. However, zero-emissions are not enough. Mankind must reduce the level of Carbon, which is already overheating the planet.

There is a way to reduce Carbon – the preservation of forests, greenery and their increase. In Scotland, for example, 22 million seedlings have been planted a year to adapt to climate change. Local forests annually extract almost 9.5 million tons of carbon dioxide from the atmosphere.

Studies show that planting additional trees to adapt to climate change in Europe can increase rainfall. According to the BBC, the conversion of agricultural land to the forest will increase the number of summer rains by an average of 7.6%. Scientists argue that additional rains may partially offset the increase in drought expected due to climate change. Conclusions on the increase in precipitation are partly based on observations of existing models. However, the main reasons are less clear - they are probably related to how forests interact with cloudy air.

Planting trees has become one of the main focuses of many countries' efforts to adapt to climate change around the world (Fig. 1.21).

Thus, in the UK by 2025 it is planned to plant about 30 million new trees annually.

Researchers have found that if forests increased by 20% evenly across Europe, it would lead to an increase in local rainfall, especially in winter and with a large impact that would be felt in coastal regions. In addition to local rains, planting new forests affects the leeward side. Scientists have found that rainfall in these places has increased, especially in the summer months. Combining these two effects, it was found that the total amount of precipitation in the summer increased by 7.6%.

The global initiative to plant a billion trees could be the most powerful way to address the climate crisis. In addition, increasing the number of trees can reduce the amount of carbon dioxide in the atmosphere.

Forests help reduce soil erosion, increase rainfall and therefore can guarantee

the sustainable development of the biosphere. Deforestation will not only have a positive impact on the planet's biodiversity, but will also help stabilize the planet's climate and freshwater levels, as well as benefit food and other resources.



Fig. 1.21. Planting trees has become one of the main focuses of many countries' efforts to adapt to climate change around the world.

Another very simple transformation will help humanity stay within planetary boundaries. This is a change in diet, namely, a reduction in the consumption of red meat, more vegetable protein, fruits, nuts, less food containing starch. If you follow this diet, you can also approach a safe zone not only for climate but also for biodiversity, nitrogen and phosphorus levels. Interestingly, a healthy diet can be the most effective way to adapt to climate change.

The next important transformation that will help return the panel to a security environmental zone is zero waste.

The next important transformation that will help return the panel to a safe ecological zone is zero waste. Therefore, a closed-loop economy (circular green economy) is fundamental to the sustainable development of the planet's ecosystem.

Circular (green) economy is based on the restoration and rational consumption of resources, an alternative to a traditional, linear, economy. It is characterized by the creation of new alternative economic approaches, the task of which is to minimize the negative human impact on the environment. The closed-loop economy is designed to change the classic linear model of production, focusing on products and services that minimize waste and other types of pollution. The basic principles of the closed-loop economy are based on the recovery of resources, recycling, the transition

from fossil fuels to the use of renewable energy sources. This type of economy is seen as part of the Fourth Industrial Revolution, which will increase the overall rational use of resources, including natural resources, the economy will be more transparent, predictable, and its development systemic.

Waste minimization, as well as their complete elimination, will allow humanity to achieve a secure environmental zone, reduce the pressure on biodiversity and reduce nutrient consumption.

Planetary boundaries, in other words environmental risks, have identified ways to restore and conserve biodiversity. Things like using renewable energy, eating healthy food, planting trees, disposing of waste can change the future of the Earth. Such transformations will already help to improve the environmental situation, both locally and globally. Returning to the planetary borders will be a guarantee of sustainable development of society in all its forms, especially environmental, as well as economic and social. This will reduce the risks of conflict and instability in the regions.

What will humanity do in the next 10 years? Given the current environmental challenges, this will be a crucial decade for the future of human society. Thus, the future of the planet for the next century depends on the choice of direction for the current 10 years. The issue of planned borders must become a priority at the highest level in the world, developed by the UN Security Council.

Today, human society dominates the planet, which has not been observed for 4.5 billion years. Scientists have learned to observe planned processes, to determine their ecological status. The digitalization and hyperconnectivity of world science determine the complex knowledge of the planet. Today there is a new geological epoch, which is determined not only by the physical content, but also by the creation of a new consciousness, which will be built into the future vector of development of the planet.

Conclusions



So, our planet has several boundaries, beyond which there are certain global environmental risks. These are the problems of the ozone layer; freshwater; ocean acidification; air pollution by aerosols; climate; reduction of forest area; nutrient

intake; biodiversity conservation.

So far, humanity is in a safe zone against the problems of the ozone layer, the acidification of the ocean and freshwater. The risks to air polluted by the new compounds are still unknown. However, humanity has already crossed dangerous zones of environmental risk in terms of climate, forests, nutrient supply and biodiversity conservation.

Currently, scientists have defined a clear structure of planetary boundaries. There is strong evidence that humanity is at risk of climate change and biodiversity loss. There is a frequency of droughts, the number of fires on many continents, the negative impact on tropical forests, the acceleration of melting glaciers, the catastrophic state of coral reefs.

Under conditions of global warming there is a mass extinction of corals. The effects of discoloration are 10 times greater than those of a large-scale tropical cyclone of the fifth category.

The planet will experience harsher and more devastating weather events over the next 30 years. Floods, fires and storms, along with melting glaciers, rising sea levels, the disappearance of coral reefs and the spread of deserts, may be the norm.

To stop the deterioration of weather conditions by 2050, the increase in global temperature should be limited to about 1.5°C according to the pre-industrial level. However, the planet has already warmed up to 1.2°C, thanks to greenhouse gases.

Estimates based on countries' current promises to reduce emissions suggest that temperatures are likely to rise more than 2°C above pre-industrial levels by the middle of the century.

In such a future, most of the planet is likely to suffer from drought; tropical forests are at risk of extinction, and melting ice sheets will lead to dangerous sea levels and major changes in the behavior of ocean currents such as the Gulf Stream. In addition, the loss of ice cover will cause the oceans to absorb more solar radiation, while the melting of permafrost will lead to increased methane emissions. The inevitable temperature will rise even more.

Mankind's primary goal is to achieve zero carbon emissions. Of the energy used by mankind today, 34% of the world's energy comes from burning oil, 27% from coal, and 24% from natural gas. Nuclear energy, as well as hydroelectric power and other renewable sources, together now account for only 15%. The result of burning fossil fuels is the current industrial economy, and for the planet as a whole it is 9.5 billion tons of carbon annually, which is released from the ground into the atmosphere.

After the beginning of the industrial revolution, carbon dioxide emissions

amounted to 2,400 billion tons. In order not to exceed the threshold of 1.5°C, we must emit 300 billion tons less. If humanity continues to emit 40 billion tons of CO₂ per year, it will reach a critical level in 7 years! Currently, the Carbon cycle is unbalanced.

If by 2060 the world abandons the use of 90% of fossils compared to the current level, to balance the remaining 10% it is necessary to absorb about a billion tons of carbon per year. So far, carbon absorption systems of this magnitude are barely able to absorb only one-thousandth of this amount. Ensuring the necessary absorption by photosynthesis will require additional forest cover of large areas.

Mankind can avoid a global temperature increase of 2oC, even 1.5oC, although this possibility is incredible and requires the efforts of all countries.

Abandonment of fossil fuels could return humanity to a safe zone for climate change. This will significantly reduce air pollution, ocean acidification, and reduce the pressure on biodiversity.

There is a way to reduce Carbon - the preservation of forests, greenery and their increase. Planting additional trees to adapt to climate change in Europe can increase rainfall.

It is estimated that if forests increased by 20% evenly across Europe, this would lead to an increase in local rainfall, especially in winter and with a large impact felt in coastal regions. In addition to local rains, planting new forests affects the leeward side. Scientists have found that rainfall in these places has increased, especially in the summer months. Combining these two effects together, it was found that the total amount of precipitation in the summer increased by 7.6%.

A global initiative to plant a billion trees could be the most powerful way to address the climate crisis. In addition, increasing the number of trees can reduce the amount of carbon dioxide in the atmosphere.

Another very simple transformation will help humanity stay within planetary boundaries. This is a change in diet, namely, a reduction in the consumption of red meat, more vegetable protein, fruits, nuts, less food containing starch. If you follow this diet, you can also approach a safe zone not only for climate but also for biodiversity, nitrogen and phosphorus levels. Interestingly, a healthy diet can be the most effective way to adapt to climate change.

The next important transformation that will help return the panel to a safe ecological zone is zero waste. Therefore, a closed-loop economy (circular green economy) is fundamental to the sustainable development of the planet's ecosystem.

The basic principles of the closed-loop economy are based on the recovery of resources, recycling, the transition from fossil fuels to the use of renewable energy

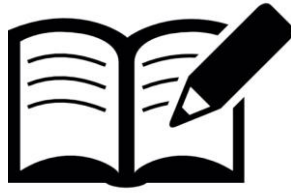
sources. This type of economy is seen as part of the Fourth Industrial Revolution, which will increase the overall rational use of resources, including natural resources, the economy will be more transparent, predictable, and its development systemic.

Waste minimization, as well as their complete elimination, will allow humanity to achieve a safe ecological zone, reduce the pressure on biodiversity and reduce nutrient consumption.

Planetary boundaries, in other words environmental risks, have identified ways to restore and conserve biodiversity. Things like the use of renewable energy, healthy eating, planting trees, waste disposal can change the future of the Earth. Such transformations will already help to improve the environmental situation, both locally and globally.

Questions for self-control

1. What factors support the stability of the Earth?
2. Define the Holocene and Anthropogenic. What is the fundamental difference between the epochs?
3. What is the main driving factor in the development of the planet?
4. Describe potential scenarios for the effects of global greenhouse gas emissions?
5. Describe the dynamics of melting glaciers?
6. What ecosystems do the biome consist of?
7. Name the basis of the biosphere.
8. What is the limit of the non-painful process of desertification?
9. What is the limit of global warming?
10. Describe the concept of water footprint.
11. Which countries in the world have the largest environmental footprint?
12. Which countries in the world are the richest in water resources?
13. Describe the unique properties of water.
14. How is the phenomenon of eutrophication related to the circulation of nutrients?
15. Name examples of "dead zones" in the oceans.
16. Describe the chemistry of the process of ocean acidification.
17. How does an increase in CO₂ affect the acidification process?
18. Describe the main air pollutants. Why are aerosols the most dangerous in terms of climate change?
19. Describe the main aspects of the ozone problem.
20. Describe the main ways to adapt to climate change.



References

1. Аналіз впливу кліматичних змін на водні ресурси України (резюме дослідження). / Сніжко С., Шевченко О., Дідовець Ю. // Під ред. Садогурської С.С. Центр екологічних ініціатив «Екодія», 2021. – 32 с.
2. Великий Бар'єрний риф не раз відроджувався після масової загибелі коралів. – [Електронний ресурс]. – Режим доступу : <https://www.unian.ua/ecology/naturalresources/10138736-velikiy-bar-yerniy-rif-ne-raz-vidrodzhuvavsy-a-pislyo-ji-zagibeli-koraliv-vcheni.html>
3. Закислення океану та Чорне море (2021). Центр екологічних ініціатив «Екодія». [Електронний ресурс]. – Режим доступу : bit.ly/zakyslenna
4. Інформаційно-аналітична довідка про стан водних ресурсів держави та особливості сільськогосподарського виробництва в умовах змін клімату. – [Електронний ресурс]. – Режим доступу : <http://naas.gov.ua/upload/iblock/78a/>
5. Лобода Н., Козлов М. (2020). Оцінка водних ресурсів річок України за середніми статистичними моделями траекторій змін клімату RCP4.5 та RCP8.5 у період 2021–2050 рр. Український гідрометеорологічний журнал. (25). – С. 93–104.
6. Мітрясова О. П. Хімічна екологія: навч. посібник / О. П. Мітрясова / видання 2-е, виправлене та доповнене. – Херсон : ОЛДІ-ПЛЮС, 2016. – 318 с.
7. Mitryasova O. Environmental Footprint Enterprise as Indicator of Balance it's Activity / Olena Mitryasova, Volodymyr Pohrebennyk, Anna Kochanek, Oksana Stepanova // Conference Proceedings [«17th International Multidisciplinary Scientific Geoconference SGEM 2017»], (Albena, Bulgaria, 29 June – 5 July 2017). – ISSUE 51. – Ecology, Economics, Education and Legislation. — Volume 17. – Ecology and Environmental Protection. – P. 371–378.
8. Мітрясова О. Екологічний інтегрований менеджмент водних ресурсів у європейських країнах: навчальний посібник / Олена Мітрясова, Віктор Смирнов, Євген Безсонов / за ред. проф. Олени Мітрясової, - Миколаїв: ЧНУ імені Петра Могили, 2020. – 288 с.

9. ООН (2017). Воздействие изменения климата и связанных с ним атмосферных изменений на океан. Технические тезисы первой Глобальной комплексной оценки состояния морской среды. [Електронний ресурс]. – Режим доступу : <https://www.un.org/regularprocess/sites/www.un.org.regularprocess/fles/17-05753-impacts-of-climate-change.pdf>
10. Побудована еталонна крива клімату від початку кайнозою до наших днів [Електронний ресурс]. – Режим доступу : <https://ecolive.com.ua/content/blogs/pobudovana-etalonna-kriva-klimatu-vid-pochatku-kaynozou-do-nashikh-dniv>
11. Посадка додаткових дерев збільшить кількість опадів в Європі [Електронний ресурс]. – Режим доступу : <https://www.meteoprog.ua/ua/news/594076-posadka-dodatkovix-derev-zbilsit-kilkist-opadiv-v-jevropi.html>
12. Скрытая угроза: мёртвые зоны в океане [Електронний ресурс]. – Режим доступу : <https://www.mytransat.com/ru/mertvye-zony-v-okeane>
13. Хільчевський В.К., Забокрицька М.Р., Кравчинський Р.Л. Екологічна стандартизація та запобігання впливу відходів на довкілля – К.: ВПЦ «Київський університет». – 2016. – 192 с.
14. Шоста хвиля вимирання: чи є шанс зупинити зникнення тварин? – Access mode: <https://hromadske.ua/posts/shosta-hvilya-vimirannya>
15. Эвтрофикация водоёмов повысит уровень парниковых газов [Електронний ресурс]. – Режим доступу : https://nomitech.ru/news/evtrofikatsiya_vodoyemov_povysit_uroven_parnikovykh_gazov/
16. Як людство змінило вуглецевий баланс атмосфери. Наслідки зміни клімату убивчі, але до кінця не зрозумілі. – [Електронний ресурс]. – Режим доступу : <https://inlnk.ru/577ZBx>
17. Alexander, K., et al., 2015. Sudden spreading of corrosive bottom water during the Palaeocene–Eocene Thermal Maximum. Nature Geoscience, 8, 458–461.
18. Carbon dioxide concentration: – Access mode: <https://www.gurumed.org/2013/05/12/le-plus-haut-niveau-de-co2-depuis-3-millions-danne/>
19. Epe, Tim Sebastian; Finsterle, Karin; Yasseri, Said. Nine years of phosphorus management with lanthanum modified bentonite (Phoslock) in a eutrophic, shallow swimming lake in Germany". Lake and Reservoir Management. 2017, 33 (2): 119–129.

20. Future greenhouse gas emissions scenarios. – Access mode: <https://ourworldindata.org/future-emissions>
21. Galdies, C., Bellerby, R., Canu, D., Chen, W., Garcia-Luque, E., Gašparović, B., Godrijan, J., ..., & Guerra, R. (2020) European policies and legislation targeting ocean acidification in European waters - Current state. *Marine Policy* 118, 103947. [Електронний ресурс]. – Режим доступу : <https://doi.org/10.1016/j.marpol.2020.103947>.
22. Hughes, T. P., Kerry, J. T., Baird, A. H., Connolly, S. R., Chase, T. J., Dietzel, A., ... & Woods, R. M. (2019). Global warming impairs stock–recruitment dynamics of corals. *Nature*, 568(7752), 387–390.
23. National Snow and Ice Data Center. Global glacier recession. *GLIMS Data at NSIDC*. – Access mode: <https://nsidc.org/data/glims>
24. Steffen, W.; Grinevald, J.; Crutzen, P.; McNeill, J. The Anthropocene: conceptual and historical perspectives // *Philosophical Transactions of the Royal Society*, 2011, 369, 843.
25. The World Bank Group. Renewable internal freshwater resources per capita (cubic meters). – Access mode: <https://data.worldbank.org/indicator/ER.H2OINTR.PC>
26. Why the Amazon rainforest important? – Access mode: https://wwf.panda.org/discover/knowledge_hub/where_we_work/amazon/about_the_amazon/why_amazonImportant/
27. Zari, M. P., Gaëll, M. Ecosystem Services Analysis in Response to Biodiversity Loss Caused by the Built Environment, *SAPIENS*, 2017, 7.1: – Access mode: <https://journals.openedition.org/sapiens/1684>

Chapter II

ENVIRONMENTAL ETHICS AND ECONOMICS AS KEY INSTRUMENTS FOR SUSTAINABLE DEVELOPMENT



In this section you will learn about

- ✓ Nowadays new challenges
- ✓ Cultural evolution
- ✓ Sustainable development – general background
- ✓ Value orientations
- ✓ Environmental Economics



Key words

sustainable development
environmental ethics
environmental economics
cultural evolution

You will learn about principles of sustainable development, including human values compatible and incompatible with sustainable development and economical aspects of sustainable development.

Exponential growth in production and consumption within the restricted Earth ecosystems is not sustainable in the long term. Therefore the international commission was established, that would attempt to do the seemingly impossible – propose how to enable people and whole nations to

develop while sustaining functioning ecosystems and a healthy environment. The efforts of the UN World Commission on Environment and Development resulted in a report called „Our Common Future“ published in 1987. The key term was „sustainable development“, a phrase central to world politics at the end of the last millennium and the beginning of the 21st century.

According to the UN World Commission on Environment and Development, sustainable development is „development that meets the needs of the present without compromising the ability of future generations to meet their own needs“. Although the concept of sustainable development has been evolving for more than 30 years, it is still extremely vague. On the other hand, despite the concept of sustainable development is far from flawless and is not a scientific theory, there is no better way to attempt to respond to the ever more acute problems of global scale.

The values which people hold and base their conduct on are probably the most important factor deciding whether we do or do not endorse sustainable development. Value orientations are likely to change over long time periods. We must strive for a substantial change in our value orientations and lifestyle if we want people in the future to have the chance to live their lives with dignity, quality, and creativity.

Economic instruments, unlike value orientations, can be implemented very quickly and they become effective virtually immediately. Nevertheless, political will is necessary to promote and adopt them. Until recently, economists and politicians focused exclusively on solving the problem of labor and capital productivity and investigating their mutual relationship. The productivity of natural riches was neglected, which led to the inefficient use of natural resources. Humanity is facing a historical turning point. For the first time in history the limits to the growth of prosperity are not caused by the lack of man-made capital, but natural capital. We are at the point where further growth of the economy does not make us richer, but poorer.

Sustainable development in this sense does not mean the end of economics. On the contrary, when economic growth reaches its limits, economics becomes a more important discipline than ever before, but it is an economics of solidarity, frugality, humility, and adaptation to the limits which nature puts to us. It is an economics which seeks quality, not expansion.

2.1. Nowadays new challenges.

„That's one small step for a man, one giant leap for mankind.“ These were the words of Neil Armstrong, the first person to set foot on the Moon on July 20, 1969. It was a triumph of human hope, will, and creativity in the best possible sense.

The Apollo 11 flight and the landing of a human on an extraterrestrial body should remind us that once people have a vision and the will to implement it, they are capable of great things.

Nowadays we are facing a similar challenge, but of a much greater, global extent. We are confronted with massive poverty in the world. More than fifty years ago we managed to send people to the Moon yet we remain unable to prevent people from dying of hunger. In many regions the environment is damaged or being destroyed. Many animal and plant species are irretrievably disappearing due to human activities. The world's population continues to grow, increasing the anthropogenic pressure on the ecosystems and natural resources.

We need a vision of what to do next, and maybe more than that. We need to search for and find (on the individual as well as societal level) the „will to meaning“. The Austrian psychiatrist Viktor Frankl (2006) says: „A society of prosperity or a nation of prosperity are able to meet basically all the needs of many, while the consumer society only generates individual needs. Alas one need remains unsatisfied – the will to meaning – a need to find a meaning in one's life, or better still in every situation – and devote oneself to it, fulfill it!“

In the history of Earth there occurred many times catastrophic situations, causing the extinction of the overwhelming majority of species. Surprisingly, however, the process of evolution was not set back by them. On the contrary, after each such „catastrophe“ life developed into higher, more diverse and more advanced forms.

The cause of these extinctions was a collision with an asteroid or intensive volcanic and tectonic activity triggered by the movement and collisions of tectonic plates.

Even today relatively common phenomena, like a hurricane or an ordinary storm, release an enormous amount of energy which has, on a local or regional basis, a considerable impact on life. A tropical hurricane can in twenty-four hours release as much energy as all the inhabitants of France use in a year. One thunderstorm can contain an amount of energy equivalent to four days' use of electricity for the whole United States.

From the beginning the Earth, and subsequently the biosphere, has been formed and influenced by a series of powerful natural elements. Life on Earth has several times been pushed to the edge of extinction, but it has never disappeared. It is human beings that have recently become another power (comparable to natural elements) influencing the state of the biosphere. From the geological point of view, their onset has been very fast.

When the Earth collided with an asteroid 65 million years ago, causing the extinction of 70 – 75 % of all animal and plant species, it was not just the annihilation of the existing state, but at the same time, a chance of creating something new.

Evolution seized the opportunity. The dominant dinosaurs disappeared from the scene, being gradually replaced by mammals.

The first ancestor of the Hominidae, which developed in the Tertiary period 15 million years ago, was the herbivorous Ramapithecus living in Africa and Asia. Seven million years ago, a new group of creatures emerged from the tropical forests of Africa and began to live on the savannahs. These were the Australopithecines, and for 5 million years they would be the world's dominant hominid species.

Between two and three million years ago, there may have been as many as six hominid types coexisting in Africa. But only one was fated to last – the genus Homo. The first member of the genus Homo was *Homo habilis*, an omnivore living in Africa about 2 – 3 million years ago. A higher species of hominid was *Homo erectus* that appeared one million years ago and gradually settled in Africa, Asia and Europe. The only living species of the genus Homo, having appeared about 200 000 – 280 000 years ago, is *Homo sapiens*. At that time also *Homo neanderthalensis* existed, which disappeared relatively recently, i.e. 24 000 years ago. Modern humans, called Cro-Magnons could make stone and bone tools and were good hunters, not only gatherers of fruit. They mastered the art of speech, which further stimulated brain development. Moreover, with the first artistic works (cave paintings and figurines) they were able to think abstractly (they probably believed in an afterlife and hence were able to contemplate the future, an ability no other species on the planet appears to have).

Modern humans show remarkably little genetic variability. The reason is that we are the descendants of a small founding population.¹

2.2. Cultural evolution.

Man is different from other creatures. Minds meet and communicate, and the feedback begins; the mind affects the body. Biological evolution is transformed in human beings into cultural evolution, which proceeds much faster.

With the Ice Age (10 000 – 12 000 years ago) coming to end, the climate underwent a change. The landscape acquired a new character and fauna and flora changed as well. As a result, man-the hunter was forced to search for additional sources of sustenance. He became a nomad and domesticated animals (dogs, sheep, goats, pigs, cattle, and others) on the way.

People developed fishing and collected grains of selected plants. This was followed by the artificial cultivation of wild growing grasses and cereals. This marked the beginning of the Neolithic (agricultural) revolution.

¹ This could be connected to the supervolcano eruption in Sumatra 75 000 years ago, followed by six global „volcanic winters“, which it is thought only a few thousand *Homo sapiens* survived. (Bryson, 2003)

People settled predominantly in warm areas. They built permanent settlements that would slowly grow larger. The new source of sustenance supported many more people than collecting and hunting ever could. Thanks to population growth, human clans united with groups of blood related families, associating in tribes and later in tribal unions. Tribe and tribal union members shared the same language, customs, religious ceremonies, and jointly defended the settled areas.

Providing the basis for future civilizations, the centers of these large communities emerged in the fertile silts of mighty rivers in the subtropical and temperate climatic zone (the Nile, Euphrates, Tigris, Indus, Ganges, Yellow River, and other rivers).

Four or five thousand years ago people began making the first tools, bronze weapons, and glass vessels. Three thousand years ago, iron was put to use. People were building farms, irrigation systems, water piping, and roads.

In those times, humans were able to adjust their environment (whether in a positive or negative way) on a regional scale. In ancient times our ancestors did not act any better or worse than we do now. However, their chances of affecting their environment were significantly more limited than ours.

In the 18th century, a „revolution“ broke out in Europe (spreading around the whole world), the importance of which can be compared to the Neolithic revolution. The symbol of the Industrial Revolution is the steam engine. But it is symbolized also by another two features: dependency on fossil fuels and exponential growth.

People were using more and more energy and so exponential growth became typical for the Industrial Revolution, whether it involved the increasing number of the population, the consumption of raw materials, energy, or pollution of the environment. Only in second half of the 20th century did people notice something was wrong and realize that this growth was not sustainable. There is a limit and exhaustion point to our space, defined approximately by the extent of the biosphere, and our stock of raw materials and energy. Therefore, the economic growth started by the Industrial Revolution must either come to an end or change in terms of quality.

The Industrial Revolution brought us much good, and the vast majority of people of the developed world now probably have a better standard of living (whether it concerns the level of hygiene, nutrition or the energy we use for heating, light, and transportation) than the one enjoyed by the nobility prior to the arrival of the industrial age. But there are two sides to every coin. We have collided with the „limits to growth“; the exponential increase in resource consumption and the related pollution production are no longer sustainable.

2.3. Sustainable development – general background.

Reports to the Club of Rome² and some other globally oriented reports of the 1970s and early 1980s demonstrated that the exponential growth in production and consumption within the restricted Earth ecosystem is not sustainable in the long term.³ It was also more and more obvious that it was necessary to respect the different views held by developed and developing countries, as the developing countries were justly expressing their wish to establish first better living conditions and only then perhaps adopt restrictions in respect of the ecosystems' sustainable capacity.

Therefore in 1983 the UN Secretary-General Javier Perez de Cuellar invited the Prime Minister of Norway (former Minister of the Environment) Gro Harlem Brundtland to establish international commission that would attempt to do the seemingly impossible – propose how to enable people and whole nations to develop while sustaining functioning ecosystems and a healthy environment. The efforts of the UN World Commission on Environment and Development over the course of four years resulted in a report called „Our Common Future“ (widely referred to as the „Brundtland Report“), published in 1987. The key term of probably the most important UN report of the 1980s was „sustainable development“, a phrase central to world politics at the end of the last millennium and the beginning of the 21st century. According to the UN World Commission on Environment and Development (1987), sustainable development is „development that meets the needs of the present without compromising the ability of future generations to meet their own needs. In its broadest sense, the strategy for sustainable development aims to promote harmony among human beings and between humanity and nature“.

The above definition is anthropocentrically oriented (meeting the needs of people) but that is not what is fundamentally wrong here. Above all, it is so vague and „all-embracing“ that it is impossible not to agree with. Its biggest deficiency is the fact that it fails to attempt to even define human needs.

No unified, generally accepted definition has been provided as yet. Instead, there are dozens and probably hundreds of various sustainable development definitions, of which many are available in the Internet. We do not intend to present and evaluate these definitions. Let us mention only few of them.

² The Club of Rome is an independent association of politicians, scientists and artists founded by the Italian industrialist Aurelio Peccei that achieved the greatest popularity in the research of the global problems of the 1970s.

³ The reports involved the first report to the Club of Rome „The Limits to Growth“ (1972) as well as some of the other reports: „Mankind at the Turning Point“ (1975), „Reshaping the International Order“ (1976), „Beyond the Age of Waste“ (1977), „Goals for Mankind“ (1977), „No Limits to Learning“ (1978), „Road Maps to the Future“ (1980). Apart from activities of the Club of Rome and its associates, other publications included e.g. „To Have or To Be“ by Erich Fromm (1976), „The Turning Point“ by Fritjof Capra (1982), „Small is Beautiful“ by Ernst Friedrich Schumacher (1973), „Gaia: A New Look at Life on Earth“ by James Lovelock (1979), „The Global 2000 Report to the President“ by Gerald O. Barney (1980) and others.

The European Parliament defines sustainable development as such development that gives rise to improvement in the living standard and welfare of people within the capacity of ecosystems while sustaining natural values and biological diversity for the present and future generations.

The Organisation of Economic Co-operation and Development (OECD) defines sustainable development as a dynamic balance between the economic, social, and environmental aspects of development in globalization, or as economically efficient, socially tolerable, and environmentally friendly development in all fields of human activity.

The former Czechoslovak Federal Minister of the Environment Josef Vavroušek (1993), defined sustainable development as follows: „Sustainable development, or a sustainable lifestyle, aims at the ideals of humanism and harmonious relationships between human beings and nature. It is a way of life that searches for a balance between the freedom and rights of each individual and his or her responsibility to other people and nature as a whole, including responsibility to future generations.“

The last definition to be mentioned is by Slovak author Ján Topercer Jr. (Topercer in Nováček, Mederly et al., 1996): „Sustainable development is a purposeful process of changes in the way human society treats itself and its environment (the land and its resources), directed at increasing the present and future potential for meeting the needs of people and other beings while respecting the capacities (limits) of the land and its resources.“

A definition should be concise and therefore can never capture the concept of sustainable development in its wider scope. In order to clarify this vague concept, the definitions are often complemented with the main principles of sustainable development.

Let us stress one principle we consider crucial – the precautionary principle. It is explicitly contained and defined also in Principle 15 of the Rio Declaration:⁴ „Where there are threats of serious or irreversible damage, lack of full scientific certainty shall not be used as a reason for postponing cost-effective measures to prevent environmental degradation.“

Although the concept of sustainable development has been evolving for more than 30 years, it is still extremely vague, which stems from the effort to capture and respond to highly complex global (not only environmental) problems. Ján Topercer Jr. (Mederly, Topercer, Nováček, 2004) characterized the key weak point of the concept of sustainable development as follows: „Sustainable development anticipates

⁴ The Rio Declaration is a non-binding convention adopted at the United Nations' Conference on Environment and Development in June 1992.

development that would not compromise the ability of future generations to meet their needs as viewed from the perspective of today's generation. This concept of development is considered desirable, which makes it assume a prescribing rather than predicting role. However, the above concept lacks a reliable basis for prescription for the following reasons:

- The idea of a universal hierarchy of needs has not been sufficiently empirically documented (Smelser, 1994), which applies to space (geographically) but perhaps even more to time.
- In addition, our standards of what is optimal and desirable develop over time.

The concept of sustainable development encompasses one of the striking forms of a universal desire held by the majority of people: the desire to see the world from the perspective of „God's eye“ (Putnam, Rorty, 1997), which is capable of an undistorted view and assessment of the needs and capacities of the past, present, and future generations.

Sustainable development can thus be preliminary classified under the category of „science&art“, i.e. among fields falling between science and art.

Although the concept of sustainable development is far from flawless and is not a scientific theory, there is no better way to attempt to respond to the ever more acute problems of global scale.

We (individuals and the society) have three options how to respond to the current global challenges:

1. We can underestimate, trivialize, or ignore the problems. We can honestly believe, that the situation (the consequences of climate change, high population increases in developing countries, resources exhaustion, poverty, etc.) is not serious and we need not worry. This logically suggests that there is no need for a response and everything can stay as it is, without any change. But that does not solve the problems. Quite the opposite, putting off an efficient action only makes them worse, while we are wasting perhaps the most precious and „exhaustible“ resource – time.

2. We can acknowledge the seriousness of the matter without trying to solve it. We fear a disaster but do not believe that our efforts could make a difference, that we ourselves could do anything to avert it. Therefore, we remain passive and resign ourselves to our fate, hoping things will sort themselves out. Or, even worse, we act regardless of what comes next, trying to seize as many pleasures as we can for ourselves before everything is lost. Thus we suppress the instinct of self-preservation and behave cruelly especially to our children, to future generations.

3. We can actively try to affect and alter the present adverse trends, to formulate and assert alternative, positive, and democratic visions of society's development. However, no one can find the answer to: „What are the chances of

success?“ The chance can be eighty percent or just one percent and still we should take it. Although as individuals we are not that responsible for the outcome (usually, our capacity to affect that is very limited), we all are definitely responsible for our individual efforts, for how much time, energy, and skills we dedicate to what.

Let us try now to sum up the main ideas contained in the definitions and principles of sustainable development into four generalizing basic requirements.

1. Requirement for all people on Earth to be able to meet their (at least elementary) needs.

The trouble starts already when trying to define elementary human needs. We need food, water, clothes, and shelter for bare survival. Just surviving on a long-term basis is naturally not an option. Despite that, unfortunately about one billion people around the world suffer from acute hunger and 1.2 billion people have no access to safe water. In developed countries, we would certainly loathe it if we could cover but the most essential needs facilitating survival. But where is the limit to human needs? Probably in „infinity“.

Are there any limits to justified human needs? And do they differ in time and space? Abraham Maslow (1954) proposed a hierarchy (pyramid) of human needs, now widely known and accepted:

- Basic physical, physiological needs.
- Need for security and safety.
- Social needs (a need for belonging and love).
- Need for esteem and respect.
- Need for self-realization.

Unfortunately, not even Maslow's hierarchy of human needs can help us determine a reasonable limit for human desires, which are often perceived as needs or even as something we are entitled to.

The communist ideology carried an appealing motto it never managed (nor was it possible) to honor: „From each according to his abilities, to each according to his needs.“ But is a car, a private yacht, a tourist trip into orbit a justifiable need?

I think the requirement for the satisfaction of needs as stated in the definition of the UN World Commission on Environment and Development is appealing but unfeasible and impossible to define. It seems more logical and adequate to condition the satisfaction of human needs by respecting the ecosystems' carrying capacity while preserving natural values and biological diversity for the present and future generations.

The elementary requirement of sustainable development should not be formed by the satisfaction of human needs but by the respect for the ecosystems' carrying

capacity upon which the activities of people living in individual regions and time periods must be based.

2. Requirement for the rights of future generations to meet their needs

This is a great new challenge. In history, various groups of inhabitants strived (whether by violent or non-violent means) to assert their rights – slaves, serfs, colonized nations, etc. Nowadays the problem is whether we will be able to respect the rights of those who are not here yet but will be – our children and all generations to come. This general statement can be specified with the help of Herman Daly's (1977, 1989) three principles suggesting how to use Earth's natural resources and ecosystems sustainably:

- a) Exploitation of renewable resources (forest, fish populations, etc.) does not exceed the rate at which they regenerate.
- b) The rate of depleting non-renewable natural resources (e.g. fossil fuels) does not exceed the rate of growth of the renewable substitutes.
- c) Waste emissions do not exceed the renewable assimilative capacity of the local environment (and therefore will not exceed the ecosystems' carrying capacity).

3. Requirement for respecting the rights of other living beings

This is another great challenge that did not receive much attention in the 20th century, when people were „conquering“ nature. Similarly to the first requirement of sustainable development, we are unable to define the optimum status here either. Should humankind use its dominant position among other living beings and act as the „lord of creation“ or should it rather be a responsible manager of this planet? Or should we consider other beings equal to us (regardless of the fact that this radical requirement could not be implemented at any rate)?

Should we differentiate between individual species depending on what place they occupy in evolution?

These are questions we have no answer to, nor can we determine clearly what is good and what is wrong. However, we should not ignore the above challenges and instead formulate the answers gradually, even if it takes decades and perhaps even longer. We should gradually approach harmony in relationships between human beings and both animate and inanimate nature, as Josef Vavroušek states in his definition. Full harmony we will probably never reach. But we can always feel respect for life and nature in the sense of the legacy of Albert Schweitzer (see the ethics of reverence for life later in this text).

4. Requirement for learning from the future

This requirement does not ensue from the aforementioned definitions but I believe that it is indispensable for the implementation of sustainable development. The report to the Club of Rome „No Limits to Learning“ (1978) elaborates on the

idea of „anticipatory learning“, that is learning based on anticipating the possible consequences of our current activities. Anticipatory learning is thus a path leading to fulfilling the key principle of sustainable development, the precautionary principle.

Throughout all their history, human beings have learnt from their past experience or the past experience of their fellow humans. This model functioned well for thousands of years, as long as the consequences of our deeds (and errors) were space and time limited. Scientific knowledge and technological development have provided us with such powers that potential errors may now lead to a severe aftermath, whether it concerns e.g. the peaceful or military use of nuclear energy, genetically modified organisms, climate change, etc. Therefore it is necessary to learn not only from the past but also from possible futures and behave and act accordingly.

Society's transition to sustainable development, to a sustainable lifestyle, implies major changes in its functioning. Owing to its importance, this transition could be called „the third global revolution“. Could such a change be truly global though? Is the vision of sustainable development applicable in various cultures and populations, despite all their dissimilarities?

If anyone will take the trouble to compare the moral teaching of, say, the ancient Egyptians, Babylonians, Hindus, Chinese, Greeks and Romans, what will really strike him will be how very like they are to each other and to our own. Men have differed as regards what people you ought to be unselfish to, whether it was only your own family, or your fellow countrymen, or everyone. But they have always agreed that you ought not to put yourself first.

Clive Staples Lewis

2.4. Value orientations.

The values which people hold and base their conduct on are probably the most important factor deciding whether we do or do not endorse sustainable development. Value orientations are likely to change over long time periods (decades to hundreds of years).

The sociologist Stanislav Hubík states that „value orientation is subject to inertia, it changes as slowly as possible and a revolution in value orientation is in progress silently, although it is the most revolutionary revolution“.

The set of principles and rules which indicate to people how they should behave in their interaction with others is called ethics. Ecological ethics, or rather environmental ethics is the set of principles and rules which indicate to people how they should behave in their interaction with the entire non-human world.

Value orientation of people in their everyday reality stems from what the phylogenesis⁵ of hunters and gatherers equipped them with. Anthropologists point out that *Homo sapiens* has spent in this evolutionary stage 90 % of the time it has existed. Therefore, we tend to see nature, the world around us, as something which not only surrounds us, but also still potentially endangers us. That is why we must fight with nature, conquer it.

The 16th and 17th centuries gradually established the conception of the world as a machine. This radical change was triggered by new discoveries in physics, astronomy, and mathematics. Galileo Galilei restricted science to the study of phenomena which could be measured and quantified.

Galileo Galilei, René Descartes and Immanuel Kant influenced our perception or the world. Descartes and Kant separated reason from nature. Kant was convinced that the only thing deserving of respect was reason, which he considered the foundation of our freedom.

Descartes narrowed the concept of reason down to a purely mathematical arrangement of ideal entities and, in nature, to the mathematical and mechanical arrangement of particles in spacetime.

The first strong opposition to the mechanistic Cartesian paradigm originates in the Romantic movement⁶ in art, literature, and philosophy. Nevertheless, a real shock for science came according to Capra, only in the 20th century when system theory was elaborated. Systems cannot be understood by means of their analyses. From the system perspective, it is the characteristics of the whole which none of its components has which are regarded as the fundamental, essential characteristics of an organism or living system. These characteristics originate in interactions among the components.

What actually makes humans fundamentally different from other living beings? According to the Judeo-Christian conception, humans, like everything else, have been created by God, but unlike animals, they possess immortal souls.

Early Modern Era the animal has ceased to be regarded as kin and a conception of the animal as raw material has been forming instead.⁷ Whether humans are created by God and whether they, unlike animals, have souls is, at least for now, a question of faith. Intellectually, we can specify three basic features of humanity:

⁵ Phylogeny (phylogenetic evolution) is the evolution of species in historical sequence as understood by the theory of evolution. In contrast, ontogeny is the development course of a human individual.

⁶ Romanticism – an artistic movement and philosophical school of thought as well as the life stance in the Euro-American culture of the end of the 18th and early 19th century.

⁷ Kohák harshly but fittingly remarks: „Many people were shocked to read, after the war, about the medical experiments on children in Nazi concentration camps. Few of them noted that the only difference between Dr. Mengele's experiments and the experiments we accept without hesitation is that Dr. Mengele drew the line between prohibited and permitted experimental animals between „Aryans“ and „non-Aryans“ while we draw it between humans and chimpanzees.“

- a) Speech – the ability to capture the fleeting moment in concepts. This ability, dramatically intensified by the written word, makes possible far more rapid and effective cumulation of knowledge than the growth of customs and tradition.
- b) Reason – because humans can capture immediate experience in words, they can grasp not only immediate spatiotemporal relations of continuity, contiguity, and resemblance, but also of logical and ideal relations. Defining ideal relations among components of experience is precisely what we call reason. There is one more thing related to reason: imagination, which is possible only because humans are capable not only of seeing a given state, but also of imagining it in ideas and concepts.
- c) Freedom – reason and imagination enable humans to recognize moral responsibility. They do not live in the innocence which modernity attributed to other animals, said to accept uncritically whatever there is. Humans are aware of moral duties and are capable of worshipping God, thereby manifesting their „immortal soul“ (or, more precisely, immortal spirit).

„Between humans and animals there is only one morally relevant difference, and that is freedom. Humans are beings who can imagine that things could be otherwise, the only beings that do not live within firmly established instinctual parameters. Freedom, though, does not mean privilege.

Peter Singer is a leading advocate of granting certain rights to other beings. In 1975 he published „Animal Liberation“, a ground-breaking study on the relationship of humans and animals. According to Singer, the ability to suffer and feel pain (which is common to humans and animals) is sufficient reason for consideration. In Singer’s conception we are equal with animals, even though it does not mean that we are the same.

None of the differences between humans and their non-human fellows is morally relevant. None justify domination and discrimination. Societies for the protection of animals generally recognize four basic needs common to all higher animals (as a matter of fact, they were denied even to African slaves as recently as two centuries ago):

1. The possibility of free movement in sufficient space.
2. The natural cycle of day and night, of activity and rest.
3. The fellowship of their kind, including family relations.
4. A diet natural to the animal.

What attitudes do people have to living and non-living nature? To put it very simply, we have three options: the anthropocentric, the biocentric, and the theocentric attitudes.

Erazim Kohák (1998) provides an alternative division which is based on ecological or, rather, environmental ethics:

1. Ethics of the fear of the Lord

The kind of short-sighted egoism which we today call „anthropocentrism“ is something we normally encounter first in highly advanced civilizations, typically as a sign of decadence.

Early humans, hunters, herdsmen, farmers, were painfully aware of their own vulnerability and unimportance. Everything appears to them as a gift. Nature, which surrounds them, appears to them as infinitely powerful, unfathomable, evoking a holy fear which in a later religious conception will figure as the fear of the Lord.

In modern terminology, it is called theocentrism⁸, its fundamental stance is that all value derives from God, and humans are but dependent parts of God´s creation.

Polish-American Catholic thinker Henryk Skolimowski (in Kohák, Kolářský and Míchal, 1996) considers contemporary fashionable attitudes, egoism, narcissism, snobbery, simply everything that leads the consumer society to destruction and self-destruction, a product of the ethical vacuum which ethical relativism generates around us.

2. Ethics of noble humanity

Annie Dillard (in Kohák, Kolářský and Míchal, 1996) and Charles Sherrington (1953) claim that nature is neither good nor evil, it is only completely insensitive. They give examples:

A wasp stings a caterpillar in seven nerve nodes to paralyze it, but not kill it. Only after that does the wasp lay eggs in the body of the caterpillar. It is necessary that the caterpillar lives long and suffers while bearing foreign eggs.

A cat plays with a mouse: it does not kill, only cripples and goes on playing.

Life is a constant escape from death. Those who survive bear the scars at the end of the summer – butterflies with torn wings, spiders missing a leg. And Mother Nature? It does not care about suffering. Only humans observing the insensitivity of nature suffer from empathy.

According to Sherrington and Dillard alike, only with humans does altruism – freedom and the ability to act for the good of nature – enter into the world.

3. The ethics of reverence for life

All life is a source of meaning and value. Albert Schweitzer (1974) developed this concept under the title „the philosophy of reverence for life“. Reverence for life began with wonder over the miracle that there is life at all. An ethics which restricts itself to human interactions with each other is incomplete. A broader outreach is

⁸ Theocentrism does not mean the centrality of God in the traditional European concept, but the centrality of sacred transcendence and awe.

needed, a reverence for all living beings. Only such a broad outreach, as wide as life itself, could provide the framework for avoiding harm and doing good as a general posture.

The ethics of reverence for life (or the biocentric approach to world) was developed by the American philosopher Paul Taylor (1986) in four propositions:

- People, animate beings of the subspecies *Homo sapiens sapiens*, are equal members of the community of all beings.
- The Earth is a web of mutual dependence.
- Every member of the biotic community is valuable simply because it is.
- The three previous propositions lead to the conclusion that the idea of human superiority is only an expression of human racism.

4. The land ethic

The land ethic comes from the work of ecological thinker Aldo Leopold.⁹ This concept is not concerned only with respect for life itself, but with respect for the presuppositions of life, the whole community of all life, and conditions of its sustainability.

Value does not derive from humans or from life. It is a function of the balance of the entire ecosystem. In Leopold's words, „a thing is right when it tends to preserve the integrity, stability, and beauty of the biotic community. It is wrong when it tends otherwise“.

5. Lifeboat ethics

Economist Kenneth Boulding (1966) pointed out that the planet ceased to be „endless“ a long time ago. He proposed the metaphor of a spaceship. Like in a spaceship, we on the Earth have only a limited amount of resources, and like in a spaceship, all our waste stays onboard. Garrett Hardin (1985) builds of Boulding with a reminder that a ship must have a captain – which the Earth does not.

Garrett Hardin concludes that where there is a surplus of demand it is essential to limit the availability of supply. Limited resources (of the planet) are incompatible with unlimited demands (of people).

The starting point of lifeboat ethics is that there are too many of us and that we share limited resources. Generosity will lead to tragedy. Therefore let us help no one, only make sure that we shall use our privileges for the preservation of common cultural values, not only personal consumption. Attempts to help others beyond that only prolong the misery. For instance the green revolution, which doubled agricultural yields, temporarily prevented famine but brought about a catastrophic

⁹ Aldo Leopold was a forester and the first American university teacher of conservation ecology as a separate subject. His most famous work is „A Sand County Almanac“ (1949).

rise in populations in which each extra mouth represents a further burden on the environment.

In addition to this division in attitudes towards nature based on Erazim Kohák, we shall also mention the concept of „deep ecology“ used first by Arne Naess (1996) from Norway in 1973. The distinction between „shallow“ and „deep“ ecologies is often used to distinguish between the ecology that is interested only in the technology of environmentally friendly production and the ecology which goes to the roots of the ecological crisis in human attitudes, especially in the consumer orientation of Euro-American civilization.

We are in the period of the sixth catastrophic extinction when species are disappearing because of the habitat loss caused by humans. Human genetic memory does not prepare humans for the conditions of a purely culturally determined life. Humans experience a deeply encoded fear of what had been dangerous in nature (e.g. of serpents). The incredible speed of modern development means, however, that humans do not even begin to develop a similar instinctive fear of far more dangerous things like automobiles and firearms.

Is it realistic to expect that values compatible with sustainable development will assert themselves in the behavior and activities of people? International long-term research conducted by Ronald Inglehart (1977, 1990) in the 1970s tried to capture the shift from material to post-material values. He performed a large-scale representative survey in all countries of Western Europe, North America, Japan, South Africa, and later in some countries of Central and Eastern Europe.

The basic finding is the gradual shift of emphasis from the needs of material nature to the non-material needs. Inglehart understands the material values primarily as material affluence and security, focus on economic prosperity, and stable economic growth. Post-material values include according to him, the unrestricted self-realization of an individual, the opportunity to participate in the administration of public affairs, to contribute to a more humane society in which ideas have higher importance than money, and also to create a better environment.

Inglehart calls this subtle but crucial change a „quiet revolution“ and demonstrates it in statistically reliable figures. He observes the shift in values especially in younger age groups. In the post-war generation, the proportion of „post-materialistic“ is already quantitatively higher than the proportion of people with a „materialistic“ orientation. A growing non-consumerist orientation can be found most frequently in the „middle class“.

With respect to a sustainable lifestyle the research revealed a problem: there is a relationship between post-materialistic attitudes and the level of gross domestic product (and the level of consumption in a given country).

This takes us back to the dilemma faced by the Brundtland Commission. What can be done to preserve a reasonable quality of the environment and at the same time allow countries to develop and prosper economically? With respect to value orientation: what can be done to shift from material towards post-material values if this shift depends on the level of GDP and 80% of the global population lives in poor, developing countries?

Values compatible and incompatible with sustainable lifestyle

Josef Vavroušek (1993) attempted to define a framework of key values which are typical for industrial society and stimulate the emergence of global and regional problems (values of type A). He assigned alternative values to them which should be compatible with a sustainable way of life (values of type B):

1. Attitude of humans to nature
 - A. Predatory attitude to nature.
 - B. Awareness of unity with nature.
2. Attitude of human individuals to society
 - A. One-sided emphasis on individualism and competitiveness (typical for „real capitalism“) as well as a one-sided emphasis on collectivism (typical for „real socialism“).
 - B. Balanced emphasis on the individual and the collective, supplementing competitiveness with cooperation.¹⁰
3. Attitude to the passage of time and a sense of history
 - A. Obsession with the ideas of quantitative growth.
 - B. Emphasis on the qualitative development of human society.
4. Attitude to the sense of our lives
 - A. Hedonistic orientation to the consumer lifestyle.
 - B. Emphasis on the quality of life, conscious modesty, and the self-denial of superfluous things.
5. Attitude to freedom and responsibility
 - A. One-sided emphasis on human rights and freedoms, the erosion of common responsibility for the course of public affairs.
 - B. Development of human rights and freedoms while respecting the symmetry between them and the responsibility which is connected with them.
6. Attitude to the level of our knowledge

¹⁰ The American ecologist Eugene P. Odum (1977) says that the relations in nature evolve from parasitism to mutualism, that is, to mutual cooperation. Alternative economists talk about a „win-win strategy“, that is, a strategy by which individual subjects gain more in the long term through mutual agreement than if they competed and lived at the expense of one another.

- A. „Pride in reason“ resting on the one-sided emphasis on rationality and on the overestimation of the complexity, depth, and reliability of our knowledge and our ability to foresee and shape future development.
- B. Caution in all interference with nature and society.
- 7. Attitude to our lives
 - A. Our alienation from our own lives, the weakening of the human instinct of self-preservation and of the feedback which makes the correction of our inappropriate or unsuccessful action possible.
 - B. Restoring the human instinct of self-preservation.
- 8. Attitude to future generations
 - A. Preference for short-term goals over long-term and permanent goals, life at the expense of future generations.
 - B. Awareness of the long-term consequences of human activities.
- 9. Attitude to other opinions and other civilizations
 - A. Lack of respect for other opinions, ideological, religious, racial, or other intolerance and the tendency to solve problems by force.
 - B. Mutual tolerance, endeavoring to understand the situation of the citizens of other countries, solving problems by negotiation.
- 10. Attitude to common issues
 - A. Withdrawal from common decision making.
 - B. Development of participatory democracy combining the advantages of representative democracy with self-government.

According to Josef Vavroušek, our future depends largely on how high we will place values of type B in our individual and group value systems and to what extent we will suppress the values of type A. Suppressing values of type A in our behavior sounds rational, but unfortunately humans often do not behave rationally. It is a race against time; time is perhaps our scarcest resource.

In conclusion we may say that we must strive for a substantial change in our value orientations and lifestyle if we want people in the future to have the chance to live their lives with dignity, quality, and creativity.

Throughout the existence of the *Homo sapiens sapiens* subspecies, humanity has been immediately and existentially dependent on the surrounding nature as children are dependent on their parents. In the course of their evolution, for millenia, people have struggled with a shortage of food, diseases, and natural disasters; they have felt constantly threatened by the surrounding natural world. Only in the last few centuries has the situation been gradually changing (especially in the developed countries). Like those who have starved and suffered for a long time have a tendency to overeat excessively, to the point where they endanger themselves, also the current

majority of society considers accumulating wealth and entering into a „paradise of consumption“ almost the meaning of life.

Today we have become the new „geological force“ on Earth; to put it arrogantly, we have become the „masters of the Earth“, with the ability to deplete the non-renewable resources of the biosphere and destroy the renewable resources of the biosphere.

Now the goal is not only to recognize our strength in time, but also admit our dependence on the surrounding environment, on nature. Similar to an individual developing from child's one-sided dependence on its parents into rebellious puberty and then into adulthood, human society too may now be experiencing the „stage of puberty“. Individuals want to outgrow their parents and become free and independent, people have the need to conquer nature, their environment. If that is the case, there will be much at stake in the first half of the 21st century.

At puberty, individuals are most vulnerable and can easily hurt themselves and others. Their outwardly self-assured and even arrogant behavior actually shows insecurity and weakness. It is this stage which substantially determines what kind of people they will become and how they will behave in adulthood, which is in fact already at the door.

If all goes well, they will recognize their power which has surpassed the power of their parents, but they will not misuse it against them. On the contrary, they will respect their parents, not as a child any more but as an equal partner. Perhaps it is possible, not only to believe, to hope, that the relationship of humanity to nature will ripen and mature, but also to actively seek to accomplish that aim, even though it will be a difficult and by no means painless process.

Shifts in value orientations – stories of success

Value orientations shift „silently“ and slowly, over decades or centuries, but there is no need to despair. There are several examples of positive changes in behavior and thoughtful readers can surely recall a few more hopeful signs from their neighborhood.

1. Abolition of slavery

Slavery has accompanied human society since time immemorial. In the United States it became the source of the most devastating war in its history, the Civil War between 1861 and 1865. When slavery was abolished, many people were afraid that the economy based on agriculture in the southern states would collapse. It did not happen. Today, one hundred and sixty years later, slavery is unacceptable from the perspective of values in the developed world. An advocate of slavery, for instance in an election campaign, would not be dangerous any more today, but ripe for the madhouse. The United States have certainly not resolved all the traumas originating

in the historically unequal and unjust relations of blacks and whites, but a shift in value orientations in a positive direction no doubt occurred.

2. Restrictions on smoking

Tobacco corporations earn billions of dollars from our addiction to smoking. When some civic initiatives in the Western countries started to campaign for restrictions on tobacco advertising in the 1970s, it had all the signs of tilting at windmills. A couple of hundred or maybe a few thousand zealots stood up against economic giants with sophisticated marketing strategies and effective lobbying. Yet it is now apparent in the developed countries that smoking has been restricted, especially there are fewer smokers among young people, and in many countries smoking is banned in public buildings and public areas where nonsmokers might be inconvenienced. This makes the multinational tobacco corporations push their way all the more aggressively into the former socialist and developing countries, but that is another story.

3. Recycling

I am convinced that if during my childhood and youth (the 1960s and 1970s) someone had suddenly started to ask people to sort waste voluntarily and for free, the results would have been woeful. Due to the increased attention to environmental issues in the following years and due to environmental education and campaigns, the sorting of waste works well in the majority of the developed countries today. Some people may take it as an alibi for an otherwise dissolute consumerist lifestyle („I sort waste, that means I have already done enough for the environment, let those who are paid for it take care of the rest.“), but nothing is perfect. I think that the recycling of waste can be included among the success stories showing a change in the behavior of people for the better which has occurred over a relatively short period of time.

4. Relations between France and Germany

I am not a historian and I may be simplifying the situation, but I chose as the last example the transformation of the relations between two powerful and ambitious nations, or rather countries. France and Germany were mortal enemies in both World Wars I and II. Millions of dead on both sides could have led to the rational assumption after World War II that there was enough hatred sown for several generations ahead. Instead of that, the two countries have been, for two decades at least, the major driving force of European integration. One of the reasons for this success is perhaps the Marshall Plan and the subsequent economic prosperity of both countries. Nevertheless, it is not important for us at this point. What is important is that the mortal enemies have become friends, or at least reliable partners in building a united Europe and that it occurred within two or three generations.

Infobox: Virtues and vices

The values of Euro-American culture and civilization stem from the heritage of Judaism and Christianity (it applies similarly to Hispanic and Orthodox civilization groups). Judaism and Christianity find fundamental ethical importance in the Ten Commandments. The fourth through the tenth commandments are generally considered in these societies (even beyond religion) the „ethical minimum“ which defines the basic human relations.

According to the Old Testament, Moses received the Ten Commandments in the Sinai desert. A brief, catechetical version of the Ten Commandments is as follows:

1. I am the Lord, your God: you shall not have strange Gods before me.
2. You shall not take the name of the Lord your God in vain.
3. Remember to keep holy the Lord's Day.
4. Honor your father and your mother, so that you may live long and that it may go well with you in the land.
5. You shall not kill.
6. You shall not commit adultery.
7. You shall not steal.
8. You shall not bear false witness against your neighbor.
9. You shall not covet your neighbor's wife.
10. You shall not covet your neighbor's goods.

Around 600 A.D. Pope Gregory I created a list of seven deadly sins. They are: pride, envy,

greed, wrath, lust, gluttony, and sloth.

Contrasting with the seven deadly sins there are seven main virtues in Christianity: humility, charity, kindness, patience, chastity, temperance, and diligence.

Moder time, however, bring new challenges and it is not easy to distinguish what is good (or what is still acceptable) and what is not. In March 2008, Gianfranco Girotti, a bishop from the Vatican, outlined in the newspaper L'Osservatore Romano which other vices connected with the process of globalization could be in the 21st century considered by the Catholic Church serious offenses against God and our neigbors.¹¹ They are: genetic engineering, experiments on humans, polluting the environment, contributing to social inequality, contributing to the poverty of others, lives in excessive wealth, drug trafficking and use.

„You offend God not only by stealing, blaspheming or coveting your neighbor's wife, but also by ruining the environment, carrying out morally debatable scientific

¹¹ It is not, of course, the official position of the Catholic Church, but the personal statement of influencial Vatican bishop.

experiments, or allowing genetic manipulations that alter DNA or compromise embryos“, says Bishop Girotti.¹²

Some of these „new sins“ are hard to define because in the developed countries we are all contributing to social inequality and the degradation of the environment in the developing countries by buying cheap products which people in the developing countries have produced in appalling social conditions and the production of which is damaging the local environment. Nevertheless, it is certainly positive that after 14 centuries the Catholic Church (and let us hope not only it) seems to be opening a debate on the ethical aspects of emerging development opportunities and threats.

Hans Küng (1992, 1997, 2000) deals with values and ethical principles in his work devoted to the world’s ethos. He mentions „the golden rule of humanity“, encountered in all major religious and ethical traditions. It can be worded negatively („Do not treat others in ways you would not like to be treated“) or positively („Treat others as you would like them to treat you“). Hans Küng lists variations of this message as it appears in various environments which differ historically, culturally, and religiously:

- Confucius (c. 551 – 489 BC): „What you yourself do not want, do not do to another person“ (Sayings 15, 23).
- Rabbi Hilel (60 BC – 10 AD): „Do not do to others what you would not want them to do to you“ (Shabbat 31a).
- Jesus of Nazareth: „Whatever you want people to do to you, do also to them“ (Matt. 7.12; Luke 6.31)
- Islam: „None of you is a believer as long as he does not wish his brother what he wishes himself“ (Forty Hadith of an-Nawawi, 13).
- Jainism: „Human beings should be indifferent to worldly things and treat all creatures in the world as they would want to be treated themselves“ (Sutrakritanga I, 11, 33).
- Buddhism: „A state which is not pleasant or enjoyable for me will also not be so for him, and how can I impose on another a state which is not pleasant or enjoyable for me?“ (Samyutta Nikaya V, 353.35 – 342.2).
- Hinduism: „One should not behave towards others in a way which is unpleasant for oneself: that is the essence of morality“ (Mahabharata XIII 114,8).

2.5. Environmental Economics.

Economics is the science of the economy of human society. Economics attempts to discover and formulate the laws governing economic activity in society.

¹² Taken from an article „Seven new deadly sins: are you guilty?“ published in the Times on March 10, 2008.

As the economist Zdeněk Štěpánek (1997) puts it, economics is the science which primarily deals with the issue of how different societies use scarce resources to produce useful goods and how they distribute them among various population groups. Environmental economics developed relatively recently. It studies the ways in which the main economic activities (the production and consumption of goods and services) influence the environment, as well as the ways in which the condition of the environment and its protection influence the economy (economic growth, resource availability, distribution of goods, etc.).

Economic instruments, unlike value orientations, can be implemented very quickly and they become effective virtually immediately. Nevertheless, political will is necessary to promote and adopt them.

Arthur Rich (1994) distinguishes four purposes of the economy: fundamental, humane, social and environmental.

a) The fundamental purpose of the economy

The most fundamental need of humans is the need to live, to grow, to develop themselves, which are basically concepts synonymous with life. We share this need with plants and animals.

The purpose of the economy is satisfying basic existential needs. The truest purpose of the economy therefore rests in service to life and because it has a service purpose, the economy must be oriented towards the needs of humans, not humans towards the needs of the economy. The economy must always be only a means, not an end.

b) The humane purpose of the economy

The human purpose of the economy is connected with the efficiency and organization of work. Humans need an efficient economy which is able to secure their material basis of life, but they also need an economy with a humane structure which gives them room for the development of their personalities: personalities created in the image of God, not humanly stunted robots.

c) The social purpose of the economy

If an economy creates on a national or global scale social inequality of such a kind that there exists, on the one hand, an unnecessary surplus and, on the other hand, a shortage of the most necessary goods, it is experienced as an absurd, unjust, and unsustainable state.

d) The ecological purpose of the economy

It is the nature of humans that they are a part of creation, embedded in the ecological cycle of nature, in which everything is related to everything else. It is also their nature to have a special place within creation that enables them to intervene in nature. Insofar as we find the purpose of the economy in using natural resources for

the good of humans without thereby endangering or even destroying nature as the universal basis of life, we can speak of the ecological purpose of the economy. Natural resources should, not only be used in the service of life, but also carefully preserved.

If the economy grows, the fundamental and social purpose converge, but it can also mean a divergence from the humane or ecological purpose of the economy. For instance, an increase in the economic efficiency of a company may eliminate jobs, deprive work of its content, or strengthen the burden of the already overloaded ecosystems.

Complete harmony among the different purposes of the economy may not be possible, but humans are certainly capable of reducing the tension and eliminating what Rich calls the „imperialism of a single purpose“.

As Arthur Rich distinguishes several purposes of the economy, it is useful to distinguish several kinds of capital. Traditionally, capital is understood as resources (material goods, means of production, money, shares, etc.) which are not consumed by their owner, but used to generate profits.

, Lovins and Lovins (2003) distinguish four kinds of capital:

- Human capital – in the form of labor, intelligence, culture, and organization.
- Financial capital – consisting of cash, investments, and monetary instruments.
- Manufactured capital – including infrastructure (transport, energy, etc.), machines, tools, and factories.
- Natural capital – made up of the resources of living systems and the services provided by the ecosystem.

This list needs complementation with an additional item: social capital, which can be characterized as a set of social contacts and relationships. Robert Putnam defines it as „features of social organization, such as networks, norms, and trust, that facilitate coordination and cooperation for mutual benefit“.

Especially natural capital has been neglected up to now despite it plays a key role in sustainable development.

Natural capital includes water, minerals, fossil fuels, fish, soil, air, etc. But it also encompasses living systems, which include grasslands, savannas, wetlands, estuaries, oceans, coral reefs, riparian corridors, tundras, rainforest, and so on.

The Czech economist Zdeněk Štěpánek (1997) presents similar ideas when outlining what we gain from a balanced natural system which has been evolving for hundreds of millions of years:

- protection against cosmic influences;
- relatively stable physical and chemical conditions for life;
- clean water provided by the natural water cycle;

- material resources;
- natural decontamination;
- fertile soils;
- energy resources;
- biological resources;
- room for life.

Herman E. Daly (1996) claims that until recently, economists and politicians focused exclusively on solving the problem of labor and capital productivity and investigating their mutual relationship. The productivity of natural riches was neglected, which led to huge wastage and the inefficient use of natural resources. In the past, this approach had its logic. The resources of energy and raw materials were seemingly inexhaustible and ecosystems were able to absorb waste and gas emissions. Today the situation is different.

The scarcest (because the shortest in supply) factor today is not man-made capital (such as fishing boats and chainsaws) but the remaining natural capital (such as the remaining fish populations and forests). Larger amounts of capital (chainsaws, fishing boats) cannot replace the decreasing amounts of resources (forests, fish populations). As Daly points out: „You cannot make the same house by substituting more saws for less lumber.“

If we accept the argument that natural capital and man-made capital are complements rather than substitutes, then the factor in shortest supply (the scarcest) will also be the limiting factor.

Keller, Gál, and Frič (1996) argue that conventional economists reduced nature to many isolated items, like soil, raw materials, food, and most recently biotechnology. Ignoring the unity and uniqueness of nature, reducing it to a sum of mere objects to be possessed did not reflect the most fundamental quality of nature – its powerful productive capacity.

The physical growth of the economy leads to the transformation of natural capital into man-made capital. When we cut down a tree, we can make a table from it. We gain the benefits which the table provides. On the other hand we lose the benefits which the tree had provided before. In a sparsely populated world with limited economic activity, the benefits we lost by cutting down a couple of trees was insignificant, but the benefits we gained by the production of tables was significant. However, in today's densely populated world with high economic activity the more trees we cut down, the more problems related to their shortage (and the shortage of the benefits they provide) we cause.

Growing total consumption (the total scale of the economy) is linked to both costs and benefits. Benefits are services which a greater number of tables provide us.

Costs arise from the inability of the ecosystem to continue providing certain services (cutting down trees leads to an increase in CO₂ emissions, the loss of biodiversity, soil erosion, etc.).

With growing consumption marginal costs tend to increase and marginal utility tends to decrease. If the value of marginal costs equals the value of marginal utility, the scale has reached its optimum and further growth of the economic scale (total consumption) would be uneconomical. The more the economy grows, the higher are the costs of its reproduction.

Traditional economists believe that we consume only the value that we ourselves have added to the natural riches. In their model we first add the value, subsequently we consume it, and this cycle is repeated again and again. All attention is focused on the added value, but the object to which the value is added, i.e. nature with its riches, suffers somewhat from a lack of interest.

The exploitation of nature, or more precisely natural capital, is analogous to the depreciation of man-made capital. Daly distinguishes two categories of natural capital: geological (non-renewable) and biological (renewable). Both these categories are exhaustible.

According to Keller, Gál, and Frič (1996), as a result of our treatment nature loses its productive capacity. All our wealth originates in nature and in human labor, whether physical or mental. Conventional economists know that the productivity of human labor can be sustained only if employees can renew their physical and mental strength, their productivity, but classical economic theory denies nature any means of sustaining its productivity. Nature is expected to regenerate somehow by itself, no matter how much we squeeze out of it for our needs.

Each employee under such treatment would have died from exhaustion a long time ago. In this respect, the ecological crisis is the cruel suffering of exhausted nature which has neither the means nor the time to regenerate its productivity. It means the end of the period in which man-made capital was the limiting factor and the beginning of the phase where it is the remaining natural capital which becomes the limiting factor. „The production of caught fish is currently limited by remaining fish populations, not by the number of fishing boats; timber production is limited by reamining forests, not by sawmills; barrels of pumped crude oil is limited by petroleum deposits (or perhaps more stringently by the capacity of the atmosphere to absorb CO₂), not by pumping capacity; and agricultural production is frequently limited by water availability, not by tractors, harvesters, or even land area.

According to Daly (1996), humanity is facing a historical turning point. For the first time in history the limits to the growth of prosperity are not caused by the lack of man-made capital, but natural capital. Whenever new limiting factors have appeared

in history, the economy has usually undergone a profound restructuring in response. We are once again in a period of restructuring.

When something grows it gets quantitatively bigger; when it develops it gets qualitatively better, or at least different.

Quantitative growth and qualitative improvement follow different laws. Our planet develops over time without growing. Our economy, a subsystem of the finite and non-growing Earth, must eventually adapt to a similar pattern of development. While there are limits to growth, it is necessary that there are no limits to development.

The American economist Kenneth Boulding (1966) distinguished between a „cowboy economy“ and a „spaceman economy“. Cowboys on the endless plains lived from the one-way flow of materials and energy in the ecosystem from the original source to the outlet holes. They did not need to recycle anything. By contrast, the crew of a spaceship lives in a small cabin which has a fixed and very limited cycle of material in a system of immediate feedback. It is therefore necessary to have everything under control, economize processes and make them efficient. While expense is irrelevant for the cowboy, it is absolutely essential for the crew of the spaceship.

The market is competent to solve the problem of optimal resource allocation but it is not able to solve the problem of optimal resource distribution (redistribution) and especially the optimal scale of economic activities.

The above mentioned is not an attempt to reject the market economy as the most perfect instrument known which serves the optimal distribution of resources among different uses. However, there is no type of economy, not even the market economy itself, with built-in sensors which would signal to us that the scope of our activities has already exceeded the carrying capacity ensuring the survival of the surrounding natural systems. The absence of such sensors is the more dangerous the more rapidly the economy turns natural resources into waste.

Economic growth in the physical sense does not generate only positives. It can cause the environmental costs (damage) to grow faster (and their extent to be much more serious) than the resulting benefits. In that case, we are in fact not getting richer, but poorer. So the question is whether such growth can still be called economic and whether the term „uneconomic growth“ would not be more appropriate. There may be nothing bad about getting rich at all. What is bad is when people get poorer due to uneconomical growth while it looks as if it was economic growth.

Alternative economists believe that the first thing which must be changed in economic theory is the conception of the economic process as a separate cycle

completely independent of its environment which does not mention the input and output of raw materials and energy. It is the same as if a biologist describing the body of an animal gave a detailed description of the circulatory system without mentioning the digestive track. An animal with an isolated circulatory system without a digestive tract would be a kind of a perpetual motion machine.

Together with Herman Daly, we can conclude these considerations by saying that we are at the point where further growth of the economy does not make us richer, but poorer. It seems that redistributive policies, a comprehensive (ecological) tax reform, and the efficient use of resources will have to be implemented as instrument for eliminating poverty.

Sustainable development in this sense does not mean the end of economics. On the contrary, when economic growth reaches its limits, economics becomes a more important discipline than ever before, but it is a subtle and complex economics of cultivation and quality improvements, an economics of solidarity, frugality, humility, and adaptation to the limits which nature puts to us. It is an economics which seeks quality, not expansion.

Ecological tax reform

Ecological tax reform occupies the prominent position among the environmental and sustainable development economic instruments. The idea is one hundred years old and its originator was the economist Cecil Pigou (so called Pigou tax).

The essence of the ecological tax reform is to shift the tax burden from what we want to have in sufficient amounts (e.g. labor) onto what we want to have in minimal amounts (e.g. depletion of natural resources). It therefore means gradual (long term) significant taxation and also an increase in the prices of energy and raw material resources which would, however, be balanced by the lower or even zero taxation of labor.

The principle of the ecological tax reform is fiscal (budget) neutrality. That is, what the state obtains from the higher taxation of natural resources is „dissolved“ in a decrease in labor taxes. It is therefore not a new tax, but a comprehensive tax reform which would increase primarily excise duty and environmental protection taxes and reduce (or even revoke) income tax and value added tax.

The ecological tax reform is a complicated strategic gambit. Therefore it is envisaged that the start of the ecological tax reform would be gradual and might take over a decade.¹³

¹³ If, for example, the prices of energy and raw materials increased by 5 % annually, they would double in 14 years and they would increase four times compared with the original levels in 28 years.

The long implementation of the ecological tax reform is, however, also an obstacle to its political implementation. In democratic systems politicians are elected for 4 – 5 years and their considerations are bound to this time limit. It is difficult for them to embrace a comprehensive tax reform the significant benefits of which may materialize far beyond their mandate.

Another obstacle to the implementation of the ecological tax reform is that it should be introduced at one moment in a large and robust economic space. Ideally, it should be introduced globally, but this is unrealistic with respect to the present day profound economic, political and cultural differences. Considering this, it is perhaps the European Union that has the greatest chance for the implementation of the ecological tax reform. It is strong enough economically to implement it and prevent the collapse of its trade balance with those countries and regions which will not introduce the reform.

It may be expected that the benefits resulting from the implementation of a comprehensive ecological tax reform would significantly outweigh the potential risks and costs. The clear consequence of the reform would be that businesses and households would use natural resources in a more efficient way. Businesses would be motivated to use modern, more efficient technologies, households would invest primarily in energy savings (insulation of houses and apartments, energy efficient light bulbs etc.). The introduction of the ecological tax reform would provide a new impetus for using renewable energy resources, for the more thorough recycling of materials and for longer product lifetime. Nor can we forget the support of employment, because human labor subjected to lower taxation will be cheaper.

Carbon tax

The system of excise duties is a widely accepted tool for regulating human behavior. A carbon tax, i.e. a tax on fossil fuels the burning of which produces the greenhouse gas carbon dioxide could work similarly to excise duties. People whose lifestyle produces high CO₂ should pay by means of the carbon tax and its redistribution to people who do not produce such large quantities of CO₂.

The carbon tax should encourage not only the replacement of highly polluting sources with less polluting ones, but also savings.

It is desirable to introduce and gradually increase the carbon tax on fossil fuels to a level at which the price of energy generated from fossil fuels equals the price of energy from highly efficient renewable energy sources. Under such conditions, each subject will perceive the cost of energy as very high. It will increase the overall demand for efficient energy saving measures.

The patterns of human behavior will change in favor of lower energy demands and energy generating facilities using fossil fuels will be replaced with efficient sources employing renewable energy.

It is advisable to outline the carbon tax project on a worldwide scale, because climate change occurs globally as well. The tax should be collected by a „central world bank“ at the moment of fossil fuel extraction. Because the number of mining companies in the world is relatively small, it should be feasible to control the collection of taxes. After that, fossil fuels would be traded with the burden of the carbon tax, which would prevent tax evasion on imports and exports.

Initially, the carbon tax should be low in order to allow smooth reactions to various unexpected and unintended effects. It would grow gradually to an estimated target level somewhere between USD 100 – 200 per ton of CO₂.

The mechanism of carbon tax redistribution would include the principle of solidarity. Maximum solidarity would be achieved through the flat redistribution of the collected tax, i.e. each person in the world would receive the same amount. This would reflect the „right“ of everyone to contribute to CO₂ emissions produced by the country. The even distribution of the collected tax among the citizens could be administered through an increase in pensions and for working people through income tax deductions proportional to the number of their dependents.

The carbon tax would solve many social problems of a local and global character. It would create a flow of money from the rich countries producing large amounts of CO₂ emissions to the poor countries with low CO₂ production. If 80 % of the carbon tax was distributed by the amount of CO₂ emissions produced in the given country and 20 % by the size of the population, the carbon tax would bring benefit to everyone in a high CO₂ emission country who consumed less than 80 % of the countrywide average of CO₂ emissions. Because the majority of the population consumes less than 80 % of the countrywide emission average, this model could be politically acceptable.

The introduction of the carbon tax would change the market environment in favor of energy savings and low carbon technologies. It could also reduce the bureaucracy which has sprouted up around the problems associated with global climate change.

The introduction and gradual increase of the carbon tax would necessitate the discontinuation of all subsidies. Also, in a system with no subsidies, institutions which distribute them would become unnecessary.

Conclusion



If we are to ponder the concept of sustainable development thoroughly and honestly, we cannot avoid the elementary questions accompanying the pilgrimage of human life. Who are we? Where do we come from? Where are we going?

It all began with the Big Bang more than 13 billion years ago and with the formation of inanimate matter, which took 9 billion years. Then, less than a billion years after the planet Earth was born, 3,85 billion years ago the first transgression took place: the evolution of inanimate matter transformed into biological evolution. The latter has been proceeding on Earth ever since and in spite of numerous turbulences and „disasters“ it has never stopped.

Life has been developing genetically, that is in information (genes) encoded in chromosomes, which govern the individual's development from cell fertilization until the adult stage. In higher animals this development has continued even paragenetically, when the new individual must first learn from its parents or the species group to survive in the environment.¹⁴ The third stage is metagenetic evolution, applicable only to humans.

The moment the „human mind evoked“ the second transgression took place: biological evolution transformed into cultural evolution (materialized through humans). Cultural evolution runs from the development of tools, the use of fire, agriculture, architecture, the invention of writing, philosophy, and science to the rapid expansion of the homosphere and subsequently the noosphere.¹⁵

In the noosphere, information, knowledge, and the ability to communicate spread breathtakingly fast. We have reached a technological stage when each of us can be identified at any given moment anywhere around the globe. We live in a stage of total globalization. This situation has two possible outcomes; either self-destruction or the third transgression and a shift to the next evolutionary stage, the stage of spiritualization.

¹⁴ For example, a young bird of prey learns how to catch prey from its parents. The higher the organism, the longer the „education“ of the young ones takes.

¹⁵ The homosphere is defined by the presence of humans and the extent of their influence. The homosphere is where the presence and influence of human beings predominates. The noosphere originates when the power of human intellect transforms the biosphere. It is the sum of knowledge and information accumulated by people throughout history. Human beings use this knowledge and information to change and transform their environment (biosphere).

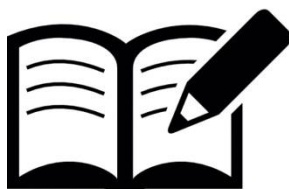
This stage (if people manage to successfully enter it) should witness the realization of the biosociological self-organization of humankind, when people start determining and controlling their further development.

It is hard to imagine that one day the mind should prevail over matter, the spiritual over the physical world. In other words, human nature should transform. Perhaps this is precisely the meaning and final purpose of the extremely long process of transformations from the mineral, i.e. inorganic sphere Alpha (from the sphere of the inanimate physical world) through the biosphere (the revived world) to Omega, the sphere of spiritualization and pure spirit. Teilhard de Chardin¹⁶ posits that arriving at the Omega Point is the ultimate goal of the evolution of the universe.

In order to eliminate risks, harm, and suffering as much as possible on our path to controlled evolution we need to change course. Changing course will require an immense amount of energy. Not the energy that comes from coal, gas, oil, or even nuclear fuel, but rather spiritual and emotional energy, enough to change the thinking and lives of more than eight billion people.

Questions for self-control

1. What is definition of sustainable development?
2. What are three basic features of humanity?
3. What are five different approaches to environmental ethics?
4. What are examples of positive shifts in value orientations?
5. What are four purposes of the economy according to Arthur Rich?
6. What are principal ideas of ecological tax reform and carbon tax?



References

1. Barney, G., O. The Global 2000 Report to the President. Pergamon Press, Oxford, 1980
2. Barney, G., O., Blewett, J., Barney, K., R. Global 2000 Revisited. Millennium Institute, Arlington, 1993

¹⁶ Pierre Teilhard de Chardin (1881 – 1955) was a Jesuit who trained as geologist and paleontologist. In his important book „The Phenomenon of Man“ (1989) he introduces an original synthesis of the biblical idea of Creation and the end of the world with an evolutionary concept of development.

3. Bible: Písmo svaté Starého a Nového zákona. Ekumenický překlad. Česká katolická charita, Praha (in Czech), 1987
4. Botkin, J., Elmandjra, M., Malitza, M. No Limits to Learning. Pergamon Press, Oxford, 1978
5. Boulding, K. The Economics of the Coming Spaceship Earth. In: Jarrett, H., ed.: Environmental Quality in a Growing Economy. John Hopkins Press, Baltimore, pp. 3 – 14, 1966
6. Bryson, B. A Short History of Nearly Everything. Broadway Books, New York, 2003
7. Capra, F. The Turning Point: Science, Society, and the Rising Culture. Simon&Schuster, New York, 1982
8. Capra, F. The Web of Life. Anchor Books, Doubleday, New York, 1996
9. Daly, H., E. Steady-State Economics. Freeman, San Francisco, 1977
10. Daly, H., E. Beyond Growth. Beacon Press, Boston, 1996
11. Daly, H., E., Cobb, B., J. For the Common Good. Redirecting the Economy toward Community, the Environment, and a Sustainable Future. Beacon Press, Boston, 1989
12. Frankl, V. Vůle ke smyslu. Vybrané přednášky o logoterapii. Cesta, Praha (in Czech), 2006
13. Fromm, E. To Have or to Be? Abacus, London, 1976
14. Gabor, D., et al. Beyond the Age of Waste. Pergamon Press, Oxford, 1978
15. Georgescu-Roegen, N. The Entropy Law and the Economic Process. Harvard University Press, Cambridge, 1999
16. Hardin, G. Filter against Folly: How to Survive Despite Economics, Ecologists and the Merely Eloquent. Viking, New York, 1985
17. Hawken, P., Lovins, A., Lovins, H., L. Přírodní kapitalismus. Jak se rodí další průmyslová revoluce. Mladá fronta, Praha (in Czech), 2003
18. Hawrylyshyn, B. Road Maps to the Future. Towards More Effective Societies. Pergamon Press, Oxford, 1980
19. Inglehart, R. The Silent Revolution. Princeton University Press, Princeton, 1977
20. Inglehart, R. Culture Shift in Advanced Industrial Society. Princeton University Press, Princeton, 1990
21. Jarrett, H., ed. Environmental Quality in a Growing Economy. John Hopkins Press, Baltimore, 1966
22. Keller, J., Gál, F., Frič, P. Hodnoty pro budoucnost. G plus G, Praha (in Czech), 1996
23. Kohák, E. Zelená svatozár. Sociologické nakladatelství, Praha (in Czech), 1998

24. Kohák, E., Kolářský, R., Míchal, I. Závod s časem. Texty z morální ekologie. Ministerstvo životního prostředí ČR, Praha, 1996
25. Küng, H. Světový étos projekt. Archa, Zlín (in Czech), 1992
26. Küng, H. Prohlášení ke světovému étosu – Deklarace Parlamentu světových náboženství. Centrum pro studium demokracie a kultury, Brno (in Czech), 1997
27. Küng, H. Světový étos pro politiku a hospodářství. Vyšehrad, Praha (in Czech), 2000
28. Laszlo, E., et al. Goals for Mankind. Dutton, New York, 1977
29. Leopold, A. A Sand County Almanach. Ballantine Books, New York, 1949
30. Lewis, C., S. K jádru křesťanství. Návrat domů, Praha (in Czech), 1993
31. Librová, H. Pestří a zelení. Veronica, Hnutí Duha, Brno (in Czech), 1992
32. Lovelock, J. Gaia: A New Look at Life on Earth. Oxford University Press, Oxford, 1979
33. Maslow, A., H. Motivation and Personality. HarperCollins, London, 1954
34. Meadows, D., Meadows, D., Randers, J. The Limits to Growth. Universe Books, New York, 1972
35. Meadows, D., Meadows, D., Randers, J. Limits to Growth – the 30-Year Update. Chelsea Green Publishing Co, Vermont, 2004
36. Mederly, P., Topercer, J., Nováček, P. Indikátory kvality života a udržitelného rozvoje. Kvantitativní, vícerozměrný a variantní přístup. UK FSV CESES, Praha (in Czech), 2004
37. Mesarovic, M., Pestel, E. Mankind at the Turning Point. Dutton, New York, 1975
38. Naess, A. Ekologie, pospolitost a životní styl. ABIES, Tulčík u Prešova (in Czech), 1996
39. Nováček, P., Mederly, P. Strategie udržitelného rozvoje. G plus G, Praha (in Czech), 1996
40. Nováček, P., Vavroušek, J., eds. Lidské hodnoty a trvale udržitelný způsob života. Sborník přednášek. Vydavatelství Univerzity Palackého, Olomouc (in Czech), 1993
41. Odum, E., P. Základy ekologie. Academia, Praha (in Czech), 1977
42. Putnam, R. The Prosperous Community: Social Capital and Public Life. In: American Prospect, Vol. 13, pp. 35 – 42, 1993
43. Putnam, H., Rorty, R. Co po metafyzice? (Hilary Putnam a Richard Rorty o realismu a relativismu.) Archa, Bratislava (in Slovak), 1997
44. Rich, A. Etika hospodářství. Oikúmené, Praha (in Czech), 1994
45. Schweitzer, A. Nauka úcty k životu. Lyra pragensis, Praha (in Czech), 1974
46. Schumacher, E., F. Small is Beautiful. A Study of Economics as if People Mattered. Bond and Briggs, London, 1973

47. Sherrington, Ch. *Man on his Nature*. Doubleday, New York, 1953
48. Singer, P. *Animal Liberation*. Avon Books, New York, 1975
49. Smelser, N., J. *Sociology*. Blackwell, Cambridge, 1994
50. Svoboda, J., Nováček, P. *Rozhovory od Bakerova jezera. Na hranici reality, metareality a fikce*. Atelier IM, Luhačovice (in Czech), 2002
51. Svoboda, J., Svobodová, J. Uhlíková daň. Podceňovaný nástroj boje proti globální změně klimatu. In: *Vesmír*, No. 9, 616 – 621 (in Czech), 2008
52. Štěpánek, Z. *Ekonomické souvislosti ochrany životního prostředí*. Vydavatelství Univerzity Palackého, Olomouc (in Czech), 1997
53. Taylor, P. *Respect for Nature*. Princeton University Press, Princeton, 1986
54. Teilhard de Chardin, P. *Vesmír a lidstvo*. Vyšehrad, Praha (in Czech), 1989
55. Tinbergen, J. *RIO Report: Reshaping the International Order*. Dutton, New York, 1976
56. United Nations World Commission on Environment and Development. *Our Common Future*. Oxford University Press, Oxford, 1987
57. Vavroušek, J. Perspektivy lidských hodnot slučitelných s trvale udržitelným způsobem života. In: Nováček, P., Vavroušek, J., eds.: *Lidské hodnoty a trvale udržitelný způsob života. Sborník přednášek*. Vydavatelství Univerzity Palackého, Olomouc, 91 – 100 (in Czech), 1993
58. Wilson, E., O. *Rozmanitost života*. Nakladatelství Lidové noviny, Praha (in Czech), 1995

Chapter III

INLAND WATERS: TYPES, THREATS, CHALLENGES



In this section you will learn about

- ✓ Inland water resources
- ✓ Hydrological and ecological characteristics of artificial water reservoirs.
- ✓ Large and small retention
- ✓ Types of artificial retention reservoirs
- ✓ Quality of inland waters
- ✓ The role of bottom sediments in the aquatic ecosystem
- ✓ Technological possibilities of removing organic pollutants from bottom sediments



Key words:

Inland water
Quality of inland waters
Organic pollutants
Bottom sediments

Inland waters are aquatic environments within land boundaries. This definition also covers transitional waters in coastal areas, even in the vicinity of marine environments. Inland water systems can be fresh, brine or mixed. Inland waters should not be equated with freshwater only. According to the common systematics, the Caspian Sea (freshwater) and the Dead Sea should be classified as such, while the Baltic Sea (also largely freshwater) will be excluded from this classification (UN 1982). In practice, however, inland water conditions focus on freshwater, in large part because freshwater

environments dominate inland waters, but also because of the importance of freshwater in the world. This definition covers all possible types of landward water bodies, including groundwater and groundwater. From an ecological and hydrological point of view, all groundwater and groundwater form an integral part of the inland water ecosystem, as freshwater from precipitation flows down the ground and feeds rivers, lakes and wetlands.

Inland waters, especially rivers, are part of all landscapes. On a smaller scale, inland aquatic ecosystems are also found in all terrestrial biomes - including meadows, mountains, forests, islands, agricultural areas, inland stretches of coastal zones, and deserts, where oases and seasonal or transitional rivers sustain life. Inland waters thus include lakes, rivers, ponds, streams, groundwater, springs, flood plains, as well as peatlands, wetlands and swamps that are traditionally grouped as inland wetlands.

Exploitation of water resources and neglect of issues related to their protection contributed to the progressive degradation of the environment. One of the main determinants of the severity of anthropopressure is the presence of organic and inorganic compounds in the bottom sediments, including heavy metals. They are not biodegradable but only biotransformed and can be immobilized in bottom sediments for a long time. However, the disruption of the structure of bottom sediments causes them to move to the upper layers of the water and to transport and deposit elsewhere. For this reason, pollution of bottom sediments is one of the most important environmental problems.

The coming years will be a time when Europe will be guided by the policy of the Green Deal. Its main goal is to reduce pollution by investing in environmentally friendly technologies. In recent years, there has been a significant increase in interest in the possibilities of stopping or reversing the ongoing degradation of the natural environment, caused by anthropogenic factors. The removal of pollutants from the aquatic environment is generally costly and very difficult. Effective activities in this area require knowledge of the types of pollution, in particular their physicochemical properties, as well as the geological structure of the catchment area, hydrological conditions of the water ecosystem, and the scope of activities and objectives required to achieve. Most anthropogenic chemicals, such as pesticides, phthalic acid esters, polycyclic aromatic hydrocarbons (PAHs) and many others, are poorly disposed of by conventional processes. As a result, new technologies based on the concept of green chemistry are implemented.

3.1. Inland water resources.

The earth's water resources are very large - but most of it is salt water in the oceans. Salt waters account for over 97% of the Earth's water resources. The remaining 3% is fresh water, which is largely trapped in glaciers and polar snows. Groundwater accounts for slightly more than 0.5% of water, and only 0.1% of water in rivers, although it is estimated that the outflow of inland waters to the seas this way

is approximately 37,000 km³ annually (PFOZ 2019). About 0.4% of the world's water resources are closed in natural lakes, but interestingly, about 20-25% of this resource is retained in Lake Baikal, which, according to estimates, can provide a permanent water supply for over a billion people (PWN 2019). Tables 3.1 and 3.2 summarize the total distribution of waters and fresh waters in individual geocomponents occurring on the Earth.

Table 3.1**The world's water resources (Małecka and Staszewski 2015)**

Types of waters	Volume x 1000 km³	% of the total
The waters of the world ocean	1338000.0	96.5
Glaciers and permanent snow cover	26064.1	1.74
Groundwater	23400.0	1.7
including active waters (up to 100 m)	10530.0	0.76
Permafrost	300.0	0.022
Lakes	176.4	0.013
Soil waters	16.5	0.001
Water vapor in the atmosphere	12.9	0.001
Swamps	11.47	0.0008
Rivers	2.12	0.0002
Biological water	1.12	0.0001
Total waters of the hydrosphere	1385984.0	100.0

Table 3.2**Freshwater resources (Małecka and Staszewski 2015)**

Types of waters	Volume x 1000 km³	% of the total
Glaciers and permanent snow cover	24064.1	68.7
Groundwater	10530.0	30.1
Permafrost	300.0	0.86
Sweet lakes	91.0	0.26
Soil moisture	16.5	0.05
Water vapor in the atmosphere	12.9	0.037
Swamps	11.47	0.03
Rivers	2.12	0.006
Biological water	1.12	0.003
Total freshwaters	35029.21	100.0

All inland freshwater resources of the Earth could be sufficient to meet the needs of the entire population, but their uneven distribution and irrational management make the supply of people with water a huge problem in many countries

of the world. The countries of Central and Northern Africa, Central Asia and South America suffer the most from the water deficit. It is estimated that many European countries will soon struggle with the shortage of drinking water.

Poland's surface water resources vary from 40 km³ in an extremely dry year to 90 km³ in an extremely wet year, with an average value of 63 km³. In turn, the amount of groundwater is estimated at 15 km³, of which 2 km³ is available. Approximate water availability for one inhabitant is about 1600 m³ of water per year and is up to 4.5 times lower than the global average. Additionally, access to these resources is heterogeneously distributed both seasonally and spatially. Most of the areas of the Polish Lowlands struggle with the deficit in the water balance for 6-9 months a year. On the other hand, the outflow from the submontane catchments during periods of intense rainfall or snowmelt results in a strong flood wave. The value of river outflow from Poland per capita in the nineties ranged between 1.1 and 1.9 thousand km³, and only 6% of this load was retained under artificial conditions. The described situation determines the necessity to build water retention systems both as protection against drought and floods.

The climatic changes observed in recent years and the rationalization of the use of existing water resources, forced by increasing costs, determine the search for new water sources and ways of retaining rainwater and seasonal waters. The basic method of water retention is the construction of dam reservoirs. It is also connected with an additional element of eco-development, i.e. obtaining clean electricity for the needs of the developing world economy. Recognition and understanding of limnological and hydrological processes observed in dam reservoirs treated as river-lake ecosystems, will enable an appropriate policy of exploitation and protection of these objects. Human activity can significantly change the amount of natural retention of a specific area or element involved in the water cycle in nature.

There are different forms of water retention. The basic systematics distinguish between natural and artificial retention. Natural retention is created by natural landscape elements, such as forests and smaller trees or shrubs, peat bogs and swamps, lakes and ponds, but also snow and glaciers. It plays a huge role in the water management of the catchment area. Artificial retention is identified with the construction of artificial water reservoirs, but these are also agrotechnical or drainage treatments resulting in the accumulation of water in the environment. Artificial water reservoirs play a significant role. They improve the water balance of the catchment area by influencing the biological quality of the surroundings. Additionally:

- they can stop water rising;
- they play an important economic role as sources of municipal and irrigation water;

- are an element diversifying the landscape
- they form a permanent element of tourism infrastructure.

However, it should be remembered that artificial aquatic ecosystems radically change the nature of the catchment area. This change can be both beneficial and unfavorable for the environment and people. It is important to balance the needs and effects of building a water reservoir in accordance with the principles of sustainable development.

3.2. Hydrological and ecological characteristics of artificial water reservoirs.

As already mentioned, dam reservoirs are built for the purpose of storing water in connection with providing it for municipal and energy needs, or preventing floods. The unevenness of water supply and outflow related to these tasks causes that the water retention time in reservoirs is shorter than in natural lakes with similar morphometric parameters. Most often, within the reservoirs, the river zone (in the region of tributaries) and the lake zone (lacustral – in the region of the outflow) are distinguished. Polish dam reservoirs are classified as flowing waters, because this is the treatment of water reservoirs with a continuous inflow or outflow of surface waters, as well as artificial water reservoirs located in waters with variable flow. However, from the hydrological and ecological point of view, in some reservoirs, especially deep ones with a long retention time, conditions and phenomena similar to those in natural lakes, e.g. stratification or mixing. The basic features that distinguish dam reservoirs from natural lakes are (Fig. 3.1):

- one large, anthropogenically controlled runoff, located in the deepest part of the reservoir;
- deep water discharge, partially disturbing the stratification;
- seasonal, several-meter fluctuations in water level;
- depth systematically increasing from the inflow (tributaries) to the outflow;
- physico-chemical and biological parameters of the ecosystem changing along the reservoir, from purely river to lake;
- a long coastline, usually devoid of a littoral zone;
- catchment area, even several dozen times larger than the surface of the reservoir;
- duration (existence) of the order of only several dozen years due to faster sedimentation rates and siltation due to sediment deposition and eutrophication.

Some of these differences negatively affect the usability of the reservoirs. The fact that the freely flowing river is blocked by a dam causes that the resulting reservoir has a catchment area with a large area and often with a high degree of

development. This results in a significant load on its surface not only with solid material from soil erosion, but also a large supply of chemical compounds in a dissolved state, including biogenic ones.

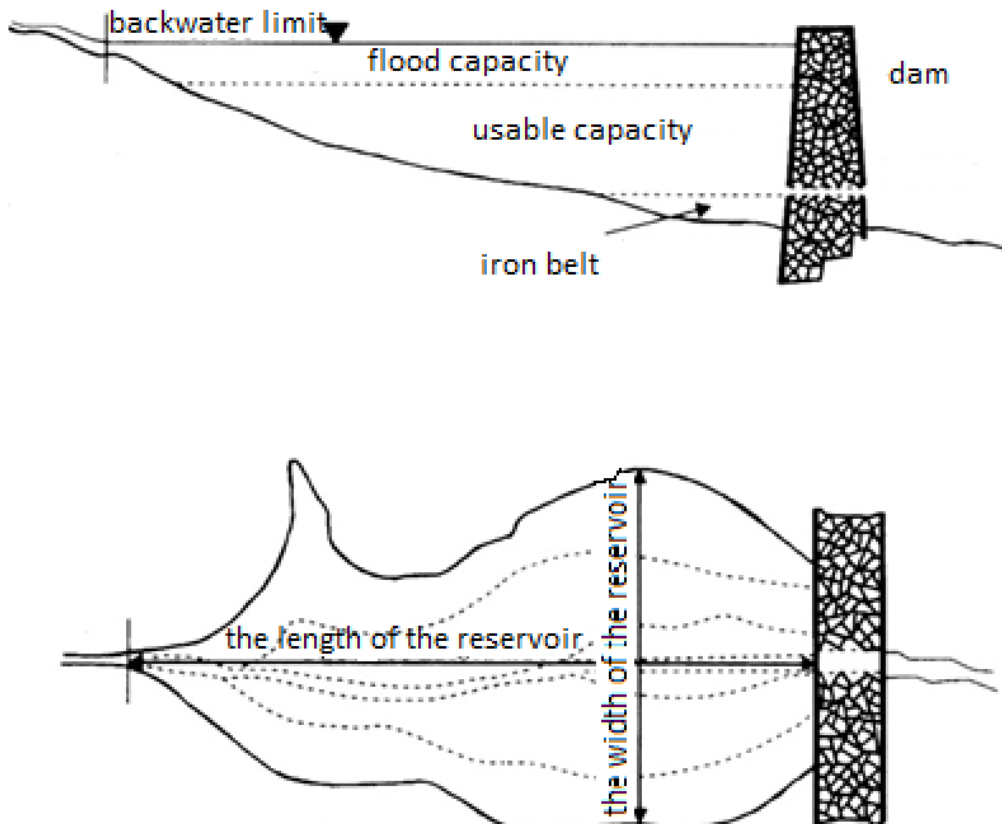


Fig. 3.1. Morphological and hydrological characteristics of dam reservoirs (Szczerbowski, 2008)

The consequence of this is the retention and deposition in the ecosystem of suspension particles supplied from the outside, as well as those produced as a result of autotrophic processes (e.g. eutrophication). Eutrophication is the most common and the most damaging anthropogenic disruption of the functioning of aquatic ecosystems. The waters are characterized by a different trophic state which determines the intensity of primary production. This leads to the formation of bottom sediments and a reduction in the usable capacity of the reservoirs. The process of shallowing having an external origin may be accelerated as a result of the accumulation of matter resulting from the processes of primary production processes in the waters (eutrophication). The time of water retention in the flooded section also increases, which further stimulates the processes of organic matter formation inside ecosystems. In this situation, the oxygen conditions in the tank deteriorate.

Reduction of water saturation with oxygen is most often observed in those

zones of reservoirs that are located closer to the dam, and is caused by its use for the degradation of indigenous matter, additional to the external matter supplied so far. This situation brings about three basic ecological problems that determine the need to balance both engineering and limnological activities at the stage of designing, building and operating reservoirs.

These problems are:

- the release of heavy metals from bottom sediments;
- emission of greenhouse gases to the atmosphere;
- modifications in the natural biogeochemical cycles of biogenic elements.

In the case of metals, one of the main issues currently being raised is the role of dam reservoirs as a specific source of mercury enriching the waters below them. This is especially true of newly built tanks. Inorganic mercury contained in flooded soils in concentrations that are often consistent with the geochemical background, undergoes biochemical transformation under anoxic conditions into the toxic mercury methyl (CH_3Hg^+), which is well soluble in the aquatic environment and undergoes bioaccumulation and biomagnification, constituting a very serious toxicological contamination.

Under low oxygenation conditions, the biomass delivered or produced within the reservoirs is decomposed into both carbon dioxide(IV) and methane. Also in this case, the production and emission of gases is intensified in the initial years of the dam reservoir's existence due to the decomposition of labile forms of terrestrial matter contained in flooded soils. A large amount of this matter determines the rapid depletion of oxygen, thanks to which the share of the fermentation product, which is methane, increases. In tropical ecosystems, greenhouse gas emission processes are intensified in the first 20 years of the reservoir's existence, for the temperate zone it may be even several dozen years.

The emission of carbon gases from dam reservoirs may constitute about 7% of the global production, and by about 60% exceeds the amount of coal retained within the reservoirs. The production of CO_2 and CH_4 is related to respiration and fermentation, respectively. The deterioration of the oxygen conditions of the reservoir shifts the balance of early diagenesis processes towards fermentation, which means that some other biogenic compounds bound in organic matter are retained in the bottom sediments or transformed into undesirable substances (e.g. S^{2-} instead of SO_4^{2-} or NH_4^+ instead of NO_3^-).

Modification of the natural cycles of transformation of biogenic elements is closely related to their easier inclusion in the trophic chain in lake ecosystems than in river ecosystems. In a sense, it is a positive phenomenon, because the excess loads of nutrients flowing from the overfertilised catchments are reduced, and the waters

leaving the reservoir are usually poorer in these compounds than the river before the dam was built. On the other hand, the collection of these elements for the purposes of biological production is associated with easier sedimentation, and the accumulated biogenic compounds cause the degradation of the ecosystem in which they have been retained. Anyway, many dam reservoirs are built precisely to retain nitrogen or phosphorus and protect other reservoirs/lakes/seas located below. The mechanisms of biogenic elements retention in dam reservoirs are similar to those that determine this phenomenon in other types of surface waters. Due to the widely observed anthropopressure in various ecosystems, they may be of different quantitative and qualitative nature.

A key and often unfavorable phenomenon accompanying the construction of artificial reservoirs is also the rising of the groundwater table in their vicinity and depends on the relief of the coastal zone, geological structure, as well as the damming height and the water management regime, i.e. damming and draining water. Preventing this negative phenomenon is difficult, costly and not always positive, therefore rational drainage solutions are needed in the adjacent areas.

3.3. Large and small retention.

In the hydrological nomenclature, there are non-standardized concepts of small and large retention. Small retention is described as a set of measures aimed at slowing down the runoff of rainwater from the catchment area, without the possibility of regulating the retained resource. Therefore, small retention is not only water reservoirs, but also all melioration activities resulting in an increase in the efficiency of soil and forest retention or regulation of watercourses. The most common border parameter to distinguish between low and large retention is retention capacity. It is considered that up to 5 million m³, small retention should be considered, and above this value – high.

The working capacities of large retention reservoirs depend on their intended use and field conditions. Typically, reservoirs built for flood protection retain the largest amounts of water. They are located in the upper, i.e. mountain, parts of the catchment area, which means that, given their large capacity, the water surface area is not always very large. The formation of flooded mountain river valleys favors additional use for energy production. By the way, recreational functions of such reservoirs appear. The dams of the mountain reservoirs are tall but relatively short. They are deep tanks. Even slight fluctuations in the water level in these reservoirs expose the banks, thus preventing the formation of a littoral zone.

In Poland, examples of such reservoirs are the Solina-Myczkowce complexes on the San River (Fig. 3.2), Czorsztyn-Sromowce on the Dunajec River or Tresna-

Porąbka-Czaniec on the Sola River. Lowland reservoirs usually have a smaller capacity, but a larger area than mountain reservoirs. They are most often built in connection with the need to provide municipal water, e.g. Goczałkowice for Upper Silesia, Sulejów for Łódź or Dobczyce for Cracow.



Fig. 3.2. Solina high retention reservoir. Below the dam, the power plant with the upper part of the Myczkowce equalizing reservoir (photo by L. Mnich)

However, the lower the basin a reservoir is built, the greater the probability of contamination of its waters, mainly as a result of the application of eroded soil particles from the basin and eutrophic processes. Unlike natural lakes, they have drainage basins much larger than their own, which results in the deposition of large amounts of the above-mentioned pollutants and river sediment. The lower part of these types of tanks is often bounded by reverse shafts. Their dams are not high, but long. Fluctuations in the water level are smaller, lowering the damming level usually exposes large areas of the bottom of the reservoir (Fig. 3.3).



Fig. 3.3. Small retention water reservoir on the Służewiecki stream in Warsaw

3.4. Types of artificial retention reservoirs

The criteria for the division of tanks given in the literature mainly take into account the functions and tasks of tanks, as well as their parameters, location, geodynamic processes, and the method of obtaining capacity. Most of the large retention reservoirs that are currently being built are most often multi-purpose facilities, providing at the same time several detailed basic needs, including:

- electricity production;
- a place of rest and recreation;
- regulation of water conditions in the field (stabilization of the groundwater table);
- protection against floods and droughts by regulating flows;
- water supply for municipal needs;
- protection of rivers/reservoirs/lakes below.

On the other hand, small retention tanks are usually built to meet one or two of the above-mentioned needs. Due to the multiple water exchange, according to the systematics proposed by Starmach et al. 1978, there are rheolymnic (flow) and limnic (low flow) tanks. The multiple of the total water change during the year was assumed as the dividing line between these types of reservoirs. Water in rheolimic reservoirs is changed more than 10 times a year, while in limnic reservoirs less than 10 times a year. For these hydrological reasons, liminal reservoirs retain organic matter in bottom sediments, as opposed to rheolymic, where this retention is significantly lower. The division of reservoirs into rheolimic and limnic refers to both mountain and lowland reservoirs.

Flood protection reservoirs are designed to reduce the risk of flooding below the reservoir as a result of stopping and delaying the outflow of raised waters. In Poland, all major retention reservoirs are used for active flood protection. It is assumed that approximately 145 reservoirs and over-dammed lakes are used for this purpose. The total amount of the flood reserve in Poland amounts to about 800 million m³, and it is at least twice lower than the needs.

Most of the flood control reservoirs are built as "wet" reservoirs with a fixed filling, but also "dry" reservoirs. They are mono-functional objects and their task is only to reduce the height of the flood wave. "Dry" tanks are created thanks to the construction of dams or dams, the overflows and outlets of which are not closed. In the periods between floods, the water flows naturally through the reservoir's bowl and outlets. When water flows into the tank with a flow exceeding its capacity, water accumulates in the tank. With large tributaries, water can also flow through surface overflows. Reducing the amount of water inflow from the catchment area leads to the emptying of the reservoir (Fig. 3.4).

In 2015, in the Podkarpackie Province, a "dry" reservoir with a capacity of up to 3.25 million m³ was commissioned, near the town of Kańczuga on the Mleczka River. Currently, about 20 flood protection reservoirs are being built in Poland, including large ones, such as Świnna-Poreba (up to 160 million m³), and projects of others, such as Kąty-Myscowa (up to 19.5 million m³), are advanced, although the conclusions after the great flood from in 1997 indicated the need for much more intensive activities in this direction.

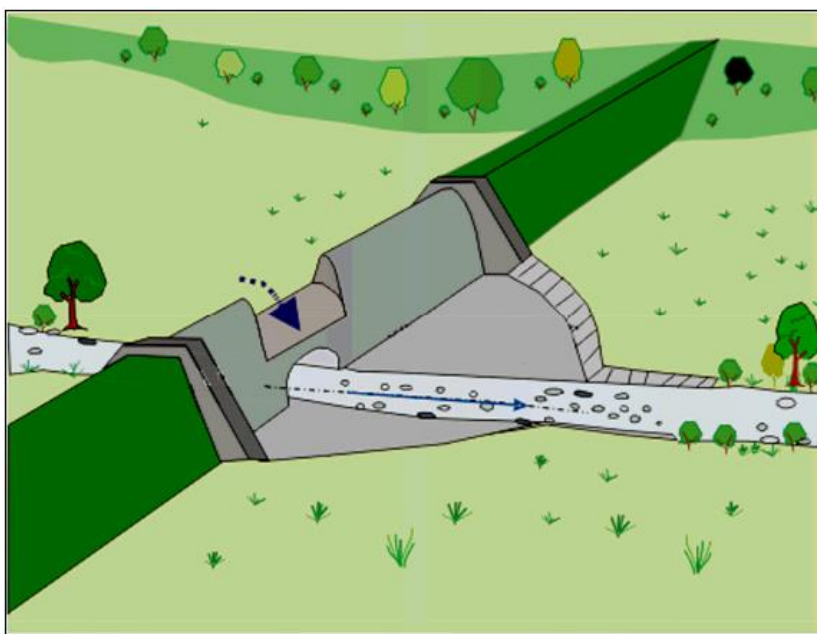


Fig. 3.4. The principle of operation of a dry reservoir dam with a central overflow

Utility tanks can be used for industrial, municipal, agricultural (irrigation), energy, shipping and recreational purposes. Industrial tanks collect water for production purposes. This water should be of a certain quality and must be supplied in the right quantity and at the right time depending on its production profile. The required capacity of the tank is determined on the basis of the projected and actual water consumption by its owner. These types of tanks, due to their work as part of the technological line, are exposed to contamination. A good example is the Rybnik reservoir, built in the 1970s as a power plant facility (at the normal water level, it has a capacity of 22 million m³). It is a source of cooling water for the power plant, therefore the waste water returned to the reservoir is enriched with heavy metals and biogenic forms and with a stable (increased) temperature throughout the year, as a result of which contamination of bottom sediments and increased trophic status are observed.

Municipal reservoirs collect water for the purposes of supplying the population and small production plants located in cities and housing estates. The development and functioning of large cities, urban agglomerations and industry

requires water supply of appropriate quality and quantity. In Poland, about 70% of municipal water is provided by underground sources. However, for many, also large administrative units, surface waters are the main source. The Dobczyce reservoir (127 million m³) provides about 55% of the water demand for Cracow. Additionally, it accumulates Raba's floods and supplies the hydroelectric power plant. Due to its tasks, it does not fulfill recreational functions.

Agricultural tanks are intended for storing water for irrigation and fish farming. The capacities of these tanks are in a wide range from 0.01 million m³ to over 50 million m³. Irrigation tanks store water in the autumn and winter period, while its use takes place in the period from May to September. Agricultural tanks are characterized by a large working layer and thus significant fluctuations in water levels. They influence the microclimate and the condition of water resources in the catchment area. They constitute a refuge for water and marsh birds and are an important element of the countryside landscape. In Poland, a model example of this type of tanks is Siemianówka on Narew. This lowland reservoir collects approx. 60–80 million m³ of water, ensuring the irrigation of approx. 15 thousand. hectares of arable land and 20 thousand. hectares of valuable natural areas. At the same time, the reservoir is a habitat for numerous species of birds, including those protected as the black stork, and also provides about 15–30 tons of fish per year. It is a significant element of recreational infrastructure and cooperates with a hydroelectric plant.

In a large number of countries, dam lakes are the basis for the development of energy that uses the energy potential of rivers. Where energy is based on thermal or nuclear power plants, dam lakes together with hydroelectric power plants supplement the energy base. Compared to other utilities, hydropower plants deliver significant amounts of energy at low cost (Sørensen, 2004). Electricity from hydropower plants is classified as a renewable energy resource, although, as described above, it cannot be said that it is a zero-emission technology from the point of view of greenhouse gas emissions.

There are several types of hydroelectric power stations. Run-of-river power plants use the natural flow of water in slope conditions and do not require back-up and construction of a reservoir or reservoir. This technology is applicable to both large and small local (less than 5MW) power plants. The situation is slightly different in the case of pumped storage power plants, which include at least two tanks, upper and lower (equalizing). In the period of low energy demand, water from the lower reservoir is pumped to the upper reservoir, and in the period of peak energy demand, the drain from the upper reservoir generates energy production (Fig. 3.5).

The Solina and Myczkowce reservoirs located in the Podkarpackie Voivodeship together with the technical infrastructure constitute an element of the

Solina-Myczkowce S.A. Hydroelectric Power Plant Complex, which can provide an average of 262 GWh of ecologically clean electricity. It allows to save about 120 thousand tons of carbon and eliminate from the environment about 32 thousand tons of carbon(IV) oxide and 320 tons of sulfur(IV) oxide. Outflow from the upper reservoir, and thus supply to the lower one, are carried out through three overflow sections with overflows for emptying water or through the above-mentioned four pipelines concreted at a depth of 40 m with installed turbine sets. Discharges from the Solina Reservoir constitute about 90% of the total hydraulic load supplying the Myczkowce Reservoir, which means that its waters are characterized by low temperatures in summer and warmer in winter. Both reservoirs accumulate up to 500 million m³ of water, which accounts for approx. 15% of the total artificial water retention in Poland.

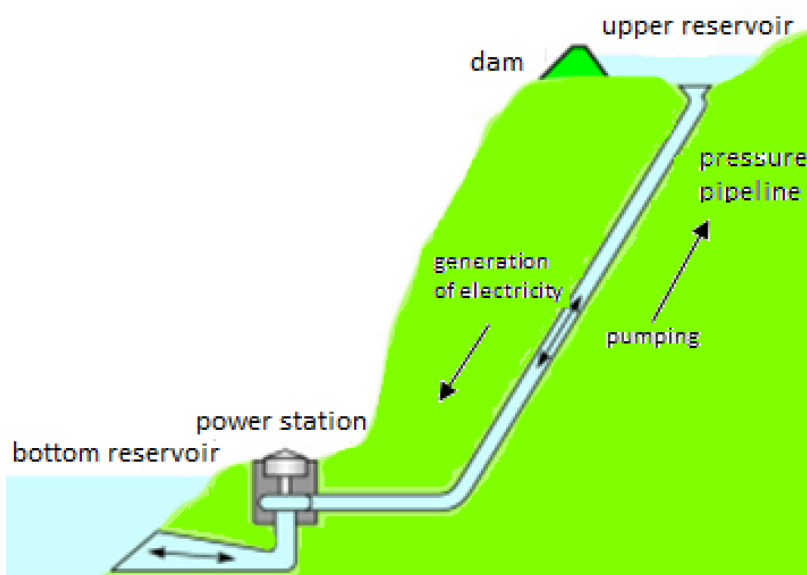


Fig. 3.5. Principle of water operation of a pumped storage power plant

3.5. Quality of inland waters.

Changes in the quality of inland waters

Quantitative and qualitative degradation of inland water systems has been initiated by many factors acting individually and synergistically or also cumulatively. Directly responsible are the changes resulting from the functioning of agriculture (irrigation, but also drainage), the spread of urban, industrial, tourist and recreational infrastructure. These changes mainly affect salinity and eutrophication. Global climate change, perceptible in recent decades, is likely to lead to even further degradation and exacerbation of existing pressures. Two phenomena are being observed and will continue to be: (i) changes in species diversity within aquatic habitats; (ii) emergence of new pollutants having a therapeutic effect at micro or nano

concentrations per dm³.

Changes in species diversity within aquatic habitats are well described by the Living Planet Index (LPI) developed by the United Nations Environment Program. The LPI shows changes in 3,000 populations of 1,145 vertebrate species worldwide and in different types of aquatic habitats. For freshwater habitats, 93 populations of fish species, 67 amphibians, 16 reptiles, 136 birds and 11 mammals were observed. The LPI shows that freshwater populations declined systematically at a faster rate than other species groups, with an average decline of 50% between 1970 and 2000. In the same period, both land and marine fauna decreased by only 30% (Fig. 3.6). This is an extremely negative trend that proves that inland waters are becoming a habitat difficult to live in. The Water Framework Directive contains regulations based on many years of observations of the impact of chemical environmental pollutants on populations and species diversity. On this basis, the principles of monitoring the aquatic environment have been developed, where biological elements (indicators) determine the classification of the ecological status of surface waters, while physicochemical indicators - often treated as decisive - are only supporting elements (GIOŚ 2015).

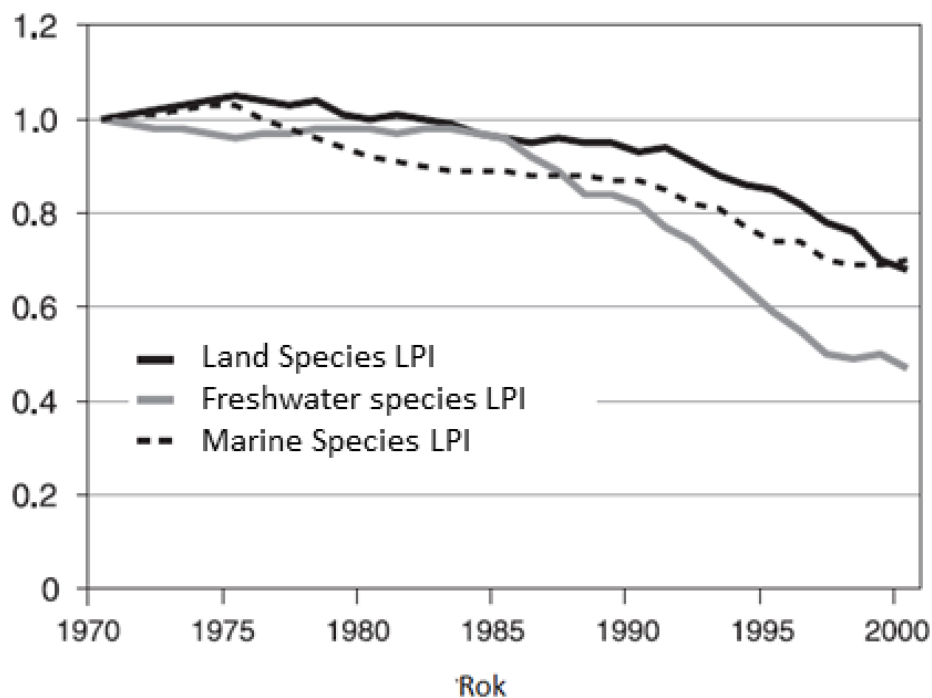


Fig. 3.6. Changes in the Living Planet Index for different types of water

It is well known that nutrient concentrations have increased significantly in inland waters around the world, resulting in progressive eutrophication, harmful algae blooms, and high levels of nitrate in drinking water. In industrialized countries, pollution with municipal wastewater has been largely eliminated, but unfortunately, more and more pollutants are appearing, the negative impact of which on the

condition of aquatic environments is still unknown. Developing countries, apart from growing micropollutants, are still struggling with large loads of biogenic compounds polluting surface waters. In Europe, it is believed that the agricultural sector generates around 50% of the total nitrogen and phosphorus load that feeds rivers. Municipal sources account for around 25%, and industry and atmospheric deposition for another 25%.

Meybeck (2003) provides an overview of water pollution problems in inland waters (Table 3.3). It is clearly visible that organic micropollutants are becoming a global problem. Identification of sources of origin and methods of their elimination in situ are today one of the main elements of water protection.

The reasons for the deterioration of inland water quality

(Meybeck 2003, Finlayson et al. 2006)

Contaminant	Rivers	Lakes	Artificial tanks	Groundwater
Pathogens	xxx	x	x	xx
Suspensions	xx	na	x	na
Decomposable organic matter	xxx	x	xx	x
Eutrophication	x	xx	xxx	nd
Nitrates	x	0	0	xxx
Salinity	x	0	x	xxx
Heavy metals	xx	xx	xx	xx
Organic micropollutants	xxx	xx	xx	xxx
Acidification	x	x	xx	0
xxx – a serious global threat xx – significant threat x – occasional regional threat 0 – slight threat nd – not applicable				

Newly emerging pollutants

Reports on the presence of other, unusual pollutants in aquatic ecosystems are increasingly appearing in the scientific literature. These compounds are referred to as "emerging pollutants" (EC's), less frequently "emerging contaminants", "emerging substances", "contaminants of emerging concern". In Polish, they are most commonly referred to as "newly emerging pollutants/micropollutants".

'Newly emerging micropollutants' are trace pollutants, recently introduced or

found in the environment, largely due to the development of new analytical techniques that have allowed a significant reduction in the detection limit of micropollutants in environmental samples. Micropollutants in the environment appear and often have a therapeutic effect at the level of trace concentrations ranging from μg to below ng . Despite the fact that most of these substances are present in very low concentrations, they are a great threat to the environment because they are resistant to biodegradation and have a negative impact on living organisms. These are substances of both natural and anthropogenic origin, but the main threat to human health and life and to fauna and flora are anthropogenic micro-pollutants, which are part of products produced industrially on a large scale. Table 3.4 presents the main groups of newly emerging anthropogenic micropollutants detected in the environment and their exemplary impact on living organisms.

Table 3.4
Examples of newly emerging micropollutants in the environment and their impact on living organisms (Ziembowicz 2018)

Group of micropollutants	Examples of substances	Effect on living organisms
Antibiotics	Tetracycline, Erythromycin	Resistance to antibiotics
Disinfectants and disinfection by-products	Alcohols, aldehydes, oxidants and trihalomethanes	Genotoxicity, cytotoxicity, carcinogenicity
Personal hygiene products	Parabens	Bacterial resistance, endocrine disorders
Flame retardants	Polybrominated diphenyl ethers	Endocrine disorders, indicating an increased risk of cancer
Pesticides and insecticides	Permetryna, Fenitrotion	Zakłócenia endokrynologiczne
Plastyfikatory	Diethyl phthalate, dibutyl phthalate, di(2-ethylhexyl) phthalate	Endocrine disorders, indicating an increased risk of cancer
Perfluorinated organic compounds	Perfluorooctanoic acid, perfluorooctane sulfonic acid	Hepatotoxic and teratogenic effects, negative influence on the reproductive and endocrine systems
Benzotriazoles	1H-benzotriazole, 5-methylbenzotriazole	Toxic, mutagenic and carcinogenic properties

The presence of groups of organic micropollutants in surface waters proves that conventional methods of wastewater treatment are insufficient and research on the development of an effective method of elimination of these compounds, which

are often very dangerous and toxic to the environment in small amounts, remains valid. Anthropogenic micropollutants most often do not biodegrade and are classified as difficult or non-degradable compounds. They are characterized by relatively long decay times, which depends on the type of pollution and natural conditions.

Due to the fact that the anthropogenic micropollutants occurring in the environment are very diverse in terms of their chemical structure, and thus – they have different physicochemical properties and have a different effect on living organisms present in the environment, there is no single pathway for the transformation of these pollutants in the aquatic environment. Under environmental conditions, they undergo multidirectional changes under the influence of physical, chemical and biological factors. Microorganisms play the main role in the mineralization of organic pollutants in the environment, however, the products of biological transformation may be more toxic than the original product. Transformation of pollutants in the environment may also occur as a result of abiotic factors, such as: UV radiation, free radicals or temperature.

In order to systematize the type and harmfulness of chemical compounds introduced into the aquatic ecosystem and measures aimed at counteracting the pollution of waters and bottom sediments, Directive 2000/60/EC of the European Parliament and of the Council of 23 October 2000 (Water Framework Directive) establishing the framework for Community action was developed in the field of water policy. This document obliges the EU Member States, *inter alia*, to monitor surface and groundwater, especially bearing in mind the developed list of 33 basic pollutants that significantly affect the quality of the aquatic environment. Among these chemical compounds, a group of hazardous priority substances has been distinguished. Some assumptions of Directive 2000/60/EC have been changed by Directive 2008/105/EC of December 16, 2008. Introduced, among others Environmental Quality Standards (EQS) for priority substances and other pollutants. If the EQS value is exceeded, it is impossible to achieve good status for selected rivers and lakes and related artificial or strongly changed water bodies.

The current legal act is Directive 2013/39/EU of 12 August 2013, which introduces the obligation to test the levels of certain hazardous chemical compounds in matrices other than waters, such as bottom sediments, fauna and flora, because the concentrations of pollutants in the water phase do not reflect the actual state. This document also updates the list of hazardous priority substances, recognizing, *inter alia*, di(2-ethylhexyl) phthalate is environmentally hazardous. Directive 2013/39/EU also extends the list of monitoring priority substances by another 12 substances or groups of substances, and tightens the environmental quality standards for seven applicable pollutants, and at the same time introduces the obligation to monitor

chemical compounds from the so-called watch list that may pose a risk to the aquatic environment. Some of them are also included in the so-called persistent organic pollutants (POPs), covered by the provisions of the Stockholm Convention, on the basis of which Regulation EC No 850/2004 and the amendment to Directive 79/117/EEC were developed. The first list contained twelve substances, most of which belong to the group of pesticides and PAHs. The list of these contaminants is open, and the most important are pharmaceuticals and substances contained in cosmetics, anti-ignition impregnates, products produced during water treatment (UPU) and water disinfection (UPD).

The harmfulness of pollutants on the natural environment is determined by many factors. One of the most important is the impact of pollutants on plant and animal organisms and on humans. Monitoring the pollution of bottom sediments allows for early identification of undesirable changes in the water ecosystem and for taking measures to reduce and eliminate pressures and negative environmental impacts. The greatest threat are organic substances such as phthalic acid esters, pesticides, polycyclic aromatic hydrocarbons (PAHs), polychlorinated biphenyls (PCBs), polychlorinated dibenzofurans (PCDFs), polychlorinated dibenzodioxins (PCDDs), etc.

The presence of phthalic acid esters in bottom sediments can, to a large extent, select the biocenosis. Exposure to these types of compounds is related to, inter alia, with hormonal imbalance, reduced survival of aquatic organisms and reproductive problems. Phthalates belong to the group of exogenous endocrine disrupters (EDs), which disrupt the functioning of the endocrine glands and are toxic to the reproductive system of mammals. Changes in the species composition of benthos mean that some environmental processes, such as biodegradation and productivity, may be seriously disrupted. The loss of any population that is part of the biocenosis can directly or indirectly affect other components of the ecosystem. The extinction of species sensitive to the increase in environmental pollution may also lead to the dominance of species tolerating hazardous substances, which in turn may disturb the natural competitiveness and affect the dynamics of the population of higher organisms.

Contaminated sediment not only causes disease and extinction of aquatic species, but also poses a danger to humans and animals consuming contaminated fish flesh. Phthalic acid esters enter the human body mainly through the alimentary system, through the skin and as a result of inhalation. The amount of a substance that can be taken up by the human body is an indicator of exposure to a given chemical pollutant. Based on the measurements of the concentration of this substance in the environment, body weight and exposure time, it is possible to estimate the daily dose

of the substance taken up by the body. The tolerable daily intake (TDI) for DEHP is in the range of 40 - 140 µg/kg body weight/day. An example of a daily human consumption of di(2-ethylhexyl) phthalate is summarized in Table 3.5. The presence of DEHP in the highest levels has been found in dairy products, meat and fish, as well as in other products characterized by a high fat content.

Table 3.5**Human consumption of DEHP by age group (IARC, 2013)**

Matrix	DEHP dose (ng/kg body weight/day)				
	0 – 0.5 years	0,5 – 4 years	5 – 11 years	12 – 19 years	20 – 70 years
Air	0.03 – 0.3	0.03 – 0.3	0.04 – 0.4	0.03 – 0.3	0.03 – 0.3
The air inside	860	990	1200	950	850
Drinking water	130 – 380	60 – 180	30 – 100	20 – 70	20 – 60
Food	7900	18000	13000	7200	4900
Soil	0.064	0.042	0.014	0.04	0.03
Sum	8900 – 9100	19000	14000	8200	5800

The only survey of the Polish population so far conducted by Struciński et al. (2006) showed that in all analyzed blood samples significant amounts of the most commonly used phthalates were found. The concentration of DEHP in most of the analyzed samples ranged from 49 to 293 ng/g of blood. According to the US EPA, phthalates are among the substances that are possibly carcinogenic to humans. Therefore, the EU Commission Regulation No. 143/2011 of February 17, 2011 on the Registration, Evaluation, Authorization and Restriction of Chemicals (REACH) included six substances on the list, of which DEHP, DBP and BBP meet the criteria, which allow their classification as toxic for reproduction - category 1B. In addition, DNA damage has been found in humans exposed to these substances. Some of them cause genetic aberrations, adversely affect reproduction and further development, and lead to endocrine disorders. Phthalic acid esters block testosterone production in men, causing fertility problems, and in women, they lead to premature puberty. Exposure to phthalates in pregnant women is a significant concern as they are able to cross the placental barrier and easily enter the developing fetus. They disrupt the development of reproductive organs in male fetuses, in children they affect the development of the

brain and changes in the lungs.

Experiments by Swan et al. (2005) unequivocally showed that phthalic acid esters passing through the placenta into the child's body are metabolized much slower and their concentrations are twice as high as compared to the mother's body. Epidemiological data published in 2012 confirmed the role of di(2-ethylhexyl) phthalate in the development of mental disorders in children, such as autism and attention deficit hyperactivity disorder (ADHD). However, the role of phthalates in the formation of these disorders has not been clarified so far, as has the mechanism of their action in the nervous system. In addition, phthalates are toxic to the liver and kidneys, possibly increasing the risk of breast cancer, asthma and allergies. Exposure to phthalate metabolites has been associated with the observed infertility, toxicity and malformations in animals. Although di(2-ethylhexyl) phthalate is characterized by a lower acute toxicity compared to MEHP - the lethal dose of LD50 for rats is 25 g DEHP/kg body weight and 1.5 g MEHP/kg body weight, it should be taken into account that people are chronically exposed to DEHP throughout their lives.

3.6. The role of bottom sediments in the aquatic ecosystem

Bottom sediments are one of the elements of the environment into which the most pollutants are introduced and their number continues to increase in the environment. Additionally, bottom sediments are one of the most important components of any aquatic ecosystem. They arise as a result of the accumulation of allochthonous substances that flow into the water reservoir from the surrounding catchment area, and of indigenous substances, i.e. matter formed from mineral substances precipitated from the water phase and undecomposed organic matter. As a result of sedimentation of material suspended in the water column, sedimentary matter is formed, the three-phase structure of which makes it a natural geosorbent, accumulating pollutants introduced into the aquatic environment.

The content of pollutants in bottom sediments is influenced by a number of natural and anthropogenic factors. Among the natural ones, the lithological structure of the catchment, the type of soil cover, the topography and climatic conditions play a major role. These factors determine the course of the weathering processes, the activation of elements as well as their migration and accumulation in the environment. In particular, the content of trace elements and organic impurities in the surface layer of the sediments is constantly changing. It is a consequence of the decomposition of organic matter, precipitation and exchange of components during the course of processes such as sorption – desorption, dissolution - precipitation, which are related to the change of physicochemical conditions (salinity, pH, temperature, oxygenation).

The chemical composition of bottom sediments is also significantly influenced by changes in the degree of water oxygenation, water balance, primary production and the intensity of photosynthesis processes, especially the persistence of periodic advantage of evaporation over supply and changes in the intensity of denudation in the catchment area, directly affecting the sedimentation rate. The method of the catchment management also determines the quality of bottom sediments. In urbanized areas, the composition of bottom sediments depends primarily on human economic activity conducted in the water reservoir catchment area. Discharges of both industrial and municipal wastewater, leaks from landfills as well as gas and dust pollution of the atmosphere are the source of information on the degree of anthropopressure in the water ecosystem. In turn, the analysis of the content of pollutants in bottom sediments is an important source of information to determine the origin, speed and distribution routes of chemical compounds in the aquatic ecosystem. Particularly high concentrations of chemicals in the sediments are detected near anthropogenic sources of pollution (Table 3.6).

Table 3.6
The origin of selected organic pollutants (Siebielec et al., 2015)

Organic pollutants	Source
organochlorine pesticides	plant protection products
polycyclic aromatic hydrocarbons (PAHs)	transport; hard coal processing; incineration of municipal waste; fires; crude oil processing
polychlorinated biphenyls (PCBs)	incineration of hospital waste; coal combustion in power plants; transport; technological processes; leaks from heat exchangers
phthalic acid esters (phthalates)	production of plastics; production of floors, roofs, walls, cable covers; medical devices

Although a significant part of low-solubility and low-degradable inorganic and organic pollutants entering the aquatic environment are retained in the bottom sediments at the final stage of the self-purification processes, some of them may be re-activated into the water phase as a result of the sediments of chemical and biochemical processes (molecular diffusion, dispersion, resuspension, bioturbation). The process of releasing the ingredients into the water column can be triggered, among others, by as a result of mechanical disturbance of the sediment structure as a result of natural processes (flood, high water levels, wind waves). Moreover, during a flood, contaminated sediments can be transported and deposited in other places, also

not included in the water ecosystem (except for the river bed in floodplains).

Another significant problem is the excessive accumulation of bottom sediments, which causes a number of adverse effects in water reservoirs, hindering their proper functioning. The results of the research on the silting process of medium and large dam reservoirs located in Poland confirm the occurrence of operational problems. The accumulation of bottom sediments is the basic factor influencing their service life. The increase in the thickness of bottom sediments primarily contributes to the reduction of the capacity and depth, limiting the usability of water reservoirs. In the part of the inlet to the water reservoir, there is shallowing and intensive overgrowing with vegetation, which contributes to flooding or flooding of the adjacent areas during floods. The retention capacity also decreases - it is especially important for reservoirs whose primary function is flood protection. On the other hand, at low water levels, contaminated bottom sediments have a negative impact on its quality, which is particularly important in the case of reservoirs that are a source of drinking water, and which are not adapted to remove micropollutants. Recreational functions are also limited and, above all, it is difficult to properly conduct water management.

The intensity of silting of a water reservoir depends on many factors, resulting from the complex relations between the shape and surface of the catchment, the nature of its use, climate and the fluvial system (Table 3.7).

Table 3.7
The main factors influencing the silting process (Gwóźdż, 2007)

Hydrological parameters and hydrographic catchments	Reservoir geomorphology	The geological structure of the catchment area
<ul style="list-style-type: none"> • catchment area • way of using the catchment area • river network density • the state of watercourse regulation • basin hypsometry • the amount of rainfall in the catchment area 	<ul style="list-style-type: none"> • development of edge abrasion 	<ul style="list-style-type: none"> • susceptibility of the substrate to the development of erosive processes • mineral and petrographic composition of the substrate

These factors affect the course of erosion processes in the catchment area, the amount of sediment runoff denudation and ultimately the amount of mineral material flowing into the water reservoir. However, the accumulation of bottom sediments is primarily determined by the intensity of transport of particularly suspended sediment

and the ability of a water reservoir to retain it.

The phenomenon of reservoir silting has both a geochemical and a technical aspect and is often analyzed in terms of quantity and quality. Qualitative research includes, among others, the determination of the physical and chemical properties of bottom sediments and the assessment of their variability as they move away from the reservoir feeding point. In terms of quantity, changes in the thickness of sediments accumulated in the reservoir at specific intervals are determined. This allows to characterize the sedimentation dynamics and forecast the rate of decrease of the reservoir capacity during its operation.

Small retention reservoirs are characterized by more intense silting compared to large retention dam reservoirs. Measurements of the volume of river sediment retained in the reservoir were made after 10, 13 and 14 years of operation. The degree of silting was respectively 13.08%, 15.79% and 16.20%, while the annual average was 0.87%. For small reservoirs, these values are in the range of 1.87–5.08%. For comparison, the average annual silting rate of reservoirs, which belong to the global average category, is in the range of 0.02– 0.58%. The low value of the silting degree of the Wilcza Wola Reservoir, which is classified as a small water reservoir, despite the high intensity of transported sediment, may result from its considerable capacity (3,860,000 m³).

Research aimed at determining the thickness increment of bottom sediments was also carried out by Madeyski et al. (2008), according to which the silting degree for the Rzeszów reservoir was 66% after 13 years of operation (average annual - 5.07%). The Brzóza Stadnicka reservoir is also characterized by a high degree of silting, for which this value after 7 years of operation was 44.66% (average annual - 6.38%), while after 16 years it was over 80%. If the capacity of the tank is reduced by 80%, it does not fulfill its function. On the other hand, the functions of small water reservoirs are limited as soon as the capacity is reduced in the range of 40–60%. As a consequence of this, silting of water reservoirs necessitates the removal of sediments from the bottom, which primarily includes such aspects as: protection of water reservoirs against decreasing usable capacity, the need for proper management of the efficiency of watercourses to facilitate water outflow, optimal management in fish ponds, optimization of retention in reservoirs industrial and reducing clogging of infiltration ponds.

The restoration of the original capacity of the reservoir is carried out mainly by mechanical removal of sediments, less often they are biological or chemical methods. Desludging of dam reservoirs can be accomplished by:

- digging with excavators from the exposed bottom of the tank,
- dredging – mechanical removal with grab or multi-bucket dredgers, suction of

water with sediments using suction dredgers (dredgers), suction of water with sediments using a siphon thrown over the dam,

- draining water from the tank assisted by mechanical or hydraulic disturbance of sediments,
- quick drainage of water from the reservoir during high water levels or through large bottom flushing outlets,
- slowly draining the water from the reservoir and flushing with the natural flow of the river,
- controlled drainage of water from the tank through the rinsing outlet.

Removal of bottom sediments is considered to be one of the most effective methods of reclamation of water reservoirs, especially in the case of persistent organic pollutants, biogenic elements and heavy metals. Chmisi and Hämerling (2016) analyzed the five most commonly used methods of reservoir rehabilitation (biomanipulation, dredging, biostructures, bottom layer oxygenation and phosphorus inactivation) to determine the most effective. The criteria to be assessed were the individual type of reservoir, the effectiveness of the treatments due to the reason for degradation, the cost of works, the time needed to carry out the process and the source of contamination. Due to the time needed to achieve the intended goal, the immediate effect guarantees the correct removal of bottom sediments. On the other hand, the prospect of achieving the intended goal within a few years is realistic with the use of phosphorus inactivation. In the case of urbanized areas, which provide pollutants that are difficult to biodegrade in the biological way, it is necessary to use primarily mechanical methods, such as dredging. According to the authors, taking into account the overall assessment, dredging was the second best reclamation method, while the oxygenation of the bottom layers was considered the least effective. The use of off-tank removal methods is advisable for environmental and financial benefits. Research carried out on Lake Trummen in southern Sweden also shows the effectiveness of this procedure in the rehabilitation of water reservoirs. The research was carried out to observe the level of pollution with nitrogen and phosphorus compounds. After removing the sediments, a decrease in nitrogen concentration by about 80% and phosphorus by about 90% was observed, and an increase in water transparency from 0.2 m to 0.6–0.8 m. Currently, bottom sediments are removed only because of the excessive accumulation of matter in lakes, reservoirs or, if necessary, to restore the rivers. Unfortunately, the main reason for the removal of sediments from the seabed is not due to the presence of a large amount of contaminants.

Dredging water reservoirs is a necessary and commonly used procedure that allows to keep them in such a state that they fulfill their economic and economic

functions. First of all, it is an attractive method in many respects to remove dangerous organic pollutants from the aquatic ecosystem. During the implementation of this method, it is important to determine the physical and chemical properties of bottom sediments, which may indicate their ecological condition and the possibilities of their management.

3.7. Technological possibilities of removing organic pollutants from bottom sediments.

General characteristics

The decision to remove bottom sediments from the water ecosystem is made in the case of excessive shallowing of reservoirs, lakes or the necessity to restore the rivers. However, due to the rarity of implementing such a solution, there are few studies in the literature on the removal of organic pollutants from bottom sediments. The elimination of harmful pollutants from bottom sediments and their subsequent management is more advantageous than storage, taking into account the financial and environmental aspects. The technologies used for soil remediation were the basis for the development of methods for the treatment of bottom sediments. Physical, chemical, thermal, biological and combined methods are used for the treatment of bottom sediments extracted from the bottom of the aquatic ecosystem (ex situ methods). The processes of cleaning sludge from contamination are carried out on a specially prepared technological stand. The advantage of such a solution is the ease of their control and relatively short time of the process. In situ methods for removing pollutants from bottom sediments can also be carried out. Treatment of bottom sediments based on in situ methods, compared to ex situ methods, is much more difficult to implement and sometimes more expensive, which results, among others, from the necessity to use environmentally non-invasive methods of cleaning and establishing and maintaining a base near the reservoir.

Biological methods are the most popular for removing contaminants from bottom sediments. However, the high content of hazardous organic substances makes it impossible to apply these methods. For example, the presence of heavy metals in bottom sediments has a toxic effect on organisms that prevent their development and, as a result, limit the possibility of removing pollutants from. The content of phthalic acid esters in the soil at the level of about 100 mg/kg inhibits the growth of microorganisms and the activity of the catalase enzyme. On the other hand, the increase in the content of diesel oil from 2,500 mg/kg to 20,000 mg/kg resulted in a decrease in the efficiency of bioremediation by 60% in soil.

The physicochemical parameters of the analyzed soil have a key impact on the process of removing both diesel oil and other pollutants. The optimal pH for the

effective course of soil bioremediation from petroleum products is 7.5. Extreme pH values resulted in a reduction in the activity of soil microorganisms towards the degradation of these products. Water content is also important in the biodegradation process. The humidity should be about 80% of the water capacity, the relative humidity should not be less than the value of 15%. Despite many advantages, in order to obtain satisfactory results of contamination removal, biological methods require a long process time (even several years). In this case, physical, chemical or physicochemical methods can be used first for the treatment of bottom sediments, followed by biological methods.

Thermal methods are considered to be one of the most effective methods for removing pollutants from bottom sediments. They are characterized by a short process time and are easy to carry out. A huge challenge for the design of these methods is the prevention of air pollution generated during the process. To protect the air, install scrubbers that clean the air before releasing the resulting gases into the atmosphere.

Another disadvantage of incineration of bottom sediments is also the excessive consumption of energy necessary to heat the soil to the required temperature and the presence of water, which significantly reduces the efficiency of the process. Thermal methods include the use of microwave radiation. The downside of this process is significant energy consumption and health risks. This method may also pose a safety risk, especially in the case of the remediation of bottom sediments rich in organic components. In order to use this process efficiently, further research on heat recovery is required.

There are also some promising methods to remove a specific pollutant or group of substances in the literature, but these are ongoing studies that require additional analyzes. An example might be:

- remediation of bottom sediments by resuspension,
- in situ removal of pesticides with the use of activated carbon and carbon nanotubes,
- in situ removal of petroleum substances with the use of zeolites combined with microbial decomposition.

The use of chemical methods, above all, increases the bioavailability of hazardous and hardly biodegradable chemical compounds by reducing their toxicity. Moreover, chemical methods very often completely decompose pollutants into simple products such as carbon(IV) oxide and water. In this case, the so-called advanced oxidation methods (AOPs). Unlike most methods, they do not transfer pollutants to another environment, but contribute to their degradation and are safe for the environment, which is a clear advantage over other methods used.

The effectiveness of APOs depends mainly on the type and concentration of the substance to be removed and the presence of other organic and mineral compounds. The hydroxyl radicals present in this process react quickly and non-selectively with almost all organic compounds. Thus, leading to their mineralization, therefore other substances present in the bottom sediments will compete with each other for the possibility of reacting with them, acting as the so-called HO radical scavenger.

Advanced oxidation methods use different oxidation systems that can be divided into three groups:

- chemical processes, which include oxidation with ozone, hydrogen peroxide or the simultaneous use of both of these reagents, the Fenton reaction with the use of iron (II) ions and hydrogen peroxide, supercritical water oxidation (SCWO), wet air oxidation (WAO) and Fenton's reagent assisted by ultrasound,
- processes using electromagnetic radiation with the use of electrodes with a high oxygen evolution overvoltage and Fenton's reagent assisted with electric current,
- photochemical processes, including photocatalytic degradation in aqueous semiconductor suspensions, Fenton's reagent assisted with UV light.

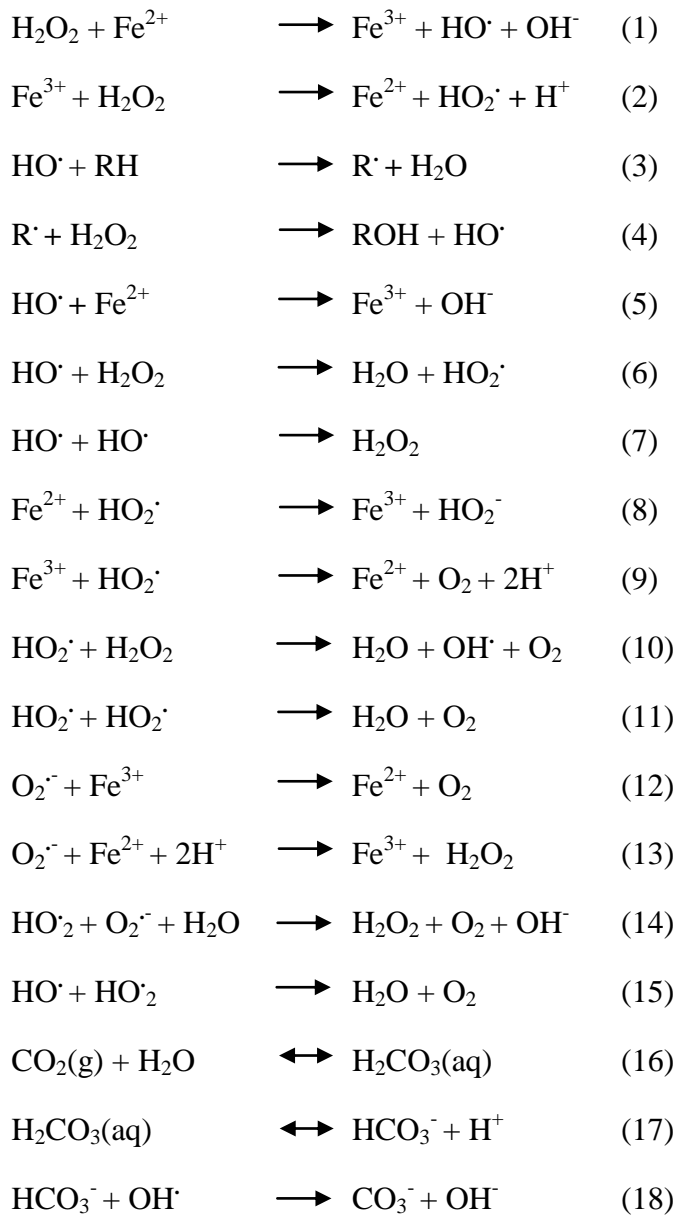
Each method has its limitations, which is why new and better solutions are constantly searched for. In order to obtain satisfactory final results, in many cases it is necessary to use several methods together.

The Fenton process in the remediation of bottom sediments

Due to the simple technological solution, the most popular method among AOPs is the Fenton reaction. It was first used to oxidize toxic pollutants in the 1960s. However, research on the application of this process in soil remediation began only at the end of the 20th century. Among the undisputed advantages of the Fenton process is the lack of formation of harmful products, which are formed, for example, in the case of chlorination and ozonation. It is believed that the Fenton reaction is particularly effective in degrading most pollutants and competitive with other advanced oxidation methods due to its simplicity, general availability of reagents and no need for specialized equipment. The mechanism of the classic Fenton reaction leads to the catalytic decomposition of hydrogen peroxide in the presence of iron ions, during which hydroxyl radicals are generated. The mixture of hydrogen peroxide and iron ions forms the so-called Fenton's reagent. Hydrogen peroxide is called the green oxidant because the by-product of the reactions involving water and oxygen. Moreover, it is relatively cheap and readily available in large quantities, and its use is an environmentally friendly alternative as opposed to oxidants such as ozone, $KMnO_4$, $K_2Cr_2O_7$. Hydrogen peroxide and other oxidants can also be used individually, but often turn out to be too weak to effectively degrade chemical

compounds that are difficult to decompose (Ferrarese et al. 2008). Therefore, iron ions are usually used which activate the decomposition of hydrogen peroxide and accelerate the overall rate of oxidation. Hydroxyl radicals formed in this process in an acidic environment (recommended pH in the range 2–4) oxidize organic substances with the diffusion rate in water 109–1010 1/M·s. At the same time, the addition of iron ions is not always necessary in the remediation of bottom sediments or soil, because the natural admixture of iron also takes part in the Fenton reaction.

The Fenton reaction is a complex process in which many side reactions take place. In soil, bottom sediment, these reactions include basic radical initiation (reactions (1) and (2), propagation (reactions (3) and (4) and termination (reactions (5)–(7) as well as with intermediates (reactions (8)–(15), with carbonate and bicarbonate ions (reactions (16)–(21) and with natural organic matter (NOM) (reaction (22).





In addition to hydroxyl radicals, the process produces hydroperoxide radicals, superoxide anion radicals and hydroperoxide anions, which can act as their scavengers and have a very small share in the direct oxidation of organic pollutants, because they are much less reactive than OH radicals. An excess of hydrogen peroxide can lead to the formation of HO₂ radicals. Like too many Fe²⁺ and H⁺ ions, it can also bind hydroxyl radicals. Bicarbonate and carbonate ions also act as radical scavengers. The radicals – carbonate ions produced in these reactions are also oxidants, and they are more selective, but much weaker than HO radicals. Natural organic matter present in bottom sediments also usually inhibits the action of hydroxyl radicals.

Hydroxyl radicals are formed not only in the presence of iron(II) ions. Iron(III) ions can also be used as a catalyst for the generation of hydroxyl radicals. Any change in the classic Fenton reaction is referred to as a "modified Fenton". The radicalation processes in this case take place in two or three stages, as a result of a slow reaction between H₂O₂ and Fe³⁺, and then a rapid reaction between the produced ferrous ions and H₂O₂. The efficiency of removing petroleum products was higher in the case of using iron(III) ions as a catalyst compared to iron(II) ions. According to the authors, the reason for this is the partial loss of hydrogen peroxide in the oxidation phase of iron(II) to iron(III).

The use of the Fenton process is recommended in the remediation of soil and bottom sediments. However, usually the kinetics of the classical Fenton reaction is too slow to degrade the highly absorbed pollutants in soils and bottom sediments, and the heterogeneity of these matrices makes the process difficult. For example, the efficiency of removing 24 substances from the PAH group from the soil after 24 hours using the Fenton process ranged from 8.8 to 43% (Jonsson et al. 2007). In turn, Silva et al. (2009) achieved a degradation of phenanthrene in soil with a starting concentration of 700 mg/kg at 94%, but the content of pyrene (615 mg/kg) was only almost halved. At a comparable level (44%), the authors reported pyrene removal efficiency using photocatalytic degradation in the presence of TiO₂ after 25 hours, with the initial pyrene concentration being only 40 mg/kg.

In soil remediation, the Fenton process is especially recommended for the removal of pesticides. One of the first studies in this direction was conducted by

Miller et al. (1996). According to their reports, the efficiency of degradation of pendimethalin belonging to the group of herbicides as a result of the classic Fenton reaction was over 99%. Further studies confirmed the usefulness of this method for removing substances belonging to the group of pesticides. Although the effectiveness of the Fenton process in soil remediation is satisfactory, there are still limitations in applying this process individually. Sometimes, much higher doses of the oxidant are required due to the presence of natural organic matter in the soil, which may also undergo oxidation.

In order to eliminate or minimize disadvantages and limitations, various integrated methods using biological, physical and chemical methods in combination with the Fenton process are constantly being developed. Modifications of this process in soil remediation are mainly due to the lower availability of pollutants due to sorption on solid particles and the impeded operation of the iron catalyst in the natural soil environment. In the conventional Fenton reaction, the problem is the required low soil pH, which negatively affects the quality and properties and is incompatible with subsequent biodegradation. To extend the application of this method at a higher pH, a solution may be the use of chelating agents (e.g. EDTA, pyrocatechin) which keep the Fe³⁺ ions formed under these conditions in a dissolved form. The influence of these substances on the removal of pollutants from soil during the application of the Fenton process was investigated, among others. In many cases, however, the use of chelating substances is insufficient and it is necessary to use several methods together to obtain the desired end effects. For example, in the photo-Fenton reaction, hydroxyl radicals are formed under the influence of UV radiation and at the same time photo-reduction of iron(III) to (II) ions takes place, during which HO radicals are formed. In turn, in the electro-Fenton method, hydrogen peroxide is generated electrochemically or ions are formed iron(II) or combinations thereof. In soil remediation, however, the most popular is the use of biological methods in combination with chemical methods.

Ultrasonic field in the remediation of bottom sediments

A new method in the remediation of bottom sediments is the use of ultrasound (sonication), which can also be successfully used *in situ*. In environmental engineering, the ultrasonic field in the range of 20–100 kHz is most often used. This method is based on emitting ultrasounds to the water phase, which in contact with it cause the phenomenon of cavitation. The cavitation process consists in the formation of pulsating vacuum bubbles in the liquid or filled with gas dissolved in the liquid or with saturated vapor (Fig. 3.7).

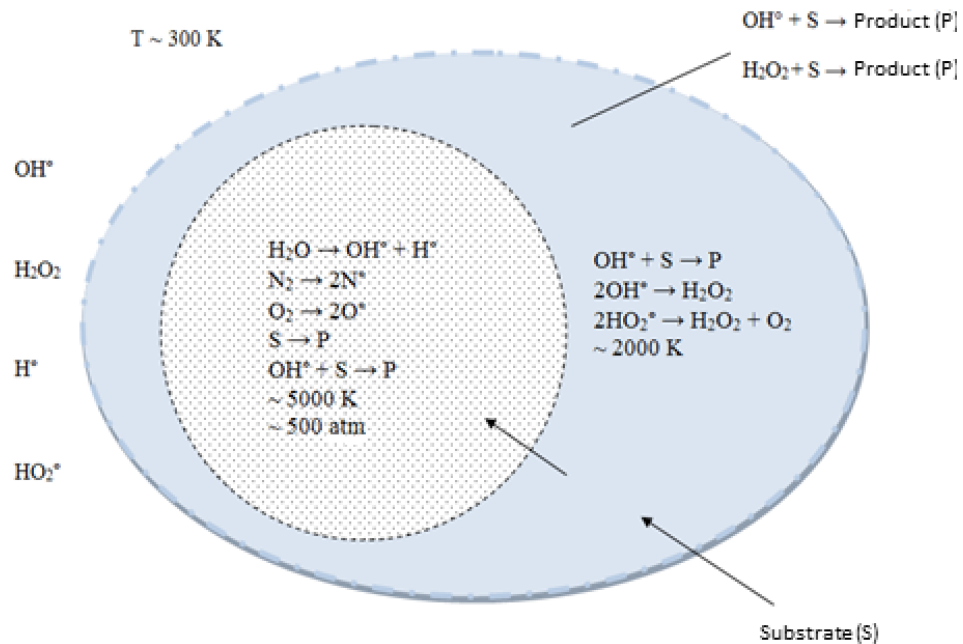
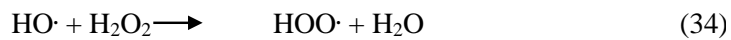
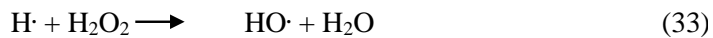
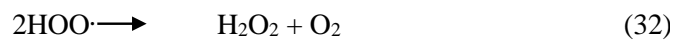
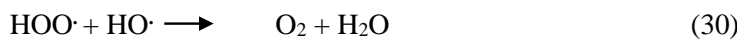
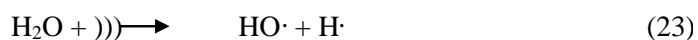


Fig. 3.7. Cavitation bubble (own elaboration based on Adewuyi, 2001)

Cavitation bubbles appear as a result of local ruptures of the medium under the influence of high tensile forces. During the operation of the ultrasonic field, the cavitation bubbles increase their radius twice or more. They then collapse rapidly, releasing a large amount of energy, resulting in a local increase in temperature and pressure. The rapid increase in pressure inside the bubble causes them to burst and the formation of a hydrodynamic shock wave. Extreme conditions are the cause of the thermal breakdown of water molecules, during which hydroxyl radicals are formed, which are the main source of the so-called sonochemical reactions (reactions 23–35). This phenomenon significantly accelerates the course of chemical and physical reactions.



Reactions that are initiated by cavitation can occur in three different areas. The interior of the collapsing bubble, subject to extreme pressure and temperature conditions, is the first area where the resulting hydroxyl radicals react with substances present in the gas phase as a result of thermal dissociation of water. The second area is the gas-liquid interface. There is still high temperature and pressure between the collapsing bubble and the liquid, but even low-volatile substances pyrolyze under these conditions. The effectiveness of thermal degradation of dissolved non-volatile substances depends mainly on their hydrophobicity and the activation energy necessary to break the bond. In turn, in the third area, which is the solution at ambient temperature, the hydroxyl radicals formed in the cavitation bubbles, which did not react in the border zone, react with the substance dissolved in the solution.

The production of hydroxyl radicals depends on many factors. Particular attention to the influence of pH, temperature, physicochemical properties of the removed substances, time, intensity and frequency of the ultrasonic field and the presence of inhibitory substances. According to his research, the pH is irrelevant to the amount of generated hydroxyl radicals and hydrogen peroxide. The impact of this parameter depends on the structure and chemical structure of the substance to be removed, it is important when the organic substance has a molecular and ionic form. The substance in the ionic form shows lower hydrophobicity, therefore its decomposition takes place in the third region (apart from the cavitation bubble), where less favorable conditions occur. In order for the degradation of the contaminant to take place inside the cavitation bubble, this substance must be present in the solution in a molecular form.

Henry's solubility and constant value are also important in this process. Temperature is also of great importance for the effectiveness of the removal of substances during the operation of the ultrasonic field. The increase in temperature causes an increase in the amount of cavitation bubbles, but they are filled with water vapor, which causes a decrease in the intensity of bubble collapse after exceeding the optimal temperature, which depends on the physicochemical properties of the pollutant removed. An increase in the process temperature from 15 to 35 °C has a positive effect on the efficiency of naproxen and paracetamol removal, while above 35°C a decrease in the amount of hydroxyl radicals was observed.

The literature also confirms the influence of the frequency of the ultrasound wave on the efficiency of pollutant removal. By using ultrasonic waves in the frequency range of 200–400 kHz, the best results are obtained for the decomposition of low-volatile substances. On the other hand, for volatile substances, increasing the frequency increases the efficiency of removal. The use of the ultrasonic field to

remove impurities that are difficult to decompose is a promising and recommended method, because ultrasounds, due to its high efficiency, significant reduction of the time of unit processes and low instrumental requirements, are treated as "green" technologies. The process can be carried out using a special sonotrode or in ultrasonic cleaners equipped with an ultrasonic transducer.

The available studies confirm the positive effect of sonochemical methods on the degradation of many organic compounds. Naddeo et al. (2007) analyzed the possibility of removing natural organic matter (NOM) from an aqueous solution as a result of an ultrasonic field with a frequency of 20 kHz and a field strength of 7 to 42 W/cm². The authors noted a reduction in the concentration of humic acids within the range of 24.5–34.9%. The degree of removal of these impurities depended on the intensity and duration of sonication. In turn, Shemer and Narkis (2005), using ultrasound with a field strength of 3.75 W/cm² and a frequency of 20 kHz, removed trihalomethanes from an aqueous solution. The efficiency obtained in these studies, during 180 min, was 100% for CHCl₃ (chloroform).

On the other hand, the removal of pollutants from soil and bottom sediments using an ultrasonic field was carried out by Collings et al. (2006). PCB 1254 removal efficiency from soil was 99% in 7–10 min (90% after 2 min), initial concentration - 45 ppm. The effectiveness of removing selected substances from the PAH group from bottom sediments was 70% after 2 minutes of sonication (initial concentration – 400 ppm). The research was carried out with the use of an ultrasound generator with high electrical power equal to 1.5 kW. According to the authors, this method is promising due to its high efficiency in removing pollutants, no formation of toxic by-products, and low energy consumption, assuming that similar results can be obtained on an industrial scale. The technology is also easy to move and, above all, it is possible to hydraulically transport the soil to the reactor. Moreover, during the process in suspension, the cavitation bubble collapses asymmetrically towards the surface of the solid. The shock waves generated as a result of this phenomenon are the cause of extreme conditions on the surface of the solid, which the fracture of the solids and the breakdown of the contaminants that are normally adsorbed on the solids. Mason et al. (2004) used the soil washing method to remove contaminants. Supporting this process with ultrasound significantly improves the efficiency of removing pollutants, e.g. as a result of the capillary phenomenon in the formed pores and crevices of solid particles.

Nevertheless, this method does not always produce satisfactory results, therefore a promising alternative in relation to conventional and unit oxidation methods is the combination of processes, e.g. the use of an ultrasonic field in combination with the application of the H₂O₂ oxidant or the Fenton process. A good

example is the research, where using the ultrasonic field to remove dichlorvos (insecticide) from an aqueous solution with an initial concentration of 20 mg/dm^3 , achieved the removal efficiency of 6.4% after 120 minutes of sonication. As a result of the addition of hydrogen peroxide (500 mg/dm^3), this value increased to 20% using the Fenton process ($80 \text{ mg H}_2\text{O}_2/\text{dm}^3$, $80 \text{ mg Fe}^{2+}/\text{dm}^3$) – 81.2%.

The combined process allows, among others to a significant increase in the efficiency of pollutants removal compared to a unit process, often shortening the time and, depending on the processes used, reducing the dose of oxidant and catalyst.

Conclusions

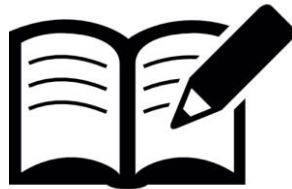


The analysis of the available data shows that both the qualitative and quantitative degradation of inland waters is progressing independently of the implementation of remedial programs, e.g. the Water Framework Directive, the slowing effect of which is visible mainly in developed countries. The protection and use of good-quality inland water resources is a constant challenge for societies, as is reducing the negative consequences of inland water degradation. Failure to act to reduce and reverse the processes of qualitative and quantitative degradation of inland water systems will have far-reaching consequences for humans, as this problem is both environmental and social – it can determine political consequences such as migration and wars.

Questions for self-control

1. What methods can we use to remove impurities that are difficult to decompose in bottom sediments?
2. What is the Fenton process?
3. What is the function of bottom sediments in the aquatic ecosystem?
4. What are the benefits of water retention?
5. What groups of organic pollutants are classified as difficult to degrade in the aquatic ecosystem?
6. Short describe the technological possibilities of removing organic pollutants from bottom sediments.

7. What is the technological possibility of removing organic pollutants from bottom sediments more effective?
8. What is the sence of the Fenton process in the remediation of bottom sediments?



References

1. Adewuyi Y. G., Sonochemistry: environmental science and engineering applications, *Industrial & Engineering Chemistry Research*, 2001, 40(22), 4681–4715.
2. Agarwal A., Liu Y., Remediation technologies for oil-contaminated sediments. *Marine pollution bulletin*, 2015, 101(2), 483–490.
3. Akcil A., Erust C., Ozdemiroglu S., Fonti V., Beolchini F., A review of approaches and techniques used in aquatic contaminated sediments: metal removal and stabilization by chemical and biotechnological processes. *Journal of Cleaner Production*, 2015, 86, 24–36.
4. Andreozzi R., Di Somma I., Marotta R., Pinto G., Pollio A., Spasiano D., Oxidation of 2, 4-dichlorophenol and 3, 4-dichlorophenol by means of Fe(III) – homogeneous photocatalysis and algal toxicity assessment of the treated solutions. *Water research*, 2011, 45(5), 2038–2048.
5. Anthony E. J., Wang J., Pilot plant investigations of thermal remediation of tar-contaminated soil and oil-contaminated gravel. *Fuel*, 2006, 85(4), 443–450.
6. Avilés A., Niell F. X., *The control of a small dam in nutrient inputs to a hypertrophic estuary in a Mediterranean climate*, *Water Air Soil Pollution*, 180, 2007, pp. 97-108.
7. Bajkiewicz-Grabowska E., Mikulski Z., *Hydrologia ogólna*, Wydawnictwa Naukowe PWN, wyd. IV, Warszawa 2007.
8. Baran A., Tarnawski M., Zawartość metali ciężkich w wyciągach wodnych sporządzonych z osadów dennych zbiornika rzeszowskiego. *Proceedings of ECOpole*, 2012, 6(2), 671–675.

9. Barbusiński K., Intensyfikacja procesu oczyszczania ścieków i stabilizacji osadów nadmiernych z wykorzystaniem odczynnika Fentona. Zeszyty Naukowe. Inżynieria Środowiska/Politechnika Śląska, 2004, 50, 7–169.
10. Bednarczyk S., Jarzębińska T., Mackiewicz S., Wołoszyn E., *Vademecum ochrony przeciwpowodziowej*, Krajowy Zarząd Gospodarki Wodnej, Gdańsk 2006.
11. Bełdowski J., Arktyka Europejska – morski przewodnik użytkowania. Wymiana chemiczna między wodą i osadami, Instytut Oceanologii PAN, Sopot, 2012.
12. Bengtsson L., Fleischer S., Lindmark G., Ripl W., Lake Trummen restoration project I. Water and sediment chemistry: With 5 figures and 2 tables in the text. Internationale Vereinigung für theoretische und angewandte Limnologie: Verhandlungen, 1975, 19(2), 1080–1087.
13. Bogacki J., Naumczyk J., Fizykochemiczne metody ex-situ oczyszczania osadów dennych z metali ciężkich. Gaz, Woda i Technika Sanitarna, 2009, 11, 3–42.
14. Bojakowska I., Geochemia osadów powierzchniowych Morza Bałtyckiego. Rozdział 2.4. Państwowy Instytut Geologiczny – Państwowy Instytut Badawczy, pod redakcją S. Uścinowicz, Warszawa, 2011.
15. Borghi C. C., Fabbri M., Fiorini M., Mancini M., Ribani P. L., Magnetic removal of surfactants from wastewater using micrometric iron oxide powders. Separation and Purification Technology, 2011, 83(15), 180–188.
16. Borówka R. K., Geochemiczne badania osadów jeziornych strefy umiarkowanej. Studia Limnologica et Telmatologica, 2007, 1, 33–42.
17. Brooke L., Thursby G., Ambient aquatic life water quality criteria for nonylphenol. Report for the United States EPA, Office of Water, Office of Science and Technology, Washington, DC, USA, 2005.
18. CBD 2019 [strona w internecie]. Convention on Biological Diversity; 2019 [cytowana 12 maja 2019]. Dostępna z <https://www.cbd.int/waters/about.shtml>
19. Chang H. J., Jou C. J. G., Lee C. L., Treatment of heavy oil contaminated sand by microwave energy. Environmental Engineering Science, 2011, 28(12), 869–873.
20. Chanson H., *Extreme reservoir sedimentation in Australia, A review*, International Journal of Sediment Research, 13(3), 1998, pp. 55-63.
21. Cheng M., Zeng G., Huang D., Lai C., Xu P., Zhang C., ... & Zhu Y., Degradation of atrazine by a novel Fenton-like process and assessment the influence on the treated soil. Journal of hazardous materials, 2016, 312, 184–191.

22. Chmist J., Hä默ling M., Wybór najskuteczniejszej metody rekultywacji zbiorników wodnych z wykorzystaniem metody AHP. *Acta Sci. Pol., Formatio Circumiectus*, 2016, 15(2), 27–39.
23. Chu K. H., Al – Hamadani Y. A., Park C. M., Lee G., Jang M., Jang A., ... & Yoon Y., Ultrasonic treatment of endocrine disrupting compounds, pharmaceuticals, and personal care products in water: a review. *Chemical Engineering Journal*, 2017, 327, 629–647.
24. Collings A. F., Farmer A. D., Gwan P. B., Pintos A. S., Leo C. J., Processing contaminated soils and sediments by high power ultrasound. *Minerals engineering*, 2006, 19(5), 450–453.
25. Corada–Fernández C., Lara–Martín P. A., Candela L., González–Mazo E., Vertical distribution profiles and diagenetic fate of synthetic surfactants in marine and freshwater sediments. *Science of The Total Environment*, 2013, 1 (461–462), 568–575.
26. Dąbkowski S. L., Pawłat–Zawrzykraj A., Wybrane właściwości chemiczne osadów dennych wód otwartych w zlewni Raszynki. *Woda–Środowisko–Obszary Wiejskie*, 2003, 3(6), 141–148.
27. Depczyński W, Szamowski A., *Budowle i zbiorniki wodne*, Oficyna Wydawnicza Politechniki Warszawskiej, Warszawa 1999.
28. Deveci H., Alp I., Uslu T., Generation of hydrogen peroxide and removal of cyanide from solutions using ultrasonic waves. *Desalination*, 2007, 216(1–3), 209–221.
29. Eymontt A., Wierzbicki K., Nowa technologia usuwania antropogenicznych osadów dennych. *Problemy Inżynierii Rolniczej*, 2013, 4(82), 129–138.
30. Falciglia P. P., Malarbì D., Maddalena R., Greco V., Vagliasindi F. G., Remediation of Hg – contaminated marine sediments by simultaneous application of enhancing agents and microwave heating (MWH). *Chemical Engineering Journal*, 2017, 321, 1–10.
31. Ferrarese E., Andreottola G., Oprea I. A., Remediation of PAH-contaminated sediments by chemical oxidation. *Journal of Hazardous Materials*, 2008, 152(1), 128–139.
32. Finlayson M, Brouwer J, Aladin NW, Davidson NC. Inland Water System. W: Hassan R, Scholes R, Ash N, redaktorzy. *Ecosystems and Human Well-Being: Current State and Trends*. Washington: Island Press; 2006.
33. Fonti V., Dell'Anno A., Beolchini F., Does bioleaching represent a biotechnological strategy for remediation of contaminated sediments? *Science of the Total Environment*, 2016, 563, 302–319.

34. Gajewska M., Kopeć Ł., Obarska-Pempkowiak H., Operation of small wastewater treatment facilities in a scattered settlement. Rocznik Ochrona Środowiska (Annual Set the Environment Protection), 2011, 13(1), 207–225.
35. Gałka B., Ocena stopnia zanieczyszczenia i możliwości zagospodarowania osadów dennych z małych obiektów wodnych w parku we Wrocławiu-Pawłowicach. Ochrona Środowiska i zasobów naturalnych, 2010, 42, 233–239.
36. Gałka B., Wiatkowski M., Charakterystyka osadów dennych zbiornika zaporowego Młyny oraz możliwość rolniczego wykorzystania. Woda–Środowisko–Obszary Wiejskie, 2010, 4(32), 53–63.
37. Gan S., Ng H. K., Inorganic chelated modified – Fenton treatment of polycyclic aromatic hydrocarbon (PAH) – contaminated soils. Chemical Engineering Journal, 2012, 180, 1–8.
38. Geissen V, Mol H, Klumpp E, Umlauf G, Nadal M, van der Ploeg M, van der Zee S, Ritsema CJ. Emerging pollutants in the environment: a challenge for water resource management. International Soil and Water Conservation Research. 2015; 3(1): 57-65.
39. GIOŚ 2015 [strona w internecie]. Program Państwowego Monitoringu Środowiska na lata 2016-2020; 2015 [cytowana 09 maja 2019]. Dostępna z http://www.gios.gov.pl/images/dokumenty/pms/pms/PPMS_2016-2020.pdf
40. Gorączko M., Woziwodzki Z., Zawalski A., Dzieweczyński P., Ocena możliwości oczyszczania dna zbiornika wodnego za pomocą spustu rurowego w korpusie grobli. Journal of Civil Engineering, Environment and Architecture JCEEA, 2016, 63 (1/II/16), 9–16.
41. Gruca-Rokosz R., Tomaszek J. A., *Temperature and oxygen profiles in the Solina reservoir*, Environment Protection Engineering, 28(1), 2002, pp. 81-89.
42. Gruca-Rokosz R., *Zbiorniki zaporowe jako źródło emisji gazów cieplarnianych*, Inżynieria i Ochrona Środowiska, 15(1), 2012, str. 51-65.
43. Gutry-Korycka M, Sadurski A., Pociask-Karteczka J., Skrzypczyk L. Zasoby wodne a ich wykorzystanie. Nauka. 2014; 1: 77-98.
44. Gwóźdź R., Właściwości osadów spoistych Jeziora Rożnowskiego w aspekcie ich geotechnicznego wykorzystania. Praca doktorska. Politechnika Krakowska, 2007.
45. Hartung F., Ursache und Verhuetung der Staumraumverlandung bei Talsperren. Wasserwirtschaft, 1959, 1, 3–13.
46. IARC Working Group on the Evaluation of Carcinogenic Risks to Humans, Some chemicals present in industrial and consumer products, food and drinking-water. IARC monographs on the evaluation of carcinogenic risks to humans, 2013, 101, 9.

47. Im, J. K., Heo, J., Boateng, L. K., Her, N., Flora, J. R., Yoon, J., ... & Yoon, Y., Ultrasonic degradation of acetaminophen and naproxen in the presence of single-walled carbon nanotubes. *Journal of hazardous materials*, 2013, 254, 284–292.
48. Jonsson S., Persson Y., Frankki S., van Bavel B., Lundstedt S., Haglund P., Tysklind, M., Degradation of polycyclic aromatic hydrocarbons (PAHs) in contaminated soils by Fenton's reagent: a multivariate evaluation of the importance of soil characteristics and PAH properties. *Journal of hazardous materials*, 2007, 149(1), 86–96.
49. Jorfi S., Rezaee A., Moheb-ali G. A., alah Jaafarzadeh N., Pyrene removal from contaminated soils by modified Fenton oxidation using iron nano particles. *Journal of Environmental Health Science and Engineering*, 2013, 11(1), 17.
50. Kaleta, J., Kida, M., Koszelnik, P., Papciak, D., Puszkarewicz, A., & Tchórzewska-Cieślak, B. The use of activated carbons for removing organic matter from groundwater. *Archives of Environmental Protection*, 2017, 43(3), 32–41.
51. Kasperek R., Rosik-Dulewska C., Wiatkowski M., Badania osadów dennych w rejonie granicznych meandrów Górnnej Odry. *Rocznik Ochrona Środowiska*, 2007, 9, 293–302.
52. Kennedy, R. H., Tundisi J. G., Straškrábová V., Lind O. T, Hejzlar J. Reservoirs and the limnologist's growing role in sustainable water resource management. *Hydrobiologia*. 2003; 504: xi-xii.
53. Kida M., Wykorzystanie pola ultradźwiękowego w procesach chemicznego usuwania ftalanu di(2-etyloheksylu) w matrycach osadów dennych. *Rozprawa doktorska*, Rzeszów: Politechnika Rzeszowska; 2018.
54. Kida M., Ziembowicz S., Koszelnik P., Contaminated Bottom Sediments - Methods of Reducing the Environmental Impact [in] Proceedings of the International Forum on Climate Change and Sustainable Development: New Challenges of the Century, 2021.
55. Kondo F., Ikai Y., Hayashi R., Okumura M., Takatori S., Nakazawa H., ... & Makino T., Determination of five phthalate monoesters in human urine using gas chromatography – mass spectrometry. *Bulletin of environmental contamination and toxicology*, 2010, 85(1), 92–96.
56. Kostecki M., *Alokacja i przemiany wybranych zanieczyszczeń w zbiornikach zaporowych hydrowęzła rzeki Kłodnicy i Kanale Gliwickim*, IPIŚ PAN Prace i Studia, Zabrze, 2003, str. 1-124.

57. Kostecki M., Nocoń W., Nocoń K., *Możliwość usuwania metali ciężkich z ekosystemu limnicznego poprzez usunięcie biomasy planktonu na przykładzie rybnickiego zbiornika zaporowego*, Zeszyty Naukowe Politechniki Rzeszowskiej Nr 276, Budownictwo i Inżynieria Środowiska, z. 58 (4/11), 2011, str. 89-98.
58. Koszelnik P., Krupa J., Rymar S., Szpara K. Woda, Żywność, Turystyka – regionalne uwarunkowania zrównoważonego rozwoju obszarów południowo-wschodniej Polski, (pod red. J. Krupa). Dynów: Związek Gmin Turystycznych Pogórza Dynowskiego; 2016.
59. Koszelnik, P., Tomaszek J. A., *The influence of reservoir morphometry on nitrogen retention*. W, C. A. Brebbia, D. Almorza, D. Sales, Water Pollution VII, Modelling, Measuring and Prediction, Witt Press, Southampton, 2003, ss. 261-269.
60. Koś K., Zawisza E., Stabilization of bottom sediments from Rzeszowski Reservoir, Annals of Warsaw University of Life Sciences – SGGW Land Reclamation, 2015, 47(2), 127–137.
61. Krasicki R., Wojtanowski A., *Modernizacja obiektów i urządzeń Zespołu Elektrowni Wodnych Solina-Myczkowce jako inwestycja korzystna ekologicznie*, Materiały z II Ogólnopolskiej Konferencji Naukowo-Technicznej pn.: „Postęp w Inżynierii Środowiska”, Oficyna Wydawnicza Politechniki Rzeszowskiej, Rzeszów, 2001, str. 370-373 (suplement).
62. Król M, Dudziak M. Występowanie i oznaczanie wybranych grup mikrozanieczyszczeń regulowanych dyrektywą 2000/60/WE w środowisku wodnym. Ecological Engineering, 2018; 19(2): 38-47.
63. Kuczyńska A., Wyniki pilotażowego badania zawartości substancji czynnych farmaceutyków w wodach podziemnych w próbkach wody pobranych z krajowej sieci monitoringu wód podziemnych. Przegląd Geologiczny, 2017, 65(11/1), 1096–1103.
64. Kudlek E, Dudziak M. Degradation pathways of pentachlorophenol and benzo(a)pyrene during heterogeneous photocatalysis. Water Science and Technology. 2018; 77(10): 2407-2414
65. Kwarciak-Kozłowska A., Krzywicka A., Effect of ultrasonic field to increase the biodegradability of coke processing wastewater. Archives of Waste Management and Environmental Protection, 2015, 17(3), 133–142.
66. Lenar-Matyas A., Poulard Ch., Ratomski J., Royet P., *Konstrukcja i działanie suchych zbiorników przeciwpowodziowych o różnej charakterystyce i lokalizacji*, Infrastruktura i Ekologia Terenów Wiejskich, 9, 2009, str. 115–129.

67. Lewis S., Lynch A., Bachas L., Hampson S., Ormsbee L., & Bhattacharyya D. (2009). Chelate – modified Fenton reaction for the degradation of trichloroethylene in aqueous and two – phase systems. *Environmental Engineering Science*, 26(4), 849–859.
68. Lim M. W., Von Lau E., Poh P. E., A comprehensive guide of remediation technologies for oil contaminated soil—present works and future directions. *Marine pollution bulletin*, 2016, 109(1), 14–45.
69. Lim M. W., Von Lau E., Poh P. E., A comprehensive guide of remediation technologies for oil contaminated soil—present works and future directions. *Marine pollution bulletin*, 2016, 109(1), 14–45.
70. Loh J, Wackernagel M. The Living Planet Report 2004. Gland: World Wide Fund for Nature; 2004.
71. Madeyski M., Michalec B., Tarnawski M., Zamulanie małych zbiorników wodnych i jakość osadów dennych. *Infrastruktura i Ekologia Terenów Wiejskich*, 2008, 11.
72. Madeyski M., Tarnawski M., Ocena stanu ekologicznego osadów dennych wybranych małych zbiorników wodnych. *Infrastruktura i Ekologia Terenów Wiejskich*, 2006, 4(3), 107–116.
73. Maj K., Koszelnik P., Metody zagospodarowania osadów dennych. *Journal of Civil Engineering, Environment and Architecture JCEEA*, 2016, 63 (2/I/16), 157–169.
74. Malina G., Likwidacja zagrożenia środowiska gruntowo-wodnego na terenach zanieczyszczonych. *Polskie Zrzeszenie Inżynierów i Techników Sanitarnych Oddział Wielkopolski*, Poznań, 2011.
75. Małecka I, Staszewski Z. Woda czynnikiem życia każdego organizmu. *Zeszyty Naukowe. Inżynieria Lądowa i Wodna w Kształtowaniu Środowiska*. 2015;(13):101-107.
76. Margesin R., Hämmeler M., Tscherko D., Microbial activity and community composition during bioremediation of diesel-oil-contaminated soil: effects of hydrocarbon concentration, fertilizers, and incubation time. *Microbial Ecology*, 2007, 53(2), 259-269.
77. Mason T. J., Collings A., Sumel, A., Sonic and ultrasonic removal of chemical contaminants from soil in the laboratory and on a large scale. *Ultrasonics Sonochemistry*, 2004, 11(3–4), 205–210.
78. McGoldrick D. J., Pelletier M., de Solla S. R., Marvin C. H., Martin P. A., Legacy of legacies: Chlorinated naphthalenes in Lake Trout, Walleye, Herring Gull eggs and sediments from the Laurentian Great Lakes indicate possible

- resuspension during contaminated sediment remediation. *Science of The Total Environment*, 2018, 634, 1424–1434.
79. Meybeck M. Global analysis of river systems: from Earth system controls to Anthropocene syndromes. *Philosophical Transactions of the Royal Society of London. Series B: Biological Sciences*, 2003(358/1440):1935-1955.
 80. Michalec B., Określenie stopnia zamulenia zbiornika wodnego w Krempnej i ocena wpływu jego przebudowy na proces zamulania. *Infrastruktura i Ekologia Terenów Wiejskich*, 2010, 4(3), 107–116.
 81. Michalec B., Określenie żywotności małych zbiorników wodnych. *Infrastr. Ekol. Ter. Wiejs.*, 2012, 3(4), 119–129.
 82. Mielczarek M., Szydłowski K., Rola, podział oraz klasyfikacja jakości osadów dennych zbiorników wodnych. *Inżynieria Ekologiczna*, 2017, 18(3) 194–201.
 83. Miksch K, Felis E, Kalka J, Sochacki A, Drzymała J. Micropollutants in the environment: occurrence, interactions and elimination. *Rocznik Ochrona Środowiska*. 2016; 3: 1-84.
 84. Miller C. M., Valentine R. L., Roehl M. E., Alvarez P. J., Chemical and microbiological assessment of pendimethalin-contaminated soil after treatment with Fenton's reagent. *Water Research*, 1996, 30(11), 2579–2586.
 85. Miłowska K., Ultradźwięki – mechanizmy działania i zastosowanie w terapii sonodynamicznej Ultrasound–mechanisms of action and application in sonodynamic therapy. *Postępy Hig Med Dosw.(online)*, 2007, 61, 338–349.
 86. Mioduszewski W. Mała retencja w lasach elementem kształtowania i ochrony zasobów wodnych. *Studia i Materiały Centrum Edukacji Przyrodniczo-Leśnej*. 2008, R. 10. Zeszyt 2 (18): 33-48.
 87. Mioduszewski W., *Mała retencja w lasach elementem kształtowania i ochrony zasobów wodnych*, Studia i Materiały Centrum Edukacji Przyrodniczo-Leśnej, R. 10. Zeszyt 2 (18), 2008, str. 33-48.
 88. Molisani M. M., Kjerfve B., Barreto R., De Lacerda L. D., *Land–sea mercury transport through a modified watershed, SE Brazil*. *Water Research*, 41(9), 2007, pp. 1929-1938.
 89. Moreau M., Leonard J., Phillips K. A., Campbell J., Pendse S. N., Nicolas C., ... & Pudukodu H., Using exposure prediction tools to link exposure and dosimetry for risk-based decisions: A case study with phthalates. *Chemosphere*, 2017, 184, 1194–1201.
 90. Morillo E., Villaverde J., Advanced technologies for the remediation of pesticide-contaminated soils. *Science of the Total Environment*, 2017, 586, 576–597.

91. Naddeo V., Belgiorno V., Napoli R. M., Behaviour of natural organic matter during ultrasonic irradiation. *Desalination*, 2007, 210(1–3), 175–182.
92. Pardo F., Rosas J. M., Santos A., Romero A., Remediation of a biodiesel blend-contaminated soil by using a modified Fenton process. *Environmental Science and Pollution Research*, 2014, 21(21), 12198–12207.
93. Patil P. N., Gogate P. R. , Degradation of dichlorvos using hybrid advanced oxidation processes based on ultrasound. *Journal of Water Process Engineering*, 2015, 8, 58–65.
94. Peng F., Ji W., Zhu F., Peng D., Yang M., Liu R., ... & Yin L., A study on phthalate metabolites, bisphenol A and nonylphenol in the urine of Chinese women with unexplained recurrent spontaneous abortion. *Environmental research*, 2016, 150, 622–628.
95. Pétrier C., The use of power ultrasound for water treatment. In *Power Ultrasonics*, 2015, 939–972.
96. PFOZ 2019 [website]. Polska Fundacja Ochrony Zasobów Wodnych; 2019 [access: 28.11.2021]. <http://www.pfozw.org.pl/>
97. PGE Energia Odnawialna S.A., <http://www.pgeeo.pl/nasze-obiekty/elektrownia-wodna-w-solinie> (dostęp: 3.01.2016).
98. Pourabadehei M., Mulligan C. N., Resuspension of sediment, a new approach for remediation of contaminated sediment. *Environmental pollution*, 2016, 213, 63–75.
99. Przedsiębiorstwo Produkcyjno–Usługowe Form-Awa Sp. z o.o., <http://formawa.pl/realizacje-form-awa-sp-z-o-o-2> (dostęp: 3.01.2016).
100. PWN 2019. Encyklopedia PWN; (access: 29.11.2021). <https://encyklopedia.pwn.pl/haslo/Bajkal;3873443.html>
101. Rahman K. S. M., Thahira–Rahman J., Lakshmanaperumalsamy P., Banat I. M., Towards efficient crude oil degradation by a mixed bacterial consortium. *Bioresource technology*, 2002, 85(3), 257–261.
102. Ravikumar J. X., Gurol M. D., Chemical oxidation of chlorinated organics by hydrogen peroxide in the presence of sand. *Environmental science & technology*, 1994, 28(3), 394–400.
103. Regionalny Zarząd Gospodarki Wodnej w Krakowie, http://www.krakow.rzgw.gov.pl/download/obwieszczenia/susza/gorna_wisla/zal_3-7.pdf. (access: 28.11.2021).
104. Reis E., Lodolo A., Miertus S., Survey of sediment remediation technologies: International Centre for Science and High Technology (ICS). Google Scholar. 2007.

105. Rozporządzenie (WE) nr 1907/2006 Parlamentu Europejskiego i Rady z dnia 18 grudnia 2006 r. (Dz.U. 1 396 z 30.12.2006) w sprawie rejestracji, oceny, udzielania zezwoleń i stosowanych ograniczeń w zakresie chemikaliów (REACH) i utworzenia Europejskiej Agencji Chemikaliów, zmieniające dyrektywę 1999/45/WE oraz uchylające rozporządzenie Rady (EWG) nr 793/93 i rozporządzenie Komisji (WE) nr 1488/94, jak również dyrektywę Rady 76/769/EWG i dyrektywy Komisji 91/155/EWG, 93/67/EWG, 93/105/WE i 2000/21/WE.
106. Schenkel R., Carl M. P., European Union Risk Assessment Report: Bis (2-Ethylhexyl) Phthalate (DEHP), 2008.
107. Shemer H., Narkis N., Sonochemical removal of trihalomethanes from aqueous solutions. *Ultrasonics sonochemistry*, 2005, 12(6), 495–499.
108. Siebielec S., Siebielec G., Smreczak B., Zanieczyszczenia osadów dennych rzek i zbiorników wodnych. *Studia i Raporty IUNG-PIB*, 2015, 46(20), 163–181.
109. Silva V.L.D., Neto B.D.B., Simonnot M.O., Phenanthrene and pyrene oxidation in contaminated soils using Fenton's reagent. *J. Hazard. Mater.* 2009, 161: 967–973.
110. Sørensen B., *Renewable Energy: Its Physics, Engineering, Use, Environmental Impacts, Economy, and Planning Aspects*, Academic Press, 2004, pp. 556.
111. St. Louis V. L., Kelly C. A, Duchemin E., Rudd J. W. M., Rosenberg D. M., *Reservoir surfaces as sources of greenhouse gases to the atmosphere: a global estimate*, BioScience, 50, 2000, pp. 766-775.
112. Starmach K., Wróbel S., Pasternak K., *Hydrobiologia, Limnologia*, PWN, Warszawa, 1978, ss. 1-621.
113. Straskraba M. Limnological differences between deep valley reservoirs and deep lakes. *International Review of Hydrobiology*. 1998; 83(special issue): 1-12.
114. Straskraba M., *Limnological differences between deep valley reservoirs and deep lakes*, International Review of Hydrobiology, 83(special issue), 1998, pp. 1-12.
115. Struciński P., Góralczyk K., Ludwicki J. K., Czaja K., Hernik A., Korcz, W. (2006). Poziomy wybranych insektycydów chlороorganicznych, polichlorowanych bifenyli, ftalanów i perfluorowanych związków alifatycznych we krwi – badanie WWF. *Roczn. PZH*, 57(2), 99–112.

116. Swan S. H., Main K. M., Liu F., Stewart S. L., Kruse R. L., Calafat A. M., ... & Teague J. L., Decrease in anogenital distance among male infants with prenatal phthalate exposure. *Environmental health perspectives*, 2005;113(8), 1056.
117. Szarek-Gwiazda E., *The effect of abiotic factors on the content i mobility of heavy metals in the sediment of a eutrophic dam reservoir (Dobczyce Reservoir, southern Poland)*, Acta Hydrobiologica, 40, 1998, pp. 121-129.
118. Szczerbowski J. A. (red.). *Rybactwo śródlądowe*, Instytut Rybactwa Śródlądowego, Olsztyn 2008.
119. Szydłowski K., Podlasińska J., Charakterystyka osadów dennych oczek wodnych. *Inżynieria Ekologiczna*, 2016, 47, 40–46.
120. Tarnawski M., Baran A., Jasiewicz C., Ocena właściwości fizyczno-chemicznych osadów dennych zbiornika Chańcza. *Proceedings of ECOpole*, 2012, 6(1), 305–311.
121. Tarnawski M., Michalec B., Charakterystyka ilościowa i jakościowa osadów dennych zbiornika wodnego w Wilczej Woli. *Infrastruktura i Ekologia Terenów Wiejskich*, 2006, 3(1), 31–43.
122. Tatano F., Felici F., Mangani F., Lab-scale treatability tests for the thermal desorption of hydrocarbon-contaminated soils. *Soil and Sediment Contamination: An International Journal*, 2013, 22(4), 433–456.
123. Testa C., Nuti F., Hayek J., De Felice C., Chelli M., Rovero P., Latini G., Papini A.M., Di-(2-ethylhexyl) phthalate and autism spectrum disorders. *ASN Neuro*, 2012, 4, 223–229.
124. Tienpont B. Determination of phthalates in environmental, food and biomatrices: an analytical challenge (Doctoral dissertation, Ghent University), 2004.
125. Trellu C., Mousset E., Pechaud Y., Huguenot D., Van Hullebusch E. D., Esposito G., Oturan M. A., Removal of hydrophobic organic pollutants from soil washing/flushing solutions: a critical review. *Journal of hazardous materials*, 2016, 306, 149–174.
126. UN 1982 [strona w internecie]. United Nations Convention on the Law of the Sea; 1982 [cytowana 10 maja 2019] Dostępna z https://www.un.org/Depts/los/convention_agreements/texts/unclos/closindx.htm
127. Vicente F., Rosas J. M., Santos A., Romero A., Improvement soil remediation by using stabilizers and chelating agents in a Fenton-like process. *Chemical Engineering Journal*, 2011, 172(2–3), 689–697.

128. Vicente F., Santos A., Sagüillo E. G., Martínez–Villacorta Á. M., Rosas J. M., Romero A., Diuron abatement in contaminated soil using Fenton-like process. *Chemical Engineering Journal*, 2012, 183, 357–364.
129. Wang M., Zhu Y., Cheng L., Andserson B., Zhao X., Wang D., & Ding A., Review on utilization of biochar for metal-contaminated soil and sediment remediation. *Journal of Environmental Sciences*, 2018, 63, 156–173.
130. Ward MH, Jones RR, Brender JD, de Kok TM, Weyer PJ, Nolan BT, Villanueva CM, van Breda SG. Drinking Water Nitrate and Human Health: An Updated Review. *International Journal of Environmental Research and Public Health*, 2018;(15/7):1557.
131. Watts R. J., Dilly S. E., Evaluation of iron catalysts for the Fenton-like remediation of diesel-contaminated soils. *Journal of Hazardous Materials*, 1996, 51(1–3), 209–224.
132. Watts R. J., Smith B. R., Miller G. C., Catalyzed hydrogen peroxide treatment of octachlorodibenzo-p-oxin (OCCD) in surface soils. *Chemosphere*, 1991, 23(7), 949–955.
133. Watts R. J., Spencer C. J., Stanton P. C., On-site treatment of contaminated soils using catalyzed peroxide. Final report (No. PB-95-111365/XAB). Washington State Transportation Center, Pullman, WA (United States), 1994.
134. Watts R. J., Udell M. D., Monsen R. M., Use of iron minerals in optimizing the peroxide treatment of contaminated soils. *Water Environment Research*, 1993, 65(7), 839–844.
135. WHO 2019 [strona w internecie]. World Health Organization; 2019 [cytowana 09 maja 2019]. Dostępna z <https://www.who.int/news-room/fact-sheets/detail/drinking-water>
136. Wiatkowski M., *Wpływ zbiorników wstępnych na zmiany jakości wód retencjonowanych w zbiornikach głównych*, Instytut Podstaw Inżynierii Środowiska Polskiej Akademii Nauk, 2006, str. 29-34.
137. Włodarczyk-Makuła M. Wybrane mikrozanieczyszczenia organiczne w wodach i glebach. Częstochowa: Wydawnictwo Politechniki Częstochowskiej, 2013.
138. Włodarczyk-Makuła M., Wybrane mikrozanieczyszczenia organiczne w wodach i glebach. Wydawnictwo Politechniki Częstochowskiej, Częstochowa, 2013.
139. Włodarczyk-Makuła, M., Rola rodników hydroksylowych w utlenianiu mikrozanieczyszczeń organicznych. *LAB Laboratoria, Aparatura, Badania*, 2015, 20.

140. Xu L. J., Chu W., Graham N., A systematic study of the degradation of dimethyl phthalate using a high-frequency ultrasonic process. *Ultrasonics sonochemistry*, 2013, 20(3), 892–899.
141. Yap C. L., Gan S., Ng H. K., Fenton based remediation of polycyclic aromatic hydrocarbons-contaminated soils. *Chemosphere*, 2011, 83(11), 1414–1430.
142. Zalewski M. Flood pulses and river ecosystem robustness. W: Tchiguirinskaia I, Thein KNN, Hubert P, redaktorzy. *Frontiers in Flood Research*. Paris: IAHS Publication 2006, pp. 143-154.
143. Zalewski M., *Flood pulses and river ecosystem robustness*, W, I. Tchiguirinskaia, K. N. N. Thein, P. Hubert, *Frontiers in Flood Research*, IAHS Publication 305, Paris, 2006, pp. 143-154.
144. Zawadzki P., Błażejewski R., Pawlak M., Przegląd metod odmulania zbiorników wodnych. *Acta Scientiarum Polonorum. Formatio Circumiectus*, 2017, 16(2), 217–228.
145. Zhao G., Sheng Y., Wang C., Yang J., Wang Q., Chen L., In situ microbial remediation of crude oil-soaked marine sediments using zeolite carrier with a polymer coating. *Marine pollution bulletin*, 2018, 129(1), 172–178.
146. Zhou H., Sun Q., Wang X., Wang L., Chen J., Zhang J., Lu X., Removal of 2,4-dichlorophenol from contaminated soil by a heterogeneous ZVI/EDTA/Air Fenton-like system. *Separation and Purification Technology*, 2014, 132, 346–353.
147. Ziembowicz S, Kida M, Koszelnik P. Selected EPs in the water of certain Polish lakes and rivers. *E3S Web of Conferences*. 2018, 49: 00136.
148. Ziembowicz S. Wykorzystanie alternatywnych katalizatorów w procesach chemicznego usuwania ftalanu di-n-butylu z roztworów wodnych. Rozprawa doktorska. Rzeszów: Politechnika Rzeszowska; 2018.

Chapter IV

WATER MANAGEMENT: HISTORY; WATER PURIFICATION; WASTEWATER AND SEWAGE TREATMENT



In this section you will learn about

- ✓ History of water supply and sanitation.
- ✓ Water purification.
- ✓ Wastewater and sewage treatment.



Key words:

Water supply systems, aqueducts
Cloaca Maxima
Sewage farms, indoor plumbing
Biological treatment and activated sludge process
Water purification, underground and surface waters
Water pretreatment, sedimentation, coagulation and flocculation
Water softening, pH adjustment, disinfection, drinking water quality
Solids, microorganisms, dissolved inorganic and organic substances

Sewage or municipal wastewater treatment
Sewage pretreatment: screening, grit, fat and grease removal, flow equalization
Primary and secondary clarifiers, activated sludge process
Nutrients removal and sludge handling

Major human settlements could initially develop only where fresh surface water was plentiful, such as near rivers or natural springs. Throughout history, people have devised systems to make getting water into their communities. Early human habitations were often built next to water sources. Rivers would often serve as a crude form of natural sewage disposal.

During the Neolithic era, humans dug the first permanent water wells, from where vessels could be filled and carried by hand. The size of human settlements was largely dependent on nearby available water.

Water purification means the process of removing undesirable chemicals, biological contaminants, suspended solids, and gases from water. The goal is to produce water that is fit for specific purposes.

The history of water purification includes a wide variety of methods. The methods used include physical processes such as filtration, sedimentation, and distillation and chemical processes such as slow sand filters or active carbon, flocculation and the use of electromagnetic radiation such as ultraviolet light. Water purification may reduce the concentration of particulate matter including suspended particles, parasites, bacteria, algae, viruses, and fungi as well as reduce the concentration of a range of dissolved and particulate matter. Simple procedures such as boiling or the use of a household activated carbon filter are not sufficient for treating all possible contaminants that may be present in water from an unknown source. Even natural spring water, considered safe for all practical purposes in the 19th century, must now be tested before determining what kind of treatment, if any, is needed. Chemical and microbiological analysis, while expensive, are the only way to obtain the information necessary for deciding on the appropriate method of purification.

The standards for drinking water quality are typically set by governments or by international standards. These standards usually include minimum and maximum concentrations of contaminants, depending on the intended use of the water.

Widely varied techniques are available to remove contaminants like fine solids, micro-organisms and some dissolved inorganic and organic materials, or environmental persistent pharmaceutical pollutants. The choice of method will depend on the quality of the water being treated, the cost of the treatment process and the quality standards expected of the processed

water. The processes below are the ones commonly used in water purification plants.

Sewage treatment (or domestic wastewater treatment, municipal wastewater treatment) is a type of wastewater treatment which aims to remove contaminants from sewage to produce an effluent that is suitable for discharge to the surrounding environment or an intended reuse application, thereby preventing water pollution from raw sewage discharges. Sewage contains wastewater from households and businesses and possibly pre-treated industrial wastewater. There are a high number of sewage treatment processes to choose from. These can range from decentralized systems (including on-site treatment systems) to large centralized systems involving a network of pipes and pump stations (called sewerage) which convey the sewage to a treatment plant. For cities that have a combined sewer, the sewers will also carry urban runoff (stormwater) to the sewage treatment plant. Sewage treatment often involves two main stages, called primary and secondary treatment, while advanced treatment also incorporates a tertiary treatment stage with polishing processes and nutrient removal. Secondary treatment can reduce organic matter (measured as biological oxygen demand) from sewage, using aerobic or anaerobic biological processes. With regards to biological treatment of sewage, the treatment objectives can include various degrees of the following: transform dissolved and particulate biodegradable components (especially organic matter) into acceptable end products, transform and remove nutrients (nitrogen and phosphorus), remove or inactivate pathogenic organisms, and remove specific trace organic constituents (micropollutants). Some types of sewage treatment produce sewage sludge which can be treated before safe disposal or reuse. Under certain circumstances, the treated sewage sludge might be termed "biosolids" and can be used as a fertilizer.

Sewerage (or sewage system) is the infrastructure that conveys sewage or surface runoff (stormwater, meltwater, rainwater) using sewers. It encompasses components such as receiving drains, manholes, pumping stations, storm overflows, and screening chambers of the combined sewer or sanitary sewer. Sewerage ends at the entry to a sewage treatment plant or at the point of discharge into the environment. It is the system of pipes, chambers, manholes, etc. that conveys the sewage or storm water.

4.1. History of Water Supply and Sanitation.

Wastewater reuse activities and drinking water supply since prehistoric time.

Reuse of untreated municipal wastewater has been practiced for many centuries with the objective of diverting human waste outside of urban settlements. Likewise, land application of domestic wastewater is an old and common practice, which has gone through different stages of development.

Domestic wastewater was used for irrigation by prehistoric civilizations (e.g. Mesopotamian, Indus valley) since the Bronze Age (ca. 3200-1100 BC). Thereafter, wastewater was used for disposal, irrigation, and fertilization purposes by Hellenic civilizations and later by Romans in areas surrounding cities (e.g. Athens and Rome).

The ca. 2400 BCE, Pyramid of Sahure, and adjoining temple complex at Abusir, was discovered to have a network of copper drainage pipes.

Some of the earliest evidence of water wells are located in China. The Neolithic Chinese discovered and made extensive use of deep drilled groundwater for drinking. Archaeological evidence and old Chinese documents reveal that the prehistoric and ancient Chinese had the aptitude and skills for digging deep water wells for drinking water as early as 6000 to 7000 years ago.

Devices such as shadoofs were used to lift water to ground level. Ruins from the Indus Valley Civilization had settlements with some of the ancient world's most sophisticated sewage systems. They included drainage channels, rainwater harvesting, and street ducts.

The ancient Greek civilization of Crete was the first civilization to use underground clay pipes for sanitation and water supply. Their capital had a well-organized water system for bringing in clean water, taking out waste water and storm sewage canals for overflow when there was heavy rain. It was also one of the first uses of a flush toilet, dating back to the 18th century BC. In addition to sophisticated water and sewer systems they devised elaborate heating systems.

The Ancient Greeks of Athens and Asia Minor also used an indoor plumbing system, used for pressurized showers. The Greek inventor Heron used pressurized piping for fire fighting purposes in the City of Alexandria. The Mayans were the third earliest civilization to have employed a system of indoor plumbing using pressurized water.

An inverted siphon system, along with glass covered clay pipes, was used for the first time in the palaces of Crete, Greece. It is still in working condition, after about 3000 years (Fig. 4.1).



Fig. 4.1. Pont du Gard, a Roman aqueduct in France.

In ancient Rome, the Cloaca Maxima, considered a marvel of engineering, discharged into the Tiber. Public latrines were built over the Cloaca Maxima (Fig. 4.2).

Beginning in the Roman era a water wheel device known as a noria supplied water to aqueducts and other water distribution systems in major cities in Europe and the Middle East.

The Roman Empire had indoor plumbing, meaning a system of aqueducts and pipes that terminated in homes and at public wells and fountains for people to use. Rome and other nations used lead pipes; while commonly thought to be the cause of lead poisoning in the Roman Empire, the combination of running water which did not stay in contact with the pipe for long and the deposition of precipitation scale actually mitigated the risk from lead pipes.

Roman towns and garrisons in the United Kingdom between 46 BC and 400 AD had complex sewer networks sometimes constructed out of hollowed-out elm logs, which were shaped so that they butted together with the down-stream pipe providing a socket for the upstream pipe.

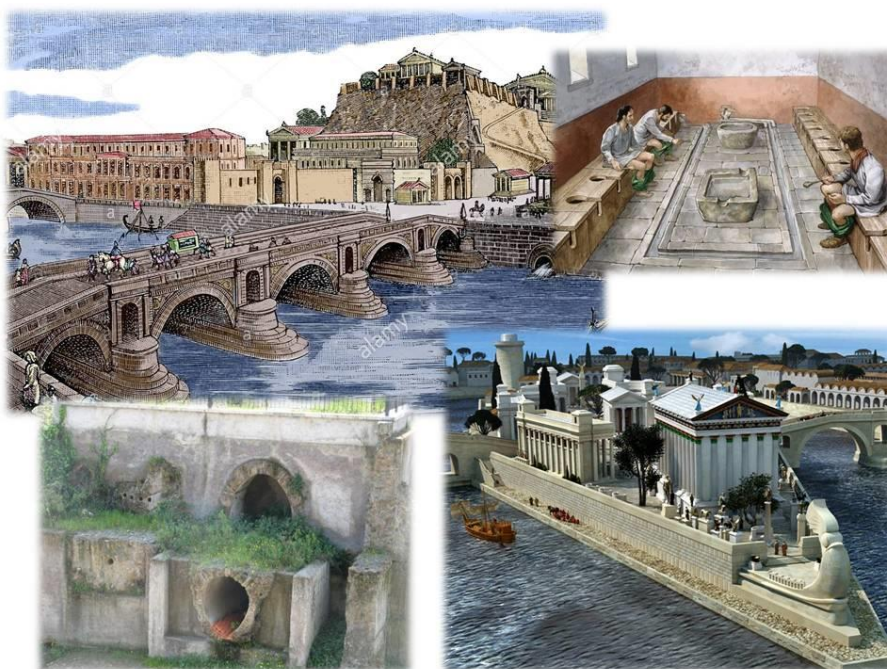


Fig. 4.2. Ancient Rome factual approximation

There is little record of other sanitation systems (apart of sanitation in ancient Rome) in most of Europe until the High Middle Ages. Unsanitary conditions and overcrowding were widespread throughout Europe and Asia during the Middle Ages. This resulted in pandemics which killed tens of millions of people. Very high infant and child mortality prevailed in Europe throughout medieval times, due partly to deficiencies in sanitation.

In medieval European cities, small natural waterways used for carrying off wastewater were eventually covered over and functioned as sewers. London's River Fleet is such a system. Open drains, or gutters, for waste water run-off ran along the center of some streets. These were known as canals, channels and in Paris were sometimes known as "split streets," as the waste water running along the middle physically split the streets into two halves. The first closed sewer constructed in Paris was designed by Hugues Aubird in 1370 on Montmartre Street and was 300 meters long. The original purpose of designing and constructing a closed sewer in Paris was less-so for waste management as much as it was to hold back the stench coming from the odorous waste water. In Dubrovnik, then known as Ragusa (Latin name), the Statute of 1272 set out the parameters for the construction of septic tanks and channels for the removal of dirty water. Throughout the 14th and 15th century the sewage system was built, and it is still operational today, with minor changes and repairs done in recent centuries. Pail closets, outhouses, and cesspits were used to collect human waste. The use of human waste as fertilizer was especially important in China and Japan, where cattle manure was less available. However, most cities did not have a functioning sewer system before the Industrial era, relying instead on nearby rivers or occasional rain showers to wash away the sewage from the streets. In some places, waste water simply ran down the streets, which had stepping stones to keep pedestrians out of the muck, and eventually drained as runoff into the local watershed.

In the 16th century, Sir John Harington invented a flush toilet as a device for Queen Elizabeth I (his godmother) that released wastes into cesspools. After the adoption of gunpowder, municipal outhouses became an important source of raw material for the making of saltpeter in European countries. In London, the contents of the city's outhouses were collected every night by commissioned wagons and delivered to the nitrite beds where it was laid into specially designed soil beds to produce earth rich in mineral nitrates. The nitrate rich-earth would be then further processed to produce saltpeter, or potassium nitrate, an important ingredient in black powder that played a part in the making of gunpowder.

Sewage farms (i.e. wastewater application to the land for disposal and agricultural use) were operated in Silesia in 1531, in Scotland in 1650, in Paris in 1868, in Berlin in 1876 and in different parts of the USA since 1871, where wastewater was used for beneficial crop production. In the 16th and 18th centuries in many rapidly growing countries/cities of Europe (e.g. Germany, France) and the United States, "sewage farms" were increasingly seen as a solution for the disposal of large volumes of the wastewater, some of which are still in operation today. Irrigation with sewage and other wastewater effluents has a long history also in China and

India; while also a large “sewage farm” was established in Australia in 1897 (Fig. 4.3).

Modern age. Sewer systems

A significant development was the construction of a network of sewers to collect wastewater. In some cities, including Rome, Istanbul (Constantinople) networked ancient sewer systems continue to function today as collection systems for those cities modernized sewer systems. Instead of flowing to a river or the sea, the pipes have been re-routed to modern sewer treatment facilities.

Basic sewer systems were used for waste removal in ancient Mesopotamia, where vertical shafts carried the waste away into cesspools. Similar systems existed in the Indus Valley civilization in modern-day India and in Ancient Crete and Greece. In the Middle Ages the sewer systems built by the Romans fell into disuse and waste was collected into cesspools that were periodically emptied by workers known as 'rakers' who would often sell it as fertilizer to farmers outside the city.

The tremendous growth of cities in Europe and North America during the Industrial Revolution quickly led to crowding, which acted as a constant source for the outbreak of disease. As cities grew in the 19th century concerns were raised about public health. As part of a trend of municipal sanitation programs in the late 19th and 20th centuries, many cities constructed extensive gravity sewer systems to help control outbreaks of disease such as typhoid and cholera. Storm and sanitary sewers were necessarily developed along with the growth of cities. By the 1840s the luxury of indoor plumbing, which mixes human waste with water and flushes it away, eliminated the need for cesspools.

Modern sewerage systems were first built in the mid-nineteenth century as a reaction to the exacerbation of sanitary conditions brought on by heavy industrialization and urbanization. Baldwin Latham, a British civil engineer contributed to the rationalization of sewerage and house drainage systems and was a pioneer in sanitary engineering. He developed the concept of oval sewage pipe to facilitate sewer drainage and to prevent sludge deposition and flooding. Due to the contaminated water supply, cholera outbreaks occurred in 1832, 1849 and 1855 in London, killing tens of thousands of people. This, combined with the Great Stink of 1858, when the smell of untreated human waste in the River Thames became overpowering, and the report into sanitation reform of the Royal Commissioner Edwin Chadwick, led to the Metropolitan Commission of Sewers appointing Joseph Bazalgette to construct a vast underground sewage system for the safe removal of waste. Contrary to Chadwick's recommendations, Bazalgette's system, and others later built in Continental Europe, did not pump the sewage onto farm land for use as

fertilizer; it was simply piped to a natural waterway away from population centres, and pumped back into the environment.

From as early as 1535 there were efforts to stop polluting the River Thames in London. Beginning with an Act passed that year that was to prohibit the dumping of excrement into the river. Leading up to the Industrial Revolution the River Thames was identified as being thick and black due to sewage, and it was even said that the river “smells like death.” As Britain was the first country to industrialize, it was also the first to experience the disastrous consequences of major urbanization and was the first to construct a modern sewerage system to mitigate the resultant unsanitary conditions. During the early 19th century, the River Thames was effectively an open sewer, leading to frequent outbreaks of cholera epidemics. Proposals to modernize the sewerage system had been made during 1856 but were neglected due to lack of funds. However, after the *Great Stink* of 1858, Parliament realized the urgency of the problem and resolved to create a modern sewerage system.

Joseph Bazalgette, a civil engineer and Chief Engineer of the Metropolitan Board of Works, was given responsibility for the work. He designed an extensive underground sewerage system that diverted waste to the Thames Estuary, downstream of the main center of population. Six main interceptor sewers, totaling almost 160 km in length, were constructed, some incorporating stretches of London's 'lost' rivers. Three of these sewers were north of the river, the southernmost, low-level one being incorporated in the Thames Embankment. The Embankment also allowed new roads, new public gardens, and the Circle Line of the London Underground.

The intercepting sewers, constructed between 1859 and 1865, were fed by 720 km of main sewers that, in turn, conveyed the contents of some 21000 km of smaller local sewers. Construction of the interceptor system required 318 million bricks, 2.7 million cubic metres of excavated earth and 670000 cubic metres of concrete. With only minor modifications, Bazalgette's engineering achievement remains the basis for sewerage design up into the present day.

In 1802, Napoleon built the Ourcq canal which brought 70 000 cubic meters of water a day to Paris, while the Seine river received up to 100 000 cubic meters of wastewater per day. The Paris cholera epidemic of 1832 sharpened the public awareness of the necessity for some sort of drainage system to deal with sewage and wastewater in a better and healthier way. Between 1865 and 1920 Eugene Belgrand lead the development of a large scale system for water supply and wastewater management. Between these years approximately 600 kilometers of aqueducts were built to bring in potable spring water, which freed the poor quality water to be used for flushing streets and sewers. By 1894 laws were passed which made drainage

mandatory. The treatment of Paris sewage was left to natural devices as 5000 hectares of land were used to spread the waste out to be naturally purified.

The first comprehensive sewer system in a German city was built in Hamburg in the mid-19th century. In 1863, work began on the construction of a modern sewerage system for the rapidly growing city of Frankfurt am Main, based on design work by William Lindley. 20 years after the system's completion, the death rate from typhoid had fallen from 80 to 10 per 100 000 inhabitants.

The first sewer systems in the United States were built in the late 1850s in Chicago and Brooklyn. Initially the gravity sewer systems discharged sewage directly to surface waters without treatment. Later, cities attempted to treat the sewage before discharge in order to prevent water pollution and waterborne diseases. During the half-century around 1900, these public health interventions succeeded in drastically reducing the incidence of water-borne diseases among the urban population, and were an important cause in the increases of life expectancy experienced at the time.

Early techniques for sewage treatment involved land application of sewage on agricultural land. One of the first attempts at diverting sewage for use as a fertilizer in the farm was made by the cotton mill owner James Smith in the 1840s. He experimented with a piped distribution system initially proposed by James Vetch that collected sewage from his factory and pumped it into the outlying farms, and his success was enthusiastically followed by Edwin Chadwick and supported by organic chemist Justus von Liebig.

The idea was officially adopted by the Health of Towns Commission, and various schemes (known as sewage farms) were trialled by different municipalities over the next 50 years. At first, the heavier solids were channeled into ditches on the side of the farm and were covered over when full, but soon flat-bottomed tanks were employed as reservoirs for the sewage; the earliest patent was taken out by William Higgs in 1846 for tanks or reservoirs in which the contents of sewers and drains from cities, towns and villages are to be collected and the solid animal or vegetable matters therein contained, solidified and dried. Improvements to the design of the tanks included the introduction of the horizontal-flow tank in the 1850s and the radial-flow tank in 1905. These tanks had to be manually de-sludged periodically, until the introduction of automatic mechanical de-sludgers in the early 1900s.

Chemical treatment and sedimentation

As pollution of water bodies became a concern, cities attempted to treat the sewage before discharge. In the late 19th century some cities began to add chemical treatment and sedimentation systems to their sewers. In the United States, the first sewage treatment plant using chemical precipitation was built in Massachusetts in 1890. During the half-century around 1900, these public health interventions

succeeded in drastically reducing the incidence of water-borne diseases among the urban population, and were an important cause in the increases of life expectancy experienced at the time.



Fig. 4.3. A Chinese ceramic model of a well with a water pulley system, excavated from a tomb of the Han Dynasty (202 BC - 220 AD) period (left) and typical old medieval water wells (right).

Odor was considered the big problem in waste disposal and to address it, sewage could be drained to a lagoon, or "settled" and the solids removed, to be disposed of separately. This process is now called "primary treatment" and the settled solids are called "sludge." At the end of the 19th century, since primary treatment still left odor problems, it was discovered that bad odors could be prevented by introducing oxygen into the decomposing sewage. This was the beginning of the biological aerobic and anaerobic treatments which are fundamental to wastewater processes.

The precursor to the modern septic tank was the cesspool in which the water was sealed off to prevent contamination and the solid waste was slowly liquified due to anaerobic action; it was invented by L.H Mouras in France in the 1860s. Donald Cameron, as City Surveyor for Exeter patented an improved version in 1895, which he called a 'septic tank'; septic having the meaning of 'bacterial'. These are still in worldwide use, especially in rural areas unconnected to large-scale sewage systems.

Biological treatment

It was not until the late 19th century that it became possible to treat the sewage by biologically decomposing the organic components through the use of microorganisms and removing the pollutants. Land treatment was also steadily becoming less feasible, as cities grew and the volume of sewage produced could no longer be absorbed by the farmland on the outskirts.

Edward Frankland conducted experiments at the sewage farm in England, during the 1870s and was able to demonstrate that filtration of sewage through porous gravel

produced a nitrified effluent (the ammonia was converted into nitrate) and that the filter remained unclogged over long periods of time. This established the revolutionary possibility of biological treatment of sewage using a contact bed to oxidize the waste.

From 1885 to 1891 filters working on this principle were constructed throughout the UK and the idea was also taken up in the US at the Lawrence Experiment Station in Massachusetts, where Frankland's work was confirmed. Contact beds were tanks containing an inert substance, such as stones or slate, that maximized the surface area available for the microbial growth to break down the sewage. The sewage was held in the tank until it was fully decomposed and it was then filtered out into the ground.

Activated sludge process

Most cities in the Western world added more expensive systems for sewage treatment in the early 20th century, after scientists at the University of Manchester discovered the sewage treatment process of activated sludge in 1912.

The activated sludge process was discovered in 1913 in the United Kingdom by two engineers, Edward Ardern and W.T. Lockett, who were conducting research for the Manchester Corporation Rivers Department. In 1912, Dr. Gilbert Fowler, a scientist at the University of Manchester, observed experiments being conducted at the Lawrence Experiment Station at Massachusetts involving the aeration of sewage in a bottle that had been coated with algae. Fowler's engineering colleagues, Ardern and Lockett, experimented on treating sewage in a draw-and-fill reactor, which produced a highly treated effluent. They aerated the waste-water continuously for about a month and were able to achieve a complete nitrification of the sample material. Believing that the sludge had been activated the process was named *activated sludge*. Not until much later was it realized that what had actually occurred was a means to concentrate biological organisms, decoupling the liquid retention time from the solids retention time. Their results were published in their seminal 1914 paper, and the first full-scale continuous-flow system was installed at Worcester two years later.

Water treatment

The first documented use of sand filters to purify the water supply dates to 1804, when the owner of a bleachery in Scotland, John Gibb, installed an experimental filter, selling his unwanted surplus to the public. This method was refined in the following two decades by engineers working for private water companies, and it culminated in the first treated public water supply in the world, installed by engineer James Simpson for the Waterworks Company in London in 1829. This installation provided filtered water for every resident of the area, and the

network design was widely copied throughout the United Kingdom in the ensuing decades. Early attempts at implementing water chlorination at a water treatment plant were made in 1893 in Germany, and in 1897 in England, was the first to have its entire water supply treated with chlorine. Permanent water chlorination began in 1905, when a faulty slow sand filter and a contaminated water supply led to a serious typhoid fever epidemic in England. Founders of microscopy, Antonie van Leeuwenhoek and Robert Hooke, used the newly invented microscope to observe for the first time small material particles that were suspended in the water, laying the groundwork for the future understanding of waterborne pathogens and waterborne diseases.

Water supply and sanitation in medieval Pressburg (Bratislava)

During the 16th century Pressburg (Bratislava) inhabitants used plenty wells, such as on the streets Hlavné námestie, Zámocká, Kapitulská, Michalská brána and the others (Fig. 4.4; 4.5.).



Fig. 4.4. The first digged well on the Sihot' Island for Pressburg (upper left), Water Works at the Sihot'(upper right), Inventor of drinking water pumping to the castle of Pressburg Wolfgang von Kempelen (lower left) and Company which constructed the first 4.1 km of sewerage for the city of Pressburg (lower right).

Drinking water was supplied also from surrounded Malé Karpaty mountains using for transportation firstly stone and wooden and later on copper pipes and

troughs. Around the year 1760 there was dug some well on the Danube river embankment which supplied with drinking water and horse drive the castle reservoir. Construction of the first objects of the city plumbing was started on the August 25, 1884 by C. Corte Company which managed Bernard Salbach. Since the February 1886 started the operation of the first city plumbing for 50 000 inhabitants with the capacity of $1059 \text{ m}^3/\text{d}$ (20 liter/d/inhabitant) using the steam pump.

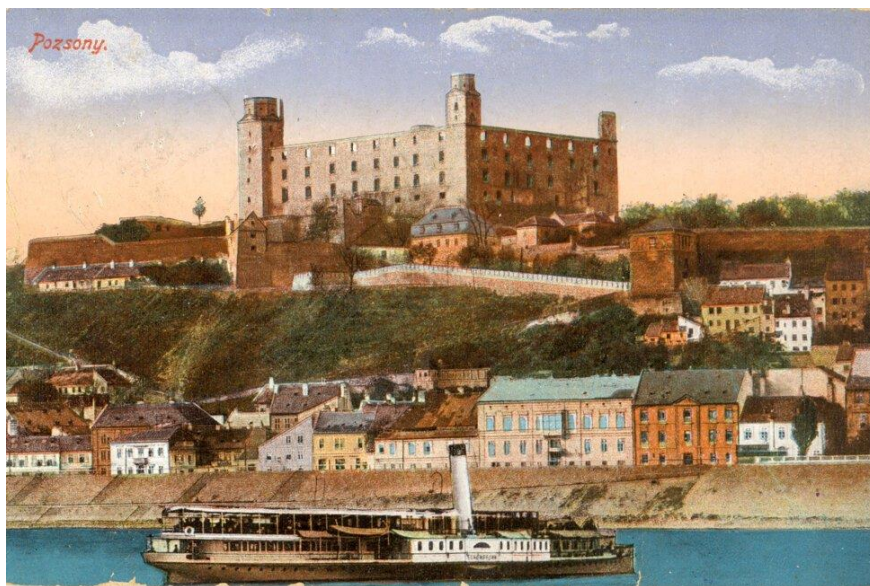


Fig. 4.5. Prešporok (Bratislava), Pressburg, Pozson in the middle-age time.

The first water pumping station was constructed on the left bank of the Danube River in Karlova Ves in 1886. Together with the well on the island of Sihot' and the water reservoir near Bratislava Castle, the pumping station forms the base of the waterworks for Bratislava.

Drinking water was supplied from underground sources on the island of Sihot'. These sources have been rich in naturally filtered water from the Danube. Water was supplied from the water well on Sihot' to the main pumping station in Karlova Ves via a 1.7 km pipeline. From there, water was distributed by steam pumps to the entire city and then into the main water reservoir near Bratislava Castle. Designed and engineered by Bernhard Salbach and Zdenko Ritter von Wessely, Bratislava's waterworks use a pressure-gravity system and were the first of their kind in Slovakia. The island's first water well from 1886 is surrounded by a high bank and lined with granite to protect it from floods (Fig. 4.4.). In the past, 3000 m^3 of water could be pumped from this well. The first pumping station with electric pumps was built on the island in 1912. Leading from here is a 100 meter concrete tunnel with water pipes, located beneath the arm of the Danube river. The Karloveské rameno is one of the few free-flowing arms of the Danube along the entire section of the

Danube flowing through Slovakia. Its total length is 4 800 m and it flows around the island of Sihot', one of the most important sources of drinking water in Bratislava. The original vegetation of the floodplain forest and natural willow-poplar forests which complement it are preserved in the surroundings of the Karloveské rameno. It is the home of many rare plant and animal species.

The first 4.1 km long sewerage system was constructed in Pressburg (old Bratislava) during the years 1897 – 1900 by Pittel & Brausenwetter Company (Fig. 4.4. and 4.5.).

3.2. Water purification.

Water purification means the process of removing undesirable chemicals, biological contaminants, suspended solids, and gases from water. The goal is to produce water that is fit for specific purposes. The history of water purification includes a wide variety of methods. The methods used include physical processes such as filtration, sedimentation, and distillation and chemical processes such as slow sand filters or active carbon, flocculation and the use of electromagnetic radiation such as ultraviolet light. Water purification may reduce the concentration of particulate matter including suspended particles, parasites, bacteria, algae, viruses, and fungi as well as reduce the concentration of a range of dissolved and particulate matter. Simple procedures such as boiling or the use of a household activated carbon filter are not sufficient for treating all possible contaminants that may be present in water from an unknown source. Even natural spring water, considered safe for all practical purposes in the 19th century, must now be tested before determining what kind of treatment, if any, is needed. Chemical and microbiological analysis, while expensive, are the only way to obtain the information necessary for deciding on the appropriate method of purification.

The standards for drinking water quality are typically set by governments or by international standards. These standards usually include minimum and maximum concentrations of contaminants, depending on the intended use of the water. Table 4.1. illustrates individual element concentrations valid according to Slovak Water Act in drinking water.

Widely varied techniques are available to remove contaminants like fine solids, micro-organisms and some dissolved inorganic and organic materials, or environmental persistent pharmaceutical pollutants. The choice of method will depend on the quality of the water being treated, the cost of the treatment process and the quality standards expected of the processed water. The processes below are the ones commonly used in water purification plants.

Pretreatment of water

The majority of water must be pumped from its source or directed into pipes or holding tanks. To avoid adding contaminants to the water, this physical infrastructure must be made from appropriate materials and constructed so that accidental contamination does not occur. The first step in purifying surface water is to remove large debris such as sticks, leaves, rubbish and other large particles which may interfere with subsequent purification steps. Most deep groundwater does not need screening before other purification steps.

Table 4.1
Drinking water quality indicators (physico-chemical) according to Slovak Water Act

Drinking water quality needs to fulfil legislations, in SR Act No.364/2004 according to WHO (Act 184/2002; Novels 308/2012; 409/2014 and 247/2017 Z.z)

T = 8-12°C chloride=100mg/l zinc=0.3mg/l
 conductivity=1000 µS/cm sulfate=250mg/l copper=1mg/l
 pH=6.5-8.5 nitrate =50mg/l lead=0.01mg/l
 COD=3 mg/l nitrite =0.1mg/l mercury=0.001mg/l
 Ca=175mg/l NMH ammonia=0.5mg/l (phosphate=2.5mg/l,NMH 6,7)
 Mg=125mg/l MH iron=0.2(0.5)mg/l chromium=0.05mg/l
 Mn=0.05 (0.2)mg/l aluminum =0.2mg/l antimony=0.005mg/l
 boron=1 mg/l (NMH)

(min. content Ca in drinking water 30 mg/l; Ca : Mg = 2 : 1)

Min. 26 and max. 83 indicators

MH = limit value

Mg: 20-30 mg/l Ca: 40-80 mg/l, optimum 50 mg/l

NMH = max. limit value

Sedimentation

Waters exiting the flocculation basin may enter the sedimentation basin, also called a clarifier or settling basin (Fig. 4.6). It is a large tank with low water velocities, allowing floc to settle to the bottom. The sedimentation basin is best located close to the flocculation basin so the transit between the two processes does not permit settlement or floc break up. Sedimentation basins may be rectangular, where water flows from end to end, or circular where flow is from the centre outward. Sedimentation basin outflow is typically over a weir so only a thin top layer of water - that furthest from the sludge - exits. In general, sedimentation basin efficiency is not a function of detention time or depth of the basin. Although, basin depth must be sufficient so that water currents do not disturb the sludge and settled particle interactions are promoted. As particle concentrations in the settled water

increase near the sludge surface on the bottom of the tank, settling velocities can increase due to collisions and agglomeration of particles. Typical detention times for sedimentation vary from 1.5 to 4 hours. As particles settle to the bottom of a sedimentation basin, a layer of sludge is formed on the floor of the tank which must be removed and treated. The amount of sludge generated is significant, often 3 to 5 percent of the total volume of water to be treated. The cost of treating and disposing of the sludge can impact the operating cost of a water treatment plant. The sedimentation basin may be equipped with mechanical cleaning devices that continually clean its bottom, or the basin can be periodically taken out of service and cleaned manually.

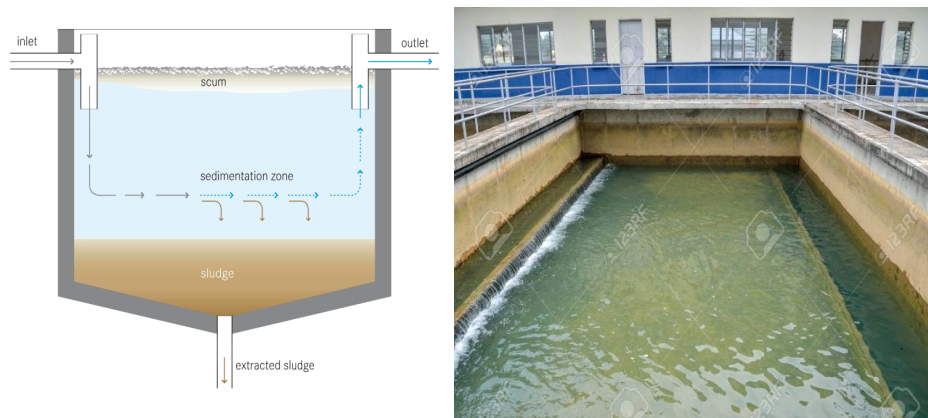


Fig. 4.6. Sketch of sedimentation tank (left) and sedimentation basin in real waterworks (right).

Sand filtration

The most common type of filter is a rapid sand filter. Water moves vertically through sand which often has a layer of activated carbon or anthracite coal above the sand. The top layer removes organic compounds, which contribute to taste and odour. The space between sand particles is larger than the smallest suspended particles, so simple filtration is not enough. Most particles pass through surface layers but are trapped in pore spaces or adhere to sand particles. Effective filtration extends into the depth of the filter. This property of the filter is key to its operation. If the top layer of sand were to block all the particles, the filter would quickly clog (Fig. 4.7).

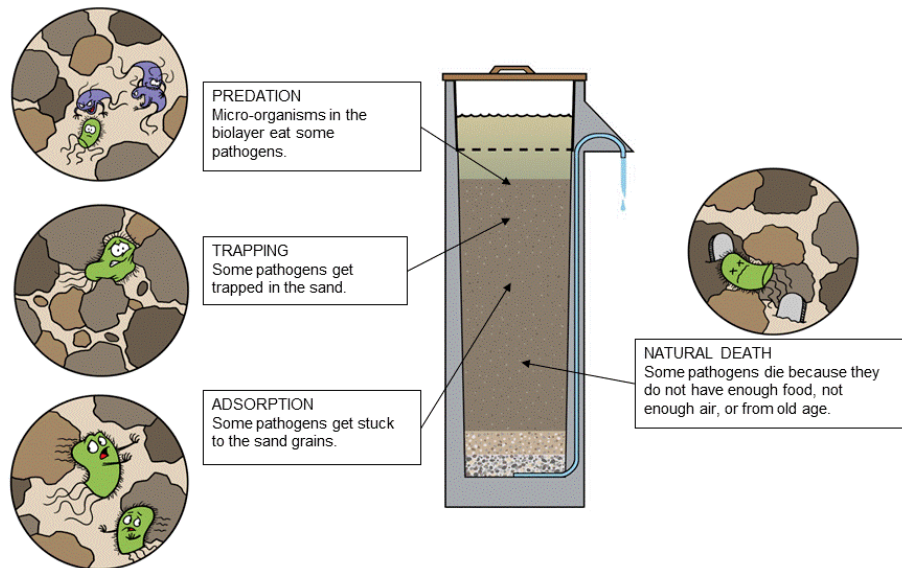


Fig. 4.7. Principle of mechanical sand filtration.

To clean the filter, water is passed quickly upward through the filter, opposite the normal direction (called *backwashing*) to remove embedded or unwanted particles. Prior to this step, compressed air may be blown up through the bottom of the filter to break up the compacted filter media to aid the backwashing process; this is known as *air scouring*. This contaminated water can be disposed of, along with the sludge from the sedimentation basin, or it can be recycled by mixing with the raw water entering the plant although this is often considered poor practice since it re-introduces an elevated concentration of bacteria into the raw water. Slow sand filters may be used where there is sufficient land and space, as the water flows very slowly through the filters. An effective slow sand filter may remain in service for many weeks or even months, if the pretreatment is well designed, and produces water with a very low available nutrient level which physical methods of treatment rarely achieve. Some water treatment plants employ pressure filters (Fig. 4.8). These work on the same principle as rapid gravity filters, differing in that the filter medium is enclosed in a steel vessel and the water is forced through it under pressure.

Coagulation and flocculation

One of the first steps in most conventional water purification processes is the addition of chemicals to assist in the removal of particles suspended in water. Particles can be inorganic such as clay and silt or organic such as algae, bacteria, viruses, protozoa and natural organic matter. Inorganic and organic particles contribute to the turbidity and color of water.

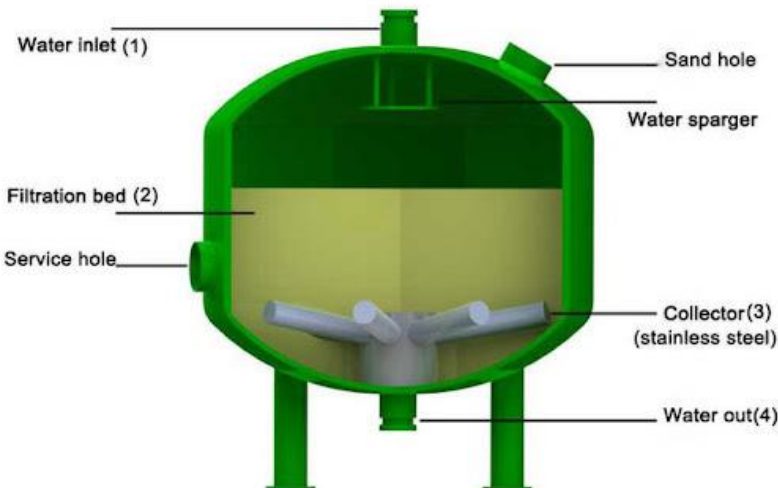


Fig. 4.8. Commercial steel pressure filter composition.

The addition of inorganic coagulants such as aluminum sulfate (or alum) or iron(III) salts such as iron(III) chloride cause several simultaneous chemical and physical interactions on and among the particles. Within seconds, negative charges on the particles are neutralized by inorganic coagulants. Also within seconds, metal hydroxide precipitates of the iron and aluminium ions begin to form (Fig. 4.9.).

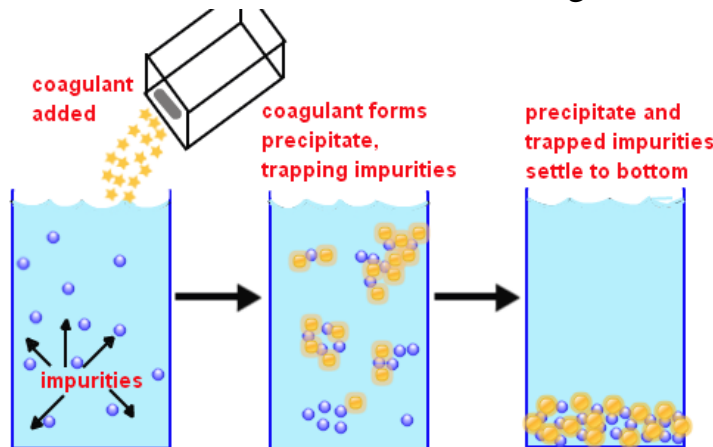


Fig. 4.9. Basic process explanation for coagulation and flocculation.

These precipitates combine into larger particles under natural processes such as Brownian motion and through induced mixing which is sometimes referred to as flocculation. Amorphous metal hydroxides are known as "floc". Large, amorphous aluminum and iron (III) hydroxides adsorb and enmesh particles in suspension and facilitate the removal of particles by subsequent processes of sedimentation and filtration. Aluminum hydroxides are formed within a fairly narrow pH range, typically: 5.5 to about 7.7. Iron (III) hydroxides can form over a larger pH range including pH levels lower than are effective for alum, typically 5.0 to 8.5. In water purification plants, there is usually a high energy, rapid mix unit process (detention

time in seconds) whereby the coagulant chemicals are added followed by flocculation basins (detention times range from 15 to 45 minutes) where low energy inputs turn large paddles or other gentle mixing devices to enhance the formation of floc. In fact, coagulation and flocculation processes are ongoing once the metal salt coagulants are added (Fig. 4.10. and Fig. 4.11).

Organic polymers were developed in the 1960s as aids to coagulants and, in some cases, as replacements for the inorganic metal salt coagulants. Synthetic organic polymers are high molecular weight compounds that carry negative, positive or neutral charges. When organic polymers are added to water with particulates, the high molecular weight compounds adsorb onto particle surfaces and through interparticle bridging coalesce with other particles to form floc.

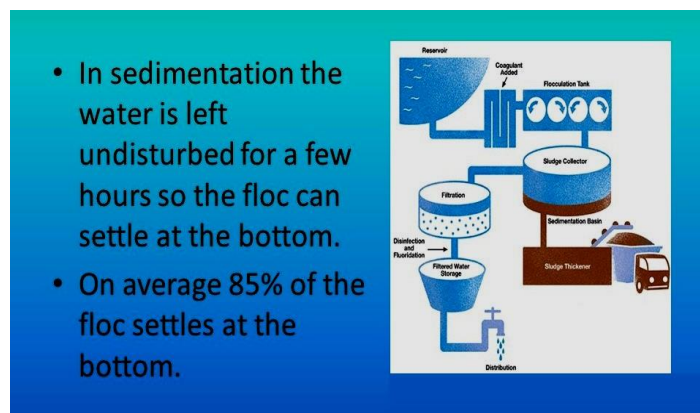


Fig. 4.10. Sketch of surface water purification incl. coagulation and flocculation.



Fig. 4.11. View of coagulation & flocculation process in real waterworks.

Water softening

Water softening is the removal of calcium, magnesium, and certain other metal cations in hard water. The resulting soft water requires less soap for the same cleaning effort, as soap is not wasted bonding with calcium ions. Soft water also extends the lifetime of plumbing by reducing or eliminating scale build-up in pipes and fittings. Water softening is usually achieved using lime softening or ion-

exchange resins but is increasingly being accomplished using nanofiltration or reverse osmosis membranes. Hard water contains calcium or magnesium ions that form insoluble salts upon reacting with soap, leaving a coating of insoluble stearates on tub and shower surfaces, commonly called soap scum (Fig. 4.12 and 4.13).

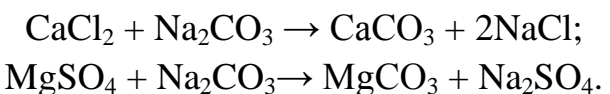


Fig. 4.12. Limescale in a PVC pipe.



Fig. 4.13. Ion exchange resin in the form of beads.

Water rich in hardness (calcium and magnesium ions) is treated with lime (calcium oxide) and/or soda-ash (sodium carbonate) to precipitate calcium carbonate out of solution utilizing the common-ion effect. Lime softening is the process in which lime is added to hard water to make it softer. It has several advantages over the ion-exchange method but is mainly suited to commercial treatment applications. In this method, water is treated with a calculated amount of washing soda (Na_2CO_3), which converts the chlorides and sulfates of calcium and magnesium into their respective carbonates, which get precipitated:



Ion exchange resins in the form of beads (Fig. 4.12) are organic polymers containing anionic functional groups to which the divalent cations (Ca^{2+}) bind more strongly than monovalent cations (Na^+). Inorganic materials called zeolites also exhibit ion-exchange properties (Fig. 4.14). These minerals are widely used in laundry detergents. Resins are also available to remove the carbonate, bicarbonate, and sulfate ions that are absorbed and hydroxide ions that are released from the resin.

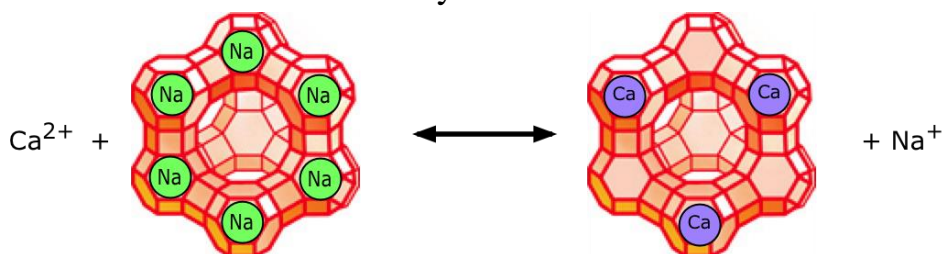


Fig. 4.14. Synthetic zeolites NaA, NaX or NaP in micrometric size used to be applied for detergents production since 1970.

When all the available Na^+ ions have been replaced with calcium or magnesium ions, the resin must be recharged by eluting the Ca^{2+} and Mg^{2+} ions using a solution of sodium chloride or sodium hydroxide, depending on the type of resin used. For anionic resins, regeneration typically uses a solution of sodium hydroxide (lye) or potassium hydroxide. The waste waters eluted from the ion-exchange column containing the unwanted calcium and magnesium salts are typically discharged to the sewage system.

pH adjustment

Pure water has a pH close to 7 (neither alkaline nor acidic). Sea water can have pH values that range from 7.5 to 8.4 (moderately alkaline). Fresh water can have widely ranging pH values depending on the geology of the drainage basin or aquifer and the influence of contaminant inputs (acid rain). If the water is acidic (lower than 7), lime, soda ash, or sodium hydroxide can be added to raise the pH during water purification processes. Lime addition increases the calcium ion concentration, thus raising the water hardness. For highly acidic waters, forced draft degasifiers can be an effective way to raise the pH, by stripping dissolved carbon dioxide from the water. Making the water alkaline helps coagulation and flocculation processes work effectively and also helps to minimize the risk of lead being dissolved from lead pipes and from lead solder in pipe fittings. Sufficient alkalinity also reduces the corrosiveness of water to iron pipes. Acid (carbonic acid, hydrochloric acid or sulfuric acid) may be added to alkaline waters in some circumstances to lower the pH. Alkaline water (above pH 7.0) does not necessarily mean that lead or copper from the plumbing system will not be dissolved into the water. The ability of water to precipitate calcium carbonate to protect metal surfaces and reduce the likelihood of toxic metals being dissolved in water is a function of pH, mineral content, temperature, alkalinity and calcium concentration.

Disinfection

Disinfection is accomplished both by filtering out harmful micro-organisms and by adding disinfectant chemicals. Water is disinfected to kill any pathogens which pass through the filters and to provide a residual dose of disinfectant to kill or inactivate potentially harmful micro-organisms in the storage and distribution systems. Possible pathogens include viruses, bacteria, including *Salmonella*, *Cholera*, *Campylobacter* and *Shigella*, and protozoa, including *Giardia lamblia* and other *cryptosporidium*.

After the introduction of any chemical disinfecting agent, the water is usually held in temporary storage, often called a contact tank or clear well, to allow the disinfecting action to complete. The most common disinfection method involves some form of chlorine or its compounds such as chloramine or chlorine dioxide.

Chlorine is a strong oxidant that rapidly kills many harmful micro-organisms. Because chlorine is a toxic gas, there is a danger of a release associated with its use.

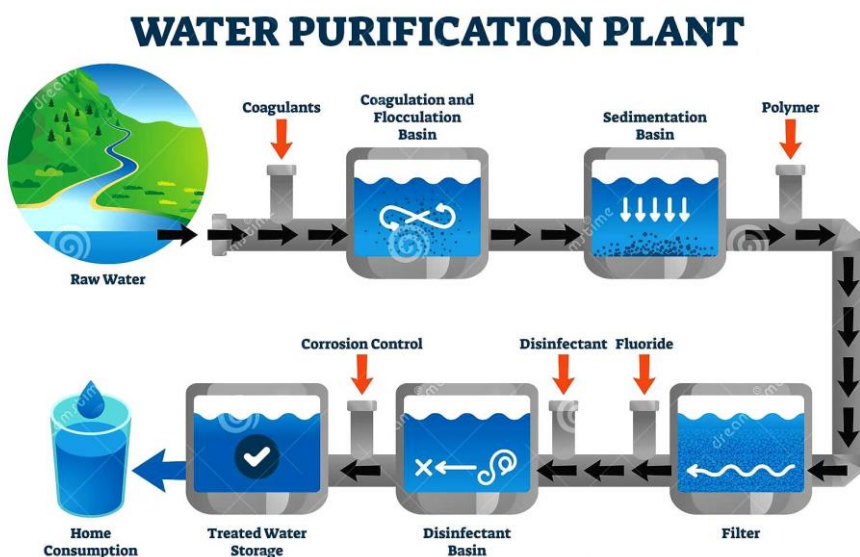


Fig. 4.15. Scheme of conventional surface water purification in waterworks (upper figure a typical surface water pumping into waterworks from the middle of reservoir).

This problem is avoided by the use of sodium hypochlorite, which is a relatively inexpensive solution used in household bleach that releases free chlorine when dissolved in water. Chlorine solutions can be generated on site by electrolyzing common salt solutions. A solid form, calcium hypochlorite, releases chlorine on contact with water. Handling the solid, however, requires more routine human contact through opening bags and pouring than the use of gas cylinders or bleach, which are more easily automated. The generation of liquid sodium hypochlorite is inexpensive and also safer than the use of gas or solid chlorine. Chlorine levels up to

4 milligrams per liter are considered safe in drinking water. One drawback is that chlorine from any source reacts with natural organic compounds in the water to form potentially harmful chemical by-products. These by-products, trihalomethanes (THMs) and haloacetic acids (HAAs), are both carcinogenic in large quantities. Although chlorine is effective in killing bacteria, it has limited effectiveness against pathogenic protozoa that form cysts in water such as *Giardia lamblia* and *Cryptosporidium*.

Chlorine dioxide is a faster-acting disinfectant than elemental chlorine. It is relatively rarely used because in some circumstances it may create excessive amounts of chlorite, which is a by-product regulated to low allowable levels. Chlorine dioxide can be supplied as an aqueous solution and added to water to avoid gas handling problems. Ultraviolet light (UV) is very effective at inactivating cysts, in low turbidity water. UV light's disinfection effectiveness decreases as turbidity increases, a result of the absorption, scattering, and shadowing caused by the suspended solids. The main disadvantage to the use of UV radiation is that, like ozone treatment, it leaves no residual disinfectant in the water; therefore, it is sometimes necessary to add a residual disinfectant after the primary disinfection process.

3.3. Wastewater and sewage treatment

Sewage treatment (or domestic wastewater treatment, municipal wastewater treatment) is a type of wastewater treatment which aims to remove contaminants from sewage to produce an effluent that is suitable for discharge to the surrounding environment or an intended reuse application, thereby preventing water pollution from raw sewage discharges. Sewage contains wastewater from households and businesses and possibly pre-treated industrial wastewater. There are a high number of sewage treatment processes to choose from. These can range from decentralized systems (including on-site treatment systems) to large centralized systems involving a network of pipes and pump stations (called sewerage) which convey the sewage to a treatment plant. For cities that have a combined sewer, the sewers will also carry urban runoff (stormwater) to the sewage treatment plant. Sewage treatment often involves two main stages, called primary and secondary treatment, while advanced treatment also incorporates a tertiary treatment stage with polishing processes and nutrient removal. Secondary treatment can reduce organic matter (measured as biological oxygen demand) from sewage, using aerobic or anaerobic biological processes. With regards to biological treatment of sewage, the treatment objectives can include various degrees of the following: transform dissolved and particulate biodegradable components (especially organic matter) into acceptable end products, transform and remove nutrients (nitrogen and phosphorus), remove or inactivate

pathogenic organisms, and remove specific trace organic constituents (micropollutants). Some types of sewage treatment produce sewage sludge which can be treated before safe disposal or reuse. Under certain circumstances, the treated sewage sludge might be termed "biosolids" and can be used as a fertilizer.

Sewerage (or sewage system) is the infrastructure that conveys sewage or surface runoff (stormwater, meltwater, rainwater) using sewers. It encompasses components such as receiving drains, manholes, pumping stations, storm overflows, and screening chambers of the combined sewer or sanitary sewer. Sewerage ends at the entry to a sewage treatment plant or at the point of discharge into the environment. It is the system of pipes, chambers, manholes, etc. that conveys the sewage or storm water.

Types of treatment processes

Sewage can be treated close to where the sewage is created, which may be called a "decentralized" system or even an "on-site" system (on-site sewage facility, septic tanks, etc.). Alternatively, sewage can be collected and transported by a network of pipes and pump stations to a municipal treatment plant (Fig. 4.16).

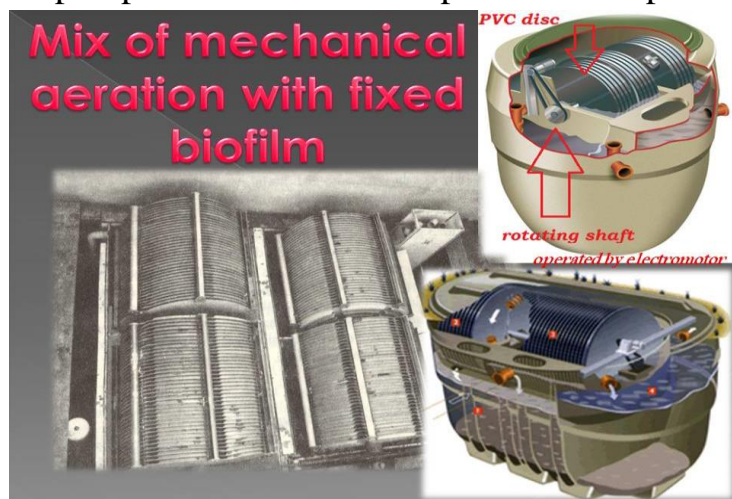


Fig. 4.16. Municipal wastewater treatment using biodiscs.

This is called a "centralized" system (see also sewerage and pipes and infrastructure). A large number of sewage treatment technologies have been developed, mostly using biological treatment processes (see list of wastewater treatment technologies). Very broadly, they can be grouped into high tech (high cost) versus low tech (low cost) options, although some technologies might fall into either category. Other grouping classifications are "intensive" or "mechanized" systems (more compact, and frequently employing high tech options) versus "extensive" or "natural" or "nature-based" systems (usually using natural treatment processes and occupying larger areas) systems. This classification may be sometimes oversimplified, because a treatment plant may involve a combination of processes,

and the interpretation of the concepts of high tech and low tech, intensive and extensive, mechanized and natural processes may vary from place to place.

There are other process options which may be classified as disposal options, although they can also be understood as basic treatment options. These include: Application of sludge, irrigation, soak pit, leach field, fish pond, floating plant pond, water disposal/groundwater recharge, surface disposal and storage. Application of sewage to land can be considered as a form of final disposal or of treatment, or both. It leads to groundwater recharge and/or to evapotranspiration. Land application include slow-rate systems, rapid infiltration, subsurface infiltration, overland flow. It is done by flooding, furrows, sprinkler and dripping. It is a treatment/disposal system that requires a large amount of land per person.

Population equivalent

The "per person organic matter load" is a parameter used in the design of sewage treatment plants. This concept is known as population equivalent (PE). The base value used for PE can vary from one country to another. Commonly used definitions used worldwide are: 1 PE equates to 60 gram of BOD per person per day, and it also equals 200 liters of sewage per day. This concept is also used as a comparison parameter to express the strength of industrial wastewater compared to sewage.

Available process steps

Sewage treatment often involves two main stages, called primary and secondary treatment, while advanced treatment also incorporates a tertiary treatment stage with polishing processes. Different types of sewage (Fig. 4.17) treatment may utilize some or all of the process steps listed below. Preliminary treatment (sometimes called pretreatment) removes coarse materials that can be easily collected from the raw sewage before they damage or clog the pumps and sewage lines of primary treatment clarifiers.

Screening and grit removal

The influent in sewage water passes through a bar screen to remove all large objects like cans, rags, sticks, plastic packets, etc. carried in the sewage stream. This is most commonly done with an automated mechanically raked bar screen in modern plants serving large populations, while in smaller or less modern plants, a manually cleaned screen may be used. The raking action of a mechanical bar screen is typically paced according to the accumulation on the bar screens and/or flow rate. The solids are collected and later disposed in a landfill, or incinerated. Bar screens or mesh screens of varying sizes may be used to optimize solids removal. If gross solids are not removed, they become entrained in pipes and moving parts of the treatment plant, and can cause substantial damage and inefficiency in the process (Fig. 4.17).

Grit consists of sand, gravel, rocks, and other heavy materials. Preliminary treatment may include a sand or grit removal channel or chamber, where the velocity of the incoming sewage is reduced to allow the settlement of grit. Grit removal is necessary to (1) reduce formation of deposits in primary sedimentation tanks, aeration tanks, anaerobic digesters, pipes, channels, etc. (2) reduce the frequency of tank cleaning caused by excessive accumulation of grit; and (3) protect moving mechanical equipment from abrasion and accompanying abnormal wear. The removal of grit is essential for equipment with closely machined metal surfaces such as comminutors, fine screens, centrifuges, heat exchangers, and high pressure diaphragm pumps.



Fig. 4.17. Manually-cleaned screens (left); sewage pumping into the next technology units of wastewater treatment plant (middle); horizontal flow grit chambers (right).

Grit chambers come in three types: horizontal grit chambers, aerated grit chambers, and vortex grit chambers. Vortex grit chambers include mechanically induced vortex, hydraulically induced vortex, and multi-tray vortex separators. During periods of high flow deposited grit is resuspended and the quantity of grit reaching the treatment plant increases substantially. It is therefore important that the grit removal system not only operates efficiently during normal flow conditions but also under sustained peak flows when the greatest volume of grit reaches the plant.

Flow equalization

Equalization basins can be used to achieve flow equalization, with the aim to reduce peak dry-weather flows or peak wet-weather flows in the case of combined sewer systems. The benefits are performance improvements of the biological treatment processes, the secondary clarifiers and any effluent filtration equipment.

Disadvantages include the basins' capital cost and space requirements. Basins can also provide a place to temporarily hold, dilute and distribute batch discharges of toxic or high-strength wastewater which might otherwise inhibit biological secondary treatment (such was wastewater from portable toilets or fecal sludge that is brought to the sewage treatment plant in vacuum trucks). Flow equalization basins require variable discharge control, typically include provisions for bypass and cleaning, and may also include aerators and odor control.

Fat and grease removal

In some larger plants, fat and grease are removed by passing the sewage through a small tank where skimmers collect the fat floating on the surface. Air blowers in the base of the tank may also be used to help recover the fat as a froth. Many plants, however, use primary clarifiers with mechanical surface skimmers for fat and grease removal.

Primary treatment

Primary treatment is the "removal of a portion of the suspended solids and organic matter from the sewage". It consists of allowing sewage to pass slowly through a basin where heavy solids can settle to the bottom while oil, grease and lighter solids float to the surface and are skimmed off (Fig. 4.18). These basins are called "primary sedimentation tanks" or "primary clarifiers" and typically have a hydraulic retention time of 1.5 to 2.5 hours. The settled and floating materials are removed and the remaining liquid may be discharged or subjected to secondary treatment. Primary settling tanks are usually equipped with mechanically driven scrapers that continually drive the collected sludge towards a hopper in the base of the tank where it is pumped to sludge treatment facilities.



Fig. 4.18. Primary clarifier.

Secondary treatment

The main processes involved in secondary sewage treatment are designed to remove as much of the solid material as possible. They use biological processes to digest and remove the remaining soluble material, especially the organic fraction. This can be done with either suspended-growth or biofilm processes. The microorganisms that feed on the organic matter present in the sewage grow and multiply, constituting the biological solids, or biomass. These grow and group together in the form of flocs or biofilms and, in some specific processes, as granules. In several treatment processes, the biological floc or biofilm and remaining fine solids can then be settled as a sludge, leaving a liquid substantially free of solids, and with a greatly reduced concentration of pollutants.

Secondary treatment can reduce organic matter (measured as biological oxygen demand) from sewage, using aerobic or anaerobic processes. The organisms involved in these processes are sensitive to the presence of toxic materials, although these are not expected to be present at high concentrations in typical municipal sewage (Figs. 4.19 and 4.20).



Fig. 4.19. Sketch of secondary sewage treatment in activated sludge tank connected with secondary clarifier (activation – intensification of processes ongoing in nature).

Secondary treatment is the removal of biodegradable organic matter (in solution or suspension) from sewage or similar kinds of wastewater. The aim is to achieve a certain degree of effluent quality in a sewage treatment plant suitable for the intended disposal or reuse option. A "primary treatment" step often precedes secondary treatment, whereby physical phase separation is used to remove settleable solids. During secondary treatment, biological processes are used to remove

dissolved and suspended organic matter measured as biochemical oxygen demand (BOD). These processes are performed by microorganisms in a managed aerobic or anaerobic process depending on the treatment technology. Bacteria and protozoa consume biodegradable soluble organic contaminants (e.g. sugars, fats, and organic short-chain carbon molecules from human waste, food waste, soaps and detergent) while reproducing to form cells of biological solids. Secondary treatment is widely used in sewage treatment and is also applicable to many agricultural and industrial wastewaters.

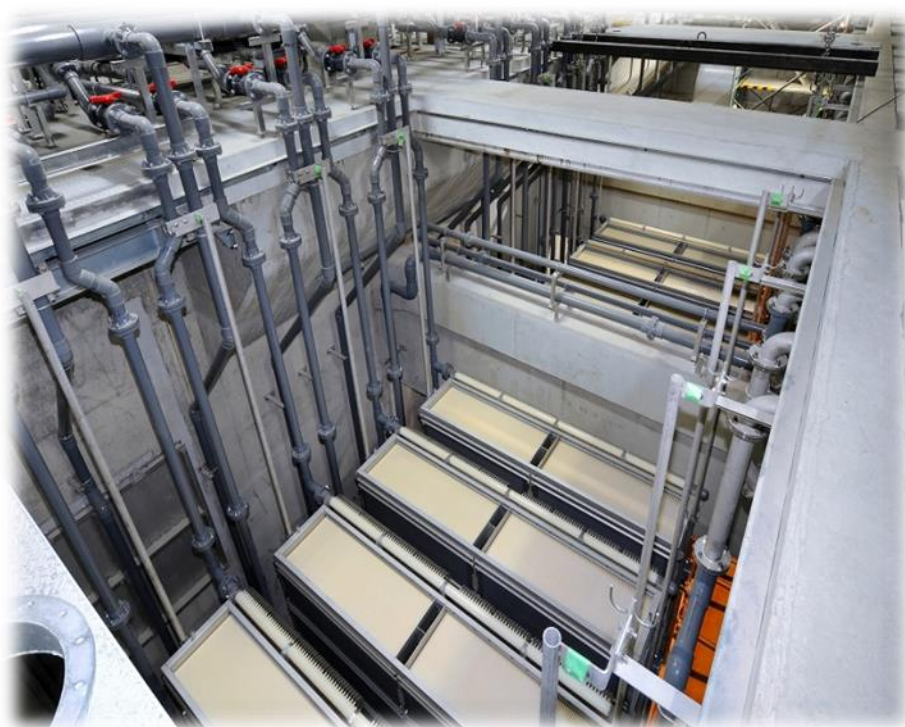


Fig. 4.20. Plate membrane reactor for N – microorganisms retention and high sludge age reaching (simultaneously cleaned using the air).

Biological nutrient removal

Excessive release to the environment can lead to nutrient pollution, which can manifest itself in eutrophication. This process can lead to algal blooms, a rapid growth, and later decay, in the population of algae. In addition to causing deoxygenation, some algal species produce toxins that contaminate drinking water supplies. Ammonia nitrogen, in the form of free ammonia (NH_3) is toxic to fish. Ammonia nitrogen, when converted to nitrite and further to nitrate in a water body, in the process of nitrification, is associated with the consumption of dissolved oxygen. Nitrite and nitrate may also have public health significance if concentrations are high in drinking water, because of a disease called metahemoglobinemia.

Phosphorus removal is important as phosphorus is a limiting nutrient for algae growth in many fresh water systems. Therefore, an excess of phosphorus can lead to eutrophication. It is also particularly important for water reuse systems where high phosphorus concentrations may lead to fouling of downstream equipment such as reverse osmosis. A range of treatment processes are available to remove nitrogen and phosphorus. Biological nutrient removal is regarded by some as a type of secondary treatment process, and by others as a tertiary (or "advanced") treatment process.

Nitrogen removal

Nitrogen is removed through the biological oxidation of nitrogen from ammonia to nitrate (nitrification), followed by denitrification, the reduction of nitrate to nitrogen gas. Nitrogen gas is released to the atmosphere and thus removed from the water. Nitrification itself is a two-step aerobic process, each step facilitated by a different type of bacteria. The oxidation of ammonia (NH_4^+) to nitrite (NO_2^-) is most often facilitated by bacteria such as *Nitrosomonas*, *Nitrosocystis*, *Nitrosospira*. Nitrite oxidation to nitrate (NO_3^-), though traditionally believed to be facilitated by *Nitrobacter* (Figs. 4.21 and 4.22).

Denitrification requires anoxic conditions to encourage the appropriate biological communities to form. "Anoxic conditions" refers to a situation where oxygen is absent but nitrate is present. Denitrification is facilitated by a wide diversity of bacteria. The activated sludge process, sand filters, waste stabilization ponds, constructed wetlands and other processes can all be used to reduce nitrogen.



Fig. 4.21. Layout of nitrification process by chemical equations.

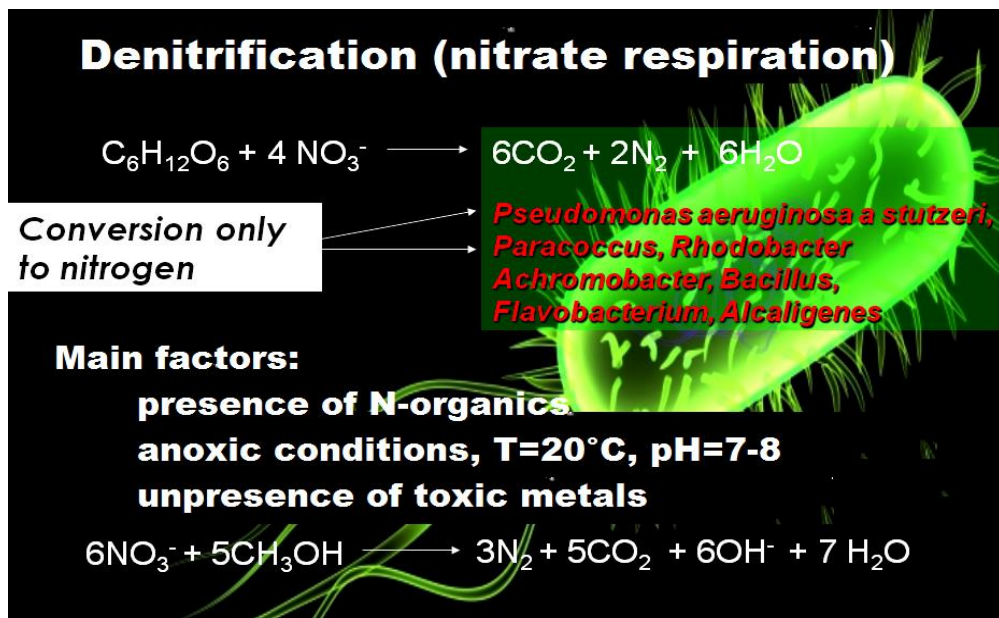


Fig. 4.22. Layout of denitrification process by chemical equations.

Since denitrification is the reduction of nitrate to dinitrogen (molecular nitrogen) gas, an electron donor is needed. This can be, depending on the wastewater, organic matter (from the sewage itself), sulfide, or an added donor like methanol. The sludge in the anoxic tanks (denitrification tanks) must be mixed well (mixture of recirculated mixed liquor, return activated sludge, and raw influent) e.g. by using submersible mixers in order to achieve the desired denitrification. Over time, different treatment configurations for activated sludge processes have evolved to achieve high levels of nitrogen removal. An initial scheme placed an anoxic treatment zone before the aeration tank and clarifier, using the return activated sludge from the clarifier as a nitrate source. The sewage (either raw or as effluent from primary clarification) serves as the electron source for the facultative bacteria to metabolize carbon, using the inorganic nitrate as a source of oxygen instead of dissolved molecular oxygen (Figs. 4.22 and 4.23).

Phosphorus removal

Phosphorus can be removed biologically in a process called enhanced biological phosphorus removal. In this process, specific bacteria, called polyphosphate-accumulating organisms (PAOs), are selectively enriched and accumulate large quantities of phosphorus within their cells (up to 20 percent of their mass) – Fig.4.24.

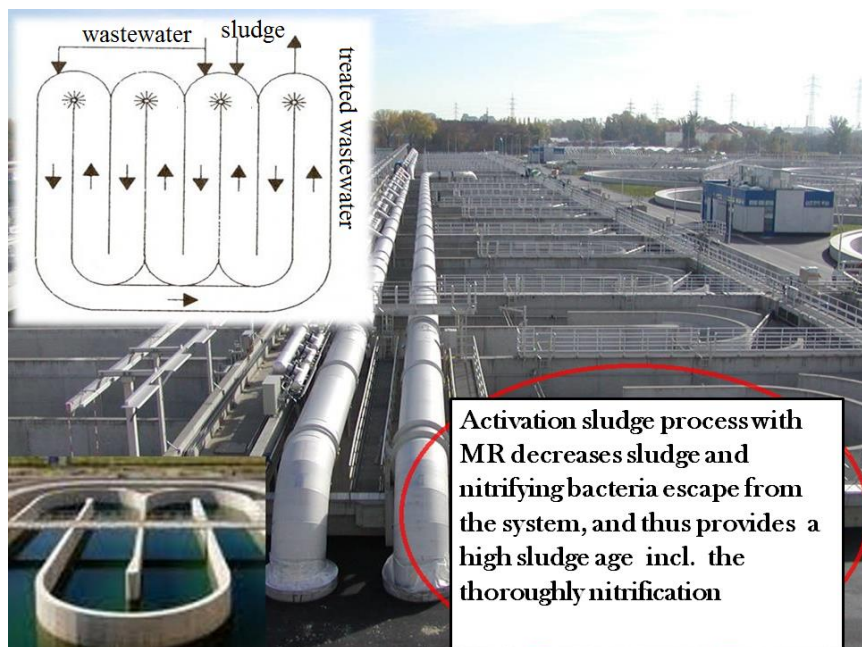


Fig. 4.23. Carrousel system as the most simple arrangement for the carbonisation, nitrification and denitrification of wastewater in wastewater treatment plants.

Phosphorus removal can also be achieved by chemical precipitation, usually with salts of iron (e.g. ferric chloride) or aluminum (e.g. alum), or lime. This may lead to a higher sludge production as hydroxides precipitate and the added chemicals can be expensive. Some systems use both biological phosphorus removal and chemical phosphorus removal. The chemical phosphorus removal in those systems may be used as a backup system, for use when the biological phosphorus removal is not removing enough phosphorus, or may be used continuously. In either case, using both biological and chemical phosphorus removal has the advantage of not increasing sludge production as much as chemical phosphorus removal on its own, with the disadvantage of the increased initial cost associated with installing two different systems.

Advanced and complementary sewage treatments

Advanced sewage treatment generally involves three main stages, called primary, secondary and tertiary treatment but may also include intermediate stages and final polishing processes. The purpose of tertiary treatment (also called "advanced treatment") is to provide a final treatment stage to further improve the effluent quality before it is discharged to the receiving water body or reused. More than one tertiary treatment process may be used at any treatment plant. If disinfection is practiced, it is always the final process. It is also called "effluent polishing". Tertiary treatment may include disinfection and removal of micropollutants, such as environmental persistent pharmaceutical pollutants.

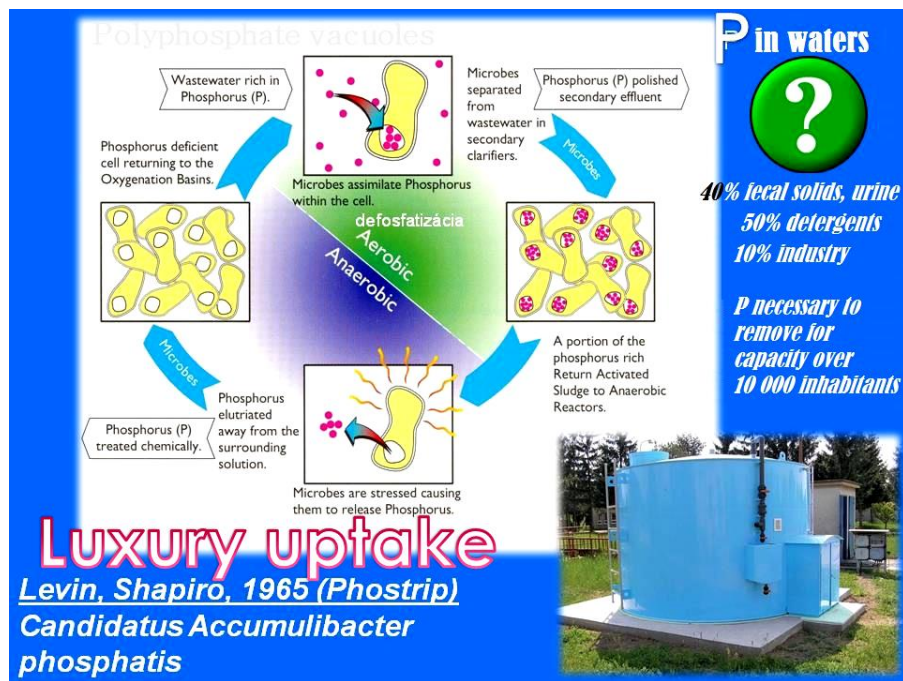


Fig. 4.24. Scheme of Luxury uptake phosphorus removal.

Advanced sewage treatment is defined as anything more than primary and secondary treatment in order to allow discharge into a highly sensitive or fragile ecosystem such as estuaries, low-flow rivers or coral reefs. Treated water is sometimes disinfected chemically or physically (for example, by lagoons and microfiltration) prior to discharge into a stream, river, bay, lagoon or wetland, or it can be used for the irrigation of a golf course, greenway or park (Fig. 4.25). If it is sufficiently clean, it can also be used for groundwater recharge or agricultural purposes.

Sand filtration removes much of the residual suspended matter. Filtration over activated carbon, also called carbon adsorption, removes residual toxins. Micro filtration or synthetic membranes are also used, for example in membrane bioreactors which also remove pathogens. Settlement and further biological improvement of treated sewage may be achieved through storage in large man-made ponds or lagoons. These lagoons are highly aerobic, and colonization by native macrophytes, especially reeds, is often encouraged.

Disinfection

Disinfection of treated sewage may be attempted to kill pathogens (disease-causing microorganisms) prior to disposal, and is increasingly effective after more elements of the foregoing treatment sequence have been completed. The purpose of disinfection in the treatment of sewage is to substantially reduce the number of pathogens in the water to be discharged back into the environment or to be reused. The effectiveness of disinfection depends on the quality of the water being treated (e.g. turbidity, pH, etc.), the type of disinfection being used, the disinfectant dosage

(concentration and time), and other environmental variables. Water with high turbidity will be treated less successfully, since solid matter can shield organisms, especially from ultraviolet light or if contact times are low. Generally, short contact times, low doses and high flows all militate against effective disinfection. Common methods of disinfection include ozone, chlorine, ultraviolet light, or sodium hypochlorite. Monochloramine, which is used for drinking water, is not used in the treatment of sewage because of its persistence.



Fig. 4.25. Further biological improvement of treated sewage may be achieved through storage in large man-made ponds or lagoons.

Chlorination remains the most common form of treated sewage disinfection in many countries due to its low cost and long-term history of effectiveness. One disadvantage is that chlorination of residual organic material can generate chlorinated-organic compounds that may be carcinogenic or harmful to the environment. Residual chlorine or chloramines may also be capable of chlorinating organic material in the natural aquatic environment. Further, because residual chlorine is toxic to aquatic species, the treated effluent must also be chemically dechlorinated, adding to the complexity and cost of treatment.

Ultraviolet (UV) light can be used instead of chlorine, iodine, or other chemicals. Because no chemicals are used, the treated water has no adverse effect on organisms that later consume it, as may be the case with other methods. UV radiation causes damage to the genetic structure of bacteria, viruses, and other pathogens, making them incapable of reproduction. The key disadvantages of UV disinfection are the need for frequent lamp maintenance and replacement and the need for a highly treated effluent to ensure that the target microorganisms are not shielded from the UV radiation (i.e., any solids present in the treated effluent may protect microorganisms from the UV light). In many countries, UV light is becoming the most common means of disinfection because of the concerns about the impacts of

chlorine in chlorinating residual organics in the treated sewage and in chlorinating organics in the receiving water.

Membranes can also be effective disinfectants, because they act as barriers, avoiding the passage of the microorganisms (Fig. 4.26). As a result, the final effluent may be devoid of pathogenic organisms, depending on the type of membrane used. This principle is applied in membrane bioreactors.

Micropollutants such as pharmaceuticals, ingredients of household chemicals, chemicals used in small businesses or industries, environmental persistent pharmaceutical pollutants or pesticides may not be eliminated in the commonly used sewage treatment processes and therefore lead to water pollution. Although concentrations of those substances and their decomposition products are quite low, there is still a chance of harming aquatic organisms. For pharmaceuticals, the following substances have been identified as "toxicologically relevant": substances with endocrine disrupting effects, genotoxic substances and substances that enhance the development of bacterial resistances. Techniques for elimination of micropollutants via a fourth treatment stage during sewage treatment are implemented in Germany, Switzerland, Sweden and the Netherlands and tests are ongoing in several other countries. Such process steps mainly consist of activated carbon filters that adsorb the micropollutants (Fig. 4.27). The combination of advanced oxidation with ozone followed by granular activated carbon has been suggested as a cost-effective treatment combination for pharmaceutical residues. For a full reduction of microplastics the combination of ultrafiltration followed by GAC has been suggested.

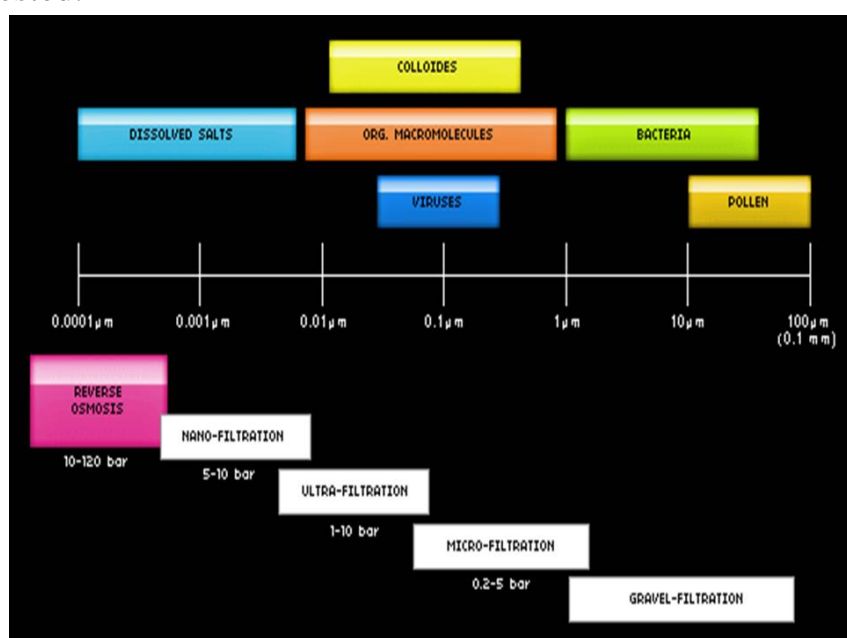


Fig. 4.26. Depending on the type of membrane used various pollutants incl. microplastics can be removed from water.



Fig. 4.27. Principal sketch of pressure filter (left) which may be filled with activated carbon (right).

Sewage sludge treatment and disposal

Sewage sludge treatment describes the processes used to manage and dispose of sewage sludge produced during sewage treatment. Sludge treatment is focused on reducing sludge weight and volume to reduce transportation and disposal costs, and on reducing potential health risks of disposal options. Water removal is the primary means of weight and volume reduction, while pathogen destruction is frequently accomplished through heating during thermophilic digestion, composting, or incineration. The choice of a sludge treatment method depends on the volume of sludge generated, and comparison of treatment costs required for available disposal options. Air-drying and composting may be attractive to rural communities, while limited land availability may make aerobic digestion and mechanical dewatering preferable for cities, and economies of scale may encourage energy recovery alternatives.

Sludge is mostly water with some amounts of solid material removed from liquid sewage. Primary sludge includes settleable solids removed during primary treatment in primary clarifiers. Secondary sludge is sludge separated in secondary clarifiers that are used in secondary treatment bioreactors or processes using inorganic oxidizing agents. In intensive sewage treatment processes, the sludge produced needs to be removed from the liquid line on a continuous basis because the volumes of the tanks in the liquid line have insufficient volume to store sludge. This is done in order to keep the treatment processes compact and in balance (production of sludge approximately equal to the removal of sludge).

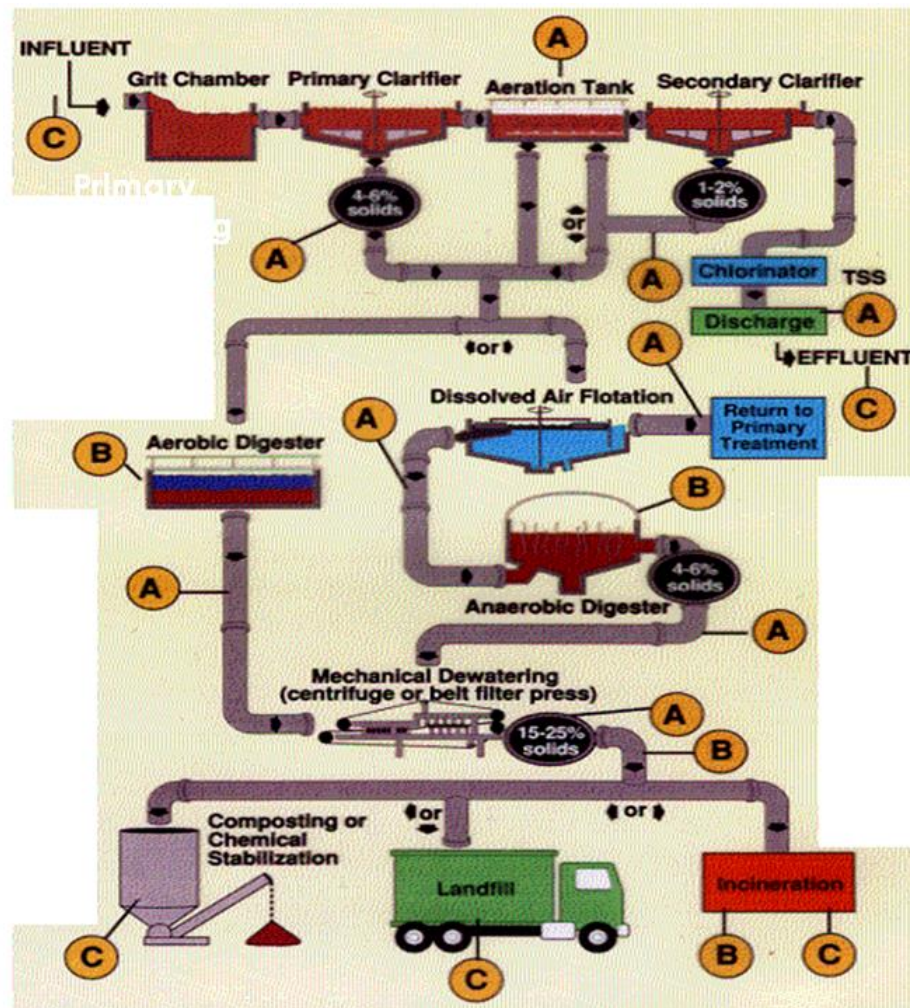


Fig. 4.28. Scheme of the entire wastewater treatment plant incl. sludge handling.

The sludge removed from the liquid line goes to the sludge treatment line. Aerobic processes (such as the activated sludge process) tend to produce more sludge compared with anaerobic processes. On the other hand, in extensive (natural) treatment processes, such as ponds and constructed wetlands, the produced sludge remains accumulated in the treatment units (liquid line) and is only removed after several years of operation.

Sludge treatment options depend on the amount of solids generated and other site-specific conditions. Composting is most often applied to small-scale plants with aerobic digestion for mid-sized operations, and anaerobic digestion for the larger-scale operations (Figs. 4.28 and 4.29). The sludge is sometimes passed through a so-called pre-thickener which de-waters the sludge. Types of pre-thickeners include centrifugal sludge thickeners, rotary drum sludge thickeners and belt filter presses. Dewatered sludge may be incinerated or transported offsite for disposal in a landfill or use as an agricultural soil amendment (Fig. 4.30).

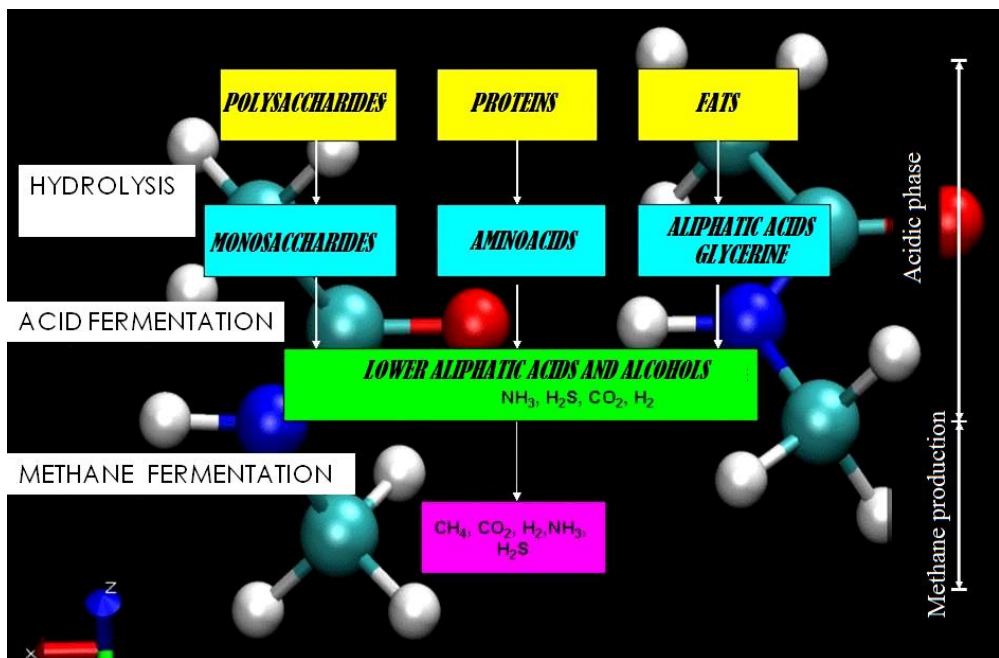


Fig. 4.29. Biochemical process layout for the anaerobic digestion.

Energy requirements

The energy requirements vary with type of treatment process as well as sewage strength. For example, constructed wetlands and stabilization ponds have low energy requirements, associated mainly with the occasional presence of pumps and other equipment. On the other hand, the activated sludge process includes an aeration step, which is highly energy consuming. Sewage treatment plants that produce biogas in their sewage sludge treatment process with anaerobic digestion can produce enough energy to meet most of the energy needs of the sewage treatment plant itself (Fig. 4.31). Most of this electricity is used for aeration, pumping systems and equipment for the dewatering and drying of sewage sludge. Advanced sewage treatment plants, e.g. for nutrient removal, require more energy than plants that only achieve primary or secondary treatment. Small rural plants using trickling filters may operate with no net energy requirements, the whole process being driven by gravitational flow, including tipping bucket flow distribution and the desludging of settlement tanks to drying beds. This is usually only practical in hilly terrain and in areas where the treatment plant is relatively remote from housing because of the difficulty in managing odors.



Fig. 4.30. Sewage sludge dewatering.

Co-treatment of industrial effluent

In highly regulated developed countries, industrial wastewater usually receives at least pretreatment if not full treatment at the factories themselves to reduce the pollutant load, before discharge to the sewer. The pretreatment has the following aims: to remove constituents that may pose risks to the sewerage system and its workers; prevent toxic or inhibitory compounds to the microorganisms in the biological stage in the municipal treatment plant; hinder beneficial use of the produced sewage sludge; or that will still be present in the final effluent from the treatment plant. Some industrial wastewater may contain pollutants which cannot be removed by sewage treatment plants. Also, variable flow of industrial waste associated with production cycles may upset the population dynamics of biological treatment units.



Fig. 4.31. Anaerobic digestion towers (upper figure municipal wastewater treatment plant for the city residence Petržalka of Bratislava capital where biogas production during sludge digestion process is combined with electricity co-generation unit).

Environmental impacts

Sewage treatment plants can have significant effects on the biotic status of receiving waters and can cause some water pollution, especially if the treatment process used is only basic. For example, for sewage treatment plants without nutrient removal, eutrophication of receiving water bodies can be a problem.

Water pollution (or aquatic pollution) is the contamination of water bodies, usually as a result of human activities, in such a manner that negatively affects its legitimate uses. Water pollution reduces the ability of the body of water to provide the ecosystem services that it would otherwise provide. Water bodies include for example lakes, rivers, oceans, aquifers, reservoirs and groundwater. Water pollution results when contaminants are introduced into these water bodies. For example, releasing inadequately treated wastewater into natural waters can lead to degradation of these aquatic ecosystems. All plants and organisms living in or being exposed to polluted water bodies can be impacted. The effects can damage individual species and impact the natural biological communities they are part of. Water pollution can also lead to water-borne diseases for people using polluted water for drinking, bathing, washing or irrigation.

Increasingly, people use treated or even untreated sewage for irrigation to produce crops. Cities provide lucrative markets for fresh produce, so are attractive to farmers. Because agriculture has to compete for increasingly scarce water resources with industry and municipal users, there is often no alternative for farmers but to use water polluted with sewage directly to water their crops. There can be significant health hazards related to using water loaded with pathogens in this way. The World Health Organization developed guidelines for safe use of wastewater in 2006. They advocate a ‘multiple-barrier’ approach to wastewater use, where farmers are encouraged to adopt various risk-reducing behaviors. These include ceasing irrigation a few days before harvesting to allow pathogens to die off in the sunlight, applying water carefully so it does not contaminate leaves likely to be eaten raw, cleaning vegetables with disinfectant or allowing fecal sludge used in farming to dry before being used as a human manure.

Water reclamation (also called wastewater reuse, water reuse or water recycling) is the process of converting municipal wastewater (sewage) or industrial wastewater into water that can be reused for a variety of purposes. Types of reuse include: urban reuse, agricultural reuse (irrigation), environmental reuse, industrial reuse, planned potable reuse, de facto wastewater reuse (unplanned potable reuse). For example, reuse may include irrigation of gardens and agricultural fields or replenishing surface water and groundwater (i.e., groundwater recharge). Reused water may also be directed toward fulfilling certain needs in residences (e.g. toilet

flushing), businesses, and industry, and could even be treated to reach drinking water standards. Treated municipal wastewater reuse for irrigation is a long-established practice, especially in arid countries. Reusing wastewater as part of sustainable water management allows water to remain as an alternative water source for human activities. This can reduce scarcity and alleviate pressures on groundwater and other natural water bodies.

Global targets

Sustainable Development Goal has a Target which is formulated as follows: "By 2030, improve water quality by reducing pollution, eliminating dumping and minimizing release of hazardous chemicals and materials, halving the proportion of untreated wastewater and substantially increasing recycling and safe reuse globally." The corresponding Indicator is the "proportion of wastewater safely treated". Data in 2020 showed that there is still too much uncollected household wastewater: Only 66% of all household wastewater flows were collected at treatment facilities in 2020 (this is determined from data from 128 countries). Based on data from 42 countries in 2015, the report stated that "32 per cent of all wastewater flows generated from point sources received at least some treatment". For sewage that has indeed been collected at centralized sewage treatment plants, about 79% went on to be safely treated in 2020.

Conclusions



Early human habitations were often built next to water sources. Rivers would often serve as a crude form of natural sewage disposal. Some of the earliest evidence of water wells are located in China. The Roman Empire had indoor plumbing, meaning a system of aqueducts and pipes that terminated in homes and at public wells and fountains for people to use. Rome and other nations used lead pipes; while commonly thought to be the cause of lead poisoning in the Roman Empire, the combination of running water which did not stay in contact with the pipe for long and the deposition of precipitation scale actually mitigated the risk from lead pipes. In the 16th and 18th centuries in many rapidly growing countries/cities of Europe (e.g. Germany, France) and the United States, "sewage farms" were increasingly seen as a solution for the disposal of large volumes of the wastewater, some of which are still in operation today. Irrigation with sewage and other wastewater effluents has a long

history also in China and India; while also a large “sewage farm” was established in Australia in 1897. It was not until the late 19th century that it became possible to treat the sewage by biologically decomposing the organic components through the use of microorganisms and removing the pollutants. The activated sludge process was discovered in 1913 in the United Kingdom by two engineers, Edward Ardern and W.T. Lockett, who were conducting research for the Manchester Corporation Rivers Department.

The water emerging from some deep ground water may have fallen as rain many tens, hundreds, or thousands of years ago. Soil and rock layers naturally filter the ground water to a high degree of clarity and often, it does not require additional treatment besides adding chlorine as secondary disinfectant. Such water may emerge as springs, artesian springs, or may be extracted from boreholes or wells. Deep ground water is generally of very high bacteriological quality (i.e. pathogenic bacteria or the pathogenic protozoa are typically absent), but the water may be rich in dissolved solids, especially carbonates and sulfates of calcium and magnesium. Depending on the strata through which the water has flowed, other ions may also be present including chloride and bicarbonate. There may be a requirement to reduce the iron or manganese content of this water to make it acceptable for drinking, cooking, and laundry use. Primary disinfection may also be required. Typically located in the headwaters of river systems, upland reservoirs are usually sited above any human habitation and may be surrounded by a protective zone to restrict the opportunities for contamination. Bacteria and pathogen levels are usually low, but some bacteria, protozoa or algae will be present. Where uplands are forested or peaty, humic acids can colour the water. Many upland sources have low pH which require adjustment. Sewage (or domestic wastewater) consists of wastewater discharged from residences and from commercial, institutional and public facilities that exist in the locality. Sewage is a mixture of water (from the community's water supply), human excreta (feces and urine), used water from bathrooms, food preparation wastes, laundry wastewater, and other waste products of normal living. Sewage from municipalities contains wastewater from commercial activities and institutions, e.g. wastewater discharged from restaurants, laundries, hospitals, schools, prisons, offices, stores and establishments serving the local area of larger communities. Sewage can be distinguished into "untreated sewage" (also called "raw sewage") and "treated sewage" (also called "effluent" from a sewage treatment plant).

The term "sewage" is nowadays often used interchangeably with "wastewater" - implying "municipal wastewater" – in many textbooks, policy documents and the literature. To be precise, wastewater is a broader term, because it refers to any water after it has been used in a variety of applications. Thus it may also refer to "industrial

wastewater", agricultural wastewater and other flows that are not related to household activities.

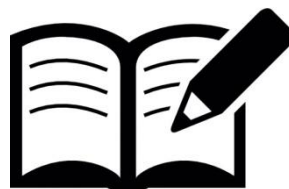
The sewage is composed of around 99.9% pure water, and the remaining 0.1% are solids, which can be in the form of either dissolved solids or suspended solids. The suspended and dissolved solids include organic and inorganic matter plus microorganisms. About one-third of this solid matter is suspended by turbulence, while the remainder is dissolved or colloidal. The organic matter in sewage can be classified in terms of form and size: Suspended (particulate) or dissolved (soluble). Secondly, it can be classified in terms of biodegradability: either inert or biodegradable. The organic matter in sewage consists of protein compounds (about 40%), carbohydrates (about 25–50%), oils and grease (about 10%) and urea, surfactants, phenols, pesticides and others (lower quantity).

In order to quantify the organic matter content, it is common to use "indirect methods" which are based on the consumption of oxygen to oxidize the organic matter: mainly the Biochemical Oxygen Demand (BOD) and the Chemical Oxygen Demand (COD). These indirect methods are associated with the major impact of the discharge of organic matter into water bodies: the organic matter will be food for microorganisms, whose population will grow, and lead to the consumption of oxygen, which may then affect aquatic living organisms. In raw sewage, nitrogen exists in the two forms of organic nitrogen or ammonia. The ammonia stems from the urea in urine. Urea is rapidly hydrolyzed and therefore not usually found in raw sewage. Total phosphorus is mostly present in sewage in the form of phosphates. They are either inorganic (polyphosphates and orthophosphates) and their main source is from detergents and other household chemical products. In most practical cases, pathogenic organisms are not directly investigated in laboratory analyses. An easier way to assess the presence of fecal contamination is by assessing the most probable numbers of fecal coliforms (called thermotolerant coliforms), especially *Escherichia coli*. *Escherichia coli* are intestinal bacteria excreted by all warm blooded animals, including human beings, and thus tracking their presence in sewage is easy, because of their substantially high concentrations (around 10 to 100 million per 100 ml).

Questions for self-control

1. How can you characterize history of water supply and sanitation?
2. What do you understand under the Cloaca Maxima?
3. How can you define sewage farms and how cesspool?
4. Who are inventors of activated sludge process?
5. Define sewage system and population equivalent.

6. Which preliminary sewage treatment steps do you know?
7. Describe sewage primary and secondary treatment in wastewater treatment plant.
8. How would you explain biological nutrient removal in wastewater treatment plant?
9. Which advanced and complementary sewage treatments do you know?
10. How would you remove contaminants like fine solids, micro-organisms and some dissolved inorganic and organic substances from waters?
11. Describe individual treatment steps in conventional water purification process.
12. Explain the principle of coagulation and flocculation process.
13. What means disinfection and which disinfectants do you know?
14. Define sewage system and population equivalent.
15. Which preliminary sewage treatment steps do you know?
16. Describe sewage primary and secondary treatment in wastewater treatment plant.
17. How would you explain biological nutrient removal in wastewater treatment plant?
18. Which advanced and complementary sewage treatments do you know?



References

1. Andersson, K., Rosemarin, A., Lamizana, B., Kvarnström, E., McConville, J., Seidu, R., Dickin, S. and Trimmer, C. (2016). Nairobi and Stockholm: United Nations Environment Programme and Stockholm Environment Institute. ISBN 978-92-807-3488-1.
2. Angelakis, Andreas N. Snyder, Shane A. (2015). Wastewater treatment and reuse: Past, Present and Future. *Water*. 7 (9): 4887–4895.
3. Ashkenazi, Eli. "Ancient well reveals secrets of first Jezreel Valley farmers". Haaretz.com. Haaretz. Archived from the original on 29 March 2014.
4. The Art of Plumbing as Recorded through History. www.academia.edu. 2016.
5. Burney, Charles (2004). Historical Dictionary of the Hittites. Scarecrow Press.

- ISBN 978-0-8108-6564-8. Archived from the original on 7 November 2020.
6. Bunson, Margaret (2014). Encyclopedia of Ancient Egypt. Infobase Publishing. p. 6. ISBN 978-1-4381-0997-8.
 7. BVS Bratislava, Waterworks Museum. – Accessed: www.vodarenskemuzeum.sk November 25, 2021.
 8. Borea, Laura; Ensano, Benny Marie B.; Hasan, Shadi Wajih; Balakrishnan, Malini; Belgioro, Vincenzo; de Luna, Mark Daniel G.; Ballesteros, Florencio C.; Naddeo, Vincenzo (2019). Are pharmaceuticals removal and membrane fouling in electromembrane Bioreactor. *Science of the Total Environment*. 692: 732–740.
 9. Carlo M. Cipolla, Before the Industrial Revolution: European Society and Economy 1000—1700, W.W. Norton and Company, London (1980) ISBN 0-393-95115-4.
 10. Childe, V.; Paterson, J.; Thomas, Bryce (1929). Provisional Report on the Excavation at Skara Brae and on Finds from the 1927 and 1928 Campaigns with a Report on Bones. *Proceedings of the Society of Antiquaries of Scotland*. 63: 225–280, 2020.
 11. Colin Chant, David Goodman (2005). Pre-Industrial Cities and Technology. Routledge. pp. 136–8. ISBN 1134636202.
 12. Chowdhry, S., Koné, D. (2012). Business Analysis of Fecal Sludge Management: Emptying and Transportation Services in Africa and Asia – Draft final report. Bill & Melinda Gates Foundation, Seattle, USA.
 13. Colin A. Russell (2003). Edward Frankland: Chemistry, Controversy and Conspiracy in Victoria England. Cambridge University Press. pp. 372–380. ISBN 978-0-521-54581-5.
 14. "Drinking Water Contaminant Candidate List (CCL) and Regulatory Determination | US EPA Water.epa.gov. 2016-05-09.
 15. The Editors of Encyclopædia Britannica (1998). Hard water. ISBN: 9781593392925.
 16. Eckenfelder, W. Wesley (2000). "Water, Pollution". Kirk-Othmer Encyclopedia of Chemical Technology. ISBN 9780471484943.
 17. Filtration Facts (2005) U.S. Environmental Protection Administration, pp. 6-7. Accessed 6 January 2013.
 18. George Commair, "The Waste Water Network: and underground view of Paris," in Great Rivers History: Proceedings and Invited Papers for the EWRI Congress and History Symposium, May 17–19, 2009, Kansas City, Missouri, ed. Jerry R. Roger, (Reston: American Society of Civil Engineers, 2009), 91–96.
 19. Grant, Walter G., F.S.A.ScoT.; Childe, V. G., F.S.A.ScoT. (A Stone-age settlement at the Braes of Rinyo, Rousay, Orkney (First Report). *Proceedings*

- of the Society of Antiquaries of Scotland. Archived from the original on 3 October 2020.
20. Galvão, A; Matos, J; Rodrigues, J; Heath, P (2005). Sustainable sewage solutions for small agglomerations. *Water Science & Technology*. 52 (12): 25–32.
 21. "How to Achieve Optimal Softener Performance". Chem Aqua, Inc. 2020. Retrieved December 21, 2020.
 22. Henze, M.; van Loosdrecht, M. C. M.; Ekama, G.A.; Brdjanovic, D. (2008). Biological Wastewater Treatment: Principles, Modelling and Design. IWA Publishing (Spanish and Arabic versions are available online for free). ISBN 978-1-78040-186-7.
 23. Henze, M.; van Loosdrecht, M. C. M.; Ekama, G.A.; Brdjanovic, D. (2008). Biological Wastewater Treatment: Principles, Modelling and Design. IWA Publishing. ISBN 978-1-78040-186-7.
 24. Harshman, Vaughan; Barnette, Tony (2000). "Wastewater Odor Control: An Evaluation of Technologies. Water Engineering & Management. ISSN 0273-2238.
 24. "Ion Exchange Treatment of Drinking Water" (PDF). Des.nh.gov. 2009. Retrieved 2016-07-23.
 25. Israr Hasan (2006), Muslims in America, p. 144, ISBN 978-1-4259-4243-4, archived from the original on 7 November 2020.
 26. Jaffe, Eric. "Old World, High Tech". smithsonianmag.com. Smithsonian Magazine. Archived from the original on 9 April 2020.
 27. Jones, Edward R.; van Vliet, Michelle T. H.; Qadir, Manzoor; Bierkens, Marc F. P. (2021). "Country-level and gridded estimates of wastewater production, collection, treatment and reuse. Earth System Science Data. 13 (2): 237–254.
 28. Judith Kidd, Rosemary Rees, Ruth Tudor (2000). Life in Medieval Times. Heinemann. p. 165. ISBN 0435325949.
 29. Khan, Saifullah. 1 Chapter 2 Sanitation and wastewater technologies in Harappa/ Indus valley civilization (ca. 2600 -1900 BC). Academia.edu. Archived from the original on 9 April 2020.
 30. Khouri, N; Kalbermatten, J. M.; Bartone, C. R. Reuse of wastewater in agriculture: A guide for planners. Archived (PDF) from the original on 5 May 2020. Retrieved 29 July 2016.
 31. Khopkar, S.M. (2004). Environmental Pollution Monitoring And Control. New Delhi: New Age International. p. 299. ISBN 978-81-224-1507-0.
 32. Kuhn, Oliver (2004). "Ancient Chinese Drilling". Canadian Society of Exploration Geophysicists. 29 (6).
 33. Layton, Lyndsey (2010). "FDA plans to limit amount of salt allowed in processed foods for health reason, Washingtonpost.com.

34. Lienert, J.; Bürki, T.; Escher, B.I. (2007). Reducing micropollutants with source control: Substance flow analysis of 212 pharmaceuticals in faeces and urine. *Water Science & Technology*. 56 (5): 87–96.
35. Majeed, Azeem (2005). "How Islam changed medicine". *BMJ*. 331 (7531): 1486–1487. ISSN 0959-8138.
36. Metcalf & Eddy (2014). *Wastewater engineering : treatment and resource recovery*. George Tchobanoglous, H. David Stensel, Ryujiro Tsuchihashi, Franklin L. Burton, Mohammad Abu-Orf, Gregory Bowden (Fifth ed.). New York, NY. ISBN 978-0-07-340118-8.
37. Mitchell, Piers D. (2016). *Sanitation, Latrines and Intestinal Parasites in Past Population*. Routledge. p. 22. ISBN 978-1-317-05953-0.
38. Rodda, J. C. and Ubertini, Lucio (2004). *The Basis of Civilization - Water Science?* pg 161. International Association of Hydrological Sciences (International Association of Hydrological Sciences Press 2004).
39. Rowe, Gary (1988). "Well Contamination By Water Softener Regeneration Discharge Water". *Journal of Environmental Health*. 50 (5): 272–276.
40. Sercombe, Derek C. W. (1985). The control of septicity and odours in sewerage systems and at sewage treatment works operated by Anglian Water Services Limited. *Water Science & Technology*. 31 (7): 283–292.
41. Sharma, Sanjay Kumar; Sanghi, Rashmi (2012). *Advances in Water Treatment and Pollution Prevention*. Springer Science & Business Media. ISBN 978-94-007-4204-8.
42. Shuval, H. *Wastewater recycling and reuse as a water source for Mediterranean countries: Hygienic and technological aspects*. www.oieau.fr. Archived from the original on 14 June 2015. Retrieved 29 July 2016.
43. Stephen Lower (2007). "Hard water and water softening". Retrieved 2007-10-08.
44. Spuhler, Dorothee; Germann, Verena; Kassa, Kinfe; Ketema, Atekelt Abebe; Sherpa, Anjali Manandhar; Sherpa, Mingma Gyalzen; Maurer, Max; Lüthi, Christoph; Langergraber, Guenter (2020). Developing sanitation planning options: A tool for novel Systematic technologies. *J. Environmental Management*. 271: 111004.
45. Spuhler, Dorothee; Scheidegger, Andreas; Maurer, Max (2020). Comparative analysis of sanitation systems for resource recovery: Influence of configurations and single technology components. *Water Research*. 186: 116281.
46. Tahāra. Encyclopedia Britannica. Archived from the original on 16 March 2020. Retrieved 7 September 2019.
47. Tilley, E., Ulrich, L., Lüthi, C., Reymond, Ph., Zurbrügg, C. (2014). *Compendium of Sanitation Systems and Technologies – (2nd Revised ed.)*. Swiss Federal Institute of Aquatic Science and Technology (Eawag),

- Duebendorf, Switzerland. ISBN 978-3-906484-57-0.
48. Tzanakakis, V. E.; Paranychianaki, N. V.; Angelakis, A. N. (2007). "Soil as a wastewater treatment system: historical development". *Water Science and Technology: Water Supply*. 7 (1): 67–75. ISSN 1606-9749.
49. Von Sperling, M. (2015). "Wastewater Characteristics, Treatment and Disposal". *Water Intelligence Online*. 6: 9781780402086. ISSN 1476-1777.
50. Von Sperling, M. (2015). "Wastewater Characteristics, Treatment and Disposal". *Water Intelligence Online*. 6. ISBN 9781780402086.
51. Von Sperling, M. (2015). "Activated Sludge and Aerobic Biofilm Reactors". *Water Intelligence Online*. 6: 9781780402123. ISSN 1476-1777.
52. Wang, Shaobin; Peng, Yuelian (2009). Natural zeolites as effective adsorbents in water & wastewater treatment. *Chemical Engineering Journal*. 156 (1): 11–24.
53. Walker, James D. and Welles Products Corporation (1976)."Tower for removing odors from gases. U.S. Patent No. 4421534.
54. "Water Softeners". Canadian Mortgage and Housing Corporation. Archived from the original on October 10, 2006.
55. Wood, R. B.; McAtamney, C.F. (December 1996). "Constructed wetlands for waste water treatment: the use of laterite in the bed medium in phosphorus and heavy metal removal". *Hydrobiologia*. 340 (1–3): 323–331.

Chapter V

SUSTAINABLE AND ENVIRONMENTAL LAND MANAGEMENT



In this section you will learn about

- ✓ Soil ecosystem: definition, composition and its functions
- ✓ Soil physical, chemical and biological properties
- ✓ Contamination in soil ecosystem: the sources of pollution, causes of contamination and the reducing of soil contamination
- ✓ Soil degradation: definition and what can involve
- ✓ Soil quality indicators of sustainable soil management
- ✓ General principles of sustainable land management



Key words:

Soil ecosystem
Indicators of soil quality
Soil degradation
Soil sustainability

Soil is one of the earth's most important natural resources. It is a biologically active, complex mixture of minerals, organic materials, living organisms, air and water. It underpins human food production systems, supports the cultivation of vegetation for feed, fibre and fuel, and has the potential to help combat and mitigate climate change. Human activity and related land use changes are the primary cause of soil degradation, which has substantial implication for nutrient and carbon cycling, land productivity and in turn, worldwide socio-economic conditions. Land occupies 38% of the total space, where approximately 30% represents agricultural land, approximately 30% represents forest ecosystem, 36% is represented by

deserts and 4% represents other land (rocks etc.). More than 90% of our food is grown on soil. One hectare of fertile, no compacted soil can cover the annual bread consumption of more than 120 people. Many hectares of fertile soil in Europe are still transformed into settlement and circulation areas every day. Nearly half of that area is sealed: streets, paths, parking lots and buildings are erected, asphalted, covered in concrete, paved or compacted. These settlement and circulation areas are then lost for the cultivation of agricultural or forestry products.

After reading this chapter, we hope you will have a greater appreciation and understanding of soil ecology, the function of soil in the natural environment and the role of soil organisms in affecting our daily lives.

5.1. Soil ecosystem: definition and function.

Soil is the biologically active, porous medium that has developed in the uppermost layer of Earth's crust. It is one of the principal component of life on Earth, serving as a reservoir of water and nutrients, as a medium for the filtration and breakdown of injurious wastes, and as a participant in the cycling of carbon and other elements through the global ecosystem. It arises at the interface of the atmosphere, lithosphere, hydrosphere and the biosphere, and thus its composition is significantly affected. In soil-forming processes, abiotic and biotic environmental factors are applied, and the result of their action is the component of the environment - **soil**.

Soil is a material composed of five ingredients — **minerals**, **soil organic matter**, **living organisms**, **gas** (soil air), and **water** (Fig. 5.1). Soil minerals are divided into three size classes — clay, silt, and sand, the percentages of particles in these size classes is called soil texture. Mineral matter contains three fraction: *sand*, *silt*, and *clay*. Organic matter contains appreciable quantities of nitrogen, phosphorus and sulphur. Soil organic matter consists of:

1. **Litter** – plant debris, animal carcasses, excreta,
2. **Leachates** – soluble organic compounds,
3. **Roots**,
4. **Soil organisms** – e.g. bacteria, acetomycetes, fungi, algae, protozoa.

Air and water occupy pore spaces in soil. Soil water we can be devided into two groups:

1. **Gravitational water** – it fills all the pore-space, and leaves no room for oxygen and gaseous exchange,
2. **Capillary water** – is held in pores that are small enough to hold water against gravity, but not so tightly, that roots cannot absorb it. This water occurs as a film around soil particles and in the pores between them and is the main source of plant moisture.

3. Hygroscopic water – this water is held so tight (by surface tension) to the soil particles that the plant roots cannot take it up.

The main abiotic factors involved in soil formation include *parent material* (soil forming material), *relief*, *water* and *climatic conditions*.

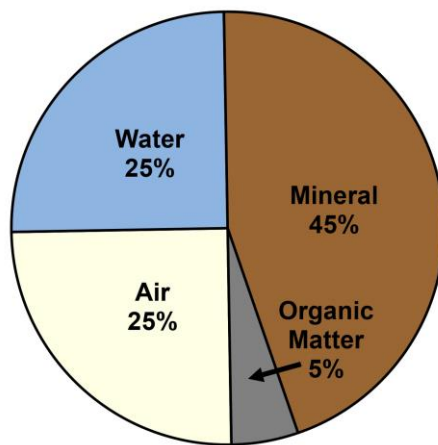


Fig. 5.1. Soil composition

The **chemical composition** of the soil depends mainly on the parent material from which the soil originated, from the processes taking place in the soil and from the human activities. The soil contains the most oxygen (about 50%) and silicon (about 25%), of the other elements it is mainly aluminium (clay), iron, calcium (limestone, gypsum), sodium, potassium, magnesium, hydrogen, titanium, in small amounts carbon, chlorine, phosphorus, sulphur and manganese.

Biotic factors include soil edaphon. These factors are called soil-forming factors. Edaphone is a living component of the soil. It is a set of soil microorganisms, fungi, plants and animals. Soil organisms (geobionts) live in washed-up crevices in soil air or water, especially in the topsoil. For humification processes are the most important plants, bacteria and mycophytes. Bacteria decompose organic matter in the soil. Both autotrophic and heterotrophic bacteria are found in the soil and can have a variety function in the soil ecosystem.

Decomposition of animal, plant and microbial residues is performed by heterotrophic bacteria. Chemoautotrophic bacteria are predominant in the soil that are represented by nitrifying bacteria and iron (Fe) oxidising bacteria. The most common microbial cells in the soil system are unicellular prokaryotes. Despite their high concentration in soil, fungal biomass predominates over bacterial biomass. Soil bacterial flora is extremely diverse, but fungal groups dominate in the soil in terms of biomass. They are eukaryotic organisms and have a mycelial morphology consisting of the mycelium that surrounds the multinucleated cytoplasm. They live in symbiosis

with most plant roots providing increased water and nutrient absorption capabilities. The production of spores by soil fungi allows them to survive to a certain extent adverse soil conditions. Fungi also include many important plant pathogens. Bacteria, worms, insects and other animals process plant residues in healthy soil. This is how the soil is enriched with substances that are vital for vegetation. However, if the soil is acidified by the rain, the animals cannot live in it. In this case, dead plant material remain lying down on earth, no nutrients are produced for the animals and the food chain is broken.

Healthy soil is the foundation of agriculture and as essential resource to ensure human needs in the 21st century, such as food, feed, fibre, clean water and clean air. It is vital part of ecosystem and earth system functions that support the delivery of primary ecosystem services. Soil have various unique **soil functions**. It is:

1. an essential natural resource,
2. an integrator of all parts of ecosystems,
3. a medium for plant growth,
4. a home for organisms,
5. a storehouse of water, heat and chemicals,
6. a decomposing medium for wastes,
7. a source material for construction of shelter and
8. a buffer system to neutralize harsh environmental changes.

5.2. Soil physical, chemical and biological properties.

There are three basic categories of soil properties that include:

1. **Physical properties** – texture, structure, bulk density, moisture, infiltration, porosity, water holding capacity, temperature, colour, etc.;
2. **Chemical properties** – nutrient content, salinity, pH, organic matter content, mineral content, cation exchange capacity, calcium carbonate content, etc.;
3. **Biological properties** – activity of microbes (bacteria, fungi), microbial biomass, biodiversity, biological activity (e.g. soil enzymatic activity).

Soil physical properties

Soil texture represents the relative proportion of sand, silt, and clay in the soil. These proportions affect how soil feels to the touch, thus the term texture. Sand are the largest particles, silt are medium sized and clay are the smallest sized particles. The proportion of different sized mineral particles in the soil or the relative amount of sand, silt, and clay present in the soil is expressed as percentage. On this base, we can recognize 12 textural class categories (Fig. 5.2.).

Soil structure refers to how particles of soil are grouped together into aggregates. They are cemented or bound together by physical, chemical and biological processes. Together, soil structure and texture have the greatest influence on pore spaces in soil, and how easily air, water, and roots can move through a soil. Soil structure is classified by type (shape) of peds, and grade (strength of cohesion) of aggregates. Soil aggregate stability is an indicator of organic matter content, biological activity and nutrient cycling. It is important for many other physical properties, such as infiltration and water movement, root penetration and growth, resistance to erosive forces of wind and water.

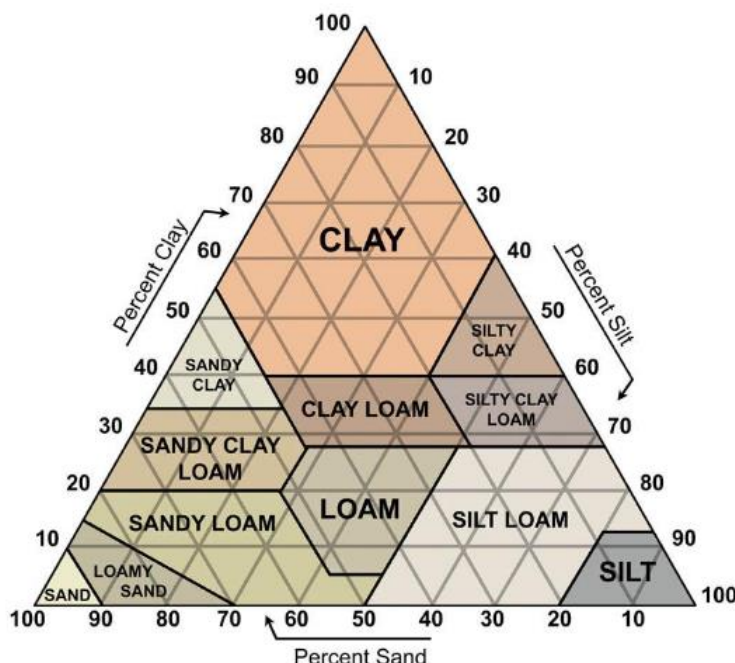


Fig. 5.2. Soil structure (Rowell, 1994)

Soil bulk density is defined as the dry weight of soil per unit volume of soil. Bulk density considers both the solids and pore spaces, whereas, particle density considers only the mineral solids. It is the indicator of soil compaction and tends to increase with the soil depth. Most soils have bulk densities between 1 and 2 g/cm³. Soils with bulk densities higher than 1.6 g/cm³ tend to restrict root growth.

Soil chemical properties

Soil reaction (soil pH) is an indication of the acidity or alkalinity of soil and is measured in pH units. Soil pH is defined as the negative logarithm of the hydrogen ion concentration. The pH scale goes from 0 to 14, with pH 7 as the neutral point (Table 1.). The effect of soil pH is great on the solubility of minerals or nutrients. Before a nutrient can be used by plants it must be dissolved in the soil solution. Most minerals and nutrients are more soluble or available in acid soils

than in neutral or slightly alkaline soils. Extremely and strongly acid soils (pH 4.0-5.0) can have high concentrations of soluble aluminium, iron and manganese that may be toxic to the growth of some plants. The soil pH can also influence plant growth by its effect on activity of beneficial microorganisms. Bacteria that decompose soil organic matter are hindered in strong acid soils. This prevents organic matter from breaking down, resulting in an accumulation of organic matter and the tie up of nutrients, particularly nitrogen, that are held in the organic matter. Soils tend to become acidic as a result of:

1. rainwater leaching away basic ions (calcium, magnesium, potassium and sodium);
2. carbon dioxide from decomposing organic matter and root respiration dissolving in soil water to form a weak organic acid;
3. formation of strong organic and inorganic acids, such as nitric and sulphuric acid, from decaying organic matter and oxidation of ammonium and sulphur fertilizers.

Strongly acid soils are usually the result of the action of these strong organic and inorganic acids. Generally, at low pH, many nutrients become very soluble and are readily leached from the soil profile. At high pH, nutrients become insoluble and plants cannot readily extract them. Maximum soil fertility occurs in the range 6.0 to 7.2 (Table 5.1).

Table 5.1

Soil quality categories based to pH index

Soil Category	pH/H₂O	pH/KCl, CaCl₂
Extremely acid	< 3.5	< 4.5
Very strong acid	3.5-4.5	4.6-5.0
Strongly acid	4.6-5.5	5.1-5.5
Moderately acid	5.6-6.5	5.6-6.5
Slightly acid to neutral	6.6-7.2	6.6-7.2
Slightly alkaline	7.3-8.5	7.3-7.7
Alkaline	> 8.5	> 7.7

Organic matter content (soil humus) makes up just 2-10% of most soils mass and has an important role in the physical, chemical and biological function of agricultural soils. Organic matter contributes to nutrient retention and turnover, soil structure, moisture retention and availability, degradation of pollutants, and carbon sequestration. Soil organic matter is composed mainly of carbon, hydrogen and oxygen, and has small amounts of other elements, such as nitrogen,

phosphorous, sulphur, potassium, calcium and magnesium contained in organic residues. It is divided into '*living*' and '*dead*' components and can range from very recent inputs, such as stubble, to largely decayed materials that are thousands of years old. About 10% of belowground soil organic matter, such as roots, fauna and microorganisms, is '*living*'.

Cation exchange capacity (CEC) is the maximum quantity of total cations that a soil is capable of holding, at a given pH value, available for exchange with the soil solution. CEC is used as a measure of fertility, nutrient retention capacity, and the capacity to protect groundwater from cation contamination. It is expressed as centimol of Hydrogen per kg (cmol_c/kg or 100 meq_c/100g). Most of the soil's CEC occurs on clay and humus.

Calcium carbonate content CaCO₃ is a salt that is not very soluble and occurs in various forms and concentration in soils. Calcium carbonate in moderate amounts is favourable for soil structure and is often used to correct the pH of acidic soils, but when the level of calcium in the soil exceeds the capacity of the soil to absorb it, it binds with other elements and forms insoluble compounds that are difficult for plants to absorb. Excess amounts of calcium may restrict the availability of phosphorous, boron and iron to plants.

Soil biological properties

Soil biota consist of the:

1. **Micro-biota** – soil algae, bacteria, fungi, archaea, protozoa;
2. **Meso-biota** – nematodes, oligochaetes, insect larvae, collembolan;
3. **Macro-biota** – earthworms, rats, snakes.

As soil organisms consume organic matter and each other, nutrients and energy are exchanged through the food web and are made available to plants. Each soil organism plays a role in the decomposition of plant residue, dead roots, and animal remains. Soil biota depend on the soil environment for their energy and nutrient supply. Five **functions** mediated by the soil biota are:

1. The formation and turnover of soil organic matter that includes mineralization and sequestration of carbon;
2. Nutrient cycling;
3. Disease transmission and prevention;
4. Improvement of soil structure.

The soil environment hosts a complex and diverse biological community likely because of its extremely high physical and chemical heterogeneity at small scales, microclimatic characteristics, and phenologies of organisms that promote the development and maintenance of an extremely large number of niches. Soil organisms have been classified on the basis of body width into **microflora** (1–100

μm , e.g. bacteria, fungi), **microfauna** (5–120 μm , e.g. protozoa, nematodes), **mesofauna** (80 μm –2 mm, e.g. collembola, acari) and **macrofauna** (500 μm –50 mm, e.g. earthworms, termites) (Fig. 5.3.).

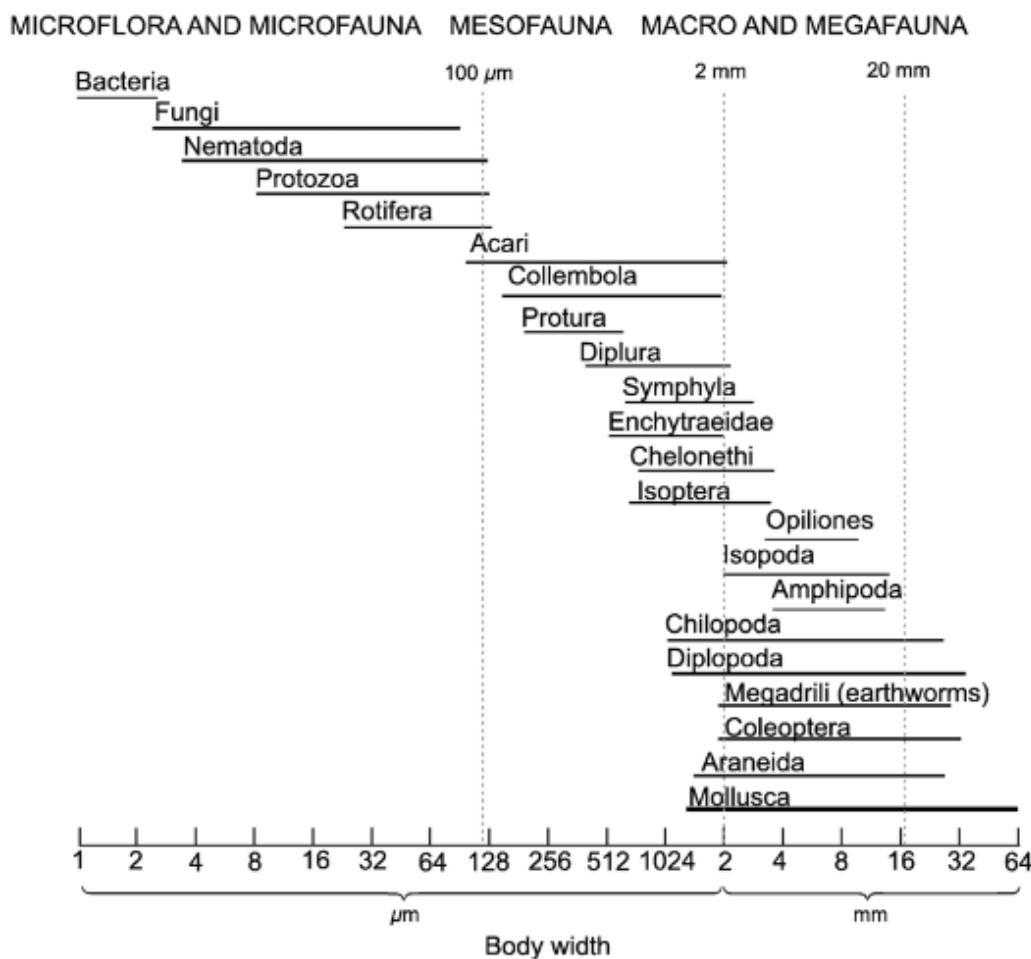


Fig. 5.3. Size classification of soil organisms according to body width
(Swift et al., 1979)

Soil biodiversity is probably the most important for maintaining ecosystem function in a disturbed environment and can be measured directly (as species richness) or indirectly using standardized procedures (various indices). The functionality of soil processes can be measured by determining the activity of soil enzymes, nutrient mineralization, potential nitrification, soil respiration, etc. Representatives of various classes are used as bioindicators of the soil environment and evaluation of its quality. A suitable indicator of soil quality is the use of nematodes, mites, springtails, earthworms, etc. Very suitable indicator of an active nematode community, microflora and decomposition activity in grasslands is the high diversity of nematodes. These communities can also serve as bioindicators of climate change. The influence of heavy metals can also be determined on the basis of changes

in the occurrence of nematode groups. They react very sensitively to the content of SO₂ in the soil and sludge, which can signal environmental stresses in the soil ecosystem in time. Some representatives of mites are considered to be bioindicators of habitat and soil conditions and, together with springtails, they are among the most numerous representatives of soil fauna. Due to the fact that they accumulate heavy metals, they are suitable for bioindication of metal contaminated soils. Earthworms are considered to be the best indicators of soil quality due to their easy identification. They can be used as biomarkers to detect the effects of pollutants or to monitor sublethal doses of toxicants. Some types of earthworms are able to increase the availability of nutrients in the soil (phosphorus and potassium) to plants, increase soil pH, and thus immobilize heavy metals in the soil (lead and zinc), probably through the release of substances formed by specific processes within their body.

Biological properties in soil ecosystem represent the direct and indirect influence of the living organisms habituating a particular soil. They reflect how well suited a soil is to support life. Most of the properties require specialized and high powered equipment for observations or measurements.

Mineralization of carbon (soil respiration) is a measure of the metabolic activity of the soil microbial community. It is measured by capturing and quantifying carbon dioxide (CO₂) released from soil. Respiration is a direct measurement of biological activity, integrating abundance and activity of microbial life. Thus, it is an indicator of the biological status of the soil community, which can give insight into the ability of soils microbial community to accept and use residues or amendments, to mineralize and make nutrients available from them to plants and other organisms, to store nutrients and thus buffer their availability over time, and to develop good soil structure, among other important functions. Soil biological activity influences key physical, biological and chemical soil processes, and is also influenced by constraints in physical and chemical soil functioning. The source of soil respiration is the decomposition of soil organic waste, respiration of roots, respiration of microorganisms in the rhizosphere and oxidation of soil organic matter. Its change is greatly influenced by temperature, humidity and the presence of the substrate. All CO₂ produced by microorganisms does not enter the atmosphere, but some remains in the soil, where it performs important functions. Soil respiration is positively correlated with soil organic matter content, microbial biomass and microbial activity (e.g. soil enzyme activity). It is highly variable and may indicate natural fluctuation depending on a number of environmental factors.

Mineralization of nitrogen is the process by which inorganic nitrogen is obtained by decomposition of dead organisms and degradation of organic nitrogenous compounds. As this process releases ammonium, it is also known as ammonification,

although this term is also used for other dissimilatory processes.

Nitrification is the biological oxidation of ammonia to nitrite followed by the oxidation of the nitrite to nitrate occurring through separate organisms or direct ammonia oxidation to nitrate in comammox bacteria. The transformation of ammonia to nitrite is usually the rate-limiting step of nitrification. Nitrification is an important step in the nitrogen cycle in soil. Nitrification is an aerobic process performed by small groups of autotrophic bacteria and archaea.

Soil enzymatic activity are the indicators of microbial community and functions. They reflect changes in soil biochemical processes and soil organic matter dynamics attributed to human-induced variation in abiotic and biotic factors in soil. Activity of soil enzymes is proposed to be an important determinant of soil and water quality improvement in different types of ecosystems and is affected by many factors, including biological (microbial population, higher taxa and fauna), physico-chemical properties (pH value, organic matter content, nutrient composition, depth, etc.) and climate. Soil enzymes participate in nutrient cycles, such as carbon (beta-glucosidase), nitrogen (urease) and phosphorus (phosphatases). These enzymes transfer energy through organic matter decomposition and nutrients are released to be available for plant growth. Enzymes indicate the rate of important microorganism-mediated processes in soil. That makes them suitable indicators of biological activity; energy transfer; detoxification of contaminants; or immobilisation of heavy metals, plant production and the turnover of nutrients. Diversity of soil enzymes is very high and it correlates with the diversity of soil microbial community because the most enzymes originated with microorganisms. The presence and activity of soil enzymes are related to soil physical and chemical properties, microbial population composition, vegetative cover, land management, land use, etc. There are more than 500 enzymes in soil systems that play a role in soil cycles C, N, P and S. The high diversity of enzymes existing in the soil correlates with the diversity of soil microbial communities, as most enzymes come from microorganisms.

Microbiological characteristics are very often and effectively used as soil quality indicators, because the large surface area, reactivity, distribution, generation time and diversity of the soil microflora allow a virtually immediate response to any stimulus. Microbial parameters (e.g. soil respiration, soil microbial biomass, soil enzyme activity, fixation of biological N₂, etc.) appear to be useful in monitoring soil contamination by heavy metals, but the determination of only one attribute has no significance for soil and its changes in the environment. Therefore, several important microbial activities need to be taken into account. The soil environment is the largest complex of the biological community, which is highly diverse and contributes to a wide range of services for the soil ecosystem, which is beneficial for the sustainable

living of the natural and managed ecosystem. Activities of soil biota contribute significantly to increasing the quality and fertility of the soil. Most of these soil organisms are sensitive to various changes and are therefore used in soil biomonitoring. The most active component of soil biocenosis is microorganisms and their role in the soil ecosystem is irreplaceable.

5.3. Contamination in soil ecosystem: the sources of pollution, causes of contamination and the reducing of soil contamination

Soil contamination (soil pollution, land pollution) is the presence of man-made chemicals or other alteration to the natural soil environment. There is urgency in controlling the soil pollution in order to preserve the soil fertility and increase the productivity. Pollution may be defined as an undesirable change in the physical, chemical and biological characteristics of air, water and soil that affect human life, lives of other useful living plants and animals, industrial progress, living conditions and cultural assets. It is typically caused by industrial activity, agricultural chemical, or improper disposal of waste. The biggest risks for soil contamination are in urban areas and former industrial sites. The most common chemical of soil contamination are Petroleum hydrocarbons, heavy metals, pesticides and solvents. The most sources of contaminants are:

1. **Industrial pollution** – active mines, solid wastes, waste waters, etc.;
2. **Oil pollution** – consumption of fossil fuels;
3. **Agricultural pollution** – pesticides, fertilizers.

Sources of solid wastes that cause land pollution include wastes from *agriculture* (crop and farm residues, animal manure), wastes from *mining* (coal wastes, metal ore wastes), *industrial* wastes (solvents chemicals, paints), *solids* from sewage treatments-biomass sludge, settled solids, *ashes* (residues from solid fuels) and *garbage* (glass, metals, clothes, plastic, wood, papers).

When soil is contaminated with these substances, it can hurt the native environment. Many of these substances are just as toxic to plants as they are to humans. In addition, since soil is the “*earth’s kidney*,” contaminants can trickle through the soil and get to our water supply. Soil contamination have a strong effect on agriculture in reduced soil fertility, low crop yield, reduced soil biodiversity and reduced nitrogen fixation. Where and how much contamination is added to soils will largely determine how that contamination spreads throughout an area. The type of soil will also play a role in its distribution. For example, certain contaminants may reach groundwater sources more easily in sand than clay. This is because of faster infiltration rates of coarse-grained sandy soil types. Fine-grained clay soils or organic material in surface soils can hold contaminants tightly, which means the

contaminants will accumulate if left undisturbed. Not unexpectedly, soil contaminants can have significant deleterious consequences for ecosystems. There are radical soil chemistry changes, which can arise from the presence of many hazardous chemicals even at low concentration of the contaminant species. Effects occur to agricultural lands that have certain types of soil contamination. Contaminants typically alter plant metabolism, often causing a reduction in crop yields. This has a secondary effect upon soil conservation, since the languishing crops cannot shield the Earth's soil from erosion. Some of these chemical contaminants have long half-lives and in other cases, derivative chemicals are formed from decay of primary soil contaminants.

Contaminated or polluted soil directly affects human health through direct contact with soil or via inhalation of soil contaminants, which have vaporized. This tends to results in the development of pollution-related diseases. Exposure to heavy metals in soil and industrial toxins may cause nervous system disorders, kidney damage, liver toxicity, cancer, infertility, birth defects, and many other serious impacts on human health. There are several ways humans can be exposed to soil contaminants. The most common are:

1. Ingesting soil – the soil can be ingested in a variety of ways. Children that play in bare soil, might breathe in dust particles and if the soil is contaminated, it can cause serious problems. Contaminated soil dust may also affect our food supply. For example, contaminated soil could be present on products. If the vegetables are grown in soil with contaminants, the leaves, fruits and other parts could be covered. In addition, root crops like carrots and potatoes usually have soil on them in the store. The biggest risk of ingesting soil happens when the soil is left bare. Covering soil with grass or other plants and mulching well reduces the risk of contamination. If people are eating outdoors near windy soil on a windy day, airborne contaminants may land on food before it is eaten.

2. Breathing volatiles and dust - when soils are uncovered, small particles can become airborne with wind or other disturbance. Construction or demolition work, mining operations, or poor landscaping efforts can make soil dust. Breathing in contaminated dust may cause physical or chemical damage to humans. For example, asbestos fibres can puncture the lungs. Chemicals such as lead can hurt the nervous system, including the brain.

3. Absorbing through skin

4. Eating food grown in contaminated soil - Many vegetables and herbs can absorb contaminants as they grow. That puts us at risk if we eat them. In additon, vegetables and herbs can have soil dust on them. Without proper washing, contaminants remain.

Environmental remediation

Assessing the ecological risk of contaminated soil, pesticide application, sewage sludge amendment, and other human activities leading to exposure of the terrestrial environment to hazardous substances is a complicated task with numerous associated problems. A solution to the problem of soil contamination is **soil remediation**. Soil remediation is a way of purifying and revitalizing the soil. It is the process of removing contaminants in order to protect both the health of the population and the environment. In short, the goal of the process is to restore the soil to its natural, pollution-free state. Traditionally, there are three main soil remediation technologies: soil washing, thermal desorption and bioremediation.

Soil washing is a process that uses surfactants and water to remove contaminants from the soil. The process involves either dissolving or suspending pollutants in the wash solution and separates the soil by particle size.

In **thermal desorption**, heat is used to increase the volatility of contaminants, so that they can be separated from the solid material. The contaminants are then either collected or destroyed. Thermal desorption is the most proven and successful technology used for hydrocarbon contamination, and typically direct fired plants have been used for low levels of contamination. Lately, indirect fired units are more commonly used because of their versatility and their ability to recapture the hydrocarbons. A typical thermal desorption unit consists of two main processes. In the first, contaminated solids are heated to the boiling point of the contaminants. The volatized contaminants are then pumped to the second part of the process, where the vapour is either destroyed by a thermal oxidizer or condensed in a vapour recovery unit.

Bioremediation involves the use of living microorganisms, such as bacteria and fungi, to break down organic pollutants in the soil.

The **microbial treatment methods** appear to be more promising which can deal with whole range of organic contaminants including phenol, polychlorinated hydrocarbons, oil and oil products, dioxins, etc. There are two different ways of approaching the problems. A community of microbes already existing on the site is collected and cultured in the laboratory. Strains of microbes are developed in the laboratory that is capable of metabolizing particular chemicals. Excavation of the soil prior to treatment offers the greatest scope for creating optimum conditions. The excavated soil can be placed on thin layers to various depth using standard earth moving techniques and microbes and nutrients applied using standard agricultural techniques such as fertilizing, ploughing, harrowing, etc. Applying bio-fertilizers and manures can reduce chemical fertilizer and pesticide use. Biological methods of pest control can also reduce the use of pesticides and thereby minimize soil pollution.

5.4. Soil degradation: definition and what can involve.

Soil degradation is the physical, chemical and biological decline in soil quality. It can be the loss of organic matter, decline in soil fertility, and structural condition, erosion, adverse changes in salinity, acidity or alkalinity, and the effects of toxic chemicals, pollutants or excessive flooding. Degradation of soil is caused by soil deterioration, negative use of land management, usually for agricultural and industrial purposes. It is a serious environmental problem and the early detection of changes in the quality of the soil environment and its subsequent revitalization is crucial not only for the proper functioning of ecosystems, but also for humans. Currently, up to 60% of the world's ecosystems are reported to be degraded and exploited unsustainably. Intensification of agriculture associated with the cultivation of monocultures, intensive tillage and fertilization, application of phytopharmaceuticals, drainage activities, or biological invasions can have a dramatic impact on the activity and diversity of the natural community. In Slovakia and worldwide, ecosystems are still being destroyed, fragmented and degraded largely as a result of agricultural and forestry activities, transport and tourist infrastructure. Acidification, chemical pollution, invasive species, climate change and the growing ecological footprint also put increasing pressure on ecosystems largely. The impact of invasive plants on soil ecosystems has attracted worldwide attention in recent decades. Invasions of exotic plants often have a dramatic effect on the structure of natural vegetation and invasive plants are reported to alter soil abiotic properties, nutrient availability, organic carbon content, soil microflora composition and soil mesofauna. Particular attention is paid to the highly vulnerable and endangered ecosystems of the world, which include e.g. peat bogs, heaths, coastal ecosystems, etc. It is therefore very important to use methods that are reliable and sensitive to the early detection of adverse changes in ecosystems caused by anthropogenic influences. Soil degradation can involve:

- **water erosion** (includes sheet, rill and gully erosion),
- **wind erosion**,
- **salinity** (includes dryland, irrigation and urban salinity),
- **loss of organic matter**,
- **fertility decline**,
- **soil acidity or alkalinity**,
- **structure decline** (includes soil compaction and surface sealing),
- **mass movement**,
- **soil contamination** (including effects of toxic chemicals and pollutants).

5.5. Soil quality indicators of sustainable soil management.

Scientists use **soil quality indicators** to evaluate how well soil functions since soil function often cannot be directly measured. A **bioindicator** is defined as an organism, part of an organism, its product (e.g. enzyme), a set of organisms or a biological process that can be used to obtain information on the state and quality of all or part of the environment. The study and monitoring of these indicators is very important for understanding ecological changes within the soil ecosystem. **Principal requirements for soil indicators should:**

- be sensitive to human-induced changes to the environment,
- be simple and cost effective to measure, and applicable to the majority of soil monitoring networks,
- integrate soil physical, chemical, and biological properties and processes,
- indicate responses that can be distinguished from natural variability,
- be interpretable,
- provide both diagnostic and prognostic information.

Maintaining of soil quality is crucial for environmental sustainability. It depends partially on the natural composition of the soil, but also on changes caused by human activity and soil management. Soil quality cannot be determined directly, but must be derived from changes in its parameters or indicators. In practice, the determination of the whole spectrum of suitable indicators is used. As a rule, they should correlate with processes in the ecosystem and integrate the physical, chemical and biological properties of soils as mentioned above. The selection of key indicators and their critical limits (threshold values) that must be met for normal soil functioning are needed to monitor changes and identify trends in improving or deteriorating soil quality for different agro-ecological zones for use at national and global levels. Many soil indicators interact with each other, and therefore the value of one is affected by one or more other selected parameters.

There are three main categories of soil indicators: **chemical, physical** and **biological**. Typical soil tests only look at chemical indicators. Soil quality attempts to integrate all three types of indicators. The categories do not neatly align with the various soil functions, so integration is necessary. Some indicators are descriptive and can be used in the field as part of a health card. Others must be measured using laboratory analyses (Table 5.2).

Organic matter, or more specifically soil carbon, transcends all three indicator categories and has the most widely recognized influence on soil quality. Organic matter is tied to all soil functions. It affects other indicators, such as aggregate stability (physical), nutrient retention and availability (chemical), and nutrient cycling (biological); and is itself an indicator of soil quality.

Table 5.2

Relationship between indicator type and soil function	
Indicator category	Related soil function
Chemical	nutrient cycling, water relations, buffering
Physical	physical stability and support, water relation, habitat
Biological	biodiversity, nutrient cycling, filtering

Chemical indicators can give the information about the equilibrium between soil solution (soil water and nutrients) and exchange sites (clay particles, organic matter); plant health; the nutritional requirements of plant and soil animal communities; and levels of soil contaminants and their availability for uptake by animals and plants. **Physical indicators** provide information about soil hydrologic characteristics, such as water entry and retention that influences availability to plants. Some indicators are related to nutrient availability by their influence on rooting volume and aeration status. Other measures tell us about erosional status. **Biological indicators** can tell us about the organisms that form the soil food web that are responsible for decomposition of organic matter and nutrient cycling. Information about the numbers of organisms, both individuals and species, that perform similar jobs or niches, can indicate a soil's ability to function or bounce back after disturbance (resistance and resilience). Indicators include measures of earthworms, particulate organic matter, soil respiration, soil enzymes, total organic carbon, microbial biomass, etc.

Soil microbial and biochemical parameters in soil ecosystem monitoring

Compared to higher organisms, **microorganisms** respond very quickly to environmental stresses because they are closely related to the surrounding environment. In certain situations, changes in microbial diversity, or its activity, can lead to changes in the physical and chemical properties of the soil, leading to early detection of soil degradation. Accessibility of chemicals, such as heavy metals or pesticides, is an important soil health issue and it is microbial activity that significantly influences this process. The concentration of heavy metals in the soil does not change in a short time, but their accessibility to living organisms may change. Soil microorganisms and enzymes are the primary mediators of soil biological processes, including soil organic matter degradation, mineralization and nutrient cycling. They play an important role in maintaining the quality of the soil ecosystem and soil functional diversity. These microbiological and biochemical indicators are able to provide reliable indications of changes in soil quality and

nutrient cycles. Microorganisms are of the greatest importance in the biological cycle of substances due to their large active surfaces in relation to biomass volume, high degree of reproduction, large number of physiological groups with differentiated ability to decompose, transform and synthesize matter in the soil system. Substances that adversely affect soil organisms or alter the quality or quantity of organic matter may impair the functioning of the soil-plant system. Temperature fluctuations, extreme pH, disturbing physical factors, reduced soil gas exchange, low nutrient content and increased incidence of inhibitors, predators and antagonists are considered to be the most important environmental factors that adversely affect soil microbial biomass and its activity. Significant change of soil reaction and its reduction is also caused by lower amount of soil organic carbon, organic nitrogen, lower proportion of soil microbial biomass, changes in microbial activity and composition of microbial community, which is due to lower input of soil organic matter into acidic environment. The ecology, activity and population dynamics of microorganisms in the soil are affected by 15 environmental factors: carbon and energy sources, minerals, growth factors, ion composition, water accessibility, temperature, pressure, air composition, electromagnetic radiation, pH, redox potential, surfaces, spatial distribution, genetics of microorganisms and interactions between microorganisms. When determining soil quality and microbial soil activity, it is not appropriate to use individual microbiological and biochemical properties, because their size varies in time and space. Therefore, a combination of different soil properties is used to assess soil quality, which most closely reflects important microbiological and biochemical processes in the soil. Soil health microbial indicators include a set of microbial measurements to comprehensively assess all of their properties in the soil ecosystem. The evaluation of soil biological activity, and thus the assessment of management systems, encounters more serious problems in microbiological practice in connection with the selection and use of appropriate and available biological indicators for its monitoring. The effect on microbial activity, the movement of organic matter and the sequestration of N and C in the soil are also influenced by different tillage methods.

5.6. General principles of sustainable land management.

Sustainable land management was defined by the UN 1992 Rio Earth Summit as “*the use of land resources, including soils, water, animals and plants, for the production of goods to meet changing human needs, while simultaneously ensuring the long-term productive potential of these resources and the maintenance of their environmental functions.*” The productivity and sustainability of a land-use system is determined by the interaction between land resources, climate and human activities.

Especially in the face of climate change and variability, selecting the right land uses for given biophysical and socio-economic conditions, and implementing sustainable land management, are essential for minimizing land degradation, rehabilitating degraded land, ensuring the sustainable use of land resources (i.e. soils, water and biodiversity) and maximizing resilience (Fig. 5.4).

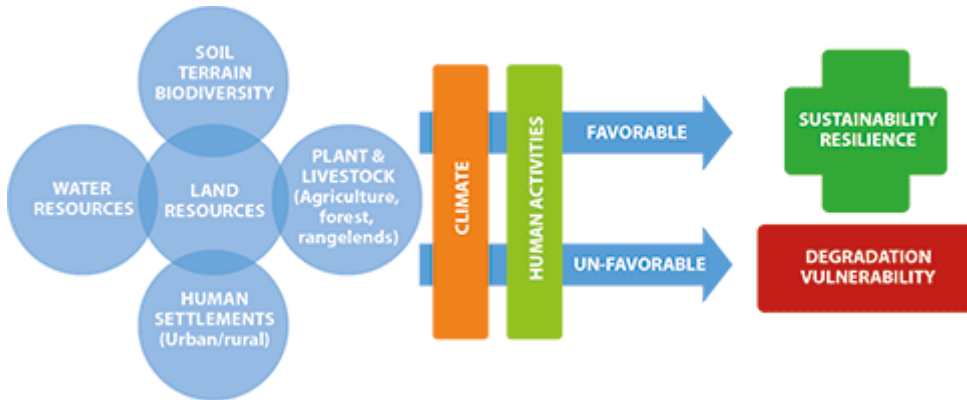


**Fig. 5.4. Sustainable soil/land management for climate-smart agriculture
(FAO, Climate-Smart Agriculture Sourcebook)**

Sustainable land management is crucial to minimizing land degradation, rehabilitating degraded areas and ensuring the optimal use of land resources for the benefit of present and future generations. Sustainable land management involves using the land within its capability to ensure the productivity and economic potential of the land is maintained, whilst its ecological function, such as the ability of the soils to retain water or the landscape to support biodiversity, is not diminished.

General land management principles includes:

1. Management the soil according to the capacity and limitations of the land - this is based on an understanding of land resource areas and ecological processes. Consider soil structure, depth and type, slope and drainage in the management decisions. Critical processes include the ability of the soil to retain water or resist erosion.

2. Ensure appropriate placement and maintenance of infrastructure - this could include roads, bridges, drains, soil conservation features such as contours and waterways, fences, yards and water points to minimise land degradation. A property management plan can guide in making these decisions from a whole of property perspective.

3. Protect and rehabilitate areas that are degraded or at risk from erosion and salinity.

4. Control weeds and pests.

5. Respect and protect Indigenous and European cultural heritage sites.

6. Manage native forests for multiple purposes - implementing sustainable forest practices can improve timber production and grazing whilst maintaining or enhancing biodiversity values.

7. Minimizing on-farm energy use and waste.

Maintaining the healthy soil is made through managing soils and pastures. Sustaining good vegetation cover helps keep soils healthy, as the roots help bind the soil together, controlling run-off and preventing erosion. The quality of groundwater and run-off water entering watercourses are also largely influenced by vegetation cover and soil health. The soil should be kept at least 90% of the soil surface covered at all times of the year by managing your stocking rate. This will help prevent erosion, improve water quality and the pasture is able to quickly respond to any rainfall.

There are also other important points to consider when **managing soils and pastures:**

- 1.** Maintaining high levels of groundcover.
- 2.** Regularly monitoring the pastures.
- 3.** Adopting grazing management practices which maintain good land condition - maintain healthy, diverse pastures dominated by perennial, productive and palatable) species by managing utilisation, matching stock numbers to available forage and routine spelling.
- 4.** Adopting sustainable cropping practices - this includes reduced tillage, stubble retention, use of green manure crops, legumes and ley pastures, crop rotations, and regular soil analysis to match inputs to crop and soil needs, prevent soil health decline, soil acidification and erosion.
- 5.** Adopting sustainable irrigation and farming practices - implement irrigation and farming practices which improve water use efficiency, minimise nutrient losses, run off and deep drainage and conserve limited water supplies.

Soil protection and sustainable land management practices for croplands are usually considered to be cost-effective. Soil protection practices are generally considered as desirable actions and an appropriate approach to prevent, reduce and reverse soil and land degradation. These practices and policies aim to maintain the long-term productivity of ecosystems through integrated management of soils, water, vegetation and biodiversity within their specific biophysical and socio-economic contexts. Managing for soil health allows producers to work with the land – not against – to reduce erosion, maximize water infiltration, improve nutrient cycling, save money on inputs, and ultimately improve the resiliency of their working land.

Moreover, healthy soils are the basis for healthy food production. It is estimated that 95% of our food is directly or indirectly produced on our soils. With a global population that is projected to exceed 9 billion by 2050, compounded by competition for land and water resources and the impact of climate change, our current and future food security hinges on our ability to increase yields and food quality using the soils that are already under production today. Healthy soils are the foundation of the food system. Our soils are the basis for agriculture and the medium in which nearly all food-producing plants grow. Healthy soils produce healthy crops that in turn nourish people and animals. Indeed, soil quality is directly linked to food quality and quantity. Farmers play a central role in this aspect. Numerous and diverse farming approaches promote the sustainable management of soils with the goal of improving productivity, for instance: agroecology, conservation agriculture, organic farming, zero tillage farming and agroforestry. Ultimately, a better understanding of the linkages between soil life and ecosystem function and the impact of human interventions will enable the reduction of negative impacts and allow to capture the benefits of soil biological activity more effectively for a more sustainable and productive agriculture.

Conclusions



Sustainable land management is proposed as a unifying theme for current global efforts on combating desertification, climate change and loss of biodiversity in any type of ecosystems. Where land is managed in a way that either conserves or enhances native vegetation, providing habitat for wildlife, the results can also be highly beneficial for sustainable farm production. A well balanced ecosystem has a key role in functions such as soil health, water quality, pest management and salinity control. Improved agronomic practices include organic fertilization, minimum soil disturbance, and incorporation of residues, terraces, water harvesting and conservation, and agroforestry. These practices can also deliver co-benefits in the form of reduced greenhouse gas emissions and enhanced carbon storage in soils and biomass. All parameters of microbial activity are more sensitive in monitoring changes in land use and such indicators are important for assessing the intensity of soil degradation as well as the other anthropogenic disturbances.

Questions for self-control

1. Define the soil system, soil function and its composition.
2. What are the main soil properties?
3. What is bioindicator and why soil biota (its activity and diversity) is considered to be the most effective indicator of soil health and quality?
4. What are the most sources of soil contamination? Think how this problem can be resolved.
5. State the general principles of sustainable soil use with the specific examples.



References

1. Ashraf, M.A., Maah, M.J., Yusoff, I. Soil Contamination, Risk Assessment and Remediation, Environmental Risk Assessment of Soil Contamination, Maria C. Hernandez-Soriano, IntechOpen, 2014, DOI: 10.5772/57287. Access mode: <https://www.intechopen.com/chapters/46032>.
2. Bardon, C., Piola, F., Bellvert, F., Haichar, F. Z., Comte, G., Meiffren, G., Pommier, T., Puijalon, S., Tsafack, N., Poly, F. Evidence for biological denitrification inhibition (BDI) by plant secondary metabolites. *New Phytologist*, 2014, 204: 620–30.
3. Barrios, E. Soil biota, ecosystem services and land productivity. *Ecological Economics*, 2007, 64: 269-285.
4. Belluck, D.A., Benjamin, S.L., Baveye, P., Sampson, J., Johnson, B. Widespread arsenic contamination of soils in residential areas and public spaces: an emerging regulatory or medical crisis? *International Journal of Toxicology*, 2003, 22: 109-128.
5. Bobuľská, L., Demková, L. Variability of soil properties in conditions of the sustainable soil utilization in Carpathian region. *Polish Journal of Natural Sciences*, 2018, 33: 215-222.
6. Bobuľská, L., Fazekašová, D., Kotorová, D., Angelovičová, L. Impact of ecological and conventional farming systems on chemical and biological soil quality indices in a cold mountain climate in Slovakia. *Biological Agriculture and Horticulture*, 2015, 31: 205-218.

7. Borelli, P., Robinson, D.A., Fleischer, L.R., Lugato, E., Ballabio, C., Alewell, C., Meusburger, K., Modugno, S., Schütt, B., Ferro, V., Bagarello, V., Van Oost, K., Montanarella, L., Panagos, P. An assessment of the global impact of 21st century land use change on soil erosion. *Nature Communication*, 2017, 8: 2013.
8. Borrelli, P., Oost, K., Meusburger, K., Alewell, C., Lugato, E., Panagos, P. A step towards a holistic assessment of soil degradation in Europe: coupling on-site erosion with sediment transfer and carbon fluxes. *Environmental Research*, 2018, 161: 291–298.
9. Branca, G., Lipper, L., McCarthy, N., Jelejole, M.C. Food security, climate change, and sustainable land management. A review. *Agronomy for Sustainable Development*, 2013, 33: 635-650.
10. Doran, J.W., Coleman, D.C., Bezdicek, D.F., Stewart, B.A. Defining soil quality for sustainable environment, Volume 35. SSSA Special Publications, 1994, 244 p.
11. Doran, J.W., Parkin, T.B. Quantitative indicators of soil quality: a minimum data set. In: Doran, J.W., Jones, A.J. (eds.). *Methods for Assessing Soil Quality*. SSSA, Inc., Madison, Wisconsin, USA, 1996, p. 25-38.
12. Doran, J.W., Zeiss, M.R. Soil health and sustainability: managing the biotic component of soil quality. *Applied Soil Ecology*, 2000, 15: 3-11.
13. Drobnič, T., Greiner, L., Keller, A., Grêt-Regamey, A. Soil quality indicators – From soil functions to ecosystem services. *Ecological Indicators*, 2018, 94: 151-169.
14. Fejér, J., Bobuľská, L. *Soil Science (in Slovak)*. University of Prešov, 2015, 121 p.
15. Ferreira, C.S.S., Walsh, R.P.D., Ferreira, A.J.D. Degradation in urban areas. *Current Opinion in Environmental Science and Health*, 2018, 5: 19–25.
16. Gardi, C., Jeffery, S., Saltelli, A. An estimate of potential threats levels to soil biodiversity in EU. *Global Change Biology*, 2013, 19: 1538–1548.
17. Lavelle, P., Bignell, D., Lepage, M., Wolters, V., Armand, R.P., Ineson, P., Heal, O.W., Dhillon, S. Soil function in a changing world: the role of invertebrate ecosystem engineers. *European Journal of Soil Biology*, 1997, 33(4): 159-193.
18. Levine, J.M., Vilà, M., D'Antonio, C.M., Dukes, J.S., Grigulis, K., Lavorel, S. Mechanisms underlying the impacts of exotic plant invasions. *Proceedings of the Royal Society of London B*, 2003, 270: 775–81.
19. Okrent, D. On intergenerational equity and its clash with intragenerational equity and on the need for policies to guide the regulation of disposal of wastes

- and other activities posing very long time risks. *Risk Analysis*, 1999, 19: 877-901.
20. Popa, D., Coyne, M. *Soil microbiology: The life beneath your feet*. Instant Publisher, Lexington, 2007, 241 p.
 21. Rowell, D. *Soil Science: Methods and Applications*. Longman Scientific and Technical, 1994, 350 p.
 22. Schloter, M., Nannipieri, P., Sørensen, A.J., Van Elsas, J.D. Microbial indicators for soil quality. *Biology and Fertility of Soils*, 2018, 54: 1-10.
 23. Stefanowicz, A.M., Stanek, M., Majewska, M.L., Nobis, M., Zubek, S. Invasive plant species identity affects soil microbial communities in a mesocosm experiment. *Applied Soil Ecology*, 2019, 136: 168–77.
 24. Sterzyńska, M., Shrubovych, J. and Nicia, P. Impact of plant invasion (*Solidago gigantea* L.) on soil mesofauna in a riparian wet meadows. *Pedobiologia*, 2017, 64: 1–7.
 25. Swift, M.J., Heal, O.W., Anderson, J.M., 1979. *Decomposition in terrestrial ecosystems*. University of California Press, Berkeley.
 26. Swift, M.J., Izac, A.M.N., van Noordwijk, M., 2004. Biodiversity and ecosystem services in agricultural landscapes — are we asking the right questions? *Agriculture, Ecosystems & Environment* 104, 113–134.
 27. Tepes, A., Galarraga, I., Markandya, A., Sánchez, M.J.S. Costs and benefits of soil protection and sustainable land management practices in selected European countries: Towards multidisciplinary insights. *Science of the Total Environment*, 2021, 756: 143925.
 28. Van Elsas, J.D., Chiurazzi, M., Mallon, C.A., Elhottova, D., Kristufek, V., Salles, J.F. Microbial diversity determines the invasion of soil by a bacterial pathogen. *Proceeding of the National Academy of Sciences of the United States of America*, 2012, 109: 1159–1164.

Chapter VI

GREEN CHEMISTRY: PRINCIPLES, METRICS, EXAMPLES



In this section you will learn about

- ✓ Principles of green chemistry
- ✓ Green chemistry metrics: Atom economy, E-factor, calculation Waste prevention
- ✓ Green solutions in the chemical syntheses.



Key words:

Green chemistry
Alternative technologies
Green chemistry metrics
Green technologies

The green chemistry movement have been obtained popularity in the early 1990s. Since that time, there have been major contributions from all around the globe, with thousands of publications in this area. Numerous scientific journals related to green chemistry have achieved high impact factors due to new trend research. The evaluation of the environmental impact of a chemical process requires the consideration of numerous factors, such as processing efficiency, safety, and cost effectiveness. These criteria have historically been the primary consideration of the development of new chemical processes. The green chemistry principles also demand a detailed

analysis of environmental and health impacts. Each of these components must be evaluated across an average of numerous synthetic steps, across a wide range of functional group transformations and considering hundreds of options for reagents, catalysts and solvents.

A chemist needs to have the tools to conduct the selection of reagents and metrics to assess the changes being made to achieve an efficient, environmentally benign synthesis.

Many tools have been developed for measuring how green the processes are during recent years. First, the concept of atom economy which measures the efficiency of raw material use was introduced. Then, the E-factor analysis that quantifies waste generation was developed. Later, twelve principles of green chemistry which claims that prevention is better than cure were formulated.

6.1. Principles of green chemistry.

The 12 Green Chemistry Principles:

1. ***Wastes prevention.*** Waste prevention is better and easier than waste treatment is the first and most important principle.

2. ***Atom economy.*** Maximal incorporation of starting materials into the final product is a fundamental principle to design and development of synthetic methods.

3. ***Safer synthesis.*** The designing of chemical methods with utilization and generation of substances with low or no toxicity to people and the environment is major priority.

4. ***Safer chemicals.*** Chemical products and side products should be designed to achieve a desired function with minimal toxicity.

5. ***Safer solvents and auxiliaries.*** Auxiliary substances such as solvents and separation agents should be minimized or eliminated whenever possible and made innocuous when used.

6. ***Energy efficiency.*** The minimization of the economic and environmental impacts associated with energy use in chemical synthesis is point of importance. The development of methods conducted at ambient temperature and pressure whenever it is possible is invited.

7. ***Renewable feedstocks.*** Starting materials from renewable origins should be used whenever economically and technically practicable.

8. ***Derivatives minimization.*** The utilization of protection/deprotection, blocking groups, and temporary modification of physical/chemical processes should be excluded or at least minimized with purposes of waste reduction.

9. ***Catalysts.*** Catalytic reagents that are engineered for high selectivity and efficiency for less waste production are needed.

10. ***Design for degradation.*** The design chemical products which break down into innocuous degradation materials at the end of their function and not dangerous for the environment is important.

11. ***Real-time analysis.*** It is important to develop and adopt real-time analytical methods that provide continuous process monitoring and control of the formation of hazardous compounds.

12. ***Accident prevention for safer chemical production.*** The potential for chemical accidents such as releases, explosions, and fires should be minimized by choosing inherently safer substances.

Following the formulation of these principles, more specific guides were published for process chemists and engineers. Efforts have continued in academia and industry to further development of metrics and educational tools that help chemists develop greener processes. Some of the recently published tools include the development of a series of solvent and reaction selection guides to help chemists during route development, even as early as the first medicinal chemistry route.

The 12 Green Principles of Chemical Processes Engineering:

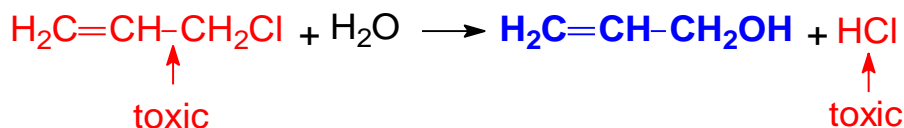
1. Designers need to ensure that material and energy sources and outputs are as non-hazardous as possible.
2. It is better to prevent the waste production than as the waste treat or clean up after it is produced.
3. The minimization of materials and energy consumption for separation and purification operations should be designed.
4. Products, processes, and systems should be designed to maximize energy, mass, time, and space efficiency.
5. Products, processes, and systems should be “output pulled” rather than “input pushed” using materials and energy.
6. Embedded entropy and complexity must be involved when making design choices on reutilization, recycling, or beneficial disposition.
7. The goal of design should be targeted durability but not immortality.
8. Developing solutions for unnecessary capacity or capacity (for example, “one size fits all”) should be considered a shortcoming of the project.
9. Diversity of materials in multi-component products should be minimized to facilitate disassembly and preservation of value.
10. The design of products, processes and systems should include integration and interconnection with existing flows of energy and materials.
11. Products, processes and systems must be designed to work in commercial “afterlife”.
12. Material and energy resources must be renewable, not depleting.

6.2. Green chemistry metrics: Atom economy, E-factor, calculation Waste prevention.

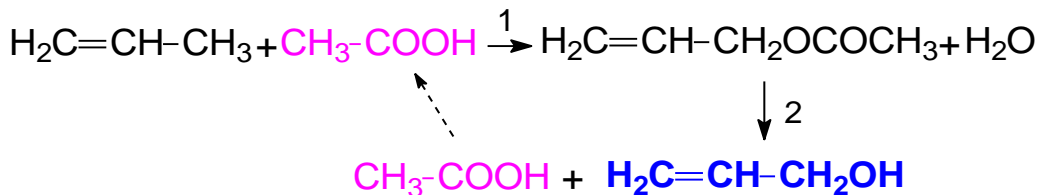
Waste prevention. The main idea is that it is better to prevent waste formation than invest to the treatment, clean up or storage of waste after it is formed. According to this principle, the traditional routes for synthesis of organic compounds must be substituted by an alternative, which minimize or even eliminate the use and production of toxic compounds.

For example, the production of allyl alcohol. The traditional route consists in hydrolysis of allyl chloride.

Despite the advantage, that this is one step production, this route involves the usage of toxic reactant (allyl chloride) and production of toxic side product (hydrochloric acid). Both compounds are toxic and harmful for the environment in case of an accidental release during the transportation, storage, or manipulation.



However, there is an alternative two step route available. Allyl alcohol can be synthesized using propylene ($\text{CH}_2=\text{CHCH}_3$), acetic acid (CH_3COOH) and oxygen.



Only the side-product (acetic acid) produced in the second reaction can be received and used again for the first reaction. Therefore, no unwanted by-product in this route.

Atom economy. Synthetic methods should maximize the incorporation of all materials used into the final product. The synthetic routes should be designed to maximize the incorporation of all materials used in the process into the final product. Several green chemistry metrics are proposed for evaluation of “greenness” of chemical production.

Percentage of yield

The selection of chemical reactions for production of chemical compounds usually is based on the Percentage of yield. This is a very important matter for a chemist that provides a means of comparison of the theoretical and actual quantity of product. Percentage of yield evaluates the reaction efficiency.

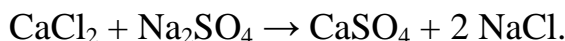
Chemists commonly calculate Percentage yield to ascertain the efficiency of a particular reaction and defined by measuring the actual amount of a product produced

in a chemical reaction and comparing it to the mass predicted from the stoichiometric yield it is possible to calculate the percent yield.

$$\text{% Yield} = \frac{\text{Actual yield}}{\text{Stoichiometric yield}} \times 100\%$$

The stoichiometric yield of a chemical reaction is the mass of product calculated from the mass of limiting reactant in a chemical reaction.

For example, the reaction below shows the formation of CaSO_4 by reacting CaCl_2 with Na_2SO_4



In one run of this reaction in a water solution, the limiting reagent is CaCl_2 . When 100 g of CaCl_2 was mixed with an extent of sodium sulphate solution, an actual yield of 120 g of the CaSO_4 participate was obtained after filtration, washing, and drying. In the begin, we need to find the stoichiometric yield. According to equation of the reaction, 1 mole of CaCl_2 transfers into 1 mole of CaSO_4 .

$$n(\text{CaCl}_2) = \frac{m(\text{CaCl}_2)}{FW(\text{CaCl}_2)} = \frac{100\text{g}}{111\text{g/mole}} = 0.9 \text{mole CaCl}_2 = n(\text{CaSO}_4)$$

where FW - formula weight of chemical compound,

n – quantity of chemical compound,

m – mass of chemical compound.

Stoichiometric yield of the reaction is

$$m(\text{CaSO}_4) = n(\text{CaSO}_4) \times FW(\text{CaSO}_4) = 0.9 \text{mole} \times 136\text{g/mole} = 122.4 \text{ g.}$$

It is the maximum possible amount of product we can get in this reaction. In terms of percentage yield, this is 100%. The Actual yield (experimental) is 120 g. Thus, the Percentage of yield is

$$\text{%Yield} = \frac{120\text{g}}{122.4 \text{ g}} \times 100\% = 98\%.$$

Such calculations show the completeness of the transformation of reagents into desired products. However, provides no information about the extent to which unwanted products are formed in the reaction pathway. In the chemical industry, there are many examples of highly “efficient” reactions that generate waste far greater in mass and volume than the desired product.

Therefore, the alternative criteria for evaluation of accordance to the Green chemistry principles were developed. One of them is Atom economy which measure the amount of atoms from the starting material that are present in the final product at the end of a chemical process. Hight Atom economy means most of the atoms of the

reactants are incorporated in the desired products. Only small amount of waste is produced, hence lesser problem of waste disposal.

The Atom economy of a process can be calculated using the following formula:

$$\text{% Atom economy} = \frac{\Sigma(\text{FW of the desired products})}{\Sigma(\text{FWs of all the reactants})} \times 100\%$$

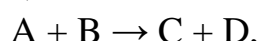
High Atom economy (100%)



where A and B are reagents,

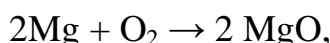
C is desired product.

Low Atom economy (<100%)



where D is side product.

Let's compare two industrial reactions. Preparation of the material for fire resistant coating (MgO)



$FW(\text{Mg}) = 24 \text{ g/mole}$; $FW(\text{O}) = 16 \text{ g/mole}$; $FW(\text{MgO}) = 40 \text{ g/mole}$.

Reagents are quantitatively transformed on the desired product.

$$\text% Atom economy = \frac{2 \times FW(\text{MgO})}{2 \times FW(\text{Mg}) + FW(\text{O}_2)} \times 100\% = \frac{80}{80} \times 100\% = 100\%.$$

Preparation of calcium oxide, the important compound for building industry

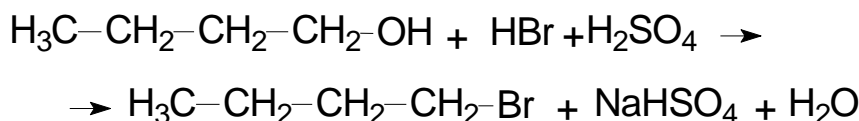


$FW(\text{CaCO}_3) = 100 \text{ g/mole}$; $FW(\text{CaO}) = 56 \text{ g/mole}$; $FW(\text{CO}_2) = 44 \text{ g/mole}$.

In addition to desired product CaO, the preparation as followed by formation of side product CO₂.

$$\text% Atom economy = \frac{FW(\text{CaO})}{FW(\text{CaCO}_3)} \times 100\% = \frac{56}{100} \times 100\% = 56\%.$$

Example 1: Conversion of butan-1-ol to 1-bromobutane



$$\begin{aligned} \text% Atom economy &= \frac{FW(\text{C}_4\text{H}_9\text{Br})}{FW(\text{C}_4\text{H}_9\text{OH}) + FW(\text{HBr}) + FW(\text{H}_2\text{SO}_4)} \times 100\% = \\ &= \frac{137}{275} \times 100\% = 49.81\%. \end{aligned}$$

Example 2: Fermentation of sugar (glucose) to ethanol:



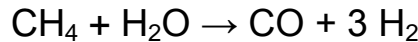
$$\text% Atom economy = \frac{2 \times FW(\text{C}_2\text{H}_5\text{OH})}{FW(\text{C}_6\text{H}_{12}\text{O}_6)} \times 100\% = \frac{2 \times 46}{180} \times 100\% = 51.1\%.$$

Example 3: Dehydration of ethanol:



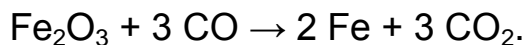
$$\% \text{ Atom economy} = \frac{\text{FW}(\text{C}_2\text{H}_4)}{\text{FW}(\text{C}_2\text{H}_5\text{OH})} \times 100\% = \frac{28}{46} \times 100\% = 60.9\%.$$

Example 4: Obtaining of the hydrogen from methane (stream methane reforming):



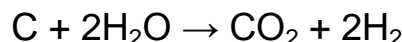
$$\% \text{ Atom economy} = \frac{3 \times \text{FW}(\text{H}_2)}{\text{FW}(\text{CH}_4) + \text{FW}(\text{H}_2\text{O})} \times 100\% = \frac{6}{34} \times 100\% = 17.6\%.$$

Example 5: Industrial production of iron:



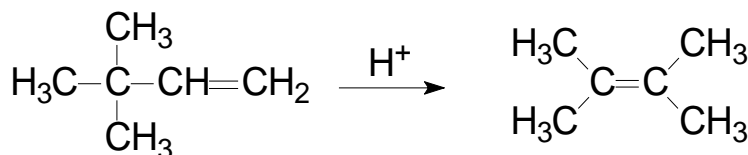
$$\begin{aligned} \% \text{ Atom economy} &= \frac{2 \times \text{FW}(\text{Fe})}{\text{FW}(\text{Fe}_2\text{O}_3) + 2 \times \text{FW}(\text{CO})} \times 100\% = \\ &= \frac{112}{244} \times 100\% = 45.9\%. \end{aligned}$$

Example 6: Production of hydrogen by reacting coal with steam:



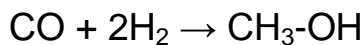
$$\% \text{ Atom economy} = \frac{2 \times \text{FW}(\text{H}_2)}{\text{FW}(\text{CO}_2) + 2 \times \text{FW}(\text{H}_2)} \times 100\% = \frac{4}{48} \times 100\% = 8.3\%.$$

Example 7: Reaction of 3,3-dimethylbutene-1:



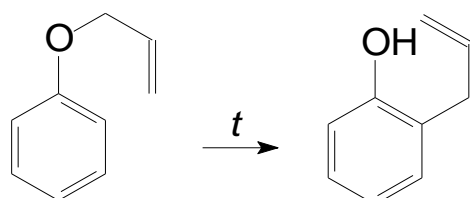
$$\% \text{ Atom economy} = \frac{\text{FW}(\text{C}_6\text{H}_{12})}{\text{FW}(\text{C}_6\text{H}_{12})} \times 100\% = \frac{84}{84} \times 100\% = 100\%.$$

Example 8: Production of methanol:



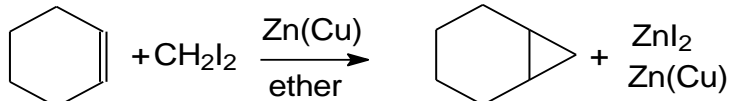
$$\% \text{ Atom economy} = \frac{\text{FW}(\text{CH}_3\text{OH})}{\text{FW}(\text{CH}_3\text{OH})} \times 100\% = \frac{32}{32} \times 100\% = 100\%.$$

Example 9: Claisen rearrangement:



$$\% \text{ Atom economy} = \frac{\text{FW}(\text{C}_9\text{H}_{10}\text{O})}{\text{FW}(\text{C}_9\text{H}_{10}\text{O})} \times 100\% = \frac{144}{144} \times 100\% = 100\%.$$

Example 10: Simmons-Smith cyclopropanation (assume the yield 87%):



When the yield is 100%, Atom economy is

$$\begin{aligned}\% \text{ Atom economy} &= \frac{\text{FW}(\text{C}_7\text{H}_{12})}{\text{FW}(\text{C}_6\text{H}_{10}) + \text{FW}(\text{CH}_2\text{I}_2) + \text{FW}(\text{Zn(Cu), ether})} \times \\ &\quad \times 100\% = \frac{96}{82 + 267 + 129} \times 100\% = 20\%.\end{aligned}$$

If the yield for target product is 87%, the obtained amount is $96 \times 87\% / 100\% = 83.5$. Then

$$\% \text{ Atom economy} = \frac{83.5}{82 + 267 + 129} \times 100\% = 17.4\%.$$

It's clear through these three calculations that the route I for bromination of stilbene is much more atom economical (100%), compared to route II (68%) and route III (90.4%). It means that 32% of the reagents used in the bromination of stilbene in route II and 9.6% in route II were wasted. Despite the fact the Atom economy is 100%, E-factor is not 1 because it considers the use of solvent.

Atom economies are theoretical but do not consider the reaction yield or selectivity, or the nature (toxic / benign) of the waste stream. It takes into account stoichiometric reagents, but do not consider the utilization of catalysts and solvents, as well as, other green chemistry concerns, e.g., energy, toxicity.

Atom economies are a useful way of comparing the waste production of alternative pathways, but other factors should still be considered.

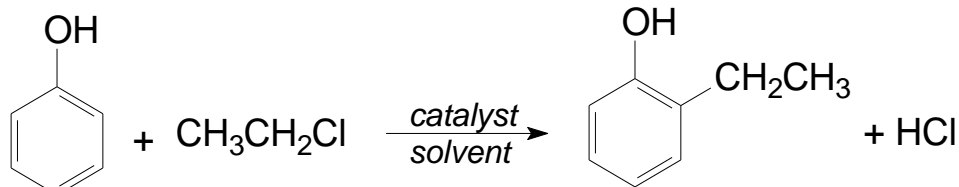
E-Factor

E-Factor (environmental factor) is another Green chemistry metric. The E-Factor is calculated as the ratio of total weight of waste generated to the total weight of product isolated.

$$\text{E - Factor} = \frac{\sum \text{m(waste)}}{\sum \text{m(desired product)}}$$

This metric allows for rapid comparison of many different routes to the same product or across multiple products. It can also serve as a metric across different organizations in a similar field.

For reaction Friedel-Craft alkylation (preparation of 2-ethylphenol)



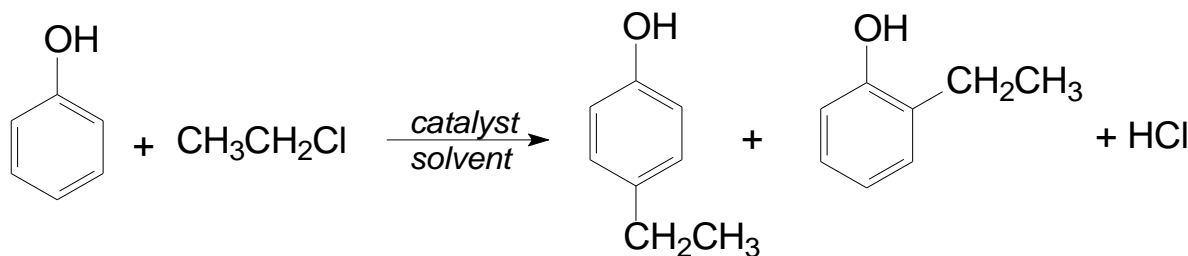
$\text{FW}(\text{C}_6\text{H}_5\text{OH}) = 94 \text{ g/mole}$; $\text{FW}(\text{CH}_3\text{CH}_2\text{Cl}) = 64.5 \text{ g/mole}$;

$FW(HCl) = 36.5 \text{ g/mole}$; $FW(OH-C_6H_4-CH_2CH_3) = 123 \text{ g/mole}$.

If the experimental data are not available, E-factor can be calculated using reaction equation. Thus, for obtaining of 1 mole of desired product, the mass of reactants and products are equal to FW multiplied on stoichiometric coefficients of equation. According to equation of reaction

$$E - Factor = \frac{m(HCl)}{m(OH-C_6H_4-CH_2CH_3)} = \frac{36.5}{123} = 0.3.$$

However, the realisation of the reaction involves the utilization of catalyst and solvent, as well as formation of 4-ethylphenol (side product):



Therefore, the more correct calculations can be done only when experimental data are available.

For example, during the synthesis of 60.0 g 2-ethylphenol, the 400 g of solvent and 2 g of catalyst were used. Additionally, 18.25 g of HCl and 63 g 4-ethylphenol (both are the side products) are obtained.

$$E - Factor = \frac{m(\text{catalyst}) + m(\text{solvent}) + m(4\text{-ethylphenol}) + m(HCl)}{m(2\text{-ethylphenol})} = \frac{2 \text{ g} + 400 \text{ g} + 63 \text{ g} + 18.25 \text{ g}}{60 \text{ g}} = 8.05.$$

Example 1: Production of hydrazine:



$FW(\text{NH}_3) = 17 \text{ g/mole}$; $FW(\text{NaOCl}) = 74.5 \text{ g/mole}$; $FW(\text{N}_2\text{H}_4) = 32 \text{ g/mole}$;

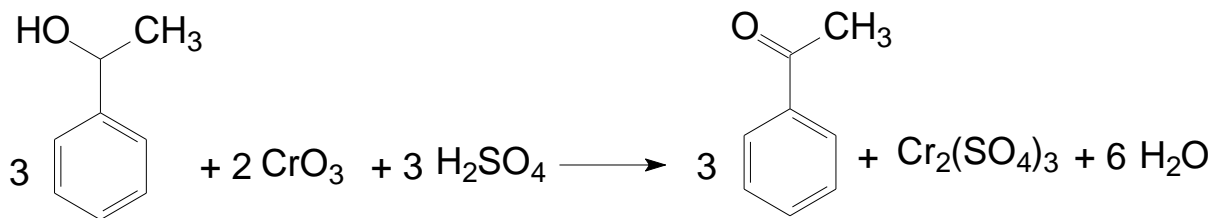
$FW(\text{NaCl}) = 58.5 \text{ g/mole}$; $FW(\text{H}_2\text{O}) = 17 \text{ g/mole}$.

$$\% \text{ Atom economy} = \frac{FW(N_2H_4)}{FW(N_2H_4) + FW(\text{NaCl}) + FW(\text{H}_2\text{O})} \times 100\% = \frac{32}{108.5} \times 100\% = 29.5\%$$

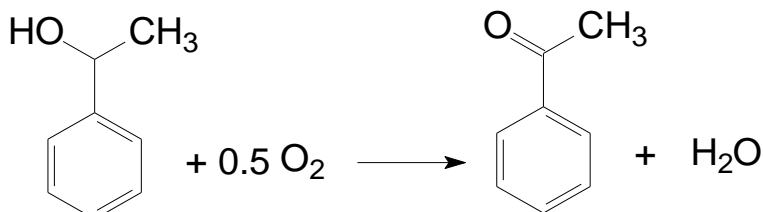
$$E - factor = \frac{FW(\text{NaCl}) + FW(\text{H}_2\text{O})}{FW(N_2H_4)} = \frac{76.5}{32} = 2.39$$

Example 2: Compare two methods of methylphenylketone production:

a) stoichiometric oxidation (Jones Reagent)



b) catalytic oxidation



$FW(\text{C}_6\text{H}_5\text{C}(\text{OH})\text{CH}_3) = 121 \text{ g/mole}$; $FW(\text{C}_6\text{H}_5\text{C}(\text{O})\text{CH}_3) = 120 \text{ g/mole}$;
 $FW(\text{O}_2) = 32 \text{ g/mole}$; $FW(\text{CrO}_3) = 100 \text{ g/mole}$; $FW(\text{H}_2\text{SO}_4) = 98 \text{ g/mole}$;
 $FW(\text{Cr}_2(\text{SO}_4)_3) = 392 \text{ g/mole}$; $FW(\text{H}_2\text{O}) = 18 \text{ g/mole}$.

Route a)

$$\begin{aligned}
 \% \text{ Atom economy} &= \frac{3 \times FW(\text{C}_6\text{H}_5\text{C}(\text{O})\text{CH}_3)}{3 \times FW(\text{C}_6\text{H}_5\text{C}(\text{O})\text{CH}_3) + FW(\text{Cr}_2(\text{SO}_4)_3) + 6 \times FW(\text{H}_2\text{O})} \times 100\% = \\
 &= \frac{360}{860} \times 100\% = 41.9\% \\
 E - \text{factor} &= \frac{FW(\text{Cr}_2(\text{SO}_4)_3) + 6 \times FW(\text{H}_2\text{O})}{3 \times FW(\text{C}_6\text{H}_5\text{C}(\text{O})\text{CH}_3)} = \frac{500}{360} = 1.39
 \end{aligned}$$

Route b)

$$\begin{aligned}
 \% \text{ Atom economy} &= \frac{FW(\text{C}_6\text{H}_5\text{C}(\text{O})\text{CH}_3)}{FW(\text{C}_6\text{H}_5\text{C}(\text{O})\text{CH}_3) + FW(\text{H}_2\text{O})} \times 100\% = \\
 &= \frac{120}{138} \times 100\% = 87.0\% \\
 E - \text{factor} &= \frac{FW(\text{H}_2\text{O})}{FW(\text{C}_6\text{H}_5\text{C}(\text{O})\text{CH}_3)} = \frac{18}{138} = 0.13
 \end{aligned}$$

It's clear through these three calculations that the route I for bromination of stilbene is much more atom economical (100%), compared to route II (68%) and route III (90.4%). It means that 32% of the reagents used in the bromination of stilbene in route II and 9.6% in route III were wasted. Despite the fact the Atom economy is 100%, E-factor is not 1 because it considers the use of solvent.

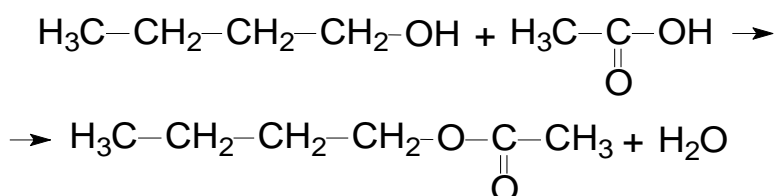
Effective Mass Yield

Effective Mass Yield (EMY) measures the environmental acceptability of a process. It is defined as the percentage of the mass of the desired product relative to mass of all non-benign materials used in its synthesis.

$$\text{EMY} = \frac{\sum m(\text{desired products})}{\sum m(\text{non - benign reagents})}$$

This metric requires further definition of a benign substance - by-products, reagents or solvents that have no environmental risk associated with them, for example, water, low-concentration saline, dilute ethanol, autoclaved cell mass, etc.". This definition is not clear, as nothing is non-benign (which is a subjective term) and the substances listed in the definition have some environmental impact associated with them. Despite the formula also fails to address the level of toxicity associated with a process, EMY can be used as one of the Green chemistry metrics.

Let consider the esterification of n-butanol with acetic acid

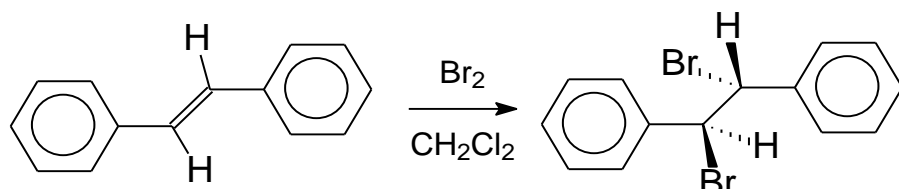


$$m(\text{C}_4\text{H}_9\text{OH}) = 74 \text{ g}; m(\text{CH}_3\text{COOH}) = 120 \text{ g}; m(\text{C}_4\text{H}_9\text{OOCCH}_3) = 80 \text{ g}.$$

$$\text{EMY} = \frac{m(\text{C}_4\text{H}_9\text{OOCCH}_3)}{m(\text{C}_4\text{H}_9\text{OH})} = \frac{80}{74} = 108\%$$

Example: Comparison of Green chemistry metrics for the different synthesis methods. Bromination of stilbene can be carried out in three different routes:

1. *Bromination in methylene chloride:*

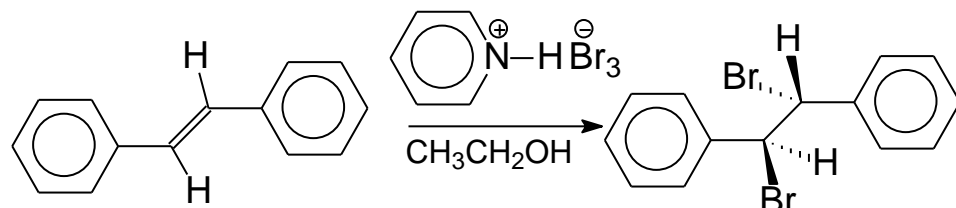


$$FW(\text{C}_{14}\text{H}_{12}) = 180.25 \text{ g/mol}, FW(\text{Br}_2) = 159.81 \text{ g/mol},$$

$$FW(\text{C}_{14}\text{H}_{12}\text{Br}_2) = 340.05 \text{ g/mol}.$$

Atom economy is 100.0%, E-factor = 7.46, EMY = 11.8%.

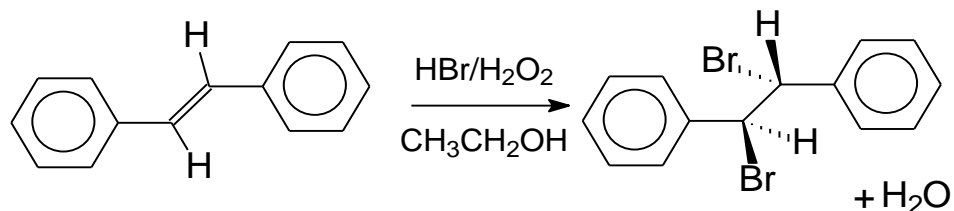
2. *Pyridinium tribromide in ethanol:*



$$FW(\text{C}_{14}\text{H}_{12}) = 180.25 \text{ g/mol}, FW(\text{C}_5\text{H}_6\text{NBr}_3) = 319.82 \text{ g/mol}, FW(\text{C}_{14}\text{H}_{12}\text{Br}_2) = 340.05 \text{ g/mol}, FW(\text{C}_5\text{H}_6\text{NBr}) = 160.01 \text{ g/mol}.$$

Atom economy is 68.0%, E-factor = 8.96, EMY = 62.3%.

3. Hydrogen bromide and hydrogen peroxide in ethanol:



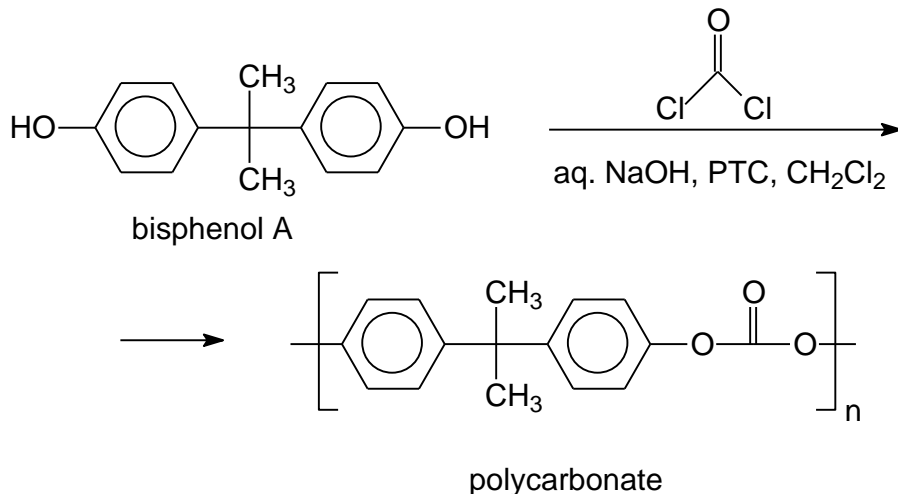
$FW(C_{14}H_{12}) = 180.25 \text{ g/mol}$, $FW(HBr) = 80.92 \text{ g/mol}$, $FW(H_2O_2) = 34.02 \text{ g/mol}$, $FW(C_{14}H_{12}Br_2) = 340.05 \text{ g/mol}$, $FW(H_2O) = 18.01 \text{ g/mol}$.

Atom economy is 90.4%, E-factor = 9.81, EMY = 11.8%.

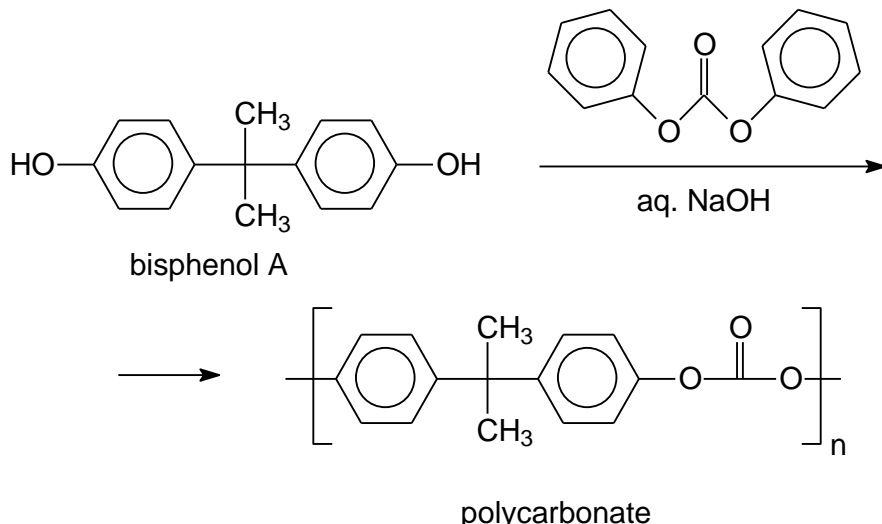
Reduced toxicity. Synthetic methods should use and generate substances that possess little or no toxicity to human health and the environment.

For example, the synthesis of polycarbonate. The first route through the phosgene process.

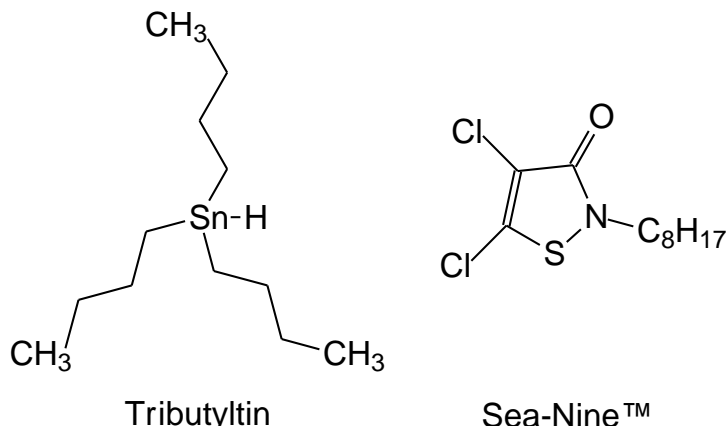
This route involves the utilization of a toxic reagent (phosgene) and large amounts of toxic solvent (dichloromethane). Produced polycarbonate is also contaminated with chlorine impurities.



An alternative route involves the use of diphenylcarbonate instead of phosgene, eliminates the use of dichloromethane and produces high-quality polycarbonates.



Another example, the tributyltin was used as an additive for ship paint to prevent the growth of marine organisms on ships. However, organotin compounds are persistent organic pollutants with extremely high toxicity for some marine organisms. Endocrine disruption is visibly expressed in gonochoristic marine snails.



A novel antifoulant Sea-Nine™ was developed, which demonstrates high acute toxicity, but no chronic toxicity.

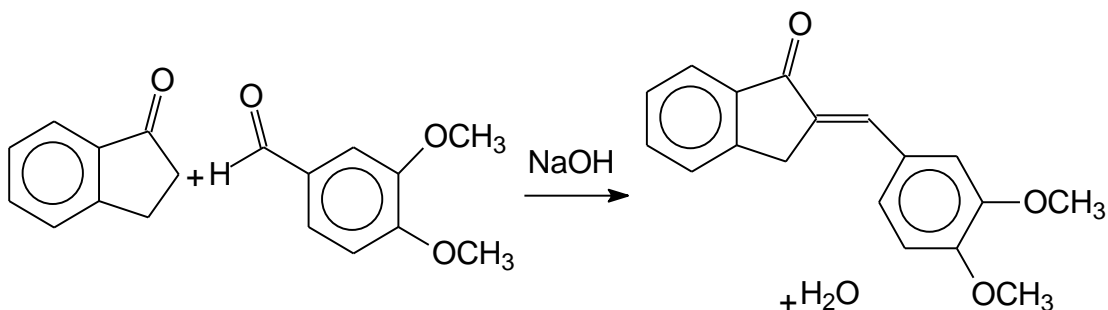
6.3. Green solutions in the chemical syntheses.

Safer solvents and auxiliaries

Organic solvents are commonly used in chemical syntheses, and these are the major sources of generated wastes. Such solvents are flammable, volatile and hazardous to human beings and the environment. There are two main approaches the problems caused due to these solvents can be solved. In the first approach, the solventless design. Many reactions can be carried out under the ‘neat’ conditions. But in solvent free techniques, many reactions are not possible, and many reagents and intermediates are not stable outside the solution.

The second approach is the replacement of organic solvents with greener solvents. Now a days, ionic liquids and supercritical fluids have been used quite commonly. There are some more compounds, which can serve as green solvents in chemical syntheses. The most popular among these green solvents are water, glycerol, polyethylene glycol, 2-methyltetrahydrofuran, cyclopentylmethyl ether, ethyl lactate, and so on.

Solventless Reactions. Solventless design of reaction can be used when all reagents and products are liquids which can react without solvent. For example, the Crossed-Aldol condensation:



Solvents are necessary for the synthesis of organic compounds, but their vapour creates air pollution. Therefore, efforts are being made to use solvents with high boiling points or to avoid solvent (solvent free reaction).

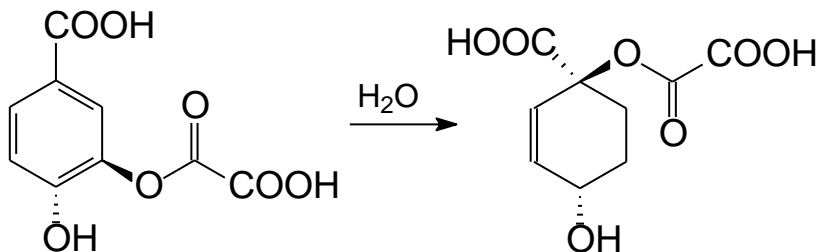
Solid state reaction is another alternative of solventless reaction. In such a situation, two fine grinded macroscopic solids interact directly and form a third, solid product without the intervention of a liquid or vapour phase (for example, oxidation, reductions, halogenations, hydrohalogenations, Aldol additions, elimination reactions, Aldol condensation reaction). However, not all reactions will work in the absence of solvent.

Green solvents

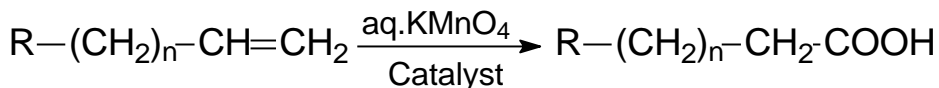
Water. Water is one of the green solvents. It is easily available, not expensive, safe, and non-hazardous to environment. Water is also a “universal solvent” in nature. Living cells represent the most complex chemical reactions (termed as biochemical reaction) and all such reactions occur in environment with >90% water. Both, inorganic and organic reactions are also carried out using water as a solvent.

Most of the important reactions in organic synthesis have been tried using water as a solvent or one of the components in the solvent mixture; of course, with some modifications in the conventional methodologies.

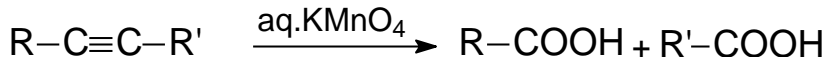
For example, in Claisen rearrangement of chorismic acid, pure water is used to promote the reaction.



Oxidation of alkene using aqueous solution of KMnO₄ and in presence of a phase transfer catalyst gives carboxylic acid with good yield.



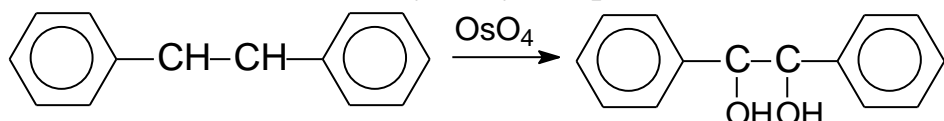
Alkynes can also be oxidized with formation of a mixture of carbonic acids



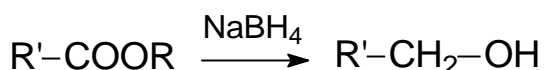
Polyethylene glycol. Polyethylene glycol is a linear polymer formed from the polymerization of ethylene oxide. It is available in a variety of molecular weights. The numerical designations of polyethylene glycol indicate the average molecular weight, for instance, PEG-200, PEG-400, PEG-2000 etc. Low molecular weight polyethylene glycols are liquid and completely miscible in water. Polyethylene glycols with high molecular weight are waxy white solids and highly soluble in water. The compound is inexpensive, non-flammable, biologically compatible, recoverable, non-toxic, thermally stable and biodegradable. Therefore, it can be considered not only as an environmentally benign solvent but also as biologically acceptable polymer, which has immense importance in drug delivery and approved for internal consumption.

Polyethylene glycols are used as the solvents for many organic reactions because they are stable to acids, bases, and high temperatures, not affected by oxygen, hydrogen peroxide or other oxidation systems.

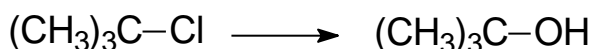
Can be used in the oxidation dihydroxy compounds of olefins



reduction of alkyl and acyl esters to the corresponding alcohols by sodium borohydride (NaBH_4)



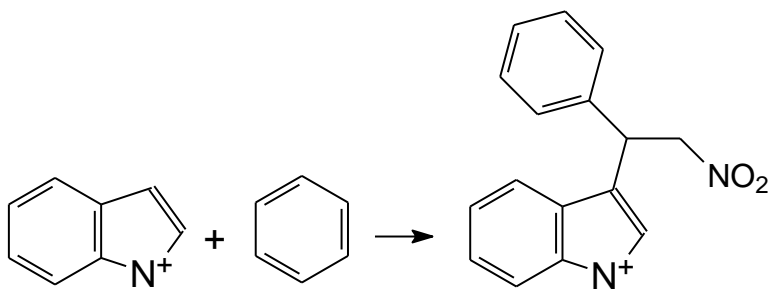
and substitution



and others.

Glycerol. Glycerol is another effective green solvent due to its polarity (capable for dissolving of polar and hydrophobic compounds low volatility (can easily be separated by distillation), low toxicity, low vapor pressure, low environmental impact, availability, easy handling, and storage).

For example, the addition reaction of indole to nitrostyrene was found with high yield under catalyst free conditions in glycerol.



Cyclopentyl methyl ether. Cyclopentyl methyl ether is new hydrophobic ether solvent with some unique properties - high hydrophobicity (simple separation and recovering from water, reduced emissions and wastewater), wide liquidity range (applications from lower to higher temperatures for accelerating reaction rate), low heat of vaporization (low energy consumption for distillation and recovery), relatively high stability to acids and bases,

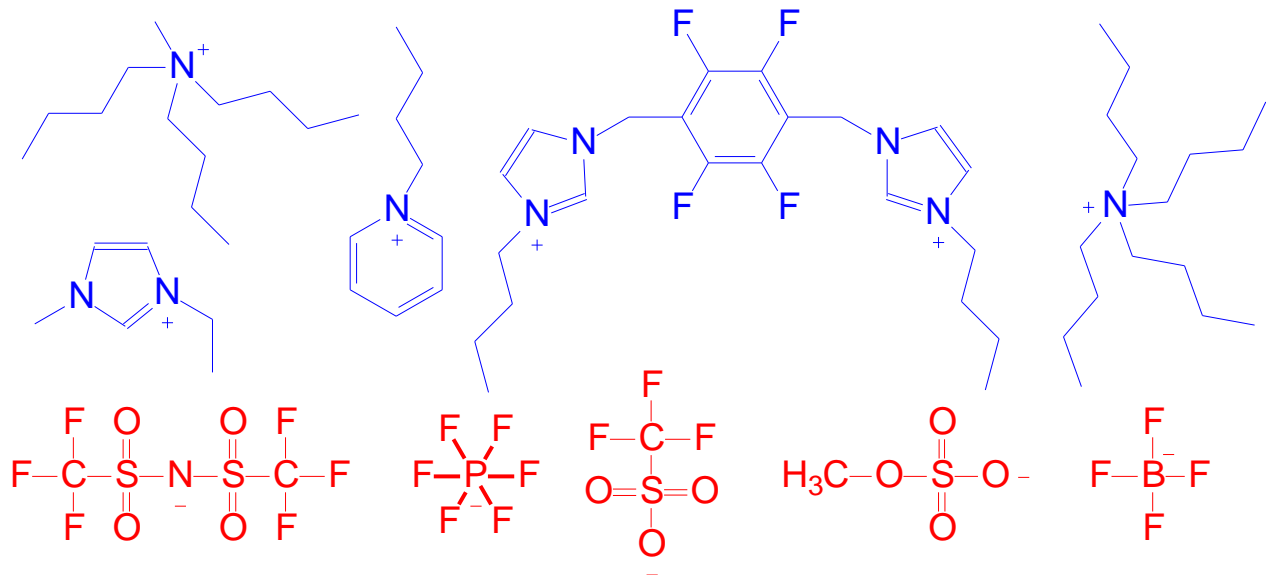
It has many properties that make it greener, easy to use and a more cost-effective process solvent for many types of synthesis.

Perfluorinated solvents. Perfluorinated solvents are highly fluorinated hydrocarbons based upon sp^3 hybridized carbon (perfluorohexane C_6F_{14} , perfluoroheptane C_7F_{16} , perfluorodecalin $\text{C}_{10}\text{F}_{18}$, perfluoromethylcyclohexane C_7F_{14} , perfluorotributyl amine $\text{C}_{12}\text{F}_{27}\text{N}$). They are found to be unique solvents due to the immiscibility with water and most of the common organic solvents and form third liquid phase, nontoxic, non-flammable, thermally stable, recyclable and having high ability to dissolve oxygen. Fluorous fluids have high density, low intermolecular interaction, low surface tension, low dielectric constant and high stability. Perfluorous liquids for example, perfluoroethers, perfluoroalkanes, perfluroamines and so on, exhibit unique characteristics, which make them suitable alternative to most of the common organic solvents. The boiling point of these liquids depend on their molar mass, and it is lower than the corresponding alkanes. The density of perfluorous alkanes is higher than water and other organic molecules. Oxygen, carbon dioxide and hydrogen like gases are highly soluble in perfluorocarbons. Thus, these perfluorinated hydrocarbons permit some selective and efficient oxidation reaction under mild conditions.

Ionic liquids. A new class of solvents has emerged, which are fluid in a wide range of the temperature. As these solvents have high boiling point, it means lower vapour pressure of that solvent, and hence, no volatile organic compounds are escaped from these liquids at lower temperatures.

Ionic liquids are made-up of two components: cations and anions, which vary with different types of groups. Some examples of most common cations (blue) and anions (red). The nature of the cations and anions has a significant influence on the properties of

these ionic liquids. The most employed ionic liquid anions are polyatomic inorganic species, halogens, and organic anions.

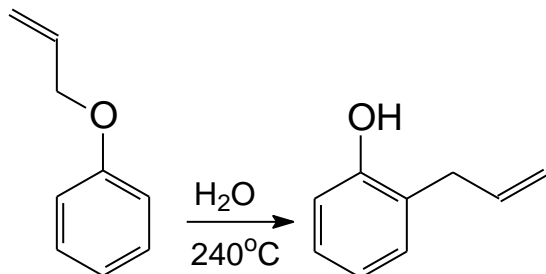


Ionic liquids are biodegraded via different pathways depending upon the length of the substituted alkyl chain. Biodegradation products are non-toxic to aquatic test organisms.

Supercritical fluids. Another green alternative of solvents are supercritical fluids. A supercritical fluid is a substance at a temperature and pressure above its critical point, where distinct liquid and gas phases do not exist. It can effuse through solids like gas and dissolve materials like a liquid. In addition, close to the critical point, small changes in pressure or temperature results in large changes in density allowing many properties of a supercritical fluid to be “fine-tuned”. Super-critical fluids are suitable as a substitute for organic solvents in a range of industrial and laboratory processes. Carbon dioxide and water are the most commonly used supercritical fluids, and also being used for decaffeination and power generation, respectively.

Water is described as superheated water, subcritical water or pressurized hot water between 100°C and its supercritical point at 370°C. Subcritical water has been used in synthetic organic chemistry because of having some unique properties different from those of ambient water. Water has similar properties to an organic solvent such as methanol, but also has some unique properties and these characteristics are lower viscosity as compared to water that results in faster diffusion of the compound, lower surface tension, higher solubility of polar compounds due to lower hydrogen bonding, increased heat capacity (in 2-5 times compared to liquid water), which improves transfer of heat, single homogeneous phase results in no interfacial mass transfer limitation.

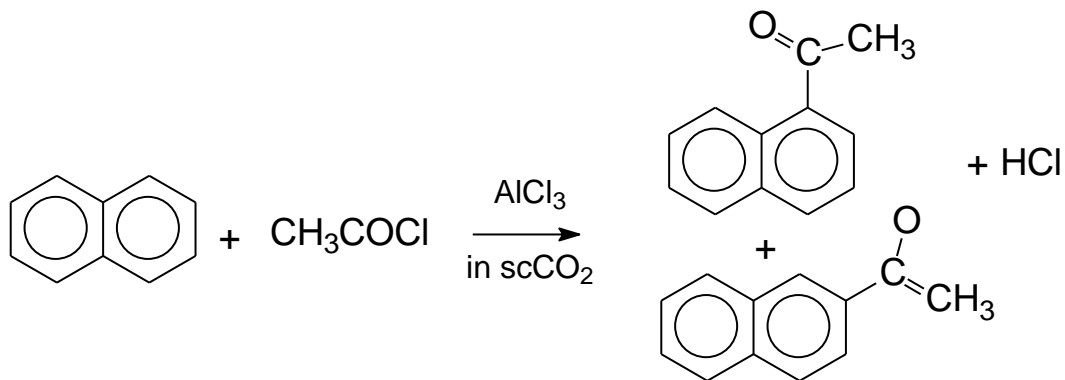
For example, Claisen rearrangement was reported in near critical water at 240°C in a microwave oven with 84% yield.



Carbon dioxide exists in three phases, that is, solid, liquid and gas. The solid phase of CO₂ is called ‘dry ice’ and it is used for cooling. The gas phase is well-known, and at atmospheric temperature and pressure the solid transforms to gas without liquification. Only in certain specified conditions, it can be liquefied. With the increasing pressure on gas or heating of solid CO₂, liquid phase can be achieved. The critical temperature of CO₂ is 31°C. At the temperature of -56°C and 5.1 atm, all three phases of carbon dioxide exist simultaneously. At 31°C and 73 atm, it exists as a supercritical fluid. At this condition, it has unique properties, that is, viscosity similar to the gas phase and density similar to the liquid phase.

Some advantages of supercritical carbon dioxide are a high diffusion rate offers potential for increased reaction rates, it has high compressibility (large changes in solvent properties with relatively small change in pressure), an excellent medium for oxidation and reduction reactions, no hydrolysis (which generally occurs in steam distillation), no thermal degradation products, high concentration of valuable ingredients and high extraction yield, environmentally benign solvent, high solubility toward hydrocarbons, ethers, esters, whereas polar compounds (sugars, tannins, glycosides etc.) are insoluble.

For example, the following transformation has been achieved by using Friedel-Crafts reaction in supercritical carbon dioxide:



The supercritical CO₂ is also used for extraction of natural products: essential oils from turmeric, coriander, ginger, ajowan, and extensively used for natural coffee decaffeination.

Renewable raw materials.

A raw material of feedstock should be renewable rather than depleting wherever technically and economically practicable. For example, plants are in use for the obtaining of pesticides, medicines or phytomediated synthesis of nanoparticles.

The production of metal and metal oxide nanoparticles is growing every year due to the interest to this kind of materials. Generally, convectional chemical methods of NPs synthesis involve using two groups of chemicals: reducing (sodium borohydride, methoxy polyethylene glycol, potassium bitartrate, hydroxylamine, and hydrazine) and stabilizing agents (polyvinyl alcohol, polyvinylpyrrolidone, hexadecyltrimethylammonium bromide). Some of them belongs to toxic compounds. This problem even more significant due to the fact, that synthesis of nanoparticles is the interaction of highly diluted solutions ($<0.001\text{ M}$). Therefore, the production of 1 g of nanoparticles resulted of large volume of solutions which are diluted but often still toxic.

Plant extracts usually contain bio-reductants, capping and stabilizing agents, obviating the need for additional reagents.

The variability of different classes of organic compounds in the plant extracts helps to design various sizes and shapes of final nanoparticles. For instance, Fig. 6.1 presents the electron transmission microscopy images of spherical silver, spherical gold and triangular gold nanoparticles prepared with various plant extracts.

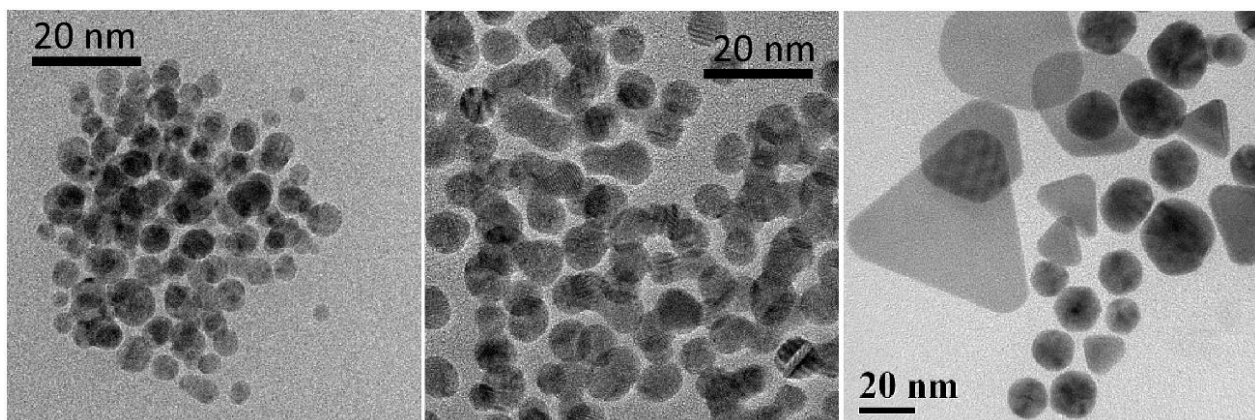


Fig. 6.1. Electron transmission microscopy images of spherical silver (left), spherical gold (middle) and triangular gold (right) nanoparticles.

The waste solutions after nanoparticle's synthesis contains the rest of plant extracts which normally are non-toxic.

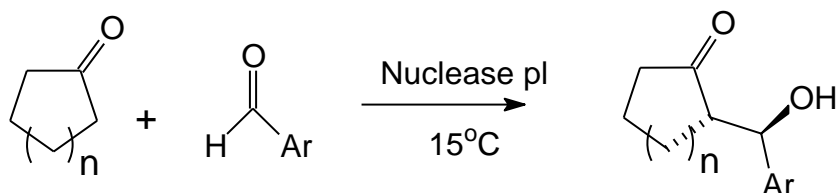
Catalysts

Many organic reactions of synthetic importance are slow, and catalyst need to be used to enhance their reaction rate. However, this catalyst may be toxic in nature, and it is important to find out some alternate catalyst, which is harmless or less toxic.

Such a job can also be done by any enzyme, which is also called biocatalyst or, in general, green catalyst.

Despite the fact, that homogeneous catalysis is preferable due to the higher reaction rate, heterogeneous catalysis, whenever possible, is a preferred and established method of waste reducing. This is because simple filtration or centrifugation facilitate the recovery of a heterogeneous catalyst from solution, leaving minimal impurities in the final product.

For example, nuclease p1 from *Penicillium citrinum* is able to catalyse asymmetric aldol reactions between aromatic aldehydes and cyclic ketones under solvent free conditions.



Green manufacturing involves production processes, which use inputs with low environmental impacts, which are highly efficient and generates little or no waste or takes care of pollution. It involves source reduction (also known as waste or pollution minimization or prevention), recycling and green product design.

Green products

Searching for green alternatives for the everyday products we consume, can have a beneficial impact on water and soil quality, reduce energy uses and the amount of pollution or waste by using concepts (catalysis by design, biodegradable consumer products) and accelerated application of green technologies and products. Therefore, the customers getting gradually concerned about the environment friendly products and the world market is drifting toward the recyclable or decomposable home appliances, hardware equipment and daily life products.

Bioplastics. Recently, the trend of plastic polybags ban occurs across the world because plastic waste are almost non-biodegradable. This have a dramatic effect on animals.

Bioplastics are a form of plastics derived from renewable biomass sources, such as vegetable fats and oils, corn starch, cellulose, biopolymers, or microbiota displays a high-market potential because of their additional advantage of biodegradability in 10–15 years. Currently used plastics derived from petrochemicals, constitute a sustainable alternative to conventional oil-based plastics, which degrade in 100–150 years.

Naturally produced bioplastics are *polyhydroxyalkanoates* (poly-3-hydroxybutyrate, polyhydroxyvalerate, polyhydroxyhexanoate) and *renewable resource* (polylactic acid etc.). A novel and cost-effective polymerization technology

has been developed to produce high-quality bioplastics, with improved thermal stability up to 200°C.

Green fuel. Hydrogen has attracted great attention of scientists, environmentalists, and industrialists as a benign fuel of future because of its capability to produce pollution free energy (no carbon emission and useful by-product of hydrogen fuel combustion that is only water) with highest energy density (140MJ/kg).

Despite that the transition will be very messy, and will take many technological paths but the hydrogen-fuel cells expected to be the future". The actual hydrogen production is derived from fossil fuels (coal, oil, and natural gas). Therefore, the success of hydrogen technology will depend on the efficient generation of hydrogen from water cleavage powered by renewable sources (such as solar or wind).

Green pesticides. The modern agriculture is dependent from the pesticides. Many of them are hazardous for human health and ecosystem. Therefore, there is a big interest to green pesticides that are derived from organic sources, which are considered environment friendly and causing less harm to human and animal health, and to habitats and the ecosystem.

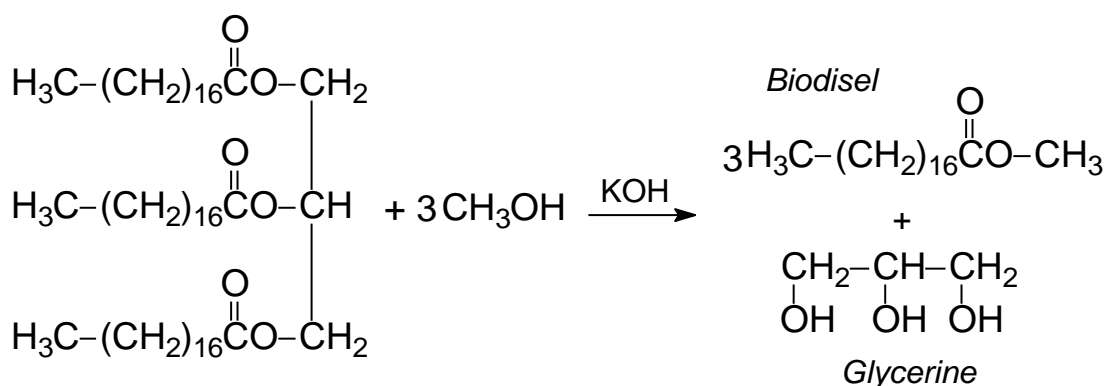
Biopesticides are generally safer than synthetic pesticides, but they are not always more safe or environment friendly than synthetic pesticides. Some examples: spinosad (shows high selectivity in destroying harmful pests and leaving beneficial insects alive), Wormwood extract, Chive extract, Summer tansy dust, Stinging nettle extract, Daffodil extract, Garlic extract, Rhubarb extract, Onion extract, Sambucus extract, Tobacco extract, and Stale beer. Sulfur (organic fungicide, pesticide, and acaricide), Bio-S (sulfur mixture), Pilzvorsorge, Spruzit, Carbofineum, Basalt dusting powder, Gene silencing pesticide, and Steam (Thermal pest control).

Green building construction materials. Green concrete (cements) is another resource saving structures with reduced environmental impact in term of CO₂ emissions, energy saving, and waste water. The traditional cement making is environmentally destructive process that includes extraction and mining of limestone, transportation of materials and high energy consumption (over 7% of all green-house gas emissions worldwide are caused from the manufacturing of Portland cement).

The utilization of alternative raw materials and energy saving strategies, like use of fly ash, waste glass, waste fibre glass, blast furnace slag, volcano ash, metakaolin or calcined clay, calcined shale, rice hull ash, calcined shale, municipal solid waste incinerated product, and alternative fuels (sewage sludge, etc.) to develop or improve cement with low energy consumption belongs to main trends in the development of a new green cements.

The new types of cement with reduced environmental impact are more cost effective and friendly to environment. For example, geopolymmer concrete. Geopolymers are amorphous alumino-silicate binding materials synthesized by polycondensation reaction of geopolymeric precursor, and alkali polysilicates. Main ingredients of geopolymers includes the fly ash, sand aggregates, alkaline liquid (sodium silicate and sodium hydroxide solution, water, and super plasticizer).

Biodiesel. One of the priorities of Green chemistry is utilization of benign and renewable feedstocks as raw materials. Therefore, combustion of fuels obtained from renewable feedstocks would be more preferable than combustion of the fossil fuels from depleting finite sources. The production of biodiesel oil is a promising green option. In this technology, fat embedded plant's oils are converted into the biodiesel via a transesterification reaction by using methanol and caustic or acid catalysts. The triglycerides are converted into the methyl ester and glycerol during these reactions. Production technology allow to use a greater range of feedstocks (i.e., used cooking oil). Another advantage, that product does not need to be washed to remove catalyst, and is it easier to design as a continuous process.



Conclusions



The green chemistry movement have been obtained popularity in the early 1990s. Since that time, there have been major contributions from all around the globe, with thousands of publications in this area. A chemist needs to have the tools to conduct the selection of reagents and metrics to assess the changes being made to achieve an efficient, environmentally benign synthesis.

Many tools have been developed for measuring how green the processes are during recent years. First, the concept of atom economy which measures the efficiency of raw material use was introduced. Then, the E-factor analysis that quantifies waste generation was developed. Later, twelve principles of green chemistry which claims that prevention is better than cure were formulated.

There are 12 Green Chemistry Principles: wastes prevention; atom economy; safer synthesis; safer chemicals; safer solvents and auxiliaries; energy efficiency; renewable feedstocks; derivatives minimization; catalyst; design for degradation; real-time analysis; accident prevention for safer chemical production.

Searching for green alternatives for the everyday products we consume, can have a beneficial impact on water and soil quality, reduce energy uses and the amount of pollution or waste by using concepts (catalysis by design, biodegradable consumer products) and accelerated application of green technologies and products. A novel and cost-effective polymerization technology has been developed to produce high-quality bioplastics, with improved thermal stability up to 200°C.

Hydrogen has attracted great attention of scientists, environmentalists, and industrialists as a benign fuel of future because of its capability to produce pollution free energy with highest energy density.

Biopesticides are generally safer than synthetic pesticides, but they are not always more safe or environment friendly than synthetic pesticides.

Green concrete (cements) is another resource saving structures with reduced environmental impact in term of CO₂ emissions, energy saving, and waste water.

The new types of cement with reduced environmental impact are more cost effective and friendly to environment. One of the priorities of Green chemistry is utilization of benign and renewable feedstocks as raw materials.

Questions for self-control

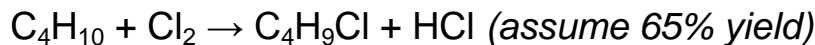
1. What is green chemistry?
2. What is the distinction between yield and atom economy?
3. What are the major basic principles of green chemistry?
4. Calculate the Atom economy and E-factor for the obtaining of hydrogen through the reaction:
 - a) C + H₂O → H₂ + CO (*assume 75% yield*),
 - b) 2H₂O → 2H₂ + O₂ (*assume 80% yield*).
5. Calculate the Atom economy and E-factor for the preparation of ethanol through the reaction:



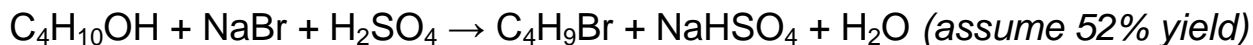
6. Calculate the Atom economy and E-factor for the synthesis of bromoethane through the reaction



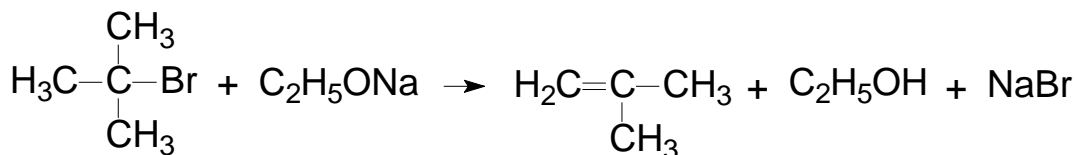
7. Calculate the Atom economy and E-factor to produce chlorobutane through the reaction



8. Calculate the Atom economy and E-factor for the preparation of bromobutane through the reaction

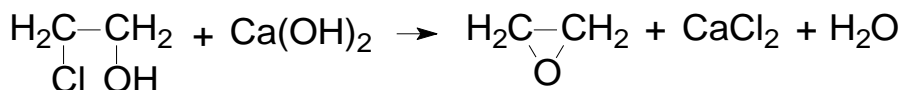
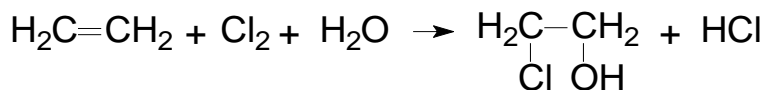


9. Calculate the Atom economy and E-factor for the obtaining of methylpropene through the reaction

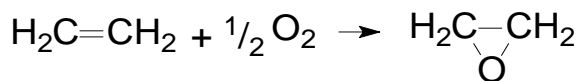


10. Compare the Atom economy and E-factor for the preparation of ethylene oxide through the different reactions:

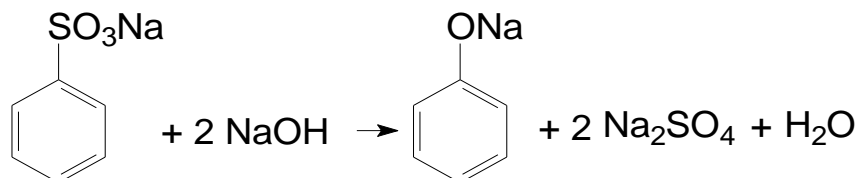
a) the chlorohydrin route (assume 52% yield)



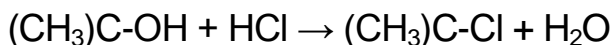
b) catalytic oxidation (assume 72% yield)



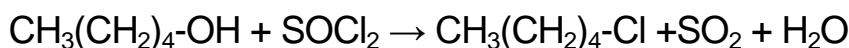
11. Calculate the Atom economy and E-factor for the preparation of sodium phenolate through the reaction



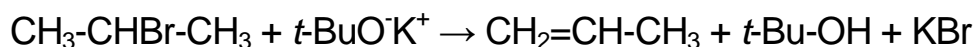
12. Calculate the Atom economy and E-factor for the synthesis of 2-chloro-2-methylpropane through the reaction



13. Calculate the Atom economy and E-factor to produce 1-chlorohexane through the reaction



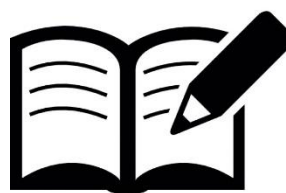
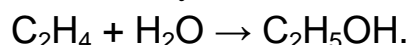
14. Calculate the Atom economy and E-factor for the synthesis of propene through the reaction



15. Compare the Atom economy of reactions of preparation of copper



16. Production of ethanol from ethylene:



References

1. Clark, James H. a Duncan J. MacQuarrie. Handbook of green chemistry and technology. Malden, MA: Blackwell Science, 2002. ISBN 0-632-05715-7.
2. Anastas, Paul T., and Warner, John C. Green Chemistry Theory and Practice, Oxford University Press, New York, 1998.
3. Ameta, Suresh C. and Rakshit Aameta. Green chemistry: Fundamentals and Applications. New York: CRC Press Taylor & Francis Group, 2013. ISBN 978-1-4665-7826-5.
4. McKenzie, Lallie C., Lauren M. Huffman and James E. HUTCHISON. The Evolution of a Green Chemistry Laboratory Experiment: Greener Brominations of Stilbene. Journal of Chemical Education. 2005, 82(2). ISSN 0021-9584. Available from: doi:10.1021/ed082p306
5. Mariychuk, R., D. Grulova, L.M. Grinchenko, R.P. Linnyk and V.V. Lisnyak. Green synthesis of non-spherical gold nanoparticles using *Solidago canadensis* L. extract. Applied Nanoscience. 2020, 10(12), 4817-4826. Available from: doi: 10.1007/s13204-020-01406-x
6. Mariychuk, R., Porubská, J., Ostafin, M., Čaplovíčová, M., Eliašová, A. Green synthesis of stable nanocolloids of monodisperse silver and gold nanoparticles using natural polyphenols from fruits of *Sambucus nigra* L. (2020) Applied Nanoscience (Switzerland), 10 (12), pp. 4545-4558. Available from: 10.1007/s13204-020-01324-y

Chapter VII

THE ROLE OF THE ENVIRONMENTAL ETHICS AND PROJECT-BASED LEARNING IN THE EDUCATION OF ENVIRONMENTAL ENGINEERS



In this section you will learn about

- ✓ Definition of environmental ethics and its trends;
- ✓ Pedagogical methods of environmental education;
- ✓ The strategy and methods of project-based education;
- ✓ Evaluation of a project based environmental course.



Keywords:

Education of environmental engineers
B.Sc. level
Ethical environmental awareness
Project-based education

The engineers can act responsibly in their profession if they manage to combine high level of expertise with principled ethical behavior. This expectation is also phrased in the Code of Ethics of the Hungarian Chamber of Engineers, as well as in the Training and Output Requirements. Our education system contains the development of competencies: high theoretical knowledge, practical trainings and ethical point of view. This study focuses on the environmental engineering education (B.Sc.) from the point of view of ethical aspects. Principles of environmental ethics, incorporated into the various disciplines, can develop environmental awareness and formation of ecological thinking. Our teaching strategies, which achieve these goals, includes development of ethical thinking as a main aspect. The project-based education system is an effective way to get high-level theoretical and practical knowledge as well as ethical attitudes

The knowledge-based society of the 21st century expects up-to-date learning from the high-level educational institutes. This learning must be appropriate to answer the challenges of environmental difficulties of the last 50 years, and to give guidelines for solutions of these problems in the present time and the future. As Schumacher showed well in its book "Small is Beautiful" : The most important role of education is to teach, what we can do in our life perspectives. The key issues are non-technical, but ethical. The lack of wisdom will cause catastrophic situations. We can survive if we gain more wisdom with ethical attitudes.

The bases of right decisions are wisdom, prudent judgment for the truth, critical thinking and responsibility for the future. The educations, mostly the high-level educations can promote to get these abilities. The Report of Club of Rome has established the importance of skills-building innovative learning in 1972 . New attitudes need to be developed, which make the humankind to be appropriated for global responsibility and solidarity. Education has crucial role to build up the following virtues: foresight, estimations of consequences of present actions. A good learning program teaches team works, to built up mutual trust, and fair share of goods of humankind. The adaptation of the new type of learning is expected as a possible way of surviving. Can the society revise its traditional thinking, and preferences, and manage the necessary alterations? Every member of human society has to develop his or her ability for making the necessary changes. One of the most important parts of new thinking is the lifelong learning practice. The previously listed skills are particularly important for environmental engineers because they can directly influence environmental transformations and preservations. Namely,

improving our environment is the most emerging task of the humankind. There is no future without accepting the sustainability concept.

It is not enough to get knowledge in technical, natural, economy and law sciences for the environmental engineers, but it is also very important to get ethical thinking for them. It is good to note: the healing of the difficulties of humankind is not possible without moral basis.

There are two basic concepts of the environmental policy: technical conditions of environmental protection and ethical attitude, which are closely connected to each others. The environmental protection cannot be successful without technical and financial background. However, the previously mentioned conditions are not enough if the environmental attitudes and environmentally conscious behavior are missing. These are the reasons why it is so important to create an ethical and ecological attitude for environmental engineers in our education system.

The role of education has been already emphasized in United Nations Conference on Environment and Development, Rio de Janeiro, Brazil, 3-14 June 1992. The agenda for 21 century shows several targets in this field. For 40 years, the scientists and authorities have done a lot to draw attention for the environmental difficulties and they solved many of them. However, a lot of troubles have been unsolved. The better education can be an appropriate solution, to improve the environmentally conscious behavior of people. It is important to emphasize the overwhelming parts of technical difficulties can be solved with recent methods, but the extinct species and ecological communities cannot be restored. Our future depends on us. The essence of the processes influencing the environment must be understood and these processes must be steered in the right direction. High-level education has a key role in the dissemination of environmental awareness attitudes and supporting the transformation of environmental ethics into social practices.

7.1. Definition of environmental ethics and its trends.

The role of the engineers is very important in environmental protections, water management, forestry, and agriculture. Namely, the environmental engineers make momentous strategic decisions, which influence of the environment to a large extent. The right decisions require deep ecological knowledge and ecological thinking. These attitudes are necessary to stop the fast destruction of natural values and other unfavorable changes in the environment.

The significant part of leading scientists and authorities have poor knowledge and sense in the field of environmental difficulties. They concentrate only on the

technical and financial aspects. Their education and socialization happened many years ago, when the troubles of the environment were not so obvious as today. This is one of the reasons why their plans decisions and actions underestimate the environmental difficulties. The troubles of environment can be solved only with new ecological sensitive thinking. To get more data is not enough to realize the real harm. New knowledge and new attitudes are required to solve the ecological difficulties. An up-to-date high-level education must emphasize the environmental issues, including environmental ethics.

The priority role of environmental ethics is to create a new type of thinking promoting the formation of an ecologically responsible society. Only a new environment conscious society can preserve our environment. For example, the water management actions must take consideration of the sport, drinking water, air quality, climatic aspects and mostly the ecological consequences. People, who build a cistern in their garden spare tap water, decreasing the volume of environment destruction water cleaning productions.

The ecological considerations have come to the forefront in the water management policy even in the inland water treatments. An inland water investment can decrease the volumes of flooded areas in the rainy periods, but these areas need water sprinklings in the dry seasons. Moreover, there are several water habitats die off, unwanted microclimatic changes happen, buffering effects of water bodies decrease toward to the point pollution sources, as a consequence of hydrological action. It is obvious a hydrological action on inland waters has ecological side effects, which can be managed with a good ecological attitude. The ecological troubles of Nasser dam are well known. Such cases can be avoided with an environmental cautious attitude in recent and future investments.

The necessity of a new environmentally friendly engineering attitude was already stated in 1931. The character of a good senior engineer consists of 50% moral strength, 25% general literacy and 25% technical knowledge. These requirements harmonize with the guidelines of the “Ethical Code of the Hungarian Chamber of Engineers”. The environmental ethics imposes obligations toward to the natural landscapes, animals, plants, and ecosystems, not only toward to humans. These are requirements that refer not only for the present, but for the future too. Environmental ethics deals with the human attitudes toward to biosphere and landscape in a philosophical basis. Its task is to judge the actions from moral aspects in the environment. The principles of environmental ethics define morally acceptable behaviors, and they can determine if an action is good or bad.

The environmental ethics has a double profile: it establishes the basic principles and judges the individual cases. The statements of the environmental ethics

are based on the scientific and social results of various branches of environmental sciences. The scientific and ethical bases are necessary to explain why something is good or bad.

The trends of various branches of environmental ethics differ from each other's in their concepts of the most important preserving goals and the moral status of a certain object. The "selfish" trend is human-centered, where the most important factor is the short-term human interests, and it does not care to much for the long-lasting effects on the environment. Ethical egoists keep the right to make decisions without caring for the environment. This trend also includes the deist concept, which declares the supernatural characters of humankind coming from divine will. The other trend is sustainability, which takes emphasized consideration to the long-lasting effects in the environment. Humanistic ethics keep in mind ecological factors emphatically.

The anthropogenic ethics concentrates for only the human beings. Biocentric environmental ethics preaches the sanctity of life, like the Buddhist philosophy. On the other hand, the ecocentric ethics trend takes care of the whole ecosystem without favoring any branch in a holistic way. The essences of this ethics is tolerance, the pursuit of understanding and cooperation, the acceptance and appreciation of the diversity of life. These factors must combine the responsible behavior and activities of the engineers. Such an ethics can be obtained effectively through a modern environmental education.

7.2. Pedagogical methods of environmental education.

The primary purposes of environmental education are environmental awareness, constructive lifestyle, high level of knowledge with high responsibility. The constructive lifestyle has a structured action scheme with responsibility in its center (Fig. 7.1).

The responsible behaviors manifest in the independence, freedom, and decisions of individuals. The self-determination expresses in self-controls, restraints, cooperation abilities and self-responsibility for actions. The individuals show-up to themselves in freedom taking consideration to the other's freedom. These individuals try to express their permanently developed inside values. They work out compromises with others. They do not subjugate the environment, but they harmonize their actions with the requirements of nature. Their deep knowledge helps them to solve the difficulties. The main aspects of cooperation are knowing and compile the disciplines without circumvention of the rules.

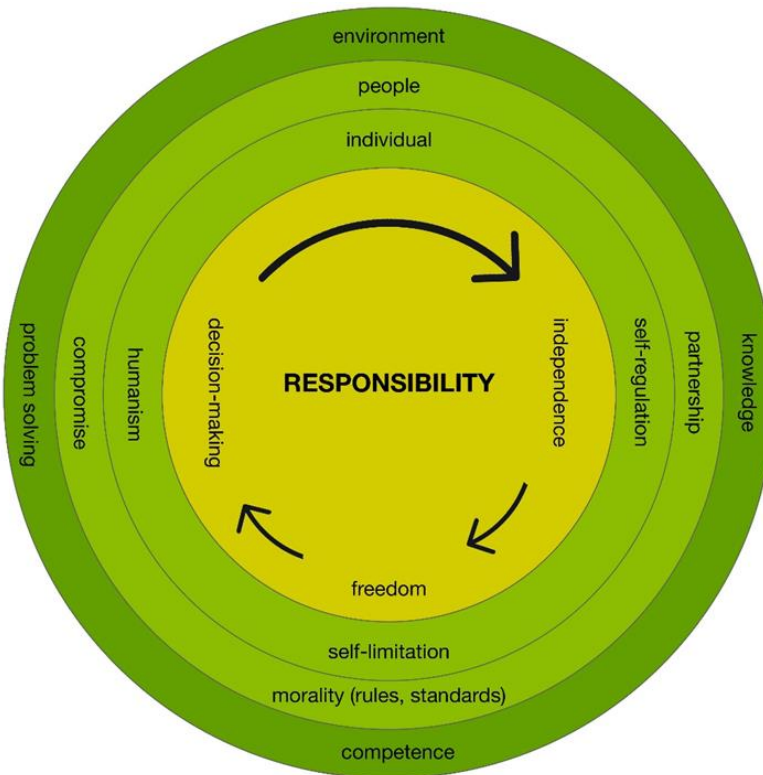


Fig. 7.1. Structure of constructive lifestyle.

The lack of deep knowledge and ecological thinking were the main reason for the red mud industrial catastrophe in Ajka. The walls of a giant storage reservoir of the red mud collapsed on 04.10.2010. The red mud flood swamped 1017 hectares and killed 10 people. The extremely alkaline flood destroyed the ecosystems along with flood (several tenths of kilometers). The catastrophe was caused by several reasons: too much amount of the highly basic mud in the cassette, lack of the alarming system, breaking several rules and standards. The ecological aspects were totally neglected, in the time of planning of the cassettes and during its operation. Moreover, the gypsum, which was applied for neutralization of basic sludge, also caused long-lasting ecological difficulties in several tenths of kilometers long. The red mud catastrophe made it obvious, that even a big economic advantage does not allow such economically dangerous practice.

Responsible people must have environmental awareness characters to avoid such catastrophes in the future. Their emotions have to play an important role. The will of preservation, protection of natural and environmental values, creativity, sense of responsibility are the most important requirements in the ecological correct actions. Deep knowledge of the environment promotes correct thinking and environmentally conscious behavior. These give appropriate behaviors toward to

environment, which are realized in moral conducts.

The basics of environmental awareness education is illustrated in Fig. 7.2.

A large amount of knowledge is required to be familiar with the environment: rules of nature, sociological aspects, economic situations, and environmental law. Understanding the theory of sustainability and the importance of lifelong learning are also crucial to make the right decisions.

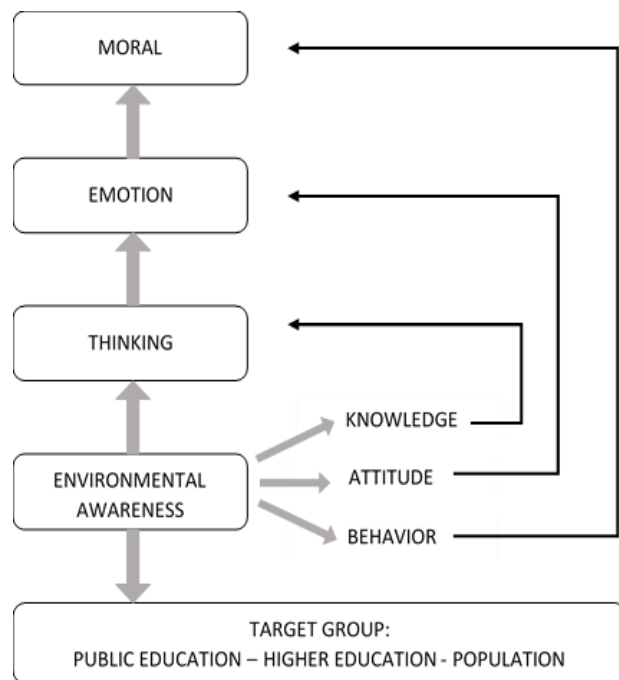


Fig. 7.2. The structure of environmental awareness education.

The theoretical knowledge is not enough for the appropriate decisions. It is necessary to learn examples, projects and tasks from real life for the decision-making persons. Experience, empathy, and self-examination are also required elements of gaining wisdom. The theoretical knowledge is crucial part of higher education, but they are not enough for wisdom. The practical trainings help to recognize the real situations and arouse the interests of students. Project-based education is an excellent method to get practical knowledge under real situations for years.

7.3. The strategy and methods of project-based education.

Project-based education is a problem-oriented open education strategy. It includes task-oriented structured student activities. These tasks improve the skills, knowledge, and abilities of students. This system guides the student from the wording of the problems to solving them. The result of the education processes is realized in successful solutions of certain problems. Moreover, project-based education helps to develop the environmental awareness attitude under real-life conditions. The

independently done explorations and solutions promote the lifelong learning attitude of the pupils. During self-regulated learning, the students can formulate their personal goals in accordance with their own needs and ability. A well-solved project gives positive motivations and suggests further learning and activity for people.

There are three well-separable activity groups during the project-based education.

1. The students choose a problem to solve which can be suggested by the teacher. The first step is to recognize and understand the subject of the project. Students have to establish the consequences of the problem to be solved. They recognize causal relationships and select the main target. The groups divide to subgroups with the determination of the responsibility and aims of different subgroups. Every individual gets their own defined task in the subgroups. Of course, the targets must be in accordance with conditions (time, money, instrumentation knowledge etc.).

2. The next steps are the detailed planning and workout periods of the actions. The detailed plan is constructed for the solution of the subtask. Data are collected, activities are divided to different persons, the appropriate experiments are chosen, timetables are laid down (what, who, how) in these periods. The group leaders and responsible persons are selected by participants. If it is necessary, some modifications are taken in the subtasks.

3. The gained data are collected, sorted, understood, and evaluated. Finally, the results are presented

The Table 7.1 summarizes the main features of project-based education methods in the different phases.

Table 7.1
The summary of project-based education

The systematic structures of project-based education			
Activities	Tasks	Methods	
Drafting of the project	Definition of problem Determination of target Choosing theme Designations of main	Methods to help learn individual goals	consultative thinking
			retrospective judges
			target in a broader view
			chats
			prepared discussions
			definition of the target
			small lectures of the students
			role plays

	and sub-objectives		reports explanations illustrations
			observations experiments measurements collections analyses planning's investigations data processing interpretations, comparisons sorting research surveys interviews explorations field works creations case studies learning contracts homework impact assessment
Planning, elaboration	Gaining experiences Data collections Determination of duties Wording of causal relationships Sharing the tasks	Methods that promote independence, creativity and research	
Implementation	Analysis and interpretation of data, Data processing, systematizations Problem solving Product preparations	Methods of cooperation's	project methods cooperative actions Games role plays situation role plays field practices quizzes competitions guided tours event organizations

7.4. Evaluation of a project based environmental course.

A project-based education program was launched for B.Sc. environmental engineer students, pursued the guidelines of table 7.1. The title of the project was “Evaluation of water pollution of a low water stream”.

The project emphasized the following educational purposes:

- built-up and further develop the ecological thinking,
- acquisition the environmentally conscious behavior and lifestyles,
- adaptation of the systematic working approach,
- developing a holistic and global approach,
- educating theory of sustainability and promoting to accept its principles,
- teaching the environmental ethics to adopt the ethical engineering attitudes,
- developing tolerance and a supportive lifestyle,
- creating civic responsibility.
- developing the ability to recognize causal relationships,
- problem-solving thinking, development of decision-making skills,
- improving the communication skills,
- developing cooperative skills and helpfulness skills,
- building-up organizational skills, strengthening self-confidence,
- developing the critical thinking and creative problem solving,
- creating and developing the responsibility attitudes.

The actions of our project aimed at the observation of the sustainable use of water, recycling the water, and protection of ecosystems of water. These activities strengthened the environmentally conscious attitudes, ecological point of view, and environmental responsible characters of students.

The final result of the project showed the ecological status and ecological mapping of the chosen low water stream (Aranyhegyi patak). The project was made according to the guidelines of water framework directives (WFD), showing a good example for the survey of other low water streams.

The used methods followed the figures of table 7.1. because they were well constructed and practical orientated. The crucial parts of the project were the field surveys, field, and laboratory measurements of the students. The pupils could get experiences under realistic conditions, which will be useful in their further careers. The raw data were the measured, observed and literature parameters. The data were compared to the previous measurements and legal limits. Such comparisons show the ecological and chemical status of this low water stream.

The project significantly improved the positive attitudes of the students. They could also explore causal relationships, which were one of the most important duties of environmental engineers.

This case study guided the students from the recognition to the solution of a problem. This case study can be a supplement of the CV of the students. The objectivity, reliability, decision making ability characters of the students improved during the project, moreover they got a lot of knowledge.

The students worked independently on their chosen topics, but they consulted each other's to reach the common goals. The personal duties improved their sense of responsibility and sense of reliability.

The pupils learned cooperation during the group activity, recognizing the importance of common work to achieve their targets. The common activity helped the development of helpfulness tolerance emphatic characters. This cooperation ability will be also useful on their workplaces, to solve personal conflicts too.

The consultative thinking promoted opinion-forming, judgment-making, and step-by-step thinking methods. Listening to other opinions improved the tolerance, discussion skill, cooperation ability of members of the groups.

The intrinsic motivation method promoted getting as much knowledge as possible. This also supported the adaptation of the lifelong learning practice.

Project evaluation tasks were also very important. The lectures improved structured communication, verbal expressiveness, and willingness to debate. The written works helped to develop the structured presentation, systematic writing, structured well readable style and editorial skills. The statistical evaluations taught the student for using data sources, and the validation of their own data.

The success of the completed work gave pleasure, increased the student's self-confidence, and aroused the desire to do another research and work. The developed skills will be also realized in the future careers of the participants of the project.

Conclusions



One of the crucial requirements of engineering education is to harmonize theoretical knowledge to practical-orientated skills. These expectations are more emphasized in the education of environmental engineers because several of them will do fieldwork. Their educations must include environmental awareness, ethical thinking too. The unsolved environmental difficulties of the last decades draw our attention for the necessity of environmentally conscious attitudes. Probably the overwhelming part of the environmental difficulties do not result of the lack of appropriate technological knowledge.

The reason of these difficulties came from the lack of sense of responsibility toward to environment. The ethical attitude, the main competence, can only be the key to our survival in the future. According to the leading scientists, technical

knowledge is not enough for solving environmental troubles, but ethical attitudes are also necessary for success. The environmental ethics is dealing with not only humans, but the natural environment, animals, plants, whole ecosystem has also a central role in it. Moreover, the environment ethics takes into consideration the present as well as future. “We do not inherit the earth from our ancestors; We borrow it from our children”

The ethical aspects are very important in the engineer practices, and in more emphasized the way in the works of environmental engineers works. The ethical attitudes of environmental engineers must be evolved during their education. Competence-based higher education is an effective way to create ethical environmental attitudes. The effective environmental protection requires high-level professional knowledge, deep scientific background and ethical thinking.

Project-based education is appropriate to give theoretical knowledge as well practical skills. A project-based course combines the classroom, literature search, field practice, laboratory measurements, data processing, data evaluation, report writing and presentation studies. The students become also familiar with effective cooperation, good communication, realistic timing, and program management under realistic conditions. Project-based education is also an effective method to build up the environmental ethic attitudes of the students.



Questions for self-control

1. What is the environmental ethics?
2. Describe trends of the environmental ethics.
3. What pedagogical methods of environmental education do you know?
4. Short describe the strategy of the project-based education.
5. What are the major methods of project-based education?
6. What are the steps of the evaluation of a project based environmental course?
7. Formulate the essence of project-based education.

References

1. Abdel-Aziz I. Kashef, Technical and ecological impacts of the High Aswan Dam, Journal of Hydrology, 53, (1981) pp.73-84, [https://doi.org/10.1016/0022-1694\(81\)90037-8](https://doi.org/10.1016/0022-1694(81)90037-8)
2. Carolyn McGibbon, Jean-Paul Van Belle, Integrating environmental sustainability issues into the curriculum through problem-based and project-based learning: a case study at the University of Cape Town, Current Opinion in Environmental Sustainability 16 (2015) pp. 81–88, <https://doi.org/10.1016/j.cosust.2015.07.013>
3. Environmental Ethics, ed. Michael Boylan, 2014, Wiley, ISBN10 1119635063
4. Ernst F. Schumacher, Small is beautiful, 1973, Oekom Verlag, ISBN: 3962381368
5. Donella H. Meadows, et al., The Limits to Growth, 1972, Potomac Associates, ISBN: 0-87663-165-0
6. International Labour Office (ILO), Working towards sustainable development: opportunities for decent work and social inclusion in a green economy, 2012 <http://hdl.voced.edu.au/10707/217389>
7. James W. Botkin, Mahdi Elmandrija, Miecea Malitzia, No Limits to Learning, 1979, Elsevier, ISBN: 9781483297330
8. Jenő Gy.FEKETE, Gondolatok a környezetmérnök oktatásról (Thoughts of education of environmentl engineers), Környezetvédelem (2010/3) pp. 26.
9. Leon Guillet, Bul.Soc.Pol., 45(1931) pp. 932–939.
10. Magyar Mérnöki Kamara Etikai-Fegyelmi Szabályzata (Ethical-Disciplinary Regulations of the Hungarian Chamber of Engineers) 2012, <https://www.mmk.hu/.../szabalyzatok/etikai-fegyelmi-szabalyzat-regi-2012-12-08-ig.p>.
11. Mária KOVÁTS-NÉMETH Mária et al., Az erdőpedagógiától a környezetpedagógiáig, (From the forestry pedagogyto environmental pedagogy) 2010, Comenius Kft., ISBN: 978-963-9687-18-9.
12. Mária Kováts-Németh, Rita Bodáné Kendrovics, Zoltán Juvancz, Environmental Pedagogy for Sustainability E-CONOM 4 (2015) pp. 2-16, DOI:10.17836/EC.2015.1.002.
13. Murat Genc The project-based learning approach in environmental education, International Research in Geographical and Environmental Education, 24 (2015) pp. 105-117, DOI: 10.1080/10382046.2014.993169.
14. Ott Konrad (2020): Environmental ethics, inOnline Encyclopedia

Philosophy of Nature, ed. In: Thomas Kirchhoff, 2019,
 doi.org/10.11588/oepn.2020.0.71420.

15. Pankaj Kumar, et al. Integrated water resources management for an inland river basin in China, *Watershed Ecology and the Environment*, 1 (2019) pp 33-38 doi.org/10.1016/j.wsee.2019.10.002

16. Rita Bodáné-Kendrovics, Develop practical education method in higher engineering education for water quality protection subject (Based on water quality assessment exercise of Aranyhegyi stream), Thesis, 2012, Nyugatmagyarországi Egyetem, Sopron.

17. Rita Bodáné Kendrovics, Results of project pedagogy at environmental engineering education of Óbuda University, *ACTA MECHANICA SLOVACA* 16: (2012/3) pp. 52-61. DOI: 10.21496/ams.2012.030.

18. Stephen Tinsley, Ilona Pillai, *Environmental Management Systems*, 2016, Taylor & Francis, ISBN: 9781138968912.

19. The EU Water Framework Directive - integrated river basin management for Europe, „Directive 2000/60/EC of the European Parliament and of the Council establishing a framework for the Community action in the field of water policy”, 2000, https://ec.europa.eu/environment/water/water-framework/index_en.html.

20. United Nations Conference on Environment & Development, Rio de Janeiro, Brazil, 3 to 14 June 1992, AGENDA 21, <https://sustainabledevelopment.un.org/content/documents/Agenda21.pdf>

21. Vera Istvánovics, László Somlyódi, Ökológia és természetvédelem (Ecology and environmental protection, in: Hazai vízgazdálkodás stratégiai kérdései, ed. László Somlyódi, 2002, Magyar Tudományos Akadémia, Budapest, ISBN: 963-508-333-5

22. Zoltán Illés, Dezső Mikus, Red Mud Accident in Ajka and geospatial solutions in pre/post- disaster management, Central European University, Tuesday, March 13, 2018, Budapest, <https://events.ceu.edu/2018-03-13/red-mud-accident-ajka-and-geospatial-solutions-prepost-disaster-management>.

Education publication

Climate Change & Sustainable Development: New Challenges of the Century: textbook

Chapter I. – prof. Olena Mitryasova; Chapter II – assoc. prof. Pavel Nováček;

Chapter III. – prof. Piotr Koszelnik, Ph.D Małgorzata Kida;

Chapter IV. – prof. Eva Chmielewská; Chapter V. – Ph.D Lenka Bobušká;

Chapter VI. – assoc. prof. Ruslan Mariychuk;

Chapter VII. – assoc. prof. Rita Bodáné-Kendrovics; emeritus prof. Zoltán Juvancz.

Editor: prof. Olena Mitryasova

Technical editor:
Andrii Mats

Design and layout *Pavel Usik*

The authors of the sections are responsible for the reliability of the content.

*The textbook prepared and funded under Visegrad Project.
This project was made possible though Grant #22110149 from
International Visegrad Fund.*

• *supported by*

• **Visegrad Fund**

• •

Publisher:

Petro Mohyla Black Sea National University, Ukraine
10, 68-Desantnykiv St., Mykolaiv, 54003, Ukraine

tel.: +380512765568

e-mail: rector@chdu.edu.ua; <http://www.chdu.edu.ua>

Publisher and Printed by: PE "Publisher "BONA", Phone: +38 (032) 234-04-12;
Certificate subject publishing DK №4275 from 06/03/2012.
Naukova St., Lviv, Ukraine, 79060

The authors of the sections are responsible for the reliability of the results.

The project is co-financed by the Governments of Czechia, Hungary, Poland and Slovakia through Visegrad Grant from International Visegrad Fund. The mission of the fund is to advance ideas for sustainable regional cooperation in Central Europe.

All rights reserved. No part of this publication may be reproduced, stored in a retrieval system or transmitted in any form or by any means, electronic, mechanical, photocopying, recording or otherwise without the prior permission of the publisher.

Circulation: 100 hard copies



ISBN 978-617-8097-01-1



- *supported by*
- Visegrad Fund
- •

Renewable Energy: Generation and Application ICREGA'24

7th International Conference on Renewable Energy:
Generation and Application, PMU campus, Al Khobar,
Kingdom of Saudi Arabia, April 21-24, 2024



PRINCE MOHAMMAD BIN FAHD
UNIVERSITY

UAEU



Edited by
Ala A. Hussein

M|R|F

Renewable Energy: Generation and Application ICREGA'24

ICREGA'24

7th International Conference on Renewable Energy: Generation and Application, PMU campus, Al Khobar, Kingdom of Saudi Arabia, April 21st to 24th, 2024

Editors
Ala A. Hussein

Prince Mohammad Bin Fahd University, Khobar, Saudi Arabia

Peer review statement

All papers published in this volume of “Materials Research Proceedings” have been peer reviewed. The process of peer review was initiated and overseen by the above proceedings editors. All reviews were conducted by expert referees in accordance to Materials Research Forum LLC high standards.

Copyright © 2024 by authors

 Content from this work may be used under the terms of the Creative Commons Attribution 3.0 license. Any further distribution of this work must maintain attribution to the author(s) and the title of the work, journal citation and DOI.

Published under License by **Materials Research Forum LLC**
Millersville, PA 17551, USA

Published as part of the proceedings series
Materials Research Proceedings
Volume 43 (2024)

ISSN 2474-3941 (Print)
ISSN 2474-395X (Online)

ISBN 978-1-64490-320-9 (Print)
ISBN 978-1-64490-321-6 (eBook)

This book contains information obtained from authentic and highly regarded sources. Reasonable efforts have been made to publish reliable data and information, but the author and publisher cannot assume responsibility for the validity of all materials or the consequences of their use. The authors and publishers have attempted to trace the copyright holders of all material reproduced in this publication and apologize to copyright holders if permission to publish in this form has not been obtained. If any copyright material has not been acknowledged please write and let us know so we may rectify in any future reprint.

Distributed worldwide by

Materials Research Forum LLC
105 Springdale Lane
Millersville, PA 17551
USA
<https://www.mrforum.com>

Manufactured in the United State of America
10 9 8 7 6 5 4 3 2 1

Table of Contents

Preface

Committees

Cyclic voltammetric and characterization studies of electrodeposited copper-indium for thin-film solar cell application

Leher Farooq 1

Electroluminescence image-based defective photovoltaic (solar) cell detection using a modified deep convolutional neural network

Hiren MEWADA, L. SYAMSUNDAR, Hiren Kumar THAKKAR, Miral DESAI 13

Analysis of thermal efficiency of solar flat plate collector working with hybrid nanofluids: An experimental study

Solomon MESFIN, Veeredhi VASUDEVA RAO, L. Syam SUNDAR 21

Green and environmental-friendly material for sustainable buildings

Noura Al-MAZROUEI, Amged ELHASSAN, Waleed AHMED, Ali H. Al-MARZOUQI, Essam ZANELDIN 31

Techno-economic comparison between PV and wind to produce green hydrogen in Jordan

Zaid HATAMLEH, Ahmad AL MIAARI 36

Analytical and numerical evaluation for wind turbine aerodynamic characteristics

Ashraf Abdelkhalig, Mahmoud Elgendi, Mohamed Y.E. Selim, Maryam Nooman AlMallahi, Sara Maen Asaad 44

Sustainability policies and regulation challenges in recycling EV batteries

Afnan KHALIL, Mousa HUSSEIN, Essam ZANELDIN, Waleed AHMED 51

Renewable energy sources, sustainability aspects and climate alteration: A comprehensive review

M. Amin Mir, M. Waqar Ashraf, Kim Andrews 60

Potential uses of renewable energy in construction: Advantages and challenges

Essam ZANELDIN, Waleed AHMED, Betiel PAULOS, Feruz GABIR, Makda ARAYA, El Bethel MULUYE, Deborah DEBELE3 66

Adaptive cooling framework for Photovoltaic systems: A seasonal investigation under the terrestrial conditions of Sharjah, UAE

Mena Maurice FARAG, Abdul-Kadir HAMID, Mousa HUSSEIN 73

A novel approach to address reliability concerns of wind turbines

Sorena ARTIN 82

Solar radiation forecasting using attention-based temporal convolutional network

Damilola OLAWOYIN-YUSSUF, Mohamad MOHANDES, Bo LIU, Shafiqur REHMAN 88

Application of artificial intelligence (AI) in wind energy system with a case study

Fay ALZAHRANI, Feroz SHAIK, Nayeemuddin MOHAMMED, Nasser Abdullah Shinoon AL-NA'ABI 96

Prediction of distillate output in photocatalytic solar still using artificial intelligence (AI)

Reyrouf ALQAHTANI, Feroz SHAIK, Nayeemuddin MOHAMMED, Mohammad Ali KHASAWNEH, Tasneem SULTANA 104

Power systems stability of high penetration of renewable energy generations	
Ahmad HARB, Hamza NAWAFLEH	112
Assessment of utilizing solar energy to enhance the performance of vertical aeroponic farm	
Esam Jassim, Bashar Jasem, Faramarz Djavanroodi	118
Energy efficiency and sustainability enhancement of electric discharge machines by incorporating nano-graphite	
Asaad A. ABBAS, Raed R. SHWAISH, Shukry H. AGHDEAB, Waleed AHMED	124
Exploring sustainable micro milling: Investigating size effects on surface roughness for renewable energy potential	
Ahmet HASCELIK, Kubilay ASLANTAS, Waleed AHMED.....	132
From smart soles to green goals, interlacing sustainable innovations in the age of smart health: An exploratory search	
Fahd KORAICHE, Amine DEHBI, Rachid DEHBI.....	140
Water and electricity consumption management architectures using IoT and AI: A review study	
Oumaima RHALLAB, Amine DEHBI, Rachid DEHBI.....	148
A comprehensive review on computing methods for the prediction of energy cost in Kingdom of Saudi Arabia	
Nayeemuddin MOHAMMED, Andi ASIZ, Mohammad Ali KHASAWNEH, Feroz SHAIK, Hiren MEWADA, Tasneem SULTANA	156
Vibration analysis of 3D printed PLA beam with honeycomb cell structure for renewable energy applications and sustainable solutions	
Kubilay ASLANTAS, Ekrem ÖZKAYA, Waleed AHMED	164
Potential use of reject brine waste as a sustainable construction material	
Seemab TAYYAB, Essam ZANELDIN, Waleed AHMED, Ali AL MARZOUQI	172
Bidding optimization for a reverse osmosis desalination plant with renewable energy in a day ahead market setting	
Ebaa Al Nainoos, Ali Al Awami	179
Adaptive neuro-fuzzy inference system for DC power forecasting for grid-connected PV system in Sharjah	
Tareq SALAMEH, Mena Maurice FARAG, Abdul Kadir HAMID, Mousa Hussein	188
Robust testing requirements for Li-ion battery performance analysis	
Muhammad SHEIKH, Muhammad RASHID, Sheikh REHMAN	197
Date fruit type classification using convolutional neural networks	
Abdullah ALAVI, Md Faysal AHAMED, Ali ALBELADI, Mohamed MOHANDES	205
Bidding optimization for hydrogen production from an electrolyzer	
Nouf M. ALMUTAIRY, Ali T. ALAWAMI	214
Li-ion batteries life cycle from electric vehicles to energy storage	
Muhammad RASHID, Muhammad SHEIKH, Sheikh REHMAN	223

AI-Based PV Panels Inspection using an Advanced YOLO Algorithm	
Agus HAERUMAN, Sami UI HAQ, Mohamed MOHANDES, Shafiqur REHMAN, Sheikh Sharif Iqbal MITU.....	230
Impact of artificial intelligence (AI) in Martian architecture (exterior and interior)	
Lindita Bande, Jose Berengueres, Aysha Alsheraifi, Anwar Ahmad, Saud Alhammadi, Almaha Alneyadi, Amna Alkaabi, Maitha Altamimi, Yosan Asmelash.....	238
Sliding mode control for grid integration of point absorber type wave energy converter	
Abdin Y. ELAMIN, Addy WAHYUDIE.....	246
Design and fabrication of low temperature flat plate collector for domestic water heating	
Abdulkrim Almutairi, Abdulrahman Almarul, Riyadh Alnafessah, Abbas Hassan Abbas Atya, Sherroz Khan, Noor Maricar.....	254
The utilization of IoT-based humidity monitoring method and convolutional neural networks for orchid seed germination	
Muhammad Ridhan FIRDAUS, Hilal H. NUHA, Mohamed MOHANDES, Agus HAERUMAN	261
Intelligent solutions for modern agriculture: Leveraging artificial intelligence in smart farming practices	
Fatima Zahrae BERRAHAL, Amine BERQIA	269
On the performance assessment of King Faisal University grid-connected solar PV facility	
Mounir BOUZGUENDA	277
Solar energy powered smart water heating system	
Ahmed ALTURKI, Yahya ALMAHZARI, Majid ALBLOOSHI, Faris ALGHAMDI, Ahmed A. HUSSAIN, Ala A. HUSSEIN, Jamal NAYFEH	285
Experimental investigation on the thermal and exergy efficiency for a 2.88 kW grid connected photovoltaic/thermal system	
Mena Maurice FARAG, Tareq SALAMEH, Abdul Kadir HAMID, Mousa Hussein	290
Solar PV based charging station for electric vehicles (EV)	
Raghad ALGHAMDI, Batool ALSUNBUL, Raghad ALMUTAIRI, Rania ALNASSAR, Maha ALHAJRI, Saifullah SHAFIQ, Samir EL-Nakla, Ahmed ABUL HUSSAIN, Jamal NAYFEH	299
Role of renewable energy in decarbonisation process: Case study in KSA	
Samar DERNAYKA, Saidur R. CHOWDHURY, Mohammad Ali KHASAWNEH.....	307
An automated and cost-efficient method for photovoltaic dust cleaning based on biaxially oriented polyamide coating material	
Said Halwani, Mena Maurice Farag, Abdul-Kadir Hamid, Mousa Hussein.....	316
Vibration harvesting techniques for electrical power generation: A review	
Omar D. MOHAMMED, Isha BUBSHAIT, Reyouf ALQAHTANI, Kawther ALMENAYAN, Semat ALZAHER, Reem ALHUSSAIN	324
Multiport universal solar power bank	
Abdullah ALTELMESSANI, Abdulqader ALJABER, Turki ALTUWAIRQI, Ala A. HUSSEIN, Jamal NAYFEH	332

Electricity sector reforms in Saudi Arabia and their impact on demand growth and development of renewable energy	
Samir El-NAKLA, Chedly Belhadj YAHYA, Jamal NAYFEH.....	337
Optimising solar: A techno-economic assessment and government facility compensation framework power generation	
Navaid ALI, Faheem Ullah SHAIKH, Laveet KUMAR	345
A developed system design for blue energy generation	
Omar D. MOHAMMED, Saud ALHARBI, Shoja ALHARBI, Waleed ALDHUWAIHI, Nasser BINI HAMEEM	355
A review of the renewable energy technologies and innovations in geotechnical engineering	
Eman J. Bani ISMAEEL, Samer RABABAH, Mohammad Ali KHASAWNEH, Nayeemuddin MOHAMMED, Danish AHMED	360
Theoretical modeling to analyze the energy and exergy efficiencies of double air-pass solar tunnel dryer with recycled organic waste material	
Dagim Kebede GARI, A. Venkata RAMAYYA, L. Syam SUNDAR	368
Renewable energy in pavement engineering and its integration with sustainable materials: A review paper	
Mohammad Ali KHASAWNEH, Danish AHMED, Fawzyah ALKHAMMAS, Zainab ALMSHAR, Maryam HUSSAIN, Dalya ALSHALI, Maryam ALKHURAIM, Rana, ALDAWOOD, Hidaia ALZAYER, Nayeemuddin MOHAMMED.....	377

Keyword index

Preface

Renewable energy represents a pivotal shift in our approach to generating power, emphasizing sustainability and environmental responsibility. Unlike finite fossil fuels, renewable energy sources such as solar, wind, hydro, and geothermal power harness naturally replenishing elements of the Earth's ecosystem. This shift not only addresses the urgent need to mitigate climate change but also offers diverse applications across various sectors. From powering homes and businesses to driving transportation and industrial processes, renewable energy technologies are pivotal in shaping a cleaner, more resilient energy future.

Renewable energy generation involves harnessing naturally occurring and replenishing resources to produce electricity or heat. The main sources include:

- Solar Energy: Generated from sunlight through photovoltaic (PV) cells or concentrated solar power (CSP) systems. Solar energy is versatile, used in residential, commercial, and utility-scale applications for electricity generation and heating.
- Wind Energy: Captured by wind turbines that convert kinetic energy into electricity. Wind farms are increasingly common in areas with consistent wind patterns, contributing significantly to global electricity supply.
- Hydropower: Generated from flowing water in rivers, streams, and oceans. Hydroelectric dams and run-of-river systems convert water's gravitational energy into electricity, providing consistent, baseload power.
- Geothermal Energy: Extracted from heat stored beneath the Earth's surface. Geothermal power plants use steam or hot water to generate electricity and provide direct heating for buildings.
- Biomass Energy: Derived from organic materials such as wood, agricultural residues, and organic waste. Biomass can be burned directly for heat or converted into biogas or biofuels for electricity generation and heating.

Applications of renewable energy extend across various sectors:

- Electricity Generation: Renewable energy contributes to grid power, reducing reliance on fossil fuels and mitigating greenhouse gas emissions.
- Transportation: Electric vehicles (EVs) powered by renewable electricity are reducing emissions in the transportation sector.
- Heating and Cooling: Renewable energy sources like solar thermal and geothermal heat pumps provide efficient heating and cooling solutions for residential and commercial buildings.
- Industrial Processes: Renewable electricity and heat are used in industrial applications, reducing carbon footprints and enhancing sustainability.

- Rural Electrification: Off-grid renewable energy systems bring electricity to remote areas without access to traditional power grids, improving quality of life and economic opportunities.

The development and adoption of renewable energy technologies are crucial in combating climate change, enhancing energy security, and fostering sustainable development globally. In fact, renewable energy has a rich history of development and adoption worldwide, driven by technological advancements, environmental concerns, and energy security considerations. Here's an overview of its evolution and current status globally:

History of Renewable Energy:

- Early Use: Humans have utilized renewable energy sources for millennia, such as wind for sailing ships and grinding grain, and biomass for cooking and heating.
- Industrial Revolution: The 19th century saw increased use of hydropower for mechanical tasks and later for electricity generation as turbines were developed.
- 20th Century: The early 20th century saw the rise of hydropower and biomass as significant energy sources. In the mid-20th century, solar photovoltaic (PV) technology and wind turbines began development.
- Late 20th Century: The energy crises of the 1970s spurred interest in renewable energy, leading to government incentives and research in solar, wind, and geothermal energy.
- 21st Century: Rapid technological advancements, declining costs, and environmental concerns have accelerated the deployment of renewables globally.

Current Status Worldwide:

- Electricity Generation:
 - Solar PV: Solar energy capacity has grown significantly, with large-scale installations in countries like China, the United States, and India.
 - Wind Power: Wind turbines contribute a substantial portion of electricity in many countries, particularly in Europe and North America.
 - Hydropower: Remains a significant source, especially in countries like China, Brazil, and Canada.
- Policy Support: Many countries have implemented policies to promote renewable energy, including feed-in tariffs, tax incentives, and renewable portfolio standards.
- Technological Advancements: Advances in energy storage, grid integration, and efficiency improvements have bolstered renewable energy's viability and reliability.
- Global Growth: The International Renewable Energy Agency (IRENA) reports that renewable energy capacity has grown rapidly, with substantial investments in solar, wind, and other technologies.

- Challenges: Despite growth, challenges remain, including intermittency issues with solar and wind, grid integration challenges, and varying policy support across different regions.
- Future Outlook: The transition to renewables is expected to continue, driven by climate goals under the Paris Agreement, technological innovation, and economic competitiveness.

In summary, renewable energy has evolved from traditional uses to a pivotal component of global energy systems. Its history reflects a trajectory of technological innovation, policy support, and increasing global adoption, positioning it as a key solution in addressing climate change and achieving sustainable development goals worldwide. And, as technology advances and economies of scale improve, renewable energy continues to play a pivotal role in shaping a cleaner and more resilient energy landscape for the future.

Committees

HONORARY CHAIR

Dr. Issa H. Alansari, President, Prince Mohammed Bin Fahd University

CONFERENCE CHAIR

Dr. Faisal Yousif Al Anezi, Vice President, Prince Mohammed Bin Fahd University

TECHNICAL PROGRAM CHAIRS

Dr. Ala A. Hussein, Prince Mohammed Bin Fahd University, Saudi Arabia

Dr. Samir El Nakla, Prince Mohammed Bin Fahd University, Saudi Arabia

Dr. Mousa Hussein, United Arab Emirates University, United Arab Emirates

TECHNICAL PROGRAM COMMITTEE

Dr. Jamil Mosallam Bakhshwain, Prince Mohammed Bin Fahd University, Saudi Arabia

Dr. Jawad Al Asad, Prince Mohammed Bin Fahd University, Saudi Arabia

Dr. Sadiq Al Huwaidi, Prince Mohammed Bin Fahd University, Saudi Arabia

Dr. Christakis Papageorgiou, Prince Mohammed Bin Fahd University, Saudi Arabia

Dr. Hiren Mewada, Prince Mohammed Bin Fahd University, Saudi Arabia

Dr. Hussain Shareef, United Arab Emirates University, United Arab Emirates

Dr. Imad Barhumi, United Arab Emirates University, United Arab Emirates

Dr. Addy Wahyudie, United Arab Emirates University, United Arab Emirates

Dr. Nasir Saeed, United Arab Emirates University, United Arab Emirates

Dr. Waleed Ahmed, United Arab Emirates University, United Arab Emirates

Dr. Said Al-Hallaj, University of Illinois at Chicago, USA

Dr. Issa Batarseh, University of Central Florida, USA

Dr. Mohamed Farid, The University of Auckland

Dr. Yahya Meziani, Universidad de Salamanca, Spain

ORGANIZING COMMITTEE

Dr. Samir El Nakla, Prince Mohammed Bin Fahd University, Saudi Arabia

Dr. Ala Hussein, Prince Mohammed Bin Fahd University, Saudi Arabia

Dr. Christakis Papageorgiou, Prince Mohammed Bin Fahd University, Saudi Arabia

Dr. Jawad Al Asad, Prince Mohammed Bin Fahd University, Saudi Arabia

Dr. Sadiq Al Huwaidi, Prince Mohammed Bin Fahd University, Saudi Arabia

Dr. Hiren Mewada, Prince Mohammed Bin Fahd University, Saudi Arabia

Dr. Ghida Alzohbi, Prince Mohammed Bin Fahd University, Saudi Arabia

Dr. Mousa Hussein, United Arab Emirates University, United Arab Emirates

Dr. Amine El Moutaouakil, United Arab Emirates University, United Arab Emirates

Dr. Atef Abdrabou, United Arab Emirates University, United Arab Emirates

Dr. Mohammed Noor Al Tarawneh, United Arab Emirates University, United Arab Emirates

Dr. Rachid Errouissi, United Arab Emirates University, United Arab Emirates

Dr. Falah Awwad, United Arab Emirates University, United Arab Emirates

Mr. Ahmed Abul Hussain, Prince Mohammed Bin Fahd University, Saudi Arabia

Mr. Adil Humayun Khan, Prince Mohammed Bin Fahd University, Saudi Arabia

Mr. Wael Suliman, Prince Mohammed Bin Fahd University, Saudi Arabia

Cyclic voltammetric and characterization studies of electrodeposited copper-indium for thin-film solar cell application

Leher Farooq^{1,a*}

¹Department of Chemical & Petroleum Engineering, United Arab Emirates University, Abu Dhabi - 15551, UAE

^a201570178@uaeu.ac.ae

Keywords: Electrodeposition, Copper Indium Diselenide, Thin-Film Solar Cells, Complexing Agents, Cyclic Voltammetry, Energy Dispersive X-Ray Spectroscopy, X-Ray Diffraction, Scanning Electron Microscopy

Abstract. Copper-indium layers were grown on a carbon substrate by a one-step electrodeposition technique. Four deposition electrolytes were prepared: Two unitary electrolytes comprising of 300 mM copper (II) chloride and 700 mM trisodium citrate and 300 mM indium (III) chloride and 700 mM trisodium citrate; two binary electrolytes comprising of 300 mM copper (II) chloride, 300 mM indium (III) chloride and 700 mM trisodium citrate for deposition at potentials of -0.6 V and -0.9 V, respectively. The pH of the solution was left unaltered at 4.8. X-ray diffraction studies showed the produced copper indium layers had an amorphous structure. From the scanning electron microscopy studies, it was found that copper indium layers indicated a small grain size and grain shape was irregular. The structure was not compact. Energy dispersive spectroscopy showed presence of low percentages of copper and indium in all four samples and stoichiometric molar ratios of Cu:In of 1:1 can be achieved using deposition potentials between -0.6 to -0.9 V. SEM, EDS and XRD characterization helps in the identification of the reaction mechanism, the structure and morphology of the films deposited under different conditions. These characterization studies will assist in enhancing the efficiency of the thin-films deposited for maximum conversion of sunlight to electricity using this sustainable method. In this present study, an attempt has been made to obtain near stoichiometric films for higher efficiencies.

Introduction

The direct conversion of sunlight into electricity (photovoltaics) may be the most prevailing and potential alternative to the utilization of fossil fuels. Primary energy consumption decreased by 4.5% last year, which is the first decline since 2009. Nevertheless, alternative forms to fossil fuel are in dire need to protect the environment from global warming. Copper indium diselenide (CIS) and copper indium gallium diselenide (CIGS) are two of the most favorable absorber materials for low cost photovoltaics or thin film solar cells and extensive research is being conducted in the development of these thin film solar cells [1]–[4]. Copper indium diselenide has a I-III-VI₂ ternary chalcopyrite structure and possesses desirable physical properties such as a direct band gap at ~1 eV and a high absorption coefficient of greater than 10⁵ cm⁻¹ at photon energies above the band gap. CIS thin film of about 1 μm thickness absorbs 90% of the incident sunlight with photon energy greater than its band gap. The best CIGS solar cells have the following layer structure: Mo (1 μm) coated glass/CIGS absorber/CdS buffer layer/CdS-ZnO window layer/MgF₂ antireflection coating/Ni-Al alloy grid [5]. These qualities make it ideal for fabrication of high efficiency polycrystalline thin film photovoltaic devices [6]. Several techniques are present for the preparation of CIS thin films including co-evaporation [7], sputtering [8]–[10], spray pyrolysis [11]–[13], electrodeposition [1], [3], [14], molecular beam epitaxy [15], etc. The highest efficiency achieved for CIS thin-film solar cell is 23.35% reported by Solar Frontier in 2019 [16]. The



conductivity of this ternary semiconductor can be either n- or p-type which depends on the synthesis method and the composition of the constituent elements in the structure [17].

Several works have been published on chalcopyrite materials which have primarily used one-step electrodeposition process instead of physical vapor deposition because it allows achievement of low production cost, higher deposition speed and negligible waste of chemicals [18]. Owing to the reasoning that the co-electrodeposition process does not require very sophisticated equipment and is easy to use, this technique where the Cu-In-Ga-Se species are present in the same chemical bath is one of the suitable techniques to prepare low cost thin films [19]. PVD technique produces high quality films but is difficult to scale up. Co-electrodeposition process can be identified into two types: (1) where the elements involved have almost the same order of electrode potential, and (2) where the elements involved have different electrode potentials. In the cases where the elements involved have different electrode potentials, complexing agents such as trisodium citrate or EDTA can be utilized to reduce the difference in the deposition potentials.

Considerable amount of work has been done on the electrodeposition of CIS which includes a few studies devoted to the mechanism of CIS formation. Carboneille and Lamberts conducted an elementary study as well as the first step in understanding the mechanism of copper selenide electrodeposition to understanding the copper indium diselenide deposition from a ternary bath. Their results found that copper selenide is an intermediate or precursor for the formation of copper indium diselenide deposition [20].

The formation of the electrodeposited CIGS on the cathodic (working electrode) surface within an electrolysis cell typically depends on the pH level, redox (standard reduction) potential, deposition time, applied potential and the initial solution concentration along with some other factors [21]. In this paper, the final composition of the deposited film is determined using EDS analysis by studying the effects of initial concentrations of the electrolyte as well as the deposition potentials at which the reduction occurs. A detailed study through cyclic voltammetry, Energy Dispersive Spectroscopy, X-Ray Diffraction and Scanning Electron Microscopy is conducted in order to study the specific initial concentration of the electrolyte.

Materials and methods

Materials preparation

Copper (II) chloride (CuCl_2), indium (III) chloride (InCl_3) and trisodium citrate ($\text{Na}_3\text{C}_6\text{H}_5\text{O}_7$) were all purchased from Sigma-Aldrich. All chemicals were used as received and deionized water was used for the deposition bath. A small circular carbon electrode with dimensions of 2 mm in diameter was used as the substrate. The electrodeposition was carried out potentiostatically in a three-electrode cell configuration. The reference electrode was silver/silver chloride electrode and the working and counter electrodes were made up of carbon. All substrates were cleaned with acetone and rinsed with deionized water, and subsequently dried. The electrolyte bath contained 100 ml deionized water and 300 mM copper (II) chloride, 300 mM indium (III) chloride and 700 mM trisodium citrate. The pH of the solution was 4.8. With the aim of checking the stability of the electrolyte solutions prepared, they were stored for at least 20 days at room temperature and pressure and their final stability at the end of 20 days was observed before usage. The pH of the electrolytes were not altered using any acidic agents such as hydrochloric acid or sulphuric acid.

Characterization

A Solartron ModuLab XM ECS potentiostat/galvanostat was used for the film depositions and cyclic voltammetry studies. The cyclic voltammograms were measured at a scan rate of 15 mV/s and were scanned only in the negative potential region. The cathodic potentials have been fixed at -0.6 V and -0.9 V for copper and indium deposition, respectively. The deposition time has been at

15 min. All film depositions and cyclic voltammogram measurements were performed in a stagnant bath at room temperature.

The surface morphology, chemical composition and crystalline properties of the electrodeposited films were characterized by scanning electron microscopy (SEM, Jeol JSM-6010PLUS/LA), energy dispersive X-ray spectroscopy and X-ray diffraction (XRD, X' Pert PRO MRD XL XRD system from Panalytical), respectively.

Results and discussion

The deposition solutions containing electrochemically active species Cu^{2+} and In^{3+} in the presence of trisodium citrate as a complexing agent are stable for a long time. Different potentials were employed to produce Cu-rich and Cu-poor deposition layers. Cu-rich layers were produced in a binary solution containing copper (II) chloride and indium (III) chloride along with trisodium citrate at a cathodic potential of -0.6 V and Cu-poor layers were produced at a cathodic potential of -0.9 V. Both the electrolytes for the electrochemical experiments at -0.6 V and -0.9 V have the same $[\text{Cu}^{2+}]/[\text{In}^{3+}]$ initial ratios. Electrodeposition was carried out without agitation. The chemical composition of the unitary deposits of copper and indium and binary deposit of copper-indium were analyzed by EDS. The results of the chemical compositional analysis of copper at -0.6 V, indium at -0.9 V and copper-indium layer at -0.6 V and -0.9 V are shown in table 1, 2, 3 and 4, respectively. One can observe the presence of copper, indium, sodium, chloride and oxygen atoms in the deposited layer. Apart from copper and indium, the other elements present are due to improper washing of the deposited layers.

Table 1 – Chemical composition of the synthesized layer of copper at -0.6V

Formula	mass%	Atom%
O	10.50	18.87
Na	32.71	40.94
Cl	40.35	32.75
Cu	16.44	7.44
Total	100.00	100.00

Table 2 – Chemical composition of the synthesized layer of indium at -0.9V

Formula	mass%	Atom%
O	52.12	67.91
Na	28.61	25.95
Cl	6.50	3.82
In	12.77	2.32
Total	100.00	100.00

Table 3 – Chemical composition of the synthesized layer of copper-indium at -0.6V

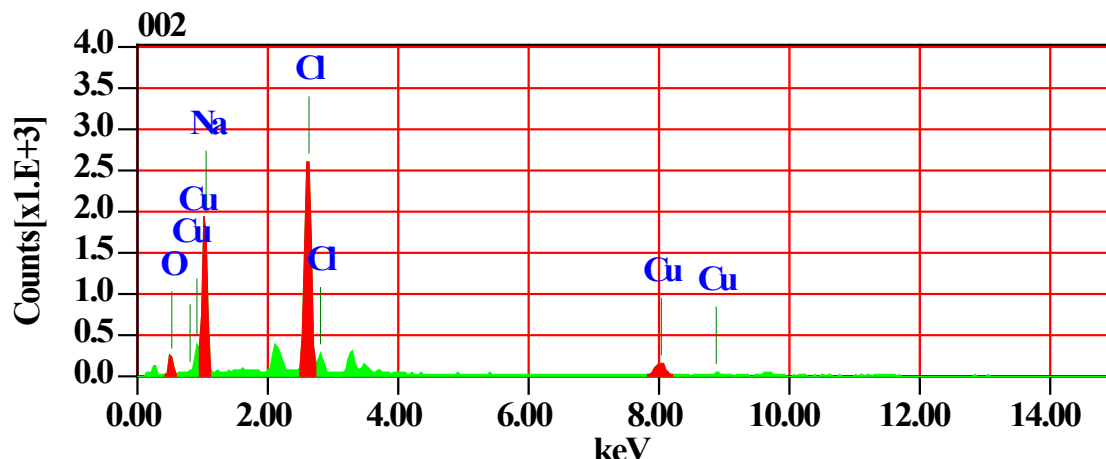
Formula	mass%	Atom%
O	30.27	49.45
Na	26.39	30.01
Cl	14.37	10.59
Cu	18.25	7.51
In	10.72	2.44
Total	100.00	100.00

Table 4 – Chemical composition of the synthesized layer of copper-indium at -0.9V

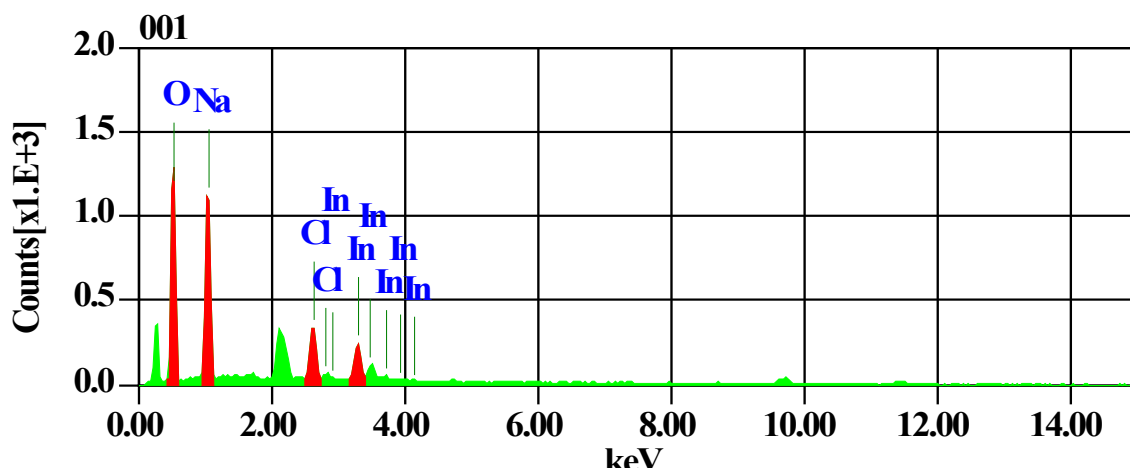
Formula	mass%	Atom%
O	29.27	50.13
Na	18.62	22.19
Cl	26.24	20.28
Cu	6.35	2.74
In	19.52	4.66
Total	100.00	100.00

Four cyclic voltammetric experiments were conducted: copper electrodeposition at -0.6 V, indium electrodeposition at -0.9 V, copper indium electrodeposition at -0.6 V and -0.9 V. The molar ratio of Cu:In at a deposition potential of -0.6V was found to be approximately 2:1. The molar ratio of Cu:In at a deposition potential of -0.9V was found to be approximately 1:3. Thus, to obtain stoichiometric molar ratio of Cu:In = 1:1, a deposition potential between -0.6 V and -0.9 V must be chosen. The atomic ratio for Cu:In at a deposition potential of -0.6 V was found to be 3:1 and at -0.9 V is approximately 3:2. Therefore, to obtain stoichiometric atomic ratio of Cu:In = 1:1, a more negative deposition potential should be selected. Figure 1 shows the EDS diagrams and indicates that the rates of Cu and In components obtained in this study are seen to be low which matches the data obtained from the compositional analysis.

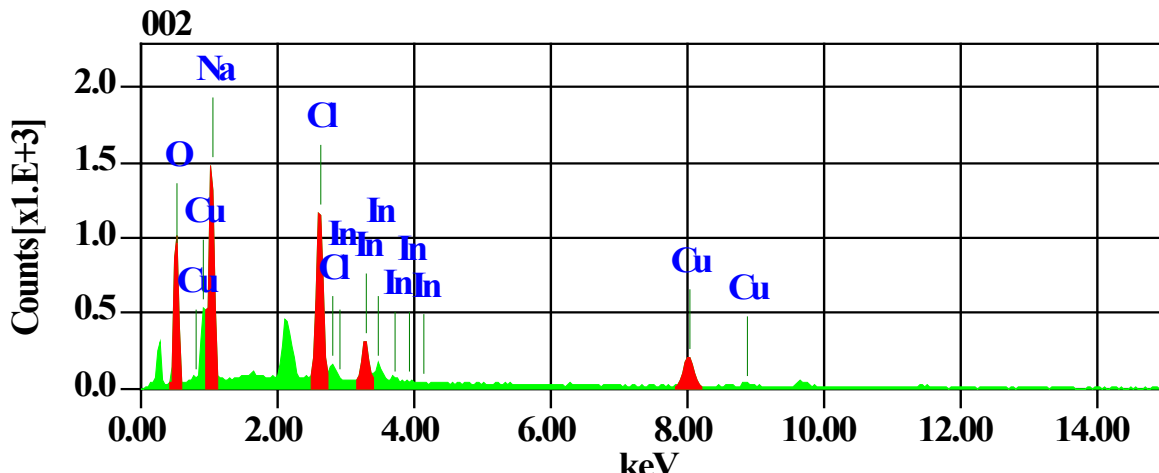
(a)



(b)



(c)



(d)

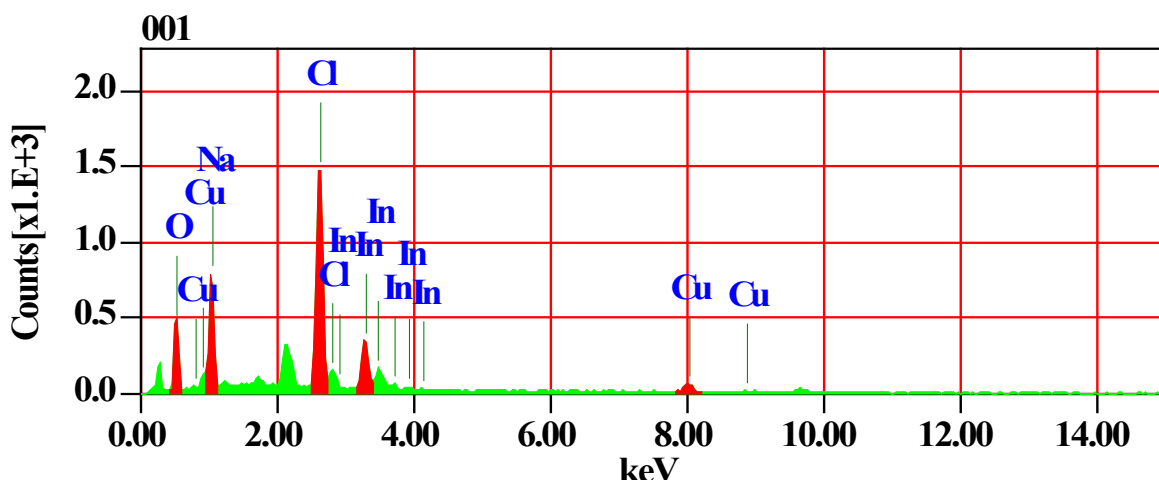


Fig. 1. EDS of the copper-indium layers.

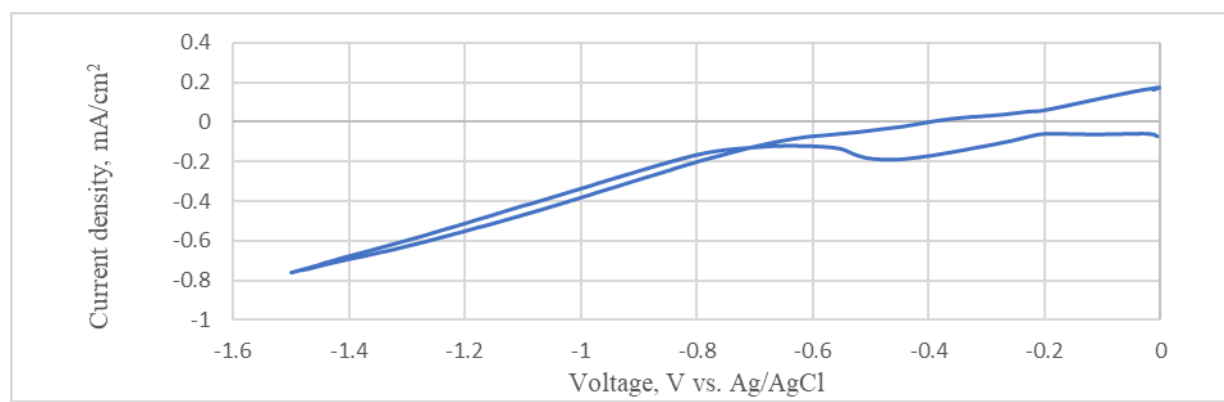


Fig. 2. 300 mM CuCl_2 + 300 mM InCl_3 without any complexing agent.

Fig. 2. shows no prominent peak for indium obtained in a binary solution of 300 mM copper (II) chloride and 300 mM indium (III) chloride without the usage of any complexing agents.

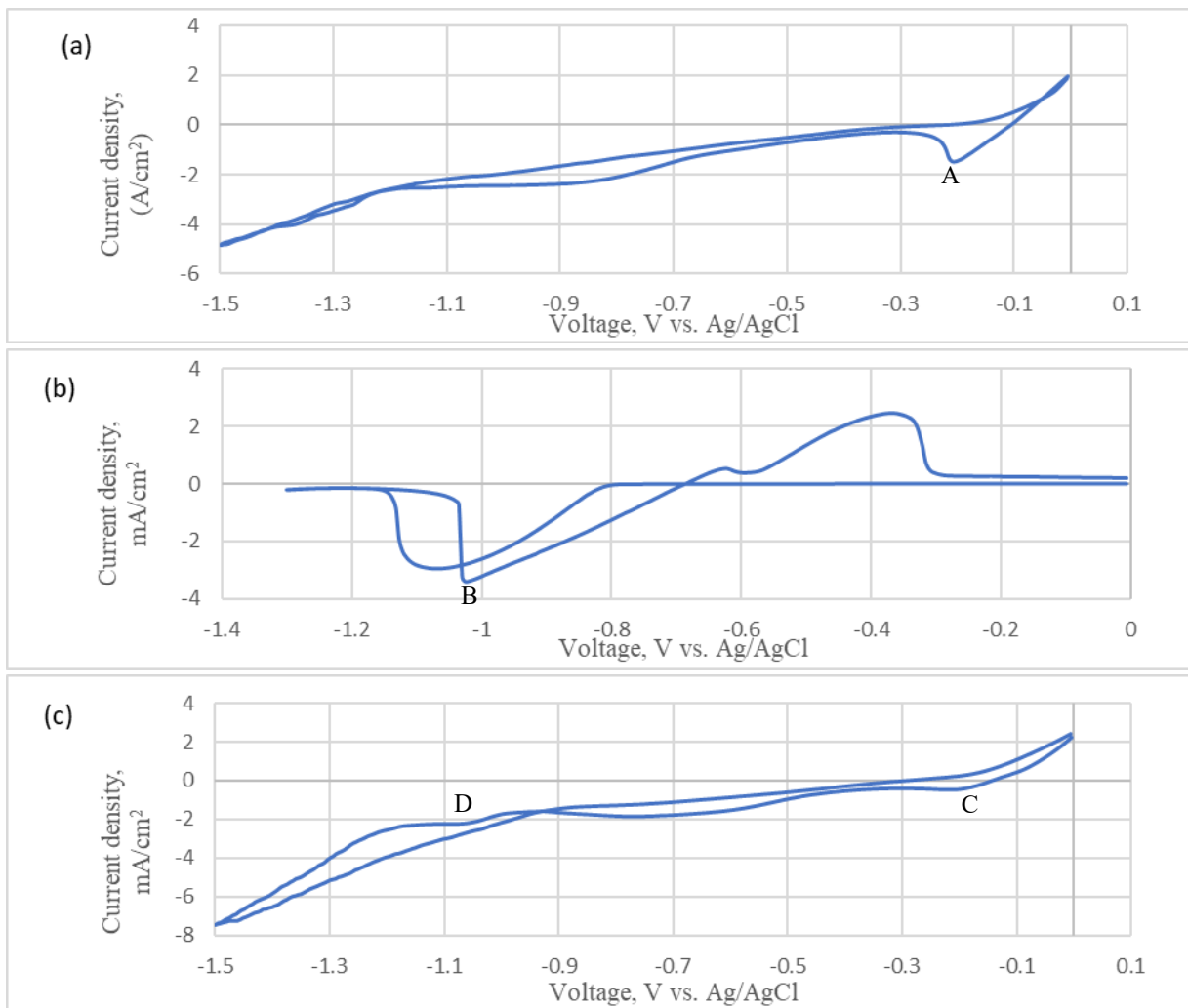


Fig. 3. Cyclic voltammograms of a Carbon electrode in (a) 300 mM CuCl₂ + 700 mM Trisodium Citrate, (b) 300 mM InCl₃ + 700 mM Trisodium Citrate and (c) 300 mM CuCl₂ + 300 mM InCl₃ + 700 mM Trisodium Citrate.

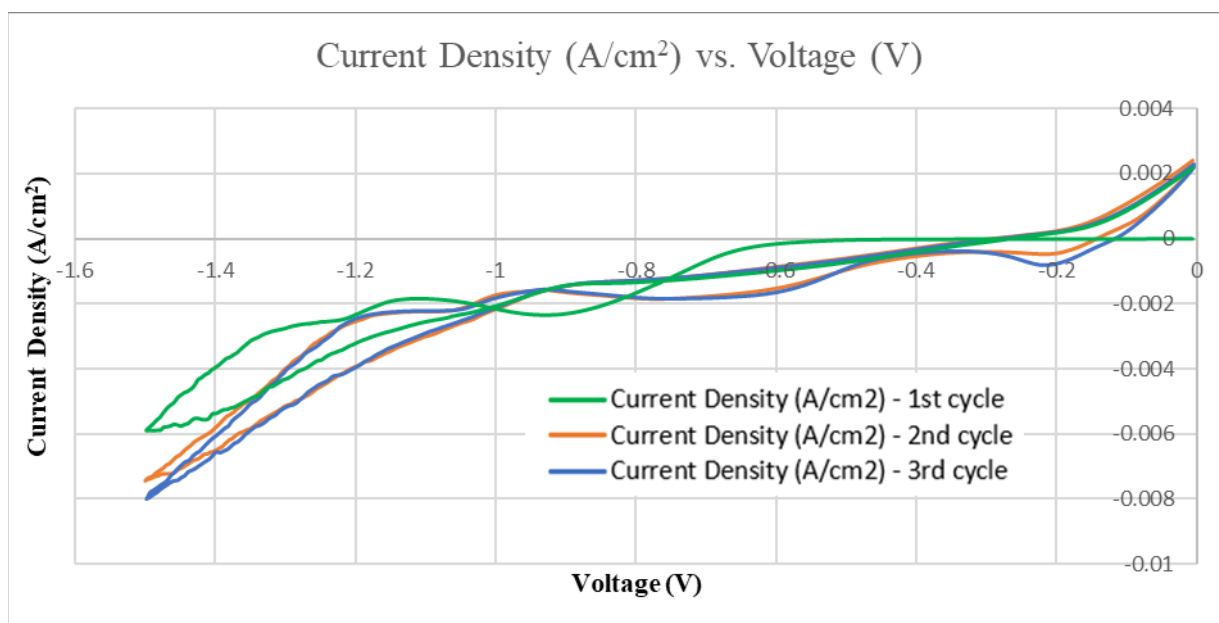


Fig. 4. Three cycles of cyclic voltammograms for binary solution of copper (II) chloride + indium (III) chloride and trisodium citrate.

On juxtaposing the successive cyclic voltammograms, slight differences are observed in the three cycles. As observed in Figure 4, for the third successive cycle, no copper peak is observed whereas an indium peak is observed but it seems to appear shifted to more negative deposition potential. Not much difference in the peaks is observed for the first and second cycles. The explanation for this could be that some copper is not oxidized back into copper ions and some nucleation sites are left covered on the carbon electrode by copper which reduces the number of nucleation sites available for copper reduction. This is known as the surface effect.

The charge transfer reaction corresponding to the peaks A and B in Figure 3 (a) and (b) at -0.2 V and -1 V potentials respectively must be related to the electrodeposition of copper and indium respectively. Cathodic peaks C and D are attributed to copper and indium electrodeposition in the binary electrolyte. These plots are for unitary solutions of copper (II) chloride and indium (III) chloride containing trisodium citrate as the complexing agent. For binary solution, respective peaks for copper and indium were found at -0.2 V and -1 V as well. For Figure 3 (a), (b) and (c), the voltammogram shows a badly defined hump at -0.8 V, -0.6 V and -0.6 V, respectively which might be attributed to the hydrogen evolution reaction. On juxtaposing Figures 2 and 3 which are cyclic voltammograms for the electrolytes in the absence and presence of the complexing agent, respectively, obtained in similar conditions, a negative shift in the peak potential of the respective element is observed by a degree of 0.2 V. This seems to suggest that some kind of complexation between the citrate anion and copper (II) and indium (III) cation occurs.

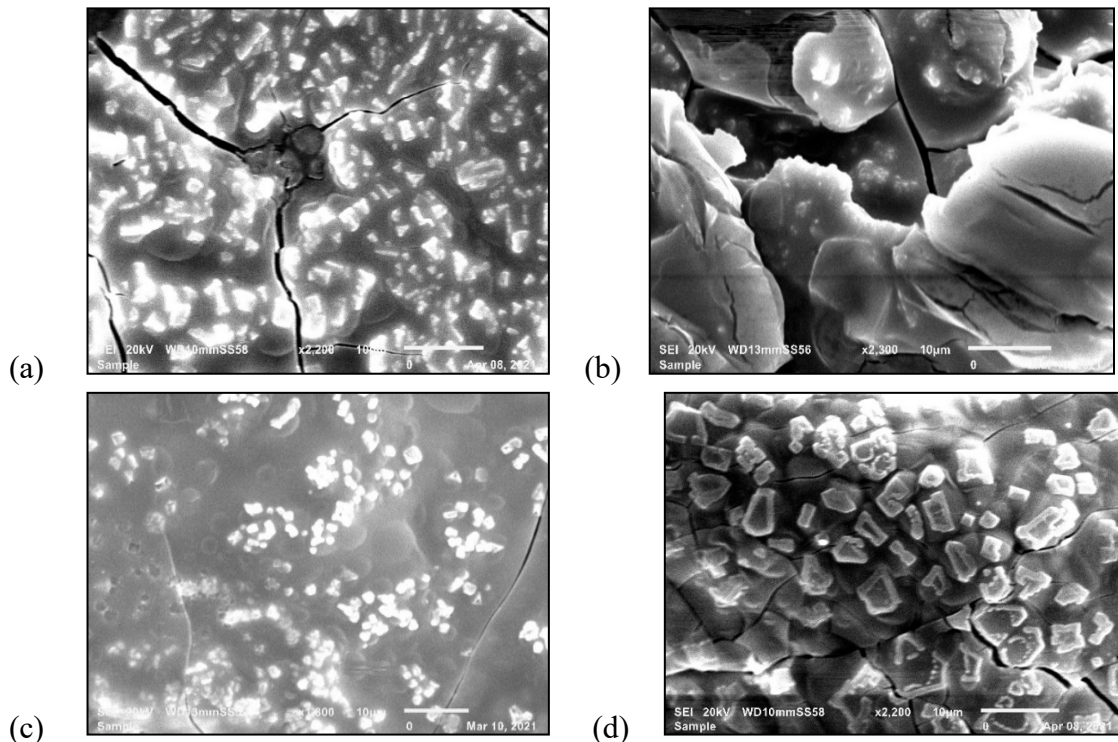
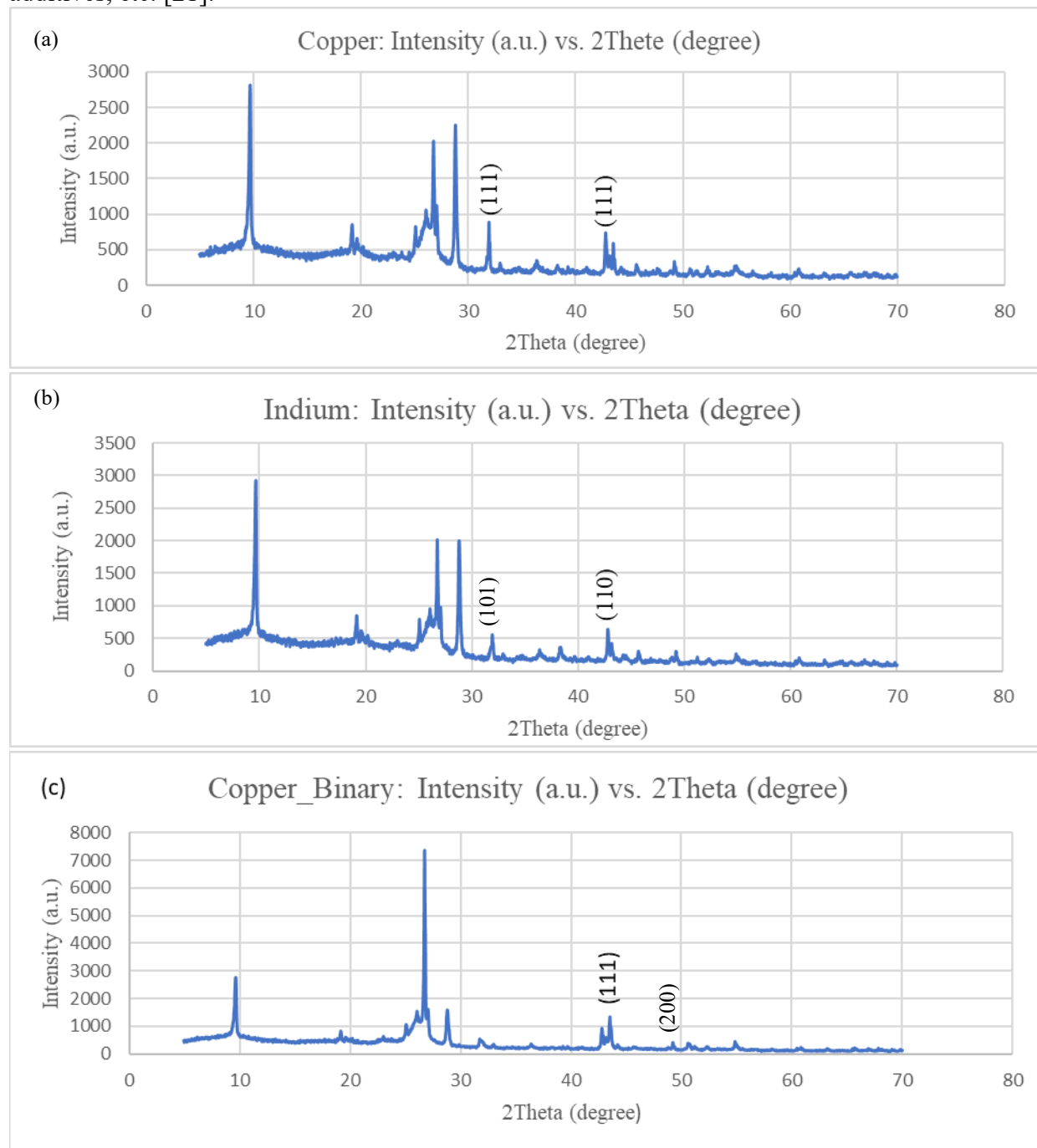


Fig. 5. SEM micrographs of (a) copper deposits at -0.6 V (*2200), (b) indium deposits at -0.9 V (*2300), (c) copper-indium deposits at -0.6 V (*1800) and (d) copper-indium deposits at -0.9 V (*2200).

High resolution scanning electron microscopy micrographs were recorded to investigate electrodeposited films of copper, indium and copper-indium. The copper films deposited at room temperature consisted mainly of grains with diameter varying about $2\text{-}4\text{ }\mu\text{m}$ as seen in Figure 5 (a). A few rods are also observed with the mean length $5\text{ }\mu\text{m}$ randomly oriented. Grains shape and size is irregular. SEM for copper film deposited at -0.6 V show crystallite structure compared to cauliflower-like structure produced in literature which could be a result of not washing the deposits after electrodeposition. Similar grain sizes and structure have been reported in literature. As can be seen from the surface morphology, the film deposit is not crack-free. Indium particles seem to be bigger than copper particles with their average size being $20\text{ }\mu\text{m}$ as compared to copper average particle size being around $2\text{ }\mu\text{m}$ as seen in Figure 5 (b). For indium, litterature has reported densely packed particles whereas those shown in Figure 5 (c) are more compact. Shape and size of the particles is more irregular. In litterature, grains had more regular circular shape [22]. The surface morphology of the Indium deposit also shows cracks on the surface. SEM depicted in Figure 5 (c) indicates smaller grain size when compared to copper alone. Again it seems that the particles are in the initial stages of nucleation. The small grains is irregular in shape and size. The size ranged from 1 to $3\text{ }\mu\text{m}$. The surface morphology examination from the $\times 900$ magnification shows a lot of cracks on the surface. Having cracks on the surface is not recommended and needs to be corrected by altering the deposition conditions such as deposition time, pH, concentration of electrolytes and potential. Figure 24 (a) and (b) indicates large indium particles as compared to copper deposition in the previous case. From the SEM morphology diagrams in figure 24 (c) and (d), it can be observed that copper and indium suppress each other's formation. Grain size and shape is irregular, and the average size is $5\text{ }\mu\text{m}$. Similar to the previous SEMs for the different deposits, cracks are observed on the surface. From literature, these cracks could be avoided by improving the process

conditions of the bath such as pH, deposition time, deposition voltage, bath composition, bath additives, etc. [21].



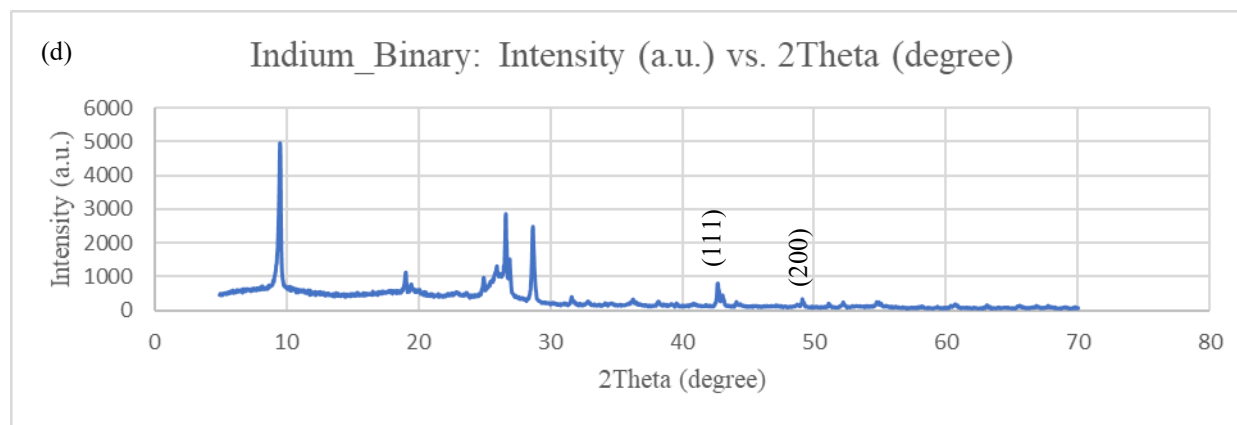


Fig. 6. X-ray diffraction patterns of the copper-indium layers at different deposition potentials.

Figure 6 depicts the X-ray diffractograms of the four deposited layers. XRD figures indicate a more amorphous structure. Figure 6 (c) and (d) show the presence of copper-indium at 2theta of 49° at a preferential plane of (200) to the growth of copper-indium. The XRD diffraction patterns cannot be compared with the JCPDS database owing to the small amount of the substance present in the deposited layer analyzed.

Conclusion

The study reports non-vacuum and easy production of copper indium layers by the co-deposition method. In this paper, the electrodeposition process for the fabrication of copper-indium has been studied which includes cyclic voltammetry, X-ray diffraction, scanning electron microscopy and energy dispersive X-ray spectroscopy. Results can be used in further studies to determine the structure, morphology and reaction mechanism of the films deposited. It can be concluded that best results are obtained at a deposition potential of -0.8 V by comparing the results of the cyclic voltammograms for the binary solutions at -0.6 V and -0.9 V. SEM characterization studies showed cracks on the surface for all four samples and irregular grain shape and size between 2-20 µm. X-ray diffraction studies indicate the presence of copper-indium at 2theta of 49° at a preferential plane of (200) to the growth of copper indium. EDS studies indicate a relatively low amount of copper and indium and that a 1:1 ratio of Cu:In will be obtained at approximately -0.8 V. This study is a good elementary study which can be used to determine which composition of the final deposited layer give maximum conversion efficiency.

References

- [1] L. Farooq, A. Alraeesi, and S. Al Zahmi, "A review on the Electrodeposition of CIGS Thin-Film Solar Cells," in *Proceedings of the International Conference on Industrial Engineering and Operations Management*, 2019, pp. 158–186.
- [2] V. S. Saji, I. H. Choi, and C. W. Lee, "Progress in electrodeposited absorber layer for CuIn(1-x)Ga_xSe₂ (CIGS) solar cells," *Sol. Energy*, vol. 85, no. 11, pp. 2666–2678, 2011, <https://doi.org/10.1016/j.solener.2011.08.003>
- [3] Y.-S. Chiu, M.-T. Hsieh, C.-M. Chang, C.-S. Chen, and T.-J. Whang, "Single-step electrodeposition of CIS thin films with the complexing agent triethanolamine," *Appl. Surf. Sci.*, vol. 299, pp. 52–57, 2014. <https://doi.org/10.1016/j.apsusc.2014.01.184>
- [4] R. Chandran, R. Pandey, and A. Mallik, "One step electrodeposition of CuInSe₂ from an acidic bath: A reduction co-deposition study," *Mater. Lett.*, vol. 160, pp. 275–277, 2015. <https://doi.org/10.1016/j.matlet.2015.07.132>

- [5] M. E. Calixto and P. J. Sebastian, "Solartron analytic," *Sol. Energy Mater. Sol. Cells*, vol. 63, no. 4, pp. 335–345, 2000. [https://doi.org/10.1016/S0927-0248\(00\)00053-2](https://doi.org/10.1016/S0927-0248(00)00053-2)
- [6] A. Luque and S. Hegedus, "Handbook of Photovoltaic Science and Engineering," *John Wiley Sons, Ltd*, pp. 92–100, Jan. 2003.
- [7] S. Ruffenach, Y. Robin, M. Moret, R.-L. Aulombard, and O. Briot, "(112) and (220)/(204)-oriented CuInSe₂ thin films grown by co-evaporation under vacuum," *Thin Solid Films*, vol. 535, pp. 143–147, 2013. <https://doi.org/10.1016/j.tsf.2013.01.053>
- [8] M. Li *et al.*, "CIS and CIGS thin films prepared by magnetron sputtering," *Procedia Eng.*, vol. 27, pp. 12–19, 2012. <https://doi.org/10.1016/j.proeng.2011.12.419>
- [9] S. Seeger and K. Ellmer, "Reactive magnetron sputtering of CuInS₂ absorbers for thin film solar cells: Problems and prospects," *Thin Solid Films*, vol. 517, no. 10, pp. 3143–3147, 2009. <https://doi.org/10.1016/j.tsf.2008.11.120>
- [10] H. L. Hwang, C. L. Cheng, L. M. Liu, Y. C. Liu, and C. Y. Sun, "Growth and properties of sputter-deposited CuInS₂ thin films," *Thin Solid Films*, vol. 67, no. 1, pp. 83–94, 1980. [https://doi.org/10.1016/0040-6090\(80\)90291-6](https://doi.org/10.1016/0040-6090(80)90291-6)
- [11] M. Hashemi, S. M. Bagher Ghorashi, F. Tajabadi, and N. Taghavinia, "Aqueous spray pyrolysis of CuInSe₂ thin films: Study of different indium salts in precursor solution on physical and electrical properties of sprayed thin films," *Mater. Sci. Semicond. Process.*, vol. 126, p. 105676, 2021. <https://doi.org/10.1016/j.mssp.2021.105676>
- [12] M. Esmaeili-Zare and M. Behpour, "Influence of deposition parameters on surface morphology and application of CuInS₂ thin films in solar cell and photocatalysis," *Int. J. Hydrogen Energy*, vol. 45, no. 32, pp. 16169–16182, 2020. <https://doi.org/10.1016/J.IJHYDENE.2020.04.106>
- [13] J. Leng *et al.*, "Advances in nanostructures fabricated via spray pyrolysis and their applications in energy storage and conversion," *Chem. Soc. Rev.*, vol. 48, no. 11, pp. 3015–3072, 2019. <https://doi.org/10.1039/C8CS00904J>
- [14] M. E. Calixto, P. J. Sebastian, R. N. Bhattacharya, and R. Noufi, "Compositional and optoelectronic properties of CIS and CIGS thin films formed by electrodeposition," *Sol. Energy Mater. Sol. Cells*, vol. 59, no. 1, pp. 75–84, 1999. [https://doi.org/10.1016/S0927-0248\(99\)00033-1](https://doi.org/10.1016/S0927-0248(99)00033-1)
- [15] K. Abderrafi *et al.*, "Epitaxial CuInSe₂ thin films grown by molecular beam epitaxy and migration enhanced epitaxy," *J. Cryst. Growth*, vol. 475, pp. 300–306, 2017. <https://doi.org/10.1016/j.jcrysgro.2017.07.010>
- [16] "Solar Frontier Achieves World Record Thin-Film Solar Cell Efficiency of 23.35%." .
- [17] S. K. Deb, "Thin-film solar cells: An overview," *Renew. Energy*, vol. 8, no. 1, pp. 375–379, 1996. [https://doi.org/10.1016/0960-1481\(96\)88881-1](https://doi.org/10.1016/0960-1481(96)88881-1)
- [18] O. Meglali, N. Attaf, A. Bouraiou, J. Bougdira, M. S. Aida, and G. Medjahdi, "Chemical bath composition effect on the properties of electrodeposited CuInSe₂ thin films," *J. Alloys Compd.*, vol. 587, pp. 303–307, 2014. <https://doi.org/10.1016/j.jallcom.2013.10.100>

- [19] J. Herrero and C. Guillén, "Study of the optical transitions in electrodeposited CuInSe₂ thin films," *J. Appl. Phys.*, vol. 69, no. 1, pp. 429–432, Jan. 1991.
<https://doi.org/10.1063/1.347734>
- [20] K. K. Mishra and K. Rajeshwar, "A voltammetric study of the electrodeposition chemistry in the Cu + In + Se system," *J. Electroanal. Chem. Interfacial Electrochem.*, vol. 271, no. 1, pp. 279–294, 1989. [https://doi.org/10.1016/0022-0728\(89\)80082-8](https://doi.org/10.1016/0022-0728(89)80082-8)
- [21] A. M. Fernández and R. N. Bhattacharya, "Electrodeposition of CuIn_{1-x}GaxSe₂ precursor films: optimization of film composition and morphology," *Thin Solid Films*, vol. 474, no. 1, pp. 10–13, 2005. <https://doi.org/10.1016/j.tsf.2004.02.104>
- [22] A. A. C. Alcanfor, L. P. M. dos Santos, D. F. Dias, A. N. Correia, and P. de Lima-Neto, "Electrodeposition of indium on copper from deep eutectic solvents based on choline chloride and ethylene glycol," *Electrochim. Acta*, 2017. <https://doi.org/10.1016/j.electacta.2017.03.082>

Electroluminescence image-based defective photovoltaic (solar) cell detection using a modified deep convolutional neural network

Hiren MEWADA^{1,a*}, L. SYAMSUNDAR^{2,b}, Hiren Kumar THAKKAR^{3,c} and Miral DESAI^{4,d}

¹Electrical Engineering Department, Prince Mohammad Bin Fahd University, P.O. Box 1664, Al Khobar 31952, Kingdom of Saudi Arabia

²Mechanical Engineering Department, Prince Mohammad Bin Fahd University, P.O. Box 1664, Al Khobar 31952, Kingdom of Saudi Arabia

³Department of Computer Science and Engineering, School of Technology, Pandit Deendayal Energy University, Gandhinagar, Gujarat, India, 382421

⁴V. T. Patel Department of Electronics and Communication Engineering, Chandubhai S Patel Institute of Technology, Charotar University of Science and Technology, Changa, Gujarat, India

^ahmewada@pmu.edu.sa, ^bslingala@pmu.edu.sa, ^chiren.pdeu@gmail.com,
^dmiraldesai.ec@charusat.ac.in

Keywords: Renewable Energy, Photovoltaic Solar Panels, Deep Convolution Neural Network, Image Classification

Abstract. Electroluminescence (EL) imaging of photovoltaic solar cells can detect and classify solar panel faults. This method allows technicians and manufacturers to identify defective panels that may affect performance and longevity. However, noise in EL images and solar cell silicon granularity make this process difficult. The paper presents an automated deep-learning framework to identify faulty and normal solar cells from images. Xception, a popular CNN network, is modified to reduce complexity and solve overfitting issues. Few separable convolution layers were removed from the original Xception network, and lateral dropout layers were added. The proposed deep CNN is tested on ELVP. To balance two classes, images are augmented with two rotations and dimensional shifting. Finally, the proposed model is compared to a pretrained CNN network and leading methods. The quantitative analysis showed that the model performed better than previous methods, with 94.382% accuracy, 92% precision, 95.12% recall rate, and 93.53% F1 score. Module fault identification helps with maintenance planning. Solar energy's widespread adoption and growth as a renewable and sustainable power source may result.

Introduction

Solar power has grown in popularity as a renewable energy source. Over the past decade, massive solar power plants worldwide have enabled large-scale solar energy component production. The photovoltaic (PV) module is essential to solar power. How well solar energy systems work depends on solar module efficiency. Crystalline silicon (c-Si) photovoltaic (PV) modules are the most popular due to their low cost per watt and well-established manufacturing process. Tang et al. [1], say this technology accounts for 97% of monocrystalline and polycrystalline module sales.

Solar panel fault classification is necessary for several reasons. First, a solar panel fault can reduce energy output. It streamlines maintenance planning and resource allocation. Technicians can optimize their efforts and address critical issues quickly by categorizing and prioritizing faults by severity and impact. Additionally, fault classification in electroluminescent solar panels has helped develop predictive maintenance strategies. By analyzing historical fault data and understanding patterns and trends, predictive models can predict and prevent faults. In solar panel manufacturing, fault classification is crucial to quality control. Before deployment, manufacturers can identify and classify panel defects using imaging. This ensures customers receive high-quality

panels, improving satisfaction and reducing the risk of premature failure or performance degradation.

These solar panel faults can be identified using I-V curve measurements, thermal-infrared imaging (IR), and electroluminescence (EL) imaging. The I-V curve approach utilizes graphs to display PV module voltage and current output under specific radiation conditions. While the I-V curve can show module status, it cannot identify faulty cells or their locations. Using infrared imaging to monitor solar modules and cells is another popular method. An open circuit can cool a place, while a large current can heat it. IR imaging can detect dead cells, hot spots, and short circuits. However, thermal cameras' low resolution prevents them from detecting microcracks [2]. Such issues can be resolved via EL imaging. One nondestructive way to detect PV module defects is with an EL test. EL imaging can discover faulty cells and regions with ease and provide a thorough evaluation of all PV module cells. The overall status and longevity of the module can be determined at any stage[3].

Electroluminescence (EL) imaging is useful for fault detection and characterization in PV panels. As solar energy becomes more popular as a clean and sustainable power source, PV panel performance and longevity are crucial. Solar panel faults can be identified and classified noninvasively and efficiently using EL imaging, maximizing energy generation and maintenance. Images of solar cells' electroluminescent response to an electric field are captured using EL imaging. These images allow the detection of cracks, hotspots, and degradation patterns that may not be visible to the naked eye.

Some common fault types observed in EL images include cracks, i.e., visible breaks in solar cell structures, localized areas of high temperature, referred to as hotspots, and degradation patterns. This leads to reduced efficiency, resulting in diminished power output. By classifying these faults, technicians can identify the severity of the issue and take appropriate actions to rectify or mitigate its impact.

There are key challenges associated with fault classification. Manually inspecting and classifying faults in each panel is time-consuming and impractical as the number of solar panels in large-scale installations increases. Automating the classification process through the development of intelligent systems and algorithms is crucial for efficiently handling the volume of data generated by multiple panels. Thus, there is a need to create an automated classification system that can effectively categorize and differentiate between various fault types, which requires a deep understanding of the underlying physics and characteristics of each fault. Deep learning has emerged as a powerful data-driven approach for image classification applications because it can learn directly from a set of images. However, there are certain challenges associated with using deep learning for EL image classification. The limited spatial resolution, lack of color information, presence of noise and artifacts in images and limited spectral information are the major challenges associated with the use of deep learning for accurate classification.

There are many studies on EL imaging-based faulty panel identification. Overall, these methods can be categorized into traditional and machine learning algorithms. Several of the traditional methods include a logical gate-based image processing algorithm to enhance the crack regions [4], independent component analysis [5] and an anisotropic filter-based SVM approach for crack detection [6]. In this section, we review machine learning approaches. Zhang et al. [7] proposed a lightweight CNN with a size of 1.85 M learnable parameters based on the ResNet architecture for EL image classification. Based on the probability values, the overall set of images is divided into two classes, where panels are considered defective if their probability values are greater than 0.5. Their model achieved a maximum classification accuracy of 91.74%. In [8], the EL images were enhanced by equalizing the histogram of the images. Then, global information using the GCAM algorithm was integrated into an EfficientNet architecture to detect types of cracks or defects in the images. Attention-based deep learning was used in [9] to identify faulty panels from surface

images of panels and achieved 98.66% accuracy. An RGB dataset of panels with dust, cement, cracks, etc., are classified as faulty types in this research. The dataset contains dusty panel images that cannot be considered defective panels. In [10], the authors prepared their dataset using an OPT-M311 camera. They used image augmentation with rotation, brightness adaptation and mirror shifting. This dataset was used to train the CNN network. Their network performed well, with 98.40% accuracy. However, validation on open-source datasets was not presented in the paper. Rahman et al. [11] tested various pretrained CNN architectures, including VGG and its variant, ResNet50 variant and the Xception network, to identify defective panels from a set of images. In their experiment, they sorted images into three categories, i.e., uncracked, cracked and unsure, which are too distorted. Although unsure images have notation, due to large distortions, they differentiate them from a set of functional and defective images. The Inception V3 network achieved 96% accuracy on monocrystalline panels, and VGG16 achieved 91.2% accuracy on polycrystalline panels. The limitation of this work is that the overall accuracy of combining both methods was not presented in the paper.

This paper presents a low-complexity, resource-efficient deep convolution network for EL image classification. We modified the Xception network to classify EL images into two classes, i.e., normal or defective. The major challenges in EL images are their low resolution and lack of spectral information. The use of a depthwise separable convolution layer in the Xception network allows efficient modeling of spatial relations within images that capture both global and local features. Therefore, we modified an Xception network by reducing its learning parameters and providing efficient classification with a small dataset. The remainder of this paper is organized as follows: Section 2 presents the proposed modified Xception network for EL image classification. Section 3 discusses the dataset and results using the proposed network. Finally, a conclusion is established based on the experimental results.

Proposed Methodology

The deep neural network plays a vital role in image categorization. A wide variety of pretrained networks are available for use in image classification. However, the types of images are the key aspect of selecting the CNN network. As explained in Section 1, electroluminescence imaging is a better choice for detecting faults within the cell of a PV module. However, the lack of spectral information and resolution makes this process challenging. A traditional CNN applies a set of filters K to the input feature map X with dimensions $H \times W \times C$, where H represents the height, W represents the width, and C represents the number of input channels. For the EL images, C is 1. Each filter has dimensions $F \times F \times C$, where F represents the filter size. The convolution operation is performed by sliding each filter across the input feature map, computing the elementwise multiplication between the filter and the corresponding spatial region of the input, and summing the results to produce an output feature map.

The Xception network modifies this convolutional operation by separating the spatial and channelwise information. It introduces two separate convolutional operations: depthwise convolution and pointwise convolution. The depthwise convolution operates on each input channel independently. It applies a set of depthwise filters, denoted as K_d , to each input channel of the feature map X . The depthwise filters have dimensions $F \times F \times 1$, where 1 represents the number of input channels. The depthwise convolution produces a set of intermediate feature maps, denoted as M , with dimensions $H \times W$. Mathematically, the depthwise convolution can be represented as:

$$M = \text{DepthwiseConv}(X, K_d) \quad (1)$$

The pointwise convolution performs a 1×1 convolution on the intermediate feature maps M obtained from the depthwise convolution. It applies a set of pointwise filters, denoted as K_p , to combine and transform the intermediate feature maps. The pointwise filters have dimensions of $1 \times 1 \times C'$, where C' represents the number of output channels. The pointwise convolution produces

the final output feature map, denoted as Y , with dimensions $H \times W \times C'$. Mathematically, it can be represented as:

$$Y = \text{PointwiseConv}(M, K_p) \quad (2)$$

By separating the spatial and channelwise convolutions, the Xception network reduces the number of parameters and computations compared to standard convolutions. This parameter efficiency makes the Xception network computationally efficient and suitable for deep learning tasks with limited computational resources. The Xception network architecture repeats the depthwise and pointwise convolutions in multiple layers, enabling the network to learn hierarchical representations of features at different scales and complexities. Additionally, the Xception network often incorporates other common components found in deep neural networks, such as pooling layers, activation functions, and fully connected layers, to further enhance its performance. The structure of the Xception network, shown in Figure 1, is established based on the experimental results.

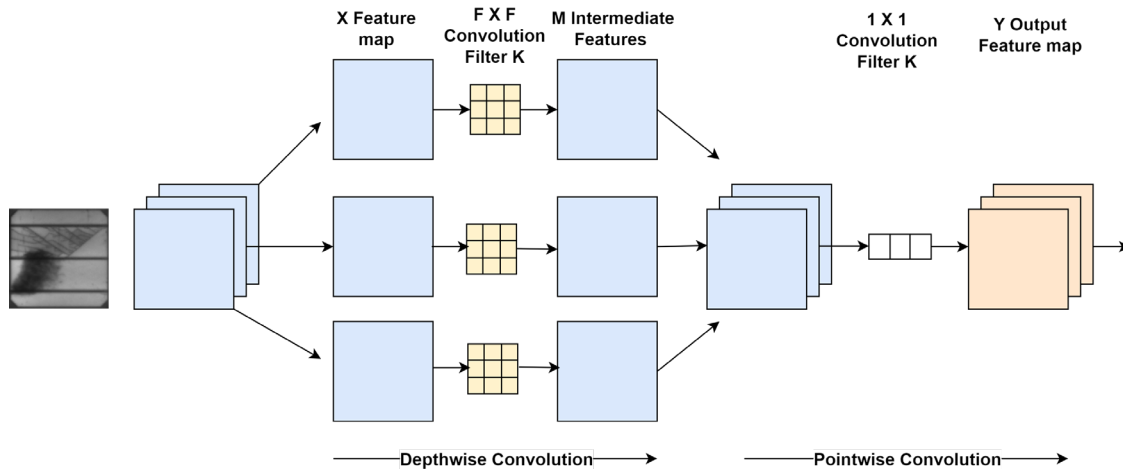


Figure 1 Xception network structure for convolution operation

The Xception network is built using stacking depth-separable convolution and comprises 14 modules, each with 36 convolutional layers. All of the layers utilize this technique except for the first 2 and the ones linked by residuals; the basic network is also built using this method. The pretrained Xception network has 170 deep layers with 22.9 million learnable parameters. The internal structure represented in Figure 2 is repeated 12 times with additional separable convolution layers in a few of the blocks. Here, this network is modified to classify grayscale EL images. In the proposed network, the initial layer is modified for grayscale images. The initial 80 layers of the pretrained Xception network are the same as those of the proposed network. The size of the network is reduced by removing the last four blocks. In addition, dropout layers are added to block 7 and the last block of the structure to reduce the feature size. These dropout layers help to solve the problem of network overfitting. The overall proposed structure has 120 layers with 14.3 M learnable parameters.

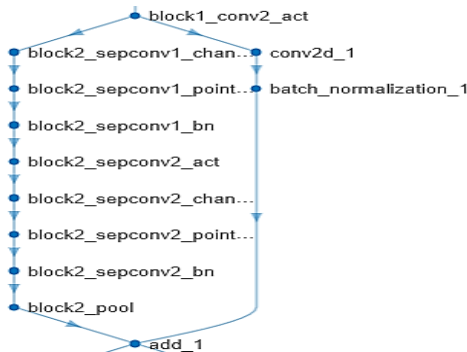


Figure 2 One block of convolution operations in the Xception network

Result Analysis and Discussion

Dataset

There is a wide variety of PV cell faults; however, not all of them will cause a significant drop in power output. The power output of the module is unaffected by some flaws, but it can be reduced over time, or the cells can disengage from the module due to others [12]. EL imaging can reveal cracks, microcracks, fractures, disconnections, silicone material flaws, finger disruptions, and unconnected cells. In this study, overall, PV cells were classified into two categories, i.e., normal and defective, if the panel had any of the above abnormalities. The ELVP dataset prepared using 18 monocrystalline and 26 polycrystalline PV panels from [13] was used in the experiments. A total of 2624 EL solar cell images, including 1508 normal images and 1116 defective images, are available in this dataset. Out of 1116 defective images, 715 images are faulty with 100% probability, and the remaining images have a lower probability of being faulty. Therefore, in the experiment, we used 1508 normal images and 716 defective images. We divided the EL images into a training set consisting of 80% (1206 normal and 573 defective) and a test set consisting of 20% for dataset partitioning. The sample images of both the normal and defective panels are shown in Figure 3.

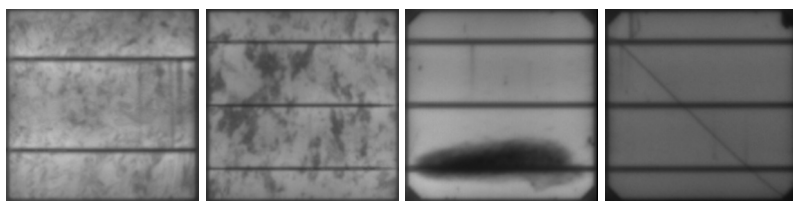


Figure 3 Sample images from the dataset (the left two images are normal panels, and the right two images are defective panels)

The small size of the dataset causes overfitting. Therefore, before using this dataset, an augmentation of images is used to enlarge the dataset. The dataset used had perfectly aligned EL images. Therefore, during the augmentation process, rotations of 90° and 180° were used. In addition, random shifting in both the X-direction and Y-direction is performed by increasing the set of training and testing images. This also helps to address the imbalance between the two classes.

Results and Discussion

The ADAM optimizer is used in a modified Xception network. The learning rate is initialized to 0.0001. The maximum number of epochs used is 10, and 64 is selected for the mini-batch size. Images are shuffled at every epoch for better network performance. We decided to quantify the classification effect and performance of our suggested model using accuracy, recall, precision, and F1 score, which are four commonly used metrics for evaluating and comparing effective models. In particular, higher values indicate better results for F1, recall, accuracy, and precision. If true positives (TPs) and true negatives (TNs) represent the number of positive results, for example, corrected detection of normal and defective panels, whereas false positives (FPs) and false negatives (FNs) represent the number of negative results, then these matrices can be calculated as follows:

$$\text{Precision} = \frac{TP}{TP+FP},$$

$$\text{Accuracy} = \frac{TP+TN}{TP+TN+FP+FN}$$

$$\text{Recall} = \frac{TP}{TP+FN} \quad (3)$$

$$\text{F1 Score} = \frac{2 \times \text{Precision} \times \text{Recall}}{\text{Precision} + \text{Recall}} \quad (4)$$

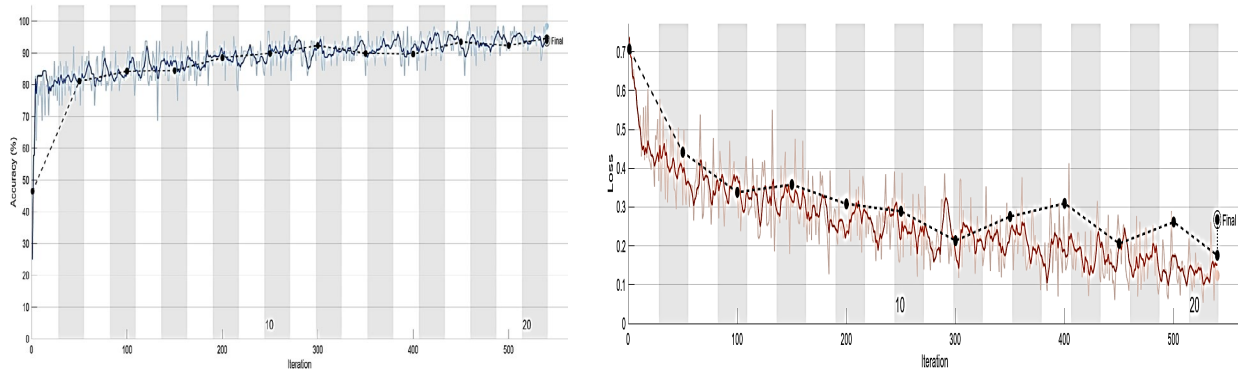


Figure 4 Accuracy and loss variation over time for the training and test datasets

The normal PV cell EL images had a uniform surface, but they had shadowed areas or impurities in the background. The backgrounds were clear and textured, but they were not defective; this put some pressure on the model to find defects. It was challenging to differentiate the surface defects of aberrant PV cells from the background in the EL image because they looked so similar to the background in the original image. The accuracy and loss analysis over the epochs for the training dataset are shown in Figure 4. Figure 4 shows that the model succeeded in achieving 93.93% accuracy with a training loss of less than 0.2.

The confusion matrix represents the TP, TN, FP and FN results of the network. Figure 5 shows the confusion matrix of the proposed network for the training dataset.

Output Class			Defective	Normal
	Defective	Normal		
Defective	122 27.4%	4 0.9%	96.8% 3.2%	
Normal	21 4.7%	298 67%	93.4% 6.6%	
	85.3% 14.7%	98.7% 1.3%	94.4% 5.6%	
Target Class				

Figure 5 Confusion matrix of the modified Xception network

In Figure 5, the first two diagonal cells show the number and percentage of correct classifications by the network. For example, 122-panel images are correctly classified as defective. This corresponds to 27.4% of all test set images. Similarly, 298 cases are correctly classified as normal. This corresponds to 67% of all test images. Twenty-one of the defective panels are incorrectly classified as normal, which corresponds to 4.7% of all images. Out of 302 normal test images, 98.7% are correct and 1.3% are incorrect. Overall, 94.4% of the predictions are correct, and 5.6% are wrong.

Some of the most successful approaches to PV defect detection in the past few years were compared to our model. We selected these approaches for testing and assessment on the same dataset as our proposed model to ensure a fair comparison; Table 1 displays the results of the method comparison.

Table 1 Comparison of the experimental results with those of other methods

Model	Accuracy	Precision	Recall	F1 Score
CNN [14]	78.38	77.86	70.10	71.84
VGG16 [14]	84.01	82.26	80.31	81.15
InceptionV3 [14]	88.96	87.73	86.72	87.20
SVM [15]	82.44	-	-	85.52
CNN [15]	88.42	-	-	88.39
L-CNN [16]	89.33	90.44	95.42	92.86
Our network	94.382	92	95.12	93.53

As shown in Table 1, pretrained networks, including CNN, VGG16 and InceptionV3, were tested in [14], and their models were compared. The presence of noise makes it challenging, and therefore, these models struggle to classify faulty panels from the set of images. In [15], the authors extracted various VGG-based CNN features, and SVM was used as a classifier. A validation of the experiment using mono-, poly- and the overall set of images was presented in the paper. However, their accuracy was limited to 88.42 max when using a CNN. In [16], a lightweight convolutional neural network was presented. They trained it from scratch, and a comparison with a support vector machine was presented in their work. Their light CNN succeeded at 89.33% accuracy for two-class classification. In contrast, the modification of the Xception network with the removal of a few separable convolution layers and the introduction of dropout layers performed well on augmented images and achieved 90% accuracy.

Conclusion

Solar cells have crystal grain boundaries due to the intrinsic silicon structure, and the presence of noise in EL images causes ambiguity in distinguishing minor cracks. In addition, EL images lack spectral information. These characterizations impose a challenge to applying conventional CNN networks to identify faulty cells from normal cells. In this paper, we used the Xception network to determine whether a panel is defective. The large number of layers in deep CNNs increases the complexity of the network; hence, the network cannot learn well from grayscale images. Therefore, the network is minimized by removing repetitive separable convolution layers. Furthermore, dropout layers are introduced in the Xception network to solve the overfitting problem, and the experimental results and a comparison with state-of-the-art methods suggest that the model's classification accuracy is improved. The experimental results are validated for binary classification only. Therefore, further validation of the network for multiclass classification will be performed in the future.

References

- [1] W. Tang, Q. Yang, K. Xiong, and W. Yan, "Deep learning based automatic defect identification of photovoltaic module using electroluminescence images," *Solar Energy*, vol. 201, pp. 453–460, May 2020. <https://doi.org/10.1016/j.solener.2020.03.049>
- [2] M. W. Akram *et al.*, "CNN based automatic detection of photovoltaic cell defects in electroluminescence images," *Energy*, vol. 189, p. 116319, Dec. 2019.
- [3] U. Jahn, M. Herz, M. Köntges, D. Parlevliet, M. Paggi, and I. Tsanakas, *Review on infrared and electroluminescence imaging for PV field applications: International Energy Agency Photovoltaic Power Systems Programme: IEA PVPS Task 13, Subtask 3.3: report IEA-PVPS T13-12:2018*. Paris: International Energy Agency, 2018.
- [4] M. Dhimish, V. Holmes, and P. Mather, "Novel Photovoltaic Micro Crack Detection Technique," *IEEE Trans. Device Mater. Relib.*, vol. 19, no. 2, pp. 304–312, Jun. 2019. <https://doi.org/10.1109/TDMR.2019.2907019>

- [5] D.-M. Tsai, S.-C. Wu, and W.-Y. Chiu, “Defect Detection in Solar Modules Using ICA Basis Images,” *IEEE Trans. Ind. Inf.*, vol. 9, no. 1, pp. 122–131, Feb. 2013.
<https://doi.org/10.1109/TII.2012.2209663>
- [6] S. A. Anwar and M. Z. Abdullah, “Micro-crack detection of multicrystalline solar cells featuring an improved anisotropic diffusion filter and image segmentation technique,” *J Image Video Proc.*, vol. 2014, no. 1, p. 15, Dec. 2014. <https://doi.org/10.1186/1687-5281-2014-15>
- [7] J. Zhang, X. Chen, H. Wei, and K. Zhang, “A lightweight network for photovoltaic cell defect detection in electroluminescence images based on neural architecture search and knowledge distillation,” *Applied Energy*, vol. 355, p. 122184, Feb. 2024.
- [8] Q. Liu, M. Liu, C. Wang, and Q. M. J. Wu, “An efficient CNN-based detector for photovoltaic module cells defect detection in electroluminescence images,” *Solar Energy*, vol. 267, p. 112245, Jan. 2024. <https://doi.org/10.1016/j.solener.2023.112245>
- [9] D. Dwivedi, K. V. S. M. Babu, P. K. Yemula, P. Chakraborty, and M. Pal, “Identification of surface defects on solar PV panels and wind turbine blades using attention based deep learning model,” *Engineering Applications of Artificial Intelligence*, vol. 131, p. 107836, May 2024.
<https://doi.org/10.1016/j.engappai.2023.107836>
- [10] M. Sun, S. Lv, X. Zhao, R. Li, W. Zhang, and X. Zhang, “Defect Detection of Photovoltaic Modules Based on Convolutional Neural Network,” in *Machine Learning and Intelligent Communications*, vol. 226, X. Gu, G. Liu, and B. Li, Eds., in Lecture Notes of the Institute for Computer Sciences, Social Informatics and Telecommunications Engineering, vol. 226. , Cham: Springer International Publishing, 2018, pp. 122–132. https://10.1007/978-3-319-73564-1_13
- [11] Md. R. Rahman, S. Tabassum, E. Haque, M. M. Nishat, F. Faisal, and E. Hossain, “CNN-based Deep Learning Approach for Micro-crack Detection of Solar Panels,” in *2021 3rd International Conference on Sustainable Technologies for Industry 4.0 (STI)*, Dhaka, Bangladesh: IEEE, Dec. 2021, pp. 1–6. doi: 10.1109/STI53101.2021.9732592
- [12] M. Köntges, S. Kurtz, C. Packard, U. Jahn, K. A. Berger, and K. Kato, *Performance and reliability of photovoltaic systems: subtask 3.2: Review of failures of photovoltaic modules: IEA PVPS task 13: external final report IEA-PVPS*. Sankt Ursen: International Energy Agency, Photovoltaic Power Systems Programme, 2014.
- [13] L. Pratt, J. Mattheus, and R. Klein, “A benchmark dataset for defect detection and classification in electroluminescence images of PV modules using semantic segmentation,” *Systems and Soft Computing*, vol. 5, p. 200048, Dec. 2023.
<https://doi.org/10.1016/j.sasc.2023.200048>
- [14] J. Wang *et al.*, “Deep-Learning-Based Automatic Detection of Photovoltaic Cell Defects in Electroluminescence Images,” *Sensors*, vol. 23, no. 1, p. 297, Dec. 2022.
<https://doi.org/10.3390/s23010297>
- [15] S. Deitsch *et al.*, “Automatic classification of defective photovoltaic module cells in electroluminescence images,” *Solar Energy*, vol. 185, pp. 455–468, Jun. 2019.
<https://doi.org/10.1016/j.solener.2019.02.067>
- [16] M. Y. Demirci, N. Beşli, and A. Gümüşçü, “Efficient deep feature extraction and classification for identifying defective photovoltaic module cells in Electroluminescence images,” *Expert Systems with Applications*, vol. 175, p. 114810, Aug. 2021.
<https://doi.org/10.1016/j.eswa.2021.114810>

Analysis of thermal efficiency of solar flat plate collector working with hybrid nanofluids: An experimental study

Solomon MESFIN^{1,a}, Veeredhi VASUDEVA RAO^{2,b}, L. Syam SUNDAR^{3,c,*}

¹Department of Mechanical Engineering, University of Gondar, Gondar, Ethiopia

²Department of Mechanical Engineering, School of Engineering, CSET, University of South Africa (UNISA), South Africa

³Department of Mechanical Engineering, College of Engineering, Prince Mohammad Bin Fahd University, Al-Khobar, Saudi Arabia

^asolomonmesfin5@gmail.com, ^bvasudvr@unisa.ac.za, ^csslingala@gmail.com

Keywords: Thermal Efficiency, Flat Plate Collector; Hybrid Nanofluids; Augmentation, Solar Energy

Abstract. Thermal efficiency of solar flat-plate collector (SFPC) was analyzed experimentally through water-based mono Al₂O, CuO, and hybrid Al₂O₃-CuO nanofluids. The particle loadings used for the analysis are 0.048%, 0.096%, 0.144%, 0.192% and 0.24%, respectively. The experiments were conducted at a flow rate of 0.008 kg/s of mono, and hybrid nanofluids. The experimental outcomes indicate, the thermal efficiency of mono and hybrid nanofluids raised under the larger volume loadings in comparison with water. Results show, that the Al₂O₃-CuO hybrid nanofluid offered higher thermal efficiency values than mono Al₂O₃ and CuO nanofluids. Thermal efficiency of SFPC was found to get enhanced by 57.66%, 66.58% and 73.75% at 0.24 vol.% Al₂O₃, CuO, and Al₂O₃-CuO hybrid nanofluids, over the water data, respectively, at solar noon time of 12:00 P.M.

Introduction

The depletion of fossil resources has resulted in a global energy shortage. In the current situation, energy is critical to industrial and economic development, hence efforts must be necessary to fix the problem of using fossil fuels with alternative fuels. The ongoing movement in development toward sustainability and better environmental responsibility connected with future development, emphasizes the need for renewable energy.

Renewable energy is a rapidly growing industry, with numerous innovations and applications emerging. The concept of localized renewable energy systems has been recognized as a solution to industries and residential energy demands. The depletion of natural resources and the growing demand for traditional energy have prompted planners and decision-makers to look into other sources. As the cost of conventional energy sources rises, there is a growing interest in renewable energy sources. Recently, there has been a great deal of effort in the field of renewable energy source engineering, particularly in the generation of solar energy. Unfortunately, the spectrum of feasible applications is limited to large-output arrays, prohibitively expensive technology, and massive assemblies requiring large parcels of land and expenses because a significant portion of the development of said renewable energy generation has not been for utilities.

The sun emits solar energy into space, but only 1367 W/m² penetrates Earth's atmosphere [1]. The energy received from the solar mean in a certain time interval of time on a 1 m² area can be estimated that, the radiation during that particular time period, which is known as solar radiation or insulation. This is called as direct and diffuse solar radiation [2]. Three major criteria influencing the performance of solar energy systems in converting direct and diffuse sunlight into useable energy are a given location's geographical coordinates, topography, and climatic conditions [3].

Thermal converters capture thermal energy, which is then transferred to a fluid that circulates through the panel. The solar radiation concentrators are non-concentrator type, i.e. flat plate or vacuum tubes, and concentrated type collectors. Flat non-concentrated heat collectors (which require pipes to connect the two components) are made up of numerous parts: a transparent glass cover, pipes, absorbers, and a thermal insulating layer. In contrast, the vacuum tubes' solar thermal collector is made up of absorbers, glass tubes, heat pipes, and an insulated casing [4]. In both systems, the absorber is critical to the heat transfer process, which requires high thermal conductivity. To limit the heat losses, the insulation between absorber and collector housing must be adjusted. Such factors necessitate the use of high price materials, raising the initial cost of collectors [5].

Literature review

Solar flat plate collectors (SFPC) consist of a heat-absorbing plate, serpentine tube, insulation and a heat transmitting cover. Solar energy falls on the absorber plate, and which is transmitted into the working fluid in a tube based on the convection mode of heat transfer. The absorber is made from high thermal conductivity aluminum metal sheet. Even though these SFPC are used commonly, further larger in thermal efficiency of these collectors is necessary, because they are still under low thermal efficiencies [6]. Studies to improve the thermal efficiency of SFPC have included the redesigning of riser's channels [7], re-designing the top glazing in the collector and changing the heat-transfer fluid.

One of the most convenient and successful methods for increasing the improvement of SFPC is to introduce the nanofluids into the collector's tubes instead of standard heat transfer fluids such as water. Choi and Eastman introduced the term "nanofluid" for the first time [8]. The nanofluid is a colloidal dispersion of nanoparticles in base fluids (size less than 100 nm). Dispersing solid nanoparticles into the base fluid improved thermal conductivity. Nanofluids can dramatically increase thermal conductivity and heat transfer coefficient [9]. Nanofluids have a larger density and a lower specific heat, which leads to increased thermal efficiency. As a result, it minimizes the solar collector's area, weight, energy, and manufacturing costs.

Nanofluids are classified into mono and hybrid nanofluids [10]. The hybrid nanofluids are new generation and homogeneous mixture fluids which can be prepared by suspending different types (two or more than two) of nanoparticles in base fluid with developed physical and chemical bonds. Due to synergistic effect, the thermal conductivity and heat transfer of hybrid nanofluids are higher than individual nanofluids [11], Lee and Sharma [12]. Experimental results show that ethylene glycol as heat transfer fluid (HTF) in active solar flat plate heat (SFPH) system is good for cold climate countries due to its antifreeze properties.

Geovo et al. [13] considered experimental data of water diluted MgO nanofluids in SFPC for the purpose of comparison with the MATLAB software. They noticed maximum relative error of 5.36% and minimum relative error of 0.20% between experimental and software data. Choudhary et al. [14] obtained thermal efficiency increase of 16.7% for MgO-ethylene glycol/distilled water nanofluids in a FPSC under 0.2 vol% at a flow rate of 1.5 L/min. Verma et al. [15] used different nanofluids in a FPSC and analyzed energetic and exergetic parameters and obtained 23.47% increase of thermal efficiency at 0.75 vol% and at a flow rate of 0.025 kg/s for MNCNT/water as the working fluid. Moghadam et al. [16] considered water mixed CuO nanofluids in a FPSC and seen 21.8% of increase of thermal efficiency at vol. of 0.4 and at 3 kg/min. Yousefi et al. [17] found 28.3% increase of collector thermal efficiency by using Al₂O₃/water nanofluids in a FPSC. In another analysis, Yousefi et al. [18] analyzed the collector thermal efficiency by changing the nanofluids pH value, and they mentioned that, nanofluid pH also one of the influencing parameters for the collector efficiency. Belkassmi et al. [19] obtained efficiencies of 4.45%, 4.28%, and 4.22% at 2.0 lit/min, based on the experimental data of water dispersed Cu, CuO, and Al₂O₃ nanofluids in FPSC, respectively.

With the utilization of mono nanofluids, the collector thermal efficiency is enhanced. Similarly, researchers have concentrated the use of hybrid nanofluids in FPC. Elshazly et al. [20] seen an enhanced thermal efficiency of 26% by using hybrid nanofluids of MWCNT/Al₂O₃ (50:50%) in a FPSC at 1.5 lit/min.

This work is to estimate experimentally the thermal efficiency of water diluted Al₂O₃-CuO nanofluids flow in a FPSC with various volumetric concentrations. In addition to the above, the study is also focused on to investigation of efficiency of water-based copper oxide (CuO) and aluminum oxide (Al₂O₃) nanofluids alone and compare with the Al₂O₃-CuO water based nanofluid at constant mass flow rate to get the required amount of heat for water heating applications.

Experimental study

Preparation of nanofluids

The nanofluids are prepared by mixing the nanoparticles with water. Table 1 is the physical properties of Al₂O₃, CuO and water, and Table 2 is the weights of CuO and Al₂O₃ nanoparticles used for water for development of various nanofluids. Step-by-step procedure of nanofluids preparation is mentioned in Fig. 1.

Table 1: The physical properties of Al₂O₃, CuO and water.

Nanoparticle/ base fluid	ρ , kg/m ³	C_p , (J/kgK)	k , (W/mK)	Color	Diameter, (nm)
Al ₂ O ₃	3900	785.2	30	White	50
CuO	6510	540	33	Black	27
Water	1000	4179	0.613	---	---

Table 2: Weights of CuO, and Al₂O₃ nanoparticles used for water for the preparation of various nanofluids.

Mass of nanoparticles (g)	Particle volume loading (%)				
	$\phi = 0.048\%$	$\phi = 0.096\%$	$\phi = 0.144\%$	$\phi = 0.192\%$	$\phi = 0.24\%$
CuO (g)	25	50	75	100	125
Al ₂ O ₃ (g)	15	30	45	60	75
Al ₂ O ₃ -CuO, (g)	20	40	60	80	100
Water (lit)	8	8	8	8	8

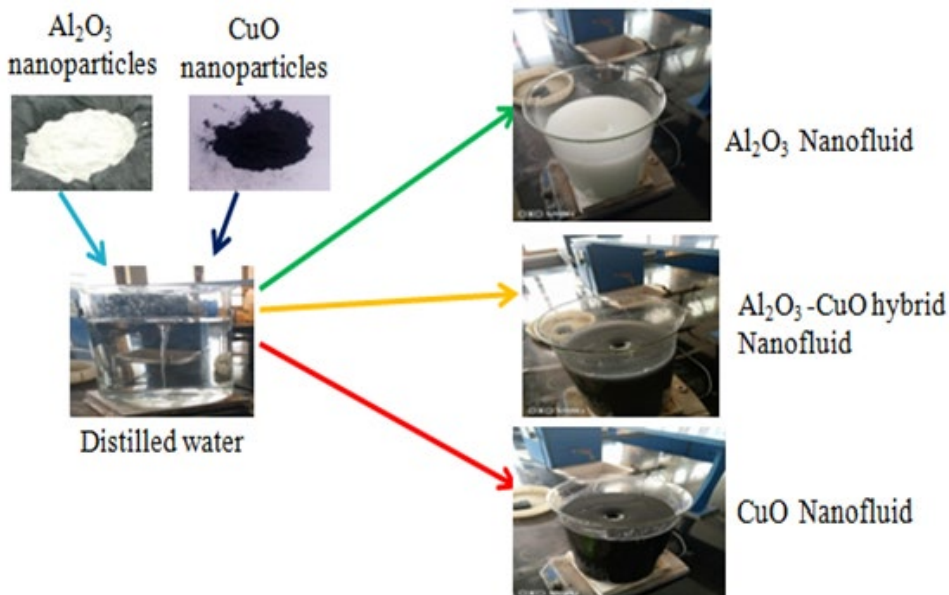


Fig. 1: Preparation of water-based mono and hybrid nanofluids.

Flat plate collector

The experimental set-up of flat plate collector is shown in Fig. 2, and which is used for water, mono, and hybrid nanofluids and its thermal efficiency is estimated. The solar collector was placed in the Gondar town, Ethiopia, which is located on 12.6° N latitude and 37.47° E longitude in the northern hemisphere with an elevation of 2133 meters above sea level. For maximum captured radiation, the flat plate solar collector was installed at 27.6° tilt angle. The set-up mainly consists of an absorber plate to absorb incident solar radiation, a single glass cover to protect collector heat loss, serpentine tube for fluid passage through the solar collector, storage tank to store working fluids for experimentation and used as heat exchanger, a pump capable to deliver the fluid to the serpentine pips, by-pass valve for returning of fluids after adjusting the control valve, adjustable valves to control flow rate one at the main flow loop and the other at the by-pass line, flow meter to measure the fluid flow rate, cold water storage tank, table to support water tank, and collector support to carry the flat plate solar collector. During the experimental test, the glass temperature, plate temperature, inlet and outlet temperatures and mass flow rates of the working fluids are measured to obtain the thermal efficiency of the flat plate solar collector.

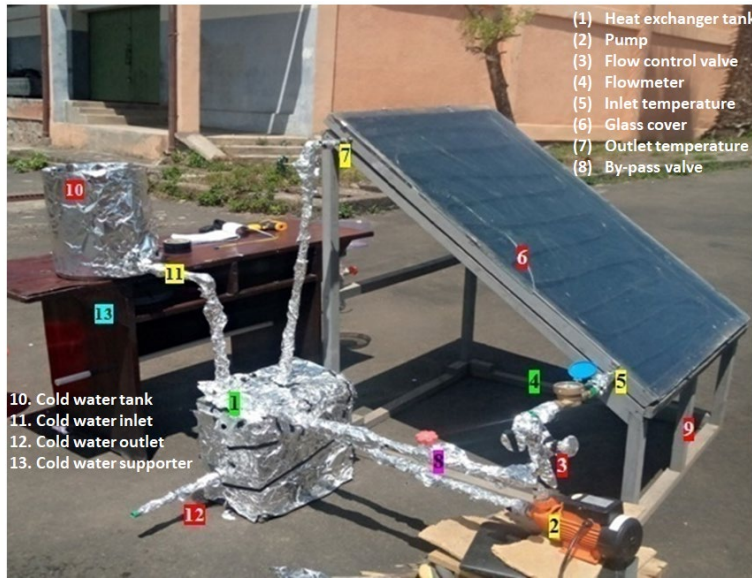


Fig. 2: Photograph of flat plate collector.

Data analysis

Collector thermal efficiency analysis

Thermal performance of solar collector is evaluated through the instantaneous collector efficiency, which requires the amount of solar radiation attracted by the collector. The useful heat energy of the working fluid is determined by the following equations.

$$Q_u = \dot{m}C_{pf}(T_o - T_i) \quad (1)$$

$$\eta_{th} = \frac{Q_u}{A_c I_T} \quad (2)$$

$$\eta_{th} = \frac{\dot{m}C_{pf}(T_o - T_i)}{A_c I_T} \quad (3)$$

Where, C_p is specific heat (KJ/kgK), T_o is outlet temperature (K), T_i is inlet temperature (K), η_{th} is the thermal efficiency, and Q_u useful heat energy or the incident solar energy, A_c is absorber area (m^2), and I_T is the incident solar energy (W/m^2).

Results and discussion

Temperature distribution

In Fig. 3, it is seen that the highest outlet temperature at solar noon for 0.24% volumetric concentrations of Al_2O_3 , CuO and Al_2O_3-CuO hybrid water based nanofluids are 62.4 °C, 69 °C, and 86.7 °C, respectively. From the above experimental readings it is noticed that the Al_2O_3-CuO hybrid nanofluids outlet temperatures of flat plate solar water heating is higher than individual nanofluids and CuO nanofluid outlet temperatures is also higher than Al_2O_3 and base fluid. Due to larger random collisions of nanoparticles in base fluid, the outlet temperature of the nanofluid is raised. Therefore, increasing the volume particle concentrations of nanofluids and hybridizing the nanoparticles raises the exit temperature of the fluid by increasing the absorptivity of SFPC.

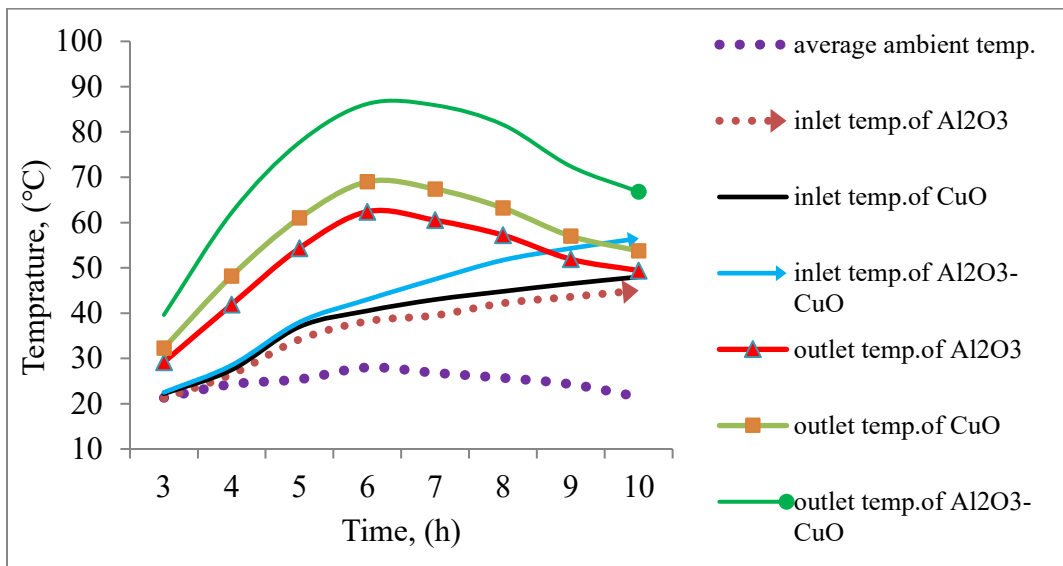


Fig. 3: Temperature records at $\phi = 0.24\%$ particle concentration nanofluids with time.

Heat gain in the collector

Fig. 4 gives compression of useful heat gained by the distilled water and 0.048% nanoparticle concentration of single and hybrid water-based nanofluids at constant mass flow rate of 0.008 kg/s. Maximum useful energy of distilled water and 0.048% particle volume concentration of Al₂O₃, CuO and Al₂O₃-CuO hybrid water based nanofluids are 574.15 W/m², 627.76 W/m², 691.82 W/m², and 799.72 W/m² respectively. This shows that useful heat energy of distilled water was less with the same mass flow rate compared to 0.048% Al₂O₃/water nanofluid and the useful heat energy of CuO nanofluid is greater over Al₂O₃ nanofluid under a fixed particle volume loading and fluid flow rate, also, useful heat energy of Al₂O₃-CuO/water hybrid nanofluid was very high with the same mass flow rate and particle volume concentration compare to CuO/water nanofluid.

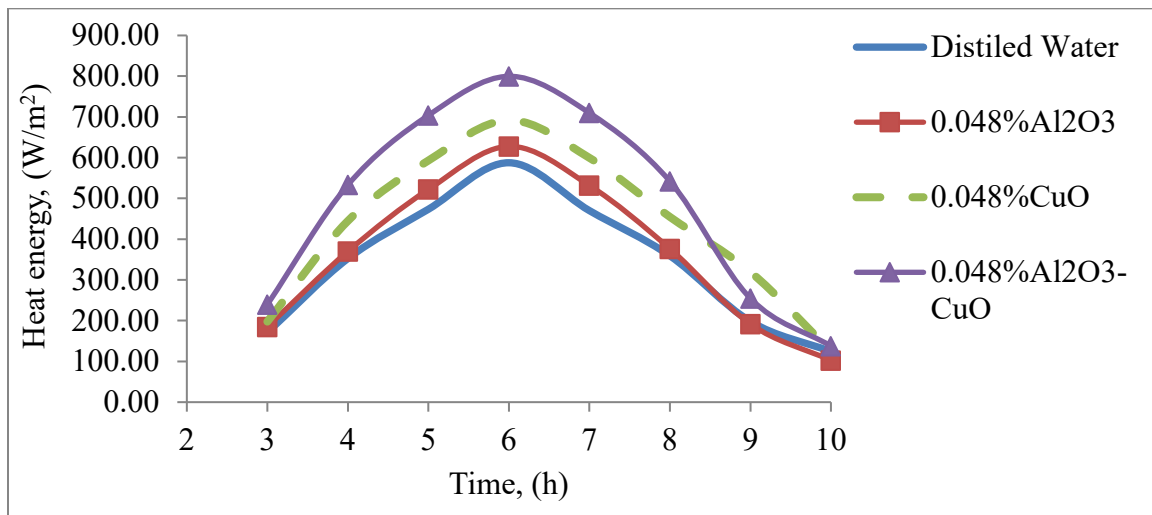


Fig. 4: Hourly variation of heat energy of water and nanofluids ($\phi = 0.048\%$) with time.

From Fig. 5 it is seen that the maximum useful heat energy with 0.096% particle volume concentration and constant mass flow rate of Al₂O₃, CuO and Al₂O₃-CuO hybrid water based nanofluids were 650.28 W/m², 738.58 W/m² and 834.73 W/m², respectively.

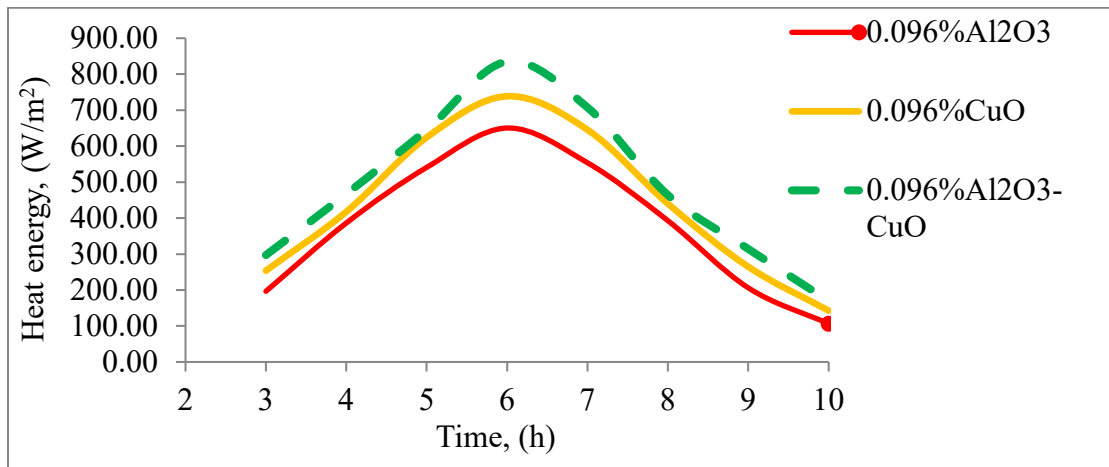


Fig. 5: Hourly variation of heat energy for ($\phi = 0.096\%$) nanofluids with time.

From Fig. 6, it can be seen that the maximum thermal efficiency of flat plate solar collector was 57.66%, 66.58% and 73.75% for 0.24% particle concentration of Al₂O₃, CuO and Al₂O₃-CuO hybrid water based nanofluids respectively at fixed 0.008kg/s mass flow rate. The experimental results indicated that due to the increased interactions of nanoparticles in base fluid, the efficiency of flat plate solar collector increased with percentage volume concentration of all nanofluids. Furthermore, because of the rise in internal energy between particles and reduction in agglomeration, hybrid nanofluid has higher collector efficiency than the isolations. The result is also understood that CuO/water nanofluid has greater collector efficiency than Al₂O₃/water nanofluid due to the higher thermal conductivity properties of copper oxide nanoparticles.

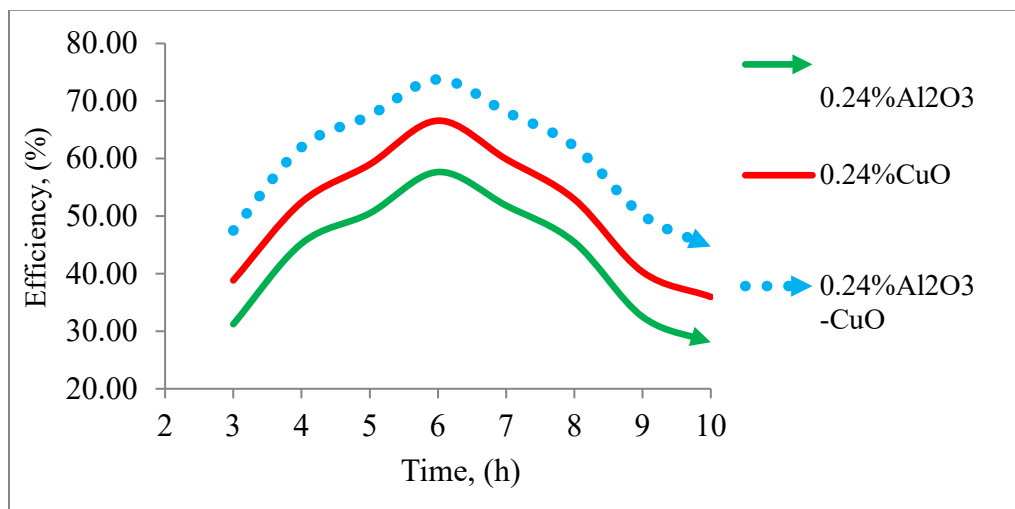


Fig. 6: Hourly variation thermal efficiency comparisons of nanofluids at ($\phi = 0.24\%$).

Figure 7 gives the data related to the thermal efficiency of mono, and hybrid nanofluids in a FPSC. Experimental results showed that at constant flow rate, the efficiency of flat plate solar

collector was improved in all nanofluids with the increase in volumetric concentrations of nanoparticles in base fluids. The lowest thermal efficiency of the solar collector was observed about 48.32% for distilled water. The maximum thermal efficiency improvements of flat plate solar collector with 0.24 percentage nanoparticle concentration of Al_2O_3 , CuO , and $\text{Al}_2\text{O}_3\text{-CuO}$ hybrid nanofluids were 9.34%, 18.26% and 25.43% respectively compared to base fluid i.e., distilled water. Moreover, from the results it is noticed that hybrid nanofluid is more efficient than the individual nanofluids. The results are also shown that, the thermal efficiency of CuO nanofluid is higher than Al_2O_3 nanofluid and base fluid. Therefore, hybridizing nanoparticles and increasing nanoparticle concentrations from 0.048 to 0.24% improved the thermal efficiency of SPFC.

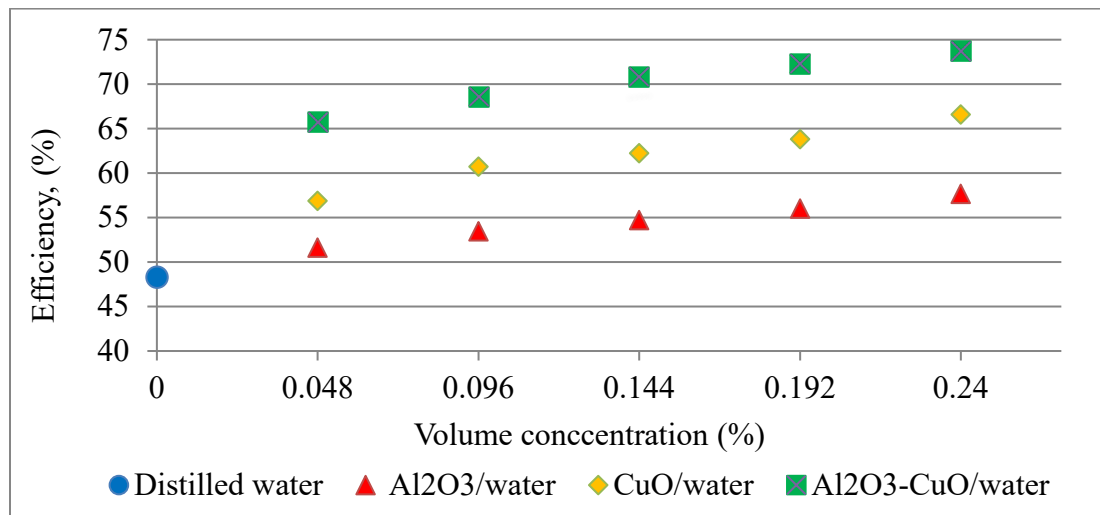


Fig. 7: Thermal efficiencies of working fluids as function of nanoparticle concentration.

Conclusions

In this research the thermal efficiency of flat plate solar collector with $\text{Al}_2\text{O}_3/\text{water}$, CuO/water and $\text{Al}_2\text{O}_3\text{-CuO}/\text{water}$ hybrid nanofluid, the effect of particle volume concentrations and the two-step preparation methods were studied. Efficiencies of FPSC with each working fluid at various nanoparticle concentrations and constant flow rate 0.008kg/s were compared. The thermal efficiency of flat plate solar collectors is show to increase with the increase in nanoparticle concentration of the nanofluids. The maximum thermal efficiency of the flat plate solar collector for water and 0.24% Al_2O_3 , CuO and $\text{Al}_2\text{O}_3\text{-CuO}$ hybrid nanofluids was 48.32%, 57.66%, 66.58% and 73.75% respectively at constant flow rate 0.008 kg/s. From this, mixing of Al_2O_3 nanoparticles in water enhances the collecor efficiecy by 9.34% as compared to pure water. The SFPC with CuO nanofluid is better than Al_2O_3 nanofluid by 8.92%. Thermal efficiency SPFC wokirng with $\text{Al}_2\text{O}_3\text{-CuO}$ hybrid nanofluid is higher than CuO/water nanofluid by 7.17%. Therefore from the 0.24 vol. % data, volume concentration of $\text{Al}_2\text{O}_3\text{-CuO}/\text{water}$ hybrid nanofluid and 0.008kg/s, the thermal efficiency of SPFC raises upto 73.75%, which was 25.43% higher than the pure water.

References

- [1] F. Yang, J. Liu, Q. Sun, L. Cheng, R. Wennersten, Simulation analysis of household solar assistant radiant floor heating system in cold area, Energy Procedia 158 (2019) 631-636. doi: 10.1016/j.egypro.2019.01.166
- [2] M. Ammar, A. Mokni, H. Mhiri, P. Bournot, Parametric investigation on the performance of natural convection flat plate solar air collector with additional transparent insulation material parallel slats (TIM-PS), Solar Energy 231 (2021) 379-401.
<https://doi.org/10.1016/j.solener.2021.11.053>

- [3] A.C.M. Ango, M. Medale, C. Abid, Optimization of the design of a polymer flat plate solar collector, *Solar Energy* 87(2013) 64-75. <https://doi.org/10.1016/j.solener.2012.10.006>
- [4] M. Hosseinzadeh, A. Salari, M. Sardarabadi, M. Passandideh-Fard, Optimization and parametric analysis of a nanofluid based photovoltaic thermal system: 3D numerical model with experimental validation, *Energy Convers. Manag.* 160 (2018) 93-108. <https://doi.org/10.1016/j.enconman.2018.01.006>
- [5] Z. Jiandong, T. Hanzhong, C. Susu, Numerical simulation for structural parameters of flat-plate solar collector, *Solar Energy* 117 (2015) 192-202. <https://doi.org/10.1016/j.solener.2015.04.027>
- [6] Z. Wang, W. Yang, F. Qiu, X. Zhang, X. Zhao, Solar water heating: From theory, application, marketing and research, *Renew. Sustain. Energy Rev.* 41 (2015) 68-84. <https://doi.org/10.1016/j.rser.2014.08.026>
- [7] Y. Deng, Y. Zhao, W. Wang, Z. Quan, L. Wang, D. Yu, Experimental investigation of performance for the novel flat plate solar collector with micro-channel heat pipe array, *Appl. Therm. Eng.* 54 (2013) 440-449. <https://doi.org/10.1016/j.applthermaleng.2013.02.001>
- [8] S.U.S. Choi, Enhancing thermal conductivity of fluids with nanoparticles, *Am. Soc. Mech. Eng. Fluids Eng. Div. FED*, 231 (1995) 99-105.
- [9] T. Yousefi, E. Shojaeizadeh, F. Veysi, S. Zinadini, An experimental investigation on the effect of pH variation of MWCNT-H₂O nanofluid on the efficiency of a flat-plate solar collector, *Sol. Energy*, 86 (2012) 771-779. <https://doi.org/10.1016/j.solener.2011.12.003>
- [10] M.H. Ahmadi, A. Mirlohi, M. Alhuyi Nazari, R. Ghasempour, A review of thermal conductivity of various nanofluids, *J. Mol. Liq.* 265 (2017) 181–188. <https://doi.org/10.1016/j.molliq.2018.05.124>
- [11] H. Chen, Y. Ding, Y. He, C. Tan, Rheological behaviour of ethylene glycol based titania nanofluids, *Chem. Phys. Lett.* 444 (2007) 333-337. <https://doi.org/10.1016/j.cplett.2007.07.046>
- [12] D.W. Lee, A. Sharma, Thermal performances of the active and passive water heating systems based on annual operation, *Sol. Energy* 81 (2007) 207-215. <https://doi.org/10.1016/j.solener.2006.03.015>
- [13] L. Geovo, G.D. Ri, R. Kumar, S.K. Verma, J.J. Roberts, A.Z. Mendiburu, Theoretical model for flat plate solar collectors operating with nanofluids: Case study for Porto Alegre, Brazil, *Energy* 263 Part B (2023) 125698, <https://doi.org/10.1016/j.energy.2022.125698>
- [14] S. Choudhary, A. Sachdeva, P. Kumar, Investigation of the stability of MgO nanofluid and its effect on the thermal performance of flat plate solar collector, *Renewable Energy* 147 Part 1 (2020) 1801-1814.
- [15] S.K. Verma, A.K. Tiwari, S. Tiwari, D.S. Chauhan, Performance analysis of hybrid nanofluids in flat plate solar collector as an advanced working fluid, *Solar Energy* 167 (2018) 231-241.
- [16] A.J. Moghadam, M. Farzane-Gord, M. Sajadi, M. Hoseyn-Zadeh, Effects of CuO/water nanofluid on the efficiency of a flat-plate solar collector. *Experimental Thermal and Fluid Science*, 58 (2014) 9-14.
- [17] Yousefi, T., Veysi, F., Shojaeizadeh, E., & Zinadini, S. (2012). An experimental investigation on the effect of Al₂O₃-H₂O nanofluid on the efficiency of flat-plate solar collectors. *Renewable Energy*, 39(1), 293-298.
- [18] Yousefi, T., Veisy, F., Shojaeizadeh, E., & Zinadini, S. (2012). An experimental

investigation on the effect of MWCNT-H₂O nanofluid on the efficiency of flat-plate solar collectors. *Experimental Thermal and Fluid Science*, 39, 207-212.

[19] Belkassmi, Y., Gueraoui, K., El maimouni, L. *et al.* Numerical Investigation and Optimization of a Flat Plate Solar Collector Operating with Cu/CuO/Al₂O₃-Water Nanofluids. *Trans. Tianjin Univ.* 27, 64–76 (2021). <https://doi.org/10.1007/s12209-020-00272-6>.

[20] E. Elshazly, A.A. Abdel-Rehim, I. El-Mahallawi, 4E study of experimental thermal performance enhancement of flat plate solar collectors using MWCNT, Al₂O₃, and hybrid MWCNT/ Al₂O₃ nanofluids, *Results in Engineering* 16 (2022) 100723.

Green and environmental-friendly material for sustainable buildings

Noura AI-MAZROUEI^{1,a*}, Amged ELHASSAN^{2,b}, Waleed AHMED^{3,c*},
Ali H. AI-MARZOUQI^{1,d}, Essam ZANELDIN^{4,e}

¹ Chemical and Petroleum Engineering Department, COE, UAE University, Al Ain, UAE

² Mechanical and Aerospace Engineering Department, COE, UAE University, Al Ain, UAE

³ Engineering Requirements Unit, COE, UAE University, Al Ain, UAE

⁴ Civil and Environmental Engineering Department, COE, UAE University, Al Ain, UAE

^a201311706@uaeu.ac.ae, ^b201450104@uaeu.ac.ae, ^cw.ahmed@uaeu.ac.ae,
^dhassana@uaeu.ac.ae, ^eessamz@uaeu.ac.ae

Keywords: Natural Binder, Sustainable Material, Composite, Construction

Abstract. In construction, incorporating waste materials such as bio-binders and fine aggregates plays a vital role in promoting environmentally friendly building methods. Utilizing these materials for a second time reduces waste generation, contributing to conserving valuable natural resources. This underscores the importance of sustainable construction practices. This study outlines the experimental results concerning the mechanical attributes when employing a combination of micro sand silica and a bio-binder, specifically *Abelmoschus esculentus*. The investigated mechanical properties in this study encompass modulus, strength, and toughness. The experimentation involved mixing *Abelmoschus esculentus* with varying weight percentages and three distinct micro-size particles and then compressing them into cylindrical samples. *Abelmoschus esculentus* demonstrated favorable adhesion properties with sand silica particles, and the findings suggest a noteworthy impact on the mechanical properties upon its addition. Overall, it was observed that the optimal mechanical properties were attained with a 15% weight ratio of *Abelmoschus esculentus* bio-binder at a particle size of 250 µm.

Introduction

Eco-friendly building materials could be created by combining aggregates with bio-binders derived from natural resources, such as agricultural waste. This eco-friendly strategy reduces landfill trash in addition to carbon emissions. This environmentally conscious alternative to conventional cement manufacturing has the potential to make a substantial impact on mitigating global warming. The conversion of biomass stands out as a promising alternative energy solution because of its minimal greenhouse gas emissions and the generation of substitutes for petroleum. This renders it a valuable, abundant, cost-effective renewable energy source [1]. The adaptability of biomass utilization, enabling its direct use as a fuel source and transformation into diverse forms of energy, stands out as a significant advantage. In 2030, biomass is expected to increase for the world energy supply, making it the leading renewable energy source, according to IRENA research on the subject [2]. In light of the current imperative for environmental sustainability amid escalating energy demands, biomass emerges as an alternative fuel capable of displacing fossil fuels and promoting sustainability. Wood, agricultural and animal waste, energy crops, and industrial waste are examples of potential biomass sources for renewable energy [3]. One way to limit the use of natural resources and reduce energy usage is to produce eco-friendly construction materials from agricultural waste [4]. Furthermore, one effective way to use agricultural waste is to use plant leftovers as a bio-binder. This knowledge is anticipated to lead to a broader acceptability of using agricultural wastes in construction applications [5]. Different research has called building materials with minimal carbon emissions, sustainability, and many uses

"agricultural concrete" [6]. Building waste, in particular, has a significant percentage of heavy metals, including massive solid garbage. Consequently, increased soil heavy metal concentration risks soil quality due to various biochemical processes [7]. Furthermore, the accumulation of waste generated from construction projects leads to the decomposition of specific organic substances, emitting harmful gasses that add to environmental pollution. Furthermore, air quality can be negatively impacted by pathogens and particles from garbage spreading through the atmosphere [8]. Consequently, choosing agricultural materials like *Abelmoschus esculentus* can help diminish the generation of construction waste, exercising control over releasing dangerous compounds into the environment and damaging pollutants. Since silica dioxide (SiO_2) makes up the majority of sand, it is frequently included as a filler in studies. When creating composite materials, one or several filler substances are combined with a matrix material, such as ceramic or polymer, sand is typically used as a filler. Strength, stiffness, toughness, and thermal stability are among the mechanical and physical properties of the composite that are improved by the use of sand as a filler. Sand is a valuable filler material in many industrial and scientific applications because of its availability, affordability, and compatibility with various matrix substances. Composite materials' mechanical and physical characteristics can be improved by adding sand as a filler, making them more appropriate for a broader range of uses. Despite its crystalline form, SiO_2 , considered physiologically benign, finds uses in the pharmaceutical and agricultural industries with no known health hazards. In general, silica has qualities that allow it to work well with various polymeric materials, improving their overall qualities. Furthermore, a lot of filler is made of silica to improve the mechanical performance of polymeric substances [9]. SiO_2 nanoparticles are easily synthesized and are reasonably priced, making them useful in chromatography, chemical sensors, catalysts, and ceramics. *Abelmoschus esculentus* gum, commercially known as *Abelmoschus esculentus*, demonstrated noteworthy results as a tablet binder, suggesting its viability as an alternative for compositions [10]. *Abelmoschus esculentus*, a plant commonly cultivated in Africa and Asia, offers a natural, cost-effective, and non-toxic extract, showing promise across various industries. This plant's various components have long been used in medicine traditionally as fight cancer medication, antibacterial, and antidiabetic [11]. This research aims to evaluate the effects of various *Abelmoschus esculentus* weight percentages on the mechanical characteristics of a composite containing sand silica particles of various sizes. This study aims to evaluate this composite's potential as an ecologically friendly building material. Furthermore, TGA, XRD, and SEM investigations were performed to characterize the produced materials.

Materials and Process

The research examined the compressive strength of multiple samples produced by mixing silica sand with *Abelmoschus esculentus* at several ratios (five, ten, and fifteen percent). The silica sand samples were placed on an automatic sieve shaker to remove impurities from their surfaces and allowed to sit for ten minutes. A range of sieves with square mesh sizes of 250 μm , 425 μm , and 850 μm were used in this shaker. A volume of 15×10^4 Liter was achieved by adding deionized water. After agitating the mixture for five minutes at room temperature, the mixture was poured into a precisely cylindrical mold with a 0.5-inch diameter and 1-inch height made of stainless steel base don ISO 604 [12]. A mold releaser was applied to prevent adhesion to the mold surfaces, and the samples were cured for 30 minutes at 176 °F with a 49 N/mm² load using a heated mechanical press. After adopting a drying process by an oven, the samples were placed in glass incubators for cooling, and their compressive mechanical properties were examined using a general Tensile Testing Machine at a 0.4 mm/min load rate.

Results and Discussion

As depicted in Figure 1, adding *Abelmoschus esculentus* at weight percentages of five, ten, and fifteen percent addition by weight led to an approximately thirty-five percent increase in compressive strength due to the increased number of granules of silica sand in a medium size. The silica sand mixture's compressive strength was increased by the addition of *Abelmoschus esculentus*, which also enhanced sand particle adherence. This enhancement can be attributed to the high concentration of galactose, rhamnose, and galacturonic acid in *Abelmoschus esculentus*, which enhance adhesive qualities and have crosslinking characteristics. Furthermore, for all weight percentages of additional *Abelmoschus esculentus*, it was depicted that the strength dropped by forty percent between 250 μm and 425 microns. The adhesion between particles can be affected by the size of the particles and the applied constant load. Unexpectedly, 850-micron silica sand particles had the lowest compressive strength, even with *Abelmoschus esculentus* injected in trace amounts. Evidence shows that the silica particle size noticeably affects the composite's overall strength. A noteworthy discovery was made when it was discovered that adding ten percent by weight of *Abelmoschus esculentus* to 850 μm silica sand may boost compressive strength by twenty-one percent. There appears to be a correlation between the amount of *Abelmoschus esculentus* added and the silica sand mix particle size in the elastic modulus section. An average of twenty seven percent less *Abelmoschus esculentus* is added to the mixture as the particle size increases from 425 to 850 microns. Including *Abelmoschus esculentus* raises the elastic modulus of silica sand because it strengthens the links between the particles in the composite. Particle size, in particular, does not affect a composite's Young's modulus, especially when working with micron-sized particles, as this instance shows [13]. At the nanoscale, the composite's Young's modulus may be enhanced by reducing the size of the particles [14]. The 850 μm silica sand had the lowest elastic modulus of all sizes of silica particles, mainly due to the large dust particles that affected its mechanical properties. By contrast, regardless of the amount of *Abelmoschus esculentus* added to the combination, the silica particle size of 250 microns demonstrated the highest elastic modulus.

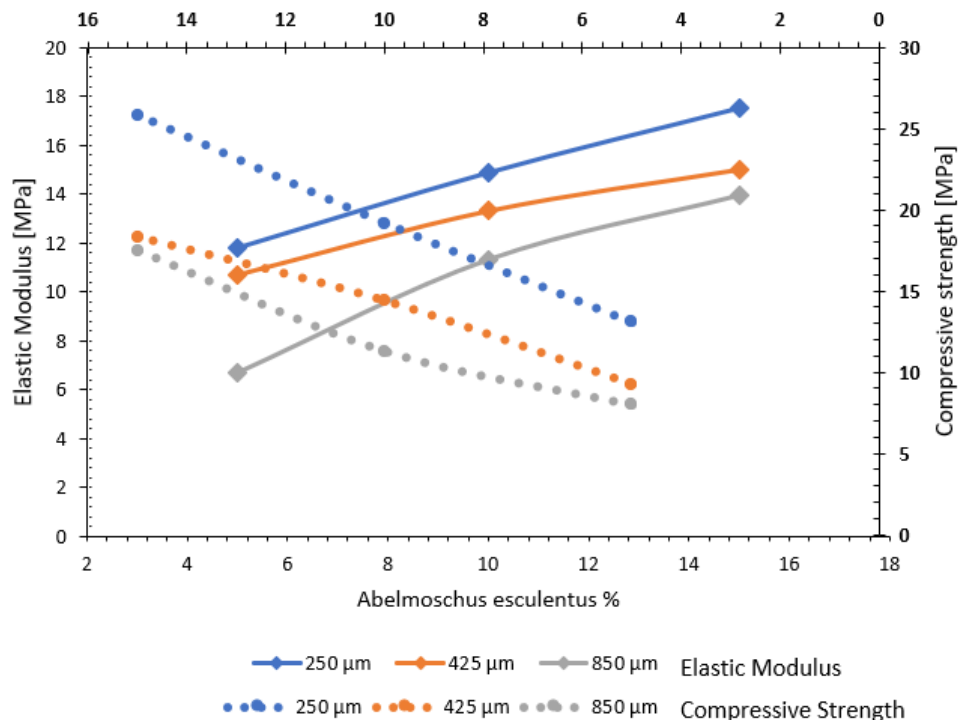


Figure 1 Elastic Modulus and Compressive Strength

Conclusion

The modulus and compressive strength of *Abelmoschus esculentus*, as well as the mechanical characteristics of micro silica sand, were thoroughly examined in the experiment findings. The particle size emerged as a crucial factor influencing the strength of particulate composites. Specifically, the composite exhibited the highest compressive mechanical properties at fifteen percent by weight of *Abelmoschus esculentus* with a particle size of 250 microns. The maximum recorded compressive strength reached 26 MPa, while the peak elastic modulus reached 178 MPa. The potential of silica sand and *Abelmoschus esculentus* composites in creating environmentally friendly building materials is highlighted by this study.

References

- [1] Huang, Y., Wang, Y. D., Rezvani, S., McIlveen-Wright, D. R., Anderson, M., Mondol, J., Zacharopolous, A., & Hewitt, N. J. (2013). A techno-economic assessment of biomass fuelled trigeneration system integrated with organic rankine cycle. *Applied Thermal Engineering*, 53(2), 325–331. <https://doi.org/10.1016/j.applthermaleng.2012.03.041>
- [2] Muniyappan, D., Pereira Junior, A. O., M, A. V., & Ramanathan, A. (2023). Synergistic recovery of renewable hydrocarbon resources via microwave co-pyrolysis of biomass residue and plastic waste over spent toner catalyst towards sustainable solid waste management. *Energy*, 278. <https://doi.org/10.1016/j.energy.2023.127652>
- [3] Di Fraia, S.; Fabozzi, S.; Macaluso, A.; Vanoli, L. Energy potential of residual biomass from agro-industry in a Mediterranean region of southern Italy (Campania). *J. Clean. Prod.* 2020, 277, 124085. <https://doi.org/10.1016/j.jclepro.2020.124085>
- [4] Bumanis, G.; Vitola, L.; Pundiene, I.; Sinka, M.; Bajare, D. Gypsum, Geopolymers, and Starch—Alternative Binders for Bio-Based Building Materials: A Review and Life-Cycle Assessment. *Sustainability* 2020, 12, 5666. <https://doi.org/10.3390/su12145666>
- [5] Sayed, M. A., El-Gamal, S. M. A., Mohsen, A., Ramadan, M., Wetwet, M. M., Deghiedy, N. M., Swilem, A. E., & Hazem, M. M. (2024). Towards a green climate: production of slag-red brick waste-based geopolymer mingled with WO_3 nanoparticles with bio-mechanical achievements. *Construction and Building Materials*, 413 <https://doi.org/10.1016/j.conbuildmat.2024.134909>
- [6] Ingrassia, L.P.; Cardone, F.; Canestrari, F.; Lu, X. Experimental investigation on the bond strength between sustainable road bio-binders and aggregate substrates. *Mater. Struct.* 2019, 52, 80. <https://doi.org/10.1617/s11527-019-1381-6>
- [7] Ding, Z.; Gong, W.; Li, S.; Wu, Z. System Dynamics versus Agent-Based Modeling: A Review of Complexity Simulation in Construction Waste Management. *Sustainability* 2018, 10, 2484. <https://doi.org/10.3390/su10072484>
- [8] Othman, A. A. E., & Abdelrahim, S. M. (2019). Achieving sustainability through reducing construction waste during the design process. *Journal of Engineering, Design and Technology*, 18(2), 362–377. <https://doi.org/10.1108/JEDT-03-2019-0064>
- [9] Ahmed, W.; Siraj, S.; Al-Marzouqi, A.H. 3D printing PLA waste to produce ceramic based particulate reinforced composite using abundant silica-sand: Mechanical properties characterization. *Polymers* 2020, 12, 2579. <https://doi.org/10.3390/polym12112579>
- [10] Zaharuddin, N. D., Noordin, M. I., & Kadivar, A. (2014). The use of *hibiscus esculentus* (okra) gum in sustaining the release of propranolol hydrochloride in a solid oral dosage form. *Biomed Research International*, 2014, 735891–735891. <https://doi.org/10.1155/2014/735891>

- [11] Elkhalifa, A. E. O., Alshammari, E., Adnan, M., Alcantara, J. C., Awadelkareem, A. M., Eltoum, N. E., Mehmood, K., Panda, B. P., & Ashraf, S. A. (2021). Okra (*abelmoschus esculentus*) as a potential dietary medicine with nutraceutical importance for sustainable health applications. *Molecules* (Basel, Switzerland), 26(3). <https://doi.org/10.3390/molecules26030696>
- [12] International Organization for Standardization. ISO 604: Plastics — Determination of compressive properties. Geneva, Switzerland: ISO, 2022.
- [13] Cho, J.; Joshi, M.S.; Sun, C.T. Effect of inclusion size on mechanical properties of polymeric composites with micro and nano particles. *Compos. Sci. Technol.* 2006, 66, 1941–1952. <https://doi.org/10.1016/j.compscitech.2005.12.028>
- [14] Fan, S.; Cheng, Z. A micropolar model for elastic properties in functionally graded materials. *Adv. Mech. Eng.* 2018. <https://doi.org/10.1177/1687814018789520>

Techno-economic comparison between PV and wind to produce green hydrogen in Jordan

Zaid HATAMLEH^{1,a*}, Ahmad AL MIAARI^{1,b}

¹Mechanical Engineering Department, King Fahd University of Petroleum and Minerals, Dhahran, Saudi Arabia

^azaidhatamleh08@outlook.com, ^bbahmad.miaari@gmail.com

Keywords: Hydrogen, Green Hydrogen, Renewable Energy, Photovoltaic Energy, Wind Energy, Levelized Cost of Hydrogen (LCOH)

Abstract. The world has begun to move towards searching for the best ways and means to be able to produce hydrogen gas in a healthy and environmentally friendly manner. Especially after manufacturing cars that run on hydrogen, many home appliances in the future would operate using hydrogen. This research paper aims to provide a detailed study and comparison for the potential of photovoltaic energy and wind energy in hydrogen gas production using electrolyzes technology for home applications. In this study, a mathematical model is proposed to predict hydrogen production by means of the two renewable energy sources. Furthermore, the mathematical model computes the electrical energy produced from the fuel cells using the produced hydrogen gas and evaluate its leveled cost. The study was conducted based on the technical specifications based on Jordanian codes and conditions. Results showed that photovoltaic energy system is the best solution compared to other proposed systems which can produce 30,140.5252 kg of hydrogen and produce 1,264,551 kWh/year with the lowest hydrogen leveled cost of 13.262 \$/kg.

Introduction

Green hydrogen, a clean energy carrier, is crucial to decarbonization, but its cost is currently high[1]. This is mainly due to the cost of electrolyzers, which split water into hydrogen and oxygen [2]. However, electrolyzer costs are expected to decline significantly in the coming years, making green hydrogen more competitive[2]. Innovation is one of the key factors in reducing electrolyzer costs. This includes developing cheaper electrodes and catalyst materials, and increasing production volumes [2]. By 2030, green hydrogen could be cost-competitive with blue hydrogen in many countries [3]. Another important consideration is the use of renewable energy sources specifically for hydrogen production [4]. This would help reduce the overall cost of green hydrogen. Other challenges include taking into account weather fluctuations and hourly electricity consumption in the system design [5].As well as assessing the environmental impact of the entire production chain, not just the electrolyzers [6]. In addition to incorporating energy storage to manage intermittent renewable energy sources [7]. Research is ongoing to address these challenges and further reduce the cost of green hydrogen. This includes optimizing system design, developing advanced energy storage solutions, and making realistic comparisons of solar and wind energy for hydrogen production [8], [9].

Green hydrogen has the potential to play a major role in decarbonizing the energy sector. Continued research and development efforts are essential to make this a reality. The success of this technology highly depends on the hydrogen production cost per one kilogram [10]. The main idea of this study is to make a real comparison between solar energy and wind energy in hydrogen production and its cost based on Jordanian conditions and policies. The study is done by using mathematical models and using Homer program. This study aims to give a valuable insight that helps policymakers in decision making for selecting and implementing the optimal renewable hydrogen powered home[11].

Methodology

Based on what was mentioned, mathematical calculations and simulations of two different systems will be performed. The first system will be hydrogen production through photovoltaic panels. The second system is hydrogen production through wind turbines.

1) electrical load estimation

Electricity consumption bills for 12 months are used to determine the load of a single house. The energy consumption of different appliances and their operating hours are proposed in table 1.

The total annual home energy consumption for a single house in Jordan is calculated using equation 1.

Table 1 Annual Electricity Consumption for the Electrical Appliances`

DATA	Summe r Hours	Winte r Hours	Unit s	Ratin g (W)	Summer Consum- ption/da y	Winter Consum- ption/day	Annual Energy Consumption (kWh)
Small LED Spots	3	5	15	11.5	0.52	0.86	251.9
LED Smart TV	5	5	2	150	1.5	1.5	547.5
Air Conditioner	2	1	1	3000	6	3	1642.5
LED Bulbs	3	5	40	15	1.8	3	876
Phone Charger	3	3	5	25	0.38	0.38	136.9
Laptop Charger	5	5	5	65	1.63	1.63	593.1
Printer	0.5	0.5	1	1.27	0	0	0.23
Suction Fan	0.4	0.5	4	60	0.1	0.12	39.42
Speed Water Heater	0.1	0.4	1	5500	0.55	2.2	501.9
Washing Machine	1.5	1.2	1	1500	2.25	1.8	739.1
Fridge	6	6	2	600	7.20	7.2	2628
Water Pump	0.7	0.4	1	550	0.39	0.22	110.4
Water Cooler	6	6	1	5	0.03	0.03	10.9
Water Heater	0	5	1	1500	0	7.50	1368.8
Food Processor	0.1	0.1	1	250	0.03	0.03	9.1
Grill	0.1	0.4	1	1400	0.14	0.56	127.8
Water Filter (RO)	4	2	1	750	3.00	1.50	821.3

Air Fresher (Suction Duct)	0.2	0.2	1	200	0.04	0.04	14.6
Drying Machine	0	1	1	2700	0	2.7	492.8
Stand Blender	0.1	0.1	1	250	0.03	0.03	9.1

$$\text{Energy (kW/h)} = \text{Power (kW)} * \text{Time (h)} \quad (1)$$

The total annual electricity consumption for each home in Jordan based on the above loads is estimated to be $10921 \frac{\text{kWh}}{\text{Year Home}}$, resulting in a total of 1,092,100 kWh/year for a hundred homes.

2) hydrogen production

The amount of hydrogen production that can satisfy the annual electricity consumption for 100 homes can be calculated from equation 2 [12].

$$\text{Hydrogen (kg)} = \frac{\text{Electricity (kWh)}}{\text{Heating Value } (\frac{\text{MJ}}{\text{kg}}) * \text{Fuel Cell Efficiency (\%)} * \text{Electrochemical Conversion (\%)} * \text{Conversion Factor } (\frac{\text{MJ}}{\text{kWh}})} \quad (2)$$

A solid oxide hydrogen fuel cell from Bloom energy company was chosen for this particle study, due to its high efficiency, fuel flexibility and low emissions. The selected fuel cell has a high efficiency and electrochemical conversion of 52 % and 80% respectively. The total amount of hydrogen produced by the selected fuel cell to satisfy the annual electricity of 100 homes is calculated to be 18817.1 kg/year when using hydrogen with a heating value of 119.96 MJ/kg [13].

3) photovoltaic energy system's design

Photovoltaics are an important technology for generating electricity using solar energy[14]. This technology can be integrated in many applications such as greenhouses[15], and battery charging[16]. The photovoltaic system capacity highly depends on the sunny hours. Based on the Energy and Minerals Regulatory Commission (EMRC) in Jordan, the useful sunny hours during the year in Jordan is around 1540 h/year. The power needed to run a 100 house in Jordan can be calculated from equation 3.

$$\text{Power} = \frac{\text{Energy}}{\text{Time}} \quad (3)$$

To generate electricity with a capacity of 709 kW that satisfies the demand. A commercial photovoltaic panel Trina Vertex with a capacity of 555 W is chosen for this application. Trina is considered a well-known and trustable brand that is widely found in Jordanian market. A total of 1273 panels are needed for the one hundred houses.

The price and cost of the selected solar panels are established by the Consolidated Energy and Economic Engineering Company. Table 2 shows the cost of the suggested PV panels, where the cost of each Watt of (Trina Vertex 555W) is 0.27 \$/Watt.

Table 2 PV Panel Cost

Capital Cost (\$/KW)	Replacement (\$/KW)	O&M (\$/Year)	System Life Time (Years)	Derating Factor (%)
270	270	10	25	84.8

For the AC side of the whole PV system SMA inverters were used with 1.5 (*DC/AC*) ratio to ensure the highest number of operating hours for the solar inverters at their maximum power point tracking.

Regarding the cost of the solar inverters, SMA solar inverters are priced also by the Consolidated Energy and Economic Engineering Company and can be presented in table 3.

Table 3 Solar Inverter Cost

Capital Cost (\$/KW)	Replacement (\$/KW)	O&M (\$/Year)	System Life Time (Years)
174	174	5	25

4) Wind energy system's design

The design of wind energy system highly depends on the wind speed. According to Wind Atlas software the average wind speed in Amman-Jordan is 7.12 m/s. The available wind power potential can be calculated using equation 4.

$$\dot{W}_{Available} = 0.5 * \rho * A * V^3 \quad (4)$$

Where ρ is the density of the air at specific temperature, A is the wind turbine swept area, and V is the average wind speed.

For this specific study Vestas V82-1.65 is selected. The wind turbine is manufactured by Vestas company with a swept area of 5281.01 m² and power performance presented in figure 1.

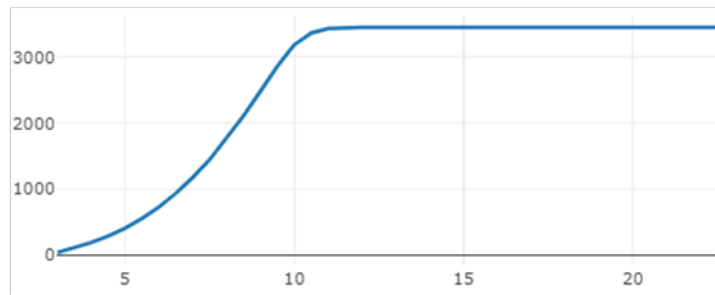


Fig. 1 Vestas V82-1.65 Power Curve

The selected wind turbine was priced by Al-Fujeij Wind Energy Company and summarized in table 4.

Table 4 Wind Turbine Specification and Cost

System Capacity (One Turbine)	Hub Height (m)	Capital Cost (\$/Turbine)	Replacement (\$/Turbine)	O&M (\$/Year)	System Life Time (Years)
1650 kW	100	1,980,000	1,980,000	20,000	20

Results and Discussions

Energy and economic comparison for the two proposed renewable energy systems is done using Homer software [11]. Various results concerning the system potential, costs, and technical specifications are reached and discussed. The first section delves into the results of integrating the system with the PV system, while the other section discusses the results of integrating the system with wind system.

1) PV system

The PV/hydrogen proposed system consists of five main components which are the electrolyzer, PV, inverter, grid, and hydrogen tank. These components relate to each other as shown in figure 2.

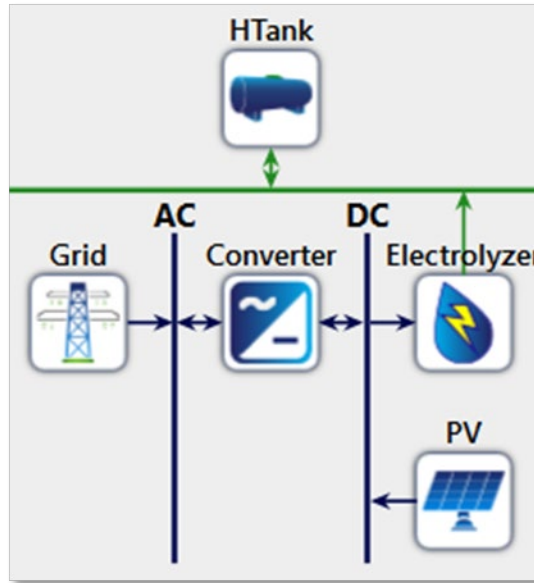


Fig. 2 PV System Schematic Diagram

The results from the mathematical models in the previous section are considered as an input for Homer software [11]. The main idea of these calculations is to reduce the size of the system as much as possible to fit the loads without creating any excess production beyond the energy-consuming facility's need. Important results after running the software can be summarized in table 5.

Table 5 Calculated PV System Output Data

Data	Unit	Value
Net Present Cost	(\\$)	312,062
Levelized Cost of Energy (LCOE)	(\\$/kWh)	0.0104
Payback Period	(years)	1.49
CO₂ Emissions	(kg/year)	388,581
Renewable Fraction	(%)	64.9
Annual PV Production	(KWh/year)	1,264,551
Grid Purchases	(KWh/year)	614,844
Total Hydrogen Production	(kg)	30,140.5252
Hydrogen Produced using PV (Green Hydrogen)	(kg)	21,788.2137
Levelized Cost of Hydrogen	(\\$/Kg)	13.262

Table 5 represents the simulation results of the first experiment of this study, the amount of electrical energy produced from photovoltaic panels is considered appropriate and sufficient to cover the needs of electrical energy consumption in operating the electrolyzers for the purposes of producing green hydrogen while considering the losses during energy transmission, distribution, and losses inside the electrolyzers.

2) Wind Turbines

The wind/hydrogen proposed system consists of five main components which are the electrolyzer, wind turbine, inverter, grid, and hydrogen tank. These components relate to each other as shown in figure 3.

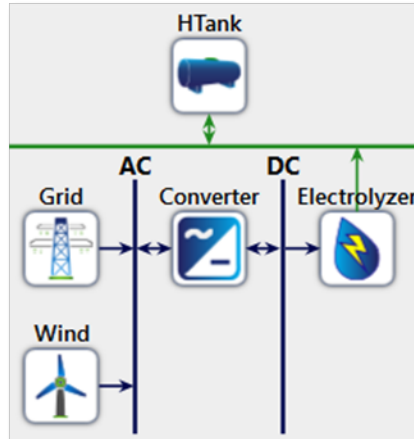


Fig. 3 Wind System Schematic Diagram

A wind farm is suggested to be in Al-Muwaqqar area in Amman, which is known for its low population density. The clean energy from the farm can be used to operate the electrolyzers to produce green hydrogen. The technical specifications and costs of the wind turbines mentioned in previous sections are also considered as an input for Homer software [11]. Different results are obtained and can be presented in table 6.

Table 6 Monthly Electric Production for the Wind System

Data	Unit	Value
Net Present Cost	(\\$)	984,785,100
Levelized Cost of Energy (LCOE)	(\\$/kWh)	0.1379
Payback Period	(years)	1.94
CO₂ Emissions	(kg/year)	63,533
Renewable Fraction	(%)	100
Annual Wind Production	(KWh/year)	552,150,642
Grid Purchases	(KWh/year)	100,527
Total Hydrogen Production	(kg)	9,515,287.625
Hydrogen Produced using Wind (Green Hydrogen)	(kg)	9,513,555.562
Levelized Cost of Hydrogen	(\\$/Kg)	26.7368

It is noted from table 6 that the option of using wind turbines is considered very expensive in terms of the initial cost. Moreover, wind turbines located in Jordanian capital is not considered a good

Approach, as the wind speed inside the region does not exceed 10 m/s which is considered low compared to other locations. The turbine will not reach its natural production capacity. The high cost of producing electricity also leads to a significant increase in the cost of hydrogen.

In terms of levelized cost and hydrogen production the PV/hydrogen system is considered a better option compared to wind/Hydrogen system, where the levelized cost of the first system is 13.5 \\$/ kg less than of that of wind/hydrogen system.

Conclusion

A techno-economic investigation for hydrogen powered homes in Amman-Jordan based on solar energy and wind energy is presented in this study. The study utilizes mathematical models and Homer software to explore electricity, hydrogen production, and evaluate hydrogen leveled cost. The study is conducted based on Jordanian technical specifications and conditions. Based on the results it is concluded that PV integrated with hydrogen system is a better option than wind turbine integrated with hydrogen system. This is due to the ability of the system to meet the electrical load correctly without causing any disturbances in the network, while also producing 30,140.5252 kg of hydrogen at a low hydrogen leveled cost and payback period of 13.262 \$/kg and 1.49 years respectively. The CO₂ emitted from the PV/hydrogen system is considered greater than from Wind turbine/ hydrogen system which was 63,533 kg/year. This high amount of CO₂ emissions is due to the electricity purchase from the grid.

References

- [1] M. T. Muñoz Díaz, H. Chávez Oróstica, and J. Guajardo, "Economic Analysis: Green Hydrogen Production Systems," *Processes*, vol. 11, no. 5, p. 1390, May 2023. <https://doi.org/10.3390/pr11051390>
- [2] O. Schmidt, A. Gambhir, I. Staffell, A. Hawkes, J. Nelson, and S. Few, "Future cost and performance of water electrolysis: An expert elicitation study," *Int. J. Hydrogen Energy*, vol. 42, no. 52, pp. 30470–30492, Dec. 2017. <https://doi.org/10.1016/j.ijhydene.2017.10.045>
- [3] M. Shahabuddin, M. A. Rhamdhani, and G. A. Brooks, "Technoeconomic Analysis for Green Hydrogen in Terms of Production, Compression, Transportation and Storage Considering the Australian Perspective," *Processes*, vol. 11, no. 7, p. 2196, Jul. 2023. <https://doi.org/10.3390/pr11072196>
- [4] M. S. Herdem *et al.*, "A brief overview of solar and wind-based green hydrogen production systems: Trends and standardization," *Int. J. Hydrogen Energy*, vol. 51, pp. 340–353, Jan. 2024. <https://doi.org/10.1016/j.ijhydene.2023.05.172>
- [5] I. Ourya, N. Nabil, S. Abderafi, N. Boutammachte, and S. Rachidi, "Assessment of green hydrogen production in Morocco, using hybrid renewable sources (PV and wind)," *Int. J. Hydrogen Energy*, vol. 48, no. 96, pp. 37428–37442, Dec. 2023. <https://doi.org/10.1016/j.ijhydene.2022.12.362>
- [6] L. B. B. Maciel, L. Viola, W. de Queiróz Lamas, and J. L. Silveira, "Environmental studies of green hydrogen production by electrolytic process: A comparison of the use of electricity from solar PV, wind energy, and hydroelectric plants," *Int. J. Hydrogen Energy*, vol. 48, no. 93, pp. 36584–36604, Dec. 2023. <https://doi.org/10.1016/j.ijhydene.2023.05.334>
- [7] L. Al-Ghussain, A. D. Ahmad, A. M. Abubaker, K. Hovi, M. A. Hassan, and A. Annuk, "Techno-economic feasibility of hybrid PV/wind/battery/thermal storage trigeneration system: Toward 100% energy independency and green hydrogen production," *Energy Reports*, vol. 9, pp. 752–772, Dec. 2023. <https://doi.org/10.1016/j.egyr.2022.12.034>
- [8] Y. Ren *et al.*, "Modelling and capacity allocation optimization of a combined pumped storage/wind/photovoltaic/hydrogen production system based on the consumption of surplus wind and photovoltaics and reduction of hydrogen production cost," *Energy Convers. Manag.*, vol. 296, p. 117662, Nov. 2023. <https://doi.org/10.1016/j.enconman.2023.117662>
- [9] M. Nasser and H. Hassan, "Thermo-economic performance maps of green hydrogen production via water electrolysis powered by ranges of solar and wind energies," *Sustain. Energy Technol. Assessments*, vol. 60, p. 103424, Dec. 2023. <https://doi.org/10.1016/j.seta.2023.103424>

- [10] O. A. Dabar, M. O. Awaleh, M. M. Waber, and A.-B. I. Adan, “Wind resource assessment and techno-economic analysis of wind energy and green hydrogen production in the Republic of Djibouti,” *Energy Reports*, vol. 8, pp. 8996–9016, Nov. 2022.
<https://doi.org/10.1016/j.egyr.2022.07.013>
- [11] HOMER Pro, “Microgrid Software for Designing Optimized Hybrid Microgrids n.d.”
<https://homerenergy.com/products/pro/index.html>
- [12] K. W. Harrison, R. Remick, G. D. Martin, and A. Hoskin, “Hydrogen Production: Fundamentals and Case Study Summaries e Preprint,” 2010. [Online]. Available: <http://www.osti.gov/bridge>
- [13] *The Hydrogen Economy*. Washington, D.C.: National Academies Press, 2004.
<https://doi.org/10.17226/10922>
- [14] A. Al Miaari and H. M. Ali, “Technical method in passive cooling for photovoltaic panels using phase change material,” *Case Stud. Therm. Eng.*, vol. 49, p. 103283, Sep. 2023.
<https://doi.org/10.1016/j.csite.2023.103283>
- [15] A. Al Miaari, A. El Khatib, and H. M. Ali, “Design and thermal performance of an innovative greenhouse,” *Sustain. Energy Technol. Assessments*, vol. 57, p. 103285, Jun. 2023.
<https://doi.org/10.1016/j.seta.2023.103285>
- [16] A. Al Miaari and H. M. Ali, “Batteries temperature prediction and thermal management using machine learning: An overview,” *Energy Reports*, vol. 10, pp. 2277–2305, Nov. 2023.
<https://doi.org/10.1016/j.egyr.2023.08.043>

Analytical and numerical evaluation for wind turbine aerodynamic characteristics

Ashraf Abdelkhalig^{1,2,a}, Mahmoud Elgendi^{1,3,b*}, Mohamed Y.E. Selim^{1,3,c},
Maryam Nooman AlMallahi^{1,d}, Sara Maen Asaad^{4,e}

¹ Department of Mechanical and Aerospace Engineering, College of Engineering, United Arab Emirates University, Al Ain, UAE

² Aeronautical Engineering Department, College of Engineering, Sudan University of Science and Technology, Khartoum, Sudan

³ National Water and Energy Center, United Arab Emirates University, Al Ain, P.O. Box 15551, United Arab Emirates

⁴ Sustainable Energy and Power Systems Research Center, Research Institute of Science and Engineering (RISE) Engineering Sharjah, UAE

^a ashraf891@hotmail.com, ^b mahgendi@uaeu.ac.ae, ^c mohamed.selim@uaeu.ac.ae,
^d 700039403@uaeu.ac.ae, ^e smaen@sharjah.ac.ae

Keywords: Renewable Energy, Wind Turbine, Aerodynamics

Abstract. Energy lies at the core of ultramodern society, empowering everything from heating, lighting, computers, and food products to manufacturing and transport. A rising realization of the harmful climatic belongings of anthropogenic greenhouse gas emissions is boosting governmental pressure to alleviate or avoid CO₂ discharge into the ambiance. Wind turbines are one of the most likely initial applications for renewable sources. The major challenge in the wind turbine field is designing a machine that performs efficiently, boosting its reliability and producing power. The necessity for computational and experimental proceedings for probing aeroelastic stability has increased with the increase in output power and the size of the turbines. Due to the complexity and high costs of experimental investigations, several modeling methods have been practical solutions for design and analysis objectives. In this context, this paper presents an evaluation study for the aerodynamic performance of wind turbines - by concentrating on analyses of aerodynamic workforces that act on the rotor, employing Blade Element Momentum (BEM) and with the usage of the Computational Fluid Dynamic (CFD) solver. The computed results show a reasonable agreement with the previous results found in the literature. This indicates that it is possible to predict the characteristics of wind turbines from analytical and numerical approaches with plausible reliability.

Introduction

The conversion of wind power into beneficial power has placed the foundations for one of the most significant technological progress of the 20th century. Wind turbines—elaborated to harness and utilize wind power to generate electricity—are the technology behind one of the speedy promoting industries for power production. They are currently an ordinary sight worldwide in the countryside and urban regions [1].

For successful and outsize wind energy employment, the cost of wind turbines must be reduced to be competitive with the instant options. The conduct of a wind turbine is formed by a complicated relationship of elements and sub-systems [2]. The main parts are the rotor, tower, hub, and nacelle. Extrapolating the interactive actions between the parts provides the basics for trusty design computations, optimized machine arrangements, and reduced wind electricity expenses [30]. In the aspect of rotor aerodynamics, many phenomena (e.g., atmospheric boundary layer

flow) still need to be fully understood. Consequently, some methods are used to analyze the aerodynamic performance, such as wind tunnel tests or field measurements, analytical models, and Computational Fluid Dynamics (CFD) [3].

Many researchers [4-7] provided extensive surveys of the literature on the analytical and semi-empirical models (e.g., Blade Element Momentum (BEM) model). However, CFD is a vital tool for flow simulation in different cases [8–17]. With the evolution of computing implementations, using the CFD approach makes it possible to resolve wind turbine rotors fully. In this context, Ferziger and Peric [19], Jorge et al. [20], and Jiyuan et al. [21] explored the dynamic capability of CFD. They pointed out the descriptions of fundamental theories, basic techniques, and practical guidelines.

The present work aims to examine the performance characteristics of the HAWT rotor from an aerodynamics perspective and, in general, to validate the capabilities of BEM and CFD techniques applied in the wind energy field.

Method of Analysis

Analytical Study

The wind turbine performance can be predicted analytically by applying the BEM theory. In this approach, the blade is split into several separated parts along with the spread of the blade. For every part, a force equilibrium is utilized concerning two-dimensional lift and drag with the thrust and torque delivered by the part. Simultaneously, an equilibrium of axial and angular momentum applies to it. This outputs several equations that can be resolved iteratively [22]. The equations of the BEM theory given by [6] are utilized to compute the output power of the NREL turbine (see Table 1), and the details about the blade and measurement conventions can be found in [23].

Table 1. Characteristics of NREL Phase VI wind turbine [23].

Blades number	2
Blade profile	S809
Rotor radius	5.029 m
Rotational speed	72 rpm
Turbine power	19.8 kW
Power regulation	Stall

Numerical Study

Here, we investigate the aerodynamic characteristics of the S809 airfoil, represented in the blade profile. A commercial, finite volume-based solver has been used to implement this analysis. Generally, three main configurations point out commercial CFD codes corresponding to three stages of problem-solving- pre-processor, solver, and post-processor [24]. The computational domain for 2D airfoil analysis is shown in Fig 1. During the creation of the mesh around the airfoil, great care must be taken in the vicinity close to the airfoil surface to consider the boundary layer flow that might be formed, as illustrated in Fig 2. Also, the k- ϵ model is applied as a turbulence model.

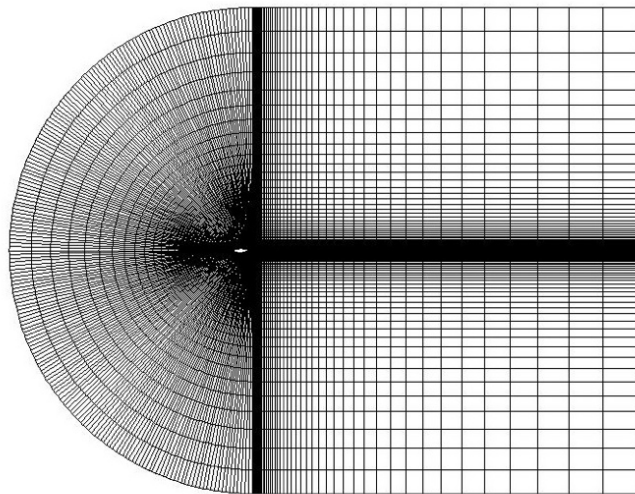


Fig. 1. Mesh generated for the airfoil section

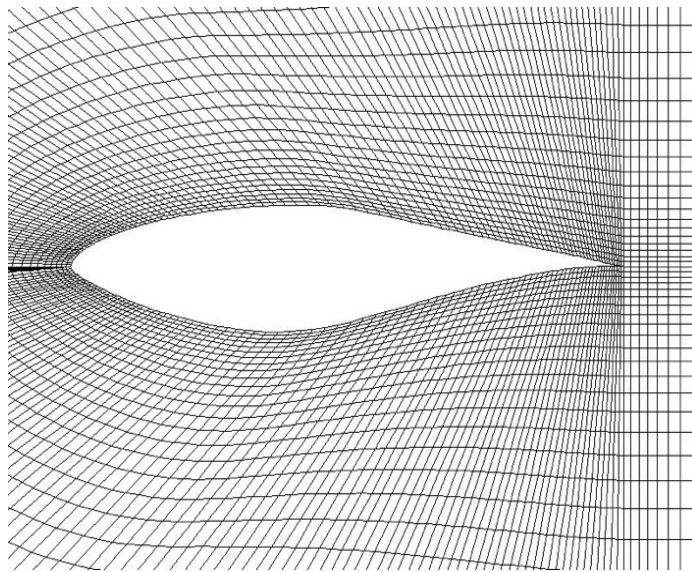


Fig. 2. Concentrated mesh generated around the airfoil.

Results and Discussion

BEM code results

The BEM code splits the blade into ten elements to determine the power generated over a range of wind speeds for each element. This has been done at wind speeds ranging from 5 to 15 m/s. Fig. 3 shows the comparison of present code results (BEM) with measured data (Exp.) [25] and other BEM predictions [26, 27] for the NREL Phase VI rotor.

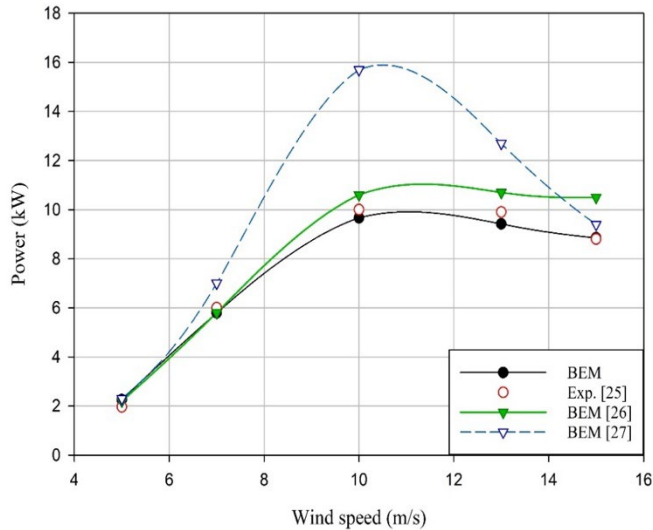


Fig. 3. Power predicted at different wind speeds.

It is illustrated by Fig. 3 that the power computed from the present BEM code compared well with experimental results at all wind velocities, except at 13m/s, where an under-prediction of 13% is realized.

2D Airfoil analysis results

Fig. 4 shows the computed pressure coefficient (C_p) distribution in the present analysis (CFD) at zero angles of attack (AOA) and 106 Reynolds number, compared with experimental data (Exp.) [28] and another computational study CFD [28] for the same airfoil and operating conditions.

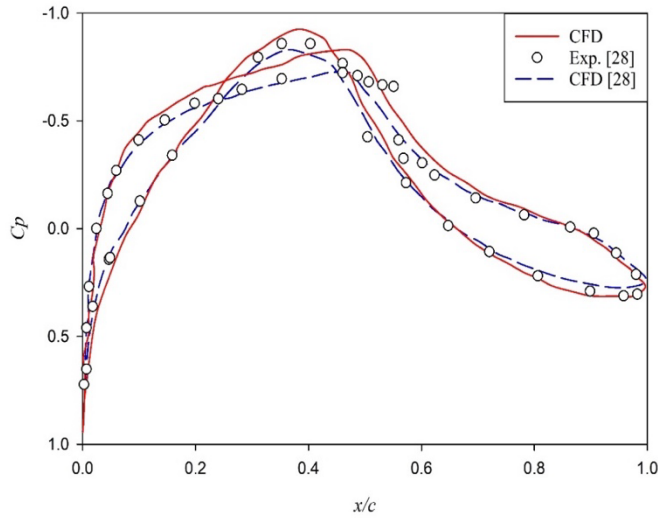


Fig. 4. Pressure coefficient for S809 airfoil.

The distribution of C_p with referenced data was validated on both airfoil surfaces. In addition, table 2 compares the numerical and experimental lift coefficient (C_l) and drag coefficient (C_d), calculated at 2×10^6 Reynolds number and different attack angles. Lift coefficient results are very close to the experimental data at all AOA (within 8%), while the predicted drag coefficients are up to 40% higher than the experiment results. This over-prediction of drag could be reasonable due to the laminar flow over the airfoil's forward half.

Fig. 5 (a) displays the pressure contours over the airfoil for the zero-degree angle of attack. The maximum pressure is generated at the airfoil leading edge. Also, negative pressure is created at both airfoil surfaces (i.e., top and bottom). The variation between these pressures is the source of the lift force. With the increase of AOA (Fig. 5 (b)), the negative pressure at the upper surface increases, while the negative pressure at the lower surface decreases, so the lift increases (and consequently, the lift coefficient, as indicated in Table 2).

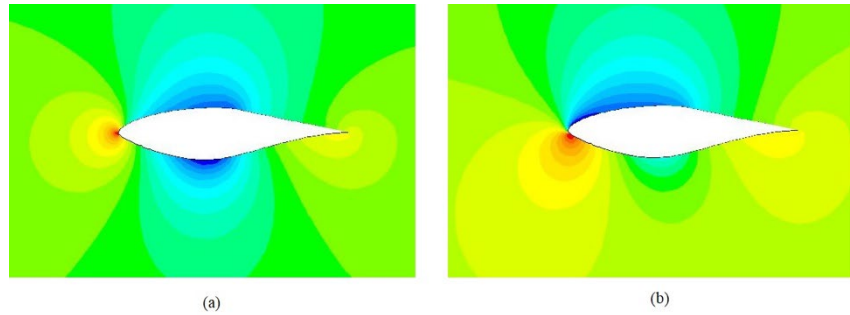


Fig. 5. Pressure contours of S809 at 2×10^6 Reynolds number for (a) 0 and (b) 5.13 AOA

Table 2. Comparisons between CFD and experimental C_l and C_d [28].

AOA (deg)	C_l					C_d				
	Exp. [28]	CFD	%	CFD [28]	% Error	Exp. [28]	CFD	%	CFD [28]	% Error
			Error					Error		
0.00	0.1469	0.152482	4	0.1324	-10	0.0070	0.012092	42	0.0108	54
1.02	0.2716	0.267285	-2	0.2492	-8	0.0072	0.012463	42	0.0110	53
5.13	0.7609	0.70615	-8	0.7123	-6	0.0070	0.018062	61	0.0124	77

Conclusion

The main goal of this paper is to carry out a characteristic aerodynamic evaluation of the blade of a HAWT. For this, the NREL Phase VI blade is analyzed analytically using the BEM method and numerically using the CFD. The results were quite satisfactory and can represent a well-grounded basis for coming research in this field. Fundamentally, the effects of changing the geometric and aerodynamic factors on the performance of wind turbines could be understood through BEM theory. More importantly, the reliability of CFD for calculating performances on a HAWT blade was confirmed. As evident from this work, the numerical investigations involved the assumption of a fully turbulent flow using the k- ϵ model. Nonetheless, a more advanced model with different setups needs to be considered to obtain optimal results.

References

- [1] Bakırıcı M and Yılmaz S 2018 Eng. Sci. Technol, an International J. 21 1128–42.
<https://doi.org/10.1016/j.jestch.2018.05.006>
- [2] Abdelrahim A and Seory A 2017 Proc. 10th Biennial International Workshop Advances in Energy Studies BIWAES2017 (Naples, Italy)
- [3] Sørensen J and Shen W 2002 J. Fluid Engineering 124 393–9.
<https://doi.org/10.1115/1.1471361>
- [4] Gordon L 2011 *Aerodynamics of Horizontal Axis Wind Turbines*, In: *Advances in Wind Energy Conversion Technology*, ed Mathew S and Philip G, Springer.
- [5] Pramod J 2011 *Wind Energy Engineering* (London: McGraw-Hill)

- [6] Hansen M 2008 *Aerodynamics of Wind Turbines* 2nd ed (London: Earthscan)
- [7] Manwell J, McGowan J and Rogers A 2002 *Wind Energy Explained* (John Wiley & Sons Ltd). <https://doi.org/10.1002/0470846127>
- [8] Mekhail T, Dahab O, Sadik M, El-Gendi M and Abdel-Mohsen H 2015 *Open J. Fluid Dyn.* **05** 224–37. <https://doi.org/10.4236/ojfd.2015.53025>
- [9] El-Gendi M, Ibrahim M, Mor K and Nakamura Y 2010 *Trans. Jpn. Soc. Aeronaut. Space Sci.* **53** 122–9. <https://doi.org/10.2322/tjsass.53.122>.
- [10] El-Gendi M, Ibrahim M, Mor K and Nakamura Y 2009 *Trans. Jpn. Soc. Aeronaut. Space Sci.* **52** 206–12. <https://doi.org/10.2322/tjsass.52.206>
- [11] El-Gendi M, Do K, Ibrahim M, Mor K and Nakamura Y 2010 *Trans. Jpn. Soc. Aeronaut. Space Sci.* **53** 171–9. <https://doi.org/10.2322/tjsass.53.171>
- [12] El-Gendi M, Lee S, Joh C, Lee G, Son C, Chung W 2013 *Trans. Jpn. Soc. Aeronaut. Space Sci.* **56** 82–9. <https://doi.org/10.2322/tjsass.56.82>
- [13] El-Gendi M 2018 *Int. J. Therm. Sci.* **125** 369–80.
<https://doi.org/10.1016/j.ijthermalsci.2017.12.012>
- [14] El-Gendi M and Aly A 2017 *Int. J. Numer. Methods Heat Fluid Flow* **27** 2508–27.
<https://doi.org/10.1108/HFF-10-2016-0376>
- [15] El-Gendi M, Do K, Ibrahim M, Mor K and Nakamura Y 2010 *Trans. Jpn. Soc. Aeronaut. Space Sci.* **53** 171–9. <https://doi.org/10.2322/tjsass.53.171>
- [16] El-Gendi M, Lee S and Son C 2011 *J. Korean Soc. Mar. Eng.* **35** 938–45.
<https://doi.org/10.5916/jkosme.2011.35.7.938>
- [17] Cheng S, Elgendi M, Lu F and Chamorro L 2021 *Energies* **14** 7204.
<https://doi.org/10.3390/en14217204>
- [18] Abdelkhalig A, Elgendi M and Sliem M 2022 In: *2022 AUA Acad. Conf. Sustain. Energy Green Technol., IOP-EES*
- [19] Ferziger J and Peric M 1999 *Computational Methods for Fluid Dynamics* (Berlin: Springer-Verlag). <https://doi.org/10.1007/978-3-642-98037-4>
- [20] Jorge C, Achim H, Florian M, Thomas E and Antoine L 2001 *Advanced CFD Analysis of using Aerodynamics Using CFX* (AEA Technology GmbH)
- [21] Jiyuan T, Guan H and Chaoqun L 2008 *Computational Fluid Dynamics: A Practical Approach* (Elsevier Inc.)
- [22] Grant I 2005 *Wind Turbine Blade Analysis using the Blade Element Momentum Method Version 1.0* School of Engineering (Durham: Durham University)
- [23] Hand M, Simms D, Fingersh L, Jager D, Cotrell JSchreck S and Larwood S 2001 *NREL Technical Report/TP-500-29955* (Golden, Colorado)
- [24] Versteeg H and Malalasakera W 1995 *An Introduction to Computational Fluid Dynamics: The Finite-Volume Method* (New York: Longman Scientific & Technical)
- [25] Leclerc C and Masson C 2005 *J. Sol. Energy Eng. Trans.-ASME* **127** 200–8.
<https://doi.org/10.1115/1.1889466>
- [26] Maria M and Jacobson M 2009 *Energies* **2** 816–38. <https://doi.org/10.3390/en20400816>
- [27] Yelmule M and Anjuri E 2013 *Int. J. Renew. Energy. Res.* **3** 261–9
- [28] Wolfe W and Ochs S 1997 *AIAA-97-0973*

[29] Elgendi, M., AlMallahi, M., Abdelkhalig, A. and Selim, M.Y., 2023. A review of wind turbines in complex terrain. International Journal of Thermofluids, p.100289.
<https://doi.org/10.1016/j.ijft.2023.100289>

[30] Abdelkhalig, A., Elgendi, M., & Selim, M. Y. (2022, August). Review on validation techniques of blade element momentum method implemented in wind turbines. In IOP Conference Series: Earth and Environmental Science (Vol. 1074, No. 1, p. 012008). IOP Publishing. <https://doi.org/10.1088/1755-1315/1074/1/012008>

Sustainability policies and regulation challenges in recycling EV batteries

Afnan KHALIL^{1,a*}, Mousa HUSSEIN^{2,b}, Essam ZANELDIN^{3,c}, Waleed AHMED^{4,d}

¹ Chemical and Petroleum Engineering Department, COE, UAE University, Al Ain, UAE

² Electrical and Communication Engineering Department, COE, UAE University, Al Ain, UAE

³ Civil and Environmental Engineering Department, COE, UAE University, Al Ain, UAE

⁴ Engineering Requirements Unit, COE, UAE University, Al Ain, UAE

^a700043891@uaeu.ac.ae, ^bmihussein@uaeu.ac.ae, ^cessamz@uaeu.ac.ae,
^dw.ahmed@uaeu.ac.ae

Keywords: EV, Recycling, Policies, Regulations, Batteries

Abstract. The increasing use of electric vehicles has brought the critical issue of recycling the batteries of electric cars to the forefront. This paper explores the challenges posed by current recycling policies, emphasizing the gaps in regulations and the pressing need for effective authorities involvement. The complications surrounding the recycling policies of electric car batteries are explored, shedding light on the disadvantages that may restrict successful implementation. The paper underscores the importance of addressing these challenges to ensure sustainable and responsible management of electric car batteries, emphasizing the shared responsibility between authorities, manufacturers, and other stakeholders. Examining existing policies and identifying areas for improvement will contribute to the ongoing discourse on developing comprehensive and effective electric car battery recycling frameworks and a sustainable and environmentally responsible approach to the end-of-life management of electric vehicle batteries. Recommendations on how to address this crucial issue are also presented.

Introduction

Sustainability incorporates maintaining or preserving a process over an extended period of time. In commerce and policy, sustainability is driven by protecting natural and physical resources to ensure their availability for an extended duration [1]. However, the actual core of sustainable strategies goes beyond resource conservation since it prioritizes an in-depth consideration of how specific policies or corporate practices will impact not only the durability of resources but also the well-being of people, the resilience of ecosystems, and the overall stability of the economy in the future [2]. Sustainability is grounded in a reflective understanding that the Earth faces the risk of irreversible damage if substantial changes are not instituted in its management. It highlights the resolution of responsible and forward-thinking practices to safeguard the planet for future generations. As we inspect the context of fuel-powered vehicles through the lens of sustainability, a reality emerges they employ a considerable environmental impact. The emissions from conventional vehicles, including pollutants like smog, carbon monoxide, and other harmful substances, pose a significant threat to human beings and the environment [3]. What exacerbates this concern is that these emissions derive from street vehicles, directly exposing people to contaminated air that is inhaled into their lungs. This proximity increases the health risks, making vehicle emissions a pressing and immediate concern, unlike pollutants released at higher altitudes from industrial smokestacks. In fact, the sustainability discourse demands a critical evaluation of our choices, particularly in the context of transportation. Recognizing the contrary effects of conventional vehicles on human health and the environment underlines the imperative to transition to more sustainable alternatives, such as electric vehicles, as a crucial step toward mitigating the

harmful impact on our planet [4]. This shift aligns with the broader principles of sustainability, emphasizing responsible resource management and the preservation of ecosystems for the long-term well-being of our planet and its inhabitants. In pursuing a sustainable future in the automotive industry, shifting from traditional internal combustion engine vehicles to electric vehicles (EVs) is a pivotal transformation in the automotive landscape [5]. Figure 1 illustrates the design of a modern electrical car.



Figure 1: A modern electric vehicle.

Beyond reducing emissions, this transition promises a comprehensive reimaging of our mobility and environmental responsibility approach. At the core of the move to electric vehicles is a significant reduction in greenhouse gas emissions, as EVs operate with zero tailpipe emissions. This shift reflects a commitment to a cleaner atmosphere and a more sustainable global ecosystem [7]. In densely populated urban areas, where air quality is a growing concern, adopting electric vehicles contributes to a healthier living environment. The zero-emission operation of EVs takes precautions against the pollutants that compromise air quality and impact human health and the environment [8]. Electric vehicles redefine transportation efficiency by significantly reducing the overall energy consumption compared to traditional combustion engines. This brings cost savings for users and aligns with the principles of resource efficiency, promoting responsible energy use and conservation. As the world acknowledges the finite nature of fossil fuel resources, the transition to electric vehicles strategically lessens dependence on exhaustible fuels. This move toward energy diversification supports a more sustainable energy mix, integrating renewable sources like solar and wind into our transportation infrastructure [9]. The shift to electric vehicles catalyzes technological innovation, particularly in battery technology, energy storage, and charging infrastructure. This combined effect fosters a cycle of innovation, propelling advancements in sustainable practices and contributing to a more sustainable technological landscape [10]. The desire for electric vehicles is booming as more people seek eco-friendly transportation options and governments push for cleaner mobility solutions. This rising demand for EVs reflects a global shift towards sustainable transportation fueled by lower operating costs, technological advancements, and environmental consciousness. Figure 2 shows the increase in the EV demand.

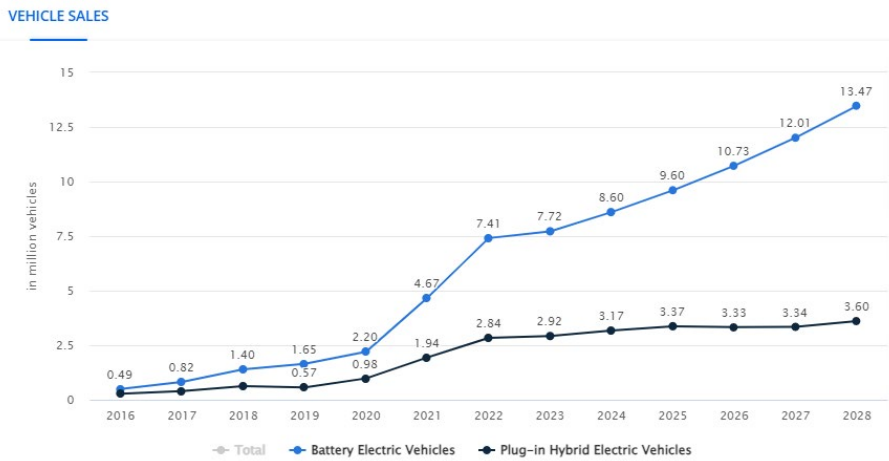


Fig. 2 Demand statistics on EV. [11]

In general, embracing electric vehicles transcends the conventional boundaries of transportation revolutions. It signifies a conscious choice towards a future where sustainability is not just an aspiration but an integral part of our collective journey. As the automotive industry accelerates towards electric mobility, incorporating these advantages holds the potential to usher in a transformative era of environmental harmony and sustainable living [12]. Despite all the benefits of this transformation from traditional vehicles to electric vehicles, the recycling of electric vehicles batteries remains a high concern. The increasing demand for electric vehicle (EV) batteries is driven by the production of new EV cars and the need for spare parts, reflecting the growing adoption of electric mobility worldwide. As more EVs hit the roads and manufacturers expand their product lines, the demand for reliable and efficient batteries continues to surge, highlighting the critical role of battery technology in the transition to sustainable transportation. Figure 3 depicts the demand and supply of lithium for batteries by sector.

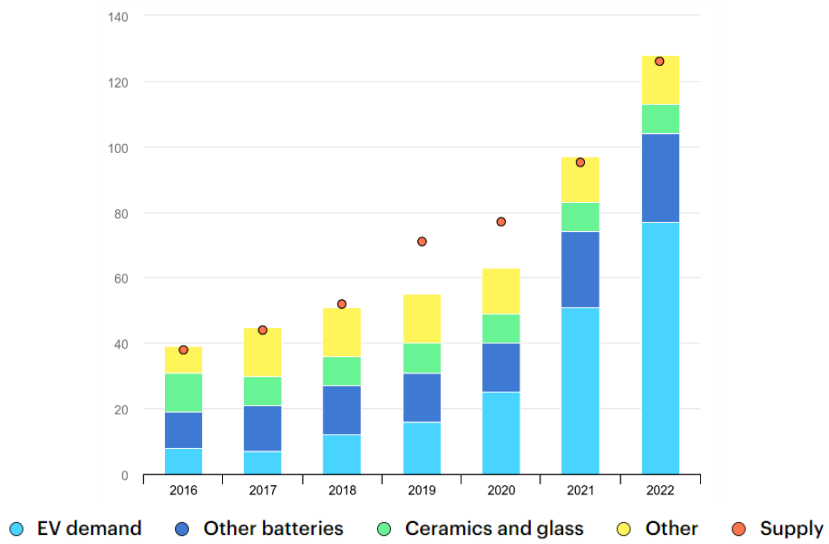


Fig. 3 Overall supply and demand of lithium for batteries by sector, 2016-2022 [13].

This article aims to understand the difficulties in recycling electric vehicle batteries by looking at different angles, particularly on how policies play a significant role. Our goal is to break down and study the complex process of recycling EV batteries, highlighting the challenges from different

viewpoints and exploring how policies significantly impact the sustainable handling of these crucial components.

Challenges, Regulations, Responsibilities, and Disadvantages

In this review, our goal is to tackle the challenges, regulations, responsibilities, and disadvantages associated with the shift to electric vehicles. This involves a comprehensive understanding of the extent of the problem by exploring these essential aspects. The complicated manufacturing details of electric vehicle batteries and the absence of a well-established recycling infrastructure provide several difficulties for the recycling industry [14]. The following subsections highlight some significant obstacles to recycling policies for batteries used in electric vehicles:

Challenges in Recycling Policies

In the field of chemical complexity, lithium, cobalt, nickel, and other rare earth elements are among the valuable and potentially dangerous compounds commonly found in electric vehicle batteries. These materials must be extracted and separated for recycling, a complicated operation requiring specialized technologies. Considering that recycled materials must adhere to strict requirements to be used in creating new batteries, the complexity stems from the necessity to separate and recover these materials without sacrificing their quality [15]. Lithium-ion battery recycling may not be possible using conventional techniques like shredding and melting because of the possibility of losing essential materials and associated safety risks. Moreover, the infrastructure for recycling lithium-ion batteries is less developed than that of classic lead-acid batteries, which have clear and well-established recycling procedures. A robust collecting and transportation system and the expansion of recycling facilities are required to handle the growing quantity of end-of-life electric car batteries [16]. Considering transportation logistics as a critical point, batteries must be delivered to recycling centers properly and safely. The absence of a dedicated infrastructure for the transportation of batteries for electric vehicles might lead to higher expenses and more complicated logistics. Transportation must be safe and legal to prevent incidents and harmful emissions [17]. Besides the policy and regulation gaps, there might be exceptions to the rules and laws concerning the recycling of electric vehicle batteries in specific areas. Clear rules, rewards, and restrictions can be established to encourage producers and customers to engage in recycling initiatives in extended procedure responsibility [18]. Sustainable battery recycling depends on end-of-life extended producer responsibility (EPR) plans, which enable proper collection and disposal of items at the end of their useful lives by assuring responsible manufacturing procedures and methods. However, gaps in accountability and recycling programs may result from the lack of widespread adoption of EPR regulations for batteries used in electric vehicles [19].

Gaps in Recycling Regulations

One major obstacle to efficiency, safety, and the creation of an international framework for sustainable practices in the recycling of electric vehicles batteries is the absence of standards. Significant elements of the lack of standards are various battery layouts, where battery designs used by manufacturers of electric vehicles frequently differ in terms of cell shapes, packaging, and thermal management mechanisms. Developing consistent recycling procedures and technology is challenging due to the absence of uniformity in these design elements. In contrast, when we come to uncertain responsibilities, there may not have been a clear definition of who is responsible for what at each stage of the battery life cycle, including recycling. Roles and duties must be clearly defined to prevent gaps in the performance of recycling procedures. However, clarity regarding the obligations of manufacturers, consumers, and recycling facilities for the disposal of electric car batteries at the end of their useful lives is lacking in many countries. Controlling the disposal of electric vehicle (EV) batteries in landfills is crucial to prevent environmental contamination and maximize resource recovery. Implementing strict regulations, promoting battery recycling

programs, and incentivizing proper disposal methods are essential steps in managing the end-of-life cycle of EV batteries and mitigating potential ecological risks. Figure 4 illustrates the expected future landfill caused by EVs batteries disposals.



Fig. 4 Future landfill of EV battery disposals [6]

Well-defined policies are necessary to create accountability and encourage ethical recycling methods. Policies and guidelines for achieving goals without opposing or distancing specific technologies are known as technology-neutral guidelines. Technology-neutral policies are intended to establish fair and equal opportunities for various recycling techniques and technologies in electric car battery recycling. Among the crucial issues that should be addressed is the need to promote innovation. Technology-neutral policies promote constant creativity in the field of recycling electric vehicles batteries without favoring any particular technology over other technologies. With this strategy, the industry is free to experiment with and implement modern eco-friendly techniques without being restricted by outdated rules. In addition to the approach based on objectives, technology-neutral regulations place a greater value on the intended results and environmental goals than on recommending techniques or tools. This makes it possible to be adaptable and flexible as recycling technologies develop over time.

Authority Responsibilities and Commitments

Authorities are essential when developing and implementing efficient rules for recycling electric car batteries. In this area, authorities are primarily responsible for legislation and regulations, which are vital in controlling and directing numerous aspects of society, including sectors like the recycling of electric vehicle batteries. Regulations and legality are essential for maintaining safety, ecological sustainability, and end-of-life management of electric vehicle batteries. Legislative frameworks may require public awareness campaigns and educational programs to educate customers, companies, and other stakeholders on the significance of responsibly disposing of and recycling batteries [20]. This brings us to the matter of public awareness and education requirements. Promoting active involvement in recycling programs and developing a sustainable culture requires education. Regarding recycling electric vehicles batteries, regulations and laws seek to establish an organized, secure, and long-lasting system that handles environmental issues, encourages creativity, and guarantees the proper handling of batteries that have reached the end of their useful lives. To keep up with changes in consumption habits and technological advances, these frameworks need to be updated regularly. Furthermore, tracking and enforcing procedures are essential elements of successful legislation in the context of recycling electric car batteries. These features guarantee that set guidelines and regulations are followed, encouraging environmental sustainability, safety, and appropriate disposal of spent batteries. However, inspecting procedures are required, and supervision includes creating and applying inspection

protocols. The guidelines define the standards for evaluating consistency, influencing safety rules, ecological consequences, and conformity to recycling techniques. Inspections can occur during transportation, recycling locations, and factories. Additionally, safety inspections are required in battery recycling situations where safety is a top priority. Regulatory agencies conduct safety checks to evaluate whether companies follow safety procedures when gathering, moving, and handling wasted batteries [21]. The purpose of these examinations is to stop hazardous material releases, fires, and accidents.

Disadvantages of Recycling Policies

There are significant drawbacks to recycling regulations for electric vehicles batteries, even though they are essential for managing the end-of-life phase of these batteries and resolving environmental concerns. It's critical to recognize these difficulties to guide continuing efforts toward progress. Creating and applying innovative recycling technology for electric vehicle batteries can be quite costly. Compared to alternative approaches, including raw material extraction, recycling may not be as financially practical due to the expensive costs involved in the process and the requirement for specialized equipment and qualified employees. Also, it may fall under the field of energy efficiency of recycling. The energy intensity of recycling is the energy needed to gather, process, and repurpose wasted materials into new goods. The recycling process for electric car batteries can be expensive in terms of energy, affecting the sustainability of recycling programs from an environmental and financial perspective. There are some energy-intensive battery recycling procedures for electric vehicles. The energy obtained from sources that are not renewable may cause some of the environmental advantages of recycling to be outweighed by the energy needed to extract valuable components from utilized batteries. As well as, by carrying out a life cycle assessment, the environmental impact of the battery lifecycle from production and usage to recycling can be thoroughly examined, including the energy intensity of the process. Lifecycle assessment helps find ways to make the recycling process more energy-efficient and cost-effective. In addition, customer engagement and understanding are other vital points where insufficient consumer knowledge about the value of recycling and the accessibility of appropriate disposal methods may result in low customer engagement. The success of a recycling policy depends on educating customers about proper battery disposal. Policies aimed at recycling the batteries used in electric cars must succeed in raising consumer knowledge and awareness and encouraging their involvement. Increasing consumer awareness of the value of adequately disposing and recycling EV batteries can significantly impact recycling rates and help create a more sustainable end-of-life battery management strategy [22]. Yet, customers must understand how incorrect disposal of electric car batteries affects their health and the environment. If recycled improperly, the compounds found in used batteries have the potential to cause serious environmental harm. Encouraging environmentally responsible behavior among consumers involves educating them about the potential implications of improper disposal. Also, battery manufacturers may help by clearly identifying their products, emphasizing the need for recycling, and offering guidance on how to do so. Consumers may make educated decisions and comprehend their part in the recycling process with straightforward information. Lastly and most importantly, using social media channels to interact with customers and share information about recycling batteries is a good strategy. Programs on social media can increase awareness, provide information, and promote community engagement in sustainability initiatives.

Recommendations

Typically, a lithium-ion battery can last between 8 to 10 years or 100,000 to 200,000 miles, whichever comes first. However, several factors can affect the life of an EV battery. Some factors contributing to reducing the EV battery's lifespan include frequent fast charging, high-speed driving, and exposure to extreme temperatures. It is always recommended to regularly check the

battery's state of charge and identify issues before they become severe. It is also recommended that the battery be appropriately charged to only 80% of its capacity and that frequent fast charging is avoided. Despite all these preventive measures to increase the battery's lifespan, the life of the EV battery will end and proper recycling should be implemented [23]. Some of the recommendations to optimally recycle EV batteries with the objective of conserving resources, reducing environmental impact, improving energy efficiency, and minimizing waste include:

1. Develop efficient and environmentally friendly recycling techniques for EV batteries.
2. Ensure collaboration between industries, governments, and researchers and continuously introduce innovative methods to drive the development of more effective recycling processes.
3. Develop consistent and clear technology-neutral recycling policies and guidelines. These policies should clearly define the responsibilities at each stage of the battery life cycle, including the recycling stage, roles and duties, and accountability and obligations of manufacturers, consumers, and recycling facilities to dispose of the batteries at the end of their useful lives.
6. Reduce waste, conserve resources, and promote a greener and more sustainable future by giving used EV batteries a second life.
7. Educate customers about proper battery disposal. Increasing consumer awareness of the value of properly disposing of and recycling batteries helps create a more sustainable end-of-life battery management strategy.

Concluding Remarks

In summary, it emphasizes an urgent need for comprehensive and effective sustainability policies and regulations to address the challenges of recycling electric vehicle (EV) batteries. The complexities arising from chemical composition, the lack of infrastructure, and regulatory gaps pose significant barriers. Clear roles, technology-neutral guidelines, and active involvement of authorities are highlighted as essential components. Despite the importance of recycling regulations, challenges such as high costs and energy-intensive processes exist. Consumer education and engagement are crucial for the success of recycling initiatives. Collaborative efforts among authorities, manufacturers, and consumers are imperative to develop and implement sustainable and responsible recycling frameworks for EV batteries. This is crucial for mitigating environmental impact, fostering innovation, and ensuring responsible end-of-life management in the era of electric mobility.

References

- [1] Kuhlman, T.; Farrington, J. What is Sustainability? *Sustainability* 2010, 2, 3436-3448.
<https://doi.org/10.3390-su2113436>
- [2] Anne P.M. Velenturf, Phil Purnell, Principles for a sustainable circular economy, *Sustainable Production and Consumption*, Volume 27, 2021, Pages 1437-1457.
<https://doi.org/10.1016/j.spc.2021.02.018>
- [3] Perera, F. Pollution from Fossil-Fuel Combustion is the Leading Environmental Threat to Global Pediatric Health and Equity: Solutions Exist. *Int. J. Environ. Res. Public Health* 2018, 15, 16. <https://doi.org/10.3390/ijerph15010016>
- [4] Anenberg, S.; Miller, J.; Henze, D.; Minjares, R. A global snapshot of the air pollution-related health impacts of transportation sector emissions in 2010 and 2015.
- [5] Pavlínek, P. Transition of the automotive industry towards electric vehicle production in the east European integrated periphery. *Empirica* 50, 35–73 (2023). <https://doi.org/10.1007/s10663-022-09554-9>
- [6] <https://www.imagine.art/>, Text to image with AI Art Generator, accessed on 24-March-2024.

- [7] Gao, Z., Xie, H., Yang, X., Zhang, L., Yu, H., Wang, W., Liu, Y., Xu, Y., Ma, B., Liu, X., & Chen, S. (2023). Electric vehicle lifecycle carbon emission reduction: A review. *Carbon Neutralization*, 2(5), 528-550. <https://doi.org/10.1002/cnl2.81>
- [8] Peters, D. R., Schnell, J. L., Kinney, P. L., Naik, V., & Horton, D. E. (2020). Public Health and Climate Benefits and Trade-Offs of U.S. Vehicle Electrification. *GeoHealth*, 4(10). <https://doi.org/10.1029/2020GH000275>
- [9] Jamil, M., Ahmad, F., & Jeon, Y. (2016). Renewable energy technologies adopted by the UAE: Prospects and challenges – A comprehensive overview. *Renewable and Sustainable Energy Reviews*, 55, 1181-1194. <https://doi.org/10.1016/j.rser.2015.05.087>
- [10] Bustinza, O. F., Vendrell-Herrero, F., & Chiappetta Jabbour, C. J. (2024). Integration of product-service innovation into green supply chain management: Emerging opportunities and paradoxes. *Technovation*, 130, 102923. <https://doi.org/10.1016/j.technovation.2023.102923>
- [11] <https://www.statista.com/outlook/mmo/electric-vehicles/worldwide#unit-sales>, online statistics portal that provides access to a vast array of data and insights across various industries and topics, accessed on 24-March-2024.
- [12] Wellbrock, W., Ludin, D., Röhrle, L., & Gerstlberger, W. (2020). Sustainability in the automotive industry, importance of and impact on automobile interior – insights from an empirical survey. *International Journal of Corporate Social Responsibility*, 5(1), 1-11. <https://doi.org/10.1186/s40991-020-00057-z>
- [13] <https://www.iea.org/data-and-statistics/charts/overall-supply-and-demand-of-lithium-for-batteries-by-sector-2016-2022>, The International Energy Agency (IEA) is a prominent organization focused on energy policy and analysis, accessed on 24-March-2024.
- [14] Costa, C., Barbosa, J., Gonçalves, R., Castro, H., Campo, F. D., & Lanceros-Méndez, S. (2021). Recycling and environmental issues of lithium-ion batteries: Advances, challenges and opportunities. *Energy Storage Materials*, 37, 433-465. <https://doi.org/10.1016/j.ensm.2021.02.032>
- [15] Kang, Z., Huang, Z., Peng, Q., Shi, Z., Xiao, H., Yin, R., Fu, G., & Zhao, J. (2023). Recycling technologies, policies, prospects, and challenges for spent batteries. *IScience*, 26(11), 108072. <https://doi.org/10.1016/j.isci.2023.108072>
- [16] Neumann, J., Petranikova, M., Meeus, M., Gamarra, J. D., Younesi, R., Winter, M., & Nowak, S. (2022). Recycling of Lithium-Ion Batteries—Current State of the Art, Circular Economy, and Next Generation Recycling. *Advanced Energy Materials*, 12(17), 2102917. <https://doi.org/10.1002/aenm.202102917>
- [17] Slattery, M., Dunn, J., & Kendall, A. (2021). Transportation of electric vehicle lithium-ion batteries at end-of-life: A literature review. *Resources, Conservation and Recycling*, 174, 105755. <https://doi.org/10.1016/j.resconrec.2021.105755>
- [18] Albertsen, L., Richter, J. L., Peck, P., Dalhammar, C., & Plepys, A. (2021). Circular business models for electric vehicle lithium-ion batteries: An analysis of current practices of vehicle manufacturers and policies in the EU. *Resources, Conservation and Recycling*, 172, 105658. <https://doi.org/10.1016/j.resconrec.2021.105658>
- [19] Skeete, J., Wells, P., Dong, X., Heidrich, O., & Harper, G. (2020). Beyond the EVent horizon: Battery waste, recycling, and sustainability in the United Kingdom electric vehicle transition. *Energy Research & Social Science*, 69, 101581. <https://doi.org/10.1016/j.erss.2020.101581>

- [20] Xie, Y., Yu, H., & Changdong, L. (2016). Research on systems engineering of recycling ev battery. <https://doi.org/10.2991/ameii-16.2016.291>
- [21] Loganathan, M., Anandarajah, G., Tan, C., Msagati, T., Das, B., & Hazarika, M. (2022). Review and selection of recycling technology for lithium-ion batteries made for ev application - a life cycle perspective. Iop Conference Series Earth and Environmental Science, 1100(1), 012011. <https://doi.org/10.1088/1755-1315/1100/1/012011>
- [22] Wang, S. (2022). Multi-angle analysis of electric vehicles battery recycling and utilization. Iop Conference Series Earth and Environmental Science, 1011(1), 012027. <https://doi.org/10.1088/1755-1315/1011/1/012027>
- [23] Luo, C., Zhang, Z., Qiao, D., Lai, X., Li, Y., & Wang, S. (2022). life prediction under charging process of lithium-ion batteries based on automl. Energies, 15(13), 4594. <https://doi.org/10.3390/en15134594>

Renewable energy sources, sustainability aspects and climate alteration: A comprehensive review

M. Amin Mir^{1,a*}, M. Waqar Ashraf^{1,b}, Kim Andrews^{1,c}

¹Department of Mathematics & Natural Sciences, Prince Mohammad Bin Fahd University, Al-Khobar, Saudi Arabia

^ammir@pmu.edu.sa, ^bmashraf@pmu.edu.sa, ^ckandrews@pmu.edu.sa

Keywords: Sustainability, Renewable Energy, Climate, Future, Environment

Abstract. The increasing global demand for energy is transforming our world into a closely connected community, yet the Earth remains unchanged in its capacity. As the world population seeks more energy to fuel social, economic, and developmental needs, along with health and well-being, the call for sustainable solutions intensifies. Unfortunately, escalating energy consumption contributes to rising greenhouse gas emissions and environmental harm. Embracing renewable energies becomes crucial for combating climate change, but such a shift must be sustainable to fulfill the energy requirements of future generations. A comprehensive strategy combining energy management and renewable sources is required to address these issues. An overview of current energy consumption trends, energy management techniques, and renewable energy sources is provided in this article. The results show that an integrated strategy that includes renewable energy sources and energy management techniques can dramatically reduce energy consumption and greenhouse gas emissions while also providing economic benefits. The article's conclusion highlights how important it is to implement an integrated strategy for energy management and renewable energy sources in order to achieve efficient and sustainable energy use.

Introduction

Global energy consumption has surged due to increased urbanization, industrialization, and population growth, causing adverse environmental effects such as climate change, air pollution, and resource depletion [1]. An integrated strategy including energy management techniques and renewable energy sources is necessary to address these issues [2]. An extensive analysis of energy use, energy management techniques, and renewable energy sources is given in this article. Analyzing recent studies, case studies, and assessing the efficacy of different energy management and renewable energy technologies are all part of the study technique [3]. Energy is essential for economic expansion, but the present fossil fuel dependency is unsustainable, requiring a move to renewable alternatives in order to lessen environmental effects [4]. Energy consumption and greenhouse gas emissions can be considerably decreased while providing economic advantages by putting energy management concepts into practice and switching to renewable energy sources. Strategies include using energy-efficient technologies, adopting practices, and employing management systems for monitoring and controlling energy usage [5]. Renewable sources like solar, wind, hydro, and geothermal provide sustainable alternatives, with global adoption increasing due to government incentives and declining technology costs [6]. Energy consumption, particularly in sectors like transportation, residential, commercial, and industrial, contributes significantly to greenhouse gas emissions. The International Energy Agency (IEA) reported a 2.3% global energy consumption increase in 2019, with the transportation sector leading at 32%, followed by residential (23%), commercial (12%), and industrial (37%) sectors. Fossil fuels, constituting coal, oil, and natural gas, accounted for 84% of global energy consumption in 2019 [7].



Sources of Renewable Energy

Renewable energy emerges as a pivotal solution to address these challenges [8]. Notably, in 2012, these sources contributed 22% to global energy generation, indicating a significant shift. Reliable energy supply is indispensable for heating, lighting, industry, and transportation, playing a crucial role in global economies. The substitution of fossil fuels with renewables substantially reduces greenhouse gas emissions. However, challenges like intermittent generation due to seasonal variations exist, necessitating intricate design and optimization methods. Fortunately, advancements in computer hardware and software empower researchers to overcome these challenges, fostering progress in the renewable and sustainable energy field [9].

Technology and Renewable Energy

Renewable energy sources derive from continual natural energy flows in our environment: bioenergy, solar, geothermal, hydropower, wind, and ocean energy.

Hydro energy. One important energy source that is obtained from the flow of water from higher to lower elevations is hydropower, which is mainly used to turn turbines and produce electricity. There are many different types of hydropower projects, such as in-stream projects, run-of-river projects, and dam projects with reservoirs. Hydropower is a technologically advanced resource that uses a variable resource over time. Hydropower reservoirs are used for navigation, irrigation, drinking water production, flood and drought control, and other uses. The main source of energy for hydropower is gravity plus the height at which the water descends onto the turbine. The potential energy relies on the mass of the water, the gravity factor ($g = 9.81 \text{ ms}^{-2}$), and the head, defined as the difference between the dam and tail water levels. Turbines are engineered to accommodate an optimal water flow. Hydropower exhibits minimal particulate pollution, rapid upgradability, and the capability to store energy for extended periods.

Energy of Biomass. Bioenergy, a renewable energy source sourced from biological materials, plays a vital role in various applications. It serves as a versatile energy provider for transportation through biodiesel, electricity generation, and heating for cooking. Electricity derived from bioenergy encompasses diverse sources like wood residues from forests, agricultural byproducts such as sugar cane waste, and animal husbandry residue like cow dung. A notable advantage lies in the fact that the fuel for biomass-based electricity often originates from by-products or waste, avoiding competition between land designated for food and that for fuel. While global biofuel production is currently modest, it exhibits a continuous upward trend. In the United States, annual biodiesel consumption reached 15 billion liters in 2006, with a growth rate of 30–50% annually, aiming for 30 billion liters by the end of 2012 [10].

Solar Power. "Direct" solar energy pertains to renewable energy technologies that directly harness the Sun's energy. Unlike some renewables like wind and ocean thermal, which utilize solar energy after its absorption on Earth, solar energy technologies directly capture sunlight. Photovoltaic (PV) systems convert solar irradiance into electricity, and concentrating solar power (CSP) generates thermal energy. Solar energy not only fulfills direct lighting needs but also has the potential to produce fuels for transportation and other purposes [11]. The World Energy Council (2013) notes that solar radiation falling on Earth exceeds 7,500 times the world's annual primary energy consumption of 450 EJ [9].

Geothermal power. Geothermal power is harnessed from the interior of the earth as a natural source of energy, rooted in the planet's internal structure and associated physical processes. Despite substantial heat existing in the Earth's crust, it is often not equally distributed, hardly concentrated, and frequently lies at depths challenging for mechanical exploitation. The geothermal gradient, averaging about $30 \text{ }^{\circ}\text{C/km}$, varies across the Earth's interior, with some regions attainable by digging exhibiting gradients well above average [12]. Geothermal reservoirs, mined for heat through wells and other methods, include naturally hot and permeable hydrothermal reservoirs and enhanced geothermal systems (ESG), which are sufficiently hot but benefit from hydraulic

stimulation. Extracted fluids, varying in temperature, can then be used for electricity generation and other applications requiring heat energy [9].

Wind energy. Wind has emerged as a leading global energy source among renewables due to its widespread presence, especially in areas with substantial energy density [13]. Harnessing kinetic energy from moving air, wind energy is vital for mitigating climate change by generating electricity through large turbines positioned onshore or offshore [14]. Large-scale production and implementation of onshore wind technology have previously occurred [9]. Wind turbines efficiently convert wind energy into electricity, marking a significant stride in renewable energy solutions.

Ocean energy (tide and wave). Surface waves form when wind moves over water, particularly in the ocean. The duration, speed, and distance of sustained wind directly impact wave height and the energy produced. The ocean possesses vast energy potential stored in waves, tides, currents, and temperature differences. In 2008, the first commercial sea energy devices debuted with installations like the UK's SeaGen and Portugal's Pelamis. Currently, ocean energy areas are derived through wind, tides, waves, and thermal disparities between deep and shallow sea water [15].

Sustainable development and Renewable energy

Because it promotes economic productivity and human growth, renewable energy is essential to sustainable development. Prospects for energy security, social and economic advancement, increased energy accessibility, reducing the effects of climate change, and improving the environment and human health are presented by these energy sources [16].

Energy security. The concept of energy security lacks a universally agreed-upon definition, leading to varied interpretations. Nevertheless, the underlying concern for energy security revolves around ensuring a continuous and reliable energy supply, a fundamental requirement for sustaining economic operations [17]. Given the intrinsic connection between economic growth and energy consumption, maintaining stable energy access is a significant challenge for both developed and developing nations, posing potential economic and functional challenges in case of prolonged disruptions [15]. Renewable energy sources, unlike fossil fuels, are globally distributed and less subject to market trading. Introducing renewables not only reduces dependence on energy imports but also diversifies the supply portfolio, lessening vulnerability to price volatility and fostering global energy security. Additionally, renewable energy integration enhances the reliability of energy services, particularly in areas with inadequate grid access, contributing to overall energy security through a well-managed and diversified energy portfolio [16].

Economic and Social development. Economic growth and rising energy consumption have historically been strongly correlated, making the energy sector essential to economic development. Per capita income and energy consumption are positively correlated globally, indicating that economic expansion is the main cause of the recent increase in energy consumption. This growth also generates employment, with a 2008 study indicating around 2.3 million jobs worldwide in renewable energy technologies, contributing to enhanced health, education, gender equality, and environmental safety [9].

Energy access. Sustainable Development Goal Seven focuses on ensuring universal access to clean, affordable, and available energy. The use of renewable energy sources, widely distributed globally, is key to achieving this goal. Addressing access discrepancies requires a local understanding, particularly in regions like sub-Saharan Africa and South Asia, where urban and rural electrification differences are evident [18]. Renewable energy-based distributed grids prove more competitive in rural areas, offering substantial opportunities for mini-grid systems to enhance electricity access.

Effect of Climate change on Environmental and health. The renewable energy source utilization in power generation plays a pivotal role in curbing the emission of greenhouse gases,

mitigating climate change, and lessening effect on environment and health associated with fossil fuel-derived pollutants. GHG emissions per capita also saw a 22% reduction from 1990 to 2012, as shown in Figure 3 (EEA, 2016). As mentioned carbon dioxide emissions in the United States from 1990 to 2013, exemplifying a decrease in CO₂ levels due to a transition from fossil fuels to available energy sources [19].

Renewable Energy Source Challenges

In low-carbon economies, renewable energy sources have the potential to dominate the energy supply, requiring significant adjustments to all energy systems. The main problem of the first half of the twenty-first century is generally recognized to be the shift from non-sustainable to renewable energy [20]. Notably, a country's policies and instruments significantly impact the adoption of renewable energy, influencing costs and technological advancements. Technological innovations, in turn, influence costs, contributing to market failures and limited adoption. An effective renewable energy policy must consider these interconnected factors to foster sustainability.

The study proposes several policy recommendations to effectively alleviate changes in climate and its impacts.

- Encourage all fields and areas to invest in technologies of renewable energy and adopt policies promoting their use, fostering a collective effort in reducing carbon emissions.
- Advocate for lifestyle and behavioral changes to reduce individual carbon footprints, emphasizing the significant contribution of personal choices to climate change mitigation.
- Support research into revolution and mechanries that minimize land use, prevent accidents associated with renewable energy sources, and address resource competition, particularly in bioenergy where food production competes with energy generation.
- Strengthen international collaboration and assistance for developing countries, facilitating infrastructure expansion and technology upgrades to enable modern and sustainable energy services. This approach aims to mitigate climate change and its adverse effects on a global scale.

Conclusion

Energy is a fundamental requirement in our daily lives, crucial for human development, economic growth, and productivity. Shifting towards renewable energy is recognized as a significant step in mitigating climate change, but its sustainability is paramount for securing a future that meets energy needs for generations to come. The goal of this study is to ascertain the sustainability of renewable sources and their potential to mitigate the effects of climate change by examining the relationship between sustainable development and green energy. Qualitative research was conducted through a comprehensive review of relevant literature within the study's scope. While renewable energy sources exhibit no net emissions throughout their lifecycle, barriers such as cost, pricing structures, political environments, and market conditions hinder their full utilization in emerging, minimum-developed, and developed nations. To address these challenges, the study advocates for the creation of global opportunities through international interactions. Supporting developing nations in accessing green energy, enhancing energy productivity, investing in clean energy utilization, and encouraging research and energy infrastructure to lower the cost of renewable energy and remove inefficiencies, and contribute to climate change mitigation. Opportunities related to renewable energy sources are identified in the report, including enhanced energy security, social and economic development, and climate change mitigation. However, obstacles like communication gaps, market failures, raw material availability issues, and inefficient energy use pose a danger to renewable energy's sustainability and ability to mitigate climate change.

Future Recommendations

Policy formulation and technological improvement: Encourage policy discussions across sectors to enhance technologies in the renewable sector for sustained development.

- Advocate for more efficient energy use at individual and global levels. Implement global energy efficiency programs, offering tax exemptions for energy-efficient initiatives and product designs.
- Invest in research to address concerns and potential risks associated with renewable energy.
- Raise public knowledge and education about effect reduction, adaptation, and mitigation of climate change.

In addition to addressing the sustainability of renewable energy, putting these recommendations into practice would support the seventh and thirteenth goals of sustainable development, which call for preventing climate change and its effects as well as guaranteeing that everyone has access to affordable, dependable, and sustainable energy.

References

- [1] Tomin, Nikita, et al. "Design and optimal energy management of community microgrids with flexible renewable energy sources." *Renewable Energy* 183 (2022): 903-921.
<https://doi.org/10.1016/j.renene.2021.11.024>
- [2] Kartal, Mustafa Tevfik, et al. "Do nuclear energy and renewable energy surge environmental quality in the United States? New insights from novel bootstrap Fourier Granger causality in quantiles approach." *Progress in Nuclear Energy* 155 (2023): 104509.
<https://doi.org/10.1016/j.pnucene.2022.104509>
- [3] Tiwari, Sunil, Joanna Rosak-Szyrocka. Internet of things as a sustainable energy management solution at tourism destinations in India." *Energies* 15.7 (2022): 2433.
<https://doi.org/10.3390/en15072433>
- [4] Natarajan, B., Obaidat, M.S., Sadoun, B., Manoharan, R. New Clustering-Based Semantic Service Selection and User Preferential Model. *IEEE Systems Journal*, (200).
- [5] Sadiq, Muhammad, et al. "The influence of economic factors on the sustainable energy consumption: evidence from China." *Economic research-Ekonomska istraživanja* 36.1 (2023): 1751-1773. <https://doi.org/10.1080/1331677X.2022.2093244>
- [6] M. Amin Mir. Adsorption of Heavy Metals by Chopped Human Hair: An Equilibrium and Kinetic Study. *Asian Journal of Chemistry*. 35(6). (2023). 1458 – 1462.
<https://doi.org/10.14233/ajchem.2023.27653>
- [7] Wang, Shuguang, Luang Sun, and Sajid Iqbal. "Green financing role on renewable energy dependence and energy transition in E7 economies." *Renewable Energy* 200 (2022): 1561-1572.
<https://doi.org/10.1016/j.renene.2022.10.067>
- [8] Tiwari, G. N., & Mishra, R. K. Advanced renewable energy sources. Royal Society of Chemistry. (2011). P007-P015. <https://doi.org/10.1039/9781849736978-FP007>
- [9] Banos, R., Manzano-Agugliaro, F., Montoya, F., Gil, C., Alcayde, A., & Gómez, J. (2011). Optimization methods applied to renewable and sustainable energy: A review. *Renewable and Sustainable Energy Reviews*, 15, 1753–1766. <https://doi.org/10.1016/j.rser.2010.12.008>
- [10] Ayoub, M., & Abdullah, A. Z. Critical review on the current scenario and significance of crude glycerol resulting from biodiesel industry towards more sustainable renewable energy

industry. *Renewable and Sustainable Energy Reviews*, 16, (2012). 2671–2686.
<https://doi.org/10.1016/j.rser.2012.01.054>

[11] Edenhofer, O., Pichs-Madruga, R., Sokona, Y., Seyboth, K., Matschoss, P., Kadner, S., ... von Stechow, C. *Renewable Energy Sources and Climate Change Mitigation*. Cambridge: Cambridge University Press. (2011). <https://doi.org/10.1017/CBO9781139151153>

[12] Barbier, E. Geothermal energy technology and current status: An overview. *Renewable and Sustainable Energy Reviews*, 6, (2002). 3–65. [https://doi.org/10.1016/S1364-0321\(02\)00002-3](https://doi.org/10.1016/S1364-0321(02)00002-3)

[13] M. Amin Mir, Waqar Ashraf M. The challenges and potential strategies of Saudi Arabia's water Resources: A review in analytical way. *Environmental Nanotechnology, Monitoring and Management*, 20 (2023). <https://doi.org/10.1016/j.enmm.2023.100855>

[14] Asumadu-Sarkodie, S., & Owusu, P. A. The potential and economic viability of wind farms in Ghana Energy Sources, Part A: Recovery, Utilization, and Environmental Effects. (2016). <https://doi.org/10.1080/15567036.2015.1122680>

[15] Esteban, M., & Leary, D. Current developments and future prospects of offshore wind and ocean energy. *Applied Energy*, 90, 128–136. (2012).
<https://doi.org/10.1016/j.apenergy.2011.06.011>

[16] Asumadu-Sarkodie, S., & Owusu, P. ACarbon dioxide emissions, GDP, energy use and population growth: A multivariate and causality analysis for Ghana, (2016). 1971–2013. *Environmental Science and Pollution Research International*. <https://doi.org/10.1007/s11356-016-6511-x>

[17] Kruyt, B., van Vuuren, D. P., de Vries, H., & Groenenberg, H. Indicators for energy security. *Energy Policy*, 37, (2009). 2166–2181. <https://doi.org/10.1016/j.enpol.2009.02.006>

[18] Brew-Hammond, A. Energy access in Africa: Challenges ahead. *Energy Policy*, 38, (2010). 2291–2301. <https://doi.org/10.1016/j.enpol.2009.12.016>

[19] United States Environmental Protection Agency. Carbon dioxide emissions.2, (2015)
<http://www3.epa.gov/climatechange/ghgemissions/gases/co2.html>

[20] Frederick Verbruggen, Adam R Aron, Michaël A Stevens, Christopher D Chambers. Theta burst stimulation dissociates attention and action updating in human inferior frontal cortex. *Proc Natl Acad Sci U S A*, (2010) 3;107(31):13966-71. <https://doi.org/10.1073/pnas.1001957107>

Potential uses of renewable energy in construction: Advantages and challenges

Essam ZANELDIN^{1,a*}, Waleed AHMED^{2,b}, Betiel PAULOS^{3,c}, Feruz GABIR^{3,d},
Makda ARAYA^{3,e}, El Bethel MULUYE^{3,f} and Deborah DEBELE^{3,g}

¹Associate Professor, Department of Civil and Environmental Engineering, United Arab Emirates University, Al-Ain, United Arab Emirates

²Assistant Professor, Engineering Requirements Unit, United Arab Emirates University, Al-Ain, United Arab Emirates

³Student, College of Engineering, United Arab Emirates University, Al-Ain, United Arab Emirates

^aessamz@uaeu.ac.ae, ^bw.ahmed@uaeu.ac.ae, ^c201950002@uaeu.ac.ae,

^d201950008@uaeu.ac.ae, ^e201950013@uaeu.ac.ae, ^f201950311@uaeu.ac.ae,
^g201950305@uaeu.ac.ae

Keywords: Construction Industry, Green Buildings, Renewable Energy, Sustainability

Abstract. The construction industry accounts for a high percentage of the total global energy consumption, placing it among the main sectors contributing to climate change, pollution, and energy-related problems. This fact has placed tremendous pressure on the construction industry to find solutions to this crucial problem and shift to more sustainable, energy-efficient, and cost-effective construction practices. In this study, the importance of using renewable energy in the construction sector, particularly building construction, is highlighted and a review of some emerging practices in using renewable energy in construction is presented. The paper also presents the various sources of renewable energy and their applications in construction along with their advantages and drawbacks. The paper highlights the importance of establishing standards and regulations related to the use of renewable energy in building projects.

Introduction

With the exponential growth of population in the world coupled with the increased needs of humans, the global consumption of energy is growing rapidly at an average annual rate of 2.2% [1, 2] and the construction industry accounts for around 40% of the total global energy consumption and 30% of global carbon dioxide emissions, placing it among the main sectors responsible for air pollution and environmental instability [1]. As a result of the rapid growth of population, more buildings will be needed and, if built using the old traditional construction methods, the result will be more carbon emissions and environmental instability, such as the greenhouse effect and the extreme weather caused by energy. This has stimulated the importance of using green, low-carbon, sustainable, and other forms of renewable energy in construction. Serving the same purpose, the International Energy Agency has set a goal of net zero emissions by 2050, placing the construction industry under intense pressure to achieve this target [3]. To this end, a number of countries are announcing initiatives to achieve net zero emissions by 2050. However, the world is still behind in terms of the implementation of a clear and well-defined policy to achieve this objective, particularly in the construction industry. Europe and the USA, for example, have redefined regulations and policies related to the development of near-zero-energy buildings for the development of renewable energy [4, 5]. China is also committed to reaching peak carbon by 2030 and carbon neutrality by 2060 [6]. With the construction sector being a main player in this context, the application of renewable energy in construction to produce energy-

efficient buildings by using natural materials has become a major driver to reduce the contribution of the building sector to climate change and energy use and promote sustainability [7].

It is well established in the literature that natural materials are good sources of renewable energy since they are green, environmentally friendly, and serve as an alternative to traditional energy sources [7, 8]. The use of renewable energy in construction projects becomes eminent as it promotes sustainability and reduces environmental impacts. This is clearly important considering the increasing need to reduce carbon emissions by mitigating the impact of construction activities on the environment. In building construction, renewable energy is an integration of sustainable sources of energy, such as water, wind, solar, plants, biomass, and geothermal in the building life cycle stages, including design, construction, and operation and maintenance to reduce the use of traditional sources of energy and, therefore, mitigate climate change and promote the environmental sustainability of buildings [7, 9, 10]. With the increasing awareness of the use of renewable energy in building construction, its application in modern buildings has also gained momentum. Architects, for example, have designed buildings with proper orientation to facilitate the use of natural sunlight for heating and ventilating [11, 12]. Other engineers involved in the design of buildings are also using sustainable sources in their designs such as solar panels to generate electricity, natural fibers and materials to replace traditional construction materials, and biomass boilers and heating systems to provide sustainable heating and hot water solutions contributing to energy efficiency and reducing carbon emissions. However, the application of renewable energy in buildings depends on the type of the source of energy and the characteristics of energy. As reported by Khan and Al-Ghamdi [9] and Wu and Skye [10], renewable energy sources such as solar, geothermal, wind, and biomass energy have the potential to satisfy the sustainable energy needs of buildings.

Potential Uses of Sustainable Renewable Energy Sources in Construction

The use of renewable energy sources has become a viable solution to the problem of air pollution and environmental instability resulting from construction projects. In this section, the most important renewable energy sources that can be utilized in the construction of buildings to promote sustainability and reduce environmental impact are presented. As shown in Fig. 1, renewable energy sources include solar energy, biomass energy, geothermal energy, wind energy, and hydro energy, in addition to the hybrid renewable energy systems.

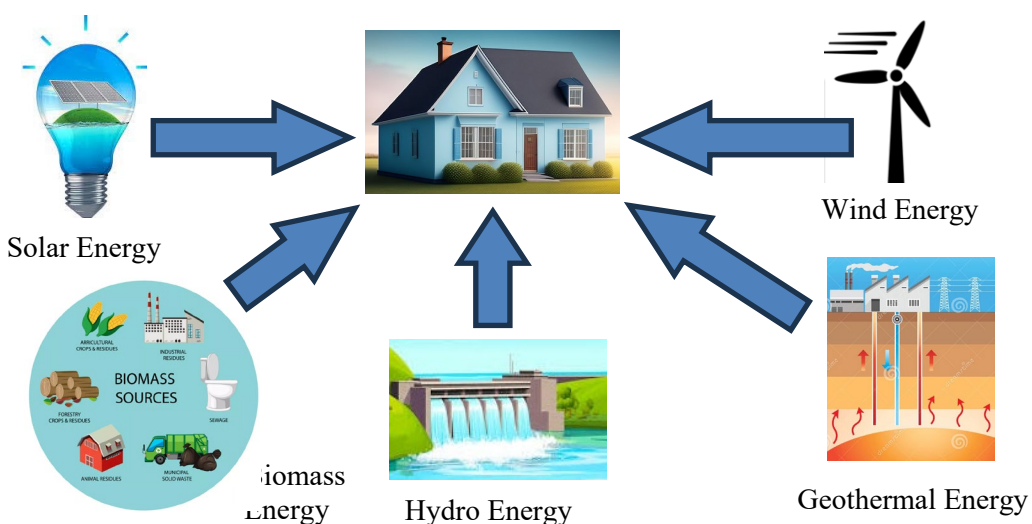


Fig. 1: Major Sources of Renewable Energy Used in Building Construction.

Solar Energy

It is well established that solar energy is the most commonly used source of renewable energy [7]. It is generated for building construction using a range of technologies such as solar power to generate electricity and solar thermal energy, including solar water heating. Solar energy technologies are either passive or active, depending on how they capture and distribute solar energy and convert it into solar power. Active techniques include the use of photovoltaic systems, concentrated solar power, and solar water heating to generate energy while passive techniques include the optimal building orientation towards the sun, selection of materials with favorable thermal mass or light dispersing properties, thermal biomass, and the design of spaces with natural air circulation [8]. Solar energy is known for its environmentally friendly attributes and unlimited supply, placing it among the leading and widely used sources of renewable energy in the world [13]. In the USA, for example, solar energy accounts for 31% of the total energy consumption [10].

Several researchers have addressed the use of solar energy to improve the environmental performance of buildings and facilitate climate circulation. Vassiliades et al. [14], for example, noticed that the use of solar energy in buildings helps reduce the negative impacts of building on the climate and the use of photovoltaic technology improves the energy utilization efficiency and reduces the consumption of energy. Another study by [15] showed that the use of solar systems in buildings can increase the renewable energy factor to 83% and reduce energy demand by 48%. It is, therefore, important to maximize the use of solar energy in buildings during the design phase as this will result in improved efficiency, reduce the operating costs, and enhance the functionality of buildings, in addition to its main benefit of being environmentally friendly as it does not produce greenhouse emissions. Despite all these advantages, the use of solar energy results in high maintenance costs and requires technological advancements.

Biomass Energy

Biomass is an organic material extracted from living organisms such as plants, animals, or microorganisms. Biomass is the oldest renewable energy source used by humans [16]. To lower emissions and reduce dependence on fossil fuels, biomass is usually utilized in the form of biomaterials in structural or non-structural elements of buildings. Biomass energy relies, in general, on natural resources such as wood, plant fibers, and organic waste materials, coming from human, plant, and animal wastes. Biomass includes other materials such as construction waste and animal excreta, which can also be used to generate electricity [9]. Several research efforts investigated the use of biomass energy in buildings. Rahman et al. [17] investigated the possibility of using biomass energy as the main source of power for a residential building. Allouhi et al. [18] and Wu and Skye [10] indicated that biomass can have different uses in buildings including utilizing it as gas, fuel, heat, and power generation. In addition, biomass is carbon-neutral efficient source of energy, and its efficiency can be further enhanced by compressing biomass wood into pellets under high pressure and temperature [19]. However, biomass combustion can lead to corrosion on heating surfaces due to boiler deposits [7]. While woodchip boilers improve local air quality and reduce local ground-level particulate matter concentrations, it may not be as environmentally friendly as compared to natural gas boilers. In addition to its use in buildings as a source of energy, biomass can also be used as a thermal insulation material or as a structural element in building construction, providing a sustainable and green alternative to some traditional building components, and improving energy supply chains by reducing dependence on imported fossil fuels [20].

Despite all the benefits resulting from the use of biomass in buildings, it is important to note that some biomass materials may be less durable and less resistant to some factors such as moisture, fire, and pests as compared to conventional building materials. This is in addition to the

fact that biomass materials have limited availability and may vary in performance and quality [21]. To address these concerns, additional treatment and protection measures may be required.

Geothermal Energy

The stored internal heat of earth contributes to the generation of geothermal energy, which is a renewable source of energy that is not dependent on climate or time of day and can supply energy all day long, independently of external conditions [6]. Geothermal energy is mainly used for heat production and cooling and can work in combination with other energy systems, such as solar energy. Geothermal energy systems can improve energy efficiency while reducing energy costs and greenhouse gas emissions, as compared to traditional heating and cooling systems. A study by [22] confirmed that the use of geothermal energy significantly reduces energy demand, cost, and CO₂ emissions, as compared to conventional gas boilers, demonstrating its effective contribution to achieve the goal of net-zero-energy buildings. In addition to these advantages, geothermal systems require a relatively small land area, operate quietly without the noise generated by traditional HVAC systems, and provide design flexibility as they can be used with different architectural designs. Despite the mentioned advantages of geothermal energy systems, their installation cost is relatively high and the underground site conditions determine if a geothermal system is feasible or not [7]. It is, therefore, important to conduct a precise study on the subsurface conditions of the site to investigate the costs associated with installing a geothermal energy system for a building. This is in addition to the environmental impact of installing and operating geothermal systems, which are resulting from the noise associated with the installation of the systems and the treatment of geothermal fluids.

Wind Energy

The use of wind energy in buildings is considered one of the most widely used source of renewable energy sources [23]. The wind energy system consists of wind turbines, mechanical energy, heat pumps, and other required energy using wind vortex machines [7]. The most important advantage of using wind energy, as a source of renewable energy, is to reduce carbon emissions and consumption of energy. Statistics indicate that, as of 2017, the use of wind energy has reduced greenhouse gas emissions by at least 600 million tons [7]. According to [24], wind energy can provide around 15% of buildings' energy needs. To best utilize wind energy, architects design buildings in a way that they use natural ventilation for air circulation through natural wind power, which reduces the use of the air conditioning systems and, consequently, reduces energy consumption.

However, equipment needed to generate wind energy require high initial investment and maintenance cost, as compared with traditional energy sources. Another concern is the noise generated by the wind turbines, in addition to the fact that buildings layout limits the use of wind energy since the wind direction and speed between buildings may be affected by turbulence and blocking, which results in a reduced efficiency of generating the wind power [24]. In addition, the uncertain characteristics of wind make the power generated by wind irregular. It is, therefore, important to explore other new technologies to improve the efficiency of wind energy.

Hydro Energy

Hydropower is an energy generated by water. Hydropower is derived from the kinetic energy of falling or flowing water. It can be generated from streams, lakes and rivers or man-made structures such as dams, lagoons and reservoirs. It relies on the water cycle, which is driven by the sun, making it a clean and renewable source of energy. Hydropower is used to generate low-cost electricity, provide flood control, support irrigation, and produce clean drinking water. provides low-cost electricity and durability over time compared to other sources of energy. While

the initial construction cost of hydropower systems can be costly, the cost can be reduced by using existing structures such as bridges, tunnels, and dams. However, the amount of energy extracted from the water depends on the available water volume and the difference in height between the turbines and the elevated source, known as the hydraulic head.

Hybrid Renewable Energy Systems

Hybrid energy systems combine different energy technologies to reduce costs, reduce greenhouse gas emissions, and improve capability, value, energy efficiency, or environmental performance of buildings as compared with the use of independent renewable energy systems. Hybrid energy systems combine multiple sources of energy with traditional electricity to meet the energy demands of buildings. Examples of hybrid energy systems include combining solar energy with wind energy, solar energy with hydrogen energy, wind energy with hydrogen energy, geothermal energy with hydrogen energy, etc. Hydrogen hybrid energy, for example, can be used for heating houses, supplying hot water, cooking, and meeting electricity needs. The solar-hydrogen hybrid system, for example, is considered the most efficient system of generating renewable energy. As the benefits of hybrid energy systems become more widely recognized, they are becoming increasingly popular in residential commercial and buildings to reduce energy costs and to promote sustainable construction.

Summary and Concluding Remarks

The use of renewable energy in buildings directly addresses the increasing demand of energy worldwide and mitigates the crucial concern of global warming. This paper presents the various types of renewable energy and their application in construction, including energy sources such as solar, biomass, geothermal, wind, and hydro energy, in addition to the hybrid sources of renewable energy. It is quite obvious that each of these sources offer sustainable and environmentally friendly advantages that enhance building energy efficiency and reduce operational costs. However, it is highly recommended to formulate standards and regulations related to renewable energy that can be followed by construction practitioners. The implementation of such standards and regulations will encourage the development of renewable energy in the construction industry and promote sustainability and innovation. It is also important to note that the application of hybrid renewable energy systems in buildings can provide designers and constructors with alternative and cost-effective renewable energy solutions. This study provides construction practitioners with information about the various renewable energy systems that can be used in the design and construction of buildings along with their benefits, challenges, and disadvantages.

References

- [1] M. Nazari-Heris, A.T. Esfahanlatah, P. Ifaei, Hybrid energy systems for buildings: a techno-economic-enviro systematic review, *energies.* 16(12) (2022).
<https://doi.org/10.3390/en16124725>
- [2] R.A. Salam, K.P. Amber, N.I. Ratyal, M. Alam, N. Akram, C.Q.G. Munoz, F.P.G. Marquez, An overview on energy and development of energy integration in major South Asian Countries: the building sector, *Energies.* 13 (2000). <https://doi.org/10.3390/en13215776>
- [3] S. Zhang, P. Oclon, J.J. Klemes, P. Michorczyk, K. Pielichowska, K. Pielichowski, Renewable energy systems for building heating, cooling and electricity production with thermal energy storage, *Renew Sustain Energy Rev.* 165 (2022) 112560. <https://doi.org/10.1016/j.rser>.
- [4] B. Liu, D. Rodriguez, Renewable energy systems optimization by a new multi-objective optimization technique: a residential building, *J Build Eng.* 35 (2021) 102094.
<https://doi.org/10.1016/j.jobe>.

- [5] M. Yang, L. Chen, J. Wang, G. Msigwa, A.I. Osman, S. Fawzy, D.W. Rooney, P-S Yap, Circular economy strategies for combating climate change and other environmental issues, *Environ Chem Lett.* (2022). <https://doi.org/10.1007/s10311-022-01499-6>
- [6] A.I. Osman, L. Chen, M. Yang, G. Msigwa, M. Farghali, S. Fawzy, D.W. Rooney, P-S Yap, Cost, environmental impact, and resilience of renewable energy under a changing climate: a review, *Environ Chem Lett* 21 (2023) 741–764. <https://doi.org/10.1007/s10311-022-01532-8>
- [7] L. Chen, Y. Hu, R. Wang, X. Li, Z. Chen, J. Hua, A. I. Osman, M. Farghali, L. Huang, J. Li, L. Dong, D.W. Rooney, P-S Yap, Green building practices to integrate renewable energy in the construction sector: a review, *Environmental Chemistry Letters.* (2023). <https://doi.org/10.1007/s10311-023-01675-2>
- [8] S. Dey, A. Sreenivasulu, G.T.N. Veerendra, K.V. Rao, P.S. Babu, Renewable energy present status and future potentials in India: overview, *Innov Green Dev.* (2022). <https://doi.org/10.1016/j.igd.2022>
- [9] S.A. Khan, S.G. Al-Ghamdi, Renewable and integrated renewable energy systems for buildings and their environmental and socio-economic sustainability assessment, In: (ed) Springer. (2021) 127–144. https://doi.org/10.1007/978-3-030-67529-5_6
- [10] W. Wu, H.M. Skye, Residential net-zero energy buildings: review and perspective, *Renew Sustain Energy Rev.* 142 (2021). <https://doi.org/10.1016/j.rser.2021.110859>
- [11] Q. Gong, F. Kou, X. Sun, Y. Zou, J. Mo, X. Wang, Towards zero energy buildings: a novel passive solar house integrated with flat gravity-assisted heat pipes, *Appl Energy.* 306 (2022). <https://doi.org/10.1016/j.apenergy.2021.117981>
- [12] C. Ionescu, T. Baracu, G.E. Vlad, H. Necula, A. Badea, The historical evolution of the energy efficient buildings, *Renew Sustain Energy Rev.* 49 (2015) 243–253. <https://doi.org/10.1016/j.rser.2015.04.062>
- [13] S.R. Aldhshan, K.N. Maulud, W.S. Jaafar, O.A. Karim, B. Pradhan, Energy consumption and spatial assessment of renewable energy penetration and building energy efficiency in Malaysia: a review, *Sustainability.* 13 (2021). <https://doi.org/10.3390/su13169244>
- [14] C. Vassiliades, A. Savvides, A. Buonomano, Building integration of active solar energy systems for facades renovation in the urban fabric: effects on the thermal comfort in outdoor public spaces in Naples and Thessaloniki, *Renew Energy.* 190 (2022) 30–47. <https://doi.org/10.1016/j.renene.2022.03.094>
- [15] M. Bilardo, M. Ferrara, E. Fabrizio, Performance assessment and optimization of a solar cooling system to satisfy renewable energy ratio (RER) requirements in multi-family buildings, *Renew Energy.* 155 (2020) 990–1008. <https://doi.org/10.1016/j.renene.2020.03.044>
- [16] C. Yang, H. Kwon, B. Bang, S. Jeong, U.D. Lee, Role of biomass as low-carbon energy source in the era of net zero emissions, *Fuel.* 328 (2022). <https://doi.org/10.1016/j.fuel.2022.125206>
- [17] H. Rahman, M.R. Sharif, R. Ahmed, T. Nijam, M.A. Shoeb, Designing of biomass-based power plant for residential building energy system, International conference on electrical engineering and information communication technology (ICEEICT), 2015, pp. 1–6. <https://doi.org/10.1109/ICEEICT.2015.7307366>

- [18] A. Allouhi, S. Rehman, M. Krarti, Role of energy efficiency measures and hybrid PV/biomass power generation in designing 100% electric rural houses: a case study in Morocco, *Energy Build.* 236 (2021). <https://doi.org/10.1016/j.enbuild.2021.110770>
- [19] H. Hartmann, V. Lenz, Biomass energy heat provision in modern small-scale systems. In: Kaltschmitt M (ed) Springer New York, New York, NY, 2019, pp. 533–586.
https://doi.org/10.1007/978-1-4939-7813-7_248
- [20] A. Behzadi, E. Thorin, C. Duwig, S. Sadrizadeh, Supply-demand side management of a building energy system driven by solar and biomass in Stockholm: a smart integration with minimal cost and emission. *Energy Convers Manag.* 292 (2023).
<https://doi.org/10.1016/j.enconman.2023.117420>
- [21] M. Hiloidhari, M.A. Sharno, D.C. Baruah, A.N. Bezbaruah, Green and sustainable biomass supply chain for environmental, social and economic benefits, *Biomass Bioenerg.* 175 (2023).
<https://doi.org/10.1016/j.biombioe.2023.106893>
- [22] D. D'Agostino, F. Minichiello, F. Petito, C. Renno, A. Valentino, Retrofit strategies to obtain a NZEB using low enthalpy geothermal energy systems. *Energy.* 239 (2022).
<https://doi.org/10.1016/j.energy.2021.122307>
- [23] Z. Zhang, X. Liu, D. Zhao, S. Post, J. Chen, Overview of the development and application of wind energy in New Zealand, *Energy Built Environ.* 4 (2023) 725–742.
<https://doi.org/10.1016/j.enbenv.2022.06.009>
- [24] K.C. Kwok, G. Hu, Wind energy system for buildings in an urban environment. *J Wind Eng Ind Aerodyn.* 234 (2023). <https://doi.org/10.1016/j.jweia.2023.105349>

Adaptive cooling framework for Photovoltaic systems: A seasonal investigation under the terrestrial conditions of Sharjah, UAE

Mena Maurice FARAG^{1,a*}, Abdul-Kadir HAMID^{1,b*}, Mousa HUSSEIN^{2,c}

¹Department of Electrical Engineering, College of Engineering, University of Sharjah, Sharjah, UAE

²Department of Electrical and Communication Engineering, College of Engineering, United Arab Emirates University, Al Ain, UAE

^au20105427@sharjah.ac.ae, ^bakhamid@sharjah.ac.ae, ^cmihussein@uaeu.ac.ae

Keywords: Adaptive Cooling, Photovoltaic Systems, Solar Energy, Temperature Regulation, Photovoltaic-Thermal Applications

Abstract. The increment of PV operating temperature has a significant impact on the overall efficiency, longevity, and degradation of PV systems. In this notion, researchers have sought to investigate different cooling methodologies to minimize the impact of abrupt operating temperatures. However, most investigations discuss the impact of the working base fluid in small periods without proposing methods for temperature regulation based on defined thresholds. In this study, an adaptive cooling framework is proposed through thermal and electrical modeling to examine the cooling effect on a 2.88 kW grid-connected PV system installed in Sharjah, UAE. An operating temperature threshold of 55°C is considered based on the annual average operating temperature, to facilitate adaptive cooling. The framework is modeled based on heat transfer thermodynamic laws and implemented on MATLAB using experimentally driven measurements collected from the above-mentioned system for December, March, June, and September. As a result, the proposed framework has presented notable merits in terms of electrical and thermal characteristics across the four different seasons. The highest heat extraction was observed in September, where a reduction of 25.36% was observed in PV operating temperature, showing the effectiveness of temperature regulation in harsh weather conditions. As a result, the electrical characteristics have improved significantly leading to an 8.79%, 6.39%, and 6.58% enhancement in maximum power output, maximum voltage, and electrical efficiency, respectively.

Introduction

The continuous depletion of conventional energy resources has led to the introduction of clean and renewable energy resources (RES) to tackle the escalating consequences of climate change [1–3]. Solar energy has been popular amongst other RES due to its reliability, abundance, and zero-net fuel dependence, hence leading the way for the development of photovoltaic (PV) systems for clean electricity generation [4].

PV modules generate electrical energy based on two environmental factors, solar irradiance, and ambient temperature [5]. Typically, there is a direct proportionality for power with respect to solar irradiance [6], while there is an indirect proportionality with respect to the ambient temperature [7]. The PV cell performance is heavily dependent on environmental conditions, specifically operating temperature [8]. The increment of the PV module operating temperature dramatically reduces the overall efficiency of the PV panel. In this notion, cooling of PV modules is essential to sustain the PV system's longevity and performance. The extraction of dissipated heat from PV modules is critical to enhancing the operation of the PV cell [9]. The employment of water as a working base fluid has been a popular and viable cooling technique amongst other available techniques due to its feasibility on different system levels [10].



Several studies in the literature have reported the enhancement in PV module performance through the significant reduction in PV module operating temperature. A study reported by [11], investigated the impact of temperature of the PV cell on its performance through a range of 25°C – 60°C while maintaining a constant solar irradiance exposure. A laboratory-based experiment also conducted in [12], investigated the impact of operating temperature from a range of 25°C – 55°C while maintaining a 1000 W/m² solar irradiance. A simulation study reported by [13], combined artificial neural networks (ANN) and capabilities of reduced module operating temperature. The study demonstrated that with a reduction of 10°C in module operating temperature, the number of PV modules can be reduced by 12 % while supplying the same electrical capacity. An experimental study reported in [14], investigated the impact of water as a working base fluid for front surface heat extraction on a large-scale PV system. The study reported an increase of 9.76% in output power generation and a maximum efficiency of up to 13.47% while generating a thermal difference of 2.3°C. A study investigated under both laboratory and experimental conditions is reported in [15]. The validation of the effectiveness of water as a working base fluid was observed as a reduction of 24 K in PV module operating temperature was observed. As a result, the output power was enhanced by 10% as compared to the uncooled PV module. The employment of water as the cooling technique was experimentally investigated during July as reported in [16]. The study reported that a 10% increase in PV output power was observed due to the reduction of 20% in PV surface temperature, thus improving the PV module conversion efficiency by 14%. Additionally, the optimization of the water cooling process during the harsh climatic conditions in the UAE is reported [17]. The experimental investigation proposes an adaptive technique based on a defined 55°C temperature threshold to facilitate automated front surface cooling. As a result, a decrement of 17.3°C in PV module operating temperature was observed with an extracted heat of 15.41°C. In this notion, the output power and output voltage increased by 39.21% and 16.31%, respectively achieving a 12.5% electrical conversion efficiency. Another study reported the employment of automated timers for the automatic pumping of water for the cooling process as reported in [18]. Under summer conditions of the UAE, the experimental study is conducted to reveal the performance of a timed cooling operation on PV module performance. As a result, the average output power increased by 1.6 %, while decreasing the operating temperature by 6% on average. Additionally, the investigation of a small-scale controlled water spraying system was investigated by [19]. The self-cleaning methodology observed an improved electrical efficiency of 2.53% and an overall system efficiency of 83.3%.

The scientific literature explored the significant impact of deploying water as a working base fluid to enhance the performance of PV systems, especially in harsh and arid weather conditions. However, most investigations report the operation of water as a working base fluid for a specific day of the year, while the performance may vary throughout the entire year. The concept of investigating water as a working base fluid for different seasons of the year as well under defined temperature thresholds needs to be highlighted, to optimize the cooling procedure.

In this notion, this study presents a modeling approach to characterize the thermal properties of water as a working base fluid, illustrating the cooling effect and its impact on the PV module's electrical and thermal properties. The developed model is based on a 55°C temperature threshold, which operates as a gradient for facilitating an adaptive cooling effect, to optimize the cooling process when operating temperature is critical. Moreover, the study considers a 2.88 kW grid-connected PV system as a practical case study installed in Sharjah, United Arab Emirates, to model the impact of adaptive front surface cooling across four different seasons based on experimental measurements retrieved from the system, presenting variable weather conditions.

Dependence of electrical performance on thermal parameters

Environmental parameters have a prominent impact on the electrical conversion efficiency of PV systems, and their irregularity leads to deviation and instability in their overall performance. The United Arab Emirates is blessed with large exposure to solar irradiance of an average of 2285 kWh/m² annually, presenting the promise of PV system deployment [20]. However, 20% of sunlight is converted and generated into electricity, while the remainder is dissipated as waste heat leading to degradation in PV system performance and lifespan. PV cell technologies are defined with a power temperature coefficient (β), that demonstrates a degradation rate in %/°C with every 1°C above the standard testing conditions (STC) i.e., 25°C.

The dramatic impact of temperature can be observed during the summer periods, when the PV module operating temperature may reach up to 70°C. Such abrupt operating temperature leads to a significant reduction in output power generation. A comparison between summer and winter temperature profiles for July and December, respectively as illustrated in Fig. 1.

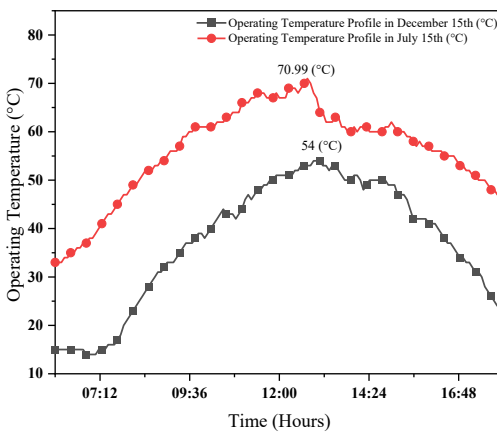


Fig. 1. PV module operating temperature profile comparison between summer and winter seasons for July 15th and December 15th.

In this notion, critical electrical parameters have been defined based on theoretical and mathematical interpretations as reported in [21], demonstrating the impact of temperature on maximum power output, maximum voltage output, and the electrical conversion efficiency for PV modules.

The maximum power output (P_{mpp}) at a single interval is demonstrated by Eq. 1 as follows:

$$P_{mpp} = P_{STC} \times \frac{G}{G_{STC}} \times [1 + \beta_{STC} (T_{PV} - T_{STC})] \quad (1)$$

where P_{STC} is the power prescribed by the manufacturer at standard testing conditions (STC), G is the solar irradiance measured at actual conditions, G_{STC} is the solar irradiance at STC conditions, which coincides to 1000 W/m², β_{STC} represents the power temperature coefficient that typically represents a negative decrement in power by %/1°C as the operating PV temperature surpasses the prescribed STC conditions, i.e., 25°C. This metric is usually mentioned by the PV manufacturer and is dependent on the T_{PV} representing the measured operating PV module temperature and T_{STC} is the operating PV module temperature at STC conditions, which coincides to 25°C. The power temperature coefficient typically varies between various PV technologies as previously discussed in Table 1.

Similarly, the maximum voltage output (V_{mpp}) at a single interval is demonstrated by Eq. 2 as follows:

$$V_{mpp} = V_{STC} \times \frac{G}{G_{STC}} \times [1 + \gamma_{STC} (T_{PV} - T_{STC})] \quad (2)$$

where V_{STC} is the voltage prescribed by the manufacturer at STC conditions, which coincides with the open circuit voltage (V_{oc}), γ_{STC} represents the V_{oc} temperature coefficient that typically represents a negative decrement in voltage by %/1°C as the operating PV temperature surpasses the prescribed STC conditions, i.e., 25°C.

Furthermore, the electrical conversion efficiency (η) at a single interval is demonstrated by Eq. 3 as follows

$$\eta = \eta_{STC} \times [1 + \beta_{STC} (T_{PV} - T_{STC})] \quad (3)$$

where η is the electrical efficiency prescribed by the manufacturer at STC conditions.

Research Methodology

Experimental State-of-the-art

A 2.88 kW grid-connected PV system is established at the University of Sharjah main campus on the rooftop of the W-12 building (Lat. 25.34° N; Long. 55.42° E) as illustrated in Fig. 2. The system operates through a real-time data acquisition system, for instantaneous access of system data [22]. The system was previously discussed for its operation both in small and large periods, showing superior data recording capability and complete infrastructure [23]. In addition, the system operates as a complete grid-connected PV system, injecting AC electrical energy to the 3-phase local utility grid. Moreover, the on-grid PV system records electrical and environmental parameters at 5-minute intervals.

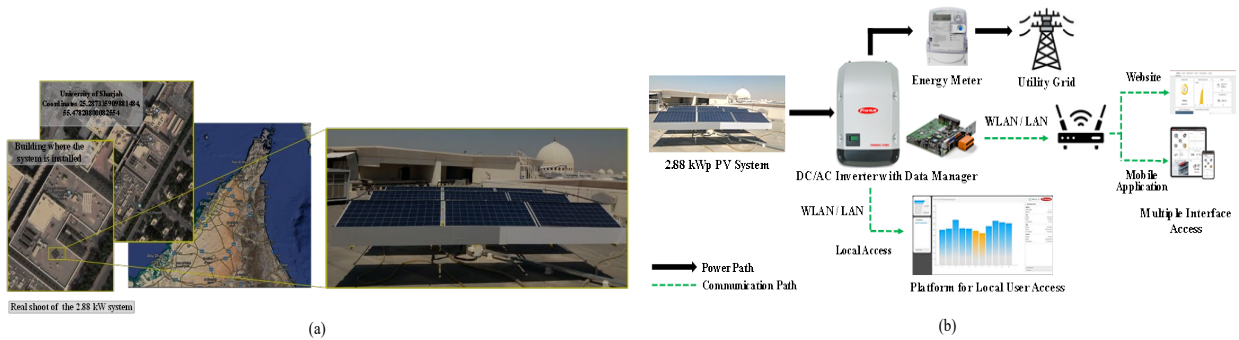


Fig. 2. Demonstration of (a) Established on-grid PV system (b) Power and Communication Loop

Adaptive Cooling Framework model

Based on the previously discussed state-of-the-art, a model is proposed and simulated through MATLAB, to depict the characteristics of water as a working base fluid based on the annual measured data retrieved from the real-time data acquisition hub. Water is selected as a working fluid due to its exceptional heat transfer characteristics and feasible implementation. The constant thermophysical properties are considered to show a uniform effect across all months, except with the change in inlet water temperature as per the given month. The months selected for data variability are December, March, June, and September demonstrating the variability in PV module operating temperature, validating the impact of the proposed temperature regulation technique.

The thermal modeling of water as a working base fluid is defined based on a set of thermodynamic laws, to depict the behavior of water. The heat absorption energy (Q) is defined by Eq. 4 as follows:

$$Q = m \times c \times \Delta T = m \times c \times (T_{PV} - T_{in}) \quad (4)$$

Where m is the mass of the water in kg, c is the specific heat of the water in J/kg.k, and ΔT is the temperature difference between the operating temperature and the water temperature in the Inlet tank assumed by its respective weather conditions.

The mass of water (m) is computed based on Eq. 5 as follows:

$$m = \rho \times A \times d \quad (5)$$

Where ρ is the density of water in kg/m^3 , A is the surface area of the PV system in m^2 , and d is the thickness of the water film in millimeters (mm).

Therefore, the temperature reduction ($T_{\text{reduction}}$) is computed through Newton's law of cooling as depicted in Eq. 6 as follows:

$$T_{\text{reduction}} = \frac{Q}{h \times A \times t} \quad (6)$$

Where h represents the convective heat transfer coefficient in $\text{W/m}^2\text{K}$, and t represents the time in seconds over which cooling occurs. The value considered is $250 \text{ W/m}^2\text{K}$ since it is typical for harsh weather conditions such as the UAE, where it typically ranges from $50 - 300 \text{ W/m}^2\text{K}$.

In this notion, the thermal model proposed will simulate the cooling effect under a temperature threshold of 55°C , which is selected based on the annual average temperature. The parameters of the thermal model are selected and presented in Table 1, which is based on the experimental conditions and location of Sharjah, UAE.

Table 1. Selected thermal parameters for the proposed adaptive cooling framework

Description	Value
Specific Heat [J/kg.K]	4186
Density [kg/m^3]	1000
Convective heat transfer coefficient [$\text{W/m}^2/\text{k}$]	250
Surface Area of PV system [m^2]	18.5
Thickness of water film [mm]	1
Time over which cooling occurs [s]	19.55
Average water temperature for cooling per month [$^\circ\text{C}$]	December: 24.5 March: 32.5 June: 34.5 September: 34.5

Results and Discussion

The experimental data measured from the on-grid PV system is considered across an entire day from 6 AM to 6 PM during four distinct months. In principle, the thermodynamic laws discussed are implemented using MATLAB to assess the performance of the PV system across four distinct months both electrically and thermally, through the MATLAB script development.

The PV module operating temperature is the primary figure of merit to be assessed based on the proposed framework. Based on the computations discussed above, longer periods of cooling are required during June and September as compared to December and March. Thus, an average PV operating temperature reduction of 20.43% and 25.35% is observed during June and September, respectively. The reduction in operating temperature is illustrated in Fig 3 and a summary of the temperature reduction is presented in Table 2, presenting the notable heat extraction during all four seasons using the above-mentioned thermodynamic laws.

Moreover, the relative decrease in operating temperature has led to an increment in the maximum power point. The maximum power output as computed in Eq. 1, presents an average increment of 6.3% and 8.8% in June and September, respectively, as demonstrated in Fig. 4.

The relative enhancement is also observed across other parameters such as the maximum operating voltage and electrical conversion efficiency as computed by Eqs. (2)-(3), presenting the adaptability of temperature regulation across different seasons for maintaining PV system lifetime and longevity. Thus, the proposed adaptive cooling framework proves viability when implemented practically on large-scale PV systems. The performance assessment of the proposed adaptive cooling framework is presented in Table 3, providing improved electrical performance across all seasons of the year, and maintaining high electrical efficiency at longer periods.

Table 2. Summary of operating temperature assessment based on proposed adaptive cooling framework for large-scale on-grid PV system

Description	Period of Adaptive Cooling [Hours]	Operating Temperature [°C]		
		Uncooled	Cooled	Average Decrement
		Average	Average	
December	10:40 AM – 2:20 PM	41.05	32.78	20.13%
March	11:05 AM – 2:05 PM	45.24	40.98	9.41%
June	9:10 AM – 4:20 PM	54.24	43.16	20.43%
September	8:55 AM – 3:50 PM	55.32	41.29	25.36%

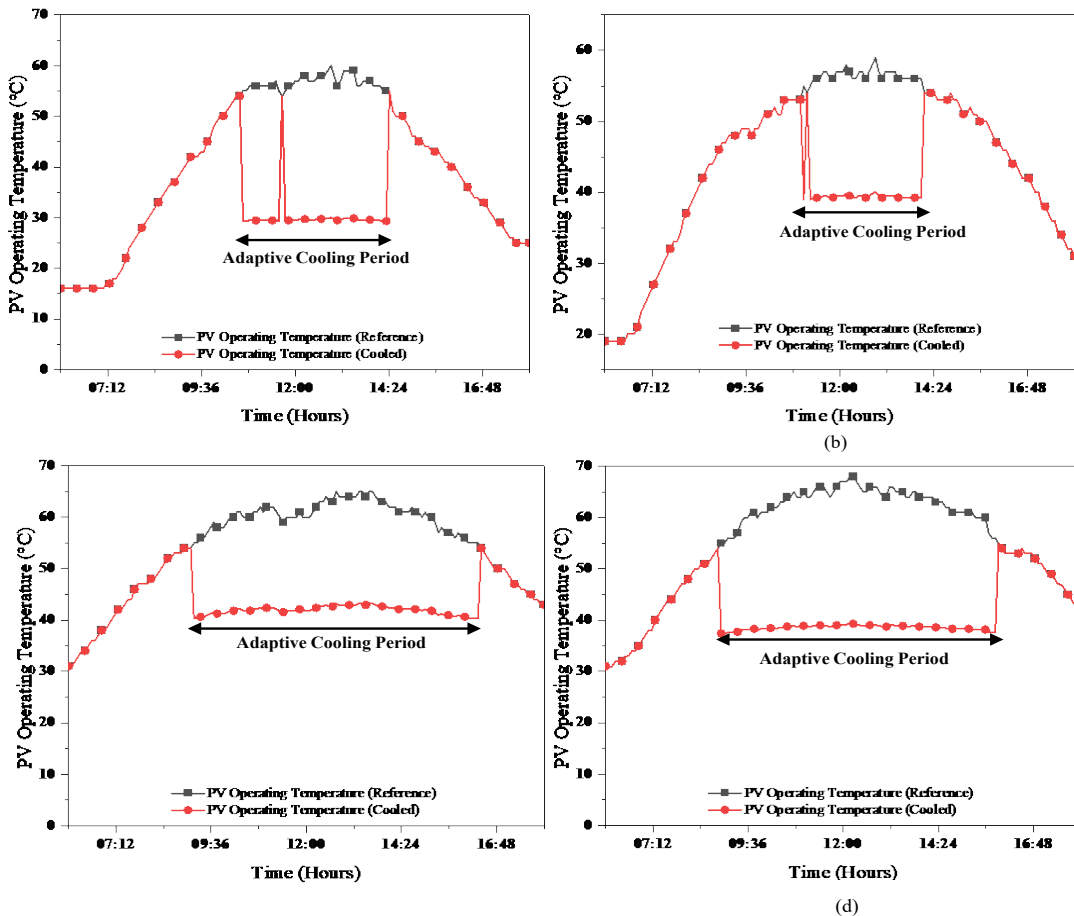


Fig. 3. Comparative assessment of operating temperature reduction during adaptive cooling process for large-scale on-grid PV system during selected days from (a) December (b) March (c) June (d) September

Table 3. Summary of electrical characteristics based on proposed adaptive cooling framework for large-scale on-grid PV system

Description	Maximum Power Point [W]			Maximum Operating Voltage [V]			Electrical Conversion Efficiency [%]		
	Uncooled	Cooled	Average	Uncooled	Cooled	Average	Uncooled	Cooled	Average
	Average	Average	Increment	Average	Average	Increment	Average	Average	Increment
	December	1411.73	1497.88	6.10%	168.12	175.67	4.49%	15.42%	15.96%
March	1656.48	1700.73	2.67%	197.39	201.26	1.96%	15.21%	15.41%	1.31%
June	1553.70	1651.51	6.30%	186.71	195.29	4.59%	14.51%	15.26%	5.17%
September	1661.28	1807.34	8.79%	200.35	213.16	6.39%	14.44%	15.39%	6.58%

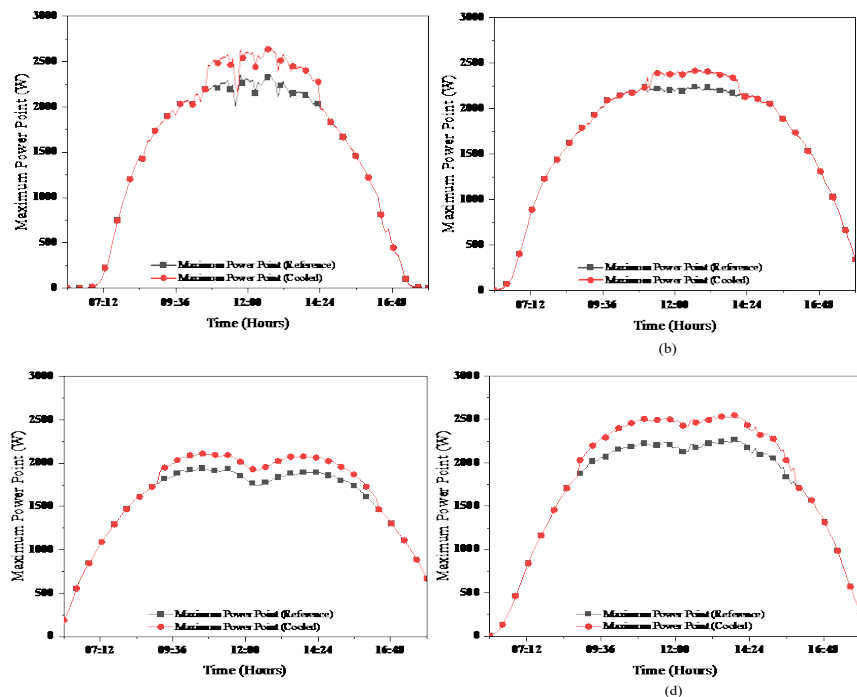


Fig. 4. Comparative assessment of MPP during adaptive cooling process for large-scale on-grid PV system during selected days from (a) December (b) March (c) June (d) September

Summary

This paper proposed a modeling framework for facilitating adaptive cooling for photovoltaic systems, for enhancing system efficiency and longevity. The proposed framework was implemented using MATLAB and experimentally driven environmental conditions, to simulate the thermal and electrical characteristics of a 2.88 kW grid-connected PV system in Sharjah, UAE. A temperature regulating threshold of 55°C was considered, to simulate the system characteristics for December, March, June, and September, providing a wide range of variability in PV module operating temperatures. The highest operating temperature reduction was observed in September with 25.36%, showing the effectiveness of temperature regulation in harsh weather conditions. As a result, the electrical characteristics have improved significantly leading to an 8.79%, 6.39%, and 6.58% enhancement in maximum power output, maximum voltage, and electrical efficiency, respectively. As a future work, the temperature threshold response time will be validated under experimental conditions and incorporation of advanced hardware. Additionally, the utilization of machine learning techniques to optimize the necessary thermal parameters will be investigated for improved energy efficiency and usage.

References

- [1] N. Novas, R.M. Garcia, J.M. Camacho, A. Alcayde, Advances in Solar Energy towards Efficient and Sustainable Energy, *Sustainability*. 13 (2021) 6295. <https://doi.org/10.3390/su13116295>
- [2] S. Paraschiv, L.S. Paraschiv, Trends of carbon dioxide (CO₂) emissions from fossil fuels combustion (coal, gas and oil) in the EU member states from 1960 to 2018, *Energy Reports*. 6 (2020) 237–242. <https://doi.org/10.1016/j.egyr.2020.11.116>
- [3] M.M. Farag, R.A. Alhamad, A.B. Nassif, Metaheuristic Algorithms in Optimal Power Flow Analysis: A Qualitative Systematic Review, *Int. J. Artif. Intell. Tools*. 32 (2023). <https://doi.org/10.1142/S021821302350032X>
- [4] E. Kabir, P. Kumar, S. Kumar, A.A. Adelodun, K.-H. Kim, Solar energy: Potential and

- future prospects, *Renew. Sustain. Energy Rev.* 82 (2018) 894–900.
<https://doi.org/10.1016/j.rser.2017.09.094>
- [5] M.M. Farag, N. Patel, A.-K. Hamid, A.A. Adam, R.C. Bansal, M. Bettayeb, A. Mehiri, An Optimized Fractional Nonlinear Synergic Controller for Maximum Power Point Tracking of Photovoltaic Array Under Abrupt Irradiance Change, *IEEE J. Photovoltaics.* 13 (2023) 305–314.
<https://doi.org/10.1109/JPHOTOV.2023.3236808>
- [6] M.M. Farag, F. Faraz Ahmad, A.K. Hamid, C. Ghenai, M. AlMallahi, M. Elgendi, Impact of Colored Filters on PV Modules Performance: An Experimental Investigation on Electrical and Spectral Characteristics, in: 50th Int. Conf. Comput. Ind. Eng., 2023: pp. 1692–1704.
- [7] T. Salameh, A.K. Hamid, M.M. Farag, E.M. Abo-Zahhad, Energy and exergy assessment for a University of Sharjah's PV grid-connected system based on experimental for harsh terrestrial conditions, *Energy Reports.* 9 (2023) 345–353.
<https://doi.org/10.1016/j.egyr.2022.12.117>
- [8] N.K. Almarzooqi, F.F. Ahmad, A.K. Hamid, C. Ghenai, M.M. Farag, T. Salameh, Experimental investigation of the effect of optical filters on the performance of the solar photovoltaic system, *Energy Reports.* 9 (2023) 336–344.
<https://doi.org/10.1016/j.egyr.2022.12.119>
- [9] T. Salameh, A.K. Hamid, M.M. Farag, E.M. Abo-Zahhad, Experimental and numerical simulation of a 2.88 kW PV grid-connected system under the terrestrial conditions of Sharjah city, *Energy Reports.* 9 (2023) 320–327. <https://doi.org/10.1016/j.egyr.2022.12.115>
- [10] H.M.S. Bahaidarah, A.A.B. Baloch, P. Gandhidasan, Uniform cooling of photovoltaic panels: A review, *Renew. Sustain. Energy Rev.* 57 (2016) 1520–1544.
<https://doi.org/10.1016/j.rser.2015.12.064>
- [11] S. Chander, A. Purohit, A. Sharma, Arvind, S.P. Nehra, M.S. Dhaka, A study on photovoltaic parameters of mono-crystalline silicon solar cell with cell temperature, *Energy Reports.* 1 (2015) 104–109. <https://doi.org/10.1016/j.egyr.2015.03.004>
- [12] M. Al-Maghalseh, Experimental study to investigate the effect of dust, wind speed and temperature on the PV module performance, *Jordan J. Mech. Ind. Eng.* 12 (2018) 123–129.
- [13] H. Attia, K. Hossin, Integrated Renewable PV System through Artificial Neural Network Based MPPT and Water Cooling Treatment, in: 2019 Int. Conf. Electr. Comput. Technol. Appl., IEEE, 2019: pp. 1–5. <https://doi.org/10.1109/ICECTA48151.2019.8959581>
- [14] M.M. Farag, F.F. Ahmad, A.K. Hamid, C. Ghenai, M. Bettayeb, M. Alchadirchy, Performance Assessment of a Hybrid PV/T system during Winter Season under Sharjah Climate, in: 2021 Int. Conf. Electr. Comput. Commun. Mechatronics Eng., IEEE, 2021: pp. 1–5.
<https://doi.org/10.1109/ICECCME52200.2021.9590896>
- [15] K. Sornek, W. Goryl, R. Figaj, G. Dąbrowska, J. Brezdeń, Development and Tests of the Water Cooling System Dedicated to Photovoltaic Panels, *Energies.* 15 (2022) 5884.
<https://doi.org/10.3390/en15165884>
- [16] M. Al-Odat, Experimental Study of Temperature Influence on the Performance of PV/T Cell under Jordan Climate Conditions, *J. Ecol. Eng.* 23 (2022) 80–88.
<https://doi.org/10.12911/22998993/152283>
- [17] M.M. Farag, A.K. Hamid, Performance assessment of rooftop PV/T systems based on adaptive and smart cooling facility scheme - a case in hot climatic conditions of Sharjah, UAE, in: 3rd Int. Conf. Distrib. Sens. Intell. Syst. (ICDSIS 2022), Institution of Engineering and Technology, 2022: pp. 198–207. <https://doi.org/10.1049/icp.2022.2448>
- [18] H. Attia, K. Hossin, M. Al Hazza, Experimental investigation of photovoltaic systems for

performance improvement using water cooling, *Clean Energy.* 7 (2023) 721–733.
<https://doi.org/10.1093/ce/zkad034>

[19] K. Mostakim, M.R. Akbar, M.A. Islam, M.K. Islam, Integrated photovoltaic-thermal system utilizing front surface water cooling technique: An experimental performance response, *Heliyon.* 10 (2024) e25300. <https://doi.org/10.1016/j.heliyon.2024.e25300>

[20] M.M. Farag, R.C. Bansal, Solar energy development in the GCC region – a review on recent progress and opportunities, *Int. J. Model. Simul.* 43 (2023) 579–599.
<https://doi.org/10.1080/02286203.2022.2105785>

[21] D.L. Evans, L.W. Florschuetz, Terrestrial concentrating photovoltaic power system studies, *Sol. Energy.* 20 (1978) 37–43. [https://doi.org/10.1016/0038-092X\(78\)90139-1](https://doi.org/10.1016/0038-092X(78)90139-1)

[22] M.M. Farag, F.F. Ahmad, A.K. Hamid, C. Ghenai, M. Bettayeb, Real-Time Monitoring and Performance Harvesting for Grid-Connected PV System - A Case in Sharjah, in: 2021 14th Int. Conf. Dev. ESystems Eng., IEEE, 2021: pp. 241–245.
<https://doi.org/10.1109/DeSE54285.2021.9719385>

[23] M.M. Farag, A.K. Hamid, Experimental Investigation on the Annual Performance of an Actively Monitored 2.88 kW Grid-Connected PV System in Sharjah, UAE, in: 2023 Adv. Sci. Eng. Technol. Int. Conf., IEEE, 2023: pp. 1–6.
<https://doi.org/10.1109/ASET56582.2023.10180880>

A novel approach to address reliability concerns of wind turbines

Sorena ARTIN^{1,a*}

¹Prince Mohammad Bin Fahd University, Al Khobar, Eastern Province, Saudi Arabia

^asartin@pmu.edu.sa

Keywords: Wind Turbines, Reliability Analysis, Random Variables, Renewable Energy

Abstract. Designing and manufacturing a system in the current industrial world cannot be accomplished without addressing safety related issues. For this purpose, system reliability is a powerful tool to ensure that failure probability of the system is below an accepted level while the system is operational. A commonly used approach to deal with these considerations is to define a performance function for the system in order to investigate its reliability. In this case, renewable energy systems (RESs) are not different. When a wind turbine, as a RES, is designed, its reliability cannot be ignored or underestimated. Therefore, stable and efficient models are needed to make sure that the turbine remains operational and is able to safely generate electricity power. In this paper, a new approach is proposed to set up a reliability analysis model for the wind turbines. The introduced model takes two important factors, i.e. the wind speed and the wind angle, and their probability distributions into account. These two factors are indeed considered as random variables to design a new system performance function and set up the new model in order to investigate wind turbine's reliability.

Introduction

Climate change has recently attracted attentions around the world. This has made many researchers and organizations to focus on renewable energy systems (RESs) and their related issues. However, fossil fuels still play important roles, either in financial markets and/or international relationships, as RESs, such as wind turbines and solar panels, are not yet efficient enough to replace fossil fuels in a foreseeable future [1, 2].

There are always challenges when designing every single RES, regarding their economic feasibility, safety checks, engineering design, reliability features, etc. These challenges need to appropriately be addressed as otherwise they could bring catastrophic consequences, like shutting down entire renewable energy station [3].

Renewable energy resources often have random behavior. For instance, there needs to be irradiance and wind available and this availability depends on randomness of the resources. Data mining and machine learning techniques are often employed to predict this availability in order to investigate the system's behavior in the future [4, 5].

Moreover, the Internet of Things (IoT) has been used to oversee solar power stations [4]. As these panels often need a vast area to install large-scale systems, it is crucial to find the right place and also analyze functionality of the panels in real-time tasks. To do this, there are some algorithms which employ the IoT techniques to improve these systems' reliability. Also, a widely applied technique is to estimate their parameters in order to formulate deterministic optimization models of solar panels. A method has been introduced that uses stochastic fractal search algorithms to estimate current-voltage parameters for modelling purposes [6].

Also, various data mining methods are used to predict solar cell's energy production. However, a new finding proposes a hybrid method incorporating machine learning algorithms and statistical methods is going to perform better in terms of PV energy predictions [4, 5, 7].

Other RESs have their own associated challenges and risks. However, the main challenges to generate electricity power by wind turbines are again related to randomness of the main factor; i.e.

the wind. It has been reported that wind turbines have great potentials to generate green energy and help environment, as they produce low emission compared with traditional fossil fuels. On the other hand, there are new barriers to research and industry in order to design these systems due to randomness and intermittent characteristics associated with these turbines. As a result of these challenges, uncertainty level is high that needs to be addressed by introducing efficient reliability analysis models and methods [8].

Further, many researches work on offshore wind power stations as another way to produce renewable energy. It has been found that many untouched offshore locations are rich in terms of resources of available wind. Among available structures for offshore wind turbine stations, fixed structures, such as monopile, jacket and tripod support are often preferred. These structures however do have uncertainty problems. It has been reported that uncertainty of these systems can be considered by using semi-probabilistic nature of the existing frameworks [9].

There are also researches that have found offshore wind turbines would bring more reliability related consideration into energy production process. It has been reported that the Gaussian process regression is of the most stable and efficient methods to handle these problems [10]. Although it is believed that offshore wind resources have great potential for energy production, these stations often require huge maintenance costs which means it could be very challenging to deal with these systems and therefore there are projects have been abandoned due to the financial problems [11].

Wind Turbines' Reliability Considerations

Moving towards renewable energy has motivated researchers to work on mathematical models of RESs. It is reported that hybrid renewable energy systems (HRESs) could be more efficient than single renewable source systems. However, more challenging problems are expected when working with a HRES. This often happens due to a large number of factors that need to be considered to set up HRESs' mathematical models.

Reliability related issues are of the highest importance when it comes to developing new systems. In this case, reliability concerns of RESs are mainly originating from random nature of their required natural resources [12, 13]. A system's reliability is often studied by employing a reliability function which can be defined by the system's failure rate λ as below [14]:

$$R(t) = e^{-\lambda t} \quad (1)$$

Reliability analysis problems are another tool to investigate a system's reliability. For this purpose, a reliability analysis problem, as an optimization problem, needs to be solved in order to find a reliability index. Analytical and simulation approaches are widely used to perform a reliability analysis problem, either by using a mathematical model to evaluate system reliability or by applying simulation techniques to approximate the reliability index [15].

A wind energy conversion system (WECS) can also be used to formulate a wind turbine's reliability analysis problem [12]. The wind speed is a major factor in this system and so its probability distribution needs to be determined. It has been reported that the Weibull distribution is an appropriate choice for this purpose, which is often shown as a matrix representing time. α_w and β_w , as a scale parameter and a shape parameter respectively, are applied in the Weibull density and distribution functions.

$$f_v(v) = \frac{\beta_w}{\alpha_w^{\beta_w}} v^{\beta_w - 1} e^{-\frac{v}{\alpha_w \beta_w}} \quad (2)$$

$$F_v(v) = 1 - e^{-\frac{v}{\alpha_w \beta_w}} \quad (3)$$

As random variables play significant roles in reliability analysis problems, it would be crucial to find these variables for a wind turbine reliability model. It is reported that wind speed and wind angle are two random variables of a reliability analysis problem of wind turbines [16]. To work out these variables, two boundaries of the wind speed must be considered as cut-in V_{ci} and cut-off speeds V_{co} . If the wind speed was below V_{ci} or above V_{co} , then wind turbine would stop working (either due to the lack of enough energy or because of safety concerns) [12, 13, 17]. The power generated by the turbine can be worked out as:

$$P_w(v) = \begin{cases} 0 & \text{if } v < V_{ci} \\ \frac{v - V_{ci}}{V_R - V_{ci}} P_R & \text{if } V_{ci} \leq v \leq V_R \\ P_R & \text{if } V_R \leq v \leq V_{co} \\ 0 & \text{if } V_{co} < v \end{cases} \quad (4)$$

The coefficient $\frac{v - V_{ci}}{V_R - V_{ci}}$ could be replaced by a quadratic polynomial and multiplied into the rated capacity [18].

Wind Turbines' Performance Function

A system performance function, which is also known as a limit-state function, is often employed to set up a reliability analysis problem and a reliability-based design optimization (RBDO) problem [19]. Once random variables of a wind turbine were determined, they would be used to define the system performance function. A probabilistic constraint as $P[G(t) \leq 0] \leq \Phi(-\beta)$ is then formulated in an RBDO problem to take reliability concerns into account.

This performance function is then used to setting up a reliability analysis problem for the wind turbine. A first-order direct reliability analysis problem is defined as below [20]:

$$\begin{aligned} \min & \| (u_1, u_2, \dots, u_n) \| \\ \text{s.t. } & G_U(u_1, u_2, \dots, u_n) = 0 \end{aligned} \quad (5)$$

where (u_1, u_2, \dots, u_n) represents standard normalized design variable and G_U is standard normalized system performance function. It has been reported that the conjugate gradient direction-based (CGDB) method is the most stable and efficient method to solve this problem and find a reliability index β [21].

Probability distribution and also their relevant density function are the basis of all reliability analysis problems. In this case, for power generated by the WECS, the following density function is available, in which F_v shows the probability distribution function of the WECS [12]:

$$f_{P_w}(P_w) = \begin{cases} F_1 = 1 - F_3 & \text{if } P_w = 0 \\ F_2 & \text{if } V_{ci} \leq v \leq V_R \\ F_3 & \text{if } P_w = P_R \end{cases} \quad (6)$$

where

$$F_2 = \frac{V_R - V_{ci}}{P_R} \frac{\beta_w}{\alpha_w^{\beta_w}} (V_{ci} + (V_R - V_{ci}) \frac{P_w}{P_R})^{\beta_w-1} e^{-\left(\frac{V_{ci} + (V_R - V_{ci}) \frac{P_w}{P_R}}{\alpha_w}\right) \beta_w}$$

and

$$F_3 = F_v(V_F) - F_v(V_{ci})$$

It is found that the random variable v in the above function can follow two probability distribution functions as the Weibull distribution [12] or the Normal distribution [22]. In the next section, it will be shown how to set up a reliability analysis problem of wind turbines based on the random variables and probability distributions discussed in this paper.

Introducing Reliability Analysis Problems for Wind Turbines

To investigate reliability concerns of a wind turbine, a performance function should first be defined. It is elaborated here how to formulate such a system performance function based on two previously discussed random variables and then a new approach is proposed to set up new reliability analysis problems for wind turbines.

Random Variables

The first task is to determine random variables. The wind speed and the wind angle are considered in this paper as two random variables of a wind turbine using which a performance function can be formulated. Once the performance function was available, then a reliability analysis problem can be set up.

It is required to find (or identify) probability distribution function(s) of each random variable. It is already known that the wind turbine, as the first random variable, may follow two probability distributions, either the Gaussian distribution (also known as the Normal distribution) or the Weibull distribution. Data collected in different geographical locations prove that these two distributions are appropriate choices to explain behavior of the wind speed.

The second random variable would be the wind angle. However, no valid data is yet available for this variable to determine its probability distribution function. Therefore, it remains a big challenge to determine the wind angle's distribution in order to set up a wind turbine's reliability analysis problem.

System Safety and Failure

The cut-in speed V_{ci} and the cut-off speed V_{co} should also be considered when setting up the reliability analysis problem. Considering V_{ci} and V_{co} as two thresholds and given the wind speed v must be between these thresholds, the system safety and system failure could be defined for a wind turbine.

Based on the Eq. 4, a turbine is supposed to work properly when $V_{ci} \leq v \leq V_{co}$. Therefore, this condition is assumed as system's safety which means the turbine is able to generate electricity power only if the wind speed is between its boundaries. However, when the wind speed is out of the above-mentioned range, i.e. $V_{co} < v$ or $v < V_{ci}$, then the turbine stops working and no power could be generated, and so it would be considered as system failure.

However, it must be mentioned that total failure of the system, which means the turbine needs maintenance or replacement, is different from the system failure defined in this Section.

For simplicity reasons, let's assume x is a random variable representing the wind speed. Also, d_1 and d_2 are the thresholds of random variable x , which represent the cut-in and cut-off speeds, respectively. Then, the discussed safety and failure conditions can be used to formulate the wind turbine's performance function(s) as below:

$$G_1(x) = x - d_1 \quad (7)$$

$$G_2(x) = d_2 - x \quad (8)$$

Therefore, $G_1(x) > 0$ and $G_2(x) > 0$ show the system safety which means electricity power can be generated, and so $G_1(x) < 0$ and $G_2(x) < 0$ indicate system failure meaning no power can be generated.

So, the failure surface of a reliability analysis problem (such as Eq. 5) or the probabilistic constraint of an RBDO problem for wind turbines can be set up as $G_1(x) = 0$ and $G_2(x) = 0$.

Future Works and Conclusion

Reliability has always been one of the most important considerations when designing any new system, and in this case, the RESs in general and wind turbines in particular are not different. In this paper, new approaches are proposed to deal with reliability issues of wind turbines.

The main focus here is to identify random variables of the system, i.e. a wind turbine, and then employ them to define a performance function for the turbine. This performance function can then be used to design a direct reliability analysis problem, or an inverse reliability analysis problem, or even an RBDO problem.

Based on the discussions on reliability issues in the previous Section, it can be concluded that an important step in the future works to setting up the required problem(s) is to figure out probability distribution of the wind angle, as a random variable of the system. The other random variable is the wind speed for which at least two probability distributions are available. Once probability distribution and statistical data of both random variables were available, then they can be used to set up a system performance function.

The wind speed characteristics, such as the cut-in and cut-off speeds, and the power function can also be used to define a performance function for a wind turbine. In all these cases, the wind turbine's performance function should be set up based on the safety conditions to ensure electricity power can be generated.

Once a system performance function was formulated using any of the above approaches, a reliability analysis problem, either direct or inverse, and/or an RBDO problem can be modeled to address reliability issues of a wind turbine.

References

- [1] B. Morawski; Global Wind, Solar Production Hit Highest Benchmarks Ever in 2021, But Coal Also Kept Pace; World Economy Forum (2022).
- [2] S. Costello; Neighbourhood Dispute Erupts Over Man's Backyard Wind Turbine; Nine News Australia (2022).
- [3] J. Hill; Swedish Wind Turbine Collapses Days After Wind Farm Inauguration; Renew Economy (2022).
- [4] S. Shakya; A self-monitoring and analysing system for solar power station using IoT and data mining algorithms. *Journal of Soft Computing Paradigm*, 3(2) (2021), 96-109. <https://doi.org/10.36548/jscp.2021.2.004>
- [5] C. Vennila, A. Titus, T. Sri Sudha, U. Sreenivasulu, R. Pandu Ranga Reddy, K. Jamal, A. Belay; Forecasting Solar Energy Production Using Machine Learning; *International Journal of Photoenergy*, 7797488 (2022). <https://doi.org/10.1155/2022/7797488>
- [6] H. Rezk, T. Sudhakar Babu, M. Al-Dhaifallah, H. Zeidan; A Robust Parameter Estimation Approach Based on Stochastic Fractal Search Optimization Algorithm Applied to Solar PV Parameters; *Energy Reports*, 7 (2021), 620-640. <https://doi.org/10.1016/j.egyr.2021.01.024>
- [7] S. Artin; Reliability Enhancement of Solar Panels based on the Photocurrent Equality; 2023 Asia-Pacific Conference on Applied Mathematics and Statistics; Nanjing, China, June 2023.
- [8] J. Deng, H. Li, J. Hu, Z. Liu; New Wind Speed Scenario Generation Method Based on Spatiotemporal Dependency Structure; *Renewable Energy*, 163 (2021), 1951-1962. <https://doi.org/10.1016/j.renene.2020.10.132>

- [9] S. Okpokparoro, S. Sriramula; Uncertainty Modelling in Reliability Analysis of Floating Wind Turbine Support Structure; *Renewable Energy*, 165 (2021), 88-108. <https://doi.org/10.1016/j.renene.2020.10.068>
- [10] D. Wilkie, C. Galasso; Gaussian Process Regression for Fatigue Reliability Analysis of Offshore Wind Turbines; *Structural Safety*, 88 (2021), 102020. <https://doi.org/10.1016/j.strusafe.2020.102020>
- [11] C. Clark, B. DuPont; Reliability-Based Design Optimization in Offshore Renewable Energy Systems; *Renewable and Sustainable Energy Reviews*, 97 (2018), 390-400. <https://doi.org/10.1016/j.rser.2018.08.030>
- [12] G. Tina, S. Gagliano, S. Raiti; Hybrid Solar/Wind Power System Probabilistic Modelling for Long-Term Performance Assessment; *Solar Energy*, 80 (2006), 578-588. <https://doi.org/10.1016/j.solener.2005.03.013>
- [13] S. Eryilmaz, I. Bulanik, Y. Devrim; Reliability Based Modelling of Hybrid Solar/Wind Power System for Long Term Performance Assessment; *Reliability Engineering and System Safety*, 209 (2021), 107478. <https://doi.org/10.1016/j.ress.2021.107478>
- [14] G. Ezzati, A. Rasouli; Evaluating System Reliability Using Linear-Exponential Distribution Function; *International Journal of Advanced Statistics and Probability*, 3(1) (2015), 15-24. <https://doi.org/10.14419/ijasp.v3i1.3927>
- [15] M. Zarmai, C. Oduoza; Impact of Intermetallic Compound Thickness on Thermo-Mechanical Reliability of Solder Joints in Solar Cell Assembly; *Microelectronics Reliability*, 116 (2021), 114008. <https://doi.org/10.1016/j.microrel.2020.114008>
- [16] S. Al Sanad, L. Wang, J. Parol, A. Kolios; Reliability-Based Design Optimization Framework for Wind Turbine Towers; *Renewable Energy*, 167 (2021), 942-953. <https://doi.org/10.1016/j.renene.2020.12.022>
- [17] A. Askarzadeh, L. Coelho; A Novel Framework for Optimization of a Grid Independent Hybrid Renewable Energy System: A Case Study of Iran; *Solar Energy*, 112 (2015), 383-396. <https://doi.org/10.1016/j.solener.2014.12.013>
- [18] B. Zhang, M. Wang, W. Su; Reliability Analysis of Power Systems Integrated with High-Penetration of Power Converters; *IEEE Transactions on Power Systems*, 36(3) (2021), 1998-2009. <https://doi.org/10.1109/TPWRS.2020.3032579>
- [19] G. Ezzati; A Reliability-Based Design Optimization Model for Electricity Power Networks; *Dynamics of Continuous, Discrete and Impulsive Systems, Series B: Applications & Algorithms*, 22 (2015), 339-357.
- [20] G. Ezzati, M. Mammadov, S. Kulkarni; Solving Reliability Analysis Problems in the Polar Space; *International Journal of Applied Mathematical Research*, 3(4) (2015), 353-365. <https://doi.org/10.14419/ijamr.v3i4.3302>
- [21] S. Artin, S. Salimzadeh; A Conjugate Gradient Direction-Based Method to Evaluate Reliability Analysis Problems; *IAENG International Journal of Applied Mathematics*, 52(3) (2022), 659-666.
- [22] G. Ochoa, J. Alvarez, M. Chamorro; Data Set on Wind Speed, Wind Direction and Wind Probability Distributions in Puerto Bolivar – Colombia; *Data in Brief*, 27 (2019). <https://doi.org/10.1016/j.dib.2019.104753>

Solar radiation forecasting using attention-based temporal convolutional network

Damilola OLAWOYIN-YUSSUF^{1,a}, Mohamad MOHANDES^{1,b*}, Bo LIU^{1,c}, and Shafiqur REHMAN^{1,d}

¹Department of Electrical Engineering, King Fahd University of Petroleum and Minerals, Academic Belt Road, Dhahran, 31261, Eastern Region, Saudi Arabia

^ag202110610@kfupm.edu.sa, ^bmohandes@kfupm.edu.sa, ^cboliu@kfupm.edu.sa,
^dsrehman@kfupm.edu.sa

Keywords: Global Solar Radiation, Temporal Convolutional Network (TCN), LSTM

Abstract. Solar energy, an inexhaustible and pristine power source, harbors the capability to mitigate the emissions of greenhouse gases and the dependency on fossil fuels, thereby playing a pivotal role in the conservation of our ecosystem. Nevertheless, the process of harnessing solar energy from sunlight is subject to the capricious characteristics of weather conditions, which include variables such as the density of cloud cover, levels of atmospheric moisture, and fluctuations in temperature. Hence, the task of prognosticating solar radiation holds significant importance for the strategic planning and efficient management of solar power systems. The current machine-learning methods for predicting global solar radiation make use of recurrent networks. One major downside of recurrent-based models is that they are exposed to vanishing gradients and stagnant performance over longer available input sequences. The model showcased is an attention-fueled Temporal Convolutional Network (TCN) intertwined with Convolutional Neural Network (CNN). The suggested method merges the advantages of the feature extraction proficiencies of a TCN and the aggregation capabilities of a CNN. The method has been tested for up to 24 hours of future time sequence prediction and it has been noted that its performance is unmatched.

Introduction

Owing to the unpredictable characteristics of weather conditions, the production of solar energy harnessed from sunlight cannot be pre-established with absolute certainty. Many methods for predicting solar radiation have been employed because it is critical in many industries, including solar energy production, agriculture, and weather forecasting[1]. Accurate predictions of solar radiation help these industries to plan and make informed decisions. Historically, the prediction of solar radiation was reliant on physical models that considered a multitude of factors. These included the position of the sun, the angle of incidence, the extent of cloud cover, and the prevailing atmospheric conditions [1]. These models require significant expertise and resources to develop, and the quality and availability of input data can limit their accuracy. Furthermore, they may be unable to capture the complex relationships between input variables and output predictions [1]. In recent years, there has been a growing interest in using machine learning (ML) algorithms to improve solar radiation prediction [2]. ML algorithms can model complex relationships between input and output by learning from the provided data. An ML technique that has an effective handle on getting better performance with big data is deep learning because of its ability to incorporate large datasets and interpret complicated correlations between variables in a versatile, trainable way [3]. Deep learning techniques like multi-layered perceptron [4], convolutional neural networks [5], and recurrent neural network [6, 7] have been used to explore predicting global solar radiation. While these methods have no doubt produced encouraging results, they do so with some challenges. Firstly, some of the methods used in predicting solar radiation fail to provide an

estimation over multiple time steps. Multiple-time step prediction provides the advantage of being used in early warning applications and predictive planning. Secondly, although other models based on recurrent networks like Recurrent Neural Network (RNN), Long Short-Term Memory (LSTM), and gated recurrent units (GRUs) have the capability of storing significant information and prediction over multiple time steps, they do suffer from degradation when making predictions over multiple time steps.

In response to these challenges, a multi-time step prediction architecture is proposed using a two-stage approach. The first stage extracts feature from the input dataset by using an attention mechanism with a temporal convolutional network (TCN) backbone. The first stage acts as an encoder as it outputs a fixed-length representation of the input. The second stage acts as a decoder using the fixed length representation to predict the desired output. It does so by leveraging a CNN and a dense layer to forecast solar radiation for multiple time steps.

Related Work

The application of ML techniques has brought about significant advancements in the study of solar radiation [8]. ML, a smaller category under artificial intelligence, revolves around the principle of instructing algorithms to identify patterns and formulate predictions predicated on data. These algorithms, with their ability to learn and adapt, offer a more efficient and precise approach to data analysis compared to traditional methods. [9] proposed a novel data preprocessing approach that aims to reduce forecasting errors, which are often associated with traditional prediction methods such as Markov chains or k-Nearest Neighbors (KNN). They engineered an enhanced multi-layer perceptron (MLP) model, incorporating three neurons within the concealed layer. This model demonstrated the capacity to yield predictions that were on par, if not surpassing, those generated by techniques such as Bayesian inference, Markov chains, and the KNN algorithm. Xing et al. introduced an innovative hybrid stack autoencoder LSTM (SAELSTM) architecture, specifically designed for predicting daily global solar radiation (GSR) [10]. This architecture harnesses the power of deep learning and incorporates a feature selection technique grounded on Manta Ray Foraging Optimization (MRFO). The utilization of this architecture in the context of GSR forecasting is further elaborated in the work of Ghimire et al. [11]. The deep learning hybrid SAELSTM model outperformed other models and persistence methods in simulations in terms of accuracy. The model generates intervals for high-quality solar energy predictions with a high likelihood of coverage and minimal interval errors. The study found that deep learning models, such as Bidirectional LSTM [12], perform better than traditional ML for forecasting daily GSR models. In a study conducted by Alizamir et al., wavelet transformation was utilized to break down different meteorological parameters to predict daily solar radiation [7]. The decomposed signals were then used as input into an LSTM recurrent network. While this approach improved network performance, it also increased the number of input parameters needed, thereby increasing the complexity of the optimization process. In another study, [13] employed CNN and an amalgamation of CNN and LSTM to predict monthly radiation at multiple steps. The study inferred that CNN outperformed other models such as MLP, LSTM, GRU, and CNN-LSTM. However, it's important to note that the receptive fields of CNN do not consider the sequence progression of time series data, which could limit its effectiveness in certain applications. Ghimire et al. predicted solar radiation by selecting features using a random forest recursive feature elimination [5]. The convolutional neural network extracted features which were then fed as input to a multilayer perceptron to generate a predicted output. However, using a multilayer perceptron for prediction limited the model's capability of predicting global solar radiation over multiple time steps. This highlights the need for models that can effectively handle time series data and make accurate predictions over multiple time steps.

Methodology

Symbol Definitions and Issue Formulation:

Consider an exogenous series, denoted as $X = (X_1, X_2, \dots, X_n)$ and $X \in \mathbb{R}^{T \times n}$ where n represents the number of features and T signifies the time steps. The i -th exogenous series, expressed in terms of time steps, can be represented as $X_i = (X_i^1, X_i^2, \dots, X_i^T)$ or $X_i \in \mathbb{R}^T$. The objective of a time series prediction network is to train a function that, given a specific set of previous time series features $X = (X_1, X_2, \dots, X_n)$ and their corresponding outputs within that time steps $\hat{Y} = \hat{y}^{T+1}, \hat{y}^{T+2}, \dots, \hat{y}^{T+k}$ where $Y \in \mathbb{R}^k$. This can be mathematically expressed as:

$$\hat{y}^{T+1}, \hat{y}^{T+2}, \dots, \hat{y}^{T+k} = F(X^1, X^2, \dots, X^T, Y) \quad (1)$$

In this equation, the function $F(\cdot)$ is the function whose parameters are learnable. This means that the function can adapt and improve its performance based on the data it is trained on, thereby enhancing the accuracy of the predictions it makes.

Model:

The design of the proposed model as outlined in Figure 1 takes a series of driving input sequences as its input. These sequences are then passed through an LSTM block, which acts like a translator, converting the input sequences into a form that the model can understand better; this

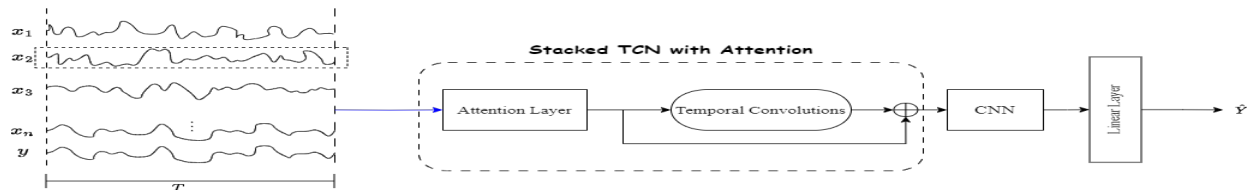


Figure 1 Graphical illustration of the proposed model architecture. It consists of an input layer (the blue line leading to the attention block signifies an LSTM layer used for embedding input), a stacked attention based TCN, a CNN block for merging the TCN output, and finally a linear output layer.

is known as embedding. The decision to use recurrent layers for extracting embeddings was inspired by the work of Gugulothu et al., where GRUs were utilized to generate embeddings for decoding multiple sequences in a multivariate time series network [14].

The output gate of an LSTM is expressed as:

$$o_n = F_{emb}(\cdot) = \sigma(W_o * X_n + U_o * h_{n-1} + b_o) \quad (2)$$

X_n : the input vector at time n

h_n : the hidden state vector at time n

W : input-to-hidden weight matrix

b : hidden layer bias vector

σ : sigmoid activation functions.

From equation 2, the output o_n gives the temporal input embedding. The temporal input can be rewritten as:

$$x_{emb,i} = F_{emb}(X_i^1, X_i^2, \dots, X_i^T) \quad (3)$$

The embedded input is then fed into a feature extraction network. This network is made up of an attention block stacked on top of a temporal convolution network.

Attention Block:

The Attention Block [15], works by first obtaining an attention weight vector from the provided input. This input could be represented as $x_{emb,i} = F_{emb}(X_{emb,i}^1, X_{emb,i}^2, \dots, X_{emb,i}^T)$. The attention block helps the model focus on the most important parts of the input. It's postulated that the embeddings possess the same dimensional attributes as the input, albeit this is typically not the scenario. The attention weight vectors are calculated using the following equations:

$$u_i = W_u^T x_{emb,i} + b_u \quad (4)$$

Where $W_u \in \mathbb{R}^{T \times 1}$, and $b_u \in \mathbb{R}$ are parameters to be learned. These attention weight vectors are then normalized using a SoftMax function to ensure they all sum to unity. The normalization SoftMax functions can be expressed as:

$$\mu_i^t = \frac{\exp(u_i^t)}{\sum_{t=1}^T \exp(u_i^t)} \quad (5)$$

where $t \in [1, T]$. These normalized softmax values represent the distribution of the input that should be paid attention to. The attention output, defined by the function $F_{att}(\cdot)$, can be calculated by multiplying the normalized SoftMax by the input:

$$x_{att,i} = \mu_i^t \cdot x_{emb,i} \quad (6)$$

Extracting Features with TCN:

In sequence modelling, recurrent networks such as RNN and its variants have been traditionally used until Bai et al. introduced the concept of using generic convolutional networks for sequence modelling tasks. This new approach, called Temporal Convolutional Networks (TCN), outperformed the LSTM [16]. The structure of the TCN is a simple modification of the conventional CNN. The TCN uses causal convolutions, which ensure that the model's prediction at a given time does not depend on future values of the input and makes them much faster to train compared to recurrent models as they do not have recurrent connections. A further enhancement of the causal convolution, known as dilated causal convolution, allows convolution over a wider window by skipping some input values. The receptive field of the dilated causal convolution is much wider than that of the causal convolution, making it more efficient. Figure 2 shows the dilated causal convolutions for different levels of dilation. Given the input $x \in \mathbb{R}^T$ and a filter $f : \{0, \dots, a, \dots, m-1\}$ of size m , the dilation convolution operator on a within the sequence can be defined as:

$$F_{TCN}(a) = \sum_{j=0}^{m-1} f(j) \cdot x^{(a-d \cdot j)} \quad (7)$$

Where d is the dilation factor, and $a - d \cdot j$ explains the orientation of the past.

The Temporal Convolutional Network (TCN) block, as depicted in figure 1, is a composite of several components. These encompass a dilated causal convolution, weight standardization, a Rectified Linear Unit (ReLU) activation function, and dropout strata incorporated to augment the resilience of the network. The extent of the TCNs could potentially cause the vanishing gradient problem. This is a difficulty encountered during the training of artificial neural networks with gradient-based learning methods and backpropagation. To mitigate this, a skip or residual connection has been incorporated. In a residual block, as described by He et al. [17], there's a pathway that leads us through a series of transformations, denoted as F_o . The results of these transformations are then seamlessly integrated with the block's original input, x . The output after a residual connection, O_{res} , is given by the equation:

$$O_{res} = \sigma(x + F_o(x)) \quad (8)$$

Here, σ represents the activation function. This function introduces non-linearity into the output of a neuron. This non-linearity helps the network learn from the error so that the model can classify inputs that are not linearly separable.

Aggregating extracted features with CNN:

The output from the stack of attention TCN block is of the form $\mathbb{R}^{N \times T \times L}$ where N is the batch size, T is the number of the input sequence, and L is the number of channels in each TCN layer. There exists a requirement to transform the output of this Temporal Convolutional Network (TCN)

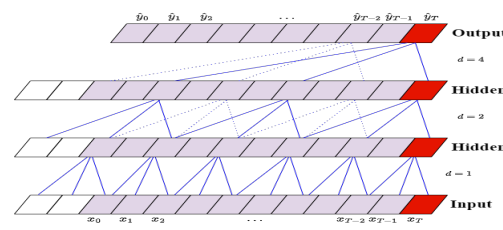


Figure 2 TCN Architecture

into a vector of dimension $\mathbb{R}^{N \times 1 \times K}$, where K signifies the number of anticipated output sequences. To achieve an output of this dimension two different approaches can be followed: flattening the last two dimensions and using a linear layer, or a convolutional layer. In this study, the path of using a convolutional layer was followed because of the added advantage of reducing the number of parameters needed for computation. If a linear layer was used, the number of parameters required would be of dimension $T \times L \times K$ while when a 1-dimensional convolutional layer is used the number of weights required would be $(L \times m) + (L \times K) = L \times (m + K)$, where m is the size of kernel used in the convolutional layer. The $L \times K$ accounts for the number of weights needed in the linear layer for the output to be in the right dimension after the convolutional layer. The convolution operation over an input X can be expressed mathematically as:

$$O_{conv} = \sigma_{lr}(W_{conv}X + B_{conv}) \quad (9)$$

where σ_{lr} is the leaky rectified linear unit (leakyReLU) activation function, W_{conv} is the convolutional weight, and B_{conv} is the convolutional bias. The dense layer utilized after the CNN is an affine amalgamation of the output after the convolution layer and a certain bias, devoid of an activation layer.

Experimental data description, training settings, and evaluation metrics

The empirical dataset employed in this investigation, amassed in the northern region of Saudi Arabia, comprises 75133 data entries encapsulating variables such as solar radiation, atmospheric temperature, relative humidity, velocity and direction of wind, and precipitation, extending over a period from 2012 to 2021. However, it's important to note that there are gaps in the dataset between

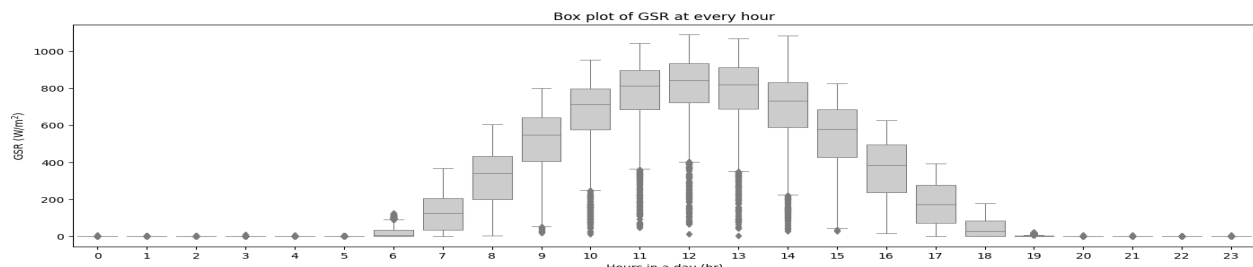


Figure 3 Box plots of GSR at every hour of the day.

October 3rd, 2019, and January 1st, 2020, as well as between March 29th, 2020, and June 4th, 2020. Given the sequential nature of the dataset, the data was not shuffled when loaded and was divided into training, validation, and testing portions. The split was done in a 70:15:15 ratio, ensuring a substantial amount of data for each phase of the model development and evaluation process.

In this study, we considered the lags of Global Solar Radiation (GSR) as input to the model, to envisage the next one hour, six hours, 12 hours, and 24 hours respectively. The lags used are 24, 48, and 72 hours respectively, or in mathematical notation as $T \in \{24, 48, 72\}$. To understand the effect of the time of day on global solar radiation, a box plot showing the distribution of GSR at every hour of the day is presented in Figure 3. The time of day significantly affects global solar radiation, with some outliers observed. A comparison of the maximum values of the variables in our dataset reveals the need for input scaling. Various scaling methods like the standard scaler, robust scaler, and min-max scaler have been used in different studies [18]. The best scaling method for a dataset depends on the variable distribution in that dataset, which can be visualized using box plots. The robust scaler, which uses the interquartile range and median, is used for this problem. The robust scaler calculates the scaled value of an item V in a series of inputs as:

$$V_{scaled} = \frac{V_{original} - \tilde{\eta}}{IQR} \quad (10)$$

where the scaled value is V_{scaled} , the original value is $V_{original}$, $\tilde{\eta}$ represents the input median, and IQR is the input's interquartile range.

The forecast was made for the upcoming 1, 6, 12, and 24 hours, focusing on the variable k in equation 1, where k can be any of the values 1, 6, 12, or 24. This was done to test the theory of

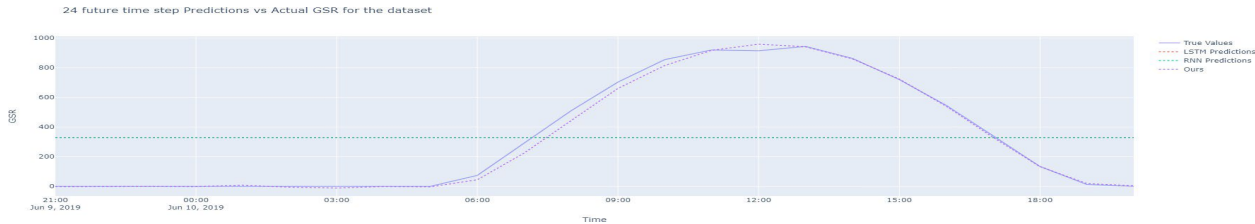


Figure 4 Prediction results for 24 future time steps.

Temporal Convolutional Network (TCN) structure. The model's hidden size was determined to be 64 through a grid search, and this size was also used for the RNN and LSTM models. The model structure consists of 1 CNN layer and 6 TCN blocks each having a dropout rate of 0.2. An Adam optimizer with weight decay of 1×10^{-6} was used with a learning rate scheduler having a patience of 2, and a threshold of 0.01. All models underwent training under homogeneous conditions, commencing with a learning rate of 1×10^{-3} and persisting for 40 epochs within a Google Colab environment, utilizing the Torch library of Python-3. A v100 GPU with a 15GB RAM infrastructure was used for the entire experiment. To evaluate the models, three widely used metrics for time series prediction were employed: R-squared, Mean Absolute Error (MAE), and Root Mean Squared Error (RMSE). Lower values of RMSE and MAE and a higher R-squared indicate a better model.

Results

The outcomes of applying the proposed model to predict global solar radiation over several time steps are detailed in Table 1 and Figure 5. It's plausible that employing exclusively recurrent architectures, such as LSTM and RNN, might culminate in optimal outcomes for a solitary temporal increment. However, it's also arguable that the model introduced here can confidently compete at that single time step. When predictions are made over multiple time steps like that shown in Figures 4, and regardless of the amount of historical time sequence data used as input, the performance of the recurrent models (i.e., LSTM and RNN) declines significantly. The extent to which they are less accurate compared to the proposed model is quite substantial. There were some unexpected performances when the RNN was predicting 12 future time steps, and the LSTM was predicting 6-time steps. Even under these conditions, the proposed model achieved performance measures close to the best possible outcomes. The consistent performance of this model, either close to the best or the best, attests to its balance and robustness.

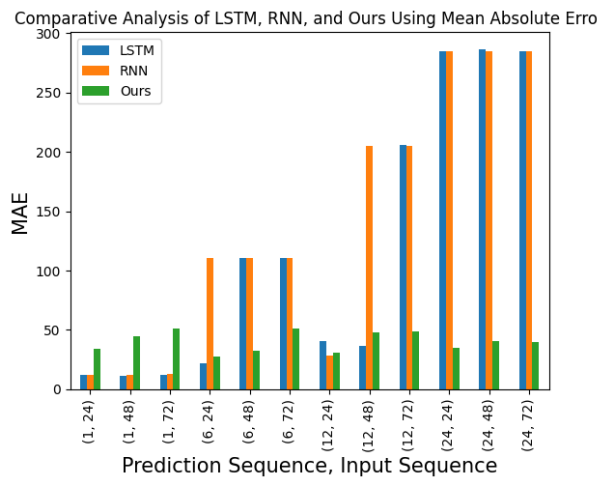


Figure 5 MAE Comparison

Table 1. Juxtaposition of Different Methods with 1 and 6 Prediction Steps.

Mthds	Pred. Steps	1			6			12			24		
		24	48	72	24	48	72	24	48	72	24	48	72
	Metric												
LSTM	RMSE	35.765	39.639	38.988	55.651	158.812	159.395	84.145	89.088	259.090	323.678	323.688	323.576
	MAE	11.719	11.400	11.699	21.768	110.315	110.644	40.773	36.344	206.024	284.396	286.481	284.912
	R-Sq.	0.988	0.985	0.986	0.971	0.735	0.733	0.932	0.926	0.345	0.032	0.031	0.032
RNN	RMSE	30.437	32.067	33.161	159.285	159.385	159.293	67.259	258.887	258.753	323.627	323.554	323.531
	MAE	12.195	12.0160	12.911	110.162	110.404	110.693	27.966	204.729	205.334	284.612	284.856	284.684
	R-Sq.	0.991	0.990	0.990	0.733	0.733	0.733	0.957	0.345	0.347	0.032	0.032	0.0319
Ours	RMSE	71.96	95.539	107.244	72.619	72.770	87.462	75.711	87.858	81.709	79.112	81.334	91.994
	MAE	33.81	44.961	51.358	27.406	32.155	51.358	30.793	47.847	48.853	35.018	40.539	39.420
	R-Sq.	0.952	0.915	0.893	0.951	0.951	0.928	0.946	0.928	0.938	0.941	0.938	0.921

Conclusion

This work suggested the application of an attention-fueled temporal convolutional network in conjunction with a convolutional neural network to predict global solar radiation (GSR). This approach is particularly effective when the accessible historical sequence of GSR spans durations of 24, 48, and 72 hours. We then compared the proposed model with other ML models used for GSR, including RNN and LSTM. The models were evaluated using RMSE, MAE, and R2 metrics. The empirical findings demonstrated that the suggested model exhibited superior performance compared to other models in most of the instances. Potential avenues for subsequent research could encompass broadening the temporal scope of the models to forecast one week or one month into the future and juxtaposing their performance with other established methodologies. Another direction is to investigate further feature generation and manipulation and to include other meteorological variables as input features for the models.

References

- [1] Makade, R.G., Chakrabarti, S., Jamil, B.: Development of global solar radiation models: A comprehensive review and statistical analysis for Indian regions. *Journal of Cleaner Production* 293, 126208 (2021) <https://doi.org/10.1016/j.jclepro.2021.126208>
- [2] Solano, E.S., Dehghanian, P., Affonso, C.M.: Solar radiation forecasting using machine learning and ensemble feature selection. *Energies* 15(19), 7049 (2022). <https://doi.org/10.3390/en15197049>
- [3] Ngiam, K.Y., Khor, W.: Big data and machine learning algorithms for health-care delivery. *The Lancet Oncology* 20(5), 262–273 (2019). [https://doi.org/10.1016/S1470-2045\(19\)30149-4](https://doi.org/10.1016/S1470-2045(19)30149-4)
- [4] Rehman, S., Mohandes, M.: Artificial neural network estimation of global solar radiation using air temperature and relative humidity. *Energy policy* 36(2), 571–576 (2008). <https://doi.org/10.1016/j.enpol.2007.09.033>
- [5] Ghimire, S., Nguyen-Huy, T., Prasad, R., Deo, R.C., Casillas-Perez, D., Salcedo-Sanz, S., Bhandari, B.: Hybrid convolutional neural network-multilayer perceptron model for solar radiation prediction. *Cognitive Computation* 15(2), 645–671 (2023). <https://doi.org/10.1007/s12559-022-10070-y>

- [6] Pang, Z., Niu, F., O'Neill, Z.: Solar radiation prediction using recurrent neural network and artificial neural network: A case study with comparisons. *Renewable Energy* 156, 279–289 (2020). <https://doi.org/10.1016/j.renene.2020.04.042>
- [7] Alizamir, M., Shiri, J., Fard, A.F., Kim, S., Gorgij, A.D., Heddam, S., Singh, V.P.: Improving the accuracy of daily solar radiation prediction by climatic data using an efficient hybrid deep learning model: Long short-term memory (lstm) network coupled with wavelet transform. *Engineering Applications of Artificial Intelligence* 123, 106199 (2023). <https://doi.org/10.1016/j.engappai.2023.106199>
- [8] Ali-Ou-Salah, H., Oukarfi, B., Bahani, K., Moujabbir, M.: A new hybrid model for hourly solar radiation forecasting using daily classification technique and machine learning algorithms. *Mathematical Problems in Engineering* 2021, 1–12 (2021). <https://doi.org/10.1155/2021/6692626>
- [9] Paoli, C., Voyant, C., Muselli, M., Nivet, M.-L.: Forecasting of preprocessed daily solar radiation time series using neural networks. *Solar energy* 84(12), 2146–2160 (2010). <https://doi.org/10.1016/j.solener.2010.08.011>
- [10] Xing, X., Li, Z., Xu, T., Shu, L., Hu, B., Xu, X.: Sae+ lstm: A new framework for emotion recognition from multi-channel eeg. *Frontiers in neurorobotics* 13, 37 (2019). <https://doi.org/10.3389/fnbot.2019.00037>
- [11] Ghimire, S., Deo, R.C., Wang, H., Al-Musaylh, M.S., Casillas-Perez, D., SalcedoSanz, S.: Stacked lstm sequence-to-sequence autoencoder with feature selection for daily solar radiation prediction: a review and new modeling results. *Energies* 15(3), 1061 (2022). <https://doi.org/10.3390/en15031061>
- [12] Liu, G., Guo, J.: Bidirectional lstm with attention mechanism and convolutional layer for text classification. *Neurocomputing* 337, 325–338 (2019). <https://doi.org/10.1016/j.neucom.2019.01.078>
- [13] Azizi, N., Yaghoubirad, M., Farajollahi, M., Ahmadi, A.: Deep learning based long-term global solar irradiance and temperature forecasting using time series with multi-step multivariate output. *Renewable Energy* 206, 135–147 (2023). <https://doi.org/10.1016/j.renene.2023.01.102>
- [14] Gugulothu, N., Tv, V., Malhotra, P., Vig, L., Agarwal, P., Shroff, G.: Predicting remaining useful life using time series embeddings based on recurrent neural networks. *arXiv preprint arXiv:1709.01073* (2017)
- [15] Vaswani, A., Shazeer, N., Parmar, N., Uszkoreit, J., Jones, L., Gomez, A.N., Kaiser, L., Polosukhin, I.: Attention is all you need. *Advances in neural information processing systems* 30 (2017)
- [16] Bai, S., Kolter, J.Z., Koltun, V.: An empirical evaluation of generic convolutional and recurrent networks for sequence modeling. *arXiv preprint arXiv:1803.01271* (2018)
- [17] He, K., Zhang, X., Ren, S., Sun, J.: Deep residual learning for image recognition. In: *Proceedings of the IEEE Conference on Computer Vision and Pattern Recognition*, pp. 770–778 (2016). <https://doi.org/10.1109/CVPR.2016.90>
- [18] Balabaeva, K., Kovalchuk, S.: Comparison of temporal and non-temporal features effect on machine learning models quality and interpretability for chronic heart failure patients. *Procedia Computer Science* 156, 87–96 (2019). <https://doi.org/10.1016/j.procs.2019.08.183>

Application of artificial intelligence (AI) in wind energy system with a case study

Fay ALZAHRANI^{1,a}, Feroz SHAIK^{1,b*}, Nayeemuddin MOHAMMED^{2,c},
Nasser Abdullah Shinoon AL-NA'ABI^{3,d}

¹Department of Mechanical Engineering, Prince Mohammad Bin Fahd University, Al Khobar, Kingdom of Saudi Arabia

²Department of Civil Engineering, Prince Mohammad Bin Fahd University, Al Khobar, Kingdom of Saudi Arabia

³Department of Mechanical Engineering, University of Technology and Applied Sciences, Sultanate of Oman

202000892@pmu.edu.sa^a; fshaik@pmu.edu.sa^b, mnayeemuddin@pmu.edu.sa^c;
nasser.alnaabi@utas.edu.om^d

Keywords: Wind Energy, Artificial Intelligence, Wind Turbine, Windmill, Genetic Algorithm, Wind Speed, Current Output

Abstract. Renewable energy is the fastest growing source of clean energy worldwide. The employment of wind energy is expected to increase dramatically over the next few years. There is a good source of wind power on the highways due to the movement of vehicles. A small windmill could utilize the wind power generated by passing vehicles and produce electricity that can power the lights on the highway. This paper presents the application of artificial intelligence to predict the current output from a small windmill placed on the highway. The results show a good concurrence between the experimental and predicted values.

Introduction

The main energy source is from fossil fuels, which is extensively used to meet the demand. The usage of fossil fuels directly harms the clean environment and also leads to global warming. Fossil fuels are non-renewable and get depleting, which makes people to focus on renewable energy sources. All over the world harnessing of solar and wind as a sustainable source of energy gained popularity to curtail the heavy dependency on fossil fuels and also to counter the global warming. When wind energy is used to produce electricity, less pollution from conventional power plants will be released into the environment. The need of concentrating on renewable energy resources has increased, particularly in the wake of the Gulf of Mexico oil leak and the Japanese nuclear accident. The installed wind energy capacity reached 196,630 MW globally in 2010, with 37,642 MW added in that year, according to the World Energy Association's report on wind energy for 2010. Enhancing wind farm design and layout; boosting wind turbine accessibility, dependability, and efficiency; streamlining the upkeep, assembly, and installation of offshore and onshore turbines and their substructures; showcasing massive wind turbine prototypes and expansive, interconnected wind farms, etc. are the main research areas that should be prioritized in the wind energy industry [1]. The first wind-powered generator was invented by Charles F. Brush, an electrical pioneer from America, and it produced energy in his backyard. He built a windmill that was 40 tons in weight and stood 60 feet tall. The actual wind mill measured 56 feet in diameter. The wind mill had a total of 144 separate blades. 500 revolutions per minute was the turbine's peak rotational speed. Everything in his basement was wired up to 408 batteries. With this technology, he was able to power his entire house, including the lab. Up until 1909, his wind mill operated for 20 years [2].

The wind turbine's size is determined by its intended use. Typically, tiny turbines have a power output between 20 and 100 kW. The 20- to 500-watt "micro" turbines are smaller and have a wider range of uses, including the charging of sailboat and recreational vehicle batteries. Water pumping is one use for turbines ranging from one to ten kW. Grain mills and water pumps have been powered by wind for millennia. While mechanical windmills remain a cost-effective and practical choice for water pumping in wind-free regions, farmers and ranchers are discovering that wind-electric pumping offers greater versatility and doubles the volume of water pumped for the same initial outlay. Furthermore, mechanical windmills have to be positioned straight above the well, which could not maximize the wind resources that are available. Electric cables can be used to link wind-electric pumping systems to the pump motor, which can be installed where the best wind resource is available. Depending on how much power you wish to create, household turbines can range in size from 400 watts to 100 kW (100 kW for extremely big loads). An average household consumes around 10,000 kWh (kilowatt-hours) of power year, or 830 kWh each month. To significantly meet this requirement, a wind turbine with a rating of between 5 and 15 kW would be needed, depending on the typical wind speed in the region. If the average yearly wind speed in the area is 14 miles per hour (6.26 meters per second), a 1.5 kW wind turbine can supply the energy needed for a house that uses 300 kWh per month. Automatic overspeed-governing mechanisms are included in most turbines, which prevent the rotor from spinning uncontrollably in extremely strong winds [3].

Harrous and Ahshan [4], [5] developed a hybrid solar/wind system for his home. The hybrid system consists of Bergey XL-1, a 1000-watt wind generator mounted on a tower 104 feet tall along with 300 watts of solar, which is a stand-alone system with batteries. The battery bank is a 220-amp system made up of eight 6-volt batteries wired as a 24-volt system. The system runs incandescent lights and a well pump at the barn, as well as water through heaters. The cost of the complete system was around \$ 10,000 including equipment, trenching for wires, building permit, etc. For wind energy uses, there must be open space or accessible coastlines for wind energy plants. Saudi Arabia is a large nation with extensive coastlines and open spaces. In the majority of these locations, the wind speed is sufficiently high to make using wind energy cost-effective. Saudi Arabian authorities will invest billions in this potential field of electricity since they understand the value of renewable energy, particularly wind energy. Despite its vast oil reserves, Saudi Arabia is very interested in actively participating in the development of new technologies for the exploitation and use of renewable energy sources. Despite Saudi Arabia's substantial wind resource potential, there are several obstacles to its development. These comprise the resource's erratic nature, its seasonal and diurnal fluctuations, its isolated geographic position, and the electrical grid infrastructure required to transfer wind energy to load regions. Significant technological obstacles must be overcome in order to fully utilize Saudi Arabia's wind potential. The energy balance between the needed load and the generated power, as well as the matching of the wind turbine and location with an appropriate economic position, remain a significant problem. By matching the locations and wind turbines, the researcher created an extensive computer program that does all the calculations and optimization needed to precisely build the Saudi Arabian wind energy system [6].

Eltamaly et al [7] built and examined the dynamic performance of a novel wind turbine producing system using a thyristor inverter. The system is basically based on shaft generators, which are highly reliable and produce high-quality power output and are frequently employed in big ships. It was looked into if this innovative method could provide low-distortion electric power at a steady frequency even when the natural wind's velocity fluctuated. Additionally, a dynamic model was created, and it was discovered to have good agreement with the system's experimental and simulated results. Zemamou et al [8] investigated the remarkable performance of savonius wind turbines and how they might be used as an alternative to normal wind turbines to extract

valuable energy from air streams. Some benefits of employing this kind of machine include its straightforward design, high starting and full operation moment, ability to receive wind from any direction, minimal noise and angular velocity when operating, and reduced wear on moving components. There have been many suggested modifications for this gadget over time. Another benefit of employing such a machine is the range of possible rotor designs. The performance of a Savonius rotor is impacted by each configuration. The performance of a Savonius rotor is influenced by air flow, geometric, and operational factors. For the majority of settings, the quoted range for the highest averaged power coefficient is between 0.05 and 0.30. The usage of stators has also been shown to result in performance increases of up to 50% for the tip speed ratio of the highest averaged power coefficient.

Renewable energy technologies affect how household power demands are met. Since most of the energy produced by fossil fuels is used in buildings and their unchecked use is linked to environmental risks, global warming, and the possibility of their depletion, it will be advantageous to replace the conventional energy generation system with renewable energy sources [9]. Globally, there is a growing need to transition from fossil fuels to renewable energy sources. The main causes of this transformation are the lack of fossil fuels and their detrimental consequences on the environment, particularly the climate. As a result, interest in renewable energy sources such as solar, wind, and wave energy is growing around the world [10]. Converters for multiphase generators, back-to-back linked converters, passive generator-side converters, and converters without an intermediary dc-link for high-power wind energy conversion systems (WECS) are all included in the low and medium voltage category. The series/parallel connection of wind turbine ac/dc output terminals and high voltage ac/dc gearbox are taken into consideration while evaluating the onshore and offshore wind farm layouts [11].

Artificial Intelligence (AI) in Wind Energy Systems

The majority of wind farms are situated in isolated areas or several miles offshore, thus it is vital to monitor their mechanical parts for maintenance in order to keep them from breaking down mechanically and perhaps cutting themselves off from the electricity grid [12]. Machine learning algorithms, particularly artificial neural network ANNs, are commonly used to process gathered data. The ANN's structure is inspired by real neurons, with basic processing units coupled by weighted linkages. It contains three major layers: input, concealed, and output. Furthermore, the number of hidden layers may be increased to construct the deep neural network (DNN) architecture [13]. The Artificial Neural Network (ANN), Backpropagation Neural Network (BPNN), Adaptive Neuro-Fuzzy Inference System (ANFIS), and Genetic Algorithm (GA) are some of the most often used and proven AI approaches. The level of technology today and potentially uses tried-and-true methods to create AI-powered renewable energy systems, particularly solar energy systems. To ascertain the state and progress of AI approaches in the field of renewable energy systems (RES), particularly solar power systems, a number of peer-reviewed journal publications were analyzed [14].

The physical methods forecast wind energy using meteorological data, such as topography, atmospheric pressure, and ambient temperature; the hybrid methods combine the advantages of multiple single forecasting models to obtain the final prediction results through various weighting strategies; and the intelligent methods process and optimize the integration of external and internal big data to estimate future wind energy. The statistical approaches anticipate wind energy time series by an assessment of the probability distribution and random process of the samples. Since intelligent approaches and AI-based hybrid methods are more efficient at analyzing the complex connections present in huge data sets, they are essential for increasing energy efficiency, decreasing energy usage, and allowing real-time decision-making in the wind energy business. [15].

Case Study

A small wind mill was fabricated using wind turbine mounted inside the tube, generator and a battery pack. The fabricated tubular wind mill was flexible and can withstand turbulence. The turbine inside the tube rotates in the direction of wind turbulence. Standard generator system was used which can deliver a power output of 1 kW along with a maintenance free battery pack, inverter and charge controller. Figure 1 shows the schematic diagram of the wind mill. Experimental data was recorded by keeping the wind mill on road side platform based on vehicular movements for 7 days. Duration of data recording on each day varies from 30 to 180 min.

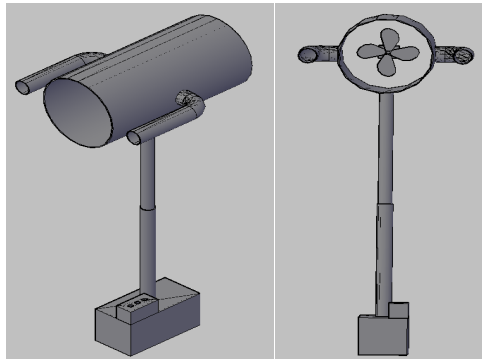


Fig 1. Schematic Diagram of Wind Mill

Artificial Neural Networks (ANN) use genetic algorithms that make use of adaptive heuristic search methods. A genetic algorithm is a better method for achieving the global optimum's convergence. Chromosome initialization is the first step in the genetic algorithm's operation, after which fitness is assessed using an objective function [16]. Chromosomes are genetically propagated by first selecting the most fit individuals and then using operators such as crossover and mutation. A multi-objective solution from the optimization toolkit and a genetic algorithm were used to optimize the process output variable models [17]. Ten neurons or nodes made up the hidden layer, the output current serving as the dependent output neuron, and time and wind speed serving as independent input variables were used to create the ANN network model [18]. Ten neurons made up the hidden layer of the neural network, which was trained until the mean squared error between the target and model output was as little as possible. The comparison between the goal values of the present output and the output values of the ANN network model is displayed in Figure 2 [19]. A high correlation coefficient value across training, validation, testing, and overall comparison shows that the model can accurately forecast the wind mill's current production value. The comparison output variables between the experimental investigations and the ANN-GA projected values are displayed in Table 1 [20], [21].

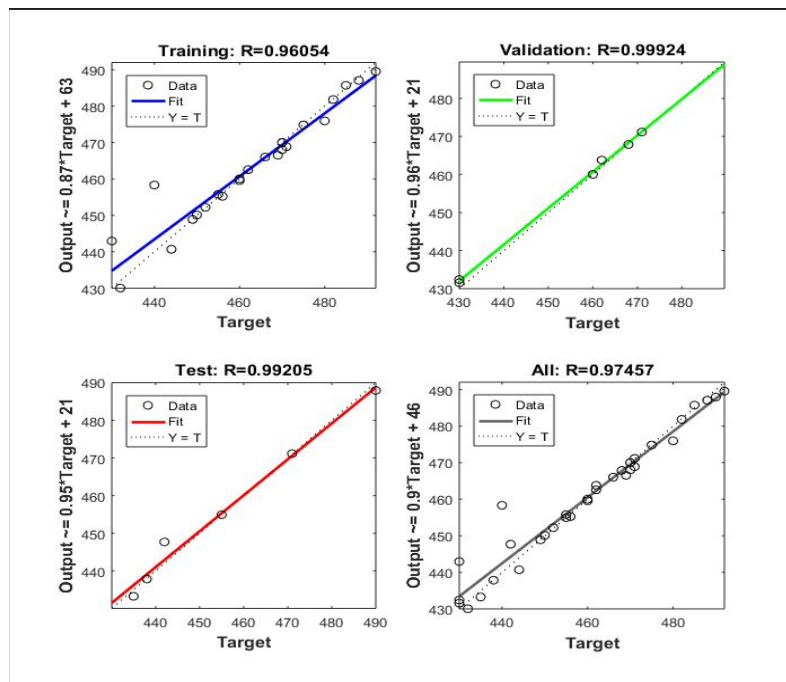


Fig 2. ANN network model output values and the target values of the current output

Table 1. Experimental data and ANN-GA (Genetic Algorithm) Predicted Data

Time	Wind Speed [m/s]	Current [Amp] (Experimental)	Current [Amp] (Predicted from ANN)
30	6.44	460	459.562
60	6.58	470	469.965
90	6.86	490	487.948
120	6.72	480	475.955
150	6.58	470	470.052
180	6.78	485	485.718
30	6.3	450	450.116
60	6.37	455	455.799
90	6.52	466	466.029
120	6.47	462	463.786
150	6.44	460	460.033
180	6.59	471	471.153
30	6.88	492	489.558
60	6.83	488	487.069
90	6.59	471	468.879
120	6.56	469	466.526

150	6.32	452	452.211
180	6.28	449	448.877
30	6.44	460	459.562
60	6.02	430	431.558
90	6.04	432	430.039
120	6.09	435	433.239
150	6.13	438	437.854
180	6.18	442	447.680
30	6.38	456	455.237
60	6.37	455	455.799
90	6.55	468	467.877
120	6.58	470	468.046
150	6.65	475	474.828
180	6.74	482	481.832
30	6.37	455	454.937
60	6.16	440	458.332
90	6.21	444	440.683
120	6.02	430	432.400
150	6.44	460	460.033
180	6.02	430	442.955
30	6.3	450	450.116
60	6.37	455	455.799
90	6.52	466	466.029
120	6.46	462	462.543
150	6.44	460	460.033
180	6.59	471	471.153

Results and Discussion

The simple design of rotor blades enhanced the wind velocity and thereby generate high currents. Artificial Intelligence (AI) methods, including machine learning and neural networks, have been used successfully to improve wind turbine performance and efficiency. The implementation of AI in wind energy systems has shown promising outcomes, as demonstrated by the case study done in this paper. The case study entailed gathering real-time data from a wind turbine and using AI models to forecast wind speed and direction, optimize turbine performance, and boost energy output. It was shown by the results that artificial intelligence (AI) may greatly raise the overall efficiency of wind energy systems, which will raise output and lower operating expenses. Additionally, by offering more precise forecasts and enhanced grid stability, AI can help with the better integration of wind energy into the system. In summary, this study shows how artificial

intelligence (AI) has the power to completely transform the wind energy industry, making it more dependable, effective, and sustainable.

Conclusions

A small fabricated windmill was used to measure the current out on a highway during vehicle movement. The experimental data for seven days at an interval of 30 min. The obtained data was used in Artificial Neural Network-Genetic Algorithm and training and testing. The ANN predicted values were found to be in good concurrence with the experimental data.

References

- [1] Y. Eroğlu and S. U. Seçkiner, "Wind farm layout optimization using particle filtering approach," *Renewable Energy*, vol. 58, pp. 95–107, Oct. 2013.
<https://doi.org/10.1016/j.renene.2013.02.019>
- [2] National Renewable Energy Laboratory (NREL), Golden, CO., "Small Wind Electric Systems: An Ohio Consumer's Guide," DOE/GO-102005-2077, 15016004, Mar. 2005.
<https://doi.org/10.2172/15016004>
- [3] T. J. Wenning and J. K. Kissock, "Methodology for Preliminary Assessment of Regional Wind Energy Potential," in *ASME 2009 3rd International Conference on Energy Sustainability, Volume 2*, San Francisco, California, USA: ASMEDC, Jan. 2009, pp. 1031–1040.
<https://doi.org/10.1115/ES2009-90469>
- [4] A. Harrouz, I. Colak, and K. Kayisli, "Control of a small wind turbine system application," in *2016 IEEE International Conference on Renewable Energy Research and Applications (ICRERA)*, Birmingham, United Kingdom: IEEE, Nov. 2016, pp. 1128–1133.
<https://doi.org/10.1109/ICRERA.2016.7884509>
- [5] R. Ahshan, A. Al-Badi, N. Hosseinzadeh, and M. Shafiq, "Small Wind Turbine Systems for Application in Oman," in *2018 5th International Conference on Electric Power and Energy Conversion Systems (EPECS)*, Kitakyushu, Japan: IEEE, Apr. 2018, pp. 1–6.
<https://doi.org/10.1109/EPECS.2018.8443520>
- [6] P. Rogowski, M. Rogowska, T. Smaz, and F. Grapow, "Small Wind Turbine Off-Grid Power Generation Optimization," in *2021 IEEE 4th International Conference on Renewable Energy and Power Engineering (REPE)*, Beijing, China: IEEE, Oct. 2021, pp. 355–359.
<https://doi.org/10.1109/REPE52765.2021.9617019>
- [7] A. M. Eltamaly, "Design and implementation of wind energy system in Saudi Arabia," *Renewable Energy*, vol. 60, pp. 42–52, Dec. 2013. <https://doi.org/10.1016/j.renene.2013.04.006>
- [8] M. Zemamou, M. Aggour, and A. Toumi, "Review of savonius wind turbine design and performance," *Energy Procedia*, vol. 141, pp. 383–388, Dec. 2017.
<https://doi.org/10.1016/j.egypro.2017.11.047>
- [9] S. Vahdatpour, S. Behzadfar, L. Siampour, E. Veisi, and M. Jahangiri, "Evaluation of Off-grid Hybrid Renewable Systems in the Four Climate Regions of Iran," *JREE*, vol. 4, no. 1, Feb. 2017. <https://doi.org/10.30501/jree.2017.70107>
- [10] M. Abdulateef Mostafa, E. A. El-Hay, and M. M. ELkholy, "Recent Trends in Wind Energy Conversion System with Grid Integration Based on Soft Computing Methods: Comprehensive Review, Comparisons and Insights," *Arch Computat Methods Eng*, vol. 30, no. 3, pp. 1439–1478, Apr. 2023. <https://doi.org/10.1007/s11831-022-09842-4>
- [11] V. Yaramasu, B. Wu, P. C. Sen, S. Kouro, and M. Narimani, "High-power wind energy conversion systems: State-of-the-art and emerging technologies," *Proc. IEEE*, vol. 103, no. 5, pp. 740–788, May 2015. <https://doi.org/10.1109/JPROC.2014.2378692>

- [12] N. O. Farrar, M. H. Ali, and D. Dasgupta, "Artificial Intelligence and Machine Learning in Grid Connected Wind Turbine Control Systems: A Comprehensive Review," *Energies*, vol. 16, no. 3, p. 1530, Feb. 2023. <https://doi.org/10.3390/en16031530>
- [13] F. Elyasichamazkoti and A. Khajehpoor, "Application of machine learning for wind energy from design to energy-Water nexus: A Survey," *Energy Nexus*, vol. 2, p. 100011, Dec. 2021. <https://doi.org/10.1016/j.nexus.2021.100011>
- [14] J. T. Dellosa and E. C. Palconit, "Artificial Intelligence (AI) in Renewable Energy Systems: A Condensed Review of its Applications and Techniques," in *2021 IEEE International Conference on Environment and Electrical Engineering and 2021 IEEE Industrial and Commercial Power Systems Europe (EEEIC / I&CPS Europe)*, Bari, Italy: IEEE, Sep. 2021, pp. 1–6. <https://doi.org/10.1109/EEEIC/ICPSEurope51590.2021.9584587>
- [15] E. Zhao, S. Sun, and S. Wang, "New developments in wind energy forecasting with artificial intelligence and big data: a scientometric insight," *Data Science and Management*, vol. 5, no. 2, pp. 84–95, Jun. 2022. <https://doi.org/10.1016/j.dsm.2022.05.002>
- [16] N. Mohammed, P. Palaniandy, and F. Shaik, "Pollutants removal from saline water by solar photocatalysis: a review of experimental and theoretical approaches," *International Journal of Environmental Analytical Chemistry*, vol. 103, no. 16, pp. 4155–4175, Dec. 2023. <https://doi.org/10.1080/03067319.2021.1924160>
- [17] N. Mohammed, A. Asiz, M. A. Khasawneh, H. Mewada, and T. Sultana, "Machine learning and RSM-CCD analysis of green concrete made from waste water plastic bottle caps: Towards performance and optimization," *Mechanics of Advanced Materials and Structures*, pp. 1–9, Aug. 2023. <https://doi.org/10.1080/15376494.2023.2238220>
- [18] N. Mohammed, P. Palaniandy, F. Shaik, and H. Mewada, "Experimental and computational analysis for optimization of seawater biodegradability using photo catalysis," *IIUMEJ*, vol. 24, no. 2, pp. 11–33, Jul. 2023. <https://doi.org/10.31436/IIUMEJ.v24i2.2650>
- [19] N. Mohammed, P. Palaniandy, F. Shaik, H. Mewada, and D. Balakrishnan, "Comparative studies of RSM Box-Behnken and ANN-Anfis fuzzy statistical analysis for seawater biodegradability using TiO₂ photocatalyst," *Chemosphere*, vol. 314, p. 137665, Feb. 2023. <https://doi.org/10.1016/j.chemosphere.2022.137665>
- [20] N. Mohammed, P. Palaniandy, F. Shaik, B. Deepanraj, and H. Mewada, "Statistical analysis by using soft computing methods for seawater biodegradability using ZnO photocatalyst," *Environmental Research*, vol. 227, p. 115696, Jun. 2023. <https://doi.org/10.1016/j.envres.2023.115696>
- [21] N. Mohammed, P. Palaniandy, F. Shaik, and H. Mewada, "Statistical Modelling of Solar Photocatalytic Biodegradability of Seawater Using Combined Photocatalysts," *J. Inst. Eng. India Ser. E*, Sep. 2023. <https://doi.org/10.1007/s40034-023-00274-8>

Prediction of distillate output in photocatalytic solar still using artificial intelligence (AI)

Reyoud ALQAHTANI^{1,a}, Feroz SHAIK^{1,b*}, Nayeemuddin MOHAMMED^{2,c},
Mohammad Ali KHASAWNEH^{2,d}, Tasneem SULTANA^{3,e}

¹Department of Mechanical Engineering, Prince Mohammad Bin Fahd University, Al Khobar,
Kingdom of Saudi Arabia

²Department of Civil Engineering, Prince Mohammad Bin Fahd University, Al Khobar, Kingdom
of Saudi Arabia

³Artificial Intelligence and Machine Learning, Godutai Engineering College for Women,
Sharnbasva University, Kalaburagi, India

202000155@pmu.edu.sa^a; fshaik@pmu.edu.sa^{b*}, mnayeemuddin@pmu.edu.sa^c;
mkhasawneh@pmu.edu.sa^d, tasneemsultana841@gmail.com^e

Keywords: Solar Still, Photocatalytic, Artificial Intelligence, Distillate, Desalination

Abstract. Solar desalination is widely employed technology to separate potable water from saline water. In this study a solar still with one slope was employed to desalinate the saline water. The bottom plate of the solar still was coated with titanium dioxide to improve its performance. The distillate output was collected at three depths of water level in the still for different time intervals. Artificial Intelligence-Levenberg Marquardt (AI-LM) method was employed to predict the distillate output. The predicted values for the response were found to be in good agreement ($R^2 = 0.997$) with the experimental data.

Introduction

Water is one of the most abundant resources on Earth since it is necessary for human activity and all ecosystems. As the population grows, so does the demand for drinkable water. Large amounts of fresh water are required in every corner of the world for agricultural, industrial, and household purposes [1]. Oceans are a large supply of water, but they are not suitable for human consumption due to their salt [2]. Several writers reported on research in the field of solar desalination, which is the most prominent and cost-effective method, requiring simple technology and maintenance [3]. A single slope solar still is one of the best solar desalination devices, and numerous efforts are being made to improve its productivity [4].

The light absorber's evaporation efficiency remained practically unchanged after thirty cycles of evaporation and condensation. The photothermal layer's excellent light-harvesting properties, its ability to withstand heat, and the substrate's abundance of open channels allow for the system's exceptional photothermal performance for long-term solar desalination [5]. As the contact period extended up to six hours, the salt content progressively reduced by more than 25%. There is no discernible shift in the water's pH has occurred. Salinity in seawater can be efficiently decreased by the hybrid titanium di oxide (TiO_2) [6]. The combined photocatalytic and photothermal system has a high solar energy utilization efficiency and may be used to clean wastewater and produce potable water in one unit [7]. The cost of generating water using solar-based desalination techniques remains greater than that of typical fossil-fuel-based desalination facilities, owing mostly to the high cost of solar collectors. This is one of the primary issues limiting commercialization rates. Residue removal may be expensive in terms of water use and have unfavorable consequences on the environment [8].



Due to the synergistic impact of Polydopamine (PDA) / TiO₂ nanoparticles, the Janus evaporator can breakdown over 95% of organic dyes (such as Congo red and trypan blue) and efficiently desalinate and purify other unusual water sources. Potential uses for this Janus structured hydrogel evaporator include desalination and wastewater treatment [9]. The most intriguing aspect is that the solar-driven photothermal effect may potentially be used by a number of other water purification technologies [10]. With the help of an efficient monolithic material platform and a straightforward, reusable, portable, and reasonably priced solar thermal water purification system, water filtration for a range of environmental conditions is revolutionized [11].

Under the sun (i.e., 1 kW m⁻²), the TiO₂-CuO-Cufoam evaporator concurrently exhibits high solar evaporation efficiency of 86.6% and efficiency of 80.0% for the elimination of volatile organic compounds (VOCs) [12]. The photocatalytic hydrogen generation process is a straightforward and economical technique used to produce solar hydrogen by imitating artificial photosynthesis [13]. The traditional method of desalination using passive solar stills relies solely on sun radiation as a source of thermal energy [14]. Seawater desalination by membrane distillation is believed to be attainable by the direct joule heating of the water-hydrophobic membrane interface utilizing a porous thin-film carbon nanotube [15].

Artificial Intelligence-Levenberg Marquardt (AI-LM) in Solar Still Systems

An artificial neural network (ANN) was created to investigate the role of the photocatalyst in the desalination process and supply the quantity of distillate needed for solar photocatalytic modelling. Water is produced via desalination for a variety of uses, including home usage, industrial processing, and water delivery [16]. Desalination methods most commonly used include membrane processes Reverse Osmosis (RO) or thermal desalination [17]. Three data sets training, validation, and test were created using the Fujairah sea water reverse osmosis (SWRO) plant's one-year operating data ($n = 200$) in order to create the ANN model. Good agreement was produced between the simulated and observed data in the test data set by the trained ANN model (TDS: $R^2 = 0.96$; flow rate: $R^2 = 0.75$) [18].

Reverse/Back propagation radial basis function (RBF) neural networks and a multilayer perception (MLPs) trained with the Rprop approach are used to forecast pH values. When the created models were compared to the linear regression methodology, it was found that the MLP and RBF neural network forecasts outperformed those of the conventional methods [19]. An effective method for handling complex and stochastic systems that only accept time series data as input variables and don't fully comprehend physical or hydrogeological components is the artificial neural network (ANN) [20]. With the Nash-Sutcliffe efficiency coefficient of 0.964, the correlation coefficient of 0.983, and the root mean square error of 1.052 km², the integrated model showed that this approach effectively reproduced static integrated analysis (SIA) variations [21]. Moreover, the ANN algorithm's performance was assessed in October 1999, during a super storm over the Bay of Bengal [22].

Al-Ghamdi et al., assess the effectiveness of ANNs for short-term water demand forecasting in Jeddah, Saudi Arabia, using a variety of normalization techniques (min-max, z-score, decimal, median, and Median Absolute Deviation (MAD) [23]. The ANN approach has been used to the calibration of an industrial prototype microwave six-port equipment, yielding great accuracy across a broad dynamic range [24] and [25]. Freshwater shortage is a major global concern due to the dramatic increase in demand for freshwater for drinking and personal use that has occurred as a result of population growth. The usefulness of machine learning in forecasting the performance of solar stills has been updated to the point where it is now a central component of numerous studies. Regardless of the size of the dataset, multiple regression models can display a moderate level of prediction accuracy. As opposed to multiple regression models, ANN (Artificial Neural Network) models have an accuracy that is greater and are influenced by dataset sizes ranging from 100 to 400. The models varied in terms of prediction accuracy. Support vector machines, artificial

neural networks (ANNs), back-propagation ANNs, and random forests based on Bayesian optimization demonstrated strong prediction ability for hemispheric, inched, tubular, double-slope, and single-slope SSs, respectively. Several models were tested to anticipate thermal efficiency; the highest accurate prediction was produced at six input neurons using an ANN in combination with the Imperialist Competition Algorithm, with an RMSE (root mean square error) of 1.3673 [26].

To anticipate the solar still performance characteristics, a back propagation artificial neural network model was created. For the purpose of predicting solar still performance, the applicability and efficacy of artificial neural networks (ANNs) considering a number of operational and meteorological factors have been assessed. The five input variables pertaining to weather conditions were air temperature (T_o), relative humidity (RH), wind speed (U), solar radiation (Rs), and ultraviolet index (UVI); the four variables pertaining to system operational conditions were brine temperature, feed water temperature, total dissolved solids of brine (TDSB), and brine temperature. The last variable was the number of days, or Julian day (J). Testing and validation processes utilizing statistical criteria indicate that the created artificial neural network (ANN) model may provide extremely high efficiency results, confirming its usability and usefulness in solar desalination prediction. These results bolster the hypothesis that the built artificial neural network (ANN) model correctly anticipated the performance parameters of the solar still.

The primary advantage of the artificial neural network (ANN) model for solar desalination performance prediction is its ease of use, since it can be implemented with ease using any spreadsheet or computer language. The ANN model produced the contribution ratio, which shows how each input variable affects the outputs. In the ANN model for MD and gth prediction, TF is the input parameter with the highest contribution ratio. However, when it comes to objective response rate (ORR) prediction, ultra violet index (UVI) has the biggest contribution ratio. The study also demonstrated the usefulness and effectiveness of artificial neural networks (ANNs), which can forecast solar still performance without the need for additional trials and may result in time, effort, and resource savings [27].

Artificial neural networks, or ANNs, are sophisticated mathematical representations of the nervous system of humans. Over the last three decades, there has been a noticeable surge in the use of artificial neural networks (ANNs) for problem classification, pattern recognition, regression, and forecasting. The input layer, which is the initial layer in a multilayer perception (MLP) architecture, provides input variables to the network. The layers that are located between the input and output levels are known as hidden layers, and the output layer is the last layer. One of the most popular FFNNs is the multilayer perceptron (MLP) neural network. In multilevel perception (MLP), the unidirectional connections between neurons are represented by weights, which are the actual numbers present in the interval [28].

A thorough analysis of recent advancements using Nano/micro materials in solar stills is given. The majority of current efforts have focused on enhancing solar evaporation, which is only one of the fundamental processes in a solar still. To increase the system's productivity and efficiency, a variety of materials were used, including paper-based film, synthetic aerogel, and natural biomaterials. When combined with optimum thermal design and heat localization at the air-water interface, suitable materials can potentially attain an efficiency of over 90% when exposed to 1 kw/m² of solar energy. However, even with the application of these materials, productivity is still low. This demonstrates how different solar evaporation systems are from sun stills [30].

Case Study

The still was filled with saline water and exposed to natural sunlight. Three different levels of water were considered and at each level the distillate output was measured for various time intervals. The bottom plate of the still was coated with photocatalyst (Titanium dioxide) to enhance the performance of the still. Figure 1 displays the schematic diagram for the still.

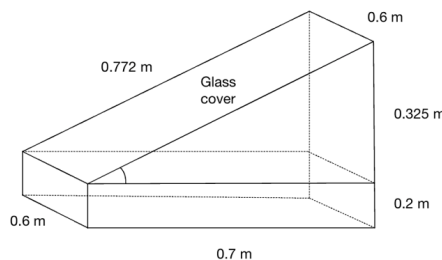


Fig 1. Schematic Diagram of Solar Still

The experimental data was utilized to test, train and predict the distillate output using ANN-LM algorithm. The Levenberg-Marquardt algorithm (LM) and damped least squares (DLS) approach were utilized in MATLAB R2023 by Math Works, Inc. to optimize the input variables [31]. A MATLAB tool called the Artificial Neural Network is used to computationally model data variables in order to investigate the links between input and output in systems or processes [32]. The size of the network is similar to the number of neurons in the brains of living beings that enable intelligent behavior. It consists of input nodes for the input independent variables of the experimental data and output nodes for the factors or dependent variables of the response [33]. S neurons, multilayer neural networks, and a multi-layer network with R input components were all used in the current optimization technique. Three subsets of the data were used, comprising of 70%, 15%, and 15% of the total [34]. Two subsets are utilized for testing and validation, and the first subset is used for training. The distillation target values and model output are displayed in Figure 2. The comparison of the experimental and expected values is displayed in Table 1.

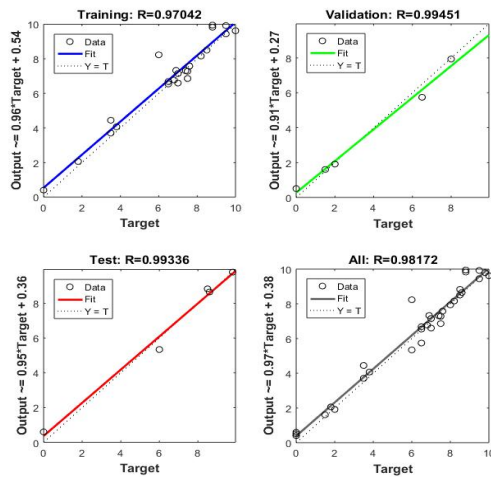


Fig 2. ANN network model output values and the target values of distillate still

Table 1. Experimental and ANN-LM Predicted Data

Depth, m	Time, hours	Solar Radiation W/m ²	Amount of Distillate m ³	Prediction
0.0333	8	500	0	0.00000402
0.0333	9	727	0.000015	0.00001605
0.0333	10	932	0.000035	0.00003705
0.0333	11	1045	0.00006	0.00005340
0.0333	12	1136	0.000065	0.00006545
0.0333	13	1114	0.00008	0.00007937

0.0333	14	1023	0.000095	0.00009445
0.0333	15	886	0.000085	0.00008508
0.0333	16	682	0.000075	0.00006860
0.0333	17	409	0.00007	0.00007149
0.0333	18	200	0.00006	0.00008233
0.025	8	500	0	0.00000509
0.025	9	727	0.00002	0.00001913
0.025	10	932	0.000038	0.00004068
0.025	11	1045	0.000065	0.00005742
0.025	12	1136	0.000075	0.00007279
0.025	13	1114	0.000085	0.00008831
0.025	14	1023	0.000098	0.00009792
0.025	15	886	0.000088	0.00009828
0.025	16	682	0.000076	0.00007577
0.025	17	409	0.00007	0.00006599
0.025	18	200	0.000065	0.00006684
0.0133	8	500	0	0.00000598
0.0133	9	727	0.000018	0.00002056
0.0133	10	932	0.000035	0.00004447
0.0133	11	1045	0.000068	0.00006771
0.0133	12	1136	0.000086	0.00008650
0.0133	13	1114	0.0001	0.00009622
0.0133	14	1023	0.000095	0.00009924
0.0133	15	886	0.000088	0.00009948
0.0133	16	682	0.000082	0.00008161
0.0133	17	409	0.000074	0.00007310
0.0133	18	200	0.000069	0.00007328

Results and Discussion

The use of Artificial Intelligence (AI) Levenberg Marquardt method in predicting the distillate output for a photocatalytic solar still has yielded promising results. The AI models, including machine learning algorithms and neural networks, demonstrated high accuracy in forecasting distillate output based on various input parameters such as time and solar radiation. These models were able to effectively capture the complex relationships between these factors and distillate output, leading to precise predictions. The application of AI in this context offers several advantages, including improved operational efficiency, better planning of distillation processes, and enhanced performance of photocatalytic solar stills.

Conclusion

Solar photocatalytic still was employed to desalinate the saline water. The output distillate was collected at three depths of water levels for various time intervals. The experimental data was utilized to train, test and predict the distillate output using artificial neural network-Levenberg Marquardt ANN-LM algorithm. The expected values and the experimental values were found to be in good agreement for the response with an average of $R^2 = 0.997$.

References

- [1] N. Mohammed, P. Palaniandy, F. Shaik, and H. Mewada, "Statistical Modelling of Solar Photocatalytic Biodegradability of Seawater Using Combined Photocatalysts," *J. Inst. Eng. India Ser. E*, Sep. 2023. <https://doi.org/10.1007/s40034-023-00274-8>
- [2] N. Mohammed, P. Palaniandy, F. Shaik, H. Mewada, and D. Balakrishnan, "Comparative studies of RSM Box-Behnken and ANN-Anfis fuzzy statistical analysis for seawater biodegradability using TiO₂ photocatalyst," *Chemosphere*, vol. 314, p. 137665, Feb. 2023. <https://doi.org/10.1016/j.chemosphere.2022.137665>
- [3] F. Shaik, S. S. R. Al Siyabi, N. Mohammed, and M. Eltayeb, "Assessment of ground and surface water quality and its contamination," *International Journal of Environmental Analytical Chemistry*, vol. 103, no. 6, pp. 1449–1467, May 2023. <https://doi.org/10.1080/03067319.2021.1873975>
- [4] N. Mohammed, P. Palaniandy, F. Shaik, and H. Mewada, "EXPERIMENTAL AND COMPUTATIONAL ANALYSIS FOR OPTIMIZATION OF SEAWATER BIODEGRADABILITY USING PHOTO CATALYSIS," *IJUMEJ*, vol. 24, no. 2, pp. 11–33, Jul. 2023. <https://doi.org/10.31436/ijumej.v24i2.2650>
- [5] M. Shafaee, E. K. Goharshadi, M. M. Ghafurian, M. Mohammadi, and H. Behnejad, "A highly efficient and sustainable photoabsorber in solar-driven seawater desalination and wastewater purification," *RSC Adv.*, vol. 13, no. 26, pp. 17935–17946, 2023. <https://doi.org/10.1039/D3RA01938A>
- [6] R. Isha and N. H. Abd Majid, "A Potential Hybrid TiO₂ in Photocatalytic Seawater Desalination," *AMR*, vol. 1113, pp. 3–8, Jul. 2015. <https://doi.org/10.4028/www.scientific.net/AMR.1113.3>
- [7] L. Shi *et al.*, "An Integrated Photocatalytic and Photothermal Process for Solar-Driven Efficient Purification of Complex Contaminated Water," *Energy Tech*, vol. 8, no. 9, p. 2000456, Sep. 2020. <https://doi.org/10.1002/ente.202000456>
- [8] Y. Zhang, M. Sivakumar, S. Yang, K. Enever, and M. Ramezanianpour, "Application of solar energy in water treatment processes: A review," *Desalination*, vol. 428, pp. 116–145, Feb. 2018. <https://doi.org/10.1016/j.desal.2017.11.020>
- [9] J. Wen *et al.*, "Architecting Janus hydrogel evaporator with polydopamine-TiO₂ photocatalyst for high-efficient solar desalination and purification," *Separation and Purification Technology*, vol. 304, p. 122403, Jan. 2023. <https://doi.org/10.1016/j.seppur.2022.122403>
- [10] Y. Lu, H. Zhang, D. Fan, Z. Chen, and X. Yang, "Coupling solar-driven photothermal effect into photocatalysis for sustainable water treatment," *Journal of Hazardous Materials*, vol. 423, p. 127128, Feb. 2022. <https://doi.org/10.1016/j.jhazmat.2021.127128>
- [11] Y. Yang *et al.*, "Graphene-Based Standalone Solar Energy Converter for Water Desalination and Purification," *ACS Nano*, vol. 12, no. 1, pp. 829–835, Jan. 2018. <https://doi.org/10.1021/acsnano.7b08196>
- [12] Y. Tian *et al.*, "High-performance water purification and desalination by solar-driven interfacial evaporation and photocatalytic VOC decomposition enabled by hierarchical TiO₂-CuO nanoarchitecture," *Intl J of Energy Research*, vol. 46, no. 2, pp. 1313–1326, Feb. 2022. <https://doi.org/10.1002/er.7249>
- [13] M. S. Yesupatham *et al.*, "Photocatalytic seawater splitting for hydrogen fuel production: impact of seawater components and accelerating reagents on the overall performance," *Sustainable Energy Fuels*, vol. 7, no. 19, pp. 4727–4757, 2023. <https://doi.org/10.1039/D3SE00810J>

- [14] R. Djellabi *et al.*, "Recent advances and challenges of emerging solar-driven steam and the contribution of photocatalytic effect," *Chemical Engineering Journal*, vol. 431, p. 134024, Mar. 2022. <https://doi.org/10.1016/j.cej.2021.134024>
- [15] M. Fujiwara and M. Kikuchi, "Solar desalination of seawater using double-dye-modified PTFE membrane," *Water Research*, vol. 127, pp. 96–103, Dec. 2017. <https://doi.org/10.1016/j.watres.2017.10.015>
- [16] N. Mohammed, A. Asiz, M. A. Khasawneh, H. Mewada, and T. Sultana, "Machine learning and RSM-CCD analysis of green concrete made from waste water plastic bottle caps: Towards performance and optimization," *Mechanics of Advanced Materials and Structures*, pp. 1–9, Aug. 2023. <https://doi.org/10.1080/15376494.2023.2238220>
- [17] N. Mohammed, P. Palaniandy, and F. Shaik, "Pollutants removal from saline water by solar photocatalysis: a review of experimental and theoretical approaches," *International Journal of Environmental Analytical Chemistry*, vol. 103, no. 16, pp. 4155–4175, Dec. 2023. <https://doi.org/10.1080/03067319.2021.1924160>
- [18] Y. G. Lee *et al.*, "Artificial neural network model for optimizing operation of a seawater reverse osmosis desalination plant," *Desalination*, vol. 247, no. 1–3, pp. 180–189, Oct. 2009. <https://doi.org/10.1016/j.desal.2008.12.023>
- [19] H. Adel Zaqoot, A. Baloch, A. Khalique Ansari, and M. Ali Unar, "APPLICATION OF ARTIFICIAL NEURAL NETWORKS FOR PREDICTING pH IN SEAWATER ALONG GAZA BEACH," *Applied Artificial Intelligence*, vol. 24, no. 7, pp. 667–679, Aug. 2010. <https://doi.org/10.1080/08839514.2010.499499>
- [20] S. Al Ajmi, M. Ali Syed, F. Shaik, M. Nayeemuddin, D. Balakrishnan, and V. R. Myneni, "Treatment of Industrial Saline Wastewater Using Eco-Friendly Adsorbents," *Journal of Chemistry*, vol. 2023, pp. 1–11, Apr. 2023. <https://doi.org/10.1155/2023/7366941>
- [21] D. Li *et al.*, "Simulation of Seawater Intrusion Area Using Feedforward Neural Network in Longkou, China," *Water*, vol. 12, no. 8, p. 2107, Jul. 2020. <https://doi.org/10.3390/w12082107>
- [22] B. Jena, D. Swain, and A. Tyagi, "Application of Artificial Neural Networks for Sea-Surface Wind-Speed Retrieval From IRS-P4 (MSMR) Brightness Temperature," *IEEE Geosci. Remote Sensing Lett.*, vol. 7, no. 3, pp. 567–571, Jul. 2010. <https://doi.org/10.1109/LGRS.2010.2041632>
- [23] A.-B. Al-Ghamdi, S. Kamel, and M. Khayyat, "Evaluation of Artificial Neural Networks Performance Using Various Normalization Methods for Water Demand Forecasting," in *2021 National Computing Colleges Conference (NCCC)*, Taif, Saudi Arabia: IEEE, Mar. 2021, pp. 1–6. <https://doi.org/10.1109/NCCC49330.2021.9428856>
- [24] Yi Liu, "Calibrating an industrial microwave six-port instrument using the artificial neural network technique," *IEEE Trans. Instrum. Meas.*, vol. 45, no. 2, pp. 651–656, Apr. 1996. <https://doi.org/10.1109/19.492804>
- [25] N. N, A. Siva Kumaran K, A. A, A. V. S, and B. M. J, "Convolutional Neural Networks (CNN) based Marine Species Identification," in *2022 International Conference on Automation, Computing and Renewable Systems (ICACRS)*, Pudukkottai, India: IEEE, Dec. 2022, pp. 602–607. <https://doi.org/10.1109/ICACRS55517.2022.10029109>
- [26] A. F. Mashaly, A. A. Alazba, A. M. Al-Awaadh, and M. A. Mattar, "Predictive model for assessing and optimizing solar still performance using artificial neural network under hyper arid environment," *Solar Energy*, vol. 118, pp. 41–58, Aug. 2015. <https://doi.org/10.1016/j.solener.2015.05.013>

- [27] F. A. Essa, M. Abd Elaziz, and A. H. Elsheikh, "An enhanced productivity prediction model of active solar still using artificial neural network and Harris Hawks optimizer," *Applied Thermal Engineering*, vol. 170, p. 115020, Apr. 2020.
<https://doi.org/10.1016/j.applthermaleng.2020.115020>
- [28] A. O. Alsaiari, E. B. Moustafa, H. Alhumade, H. Abulkhair, and A. Elsheikh, "A coupled artificial neural network with artificial rabbits optimizer for predicting water productivity of different designs of solar stills," *Advances in Engineering Software*, vol. 175, p. 103315, Jan. 2023. <https://doi.org/10.1016/j.advengsoft.2022.103315>
- [29] G. Peng *et al.*, "Micro/nanomaterials for improving solar still and solar evaporation -- A review." arXiv, Jun. 20, 2019. <https://doi.org/10.48550/arXiv.1906.08461>
- [30] G. Peng *et al.*, "Potential and challenges of improving solar still by micro/nano-particles and porous materials - A review," *Journal of Cleaner Production*, vol. 311, p. 127432, Aug. 2021. <https://doi.org/10.1016/j.jclepro.2021.127432>
- [31] N. Mohammed, P. Palaniandy, and F. Shaik, "Optimization of solar photocatalytic biodegradability of seawater using statistical modelling," *Journal of the Indian Chemical Society*, vol. 98, no. 12, p. 100240, Dec. 2021. <https://doi.org/10.1016/j.jics.2021.100240>
- [32] N. Mohammed, P. Palaniandy, F. Shaik, B. Deepanraj, and H. Mewada, "Statistical analysis by using soft computing methods for seawater biodegradability using ZnO photocatalyst," *Environmental Research*, vol. 227, p. 115696, Jun. 2023.
<https://doi.org/10.1016/j.envres.2023.115696>
- [33] N. Mohammed, P. Palaniandy, and F. Shaik, "Solar photocatalytic biodegradability of saline water: Optimization using RSM and ANN," *AIP Conference Proceedings*, vol. 2463, no. 1, p. 020027, May 2022. <https://doi.org/10.1063/5.0080297>
- [34] N. Mohammed, P. Palaniandy, and F. Shaik, "Advanced Oxidation Processes for the Treatment of Pollutants from Saline Water," *Removal of Pollutants from Saline Water: Treatment Technologies*, p. 95, 2021.

Power systems stability of high penetration of renewable energy generations

Ahmad HARB^{1,a*}, Hamza NAWAFLEH^{2,b}

¹ German Jordanian University, Amman-Jordan

²University of Wisconsin Milwaukee, USA

^aahmad.harb@gju.edu.jo, ^bAlnawf2@uwm.edu

Keywords: Power Systems Stability, Renewable Energy, Impacts of Renewable Energy on Power Systems

Abstract. In this Paper a comprehensive analysis of the Jordanian Power Grid (JPG)'s stability under various practical scenarios, including load disturbances and the integration of Renewable Energy Sources (RES). A key focus of the study is the impact of RES on the stability of the JPG, especially during unexpected disturbances. The findings reveal a notable trend: higher RES integration tends to decrease the grid's stability under certain conditions. Additionally, the report explores the effects of interconnecting the JPG with neighboring countries, such as Egypt. This connection is shown to potentially enhance the JPG's stability, both with and without the involvement of RES. The report delves into numerous cases, providing detailed discussions and insights. The conclusions drawn emphasize the critical importance of carefully managing the proportion of RES in the JPG to maintain its stability against various disturbances. This study offers valuable recommendations for future strategies to ensure the robustness and reliability of the Jordanian Power Grid in the face of evolving energy landscapes.

Introduction

The Hashemite Kingdom of Jordan is significantly reliant on foreign energy sources, with an import ratio of approximately 92% [1]. The country's energy demand is on the rise, spurred by factors such as population growth and the influx of refugees from neighboring regions. Jordan faces substantial challenges in meeting its electricity needs due to limited local fossil fuel resources, inadequate conversion capacities, and the financial constraints of its energy sector. Renewable Energy Sources (RES) have emerged as a pivotal solution for Jordan, offering a means to secure electricity supply while protecting the environment [2–4]. The nation's abundant solar and wind resources make this a particularly viable option. While RES contributes to reducing emissions and enhancing supply security, they also introduce greater uncertainty and variability in the transmission and distribution of power [5 - 7]. This dynamic has been complicated by the current economic impracticality of large-scale energy storage, which exacerbates the challenge of balancing generation with real-time demand. Moreover, while Distributed Generation curtails losses associated with electricity transport and transformation, it adds complexity to the system, necessitating advanced, research-based solutions [8 - 10].

Globally, there is a growing interest in transitioning to RES, and Jordan has made significant strides in this direction. Over the past decade, approximately 3500 MW of RES has been integrated into the Jordanian Power Grid (JPG), accounting for 30% of total generation as of 2022 [8 - 10]. However, this increased reliance on RES presents operational challenges for the JPG. The main objective of this research is to investigate the effects of integrating large-scale renewable energy sources on the transient behavior and sustainability of the JPG. Utilizing the Power analysis program DIGSILENT, along with current system steady-state and dynamic models, this study will focus on the impacts of RES integration on JPG's voltage profile, sustainability, and overall

stability. The analysis will shed light on the challenges and dynamics introduced by the increased share of renewable energy within the Jordanian power landscape.

Methodology

The methodology of this study centers on evaluating the stability of the Jordanian Power Grid (JPG) with a high Renewable Energy Sources (RES) share. To achieve this, the study employs DIGSILENT power software, a tool adept at assessing electrical systems, particularly in power transmission and distribution contexts. The JPG's operational model is meticulously simulated within DIGSILENT to investigate whether the system can maintain synchronism following significant transient disturbances. The key to this study is the simulation and analysis of various challenging scenarios, such as abrupt generation loss and frequency mismatches, within the JPG model. The robustness of the system's synchronism is rigorously tested under scenarios like sudden loss of generation. These tests are conducted across different grid load conditions—specifically peak and low load periods—under high RES integration scenarios. Additionally, the stability of the system's frequency is thoroughly examined. This aspect is crucial, given that system frequency significantly influences the performance of power generating units at all voltage levels, especially during extreme imbalances.

Results and Discussions

In this section, we explore two distinct scenarios simulated for the Jordanian Power Grid (JPG) in the year 2025, under conditions of high Renewable Energy Sources (RES) integration. These simulations are aimed at assessing the impact of increased RES on the stability of the JPG.

Case 1: Peak Load Scenario in 2025

Under peak load conditions with high integration of renewable projects, the network analysis reveals a robust system. A hypothetical disturbance, such as a complete loss of power generation from all wind farms due to a wind storm, was simulated. Despite this extreme scenario, the Jordanian electrical system maintained stable performance in terms of voltage, frequency, and generator power angles and speeds. No Under Frequency Load Shedding (UFLS) was necessary as the frequency remained above the critical threshold. The National Grid summary for this category in Year 2025 in peak load situation and high renewable projects integration is shown in Table 1.

Table 1: JPG summary for case 1

National Grid summary	
Grid Demand	4670MW
Total Installed Capacity	8200MW
Wind integration	774MW
Solar integration	1710MW
Spinning Reserve	820 MW
Grid Losses	96 MW
External In feed (Egypt)	7MW (to Egypt)

In this specific case, no major problems have been detected and the Jordanian electrical system shows stable behavior in voltage, frequency and generators power angle and speed, No UFLS detected since the frequency did not reach or drop below the first stage threshold of 49.1HZ, as shown in Figs1, 2, and 3.

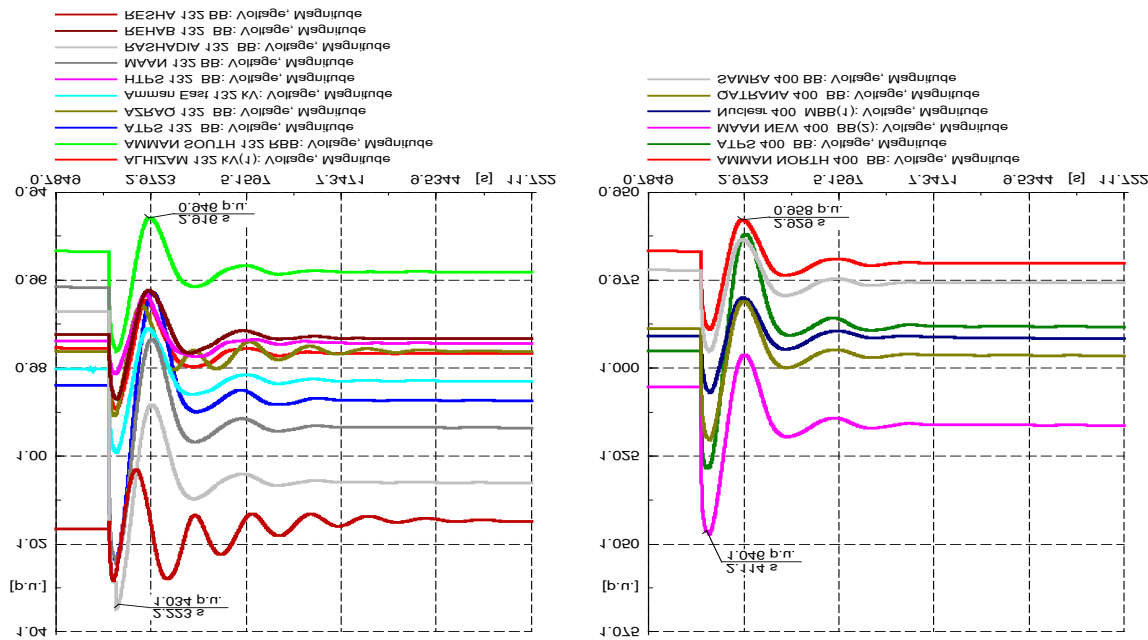


Figure 1: Voltage behavior for selected 132kV and 400kV busbars in the JPG [10]

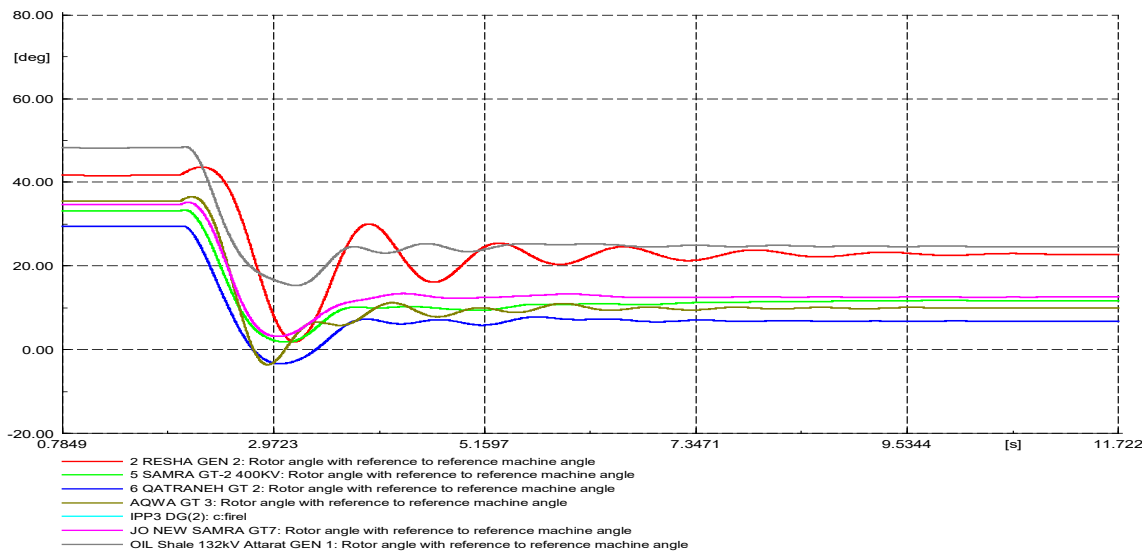


Figure 2: Power angle with reference to reference machine for several generators in the JPG

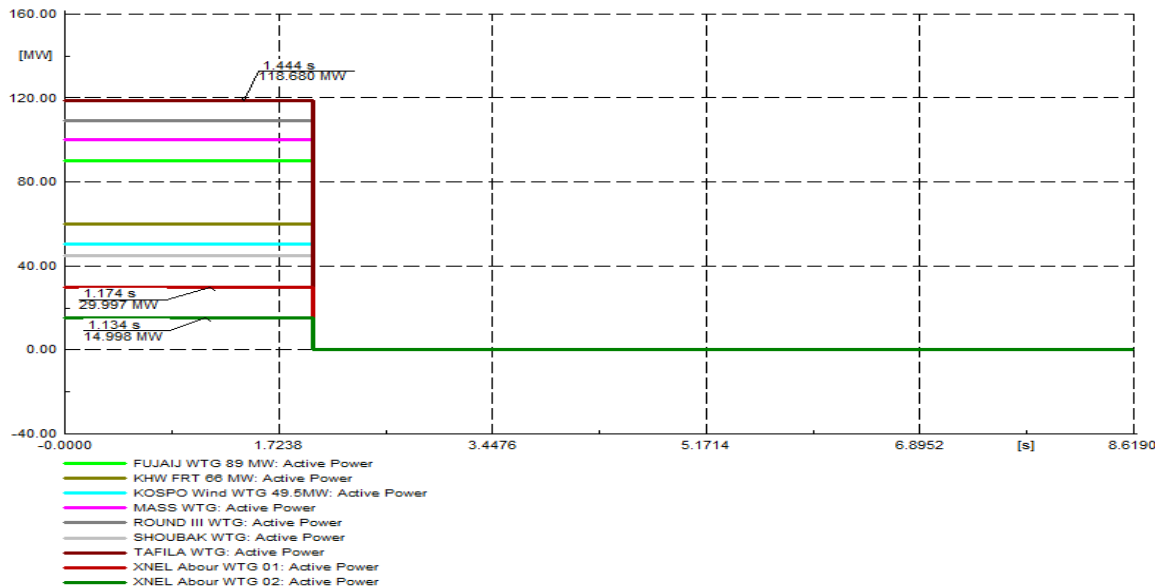


Figure 3: wind farms response after Loss of generation case [10]

Case 2: Low Load Scenario in 2025

In this scenario, the study considers a low load situation with high RES integration. The simulation predicts an increased reliance on RES, including wind and solar, alongside new primary energy resources like oil shale and nuclear power. When simulating a complete loss of power generation from all wind farms during a wind storm, it was observed that the system could handle the disturbance without major issues. The JPG summary for this category in Year 2025 low load situation and high renewable projects integration is shown in Table 2 below.

Table 2: JPG summary in 2025

National Grid summary	
Grid Demand	2100MW
Total Installed Capacity	8200MW
Wind integration	774MW
Solar integration	1710MW
Spinning Reserve	930MW
Grid Losses	91.4MW
External In feed (Egypt)	200MW (to Egypt)

In case the system forced to operate at 80% of renewable integration where only 500MW of conventional generation presented and the rest of power is covered by wind and PV, (the planning value of renewable is about 3000MW of approved projects until year 2025), the system will never converge or solve, the below errors as shown in Figure 4 will occur, where the inertia in the system is not sufficient to develop any response to the studied events [10]

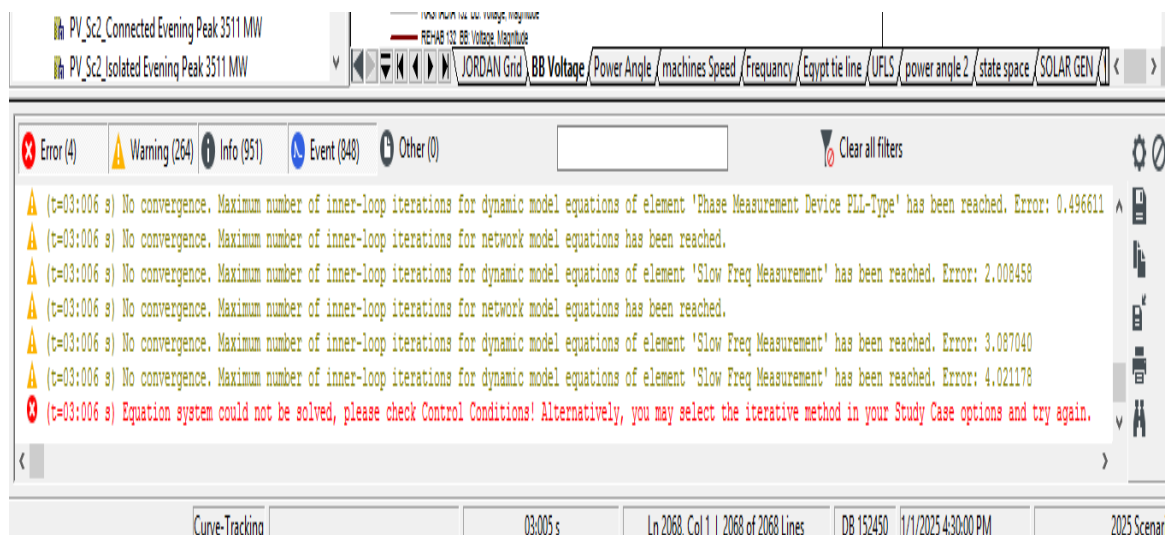


Figure 4: Error message in Simulation of 80% RES (Wind and PV integration).

In this case the assumption is to operate several conventional generation in the system in the minimum possible power dispatch condition in order to start the initial condition for simulation and to increase system inertia, the simulation is started with 57% of RES integration by making some of wind farms in the southern area in operation condition and switching off more PV projects in the grid, then implement wind and Solar power curtailment scheme, Results of case 4 (loss of several wind farms) are shown below, in this case the system is considered stable after loss of wind event.

Here below selected monitored elements and simulation results are shown. In this specific case, no major problems have been detected and the Jordanian electrical system shows stable behavior in voltage, frequency and generators power angle and speed, No UFLS detected even the frequency drop below the fourth stage threshold of 48.4HZ but the drop duration was less than 0.2 seconds. The simulation results of this case are presented, for low spring load of 2150MW in year 2025 with maximum RES integration. The most critical contingency in the low load condition appears to be the simultaneous trip of all wind farms, particularly in the southern green corridor. This leads to a significant power deficit of 612 MW. Nevertheless, the system's resilience is primarily due to the support from interconnected systems, namely Egypt and Syria. The simulation results show that peak power transfers, particularly from the Egyptian system, could exceed protective settings, posing a risk of separation from the Egyptian grid. This highlights the importance of careful management and coordination in interconnected grid operations, especially under high RES integration scenarios.

Conclusion

The study of the Jordanian Power Grid (JPG) for 2025 underlines its robustness amidst high Renewable Energy Sources (RES) integration. While the grid-maintained stability during peak loads even with extreme disruptions like total wind power loss, challenges arose in low load conditions at 80% RES integration due to insufficient system inertia. Strategic adjustments, including a balanced mix of renewable sources and curtailment strategies, were key to stabilizing the grid. The study highlights the grid's vulnerability to simultaneous wind farm disconnections, underscoring the importance of meticulous planning, balanced energy mix, and strong interconnectivity protocols in ensuring grid resilience in a renewable-dominant future.

References

- [1] H. Alnawafah and A. Harb, "Modeling and Control for Hybrid Renewable Energy System in Smart Grid Scenario - A Case Study Part of Jordan Grid," in 2021 12th International Renewable Energy Congress (IREC), 2021, pp. 1–6. <https://doi.org/10.1109/IREC52758.2021.9624739>
- [2] L. Xiong, X. Liu, D. Zhang, and Y. Liu, "Rapid Power Compensation Based Frequency Response Strategy for Low Inertia Power Systems," IEEE J Emerg Sel Top Power Electron, vol. 6777, no. c, pp. 1–1, 2020. <https://doi.org/10.1109/jestpe.2020.3032063>
- [3] L. Xiong, X. Liu, D. Zhang, and Y. Liu, "Rapid Power Compensation-Based Frequency Response Strategy for Low-Inertia Power Systems," IEEE J Emerg Sel Top Power Electron, vol. 9, no. 4, pp. 4500–4513, Aug. 2021. <https://doi.org/10.1109/JESTPE.2020.3032063>
- [4] M. Alkasrawi, E. Abdelsalam, H. Alnawafah, F. Almomani, M. Tawalbeh, and A. Mousa, "Integration of solar chimney power plant with photovoltaic for co-cooling, power production, and water desalination," Processes, vol. 9, no. 12, 2021. <https://doi.org/10.3390/pr9122155>
- [5] B. Kroposki et al., "Achieving a 100% Renewable Grid: Operating Electric Power Systems with Extremely High Levels of Variable Renewable Energy," IEEE Power and Energy Magazine, vol. 15, no. 2, pp. 61–73, Mar. 2017. <https://doi.org/10.1109/MPE.2016.2637122>
- [6] M. Velasco, P. Martí, J. Torres-Martinez, J. Miret, and M. Castilla, "On the optimal reactive power control for grid-connected photovoltaic distributed generation systems," in IECON 2015 - 41st Annual Conference of the IEEE Industrial Electronics Society, IEEE, Nov. 2015, pp. 003755–003760. <https://doi.org/10.1109/IECON.2015.7392686>
- [7] E. Abdelsalam et al., "Performance analysis of hybrid solar chimney–power plant for power production and seawater desalination: A sustainable approach," Int J Energy Res, vol. 45, no. 12, pp. 17327–17341, 2021. <https://doi.org/10.1002/er.6004>
- [8] Hamza Alnawafah, "MODELING AND CONTROL FOR HYBRID RENEWABLE ENERGY SYSTEM IN SMART GRID SCENARIO A CASE STUDY PART OF JORDAN GRID," German Jordanian University, Amman, 2020. Accessed: Sep. 08, 2023. [Online]. Available: http://hip.jopuls.org.jo/c/portal/layout?p_1_id=PUB.1009.1&p_p_id=search_WAR_fusion&p_p_action=1&p_p_state=normal&p_p_mode=view&p_p_col_id=column-1&p_p_col_pos=0&p_p_col_count=2&_search_WAR_fusion_action=navigate&_search_WAR_fusion_navigationData=search%7E%3D1%7E%21BIB%7E%212147483647%7E%217123071
- [9] H. Alnawafah, R. Sarrias-Mena, A. Harb, L. M. Fernández-Ramírez, and F. Llorens-Iborra, "Evaluating the inertia of the Jordanian power grid," Computers and Electrical Engineering, vol. 109, Aug. 2023. <https://doi.org/10.1016/j.compeleceng.2023.108748>
- [10] A. T. M. Abu Dyak, "The Effect of Connecting Large Scale Renewable Project on Power Quality And Voltage Control Of The Jordanian Electrical Grid," German Jordanian University, Amman, 2017.

Assessment of utilizing solar energy to enhance the performance of vertical aeroponic farm

Esam Jassim^{1,a,*}, Bashar Jasem^{2,b}, Faramarz Djavanroodi^{1,c}

¹College of Engineering, Prince Muhammad Bin Fahd University, 31952 Al-Khobar, Kingdom of Saudi Arabia

²Department of Computer Technology, Al-Hadba University College, Mosul, Iraq.

^aejassim@pmu.edu.sa, ^badamatzuhairee@gmail.com, ^cfdjavanroodi@pmu.edu.sa

Abstract. The manuscript presents the significance of utilizing renewable energy in vertical aeroponic farming system. Components such as the tower garden, the solar panels, the water pump, and the control unit are integrated and designed to generate sufficient solar energy to power the system. The environmental conditions inside the chamber are optimized for plant growth, to maintain 18-24 °C temperature and relative humidity of 75-85 %. The paper also discusses the challenges, limitations, and future recommendations for improving the system. Finally, the paper provides some future recommendations for improving the design and performance of the solar powered vertical farm.

Introduction

Vertical farming (VF) is a process to produce food via utilizing vertical dimension for hydroponic growing of crops with indoor controlled-environment agriculture. Vertical gardens play a key role in tackling the ongoing challenges that modern cities encounter, due to a rapid growing in urban environment associated with the scarcity of water and the major growing in population, crises in food demand are emerged. Researchers predict about 25%-70% increasing in the crops needs by 2050 [1]. However, with the decrement in the availability of growing lands together with the worsen of climate condition, rises the demand of VF. The term "vertical farming" refers to the utilization of several vertical layers of crops planted within a warehouse to create an artificial growth environment that mimics horizontal farming.

Food costs remain augmented for several factors such as including population growing and food shortage. Although traditional Horizontal Farming HF are less expensive to maintain and build than greenhouses, such method still requires large landscape and fertilized soil. VF, on the other hand, is notorious for using a large amount of electricity, triggering the alarm of the essential of finding alternative source of energy. Renewable resources are currently drawing attention to sub the conventional electrical power. Hence, solar power became a popular choice for supplying energy to such devices since it is both practical and readily available. Solar lighting systems have a lot of promise, as demonstrated by a UK research that examined the potential cost reductions associated with their use. The analysis reveals 56% to 89% of possible savings [2]. The use of solar energy in vertical farming would thus benefit the entire process and make it even more dependable and sustainable.

Incorporating solar energy into vertical farming systems is a sustainable approach that enhances the overall efficiency and environmental impact of the agricultural process. Research indicates that integrating solar panels into vertical farming structures can provide a reliable and renewable energy source, powering LED lights, climate control systems, and other essential equipment. Such incorporation not only reduces the dependence on conventional energy grids but also mitigates the contribution of carbon by-product associated with the production of food. However, power intermittency and energy storage of solar panels are still of ongoing challenges, in particular integration into vertical farming. Hence, more studies are in need to optimize a sustainable and self-sufficient agricultural model.

Furthermore, studies emphasized that the incorporation of solar energy in vertical farming can lead to increased energy autonomy and cost-effectiveness over the long term. Solar panels strategically positioned on the vertical farming structures, harness sunlight for electricity and minimizing reliance on conventional power sources. This sustainable energy approach associates with the continuous demand for eco-friendly agricultural practices, addressing concerns related to climate change and conventional energy consumption in food production.

Innovations in solar technology, such as advancements in photovoltaic efficiency and energy storage solutions, are crucial in overcoming challenges associated with intermittent sunlight availability. Ongoing research explores the optimization of energy capture and storage mechanisms to ensure continuous and reliable power supply, regardless of weather conditions or time of day.

Moreover, incorporating solar energy in vertical farming is vital to the development of off-grid farming solutions, particularly in remote areas. This approach not only facilitates increased food production in regions with limited access to conventional power but also promotes sustainable agriculture practices that prioritize environmental stewardship.

As the field continues to evolve, interdisciplinary collaboration between agriculture, engineering, and renewable energy sectors becomes pivotal. This collaborative effort aims to refine and scale up solar-powered vertical farming systems, fostering a more feasible and sustainable future for agriculture.

Although one of the most flaws in VF systems is the high energy consumption, incorporation of renewable energy sources (RE) such as solar and wind could mitigate the capital and operation costs. Hence, utilizing renewable energy in VF systems have intensively addressed by recent literatures to assess the promotion of sustainability in urban agriculture.

System design

The prototype was initially built based on the standards of greenhouses, but it was customized to meet certain specifications. The final dimensions and design of the building are illustrated in Fig (1). Carbon steel, a material with high tensile strength and rigidity, was selected as the main structural material for the prototype. Insulation was selected to minimize the energy interaction between the system and the surroundings. Factors such as thermal resistance, ageing, moisture accumulation and thickness are prioritized during the selection process.

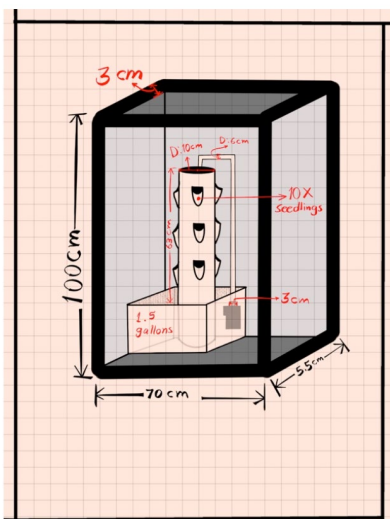


Fig. (1) Dimensions of the Tower Farm

LED lighting is the best choice for indoor farming for various reasons. It can reduce energy consumption for different crops as well as easy to control. The quality can be tailored to suit the photosynthetic pigments and photoreceptors of the crop by adjusting its intensity and spectrum[2]. This is important in vertical farming since plants can sense and respond to changes in light intensity and illuminance. LED lights can also influence the flavor, nutritional value and shelf life of crops.

Red/blue LED lights can enhance the growth and biomass of C. LED lights can also improve the growth, color, flavor, and phytonutrient content of leafy greens in controlled environments by adjusting the light spectrum [2].

Furthermore, LED lights are more energy-efficient than other forms of lighting, as they consume less energy for running lights and climate management [3]. LED lights also affect the heat load of the room. The heat load was lower when LED lights were off, and higher when they were on [4].

A recent experiment showed that LED grow lights accounted for 78% of the daily heat load on average, and also accelerated the processes of respiration and evaporation in plants. Moreover, an energy balance analysis revealed that LED lighting increased the evapotranspiration and heat loads by up to five times compared to a scenario without LED lighting. Therefore, it is important to choose the right type and intensity of LED grow lights for different plants and growth stages [4].

Solar resource assessment

Saudi Arabia, has an excellent solar power potential due to its long hours of light, few days with clouds (particularly, in eastern province) , and elevated Direct Normal radiation DNI, which reaches a peak power density of 4800 kWh/m²/year [5].

Such places are viable and highly positioned among the forefront of countries with the ability to produce electrical power using solar energy [6].

The DNI is a crucial factor to consider when evaluating the viability of a geographical area for the implementation of CSP technology. It is worth mentioning that CSP systems are generally considered viable in locations where the direct normal irradiance (DNI) surpasses 1800 kWh/m²/year [7, 8].

FPS modeling:

This section examines the viability of the suggested FSP systems according to the conditions of east province in Saudi Arabia. Annual energy output (GWh), which refers to the sum of the hourly energy produced over the course of a year. The following equation is used to calculate annual energy output:

$$AE = \sum_{t=1}^{t=8760} Q_t$$

where t represents time (hour) and Q_t stand for the generated energy. The capacity factor, defined as a ratio of the total number of hours of electricity generated in an FSP plant relative to its nominal capacity over the course of one year, can be computed by the following equation:

$$\text{Capacity Factor} = \frac{\text{Net Annual Energy}}{\frac{\text{System Capacity (kWh}_ac\text{)}}{8760}}$$

$$CF = \frac{AE}{\frac{\text{system capacity}}{8760 (\text{hr/year})}}$$

The annual energy and capacity factor in eastern province in Saudi Arabia are determined to be 209 GWhr and 72.5% respectively.

Two 300-watt solar panels were utilized to provide the power demanded by the VF system. The size of each panel is 164 x 99.2 x 4 cms. The output electrical energy (E), in kWh, is determined from the following expression:

$$E = A \times \eta \times I \times PR$$

where: A = area of the solar panel;

η = solar panel efficiency (roughly 15%);

I = average annual solar radiation on titled panels (5.337 kWh/m² day for the optimal tilt angle 20.833°)

PR = performance ratio (average value = 0.75)

Results and discussion

A series of tests have been conducted on the system, including lighting, cooling, humidifier, dehumidifier and irrigation system, as illustrated in Fig. (2). The system run twice for each test: full day and half day. To create a suitable environment for lettuce growth, Styrofoam insulation was utilized to line a wooden frame that holds the nutrient solution as well as serves as a floating platform for the plants. Since the optimal conditions for lettuce are 75-85% humidity and 18-24 °C temperature, growth lights, an evaporative cooler, a humidifier, and a dehumidifier were installed to control the system thermal conditions. The growth lights have a power of 16W, while the evaporative cooler consumes 65W. A submersible pump utilized to circulate the nutrient solution requires 13W to operate at maximum flow rate of 700L/h and vertical head (H_{max}) of 1.0m. The humidifier has a wattage of 25W, and it can filter impurities from water and adjust the fog intensity. The dehumidifier, on the other hand, operates at consumption up to 25W and it can recover about 0.4kWh to dry.

The nutrient solution was pumped from the reservoir to the top of the garden tower, where it drips down over the exposed roots of the plants. A timer ensures that this process is repeated regularly to provide adequate oxygen, water, and nutrients to the plants.

The energy produced by each panel with specification elaborated earlier is 0.977 kWhr for a total of 1.95 kW hr. Equipment of the system needs 1.728 kWhr to operate at full load condition for 12 hrs. Hence, the system is durable and the technologies performed well from both the intended purpose and the eco-friendly environment.



Fig. (2) Lighting and humidification processes

Conclusion

This paper presents a design of a solar powered vertical farm that uses aeroponic tower garden technology to grow lettuce in a closed chamber. The main objectives of this design are to address the scarcity of power source in remote area, the reduction of environmental impact resulted by conventional agriculture, and the provision of fresh and healthy food for local consumption by incorporating of renewable energy. The paper describes the design process, the prototype fabrication, and the testing and analysis of the system. The design process involved selecting the appropriate materials and components for the aeroponic tower garden, the solar system, and the control system. The aeroponic tower garden consists of a vertical structure with multiple planting ports that spray nutrient-rich water to the roots of the plants. Design of the solar system consists of photovoltaic panels, batteries, charge controller, and inverter that provide electricity to power the pumps, AC, humidifier, dehumidifier, sensors, and lights.

The prototype was tested twice and produced the required environment for producing healthy and fresh lettuce. The paper discusses the results and analyses of the prototype performance, comparing it with other similar systems and highlighting its advantages and limitations.

References

- [1] Yahya, O., Yahya, G., Al-Omair, A., Yahya, E., Jassim, E., Djavanroodi, F. (2023). "Aeroponic tower garden solar powered vertical farm". Volume 31, Pages 287 - 2982023 International Conference on Advanced Topics in Mechanics of Materials, Structures and

Construction, AToMech1 2023 Al Khobar 12 March 2023.

<https://doi.org/10.21741/9781644902592-30>

[2] Jahan, N., Moody, B., Kerr, J., Cynthia, D, & Lawson, C. “Grow lights for your vertical garden: A complete guide. Garden Tabs. Retrieved”, February 16, 2022.

[3] SharathKumar, M., Heuvelink, E., & Marcelis, L. F. M. (2020). Vertical Farming: Moving from Genetic to Environmental Modification. Trends in Plant Science, 25(8), 724–727.

<https://doi.org/10.1016/j.tplants.2020.05.012>

[4] Omar Yahya, Gharam Yahya, Ahmad Al-Omair, Emad Yahya, Esam Jassim, Faramarz Djavanroodi, Aeroponic tower garden solar powered vertical farm, Materials Research Proceedings, Vol. 31, pp 287-298, 2023. <https://doi.org/10.21741/9781644902592-30>

[5] Esam Jassim, “Improvement of Indoor Air Distribution by Utilizing Small Fans Powered by Solar Energy”, International Journal of Computational Physics Series 1(2), 1-8, 2017.
<https://doi.org/10.29167/A1I2P1-8>

[6] Kazem, Hussein A., et al. "A review of dust accumulation and cleaning methods for solar photovoltaic systems." *Journal of Cleaner Production* 276 (2020): 123187.
<https://doi.org/10.1016/j.jclepro.2020.123187>

[7] Erica Zell, Sami Gasim, Stephen Wilcox, Suzan Katamoura, Thomas Stoffel, Husain Shibli, Jill Engel-Cox, Madi Al Subie, “Assessment of solar radiation resources in Saudi Arabia”, *Solar Energy*, Volume 119, 2015, Pages 422-438. <https://doi.org/10.1016/j.solener.2015.06.031>

[8] M. Enjavi-Arsanjani, K. Hirbodi, M. Yaghoubi, “Solar Energy Potential and Performance Assessment of CSP Plants in Different Areas of Iran”, *Energy Procedia*, Volume 69, 2015, Pages 2039-2048. <https://doi.org/10.1016/j.egypro.2015.03.216>

Energy efficiency and sustainability enhancement of electric discharge machines by incorporating nano-graphite

Asaad A. ABBAS^{1,a}, Raed R. SHWAISH^{1,b*}, Shukry H. AGHDEAB^{1,c}, and Waleed AHMED^{2,d*}

¹Production Engineering and Metallurgy Department University of Technology- Iraq, Baghdad, Iraq

²ERU, COE, UAE University, Al Ain, UAE

^a asaad.a.abbas@uotechnology.edu.iq, ^b raed.r.shwaish@uotechnology.edu.iq,
^c Shukry.H.Aghdeab@uotechnology.edu.iq, ^d w.ahmed@uaeu.ac.ae

Keywords: EDM, Nano-Powder Mixed Electro-Discharge Machining, Electrode Wear Rate, Full Factorial

Abstract. The research paper endeavored to significantly improve the energy efficiency and sustainability of the electrode wear rate (EWR) in electric discharge machining (EDM) through a particular exploration of various parameters. These parameters included nano-powder concentration, electric current, and pulse-on time. By systematically analyzing and manipulating these variables, the study aimed to optimize the EDM process, thereby reducing energy consumption and enhancing the overall sustainability of the machining operation. We employed the Powder Mixed Electro-Discharge Machining (PMEDM) technique, a refined iteration of electric discharge machining. This innovative method blended graphite nano-powder with transformer oil to serve as the dielectric medium. The primary objective of this investigation is to examine the outcomes concerning crucial process parameters such as graphite powder concentration, electric current, and pulse-on time when machining high-speed steel, focusing mainly on electrode wear rate (EWR). Incorporating nano graphite (Gr) mixed powders into dielectric liquids has demonstrated a discernible enhancement in EWR across diverse operational conditions. The study found that the electrode wear rate (EWR) varied based on nano-powder concentration, electric current, and pulse-on time. Maximum EWR was observed at a concentration of 10 g/L, a current of 30 A, and a pulse-on time of 70 µs, while minimum EWR occurred at 0 g/L, 10 A, and 60 µs. The Full Factorial design, executed with MINITAB 17 software, validated these findings. The optimal EWR recorded was 1.154 mm³/min. The coefficient of determination (R-sq) for surface roughness prediction also stood at 91.15%.

Introduction

An essential player in non-traditional machining methodologies, electrical discharge machining (EDM) stands out as a proven, logical, and economical approach to the precision machining newly developed high-strength alloys. Its success lies in delivering tailored machining solutions with exceptional dimensional accuracy while reducing production costs. This technology holds promise in enhancing energy efficiency and sustainability in manufacturing processes due to its precise material removal capabilities and potential for optimizing resource utilization. Despite their inherent hardness and brittleness, conductive materials can undergo efficient and effective thermal energy treatment. This method mitigates wear and minimizes the expenses typically incurred in conventional machining processes. Ceramics, titanium, and steel are just a few materials amenable to this treatment [1]. Leveraging thermal energy in material treatment enhances the machining process and potentially reduces energy consumption and environmental impact, contributing to sustainability in manufacturing practices. Emerging materials with challenging machining

characteristics continually evolve within electric discharge machining (EDM). These encompass ceramics, tool steel, superalloys, carbides, stainless steel, heat-resistant steel, and more. Widely applied across diverse sectors, including aerospace, nuclear, and die and mold-making industries, these materials pose intricate machining demands and underscore the necessity for advanced EDM techniques and technologies. By addressing the machining complexities of these materials, EDM plays a pivotal role in facilitating innovation and progress across various industrial domains. Furthermore, electric discharge machining (EDM) extends its influence into novel domains, encompassing sports equipment, medical and surgical instruments, optical devices, dental appliances, and jewelry manufacturing. Moreover, it permeates the research and development sector of the automotive industry [2-6]. This broadening scope reflects EDM's adaptability and versatility in addressing diverse machining needs across various industries, driving innovation and advancements in different sectors beyond traditional manufacturing applications. The swift solidification during the erosion process induces substantial internal thermal stress within the upper layers of the workpiece surface, thereby influencing the component properties. The cessation of discharge during erosion fundamentally characterizes a thermal erosion process [7]. This phenomenon underscores the intricate interplay between thermal dynamics and material behavior, highlighting the importance of understanding and managing thermal effects in erosion processes for effective material treatment and component performance enhancement.

Erosion arises from heat generation. Abrupt temperature surges in the machining process profoundly impact the physical attributes of the machined surface layer, leading to residual stress. This pivotal factor significantly influences machined surfaces quality and functional attributes, underscoring its importance in surface engineering and manufacturing practices. Understanding and effectively managing these thermal effects are paramount for achieving desired surface characteristics and optimal component performance [8-10]. A recent advancement in electric discharge machining technology is powder-mixed electric discharge machining (PMEDM). The finely graded powder material is meticulously mixed with the dielectric liquid to enhance its breakdown characteristics [11]. The study explored the effects of blending an Al and Cr powder mixture with kerosene. Findings indicated that this combination decreased the thermal insulating properties of the kerosene while widening the spark gap. Consequently, this stabilized the machining process and significantly boosted the material removal rate (MRR). Tzeng and Lee delved into the influence of different powder characteristics on the machining of SKD11 materials, which are equivalent to AISI H13 tool steel [12]. Despite promising results, the adoption of powder mix EDM in the industry has been gradual. A key contributing factor is the lack of clarity surrounding various aspects of this emerging technology, including the editing process. To address this gap, researchers employed response surface methodology (RSM) to examine the effects of process variables such as peak powder concentration, tool diameter, and current on the material removal rate (MRR) for EN8 steel [13], [14]. Researchers investigated the influence of fine metal powder grains such as aluminum (Al) and copper (Cu) when introduced into dielectric fluids during the EDM process of AISI D3 and EN31 steels using Taguchi design experiments. Numerous endeavors have aimed to simulate the EDM process and evaluate its effectiveness [15].

This study aimed to analyze the impact of EDM parameters on the induced electrode wear rate when employing copper electrodes, with or without the incorporation of Nano-graphite powder mixed in transformer oil dielectric, for A 240 stainless steel 304. The experimental design matrices for the materials were generated using the Full Factorial Design (FFD) approach. The electrode wear rate was analyzed using ANOVA models, with separate models developed for two sets of trials. The first set utilized transformer oil as the dielectric, while the second set employed nano-graphite particles mixed with the dielectric fluid (PMEDM) at concentrations of 5 and 10 g/l. This

approach aimed to enhance machining efficiency, mitigate instability in arcing effects, and analyze the electrode wear rate resulting from process modifications.

Experimental work

As depicted in Figure 1, an experimental investigation was conducted using a CHEMER EDM machine (CM323C). The workpiece employed in the experiment was stainless steel 304, ASTM A 240, measuring (40 x 30 x 1.7 mm) in dimensions.

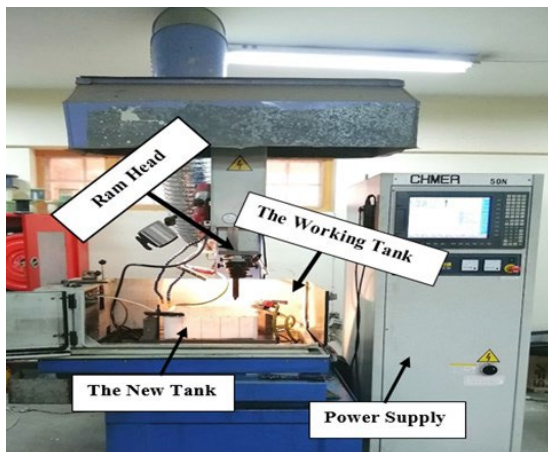


Fig. 1. Model of the EDM machine (CM 323C).

Chemical composition percentages of the 304 stainless steel workpiece materials per the ASTM E415 standard are summarized in Table 1 (tested at the Central Organization for Standardization and Quality Control Center).

TABLE 1. Stainless steel 304 Chemical composition of samples.

Material	C	Si	Mn	P	S	V	Cr	Mo	Ni	Fe
Weight (%)	0.06	0.6	1.1	0	0	0.14	19	0.2	9	Balance

Table 2 outlines numerous mechanical and physical characteristics of the workpiece. The electrode comprises 99.74% pure copper and possesses a diameter of 5 mm. Additionally, the dielectric solution, a form of transformer oil, incorporates a nano-powder mix of graphite .

TABLE 2. The mechanical and physical characteristics of the samples

Ultimate Strength	621 MPa
Density	8030 kg/m ³
Hardness	1667 N/ mm ²
Ductility	60 mm/mm
Melting point	2552-2642°F

The experiment occurred in a newly designed tank, which housed a blend of graphite nano-powder and transformer oil. A small pump was integrated into the reservoir to put off powder accumulation at the bottom or the formation of insulating surface deposits. This measure ensured the efficient separation of the internally mixed nano-powder. The viscosity of the transformer oil used in the practical experiments was measured at 28.01 Pa.s at a room temperature of 23°C. A sample of graphite nano-powder was obtained, with particle sizes measuring 80 nanometers. Before and after

machining, the weight of the sample and electrode was thoroughly determined using an electronic weighing scale at a precision of 0.0001g. Following NPMEDM machining, the surface roughness of each workpiece was evaluated using a portable surface roughness tester, boasting an accuracy of 0.05 µm. The operational mechanism of nano-powder-mixed EDM is depicted in the following figure.

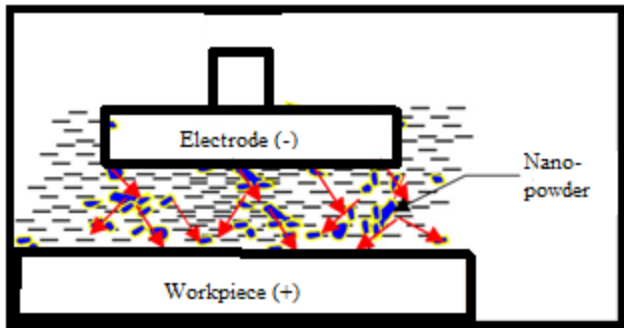


Fig. 2. Mechanism of nano-powder-mixed EDM.

The machining parameters encompassed varying concentrations of nano-powder (graphite), current, pulse-on time, and pulse-off time. Besides, nano-powder graphite concentrations ranged from 0, 5, to 10 g/l, while 10, 20, and 30 amperes discharge currents were employed. Furthermore, pulse-on times were selected at 50, 60, and 70 µs, with a pulse-off time set at 55 µs. Following the manufacturer guidelines, the remaining electric impulse parameters were maintained constant, including an open gap voltage of 140V and a negative tool electrode polarity. The goal is to explore the impact of nano-powder-mixed dielectric on the electrode wear rate (EWR) by varying input machining parameters. Table 3 shows the three parameters used in this study, each with three levels. Furthermore, Table 4 displays the input machining settings that haven't changed.

TABLE 3. Machining Parameters and their corresponding stages.

Parameters	Stages		
Concentration (Nano-Graphite), gram/Liter	1	2	3
Current, Ampere	0	5	10
Pulse-on time, micro-Second	10	20	30
	50	60	70

TABLE 4. unchanged input parameters.

Workpiece polarity	Positive
Electrode polarity	Negative
Dielectric fluid	Transformer oil with Mixture nano-powder of Gr
High voltage	140 V 1.2 A
Pulse-off time	25 µsec
Working time	5.0 sec
Jumping time	2.0 mm
Depth of cut	1 mm
Gap code	10
Servo feed	75 %

Results and discussion

The impact of process variables like powder concentration, discharge current, and pulse-on time on the response variable, namely the electrode wear rate (EWR), was investigated. Analysis of variance (ANOVA) was conducted using MINITAB 17 software to analyze the experimental data and ascertain the significance of these factors on EWR. The conclusions of the ANOVA analysis for EWR are presented in Table 5. ANOVA was employed to assess the importance of the model. Model terms are considered statistically significant if their "P-Value" is below 0.05, indicating a 95 percent confidence interval [16]. Furthermore, Table 6 presents the model summary, including the coefficients associated with the terms (Coef.), the standard error of each coefficient (SE Coeff), the t-statistic, and the p-value of each term. These values aid in assessing whether to accept or reject an invalid assumption. All of the terms' p-values are below the predetermined threshold, indicating their significance within the model. An R-squared value of 91.15% suggests that the predictors or factors in the model elucidate 91.15% of the total variance in the response. Additionally, the adjusted R-squared value of 88.50% factors in the number of predictors in the model and defines the significance of the association.

TABLE 5. Analysis of Variance for EWR

Source	Model	Linear	Nano Powder	Current	Ton	Error	Total
DF	6	6	2	2	2	20	26
Adj SS	15.741	15.741	7.727	3.033	4.981	1.528	17.269
Adj MS	2.62355	2.62355	3.86353	1.51673	2.49039	0.0764	
F-Value	34.34	34.34	50.57	19.85	32.6		
P-Value	0	0	0	0	0		

TABLE 6. Model summary

Term	Coeff	SE Coeff	T-Value	P-Value
Constant	2.7952	0.0532	52.55	0.000
Nano Graphite				
0	-0.6612	0.0752	-8.79	0.000
5	0.0121	0.0752	0.16	0.873
Current				
10	-0.3691	0.0752	-4.91	0.000
20	0.0731	0.0752	-0.97	0.343
Ton				
50	-0.5153	0.0752	-6.85	0.000
60	-0.0209	0.0752	-0.28	0.784
S	R-sq	R-sq (adj)	R-sq (pred)	
0.276406	91.15%	88.50%	83.87%	

The significant effects plot of the electrode wear rate (EWR) revealed that an increase in nano-powder concentration correlates with higher EWR. Similarly, elevating both currents (10, 20, and 30 A) and pulse-on times (50, 60, and 70 μ s) and maintaining a pulse-off time of 55 μ s contributed to this trend. This phenomenon can be attributed to the heightened spark energy between the workpiece and electrode due to increased temperature on the workpiece, resulting in an escalation of the EWR. Moreover, the longest pulse-off time (Toff) corresponds to the highest electrode wear rate (EWR) due to its role in prolonging the re-solidification period within the dielectric medium. This extension results in larger surface grains, leading to a higher EWR. Nano-powder

concentration, current, and pulse-on time (T_{on}) are also observed to influence EWR, as depicted in Figure 3.

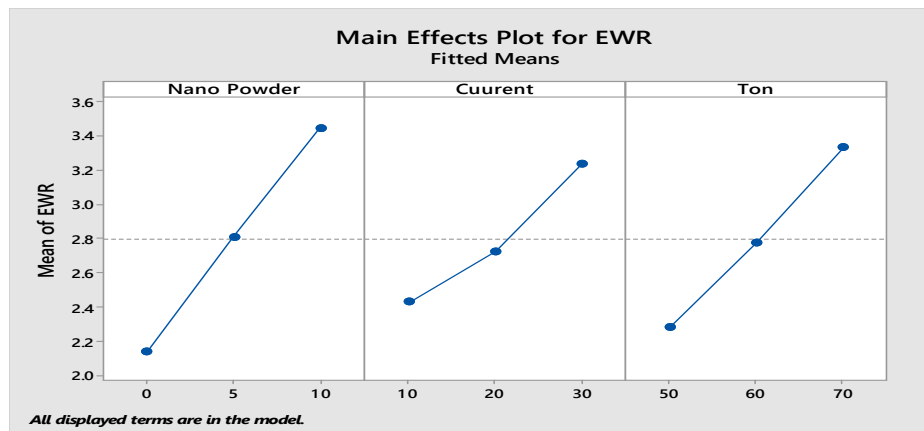


Fig. 3. Impact of Nano-graphite concentration, plus, and current on time on EWR

The nano-powder concentration correlates with the enhanced electrode wear rate (EWR) of the workpiece, along with increasing currents (10, 20, and 30 A) and pulse-on times (50, 60, and 70 μ s). The impact of nano-graphite concentration, pulse-on time, and current on EWR is depicted in Figure 4.

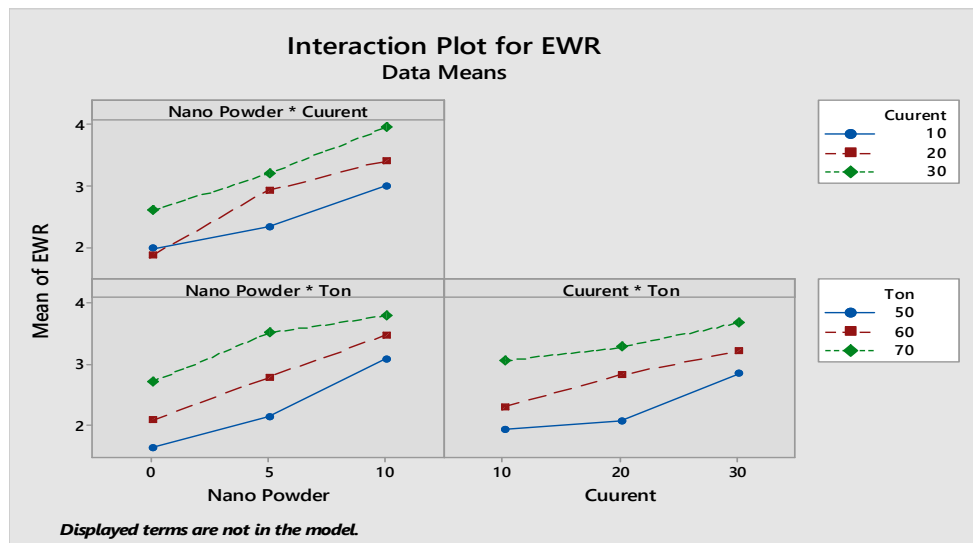


Fig. 4. The effect of Nano-graphite concentration, current, and pulse on time (T_{on}) on EWR.

Conclusions

In addition to exploring the impact of electrical process variables on the electrode wear rate (EWR) for high-speed steel with pure copper electrodes, this investigation highlights critical factors influencing machining efficiency and sustainability. The findings emphasize the significance of nano-powder concentration in transformer oil as a crucial determinant of electrode wear, with higher concentrations correlating with increased wear rates. Notably, the study reveals that the highest EWR occurs at ten g/l concentration, 70 μ s at pulse-on time, and 30 Amp, current, emphasizing the sophisticated relationship of process parameters. Moreover, employing a Full Factorial design executed with MINITAB 17 software enhances our understanding of the machining process, facilitating the identification of optimal conditions for minimizing electrode wear. The finding of an optimal EWR value of 1.154 mm³/min points out the potential for enhancing energy efficiency and sustainability in machining operations. The high coefficient of

determination (R-sq) of 91.15% indicates the robustness of the predictive model, offering valuable understanding into future machining industries aimed at reducing wear rates while optimizing resource utilization. As industries strive for eco-friendly manufacturing practices, these findings provide a crucial foundation for developing more sustainable machining techniques that align with environmental and energy efficiency goals.

References

- [1] Y. H. Guu, H. Hocheng C. Y. Chou and C. S. Deng, "Effect of electrical discharge machining on surface characteristics and machining damage of AISI D2 tool steel", Materials Science and Engineering, A 358, pp. 37-43, 2003. [https://doi.org/10.1016/S0921-5093\(03\)00272-7](https://doi.org/10.1016/S0921-5093(03)00272-7)
- [2] Sundaram M. M. and K. Rajurkar, "Electrical and Electrochemical Processes, in Intelligent Energy Field Manufacturing", CRC Press. p. 173-212, 201, 2011.
<https://doi.org/10.1201/EBK1420071016-c6>
- [3] Klocke F., Zeis M., Klink A. and Veselova D., "Technological and Economical Comparison of Roughing Strategies via Milling, EDM and ECM for Titanium- and Nickelbased Blisks", Proceedings of the 1st CIRP Global Web Conference on Interdisciplinary Research in Production Engineering, Vol. 2, pp. 98-101, 2012. <https://doi.org/10.1016/j.procir.2012.05.048>
- [4] Gu L., Le. L., Zhao W., and Rajurkar K. P., "Electrical Discharge Machining of Ti6Al4V with Bundled Electrode", International Journal of Machine Tools and Manufacturing, Vol. 53, pp. 100- 106, 2012. <https://doi.org/10.1016/j.ijmachtools.2011.10.002>
- [5] Jahan M., Malshe A. and Rajurkar K., "Experimental Investigation and Characterization of Nano-scale Dry Electro-machining", Journal of Manufacturing Processes, Vol. 14 pp. 443-451, 2012. <https://doi.org/10.1016/j.jmapro.2012.08.004>
- [6] Klocke F., "EDM Machining Capabilities of Magnesium (Mg) Alloy WE43 for Medical Applications", Procedia Engineering, Vol. 19(0): pp. 190-195, 2011.
<https://doi.org/10.1016/j.proeng.2011.11.100>
- [7] H. Singh, "Experimental study of distribution of energy during EDM process for utilization in thermal models", International Journal of Heat and Mass Transfer, 2012.
<https://doi.org/10.1016/j.ijheatmasstransfer.2012.05.004>
- [8] Ahmed N. Al-Khazraji, Samir A. Al-Rabii and Ali H. Al-Jelehawy, " Fe Analysis of Residual Stresses Induced by Spot Welding of Stainless-Steel Type AISI 316" Engineering and Technology Journal, Vol. 32, Part (A), No. 2, 2014. <https://doi.org/10.30684/etj.32.2A.7>
- [9] Ahmed N. Al-Khazraji, Farag M. Mohammed and Ali Riyadh A. Al-Taie, " Residual Stress Effect on Fatigue Behavior of 2024- Aluminum Alloy" Engineering and Technology Journal, Vol. 29, No. 3, 2011. <https://doi.org/10.30684/etj.29.3.13>
- [10] Ahmed N. Al-Khazraji, Samir A. Al-Rabii and Ali H. Fahem, " Formation of Compressive Residual Stresses by Shot Peening for SpotWelded Stainless Steel Plates" Engineering and Technology Journal, Vol. 31, Part (A), No. 11, 2013. <https://doi.org/10.30684/etj.31.11A14>
- [11] Wang, C. H., Lin, Y. C., Yan, B. H. and Huang, F. Y., "Effect of characteristics of added powder on electric discharge machining", J. Jpn. Inst. Light Met., Vol. 42 (12), pp. 2597–2604, 2001. <https://doi.org/10.2320/matertrans.42.2597>
- [12] Tzeng, Y. F., Lee, C. Y., "Effects of powder characteristics on electro-discharge machining efficiency", Int. J. Adv. Manuf. Technol., Vol. 17, pp. 586–592, 2001.
<https://doi.org/10.1007/s001700170142>

- [13] C. Huang, J. Wang and X. Li, "Powder Mixed near Dry Electrical Discharge Machining", Advanced Materials Research, Vol. 500, 2012.
<https://doi.org/10.4028/www.scientific.net/AMR.500.253>
- [14] N. S. Khundrakpam, H. Singh, S. Kumar, and G. S. Brar," Investigation and Modeling of Silicon Powder Mixed EDM using Response Surface Method", International Journal of Current Engineering and Technology, Vol.4, No.2 (April 2014).
- [15] B. Reddy, G.N. Kumar, and K. Chandrashekhar, "Experimental Investigation on Process Performance of Powder Mixed Electric Discharge Machining of AISI D3 steel and EN-31 steel", International Journal of Current Engineering and Technology, Vol. 4, No. 3, June 2014.
- [16] S. Assarzadeh and M. Ghoreishi, "A dual response surface-desirability approach to process modeling and optimization of Al₂O₃ powder-mixed electrical discharge machining (PMEDM) parameters," The International Journal of Advanced Manufacturing Technology, Vol. 64, No. 9-12, pp. 1459-1477, 2013. <https://doi.org/10.1007/s00170-012-4115-2>

Exploring sustainable micro milling: Investigating size effects on surface roughness for renewable energy potential

Ahmet HASCELIK^{1,a*}, Kubilay ASLANTAS^{2,b}, Waleed AHMED^{3,c*}

¹ Department of Mechanical and Metal Technology, Iscehisar Vocational School of Higher Education, Afyon Kocatepe University, Afyonkarahisar, Turkey

² Department of Mechanical Engineering, Faculty of Technology, Afyon Kocatepe University, Afyonkarahisar, Turkey

³ ERU, College of Engineering, UAE University, Al Ain, UAE

^aahascelik@aku.edu.tr, ^baslantas@aku.edu.tr, ^cw.ahmed@uaeu.ac.ae

Keywords: Sustainable Micro-Milling, Size Effect, Surface Roughness, Minimum Chip Thickness

Abstract. Micromilling is a helpful process empowering the fabrication of small-scale components characterized by complex geometries, heightened precision, and superior surface integrity. Widely embraced across aerospace, biomedical, and electronics sectors, it characterizes efficiency and sustainability in modern manufacturing paradigms. However, fundamental instabilities emerge during the cutting phase, particularly when the size effect diminishes below a critical threshold termed the minimum chip thickness, a parameter linked to the cutting-edge radius and feed rate dynamics. The micro-milling process enables the production of small-scale parts with complex geometries, high precision, and optimal surface quality. It stands as a preferred production method not only in the aerospace, biomedical, and electronics industries but also in the renewable energy sector, where its ability to create intricate components with precise dimensions and superior surface quality is crucial for optimizing efficiency and sustainability in energy harvesting and storage technologies. Instabilities are observed in the cutting process when the size effect falls below a critical value known as the minimum chip thickness. This critical value is related to the cutting-edge radius and feed rate. This study investigates the effect of size on surface roughness in micro-milling of Al6061-T6 workpiece. The results show that surface roughness is high at feed rates below the minimum chip thickness due to the ploughing mechanism. The shear mechanism is active at feed rates above the minimum chip thickness, but the ploughing effect is still observed at the 100µm edge of the cutting channel. The study revealed that surface roughness and height differences were high at feed rates significantly below or above the minimum chip thickness. However, surface quality was optimal at feed rates near the minimum chip thickness. Nevertheless, the study highlights an optimal peak in surface quality achieved at feed rates close to the minimum chip thickness, explaining a relationship between operational efficiency and sustainability in micro-milling endeavours.

Introduction

The demand for precision and small-scale parts in various industries, including electronics, medicine, biomedicine, aerospace, automotive, and telecommunications, is on the rise [1]. Micro-mechanical machining methods have been developed to meet these demands and produce parts with high precision and small dimensions [2]. Among these methods, micro-milling stands out as a way to produce precise and complex parts at a micro scale [3]. The micro-milling method is commonly utilised in various applications, including precision integrated circuits, microelectronic and medical devices, biomedical implants, and optical components like micro mirrors, micro lenses, sensors, microchips, micro propellers, and blades [1]. The micro-milling process differs

fundamentally from conventional milling due to the size effect [4]. When the feed rate per tooth (f_z) falls below a critical value, which depends on the cutting tool and workpiece pair, instabilities occur in the cutting process and surface roughness increases. The optimal ratio between the cutting tool's edge radius (R_e) and the feed rate per tooth determines the critical value. The ratio defining the minimum chip thickness is called h_{min} [5]. In micromachining, the uncut chip thickness (h) is kept below h_{min} , and the negative rake angle effect caused by the cutting-edge radius results in ploughing during the cutting process [6, 7]. Experimental studies have been conducted to determine the minimum chip thickness. According to the literature, the minimum chip thickness varies between 20% and 30% of the cutting-edge radius [8]. In titanium alloys, this ratio is 30% [9], while in aluminium alloys, it can go up to 35-40% [10, 11]. Wu et al. (2020) discovered that the minimum chip thickness is 17% of the edge radius [12]. It is a well-established fact that cutting forces display unstable behaviour at feed rates below the minimum chip thickness [13, 14]. This is attributed to the ploughing mechanism that becomes active at feed rates below the minimum chip thickness during the cutting process. Figure 1a provides a schematic representation of full slot machining in the micro milling process, while Figure 1b illustrates the variation of the chip thickness based on the position of the cutting edge and the feed rate per tooth. As is commonly understood, the thickness of the chip during milling varies depending on the position of the tool. Initially, when the tool first makes contact with the workpiece, the chip thickness is almost zero. As the angular position of the cutting edge (ϕ) increases, the value of h also increases. When $\phi=90^\circ$, $h=f_z$. If $h < h_{min}$, ploughing occurs, which results in a decrease in the quality of the machined surface and an increase in the amplitude of the cutting forces [15]. This study aimed to establish a relationship between the angular position of the tool (represented by the symbol ϕ) and the ploughing length (w_p) by examining the change in surface roughness on the machined slot surface (Fig. 1).

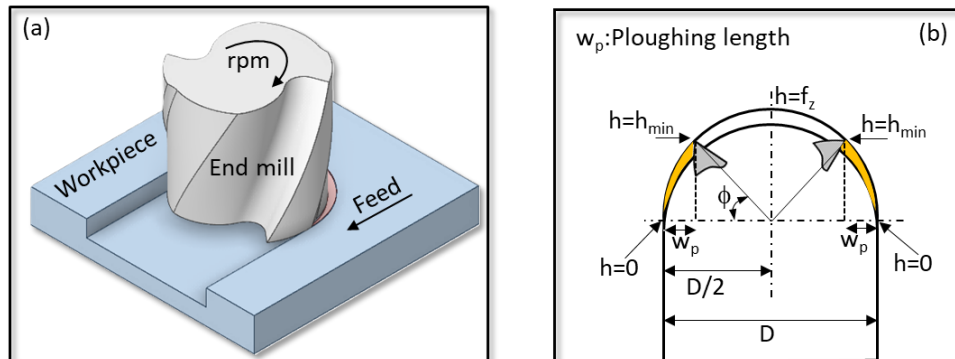


Figure 1. Relationship between uncut and minimum chip thickness.

The use of the ploughing mechanism instead of the shear mechanism during the cutting process has a negative impact on the surface quality of the workpiece. The high feed rate results in increased cutting forces, which in turn leads to a deterioration of the surface quality and an increase in surface roughness. To achieve the best surface quality during the cutting process, it is essential to use a feed rate that is large enough to prevent ploughing, yet small enough to keep cutting forces low. This study investigates the effect of size on surface roughness in the micro-milling process. Surface roughness measurements were taken from the cutting grooves of the micro-milled workpiece at different feed rates. The minimum chip thickness was determined, and the ploughing effect was identified.

Material and Method

This study used Al6061-T6 alloy, commonly used in the production of micro equipment in the defence, aerospace, and electronics sectors. Aluminium alloys are widely used due to their formability, light weight, high strength, and corrosion resistance. The T6 heat treatment improved

the mechanical and physical properties of the alloy. Compared to other aluminum alloys, Al6061-T6 stands out due to its high toughness, superior corrosion resistance, low density, high thermal conductivity, and low cost [17]. Table 1 shows the alloy's chemical and basic mechanical properties, where 10 mm x 10 mm x 15 mm specimens were used in cutting tests.

Table 1. Chemical composition and mechanical properties of Al6061-T6 material [17].

Elements	Chemical Composition						Mechanical Properties			
	Al	Mg	Fe	Cu	Zn	Si	Mn	UTS (MPa)	YS (MPa)	%Elongation
Alloying elements(%)	Rest	1.14	0.35	0.3	0.25	0.67	0.12	307	275	20

The cutting tests employed a 975 μm diameter, 2-flute tungsten carbide cutting tool with AlTiSiN coating. The tool has a helix angle of 30°, a helix length of 2 mm, an edge radius of 5 μm , a rake angle of 0°, and a clearance angle of 15°. The geometrical properties of the cutting tool were determined by measuring its features from scanning electron microscope images (Fig. 2).

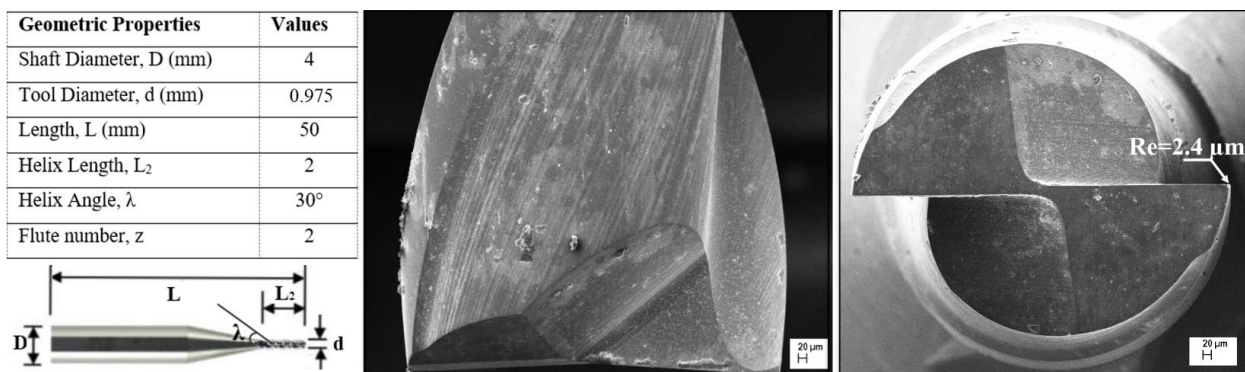


Figure 2. SEM image of the diameter and edge radius of the cutting tool used in cutting experiments.

Cutting tests were conducted at various feed rates under dry cutting conditions using a triaxial test rig to determine the minimum chip thickness. The cutting tool was secured to the IMT spindle with a collet, and axis movements were set using Thorlabs software. The workpiece was held in place with a Kistler-9119AA1 mini dynamometer to measure the instantaneous cutting forces. The cutting force signals were transferred to the computer via an amplifier and converted into force measurements using Dynoware software. The cutting tool movements and cutting zone were observed using a USB microscope during the cutting process (Fig. 3).

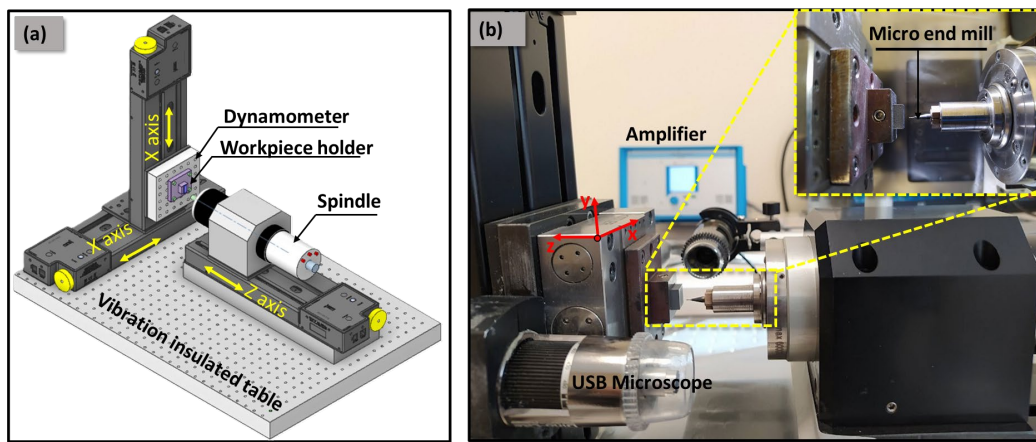


Figure 3. a) Schematic representation of the experimental setup used in cutting experiments, b) a general view and positioning of the cutting tool-workpiece on the experimental setup.

Micro milling experiments were conducted at a constant depth of cut (100 μm) and speed (30000 rpm) to determine the minimum chip thickness and observe the effect of feed rate differences per tooth on surface roughness. Ten different feed rates (0.1, 0.25, 0.5, 0.75, 1, 2, 4, 6, 8, 10 $\mu\text{m}/\text{tooth}$) were used to determine the dominant cutting process mechanism between shear and ploughing. The Nanovea 3D ST400 optical surface profilometer was used to take measurements by scanning the cutting grooves. The scanning distance was 1.2 mm x 0.6 mm with a scanning step of 3 μm . Measurements were taken from the inside of the channel at a distance of 970 μm x 600 μm . The resulting Sa (areal average surface roughness) and Sz (areal maximum surface roughness) surface roughness values were compared at different feed rates. Additionally, Ra measurements were taken parallel to the feed direction across the width of the machined channel. This revealed the impact of differences in feed rate on surface roughness for two distinct levels of roughness.

Results and Discussion

Sa and Sz values were determined at different feed rates through cutting tests and surface roughness scanning. Measurements were taken from at least three different areas of the cutting grooves, and the averages of these measurements are presented in Figure 4. A detailed graph for $f_z=2\mu\text{m}/\text{tooth}$ is also provided in Figure 4. The results indicate a significant increase in both Sa and Sz values for $f_z < 0.5\mu\text{m}/\text{tooth}$, which is defined as the Ploughing zone in both graphs. In micro milling, a negative rake angle effect occurs at the cutting edge when the feed per tooth is smaller than the minimum chip thickness. This effect makes the cutting process difficult, increases cutting forces, and causes deterioration of the machined surface quality and burr formation. Figure 4 shows a significant difference between the error bars for 0.1 and 0.25 $\mu\text{m}/\text{tooth}$, indicating a high degree of surface variability. For f_z greater than 0.5 $\mu\text{m}/\text{tooth}$, the milling process achieves cutting through a shear mechanism. Similar to conventional milling, increasing the feed rate results in an increase in surface roughness. As the cutting edge radius measures 2.4 μm (Fig. 2), the minimum chip thickness corresponds to 21% of the cutting edge radius, based on the surface roughness results. The Sa and Sz values at the minimum feed rate (0.1 $\mu\text{m}/\text{tooth}$) are higher than those at the maximum feed rate (10 $\mu\text{m}/\text{tooth}$), indicating that the ploughing mechanism has a significant effect on surface roughness.

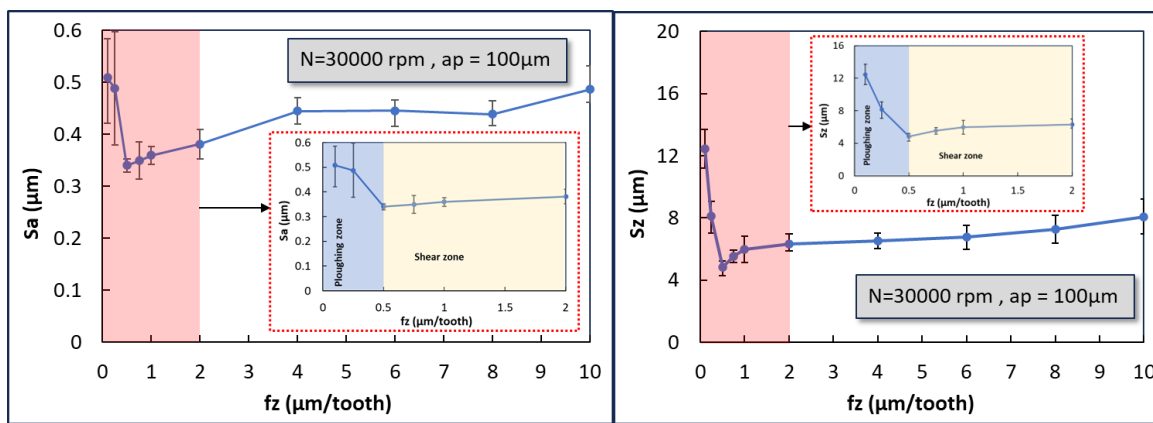


Figure 4. Variation of S_a and S_z surface roughnesses as a function of feed rate.

Figure 5 displays the surface topographies of the machined slots, illustrating the impact of the ploughing and shear mechanism on the surface in micro milling. Additionally, the two-dimensional variation plot along the slot width is presented. When the feed rate is below the minimum chip thickness ($0.1 \mu\text{m}/\text{tooth}$ is provided as an example), a non-uniform surface topography is observed. The cutting marks of the cutting tool are faint and only located in the center of the slot, across its width. The surface irregularity and height difference increase towards the edges of the slot, as shown in the linear variation plot. When using $f_z=1 \mu\text{m}/\text{tooth}$, the cutting marks on the surface are more pronounced, and the height difference (h_{pv}) at the edges of the slot is smaller compared to $f_z=0.1 \mu\text{m}/\text{tooth}$. Additionally, the height difference (h_{pv}) of the surface marks between the edges and the middle region of the slot is also smaller for $f_z=1 \mu\text{m}/\text{tooth}$. At a f_z of $1 \mu\text{m}/\text{tooth}$, the cutting in the middle region of the slot ($100 \mu\text{m} < w_s < 800 \mu\text{m}$) is achieved through shear mechanism. However, there is a height difference between the edges and the center of the slot, indicating ploughing occurs at the edges. At a f_z of $10 \mu\text{m}/\text{tooth}$, the cutting process is also achieved through shear mechanism. The high feed rate resulted in an increase in surface roughness. Figure 5 shows that the h_{pv} values for 0.1 and $10 \mu\text{m}/\text{tooth}$ are similar, indicating a deterioration of surface quality caused by milling with ploughing.

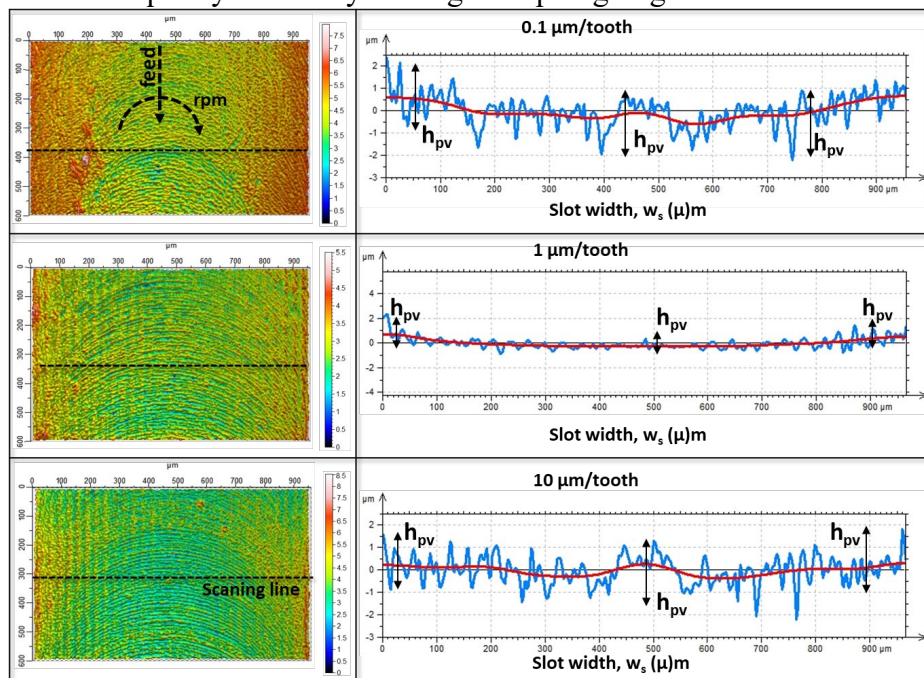


Figure 5. 3D surface topographies from the optical profilometer.

Figure 6 illustrates the variation of two-dimensional surface scanning results parallel to the feed direction with slot width. The surface roughness is high at the edges and in the middle regions in cutting processes with $f_z=0.1$ and $0.25 \mu\text{m}/\text{tooth}$ due to the ploughing mechanism effect since $h < h_{\min}$ along the cutting channel. However, in cutting processes with feed rates of 0.5 , 0.75 and $1 \mu\text{m}/\text{tooth}$, R_a is minimum in the middle region of the cutting channel ($100 \mu\text{m} < w_s < 800 \mu\text{m}$). In contrast, R_a increases near the starting ($w_s < 100 \mu\text{m}$) and ending edges ($w_s > 900 \mu\text{m}$) of the slot due to ploughing. The chip thickness is initially close to zero and increases with the rotation of the tool during cutting, even for $f_z=0.5 \mu\text{m}/\text{tooth}$, where the surface roughness is minimum. However, the chip thickness at the beginning and end of the cutting process is less than the minimum chip thickness, causing ploughing. Figure 6 shows that the length at which ploughing occurs is about $100 \mu\text{m}$. At $f_z=0.1$ and $0.25 \mu\text{m}/\text{tooth}$, the R_a value varies across the entire width of the groove, with the maximum R_a value being at the edge and in the center of the groove. At higher feed rates ($f_z=8$ and $10 \mu\text{m}/\text{tooth}$), the R_a value is higher in the center of the slot ($200 \mu\text{m} < w_s < 800 \mu\text{m}$). However, the R_a value is low at the beginning ($w_s < 100 \mu\text{m}$) and end edges ($w_s > 900 \mu\text{m}$) of the slot.

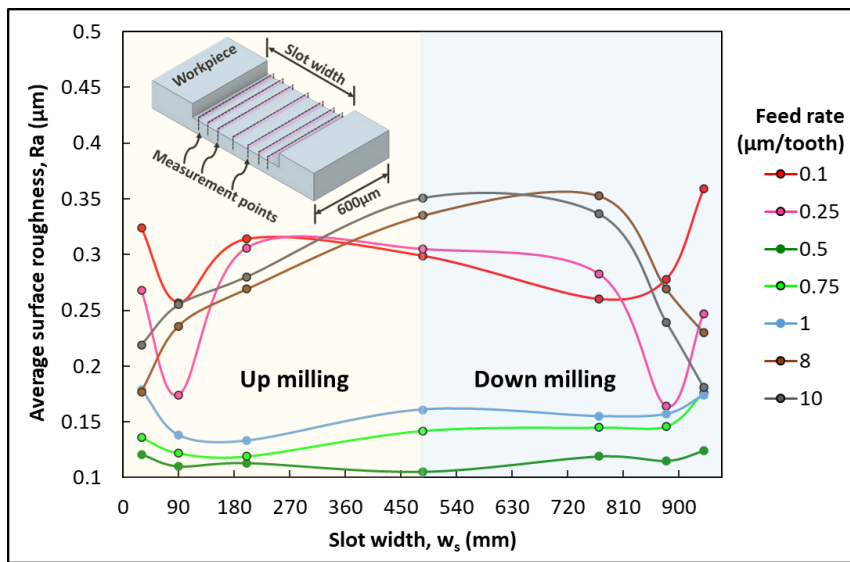


Figure 6. Two-dimensional surface topographies from the optical profilometer.

Conclusion

This study observes the size effect in the micro milling process and investigates the impact of different feed rates on surface roughness due to ploughing and shear mechanisms. The obtained results are listed below.

- Based on the surface roughness results obtained at different feed rates, it was determined that the critical feed rate was approximately $f_z=0.5 \mu\text{m}/\text{tooth}$.
- It was observed that when feed rates fall below the minimum chip thickness, the ploughing mechanism significantly increases surface roughness.
- At feed rates higher than the minimum chip thickness, the surface roughness increases linearly with the feed rate because the shear mechanism is active.
- At feed rates where the shear mechanism is active, the surface roughness is higher at the starting and ending edges of the $100 \mu\text{m}$ slot than in the middle regions due to the ploughing effect.
- At high feed rates, the surface roughness in the middle regions of the slot ($200 \mu\text{m} < w_s < 800 \mu\text{m}$) is higher than the edge regions ($w_s < 100 \mu\text{m}$). The R_a value increases

with increasing feed rate, which is more effective than the increase due to ploughing in the edge regions.

- At feed rates lower than the minimum chip thickness and at high feed rates, there are greater height differences in the surface topography.

Moreover, these findings hold promising implications for renewable energy applications. Understanding the interaction between feed rates and surface roughness enhances manufacturing efficiency and has significance in the fabrication of micro-components crucial for renewable energy technologies. Manufacturers can achieve smoother surfaces and improved energy conversion efficiencies in micro-devices utilized in solar panels, wind turbines, and other renewable energy systems by optimizing milling parameters to minimize plowing effects and maximize shear mechanisms. This emphasizes the pivotal role of micro-milling in advancing sustainable energy solutions.

References

- [1] Aslantas, K., Demir, B., Guldibi, AS., Niinomi, M, Dikici, B., A comparative study on the machinability of β -type novel Ti29Nb13Ta4.6Zr (TNTZ) biomedical alloys under micro-milling operation, *Journal of Manufacturing Processes* 92 (2023) 135-146.
<https://doi.org/10.1016/j.jmapro.2023.02.043>
- [2] Boswell, B., Islam, M.N., Davies, I.J., A review of micro-mechanical cutting, *Int. J. Adv. Manuf. Technol.* 94 (2018) 789-806. DOI: 10.1007/s00170-017-0912-y
- [3] Balazs, B.Z., Geier, N., Takacs, M., Davim, J.P., A review on micro-milling: recent advances and future trends, *Int. J. Adv. Manuf. Technol.* 112 (2020) 655-84. DOI: 10.1007/s00170-020-06445-w
- [4] Fu, M.W., Wang, J.L., Size effects in multi-scale materials processing and manufacturing, *Int. J. Mach. Tool. Manuf.* 167 (2021) 103755. DOI: 10.1016/j.ijmachtools.2021.103755
- [5] Dib, M.H.M., Duduch, J.G., Jasinevicius, R.G., Minimum chip thickness determination by means of cutting force signal in micro endmilling, *Precis. Eng.* 51 (2018) 244–62.
10.1016/j.precisioneng.2017.08.016
- [6] Wan, M., Ma, Y.C., Feng, J., Zhang, W.H., Study of static and dynamic ploughing mechanisms by establishing generalized model with static milling forces, *Int. J. Mech. Sci.*, 114 (2016) 120-31.
- [7] Krajewska-Spiewak, J., Maruda, R.W., Krolczyk, G.M., Nieslony, P., Wieczorowski, M., Gawlik, J. Wojciechowski, S., Study on ploughing phenomena in tool flank face - workpiece interface including tool wear effect during ball-end milling, *Tribology International* 181 (2023) 108313.
- [8] Cheng, K., Huo, D., Micro-cutting: fundamentals and applications (First Edition), Chichester UK, John Wiley & Sons Ltd. (2013). DOI: 10.1002/9781118536605
- [9] Aslantas, K., Danish, M., Hasçelik, A., Mia M., Gupta M., Ginta T., Ijaz H., Investigations on Surface Roughness and Tool Wear Characteristics in Micro-turning of Ti-6Al-4V Alloy, *Materials* 13 (2020) 2998. <https://doi.org/10.3390/ma13132998>
- [10] Park, S. S., Malekian, M., Mechanistic Modeling and Accurate Measurement of Micro End Milling Forces, *CIRP Annals-Manufacturing Technology* 58 (2009) 49-52.
<https://doi.org/10.1016/j.cirp.2009.03.060>

- [11] Chen, Y., Wang, T., Zhang, G., Research on Parameter Optimization of Micro-Milling Al7075 Based on Edge-Size-Effect, *Micromachines* 11 (2020) 197.
<https://doi.org/10.3390/mi11020197>
- [12] Wu, X., Liu, L., Du, M., et al., Experimental Study on the Minimum Undeformed Chip Thickness Based on Effective Rake Angle in Micro Milling, *Micromachines* 11 (2020) 924.
<https://doi.org/10.3390/mi11100924>
- [13] Chae, J., Park, S.S., Freiheit, T., Investigation of Micro-Cutting Operations, *International Journal of Machine Tools and Manufacture* 46 (2006) 313-332.
<https://doi.org/10.1016/j.ijmachtools.2005.05.015>
- [14] Sun, X., Cheng, K., Micro/Nano-Machining through Mechanical Cutting (2010).
<http://dx.doi.org/10.1016/B978-0-8155-1545-6.00002-8>
- [15] Sun, Z., To, S., Zhang, S., Zhang G., Theoretical and experimental investigation into non-uniformity of surface generation in micro-milling, *International Journal of Mechanical Sciences*, 140 (2018) 313-324. <https://doi.org/10.1016/j.ijmecsci.2018.03.019>
- [16] Akram, S., Jaffery, S., Khan, M., et.al., Numerical and experimental investigation of Johnson–Cook material models for aluminum (Al 6061-T6) alloy using orthogonal machining approach, *Advances in Mechanical Engineering* 10 (2018) 1-14.
<https://doi.org/10.1177/1687814018797794>
- [17] Wakchaure, K., Chaudhari, R., Thakur, A., Fuse, K., Lopez de Lacalle, L.N., Vora, J., The Effect of Cooling Temperature on Microstructure and Mechanical Properties of Al 6061-T6 Aluminum Alloy during Submerged Friction Stir Welding, *Metals* 13 (2023) 1159.
<https://doi.org/10.3390/met13071159>

From smart soles to green goals, interlacing sustainable innovations in the age of smart health: An exploratory search

Fahd KORAICHE^{1,a *}, Amine DEHBI^{2,b} and Rachid DEHBI^{1,c}

¹Research Laboratory of Computer Science (LIS), Faculty of Science Ain Chock, Casablanca, Morocco

²Research Laboratory of Mathematics and Computer Science (LTI), Faculty of Science Ben M'Sick, Casablanca, Morocco

^afahd.koraiche@gmail.com, ^bdehbiamine1@gmail.com, ^cdehbirac@yahoo.fr

Keywords: Energy Consumption, IoT, IoMT, Healthcare, Smart Health

Abstract. Health goes beyond the mere absence of illness. It's arguably a state that encompasses a whole spectrum of physical, social, and mental well-being. It involves not only curing sickness but also promoting healthy lifestyles, behaviors, and environments that enable individuals to thrive. Health interventions can be formalized through medicine, but they can also take on a broader spectrum of approaches, including prevention, early detection, and management of diseases. By acknowledging this broader vision of health, we can see that it influences various aspects of our lives, including our work, education, relationships, food, clothes, and recreational activities. It also impacts our communities and cultures, affecting social norms, policies, and practices that shape our health outcomes. Therefore, health is not just an individual concern but also a collective one. Furthermore, the integration of health into technological practices can have a significant impact on our well-being. It can facilitate access to health information, resources, and services, enable remote monitoring and diagnosis, and enhance communication and social support networks.

Introduction

In an era where technology and health converge, the paradigm of smart health not only reshapes how we monitor well-being but also holds the potential to redefine our relationship with the environment. Smart health technologies, in addition to revolutionizing well-being management, present auspicious avenues for ameliorating our environmental footprint.

Concurrently, the urgency of mitigating climate change compels us to explore innovative solutions that optimize resource consumption and minimize environmental impact. This article delves into the intricate nexus of these two critical domains, exploring how smart health advancements can foster both individual well-being and environmental responsibility.

This article encapsulates a journey into the synergy between cutting-edge healthcare technologies and a commitment to environmental sustainability. This exploratory search navigates through the intricate tapestry of interconnected themes. We will first delve into the profound connections between sustainability practices and individual well-being. From exploring how smart shoes contribute to holistic health monitoring to the impact of programming languages on carbon emissions, we dissect the intricate threads that weave together a narrative of interconnected health and environmental consciousness.

Literature Study

Zahid et al. [1] responded to the primary weakness of Body Sensors Area Networks (BSNs) which is energy consumption which is due to their small size and limited lifetime batteries, they wrote a paper that presents two contributions. First, they propose an adaptive duty-cycle optimization algorithm (ADO) that enhances the devices' active time by taking into consideration the exact

power level that saves more energy, unlike traditional methods that increase the sleep period. Second, they propose a joint Sustainable and Green smart-health framework. They conducted a thorough experimental and theoretical analysis through real-time data. The results showed that the algorithm enhances energy and reliability savings by 36.54% and 24.43%, respectively. Therefore, they concluded that the algorithm is more promising for energy-limited sensor devices in healthcare-connected platforms.

Abdellatif et al. [2] have proposed an architecture that uses wireless technologies and sensors to connect patients with medical healthcare. This framework differs from previous work in this field by using various wireless networks to optimize medical data delivery. The team aims to reduce the size of transmitted data while maintaining reliable real-time healthcare services. They have developed an energy-efficient s-Health system by incorporating wireless network components with application characteristics and using the spectrum across multiple radio access technologies to fulfill the applications' Quality of Service (QoS). The proposed MEC-based system architecture meets all s-Health requirements. The team has used intelligent data processing techniques at the network edge to achieve this. They have also introduced some edge computing techniques, such as adaptive in-network compression, event detection, and network-aware optimization, which enable MEC-based system architecture to fulfill all s-Health requirements. In addition, the team has discussed the challenges and open issues for utilizing the MEC paradigm in s-Health. This includes the use of cooperative edges to improve energy and spectrum efficiency, as well as the need and benefit of combining heterogeneous data sources at the edge.

D. Laxma Reddy et al. [4] mainly focused on finding the best Cluster Head for an energy-efficient routing protocol in Wireless Sensor Networks (WSN). The paper proposes a new hybrid algorithm called Ant Colony Optimization (ACO) integrated Glowworm Swarm Optimization (GSO) approach (ACI-GSO) as a solution for Cluster Head Selection (CHS). The main objective of CHS is to reduce the distance between the selected Cluster Head nodes. To achieve this, the fitness function uses multiple objectives such as distance, delay, and energy. Finally, the proposed work was evaluated and proved to be more effective compared to other conventional methods.

Intertwining Sustainability and Well-being

In this chapter, we delve into the intricate connections between sustainability and well-being, exploring how sustainable innovations can significantly impact and promote overall health and wellness. By examining the interplay between sustainable practices and well-being, we aim to uncover the profound implications of sustainability on fostering a healthier and more environmentally conscious future. For example, hospitals have started installing solar energy systems to meet part of their energy needs. Others have implemented waste management programs to minimize their impact on the environment.

A. Sustainable Waste Management Optimization

Sustainable waste management (SWM) optimization in the context of smart health involves leveraging technology to minimize waste generation, maximize resource efficiency, and reduce environmental impact within healthcare settings. Here's how it works:

1) Reducing Medical Waste:

Smart health technologies can help streamline healthcare processes, leading to reduced medical waste generation. For example, digital health records and telemedicine platforms eliminate the need for paper-based records and unnecessary in-person visits, thereby reducing paper and plastic waste.

2) Optimizing Resource Utilization:

Smart sensors and IoT devices can monitor resource usage in healthcare facilities, such as energy, water, and medical supplies. By analyzing real-time data, healthcare providers can identify inefficiencies and implement strategies to optimize resource utilization, thereby reducing waste [1]. In 2017, the Republic of Türkiye's Ministry of Environment, Urbanization, and Climate Change launched the "Zero Waste Project." The project aims to prevent waste generation, reduce waste, recycle waste at its source, prevent wastage, and utilize natural resources more efficiently [5].

3) Recycling and Reuse:

Smart health technologies can facilitate the recycling and reuse [19] of medical equipment and supplies. For instance, smart inventory management systems can track the usage of medical supplies and identify items that can be recycled or sterilized for reuse, reducing the need for single-use items.

4) Waste Segregation and Disposal:

Smart waste management systems can automate the segregation and disposal of different types of waste in healthcare facilities. By using sensors and AI algorithms, these systems can identify recyclable, hazardous [18], and non-recyclable waste, ensuring proper disposal and minimizing environmental contamination.

The Green Grid of Health with Smart Technologies

We'll break down the intricate connections between smart health and sustainability, demystifying the technologies and highlighting their potential to revolutionize both our well-being and the health of our planet. In this context, it is evident that green technologies have been implemented to enhance the quality of healthcare, or at least support for energy consumption measurement should be provided [12]. Hospitals are now utilizing air quality monitoring systems to ensure a healthy environment for both patients and staff. Additionally, energy-efficient medical equipment is being used to reduce energy consumption and costs. There are many other initiatives as well [7][8].

A. Harvesting the Planet for a healthier life

1) How Smart Shoes are Paving the Way for a More Active and Earth-Conscious Future

- **Promoting Physical Activity:** Embedded sensors can track steps, distance, and calories burned, motivating users to embrace healthier lifestyles and reduce reliance on carbon-heavy transportation.

- **Encouraging Sustainable Choices:** Gamified fitness apps linked to smart shoes can incentivize walking and cycling over car travel, reducing individual carbon footprints [12].

- **Generating Green Energy:** Kinetic energy from footsteps can be harvested to power the shoes themselves or even contribute to a microgrid for other smart health devices, eliminating reliance on batteries [8][17]. Also, wave generators and turnstiles are innovative ways to generate renewable and sustainable energy. Wave generators use natural resources like oceans' wave movement, while turnstiles [25] generate electricity each time someone passes through them, they are usually put in a population-dense area.

2) Solar Panels as a Sustainable Powerhouse:

- **Green Energy Source:** Embedded solar panels can power healthcare facilities (Points Of Care) and health devices, minimizing dependence on conventional electricity [11], and reducing greenhouse gas emissions.

- **Decentralized Power:** Distributed solar energy collection in smart shoes and wearable devices lowers reliance on centralized grids, increasing resilience and sustainability.



Fig 1. Planetary Health pathway

- **Personal Empowerment:** Individuals gain autonomy over their energy needs, promoting environmental consciousness and fostering a sense of self-reliance.

In other words, smart shoes [17] play a multifaceted role in promoting physical activity, tracking environmental data, and contributing to sustainable transportation choices. Additionally, smart panels offer a renewable energy source for smart health monitoring systems, with the challenge lying in finding the right balance between device performance and energy consumption through thoughtful optimization strategies.

B. Invisible Footprint: Green Programming for a Healthier Planet

The digital world might seem intangible, but the lines between its code and our planet's health are not. Programming languages, software architectures, and middleware, though seemingly technical aspects of software development, hold hidden implications for CO₂ emissions and ultimately, the well-being of our planet and its inhabitants [1].

1) The Impact on Planetary and Human Health:

- **Climate Change:** Increased CO₂ emissions contribute to global warming, rising sea levels, extreme weather events, and ecosystem disruption, impacting food security, water resources, and public health.

- **Air Pollution:** Data centers rely on energy sources that often result in air pollution, exacerbating respiratory illnesses and cardiovascular diseases.

- **Mental and Social Impacts:** The relationship between our health and that of the planet is very tight, any disturbance in the planet's ecosystem is a disturbance to humanity, for instance, Climate change and its consequences pose mental health [16] challenges as well as displacement and social unrest, creating a chain reaction of suffering.

- **Data Centers and Cloud Services Energy Consumption:** Large-scale data centers that host software applications and cloud services consume significant amounts of energy. Inefficiently designed software can contribute to higher energy needs in data centers, amplifying the environmental footprint and impacting planetary health.

- **Electronic Waste (E-Waste) & Short Lifecycle:** Poorly designed software may lead to faster hardware obsolescence, contributing to the generation of e-waste. E-waste disposal has environmental consequences, with improper disposal methods leading to soil and water pollution, negatively affecting planetary health.

2) Programming languages for a sustainable future:

Different programming languages have varying levels of energy efficiency. For instance, languages that demand more computational resources may contribute to higher energy consumption during program execution. The choice of programming language affects the energy requirements of software systems and subsequently influences CO₂ emissions.

- **Software Architectures:** The design and architecture of software systems determine how efficiently resources, including processing power and memory, are utilized. Poorly optimized software architectures can result in excessive resource usage, leading to higher energy consumption and increased CO₂ emissions [1][3].



Fig 2. Illustration of Green Technologies impact

- **Middleware and communication efficiency(Green middleware):** Opting for lightweight, energy-efficient middleware solutions can streamline data communication and management while maximizing sustainability. Inefficient middleware can lead to higher data transfer loads, requiring more energy for communication processes and contributing to increased CO₂ emissions [2][3].
- **Code-Level Awareness:** Educating developers about the environmental impact of their code choice.
 - **Algorithmic Efficiency:** Optimizing algorithms for reduced processing power and minimizing unnecessary computations can significantly decrease energy consumption [2] [3][4].
 - **Lightweight Architectures:** Choosing leaner frameworks, optimizing server usage, and minimizing geographic distribution can help reduce the carbon footprint of software systems [3].

By acknowledging the link between programming and planetary health, we can weave a new narrative. By optimizing code, architectures, and middleware, we can rewrite our digital footprint and contribute to a future where technology complements, not threatens, the well-being of our planet and its inhabitants(Global Health). Let's remember, that every line of code has the potential to leave a mark, not just on a screen, but on the very fabric of our planet's health.

C. The Tradeoff of Performance vs. Energy Consumption

1) Optimizing the Performance-Energy Trade-off:

The quest for powerful smart devices often comes at the cost of high energy consumption. However, several strategies can strike a balance:

- **Sensor Optimization:** Employing energy-efficient sensors and utilizing them strategically can significantly reduce power consumption without compromising data accuracy.
- **Low-Power Processors:** Implementing specialized, low-power processors specifically designed for wearables can further enhance energy efficiency.
- **Cloud-Based Processing:** Offloading data processing to the cloud reduces on-device energy needs, enabling more powerful features while extending battery life.
- **Adaptive Algorithms:** Developing algorithms that adjust processing power based on activity level can optimize performance while ensuring efficient energy use [2].

2) Addressing Concerns about Smart Health Device Electromagnetic Frequency Radiation

Smart devices, including wearables, emit non-ionizing radiation in the radiofrequency (RF) range. Unlike ionizing radiation (e.g., X-rays) which can damage DNA, RF radiation is generally considered safe at low levels. However, concerns remain about the potential long-term health effects of chronic exposure, particularly with the increasing number of devices we interact with daily.

• **Safety Standards and Research:** International safety guidelines, such as those set by the International Commission on Non-Ionizing Radiation Protection (ICNIRP), exist to limit exposure to RF radiation. Device manufacturers must adhere to these standards, ensuring emissions remain within safe thresholds. Ongoing research continues to investigate the potential health effects of chronic RF exposure. While some studies haven't found conclusive evidence of harm, others suggest a weak link between certain types of RF radiation and increased risk of certain cancers, like brain tumors. However, it's important to note that these studies are often complex, with confounding factors and limitations, making it difficult to establish definitive causal relationships.

• **Exposure Levels and Health Effects:** Prolonged exposure to electromagnetic frequency (EMF) radiation from smart devices, including wearables, raises concerns about its impact on human health. While EMF is a fundamental aspect of technology, addressing concerns involves understanding potential risks associated with extended exposure. Some studies suggest a possible link between long-term exposure to EMF radiation and health issues such as headaches, sleep

disturbances, and potential implications for fertility. Ongoing research aims to clarify these potential health effects and establish clear causal relationships.

• **Navigating the Uncertainty:** While uncertainty persists, responsible use of smart devices can help mitigate potential risks like minimizing Exposure; and limit the time spent close to the device, particularly when it's actively transmitting data. For example, don't sleep with your phone under your pillow or keep it directly against your body for extended periods. Opt for Airplane Mode; When not in use, turn off wireless features like Bluetooth and Wi-Fi to minimize unnecessary exposure. Choose Eco-Friendly Devices; Some devices offer lower-power modes or settings that can reduce radiation emissions. Stay Informed; Follow reputable sources, like international health organizations, for updates on research findings and safety recommendations.

• **Vulnerability and Specific Absorption Rate(SAR):** SAR measures the rate at which the body absorbs radiofrequency (RF) energy from a device. Regulatory bodies set SAR limits to prevent excessive RF energy absorption and minimize potential health risks. Also, vulnerable populations, such as pregnant individuals and children, are of particular concern due to potential sensitivity to radiation. Recognizing the need for caution, especially for those more susceptible, underscores the importance of safety standards.

Discussion

In a tapestry woven from the threads of science, technology, and environmental consciousness, our article has explored the intricate connections between individual well-being, sustainable practices, and the health of our planet. In exploring the realm of smart health and sustainable innovations, we've delved into a diverse array of topics. From the foundational concerns surrounding electromagnetic frequency radiation emitted by smart devices to the intricate interplay between programming languages, software architectures, and CO₂ emissions, the journey has been comprehensive. Our study extended to the pivotal role of smart shoes in promoting physical activity and sustainable transportation choices, not forgetting their potential to generate green energy [11]. However, the reviewed literature showcases commendable efforts to address key challenges in smart health systems, particularly focusing on energy consumption efficiency and sustainable energy. While each work contributes significantly to the field, further collaborative research could explore synergies between these approaches, potentially offering holistic solutions for the evolving landscape of smart health systems. For instance, a combination of these approaches applied for a Wearable Area Sensors Network, that can rely on self-energy generation from human motion would be the most efficient, like energy-harvesting shoes.

Conclusion and Future Perspective

Our exploration of the intricate nexus between smart health technologies, green solutions, and language processing reveals a promising avenue toward a sustainable future. Intertwined threads of smart health innovation, from nuanced personal well-being monitoring to the interplay of connectivity protocols, frequency radiations, and language processing, unveil a tapestry of profound interconnectedness. The symbiotic relationship between these technological advancements and environmental stewardship offers a blueprint for a future where technological progress and ecological responsibility coexist harmoniously.

Future work may include a novel approach that follows this study to implement a greener and more sustainable Smart Health Monitoring System that monitors both human and planetary health.

References

- [1] Zahid, N., Sodhro, A. H., Al-Rakhami, M. S., Wang, L., Gumaei, A., & Pirbhulal, S. (2021). An Adaptive Energy Optimization Mechanism for Decentralized Smart Healthcare Applications. 2021 IEEE 93rd Vehicular Technology Conference (VTC2021-Spring).
<https://doi.org/10.1109/vtc2021-spring51267.2021.9448673>

- [2] Abdellatif, A. A., Mohamed, A., Chiasserini, C. F., Erbad, A., & Guizani, M. (2020). Edge computing for energy-efficient smart health systems. *Energy Efficiency of Medical Devices and Healthcare Applications*, 53–67. <https://doi.org/10.1016/b978-0-12-819045-6.00003-0>
- [3] Natarajan, Rajesh & H L, Gururaj & Flammini, Francesco & Premkumar, Anitha & Kumar, V Vinoth & Gupta, Dr-Shashi. (2023). A Novel Framework on Security and Energy Enhancement Based on Internet of Medical Things for Healthcare 5.0. *Infrastructures*. 8. 22. <https://doi.org/10.3390/infrastructures8020022>
- [4] Reddy, D.L.; Puttamadappa, C.; Suresh, H.N. Merged glowworm swarm with ant colony optimization for energy-efficient clustering and routing in the wireless sensor network. *Pervasive Mob. Comput.* 2021, 71, 101338.
- [5] Aykal, Güzin. (2023). Green transformation in the health sector and medical laboratories, adaptation to climate change in Türkiye. *Turkish Journal of Biochemistry*. <https://doi.org/10.1515/tjb-2023-0207>
- [6] EFLM Green Labs [Internet]. <https://greenlabs.eflm.eu/> [Accessed Jan 2024].
- [7] Ghernouk, Chaimae & Marouane, Mkik & Dalili, Saad & Boutaky, Soukaina & Hebaz, Ali & Mchich, Hamza. (2023). The Attractive Determinants of Green Technologies: The Case of The Health Sector in Morocco. 21. 1759-1774. <https://doi.org/10.55365/1923.x2023.21.192>
- [8] Sadegh Seddighi, Edward J. Anthony, Hamed Seddighi, Filip Johnsson, The interplay between energy technologies and human health: Implications for energy transition, *Energy Reports*, Volume 9, 2023, Pages 5592-5611, ISSN 2352-4847, <https://doi.org/10.1016/j.egyr.2023.04.351>
- [9] Prajapati, Sunil & Dayal, Parmeswar & Kumar, Vipin & Gairola, Ananya & Sustain, Agri. (2023). Green Manuring: A Sustainable Path to Improve Soil Health and Fertility. 01. 24-33. <https://doi.org/10.5281/zenodo.10049824>
- [10] Cardinali, Marcel & Balderrama, Alvaro & Arztmann, Daniel & Pottgiesser, Uta. (2023). Green Walls and Health: An umbrella review. *Nature-Based Solutions*. 3. <https://doi.org/100070>. <https://doi.org/10.1016/j.nbsj.2023.100070>
- [11] Li, Meng & Geng, Yong & Zhou, Shaojie & Sarkis, Joseph. (2023). Clean energy transitions and health. *Heliyon*. 9. e21250. <https://doi.org/10.1016/j.heliyon.2023.e21250>
- [12] Aripriharta, Aripriharta. (2023). Performance Analysis Smart-Shoes To Measure the Pulse in Dorsalis Pedis Artery. *Fidelity : Jurnal Teknik Elektro*. 5. 21-30. <https://doi.org/10.52005/fidelity.v5i2.146>
- [13] Li, Qiangyi & Liu, Yangqing & Yang, Lan & Ge, Jiexiao & Chang, Xiaona & Zhang, Xiaohui. (2023). The impact of urban green space on the health of middle-aged and older adults. *Frontiers in Public Health*. 11. <https://doi.org/10.3389/fpubh.2023.1244477>
- [14] Revich, B.A.. (2023). The significance of green spaces for protecting health of urban population. *Health Risk Analysis*. 168-185. <https://doi.org/10.21668/health.risk/2023.2.17.eng>
- [15] Rathnayke, Saumya & Amofah, Seth. (2023). Health and Wellbeing Implications of Urban Green Exposure on Young Adults in a European City. *Journal of Advanced Research in Social Sciences*. 6. 53-70. <https://doi.org/10.33422/jarss.v6i4.1136>
- [16] Zhang, Jun & Jin, Jinghua & Liang, Yimeng. (2024). The Impact of Green Space on University Students' Mental Health: The Mediating Roles of Solitude Competence and Perceptual Restoration. *Sustainability*. 16. 707. <https://doi.org/10.3390/su16020707>

- [17] Kurita, Hiroki & Katabira, Kenichi & Yoshida, Yu & Narita, Fumio. (2019). Footstep Energy Harvesting with the Magnetostrictive Fiber Integrated Shoes. *Materials*. 12. 2055. <https://doi.org/10.3390/ma12132055>
- [18] Ugooze, Kenneth & Alalor, Christian & Ibezim, Chidozie & Chinko, Bruno & Owonaro, Peter & Anie, Clement & Okoronkwo, Ngozi & Mgbahurike, Amaka & Ofomata, Chijioke & Alfred-Ugbenbo, Deghinmotei & Ndukwu, Geraldine. (2024). Environmental and Human Health Impact of Antibiotics Waste Mismanagement: A Review. *Advances in Environmental and Engineering Research*. 05. 1-21. <https://doi.org/10.21926/aeer.2401005>
- [19] Mohd Nawi, Mohd Nasrun & Mohd Nasir, Najuwa & Abidin, Rahimi & Salleh, Nurul & Harun, Aizul & Osman, Wan & Ahmad, M.. (2018). Enhancing construction health and safety through the practices of reuse and recycle in waste management among Malaysian contractors. *Indian Journal of Public Health Research & Development*. 9. 1521. <https://doi.org/10.5958/0976-5506.2018.01664.9>
- [20] Haustein, Sonja & Koglin, Till & Nielsen, Thomas & Svensson, Åse. (2019). A comparison of cycling cultures in Stockholm and Copenhagen. *International Journal of Sustainable Transportation*. 14. 1-14. <https://doi.org/10.1080/15568318.2018.1547463>
- [21] Wang, Junlin & Mukhopadhyaya, Phalguni & Valeo, Caterina. (2023). Implementing Green Roofs in the Private Realm for City-Wide Stormwater Management in Vancouver: Lessons Learned from Toronto and Portland. *Environments*. <https://doi.org/10.3390/environments10060102>
- [22] Zhu, Wenhao. (2023). Vertical Farms: A Sustainable Solution to Urban Agriculture Challenges. *Highlights in Science, Engineering and Technology*. 75. 80-85. <https://doi.org/10.54097/4n06rw70>
- [23] Marques, Bruno & McIntosh, Jacqueline & Popoola, Tosin. (2018). Green Prescriptions and Therapeutic Landscapes: A New Zealand Study. *International Journal of Behavioral Medicine*. 25. 21.
- [24] Taylor, Bron. (2013). Kenya's green belt movement: Contributions, conflict, contradictions, and complications in a prominent environmental non-governmental organization (ENGO). <https://doi.org/10.1515/9780857457578-009>
- [25] Penagos, Hernán. (2020). Electric power generation from a turnstile. *Dyna (Medellín, Colombia)*. 87. 156-162. <https://doi.org/10.15446/dyna.v87n215.86789>

Water and electricity consumption management architectures using IoT and AI: A review study

Oumaima RHALLAB^{1,a*}, Amine DEHBI^{2,b*} and Rachid DEHBI^{1,c}

¹ Research laboratory of computer science (LIS) Faculty of Sciences Aïn Chock Casablanca, Morocco

² Research laboratory of mathematics and computer science (LTI) Faculty of Sciences Ben M'Sick Casablanca, Morocco

^aoumaimarhallab2@gmail.com, ^bdehbiamine1@gmail.com, ^c dehbirac@yahoo.fr

Keywords: Water and Electricity Management, Internet of Things (IoT), Artificial Intelligence (AI), Resource Management

Abstract. This in-depth article delves into the implemented architectures aimed at optimizing water and electricity consumption through the integration of the Internet of Things (IoT) and artificial intelligence (AI). It provides a detailed analysis of various developments, trends, and key technologies shaping this rapidly evolving field. The article meticulously examines background research and scrutinizes the architecture, thus offering profound insights into the technical challenges, potential benefits, and implementation obstacles of leveraging IoT and AI in resource management. By exploring these architectures, the article highlights significant advancements in terms of efficiency, resource utilization, and predictive capabilities within integrated systems. Convincing results demonstrate the positive impact of this technological convergence on environmental sustainability, waste reduction, and resource optimization, thus offering a promising vision for the future of resource management. Furthermore, an extensive discussion section critically evaluates the discussed approaches, pinpointing the strengths and weaknesses of each method and proposing avenues for improvement and development. This nuanced analysis provides a solid foundation for future research and continuous innovation in the field of resource management. This article serves as an essential resource for professionals and researchers working in the fields of water, energy, and IoT/AI. It offers an in-depth understanding of the challenges and opportunities associated with integrating these technologies and provides strategic guidance for effective and sustainable resource management in the digital age.

Introduction

In a context where the challenges of managing resources such as water and electricity are becoming increasingly pressing, advancements in the fields of the Internet of Things (IoT) and artificial intelligence (AI) offer intriguing prospects for addressing these challenges in innovative and efficient ways. This article delves deep into this technological convergence, exploring various strategies and architectures implemented to optimize water and electricity consumption. The meticulous examination of existing methodologies reveals a wealth of possibilities and complexities. Approaches such as smart telemetry, interconnected sensor networks, and AI-based predictive systems hold considerable promise for real-time monitoring, precise control, and proactive prediction of consumption patterns. These technological advancements pave the way for more efficient and sustainable resource management, with potentially revolutionary implications for industries, municipalities, and households. However, this landscape of innovation is not without its challenges. Data privacy and cybersecurity issues emerge as systems become more interconnected and data volumes increase. Moreover, the need to ensure equitable access to these technologies raises concerns about digital divides and social exclusion. Beyond technological

considerations, it is crucial to examine the socio-economic and environmental implications of these advancements. How do these technologies affect the livelihoods of populations, local economies, and the health of our planet as a whole? How can we ensure that the benefits of these innovations accrue to all, without compromising fundamental rights and long-term sustainability? In this quest to address these challenges, a collaborative and interdisciplinary approach is indispensable. Policymakers, scientists, engineers, sociologists, and environmental advocates must come together to design integrated and equitable solutions. It is imperative to adopt a long-term perspective, balancing current needs with the ability of future generations to meet their own.

Literature Review

Fuentes, H[1], proposes an innovative IoT framework for water consumption management. It emphasizes secure data capture through encryption, local preprocessing of consumption data, physical security of devices, Recording and displaying water usage patterns, along with identifying leaks through the implementation of the Water Leak Algorithm. This system involves five primary elements for the collection, retention, examination, and representation of water consumption data. In the "House Data Collection" module, a smart meter captures water usage data at each T1 moment, transmitted to the "Edge Gateway" for archival, with a security feature to detect unauthorized manipulations. Cumulative consumption is sent to the Cloud at broader intervals (T2), stored with user location data obtained from their phone's GPS. The data undergoes analysis for leak detection at the Cloud, and users can visualize real-time water consumption through a web portal. This framework provides a comprehensive solution for gathering, safeguarding, storing, analyzing, and presenting water consumption data, integrating security measures for data integrity and proactive leak detection. The study offers a detailed technological overview, emphasizing the five essential elements, specifying software, programming languages, databases, and operating systems associated with each component.

Paramasivan's [2] proposed system introduces an inventive resolution for implementing prepaid energy supply while consolidating the oversight of all energy meters. The primary aim is to thwart unauthorized tampering with electricity at consumer premises while concurrently curbing labor expenses associated with billing. The GSM unit establishes a connection with the intelligent meter installed in individual residences, with each meter being allocated a unique quantity by electricity suppliers. The intelligent meter consistently records electricity usage and displays the consumed units on an LCD screen linked to the meter. The microcontroller diminishes the unit quantity in response to consumption. Upon a request from the electricity provider's server, the GSM modem is prompted to instruct the microcontroller to take necessary actions. The MAX232 module facilitates communication between the microcontroller and the GSM modem. The GSM plays a vital role in furnishing information about electricity consumption to both the electricity provider and the consumer, in real-time or as required. The GSM assumes a pivotal role in disseminating information about energy consumption to the application management and the consumer, as needed. The aerial container, affixed on or near the meter, heightens GSM communication for effective energy monitoring.

The advanced system, introduced by Ramadhan and Ali [3], offers a sophisticated solution for the cost-effective surveillance of water quality in a minimum of five water treatment stations. Its design ensures prolonged and uninterrupted operation through low energy consumption, facilitated by solar panels. Precise monitoring of water quality parameters is achieved through the utilization of ten specific sensors within the system. These parameter values are promptly displayed in real-time on a dedicated web page, providing immediate insights into the water quality across the monitored areas. The system possesses the capability to issue real-time alerts to relevant personnel via SMS and emails when abnormal or problematic values are detected. The recorded data is also archived for subsequent statistical analysis. The sensors employed in this system have undergone rigorous laboratory testing, demonstrating exceptional performance in terms of accuracy and

reliability. The monitoring system is composed of three primary components: the detection node (SN), the data router (DR), and the website (WS), seamlessly integrated. Each water station is represented by a detection node (SN), and each node comprises four fundamental elements: the control unit, sensors, transceiver, and power unit. The control unit is facilitated by a programmable logic controller (PLC) of the CONTROLLINO MEGA type.

Segun O. Olatinwo [4] introduces a pioneering system architecture that integrates a Wireless Sensor Network (WSN) with multiple sensors categorized into two groups: Group 1 and Group 2. The classification is based on their prioritized schedule for information transmission, determined by a sequential data transmission method. Group 1, consisting of sensors i , becomes active during the initial cycle of the Up-Link (UL) transmission phase, while Group 2, comprising sensors q , is designated for transmitting data regarding the quality of water. In the subsequent cycle of the UL phase. Consequently, sensors from both Group 1 and Group 2 engage in data communication. To efficiently oversee the concurrent transfer of water quality data from every sensor group to a designated receiving node., a Successive Interference Cancellation (SIC) mechanism is implemented at the receiver. This mechanism acts as a congestion control measure, facilitating the separation of data emitted simultaneously by the sensors. The sensor nodes utilized in this system are Water Quality Sensors (WQS) designed to measure essential microbiological and chemical properties of water at treatment stations. These nodes are powered by Distributed Power Sources (DPS) equipped with omnidirectional antennas. The system controller possesses extensive knowledge of network resources, sensors in Groups 1 and 2, and a scheduler for activating Group 1 or Group 2 based on a predefined priority.

The architecture of the IoT application has been organized to facilitate sequential sharing of functions among all components, as suggested by Khan, M.A [5], starting from current IoT devices to the Managed-Cloud, in which data undergoes processing for making insightful decisions. The smart circuit is designed to enable the sequential measurement of current and voltage for three household appliances, utilizing ACS712 current sensors and ZMPT101B voltage sensors. Once the measured data is acquired, it is transmitted towards inputs of a Wi-Fi access controller, such as an ESP8266 module. This module, known for its online monitoring and control capabilities, is chosen for its power efficiency and affordability. Following data processing, it is forwarded to an MQTT server in the cloud, serving as a intermediary between the user and the loads. This cloud server facilitates multiple clients/users to connect and access the data. Users can oversee and control the data through a HumanMachine-Interface using either a personal computer and/or a mobile app. Furthermore, there are two additional loads included to indicate power and detect overloads. Initially linked to the power using a 4- channel relay, these loads can function in two modes: "normally open (NO)" and "normally closed (NC)." To prioritize safety, the initial configuration is set to "NO," and the voltages are consistently maintained at 220 V.

Liu, Yi [6] introduces a system proposing A framework for energy management built upon the Internet of Things (IoT), integrating advanced computing technologies and a Deep Reinforcement Learning (DRL) network. The structure is composed of three primary elements: energy devices, energy edge servers, and energy cloud servers. In this design, data is processed locally by energy edge servers and then sent via the central network to the cloud server. Agents for Deep Reinforcement Learning (DRL) are installed on edge and cloud servers. When a computing task is needed, an energy device sends it to the closest edge server, where the edge DRL agent does the task computation. Deep neural network (DNN) weight pre-training can be done in the energy cloud server to improve energy consumption in the edge server. After training, the DNN advances to the boundary, where Deep Q-Learning assumes control. Edge servers collect data from devices and transmit it to the cloud for effective processing, hence reducing energy consumption.

Background study

1. Data Sources for Adaptive Water-Electricity Management

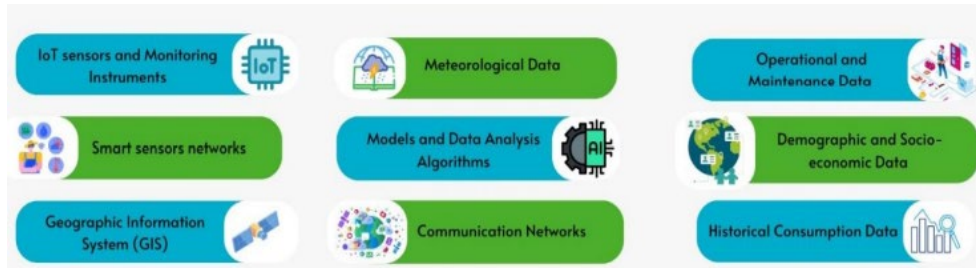


Figure 1: Data Sources for Adaptive Water-Electricity Management

Leveraging diverse data sources is vital for adaptive water and electricity system management to optimize processes, enhance efficiency, and enable informed decision-making. Common data sources for adaptive approaches in water and electricity management include:

- **IoT Sensors and Monitoring Instruments:** Real-time data on consumption, quality, temperature, water levels, and pressure [7, 8] can be obtained using sensors deployed in distribution infrastructures. Smart Sensor Networks creating distributed monitoring systems with interconnected smart sensor networks allows for extensive data collection from multiple points [9].
- **Geographic Information Systems (GIS):** GIS provides spatial information to analyze geographical distribution, plan maintenance routes, and optimize resource management [10].
- **Meteorological Data:** Crucial for anticipating electricity demand, especially for renewables [11], and predicting weather conditions impacting water resources.
- **Historical Consumption Data:** Analyzing past consumption patterns is vital for forecasting future demand and planning capacity [12].
- **Communication Networks:** Wired and wireless networks facilitate reliable data transmission between system components [13].
- **Operational and Maintenance Data:** Information on infrastructure operations, maintenance reports, downtime, and equipment performance is crucial for optimizing processes [14].
- **Demographic and Socio-economic Data:** Understanding population factors helps tailor management strategies to changing water and electricity demand [15].

2. Data transmission protocols

The data pathway in adaptive management of water and electricity systems can traverse various channels, with certain methods evolving in prominence [16]. Contemporary implementations predominantly leverage Bluetooth and Wi-Fi transmissions. Some systems embrace standard wireless technologies like ZigBee, XBee, and ZWave. While GSM has historically offered stability in mobile communication, it has witnessed a decline in use, being superseded by advanced cellular standards such as 3G, 4G, and 5G, offering enhanced data transfer speeds. It's noteworthy that Table 1 illustrates a comparison between some protocols [17], highlighting their distinct characteristics and functionalities.

3. Data Storage

In IoT systems dedicated to monitoring water and electricity consumption in Morocco, the data aggregation phase assumes a pivotal role. This stage involves consolidating information from multiple sensors through intelligent IoT gateways, creating a unified representation for simplified

processing and analysis [18]. Utilizing buffers or local databases ensures data availability during temporary network disruptions. This approach optimizes data transmission to the central platform, maintaining efficient information flow despite potential connectivity fluctuations. Upstream of in-depth analysis, data preprocessing becomes instrumental. This stage involves processes like noise filtering, normalization of measurement units, and error correction, refining raw data quality for consistency and readiness in advanced analyses [19]. Some systems employ local storage at the sensor or gateway level, ensuring immediate data availability even without connectivity. Simultaneously, a cloud-first architecture allows direct transmission of other data to the cloud [20]. This hybrid strategy accommodates the specific constraints of each system, facilitating effective information management aligned with infrastructure needs and capabilities [21].

Table 1: Comparison between data transmission protocols

Specifications	Wi-Fi	Bluetooth	GSM	Zigbee
Network type	Point-to-point, WLAN, WAN, Mesh, Point-to- multipoint	PAN	Cellular network	Mesh network
Communication	Radio Frequency, Protocols (IEEE 802.11, 802.11b, 802.11g,...)	Wireless	Wireless	Wireless
Security	Protocol (WEP, WPA, and WPA2/WPA3),	Encryption methods	Encryption methods	Encryption methods
Range	Up to 100 meters	Up to 10 meters	Several kilometers	from 10 to 100 meters
Frequency	2.4 GHz and 5 GHz	2.4 GHz	900 MHz and 1800 MHz	2.4 GHz
Bit rate	From 11Mbps to up than 9,6 Gbps depending on the Wi- Fi standard being used	Depends on the Bluetooth version, ranging from 1 Mbps to 3 Mbps.	Up to 9.6 kbps	Between 20 and 250 kbps
Continuous sampling	Yes	Yes	NO	Yes
Interoperability	Different and same devices	Compatible devices	GSM compatible devices	Same devices

4. AI Processing:

Table 2: The processing AI steps

Phase	Description
Retrieval and Preparation	Following the Storage of data, the AI-driven processing phase commences with the retrieval of stored information. The data is subsequently prepared for analysis, encompassing tasks such as formatting, structuring, and ensuring compatibility with AI algorithms [22].
Preprocessing with AI	AI is utilized for intricate preprocessing tasks, where machine learning models can autonomously identify patterns, outliers, and anomalies within the stored data. This step guarantees that the data is refined and well-prepared for more sophisticated analyses [23].
Predictive Analytics	AI algorithms, encompassing machine learning and predictive modeling [24], come into play for forecasting future trends based on historical data [25] [26]. This facilitates proactive decision-making and resource planning in response to anticipated consumption patterns.
Real-time Insights	AI transcends traditional batch processing limitations, enabling real-time analytics [27]. Continuously analyzing incoming data, AI algorithms furnish immediate insights into consumption patterns, potential inefficiencies, or abnormalities.

Continuous Improvement

In the realm of data processing, AI systems are engineered for continuous improvement [28]. Employing feedback loops and continuous learning mechanisms, these models evolve over time, progressively enhancing their accuracy and efficacy in dealing with a myriad of data scenarios.

Conclusion

In conclusion, this comprehensive study delved into water and electricity management architectures integrating AI and IoT, providing insights into current trends and key technologies. The background research highlighted the diverse data sources used in these architectures, emphasizing IoT sensors, communication networks, and other advanced technologies. Transmission protocols were scrutinized, comparing multiple options to inform implementation choices. It is crucial to acknowledge that this study presents findings based on the examination of six specific architectures and the comparison of four transmission protocols. The conclusions indicate significant advancements in terms of efficiency, resource utilization, and predictive capabilities in these integrated systems. However, certain limitations need to be emphasized. The restriction to six architectures and four protocols may not cover all possible variants. For a more comprehensive and nuanced understanding, future research could explore a broader range of architectures and protocols. As for future perspectives, an in-depth bibliometric study on water and electricity consumption topics, integrating AI and IoT, could provide a more holistic view of the field. This would help identify emerging trends, gaps in current research, and guide future work towards areas of innovation and particular importance.

References

- [1] Fuentes, H., & Mauricio, D. (2020). Smart water consumption measurement system for houses using IoT and cloud computing. *Environmental Monitoring and Assessment*, 192, 1-16. <https://doi.org/10.1007/s10661-020-08535-4>
- [2] Rajesh, M. (2021). GSM Based Smart Energy Meter System.
- [3] Ramadhan, A. J., Ali, A. M., & Kareem, H. K. (2020). Smart waterquality monitoring system based on enabled real-time internet of things. *J. Eng. Sci. Technol*, 15(6), 3514-3527.
- [4] Olatinwo, S. O., & Joubert, T. H. (2020). Energy efficiency maximization in a wireless powered IoT sensor network for water quality monitoring. *Computer Networks*, 176, 107237. <https://doi.org/10.1016/j.comnet.2020.107237>
- [5] Khan, M. A., Sajjad, I. A., Tahir, M., & Haseeb, A. (2022). IoT application for energy management in smart homes. *Engineering Proceedings*, 20(1), 43. <https://doi.org/10.3390/engproc2022020043>
- [6] Liu, Y., Yang, C., Jiang, L., Xie, S., & Zhang, Y. (2019). Intelligent edge computing for IoT-based energy management in smart cities. *IEEE network*, 33(2), 111-117. <https://doi.org/10.1109/MNET.2019.1800254>
- [7] Ibrahim, S. N., Asnawi, A. L., Abdul Malik, N., Mohd Azmin, N. F., Jusoh, A. Z., & Mohd Isa, F. N. (2018). Web based Water Turbidity Monitoring and Automated Filtration System: IoT Application in Water Management. *International Journal of Electrical & Computer Engineering* (2088-8708), 8(4). <https://doi.org/10.11591/ijece.v8i4.pp2503-2511>
- [8] Li, J., Herdem, M. S., Nathwani, J., & Wen, J. Z. (2023). Methods and applications for Artificial Intelligence, Big Data, Internet of Things, and Blockchain in smart energy management. *Energy and AI*, 11, 100208. <https://doi.org/10.1016/j.egyai.2022.100208>

- [9] Jaradat, M., Jarrah, M., Bousselham, A., Jararweh, Y., & AlAyyoub, M. (2015). The internet of energy: smart sensor networks and big data management for smart grid. *Procedia Computer Science*, 56, 592-597. <https://doi.org/10.1016/j.procs.2015.07.250>
- [10] Zulkifli, C. Z., Garfan, S., Talal, M., Alamoodi, A. H., Alamleh, A., Ahmaro, I. Y., ... & Chiang, H. H. (2022). IoT-based water monitoring systems: a systematic review. *Water*, 14(22), 3621. <https://doi.org/10.3390/w14223621>
- [11] Saheb, T., Dehghani, M., & Saheb, T. (2022). Artificial intelligence for sustainable energy: A contextual topic modeling and content analysis. *Sustainable Computing: Informatics and Systems*, 35, 100699. <https://doi.org/10.1016/j.suscom.2022.100699>
- [12] Rochd, A., Benazzouz, A., Abdelmoula, I. A., Raihani, A., Ghennoui, A., Naimi, Z., & Ikken, B. (2021). Design and implementation of an AI-based & IoT-enabled Home Energy Management System: A case study in Benguerir—Morocco. *Energy Reports*, 7, 699-719. <https://doi.org/10.1016/j.egyr.2021.07.084>
- [13] Rahmadya, B., Zaini, Z., & Muhamram, M. (2020). IoT: A mobile application and multi-hop communication in wireless sensor network for water monitoring. <https://doi.org/10.3991/ijim.v14i11.13681>
- [14] Krishnan, S. R., Nallakaruppan, M. K., Chengoden, R., Koppu, S., Iyapparaja, M., Sadhasivam, J., & Sethuraman, S. (2022). Smart water resource management using Artificial Intelligence—A review. *Sustainability*, 14(20), 13384. <https://doi.org/10.3390/su142013384>
- [15] Ansari, S., Ayob, A., Lipu, M. S. H., Saad, M. H. M., & Hussain, A. (2021). A review of monitoring technologies for solar PV systems using data processing modules and transmission protocols: Progress, challenges and prospects. *Sustainability*, 13(15), 8120. <https://doi.org/10.3390/su13158120>
- [16] Kanellopoulos, D., Sharma, V. K., Panagiotakopoulos, T., & Kameas, A. (2023). Networking Architectures and Protocols for IoT Applications in Smart Cities: Recent Developments and Perspectives. *Electronics*, 12(11), 2490. <https://doi.org/10.3390/electronics12112490>
- [17] Dehbi, A., Bakhouyi, A., Dehbi, R., & Talea, M. (2024). Smart Evaluation: A New Approach Improving the Assessment Management Process through Cloud and IoT Technologies. *International Journal of Information and Education Technology*, 14(1), 107-118. <https://doi.org/10.18178/ijiet.2024.14.1.2030>
- [18] Bedi, P., Goyal, S. B., Rajawat, A. S., Shaw, R. N., & Ghosh, A. (2022). Application of AI/IoT for smart renewable energy management in smart cities. *AI and IoT for Smart City Applications*, 115-138. https://doi.org/10.1007/978-981-16-7498-3_8
- [19] Goudarzi, S., Anisi, M. H., Soleymani, S. A., Ayob, M., & Zeadally, S. (2021). An IoT-based prediction technique for efficient energy consumption in buildings. *IEEE Transactions on Green Communications and Networking*, 5(4), 2076-2088. <https://doi.org/10.1109/TGCN.2021.3091388>
- [20] LakshmiKantha, V., Hiriyannagowda, A., Manjunath, A., Patted, A., Basavaiah, J., & Anthony, A. A. (2021). IoT based smart water quality monitoring system. *Global Transitions Proceedings*, 2(2), 181-186. <https://doi.org/10.1016/j.gltip.2021.08.062>
- [21] Praveena, D., Thanga Ramya, S., Gladis Pushparathi, V. P., Bethi, P., & Poopandian, S. (2021). Hybrid Cloud Data Protection Using Machine Learning Approach. In *Advanced Soft*

- Computing Techniques in Data Science, IoT and Cloud Computing (pp. 151- 166). Cham: Springer International Publishing. https://doi.org/10.1007/978-3-030-75657-4_7
- [22] Bourechak, A., Zedadra, O., Kouahla, M. N., Guerrieri, A., Seridi, H., & Fortino, G. (2023). At the Confluence of Artificial Intelligence and Edge Computing in IoT-Based Applications: A Review and New Perspectives. *Sensors*, 23(3), 1639. <https://doi.org/10.3390/s23031639>
- [23] Himeur, Y., Elnour, M., Fadli, F., Meskin, N., Petri, I., Rezgui, Y., ... & Amira, A. (2023). AI-big data analytics for building automation and management systems: a survey, actual challenges and future perspectives. *Artificial Intelligence Review*, 56(6), 4929-5021. <https://doi.org/10.1007/s10462-022-10286-2>
- [24] Rajawat, A. S., Mohammed, O., Shaw, R. N., & Ghosh, A. (2022). Renewable energy system for industrial internet of things model using fusion-AI. In Applications of AI and IOT in Renewable Energy (pp. 107-128). Academic Press. <https://doi.org/10.1016/B978-0-323-91699-8.00006-1>
- [25] Jiang, D., Lian, M., Xu, M., Sun, Q., Xu, B. B., Thabet, H. K., ... & Guo, Z. (2023). Advances in triboelectric nanogenerator technology—Applications in self-powered sensors, Internet of things, biomedicine, and blue energy. *Advanced Composites and Hybrid Materials*, 6(2), 57. <https://doi.org/10.1007/s42114-023-00632-5>
- [26] Olatinwo, S. O., & Joubert, T. H. (2023). Resource Allocation Optimization in IoT-Enabled Water Quality Monitoring Systems. *Sensors*, 23(21), 8963. <https://doi.org/10.3390/s23218963>
- [27] Nasiri, F., Ooka, R., Haghigat, F., Shirzadi, N., Dotoli, M., Carli, R., ... & Sadrizadeh, S. (2022). Data analytics and information technologies for smart energy storage systems: A state-of-the-art review. *Sustainable Cities and Society*, 84, 104004. <https://doi.org/10.1016/j.scs.2022.104004>
- [28] Kamyab, H., Khademi, T., Chelliapan, S., SaberiKamarposhti, M., Rezania, S., Yusuf, M., ... & Ahn, Y. (2023). The latest innovative avenues for the utilization of artificial Intelligence and big data analytics in water resource management. *Results in Engineering*, 101566. <https://doi.org/10.1016/j.rineng.2023.101566>

A comprehensive review on computing methods for the prediction of energy cost in Kingdom of Saudi Arabia

Nayeemuddin MOHAMMED^{1,a}, Andi ASIZ^{1,b}, Mohammad Ali KHASAWNEH^{1,c},
Feroz SHAIK^{2,d}, Hiren MEWADA^{3,e}, Tasneem SULTANA^{4,f*}

¹Department of Civil Engineering, Prince Mohammad Bin Fahd University, Al Khobar, Kingdom of Saudi Arabia

²Department of Mechanical Engineering, Prince Mohammad Bin Fahd University, Al Khobar, Kingdom of Saudi Arabia

³Department of Electrical Engineering, Prince Mohammad Bin Fahd University, Al Khobar, Kingdom of Saudi Arabia

⁴Artificial Intelligence and Machine Learning, Godutai Engineering College for Women, Sharnbasva University, Kalaburagi, India

mnayeemuddin@pmu.edu.sa^a, aasiz@pmu.edu.sa^b mkhawneh@pmu.edu.sa^c,
fshaik@pmu.edu.sa^d, hmewada@pmu.edu.sa^e, tasneemsultana841@gmail.com^{f*}

Keywords: Energy, Artificial Neural Network, Prediction Models, Regression, Statistical, Deep Learning

Abstract. Addressing the increasing demand for energy in the Kingdom of Saudi Arabia (KSA) poses challenges and opportunities. This necessitates effective energy planning, diversification of energy sources, and implementation of energy-efficient technologies. This study presents the energy scenario in the KSA. Later, various technical algorithms used for energy prediction from past data, including regression models, statistical models, machine learning and deep learning networks, are presented. The present study revealed that learnable models, specifically neural networks, outperformed statistical and regression networks in predicting energy demands. In addition, statistical models lack predictability and lack adoption with new data.

Introduction

Power is an exceptional resource. There must be an ongoing equilibrium between production and consumption for the power system to be stable, and this equilibrium is economically unstoreable. Concurrently, the amount of economic and daily activity during off-peak and peak hours, on weekdays and weekends, etc., and weather-related factors, e.g., temperature, wind speed, precipitation, etc., determine energy demand. The forecasting of electricity is a fundamental need at the government and corporate levels for the decision-making process. Market players hedge against both volume risk and price fluctuations due to the extreme volatility of prices, which can be two orders of magnitude greater than that of any other financial asset or commodity. Thus, forecasting energy costs for a single country is valuable for several reasons. Accurate energy cost predictions enable governments and policymakers to plan for the economic development of a country. Energy costs have a significant impact on various sectors, such as manufacturing, transportation, and agriculture. By forecasting energy costs, governments can assess the competitiveness of industries, attract investments, and develop strategies to ensure an affordable and reliable energy supply. By understanding future energy costs, governments can assess the availability and affordability of energy sources. This knowledge helps in diversifying the energy supply, reducing dependence on volatile or geopolitically unstable sources, and developing strategies to maintain a stable and reliable energy infrastructure.

Predictions of energy costs are essential for developing energy legislation and policy. With the help of these forecasts, governments can create energy-saving policies, incentives, or subsidies that encourage the use of renewable energy sources and sustainable energy practices. Accurate predictions can help policymakers understand the potential impact of policy changes on energy costs for consumers and businesses. By predicting energy costs for a specific country, stakeholders can gain valuable insights for economic planning, energy security, policy formulation, consumer decision-making, and market analysis. These insights contribute to efficient energy management, sustainable development, and the overall well-being of the country and its citizens. There are several methods for predicting the energy cost. A few popular methods are regression analysis, time-series analysis, machine learning approaches, data mining and optimization algorithms. The accuracy and effectiveness of these methods depend on the availability and quality of the data, as well as the specific characteristics of the energy system being analyzed. In practice, a combination of multiple methods or an ensemble approach may be employed to improve the prediction accuracy.

In regard to global power consumption, the Kingdom of Saudi Arabia (KSA) ranks fourteenth. There has recently been remarkable growth in every sector of the Saudi Arabian economy, but the generation and consumption of electrical power have been particularly impressive. The government is currently working on strategies to improve this industry in the future. This is because it is crucial to sustainable development goals and because Vision 2030 requires the use of renewable energy to power the nation. Saudi Arabia generated an estimated 374 tera watt hours (TWh) of electricity in 2022, up 2% from 367 TWh in 2021 [1].

This paper presents recent algorithms used for energy prediction. Initially, an energy scenario in the KSA and various developed countries was presented. This paper focuses on various algorithms presented in the literature for accurate energy forecasting. Finally, limitations were presented.

Energy scenario in KSA

Resources for renewable and sustainable energy (RnSE) have gained prominence recently as being essential to the stability of economies throughout the world. Recent research has identified renewable and sustainable energy (RnSE) resources as a critical component of a healthy global economy, especially in industrialized nations like the Kingdom of Saudi Arabia (KSA) [2]. Saudi Arabia, as the biggest economy in the GCC, is heavily dependent on non-renewable resources for its economic growth. As such, it is imperative that the country look into alternate energy sources. In the region, using solar applications especially photovoltaics is seen to be the most cost-effective way to supply basic energy services [3]. Residential structures have received the majority of attention, although commercial and educational building construction is rapidly increasing [4]. The leveled cost of energy and the net present cost are used to compare the photovoltaic (PV) energy outputs of the Kingdom of Saudi Arabia with those of potential PV energy customers, such as European countries, China, India, and Pakistan [5]. Compared to the Mass Burn with recycling scenario, the Mass Burn scenario may yield twelve times as much. To compare the two situations in terms of economic, social, technological, and environmental factors need required another studies [6].

Future substantial expansion in the country's energy consumption is predicted due to a number of variables, including cheap energy prices, high economic growth, and a growing population [7]. After the construction and industrial sectors in Saudi Arabia, the electricity industry as a whole had the second-highest carbon emissions in 2018 [8].

Energy Cost Prediction Models

The Gaussian process creates a prediction function for the energy consumption with confidence bounds by modelling the intricate interactions between the input machining parameters and the

output energy consumption. Prediction models that consider various operations and process characteristics may be created using sophisticated data collecting and processing techniques to estimate a machine tool's energy usage [9]. Predicting energy usage in office buildings in cold climates was done using neural network prediction models based on evolutionary algorithms and back propagation. The highest RMSE value of the enhanced GA-BP neural network was 0.36, and the maximum MAPE value was 0.29%; both evaluation indicators were less than those of the BP prediction technique [10].

The prediction algorithm was built using two available datasets of residential and commercial structures. Accurate assessment of the energy consumption in buildings is essential for both energy policy and building energy management. The main difference between this model and the shallow machine learning (ML) model is the quantity of linear or non-linear transformations applied to the input data. The deep neural network model often makes numerous modifications to the input data before generating an output. The planned design model for the ANN-Levenberg Marquardt tool, which is employed in ANN. 3 hidden layers, with 3 inputs employed to design the model for regression and optimization using artificial neural network Levenberg Marquardt tool in MATLAB application. Each layer has different neurons such as 35, 20 and 10 were suggested to get more accuracy of prediction as shown in Figure 1 [11]. Cao et al., created and evaluated an integrated learning method that uses data permutation to gauge the significance of features in order to reduce the instability issue with building management systems [12], [13].

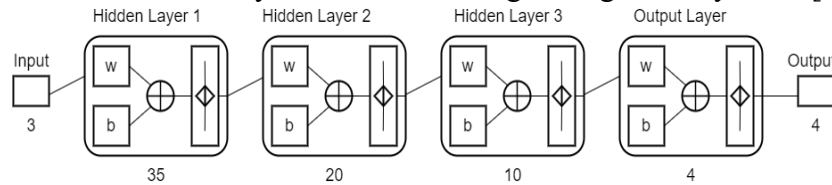


Fig 1. Design modeling for ANN-LM tool in ANN [13]

Kim et al., investigated and used the response surface approach in conjunction with the statistical method to create a prediction model for residential building energy consumption. In Seoul and Busan apartment buildings, higher window and wall thermal transmittances and infiltration rates led to higher heating energy consumption; conversely, higher SHGC was linked to reduced cooling energy consumption [14]. The suggested deep learning technique was used to forecast the energy usage of a particular building for which data on energy use over a 12-month period was gathered. The results of the experiment and comparison show that the deep learning approach performs better than a number of well-liked conventional machine learning techniques [15], [16].

Limitations in Energy Cost Prediction Models

When comparing the ANN to the BP neural network, the ELM significantly enhanced it. In contrast to typical feedforward neural networks, the ELM randomizes the network weight of a single hidden layer. The inverse matrix of Moore-Penrose is used to determine the outputs. As a result, the output calculation speed and generalization precision are rather high, and it is difficult to reach a local maximum [17]. Support vector machines (SVM), artificial neural networks (ANN), decision trees, and other statistical methods are examples of learning algorithms [18],[19]. Building and region scales are examples of spatial scales. Both short-term and long-term temporal granularities are available. There are several types of energy consumption forecast, such as total, heating, cooling, and lighting. Real and simulated datasets are two examples of dataset types [20].

Energy Cost Prediction Models Applied to KSA Scenario

The Kingdom of Saudi Arabia, an expanding nation, is seeing remarkable developments in a range of fields, such as the medical, educational, engineering, and urban sectors, particularly in the economic and industrial realms. Planning for capacity, transmission, and price all depend on the

ability to forecast energy use. The aspects of power consumption forecasting vary depending on the prediction perspective. Almuhaini's research forecasted annual TEC using statistical and machine learning techniques, namely ARIMAX, BOA-SVR, and BOA-NARX models [21]. ANFIS combines fuzzy logic and neural networks, it usually consists of five layers: fuzzification, fuzzy rule evaluation, normalization, defuzzification, and output. Each layer performs a specific function in the inference process [22]. Training includes the ANFIS model using a hybrid learning algorithm that combines gradient descent and least squares estimation. Figure 2 shows the design modelling steps involved in ANFIS method of prediction [23], [24]. These tactics function even in the absence of prior understanding of the previously outlined systems. By correctly analyzing a dataset that includes obtained output and input parameters, they try to understand the link between outputs and inputs [25], [26].

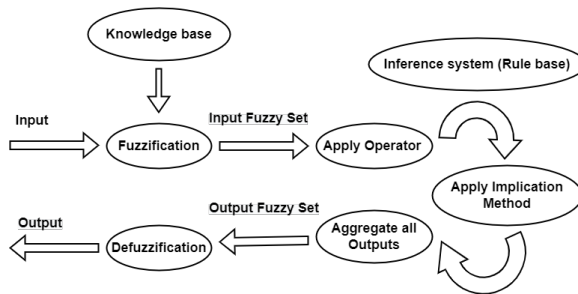


Fig 2. Design modeling for ANFIS tool in ANN [26]

A government agent may utilize the generated energy prediction model to help them plan corrective steps for future school building, design with minimal energy consumption, and make the most use of their limited finances [27]. Model accuracy and computing capacity are increased by new technological advancements including parametric modelling, simulation, and artificial neural networks (ANNs). Elbeltagi et al., used ANN application to forecast the energy demand for residential structures. Artificial neural networks (ANNs), simulation, and parametric modelling are examples of recent technology developments that improve model accuracy and processing power [28], [24]. Table 1 shows the renewable energy cost aspects and prediction of models applied in Kingdom of Saudi. Table 2 shows the study of various ANN and machine learning network used successfully in forecasting the energy consumption within different zone of Saudi Arabia. Table 2 shows deep network [29] performed best in compared to machine learning with least error in the prediction over large-scale dataset.

Table 1 Displays the detailed renewable energy cost aspects and prediction

	Aspects	Description	Ref.
Energy Scenario	Energy Production	Significant investments in renewable energy, particularly solar energy	[30]
	Renewable Energy	Ambitious plans to develop renewable energy sector, with a focus on solar and wind energy	[31]
Energy Cost Prediction models	Artificial Neural Networks (ANN)	Machine learning models that can capture complex relationships in energy cost data	[32]
	Support Vector Machines (SVM)	Machine learning models that can analyze and forecast energy costs based on historical data	[33]

Limitations in energy cost prediction models	Data Availability	Limited availability of high-quality historical data, especially for newer technologies and renewable sources	[34]
Prediction models applied in K. S. A	Hybrid Models	Combine multiple approaches (e.g., regression, machine learning) for more accurate energy cost predictions	[36]

Table 2 Analysis of various prediction algorithm adopted for electricity cost analysis in KSA

Ref	Goal	Analysis
[39]	Energy const prediction using ANN/BIM model for residential building in KSA	Design Builder was used to create a 3D model, and the energy usage was determined. The dataset covers building area, type of air conditioning, glazing system, and envelope system.
[40]	Energy consumption in school building in Riyadh, KSA	To find the best network model, several neural network (NN) design topologies were tested. The developed model had an accuracy of roughly 87.5%.
[41]	Photovoltaic power output prediction in Jubail Industrial City, KSA.	Optimal database finding suitable merit indicator can enhance the performance.
[29]	Forecasting annual electricity consumption in Saudi Arabi	A Bayesian optimized non-linear autoregressive network was developed for forecasting energy consumption.

Conclusion

Advancements in infrastructure and laying down new large projects and increasing populations in the KSA led to increased energy demands. Vision 2030 is nominated with a large number of new projects; therefore, it is necessary to forecast future energy demands. We presented a scenario in which energy requirements are met in the KSA. Later, the various algorithms presented in the literature for energy forecasting were presented. The algorithms were categorized into statistical models, i.e., ARIMAX and BOA; machine learning algorithms, including regression networks; KNN and SVM; and ANN networks, which include deep CNNs, BPNs, ANNs, and long short-term memory (LSTM). The study revealed that deep CNN performance is better than that of statistical models, which lack accuracy and adaptivity.

References

- [1] “U.S. Energy Information Administration,” International Energy Statistics. Accessed: Feb. 20, 2024. [Online]. Available: Energy Institute, Statistical Review of World Energy, 2023
- [2] Y. H. A. Amran, Y. H. M. Amran, R. Alyousef, and H. Alabduljabbar, “Renewable and sustainable energy production in Saudi Arabia according to Saudi Vision 2030; Current status and future prospects,” *Journal of Cleaner Production*, vol. 247, p. 119602, Feb. 2020. <https://doi.org/10.1016/j.jclepro.2019.119602>
- [3] M. A. Salam and S. A. Khan, “Transition towards sustainable energy production – A review of the progress for solar energy in Saudi Arabia,” *Energy Exploration & Exploitation*, vol. 36, no. 1, pp. 3–27, Jan. 2018. <https://doi.org/10.1177/0144598717737442>
- [4] M. Abdul Mujeebu and O. S. Alshamrani, “Prospects of energy conservation and management in buildings – The Saudi Arabian scenario versus global trends,” *Renewable and*

Sustainable Energy Reviews, vol. 58, pp. 1647–1663, May 2016.

<https://doi.org/10.1016/j.rser.2015.12.327>

[5] M. Zubair, A. B. Awan, R. P. Praveen, and M. Abdulbaseer, “Solar energy export prospects of the Kingdom of Saudi Arabia,” *Journal of Renewable and Sustainable Energy*, vol. 11, no. 4, p. 045902, Jul. 2019. <https://doi.org/10.1063/1.5098016>

[6] O. K. M. Ouda, H. M. Cekirge, and S. A. R. Raza, “An assessment of the potential contribution from waste-to-energy facilities to electricity demand in Saudi Arabia,” *Energy Conversion and Management*, vol. 75, pp. 402–406, Nov. 2013.

<https://doi.org/10.1016/j.enconman.2013.06.056>

[7] F. Alrashed and M. Asif, “Prospects of Renewable Energy to Promote Zero-Energy Residential Buildings in the KSA,” *Energy Procedia*, vol. 18, pp. 1096–1105, Jan. 2012. <https://doi.org/10.1016/j.egypro.2012.05.124>

[8] S. Alsulamy, A. S. Bahaj, P. James, and N. Alghamdi, “Solar PV Penetration Scenarios for a University Campus in KSA,” *Energies*, vol. 15, no. 9, Art. no. 9, Jan. 2022. <https://doi.org/10.3390/en15093150>

[9] R. Bhinge, J. Park, K. H. Law, D. A. Dornfeld, M. Helu, and S. Rachuri, “Toward a Generalized Energy Prediction Model for Machine Tools,” *Journal of Manufacturing Science and Engineering*, vol. 139, no. 041013, Nov. 2016. <https://doi.org/10.1115/1.4034933>

[10] J. Huang, H. Lv, T. Gao, W. Feng, Y. Chen, and T. Zhou, “Thermal properties optimization of envelope in energy-saving renovation of existing public buildings,” *Energy and Buildings*, vol. 75, pp. 504–510, Jun. 2014. <https://doi.org/10.1016/j.enbuild.2014.02.040>

[11] N. Mohammed, P. Palaniandy, and F. Shaik, “Solar photocatalytic biodegradability of saline water: Optimization using RSM and ANN,” presented at the AIP Conference Proceedings, AIP Publishing, 2022.

[12] W. Cao *et al.*, “Short-term energy consumption prediction method for educational buildings based on model integration,” *Energy*, vol. 283, p. 128580, Nov. 2023. <https://doi.org/10.1016/j.energy.2023.128580>

[13] N. Mohammed, P. Palaniandy, and F. Shaik, “Optimization of solar photocatalytic biodegradability of seawater using statistical modelling,” *Journal of the Indian Chemical Society*, vol. 98, no. 12, p. 100240, Dec. 2021. <https://doi.org/10.1016/j.jics.2021.100240>

[14] D. D. Kim and H. S. Suh, “Heating and cooling energy consumption prediction model for high-rise apartment buildings considering design parameters,” *Energy for Sustainable Development*, vol. 61, pp. 1–14, Apr. 2021. <https://doi.org/10.1016/j.esd.2021.01.001>

[15] C. Li, Z. Ding, D. Zhao, J. Yi, and G. Zhang, “Building Energy Consumption Prediction: An Extreme Deep Learning Approach,” *Energies*, vol. 10, no. 10, Art. no. 10, Oct. 2017. <https://doi.org/10.3390/en10101525>

[16] N. Mohammed, P. Palaniandy, F. Shaik, B. Deepanraj, and H. Mewada, “Statistical analysis by using soft computing methods for seawater biodegradability using ZnO photocatalyst,” *Environmental Research*, vol. 227, p. 115696, Jun. 2023. <https://doi.org/10.1016/j.envres.2023.115696>

[17] Z. Geng, Y. Zhang, C. Li, Y. Han, Y. Cui, and B. Yu, “Energy optimization and prediction modeling of petrochemical industries: An improved convolutional neural network based on cross-feature,” *Energy*, vol. 194, p. 116851, Mar. 2020. <https://doi.org/10.1016/j.energy.2019.116851>

[18] N. Mohammed, “Characterization of sustainable concrete made from wastewater bottle caps using a machine learning and RSM-CCD: towards performance and optimization,” presented at

- the AToMech1-2023 Supplement, Nov. 2023, pp. 38–46. <https://doi.org/10.21741/9781644902790-4>
- [19] N. Mohammed, P. Palaniandy, F. Shaik, and H. Mewada, “EXPERIMENTAL AND COMPUTATIONAL ANALYSIS FOR OPTIMIZATION OF SEAWATER BIODEGRADABILITY USING PHOTO CATALYSIS,” *IIUM Engineering Journal*, vol. 24, no. 2, pp. 11–33, Jul. 2023. <https://doi.org/10.31436/iiumej.v24i2.2650>
- [20] K. Amasyali and N. El-Gohary, “Machine learning for occupant-behavior-sensitive cooling energy consumption prediction in office buildings,” *Renewable and Sustainable Energy Reviews*, vol. 142, p. 110714, May 2021. <https://doi.org/10.1016/j.rser.2021.110714>
- [21] S. H. Almuhaini and N. Sultana, “Forecasting Long-Term Electricity Consumption in Saudi Arabia Based on Statistical and Machine Learning Algorithms to Enhance Electric Power Supply Management,” *Energies*, vol. 16, no. 4, Art. no. 4, Jan. 2023. <https://doi.org/10.3390/en16042035>
- [22] N. Mohammed, P. Palaniandy, and F. Shaik, “Pollutants removal from saline water by solar photocatalysis: a review of experimental and theoretical approaches,” *International Journal of Environmental Analytical Chemistry*, vol. 103, no. 16, pp. 4155–4175, Dec. 2023. <https://doi.org/10.1080/03067319.2021.1924160>
- [23] A. Abubakar Mas’ud, “Comparison of three machine learning models for the prediction of hourly PV output power in Saudi Arabia,” *Ain Shams Engineering Journal*, vol. 13, no. 4, p. 101648, Jun. 2022. <https://doi.org/10.1016/j.asej.2021.11.017>
- [24] N. Mohammed, A. Asiz, M. A. Khasawneh, H. Mewada, and T. Sultana, “Machine learning and RSM-CCD analysis of green concrete made from waste water plastic bottle caps: Towards performance and optimization,” *Mechanics of Advanced Materials and Structures*, pp. 1–9, Aug. 2023. <https://doi.org/10.1080/15376494.2023.2238220>
- [25] N. Mohammed, P. Palaniandy, and F. Shaik, “Optimization of solar photocatalytic biodegradability of seawater using statistical modelling,” *Journal of the Indian Chemical Society*, vol. 98, no. 12, p. 100240, Dec. 2021. <https://doi.org/10.1016/j.jics.2021.100240>
- [26] N. Mohammed, P. Palaniandy, F. Shaik, H. Mewada, and D. Balakrishnan, “Comparative studies of RSM Box-Behnken and ANN-Anfis fuzzy statistical analysis for seawater biodegradability using TiO₂ photocatalyst,” *Chemosphere*, vol. 314, p. 137665, Feb. 2023. <https://doi.org/10.1016/j.chemosphere.2022.137665>
- [27] A. Alshibani, “Prediction of the Energy Consumption of School Buildings,” *Applied Sciences*, vol. 10, no. 17, p. 5885, Aug. 2020. <https://doi.org/10.3390/app10175885>
- [28] E. Elbeltagi and H. Wefki, “Predicting energy consumption for residential buildings using ANN through parametric modeling,” *Energy Reports*, vol. 7, pp. 2534–2545, Nov. 2021. <https://doi.org/10.1016/j.egyr.2021.04.053>
- [29] S. H. Almuhaini and N. Sultana, “Forecasting Long-Term Electricity Consumption in Saudi Arabia Based on Statistical and Machine Learning Algorithms to Enhance Electric Power Supply Management,” *Energies*, vol. 16, no. 4, Art. no. 4, Jan. 2023. <https://doi.org/10.3390/en16042035>
- [30] J. B. Smith and J. Ming, “Renewable energy research leases: Prospects and opportunities on the Hawaiian Outer Continental Shelf (OCS),” in *OCEANS’11 MTS/IEEE KONA*, Sep. 2011, pp. 1–5. <https://doi.org/10.23919/OCEANS.2011.6107285>
- [31] W. Strielkowski, L. Civín, E. Tarkhanova, M. Tvaronavičienė, and Y. Petrenko, “Renewable Energy in the Sustainable Development of Electrical Power Sector: A Review,” *Energies*, vol. 14, no. 24, Art. no. 24, Jan. 2021. <https://doi.org/10.3390/en14248240>

- [32] B. Bush, N. Brunhart-Lupo, B. Bugbee, V. Krishnan, K. Potter, and K. Gruchalla, “Coupling visualization, simulation, and deep learning for ensemble steering of complex energy models,” in *2017 IEEE Workshop on Data Systems for Interactive Analysis (DSIA)*, Oct. 2017, pp. 1–5. <https://doi.org/10.1109/DSIA.2017.8339087>
- [33] J. Zhang, Q. Liu, Q. Wang, R. Tang, Y. He, and N. Tai, “Data-Driven Intelligent Fault Diagnosis Technology for Transmission Lines of Wind Power Renewable Energy System,” in *2023 3rd International Conference on Energy, Power and Electrical Engineering (EPEE)*, Sep. 2023, pp. 246–251. <https://doi.org/10.1109/EPEE59859.2023.10351976>
- [34] X. Yang *et al.*, “Optimal Distribution Network Planning with CVaR Model Considering Renewable Energy Integration,” in *2018 2nd IEEE Conference on Energy Internet and Energy System Integration (EI2)*, Oct. 2018, pp. 1–6. <https://doi.org/10.1109/EI2.2018.8582256>
- [35] K. Kampouropoulos, F. Andrade, E. Sala, A. G. Espinosa, and L. Romeral, “Multiobjective Optimization of Multi-Carrier Energy System Using a Combination of ANFIS and Genetic Algorithms,” *IEEE Transactions on Smart Grid*, vol. 9, no. 3, pp. 2276–2283, May 2018. <https://doi.org/10.1109/TSG.2016.2609740>
- [36] M. M. Samy, H. H. Sarhan, S. Barakat, and S. A. Al-Ghamdi, “A Hybrid PV-Biomass Generation Based Micro-Grid for the Irrigation System of a Major Land Reclamation Project in Kingdom of Saudi Arabia (KSA) - Case Study of Alba Area,” in *2018 IEEE International Conference on Environment and Electrical Engineering and 2018 IEEE Industrial and Commercial Power Systems Europe (EEEIC / I&CPS Europe)*, Jun. 2018, pp. 1–8. <https://doi.org/10.1109/EEEIC.2018.8494543>
- [37] Y. Bhandari, S. Chalise, J. Sternhagen, and R. Tonkoski, “Reducing fuel consumption in microgrids using PV, batteries, and generator cycling,” in *IEEE International Conference on Electro-Information Technology , EIT 2013*, May 2013, pp. 1–4. <https://doi.org/10.1109/EIT.2013.6632692>
- [38] M. Patterson, N. F. Macia, and A. M. Kannan, “Hybrid Microgrid Model Based on Solar Photovoltaic Battery Fuel Cell System for Intermittent Load Applications,” *IEEE Transactions on Energy Conversion*, vol. 30, no. 1, pp. 359–366, Mar. 2015. <https://doi.org/10.1109/TEC.2014.2352554>
- [39] A. Alshibani and O. S. Alshamrani, “ANN/BIM-based model for predicting the energy cost of residential buildings in Saudi Arabia,” *Journal of Taibah University for Science*, vol. 11, no. 6, pp. 1317–1329, Nov. 2017. <https://doi.org/10.1016/j.jtusci.2017.06.003>
- [40] A. Alshibani, “Prediction of the Energy Consumption of School Buildings,” *Applied Sciences*, vol. 10, no. 17, Art. no. 17, Jan. 2020. <https://doi.org/10.3390/app10175885>
- [41] A. Abubakar Mas’ud, “Comparison of three machine learning models for the prediction of hourly PV output power in Saudi Arabia,” *Ain Shams Engineering Journal*, vol. 13, no. 4, p. 101648, Jun. 2022. <https://doi.org/10.1016/j.asej.2021.11.017>
- [42] T. Alquthami and A. Alaraishy, “Comprehensive Energy and Cost evaluation through detailed Auditing and Modeling for Mosque in Saudi Arabia,” vol. 16, no. 9, 2021.

Vibration analysis of 3D printed PLA beam with honeycomb cell structure for renewable energy applications and sustainable solutions

Kubilay ASLANTAS^{1,a*}, Ekrem ÖZKAYA^{2,b}, Waleed AHMED^{3,c,*}

¹ Department of Mechanical Engineering, Faculty of Technology, Afyon Kocatepe University, Afyonkarahisar, Turkey

² Faculty of Engineering - Department of Mechanical Engineering, Turkish-German University, 34820 Beykoz / İSTANBUL, Turkey

²Mechanical Engineering Department College of Engineering, UAE University, Al Ain, Abu Dhabi; UAE

^aaslantas@aku.edu.tr, ^bekrem.oezkaya@tau.edu.tr, ^cw.ahmed@uaeu.ac.ae

Keywords: Additive Manufacturing, Vibration Analysis, Finite Element Method

Abstract. Research shows a lack of vibration analyses of structures produced by 3D printing. This study, therefore, investigates the vibration behavior of honeycomb structures made of polylactic acid (PLA) using the additive manufacturing process fused deposition modeling (FDM) in a beam element. Based on an experimental modal analysis and the determination of the damping rate, a FEM reference simulation model is created, and the results are validated with the data from the experiment. The original honeycomb structure was numerically varied in its density, i.e., in the thickness (*t*) of the cell wall, in the length (*L*) of the regular hexagons, and in its degree of filling. The results showed that the density of the honeycombs at a filling level of 19% has a marginal influence on the vibration behavior. The vibration behavior was reduced only when the filling level was increased to 30%. This study has implications for many areas of research in which vibrations play a significant role in technical applications. These findings highlight the potential for integrating renewable energy applications with sustainable solutions, emphasizing the importance of vibration dynamics in advancing environmentally friendly technologies.

Introduction

Digital manufacturing technology, also known as 3D printing or additive manufacturing, has revolutionized the field of manufacturing. It allows for the production of complex structures with high precision and customization by successively adding materials based on three-dimensional computer-aided design (CAD) data [1]. Various techniques are available for 3D printing, with the most common being powder bed fusion (PBF) and fused deposition modeling (FDM) [2]. The ability to use various materials, including thermoplastics, ceramics, graphene-based materials, and metals, offers numerous application possibilities [3]. An overview of significant advances, typical applications, current challenges, advantages, and disadvantages of 3D printing processes, and a comprehensive description of various materials can be found in [4-5]. The use of plastics is becoming increasingly popular due to their excellent properties (high strength-to-mass ratio, low cost, durable, relatively impermeable, sterilizable) with controllable flexibility. In particular, there is growing interest in the use of biodegradable polymers. The most extensively investigated (bio)degradable thermoplastic polymers, which are also suitable for additive manufacturing technologies, are polyesters such as polylactic acid (PLA), polycaprolactone (PLC), and polyhydroxyalkanoates (PHA) [6]. Polylactic acid (PLA), a biodegradable and environmentally friendly thermoplastic, has emerged as a popular choice for 3D printing due to its ease of use and versatility [7]. The properties of PLA can also be chemically altered through synthesis or physical modifications [8-9]. The integration of honeycomb geometries into structural components has been

found to be applicable in many industries due to its potential to improve strength-to-weight ratios and overall mechanical efficiency [10]. However, the addition of internal honeycomb cell structures (which have good energy absorption properties) can add a layer of complexity to the material, influencing its dynamic response to external stimuli, especially vibrations. Geometric revisions to the extruded honeycomb structures will also significantly affect the vibration characteristics of the structure. The modal analysis technique is often used to determine the dynamic characterization of a structure or a machine element. Modal analysis determines a system's natural frequencies, mode shapes, and damping characteristics. The basic concept of modal analysis lies in representing the vibration response of a time-invariant linear dynamic system as a linear combination of a series of simple harmonic motions called natural modes of vibration. Modal analysis is an experimental approach that a hammer impact test or a vibration shaker can perform. Modal analysis of any structure or component must not be performed experimentally. When appropriate boundary conditions are defined, modal analysis can be performed using the finite element technique (FEM) to obtain the mode shapes and frequencies of the structure. With the widespread use of additive manufacturing in the last decade, porous structures' vibration-damping properties have been modeled experimentally and numerically. To increase the impact or vibration-damping properties of a structure, the pore structures shown in Figure 1 are widely used. Honeycomb geometry is frequently used in sandwich panels, and these structures' vibration behavior has been the subject of many studies [5].

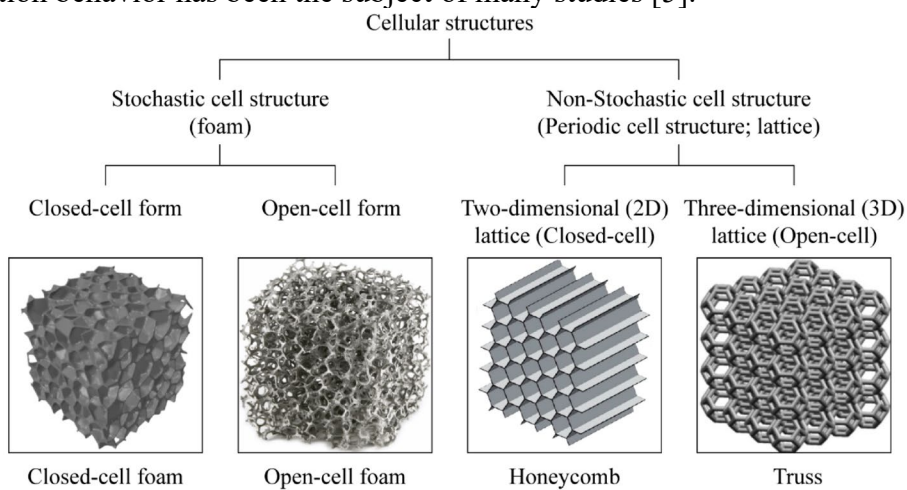


Fig. 1. Categories of cellular structures [12].

There is a lack of vibration analyses of structures produced using 3D printing in research. Understanding such structures' vibration characteristics is essential to ensure optimum performance in practical applications. This study investigates the effect of the honeycomb lattice structure on the vibration behaviour of a beam made of PLA material. In the study, firstly, a 3D printed PLA beam was produced by taking the edge length (L) and thickness (t) of the honeycomb lattice geometry as constant, and the damping ratio and resonant frequencies were found by performing a hammer test. The mode frequencies and vibration amplitudes obtained by numerical modeling are compared. FE analyses are extended for different values of L and t of the honeycomb geometry.

Material and Method

In the first stage of the study, a sample of PLA material was produced using the FDM method. The hammer test was performed on this sample, and the damping ratio of the material was determined. The damping ratio was used as input for harmonic analysis.

Sample Preparation

In this part of the study, the computer-aided design of the specified honeycomb geometry and the whole beam was carried out first. SpaceClaim software was used for the design. The 25 mm part of the beam (A region) is modeled as solid and is used to stabilize the beam (Fig. 2). The B region of the beam has a wall thickness of 0.75 mm and is filled with honeycomb. The dimensions of the honeycomb used are also given in Figure 2.

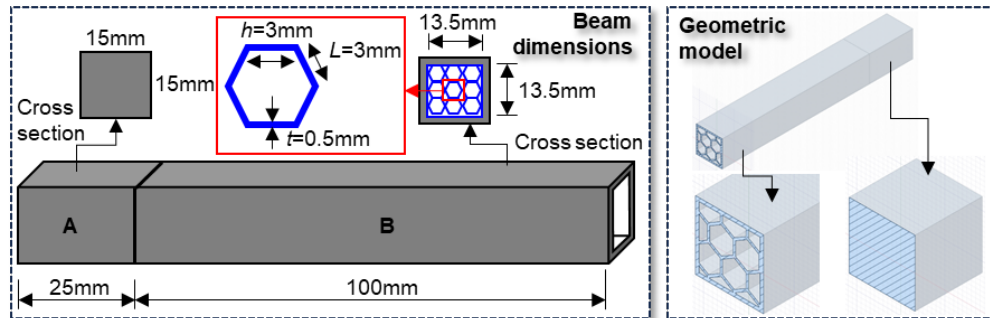


Fig.1. Dimensions and geometrical modeling of the beam

Experimental analysis

Figure 3 shows a schematic representation of the experimental procedure used in the study. The 3D-printed specimen was fixed from the A region (Fig. 2) employing a vice. An accelerometer was connected to the tooltip to measure the natural frequencies of the specimen. A Dytran brand hammer with model number 5800B4 was used for tap testing. A Dytran accelerometer (322F1) was mounted at the relevant position to measure the frequency response. A four-channel data acquisition system (Novian, model number S04) was used in conjunction with the Tap Testing measurement module of the CutPRO software to obtain the results of the vibration characteristics of the specimen. After the measurement, force-time, acceleration-time graphs and real-frequency and imaginary-frequency changes were obtained. In addition, the amplitude value occurring in the sample at the first mode frequency was also obtained. For numerical modeling, the damping ratio value of the sample must be known. The damping ratio of the sample was calculated using the real-frequency change obtained after the tap testing (Fig. 4).

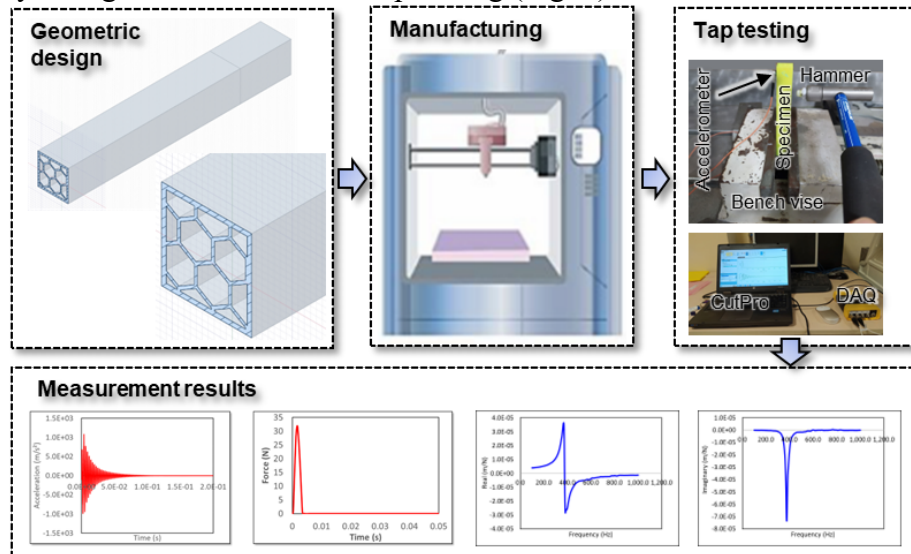


Fig. 3. Schematic representation of the experimental procedure used in the study

The specimen's real and imaginary part curves were obtained after the hammer test. The peak points (ω_1 and ω_2) in the real part curve and the values corresponding to the natural frequency (ω_n) were used. The damping ratio value of the specimen was calculated using Eq. 1.

$$\zeta = \frac{\omega_2 - \omega_1}{2 \cdot \omega_n} \quad (1)$$

Numerical modeling

Ansys software was used for FE analysis, and SpaceClaim software was preferred for geometric design. After the geometric model was imported to Ansys software [13], modal analysis was performed to find the mode frequencies. Afterward, the frequency response of the sample was obtained by performing harmonic analysis. In both analyses, part A of the specimen was fixed as anchored. In the harmonic analysis, the load was applied in the direction of the hammer load. Prior to numerical modeling, mesh convergence analysis was performed to determine the sufficient number of elements and nodes. Figure 5 shows the steps of the numerical modeling process used in the study. The modulus of elasticity of the PLA material used was taken as 2350 MPa, Poisson's ratio as 0.39, and density as 1.25 g/cm³. In addition, the damping ratio was obtained as 0.022 using the method mentioned in the previous section. In the modeling, 31752 elements (tetrahedrons with 10 nodes) and 56764 nodes were used.

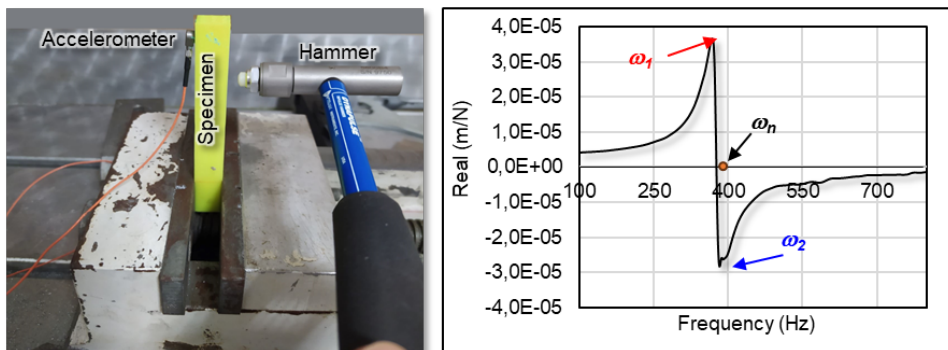


Fig. 4. Tap testing test setup and real part graph used to calculate the damping ratio.

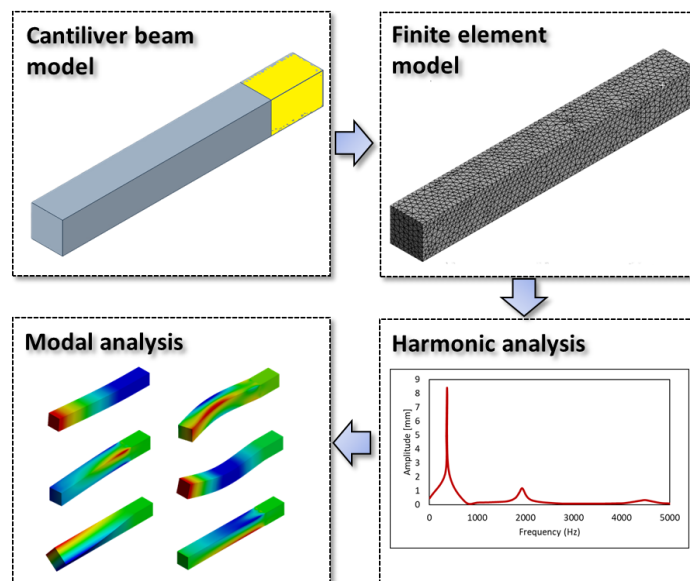


Fig. 5. Schematic representation of the steps used in numerical modeling

Results and Discussion

Tap testing results and verification of the FE model

In the study, experimental studies were first completed, and the value of the damping ratio required for numerical modeling was determined. Frequency values in each mode were obtained by hammer test. The frequency values for each mode obtained after numerical modeling were compared with the experimental results (Table 1). As can be seen from Table 1, there is a good agreement in the other frequency values except the 2nd mode value. The high margin of error in the 2nd mode frequency value may be due to two reasons. The first is that the point where the load is applied during the hammer test is not the same every time. The second is the minor dimensional errors caused during the production of the specimen. In particular, even slight differences in the wall thickness of the honeycomb may have caused this error.

Table 1. Comparison of experimental and numerical results and mode shapes

Mode No	Experimental	Modelling	Error (%)	Mode shape
1	363	364.8	0.5	
2	447.6	376.6	-18.8	
3	1687.9	1768.8	4.6	
4	1998.1	1952.4	-2.3	
5	2046.5	1986.1	-3	
6	3494.4	3435.5	-1.7	

After numerical modeling, the amplitude-frequency variation obtained for the 1st mode was compared with the experimental result (Fig. 6). As seen from Figure 6, the experimental and numerical modeling results agree very well. This shows the accuracy of the FE model and the boundary conditions used. It is seen that the maximum amplitude value occurs as 0.165 mm at 363 Hz in the experimental study, while it occurs as 0.166 mm at 364.8 Hz in the FE analysis.

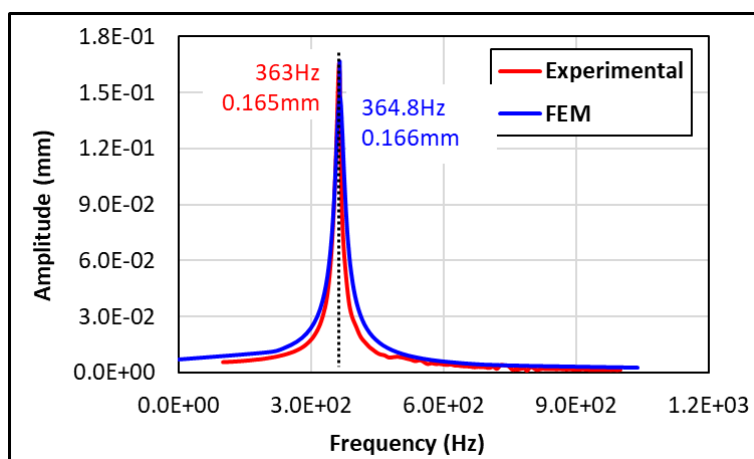


Fig. 6. Comparison of amplitude-frequency variation results in the beam

Vibration behavior of the revised honeycomb geometry

In the previous section, the vibration behavior of the honeycomb-filled PLA beam was obtained by hammer-impactor test, and the FE model was also validated. In this section, geometrical revisions were made to the honeycomb geometry, and the effects of the honeycomb's edge length, thickness, and filling rate were investigated. In lattice structures, changing the dimensions of the cell geometry causes a change in the filling rate. The FE analyses carried out in this section were performed for three different cell sizes, two different filling rates, and solid and hollow cases of the beam. Modal and then harmonic analyses were performed for the geometrical models. Thus, it was possible to calculate how much the revision in the honeycomb geometry affects the vibration amplitude and 1st mode frequency. Figure 7 shows different sections of the beam geometry used in the FE analysis. The effect of the change in cell edge length (L), cell edge thickness (t), and filling rate was investigated.

Filling rate (%)	100	--	19			30
Description	Solid beam	Hollow beam	$L=1.5\text{mm}$ $t=0.25\text{mm}$	$L=3\text{mm}$ $t=0.5\text{mm}$	$L=4\text{mm}$ $t=0.67\text{mm}$	$L=1.7\text{mm}$ $t=0.5\text{mm}$
Cross section						

Fig. 7. Cross sections of the beam geometry used in FE analysis

Figure 8 shows the amplitude-frequency variation obtained as a result of the harmonic analysis. Since the maximum amplitude occurs in the 1st mode in the beam, only 1st mode values are given in Figure 8. The hollow beam has the lowest stiffness among the analyzed sections. As expected, the maximum amplitude occurred in the hollow beam. All three sections' 1st mode frequency values with a filling rate of 19 are very close. In the inner graph in Figure 8, the graph for the % filling rate of 19% is detailed. As can be seen, the maximum amplitude was realized at $L = 4 \text{ mm}$ and $t = 0.67 \text{ mm}$.

On the other hand, the maximum frequency was obtained for $L = 1.5 \text{ mm}$ and $t = 0.25 \text{ mm}$. According to these three results, where the filling rate is constant, the variation of L and t does not affect the vibration amplitude and frequency much. When the filling rate ratios are compared, the amplitude value obtained for 30% is lower than 19%. On the other hand, the frequency value for 30% is lower than 19%. The amplitude value is minimum since the solid beam is the section geometry with the highest stiffness. However, the solid beam is the cross-section with the lowest 1st mode frequency value.

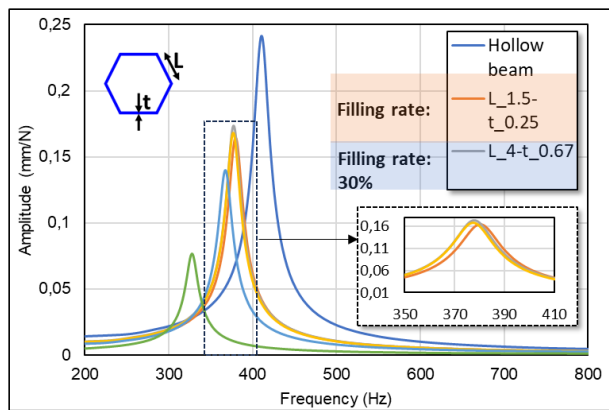


Fig. 8. Comparison of amplitude-frequency

Conclusion

This study thoroughly examined the impact of utilizing honeycomb geometry as a filling element within the beam structure. Experimental samples, crafted from PLA material with $L=3$ mm and $t=0.5$ mm (filling rate: 19%), were rigorously analyzed and validated through FE analysis. The validated FE simulation model enabled the exploration of varying densities (different L and t values) at 19% and 30% filling rates, shedding light on critical findings:

- The resonance frequency values obtained experimentally and numerically exhibited strong agreement, validating the reliability of the analysis.
- Maximal resonance amplitudes occurred at the 1st mode frequency, consistently verified through experimental and numerical approaches.
- Variations in L and t ratios, while holding the filling rate constant, minimally affected both amplitude and frequency.
- Increasing the filling rate resulted in decreased vibration amplitudes and frequencies, highlighting the role of density in vibration behavior.

The validated FE simulation model serves as a robust foundation for future investigations. Subsequent studies will explore diverse materials, filling structures, and structural densities while examining the influence of various pressure parameters. These efforts aim to advance sustainable practices and renewable energy applications, contributing to the ongoing evolution of environmentally conscious engineering solutions.

The research highlights the potential of 3D-printed honeycomb structures for renewable energy applications. Their vibration behavior, characterized through experimental analysis, offers opportunities for enhancing efficiency in energy harvesting devices and damping mechanisms. The structures' adaptability and lightweight nature make them suitable for components in wind turbines, solar panels, and energy storage systems. Integrating these structures into renewable energy technologies holds promise for advancing sustainable solutions and improving overall system performance.

References

- [1] A. M. T. Syed, P. K. Elias, B. Amit, B. Susmita, O. Lisa, & C. Charitidis, "Additive manufacturing: scientific and technological challenges, market uptake and opportunities," Materials today, Vol. 1, pp. 1-16, 2017
- [2] Shulman, H.; Spradling, D.; and Hoag, C.: Introduction to additive manufacturing, Ceram. Indus. 162:15-21, 2012.

- [3] N. Shahrubudin, T.C. Lee, R. Ramlan, An Overview on 3D Printing Technology: Technological, Materials, and Applications, Procedia Manufacturing, Volume 35, 2019, Pages 1286-1296. <https://doi.org/10.1016/j.promfg.2019.06.089>
- [4] Ji-chi Zhang, Kuai He, Da-wei Zhang, Ji-dong Dong, Bing Li, Yi-jie Liu, Guo-lin Gao, Zai-xing Jiang, Three-dimensional printing of energetic materials: A review, Energetic Materials Frontiers, Volume 3, Issue 2, 2022, Pages 97-108,7. <https://doi.org/10.1016/j.enmf.2022.04.001>
- [5] Anketa Jandyal, Ikshita Chaturvedi, Ishika Wazir, Ankush Raina, Mir Irfan Ul Haq, 3D printing – A review of processes, materials and applications in industry 4.0, Sustainable Operations and Computers, Volume 3, 2022, Pages 33-42.
<https://doi.org/10.1016/j.susoc.2021.09.004>
- [6] Jennifer Gonzalez Ausejo, Joanna Rydz, Marta Musioł, Wanda Sikorska, Henryk Janeczek, Michał Sobota, Jakub Włodarczyk, Urszula Szeluga, Anna Hercog, Marek Kowalcuk, Three-dimensional printing of PLA and PLA/PHA dumbbell-shaped specimens of crisscross and transverse patterns as promising materials in emerging application areas: Prediction study, Polymer Degradation and Stability, Volume 156, 2018, Pages 100-110.
<https://doi.org/10.1016/j.polymdegradstab.2018.08.008>
- [7] Iftekhar, S.F.; Aabid, A.; Amir, A.; Baig, M. Advancements and Limitations in 3D Printing Materials and Technologies: A Critical Review. *Polymers* **2023**, *15*, 2519.
<https://doi.org/10.3390/polym15112519>
- [8] Rasal RM, Janorkar AV, Hirt DE. Poly(lactic acid) modifications. *Prog Polym Sci* 2010;35:338-356. <https://doi.org/10.1016/j.progpolymsci.2009.12.003>
- [9] Arrieta MP, López J, Hernández A, Rayón E. Ternary PLA-PHB-limonene blends intended for biodegradable food packaging applications. *Eur Polym J* 2014;50:255-270.
<https://doi.org/10.1016/j.eurpolymj.2013.11.009>
- [10] Hossein Mohammadi, Zaini Ahmad, Michal Petrů, Saiful Amri Mazlan, Mohd Aidy Faizal Johari, Hossein Hatami, Seyed Saeid Rahimian Koloor, An insight from nature: honeycomb pattern in advanced structural design for impact energy absorption, Journal of Materials Research and Technology, Volume 22, 2023, Pages 2862-2887.
<https://doi.org/10.1016/j.jmrt.2022.12.063>
- [11] Zippo, A.; Iarricchio, G.; Pellicano, F.; Shmatko, T. Vibrations of Plates with Complex Shape: Experimental Modal Analysis, Finite Element Method, and R-Functions Method. *Shock. Vib.* **2020**, 8882867. <https://doi.org/10.1155/2020/8882867>
- [12] Park, K.-M.; Min, K.-S.; Roh, Y.-S. Design Optimization of Lattice Structures under Compression: Study of Unit Cell Types and Cell Arrangements. *Materials* **2022**, *15*, 97.
<https://doi.org/10.3390/ma15010097>
- [13] ANSYS Inc. (2022). ANSYS Software. Retrieved from <https://www.ansys.com>

Potential use of reject brine waste as a sustainable construction material

Seemab TAYYAB^{1,a}, Essam ZANELDIN^{2,b*}, Waleed AHMED^{3,c}, and Ali AL MARZOUQI^{4,d}

¹Research Assistant, Department of Civil and Environmental Engineering, United Arab Emirates University, Al-Ain, United Arab Emirates

²Associate Professor, Department of Civil and Environmental Engineering, United Arab Emirates University, Al-Ain, United Arab Emirates

³Assistant Professor, Engineering Requirements Unit, United Arab Emirates University, Al-Ain, United Arab Emirates

⁴Professor, Department of Chemical and Petroleum Engineering, United Arab Emirates University, Al-Ain, United Arab Emirates

^atayyabseemab14@gmail.com, ^bessamz@uaeu.ac.ae, ^cw.ahmed@uaeu.ac.ae,
^dhassana@uaeu.ac.ae

Keywords: Reject Brine, Desalination, Sustainable Construction, Resource Utilization, Environmental Impact

Abstract. In countries near the ocean, the majority of the water used for household, agricultural, and industrial purposes is attained through seawater desalination. Desalination produces highly salty water, commonly known as reject brine, which can have many drastic, negative effects on the environment. The waste results in both an environmental challenge and an opportunity for sustainable resource utilization. This research work is a literature study to investigate the feasibility and potential benefits of utilizing reject brine waste as a sustainable construction material. The results revealed that reject brine has a prodigious possibility to be used as a binder, and in place of water in concrete. The use of reject brine in cementitious composites decreases CO₂ emissions and makes them economical. Also, reject brine is fruitful in the stabilization of soil by increasing the mechanical properties and enhance the strength of soil. In essence, the use of reject brine from water desalination in construction is a sustainable and environment-friendly approach.

Introduction

Water is life. Fresh water is essential for living organisms to survive on earth and is increasingly depleted. The increase in population and industrialization lead to an increase in demand for water. About 1.8 billion people around the world will face water shortage by the end of the year 2025 [1]. The countries near the ocean (e.g., gulf countries) lack fresh water and frequently use desalination techniques to produce drinkable water. The produced water is used by human beings and for construction practices as well. Desalination methods include reverse osmosis, multistage flash evaporation, multi-effect distillation, and electrodialysis [2]. These techniques produce pure water but at the same time result in the production of a by-product waste with a high concentration of salt called reject brine. Only 35-45% of freshwater is recovered from the sea, while the remaining 55-65% of gross feed comes out of the desalination plant as waste brine [3]. It is estimated that Gulf countries produce more than 60% of the world's desalinated water with UAE's contribution alone around 13% [4]. The waste is disposed of in open sea and in valuable lands which is a major threat to aquatic life and sustainable development.

Concrete is the 2nd most widely used material after water on Earth. It is an old material consisting of cement, sand, aggregate, water, and suitable admixtures that have been in use for

many centuries. The large-scale consumption of ordinary Portland cement (OPC) as a binding agent in concrete results in serious environmental challenges and issues because of the significant CO₂ emissions associated with its production. Every 1kg of cement production results in 0.9kg production of CO₂ to the environment [5-7]. The natural fine and coarse aggregates (sand, gravel, etc.) used in concrete synthesis result in their depletion with time. Concrete is a thirsty behemoth, sucking up almost 1/10th of the total world's industrial water usage. By 2050, 75% of infrastructure water demand is expected to occur in areas expected to experience water stress [8]. Therefore, in the past, various research efforts have been devoted to producing substitute construction materials in place of natural ingredients without compromising the strength, durability, and economy to promote sustainable development. A brief description of some of the studies is given in Table 1.

Table 1: A literature review of the use of different alternatives partially in place of cement, sand, and water in concrete

Material to be replaced	Material replaced with	Procedure	Result	Reference
Cement	Waste brick powder	Prepared concrete specimens using 5% and 10% of WBP in place of cement	Workability and compressive strength increased due to the shape and particle size of WBP	[9]
Cement	Marble dust	Studied the use of marble dust collected from marble blocks in concrete mixtures by 5, 10, 15, and 20%	The mechanical properties of concrete increased significantly compared to the control sample	[10]
Cement	Rice husk ash	Addressed the strength characteristics of cement mortar containing 0, 2.5, 5, 7.5, 10, 12.5, 15% RHA	Compressive strength of hardened concrete decreases with increasing RHA percentage	[11]
Sand	Coal bottom ash	Studied the effect of CBA as a replacement of sand in concrete with dosage at 20, 30, 40, 50, 75, and 100%	Workability and bleeding decreased, compressive and splitting strength of concrete did not change significantly	[12]
Sand	Recycled plastic waste	Evaluated the performance of concrete with RPW as a partial replacement of sand in different proportions	Replacing 10% of sand by volume is the best solution, saving 0.820 billion tons of sand every year	[13]
Sand	Fly ash	Concrete samples containing FA in amounts 20, 40, 60, 80, and 100% were cast and tested	Compressive strength, split tensile strength, and modulus of elasticity increased up to an optimum dosage of 40%	[14]
Water	Polyvinyl acetate resins waste waster	Used the industrial wastewater discharged to replace the water in concrete completely	While compressive strength and density increased slightly, the values of slump decreased	[15]
Water	Treated Water and Waste Water	Assessed the strength of concrete using treated water and wastewater	The strength of concrete samples decreased using wastewater but the value is above the standard requirement	[16]

Desalination of Seawater

The amount of calcium, chloride, magnesium, potassium, sodium, and sulphates in seawater are 412, 19500, 1290, 380, 10770, and 905mg/L as compared to potable water containing these minerals in compositions of 75, 250, 50, 10, 200, and 400mg/L respectively. Also, the amount of total dissolved solids in seawater is 33387pm as compared to 500pm in drinkable water [17]. Desalination is the process of removing minerals from salt water. Saltwater is desalinated in order to produce water suitable for human household consumption or irrigation purposes. The formation of reject brine takes place as a byproduct of desalination. There are different methods used for the desalination process all over the world as shown in Figure 1. They meet the needs of more than 300 million people by producing 87 million cubic meters of clean water every day [18]. The schematic procedure of reject brine formation is shown in Figure 2.

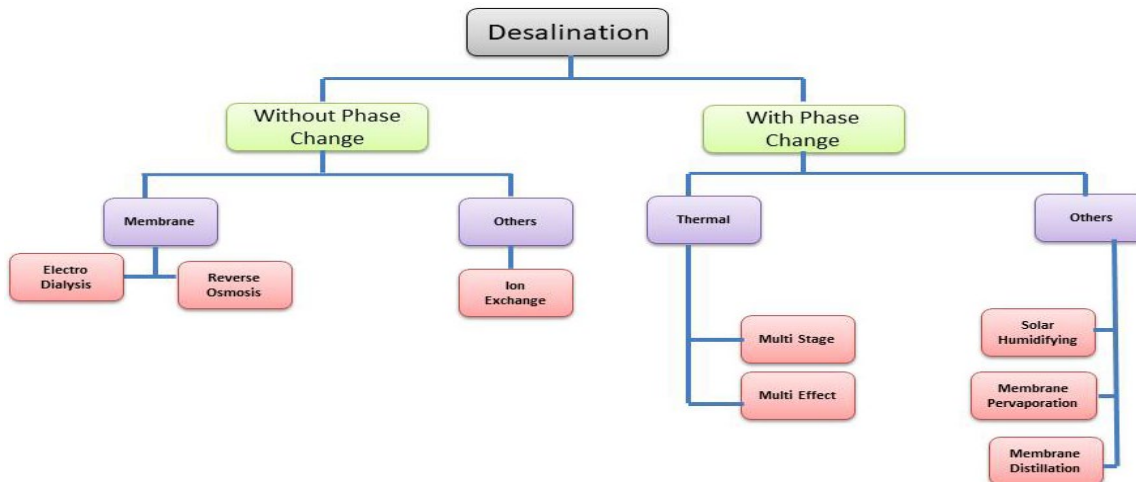


Figure 1: Processes used for desalination [19]

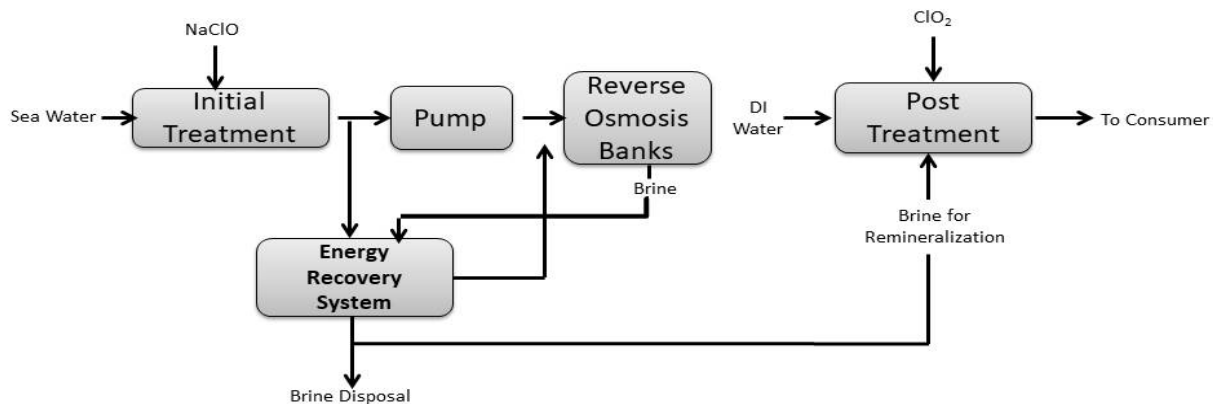


Figure 2: Schematic diagram of reject brine formation [20]

Reject Brine Use in Construction

The study of the feasibility of using desalination reject brine in construction materials has become of growing interest in this modern era. The use of reject brine in making construction materials like concrete, mortar, bricks, blocks, soils, etc. will serve two main purposes. First, natural ingredients consumption in the construction industry will decrease, releasing some pressure on the natural resources which are limited and depleting with time. Second, the brine's harmful ecological and physiochemical influences on the receiving aquatic bodies will be reduced.

Reject Brine as a Binder in Concrete

Cement is the binding agent used in construction projects obtained through the chemical process of limestone, clay, magnesia, silica, alumina, etc. [21]. It gives stability, strength, and durability to materials to guarantee they stay longer. The presence of an optimum percentage of MgO in cement ensures the setting time and strength of the composites [22]. Due to its high magnesium content (Mg^{2+}), waste brine has the character to be used as an eco-friendly and sustainable cause for cement production. S. Ruan et al. (2021) highlighted problems shown with increased emissions of magnesium oxide and carbon dioxide from brine waste. They examined the possibility of producing cement containing MgO (from brine waste) and analyzed its use as a binding agent compared to commercial MgO. The mechanical properties of the specimens were evaluated along with microstructural analysis using X-ray diffraction (XRD), thermogravimetric analysis/differential scanning calorimetry (TGA/DSC), etc. Samples containing higher reactivity magnesium oxide products were found to be stronger than samples containing commercial magnesium oxide products. The increased solubility of synthetic magnesium oxide leads to better hydration and carbonation, leading to a denser structure and structures with improved properties [23].

Reject Brine in Place of Water in Concrete

The process of hydration of cement in cementitious composites is due to the presence of water. Using salt water to prepare concrete is not a new procedure. MS. Islam et al. (2010) emphasized the effect on the setting time of concrete by partially using saline water in place of ordinary portable water [24]. Mori et al. (1981) prepared concrete samples containing fresh water and saline water. They observed a comparatively minor alteration between the mechanical strength of concrete prepared with fresh water and concrete produced with saline water [25]. However, Yamamoto et al. (1980) found that concrete prepared with salty or saline water confirms higher strength compared to concrete containing fresh water [26]. To prevent the chances of metal erosion, V. Kumar et al. (1998) suggested avoiding the use of salty water for reinforced concrete (RC) [27]. However, Dang et al. (2022) studied the long-term concrete exposure to chloride (Cl^-) ions and exhibited that the effect of chloride (Cl^{-1}) ions in concrete production from seawater is quite small or insignificant [28]. In another study, F. Qu et al. (2021) determined that corrosion of steel in reinforced concrete (RC) structures is because of sulphate attack occurs not due to the presence of chloride ions (Cl^{-1}) in seawater, but due to the harsh marine environment in which the sample is located [29].

Reject Brine to Minimize CO₂ Emissions from Cementitious Composites

Cement is an important building binding material and its production accounts for 5% of the world's CO₂, a powerful greenhouse gas. With the dedication of reducing the carbon footprint of the process of concrete preparation using reject brine, Fattah et al. (2017) conducted research to determine the impact of CO₂ emissions by using brine waste as water and ground-granulated-blast-furnace slag (GGBS) as a cement substitute. Concrete specimens containing different percentages of cement were prepared using ordinary portable water and wastewater containing brine. The results exhibited that the use of reject brine and GGBS enhanced the mechanical strength of concrete formed, because of the high filling character of GGBS. Consuming reject brine as the potential water source and replacing 50% of the cement with GGBS can reduce 3.74–7.5 lbs. of CO₂/cubic meter of concrete, and 388 lbs. of CO₂/cubic meter of concrete respectively. The waste reject brine usage in cementitious composites is an economical approach as it can save about AED 625–1250 per cubic meter of concrete prepared [30].

Reject Brine to Enhance the Strength of Soil

Soil is an important engineering material that serves a major role in the construction of foundations, roadbeds, dams, and buildings [31]. Mathew et al. (2012) studied the effect of increasing brine concentration on soil-bearing capacity. The samples with and without reject brine were prepared and their shear strength parameters were monitored for 364 days. The soil's bearing capacity was calculated using numerical equations. The more the contamination of soil with brine, the more decrease in the bearing capacity [32]. Kuriakose et al. (2022) researched to make use of the brine waste generated from the desalination of water for the steadiness of soil. The brine sludge was mixed with marine clay at various percentages by the dry weight of the moist clay. It was found that brine sludge can be used as a substitute in the stabilization of soft clays as it improves the geotechnical properties of soil [33]. S.L. Barbour et al. (1993) evaluated the geotechnical properties of two Ca-montmorillonite clayey soils having brine adulteration. The changes in mechanical properties (shear strength, bearing capacity, etc.), index properties (liquid limit, plastic limit, etc.), and hydraulic properties by the incorporation of reject brine were determined. A significant increase in shear strength and bearing capacity was reported [34].

Conclusion

In conclusion, this study proved that reject brine has great potential to be used in construction materials, in the formation of cement, mortar, concrete, bricks, soils, etc. It will be a great source to enhance the mechanical and durability properties of cementitious composites and also make them economical. This will in turn reduce the consumption of natural water and get rid of waste brine which is a serious concern in this modern era for the countries near the ocean. The use of reject brine in the construction industry will surely be a sustainable and environment-friendly approach in the future. Future studies by the research team are directed at defining the long-term performances of reinforced cementitious materials through carbonation tests, freeze and thaw tests, sulphate attack tests, rapid chloride ion penetration tests, sorption tests, etc. There is a great possibility of checking the feasibility of reject brine in the manufacture of bricks and also the treatment of soil with brine might enhance its properties.

References

- [1] Chakraborti, R.K., Kaur, J. and Kaur, H., 2019. Water Shortage Challenges and a Way Forward in India. Journal: American Water Works Association, 111(5). <https://doi.org/10.1002/awwa.1289>
- [2] Thimmaraju, M., Sreepada, D., Babu, G.S., Dasari, B.K., Velpula, S.K. and Vallepu, N., 2018. Desalination of water. Desalination and water treatment, pp.333-347. <https://doi.org/10.5772/intechopen.78659>
- [3] Khan, M. and Al-Ghouti, M.A., 2021. DPSIR framework and sustainable approaches of brine management from seawater desalination plants in Qatar. Journal of Cleaner Production, 319, p.128485. <https://doi.org/10.1016/j.jclepro.2021.128485>
- [4] Jones, E., Qadir, M., van Vliet, M.T., Smakhtin, V. and Kang, S.M., 2019. The state of desalination and brine production: A global outlook. Science of the Total Environment, 657, pp.1343-1356. <https://doi.org/10.1016/j.scitotenv.2018.12.076>
- [5] Imbabi, M.S., Carrigan, C. and McKenna, S., 2012. Trends and developments in green cement and concrete technology. International Journal of Sustainable Built Environment, 1(2), pp.194-216. <https://doi.org/10.1016/j.ijsbe.2013.05.001>
- [6] Ibeto, C.N., Obiefuna, C.J. and Ugwu, K.E., 2020. Environmental effects of concrete produced from partial replacement of cement and sand with coal ash. International Journal of Environmental Science and Technology, 17, pp.2967-2976. <https://doi.org/10.1007/s13762-020-02682-4>
- [7] Ummi, R.K., 2017, July. A Comparative Study of Green Technology in Cement Industry. In ASEAN/Asian Academic Society International Conference Proceeding Series.

- [8] Miller, S.A., Horvath, A. & Monteiro, P.J.M. Impacts of booming concrete production on water resources worldwide. *Nat Sustain* 1, 69–76 (2018). <https://doi.org/10.1038/s41893-017-0009-5>
- [9] Arif, R., Khitab, A., Kırız, M.S., Khan, R.B.N., Tayyab, S., Khan, R.A., Anwar, W. and Arshad, M.T., 2021. Experimental analysis on partial replacement of cement with brick powder in concrete. *Case Studies in Construction Materials*, 15, p.e00749. <https://doi.org/10.1016/j.cscm.2021.e00749>
- [10] Vaidevi, C., 2013. Study on marble dust as partial replacement of cement in concrete. *Indian journal of engineering*, 4(9), pp.14-16.
- [11] Bawankule, S.P. and Balwani, M.S., 2015. Effect of partial replacement of cement by rice husk ash in concrete. *Int. J. Sci. Res*, 4, pp.1572-1574.
- [12] Singh, M., 2018. Coal bottom ash. In *Waste and Supplementary Cementitious Materials in Concrete* (pp. 3-50). Woodhead Publishing. <https://doi.org/10.1016/B978-0-08-102156-9.00001-8>
- [13] Thorneycroft, J., Orr, J., Savoikar, P. and Ball, R.J., 2018. Performance of structural concrete with recycled plastic waste as a partial replacement for sand. *Construction and Building Materials*, 161, pp.63-69. <https://doi.org/10.1016/j.conbuildmat.2017.11.127>
- [14] Majhi, R.K., Nayak, A.N. and Mukharjee, B.B., 2020. An overview of the properties of sustainable concrete using fly ash as replacement for cement. *International Journal of Sustainable Materials and Structural Systems*, 4(1), pp.47-90. <https://doi.org/10.1504/IJSMSS.2020.106418>
- [15] Ismail, Z.Z. and Al-Hashmi, E.A., 2011. Assessing the recycling potential of industrial wastewater to replace fresh water in concrete mixes: application of polyvinyl acetate resin wastewater. *Journal of Cleaner Production*, 19(2-3), pp.197-203. <https://doi.org/10.1016/j.jclepro.2010.09.011>
- [16] Mahasneh, B.Z., 2014. Assessment of replacing wastewater and treated water with tap water in making concrete mix. *Electron. J. Geotech. Eng*, 19, pp.2379-2386.
- [17] Malek, A., Hawlader, M.N.A. and Ho, J.C. Large -scale seawater desalination: a technical and economic review. *ASEAN J. Sci. Technol. Development* Vol. 9 No. 2. pp 41-61, 1992
- [18] Alix, Alexandre; Bellet, Laurent; Trommsdorff, Corinne; Audureau, Iris, eds. (2022). Reducing the Greenhouse Gas Emissions of Water and Sanitation Services: Overview of emissions and their potential reduction illustrated by utility know-how. <https://doi.org/10.2166/9781789063172>
- [19] IDA 2004: Desalination Business Stabilized on a High Level, *Int. Desal. Water Reuse*, Vol. 14 (2), pages.14–17.2004.
- [20] Burke, L., Chen, C., Jamil, O. and Majewska, N., 2016. Desalination-Team B.
- [21] Gartner, E. and Sui, T., 2018. Alternative cement clinkers. *Cement and concrete research*, 114, pp.27-39. <https://doi.org/10.1016/j.cemconres.2017.02.002>
- [22] Kara, S., Erdem, S. and Lezcano, R.A.G., 2021. MgO-based cementitious composites for sustainable and energy efficient building design. *Sustainability*, 13(16), p.9188. <https://doi.org/10.3390/su13169188>
- [23] Ruan, S., Yang, E.H. and Unluer, C., 2021. Production of reactive magnesia from desalination reject brine and its use as a binder. *Journal of CO2 Utilization*, 44, p.101383. <https://doi.org/10.1016/j.jcou.2020.101383>

- [24] Islam, M.S., Mondal, B.C. and Islam, M.M., 2010. Effect of sea salts on structural concrete in a tidal environment. Australian Journal of Structural Engineering, 10(3), pp.237-252. <https://doi.org/10.1080/13287982.2010.11465048>
- [25] Mori, Y. et. al. (1981). "10 years exposure test of concrete mixed with seawater under marine environment", Journal of Cement Association, Vo.35, pp.341-344 (in Japanese).
- [26] Mehta, P.K. and Malhotra, V.M., 1980. Performance of concrete in marine environment. ACI SP-65, pp.1-20.
- [27] Kumar, V., 1998. Protection of steel reinforcement for concrete-A review. Corrosion Reviews, 16(4), pp.317-358. <https://doi.org/10.1515/CORRREV.1998.16.4.317>
- [28] Dang, V.Q., Ogawa, Y., Bui, P.T. and Kawai, K., 2022. Effects of chloride ion in sea sand on properties of fresh and hardened concrete incorporating supplementary cementitious materials. Journal of Sustainable Cement-Based Materials, 11(6), pp.439-451. <https://doi.org/10.1080/21650373.2021.1992683>
- [29] Qu, F., Li, W., Dong, W., Tam, V.W. and Yu, T., 2021. Durability deterioration of concrete under marine environment from material to structure: A critical review. Journal of Building Engineering, 35, p.102074. <https://doi.org/10.1016/j.jobe.2020.102074>
- [30] Fattah, K.P., Al-Tamimi, A.K., Hamweyah, W. and Iqbal, F., 2017. Evaluation of sustainable concrete produced with desalinated reject brine. International Journal of Sustainable Built Environment, 6(1), pp.183-190. <https://doi.org/10.1016/j.ijsbe.2017.02.004>
- [31] Dauncey, P.C., Bates, A.D., Poole, A.B. and Engineering Group Working Party, 2012. Chapter 10 Engineering design and construction. Geological Society, London, Engineering Geology Special Publications, 25(1), pp.347-392. <https://doi.org/10.1144/EGSP25.10>
- [32] AYININUOLA, G.M. and AGBEDE, O.A., 2012. EFFECT OF BRINE INTRUSION ON SOIL BEARING CAPACITY.
- [33] Kuriakose, M., Athira, K.N., Abraham, B.M. and Cyrus, S., Utilization of Brine Sludge to Improve the Strength and Compressibility Characteristics of Soft Clays.
- [34] Barbour, S.L. and Yang, N., 1993. A review of the influence of clay-brine interactions on the geotechnical properties of Ca-montmorillonitic clayey soils from western Canada. Canadian Geotechnical Journal, 30(6), pp.920-934. <https://doi.org/10.1139/t93-090>

Bidding optimization for a reverse osmosis desalination plant with renewable energy in a day ahead market setting

Ebaa Al Nainoon^{1,a*} and Ali Al Awami^{2,b}

¹Electrical Engineering Department, KFUPM, Dhahran, Saudi Arabia

²K.A.CARE Energy Research & Innovation Center, Dhahran, Saudi Arabia

^ag202202180@stu.kfupm.sa, ^baliawami@kfupm.edu.sa

Keywords: Generation, PV, RO, Desalination, Electricity Market, Bidding, Strategy, Renewable Energy, Maximizing Profits, Optimization, Coordination, Flexibility, Revenue, Production, Water Power Nexus, Day Ahead Market

Abstract. This study explores the relationship between power system electrical generation with PV and grid-connected reverse osmosis (RO) water desalination plants in an electricity market setting. It aims to optimize bidding strategies for renewable energy companies in this market, maximizing profits by optimizing coordination and utilizing the flexibility of RO desalination facilities. The research aims to improve economic efficiency, revenue production, and promote renewable energy resource exploitation through better coordination and integration of water desalination processes.

Introduction

Water scarcity presents a global challenge, necessitating the development of sustainable water production solutions. Grid-connected RO desalination, powered by renewable energy sources like PV, offers a promising approach. This research aims to investigate the interdependent relationship between a power system with PV generation and grid-connected reverse osmosis (RO) water desalination plants in an electricity market setting. It will examine how to best bid for a renewable energy generation company and reverse osmosis (RO) desalination plant in a future market setting with an objective to maximize profits by optimizing the coordination of PV as well as leveraging the inherent flexibility of RO plants within the bidding strategy.

Hence, this research aims to present an optimization case study with an objective to improve economic efficiency in the electrical market, maximize revenue production, and promote the exploitation of renewable energy resources through better coordination and enhanced integration of water desalination processes within an electricity market.

Literature Review

Water scarcity is a major worldwide crisis as per the United Nations as reported in [1] that around 2 billion individuals which comprise 26% of the global population didn't have access to clean, readily available drinking water on-site. Even basic access to drinking water was unavailable to 771 million people. Eight in ten were from rural areas. The majority of them were in least developed nations. In order to ensure that everyone has access to safely managed drinking water by 2030, current rates of progress must be quadrupled. Pollution and climate change are the main reasons why freshwater resources are insufficient. This imposes the development of efficient and sustainable water production technologies. Among these technologies Reverse Osmosis (RO) desalination has become a well-known technology solution to address the growing need for freshwater in coastal and dry locations. In order to guarantee economical and ecologically sustainable water production, it is crucial to investigate the operational elements of RO desalination plants and their integration into the energy market as the demand for freshwater rises [2,3].

This literature review explores RO desalination plant operational features, energy consumption, cost structures, and flexibility, and their integration into renewable energy generation companies' bidding strategies, aiming to understand system operation and market dynamics. [3]. The primary sources of cost in any of these processes that produce water are energy, operating and maintenance expenses, and capital investments. This is the case in many countries around the world where water production process consume hefty amounts of electricity [4,5]. Thermal and membrane water desalination facilities are the main types of water desalination facilities. Thermal WDP uses steam to produce saline water, which is then condensed to create freshwater. Some steam is fed into steam turbines to generate energy, enabling simultaneous generation of electricity and desalinated water. The energy for heating steam can be produced off-grid using renewable resources or fossil fuels. [6].

Reverse Osmosis (RO) water desalination uses a semi-permeable membrane filter to filter out salt, resulting in concentrated water on the membrane's high-pressure side. Electricity powers the pump, which produces the pressure needed to push water through the membrane. The desalination pressure ranges from 17 to 27 bars for brackish water and 55 to 82 bars for seawater. [7,8] Renewable energy sources like solar thermal, photovoltaic, wind, and geothermal technologies can be used as energy suppliers in water desalination plants, especially in remote areas with acute water shortages where public electricity grid connections are not practical or cost-effective. Ghaithan et.al [3] offered a multi-objective model for a grid-connected photovoltaic-wind system that would supply energy to a Saudi Arabian RO desalination plant. The model aims to reduce life cycle costs and greenhouse gas emissions by considering economic and non-economic factors. It selects three Pareto-optimal solutions and provides management insights from economic and environmental perspectives. Additionally, in their study referenced as [9] The authors introduced the two-stage pricing (TSP) method for Northeast China's electric power auxiliary service market. This involves a freshwater supply and demand balance model, upper-level optimization, and low-level wind power pricing to maximize profits and enhance energy flexibility. In addition, Authors from Malaysia in [10] designed a mini-grid hybrid power system for rural communities and emergency relief situations. This system relies solely on solar power as its primary source and incorporates renewable energy applications to minimize greenhouse gas emissions. In a pool-based energy market, retailers of electricity face several uncertainties, including those related to market pricing and demand [11]. The integration of hybrid energy sources with energy storage devices in micro-grid operations is complicated by the intermittent nature of renewable energy sources. This challenge leads retailers to face difficulties in maintaining a real-time supply-demand balance, as highlighted by Chakraborty and colleagues [12]. The authors reviewed optimization approaches aimed at achieving accurate load forecasting and maximizing profits for retailers and energy users, with the goal of reducing electricity bills. In addition, in [13] Parvania and Oikonomou discussed using desalination plants to help meet electricity demand. It discusses the challenges of desalination plants' high electricity consumption and proposes a model to optimize their participation in electricity markets. Operators of water distribution systems would be able to offer the flexibility of desalination plants in energy markets thanks to the approach. This would help to offset the costs of desalination and make it more sustainable. The model also considers the hydraulic constraints of the water distribution system and the availability of freshwater resources. Elsir and colleagues [13] Also discuss coordinating the water desalination and demand response facilities' day-ahead operation scheduling in smart grids. It talks on the necessity of water desalination and the difficulties in incorporating renewable energy sources. The authors propose a market-clearing mechanism that maximizes the performance of renewable-rich power systems and grid-connected reverse osmosis water desalination plants (RO-WDPs). The study uses a mixed-integer linear programming problem to develop a market clearing method that integrates electric

demands into demand response programs, improving system efficiency without compromising water supply-demand balance.

This literature review highlights the growing need for sustainable water production and the potential of integrating grid-connected RO desalination with renewable energy like PV. It goes over the energy dependence of RO plants, integration challenges in micro-grids, and existing optimization approaches for cost reduction and profit maximization. This knowledge lays the foundation for developing an effective bidding strategy that leverages the flexibility of RO desalination within an electricity market, ultimately maximizing profits for renewable energy companies while promoting sustainable water production.

Methodology and Problem Formulation

This study aims to develop the optimal bidding strategy for renewable energy companies with RO desalination plants. It focuses on how these businesses can optimize their bidding techniques to maximize profits in the electricity market and utilize the flexibility of desalination facilities. The study examines a generation company entering the power market with renewable resources and desalination facilities in a future market setting. Our example will represent the future electricity market pool of Bahrain.

This section discusses the mathematical equations for optimizing bidding in an electricity market, focusing on cost-effective and sustainable desalination operations. The formulation uses renewable energy resources and RO flexibility, and employs the General Algebraic Modeling System (GAMS) to optimize the bidding strategy, considering energy consumption, cost structures, and market dynamics.

Profit Cost function. The problem formulation involves creating a profit cost function that considers variable operation and maintenance costs to accurately reflect the desalination plant's operation viability. This function captures the interplay between energy prices, renewable energy generation, and electricity market dynamics, allowing for optimized bidding strategies. The goal is to maintain water sales revenue while minimizing variable costs to enhance the desalination plant's profitability.

$$\text{Profit} = RT - CT \quad (1)$$

Where RT in Equation. 1 is the total revenue and CT is the total cost. calculated as:

$$R_T = \sum_{t=t_0}^{t_f} (R_{\text{Electricity}}(t) + R_{\text{Water}}(t)) \quad (2) \quad C_T = \sum_{t=t_0}^{t_f} (C_{\text{Electricity}}(t) + C_{\text{Water}}(t)) \quad (3)$$

Where $R_{\text{Electricity}}(t) = E_{\text{Surplus}}(t) \times \pi_E(t)$ and $R_{\text{Water}}(t) = V_{\text{demand}}(t) \times \pi_W(t)$

And $C_{\text{Electricity}}(t) = E_{\text{deficit}}(t) \times \pi_E(t)$ and $C_{\text{Water}}(t) = V_{\text{RO}}(t) \times MC$

$\pi_E(t)$ represents the Price of electricity for hour t and $\pi_W(t)$ represents the price of water, while MC represents the variable Maintenance Cost per m³ of Water Produced.

The energy requirement will be represented by the energy balance equation:

$$E_{\text{RO}}(t) = E_{\text{PV}}(t) + E_{\text{deficit}}(t) - E_{\text{Surplus}}(t) \quad (4)$$

These equations will be further elaborated in the relevant following subsections.

RO Water Desalination Energy Consumption and Cost structure. Reverse osmosis (RO) is a process that removes impurities from water by pressurizing it through a semipermeable membrane, leaving only pure water. The energy input for RO water production is influenced by the pressure needed to overcome osmotic pressure. This text presents a straightforward mathematical generalization of energy use, cost structures, and the adaptability of RO.

In terms of Energy Consumption RO systems require energy to operate the high-pressure pumps that push water through the membrane. The energy consumption of an RO system depends on various factors such as feed water quality, system design, and recovery rate [7]. RO systems consume significant energy, especially in large-scale applications. Advancements in technology have led to more energy-efficient membranes. The cost structure of an RO system includes capital and operating expenses, including equipment, energy, membrane replacement, sanitization, and monitoring. The complexity and capacity of the system influence these costs. Capital costs are disregarded for bidding purposes. A simplified equation for RO water production accounting for operating costs and energy consumption with temperature can be obtained using the following formulation.

$$\text{Operational Cost} = \text{Energy Cost} + \text{Maintenance Cost}$$

The energy cost component is reliant on the RO system's energy consumption, which is impacted by the surrounding ambient temperature. Higher or lower temperatures may increase energy requirements due to reduced water flux and increased osmotic pressure whenever you deviate from the optimal operating temperatures [14,15,16].

The connection between the production of water in RO and energy input is referred to as specific energy consumption (SEC). Which measures the energy needed to use the RO process to generate a specific volume of purified water. Usually, it is given as (kWh/m³) or kWh/gal. [7].

$$E_{RO}(t) = SEC(t) \times V_{RO}(t) \quad (5) \quad C_{Water}(t) = V_{RO}(t) \times MC \quad (6)$$

The calculation of energy requirement as depicted in Equation. 5 will involve multiplying the SEC (kWh/m³) by the volume of water produced in m³ to obtain the total energy input needed at a certain hour to produce the desired water output, which is part of the energy balance in Equation 4. In addition, the costs of replacing membranes, cleaning, sanitizing, and other regular maintenance tasks are included in the maintenance cost component. An estimate of the maintenance cost (MC) for a certain RO system can be made using industry standards or historical data. It can be stated as a price per generated unit of filtered water (cost/m³) for example as in Equation. 6 Above. As such, Total cost of RO Water Production was summarized in Equation. 3.

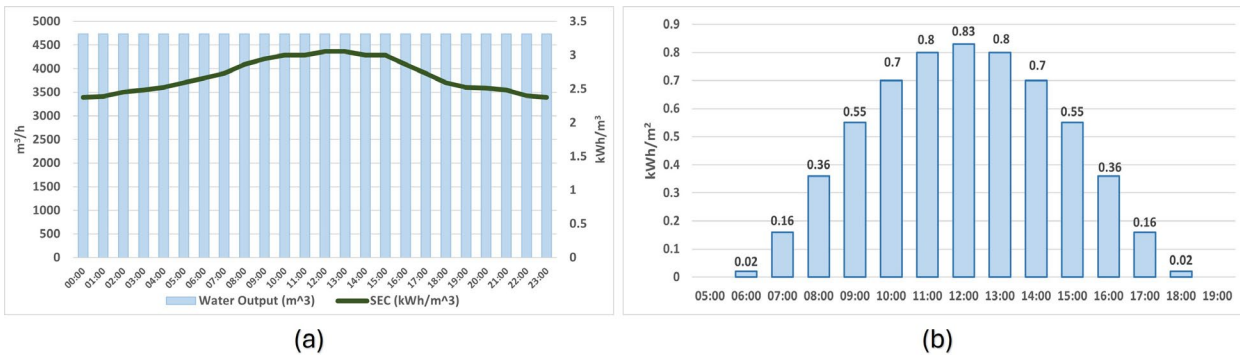


Figure 1. (a) Relationship between SEC and output of a SWRO plant (b) Average energy output for solar PV system in Bahrain [19].

We mentioned that SEC can be affected by ambient temperature, therefore for a summer day in GCC greater SEC would be required for hotter times of day to produce the same water output. This shall be taken into account while scaling SEC input parameters. For this proposal, since it is in a future market setting we will scale data for a current IPWP in Bahrain. This IPWP has a generation capacity of 50 MIGD for Sea Water RO (SWRO) which is equal to 227,304.5 m³/day and is expected to keep an almost constant water production in its two production blocks throughout the day with an average of 9,471.02 m³/hr [17] total and 4,735.51 per block. Therefore the expected

water output for 1 block vs. SEC should look like the graph in Fig. (1a) for 24 hours if we take into consideration the effect of ambient temperature on SEC and an average SEC of 2.374 kWh/m³ for seawater [7].

In addition, the Maintenance cost has been approximated by averaging the cost of replacement of different kinds of membranes as stated in [18] which came to about 0.1638 \$/m³ and it was rounded to 0.2 \$/m³ to account for other maintenance or operational aspects.

PV Generation and Cost structure. The variable cost of PV power production requires precise data collection and analysis, tailored to the specific PV system. The capacity, efficiency, sun irradiation, and ambient temperature of a photovoltaic system are some of the elements that affect its energy generation rate. A generic formula will be examined, considering operational expenses and energy generation, for simplicity. Since the company already owns the PV panels Energy costs for PV will be very minimal and Maintenance costs (MC) are relatively very small and thus can be ignored. For this problem we will use the simulated data for the solar system which is already deployed in Bahrain as seen in [19] to more realistically tailor the optimization problem for an IPWP in Bahrain.

The Energy output of the PV will be calculated for this proposal using the previously stated PV system data in [19] which has the energy output in Fig. 3 per m². In order to calculate the Relevant Energy production for the IPWP we are studying, we will assume that PV panels are installed on 60% of the total land area of the power plant, where the total area for the IPWP in the proposal is approximately 32,400 m² according to coordinates. Therefore, we'll assume the total area of PV installation is around 19,440 m² and we'll assume a higher efficiency of PV panels (10%) since it is a future application. As observed in Figure. (1a) we can achieve higher energy output with higher ambient temperatures, since higher temperature is usually correspondent with higher solar irradiance. which is where the PV characteristics can nicely align with optimal generation for an RO facility in the summer during higher SEC hours.

Problem Definition

The above equations have been used to formulate the profit maximization objective function with constraints and relevant variables. Thus, the problem formulation will be as follows:

Maximize Equation. (1) $Profit = RT - CT$

subject to:

Eqution. (4) and Eqution. (5)

$$E_{deficit}(t) \cdot E_{surplus}(t) \leq 0$$

$$V_{demand}(t) = \text{Hourly Demand Target}$$

$$V_{RO}(t) \leq \text{Production Block Maximum}$$

$$V_{tank}(t) \leq \text{Tank Storage Capacity}$$

$$V_{RO}(t) \cdot V_{tank}(t) \geq 0$$

$$V_{tank}(t) = V_{tank}(t-1) + V_{RO}(t) - V_{demand}(t)$$

where t ranges between $t_o = 1$ and $t_f = 24$ for a 24 hour time period.

Since Bahrain doesn't currently have a market setting and hourly pricing, we will use Day ahead hourly market prices available in [20] and scale it with the same pattern to match the regional prices in GCC. As for the water price, a constant value of \$2.012/m³ will be considered.

Table 1. Optimization Problem Input Parameters

t	EPV	\$/MWh	\$/m³	t	EPV	\$/MWh	\$/m³	t	EPV	\$/MWh	\$/m³
1	0	39.698	2.012	9	8.9813	75.267	2.012	17	8.9813	87.658	2.012
2	0	48.52	2.012	10	13.721	78.533	2.012	18	3.9917	105.22	2.012
3	0	47.522	2.012	11	17.464	78.753	2.012	19	0.499	111.18	2.012
4	0	39.698	2.012	12	19.958	80.718	2.012	20	0	101.36	2.012
5	0	42.268	2.012	13	20.707	78.042	2.012	21	0	92.534	2.012
6	0	54.16	2.012	14	19.958	82.669	2.012	22	0	84.075	2.012
7	0.499	67.571	2.012	15	17.464	83.19	2.012	23	0	76.469	2.012
8	3.9917	75.819	2.012	16	13.721	85.64	2.012	24	0	73.77	2.012

Table. 1 Displays the expected output of the PV panels EPV values and market day ahead prices of power and water for the time frame of 24 hours. 4 scenarios of power/water exchange dynamics have been considered as follows.

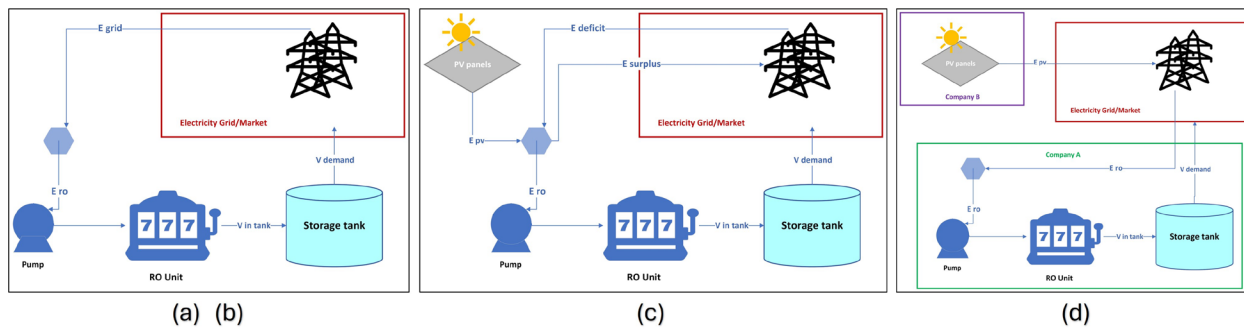


Figure 2. Modeling Scenarios

Scenario A in Fig 2a. represents the basic, classical Energy in - Water out RO system where no optimization can be done, and you have to operate the system in the same way to produce the same output regardless of energy prices or system conditions (no storage tank). On the other hand, Scenario B is an upgrade to the basic system in which a water storage tank is added to the system allowing some degree of flexibility in production.

Thirdly, Scenario C considers the full PV-RO system in which there is one main company that owns both RO facilities and PV facilities. The optimization problem will revolve around how the energy cost efficiency with the addition of PV and flexibility of RO can be maximized.

For the last case, Case D, the PV and RO facilities are owned by two separate companies that bid separately into the electricity market.

Each of the above cases will be examined in terms of profit and cost vs. revenue to observe the optimization process for each configuration.

Results and Discussion

The Four above Scenarios were simulated using GAMS software to obtain the profit maximization results while considering a 24-hour time period.

Table 2. Scenario Comparison of Cases A and B

Variable	Total Cost	Total Revenue	Total Profit
Scenario A	\$28,994.91	\$144,864.00	\$115,869.09
Scenario B	\$27,446.62	\$144,864.00	\$117,417.38

As can be seen from the table when the storage was added in scenario B the flexibility of the RO allowed for reduced water production during higher price periods while still maintaining the supply demand. This is done by increasing the water production during the periods of time where the electricity is cheaper and then utilizing the water storage to maintain demand during the pricye hours to buy less electricity. Hence, the cost reduced for scenario B allowing for increased profits for the same revenue and demand.

This process can be observed in Table. 3 with details about charging, discharging, electricity price and SEC for the 24 h period.

Table 3. Variation of storage tank with respect to time

t	\$/MWh	SEC	in tank	out tank	Tank (t)	t	\$/MWh	SEC	in tank	out tank	Tank (t)
1	39.69756	0.002374	4735.51	3000	1735.51	13	78.04188	0.003056	4735.51	3000	9000
2	48.52008	0.002388	4735.51	3000	3471.02	14	82.6686	0.003056	1264.49	3000	7264.49
3	47.52216	0.002456	4735.51	3000	5206.53	15	83.19024	0.003002	4735.51	3000	9000
4	39.69756	0.002483	4735.51	3000	6942.04	16	85.63968	0.003002	0	3000	6000
5	42.26796	0.002524	4735.51	3000	8677.55	17	87.6582	0.002865	4735.51	3000	7735.51
6	54.15984	0.002592	3322.45	3000	9000	18	105.2201	0.002729	0	3000	4735.51
7	67.57128	0.002661	3000	3000	9000	19	111.1774	0.002592	0	3000	1735.51
8	75.81924	0.002729	3000	3000	9000	20	101.3645	0.002524	1264.49	3000	0
9	75.26736	0.002865	3000	3000	9000	21	92.5344	0.00251	3000	3000	0
10	78.53328	0.002947	3000	3000	9000	22	84.07476	0.002483	3000	3000	0
11	78.75252	0.003002	3000	3000	9000	23	76.4694	0.002401	3000	3000	0
12	80.71812	0.003002	1264.49	3000	7264.49	24	73.77048	0.002374	3000	3000	0

In the (out tank) column of Table. 3 we see that the number is constant which is the water demand that should be supplied at all times, and you can notice the relationship between state of storage and electricity price. Moreover, tank capacity can also play a role in the optimization process. Therefore, Scenario B has been simulated considering 3 different water tank capacities.

Table 4. Scenario B: Capacity Comparison

Capacity	9000 m ³	18000 m ³	36000 m ³
Total Cost	\$27,446.62	\$26,978.74	\$26,950.05
Total Revenue	\$144,864.00	\$144,864.00	\$144,864.00
Total Profit	\$117,417.38	\$117,885.26	\$117,913.95

As observed from Table 4 increasing the capacity can increase the profits due to the added flexibility, however at some point increasing the capacity beyond a certain volume will be unprofitable. Increasing the capacity from 18000 m³ to 36000 m³ will only increase the profits by \$ 28.69 per day, this small increase in profit will likely only be worth it if the cost of upgrading the tank can be justified.

Meanwhile, for scenarios C and D, it can be noticed that there is an extra source of revenue. Therefor in Table. 5 for C not only did the cost reduce significantly due to utilizing energy from PV, but the revenues have also increased as the company can sell excess PV energy to the grid.

Table 5. Scenario Comparison of Cases C and D

Variable	Total Cost (W)	Total Revenue	PV Revenue	RO Revenue	Total Profit	RO Profit
Case C	\$21,469.325	\$150,007.47	\$5,143.47	\$144,864	\$128,538.144	\$123,394.675
Case D	\$27,446.623	\$155,984.77	\$11,120.767	\$144,864	\$128,538.14	\$117,417.38

Moreover, for scenario D this will be different, as PV is no longer part of the same company and is selling energy separately to the grid, the interesting thing is, that both scenarios C and D have reached the same optimal profit value for the total system. However, the profits here are divided between 2 companies, the revenues from selling PV power have increased because the output of the PV is sold entirely to the grid. But, for the RO company the costs saw an increase, as there is no longer a free energy source to use, and more must be bought from the grid. This is probably due to the balance of Energy bought and sold, as the same amount of energy is still being exchanged however it is in different directions (for different beneficiaries). Assuming, Company B were to sell Electricity to Company A directly under a predetermined contract, profits might improve because both parties would be able to take advantage of the flexibility of these resources accessible for their best interests.

Conclusion

The study examined the connection between power system electrical generation, PV, and grid-connected reverse osmosis (RO) water desalination plants in an electricity market setting, aiming to maximize profits by optimizing RO facility coordination and flexibility. The study examined four scenarios: basic RO system, RO with water storage tank, combined PV-RO system, and Separate PV-RO system with energy optimization. It found that incorporating a water storage tank and using PV energy during daylight hours can reduce costs, increase revenues and profits. Moreover, while bidding the PV separately can result in the same combined profits it would mean compromising on some profits for the RO owner compared to the combined system. Additionally, the simulation considered different water tank capacities where the results indicated that increasing the capacity can enhance profits and earnings only up to a certain point, beyond which incremental benefits become negligible.

The study highlights the economic benefits of integrating RO desalination plants into renewable energy generation companies' bidding strategies. It emphasizes the cost reduction and revenue maximization benefits of water storage and PV energy utilization, while balancing profits and costs in a day ahead electricity Market setting.

References

- [1] UN-Water, "Summary progress update 2021: Sdg 6 - water and sanitation for all," Online, 2021. [Online]. Available: <https://www.unwater.org/sites/default/files/app/uploads/2021/12/SDG-6-SummaryProgress-Update-2021 Version-July-2021a.pdf>
- [2] M. Rouholamini, C. Wang, C. J. Miller, and M. Mohammadian, "A review of water/energy co-management opportunities," in 2018 IEEE Power & Energy Society General Meeting (PESGM), 2018, pp. 1–5. <https://doi.org/10.1109/PESGM.2018.8586013>
- [3] A. M. Ghaithan, A. Mohammed, A. Al-Hanbali, A. M. Attia, and H. Saleh, "Multi-objective optimization of a photovoltaic-wind- grid connected system to power reverse osmosis desalination plant," Energy, vol. 251, p. 123888, 2022. <https://doi.org/10.1016/j.energy.2022.123888>
- [4] S. Shu, D. Zhang, S. Liu, M. Zhao, Y. Yuan, and H. Zhao, "Power saving in water supply system with pump operation optimization," in 2010 Asia-Pacific Power and Energy Engineering Conference, 2010, pp. 1–4. <https://doi.org/10.1109/APPEEC.2010.5449192>
- [5] A. Siddiqi and L. D. Anadon, "The water–energy nexus in middle east and north africa," Energy Policy, vol. 39, no. 8, pp. 4529–4540, 2011, at the Crossroads: Pathways of Renewable and Nuclear Energy Policy in North Africa. <https://doi.org/10.1016/j.enpol.2011.04.023>
- [6] M. Elsir, A. T. Al-Awami, M. A. Antar, K. Oikonomou, and M. Parvania, "Risk-based operation coordination of water desalination and renewable-rich power systems," IEEE Transactions on Power Systems, vol. 38, no. 2, pp. 1162–1175, 2023.
- [7] A. Karabelas, C. Koutsou, M. Kostoglou, and D. Sioutopoulos, "Analysis of specific energy consumption in reverse osmosis desalination processes," Desalination, vol. 431, pp. 15–21, 2018, "Desalination, energy and the environment" in honor of Professor Raphael Semiat. <https://doi.org/10.1016/j.desal.2017.04.006>
- [8] A. Al-Karaghoubi and L. L. Kazmerski, "Energy consumption and water production cost of conventional and renewable energy powered desalination processes," Renewable and Sustainable Energy Reviews, vol. 24, pp. 343–356, 2013. <https://doi.org/10.1016/j.rser.2012.12.064>

- [9] S. Chu, S. Zhang, W. Ge, G. Cai, and Y. Li, “The pricing method for abandoned wind power contract between wind power enterprises and desalination plants in bilateral transactions,” Electric Power Systems Research, vol. 214, 2023. <https://doi.org/10.1016/j.epsr.2022.108918>
- [10] N. Baharudin, T. Mansur, R. Ali, A. Wahab, N. Rahman, E. Ariff, and A. Ali, “Minigrid power system optimization design and economic analysis of solar powered sea water desalination plant for rural communities and emergency relief conditions,” in 2012 IEEE International Power Engineering and Optimization Conference Melaka, Malaysia, 2012, pp. 465–469.
- [11] S. M. Mousavi, T. Barforoushi, and F. H. Moghimi, “A decision-making model for a retailer considering a new short-term contract and flexible demands,” Electric Power Systems Research, vol. 192, p. 106960, 2021. <https://doi.org/10.1016/j.epsr.2020.106960>
- [12] N. Chakraborty, N. B. D. Choudhury, and P. K. Tiwari, “Profit maximization of retailers with intermittent renewable sources and energy storage systems in deregulated electricity market with modern optimization techniques: A review,” Renewable Energy Focus, vol. 47, p. 100492, 2023. <https://doi.org/10.1016/j.ref.2023.100492>
- [13] K. Oikonomou and M. Parvania, “Optimal participation of water desalination plants in electricity demand response and regulation markets,” IEEE Systems Journal, vol. 14, no. 3, pp. 3729–3739, 2020.
- [14] C. Koutsou, E. Kritikos, A. Karabelas, and M. Kostoglou, “Analysis of temperature effects on the specific energy consumption in reverse osmosis desalination processes,” Desalination, vol. 476, p. 114213, 2020. <https://doi.org/10.1016/j.desal.2019.114213>
- [15] M. M. Armendáriz-Ontiveros, G. E. Dévora-Isiordia, J. Rodríguez-López, R. G. Sánchez-Duarte, J. Álvarez Sánchez, Y. Villegas-Peralta, and M. d. R. Martínez-Macias, “Effect of temperature on energy consumption and polarization in reverse osmosis desalination using a spray cooled photovoltaic system,” Energies, vol. 15, no. 20, 2022. <https://doi.org/10.3390/en15207787>
- [16] S. Yagnambhatt, S. Khanmohammadi, and J. Maisonneuve, “Reducing the specific energy use of seawater desalination with thermally enhanced reverse osmosis,” Desalination, vol. 573, p. 117163, 2024. <https://doi.org/10.1016/j.desal.2023.117163>
- [17] “NOMAC - AL DUR PHASE II IWPP,” NOMAC. [Online]. Available: <https://www.nomac.com/en/our-operations/nomac-globally/al-dur2-iwpp/>.
- [18] S. Avlonitis, K. Kouroumbas, and N. Vlachakis, “Energy consumption and membrane replacement cost for seawater RO desalination plants,” Desalination, vol. 157, no. 1, pp. 151–158, 2003, desalination and the Environment: Fresh Water for all. [https://doi.org/10.1016/S00119164\(03\)00395-3](https://doi.org/10.1016/S00119164(03)00395-3)
- [19] W. Alnaser, N. Alnaser, and I. Batarseh, “Bahrain’s bapco 5mw pv grid-connected solar project,” Int. J. Power Renew. Energy Syst., vol. 1, pp. 72–84, 01 2014.
- [20] “Market data - Nord Pool,” Nord Pool. [Online]. Available: <https://www.nordpoolgroup.com/en/Market-data/GB/Auction-prices/UK/Hourly/?view=table>.

Adaptive neuro-fuzzy inference system for DC power forecasting for grid-connected PV system in Sharjah

Tareq SALAMEH^{1,2,a}, Mena Maurice FARAG^{2,3,b*}, Abdul Kadir HAMID^{2,3,c*},
Mousa Hussein^{4,d}

¹Department of Sustainable and Renewable Energy Engineering, College of Engineering,
University of Sharjah, United Arab Emirates

²Sustainable Energy and Power Systems Research Centre, Research Institute for Sciences and
Engineering (RISE), University of Sharjah, Sharjah, United Arab Emirates

³Department of Electrical Engineering, College of Engineering, University of Sharjah, Sharjah,
United Arab Emirates

⁴Department of Electrical and Communication Engineering, College of Engineering, United Arab
Emirates University, Al Ain, UAE

^atsalameh@sharjah.ac.ae, ^bu20105427@sharjah.ac.ae, ^cakhamid@sharjah.ac.ae,
^dmihussein@uaeu.ac.ae

Keywords: Artificial Intelligence, ANFIS, Solar Energy, PV Systems

Abstract. Solar energy forecasting is essential to maintain PV system's performance in uncertain environmental conditions. Factors such as module temperature, ambient temperature, solar irradiance, and wind speed contribute to the DC current generated by PV systems. In this study, an adaptive neuro-fuzzy inference system (ANFIS) is developed on MATLAB to study a 2.88 kW grid-connected PV system in the harsh weather conditions of Sharjah. Solar irradiance, ambient temperature, module temperature, and wind speed are considered as the input membership functions in the developed ANFIS model. The output parameter considered in this study is the current DC generation, which critically depends on the defined membership functions. The accuracy of the model was determined based on the comparison with the experimental dataset. The R^2 value has shown that the proposed model can forecast the DC current with minimal error, with a value of 99.12% and 99.13% for training and testing, respectively. Moreover, the spatial 3-D surface has shown that the optimum DC current generation is achieved at the highest solar irradiance and ambient temperature while minimizing the module temperature for enhanced electrical efficiency.

Introduction

Conventional energy resources have been the main contributors to global warming and climate change, leading to the integration of clean energy sources [1]. Solar emissions received yearly present a huge portion of clean energy resources, making solar energy a remarkable source of alternate energy [2]. Photovoltaic (PV) systems have been designed to utilize solar emissions for clean electricity generation, therefore reducing carbon emissions and maintaining a clean economy [3].

Renewable Energy Sources (RES) have been increasingly integrated into the energy mix, specifically in oil-dependent countries such as the United Arab Emirates [4]. Moreover, solar irradiance exposure globally counts to 1367 W/m^2 , which is sufficient to meet the electrical energy demand requirements worldwide [5,6].

However, to successfully integrate solar energy within the energy mix and attain electricity demands, its accurate prediction is necessary to ensure stability in power generation and injection into the energy grid [7,8]. Power generation from PV plants is known to be dynamic due to weather

conditions dependency, presenting potential effects in its coupling with electrical networks [9]. In this notion, it's essential to forecast PV power plant generation to boost solar energy use and maintain electrical network stability. In principle, forecasting based on time-series data is extracted based on numerous amounts of sensors, guaranteeing precise data production and interval-based data measurement [10].

The accurate prediction of PV plants' performance is a critical task since weather conditions drive the operating conditions of PV plants. The dynamic change in solar irradiance causes fluctuation in PV power generation, leading to inconsistent electricity production. Multiple forecasting models are proposed to accurately predict PV plant generation [11]. Precise prediction of DC power generation requires the employment of machine learning (ML) techniques to enable learning complex pattern recognition and regression analysis [12]. Multiple forecasting models have been developed in the scientific literature such as ARIMA [13], support vector regression (SVR) [14], artificial neural network (ANN) and ANN-based hybrid models [15], hybrid intelligent system (HIS), Convolutional Neural Networks (CNN) [16], Long Short-Term Memory (LSTM) [17], and numerous other forecasting models.

The amalgamation of more than one forecasting offers an efficient compromise between prediction accuracy, computation time, and direct forecasting of PV plant power generation. Recently, ANN has been designed and modeled using a Fuzzy Inference System to develop an Adaptive Neuro Fuzzy Inference System (ANFIS) [18]. ANFIS and Support Vector Machine (SVM) have been popular tools for forecasting techniques and applications. However, ANFIS has proven to be precise as compared to SVM. Several studies discussed the employment of ANFIS in many fields of sciences [19,20], and as a model for accurate PV plant generation forecasting, proving its feasibility [21].

In this study, ANFIS has been employed to predict the performance of a 2.88 kW on-grid PV system installed in the terrestrial conditions of Sharjah, UAE. The forecasting of DC current is considered the main factor affecting PV power generation and therefore is considered in this study. Moreover, the relationship between the DC current and environmental factors such as solar irradiance, ambient temperature, module temperature, and wind speed is established. Therefore, the forecasting results are compared with the experimental results measured by the system to demonstrate the accuracy of the proposed model.

Experimental Setup

As seen in Fig. 1, a 2.88 kW on-grid photovoltaic system is installed on the rooftop of the W-12 central laboratories building at the University of Sharjah's main campus (Lat. 25.34° N; Long. 55.42° E) [22,23]. For immediate access to system data, the system is powered by a real-time data capture system [24]. The system's potential to function over short and long-time spans, together with its comprehensive infrastructure and improved data recording capabilities, were previously highlighted [25,26]. Furthermore, the system functions as a comprehensive grid-connected photovoltaic system, contributing AC electrical energy to the three-phase local utility grid. In addition, the on-grid photovoltaic system logs environmental and electrical characteristics every five minutes [27]. Table 1 represents the technical specifications of the on-grid PV system state-of-the-art.

Table 1. Technical Specifications of the 2.88 kW on-grid PV system

Equipment	Specifications
On-grid PV system State-of-the-Art	<ul style="list-style-type: none"> - 9 PV modules of 320 W electrical capacity. - Single Axis azimuth tracking. - 3.7 kWac Grid Inverter for Electrical Network Coupling and Synchronization. - Data manager for centralization system measurements on a common online interface.
Sensor Box	<p>Responsible for coupling environmental sensors such as:</p> <ul style="list-style-type: none"> - PT1000 thermocouples for module and ambient temperature measurement. - Irradiation sensor for solar insolation measurement. - Anemometer for wind speed measurement.

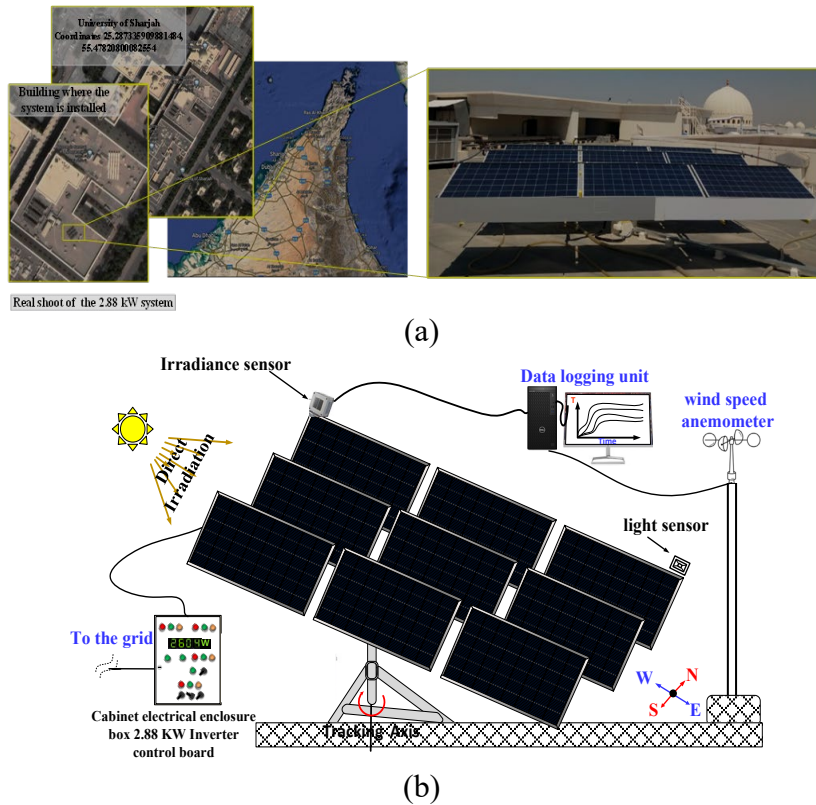


Fig 1. Illustration of 2.88 kW on-grid PV system (a) experimental setup (b) system visualization.

Adaptive network-based fuzzy inference system (ANFIS)

Deployment of fuzzy logic (FL) in control research has grown daily since the 1960s. The FL's foundation is expanding the well-known Boolean logic operations. The FL employs binary systems (0 and 1) during the modeling procedure. Moreover, FL deals with multi-valued interpretation, which ranges from 0 to 1, just like in human perception. In the 1990s of this centuries, Jang created an Adaptive Network-based Fuzzy Inference System (ANFIS) based on the artificial neural network (ANN) and the fuzzy inference system (FIS) [28]. ANFIS can demonstrate a complicated system with extreme nonlinearity. The FL structure consists of three primary components: defuzzification, inference, and fuzzification.

In ANFIS, two different kinds of structures are combined to produce a fuzzy rule. The first kind is called Mamdani, and it was established in 1975 for the controller layout of heat transfer techniques where the Center of Gravity (COG) is the best defuzzifier. The second type, Sugeno (TSK), uses Weighted Average (Wtaver) as a defuzzifier. Eqs. (1) and (2) illustrate how these two types differ for fuzzy systems with two inputs and one output.

Should A be MF_A and B be MF_B , then C is the MF_C Mamdani form. (1)

In the event when A is MF_A and B is MF_B , $C = F(A, B)$ Form of Sugeno (2)

MF_A and MF_B represent fuzzy membership functions (MFs) for A and B, respectively. A and B are the two input (antecedent) fuzzy systems. The membership functions for the Mamdani form are MFC , the membership functions for the Sugeno form are $F(A, B)$, and the output (consequence) fuzzy system is C. For A and B as input factors, $F(A, B)$ can be either a linear or nonlinear function [29].

In this study, since DC current generated from PV systems is critically dependent on several environmental factors such as solar irradiance, ambient temperature, and module temperature, the compound Sugeno form (TSK) model is considered to represent a nonlinear function and is studied. The phases of fuzzification and defuzzification were translated using the membership functions, respectively. To carry out this translation, the input and output values were converted from crisp to fuzzy during the fuzzification stage and from fuzzy to crisp during the defuzzification step.

The study's data was used to extract the rules. As indicated by Eq. 3, the total output value was computed using the number of input variables and the quantification of rules implemented.

$$y(x) = \frac{\sum_{i=1}^n w_i y_i(x)}{\sum_{i=1}^n w_i} \quad (3)$$

where the i^{th} fuzzy rule's weight, input, and output are represented by the variables y_i , x , and w_i , respectively. The weight of the i^{th} fired rule has a range of [0 1].

A dataset of experimental measurements is used for the training and testing phases of 601 data points. With four input parameters, training and testing data were done for every fuzzy model output. Table 2 demonstrates every detail of the fuzzy model that was used in this investigation.

Table 2. Specifications of the developed fuzzy model

Fuzzy component	Type	Details
Inputs	Variables	4
Epochs	Number of Training Data	410
	Number of Testing Data	191
Rule	Number	4
	Base builder	SC
	ANDing Operation	Product
	ORing Operation	Probabilistic OR
	Implication	Min
	Aggregation	Max
	Defuzzification	Wtaver
	Output	Function
		Linear

Results and Discussion

A large data set of experimental data was employed for the developed ANFIS model. The prediction of DC current by the ANFIS model under the terrestrial conditions of Sharjah during harsh weather conditions is demonstrated in Fig 3. Moreover, the accuracy and precision of the proposed model according to the R^2 value, as presented in Fig 3, represent 99.1% accuracy. The ANFIS model can sufficiently forecast the DC current with respect to the experimental data that is measured from the system, as presented in Fig 2 and Fig 3.

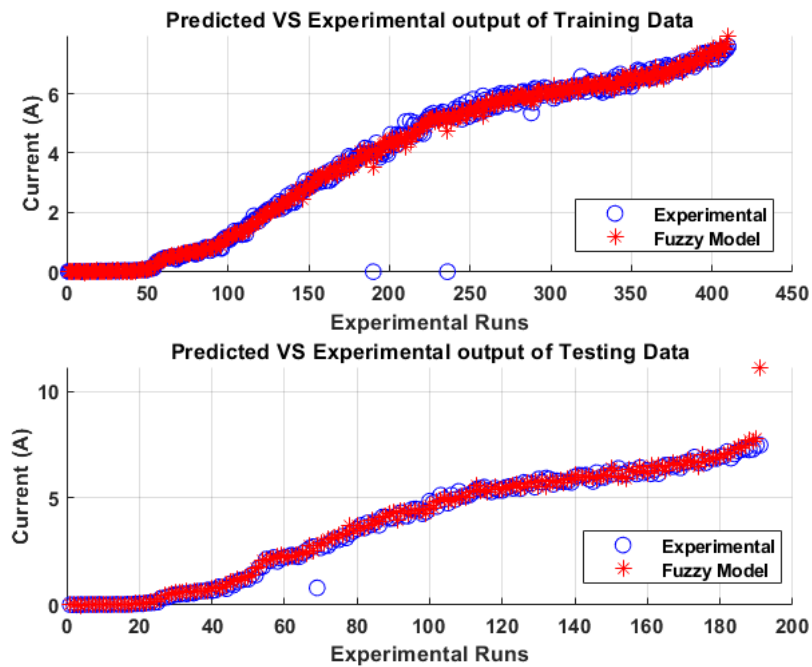


Fig 2. ANFIS model predictions for training and testing datasets for the experimental data.

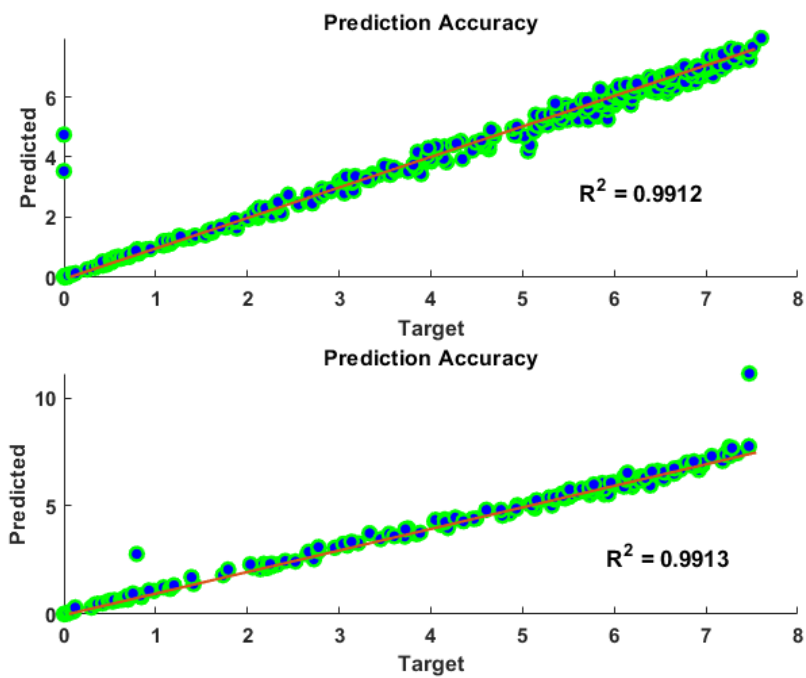


Fig 3. Forecasting accuracy for training data (above) and testing data (below).

The input parameter membership functions that are employed in this investigation are presented in Fig 4. These functions are typically used as rules to convert between the fuzzification and defuzzification procedures. The different colors represent the various membership functions that are utilized to connect the fuzzification and defuzzification procedures within the fuzzy inference system architecture.

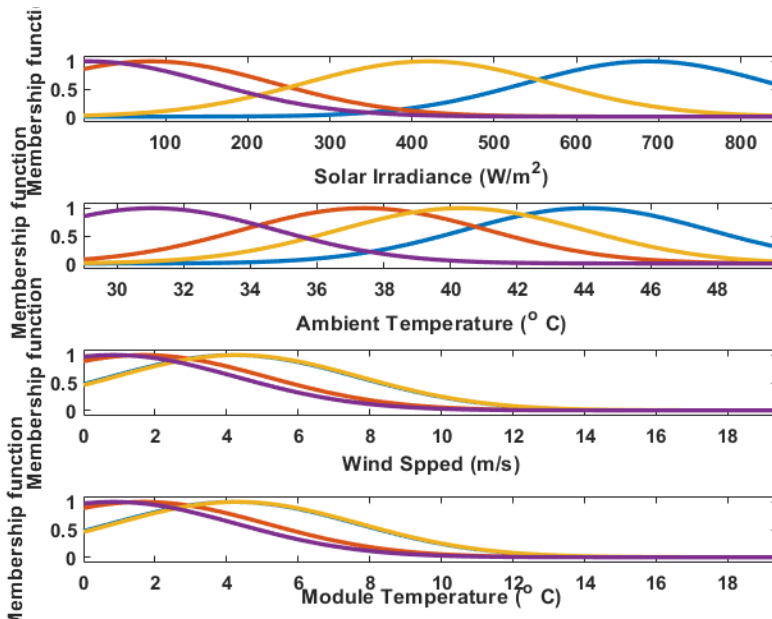


Fig 4. Membership Functions for input parameters for the developed ANFIS model.

Figs. 5 (a)-(e) represent the spatial 3-D surface for the DC Current (A) for the given PV system for each combination of the input parameters of the developed fuzzy model. The effect of ambient temperature, module temperature, and solar irradiance on the DC current generation is demonstrated in Fig. 5 (a) and (b), respectively. A direct relationship is observed with respect to ambient temperature and solar irradiance on the DC current generation. However, as module temperature increases significantly, the DC current is observed to reduce due to the reduction in the overall electrical efficiency of the system.

Moreover, Fig. 5 (c) depicts the impact of wind speed and ambient temperature on DC current generation. The spatial 3-D surface further demonstrates the direct relation of ambient temperature with DC current generation, while wind speed does not influence the DC current generation much.

Moreover, Figs. 5 (d) and (e) demonstrate the adverse impact of module temperature on the DC current generation as it increases significantly. The relative decrement in module temperature and maximizing the ambient temperature demonstrates an increase in the DC current generation as observed in Fig 5 (d). Furthermore, the minimal effect of wind speed on the DC current generation further confirms the findings presented in Fig 5 (c).

Therefore, the developed ANFIS model has demonstrated the performance of the demonstrated PV system based on four input variables. The DC current generation yield is at its highest when ambient temperature and solar irradiance are maintained at peak, while module temperature is minimized to attain maximum yield. This demonstrates the importance of incorporating cooling techniques to improve the PV system's electrical yield, sustaining its performance under harsh weather conditions.

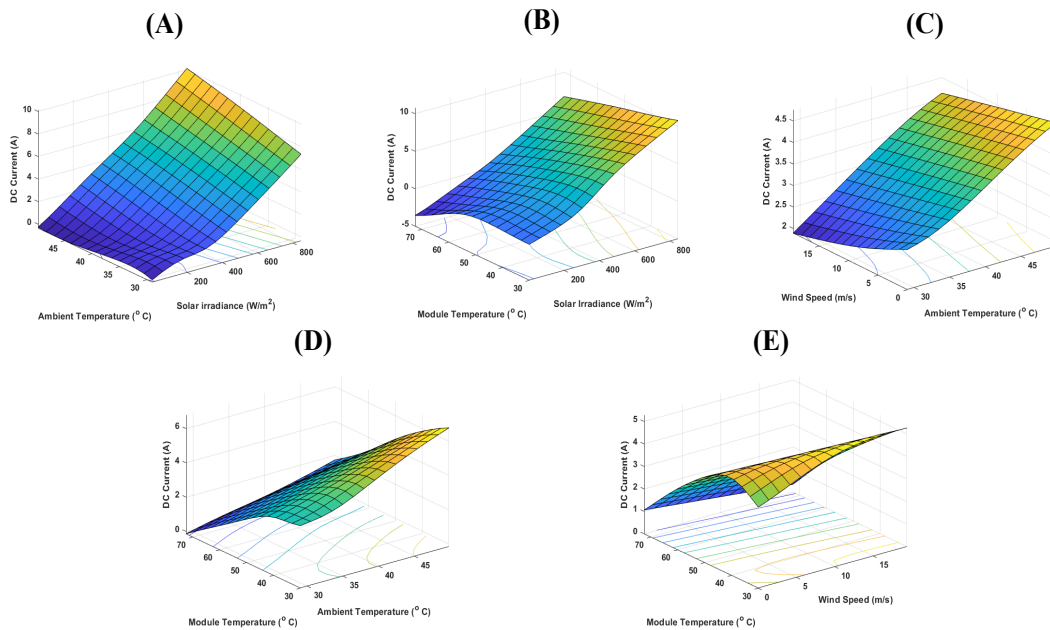


Fig 5. Spatial 3-D surface representation of DC current with respect to membership functions

Summary

PV System's DC current generation is affected by several environmental factors such as module temperature, ambient temperature, solar irradiance, and wind speed. In this study, the Adaptive Neuro-Fuzzy Inference System (ANFIS) model was developed to forecast the performance of a 2.88 kW on-grid PV system in the terrestrial conditions of Sharjah, UAE. The model adopted four input membership functions that relate to the DC current output power generation. DC current generation has observed a direct proportional relationship with respect to solar irradiance and ambient temperature, while module temperature presents an indirect relationship. This presents that DC current is improved at lower module temperatures while maintaining high solar irradiance exposure to enhance the electrical efficiency of the PV system. Moreover, the model presented a notable prediction accuracy and a significant correlation based on the least error, as the R^2 value corresponded to 99.12% and 99.13% for training and testing, respectively. Optimization techniques will be incorporated and tested in future work to improve the forecasting accuracy for larger datasets.

References

- [1] J.L. Holechek, H.M.E. Geli, M.N. Sawalhah, R. Valdez, A Global Assessment: Can Renewable Energy Replace Fossil Fuels by 2050?, *Sustainability*. 14 (2022) 4792. <https://doi.org/10.3390/su14084792>
- [2] T. Güney, Solar energy, governance and CO₂ emissions, *Renew. Energy*. 184 (2022) 791–798. <https://doi.org/10.1016/j.renene.2021.11.124>
- [3] A. Mehmood, J. Ren, L. Zhang, Achieving energy sustainability by using solar PV: System modelling and comprehensive techno-economic-environmental analysis, *Energy Strateg. Rev.* 49 (2023) 101126. <https://doi.org/10.1016/j.esr.2023.101126>
- [4] M.M. Farag, R.C. Bansal, Solar energy development in the GCC region – a review on recent progress and opportunities, *Int. J. Model. Simul.* 43 (2023) 579–599. <https://doi.org/10.1080/02286203.2022.2105785>
- [5] M. Jamei, M. Karbasi, M. Ali, A. Malik, X. Chu, Z.M. Yaseen, A novel global solar exposure forecasting model based on air temperature: Designing a new multi-processing ensemble deep learning paradigm, *Expert Syst. Appl.* 222 (2023) 119811.

<https://doi.org/10.1016/j.eswa.2023.119811>

- [6] M.M. Farag, A.K. Hamid, T. Salameh, E.M. Abo-Zahhad, M. AlMallahi, M. Elgendi, ENVIRONMENTAL, ECONOMIC, AND DEGRADATION ASSESSMENT FOR A 2.88 KW GRID-CONNECTED PV SYSTEM UNDER SHARJAH WEATHER CONDITIONS, in: 50th Int. Conf. Comput. Ind. Eng., 2023: pp. 1722–1731.
- [7] C. Scott, M. Ahsan, A. Albarbar, Machine learning for forecasting a photovoltaic (PV) generation system, *Energy*. 278 (2023) 127807. <https://doi.org/10.1016/j.energy.2023.127807>
- [8] U.K. Das, K.S. Tey, M. Seyedmahmoudian, S. Mekhilef, M.Y.I. Idris, W. Van Deventer, B. Horan, A. Stojcevski, Forecasting of photovoltaic power generation and model optimization: A review, *Renew. Sustain. Energy Rev.* 81 (2018) 912–928. <https://doi.org/10.1016/j.rser.2017.08.017>
- [9] M.M. Farag, N. Patel, A.-K. Hamid, A.A. Adam, R.C. Bansal, M. Bettayeb, A. Mehiri, An Optimized Fractional Nonlinear Synergic Controller for Maximum Power Point Tracking of Photovoltaic Array Under Abrupt Irradiance Change, *IEEE J. Photovoltaics*. 13 (2023) 305–314. <https://doi.org/10.1109/JPHOTOV.2023.3236808>
- [10] E. Kim, M.S. Akhtar, O.-B. Yang, Designing solar power generation output forecasting methods using time series algorithms, *Electr. Power Syst. Res.* 216 (2023) 109073. <https://doi.org/10.1016/j.epsr.2022.109073>
- [11] A. Alcañiz, D. Grzebyk, H. Ziar, O. Isabella, Trends and gaps in photovoltaic power forecasting with machine learning, *Energy Reports*. 9 (2023) 447–471. <https://doi.org/10.1016/j.egyr.2022.11.208>
- [12] F. Pereira, C. Silva, Machine learning for monitoring and classification in inverters from solar photovoltaic energy plants, *Sol. Compass*. 9 (2024) 100066. <https://doi.org/10.1016/j.solcom.2023.100066>
- [13] Y. Chen, M.S. Bhutta, M. Abubakar, D. Xiao, F.M. Almasoudi, H. Naeem, M. Faheem, Evaluation of Machine Learning Models for Smart Grid Parameters: Performance Analysis of ARIMA and Bi-LSTM, *Sustainability*. 15 (2023) 8555. <https://doi.org/10.3390/su15118555>
- [14] M. Jobayer, M.A.H. Shaikat, M. Naimur Rashid, M.R. Hasan, A systematic review on predicting PV system parameters using machine learning, *Heliyon*. 9 (2023) e16815. <https://doi.org/10.1016/j.heliyon.2023.e16815>
- [15] S. Pereira, P. Canhoto, R. Salgado, Development and assessment of artificial neural network models for direct normal solar irradiance forecasting using operational numerical weather prediction data, *Energy AI*. 15 (2024) 100314. <https://doi.org/10.1016/j.egyai.2023.100314>
- [16] S.B. Bashir, M.M. Farag, A.K. Hamid, A.A. Adam, A.G. Abo-Khalil, R. Bansal, A Novel Hybrid CNN-XGBoost Model for Photovoltaic System Power Forecasting, in: 2024 6th Int. Youth Conf. Radio Electron. Electr. Power Eng., 2024. <https://doi.org/10.1109/REEPE60449.2024.10479878>
- [17] M.S. Ibrahim, S.M. Gharghory, H.A. Kamal, A hybrid model of CNN and LSTM autoencoder-based short-term PV power generation forecasting, *Electr. Eng.* (2024). <https://doi.org/10.1007/s00202-023-02220-8>
- [18] G. Perveen, M. Rizwan, N. Goel, An ANFIS-based model for solar energy forecasting and its smart grid application, *Eng. Reports*. 1 (2019). <https://doi.org/10.1002/eng2.12070>
- [19] T.M.M. Abdellatif, M.A. Ershov, V.M. Kapustin, E.A. Chernysheva, V.D. Savchenko, T. Salameh, M.A. Abdelkareem, A.G. Olabi, Uniqueness technique for introducing high octane environmental gasoline using renewable oxygenates and its formulation on Fuzzy modeling, *Sci. Total Environ.* 802 (2022) 149863. <https://doi.org/10.1016/j.scitotenv.2021.149863>

- [20] T.M.M. Abdellatif, M.A. Ershov, V.M. Kapustin, E.A. Chernysheva, V.D. Savelenko, T. Salameh, M.A. Abdelkareem, A.G. Olabi, Novel promising octane hyperboosting using isoolefinic gasoline additives and its application on fuzzy modeling, *Int. J. Hydrogen Energy.* 47 (2022) 4932–4942. <https://doi.org/10.1016/j.ijhydene.2021.11.114>
- [21] T. Salameh, E.T. Sayed, A.G. Olabi, I.I. Hdaib, Y. Allan, M. Alkasrawi, M.A. Abdelkareem, Adaptive Network Fuzzy Inference System and Particle Swarm Optimization of Biohydrogen Production Process, *Fermentation.* 8 (2022) 483. <https://doi.org/10.3390/fermentation8100483>
- [22] M.M. Farag, F.F. Ahmad, A.K. Hamid, C. Ghenai, M. Bettayeb, M. Alchadirchy, Performance Assessment of a Hybrid PV/T system during Winter Season under Sharjah Climate, in: 2021 Int. Conf. Electr. Comput. Commun. Mechatronics Eng., IEEE, 2021: pp. 1–5. <https://doi.org/10.1109/ICECCM52200.2021.9590896>
- [23] F.F. Ahmad, M. Abdelsalam, A.K. Hamid, C. Ghenai, W. Obaid, M. Bettayeb, Experimental Validation of PVSYST Simulation for Fix Oriented and Azimuth Tracking Solar PV System, in: 2020: pp. 227–235. https://doi.org/10.1007/978-981-15-4775-1_25
- [24] M.M. Farag, F.F. Ahmad, A.K. Hamid, C. Ghenai, M. Bettayeb, Real-Time Monitoring and Performance Harvesting for Grid-Connected PV System - A Case in Sharjah, in: 2021 14th Int. Conf. Dev. ESystems Eng., IEEE, 2021: pp. 241–245. <https://doi.org/10.1109/DeSE54285.2021.9719385>
- [25] T. Salameh, A.K. Hamid, M.M. Farag, E.M. Abo-Zahhad, Energy and exergy assessment for a University of Sharjah's PV grid-connected system based on experimental for harsh terrestrial conditions, *Energy Reports.* 9 (2023) 345–353. <https://doi.org/10.1016/j.egyr.2022.12.117>
- [26] T. Salameh, A.K. Hamid, M.M. Farag, E.M. Abo-Zahhad, Experimental and numerical simulation of a 2.88 kW PV grid-connected system under the terrestrial conditions of Sharjah city, *Energy Reports.* 9 (2023) 320–327. <https://doi.org/10.1016/j.egyr.2022.12.115>
- [27] M.M. Farag, A.K. Hamid, Experimental Investigation on the Annual Performance of an Actively Monitored 2.88 kW Grid-Connected PV System in Sharjah, UAE, in: 2023 Adv. Sci. Eng. Technol. Int. Conf., IEEE, 2023: pp. 1–6. <https://doi.org/10.1109/ASET56582.2023.10180880>
- [28] J.-S.R. Jang, ANFIS: adaptive-network-based fuzzy inference system, *IEEE Trans. Syst. Man. Cybern.* 23 (1993) 665–685. <https://doi.org/10.1109/21.256541>
- [29] T. Salameh, P.P. Kumar, E.T. Sayed, M.A. Abdelkareem, H. Rezk, A.G. Olabi, Fuzzy modeling and particle swarm optimization of Al₂O₃/SiO₂ nanofluid, *Int. J. Thermofluids.* 10 (2021) 100084. <https://doi.org/10.1016/j.ijft.2021.100084>

Robust testing requirements for Li-ion battery performance analysis

Muhammad SHEIKH^{1,a *}, Muhammad RASHID^{1,b} and Sheikh REHMAN^{2,c}

¹WMG, The University of Warwick, Coventry, UK

²School of Computing, Engineering and Digital Technologies. Teesside University,
Middlesborough, UK

^amohammad.sheikh@warwick.ac.uk, ^bR.Muhammad.1@warwick.ac.uk, ^cS.Rehman@tees.ac.uk

Keywords: Battery Degradation, Capacity Fade, Failure Analysis, Testing and Characterization, Test Matrix Design, Design and Development

Abstract. Lithium-ion batteries are considered reliable option for Electric vehicle propulsion and portable applications. Various battery chemistries are being developed to enhance safety and performance of batteries to improve lifespan and reliability. Battery use case scenario often dictate requirements of different li-ion battery types. When target applications are fulfilled, other key considerations are implemented which include testing and characterisation to understand useful performance indicators from chosen battery type. This paper investigates current testing and characterisation needs to understand capacity fade and battery degradation with respect to temperature variations. Cycling tests followed by reference performance tests are used to analyse capacity fade. Due to limitation for the paper size only capacity fade analysis along with immersed test setup are focused to understand battery degradation with respect to various C-rates. Key findings are discussed, and comparative analysis is provided with future recommendations.

Introduction

Lithium-Ion batteries (LIBs) have attracted more attention due to their great energy storage capacity, high current density, extended lifespan, low self-discharge, lack of memory effects, and minimal environmental impact [1]. LIBs are mostly used in portable electronics, energy storage systems, and electric vehicles (EVs) throughout a variety of industries, including transportation and aerospace [2][3], such as Tesla (Model 'S' and Roadster) and Nissan (Leaf) are among the main automotive manufacturers using LIBs for their fleets [4]. LIBs are the widely used technology for energy storage applications, despite the existence of alternative technologies [5]. This is due to their ability to fast-charging capacity with higher cycle life and energy density when compared to established technologies that are available commercially [6]–[8].

Battery Safety

LIBs are an effective energy source for present electric vehicles (EVs), their safety must be taken into consideration before these batteries are large-scale deployment. One of the issues is short circuits in batteries, which can propagate fast within battery packs or modules if they are not managed at the cell level [9]. Battery failures are evident once they are exposed to abusive conditions, however, when using test and validation techniques to determine battery potential, predicting these failures before the time is extremely essential [10]. Various LIBs have been recalled in recent years as a result of explosion and fire incidents [12–15], significantly damaging LIBs reputation and causing serious economic problems for associated market sectors [11].

Although LIBs provide many advantages, it is important to carefully assess their durability and safety [12]. When a battery's capacity approaches 80% of its initial value, battery is at the end of its life. Excessive use of a battery beyond its end-of-life (EOL) specifications can result in bad system performance and occasionally catastrophic events [13][14]. Remaining usable life (RUL) prediction is therefore required to ensure battery safety and reliable operation. Battery's operation

can be managed via a battery management system (BMS), based on the RUL prediction results. Accurately estimating the state of health (SOH) of lithium batteries has become difficult, because of the uncertainty and diversity of their internal side reactions and external working conditions [15].

The chemistry of the battery [16][17], its working environment, and its abuse tolerance [18] all have a significant impact on battery safety. Electrochemical system instability is the root cause of a LIBs internal failure [19]. Optimising battery design and making thoughtful selections regarding electrode materials, separators, and electrolytes can greatly increase LIB safety and performance stability. In typical circumstances, external techniques such as cell balancing and cooling can also significantly improve LIBs safety performance [11]. Therefore, it is essential to include appropriate safety precautions in the design, manufacture, and second life of LIBs, such as through the appropriate design of short circuit protection or temperature management systems [20].

Capacity degradation

The actual capacity degrades as the battery cycles, It affects the vehicle's driving range and increases "range anxiety"[21]. Repeated cycles of charging and discharging can cause LIBs to degrade over time in terms of their durability. This might affect their charge retention capacity and their lifespan. Cycle-life performance of LIBs is intrinsically correlated to the fundamental understanding of ageing mechanisms [22]. Therefore, continuous research is carried out to advancements in materials, battery management systems and electrode designs. The goal of LIB development is to increase their efficiency by using eco-friendly components [23]. Batteries can fail at any point in their life cycle for several reasons, including degradation, abuse conditions, and manufacturing errors. Battery abuse loads, both mechanical and thermal, have been simulated through the development of tests [24]. In the EV industry, new techniques that enable continuous battery condition monitoring are currently being used [12].

Literature shows that the causes of capacity fade can be classified into two groups namely calendar ageing and cycling ageing. Whereas cycling ageing is usually influenced by ambient temperature, the number of charge cycles or charge throughput, C-rate, and DoD, calendar ageing is generally primarily affected by the storing temperature, SoC, and time, which represents how long the battery placed in the storage or in resting state [25].

Battery Capacity Fading

Battery capacity fading can be divided into three stages; constant capacity fading, rapid capacity fading, and repetition between capacity increase and decrease [26]. According to Jialong et al, they used incremental capacity analysis and electrochemical impedance spectroscopy to investigate relevant aging mechanisms in their experiment work [27]. They found; The formation of solid electrolyte interface (SEI) films causes a rapid decrease in capacity during the first stage. The capacity decreases slowly due to the stable state of the lithium-ion battery in the second stage. In the third stage, the capacity decreases rapidly again due to the decrease in charge acceptance capability and damage to active materials.

To optimise battery design, management, and operation, precise measurement and prediction of LIBs performance and degradation are essential. As a result, a lot of study has been done to look at the models and testing procedures used to determine the lifetime and capacity fading of LIBs. Several tests to identify capacity fading have been suggested in the literature such as tests based on electrochemical models [28], equivalent circuit models [29], an analytical model with empirical data fitting [30], and performance-based models have been proposed. Safari et al created an electrochemical model to investigate how ageing affects impedance rise and capacity fading [31]. Wang et al proposed advanced data-driven methods for predicting the remaining useful life (RUL) and whole life cycle state of charge (SOC) of lithium-ion batteries [32]. Selcuk et al; presented a novel ageing mechanism, this mechanism improves upon the standard approach of

transport limited models that incorporates (i) multi-layered SEI, (ii) lithium-plating, and (iii) reduction of anode porosity. This method attempted to represent more realistic ageing kinetics in order to obtain an understanding of linear and nonlinear capacity fading [22]. Muhammad et al developed dataset for rapid state of health estimation of lithium batteries using EIS and machine learning, this dataset encompasses all ageing statistics for commercially accessible and commonly used lithium-ion batteries. It also evaluates how increased charge throughput (ageing) affects the cell's retained energy capacity and impedance. The dataset quantifies the inter-dependency between LIB impedance's temperature and SOC at various ageing states between 100% and 80% SOH [33]. A variety of scientists and engineers working on battery-related projects can use the datasets. Truong et al. report a thorough investigation on decreased lithium-ion battery degradation, through state-of-charge pre-conditioning techniques that enable an electric car to engage in vehicle-to-grid activities when the vehicle is parked [34].

Test procedure and experimental results

This section provides details of the test procedures used on the cells under examination for ageing analysis. These include cycle ageing at various charge/discharge rates and temperatures. Preconditioning and characterisation of cells are done prior to cell testing. The experiment conditions were selected from an originally more comprehensive test matrix.

When conducting long term ageing tests, equipment selection is crucial as it has direct impact on cell performance estimation. To overcome the high-temperature issue and ensure the safety of cells, schematic of a fully immersed setup is shown in figure 1(a), where dielectric oil (Kryo-51) is used and cell fixtures are shown in figure 1(b). The initial characterisation tests proved this method of thermal management more effective, enabling improved temperature control throughout the test.

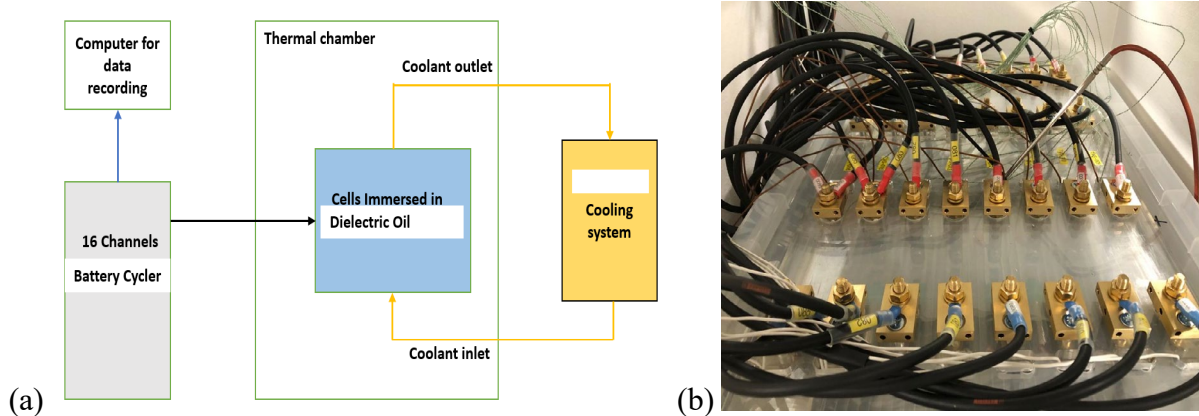


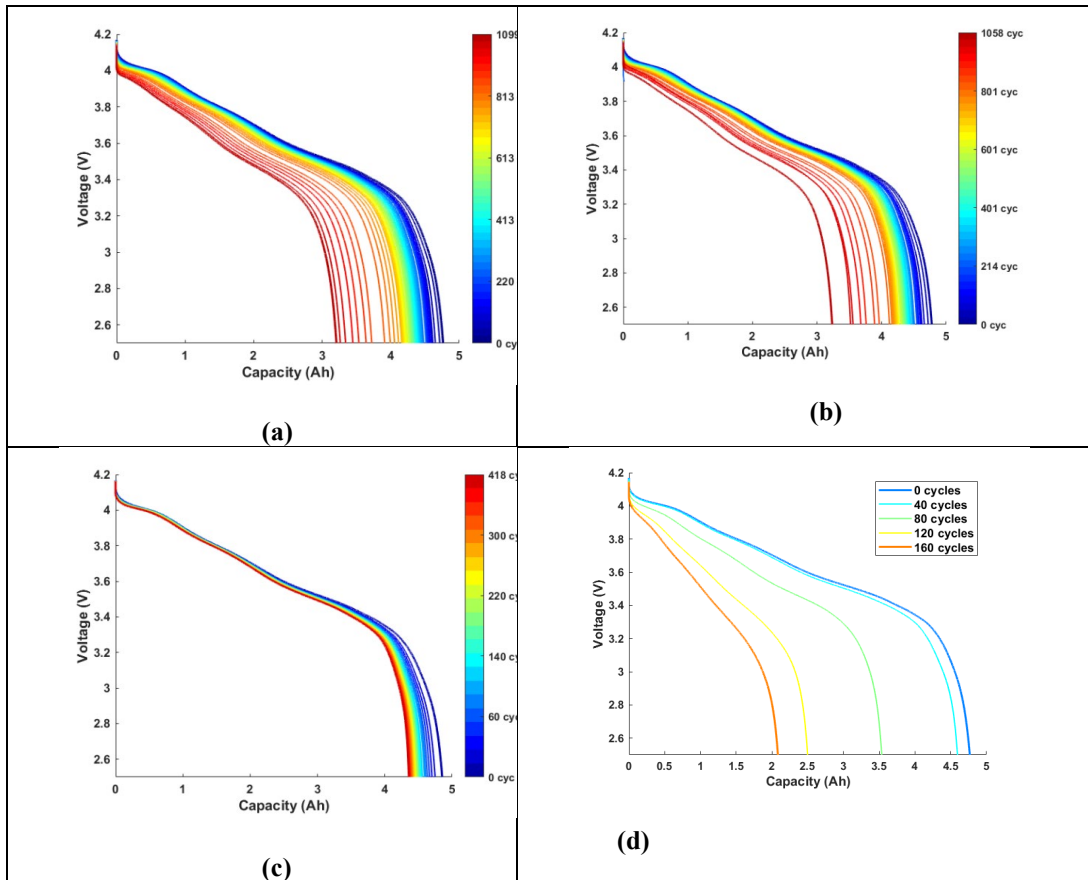
Figure 1: (a) Schematic of fully immersed test setup, (b) Cell fixtures for immersed setup

To record capacity variations, reference performance tests (RPT) are recorded periodically, and the data is analysed according to the ageing test conditions. The results are discussed in detail in the following sections. The cell capacity is tracked periodically to analyse capacity fade to a given usage profile, with uncertainty intervals based on the four cells used per experiment. To ensure the safe running of the tests, routine monitoring of the oil-rig test setup, running programs and the live readings of the cycler data are performed.

Table 1: Summary of the cycle ageing tests performed

Full Charge-Discharge cycling			
Temperature/Rate	0.3C Charge-0.3C Discharg	0.5C Charge-0.3C Discharge	0.7C Charge- 0.3C Discharge
0°C	4 cells	4 cells	4 cells
10°C	4 cells	4 cells	4 cells
25°C	4 cells	4 cells	4 cells

Table 1 provide details of ageing test conditions used where three temperature conditions are monitored with different charge and discharge currents applied. The battery investigated was a 5Ah, 21700 cylindrical cell manufactured by LG Chem. This cell utilises nickel-rich NMC811 and SiOy-graphite active materials. For cycle ageing testing we have considered three test conditions which are 0.3C charge-0.3C discharge, 0.5C charge-0.3C discharge, 0.7C charge-0.3C discharge, and three temperature conditions at 0°C, 10°C, and 25°C. Four cells are used for each cycling ageing test condition and the same cell numbers are used throughout this work. Capacity checks are done after one week of cycling for all temperatures. The End-of-Life (EoL) for these cells are defined as 80% capacity compared to the initial capacity (5Ah). Figure 2 shows voltage vs capacity changes with respect to total number of cycles for each cycling condition underwent before reaching EoL.



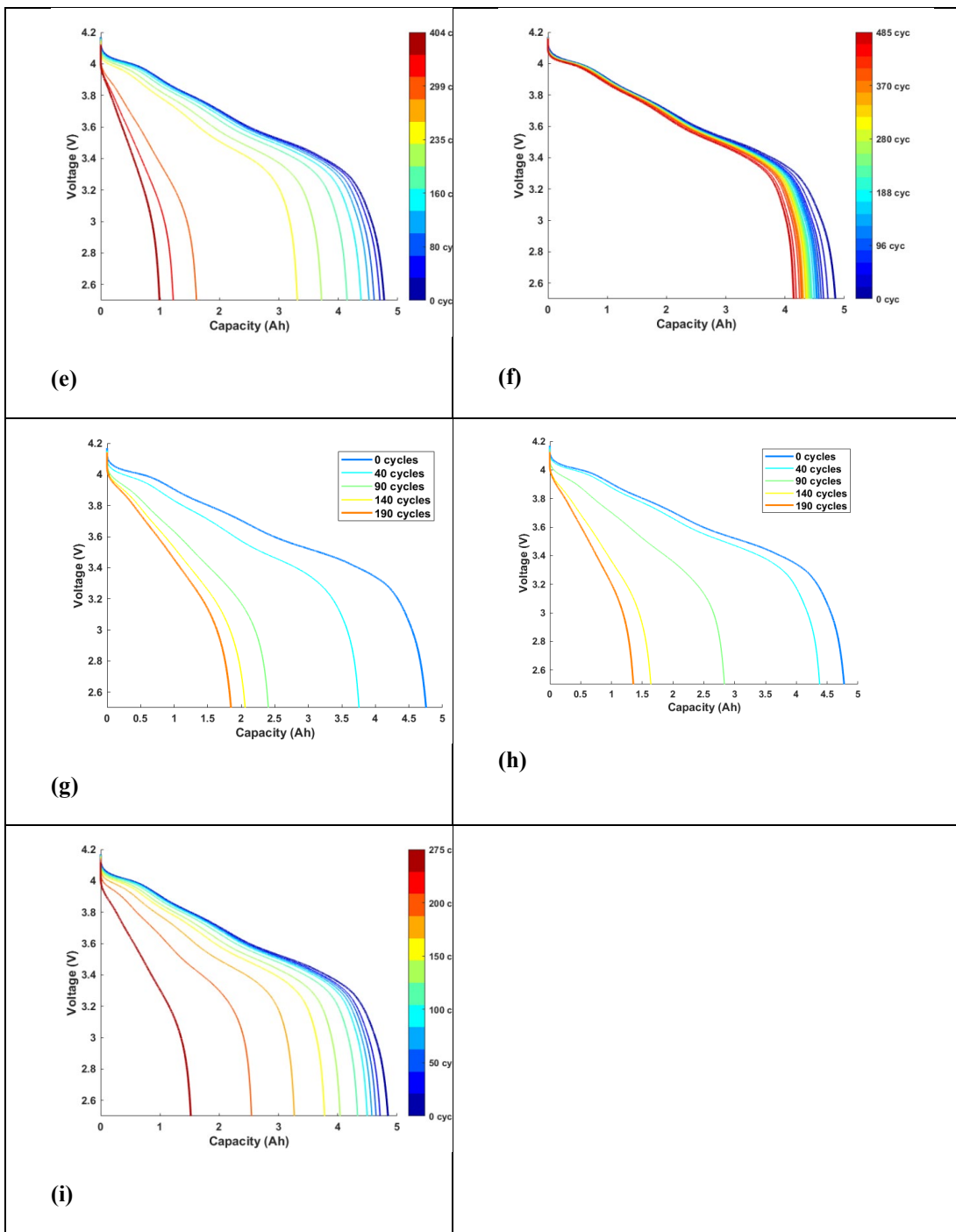


Figure 2: Capacity Test Voltage Curves (a) 0.3C/0.3C-0°C (b) 0.3C/0.3C-10°C (c) 0.3C/0.3C-25°C (d) 0.5C/0.3C-0°C (e) 0.5C/0.3C-10°C (f) 0.5C/0.3C-25°C (g) 0.7C/0.3C-0°C (h) 0.7C/0.3C-10°C (i) 0.7C/0.3C-25°C

Figures 2(a-c), show there is less affect of immersed temperature with low charge-discharge currents (1.67A). Analysis is further broaden to compare number of cycles and at the same number of cycles (418 cycles) we have same capacity fade. When charge current is increased and testing is done at 0.5C (2.5A) charge and 0.3C (1.67A) discharge as shown in figures 2(d-f), we can see less number of cycles are completed at 0°C and 10°C and capacity fade is rapid which, but at 25°C high number of cycles are achieved and capacity fade is lower which is only 20% after 485 cycles.

Figures 2(g-i) show that fewer cycles are achieved with the 0.7C charge (3.5A) and 0.3C discharge (1.67A) for all temperature cases.

Overall, it can be observed that with the low charge current (0.3C) condition, degradation has occurred more slowly compared with high charge currents (0.5C and 0.7C) for all temperature conditions except 25°C, whereby the performance becomes more comparable. However, ordinarily at lower temperatures, the diffusion kinetics for Li are slower and there is an inevitable trade-off in some performance level. Thus, higher cycling currents would not be sustainable to achieve a long lifespan.

Summary

This paper investigated current testing and characterisation needs to understand capacity fade, battery degradation and temperature dependance. Capacity fade analysis along with immersed test setup is provided to understand battery degradation with respect to various C-rates. Low temperatures in general, can induce deterioration in battery performance for a whole host of reasons; ultimately reducing the discharge voltage and accelerating capacity decay. The most severe capacity fading process has been reported to relate to effects from Li-plating on the anodes. This will result in lowered lithium inventory and reductions in accessible active material – capacity decay will thus continue. This at first may appear counterintuitive; however, this indicates that while cycling within the maximum and minimum voltage limits, the lower discharge current causes lower voltage losses in the battery and allows a higher utilisation of the electrodes. As a result, the charge throughput increases and the cells are worked harder while operating with the constant discharge, resulting in fewer cycles to reach EoL.

Author Contributions

Methodology, M.S.; formal analysis, M.S. and S.R.; investigation M.S. and M.R.; writing—original draft, M.S., M.R. and S.R., writing—review and editing, M.S. All authors have read and agreed to the published version of the manuscript.

References

- [1] S. Windisch-Kern *et al.*, “Recycling chains for lithium-ion batteries: A critical examination of current challenges, opportunities and process dependencies,” *Waste Manag.*, vol. 138, pp. 125–139, 2022. <https://doi.org/10.1016/j.wasman.2021.11.038>
- [2] Z. Cui, L. Wang, Q. Li, and K. Wang, “A comprehensive review on the state of charge estimation for lithium-ion battery based on neural network,” *Int. J. Energy Res.*, vol. 46, no. 5, pp. 5423–5440, 2022. <https://doi.org/10.1002/er.7545>
- [3] R. Gong *et al.*, “A sustainable closed-loop method of selective oxidation leaching and regeneration for lithium iron phosphate cathode materials from spent batteries,” *J. Environ. Manage.*, vol. 319, no. March 2022, p. 115740, 2022. <https://doi.org/10.1016/j.jenvman.2022.115740>
- [4] M. Sheikh, S. Rehman, and M. Elkady, “Numerical simulation model for short circuit prediction under compression and bending of 18650 cylindrical lithium-ion battery,” *Energy Procedia*, vol. 151, pp. 187–193, 2018. <https://doi.org/10.1016/j.egypro.2018.09.046>
- [5] G. E. Blomgren, “The Development and Future of Lithium Ion Batteries,” *J. Electrochem. Soc.*, vol. 164, no. 1, pp. A5019–A5025, 2017. <https://doi.org/10.1149/2.0251701jes>
- [6] S. S. Rangarajan *et al.*, “Lithium-Ion Batteries—The Crux of Electric Vehicles with Opportunities and Challenges,” *Clean Technol.*, vol. 4, no. 4, pp. 908–930, 2022. <https://doi.org/10.3390/cleantechnol4040056>
- [7] Y. Bai, N. Muralidharan, Y. K. Sun, S. Passerini, M. Stanley Whittingham, and I. Belharouak, “Energy and environmental aspects in recycling lithium-ion batteries: Concept of

- Battery Identity Global Passport," *Mater. Today*, vol. 41, no. December, pp. 304–315, 2020.
<https://doi.org/10.1016/j.mattod.2020.09.001>
- [8] Y. Liang *et al.*, "A review of rechargeable batteries for portable electronic devices," *InfoMat*, vol. 1, no. 1, pp. 6–32, 2019. <https://doi.org/10.1002/inf2.12000>
- [9] M. Sheikh, A. Elmarakbi, and S. Rehman, "A combined experimental and simulation approach for short circuit prediction of 18650 lithium-ion battery under mechanical abuse conditions," *J. Energy Storage*, vol. 32, no. August, p. 101833, 2020.
<https://doi.org/10.1016/j.est.2020.101833>
- [10] M. Sheikh; M. Elmarakbi; S. Rehman and A. Elmarakbi, "Internal Short Circuit Analysis of Cylindrical Lithium-Ion Cells Due to Structural Failure," *J. Electrochem. Soc.*, 2021.
- [11] Y. Chen *et al.*, "A review of lithium-ion battery safety concerns: The issues, strategies, and testing standards," *J. Energy Chem.*, vol. 59, pp. 83–99, 2021.
<https://doi.org/10.1016/j.jecchem.2020.10.017>
- [12] X. C. A. Chacón, S. Laureti, M. Ricci, and G. Cappuccino, "A Review of Non-Destructive Techniques for Lithium-Ion Battery Performance Analysis," *World Electr. Veh. J.*, vol. 14, no. 11, 2023. <https://doi.org/10.3390/wevj14110305>
- [13] X. Li, D. Yu, V. Søren Byg, and S. Daniel Ioan, "The development of machine learning-based remaining useful life prediction for lithium-ion batteries," *J. Energy Chem.*, vol. 82, pp. 103–121, 2023. <https://doi.org/10.1016/j.jecchem.2023.03.026>
- [14] Q. Yu, C. Wang, J. Li, R. Xiong, and M. Pecht, "Challenges and outlook for lithium-ion battery fault diagnosis methods from the laboratory to real world applications," *eTransportation*, vol. 17, no. May, p. 100254, 2023. <https://doi.org/10.1016/j.etran.2023.100254>
- [15] Y. Wang, X. Zhang, K. Li, G. Zhao, and Z. Chen, "Perspectives and challenges for future lithium-ion battery control and management," *eTransportation*, vol. 18, no. June, p. 100260, 2023. <https://doi.org/10.1016/j.etran.2023.100260>
- [16] Q. Zhao *et al.*, "Hierarchical flower-like spinel manganese-based oxide nanosheets for high-performance lithium ion battery," *Sci. China Mater.*, vol. 62, no. 10, pp. 1385–1392, 2019.
<https://doi.org/10.1007/s40843-019-9442-x>
- [17] X. Chen, H. Li, Z. Yan, F. Cheng, and J. Chen, "Structure design and mechanism analysis of silicon anode for lithium-ion batteries," *Sci. China Mater.*, vol. 62, no. 11, pp. 1515–1536, 2019.
<https://doi.org/10.1007/s40843-019-9464-0>
- [18] L. Wang *et al.*, "Unlocking the significant role of shell material for lithium-ion battery safety," *Mater. Des.*, vol. 160, pp. 601–610, 2018. <https://doi.org/10.1016/j.matdes.2018.10.002>
- [19] Y. Kang, C. Deng, X. Liu, T. Liang, Zheng; Li, Q. Hu, and Y. Zhao, "Binder-Free Electrode based on Electrospun-Fiber for Li Ion Batteries via a Simple Rolling Formation," *Scopus*, 2020.
- [20] A. G. Olabi *et al.*, Battery thermal management systems: Recent progress and challenges, vol. 15, no. June. Elsevier Ltd, 2022.
- [21] R. Xiong, Z. Li, R. Yang, W. Shen, S. Ma, and F. Sun, "Fast self-heating battery with anti-aging awareness for freezing climates application," *Appl. Energy*, vol. 324, no. 5, p. 119762, 2022. <https://doi.org/10.1016/j.apenergy.2022.119762>
- [22] S. Atalay, M. Sheikh, A. Mariani, Y. Merla, E. Bower, and W. D. Widanage, "Theory of battery ageing in a lithium-ion battery: Capacity fade, nonlinear ageing and lifetime prediction," *J. Power Sources*, vol. 478, p. 229026, 2020. <https://doi.org/10.1016/j.jpowsour.2020.229026>

- [23] J. C. Barbosa, R. Gonçalves, C. M. Costa, and S. Lanceros-Mendez, “Recent advances on materials for lithium-ion batteries,” *Energies*, vol. 14, no. 11, 2021.
<https://doi.org/10.3390/en14113145>
- [24] H. Wang, E. Lara-Curzio, E. T. Rule, and C. S. Winchester, “Mechanical abuse simulation and thermal runaway risks of large-format Li-ion batteries,” *J. Power Sources*, vol. 342, pp. 913–920, 2017. <https://doi.org/10.1016/j.jpowsour.2016.12.111>
- [25] A. Ahmadian, M. Sedghi, A. Elkamel, M. Fowler, and M. Aliakbar, “Plug-in electric vehicle batteries degradation modeling for smart grid studies : Review , assessment and conceptual framework,” *Renew. Sustain. Energy Rev.*, vol. 81, no. June 2017, pp. 2609–2624, 2018.
<https://doi.org/10.1016/j.rser.2017.06.067>
- [26] B. Xu, A. Oudalov, A. Ulbig, G. Andersson, and D. S. Kirschen, “Modeling of lithium-ion battery degradation for cell life assessment,” *IEEE Trans. Smart Grid*, vol. 9, no. 2, pp. 1131–1140, 2018. <https://doi.org/10.1109/TSG.2016.2578950>
- [27] J. Liu *et al.*, “Capacity fading mechanisms and state of health prediction of commercial lithium-ion battery in total lifespan,” *J. Energy Storage*, vol. 46, no. December 2021, p. 103910, 2022. <https://doi.org/10.1016/j.est.2021.103910>
- [28] A. Khalid and A. I. Sarwat, “Fast charging li-ion battery capacity fade prognostic modeling using correlated parameters’ decomposition and recurrent wavelet neural network,” *2021 IEEE Transp. Electrif. Conf. Expo, ITEC 2021*, pp. 27–32, 2021.
<https://doi.org/10.1109/ITEC51675.2021.9490177>
- [29] D. Andre, C. Appel, T. Soczka-Guth, and D. U. Sauer, “Advanced mathematical methods of SOC and SOH estimation for lithium-ion batteries,” *J. Power Sources*, vol. 224, pp. 20–27, 2013. <https://doi.org/10.1016/j.jpowsour.2012.10.001>
- [30] K. M. Tsang and W. L. Chan, “State of health detection for Lithium ion batteries in photovoltaic system,” *Energy Convers. Manag.*, vol. 65, pp. 7–12, 2013.
<https://doi.org/10.1016/j.enconman.2012.07.006>
- [31] M. Safari; C. Delacourt, “Simulation-Based Analysis of Aging Phenomena in a Commercial Graphite/LiFePO₄ Cell,” *J. Electrochem. Soc.*, vol. 158, no. 12, 2011.
- [32] S. Wang, P. Takyi-Aninakwa, S. Jin, C. Yu, C. Fernandez, and D. I. Stroe, “An improved feedforward-long short-term memory modeling method for the whole-life-cycle state of charge prediction of lithium-ion batteries considering current-voltage-temperature variation,” *Energy*, vol. 254, p. 124224, 2022. <https://doi.org/10.1016/j.energy.2022.124224>
- [33] M. Rashid, M. Faraji-niri, J. Sansom, M. Sheikh, D. Widanage, and J. Marco, “Dataset for rapid state of health estimation of lithium batteries using EIS and machine learning : Training and validation,” *Data Br.*, vol. 48, p. 109157, 2023. <https://doi.org/10.1016/j.dib.2023.109157>
- [34] T. M. N. Bui *et al.*, “A Study of Reduced Battery Degradation Through State-of-Charge Pre-Conditioning for Vehicle-to-Grid Operations,” *IEEE Access*, vol. 9, pp. 155871–155896, 2021.
<https://doi.org/10.1109/ACCESS.2021.3128774>
- [35] Y. Tian, Q. Wang, and J. Liu, ‘Analysis of Lithium-Ion Battery through Direct Current Internal Resistance Characteristic’, *SAE International Journal of Electrified Vehicles*, vol. 12, no. 2, pp. 173–184, Apr. 2022. <https://doi.org/10.4271/14-12-02-0009>

Date fruit type classification using convolutional neural networks

Abdullah ALAVI^{1,a}, Md Faysal AHAMED^{1,b}, Ali ALBELADI^{1,c},
Mohamed MOHANDES^{1,d}*

¹King Fahd University of Petroleum and Minerals, Department of Electrical Engineering,
Dhahran, Saudi Arabia

^ag202313690@kfupm.edu.sa, ^bg202309930@kfupm.edu.sa, ^calbeladi@kfupm.edu.sa,
^dmohandes@kfupm.edu.sa

Keywords: Date Fruit Type Classification, Convolutional Neural Network, SqueezeNet, Pretrained Network, Transfer Learning

Abstract. Classification of objects is an important task for convolutional neural networks (CNNs). They have been applied to numerous fields with excellent results. In this study, we use CNNs to classify five categories of Sukkari dates, namely Galaxy, Mufattal, Nagad, Qishr, and Ruttab. Transfer learning is when a pretrained model is taken and only the final layers are trained to make a prediction. In this paper, we used the following five models: SqueezeNet, GoogLeNet, EfficientNet-b0, ShuffleNet, and MobileNet V2. The results show that SqueezeNet outperforms the other networks with a classification accuracy of 92% on the testing set. The testing accuracy for GoogLeNet, EfficientNet-b0, ShuffleNet, and MobileNet V2, on the other hand are 85.14%, 82.86%, 89.14%, and 87.43%, respectively. As this is a classification task, other metrics like precision, recall, and F1 score are also evaluated. These values for the SqueezeNet on the testing set are 92.67%, 92%, and 92.33%, respectively. ShuffleNet was second with values of 89.41%, 89.14%, and 89.28%, respectively. EfficientNet scored the lowest with 83.10%, 82.86%, and 82.98%, respectively.

Introduction

The recent breakthroughs in computer vision and artificial intelligence (AI) have led to myriad applications, ranging from facial recognition to self-driving cars. All such applications have a common theme, that it is relatively easy for people to solve with good accuracy but nearly impossible to program and implement on a computer [1]. To solve this problem, AI-based systems need to possess the ability to extract the patterns from the raw data and produce an output based on this knowledge [1, 2, 3, 4]. Agriculture is one of the areas that fall in this category and has benefitted from the developments of computer vision. Applications include machines to sort fruits, automatic fruit harvesting, and fruit scanners in markets [5, 6].

Deep Learning (DL) is a subset of AI that has gained significant popularity in recent years. It has a high level of abstraction and can automatically learn patterns from images [7]. Convolutional Neural Network (CNN) [8] is a popular architecture for applications that involve image processing [1, 4, 9, 10]. CNNs use a convolution operation in at least one of the layers [1, 11]. CNNs have started to gain popularity after 2012, when Krizhevsky et al. [12] won the ILSVRC competition on ImageNet [13]. Since then, they have found various applications in computer vision including fruit classification and detection [14, 15, 16, 17, 18].

Dates fruits are popular in the Middle East, North Africa, and Southwest Asia [19]. In the Kingdom of Saudi Arabia (KSA), date palm trees occupy nearly a quarter of the total cultivated land [20]. Various types of dates are cultivated and they vary greatly in terms of their size, color, and taste [21]. The recent success of AI and DL on inspecting a variety of fruits has inspired a number of works pertaining to date fruits. Date fruit quality classification, for instance, has gained traction among several researchers [22, 23]. Alresheedi et al. [24] compared the accuracy of several

machine learning models with CNN. The dataset consisted of nine classes of date fruits. The authors found that the CNN model boasted the highest accuracy. In [25], a framework is proposed for date recognition. 500 images of three types of date fruits were used. The framework was based on a deep CNN and achieved an accuracy of 89.2%. In [20], Faisal et al. proposed a solution consisting of three estimation functions to classify date fruits based on maturity, type, and mass. The work used a Support Vector Machine (SVM) and achieved an accuracy of 99% among all the estimation functions. In [26], the authors focused on sorting dates based on their health and maturity. Four date types in different maturity stages along with defective dates were used in a CNN model based on VGG-16. The accuracy reported was 97%. In [27], Perez et al. used Medjool dates to compare the performance of eight different CNNs. The target was to sort the dates based on maturity stage. Out of all models, VGG-19 performed the best with an accuracy of 99.32%. In [26], the authors used transfer learning with fine-tuning using two pretrained networks, namely AlexNet and VGGNet. They used a dataset of 8,000 images separated into 5 classes and achieved an accuracy of 97.25%. In [28], the authors implemented a machine vision framework to deploy in a harvesting robot. The framework used three models to classify according to the type, maturity, and harvesting decision. The models are based on pretrained AlexNet and VGG-16. The VGG-16 model achieved accuracy of 99.01%, 97.25%, and 98.59% on date type, maturity, and harvesting decision classification, respectively. In [29], the authors used a dataset of 1,658 images belonging to nine categories of dates. The model used MobileNet V2 and resulted in an accuracy of 96%.

Although, numerous works have been published using individual pretrained models, there has been very little regarding the comparison of the performances of these various pretrained state-of-the-art models. Hardware and datasets for training and testing are different in published works, which make it unfair to compare performances. In this work, we present a comparison between various pretrained CNN models and observe how they perform on the same dataset. The goal of the CNN models is to classify five subclasses of dates of the same family. The paper is organized as follows. Section II describes the CNN models used. Section III explains the dataset and the methodology. Section IV discusses the results. Finally, the conclusion is presented in Section V.

Overview of the CNN Models

A number of popular state-of-the-art pretrained networks like VGG-16, ResNet, Inception, and AlexNet are implemented frequently. However, due to their great number of layers, they usually require a long time to train even on powerful hardware. To mitigate this issue, researchers are looking for ways to minimize the size and training time by restructuring the CNN in various ways while maintain a comparable accuracy. In this paper, we implemented five such models and compared their performance in this classification task. The models are SqueezeNet [30], GoogLeNet [31], EfficientNet-b0 [32], ShuffleNet [33], and MobileNet V2 [34]. A brief summary is provided below about each model and the techniques they used to improve the efficiency.

In SqueezeNet, the authors achieved accuracy comparable to that of AlexNet [12] while using 1/50th of its parameters. They also reduced the size to less than 0.5 MB, which is 510 times smaller than AlexNet. They achieved this by replacing the 3x3 filters with 1x1 filters. They also decreased the number of input channels and down sampling the later layers in the network. These strategies were then incorporated with other modifications and packed in what is known as a *Fire module*.

In GoogLeNet, the authors managed to increase the depth and width of the network without increasing the computational demand. They have achieved this by implementing the *Inception module*. This module applies 1x1, 3x3, 5x5 parallel convolutions along with dimensionality reduction. This helped in capturing details of varying sizes.

In EfficientNet, the primary motivation was how to scale up a CNN. Generally, CNNs are developed with certain computational constraint in mind. If the model performs satisfactorily, then it is scaled up to further increase the accuracy. Scaling up can be done by increasing the depth,

width or resolution. Instead of scaling up arbitrarily, the authors proposed a relationship between the three parameters known as *compound coefficient*. Using this technique, they have managed to reduce the size and increase the speed when compared to existing state-of-the-art CNNs.

In ShuffleNet, the primary motivation was to design a CNN that can run on mobile devices with extremely limited hardware. They used two new operations, namely pointwise group convolutions and channel shuffling. Using this, the ShuffleNet architecture achieved a superior performance, outperforming MobileNet in terms of accuracy in the ImageNet top-1 error on a computational power of 40 MFLOPS. On ARM-based computing hardware, ShuffleNet achieved a 13x speedup over AlexNet while maintaining a similar level of accuracy.

In MobileNetV2, the authors implemented what is known as an inverted residual structure. In this structure, the shortcut connections are between the thin bottleneck layers. Then, in the intermediate expansion layers, lightweight depth wise convolutions are performed to filter features in order to introduce non-linearity. Also, in the narrow layers, they discovered that it is important to remove non-linearities. This helped in maintaining representational power. On the ImageNet dataset, the MobileNet architecture improved the state-of-the-art on various performance measures in addition to reducing the model complexity.

Dataset and Methodology

The dataset used in this paper came from a real date palm plantation. It consists of images of dates that belong to five subcategories of Sukkari dates. They are known as Galaxy, Ruttab, Mufattal, Qishr, and Nagad. The original images were cropped to 500 by 500 pixels with RGB channels of size 8 bits each with white background. The images were then down sampled to 250 by 250 to reduce the size. Fig. 1 illustrates the five classes of images. As can be observed, the subclasses bear similar resemblance to each other. However, upon closer inspection, it can be seen that they have slightly different texture.

The dataset contains a total of 1,689 images that include the five classes of dates mentioned above. The images were not equally divided between the five classes, rather each class had roughly 400-440 images. For testing, a total of 175 images were set aside from the 1,689 images, and each class contained 35 images. The remaining images were used for training and validation with a split of 80% for training and 20% for validation, respectively. After splitting the dataset, the five CNNs mentioned in the previous section are loaded and trained. Fig. 2 illustrates the flowchart of the overall process of the collection of the images, cropping and down sampling, and the training phase of the CNNs.

The pretrained CNNs were originally trained on the ImageNet dataset [35]. For this study, only the final convolutional, classification and softmax layer were modified to produce the outputs of 5 classes. Also, the learning rate of the final layers were increased. This is discussed further in the next section. Apart from that, no other parameters of the CNNs were modified and the default values were used for simulation. The size of the input layers and the subsequent layers and their connections were also kept the same. During the training, validation, and testing phase, the images were automatically resized to fit the size of the default input layer of the pretrained networks.

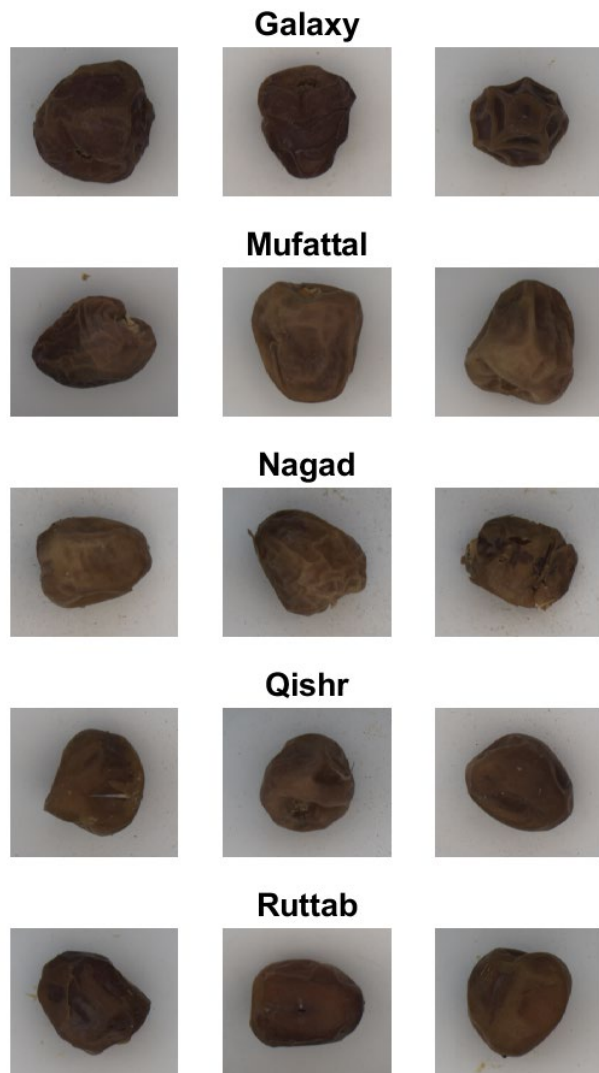


Fig. 1. Five classes of dates.

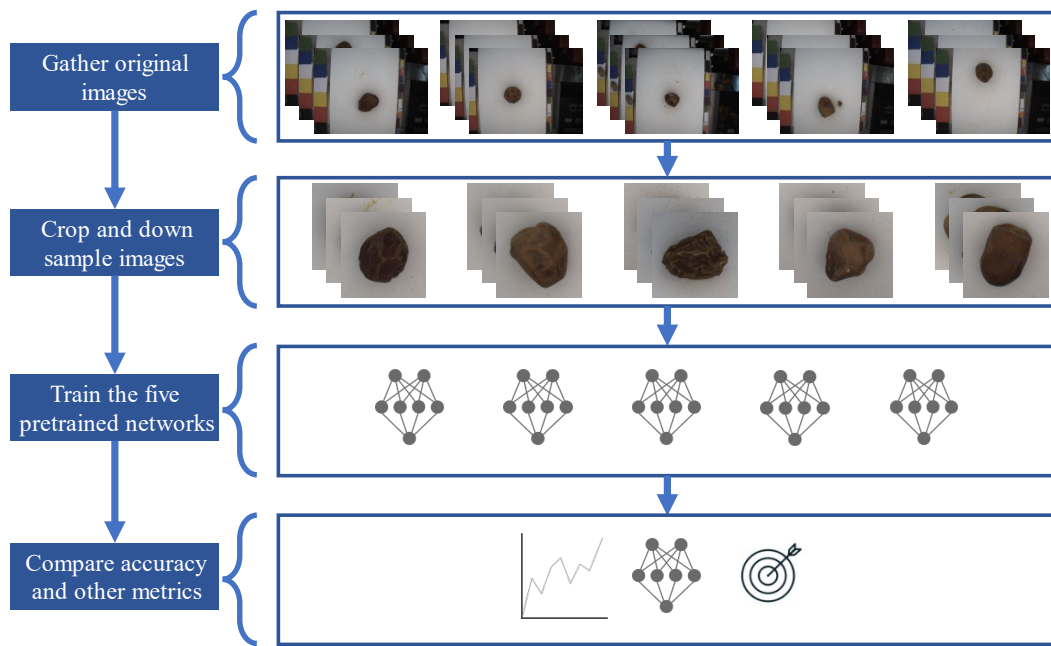


Fig. 2. Flowchart of the overall simulation.

Simulation Results

The results of the simulation provide an overview of the performances of the various networks. MATLAB 2023b along with the built-in Deep Learning Toolbox were used to train, validate, and test the networks. The networks were trained on a Lenovo IdeaPad Gaming 3 laptop. The networks were specifically trained on the GPU only. The GPU on the laptop is Nvidia GeForce RTX 4050 (6 GB). The CPU is an AMD Ryzen 7-7735HS. The RAM is 16 GB. As the networks are pretrained, the training does not need to be as extensive because the previous layers have already learned the detailed features. The epochs have been set to 10 with a batch size of 32 images. The validation frequency has been set to every two iterations. Cross-entropy loss was used with a train-test-validation split of 72-18-10, respectively. The learning rate for all layers except the last layer has been set to 0.0001. For the final layer, it has been set to 10 for both the weights and biases. For augmenting the images, random X and Y-reflections were applied. Also, random X and Y-translation has been applied varying from -30 to 30 pixels. Table 1 summarizes the parameters used for the training of the network.

Table 1. Training parameters for the CNNs.

Training Parameters	Setting
Epochs	10
Mini Batch Size	32
Total Iterations	480
Validation Frequency (Iterations)	2
Train-Val-Test Split	72-18-10
Loss Function	Cross-entropy
Overall Learning Rate	0.0001
Final Layer Weight and Bias Learning Rate	10
Image Augmentation	X-reflection
	Y-reflection
	X-translation (30 to -30 pixels)
	Y-translation (30 to -30 pixels)

Table 2 summarizes the results of the testing for all the models. The primary metric is the accuracy. However, as the task is classification, other metrics such as precision, recall and F1 score are also of great significance. The training time is also included in the table. The results on the test set indicate that SqueezeNet outperforms the other networks. The overall accuracy of SqueezeNet is 92%, with precision, recall, and F1 score of 92.67%, 92%, and 92.33%, respectively. In the second place was ShuffleNet with an accuracy of 89.14%, with precision, recall, and F1 score of 89.41%, 89.14%, and 89.28%, respectively. EfficientNet recorded the lowest accuracy at 82.86%, with precision, recall, and F1 score of 83.10%, 82.86%, and 82.98%, respectively. In terms of the training time, SqueezeNet was also the quickest, taking 9 minutes and 17 seconds to train. GoogLeNet was the second at 14 minutes and 46 seconds. EfficientNet took the longest with 34 minutes and 17 seconds.

Table 2. Summary of the results of testing and training time.

CNN	Accuracy (%)	Precision (%)	Recall (%)	F1 Score (%)	Training Time (mm:ss)
SqueezeNet	92	92.67	92	92.33	09:17
ShuffleNet	89.14	89.41	89.14	89.28	15:20
MobileNet	87.43	87.65	87.43	87.54	21:05
GoogLeNet	85.14	85.68	85.14	85.41	14:46
EfficientNet	82.86	83.10	82.86	82.98	34:17

Fig. 3 illustrates the confusion matrix for SqueezeNet in the test set. The vertical axis is the actual class. The horizontal axis is the predicted class. The diagonal elements represent the correct predictions while the off-diagonal elements represent the misclassified predictions. The outer horizontal percentages give the precision for each class, whereas the vertical percentages give the recall for each class.

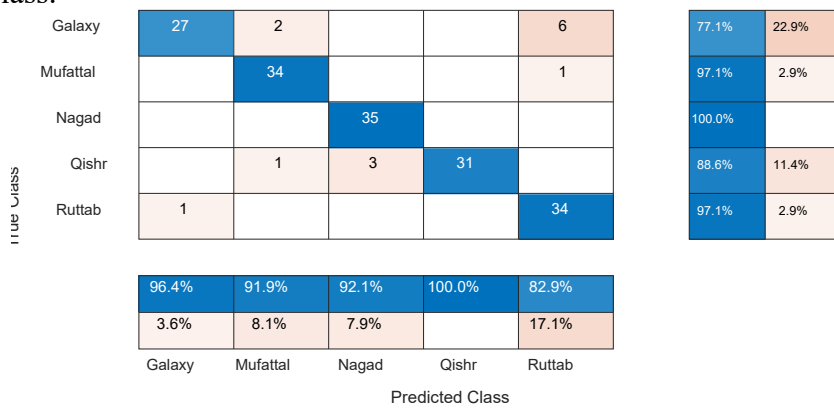


Fig. 3. Confusion matrix for SqueezeNet in the Test set.

Fig. 4 illustrates how the accuracy of the SqueezeNet evolved as the training and validation iterations progress. The number of iterations for the 10 epochs is 480 (for batch size of 32 images). As can be seen, the model converges quickly as it is a pretrained network. Fig. 5 illustrates the loss vs. the iterations. The loss will decrease as the iterations progress. Accuracy and loss are inversely related. Therefore, as accuracy increases, loss decreases.

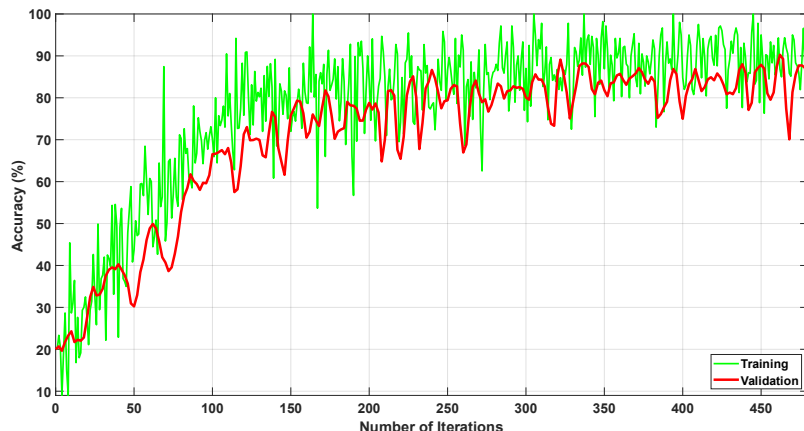


Fig. 4. Accuracy of SqueezeNet vs. the number of iterations.

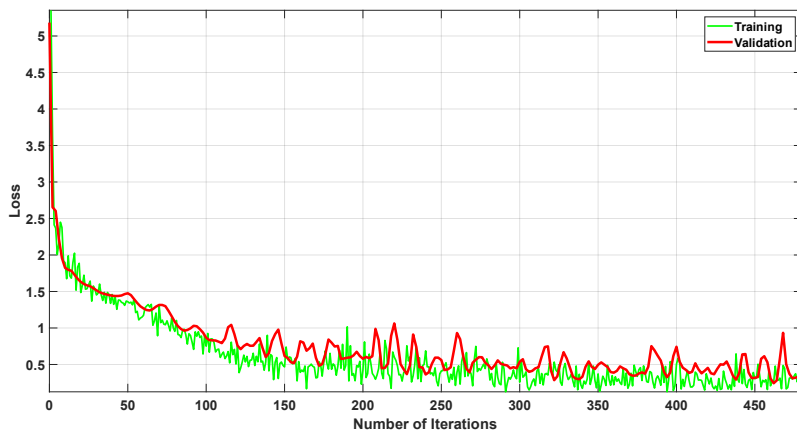


Fig. 5. Loss of SqueezeNet vs. the number of iterations.

Conclusion

Fruit classification is an important area of research for industries as they proceed towards automating the classification process. Various researches have been published in this area using various fruit datasets. However, most studies either include a single model or train a model from scratch. Comparisons between various papers on different models are usually not homogeneous in nature as they are trained on different datasets and/or different hardware which can significantly affect the results. In this study, we used transfer learning on five popular pretrained CNNs to classify five subcategories of Sukkari dates. We used the same dataset of 1,689 regular RGB images and run the simulation on the same hardware for an even comparison. Comparing the results of the training for the CNNs, it is observed that SqueezeNet performs the best in terms of classification accuracy and the training time. The overall testing accuracy of SqueezeNet is 92% and took 9 minutes and 17 seconds to train on Nvidia GeForce RTX 4050 (6 GB) GPU. The second highest accuracy recorded was the ShuffleNet with a testing accuracy of 89.14%, whereas the second fastest in terms of training time was the GoogLeNet with a training time of 14 minutes and 46 seconds. For the future, we plan to perform further studies on how to improve the accuracy of these models and include other types of date fruits.

References

- [1] I. Goodfellow, Y. Bengio, and A. Courville, Deep Learning. MIT Press, 2016.
- [2] B. Coppin, Artificial intelligence illuminated. Jones & Bartlett Learning, 2004.

- [3] M. I. Jordan and T. M. Mitchell, "Machine learning: Trends, perspectives, and prospects," *Science* (1979), vol. 349, no. 6245, pp. 255–260, 2015. <https://doi.org/10.1126/science.aaa8415>
- [4] Y. LeCun, Y. Bengio, and G. Hinton, "Deep learning," *Nature*, vol. 521, no. 7553, pp. 436–444, 2015. <https://doi.org/10.1038/nature14539>
- [5] E. Rachmawati, I. Supriana, and M. L. Khodra, "Toward a new approach in fruit recognition using hybrid RGBD features and fruit hierarchy property," in 2017 4th International Conference on Electrical Engineering, Computer Science and Informatics (EECSI), 2017, pp. 1–6. <https://doi.org/10.1109/EECSI.2017.8239110>
- [6] Y. Tao and J. Zhou, "Automatic apple recognition based on the fusion of color and 3D feature for robotic fruit picking," *Comput Electron Agric*, vol. 142, pp. 388–396, 2017. <https://doi.org/10.1016/j.compag.2017.09.019>
- [7] J. Naranjo-Torres, M. Mora, R. Hernández-Garcia, R. J. Barrientos, C. Fredes, and A. Valenzuela, "A review of convolutional neural network applied to fruit image processing," *Applied Sciences*, vol. 10, no. 10, p. 3443, 2020. <https://doi.org/10.3390/app10103443>
- [8] Y. LeCun, L. Bottou, Y. Bengio, and P. Haffner, "Gradient-based learning applied to document recognition," *Proceedings of the IEEE*, vol. 86, no. 11, pp. 2278–2324, 1998. <https://doi.org/10.1109/5.726791>
- [9] Y. Guo and others, "Deep learning for visual understanding." *Neurocomput*, 2017.
- [10] M. D. Zeiler and R. Fergus, "Visualizing and understanding convolutional networks," in *Computer Vision–ECCV 2014: 13th European Conference, Zurich, Switzerland, September 6–12, 2014, Proceedings, Part I* 13, 2014, pp. 818–833. https://doi.org/10.1007/978-3-319-10590-1_53
- [11] R. Singh and S. Balasundaram, "Application of extreme learning machine method for time series analysis," *International Journal of Computer and Information Engineering*, vol. 1, no. 11, pp. 3407–3413, 2007.
- [12] A. Krizhevsky, I. Sutskever, and G. E. Hinton, "Imagenet classification with deep convolutional neural networks," *Adv Neural Inf Process Syst*, vol. 25, 2012.
- [13] O. Russakovsky et al., "Imagenet large scale visual recognition challenge," *Int J Comput Vis*, vol. 115, pp. 211–252, 2015. <https://doi.org/10.1007/s11263-015-0816-y>
- [14] Y. Lu, "Food image recognition by using convolutional neural networks (cnns)," *arXiv preprint arXiv:1612.00983*, 2016.
- [15] Y.-D. Zhang et al., "Image based fruit category classification by 13-layer deep convolutional neural network and data augmentation," *Multimed Tools Appl*, vol. 78, pp. 3613–3632, 2019. <https://doi.org/10.1007/s11042-017-5243-3>
- [16] J. Steinbrener, K. Posch, and R. Leitner, "Hyperspectral fruit and vegetable classification using convolutional neural networks," *Comput Electron Agric*, vol. 162, pp. 364–372, 2019. <https://doi.org/10.1016/j.compag.2019.04.019>
- [17] S. W. Chen et al., "Counting apples and oranges with deep learning: A data-driven approach," *IEEE Robot Autom Lett*, vol. 2, no. 2, pp. 781–788, 2017. <https://doi.org/10.1109/LRA.2017.2651944>
- [18] S. Bargoti and J. Underwood, "Deep fruit detection in orchards," in 2017 IEEE international conference on robotics and automation (ICRA), 2017, pp. 3626–3633. <https://doi.org/10.1109/ICRA.2017.7989417>
- [19] K. Albarak, Y. Gulzar, Y. Hamid, A. Mehmood, and A. B. Soomro, "A deep learning-based model for date fruit classification," *Sustainability*, vol. 14, no. 10, p. 6339, 2022. <https://doi.org/10.3390/su14106339>
- [20] M. Faisal, F. Albogamy, H. Elgibreen, M. Algabri, and F. A. Alqershi, "Deep learning and computer vision for estimating date fruits type, maturity level, and weight," *IEEE Access*, vol. 8, pp. 206770–206782, 2020. <https://doi.org/10.1109/ACCESS.2020.3037948>

- [21] A. Alsirhani, M. H. Siddiqi, A. M. Mostafa, M. Ezz, and A. A. Mahmoud, “A novel classification model of date fruit dataset using deep transfer learning,” *Electronics (Basel)*, vol. 12, no. 3, p. 665, 2023. <https://doi.org/10.3390/electronics12030665>
- [22] D. Chaudhari and S. Waghmare, “Machine vision based fruit classification and grading—a review,” in *ICCCCE 2021: Proceedings of the 4th International Conference on Communications and Cyber Physical Engineering*, 2022, pp. 775–781. https://doi.org/10.1007/978-981-16-7985-8_81
- [23] T. Shoshan, A. Bechar, Y. Cohen, A. Sadowsky, and S. Berman, “Segmentation and motion parameter estimation for robotic Medjoul-date thinning,” *Precis Agric*, vol. 23, no. 2, pp. 514–537, 2022. <https://doi.org/10.1007/s11119-021-09847-2>
- [24] K. M. Alresheedi, S. Aladhadh, R. U. Khan, and A. M. Qamar, “Dates Fruit Recognition: From Classical Fusion to Deep Learning.,” *Computer Systems Science & Engineering*, vol. 40, no. 1, 2022. <https://doi.org/10.32604/csse.2022.017931>
- [25] A. Magsi, J. A. Mahar, S. H. Danwar, and others, “Date fruit recognition using feature extraction techniques and deep convolutional neural network,” *Indian J Sci Technol*, vol. 12, no. 32, pp. 1–12, 2019. <https://doi.org/10.17485/ijst/2019/v12i32/146441>
- [26] A. Nasiri, A. Taheri-Garavand, and Y.-D. Zhang, “Image-based deep learning automated sorting of date fruit,” *Postharvest Biol Technol*, vol. 153, pp. 133–141, 2019. <https://doi.org/10.1016/j.postharvbio.2019.04.003>
- [27] B. D. Pérez-Pérez, J. P. Garcia Vazquez, and R. Salomón-Torres, “Evaluation of convolutional neural networks’ hyperparameters with transfer learning to determine sorting of ripe medjool dates,” *Agriculture*, vol. 11, no. 2, p. 115, 2021. <https://doi.org/10.3390/agriculture11020115>
- [28] H. Altaheri, M. Alsulaiman, and G. Muhammad, “Date fruit classification for robotic harvesting in a natural environment using deep learning,” *IEEE Access*, vol. 7, pp. 117115–117133, 2019. <https://doi.org/10.1109/ACCESS.2019.2936536>
- [29] M. F. Nadhif and S. Dwiasnati, “Classification of Date Fruit Types Using CNN Algorithm Based on Type,” *MALCOM: Indonesian Journal of Machine Learning and Computer Science*, vol. 3, no. 1, pp. 36–42, 2023. <https://doi.org/10.57152/malcom.v3i1.724>
- [30] F. N. Iandola, S. Han, M. W. Moskewicz, K. Ashraf, W. J. Dally, and K. Keutzer, “SqueezeNet: AlexNet-level accuracy with 50x fewer parameters and< 0.5 MB model size,” *arXiv preprint arXiv:1602.07360*, 2016.
- [31] C. Szegedy et al., “Going deeper with convolutions,” in *Proceedings of the IEEE conference on computer vision and pattern recognition*, 2015, pp. 1–9. <https://doi.org/10.1109/CVPR.2015.7298594>
- [32] M. Tan and Q. Le, “Efficientnet: Rethinking model scaling for convolutional neural networks,” in *International conference on machine learning*, 2019, pp. 6105–6114.
- [33] X. Zhang, X. Zhou, M. Lin, and J. Sun, “Shufflenet: An extremely efficient convolutional neural network for mobile devices,” in *Proceedings of the IEEE conference on computer vision and pattern recognition*, 2018, pp. 6848–6856. <https://doi.org/10.1109/CVPR.2018.00716>
- [34] M. Sandler, A. Howard, M. Zhu, A. Zhmoginov, and L.-C. Chen, “Mobilenetv2: Inverted residuals and linear bottlenecks,” in *Proceedings of the IEEE conference on computer vision and pattern recognition*, 2018, pp. 4510–4520. <https://doi.org/10.1109/CVPR.2018.00474>
- [35] “Pretrained Deep Neural Networks.” Accessed: Feb. 25, 2024. [Online]. Available: <https://www.mathworks.com/help/deeplearning/ug/pretrained-convolutional-neural-networks.html>

Bidding optimization for hydrogen production from an electrolyzer

Nouf M. ALMUTAIRY^{1,a*}, Ali T. ALAWAMI^{2,b}

¹Department of Electrical Engineering, King Fahd University of Petroleum and Minerals , Saudi Arabia

²Department of Electrical Engineering, King Fahd University of Petroleum and Minerals , Saudi Arabia

^a nouf459@gmail.com, ^b aliaawami@kfupm.edu.sa

Keywords: Hydrogen Production, Electrolyzer, Bidding Optimization, Sustainability

Abstract. This paper presents a comprehensive study on the bidding optimization for hydrogen production from an electrolyzer, focusing on a single day comprising 24 hours. With the rising demand for clean energy sources, the research aims to optimize profitability and efficiency in hydrogen production. The primary objective is to maximize profit while ensuring the fulfillment of the targeted hydrogen production by the end of the day. The optimization formulation incorporates electrolyzer maintenance, electricity, and water consumption costs. The model considered two cases with different electrolyzer efficiency values to optimize power usage, allowing for a comprehensive analysis of hydrogen production optimization. Ramping limits are imposed to maintain power system stability and reliability, preventing sudden fluctuations. By solving the formulated equations and considering factors such as energy and water prices, the research findings demonstrate the effectiveness of the bidding optimization approach in optimizing resource utilization and maximizing profit. Notably, the model successfully achieves the targeted hydrogen production by the end of the day while maximizing profit. This research contributes valuable insights into the bidding optimization process for hydrogen production, highlighting the potential for economic and sustainable hydrogen generation from electrolyzers.

Introduction

Climate change necessitates a shift to clean, sustainable energy sources to mitigate its environmental impact. Hydrogen, as a clean and efficient energy carrier, has garnered attention in the energy industry. However, traditional hydrogen production from fossil fuels without carbon capture contributes to greenhouse gas emissions. The shift towards hydrogen produced from fossil fuels with carbon capture, utilization, and storage (CCUS) offers a viable alternative, considering the high carbon production from natural gas and coal sources. This transition is crucial in combating climate change. Hydrogen can contribute to a resilient and sustainable energy future by utilizing alternative and cleaner production methods and diversifying its sources. Additionally, hydrogen can be utilized in new applications and complement electricity use, enhancing its potential. Today, more countries invest in hydrogen technologies since they recognize their importance for the future of energy. Austria announced that as part of the Austrian Climate and Energy Strategy for 2030, a hydrogen strategy based on renewable electricity would be developed. Even in Saudi Arabia, Saudi Aramco and Air Products announced their plans to construct Saudi Arabia's first hydrogen refueling station. Thus, this paper focuses on the bidding optimization for hydrogen production from an electrolyzer. [1]

To produce hydrogen as an energy carrier, an electrolyzer is required. This device utilizes electricity to split water into hydrogen and oxygen through an electrochemical process called electrolysis. The electrolyzer connects to an external circuit to provide the required electric current for electrolysis. This process makes water break down into its constituent elements of hydrogen and oxygen gases. The electrolyzer consists of an anode and a cathode. At the anode, a process

called oxidation takes place. Water molecules near the anode lose electrons and form oxygen gas (O_2) and positively charged hydrogen ions (H^+). The cathode attracts hydrogen ions (H^+) from the electrolyte. At the cathode, the hydrogen ions gain electrons from the external circuit and combine to form hydrogen gas (H_2) in a reduction process. [2]

Bidding optimization is identifying the optimal bidding strategy in energy markets to maximize profits. Optimizing bidding for hydrogen production from an electrolyzer is crucial for a greener future and for addressing carbon emissions. Developing bidding strategies considering market prices for hydrogen, electricity, and electrolyzer costs can maximize revenue and profitability as hydrogen production gains traction. Hydrogen plants play a vital role in the clean energy sector, making bid optimization for electrolyzer-based hydrogen production a focal point. With the growing interest in hydrogen as a sustainable energy alternative, bid optimization can significantly contribute to the global transition toward a greener future [3].

Several studies have focused on hydrogen production from electrolyzer. Study [4] provides an overview of water electrolysis-based systems for hydrogen production, particularly those utilizing hybrid/solar/wind energy sources. The article emphasizes the importance of hydrogen as a clean energy carrier and discusses system configurations, electrolyzer types, catalysts, and energy sources. Study [5] delves into the role of catalysts in enhancing the efficiency and performance of electrolyzers for hydrogen production, exploring different types of catalysts and recent advancements in catalyst design. In [6], the focus is on a membrane-based seawater electrolyzer that directly splits seawater into hydrogen and oxygen using a proton-conducting membrane.

Recent studies have focused on optimization for hydrogen production from electrolyzer. In a study [7], this paper discusses optimizing a high-temperature electrolysis system for hydrogen production, considering the degradation of cell materials. It explores the factors causing degradation and investigates the influence of operating conditions on the degradation process. The paper also proposes operation strategies to balance hydrogen production efficiency and the lifespan of the stack. In the study [8], this paper's primary emphasis is modeling and enhancing an alkaline water electrolysis system employed for hydrogen generation. The study extensively covers the design and operational aspects of the electrolyzer, along with an exploration of diverse optimization methodologies. This research aims to improve hydrogen production efficiency and cost-effectiveness through electrolysis.

Optimizing bidding strategies is crucial for maximizing profits in electrolyzer-based hydrogen production, and it has gained significant research attention. In the study [9], an optimal bidding strategy is developed for hydrogen production from electrolyzers in renewable energy systems. The proposed mathematical model considers uncertainties in renewable energy generation and electricity prices to maximize profit. The results demonstrate the effectiveness of the strategy in maximizing profit. In [10], the potential participation of virtual power plants (VPPs) with hydrogen energy storage in multi-energy markets is discussed. The study highlights the role of hydrogen storage in VPPs and presents a two-layer optimization model considering resource complementarity and external market bidding strategies.

In addition to previous studies on hydrogen production from electrolyzers, it is essential to understand the motivation behind this research. Electrolyzers are electric loads that require electric energy to produce hydrogen (H_2). However, hydrogen production plants' storage capacity allows them to schedule their operations based on electricity prices. The lack of an optimization framework integrating bidding prices presents a research gap in hydrogen production from electrolyzers. This aspect is crucial in optimizing the operational scheduling of electrolyzers. Therefore, the objective is to integrate bidding prices into the optimization process and identify the most effective strategy for achieving maximum profit while meeting the targeted hydrogen production quota. The study will utilize the GAMS software for accurate and reliable results.

Methodology

A. Objective function

The study utilizes a bidding optimization model to maximize the profit from hydrogen production. This bidding optimization model is achieved through (1), which explains that the optimization model will maximize the profit. In this equation, F represents the profit, R represents the revenue from hydrogen production, and C represents the cost of the electrolyzer needed to produce hydrogen.

$$\max F = R - C \quad (1)$$

The analysis assumes that the demand for hydrogen is already established, which allows for revenue calculation using (2). As reference [11] indicates, the selling price has been set at \$11 per kilogram. The study target for hydrogen production is 1000 kilograms, resulting in a total revenue of 11000 dollars.

$$R = \text{selling price} * \text{quantity of hydrogen target} \quad (2)$$

Eq. 3 represents the cost function for the electrolyzer. In this equation, C_M represents the maintenance cost for the electrolyzer, as derived from the reference paper [10]. According to formula 4, C_M can be calculated as 2% of the electrolyzer capital cost.

Eq. 5 to 6 illustrate the cost functions for electricity and water consumption, respectively. These equations quantify the expenses associated with utilizing an electrolyzer to produce hydrogen.

$$C = C_E + C_W + C_M \quad (3)$$

$$C_M = 2\% \times \text{capital cost} \quad (4)$$

$$C_M = 2\% \times 1765 \$/\text{kW} = 35.3 \$/\text{kW}$$

Eq. 5 defines the cost function for electricity consumption. In this equation, $P(t)$ represents the decision variable denoting the electricity required at each time interval, covering the 24-hour duration of the study. The variable Energy price(t) represents the corresponding energy price for each specific time interval. The data used for the energy price, expressed in \$/kWh, was sourced from Norway on December 5, 2023 [12].

$$C_E = \sum_{t=1}^{24} P(t) * \text{energy price}(t) \quad (5)$$

Eq. 6 defines the cost function for water consumption. In this equation, $W(t)$ represents the decision variable indicating the water required at each time interval within the 24-hour study period. The variable water price(t) represents the corresponding water price for each specific time interval. The water price data, equal to 0.00669 \$/kg, is sourced from Norway [13].

$$C_W = \sum_{t=1}^{24} W(t) * \text{water price}(t) \quad (6)$$

B. Equality constraints:

1. Constraint for Electricity Consumption:

The model considers two cases for electricity consumption related to the efficiency of the electrolyzer. The electrolyzer efficiency is set at 70% in the first case, as referenced in [9]. Eq. 7 establishes the relationship between the power input to the electrolyzer and the resulting hydrogen production. The decision variable $H(t)$ represents the hydrogen produced at each time interval. In the second case, the efficiency is assumed to be 80%. Analyzing these two cases allows the model

to explore the impact of different electrolyzer efficiencies on electricity consumption and hydrogen production.

$$P(t) = \frac{50 * H(t)}{\text{efficiency of electrolyzer}} \quad (7)$$

2. Constraint for Water Consumption:

The model includes a constraint on water consumption, which defines the relation between the water consumption and hydrogen production decision variables, shown in Eq.8.

Additionally, the water needed in kg to produce 1 kg of hydrogen is 9 kg [15].

$$W(t) = 9 * H(t) \quad (8)$$

3. Constraint for the hydrogen tank:

Eq. 9 represents a constraint that governs the hydrogen storage in the tank at a specific time t. It ensures that the amount of hydrogen stored in the tank at time t is determined by the sum of the hydrogen storage in the tank at the previous time and the amount of hydrogen produced during time t. This constraint captures the dynamics of the hydrogen storage system, where the current storage level depends on the previous storage level and the hydrogen production during the current period.

$$\text{TankStore}(t) = \text{TankStore}(t - 1) + H(t) \quad (9)$$

C. Inequality constraints:

1. Maximum and Minimum Consumption:

The proposed model incorporates certain constraints to ensure electricity and water consumption remain within certain limits. Specifically, the model uses inequality constraints to set the upper and lower limits on electricity consumption as shown in Eq. 10 and water consumption as shown in Eq. 11. The model's maximum allowable electricity consumption (P_{\max}) is 6000 kWh, while the minimum allowable consumption (P_{\min}) is zero. Similarly, the maximum allowable water consumption (W_{\max}) is assumed to be 3000 kg, while the minimum allowable consumption (W_{\min}) is also zero.

$$0 \leq P(t) \leq 6000 \quad (10)$$

$$0 \leq W(t) \leq 3000 \quad (11)$$

2. Constraint for the hydrogen target:

Eq. 12 represents a target constraint that ensures the cumulative sum of $H(t)$ over all periods is greater than or equal to the target hydrogen value. This constraint ensures that the total hydrogen produced throughout all periods meets or exceeds the desired target value.

$$\text{Target} \leq \sum_{t=1}^{24} H(t) \quad (12)$$

3. Ramping constraints:

Ramping limits play a crucial role in maintaining power system stability and reliability. These limits constrain the rate of change of electricity, hydrogen production, and water consumption rates, preventing sudden and excessive fluctuations. Ramping limits help optimize resource utilization and mitigate the risk of disruptions or imbalances by ensuring a gradual and controlled adjustment of these variables over consecutive periods. The constraints from Eq. 13 to 15 define allowable changes in electricity consumption, hydrogen production rate, and water consumption

rate between periods. They set bounds on the differences between current and previous values, preventing rapid increases or decreases. Enforcing these ramping limits supports grid stability and enhances overall system performance.

$$-355.5 \leq P(t) - P(t-1) \leq 355.5 \quad (13)$$

$$-25 \leq H(t) - H(t-1) \leq 25 \quad (14)$$

$$-100 \leq W(t) - W(t-1) \leq 100 \quad (15)$$

Results and discussion

The bidding optimization model for hydrogen production from the electrolyzer was solved using the General Algebraic Modeling System (GAMS), with the solver of choice being a linear Programming (LP) solver. This approach efficiently optimized the model, determining optimal values for decision variables and constraints. The results provided insights into maximizing profit from hydrogen production. For each period, optimal values for decision variables, including electricity consumption, water consumption, and hydrogen production, were determined. To optimize power usage, the model considered two cases with different electrolyzer efficiency values.

A. Case 1: Electrolyzer efficiency equals 70%.

In this scenario, the electricity consumption formula considers an electrolyzer efficiency of 70%. Based on Table 1, the objective function aims to maximize profit and minimize total cost. Table 2 displays the results for $H(t)$, $W(t)$, $P(t)$, and Tank Storage(t), satisfying all constraints. The table confirms that the hydrogen target is achieved in the hydrogen tank at $t=24$. The results demonstrate the successful consideration of the dynamics of the hydrogen storage system in the bidding optimization model. Eq. 10 ensures that the amount of hydrogen stored in the tank at each time $TankStore(t)$ is accurately calculated based on the previous storage level $TankStore(t-1)$ and the current hydrogen production ($H(t)$). This enables informed decision-making for optimal hydrogen production scheduling.

Table 1. Output parameters in dollars for case 1.

Profit	Revenue	Total cost	C _E	C _w	C _M
\$1497.799	\$11000	\$9502.201	\$9406.691	\$60.210	\$35.500

The model successfully satisfied the inequality constraints (Eq. 11-12) on electricity and water consumption, ensuring they remained within the specified limits. Additionally, the optimized hydrogen production ($H(t)$) adhered to the ramping constraint (Eq. 15), maintaining a controlled rate of change between consecutive periods. Figures 1 and 2, corresponding to Table 2, illustrate the 24-hour trends in electricity usage and hydrogen tank storage. Figure 1 shows that $P(t)$ steadily increases as time progresses and then slightly decreases due to the increase in energy prices. Subsequently, hydrogen production increases, leading to simultaneous increases in $P(t)$ and $W(t)$. The initial hydrogen production is recorded as 4.977 kg, reaching a maximum value of 77.117 kg after 24 hours.

Table 2. Hourly output parameters for case 1.

Time [hr]	1	2	3	4	5	6	7	8	9	10	11	12
H(t)	4.98	9.95	14.93	19.91	24.89	29.8 6	34.84	39.82	44.79	49.77	52.23	47.26
Tank storage (t)	4.98 3	14.9 3	29.86	49.77	74.66	104. 5	139.3 6	179.1 7	223.97	273.7 4	325.97	373.2 2
P(t)	355.5 0	711. 00	1066. 50	1422. 00	1777. 50	2133 .00	2488. 50	2844. 00	3199.5 0	3555. 00	3730.8 3	3375. 33
W(t)	44.79 9	89.5 8	134.3 8	179.1 7	223.9 7	268. 76	313.5 5	358.3 4	403.14	447.9 3	470.08	425.2 9
Time [hr]	13	14	15	16	17	18	19	20	21	22	23	24
H(t)	42.28 0	37.3 0	32.32	37.30	42.28	47.2 6	52.23	57.21	62.19	67.16	72.14	77.12
Tank storage (t)	415.5 0	452. 80	485.1 2	522.4 2	564.7 0	611. 96	664.1 9	721.4 0	783.58	850.7 4	922.88	1000. 000
P(t)	3019. 83	2664 .33	2308. 83	2664. 33	3019. 83	3375 .33	3730. 83	4086. 33	4441.8 3	4797. 33	5152.8 3	5508. 33
W(t)	380.4 9	335. 71	290.9 1	335.7 1	380.5 0	425. 29	470.0 8	514.8 8	559.67	604.4 6	649.26	694.0 5

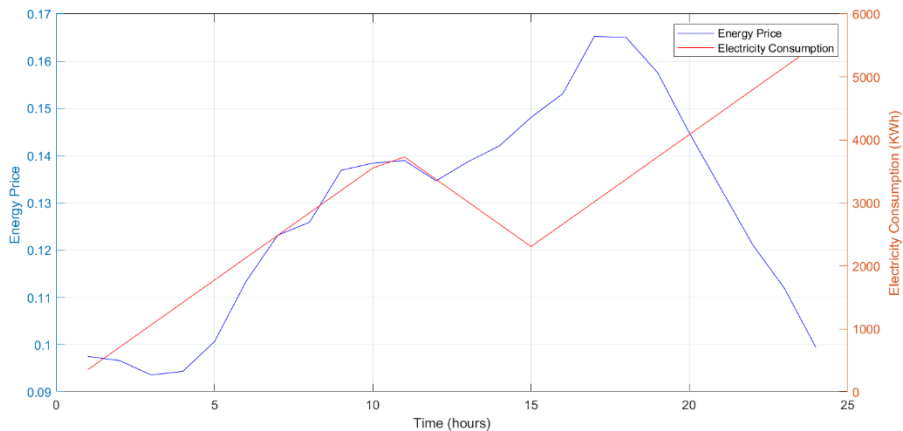


Figure 1. Electricity consumption and energy price for case 1.

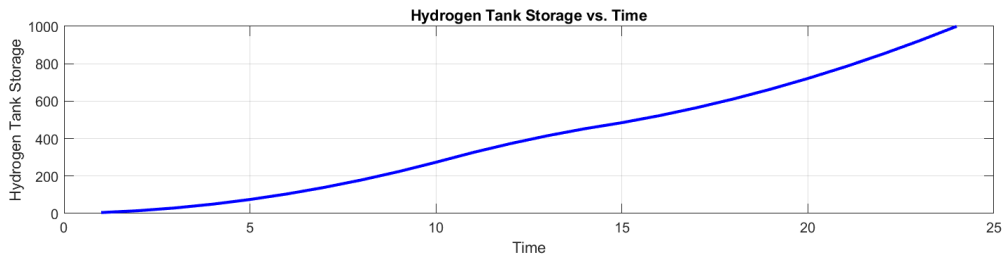


Figure 2. Hydrogen Tank Storage for case 1.

B. Case two : electrolyzer efficiency equals 80%.

In this scenario, the electricity consumption equation considers an electrolyzer efficiency of 80%. According to the results presented in Table 3, the objective function achieved in this case,

considering both maximum profit and minimum total cost, shows improvement compared to case 1. The profit is higher, while the total cost of the electrolyzer is reduced.

Table 3. Output parameters in dollars for case 2.

Profit	Revenue	Total cost	C _E	C _w	C _M
\$ 2743.899	\$11000	\$ 8256.101	\$ 8160.591	\$ 60.210	\$35.500

The results for H(t), W(t), P(t), and Tank Storage(t) are shown in Table 4. All the constraints were satisfied for all the variables. Fig. 3 visualizes the trends in electricity consumption with energy prices over time. As depicted in the figure, P(t) steadily increases as time progresses until reaching a stable point. Subsequently, it decreases due to the rise in energy prices. However, when the energy prices start decreasing, P(t) steadily increases again. In this scenario, hydrogen production ranges between 5.688 kg and 78.043 kg. Notably, the hydrogen production range is more significant than in case 1, highlighting the improved flexibility and variability in hydrogen production achieved through the optimization framework.

Table 4. Hourly output parameters for case 2.

Time [hr]	1	2	3	4	5	6	7	8	9	10	11	12
H(t)	5.69	11.38	17.0 6	22.75	28.44	34.13	39.82	45.50	51.19	55.29	49.60	43.92
Tank storage (t)	5.69	17.06	34.1 3	56.88	85.32	119.4 5	159.2 6	204.7 7	255.96	311.2 5	360.85	404.7 7
P(t)	355.5 0	711.0 0	1066. .50	1422. .00	1777. .50	2133. .00	2488. .50	2844. .00	3199.5 0	3455. 67	3100.1 7	2744. 67
W(t)	51.19	102.3 8	153. 58	204.7 7	255.9 6	307.1 5	358.3 4	409.5 4	460.73	497.6 2	446.42	395.2 3
Time [hr]	13	14	15	16	17	18	19	20	21	22	23	24
H(t)	38.23	32.54	26.8 5	32.54	38.23	43.92	49.60	55.29	60.98	66.67	72.36	78.04
Tank storage (t)	442.9 9	475.5 3	502. 38	534.9 2	573.1 5	617.0 6	666.6 7	721.9 6	782.94	849.6 0	921.96	1000. 00
P(t)	2389. 17	2033. 67	1678 .17	2033. 67	2389. 17	2744. 67	3100. 17	3455. 67	3811.1 7	4166. 67	4522.1 7	4877. 67
W(t)	344.0 4	292.8 5	241. 66	292.8 5	344.0 4	395.2 3	446.4 2	497.6 2	548.81	600.0 0	651.19	702.3 8

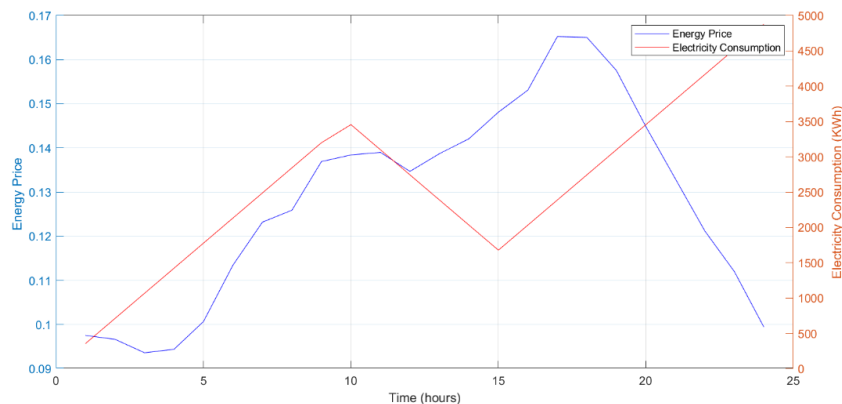


Figure 3: Electricity Consumption and Energy price for case 2.

Conclusion

In conclusion, this research paper has presented a comprehensive study on optimizing the bidding process for hydrogen production through an electrolyzer. The primary objective was to develop an optimization framework that maximizes profitability while meeting the targeted hydrogen production quota. Two cases were considered: Case 1, which incorporated an electrolyzer efficiency of 70% in the electricity consumption equation, and Case 2, where electrolyzer efficiency was 80%. For Case 1, hydrogen production started at 4.977 kg and reached 77.117kg after 24 hours. However, Case 2, which considered 80% electrolyzer efficiency, yielded improved outcomes regarding maximum profit and minimum total cost. Hydrogen production ranged from 5.688 kg to 78.043 kg., with higher profitability achieved. These results emphasize the importance of considering various factors, such as electrolyzer efficiency, in the bidding optimization process. Overall, this research emphasizes the importance of bidding optimization in hydrogen production, offering valuable insights for the energy industry's transition towards sustainable and economically viable hydrogen generation.

References

- [1] IEA. (2019). The Future of Hydrogen, Report Prepared by the IEA for the G20, Japan. Seizing Today's Opportunities.
- [2] What is an electrolyzer and what is it used for? | Accelera. Available at: <https://www.accelerazero.com/news/what-is-an-electrolyzer-and-what-is-it-used-for> (Accessed: 10 November 2023).
- [3] Kim, M., & Kim, J. (2016). Optimization model for the design and analysis of an integrated renewable hydrogen supply (IRHS) system: Application to Korea's hydrogen economy. International Journal of Hydrogen Energy, 41(38), 16613-16626. <https://doi.org/10.1016/j.ijhydene.2016.07.079>
- [4] Nasser, M., Megahed, T. F., Ookawara, S., & Hassan, H. (2022). A review of water electrolysis-based systems for hydrogen production using hybrid/solar/wind energy systems. Environmental Science and Pollution Research, 29(58), 86994-87018. <https://doi.org/10.1007/s11356-022-23323-y>
- [5] Wang, S., Lu, A., & Zhong, C. J. (2021). Hydrogen production from water electrolysis: role of catalysts. Nano Convergence, 8, 1-23. <https://doi.org/10.1186/s40580-021-00254-x>
- [6] Xie, H., Zhao, Z., Liu, T., Wu, Y., Lan, C., Jiang, W., ... & Shao, Z. (2022). A membrane-based seawater electrolyser for hydrogen generation. Nature, 612(7941), 673-678. <https://doi.org/10.1038/s41586-022-05379-5>
- [7] Yuan, J., Li, Z., Yuan, B., Xiao, G., Li, T., & Wang, J. Q. (2023). Optimization of High-Temperature Electrolysis System for Hydrogen Production Considering High-Temperature Degradation. Energies, 16(6), 2616. <https://doi.org/10.3390/en16062616>
- [8] K. Stewart et al., "Modeling and Optimization of an Alkaline Water Electrolysis for Hydrogen Production," 2021 IEEE Green Energy and Smart Systems Conference (IGESSC), Long Beach, CA, USA, 2021, pp. 1-6. <https://doi.org/10.1109/IGESSC53124.2021.9618679>
- [9] Morton, E. M., Deetjen, T. A., & Goodarzi, S. (2023). Optimizing hydrogen production capacity and day ahead market bidding for a wind farm in Texas. International Journal of Hydrogen Energy, 48(46), 17420-17433. <https://doi.org/10.1016/j.ijhydene.2022.12.354>
- [10] Zhang, W., Shen, Y., Wang, X., Li, M., Ren, W., Xu, X., & Zhang, Y. Research on multi-market strategies for virtual power plants with hydrogen energy storage. Frontiers in Energy Research, 11, 1260251. <https://doi.org/10.3389/fenrg.2023.1260251>

- [11]Economics SGH2 Energy. Available at : <https://www.sgh2energy.com/economics> (Accessed: 05 December).
- [12]Market data | Nord Pool. Available at: <https://www.nordpoolgroup.com/en/Market-data1/Dayahead/Area-Prices/de-lu/hourly/?view=table> (Accessed: 05 December 2023).
- [13] Salas, E.B. (2023) Europe: Tap water prices in select cities , Statista. Available at: <https://www.statista.com/statistics/1232847/tap-water-prices-in-selected-european-cities/> (Accessed: 5 December 2023).
- [14] KURRER, C. M. (2020). The potential of hydrogen for decarbonising steel production.
- [15] Saulnier, R., Minnich, K., & Sturgess, P. K. (2020). Water for the hydrogen economy

Li-ion batteries life cycle from electric vehicles to energy storage

Muhammad RASHID^{1,a*}, Muhammad SHEIKH^{1,b} and Sheikh REHMAN^{3,c}

¹WMG, The University of Warwick, Coventry, UK

²School of Computing, Engineering and Digital Technologies. Teesside University,
Middlesborough, UK

^aR.Muhammad.1@warwick.ac.uk, ^bmuhammad.sheikh@warwick.ac.uk,
^cS.Rehman@tees.ac.uk

Keywords: Li-ion Battery, State of Health (SOH), Retired Batteries, 2nd Life Application, Energy Storage Systems (ESS)

Abstract. Vehicle electrification is an emerging solution to reduce fossil fuel dependence and the environmental pollution caused by automobile emissions. Electric vehicles (EVs) are powered by Li-ion batteries which degrade with use and time, and once their state of health (SOH, ratio of current capacity to the initial capacity) reaches 80% they retire from the EVs and need a replacement. In this study, battery degradation behaviour has been investigated and demonstrated under different electrical and thermal loading conditions. A different rate of cell degradation has been observed with different environmental and electrical loading conditions. The rate of degradation of the cells is higher at low temperatures and at high current charging conditions. Additionally, it has been demonstrated that the temperature of the cells within a battery module is different across the 6S2P battery module which would be significantly higher in the case of a bigger battery module. Hence for the potential second-life applications of the retired electric vehicle batteries, knowing the correct cell SOH is highly essential to grouping them which will lead to optimized use of this battery in 2nd life applications.

Introduction

Government and policymakers are continuously promoting vehicle electrification to reduce fossil fuel dependency and minimize carbon emissions [1]. Li-ion batteries are the key contender to power EVs and HEVs (hybrid electric vehicles) due to their high gravimetric and volumetric energy density. However, the bottleneck with LIB is its endurance with time [1-3] which is caused by the capacity degradation due to repeated charge/discharge and storage. This degradation leads to a reduction in the driving range of the vehicle and eventually makes the LIBs incompatible with EVs when they reach 80% SOH (varying with the EV manufacturer and government regulations) [2-5]. At this stage, the battery needs to be replaced which costs significantly to the EV owners and the disposal of the retired batteries is hazardous to the environment [4-5]. The replacement cost of EV batteries could be reduced by selling the batteries to the businesses involved in utilizing the retired batteries in low-power and stationery applications [3,5]. Hence the selection of batteries from the first life and their SOH investigation and finally categorizing and grouping them for the potential second life is an open challenge which needs significant researchers' attention [1-6].

Since the cycle and the shelf life of each cell within a battery pack are dictated by the rate of capacity degradation and operational conditions. In the case of EVs and HEVs, multiple cells are arranged in series, parallel and mixed connections to achieve the desired voltage and current [1,4]. Hence, (i) cells within a battery pack have variations in electrical loading based on the series-parallel architecture of the battery systems and (ii) they would have different temperature conditions based on their location within the pack thermal management system [5-8]. These two variations lead to the uneven degradation of the cells across the battery pack [5-8]. However, the SOH of the pack is specified by the weakest cell [6,7] which has faster degradation due to the

nonhomogeneous electrical loading or due to the manufacturing defect caused by slower ionic/charge transport [9,10]. Hence, an understanding of the cell behaviour in parallel to the battery pack is highly needed to pinpoint the root causes of the pack failure. Identifying weak cells within the battery pack can facilitate the replacement of that module/cell containing dead cells and can improve the capacity utilization of the battery pack.

Battery End of Life, Reuse and Recycling

End-of-life (EOL) of EVs and HEVs battery systems are considered once they hit 80% SOH, however, these retired batteries have significant leftover energy [11] which must be utilized by some means otherwise will go to waste [9-13]. An EOL of the EV batteries will strongly impact the economic, environmental, and political dynamics of the nation because the battery raw materials are not evenly accessible across the globe [1-3]. Hence, reuse of the batteries for Energy storage systems (ESS) can minimize that impact by offering significant economic and environmental benefits [9-10]. ESS is an essential factor for the smart grid which helps store energy at times of load shifting and low energy demands and supply at times of high energy demand and saves the cost for the consumers and suppliers. For instance, reusing these batteries in utilities can provide energy at the time of the fluctuations since the cost of the retired batteries ranges from \$38-\$147/kWh as compared to new LIBs ~\$209/kWh [14]. However, the application of the retired batteries needs to be encouraged by the policymakers by providing funds to the new businesses [7,9,14]. Major areas of battery 2nd life application are:

- Low-speed EVs
- Mobile power
- Energy storage for home use
- Backup power and energy storage sites

2nd life application of the batteries can encourage business model innovation which will link transportation with other energy applications [1,4]. These applications could reduce the effective price of EVs and reduce its life cycle impacts on the EV owners. Reuse of the batteries will promote the EVs uses on the road which can also greatly reduce CO₂ emissions and improve air quality using retired batteries in the grid application and UPSs [10]. Since batteries are not simple waste which can be disposed of anywhere, they are electrochemical systems which if not disposed of safely might cause accidents and fire [12]. Therefore, its disposal is also expensive which generates various harmful gases which pollute the environment and atmosphere and this can be minimized by the reuse of the battery systems [2,13-14].

Battery SOH and Capacity Estimation

Battery pack SOH and rate of capacity degradation estimation are essential for the appropriate 2nd life applications or subsequent recycling. For 2nd life applications of the batteries, it is highly desirable to have a similar rated capacity and comparable SOH and, also have a capacity greater than 50% of the original capacity [7-8]. A dissimilarity in cell SOH within a pack leads to incomplete utilization of the battery pack since the battery capacity is defined by the capacity of the weakest cell connected in a series [9]. Since the SOH of the battery pack is determined by the SOH of the weakest cell it is inadequate to maximize the energy utilization of the entire pack [4,6]. Therefore, identification of the cell SOH is highly desirable for the best possible uses, because the parallelly connected cells undergo different currents due to varying internal resistance which leads to different degradation rates [10,11]. Even cells in a series connection can have different SOH and degradation rates. Therefore, the SOH and capacity estimation of the pack without knowing the SOH of the cell is misleading information about the battery systems. For the 2nd life application, cells from the same SOH and internal resistance are recommended even in case of parallel connections [12,13]. There are a variety of SOH assessment techniques reported in the literature, however, either they are time-consuming or are not accurate enough [6-8, 15-18]. The SOH

methods must be cheap and fast enough to reduce the SOH testing apparatus time as well as cost which makes it economical and benign [1,8,9]. Battery SOH is widely assessed by a series of charge/discharge cycles which take several hours to conduct and are hence time-consuming and costly [4,8-9]. However, because of 2nd life application, a fast-screening method with high accuracy is highly desirable to make the reuse of EV batteries sustainable. In this study, battery degradation behavior has been investigated and demonstrated under different electrical and thermal loading conditions. Additionally, a simulation of thermal gradients for a 6S2P battery module has been conducted to demonstrate temperature variation within the cells and across the module.

Test Methodology and Data Collection

To conduct the test, fresh batteries are aged under various loading and operational conditions up to the EOL. This process involves initial electrochemical milling/formation of the cells, followed by a reference capacity test (RCT) within a thermal chamber using a battery cycler at 25°C. To accurately assess the cells' performance, we aged them through mild and aggressive electrochemical cycling and various drive cycles, simulating temperature conditions ranging from 0-25°C. To achieve the required thermal environment, the batteries are placed within an incubator to imitate the real-use scenarios. By regularly conducting RCTs, we monitored the SOH and performance of the cells throughout their first life until the cells reached their EOL. With this approach, battery ageing data was collected and analyzed, which are discussed in the results section.

Results and Discussion

In this section, discussion of the cycling behavior of LGM50 commercial cell is presented. Figure 1 shows the variation in cell capacity with respect to cycling at different temperature conditions which is 0, 10 and 25°C. As can be seen, the cycling behavior of the cell is impacted by the environmental temperature. Three different charging conditions have been used which are 0.3C, 0.5C and 0.7C, however the discharge current is 0.3C for all the cases. Observing the discharge behaviour of the cell it is evident that cell degradation is highly dependent on temperature conditions as well as applied current which indicates the loading condition of the cell. Additionally, for similar cycling/environmental conditions there is significant cell-to-cell variation. Even in similar test conditions cell performance and cell degradation would be different, which indicates that even within the same battery module in a real use case scenario the cells within a battery module will degrade differently just because of different loading conditions. Hence talking about Figure 1(a) cells at 0.3C charge condition for all the temperature conditions have shown less degradation even after 800 cycles compared to 1000 cycles. After 800 cycles cell has lost only 15% of its capacity. Furthermore, before the occurrence of the knee point cell-to-cell variation for the capacity degradation is minimal however after the knee point significant variation between cell-to-cell is observed which is highest at 0°C and 10°C.

After further analyzing the capacity variation of the cell with cycling at 0.7C charge condition for the similar temperature conditions we can see that cells lose their capacity rapidly for all the temperature conditions. It is also observed that the rate of degradation is highest in case of 0°C as can be seen in the figure 1(b). For this condition the degradation behavior at 25°C is significantly less as compared to 0°C and 10°C. Cell lose 20% of SoH after 200 cycles however in case of 10°C and 0°C cell lose 50% of SoH within 70 and 80 cycles respectively. Aging these cells further even after losing 20% of its SoH, we can see the cells lose around 60% and 70% of SoH within 200 cycles for 0°C and 10°C, however at 25°C cell can go up to 300 cycles before it loses 70% SoH. This degradation at low temperature is attributed to the slower reaction kinetics and transport limitations for ions and electrons and lower diffusivity of lithium ions within the cathode and anode.

Further analysing the resistance rise in the cells with cycling condition at 0.3C charge for all the temperature conditions we can see that the rate of rise of cell resistance is quite consistent for all the temperature conditions up to 800 cycles. Additionally, the cell-to-cell variation in internal resistance of the cells is quite minimal up to 800 cycles, however after 800 cycles the rate of rise of the cell resistance is significantly higher, which is also a variation in rate of rise for different temperature conditions as can be seen in the figure 2. For capacity variation with cycling, we can see that the rate of rise in cell resistance at 10°C is significantly higher than the other two temperature conditions including higher cell-to-cell variation. Rapid resistance increases after 800 cycles support the previous discussion and the plots shown in Figure 1(a).

In Figure 1(d) we see variation in cell resistance with cycling at 0.7 C charging current and with 0.3C discharging current at 0, 10 and 25° C temperature conditions, all other conditions are the same for all the cells. The rate of resistance rise in the cell at 25°C is very minimal as compared to 0°C and 10°C up to 170 cycles however after that a significant rise in resistance can be observed even at 25°C. Looking for the resistance rise at 0 and 10° C we can see a significant rise even in less than 50 cycles with 40% and 50% as compared to 1.5% in the case of 25° C. With further cycling the rate of rise of the cell resistance is high in cases of 0 and 10°C and within 180 cycles the cell resistance is 2.6 and 2.8 times the initial resistance of the cell. However, in the case of 25°C cell resistance is up to 2.6 times which shows a rapid increase after 250 cycles. By analyzing the cell resistance, it is observed that a variable rate of cell degradation for different temperature conditions is shown in Figure 1(c).

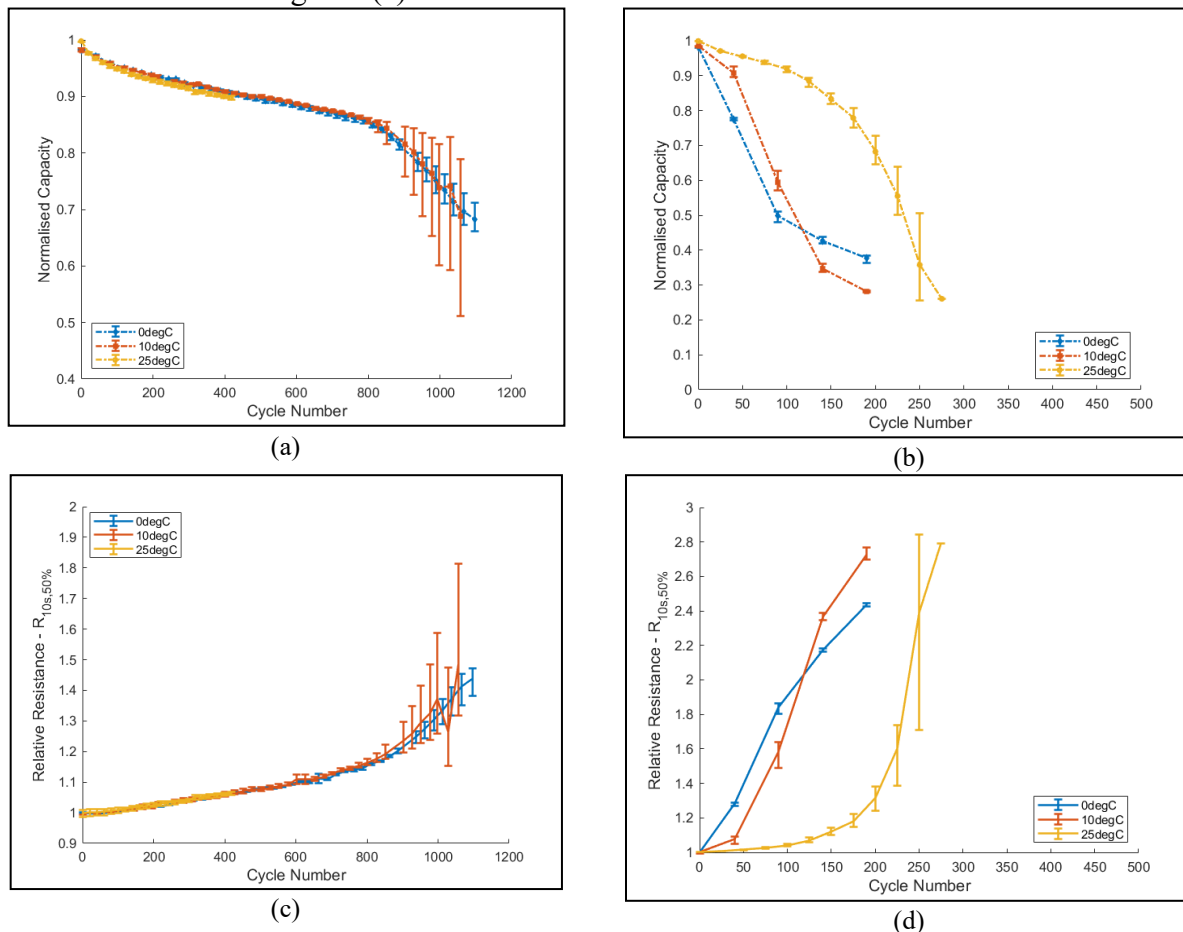


Figure 1: Discharge capacity vs cycle Number (a) 0.3C and (b) 0.7C charging current, cell resistance with cycle number (c) 0.3C and (d) 0.7C charging current at 0, 10, 25°C. Discharge current for all the cases is 0.3C.

In figure 2 variation in thermal condition across a battery module with 6S2P configuration has been shown. As can be seen, the temperature of the individual cells depends on the location within a battery module. Hence, for a same thermal management system of the battery module we can see a significant variation between cell temperature within the cell as well as across the battery module. Even for a small battery module (figure 2) this much variation in temperature can be seen, hence, in case of a commercial module/pack significant variation in temperature can happen which may lead to different rate of degradation of the cells for similar electrical loading. Further on, cells within a module or a battery pack would have different electrical loading conditions due to different SP architects which may lead to different rate of heat generation within the cells which will degrade cells differently. As discussed in the results shown in Figure 1 that the rate of degradation of the cells are highly dependent of temperature conditions as well as electrical loading. And figure 2 dominates a significant temperature variation which will lead to significantly different rate of degradation of the cells within a battery module. Hence at the rate retired stage of the battery happens when battery reaches 80% SOH because of the weakest cells. These retired modules would have a significant number of cells with higher SOH. With this study, it has been demonstrated the importance of identification of the SOH of the cells for potential 2nd life applications. For an effective utilization of the remaining capacity of the retired cells, cells with capacity need to be grouped and utilized in secondary applications.

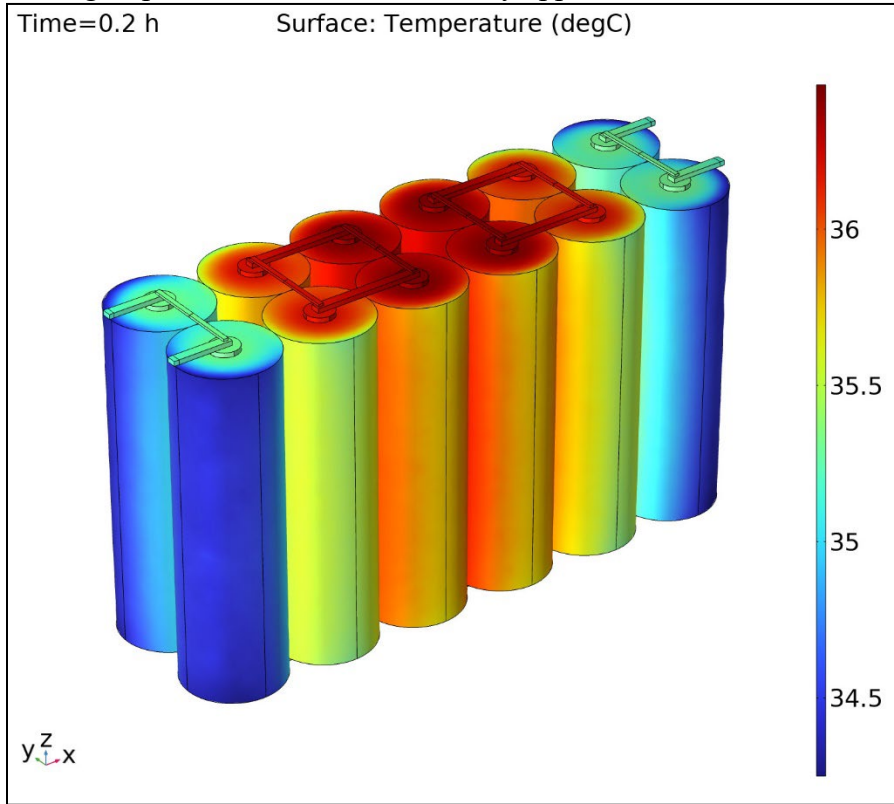


Figure 2: Demonstration of thermal gradient for 6S2P module across the cells.

Conclusion

In conclusion, a different rate of cell degradation has been observed with different environmental and electrical loading conditions. The rate of degradation of the cells is higher at low temperature and at high current charging conditions. In case of 0.3C charging conditions the rate of degradation is slower and after that and after the knee point is reached, the rate of degradation is steep. However, in case of 0.7C charging condition the rate half degradation is steep from the early stage of the cycling. Additionally, it has been demonstrated that the temperature of the cells within a

battery module is different across the 6S2P battery module which would be significantly higher in case of a bigger battery module. This temperature condition will lead to a different rate of degradation of the cells within a battery module. Hence for the potential second life applications of the retired electric vehicle batteries, knowing correct cell SOH is highly essential to group them which will lead to optimized use of these battery in 2nd life application. Therefore, future scope of this study is to develop a rapid state of health measurement or estimation technique which can be effectively utilized to grade and group cells with similar SOH for the potential second life applications which can be utilized in energy storage applications or renewable energy storage applications and remote areas. With this method the battery's SOH can be assessed within a short period (<60 seconds).

References

- [1] Li, X., Zhang, L., Liu, Y., Pan, A., Liao, Q., & Yang, X. (2020). A fast classification method of retired electric vehicle battery modules and their energy storage application in photovoltaic generation. *International Journal of Energy Research*, 44(3), 2337–2344.
<https://doi.org/10.1002/er.5083>
- [2] Liao, Q., Mu, M., Zhao, S., Zhang, L., Jiang, T., Ye, J., Shen, X., & Zhou, G. (2017). Performance assessment and classification of retired lithium-ion battery from electric vehicles for energy storage. *International Journal of Hydrogen Energy*, 42(30), 18817–18823.
<https://doi.org/10.1016/j.ijhydene.2017.06.043>
- [3] Xu, Z., Wang, J., Lund, P. D., & Zhang, Y. (2021). Estimation and prediction of state of health of electric vehicle batteries using discrete incremental capacity analysis based on real driving data. *Energy*, 225, 120160. <https://doi.org/10.1016/j.energy.2021.120160>
- [4] Braco, E., San Martín, I., Berrueta, A., Sanchis, P., & Ursúa, A. (2020). Experimental assessment of cycling ageing of lithium-ion second-life batteries from electric vehicles. *Journal of Energy Storage*, 32(May), 101695. <https://doi.org/10.1016/j.est.2020.101695>
- [5] Zheng, Y., Wang, J., Qin, C., Lu, L., Han, X., & Ouyang, M. (2019). A novel capacity estimation method based on charging curve sections for lithium-ion batteries in electric vehicles. *Energy*, 185, 361–371. <https://doi.org/10.1016/j.energy.2019.07.059>
- [6] Xu, Z., Wang, J., Lund, P. D., Fan, Q., Dong, T., Liang, Y., & Hong, J. (2020). A novel clustering algorithm for grouping and cascade utilization of retired Li-ion batteries. *Journal of Energy Storage*, 29, 100303. <https://doi.org/10.1016/j.est.2020.101303>
- [7] Lai, X., Qiao, D., Zheng, Y., & Yi, W. (2018). A novel screening method based on a partially discharging curve using a genetic algorithm and back-propagation model for the cascade utilization of retired lithium-ion batteries. *Electronics*, 7, 399.
<https://doi.org/10.3390/electronics7120399>
- [8] Lai, X., Deng, C., Li, J., Zhu, Z., Han, X., & Zheng, Y. (2021). Rapid Sorting and Regrouping of Retired Lithium-Ion Battery Modules for Echelon Utilization Based on Partial Charging Curves. *IEEE Transactions on Vehicular Technology*, 70(2), 1246–1254.
<https://doi.org/10.1109/TVT.2021.3055068>
- [9] Zhou, Z., Ran, A., Chen, S., Zhang, X., Wei, G., Li, B., Kang, F., Zhou, X., & Sun, H. (2020). A fast-screening framework for second-life batteries based on an improved bisecting K-means algorithm combined with fast pulse test. *Journal of Energy Storage*, 31, 101739.
<https://doi.org/10.1016/j.est.2020.101739>
- [10] Zhou, P., He, Z., Han, T., Li, X., Lai, X., Yan, L., & Lv, T. (2020). A rapid classification method of the retired LiCo_xNi_yMn_{1-x-y}O₂ batteries for electric vehicles. 6, 672–683.

- [11] Lai, X., Qiao, D., Zheng, Y., Ouyang, M., Han, X., & Zhou, L. (2019). A rapid screening and regrouping approach based on neural networks for large-scale retired lithium-ion cells in second-use applications. *Journal of Cleaner Production*, 213, 776–791.
<https://doi.org/10.1016/j.jclepro.2018.12.210>
- [12] Zhang, Q., Li, X., Du, Z., & Liao, Q. (2021). Aging performance characterization and state-of-health assessment of retired lithium-ion battery modules. *Journal of Energy Storage*, 40, 102743. <https://doi.org/10.1016/j.est.2021.102743>
- [13] Enache, B., Seritan, G., Grigorescu, D., Cepisca, C., Argatu, V., & Voicila, T. I. (2020). A Battery Screening System for Second Life LiFePO₄ Batteries. *EPE*, 298–301.
<https://doi.org/10.1109/EPE50722.2020.9305538>
- [14] Kamath, D., Arsenault, R., Kim, H. C., & Anctil, A. (2020). Economic and Environmental Feasibility of Second-Life Lithium-Ion Batteries as Fast-Charging Energy Storage. *Environmental Science & Technology*, 54, 6878–6887. <https://doi.org/10.1021/acs.est.9b05883>
- [15] Li, J., Wang, Y., & Tan, X. (2017). Research on the Classification Method for the Secondary Uses of Retired Lithium-ion Traction Batteries. *Energy Procedia*, 105, 2843–2849.
<https://doi.org/10.1016/j.egypro.2017.03.625>
- [16] Luo, F., Huang, H., Ni, L., & Li, T. (2021). Rapid prediction of the state of health of retired power batteries based on electrochemical impedance spectroscopy. *Journal of Energy Storage*, 41, 102866. <https://doi.org/10.1016/j.est.2021.102866>
- [17] Enache, B., Seritan, G., Cepisca, C., Grigorescu, S. Florin-Ciprian, A., Felix-Constantin, A., Teodor, V., (2020). Comparative study of screening methods for second life lifepo₄ batteries. *Rev. Roum. Sci. Technn. -Électrotechn. et Énerg.*, 65, 71–74.
- [18] Braco, E., Martin, I. S., Sanchis, P., & Ursúa, A. (2019), Characterization and capacity dispersion of lithium ion second-life batteries from electric vehicles. *Proceedings - 2019 IEEE International Conference on Environment and Electrical Engineering and 2019 IEEE Industrial and Commercial Power Systems Europe, EEEIC/I and CPS Europe 2019*.
<https://doi.org/10.1109/EEEIC.2019.8783547>
- [19] Patil, M. A. et al., (2015), A novel multistage Support Vector Machine based approach for Li ion battery remaining useful life estimation. *Appl. Energy* 159, 285–297.
<https://doi.org/10.1016/j.apenergy.2015.08.119>

AI-Based PV Panels Inspection using an Advanced YOLO Algorithm

Agus HAERUMAN^{1,2,a}, Sami UI HAQ^{1,3,b}, Mohamed MOHANDES^{1,4,c*},
Shafiqur REHMAN^{1,5,d} and Sheikh Sharif Iqbal MITU^{1,4,e}

¹SDAIA- KFUPM Joint Research Center for Artificial Intelligence (JRC-AI) grant No. JRCAI-UCG-03

²Mechanical Engineering Department, King Fahd University of Petroleum and Minerals (KFUPM),
Dahran, Saudi Arabia

³Computer Engineering Department, King Fahd University of Petroleum and Minerals (KFUPM), Dahran,
Saudi Arabia

⁴Electrical Engineering Department, King Fahd University of Petroleum and Minerals (KFUPM), Dahran,
Saudi Arabia

⁵Research Institute, King Fahd University of Petroleum and Minerals (KFUPM), Dahran, Saudi Arabia

^ag202208480@kfupm.edu.sa, ^bg202315350@kfupm.edu.sa, ^cmohandes@kfupm.edu.sa,
^dsrehman@kfupm.edu.sa, ^esheikhshi@kfupm.edu.sa

Keywords: Solar Energy, PV Panel Thermal Inspection, Artificial Intelligence, Deep Learning, Object Detection, YOLOv7

Abstract. The rapid growth of solar photovoltaic (PV) systems as green energy sources has gained momentum in recent years. However, the anomalies of PV panel defects can reduce its efficiency and minimize energy harvesting from the plant. The manual inspection of PV panel defects throughout the plant is costly and time-consuming. Thus, implementing more intelligent ways to inspect solar panel defects will provide more benefits than traditional ones. This study presents an implementation of a deep learning model to detect solar panel defects using an advanced object detection algorithm called You Look Only Once, version 7 (YOLOv7). YOLO is a popular algorithm in computer vision for classification and localization. The dataset utilized in this study was sourced from ROBOFLOW, consisting of 1660 infrared images showcasing thermal defects in PV panels. The model was constructed to identify a broader range of images with heterogeneity, leveraging the aforementioned dataset. Following validation, the model demonstrates a mean Average Precision (mAP) of 85.9%. With this accuracy, the model is relevant for real-world applications. This assertion is affirmed by testing the model with additional data from separate video-capturing PV panels. The video was recorded using a drone equipped with a thermal camera.

Introduction

The increase in energy demand due to massive population growth and the requirement to minimize greenhouse gas emissions have motivated novel approaches to utilizing more clean and sustainable energy. Solar energy is one of the most abundant renewable energy sources. It has now become popular due to the increase in its efficiency and lower cost compared to the last decades. However, maintaining photovoltaic modules is essential to maximize energy harvesting and gain more efficiency.

Defects in PV modules, whether arising from installation or operational factors, can significantly reduce their power generation efficiency. Despite features such as frames made up of Aluminum or glass-lamination that protect panels from environmental factors like rain, wind, and snow, they may not be able to completely protect panels from mechanical stress during transport or in extreme weather conditions like hail [1]. In addition, manufacturing defects such as defective soldering or faulty wiring can also affect the efficiency of PV modules [2]. Thus, it is vital to



employ timely and dependable inspection methods to evaluate and uphold the peak functioning of PV modules, ensuring the utmost effectiveness of solar PV plants.

Implementing more intelligent ways of detecting PV panel defects is one of the most important topics to be discussed. Some researchers have implemented an AI-based method for detecting PV panel defects. Akram et al., for instance, proposed isolated deep learning techniques and developed model transfer deep learning techniques for the detection of PV module defects [3]. Both methods require low computational costs and less time, so they are suited for hardware with less memory installed. Herraiz et al. presented a novel approach to identifying PV panel defects using convolutional neural networks (CNN). They combined thermography and telemetry data to monitor panel conditions [4]. Various alternative strategies employing deep learning have been introduced for the identification of flaws in solar-cell panels. These strategies encompass the application of transfer learning methods utilizing various architectures such as VGG16 [5], VGG19 [6], GoogLeNet [7], ResNet18 [8], Unet [9], FPN [10], LinkNet [11], and EfficientNet [12] to identify anomalies on solar-cell panels [13].

This study delves into the application of an advanced Object Detection Algorithm, specifically YOLOv7, in the thermal inspection of PV panels. The utilization of AI through YOLOv7 aims to revolutionize the detection and classification of potential issues, offering a faster and more precise alternative to conventional inspection techniques. The choice of YOLOv7 architecture for this study is motivated by its reputation for real-time object detection capabilities. YOLOv7 works by dividing the input image into grids, enabling simultaneous prediction of bounding boxes and class probabilities, thus streamlining the detection process. This approach aligns with the demands of thermal inspection for PV panels, where swift and accurate identification of anomalies is crucial for maintaining the efficiency and reliability of solar energy systems. Furthermore, YOLOv7 performs single forward-pass neural networks, thus making it faster and more efficient compared to the other object detection algorithms.

The remaining parts of this paper are organized as follows: Section II presents a comprehensive literature analysis, outlining existing approaches for PV panel inspection and emphasizing advances in AI applications for similar goals. Section III describes the materials and methods utilized in the implementation of the YOLOv7 architecture for thermal inspection, including the dataset and training procedure. Section IV includes the experiment data and analysis, evaluating the performance of the proposed AI-based thermal inspection approach. Section V finishes the work with a summary of major findings, consequences, and future research directions.

Literature Review

Recently, machine learning has grown in popularity as a method for studying PV panels. Various researchers used different ways to inspect and maintain the quality of PV panel modules. Visual inspection, current-voltage (I-V) curve analysis, infrared thermography, and Electroluminescence (EL) testing are among these methods. For instance, in [14], the author utilized a multi-scale CNN model in two modes: transfer learning-based (using two selected DNNs) and independent light-depth (CNN-ILD) CNN. The experimental data using the open ELPV dataset shows promising classifications for PV panel defects in EL images. However, the EL imaging system assesses the photovoltaic (PV) system in low-light conditions, concurrently administering a direct current (DC) to the PV. This approach enables the detection of minor defects, disconnected cell regions, shunts, and similar issues within the PV cells, making it well-suited for indoor inspections. Nevertheless, employing this method outdoors for extensive objects presents notable challenges [15].

Many researchers have also used other types of machine learning to classify solar panel flaws according to attributes extracted from EL images, including Support Vector Machines, Random Forests, and K-Nearest Neighbors [16], [17], and [18]. These methods require manual feature extraction, in which relevant features that capture the traits of various fault kinds are designed using domain expertise. However, these approaches' effectiveness usually depends on how well-

engineered the features are, so they could not be as effective as deep learning approaches, in which the features can automatically learned. [19] and [20]. Similarly, several research studies have been done on deep learning techniques for detecting PV panel defects using EL and IR images. For example, in [15], the author proposed a remote sensing method using infrared radiation cameras installed on unmanned aerial vehicles (UAV) to capture images of solar panels and detect anomalies using CNN. Likewise, [21] proposed a deep-learning method to detect defective solar panels in EL images. They utilize two CNN architectures: a fine-tuned VGG16 model for classification and a lightweight CNN model created from scratch for baseline comparison. The proposed method achieved a 95.2% accuracy on the test dataset. However, these approaches have their limitations. The fine-tuned VGG16 model, while effective in classification, may face challenges in real-time performance, potentially hindering its practicality for dynamic PV panel inspections. On the other hand, the lightweight CNN model, though created for efficiency, might struggle to achieve the same level of accuracy as more established architectures, impacting its reliability in defect detection tasks. These drawbacks influenced our decision to explore alternative solutions better suited for the real-time and accuracy demands of our project.

While several research studies have delved into deep learning techniques for detecting defects in PV panels using EL and IR images, our focus on thermal IR image-based defect detection led us to explore alternatives better aligned with the real-time and accuracy demands of our project. Contrary to the drawbacks associated with the existing methods mentioned above, we opted for YOLOv7 for several reasons. Compared to [15], YOLOv7 provides better object recognition performance for outdoor PV panel inspection, with higher label assignment and bounding box localization. YOLOv7 is also based on neural network architectures that require no feature selection, as mentioned in [16], [17], and [18], which are based on Machine Learning models. The last thing to note here is that, compared to other deep learning models such as mentioned in [21], YOLOv7 requires much less computational cost, making it learn much faster with smaller datasets without pre-training needed. [22].

Methodology and Experiments

The dataset for this project was obtained from ROBOFLOW, an online resource for open-source datasets for computer vision. The dataset comprising thermal images of PV panels acquired by UAV was downloaded in YOLOv7 format. The dataset contains 5313 labeled images [23]. The label contains a bounding box information of the object, such as x-center, y-center, height, width, and the PV panel's status. This format is required for YOLOv7 to detect the object and do localization. Before training the model, the dataset was pre-processed. We chose only 1660 images for this study and removed those images that were taken from a short-distance shoot.

The dataset was then split into training, validation, and testing with a ratio of 70%, 20%, and 10% for training, validation, and testing, respectively. During the training process, we used only the training and validation dataset, while we reserved the testing dataset for testing unseen data.

Fig. 1a shows a sample PV panel thermal image with a single hot spot, while Fig. 1b shows the PV panel with a multi-hot spot. The brighter spots in the panels are the defective cells of the panel due to heat dissipation, and this phenomenon can decrease the efficiency of the panel. All the image sizes are 640x640 pixels.

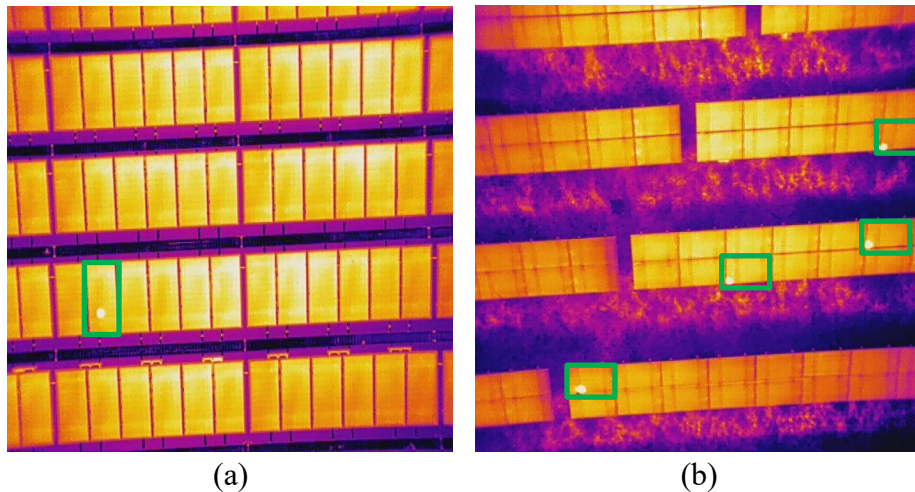


Fig. 1 Sample of images. (a) Image with single hotspot. (b) Image with multiple hotspots [23].

YOLOv7 is the most updated version of the YOLO family from the original authors of the YOLO architecture. This model outperformed all known predecessor object detectors in speed and accuracy, such as YOLOR, YOLOX, YOLOv5, Scaled-YOLOv4, and PPYOLOE. It has reduced a significant number of parameters and computational costs, leading to faster inference speeds and higher detection accuracy. The Basic YOLO Architecture is described in Fig. 2, and the YOLOv7 introduced some major changes in its new architecture, including the Extended Efficient Layer Aggregation Network (E-ELAN), compound model scaling, planned re-parameterized convolution, and coarse-to-fine lead guided assigner [24].

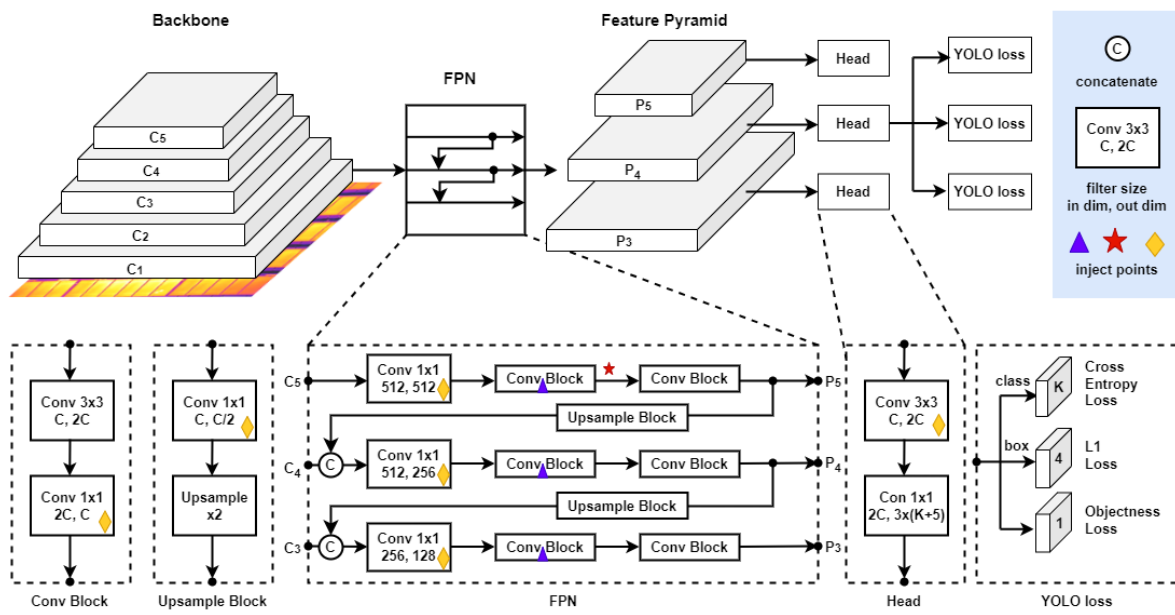


Fig. 2 Basic YOLO Architecture [25].

In this study, we built the model based on YOLOv7 using the mentioned dataset. We used the Nvidia GPU to accelerate the training process and a specific project directory in Google Drive mounted to the Google Colab. All the datasets were put in this directory. The original YOLOv7 repository and the pre-trained model were then acquired. With some adjustments to the dataset and

label information in the COCO.yaml and YOLOv7.yaml files, the models were then trained. The parameters used during the experiment can be seen in Table 1. The Performance metrics we used to evaluate the accuracy of the model's performance are mAP, precision, and recall. Mean Average Precision (mAP) is commonly used to evaluate the model, with ranges of the evaluation from 0 to 1. On the other hand, we also use precision to indicate the accuracy of the detected objects, calculating how many detections were correct, while recall gives information about the ability of the model to identify all instances of objects in the images.

Table 1. Training parameters of the models.

Batch Number	Learning Rate	Momentum	Weight Decay	Number of epochs
8	0.01	0.937	0.0005	200

Result and Discussion

The objective was to evaluate the model's accuracy and investigate its performance in real-life applications. The model was built using heterogeneous images with different elevation drone cameras and more angles. When we test the model using testing data, it can be seen that the model can detect PV panel defects from various images. The data was split into 1170 training data points, 330 validation data points, and 160 testing data points. The batch size was 8, with a learning rate of 0.01, a momentum of 0.937, a weight decay of 0.0005, and a running of 200 epochs. After running the testing with the best weight, it yielded the mAP of 85.9% for threshold 0.5 IoU, the R-value of 83.2%, and the P-value of 75.9%, with 322 defect panels detected from 160 images, as described in Tabel 2. The sample of the testing image was used to see the performance of the model in detecting PV panel defects, as we described in Fig 3. It can be observed that the model performed well in detecting PV panel defects, with three bounding boxes detected with an IoU of 0.71, 0.79, and 0.80.

Table 2. Testing Result of the Model.

Images	Labels	Precision	Recall	mAP@0.5
160	322	0.759	0.832	0.859

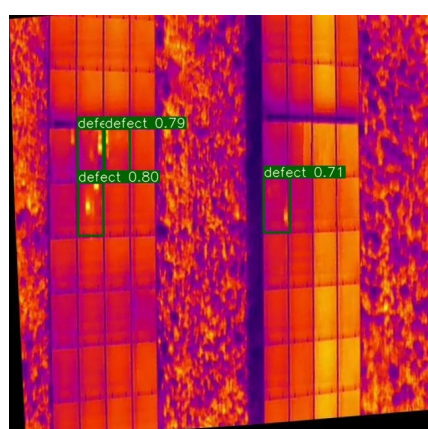


Fig. 3. Model performance for the testing image.

To see the performance of the models for a real-life application, the model was tested to run on a video file obtained from [26]. It was found that the Model performed well in the detection of PV panel defects, as can be seen in Fig. 4. This Model can also be applied for the online monitoring of PV panel defects when it is used to detect the panel using a drone-embedded camera during PV panel inspection.

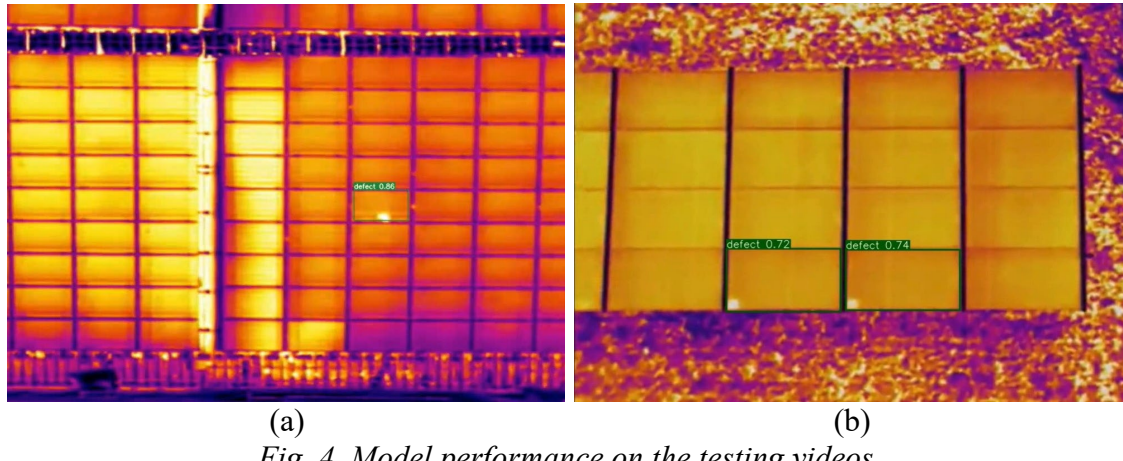


Fig. 4. Model performance on the testing videos.

Conclusion

Solar energy is one of the most popular renewable energy resources, and many countries are now utilizing photovoltaic (PV) panels to harvest energy from the sun. However, the occurrence of PV panel defects can reduce its efficiency and decrease power output. To address this challenge, a lot of research has been conducted to alternate manual PV panel inspection with the most effective and intelligent methods. This study presented an implementation of artificial intelligence, especially deep learning architecture for object detection, known as You Look Only Once, version 7 (YOLOv7). The object detection model was developed using a dataset comprising 1660 data points, achieving an mAP of 85.9%. The model can effectively learn a diverse set of images suitable for real-life applications. This capability was confirmed during testing on unseen images, where the model demonstrated good performance. Furthermore, the model underwent evaluation with a video file for real-life applications. To extend this study to future works, the model can be developed with more heterogeneous images with variations in elevations and angles to perform much better for online applications, especially when it comes to deploying the system in edge artificial intelligence environments.

Acknowledgment

The authors would like to acknowledge the support provided by Saudi Data & AI Authority (SDAIA) and King Fahd University of Petroleum & Minerals (KFUPM) under SDAIAKFUPM Joint Research Center for Artificial Intelligence (JRCAI) grant No. JRCAI-UCG-03.

References

- [1] S. Djordjevic, D. Parlevliet, and P. Jennings. Detectable faults on recently installed solar modules in Western Australia. *Renewable Energy*, 67:215-221, 2014.
<https://doi.org/10.1016/j.renene.2013.11.036>
- [2] Ronnie O Serfa Juan and Jeha Kim. Photovoltaic cell defect detection model based on extracted electroluminescence images using SVM classifier. In 2020 International Conference on Artificial Intelligence in Information and Communication (ICAIIC), pages 578-582. IEEE, 2020.
<https://doi.org/10.1109/ICAIIC48513.2020.9065065>

- [3] M Waqar Akram, Guiqiang Li, Yi Jin, Xiao Chen, Changan Zhu, and Ashfaq Ahmad. Automatic detection of photovoltaic module defects in infrared images with isolated and develop-model transfer deep learning. *Solar Energy*, 198:175-186, 2020.
<https://doi.org/10.1016/j.solener.2020.01.055>
- [4] Alvaro Huerta Herraiz, Alberto Pliego Marugan, and Fausto Pedro Garcia Marquez. Photovoltaic plant condition monitoring using thermal images analysis by convolutional neural network-based structure. *Renewable Energy*, 153:334-348, 2020.
<https://doi.org/10.1016/j.renene.2020.01.148>
- [5] Karen Simonyan and Andrew Zisserman. Very deep convolutional networks for large-scale image recognition. *arXiv preprint arXiv:1409.1556*, 2014.
- [6] Long Wen, X Li, Xinyu Li, and Liang Gao. A new transfer learning based on VGG-19 network for fault diagnosis. In 2019 IEEE 23rd international conference on computer supported cooperative work in design (CSCWD), pages 205-209. IEEE, 2019.
<https://doi.org/10.1109/CSCWD.2019.8791884>
- [7] Christian Szegedy, Wei Liu, Yangqing Jia, Pierre Sermanet, Scott Reed, Dragomir Anguelov, Dumitru Erhan, Vincent Vanhoucke, and Andrew Rabinovich. Going deeper with convolutions. In *Proceedings of the IEEE conference on computer vision and pattern recognition*, pages 1-9, 2015. <https://doi.org/10.1109/CVPR.2015.7298594>
- [8] Kaiming He, Xiangyu Zhang, Shaoqing Ren, and Jian Sun. Deep residual learning for image recognition. In *Proceedings of the IEEE conference on computer vision and pattern recognition*, pages 770-778, 2016.
- [9] Olaf Ronneberger, Philipp Fischer, and Thomas Brox. U-Net: Convolutional networks for biomedical image segmentation. In *Medical Image Computing and Computer-Assisted Intervention—MICCAI 2015: 18th International Conference, Munich, Germany, October 5-9, 2015, Proceedings, Part III 18*, pages 234-241. Springer, 2015. https://doi.org/10.1007/978-3-319-24574-4_28
- [10] Tsung-Yi Lin, Piotr Dollar, Ross Girshick, Kaiming He, Bharath Hariharan, and Serge Belongie. Feature pyramid networks for object detection. In *Proceedings of the IEEE conference on computer vision and pattern recognition*, pages 2117-2125, 2017.
- [11] Abhishek Chaurasia and Eugenio Culurciello. Linknet: Exploiting encoder representations for efficient semantic segmentation. In *2017 IEEE visual communications and image processing (VCIP)*, pages 1-4. IEEE, 2017. <https://doi.org/10.1109/VCIP.2017.8305148>
- [12] Mingxing Tan and Quoc Le. Efficientnet: Rethinking model scaling for convolutional neural networks. In *International conference on machine learning*, pages 6105-6114. PMLR, 2019.
- [13] Minhhuy Le, Dang Khoa Nguyen, Van-Duong Dao, Ngoc Hung Vu, Hong Ha Thi Vu, et al. Remote anomaly detection and classification of solar photovoltaic modules based on deep neural network. *Sustainable Energy Technologies and Assessments*, 48:101545, 2021.
<https://doi.org/10.1016/j.seta.2021.101545>
- [14] Hazem Munawer Al-Otum. Deep learning-based automated defect classification in electroluminescence images of solar panels. *Advanced Engineering Informatics*, 58:102147, 2023. <https://doi.org/10.1016/j.aei.2023.102147>

- [15] Minhhuy Le, DucVu Le, and Hong Ha Thi Vu. Thermal inspection of photovoltaic modules with deep convolutional neural networks on edge devices in AUV. *Measurement*, 218:113135, 2023. <https://doi.org/10.1016/j.measurement.2023.113135>
- [16] Mustafa Yusuf Demirci, Nurettin Besli, and Abdulkadir Gumuscu. Efficient deep feature extraction and classification for identifying defective photovoltaic module cells in electroluminescence images. *Expert Systems with Applications*, 175:114810, 2021. <https://doi.org/10.1016/j.eswa.2021.114810>
- [17] Stefan Bordihn, Andreas Fladung, Jan Schlipf, and Marc Kontges. Machine learning based identification and classification of field-operation caused solar panel failures observed in electroluminescence images. *IEEE Journal of Photovoltaics*, 12(3):827-832, 2022. <https://doi.org/10.1109/JPHOTOV.2022.3150725>
- [18] Harsh Rajesh Parikh, Yoann Buratti, Sergiu Spataru, Frederik Villebro, Gisele Alves Dos Reis Benatto, Peter B. Poulsen, Stefan Wendlandt, Tamas Kerekes, Dezso Sera, and Ziv Hameiri. Solar cell cracks and finger failure detection using statistical parameters of electroluminescence images and machine learning. *Applied Sciences*, 10(24), 2020. <https://doi.org/10.3390/app10248834>
- [19] Ronnie O. Serfa Juan and Jeha Kim. Photovoltaic cell defect detection model based on extracted electroluminescence images using SVM classifier. In 2020 International Conference on Artificial Intelligence in Information and Communication (ICAIIC), pages 578-582, 2020. <https://doi.org/10.1109/ICAIIC48513.2020.9065065>
- [20] Sergiu Deitsch, Vincent Christlein, Stephan Berger, Claudia BuerhopLutz, Andreas K. Maier, Florian Gallwitz, and Christian Riess. Automatic classification of defective photovoltaic module cells in electroluminescence images. *ArXiv*, abs/1807.02894, 2018.
- [21] Abraham Kaligambe and Goro Fujita. A deep learning-based framework for automatic detection of defective solar photovoltaic cells in electroluminescence images using transfer learning. In 2023 4th International Conference on High Voltage Engineering and Power Systems (ICHVEPS), pages 81-85, 2023. <https://doi.org/10.1109/ICHVEPS58902.2023.10257399>
- [22] Christine Dewi, Abbott Po Shun Chen, and Henoch Juli Christanto. Deep learning for highly accurate hand recognition based on yolov7 model. *Big Data and Cognitive Computing*, 7(1), 2023. <https://doi.org/10.3390/bdcc7010053>
- [23] Solveview. Thermal defects dataset. <https://universe.roboflow.com/solveview/thermal-defects>, Aug 2023. visited on 2023-11-20.
- [24] Chien-Yao Wang, Alexey Bochkovskiy, and Hong-Yuan Mark Liao. Yolov7: Trainable bag-of-freebies sets new state-of-the-art for real-time object detectors. In Proceedings of the IEEE/CVF Conference on Computer Vision and Pattern Recognition, pages 7464-7475, 2023.
- [25] Xiang Long, Kaipeng Deng, Guanzhong Wang, Yang Zhang, Qingqing Dang, Yuan Gao, Hui Shen, Jianguo Ren, Shumin Han, Errui Ding, et al. Pp-yolo: An effective and efficient implementation of object detector. *arXiv preprint arXiv:2007.12099*, 2020.
- [26] www.ThermalCamUSA.com. Infrared solar panel inspection by drone. https://www.youtube.com/watch?v=1E-_N-KtQTQ, Feb 2018. visited on 2023-11-20.

Impact of artificial intelligence (AI) in Martian architecture (exterior and interior)

Lindita Bande^{1,a*}, Jose Berengueres¹, Aysha Alsheraifi¹, Anwar Ahmad¹,
Saud Alhammadi¹, Almaha Alneyadi¹, Amna Alkaabi¹, Maitha Altamimi¹,
Yosan Asmelash¹

¹ United Arab Emirates University, UAE

^alindita.bande@uaeu.ac.ae

Keywords: Martian Architecture, AI Tool, Critical Thinking, RHINO/Grasshopper

Abstract. Martian architecture has gained interest in the recent year. Several grand architectural studios have designed hypothetical buildings as part of a colony of the red planet. This study is a continuation of a previous research on mars Habitat. The use of AI to generate alternatives of design based on an initial idea gives insight of how technology can assist us in such major projects. The methodology followed in this study is as per the below steps: 1- General Description of the initial concept: Organic Architecture, 2- General Description of the initial concept: Minimal Architecture, 3- Use of AI in the selected projects, tool description, 4- Results: Outcomes of AI Applications. The aim of this study is to investigate the impact of the AI on Space Architecture, more specifically Martian Architecture. The initial step in the methodology is to design a colony that connects together but as also well distributed in the plan. The following step is using an AI tool to generate processed (rendered) images of the base image. These AI renders will then be analyzed and the final implication of the findings for the project will be described. The findings of this study can be relevant to relevant authorities in space exploration and space architecture with the help of AI tools.

Introduction

All manuscripts must be in English, also the table and figure text.

A new research outlines the design of Martian Habitat Units (MHUs) for extended human missions on Mars, prioritizing functionality, and aesthetics. Circular clusters of MHUs, each accommodating nine crew members, incorporate solar farms, nuclear fission, and wind turbines for energy. Lighting simulations demonstrate that a radial configuration maximizes natural light usage, meeting 36–44% of the lighting load. This information is crucial for planning energy-efficient systems on Mars. [1]

As per a recent article that discusses the design of a Mars research base for long-term habitation, incorporating art and architecture for a thriving lifestyle. Martian Habitat Units (HMUs) are designed with nuclear power, solar farms, and wind turbines, utilizing innovative features like Anti-Dust Settlement Membranes (ADSMs) for solar farm maintenance. The construction involves local grain 3D-printing, and the design prioritizes fail-safe procedures for crew safety. The technologies are based on current advancements, with potential reconsideration closer to the mission date. [2]

The text underscores escalating challenges in Mars missions due to increasing distance from Earth, jeopardizing ground support and crew capabilities. While fast-transit solutions may alleviate some hazards, they introduce novel risks and complexity. Extended exposure to microgravity raises concerns, requiring research into effective countermeasures. The communication delay and resupply constraints necessitate a shift towards autonomous human-system integration, urging urgent attention to develop and validate suitable architectures. [3]

The Mars Quantum Gravity Mission (MaQuIs) focuses on exploring Mars' gravitational field to study subsurface water occurrences and planetary dynamics. The paper outlines current knowledge, proposes satellite gravimetry using quantum technologies, and discusses scenarios for mission simulation. Authors highlight roles in assembling the consortium, estimating gravitational signals, and detailing inertial measurement systems for the mission. Future steps involve simulation scenarios, evaluating dependencies, and identifying limiting factors for the mission concept and technologies in the Martian environment. [4]

The passage highlights the application of machine learning in processing mass spectrometry data for future space missions. By using various artificial intelligence models, accurate results can be obtained quickly, benefiting in-flight processing. Root transformation and 2D spectrograms enhance accuracy, and pretrained convolutional neural networks (CNNs) perform exceptionally well. Generalization, model assembling, and proper training procedures are essential for small datasets. Increased data availability is crucial for further improvement, and machine learning analysis can be effectively run on the edge for future missions, particularly in analyzing sediments from Mars and other celestial bodies. [5]

The article introduces a GeoAI framework for accurate crater detection by integrating domain knowledge and scale-aware learning. Collaboration between computer scientists and Earth/space scientists enhances object detection models. The methodology aims to reduce the time for cataloging new craters, with future improvements planned for data completeness and efficiency optimization. The research envisions incorporating multi-source data to enhance detection accuracy, and the model and data will be open-sourced to encourage collaborative research in the field. [6]

A new research explores the application of AI methods for cyber risk analytics in extreme environments like outer space. It emphasizes adapting data strategies for collecting relevant cyber-risk data and leveraging IoT systems for diverse data streams. The review identifies potential impact assessment approaches, and the conclusion introduces a quantitative version of the NIST 'traffic lights' system with multiple risk calculation metrics, enhancing cost and risk evaluation. The study presents a mathematical formula for future cyber risk developments, focusing on coordination and reliability in AI/ML-based cyber protection for supply and control systems while anonymizing risk data. [7]

Referring to an article that highlights the rapid growth in conversational studies, particularly in open-domain dialogue systems, with a thriving research community and increased industry efforts. The overview summarizes current progress and anticipates a promising future in the AI era, characterized by abundant data and powerful learning techniques. Despite facing challenges in improving conversational AI, the authors express optimism about advancing dialogue systems through dedicated efforts and resolving key issues. [8]

New research argues that despite a deep faith in human reason and experience, the main obstacle to a human mission to Mars is a technological barrier, compounded by increasing threats and risks. The author questions the urgent need for a long-term interplanetary program, citing challenges such as overpopulation, limited resources, and climate change. Additionally, the psychological challenges of living in a confined space, whether on Earth or in space, are highlighted, raising ethical questions about the quality of life in such conditions. The author suggests that mission planners should prioritize the human factor and consider broader interconnected factors in their planning. [9]

As per a new article reviews the current applications of Artificial Intelligence (AI) in environmental disciplines, emphasizing its role in managing and analyzing large datasets related to demographics, traffic, and energy usage. The integration of big data and AI provides new opportunities for environmental tasks such as modeling, monitoring, and research. AI tools, particularly machine learning algorithms, contribute to real-time monitoring of air and water

quality, prediction of future trends, accurate detection of key fish species, and optimization of energy efficiency. Collaborations between ecology and data science are highlighted as crucial for effective conservation efforts. [10]

Methodology

This study is a continuation of a previous research on Mars Habitat. The use of AI to generate alternatives of design based on an initial idea gives insight of how technology can assist us in such major projects.

The methodology followed in this study is as per the below steps:

- General Description of the initial concept: Organic Architecture,
- General Description of the initial concept: Minimal Architecture,
- Use of AI in the selected projects, tool description.
- Results: Outcomes of AI Applications

General Description of the initial concept: Organic Architecture

The Martian Habitat based on Space Architecture concepts, designed in the likeness of flower petals, symbolizes the resilience of life in the Martian setting. It communicates a powerful message, affirming the existence and vitality of life in this challenging environment (figure 1-5).

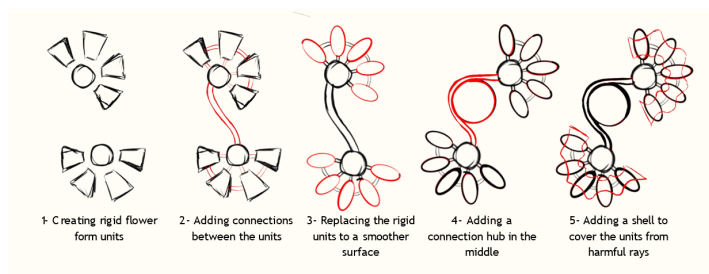


Figure 1. The design concept.

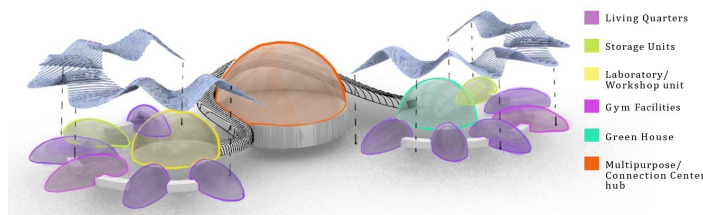


Figure 2. Function distribution in 3D.

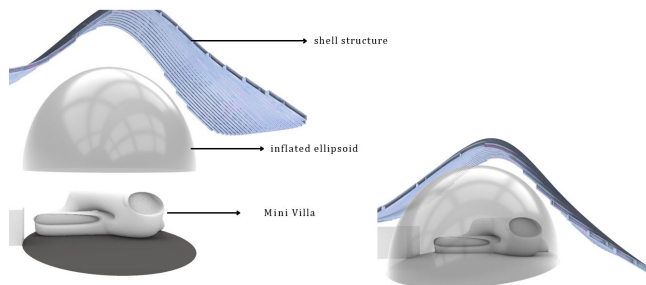


Figure 3. Unit Development, Exterior-Interior.

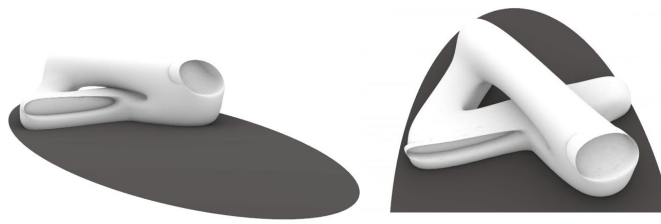


Figure 4. Intereror development, concept.

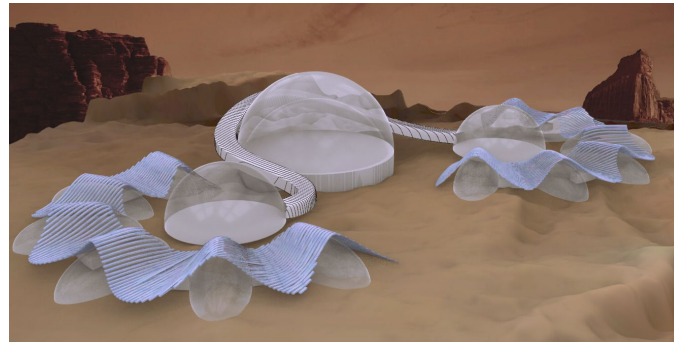


Figure 5. 3D Model from Rhino/Grasshopper, view 1.

General Description of the initial concept: Minimal Architecture

The minimalist Architectural approach uses the dome as the main element of construction. Considering the high radiation in the red planet this shape seems to be the most functional one on an initial stage. Furthermore, much deeper investigation is needed to explore the nature of the materials on the planet, their resistance, endurance, lifecycle. For the current study this particular process is focused on the design of the unit that would create a colony of humans.

Use of AI in the selected projects, tool description.

The use of AI to generate renders based on figure 5 was quite interesting. By adding several keywords and uploading the image the tool generated renders that are shown in the results. In this trial 8 options were selected for the evaluation. There are several options how an image is processed, realistic, creative, more [AI Render tools - https://mnml.ai/app/exterior-ai](https://mnml.ai/app/exterior-ai) (table 1).

Table 1. Keywords used in the AI Tool.

Options	Keywords
Organic Architecture	
Option 1	Martian architecture, desert landscape, universal light, rocks
Option 2	Islamic architecture, mountain view, desert landscaping and bright light
Option 3	modern architecture, desert view, hard landscape and day light
Option 4	parametric architecture, desert view, soft landscape and evening light
Option 5	minimal architecture, grey field view, soft landscape and morning light
Option 6	classic architecture, desert view, hard landscape and morning light

Option 7	concrete facade, modern architecture, rock landscape and evening light
Option 8	concrete facade, modern architecture, desert view, hard landscape and evening light

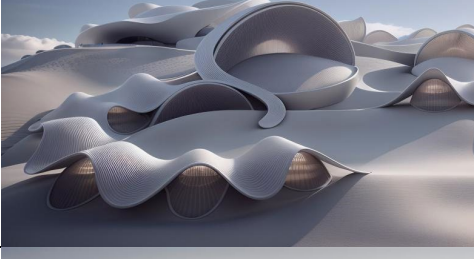
Meanwhile the tool used for the Minimalistic Design is PromeAI (Free AI art generator). The use of AI in architecture helps the designer to visualize and get a creative idea easily and continuously, with just a simple image you can create different buildings using different architectural styles. Everyone can create shapes using any 3d software like Revit or SketchUp and insert it in any AI rendering tools like Prome AI or ReRender AI and write any keyword like modern or classic and decide if the AI tool should change the shape and decide if the AI tool should be creative completely or to keep the shape but just put some ideas to the shape. AI tool will generate images that would save the architect some time in rendering because the architect will have a reference images. Prome AI allow you to generate 200 images every day, but the architect or student that have a membership in the website the images that is generated using the tool will be unlimited. Prome AI generate 3 images so that you choose the best one. There are many tools in the Prome AI for example erase and replace tool which you can select what you want to change in the image. 2d images also can be used in AI tools to generate a creative piece of art. Choosing the mood and the place that you want the building to be in can be easily created using AI for example of you want the building to be in mars AI can make it happen. For example, if you want the building to float in the sea AI will generate it to your imaginations. Some AI tool have some restrictions to what you can do with them (number of images to generate, the architecture style, the creativity, Etc.).

Results

The results of the 8 trials in organic architecture and minimalistic architecture are shown in table 2. Each option has a different outcome impacting the shape of the building, the openings, the relation to the outdoor. However, the shell structure remains in both scenarios.

Table 2. Ai Generated images from AI Tool

Ai Generated images from AI Tool		
Organic Architecture	Minimal Architecture	
Option 1		
Option 2		

Option 3		
Option 4		
Option 5		
Option 6		
Option 7		
Option 8		

Discussion and Conclusions

Discussions

This study highlights the benefits of AI tools in architectural education, demonstrating how it can assist students, especially in designing sustainable houses in challenging environments like the Mars. The results are in agreement with similar studies elsewhere (Tholander et al. 2023; Ildirim et al. 2023). Said tools offer a variety of design options, which are instrumental in aiding critical assessment and decision-making. Regarding the implications for Martian architecture itself, the results underscore an awareness for the need for energy-efficient design while considering Mars' unique environmental challenges, such as radiation and dust storms. We note the ability of AI generated designs to incorporate and balance both functionalities, like energy systems and dust protection, and aesthetics. Furthermore, the broader implications of these findings extend beyond academic settings. They offer valuable insights for the space exploration industry, indicating that AI tools can significantly enhance the added value of the design process (figure 6).

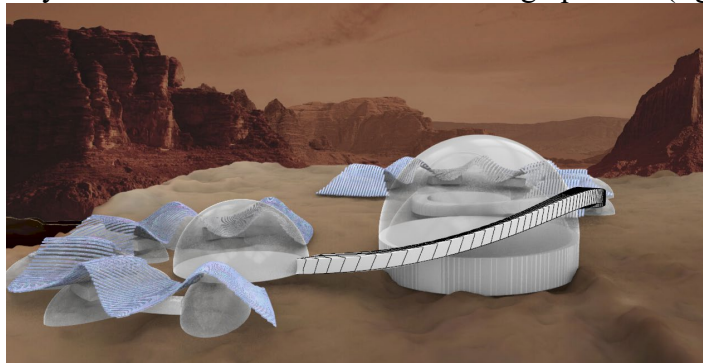


Figure 6. 3D Model from Rhino/Grasshopper, view 2.

Conclusions

The profound impact of Martian exploration efforts in driving progress is undeniably significant. Similar to the Apollo missions five decades ago, as noted by Comstock (2007), the research and development (R&D) outcomes from Mars missions are anticipated to enhance life quality on Earth as well. For instance, the development of computers is attributed to the Apollo space missions. Notably, the Apollo 11 moon landing in 1969 played a crucial role, perhaps unintentionally, in advancing computer technology. The Apollo Guidance Computer (AGC), created for the Apollo program to navigate and guide spacecraft, was among the first to incorporate integrated circuits (ICs). Other notable developments from the Apollo missions included advancements in satellite TV, water purification systems, and new insulating materials for spacecraft, now utilized in building construction (Denver et al., 1981). These findings hold particular relevance for space exploration authorities and architectural firms specializing in extreme environments, demonstrating, as corroborated by other sources, the potential of AI to enhance creative processes. (figure 7).

References

- [1] Amini, K., Janabadi, E.D. and Fayaz, R. (2022) 'Lighting and illumination investigation of long-term residence on Mars for the case of a set of designed martian habitat units (mhus)', *Acta Astronautica*, 192, pp. 210–232. <https://doi.org/10.1016/j.actaastro.2021.12.021>
- [2] Amini, K. et al. (2022) 'Design of a set of habitat units and the corresponding surrounding cluster for long-term scientific missions in the pre-terraforming era on Mars', *Icarus*, 385, p. 115119. <https://doi.org/10.1016/j.icarus.2022.115119>
- [3] Valinia, A. et al. (2023) 'Risk trade-space analysis for Safe Human Expeditions to Mars', *Acta Astronautica*, 211, pp. 192–199. <https://doi.org/10.1016/j.actaastro.2023.05.039>

- [4] Wörner, L. et al. (2023) ‘Maquis—concept for a mars quantum gravity mission’, Planetary and Space Science, 239, p. 105800. <https://doi.org/10.1016/j.pss.2023.105800>
- [5] Nasios, I. (2024) ‘Analyze mass spectrometry data with artificial intelligence to assist the understanding of past habitability of Mars and provide insights for future missions’, Icarus, 408, p. 115824. <https://doi.org/10.1016/j.icarus.2023.115824>
- [6] Hsu, C.-Y., Li, W. and Wang, S. (2021) ‘Knowledge-driven geoai: Integrating spatial knowledge into multi-scale deep learning for Mars Crater Detection’, Remote Sensing, 13(11), p. 2116. <https://doi.org/10.3390/rs13112116>
- [7] Radanliev, P. et al. (2020) ‘Design of a dynamic and self-adapting system, sup-ported with Artificial Intelligence, machine learning and real-time intelligence for predictive cyber risk analytics in extreme environments – cyber risk in the colonization of Mars’, Safety in Extreme Environments, 2(3), pp. 219–230. <https://doi.org/10.1007/s42797-021-00025-1>
- [8] Yan, R. and Wu, W. (2021) ‘Empowering conversational AI is a trip to Mars: Progress and future of open domain human-computer dialogues’, Proceedings of the AAAI Conference on Artificial Intelligence, 35(17), pp. 15078–15086. <https://doi.org/10.1609/aaai.v35i17.17771>
- [9] Szocik, K. (2019) ‘Should and could humans go to Mars? yes, but not now and not in the near future’, Futures, 105, pp. 54–66. <https://doi.org/10.1016/j.futures.2018.08.004>
- [10] Konya, A. and Nematzadeh, P. (2024) ‘Recent applications of AI to Environmental Disciplines: A Review’, Science of The Total Environment, 906, p. 167705.
<https://doi.org/10.1016/j.scitotenv.2023.167705>

Sliding mode control for grid integration of point absorber type wave energy converter

Abdin Y. ELAMIN^{1,a} and Addy WAHYUDIE^{1,b*}

¹Department of Electrical and Communication Engineering, United Arab Emirates University (UAEU), Al Ain, United Arab Emirates

^a201890100@uaeu.ac.ae, ^baddy.w@uaeu.ac.ae

Keywords: Current Controllers, DC Bus Regulation, Grid Integration, Phase Locked Loop Point Absorber, Resistive Loading, Sliding Mode Control, Wave Energy

Abstract. This paper addresses the integration of a point absorber type wave energy converter into power grids, a process complicated by wave energy's intermittent and unpredictable nature. It proposes a sliding mode control strategy with an exponential reaching law in a voltage-oriented control architecture for the grid-side converter of the point absorber. The control objective is to maximize the transfer of generated power to the electrical grid, while concurrently stabilizing the DC bus voltage at a predetermined value and achieving a unity power factor. Results from simulations conducted within a MATLAB framework underscore the efficacy of the sliding mode control approach in sustaining specified DC bus voltage values, and in regulating the direct and quadrature currents by minimizing their respective tracking errors.

Introduction

Wave energy has a potential of 0.534 to 17.5 PWh/year and offers a high energy density with minimal environmental impact [1]. Its availability rate of up to 90% is significantly greater than the 20%-30% of solar and wind energies [2-3]. Wave energy converters (WECs), including various types such as point absorbers (PAs), are used to transform wave energy into electricity. Despite its benefits, wave energy's integration into power grids faces challenges due to its intermittent and unpredictable nature, causing fluctuations in power output that lack synchronization with key grid parameters, such as voltage, phase angle, and frequency. Asynchronization can significantly degrade grid stability and may introduce unwanted effects such as harmonics, frequency deviation and voltage collapse. The criticality of this issue escalates when the grid faces disturbances and unbalanced faults. The back to back converter topology is particularly effective for ensuring the poor power quality of the WEC doesn't propagate into the grid.

The role of the machine-side converter (MSC), i.e., AC/DC converter, is to maximize wave energy extraction, while the grid-side converter (GSC), i.e., DC/AC converter, is tasked with ensuring the synchronization of a constant voltage and frequency to the grid. In terms of GSC control strategies, Proportional-Integral (PI) controllers have been popularly suggested for regulating DC bus voltage and ensuring unity power factor by synchronizing current waveforms with the grid's frequency [4]. However, their performance is constrained by their reliance on linear models and sensitivity to parameter variations. Given the strongly coupled and nonlinear nature of the GSC system, a nonlinear control strategy could potentially enhance both static and dynamic performance. A study in [5] proposed a Lyapunov-based nonlinear controller for active power regulation and zero reactive power injection into the grid.

Sliding mode control (SMC) techniques have been used extensively as nonlinear controllers in GSCs for wind energy and photovoltaic applications [6], yet they haven't been implemented in WEC systems. Their robustness to parameter variations and disturbances [7], make them prime candidates in grid tied WEC applications. This paper proposes a SMC strategy for a GSC in a PA,

utilizing a voltage-oriented control (VOC) architecture. The VOC incorporates two cascaded control loops, with the outer-loop focusing on DC bus voltage regulation. The inner-loop ensures that the GSC output currents accurately track the reference currents from the upper-loop and are synchronized with the grid frequency. A phase-locked-loop (PLL) is adopted for grid synchronization. The resistive loading control employed by the MSC for maximum wave energy absorption is not discussed in this paper, with a comprehensive explanation available in [8]. The paper is organized in the following manner: Initially, it provides a comprehensive model of the PA system from wave to grid. Subsequently, it delves into the design aspects of the GSC control strategy. This is followed by an analysis of simulation results. Finally, the paper ends with a conclusion.

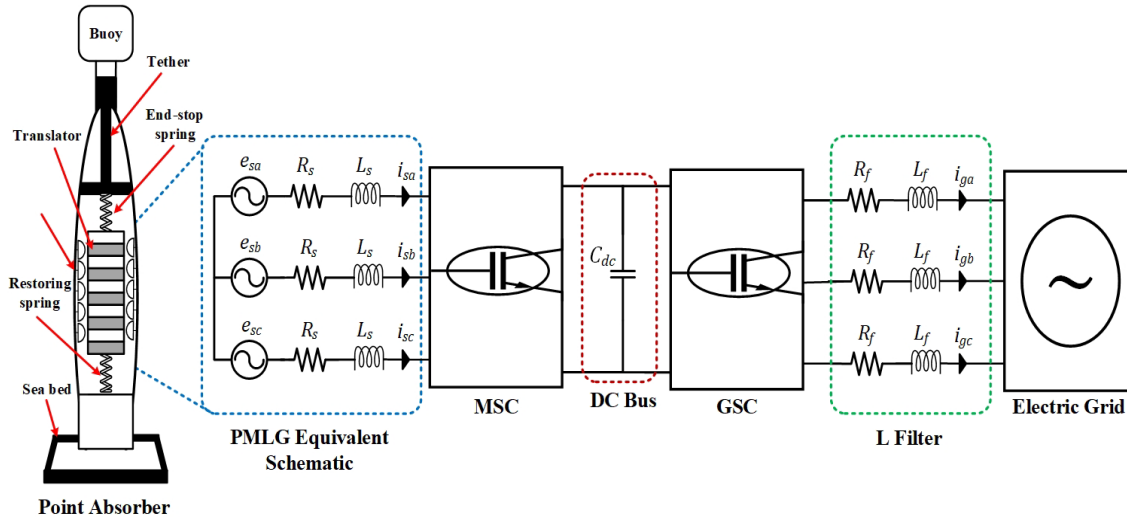


Figure 1: Point absorber system schematic.

System Model

A visual description of the PA system is shown in Fig.1. The PA consists of a floating cylindrical buoy, tethered to a three-phase permanent magnet linear generator (PMLG). A back-to-back converter topology, linking the MSC and GSC via a DC bus, serves as the intermediary between the PA and the electrical grid. Finally, an L filter is used to mitigate the harmonics distortion in the GSCs' output. This topology offers the ability to decouple the PA from the grid, enabling the system model to be split into two independent subsystems: the machine-side and the grid-side.

Machine-side Model

The machines-side model incorporates the wave-buoy hydrodynamic interaction and the electrical dynamics of the PMLG. By assuming only linear forces, the buoy heaving motion during wave interaction can be formulated using Newton's second law of motion given by

$$M\ddot{z}(t) = f_{ex}(t) - f_r(t) - f_b(t) - f_{rs}(t) + f_u(t). \quad (1)$$

where M being the buoy mass, and $\ddot{z}(t)$ is the heave acceleration. $f_{ex}(t)$ corresponds to the wave excitation force, $f_r(t)$ to the radiation force, $f_b(t)$ to the hydrostatic buoyancy force, $f_{rs}(t)$ to the restoring spring force, and $f_u(t)$ to the electromagnetic control force exerted by the PMLG.

The translator in the PMLG is mechanically linked to the buoy, thereby mirroring its heave motion. Consequently, this translator movement induces electromotive force (EMF) voltages in the stationary windings of the PMLG. The PMLG model in the abc frame is given as

$$\mathbf{e}_s(t) = R_s \mathbf{i}_s(t) + j\omega_e(t) L_s \mathbf{i}_s(t) + \mathbf{v}_s(t). \quad (2)$$

where $\mathbf{e}_s(t) = [e_{sa}(t) \ e_{sb}(t) \ e_{sc}(t)]^T$, $\mathbf{i}_s(t) = [i_{sa}(t) \ i_{sb}(t) \ i_{sc}(t)]^T$, R_s , L_s and $\mathbf{v}_s(t) = [v_{sa}(t) \ v_{sb}(t) \ v_{sc}(t)]^T$ are the three phase EMF voltage, stator currents, stator resistance, stator inductance and the three phase voltage terminals. The resistance and inductance represent the internal losses of the generator due to the copper windings and the magnetic field, respectively. By applying Park transformation to Eq. 2 and including the MSC switching inputs, the machine-side model can be expressed in the synchronous reference (d-q) frame as

$$\frac{di_{sd}(t)}{dt} = \frac{-R_s i_{sd}(t)}{L_s} + \omega_e(t) i_{sq}(t) - \frac{u_{sd}(t)}{L_s}. \quad (3)$$

$$\frac{di_{sq}(t)}{dt} = \frac{-R_s i_{sq}(t)}{L_s} - \omega_e(t) i_{sd}(t) - \frac{\omega_e(t)}{L_s} \varphi_{pm} - \frac{u_{sq}(t)}{L_s}. \quad (4)$$

where $i_{sd}(t)$ and $i_{sq}(t)$ are the direct and quadrature components of the stator current, whereas $u_{sd}(t)$ and $u_{sq}(t)$ are the d-q components of MSC switching signals. The flux linkage is denoted by φ_{pm} and the angular frequency $\omega_e(t)$ is obtained as follows

$$\omega_e(t) = \frac{\pi}{\tau_p} \dot{z}(t). \quad (5)$$

with $\dot{z}(t)$ and τ_p being the heave velocity and the PMLG pole pitch, respectively. The captured wave power $P_m(t)$ and PA generated electrical power $P_e(t)$ are given by

$$P_m(t) = f_u(t) \dot{z}(t) = \frac{3\pi\varphi_{pm}}{2\tau_p} i_{sq}(t) \dot{z}(t). \quad (6)$$

$$P_e(t) = \frac{3}{2} (v_{sd}(t) i_{sd}(t) + v_{sq}(t) i_{sq}(t)) = v_{dc}(t) i_{dc}(t). \quad (7)$$

with $v_{dc}(t)$ and $i_{dc}(t)$ being DC bus voltage and DC current output of the MSC, respectively.

Grid-side Model

The grid-side model includes the GSC, L filter and electric grid. The grid is modeled as a voltage source in series with an impedance based on its Thevenin equivalent circuit. The impedance consists of a resistor R_g and inductance L_g to account for transmission line and power transformer effects. The grid-side model can be written using Kirchhoff's laws as follows

$$\mathbf{v}_g(t) = (R_f + R_g) \mathbf{i}_g(t) + (L_f + L_g) \frac{di_g(t)}{dt} + \mathbf{e}_g(t). \quad (8)$$

where $\mathbf{e}_g(t) = [e_{ga}(t) \ e_{gb}(t) \ e_{gc}(t)]^T$, $\mathbf{i}_g(t) = [i_{ga}(t) \ i_{gb}(t) \ i_{gc}(t)]^T$ and $\mathbf{v}_g(t) = [v_{ga}(t) \ v_{gb}(t) \ v_{gc}(t)]^T$ are the three phase grid voltages, grid currents and GSC voltage output, respectively. R_f represents a small resistor to account for losses in the filter. By applying Park transformation to Eq. 8, the grid-side model in the (d-q) frame at grid voltage frequency ω_g is given by

$$\frac{di_{gd}(t)}{dt} = \frac{-(R_f + R_g)i_{gd}(t)}{(L_f + L_g)} - \frac{e_{gd}(t)}{(L_f + L_g)} + \frac{u_{gd}(t)}{(L_f + L_g)} + \omega_g(t) i_{gq}(t). \quad (9)$$

$$\frac{di_{gq}(t)}{dt} = \frac{-(R_f + R_g)i_{gq}(t)}{(L_f + L_g)} - \frac{e_{gq}(t)}{(L_f + L_g)} + \frac{u_{gq}(t)}{(L_f + L_g)} - \omega_g(t) i_{gd}(t). \quad (10)$$

here, $i_{gd}(t)$, $i_{gq}(t)$, $e_{gd}(t)$, $e_{gq}(t)$, $u_{gd}(t)$ and $u_{gq}(t)$ are the d-q components of the grid currents, grid voltages and GSC switching signals, respectively. The active and reactive power delivered to the grid are given respectively by

$$P_g(t) = \frac{3}{2} (e_{gd}(t)i_{gd}(t) + e_{gq}(t)i_{gq}(t)). \quad (11)$$

$$Q_g(t) = \frac{3}{2} (e_{gq}(t)i_{gd}(t) - e_{gd}(t)i_{gq}(t)). \quad (12)$$

Finally, the power exchange in the DC bus can be expressed as follows

$$C_{dc} v_{dc}(t) \frac{dv_{dc}(t)}{dt} = P_e(t) - P_g(t). \quad (13)$$

where C_{dc} represents the DC bus capacitor.

Controller Design

The objective of the SMC is to govern the GSC operations to ensure the PA output power is grid compatible in terms of frequency synchronization, while regulating the DC bus voltage. Assuming no limitations on the grid power intake, the PA operates at peak generation capacity. A schematic of the SMC strategy in a VOC architecture is illustrated in Fig. 2.

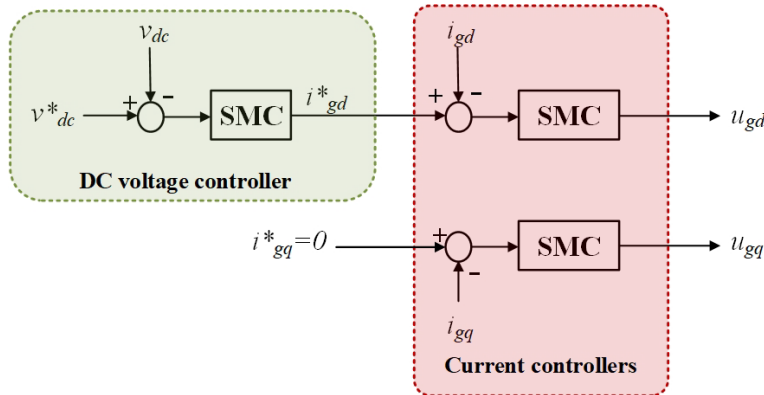


Figure 2: proposed GSC control strategy.

Outer Voltage Control Loop

As observed in Fig. 2, the voltage controller's output is the direct current reference $i_{gd}^*(t)$, which dictates the power level the GSC must either supply or absorb to keep the DC bus voltage at a fixed level. The quadrature current reference $i_{gq}^*(t)$ is set to zero to attain a unity power factor. Substituting Eq. 7 and Eq. 11 into Eq. 13, and simplifying that the quadrature grid voltage is zero ($e_{gq}(t) = 0$), the DC voltage can be written as

$$\frac{dv_{dc}(t)}{dt} = \frac{1}{C_{dc}} i_{dc}(t) - \frac{3}{2C_{dc}v_{dc}(t)} e_{gd}(t)i_{gd}(t). \quad (14)$$

The SMC design requires formulating a sliding surface function $S_v(t)$ of the following form

$$S_v(t) = e_v(t) + \lambda_v \int e_v(t) dt. \quad (15)$$

here, $e_v(t)$ and λ_v are the voltage tracking error and convergence rate of $S_v(t)$. The tracking error $e_v(t)$ and its derivative are given by

$$e_v(t) = v_{dc}^*(t) - v_{dc}(t), \quad \dot{e}_v(t) = \dot{v}_{dc}^*(t) - \dot{v}_{dc}(t). \quad (16)$$

where $v_{dc}^*(t)$ is the DC voltage reference. Based on Eq. 14, $\dot{e}_v(t)$ can be expressed as

$$\dot{e}_v(t) = \dot{v}_{dc}^*(t) - \frac{1}{C_{dc}} i_{dc}(t) + \frac{3}{2C_{dc}v_{dc}(t)} e_{gd}(t)i_{gd}(t). \quad (17)$$

By differentiating Eq. 15, yields the following

$$\dot{S}_v(t) = \dot{v}_{dc}^*(t) - \frac{1}{C_{dc}} i_{dc}(t) + \frac{3}{2C_{dc}v_{dc}(t)} e_{gd}(t)i_{gd}(t) + \lambda_v e_v(t). \quad (18)$$

Equating Eq. 18 to zero, and solving for $i_{gd}(t)$, yields the equivalent direct current reference $i_{gd,eq}^*(t)$ as follows

$$i_{gd,eq}(t) = \frac{2v_{dc}(t)}{3e_{gd}(t)} i_{dc}(t) - \frac{2C_{dc}v_{dc}(t)}{3e_{gd}(t)} (\dot{v}_{dc}^*(t) + \lambda_v e_v(t)). \quad (19)$$

Adding the exponential reaching law found in [7] to Eq. 19, gives the direct current reference $i_{gd}^*(t)$ as

$$i_{gd}^*(t) = \frac{2v_{dc}(t)}{3e_{gd}(t)} i_{dc}(t) - \frac{2C_{dc}v_{dc}(t)}{3e_{gd}(t)} (\dot{v}_{dc}^*(t) + \lambda_v e_v(t)) - \varepsilon_v \operatorname{sgn}(S_v(t)) - k_v S_v(t). \quad (20)$$

with ε_v and k_v being positive tuning variables used to guarantee faster convergence speed, and the notation $\operatorname{sgn}(S_v(t))$ represents the signum function of $S_v(t)$.

Inner Current Control Loop

Similar to the voltage controller, the current controllers require defining the d-q current tracking errors given by

$$e_{id}(t) = i_{gd}^*(t) - i_{gd}(t), \quad e_{iq}(t) = i_{gq}^*(t) - i_{gq}(t). \quad (21)$$

The sliding surface functions can be defined as

$$S_d(t) = e_{id}(t) + \lambda_i \int e_{id}(t) dt, \quad S_q(t) = e_{iq}(t) + \lambda_i \int e_{iq}(t) dt. \quad (22)$$

where i_{gd}^* and i_{gq}^* represent the d-q stator current references, whereas λ_i denote the convergence rate of the sliding functions $S_d(t)$ and $S_q(t)$. The derivatives of Eq. 22 using Eq. 9, Eq. 10 and Eq. 21 is given by

$$\dot{S}_d(t) = i_{gd}^*(t) + \frac{(R_f+R_g)i_{gd}(t)}{(L_f+L_g)} + \frac{e_{gd}(t)}{(L_f+L_g)} - \frac{u_{gd}(t)}{(L_f+L_g)} - \omega_g(t)i_{gq}(t) + \lambda_i e_{id}(t). \quad (23)$$

$$\dot{S}_q(t) = i_{gq}^*(t) + \frac{(R_f+R_g)i_{gq}(t)}{(L_f+L_g)} + \frac{e_{gq}(t)}{(L_f+L_g)} - \frac{u_{gq}(t)}{(L_f+L_g)} + \omega_g(t)i_{gd}(t) + \lambda_i e_{iq}(t). \quad (24)$$

Assuming $\dot{S}_d(t)$ and $\dot{S}_q(t)$ equal zero and incorporating the exponential reaching law, as delineated in [7], give the following GSC switching signals

$$u_{gd}(t) = (R_f + R_g)i_{gd}(t) + e_{gd}(t) - (L_f + L_g)(i_{gd}^*(t) - \omega_g(t)i_{gq}(t) + \lambda_i e_{id}(t)) - \varepsilon_i \operatorname{sgn}(S_d(t)) - k_i S_d(t). \quad (25)$$

$$u_{gq}(t) = (R_f + R_g)i_{gq}(t) + e_{gq}(t) - (L_f + L_g)(i_{gq}^*(t) + \omega_g(t)i_{gd}(t) + \lambda_i e_{id}(t)) - \varepsilon_i \operatorname{sgn}(S_q(t)) - k_i S_q(t). \quad (26)$$

here, ε_i and k_i are the tuning parameters for increasing the convergence rate.

Simulation Results

To assess the efficacy of the proposed SMC approach for GSC control, computational simulations were performed within a MATLAB framework. The voltage and current controllers operate at a sampling period of 1ms and their tuning parameters are set as $\lambda_v = 5$, $\lambda_i = 30$, $\varepsilon_v = \varepsilon_i = 3$ and $k_v = k_i = 1$. The system parameters used in this paper are depicted in Table 1.

Table 1: System parameters.

Subsystem	Specifications		
	Parameter	Symbol	Value
Machine-side	Total mass	m	3×10^4 kg
	PMLG flux linkage	φ_{pm}	19.8 Wb
	PMLG pole pitch	τ_p	0.045 m
	PMLG impedance	R_s, L_s	$2 \Omega, 32$ mH
	DC bus capacitor	C_{dc}	2.7 mF
	Nominal DC bus voltage	v_{dc}	2000 V
Grid-side	L filter inductance	L_f	2 mH
	L filter resistance	R_f	40 mΩ
	Grid RMS voltage (line to line)	E_{gn}	563.4 V
	Grid frequency	f_g	50 Hz
	Grid impedance	R_g, L_g	20 mΩ, 0.1 mH

Fig. 3 demonstrates the efficacy of the voltage controller in the presence of polychromatic wave of significant height 4 m and dominant frequency 0.65 rad/s. As evidenced in Fig. 3a, the DC voltage controller successfully sustained the bus voltage at its desired reference level of 2000 V. Voltage fluctuations were noted, particularly a 1.84 V increase at 87.5 s, due to P_e exceeding P_g by 8.28 kW, as shown in Fig. 3b. Throughout the simulation from 60 s to 140 s, the PA generated an average power output of 3.59 kW and delivered an average power of 3.53 kW to the electrical grid. This confirms that a majority of generated power is efficiently transferred to the grid with minor discrepancies due to switching losses.

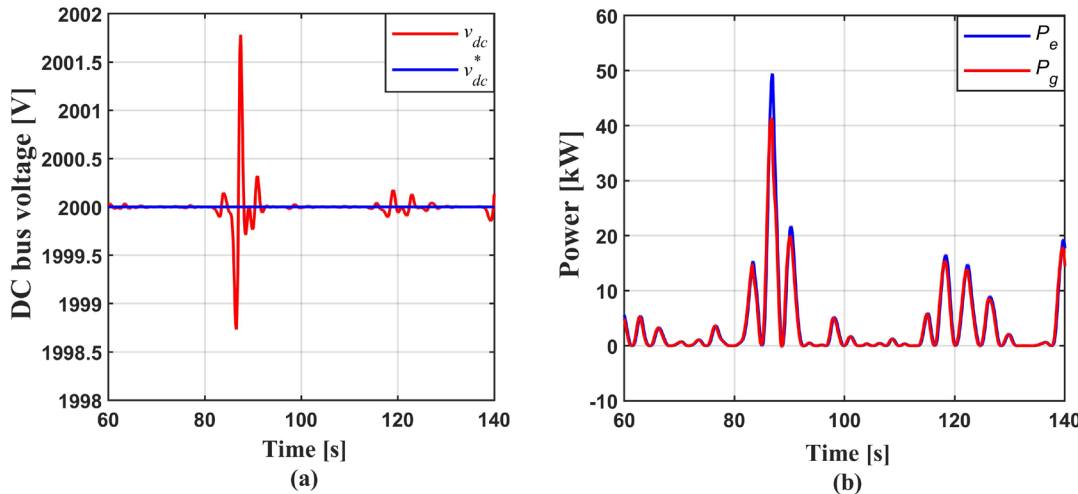


Figure 3: The voltage control loop performance: (a) DC voltage (b) power plots.

Fig. 4a and 4b show the performance of the low-level controllers for direct and quadrature currents, respectively. The direct current reference i_{gd}^* is determined by the DC voltage controller, which augments its value in response to a rise in DC voltage, thereby boosting the power injected into the electrical grid. The direct current reached a maximum peak of 86.7 A in reaction to the highest DC bus voltage at 87.5 s. The quadrature current controller managed to regulate its respective current i_{gq} to zero to ensure a unity power factor. However, minor oscillations in both positive and negative directions were observed, attributable to the coupling effects between i_{gq} .

and i_{gd} , especially at peak values of i_{gd} . Fig. 5 shows the power quality at the point of common coupling, with Fig. 5a displaying the three-phase grid injected currents and Fig. 5b confirming voltage and current of Phase A are synchronized for a unity power factor.

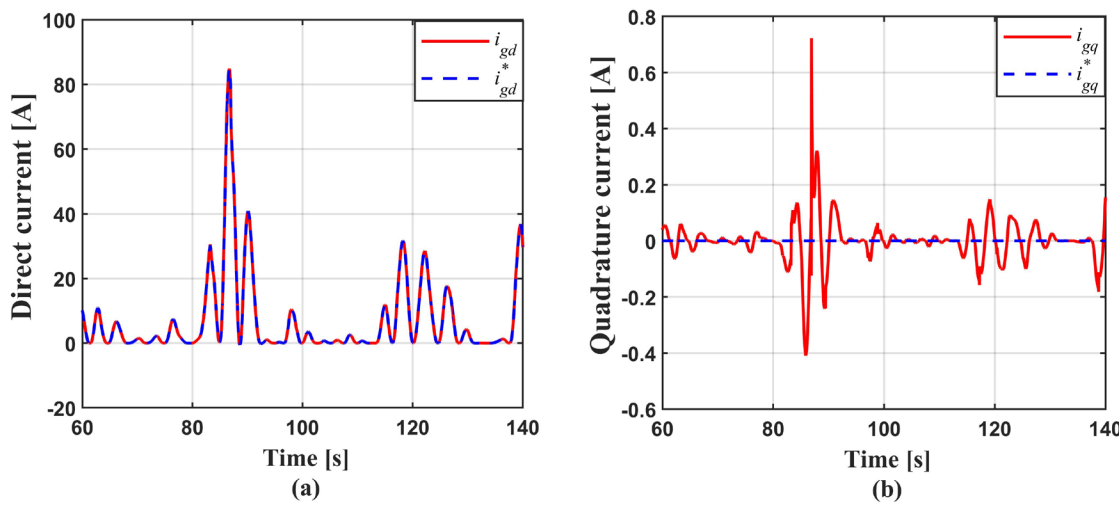


Figure 4: The current control loop performance: (a) direct current (b) quadrature current.

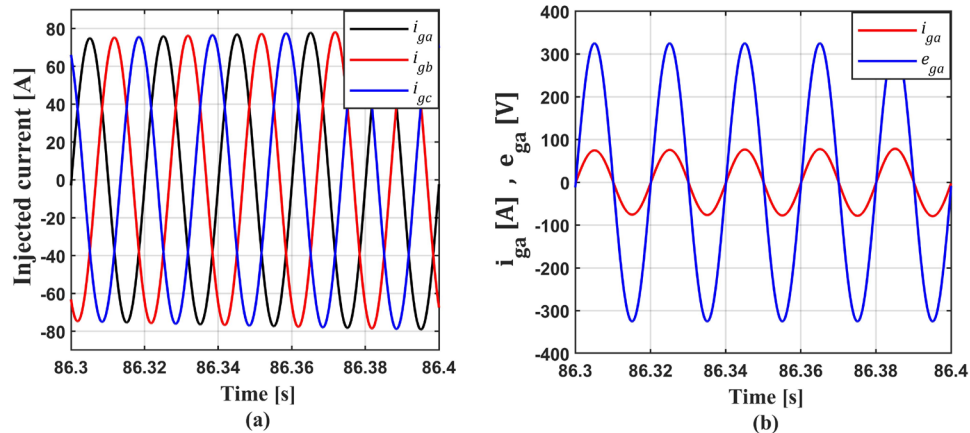


Figure 5: Power quality: (a) three phase injected current (b) grid voltage and current at phase A

Conclusion

This paper highlights the effectiveness of a sliding mode control strategy, incorporating an exponential reaching law within a voltage-oriented control architecture, for integrating a PA type WEC into the power grid. The study's primary goal was to enhance the transfer of generated power to the grid while maintaining the DC bus voltage at a set level and securing a unity power factor, addressing the inherent challenges posed by the variable nature of wave energy. Simulation outcomes, achieved through a MATLAB environment, validate the proposed control strategy's ability to maintain designated DC bus voltage levels and manage the direct and quadrature currents effectively by reducing tracking errors. This research contributes to the field by providing a robust control solution that can improve the reliability and efficiency of wave energy conversion systems when integrated into electrical grids.

References

- [1] A. Wahyudie and M. Jama, "Perspective on damping control strategy for heaving wave energy converters," *IEEE Access*, vol. 5, 99. 22224-22233, 2017.
<https://doi.org/10.1109/ACCESS.2017.2757278>

- [2] O. Saeed *et al.*, "Simple resonance circuit to improve power conversion in a two-sided planar permanent magnet linear generator for wave energy converters," *IEEE Access*, vol. 5, pp. 18654-18664, 2017. <https://doi.org/10.1109/ACCESS.2017.2752466>
- [3] M. Jama *et al.*, "Self-tunable fuzzy logic controller for optimization of heaving wave energy converters," *in proc. of ICRERA 2012*, pp. 6477273, 2012.
<https://doi.org/10.1109/ICRERA.2012.6477273>
- [4] S. Rasool *et al.*, "Coupled modeling and advanced control for smooth operation of a grid-connected linear electric generator based wave-to-wire system," *IEEE Transactions on Industry Applications*, vol. 56, no. 5, pp. 5575-5584, 2020. <https://doi.org/10.1109/TIA.2020.3004759>
- [5] H. A. Said, D. García-Violini, and J. V. Ringwood, "Wave-to-grid (W2G) control of a wave energy converter," *Energy Conversion and Management: X*, vol. 14, p. 100190, 2022.
<https://doi.org/10.1016/j.ecmx.2022.100190>
- [6] K. Zeb *et al.*, "A comprehensive review on inverter topologies and control strategies for grid connected photovoltaic system," *Ren. and Sust. Energy Reviews*, vol. 94, pp. 1120-1141, 2018.
<https://doi.org/10.1016/j.rser.2018.06.053>
- [7] J. Liu, *Sliding mode control using MATLAB*. Academic Press, 2017.
<https://doi.org/10.1016/B978-0-12-802575-8.00005-9>
- [8] A. Y. Elamin *et al.*, "Real-time Model Predictive Control Framework for a Point Absorber Wave Energy Converter with Excitation Force Estimation and Prediction," *IEEE Access*, 2023.
<https://doi.org/10.1109/ACCESS.2023.3347731>

Design and fabrication of low temperature flat plate collector for domestic water heating

Abdulkrim Almutairi^{1,a*}, Abdulrahman Almarul^{1,b}, Riyadh Alnafessah^{1,c},
Abbas Hassan Abbas Atya^{1,d}, Sheroz Khan^{1,e}, Noor Maricar^{1,f}

¹Department of Electrical Engineering, College of Engineering and Information Technology,
Onaizah Colleges, 56447, Al Qassim, Saudi Arabia

^a432110787@oc.edu.sa, ^b122382024@oc.edu.sa, ^c401100108@oc.edu.sa,
^dabbas.atya@oc.edu.sa, ^ecnar32.sheroz@gmail.com, ^fnmmaricar@yahoo.com

Keywords: Flat Plate Collector, Glazed, Unglazed, Daylight Time, Heat Transfer Rate, Mass Flow, Solar Irradiation, Specific Heat, Headers, Raisers, Thermal Conductivity, Apparent Solar Time, Absorber Plate

Abstract. Solar energy, specifically using flat plate collectors, shows very promising as a renewable energy source for meeting global energy demands. These collectors, commonly used to capture solar energy and convert it into heat for various purposes, offer advantages over conventional water heaters in terms of lifespan and energy consumption. This study focuses on understanding flat plate collectors with region specific parameters for domestic use in Onaizah, Saudi Arabia. It includes a detailed design process based on site-specific data and featured with settings adjustable for different seasons. The use of double glazing with a gap between glass panels provides heat insulation from the front. Initial experiments conducted involved temperature measurements of outlet water and calculation of the solar collector's efficiency, resulting in the highest temperature recorded at 62.3°C and an efficiency of 53.5%.

Introduction

Traditional water heaters rely on burning fossil fuels or using resistive heating elements, leading to carbon emissions or wastage of electrical energy. They struggle to meet hot water demands efficiently, resulting in unnecessary energy consumption. These systems also have maintenance issues and a shortened lifespan [1]. Flat plate collectors (FPCs) have undergone significant developments to improve performance. Researchers have worked on enhancing efficiency, minimizing thermal losses, advancing materials and coatings, and exploring innovative designs. The performance of FPCs depends on factors such as solar irradiance, temperature, design, and operating conditions [2, 5]. With history dating back to early 20th century, FPCs water heaters gained popularity in the 1940s and 1950s. Researchers then focused on selective coatings and improved glazing materials leading to efforts to improve insulation with materials of fiberglass, polyurethane foam, and mineral wool. Potential strategies and research directions included cost reduction, performance enhancement, and integration with energy storage systems [5, 9].

Advancements in materials science, manufacturing techniques, and system designs have continued to shape and optimize the FPCs technology, developing high-performance absorber coatings, exploring novel materials, and optimizing the design of flow channels. Innovations included integral collector-storage systems (ICS) and evaluated flat plate collectors (EFPCs), offering improved thermal performance and energy storage capabilities [12]. The orientation and tilt angle of FPCs play crucial role in their performance, typically aligned to the latitude of the location [13].

Calculations are used to determine the performance and heat output of FPCs, taking into account incident solar radiation, fluid flow rate, temperature differentials, and heat transfer coefficients.



Despite having advantages, FPCs have weather-coupled limitations of lower efficiency, having thus different types, including glazed, unglazed, hybrid, and high-temperature collectors [11,13].

FPCs are used in various applications such as residential water heating, space heating, commercial water heating, manufacturing processes, greenhouse heating, pool heating, and solar desalination. However, there are challenges that include improving thermal efficiency, minimizing heat losses, reducing costs, and developing efficient thermal energy storage systems. Supportive policies, financial incentives, and public awareness campaigns are important to promote the use of FPCs and maximize their potential usages. Continued research and collaboration among stakeholders are key to addressing these challenges and advancing FPC technology [10,13].

Problem:

The problem under focus inefficiency and high energy consumption associated with conventional water heaters used for residential and commercial purposes. Traditional water heaters often rely on fossil fuels or electric resistance heating elements. An ideal water heater should prioritize energy efficiency by utilizing renewable energy sources [13].

Objectives:

To determine the optimal design parameters for flat plate collectors in terms of the angle at which they are tilted to maximize solar energy absorption and overall system performance.

To assess the energy efficiency of flat plate collectors for domestic water heating by measuring heat absorption, transfer, and overall system efficiency under varying weather and operating conditions.

Significance of study

The significance of the study lies in addressing local needs by designing a flat plate collector tailored to the specific requirements and climatic conditions of the Qassim Region. Improving thermal performance using double glazing with a vacuum, reducing heat loss, and increasing overall system efficiency. Providing cost savings and affordability by reducing reliance on conventional energy sources and lowering utility bills. Supporting environmental sustainability by utilizing solar energy as a renewable and clean energy source.

Methodology

The design process involves considering various factors such as collector area, materials, fluid selection, and system configuration. The absorber plate area is a critical design parameter that determines the amount of solar energy that can be captured [12]. The solar radiation incident is measured throughout the day. For our application we need the measurements for a certain area in wintertime. Since, in Saudi Arabia the water heaters only needed in winter we need to take into consideration Daylight Time. Daylight Time in Saudi Arabia is 10 hours, this information can be used to calculate solar radiation incident on a specific area [6]. From the information about the location, we designed our collector for this application using equation (1).

$$A = \frac{Qu}{G\eta} \quad (1)$$

Where A is the collector area in square meters, Qu is the desired heat output in Watts, G is the solar radiation incident on the collector in watts per square meter, and η is the collector's thermal efficiency as in equation (2).

$$Qu = \dot{m} C_p (T_{out} - T_{in}) \quad (2)$$

Where \dot{m} is the mass flow rate of the fluid in kilograms per second, C_p is the specific heat capacity of the fluid in joules per kilogram per °C for water, T_{out} is the outlet temperature of the

fluid in degrees Celsius and T_{in} is the inlet temperature. The mass flow rate can be calculated from the capacity of the flat plate collector. If we assume that the capacity for our tank is 20 liters. To determine the required area for FPC, factors such as solar insolation data, daily energy demand, and assumed efficiency are considered. Design parameters of diameter, spacing, and number is crucial. The riser diameter is chosen based on cost, flow rate, and efficiency. A diameter of 9mm is selected in this case. The spacing between risers is decided on heat transfer, pressure drop, and cost. The number of risers is calculated based on the width of the absorber plate, riser diameter, and spacing. These parameters optimize performance, efficiency, and cost-effectiveness. Fig.1 shows a wooden case with insulation, absorber plate, pipes, and glazing.

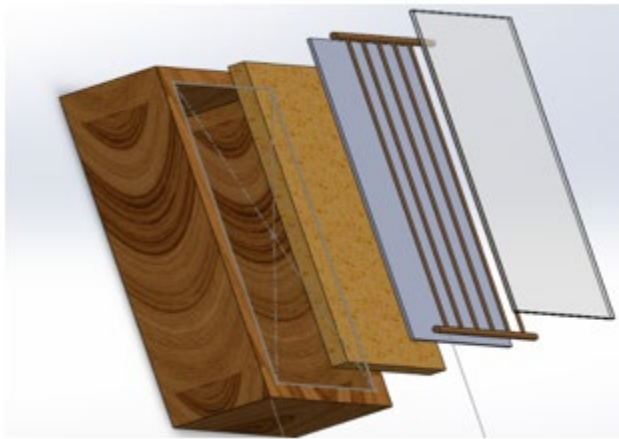


Figure 1: The rendering of the flat plate collector configuration

Material Selection

The selection of materials is important when designing a flat plate solar collector. Factors like cost, availability, installation ease, and lifespan should be considered. Copper, aluminum, steel, and stainless steel are common materials for the absorber plate, each offering different thermal conductivity and corrosion resistance properties. Risers and headers are typically made of copper, aluminum, or stainless steel. Insulation materials like rock wool, cellulose, Styrofoam, polyurethane foam, and polyisocyanurate foam are commonly used. Glazing options include tempered glass, low-iron glass, and polycarbonate. The orientation of a solar collector should be such that it faces south for maximum solar radiation with tilt angle at around $26^\circ \pm 5^\circ$ from the horizontal plane, with adjustable mechanisms. The apparent solar time can be determined by considering the time zone offset and longitude.

Results

The design of the solar water heater is based on the region average solar irradiation, which stands at 6000 kWh per day for Onaizah, and since the heater is used in the winter, which has ten hours of daylight, the average solar radiation per hour is 600 kW [14]. Assumptions are made for the inlet temperature (25°C), outlet temperature (70°C), and operation time (five hours). Assuming an efficiency of 50%, the area of the collector is calculated to be 0.6 square meters. The dimensions of the collector, including the number of risers, flow rate, and absorber plate area, are determined based on the desired specifications. The chosen dimensions for the design are 1m x 0.6m (length x width), with a header diameter of 22.225mm, riser diameter of 9mm, and a spacing of 90mm.

Copper is often chosen for risers and headers due to its high thermal conductivity and corrosion resistance. To enhance thermal absorability, the plate and pipes are usually painted black. Insulation materials such as rock wool, cellulose, Styrofoam, polyurethane foam, and polyisocyanurate foam are considered, with the choice depending on factors such as thermal

conductivity, moisture resistance, and cost. Rock wool is typically chosen when balancing these factors. For glazing material, options include tempered glass, low-iron glass, and polycarbonate.

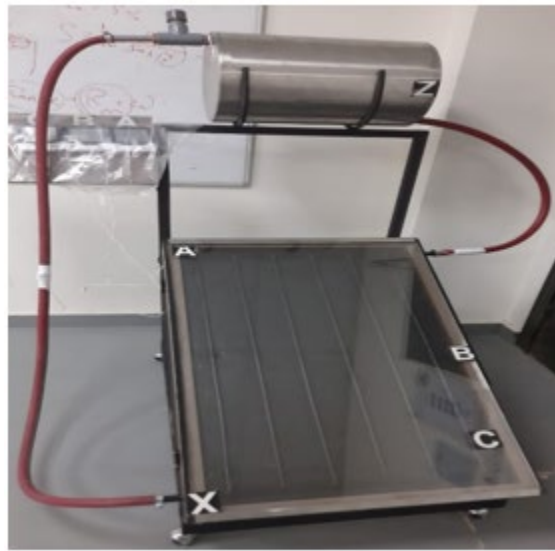


Figure 2: The fabrication of the design

Each offers advantages in terms of durability, transparency, and solar transmittance. The recommended spacing usually ranges from 10 to 25mm. In the described design, the spacing is 10mm and vacuumed to minimize heat loss from the glazing [13].

There are several different mechanisms that can be used to change the tilt angle of a flat plate solar collector. This design's mechanism is manual since it is the most reliable and can withstand the weight of the collector. The mechanism is two sets of steel tubes. One set is attached to the collector by a T-joint. And the other set is attached to a steel base holding the collector by a T-joint. As shown in Fig 3.



Figure 3: The mechanism of angle change.

The tank has many configurations based on the system design expected pressure and temperature. The tank is made from two sheets of galvanized steel and a layer of rock wool for insulation. The tank has an inlet at the bottom and an outlet at the top. From the picture below in Fig 4 it is demonstrated that the tank is connected to the collector through two hoses. The hoses are flexible to move with collector when changing the angle.



Figure 4: The tank for the

There are five sensors in the collector which are A, B, C, Z, and X as illustrated in Fig. 1. Sensors A, B, and C are temperature sensors on the plate, which provide the average temperature of the absorber plate. Sensors Z and X are the outlet and inlet sensors, respectively. All five monitors for the sensors are on the board on the side of the collector.

On Wednesday the twenty-first of February 2024 a preliminary test was performed on the collector. From this test the efficiency of the collector is calculated. The water outlet temperature increased to maximum value 62.3°C at around 4:00 PM and then decreased as shown in Fig. 5. As shown in Fig. 6 the efficiency of the collector increased with time and reached its maximum value 53.5% around 4:00 PM and then decreased.

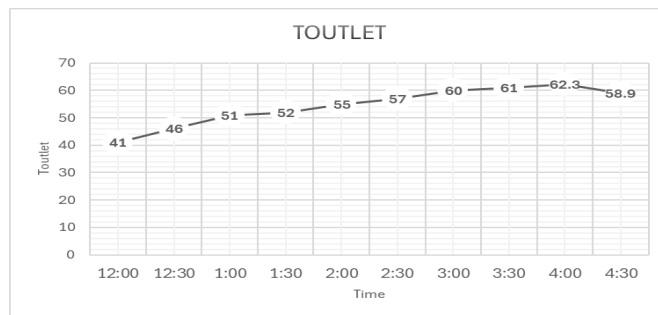


Figure 5: The temperature in the outlet vs

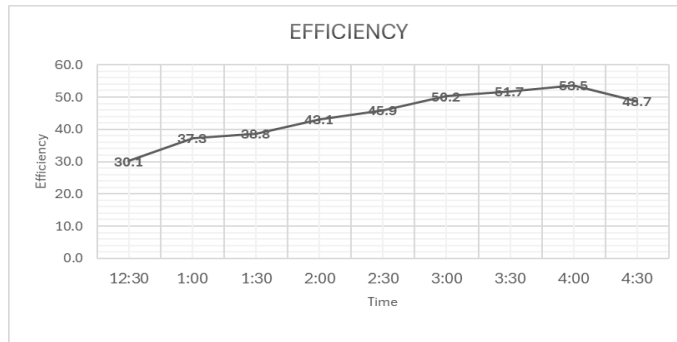


Figure 6: The Efficiency VS time chart.

Recommendations

The performance of the flat plate collector has been assessed after fabrication and testing, where its efficiency is a key factor. The actual collector efficiency may differ from the theoretical

efficiency depending on the design, mainly due to system losses. These losses can vary across regions and collectors but can be evaluated using specific criteria. These parameters must be tested in different conditions and in different seasons. The performance of a flat plate solar collector is evaluated based on its efficiency, which can vary from theoretical values due to system losses. These losses can be assessed using specific criteria such as the useful thermal load, thermal losses, and the heat removal factor. The useful thermal load refers to the amount of thermal energy provided by the collector to meet the desired demand, taking into account the heat energy transferred from the collector to the load. It depends on various factors including the collector's performance, heat transfer characteristics, specific requirements, and thermal losses within the system. The thermal losses are determined by calculating the overall heat loss coefficient, which considers the major areas of heat loss in the collector such as the top, bottom, and sides. The heat removal factor measures how effectively the collector transfers heat from the absorber plate to the heat transfer fluid, and it is calculated as the ratio of the actual heat transfer rate to the maximum possible rate under ideal conditions. This factor can be used to determine the absorbed useful energy by considering parameters such as the collector area, irradiance, absorptance and transmittance of the collector, overall heat loss coefficient, and the temperature difference between the fluid inlet and ambient temperature. These parameters should be tested under different conditions and seasons to accurately evaluate the performance of the flat plate collector.

Conclusion

In summary, the design and optimization of a flat panel solar collector involves various considerations. The collector is oriented south-ward to maximize solar radiation, with the tilt angle manually adjusted based on the latitude of Onizah, Saudi Arabia. Dimensions are determined based on the number of risers, water flow rate, and absorption plate area. Vertical orientation is preferred, with dimensions of 1m x 0.6m. Copper is chosen for risers and headers because of its thermal conductivity and resistance to corrosion. Black coating enhances thermal absorption ability. Rock wool insulation provides thermal insulation and moisture resistance. Tempered glass serves as glazing material to ensure durability and transparency. A 10mm vacuum gap between the glazing and absorber plate reduces heat loss. Manual adjustment includes two sets of steel tubes and a steel base to reliably change the tilt angle. Flexible hoses connect the collector to the tank, allowing for angle adjustments. Sensors monitor temperature variations. Initial tests show a maximum efficiency of 53.5%. Calculations evaluate thermal load and losses. This optimized collector effectively harnesses solar energy for domestic water-heating applications, providing a sustainable and cost-effective solution for the region's thermal energy requirements.

Acknowledgement

The authors express their gratitude to Department of Electrical Engineering, College of Engineering and Information Technology, Onaizah Colleges, Qassim, Saudi Arabia, for their laboratory/library support throughout the analytical derivation and design implementation.

References

- [1] D. A. Bainbridge, The Integral Passive Solar Water Heater Book: Breadboxes, Batchers, and Other Types of Simple Solar Water Heaters. Davis, CA.: Passive Solar Institute, 1981.
- [2] Y. Tripanagnostopoulos, M. Souliotis, and T. Nousia, "Solar collectors with colored absorbers," *Solar Energy*, vol. 68, no. 4, pp. 343–356, 2000. [https://doi.org/10.1016/s0038-092x\(00\)00031-1](https://doi.org/10.1016/s0038-092x(00)00031-1)
- [3] K. Patel, "Comparative analysis of solar heaters and heat exchangers in residential water heating," *International Journal of Science and Research Archive*, vol. 9, no. 2, pp. 830–843, 2023. <https://doi.org/10.30574/ijsra.2023.9.2.0689>

- [4] Shamsul Azha, Nurril Ikmal, Hilmi Hussin, Mohammad Shakir Nasif, and Tanweer Hussain. "Thermal performance enhancement in flat plate solar collector solar water heater: A review." *Processes* 8, no. 7 (2020): 756.
- [5] El-Sebaee, I. M. "Develop of Local Flat Plate Solar Heater." *Journal of Soil Sciences and Agricultural Engineering* 12, no. 5 (2021): 385-390.
- [6] L. C. Spencer, "A comprehensive review of small solar-powered heat engines: Part I. A history of solar-powered devices up to 1950," *Solar Energy*, vol. 43, no. 4, pp. 191–196, 1989. [https://doi.org/10.1016/0038-092x\(89\)90019-4](https://doi.org/10.1016/0038-092x(89)90019-4)
- [7] J. W. Twidell and A. D. Weir, *Renewable Energy Resources*. London: Taylor & Francis Ltd, 2015
- [8] F. Struckmann, "Analysis of a Flat-plate Solar Collector," Academia, <https://www.academia.edu/download/44502033/Fabio.pdf> (accessed Sep. 19, 2023).
- [9] H. Dagdougui, A. Ouammi, M. Robba, and R. Sacile, "Thermal analysis and performance optimization of a solar water heater flat plate collector: Application to Tétouan (Morocco)," *Renewable and Sustainable Energy Reviews*, vol. 15, no. 1, pp. 630–638, 2011. <https://doi.org/10.1016/j.rser.2010.09.010>
- [10] L. C. Spencer, "A comprehensive review of small solar-powered heat engines: Part I. A history of solar-powered devices up to 1950," *Solar Energy*, vol. 43, no. 4, pp. 191–196, 1989. [https://doi.org/10.1016/0038-092x\(89\)90019-4](https://doi.org/10.1016/0038-092x(89)90019-4)
- [11] Putra, Andika, K. Arwizet, Yolli Fernanda, and Delima Yanti Sari. "Performance Analysis of Water Heating System by Using Double Glazed Flat Plate Solar Water Heater." *Teknometrik* 4, no. 1 (2021): 1-7.
- [12] S. Algarni, "Evaluation and optimization of the performance and efficiency of a hybrid flat plate solar collector integrated with phase change material and heat sink," *Case Studies in Thermal Engineering*, vol. 45, p. 102892, 2023. <https://doi.org/10.1016/j.csite.2023.102892>
- [13] P. Khobragade, P. Ghutke, V. P. Kalbande and N. Purohit, "Advancement in Internet of Things (IoT) Based Solar Collector for Thermal Energy Storage System Devices: A Review," 2022 2nd International Conference on Power Electronics & IoT Applications in Renewable Energy and its Control (PARC), Mathura, India, 2022, pp. 1-5. <https://doi.org/10.1109/PARC52418.2022.9726651>
- [14] "Solar Resource Maps of Saudi Arabia," solargis.com. <https://solargis.com/maps-and-gis-data/download/saudi-arabia> (accessed Oct. 25, 2023).

The utilization of IoT-based humidity monitoring method and convolutional neural networks for orchid seed germination

Muhammad Ridhan FIRDAUS^{1,a}, Hilal H. NUHA^{1,b}, Mohamed MOHANDES^{2,c*},
and Agus HAERUMAN^{2,d}

¹Telkom University, Bandung, Indonesia

²King Fahd University of Petroleum and Minerals (KFUPM), Dhahran, Saudi Arabia
(KFUPM), Dhahran, Saudi Arabia

^aridhanfirdaus@student.telkomuniversity.ac.id, ^bhilalnuha@ieee.org,
^cmohandes@kfupm.edu.sa, ^dg202208480@kfupm.edu.sa

Keywords: CNN, IOT, Orchid Seeding

Abstract. This research endeavors to advance orchid seed germination efficiency through the development of an Internet of Things (IoT)-based humidity monitoring system integrated with Convolutional Neural Networks (CNN). Recognizing the pivotal role of proper humidity in orchid seed sowing, the proposed system employs humidity sensors connected to an IoT platform for real-time data collection. The collected data undergoes analysis and prediction by CNN, elucidated through graphical representations such as histograms, line charts, and scatterplot charts. By synergizing IoT technology with artificial intelligence, this innovative system contributes positively to orchid seed sowing efficiency, empowering farmers and orchid cultivators to optimize plant growth conditions. Furthermore, the adaptability of this approach extends beyond orchids, making it applicable to various crop seeding applications through parameter modifications tailored to specific needs.

Introduction

Smart farming is taken from the word 'smart' in smart city, smart farming which was originally called 'precision farming' will become a mandatory agricultural concept in the future due to limited land. Smart farming utilizes technology such as big data, GPS, and the Internet of Things (IoT) to improve the quality and quantity of production in the agricultural industry. Things like this should help simplify and streamline all agricultural processes from production to marketing [1].

The Smart Farming concept began to be developed as an effort to increase the efficiency and productivity of the agricultural sector which is still dominated by traditional methods. Rapid technological developments enable farmers to utilize technological information and communication in agricultural land management, production and marketing of agricultural products. Smart Farming has many benefits, including increasing the efficiency of using resources such as air and energy, increasing the quality and quantity of harvests, reducing production costs, and minimizing negative impacts on the environment. Apart from that, Smart Farming can also help farmers integrate and control the agricultural environment in real-time, which can help in overcoming problems that arise quickly and in a timely manner [2][3].

Convolutional Neural Networks (CNN) is a method of smart farming. CNN itself is a type of neural network commonly used on image data. CNN can be used to detect and recognize objects in an image. CNN is a technique inspired by the way mammals — humans, produce visual perception.

In general, a Convolutional Neural Network (CNN) is not much different from a regular neural network (NN). NNs typically transform input by passing it through a series of hidden layers. Each layer consists of a collection of neurons, where each layer is fully connected to all the neurons in

the previous layer. Finally, a fully connected layer (output layer) is used to represent the predictions. The CNN consists of neurons that have weights, biases and activation functions. Convolutional layers also consist of neurons arranged in such a way as to form a filter with length and height (pixels) and CNN utilizes the convolution process by moving a convolution kernel (filter) of a certain size to an image, the computer obtains new representative information from the results of multiplying parts of the image depending on the filter used [4][5]. CNN is used for sowing orchid seeds, because CNN can help with visual analysis, such as identifying problems, and providing information for the maintenance and development of orchid seeds.

The paper is organized into distinct sections to present the research on utilizing an Internet of Things (IoT)-based humidity monitoring system combined with Convolutional Neural Networks (CNN) for efficient orchid seed germination. The abstract succinctly introduces the research, highlighting the integration of humidity sensors with CNN analysis for optimal orchid seeding conditions. The introduction outlines the significance of smart farming, emphasizing the role of technology, particularly CNN, in agricultural advancements. The literature review delves into the importance of real-time humidity monitoring, the challenges in orchid cultivation, and the application of IoT and CNN in the context of smart farming. The methodology section details the problem identification process, the seven research stages, and the selection of evaluation metrics, showcasing the comprehensive approach taken. Device design elucidates the essential tools—NodeMCU, Water Pump DC 12V, and DHT11—employed in the research. Algorithm design provides a visual representation of the analysis method used in the Temporary Immersion System. The results section showcases temperature and humidity data, with a focus on accuracy testing using CNN and comparisons with other methods. The conclusion summarizes key findings, emphasizing the high accuracy of the IoT and CNN-based humidity monitoring methods and their potential applications in optimizing orchid seed sowing.

Literature Review

Moisture Monitoring. Monitoring soil moisture is very important in crop cultivation, especially at the time of planting. Proper soil moisture can increase the success of plant growth and reduce the risk of growth failure. The use of IoT sensor technology can monitor soil moisture in real-time and accurately [6][7].

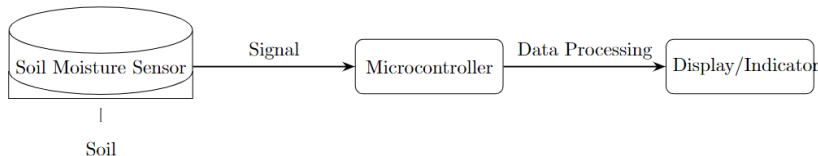


Fig. 1 Humidity Monitoring [6].

Orchid Cultivation. Orchids are a type of ornamental plant that is very popular and has high economic value. However, orchid cultivation requires careful care and supervision, especially when sowing seeds. Real-time and accurate monitoring of humidity can help increase the success of sowing orchid seeds.

Internet of Things (IoT). IoT is a concept where electronic devices connected to the internet can communicate with each other and exchange data. In this case, the use of IoT sensor technology can monitor soil moisture in real-time and send data to a server that can be accessed from anywhere.

Convolutional Neural Network (CNN). CNN is one of the most popular types of Deep Learning algorithms in image processing. CNN can learn complex patterns in images and classify images into appropriate categories based on the learned features. In this case, CNN can be used to process humidity data from IoT sensors and classify humidity status to predict the success of orchid seed sowing [8][9].

Methodology

Identification of problems. The utilization of Root Mean Square Error (RMSE) is imperative in addressing the inherent challenges associated with orchid seed germination, particularly the unpredictability in factors influencing orchid growth outcomes. Orchid seeds pose unique difficulties in prediction due to various uncontrollable variables. Traditional prediction methods often fall short in accurately foreseeing the results of observed plant behavior, leading to suboptimal predictions. RMSE serves as a valuable metric, specifically gauging plant quality, enabling researchers to set high expectations for seeds predicted to be superior while discerning and discarding those anticipated to yield damaged or compromised outcomes. This strategic application of RMSE not only enhances predictive accuracy but also aids in making informed decisions regarding seed quality and subsequent plant development.

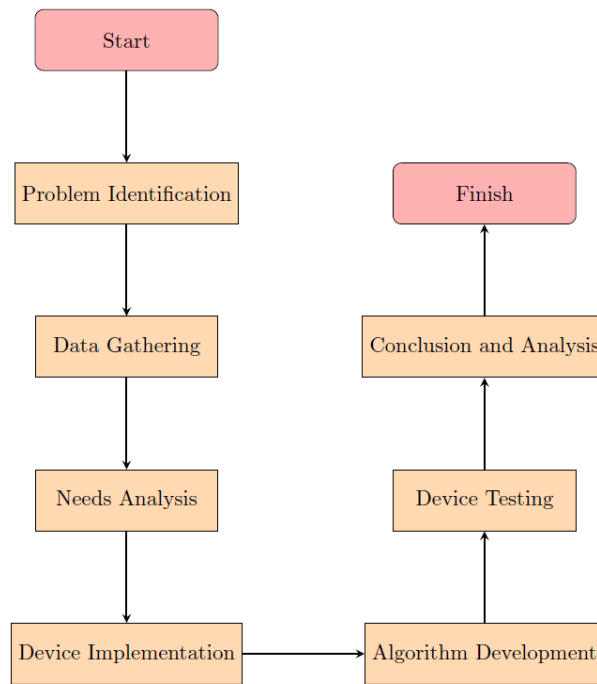


Fig. 2 Research Flow Diagram.

Research Stages. This research includes seven research stages which can be seen in Fig. 2. The beginning of this research is the problem identification process. After that, the data collection stage is carried out to process the information, then analyze the requirements needed to design the tool, including hardware, sensors and other components, with the aim of preventing errors when making the tool. After the tool has been successfully created, the research will proceed to the testing stage using the Convolutional Neural Network (CNN) method and making comparisons with other methods.

Method Selection. Mean Squared Error (MSE) is not a direct part of Convolutional Neural Networks (CNN), but MSE is one of the evaluation metrics commonly used in training and evaluating CNN models. Root Mean Square Error (RMSE) is a standard way to measure the error of a model in predicting quantitative data.

$$RMSE = \sqrt{\sum_{k=1}^K \frac{(\hat{y}_k - y_k)^2}{K}} \quad (1)$$

MAE is one of the evaluation methods commonly used in data science. MAE calculates the average of the absolute differences between predicted and actual values.

$$MAE = \frac{1}{K} \sum_{k=1}^K |\hat{y}_k - y_k| \quad (2)$$

R^2 is basically used to see how adding independent variables helps explain the variance of the dependent variable.

$$R^2 = 1 - \frac{SSR}{SST} \quad (3)$$

where R^2 is the coefficient of determination, RSS is the sum of squares of residuals, and TSS is total sum of squares.

Device Design. Following items are some of the tools needed in designing:

NodeMCU [10] (Fig. 3a) is an open source IoT platform. Consists of hardware and software. The hardware is a development board integrated with an ESP8266 microcontroller and a USB to serial communication chip. The software is firmware that is compatible with the Arduino IDE. Water Pump DC 12V (Fig. 3b). This type of pump is operated by immersing it in water and cannot work outside the water. The water pump in this design is designed to flow air from tank 1 to tank 2 periodically.

DHT11 [11] (Fig. 3c) is a sensor that can detect temperature and humidity around the area where the sensor is placed. This sensor consists of a thermistor which functions to measure temperature and a capacitive sensor which is used to measure humidity levels. Generally, this sensor is integrated in a module which is equipped with sensors and chips to convert analog signals into digital signals.

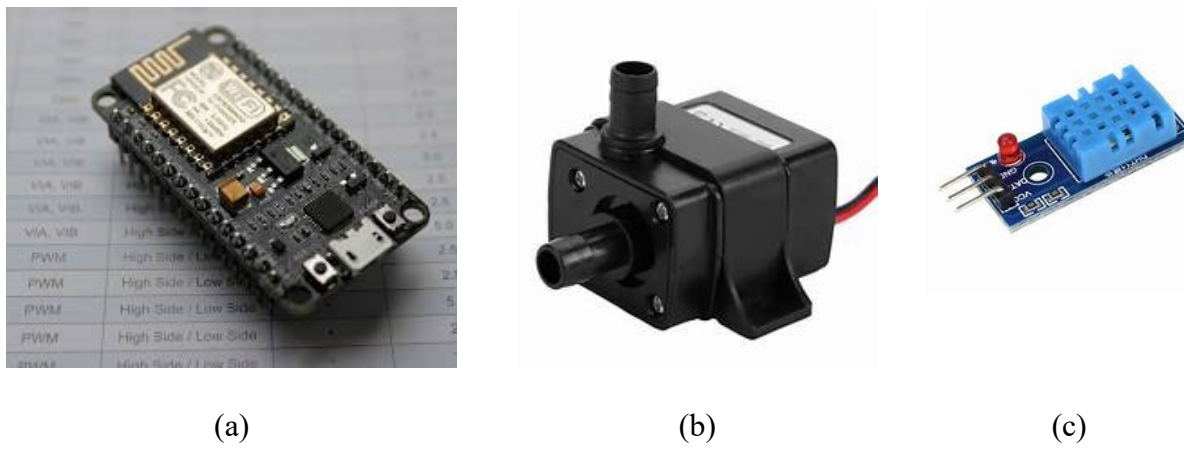


Fig. 3 Components (a) NodeMCU, (b) Water Pump, and (c) DHT11

Algorithm Design. In analyzing the impact of the time and frequency of watering in the Temporary Immersion System on the growth of orchid seeds and sowing orchid seeds, the algorithm method as depicted in Fig. 4 is used.

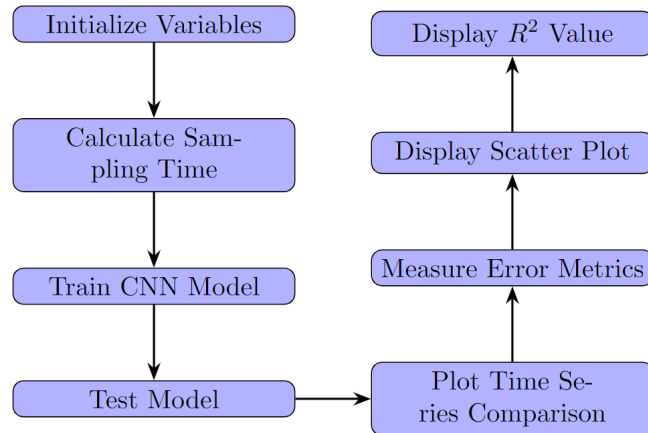


Fig. 4 Research Algorithm.

Based on the algorithm in Fig. 4, it can be explained that the code uses the predict() function to predict air humidity for each data in Xts. This function returns predicted values in vector form. The code uses the functions mse(), nmse(), rmse(), nrmse(), mae(), and mbe() to calculate various error measures between predictions and actual data. The first plot shows the actual and predicted humidity values for the first 500 minutes. The second plot shows the actual and predicted humidity values for the first 200 minutes. The R-squared value calculated with the code is 0.95, which means that the machine learning model can predict humidity with high accuracy.

Result and Discussion

Measurement results. During the period from 7 to 10 November 2023, measurements were carried out periodically every 10 seconds using the ESP32 device. A total of 4000 data were collected to record the temperature and humidity in vessel 1. The aim of this observation was to gain deeper insight into changes in temperature and humidity, especially in the context of vessel 1. The data processing was carried out using the Matlab application.

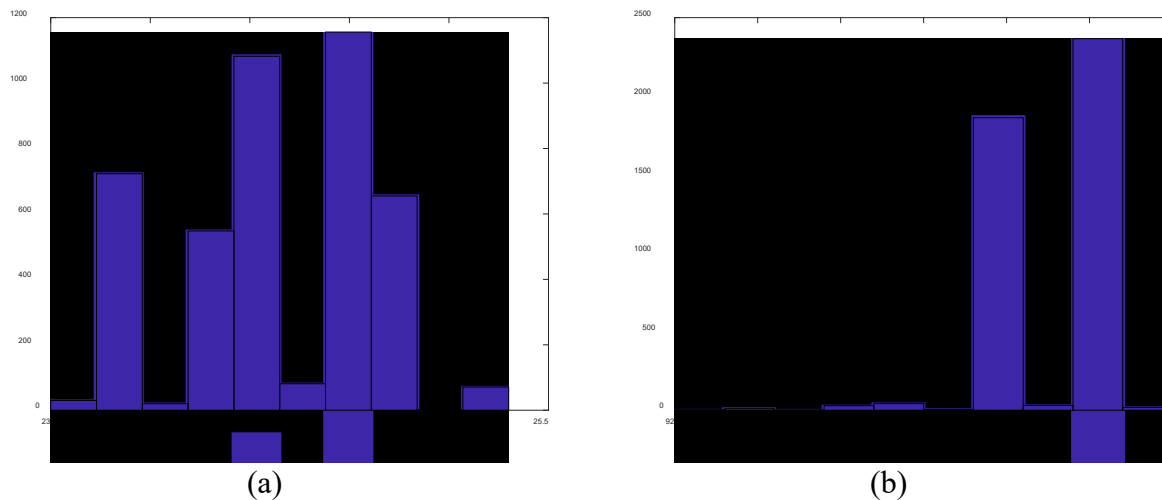


Fig. 5 Histogram of (a) Temperature and (b) Humidity Data.

Fig. 5(a) depicts a detailed graphical representation of the results of temperature measurements in vessel 1 during the observation period. The recorded temperature range was between 23° to 25.5° Celsius, providing a comprehensive picture of the temperature variations in the room. The peak frequency occurred at a temperature of 24.5° Celsius, with the amount of data reaching 1150,

followed by a temperature of 24° Celsius which reached a frequency of 1100 data. Apart from that, a temperature of 23.3° Celsius was also recorded with a frequency of 750 data.

Fig. 5(b) depicts a detailed graphical representation of the measurement results of humidity in vessel 1. The data presented via a histogram highlights the humidity value range between 92% to 98%. From the analysis carried out, it can be seen that the dominant humidity in vessel 1 reached 97%, with a measurement frequency reaching 2400 data. Apart from that, humidity at the 96% level also shows significance, measured by a measurement frequency of 1800 data.

Accuracy Test Results Using CNN. In the framework of this research, accurate measurements were carried out using the CNN method, and the results were compared with several other methods. The goal of this comparison is to gain a thorough understanding of the performance of tree regression methods on accuracy measurements.

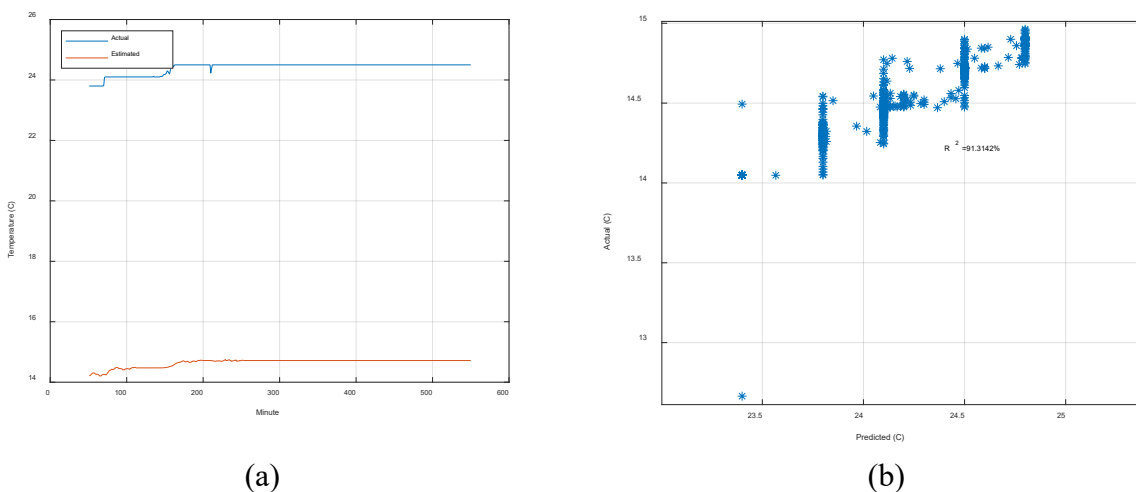


Fig. 6 (a) Comparison of Estimated Temperature Prediction Results Using CNN and (b) its Scatter Plot

The graph presented in Figure 6(a) illustrates a discrepancy between actual and predicted temperatures at the 50th minute, with the actual temperature recorded at 23.8 Celsius and the predicted temperature at 14.2 Celsius. The actual temperature exhibited a gradual increase, in contrast to the forecasted temperature, which rose in an erratic manner. By the 250th minute, both temperatures had stabilized, with the actual temperature reaching 24.5 Celsius and the forecasted temperature leveling off at 14.7 Celsius. The graph features a red line representing the predicted temperature, which does not run parallel to the blue line that indicates the actual temperature, highlighting the inaccuracy of the temperature predictions. Furthermore, the temperature prediction scatter plot, as shown in Figure 6(b), reveals that the CNN method's tests display a general trend of rising actual temperature values in conjunction with increases in estimated temperatures, despite the fluctuations in this ascent.

In Figure 7(a), during the 50th minute, 9 different tests were conducted, revealing a discrepancy between the actual and the predicted humidities, despite their nearly identical graphical representations. The actual humidity was recorded at 97%, while the predicted humidity was slightly lower at 94.05%. Both humidities experienced a decline at the 237th minute, with the actual humidity dropping to 96% and the predicted humidity to 93.3%. By the 250th minute, humidities began to rise, eventually stabilizing at the original levels by the 270th minute. This pattern indicates a slight increase in the second humidity measurement before it too stabilized at the initial level, suggesting that the predictions do not perfectly align with the actual humidities. The Scatter Plot of the humidity prediction is shown in Fig. 7(b). The humidity accuracy test appears almost rectangular, with humidity values fluctuating between 93.3% and 94.2%, and

reaching a peak at 94.6%. Concurrently, the CNN method achieved a high accuracy level, attaining 91.383%. Scatterplot analysis indicates a positive correlation between the actual and estimated humidity values.

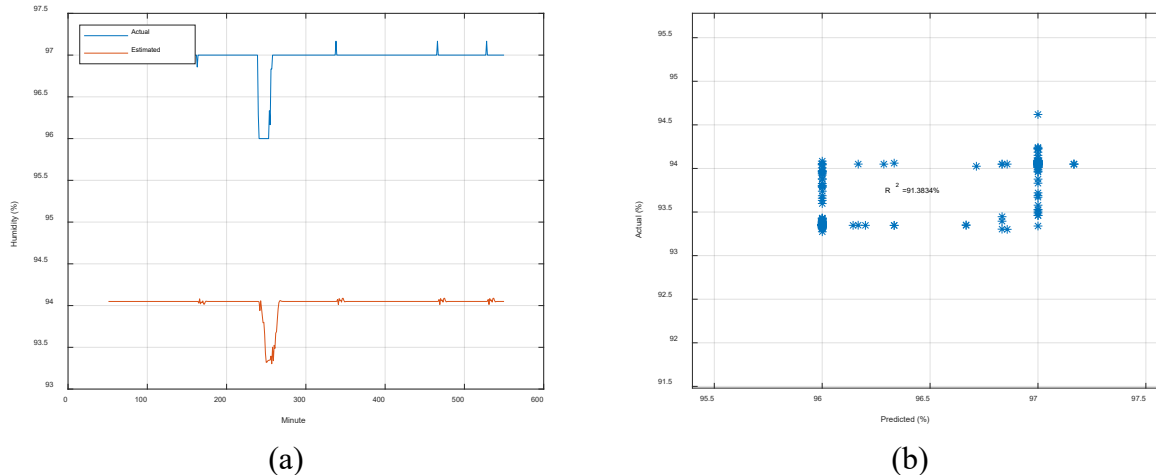


Fig. 7 (a) Comparison of Humidity Prediction using the CNN Method and (b) its Scatter Plot.

Comparison of Results. Table I demonstrates that the training method outperforms the testing method in forecasting temperature and humidity levels. This superiority is evidenced by the higher values of R₂, MSE, RMSE, MAE, MBE, NRMSE, and NMSE for the training method compared to those for the testing method. The overall analysis of the table within the figure suggests that the R₂ method is more effective in predicting air temperature and humidity.

Table 1. Comparison of Results.

Method	Temperature			Humidity		
	Train	Validation	Test	Train	Validation	Test
R ₂	0.95	0.71	0.91	0.94	0.5	0.91
MSE	93.3	1.81	93.7	7.74	8.65	8.07
RMSE	9.66	13.4	9.68	2.78	93.01	284
MAE	9.65	13.4	9.68	2.77	93.01	28.3
MBE	-9.65	13.4	-9.68	-2.77	93.01	-28.3
NMSE	0.15	2.01	0.15	8.33	8.84	8.64
NRMSE	4.2	3.09	6.91	0.55	9.11	2.43

Conclusion

In conclusion, this study successfully demonstrates the efficacy of an Internet of Things (IoT) and Convolutional Neural Networks (CNN)-based air humidity monitoring approach for enhancing orchid seed germination. The research findings affirm that the integrated system, utilizing real-time data collection and CNN analysis, achieves a notable accuracy level, particularly highlighted by a 91.383% success rate in humidity prediction. The insights gained from this study offer valuable information for farmers, enabling them to make informed decisions about optimal watering schedules and nutrient supplementation, thereby increasing the likelihood of successful orchid seed sowing. Moreover, the adaptability of this method for broader agricultural applications underscores its potential as a transformative tool in smart farming practices. By promoting increased productivity, improved crop quality, and reduced risks of failure, the IoT and CNN-

based humidity monitoring approach emerges as a promising avenue for sustainable agricultural practices.

References

- [1] Adminlp2m, Application of Smart Farming 4.0 in Current Agricultural Technology, 5 November 2020. <https://lp2m.uma.ac.id/2021/11/05/penerapan-smart-farming-4-0-dalam-teknologi-pertanian-masa-kini/>
- [2] Gifari Zakawali. Getting to Know Digital Farming, Here are the Benefits for Farmers, 21 November 2022. <https://store.sirclo.com/blog/benefits-digital-farming/>
- [3] Advantages Of Smart Agriculture | Disadvantages Of Smart Agriculture. 28 January 2024. <https://www.rfwireless-world.com/Terminology/Advantages-and-Disadvantages-of-SmartAgriculture-Farming.html>
- [4] Qolbiyatul Lina. Neural Networks Conclusion What Is It. 2 Jan 2019. <https://medium.com/@16611110/apa-itu-convolutional-neural-network-836f70b193a4>
- [5] Trivusi. Understanding and How the Convolutional Neural Network (CNN) Algorithm Works. 28 July 2022. <https://www.trivusi.web.id/2022/04/algoritma-cnn.html>.
- [6] Fig. Soil Monitoring with IoT – Smart Agriculture. February 24, 2021. <https://www.manxtechgroup.com/soil-monitoring-with-iot-smart-agri>.
- [7] Irenasari, Almira Harwidya, and Soemarno Soemarno. "Soil Moisture Assessment Using Soil Moisture Index (SMI) Method at the Bangelan Coffee Plantation, Malang Regency, East Java." Jurnal Tanah dan Sumberdaya Lahan 9, no. 1 (2022): 1-12. <https://doi.org/10.21776/ub.jtsl.2022.009.1.1>
- [8] Errissya Rasywir, Rudolf Sinaga, Yovi Pratama. Analysis and Implementation of Palm Disease Diagnosis using the Convolutional Neural Network (CNN) Method. September 2, 2020. <https://doi.org/10.31294/p.v22i2.8907>.
- [9] Ibrahim, Shafaf, Noraini Hasan, Nurbaitu Sabri, Khyrina Airin Fariza Abu Samah, and Muhamad Rahimi Rusland. "Palm leaf nutrient deficiency detection using convolutional neural network (CNN)." International Journal of Nonlinear Analysis and Applications 13, no. 1 (2022): 1949-1956.
- [10] Global Studio Center. Arduino Series – 053: Soil Moisture Sensor Module. 12 April 2022. https://www.youtube.com/watch?v=0_dsTgPVado.
- [11] Sintia, Wulantika, Dedy Hamdani, and Eko Risdianto. "Design of a Soil Moisture and Air Temperature Monitoring System Based on GSM SIM900A AND ARDUINO UNO." Jurnal Kumparan Fisika 1, no. 2 Agustus (2018): 60-65. <https://doi.org/10.33369/jkf.1.2.60-65>

Intelligent solutions for modern agriculture: Leveraging artificial intelligence in smart farming practices

Fatima Zahrae BERRAHAL^{1,a*}, Amine BERQIA^{2,b}

¹Smart Systems Laboratory, ENSIAS Mohammed V University in Rabat, Morocco

^afatimazahrae_berrahal@um5.ac.ma, ^bamine.berqia@ensias.um5.ac.ma

Keywords: Artificial Intelligence, Smart Agriculture, Machine Learning, Sustainable Agriculture, Precision Farming

Abstract. Rising global populations and climate change pose significant challenges to traditional farming methods. To address these issues, artificial intelligence (AI) is emerging as a transformative force in agriculture, often referred to as "Smart Agriculture" or "AI-powered Agriculture." This paper examines the multifaceted role of AI in revolutionizing farming processes. By leveraging AI technologies; farmers can enhance productivity, efficiency, and sustainability. This paper analyzes the diverse applications of AI in Agriculture, highlighting its potential to overcome critical farming challenges. It also explores the opportunities for AI-driven innovation in shaping the future of agriculture. With a specific focus on precision farming techniques, the paper investigates the implications and potential benefits of AI integration. This exploration sheds light on how AI can transform agricultural practices for a more sustainable future. This paper makes a comprehensive summary of the research on artificial intelligence technology in agriculture.

Introduction

Intelligent farming represents a cutting-edge approach to modern agriculture, leveraging advanced technologies such as Artificial Intelligence (AI) and Machine Learning (ML). This innovative farming paradigm marks a significant departure from traditional agricultural methods, harnessing the power of data-driven decision-making and precision techniques.

This paper delves into the convergence of smart agriculture and AI, revealing its potential to transform conventional agricultural practices and lay the groundwork for eco-conscious and more fruitful approaches.

The expansion of available land is vital to human survival and plays a crucial role in fostering economic growth and development [1]. Undoubtedly, this domain stands out as humanity's top priority, given that the overwhelming majority of our food supply relies on agriculture [2] Farming holds a vital position in the economy, acting as the bedrock of our monetary system. It serves as a fundamental pillar that supports the financial framework of our society.

With the growing unpredictability of environmental conditions, fulfilling the ever-increasing food requirements has become a progressively daunting task. Consequently, smart agriculture has emerged as a pivotal technology aimed at addressing these challenges [3].The agricultural industry is currently facing considerable obstacles due to various emerging factors, including global expansion, interests in food production, and the globalization of food markets, the unpredictability of food prices. Ensuring nutritional assurance has become a crucial goal, aiming to provide all individuals with consistent right to plentiful, nourishing sustenance. Therefore, the objective of infusing AI into cultivation techniques is to leverage AI to enhance and optimize assorted facets of farming and crop production practices.



Smart agriculture

Smart agriculture, as a comprehensive concept, incorporates a diverse array of technological innovations [4]. The blending of contemporary information technology and conventional farming has led to Agriculture 4.0, known as smart agriculture. This era represents a seamless integration of advanced technologies into farming practices, offering intelligent solutions and automation to address various agricultural needs [5]. The challenge posed by the spike in population and constrained grain production is sparking an increasing fascination with intelligent agriculture, leading to an upsurge in research in this area. The progress of agriculture relies on balancing productivity improvements with the constraints of the present era, and it is science and technology advancements that fuel the ongoing revolution in the agricultural sector [6]. The growing Tech-driven transition of farming procedures is generating a need for cutting-edge technologies capable of facilitating the shift to Intelligent farming. The agriculture of the future is no longer solely about planting, fertilizers, and irrigation, but also about algorithms and Artificial Intelligence.

Artificial Intelligence(AI)

AI, also known as Artificial Intelligence, entails the programming of machines to simulate human intelligence and learning abilities. Since its inception, it has deeply influenced various scientific fields and everyday life for all individuals. Its fundamental components are increasingly acknowledged as vital in our society, and we frequently embrace the advantages it provides, often without even realizing it.

The IA can potentially elevate agricultural techniques. It can contribute to increased yields by helping them make informed choices about the most appropriate crop varieties, embracing enhanced soil and nutrient management methods, efficiently controlling pests and diseases, estimating crop production, and predicting market prices. To attain these goals, AI employs sophisticated tools such as machine learning. These forefront tactics allow AI to confront the agricultural obstacles. Consequently, Growers have the chance to reap the advantages from Live surveillance of key agricultural variables. For instance climate, heat and water utilization, enabling them to make more informed choices [7].

The figure 1 illustrates the extensive application of artificial intelligence (AI) in agriculture, AI is revolutionizing how farmers make decisions and manage their operations. The figure likely depicts AI-driven solutions such as soil Management, crop Disease Detection Through Machine Learning and Deep Learning, climate and Weather Forecasting, Stronger and more resilient crop harvests, smart irrigation, locating suitable areas for planting particular crops and Enhance Decision-Making for Sustainable Solutions .

To adequately feed the population, it has been calculated that global food production will need to increase by a margin of 60-110% [8]. The realms of agricultural entrepreneurship, concentrate on enhancing their performance To fulfill the requirements of a burgeoning human civilization.

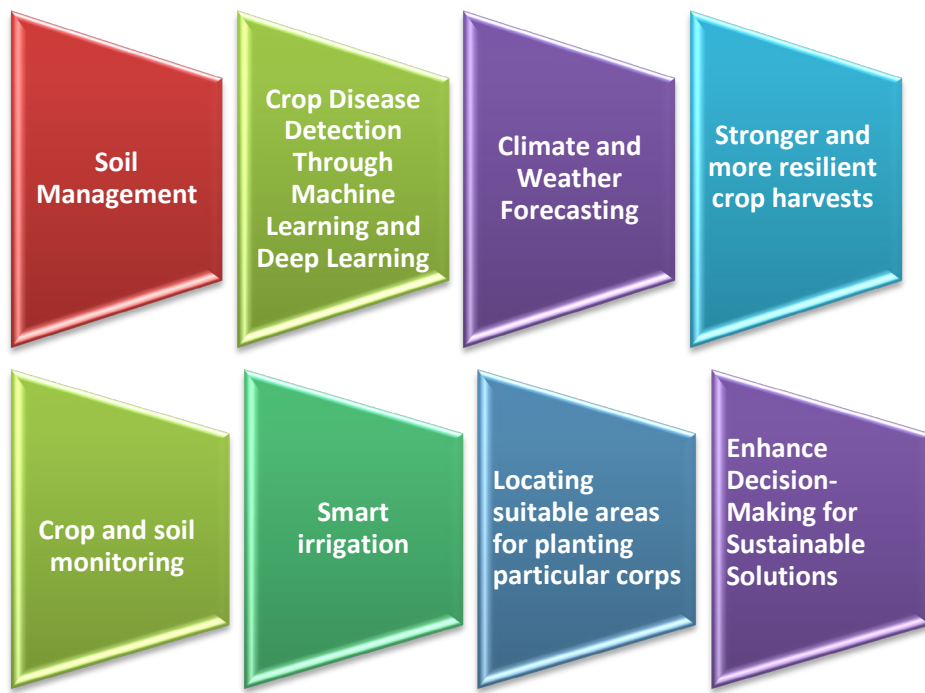


Fig.1 AI Harvest: Mapping the Pioneering Applications in Agriculture.

Unveiling the Promise of Artificial Intelligence in the Agrarian Sphere

Soil Management

Soil and crop management encounter various challenges, notably an escalating demand to sustain a burgeoning population and enhance food safety standards.

Precision farming employs advanced sensors and Forecasting analysis predictive analytics To capture instantaneous data related to soil information, Harvest readiness, Atmospheric condition, and Accessibility to improve crop production [9]. Precision spraying technology can lead to the use of unnecessary herbicide applications in redundant areas, potentially resulting in excessive herbicide consumption. However, this technology also offers the advantage of significantly, lowering the complete herbicide volume. When herbicides are used selectively in areas where weeds are present, it becomes feasible to lessen the environmental repercussions, cut costs, decrease crop damage to lessen the danger of chemical residue [10].The implementation of robots equipped with computer vision and artificial intelligence, which monitor and spray weeds, has the potential to reduce the current herbicide usage on crops by 80% .In precision fertilization,

A fertilizer dosage model is employed to calculate the necessary quantity of fertilizer, which is then administered through a variable-rate applicator [11].

Crop Disease Detection Through Machine Learning and Deep Learning

Plant diseases can significantly reduce crop yields, exerting direct repercussions on food production systems at both the national and global scales. The improper utilization of pesticides could lead to the development of long-term pathogen resistance, significantly reducing our ability to effectively combat them. This underscores the importance of precision farming as one of its key pillars [12].

Machine learning techniques have found significant uses in the agricultural industry, particularly in the analysis of soil fertility. The agricultural industry has consistently been a focal point for research in this domain [13].Automated techniques for plant disease detection are highly beneficial as they significantly reduce the extensive monitoring work required in large crop farms and enable the early detection of disease symptoms. Approximately 13% of global crop yield loss

is attributed to plant diseases. The potential of machine learning in revolutionizing the way plant diseases are detected and managed became evident, leading to further exploration and development in this field [14].

Climate and Weather Forecasting

In the field of weather forecasting, machine learning has established itself as a powerful tool, revolutionizing how meteorologists analyze and predict weather patterns. Thanks to its ability to process vast amounts of atmospheric data, machine learning algorithms excel at capturing the intricacies of weather phenomena. AI techniques play a crucial role in analyzing vast quantities of unstructured and diverse data, enabling the identification and utilization of intricate relationships within this data, all without relying on explicit analytical methods. Embracing these AI techniques becomes essential to comprehend the ever-growing data influx and effectively meet the demanding requirements in Weather Forecasting [15].

Stronger and more resilient crop harvests

AI technology is being adopted by the agricultural industry to foster healthier crop production, managing pests and overseeing soil and growth conditions. With changing weather patterns and increasing pollution posing challenges for agriculturist to identify the ideal timing for sowing grains, AI, in conjunction with weather forecasts, can be used to analyze weather conditions. By utilizing AI and weather data, farmers can plan the type of crops to cultivate and identify the most favorable planting times, ultimately improving their crop selection and increasing potential profitability [16].

Crop and soil monitoring

Evaluating and closely observing the effects of agricultural systems on soil quality is crucial to establish optimal management methods and sustainable land utilization. This is essential for addressing climate change, preserving biodiversity, and ensuring food and energy security. Artificial Intelligence (AI) has diverse applications in the monitoring of crops and soil, leveraging technologies such as drones. AI-based apps then analyze this data to identify optimal solutions [17,18]. These applications improve the comprehension of the comprehensive condition and quality of the soil. AI can predict and identify potential pest attacks by analyzing satellite or drone images and tracking trends in pest activity. The system continually monitors incoming data to detect early signs of an impending infestation [19].

Smart irrigation

The adoption of innovations in irrigation systems is crucial for improving water-use efficiency and aligning with Sustainable Development Goals, contributing significantly to this effort.

Traditional irrigation methods frequently face inefficiencies and experience water wastage, resulting in significant economic and environmental difficulties [20].

Smart irrigation control systems have emerged as a promising solution to address these challenges. These systems leverage advanced technologies to optimize irrigation practices, resulting in decreased water consumption and improved crop productivity. Through the integration of sensors, actuators, and intelligent algorithms, smart irrigation control systems facilitate precise and timely water delivery, based on the specific needs of crops. The core of these systems is sensor-based irrigation scheduling, where soil moisture sensors, for example, offer real-time measurements of soil moisture content. As a result, farmers can make informed decisions about their crops' water requirements, leading to efficient water usage and optimal crop growth [21].

Locating suitable areas for planting particular crops

Artificial intelligence, leveraging drone-captured imagery, offers invaluable support to agricultural workers by aiding in the identification of optimal crop planting locations, considering geographical attributes, soil conditions, and pertinent variables. Utilizing supervised machine learning algorithms, AI facilitates the assessment of seed quality and recognizes pre-existing crops. Before the sowing process commences, AI scrutinizes seed images, juxtaposing them with visuals of healthy seeds to guarantee the most favorable planting conditions [22].

Enhance Decision-Making for Sustainable Solutions

The integration of AI technology within the agriculture sector is experiencing a notable surge, facilitating enhanced decision-making processes. A growing reservoir of data is being harnessed and processed to inform agricultural strategies. This advancement is fueled by a range of industry innovations, including the widespread deployment of sensors, expedited access to satellite imagery, lowered expenses associated with data loggers, increased utilization of drones, and improved accessibility to data repositories. Collectively, these developments are instrumental in refining irrigation methodologies and practices [23].

Discussion

The combination of smart agriculture and AI has revolutionized the traditional farming methods, offering farmers and stakeholders valuable tools and solutions to overcome challenges posed by the ever-increasing global population, climate change, and limited natural resources.

This paper provides a comprehensive discussion of the various applications and innovations in smart agriculture through the lens of artificial intelligence.

AI continues to make significant strides in revolutionizing the agricultural sector, enabling farmers to optimize their processes and increase productivity. Precision farming remains one of the primary applications of AI in agriculture. AI-powered sensors and drones collect vast amounts of data, including soil quality, weather patterns, and crop health. Machine learning algorithms then analyze this data to provide valuable insights for farmers, helping them make data-driven decisions about irrigation, fertilization, and pest control. This precise approach results in more efficient resource utilization and reduced environmental impact. AI-powered autonomous farm machinery is also gaining momentum. These machines can perform tasks such as planting, harvesting, and weeding with high precision and minimal human intervention. This technology significantly alleviates the labor burden on farmers and allows them to focus on more strategic aspects of their operations. Crop disease detection is another noteworthy application. AI algorithms trained on extensive datasets of diseased and healthy crops can quickly identify and diagnose diseases in plants, facilitating early intervention and preventing widespread outbreaks. However, despite the promising innovations, there are challenges and potential implications that need to be addressed. Data privacy and ownership remain a concern, with questions about who controls and accesses the sensitive information generated by AI technologies.

The digital divide in agriculture is another significant issue. Smaller farmers and those in remote areas might lack access to the necessary infrastructure and training to adopt AI technologies, creating a disparity between tech-savvy and traditional farming practices. Moreover, ethical considerations surround the use of AI in agriculture, particularly in relation to genetically modified crops and altering the natural course of farming practices.

In conclusion, in the present time, AI continues to offer immense potential to revolutionize smart agriculture. However, it is essential to address the challenges and implications thoughtfully and responsibly. Integrating AI technologies into agriculture in a sustainable, inclusive, and ethical manner is crucial to harnessing its benefits for the long-term development of the agricultural sector.

Feature direction and issues:

The future of agriculture gleams with the emergence of artificial intelligence (AI) as a powerful tool. There is also some feature direction and some issues for further exploration:

Feature direction:

- ✓ Develop AI algorithms for image recognition that can automatically detect pests and diseases in crops through drone or ground-based cameras, enabling early intervention.
- ✓ Train AI models on historical data to predict potential pest or disease outbreaks based on weather patterns and crop types, allowing for preventative measures.
- ✓ Train AI models to analyze soil sensor data and satellite imagery to identify nutrient deficiencies and create customized fertilizer plans for different zones within a field.
- ✓ Integrate AI with drone-based imaging or spectral sensors to identify nutrient stress symptoms in crops and deliver targeted fertilizer applications.
- ✓ Explore AI-powered robotic systems or smart applicators that can deliver precise fertilizer amounts based on real-time plant needs.
- ✓ Develop AI models to predict water needs based on weather forecasts, crop growth stages, and historical data. This allows for proactive irrigation adjustments.
- ✓ Refine AI-controlled robots for tasks like harvesting.

Issues for Further Exploration:

- ✓ Standardizing data formats and ensuring data quality across different farms and regions is crucial for accurate AI model training and application. Developing robust security protocols to protect sensitive agricultural data from cyberattacks and ensuring farmer privacy is essential.
- ✓ Developing AI models that are interpretable and transparent to farmers allows for trust and informed decision-making.
- ✓ Accessibility and affordability: Bridge the digital divide by creating user-friendly interfaces and affordable AI technology for small and medium-scale farmers.
- ✓ Focus on human-centered AI design that empowers farmers and leverages their expertise alongside AI capabilities.
- ✓ Environmental impact assessment: Develop AI tools to optimize resource use and minimize environmental footprint associated with agricultural practices.

Conclusion

The growth of artificial intelligence (AI) is exponential and impacting numerous sectors, the swift advancement of information technology and data processing capabilities has given rise to a set of innovative tools commonly known as artificial intelligence (AI). The digital transformation occurring across all sectors is also making its way into agriculture. Farmers' living and working conditions are changing, thanks to new technologies.

As the world population continues to grow, agriculture plays a vital role in the future of our planet. Making it even more sustainable, efficient and productive is crucial, despite all structural and technological changes. One of the most powerful levers for action is the development of agriculture through artificial intelligence.

In conclusion, smart agriculture powered by AI holds immense potential for transforming the agricultural sector and addressing the challenges of food security and sustainability. However, to realize these benefits, it is crucial to address the challenges mentioned above and foster an enabling environment through collaboration between agricultural stakeholders, technology developers, and research institutions. By overcoming these obstacles, we can harness the power of AI to build a more efficient, resilient, and sustainable future for agriculture.

References

- [1] Sarfraz S, Ali F, Hameed A, Ahmad Z, Riaz K.: Sustainable agriculture through technological innovations. Sustainable agriculture in the era of the OMICs revolution, 2023, pp. 223-239. https://doi.org/10.1007/978-3-031-15568-0_10
- [2] Sitharthan R, Rajesh M, Vimal S, Saravana Kumar E, Yuvaraj S, Abhishek Kumar, Jacob Raglend I, Vengatesan K.: A novel autonomous irrigation system for smart agriculture using AI and 6G enabled IoT network, Microprocessors and Microsystems, Volume 101, 2023, 104905. <https://doi.org/10.1016/j.micpro.2023.104905>
- [3] Ganesh Gopal Devarajan, Senthil Murugan Nagarajan, Ramana T.V., Vignesh T., Uttam Ghosh, Waleed Alnumay, DDNSAS: Deep reinforcement learning based deep Q-learning network for smart agriculture system, Sustainable Computing: Informatics and Systems, Volume 39, 2023, 100890. <https://doi.org/10.1016/j.suscom.2023.100890>
- [4] Stefano Cesco, Paolo Sambo, Maurizio Borin, Bruno Basso, Guido Orzes, Fabrizio Mazzetto, Smart agriculture and digital twins: Applications and challenges in a vision of sustainability, European Journal of Agronomy, Volume 146, 2023, 126809. <https://doi.org/10.1016/j.eja.2023.126809>
- [5] Xing Yang, Lei Shu, Jianing Chen, Mohamed Amine Ferrag, Jun Wu, Edmond Nurellari and Kai Huang, "A Survey on Smart Agriculture: Development Modes, Technologies, and Security and Privacy Challenges," IEEE/CAA J. Autom. Sinica, vol. 8, no. 2, pp. 273-302, Feb. 2021. <https://doi.org/10.1109/JAS.2020.1003536>
- [6] Y. Liu, X. Ma, L. Shu, G. P. Hancke, and A. M. Abu-Mahfouz, "From industry 4.0 to agriculture 4.0: current status, enabling technologies, and research challenges," IEEE Trans. Ind. Informat., 2020. <https://doi.org/10.1109/TII.2020.3003910>
- [7] S. Y. Liu, "Artificial Intelligence (AI) in Agriculture," in IT Professional, vol. 22, no. 3, pp. 14-15, 1 May-June 2020. <https://doi.org/10.1109/MITP.2020.2986121>
- [8] J. Rockstrom, J. Williams, G. Daily et al., "Sustainable intensification of agriculture for human prosperity and global sustainability," Ambio, vol. 46, no. 1, pp. 4–17, 2017. <https://doi.org/10.1007/s13280-016-0793-6>
- [9] Ampatzidis Y, Partel V, Costa L (2020) Agroview: cloud-based application to process, analyze and visualize UAV-collected data for precision agriculture applications utilizing artificial intelligence. Comput Electron Agric 174:105457. <https://doi.org/10.1016/j.compag.2020.105457>
- [10] Balafoutis A, Beck B, Fountas S, Vangeyte J, Wal TV, Soto I, Gómez-Barbero M, Barnes A, Eory V (2017) Precision agriculture technologies positively contributing to GHG emissions mitigation. Farm Prod Econ Sustain 9:1339. <https://doi.org/10.3390/su9081339>
- [11] Elbeltagi A, Kushwaha NL, Srivastava A, Zoof AT (2022) Chapter 5: artificial intelligent-based water and soil management. Deep Learning for Sustainable Agriculture 2022:129–142. <https://doi.org/10.1016/B978-0-323-85214-2.00008-2>
- [12] Kaur, S., Pandey, S. & Goel, S. Plants Disease Identification and Classification Through Leaf Images: A Survey. Arch Computat Methods Eng 26, 507–530 (2019). <https://doi.org/10.1007/s11831-018-9255-6>
- [13] P. Tamsekar, N. Deshmukh, P. Bhalchandra, G. Kulkarni, K. Hambarde, S. Husen, Comparative analysis of supervised machine learning algorithms for GIS-based crop selection

- prediction model, in: Computing and Network Sustainability, Springer, 2019, pp. 309–314.
https://doi.org/10.1007/978-981-13-7150-9_33
- [14] Witten, I.H., Holmes, G., McQueen, R.J., Smith, L.A., & Cunningham, S.J. (1993). Practical machine learning and its application to problems in agriculture.
- [15] Dewitte, S.; Cornelis, J.P.; Müller, R.; Munteanu, A. Artificial Intelligence Revolutionises Weather Forecast, Climate Monitoring and Decadal Prediction. *Remote Sens.* 2021, 13, 3209.
<https://doi.org/10.3390/rs13163209>
- [16] Sharma S, Gahlawat VK, Rahul K, Mor RS, Malik M. Sustainable innovations in the food industry through artificial intelligence and big data analytics. *Logistics.* 2021; 5(4):66.
<https://doi.org/10.3390/logistics5040066>
- [17] Lowe M, Qin R, Mao X. A review on machine learning, artificial intelligence, and smart technology in water treatment and monitoring. *Water.* 2022;14(9):1384.
<https://doi.org/10.3390/w14091384>
- [18] Shelake S, Sutar S, Salunkher A, et al. Design and implementation of artificial intelligence powered agriculture multipurpose robot. *International Journal of Research in Engineering, Science and Management.* 2021;4(8):165–167.
- [19] Marcu IM, Suciu G, Balaceanu CM, Banaru A. IoT-based system for smart agriculture. In: 2019 11th International Conference on Electronics, Computers And Artificial Intelligence (ECAI). IEEE; 2019, June:1–4. <https://doi.org/10.1109/ECAI46879.2019.9041952>
- [20] C.A. Buckner, R.M. Lafrenie, J.A. D'enomm'ee, J.M. Caswell, D.A Want, Complementary and alternative medicine use in patients before and after a cancer diagnosis, *Curr Oncol* 25 (2018) e275-81. Available from, <https://www.intechopen.com/chapters/83182>.
<https://doi.org/10.3747/co.25.3884>
- [21] Y.D. Wu, Y.G. Chen, W.T. Wang, K.L. Zhang, L.P. Luo, Y.C. Cao, et al., Precision fertilizer and irrigation control system using open-source software and loose communication architecture, *J. Irrig. Drain. Eng.* 148 (2022) 1–9. [https://doi.org/10.1061/\(ASCE\)IR.1943-4774.0001669](https://doi.org/10.1061/(ASCE)IR.1943-4774.0001669)
- [22] Sane TU, Sane TU. Artificial intelligence and deep learning applications in crop harvesting robots-A survey. In: 2021 International Conference on Electrical, Communication, and Computer Engineering (ICECCE). IEEE; 2021, June:1–6.
<https://doi.org/10.1109/ICECCE52056.2021.9514232>
- [23] Banthia V, Chaudaki G. The study on use of artificial intelligence in agriculture. *J. Adv. Res. Appl. Artif. Intell. Journal of Advanced Research in Applied Artificial Intelligence and Neural Network.* 2022;5(2):18–22.

On the performance assessment of King Faisal University grid-connected solar PV facility

Mounir BOUZGUENDA

Department of Electrical Engineering, College of Engineering, King Faisal University,
Al- Hassa, PC 39182, Saudi Arabia

mbuzganda@kfu.edu.sa

Keywords: Energy Performance Index, Array Yield, Final Yield, Performance Ratio, Capacity Factor, System Efficiency, KSA 2030 Vision

Abstract. This paper evaluates the performance of the 9.8 kW grid-connected solar photovoltaic (PV) system mounted on the rooftop of the College of Engineering within the King Faisal University campus. The facility consists of four fields rated 2.45 kW each. Each field consists of ten 10 solar panels connected to a 3kW. The collected data include hourly and sub-hourly measurements of the radiation, ambient and module temperatures, AC and DC voltages, currents, and power outputs. Other measurements include cumulative produced energy and CO₂ savings. The assessed parameters of the PV facility include daily, and monthly energy, final yield, efficiency, and module performance ratio (PR). Aggregate performance analysis results show that the station operated as planned. The annual radiation measured in 2017 reached 2449 kWh/m² with a daily average of 6.710 kWh/m². The annual energy production reached 16.047 MWh with an average of 43.964 kWh/day. The system efficiency and capacity factor are 11.22% and 17.25%, respectively.

Introduction

Saudi Arabia's wealth in natural gas and oil has contributed to the country's rapid economic expansion over the last three decades. But the nation also produces the most carbon dioxide emissions, which suggests that it is becoming more and more dependent on gas and oil for electricity production. Saudi Arabia, having the biggest economy in the GCC, is heavily reliant on non-renewable energy sources, which makes the quest for alternate energy sources necessary. Saudi Arabia is viewed by experts as a potential hub for the production of photovoltaic solar energy. The European Commission Institute for Energy estimates that 0.3% of the light falling on the Middle East and Sahara deserts might supply Europe. Saudi Arabia, one of the largest developing countries, ranks eleventh in terms of electricity production globally. In particular, the oil and gas fuels dominate its electricity mix.

Meanwhile, evidence has shown that monitoring and performance analysis of both grid-connected and off-grid solar PV systems improve the performance of such systems. Several factors have a determinant impact on the performance of a PV system. Some of these factors have positive effects on performance while others have negative effects. Such factors and performance metrics are undertaken in this study.

The paper is organized as follows. Section 2 is devoted to Saudi Arabia's 2030 Vision and its renewable energy initiatives. The background, the motivation, and the objective of the present study are briefly introduced in this section. In Section 3, renewable energy prospects and operating large-scale facilities are discussed. In Section 4, solar PV performance metrics are discussed. Meanwhile, Section 5 and Section 6 are devoted to the analysis method and results discussion, respectively.



Renewable Energy Initiatives in KSA

Substantial evidence indicates that the shift to sustainable sources of energy will address environmental issues such as greenhouse gas emissions, air pollution, and climate change to a certain extent. This shift is occurring at a considerable rate in developing countries [1]. As a result of recognizing the need to diversify its energy sources, reduce its carbon footprint, and create a more sustainable and resilient energy sector, Saudi Arabia has launched ambitious renewable energy programs based on eight pillars.

- The Saudi Vision 2030 is a plan that aims to reduce the country's dependence on oil transform its economy and increase the contribution of renewable energies.
- The second pillar is the National Renewable Energy Program (NREP), initiated in 2017 and aims to add significant renewable energy capacity to the Saudi grid. Such projects include the Sakaka solar power plant, one of the country's first major solar projects.
- The King Salman Renewable Energy Initiative. It aims to install 41 GW of solar PV by 2032.
- The Renewable Energy Project Development Office (REPDO) was established to supervise and manage the development of renewable energy projects in the country. REPDO plays a crucial role in the acquisition and execution of renewable energy projects.
- The focus on solar and wind energy is due to KSA's abundant natural resources in these areas. Solar projects include photovoltaic and concentrated solar power systems, while wind projects utilize the country's coastal and inland wind resources.
- The Energy Efficiency and Conservation initiative to increase renewable energy capacity by focusing on improving energy efficiency in the construction, transport, and industry sectors.
- Diversification of energy sources: The government has been working to diversify its energy resources by integrating renewable energy into its energy mix and developing infrastructure for electricity storage and grid integration.

As a result of the framework of the National Renewable Energy Program, the number of renewable energy projects reached 13 projects with a total capacity of 4,470 MW of PV and 40 MW of wind. The expected annual energy produced amounts to 15,109 GWh with an estimated CO₂ emission reduction of 9,828,156 Ton/year by 2024. Table 1 lists some of the grid-connected PV systems in the country. With the increasing role of solar energy in meeting the kingdom's need for energy and the installation of many solar PV projects in the kingdom, it is necessary to assess the performance of existing and future off-grid and grid-connected solar PV systems in the kingdom. The proposed method has been applied in many countries and the study results will be compared to current studies in the field of solar PV system performance assessment.

Methodology

Research has been conducted recently to examine the effectiveness of grid-connected solar PV power systems in various settings. Reference yield, array yield, final array yield, capture losses, system losses, and performance ratio were among the performance metrics that were computed. Furthermore, it has been demonstrated that doing a performance analysis of the actual efficiency of photovoltaic installations is a difficult undertaking since it necessitates processing data from solar PV system operation monitoring. Procedures were therefore developed to assess solar power plant performance using data from actual system monitoring. Monitored data include radiation, ambient and module temperatures, AC voltage/current, DC voltage/current, and DC/AC power. Assessed parameters include daily, and monthly energy, final yield, efficiency, and module performance ratio (PR).

Table 1: Major solar PV projects in KSA [2]

Plant Name	Location	Size (MW)	Starting Year
Sakaka Solar PV Park	Al Jouf	405	2020
Haradh Solar PV Park	E. Province	30	2021
King Abdulaziz International Airport Solar PV Park	E. Province	10.5	2013
King Abdullah Petroleum Studies and Research Center Solar Park	E. Province	3	2013
King Abdullah Univ. of Science and Tech.-Solar Park	Jeddah	2	2010
Saudi Aramco Park Project	Khobar	10.5	2012
Al Fanar Jinko Solar PV Plant	Makkah	5.4	2018
Al Kharj Solar PV Park	Riyadh	15	2019
Matco Solar PV Plant	Riyadh	3.5	2019

Performance Assessment of PV Power Plant Performance Using Metric Indicators

IEC61724 standard mandates that the final yield (Y_f), array yield (Y_a), reference yield (Y_r), energy efficiency (η), and the total energy generated by the PV system E_{AC} , are used to evaluate the performance of a grid-connected PV installation.

Array yield.

The array yield (Y_a) is the ratio of the DC energy output delivered by the PV modules over a defined period divided by the PV-rated power and is given as [4]:

$$Y_a = \frac{E_{DC} (\text{kWh})}{PV_{Rated} (\text{kWp})} \quad (1)$$

The daily array yield ($Y_{a,d}$) and the monthly average array yield ($Y_{a,m}$) are given as [4]:

$$Y_{a,d} = \frac{E_{DC} (\text{kWh/day})}{PV_{Rated} (\text{kWp})} \quad (2)$$

$$Y_{a,m} = \frac{1}{N} \sum_{d=1}^N Y_{a,d} \quad (3)$$

E_{DC} is the DC energy output delivered by the PV modules (kWh) and N is the number of days in the month.

Final yield

The final yield is the total AC energy during a specific period divided by the rated power of the PV system. This metric is used to compare a given PV system with other existing PV systems.

The daily array yield ($Y_{f,d}$) and the monthly average array yield ($Y_{f,m}$) are given as: [5]

$$Y_{f,d} = \frac{E_{AC} (\text{kWh/day})}{PV_{Rated} (\text{kWp})} \quad (4)$$

$$Y_{f,m} = \frac{1}{N} \sum_{d=1}^N Y_{f,d} \quad (5)$$

E_{AC} is the AC energy output delivered by the PV modules to the grid (kWh) and N is the number of days in the month.

$$E_{AC,m} = \frac{1}{N} \sum_{d=1}^N E_{AC,d} \quad (6)$$

With $E_{AC,m}$ being the monthly AC energy output and N the number of days in a month.

Reference yield

The reference yield is the ratio of the global solar radiation H_t (kWh/m²) and the PV's reference irradiance. The reference yield is given as [6]:

$$Y_r = \frac{H_t (kWh/m^2)}{H_g} \quad (7)$$

In this case, $H_g=1 \text{ kW}/m^2$

Performance ratio

The performance ratio (PR) depends on the total losses by the PV system components (modules, inverters, trackers, and cables) and losses due to weather conditions such as ambient temperature, rain, shade, etc. The performance ratio (PR) is defined as the final yield divided by the reference yield and is expressed as:

$$PR = \frac{Y_f}{Y_r} \quad (8)$$

Array capture losses.

The array capture losses (L_C) are due to the PV array losses and are expressed as:

$$L_C = Y_r - Y_a \quad (9)$$

System losses

The system losses (L_S) are caused by inverter losses.

$$L_S = Y_a - Y_f \quad (10)$$

Capacity factor

The annual capacity factor (CF) is:

$$CF = \frac{E_{AC}}{8760 * P_{PV, rated}} \quad (11)$$

Where E_{AC} is the annual energy produced by the system and $P_{PV, \text{rated}}$ is the PV rated capacity.

System efficiencies

The system efficiencies consist of 3 components-namely the PV module efficiency, the inverter efficiency and the system efficiency. The PV module efficiency is expressed:

$$\eta_{PV} = \frac{100 * E_{AC}}{S * H_t} (\%) \quad (12)$$

The monthly PV module efficiency ($\eta_{PV,m}$) expression is:

$$\eta_{PV,m} = \frac{\sum_{i=1}^n E_{DC}}{S * \sum_{i=1}^N H_t} (\%) \quad (13)$$

Where E_{DC} is the total energy produced by solar PV modules, N is the number of days in a month and, and S is the total PV module surface (m^2).

The inverter efficiency is given as

$$\eta_{PV} = \frac{100 * E_{AC}}{E_{DC}} (\%) \quad (14)$$

The temperature loss coefficient (η_{tem}) is

$$\eta_{tem} = 1 + \alpha_P (T_c - T_{C,STC}) \quad (15)$$

$$P_{PV} = Y_{PV} f_{PV} \left(\frac{G_T}{G_{C,STC}} \right) [1 - \alpha_P (T_c - T_{C,STC})] \quad (16)$$

Where α_P indicates the power temperature coefficient ($^{\circ}/\text{C}$), T_c is the PV cell temperature ($^{\circ}\text{C}$), and $T_{C,STC}$ is PV cell temperature at STC ($^{\circ}\text{C}$).

$$T_c = T_a + \frac{P}{800} (T_{NOCT} - 20) \quad (17)$$

Where P is the power density at a specific time and T_{NOCT} is the normal operating cell temperature.

Description of KFU 9.8kW PV Facility

The 9.80 kW grid-connected PV facility has been operating since 2014. The facility consists of four arrays rated 2.45 kW each. Each array is made of ten 245Wp panels with two different solar cell specifications: efficiency and robustness in harsh weather conditions. Each field is connected to a 3-kW inverter with an efficiency of 97%. The characteristics of the solar panel technologies are listed in Table 2 . The detailed performance analysis was done for Array 1.

Table 2. Characteristics of the Solar Modules

Parameter	SM-D245PC2 (Arrays 1@2)	SM-245PC8 (arrays 3&4)
Rated power (Pmax)	245W	245W
Voltage at Pmax (Vmp)	30.4V	30.4V
Current at Pmax (Imp)	8.06A	8.08A
Warranted minimum Pmax	245W	245 W
Short-circuit current (Isc)	8.39A	8.63A
Open-circuit voltage (Voc)	37.8V	37.4V
Module efficiency	14.91%	14.72%
Operating module temperature	-40°C to + 85°C	-40°C to + 85°C
Isc Temperature coefficient	0.061%/°C	0.052%/°C
Voc Temperature Coef.	-0.345%/°C	-0.312%/°C
Power Temperature Coef.	-0.458%/°C	-0.429%/°C
Inverter Efficiency	97%	97%

Performance Analysis

As discussed earlier, the solar PV facility consists of four arrays. Each array consists of 10 solar panels connected in series yielding a peak power of 2.45 kW. The first part of the performance analysis focuses on Array 1. Therefore, a detailed performance analysis is carried out. The second part of the analysis includes the system aggregate efficiency and capacity factor for all four arrays. Figure 2 displays (a) the daily AC energy produced in May 2017, (b) the weather statistics for June 13, 2017 and (c) that the cumulative energy produced by Array 2 reached 17.5 MWh in June.

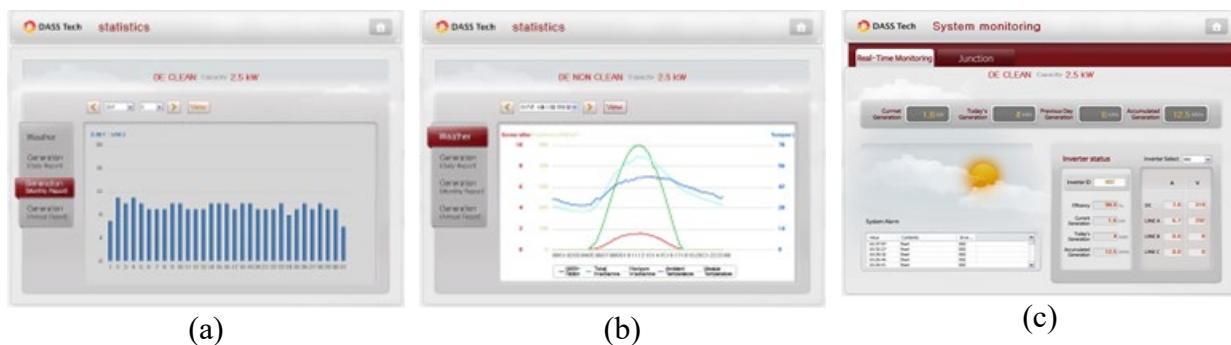


Figure 1: Array 2 Performance and Monitoring statistics (a) Daily AC energy (kWh) statistics May 2017.(b) Weather statistics, June 13, 2017. (c) Monitoring statistics, June 1, 2017.

Array 1 Performance Analysis

The nameplate efficiency of Array 1 is 14.91%. Tables 3 and 4 display the 2017 performance analysis results for Array 1. Based on these tables, the following observations are worth mentioning:

- The average plane of array radiation is 181 kWh/m². This is equivalent to 5.94 kWh/m²/day.
- Maximum power output ranges from 1.60 kW to 2.40 kW in March 2017.
- The highest monthly AC energy output of 400 kWh was produced in March and July.

- The annual AC energy output is 3.8 MWh. This is equivalent to an average of 10.42 kWh/day.
- The average efficiency exceeded 100%. This was because data are measured within one decimal point, which resulted in roundup and round-down errors. This has impacted the overall system efficiency and rendered higher than the solar conversion itself. In this case, the overall efficiency varied from 9.36% to 14.25%.
- The average performance varied from 55.8% to 84.9% with an overall average of 74.2%. The average monthly capacity factor varied from 13.97% to 21.59%.
- As seen in Tables 3 and 4 the obtained results of the capacity factors are aligned with the geographical location of the PV system and the harsh weather conditions. The system efficiency and capacity factors are compared with PV GIS based simulation results.
- The comparison results are shown in the last two rows of Table 4. The measured and simulated efficiency/capacity factor are slightly different with moderate deviation. However, they vary from one month to another.

Table 3: Array 1 Monthly Energy ambient and module temperatures

Month	Jan.	Feb.	Mar.	April	May	June	July	Aug.	Sept.	Oct.	Nov.	Dec.	Annual
POA (kWh/m ²)	160.6	130.8	162.3	204.7	209.4	188	209.9	211	211.4	214.1	169.8	188.8	181 ^y
Pac_max (kW)	2.1	2.3	2.4	2.1	2.2	1.7	1.6	1.6	1.6	1.6	2	2.1	2.4*
POA_max (kWh/m ²)	1.000	1.041	1.041	1.041	1.041	1.008	1.004	1.041	1.041	1.041	1.041	1.041	1.041*
T_mod_max (°C)	47.7	53.4	60.4	69.1	67.5	66.1	70.1	71.5	70.4	63.8	55.9	52.2	71.5*
T_amb_max (°C)	31	30	37.8	48.1	48.8	50.1	53.3	53.2	50.8	44.3	37.6	33.8	53.23*
DC Energy (kWh)	302	275	322	381	351	352	336	331	312	293	246	350	321 ^y
AC Energy (kWh)	300	200	400	300	400	300	400	300	300	300	300	300	317 ^y

*Maximum value ^yaverage value

Table 4: Array 1 efficiencies, performance ratio and capacity factor for 2017.

Month	Jan.	Feb.	Mar.	Apr.	May	June	July	Aug.	Sept.	Oct.	Nov.	Dec.	Annual
Eff_PV (%)	12.68	14.17	13.54	12.68	11.37	12.71	10.85	10.67	10.02	9.27	9.84	12.62	12.65
Eff_Inv (%)	100.3	100.6	100.3	100.5	100.9	100.9	101.0	100.8	100.9	100.9	101.0	100.7	99.5
Eff_sys (%)	12.72	14.25	13.59	12.75	11.47	12.82	10.96	10.76	10.12	9.36	9.94	12.71	12.44
Y _{a,m} (kWh)	121.2	109.4	127.3	152.0	139	142.4	133.1	131.4	123.5	114.2	95.7	136.6	127.2
Y _{f,m} (kWh)	122.1	111.1	131.4	155.5	143.1	143.7	137.1	135.3	127.4	119.4	100.6	143.0	129.0
Y_ref	160.6	130.8	162.3	204.7	209.4	188.0	209.9	211.0	211.4	214.1	169.8	188.8	181.0
P.R.(%)	76.1	84.9	81.0	76.0	68.3	76.4	65.3	64.1	60.3	55.8	59.2	75.7	74.2
C.F. (%)	16.42	16.53	17.66	21.59	19.23	19.95	18.43	18.18	17.7	16.05	13.97	19.22	18.61
Simulated Eff_PV (%)	13.6	13.2	12.7	12.4	11.9	11.6	11.6	11.8	12.0	12.4	13.1	13.5	12.4
Simulated C.F. (%)	18.6	18.2	20.5	18.7	19.8	19.7	20.1	20.9	21.2	21.5	18.2	19.0	19.7

Aggregate Performance Analysis

An aggregate performance analysis of the entire PV facility was conducted considering all four fields. The results are shown in Tables 5 and 6.

- Table 5 displays the monthly efficiency and the capacity factor for each of the four arrays. Array 4 has the highest annual values of 12.26% and 18.85%, respectively. Meanwhile, Array 2 has the lowest annual values of 9.67% and 14.87%, respectively.
- According to Table 6, the highest efficiency and the highest capacity factor were obtained in February and April, respectively. The annual efficiency and capacity factor were 11.22%

and 17.25%, respectively. Compared to reported capacity factors around the world shown in Figure 2, the recorded capacity factor at KFU is slightly below KSA figures and other countries.

Table 5. Aggregate Performance of the Entire Grid Connected PV Facility.

	Array 1		Array 2		Array 3		Array 4	
Month	Eff sys (%)	C.F. (%)						
Jan.	12.84	16.51	10.49	13.50	12.20	15.69	16.12	20.74
Feb.	14.40	16.70	11.99	13.91	13.82	16.03	17.91	20.77
Mar.	13.76	17.88	11.52	14.98	13.17	17.12	15.99	20.79
April	12.78	21.66	10.64	18.03	12.31	20.86	12.71	21.54
May	11.58	19.42	9.45	15.85	11.12	18.65	11.55	19.37
June	12.82	19.95	10.49	16.33	9.44	14.68	12.64	19.67
July	11.03	18.54	9.04	15.20	13.05	21.94	9.53	16.02
Aug.	10.84	18.32	8.80	14.87	10.39	17.56	6.69	11.30
Sept.	10.21	17.86	8.49	14.80	9.72	17.01	11.31	19.78
Oct.	9.44	16.18	7.68	13.17	8.93	15.31	13.47	23.10
Nov.	10.08	14.17	8.15	11.45	9.48	13.32	9.96	14.00
Dec.	12.81	19.37	10.74	16.24	12.26	18.54	12.75	19.27
Annual	11.74	18.06	9.67	14.87	11.21	17.24	12.26	18.85

Table 6. Aggregate Performance Analysis of the PV Facility.

Month	POA (kWh/m²)	Monthly Energy (kWh)	Daily Energy (kWh)	System efficiency η_{sys} (%)	Capacity Factor (%)
Jan.	160.6	1211.0	39.06	10.49	13.50
Feb.	130.8	1110.0	39.64	11.99	13.91
Mar.	162.3	1290.0	41.61	11.52	14.98
April	204.7	1448.0	48.27	10.64	18.03
May	209.4	1336.0	43.10	9.45	15.85
June	188.0	1246.0	41.53	10.49	16.33
July	209.9	1307.0	42.16	9.04	15.20
Aug.	211.0	1131.0	36.48	8.80	14.87
Sept.	211.4	1226.0	40.83	8.49	14.80
Oct.	214.1	1235.0	39.84	7.68	13.17
Nov.	169.8	934.0	31.13	8.15	11.45
Dec.	188.8	1338.3	43.17	10.74	16.24
Annual	188.4	1234.4	40.57	11.22	17.25

Summary

In this paper, a 9.8 kW grid-connected PV system in the College of Engineering Building at King Faisal University has been monitored since its commission. In particular, the 2017 performance was assessed on a daily, monthly, and annual basis. Array 1 performance analysis results show that this array's annual efficiency and capacity factor are 12.44% and 19.22%, respectively. The aggregate performance analysis results show that the station operated as planned. The overall efficiency and capacity factors are 11.22% and 17.25%. This is because Array 1 performed less than the other three arrays. The annual radiation measured in 2017 reached 2.449 kWh/m² with a daily average of 6.710 kWh/m². The annual energy production reached 16.047 MWh with a daily average of 43.964 kWh/day. Overall, the KFU facility capacity factor is slightly below KSA reported capacity factors. Further studies deem necessary to investigate the deviation of the capacity factor from KSA reported results.

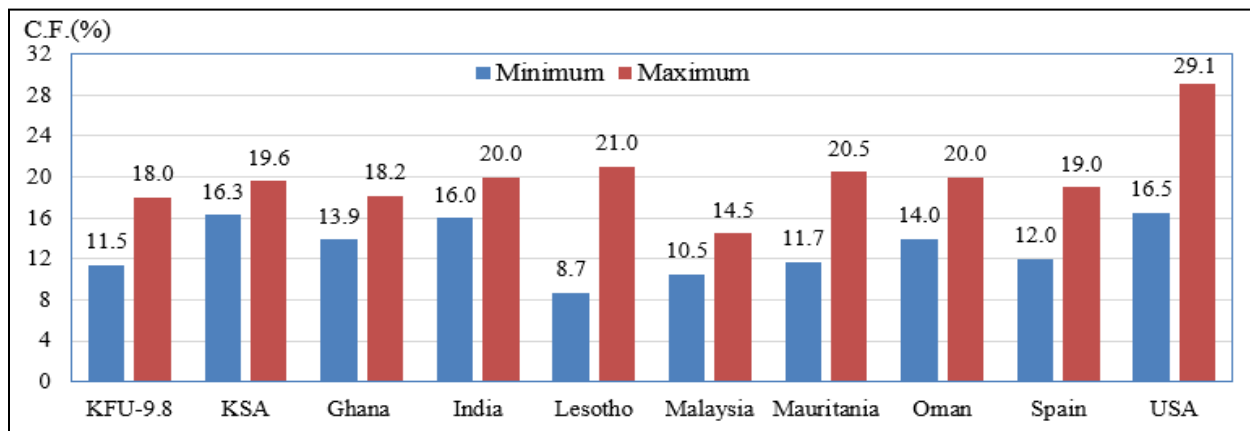


Figure 2: Capacity Factor for Selected Grid Connected PV Systems around the world [8-11].

References

- [1] Maennel, Alexander, and Hyun-Goo Kim. "Comparison of greenhouse gas reduction potential through renewable energy transition in South Korea and Germany." Energies 11.1 (2018): 206. <https://doi.org/10.3390/en11010206>
- [2] GlobalData's Saudi Arabia Solar PV Analysis: Market Outlook to 2035 report
- [3] AlOtaibi, Z.S., Khonkar, H.I., AlAmoudi, A.O. et al., "Current status and future perspectives for localizing the solar photovoltaic industry in the Kingdom of Saudi Arabia", Energy Transit 4, 1-9 (2020). <https://doi.org/10.1007/s41825-019-00020-y>
- [4] Vikrant Sharma, S.S. Chandel, "Energy Performance analysis of a 190 kWp grid interactive solar photovoltaic power plant in India", Energy, Volume 55, 15 June 2013, Pages 476-485? <https://doi.org/10.1016/j.energy.2013.03.075>
- [5] Ayompe, et al., "Measured performance of a 1.72 kW rooftop grid connected photovoltaic system in Ireland", Energy Convers. Management 52, ??816-825. <https://doi.org/10.1016/j.enconman.2010.08.007>
- [6] Emmanuel Kymakis et. Al., "Performance analysis of a grid connected photovoltaic park on the island of Crete", Energy Conversion and Management, Volume 50, Issue 3, March 2009, Pages 433-438. <https://doi.org/10.1016/j.enconman.2008.12.009>
- [7] Ahmed Bilal et al. "Solar Energy Resource Analysis and Evaluation of Photovoltaic System Performance in Various Regions of Saudi Arabia", Sustainability 2018, 10, 1129. <https://doi.org/10.3390/su10041129>
- [8] Nibras et al., "Performance Analyses of 15 kW Grid-Tied Photovoltaic Solar System Type under Baghdad city climate", Journal of Engineering 26(4):21-32, March 2020. <https://doi.org/10.31026/j.eng.2020.04.02>
- [9] A.H. Al-Badi et al., "Economic perspective of PV electricity in Oman", Energy, Volume 36, Issue 1, January 2011, Pages 226-232. <https://doi.org/10.1016/j.energy.2010.10.047>
- [10] Cristobal et al., "Self-consumption for energy communities in Spain: A regional analysis under the new legal framework", Energy Policy, March 2021, 150(4):112144. <https://doi.org/10.1016/j.enpol.2021.112144>
- [11] Today in Energy, "Southwestern states have better solar resources and higher solar PV capacity, factors", <https://www.eia.gov/todayinenergy/detail.php?id=39832>

Solar energy powered smart water heating system

Ahmed ALTURKI^{1,a}, Yahya ALMAHZARI^{1,b}, Majid ALBLOOSHI^{1,c},
Faris ALGHAMDI^{1,d}, Ahmed A. HUSSAIN^{1,e}, Ala A. HUSSEIN^{1,f}, Jamal NAYFEH^{1,g}

¹Department of Electrical Engineering, Prince Mohammad Bin Fahd University, Khobar, Saudi Arabia

^a201900814@pmu.edu.sa, ^b201701039@pmu.edu.sa, ^c201502824@pmu.edu.sa,

^d201700894@pmu.edu.sa, ^eahussain1@pmu.edu.sa, ^fahussein@pmu.edu.sa,

^gjnayfeh@pmu.edu.sa

Keywords: Photovoltaic (PV), Solar Energy, Temperature Control

Abstract. This paper proposes a smart system for controlling the temperature of a water heating system. The proposed system is powered by solar energy and it allows cooling and heating the water used in households throughout the year, particularly, when the outside temperature goes to extreme highs and lows. The system is equipped with sensors to measure the temperature of water inside the tank and show the range of water. A mobile application is developed to monitor and control the water temperature around the clock.

Introduction

Today, a country's Gross Domestic Product (GDP) is directly correlated with its energy consumption, which serves as a measure of that country's prosperity. As a result, the need for energy resources is growing every day. Energy resources come in many different forms, but they are primarily grouped into two categories: renewable energy sources (solar, air, and wind) and non-renewable energy sources (coal, petroleum).

Non-renewable energy resources speed up industrial expansion, but their supply is finite by nature. In order to meet the energy needs of the present and future generations, it is vital to find alternative energy sources due to the quick depletion of fossil fuel resources. Solar energy stands out among several options as having the best long-term prospects for supplying the world's rising energy needs. This resource's main shortcomings are its low intensity, sporadic nature, and nighttime non-availability.

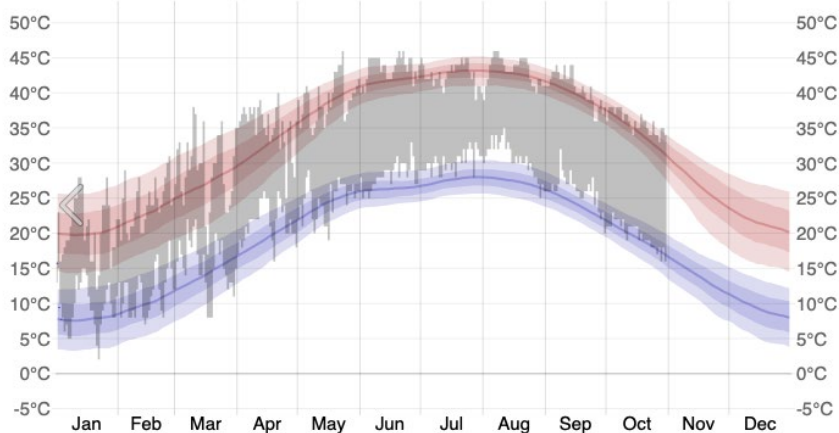


Figure 1. Temperatures throughout the year in Saudi Arabia year (2022).

Despite these drawbacks, solar energy still seems to hold the most promise of all the available renewable energy sources. Solar power is an abundant source of energy. Large amounts of renewable solar energy are produced by the sun and can be captured and used to generate heat and power. Water heating, air heating, building air conditioning, solar refrigeration, photovoltaic cells, greenhouses, photo-chemical power production, solar furnaces, and photo-biological co-versions are just a few of the many potentials uses for solar energy. The weather inside Saudi Arabia in the summer is excessively hot, which effects the water temperature inside the tanks, therefore it is difficult for people to take showers, use the toilet, do the dishes etc., therefore there is a high demand of water cooling systems, but a smart system does not exist, as a group we will design a smart system that solves this problem and make it easier for consumers to use them at home and make water more efficient which can be accessed at all times during the day.

The proposed system has several advantages over other similar systems proposed in [1] – [4]. The system in [1] is not solar powered, while the system in [2] does not have cooling feature, and it has no monitoring mechanism. The system in [3] allows heating and is solar powered, however, it has no cooling or monitoring features. In contrast, the proposed system allows both water cooling and heating. Also, it allows monitoring through a mobile application, and furthermore, it is solar powered. Details on the proposed system followed by technical specifications are demonstrated in the next section, followed by results, analysis and conclusion.

Proposed System

The block diagram of the proposed system is shown in Figure 2 below.

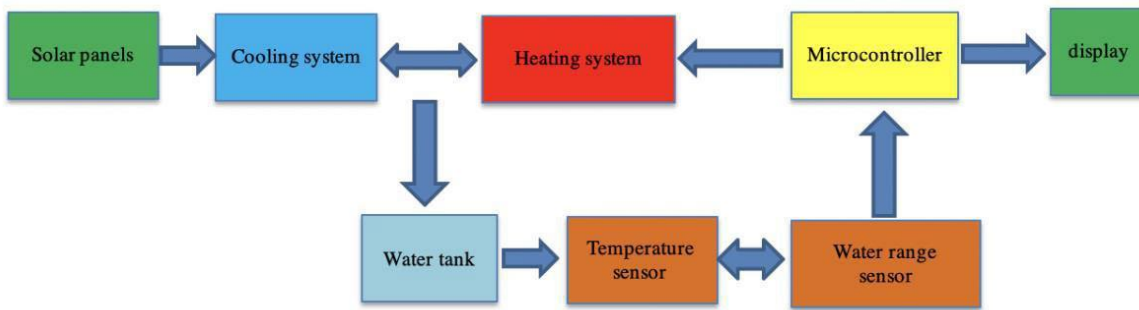


Figure 2. A block diagram of the proposed system.

The proposed system is divided into three subsystems as illustrated in Figure 3. Each of the subsystems are described in detail below.

A. Subsystem I: (Heating and Cooling System)

The majority of hot water systems include a central boiler where water is heated to a temperature between 60 and 83 °C (140 to 180 °F) before being routed through pipes to various rooms' coil units, such as radiators. Both pressure and gravity may circulate hot water, but forced circulation with a pump is more effective since it offers flexibility and control.

Hot-water systems circulate heated water using either a one-pipe or a two-pipe system. Compared to a two-pipe system, the one-pipe method utilizes fewer pipes; therefore, to accomplish the proper water temperature, we will be using the two-pipe system with cool water to achieve the water temperature that the user chose.

This system is also focused on finding the right size of cooling AC for water tanks; a cool water system should operate at a temperature between 5 to 40 °C (41 to 140°F), also finding a system that consumes the least amount of power that works on solar panels and combining this system to heating system; for finding the right water temperature that is needed. Major components used: Heating system, Cooling system, Water tank, Pipes

B. Subsystem II: (Photovoltaic System)

A photovoltaic (PV) system is made up of one or more solar panels, an inverter, and other mechanical and electrical components that harness solar energy to produce electricity. PV systems come in a wide range of sizes, from small rooftop or portable units to enormous utility-scale power plants. Although PV systems can function independently as off-grid PV systems, this article concentrates on grid-tied PV systems, which are PV systems that are linked to the utility grid.

The photovoltaic effect is the mechanism through which sunlight, composed of energy packets called photons, strikes a solar panel and generates an electric current. Each panel generates a very small quantity of electricity, but when connected to other panels, a solar array may generate much more energy.

To use all the systems on solar energy, we will need to calculate and test each system on how much power is being used; therefore, we will do the calculations and work out how many solar panels are needed and connect them to the system. Major components used: Solar panels, Inverter, Batteries, Charge controller.

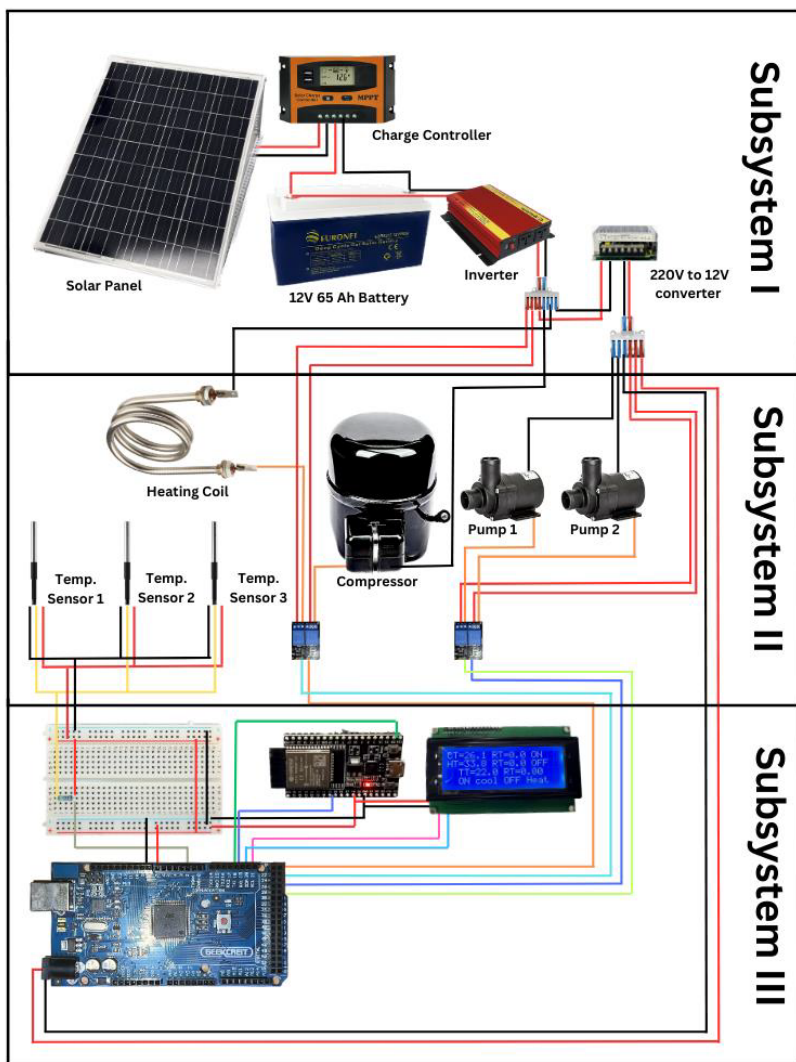


Figure 3. Project subsystems, components, and their interconnections.

C. Subsystem III: (Microcontroller and Communication System)

Information exchange between two points is described by the communication system. Communication is the process of sending and receiving information. The information transmitter,

the channel or medium of communication, and the information receiver are the three main components of communication.

To control a single device function, a microcontroller is integrated into the system. It accomplishes this by utilizing its core CPU to evaluate data that it receives from its I/O peripherals.

The microcontroller receives temporary data that is stored in its data memory, where the processor accesses it and employs program memory instructions to interpret and apply the incoming data. It then communicates and takes the necessary action via its I/O peripherals. Major components used: Sensors, Transmitter, Receiver, Arduino mega

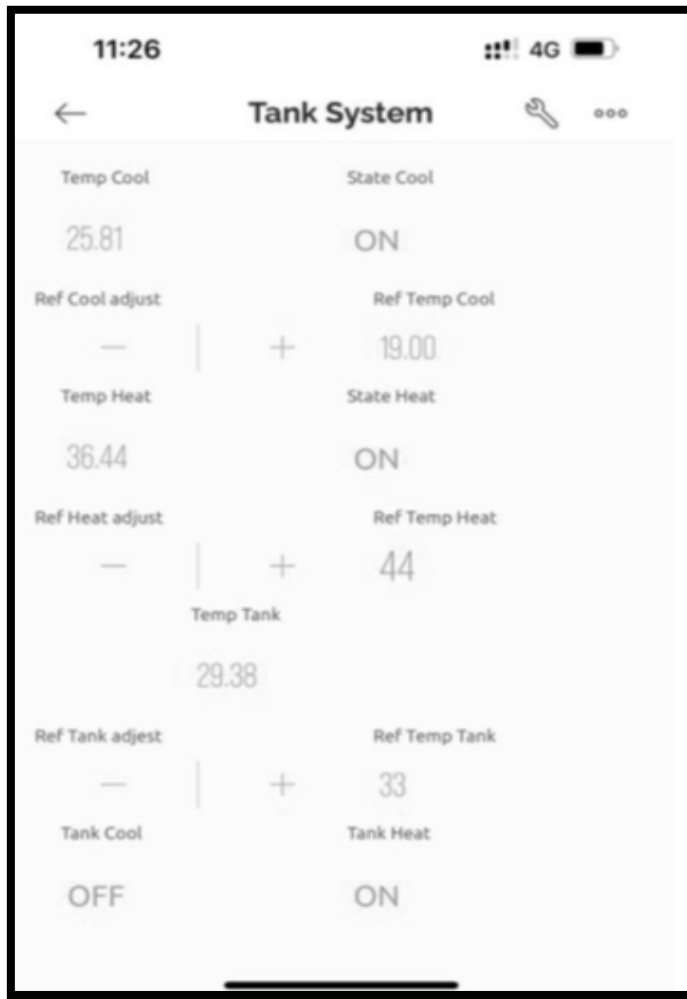


Figure 4. Mobile app UI for temperature monitoring and control.

Summary

This paper proposed a smart and efficient system for controlling and maintaining the temperature of water heating systems in residential units. It uses a renewable energy source to power the system making it environmentally friendly and sustainable. Since water-heating systems consume a lot of energy, the proposed system can help in significantly reducing the energy footprint and thus reduce the energy bills paid by the consumers.

References

- [1] Water Tank System Using System Identification Method, International Journal of Engineering and Advanced Technology (IJEAT), Malaysia, 2013.
- [2] Solar Water Heater Design, Al Akhawayn University, Morocco, 2019.

- [3] Solar Water Heater Geyser, Undergraduate Senior Design Project, Prince Mohammed Bin Fahd University, Saudi Arabia, 2020.
- [4] Powerful Tank Water Cooling Device, Global consumer bureau, Saudi Arabia, 2022.
- [5] Choudhary, M., & Singh, R. (2018). Smart Water Heating System Using Internet of Things. In Proceedings of the International Conference on Information Systems Design and Intelligent Applications (pp. 573-582). Springer, Singapore.
- [6] Li, X., Chen, X., & Li, M. (2018). Smart Water Heater Control System Based on Internet of Things. In 2018 International Conference on Computer, Information and Telecommunication Systems (CITS) (pp. 1-5). IEEE.
- [7] Nikolic, I., & Nikolic, D. (2017). Smart Water Heating Systems—A Review. In 2017 5th Mediterranean Conference on Embedded Computing (MECO) (pp. 1-4). IEEE.
- [8] Kumar, A., & Garg, R. (2019). Design and Implementation of a Smart Water Heating System Using IoT. In 2019 4th International Conference on Internet of Things: Smart Innovation and Usages (pp. 1-5). IEEE.
- [9] Dervisoglu, E., & Karakose, M. (2020). Design and Implementation of a Smart Water Heating Control System Based on IoT. In 2020 5th International Conference on Computer Science and Engineering (UBMK) (pp. 1-5). IEEE.
- [10] Chen, G., Zhang, X., & Liu, J. (2019). Design and Implementation of a Smart Water Heater Control System Based on IoT. IOP Conference Series: Earth and Environmental Science, 242(1), 012067.

Experimental investigation on the thermal and exergy efficiency for a 2.88 kW grid connected photovoltaic/thermal system

Mena Maurice FARAG^{1,2,a*}, Tareq SALAMEH^{1,3,b}, Abdul Kadir HAMID^{1,2,c*},
Mousa Hussein^{4,d}

¹Sustainable Energy and Power Systems Research Centre, Research Institute for Sciences and Engineering (RISE), University of Sharjah, Sharjah, United Arab Emirates

²Department of Electrical Engineering, College of Engineering, University of Sharjah, Sharjah, United Arab Emirates

³Department of Sustainable and Renewable Energy Engineering, College of Engineering, University of Sharjah, United Arab Emirates

⁴Department of Electrical and Communication Engineering, College of Engineering, United Arab Emirates University, Al Ain, UAE

^au20105427@sharjah.ac.ae, ^btsalameh@sharjah.ac.ae, ^cakhamid@sharjah.ac.ae,
^dmihussein@uaeu.ac.ae

Keywords: Photovoltaic-Thermal, Thermal Efficiency, Electrical Efficiency, Exergy Efficiency

Abstract. Photovoltaic-thermal (PV/T) systems have been introduced recently for waste heat extraction, to improve electricity generation from photovoltaic (PV) systems and simultaneously utilize it for potential hot water for domestic or industrial use. This study investigated a 2.88 kW grid-connected PV/T system in the terrestrial weather conditions of Sharjah, UAE. The study was experimentally investigated during December when water as a working base fluid was evaluated for waste heat recovery. The electrical, thermal, and exergy efficiencies were examined for the given system, under five different hourly intervals across the experimental period. The results have shown a notable effect of the PV/T cooling method on the terrestrial weather conditions of the UAE. A peak total efficiency of 60% was observed, showing the effectiveness in improved thermal performance because of the active cooling procedure.

Introduction

Coal, oil, and natural gas are examples of fossil fuel resources that have actively supported the world's need to produce power [1]. Because of the world's population growth, it is predicted that this demand will increase by 48% in the next 20 years [2]. Global energy demand has accelerated the use of fossil fuels and their depletion, which has accelerated the rise in carbon emissions which has been a major factor in the phenomenon of global warming [3–5]. The rapid rise in global warming has resulted in significant changes to the climate that have been observed globally over the last ten years.

Solar technologies are now a vital source of electricity production for consumers, having advanced and grown tremendously over the last ten years [6]. To address the negative effects that fossil fuels have on pollution and climate change, photovoltaic plants have been installed and deployed at a rapid pace throughout the world [7]. Photovoltaic (PV) technology has become the dominant low-carbon technology in the world due to a noticeable drop in development costs. By the end of 2020, 627 GW of PV system installations are expected to have been installed globally. PV system installations have been deployed more often. It is anticipated that within five years, the ambitious deployment of PV system installations will rise globally by at least an average of 125 GW [8].

However, PV system technologies are highly dependent on environmental parameters particularly module temperature, which contributes to their degradation and longevity [9–11]. Photovoltaic-thermal (PV/T) systems have been introduced to tackle such a dilemma by introducing cooling methods to extract the dissipated heat generated from the PV cell's surface [12–14]. Various studies have demonstrated the use of PV/T systems using different cooling methodologies to discuss the thermal and electrical efficiencies of their demonstrated systems. A study was conducted by [15] demonstrating the performance of a PV/T system under open-loop and closed-loop connections. The study demonstrated the impact of open loop configuration in improving overall thermal efficiency. Another study demonstrated the use of nanofluids to observe the efficiencies of a PV/T system [16]. The study demonstrated that the exergy efficiency was 50% higher as compared to the non-cooling conditions. The demonstration of PV/T heat pipe for heat extraction was demonstrated in [17]. The useful exergy generated by the system were considered as objective functions, to assess the performance of the optimal systems. The optimal PVHT system demonstrated a 5.1% higher exergy as compared to other proposed designs. Moreover, a spray cooling-based system is proposed as a PV/T and heat recovery system for domestic applications, as reported in [18]. The exergy losses were computed based on simulation for four different seasons. A numerical and experimental investigation of a PV/T system was studied by [19]. The study utilized a mini-channel PV/T for waste heat recovery. The results demonstrated an electrical and thermal efficiency of 12% and 47%, respectively.

The literature has demonstrated that PV/T systems present large potential, particularly for harsh regions such as the United Arab Emirates [20]. The review didn't show a prior study discussing the electrical, thermal, and exergy efficiency of a PV/T system in the UAE. Therefore, this paper experimentally investigates the performance of a 2.88 kW PV/T system installed in the University of Sharjah main campus, in the terrestrial weather conditions of Sharjah, UAE. The system is exposed to the UAE weather conditions and examined using water as a cooling fluid.

Methodology

The University of Sharjah is located at the main campus in Sharjah, United Arab Emirates. The experimental setup was built on the rooftop of the central laboratories W12 building [21]. The site of the setup is located at a latitude coordinate of 25.34° N, whereas the longitude coordinate is 55.42° E [22]. The demonstrated PV/T system has of 2.88 kW capacity, where the system is connected to the local electrical grid for clean electricity supply [23–25]. Two separate PV modules of 320 W electrical rating are used during experimentation. The PV modules are raised above the ground with a tilt angle of 20°, to ensure the stable flow of fluid on the front surface of the PV module.

Experimental Procedure

The experimental measurements were conducted during the winter weather conditions, in December. The cooling methodology was conducted across five hourly intervals between 10 AM to 2 PM, for observation of thermal and electrical characteristics.

The electrical measurements are continuously measured through a Profitest PV analyzer, which provides an accurate capacitive load for DC power, voltage, and current measurements. Whereas K-type thermocouples are utilized to measure the thermal parameters such as inlet and outlet fluid temperature, PV module front and back surface temperature, and ambient temperature. A demonstration of the experimental procedure is presented in Fig. 1. Moreover, Table 1 briefly demonstrates the technical specifications utilized for the experimentation.

Table 1. Technical Specifications of 2.88 kW PV/T system experimental setup

Description	Specifications
PV Modules	Nine PV modules are connected in series. 320 W electrical rating per module. Tilt Angle 20°
Cooling Method	Fluid Type: Water. Inlet/Outlet Fluid Tank Capacity: 200 Gal. Inlet/Outlet Pump Capacity: 1 hp
Proftest PV Analyzer	P-V and I-V curve tracing
K-Type Thermocouples	Measurement range between -200°C to 1300 °C
HPS3008 Data logger	Temperature Data logging (8 Channels)
Irradiance Sensor	Solar Irradiance measurement (W/m ²)
Anemometer	Wind speed measurement (m/s)



Fig. 1. Demonstration of Experimental Setup for the 2.88 kW PV/T system

Mathematical Model

The analysis results displayed in the subsequent sections are obtained by applying the following mathematical relations, equations, and formulas.

Electrical Performance

The solar-generated power (P_{in}) is a product of the solar irradiance (G) and the module area (A), which is expressed as follows:

$$P_{in} = G A \quad (1)$$

The maximum theoretical power (P_{theo}) can be computed based on the open circuit voltage (V_{oc}) and the short circuit current (I_{sc}), which is expressed as follows:

$$P_{theo} = I_{sc} V_{oc} \quad (2)$$

Similarly, the maximum output power (P_{max}) is computed based on the product of the maximum output voltage (V_{mp}) and maximum output current (I_{mp}), which is presented as follows:

$$P_{max} = I_{mp} V_{mp} \quad (3)$$

The electrical efficiency (η) is expressed as a ratio between P_{max} and P_{in} , represented as follows:

$$\eta_{Electrical} = P_{max}/P_{in} \quad (4)$$

Fill factor can be derived from the following equation:

$$FF = P_{max}/P_{theo} \quad (5)$$

Thermal Performance

Eq. 6 is used to determine the amount of solar heat Q_{solar} that the cooling water has captured. After differentiating it with respect to time, $m = \rho \dot{V}$, the mass flow rate, m, is computed using the mass formula. The volumetric flow rate is represented by \dot{V} , while the water density is denoted by ρ .

The specific heat capacity at constant pressure, $c_p = 4.18 \text{ [J/kg.C]}$, is used to analyze the heated property of water. By deducting the outflow temperature (T_{out}) and the input temperature (T_{in}), one may find the temperature difference (ΔT), which is then equal to $T_{out} - T_{in}$

$$Q_{solar} = m c_p \Delta T \quad (6)$$

Thermal Efficiency (η_t) can be computed through the following expression:

$$\eta_t = m c_p \Delta T / G A \quad (7)$$

The overall efficiency (U_F) by summing both electrical and thermal efficiencies can be described as the utilization factor as follows:

$$U_F = \eta_{Electrical} + \eta_{Thermal} \quad (8)$$

This overall efficiency represents the energy analysis that comprises of the electrical, thermal, and total efficiencies of the PV/T system.

Exergy Analysis

In this work, the second law of thermodynamics is utilized to perform exergy analysis. Calculating exergy is useful for energy systems to improve the sustainability and efficiency of the system, therefore utilizing the resources effectively and reducing the impact on the environment. The exergy analysis is typically used to mate the available energy. Therefore, the overall exergy balance for the given PV/T system is defined based on the following expression:

$$\begin{aligned} \sum \dot{Ex}_{in} &= \sum \dot{Ex}_{out} + \sum \dot{Ex}_{loss} \\ \Rightarrow \dot{Ex}_{sun} + \dot{Ex}_{mass,in} &= \dot{Ex}_{elec} + \dot{Ex}_{mass,out} + \dot{Ex}_{loss} \end{aligned} \quad (9)$$

The in and out exergies are represented as Ex_{in} and Ex_{out} , respectively, the exergy destruction (Entropy) due to irreversibility is described as the exergy loss Ex_{loss} . Entropy is a measure of the disorder or randomness in an energy system due to irreversibility, such as heat transfer across finite temperature gradients, friction, and mixing; the relationship between exergy and entropy can be understood from the second law of thermodynamics. This irreversibility leads to the loss of available work (exergy) and increased entropy. This study used the Petela exergy conversion coefficient [26], which is described in the following expression:

$$\psi_s = 1 - \frac{4}{3} \left(\frac{T_{out}}{T_s} \right) + \frac{1}{3} \left(\frac{T_{out}}{T_s} \right)^4 \quad (10)$$

T_s represents the solar radiation temperature from the sun, which is previously reported to be equivalent to 5777 [K] as reported in [27,28]:

$$\begin{aligned} \dot{Ex}_{in} &= \dot{Ex}_{sun} = \psi_s AG \\ \text{Or } \dot{Ex}_{sun} &= G \left(1 - \frac{T_{amb}}{T_{sun}} \right) \end{aligned} \quad (11)$$

The thermal exergy \dot{Ex}_{th} typically represents the heat loss from the PV system exterior surfaces to the cooling fluid and ambient, which can be described as follows:

$$\begin{aligned} \dot{Ex}_{mass,out} - \dot{Ex}_{mass,in} &= \dot{Ex}_{th} = \dot{m}_{f,out} [(h_{f,out} - h_{f,in}) - T_{amb} (s_{f,out} - s_{f,in})] \\ h_{f,out} - h_{f,in} &= C_{p,f} (T_{f,out} - T_{f,in}) \\ s_{f,out} - s_{f,in} &= C_{p,f} \ln \left(\frac{T_{f,out}}{T_{f,in}} \right) \\ \dot{Ex}_{th} &= \dot{m}_{f,out} \left[C_{p,f} (T_{f,out} - T_{f,in}) - T_{amb} C_{p,f} \ln \left(\frac{T_{f,out}}{T_{f,in}} \right) \right] \end{aligned} \quad (12)$$

The exergy output for PV systems is typically equivalent to the total electrical energy \dot{Ex}_{elec} , which can be described as follows:

$$\dot{Ex}_{ele} = V_m I_m \quad (13)$$

Therefore, the exergy losses of the PV system can be computed through the following expression:

$$\dot{Ex}_{loss} = \left(1 - \frac{T_{amb}}{T_{sun}}\right) G - \dot{Ex}_{ele} - \dot{m}_{f,out} \cdot C_{p,f} \left[(T_{f,out} - T_{f,in}) - T_{amb} \ln \left(\frac{T_{f,out}}{T_{f,in}} \right) \right] \quad (14)$$

Therefore, the computation of entropy generation by the PV system can be done as follows:

$$\dot{S}_{gen} = \frac{\dot{Ex}_{loss}}{T_{amb}} \quad (15)$$

As a result, the thermal and electrical exergy efficiencies can be computed based on the following equations:

$$\xi_{th} = \frac{\dot{Ex}_{th}}{\dot{Ex}_{sun}} \quad (16)$$

$$\xi_{ele} = \frac{\dot{Ex}_{ele}}{\dot{Ex}_{sun}} \quad (17)$$

Finally, the overall exergetic efficiency ξ of the PV/T system is computed based on a ratio of the output and input exergies of the system

$$\xi_{total} = \frac{\dot{Ex}_{ele} + \dot{Ex}_{th}}{\dot{Ex}_{sun}} \quad (18)$$

Results and Discussion

The closed-loop tests for front surfacing cooling are presented in Table 2. The experimental test was conducted on a fixed tilt angle of 20°. The experimental parameters are variable with time as demonstrated in Table 2, demonstrating the variability of different environmental and electrical parameters with time. Moreover, the weather profile is presented in Fig. 2(a), presenting a peak solar irradiance at noon.

The experimental measurements show the effectiveness of water as a working base fluid, by maintaining low front and back surface temperatures. This would reflect on enhancing the electrical efficiency of the PV/T system as illustrated in Fig. 2(b). The electrical efficiency (η) can be computed based on the numerical relations that were discussed in the previous section.

As demonstrated in Fig. 4, the PV/T system under cooling conditions would contribute significantly to maintaining high electrical efficiency, with a peak of 14.5%. Thereby, the effectiveness of water as a working base fluid can be attributed to the increase in electrical efficiency throughout the day, through the maintenance of the front and back surface temperatures. An inverse relationship between the module temperature and electrical efficiency can be observed, hence its reduction as the experimentation approaches noon time.

The observation of thermal performance is essential when discussing the performance of PV/T systems. The thermal study is conducted on the given PV/T system, as demonstrated in Fig. 3. The thermal investigation is computed based on the numerical equations presented in Eq. 6-7. Commenting on Fig. 3, an inversely proportional relationship between the thermal efficiency and the thermal energy losses can be observed. The highest losses are experienced during noon time due to the reduction of the cooling effect because of the increase in water temperature, thereby affecting the thermal and total efficiency of the system.

Table 2. Experimental measurements from 2.88 kW PV/T system

Experimental Measurements								
Time	G [W/m ²]	T _A [°C]	T _{in} [°C]	T _{out} [°C]	T _{PVB} [°C]	T _{PFV} [°C]	I _{sc} [A]	V _{oc} [V]
10.00	709.81	23.01	20.32	21.84	25.75	22.52	6.48	45.02
11.00	800.02	21.07	20.61	21.57	26.58	23.03	7.27	44.79
12.00	820.50	22.89	24.80	25.78	30.60	26.17	7.53	44.51
13.00	765.24	26.05	25.16	26.28	32.87	28.00	6.94	44.15
14.00	639.94	26.83	26.17	27.38	33.46	29.54	5.24	43.87

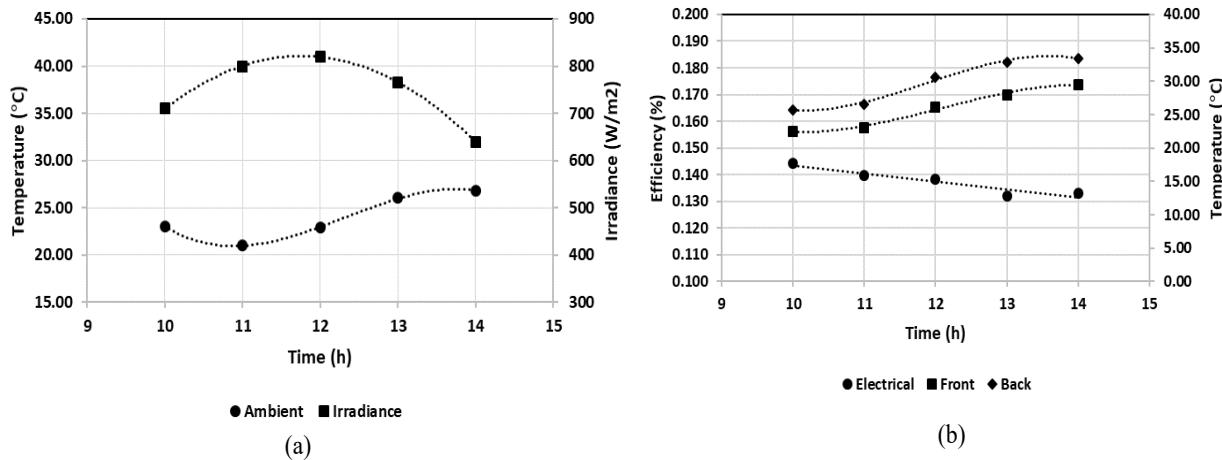


Fig. 2. Demonstration of (a) Weather profile for day of experimentation (b) Comparison of electrical efficiency with front and back module temperature

The exergy efficiency was computed based on the previously discussed numerical equations and illustrated in Fig. 4. A negative relation is presented between the exergy efficiency and exergy destruction, which are lost due to the irreversibility effect. Similarly, the highest exergy destruction is experienced during noon time, presenting the minimum exergy efficiency. In this notion, the thermal efficiency demonstrates the experimental test at the given weather conditions. Therefore, as the ΔT between inlet and outlet water temperature is significantly large, the higher the thermal efficiency. Additionally, ambient conditions are to be considered a critical factor for the thermal performance of any PV/T system.

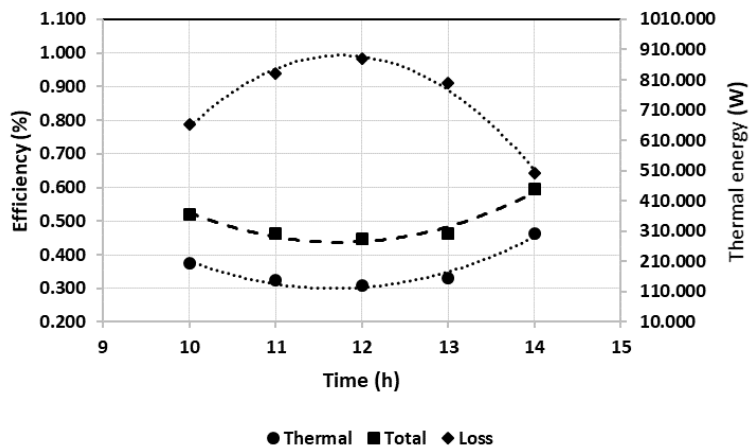


Fig. 3. Thermal performance across the period of experimentation

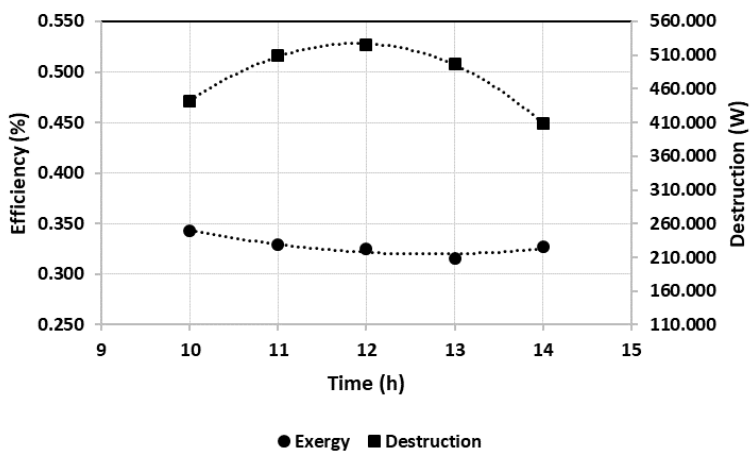


Fig. 4. Comparison of exergy efficiency with exergy destruction

Summary

This study discussed the electrical, thermal, and exergy performance of a 2.88 kW PV/T system in the terrestrial conditions of Sharjah, UAE. The experimental study was conducted during the winter conditions to assess the impact of water as a cooling fluid on both electrical and thermal efficiencies. The experimental measurements have concluded the inverse proportionality of the electrical efficiency with respect to the operating temperature, with a starting peak of 14.5%, which is close module efficiency described by the manufacturer. Moreover, a peak thermal efficiency of 48% is achieved, showing the beneficial use of PV/T systems in capturing waste heat for potential domestic applications. As a future work, the exergy analysis can be conducted for different seasons, to assess the significance of temperature difference in waste heat recovery, for total system efficiency enhancement.

References

- [1] M.H. Mostafa, S.H.E. Abdel Aleem, S.G. Ali, A.Y. Abdelaziz, Energy-management solutions for microgrids, in: Distrib. Energy Resour. Microgrids, Elsevier, 2019: pp. 483–515. <https://doi.org/10.1016/B978-0-12-817774-7.00020-X>
- [2] P. Moodley, C. Trois, Lignocellulosic biorefineries: the path forward, in: Sustain. Biofuels, Elsevier, 2021: pp. 21–42. <https://doi.org/10.1016/B978-0-12-820297-5.00010-4>
- [3] M.M. Farag, F. Faraz Ahmad, A.K. Hamid, C. Ghenai, M. AlMallahi, M. Elgendi, Impact of Colored Filters on PV Modules Performance: An Experimental Investigation on Electrical and Spectral Characteristics, in: 50th Int. Conf. Comput. Ind. Eng., 2023: pp. 1692–1704.

- [4] K.R. Abbasi, M. Shahbaz, J. Zhang, M. Irfan, R. Alvarado, Analyze the environmental sustainability factors of China: The role of fossil fuel energy and renewable energy, *Renew. Energy.* 187 (2022) 390–402. <https://doi.org/10.1016/j.renene.2022.01.066>
- [5] M. Al-chaderchi, K. Sopain, M.A. Alghoul, T. Salameh, Experimental study of the effect of fully shading on the Solar PV module performance, *E3S Web Conf.* 23 (2017) 01001. <https://doi.org/10.1051/e3sconf/20172301001>
- [6] M.M. Farag, R.C. Bansal, Solar energy development in the GCC region – a review on recent progress and opportunities, *Int. J. Model. Simul.* 43 (2023) 579–599. <https://doi.org/10.1080/02286203.2022.2105785>
- [7] M.M. Farag, N. Patel, A.-K. Hamid, A.A. Adam, R.C. Bansal, M. Bettayeb, A. Mehiri, An Optimized Fractional Nonlinear Synergic Controller for Maximum Power Point Tracking of Photovoltaic Array Under Abrupt Irradiance Change, *IEEE J. Photovoltaics.* 13 (2023) 305–314. <https://doi.org/10.1109/JPHOTOV.2023.3236808>
- [8] M.M. Farag, A.K. Hamid, T. Salameh, E.M. Abo-Zahhad, M. AlMallahi, M. Elgendi, ENVIRONMENTAL, ECONOMIC, AND DEGRADATION ASSESSMENT FOR A 2.88 KW GRID-CONNECTED PV SYSTEM UNDER SHARJAH WEATHER CONDITIONS, in: 50th Int. Conf. Comput. Ind. Eng., 2023: pp. 1722–1731.
- [9] T. Salameh, A.K. Hamid, M.M. Farag, E.M. Abo-Zahhad, Energy and exergy assessment for a University of Sharjah's PV grid-connected system based on experimental for harsh terrestrial conditions, *Energy Reports.* 9 (2023) 345–353. <https://doi.org/10.1016/j.egyr.2022.12.117>
- [10] T. Salamah, A. Ramahi, K. Alamara, A. Juaidi, R. Abdallah, M.A. Abdelkareem, E.-C. Amer, A.G. Olabi, Effect of dust and methods of cleaning on the performance of solar PV module for different climate regions: Comprehensive review, *Sci. Total Environ.* 827 (2022) 154050. <https://doi.org/10.1016/j.scitotenv.2022.154050>
- [11] H. Rezk, I.Z. Mukhametzyanov, M.A. Abdelkareem, T. Salameh, E.T. Sayed, H.M. Maghrabie, A. Radwan, T. Wilberforce, K. Elsaied, A.G. Olabi, Multi-criteria decision making for different concentrated solar thermal power technologies, *Sustain. Energy Technol. Assessments.* 52 (2022) 102118. <https://doi.org/10.1016/j.seta.2022.102118>
- [12] M.M. Farag, A.K. Hamid, Performance assessment of rooftop PV/T systems based on adaptive and smart cooling facility scheme - a case in hot climatic conditions of Sharjah, UAE, in: 3rd Int. Conf. Distrib. Sens. Intell. Syst. (ICDSIS 2022), Institution of Engineering and Technology, 2022: pp. 198–207. <https://doi.org/10.1049/icp.2022.2448>
- [13] N.K. Almarzooqi, F.F. Ahmad, A.K. Hamid, C. Ghenai, M.M. Farag, T. Salameh, Experimental investigation of the effect of optical filters on the performance of the solar photovoltaic system, *Energy Reports.* 9 (2023) 336–344. <https://doi.org/10.1016/j.egyr.2022.12.119>
- [14] T. Salameh, M. Tawalbeh, A. Juaidi, R. Abdallah, S. Issa, A.H. Alami, A novel numerical simulation model for the PVT water system in the GCC region, in: 2020 Adv. Sci. Eng. Technol. Int. Conf., IEEE, 2020: pp. 1–5. <https://doi.org/10.1109/ASET48392.2020.9118264>
- [15] A. Alkhaldi, T. Salameh, A. Al Makky, Experimental investigation thermal and exergy efficiency of photovoltaic/thermal system, *Renew. Energy.* 222 (2024) 119897. <https://doi.org/10.1016/j.renene.2023.119897>
- [16] S. Aberoumand, S. Ghamari, B. Shabani, Energy and exergy analysis of a photovoltaic thermal (PV/T) system using nanofluids: An experimental study, *Sol. Energy.* 165 (2018) 167–177. <https://doi.org/10.1016/j.solener.2018.03.028>

- [17] A. Shahsavar, M. Arıcı, Energy and exergy analysis and optimization of a novel heating, cooling, and electricity generation system composed of PV/T-heat pipe system and thermal wheel, *Renew. Energy.* 203 (2023) 394–406. <https://doi.org/10.1016/j.renene.2022.12.071>
- [18] H. Ma, Y. Xie, S. Wang, Y. Liu, R. Ding, Exergy analysis of a new spray cooling system-based PV/T and heat recovery with application in sow houses, *Sol. Energy.* 262 (2023) 111828. <https://doi.org/10.1016/j.solener.2023.111828>
- [19] J. Zhou, X. Zhao, Y. Yuan, Y. Fan, J. Li, Mathematical and experimental evaluation of a mini-channel PV/T and thermal panel in summer mode, *Sol. Energy.* 224 (2021) 401–410. <https://doi.org/10.1016/j.solener.2021.05.096>
- [20] A. Mokri, M. Aal Ali, M. Emziane, Solar energy in the United Arab Emirates: A review, *Renew. Sustain. Energy Rev.* 28 (2013) 340–375. <https://doi.org/10.1016/j.rser.2013.07.038>
- [21] M.M. Farag, A.K. Hamid, Experimental Investigation on the Annual Performance of an Actively Monitored 2.88 kW Grid-Connected PV System in Sharjah, UAE, in: 2023 Adv. Sci. Eng. Technol. Int. Conf., IEEE, 2023: pp. 1–6. <https://doi.org/10.1109/ASET56582.2023.10180880>
- [22] S.B. Bashir, M.M. Farag, A.K. Hamid, A.A. Adam, A.G. Abo-Khalil, R. Bansal, A Novel Hybrid CNN-XGBoost Model for Photovoltaic System Power Forecasting, in: 2024 6th Int. Youth Conf. Radio Electron. Electr. Power Eng., 2024. <https://doi.org/10.1109/REEPE60449.2024.10479878>
- [23] M.M. Farag, F.F. Ahmad, A.K. Hamid, C. Ghenai, M. Bettayeb, Real-Time Monitoring and Performance Harvesting for Grid-Connected PV System - A Case in Sharjah, in: 2021 14th Int. Conf. Dev. ESystems Eng., IEEE, 2021: pp. 241–245. <https://doi.org/10.1109/DeSE54285.2021.9719385>
- [24] M.M. Farag, F.F. Ahmad, A.K. Hamid, C. Ghenai, M. Bettayeb, M. Alchadiry, Performance Assessment of a Hybrid PV/T system during Winter Season under Sharjah Climate, in: 2021 Int. Conf. Electr. Comput. Commun. Mechatronics Eng., IEEE, 2021: pp. 1–5. <https://doi.org/10.1109/ICECCME52200.2021.9590896>
- [25] T. Salameh, A.K. Hamid, M.M. Farag, E.M. Abo-Zahhad, Experimental and numerical simulation of a 2.88 kW PV grid-connected system under the terrestrial conditions of Sharjah city, *Energy Reports.* 9 (2023) 320–327. <https://doi.org/10.1016/j.egyr.2022.12.115>
- [26] R. Petela, Exergy of undiluted thermal radiation, *Sol. Energy.* 74 (2003) 469–488. [https://doi.org/10.1016/S0038-092X\(03\)00226-3](https://doi.org/10.1016/S0038-092X(03)00226-3)
- [27] M. Romero, A. Steinfeld, Concentrating solar thermal power and thermochemical fuels, *Energy Environ. Sci.* 5 (2012) 9234. <https://doi.org/10.1039/c2ee21275g>
- [28] E. Masana, C. Jordi, I. Ribas, Effective temperature scale and bolometric corrections from 2MASS photometry, *Astron. Astrophys.* 450 (2006) 735–746. <https://doi.org/10.1051/0004-6361:20054021>

Solar PV based charging station for electric vehicles (EV)

Raghad ALGHAMDI^{1,a}, Batool ALSUNBUL^{1,b}, Raghad ALMUTAIRI^{1,c},
Rania ALNASSAR^{1,d}, Maha ALHAJRI^{1,e}, Saifullah SHAFIQ^{1,f}, Samir EL-Nakla^{1,g *},
Ahmed ABUL HUSSAIN^{1,h}, Jamal NAYFEH^{1,j}

¹ Electrical Engineering Department, Prince Mohammad Bin Fahd University, P.O. Box 1664, Al Khobar 31952, Saudi Arabia

^a201700819@pmu.edu.sa, ^b201700766@pmu.edu.sa, ^c201701747@pmu.edu.sa,

^d201701166@pmu.edu.sa, ^e201701472@pmu.edu.sa, ^fsshafiq@pmu.edu.sa,

^gsnakla@pmu.edu.sa, ^hahussain1@pmu.edu.sa, ^jnayfeh@pmu.edu.sa

Keywords: Renewable Energy, Solar Energy, Electric Vehicle Charging, Batteries

Abstract. Electric Vehicles (EV) have been rapidly gaining attraction owing to their use of clean energy. The use of renewable energy sources, such as solar energy, is readily available to a wider community because of the falling costs of installing PV panels per watt. Saudi Arabia's Vision 2030, a sustainable vision for the future of Saudi Arabia focuses on new environmental and sustainable policies that are being developed to reduce carbon emissions, and to achieve that, there is a strong motivation to use clean energy and resources such as solar and wind energy. This paper presents the design of a stand-alone solar PV charging station for EV which includes additional features that allow the users to monitor the charging status of an EV via a smartphone application.

Introduction

Global warming is a fact, and the weather is becoming increasingly unpredictable as air is getting highly polluted. It is concerning that the world will address the climate situation too late, resulting in irreparable consequences. The dependence on non-renewable energy has been the major contributor of climate change since it results in the emission of greenhouse gasses [1,2].

Global electricity demand and cost is growing more rapidly as compared to renewables, driving a strong increase in the consumption of fossil fuels. According to EIA (Energy Information Administrations), the demand in energy keeps increasing higher than the global population, resulting in a rise in the average amount of power consumed for each person [3,4]. Another problem is the existing charging systems are overloading the grid, if several EV's are charged at the same time in the same place the power system may face excessive demands because the modern EV's consume more power equivalent to 10 homes [5,6].

The implementation of an off-grid power generation system can help resolve the problem of grid overloading as well as provide power in remote locations, where grid connectivity is an issue. Enhancing energy efficiency and lowering the grid energy demand are commonly regarded as the most valuable, quickest, least expensive, and safest way to fight climate change. EV charging reduces on-grid energy consumption by using solar panels and other renewable energy sources.

Shatnawi et al. presented a work of battery charging technologies and recent EV charging approaches and discussed the technical challenges in this field. The paper illustrated the importance of integrating renewable energy resources, particularly solar energy in the UAE and the Arab World, to provide clean and cost-effective public and private EV charging stations [7]. Another work conducted by Madhu et al. to design a smart charging station using Arduino and a range of sensors brings numerous advantages and functionalities. Through the integration of comprehensive sensors such as current, voltage, and temperature sensors, the charging station becomes capable of effectively monitoring and regulating the charging process, ensuring optimal battery conditions and charging safety [8].

A work done by Ballaji et al. investigated the simulation of an EV charging system. The system considered the EV battery as load and studied the effect of changing conditions in the environment due to varying irradiance throughout the day [9].

This paper presents the design of a stand-alone solar photovoltaic (PV) based charging station for an electric vehicle (EV) with multiple functions and features. It allows monitoring of the charging status through a mobile phone application with automated charging to prolong EV's battery life. It also monitors solar irradiance and related weather parameters such as ambient temperature and relative humidity that may affect the overall performance of the system. The proposed system has efficient maintenance and troubleshooting characteristics as different hardware modules of the system can be isolated for safety purposes, which can be handled by hardware means or through the mobile application.

The proposed system

The block diagram of the proposed system is shown in Fig. 1 which illustrates the overall design of the EV charging station. The proposed system consists of solar panels, a battery bank (battery storage system), an EV charger, and a DC/AC inverter.

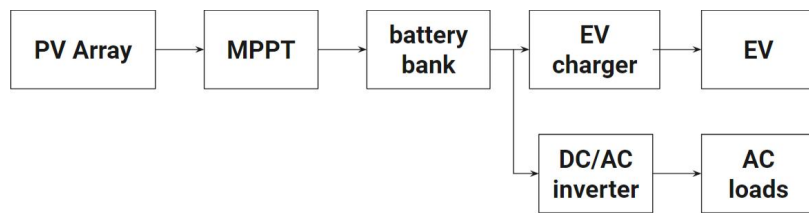


Figure 1: Overall Block Diagram of EV Charging Station System

The flow of the system shown in Fig. 1 above starts with the PV array connected to an MPPT charge controller that draws maximum power from the solar panels to be fed on to the battery bank. The battery bank acts as a solar energy storage system that provides a backup source of power on cloudy days or at night and to overcome the variation of power being produced by solar systems. It is necessary to include a battery bank especially when using a grid-independent (Off-grid) system. The system includes two types of loads, a DC load (EV battery) and an AC load (electrical appliances in the station). The EV charger consists of a DC-DC boost converter which operates as a step-up converter. Lastly, the system incorporates a DC/AC inverter that converts the DC output of the solar panels and battery bank to AC in order to power up appliances that are plugged in the station.

The EV charger is provisioned in the carport structure. The EV charger uses voltage and current sensors to measure the charging current and voltage in order to calculate the charging power. Additionally, the EV charger includes a battery monitoring system that displays to the user the charging status of the EV. The carport mounted solar panels provide an optimized fixed angle of 26 degrees for maximum sunlight collection.

System implementation

In order to design the system, it is essential to identify the loads first. The station is designed to charge an EV of 48V 7Ah and power up AC loads up to 150W minimum.

Storage batteries are needed because PV modules can generate power only when it is exposed to sunlight. They store the energy that is being generated by the PV modules during periods of high irradiance and make it available at night as well as during overcast periods. The batteries selected are two Lead-calcium batteries 12V 60Ah each, and they are connected in series as shown in Fig. 2. All the batteries used in a battery bank are the same type, same manufacturer, same age, and are maintained at equal temperature. Furthermore, the batteries have the same charge and

discharge properties under these circumstances. If the above characteristics do not match, there is a high probability of huge energy loss within the battery bank.



Figure 2: Storage battery connection

MPPT charge controller is used to maximize the power transfer from the PV array to the battery bank. Next is a DC to AC inverter which is a 24V 3 kVA pure sine wave inverter as shown in Fig. 3.



Figure 3: (left) and MPPT

The EV charger is a DC to DC boost converter that will boost the voltage of the battery bank and match it to the voltage of the EV batteries and decrease the current to the rated charging current of the EV batteries. The design is developed using LM2588 5-A Flyback Regulator [10].

The method that was used for charging was the constant voltage (CV) charging method because it is the optimal method to get the most out of the batteries in terms of service life and capacity, as well as a reasonable recharge time and cost. A DC voltage between (50.1 V) and (50.4 V) is applied to the input terminals of the CV charge controller and the output terminals are connected to a (48V 7 Ah) lead acid battery to charge it.

To start wiring the components within the system, a wiring diagram and wire sizing are made in order to visualize the connection of the system components. The wiring diagram of the system is shown in Fig. 4.

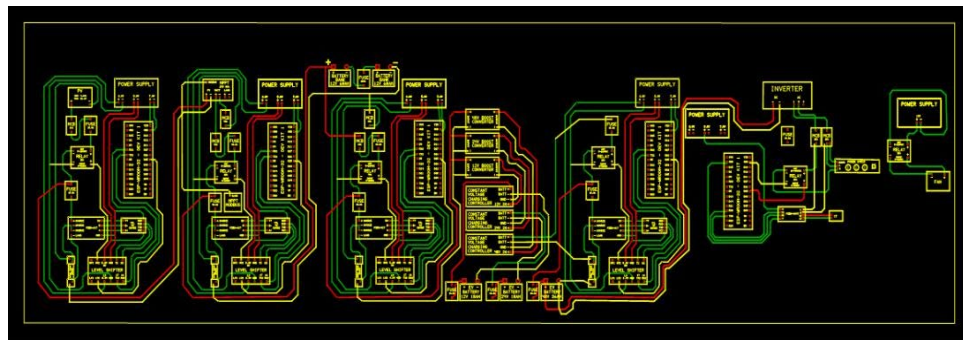


Figure 4: Wiring diagram

To display the charging status of the EV through a mobile application, a Raspberry Pi processor was used as a central server to record all the sensor readings and display them on the mobile platform to be accessed at any given time. The Raspberry Pi together with a home automation software as a server can also send data to the cloud which enables the user to view all sensor readings and to control the different parameters in the system even outside the local area network as shown in Fig. 5.



Figure 5: Mobile application user interface

Another set of parameters that was monitored in the system was the sensor outputs. The sensors include a light sensor, humidity and temperature sensor, pressure sensor, and an accelerometer sensor as shown in Fig. 6. The light sensor used is a BH1750 that measures the illuminance level of the light going to the solar panels. The humidity and temperature sensor used is DHT22 that will measure the humidity and temperature to be displayed to the user. In addition, a barometric pressure sensor BMP280 was used that detects the atmospheric pressure for weather forecasting. Lastly, an accelerometer & gyroscope (3-axis) sensor was used to measure the angle at which the solar panels will be adjusted to for maximum power.

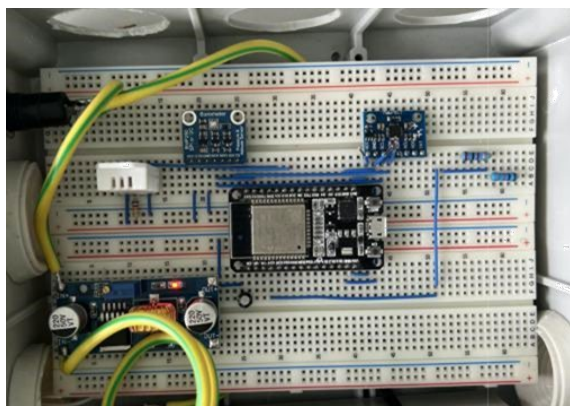


Figure 6: Sensors Circuit

Finally, the structure of the charging station and electrical enclosure which is designed using Solid Works software and a ventilation system is added to maintain the ideal working temperature for the electronic components. Dimensions are 0.81 m in height, 1.76 m in width, and 0.3 m depth. All components were placed within a factory fabricated electrical enclosure as in Fig. 7. After that, the structure of the charging station was made whose dimensions are 2.47 m in height, 2 m in width, and 1.5 m depth, as shown in Fig. 8. The solar panels were placed at an angle of 26 degrees.



Figure 7: Electrical Enclosure



Figure 8: Charging Station & Carport

Testing and Results

The angle on which the PVs are mounted is a critical consideration on any solar power system installation. After positioning the panels at different angles during months of March and April, different output ratings were obtained as shown in Table 1. It was found that the optimum tilt angle for our location is 26 degrees to pull out every single watt hour out of the system.

Table 1: Test result of solar panels

Angle	Voltage (V)	Current (A)
22°	21.5	3.64
23°	21.5	3.67
24°	21.5	3.72
25°	21.5	3.77
26°	21.5	3.81

For the boost converter, all of the specifications stated previously have been met. The output voltage across the output capacitor is 54 V with no load and 50 V with load connected. To get the efficiency, the test was performed using 4 wire measurement method to get accurate data. All DC measurements were taken using a multimeter and electronic DC load tester as well as an infrared thermometer was used to get the temperature output of the circuit shown in Fig. 9. The below tables show the result of the boost converter when testing with a fan and without a fan.

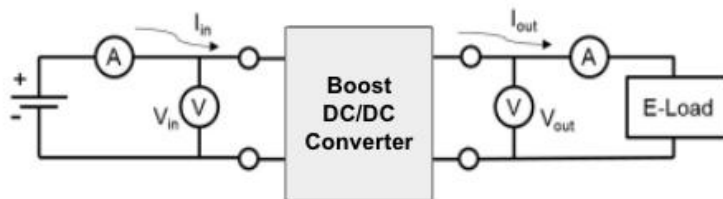


Figure 9: Testing converter

The results of the boost converter testing with a fan and without a fan were recorded as shown in Table 2 and Table 3 which show only the minimum and maximum readings recorded.

Table 2: Results of testing converter with fan

Vin(V)	In (A)	Pin (W)	Temp (C)	Vout (V)	Iout (A)	Iset (A)	Pout(W)	EFF %
24	0.37	8.88	25.4	50.4	0.15	0.15	7.56	85.13
24	1.45	34.8	24.4	50.4	0.65	0.65	32.76	94.13

Table 3: Results of testing converter without fan

Vin(V)	In (A)	Pin (W)	Temp (C)	Vout (V)	Iout (A)	Iset (A)	Pout(W)	EFF %
24	0.24	5.76	25.5	50.3	0.1	0.1	5.03	87.32
24	2.1	50.4	27.8	49.6	1	1	49.6	98.41

The converter with fan reached a maximum efficiency of 94.13%, and minimum of 85.13%. On the other hand, the converter without fan reached the maximum efficiency of 100.98%, and minimum of 100.87%. However, the converter without a fan is not efficient, it will stop working at some point as temperature increases the output voltage will decrease, and will not be able to give the desired output as well as the ICs will get damaged. The result shows the addition of a small fan played a very important role as the heat sink alone gets hot during operation and this

can damage the ICs without a fan. The efficiency vs output current graph was generated as shown in Fig. 10 with average efficiency of converter of 92.47%.

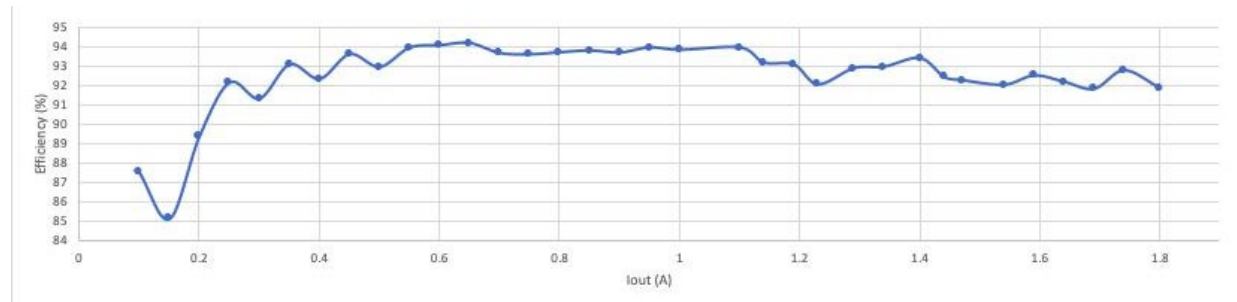


Figure 10: Efficiency Vs Output Current

The last part of the system is hardware and software integration. The circuits for all the parameters that should be monitored in our system were completed. Later, the sensors and communication modules were programmed to display the information to the user wirelessly.

Testing the battery status of the EV battery when charged, gave us accurate voltage readings for the battery used which was around 50.1 V as illustrated in Fig. 11 (a).

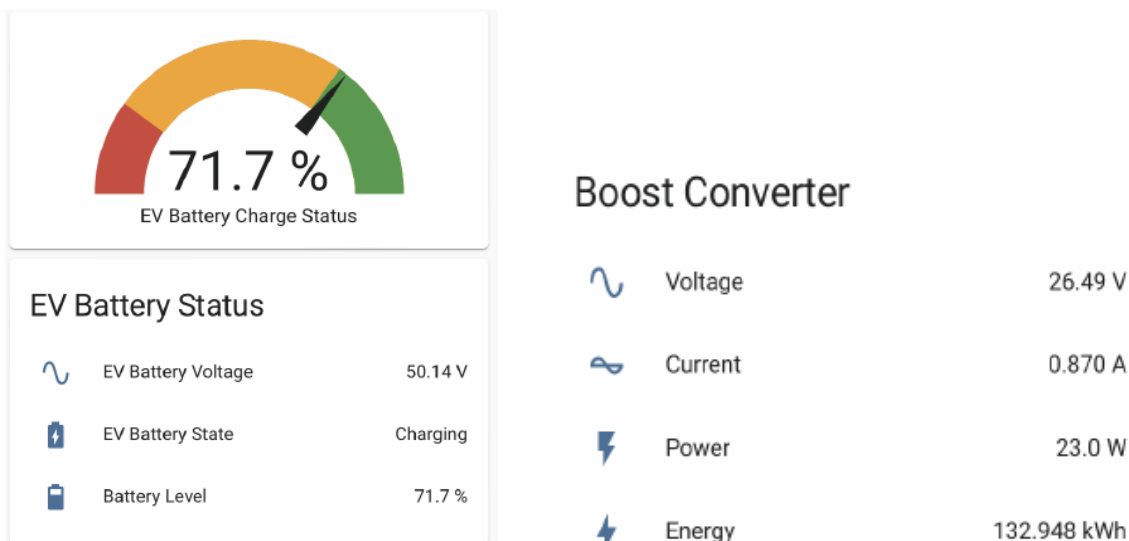


Figure 11: (a) EV Battery Status, (b) Boost Converter Energy Monitoring

The boost converter readings display the input coming from the battery bank entering the boost converter. Theoretically, the voltage of the boost converter should be 24 V. However, considering that 12 V batteries can go as high as 13.2 V when fully charged, when two 13.2 V batteries are connected in series as in our case it will give us a maximum output of 26.4 V, which can be observed in Fig. 11 (b) above.

Summary

The project involved building an off-grid solar based charging station for electric vehicles by fabricated the whole system design of the charging station as well as building the user interface of mobile application. Some important features that we included in our project is the monitoring of the charging status of the EV battery as well as the power consumption within the system. It also allows control of components and displays readings of the illuminance levels, temperature and humidity, etc.

For future work, the team will look to extend the current charging time of project which is around 3.7 hours to charge an EV to include fast charging methods for the battery to charge in a shorter period of time.

References

- [1] Biya, T. S., & Sindhu, M. R., Design and power management of Solar Powered Electric Vehicle Charging Station with energy storage system. 2019, 3rd International Conference on Electronics, Communication and Aerospace Technology (ICECA).
<https://doi.org/10.1109/iceca.2019.8821896>
- [2] Information on <https://climate.nasa.gov/evidence>
- [3] MOHAMED, K., etal, Opportunities for an off-grid solar PV assisted Electric Vehicle Charging Station. 2020, 11th International Renewable Energy Congress (IREC).
<https://doi.org/10.1109/irec48820.2020.9310376>
- [4] Information on [www.who.int/news-room/air-quality-guidelines/ambient-\(outdoor\)-air-quality-and-health](http://www.who.int/news-room/air-quality-guidelines/ambient-(outdoor)-air-quality-and-health)
- [5] Information on <https://www.eia.gov/outlooks/ieo/>
- [6] U.S. Department of Energy, Electric Vehicle Charging Infrastructure Analysis: A Case Study of California's Transportation Electrification. (2021)
- [7] M. Shatnawi, K. B. Ari, K. Alshamsi, M. Alhammadi and O. Alamoodi, Solar EV Charging, 2021 6th International Conference on Renewable Energy: Generation and Applications (ICREGA), Al Ain, United Arab Emirates, 2021, pp. 178-183,
<https://doi.org/10.1109/ICREGA50506.2021.9388301>.
- [8] Madhu B. R, Anitha G. S, Mahantesha H. and Krishna S, "Smart Charging Station for Electric Vehicles Using Solar Power," 2023 7th International Conference on Computation System and Information Technology for Sustainable Solutions (CSITSS), Bangalore, India, 2023, pp. 1-5. <https://doi.org/10.1109/CSITSS60515.2023.10334142>
- [9] A. Ballaji, R. Dash, V. Subburaj, K. J. Reddy, S. C. Swain and M. Bharat, "Design and analysis of EV Charging Station using PV Integrated Battery Sytsem," 2022 International Conference on Smart Generation Computing, Communication and Networking (SMART GENCON), Bangalore, India, 2022, pp. 1-6.
<https://doi.org/10.1109/SMARTGENCON56628.2022.10083931>
- [10] LM25885-A Flyback Regulator with Shutdown datasheet
<https://www.ti.com/lit/gpn/LM2588>

Role of renewable energy in decarbonisation process: Case study in KSA

Samar DERNAYKA^{1,a}*, Saidur R. CHOWDHURY^{1,b} and
Mohammad Ali KHASAWNEH^{1,c}

¹Prince Mohammad Bin Fahd University, Civil Engineering Department, KSA

^asdernayka@pmu.edu.sa, ^bschowdhury1@pmu.edu.sa, ^cmkhasawneh@pmu.edu.sa

Keywords: Renewable, Wind Turbine, Photovoltaic, Solar, Carbon Emissions

Abstract. Currently, most countries are replacing the fossil fuel electricity generation with renewable technologies for their crucial role in mitigating the greenhouse gas emissions. This paper discusses the implementation of three power plants in Al Aziziya in the eastern province of KSA by deploying three different renewable technologies 1) Photovoltaic 2) Solar thermal power and 3) Wind turbine. Both the energy performance and rate of electricity exported to grid were predicted when the capacity varies from 1000 to 1000,000 KW. In addition, the role of the three different renewable technologies in the decarbonization process has been evaluated.

Introduction

Over the last century, the greenhouse gases including atmospheric carbon dioxide (CO₂) have potentially grown with the energy production, especially by burning fossil fuels to generate electricity. In fact, fossil fuel materials like oil and gas stand behind 75% of the global greenhouse gas emissions and almost 90% of carbon dioxide emissions [1]. The data analysis in [2] have shown that greenhouse gas emissions were raised by 4298.05 (MTCO₂e) between 1990 and 2016 due to the tremendous electric energy consumption, which accounts of 40% of the total GHG emissions. The Kingdom faces relatively high-energy demands of energy in industrial as well as residential spots. According to The King Abdullah Petroleum Studies and Research Center (KAPSARC) Residential Energy Model (REEM), a residential Villa in Dhahran area consumes an average of 24,900 KWh annually, while apartments use around 17,200 KWh [3]. Further, a study conducted in 2012 shows that the annual average electricity consumption hits 176.5 kWh/m², exceeding international energy-efficiency benchmarks. This translates to around 21,180 kWh per year for a 120-m² house [4]. Internationally, a household consumes, on average 9,600 to 12,000 kWh annually. This translates to an average daily energy consumption of about 26 to 33 kWh, equivalent to 26,000 to 33,000 watt-hours [5].

Hence, promoting the decarbonisation concept becomes a necessity. This process is achieved either by reducing the energy consumption, or by applying efficient practice and technologies through Renewable energy [6, 7]. For a one percent shift away from the usage of oil, it is possible to reduce the carbon emissions by 1.288 [8]. With the growth of Energy demand, the decarbonisation process consists of reducing or cutting the greenhouse gas emissions, which can be achieved through zero-carbon renewable energy sources such as wind, Solar, Hydropower, Geothermal and Biomass. Simultaneously, the available carbon and methane in the atmosphere shall be continually captured, and stored to counter balance the released toxic gases. The implementation of renewable technologies is required to be in correlation with the actual needs and peak demands of power. Currently, Wind and Solar are two main clean energy resources that can be used to generate electricity with zero carbon emissions and consequently less greenhouse effect. The deployment of key technologies such as solar PV or Wind turbines is on track in many countries and it proved to present a beneficial role in the decarbonisation process. According to



[9], the slice of renewables in power production will rise from around one-quarter in 2015 to around 60% by 2030 and 85% by 2050 for energy sector decarbonisation. In Russia, the implementation of wind and solar have contributed to more than 5 GW since 2013 which is likely to exceed the targeted capacity of 5.9 GW in 2024. For Middle Eastern countries, Turkey is urging to increase the share of solar and wind as well to cover its demand of imported energy [10].

The Kingdom of Saudi Arabia has ongoing plans to halt the rise of greenhouse gas emissions, and contribute to decarbonisation in order to reach the zero-carbon emission target by 2060. The main milestone for this is certainly to generate electric power by shifting away from petroleum and fossil fuel towards Renewable energy sources. Yet, such projects are still challenging and they are affected by many factors such as the location of the facility, meteorological parameters, connections to grid and mostly the efficiency of the technology. The scope of this paper is to discuss the implementation of electric power plant based on three renewable technologies 1) Photovoltaic 2) Solar thermal power and 3) Wind turbine in Al Aziziyah, located in Dhahran, the eastern province of Saudi Arabia. The performance of the three different power plants is predicted by using Retscreen Expert, a clean energy management software that has been validated by a team of experts in the Canadian government [11] in addition to HOMER Energy software. The analysis of the results presents evaluation of the electric power exported to the grid as well as the role of the three renewable technologies in the decarbonization process.

Renewable Energy Technologies

Photovoltaic

A Solar PV system consists of panels that convert electromagnetic wave of sunlight into electricity using the photovoltaic (PV) effect. The PV modules are made up of multiple (series and parallel) interconnected solar cells, which are typically formed of semiconductor material such as silicon. When sunlight hits these cells, it excites electrons, generating an electric current. Connecting cells in series increases the voltage and connecting them in parallel increases the current of the panel [12, 13]. Solar PV capacity has experienced a growth more than any other source of electricity generation [7]. In general, the PV size is chosen based on the energy and power consumption. The process of calculation of solar photovoltaic modular system involves the following steps: 1) Determine electricity consumption by calculating the total amount of electricity appliances to be powered in kilowatt-hours (kWh). An electricity bill provides a preliminary idea of the average monthly or yearly consumption. (2) Assess the solar irradiation which depends on the geographic location, time of year, and weather conditions. (3) Account for system losses: These can typically range from 10% to 20% including shading, wiring losses, inverter efficiency, etc. (4) Calculate the required capacity as in Eq. 1 and Eq. 2 (5) Determine the number of panels based on Eq. 3 [14, 15]. The efficiency of a solar panel refers to the amount of sunlight it can convert into electricity. The average efficiency for most commercial solar panels is ranging between 15% and 20%. The typical power output of a standard solar panel is around 250 to 400 watts [12, 13 & 16]. Advanced PV modules can produce over 400 watts power with maximum efficiency that reaches 40%.

$$\text{Required Capacity (kW)} = \frac{\text{Electricity Consumption(kWh)}}{\text{Solar irradiation} * \text{System Losses}} \quad (1)$$

$$\text{Solar Irradiation per day} = \frac{P}{A} = \epsilon \sigma T^4 \quad (2)$$

$$\text{Number of panels} = \text{Required Capacity(kW)} / \text{Panel power Output(kW)} \quad (3)$$

Where, P and A represent solar power and Area; ϵ , σ and T indicate emissivity, Stefan-Boltzmann constant and surface temperature, respectively.

Solar Thermal Panel

A solar thermal panel absorbs the incoming solar radiation, converts it into heat [17, 18], and transfers this heat to a fluid (usually air, water, or oil) that flows and circulates (by mechanical component, such as a fan or pump) through the collector. A solar heating system utilizes solar heat (concentrated or not) without conversion in order to supply residential and commercial purposes [19]. The common types of solar panel or collectors are flat plate collector, integral collector-storage (ICS), double -glass solar collectors, compound parabolic collectors and evacuated tube collectors etc. [17, 18]. The concentration ratio, fluid flow velocity, and surface area would all have a significant influence on the collector's efficiency and heat removal factor. Compared to solar PV panels, solar thermal panels are more efficient, converting 70–90% of the energy input into heat, and they require less area. However, the capacity factor of the overall power utilization is in the range of 20 to 30% due to the intermittency of the naturel resources. Flat panel or collector, typically measuring one meter by two meters, is the most popular kind of solar thermal panel [20]. Figure 1 shows the system to convert sunlight to heat.

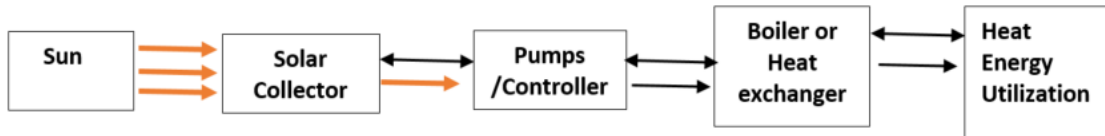


Figure 1 Converting sunlight to heat system

Again, concentrated solar power (CSP), a high temperature solar thermal system, uses groups of mirrors to concentrate solar energy at central collector. This produces a temperature high enough to generate steam, which then turns a turbine, driving a generator to produce electricity [19]. Electricity from a solar thermal system is an opto-caloric system that depends on solar radiation and its capture's capacity. Figure 2 shows the flow chart of electricity generation from solar radiation (by converting solar thermal radiation into electricity) with the support of a solar collector and other mechanical components.



Figure 2 Electricity generation from solar radiation using solar heat

High temperatures that are required to achieve the utmost efficiency can be obtained by increasing the energy flux density of the solar radiation incident on a collector. According to Lupu et al. [20] energy efficiency of a solar thermal collector is:

$$\eta_{en} = \frac{\dot{Q}_u}{GA_c} \quad (4)$$

Q_u useful heat rate absorbed by the fluid; incident solar radiation, G (average 240W/m²), A_c is area of the collector. C_p , m, and T are latent heat, mass of plate, and temperature, respectively. The useful heat rate absorbed by the fluid [20], Q_u , is

$$\dot{Q}_u = \dot{m}C_p(T_{fl,out} - T_{fl,in}) \quad (5)$$

Wind turbine

Wind turbines harness the natural wind energy to generate electricity. The blades start to rotate when they are stimulated by the wind's kinetic energy. The resulting mechanical energy created over a drive shaft is then converted to electric energy through a generator. A basic wind speed of 3 to 5m/s at 10m height is usually sufficient to have potential wind resource. The efficiency of a wind turbine is measured by calculating its capacity factor as per Eq. (6) [21].

$$C_p = \frac{\text{Actual Electricity Output (kWh)}}{\text{Maximum Electricity Output}} \quad (6)$$

$$\text{Maximum Electricity Output (kWh)} = \text{Capacity(kW)} * \text{hours per year} \quad (7)$$

The capacity factor indicates how fully the wind turbine capacity is used. It is affected by the availability of wind, the hub height, swept area of the unit and the size of its generator. The capacity factor ranges between 20 to 35% and it can go up to 52% for new giant devices.

Data Assessment

The potential electric power plants are located in Al-Aziziyah, in the vicinity of Dhahran, the eastern province of Saudi Arabia. The latitude and longitude for the facility location are 26.2 and 50.2 respectively. The climate zone is estimated to be extremely hot – Dry. The preliminary climate assessment is based on the meteorological data and NASA provided by RetScreen Expert Clean Energy Management Software platform. Fig.3 shows two meteorological parameters: the daily solar radiation and wind speed at 10m height above the ground.

The daily solar radiation ranges between 3.2 and 8 KWh/m². It is the global horizontal irradiance that presents the total solar radiation falling on a horizontal surface. The peak value of 7.8 KWh/m²/d attained in the month of June refers to 7.8 hours of sun received per day at 1 KWh/m² during this month. The extreme value of the annual average irradiance of 5.6 KWh/m²/d as per NASA as well as the high temperatures (above 30°C) make the area an excellent resource for solar applications. The annual wind speed variation shows an average of 4.4 m/s, which favors the installation of wind turbines. Besides, Dhahran area belongs to the moderate to good wind resource as per [22].

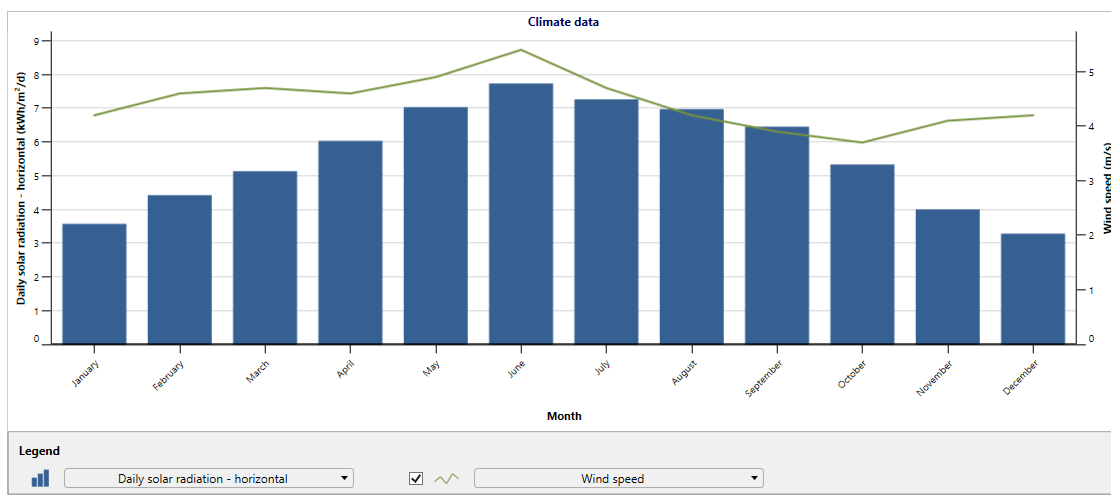


Figure 3- Daily Solar Radiation and Wind Speed in Dhahran area

RetScreen-Software based Simulation

The simulation of the three different renewable power plants has been conducted in RetScreen. Each RetScreen Technology model is developed within a workbook file that is been validated by

modelling experts and other simulation software. RetScreen evaluates the implementation of a renewable project based on several aspects: 1) Energy performance 2) Cost analysis 3) GHG emissions 4) Financial Summary and 5) Risk Analysis. The input data is relatively small since RetScreen contains integrated products, cost and weather databases. The data that is required cover the location of the facility, climate data (hourly wind Speed for wind), selected technology (Manufacturer and model) and economic input data (Table 1). Other variables that are relevant to the energy pricing can also be filled by the user.

Table 1- Financial Indicators considered in RetScreen Simulation for the current simulation

Inflation rate: 2%	Debt Interest rate: 7%	Electricity Export rate: 0.10 \$/kWh
Discount rate: 9%	Project Life: 20 years	Electricity Export Escalation rate: 2%

Results and Discussion

Renewable Energy Systems

Table 2 shows the technical specifications for the renewable technologies implemented in four potential power plants with different capacity each. Based on RetScreen predictions, the number of solar thermal and photovoltaic units is raised with the increase of the required capacity. For wind turbines, a larger electricity output is generated when the hub height increases and more turbines are added; which results in higher capacity factor. The gross energy production per turbine GE is different for each device model. For 1000,000 KW capacity, there is need for vast wind farm with 500 ENERCON 82 E2 2MW wind turbines at 138 m height. The solar thermal system presents the same performance for all capacities: 30% while photovoltaic cells have the least efficiency: the rate of miscellaneous losses considered is 15%, while the inverter capacity is 95%.

Table 2 – Technical Specifications for considered renewable based Power Plant

Capacity (KW)	Solar Thermal	Photovoltaic	Wind Turbine
1000	Abengoa Solar PS10 with parabolic mirrors Capacity factor: 30%	5000 units mono-Si Solar Collector: 3333 m ² Efficiency: 17%	2 ENERCON 53 – 73m Capacity Factor: 25%
10,000	Abengoa Solar PS10 with parabolic mirrors Capacity factor: 30%	50,000 units mono – Si SP150 Capacity per unit: 150 W Solar Collector: 64103 m ² Efficiency: 17.6%	5 ENERCON 82 E2 2MW – 78 m GE: 4771 MWh per turbine Capacity Factor: 24%
100,000	Abengoa Solar PS10 with parabolic mirrors Capacity factor: 30%	500,000 units mono – Si CS1H-320MS Capacity per unit: 320 W Solar Collector: 842105 m ² Efficiency: 17.6%	44 ENERCON 82 E2 – 138 m GE: 5818 MWh per turbine Capacity Factor: 25%
1000,000	Abengoa Solar PS10 with parabolic mirrors Capacity factor: 30%	5,000,000 units mono – Si CS1H-320MS Capacity per unit: 320 W Solar Collector: 8421053 m ² Efficiency: 17.6%	500 ENERCON 82 E2 2MW – 138 m GE: 5613 MWh per turbine Capacity Factor: 28%

Table 3 – Electricity outcome and CO₂ reduction for the three considered technologies

Designed Capacity (KW)	Electricity Exported to Grid (MWh)			GHG Emission Reduction (tCO ₂)		
	Solar Thermal	Photovoltaic	Wind Turbine	Solar Thermal	Photovoltaic	Wind Turbine
1000	2,628	1,543	1,968	1,243	730	1,650
10,000	26,280	11,576	20,675	13,582	5,475	9,778
100,000	26,280,000	246,950	221,668	124,291	116,795	104,837
1000,000	262,800,000	2,469,205	2,432,350	1,242,910	1,167,949	1,150,377

Table 3 shows the electricity exported to Grid as well as the rate of carbon reduction in tons of CO₂ relevant to each technology. The production of electricity from both photovoltaic and wind turbines is comparable specifically when the capacity exceeds 10,000 KW. The solar thermal system provides the highest rate of total electricity output at a specific designed capacity. It can play a pivotal role in the electricity generation in the area due to the abundance of sun and consequently the generated heat will be used in electricity generation. The electricity exported to grid will reach 262,800,000 MWh for a 1000,000 KW power plant capacity, which surpasses the output from Photovoltaic and wind. The amount of greenhouse gas displaced in tons of CO₂ is in correlation with the increase of the designed capacity. The implementation of photovoltaic results in the lowest carbon reduction rate in comparison with the solar and wind at 10 MW and smaller.

Role of Renewable energy technologies in the decarbonization process

Figure 4 shows the greenhouse gas emissions displacement with respect to the three different renewable technologies (solar thermal, Photovoltaic and Wind Turbine) in function of the required power plant capacity. At capacities equal to or lower than 10,000 KW, the solar thermal has the ability to displace the highest rate of carbon dioxide, followed by the wind turbine and then the photovoltaic system. For 100,000 and 1000, 000-KW power plants, the three technologies will result in comparable amount of greenhouse gas emissions. This is due to the expansion in the number of photovoltaic units and higher wind turbines that will capture more sun and wind and consequently release clean energy. The amount of displaced greenhouse gas emissions when setting up a 1,000,000 KW renewable power plant capacity attains 1,242,910 tCO₂, which accounts for 2,890,487 Barrels of crude oil not consumed.

The process of electricity generation by using renewable technologies instead of the conventional methods has a great impact on the decarbonization as it halts the release of toxic substances in the air. In fact, coal, natural gas or petroleum combustion are more carbon-intensive in electric power production in comparison with wind and solar as shown in Table 4. Besides, Coal combustion produces more greenhouse gases than the combustion of any other fossil fuels.

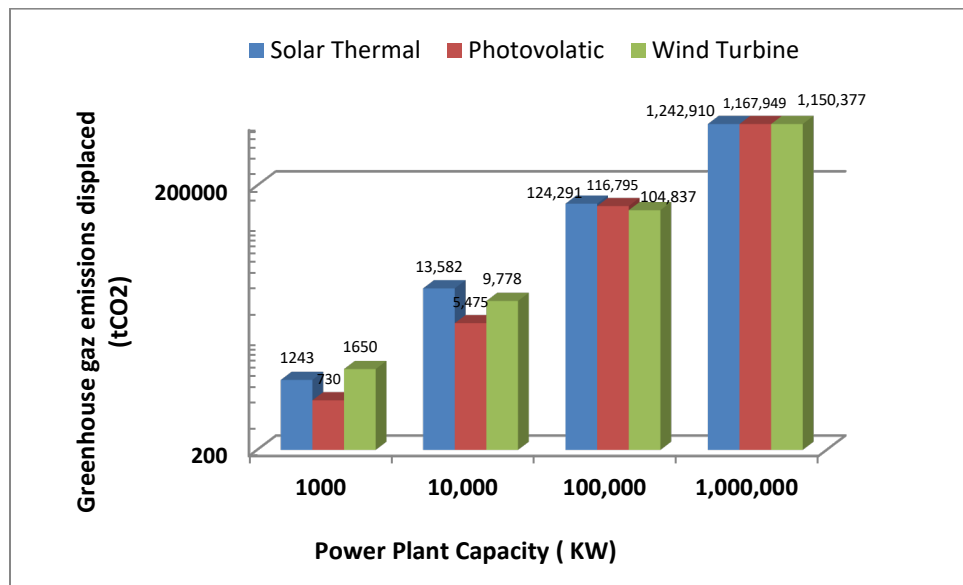


Figure 4 - Greenhouse emissions reduction with respect to renewable energy technologies (tCO₂)

Table 4 CO₂ emissions during electricity production for different energy sources (obtained from [23])

	Coal	Natural Gas	Fuel Oil	Wind	Solar	Petroleum
Electricity generation	0.88 kWh/Pound	0.13 kWh/cubic foot	12.90 kWh/gallon	2,4 kWh and 9,6 kWh/day	0.68 KWh/day	1.18 kWh/pound
CO ₂ emissions	980 g CO ₂ /kWh	465 g CO ₂ /kWh	266.5 g CO ₂ /kWh	11 g CO ₂ /kWh	41 g CO ₂ /kWh	345.0 g CO ₂ /kWh

Reducing carbon emissions from the power industry is greatly impacted by moving electricity production from fossil fuel generation sources to renewable ones. Decarbonizing the grid is one potential option that calls for international cooperation and coordination between businesses and governments in order to reduce emissions as well as follow the Paris Agreement.

Conclusion

Renewable energy sources, particularly wind and solar, provide sustainable solutions to our power needs. They present a major role in the decarbonization process especially when used in the electricity generation process. A case study conducted in Al Aziziyah in the Kingdom of Saudi Arabia reveals the most beneficial impact on displacing the greenhouse gas emissions when implementing the Solar Thermal power plant. The area, prone to continuous extreme sunlight, and good wind potential offers an efficient and sustainable alternative for producing fossil fuel based electricity and facing the high demand with minimal environment effects. Finally, while renewable energy sources like wind and solar power significantly reduce greenhouse gas emissions, they are not entirely devoid of waste generation, particularly during the manufacturing and end-of-life stages.

References

- [1] O. Edenhofer, R. P. P. Madruga, Y. Sokona, Renewable Energy Sources and Climate Change Mitigation, Cambridge University Press, New York, USA, 2012. ISBN 978-1-107-60710-1.

- [2] R. Gh. Alajmi, Factors that impact greenhouse gas emissions in Saudi Arabia: Decomposition analysis using LMDI, *Energy Policy* 156 (2021), 112454.
<https://doi.org/10.1016/j.enpol.2021.112454>
- [3] M. Aldubyan, M. Krarti,, & E. Williams, Residential Energy Model for Evaluating Energy Demand and Energy Efficiency Programs in Saudi Residential Buildings, (2020) KAPSARC, Riyadh, KSA. <https://doi.org/10.30573/KS--2020-MP05>
- [4] F. Alrashed, & M. Asif, Trends in residential energy consumption in Saudi Arabia with particular reference to the Eastern Province. *Journal of Sustainable Development of Energy, Water and Environment Systems*, 2(4) (2014), 376-387.
<https://doi.org/10.13044/j.sdewes.2014.02.0030>
- [5] <https://www.anker.com/blogs/home-power-backup/electricity-usage-how-much-energy-does-an-average-house-use>
- [6] M. Gul, Y. Kotak, & T. Muneer, Review on recent trend of solar photovoltaic technology. *Energy Exploration & Exploitation*, 34(4), (2016), 485-526.
<https://doi.org/10.1177/0144598716650552>
- [7] N. A. Ludin, N. I. Mustafa, M. M. Hanafiah, M. A. Ibrahim, M. A. Teridi, M. Sepeai & K. Sopian, Prospects of life cycle assessment of renewable energy from solar photovoltaic technologies: A review. *Renewable and Sustainable Energy Reviews*, 96 (2018) 11-28.
<https://doi.org/10.1016/j.rser.2018.07.048>
- [8] R. Gh. Alajmi, Carbon emissions and electricity generation modeling in Saudi Arabia. *Environmental Science and Pollution Research* (2022) 29:23169–23179.
<https://doi.org/10.1007/s11356-021-17354-0>
- [9] C. D. Gielena , F.Boshella , D. Sayginb , M. D. Bazilianc , N. Wagnera, R. Gorini, The role of renewable energy in the global energy transformation, *Energy Strategy Reviews* 24 (2019) 38 -50. <https://doi.org/10.1016/j.esr.2019.01.006>
- [10] D. Saygin, M. Hoffman, P. Godron, How Turkey Can Ensure A Successful Energy Transition, Center for American Progress, Washington, DC, 2018.
- [11] CLEAN ENERGY PROJECT ANALYSIS: RETSCREEN® ENGINEERING & CASES TEXTBOOK, Minister of Natural Resources Canada 2001-2005, ISBN: 0-662-39191-8 Catalogue no.: M39-112/2005E-PDF
- [12] P. K. Nayak, S. Mahesh, H. J. Snaith, & D. Cahen, Photovoltaic solar cell technologies: analysing the state of the art. *Nature Reviews Materials*, 4(4) (2019) 269-285.
<https://doi.org/10.1038/s41578-019-0097-0>
- [13] N. Rathore, N. L. Panwar, F. Yettou, & A. Gama, A comprehensive review of different types of solar photovoltaic cells and their applications. *International Journal of Ambient Energy*, 42(10) (2021) 1200-1217. <https://doi.org/10.1080/01430750.2019.1592774>
- [14] A. R. Jordehi, Parameter estimation of solar photovoltaic (PV) cells: A review. *Renewable and Sustainable Energy Reviews*, 61(2016) 354-371. <https://doi.org/10.1016/j.rser.2016.03.049>
- [15] A. A. H. Hussein, S. Harb, N. Kutkut, J. Shen, & I. Batarseh, Design considerations for distributed micro-storage systems in residential applications. In *Intelec 2010* (pp. 1-6). IEEE.
<https://doi.org/10.1109/INTLEC.2010.5525658>
- [16] G. K. Singh, Solar power generation by PV (photovoltaic) technology: A review. *Energy* 53 (2013) 1-13. <https://doi.org/10.1016/j.energy.2013.02.057>
- [17] S. A Kalogirou, Solar thermal collectors and applications. *Progress in Energy and Combustion Science* 30 (2004) 231–295. <https://doi.org/10.1016/j.pecs.2004.02.001>

- [18] L. Kumar, J. Ahmed, M.E. H. Assad, M. Hasanuzzaman. Prospects and Challenges of Solar Thermal for Process Heating: A Comprehensive Review. *Energies* 2022, 15, 8501.
<https://doi.org/10.3390/en15228501>
- [19] T. Merrigan. Solar Energy Technologies. National Renewable Energy Laboratory, U.S. Department of Energy. 2005. /https://www1.eere.energy.gov/solar/pdfs/solar_tim_merrigan.pdf
- [20] A. G. Lupu, V. M. Homutescu, D. T. Balanescu, and A. Popescu, Efficiency of solar collectors – a review. *IOP Conf. Series: Materials Science and Engineering* 444 (2018) 082015.
<https://doi.org/10.1088/1757-899X/444/8/082015>
- [21] D. Song, Y. Yang, S. Zheng, W. Tang, J. Yang, M. Su, X. Yang, J. Y. Hoon, Capacity factor estimation of variable-speed wind turbines considering the coupled influence of the QNcurve and the air density, *Energy*, Vol. (183) (2019) pp 1049 – 1060.
<https://doi.org/10.1016/j.energy.2019.07.018>
- [22] Y. El Khchin, M. Sriti, Performance Evaluation of wind turbines for energy production in Morocco's coastal regions. *Results in Engineering* 10 (2021) 100215.
<https://doi.org/10.1016/j.rineng.2021.100215>
- [23] U.S. Energy Information Administration (EIA), Electricity generation from wind. 1000 Independence Ave., SW Washington, DC 20585 (2022)
<https://www.eia.gov/energyexplained/wind/electricity-generation-from-wind>

An automated and cost-efficient method for photovoltaic dust cleaning based on biaxially oriented polyamide coating material

Said Halwani^{1,2,a*}, Mena Maurice Farag^{1,2,b*}, Abdul-Kadir Hamid^{1,2,c*},
Mousa Hussein^{3,d}

¹Sustainable Energy and Power Systems Research Centre, Research Institute for Sciences and Engineering (RISE), University of Sharjah, Sharjah, United Arab Emirates

²Department of Electrical Engineering, College of Engineering, University of Sharjah, Sharjah, United Arab Emirates

³Department of Electrical and Communication Engineering, College of Engineering, United Arab Emirates University, Al Ain, UAE

^aShalwani@sharjah.ac.ae, ^bU20105427@sharjah.ac.ae, ^cAKHAMID@sharjah.ac.ae,
^dmihussein@uaeu.ac.ae

Keywords: Dust Accumulation, Experimental Investigation, PV Systems, Cleaning Methods

Abstract. Photovoltaic (PV) systems have been at the forefront of renewable energy technologies. However, they are highly dependent on environmental parameters that affect their performance and longevity. Dust accumulation presents a critical factor in the performance of PV systems, leading to minimum system efficiency under largely dusty conditions. Several cleaning methodologies have been proposed in scientific literature to prevent dust accumulation at the forefront of PV modules. However, most cleaning methodologies are cost-consuming, time-consuming, complex in implementation, or require huge manpower to implement them. This paper proposes a cost-efficient and automated method for dust accumulation prevention and cleaning based on Biaxially Oriented Polyamide (BOPA) coating material. This transparent thin film is applied on the front surface and integrated based on an automated control scheme, for controlled rotation every 2 weeks, to prevent dust accumulation on the forefront of the PV surface. The performance of the BOPA coating film was experimentally assessed for 45 days, assessing the irradiance and electrical performance of the PV modules. The application of BOPA maintained a PV module electrical efficiency of 12.19%, while the dusty PV module electrical efficiency is reduced to 7.79% at high dust accumulation levels. Moreover, the BOPA material has demonstrated its ability in capturing solar irradiance, without losses for the visible light, hence maintaining an electrical current of 2.15 A, while the dusty PV module loses its electrical current by 40%, maintaining an electrical current of 1.28 A.

Introduction

Renewable energy resources (RES) have been at the forefront of electricity generation, due to their active contribution to clean energy generation and improved efficiency [1]. Renewable energy has been deployed due to its environmental and technical advantages in integration within the primary energy mix [2–4]. Solar energy has attracted attention in renewable energy technologies due to its abundance, reliability, and zero-cost availability [5,6]. Photovoltaic (PV) systems have been developed for the useful harvesting of solar energy, and its ability for clean energy generation and minimize the carbon footprint [7].

The global demand for solar power generation has been rapidly increasing, leading to the evolution of technology and being commercially available [8–10]. Therefore, it is essential to continuously develop the technology for efficient operation and generation [11]. Dust

accumulation on the front surface of PV modules has been a commonly reported issue in the effectiveness and applicability of PV technologies [12]. Particularly, regions such as the Middle East, China, North Africa, India, and the United States have been developing PV plants with a capacity of Gigawatts. However, such regions are exposed to dusty conditions and harsh weather conditions, leading to severe degradation in PV system performance [13–15]. Dust accumulation is considered a critical factor in regulating the electrical efficiency of a PV system, specifically when large accumulation occurs.

The scientific literature focused on several methods to clean and sustain PV modules, preventing the severe impact of soiling [16–18]. The cleaning may occur naturally through rainfall or wind. Other cleaning methods have been introduced such as manual cleaning, dry cleaning based on a robotics system, electrostatic cleaning, and preventive cleaning based on coating materials.

As aforementioned, the cleaning techniques are of many types with each having several advantages and disadvantages. Natural cleaning techniques are relatively low cost due to the utilization of the natural gravity of water or wind. However, it's not physically possible to induce rainfall or wind in specific regions, particularly depending on the dust particle volume [19,20]. Additionally, manual cleaning benefits from minimum power consumption and allows for periodical cleaning. However, high labor costs are a drawback and other potential hazards may harm the system or laborers [21]. Furthermore, the installation of sprinklers is of good beneficial ability in cleaning PV systems under short periods with feasible installation [22], however, high water consumption and non-uniform cleaning are a potential drawback [23]. Recently, the development of robots for automated cleaning has allowed for the reduction of damage on PV module surfaces and lowering the of energy consumption, through dry cleaning. However, their operation and maintenance require significant investment, and their applicability is limited to small PV plants [24]. Emerging technologies such as electrostatic cleaning and surface coating materials are still developing and need to be studied for their effectiveness due to their cost and coating properties [25–28].

This paper proposes a cost-effective and simple methodology for dust cleaning based on the application of Biaxially Oriented Polyamide (BOPA) film. A thin layer of BOPA is assessed in outdoor experimental conditions in the terrestrial conditions of Sharjah, UAE. An automated and control scheme is proposed for rotation of the transparent layer every 2 weeks, to maintain PV modules in clean conditions for 45 days. The study assesses the impact of dust accumulation on solar irradiance and electrical performance, proposing a cost-efficient solution for dust cleaning and PV module maintenance.

Research Method

This research paper presents an experimental study conducted at the University of Sharjah during solar noon in November and December 2023. The experiment involved two identical photovoltaic (PV) panels, one serving as a reference and the other coated with a colorless and thin layer of Biaxially Oriented Polyamide (BOPA). The power output of both panels was measured before and after dust accumulation. The methodology included four distinct cases: Case one involved cleaning both PV panels to determine the power reduction caused by the BOPA coating. In cases two through four, varying degrees of dust accumulation were applied to the reference panel to observe its impact on power generation. The performance of photovoltaic (PV) panels is crucial for their practical application in solar energy systems. Dust accumulation on PV panels is a common issue, particularly in arid regions like the United Arab Emirates [29,30].

Several strategies have been proposed to mitigate the effects of dust on PV panel performance, including the application of coatings. This study focuses on investigating the effectiveness of a Biaxially Oriented Polyamide (BOPA) coating in enhancing the power output of PV panels under dusty conditions. By conducting a series of experiments with controlled dust levels, this research

aims to provide empirical evidence supporting the efficacy of BOPA coatings in improving PV panel performance.

Biaxially Oriented Polyamide (BOPA) film offers a comprehensive spectrum of properties, making it a versatile choice for using it as a coat to the PV [31]. Its exceptional thermal stability ensures resilience to high temperatures, facilitating processes like heat sealing and sterilization. Coupled with impressive mechanical strength, BOPA provides robust protection during transportation and handling, ensuring the integrity of the coated PV [32]. Furthermore, its clarity and transparency options enhance product visibility and aesthetic appeal allowing the sunlight to reach the panel clearly, while its inherent chemical resistance safeguards against various substances, including oils and greases [33]. Embracing environmental sustainability, BOPA can be recycled and designed to reduce material usage, aligning with eco-conscious coating initiatives. This amalgamation of thermal resilience, strength, clarity, chemical resistance, and sustainability renders BOPA an indispensable solution across industries seeking performance and environmental responsibility in PV coating [34].

The following methodology was employed: Selection and Preparation of PV Panels: Two identical PV panels were chosen for the experiment. One panel was left uncoated (reference panel), while the other was coated with a colorless and thin layer of Biaxially Oriented Polyamide (BOPA). Both panels were cleaned thoroughly before the experiment to ensure baseline performance.

Experimental Setup

The PV panels were positioned outdoors during solar noon to receive maximum sunlight. The experimental setup included instruments for measuring the power output of the panels before and after dust accumulation. Fig. 1 demonstrates a diagram for the experiment setup.

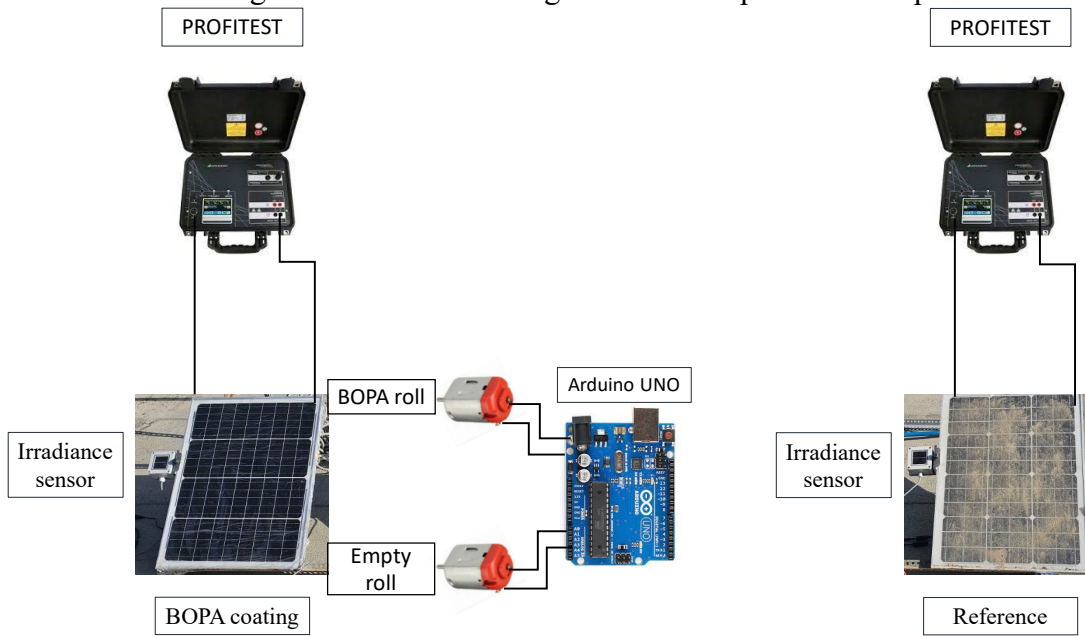


Fig. 1. Experimental setup with and without BOPA coating

The Profitest is used in this experiment to calculate the current, voltage, and power and it works as a load to the PV panel.

Dust Accumulation Procedure: Dust accumulated onto the panels for 45+ days for both panels. Four distinct cases were considered:

- Case One (Clean Panels): Both PV panels were cleaned to determine the power reduction caused by the BOPA coating alone (day 1).
- Case Two (Light Dust): After one week, the panels were subjected to light dust accumulation.

c. Case Three (Moderate Dust): The panels were exposed to a higher level of dust accumulation compared to case two after 3 weeks.

d. Case Four (Heavy Dust): The panels were heavily dusted after 45+ days.

The coating roll for the coated panel was connected to two small DC motors (6V) connected to Arduino Uno, this Arduino was programmed to power the motors for a short time allowing the coat to roll over the panel and have a new coat to the top of the panel, the number of rotation needed increases with time. The average number of rotations was measured (3.5 full rotations on average needed to cover the panel) so the motors were programmed to rotate 3.5 rotations every two weeks anticlockwise, one motor will rotate the BOPA roll and the other one will collect the dusty roll.

The coat was fully rotated and renewed every two weeks, keeping the panel clean and dust-free. The power output of both panels was measured before and after dust accumulation in each case. The data obtained were analyzed to assess the impact of the BOPA coating on PV panel performance under varying levels of dust accumulation. To calculate the cost a simple equation was used.

The number of rotations that the roll can cover the panel (R) is equal to the length of the roll (L_r) divided by the length of the panel (L_p), where the width of the roll and the panel are equal.

$$R = L_r / L_p \quad (1)$$

Then we divide R with 26.5 which is the number of weeks that the roll will rotate per year. Finally, the number of years is divided by the price of the BOPA roll, which gives 0.11 AED per rotation.

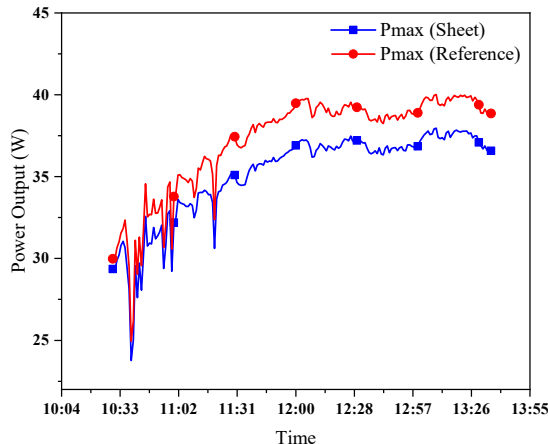
Experimental Results

The experimental results demonstrate that the BOPA-coated panel mostly produces more power than the uncoated reference panel, only after dust accumulation. These findings underscore the potential of BOPA coatings as a practical solution for optimizing PV panel performance in arid regions with high dust levels. Fig. 2 demonstrates the power produced in each case.

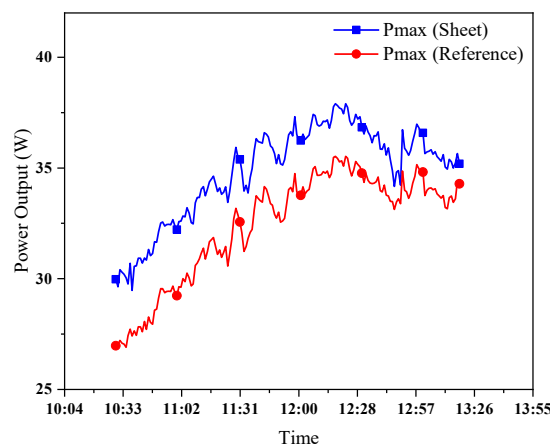
The results of the experiment indicate that the BOPA-coated panel outperformed the reference panel in all cases of dust accumulation. The reference power was more than the BOPA-coated only when both the panels were clean, because of the characteristics of the BOPA (thin and colorless) the reduction of the power was not high. The power output of the coated panel exhibited minimal reduction compared to the uncoated panel, demonstrating the effectiveness of the BOPA coating in mitigating the adverse effects of dust.

This study provides empirical evidence supporting the efficacy of BOPA coatings in enhancing the performance of photovoltaic (PV) panels under dusty conditions. The experimental results demonstrate that the BOPA-coated panel produces more power than the uncoated reference. The data in Table 1 shows that the BOPA coat is more effective when the dust accumulates, the reference power gets lower when the dust accumulation is high. The dust affected the irradiance, causing a reduction in the current and the power. In the fourth case, the efficiency was 4.4% improved with the coat, and 12.51 W increased in terms of power, even though it caused a 5°C increase in the overall temperature, and only 9 watts in 20s was the power needed for the two motors once every two weeks. Comparing other methods in the literature such as robotics systems

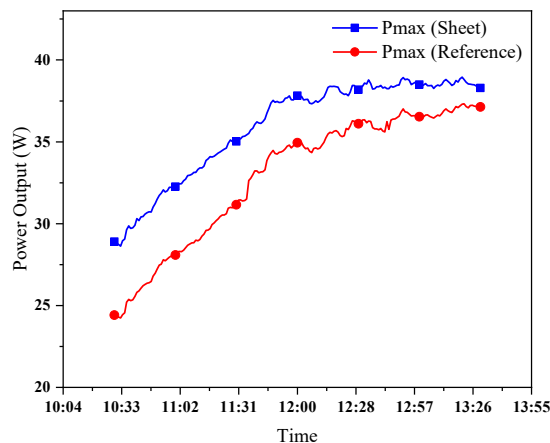
and electrostatic cleaning consume more power for a longer time and require more maintenance.



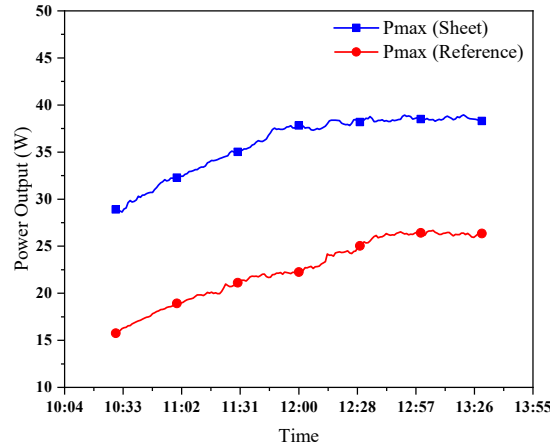
case one Both panels are clean and one is coated



case two the reference panel got light dust accumulation



case three the reference panel were subjected to higher level of dust accumulation



case four the reference panel got heavily dusted

Fig. 2. Comparison of PV modules output power generation

Table 1. Summary of solar irradiance and electrical performance for coated and reference PV module

	Case one (ref)	Case one (coated)	Case two (ref)	Case two (coated)	Case three (ref)	Case three (coated)	Case four (ref)	Case four (coated)
Current (A)	2.19	2.17	1.84	2.11	1.93	2.23	1.28	2.15
Power (watt)	37.17	35.17	32.42	34.69	32.97	35.98	22.54	35.05
Irradiance (W/m ²)	807.30	763.62	704.37	744.68	730.80	796.50	490.82	762.16
Efficiency (%)	12.93	12.24	11.53	12.00	10.95	12.35	7.79	12.19

Summary

This study has demonstrated the utilization of Biaxially Oriented Polyamide (BOPA) Coating material as a method for the prevention of dust accumulation. The proposed methodology introduced a thin film of BOPA material, optimizing the PV module performance in arid regions with high dust accumulation levels. An automated controlled scheme was integrated to allow rotation of film every 2 weeks, ensuring clean PV modules across an experimental period of 45

days. The findings suggest that BOPA coatings hold promise as a viable solution for improving the performance and longevity of PV modules under dusty conditions, through the improvement of solar irradiation exposure and electrical performance. The maximum electrical efficiency is maintained up to 12.19% with the BOPA material as compared to 7.79% under the highest dust accumulation. Additionally, solar irradiation is significantly reduced under high dust accumulation, leading to a severe reduction in electrical current, proving the viability of the proposed cleaning method. Further research may focus on optimizing the properties of BOPA coatings for maximum effectiveness and durability in real-world applications.

References

- [1] M.M. Farag, N. Patel, A.-K. Hamid, A.A. Adam, R.C. Bansal, M. Bettayeb, A. Mehiri, An Optimized Fractional Nonlinear Synergic Controller for Maximum Power Point Tracking of Photovoltaic Array Under Abrupt Irradiance Change, *IEEE J. Photovoltaics.* 13 (2023) 305–314. <https://doi.org/10.1109/JPHOTOV.2023.3236808>
- [2] Y.N. Chanchangi, A. Ghosh, S. Sundaram, T.K. Mallick, Dust and PV Performance in Nigeria: A review, *Renew. Sustain. Energy Rev.* 121 (2020) 109704. <https://doi.org/10.1016/j.rser.2020.109704>
- [3] E.T. Sayed, T. Wilberforce, K. Elsaied, M.K.H. Rabaia, M.A. Abdelkareem, K.-J. Chae, A.G. Olabi, A critical review on environmental impacts of renewable energy systems and mitigation strategies: Wind, hydro, biomass and geothermal, *Sci. Total Environ.* 766 (2021) 144505. <https://doi.org/10.1016/j.scitotenv.2020.144505>
- [4] S.B. Bashir, A.A.A. Ismail, A. Elnady, M.M. Farag, A.-K. Hamid, R.C. Bansal, A.G. Abo-Khalil, Modular Multilevel Converter-Based Microgrid: A Critical Review, *IEEE Access.* 11 (2023) 65569–65589. <https://doi.org/10.1109/ACCESS.2023.3289829>
- [5] M.M. Farag, F.F. Ahmad, A.K. Hamid, C. Ghenai, M. Bettayeb, Real-Time Monitoring and Performance Harvesting for Grid-Connected PV System - A Case in Sharjah, in: 2021 14th Int. Conf. Dev. ESystems Eng., IEEE, 2021: pp. 241–245. <https://doi.org/10.1109/DeSE54285.2021.9719385>
- [6] T. Salameh, A.K. Hamid, M.M. Farag, E.M. Abo-Zahhad, Energy and exergy assessment for a University of Sharjah's PV grid-connected system based on experimental for harsh terrestrial conditions, *Energy Reports.* 9 (2023) 345–353. <https://doi.org/10.1016/j.egyr.2022.12.117>
- [7] T. Salameh, A.K. Hamid, M.M. Farag, E.M. Abo-Zahhad, Experimental and numerical simulation of a 2.88 kW PV grid-connected system under the terrestrial conditions of Sharjah city, *Energy Reports.* 9 (2023) 320–327. <https://doi.org/10.1016/j.egyr.2022.12.115>
- [8] K. Obaideen, M. Nooman AlMallahi, A.H. Alami, M. Ramadan, M.A. Abdelkareem, N. Shehata, A.G. Olabi, On the contribution of solar energy to sustainable developments goals: Case study on Mohammed bin Rashid Al Maktoum Solar Park, *Int. J. Thermofluids.* 12 (2021) 100123. <https://doi.org/10.1016/j.ijft.2021.100123>
- [9] M.M. Farag, R.C. Bansal, Solar energy development in the GCC region – a review on recent progress and opportunities, *Int. J. Model. Simul.* 43 (2023) 579–599. <https://doi.org/10.1080/02286203.2022.2105785>
- [10] M.M. Farag, R.A. Alhamad, A.B. Nassif, Metaheuristic Algorithms in Optimal Power Flow Analysis: A Qualitative Systematic Review, *Int. J. Artif. Intell. Tools.* 32 (2023). <https://doi.org/10.1142/S021821302350032X>
- [11] A.H. Alami, M.K.H. Rabaia, E.T. Sayed, M. Ramadan, M.A. Abdelkareem, S. Alasad, A.-G. Olabi, Management of potential challenges of PV technology proliferation, *Sustain. Energy*

- Technol. Assessments. 51 (2022) 101942. <https://doi.org/10.1016/j.seta.2021.101942>
- [12] M.M. Farag, F.F. Ahmad, A.K. Hamid, C. Ghenai, M. Bettayeb, M. Alchadirchy, Performance Assessment of a Hybrid PV/T system during Winter Season under Sharjah Climate, in: 2021 Int. Conf. Electr. Comput. Commun. Mechatronics Eng., IEEE, 2021: pp. 1–5. <https://doi.org/10.1109/ICECCM52200.2021.9590896>
- [13] R. Shenouda, M.S. Abd-Elhady, H.A. Kandil, A review of dust accumulation on PV panels in the MENA and the Far East regions, J. Eng. Appl. Sci. 69 (2022) 8. <https://doi.org/10.1186/s44147-021-00052-6>
- [14] M. Rashid, M. Yousif, Z. Rashid, A. Muhammad, M. Altaf, A. Mustafa, Effect of dust accumulation on the performance of photovoltaic modules for different climate regions, Heliyon. 9 (2023) e23069. <https://doi.org/10.1016/j.heliyon.2023.e23069>
- [15] M.M. Farag, A.K. Hamid, T. Salameh, E.M. Abo-Zahhad, M. AlMallahi, M. Elgendi, ENVIRONMENTAL, ECONOMIC, AND DEGRADATION ASSESSMENT FOR A 2.88 KW GRID-CONNECTED PV SYSTEM UNDER SHARJAH WEATHER CONDITIONS, in: 50th Int. Conf. Comput. Ind. Eng., 2023: pp. 1722–1731.
- [16] A. Younis, M. Onsa, A brief summary of cleaning operations and their effect on the photovoltaic performance in Africa and the Middle East, Energy Reports. 8 (2022) 2334–2347. <https://doi.org/10.1016/j.egyr.2022.01.155>
- [17] T. Salamah, A. Ramahi, K. Alamara, A. Juaidi, R. Abdallah, M.A. Abdelkareem, E.-C. Amer, A.G. Olabi, Effect of dust and methods of cleaning on the performance of solar PV module for different climate regions: Comprehensive review, Sci. Total Environ. 827 (2022) 154050. <https://doi.org/10.1016/j.scitotenv.2022.154050>
- [18] H. Aljaghoub, F. Abumadi, M.N. AlMallahi, K. Obaideen, A.H. Alami, Solar PV cleaning techniques contribute to Sustainable Development Goals (SDGs) using Multi-criteria decision-making (MCDM): Assessment and review, Int. J. Thermofluids. 16 (2022) 100233. <https://doi.org/10.1016/j.ijft.2022.100233>
- [19] M.K. Smith, C.C. Wamser, K.E. James, S. Moody, D.J. Sailor, T.N. Rosenstiel, Effects of Natural and Manual Cleaning on Photovoltaic Output, J. Sol. Energy Eng. 135 (2013). <https://doi.org/10.1115/1.4023927>
- [20] H.A. Kazem, M.T. Chaichan, A.H.A. Al-Waeli, K. Sopian, A review of dust accumulation and cleaning methods for solar photovoltaic systems, J. Clean. Prod. 276 (2020) 123187. <https://doi.org/10.1016/j.jclepro.2020.123187>
- [21] M.Z. Al-Badra, M.S. Abd-Elhady, H.A. Kandil, A novel technique for cleaning PV panels using antistatic coating with a mechanical vibrator, Energy Reports. 6 (2020) 1633–1637. <https://doi.org/10.1016/j.egyr.2020.06.020>
- [22] M.M. Farag, A.K. Hamid, Performance assessment of rooftop PV/T systems based on adaptive and smart cooling facility scheme - a case in hot climatic conditions of Sharjah, UAE, in: 3rd Int. Conf. Distrib. Sens. Intell. Syst. (ICDSIS 2022), Institution of Engineering and Technology, 2022: pp. 198–207. <https://doi.org/10.1049/icp.2022.2448>
- [23] A. Al-Dousari, W. Al-Nassar, A. Al-Hemoud, A. Alsaleh, A. Ramadan, N. Al-Dousari, M. Ahmed, Solar and wind energy: Challenges and solutions in desert regions, Energy. 176 (2019) 184–194. <https://doi.org/10.1016/j.energy.2019.03.180>
- [24] A. Amin, X. Wang, A. Alroichdi, A. Ibrahim, Designing and Manufacturing a Robot for Dry-Cleaning PV Solar Panels, Int. J. Energy Res. 2023 (2023) 1–15. <https://doi.org/10.1155/2023/7231554>.
- [25] H. Kawamoto, Electrostatic cleaning equipment for dust removal from soiled solar panels, J.

- Electrostat. 98 (2019) 11–16. <https://doi.org/10.1016/j.elstat.2019.02.002>
- [26] N.K. Almarzooqi, F.F. Ahmad, A.K. Hamid, C. Ghenai, M.M. Farag, T. Salameh, Experimental investigation of the effect of optical filters on the performance of the solar photovoltaic system, *Energy Reports.* 9 (2023) 336–344.
<https://doi.org/10.1016/j.egyr.2022.12.119>
- [27] A. Syafiq, V. Balakrishnan, M.S. Ali, S.J. Dhoble, N.A. Rahim, A. Omar, A.H.A. Bakar, Application of transparent self-cleaning coating for photovoltaic panel: a review, *Curr. Opin. Chem. Eng.* 36 (2022) 100801. <https://doi.org/10.1016/j.coche.2022.100801>
- [28] M.M. Farag, F. Faraz Ahmad, A.K. Hamid, C. Ghenai, M. AlMallahi, M. Elgendi, Impact of Colored Filters on PV Modules Performance: An Experimental Investigation on Electrical and Spectral Characteristics, in: 50th Int. Conf. Comput. Ind. Eng., 2023: pp. 1692–1704.
- [29] M.M. Farag, A.K. Hamid, Experimental Investigation on the Annual Performance of an Actively Monitored 2.88 kW Grid-Connected PV System in Sharjah, UAE, in: 2023 Adv. Sci. Eng. Technol. Int. Conf., IEEE, 2023: pp. 1–6.
<https://doi.org/10.1109/ASET56582.2023.10180880>
- [30] M.A. M. Abdelsalam, F.F. Ahmad, A.-K. Hamid, C. Ghenai, O. Rejeb, M. Alchadirchy, W. Obaid, M. El Haj Assad, Experimental study of the impact of dust on azimuth tracking solar PV in Sharjah, *Int. J. Electr. Comput. Eng.* 11 (2021) 3671.
<https://doi.org/10.11591/ijece.v11i5.pp3671-3681>
- [31] L.-C. Liu, C.-C. Lai, M.-T. Lu, C.-H. Wu, C.-M. Chen, Manufacture of biaxially-oriented polyamide 6 (BOPA6) films with high transparencies, mechanical performances, thermal resistance, and gas blocking capabilities, *Mater. Sci. Eng. B.* 259 (2020) 114605.
<https://doi.org/10.1016/j.mseb.2020.114605>
- [32] X. Lin, Y. Wu, L. Cui, X. Chen, S. Fan, Y. Liu, X. Liu, W. Zheng, Crystal structure, morphology, and mechanical properties of biaxially oriented polyamide-6 films toughened with poly(ether block amide), *Polym. Adv. Technol.* 33 (2022) 137–145.
<https://doi.org/10.1002/pat.5497>
- [33] S. Rhee, J.L. White, Crystal structure, morphology, orientation, and mechanical properties of biaxially oriented polyamide 6 films, *Polymer (Guildf).* 43 (2002) 5903–5914.
[https://doi.org/10.1016/S0032-3861\(02\)00489-5](https://doi.org/10.1016/S0032-3861(02)00489-5)
- [34] L. Di Maio, P. Scarfato, L. Incarnato, D. Acierno, Biaxial orientation of polyamide films: processability and properties, *Macromol. Symp.* 180 (2002) 1–8. [https://doi.org/10.1002/1521-3900\(200203\)180:1<1::AID-MASY1>3.0.CO;2-X](https://doi.org/10.1002/1521-3900(200203)180:1<1::AID-MASY1>3.0.CO;2-X)

Vibration harvesting techniques for electrical power generation: A review

Omar D. MOHAMMED^{1,a,*}, Isha BUBSHAIT^{1,b}, Reyouf ALQAHTANI^{1,c},
Kawther ALMENAYAN^{1,d}, Semat ALZAHER^{1,e}, and Reem ALHUSSAIN^{1,f}

¹ Mechanical Engineering Department - Prince Mohammad bin Fahd University PMU, Khobar,
Saudi Arabia

^aosily@pmu.edu.sa, ^b202000416@pmu.edu.sa, ^c202000155@pmu.edu.sa,
^d201902471@pmu.edu.sa, ^e201901224@pmu.edu.sa, ^f201902420@pmu.edu.sa

Keywords: Vibration, Piezoelectric, Mechanisms, Power Harvesting, Energy Generation, Battery Charging

Abstract. The ongoing demands of using mechanical motion and converting it to electrical power motivated designers to find new sustainable solutions for power generation. In the current article, different techniques of clean power generation are reviewed and discussed. The reviewed techniques use mechanical vibration to produce energy. The techniques using piezoelectric and mechanical design concepts are discussed and compared. The article sheds light on the importance of these techniques and concludes with the advantages and disadvantages of each applied technique.

Introduction

There are increasing demands to find new energy sources to reduce the use of fossil fuels. The new energy source has to be of better sustainability and environmental impact. The use of clean and renewable energy has increasing demands and thus puts a lot of pressure on engineers to find new ways to generate energy. Harvesting vibration energy has obtained a lot of researchers' attention, and that led to the development of new techniques or design concepts [1,2]. The use of mechanical motion in our daily activities and converting it to electrical power has been under investigation and application. This energy harvesting concept can be applied using two main techniques, first, using mechanisms or mechanical concepts, and second, using piezoelectric transducers.

The pendulum mechanism is discussed in [3] for energy harvesting. Different pendulum configurations for energy generation were applied, for example, the multi- or single-pendulum, and modulation-based pendulums. A few combinations of piezoelectric, electromagnetic and hybrid transducers were discussed. An electromagnetic vibration-based energy generator was proposed in [4]. The technique converted the linear vibration to a rotation. Linear motion can be converted to energy using a magnet, where the rotation in the magnetic flux can generate electricity.

Piezoelectric materials can be employed as devices to generate energy from mechanical motion, which is in the form of vibrations, into electrical energy that can power other gadgets. Power harvesting is the technique of collecting energy and turning it into useful power for a system. Portable systems that don't rely on conventional power sources, such as batteries, which have a finite lifespan, can be created by putting these power harvesting devices into use [1]. The vibration energy could come from many sources, such as industrial machinery, transit networks, or even everyday activities like walking or keyboard typing. By capturing and converting these vibrations into useful electricity, we can tap into a nearly unlimited and clean energy resource. Researchers and developers aimed to turn wave energy into power. Power harvesting using piezoelectric materials has been studied for a variety of possible applications. Different power transducer techniques were applied to convert the mechanical motion to electrical energy [5]. Piezoelectric

transducers, which are small devices, can be used for energy conversion. The collected energy is usually vibrations which should be converted to electricity to be used in other daily used devices. The mechanical vibration energy is usually wasted as dissipated heat [6] but by applying vibration energy harvesting it can be converted to useful energy. However, conventional vibration energy harvesters can experience the issue of operating close to the resonance frequency and this can affect how efficient the operating range is in generating electrical energy. The overall power that can be used is small. The amount of the resulting power depends on the harvester design and also the amplitude and frequency of the vibration. Therefore, if the collected vibration energy is recorded properly the harvester must be designed and fabricated accurately for the best power results [7].

Researchers and developers aimed to turn wave energy into power. The use of piezoelectric transducers has been investigated for vibration energy harvesting in different applications. Several researchers examined the use of energy dissipated in human activities to generate energy that can power small electronic devices. Proposing Polyvinylidene fluoride films as a material for an implanted physiological power source. The prototype was shown to produce a peak voltage of 18V, corresponding to a power of around 17mW. Many researchers have also researched how to capture energy from mechanical structures. Using a piezoelectric vibrator and a steel ball to convert mechanical energy to electrical energy. Their research evaluated the amount of energy released when a steel ball struck a thin piezoelectric plate. A cantilever beam model was used in [8] for harvesting energy with piezoelectric transducers. The presented model was designed to accurately produce energy by adding the damping effect of power harvesting. A comparison approach to compare different designs and methods for vibration energy harvesting generators was presented and discussed in [9].

The unpredictability of ambient vibrations, the requirement to align the resonance frequency of the harvester with the prevailing vibration frequency, and the effective conversion and storage of the captured energy are some of the difficulties involved in vibration harvesting. Vibration harvesting has a lot of potential for powering low-power electronics, wireless sensor networks, and Internet of Things devices in applications that call for constant or long-term power sources, despite these obstacles. The goal of ongoing research and development in this area is to enhance vibration harvesting systems' scalability, dependability, and efficiency for a variety of real-world uses. The majority of research focuses on a specific technology, making it challenging to compare vastly different vibration-based energy harvesting designs and methodologies [2].

In this research paper, the process of comparing the selected harvesting energy techniques occurs. In our case, piezoelectric technique, and mechanisms technique.

Piezoelectric technique for vibration harvesting energy

Many scholars have looked into the possibility of harvesting energy from mechanical structures' ambient vibrations. The concept of a generator is examined by using a steel ball and a piezoelectric vibrator to convert mechanical energy to electrical energy. Their research measured the energy released upon the collision of a steel ball on a thin piezoelectric plate [10]. A power harvesting system model was developed and included a cantilever beam with piezoelectric patches fastened to it. Although the model's construction allowed for any combination of boundary circumstances and the piezoelectric material's position, it was tested on a cantilever beam that was suffering a base excursion from the clamped state. It was discovered that the model was accurate in estimating the energy produced and that it was also useful in illustrating how power harvesting damps energy [11]. The research that is presented in this article will concentrate on the piezoelectric techniques for vibration harvesting energy as well as utilizing the harvested energy. Fig.1 (a) demonstrates that it is based on an actual tile with a 150×150 mm² area. Fig.1 (b) demonstrates that the piezoelectric tile is made up of four supporting springs, a bottom plate, a middle plate where the piezoelectric modules are installed, and an upper plate that must be physically walked on. The

upper plate is linked to the piezo-installed layer in the middle plate. The thickness of the top and bottom plates is 10 mm apiece, and the length of the four springs is 40 mm. Fig.1 (c) provides a thorough illustration of the centre section's cross-section, showing the locations of the modules. The piezoelectric material, measuring $47 \times 32 \times 0.2$ mm³, is positioned on a stainless steel plate substrate, measuring $62 \times 37 \times 0.2$ mm³. PZT-PZNM, produced by TIOCEAN (Korea), is a thick film piezoelectric material. Fig.2 shows the experimental setup of the piezoelectric technique. The system efficiency for converting the mechanical motion to electrical power was obtained in [12]. FEA calculations were made and the results show that a bigger conversion efficiency value could be obtained with a thinner and shorter beam of a higher resonance frequency.

Different vibration harvesting energy concepts were applied for generating energy from machines, heat exchangers, compressors and motors by piezoelectric and energy harvesting devices. It was noticed that piezoelectric harvesting of energy was practically good for energy generation from vibration motion but it generated low power amount [13]. Piezoelectric energy harvesting with magnetic coupling promises a more meaningful solution to narrow bandwidth and low energy efficiency [14]. Theoretically, the cantilever beam's resonance frequency depends on its effective stiffness, effective mass, and tip mass [2]. Calculations are demonstrated regarding the beam, both effective mass and stiffness.

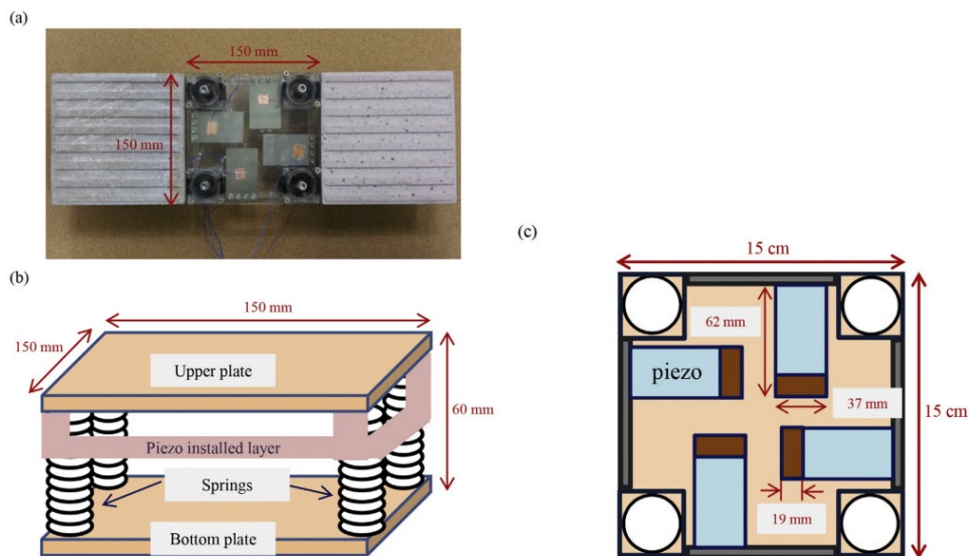


Figure 1: Piezoelectric tiles. (a) piezoelectric tile with a real tile. (b) schematic of the piezoelectric tile. (c) Piezo layer [1]

It had been selected the tip mass whose resonance frequency was closest to the tile's vibration frequency based on the experiment that was detailed [1]. Another research established a general theory containing many specifications where two piezoelectric generators were given the "effectiveness" design concept, and theoretical power outputs were computed. For one design, the power predicted by the effectiveness hypothesis was around 30% higher than the measured power output, and for the other design, it was 10% higher [10]. Three types of generators had been utilised and stated in detail initially and most importantly the piezoelectric generators, the electromagnetic generators, and the electrostatic generators. Familiarity with all types of generators is vital for predicting better alternatives depending on the required outcomes [15].

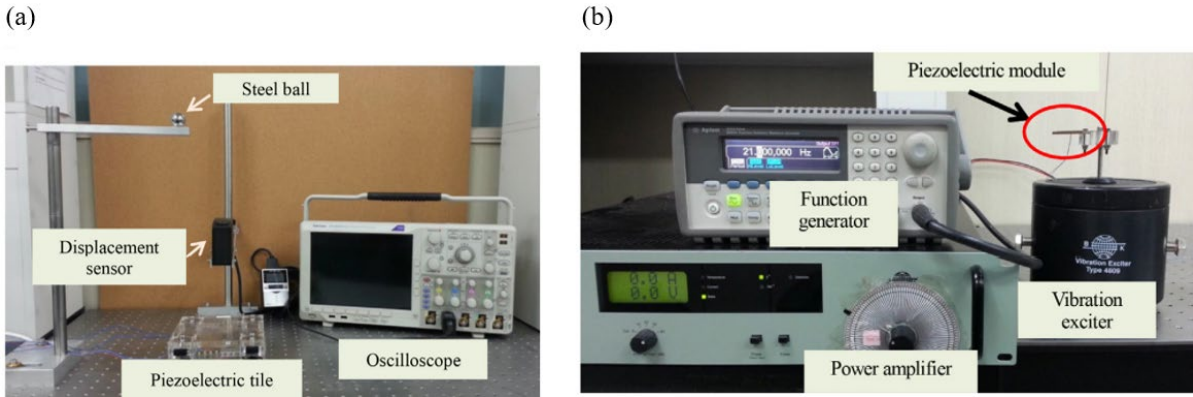


Figure 2: Piezoelectric tile system (a) vibration frequency measurement, (b) resonance frequency measurement (made by TIOCEAN CO.) [1].

While electromagnetic motors and piezoelectric materials have both been applied to vibration energy harvesting, their characteristics differ. Electromagnetic motors are velocity-induced transducers, whereas piezoelectric materials are force- or stress-induced transducers [16]. The active range of amplitude and frequency was studied in [17]. Successful lab and field tools were discussed, and the resulting energy level was compared. Keeping in mind the most recent developments in broadband energy harvesting methods, such as nonlinear methods, multimodal methods, and resonance tuning methods [18]. The application, limitations and advantages of several energy generation techniques were reviewed in [19]. Fig.3 shows a schematic diagram for two types of piezoelectric. Piezoelectric transducers were used in [20] to generate energy from a tile structure where it can produce energy when a person steps on it. A current of $140\mu\text{A}$ and power $2.8 \mu\text{W}$ could be generated. A small amount of power can be generated using piezoelectric transducers.

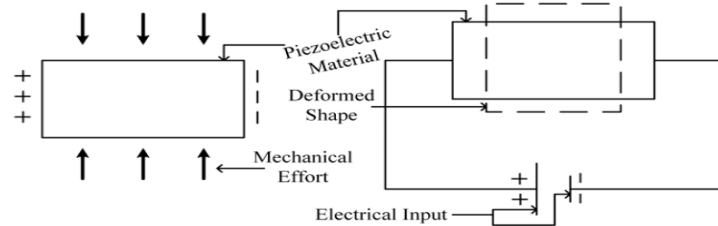


Figure 3: Piezoelectric EH types: (a) direct piezoelectric effect and (b) reverse piezoelectric effect [19].

Mechanisms technique for vibration-harvesting energy

Converting mechanical motion to electricity generation can be done by an electromagnet or a permanent magnet. Because it doesn't require power input, the permanent magnet is a better option for low-power devices than the electromagnet. Ferromagnetic or ferrimagnetic material is present in these permanent magnets. Despite producing a strong electric field, ferromagnetic materials are frequently employed because their increased electrical resistance reduces the influence of eddy currents.

A multi-degree freedom system can be introduced into an excitation structure to increase the bandwidth of the EH. Different subsystems were combined in the EH design to provide different modes. It was discovered that each resonance's average power generation by the EH differs significantly [19]. Harvesting energy response is discussed in [21], where a harvester of high sensitivity is used for generating energy. A harvesting system, including power electronics for managing the power, an electromagnetic converter and different mechanical parts was used. The

system of high sensitivity can produce useful energy using vibration shocks. Energy harvesting techniques using bi-stable systems were reviewed in [22]. Electro-mechanical systems were presented to show the practical benefits of these techniques. The different bi-stable harvesting systems use magnetic repulsion, magnetic attraction and mechanical load to induce bi-stability. Energy generation using vibration harvesting that can be applied to self-powered micro and wireless systems was reviewed in [15]. Maximum harvesting energy is analyzed and optimum results were found in single- and multi-mass systems. The system sensitivity is obtained from the implemented simulation.

Vibration harvesting energy and conversion to electricity was applied in several mechanisms, using the electromagnetic principle [4, 23-28]. As seen in Fig.4, an energy generator using a speed bump that harvests vibrational motion is presented in [23]. The model uses a mechanism of rack and pinion and clutches. The mechanism is tested in the bump impact case and power generation is examined.

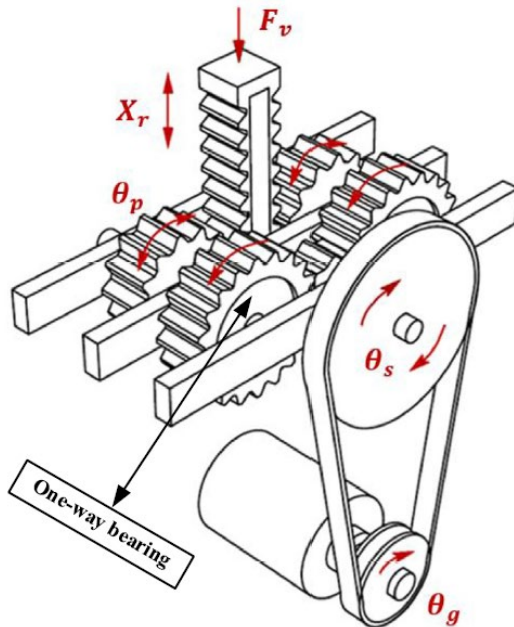


Figure 4: A speed breaker mechanism using one-way bearing [23]

Energy generation was investigated using mechanical concepts. A few mechanisms using spring were reviewed and discussed in [24]. The presented design configurations which are applied and tested work for power generation by using mechanical motion. A speed breaker design was presented and used in [25,26] for power generation. As seen in Fig.5, the mechanism can convert the linear motion of the rack to the rotary motion of the pinion and the rotational motion is converted to electrical energy using the magnetic field concept. As stated in [26], the used mechanism could produce 1.16 V, which is much higher the produced value in case of the piezoelectric. A compact energy harvesting system is presented in [27], which is an efficient, durable, and also feasible device. Modelling and simulation were used to validate the design model.

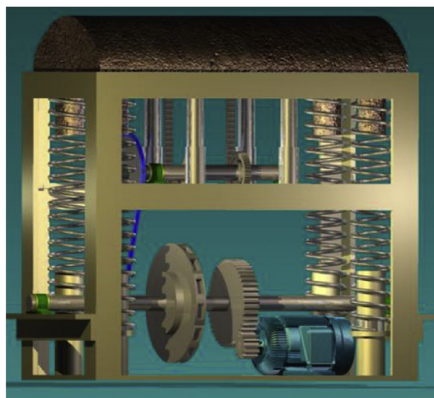


Figure 5: A speed breaker mechanism assembly [25]

Conclusions

Piezoelectric devices, which are small and light transducers, can be used to transform mechanical motion, often vibrations, into electrical energy that can power other devices used in our daily life. There are multiple energy harvesting techniques for converting vibration energy into usable electricity using mechanical design concepts. Power harvesting devices, using both piezoelectric and mechanical concepts, can be applied for vibration energy harvesting without relying on traditional energy sources, which have limited lifespans. Vibration energy is a free and sustainable source of energy that should get more attention to improve the applied techniques for increasing power generation, especially in the piezoelectric techniques. Mechanical concepts generate much higher energy than piezoelectric devices, however, they involve mainly springs, racks and gears which can result in system complexity, heavy weight, and energy losses. Moreover, the applied mechanisms can be a source of noise if the concept is applied to harvest energy from human walking. On the other hand, piezoelectric transducers, which are small and light, can produce energy with a small amplitude of vibration, but it is a much smaller amount of energy.

References

- [1] S. J. Hwang, H. J. Jung, J. H. Kim, J. H. Ahn, D. Song, Y. Song, ... & T. H. Sung, Designing and manufacturing a piezoelectric tile for harvesting energy from footsteps. *Current Applied Physics*, 15(6) (2015), 669-674. <https://doi.org/10.1016/j.cap.2015.02.009>
- [2] V. R. Challa, M. G. Prasad, Y. Shi, & Fisher, A vibration energy harvesting device with bidirectional resonance frequency tunability. *Smart Materials and Structures*, 17(1) (2008), 015035. [10.1088/0964-1726/17/01/015035](https://doi.org/10.1088/0964-1726/17/01/015035)
- [3] T. Wang. Pendulum-based vibration energy harvesting: Mechanisms, transducer integration, and applications. *Energy Conversion and Management*, (2023) 276, 15, 116469. <https://doi.org/10.1016/j.enconman.2022.116469>
- [4] Y. Wang, P. Wang, S. Li, M. Gao, H. Ouyang, Q. He, P. Wang. An electromagnetic vibration energy harvester using a magnet-array-based vibration-to-rotation conversion mechanism. *Energy Conversion and Management*, (2022) 253, 115146. <https://doi.org/10.1016/j.enconman.2021.115146>
- [5] X. Tang, & L. Zuo . Enhanced vibration energy harvesting using dual-mass systems. *Journal of sound and vibration*, 330(21) (2011), 5199-5209. <https://doi.org/10.1016/j.jsv.2011.05.019>
- [6] A. O. Odetoyan, & A. N. Ede. Energy harvesting from vibration of structures-a brief review. In IOP Conference Series: Materials Science and Engineering (Vol. 1107, No. 1, p. 012192) (2021, April). IOP Publishing. [10.1088/1757-899X/1107/1/012192](https://doi.org/10.1088/1757-899X/1107/1/012192)

- [7] T. Yildirim, M. H. Ghayesh, Li, W., & G. Alici, A review on performance enhancement techniques for ambient vibration energy harvesters. *Renewable and Sustainable Energy Reviews*, (2017). 71, 435-449. <https://doi.org/10.1016/j.rser.2016.12.073>
- [8] H. A. Sodano, D. J. Inman, & G. Park, Generation and storage of electricity from power harvesting devices. *Journal of intelligent material systems and structures*, 16(1) (2005), 67-75. <https://doi.org/10.1177/1045389X05047210>
- [9] S. Roundy, On the effectiveness of vibration-based energy harvesting. *Journal of intelligent material systems and structures*, 16(10) (2005), 809-823. <https://doi.org/10.1177/1045389X05054042>
- [10] M. Umeda, K. Nakamura, & S. Ueha, Analysis of the transformation of mechanical impact energy to electric energy using piezoelectric vibrator. *Japanese Journal of Applied Physics*, 35(5S) (1996), 3267. 10.1143/JJAP.35.3267
- [11] H. A. Sodano, G. Park, & D. J. Inman, Estimation of electric charge output for piezoelectric energy harvesting. *Strain*, 40(2) (2004), 49-58. <https://doi.org/10.1111/j.1475-1305.2004.00120.x>
- [12] D. Koyama, & K. N& Nakamura. Electric power generation using vibration of a polyurea piezoelectric thin film. *Applied Acoustics*, 71(5) (2010), 439-445. <https://doi.org/10.1016/j.apacoust.2009.11.009>
- [13] V. Jamadar, P. Pingle, & S. Kanase, Possibility of harvesting Vibration energy from power producing devices: A review. In 2016 International Conference on Automatic Control and Dynamic Optimization Techniques (ICACDOT) (2016, September) (pp. 496-503). 10.1109/ICACDOT.2016.7877635
- [14] J. Jiang, S. Liu, L. Feng, & D. Zhao, A review of piezoelectric vibration energy harvesting with magnetic coupling based on different structural characteristics. *Micromachines*, 12(4) (2021), 436. <https://doi.org/10.3390/mi12040436>
- [15] S. P. Beeby, Tudor, M. J., & White, N. M. Energy harvesting vibration sources for microsystems applications. *Measurement science and technology*, (2006).17(12), R175. 10.1088/0957-0233/17/12/R01
- [16] V. L.Kalyani, V. L., Piaus, A., & Vyas, P. Harvesting electrical energy via vibration energy and its applications. *Journal of Management Engineering and Information Technology*, (2015)2(4), 2394 - 8124.
- [17] A. Hosseinkhani, D. Younesian, P. Eghbali, A. Moayedizadeh, & A. Fassih, Sound and vibration energy harvesting for railway applications: A review on linear and nonlinear techniques. *Energy Reports*, 7 (2021), 852-874. <https://doi.org/10.1016/j.egyr.2021.01.087>
- [18] L. Tang, Y. Yang, & C. K. Soh, Broadband vibration energy harvesting techniques. *Advances in energy harvesting methods*, (2013), 17-61. 10.1007/978-1-4614-5705-3_2
- [19] R.K. Mohanty, A., Parida, S., Behera, & T. Roy. Vibration energy harvesting: A review. *Journal of Advanced Dielectrics*, (2019), 9(04), 1930001. <https://doi.org/10.1142/S2010135X19300019>
- [20] K. Al-Hamoudi, J. Almudhaki, A. Khali, A. Alqahtani. Footstep Piezo Generator. Senior Design Project, Prince Mohammad bin Fahd University. 2019.
- [21] Z. Hadas, V. Vetiska, V. Singule, O. Andrs, J. Kovar, and J. Vetiska. Energy harvesting from mechanical shocks using a sensitive vibration energy harvester. *International Journal of Advanced Robotic Systems*, (2012), 9(5), p.225. <https://doi.org/10.5772/5394>

- [22] R. L.Harne,& K. W. Wang, A review of the recent research on vibration energy harvesting via bistable systems. *Smart materials and structures*, (2013), 22(2), 023001. 10.1088/0964-1726/22/2/023001
- [23] A. Azam, A. Ahmed, N. Hayat, S. Ali, A. Khan, G. Murtaza, T. Aslam. Design, fabrication, modelling and analyses of a movable speed bump-based mechanical energy harvester (MEH) for application on road. *Energy*, (2021), 214, 118894. <https://doi.org/10.1016/j.energy.2020.118894>
- [24] A.M. Patel, A. N. Patel. A Review on Different Mechanisms Used in Power Generation Through Speed Bumps. *International Journal for Scientific Research & Development*, (2017), 5(10) 2321-0613.
- [25] J. Dara, C. Odazie, P. Okolie, A. Azaka. Design and construction of a double actuated mechanical speed breaker electricity generator. *Heliyon*, (2020), 6, e04802. <https://doi.org/10.1016/j.heliyon.2020.e04802>
- [26] A. Al-Khaldi, A. Al-Jumaah, A. Al-Mubarak. Footstep Power Generator. Senior Design Project, Prince Mohammad bin Fahd University. 2021.
- [27] N. Raj, A. Dasgotra, S. Mondal, S. Kumar, R. Patel. Deflection-Based Energy Harvesting Speed Breaker and It's Mechatronic Application. *International Journal of Sustainable Engineering*, (2021), 14 (5) 1033–1042. <https://doi.org/10.1080/19397038.2020.1862352>
- [28] X. Zhang, G. Li, W. Wang, S. Su. Study on the energy conversion mechanism and working characteristics of a new energy harvester with magnetic liquid. *Sensors and Actuators A: Physical*, (2023), 359, 114409. <https://doi.org/10.1016/j.sna.2023.114409>

Multiport universal solar power bank

Abdullah ALTELMESSANI^{1,a}, Abdulqader ALJABER^{1,b}, Turki ALTUWAIRQI^{1,c},
Ala A. HUSSEIN^{1,d}, Jamal NAYFEH^{1,e}

¹Department of Electrical Engineering, Prince Mohammad Bin Fahd University, Khobar, Saudi Arabia

^a201701254@pmu.edu.sa, ^b201902284@pmu.edu.sa, ^c201900905@pmu.edu.sa,
^dahussein@pmu.edu.sa, ^ejnayfeh@pmu.edu.sa

Keywords: IEEE Smart Village (ISV), Battery Management System (BMS), Maximum Power Point Tracking (MPPT), Perturb and Observe (P&O)

Abstract. In an era of ubiquitous electricity dependence, the need for a reliable and portable power source is increasingly vital. This proposal advocates for the development of a solar-powered portable device capable of harnessing solar energy to charge itself and subsequently supply power to various electronic devices. The envisioned solution aims to address critical scenarios such as emergencies, where access to electricity is crucial, as well as recreational activities like camping, especially in remote locations. The proposed portable power bank will be equipped with solar panels for efficient energy absorption, ensuring self-sufficiency and sustainability. The device will feature both DC and AC outputs, catering to a wide range of electronic gadgets, thereby enhancing its versatility. In the event of a disaster, this innovation could prove invaluable by providing a reliable source of electricity when traditional power infrastructure is compromised. Moreover, in recreational settings, such as desert camping in locations like Saudi Arabia, users can harness the power of the sun to charge their devices in the open, offering convenience and environmental friendliness. This solar-powered portable energy hub embodies a step towards fostering energy independence and resilience in the face of unpredictable circumstances, catering to both emergency preparedness and everyday scenarios.

Introduction

To design Multiport Universal Solar Power Bank that can use the energy of the sun with the help of a photovoltaic system such as a solar panel. The system will have some subsystems that will monitor the power level of the battery.

- Project [1] Comparison

Our solar power bank project contrasts with Project [3], which is tailored for military use. Our design boasts a cooling system and wireless monitoring, enhancing its suitability for a range of civilian applications, including emergency and outdoor use. However, it may not match the extreme condition optimization of military-spec devices. Conversely, Project [3] excels in robustness and energy density for military environments but lacks the adaptability and user-friendly features of our project, such as wireless monitoring for everyday civilian use.

- Project [2] Comparison

We see significant differences in focus and application. While their project revolves around a specific application of a mobile charger using recycled materials, our project encompasses a broader spectrum of functionalities, including a cooling system and wireless monitoring, aiming to provide versatile and accessible electricity for a variety of scenarios. Our project emphasizes

adaptability, environmental sustainability, and user-friendliness, demonstrating a comprehensive approach to portable solar energy solutions.

- Project [3] Comparison

Comparing our project with theirs, there are notable distinctions. Our project caters to a wider civilian audience, providing a versatile solar power bank with innovative features like a cooling system and wireless battery monitoring. This contrasts with the other project's military-focused design, which prioritizes high energy density and robustness for field operations. While their charger is specialized for military needs, ours is tailored for diverse environments and user convenience, highlighting our commitment to adaptable and user-friendly solar energy solutions.

- Project [4] Comparison

The SunBlazer IV focuses on larger-scale, community-based applications with a strong emphasis on scalability and modularity. It aims to empower entire communities by providing a robust, adaptable solar energy system. In contrast, our project centers on individual use with a portable solar power bank, enhanced with features like a cooling system and wireless monitoring. Our project is designed for personal convenience, adaptability, and a wide range of scenarios, whereas the SunBlazer IV caters to broader community needs and sustainable development goals.

Traditional energy sources, primarily fossil fuels, contribute significantly to carbon emissions, a leading cause of climate change. Your project, by using solar energy, helps reduce this carbon footprint. Also, fossil fuels are non-renewable and their extraction can be environmentally damaging. Solar energy, being renewable, offers a sustainable alternative. Fossil fuel combustion releases pollutants that harm air quality and public health. Solar power generation, in contrast, produces no air pollutants, making it a cleaner option.

The contributions of this research are as follows:

- **Easier access to electricity in remote areas.**
- **Use renewable resources to reduce the number of non-renewable resources used.**
- **To be used in case of a power outage.**
- **Create a solar power bank that is compatible with a wide range of electronic devices.**
- **Strive for a compact and lightweight design, making the power bank easy to carry and suitable for on-the-go activities, such as camping, or emergency situations.**
- **Implement safety features to protect both the power bank and connected devices from overcharging, overheating, and other potential risks, ensuring user safety and the longevity of the device.**

System Specifications

This project will involve the design and testing of different subsystems. Each subsystem will follow a specific job.

- Convert DC from solar panel to DC into the battery using (DC Regulator).
- Supply different voltages to different devices.
- Measures battery level.
- Can act as an AC power source with a max output of 400[W].
- The Capacity will be around 20000[mAH].
- The model will be 50[cm²] with a height of 20[cm].

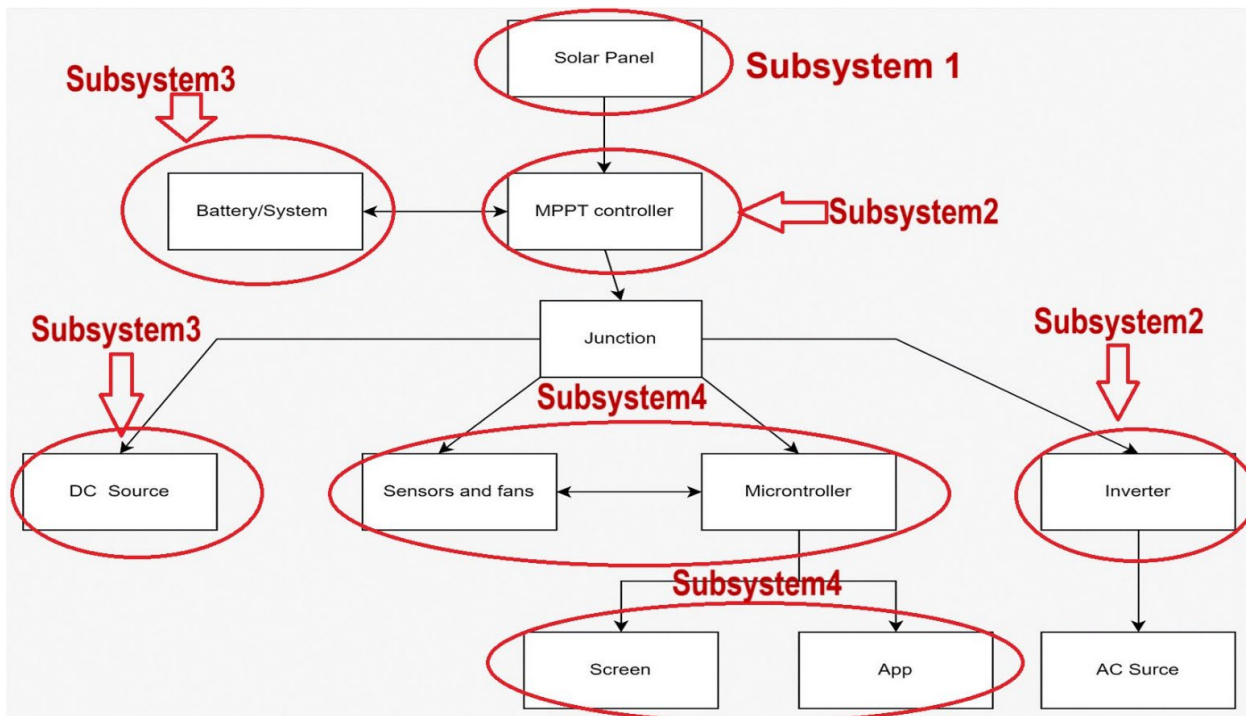


Figure 1: A block diagram of the proposed system.

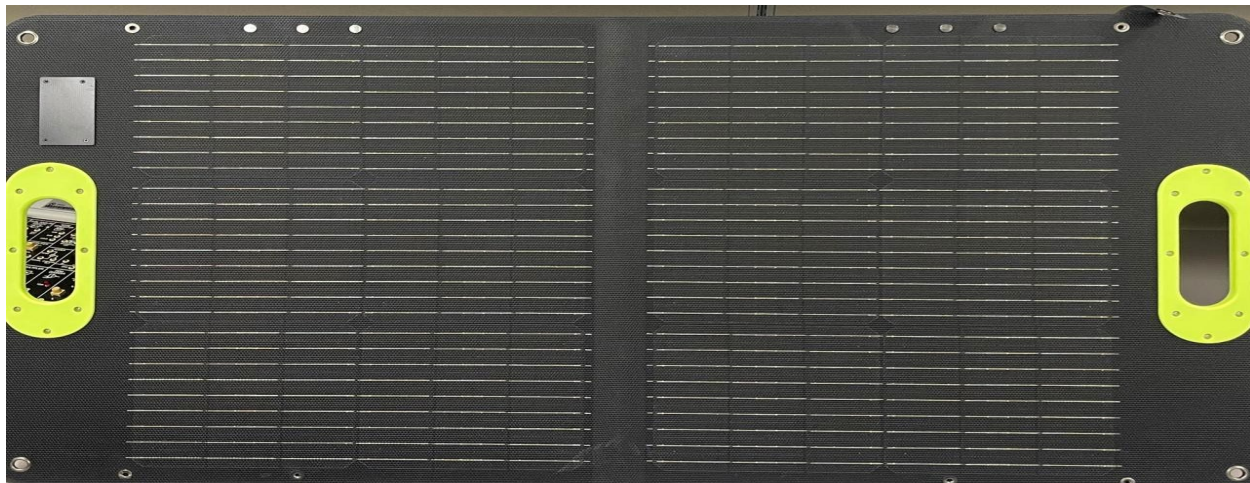


Figure 2: Solar pannel used for this project.



Figure 2: Inverter and controller used for this project.

The summary of the paper on the development of a Multiport Universal Solar Power Bank highlights the project's successful integration of innovative design, renewable energy technology, and user-centric features to address the growing need for portable, reliable, and sustainable power sources. By harnessing solar energy through efficient photovoltaic systems and incorporating versatile functionality, the project not only provides a practical solution for emergency and recreational power needs but also contributes to environmental sustainability by reducing reliance on non-renewable energy sources.

The project's emphasis on compatibility with a wide range of electronic devices, coupled with its compact and lightweight design, ensures that it meets the demands of both emergency preparedness and outdoor activities. The inclusion of safety features and adherence to engineering standards further enhances the reliability and user safety of the solar power bank.

Moreover, by focusing on sustainability through the use of renewable resources and eco-friendly materials, the project aligns with global efforts to mitigate environmental impact and promote energy independence. The consideration of economic, social, and ethical factors in the design and manufacturing processes demonstrates a comprehensive approach to addressing the multifaceted challenges of modern energy needs.

Summary and Conclusion

In summary, the Multiport Universal Solar Power Bank project represents a significant step forward in the development of portable solar energy solutions. Its ability to provide a reliable, safe, and environmentally friendly power source in a variety of scenarios underscores the potential of renewable energy technologies to improve quality of life and foster sustainable development. As the project moves forward, it holds the promise of broadening access to energy, enhancing emergency preparedness, and contributing to a more sustainable and resilient energy future. The proposed system can be used during outdoor activities, emergency cases, and backup power source for small appliances.

References

- [1] Muhseen, Z., et al., 2020. Portable smart solar panel for consumer electronics. In: 2020 International Conference on Smart Technologies in Computing, Electrical and Electronics (ICSTCEE), Bengaluru, India, pp.494-499.
<https://doi.org/10.1109/ICSTCEE49637.2020.9277123>.
- [2] Venkataraman, K., Selvan, E.V., Gandhi, R.A., Chakravarthi, M.C.A., Varunanand, V. and Vasanthakumar, B., 2022. A mobile charger through a solar panel fabricated from silicon scrap.

- In: 2022 International Conference on Power, Energy, Control and Transmission Systems (ICPECTS), Chennai, India, pp.1-4. <https://doi.org/10.1109/ICPECTS56089.2022.10047178>.
- [3] Sitbon, M., Gadelovits, S. and Kuperman, A., 2014. Multi-output portable solar charger for Li-Ion batteries. In: 7th IET International Conference on Power Electronics, Machines and Drives (PEMD 2014), Manchester, UK, pp.1-7. <https://doi.org/10.1049/cp.2014.0430>.
- [4] Larsen, R.S. and Estes, D., 2019. IEEE Smart Village launches SunBlazer IV and Smart Portable Battery Kits: Empowering remote communities. IEEE Systems, Man, and Cybernetics Magazine, 5(3), pp.49-51. <https://doi.org/10.1109/MSMC.2019.2916247>.
- [5] Rodriguez, C. and Lee, S., 2023. Advances in lithium-ion battery technology for portable solar devices. Advanced Energy Materials, 11(4), 2003035.
- [6] Johnson, K. and Patel, R., 2022. The role of renewable energy technologies in disaster risk reduction. International Journal of Disaster Risk Reduction, 49, 101925.
- [7] Tran, E. and Al Fayed, M., 2023. Impact of solar power banks on outdoor recreation and emergency preparedness. Energy Policy, 129, pp.110-121.
- [8] Doe, J. and Smith, J., 2023. On the efficiency and integration of photovoltaic systems in portable devices. Renewable Energy Focus, 30(2), pp.142-158.
- [9] Patel, A. and Chung, L.W., 2022. Sustainable materials for next-generation energy storage devices. Journal of Power Sources, 450, 227690.
- [10] Institute of Electrical and Electronics Engineers, 2024. IEEE standard for safety and performance of portable solar power systems. IEEE 1625-2024.

Electricity sector reforms in Saudi Arabia and their impact on demand growth and development of renewable energy

Samir El-NAKLA^{1,a*}, Chedly Belhadj YAHYA^{2,b}, Jamal NAYFEH^{1,c}

¹Department of Electrical Engineering, Prince Mohammad Bin Fahd University, AlKhobar, Saudi Arabia

²Electrical and Computer Engineering Technology, Chattahoochee Technical College, Marietta, GA, USA

^asnakla@pmu.edu.sa, ^bchedly.yahya@chattahoocheetech.edu, ^cjnayfeh@pmu.edu.sa

Keywords: Electricity Reforms, Demand Growth, Renewable Energy, KSA

Abstract. The Kingdom of Saudi Arabia (KSA) has experienced widespread development over the last four decades. This has resulted in tremendous increase in electricity demand. This paper reviews the status of the KSA's electricity consumption and demand to date; discusses the current and future challenges facing the Saudi electricity sector; and the Saudi government's initiatives taken to address these challenges. The study shows that KSA government started to apply the long term strategy, Vison 2030 to reduce energy consumption and high energy demand in the country. The paper evaluates the outcomes of applying the tariff reform programs that introduced in 2016 and 2018 respectively and its impact on different consuming sectors especially the residential and also the renewable energy program.

Introduction

The Kingdom of Saudi Arabia (KSA) is located in the Middle East and spread over about 2.15 million km², which constitutes around 80 percent of the Arabian Peninsula [1]. The country has a very harsh environment where the temperature varies from as high as 50°C in the shade in mid-summer to 0°C or even lower in winter. The high variation in temperature produces strong variance in electricity demand over the year resulting mainly from high demand of electricity for air conditioning during the hot weather season.

In the last four decades, KSA has witnessed massive economic development coupled with high population growth and urbanization; driven by crude oil revenues [2,3]. The population of the kingdom has grown at an annual average rate of 3% over the last 40 years. Overall, the total population has dramatically increased from 7 million in 1975 to about 34 million in mid of 2019. Furthermore, urbanization in KSA increased from 48% in the early 1970s to around 80% in the year 2000 and projected to reach 88% in 2025 [4]. High economic development as well as population and urban growth have resulted in exponential growth of the country's electricity demand [5].

In 2015, the electricity peak demand reached as high as 62.3 Gigawatt (GW). The current demand is typically met through conventional crude, heavy oil, and gas powered plants spread across the country [6]. In addition to ever-increasing electricity demand, the electricity sector in KSA is struggling with many other issues that may jeopardize the sector sustainability including: aging power plants, suboptimal electricity tariff, inefficient legal and institutional framework, and low public awareness of electricity conservation.

Moving towards a more sustainable model, the KSA government established King Abdullah City of Atomic and Renewable Energy (KACARE) with the aim to utilize the indigenous renewable energy resources through science, research and industry [6]. The ambition of KACARE program is to generate 72 GW energy from renewable energy sources such as solar, wind, nuclear and



waste-to-energy (WTE) by 2032 [7]. The performance of KACARE and the Saudi Government plan for electricity sector development have never been scientifically studied and evaluated. Additionally, there are very limited studies that document the status of electricity system in the Kingdom and little have been done to evaluate the system performance.

The Kingdom of Saudi Arabia's government has applied a new strategy for the future called Vision 2030, which was announced on April 2016, that emphasizes the challenges to meeting the future's growing requirements. The Council of Saudi Economic and Development Affairs introduced historic vision 2030 which aimed toward a number of targets and reform strategies for the Kingdom's future. Electricity demand is dramatically increasing in Saudi Arabia, with increasing peak load over the past two decades [8].

The Kingdom's energy plan is to eliminate oil overuse, to reduce subsidies by increasing the energy tariff in several stages over next ten years, and to conduct a large-scale energy reform to re-evaluate all the energy resources. The Kingdom government began its plan to reform energy prices in 2016 and 2018 which led to reduce the energy consumption [9]. The new Electricity Tariffs rate was the real challenge for the residential sector, especially for the consumer who used more than 6,000 (kWh/month) [10]. The residential sector is the main electricity consumer, constituting at least 50 percent of total consumption. Increased electricity tariffs did not affect the government and industry sectors as affected residential sector.

In order to control electricity consumption and energy management, the Kingdom government reconstructed and rehabilitated several organizations such as the Water & Electricity Regulatory Authority (WERA) which is the regulator body for electricity and water in the country and Saudi Energy Efficiency Center (SEEC) which an organization dealing with customer's awareness and educating the public.

The Saudi Energy Efficiency Center (SEEC) conducted a broad awareness campaign to educate the public about consumption reduction methods by issuing leaflets, preparing workshops that explain how to select the appropriate electrical equipment, and insisting that sales outlets adhere to the required specifications for consumption reduction [8].

In addition to the previous effective reforms implemented by energy programs, the Kingdom government launched the National Renewable Energy Program (NREP) as an essential long-term program in Future Vision 2030 which aims to substantially increase renewable energy's share in the total energy mix with carbon emission reduction [11].

The NREP during the National Transformation Program (NTP) towards which Vision 2030 will increase renewables' share in the energy mix from zero to four percent [11]. In addition, the Saudi government issued permission to households to install solar power systems. Although there are still several obstacles facing energy consumption reduction, the Kingdom's ambitious reform programs are progressing in the right direction.

The paper summarizing and presenting the data of power consumption, peak load, per capita and also looked at the consumption per different sectors within the last ten years. As tariff reforms introduced in the years 2016 and 2018, the paper looked at those increases in tariff on different consuming sector especially the residential and evaluated the impact on the government plan and vision and initiatives of renewable energy.

Challenges and Reforms

The high growth in electricity demand coupled with falling oil prices in 2014 made it very hard for the government to meet the demand without increasing help from private independent power producers (IPPs). These conditions pushed for serious reforms to tackle the demand and allowing for increased share for private sector towards a more stable and sustainable supply. Figures 1 and 2 show the growth of total electricity sold and the peak demand, the data is obtained from WERA (Water and Electricity Regulatory Authority) [5]. Both Figs. show a high growth mode up to 2015,

then from 2016 to 2021 a reduced growth mode as a result of the undertaken government reforms especially the increased tariffs as will be detailed later.

In 2010 the National Energy Efficiency Program (NEEP) was converted to the Saudi Energy Efficiency Center (SEEC) tasked with improving efficiency in buildings, transport and appliances. In coordination with MEWA and SASO (Saudi for building insulation and air conditioning Efficiency) [8]. The SASO 2662/2012 air conditioning Energy Efficiency Ratio (EER) have been Standards Organization), new standards were introduced implemented in stages beginning 2013 and by 2015 all appliances not meeting the EER requirement were taken Out from the market. Both standards on building insulation and air conditioning will have a huge impact on cutting electricity consumption since buildings (residential, commercial and government) account for up to 70% of the total electricity consumed. In addition, efficiency was targeted at the generation level by upgrading old plant and increasing the share of more efficient combined cycle (CC) turbines. The number of CC unit went from 74 in 2014 to 122 in 2017 and the share of CC increased from 8.3% in 2010 to 30.8% in 2018. The improved efficiency was directly translated into more fuel saving, so oil consumption went from 2.01 barrels per MW in 2009 to 1.71 barrels in 2017 [9].

On the restructuring side, the transmission business was separated from the Saudi Electricity Company (SEC) and named National Grid SA beginning 2012. The single buyer company was created as Saudi Company for Energy Procurement on 31/5/2017. Both companies are still 100% owned by the government. So with WERA acting as an independent regulator and the new single buyer, the electricity market became more open for competition. This resulted in IPPs share in generation increasing to about 30%. For example, Table 1 shows the list of power projects planned for 2018-20, totaling 17 GW, SEC share is only 7.5GW (44%) while the remaining 9.5GW (56%) by other companies [10]. IPPs relieve budget pressure by providing upfront capital. In addition, they are more cost competitive due to bidding process and can deliver projects faster.

Table 1. Major Projects 2018-20 [10]

Project	Capacity MW	Fuel	Startup date
PP13 (SEC)	1800	Gas	2018
Shuqaiq (SEC)	2650	Oil	2018
Waad Alshamal	1390	Gas/Solar	2018
Jizan IGCC (Aramco)	4000	-	2018
Duba 1 (SEC IPP)	550	Gas/Solar	2019
Fadhili IPP (SEC/ Aramco)	1500	Gas	2019
Sakaka 1 (REPDO IPP)	300	Solar PV	2019
PP14 (SEC)	1640	Gas	2020
Yanbu 3 (SWCC)	3100	Oil	2020
Total	16,930		

Tariff Reforms

The electricity tariff was heavily subsidized for a long period which encouraged overconsumption and inefficiency. According to WERA 2014 report, SEC collected an average of 0.138SR/ kWh, while its subsidized average cost was 0.154 SR/kWh and real unsubsidized cost was 0.80SR/kWh. This means that customers pay only 17% of the real cost on average. Table 2 shows the details of the two tariff increases beginning 2016 and 2018 for the residential sector only. The first increase (2016) only affected customers with consumption higher than 4000kWh. This increase did not bring significant income to the power companies as shown by a detailed analysis by WERA [11],

77.2 % of the residential consumption is less than 6000 kWh. For commercial sector 65.1% consume more than 6000 kWh, for government and industrial sectors 90.7% and 99.82% consume more than 8000 kWh. This explains why for the second tariff reform in 2018 the focus was on the majority consuming less than 6000 kWh to increase the income for the power companies. According to SEC 2018 report [9], the income from residential and commercial increased from about SR4.83 Billion for 2017 to SR11.8 Billion for 2018.

Table 2. Electricity Tariff Reform (Residential)

Consumption Categories (kWh)	Pre- January 2016	Jan 2016- Dec 2017	January 2018
1- 2000	5	5	
2001- 4000	10	10	18
4001- 6000	12	20	
6001-7000	15		
7001-8000	20		
8001-9000	22	30	30
9001-10000	24		
More than 10000	26		
** Tariff is in Saudi halala, 1SR=100 halala=\$0.267			

Impact of Reforms on Electricity Demand

Since the electricity sector reforms are not complete yet and the tariff major reform is less than two years old, it will be very hard to make good conclusions. Therefore, only the initial facts will be mentioned until more information becomes available.

For the impact of reforms on electricity demand, Figs. 1 and 2 clearly show that the growth started slowing after 2016 and went below 1% for the last two years. Figure 3 shows the change kWh per customer between 2009 and 2021 which supports the same trend from Figs. 1 and 2, that there is a decrease in demand growth. If we compare the change by sector, Figure 4 and 5 show the residential and commercial sectors. Again a clear reduction in growth, in particular from 2017 to 2019, the residential consumption decreased by 9.1% and commercial by 3.1%. This indicates that the tariff reform beginning 2018 had a clearer impact on residential consumers. Does this decrease in demand come from consumer reaction to tariff increase or from improved efficiency? most probably both until further information becomes available.

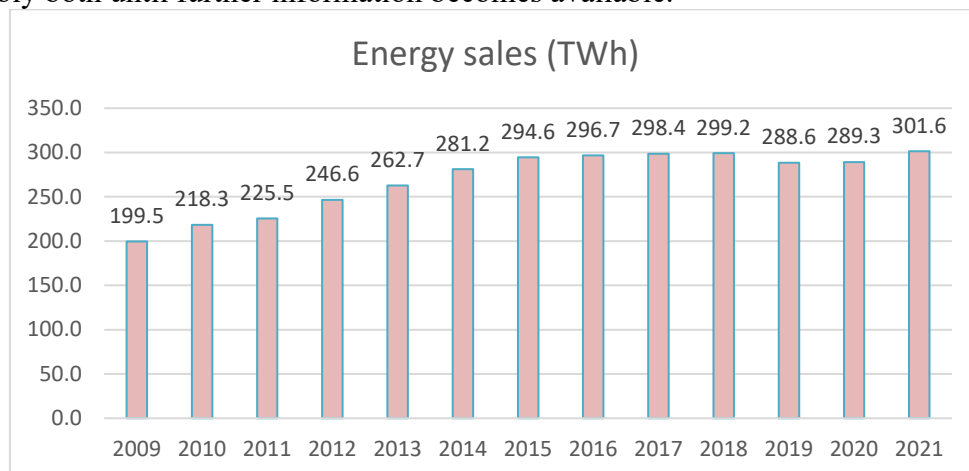


Figure 1. Total Energy Sold in TWh from 2009 to 2018 [12].

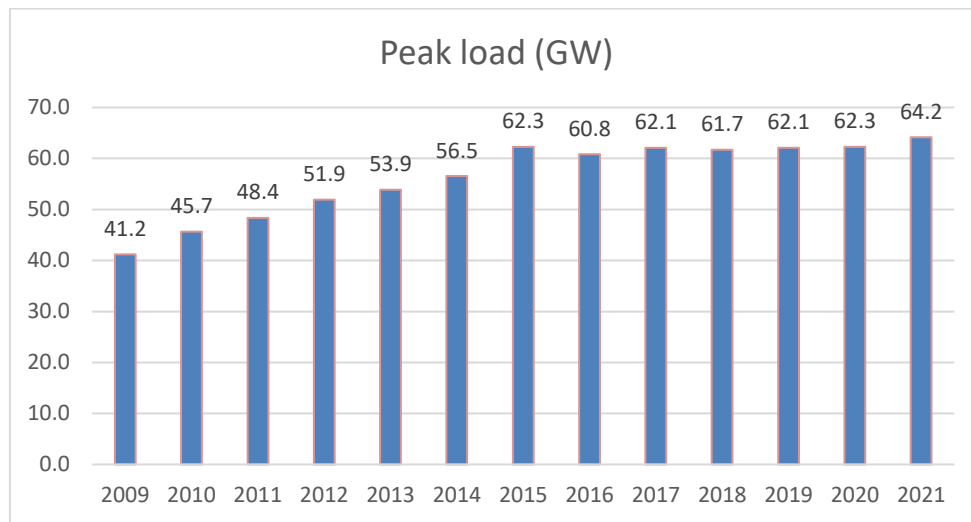


Figure 2. Peak Load in GW between 2009 and 2018 [12].

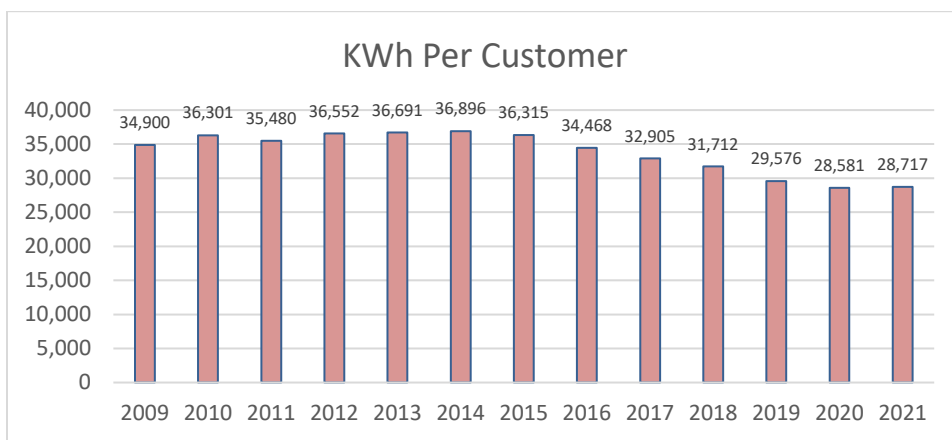


Figure 3. Consumption kWh per customer from 2009 to 2018 [12].

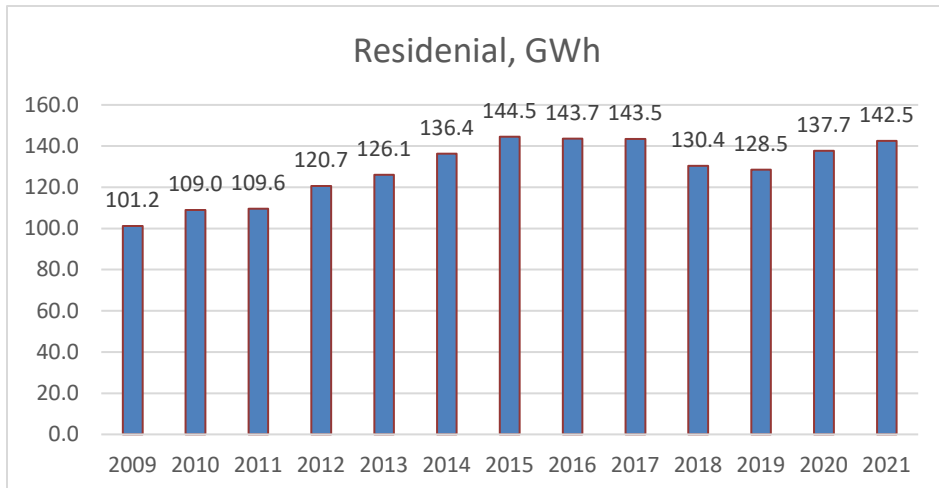


Figure 4. Residential consumption from 2009 to 2018 [12].

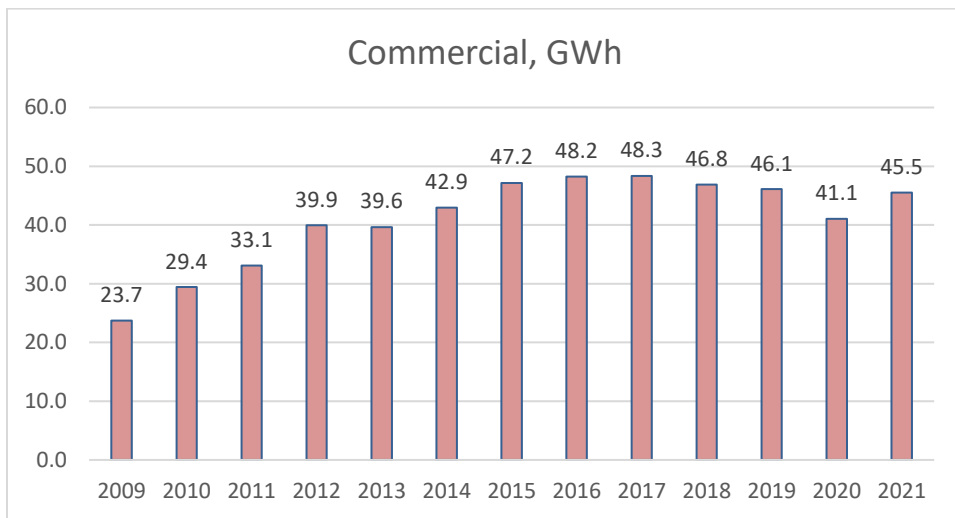


Figure 5. Commercial consumption from 2009 to 2018 [12].

Impact of reforms on Renewable Energy Program

Saudi Arabia enjoys perennial clear skies with approximately 3,000 hours of sunshine per year and annual insolation levels reaching 2450 kWh/m². In addition, KSA has empty stretches of desert that can host solar arrays and vast deposits of sand that can be used in the manufacture of silicon photovoltaic cells. As a comparison, Germany has insolation levels that barely reach 1700 kWh/m² in Freiburg and is one of the top five global leaders. As mentioned earlier, since the initial KACARE plan was announced in 2010, it experienced repeated delays and revisions. Several companies were setup in preparation for getting a share of the expected large number of solar energy projects. Some of these companies invested in factories to make photovoltaic (PV) solar cells and panels while other companies focused on solar energy project installation. Table 3 lists the main players in PV modules fabrication and project implementation.

Table 3. List of KSA Renewable Energy Companies

No.	Company	Date
1	KACST: R&D Labs	2010
2	Taqnia : Eng Solar, Wind	2014
3	AlAfandi Group: Solar (Jeddah)	2015
4	Desert Technologies (Jeddah): Solar PV Modules	2016
5	ACWA Power: Eng Projects (Riyadh)	2008

Another important strength is the establishment of research centers such as the KACST Water Energy Research Institute (WERI) and the KACST R&D Labs. The KACST WERI cooperated with the US National Renewable Energy Laboratory (NREL) to establish a network of 12 solar radiation stations spread over all KSA regions [11]. The radiation stations have been used by KACARE to produce the Renewable Resource Atlas of Saudi Arabia in support of achievement of a sustainable energy mix. The KACST R&D Labs provide another important resource that specializes in PV module testing and certification based on International Electrotechnical Commission (IEC) and newly developed desert certification procedures by KACST [13].

KSA had an early start on Solar energy (1983) compared to Gulf and MENA, but fell behind until the recent pickup in pace. After the recent tariff, regulation reforms and the decline in renewable cost, ACWA was able to complete the first large scale PV project at Sakaka (300MW) at record LCOE of 2.32 c/kWh which was completed mid November 2019 [14]. The project is a good example of IPP with a 25 years contract of power purchase. Another renewable energy

400MW wind project was awarded in July 2018 for a record LCOE of 2.13c/kWh at Dumal AlJandal (near Sakaka PV project), different renewables completed projects shown in Table 4. Figure 6 shows the revised renewable energy program for the next 5 years and 12 years [15].

Table 4. List of KSA Completed Renewable Energy Projects

No.	Project	Power	Com Date
1	KACST (Uyaynah)	350kW	1983
2	KAUST Solar Park	2 MW	2010
3	Pilot project	500 kW	2011
4	Saudi Aramco Solar Car Park	10.5 MW	2012
5	Princess Noura University (Thermal)	25 MWth	2012
6	King Abdullah Financial District	200 KW	2012
7	King Abdulaziz Int. Airport Dev Proj.	5.4 MW	2013
8	Al-Khafji PV plant (RO Desalination)	15 MW	2017
9	PV Plant at Al-Aflaj (Taqnia)	10 MW	2019
10	PV Plant at Sakaka (ACWA)	300 MW	2019
11	Dumat Al Jandal Wind Farm	400 MW	2020
12	Al Rajaf Wind Farm	400 MW	2021
13	Waad Al Shamal Solar Park	600 MW	2022
14	Sudair Solar Power Plant	1,500 MW	2022
15	Red Sea Project Solar Plant	100 MW	2022
16	Domat Al Jandal North Wind Farm	600 MW	2023
17	Al Kharsaah Solar Power Plant	1,200 MW	2023

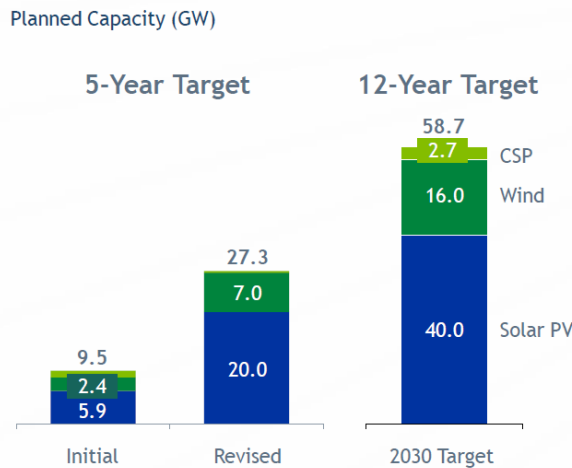


Figure 6. National Renewable Energy Program [11].

Conclusion

The research presented a review of the KSA electricity sector challenges and the government initiatives and reforms undertaken to address these challenges. Even though the reforms are in their early stages, the data shows that the reforms had a positive impact on the electricity demand growth and acceleration of renewable energy program implementation. However, more time and data are needed to have a clearer idea about the reforms impact.

References

- [1] Saudi Geological Survey. Kingdom of Saudi Arabia Numbers and Facts. Saudi Geographical Survey. 1st ed. (2012), Riyadh. KSA.
- [2] World Bank. Global Economic Prospects of the Middle East and North Africa. June 2015. <https://www.worldbank.org/content/dam/Worldbank/GEP/GEP2015b/Global-Economic-Prospects-June-2015-Middle-East-and-North-Africa-analysis.pdf>>
- [3] World Bank. “A Water Sector Assessment Report on Countries of the Cooperation Council of the Arab State of the Gulf”. Report No. 32539-MNA, (2005).
- [4] General Authority for Statistics, <https://www.stats.gov.sa/en/13>
- [5] WERA. Water & Electricity Regulatory Authority, <https://wera.gov.sa/en/DataAndStatistics/NRLList/ElectricityGeneration/Pages/default.aspx>
- [6] Ouda, Omar, KACARE (2012) presentation, “Renewable Energy- Waste to Energy, A pillar of the sustainable energy kingdom”, First International Environment Conference, King Fahd Civic Centre, Yanbu Al Sinaiyah, KSA, 20-21 November, 2012.
- [7] Royal Decree establishing King Abdullah City for Atomic and Renewable Energy (KACARE) No. A 35, 17 April 2010, <https://www.energy.gov.sa/ar/Pages/default.aspx>
- [8] Al Harbi F.” Saudi Arabia’s Electricity: Energy Supply and Demand Future Challenges”, 1st Global power, energy and communication conference (IEEE GPECOM2019) , June 2019, Turkey, <https://doi.org/10.1109/GPECOM.2019.8778554>
- [9] Energy Research: Saudi Energy price reform getting serious,” APICORP Group, Saudi Arabia, <https://www.apicorp.org/>
- [10] Saudi Electricity Company, “ Consumption Tariffs”, <https://www.se.com.sa/en/Ourservices/ColumnC/Bills-and-Consumption/ConsumptionTariffs>
- [11] National Renewable Energy Program (NREP). (<https://powersaudiarabia.com.sa/web/index.html>)
- [12] Saudi electricity company (SEC), Annual Reports. <https://www.se.com.sa/en/Investors/Reports-and-Presentations/Annual-Reports>
- [13] KACST R&D and Centers of Excellence, <https://kacst.gov.sa/>
- [14] ACWA Connects the Sakaka PV 300MW Project, <https://www.acwapower.com/news/acwa-power-connects-the-first-renewable-energy-project-in-the-kingdom-sakaka-pv-ipp-to-the-national-electricity-grid-commencing-initial-production/>,

Optimising solar: A techno-economic assessment and government facility compensation framework power generation

Navaid ALI^{1,a *}, Faheem Ullah SHAIKH^{2,b *} and Laveet KUMAR^{3,c *}

¹Directorate of Postgraduate Studies, Mehran UET, Jamshoro, Pakistan

²Department of Electrical Engineering, Mehran UET, Jamshoro, Pakistan

³Department of Mechanical Engineering, Mehran UET, Jamshoro, Pakistan

^aengrnavaid08@hotmail.com, ^bfaheemullah.shaikh@faculty.muet.edu.pk,

^claveet.kumar@faculty.muet.edu.pk

Keywords: Centralized Solar PV System, CO₂ Emissions Reduction, Government Facilities, HESCO, PVsyst

Abstract. In light of the necessity to meet growing energy demands while minimising expenses, this article examines two solar power system designs, considering peak and average load situations. The peak system, designed to handle a peak load of 190 MW with 260,568 PV panels installed, generates a significant excess of approximately 49,911 MWh annually. On the other hand, the average load design suggests a little deficit in energy. The monetary analysis reveals considerable capital expenditures for the total installation costs, totalling \$58.77 million for an average system and \$66.71 million for the peak system. However, the Levelized Cost of Energy (LCOE) rates are relatively competitive, at 0.0835 USD/kWh and 0.0736 USD/kWh respectively. Notably, the study highlights that the environmental impact analysis demonstrates a significant decrease in CO₂ emissions, with the peak system achieving a reduction of up to 3,601,588 tonnes per year. This research has explicitly validated the capabilities of centralised solar power systems in addressing the current and future energy difficulties faced by the Government of Sindh in a sustainable and economically viable manner.

Introduction

On a global scale, the energy industry faces substantial obstacles, such as the exhaustion of natural resources, environmental issues, and rising expenses, which necessitate an urgent transition to sustainable energy alternatives. Pakistan is experiencing a serious energy crisis characterised by severe power shortages, heavy dependence on non-renewable energy sources (61% thermal, 24% hydropower, 12% nuclear as of June 2023), and inadequate infrastructure [1]. Pakistan actively seeks solutions by adopting renewable energy and developing infrastructure to promote economic growth. Crucial organisations facilitate this shift, including Generation Companies (GENCOs), the Water and Power Development Authority (WAPDA), the Private Power Infrastructure Board (PPIB), National Transmission and Dispatch Company (NTDC), Distribution Companies (DISCOs), and National Electric Power Regulatory Authority (NEPRA) [2]. Following the 2010 amendment to the 1973 constitution, provinces were granted the power to generate, transmit, and distribute electricity at the provincial level. The provincial government of Sindh utilised it by implementing the Sindh Transmission and Dispatch Company (STDC) and the 100MW Nooriabad power project [3,4]. These initiatives aim to ease financial burdens by lowering power expenses. Solar and wind energy are more cost-effective than hydropower, making them good options for Pakistan's economic and operating problems. They offer a way to grow the economy and protect the environment [5]. The financial reports covering May 2021 to May 2022 reveal that Sindh's power expenditures amounted to PKR 8,704 million (\$ 31.1M) [6]. The Institute for Energy Economics and Financial Analysis (IEEFA) conducted a financial analysis of Sindh's power

expenditures, revealing that solar and wind energy is the most economically efficient, with photovoltaic power generation being the best renewable option due to affordability and low maintenance costs[7-8].

A feasibility analysis of a 100 MW_p solar power facility in Pakistan using PVSOL software was done [9]. A study assessed the facility's financial viability, encompassing revenue, operations, maintenance, interest payments, net profit, and payback period. The facility may generate 180,000 GWh/year and eliminate 90,225 tons/year of CO₂, and the payback period is 3.125 years. Based on feasibility, design, and execution, reference [10] evaluated a grid-tied 150 MW_p solar PV trial project in Karachi, Pakistan, for energy yield. In the PVsyst simulation, the average annual power generation, capacity factor, and performance ratio were 232,518 MWh/year, 17.7%, and 74.73%. Reference [11] evaluated the performance and design of a 20 MW Malaysian airport solar PV system. Power generation, performance ratio, and capacity utilisation factor (CUF) were 26,304 MWh, 76.88%, and 15.22%. A one MW PV grid-tied system in Oman was the subject of a techno-economic analysis by [12], who concluded that the system's annual yield factor was 1875 kWh/kW_p. The system indicated a capacity factor of 21.7% and an electricity production cost of roughly USD 0.2258 per kWh.

A 3 MW_p grid-connected solar PV system was tested in Karnataka, India. The annual average performance ratio was 0.7, and the power generation was 1372 kWh/kW_p [13]. An Indian grid-connected 10 MW solar PV project was assessed. The annual performance ratio, CUF, and power generation were 86.12%, 17.68%, and 15,798.19 MWh, respectively [14]. However, the techno-economic viability of Ghana's grid-connected 50 MW solar PV was examined [15]. The scientists discovered that monocrystalline, polycrystalline, and thin-film solar cells cost USD 0.124/kWh, USD 0.123/kWh, and USD 0.109/kWh, respectively, to produce power. Mono-Si, poly-Si, and CdTe systems had 75.5%, 75.7%, and 77% performance ratios. Reference [16] investigated a 12 MW_p solar-powered airport in Cochin, India. The average annual performance ratio was 86.56%, and CUF was 20.12%. This plant could produce 50,000 kWh per day. During its lifetime, the facility would reduce 12,134.26 metric tons of CO₂.

Previous studies have explored the techno-economic elements of small-scale solar PV systems, but there is a lack of research on expansive systems, especially in government facilities. This study aims to examine the economic and operational benefits of implementing 155 MW average and 190 MW peak grid-connected photovoltaic (PV) systems in Sindh, Pakistan, to address existing shortcomings such as lower energy and operational costs, energy independence, improved safety, and promote sustainability.

Methodology

A well-established technique has been employed to evaluate the feasibility of the proposed centralised solar-powered site, illustrating the sequential procedures involved in conducting the research.

i. Data Collection

The operational zone of Hyderabad Electric Supply Company (HESCO) was analysed. This analysis used HESCO and Sindh's Energy Department's Electricity Monitoring and Reconciliation Cell (EM&RC) data. Field visits to multiple places supplemented the Management Information System (MIS) data accuracy and reliability of HESCO and the energy department's electricity consumption statistics. The study examined power use data from January to December 2022 to determine energy consumption patterns—advanced data processing methods like cleaning, mining, filtering, and estimating ensured data accuracy.

Table 3 shows Sindh government-controlled power use by 75 provincials, affiliated, autonomous, and special institutions.

ii. Climatic conditions of the understudy locations

After analysing the Table 1 parameters, Manjhand, Sindh, is the best place for a solar PV installation. The location meets technical standards and supports the project's clean energy, efficiency, and sustainability goals.

iii. Simulation Tool

Solar energy companies widely use PVsyst for simulations. Solar power plants can be efficiently designed using this software for various climates, different PV modules and inverters, meteorological irradiation data, manual import data from other databases, appropriate sizes, and related components [17].

iv. Design of grid-connected large-scale solar PV system

a) Peak Load Design:

$$P_{annual} = P_{max,monthly} \times 12 \quad (1)$$

P_{annual} represents the solar PV system's projected annual peak load, measured in kilowatt-hours (kWh) and $P_{max, monthly}$ represents the highest electricity usage recorded in a month over a year.

b) Average Load Design:

$$L_{avg,monthly} = \frac{E_{total,annual}}{12} \quad (2)$$

$L_{avg, monthly}$ represents the average monthly load of the solar PV system, measured in kilowatt-hours (kWh) and $E_{total, annual}$ value represents the total yearly electricity consumption of the building (kWh).

v. Panel Generation Factor

$$PGF = \frac{\text{daily solar radiation at the site per day}}{\text{STC irradiance}} \quad (3)$$

The PGF values for Hyderabad, Thatta, Nawabshah, Manjhand, and Tharparkar are calculated as 5.69, 5.558, 5.65, 5.668 and 5.53, respectively, using the solar irradiance values.

vi. PV module selection

AE Solar's 132-AE solar modules are ideal for average and peak PV systems, offering a typical panel efficiency of 22.56% and a power rating of 700 W_p. These modules are resistant to extreme weather conditions and elevated temperatures. Table 2 of the Monocrystalline 132-AE Solar PV Module shows the technical specifications [18].

vii. Inverter Size Optimisation

It is a crucial optimisation strategy in PV systems, determining the optimal size of a solar inverter by dividing the installed DC power capacity by the AC power output rating [19]. P_{inv} represents the power rating of the inverter's AC output.

$$ILR = \frac{W_{T,peak}}{P_{inv}} \quad (4)$$

viii. Inverter selection

The chosen PVS800 ABB central inverter has a maximum system voltage rating of 1100 V_{dc}, which precisely matches the maximum input voltage rating of the inverter. The selected inverters have a frequency range of 50/60 Hz and a rated maximum power output of 1200 kW_{ac} [20].

<i>Table 1 Site selection parameters</i>						<i>Table 2 Technical specifications of solar PV module</i>	
Location	Annual Global Irradiation [kWh/m ²]	Annual PV output [kWh/kWp]	Grid Connectivity [distance, existing/new]	Annual Climatic Conditions	Infrastructure and Access	Parameters	Value (unit)
Nawabshah	2,251.4	1737.9	Approx. 250 km, new grid	35.6 [°C]	It needs to be built.	Manufacturer	AE Solar Germany
Hyderabad	2,266.5	1,754	Approx. 62 km, new grid	35 [°C]	Road access, utilities, and proximity to resources.	Model	AE700TME-132BDS
Tharparkar	2,217	1642.1	Approx. 270 km, new grid	35 [°C]	It needs to be built.	Rated maximum power capacity	700 [W]
Thatta	2221.7	1724.6	Approx. 110 km, new grid	31 [°C]	It needs to be built.	Max voltage (V _{mp})	42.10 [V]
Manjhand	2100	1744.9	Approx. 80 km, existing grid	35.1 [°C]	Road access, utilities, and proximity to resources.	Max power current (I _{mp})	16.63 [A]
						Open circuit voltage (V _{oc})	50.13 [V]
						Short circuit current I _{sc}	17.43 [A]
						Efficiency	22.56 [%]

Performance parameters for PVsyst software

In PVsyst, the required input data is reduced, calculation times are sped up, and accuracy is maintained.

1. Technical Parameters

Table 3 Performance technical parameters for PVsyst software

Parameter	Description	Equation	Unit	Reference
PV Array Yield	The array yield is the ratio of the energy output from a photovoltaic (PV) array for a specific time (such as a day, month, or year) divided by its rated power.	$Y_a = \frac{E_{DC,array}}{P_{PV,rated}}$	[kWh/k W/day]	[21]
Reference Yield	Reference yield is the ratio of solar radiation H _t (kWh/m ²) absorbed by the solar module plane to G _o (1kW/m ²). It represents a solar plant's daily peak sun hours in any location.	$Y_r = \frac{H_t}{G_o}$	[kWh/k W/day]	[21]
Specific Production	Annual energy production per kW _p is "specific production". It evaluates the plant's financial value and compares technologies and systems' operational performance.	Specific production = $\frac{\text{produced energy}}{P_o}$	[kWh/k W _p]	[21]
Performance Ratio	The ratio between the final and reference yields represents the performance ratio (PR). The PR compares installed PV systems at different places by percentage.	$PR = \frac{Y_f}{Y_r} * 100$	[%]	[21]
System Losses	The system loss L _s corresponds to the dissipation of energy on the AC side, which includes the irregular functioning of the inverter, AC transformer, and wiring.	$L_s = Y_a - Y_f$	[hour /day]	[21]
Final Yield	The final yield Y _f is the total system useable AC energy E _{grid} (kWh) over a specified period divided by the installed plant's nominal power P _o (kW _p).	$Y_f = \frac{E_{grid}}{P_o}$	[kWh/k W/day]	[21]

PV Module Efficiency (η_{PV})	The solar module's energy conversion as a percentage of available radiation is called module efficiency.	$\eta_{PV} = \frac{E_{AC}}{E_{DC}} * 100$	[%]	[21]
Inverter Efficiency (η_{inv})	The inverter generates the AC power P_{ac} fed into the grid, while the PV array produces the DC power P_{dc} .	$\eta_{inv} = S * \frac{E_{DC}}{H_t} * 100$	[%]	[21]
PV System Efficiency	The instantaneous efficiency of a photovoltaic (PV) system is determined by multiplying the efficiency of its PV module efficiency (η_{PV}) by the efficiency of the inverter efficiency (η_{inv}).	$\eta_{sys} = \eta_{PV} * \eta_{inv}$	[%]	[21]
Capacity Utilisation factor	The ratio between a PV plant's actual annual energy output and the amount of energy it would generate at nominal capacity for one year. The capacity utilisation factor of a solar PV power plant is determined by three main factors: the size of the inverter, the tracking ability, and the quality of the resource.	$CF = \frac{Y_f}{8760}$	[%]	[21]

2. Key Economics Parameters

Table 4 Key Economics Parameters for the PV Systems

Parameter	Description	Equation	Reference
Net Present Value	A project's net present value (NPV) is the difference between the present value of cash flows over the project's lifetime and the initial capital investment cost.	$NPV = \sum_{n=0}^N \frac{\text{Revenue}_n}{(1+r)^n} - \text{initial cost}$	[22]
Internal rate of return	In financial terms, the internal rate of return (IRR) is the discount rate at which a project's net present value (NPV) becomes zero.	$NPV = \sum_{n=0}^N \frac{C_n}{(1+IRR)^n}$	[22]
Simple Payback Period	The simple payback period is the duration, measured in years, required for the cash flow (minus loan payments) to equal the total investment, including debt and equity.	$SPB = \frac{\text{initial investment}}{\text{annual savings}}$	[23]
Levelised cost of energy	The levelised cost of electricity, also known as energy production cost, is the cost per unit of electricity required to achieve zero net present value.	$LCOE = \frac{\text{yearly cost} + \text{O\&M}}{\text{yearly energy system produces}}$	[24]

3. Environmental Analysis

Greenhouse gases, primarily absorbed by infrared light, are a significant contributor to global warming, causing distress to millions worldwide [25]—equation (5), which is considered to be consistent for the chosen site.

$$\text{Produced emissions} = \text{Annual generation} * CO_2/kWh \quad (5)$$

Results and Discussion

I. Technical viability under peak and average load scenario

Both peak and average simulation results reveal the techno-economics of solar PV systems. The peak system with 260,568 PV modules produces 339,721 MWh annually, or 1,863 kWh/kWp. The average system with 221,430 PV modules generates 155 MW and 288,687 MWh yearly. For both suggested systems, the performance ratio is 0.872, with an inverter output of 87.2% and a PV array

output loss of 11.3%. Calculations used a 30/180° tilt angle. The peak system's excess units may be cheaper for the facility's 289,809 MWh yearly energy needs.

Table 5 shows that PVsyst software provides the facility with the required and generated units from the average and peak PV systems. Compared to the needed units, the average solar PV system produces 1,122 MWh less yearly. During the same period, the peak solar system produced 49,911 MWh, exceeding the facility's energy needs. The analysis shows how well the solar systems perform over time and meet the facility's energy needs. Additionally, Table 6 shows the technical specifications calculated by the PVsyst software.

II. Financial analysis

Table 7 shows the average and peak PV solar system financial performance. The average PV system installation costs are 58,770,750 USD, with annual operating costs of 21,066,800 USD. The system has a 4.8-year Simple Payback Period and an LCOE of 0.0835 USD/kWh. This yields 211.3% ROI. Its IRR is 17.17%. On the other hand, Peak PV solar systems cost 66,714,400 USD to install and 21,485,900 USD to operate. Its Levelized Cost of Energy (LCOE) is 0.0736 USD/kWh and has a shorter Simple Payback Period of 6.5 years. NPV for the peak system yields 320.6% ROI and 26.10% IRR. Peak PV solar systems offer a longer payback period, higher returns, and a more favourable electricity cost than average PV systems. This study provides valuable insights for decision-makers involved in large-scale solar PV systems.

I. Environmental Analysis

Energy from solar PV facilities is not emission-free. Tables 8 and 9 break down the life cycle emissions for the system's primary components to compute a solar plant's CO₂ emissions. The average and peak PV solar systems are assessed for greenhouse gas (GHG) emissions. An average PV solar system produces 288,687.29 MWh annually, lowering CO₂ emissions by 3,853,975.3 tons. This shows its significant carbon emission reduction. Meanwhile, the system generates 333,511.75 tonnes of CO₂, totalling 3,010,449.3 tons.

In contrast, the peak PV solar system, which generates 339,720.83 MWh of electricity annually, effectively offsets 535,273.1 tonnes of CO₂. Although the system produces 333,511.75 tonnes of CO₂, it achieves a net reduction, resulting in a total CO₂ balance of 3,601,588. These findings highlight the complex interaction between emissions reduction and generation within each system, offering essential insights for sustainable energy decisions.

<i>Table 5 Comparison of generated and required units (MWh) for government facilities</i>				<i>Table 6 Technical specifications of the simulation's PV panels and inverters</i>			
Month	Units required [MWh] by the government sites	Units generated [MWh] by the average solar system	Units generated [MWh] by peak solar system	Sr no.	Parameters	Calculated values (Average)	Calculated values (Peak)
January	19,018	24,026	28,274	1	Unit Nominal Power	700 [W _p]	700[W _p]
February	18,533	22,478	26,452	2	No. of PV modules	221,430 units	260,568 units
March	19,694	27,052	31,836	3	Cell area	644,494 [m ²]	758,409 [m ²]
April	24,213	24,182	28,456	4	Module area	687,023 [m ²]	808,455 [m ²]
May	29,954	24,420	28,736	5	No. of inverters	150 units	182 units
June	29,215	24,413	28,729	6	Operating Voltage	700-1500 []V	700-1500 [V]
July	25,685	22,748	26,768	7	Nominal Power (STC)	155 [MW _p]	182.4 [MW _p]
August	24,013	22,345	26,294	8	Modules	10,065 string x 22 In series	10,857 string x 24 In series
September	22,203	24,309	28,606	9	Inverter rating	1,000 [kW _{ac}] (150 units)	1,000 [kW _{ac}] (182 units)
October	23,992	25,548	30,065	10	Inverter power	1,000 [kW _{ac}]	1,000 [kW _{ac}]
November	29,395	25,231	29,694	11	CO ₂ emissions cut	3,010,449.323 [tCO ₂ /year]	3601580.433 [tCO ₂ /year]
December	23,895	21,935	25,812				
Total	289,809	288,687	339,721				

<i>Table 7 Financial parameters of the proposed PV solar systems</i>			<i>Table 8 Peak PV Systems' Lifecycle Emissions</i>			
System parameters	Average PV Solar System	Peak PV Solar System	Item	LCE	Quantity	Subtotal [kgCO₂]
Total Installation	\$58.8 M	\$66.7 M	Modules	1713 [kgCO ₂ /kW _P]	189,998 [kW _P]	325,412,518
Operating Cost	\$21.1M [\$/year]	\$21.5 M [\$/year]	Supports	2.97 [kgCO ₂ /kg]	2,714,250 [kg]	8,056,301
Energy Generated	288,687 [MWh/year]	339,721 [MWh/year]	Inverters	294 [kgCO ₂ /Units]	182 units	53,508
LCOE	0.0835 [\$/kWh]	0.0736 [\$/kWh]	<i>Table 9 Average PV Systems' Lifecycle Emissions</i>			
Payback Period	4.8 [years]	6.5 [years]	Item	LCE	Quantity	Subtotal [kgCO₂]
NPV	\$ 124.0 M	\$213.5 M	Modules	1713 [kgCO ₂ /kW _P]	144,999 [kW _P]	248,383,287
ROI	211.3 [%]	320.6 [%]	Supports	2.97 [kgCO ₂ /kg]	2,714,250 [kg]	8,056,301
IRR	17.17 [%]	26.10 [%]	Inverters	294 [kgCO ₂ /Units]	146 units	42,924

References

- [1] D. D. A. C. Goodman Tom Prater, Joe, “The Carbon Brief Profile: Pakistan,” Carbon Brief, May 26, 2023. <https://interactive.carbonbrief.org/the-carbon-brief-profile-pakistan/>
- [2] S. A. Khatri et al., “An Overview of the Current Energy Situation of Pakistan and the Way Forward towards Green Energy Implementation,” Energies, vol. 16, no. 1, p. 423, Dec. 2022. <https://doi.org/10.3390/en16010423>
- [3] W. Rafique, “Electricity As A Subject After The 18th Amendment,” Courting The Law, Aug. 26, 2016. <https://courtingthelaw.com/2016/08/23/commentary/electricity-as-a-subject-after-the-18th-amendment/>
- [4] Information on “Nooriabad Power Company.” <https://www.snpc.com.pk/>
- [5] U. Qazi and M. Jahanzaib, “An integrated sectoral framework for the development of sustainable power sector in Pakistan,” Energy Reports, vol. 4, pp. 376–392, Nov. 2018. <https://doi.org/10.1016/j.egyr.2018.06.001>
- [6] Information on “EM&RC – SINDH ENERGY DEPARTMENT.” [Online]. Available: <https://sindhenergy.gov.pk/emrc/>
- [7] “Year Book 2022-23,” Ministry of Energy (Power Division), Nov. 28, 2023. <https://power.gov.pk/SiteImage/Publication/YearBook2022-23.pdf> (accessed Feb. 21, 2024).

- [8] M. Irfan, Z.-Y. Zhao, M. Ahmad, and M. Mukeshimana, "Solar Energy Development in Pakistan: Barriers and Policy Recommendations," *Sustainability*, vol. 11, no. 4, p. 1206, Feb. 2019. <https://doi.org/10.3390/su11041206>
- [9] N. Abas, S. Rauf, M. S. Saleem, M. Irfan, and S. A. Hameed, "Techno-Economic Feasibility Analysis of 100 MW Solar Photovoltaic Power Plant in Pakistan," *Technology and Economics of Smart Grids and Sustainable Energy*, vol. 7, no. 1, Apr. 2022. <https://doi.org/10.1007/s40866-022-00139-w>
- [10] Jamil, J. Zhao, L. Zhang, R. Jamil, and S. F. Rafique, "Evaluation of Energy Production and Energy Yield Assessment Based on Feasibility, Design, and Execution of 3×50 MW Grid-Connected Solar PV Pilot Project in Nooriabad," *International Journal of Photoenergy*, vol. 2017, pp. 1–18, 2017. <https://doi.org/10.1155/2017/6429581>
- [11] S. Sreenath, K. Sudhakar, Y. A.F., E. Solomin, and I. M. Kirpichnikova, "Solar PV energy system in Malaysian airport: Glare analysis, general design and performance assessment," *Energy Reports*, vol. 6, pp. 698–712, Nov. 2020. <https://doi.org/10.1016/j.egyr.2020.03.015>
- [12] A. Kazem, M. H. Albadi, A. H. A. Al-Waeli, A. H. Al-Busaidi, and M. T. Chaichan, "Techno-economic feasibility analysis of 1 MW photovoltaic grid-connected system in Oman," *Case Studies in Thermal Engineering*, vol. 10, pp. 131–141, Sep. 2017. <https://doi.org/10.1016/j.csite.2017.05.008>
- [13] K. Padmavathi and S. A. Daniel, "Performance analysis of a 3MWp grid-connected solar photovoltaic power plant in India," *Energy for Sustainable Development*, vol. 17, no. 6, pp. 615–625, Dec. 2013. <https://doi.org/10.1016/j.esd.2013.09.002>
- [14] B. Shiva Kumar and K. Sudhakar, "Performance evaluation of 10 MW grid-connected solar photovoltaic power plant in India," *Energy Reports*, vol. 1, pp. 184–192, Nov. 2015. <https://doi.org/10.1016/j.egyr.2015.10.001>
- [15] M. Obeng, S. Gyamfi, N. S. Derkyi, A. T. Kabo-bah, and F. Peprah, "Technical and economic feasibility of a 50 MW grid-connected solar PV at UENR Nsoatre Campus," *Journal of Cleaner Production*, vol. 247, p. 119159, Feb. 2020. <https://doi.org/10.1016/j.jclepro.2019.119159>
- [16] S. Sukumaran and K. Sudhakar, "Performance analysis of solar powered airport based on energy and exergy analysis," *Energy*, vol. 149, pp. 1000–1009, Apr. 2018. <https://doi.org/10.1016/j.energy.2018.02.095>
- [17] M. A. Anrizal Akbar, A. M. S. Yunus, and J. Tangko, "PVSYST-Based Solar Power Plant Planning," *INTEK: Jurnal Penelitian*, vol. 9, no. 1, p. 89, Apr. 2022. <https://doi.org/10.31963/intek.v9i1.3789>
- [18] "AE700TME-132BDS - AESOLAR," AESOLAR, Jan. 09, 2024. <https://ae-solar.com/products/ae700-tme-132bds/>
- [19] T. E. K. Zidane, S. M. Zali, M. R. Adzman, M. F. N. Tajuddin, and A. Durusu, "PV array and inverter optimum sizing for grid-connected photovoltaic power plants using optimisation design," *Journal of Physics: Conference Series*, vol. 1878, no. 1, p. 012015, May 2021. <https://doi.org/10.1088/1742-6596/1878/1/012015>
- [20] "Abb Solar Inverter 1000kw 1mw Pvs 800 Central Inverter Ip42 Ip65," [indiamart.com](https://www.indiamart.com/proddetail/abb-solar-inverter-1000kw-1mw-pvs-800-central-inverter-ip42-ip65-23097354773.html). <https://www.indiamart.com/proddetail/abb-solar-inverter-1000kw-1mw-pvs-800-central-inverter-ip42-ip65-23097354773.html>

- [21] N. Ahmed et al., "Techno-economic potential assessment of mega-scale grid-connected PV power plant in five climate zones of Pakistan," *Energy Conversion and Management*, vol. 237, p. 114097, Jun. 2021. <https://doi.org/10.1016/j.enconman.2021.114097>
- [22] S. Abdelhady, "Performance and cost evaluation of solar dish power plant: sensitivity analysis of levelized cost of electricity (LCOE) and net present value (NPV)," *Renewable Energy*, vol. 168, pp. 332–342, May 2021. <https://doi.org/10.1016/j.renene.2020.12.074>
- [23] M. M. Rafique and H. M. S. Bahaidarah, "Thermo-economic and environmental feasibility of a solar power plant as a renewable and green source of electrification," *International Journal of Green Energy*, vol. 16, no. 15, pp. 1577–1590, Oct. 2019. <https://doi.org/10.1080/15435075.2019.1677237>
- [24] W. Shen et al., "A comprehensive review of variable renewable energy levelized cost of electricity," *Renewable and Sustainable Energy Reviews*, vol. 133, p. 110301, Nov. 2020. <https://doi.org/10.1016/j.rser.2020.110301>
- [25] "Climate Change Indicators: Greenhouse Gases | US EPA," US EPA, Feb. 09, 2024. <https://www.epa.gov/climate-indicators/greenhouse-gases>

A developed system design for blue energy generation

Omar D. MOHAMMED^{1,a,*}, Saud ALHARBI^{1,b}, Shoja ALHARBI^{1,c},
Waleed ALDHUWAIHI^{1,d}, and Nasser BINI HAMEEM^{1,e}

¹ Mechanical Engineering Department - Prince Mohammad bin Fahd University PMU, Khobar,
Saudi Arabia

^aosily@pmu.edu.sa, ^b201801600@pmu.edu.sa, ^c202002618@pmu.edu.sa,
^d201901074@pmu.edu.sa, ^e201502982@pmu.edu.sa

Keywords. Wave Energy, Linear Generator, Power Generation, Renewable Energy

Abstract. Sustainability is an important factor in energy generation. Sea or ocean waves can be used as a sustainable source of energy generation. A technique of using buoyant floats submerged in water to drive a magnetic generator for energy conversion can be applied and studied. In the current article, a developed system design is presented for harvesting wave energy (blue energy). The wave power and generator power are calculated based on the studied model. The presented design enhances the concept of wave energy harvesting, as a renewable energy source, and shows the possibility of applying it. Applying wave energy harvesting should get more attention as a sustainable and clean source of power electricity.

Introduction

Sea or ocean wave energy, which is an abundant and untapped source of energy, can be used to reduce the use of fossil fuels. Wave energy, which can be called “blue energy”, is a clean renewable source of energy and supports sustainability. This method reduces greenhouse gas emissions and protects marine ecosystems, unlike traditional power generation. Innovation in wave energy technology boosts energy security. Waves can help coastal regions become more energy self-sufficient and less vulnerable to energy supply disruptions. Exploring and refining a linear wave energy generator advances wave energy conversion technology, potentially paving the way for future developments and commercial applications [1,2]. Electricity generation in remote or island regions often relies on imported fossil fuels. In such areas wave energy generators provide a more sustainable and independent energy source than expensive and environmentally harmful fuel imports [3]. These generators use ocean waves to provide clean renewable energy that supports the global transition to a carbon-neutral future [4]. The generator design, materials and operation, which is driven by the need for reliable and efficient wave energy converters, was discussed in [5,6]. The environmental assessments were examined to ensure sustainable ocean resource use. It helps evaluate existing technologies, identify gaps and guide this project toward a more efficient and sustainable wave energy generator [6].

A comprehensive literature review of wave energy was presented in [7] to discuss the concept development since the 1970s, highlighting its growing global importance and promise. It thoroughly examines sea wave energy understanding and use. The paper focused on wave energy resource characterization and the theoretical foundations for wave energy absorption and control hydrodynamics. The review emphasizes the complexity of wave dynamics and the theoretical frameworks needed to extract energy from ocean waves.

Wave energy using linear generator system was presented and discussed in [8,9]. Wave energy conversion and the variety of generator systems were discussed. This variety highlights the different ways to design wave energy-efficient systems. The authors discussed modern linear generator systems, including the Archimedes Wave Swing (AWS) and Uppsala systems. These systems demonstrate linear wave energy conversion technology's progress. The authors also

suggested investigating air-cored machines for integrated electrical-mechanical-structural designs suggesting a holistic generator development approach. The search for cost-effective solutions suggests exploring generator constructions that may be cheaper. This includes cylindrical generators and concentrated coil generators.

Wave energy conversion using linear generators was examined in [10]. The differences between rotary and linear generators application were discussed. The fact that linear generators convert wave energy efficiently is important in energy generation. Linear generators can adjust wave speeds unlike rotary generators. Flexible motion matches wave variations resulting in different voltages, currents and phase sequences. The peak to average power ratio increases due to this variability improving efficiency. The ocean wave energy fundamental calculations were presented in [11]. The ongoing research on wave energy at Oregon State University was summarized.

Despite the benefits of the wave energy technique, its applicability is still challenging. The device durability in harsh marine environments, cost-effectiveness, energy production and grid integration complexity still require more investigations. The previous works involved immersing the generator in the water. In the current work a new system design is developed for power generation using the wave energy. The presented system is designed to be attached to a structure above the water on the coastal wave breaker. The design concept is presented and discussed in terms of manufacturability, productivity and applicability.

System Design

In the current work a system design is developed for generating power using the wave energy. The system consists of a magnetic shaft and electric coil directly connected to a float movement. As the magnetic shaft moves inside the coil, an electrical current is generated. Electromagnetic induction generates electricity from the float's wave induced kinetic energy. Linear motion of the magnetic shaft inside the coil changes the magnetic field generating an electric current. The heart of the wave energy generator system is converting mechanical motion into electrical energy.

Fig. 1 shows the developed system model and Fig.2 shows the coil and armature used in the system. The designed model is provided by a platform to be attached to a structure above the water on the coastal wave breaker. This will provide the feasibility to locate number of the generator units for more energy generation.

The design meets practical deployment size and spatial constraints. A small footprint and streamlined design allow for efficient integration into existing marine infrastructures maximizing system effectiveness without taking up too much space.

Sustainability guides material selection and operational strategies, aiming to minimize the environmental footprint. Using eco-friendly materials and energy-efficient components creates a renewable energy and environmental preservation system. The system minimizes marine ecosystem damage. The system's deployment and operation are designed to minimize noise pollution and aquatic life disturbances to preserve marine environments. Beyond technology, by considering social impacts, the generator design concept encourages community for sustainable energy initiatives.

Efficiency and affordability are balanced by cost effectiveness. To encourage adoption, strategies optimize system efficiency while lowering manufacturing and operational costs. The system design prioritizes readily available components and construction methods for large-scale manufacturing, streamlining production for efficient and cost-effective deployment. The system's strict safety protocols and design features reduce risks for maintenance personnel and the marine environment.

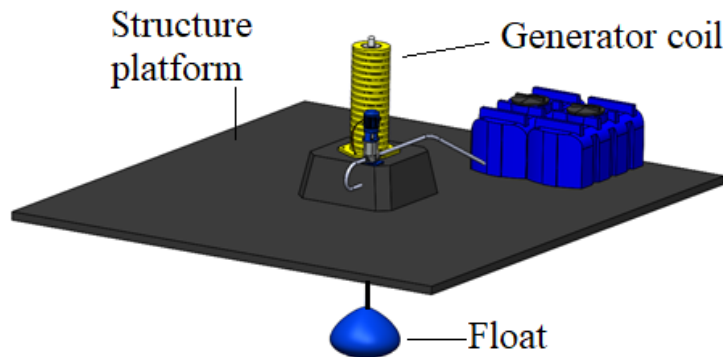


Figure 1 the developed generator system design

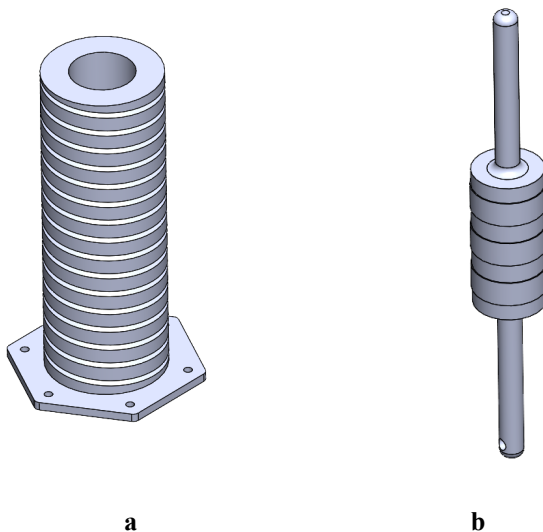


Figure 2 the generator parts, a. the generator coil, b. the magnetic armature

Theoretical Calculations

The wave motion can be characterized by the wave length or the time period (T_{wave}), and the wave height or the wave amplitude (H_{wave}). The input power to the generator is P_{wave} , which is the wave power per one meter of the wave length, can be calculated as follows [11,12,13].

$$\begin{aligned} P_{wave} &= \frac{(\rho \times g^2 \times H_{wave}^2 \times T_{wave})}{32 \pi} \\ &= 7662 \text{ W/m} \end{aligned} \tag{1}$$

Where,

The water density, $\rho = 1000 \text{ kg/m}^3$

The gravity constant, $g = 9.81 \text{ m/s}^2$

The wave amplitude, $H_{wave} = 1 \text{ m}$

The wave time period, $T_{wave} = 8 \text{ s}$

The power output of the linear generator ($P_{generator}$) can be calculated as follow.

$$\begin{aligned} P_{generator} &= \eta \times P_{wave} \\ &= 0.85 \times 7662 = 6512.8 \text{ W/m} \end{aligned}$$

Where,

The efficiency of the generator, $\eta = 0.85$

These calculations reveal wave power, linear generator output and system energy conversion efficiency.

Discussion

The system is designed to provide the feasibility to be located and attached to the wave breakers. A number of the generator units can be used for power generation and at the same time attaching the units to the wave breaker structure will give more strength to the units and will make the maintenance easier.

The buoyant float should be made of a sturdy material for hostile sea settings. Material weight, corrosion and wave resistance matter. The linear generator component selection is crucial to the subsystem. Effective electromagnetic induction is achieved by the magnetic shaft, coil and materials. Optimizing wave motion to electricity conversion demands high quality materials and precision engineering. Primary capture systems should use oscillating water columns or point absorbers to efficiently catch wave energy. In diverse wave situations, subsystem components must maximize energy absorption. Frame, bearings and anchoring systems are crucial converter components. For converter structural integrity and lifetime, durability, stability and seawater resistance are used. Controlling and converting electricity requires inverters, transformers and control units. Critical components must work well under different electrical loads and environments. These components should be chosen for performance, durability, pricing and system compatibility. The goal is an integrated system that efficiently converts wave energy into electrical power in marine conditions while being reliable and durable. Designers must choose components that enhance efficiency, safety and sustainability. To ensure alignment and functionality, the system model parts have to be fabricated, assembled and tested.

Conclusions

The wave energy converter is characterized by the aspects of innovation, perseverance and sustainability. This current work advances renewable energy and shows a shared commitment to energy issues. This work demonstrates how engineering and real-world application can use the sustainable wave energy (blue energy) for power electricity generation. A developed design is presented to use the wave energy and promote the growth of renewable energy dependency. In an age of clean energy and environmental concerns energy generation can be more sustainable. It symbolizes the commitment to fighting climate change, conserving resources and boosting economic resilience through technology. To reduce design complexity, a linear generator is applied in the project to avoid the use of extra mechanism for converting the linear motion to a rotary motion to adapt the rotary generator. Developing wave energy harvesting techniques and improving the efficiency should get more attention as a sustainable and clean source of power electricity.

References

- [1] O. Edenhofer et al. Renewable Energy Sources and Climate Change Mitigation: Special Report of the Intergovernmental Panel on Climate Change. Cambridge University Press, 2012. <https://doi.org/10.1017/CBO9781139151153>
- [2] M. Okur Dinçsoy and H. Can. Optimizing Energy Efficiency During a Global Energy Crisis. IGI Global, 2023. <https://doi.org/10.4018/979-8-3693-0400-6>
- [3] E. Hossain and S. Petrovic, Renewable Energy Crash Course: A Concise Introduction. Springer International Publishing, 2021. <https://doi.org/10.1007/978-3-030-70049-2>

- [4] F. R. Spellman and R. M. Bieber, *The Science of Renewable Energy*. CRC Press, 2016.
<https://doi.org/10.1201/b13592>
- [5] A. Pecher and J. P. Kofoed, *Handbook of Ocean Wave Energy*. Springer International Publishing, 2016. <https://doi.org/10.1007/978-3-319-39889-1>
- [6] L. Peppas. *Ocean, Tidal and Wave Energy: Power from the Sea*. Crabtree Publishing Company, 2008.
- [7] A. Falcao and s. e. reviews, *Wave energy utilization: A review of the technologies*, vol. 14, no. 3, pp. 899-918, 2010. <https://doi.org/10.1016/j.rser.2009.11.003>
- [8] H. Polinder, M. Mueller, M. Scuotto, and M. G. de Sousa Prado. Linear generator systems for wave energy conversion, in *Proceedings of the 7th European Wave and Tidal Energy Conference*, Porto, Portugal, 2007, pp. 11-14.
- [9] P. Khatri, X. Wang. Comprehensive review of a linear electrical generator for ocean wave energy conversion. *The Institution of Engineering and Technology*, 2020, vol. 14, no. 6, pp. 949-958. <https://doi.org/10.1049/iet-rpg.2019.0624>
- [10] A. A. Faiad and I. Gowaid, *Linear generator technologies for wave energy conversion applications: A review* in *2018 53rd International Universities Power Engineering Conference (UPEC)*, 2018, pp. 1-6: IEEE.
- [10] T. Brekken, A. von Jouanne, Hai Yue Han. *Ocean Wave Energy Overview and Research at Oregon State University*. 2009 *IEEE Power Electronics and Machines in Wind Applications*. <https://doi.org/10.1109/PEMWA.2009.5208333>
- [11] R. Parthasarathy. *Linear PM generator for wave energy conversion*. Louisiana State University and Agricultural and Mechanical College, Master thesis, 2012.
- [12] A. Khaligh, O. Onar. *Energy Harvesting: Solar, Wind, and Ocean Energy Conversion Systems*. Taylor and Francis Group, LLC, 2010.

A review of the renewable energy technologies and innovations in geotechnical engineering

Eman J. Bani ISMAEEL^{1,a}, Samer RABABAH^{1,b},
Mohammad Ali KHASAWNEH^{2,c}, Nayeemuddin MOHAMMED^{2,d*},
Danish AHMED^{2,e}

¹ Civil Engineering Department, College of Engineering, Jordan University of Science & Technology, Irbid 22110, Jordan

² Department of Civil Engineering, Prince Mohammad Bin Fahd University, Al Khobar, Kingdom of Saudi Arabia

^aegbaniissmaeel20@eng.just.edu.jo, ^bsrrababah@just.edu.jo, ^cmkhasawneh@pmu.edu.sa,
^dmnayeemuddin@pmu.edu.sa, ^edahmed@pmu.edu.sa

Keywords: Sustainability, Renewable Energy, Recent Trends, Fossil fuels, Climate Change, CO₂ emission

Abstract. The recent trend in the energy sector is seeking eco-friendly and cost-effective solutions. In the last few years, the globe has given attention to renewable energy resources to overcome the depletion problems of fossil fuels and take advantage of abundant natural resources such as solar, wind, and natural gas. Renewable energy resources provide a long-term efficiency solution in different applications. This review paper comprehensively reviews recent advancements in renewable energy technologies and innovations, focusing on solar energy, wind energy development, smart grid technologies, and energy storage solutions for a cleaner and more sustainable future.

Introduction

Renewable energy sources have become increasingly important in recent years [1]. They offer a solution to combat the depletion of fuels and address environmental issues like global warming [2]. Generally, energy sources can be classified into two categories: fossil fuels and renewable energy [3]. The European Union has pledged to cut its emissions by 20% in the second phase of the Kyoto Protocol. The intermittent renewable energy sources solar and wind must be transmitted and stored as effectively as feasible in order to meet this objective. Renewable energy, known for its nature, includes clean energy options [4]. With the increasing global demand for energy consumption and environmental challenges such as climate change, carbon dioxide (CO₂) emissions, and greenhouse gas (GHG) emissions, authorities are increasingly encouraged to transition from conventional energy sources, particularly fossil fuels, to clean and secure renewable energy alternative [5]. Renewable energy resources offer energy security, environmental protection, economic advantages, and a pollution-free environment. Switching from relying on fuels for energy consumption to adopting a zero-carbon emission approach marks a shift in the energy sector. The transition to renewable energy will be facilitated through the integration of smart technologies, information technology, and the implementation of clean energy policy frameworks.

The adoption of renewable energy sources has prompted the development of numerous technologies and innovations that boost progress within the energy industry. These technologies provide environmentally friendly substitutes for energy derived from fossil fuels and establish the foundation for a future distinguished by carbon-neutral energy. Recent developments in renewable energy technologies and innovations, such as advancements in solar energy, energy storage

solutions, wind energy development, and smart grid technologies, are examined in detail in this article. Moreover, this review will address the challenges and opportunities of transitioning to renewable energy.

Solar Energy Advancement

Solar energy is generated abundantly by the sun. Solar energy is considered a vital renewable resource, intercepting around 1.8×10^{14} kW on Earth. Its ubiquity, zero cost, and sustainability make it a promising solution to global energy demands. Solar energy is applicable across diverse sectors and is crucial for addressing the continuously increasing demand for energy resources. It is one of the renewable energy resources that has gained significant importance in the recent development of the energy sector [6]. Solar energy can be converted into different forms through photovoltaic (PV) systems. PV systems provide benefits such as minimal environmental impact, low maintenance expenses, and the lack of moving parts despite their typically 18-23% lower efficiency. However, numerous variables, including temperature fluctuations and solar insolation, influence the output of PV systems, resulting in power generation fluctuations. Various approaches, including maximum power point tracking (MPPT) methods and sun trackers, can increase the efficiency of a PV system [7].

The Integration of artificial intelligence (AI) into the utilization of solar energy resulted in the development of advanced solar panels optimized in structure, performance, and efficiency. [8] examined the AI can transform PV technology in the solar energy sector. According to the study, AI can potentially improve solar energy system efficiency, power grid integration, and the transition to sustainable energy. Researchers used machine learning models to accelerate the discovery of high-performance solar cell materials. These algorithms predict the material properties and searched large data sets quickly. [9] developed a solar energy tracking prototype to optimize solar energy collection using Arduino technology. The prototype could automatically adjust the position of the solar panel by utilizing servo motors and Light-Dependent Resistors (LDRs). An 18% increase in energy output compared to static panels indicates that these panels may be useful in various situations.

Advanced battery management algorithms and Neural Maximum Power Point Tracking (MPPT) control to optimize photovoltaic solar systems. This work optimized solar energy conversion to electricity by dynamically modifying the MPP and managing battery charging and discharging [10]. Thorough MATLAB/Simulink simulations showed that neural MPPT control outperforms other methods even in variable sunlight conditions. [11] investigated whether tiny machine learning (TinyML) could predict solar energy yield in real time for microcontrollers and other resource-constrained edge IoT devices. Four popular machine learning models: unidirectional long short-term memory (LSTM), bidirectional gated recurrent unit (BiGRU), bidirectional long short-term memory (BiLSTM), and simple bidirectional recurrent neural network (BiRNN) are extensively evaluated for predicting solar farm energy yield. This study adds to the body of knowledge on cost-effective IoT solutions and emphasizes edge device limitations in ML architecture selection. This makes the energy landscape more sustainable and efficient, benefiting residential and industrial sectors.

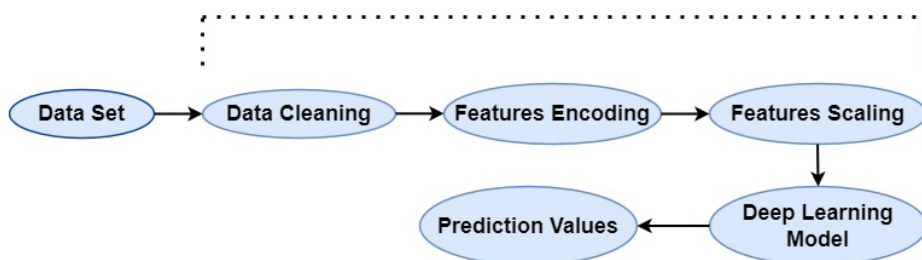


Fig. 1 shows the detail steps for ANN-ML modelling technique [11]

Wind Energy Development

Renewable energy sources, such as wind energy, offer a promising way to reduce fossil fuel dependency while mitigating environmental impact. Wind, considered an indirect derivative of solar energy, is continually replenished by natural processes driven by the sun's energy [12]. Wind energy arises from the differential heating of the Earth's surface, considered an abundant and sustainable energy resource. Estimates suggest that more than 10 million MW of energy is continuously available in the Earth's wind, significantly contributing to global energy needs [13]. The advancement in wind turbines leads to stronger, lighter, and more efficient turbine blades, which means enhancements in annual energy output and reductions in turbine weight, emission, and noise over recent years [14]. Several measurements are considered to harness wind energy's potential further, such as establishing more wind monitoring stations, enhancing turbine maintenance techniques, carefully selecting wind farm sites, adapting high-capacity machines, and using advanced design techniques. These procedures lead to optimizing wind energy generation by maximizing the turbine's efficiency, increasing machine availability, and expanding operational capacity [15].

A recent study employs computational strategies for converting wind energy into hot water. This study optimized wind farm layout, modeling and simulation systems, energy management strategy, wind resource assessment, turbine design and size, power conversion control, and layout engineering [16]. An evaluation of the semicircular wind tower blasting and painting system's potential to revolutionize conventional wind tower coating methods was conducted by [17]. Contributing to advancing the wind energy industry toward a more sustainable future, the findings of this research demonstrated that the semicircular system presents notable benefits compared to robotic arms, including a substantial enhancement in efficiency, reduced costs, and an environmentally friendly solution. In a study conducted by [18], the objective was to investigate the feasibility of utilizing wind towers as natural ventilation and cooling systems in residential buildings. The primary focus of this research was the integration of wind towers with energy storage systems and renewable energy sources to maximize their efficiency and effectively reduce greenhouse gas emissions.

Smart Grid Technologies

In general, smart grids are advanced electricity networks engineered to utilize information and communication technologies to ensure improved dependability and productivity in power delivery [19]. Promoting energy conservation and sustainability, these technologies facilitate the seamless integration and administration of renewable energy sources. Storage solutions are crucial in mitigating fluctuations in energy output, especially when considering the decentralized nature of energy production facilitated by renewable resources. In order to prevent blackouts, smart grids attempt to maintain a balance between energy supply and demand by addressing a number of issues, such as rising pressures and peak consumption [20]. Smart Grids use cutting-edge technologies like intelligent control, communication, and self-healing to advance electricity networks. Demand side management (DSM) and demand response initiatives in these power grids give consumers more control over their energy use. Meters, microgeneration, and smart appliances enable this control. Smart grids use various generator and storage technologies, including distributed generation (DG) and renewable energy sources, to reduce the environmental impact of electricity provision. They optimize asset management and delivery independently, maximizing resource use. Smart grids also ensure reliable energy supply during disasters by strengthening resilience to physical and cyber threats. Smart Grids increase supply aggregation and transmission capacity to improve power supply and market access [21].

Recent developments in smart grid technologies have been instrumental in addressing the changing demands of the power distribution sector. These developments optimize grid operations, enhance resilience to cyber and physical threats, and facilitate the integration of renewable energy

sources and energy storage solutions by utilizing cutting-edge innovations. In addition, the continuous advancement and enhancement of smart grid technologies possess tremendous potential to fortify and transform the distribution system, facilitating the transition to a future characterized by enhanced energy efficiency, dependability, and sustainability [22]. The smart grid technologies are driving significant progress toward enhancing modern power systems' reliability, sustainability, and efficiency. One notable area of advancement lies in the development of energy management systems, which play a crucial role in ensuring the seamless integration and coordination of various grid components from generation to consumption. Initiatives such as the Smart Grid Interoperability (SGIP) standards, initiated by the National Institute of Standards and Technology (NIST), have promoted interoperability among grid components and facilitated efficient planning and implementation [23].

Moreover, integrating Internet of Things (IoT) solutions has revolutionized grid communication and automation, marking an important advance in smart grid technology. IoT technologies provide greater connection and automation, allowing grid components to interact more efficiently and reliably. However, using IoT in smart grids introduces additional issues, notably regarding security and privacy. Researchers are currently addressing these problems by establishing strong security mechanisms and authentication methods to preserve the integrity and confidentiality of grid data [24]. Furthermore, big data analytics transforms smart grid operations by giving essential insights into grid efficiency and management. However, difficulties such as data storage, processing, integration, and security continue to be important emphasis areas for researchers looking to fully realize the potential of big data in smart grid technologies [25].

Energy Storage Solutions

Among the most recent developments in the renewable energy field, energy storage solutions are critical to assuring the reliability and scalability of renewable energy sources. Furthermore, this technology considerably increases energy consumption capacity. The increasing demand for sustainable and clean energy continues to rise, driving the development of new imperative solutions for energy storage [26]. This section aims to provide insights into the role of recent advancements in energy storage solutions in facilitating the transition towards a more sustainable energy landscape. The Energy PLAN modeling to find Finland's cheapest 100% renewable energy scenario by 2050. In the study, electricity and heat storage meet 15% of end-user demand, while thermal storage discharge meets 4%. High renewable energy integration requires electrical storage devices at 50% variable renewable energy penetration and seasonal storage devices at over 80% renewable energy (RE) penetration. Energy storage is crucial in Finland's 100% renewable energy system [27]. [28] analyzed the challenges during the remote Arctic region's transition from diesel and fossil fuels to renewable energy sources. Various energy storage options, including battery storage, underground solar power/storage, and hydrogen storage, are explored to achieve energy self-sufficiency at Flatey's. These energy storage options are summarized in Table 1.

Table 1: The suggested energy storage options for remote areas [28]

Storage Solution	Description
Storing Solar Power in Battery Banks	<ul style="list-style-type: none">- Utilizes battery storage in PV systems.- Flexible connection of batteries in series for larger facilities.- It requires less space than hydrogen storage.
Underground Storage Solar Power	<ul style="list-style-type: none">- Utilizes borehole thermal energy storage (BTES).- Ground source heat exchangers (BHE).- Efficiency depends on geological factors.
Storing Power by Using Hydrogen	<ul style="list-style-type: none">- Green hydrogen production through electrolysis- Challenges in storing hydrogen.- Can be stored under high pressure or in liquid form.- Utilized in fuel cells for high-efficiency electricity production.- Economic evaluation required.

Renewable Energy in geotechnical engineering applications

Geotechnical engineering is crucial in providing good foundation and anchor systems for MRE devices. Marine renewable energy (MRE) systems on a commercial scale will consist of a variety of devices secured to the bottom by foundations or anchors [29]. The renewable energy is a substitute resource to address the high demand for conventional hydrocarbon energy, reduce the impact on the environment, and ensure sustainability for many years. The review of geotechnical engineering concerns and their connection to renewable energy engineering is intended to motivate geotechnical engineers to participate in the developing area of energy research [30]. Owing to the geo-dependent nature of renewable energy, geo technology can help optimize the effective use of renewable resources. Environmental impact assessments and offshore wind turbine engineering designs both depend heavily on seabed characterization. The investigation into screw piles for the development of offshore renewable energy, significant upscaling of the currently in use onshore piles was necessary [31].

The main benefit is that it is a clean, renewable energy source with no adverse effects on the environment. In the past, Croatia's experience with geothermal energy extraction has mostly focused on the potential for deep geothermal resource extraction. "Investment Valuation Model for Renewable Energy Systems in Buildings" outlines the real options model that is being offered and identifies the special characteristics that set it apart from other valuation models [32]. The needs of a profession that will increasingly be involved in sustainable design, energy geo technology, waste management, underground utilization, enhanced/more efficient use of natural resources, and alternative/renewable energy sources must be addressed in the geotechnical engineering curriculum, from undergraduate education through continuing professional education [33]. Every technology was found to have a very wide range in terms of electricity costs, greenhouse gas emissions, and generation efficiency. This is mostly because each renewable energy source has a different geographical reliance and a different range of technological alternatives [34].

Table 2: The efficiency and cost aspect to renewable energy [35]

Aspect	Energy Production	Energy Storage	Energy Harvesting
Efficiency	-Solar Photovoltaics: 15-20% -Wind Turbines: >40%	-Lithium-ion Batteries: 80-90% -Lead-acid Batteries: 70-85%	-Photovoltaic Cells: >20% -Thermoelectric Generators: 5-10%
Cost	-Solar Photovoltaics: Decreasing, currently competitive -Wind Turbines: Decreasing.	-Lithium-ion Batteries: Decreasing, still significant cost -Lead-acid Batteries: Relatively low cost.	-Photovoltaic Cells: Decreasing, currently cost-competitive -Thermoelectric Generators: Costly,

Summary

Reviewing recent advancements in renewable energy technologies highlights the significant progress towards a sustainable energy landscape. Solar energy innovations, propelled by AI, promise enhanced efficiency and performance, while wind energy developments offer efficient and eco-friendly solutions for wind tower coatings and ventilation systems. Smart grid technologies facilitate seamless energy distribution and management, bolstering grid reliability and efficiency. Furthermore, energy storage solutions, such as thermal storage and PtG concepts, contribute to energy scalability and sustainability. These advancements underscore the critical role of renewable energy in mitigating environmental challenges and transitioning towards a greener future. Continued research and innovation in renewable energy technologies are essential to drive further progress and accelerate the global transition to clean and sustainable energy sources.

References

- [1] F. Rizzi, N. J. van Eck, and M. Frey, “The production of scientific knowledge on renewable energies: Worldwide trends, dynamics and challenges and implications for management,” *Renewable Energy*, vol. 62, pp. 657–671, 2014. <https://doi.org/10.1016/j.renene.2013.08.030>.
- [2] D. C. Mome, “Analysis of the Potential of Clean Energy Deployment in the European Union,” *IEEE Access*, vol. 6, pp. 54811–54822, 2018. <https://doi.org/10.1109/access.2018.2872786>.
- [3] N. A. Ludin *et al.*, “Prospects of life cycle assessment of renewable energy from solar photovoltaic technologies: A review,” *Renewable and Sustainable Energy Reviews*, vol. 96, pp. 11–28, 2018. <https://doi.org/10.1016/j.rser.2018.07.048>.
- [4] P. Trop and D. Goricanec, “Comparisons between energy carriers’ productions for exploiting renewable energy sources,” *Energy*, vol. 108, pp. 155–161, 2016. <https://doi.org/10.1016/j.energy.2015.07.033>.
- [5] C. Bhowmik, S. Bhowmik, A. Ray, and K. M. Pandey, “Optimal green energy planning for sustainable development: A review,” *Renewable and Sustainable Energy Reviews*, vol. 71, pp. 796–813, 2017. <https://doi.org/10.1016/j.rser.2016.12.105>.
- [6] N. Kannan and D. Vakeesan, “Solar energy for future world: - A review,” *Renewable and Sustainable Energy Reviews*, vol. 62, pp. 1092–1105, 2016. <https://doi.org/10.1016/j.rser.2016.05.022>.
- [7] R. Rajesh and M. Carolin Mabel, “A comprehensive review of photovoltaic systems,” *Renewable and Sustainable Energy Reviews*, vol. 51, pp. 231–248, 2015. <https://doi.org/10.1016/j.rser.2015.06.006>.

- [8] A. Mohammad and F. Mahjabeen, "Revolutionizing solar energy with ai-driven enhancements in photovoltaic technology," *BULLET: Jurnal Multidisiplin Ilmu*, vol. 2, no. 4, pp. 1174–1187, 2023.
- [9] A. H. Soomro, S. Talani, T. Soomro, F. A. Khushk, and A. A. Bhatti, "Prototype Development for Solar Energy Tracking Based on Arduino in QUEST Campus Larkana," *Sir Syed University Research Journal of Engineering & Technology*, vol. 13, no. 2, 2024. <https://doi.org/10.33317/ssurj.579>.
- [10] F. F. Ahmad, C. Ghenai, and M. Bettayeb, "Maximum power point tracking and photovoltaic energy harvesting for Internet of Things: A comprehensive review," *Sustainable Energy Technologies and Assessments*, vol. 47, p. 101430, 2021. <https://doi.org/10.1016/j.seta.2021.101430>.
- [11] A. M. Hayajneh, F. Alasali, A. Salama, and W. Holderbaum, "Intelligent Solar Forecasts: Modern Machine Learning Models and TinyML Role for Improved Solar Energy Yield Predictions," *IEEE Access*, vol. 12, pp. 10846–10864, 2024. <https://doi.org/10.1109/access.2024.3354703>.
- [12] M. Seif, M. A. Warsame, and W. Kasima, "Wind energy: energy sustainability perspective." Department of Technical and Vocational Education (TVE), Islamic University ..., 2013.
- [13] G. M. Joselin Herbert, S. Iniyian, E. Sreevalsan, and S. Rajapandian, "A review of wind energy technologies," *Renewable and Sustainable Energy Reviews*, vol. 11, no. 6, pp. 1117–1145, 2007. <https://doi.org/10.1016/j.rser.2005.08.004>.
- [14] J. de A. Y. Lucena, "Recent advances and technology trends of wind turbines," *Recent Advances in Renewable Energy Technologies*. Elsevier, pp. 177–210, 2021. doi: 10.1016/b978-0-323-91093-4.00009-3.
- [15] J. Charles Rajesh Kumar, D. Vinod Kumar, D. Baskar, B. Mary Arunsi, R. Jenova, and M. A. Majid, "Offshore wind energy status, challenges, opportunities, environmental impacts, occupational health, and safety management in India," *Energy & Environment*, vol. 32, no. 4, pp. 565–603, 2020. <https://doi.org/10.1177/0958305x20946483>.
- [16] P. Patil, N. Kardekar, R. Pawar, and D. Kamble, "Wind Energy-Based Hot Water Production: Computational Approaches," *International Journal of Early Childhood Special Education*, vol. 14, no. 06, Nov. 2022. <https://doi.org/10.48047/INTJECSE/V14I6.417>.
- [17] S. Nishar, "Enhancing Efficiency and Supply Chain Management in Wind Tower Fabrication through Cellular Manufacturing," *Journal of Logistics Management*, vol. 11, no. 1, pp. 1–5, 2023.
- [18] S. Dehghani, U. Daon, and M. Shariatzadeh, "Propelling a Paradigm Shift: Revolutionizing Energy Yield in Solar Photovoltaic Systems," *2023 Middle East and North Africa Solar Conference (MENA-SC)*. IEEE, 2023. doi: 10.1109/mena-sc54044.2023.10374472.
- [19] M. E. El-hawary, "The Smart Grid—State-of-the-art and Future Trends," *Electric Power Components and Systems*, vol. 42, no. 3–4, pp. 239–250, 2014. <https://doi.org/10.1080/15325008.2013.868558>.
- [20] I. Alotaibi, M. A. Abido, M. Khalid, and A. V Savkin, "A Comprehensive Review of Recent Advances in Smart Grids: A Sustainable Future with Renewable Energy Resources," *Energies*, vol. 13, no. 23, p. 6269, 2020. <https://doi.org/10.3390/en13236269>.
- [21] G. Dileep, "A survey on smart grid technologies and applications," *Renewable Energy*, vol. 146, pp. 2589–2625, 2020. <https://doi.org/10.1016/j.renene.2019.08.092>.
- [22] O. Majeed Butt, M. Zulqarnain, and T. Majeed Butt, "Recent advancement in smart grid technology: Future prospects in the electrical power network," *Ain Shams Engineering Journal*, vol. 12, no. 1, pp. 687–695, 2021. <https://doi.org/10.1016/j.asej.2020.05.004>.

- [23] V. Gupta, "Non-destructive testing of some Higher Himalayan Rocks in the Satluj Valley," *Bulletin of Engineering Geology and the Environment*, vol. 68, no. 3, pp. 409–416, Aug. 2009. <https://doi.org/10.1007/s10064-009-0211-4>.
- [24] C. Bekara, "Security Issues and Challenges for the IoT-based Smart Grid," *Procedia Computer Science*, vol. 34, pp. 532–537, 2014. <https://doi.org/10.1016/j.procs.2014.07.064>.
- [25] R. C. Qiu and P. Antonik, *Smart Grid using Big Data Analytics*. Wiley, 2017. doi: 10.1002/9781118716779.
- [26] A. N. Abdalla *et al.*, "Integration of energy storage system and renewable energy sources based on artificial intelligence: An overview," *Journal of Energy Storage*, vol. 40, p. 102811, 2021. <https://doi.org/10.1016/j.est.2021.102811>.
- [27] M. Child and C. Breyer, "The Role of Energy Storage Solutions in a 100% Renewable Finnish Energy System," *Energy Procedia*, vol. 99, pp. 25–34, 2016. <https://doi.org/10.1016/j.egypro.2016.10.094>.
- [28] M. Hjallar, E. Víðöisdóttir, and O. Gudmestad, "Transitioning towards renewable energy and sustainable storage solutions at remote communities in the Arctic, Case study of Flatey, Iceland," *IOP Conference Series: Materials Science and Engineering*, vol. 1294, p. 12035, Dec. 2023. <https://doi.org/10.1088/1757-899X/1294/1/012035>.
- [29] J. E. Heath, R. P. Jensen, S. D. Weller, J. Hardwick, J. D. Roberts, and L. Johanning, "Applicability of geotechnical approaches and constitutive models for foundation analysis of marine renewable energy arrays," *Renewable and Sustainable Energy Reviews*, vol. 72, pp. 191–204, May 2017. <https://doi.org/10.1016/j.rser.2017.01.037>.
- [30] T. S. Yun, J.-S. Lee, S.-C. Lee, Y. J. Kim, and H.-K. Yoon, "Geotechnical issues related to renewable energy," *KSCE J Civ Eng*, vol. 15, no. 4, pp. 635–642, Apr. 2011. <https://doi.org/10.1007/s12205-011-0004-8>.
- [31] M. Coughlan, M. Long, and P. Doherty, "Geological and geotechnical constraints in the Irish Sea for offshore renewable energy," *Journal of Maps*, vol. 16, no. 2, pp. 420–431, Dec. 2020. <https://doi.org/10.1080/17445647.2020.1758811>.
- [32] H. Kashani, B. Ashuri, S. M. Shahandashti, and J. Lu, "Investment Valuation Model for Renewable Energy Systems in Buildings," *Journal of Construction Engineering and Management*, vol. 141, no. 2, p. 04014074, Feb. 2015. [https://doi.org/10.1061/\(ASCE\)CO.1943-7862.0000932](https://doi.org/10.1061/(ASCE)CO.1943-7862.0000932).
- [33] R. J. Fragaszy *et al.*, "Sustainable development and energy geotechnology — Potential roles for geotechnical engineering," *KSCE J Civ Eng*, vol. 15, no. 4, pp. 611–621, Apr. 2011. <https://doi.org/10.1007/s12205-011-0102-7>.
- [34] K. Li, H. Bian, C. Liu, D. Zhang, and Y. Yang, "Comparison of geothermal with solar and wind power generation systems," *Renewable and Sustainable Energy Reviews*, vol. 42, pp. 1464–1474, Feb. 2015. <https://doi.org/10.1016/j.rser.2014.10.049>.
- [35] N. Yabuuchi, K. Kubota, M. Dahbi, and S. Komaba, "Research Development on Sodium-Ion Batteries," *Chem. Rev.*, vol. 114, no. 23, pp. 11636–11682, Dec. 2014. <https://doi.org/10.1021/cr500192f>.

Theoretical modeling to analyze the energy and exergy efficiencies of double air-pass solar tunnel dryer with recycled organic waste material

Dagim Kebede GARI^{1,a,*}, A. Venkata RAMAYYA^{1,b}, L. Syam SUNDAR^{2,c}

¹Faculty of Mechanical Engineering, Jimma Institute of Technology, Jimma University, Jimma, Ethiopia

²Department of Mechanical Engineering, College of Engineering, Prince Mohammad Bin Fahd University, Al-Khobar, Saudi Arabia

^ak.dagim82@gmail.com, ^bdra.venkata@ju.edu.et, ^csslingala@gmail.com

Keywords: Thermal Insulation Thickness; Recycled Organic Waste; Energy and Exergy; Solar Tunnel Dryer

Abstract. In this study, the effect of recycled organic waste thermal insulation materials and insulation thickness on a double air pass solar tunnel dryer performance for the charcoal briquette drying process was investigated based on the heat transfer model, that was computed with Python code. The result reveals that, an average temperature of bagasse insulated a double air pass solar tunnel dryer was higher than wood, paper, corn cop, and sawdust insulation by 17.5%, 12%, 8.3%, and 6%, and higher than rock wool, mineral wool, and glass fiber by 3.01%, 4%, and 25.41%, respectively. The energy and exergy efficiency were considerably enhanced with bagasse insulation, comparatively. Thus, the assimilation of recycled organic waste thermal insulation materials enhances the evaporation rate besides reducing energy and exergy losses to the ambient while concomitantly minimizing costs and environmental impacts.

Introduction

In recent years solar energy-driven technologies have been widely used in power generation for industrial processes, household appliances, and commercial centers and in thermal energy extraction for air, water, and process heating, drying, and cooling applications. Conventionally, solar drying and air heating systems are the most economically viable ways of solar energy conversion [1]. The significant problem encountered in solar thermal technologies is energy and exergy loss to the ambient through the bottom and edge wall [2]. This phenomenon indicates that the overall thermal and exergetic efficiency of solar thermal systems is considerably affected by heat loss [3]. Solar air heaters were analyzed in terms of exergy loss to the environment due to absorber plate temperature and the result showed that at a higher absorber plate temperature, there was an increment in the exergy and thermal energy loss [4]. In solar air heaters with double glazing, the exergy and heat loss increased as the heater surface area and absorber plate temperature increased [5].

The onion drying system was analyzed using a mathematical model in terms of exergy loss and the result indicates that the rate of exergy loss reached 28.6% of the incoming exergy in the drying chamber at a velocity and temperature of 2 m/s and 80 °C [6]. The exergy destruction of a hybrid-solar drying system for the rosemary drying process was investigated experimentally and the authors documented that the rate of exergy loss varied from 0.009 to 0.028 KW with a variation in air velocity from 1 to 2 m/s and temperature from 40 to 70 °C [7]. A solar tunnel drying system was investigated experimentally for the drying presses of orange peels and the result revealed that the average exergy loss reached 57.99% in the dryer at higher solar radiation [8]. This indicates that exergy and thermal loss increased with the increment of solar intensity. Recently, different

research has been conducted to address and improve the effect of thermal insulation materials on the heat resistance capacity in solar thermal and building technologies [9]. The performance of building elements with and without insulation material was investigated experimentally and the authors documented that using insulation materials reduces the indoor air temperature by 8 °C [10].

Besides thermos-physical properties, insulation thickness was one of the major factors that altered the performance of solar thermal systems. The effect of insulation thickness on collector efficiency of solar flat plate collectors was analyzed by ANSYS FLUENT and the result showed that the collector efficiency for 50 mm insulation thickness was higher than 35 and 25 mm by 10% and 18%, respectively [11]. The energy-saving capacity of salinity gradient solar ponds with different insulation thicknesses was analyzed using mathematical modeling and the authors reported that the energy-saving enhanced by 36.7% to 55.2% for the optimum thickness of 62 to 122 mm, respectively compared to those without insulation [12]. The energetic performance of solar water heating systems using flat plate collectors with different insulation thicknesses was analyzed by developing the thermal model and the result indicates that the energy efficiency was enhanced by 3.66% as the insulation thickness increased from 20 to 40 mm [13]. The effect of insulation thickness on energy-saving capacity and cost of the building was analyzed and the authors reported that the selection of proper insulation thickness enhances the average annual energy saving by 33.5% and the total energy saving cost by 4.4 to 53.5 \$(m²year) through the reduction energy loss factor [14].

The literature mentioned above indicates the energy efficiency, exergy efficiency, and moisture removal rate are reduced in the solar drying technologies due to the heat and exergy loss to the environment through the thermal insulation thickness [15]. Recently, recycled organic waste thermal insulation materials have promising alternatives to organic (synthetic) thermal insulation materials from the perspective of environment and sustainable development [16]. Additionally, recycled organic waste materials are widely available and economically beneficial over organic synthetic thermal insulation materials. Accordingly, this work intends to study the effect of recycled organic waste thermal insulation materials and thickness on the energy, exergy, and evaporation rate performance of a double air pass solar tunnel drying system for the drying of charcoal briquette, to reduce thermal energy loss to the ambient and environmental impacts of thermal insulation materials during the production process. Integrating recycled organic waste insulation material could reduce the material and manufacturing costs. Heat and exergy loss reduction performance and drying rate enhancement by developing heat transfer models, and the solution was computed by using Python code.

Material and methods

Dryer dimensions

This study will be investigated based on the hourly ambient parameters data of the Jimma zone, Oromia region, Ethiopia (7°40'0" N, 36°50'0"E). The hourly ambient conditions vary from 06:00 a.m. to 17:00 for 11 sunshine hours of the day. The effect of recycled organic waste thermal insulation materials and thickness were computed by developing mass and heat transfer models using the principle of exergy, mass, and energy balance. Throughout the heating and drying process, the mass flow rate of the air stream was considered constant at 0.018 and 0.035 Kg/s, at a constant velocity of 2 m/s, respectively. The influence of recycled organic waste thermal insulation materials on the energy outcomes, exergy extraction, and evaporation rate of a double air pass solar tunnel drying system (DAPSTDs) was studied by using five different materials, namely bagasse, paper, corn cop, wood, and sawdust as well as their respective thermophysical properties are listed in **Table 1**. The variation of thermal efficiency, exergy efficiency, and evaporation rate from the surface of a drying product in a DAPSTDs with the change of insulation was investigated by considering three different dimensions 0.05, 0.25, and 0.5 m.

Table 1: The recycled organic waste, and the inorganic insulation material.

Material	Density (Kg/m ³)	Specific heat (J/Kgk)	Thermal conductivity (W/Km)	Emissivity
Recycled organic waste	Bagasse	120	460	0.88
	Paper	800	1340	0.93
	Corn cop	282.38	1500	0.16
	Wood	920	1670	0.4
	Saw-Dust	415	900	0.062
Insulating material	Glass Fiber	1857	800	0.75
	Mineral Wool	200	850	0.046
	Rock Wool	200	1030	0.043

The schematic diagram of a double air pass solar tunnel drying system with the drying product and the main components is displayed in **Figure 1**. The drying system is divided into two main chambers. The heating chamber where the air stream enters through the inlet is heated by an absorber plate and the fraction of solar radiation scattered inside the chamber then flows to the next chamber. The drying chamber is where the air stream gains thermal energy from the absorber plate through convection for the second time and simultaneously, the moisture is removed from the surface of the charcoal briquette, and finally, the moist air is discharged to the ambient through, the outlet. The overall dimensions of the drying system are listed in **Table 2**.

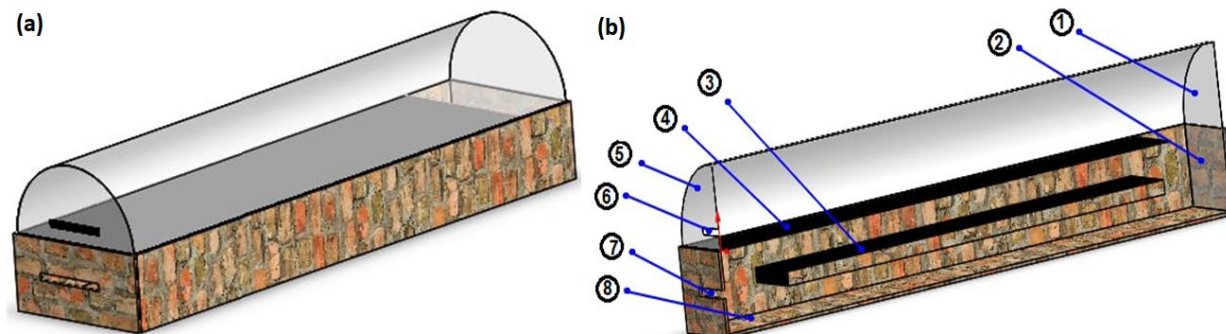


Figure 1: Schematic diagram of a double air pass solar tunnel dryer: (1) heating chamber, (2) drying chamber, (3) charcoal briquette (drying product), (4) absorber plate, (5) cover, (6) inlet, (7) outlet, and (8) floor.

Table 2: The Dimension Specification of DAPSTDs.

Parameters	Dimensions					
	Wet Base			Dry Base		
Mass of briquette	30 Kg				30 Kg	
Initial moisture content	0.5%				100%	
Final moisture content	0.1%				11.111%	
Moisture to be removed	0.4%				88.889	
Mass to be removed	12 Kg				26.667 Kg	
Parameters	Components				Chambers	
	Cover	Plate	Briquette	Floor	Heating	Drying
Length, (m)	2.4	2.25	1.6	2.4	2.4	2.4
Width, (m)	1.885	1.2	0.75	1.2	1.2	1.2
Thickness, (m)	0.0002	0.0004	0.125	0.2	0.6	0.6
Area, (m ²)	4.5	2.574	1.2	2.86	0.5652	0.72

Theoretical modeling

Modelling of the dryer

The thermal energy transfer modeling was developed by applying energy balance on the rate of thermal energy exchange between the dryer components (absorber plate, cover, and floor), Charcoal Briquette, and the air stream in both chambers, based on the schematic diagram shown in **Figure 2**. The analysis was performed using the COMSOL Multiphysics 5.2a software.

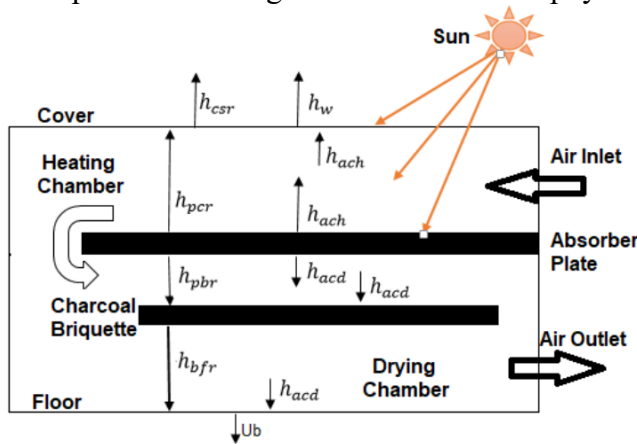


Figure 2: Schematic diagram of heat energy interaction inside the drying system.

Thermal efficiency

Energy is the ability to do work and exergy is the capacity for work extraction, which can be determined from the initial and final temperature with the corresponding time [17].

The rate of input energy (\dot{Q}_{in}) is computed as:

$$\dot{Q}_{in} = [A_{pr}I] \quad (1)$$

The amount of useful energy outcome (\dot{Q}_u) is evaluated as:

$$\dot{Q}_u = [\dot{m}_a C_{pa}(T_{ao} - T_{ai})] \quad (2)$$

The amount of heat energy loss (\dot{Q}_{loss}) is calculated as:

$$\dot{Q}_{loss} = [A_f U_b(T_{ad} - T_{ai})] \quad (3)$$

The thermal efficiency (η_{th}) is determined as:

$$\eta_{th} = \left[\frac{\dot{Q}_u}{\dot{Q}_{in}} \right] \quad (4)$$

Exergy efficiency

The rate of input exergy (\dot{Ex}_{in}) is computed as,

$$\dot{Ex}_{in} = \left[A_{pr} I \left\{ 1 - \left(\left(\frac{4}{3} \right) * \left(\frac{T_{am}}{T_{sun}} \right) \right) + \left(\left(\frac{1}{3} \right) * \left(\frac{T_{am}}{T_{sun}} \right)^4 \right) \right\} \right] \quad (5)$$

The amount of exergy outcome (\dot{Ex}_u) at a given time is computed as:

$$\dot{Ex}_u = \left[\dot{m}_a C_{pa} \left\{ (T_{ao} - T_{am}) - \left(T_{am} \log \left(\frac{T_{am}}{T_{sun}} \right) \right) \right\} \right] \quad (6)$$

The exergy efficiency (η_{ex}) is expressed by:

$$\eta_{ex} = \left[\frac{\dot{Ex}_u}{\dot{Ex}_{in}} \right] \quad (7)$$

Results and discussion

The energy outcomes, exergy extraction, and evaporation rate of the drying systems mainly depend on the ambient conditions. Thus, the mathematical model simulation was computed based on the hourly ambient parameters data of Jimma zone, Ethiopia available on 16th, March, 2023, the maximum solar intensity, temperature, and wind speed were 1051 W/m², 28 °C, and 1.61 m/s, respectively.

Air temperature at outlet

The effect of recycled organic waste thermal insulation materials on the temperature was analyzed by applying equations. The hourly variation in the temperature of the drying system under recycled organic waste thermal insulation materials was illustrated in **Figures 3(a-b)**. The average temperature achieved from the analysis in the drying and heating chamber from 09.00 AM to 17:00 PM was 52.2 (40 °C), 48 (38.4 °C), 46.5 (37.9 °C), 44.1 (37.3 °C), and 41.1°C (36.3°C) for bagasse, sawdust, corn cop, paper, and wood, respectively. The lower temperature difference was found in the morning which increased with an increment of solar insolation, then it reached the pick-point in the afternoon at higher insolation, and after that, it declined concerning the amount of solar irradiance.

The average temperature in the dryer with bagasse insulation was higher than wood, paper, corn cop, and sawdust insulation by 17.5%, 12%, 8.3%, and 6%, respectively. This shows that integrating bagasse insulation with a double-air pass solar tunnel drying system could play a role in enhancing the temperature in the heating and drying chamber during the sunshine period than other recycled organic waste insulation materials.

The comparison results of recycled organic waste material (bagasse) with inorganic materials (glass fiber, mineral wool, and rock wool) are illustrated in **Figures 3(c-d)** for similar insulation thickness. The result rivals that the average temperature from 09.00 am to 17:00 was 52.2 (40 °C), 50.63 (39.4 °C), 50.2 (39.3 °C), and 39 (35.6 °C), for bagasse, rock wool, mineral wool, and glass fiber in descending order, respectively. This indicates that the average temperature in the drying system with bagasse insulation was found higher compared to rock wool, mineral wool, and glass fiber by 3.01%, 4%, and 25.41%, respectively. This occurrence was due to bagasse having a better combination of thermos-physical properties compared to rock wool, mineral wool, and glass fiber [18]. Therefore, integrating customized recycled organic waste thermal insulation materials with a solar drying system enhances the temperature.

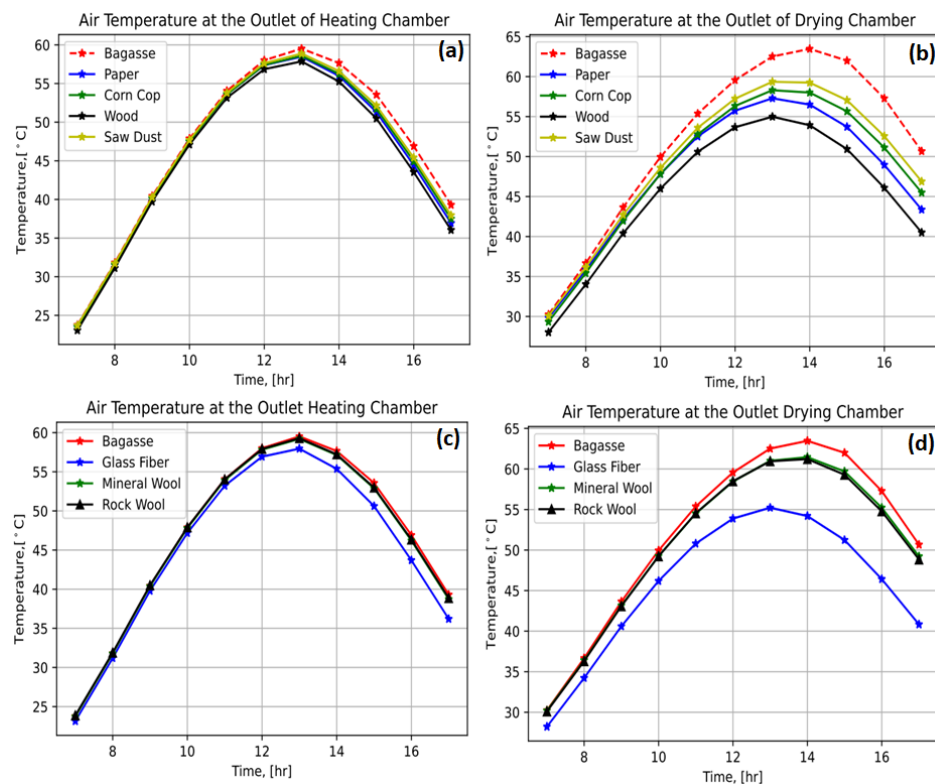


Figure 3: (a-b) Temperature in the heating and drying chamber for recycled organic waste, and (c-d) Inorganic (synthetic) thermal insulation materials.

Energy efficiency

The hourly variation of thermal efficiency in the drying system insulated with recycled organic waste thermal insulation material was displayed in **Figure 4(a)**, and the drying system insulated with inorganic thermal insulation materials was presented in **Figure 4(b)**. The result shows that the average thermal efficiency from 07:00 a.m. to 17:00 was 40.8%, 36.93%, 35.24%, 33.93%, and 30.24% for bagasse, sawdust, corn cop, paper, and wood, respectively, and for mineral wool, rock wool, and glass fiber was 39.1%, 38.76%, and 30.65%, respectively. The minimum thermal efficiency was observed at noon, where the solar insolation and the heat loss reached maximum. This phenomenon indicates that the change in thermal efficiency is due to the variation in heat loss caused by solar radiation variation with time. The result indicates that higher thermal efficiency was achieved in a drying system with bagasse than other recycled organic waste and inorganic thermal insulation materials. Because comparatively lower heat loss and higher temperature differences during the daytime were achieved in bagasse-insulated drying systems [19].

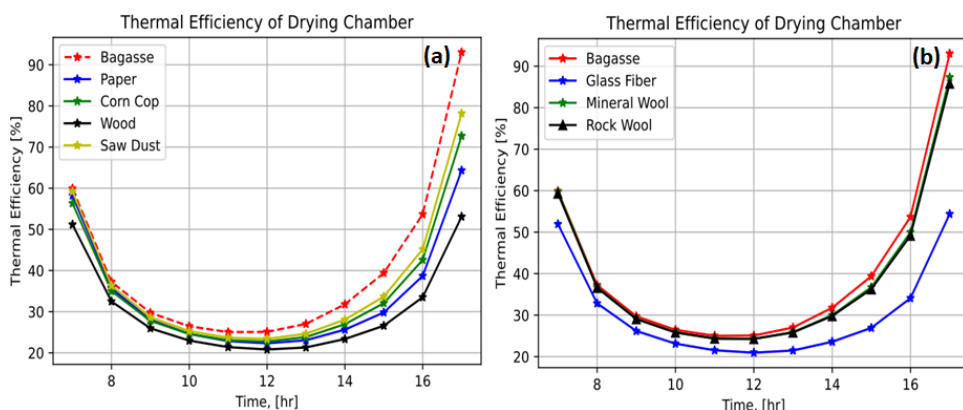


Figure 4: Thermal efficiency of the drying system with (a) recycled organic waste and (b) standard thermal insulation materials.

Exergy efficiency

The exergetic performance of the drying system integrated with recycled organic waste thermal insulation materials and for comparison with commonly used thermal insulation materials. **Figure 5(a)** and **Figure 5(b)** shows the hourly variation of the exergetic efficiency of the drying system under recycled organic waste thermal insulation material and inorganic thermal insulation materials. The average exergy efficiency from 07:00 a.m. and 17:00 was 45%, 36.76%, 33.71%, 31.35%, and 25.47% for bagasse, sawdust, corn cop, paper, and wood, respectively.

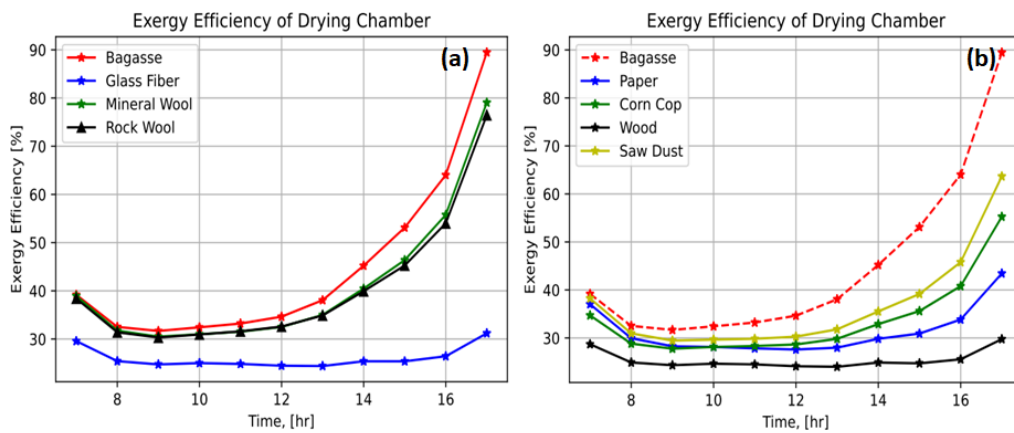


Figure 5: Exergetic efficiency of the drying system with (a) recycled organic waste and (b) standard thermal insulation materials.

The average exergy efficiency of mineral wool, rock wool, and glass fiber was 41.17%, 40.53%, and 26.08%, respectively. The useful work extraction efficiency fluctuation was considerably influenced by the input ambient condition variation during the drying period.

Comparatively, at a constant insulation thickness and emissivity of charcoal briquette, the exergetic efficiency of the dryer was higher with bagasse insulation than other recycled organic waste and inorganic thermal insulation materials. Thus, a double air pass solar tunnel drying system with bagasse insulation has a better useful work extraction capacity than other recycled organic waste standard insulation materials, because of their lower heat loss and higher temperature difference.

Energy and exergy efficiency on insulation thickness

Figures 6(a)-(b) shows the effect of insulation thickness on a double air pass solar tunnel drying system thermal efficiency and exergy efficiency investigated. The hourly average thermal efficiency was 38.5%, 40.8%, and 40.31%, and the hourly average exergy efficiency was 40.5%, 45%, and 43.88% for insulation thickness of 0.05, 0.25, and 0.5 m, respectively. The thermal and exergy efficiency enhanced until the thickness reached 0.25m due to the increment of temperature, then reduced as the thickness increased further because temperature also decreased. Thus, the maximum thermal and exergy efficiency was found when the thickness was 0.25 m.

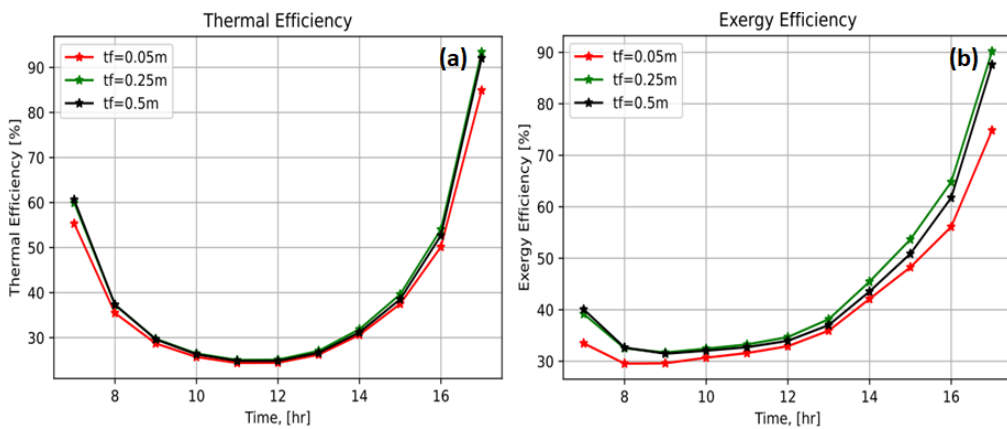


Figure 6: (a) Thermal efficiency and (b) exergy efficiency of drying system for different insulation thickness.

Conclusion

This study presents the numerical analysis of the effect of recycled organic waste thermal insulation materials and thickness on the energetic, exergetic, and evaporation rate performance of a double air pass solar tunnel drying system in terms of heat loss and environmental impact reduction for the drying process of biomass charcoal briquette. A comparative analysis of the recycled organic waste materials with commercially available thermal insulation materials and between different insulation thicknesses was investigated in terms of heat and exergy loss reduction performance and drying rate enhancement by developing mass and heat transfer models, and the solution was computed by establishing the Python code.

Comparatively, a higher temperature, thermal efficiency, and exergy efficiency were obtained in the drying system insulated with bagasse material than other recycled organic waste materials, and the most commonly used thermal insulation. Comparatively, a higher temperature, thermal efficiency, exergy efficiency, and moisture evaporation rate of the charcoal briquette were achieved at an optimum thermal insulation thickness of 0.25 m.

References

- [1] P.G. Kumar, K. Balaji, D. Sakthivadivel, V.S. Vigneswaran, M. Meikandan et al. Effect of using low-cost thermal insulation in a solar air heating system with a shot blasted V-corrugated absorber plate, *Thermal Science and Engineering Progress* 14 (2019) 100405. <https://doi.org/10.1016/j.tsep.2019.100403>
- [2] B.T.H. Huy, P. Nallagownden, R. Kannan, V.N. Dieu, Energetic optimization of solar water heating system with flat plate collector using search group algorithm, *J. Advanced Research in Fluid Mechanics and Thermal Sci.* 61 (2019) 306-322.
- [3] Q. Wu, B. Yan, Y. Gao, X. Meng, Wall adaptability of the phase-change material layer by numerical simulation, *Case Studies in Thermal Eng.* 41 (2023) 102622. <https://doi.org/10.1016/j.csite.2022.102622>
- [4] M.K. Sahu, R.K. Prasad, Exergy-based performance evaluation of solar air heater with arc shaped wire roughened absorber plate, *Renewable Energy* 96 (2016) 233–243. <https://doi.org/10.1016/j.renene.2016.04.083>
- [5] M. Hedayatizadeh, F. Sarhaddi, A. Safavinejad, F. Ranjbar, H. Chaji, Exergy loss-based efficiency optimization of a double-pass/glazed V corrugated plate solar air heater, *Energy* 94 (2016) 799–810. <https://doi.org/10.1016/j.energy.2015.11.046>

- [6] M. Castro, C. Román, M. Echegaray, G. Mazza, R. Rodriguez, Exergy Analyses of Onion Drying by Convection: Influence of Dryer Parameters on Performance, *Entropy* 20 (2018) 310. <https://doi.org/10.3390/e20050310>
- [7] H. Karami, M. Kaveh, I. Golpour, E. Khalife, R. Rusinek, B. Dobrzanski et al. Thermodynamic evaluation of the forced convective hybrid-solar dryer during drying process of rosemary (*Rosmarinus officinalis* L.) leaves, *Energies* 14 (2021) 5835. <https://doi.org/10.3390/en14185835>
- [8] A.K. Karthikeyan, R. Natarajan, Exergy analysis and mathematical modelling of orange peels drying in a mixed mode solar tunnel dryer and under the open sun: a study on performance enhancement, *Int. J. Exergy* 24 (2017) 235-253. <https://doi.org/10.1504/IJEX.2017.087695>
- [9] G. Deshmukh, P. Birwal, R. Datin, S. Patel, Thermal insulation materials: A tool for energy conservation, *J. Food Processing and Technology* 8 (2017) 670. <https://doi.org/10.4172/2157-7110.1000670>
- [10] G.K. Abdulsada, T.W. Mohammed-Salih, The impact of efficient insulation on thermal performance of building elements in hot arid region, *Renewable Energy and Environmental Sustainability* 7 (2021) 2. <https://doi.org/10.1051/rees/2021050>
- [11] M. Mastanaiah, K.R. Hemachandra, Effect of geometric and operating parameters on solar flat plate collector performance-A CFD approach, *Int. J. Research in Mechanical Engineering* 4 (2016) 6-14.
- [12] H. Beiki, E. Soukhtanlou, Determination of optimum insulation thickness for salinity gradient solar pond's bottom wall under different climate conditions, *S.N. Applied Science* 2 (2020) 1284. <https://doi.org/10.1007/s42452-020-3078-4>
- [13] T.H. Bao-Huy, P. Nallagownden, R. Kannan, V.N. Dieu, Energetic optimization of solar water heating system with flat plate collector using search group algorithm, *J. Advanced Research in Fluid Mechanics and Thermal Sci.* 61 (2019) 306-322.
- [14] M.M. Mohamed, Optimal thermal insulation thickness in isolated air-conditioned buildings and economic analysis. *J. Electronics Cooling and Thermal Control* 9 (2020) 23-45. <https://doi.org/10.4236/jectc.2020.92002>
- [15] N. Sooriyalakshmi, H.H. Jane, Thermal conductivity of insulation material: An overview, *J. Architecture and Civil Engineering* 6 (2021) 59-65. <https://doi.org/10.9734/bpi/tier/v6/2184A>
- [16] B.A. Alhabeeb, H.N. Mohammed, S.A. Alhabeeb, Thermal insulators based on waste materials. *IOP Conf. Series: Materials Science and Eng.* 1067 (2021) 012097. <https://doi.org/10.1088/1757-899X/1067/1/012097>
- [17] J.A. Duffie, W.A. Beckman, *Solar engineering of thermal processes*, John Wiley & Sons, 1991.
- [18] J.H. Watmuff, W.W.S. Charters, D. Proctor, Solar and wind induced external coefficients for solar collectors, *Cooperation Mediterraneeenne pour l'Energie Solaire, Revue Internationale d'Helio-technique* 2 (1977) 56.
- [19] A. Sotoodeh, A.S.A. Hamid, A. Ibrahim, K. Sopian, Experimental investigation on thermal efficiency of indirect forced convection solar tunnel dryer, *7th Int. Conference on Innovation in Science and Technology*. 23-25 October, 2020; Amsterdam, Netherlands.

Renewable energy in pavement engineering and its integration with sustainable materials: A review paper

Mohammad Ali KHASAWNEH^{1,a}, Danish AHMED^{1,b*}, Fawzyah ALKHAMMAS^{1,c},
Zainab ALMSHAR^{1,d}, Maryam HUSSAIN^{1,e}, Dalya ALSHALI^{1,f},
Maryam ALKHURAIM^{1,g}, Rana ALDAWOOD^{1,h}, Hidaia ALZAYER^{1,i},
Nayeemuddin MOHAMMED^{2,j}

¹Department of Civil Engineering, Prince Mohammad Bin Fahd University, Al Khobar, Kingdom of Saudi Arabia

^amkhasawneh@pmu.edu.sa, ^bdahmed@pmu.edu.sa, ^c202101603@pmu.edu.sa,
^d202001834@pmu.edu.sa, ^e202001160@pmu.edu.sa, ^f202101433@pmu.edu.sa,
^g202000692@pmu.edu.sa, ^h202101700@pmu.edu.sa, ⁱ202002635@pmu.edu.sa,
^jmnayeemuddin@pmu.edu.sa

Keywords: Renewable Energy, Pavement Engineering, Electromagnetic, Piezoelectric, Thermoelectric, Solar Panels

Abstract. Pavement engineering that incorporates renewable energy sources and uses sustainable materials has emerged as a promising path toward achieving an environmentally friendly and sustainable transportation infrastructure. An inclusive review of renewable energy applications in pavement engineering and its integration with sustainable materials is presented in this paper. The article examines various renewable energy technologies and their potential integration into pavement construction, maintenance, and operation. The findings of this review contribute to advancing sustainable practices in the transportation infrastructure sector and provide valuable insights for researchers, policymakers, and practitioners.

Introduction

Eco-friendly and sustainable transportation infrastructure can be achieved through the incorporation of sustainable materials and the use of renewable energy sources. In pavement engineering, renewable energy refers to the incorporation of energy generation technologies that utilize renewable sources of energy to power various aspects of pavement systems. By integrating renewable energy solutions, pavement engineering can contribute to sustainable and environmentally friendly transportation infrastructure. The applications of renewable energy in pavement engineering include Solar Photovoltaic (PV), Piezoelectric Energy Harvesting, thermoelectric energy harvesting, Kinetic Energy Harvesting and Geothermal Systems.

Whereas, sustainable materials refer to those that are environmentally friendly and have a reduced impact on natural resources throughout their life cycle. These materials are designed to minimize energy consumption, emissions, and waste generation during their production, use, and disposal. Sustainable materials used in pavement engineering include recycled asphalt, porous asphalt, warm mix asphalt etc. The use of sustainable materials in pavement engineering promotes resource conservation, reduces environmental impacts, and contributes to the development of more sustainable transportation infrastructure.

The combination of renewable energy in pavement engineering, along with the integration of sustainable materials, holds great importance in establishing infrastructure systems that are sustainable, resilient, cost-effective, and environmentally friendly. The objective of this study is to provide a detailed investigation of the current state of renewable energy implementation in pavement engineering, as well as its integration with sustainable materials based on existing

literature. The paper explores various renewable energy technologies and their potential for integration into pavement construction, maintenance, and operation processes.

Sustainable Materials in Pavement Engineering

Sustainable materials in pavement engineering refer to materials chosen and employed in the construction, maintenance, and rehabilitation of pavements, with the primary objective of minimizing environmental impact, preserving resources, and fostering long-term sustainability.

Yaro et al [1] provides a comprehensive exploration of the utilization of recycled waste materials and technologies in asphalt pavements, with a focus on environmental sustainability and low-carbon roads. The findings emphasize the significant environmental and economic benefits of utilizing recycled materials, including reduced reliance on virgin materials, energy savings, and lower carbon emissions. This study also illustrates that the incorporation of such materials improves the performance characteristics of asphalt pavements.

A study [2] was conducted to evaluate the performance of Asphalt Concrete using 60/70 pen asphalt and a modified binder with resin in hot mix asphalt for road pavement. The research explores the use of renewable resources as alternatives to petroleum-derived materials in bio asphalt production. Results revealed that all mixtures showed similar values for optimum bitumen content, but higher percentages of resin resulted in improved stability of the asphalt mixtures.

Praticò et al [3] presents a comprehensive life cycle assessment (LCA) of pavement technologies, specifically hot mix asphalt (HMA) and warm mix asphalt (WMA), with a focus on incorporating recycled materials such as reclaimed asphalt pavements, crumb rubber, and waste plastics. The findings demonstrate the benefits of utilizing WMA and recycled materials in reducing energy consumption and environmental effects by minimizing the use of virgin resources. It also offers cleaner production processes and significant environmental and technical benefits, including reduced energy consumption and greenhouse gas emissions, improved compaction, longer paving periods, and enhanced worker safety.

Renewable Energy Technologies in Pavement Engineering

In pavement engineering, the adoption of renewable energy technologies enhances sustainability and boosts the efficiency of transportation infrastructure by integrating sustainable energy systems into roads. By harnessing renewable energy, transportation infrastructure can become more sustainable and efficient, contributing to a greener and more effective transportation network.

Research [4] focuses on concentrated photovoltaic panels (CPPs) for pavement applications as a clean and renewable energy source in transportation. The study presents a comprehensive analysis of the structural optimization and performance testing of CPPs, demonstrating their feasibility, durability, and economic viability. Mechanical and electrical performance tests reveal the panel's strength, wear resistance, light concentration performance, and power generation capabilities. The CPP system showcases significant economic benefits, with a high return on investment and cost recovery period. Furthermore, it contributes to environmental sustainability by reducing carbon emissions.

The article by Zhou et al. [5] explores the feasibility and performance of a pavement-solar energy system through experimental analysis. The study aims to integrate solar energy collection technology into pavement systems to generate electricity and enhance environmental sustainability (Fig. 1). The experimental results demonstrate that the pavement-solar energy system effectively produces electricity from solar radiation, indicating its potential as a renewable energy source. The study emphasizes the importance of optimizing system design and orientation to improve energy harvesting.

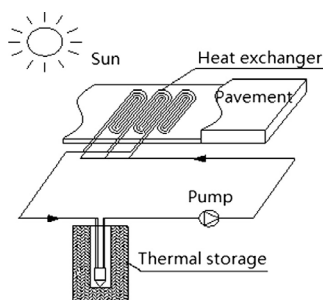


Figure 1 Harnessing solar energy through pavement infrastructure [5]

The study performed by Dunican [6] emphasizes the importance of diversifying solar power generation options in the construction sector to achieve a greener and more sustainable future. It argues that while rooftop solar solutions have become popular, alternative technologies such as transparent solar windows, solar shingles, and solar canopies offer additional opportunities to maximize renewable energy in buildings. Diversification provides benefits such as increased solar density, optimized space utilization, compliance with building codes, and design flexibility. By integrating solar technology into building materials, passive surfaces like windows can be utilized for energy production without compromising functionality.

Ma et al. [7] investigates the use of road pavements as solar energy generators in smart and sustainable cities, focusing on three pavement modules: pavement-integrated photovoltaic (PIPV), pavement-integrated solar thermal (PIST), and pavement-integrated photovoltaic thermal (PIPVT) modules (Fig. 2). PIPVT module achieves slightly higher electricity yield but lower heat yield compared to PIPV and PIST modules, with an average energy efficiency of 37.31%. All modules reduce the maximum asphalt average temperature, with PIPVT having the most significant effect, decreasing it by an average of 10.57°C. Additionally, they contribute to mitigating the urban heat island (UHI) effect, with PIPVT and PIST modules exhibiting the most and least influence, respectively.

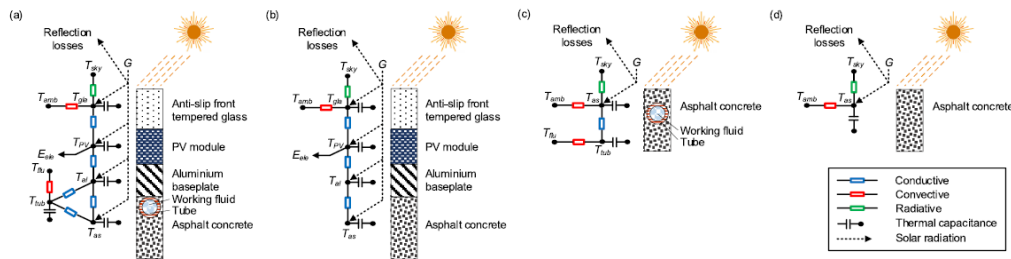


Figure 2 Thermal resistance networks of different solar energy harvesting pavements (a) PIPVT module; (b) PIPV module; (c) PIST module; (d) CP module [7]

Del Serrone et al. [8] explores the concept of utilizing photovoltaic (PV) road pavements to create low-carbon urban infrastructures. It emphasizes the importance of cool pavements in mitigating Urban Heat Islands (UHIs) and discusses the integration of PV panels into road surfaces to generate renewable energy. A case study in Rome exemplifies the potential of photovoltaic road infrastructures (Fig. 3), demonstrating their ability to generate electricity, maintain acceptable temperatures, and provide economic viability. Photovoltaic road pavements offer multiple benefits, including reduced energy consumption, enhanced microclimates, and reduced land use for solar installations.

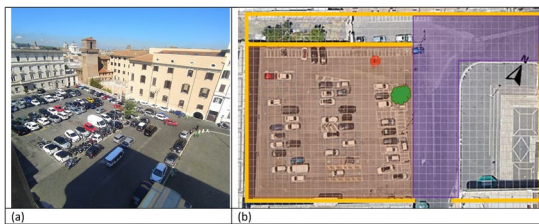


Figure 3 San Pietro in Vincola Square: (a) top view; (b) site map. [8]

Sumorek & Buczaj [9] performed the study to address the technological gap between automotive engineering and road infrastructure development by focusing on energy generation from road pavement. It evaluates the feasibility of capturing solar energy and converting it into usable electricity on the road surface, as well as harvesting mechanical vibrations energy from passing vehicles using piezoelectric transducers. The study confirms the significant potential of solar energy conversion and vibrations energy harvesting, with experimental results supporting the feasibility of converting mechanical vibrations energy into electrical energy (Fig. 4).

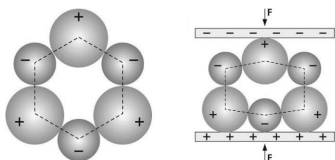


Figure 4 Mechanism of mechanical vibrations energy into electrical energy [9]

The article by Sun et al. [10] provides an in-depth exploration of green technologies for sustainable pavements, focusing on energy harvesting and permeable pavement systems. The article discussed the energy harvesting technologies including piezoelectric, solar, thermoelectric, and geothermal. Permeable pavement systems are highlighted for their ability to facilitate water infiltration, preventing urban flooding and reducing the urban heat island effect. Porous materials such as porous asphalt and concrete are examined, offering benefits like noise reduction and improved hydraulic conductivity.

Al-Qadami et al. [11] provide a systematic analysis of the existing literature on pavement geothermal energy harvesting technologies. Three main sectors are identified: piezoelectric transducer systems, thermoelectric generator systems (TEGs), and solar panel systems (Fig. 5). Piezoelectric transducer systems convert the mechanical stress from moving vehicles into electrical energy using embedded piezoelectric materials. Studies emphasize material selection, pavement design, and traffic characteristics' impact on energy generation, highlighting their potential in high-traffic areas. TEGs harness the temperature difference between the pavement surface and underlying layers to generate electricity. Research focuses on enhancing efficiency through material selection, module configuration, and optimization, indicating their integration into smart pavement systems. Solar panel systems effectively convert solar energy into electricity and can be embedded within or placed on pavement surfaces.

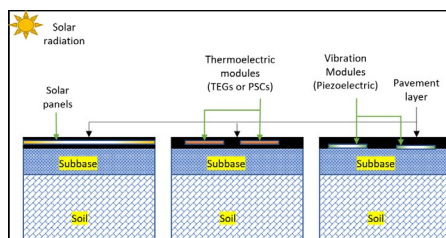


Figure 5 Pavement energy harvesting technologies [11]

Razeman et al. [12] investigated solar pavements as a means of efficiently harnessing solar energy, emphasizing sustainable conductive materials like stainless steel, copper, and aluminum. Numerical simulations are employed to optimize parameters such as pipe material, depth, arrangement, spacing, and flow rate. The results highlight serpentine copper pipe as the most efficient configuration, achieving a heat efficiency rate of 32.22% and an outlet temperature of 327.35K (54.21°C). The study underscores the benefits of solar pavement technology, reduced reliance on fossil fuels, emissions reduction, and reliable electricity generation.

Tahami et al. [13] proposed an innovative approach to harvest energy from asphalt pavements using thermoelectric technology. The findings indicate that the temperature difference in the pavement can produce sufficient electrical energy, especially in areas with intense sunlight exposure and high traffic density. The thermoelectric system demonstrated the ability to generate sustainable energy without compromising pavement performance. The authors discussed the potential applications of this technology in existing infrastructures for renewable energy generation and environmental sustainability. However, challenges such as cost-effectiveness, scaling up, and long-term durability need to be addressed for commercialization and implementation.

Gholikhani et al [14] highlights the potential of utilizing roadway pavements as a renewable energy resource through the electromagnetic speed bump energy harvester (ESE) prototype. This innovative approach aims to capture kinetic energy from passing vehicles while regulating vehicle speed. The ESE prototype absorbs the deflection caused by vehicles passing over a speed bump and converts it into rotational energy using a revolving shaft and embedded generator. Laboratory experiments demonstrate its capability to generate an average power output of up to 3.21 kW under realistic traffic loading conditions. Steel and aluminum are identified as optimal materials for the ESE's top plate due to their favorable properties.

De Fazio et al [15] explored the potential of energy harvesting from various sources on roadways, including mechanical load, solar radiation, heat, and air movement, for the development of self-sustainable smart roads. It examines different technologies such as electromagnetism, piezoelectric and triboelectric harvesters, photovoltaic modules, thermoelectric solutions, and wind turbines optimized for low-speed winds generated by vehicles. The findings emphasize the environmental benefits and potential applications of energy harvesting in the transportation sector, such as autonomous driving, real-time road condition communication, self-powered lighting systems, and security sensors.

The investigation by Saleh et al. [16] focuses on the Hydronic Asphalt Pavement (HAP) system. The HAP system utilizes a network of pipes embedded in the asphalt pavement to remove or reject heat from the pavement using a circulating fluid. The study evaluates the efficiency of the HAP system in reducing pavement surface temperature and enhancing sustainability. The results show that the HAP system successfully lowered the temperature at a depth of 2.5 cm below the surface by approximately 10°C. However, the surface temperature reduction was not significant.

Johnsson [17] study focuses on making the Coastal Highway Route E39 carbon neutral and incorporating energy output facilities. The study explores the use of renewable thermal energy to prevent road surfaces from becoming slippery, considering the warming of sidewalk surfaces and the use of solar energy to melt snow and ice. The study suggests that the proposed hydronic pavement system, when combined with BTES, can enhance winter road maintenance and safety, particularly in regions with milder winters like Scandinavia.

Charlesworth et al. [18] explores the combination of ground source heat (GSH) and pervious paving systems (PPS) to create a sustainable drainage and renewable energy solution. GSH, obtained from the ground, is a renewable energy source that can efficiently heat and cool buildings. Pervious paving systems, such as block pavers, porous asphalt, concrete, and resin, are capable of

attenuating storm surges, reducing water quantity, and improving water quality. The integration of GSH collectors with PPS allows for harnessing temperature differences within the ground.

The review paper [19] provides an overview of energy harvesting from roadways and its potential in combating the urban heat island effect. It explores various technologies, including electromagnetic, piezoelectric, thermoelectric, and solar panels, highlighting piezoelectric and thermoelectric systems as promising options. The study emphasizes the importance of hybrid systems that combine multiple energy sources for consistent power supply. Energy harvesting from roadways can reduce greenhouse gas emissions, power roadside applications, and provide electricity to roadside houses, presenting significant opportunities for sustainable energy generation. Table 1 provides a summary of literature references related to the application of renewable energy in pavement engineering.

Table 1 Application of Renewable Energy in Pavement Engineering

S. No	Reference from Literature	Application of Renewable Energy in pavement Engineering	Type of Study
1	Hu et al. [4]	Concentrated (converge sunlight) photovoltaic solar Pavement, (Concentrated photovoltaic panel (CPP) structure for pavement)	Laboratory model test and finite element numerical simulation
2	Zhou et al. [5]	Pavement-solar energy system	Experimental study
3	Ma et al. [7]	Solar energy harvesting pavements	Mathematical modeling and simulation conducted for pavement-integrated photovoltaic (PIPV) module, pavement integrated solar thermal (PIST) module, and pavement-integrated photovoltaic thermal (PIPVT) module.
4	Del Serrone et al. [8]	Utilizing photovoltaic (PV) road pavements is analyzed from the thermal and economic viewpoints	A microclimate simulation of San Pietro in Vincula Square in Rome is conducted using ENVI-Met software.
5	Sumorek & Buczaj [9]	Solar energy and vibrations energy	A combination of theoretical analysis and experimental testing
6	Sun et al. [10]	Energy harvesting technologies (Piezoelectric, solar, thermoelectric, and geothermal technologies) and permeable pavement systems	Literature review
7	Al-Qadami et al. [11]	Harvesting geothermal energy from roadway pavement (piezoelectric transducer systems, thermoelectric generator systems, and solar panel systems)	A systematic review and bibliometric analysis were conducted
8	Randriantsoa et al. [19]	Hybrid energy harvesting systems (combining piezoelectricity and thermoelectricity for pavement applications)	Bibliographic research
9	Razeman et al. [12]	Thermal energy harvesting road pavement	Numerical Simulation using ANSYS Workbench 19.2 (Fluent) and Solidworks 2020 for conducting optimization study.
10	Tahami et al. [13]	Thermoelectric generator system that utilizes the thermal gradients between the pavement surface and the soil below the pavement and converts it to electricity	Prototype testing and finite element analyses were conducted
11	Gholikhani et al. [14]	Electromagnetic speed bump energy harvester (ESE)	laboratory prototype tests and finite element analysis was conducted using software ABAQUS.
12	De Fazio et al. [11]	The study explores different technologies, including electromagnetism, piezoelectric and triboelectric harvesters, photovoltaic modules, thermoelectric solutions, and wind turbines	Literature review

Conclusion

This review paper has explored the significance of renewable energy in pavement engineering and its incorporation with sustainable materials. The utilization of renewable energy sources in pavement engineering has the potential to bring about substantial environmental and economic

benefits. By integrating sustainable materials into the design, construction, and maintenance of pavements, the sustainability of the infrastructure can further enhance.

The adoption of renewable energy technologies such as solar, Piezoelectric Energy Harvesting, thermoelectric energy harvesting, Kinetic Energy Harvesting and Geothermal Systems can significantly decrease greenhouse gas emissions associated with energy consumption in pavement construction and operation. This not only helps combat climate change but also reduces reliance on fossil fuels and promotes energy independence.

Moreover, the addition of sustainable materials in pavement engineering has been discussed as a complementary approach to renewable energy utilization. Sustainable materials, including recycled aggregates, reclaimed asphalt pavement, and bio-based binders, offer opportunities to reduce the environmental impact of pavement construction by saving natural resources and reducing waste generation. These materials can also contribute to the circular economy by promoting recycling materials within the pavement engineering.

In conclusion, the integration of renewable energy in pavement engineering, coupled with the use of sustainable materials, holds great promise for achieving a more sustainable and resilient transportation infrastructure. This combination can contribute to a more environmentally friendly and cost-effective pavements.

References

- [1] N. S. A. Yaro et al., "A Comprehensive Overview of the Utilization of Recycled Waste Materials and Technologies in Asphalt Pavements: Towards Environmental and Sustainable Low-Carbon Roads," *Processes*, vol. 11, no. 7, p. 2095, Jul. 2023.
<https://doi.org/10.3390/pr11072095>
- [2] Djumari, M. A. D. Yami, M. F. Nasution, and A. Setyawan, "Design and Properties of Renewable Bioasphalt for Flexible Pavement," *Procedia Eng.*, vol. 171, pp. 1413–1420, 2017.
<https://doi.org/10.1016/j.proeng.2017.01.458>
- [3] F. G. Praticò, M. Giunta, M. Mistretta, and T. M. Gulotta, "Energy and Environmental Life Cycle Assessment of Sustainable Pavement Materials and Technologies for Urban Roads," *Sustainability*, vol. 12, no. 2, p. 704, Jan. 2020. <https://doi.org/10.3390/su12020704>
- [4] H. Hu, X. Zha, C. Niu, Z. Wang, and R. Lv, "Structural optimization and performance testing of concentrated photovoltaic panels for pavement," *Appl. Energy*, vol. 356, p. 122362, Feb. 2024. <https://doi.org/10.1016/j.apenergy.2023.122362>
- [5] Z. Zhou, X. Wang, X. Zhang, G. Chen, J. Zuo, and S. Pullen, "Effectiveness of pavement-solar energy system – An experimental study," *Appl. Energy*, vol. 138, pp. 1–10, Jan. 2015. <https://doi.org/10.1016/j.apenergy.2014.10.045>
- [6] G. Dunican, "A diversified approach to renewable energy in the construction sector," *For Construction Pros*, Aug. 11, 2023. <https://www.forconstructionpros.com/construction-technology/article/22868964/ubiquitous-energy-a-diversified-approach-to-renewable-energy-in-the-construction-sector>
- [7] T. Ma, S. Li, W. Gu, S. Weng, J. Peng, and G. Xiao, "Solar energy harvesting pavements on the road: comparative study and performance assessment," *Sustain. Cities Soc.*, vol. 81, p. 103868, Jun. 2022. <https://doi.org/10.1016/j.scs.2022.103868>
- [8] G. Del Serrone, P. Peluso, and L. Moretti, "Photovoltaic road pavements as a strategy for low-carbon urban infrastructures," *Heliyon*, vol. 9, no. 9, p. e19977, Sep. 2023. <https://doi.org/10.1016/j.heliyon.2023.e19977>

- [9] A. Sumorek and M. Buczaj, "New technologies using renewable energy in road construction," ECONTECHMOD: an international quarterly journal on economics of technology and modelling processes, Jan. 2017.
- [10] W. Sun et al., "The State of the Art: Application of Green Technology in Sustainable Pavement," *Adv. Mater. Sci. Eng.*, vol. 2018, pp. 1–19, Jun. 2018.
<https://doi.org/10.1155/2018/9760464>
- [11] E. H. H. Al-Qadami, Z. Mustaffa, and M. E. Al-Atroush, "Evaluation of the Pavement Geothermal Energy Harvesting Technologies towards Sustainability and Renewable Energy," *Energies*, vol. 15, no. 3, p. 1201, Feb. 2022. <https://doi.org/10.3390/en15031201>
- [12] N. A. Razeman et al., "Optimization of Thermal Energy Harvesting Road Pavement using Sustainable Conductive Material in Malaysia by Numerical Simulation," *Engineering*, preprint, Jul. 2023. doi: 10.20944/preprints202307.0151.v1
- [13] S. A. Tahami, M. Gholikhani, R. Nasouri, S. Dessouky, and A. T. Papagiannakis, "Developing a new thermoelectric approach for energy harvesting from asphalt pavements," *Appl. Energy*, vol. 238, pp. 786–795, Mar. 2019. <https://doi.org/10.1016/j.apenergy.2019.01.152>
- [14] M. Gholikhani, R. Nasouri, S. A. Tahami, S. Legette, S. Dessouky, and A. Montoya, "Harvesting kinetic energy from roadway pavement through an electromagnetic speed bump," *Appl. Energy*, vol. 250, pp. 503–511, Sep. 2019. <https://doi.org/10.1016/j.apenergy.2019.05.060>
- [15] R. De Fazio, M. De Giorgi, D. Cafagna, C. Del-Valle-Soto, and P. Visconti, "Energy Harvesting Technologies and Devices from Vehicular Transit and Natural Sources on Roads for a Sustainable Transport: State-of-the-Art Analysis and Commercial Solutions," *Energies*, vol. 16, no. 7, p. 3016, Mar. 2023. <https://doi.org/10.3390/en16073016>
- [16] N. F. Saleh, A. A. Zalghout, S. A. Sari Ad Din, G. R. Chehab, and G. A. Saad, "Design, construction, and evaluation of energy-harvesting asphalt pavement systems," *Road Mater. Pavement Des.*, vol. 21, no. 6, pp. 1647–1674, Aug. 2020.
<https://doi.org/10.1080/14680629.2018.1564352>
- [17] J. Johnsson, "Winter Road Maintenance Using Renewable Thermal Energy" - ProQuest. In ProQuest. Chalmers University of Technology. Department of Civil and Environmental Engineering, (2017).
- [18] S. M. Charlesworth, A. S. Faraj-Llyod, and S. J. Coupe, "Renewable energy combined with sustainable drainage: Ground source heat and pervious paving," *Renew. Sustain. Energy Rev.*, vol. 68, pp. 912–919, Feb. 2017. <https://doi.org/10.1016/j.rser.2016.02.019>
- [19] A. N. A. Randriantsoa, D. A. H. Fakra, L. Rakotondrajaona, and W. J. Van Der Merwe Steyn, "Recent Advances in Hybrid Energy Harvesting Technologies Using Roadway Pavements: A Review of the Technical Possibility of Using Piezo-thermoelectrical Combinations," *Int. J. Pavement Res. Technol.*, vol. 16, no. 4, pp. 796–821, Jul. 2023.
<https://doi.org/10.1007/s42947-022-00164-z>

Keyword Index

2nd Life Application	223	Coordination	179
Absorber Plate	254	Copper Indium Diselenide	1
Adaptive Cooling	73	Critical Thinking	238
Additive Manufacturing	164	Current Controllers	246
Aerodynamics	44	Current Output	96
AI Tool	238	Cyclic Voltammetry	1
ANFIS	188	Date Fruit Type Classification	205
Apparent Solar Time	254	Day Ahead Market	179
Array Yield	277	Daylight Time	254
Artificial Intelligence (AI)	96, 104, 148, 188, 230, 269	DC Bus Regulation	246
Augmentation	21	Deep Convolution Neural Network	13
Batteries	51, 299	Deep Learning	156, 230
Battery Charging	324	Demand Growth	337
Battery Degradation	197	Desalination	104, 172, 179
Battery Management System (BMS)	332	Design and Development	197
Bidding Optimization	214	Distillate	104
Bidding	179	Dust Accumulation	316
Capacity Factor	277	EDM	124
Capacity Fade	197	Electric Vehicle Charging	299
Carbon Emissions	307	Electrical Efficiency	290
Centralized Solar PV System	345	Electricity Market	179
Cleaning Methods	316	Electricity Reforms	337
Climate Change	360	Electrode Wear Rate	124
Climate	60	Electrodeposition	1
CNN	261	Electrolyzer	214
CO ₂ Emission	360	Electromagnetic	377
CO ₂ Emissions Reduction	345	Energy and Exergy	368
Complexing Agents	1	Energy Consumption	140
Composite	31	Energy Dispersive X-Ray Spectroscopy	1
Construction Industry	66	Energy Generation	324
Construction	31	Energy Performance Index	277
Convolutional Neural Network	205	Energy Storage Systems (ESS)	223
		Energy, Artificial Neural Network	156
		Environment	60
		Environmental Impact	172

EV 51		KSA 2030 Vision	277
Exergy Efficiency	290	KSA	337
Experimental Investigation	316		
		Levelized Cost of Hydrogen (LCOH)	36
Failure Analysis	197	Li-ion Battery	223
Final Yield	277	Linear Generator	355
Finite Element Method	164	LSTM	88
Flat Plate Collector	21, 254		
Flexibility	179	Machine Learning	269
Fossil Fuels	360	Martian Architecture	238
Full Factorial	124	Mass Flow	254
Future	60	Maximizing Profits	179
		Maximum Power Point Tracking (MPPT)	332
Generation	179	Mechanisms	324
Genetic Algorithm	96	Minimum Chip Thickness	132
Glazed	254		
Global Solar Radiation	88	Nano-Powder Mixed Electro-Discharge Machining	124
Government Facilities	345	Natural Binder	31
Green Buildings	66		
Green Hydrogen	36	Object Detection	230
Grid Integration	246	Optimization	179
		Orchid Seeding	261
Headers	254		
Healthcare	140	Pavement Engineering	377
Heat Transfer Rate	254	Performance Ratio	277
HESCO	345	Perturb and Observe (P&O)	332
Hybrid Nanofluids	21	Phase Locked Loop Point Absorber	246
Hydrogen Production	214	Photocatalytic	104
Hydrogen	36	Photovoltaic (PV)	285, 307
		Photovoltaic Energy	36
IEEE Smart Village (ISV)	332	Photovoltaic Solar Panels	13
Image Classification	13	Photovoltaic Systems	73
Impacts of Renewable Energy on Power Systems	112	Photovoltaic-Thermal Applications	73
Internet of Things (IoT)	148	Photovoltaic-Thermal	290
IoMT	140	Piezoelectric	324
IoT	140, 261	Piezoelectric	377
		Policies	51

Power Generation	355	Solar Energy	21, 73, 188, 230, 285, 299
Power Harvesting	324	Solar Irradiation	254
Power Systems Stability	112	Solar Panels	377
Precision Farming	269	Solar Still	104
Prediction Models	156	Solar Tunnel Dryer	368
Pretrained Network	205	Solar	307
Production	179	Specific Heat	254
PV Panel Thermal Inspection	230	SqueezeNet	205
PV Systems	188, 316	State of Health (SOH)	223
PV	179	Statistical	156
Pvsyst	345	Strategy	179
		Surface Roughness	132
Raisers	254		
Random Variables	82	Sustainability	60, 66, 214, 360
Recent Trends	360	Sustainable Agriculture	269
Recycled Organic Waste	368	Sustainable Construction	172
Recycling	51	Sustainable Material	31
Regression	156	Sustainable Micro-Milling	132
Regulations	51	System Efficiency	277
Reject Brine	172		
Reliability Analysis	82	Temperature Control	285
Renewable Energy	13, 36, 44, 60, 66, 82, 112, 179, 299, 337, 355, 360	Temperature Regulation	73
Renewable	307	Temporal Convolutional Network (TCN)	88
Resistive Loading	246	Test Matrix Design	197
Resource Management	148	Testing and Characterization	197
Resource Utilization	172	Thermal Conductivity	254
Retired Batteries	223	Thermal Efficiency	21, 290
Revenue	179	Thermal Insulation Thickness	368
RHINO/Grasshopper	238	Thermoelectric	377
RO	179	Thin-Film Solar Cells	1
		Transfer Learning	205
Scanning Electron Microscopy	1		
Size Effect	132	Unglazed	254
Sliding Mode Control	246		
Smart Agriculture	269	Vibration Analysis	164
Smart Health	140	Vibration	324
Solar Energy	118		

Water and Electricity Management	148
Water Power Nexus	179
Wave Energy	36, 96, 246, 355
Wind Speed	96
Wind Turbine	44, 82, 96, 307
Windmill	96
X-Ray Diffraction	1
YOLOv7	230

PRINCIPLES of SOLAR ENGINEERING

THIRD EDITION

D. Yogi Goswami



CRC Press
Taylor & Francis Group

THIRD EDITION

PRINCIPLES OF

SOLAR

ENGINEERING

THIRD EDITION

PRINCIPLES OF SOLAR ENGINEERING

D. Yogi Goswami



CRC Press
Taylor & Francis Group
Boca Raton London New York

CRC Press is an imprint of the
Taylor & Francis Group, an **informa** business

CRC Press
Taylor & Francis Group
6000 Broken Sound Parkway NW, Suite 300
Boca Raton, FL 33487-2742

© 2015 by Taylor & Francis Group, LLC
CRC Press is an imprint of Taylor & Francis Group, an Informa business

No claim to original U.S. Government works
Version Date: 20141017

International Standard Book Number-13: 978-1-4665-6379-7 (eBook - PDF)

This book contains information obtained from authentic and highly regarded sources. Reasonable efforts have been made to publish reliable data and information, but the author and publisher cannot assume responsibility for the validity of all materials or the consequences of their use. The authors and publishers have attempted to trace the copyright holders of all material reproduced in this publication and apologize to copyright holders if permission to publish in this form has not been obtained. If any copyright material has not been acknowledged please write and let us know so we may rectify in any future reprint.

Except as permitted under U.S. Copyright Law, no part of this book may be reprinted, reproduced, transmitted, or utilized in any form by any electronic, mechanical, or other means, now known or hereafter invented, including photocopying, microfilming, and recording, or in any information storage or retrieval system, without written permission from the publishers.

For permission to photocopy or use material electronically from this work, please access www.copyright.com (<http://www.copyright.com/>) or contact the Copyright Clearance Center, Inc. (CCC), 222 Rosewood Drive, Danvers, MA 01923, 978-750-8400. CCC is a not-for-profit organization that provides licenses and registration for a variety of users. For organizations that have been granted a photocopy license by the CCC, a separate system of payment has been arranged.

Trademark Notice: Product or corporate names may be trademarks or registered trademarks, and are used only for identification and explanation without intent to infringe.

Visit the Taylor & Francis Web site at
<http://www.taylorandfrancis.com>

and the CRC Press Web site at
<http://www.crcpress.com>

Contents

Preface.....	xiii
Author.....	xvii
1. Introduction to Solar Energy Conversion.....	1
1.1 Global Energy Needs and Resources.....	2
1.1.1 Present Status and Potential of RE	3
1.1.2 Wind Power	4
1.1.3 Biomass.....	5
1.1.4 Ocean Energy Conversion	8
1.2 Solar Energy.....	8
1.2.1 Thermal Conversion	11
1.2.2 Photovoltaic Conversion	12
1.2.3 Limitations of Solar Energy.....	13
1.3 Energy Storage.....	14
1.4 Economics of Solar Systems.....	17
1.4.1 Present Worth.....	18
1.4.2 Series of Payments	18
1.4.3 Levelized Cost of Energy.....	19
1.4.4 Internal Rate of Return	19
1.5 Summary of RE Resources	24
1.6 Forecast of Future Energy Mix.....	25
References	27
2. Fundamentals of Solar Radiation	29
2.1 The Physics of the Sun and Its Energy Transport	29
2.2 Thermal Radiation Fundamentals.....	30
2.2.1 Black-Body Radiation	31
2.2.2 Radiation Function Tables	32
2.2.3 Intensity of Radiation and Shape Factor	35
2.2.4 Transmission of Radiation through a Medium	38
2.3 Sun–Earth Geometric Relationship.....	39
2.3.1 Solar Time and Angles.....	42
2.3.2 Sun-Path Diagram.....	55
2.3.3 Shadow-Angle Protractor	57
2.4 Solar Radiation	61
2.4.1 Extraterrestrial Solar Radiation	61
2.5 Estimation of Terrestrial Solar Radiation	64
2.5.1 Atmospheric Extinction of Solar Radiation	65
2.5.2 Clear-Sky Radiation Model	66

2.5.3	Solar Radiation on a Tilted Surface	68
2.5.4	Monthly Solar Radiation Estimation Models	76
2.6	Models Based on Long-Term Measured Horizontal Solar Radiation	80
2.6.1	Monthly Solar Radiation on Tilted Surfaces.....	80
2.6.2	Circumsolar or Anisotropic Diffuse Solar Radiation.....	84
2.6.3	Hourly and Daily Solar Radiation on Tilted Surfaces	85
2.6.4	Spectral Models.....	99
2.7	Measurement of Solar Radiation	99
2.7.1	Instruments for Measuring Solar Radiation and Sunshine.....	100
2.7.2	Detectors for Solar Radiation Instrumentation.....	104
2.7.3	Measurement of Sunshine Duration.....	105
2.7.4	Measurement of Spectral Solar Radiation.....	106
2.7.5	Wide Band Spectral Measurements	106
2.7.6	Solar Radiation Data.....	107
2.8	Solar Radiation Mapping Using Satellite Data	109
2.8.1	Estimation of Solar Resource from Satellite Data	110
	References	115
3.	Solar Thermal Collectors	119
3.1	Radiative Properties and Characteristics of Materials	119
3.1.1	Selective Surfaces.....	123
3.1.2	Reflecting Surfaces.....	127
3.1.3	Transparent Materials	127
3.2	Flat-Plate Collectors	129
3.2.1	Liquid-Type Collectors	130
3.2.2	Air-Type Collectors.....	130
3.2.3	Glazings.....	131
3.2.3.1	Absorbers.....	133
3.2.4	Energy Balance for a Flat-Plate Collector	134
3.2.4.1	Collector Heat-Loss Conductance	135
3.2.5	Thermal Analysis of Flat-Plate Collector–Absorber Plate.....	139
3.2.6	Collector Efficiency Factor	143
3.2.7	Collector Heat-Removal Factor	144
3.2.8	Transient Effects.....	148
3.2.9	Air-Cooled Flat-Plate Collector Thermal Analysis	151
3.2.9.1	Air-Collector Efficiency Factor	152
3.2.9.2	Air-Collector Heat-Removal Factor	152
3.3	Tubular Solar Energy Collectors.....	154
3.3.1	Evacuated-Tube Collectors.....	155
3.3.2	Thermal Analysis of a Tubular Collector	157

3.4	Experimental Testing of Collectors	158
3.4.1	Testing Standards for Solar Thermal Collectors	161
3.4.1.1	Time Constant.....	162
3.4.1.2	Thermal Performance	162
3.4.1.3	Incidence Angle Modifier	162
3.5	Concentrating Solar Collectors	162
3.5.1	Thermodynamic Limits to Concentration.....	164
3.5.2	Optical Limits to Concentrations	168
3.5.3	Acceptance of Diffuse Radiation.....	168
3.5.4	Ray Tracing Diagrams.....	169
3.5.5	Concentrator Types.....	172
3.5.6	Fixed Concentrators.....	173
3.6	Parabolic Trough Concentrator	174
3.6.1	Optical Analysis of PTC.....	174
3.6.2	Thermal Losses from PTC.....	178
3.6.3	Thermal Performance of PTC Collector	181
3.7	Compound-Curvature Solar Concentrators.....	182
3.7.1	Paraboloidal Concentrators	182
3.7.2	Spherical Concentrators	186
3.7.3	Compound Parabolic Concentrator.....	187
3.7.4	Optical Analysis of CPC Collector	188
3.7.5	Thermal Performance of the CPC Collector	192
3.8	Central Receiver Collector	193
3.9	Fresnel Reflectors and Lenses	193
3.10	Solar Concentrator Summary.....	195
	References	202
	Suggested Reading	204
4.	Thermal Energy Storage and Transport	205
4.1	Thermal Energy Storage	205
4.2	Types of TES.....	206
4.2.1	Sensible Heat Storage	206
4.2.2	Latent Heat Storage.....	207
4.2.3	Thermochemical Energy Storage	211
4.3	Design of Storage System.....	213
4.3.1	Selection of Storage Material.....	213
4.3.1.1	Solar Collection System.....	213
4.3.1.2	Application.....	213
4.3.1.3	Additional Considerations.....	214
4.3.2	Design of Containment.....	214
4.3.3	Heat-Exchanger Design.....	216
4.3.3.1	Packed Bed Storage	216
4.3.3.2	Pressure Drop in a Packed Bed	223

4.3.3.3	Flow across Tube Banks	225
4.3.3.4	Performance of Packed Bed TES Systems.....	226
4.4	Energy Transport Subsystems	229
4.4.1	Piping Systems	229
4.4.2	Pressure Drop.....	230
4.4.3	Heat Loss.....	233
4.4.4	Heat Exchangers	235
	References	252
5.	Solar Heating Systems.....	255
5.1	Calculations of Heating and Hot-Water Loads in Buildings.....	255
5.1.1	Calculation of Heat Loss.....	257
5.1.2	Internal Heat Sources in Buildings	260
5.1.3	Degree-Day Method.....	260
5.1.4	Service Hot-Water Load Calculation.....	264
5.2	Solar Water-Heating Systems	266
5.2.1	Natural Circulation Systems	266
5.2.2	Forced-Circulation Systems.....	269
5.3	Liquid-Based Solar Heating Systems for Buildings	271
5.3.1	Physical Configurations of Active Solar Heating Systems	272
5.3.2	Solar Collector Orientation.....	273
5.3.3	Fluid Flow Rates.....	273
5.3.4	Thermal Storage	274
5.3.5	Other Mechanical Components.....	276
5.3.6	Controls in Liquid Systems	277
5.3.7	Load Devices in Liquid Solar Heating Systems	277
5.4	Solar Air-Heating Systems.....	280
5.4.1	Heating System Physical Configuration.....	281
5.4.2	Collector Designs.....	283
5.4.3	Fluid Flow Rates.....	285
5.4.4	Other Mechanical Components.....	285
5.4.5	Unglazed Transpired Wall System for Air Preheating ...	286
5.5	Methods of Modeling and Design of Solar Heating Systems	288
5.5.1	Design of a Liquid-Based Solar Heating System by <i>f</i> -Chart.....	288
5.6	Long-Term Performance of Solar Heating Systems.....	302
5.6.1	Critical Solar Intensity Ratio X	302
5.6.2	Utilizability Method	303
5.6.3	Example Calculation	305
5.6.4	Collection Period (Δt_c)	307
5.6.5	Long-Term Performance of Collector Systems with Storage	308
5.7	TRNSYS Computer Simulation Program	311

5.8	Solar Industrial Process Heat	312
5.9	Examples of SIPH Systems	318
5.9.1	SIPH for Textile Industries	318
5.9.2	SIPH System for Milk Processing	322
	References	326
6.	Solar Cooling and Dehumidification	329
6.1	Solar Space Cooling and Refrigeration	329
6.1.1	Cooling Requirements for Buildings	331
6.1.2	Vapor-Compression Cycle	336
6.1.3	Absorption Air Conditioning	339
6.1.4	Mass Balance Equations.....	347
6.1.5	Ammonia–Water Refrigeration System.....	349
6.2	Solar Desiccant Dehumidification	355
6.2.1	Solid Desiccant Cooling System	356
6.2.2	Liquid Desiccant Cooling System.....	357
6.3	Summary	361
	References	365
7.	Passive Solar Heating, Cooling, and Daylighting	367
7.1	Introduction	367
7.1.1	Current Applications and Costs	367
7.2	Passive Space Heating Systems.....	368
7.2.1	Types of Passive Heating Systems.....	368
7.2.2	Fundamental Concepts for Passive Heating Design	371
7.2.3	Generalized Passive Design Methods	372
7.2.4	First Level: Rule of Thumb	373
7.2.4.1	Load.....	373
7.2.4.2	Solar Savings Fraction	373
7.2.4.3	Load Collector Ratio	373
7.2.4.4	Storage.....	374
7.2.5	Second Level: LCR Method	375
7.2.6	Third Level: SLR Method	376
7.3	Passive Space Cooling Systems	379
7.3.1	Controlling the Solar Input	379
7.3.2	Movement of Air	379
7.3.3	Evaporative Cooling	382
7.3.4	Nocturnal and Radiative Cooling Systems.....	382
7.3.5	Earth Contact Cooling (or Heating)	384
7.3.5.1	Heat Transfer Analysis	384
7.3.5.2	Soil Temperatures and Properties	387
7.3.5.3	Generalized Results from Experiments	387
7.4	Daylighting Design Fundamentals	388
7.4.1	Lighting Terms and Units.....	389

7.4.2	Economics of Daylighting.....	389
7.4.3	Daylighting Design Fundamentals	391
7.4.3.1	Architectural Features.....	391
7.4.3.2	Daylighting Geometry.....	391
7.4.4	Design Methods	393
7.4.5	Lumen Method of Sidelighting (Vertical Windows).....	393
7.4.6	Lumen Method of Skylighting.....	398
7.5	Further Information.....	405
7.5.1	General Background Information	405
7.5.2	Technical Publication Information	405
	References	408
	Suggested Readings.....	409
8.	Solar Thermal Power	411
8.1	Historical Perspective.....	411
8.2	Thermodynamic Power Cycles	414
8.2.1	Rankine Cycle.....	415
8.2.2	Supercritical Rankine Cycle	424
8.2.3	Components of a Rankine Power Plant	424
8.2.4	Choice of Working Fluid.....	425
8.3	Design of Parabolic Trough-Based Power Plants.....	428
8.3.1	Sizing and Layout of the Solar Field	428
8.3.1.1	I Field Layout	432
8.3.1.2	H Field Layout	433
8.3.2	Pressure Drop in the Solar Field.....	435
8.3.3	Expansion Tank.....	437
8.3.4	Power Block.....	438
8.3.5	Condenser	438
8.3.5.1	Air-Cooled Condensers.....	440
8.4	Examples of PTC Solar Thermal Power Plants	442
8.5	Parabolic Dish Systems	449
8.6	Stirling Cycle.....	449
8.6.1	Thermodynamics of Stirling Cycle	450
8.6.2	Piston/Displacer Drives.....	456
8.6.3	Kinematic or Free-Piston Engines	456
8.6.4	Examples of Solar Stirling Power Systems	457
8.7	Central Receiver Tower Systems	460
8.7.1	Heliostats.....	460
8.7.2	Receiver	464
8.7.2.1	External Receiver.....	464
8.7.2.2	Cavity Receivers	468
8.7.2.3	Volumetric Receivers	471
8.7.3	Design of Heliostat Field.....	473
8.7.3.1	Reflection Factor ($\eta_{\text{reflection}}$).....	475
8.7.3.2	Cosine Factor (η_{\cosine}).....	475

8.7.3.3	Atmospheric Attenuation Factor ($\eta_{\text{attenuation}}$)	476
8.7.3.4	Interception Factor ($\eta_{\text{interception}}$).....	476
8.7.3.5	Shading and Blocking Factor ($\eta_{\text{shading \& blocking}}$)	477
8.7.4	Field Layout	478
8.8	Central Receiver System (CRS) Design	480
8.9	Recent Developments in Solar Thermal Power Cycles.....	482
8.9.1	Hybrid and Combined Cycles.....	483
8.9.2	Kalina Cycle.....	484
8.9.3	Aqua–Ammonia Combined Power/Absorption Cycle...	485
8.9.4	Combined Power/Cooling Cycle	485
8.9.5	Supercritical CO ₂ Power Cycle	486
8.10	Solar Distillation of Saline Water.....	490
8.10.1	Solar-Driven Reverse Osmosis.....	496
8.10.2	RO Mathematical Model.....	497
8.11	Nonconvecting Solar Ponds.....	500
8.11.1	Introduction.....	500
8.11.2	Solar Pond Stability Criteria.....	502
8.11.3	Thermal Performance of Solar Ponds	504
	References	510
9.	Photovoltaics.....	515
9.1	Semiconductors	516
9.1.1	<i>p</i> – <i>n</i> Junction	518
9.1.2	PV Effect.....	519
9.2	Analysis of PV Cells	525
9.2.1	Efficiency of Solar Cells	530
9.2.2	Maximum Power Point Tracking.....	531
9.2.3	Multijunction Solar Cells	532
9.2.4	Thin-Film Solar Cells	533
9.2.5	Dye-Sensitized Solar Cells and Polymer Solar Cells.....	535
9.2.5.1	Fabrication of DSSC	536
9.2.6	Design of a PV System	537
9.3	Manufacture of Solar Cells and Panels.....	540
9.3.1	Single-Crystal and Polycrystalline Cells	540
9.3.2	Amorphous Silicon and Thin-Film Fabrication	543
9.4	Design for Remote PV Applications.....	544
9.4.1	Estimation of Loads and Load Profiles.....	545
9.4.2	Estimation of Available Solar Radiation.....	547
9.4.3	PV System Sizing	547
9.4.4	Water Pumping Applications.....	549
	References	557
10.	Solar Photochemical Applications	559
10.1	Photocatalytic Reactions	559
10.2	Solar Photocatalytic Detoxification	563

10.3	Solar Reactors	564
10.3.1	Concentrator Reactors	565
10.3.2	Nonconcentrating Reactors	567
10.3.3	Flat-Plate Reactors.....	568
10.3.4	Tubular Reactors	568
10.3.5	Shallow Solar Ponds	569
10.3.6	Falling Film.....	571
10.4	Kinetic Models.....	571
10.5	Useful Insolation	577
10.6	Catalyst Development	579
10.7	System Design Methodology.....	580
10.7.1	Catalyst Life	585
10.8	Gas-Phase Photocatalytic Detoxification	585
10.8.1	Photoreactors	586
10.9	Commercial/Industrial Applications	587
10.10	Solar Disinfection of Water and Air.....	590
10.11	Summary	591
	References	592
	Appendix 1: International System of Units, Fundamental Constants, and Conversion Factors.....	597
	Appendix 2: Solar Radiation Data.....	601
	Appendix 3: Supplementary Material for Chapter 3.....	669
	Appendix 4: Supplementary Material for Chapter 4.....	687
	Appendix 5: Supplementary Material for Chapter 5.....	693
	Appendix 6: Thermodynamic Data for Cooling Systems	709
	Appendix 7: Supplementary Material for Chapter 7.....	723
	Appendix 8: Supplementary Material for Chapter 8.....	751
	Appendix 9: Economic Data Tables.....	763

Preface

Almost 15 years have passed since the last edition of *Principles of Solar Engineering* was published. During this period, the price of photovoltaic (PV) panels has dropped 10 times and global deployment has increased 30 times. Of course, some of this development has occurred because of governmental incentives and economies of scale; however, a large part of the advancement has been attributed to scientific and technological developments that have improved not only conversion efficiencies but also manufacturing technologies. There have been many improvements in solar thermal technologies as well. A number of concentrating solar thermal power plants (CSPs), as large as 400 MW, have been built or are under construction or under planning stages. Developments in higher-temperature CSPs are leading to a number of other advances, especially higher-temperature heat transfer fluids and thermodynamic power cycles. Since solar power is becoming a significant part of the grid power, energy storage has assumed increased importance. As the commercial deployment of solar technologies increases, it necessitates the need for better solar resource assessment, including modeling and forecasting. All of these developments have necessitated a new edition of the book, which is thoroughly revised and updated.

The new edition has been thoroughly revised to make it useful to students all over the world, by including examples and problems for both northern and southern latitudes. Solar radiation data in the book cover most of the world and examples have been chosen to cover countries in the Northern as well as Southern Hemisphere. The book contains many examples and homework problems and is designed to be both a textbook and a reference for scientists and practicing engineers, architects, and building design and construction professionals.

Chapter 1 introduces the global energy situation and changes taking place in the distribution of available energy resources to fulfill society's needs. Significantly, the highest increase has been in the areas of wind and solar PV power installed capacities in the world. Another significant change in the first chapter from the last edition is the addition of an economic analysis of solar energy systems now with a number of solved examples. This change reflects the author's cogent practical experience in solar energy systems from the small residential scale to the multi-megawatt scale. It is critical for students to understand the importance of economic analysis of solar energy systems in addition to the science and technology. With the introduction of this economic analysis in the first chapter, as students learn about the solar energy systems in Chapters 5 through 10, they will be able to analyze these systems from an economic standpoint as well.

There are significant changes in the second chapter on solar radiation. As global investment in solar power increases, there is a realization to accurately assess solar resources. Long-term measurements provide the best “bankable” data; however, they are not available for most of the locations in the world. Therefore, solar radiation modeling methods validated with long-term measured values are very important. The revised chapter describes the modeling methods accepted by the experts in solar resource assessment.

Chapter 3 covers concentrating and nonconcentrating solar thermal collectors. Although the fundamentals are the same as in the last edition, the new edition covers the latest developments in collector materials as well as new correlations for heat transfer and thermal performance analysis. The revised chapter covers concentrating collectors in much more depth than before, especially the parabolic trough concentrator and the central receiver heliostat and its receiver/absorber. Chapter 4 covers thermal energy storage, another area that has seen significant development in the last 15 years. The new developments, including materials, analysis, and design, are thoroughly covered in the revised Chapter 4. Solar industrial process heat has been moved from Chapter 8 in the previous edition to Chapter 5 in the current edition, since these systems are more appropriate in this chapter together with the other solar heat systems. Solar refrigeration, cooling, and dehumidification are covered in Chapter 6. This chapter covers the fundamentals of the refrigeration and dehumidification cycles and their applications to building cooling and dehumidification. Chapter 7 covers passive methods of water and space heating, passive cooling, and daylighting. The revision includes a section on various computer codes and sources of information on passive system design and daylighting.

Chapters 8 and 9, covering CSP and PV power, respectively, are thoroughly edited covering the latest advancements and what students need to learn for future upcoming developments in these areas. Since solar central receiver systems, commonly known as power towers, are expected to become more prevalent in the industry than before, the new Chapter 8 covers this topic in detail, including the design of a solar heliostat field, receiver/absorber, and higher-temperature thermodynamic power cycles, especially the supercritical CO₂ cycle. Chapter 8 also covers solar desalination in detail, including thermal and reverse osmosis desalination and desalination integrated with thermodynamic power cycles as a bottoming cycle. Chapter 9 covers the latest developments in thin film solar cells, including dye-sensitized solar cells. The revised chapter also includes additional topics, such as maximum power point tracking. Since engineers use software packages for the design of solar CSP and PV plants, information about those packages is included in the chapters as well as an appendix. Finally, Chapter 10 covers environmental applications of solar energy, such as photocatalytic oxidation of environmental pollutants. This book is the only solar energy textbook that covers this topic including the fundamentals and design methods.

Because of the comprehensiveness of this book, a single course on solar energy cannot cover the entire book. Experience shows that at least two courses are necessary to cover the book, one focused on the fundamentals and the other focused on the design of systems for one or more applications, such as building heating and cooling, industrial process heat, electric power plants, or environmental applications. On the other hand, a single course could be offered covering the fundamentals and emphasis on selected applications depending on the background of the students.

The author would like to thank the coauthors of the earlier edition, Frank Kreith and Jan Kreider, for writing the original first edition that helped in the education of a large number students and professionals in the 1970s to the year 2000 when the second edition was published. The author would also like to thank Dr. Jeffrey Morehouse for writing the chapter on passive methods for heating, cooling and daylighting. Another group of persons that deserves the gratitude of the author is his current and former graduate students, colleagues, assistants, and coworkers who have helped in various ways in the revision of this book including solving examples and homework problems, updating tables of values and figures, drawing figures, combing the equations, checking reference citations, and updating the solution manual. Some of them include Ricardo Vasquez Padilla, Saeb Besarati, Gokmen Demirkaya, Chennan Li, Jamie Trahan, Phil Myers, Rachana Vidhi, Antonio Archibald Ramos, Rajeev Kamal, Samantha Wijewardane, Gunnar Tamm, Sanjay Vijayaraghavan, Chatura Wikramaratne, Mehdi Zeyghami, Yangyang Zhang, Mohammad Abutayeh, Tanvir Alam, and Abhinav Bhardwaj. The author would like to give special thanks to Gunnar Tamm and Sanjay Vijayaraghavan for preparing the solutions manual and Phil Myers for updating it for the third edition. The author would also like to thank his colleagues, Elias Stefanakos and Chand Jotshi, for numerous discussions on various topics covered in the book, and his editorial assistant, Barbara Graham, for help in the drafts of the chapters and tables.

Finally, the author would like to thank his wife, Lovely Goswami, for her encouragement, support, and patience during the preparation of this and a number of other books.

Author



D. Yogi Goswami is a Distinguished University Professor and Director of the Clean Energy Research Center at the University of South Florida. He conducts fundamental and applied research on solar thermal power and cooling, photocatalytic detoxification and disinfection, thermodynamics, third-generation photovoltaics, and hydrogen production and storage. Professor Goswami is the editor in chief of *Solar Energy* and *Progress in Solar Energy*. He has published as an author or editor 17 books and more than 350 refereed technical papers. He also holds 16 patents, some of which have been successfully commercialized.

Dr. Goswami has developed successful industrial ventures based on his inventions and other innovations and has served on the boards of many companies.

A recognized leader in professional scientific and technical societies, Prof. Goswami has served as a governor of ASME-International, president of the International Solar Energy Society (ISES), senior vice president of ASME, and president of the International Association for Solar Energy Education.

Dr. Goswami is a recipient of the highest awards of many professional societies related to solar energy including the Farrington Daniels Award from ISES, the Frank Kreith Energy award and medal from ASME, the John Yellott Award for Solar Energy from ASME, and the Charles Greely Abbott Award and Hoyt Clark Hottel Award from the American Solar Energy Society (ASES). He is a charter fellow of the National Academy of Inventors and a fellow of the American Association for the Advancement of Science, ASME International, and the ASES.

Contributing Authors

Chapter 7

Jeffrey H. Morehouse
Emeritus Professor
University of South Carolina
Columbia, South Carolina

Sections 3.6 and 8.3

Ricardo Vasquez Padilla
CSRIO
Melbourne, Australia

Section 4.33

Jamie Trahan
Clean Energy Research Center
University of South Florida
Tampa, Florida

Sections 8.7–8.9

Saeb Besarati
Clean Energy Research Center
University of South Florida
Tampa, Florida

Section 8.10

Chennan Li
GE Power & Water
Schenectady, New York

1

Introduction to Solar Energy Conversion

A thing that will assume enormous importance quite soon is the exhaustion of our fuel resources. Coal and oil have been accumulating in the earth over five hundred million years, and at the present rates of demand for mechanical power, the estimates are that oil will be all gone in about a century, and coal probably in a good deal less than five hundred years. For the present purpose, it does not matter if these are underestimates; they could be doubled or trebled and still not affect the argument. Mechanical power comes from our reserves of energy, and we are squandering our energy capital quite recklessly. It will very soon be all gone, and in the long run we shall have to live from year to year on our earnings (Darwin 1953).

Charles Galton Darwin
(grandson of Charles Darwin)

The only energy earnings or income we have is the direct radiative energy from the sun (Daniels 1964). Fossil fuels are the stored form of the sun's energy, representing our energy savings or energy capital. In addition, we have the indirect forms of solar energy (wind, biomass, ocean, and hydro), geothermal energy, and nuclear energy in radioactive materials. It is clear that we have been using the energy capital at unsustainable rates over the last 100 years while throwing away our energy earnings, the direct energy from the sun. However, there is concerted effort throughout the world to change it. As we move toward a future where solar energy will play a far greater role, education of students in the science and engineering of solar energy has become extremely important and urgent. This book fills that need.

This book assumes that the reader is familiar with traditional thermodynamics, basic heat transfer, and fluid mechanics and has knowledge of calculus and ordinary differential equations. Some elements of radiation, fluid mechanics, and heat transfer specific to solar engineering are presented in the text. The design and analysis of solar utilization schemes are approached from a systems-analysis viewpoint, which combines technical design with economic analysis. There is no single solution to a given task in solar energy utilization and each problem must be analyzed separately from fundamental principles.

1.1 Global Energy Needs and Resources

Global energy consumption in the last half-century has rapidly increased and is expected to continue to grow over the next 50 years but with significant differences. The past increase was stimulated by relatively “cheap” fossil fuels and increased rates of industrialization in North America, Europe, and Japan; yet while energy consumption in these countries continues to increase, additional factors make the picture for the next 50 years more complex. These additional complicating factors include China’s and India’s rapid increase in energy use as they represent approximately one-third of the world’s population, the expected depletion of oil resources in the near future, and the effect of human activities on global climate change. On the positive side, the renewable energy (RE) technologies of wind, biofuels, solar thermal, and photovoltaics (PV) are finally showing maturity and the ultimate promise of cost competitiveness.

The total primary energy demand in the world increased from 5536 million tons of oil equivalent (MTOE) in 1971 to 10,345 MTOE in 2002, representing an average annual increase of 2% (Figure 1.1).

By 2008, the world energy demand had increased to 12,271 MTOE, representing an average annual increase of approximately 3%. The main reason for a 50% increase in the annual rate is the fast-growing energy demand in the Asia Pacific, more specifically China. Since the per capita energy used in the most populous countries (China and India) is still very small, the global energy use may continue to increase at this extremely high rate. Since 2008,

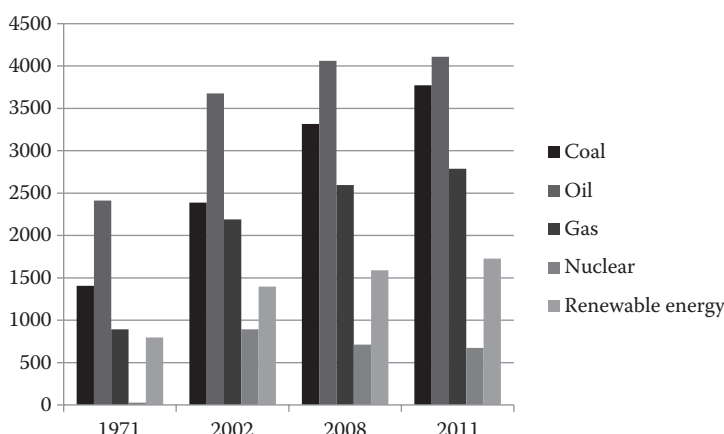


FIGURE 1.1

World primary energy demand (MTOE). (Data from IEA, *World Energy Outlook 2005*, International Energy Agency, Paris, France, 2005; IEA, *World Energy Outlook 2010*, International Energy Agency, Paris, France, 2010; IEA, *World Energy Outlook 2013*, International Energy Agency, Paris, France, 2013.)

the average annual energy increase dropped to approximately 2.1%, mainly because of the deep recession in the United States and Europe where the energy use actually went down.

Even at a 2% increase per year, the primary energy demand of 12,271 MTOE in 2008 would double by 2043 and triple by 2063. Of course, the global energy use cannot continue to increase at the same rate forever. The International Energy Agency (IEA 2010) estimated that the global energy use will increase at an average annual rate of 1.2% up to 2035. Even at that optimistic rate, the global energy use will increase by 38% by 2035, reaching a value of 16,934 MTOE per year. A review of the present energy resources and their availability (Kreith and Goswami 2007; WBGU 2003) shows that as much as 50% of the global energy use in 2050 will have to come from RE sources, a vast majority being from solar energy and wind. With a view to meet the future demand of primary energy in 2050 and beyond, it is important to know the extent of available RE resources and their ability to fulfill our energy needs for buildings, food, water, transportation, industry, and electrical power. This book presents the availability of solar energy, methods of conversion to useful forms, various applications, methods of design, and economic analysis.

1.1.1 Present Status and Potential of RE

According to the data in Table 1.1, RE accounted for 13.2% of the world's total primary energy supply in 2011. However, approximately 75% of the RE supply was from biomass, and in developing countries, it is mostly converted by traditional open combustion, which is very inefficient. Because of its inefficient use, biomass resources presently supply only approximately 20% of what they could if converted by modern, more efficient, available technologies.

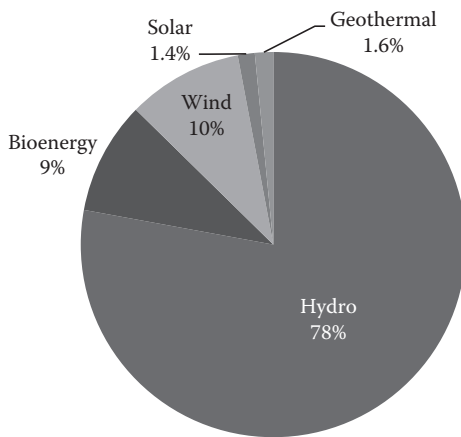
The total share of all renewables for electricity production in 2011 was approximately 20.1%, a vast majority (78%) of it being from hydroelectric power (Figure 1.2). Even though worldwide solar power capacity represented only 1.4% of the total electricity capacity, it was growing at an average annual rate of approximately 50%.

TABLE 1.1

2011 Fuel Shares in World Total Primary Energy Supply

Source	Share
Oil	31.4%
Natural gas	21.3%
Coal	28.9%
Nuclear	5.2%
Renewables	13.2%

Source: IEA, *World Energy Outlook 2013*, International Energy Agency, Paris, France, 2013.

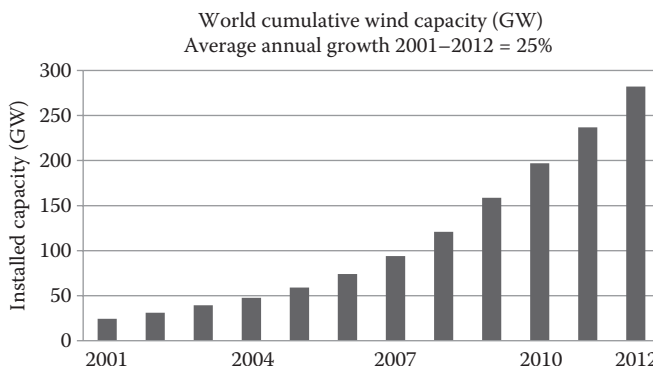
**FIGURE 1.2**

2011 Renewable resource shares in world electricity capacity. (Data from IEA, *World Energy Outlook 2013*, International Energy Agency, Paris, France, 2013.)

1.1.2 Wind Power

The utilization of wind power has been widespread since medieval times. Windmills were used in rural United States to power irrigation pumps and drive small electric generators used to charge batteries that provided electricity during the last century. A windmill or wind turbine converts the kinetic energy of moving air into mechanical motion, usually in the form of a rotating shaft. This mechanical motion can be used to drive a pump or to generate electric power. The energy content of the wind increases with the third power of the wind velocity and wind power installations are economical in regions where winds of sufficient strength and regularity occur.

Wind energy technology has progressed significantly over the last two decades. The technology has been vastly improved and capital costs have come down to as low as \$1000/kW. At this level of capital costs, wind power is already economical at locations with fairly good wind resources. Therefore, the average annual growth in worldwide wind energy capacity from 2001 to 2012 was over 25% (Figure 1.3). The average growth in the United States over the same period was 37.7%. The total worldwide installed wind power capacity, which was 24 GW in 2001 (Figure 1.3), reached a level of 282 GW in 2012 (WWEA 2012). The world's total theoretical potential for onshore wind power is around 55 TW with a practical potential of at least 2 TW (UNDP 2004), which is approximately 40% of the entire present worldwide generating capacity. The offshore wind energy potential is even larger.

**FIGURE 1.3**

World total wind power installed capacity. (From WWEA 2012, http://www.wwindea.org/webimages/WorldWindEnergyReport2012_final.pdf.)

Wind power is an indirect form of solar energy; however, it will not be covered in this book. Instead, it will be covered in detail in a companion book on RE being published separately.

1.1.3 Biomass

Although theoretically harvestable biomass energy potential is of the order of 90 TW, the technical potential on a sustainable basis is of the order of 8–13 TW or 270–450 exajoules/year. This potential is 3–4 times the present electrical generation capacity of the world. It is estimated that by 2025, even municipal solid waste (MSW) could generate up to 6 exajoules/year.

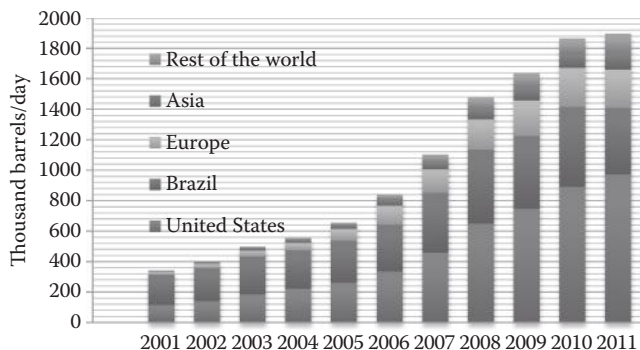
The biggest advantage of biomass as an energy resource is its relatively straightforward transformation into transportation fuels. Biofuels have the potential to replace as much as 75% of the petroleum fuels in use for transportation in the United States (Worldwatch Institute 2006). This is especially important in view of the declining oil supplies worldwide. Biofuels will not require additional infrastructure development. Therefore, development of biofuels is being viewed very favorably by governments around the world. Biofuels, along with other transportation options such as electric vehicles and hydrogen, will help diversify the fuel base for future transportation. Table 1.2 and Figure 1.4 show the global production of biofuels from 2001 to 2011. United States, Brazil, and Europe are the top producing countries and region of the world. Biofuel production grew more than 5 times in 10 years, although it started from a much smaller base. In 2005, the world ethanol production had reached approximately 36 billion liters per year while biodiesel production topped 3.5 billion liters during the same year.

TABLE 1.2

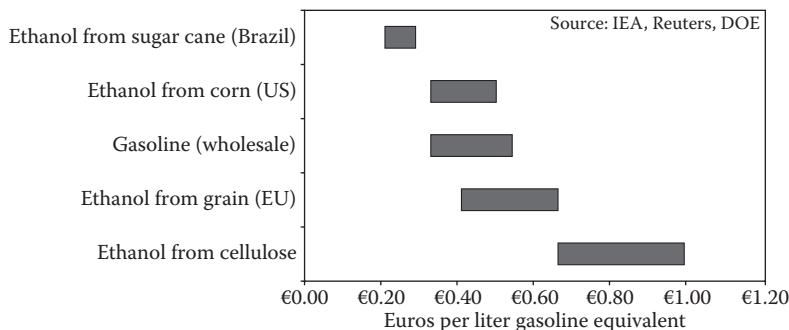
Total Biofuel Production (Thousand Barrels per Day)

	2001	2002	2003	2004	2005	2006	2007	2008	2009	2010	2011
United States	115.7	140.3	183.9	223.3	260.6	335.0	457.3	649.7	747.1	889.8	971.7
Brazil	197.6	216.9	249.4	251.7	276.4	307.3	395.7	486.3	477.5	527.1	438.1
Europe	21.2	29.3	39.3	48.9	76.8	123.9	153.8	198.1	233.2	255.2	250.5
Asia	3.1	8.3	17.2	21.1	28.2	44.9	49.2	75.6	93.8	99.8	118.2
Rest of the world	5.3	8.6	9.6	9.8	14.2	29.6	47.3	67.7	83.8	93.3	118.8
World	342.9	403.5	499.4	554.8	656.3	840.6	1103.3	1477.3	1635.4	1865.4	1897.2

Source: Enerdata, *Global Energy Statistical Yearbook 2013*, Enerdata Information Services, London, UK, 2013, <http://www.enerdata.net>; IEA, *World Energy Outlook 2013*, International Energy Agency, Paris, France, 2013.

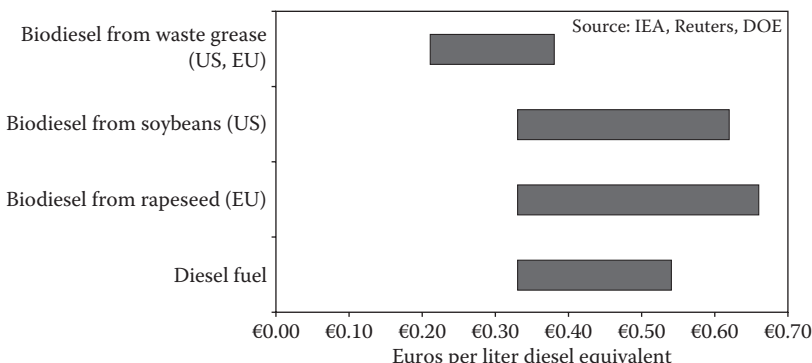
**FIGURE 1.4**

World biofuel production, 2001–2011. (From IEA, *World Energy Outlook 2013*, International Energy Agency, Paris, France, 2013.)

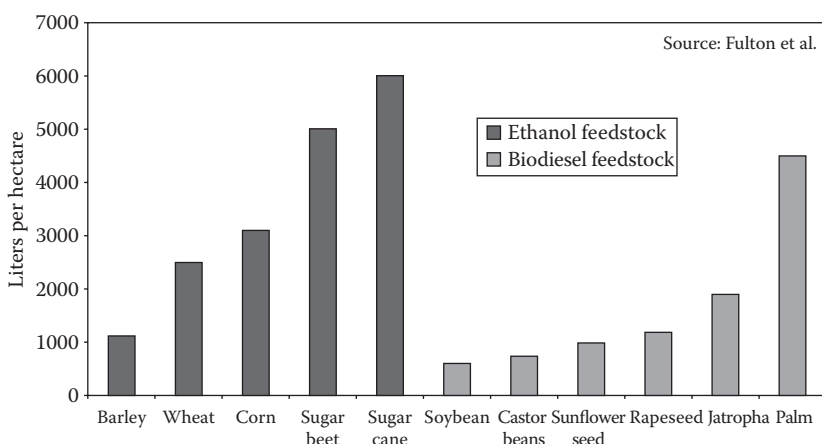
**FIGURE 1.5**

Cost ranges for ethanol and gasoline production, 2006. (From Worldwatch Institute, *Biofuels for Transportation—Global Potential and Implications for Sustainable Energy in the 21st Century*, Worldwatch Institute, Washington, DC, 2006.)

The present cost of ethanol production ranges from approximately 25 Euro cents to approximately 1 Euro per gasoline equivalent liter, as compared to the wholesale price of gasoline, which is between 40 and 60 Euro cents per liter (Figure 1.5). Biodiesel costs, on the other hand, range between 20 Euro cents to 65 Euro cents per liter of diesel equivalent (Figure 1.6). Figure 1.7 shows the feedstock used for these biofuels. An important consideration for biofuels is that the fuel should not be produced at the expense of food while there are people going hungry in the world. This would not be of concern if biofuels were produced from MSW or nonfood forest resources.

**FIGURE 1.6**

Cost ranges for biodiesel and diesel production, 2006. (From Worldwatch Institute, *Biofuels for Transportation—Global Potential and Implications for Sustainable Energy in the 21st Century*, Worldwatch Institute, Washington, DC, 2006.)

**FIGURE 1.7**

Biofuel yields of selected ethanol and biodiesel feedstock. (From Worldwatch Institute, *Biofuels for Transportation—Global Potential and Implications for Sustainable Energy in the 21st Century*, Worldwatch Institute, Washington, DC, 2006.)

According to the Worldwatch Institute report, a city of 1 million people produces approximately 1800 tons of MSW and 1300 tons of organic waste every day, which using the present-day technology could produce enough fuel to meet the needs of 58,000 persons in the United States, 360,000 in France, and nearly 2.6 million in China at current rates of per capita fuel use (Worldwatch Institute 2006).

1.1.4 Ocean Energy Conversion

Almost 71% of the world's surface is covered by oceans. Oceans serve as a tremendous storehouse of solar energy because of the temperature differences produced by the sun as well as the kinetic energy stored in the waves. There are a number of places in the ocean where temperature differences of the order of 20–25 K exist at depths of less than 1000 m, and these temperature differences could be used to operate low-pressure heat engines. Although the thermodynamic efficiency of a heat engine operating on such a small temperature difference is low, the available amount of thermal energy is very large. However, putting this energy-conversion method into practice requires the development of efficient and cheap heat exchangers that can withstand the rough marine conditions. Since heat-exchange equipment is the most expensive part of any ocean thermal conversion scheme, the cost of using the temperature gradients in the ocean for practical solar energy utilization depends largely on this development.

The second method of utilizing the oceans for energy generation is through ocean waves. Energy in ocean currents and waves is kinetic energy, which can be converted to power by specially designed turbines. Energy from tides can be harnessed by constructing a dam to hold seawater at a higher elevation when the tide is high and letting it run a turbine when the tide is low. According to an Electric Power Research Institute study, the total ocean wave and tidal power resource potential for the United States is approximately 2100 TWh/year (EPRI 2007), of which approximately 260 TWh/year could be credibly harnessed. Ocean energy conversion will not be treated in this text. Instead, it will be covered in detail in a companion text on RE conversion.

1.2 Solar Energy

The amount of solar radiant energy falling on a surface per unit area and per unit time is called *irradiance*. The mean extraterrestrial irradiance normal to the solar beam on the outer fringes of the earth's atmosphere is approximately 1.36 kW/m^2 . Since the earth's orbit is elliptical, the sun-to-earth distance varies slightly with time of year, and the actual extraterrestrial irradiance varies by $\pm 3.4\%$ during the year. The angle subtended by the sun when viewed from the earth is only 0.0093 rad (approximately 32 min of arc); the direct

beam radiation reaching the earth is therefore almost parallel. Although the brightness of the solar disc decreases from center to edge, for most engineering calculations, the disc can be assumed to be of uniform brightness. The radiant energy from the sun is distributed over a range of wavelengths, and the energy falling on a unit surface area per unit time within a particular spectral band is known as the *spectral irradiance*; its value is usually expressed in watts per square meter per nanometer of bandwidth. The extraterrestrial spectral irradiance is shown in Figure 1.8. It can be approximated by the spectrum of a black body at 5800 K. In the upper part of Figure 1.8, the wave bands typically useable for different solar applications are shown, and the lowest curve shows the spectral direct-beam irradiance at sea level on earth under clear sky conditions with the sun overhead.

The amount of sunlight striking the earth's atmosphere continuously is 1.75×10^5 TW. Considering a 60% transmittance through the atmospheric cloud cover, 1.05×10^5 TW reaches the earth's surface continuously. If the irradiance on only 1% of the earth's surface could be converted into electric energy with a 10% efficiency, it would provide a resource base of 105 TW,

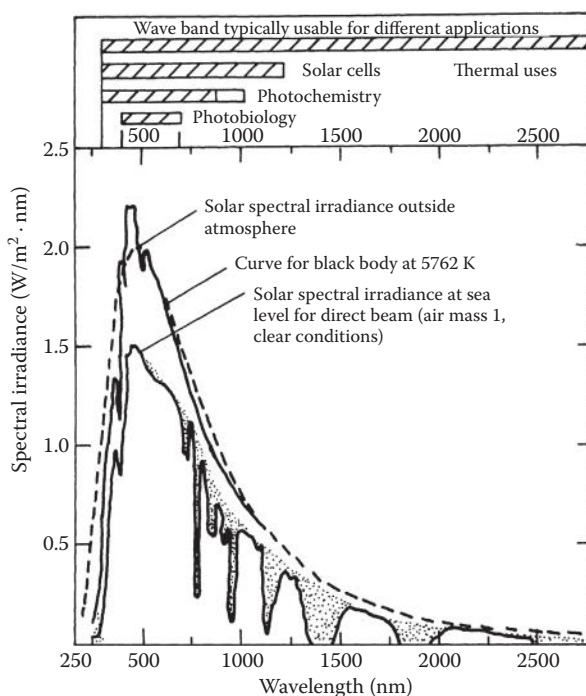


FIGURE 1.8

Spectral irradiance curves for direct sunlight are extraterrestrial and at sea level with the sun directly overhead. Shaded areas indicate absorption owing to atmospheric constituents, mainly H_2O , CO_2 , and O_3 . Wavelengths potentially utilized in different solar energy applications are indicated at the top.

while the total global energy needs for 2050 are projected to be approximately 25–30 TW. The present state of solar energy technologies is such that commercial solar panel efficiencies have reached more than 20%, laboratory multijunction solar cell efficiencies under concentrating sun have exceeded 40%, and solar thermal systems provide efficiencies of 40%–60%.

Solar PV panels have come down in cost from approximately \$30/W to approximately \$0.50/W in the last three decades. At \$0.50/W panel cost, the overall system cost is around \$2/W, which is already lower than grid electricity in the Caribbean island communities. Of course, there are many off-grid applications where solar PV is already cost-effective. With net metering and governmental incentives, such as feed-in laws and other policies, grid-connected applications such as Building-Integrated PV have become cost-effective even where grid electricity is cheaper. As a result, the worldwide growth in PV production has averaged more than 43% per year from 2000 to 2012 and 61% from 2007 to 2012 (Figure 1.9) with Europe showing the maximum growth.

Solar thermal power using concentrating solar collectors was the first solar technology that demonstrated its grid power potential. A 354 MW_e concentrating solar thermal power (CSP) plant has been operating continuously in California since 1988. Progress in solar thermal power stalled after that time because of poor policy and lack of research and development (R&D). However, the last 10 years have seen a resurgence of interest in this area and a number of solar thermal power plants around the world are under construction. The largest CSP plant with a capacity of 400 MW came on line in Nevada in February 2014. The cost of power from these plants (which is so far in the range of 12 to 16 US cents/kWh_e) has the potential to go down to 5 US cents/kWh_e with scale-up and creation of a mass market. An advantage of solar thermal power is that thermal energy can be stored efficiently, and fuels

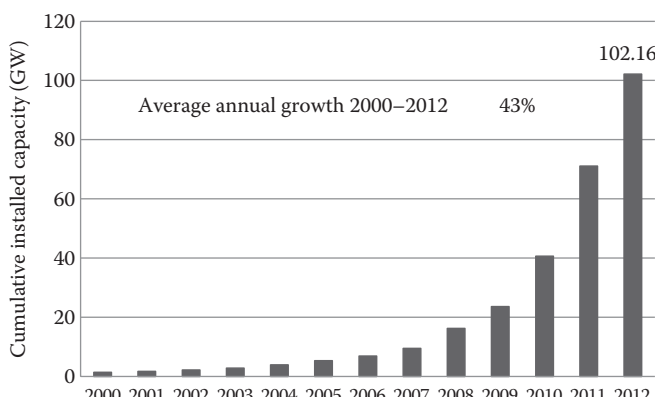
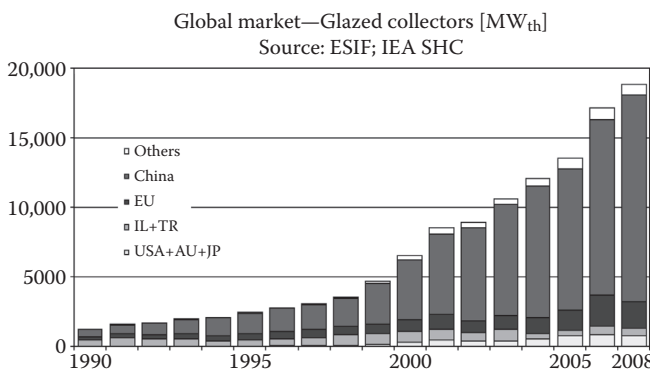


FIGURE 1.9

World solar PV production 2000–2012 (GWp). (From EPIA, *Global Market Outlook for Photovoltaics*, European Photovoltaic Industries Association, Brussels, Belgium, <http://www.epia.org/>.)

**FIGURE 1.10**

Deployment of solar heat (glazed) collectors, MW_{th}.

such as natural gas or biogas may be used as backup to ensure continuous operation. If this technology is combined with power plants operating on fossil fuels, it has the potential to extend the time frame of the existing fossil fuels.

Low-temperature solar thermal systems and applications have been well developed for quite some time. They are being actively installed wherever the policies favor their deployment. Figure 1.10 gives an idea of the rate of growth of solar thermal systems in the world.

We shall now describe, briefly, the important conversion methods.

1.2.1 Thermal Conversion

Thermal conversion is an engineering conversion method that utilizes a familiar scientific phenomenon. When a dark surface is placed in sunshine, it absorbs solar energy and heats up. Solar energy collectors working on this principle consist of a surface facing the sun, which transfers part of the energy it absorbs to a working fluid in contact with it. To reduce heat losses to the atmosphere, one or two sheets of glass are usually placed over the absorber surface to improve its efficiency. These types of thermal collectors suffer from heat losses owing to radiation and convection, which increase rapidly as the temperature of the working fluid increases. Improvements such as the use of selective surfaces, evacuation of the collector to reduce heat losses, and special kinds of glass are used to increase the efficiency of these devices.

The simple thermal conversion devices described above are called flat-plate collectors. They are available today for operation over a range of temperatures up to approximately 365 K (200°F). These collectors are suitable mainly for providing hot water service and space heating and possibly are also able to operate absorption-type air-conditioning systems.

The thermal utilization of solar radiation for the purpose of generating low-temperature heat is at the present time technically feasible and economically

viable for producing hot water and heating swimming pools. In some parts of the world, thermal low-temperature utilization is also used for heating and cooling buildings.

The generation of higher working temperatures as needed, for example, to operate a conventional steam engine requires the use of focusing devices in connection with a basic absorber–receiver. Operating temperatures as high as 4000 K (6740°F) have been achieved, and the generation of steam to operate pumps for irrigation purposes has also proved technologically feasible. At the present time, a number of focusing devices for the generation of steam to produce electric power are under construction in different regions of the world, and the cost estimates suggest that the cost of solar power in favorable locations will be no more than that of conventional thermal power when the development of these plants has been completed.

1.2.2 Photovoltaic Conversion

The conversion of solar radiation into electrical energy by means of solar cells was developed as a part of satellite and space-travel technology. The present technology utilizes the band gap of semiconductor materials to generate electrons and conduct them in a preferred direction using a p–n junction (described in detail later in the book). The theoretical maximum efficiency of single solar cells is approximately 33%, and in practice, efficiencies as high as 25% have been achieved with silicon photovoltaic devices. Multijunction solar cells can utilize a much broader spectrum of solar energy at a higher efficiency. Efficiencies as high as 44% have been achieved in the laboratory (Green et al. 2013) and the present research is aimed at efficiencies of around 50%. The overall system efficiencies of the commercially available photovoltaic panels today are in the range of 10% to 20%. With the development of thin film solar photovoltaic technologies, the costs of panels have come down from approximately \$30/W_p to as low as \$0.50/W_p. Here, W_p stands for peak watt, which means that the stated output would be expected when the solar irradiance on the panel is 1000 W/m² at standard atmospheric conditions. This level of solar radiation would be expected at a sunny location on a clear day around noon while the panel is directly facing the sun. With costs of the panels being lower than \$1/W_p, the total PV system costs are in the range of \$1.50/W_p (for multi-megawatt scale systems) to approximately \$3/W_p for residential-scale systems. Because of the reduction in costs, improvements in reliability and lifetimes, and preferential public policies, the PV industry is growing at an average annual rate of more than 50%.

Another way of direct conversion of sunlight to electricity takes advantage of the electromagnetic wave nature of sunlight as opposed to the quantum nature used in the conventional PV. This concept proposes to use nanoscale and microscale antennas (size of the order of the wavelength of radiation) to convert solar and ambient radiation into electricity (Goswami et al. 2004). The proposed panel would consist of billions of such antennas coupled with

rectifiers. The combined antenna and rectifier structure is known as a *rectenna*. The theoretical efficiency of a rectenna is in the range of 80% to 90%. An efficiency of greater than 80% was demonstrated for a rectenna converting radiation at a frequency of 2.4 GHz to electricity (Brown 1984). However, since the frequency of visible solar radiation is in the range of 300 THz, which would require a five-orders-of-magnitude size reduction of antennas and a totally different concept of the rectifier, development of this concept for converting solar energy is no simple task and is expected to take probably a decade or longer to become practical.

1.2.3 Limitations of Solar Energy

The first problem encountered in the engineering design of equipment for solar energy utilization is the low flux density, which makes necessary large surfaces to collect solar energy for large-scale utilization. Also, the larger the surfaces, the more expensive the delivered energy becomes. When the sun is directly overhead on a cloudless day, 10 m^2 of surface could theoretically provide energy at a 70% efficiency of collection and 30% conversion efficiency at a rate of approximately 2 kW. Several factors reduce this amount in practice, however.

The total solar energy reaching the earth is made up of two parts: the energy in the direct beam and the diffuse energy from the sky. The amount of direct energy depends on the cloudiness and the position of the sun and is obviously greatest on clear days. Some solar radiation falling on clouds is diffused by scattering, but clouds do not absorb all of the energy. The effect of clouds is mainly to increase the percentage of diffuse energy in the total energy reaching the surface, and diffuse irradiance in summer months with high and broken clouds can be as high as 400 W/m^2 . Thick clouds let less energy pass than thin clouds and scatter proportionally more of the total energy back into space.

The second practical limitation that is not apparent from the macroscopic energy view is that most of the solar energy falls on remote areas and would therefore require some means of transmission to be useful to the industrialized nations. The mean amount of energy available on a horizontal plane is greatest in the continental desert areas around latitudes 25°N and 25°S of the equator and falls off toward both the equator and the poles. The highest annual mean irradiance is 300 W/m^2 in the Red Sea area. Clouds reduce the mean global irradiance considerably in equatorial regions. However, whereas in northern climates the mean horizontal surface global irradiance varies from season to season, it remains relatively constant in equatorial regions. Typical values of mean annual horizontal surface irradiance are as follows: Australia, approximately 200 W/m^2 ; United States, 185 W/m^2 ; United Kingdom, 105 W/m^2 .

Table 1.3 shows the total solar electric energy potential for the solar energy-rich areas of the world. It is important to note that many of these parts of the world, for example, Saudi Arabia, central Australia, and parts of South Africa and India, are flat deserts that are practically unusable for agriculture.

TABLE 1.3

Solar-Electric Energy from Earth's High-Insolation Areas

Desert	Nominal Areas [km ²]	Nominal Annual Thermal Energy Flux [GW h(th)/km ²]	Percentage of Area Assumed Useable	Electric Energy Extracted at 25% Efficiency [GW h/year]
North Africa	7,770,000	2300	15 ^a	670,000,000
Arabian Peninsula	1,300,000	2500	30 ^b	244,000,000
Western and central Australia	1,550,000	2000	25	194,000,000
Kalahari	518,000	2000	50	129,000,000
Thar (northwest India)	259,000	2000	50	65,000,000
Mojave, southern California	35,000	2200	20	3,900,000
Vizcaino, Baja, California (Mexico)	15,500	2200	25	2,100,000
Total/average	11,447,500	2190 (average)	31 (average)	1,308,000,000

^a Parts of Arabian and Libyan deserts.^b Approximately 60% of Rub'al Khali desert.

At the same time, it should be noted that these are also regions with little or no water, which point to the need to develop dry cooling options for solar thermal electric power. Although the global distribution of solar energy does not favor the industrialized parts of the world, it is important to note that these are the regions, especially Europe, that have led in the deployment of solar power over the last decade.

The third limitation of solar energy as a large-scale source of power and heat is its intermittency. Solar energy has a regular daily cycle owing to the turning of the earth around its axis and a regular annual cycle owing to the inclination of the earth axis with the plane of the ecliptic and to the motion of the earth around the sun, and is also unavailable during periods of bad weather. It is obvious that these daily and seasonal variations in irradiance, exacerbated by variations owing to weather, introduce the need for storage or a supplementary fuel.

1.3 Energy Storage

Widespread use of solar energy systems requires satisfactory means of storing the energy once it has been collected and converted. Storage is becoming especially important for areas where grid-connected photovoltaic power capacity is increasing rapidly. Distributed grid-connected solar electric power systems require storage as a part of a *smart grid* management of

disparity between supply and demand. There are various options available for storage of solar energy before conversion to the final useful form as well as after conversion. Some are economically viable at this time, while others need more R&D and reduction in costs.

For applications such as heating and cooling of buildings, sensible heat storage in water or rocks is a reasonable solution. Passive storage in "thermal mass" in buildings is a clever method of integrating storage with buildings by incorporating additional stone, bricks, or even phase-change materials in the building components.

For electrical energy production systems, however, storage systems must be specially designed and built. Figure 1.11 shows a comparison of the energy densities of various options including liquid fuels. Figure 1.12 presents a comparison of possible energy-storage systems for various applications. The first group of storage possibilities is batteries, but only lead-acid batteries are currently available at reasonable cost, although considerable R&D is ongoing to develop more advanced battery systems. Development of supercapacitors would help in smoothing out short-term intermittency problems of storage

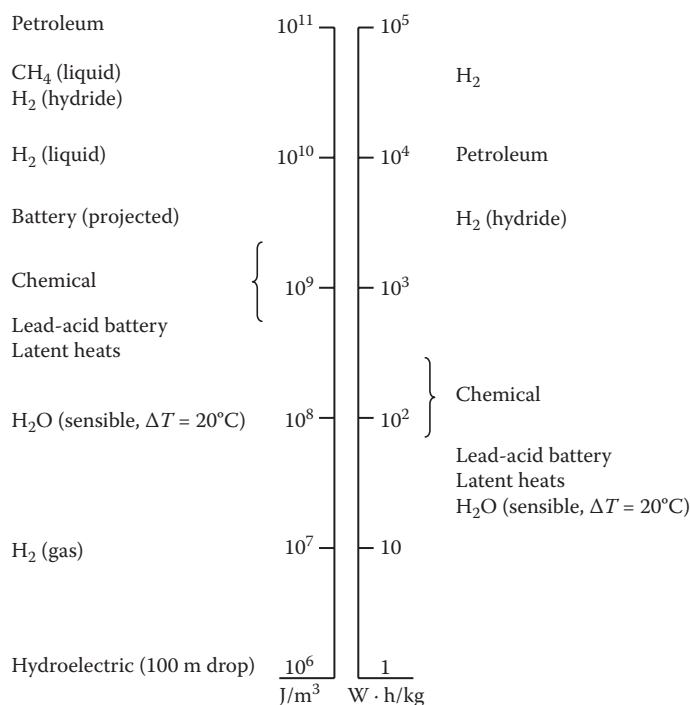
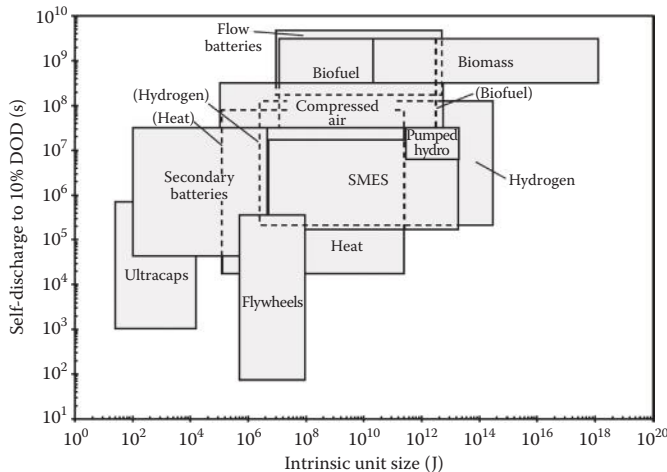


FIGURE 1.11

Mass and volumetric energy densities for typical energy-storage media. (Redrawn from Offenhardt, P.O.D., Classical methods of storing thermal energy. In: K.W. Bör (ed.), *Sharing the Sun-Solar Technology in the Seventies*, vol. 8, Solar Energy Society of Canada, Winnipeg, 1976.)

**FIGURE 1.12**

A comparison of storage technologies, mapped by self-discharge time and unit size. (Adapted from Kreith, F. and Goswami, D.Y., *Handbook of Energy Efficiency and Renewable Energy*, Chapter 18, CRC Press, Boca Raton, FL, 2007.)

especially for PV systems. However, cost-effective supercapacitors would have to be available for this to happen. Conventional electric power plants currently use hydro storage or compressed air storage where applicable. These methods could possibly be used for large solar power applications also but the plants would have to be at locations suitable for such storage systems, which put additional constraints on solar power plants. Therefore, it is unlikely that these storages would be adopted for solar power plants.

Another possibility is using solar energy to generate hydrogen and storing the energy in the gaseous or liquid phase. There appear to be no technical difficulties to the large-scale production, storage, and subsequent use of hydrogen in either liquid or gaseous form, but the hydrogen production efficiency is relatively low and, consequently, the cost of hydrogen storage and delivery systems is quite high at the present time.

High-temperature thermal energy storage is especially appropriate for concentrating solar thermal power, also known as CSP, and is already being used in large scale commercially. The present capital cost of high-temperature thermal energy storage is around \$30–\$50/kWh_{th}, which is expected to go down to below \$10/kWh_{th} with the ongoing R&D. With the capital costs of CSP plants going down from approximately \$3 M/MW_e to less than \$1.5 M/MW_e and with 6–10 h of thermal energy storage at a capital cost of approximately \$10/kWh_{th}, electricity from CSP plants can achieve grid parity in many parts of the world.

Parabolic trough-based solar thermal power plants typically operate in the range of 300°C–400°C and can use synthetic oil as the sensible heat storage

medium as well as a heat transfer fluid. However, the high cost of synthetic oil has made it necessary to look for alternatives. Molten salt, usually a mixture of potassium nitrate and sodium nitrate, is a cheaper alternative that is being considered by a number of solar power companies. Latent heat storage in phase-change materials is under development, which is expected to reduce the cost of storage to less than \$10/kWh_{th} from the present commercial storage costs of approximately \$30–\$50/kWh_{th}. Although adding storage to a CSP plant increases the capital costs of a plant, it actually reduces the leveled cost of energy (LCOE) because it allows the power block of a CSP to be used for longer number of hours. Details of these and other storage materials, components, systems, and design methods are described in detail in Chapter 4. Central receiver tower systems, also known as power tower, can achieve temperatures from 500°C to more than 1000°C, which allows them to convert thermal energy to power at much higher efficiencies than parabolic trough-based systems. Therefore, most of the future R&D and commercial activity is directed toward the power tower system.

1.4 Economics of Solar Systems

Although solar energy systems have environmental benefits that have monetary value in terms of reduced health care costs and other global climate benefits, decisions about investing in solar energy systems are rarely based on these benefits. Since these are societal benefits, sometimes the governments provide financial incentives to encourage investments in such systems. A solar energy system differs fundamentally from a fossil fuel system in a manner that requires an economic analysis reflecting the benefits accrued by solar usage throughout the lifetime of the system. Fossil fuel-based systems usually have relatively small initial costs and relatively large annual operating costs reflecting fuel costs. Solar energy systems, on the other hand, cost more initially but have much lower costs during their lifetime. Therefore, a life cycle costing approach has to be adopted to compare investment in a solar energy system with the conventional energy system.

The concept of life cycle costing includes both the initial capital costs and the year-to-year operating costs in making economic decisions. The life cycle cost of any energy system is defined as the total of the following cost components over the life of a system:

1. Initial costs including equipment, construction/installation, and land costs (if any)
2. Operating costs
3. Interest charges if money is borrowed

4. Periodic maintenance, insurance, and miscellaneous recurring charges
5. Taxes
6. Salvage value (usually a negative cost)

The costs of a solar energy system have to be weighed against the benefits, which accrue in the future as the system produces its intended output (heat, electricity, etc.). Therefore, it is necessary to convert the future benefits to their present worth (PW). The financial performance parameters most commonly used for comparing economics are *payback period*, mostly for residential and small commercial systems, and *internal rate of return* (IRR), which is used by investors for large-scale solar electric systems. These and other important concepts are described in the following.

1.4.1 Present Worth

Just as the future value X of a sum of money P invested at an annual interest rate i is

$$X = P(1 + i)^t, \quad (1.1)$$

in which t is the future time expressed in years (or other time unit corresponding to the time basis of the interest rate i), a future sum of money X with a discount rate i has a present worth P given by

$$P = X(1 + i)^{-t} = X \cdot \text{PWF}(i, t), \quad (1.2)$$

where PWF is called the present worth factor, tabulated in Table A9.1 in the Appendix. The effect of inflation on the future value of an invested sum is to reduce the future value by a factor $(1 + j)$ per year, where j is the inflation rate per year. This is important for figuring out the future savings in terms of fuel costs that are increasing at an inflation rate of j . Considering an inflation rate of j , the PWF is given by

$$\text{PWF}(i', t) = (1 + i')^{-t}, \text{ where } i' = (i - j)/(1 + j). \quad (1.3)$$

The total life cycle costs (TLCC) include the initial costs and the future costs, such as operations and maintenance, repair, and replacement costs and interest payments, all discounted to a PW.

1.4.2 Series of Payments

In many cases, a solar energy system is financed by a loan, S , at an annual interest rate of i , to be paid back with annual payments, P_{ann} over a period t years. The annual payment, P_{ann} , in such cases, is given by

$$S = P_{\text{ann}}[(1 + i)^{-1} + (1 + i)^{-2} + (1 + i)^{-3} + \dots] \quad (1.4)$$

or

$$P_{\text{ann}} = S[i/(1 - (1 + i)^{-t})] = S \cdot \text{CRF}(i, t). \quad (1.5)$$

The term in brackets in Equation 1.5 is called the *capital recovery factor*, $\text{CRF}(i, t)$, which is tabulated in Table A9.2.

1.4.3 Levelized Cost of Energy

Many governments around the world are offering *feed-in tariffs* for solar power producers, which remain fixed for certain periods, such as 10 to 25 years. In order to determine the benefit of the feed-in tariff, it is important to know the LCOE of the solar power plant. The LCOE is the cost of a unit of energy (e.g., \$/kWh_e from a PV system) produced or saved by the system over the useful life of the system, discounted back to the present. The LCOE for a system with a useful life of N years is given by the following relation:

$$\text{LCOE} = \frac{\text{TLCC}}{\sum_{n=1}^N (E_n / (1 + i)^n)}, \quad (1.6)$$

where E_n is the energy produced by the solar energy system in year n . If the solar energy system output is assumed to be the same every year, E_n in Equation 1.6 can be taken out of the summation. In that case, the remaining summation is the series $[(1 + i)^{-1} + (1 + i)^{-2} + \dots]$, which is equivalent to the ratio $[1 - (1 + i)^{-n}] / i$ or the inverse of the capital recovery factor ($\text{CRF}(i, n) = i / [1 - (1 + i)^{-n}]$). Therefore, the LCOE simplifies to

$$\text{LCOE} = \frac{\text{TLCC}}{E_n} \text{CRF}(i, n). \quad (1.7)$$

1.4.4 Internal Rate of Return

IRR is the rate of return on the initial investment needed to convert future cash flow from a project equal to the initial investment. If the initial investment is considered a negative cash flow, then IRR is the discount rate that makes the sum of all cash flows discounted to their PW equal to zero.

$$0 = \sum_{n=1}^N \frac{\text{CF}_n}{(1 + \text{IRR})^n} + \text{CI}, \quad (1.8)$$

where CF_n is the net cash flow in year n , CI is the initial capital investment, and N is the number of years of useful life of the project. CF_n is the net of the revenues (or savings) and expenses during the year n .

IRR is used by investors to compare their potential investment in a solar energy project to the same investment in another project to determine if the solar energy investment is better. For large projects, investors usually finance in part by their equity investment and the rest by debt. In such cases, the periodic debt payments including the principal and interest are considered as a part of the expenses during that year. Therefore, the IRR for the equity investment is leveraged by the debt. Since the interest on the debt is lower than the rate of return, leveraging improves the IRR of the equity investment.

Example 1.1

A homeowner in Tampa, Florida, installed a 5 kW_p PV system using crystalline silicon panels for a total cost of \$27,500. The system is connected to the grid with a net metering plan (i.e., the homeowner pays for the difference in the electricity used and that produced by the system). The system produced 7300 kWh_e in the first year. If the effective electricity rate is \$0.15/kWh and assuming the rate will increase at a rate of 5%/year, find the payback period for the system. Assume the discount rate to be 5%.

Solution

For future output from a solar system, normally we have to model the solar resource for the location and the orientation of the panels, which is covered in Chapter 2, and use it to find the output based on the system model (covered in Chapters 5 through 10 depending on the application). Since it is known in the present case that the system produced 7300 kWh_e in the first year, it is fair to assume that it will produce that amount in the future as well, modified by any expected degradation in the panel efficiency. Since the panels are crystalline silicon, their degradation will be small. Assuming that the panels will degrade at a rate of 0.25% per year, the output in the succeeding years will be

$$\text{Second year output} = 7300 \times (100 - 0.25)/100 = 7300 \times 0.9975 = 7282 \text{ kWh}_e$$

$$\text{Third year output} = 7300 \times (0.9975)^2 = 7264 \text{ kWh}_e, \text{ and so on.}$$

Since the electric rate is increasing at 5%/year, it will be $0.15 \times (1.05) = \$0.1575$ the second year. The annual savings are $7300 \text{ kWh}_e \times \$0.15/\text{kWh}_e = \$1095$ the first year and so on.

Figure 1.13 shows the calculations for 28 years, assumed as the life of the system.

On the basis of Figure 1.13, it will take approximately 17 years for a simple payback of the initial investment. However, since the investment is made in year 1, the savings must be accounted for in their PW. The PW of the savings 5 years from the initial year (taken as 0 year here) from Equation 1.2 = $\$1318 \times (1 + 0.05)^{-5} = \$1318 \times 0.7835 = \$1032$.

The factor 0.7835 can also be found from Table A9.1 as PWF(5%, 5). On the basis of the PW, the system payback time is approximately 28 years.

Year	kWh	\$/kWh	Annual savings (\$)	Cumulative annual savings (\$)	PW annual savings	PW cumulative annual savings (\$)
1	7300	0.15	1095	1095	1043	1043
2	7282	0.158	1147	2242	1040	2083
3	7264	0.165	1201	3443	1038	3121
4	7245	0.174	1258	4701	1035	4156
5	7227	0.182	1318	6019	1032	5188
6	7209	0.191	1380	7399	1030	6218
7	7191	0.201	1446	8845	1027	7245
8	7173	0.211	1514	10,359	1025	8270
9	7155	0.222	1586	11,944	1022	9292
10	7137	0.233	1661	13,605	1020	10,312
11	7120	0.244	1740	15,345	1017	11,329
12	7102	0.257	1822	17,167	1015	12,344
13	7084	0.269	1908	19,075	1012	13,356
14	7066	0.283	1999	21,074	1009	14,365
15	7049	0.297	2093	23,167	1007	15,372
16	7031	0.312	2193	25,360	1004	16,376
17	7013	0.327	2296	27,656	1002	17,378
18	6996	0.344	2405	30,061	999	18,378
19	6978	0.361	2519	32,580	997	19,375
20	6961	0.379	2638	35,219	994	20,369
21	6944	0.398	2763	37,982	992	21,361
22	6926	0.418	2894	40,877	989	22,351
23	6909	0.439	3032	43,908	987	23,338
24	6892	0.461	3175	47,083	985	24,322
25	6874	0.484	3326	50,409	982	25,304
26	6857	0.508	3483	53,892	980	26,284
27	6840	0.533	3648.14	57,540	977	27,261
28	6823	0.560	3820.97	61,361	975	28,236

FIGURE 1.13

Annual output and savings from the PV system in Example 1.1.

Example 1.2

The homeowner in Example 1.1 gets a rebate of \$2/W from the electric power company and a 30% federal income tax credit. What is the payback period now?

Solution

Total rebate for the 5 kW system = $\$2/\text{W} \times 5 \text{ kW} \times 1000 \text{ W/kW} = \$10,000$

$$\begin{aligned}\text{Federal income tax credit} &= (\text{Net total cost}) \times 0.30 \\ &= (\$27,500 - \$10,000) \times 0.3 = \$5250\end{aligned}$$

$$\text{Net total cost after tax credit} = \$17,500 - \$5250 = \$12,250.$$

Therefore, from Figure 1.13, the payback time on the basis of PW is reduced to approximately 12 years.

Example 1.3

A solar power company invests in a 1 MW_p PV system at a sunny location, where the system output is expected to be 6 MWh_e/day on the average for the whole year. The company will minimize the system degradation to less than 0.15%/year by aggressive maintenance and repairs. The company expects that the system will be down for 7 days/year for maintenance or repair. The total initial costs of the system are expected to be \$2.5 M, and the average annual maintenance/repair costs are expected to be 3% of the initial costs. The company plans to invest 30% equity and finance 70% of the capital costs as debt at 6%/year. The company expects to get feed-in tariff of \$0.22/kWh_e for 20 years. What is the LCOE for this system? What is the IRR for the system?

Solution

Capital investment for this 1 MW_e system is $\$2.5 \text{ M} \times 0.3 = \0.75 M . The rest (\$1.75 M) is debt at a rate of 6% for 20 years.

$$\text{Year 1: MWh}_e \text{ produced} = 6 \text{ MWh}_e \cdot (365 - 7) = 2148 \text{ MWh}_e$$

$$\begin{aligned} \text{Revenue} &= 2148 \text{ MWh}_e \cdot \$0.22/\text{kWh}_e \cdot (1000 \text{ kWh}_e/\text{MWh}_e) = \$472,560 \\ &\text{or } \$0.47256 \text{ M} \end{aligned}$$

$$\begin{aligned} \text{Annual debt payment from Equation 1.5, } P_{\text{ann}} &= S[i/(1 - (1 + i)^{-t})] = \\ &S \cdot CRF(i, t) \end{aligned}$$

$$P_{\text{ann}} = \$1.75 \text{ M} [0.06/(1 - (1.06)^{-20})] = \$152,573 \text{ or } \$0.152573 \text{ M}$$

$$\text{Repairs and maintenance} = \$2.5 \text{ M} \cdot 0.003 = \$0.0075 \text{ M}$$

$$\text{Cash flow} = -\$750,000 + \$472,560 - \$152,573 - \$7500 = -\$311,403$$

Year 2: Assuming that the system performance degrades 0.15% and the maintenance costs increase 5%, the calculations are as follows:

$$\text{MWh}_e \text{ produced} = 6 \text{ MWh}_e \cdot (365 - 7) (1 - 0.0015) = 2145 \text{ MWh}_e$$

$$\text{Revenue} = 2145 \text{ MWh}_e \cdot \$0.22/\text{kWh}_e \cdot (1000 \text{ kWh}_e/\text{MWh}_e) = \$471,851$$

$$\text{Repairs and maintenance} = \$2.5 \text{ M} \cdot (0.003) (1.05) = \$7875$$

$$\text{Cash flow} = \$471,851 - \$152,573 - \$7875 = \$311,403$$

Table 1.4 shows the values calculated for 20 years. The IRR calculated from Equation 1.8 is 41.26%.

For LCOE, we need to use Equation 1.6,

$$\text{LCOE} = \frac{\text{TLCC}}{\sum_1^N (E_n / (1 + i)^n)}. \quad (1.6)$$

Assuming a discount rate of 5%, the PW of the capital and interest payments is \$2,651,397, and the PW of all the repairs and maintenance costs is \$142,857.

TABLE 1.4
Annual Outputs, Revenues, Costs and Cash Flow for Example 1.3

Year	MWh _e	\$/kWh _e	Annual Revenue (\$M)	Cumulative Revenue (\$M)	PW Annual Revenue (\$M)	Cumulative Revenue (\$M)	PW Capital and Debt Payments (\$M)	Repairs and Maintenance (\$M)	Cash Flow (\$M)
1	2148	0.22	0.473	0.473	0.461	0.461	0.153	0.008	-0.750
2	2145	0.22	0.472	0.944	0.439	0.900	0.153	0.008	0.312
3	2142	0.22	0.471	1.416	0.417	1.317	0.153	0.008	0.311
4	2138	0.22	0.470	1.886	0.397	1.713	0.153	0.009	0.309
5	2135	0.22	0.470	2.356	0.377	2.090	0.153	0.009	0.308
6	2132	0.22	0.469	2.825	0.359	2.449	0.153	0.010	0.307
7	2129	0.22	0.468	3.293	0.341	2.790	0.153	0.010	0.306
8	2126	0.22	0.468	3.761	0.324	3.114	0.153	0.011	0.304
9	2122	0.22	0.467	4.228	0.308	3.423	0.153	0.011	0.303
10	2119	0.22	0.466	4.694	0.293	3.716	0.153	0.012	0.302
11	2116	0.22	0.466	5.159	0.279	3.995	0.153	0.012	0.301
12	2113	0.22	0.465	5.624	0.265	4.260	0.153	0.013	0.299
13	2110	0.22	0.464	6.088	0.252	4.513	0.153	0.013	0.298
14	2106	0.22	0.463	6.552	0.240	4.752	0.153	0.014	0.297
15	2103	0.22	0.463	7.014	0.228	4.980	0.153	0.015	0.295
16	2100	0.22	0.462	7.476	0.217	5.197	0.153	0.016	0.294
17	2097	0.22	0.461	7.938	0.206	5.404	0.153	0.016	0.292
18	2094	0.22	0.461	8.398	0.196	5.600	0.153	0.017	0.291
19	2091	0.22	0.460	8.858	0.187	5.786	0.153	0.018	0.289
20	2088	0.22	0.459	9.318	0.177	5.964	0.153	0.019	0.288
E _n							IRR		41.26%

Therefore,

$$\text{TLCC} = \$2,651,397 + \$142,857 = \$2,794,254$$

$$E_n = 42,353 \text{ MWh}_e$$

$$\text{LCOE} = \frac{\$2,794,254}{26,454.1 \text{ MWh}} = \$105.63/\text{MWh}_e \text{ or } \$0.105/\text{kWh}_e.$$

In the above example, taxes and insurance costs have been neglected.

1.5 Summary of RE Resources

By definition, the term *reserves* does not apply to renewable resources; hence, we need to look at the annual “potential” of each resource. Figure 1.14 summarizes the resource potential and the present costs and the potential future costs for each renewable resource.

Technology	Annual potential	Operating capacity 2005	Investment costs US\$ per kW	Current energy cost	Potential future energy cost
Biomass energy	276–446 EJ total or 8–13 TW MSW ~ 6 EJ				
Electricity Heat Ethanol Biodiesel		~44 GW _e ~225 GW _{th} ~36 billion lit. ~3.5 billion lit.	500–6000/kW _e 170–1000/kW _{th} 170–350/kW _{th} 500–1000/kW _{th}	3–12 ¢/kWh 1–6 ¢/kWh 25–75 ¢/lit.(ge) [*] 25–85 ¢/lit.(de)**	3–10 ¢/kWh 1–5 ¢/kWh 6–10 \$/GJ 10–15 \$/GJ
Wind power	55 TW theo. 2 TW practical	59 GW _e	850–1700	4–8 ¢/kWh	3–8 ¢/kWh
Solar energy Photovoltaics Thermal power Heat	>100 TW	5.6 GW _e 0.4 GW _e	5000–10,000 2500–6000 300–1700	25–160 ¢/kWh 12–34 ¢/kWh 2–25 ¢/kWh	5–25 ¢/kWh 4–20 ¢/kWh 2–10 ¢/kWh
Geothermal	600,000 EJ useful resource base 5000 EJ economical in 40–50 years				
Electricity Heat		9 GW _e 11 GW _{th}	800–3000 200–2000	2–10 ¢/kWh 0.5–5 ¢/kWh	1–8 ¢/kWh 0.5–5 ¢/kWh
Ocean energy Tidal Wave OTEC	2.5 TW 2.0 TW 228 TW	0.3 GW	1700–2500 2000–5000 8000–20,000	8–15 ¢/kWh 10–30 ¢/kWh 15–40 ¢/kWh	8–15 ¢/kWh 5–10 ¢/kWh 7–20 ¢/kWh
Hydroelectric	1.63 TW theo. 0.92 TW econ.	690 GW	1000–3500	2–10 ¢/kWh	2–10 ¢/kWh
Large Small		25 GW	700–8000	2–12 ¢/kWh	2–10 ¢/kWh

* ge—gasoline equivalent liter.

** de—diesel equivalent liter.

FIGURE 1.14

Potential and status of RE technologies. (From UNDP, *World Energy Assessment: Energy and The Challenge of Sustainability*, New York, 2004 [updated from the other sources].)

As in the case of other new technologies, it is expected that RE technology cost competitiveness will be achieved with R&D, scale-up, commercial experience, and mass production. Experience shows industry-wide cost reductions in the range of 10%–20% for each cumulative doubling of production for wind power, PV, ethanol, and gas turbines. Similar declines can be expected in CSP and other renewable technologies. Wind energy technologies have already achieved market maturity, and PV technologies are well on their way. CSP is expected to achieve the cost target of approximately \$0.05/kWh by the time it has an installed capacity of approximately 40 GW (GEF 2005). As a reference point, wind power achieved that capacity milestone in 2003.

1.6 Forecast of Future Energy Mix

On the basis of the information about limited oil, natural gas and nuclear resources, and the serious environmental concerns about coal, it seems logical that the RE technologies of solar, wind, and biomass not only will be essential but also will be able to fill the gap and provide a clean and sustainable energy future. There are many differing views on the future energy mix. However, we agree with the WBGU, which estimates that as much as 50% of the world's primary energy in 2050 will have to come from RE (Figure 1.15). However, achieving that level of RE use by 2050 will require a worldwide commitment and an unprecedented global effort.

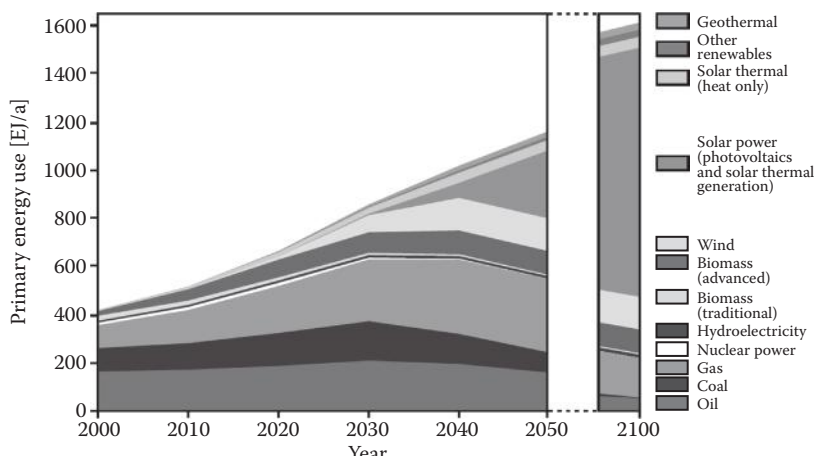


FIGURE 1.15

The global energy mix for year 2050 and 2100 according to WBGU (2003).

PROBLEMS

1. In 2011, RE provided 20.1% of the total electricity capacity of the world. Of the total electricity capacity from RE, solar power accounted for 1.4%, geothermal 1.6%, biomass 9%, and wind power accounted for 10%, the rest 78% being from hydro. On the basis of the IEA data, the annual growth rate of solar power was 50%, whereas that for biomass, wind, geothermal, and hydropower was 12%, 25%, 4%, and 2%, respectively. Assuming these annual growth rates to continue to 2025, find the fractions of each of these renewable energies in electrical power capacity in 2025, if the annual growth rate of total electricity capacity is 2.4% (based on IEA growth scenario).
2. If the total world electrical power capacity grows at a rate of 3% during this period (based on IEA growth scenario), what fraction of the total electricity capacity in 2030 will be from (a) RE and (b) solar energy?
3. Keeping the assumptions from Problem 1, find the fractions of solar, wind, biomass, and hydropower in the world electrical capacity during the present year. Compare your data with the actual available data from some source. Discuss the reasons for the differences.
4. A homeowner paid \$4000 for a solar water heater and received a tax credit of 30%. The system saves \$450 per year. Find a simple payback time. Assuming a discount rate of 5%, find the payback time based on the PW analysis.
5. A solar power company plans to build a 50 MWe solar power plant with the following information. Find the LCOE and IRR for this investment.

Location: Daggett, California (Lat. $34^{\circ} 51.8'$)
Capital costs, including site prep and construction = \$125 M (30% equity, 70% debt at 5%)
Repairs and maintenance = \$150,000/year (plant shutdown 10 days/year for maintenance and repairs)
Yearly electrical output = 300 MWh_e/day
Tariff received = \$0.15/kWh_e for the first year, with 5%/year escalation after that
Life of system = 25 years
6. Calculate the IRR if the power company gets a fixed feed-in tariff of \$0.25/kWh_e for 20 years and the salvage value of the plant after 20 years is \$20 M.

References

- Brown, W.C. 1984. The history of power transmission by radio waves. *IEEE Trans. Microw. Theory Techn.* 32: 1230–1242.
- Daniels, F. 1964. *Direct Use of Sun's Energy*. Yale University Press, New Haven, CT.
- Darwin, C.G. 1953. *The Next Million Years*. Greenwood Press Publishers, Westport, CT. Reprinted in 1973 from original publication in 1953.
- Enerdata. 2013. *Global Energy Statistical Yearbook 2013*. Enerdata Information Services, London, UK. Available at <http://www.enerdata.net>.
- EPIA (European Photovoltaic Industries Association). 2014. *Global Market Outlook for Photovoltaics*. EPIA, Brussels, Belgium. Available at <http://www.epia.org>.
- EPRI (Electric Power Research Institute). 2007. *Primer: Power from Ocean Waves and Tides*. EPRI, Palo Alto, CA. Available at <http://www.snpud.com/site/content/documents/tidal/tidalprimer.pdf>.
- Fulton, L., Hawes, T., and Hardy, J. 2004. *Biofuels for Transport—An International Perspective*. International Energy Agency, Paris, France.
- GEF (Global Environmental Facility). 2005. Assessment of the World Bank/GEF strategy for the market development of concentrating solar thermal power. GEF Report GEF/c.25/inf.11. GEF, Washington, DC.
- Goswami, D.Y. et al. 2004. New and emerging developments in solar energy. *Sol. Energy J.* 76: 1–3, 33–43.
- Green, M.A. et al. 2013. Solar cell efficiency tables. *Prog. Photovolt: Res. Appl.* 21: 1–11.
- IEA (International Energy Agency). 2005. *World Energy Outlook 2005*. International Energy Agency, Paris, France.
- IEA (International Energy Agency). 2010. *World Energy Outlook 2010*. International Energy Agency, Paris, France.
- IEA (International Energy Agency). 2013. *World Energy Outlook 2013*. International Energy Agency, Paris, France.
- Kreith, F., and D.Y. Goswami. 2007. *Handbook of Energy Efficiency and Renewable Energy*, Chapter 1. CRC Press, Boca Raton, FL.
- Offenhartz, P.O.D. 1976. Classical methods of storing thermal energy. In *Sharing the Sun-Solar Technology in the Seventies*, Vol. 8, K.W. Böer, ed. Solar Energy Society of Canada, Winnipeg.
- UNDP (United Nations Development Programme). 2004. *World Energy Assessment: Energy and The Challenge of Sustainability*. UNDP, New York.
- WBGU (German Advisory Council on Global Change). 2003. *World in Transition—Towards Sustainable Energy Systems*. WBGU, Berlin. Available at <http://www.wbgu.de>.
- Worldwatch Institute. 2006. *Biofuels for Transportation—Global Potential and Implications for Sustainable Energy in the 21st Century*. Worldwatch Institute, Washington, DC.
- WWEA (World Wind Energy Association). 2012. Available at <http://www.wwindea.org>.

2

Fundamentals of Solar Radiation

2.1 The Physics of the Sun and Its Energy Transport

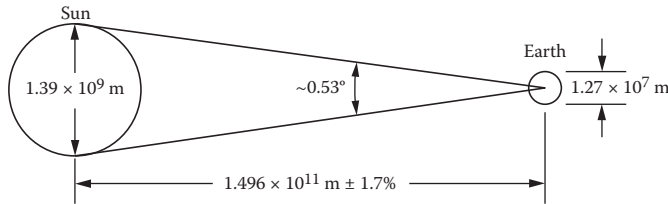
The nature of energy generation in the sun is still an unanswered question. Spectral measurements have confirmed the presence of nearly all the known elements in the sun. However, 80% of the sun is hydrogen and 19% is helium. Therefore, the remaining 100-plus observed elements make up only a tiny fraction of the composition of the sun. It is generally accepted that a hydrogen-to-helium thermonuclear reaction is the source of the sun's energy. Yet, because such a reaction has not been duplicated in the laboratory, it is unclear precisely what the reaction mechanism is, what role the turbulent flows in the sun play, and how solar prominences and sunspots are created.

The nature of the energy-creation process is of no importance to terrestrial users of the sun's radiation. Of interest is the amount of energy, its spectral and temporal distribution, and its variation with time of day and year. These matters are the main subject of this chapter.

The sun is a 13.9×10^5 km diameter sphere composed of many layers of gases, which are progressively hotter toward its center. The outermost layer, that from which energy is radiated into the solar system, is approximately at an equivalent black-body temperature of 5760 K (10,400°R). The center of the sun, however, may be at 20×10^6 K. The rate of energy emission from the sun is 3.8×10^{23} kW, which results from the conversion of 4.3×10^9 g/s of mass to energy. Of this total, only a tiny fraction, approximately 1.7×10^{14} kW, is intercepted by the earth, which is located approximately 150 million km from the sun (Figure 2.1).

Solar energy is the world's most abundant permanent source of energy. The amount of solar energy intercepted by the planet earth is 5000 times greater than the sum of all other inputs (terrestrial nuclear, geothermal and gravitational energies, and lunar gravitational energy). Of this amount, 30% is reflected to space, 47% is converted to low-temperature heat and reradiated to space, and 23% powers the evaporation/precipitation cycle of the biosphere. Less than 0.5% is represented in the kinetic energy of the wind and waves and in photosynthetic storage in plants.

Total terrestrial radiation is only approximately one-third of the extraterrestrial total during a year, and 70% of that falls on the oceans. However,

**FIGURE 2.1**

Relationship between the sun and the earth.

the remaining 1.5×10^{17} kW·h that falls on land is a prodigious amount of energy—approximately 6000 times the total energy usage of the United States in 2009. However, only a small fraction of this total can be used because of physical and socioeconomic constraints as described in Chapter 1.

2.2 Thermal Radiation Fundamentals

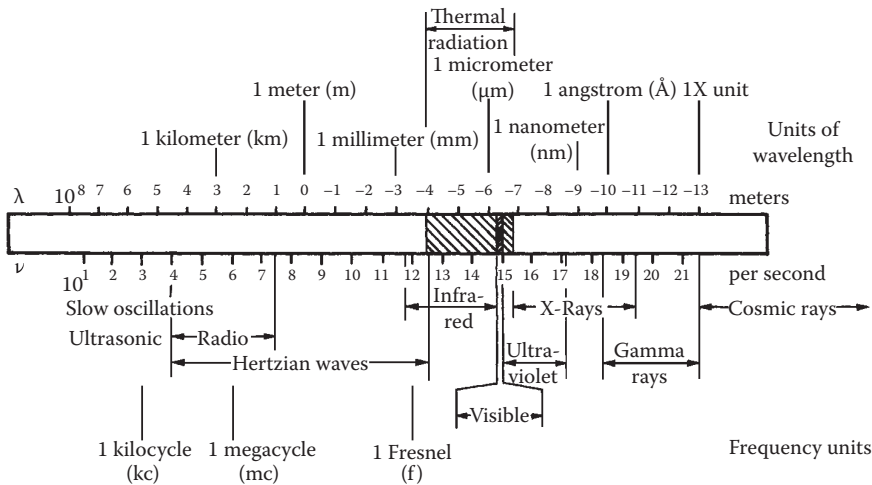
The material presented in this section has been selected from textbooks on heat transfer and radiation (e.g., Howell and Siegel 1992; Iqbal 1983; Kreith and Bohm 1993; Sparrow and Cess 1978). It provides the background needed to understand the nature of solar radiation for the engineering analysis of solar energy systems.

To begin then, all radiation travels at the speed of light, which is equal to the product of the wavelength and the frequency of radiation. The speed of light in a medium equals the speed of light in a vacuum divided by the refractive index of the medium through which it travels:

$$c = \lambda\nu = \frac{c_0}{n}, \quad (2.1)$$

where λ is the wavelength in meters (or micrometers [μm], $1 \mu\text{m} = 10^{-6}$ m), ν is the frequency (in s^{-1}), c is the speed of light in a medium (m/s), c_0 is the speed of light in a vacuum (m/s), and n is the index of refraction of the medium.

Thermal radiation is one kind of electromagnetic energy, and all bodies emit thermal radiation by virtue of their temperature. When a body is heated, its atoms, molecules, or electrons are raised to higher levels of activity called excited states. However, they tend to return to lower-energy states, and in this process, energy is emitted in the form of electromagnetic waves. Changes in energy states result from rearrangements in the electronic, rotational, and vibrational states of atoms and molecules. Since these rearrangements involve different amounts of energy changes and these energy changes are related to the frequency, the radiation emitted by a body is distributed over a range of wavelengths. A portion of the electromagnetic spectrum is shown in Figure 2.2. The wavelengths associated with the various mechanisms are not sharply defined; thermal radiation

**FIGURE 2.2**

Electromagnetic radiation spectrum.

is usually considered to fall within the band from approximately 0.1 to 100 μm , whereas solar radiation has most of its energy between 0.1 and 3 μm .

For some problems in solar energy engineering, the classical electromagnetic wave theory is not suitable. In such cases, for example, in photovoltaic or photochemical processes, it is necessary to treat the energy transport from the point of view of quantum mechanics. In this view, energy is transported by particles or *photons*, which are treated as energy units or quanta rather than waves. The energy of a photon, E_p , of frequency ν_p is

$$E_p = h\nu_p \quad (2.2)$$

where h is Planck's constant ($6.625 \times 10^{-34} \text{ J}\cdot\text{s}$).

2.2.1 Black-Body Radiation

The energy density of the radiation emitted at a given wavelength (monochromatic) by a perfect radiator, usually called a black body, is given according to the relation

$$E_{b\lambda} = \frac{C_1}{(e^{C_2/\lambda T} - 1)\lambda^5 n^2}, \quad (2.3)$$

where

$$C_1 = 3.74 \times 10^8 \text{ W}\cdot\mu\text{m}^4/\text{m}^2 \quad (1.19 \times 10^8 \text{ Btu}\cdot\mu\text{m}^4/\text{h}\cdot\text{ft}^2)$$

$$C_2 = 1.44 \times 10^4 \mu\text{m}\cdot\text{K} \quad (2.59 \times 10^4 \mu\text{m}\cdot^\circ\text{R})$$

n = refractive index of the medium = 1.0 for vacuum; n is taken to be approximately equal to 1 for air

The quantity $E_{b\lambda}$ has the unit $\text{W/m}^2\cdot\mu\text{m}$ ($\text{Btu/h}\cdot\text{ft}^2\cdot\mu\text{m}$) and is called the monochromatic emissive power of a black body, defined as the energy emitted by a perfect radiator per unit wavelength at the specified wavelength per unit area and per unit time at the temperature T .

The total energy emitted by a black body, E_b , can be obtained by integration over all wavelengths. This yields the Stefan–Boltzmann law

$$E_b = \int_0^\infty E_{b\lambda} d\lambda = \sigma T^4, \quad (2.4)$$

where σ is the Stefan–Boltzmann constant $= 5.67 \times 10^{-8} \text{ W/m}^2\cdot\text{K}^4$ ($0.1714 \times 10^{-8} \text{ Btu/h}\cdot\text{ft}^2\cdot\text{R}^4$) and T is the absolute temperature in Kelvin (or $R = 460 + {}^\circ\text{F}$).

The concept of a black body, although no such body actually exists in nature, is very convenient in engineering because its radiation properties can readily be related to those of real bodies.

2.2.2 Radiation Function Tables

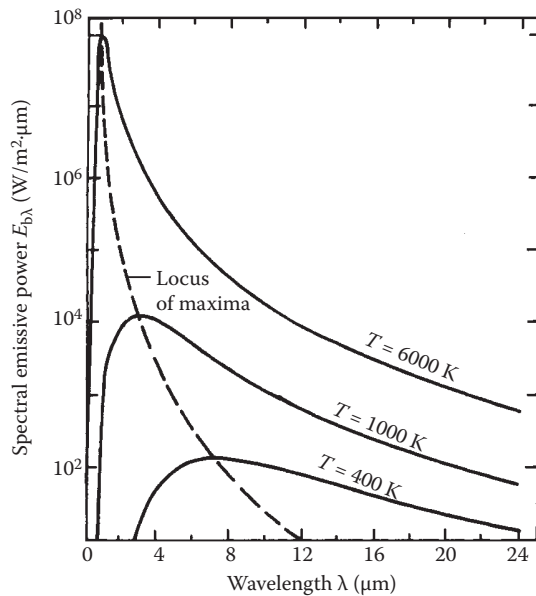
Engineering calculations of radiative transfer are facilitated by the use of radiation function tables, which present the results of Planck's law in a more convenient form than Equation 2.3. A plot of the monochromatic emissive power of a black body as a function of wavelength as the temperature is increased is given in Figure 2.3. The emissive power shows a maximum at a particular wavelength. These peaks, or inflection points, are uniquely related to the body temperature. By differentiating Planck's distribution law (Equation 2.3) and equating to zero, the wavelength corresponding to the maximum value of $E_{b\lambda}$ can be shown to occur when

$$\lambda_{\max}T = 2897.8 \mu\text{m K} \quad (5215.6 \mu\text{m R}). \quad (2.5)$$

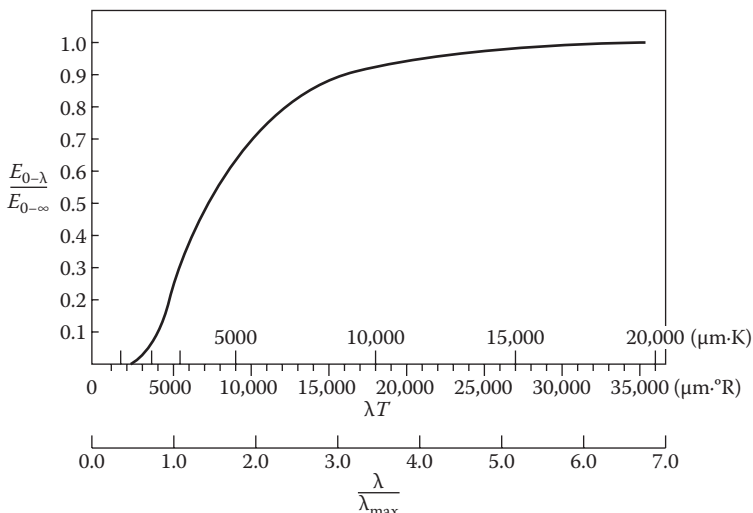
Frequently, one needs to know the amount of energy emitted by a black body within a specified range of wavelengths. This type of calculation can be performed easily with the aid of the radiation functions mentioned previously. To construct the appropriate radiation functions in dimensionless form, note that the ratio of the black-body radiation emitted between 0 and λ and between 0 and ∞ can be made a function of the single variable (λT) by using Equation 2.3 as shown below (for $n = 1$):

$$\frac{E_{b,0-\lambda}}{E_{b,0-\infty}} = \frac{\int_0^\lambda E_{b\lambda} d\lambda}{\int_0^\infty E_{b\lambda} d\lambda} = \frac{\int_0^{\lambda T} \frac{C_1 d(\lambda T)}{\sigma(\lambda T)^5 (e^{C_2/\lambda T} - 1)}}{\int_0^\infty \frac{C_1 d(\lambda T)}{\sigma(\lambda T)^5 (e^{C_2/\lambda T} - 1)}}. \quad (2.6)$$

The above relation is plotted in Figure 2.4 and the results are also shown in tabular form in Figure 2.5. In this table, the first column is the ratio of λ to

**FIGURE 2.3**

Spectral distribution of black-body radiation.

**FIGURE 2.4**

Fraction of total emissive power in spectral region between $\lambda = 0$ and λ as a function of λT and λ/λ_{\max} .

λ/λ_{\max}	$\frac{E_{b\lambda}}{E_{b\lambda,\max}}$	$\frac{E_{b\lambda,0-\lambda}}{\sigma T^4}$	λ/λ_{\max}	$\frac{E_{b\lambda}}{E_{b\lambda,\max}}$	$\frac{E_{b\lambda,0-\lambda}}{\sigma T^4}$	λ/λ_{\max}	$\frac{E_{b\lambda}}{E_{b\lambda,\max}}$	$\frac{E_{b\lambda,0-\lambda}}{\sigma T^4}$
0.00	0.0000	0.0000	1.50	0.7103	0.5403	2.85	0.1607	0.8661
0.20	0.0000	0.0000	1.55	0.6737	0.5630	2.90	0.1528	0.8713
0.25	0.0003	0.0000	1.60	0.6382	0.5846	2.95	0.1454	0.8762
0.30	0.0038	0.0001	1.65	0.6039	0.6050	3.00	0.1384	0.8809
0.35	0.0187	0.0004	1.70	0.5710	0.6243	3.10	0.1255	0.8895
0.40	0.0565	0.0015	1.75	0.5397	0.6426	3.20	0.1141	0.8974
0.45	0.1246	0.0044	1.80	0.5098	0.6598	3.30	0.1038	0.9045
0.50	0.2217	0.0101	1.85	0.4815	0.6761	3.40	0.0947	0.9111
0.55	0.3396	0.0192	1.90	0.4546	0.6915	3.50	0.0865	0.9170
0.60	0.4664	0.0325	1.95	0.4293	0.7060	3.60	0.0792	0.9225
0.65	0.5909	0.0499	2.00	0.4054	0.7197	3.70	0.0726	0.9275
0.70	0.7042	0.0712	2.05	0.3828	0.7327	3.80	0.0667	0.9320
0.75	0.8007	0.0960	2.10	0.3616	0.7449	3.90	0.0613	0.9362
0.80	0.8776	0.1236	2.15	0.3416	0.7565	4.00	0.0565	0.9401
0.85	0.9345	0.1535	2.20	0.3229	0.7674	4.20	0.0482	0.9470
0.90	0.9725	0.1849	2.25	0.3053	0.7777	4.40	0.0413	0.9528
0.95	0.9936	0.2172	2.30	0.2887	0.7875	4.60	0.0356	0.9579
1.00	1.0000	0.2501	2.35	0.2731	0.7967	4.80	0.0308	0.9622
1.05	0.9944	0.2829	2.40	0.2585	0.8054	5.00	0.0268	0.9660
1.10	0.9791	0.3153	2.45	0.2447	0.8137	6.00	0.0142	0.9790
1.15	0.9562	0.3472	2.50	0.2318	0.8215	7.00	0.0082	0.9861
1.20	0.9277	0.3782	2.55	0.2197	0.8290	8.00	0.0050	0.9904
1.25	0.8952	0.4081	2.60	0.2083	0.8360	9.00	0.0033	0.9930
1.30	0.8600	0.4370	2.65	0.1976	0.8427	10.00	0.0022	0.9948
1.35	0.8231	0.4647	2.70	0.1875	0.8490	20.00	0.0002	0.9993
1.40	0.7854	0.4911	2.75	0.1780	0.8550	40.00	0.0000	0.9999
1.45	0.7477	0.5163	2.80	0.1691	0.8607	50.00	0.0000	1.0000

λ = wavelength in micrometer.

λ_{\max} = wavelength at $E_{b\lambda,\max}$ in micrometer = $2898/T$.

$E_{b\lambda}$ = monochromatic emissive power in $\text{W}/\text{m}^2 \cdot \mu\text{m}$

$$= 374.15 \times 10^6 / \lambda^5 [\exp(14,387.9/\lambda T) - 1],$$

$E_{b\lambda,\max}$ = maximum monochromatic emissive power in $\text{W}/\text{m}^2 \cdot \mu\text{m}$

$$= 12.865 \times 10^{-12} T^5,$$

$$E_{b\lambda,0-\lambda} = \int_0^\lambda E_{b\lambda} d\lambda,$$

$$\sigma T^4 = E_{b\lambda,0-\infty} = 5.670 \times 10^{-8} T^4 \text{ W/m}^2, \text{ and}$$

T = absolute temperature in Kelvin.

FIGURE 2.5

Thermal radiation functions.

λ_{\max} from Equation 2.5, and the third column is the ratio of $E_{b,0-\lambda}$ to σT^4 from Equation 2.6. For use on a computer, Equation 2.6 can be approximated by the following polynomials:

$$\text{for } v \geq 2 \quad \frac{E_{b,0-\lambda}}{\sigma T^4} = \frac{15}{\pi^4} \sum_{m=1,2,\dots} \frac{E^{-mv}}{m^4} \left\{ [(mv+3)mv+6]mv+6 \right\}, \quad (2.7a)$$

and

$$v < 2 \quad \frac{E_{b,0-\lambda}}{\sigma T^4} = \frac{15}{1-\pi^4} v^3 \left(\frac{1}{3} - \frac{v}{8} - \frac{v^2}{60} - \frac{v^4}{5040} + \frac{v^6}{272,160} - \frac{v^8}{13,305,600} \right) , \quad (2.7b)$$

where $v = C_2/\lambda T$.

2.2.3 Intensity of Radiation and Shape Factor

The emissive power of a surface gives the total radiation emitted in all directions. To determine the radiation emitted in a given direction, we must define another quantity, the radiation intensity I . This quantity is defined as the radiant energy passing through an imaginary plane in space per unit area per unit time and per unit solid angle perpendicular to the plane as shown in Figure 2.6. I is defined by the relation

$$I = \lim_{\substack{dA \rightarrow \infty \\ d\omega \rightarrow \infty}} \frac{dE}{dA \, d\omega} \quad (2.8)$$

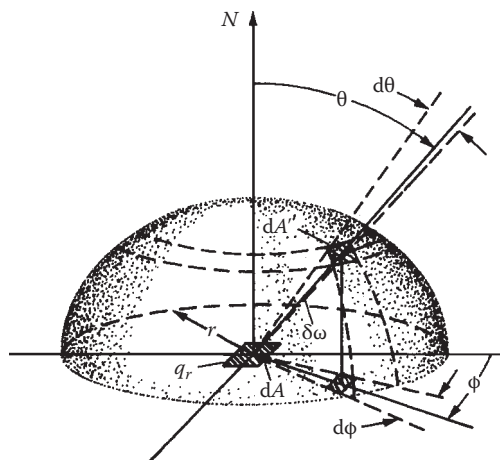


FIGURE 2.6

FIGURE 2.6 Schematic diagram illustrating radiation intensity and flux.

Radiation intensity has both magnitude and direction. It can be related to the radiation flux, defined as the radiant energy passing through an imaginary plane per unit area per unit time in all directions. Note that, whereas for the intensity, the area dA' is perpendicular to the direction of the radiation; for the flux, the area dA is at the base in the center of a hemisphere through which all of the radiation passes. Recalling that the definition for the solid angle between dA' and dA is $d\omega = dA/r^2$, the radiation flux q_r emanating from dA can be obtained by integrating the intensity over the hemisphere. As shown in Figure 2.6, the unit projected area for I is $dA \cos \theta$ and the differential area dA' on the hemisphere is $r^2 \sin \theta d\theta d\phi$; thus,

$$q_r = \int_0^{2\pi} \int_{\pi/2}^0 I \cos \theta \sin \theta d\theta d\phi. \quad (2.9)$$

If the area dA is located on a surface, the emissive power E can also be obtained from Equation 2.9. For the special case of a diffuse surface, for which I is the same in all directions, Equation 2.9 gives

$$q_r = \pi I. \quad (2.10)$$

Since all black surfaces are diffuse,

$$E_b = \pi I_b. \quad (2.11)$$

Equation 2.11 can, of course, also be written for monochromatic radiation as

$$E_{b\lambda} = \pi I_{b\lambda}. \quad (2.12)$$

In the evaluation of the rate of radiation heat transfer between two surfaces, not only their temperatures and their radiation properties but also their geometric configurations and relationships play a part. The influence of geometry in radiation heat transfer can be expressed in terms of the *radiation shape factor* between any two surfaces 1 and 2 defined as follows:

F_{1-2} is the fraction of radiation leaving surface 1 that reaches surface 2.

F_{2-1} is the fraction of radiation leaving surface 2 that reaches surface 1.

In general, F_{m-n} is the fraction of radiation leaving surface m that reaches surface n . If both surfaces are black, the energy leaving surface m and arriving at surface n is $E_{bm} A_m F_{m-n}$ and the energy leaving surface n and arriving at m is $E_{bn} A_n F_{n-m}$. If both surfaces absorb all the incident energy, the net rate of exchange $q_{m \leftrightarrow n}$ will be

$$q_{m \leftrightarrow n} = E_{bm} A_m F_{m-n} - E_{bn} A_n F_{n-m}. \quad (2.13)$$

If both surfaces are at the same temperature, $E_{bm} = E_{bn}$ and the net exchange is zero, $q_{m \leftrightarrow n} = 0$. This shows that the geometric radiation shape factor must obey the reciprocity relation

$$A_m F_{m-n} = A_n F_{n-m}. \quad (2.14)$$

The net rate of heat transfer can therefore be written in two equivalent forms:

$$q_{m \leftrightarrow n} = A_m F_{m-n}(E_{bm} - E_{bn}) = A_n F_{n-m}(E_{bm} - E_{bn}). \quad (2.15)$$

The evaluation of geometric shape factors is in general quite involved. For a majority of solar energy applications, however, only a few special cases are of interest. One of these is a small convex object of area A_1 surrounded by a large enclosure A_2 . Since all radiation leaving A_1 is intercepted by A_2 , $F_{1-2} = 1$ and $F_{2-1} = A_1/A_2$.

Another case is the exchange of radiation between two large parallel surfaces. If the two surfaces are near each other, almost all of the radiation leaving A_1 reaches A_2 and vice versa. Thus, $F_{1-2} = F_{2-1} = 1.0$, according to the definition of the shape factor. A third case of importance is the exchange between a small surface ΔA_1 and a portion of space A_2 , for example, the exchange between a flat-plate solar collector tilted at an angle β from the horizontal and the sky it can see. For this situation, we refer to the definition of radiation flux (see Figure 2.6). The portion of the radiation emitted by ΔA_1 that is intercepted by the surrounding hemisphere depends on the angle of tilt. When the surface is horizontal, $F_{1-2} = 1$; when it is vertical, $F_{1-2} = 1/2(\beta = 90^\circ)$. For intermediate values, it can be shown that (Sparrow and Cess 1978)

$$F_{1-2} = \frac{1}{2}(1 + \cos\beta) = \cos^2 \frac{\beta}{2}. \quad (2.16)$$

If the diffuse sky radiation is uniformly distributed and assumed to be black, then a small black area A_1 receives radiation at the rate

$$A_1 F_{1-sky} E_{sky} = \frac{A_1}{2}(1 + \cos\beta)\sigma T_{sky}^4 \quad (2.17)$$

whereas the net radiation heat transfer is given by

$$q_{sky-1} = A_1 F_{1-sky} \sigma (T_{sky}^4 - T_1^4). \quad (2.18)$$

If the receiving area is gray with an absorptance $\bar{\alpha}$ equal to the emittance $\bar{\epsilon}$, the net exchange is given by

$$q_{\text{sky} - 1} = A_1 F_{1-\text{sky}} \bar{\alpha} \sigma (T_{\text{sky}}^4 - T_1^4). \quad (2.19)$$

2.2.4 Transmission of Radiation through a Medium

When radiation passes through a semitransparent medium such as glass or the atmosphere, the decrease in intensity can be described by Bouger's law that assumes that the attenuation is proportional to the local intensity in the medium. If $I_\lambda(x)$ is monochromatic intensity after radiation has traveled a distance x , the law is expressed by the equation

$$-dI_\lambda(x) = I_\lambda(x) K_\lambda dx, \quad (2.20)$$

where K_λ is the monochromatic extinction coefficient assumed to be a constant of the medium. If the transparent medium is a slab of thickness L and the intensity at $x = 0$ is designated by the symbol $I_{\lambda,0}$, the monochromatic transmittance τ_λ is equal to the ratio of the intensity at $x = L$ to $I_{\lambda,0}$. An expression for $I_\lambda(L)$ can be obtained by integrating Equation 2.20 between 0 and L , which gives

$$\ln \frac{I_\lambda(L)}{I_{\lambda,0}} = -K_\lambda L \quad \text{or} \quad I_\lambda(L) = I_{\lambda,0} e^{-K_\lambda L}. \quad (2.21)$$

Then,

$$\tau_\lambda = \frac{I_\lambda(L)}{I_{\lambda,0}} = e^{-K_\lambda L}. \quad (2.22)$$

The extinction coefficient K_λ is a complex property of the medium since it combines the effects of absorption, emission, and scattering by the molecules and particles that make up the medium. Fortunately, for materials such as glass and plastics with known compositions, this coefficient can be determined accurately. Transmission of radiation through such materials will be discussed further in Chapter 3. In the present chapter, we are concerned about the transmission of solar radiation through the atmosphere. The atmosphere consists of the molecules of gases in it, such as N_2 , O_2 , CO_2 , H_2O , and so on, and aerosols such as dust particles, water droplets, and ice crystals. The extinction processes of the atmosphere consist of (a) absorption and emission by the molecules and aerosols, (b) scattering by the molecules, and (c) scattering by aerosols.

Since the atmosphere consists of a large number of components whose concentration changes as a function of time and location, determining the extinction coefficient of the atmosphere presents a formidable challenge. A major research effort is underway by scientists trying to predict global climate change. Some early attempts for the estimation of extinction coefficient for “average atmospheric conditions” were combined with an empirical approach to use the above equation for the estimation of terrestrial solar radiation resource. This approach is described later in this chapter.

2.3 Sun–Earth Geometric Relationship

Figure 2.7 shows the annual orbit of the earth around the sun. The distance between the earth and the sun changes throughout the year, the minimum

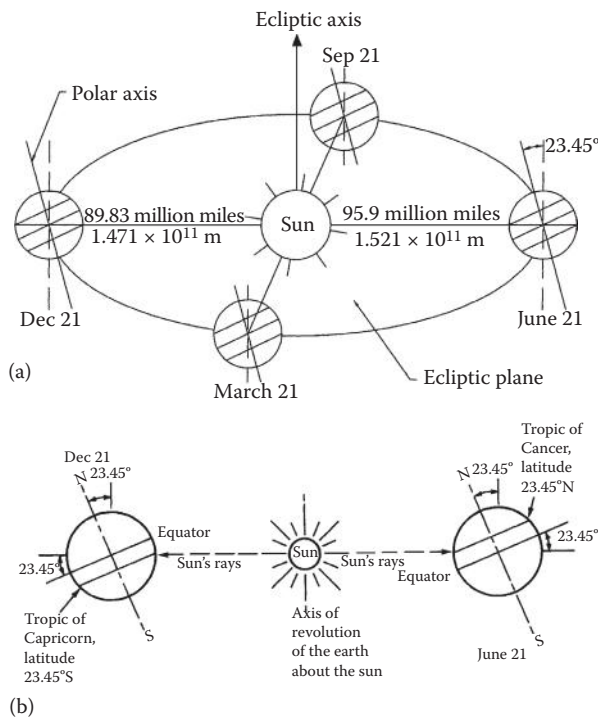


FIGURE 2.7

(a) Motion of the earth about the sun. (b) Location of tropics. Note that the sun is so far from the earth that all the rays of the sun may be considered as parallel to one another when they reach the earth.

being 1.471×10^{11} m at winter solstice (December 21) and the maximum being 1.521×10^{11} m at summer solstice (June 21). The year-round average earth–sun distance is 1.496×10^{11} m. The amount of solar radiation intercepted by the earth, therefore, varies throughout the year, the maximum being on December 21 and the minimum on June 21.

The axis of the earth's daily rotation around itself is at an angle of 23.45° to the axis of its ecliptic orbital plane around the sun. This tilt is the major cause of the seasonal variation of the solar radiation available at any location on the earth. The angle between the earth–sun line (through their centers) and the plane through the equator is called the *solar declination*, δ_s . The declination varies between -23.45° on December 21 to $+23.45^\circ$ on June 21. Stated another way, the declination has the same numerical value as the latitude at which the sun is directly overhead at solar noon on a given day. The tropics of Cancer (23.45°N) and Capricorn (23.45°S) are at the extreme latitudes where the sun is overhead at least once a year as shown in Figure 2.7. The Arctic and Antarctic circles are defined as those latitudes above which the sun does not rise above the horizon plane at least once per year. They are located, respectively, at $66\frac{1}{2}^\circ\text{N}$ and $66\frac{1}{2}^\circ\text{S}$. Declinations north of the equator (summer in the Northern Hemisphere) are designated as positive; those south, negative. The solar declination may be estimated by the relation*

$$\delta_s = 23.45^\circ \sin[360(284 + n)/365^\circ], \quad (2.23)$$

where n is the day number during a year with January 1 being $n = 1$. Approximate values of declination may also be obtained from Figure 2.8 or Figure 2.9. For most calculations, the declination may be considered constant during any given day.

For the purposes of this book, the Ptolemaic view of the sun's motion provides a simplification to the analysis that follows. It is convenient to assume the earth to be fixed and to describe the sun's apparent motion in a coordinate system fixed to the earth with its origin at the site of interest. Figure 2.10 shows an apparent path of the sun to an observer. The position of the sun can be described at any time by two angles, the altitude and azimuth angles, as shown in Figure 2.10. The *solar altitude angle*, α , is the angle between a line collinear with the sun's rays and the horizontal plane. The *solar azimuth angle*, a_s , is the angle between a due south line and the projection of the site to sun line on the horizontal plane. The sign convention used for the azimuth angle is positive west of south and negative east of south. The *solar zenith angle*, z , is the angle between the site to sun line and the vertical at the site:

$$z = 90^\circ - \alpha. \quad (2.24)$$

* A more accurate relation is $\sin \delta_s = \sin(23.45^\circ) \sin[360(284 + n)/365]^\circ$. Because the error is small, Equation 2.23 is generally used.

Date	Declination		Equation of time		Date	Declination		Equation of time	
	Deg	Min	Min	Sec		Deg	Min	Min	Sec
Jan	1	-23	4	-3	14	Feb	1	-17	19
	5	-22	42	-5	6		5	-16	10
	9	-22	13	-6	50		9	-14	55
	13	-21	37	-8	27		13	-13	37
	17	-20	54	-9	54		17	-12	15
	21	-20	5	-11	10		21	-10	50
	25	-19	9	-12	14		25	-9	23
	29	-18	9	-13	5				
Mar	1	-7	53	-12	38	Apr	1	+4	14
	5	-6	21	-11	48		5	5	46
	9	-5	48	-10	51		9	7	17
	13	-3	14	-9	49		13	8	46
	17	-1	39	-8	42		17	10	12
	21	-0	5	-7	32		21	11	35
	25	+1	30	-6	20		25	12	56
	29	3	4	-5	7		29	14	13
May	1	+14	50	+2	50	Jun	1	+21	57
	5	16	2	3	17		5	22	28
	9	17	9	3	35		9	22	52
	13	18	11	3	44		13	23	10
	17	19	9	3	44		17	23	22
	21	20	2	3	24		21	23	27
	25	20	49	3	16		25	23	25
	29	21	30	2	51		29	23	17
Jul	1	+23	10	-3	31	Aug	1	+18	14
	5	22	52	-4	16		5	17	12
	9	22	28	-4	56		9	16	6
	13	21	57	-5	30		13	14	55
	17	21	21	-5	57		17	13	41
	21	20	38	-6	15		21	12	23
	25	19	50	-6	24		25	11	2
	29	18	57	-6	23		29	9	39
Sep	1	+8	35	-0	15	Oct	1	-2	53
	5	7	7	+1	2		5	-4	26
	9	5	37	2	22		9	-5	58
	13	4	6	3	45		13	-7	29
	17	2	34	5	10		17	-8	58
	21	1	1	6	35		21	-10	25
	25	0	32	8	0		25	-11	50
	29	-2	6	9	22		29	-13	12

FIGURE 2.8

Summary of solar ephemeris. Since each year is 365.25 days long, the precise value of declination varies from year to year. *The American Ephemeris and Nautical Almanac*, published each year by the US Government Printing Office, contains precise values for each day of each year.

(Continued)

Date	Declination		Equation of time			Date	Declination		Equation of time		
	Deg	Min	Min	Sec			Deg	Min	Min	Sec	
Nov	1	-14	11	+16	21	Dec	1	-21	41	11	16
	5	-15	27	16	23		5	-22	16	9	43
	9	-16	38	16	12		9	-22	45	8	1
	13	-17	45	15	47		13	-23	6	6	12
	17	-18	48	15	10		17	-23	20	4	47
	21	-19	45	14	18		21	-23	26	2	19
	25	-20	36	13	15		25	-23	25	+0	20
	29	-21	21	11	59		29	-23	17	-1	39

FIGURE 2.8 (CONTINUED)

Summary of solar ephemeris. Since each year is 365.25 days long, the precise value of declination varies from year to year. *The American Ephemeris and Nautical Almanac*, published each year by the US Government Printing Office, contains precise values for each day of each year.

The solar altitude and azimuth angles are not fundamental angles. Hence, they must be related to the fundamental angular quantities *hour angle*, *latitude*, and *declination*. The three angles are shown in Figure 2.11. The solar hour angle h_s is based on the nominal time of 24 h required for the sun to move 360° around the earth or 15° per hour. Therefore, h_s is defined as

$$h_s = (15^\circ/h) \cdot (\text{hours from local solar noon}) = \frac{\text{minutes from local solar noon}}{4 \text{ min/degree}}. \quad (2.25)$$

Again, values east of due south, that is, morning values, are negative; and values west of due south are positive.

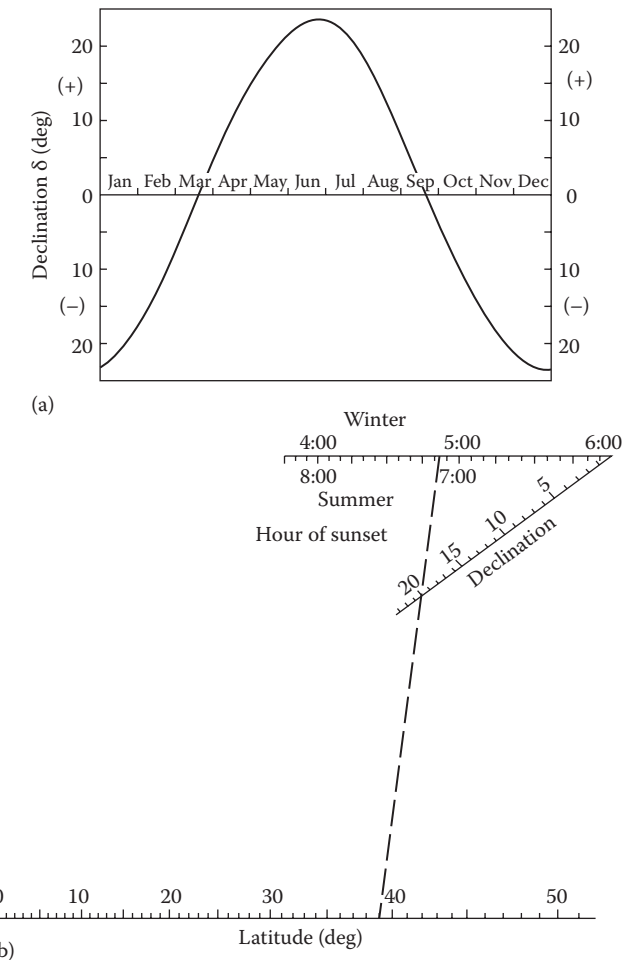
The latitude angle L is the angle between the line from the center of the earth to the site and the equatorial plane. The latitude may be read from an atlas and is considered positive north of the equator and negative south of the equator.

2.3.1 Solar Time and Angles

The sun angles are obtained from the local solar time, which differs from the local standard time (LST). The relationship between the local solar time and the LST is

$$\text{Solar time} = \text{LST} + \text{ET} + (l_{\text{st}} - l_{\text{local}}) \cdot 4 \text{ min/degree}. \quad (2.26)$$

ET is the equation of time, which is a correction factor that accounts for the irregularity of the speed of earth's motion around the sun; l_{st} is the standard

**FIGURE 2.9**

(a) Graph to determine the solar declination. (b) Sunset nomograph example. Example b shows determination of sunset time for summer (7:08 p.m.) and winter (4:52 p.m.) when the latitude is 39°N and the solar declination angle is 20°. (From Whillier, A., *Sol Energy* 9, 165–166, 1965.)

time meridian, and l_{local} is the local longitude. ET may be estimated from Figure 2.8 or calculated from the following empirical equation:

$$\text{ET (in minutes)} = 9.87 \sin 2B - 7.53 \cos B - 1.5 \sin B \quad (2.27)$$

where $B = 360(n - 81)/364$ degrees.

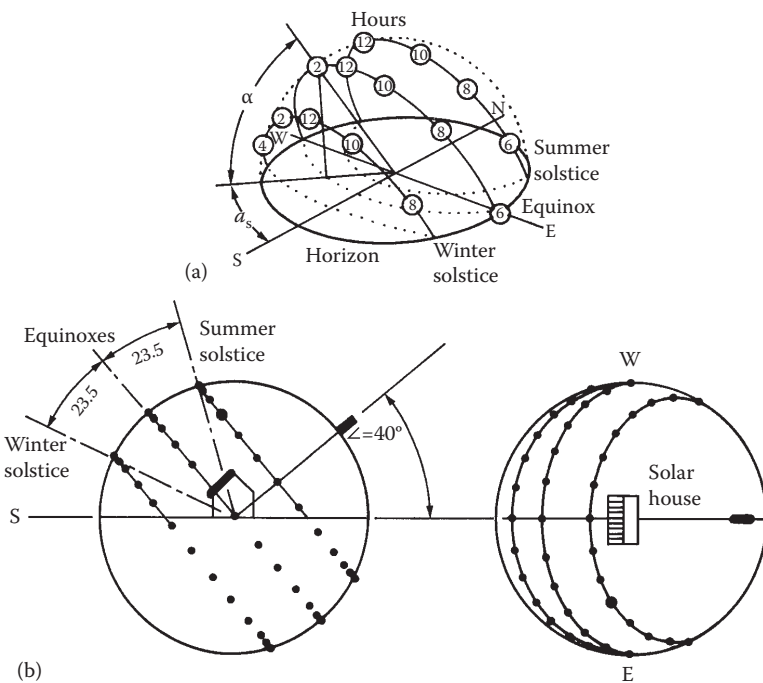


FIGURE 2.10

Sun paths for the summer solstice (6/21), the equinoxes (3/21 and 9/21), and the winter solstice (12/21) for a site at 40°N: (a) isometric view; (b) elevation and plan views.

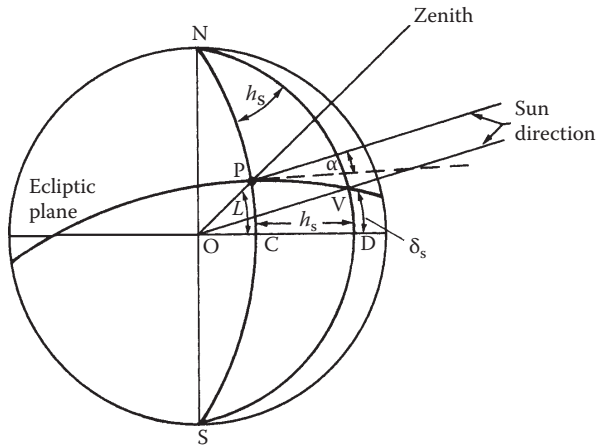


FIGURE 2.11

Definition of solar hour angle h_s (CND), solar declination δ_s (VOD), and latitude L (POC); P, site of interest. (Modified from Kreider, J.F. and F. Kreith, *Solar Heating and Cooling*, Washington, DC: Hemisphere Publ. Corp., 1982.)

The solar altitude angle, α , can be found from the application of the law of cosines to the geometry of Figure 2.11 and simplification as

$$\sin \alpha = \sin L \sin \delta_s + \cos L \cos \delta_s \cos h_s. \quad (2.28)$$

Using a similar technique, the solar azimuth angle, a_s , can be found as

$$\sin a_s = \cos \delta_s \sin h_s / \cos \alpha. \quad (2.29)$$

At local solar noon, $h_s = 0$; therefore, $\alpha = 90 - |L - \delta_s|$, and $a_s = 0$.

In calculating the solar azimuth angle from Equation 2.29, a problem occurs whenever the absolute value of a_s is greater than 90° . A computational device usually calculates the angle as less than 90° since $\sin a_s = \sin(180 - a_s)$. The problem can be solved in the following way:

For $L > \delta_s$, the solar times when the sun is due east (t_E) or due west (t_W) can be calculated by t_E or $t_W = 12:00$ noon $\mp (\cos^{-1}[\tan \delta_s / \tan L])/(15^\circ/h)$ ($-$ for t_E , $+$ for t_W).

For solar times earlier than t_E or later than t_W , the sun would be north (south in the Southern Hemisphere) of the east–west line and the absolute value of a_s would be greater than 90° , which may be calculated as $a_s = +$ or $- (180^\circ - |a_s|)$.

For $|L| \leq |\delta_s|$, the sun remains north (south in the Southern Hemisphere) of the east–west line and the true value of a_s is greater than 90° .

Sunrise and *sunset* times can be estimated by finding the hour angle for $\alpha = 0$. Substituting $\alpha = 0$ in Equation 2.28 gives the hour angles for sunrise (h_{sr}) and sunset (h_{ss}) as

$$h_{ss} \text{ or } h_{sr} = \pm \cos^{-1}[-\tan L \cdot \tan \delta_s]. \quad (2.30)$$

It should be emphasized that Equation 2.30 is based on the center of the sun being at the horizon. In practice, sunrise and sunset are defined as the times when the upper limb of the sun is on the horizon. Because the radius of the sun is $16'$, the sunrise would occur when $\alpha = -16'$. Also, at lower solar elevations, the sun will appear on the horizon when it is actually $34'$ below the horizon. Therefore, for apparent sunrise or sunset, $\alpha = -50'$.

Example 2.1a

Find the solar altitude and azimuth angles at solar noon in Gainesville, Florida, on February 1. Also find the sunrise and sunset times in Gainesville on that day.

Solution

For Gainesville,

$$\text{Latitude } L = 29^\circ + 41' \text{ N or } 29.68^\circ \text{ N.}$$

$$\text{Longitude } l_{\text{local}} = 82^\circ + 16' \text{ W or } 82.27^\circ \text{ W.}$$

On February 1, day number

$$n = 32.$$

Therefore, declination

$$\begin{aligned}\delta_s &= 23.45 \sin[360(284 + 32)/365]^\circ \\ &= -17.5^\circ\end{aligned}$$

At solar noon, $h_s = 0$. Therefore,

$$\begin{aligned}\sin \alpha &= \cos L \cos \delta_s \cos h_s + \sin L \sin \delta_s \\ &= \cos(29.68^\circ) \cos(-17.5^\circ) \cos(0) + \sin(29.68^\circ) \sin(-17.5^\circ),\end{aligned}$$

or

$$\alpha = 42.82^\circ$$

$$\sin a_s = \cos(-17.5^\circ) \sin(0) / \cos(42.8^\circ) = 0,$$

or

$$a_s = 0.$$

At solar noon, α can also be found as

$$\begin{aligned}\alpha &= 90 - |L - \delta_s|^\circ \\ &= 90 - |29.68 + 17.5|^\circ = 42.82^\circ \\ h_{ss} \text{ or } h_{sr} &= \pm \cos^{-1}[-\tan L \cdot \tan \delta_s] \\ &= \pm \cos^{-1}[-\tan(29.68^\circ) \tan(-17.5^\circ)] \\ &= \pm 79.65^\circ.\end{aligned}$$

$$\text{Time from solar noon} = \pm(79.65^\circ)(4 \text{ min/degree})$$

$$= \pm 319 \text{ min or } \pm (5 \text{ hr } 19 \text{ min}).$$

$$\text{Sunrise time} = 12:00 \text{ Noon} - (5 \text{ hr } 19 \text{ min})$$

$$= 6 \text{ hr } 41 \text{ min a.m. (solar time).}$$

$$\text{Sunset time} = 12:00 \text{ Noon} + (5 \text{ hr } 19 \text{ min})$$

$$= 5 \text{ hr } 19 \text{ min p.m. (solar time).}$$

To convert these times to local times, we need to find ET:

$$ET = (9.87 \sin 2B - 7.53 \cos B - 1.5 \sin B) \text{ min.}$$

$$\begin{aligned} B &= \frac{360}{364}(n - 81) = \frac{360}{364}(32 - 81) \\ &= -48.46^\circ. \end{aligned}$$

Therefore,

$$ET = -13.67 \text{ min.}$$

$$LST = \text{Solar time} - ET - 4(l_{st} - l_{local}).$$

Gainesville, Florida, is in the Eastern Standard Time (EST) zone, where $l_{st} = 75^\circ\text{W}$. Therefore,

$$\begin{aligned} LST &= \text{Solar time} - (-13.67 \text{ min}) - 4(75 - 82.27) \text{ min} \\ &= \text{Solar time} + 42.75 \text{ min}. \end{aligned}$$

Therefore,

$$\begin{aligned} \text{Sunrise time} &= 6:41 \text{ a.m.} + 43 \text{ min} \\ &= 7:24 \text{ a.m. EST}, \end{aligned}$$

and

$$\begin{aligned} \text{Sunset time} &= 5:19 \text{ p.m.} + 43 \text{ min} \\ &= 6:02 \text{ p.m. EST}. \end{aligned}$$

Note: Since the sunrise and sunset times are calculated when the center of the sun is at the horizon, they differ from the apparent times. If we use $\alpha = -50'$, the apparent sunrise and sunset times would be 7:20 a.m. EST and 6:06 p.m. EST, respectively.

Example 2.1b

Repeat the calculations of Example 2.1a for Canberra, Australia.

Latitude $L = 35^\circ - 18\text{ S}$ or 35.3°S .

Longitude $l_{local} = 149^\circ - 11\text{ E}$ or 149.18°E .

Standard Meridian = 150°E .

Solution

Using the values of δ_s and ET calculated in Example 2.1a, and taking the latitude and longitude as -35.3° and -149.18° , respectively, the solar angles α and a_s are found as

$$\sin \alpha = \cos(-35.3^\circ) \cos(-17.5^\circ) \cos(0) + \sin(-35.3^\circ) \sin(-17.5^\circ)$$

or

$$\alpha = 72.2^\circ.$$

$$\sin a_s = \cos(-17.5^\circ) \sin(0) / \cos(72.2^\circ)$$

or

$$a_s = 0^\circ,$$

α may also be found as

$$\begin{aligned} \alpha &= 90^\circ - |-35.3^\circ + 17.5^\circ| \\ &= 72.2^\circ. \end{aligned}$$

The hour angles for sunrise and sunset are found as

$$\begin{aligned} h_{ss}, h_{sr} &= \pm \cos^{-1}[-\tan(-35.3^\circ) \cdot \tan(-17.5^\circ)] \\ &= \pm 102.9^\circ. \end{aligned}$$

$$\begin{aligned} \text{Time from solar noon} &= \pm(102.9^\circ) \cdot (4 \text{ min/degree}) \\ &= \pm 412 \text{ min or } \pm (6 \text{ h } 52 \text{ min}). \end{aligned}$$

Sunrise time = 5:08 a.m. (solar time), and

Sunset time = 6:52 p.m. (solar time).

Take l_{st} for Canberra as -150° .
Therefore,

$$\begin{aligned} \text{LST} &= \text{Solar time} - (-13.67 \text{ min}) - 4(-150^\circ + 149.18^\circ) \text{ min} \\ &= \text{Solar time} + 17 \text{ min}. \end{aligned}$$

Therefore,

Sunrise time = 5:25 a.m. (LST)

Sunset time = 7:09 p.m. (LST)

(As explained in the previous example, the apparent sunrise and sunset times would be 5:21 a.m. and 7:13 p.m., respectively.)

Example 2.2

Find the solar altitude and azimuth angles in Tocumen (Panamá) on (a) June 1 at 7 a.m. and (b) December 1 at 2 p.m. Also find the sunrise and sunset times on these days.

Solution

For Tocumen (Panamá):

$$L = 9.05^\circ \text{ N} (+), l_{\text{local}} = 79.37^\circ \text{ W} (+), \text{ and } l_{\text{st}} = 75^\circ \text{ W} (+)$$

a. For June 1, $n = 152$.

The declination angles for this day are

$$\delta_s = 23.45^\circ \sin \frac{360}{365} (284 + 152)$$

$$\delta_s = 22.04^\circ.$$

The local time is 7:00 a.m. The solar time is given by

$$ST = LST + ET + (l_{\text{st}} - l_{\text{local}}) \cdot 4 \frac{\text{min}}{1^\circ}$$

The equation of time is

$$B = \frac{360}{364} (152 - 81) = 70.22^\circ$$

$$\begin{aligned} ET(\text{min}) &= 9.87 \sin(2 \cdot 70.22^\circ) - 7.53 \cos(70.22^\circ) - 1.5 \sin(70.22^\circ) \\ &= 2.32 \text{ min}. \end{aligned}$$

Then, the solar time is

$$\begin{aligned} ST &= 7:00 + 2.32 \text{ min} + (75^\circ - 79.37^\circ) \cdot 4 \text{ min} \\ &= 7:00 - 15.16 \text{ min} \\ &= 6:44.84 \text{ a.m.} \end{aligned}$$

The hour angle is

$$\begin{aligned} h_s &= (ST - 12) \frac{15^\circ}{h} = (6.7474 - 12) \frac{15^\circ}{h} \\ &= -78.78^\circ. \end{aligned}$$

The solar altitude angle is

$$\sin \alpha = \cos \delta_s \cos L \cos h_s + \sin \delta_s \sin L$$

$$\sin \alpha = \cos(22.04^\circ) \cos(9.05^\circ) \cos(-78.78^\circ) + \sin(22.04^\circ) \sin(9.05^\circ)$$

and

$$\alpha = 13.71^\circ.$$

The solar azimuth angles are defined by

$$\begin{aligned} \sin a_s &= \cos \delta_s \sin h_s / \cos \alpha \\ &= \cos(22.04^\circ) \sin(-78.78^\circ) / \cos(13.71^\circ) \end{aligned}$$

and

$$a_s = -69.37^\circ.$$

We need to find out if $|a_s|$ is greater than 90° . For $|L| \leq |\delta_s|$, sun is north, and $|a_s| > 90^\circ$. Therefore, the real value of a_s is

$$a_s = -180^\circ + |a_s| = -110.62^\circ.$$

The sunrise and sunset are obtained from:

$$\begin{aligned} h_{ss} \text{ or } h_{sr} &= \pm \cos^{-1}[-\tan L \tan \delta_s] \\ &= \pm 93.697^\circ \\ &= 6.247 \text{ h} \end{aligned}$$

$$h_{sr} = 12:00 - 6.247 = 5.753 \text{ a.m. (solar time)}$$

$$h_{ss} = 12:00 + 6.247 = 18.247 \text{ p.m. (solar time)}$$

$$\text{LST} = \text{ST} - \text{ET} - (L_{st} - L_{local}) \cdot 4 \frac{\text{min}}{1^\circ}$$

Then,

$$\begin{aligned} h_{sr} &= 5.753 - (-15.16) \text{ min} \\ &= 6:00:20 \text{ a.m. (local time)} \end{aligned}$$

$$\begin{aligned} h_{ss} &= 18.247 - (-15.16) \text{ min} \\ &= 18:30 \text{ p.m. (local time).} \end{aligned}$$

(As explained in the previous example, the apparent sunrise and sunset times would be 5:56 a.m. and 6:34 p.m., respectively.)

- b. For December 1, $n = 335$.

The declination angles for this day are

$$\delta_s = 23.45^\circ \sin \frac{360}{365} (284 + 335)$$

$$\delta_s = -22.10^\circ.$$

The local time is 2:00 p.m. (or 14:00 p.m.). The solar time is given by

$$ST = LST + ET + (l_{st} - l_{local}) \cdot 4 \frac{\text{min}}{1^\circ}.$$

The equation of time is

$$B = \frac{360}{364} (335 - 81) = 251.21^\circ$$

$$\begin{aligned} ET(\text{min}) &= 9.87 \sin(2 \cdot 251.21^\circ) - 7.5 \cos(251.21^\circ) - 1.5 \sin(251.21^\circ) \\ &= 9.9 \text{ min.} \end{aligned}$$

Then, the solar time is

$$\begin{aligned} ST &= 14:00 + 9.9 \text{ min} + (75^\circ - 79.37^\circ) \cdot 4 \text{ min} \\ &= 14:00 - 7.58 \text{ min} \\ &= 13:52:25 \text{ pm} \end{aligned}$$

The hour angle is

$$\begin{aligned} h_s &= (ST - 12) \frac{15^\circ}{\text{h}} = (13.873 - 12) \frac{15^\circ}{\text{h}} \\ &= 28.09^\circ. \end{aligned}$$

The solar altitude angle is

$$\begin{aligned}\sin \alpha &= \cos \delta_s \cos L \cos h_s + \sin \delta_s \sin L \\ &= \cos(-22.10^\circ) \cos(9.05^\circ) \cos(28.09^\circ) + \sin(-22.10^\circ) \sin(9.05^\circ)\end{aligned}$$

and

$$\alpha = 49.29^\circ.$$

The solar azimuth angles are defined by

$$\begin{aligned}\sin a_s &= \cos \delta_s \sin h_s / \cos \alpha \\ &= \cos(-22.10^\circ) \sin(28.09^\circ) / \cos(49.29^\circ)\end{aligned}$$

and

$$a_s = 41.99^\circ.$$

We need to find out if $|a_s|$ is greater than 90° . For $L \leq \delta_s$:

$$t_E, t_W = 12:00 \pm \cos^{-1} \frac{\tan \delta_s}{\tan L} \frac{h}{15^\circ}.$$

For this problem, $|\tan \delta_s| > |\tan L|$, which means that there is no solution for t_E or t_W . Therefore, the sun remains south and the value of a_s is the same:

$$a_s = 41.99^\circ.$$

The sunrise and sunset are obtained from

$$\begin{aligned}h_{ss} \text{ or } h_{sr} &= \pm \cos^{-1} [\tan L \tan \delta_s] \\ &= \pm 86.29^\circ \\ &= \pm 5.753 \text{ h}\end{aligned}$$

$$h_{sr} = 12:00 - 5.753 = 6.247 \text{ a.m. (solar time)}$$

$$h_{ss} = 12:00 + 5.753 = 17.753 \text{ p.m. (solar time)}$$

$$\text{LST} = \text{ST} - \text{ET} - (l_{st} - l_{local}) \cdot 4 \frac{\text{min}}{1^\circ}.$$

Then,

$$\begin{aligned} h_{sr} &= 6.247 - (-7.58) \text{ min} \\ &= 6:22:24 \text{ a.m. (local time)} \end{aligned}$$

$$\begin{aligned} h_{ss} &= 17.753 - (-7.58) \text{ min} \\ &= 17:52:46 \text{ p.m. (local time).} \end{aligned}$$

(As explained in the previous example, the apparent sunrise and sunset times would be 6:18 a.m. and 5:57 p.m., respectively.)

Knowledge of the solar angles is helpful in the design of passive solar buildings, especially the placement of windows for solar access and the roof overhang for shading the walls and windows at certain times of the year. The following example illustrates this point.

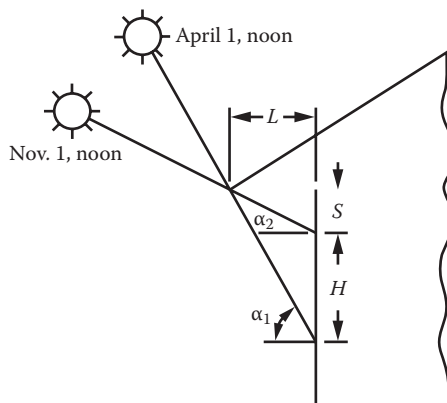
Example 2.3a

Find the roof overhang L of a south-facing window of height $H = 1 \text{ m}$, such that the window is completely shaded at solar noon on April 1 and not shaded at all at noon on November 1. Assume that the roof extends far beyond the window on either side. Location: Gainesville, Florida. Also, find the overhang if $S = 1.3 \text{ m}$.

Solution

From the geometry of the figure,

$$L = S / \tan \alpha_2.$$



Also,

$$L = (S + H)/\tan \alpha_1.$$

On April 1,

$$n = 91.$$

$$\delta_s = 23.45^\circ \sin[360(284 + 91)/365] = 4.02^\circ$$

Therefore, at solar noon,

$$\alpha_1 = 90 - |29.68 - 4.02| = 64.34^\circ.$$

On November 1,

$$n = 305.$$

$$\delta_s = 23.45^\circ \sin[360(284 + 305)/365] = -15.4^\circ.$$

Therefore,

$$\begin{aligned}\alpha_2 &= 90^\circ - |29.68^\circ + 15.4^\circ| \\ &= 44.9^\circ\end{aligned}$$

$$L = \frac{H}{\tan \alpha_1 - \tan \alpha_2} = \frac{1}{\tan(64.43^\circ) - \tan(44.9^\circ)} = 0.92 \text{ m.}$$

$$S = L \tan \alpha_2 = 0.92 \times \tan(44.9^\circ) = 0.92 \text{ m.}$$

If $S = 1.3 \text{ m}$, then,

$$L = 1.3/\tan 44.9^\circ = 1.3 \text{ m.}$$

Also,

$$L = 2.3/\tan 64.34^\circ = 1.1 \text{ m.}$$

Therefore, $1.1 \text{ m} \leq L \leq 1.3 \text{ m}$.

Example 2.3b

Repeat the above example for Canberra, Australia, for a north-facing window, such that the window is completely shaded at noon on November 1 and completely lit at noon on April 1.

Solution

The figure shown in Example 2.3a may be used if we take the solar angles α_1 and α_2 as shown in the figure to be on November 1 and April 1, respectively. From Example 2.3a,

$$\begin{aligned}\delta_s &= 4.02^\circ \text{ on April 1, and} \\ &= -15.4^\circ \text{ on November 1.}\end{aligned}$$

For Canberra, Australia, Latitude = -35.3° .
Therefore, at solar noon,

$$\begin{aligned}\alpha_1 &= 90^\circ - |-35.3^\circ + 15.4^\circ| \\ &= 70.1^\circ\end{aligned}$$

and

$$\begin{aligned}\alpha_2 &= 90^\circ - |-35.3^\circ - 4.02^\circ| \\ &= 50.68^\circ.\end{aligned}$$

Following the procedure in Example 2.3a, therefore,

$$\begin{aligned}L &= \frac{1}{\tan(70.1^\circ) - \tan(50.68^\circ)} \\ &= 0.65 \text{ m}\end{aligned}$$

and

$$\begin{aligned}S &= 0.65 \tan(50.68^\circ) \\ &= 0.79 \text{ m.}\end{aligned}$$

If S is given as 1.3 m, then,

$$L = 1.3 / \tan(50.68^\circ) = 1.07 \text{ m.}$$

Also,

$$L = 2.3 / \tan(70.1^\circ) = 0.83 \text{ m;}$$

therefore, $0.83 \text{ m} \leq L \leq 1.07 \text{ m.}$

2.3.2 Sun-Path Diagram

The projection of the sun's path on the horizontal plane is called a *sun-path diagram*. Such diagrams are very useful in determining shading phenomena

associated with solar collectors, windows, and shading devices. As shown earlier, the solar angles (α , a_s) depend upon the hour angle, declination, and latitude. Since only two of these variables can be plotted on a two-dimensional graph, the usual method is to prepare a different sun-path diagram for each latitude with variations of hour angle and declination shown for a full year. A typical sun-path diagram is shown in Figure 2.12 for 30°N latitude.

Sun-path diagrams for a given latitude are used by entering them with appropriate values of declination δ_s and hour angle h_s . The point at the intersection of the corresponding δ_s and h_s lines represents the instantaneous location of the sun. The solar altitude can then be read from the concentric circles in the diagram; the azimuth, from the scale around the circumference of the

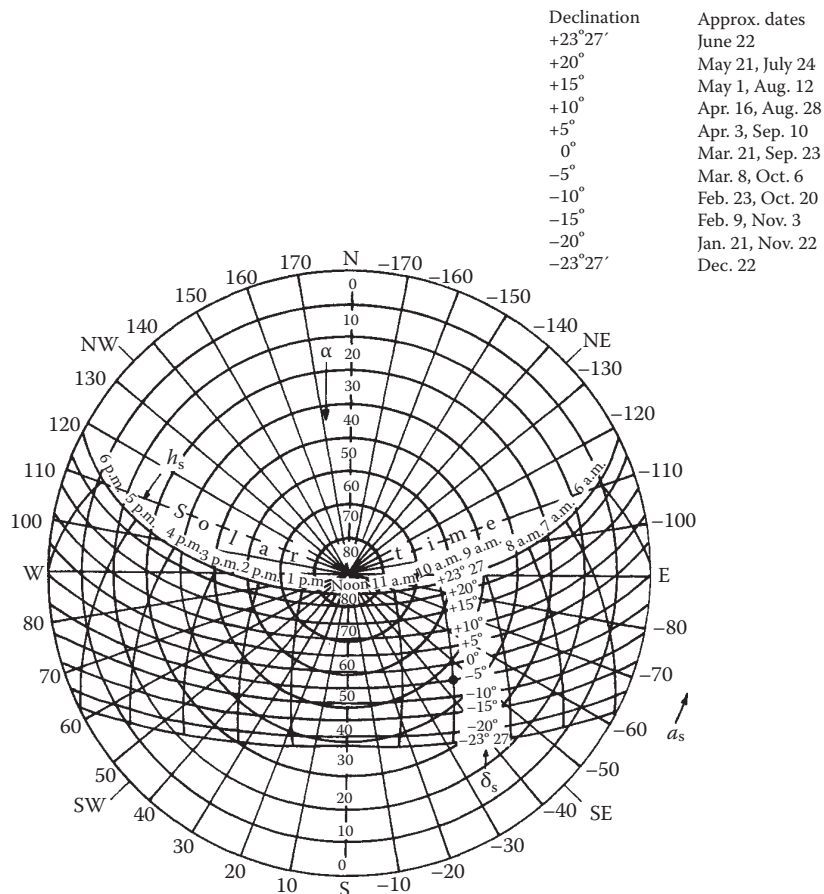


FIGURE 2.12

Sun-path diagram for 30°N latitude showing altitude and azimuth angles. (Modified from Kreider, J.F. and F. Kreith, *Solar Heating and Cooling*, revised 1st ed. Washington, DC: Hemisphere Publ. Corp., 1977.)

diagram. A complete set of sun-path diagrams is contained in Appendix 2 (Figure A2.1).

Example 2.4

Using Figure 2.12, determine the solar altitude and azimuth for March 8 at 10 a.m. Compare the results to those calculated from the basic equations (Equations 2.28 and 2.29).

Solution

On March 8, the solar declination is -5° ; therefore, the -5° sun path is used. The intersection of the 10 a.m. line and the -5° declination line in the diagram represents the sun's location; it is marked with a heavy dot in Figure 2.12. The sun position lies midway between the 40° and 50° altitude circles, say at 45° , and midway between the -40° and -50° azimuth radial lines, say at -45° . Thus, $\alpha \cong 45^\circ$ and $a_s \cong -45^\circ$. Equations 2.28 and 2.29 give precise values for α and a_s :

$$\sin \alpha = \sin(30^\circ) \sin(-5^\circ) + \cos(30^\circ) \cos(-5^\circ) \cos(-30^\circ)$$

$$\alpha = 44.7^\circ$$

$$\sin a_s = \frac{\cos(-5^\circ) \sin(-30^\circ)}{\cos(44.7^\circ)}$$

$$a_s = -44.5^\circ$$

Therefore, the calculated values are within $\pm 0.5^\circ$ (1%) of those read from the sun-path diagram.

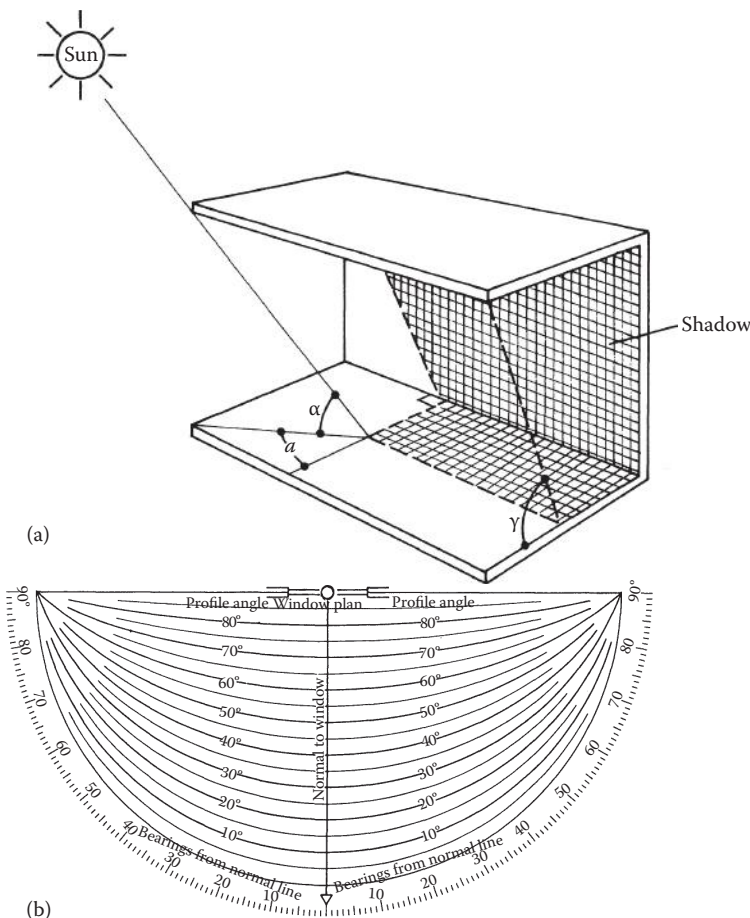
2.3.3 Shadow-Angle Protractor

The shadow-angle protractor used in shading calculations is a plot of solar altitude angles, projected onto a given plane, versus the solar azimuth angle. The projected altitude angle is usually called the *profile angle* γ . It is deemed as the angle between the normal to a surface and the projection of the sun's rays on a vertical plane normal to the same surface. The profile angle is shown in Figure 2.13a with the corresponding solar altitude angle. The profile angle, which is always used in sizing shading devices, is given by

$$\tan \gamma = \sec a \tan \alpha, \quad (2.31)$$

where a is the solar azimuth angle with respect to the wall normal.

Figure 2.13b shows the shadow-angle protractor to the same scale as the sun-path diagrams in Figure 2.12 and Appendix 2. It is used by plotting the limiting values of profile angle γ and azimuth angle a , which will start to cause shading of a particular point. The shadow-angle protractor is usually

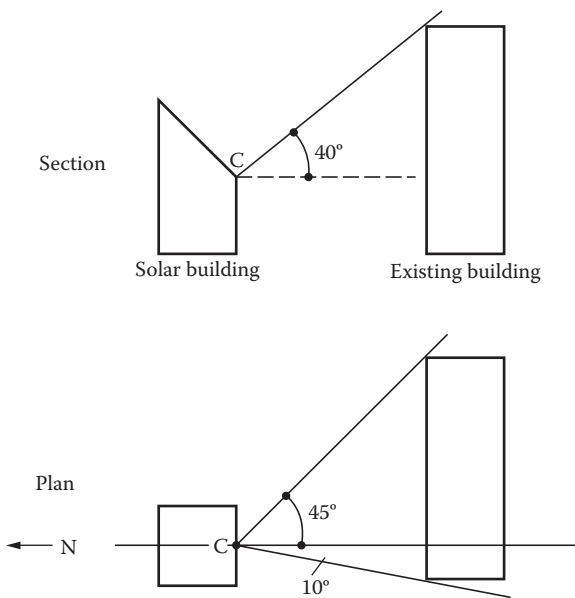
**FIGURE 2.13**

(a) Sketch showing the profile angle γ and the corresponding solar altitude angle α for a window shading device; (b) the shadow-angle protractor. (With permission from the Libby–Owens–Ford Glass Co.)

traced onto a transparent sheet so that the shadow map constructed on it can be placed over the pertinent sun-path diagram to indicate the times of day and months of the year during which shading will take place. The use of the shadow-angle protractor is best illustrated by an example.

Example 2.5

A solar building with a south-facing collector is sited to the north–northwest of an existing building. Prepare a shadow map showing what months of the year and what part of the day point C at the base of the solar collector will be shaded. Plan and elevation views are shown in Figure 2.14. Latitude = 40°N.

**FIGURE 2.14**

Plan and elevation view of proposed solar building and existing building, which may shade solar collector at point C.

Solution

The limiting profile angle for shading is 40° and the limiting azimuth angles are -45° and $+10^\circ$ as shown in Figure 2.14. These values are plotted on the shadow-angle protractor (Figure 2.15a). The shadow map, when superimposed on the sun-path diagram (Figure 2.15b), shows that point C will be shaded during the following times of day for the periods shown:

Declination	Date	Time of Day
$-23^\circ 27'$	Dec 22	8:45 a.m.–12:40 p.m.
-20°	Jan 21, Nov 22	8:55 a.m.–12:35 p.m.
-15°	Feb 9, Nov 3	9:10 a.m.–12:30 p.m.

In summary, during the period from November 3 to February 9, point C will be shaded between 3 and 4 hours. It will be shown later that this represents approximately a 50% loss in collector performance for point C, which would be unacceptable for a collector to be used for heating a building in winter.

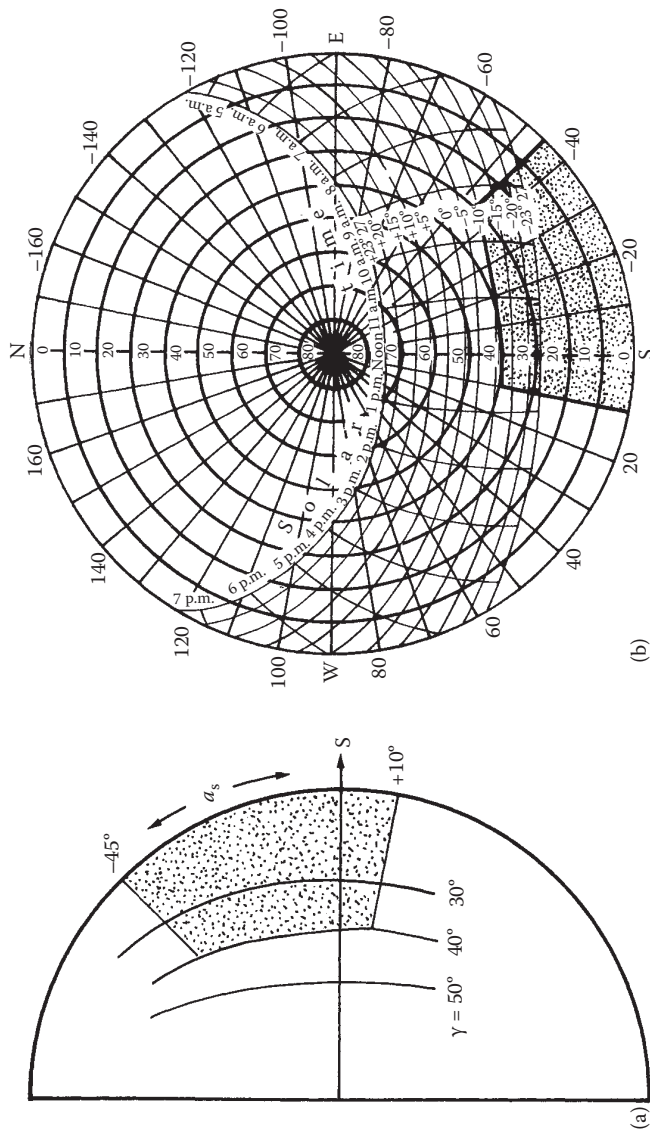


FIGURE 2.15
 (a) Shadow map constructed for the example shown in Figure 2.14; (b) shadow map superimposed on a sun-path diagram.

2.4 Solar Radiation

Detailed information about solar radiation availability at any location is essential for the design and economic evaluation of a solar energy system. Long-term measured data of solar radiation are available for a large number of locations in the United States and other parts of the world. Where long-term measured data are not available, various models based on available climatic data can be used to estimate the solar energy availability. Solar energy is in the form of electromagnetic radiation with the wavelengths ranging from approximately $0.3\text{ }\mu\text{m}$ (10^{-6} m) to over $3\text{ }\mu\text{m}$, which correspond to ultraviolet (less than $0.4\text{ }\mu\text{m}$), visible (0.4 and $0.7\text{ }\mu\text{m}$), and infrared (over $0.7\text{ }\mu\text{m}$). Most of this energy is concentrated in the visible and the near-infrared wavelength range (see Figure 2.16). The incident solar radiation, sometimes called *insolation*, is measured as irradiance, or the energy per unit time per unit area (or power per unit area). The units most often used are watts per square meter (W/m^2), British thermal units per hour per square foot ($\text{Btu}/\text{h}\cdot\text{ft}^2$), and Langleys per minute (calories per square centimeter per minute, $\text{cal}/\text{cm}^2\cdot\text{min}$).

2.4.1 Extraterrestrial Solar Radiation

The average amount of solar radiation falling on a surface normal to the rays of the sun outside the atmosphere of the earth (extraterrestrial) at mean earth-sun distance (D_0) is called the *solar constant*, I_0 . Measurements by NASA indicated the value of the solar constant to be 1353 W/m^2 ($\pm 1.6\%$), $429\text{ Btu/h}\cdot\text{ft}^2$ or

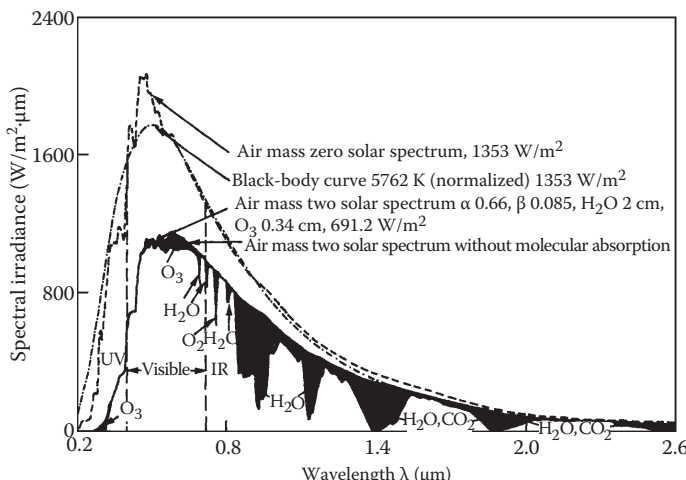


FIGURE 2.16

Extraterrestrial solar radiation spectral distribution. Also shown are equivalent black-body and atmosphere-attenuated spectra.

1.94 cal/cm²·min (Langleys/min). This value was revised upward by Frohlich et al. (1973) to 1377 W/m² or 437.1 Btu/h·ft² or 1.974 Langleys/min, which was the value used in compiling SOLMET data in the United States (Quinlan 1977, 1979). Recently, new measurements have found the value of the solar constant to be 1366.1 W/m². A value of 1367 W/m² is also used by many references.

The variation in seasonal solar radiation availability at the surface of the earth can be understood from the geometry of the relative movement of the earth around the sun. Since the earth's orbit is elliptical, the earth–sun distance varies during a year, the variation being $\pm 1.7\%$ from the average. Therefore, the extraterrestrial radiation, I , also varies by the inverse square law as below:

$$I = I_0(D_0/D)^2 \quad (2.32)$$

where D is the distance between the sun and the earth and D_0 is the yearly mean earth–sun distance (1.496×10^{11} m). The $(D_0/D)^2$ factor may be approximated as (Spencer 1971)

$$(D_0/D)^2 = 1.00011 + 0.034221 \cos(x) + 0.00128 \sin(x) \\ + 0.000719 \cos(2x) + 0.000077 \sin(2x), \quad (2.33)$$

where

$$x = 360(n - 1)/365^\circ, \quad (2.34)$$

and n = day number (starting from January 1 as 1). The following approximate relationship may also be used without much loss of accuracy:

$$I = I_0[1 + 0.034 \cos(360n/365.25)^\circ]. \quad (2.35)$$

Figure 2.17 also shows the relationship of the extraterrestrial solar radiation to the solar constant. For many solar energy applications, such as photovoltaics and photocatalysis, it is necessary to examine the distribution of energy within the solar spectrum. Table 2.1 shows the spectral irradiance at

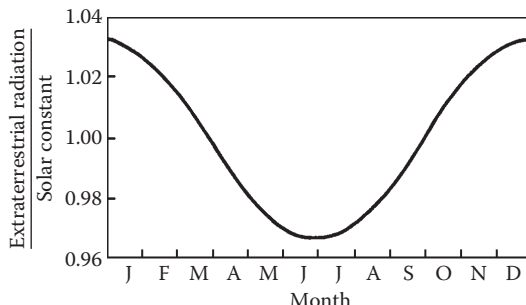


FIGURE 2.17

Effect of the time of year on the ratio of extraterrestrial radiation to the nominal solar constant.

TABLE 2.1
Extraterrestrial Solar Irradiance

λ (μm)	E_λ (W/m ² μm)	D_λ (%)	λ (μm)	E_λ (W/m ² μm)	D_λ (%)	λ (μm)	E_λ (W/m ² μm)	D_λ (%)
0.115	0.00799	3.76E-04	0.43	1.389	11.98	0.90	889.60	63.91
0.14	0.07694	1.07E-03	0.44	1848	13.25	1.00	730.70	69.84
0.16	0.20640	1.25E-03	0.45	2131	14.72	1.2	488.60	78.55
0.18	2.06	2.45E-03	0.46	2092	16.26	1.4	342.90	84.58
0.20	7.93	8.68E-03	0.47	2010	17.79	1.6	247.70	88.89
0.22	51.91	0.05	0.48	2102	19.32	1.8	168.20	91.88
0.23	59.09	0.08	0.49	2072	20.78	2.0	115.90	93.91
0.24	42.19	0.12	0.50	1932	22.24	2.2	82.58	95.35
0.25	62.28	0.16	0.51	1915	23.66	2.4	58.47	96.36
0.26	90.16	0.22	0.52	1864	25.00	2.6	43.54	97.10
0.27	297.50	0.38	0.53	1938	26.38	2.8	33.25	97.65
0.28	78.46	0.52	0.54	1813	27.78	3.0	25.60	98.08
0.29	617.70	0.74	0.55	1905	29.16	3.2	20.08	98.42
0.30	416.60	1.14	0.56	1812	30.52	3.4	15.75	98.68
0.31	464.80	1.56	0.57	1803	31.86	3.6	12.83	98.89
0.32	836.30	2.08	0.58	1818	33.19	3.8	10.39	99.06
0.33	1162	2.72	0.59	1716	34.51	4.0	8.30	99.19
0.34	1133	3.42	0.60	1737	35.80	4.5	5.03	99.43
0.35	1081	4.12	0.62	1681	38.29	5.0	3.27	99.58
0.36	1188	4.84	0.64	1591	40.68	6.0	1.64	99.75
0.37	1376	5.67	0.66	1517	42.94	7.0	0.90360	99.84
0.38	1096	6.50	0.68	1474	45.14	8.0	0.53890	99.89
0.39	1301	7.26	0.70	1413	47.25	10.0	0.22720	99.94
0.40	1727	8.12	0.72	1361	49.29	15.0	0.04418	99.98
0.41	1610	9.39	0.75	1273	52.16	20.0	0.01385	99.99
0.42	1787	10.71	0.80	1129	56.54	50.0	0.00036	100.0

Source: Adapted from Gueymard, C., *Sol Energy* 76, 423-453, 2003.

Note: Solar constant = 1366.1 W/m²; E_λ is the solar spectral irradiance; D_λ is the percentage of the solar constant associated with wavelengths shorter than λ .

the mean earth–sun distance for a solar constant of 1366.1 W/m^2 as a function of wavelength according to the standard spectrum data published by NASA. Use of the data is illustrated in the following example.

Example 2.6

Calculate the fraction of solar radiation within the visible part of the spectrum, that is, between 0.40 and $0.70 \mu\text{m}$.

Solution

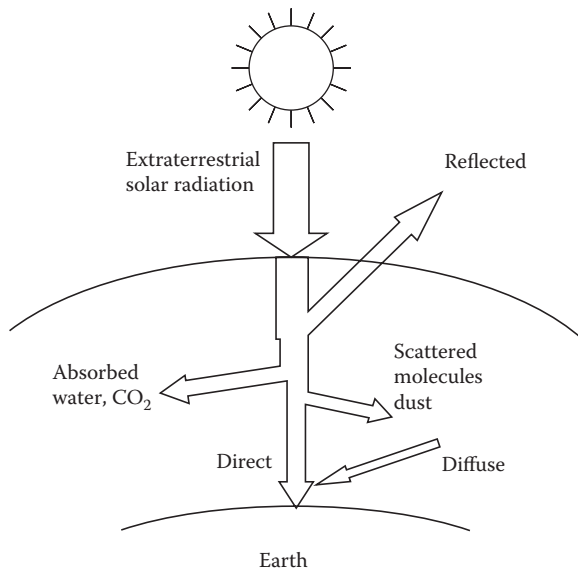
The first column in Table 2.1 gives the wavelength. The second column gives the averaged solar spectral irradiance in a band centered at the wavelength in the first column. The fourth column, $D\lambda$, gives the percentage of solar total radiation at wavelengths shorter than the value of λ in the first column. At a value of $0.40 \mu\text{m}$, 8.12% of the total radiation occurs at shorter wavelengths. At a wavelength of 0.70 , 47.25% of the radiation occurs at shorter wavelengths. Consequently, 39.13% of the total radiation lies within the band between 0.40 and $0.70 \mu\text{m}$, and the total energy received outside the earth's atmosphere within that spectral range is 534.6 W/m^2 ($169.6 \text{ Btu/h}\cdot\text{ft}^2$).

2.5 Estimation of Terrestrial Solar Radiation

As extraterrestrial solar radiation, I , passes through the atmosphere, a part of it is reflected back into space, a part is absorbed by air and water vapor, and some gets scattered by molecules of air, water vapor, aerosols, and dust particles (Figure 2.18). The part of solar radiation that reaches the surface of the earth with essentially no change in direction is called *direct* or *beam radiation*. The scattered diffuse radiation reaching the surface from the sky is called the sky *diffuse radiation*.

Although extraterrestrial radiation can be predicted with certainty,* radiation levels on the earth are subject to considerable uncertainty resulting from local climatic interactions. The most useful solar radiation data are based on long-term (30 years or more) measured average values at a location, which unfortunately are not available for most locations in the world. For such locations, an estimating method (theoretical model) based on some measured climatic parameter may be used. This chapter describes several ways of estimating terrestrial solar radiation; all have large uncertainties (as much as $\pm 30\%$) associated with them.

* The effect of sunspots, which may cause up to 0.5% variation, is neglected.

**FIGURE 2.18**

Attenuation of solar radiation as it passes through the atmosphere.

2.5.1 Atmospheric Extinction of Solar Radiation

As solar radiation I travels through the atmosphere, it is attenuated because of absorption and scattering. If K is the local extinction coefficient of the atmosphere, the beam solar radiation at the surface of the earth can be written according to Bouger's law (Equation 2.21) as

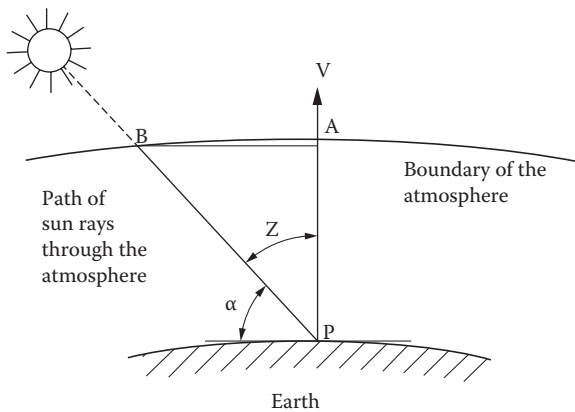
$$I_{b,N} = I e^{-\int K dx}, \quad (2.36)$$

where $I_{b,N}$ is the instantaneous beam solar radiation per unit area normal to the sun's rays and x is the length of travel through the atmosphere. If L_o is the vertical thickness of the atmosphere and

$$\int_0^{L_o} K dx = k, \quad (2.37)$$

the beam normal solar radiation for a solar zenith angle of z will be

$$I_{b,N} = I e^{-k \sec z} = I e^{-k/\sin \alpha} = I e^{-km}, \quad (2.38)$$

**FIGURE 2.19**

Air mass definition; air mass $m = BP/AP = \text{cosec } \alpha$, where α is the altitude angle. The atmosphere is idealized as a constant thickness layer.

where m is a dimensionless path length of sunlight through the atmosphere, sometimes called the *air mass ratio* (Figure 2.19).

$$m = \frac{BP}{AP} \approx \frac{1}{\cos z} \approx \frac{1}{\sin \alpha} \quad (2.39)$$

The following equation gives a more accurate value of air mass according to Kasten and Young (1989)

$$m \approx \frac{1}{\sin \alpha + 0.50572(6.07995 + \alpha)^{-1.6364}}, \quad (2.40)$$

where α is expressed in degrees.

When the solar altitude angle is 90° (sun is overhead), $m = 1$.

2.5.2 Clear-Sky Radiation Model

Gueymard and Thevenard (2009) have described a model that can be used to model solar radiation for clear days for a large number of locations in the world. This model was developed for ASHRAE to calculate the solar heat gain for fenestration; therefore, they named it the ASHRAE Clear Sky Model. This is a simple model that was developed based on a large number of simulations using sophisticated spectral simulations using the SMARTS spectral code developed by Gueymard (2000, 2005, 2008) and validating with ground-based measurements. On the basis of the detailed simulations, Gueymard developed a simple two-band solar irradiance model REST2 (Reference

evaluation of solar transmittance, 2) that can model clear-sky solar irradiance very accurately. The proposed model was developed in two steps.

1. Solar transmittance of clear sky was modeled based on two spectral bands, the first band from 0.29 to 0.7 μm , characterized by absorption by molecules and aerosols, and the second band from 0.7 to 4 μm , characterized by absorption by water vapor and CO_2 . The two-band clear-sky radiation model was used to calculate clear-sky solar irradiance for a large number of “typical” cases and compared with the data covering a large part of the world. Figure 2.20 shows the global sites used in the validation.
2. The second step consisted in developing a condensed model depending on only two monthly parameters described later in this section.

According to the ASHRAE model, the beam and diffuse components are calculated as

$$I_{b,N} = I \left(e^{-\tau_b m^b} \right) \quad (2.41)$$

$$I_{d,h} = I \left(e^{-\tau_d m^d} \right), \quad (2.42)$$

where

$I_{b,N}$: beam normal irradiance per unit area normal to the sun rays

$I_{d,h}$: diffuse horizontal irradiance per unit area on a horizontal surface

I : extraterrestrial normal irradiance

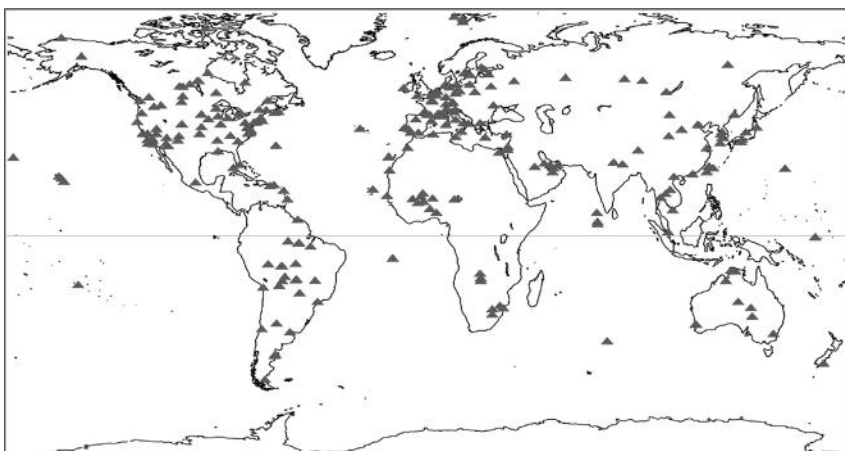


FIGURE 2.20

World sites of interest used in the model. (From Gueymard, C.A. and D. Thevenard, *Sol Energy* 83, 1998–2018, 2009.)

m: air mass

τ_b , τ_d : beam and diffuse optical depths (τ_b and τ_d are more correctly termed pseudo-optical depths, because optical depth is usually employed when the air mass coefficient is unity)

b, d: beam and diffuse air mass exponents

Values of τ_b and τ_d are location specific and vary during the year. They embody the dependence of clear-sky solar radiation upon local conditions, such as elevation, precipitable water content, and aerosols. Their average values are tabulated for the 21st day of each month for all the locations in the tables of climatic design conditions (ASHRAE NIR Fundamentals). Tables A2.2a and A2.2b give values of τ_b and τ_d for various locations in the United States and around the world, respectively.

Air mass exponents *b* and *d* are correlated to τ_b and τ_d through the following empirical relationships:

$$b = 1.219 - 0.043\tau_b - 0.151\tau_d - 0.204\tau_b \cdot \tau_d \quad (2.43)$$

$$d = 0.202 + 0.852\tau_b - 0.007\tau_d - 0.357\tau_b \cdot \tau_d \quad (2.44)$$

This radiation model describes a simple parameterization of a sophisticated broadband radiation model and provides accurate predictions of $I_{b,N}$ and $I_{d,h}$ even at sites where the atmosphere is very hazy or humid most of the time.

Solar radiation on a horizontal surface is given by

$$I_h = (I_{b,N} \sin \alpha + I_{d,h}). \quad (2.45)$$

2.5.3 Solar Radiation on a Tilted Surface

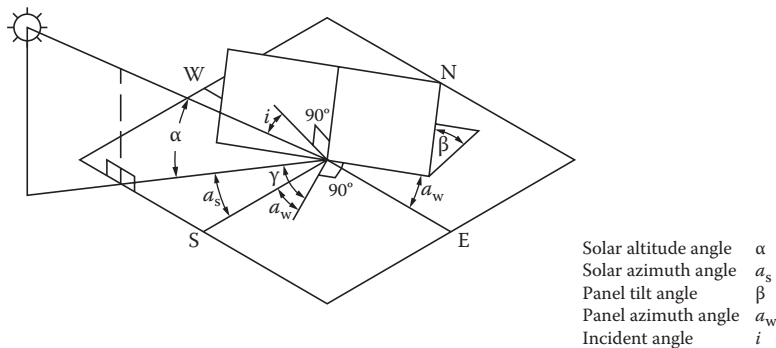
Solar radiation on an arbitrary tilted surface having a tilt angle of β from the horizontal and an azimuth angle of a_w (assumed + west of south), as shown in Figure 2.21, is the sum of components consisting of beam ($I_{b,c}$), sky diffuse ($I_{d,c}$), and ground reflected solar radiation ($I_{r,c}$):

$$I_c = I_{b,c} + I_{d,c} + I_{r,c}. \quad (2.46)$$

If *i* is the *angle of incidence* of the beam radiation on the tilted surface, it is simple to show that the instantaneous beam radiation on the surface per unit area is

$$I_{b,c} = I_{b,N} \cos i. \quad (2.47)$$

From the geometry in Figure 2.21, it can be shown that the angle of incidence *i* for the surface (angle between the normal to the surface and a line collinear with the sun's rays) is related to the solar angles as

**FIGURE 2.21**

Definitions of solar angles for a tilted surface.

$$\cos i = \cos \alpha \cos(a_s - a_w) \sin \beta + \sin \alpha \cos \beta. \quad (2.48)$$

The diffuse radiation on the surface ($I_{d,c}$) can be obtained by multiplying the sky diffuse radiation on a horizontal surface by the view factor between the sky and the surface*:

$$\begin{aligned} I_{d,c} &= I_{d,h}(1 + \cos \beta)/2 \\ &= I_{d,h} \cos^2(\beta/2). \end{aligned} \quad (2.49)$$

The ground reflected solar radiation can be found from the total solar radiation incident on a horizontal surface and the ground reflectance ρ as

$$I_{r,c} = I_h \rho. \quad (2.50)$$

The part of I_r intercepted by the tilted surface can be found by multiplying the ground reflected radiation by the view factor between the surface[†] and the ground:

$$\begin{aligned} I_{r,c} &= \rho I_h (1 - \cos \beta)/2 = \rho I_h \sin^2(\beta/2) \\ &= \rho (I_{b,N} \sin \alpha + I_{d,h}) \sin^2(\beta/2). \end{aligned} \quad (2.51)$$

For ordinary ground or grass, ρ is approximately 0.2, and for snow-covered ground, it can be taken as approximately 0.8.

* The surface has been assumed infinitely large for this view factor. See Section 2.2.3.

[†] The tilted surface and the ground in front of it have been assumed to be infinitely large for this view factor.

Example 2.7a

Find the instantaneous solar radiation at 12:00 noon EST on a solar collector surface ($\beta = 30^\circ$, $a_w = +10^\circ$) on February 1 in Tampa, Florida.

Solution

For Tampa International Airport: $L = 27.96^\circ \text{ N}$ (+), $l_{\text{local}} = 82.54^\circ \text{ W}$ (+) and $l_{\text{st}} = 75^\circ \text{ W}$ (+).

For February 1, $n = 32$.

The declination angles for this day are

$$\delta_s = 23.45^\circ \sin \frac{360}{365}(284 + 32)$$

$$\delta_s = -17.51^\circ.$$

The local time is 12:00 p.m. The solar time is given by

$$ST = LST + ET + (l_{\text{st}} - l_{\text{local}}) \cdot 4 \frac{\text{min}}{1^\circ}.$$

The equation of time is

$$B = \frac{360}{364}(32 - 81) = -48.46^\circ$$

$$\begin{aligned} ET (\text{min}) &= 9.87 \sin(2 \times (-48.46^\circ)) - 7.53 \cos(-48.46^\circ) - 1.5 \sin(-48.46^\circ) \\ &= -13.66 \text{ min}. \end{aligned}$$

Then, the solar time is

$$ST = 12:00 - 13.66 \text{ min} + (75^\circ - 82.54^\circ) \times 4 = 11:16 \text{ a.m.}$$

The hour angle is

$$h_s = (ST - 12) \frac{15^\circ}{h} = (11.26 - 12) \frac{15^\circ}{h} = -11.1^\circ.$$

The solar altitude angle is

$$\begin{aligned} \sin \alpha &= \cos \delta_s \cos L \cos h_s + \sin \delta_s \sin L \\ &= \cos(-17.51^\circ) \cos(27.96^\circ) \cos(-11.1^\circ) + \sin(-17.51^\circ) \sin(27.96^\circ) \end{aligned}$$

and

$$\alpha = 43.30^\circ.$$

The solar azimuth angle is calculated as

$$\sin a_s = \cos \delta_s \sin h_s / \cos \alpha = \cos(-17.51^\circ) \sin(-11.1^\circ) / \cos(43.30^\circ)$$

and

$$a_s = -14.61^\circ.$$

We need to find out if $|a_s|$ is greater than 90° .

For $L > \delta_s$,

$$\begin{aligned} t_E &= 12:00 - \cos^{-1} \frac{\tan \delta_s}{\tan L} \frac{h}{15^\circ} \\ &= 12:00 - \cos^{-1} \frac{\tan(-17.51^\circ)}{\tan(27.96^\circ)} \frac{h}{15^\circ} \\ &= 3.5689 \text{ h} \end{aligned}$$

Given that $ST > t_E$, the sun is south, and $a_s = -14.61^\circ$. The air mass is as follows:

$$\begin{aligned} m &= \frac{1}{\sin(43.30^\circ) + 0.50572 (6.07995 + 43.30^\circ)^{-1.6364}} \\ &= 1.4565. \end{aligned}$$

The data for the Tampa International AP, Florida, are shown in the following table:

Data for Tampa International AP, Florida

Lat: 27.96°N Long: 82.54°W Elev: 3 m

Month	Jan	Feb	Mar	Apr	May	Jun	Jul	Aug	Sep	Oct	Nov	Dec
τ_b	0.344	0.364	0.391	0.403	0.47	0.473	0.509	0.493	0.445	0.398	0.36	0.346
τ_d	2.531	2.403	2.271	2.272	2.029	2.07	1.95	2.01	2.19	2.356	2.488	2.512
$I_{b,N}$, noon (W/m^2)	902	908	899	895	831	823	793	805	836	861	876	882
$I_{d,h}$, noon (W/m^2)	94	113	134	137	174	167	188	175	143	116	97	93

Source: Data taken from ASHRAE. 2009. *Handbook of Fundamentals*. American Society of Heating Refrigeration and Air Conditioning Engineers, Atlanta, GA.

The “pseudo” optical depths are tabulated for the 21st day of each month for all the locations in the tables of climatic design. Values for other days of the year should be found by interpolation. For this example, by using linear interpolation between January and February, the pseudo optical depths are as follows:

$$\tau_b = 0.35109$$

$$\tau_d = 2.48558$$

The parameters for air mass are as follows:

$$b = 1.219 - 0.043\tau_b - 0.151\tau_d - 0.204\tau_b\tau_d = 0.6506$$

$$d = 0.202 + 0.852\tau_b - 0.007\tau_d - 0.357\tau_b\tau_d = 0.1722.$$

The extraterrestrial solar radiation is given by

$$\begin{aligned} I &= I_0 \cdot 1 + 0.034 \cos \frac{360n}{365.25} {}^\circ \\ &= 1366.1 \cdot 1 + 0.034 \cos \frac{360 \times \frac{32}{365.25}}{360} {}^\circ = 1406 \text{ W/m}^2. \end{aligned}$$

The direct solar radiation component is

$$\begin{aligned} I_{b,N} &= I e^{-\tau_b m^b} \\ &= 1406 \exp(-0.35109 \cdot 1.4565^{0.6506}) \\ &= 898 \text{ W/m}^2. \end{aligned}$$

The diffuse solar radiation on a horizontal surface is

$$\begin{aligned} I_{d,h} &= I e^{-\tau_d m^d} \\ &= 1406 \exp(-2.48558 \cdot 1.4565^{0.1722}) \\ &= 99 \text{ W/m}^2. \end{aligned}$$

The instantaneous beam radiation on the surface per unit area is given by

$$I_{b,c} = I_{b,N} \cos i.$$

For this geometry, the cosine of the angle of incidence is

$$\begin{aligned} \cos i &= \cos \alpha \cos(a_s - a_w) \sin \beta + \sin \alpha \cos \beta \\ &= \cos(43.30^\circ) \cos(-14.61^\circ - (+10^\circ)) \sin(30^\circ) + \sin(43.30^\circ) \cos(30^\circ) \\ &= 0.9248. \end{aligned}$$

Then, the beam radiation is

$$I_{b,c} = 898 \times 0.9248 = 830 \text{ W/m}^2.$$

The diffuse radiation on the collector surface will be

$$\begin{aligned} I_{d,c} &= I_{d,h} \cos^2 \frac{\beta}{2} \\ &= 99 \cos^2 \frac{30^\circ}{2} \\ &= 92 \text{ W/m}^2. \end{aligned}$$

The ground reflected solar radiation is

$$I_{r,c} = \rho(I_{b,N} \sin \alpha + I_{d,h}) \sin^2 \frac{\beta}{2} .$$

Assuming that the solar collector is surrounded by ordinary ground or grass, then $\rho \approx 0.2$

$$\begin{aligned} I_{r,c} &= 0.2(898 \sin(43.30^\circ) + 99) \sin^2 \frac{30^\circ}{2} \\ &= 10 \text{ W/m}^2. \end{aligned}$$

Finally, the total radiation on a tilted collector surface is

$$I_c = I_{b,c} + I_{d,c} + I_{r,c} = 830 + 92 + 10 = 932 \text{ W/m}^2.$$

Example 2.7b

Repeat the calculations in Example 2.6a for a north-facing solar collector ($\beta = 30^\circ$, $a_w = 10^\circ$) in Canberra, Australia (latitude = $35^\circ 18' S$, longitude = $149^\circ 11' E$, Standard Meridian = $150^\circ E$).

Solution

As the day number has not been changed, the values of the δ_s and ET remain the same.

$$\delta_s = -17.51^\circ$$

$$ET = -13.66 \text{ min.}$$

The local time is 12:00 p.m. The solar time is given by

$$ST = 12:00 - 13.66 \text{ min} + (-150^\circ + 149.18^\circ) \times 4 \frac{\text{min}}{1^\circ} = 11:43 \text{ a.m.}$$

The hour angle is

$$h_s = (ST - 12) \frac{15^\circ}{h} = (11.72 - 12) \frac{15^\circ}{h} = -4.2^\circ.$$

The solar altitude angle is

$$\begin{aligned}\sin \alpha &= \cos \delta_s \cos L \cos h_s + \sin \delta_s \sin L \\ &= \cos(-17.51^\circ) \cos(-35.3^\circ) \cos(-4.2^\circ) + \sin(-17.51^\circ) \sin(-35.3^\circ)\end{aligned}$$

and

$$\alpha = 71.82^\circ.$$

The solar azimuth angle is calculated as

$$\sin a_s = \cos \delta_s \sin h_s / \cos \alpha = \cos(-17.51^\circ) \sin(-4.2^\circ) / \cos(71.82^\circ)$$

and

$$a_s = -12.93^\circ.$$

The air mass is as follows:

$$m = \frac{1}{\sin(71.82^\circ) + 0.50572(6.07995 + 71.82^\circ)^{-1.6364}} = 1.052.$$

The data for the Canberra airport are shown in the following table:

Data for Canberra Airport

Lat: 35.30°S Long: 149.20°E Elev: 580 m

Month	Jan	Feb	Mar	Apr	May	Jun	Jul	Aug	Sep	Oct	Nov	Dec
τ_b	0.363	0.340	0.326	0.313	0.299	0.291	0.292	0.297	0.315	0.318	0.334	0.342
τ_d	2.403	2.559	2.606	2.638	2.730	2.747	2.702	2.678	2.582	2.609	2.520	2.519
$I_{b,N}$, noon (W/m ²)	972	974	952	908	871	853	869	915	948	986	995	998
$I_{d,h}$, noon (W/m ²)	126	104	94	82	69	64	70	78	94	98	111	113

Source: Data taken from ASHRAE. 2009. *Handbook of Fundamentals*. American Society of Heating Refrigeration and Air Conditioning Engineers, Atlanta, GA.

By using linear interpolation between January and February, the pseudo optical depths are as follows:

$$\tau_b = 0.3548$$

$$\tau_d = 2.4584$$

The parameters for air mass are as follows:

$$b = 1.219 - 0.043\tau_b - 0.151\tau_d - 0.204\tau_b\tau_d = 0.6546$$

$$d = 0.202 + 0.852\tau_b - 0.007\tau_d - 0.357\tau_b\tau_d = 0.1722$$

The extraterrestrial solar radiation is given by

$$I = I_0 \cdot 1 + 0.034 \cos \frac{360n}{365.25}^\circ = 1406 \text{ W/m}^2$$

The direct solar radiation component is

$$\begin{aligned} I_{b,N} &= I e^{-\tau_b m^b} \\ &= 1406 \exp(-0.3548 \times 1.052^{0.6546}) \\ &= 974 \text{ W/m}^2. \end{aligned}$$

The diffuse solar radiation on a horizontal surface is

$$\begin{aligned} I_{d,h} &= I e^{-\tau_d m^d} \\ &= 1406 \exp(-2.4584 \times 1.0521^{0.1722}) \\ &= 118 \text{ W/m}^2. \end{aligned}$$

The cosine of the angle of incidence is

$$\begin{aligned} \cos i &= \cos \alpha \cos(a_s - a_w) \sin \beta + \sin \alpha \cos \beta \\ &= \cos(71.82^\circ) \cos(-12.93^\circ - (+10^\circ)) \sin(30^\circ) + \sin(71.82^\circ) \cos(30^\circ) \\ &= 0.9665. \end{aligned}$$

Then, the beam radiation is

$$I_{b,c} = I_{b,N} \cos i$$

$$I_{b,c} = 974 \times 0.9665 = 941 \text{ W/m}^2.$$

The diffuse radiation on the collector surface will be

$$\begin{aligned} I_{d,c} &= I_{d,h} \cos^2 \frac{\beta}{2} \\ &= 118 \cos^2 \frac{30^\circ}{2} \\ &= 110 \text{ W/m}^2. \end{aligned}$$

The ground reflected solar radiation is

$$I_{r,c} = \rho(I_{b,N} \sin \alpha + I_{d,h}) \sin^2 \frac{\beta}{2} .$$

Assuming that the solar collector is surrounded by ordinary ground or grass, then $\rho \approx 0.2$

$$\begin{aligned} I_{r,c} &= 0.2(974 \sin(71.82^\circ) + 118) \sin^2 \frac{30^\circ}{2} \\ &= 14 \text{ W/m}^2 . \end{aligned}$$

Finally, the total radiation on a tilted collector surface is

$$I_c = I_{b,c} + I_{d,c} + I_{r,c} = 941 + 110 + 14 = 1065 \text{ W/m}^2.$$

2.5.4 Monthly Solar Radiation Estimation Models

One of the earliest methods of estimating solar radiation on a horizontal surface was proposed by the pioneer spectroscopist Angström. It was a simple linear model relating average horizontal radiation to clear-day radiation and to the sunshine level, that is, percent of possible hours of sunshine. Since the definition of a clear day is somewhat nebulous, Page (1966) refined the method and based it on extraterrestrial radiation instead of the ill-defined clear day:

$$\begin{aligned} \bar{H}_h &= \bar{H}_{o,h} - a + b \frac{\bar{n}}{\bar{N}} \\ &= \bar{H}_{o,h} - a + b \frac{\bar{PS}}{100} , \end{aligned} \tag{2.52}$$

where \bar{H}_h and $\bar{H}_{o,h}$ are the horizontal terrestrial and horizontal extraterrestrial radiation per day averaged for a month, \bar{PS} is the monthly averaged percent of possible sunshine (i.e., hours of sunshine/maximum possible duration of sunshine $\times 100$), a and b are constants for a given site, and \bar{n} and \bar{N} are the monthly average numbers of hours of bright sunshine and day length, respectively. The ratio \bar{n}/\bar{N} is also equivalent to the monthly average percent sunshine (\bar{PS}). $\bar{H}_{o,h}$ can be calculated by finding $H_{o,h}$ from Equation 2.53, using Equations 2.35 and 2.48 and averaging $H_{o,h}$ for the number of days in each month, or data in Appendix 2 (Table A2.1) can be used, which was developed based on I_o equal to 1366.1 W/m^2 .

$$H_{o,h} = \int_{t_{sr}}^{t_{ss}} I \sin \alpha \, dt \quad (2.53)$$

which can be written as

$$H_{o,h} = \frac{24I}{\pi} (\cos(L) \cos(\delta) \sin(h_{ss}) + h_{ss} \sin(L) \sin(\delta)) \quad (2.53a)$$

Some typical values of a and b are given in Table 2.2 (Löf et al. 1966). Additional values for worldwide locations are given in Appendix 2 (Table A2.4).

Example 2.8

Using the predictive method of Angström or Page, estimate the monthly solar radiation for the North Central Sahara Desert (Tamanrasset, Algeria, area) at latitude = 25°N. Percentages of possible sunshine and extraterrestrial radiation for this site are given in the table below.

Solution

Using the climate data given, the expected monthly average horizontal radiation for the North Sahara is calculated in the following table using $a = 0.30$ and $b = 0.43$ from Table 2.2.

Month	$\bar{H}_{o,h}^a$		\bar{H}_h	
	$\overline{PS} / 100$	$\text{kJ/m}^2\cdot\text{day}$	$\text{kJ/m}^2\cdot\text{day}$	$\text{Btu/ft}^2\cdot\text{day}$
Jan	0.88	23,902	16,215	1425
Feb	0.83	28,115	18,469	1626
Mar	0.90	32,848	22,143	1950
Apr	0.85	37,111	24,697	2174
May	0.80	39,356	25,345	2231
Jun	0.76	40,046	25,101	2210
Jul	0.86	39,606	36,528	2336
Aug	0.83	37,832	24,852	2188
Sep	0.77	34,238	21,608	1902
Oct	0.86	29,413	19,701	1735
Nov	0.85	24,909	16,577	1460
Dec	0.80	22,669	14,599	1285

^a Monthly averaged, daily extraterrestrial radiation.

TABLE 2.2Coefficients a and b in the Angström–Page Regression Equation

Location	Climate	Sunshine Hours in Percentage of Possible		a	b
		Range	Average		
Albuquerque, New Mexico	BS-BW	68–85	78	0.41	0.37
Atlanta, Georgia	Cf	45–71	59	0.38	0.26
Blue Hill, Massachusetts	Df	42–60	52	0.22	0.50
Brownsville, Texas	BS	47–80	62	0.35	0.31
Buenos Aires, Argentina	Cf	47–68	59	0.26	0.50
Charleston, South Carolina	Cf	60–75	67	0.48	0.09
Dairen, Manchuria	Dw	55–81	67	0.36	0.23
El Paso, Texas	BW	78–88	84	0.54	0.20
Ely, Nevada	BW	61–89	77	0.54	0.18
Hamburg, Germany	Cf	11–49	36	0.22	0.57
Honolulu, Hawaii	Af	57–77	65	0.14	0.73
Madison, Wisconsin	Df	40–72	58	0.30	0.34
Malange, Angola	Aw-BS	41–84	58	0.34	0.34
Miami, Florida	Aw	56–71	65	0.42	0.22
Nice, France	Cs	49–76	61	0.17	0.63
Poona, India (monsoon)	Am	25–49	37	0.30	0.51
(dry)		65–89	81	0.41	0.34
Stanleyville, Congo	Af	34–56	48	0.28	0.39
Tamanrasset, Algeria	BW	76–88	83	0.30	0.43

Source: Löf, G.O.G. et al., World distribution of solar energy. *Eng. Expt. Station Rept.* 21, University of Wisconsin, Madison, 1966. With permission.

Note: Af = tropical forest climate, constantly moist, rainfall all through the year; Am = tropical forest climate, monsoon rain, short dry season, but total rainfall sufficient to support rain forest; Aw = tropical forest climate, dry season in winter; BS = steppe or semiarid climate; BW = desert or arid climate; Cf = mesothermal forest climate, constantly moist, rainfall all through the year; Cs = mesothermal forest climate, dry season in winter; Df = microthermal snow forest climate, constantly moist, rainfall all through the year; Dw = microthermal snow forest climate, dry season in winter.

A number of researchers found Angström–Page-type correlations for specific locations, which are listed in Figure 2.22. Some of these include additional parameters such as relative humidity and ambient temperature. Correlations listed in the table may be used for the specific locations for which they were developed.

Another meteorological variable that could be used for solar radiation prediction is the opaque cloud cover recorded at many weather stations around the world. This quantity is a measure of the percent of the sky dome obscured by opaque clouds. Because this parameter contains even less solar information than sunshine values, it has not been useful in predicting long-term solar radiation values.

Authors	Measured data correlated	Correlation equations
Iqbal (1979)	Canada, 3 locations	$\frac{\bar{D}_h}{\bar{H}_h} = 0.791 - 0.635 \left(\frac{\bar{n}}{N} \right)$ $\frac{\bar{H}_d}{\bar{H}_h} = 0.163 + 0.478 \left(\frac{\bar{n}}{N} \right) - 0.655 \left(\frac{\bar{n}}{N} \right)^2$ $\frac{\bar{H}_b}{\bar{H}_{o,h}} = -0.176 + 1.45 \left(\frac{\bar{n}}{N} \right) - 1.12 \left(\frac{\bar{n}}{N} \right)^2$
Garg and Garg (1985)	India, 11 locations, 20 years' data	$\frac{\bar{H}_h}{\bar{H}_{o,h}} = 0.3156 + 0.4520 \left(\frac{\bar{n}}{N} \right)^2$ $\frac{\bar{D}_h}{\bar{H}_{o,h}} = 0.3616 - 0.2123 \left(\frac{\bar{n}}{N} \right)$ $\frac{\bar{D}_h}{\bar{H}_h} = 0.8677 - 0.7365 \left(\frac{\bar{n}}{N} \right)$
Hussain (1994)	India	$\frac{\bar{H}_h}{\bar{H}_{o,h}} = 0.394 + 0.364 \left[\frac{\bar{n}}{N'} \right] - 0.0035 W_{at}$ $\frac{\bar{D}_h}{\bar{H}_{o,h}} = 0.306 - 0.165 \left[\frac{\bar{n}}{N'} \right] - 0.0025 W_{at}$
Coppolino (1994)	Italy	$\frac{\bar{H}_h}{\bar{H}_{o,h}} = 0.67 \left(\frac{\bar{n}}{N} \right)^{0.45} \sin(\alpha_{sn})^{0.05}$ <p style="text-align: center;">α_{sn} = Solar elevation at noon on the 15th of each month, degrees</p> $0.15 \leq \frac{\bar{n}}{N} \leq 0.90$
Akinoglu and Ecevit (1990)	Italy	$\frac{\bar{H}_h}{\bar{H}_{o,h}} = 0.145 + 0.845 \left(\frac{\bar{n}}{N} \right) - 0.280 \left(\frac{\bar{n}}{N} \right)^2$
Ögelman et al. (1984)	Turkey, 2 locations, 3 years' data	$\left(\frac{\bar{H}_h}{\bar{H}_{o,h}} \right) = 0.204 + 0.758 \left(\frac{\bar{n}}{N} \right) - 0.250 \left\{ \left(\frac{\bar{n}}{N} \right)^2 + \sigma \frac{\frac{2}{n}}{N} \right\}$ $\sigma \frac{\frac{2}{n}}{N} = 0.035 + 0.326 \left(\frac{\bar{n}}{N} \right) - 0.433 \left(\frac{\bar{n}}{N} \right)^2$
Gopinathan (1988)	40 locations around the world	$\frac{\bar{H}_h}{\bar{H}_{o,h}} = a + b \left(\frac{\bar{n}}{N} \right)$ $a = -0.309 + 0.539 \cos L - 0.0639 h + 0.290 \left(\frac{\bar{n}}{N} \right)$ $b = 1.527 - 1.027 \cos L + 0.0926 h + 0.359 \left(\frac{\bar{n}}{N} \right)$

FIGURE 2.22

Angström–page-type correlations for specific locations. (\bar{H}_a , \bar{H}_b , $\bar{H}_{o,h}$, and \bar{D}_h are monthly averaged daily values; \bar{N} = maximum duration for which the Campbell–Stokes recorder can be active, that is, solar elevation $>5^\circ$; W_{at} = relative humidity $\times (4.7923 + 0.3647T + 0.055T^2 + 0.0003T^3)$; T = ambient temperature ($^\circ\text{C}$); W_{at} = g moisture/ m^3 ; h = elevation in kilometers above sea level; L = latitude.)

2.6 Models Based on Long-Term Measured Horizontal Solar Radiation

Long-term measured solar radiation data are usually available as monthly averaged total solar radiation per day on horizontal surfaces. In order to use these data for tilted surfaces, the total solar radiation on a horizontal surface must first be broken down into beam and diffuse components. A number of researchers have proposed models to do that, prominent among them being Liu and Jordan, Collares-Pereira and Rabl, and Erbs, Duffie and Klein.

2.6.1 Monthly Solar Radiation on Tilted Surfaces

In a series of papers, Liu and Jordan (1960, 1961a,b, 1963, 1967) have developed an essential simplification in the basically complex computational method required to calculate long-term radiation on tilted surfaces. This is called the LJ method. The fundamental problem in such calculations is the decomposition of long-term measured total horizontal radiation into its beam and diffuse components.

If the decomposition can be computed, the trigonometric analysis presented earlier can be used to calculate incident radiation on any surface in a straightforward manner. Liu and Jordan (LJ) correlated the diffuse-to-total radiation ratio (\bar{D}_h/\bar{H}_h) with the *monthly clearness index* \bar{K}_T , which is defined as

$$\bar{K}_T = \frac{\bar{H}_h}{\bar{H}_{o,h}}, \quad (2.54)$$

where \bar{H}_h is the monthly averaged terrestrial radiation per day on a horizontal surface. $\bar{H}_{o,h}$ is the corresponding extraterrestrial radiation, which can be calculated from Equation 2.53 by averaging each daily total for a month. The original LJ method was based upon the extraterrestrial radiation at mid-month, which is not truly an average.

The LJ correlation predicts the monthly diffuse (\bar{D}_h) to monthly total \bar{H}_h ratio. It can be expressed by the empirical equation

$$\frac{\bar{D}_h}{\bar{H}_h} = 1.390 - 4.027\bar{K}_T + 5.531\bar{K}_T^2 - 3.108\bar{K}_T^3. \quad (2.55)$$

Note that the LJ correlation is based upon a solar constant value of 1394 W/m^2 ($442 \text{ Btu/h}\cdot\text{ft}^2$), which was obtained from terrestrial observations, whereas the newer value, based on satellite data, is 1366.1 W/m^2 . The values of \bar{K}_T must be based on this earlier value of the solar constant to use the LJ method.

Collares-Pereira and Rabl (1979) conducted a study and concluded that although Liu and Jordan's approach is valid, their correlations would predict significantly smaller diffuse radiation components. They also concluded that Liu and Jordan were able to correlate their model with the measured data because they used the measured data that were not corrected for the shade ring (see solar radiation measurements). Collares-Pereira and Rabl (C-P&R) also introduced the sunset hour angle h_{ss} in their correlation to account for the seasonal variation in the diffuse component. The C-P&R correlation is

$$\frac{\bar{D}_h}{\bar{H}_h} = 0.775 + 0.347 \left(h_{ss} - \frac{\pi}{2} \right) - 0.505 + 0.0261 \left(h_{ss} - \frac{\pi}{2} \right) \cos(2\bar{K}_T - 1.8), \quad (2.56)$$

where h_{ss} is the sunset hour angle in radians. The C-P&R correlation agrees well with the correlations for India (Choudhury 1963), Israel (Stanhill 1966), and Canada (Ruth and Chant 1976) and is, therefore, preferred to Equation 2.55.

The monthly average beam component \bar{B}_h on a horizontal surface can be readily calculated by simple subtraction since \bar{D}_h is known:

$$\bar{B}_h = \bar{H}_h - \bar{D}_h. \quad (2.57)$$

It will be recalled on an instantaneous basis from Equations 2.45 and 2.47 and Figure 2.21 that

$$I_{b,N} = \frac{I_{b,h}}{\sin \alpha}, \quad (2.58)$$

$$I_{b,c} = I_{b,N} = \cos i, \quad (2.47)$$

where $I_{b,h}$ is the instantaneous horizontal beam radiation. Solving for $I_{b,c}$, the beam radiation on a surface,

$$I_{b,c} = I_{b,h} \frac{\cos i}{\sin \alpha}. \quad (2.59)$$

The ratio in parentheses is usually called the beam radiation *tilt factor* R_b . It is a purely geometric quantity that converts instantaneous horizontal beam radiation to beam radiation intercepted by a tilted surface.

Equation 2.59 cannot be used directly for the long-term beam radiation \bar{B}_h . To be strictly correct, the instantaneous tilt factor R_b should be integrated over a month with the beam component $I_{b,h}$ used as a weighting factor to

calculate the beam tilt factor. However, the LJ method is used precisely when such short-term data as $I_{b,h}$ are not available. The LJ recommendation for the monthly mean tilt factor \bar{R}_b is simply to calculate the monthly average of $\cos i$ and divide it by the same average of $\sin \alpha$. In equation form for south-facing surfaces, this operation yields

$$\bar{R}_b = \frac{\cos(L - \beta) \cos \delta_s \sin h_{sr} + h_{sr} \sin(L - \beta) \sin \delta_s}{\cos L \cos \delta_s \sin h_{sr}(\alpha = 0) + h_{sr}(\alpha = 0) \sin L \sin \delta_s}, \quad (2.60)$$

where the sunrise hour angle $h_{sr}(\alpha = 0)$ in radians is given by Equation 2.30 and h_{sr} is the min $|h_s(\alpha = 0)|, |h_s(i = 90^\circ)|$, respectively, and is evaluated at midmonth. Non-south-facing surfaces require numerical integration or iterative methods to determine \bar{R}_b . The long-term beam radiation on a tilted surface \bar{B}_c is then,

$$\bar{B}_c = \bar{R}_b \bar{B}_h, \quad (2.61)$$

which is the long-term analog of Equation 2.47. Values of \bar{R}_b are tabulated in Appendix 2, Table A2.5.

Diffuse radiation intercepted by a tilted surface differs from that on a horizontal surface, because a tilted surface does not view the entire sky dome, which is the source of diffuse radiation. If the sky is assumed to be an isotropic source of diffuse radiation, the instantaneous and long-term tilt factors for diffuse radiation, R_d and \bar{R}_d , respectively, are equal and are simply the radiation view factor from the plane to the visible portion of a hemisphere. In equation form:

$$R_d = \bar{R}_d = \cos^2 \frac{\beta}{2} = (1 + \cos \beta)/2. \quad (2.62)$$

In some cases where solar collectors are mounted near the ground, some beam and diffuse radiation reflected from the ground can be intercepted by the collector surface. The tilt factor \bar{R}_r for reflected total radiation ($\bar{D}_h + \bar{B}_h$) is then calculated to be

$$\bar{R}_r = \frac{\bar{R}}{\bar{D}_h + \bar{B}_h} = \rho \sin^2 \frac{\beta}{2} = \rho(1 - \cos \beta)/2, \quad (2.63)$$

in which ρ is the diffuse reflectance of the surface south of the collector assumed uniform and of infinite extent.

For snow, $\rho \cong 0.75$; for grass and concrete, $\rho \cong 0.2$. A more complete list of reflectances is provided in Table A2.7 of Appendix 2. The total long-term

radiation intercepted by a surface \bar{H}_c is then the total of beam, diffuse, and diffusely reflected components:

$$\bar{H}_c = \bar{R}_b \bar{B}_h + \bar{R}_d \bar{D}_h + \bar{R}_r (\bar{D}_h + \bar{B}_h). \quad (2.64)$$

Using Equations 2.62 and 2.63, we have

$$\bar{H}_c = \bar{R}_b \bar{B}_h + \bar{D}_h \cos^2 \frac{\beta}{2} + (\bar{D}_h + \bar{B}_h) \rho \sin^2 \frac{\beta}{2}, \quad (2.65)$$

in which \bar{R}_b is calculated from Equation 2.60.

Example 2.9

Using the \bar{H}_h data calculated in Example 2.7 in place of the long-term measured data for the North Central Sahara Desert at latitude 25°N, find the monthly averaged insolation per day on a south-facing solar collector tilted at an angle of 25° from the horizontal.

Solution

The solution below is for the month of January. Values for the other months can be found by following the same method.

$$\bar{H}_h = 16,215 \text{ kJ/m}^2 \cdot \text{day.}$$

From Table A2.1:

$$\bar{H}_{o,h} = 24,199.$$

Therefore,

$$\bar{K}_T = \bar{H}_h / \bar{H}_{o,h} = 0.67.$$

δ_s and h_{sr} can be found for the middle of the month (January 16).

$$\begin{aligned} \delta_s &= 23.45^\circ \sin[360(284 + 16)/365^\circ] \\ &= -21.1^\circ 1'. \end{aligned}$$

$$h_{sr}(\alpha = 0) - \cos^{-1}(-\tan L \tan \delta)$$

$$= -79.6^\circ \text{ or } -1.389 \text{ rad}$$

and $h_{ss} = 1.389$

Using CP&R correlation,

$$\begin{aligned}\frac{\bar{D}_h}{\bar{H}_h} &= 0.775 + 0.347(1.389 - 1.5708) \\ &\quad - [0.505 + 0.0261(1.389 - 1.5708)] \cos(2 \times 0.67 - 1.8) \\ &= 0.211\end{aligned}$$

Therefore,

$$\bar{D}_h = 0.211 \times 16,215 = 3421 \text{ kJ/m}^2 \cdot \text{day}$$

and

$$\bar{B}_h = \bar{H}_h - \bar{D}_h = 12,794 \text{ kJ/m}^2 \cdot \text{day}.$$

Insolation on a tilted surface can be found from Equation 2.64. We need to find \bar{R}_b from Equation 2.60.

Therefore,

$$\begin{aligned}\bar{R}_b &= \frac{\cos(0)\cos(-21.1^\circ)\sin(-79.6^\circ) - 1.389\sin(0)(-21.1^\circ)}{\cos(25^\circ)\cos(-21.1^\circ)\sin(-79.6^\circ) - 1.389\sin(25^\circ)\sin(-21.1^\circ)} \\ &= 1.47.\end{aligned}$$

$$\bar{R}_d = \cos^2(25/2) = 0.953.$$

$$\begin{aligned}\bar{R}_r &= \rho \sin^2(\beta/2) \text{ (Assume } \rho = 0.2) \\ &= 0.2 \sin^2(12.5^\circ) \\ &= 0.009.\end{aligned}$$

Therefore,

$$\begin{aligned}\bar{H}_c &= (1.47)(12,794) + 0.953(3421) + 0.009(16,215) \\ &= 22,213 \text{ kJ/m}^2\end{aligned}$$

2.6.2 Circumsolar or Anisotropic Diffuse Solar Radiation

The models described in the above sections assume that the sky diffuse radiation is isotropic. However, this assumption is not true because of circumsolar radiation (brightening around the solar disk). Although the assumption of isotropic diffuse solar radiation does not introduce errors in the diffuse values on horizontal surfaces, it can result in errors of 10% to 40% in the

diffuse values on tilted surfaces. A number of researchers have studied the anisotropy of the diffuse solar radiation because of circumsolar radiation. Temps and Coulson (1977) introduced an anisotropic diffuse radiation algorithm for tilted surfaces for clear-sky conditions. Klucher (1979) refined the Temps and Coulson algorithm by adding a cloudiness function to it:

$$R_d = \frac{1}{2}(1 + \cos\beta)M_1M_2, \quad (2.66)$$

where

$$M_1 = 1 + F \sin^3(\beta/2), \quad (2.67)$$

$$M_2 = 1 + F \cos^2 i \sin^3(z), \quad (2.68)$$

and

$$F = 1 - (D_h/H_h)^2. \quad (2.69)$$

Examining F , we find that under overcast skies ($D_h = H_h$), R_d in Equation 2.66 reduces to the isotropic term of Liu and Jordan. The Klucher algorithm reduces the error in diffuse radiation to approximately 5%.

In summary, monthly averaged, daily solar radiation on a surface is calculated by first decomposing total horizontal radiation into its beam and diffuse components using Equation 2.55 or 2.56. Various tilt factors are then used to convert these horizontal components to components on the surface of interest.

2.6.3 Hourly and Daily Solar Radiation on Tilted Surfaces

Accurate determination of the hourly solar radiation received during the average day of each month is a prerequisite in different solar energy applications. In the early 1950s, Whillier introduced the “utilizability” method to analytically predict the performance of active solar collectors. This method used a simple formulation to estimate the mean hourly radiation during each hour of an average day of the month, based on the ratio of the hourly to daily irradiation received by a horizontal surface outside of the atmosphere. The long-term models provide the mean hourly distribution of global radiation over the average day of each month.

Three methods are described below:

- Collares-Pereira and Rabl Model, CPR (Collares-Pereira and Rabl 1979)
- Collares-Pereira and Rabl Model modified by Gueymard, CPRG (Gueymard 1986)
- Daily Integration or DI Model by Gueymard (Gueymard 2000)

Given the long-term average daily total and diffuse irradiation on a horizontal surface \bar{H}_h and \bar{H}_d , it is possible to find the long-term average hourly irradiances \bar{I}_d , \bar{I}_h , and \bar{I}_b .

The ratio of the hourly diffuse to the long-term average daily diffuse irradiation on a horizontal surface, r_d , is given by (Figure 2.23)

$$r_d = \frac{I_d}{\bar{H}_d} = \frac{\pi}{24} \frac{\cos h_s - \cos h_{ss}}{\sin h_{ss} - \frac{\pi}{180} h_{ss} \cos h_{ss}}. \quad (2.70)$$

The ratio of hourly total to the long-term average daily total irradiation on a horizontal surface, r_t , is given by

$$r_t = \frac{I_h}{\bar{H}_h} = (a + b \cos(h_s)) r_d, \quad (2.71)$$

with

$$a = 0.409 + 0.5016 \sin(h_{ss} - 60^\circ)$$

$$b = 0.6609 - 0.4767 \sin(h_{ss} - 60^\circ).$$

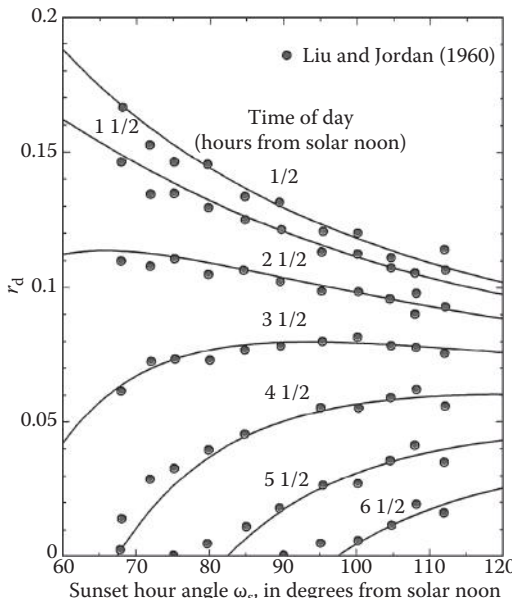


FIGURE 2.23

Collares-Pereira and Rabl Model, CPR. (Adapted from Collares-Pereira, M. and A. Rabl, *Sol Energy* 22, 155–166, 1979; Liu, B.H.Y. and R.C. Jordan, *Sol Energy* 4, 1–19, 1960. See also Liu, B.Y.H., Characteristics of solar radiation and the performance of flat plate solar energy collectors, PhD dissertation, University of Minnesota, Minneapolis, 1960.)

This fit satisfies, within 1% for all h_{ss} , the normalization condition

$$\int_{-t_s}^{t_s} I_h \, dt = \bar{H}_h. \quad (2.72)$$

For the CPRG method, the ratio of hourly total to the long-term average daily total irradiation on a horizontal surface, r_t , is given by (Gueymard 1986) (Figure 2.24)

$$r_t = \frac{I_h}{\bar{H}_h} = \frac{(a + b \cos h_s) r_d}{f_c}, \quad (2.73)$$

with

$$f_c = a + kb - \frac{\pi}{180} \left(h_{ss} - \frac{1}{2} \sin 2h_{ss} \right) \quad (2.74)$$

$$k = 2 \sin h_{ss} - \frac{\pi}{180} h_{ss} \cos h_{ss}^{-1}. \quad (2.75)$$

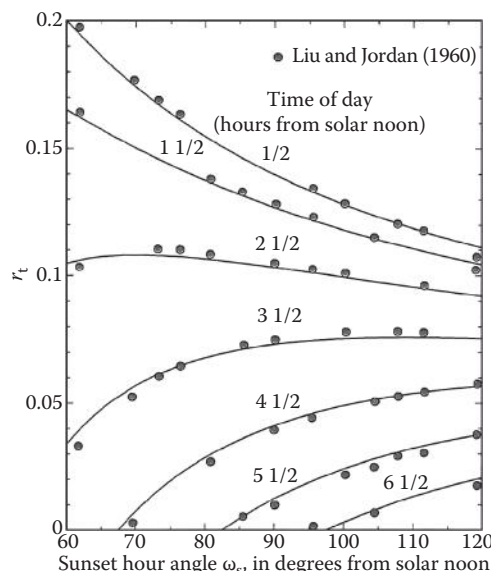


FIGURE 2.24

Collares-Pereira and Rabl Model modified by Gueymard (1986). (Adapted from Collares-Pereira, M. and A. Rabl, *Sol Energy* 22, 155–166, 1979; Liu, B.H.Y. and R.C. Jordan, *Sol Energy* 4, 1–19, 1960. See also Liu, B.Y.H., Characteristics of solar radiation and the performance of flat plate solar energy collectors, PhD dissertation, University of Minnesota, Minneapolis, 1960.)

The normalization condition is expressed by

$$\int_{-t_s}^{t_s} r_t \, dt = 1. \quad (2.76)$$

For the DI Model:

Gueymard (2000) developed the daily integration approach to predict the monthly average hourly global irradiation by using a large data set of 135 stations with diverse geographic locations (82.58°N to 67.68°S) and climates. Gueymard compared his proposed model with previous hourly radiation models, Collares-Pereira and Rabl Model CP&R (Collares-Pereira and Rabl 1979) and Collares-Pereira and Rabl Model modified by Gueymard (Gueymard 1986), and concluded that the daily integration model is the most accurate compared to the other models.

The DI model uses the same expression for r_d as above (Equation 2.70). The expression for r_t is given by

$$r_t = r_d \frac{1 + q(a_2/a_1)A(h_{ss})r_d(24/\pi)}{1 + q(a_2/a_1)B(h_{ss})/A(h_{ss})}, \quad (2.77)$$

where (a_2/a_1) represents the atmospheric extinction effect. a_1 and a_2 were obtained from a multiple least-squares fit:

$$a_1 = 0.41341K_t + 0.61197K_t^2 - 0.01886K_tS_o + 0.00759S_o \quad (2.78)$$

$$a_2 = \text{Max}(0.054, 0.28116 + 2.2475K_t - 1.7611K_t^2 - 1.84535 \sin h_o + 1.681 \sin^3 h_o) \quad (2.79)$$

and $B(h_{ss})$ is defined as

$$B(h_{ss}) = \omega_s(0.5 + \cos^2 h_{ss}) - 0.75 \sin(2 h_{ss}) \quad (2.80)$$

For all three DI, CPR, and CPRG models:

The instantaneous solar beam radiation on a horizontal surface, $I_{b,h}$, is given by

$$I_{b,h} = r_t \bar{H}_h - r_d \bar{H}_d. \quad (2.81)$$

The instantaneous solar beam radiation on a tilted surface, $I_{b,c}$, is

$$I_{b,c} = I_{b,h} \frac{\cos i}{\sin \alpha}. \quad (2.59)$$

Then, the total radiation on a tilted surface, I_c , is

$$I_c = (r_t \bar{H}_h - r_d \bar{H}_d) \frac{\cos i}{\sin \alpha} + r_d \bar{H}_d \cos^2 \frac{\beta}{2} + \rho r_t \bar{H}_h \sin^2 \frac{\beta}{2}. \quad (2.82)$$

The following websites give information about long-term database either measured or satellite solar radiation.

- Surface Meteorology and Solar Energy (Version 6.0) [<https://eosweb.larc.nasa.gov/sse/>]
- Energy Plus Weather Data [http://apps1.eere.energy.gov/buildings/energyplus/weatherdata_about.cfm?CFID=777061&CFTOKEN=999ebda95de32b46-A8949F8C-E3B6-3771-7E42A53F29DDF35C]
- National Solar Radiation Data Base, 1961–1990: Typical Meteorological Year 2 [http://webcache.googleusercontent.com/search?q=cache:http://rredc.nrel.gov/solar/old_data/nsrdb/tmy2/]
- National Solar Radiation Data Base, 1991–2005 Update: Typical Meteorological Year 3 [http://rredc.nrel.gov/solar/old_data/nsrdb/1991-2005/tmy3/]
- The Solar and Wind Energy Resource Assessment (SWERA) [<http://en.openei.org/apps/SWERA/>]
- National Renewable Laboratory (NREL) [http://www.nrel.gov/international/geospatial_toolkits.html http://www.nrel.gov/international/geospatial_toolkits.html#HOMER]

Example 2.10

Find the instantaneous solar radiation at 12:00 noon solar time on a solar collector surface (β = Latitude, $a_w = 0^\circ$) on March 21 in Las Vegas, Nevada.

Solution

For Las Vegas Mccarran Intl Ap, Nevada:

$$L = 36.08 \text{ N (+)}, l_{\text{local}} = 115.16 \text{ W (+)}, \text{ and } l_{\text{st}} = 120 \text{ W (+)}.$$

For March 21:

The declination angle for this day is

$$\delta_s = 0^\circ.$$

The hour angle is

$$h_s = (\text{ST} - 12) \frac{15^\circ}{\text{h}} = (12 - 12) \frac{15^\circ}{\text{h}} = 0^\circ.$$

The solar altitude angle is

$$\sin \alpha = \cos \delta_s \cos L \cos h_s + \sin \delta_s \sin L$$

$$\sin \alpha = \cos(0^\circ) \cos(36.08^\circ) \cos(0^\circ) + \sin(0^\circ) \sin(36.08^\circ);$$

then,

$$\alpha = 53.92^\circ.$$

The solar azimuth angle is defined by

$$\sin a_s = \frac{\cos \delta_s \sin h_s}{\cos \alpha}$$

$$\sin a_s = \frac{\cos(0^\circ) \sin(0^\circ)}{\cos(53.92^\circ)};$$

then,

$$a_s = 0^\circ.$$

We need to find out if a_s is greater than 90° .

For $L > \delta_s$,

$$t_E = 12:00 - \cos^{-1} \frac{(\tan \delta_s)}{\tan L} \frac{h}{15^\circ}$$

$$t_E = 12:00 - \cos^{-1} \frac{(\tan(0^\circ))}{\tan(36.08^\circ)} \frac{h}{15^\circ}$$

$$t_E = 6 \text{ h.}$$

Given that $ST > t_E$, the sun is south, and a_s . The air mass is calculated from

$$m = \frac{1}{\sin \alpha + 0.50572(6.07995 + \alpha^\circ)^{-1.6364}}$$

$$m = \frac{1}{\sin(53.92^\circ) + 0.50572(6.07995 + 53.92^\circ)^{-1.6364}}$$

$$m = 1.2363.$$

The data for Las Vegas Mccarran Intlp Ap, Nevada, are shown in the table below:

Data for Las Vegas Mccarran Intlp Ap, Nevada

Lat: 36.086°N Long: 115.16°W Elev: 665 m

Month	Jan	Feb	Mar	Apr	May	Jun	Jul	Aug	Sep	Oct	Nov	Dec
τ_b	0.314	0.333	0.355	0.382	0.404	0.412	0.55	0.56	0.407	0.38	0.317	0.304
τ_d	2.386	2.277	2.211	2.099	2.062	2.059	1.674	1.674	2.084	2.096	2.388	2.417
$I_{b,N}$, noon (W/m ²)	881	902	911	899	880	870	752	752	844	831	869	868
$I_{d,hv}$, noon (W/m ²)	99	119	136	159	166	167	243	243	152	139	97	92

Source: Data taken from ASHRAE. 2009. *Handbook of Fundamentals*. American Society of Heating Refrigeration and Air Conditioning Engineers, Atlanta, GA.

The pseudo optical depths are tabulated for the 21st day of each month for all the locations in the tables of climatic design. Values for other days of the year should be found by interpolation. For this example, by using linear interpolation between January and February, the pseudo optical depths are as follows:

$$\tau_b = 0.355$$

$$\tau_d = 2.211.$$

The parameters for air mass are as follows:

$$b = 1.219 - 0.043\tau_b - 0.151\tau_d - 0.204\tau_b\tau_d = 0.7097$$

$$d = 0.202 + 0.852\tau_b - 0.007\tau_d - 0.357\tau_b\tau_d = 0.2087.$$

The extraterrestrial solar radiation is given by (for March 21, $n = 80$)

$$I = I_0 \frac{D_0}{D}^2$$

$$x = \frac{360}{365} (80 - 1) = 77.91^\circ$$

$$\frac{D_0}{D}^2 = 1.00011 + 0.034221 \cos x + 0.00128 \sin x + 0.000719 \cos 2x + 0.000077 \sin 2x$$

$$\frac{D_0}{D}^2 = 1.0079.$$

Then,

$$I = 1366.1(1.0079) \frac{W}{m^2} = 1377 \frac{W}{m^2}.$$

The direct solar radiation component is

$$I_{b,N} = I e^{-\tau_b m^b}$$

$$I_{b,N} = 1377 \exp(-0.355 \times 1.2363^{0.7097}) = 911 \frac{W}{m^2}.$$

The diffuse solar radiation on a horizontal surface is

$$I_{d,h} = I e^{-\tau_d m^d}$$

$$I_{d,h} = 1377 \exp(-2.211 \times 1.2363^{0.2087}) = 137 \frac{W}{m^2}.$$

The instantaneous beam radiation on the surface per unit area is given by

$$I_{b,c} = I_{b,N} \cos i.$$

For this geometry, the cosine of the angle of incidence is

$$\cos i = \cos \alpha \cos(a_s - a_w) \sin \beta + \sin \alpha \cos \beta$$

$$\cos i = \cos(53.92^\circ) \cos(0^\circ) \sin(36.08^\circ) + \sin(53.92^\circ) \cos(36.08^\circ) = 1.0.$$

Then, the beam radiation is

$$I_{b,c} = 911(1.0) = 911 \frac{W}{m^2}.$$

The diffuse radiation on the collector surface is

$$I_{d,c} = I_{d,h} \cos^2(\beta/2)$$

$$I_{d,c} = 137 \cos^2(36.08^\circ/2) = 124 \frac{W}{m^2}.$$

The ground reflected solar radiation is

$$I_{r,c} = \rho(I_{b,N} \sin \alpha + I_{d,h}) \sin^2(\beta/2).$$

Assuming that the solar collector is surrounded by ordinary ground or grass, then $\rho \sim 0.2$

$$I_{r,c} = 0.2(911 \sin(53.92^\circ) + 137) \sin^2(36.08^\circ/2) = 17 \frac{\text{W}}{\text{m}^2}.$$

Finally, the total radiation on tilted collector surface is

$$I_c = I_{b,c} + I_{d,c} + I_{r,c}$$

$$I_c = 911 + 124 + 17 = 1052 \frac{\text{W}}{\text{m}^2}.$$

Solution by using CPRG

The sunset is given by

$$h_s = (ST - 12) \frac{15^\circ}{h} = (12 - 12) \frac{15^\circ}{h} = 0^\circ.$$

The ratio of hourly diffuse to the long-term average daily diffuse irradiation on a horizontal surface, r_d , is given by

$$r_d = \frac{\pi}{24} \frac{\cos h_s - \cos h_{ss}}{\sin h_{ss} - \frac{\pi}{180} h_{ss} \cos h_{ss}}$$

$$r_d = \frac{\pi}{24} \frac{\cos 0^\circ - \cos 90^\circ}{\sin 90^\circ - \frac{\pi}{180} 90^\circ \cos 90^\circ} = 0.1308.$$

The parameters a and b are as follows:

$$a = 0.409 + 0.5016 \sin(h_{ss} - 60^\circ)$$

$$a = 0.409 + 0.5016 \sin(90^\circ - 60^\circ) = 0.6598$$

$$b = 0.6609 - 0.4767 \sin(h_{ss} - 60^\circ)$$

$$b = 0.6609 - 0.4767 \sin(90^\circ - 60^\circ) = 0.8992$$

For CPRG, the ratio of hourly total to the long-term average daily total irradiation on a horizontal surface, r_t , is given by

$$r_t = \frac{I_h}{H_h} = \frac{a + b \cos h_s}{f_c} r_d$$

$$f_c = a + kb \frac{\pi}{180} h_{ss} - \frac{1}{2} \sin 2h_{ss} ,$$

with

$$k = 2 \sin h_{ss} - \frac{\pi}{180} h_{ss} \cos h_{ss}$$

$$k = 2 \sin 90^\circ - \frac{\pi}{180} 90^\circ \cos 90^\circ = 0.5.$$

Then,

$$f_c = 0.6598 + 0.5 \times 0.8992 \frac{\pi}{180} 90^\circ - \frac{1}{2} \sin 2 \times 90^\circ = 1.3660.$$

r_t is

$$r_t = \frac{0.6598 + 0.8992 \times \cos 0^\circ}{1.3660} \times 0.1308 = 0.1493.$$

The long-term average daily total and diffuse radiation are obtained from NASA-SSE (<http://eosweb.larc.nasa.gov/sse/>):

$$\bar{H}_h = 5.24 \frac{\text{kWh}}{\text{m}^2 \cdot \text{day}} \quad \bar{H}_d = 1.26 \frac{\text{kWh}}{\text{m}^2 \cdot \text{day}}$$

The beam radiation is

$$I_{b,c} = (r_t \bar{H}_h - r_d \bar{H}_d) \frac{\cos i}{\sin \alpha}$$

$$I_{b,c} = (0.1493 \times 5.24 - 0.1308 \times 1.26) \frac{1}{\sin 53.92^\circ} = 765 \frac{\text{W}}{\text{m}^2}.$$

The diffuse radiation on the collector surface is

$$I_{d,c} = r_d \bar{H}_d \cos^2(\beta/2)$$

$$I_{d,c} = 0.1308 \times 1.26 \cos^2(36.08^\circ/2) = 149 \frac{\text{W}}{\text{m}^2}.$$

The ground reflected solar radiation is

$$I_{r,c} = \rho r_t \bar{H}_h \sin^2(\beta/2)$$

$$I_{r,c} = 0.2 \times 0.1493 \times 5.24 \sin^2(36.08^\circ/2) = 15 \frac{\text{W}}{\text{m}^2}.$$

The total radiation on tilted collector surface is

$$I_c = I_{b,c} + I_{d,c} + I_{r,c}$$

$$I_c = 765 + 149 + 15 = 929 \frac{\text{W}}{\text{m}^2}.$$

Solution by using DI

The sunset is given by

$$h_s = (ST - 12) \frac{15^\circ}{h} = (12 - 12) \frac{15^\circ}{h} = 0^\circ.$$

The ratio of hourly diffuse to the long-term average daily diffuse irradiation on a horizontal surface, r_d , is given by

$$r_d = \frac{\pi}{24} \frac{\cos h_s - \cos h_{ss}}{\sin h_{ss} - \frac{\pi}{180} h_{ss} \cos h_{ss}}$$

$$r_d = \frac{\pi}{24} \frac{\cos 0^\circ - \cos 90^\circ}{\sin 90^\circ - \frac{\pi}{180} 90^\circ \cos 90^\circ} = 0.1308.$$

The daily-average extraterrestrial irradiation on a horizontal surface, H_o , may be calculated as a function of the solar constant, E_{sc} , as

$$H_o = \frac{24}{\pi} h_{ss} R E_{sc} \sin h_o,$$

with

$$E_{sc} = 1367 \text{ W/m}^2$$

$$R = (D_o/D)^2 = 1.0079$$

h_o is the daily average solar elevation outside of the atmosphere, defined by

$$\sin h_o = q A(h_{ss}) / h_{ss}$$

and

$$\begin{aligned} q &= \cos L \cos \delta_s = 0.8617 \\ A(h_{ss}) &= \sin h_{ss} - h_{ss} \cos h_{ss} = 1.0. \end{aligned}$$

Then,

$$\sin h_o = qA(h_{ss})/h_{ss} = 0.5485,$$

and

$$H_o = \frac{24}{\pi} h_{ss} R E_{sc} \sin h_o = 9.070 \text{ kWh/m}^2.$$

The long-term average daily total and diffuse radiation are obtained from NASA-SSE (<http://eosweb.larc.nasa.gov/sse/>):

$$\bar{H}_h = 5.24 \text{ kWh/m}^2 \cdot \text{day}$$

$$\bar{H}_d = 1.26 \text{ kWh/m}^2 \cdot \text{day}.$$

The daily average clearness index, K_t , is given by

$$K_t = \bar{H}_h / H_o = 0.5777.$$

The day length (in hours) is obtained as

$$S_o = \frac{24}{\pi} h_{ss} = 12 \text{ h}.$$

(a_2/a_1) represents the atmospheric extinction effect. a_1 and a_2 were obtained from a multiple least-squares fit:

$$a_1 = 0.41341 K_t + 0.61197 K_t^2 - 0.01886 K_t S_o + 0.00759 S_o = 0.4034$$

$$a_2 = \text{Max}\left(0.054, 0.28116 + 2.2475 K_t - 1.7611 K_t^2 - 1.84535 \sin h_o + 1.681 \sin^3 h_o\right) = 0.2569$$

$B(h_{ss})$ is defined as

$$B(h_{ss}) = \omega_s (0.5 + \cos^2 h_{ss}) - 0.75 \sin(2 h_{ss}) = 0.7853.$$

The ratio of the horizontal hourly radiation to the total horizontal daily radiation, r_t , is given by

$$r_t = r_d \frac{1 + q(90)A(h_{ss})r_d(24/\pi)}{1 + q(a_2/a_1)B(h_{ss})/A(h_{ss})}$$

$$r_t = 0.1416.$$

The beam radiation is

$$I_{b,c} = (r_t \bar{H}_h - r_d \bar{H}_d) \frac{\cos i}{\sin \alpha}$$

$$I_{b,c} = (0.1416 \times 5.24 - 0.1308 \times 1.26) \frac{1}{\sin 53.92^\circ} = 711 \frac{W}{m^2}.$$

The diffuse radiation on the collector surface is

$$I_{d,c} = r_d \bar{H}_d \cos^2(\beta/2)$$

$$I_{d,c} = 0.1308 \times 1.26 \cos^2(36.08^\circ/2) = 149 \frac{W}{m^2}.$$

The ground reflected solar radiation is

$$I_{r,c} = \rho r_t \bar{H}_h \sin^2(\beta/2)$$

$$I_{r,c} = 0.2 \times 0.1416 \times 5.24 \sin^2(36.08^\circ/2) = 14 \frac{W}{m^2}.$$

The total radiation on tilted collector surface is

$$I_c = I_{b,c} + I_{d,c} + I_{r,c}$$

$$I_c = 711 + 149 + 14 = 874 \frac{W}{m^2}.$$

Example 2.11

Calculate the monthly average normal beam radiation for Jaipur, India (Vasquez-Padilla 2011).

Solution

For Jaipur: Lat = 26°55'N and Long = 75°49'E

The input data are as follows:

Jaipur, India

Month	\bar{H}_h^a (kWh/m ² ·day)	\bar{H}_d^b (kWh/m ² ·day)
Jan	4.00	1.01
Feb	4.71	1.27
Mar	5.46	1.64
Apr	6.11	1.97
May	6.38	2.22
Jun	6.24	2.36
Jul	5.09	2.47
Aug	4.71	2.30
Sep	5.12	1.90
Oct	4.79	1.44
Nov	4.16	1.08
Dec	3.74	0.95
Annual	5.04	1.72

Source: Data taken from <http://eosweb.larc.nasa.gov/sse/>.

a Mean monthly global solar radiant exposure.

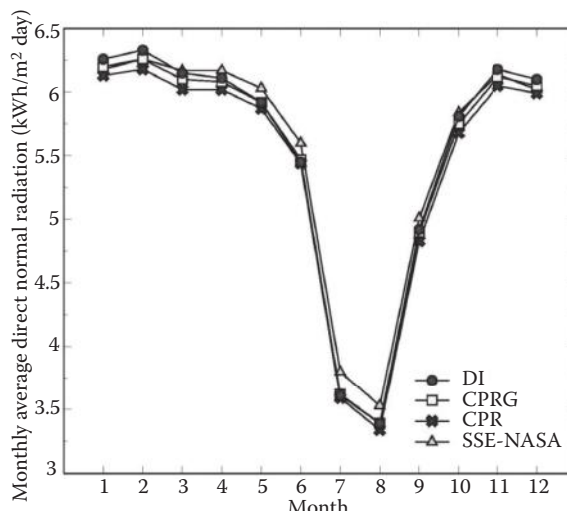
b Mean monthly diffuse solar radiant exposure.

The monthly average normal beam radiation is calculated by

$$\bar{H}_{b,N} = \int_{-t_s}^{t_s} r_t \bar{H}_h - r_d \bar{H}_d \frac{\cos i}{\sin \alpha} dt.$$

The results obtained for CPR, CPRG, and DI are as follows:

Results for Jaipur, India



2.6.4 Spectral Models

Many biological, chemical, and physical processes are activated more powerfully at some wavelengths than at others. Therefore, it is important to know the spectral characteristics of the incident radiation. In order to model spectral solar radiation at a location, radiation needs to be modeled as it travels through the atmosphere. These models are complex to begin with and are made more complex since different wavelengths are absorbed, reflected, and scattered differently in the atmosphere. Examples of radiative transfer numerical model include the Santa Barbara DISORT, atmospheric radiative transfer code (SBDART), and the moderate resolution transmission code MODTRAN. SBDART, developed at the University of California at Santa Barbara, is relatively simpler to use than MODTRAN, is freely accessible, and even has a convenient user interface online (<http://arm.mrcsb.com/sbdart/>).

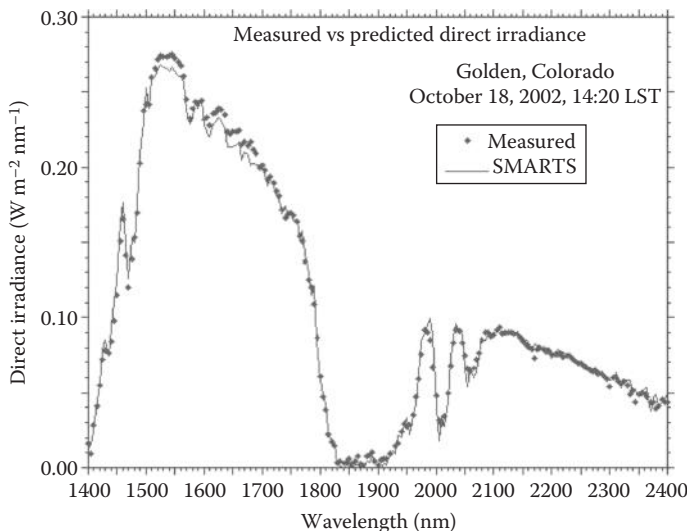
MODTRAN, developed by the Air Force Geophysical Laboratory, has a much higher resolution and is considered as the standard in atmospheric applications.

These models, however, are not convenient for solar energy or other engineering-type applications.

Bird's simple spectral model (SPCTRAL2), the spectral model of the atmospheric radiative transfer of sunshine (SMARTS), and REST2 can be used for solar engineering applications. Even though these models are limited to clear-sky conditions, they can also be empirically modified to predict spectra under cloudy conditions. The SMARTS model offers fast and accurate predictions of spectral irradiance on any tilted surface without the difficulties and limitations associated with the atmospheric models mentioned above. Sample outputs produced by SMARTS, compared with actual spectroradiometric measurements from high-performance instruments, are shown in Figures 2.25 and 2.26.

2.7 Measurement of Solar Radiation

Solar radiation measurements of importance to most engineering applications, especially thermal applications, include total (integrated over all wavelengths) direct or beam and sky diffuse values of solar radiation on instantaneous, hourly, daily, and monthly bases. Some applications such as photovoltaics, photochemical, and daylighting require knowledge of spectral (wavelength specific) or band (over a wavelength range—e.g., ultraviolet, visible, infrared) values of solar radiation. This section describes some of the instrumentation used to measure solar radiation and sunshine and some sources of long-term measured data for different parts of the world. Also described briefly in this section is the method of satellite-based measurements.

**FIGURE 2.25**

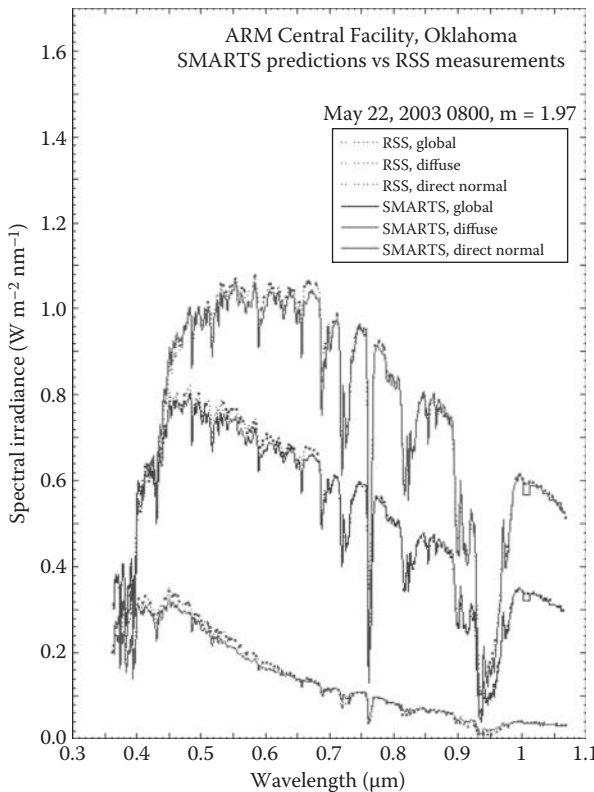
A sample spectral irradiance prediction compared with measured data for Golden, Colorado. (Taken from <http://www.solarconsultingservices.com/smarts.php>.)

2.7.1 Instruments for Measuring Solar Radiation and Sunshine

There are two basic types of instruments used to measure solar radiation, *pyranometer* and *pyrheliometer*. A pyranometer has a hemispherical view of the surroundings and therefore is used to measure total, direct, and diffuse solar radiation on a surface. A pyrheliometer, on the other hand, has a restricted view (approximately 5°) and is, therefore, often used to measure the direct or beam solar radiation by pointing it toward the sun. Pyranometers are also used to measure the sky diffuse radiation by using a shadow band to block the direct sun view. A detailed discussion of the instrumentation and calibration standards is given by Iqbal (1983) and Zerlaut (1989).

A pyranometer consists of a flat sensor/detector (described later) with an unobstructed hemispherical view, which allows it to convert and correlate the total radiation incident on the sensor to a measurable signal. The pyranometers using thermal detectors for measurements can exhibit serious errors at tilt angles from the horizontal owing to free convection. These errors are minimized by enclosing the detector in double hemispherical high-transmission glass domes. The second dome minimizes the error attributed to infrared radiative exchange between the sensor and the sky. A desiccator is usually provided to eliminate the effect of condensation on the sensor or the dome. Figure 2.27 shows pictures of typical commercially available precision pyranometers.

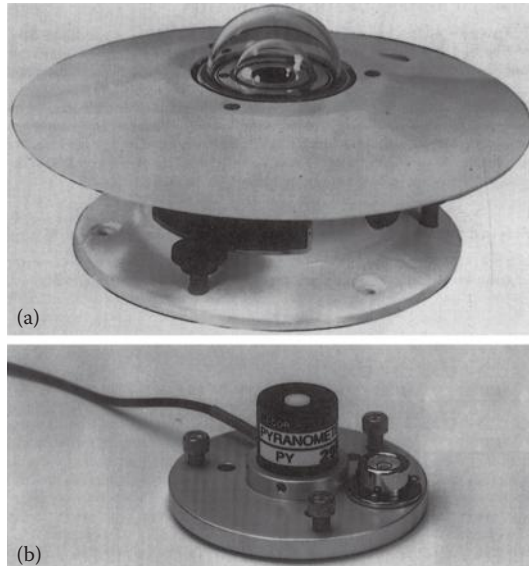
A pyranometer can be used to measure the sky diffuse radiation by fitting a shade ring to it, as shown in Figure 2.28, in order to block the beam

**FIGURE 2.26**

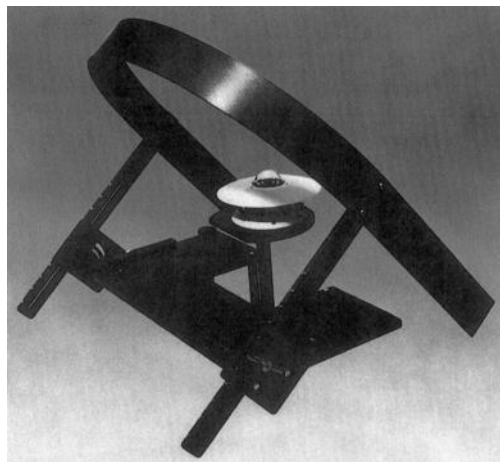
A sample prediction for direct normal, diffuse and global horizontal spectral irradiance. (Taken from <http://www.solarconsultingservices.com/smarts.php>.)

radiation throughout the day. The position of the shade ring is adjusted periodically as the declination changes. Since the shade ring obstructs some diffuse radiation from the pyranometer, correction factors must be applied.

Geometric correction factors (GCFs) that account for the part of the sky obstructed by the shade ring can be easily calculated. However, a GCF assumes isotropic sky, which results in errors because of the circumsolar anisotropy. Eppley Corp. recommends the following additional correction factors to account for anisotropy: +7% for clear sky, +4% for partly cloudy condition, and +3% for cloudy sky. Mujahid and Turner (1979) determined that these correction factors gave less than 3% errors on partly cloudy days but gave errors of -11% for clear-sky conditions and +6% on overcast days. They suggested correction factors owing to anisotropy as tabulated in Table 2.3, which reduce the errors to less than $\pm 3\%$. It must be remembered that these correction factors are in addition to the GCFs. Recently, a sun occulting disk has been employed for shading the direct sun.

**FIGURE 2.27**

Typical commercially available pyranometers with (a) thermal detector and (b) photovoltaic detector.

**FIGURE 2.28**

A pyranometer with a shade ring to measure sky diffuse radiation.

Beam or direct solar radiation is usually measured with an instrument called a pyrheliometer. Basically, a pyrheliometer places the detector at the base of a long tube. This geometry restricts the sky view of the detector to a small angle of approximately 5°. When the tube points toward the sun, the detector measures the beam solar radiation and a small part of the diffuse

TABLE 2.3

Shading Band Correction Factors Owing to Anisotropy

Solar Altitude	k_T									
Angle	0	0.1	0.2	0.3	0.4	0.5	0.6	0.7	0.8	0.9
<20°	0.0	0.0	0.0	0.0	0.015	0.06	0.14	0.23	0.24	0.24
20° to 40°	0.0	0.0	0.0	0.0	0.006	0.05	0.125	0.205	0.225	0.225
40° to 60°	0.0	0.0	0.0	0.0	0.003	0.045	0.115	0.175	0.205	0.205
>60°	0.0	0.0	0.0	0.0	0.0	0.035	0.09	0.135	0.17	0.17

Source: Mujahid, A. and Turner, W.D., Diffuse sky measurement and model. ASME Pap. no. 79-WA/Sol-5, 1979.

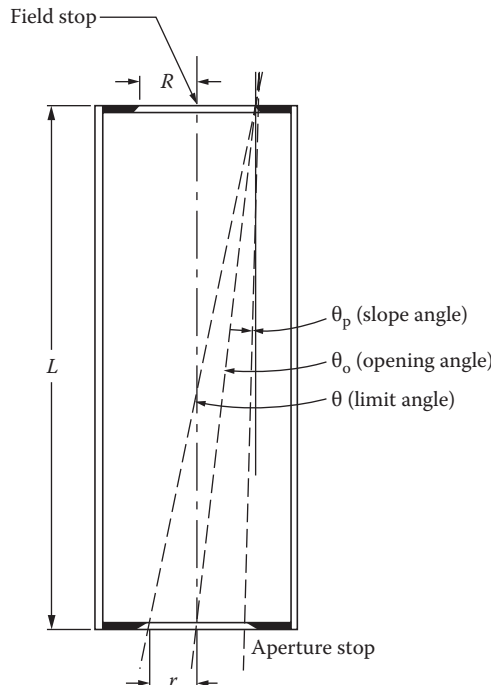
solar radiation within the view angle. Figure 2.29 shows the geometry of a pyrheliometer sky occulting tube.

In this figure, the opening half angle is

$$\theta_o = \tan^{-1} R/L. \quad (2.83)$$

The slope angle is

$$\theta_p = \tan^{-1}[(R - r)/L]. \quad (2.84)$$

**FIGURE 2.29**

Geometry of a pyrheliometer sky occulting tube.

The limit half angle is

$$\theta = \tan^{-1}[(R + r)/L]. \quad (2.85)$$

The field of view is $2\theta_0$. The World Meteorological Organization (WMO) recommends the opening half angle θ_0 to be 2.5° (Zerlaut 1989) and the slope angle θ_p to be 1° .

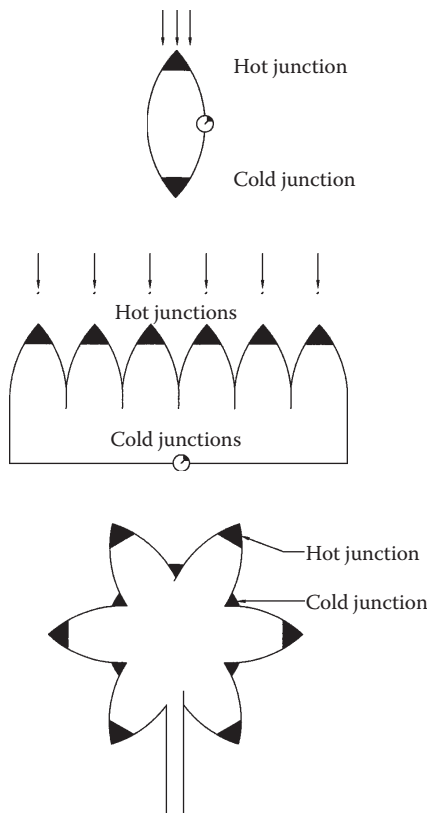
Continuous tracking of the sun is required for the accuracy of the measurements. This is obtained by employing a tracking mechanism with two motors, one for altitude and the other for azimuthal tracking. Another problem is that the view angle of a pyrheliometer is significantly greater than the angle subtended by the solar disk (approximately 0.5°). Therefore, the measurements using a pyrheliometer include the beam and the circumsolar radiation. These measurements may present a problem in using the data for central receiver systems that use only direct beam radiation. However, this is not a significant problem for parabolic trough concentrators that, in most cases, have a field of view of the order of 5° .

2.7.2 Detectors for Solar Radiation Instrumentation

Solar radiation detectors are of four basic types (Iqbal 1983; Zerlaut 1989): thermomechanical, calorimetric, thermoelectric, and photoelectric. Of these, thermoelectric and photoelectric are the most common detectors in use today.

A *thermoelectric detector* uses a thermopile that consists of a series of thermocouple junctions. The thermopile generates a voltage proportional to the temperature difference between the hot and cold junctions, which, in turn, is proportional to the incident solar radiation. Figure 2.30 shows different types of thermopile configurations. The Eppley black and white pyranometer uses a radial differential thermopile with the hot junction coated with 3M Velvet Black and the cold junction coated with a white barium sulfate paint.

Photovoltaic detectors normally use silicon solar cells measuring the short circuit current. Such detectors have the advantage of being simple in construction. Because heat transfer is not a consideration, they do not require clear domes or other convection suppressing devices. They are also insensitive to tilt as the output is not affected by natural convection. One of the principal problems with photovoltaic detectors is their spectral selectivity. Radiation with wavelengths greater than the band gap of the photovoltaic detector cannot be measured. Silicon has a band gap of 1.07 eV corresponding to a wavelength of $1.1 \mu\text{m}$. A significant portion of the infrared part of solar radiation has wavelengths greater than $1.1 \mu\text{m}$. Therefore, photovoltaic detectors are insensitive to changes in the infrared part of solar radiation.

**FIGURE 2.30**

Various thermopile configurations. (From Zerlaut, G., Solar radiation instrumentation. In *Solar Resources*, R.L. Hulstrom, ed., Cambridge, MA: MIT Press, 1989.)

2.7.3 Measurement of Sunshine Duration

The time duration of bright sunshine data is available at many more locations in the world than the solar radiation. That is why a number of researchers have used these data to estimate the available solar radiation. Two instruments are widely used to measure the sunshine duration. The device used by the US National Weather Service is called a *sunshine switch*. It is composed of two photovoltaic cells—one shaded, the other not. During daylight, a potential difference is created between the two cells, which in turn operates a recorder. The intensity level required to activate the device is that just sufficient to cast a shadow. The other device commonly used to measure the sunshine duration is called the *Campbell–Stokes sunshine recorder*. It uses a solid, clear glass sphere as a lens to concentrate the solar beam on the opposite side of the sphere. A strip of standard treated paper marked with time graduations is mounted on the opposite side of the sphere where the solar



FIGURE 2.31
Campbell-Stokes sunshine recorder.

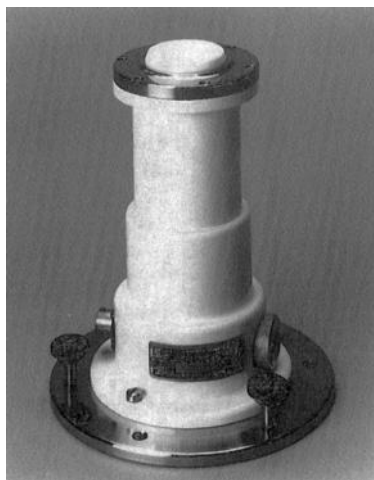
beam is concentrated. Whenever the solar radiation is above a threshold, the concentrated beam burns the paper. The length of the burned part of the strip gives the duration of bright sunshine. The problems associated with the Campbell-Stokes sunshine recorder include the uncertainties of the interpretation of burned portions of the paper, especially on partly cloudy days, and the dependence on the ambient humidity. Figure 2.31 shows a Campbell-Stokes sunshine recorder.

2.7.4 Measurement of Spectral Solar Radiation

Spectral solar radiation measurements are made with spectroradiometers. Full spectrum scanning is difficult, requires constant attention during operation, and is therefore expensive. Zerlaut (1989) has described a number of solar spectroradiometers. These instruments consist basically of a monochromator, a detector-chopper assembly, an integrating sphere, and a signal conditioning/computer package. They have the capability of measuring solar radiation in the wavelength spectrum of 280–2500 nm.

2.7.5 Wide Band Spectral Measurements

Some applications of solar energy require solar radiation data in wide band wavelength ranges such as visible, ultraviolet, and infrared rather than

**FIGURE 2.32**

Eppley TUVR Total UV Radiometer. (Courtesy of Eppley Lab.)

complete spectral data. For example, solar photocatalytic detoxification using TiO_2 as the catalyst needs data in the UV wavelength range while passive solar applications need data in the infrared wavelength range. Instruments such as pyranometers and pyrheliometers can be adapted for wide band spectral measurements by using cut-on and cut-off filters. Eppley instruments provide standard cut-off filters at the following wavelengths: 530 nm (orange), 630 nm (red), and 695 nm (dark red). They are provided as plain filters at the aperture of a pyrheliometer tube and as outer glass domes for pyranometers. Instrument manufacturers provide various interference filters peaking at different wavelengths in the solar spectrum.

Solar UV measurements are important in general since prolonged exposure to solar UV can cause skin cancer, fading of colors, and degradation of plastic materials. Such measurements have become even more important because the photocatalytic effect based on TiO_2 as a catalyst depends only on the solar UV wavelength range. Figure 2.32 shows an Eppley Model TUVR (total ultraviolet radiometer) that measures total hemispherical UV radiation from 295 to 385 nm. This radiometer uses a selenium photoelectric cell detector, a pair of band-pass filters to allow wavelengths from 295 to 385 nm to pass through, and a beveled teflon diffuser.

2.7.6 Solar Radiation Data

Measured solar radiation data are available at a number of locations throughout the world. Data for many other locations have been estimated based on measurements at similar climatic locations. Some of the available data from various locations in the world are presented in Appendix 2 (Tables A2.3a

and A2.3b). This Appendix also provides tables of modeled clear-sky data for various latitudes (Table A2.6).

Solar radiation data for the United States are available from the National Climatic Data Center of the National Oceanic and Atmospheric Administration (NOAA) and the National Renewable Energy Laboratory (NREL). In the mid-1970s, NOAA compiled a database of measured hourly global horizontal solar radiation for 28 locations for the period 1952–1975 (called SOLMET) and of data for 222 additional sites (called ERSATZ) estimated from SOLMET data and some climatic parameters such as sunshine duration and cloudiness. NOAA also has two data sets of particular interest to engineers and designers: the typical meteorological year (TMY) and the Weather Year for Energy Calculations (WYEC) data sets. The TMY data set represents typical values from 1952 to 1975 for hourly distribution of direct beam and global horizontal solar radiation. The WYEC data set contains monthly values of temperature, direct beam and diffuse solar radiation, and estimates of *illuminance* (for daylighting applications). Illuminance is solar radiation in the visible range to which the human eye responds. Recently, NREL compiled a National Solar Radiation Data Base (NSRDB) for 239 stations in the United States (Maxwell 1998; NSRDB 1992). NSRDB is a collection of hourly values of global horizontal, direct normal, and diffuse solar radiation based on measured and estimated values for the period 1961–1990. Since long-term measurements were available for only approximately 50 stations, measured data make up only approximately 7% of the total data in the NSRDB. A typical meteorological year data set from NSRDB is available as TMY2.

The data for other locations in the world are available from national government agencies of most countries of the world. Worldwide solar radiation data are also available from the World Radiation Data Center (WRDC) in St. Petersburg, Russia, based on worldwide measurements made through local weather service operations (Voeikov Main Geophysical Observatory 1999). WRDC, operating under the auspices of the WMO, has been archiving data from over 500 stations and operates a worldwide website in collaboration with NREL (<http://wrdc.mgo.nrel.gov>). Data for some cities of the world from WRDC are given in Appendix 2 (Table A2.3). An International Solar Radiation Data Base was also developed by the University of Lowell (University of Lowell Photovoltaic Program 1990).

- Surface Meteorology and Solar Energy (Version 6.0) [<http://eosweb.larc.nasa.gov/sse/>]
- Energy Plus Energy Weather Data [http://apps1.eere.energy.gov/buildings/energyplus/weatherdata_about.cfm?CFID=5019287&CFTOKEN=b54041e7be537f1f-B598302C-5056-BC19-15C492F462EE1BAC]
- National Solar Radiation Data Base, 1961–1990: Typical Meteorological Year [http://rredc.nrel.gov/solar/old_data/nsrdb/] [<http://rredc.nrel.gov/solar/pubs/NSRDB/>]

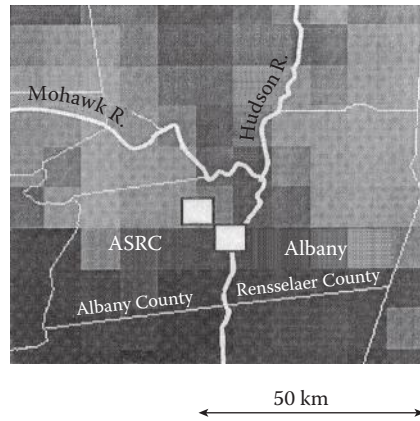
- National Solar Radiation Data Base, 1991–2005 Update: Typical Meteorological Year 3 [http://rredc.nrel.gov/solar/old_data/nsrdb/] [<http://www.nrel.gov/docs/fy12osti/54824.pdf>]
 - The Solar and Wind Energy Resource Assessment (SWERA) [[http://en.openei.org/wiki/Solar_and_Wind_Energy_Resource_Assessment_\(SWERA\)](http://en.openei.org/wiki/Solar_and_Wind_Energy_Resource_Assessment_(SWERA))]
 - National Renewable Laboratory (NREL) [<http://www.nrel.gov/>]
-

2.8 Solar Radiation Mapping Using Satellite Data

Remote sensing satellite data have been used since the early 1960s to extract quantitative and qualitative cloud data. The most important application of cloud cover mapping has been for the observation of storms, hurricanes, and so on. Recently, however, considerable interest has been developed in using the cloud mapping data to estimate terrestrial solar radiation. Since meteorological satellites from a number of countries can now cover most of the earth, the data can be used to estimate solar radiation where no measured data exist or none is being measured.

Weather satellites are available in three main orbiting configurations—equatorial, polar, and geostationary. The equatorial satellites are low-level orbiting satellites (~600 km altitude) that generally orbit the earth in a west-to-east direction in a sinusoidal path that crosses the equator at least twice per orbit. Polar satellites are also low-orbit satellites that orbit the earth from the North Pole to the South Pole while the earth rotates underneath. Sun synchronous polar orbits have their orbits synchronized with the sun such that the same point on the earth is viewed at the same time each day. Low-orbit satellites are capable of gathering high-resolution spatial data. A geostationary satellite orbits in such a way that it is always over the same point on the earth's surface. Geostationary satellites have very high altitudes (approximately 36,000 km) and can provide high temporal resolution images over a large portion of the earth's surface. A number of countries maintain geostationary satellites including the United States (GOES, longitudes 70°W and 140°W), Europe (METEOSAT, longitude 0°), India (INSAT, longitude 70°E), and Japan (GMS, longitude 140°E).

Various types of high-resolution radiometers collect radiative data images of the earth's atmosphere below. These radiometers scan spectral measurements in the wavelength ranges of shortwave (0.2–3.0 μm), longwave (6.5–25 μm), and total irradiance (0.2–100 μm). The spatial resolution of images from the satellite is given by a *pixel*, which represents the smallest area of data, generally of the order of 2 km × 2 km. However, several pixels of data are required to derive a surface value giving a surface resolution of

**FIGURE 2.33**

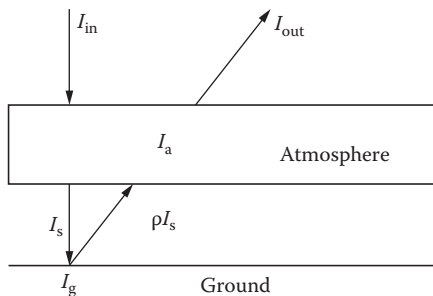
GOES-8 Intermediate resolution image close-up around Albany. (From Perez, R. et al., The strengths of satellite based resource assessment. *Proc. of the 1997 ASES Annual Conf*, pp. 303–308, Washington, DC, 1997.)

the order of $10 \text{ km} \times 10 \text{ km}$. Figure 2.33 shows an example of an intermediate resolution GOES-8 image around Albany, New York, overlaid on a local map.

2.8.1 Estimation of Solar Resource from Satellite Data

The signal recorded by a radiometer on a satellite measures the solar radiation flux reflected back from the earth's atmosphere. The basic method behind estimation of ground solar radiation from these data is to apply the principle of energy conservation in the earth-atmosphere system (Noia et al. 1993), as shown in Figure 2.34. From this figure, we can write

$$I_{\text{in}} = I_{\text{out}} + I_a + I_g \quad (2.86)$$

**FIGURE 2.34**

Solar radiation in the earth-atmosphere model.

where I_{in} represents the solar radiation incident on the atmosphere, I_{out} represents the outward radiation from the atmosphere, I_a is the radiation absorbed by the atmosphere, and I_g is the radiation absorbed by the ground.

I_g can be expressed in terms of the surface albedo* ρ (reflectivity) and the solar radiation I_s , incident on the earth's surface:

$$I_g = I_s(1 - \rho). \quad (2.87)$$

From Equations 2.82 and 2.83, we can obtain

$$I_s = (I_{\text{in}} - I_{\text{out}} - I_a)/(1 - \rho). \quad (2.88)$$

I_{out} is measured by the satellite radiometers. I_{in} depends on the sun-earth distance and the solar zenith angle and can be calculated using Equation 2.32 as

$$I_{\text{in}} = I_0(D_0/D)^2 \cdot \cos(z). \quad (2.89)$$

If we could estimate I_a , and ρ were known a priori, I_s could be estimated using Equation 2.88 from the value of I_{out} measured by a satellite. However, I_a cannot be estimated easily since it depends on the atmospheric conditions such as cloud cover, dust particles, and air mass, and surface albedo (reflectance) ρ varies for every point of the region under consideration. In order to deal with these factors, two types of empirical methods are under development. These are known as statistical and physical methods. These methods have been reviewed in detail by Schmetz (1989), Hay (1993), Noia et al. (1993), Islam (1994), and Pinker et al. (1995).

Statistical Methods. Statistical methods are based on finding a relationship between the radiative flux measured by a satellite radiometer and the simultaneous solar radiation value measured at the earth's surface in the area under consideration. Some of the models developed on statistical approach include those by Hay and Hanson (1978), Tarpley (1979), Justus et al. (1986), Cano et al. (1986), and Sorapipatana et al. (1988).

Physical Methods. Physical methods are based on the analysis of radiative processes in the atmosphere as the solar radiation passes through it. Some of the models developed with this approach include those by Gautier (1980), Moeser and Raschke (1984), Dedieu et al. (1987), and Marullo et al. (1987).

The simplest of the above models is by Hay and Hanson (1978), which gives the atmospheric transmittance T as

$$T = \frac{I_s}{I_{\text{in}}} = a - b \frac{I_{\text{out}}}{I_{\text{in}}}, \quad (2.90)$$

or $I_s = aI_{\text{in}} - bI_{\text{out}}.$

* The term *albedo* is used mostly in the field of meteorology.

The values of regression coefficients given by Hay and Hanson (1978) are as follows: $a = 0.79$, $b = 0.71$. This method is simple; however, the coefficients, particularly b , vary considerably with parameters such as cloud reflectivity. More recent investigations suggest that it is necessary to determine coefficients a and b for different locations.

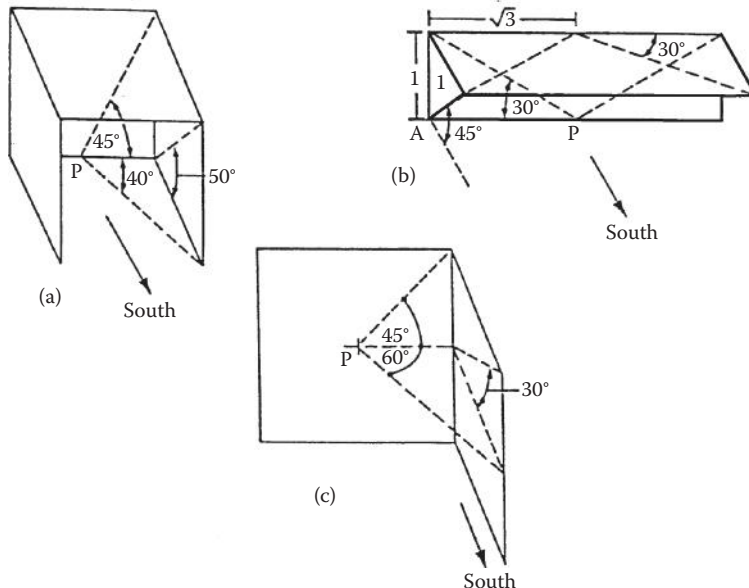
It is beyond the scope of this book to discuss all the models. It suffices, however, to point out that all the models, including the Hay and Hanson model, more or less give values within 10% of the ground measured values (Noia et al. 1993). The methods usually break down under partly cloudy conditions and under snow-covered ground conditions.

PROBLEMS

1. Spectroscopists make use the concept of wavenumber, $\tilde{\nu}$ (number of waves per unit length, $\tilde{\nu} = 1/\lambda$, to study the spectral absorption, emission, etc., of electromagnetic radiation).
 - a. For radiation in a vacuum ($n = 1$), derive an alternative form of the Planck distribution (Equation 2.3) in terms of wavenumber.
 - b. Using the results of part A, show that Wien's displacement law (Equation 2.5) can be alternatively expressed as $\tilde{\nu} = 1.93 T \text{ cm}^{-1}\text{K}$ ($3.47 \text{ cm}^{-1}\text{R}$).
2. Calculate the declination, the zenith angle, and the azimuth angle of the sun for New York City (latitude 40.77°N) on October 1 at 2:00 p.m. solar time.
3. A solar energy system in Tampa, Florida, requires two rows of collectors facing south and tilted at a fixed 30° angle. Find the minimum normalized distance at which the second row should be placed behind the first row for no shading at noon solar time at winter solstice. What percentage of the second row is shaded on the same day at 9:00 a.m. solar time?
4. Find the sunrise and sunset times for a location of your choice on September 1.
5. Construct a table of hourly sun angles for the 15th day of each month for a location of your choice. Also show the sunrise and sunset times for those days.
6. Referring to Figure 2.21, prove Equation 2.48 for the angle of incidence. (Hint: use direction cosines of the sun-ray vector and a vector normal to the tilted surface to find the angle between them. The dot product of two unit vectors gives the cosine of the angle between them.)
7. Show that the angle of incidence for a south-facing cylindrical surface (e.g., a tubular detector) can be obtained from the equation \cos^2

$i = 1 - [(\sin(\beta - L) \cos \delta_s \cos h_s + \cos(\beta - L) \sin \delta_s)]^2$. (Hint: integrate over the surface of the cylinder.)

8. Determine the following for a south-facing surface at 30° slope in Tampa, Florida (latitude = 27.97°N , longitude = 82.46°W) on September 21 at noon solar time:
 - a. Zenith angle
 - b. Angle of incidence
 - c. Beam radiation
 - d. Diffuse radiation
 - e. Reflected radiation
 - f. Total radiation
 - g. Local time
9. Show that the hourly averaged, extraterrestrial radiation for a given hour is the same, to within 1%, as instantaneous radiation at the hour's midpoint.
10. Prepare shadow maps for point P on the sun-path diagrams for 35°N and 40°N for the three geometries shown in (a), (b), and (c) below. Determine the hours of shading that occur each month.



11. Repeat Problem 10c if the surface containing point P faces due west instead of due south for a 40°N location.

12. Calculate the incidence angle at noon and 9 a.m. solar time on a fixed, south-facing flat-plate collector located at 40°N latitude and tilted 70° up from the horizontal. Find i for June 21 and December 21.
13.
 - a. If the surface in Problem 12 faces S 45°E , what are the incidence angles?
 - b. Using the results of Problem 7, determine the incidence angles for the collector in Problem 12 if it had a cylindrical surface.
14. Using a one-term Fourier cosine series, develop an empirical equation for solar declination as a function of day number counted from January 1 (see Figures 2.8 and 2.9).
15. Derive an equation for the lines of constant declination in a sun-path diagram, for example, Figure 2.12. Check your equation by plotting a few declination lines on a piece of polar coordinate graph paper.
16. Derive Equation 2.31 relating profile angle γ to azimuth angle α and altitude angle α .
17. Based on Equation 2.48, what value of β would result in the annual minimum value of the incidence angle i ? Note that this tilt angle would result in maximum collection of beam radiation on a fixed, flat, south-facing surface. (Hint: use a double integration procedure.)
18. At what time does the sun set in Calcutta (23°N) on May 1 and December 1?
19. What is the true solar time in Sheridan, Wyoming (107°W) at 10:00 a.m. Mountain Daylight Time on June 10? What is the true solar time at 10:00 a.m. Mountain Standard Time on January 10?
20. Using the Angström–Page method, calculate the average horizontal insolation in Miami, Florida, in May and in October with \bar{P}_S 60% and 70%, respectively. Compare these results to the predicted value for the 15th days of those months obtained from the ASHRAE Clear Sky Model.
21. Equation 2.55 is based on an early solar constant value of 1394 W/m^2 . Derive a modified form of Equation 2.55 based on a solar constant of 1366.1 W/m^2 .
22. Predict the hourly beam and diffuse radiation on a horizontal surface for Denver (40°N) on September 9 at 9:30 a.m. on a clear day.
23. Derive an expression for the minimum allowable distance between east–west rows of solar collectors that will assure no shading of one row by the row immediately to the south. Use the law of sines and express the result in terms of the collector tilt and face length and the controlling value of the solar profile angle.

References

- Akinoglu, B.G., and A. Ecevit. 1990. Construction of a quadratic model using modified angstrom coefficients to estimate global solar radiation. *Sol. Energy* 45: 85.
- ASHRAE. 2009. *Handbook of Fundamentals*. American Society of Heating, Refrigeration and Air Conditioning Engineers, Atlanta, GA.
- Cano, D. et al. 1986. Method for the determination of the global solar radiation from meteorological satellite data. *Sol. Energy* 37(1): 31–39.
- Choudhury, N.K.O. 1963. Solar radiation at New Delhi. *Sol. Energy* 7(44).
- Collares-Pereira, M., and A. Rabl. 1979. The average distribution of solar radiation—correlation between diffuse and hemispherical. *Sol. Energy* 22: 155–166.
- Coppolino, S. 1994. New correlation between clearness index and relative sunshine. *Renew. Energ.* 4(4): 417–423.
- Dedieu, G., P.Y. Deschamps, and Y.H. Kerr. 1987. Satellite estimation of solar irradiance at the surface of the earth and of surface albedo using a physical model applied to METEOSAT data. *J. Clim. Appl. Meteorol.* 26: 79–87.
- Frohlich, C. et al. 1973. The third international comparison of pyrheliometers and a comparison of radiometric scales. *Sol. Energy* 14: 157–166.
- Garg, H.P., and S.N. Garg. 1985. Correlation of the monthly average daily global, diffuse and beam radiation with bright sunshine hours. *Energy Convers. Manage.* 25(4): 409–417.
- Gautier, C. 1980. Simple physical model to estimate solar radiation at the surface from GOES satellite data. *J. Appl. Meteorol.* 19(8): 1005–1012.
- Gopinathan, K. 1988. A general formula for computing the coefficients of the correlation connecting global solar radiation to sunshine duration. *Sol. Energy* 41: 499.
- Gueymard, C. 1986. Mean daily averages of beam radiation received by tilted surfaces as affected by the atmosphere. *Sol. Energy* 37: 262–267.
- Gueymard, C. 2000. Prediction and performance assessment of mean hourly global radiation. *Sol. Energy* 68: 285–303.
- Gueymard, C.A. 2005. SMARTS code, version 2.9.5 User's Manual. Solar Consulting Services. Available at: <http://www.solarconsultingservices.com/smarts.php>.
- Gueymard, C.A. 2008. REST2: High performance solar radiation model for cloudless-sky irradiances, illuminance and photosynthetically active radiation; Validation with a benchmark dataset. *Sol. Energy* 82: 272–285.
- Gueymard, C.A., and D. Thevenard. 2009. Monthly average clear-sky broadband irradiance database for worldwide solar heat gain and building cooling load calculations. *Sol. Energy* 83: 1998–2018.
- Hay, J.E. 1993. Satellite based estimates of solar irradiance at the earth's surface: I. Modelling approaches. *Renew. Energ.* 3: 381–393.
- Hay, J.E., and K.J. Hanson. 1978. A satellite-based methodology for determining solar irradiance at the ocean surface during GATE. *Bull. Am. Meteorol. Soc.* 59: 1549.
- Howell, J.R., and R. Siegel. 1992. *Thermal Radiation Heat Transfer*. McGraw-Hill Book Co, New York.
- Hussain, M. 1994. Estimation of the global and diffuse irradiation from sunshine duration and atmospheric water vapor content. *Sol. Energy* 33(2): 217–220.
- Iqbal, M. 1979. Correlation of average diffuse and beam radiation with hours of bright sunshine. *Sol. Energy* 23: 169–173.

- Iqbal, M. 1983. *An Introduction to Solar Radiation*. Academic Press, New York.
- Islam, M.R. 1994. Evolution of methods for solar radiation mapping using satellite data. *RERIC Int. Energ.* J. 16(2).
- Justus, C., M.V. Paris, and J.D. Tarpley. 1986. Satellite-measured insolation in the United States, Mexico and South America. *Remote Sens. Environ.* 20: 57–83.
- Kasten, F., and A.T. Young. 1989. Revised optical air mass tables and approximation formula. *Appl. Optics* 28: 4735–4738.
- Klucher, T.M. 1979. Evaluation of models to predict insolation on tilted surfaces. *Sol. Energy* 23(2): 111–114.
- Kreith, F., and M. Bohm. 1993. *Principles of Heat Transfer*, 5th ed. West Publishing Co, St. Paul, MN.
- Liu, B.Y.H., and R.C. Jordan. 1960. The interrelationship and characteristic distribution of direct, diffuse and total solar radiation. *Sol. Energy* 4: 1–19. See also Liu, B.Y.H. 1960. Characteristics of solar radiation and the performance of flat plate solar energy collectors. PhD dissertation, University of Minnesota, Minneapolis, MN.
- Liu, B.Y.H., and R.C. Jordan. 1961a. Daily insolation on surfaces titled toward the equator. *Trans. ASHRAE* 67: 526–541.
- Liu, B.Y.H., and R.C. Jordan. 1961b. Daily insolation on surface titled toward the equator. *Trans. ASHRAE* 3(10): 53–59.
- Liu, B.Y.H., and R.C. Jordan. 1963. A rational procedure for predicting the long-term average performance of flat-plate solar energy collectors. *Sol. Energy* 7: 53–74.
- Liu, B.Y.H., and R.C. Jordan. 1967. Availability of solar energy for flat-plate solar heat collectors, Chapter 1. In *Low Temperature Engineering of Solar Energy*. ASHRAE, New York; see also 1977 revision.
- Löf, G.O.G., J.A. Duffie, and C.O. Smith. 1966. World distribution of solar energy. Eng. Expt. Station Rept. 21, University of Wisconsin, Madison.
- Marullo, S., G. Dalu, and A. Viola. 1987. Incident short-wave radiation at the surface from METEOSAT data. *Il Nuovo Cimento* 10C: 77–90.
- Maxwell, E.L. 1998. METSTAT—The solar radiation model used in the production of the national solar radiation data base (NSRDB). *Sol. Energy* 62: 263–279.
- Moeser, W., and E. Raschke. 1984. Incident solar radiation over Europe estimated from METEOSTAT data. *J. Clim. Appl. Meteorol.* 23(1): 166–170.
- Mujahid, A., and W.D. Turner. 1979. Diffuse sky measurement and model. ASME Pap. no. 79-WA/Sol-5, ASME, NY.
- Noia, M., C. Ratto and R. Festa. 1993. Solar irradiance estimation from geostationary satellite data: I. statistical models; II. physical models. *Sol. Energy* 51: 449–465.
- NSRDB. 1992. *Volume 1: Users Manual: National Solar Radiation Data Base (1961–1990), Version 1.0*. National Renewable Energy Laboratory, Golden, CO.
- Ögelman, H., A. Ecevit, and E. Tasdemiroglu. 1984. A new method for estimating solar radiation from bright sunshine data. *Sol. Energy* 33(6): 619–625.
- Page, J.K. 1966. The estimation of monthly mean values of daily total short-wave radiation on vertical and inclined surfaces from sunshine records or latitudes 40°N–40°S. *Proc. U.N. Conf. New Sources Energy* 4: 378.
- Perez, R. et al. 1997. The strengths of satellite based resource assessment. *Proc. of the 1997 ASES Annual Conf*, Washington, DC, pp. 303–308.
- Pinker, R.T., R. Frouin, and Z. Li. 1995. A review of satellite methods to derive surface shortwave irradiance. *Remote Sens. Environ.* 51: 108–124.

- Quinlan, E.T., ed. 1977. *SOLMET Vol. 1: Hourly Solar Radiation Surface Meteorological Observations*. NOAA, Asheville, NC.
- Quinlan, F.T., ed. 1979. *SOLMET Vol. 2: Hourly Solar Radiation Surface Meteorological Observations*. NOAA, Asheville, NC.
- Ruth, D.W., and R.E. Chant. 1976. The relationship of diffuse radiation to total radiation in Canada. *Sol. Energy* 18: 153.
- Schmetz, J. 1989. Towards a surface radiation climatology: Retrieval of downward irradiances from satellites. *Atmos. Res.* 23: 287–321.
- Sorapipatana, C., R.H.B. Exell and D. Borel. 1988. A bispectral method for determining global solar radiation from meteorological satellite data. *Sol. Wind Technol.* 5(3): 321–327.
- Sparrow, E.M., and R.D. Cess. 1978. *Radiation Heat Transfer*. Wadsworth Publ. Co., Belmont, CA.
- Spencer, J.W. 1971. Fourier series representation of the position of the sun. *Search* 2: 172.
- Stanhill, G. 1966. Diffuse sky and cloud radiation in Israel. *Sol. Energy* 10: 66.
- Tarpley, J.D. 1979. Estimating incident solar radiation at the surface from geostationary satellite data. *J. Appl. Meteorol.* 18(9): 1172–1181.
- Temps, R.C., and K.L. Coulson. 1977. Solar radiation incident upon slopes of different orientations. *Sol. Energy* 19(2): 179–184.
- University of Lowell Photovoltaic Program. 1990. *International Solar Irradiation Database, Version 1.0*. University of Lowell Research Foundation, Lowell, MA.
- Vasquez-Padilla, R. 2011. Simplified methodology for designing parabolic trough solar power plants. PhD dissertation, University of South Florida, Tampa, FL, USA.
- Voeikov Main Geophysical Observatory. 1999. Worldwide daily solar radiation. Available at <http://www.mgo.rssi.ru>.
- Whillier, A. 1965. Solar radiation graphs. *Sol. Energy* 9: 165–166.
- Zerlaut, G. 1989. Solar radiation instrumentation. In *Solar Resources*, R.L. Hulstrom, ed., MIT Press, Cambridge, MA.

3

Solar Thermal Collectors

Converting the sun's radiant energy to heat is very common from historical times and has evolved into a well-developed solar conversion technology today. The basic principle of solar thermal collection is that when solar radiation strikes a surface, a part of it is absorbed, thereby increasing the temperature of the surface. The efficiency of that surface as a solar collector depends not only on the absorption efficiency but also on how the thermal and reradiation losses to the surroundings are minimized and how the energy from the collector is removed for useful purposes. Various solar thermal collectors range from unglazed flat plate-type solar collectors operating at approximately 5°C–10°C above the ambient to central receiver concentrating collectors operating at above 1000°C. Table 3.1 lists various types of solar thermal collectors and their typical temperature and concentration ranges.

This chapter analyzes in detail the thermal and optical performance of several solar thermal collectors. They range from air- and liquid-cooled non-concentrating, flat-plate types to compound-curvature, continuously tracking types with concentration ratios up to 3000 or more. Applications of the energy converted by solar thermal collectors are described in Chapters 5 through 8. Section 3.1 describes some fundamental radiative properties of materials, knowledge of which helps in the design of solar thermal collectors.

3.1 Radiative Properties and Characteristics of Materials

When radiation strikes a body, a part of it is reflected, a part is absorbed and, if the material is transparent, a part is transmitted, as shown in Figure 3.1.

The fraction of the incident radiation reflected is defined as the reflectance ρ , the fraction absorbed as the absorptance α , and the fraction transmitted as the transmittance τ . According to the first law of thermodynamics, these three components must add up to unity, or

$$\alpha + \tau + \rho = 1. \quad (3.1)$$

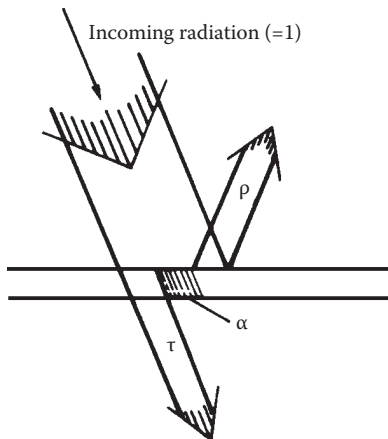
Opaque bodies do not transmit any radiation and $\tau = 0$.

The reflection of radiation can be *specular* or *diffuse*. When the angle of incidence is equal to the angle of reflection, the reflection is called specular;

TABLE 3.1

Types of Solar Thermal Collectors and Their Typical Temperature Range

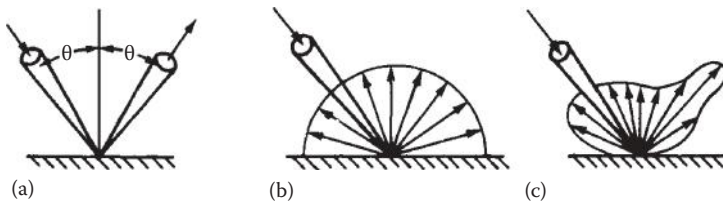
Type of Collector	Concentration Ratio	Typical Working Temperature Range (°C)
Flat-plate collector	1	≤ 70
High efficiency flat-plate collector	1	60–120
Fixed concentrator	3–5	100–150
Parabolic trough collector	10–50	150–350
Parabolic dish collector	200–500	250–700
Central receiver	500 to >3000	500 to >1000

**FIGURE 3.1**Schematic representation of transmittance τ , absorptance α , and reflectance ρ .

when the reflected radiation is uniformly distributed into all directions, it is called diffuse (see Figure 3.2). No real surface is either specular or diffuse, but a highly polished surface approaches specular reflection, whereas a rough surface reflects diffusely.

Another important radiative property is called emittance ϵ , which is the ratio of the radiative emissive power of a real surface to that of an ideal "black" surface as defined in Chapter 2.

All of the radiative properties of materials, α , τ , ρ , and ϵ , can be functions of the wavelength and direction. In fact, such dependence is used in the design of solar energy devices and systems. For example, selective absorbers are used for solar collectors and passive heating systems, and glazing materials are used for daylighting and solar collectors.

**FIGURE 3.2**

Reflections from (a) ideal specular, (b) ideal diffuse, and (c) real surfaces.

Referring to Figure 2.6, the monochromatic directional emittance of a surface at a wavelength λ , $\varepsilon_\lambda(\theta, \phi)$, in a direction signified by an azimuth angle ϕ and a polar angle θ , is

$$\varepsilon_\lambda(\theta, \phi) = \frac{I_\lambda(\theta, \phi)}{I_{b\lambda}}. \quad (3.2)$$

From the above, the total directional emittance $\varepsilon(\theta, \phi)$ over all the wavelengths or the monochromatic hemispherical emittance ε_λ can be obtained by integration of $\varepsilon_\lambda(\theta, \phi)$ over all the wavelengths or the entire hemispherical space, respectively. The overall emittance ε is found by integrating the hemispherical emittance over all the wavelengths.

$$\varepsilon = \frac{1}{\sigma T^4} \int_0^\infty \varepsilon_\lambda E_{b\lambda} d\lambda. \quad (3.3)$$

Observe that both ε_λ and ε are properties of the surface.

The next most important surface characteristic is the absorptance. We begin by defining the monochromatic directional absorptance as the fraction of the incident radiation at wavelength λ from the direction θ, ϕ that is absorbed, or

$$\alpha_\lambda(\theta, \phi) = \frac{I_{\lambda,a}(\theta, \phi)}{I_{\lambda,i}(\theta, \phi)}, \quad (3.4)$$

where the subscripts "a" and "i" denote absorbed and incident radiation, respectively. The monochromatic directional absorptance is also a property of the surface.

More important than $\alpha_\lambda(\theta, \phi)$ is the overall directional absorptance $\alpha(\theta, \phi)$, defined as the fraction of the total radiation from the direction θ, ϕ that is absorbed, or

$$\alpha(\theta, \phi) = \frac{\int_0^\infty \alpha_\lambda(\theta, \phi) I_{\lambda,i}(\theta, \phi) d\lambda}{\int_0^\infty I_{\lambda,i}(\theta, \phi) d\lambda} = \frac{1}{I_i(\theta, \phi)} \int_0^\infty \alpha_\lambda(\theta, \phi) I_{\lambda,i}(\theta, \phi) d\lambda. \quad (3.5)$$

The overall absorptance is a function of the characteristics of the incident radiation and is, therefore, unlike the monochromatic absorptance, not a property of a surface alone. It is this characteristic that makes it possible to have selective surfaces that absorb the radiation from one source at a higher rate than from another. In other words, even though according to Kirchhoff's law the monochromatic emittance at a wavelength λ must equal the monochromatic absorptance at the same wavelength

$$\alpha_\lambda(\theta, \phi) = \varepsilon_\lambda(\theta, \phi), \quad (3.6)$$

the overall emittance is not necessarily equal to the overall absorptance unless thermal equilibrium exists, and the incoming and outgoing radiation have the same spectral characteristics.

The effect of incidence angle on the absorptance is illustrated in Table 3.2 where the angular variation of the absorptance for a nonselective black surface, typical of those used on flat-plate collectors, is shown. The absorptance of this surface for diffuse radiation is approximately 0.90.

The third characteristic to be considered is the reflectance. Reflectance is particularly important for the design of focusing collectors. As mentioned previously, there are two limiting types of reflection: specular and diffuse.

TABLE 3.2

Angular Variation of Absorptance of Lampblack Paint

Incidence Angle i (°)	Absorptance $\alpha(i)$
0–30	0.96
30–40	0.95
40–50	0.93
50–60	0.91
60–70	0.88
70–80	0.81
80–90	0.66

Source: Adapted from Löf, G.O.G. and R.A. Tybout, Model for optimizing solar heating design, ASME Paper 72-WA/SOL-8, 1972.

As illustrated in Figure 3.2a, when a ray of incident radiation at an angle θ is reflected at the same polar angle and the azimuthal angles differ by 180° , as for a perfect mirror, the reflection is said to be specular. The reflection is said to be diffuse if the incident radiation is scattered equally in all directions, as shown in Figure 3.2b.

3.1.1 Selective Surfaces

Two types of special surfaces of great importance in solar collector systems are selective absorbers and reflecting surfaces. Selective absorber surfaces combine a high absorptance for solar radiation (short wavelengths) with a low emittance for the normal operating temperature of the surface. This combination of surface characteristics is possible because 98% of the energy in incoming solar radiation is contained within wavelengths below 3 μm , whereas 99% of the radiation emitted by black or gray surfaces at 400 K is at wavelengths longer than 3 μm . The dotted line in Figure 3.3 illustrates the spectral reflectance of an ideal, selective semigray surface having a uniform reflectance of 0.05 below 3 μm , but 0.95 above 3 μm . Real surfaces do not approach this performance. Figure 3.4 lists properties of some selective coatings in the normal temperature range of solar thermal collectors (below 250°C), which are reproduced from a detailed review of selective absorbers by Kennedy (2002). Performance of selective absorber coatings degrades as the temperatures increase to 400°C and above. Since the interest in concentrating solar thermal power has increased and plants as large as 300 MWe are under construction, there is a need for selective solar absorbers capable of maintaining high performance at temperatures of 400°C and above. Figure 3.5 lists some of the high-temperature selective surfaces based on the research summarized by Kennedy (2002).

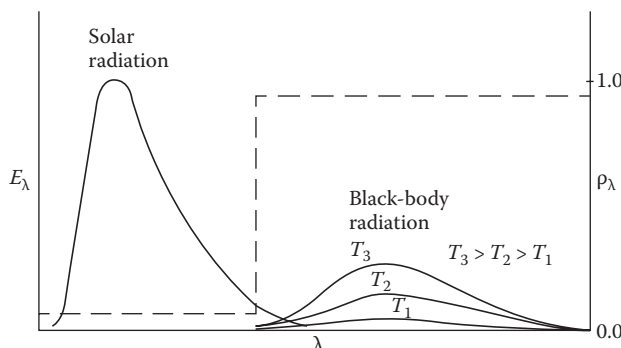


FIGURE 3.3

Illustrations of reflectance characteristics of an ideal selective surface. The figure shows radiation from ideal surfaces at different temperatures and solar radiation.

Material	Substrate	Fabrication	Stability (°C)	
			Absorptance α	Emissance ϵ (100°C)
Ni–Sn	Cu	Electrodeposition/sol–gel	0.92–0.98	0.08–0.25
Graphitic films	Cu	MF-pulsed	0.92	0.025
α -C/H/Cr	Al	PVD/PECVD	0.876	0.061
α -C/H				250
Ge in silicon binder	Cu or SS	Paint	0.91	0.7
Si			0.83	0.7
PbS			0.96	0.7
Ag dielectric	Al	Biomimetic sol–gel		300
Black copper	Cu	Electrodeposition	0.97–0.98	0.02
BiCu–Cu ₂ O/Cu				370
Black chrome	Ni–Cu	Electrodeposition	0.97	0.09
Cr–Cr ₂ O ₃	CU steel			400
Mo/Cr ₂ O ₃			0.95	<0.30
TiN _x O _y	Cu	ARE	0.92	0.06
Cr, Fe, Mo, SS, Ta, Ti, W silicides	Bulk Cu	DC reactive sputtering	0.76–0.82	0.02–0.3
Cr, Fe, Mo, SS, Ta, Ti, W carbides	Sputtered Cu		0.81–0.86	
Ni–NiO _x	Bulk Cu	DC reactive sputtering	0.76–0.81	0.02
Ni–pigmented Al ₂ O ₃	Sputtered Cu		0.84–0.90	0.035–0.06
Ni–Al	Al	Reactive sputtering	0.96	0.10
Ni–pigmented Al ₂ O ₃		Anodization	0.85–0.97	0.08–0.21
				300–400

FIGURE 3.4

Mid-temperature selective surfaces. (Adapted from Kennedy, C.E., Review of mid- to high-temperature solar selective absorber materials. Report NREL/TP-520-31267, National Renewable Energy Laboratory, Golden, CO, 2002.)

Material	Substrate	Fabrication	Absorptance α	Emissance ϵ (100°C)*	Stability (°C)	
					Vacuum	Air
Mo-Al ₂ O ₃	Ni or Al Steel	RF sputtering	0.96	0.16 (350) 0.1–0.07 (400)	350–500	
W-Al ₂ O ₃		RF sputtering	0.97–0.98	0.04	600	
W-Al ₂ O ₃	Cu	CVD	0.85	0.08	600	
Pt-Al ₂ O ₃		RF sputtering	0.90–0.98			
Al ₂ O ₃ /Pt-Al ₂ O ₃						
Double						
Mo-Al ₂ O ₃	Cu	DC sputtering	0.96	0.06 (350 _c)	500	
Mo-AlN			0.92–0.94	0.08–0.10 (350 _c)	350–500	
W-AlN					500	
Quasi-crystals multilayer cement	Cu, Si		0.90 0.86–0.92	0.025 0.031–0.05	500 500	400
Si ₃ N ₄ /Si–Ge/Ag	SS, Al	CVD	0.890	0.0389 (300) 0.545 (500)	650 (He)	
Ni:SiO ₂ Cr:SiO	Al, Cu	Reactive DC sputtering	0.90–0.96	0.03–0.14		400–800 (Ar)
Al-AlN _x –AlN	SS	Reactive DC	0.97	0.10	500	
Ag/CuO/Rh ₂ O ₃ /CeO ₂ //	SS	Organic–metallic Spray	0.9 0.86–0.88	0.1 0.1	700 775	500 550
CeO ₂ // Ag/Pt/CuO// Rh/Rh ₂ O ₃ // Ag/Pt			0.88	0.06–0.12	700	500
CeO ₂ // CuO/CoO						
Mn ₂ O ₃ /Pt						
Black cobalt						
Co ₃ O ₄ /Co			0.96–0.92	0.71–0.017		400–650
Ni–Co ₃ O ₄ /Co			0.95	0.10		

FIGURE 3.5
High-temperature selective surfaces.

(Continued)

Material	Substrate	Fabrication	Absorptance α	Emissance ϵ (100°C)*	Stability (°C)	
					Vacuum	Air
Black moly		CVD	0.94	0.30 (500 _c)	500	350
Mo-MoO ₂						
Black tungsten		CVD	0.83	0.25	800	
W-WO _x						
AU/TiO ₂	SS	Sol-gel	0.85	0.01 (400 _c)	>500	
AU/MgO	Mo/SS	RF sputtering	0.90–0.93	0.04–0.1		400
ZrC _x N _y	Al		0.85	0.074 (325 _c)	600	125
Al ₂ O ₃ /ZrC _x N _y /Ag			0.91	0.05 (325 _c)	700	175
ZrO _x /ZrC _x /Zr	SS		0.90	0.05 (20)	700	
TIN	Cu, Al	DC reactive Sputtering	0.80	0.14–0.40		500
Ti _{1-x} Al _x N						750–900
M ₃ O _c + M'Fe ₂ P ₄	Ni-Mo alloy	Painting Arc plasma	>0.90	>0.45		700 1060
VB ₂ , NbB ₂ , TaB ₂ , TiB ₂ , ZrB ₂ , LaB ₆ , WS ₂ , TiSi ₂	Glass	DC reactive sputtering	0.99	0.95–0.97	2300–3040 (MP)	
Si ₃ N ₄ AR-ZrB ₂	ZrB ₂	CVD	0.88–0.93	0.08–0.10		500
Masterbeads “paint”			0.93			<1000
Textured SS	SS		0.93 ± 0.02	0.22 ± 0.02	>440	
Textured Cr	Cr		0.80–0.90	0.10–0.30	550	<500
W whiskers			0.98	>0.26		
Mo, Rh, Pt, W, HfC, Au					>600	
NiO _x , CoO _x					800	

* Emissance values at 100°C unless indicated by a number in parenthesis. Subscript c means calculated.

FIGURE 3.5 (CONTINUED)

High-temperature selective surfaces. (Adapted from Kennedy, C.E., Review of mid- to high-temperature solar selective absorber materials. Report NREL/TP-520-31267, National Renewable Energy Laboratory, Golden, CO, 2002.)

TABLE 3.3

Specular Reflectance Values for Solar Reflector Materials

Material	ρ
Silver (unstable as front surface mirror)	0.94 ± 0.02
Gold	0.76 ± 0.03
Aluminized acrylic, second surface	0.86
Anodized aluminum	0.82 ± 0.05
Various aluminum surfaces, range	0.82–0.92
Copper	0.75
Back-silvered water-white plate glass	0.88
Aluminized type-C Mylar (from Mylar side)	0.76

3.1.2 Reflecting Surfaces

Concentrating solar collectors require the use of reflecting surfaces with high specular reflectance in the solar spectrum or refracting devices with high transmittance in the solar spectrum. Reflecting surfaces are usually highly polished metals or metal coatings on suitable substrates. With opaque substrates, the reflective coatings must always be front surfaced, for example, chrome plating on copper or polished aluminum. If a transparent substrate is used, however, the coating may be front or back surfaced. In any back-surfaced reflector, the radiation must pass through the substrate twice and the transmittance of the material becomes very important.

Table 3.3 presents typical values for the normal specular reflectance of new surfaces for beam solar radiation.

3.1.3 Transparent Materials

The optical transmission behavior can be characterized by two wavelength-dependent physical properties—the index of refraction n and the extinction coefficient k . The index of refraction, which determines the speed of light in the material, also determines the amount of light reflected from a single surface, while the extinction coefficient determines the amount of light absorbed in a substance in a single pass of radiation as described in Chapter 2.

Figure 3.6 defines the angles used in analyzing reflection and transmission of light. The angle i is called the *angle of incidence*. It is also equal to the angle at which a beam is specularly reflected from the surface. Angle θ_r is the *angle of refraction*, which is defined as shown in the figure. The incidence and refraction angles are related by Snell's law:

$$\frac{\sin(i)}{\sin(\theta_r)} = \frac{n_r}{n_i} = n_r \quad (3.7)$$

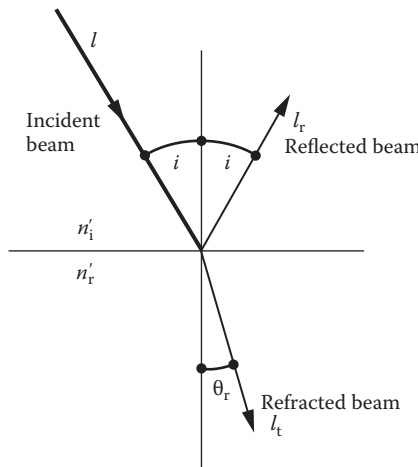
**FIGURE 3.6**

Diagram showing incident, reflected, and refracted beams of light and incidence and refraction angles for a transparent medium.

where n_i and n_r are the two refractive indices and n_r is the index ratio for the two substances forming the interface. Typical values of refractive indices for various materials are shown in Table 3.4. For most materials of interest in solar applications, the values range from 1.3 to 1.6, a fairly narrow range.

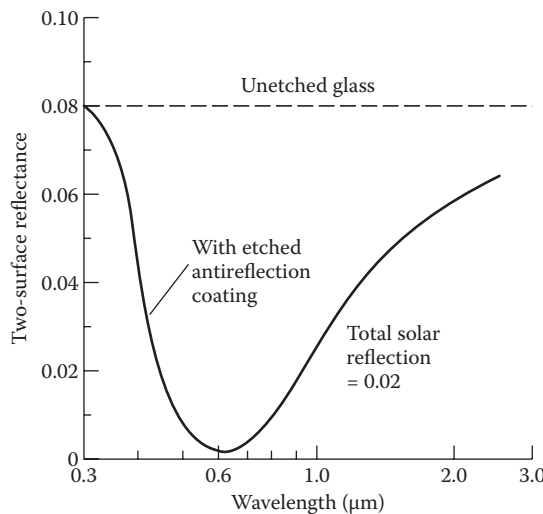
By having a gradual change in index of refraction, reflectance losses are reduced significantly. The reflectance of a glass-air interface common in solar collectors may be reduced by a factor of 4 by an etching process. If glass is

TABLE 3.4

Refractive Index for Various Substances in the Visible Range Based on Air

Material	Index of Refraction
Air	1.000
Clean polycarbonate	1.59
Diamond	2.42
Glass (solar collector type)	1.50–1.52
Plexiglass ^a (polymethyl methacrylate, PMMA)	1.49
Mylar ^a (polyethylene terephthalate, PET)	1.64
Quartz	1.55
Tedlar ^a (polyvinyl fluoride, PVF)	1.45
Teflon ^a (polyfluoroethylene-propylene, FEP)	1.34
Water—liquid	1.33
Water—solid	1.31

^a Trademark of the duPont Company, Wilmington, Delaware.

**FIGURE 3.7**

Reflection spectra for a sample of glass before and after etching.

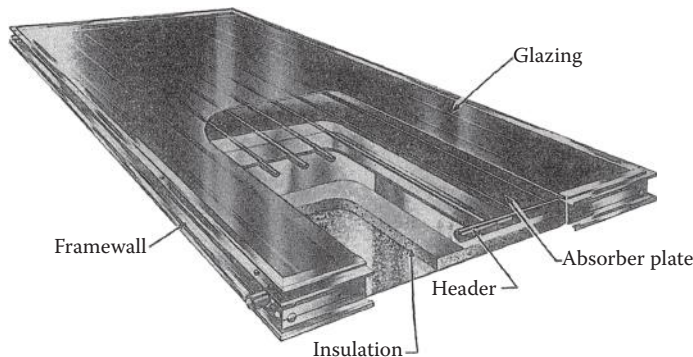
immersed in a silica-supersaturated fluosilicic acid solution, the acid attacks the glass and leaves a porous silica surface layer. This layer has an index of refraction intermediate between glass and air. Figure 3.7 shows the spectral reflectance of a pane of glass before and after etching.

3.2 Flat-Plate Collectors

A simple flat-plate collector consists of an absorber surface (usually a dark, thermally conducting surface); a trap for reradiation losses from the absorber surface (such as glass, which transmits shorter-wavelength solar radiation but blocks the longer-wavelength radiation from the absorber); a heat-transfer medium such as air, water, and so on; and some thermal insulation behind the absorber surface. Flat-plate collectors are used typically for temperature requirements up to 75°C, although higher temperatures can be obtained from high-efficiency collectors. These collectors are of two basic types based on the heat-transfer fluid:

Liquid type: where heat-transfer fluid may be water, mixture of water and antifreeze oil, and so on

Air type: where heat-transfer medium is air (used mainly for drying and space heating requirements)

**FIGURE 3.8**

Typical liquid-type flat-plate collector. (Courtesy of Morning Star Corp., Orange Park, FL.)

3.2.1 Liquid-Type Collectors

Figure 3.8 shows a typical liquid-type flat-plate collector. In general, it consists of the following:

1. *Glazing*: one or more covers of transparent material like glass, plastics, and so on. Glazing may be left out for some low-temperature applications.
2. *Absorber*: a plate with tubes or passages attached to it for the passage of a working fluid. The absorber plate is usually painted flat black or electroplated with a selective absorber.
3. *Headers* (or manifolds): to facilitate the flow of heat-transfer fluid.
4. *Insulation*: to minimize heat loss from the back and the sides.
5. *Container*: box or casing.

3.2.2 Air-Type Collectors

Air types of collectors are more commonly used for agricultural drying and space heating applications. Their basic advantages are twofold: (1) low sensitivity to leakage and (2) there is no need for an additional heat exchanger for drying and space heating applications. However, because of the low heat capacity of the air and the low convection heat-transfer coefficient between the absorber and the air, a larger heat-transfer area and higher flow rates are needed. Figure 3.9 shows some common configurations of air heating collectors. Common absorber materials include corrugated aluminum or galvanized steel sheets, black metallic screens, or simply any black painted surface.

Unglazed, transpired solar air collectors offer a low-cost opportunity for some applications such as preheating of ventilation air and agricultural drying

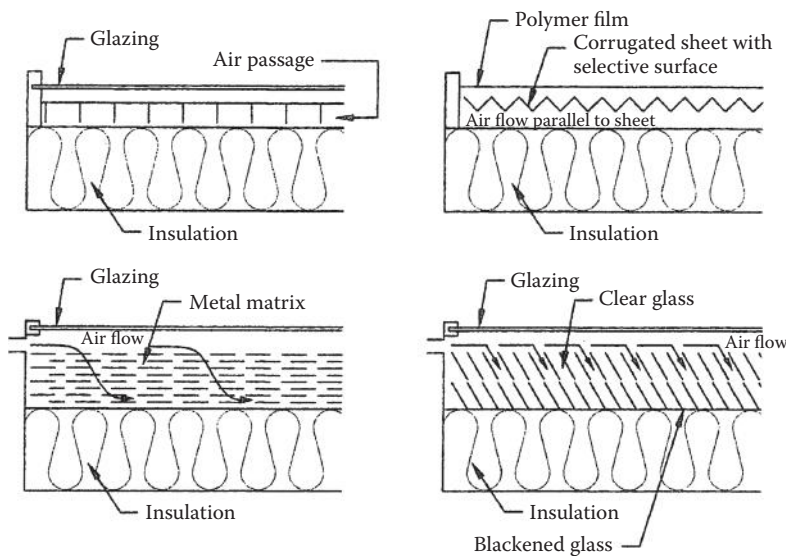


FIGURE 3.9
Some common configurations of air heating collectors.

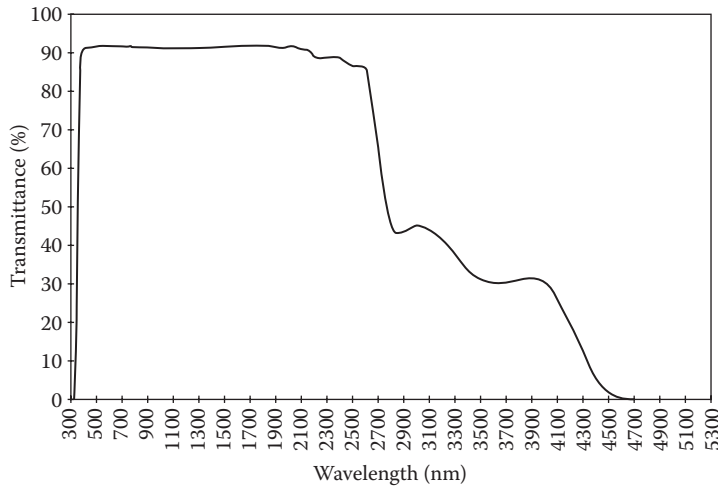
and curing (Kutcher 1996). Such collectors consist of perforated absorber sheets that are exposed to the sun and through which air is drawn. The perforated absorber sheets are attached to the vertical walls, which are exposed to the sun. Kutcher and Christensen (1992) have given a detailed thermal analysis of unglazed transpired solar collectors. (See Section 5.4.5 for additional details.)

The most important components, whose properties determine the efficiency of solar thermal collectors, are glazings and absorbers.

3.2.3 Glazings

The purpose of a glazing or transparent cover is to transmit the shorter-wavelength solar radiation but block the longer-wavelength reradiation from the absorber plate and to reduce the heat loss by convection from the top of the absorber plate. Consequently, an understanding of the process and laws that govern the transmission of radiation through a transparent medium is important. Section 3.1 describes in brief the transmission of radiation through materials.

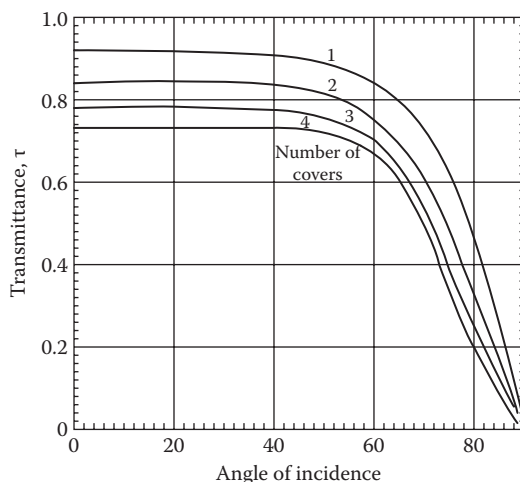
Glass is the most common glazing material. Figure 3.10 shows transmittance of glass as a function of wavelength. Transparent plastics, such as polycarbonates and acrylics, are also used as glazings for flat-plate collectors. The main disadvantage of plastics is that their transmittance in the longer wavelength is also high; therefore, they are not as good a trap as glass. Other disadvantages include deterioration over a period attributed to ultraviolet

**FIGURE 3.10**

Spectral transmittance of a 3-mm low-iron float glass.

solar radiation. Their main advantage is resistance to breakage. Although glass can break easily, this disadvantage can be minimized by using tempered glass.

In order to minimize the upward heat loss from the collector, more than one transparent glazing may be used. However, with the increase in the number of cover plates, transmittance is decreased. Figure 3.11 shows the effect of number of glass cover plates on transmittance.

**FIGURE 3.11**

Transmittance of multiple glass covers having an index of refraction 1.526".

3.2.3.1 Absorbers

The purpose of the absorber is to absorb as much of the incident solar radiation as possible, reemit as little as possible, and allow efficient transfer of heat to a working fluid. The most common forms of absorber plates in use are shown in Figure 3.12. The materials used for absorber plates include copper, aluminum, stainless steel, galvanized steel, plastics, and rubbers. Copper seems to be the most common material used for absorber plates and tubes because of its high thermal conductivity and high corrosion resistance. However, copper is quite expensive. For low-temperature applications (up to approximately 50°C or 120°F), a plastic material called ethylene propylene polymer (trade names EPDM, HCP, etc.) can be used to provide inexpensive absorber material. To compensate for the low thermal conductivity, a large surface area is provided for heat transfer. Figure 3.13 shows a typical collector made from such material.

In order to increase the absorption of solar radiation and to reduce the emission from the absorber, the metallic absorber surfaces are painted or coated with flat black paint or some selective coating. A selective coating has high absorptivity in the solar wavelength range (0.3 to 3.0 μm). Absorptivities and emissivities of some common selective surfaces are given in Figures 3.4 and 3.5.

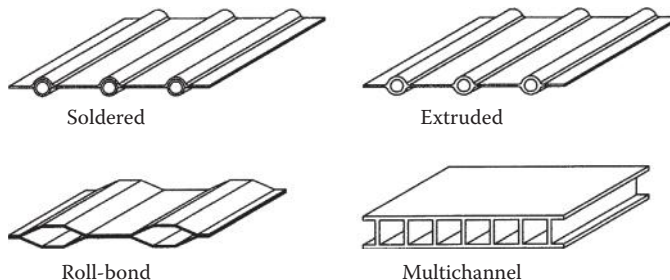


FIGURE 3.12
Common types of absorber plates.

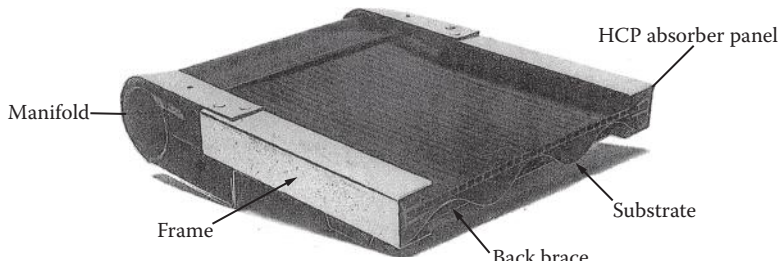


FIGURE 3.13
Cutaway view of a typical collector made from ethylene propylene polymer. (Courtesy of Sealed Air Corp., Saddle Brook, NJ.)

A simple and inexpensive collector consists of a black painted corrugated metal absorber on which water flows down open, rather than enclosed in tubes. This type of collector is called a *trickle collector* and is usually built on-site. Although such a collector is simple and inexpensive, it has the disadvantages of condensation on the glazing and a higher pumping power requirement.

3.2.4 Energy Balance for a Flat-Plate Collector

The thermal performance of any type of solar thermal collector can be evaluated by an energy balance that determines the portion of the incoming radiation delivered as useful energy to the working fluid. For a flat-plate collector of an area A_c , this energy balance on the absorber plate is

$$I_c A_c \tau_s \alpha_s = q_u + q_{\text{loss}} + \frac{de_c}{dt}, \quad (3.8)$$

where I_c is the solar irradiation on a collector surface, τ_s is the effective solar transmittance of the collector cover(s), α_s is the solar absorptance of the collector-absorber plate surface, q_u is the rate of heat transfer from the collector-absorber plate to the working fluid, q_{loss} is the rate of heat transfer (or heat loss) from the collector-absorber plate to the surroundings, and de_c/dt is the rate of internal energy storage in the collector.

The instantaneous efficiency of a collector η_c is simply the ratio of the useful energy delivered to the total incoming solar energy, or

$$\eta_c = \frac{q_u}{A_c I_c}. \quad (3.9)$$

In practice, the efficiency must be measured over a finite time period. In a standard performance test, this period is on the order of 15 or 20 min, whereas for design, the performance over a day or over some longer period t is important. Then, we have for the average efficiency

$$\eta_c = \frac{\int_0^1 q_u dt}{\int_0^1 A_c I_c dt}, \quad (3.10)$$

where t is the time period over which the performance is averaged.

A detailed and precise analysis of the efficiency of a solar collector is complicated by the nonlinear behavior of radiation heat transfer. However, a simple linearized analysis is usually sufficiently accurate in practice. In addition, the simplified analytical procedure is very important because it illustrates the parameters of significance for a solar collector and how these parameters interact. For a proper analysis and interpretation of these test results, an understanding

of the thermal analysis is imperative, although for design and economic evaluation, the results of standardized performance tests are generally used.

3.2.4.1 Collector Heat-Loss Conductance

In order to obtain an understanding of the parameters determining the thermal efficiency of a solar collector, it is important to develop the concept of *collector heat-loss conductance*. Once the collector heat-loss conductance U_c is known, and when the collector plate is at an average temperature T_c , the collector heat loss can be written in the simple form

$$q_{\text{loss}} = U_c A_c (T_c - T_a). \quad (3.11)$$

The simplicity of this relation is somewhat misleading because the collector heat-loss conductance cannot be specified without a detailed analysis of all the heat losses. Figure 3.14 shows a schematic diagram of a single-glazed collector, while Figure 3.15a shows the thermal circuit with all the elements that must be analyzed before they can be combined into a single conductance element shown in Figure 3.15b. The analysis in the following shows an example of how this combination is accomplished.

In order to construct a model suitable for a thermal analysis of a flat-plate collector, the following simplifying assumptions will be made:

1. The collector is thermally in steady state.
2. The temperature drop between the top and bottom of the absorber plate is negligible.
3. Heat flow is one-dimensional through the cover as well as through the back insulation.

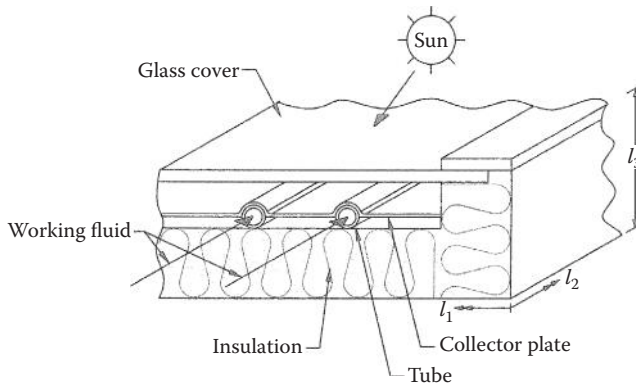
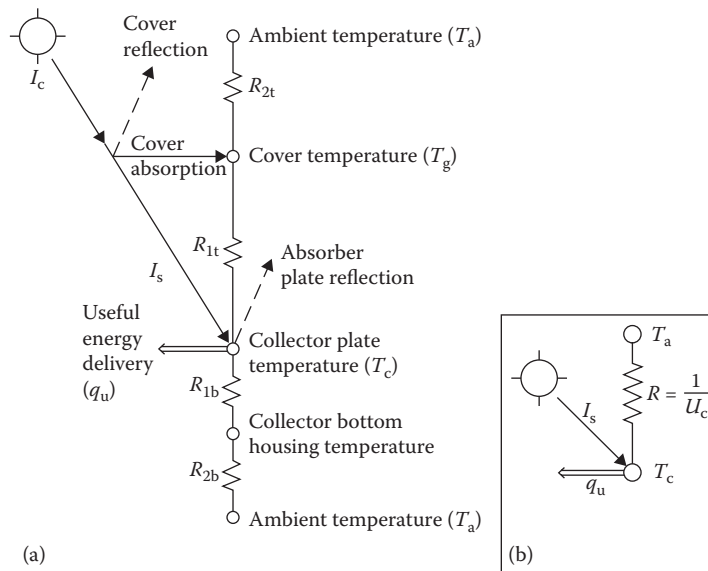


FIGURE 3.14

Schematic diagram of a solar collector.

**FIGURE 3.15**

Thermal circuits for a flat-plate collector shown in Figure 3.14: (a) detailed circuit; (b) approximate, equivalent circuit to (a). In both circuits, the absorbed energy is equal to $\alpha_s I_s$, where $I_s = \tau_s I_c$. Collector is assumed to be at uniform temperature T_c .

4. The headers connecting the tubes cover only a small area of the collector and provide uniform flow to the tubes.
5. The sky can be treated as though it were a black-body source for infrared radiation at an equivalent sky temperature.
6. The irradiation on the collector plate is uniform.

For a quantitative analysis, let the plate temperature be T_c and assume solar energy is absorbed at the rate $I_s \alpha_s$ or $I_c A_c \tau_s \alpha_s$. Part of this energy is then transferred as heat to the working fluid, and if the collector is in the steady state, the other part is lost as heat to the ambient air if $T_c > T_a$. Some of the heat loss occurs through the bottom of the collector. It passes first through the back to the environment. Since the collector is in steady state, according to Equation 3.8,

$$q_u = I_c A_c \tau_s \alpha_s - q_{\text{loss}}, \quad (3.12)$$

where q_{loss} can be determined using the equivalent thermal circuit as shown in Figure 3.15.

$$q_{\text{loss}} = U_c A_c (T_c - T_a) = \frac{A_c (T_c - T_a)}{R}. \quad (3.13)$$

There are three parallel paths to heat loss from the hot collector-absorber plate at T_c to the ambient at T_a : the top, bottom, and edges. Because the edge losses are quite small compared to the top and the bottom losses, they are quite often neglected. However, they can be estimated easily if the insulation around the edges is of the same thickness as the back. The edge loss can be accounted for by simply adding the areas of the back (A_b) and the edges (A_e) for back heat loss.

Therefore, the overall heat-loss coefficient is

$$U_c A_c = \frac{A_c}{R} = \frac{A_c}{R_{1t} + R_{2t}} + \frac{A_c + A_e}{R_{1b} + R_{2b}}. \quad (3.14)$$

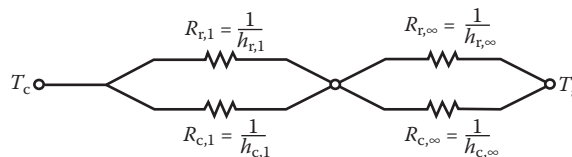
The thermal resistances can be found easily from the definition. For example,

$$R_{1b} = \frac{l_i}{k_i} \quad \text{and} \quad R_{2b} = \frac{1}{h_{c,\text{bottom}}}, \quad (3.15)$$

where k_i and l_i are, respectively, the thermal conductivity and thickness of the insulation and $h_{c,\text{bottom}}$ is the convective heat-transfer coefficient between the collector and the air below the collector. In a well-insulated collector, R_{2b} is much smaller than R_{1b} and usually neglected. Referring to Figure 3.14,

$$A_e = 2(l_1 + l_2)l_3. \quad (3.16)$$

Since the heat loss from the top is by convection and radiation, it is more complicated than the bottom heat loss. Convection and radiation provide two parallel paths for heat loss from the absorber plate at T_c to the glass cover at T_g and from the glass cover to the ambient. That is, the series resistance of R_{1t} and R_{2t} consists of



Therefore,

$$\frac{1}{R_{1t}} = \frac{1}{R_{r,1}} + \frac{1}{R_{c,1}} = h_{r,1} + h_{c,1} \quad \text{and} \quad (3.17)$$

$$\frac{1}{R_{2t}} = \frac{1}{R_{r,\infty}} + \frac{1}{R_{c,\infty}} = h_{r,\infty} + h_{c,\infty}. \quad (3.18)$$

Since thermal radiative heat transfer is proportional to the fourth power of the temperature, R_r and h_r are found as follows:

Radiative heat transfer from the plate to the glass cover

$$q_{f_{c \rightarrow R}} = \sigma A_c \frac{(T_c^4 - T_g^4)}{\left(1/\epsilon_{p,i} + 1/\epsilon_{s,i} - 1\right)} = h_{r,1} A_c (T_c - T_g), \quad (3.19)$$

where $\epsilon_{p,i}$ is the infrared emittance of the plate and $\epsilon_{g,i}$ is the infrared emittance of the glass cover.

Therefore,

$$h_{r,1} = \frac{\sigma(T_c + T_g)(T_c^2 + T_g^2)}{\left(1/\epsilon_{p,i} + 1/\epsilon_{g,i} - 1\right)}. \quad (3.20)$$

Similarly, from the radiative heat transfer between the glass plate (at T_g) and the sky (at T_s), we can find that

$$q_{r_{g \rightarrow \text{sky}}} = \epsilon_{g,i} \sigma A_c (T_g^4 - T_s^4) = h_{r,\infty} A_c (T_g - T_a), \quad (3.21)$$

or

$$h_{r,\infty} = \epsilon_{g,i} \sigma (T_g^4 - T_s^4) / (T_g - T_a). \quad (3.22)$$

Evaluation of the collector heat-loss conductance defined by Equation 3.14 requires iterative solution of Equations 3.19 and 3.21, because the unit radiation conductances are functions of the cover and plate temperatures, which are not known a priori.

Several books (Duffie and Beckman 1980; Kreith and Kreider 2012) suggest using a simplified empirical equation proposed by Klein (1975) and Agarwal and Larson (1981). However, recent studies by several researchers (Akhtar and Mullick 1999, 2007; Mahboub and Moummi 2012; Samdarshi and Mullick 1991) have shown that the empirical equation for top heat-loss coefficient could result in large errors. Therefore, Mullick and Samdarshi (1988) suggested a method to evaluate T_g accurately, which has been modified by later publications for multiple covers, large tilt angles, and V-shaped absorber surface. According to this method, the top heat-loss coefficient U_t [in $\text{W}/(\text{m}^2 \cdot \text{K})$] is

$$U_t^{-1} = \frac{\sigma(T_c^2 + T_g^2)(T_c + T_g)}{\frac{1}{\epsilon_{p,i}} + \frac{1}{\epsilon_{g,i}} - 1} + \frac{kNu}{L}^{-1} + \frac{\sigma \epsilon_{g,i} (T_g^4 - T_s^4)}{T_g - T_a}^{-1} + h_{c,\infty}^{-1} + L_g/k_g, \quad (3.23)$$

where

$$T_g = \frac{(fT_c + CT_a)}{(1+f)},$$

where

$$C = \frac{\frac{T_s}{T_a} + \frac{h_{c,\infty}}{3.5}}{1 + \frac{h_{c,\infty}}{3.5}}.$$

According to Swinbank (1963), for clear sky, T_s may be assumed to be equal to $0.0552(T_a)^{1.5}$. If T_s is assumed equal to T_a , C becomes equal to 1.

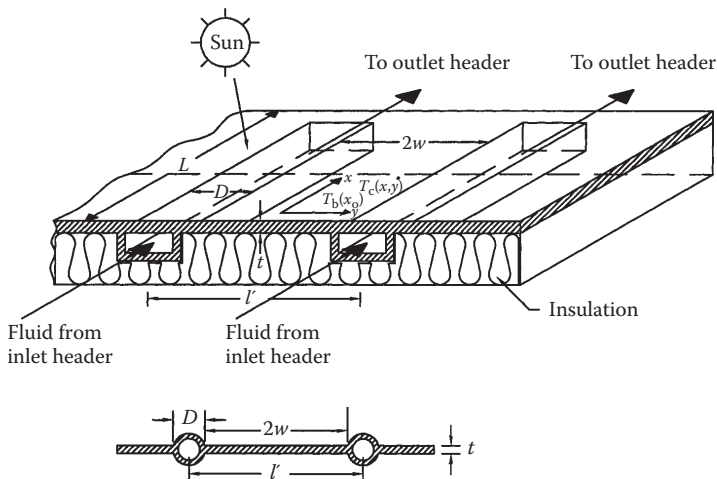
$$f = \frac{12 \times 10^{-8}(T_a + 0.2T_c)^3 + h_{c,\infty}^{-1} + 0.3L_g}{6 \times 10^{-8}(\epsilon_{p,i} + 0.028)(T_c + 0.5T_a)^3 + 0.6L^{-0.2}\{(T_c - T_a)\cos\beta\}^{0.25}^{-1}} \quad (3.24)$$

$$\text{Nu} = 1 + 1.44[1 - 1708/Ra']^+ \left\{ 1 - 1708(\sin 1.8\beta)^{1.6}/Ra' \right\}^+ + (Ra'/5830)^{1/3} - 1^+, \quad (3.25)$$

where the exponent “+” means that only positive values of the term in brackets are to be used; $Ra' = Ra \cos \beta$, where β is the collector tilt angle; k and k_g are the thermal conductivity of air and glass, respectively, in $\text{W}/(\text{m}\cdot\text{K})$; and L and L_g are the thickness of the air gap and glass, respectively, in meters.

3.2.5 Thermal Analysis of Flat-Plate Collector–Absorber Plate

In order to determine the efficiency of a solar collector, the rate of heat transfer to the working fluid must be calculated. If transient effects are neglected (Hottel and Whillier 1958; Klein 1975), the rate of heat transfer to the fluid flowing through a collector depends on the temperature of the collector surface from which heat is transferred by convection to the fluid, the temperature of the fluid, and the heat-transfer coefficient between the collector and the fluid. To analyze the rate of heat transfer, consider first the condition at a cross section of the collector with flow ducts of rectangular cross sections as shown in Figure 3.16. Solar radiant energy impinges on the upper face of the collector plate. A part of the total solar radiation falls on the upper surface of the flow channels, while another part is incident on the plates connecting any two adjacent flow channels. The latter is conducted in a transverse direction toward the flow channels. The temperature is a maximum at any midpoint between adjacent channels, and the collector plate acts as a fin attached

**FIGURE 3.16**

Sketch showing coordinates and dimensions for collector plate and fluid ducts.

to the walls of the flow channel. The thermal performance of a fin can be expressed in terms of its efficiency. The fin efficiency η_f is defined as the ratio of the rate of heat flow through the real fin to the rate of heat flow through a fin of infinite thermal conductivity, that is, a fin at a uniform temperature. We shall now derive a relation to evaluate this efficiency for a flat-plate solar collector.

If U_c is the overall unit conductance from the collector-plate surface to the ambient air, the rate of heat loss from a given segment of the collector plate at x, y in Figure 3.16 is

$$q(x, y) = U_c[T_c(x, y) - T_a] \, dx \, dy, \quad (3.26)$$

where T_c is the local collector-plate temperature ($T_c > T_a$), T_a is the ambient air temperature, and U_c is the overall unit conductance between the plate and the ambient air.

U_c includes the effects of radiation and free convection between the plates, the radiative and convective transfer between the top of the cover and the environment, and conduction through the insulation. Its quantitative evaluation has been previously considered.

If conduction in the x direction is negligible, a heat balance at a given distance x_0 for a cross section of the flat-plate collector per unit length in the x direction can be written in the form

$$\alpha_s I_s dy - U_c(T_c - T_a)dy + \left. -kt \frac{dT_c}{dy} \right|_{y, x_0} - \left. -kt \frac{dT_c}{dy} \right|_{y+dy, x_0} = 0. \quad (3.27)$$

If the plate thickness t is uniform and the thermal conductivity of the plate is independent of temperature, the last term in Equation 3.27 is

$$\frac{dT_c}{dy} \Big|_{y+dy, x_0} = \frac{dT_c}{dy} \Big|_{y, x_0} + \frac{d^2T_c}{dy^2} \Big|_{y, x_0} dy,$$

and Equation 3.27 can be cast into the form of a second-order differential equation:

$$\frac{d^2T}{dy^2} = \frac{U_c}{kt} T_c - T_a + \frac{\alpha_s I_s}{U_c} . \quad (3.28)$$

The boundary conditions for the system described above at a fixed x_0 are as follows:

1. At the center between any two ducts, the heat flow is 0, or at $y = 0$, $dT_c/dy = 0$.
2. At the duct, the plate temperature is $T_b(x_0)$, or at $y = w = (l' - D)/2$, $T_c = T_b(x_0)$ where $T_b(x_0)$ is the fin-base temperature.

If we let $m^2 = U_c/kt$ and $\phi = T_c - (T_a + \alpha_s I_s/U_c)$, Equation 3.28 becomes

$$\frac{d^2\phi}{dy^2} = m^2\phi, \quad (3.29)$$

subject to the boundary conditions

$$\frac{d\phi}{dy} = 0 \text{ at } y = 0, \text{ and}$$

$$\phi = T_b(x_0) - T_a + \frac{\alpha_s I_s}{U_c} \text{ at } y = w.$$

The general solution of Equation 3.29 is

$$\phi = C_1 \sinh my + C_2 \cosh my. \quad (3.30)$$

The constants C_1 and C_2 can be determined by substituting the two boundary conditions and solving the two resulting equations for C_1 and C_2 . This gives

$$\frac{T_c - (T_a + \alpha_s I_s/U_c)}{T_b(x_0) - (T_a + \alpha_s I_s/U_c)} = \frac{\cosh mw}{\cosh my}. \quad (3.31)$$

From the Equation 3.31, the rate of heat transfer to the conduit from the portion of the plate between two conduits can be determined by evaluating the temperature gradient at the base of the fin, or

$$q_{\text{fin}} = -kt \frac{dT_c}{dt} \Big|_{y=w} = \frac{1}{m} \{\alpha_s I_s - U_c [T_b(x_0) - T_a] \tanh mw\}. \quad (3.32)$$

Since the conduit is connected to fins on both sides, the total rate of heat transfer is

$$q_{\text{total}}(x_0) = 2w \{\alpha_s I_s - U_c [T_b(x_0) - T_a]\} \frac{\tanh mw}{mw}. \quad (3.33)$$

If the entire fin were at the temperature $T_b(x_0)$, a situation corresponding physically to a plate of infinitely large thermal conductivity, the rate of heat transfer would be a maximum, $q_{\text{total,max}}$. As mentioned previously, the ratio of the rate of heat transfer with a real fin to the maximum rate obtainable is the fin efficiency η_f . With this definition, Equation 3.33 can be written in the form

$$q_{\text{total}}(x_0) = 2w\eta_f \{\alpha_s I_s - U_c [T_b(x_0) - T_a]\}, \quad (3.34)$$

where $\eta_f \equiv (\tanh mw)/mw$.

The fin efficiency η_f is plotted as a function of the dimensionless parameter $w(U_c/kt)^{1/2}$ in Figure 3.17. When the fin efficiency approaches unity, the

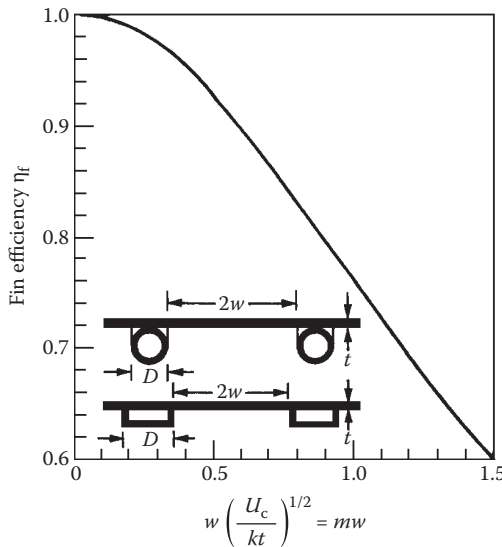


FIGURE 3.17

Fin efficiency for tube and sheet flat-plate solar collectors.

maximum portion of the radiant energy impinging on the fin becomes available for heating the fluid.

In addition to the heat transferred through the fin, the energy impinging on the portion of the plate above the flow passage is also useful. The rate of useful energy from this region available to heat the working fluid is

$$q_{\text{duct}}(x_0) = D\{\alpha_s I_s - U_c[T_b(x_0) - T_a]\}. \quad (3.35)$$

Thus, the useful energy per unit length in the flow direction becomes

$$q_u(x_0) = (D + 2w\eta)\{\alpha_s I_s - U_c[T_b(x_0) - T_a]\}. \quad (3.36)$$

The energy $q_u(x_0)$ must be transferred as heat to the working fluid. If the thermal resistance of the metal wall of the flow duct is negligibly small and there is no contact resistance between the duct and the plate, the rate of heat transfer to the fluid is

$$q_u(x_0) = P\bar{h}_{c,i}[T_b(x_0) - T_f(x_0)]. \quad (3.37)$$

where P is the perimeter of the flow duct, which is $2(D + d)$ for a rectangular duct. Contact resistance may become important in poorly manufactured collectors in which the flow duct is clamped or glued to the collector plate. Collectors manufactured by such methods are usually not satisfactory.

3.2.6 Collector Efficiency Factor

To obtain a relation for the useful energy delivered by a collector in terms of known physical parameters, the fluid temperature, and the ambient temperature, the collector temperature must be eliminated from Equations 3.36 and 3.37. Solving for $T_b(x_0)$ in Equation 3.37 and substituting this relation in Equation 3.36 gives

$$q_u(x_0) = l'F'\{\alpha_s I_s - U_c[T_f(x_0) - T_a]\}, \quad (3.38)$$

where F' is called the collector efficiency factor (Bliss 1959) and $l' = (2w + D)$. F' is given by

$$F' = \frac{1/U_c}{l - 1/(U_c(D + 2w\eta_f)) + 1/(\bar{h}_{c,i}P)}. \quad (3.39)$$

For a flow duct of circular cross section of diameter D , F' can be written as

$$F' = \frac{1/U_c}{l - 1/(U_c(D + 2w\eta_f)) + 1/(\bar{h}_{c,i}\pi D)}. \quad (3.39)$$

TABLE 3.5

Typical Values for the Parameters That Determine the Collector Efficiency Factor F' for a Flat-Plate Collector in Equation 3.39

	U_c	
2 glass covers	4 W/m ² ·K	0.685 Btu/h·ft ² ·°F
1 glass cover	8 W/m ² ·K	1.37 Btu/h·ft ² ·°F k_t
Copper plate, 1 mm thick	0.38 W/K	0.72 Btu/h·°F
Steel plate, 1 mm thick	0.045 W/K	0.0866 Btu/h·°F
		\bar{h}_{ci}
Water in laminar flow forced convection	300 W/m ² ·K	52 Btu/h·ft ² ·°F
Water in turbulent flow forced convection	1500 W/m ² ·K	254 Btu/h·ft ² ·°F
Air in turbulent forced convection	100 W/m ² ·K	17.6 Btu/h·ft ² ·°F

Physically, the denominator in Equation 3.39 is the thermal resistance between the fluid and the environment, whereas the numerator is the thermal resistance between the collector surface and the ambient air. The collector-plate efficiency factor F' depends on U_c , \bar{h}_{ci} , and η_f . It is only slightly dependent on temperature and can, for all practical purposes, be treated as a design parameter. Typical values for the factors determining the value of F' are given in Table 3.5.

The collector efficiency factor increases with increasing plate thickness and plate thermal conductivity, but it decreases with increasing distance between flow channels. Also, increasing the heat-transfer coefficient between the walls of the flow channel and the working fluid increases F' , but an increase in the overall conductance U_c will cause F' to decrease.

3.2.7 Collector Heat-Removal Factor

Equation 3.38 yields the rate of heat transfer to the working fluid at a given point x along the plate for specified collector and fluid temperatures. However, in a real collector, the fluid temperature increases in the direction of flow as heat is transferred to it. An energy balance for a section of flow duct dx can be written in the form

$$\dot{m}c_p \left(T_f|_{x+dx} - T_f|_x \right) = q_u(x)dx. \quad (3.40)$$

Substituting Equation 3.38 for $q_u(x)$ and $T_f(x) + (dT_f(x)/dx)dx$ for $T_f|_{x+dx}$ in Equation 3.40 gives the differential equation

$$\dot{m}c_p \frac{dT_f(x)}{dx} = l F \{ \alpha_s I_s - U_c [T_f(x) - T_a] \}. \quad (3.41)$$

Separating the variables gives, after some rearranging,

$$\frac{dT_f(x)}{T_f(x) - T_a - \alpha_s I_s / U_c} = \frac{l F U_c}{\dot{m} c_p} dx. \quad (3.42)$$

Equation 3.42 can be integrated and solved for the outlet temperature of the fluid $T_{f,out}$ for a duct length L and for the fluid inlet temperature $T_{f,in}$ if we assume that F' and U_c are constant, or

$$\frac{T_{f,out} - T_a - \alpha_s I_s / U_c}{T_{f,in} - T_a - \alpha_s I_s / U_c} = \exp \left(-\frac{U_c l F L}{\dot{m} c_p} \right). \quad (3.43)$$

To compare the performance of a real collector with the thermodynamic optimum, it is convenient to define the heat-removal factor F_R as the ratio between the actual rate of heat transfer to the working fluid and the rate of heat transfer at the minimum temperature difference between the absorber and the environment.

The thermodynamic limit corresponds to the condition of the working fluid remaining at the inlet temperature throughout the collector. This can be approached when the fluid velocity is very high. From its definition, F_R can be expressed as

$$F_R = \frac{G c_p (T_{f,out} - T_{f,in})}{\alpha_s I_s - U_c (T_{f,in} - T_a)}, \quad (3.44)$$

where G is the flow rate per unit surface area of collector \dot{m}/A_c . By regrouping the right-hand side of Equation 3.44 and combining with Equation 3.43, it can easily be verified that

$$\begin{aligned} F_R &= \frac{G c_p}{U_c} \left(1 - \frac{\alpha_s I_s / U_c - (T_{f,out} - T_a)}{\alpha_s I_s / U_c - (T_{f,in} - T_a)} \right) \\ &= \frac{G c_p}{U_c} \left(1 - \exp \left(-\frac{U_c l F}{G c_p} \right) \right). \end{aligned} \quad (3.45)$$

Inspection of the above relation shows that F_R increases with increasing flow rate and approaches as an upper limit F' , the collector efficiency factor. Since the numerator of the right-hand side of Equation 3.44 is q_u , the rate of useful heat transfer can now be expressed in terms of the fluid inlet temperature, or

$$q_u = A_c F_R [\alpha_s I_s - U_c (T_{f,in} - T_a)]. \quad (3.46)$$

If a glazing above the absorber plate has transmittance τ_s , then

$$q_u = A_c F_R [\tau_s \alpha_s I_c - U_c (T_{f,in} - T_a)], \quad (3.47)$$

and instantaneous efficiency η_c is

$$\eta_c = \frac{q_u}{I_c A_c} = F_R \tau_s \alpha_s - U_c (T_{f,in} - T_a) / I_c. \quad (3.48)$$

Equation 3.48 is also known as the *Hottel–Whillier–Bliss* equation. This is a convenient form for design, because the fluid inlet temperature to the collector is usually known or can be specified.

Example 3.1

Calculate the averaged hourly and daily efficiency of a water solar collector on January 15, in Boulder, Colorado. The collector is tilted at an angle of 60° and has an overall conductance of $8.0 \text{ W/m}^2\text{K}$ on the upper surface. It is made of copper tubes, with a 1-cm ID, 0.05 cm thick, which are connected by a 0.05-cm-thick plate at a center-to-center distance of 15 cm. The heat-transfer coefficient for the water in the tubes is $1500 \text{ W/m}^2\text{K}$, the cover transmittance is 0.9, and the solar absorptance of the copper surface is 0.9. The collector is 1 m wide and 2 m long, the water inlet temperature is 330 K, and the water flow rate is 0.02 kg/s. The horizontal insolation (total) I_h and the environmental temperature are tabulated in the following. Assume that the diffuse radiation accounts for 25% of the total insolation.

Solution

The total radiation received by the collector is calculated from Equation 2.46 and neglecting the ground reflected radiation:

$$I_c = I_{d,c} + I_{b,c} = 0.25 I_h \cos^2 \frac{60}{2} + (1 - 0.25) I_h R_b.$$

Time (h)	$I_h (\text{W/m}^2)$	$T_{amb} (\text{K})$
7–8	12	270
8–9	80	280
9–10	192	283
10–11	320	286
11–12	460	290
12–13	474	290
13–14	395	288
14–15	287	288
15–16	141	284
16–17	32	280

The tilt factor R_b is obtained from its definition in Chapter 2 (see Equation 2.60):

$$R_b = \frac{\cos i}{\sin \alpha} = \frac{\sin(L - \beta)\sin \delta_s + \cos(L - \beta)\cos \delta_s \cos h_s}{\sin L \sin \delta_s + \cos L \cos \delta_s \cos h_s},$$

where $L = 40^\circ$, $\delta_s = -21.1$ on January 15, and $\beta = 60^\circ$. The hour angle h_s equals 15° for each hour away from noon.

The fin efficiency is obtained from Equation 3.34:

$$\eta_f = \frac{\tanh m(l - D)/2}{m(l - D)/2}$$

where

$$m = \frac{U_c}{kt}^{1/2} = \frac{8}{390 \times 5 \times 10^{-4}}^{1/2} = 6.4, \text{ and}$$

$$\eta_f = \frac{\tanh 6.4(0.15 - 0.01)/2}{6.4(0.15 - 0.01)/2} = 0.938.$$

The collector efficiency factor F' is, from Equation 3.39,

$$F' = \frac{\frac{1/U_c}{l - 1/(U_c(D + 2w\eta_f)) + 1/(h_{c,i}\pi D)}}{\frac{1/8.0}{0.15 \cdot 1/8.0(0.01 + 0.14 \times 0.938) + 1/1500\pi \times 0.01}} = 0.92.$$

Then, we obtain the heat-removal factor from Equation 3.45:

$$F_R = \frac{Gc_p}{U_c} \left[1 - \exp \left(-\frac{U_c F}{Gc_p} \right) \right].$$

Time (h)	I_h (W/m ²)	R_b	$I_{d,c}$ (W/m ²)	$I_{b,c}$ (W/m ²)	I_c (W/m ²)	q_u (W)	T_{amb} (K)	η_c
7–8	12	4.46	2	40	42	0	270	0.000
8–9	80	2.71	15	163	178	0	280	0.000
9–10	192	2.28	36	328	364	0	283	0.000
10–11	320	2.11	60	507	567	182	286	0.160
11–12	460	2.07	86	714	800	554	290	0.346
12–13	474	2.11	89	751	840	609	290	0.363
13–14	395	2.28	74	675	749	457	288	0.305
14–15	287	2.71	54	584	638	305	288	0.239
15–16	141	4.46	26	471	498	60	284	0.060
16–17	32	0	6	0	0	0	280	0.000

$$F_R = \frac{0.001 \times 4184}{8.0} \left(1 - \exp\left(-\frac{8.0 \times 0.922}{0.01 \times 4184}\right)\right) = 0.845$$

From Equation 3.47, the useful heat delivery rate is

$$q_u = 2 \times 0.845 [I_c \times 0.81 - 8.0(T_{f,in} - T_{amb})].$$

The efficiency of the collector is $\eta_c = q_u / A_c I_c$ and the hourly averages are calculated in the table above.

Thus, $\sum I_c = 4676 \text{ W/m}^2$ and $\sum q_u = 2167 \text{ W}$. The daily average efficiency is obtained by summing the useful energy for those hours during which the collector delivers heat and dividing by the total insolation between sunrise and sunset. This yields

$$\eta_{c,day} = \frac{\sum q_u}{\sum A_c I_c} = \frac{2167}{2 \times 4676} = 0.232 \text{ or } 23.2\%.$$

3.2.8 Transient Effects

The preceding analysis assumed that steady-state conditions exist during the operation of the collector. Under actual operating conditions, the rate of insolation will vary and the ambient temperature and the external wind conditions may change. To determine the effect of changes in these parameters on the performance of a collector, it is necessary to make a transient analysis that takes the thermal capacity of the collector into account.

As shown in Klein et al. (1974), the effect of collector thermal capacitance is the sum of two contributions: the *collector storage* effect, resulting from the heat required to bring the collector up to its final operating temperature, and the *transient* effect, resulting from fluctuations in the meteorological conditions. Both effects result in a net loss of energy delivered compared with the predictions from the zero capacity analysis. This loss is particularly important on a cold morning when all of the solar energy absorbed by the collector is used to heat the hardware and the working fluid, thus delaying the delivery of useful energy for some time after the sun has come up.

Transient thermal analyses can be made with a high degree of precision (Kreith 1975), but the analytical predictions are no more accurate than the weather data and the overall collector conductance. For most engineering applications, a simpler approach is therefore satisfactory (Duffie and Beckman 1980). For this approach, it will be assumed that the absorber plate, the ducts, the back insulation, and the working fluid are at the same temperature. If back losses are neglected, an energy balance on the collector plate and the working fluid for a single-glazed collector delivering no useful energy can be written in the form

$$(\bar{mc})_p \frac{d\bar{T}_p(t)}{dt} = A_c I_s \alpha_s + A_c U_p (\bar{T}_g(t) - \bar{T}_p(t)) , \quad (3.49)$$

where $(\bar{mc})_p$ is the sum of the thermal capacities of the plate, the fluid, and the insulation; I_s is the insolation on the absorber plate; and U_p is the conductance between the absorber plate at \bar{T}_p and its cover at \bar{T}_g . Similarly, a heat balance on the collector cover gives

$$(mc)_g \frac{d\bar{T}_g(t)}{dt} = A_c U_p (\bar{T}_p(t) - \bar{T}_g(t)) - A_c U_\infty (\bar{T}_g(t) - T_a) , \quad (3.50)$$

where $U_\infty = (h_{c,\infty} + h_{r,\infty})$ (see Equation 3.18) and $(mc)_g$ is the thermal capacity of the cover plate.

Equations 3.49 and 3.50 can be solved simultaneously and the transient heat loss can then be determined by integrating the instantaneous loss over the time during which transient effects are pronounced. A considerable simplification in the solution is possible if one assumes that at any time the collector heat loss and the cover heat loss are equal, as in a quasi-steady state, so that

$$U_\infty A_c (\bar{T}_g(t) - T_a) = U_c A_c (\bar{T}_p(t) - T_a) . \quad (3.51)$$

Then, for a given air temperature, differentiation of Equation 3.51 gives

$$\frac{d\bar{T}_g(t)}{dt} = \frac{U_c d\bar{T}_p(t)}{U_\infty dt} . \quad (3.52)$$

Adding Equations 3.50, 3.51, and 3.52 gives a single differential equation for the plate temperature

$$(\bar{mc})_p + \frac{U_c}{U_\infty} (mc)_R \frac{d\bar{T}_p(t)}{dt} = \alpha_s I_s - U_c (\bar{T}_p(t) - T_a) A_c . \quad (3.53)$$

Equation 3.53 can be solved directly for given values of I_s and T_a . The solution to Equation 3.53 then gives the plate temperature as a function of time, for an initial plate temperature $T_{p,0}$, in the form

$$\bar{T}_p(t) - T_a = \frac{\alpha_s I_s}{U_c} - \frac{\alpha_s I_s}{U_c} (T_{p,0} - T_a) \exp \left(-\frac{U_c A_c t}{(\bar{mc})_p + (U_c/U_\infty)_c (mc)_g} \right) . \quad (3.54)$$

Collectors with more than one cover can be treated similarly, as shown in Collares-Pereira et al. (1977).

For a transient analysis, the plate temperature \bar{T}_p can be evaluated at the end of a specified period if the initial value of \bar{T}_p and the values of α_s , I_s , U_c , and T_a during the specified time are known. Repeated applications of Equation 3.54 provide an approximate method of evaluating the transient effects. An estimate of the net decrease in useful energy delivered can be obtained by multiplying the effective heat capacity of the collector, given by $(\bar{mc})_p + (U_c/U_\infty)(mc)_g$, by the temperature rise necessary to bring the collector to its operating temperature. Note that the parameter $[(\bar{mc})_p + (U_c/U_\infty)(mc)_g]/U_c A_c$ is the *time constant* of the collector (Collares-Pereira and Rabl 1979; Kreith 1975) and small values of this parameter will reduce losses resulting from transient effects.

Example 3.2

Calculate the temperature rise between 8 and 10 a.m. of a $1 \text{ m} \times 2 \text{ m}$ single-glazed water collector with a 0.3-cm-thick glass cover if the heat capacities of the plate, water, and back insulation are 5, 3, and 2 kJ/K , respectively. Assume that the unit surface conductance from the cover to ambient air is $18 \text{ W}/\text{m}^2 \cdot \text{K}$ and the unit surface conductance between the collector and the ambient air is $U_c = 6 \text{ W}/\text{m}^2 \cdot \text{K}$. Assume that the collector is initially at the ambient temperature. The absorbed insolation $\alpha_s I_s$ during the first hour averages $90 \text{ W}/\text{m}^2$, and that between 9 and 10 a.m., $180 \text{ W}/\text{m}^2$. The air temperature between 8 and 9 a.m. is 273 K , and that between 9 and 10 a.m., 278 K .

Solution

The thermal capacitance of the glass cover is $(mc)_g = (\rho V c_p)_g = (2500 \text{ kg}/\text{m}^3)(1 \text{ m} \times 2 \text{ m} \times 0.003 \text{ m})(1 \text{ kJ}/\text{kg}\cdot\text{K}) = 15 \text{ kJ}/\text{K}$. The combined collector, water, and insulation thermal capacity is equal to

$$(\bar{mc})_p + \frac{U_c}{U_\infty}(mc)_g = 5 + 3 + 2 + 0.3 \times 15 = 15.5 \text{ kJ}/\text{K}.$$

From Equation 3.54, the temperature rise of the collector given by

$$T_p - T_a = \frac{\alpha_s I_s}{U_c} - \frac{\alpha_s I_s}{U_c} (T_{p,0} - T_a) \exp \left[-\frac{U_c A_c t}{(\bar{mc})_p + (U_c/U_\infty)(mc)_g} \right].$$

At 8 a.m., $T_{p,0} = T_a$; therefore, the temperature rise, between 8 and 9 a.m., is

$$= \frac{90}{6} \left(1 - \exp \left[-\frac{2 \times 6 \times 3600}{15,500} \right] \right) = 15 \times 0.944 = 14.2 \text{ K}.$$

Thus, at 9 a.m., the collector temperature will be 287.2 K. Between 9 and 10 a.m., the collector temperature will rise as shown below:

$$= 278 + \frac{180}{6} - (30 - 9.2)0.056 = 306 \text{ K}$$

Thus, at 10 a.m., the collector temperature has achieved a value sufficient to deliver useful energy at a temperature level of 306 K.

3.2.9 Air-Cooled Flat-Plate Collector Thermal Analysis

The basic air-cooled flat-plate collector shown in Figure 3.18 differs fundamentally from the liquid-based collectors described in preceding sections because of the relatively poor heat-transfer properties of air. For example, in turbulent flow in a given conduit for a fixed value of Reynolds number, the convection heat-transfer coefficient for water is approximately 50 times greater than that for air. As a result, it is essential to provide the largest heat-transfer area possible to remove heat from the absorber surface of an air-heating collector.

The most common way to achieve adequate heat transfer in air collectors is to flow air over the entire rear surface of the absorber as shown. The heat-transfer analysis of such a collector does not involve the fin effect or the tube-to-plate bond conductance problem, which arises in liquid collectors. The heat-transfer process is essentially that of an unsymmetrically heated duct of large aspect ratio (typically 20–40).

Malik and Buelow (1976a,b) surveyed the fluid mechanics and heat-transfer phenomena in air collectors. They concluded that a suitable expression for the Nusselt number for a smooth air-heating collector is

$$\text{Nu}_{\text{sm}} = \frac{0.0192 \text{ Re}^{3/4} \text{ Pr}}{1 + 1.22 \text{ Re}^{-1/8} (\text{Pr} - 2)} . \quad (3.55)$$

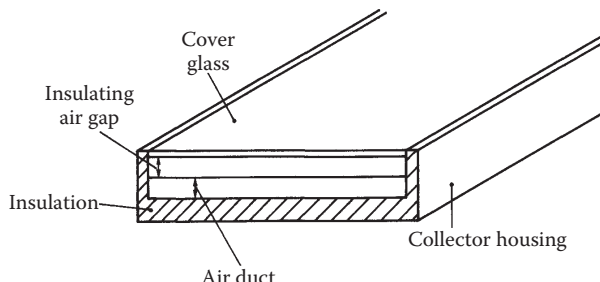


FIGURE 3.18

Schematic diagram of a basic air-heating flat-plate collector with a single glass (or plastic) cover.

If the surface is hydrodynamically rough, they recommended multiplying the smooth-surface Nusselt number by the ratio of the rough-surface friction factor f to the smooth-surface friction factor f_{sm} from the Blasius equation

$$f_{sm} = 0.079 \text{ Re}^{-1/4}. \quad (3.56)$$

The convective coefficient h_c in the Nusselt number is based on a unit absorber area but the hydraulic diameter D_H in the Nusselt and Reynolds numbers is based on the *entire duct perimeter*.

3.2.9.1 Air-Collector Efficiency Factor

The collector efficiency factor F' is defined as the ratio of energy collection rate to the collection rate if the absorber plate were at the local fluid temperature. F' is particularly simple to calculate, since no fin analysis or bond-conductance term is present for air collectors. For the collector shown in Figure 3.18, F' is given by

$$F' = \frac{\bar{h}_c}{\bar{h}_c + U_c}, \quad (3.57)$$

where U_c is calculated from Klein's equation and the duct convection coefficient h_c is calculated from Equation 3.55.

3.2.9.2 Air-Collector Heat-Removal Factor

The collector heat-removal factor is a convenient parameter, since it permits useful energy gain to be calculated by knowledge of only the easily determined fluid inlet temperature as shown in Equation 3.45. The heat-removal factor F_R for a typical air collector such as the one shown in Figure 3.18 is given by

$$F_R = \frac{\dot{m}_a c_{p,a}}{U_c A_c} \left(1 - \exp \left(- \frac{F U_c A_c}{\dot{m}_a c_{p,a}} \right) \right), \quad (3.58)$$

where F' is given by Equation 3.57, \dot{m}_a is the air flow rate (kg/s), and $c_{p,a}$ is its specific heat. The heat-removal factor for air collectors is usually significantly less than that for liquid collectors because \bar{h}_c for air is much smaller than that for a liquid such as water.

Example 3.3

Calculate the collector-plate efficiency factor F' and heat-removal factor F_R for a smooth, 1-m-wide, 5-m-long air collector with the following design. The flow rate per unit collector area is $0.7 \text{ m}^3/\text{min} \cdot \text{m}_c^2$ ($2.1 \text{ ft}^3/\text{minft}_c^2$).

The air duct height is 1.5 cm (0.6 in), the air density is 1.1 kg/m^3 (0.07 lb/ft^3), the specific heat is $1 \text{ kJ/kg}\cdot\text{K}$ ($0.24 \text{ Btu/lb}\cdot^\circ\text{F}$), and the viscosity is $1.79 \times 10^{-5} \text{ kg/m}\cdot\text{s}$ ($1.2 \times 10^{-5} \text{ lb}\cdot\text{ft}\cdot\text{s}$). The collector heat-loss coefficient U_c is $18 \text{ kJ/h}\cdot\text{m}^2\cdot\text{K}$ ($5 \text{ W/m}^2\cdot\text{K}$; $0.88 \text{ Btu/h}\cdot\text{ft}^2\cdot^\circ\text{F}$).

Solution

The first step is to determine the duct heat-transfer coefficient h_c from Equation 3.55. The Reynolds number is defined as

$$\text{Re} = \frac{\rho \bar{V} D_H}{\mu},$$

in which the average velocity \bar{V} is the volume flow rate divided by the flow area.

$$\bar{V} = \frac{0.7 \times 1 \times 5}{1 \times 0.015} = 233 \text{ m/min} = 3.89 \text{ m/s},$$

and the hydraulic diameter D_H is

$$D_H = \frac{4(0.015 \times 1)}{1 + 1 + 0.015 + 0.015} = 0.0296 \text{ m, and}$$

$$\text{Re} = \frac{(1.1)(3.89)(0.0296)}{1.79 \times 10^{-5}} = 7066.$$

From Equation 3.55, the Nusselt number is

$$\text{Nu} = \frac{0.0192(7066)^{3/4}(0.72)}{1 + 1.22(7066)^{-1/8}(0.72 - 2.0)} = 22.0.$$

The heat-transfer coefficient is

$$h_c = \text{Nu} \frac{k}{D_H} = \frac{\text{Nu} c_p}{\text{Pr} D_H}.$$

The Prandtl number for air is ~ 0.72 . Therefore,

$$\begin{aligned} h_c &= \frac{(22.0)(1.0)(1.79 \times 10^{-5})}{(0.72)(0.0296)} = 0.0185 \text{ kJ/m}^2\cdot\text{s}\cdot\text{K} \\ &= 66.5 \text{ kJ/m}^2\cdot\text{h}\cdot^\circ\text{C} (3.26 \text{ Btu/h}\cdot\text{ft}^2\cdot^\circ\text{F}). \end{aligned}$$

The plate efficiency is then, from Equation 3.57,

$$F = \frac{66.5}{66.5 + 18} = 0.787,$$

and the heat-removal factor F_R can be calculated from Equation 3.58. The mass flow rate per unit area is

$$\frac{\dot{m}}{A_c} = \rho(q/A_c) = \frac{1.1 \times 0.7}{60} = -0.128 \text{ kg/s} \cdot \text{m}_c^2.$$

Then,

$$F_R = \frac{(0.0128)(1)}{(18/3600)} \cdot 1 - \exp \left(-\frac{(0.787)(18/3600)}{(0.0128)(1)} \right) = 0.677.$$

That is, the particular collector in question can collect 67.7% of the heat it could collect if its surface were at the air-inlet temperature. F_R varies weakly with the fluid temperature through the temperature effect upon U_c .

3.3 Tubular Solar Energy Collectors

Two general methods exist for significantly improving the performance of solar collectors above the minimum flat-plate collector level. The first method increases solar flux incident on the receiver. It will be described in Section 3.5 on concentrators. The second method involves the reduction of parasitic heat loss from the receiver surface. Tubular collectors, with their inherently high compressive strength and resistance to implosion, afford the only practical means for completely eliminating convection losses by surrounding the receiver with a vacuum on the order of 10^{-4} mm Hg. The analysis of evacuated tubular collectors is the principal topic of this section.

Tubular collectors have a second application. They may be used to achieve a small level of concentration (1.5 to 2.0) by forming a mirror from a part of the internal concave surface of a glass tube. This reflector can focus radiation on a receiver inside this tube. Since such a receiver is fully illuminated, it has no parasitic "back" losses. The performance of a nonevacuated tubular collector may be improved slightly by filling the envelope with high-molecular-weight noble gases. External concentrators of radiation may also be coupled to an evacuated receiver for improvement of performance over the simple evacuated tube. Collectors of this type are described briefly below.

3.3.1 Evacuated-Tube Collectors

Evacuated-tube devices have been proposed as efficient solar energy collectors since the early 20th century. In 1909, Emmett proposed several evacuated-tube concepts for solar energy collection, two of which are being sold commercially today (Emmett 1911). Speyer (1965) also proposed a tubular evacuated flat-plate design for high-temperature operation. With the recent advances in vacuum technology, evacuated-tube collectors can be reliably mass produced. Their high-temperature effectiveness is essential for the efficient operation of solar air-conditioning systems and process heat systems.

Figure 3.19 shows schematic cross sections of several glass evacuated-tube collector concepts. The simplest design is basically a small flat-plate collector housed in an evacuated cylinder (Figure 3.19a). If the receiver is metal, a glass-to-metal seal is required to maintain a vacuum. In addition, a thermal short may occur from inlet to outlet tube unless special precautions are taken.

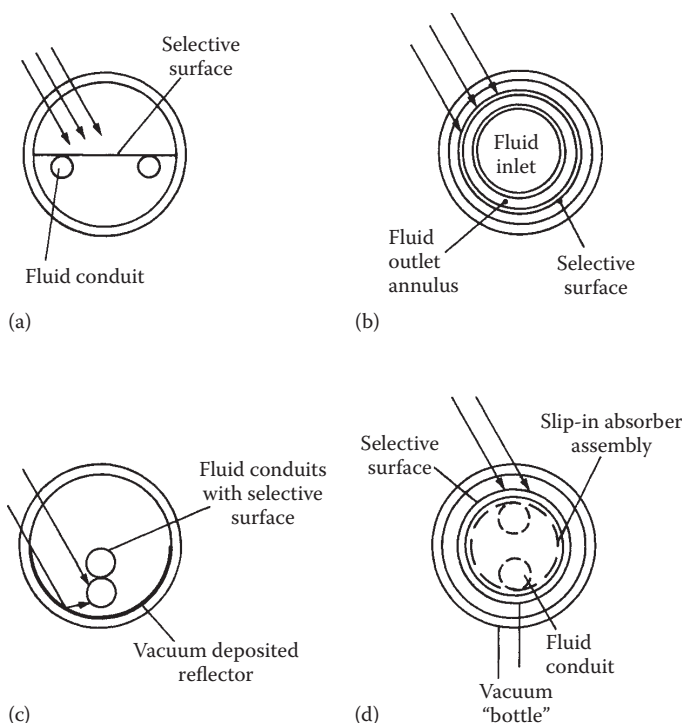


FIGURE 3.19

Evacuated-tube solar energy collectors: (a) flat plate, (b) concentric tubular, (c) concentrating, (d) vacuum bottle with slip-in heat exchanger contacting rear surface of receiver.

Mildly concentrating, tubular collectors can be made using the design of Figure 3.19c. Either a single flow-through receiver with fins or a double U tube as shown can be used.

One of Emmett's designs is shown in Figure 3.19d. It consists of an evacuated vacuum bottle much like an unsilvered, wide-mouth Dewar flask into which a metal heat exchanger is inserted. The outer surface of the inner glass tube is the absorber. The heat generated is transferred through the inner glass tube to the metal slip-in heat exchanger. Since this heat transfer is through a glass-to-metal interface that has only intermittent point contacts, significant axial temperature gradients can develop, thereby stressing the glass tube. In addition, a large temperature difference can exist between the inner and outer glass tubes. At the collector ends where the tubes are joined, a large temperature gradient and consequent thermal stress can exist.

The level of evacuation required for suppression of convection and conduction can be calculated from basic heat-transfer theory. As the tubular collector is evacuated, reduction of heat loss first occurs because of the reduction of the Rayleigh number. The effect is proportional to the square root of density. When the Rayleigh number is further reduced below the lower threshold for convection, the heat-transfer mechanism is by conduction only. For most gases, the thermal conductivity is independent of pressure if the mean free path is less than the heat-transfer path length.

For very low pressure, the conduction heat transfer in a narrow gap (Dushman 1962) is given by

$$q_k = \frac{k\Delta T}{g + 2p}, \quad (3.59)$$

where g is the gap width and p is the mean free path. For air, the mean free path at atmospheric pressure is approximately 70 μm. If 99% of the air is removed from a tubular collector, the mean free path increases to 7 mm, and conduction heat transfer is slightly affected. However, if the pressure is reduced to 10^{-3} torr, the mean free path is 7 cm, which is substantially greater than the heat-transfer path length, and conduction heat transfer is effectively suppressed. The relative reduction in heat transfer as a function of mean free path can be derived from Equation 3.59:

$$\frac{q_{vac}}{q_k} = \frac{1}{1 + 2p/g}, \quad (3.60)$$

where q_k is the conduction heat transfer if convection is suppressed and q_{vac} is the conduction heat transfer under a vacuum.

3.3.2 Thermal Analysis of a Tubular Collector

The heat loss from a tubular collector occurs primarily through the mechanism of radiation from the absorber surface. The rate of heat loss per unit absorber area q_L can then be expressed as

$$q_L = U_c(T_r - T_a). \quad (3.61)$$

Total thermal resistance $1/U_c$ is the sum of three resistances:

R_1 = radiative exchange from absorber tube to cover tube

R_2 = conduction through glass tube

R_3 = convection and radiation to environment

The overall resistance is then

$$\frac{1}{U_c} = R_1 + R_2 + R_3. \quad (3.62)$$

The conductances R_i^{-1} are given by

$$R_1^{-1} = \frac{1}{1/\epsilon_r + 1/\epsilon_e - 1} \sigma(T_r + T_{ei})(T_r^2 + T_{ei}^2), \quad (3.63)$$

$$R_2^{-1} = \frac{2k}{D_r \ln(D_{eo}/D_{ei})}, \text{ and} \quad (3.64)$$

$$R_3^{-1} = h_c + \sigma\epsilon_e(T_{eo} + T_a)(T_{eo}^2 + T_a^2) \frac{D_{eo}}{D_r}, \quad (3.65)$$

where the subscript "e" denotes envelope (tube) properties, subscripts "i" and "o" denote inner and outer surfaces of the envelope (tube), T_r is the receiver (absorber) temperature, and h_c is the external convection coefficient for the envelope. Test data have shown that the loss coefficient U_c is between 0.5 and 1.0 W/m²°C, thus confirming the analysis.

The energy delivery rate q_u on an aperture area basis can be written as

$$q_u = \tau_e \alpha_r I_{eff} \frac{A_t}{A_c} - U_c(T_r - T_a) \frac{A_r}{A_c}, \quad (3.66)$$

where I_{eff} is the effective solar radiation both directly intercepted and intercepted after reflection from the back reflector, A_t is the projected area of a

tube (its diameter), and A_r is the receiver or absorber area. The receiver-to-collector aperture area ratio is $\pi D_r/d$, where d is the center-to-center distance between the tubes. Therefore,

$$q_u = \frac{D_r}{d} [\tau_e \alpha_r I_{\text{eff}} - \pi U_c (T_r - T_a)]. \quad (3.67)$$

Beekley and Mather (1975) have shown that a tube spacing one envelope diameter D_{eo} apart maximizes daily energy gain. A specularly reflecting cylindrical back surface improves performance by 10% or more.

3.4 Experimental Testing of Collectors

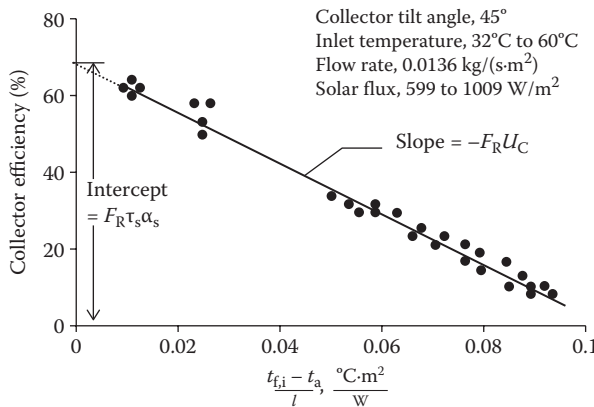
The performance of solar thermal systems for heating and cooling depends largely on the performance of solar collectors. Therefore, experimental measurement of thermal performance of solar collectors by standard methods is important and necessary. The experimentally determined performance data are needed for design purposes and for determining the commercial value of the collectors. The thermal performance of a solar collector is determined by establishing an efficiency curve from the measured instantaneous efficiencies for a combination of values of incident solar radiation, ambient temperature, and inlet fluid temperature. An instantaneous efficiency of a collector under steady-state conditions can be established by measuring the mass flow rate of the heat-transfer fluid, its temperature rise across the collector ($T_{f,out} - T_{f,in}$), and the incident solar radiation intensity (I_c) as

$$\eta_c = \frac{q_u}{A_c I_c} = \frac{\dot{m} C_p (T_{f,out} - T_{f,in})}{A_c I_c}. \quad (3.68)$$

The efficiency, η_c , of a collector under steady state can also be written according to the Hottel–Whillier–Bliss equation (Equation 3.48) as

$$\eta_c = F_R \tau_s \alpha_s - F_R U_c \frac{(T_{f,in} - T_a)}{I_c}. \quad (3.48)$$

Equation 3.48 suggests that for constant values of F_R and U_c , if η_c is plotted with respect to $(T_{f,in} - T_a)/I_c$, a linear curve will result, with a "y" intercept of $F_R \tau_s \alpha_s$ and a slope of $-F_R U_c$. Figure 3.20 shows a typical thermal performance curve for a flat-plate collector. Since τ_s and α_s can be measured independently,

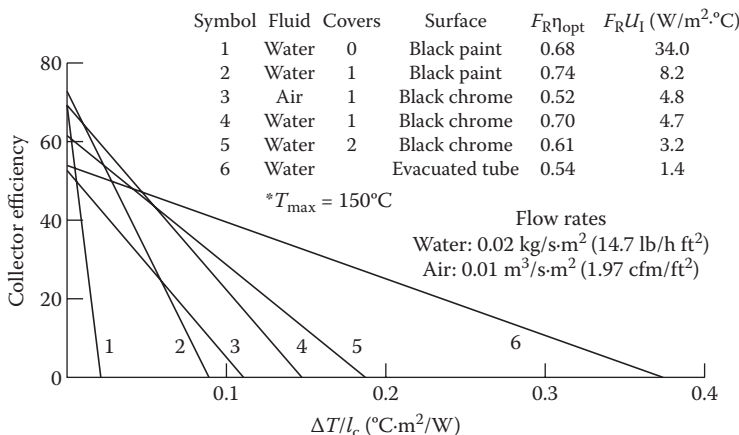
**FIGURE 3.20**

Thermal efficiency curve for a double-glazed flat-plate liquid type of solar collector.

a thermal performance curve of a flat-plate collector allows us to establish the value of F_R and U_c also. Figure 3.21 shows typical performance curves of various glazed and unglazed flat-plate solar collectors.

In Equation 3.48, the product $\tau_s \alpha_s$ will change with the angle of incidence. Since flat-plate collectors are normally fixed, the angle of incidence changes throughout the day. A relationship can be written between the actual or effective $(\tau_s \alpha_s)$ and $(\tau_s \alpha_s)_n$ for normal incidence as

$$(\tau_s \alpha_s) = (\tau_s \alpha_s)_n K_{\tau \alpha} \quad (3.69)$$

**FIGURE 3.21**

Typical performance curves for various flat-plate solar collectors.

where $(\tau_s \alpha_s)_n$ is the value of the product for normal angle of incidence and K_{ta} is called the incidence angle modifier. Therefore, the thermal performance of a flat-plate collector may be written as

$$\eta_c = F_R K_{ta} (\tau_s \alpha_s)_n - U_c \frac{(T_{f,in} - T_a)}{I_c} . \quad (3.70)$$

The thermal performance of collectors is usually found experimentally for normal angles of incidence in which case $K_{ta} = 1.0$. The incidence angle modifier is then measured separately. It has been established that K_{ta} is of the form

$$K_{ta} = 1 - b \frac{1}{\cos i} - 1 , \quad (3.71)$$

where b is a constant and i is the angle of incidence. Figure 3.22 shows a typical curve for K_{ta} .

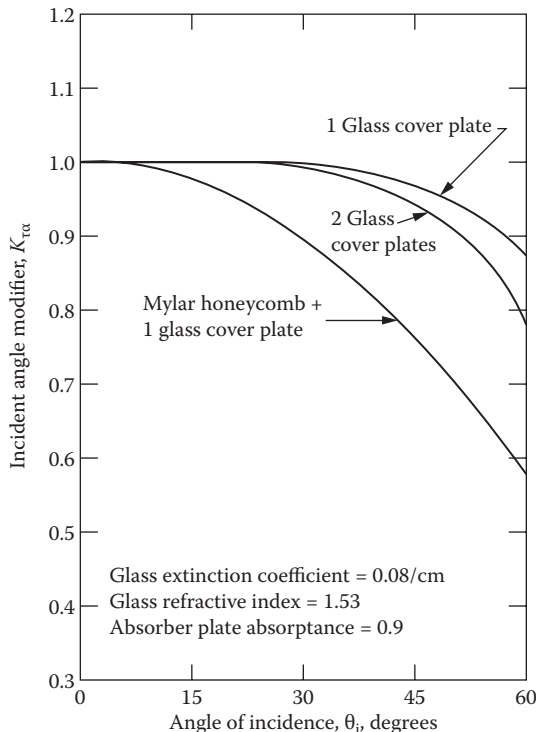


FIGURE 3.22

Incident angle modifier for three flat-plate solar collectors. (Reprinted from ASHRAE Standard 93-77, Methods of testing to determine the thermal performance of solar collectors. With permission from the American Society of Heating, Refrigerating and Air-Conditioning Engineers, Inc., Atlanta, GA.)

3.4.1 Testing Standards for Solar Thermal Collectors

Standard testing procedures adopted by regulating agencies in various countries establish ways of comparing the thermal performance of various collectors under the same conditions. In the United States, the thermal performance standards established by the American Society of Heating, Refrigeration and Air-Conditioning Engineers (ASHRAE) have been accepted for thermal performance testing of solar thermal collectors (ASHRAE 1980, 2003). Similar standards have been used in a number of countries (EN 12975-2). The standards established by ASHRAE include the following:

ASHRAE Standard 93-2003, "Methods of Testing to Determine the Thermal Performance of Solar Collectors" (ASHRAE 2003)

ASHRAE Standard 96-1980, "Methods of Testing to Determine the Thermal Performance of Unglazed Solar Collectors" (ASHRAE 1980)

ASHRAE Standard 93-2003 specifies the procedures for determining the time constant, thermal performance, and the incidence angle modifier of solar thermal collectors using a liquid or air as a working fluid. Figure 3.23 shows a schematic of a standard testing configuration for thermal performance testing. The tests are conducted under quasi-steady-state conditions

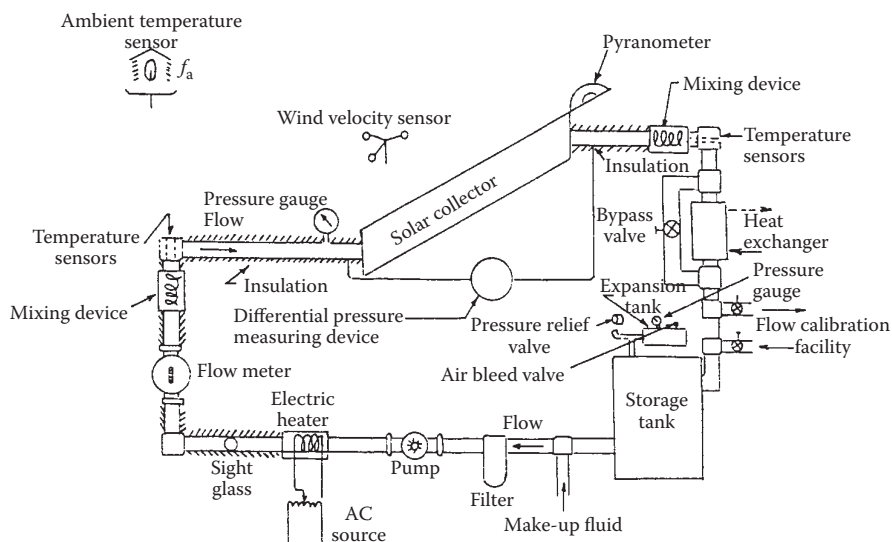


FIGURE 3.23

A testing configuration for a liquid-type solar collector. (Reprinted from ASHRAE Standard 93-77, Methods of testing to determine the thermal performance of solar collectors. With permission from the American Society of Heating, Refrigerating and Air-Conditioning Engineers, Inc., Atlanta, GA.)

3.4.1.1 Time Constant

In order to avoid the transient effects, performance of a collector is measured and integrated over at least the time constant of the collector. The time constant is measured by operating the collector under steady or quasi-steady conditions with a solar flux of at least 790 W/m^2 and then abruptly cutting the incident flux to zero, while continuing to measure the fluid inlet ($T_{f,i}$) and exit ($T_{f,e}$) temperatures. The fluid inlet temperature is maintained at $\pm 1^\circ\text{C}$ of the ambient temperature. The time constant is then determined as the time required to achieve

$$\frac{T_{f,e} - T_{f,i}}{T_{f,e,\text{initial}} - T_{f,i}} = 0.30. \quad (3.72)$$

3.4.1.2 Thermal Performance

For determining the thermal performance of a collector, ASHRAE Standard 93-2003 specifies test conditions to get at least four data points for the efficiency curve. The test conditions include the following:

1. Near normal incidence ($i \leq 5^\circ$) angle tests close to solar noon time
2. At least four tests for each $T_{f,i}$, two before and two after solar noon
3. At least four different values of $T_{f,i}$ to obtain different values of $\Delta T/I_c$, preferably to obtain ΔT at 10%, 30%, 50%, and 70% of stagnation temperature rise under the given conditions of solar intensity and ambient conditions

3.4.1.3 Incidence Angle Modifier

ASHRAE 93-2003 specifies that a curve for incidence angle modifier be established by determining the efficiencies of a collector for average angles of incidence of 0° , 30° , 45° , and 60° while maintaining $T_{f,i}$ at $\pm 1^\circ\text{C}$ of the ambient temperature. Since $(T_{f,i} - T_a) = 0$, the incident angle modifier according to Equation 3.70 is

$$K_{ta} = \frac{\eta_c}{F_R(\tau_s \alpha_s)_n}. \quad (3.73)$$

The denominator is the y intercept of the efficiency curve.

3.5 Concentrating Solar Collectors

Concentration of solar radiation is achieved by reflecting or refracting the flux incident on an aperture area A_a onto a smaller receiver/absorber area A_r .

An optical concentration ratio, CR_o , is defined as the ratio of the solar flux I_r on the receiver to the flux, I_a , on the aperture, or

$$CR_o = I_r/I_a, \quad (3.74)$$

while a geometric concentration ratio CR is based on the areas, or

$$CR = A_a/A_r. \quad (3.75)$$

CR_o gives a true concentration ratio because it accounts for the optical losses from the reflecting and refracting elements. However, since it has no relationship to the receiver area, it does not give an insight into the thermal losses that are proportional to the receiver area. In the analyses in this book, only geometric concentration ratio CR will be used.

Concentrators are inherently more efficient at a given temperature than are flat-plate collectors, since the area from which heat is lost is smaller than the aperture area. In a flat-plate device, both areas are equal in size. A simple energy balance illustrates this principle. The useful energy delivered by a collector q_u is given by

$$q_u = \eta_o I_c A_a - U_c (T_r - T_a) A_r, \quad (3.76)$$

in which η_o is the optical efficiency and other terms are as defined previously. The instantaneous collector efficiency is given by

$$\eta_c = \frac{q_u}{I_c A_a}, \quad (3.77)$$

from which, using Equation 3.76,

$$\eta_c = \eta_o - \frac{U_c (T_r - T_a)}{I_c} \frac{1}{CR}. \quad (3.78)$$

For a flat plate $CR \approx 1$, and for concentrators, $CR > 1$. As a result, the loss term (second term) in Equation 3.78 is smaller for a concentrator and the efficiency is higher. This analysis is necessarily simplified and does not reflect the reduction in optical efficiency that frequently, but not always, occurs because of the use of imperfect mirrors or lenses in concentrators. The evaluation of U_c in Equation 3.78 in closed form is quite difficult for high-temperature concentrators, because radiation heat loss is usually quite important and introduces nonlinearities ($\propto T^4$). One disadvantage of concentrators is that they can collect only a small fraction of the diffuse energy incident at their aperture. This property is an important criterion in defining the geographic limits to the successful use of concentrators.

3.5.1 Thermodynamic Limits to Concentration

A simple criterion is developed below for the upper limit of concentration (Rabl 1975) of a solar collector. Figure 3.24 is a schematic diagram of any concentrating device in which the source, aperture, and receiver are shown. The source represents a diffuse source or a diffuse-like source that could be formed by a moving point source, that is, the sun. The evaluation of the maximum achievable concentration ratio CR_{max} uses the concept of radiation exchange factors described in Chapter 2.

The factor \mathfrak{J}_{12} is defined as the fraction of radiation emitted from surface 1 that reaches surface 2 by whatever means—direct exchange, reflection, or refraction. It is shown in Chapter 2 that reciprocity relations exist for area exchange factors; for this analysis, the second law of thermodynamics requires, in addition, that

$$A_s \mathfrak{J}_{sa} = A_a \mathfrak{J}_{as} \quad (3.79)$$

and

$$A_s \mathfrak{J}_{sr} = A_r \mathfrak{J}_{rs}, \quad (3.80)$$

where “a” denotes aperture, “r” denotes receiver, and “s” denotes the source. Here, we use \mathfrak{J} symbols for exchange factor between nonblack surfaces and F symbols for black surfaces. By means of these expressions, the concentration ratio CR can be expressed as

$$CR = \frac{A_a}{A_r} = \frac{\mathfrak{J}_{sa} \mathfrak{J}_{rs}}{\mathfrak{J}_{as} \mathfrak{J}_{sr}}. \quad (3.81)$$

For the best concentrator possible, all radiation entering the aperture A_a reaches the receiver A_r ; that is,

$$\mathfrak{J}_{sa} = \mathfrak{J}_{sr}. \quad (3.82)$$

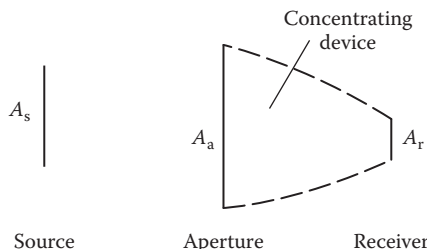


FIGURE 3.24

Generalized schematic diagram of any two-dimensional solar energy concentrating device showing source of radiation A_s , aperture A_a , and receiver A_r areas.

In addition, if the source is representable as a black body,

$$\mathfrak{F}_{as} = F_{as}, \quad (3.83)$$

where F_{as} is the radiation shape factor between two black surfaces. Using Equations 3.81 and 3.83, we have

$$CR = \frac{\mathfrak{F}_{rs}}{F_{as}}. \quad (3.84)$$

Because $\mathfrak{F}_{rs} \leq 1$ by the second law,

$$CR \leq CR_{max} = \frac{1}{F_{as}}. \quad (3.85)$$

Equation 3.85 states the simple and powerful result that the maximum concentration permitted by the second law is simply the reciprocal of the radiation shape factor F_{as} .

The shape factor F_{as} for a solar concentrator in two dimensions can be calculated from the diagram in Figure 3.25. This sketch represents a trough-like or single-curvature concentrator formed from mirrors or a linear (cylindrical) lens. It is illuminated by a line source of light of length $2r$ representing a portion of the sun's virtual trajectory. By reciprocity, we have

$$F_{as} = F_{sa} \frac{A_s}{A_a}. \quad (3.86)$$

If an angle $2\theta_{max}$ is defined as the maximum angle within which light is to be collected, we have

$$F_{as} = \sin \theta_{max} \quad (3.87)$$

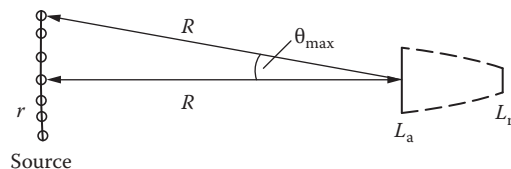


FIGURE 3.25

Schematic diagram of two-dimensional sun-concentrator geometry used to calculate shape factor F_{as} and showing acceptance half-angle θ_{max} and several positions of the sun.

from Hottel's crossed-string method (Hottel and Sarofim 1967) for $L \ll r$. The angle θ_{\max} is called the *acceptance half-angle*. From Equation 3.85, the maximum concentration is then

$$CR_{\max,2D} = \frac{1}{\sin \theta_{\max}}. \quad (3.88)$$

The term acceptance half-angle denotes coverage of one-half of the angular zone within which radiation is accepted (that is, "seen") by the receiver of a concentrator. Radiation is said to be accepted over an acceptance angle $2\theta_{\max}$ because radiation incident within this angle reaches the absorber after passing through the aperture. Practical acceptance angles range from a minimum subtending the sun's disk (approximately $1/2^\circ$) to 180° , a value characterizing a flat-plate collector accepting radiation from a full hemisphere.

Double-curvature or dish-type concentrators have an upper limit of concentration that can be evaluated by extending the method used above to three dimensions. The result of such a calculation for a compound-curvature device is given by

$$CR_{\max,3D} = \frac{1}{\sin^2 \theta_{\max}}. \quad (3.89)$$

In the above analyses, if the concentrator has an index of refraction $n > 1$, the maximum concentration will be (Welford and Winston 1989)

$$CR_{\max,2D} = \frac{n}{\sin \theta_{\max}} \quad (3.90)$$

and

$$CR_{\max,3D} = \frac{n^2}{\sin^2 \theta_{\max}}. \quad (3.91)$$

The second law prescribes not only the geometric limits of concentration as shown above but also the operating temperature limits of a concentrator. The radiation emitted by the sun and absorbed by the receiver of a concentrator q_{abs} is

$$q_{\text{abs}} = \tau \alpha_s A_s F_{\text{sa}} \sigma T_s^4, \quad (3.92)$$

where T_s is the effective temperature of the sun and τ is the overall transmittance function for the concentrator, including the effects of any lenses,

mirrors, or glass covers. If the acceptance half-angle θ_{\max} is selected to just accept the sun's disk of angular measure $\theta_s (\theta_s \sim 1/4^\circ)$, we have, by reciprocity (Equation 3.86), for a concentrator with compound curvature,

$$q_{\text{abs}} = \tau \alpha_s A_a \sin^2 \theta_s \sigma T_s^4. \quad (3.93)$$

If convection and conduction could be eliminated, all heat loss q_L is by radiation, and

$$q_L = \varepsilon_{\text{ir}} A_r \sigma T_r^4, \quad (3.94)$$

where ε_{ir} is the infrared emittance of the receiver surface. Radiation inputs to the receiver from a glass cover or the environment can be ignored for this upper limit analysis.

An energy balance on the receiver is then

$$q_{\text{abs}} = q_L + \eta_c q_{\text{abs}}, \quad (3.95)$$

where η_c is the fraction of energy absorbed at the receiver that is delivered to the working fluid. Substituting for Equations 3.93 and 3.94 in Equation 3.95, we have

$$(1 - \eta_c) \tau \alpha_s A_a \sin^2 \theta_s \sigma T_s^4 = \varepsilon_{\text{ir}} A_r \sigma T_r^4. \quad (3.96)$$

Because $CR = A_a/A_r$ and $CR_{\max} = 1/\sin^2 \theta_s$,

$$T_r = T_s (1 - \eta_c) \tau \frac{\alpha_s CR}{\varepsilon_{\text{ir}} CR_{\max}}^{1/4}. \quad (3.97)$$

In the limit as $\eta_c \rightarrow 0$ (no energy delivery) and $\tau \rightarrow 1$ (perfect optics), we have

$$\lim T_r \rightarrow T_s \frac{CR}{CR_{\max}}^{1/4}. \quad (3.98)$$

Since $\varepsilon_{\text{ir}} \rightarrow \alpha_s$ as $T_r \rightarrow T_s$, Equation 3.98 shows that

$$T_r \leq T_s, \quad (3.99)$$

as expected for an optically and thermally idealized concentrator. Equation 3.99 is equivalent to the Clausius statement of the second law for a solar concentrator.

3.5.2 Optical Limits to Concentrations

Equations 3.88 through 3.91 define the upper limit of concentration that may be achieved for a given concentration viewing angle. Of interest are the upper and lower limits of concentration defined by practical viewing angle limits—the maximum CR limited only by the size of the sun's disk and achieved by continuous tracking and the minimum CR, based on a specific number of hours of collection with no tracking.

The upper limit of concentration for two- and three-dimensional concentrators is on the order of

$$\text{CR}_{\max,2D} = \frac{1}{\sin 1/4^\circ} \approx 216 \text{ in air,}$$

$$= \frac{1.5}{\sin 1/4^\circ} \approx 324 \text{ in glass } (n = 1.5),$$

and

$$\text{CR}_{\max,3D} = \frac{1}{\sin^2 1/4^\circ} \approx 46,000 \text{ in air,}$$

$$= \frac{(1.5)^2}{\sin^2 1/4^\circ} \approx 103,500 \text{ in glass.}$$

In practice, these levels of concentration are not achievable because of the effects of tracking errors and imperfections in the reflecting- or refracting-element surface, as described later. Gleckman et al. (1989) are reported to have achieved the highest concentration of 56,000.

3.5.3 Acceptance of Diffuse Radiation

Diffuse or scattered radiation is not associated with a specific direction as is beam radiation. It is expected, therefore, that some portion of the diffuse component will fall beyond the acceptance angle of a concentrator and not be collectable. The minimum amount of diffuse radiation that is collectable can be estimated by assuming that the diffuse component is isotropic at the aperture. The exchange factor reciprocity relation shows that

$$A_a \mathfrak{I}_{as} = A_r \mathfrak{I}_{rs}. \quad (3.100)$$

For most practical concentrating devices that can accept a significant fraction of diffuse radiation, $\mathfrak{J}_{rs} = 1$. That is, all radiation leaving the receiver reaches the aperture and the environment eventually. Then,

$$\mathfrak{J}_{as} = \frac{A_r}{A_a} = \frac{1}{CR} \quad (3.101)$$

for any concentrator. Equation 3.101 indicates that at least $1/CR$ of the incident diffuse radiation reaches the receiver. In actual practice, the collectable diffuse portion will be greater than $1/CR$, since diffuse radiation is usually concentrated near the solar disk except during the cloudiest of days (see Chapter 2).

3.5.4 Ray Tracing Diagrams

Ray tracing diagrams are helpful in understanding the distribution of concentrated flux on the receiver and to design the receiver-absorber configurations. They are drawn by tracing a beam of parallel rays specularly reflected from the reflector surface. Figure 3.26 shows simple examples of ray tracing diagrams for a circular reflector and a parabolic reflector. From this figure, it is easy to understand that a receiver for a linear parabolic trough could be designed as a small diameter tube, while a larger-area rectangular surface would be required for a linear circular trough. Figure 3.27 demonstrates that the size of the receiver can be reduced, and therefore concentration increased, by using a smaller rim angle. A three-dimensional concentrator can be visualized by rotating each reflector profile about its axis. If a parabolic or circular reflecting concentrator tracks the sun in such a way that the axis of symmetry is always parallel to the solar beam, the reflected flux will be incident on the receiver. However, if the tracking is not perfect or if the concentrator is not designed to track, the beam may

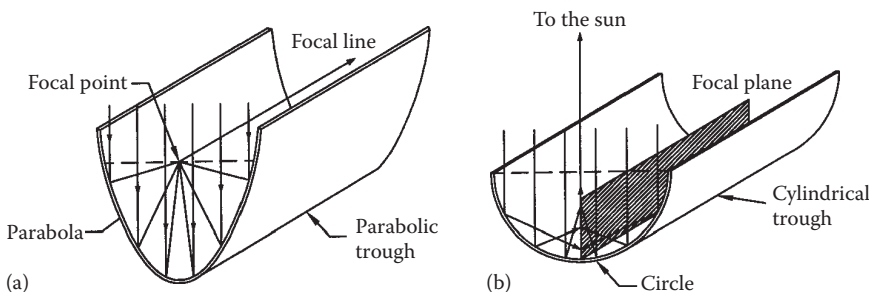
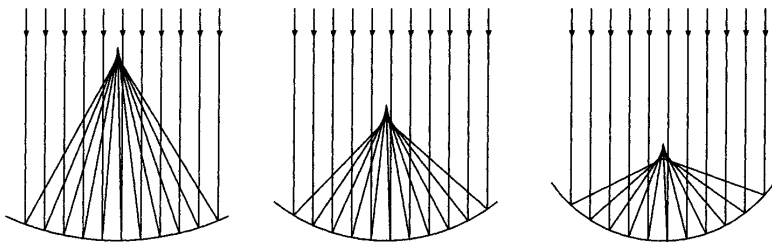
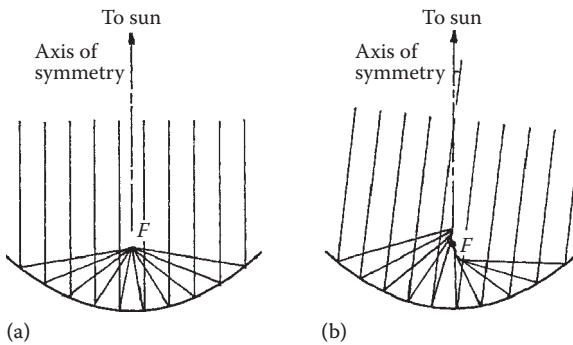


FIGURE 3.26

Examples of ray tracing diagrams for (a) a parabolic reflector and (b) a circular reflector.

**FIGURE 3.27**

Focusing of parallel rays of light using circular mirrors with different rim angles.

**FIGURE 3.28**

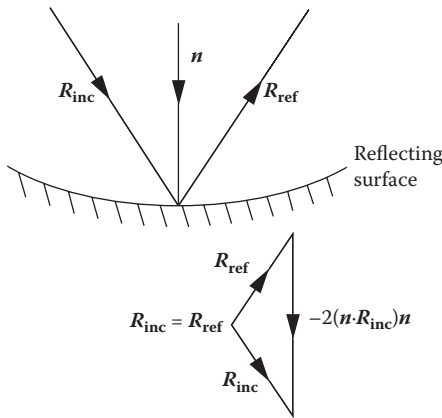
Concentration by parabolic reflector for a beam (a) parallel to the axis of symmetry and (b) at an angle to the axis.

make an angle with the axis of symmetry. In which case, the incident beam will not focus on the receiver, as demonstrated in Figure 3.28, unless the receiver design is modified. As seen from this figure, tracking errors will penalize a parabolic concentrator more severely than a circular concentrator. Therefore, a parabolic concentrator requires more accurate sun tracking for best utilization.

In order to formulate a ray tracing procedure suitable for numerical computation, laws of reflection and refraction are used in vector form as explained in detail in Welford and Winston (1989). Figure 3.29 shows the incident and reflected rays as unit vectors \mathbf{R}_{inc} and \mathbf{R}_{ref} , and a unit vector along the normal pointing into the reflecting surface is shown as \mathbf{n} . Then, according to the laws of reflection,

$$\mathbf{R}_{\text{ref}} = \mathbf{R}_{\text{inc}} - 2(\mathbf{n} \cdot \mathbf{R}_{\text{inc}})\mathbf{n}. \quad (3.102)$$

Thus, to trace a ray, we first find the incidence point at the reflecting surface, then a unit normal to the surface, and finally the reflected ray using

**FIGURE 3.29**

Vector formulation of reflection. (Adapted from Welford, W.T. and R. Winston, *High Collection Nonimaging Optics*, Academic Press, San Diego, CA, 1989.)

Equation 3.102. For example, if the reflecting surface is an ideal paraboloid with a focal length F , it can be expressed in an x, y, z coordinate system as

$$Z = \frac{x^2 + y^2}{4F}, \quad (3.103)$$

or

$$f(x, y, z) = 4Fz - x^2 - y^2. \quad (3.104)$$

The normal vector or gradient to this surface is defined as

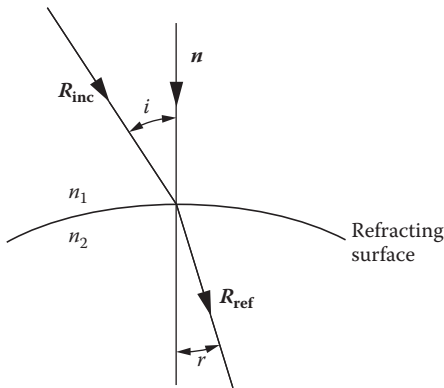
$$\mathbf{f} = \frac{df}{dx} \mathbf{i} + \frac{df}{dy} \mathbf{j} + \frac{df}{dz} \mathbf{k}. \quad (3.105)$$

Upon evaluation of the derivative ∇f from Equation 3.105, a normal to the paraboloid at x, y, z is

$$\nabla f = -2xi - 2yj + 4Fk, \quad (3.106)$$

and a unit normal is defined as

$$\mathbf{n} = \frac{\mathbf{f}}{|\mathbf{f}|}. \quad (3.107)$$

**FIGURE 3.30**

Vector formulation of refraction. (Adapted from Welford, W.T. and R. Winston, *High Collection Nonimaging Optics*, Academic Press, San Diego, CA, 1989.)

After finding n at the incidence point, R_{ref} can be found from Equation 3.102. For a refracting surface, the vector relationship between the incident and the refracted rays can be expressed as (Figure 3.30)

$$n_2 \mathbf{R}_{\text{ref}} \times \mathbf{n} = n_1 \mathbf{R}_{\text{inc}} \times \mathbf{n}. \quad (3.108)$$

The procedure to follow is similar to that for reflection. Welford (1974) gives details of the application to lens systems.

3.5.5 Concentrator Types

Concentrators can be classified according to the following:

1. Amount of tracking required to maintain the sun within the acceptance angle
2. Type of tracking—single or double axis

As shown in the preceding sections, tracking requirements depend on the acceptance half-angle θ_{max} ; the larger the θ_{max} , the less frequently and less accurately the tracker must operate. Two tracking levels may be identified:

1. Intermittent tilt change or completely fixed.
2. Continuously tracking reflector, refractor, or receiver. If oriented east–west, it requires an approximate $\pm 30^\circ/\text{day}$ motion; if north–south, an approximately $15^\circ/\text{h}$ motion.

Both must accommodate to a $\pm 23 1/2^\circ/\text{year}$ declination excursion.

The least complex concentrators are those not requiring continuous accurate tracking of the sun. These are necessarily of large acceptance angle, moderate concentration ratio, and usually single-curvature design. Because the smallest diurnal, angular excursion of the sun is in a north-south plane, the fixed or intermittently turned concentrators must be oriented with the axis of rotation perpendicular to this plane, that is, in an east-west direction, in order to capitalize on the large acceptance angles.

3.5.6 Fixed Concentrators

A simple fixed-concentrator concept is based on using flat reflectors to boost the performance of a flat-plate collector as shown in Figure 3.31. Other variations of this concept are shown in Figure 3.32. The concentration ratio of these

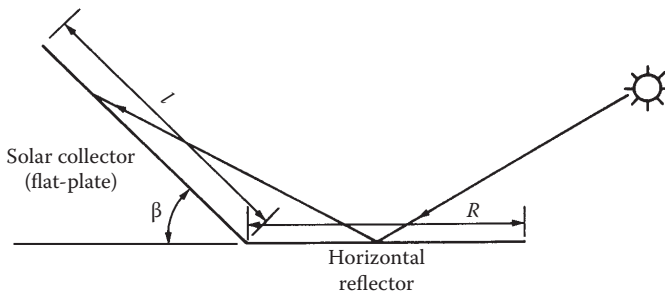


FIGURE 3.31

Horizontal reflecting surface used to boost flat-plate collector performance.

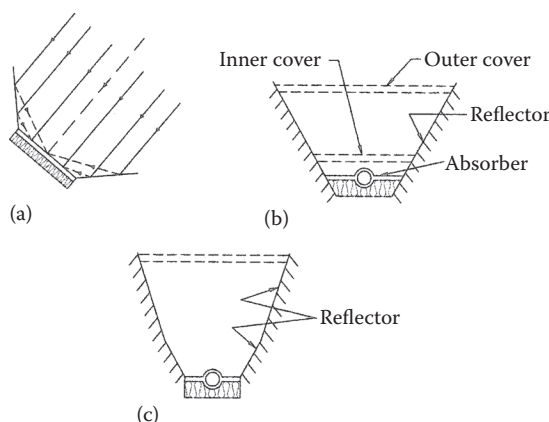


FIGURE 3.32

Examples of flat reflectors used to concentrate sunlight. (a) Flat-plate collector with reflective wings. (b) Trapezoidal design. (c) Two-facet design. (From ASHRAE 93-2003, Methods of testing to determine the thermal performance of solar collectors, ASHRAE, Atlanta, GA.)

concentrators is of the order of 1.5 to 3. For higher concentrations, spherical or parabolic reflecting or refracting surfaces are used.

3.6 Parabolic Trough Concentrator

The most common commercially available solar concentrator is the parabolic trough concentrator (PTC). Figure 3.33 shows a photograph of a commercial PTC and Figure 3.34 shows sketches of a commercial LS3 PTC. PTC collectors usually track the sun with one degree of freedom using one of three orientations: east–west, north–south, or polar. Sun tracking can be done for each by programming computers that control the tracking motors. The east–west and north–south configurations are the simplest to assemble into large arrays but have higher incidence angle cosine losses than the polar mount. Also, the polar mount intercepts more solar radiation per unit area. The absorber of a PTC is usually tubular, enclosed in a glass tube to reduce radiative and convective losses. The convective losses can be minimized by creating a vacuum in the annular space between the absorber and the glass cover.

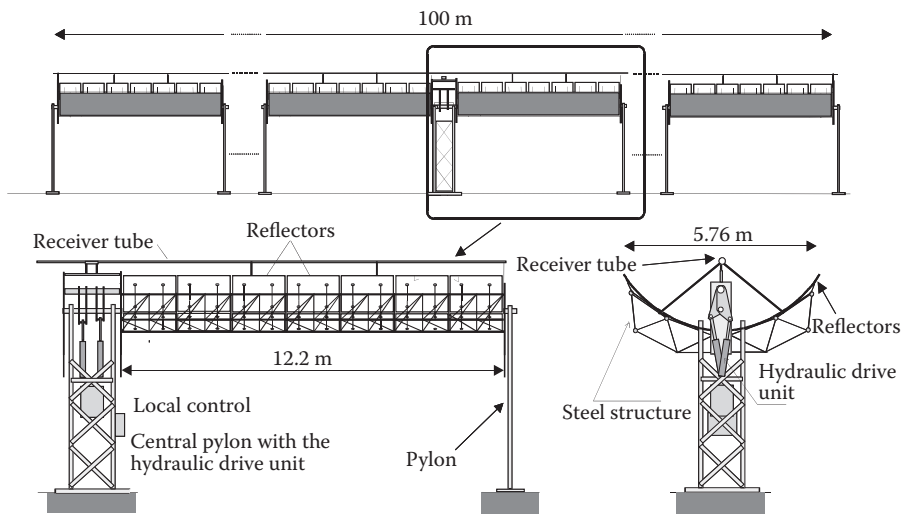
3.6.1 Optical Analysis of PTC

The peak *optical efficiency*, η_o , of a collector is the ratio of the solar radiation absorbed in the absorber to that intercepted by the collector aperture directly facing the sun. The following major optical characteristics give the optical efficiency η_o :



FIGURE 3.33

Commercial PTC. (Courtesy of Skyfuel, Inc., Arvada, CO.)

**FIGURE 3.34**

Sketches of a commercial LS3 Parabolic Trough Collector. (Adapted from Romero-Alvarez and Zarza, Concentrating Solar Power, Chapter 19 in Energy Conversion, Goswami and Kreith, eds., CRC Press, 2008.)

1. Reflectance of clean mirror, ρ . Typical clean silvered glass mirrors used in PTC have reflectance of around 0.93–0.94.
2. Transmittance of glass envelope of absorber, τ . A typical value of transmittance is 0.93. However, it can be increased to more than 0.96 by applying antireflective coatings to both sides of glass.
3. Absorptance of receiver/absorber, α . Typical values of α for selective absorbers are 0.94–0.95.
4. Intercept factor, γ , defined as the fraction of the rays reflected from the mirror that reach the absorber. A fraction of the rays reflected from the mirror do not reach the absorber because of mirror imperfections, geometrical errors in the parabolic reflector shape, mechanical deformations of the PTC during tracking, and shadowing owing to flexible bellows and the receiver supports. Neglecting the mirror imperfections, the intercept for 0° angle of incidence can be considered as made up of three factors (Vasquez-Padilla 2011): geometrical errors in parabolic trough shape, γ_1 ; shadowing by flexible bellows and receiver supports, γ_2 ; and mechanical deformation of the support structure during tracking, γ_3 . The intercept factor γ is then given by

$$\gamma = \gamma_1 \gamma_2 \gamma_3. \quad (3.109)$$

Typical values for clean PTCs are as follows: $\gamma_1 = 0.97\text{--}0.98$, $\gamma_2 = 0.96\text{--}0.97$, and $\gamma_3 = 0.99$, which gives the intercept factor γ in the range of 0.92–0.94.

Therefore, the peak optical efficiency of a parabolic trough at 0° angle of incidence

$$\eta_{o,peak} = \rho\tau\alpha\gamma. \quad (3.110)$$

During operation, the optical efficiency of a PTC is much less than peak owing to the angle of incidence, soiling of the mirrors and the glass envelope of the receiver, and end losses, which account for the fraction of a receiver, which is not illuminated by the rays incident on the aperture.

The incidence angle of the beam on the PTC aperture affects all four parameters comprising the optical efficiency. The effect is quantified by the incidence angle modifier, $K(i)$, for an angle of incidence, i , which is defined by

$$K(i) = \frac{\eta_o(i)}{\eta_o(i=0)}. \quad (3.111)$$

Table 3.6 gives the expressions for incidence angle modifiers for some popular commercially available PTC collectors (also Figure 3.35).

Another geometric factor is the end losses attributed to angle of incidence, which accounts for the fraction of the receiver tube not illuminated by the reflected radiation. From Figure 3.36, the end loss factor F_{el} is given by

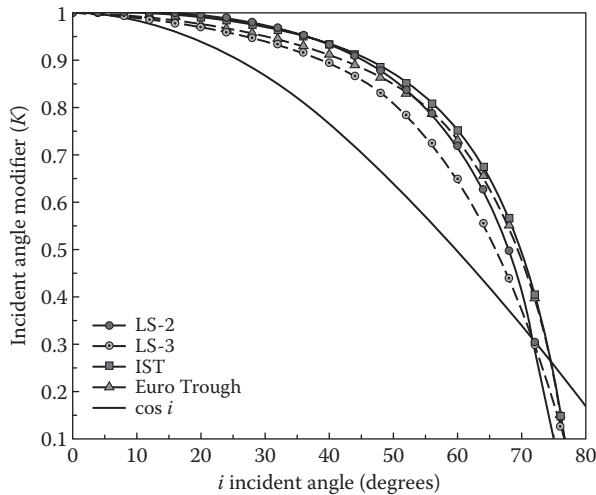
$$F_{el} = \frac{(L_c - z)}{L_c} = 1 - \frac{r}{L_c} \tan i, \quad (3.112)$$

TABLE 3.6

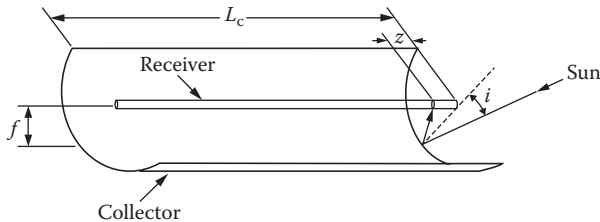
Incident Angle Modifier for Different PTC Solar Collectors

Solar Collector	Incident Angle Modifier Function, $K(i)$
LS-2	$1 + 0.000884 \frac{i}{\cos i} - 0.00005369 \frac{i^2}{\cos i}$
LS-3	$1 - 2.2307 \times 10^{-4} i - 1.1 \times 10^{-4} i^2$ + $3.18596 \times 10^{-6} i^3 - 4.85509 \times 10^{-8} i^4$
IST	$1 + 0.0003178 \frac{i}{\cos i} - 0.00003985 \frac{i^2}{\cos i}$
Euro Trough	$1 - 5.25097 \times 10^{-4} \frac{i}{\cos i} - 2.859621 \times 10^{-5} \frac{i^2}{\cos i}$

Source: Adapted from Vasquez-Padilla, R., Simplified methodology for designing parabolic trough solar power plants, PhD dissertation, University of South Florida, Tampa, FL, 2011.

**FIGURE 3.35**

Incidence angle modifier for different parabolic trough solar collectors—LS-2, LS-3, IST, and Euro Trough 9. (Adapted from Vasquez-Padilla, R., Simplified methodology for designing parabolic trough solar power plants, PhD dissertation, University of South Florida, Tampa, FL, 2011.)

**FIGURE 3.36**

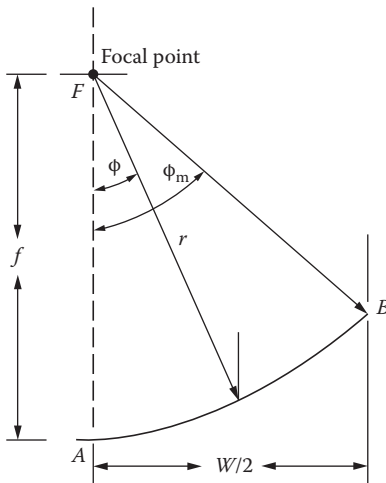
Geometrical end losses of a PTC.

where r is shown in Figure 3.37. Lippke (1995) proposed using $r = f$, which is used in many simulations (Patnode 2006; Stuetzle 2002).

Therefore,

$$F_{el} \approx 1 - \frac{f}{L_c} \tan i. \quad (3.113)$$

Gaul and Rabl (1979) suggest using an average value of r , which for a PTC of aperture width W , gives F_{el} as

**FIGURE 3.37**

Parabola geometry of a rim angle of ϕ_m . (Adapted from Lippke, F., Simulation of the part-load behavior of a 30 MWe SEGS plant. Tech. Rep., SAND-95-1293, Sandia National Labs., Albuquerque, NM, United States, 1995.)

$$F_{el} = 1 - \frac{f}{L_c} \cdot \frac{W^2}{1 + \frac{W^2}{48f^2}} \tan i. \quad (3.114)$$

Figure 3.38 shows that Gaul and Rabl's model gives slightly lower values of F_{el} .

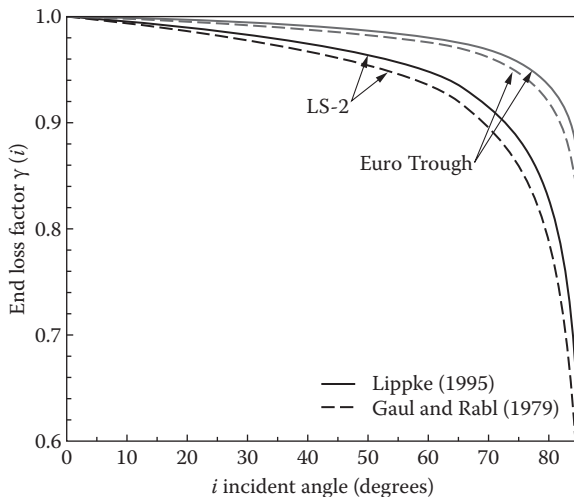
Finally, soiling of the mirror over time results in a loss, quantified by the soiling factor F_s . It is defined as the ratio of the average mirror reflectance in operation to the nominal reflectance when the mirror is clean (Zarza Moya 2012). For example, if the reflectance of the clean mirror is 0.95 and the mirror is washed when the reflectance falls to 0.9, then the average mirror reflectance is 0.925 and the F_s is $0.925/0.95 = 0.97$. Table 3.7 gives radiative properties of some heat collection elements.

Therefore, the optical efficiency of a PTC becomes

$$\eta_o = \eta_{o,peak} F_{el} F_s K(i) = \rho \tau \alpha \gamma F_{el} F_s K(i). \quad (3.115)$$

3.6.2 Thermal Losses from PTC

A major difference between a flat-plate collector and a concentrating collector, such as PTC, is that the losses for a PTC are from the receiver surface whose area is much smaller than the aperture area. However, the radiative

**FIGURE 3.38**

End loss factor for different PTC collectors based on Lippke (1995) and Gaul and Rabl (1979). (Adapted from Vasquez-Padilla, R., Simplified methodology for designing parabolic trough solar power plants, PhD dissertation, University of South Florida, Tampa, FL, 2011.)

TABLE 3.7

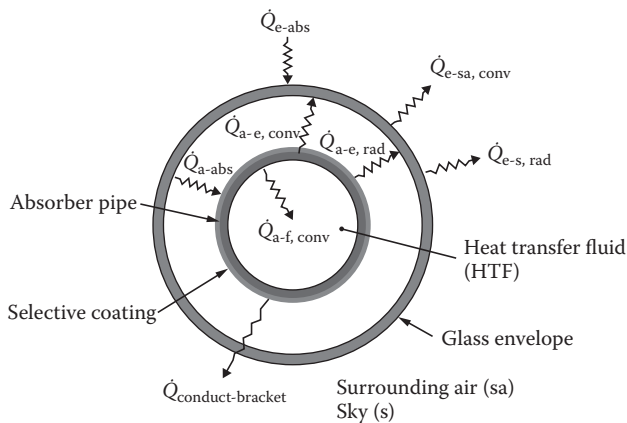
Radiative Properties for Different Heat Collection Elements

Selective Coating	Envelope Transmittance	Coating Absorptance	Coating Emittance	
			100°C	400°C
Luz black chrome	0.935	0.940	0.110	0.27
Luz cermet	0.935	0.920	0.060	0.15
Solel UVAC cermet a	0.965	0.960	0.070	0.13
Solel UVAC cermet b	0.965	0.950	0.080	0.15
Solel UVAC avg	0.965	0.955	0.076	0.14
Schott PTR70	0.96	0.95	—	0.1

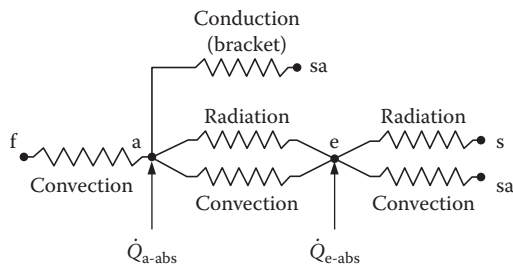
Source: Adapted from ASHRAE 96-1980, Methods of testing to determine the thermal performance of unglazed solar collectors, ASHRAE, Atlanta, GA.

losses are much higher since the receiver temperature T_r is much higher and the radiative losses are proportional to the fourth power of T_r . Figure 3.39 shows a cross section of the receiver-absorber indicating the energy transfers to and from the absorber.

A detailed heat-transfer model (see Figure 3.40) would consider the heat transfer from the absorber surface to the heat-transfer fluid (HTF) by conduction through the absorber tube and convection ($Q_{a-f, \text{conv}}$), heat loss from the

**FIGURE 3.39**

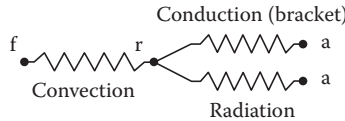
Heat transfer in a heat collection element. (Adapted from Adapted from Vasquez-Padilla, R., Simplified methodology for designing parabolic trough solar power plants, PhD dissertation, University of South Florida, Tampa, FL, 2011.)

**FIGURE 3.40**

Thermal resistance model.

absorber surface to the glass envelope by convection ($Q_{r-e, \text{conv}}$) and radiation ($Q_{r-e, \text{rad}}$), and heat transfer from the glass envelope to the ambient by convection ($Q_{e-a, \text{conv}}$) and radiation ($Q_{e-a, \text{rad}}$) including the radiative heat transmitted from the absorber through the glass. In addition, there is heat loss to the support brackets by conduction $Q_{\text{conduct-bracket}}$.

For simplification, if convective heat loss from the absorber is neglected because of vacuum, and the absorption of the glass envelope is neglected, the heat transfer could be represented by Figure 3.41 and the heat loss q_L may be written as

**FIGURE 3.41**

Simplified thermal resistance model.

$$q_L = A_k \frac{T_r - T_a}{R_k} + \varepsilon_r \sigma (T_r^4 - T_a^4) A_r, \quad (3.116)$$

where R_k is the composite thermal resistance of the support brackets and A_k is the effective area for conduction heat transfer.

3.6.3 Thermal Performance of PTC Collector

The thermal performance of a PTC collector can be analyzed similarly to that of a flat-plate collector by assuming an overall heat-loss coefficient U_c for the receiver/absorber. Therefore, the instantaneous efficiency η_c can be written as

$$\begin{aligned} \eta_c &= \frac{q_u}{I_c A_a} = \frac{q_{\text{absorbed}} - q_L}{I_c A_a} \\ &= \eta_o - U_c (T_r - T_a) A_r / I_c A_a \\ &= \eta_o - U_c \frac{T_r - T_a}{I_c} \cdot \frac{A_r}{A_a}, \end{aligned} \quad (3.117)$$

where T_r and A_r are the temperature and the area of the receiver and A_a is the aperture area of the collector.

The heat loss from a PTC depends on the absorber tube temperature and is typically measured experimentally at several temperatures in its working temperature range. Variation in the overall heat-loss coefficient is usually expressed as a second-degree polynomial equation:

$$U_c = a + b(T_r - T_a) + c (T_r - T_a)^2 \text{ W/m}^2\text{K}, \quad (3.118)$$

where coefficients a , b , and c are found experimentally. Table 3.8 gives these values for LS-3 collectors (Zarza Moya 2012). Typically, U_c for absorber tubes with good vacuum is less than 5 W/m².K.

TABLE 3.8Values of Coefficients a , b , and c for an LS-3 Collector

$T_{\text{absorber}} (\text{°C})$	a	b	c
<200	0.687257	0.001941	0.000026
>200; <300	1.433242	-0.00566	0.000046
>300	2.895474	-0.0164	0.000065

Source: Adapted from Lippke, F., Simulation of the part-load behavior of a 30 MWe SEGS plant, Tech. Rep., SAND-95-1293, Sandia National Labs., Albuquerque, NM, 1995.

3.7 Compound-Curvature Solar Concentrators

The collectors used for high-temperature solar processes are of the double-curvature type and require a tracking device with two degrees of freedom. Concentration ratios above 50 are generally used. Examples of concentrator designs include the following: spherical mirror, CR = 50–150; paraboloidal mirror, CR = 500–3000; Fresnel lens, CR = 100–1000; and Fresnel mirror, CR = 1000–3000. These concentrator types will be discussed briefly in this section.

3.7.1 Paraboloidal Concentrators

The surface produced by rotating a parabola about its optical axis is called a paraboloid. The ideal optics of such a reflector is the same, in cross section, as those of the parabolic trough described earlier in this chapter. However, owing to the compound curvature, the focus occurs ideally at a point instead of along a line. Figure 3.42 shows a commercial paraboloid collector.

**FIGURE 3.42**

Commercial paraboloidal solar concentrator.

The optical efficiency η_o (defined relative to the direct-normal solar flux) of a paraboloid is the product of six terms:

$$\eta_o = \rho \tau \alpha f \gamma(\psi_1, \psi_2) F(\psi_3), \quad (3.119)$$

where ρ is the mirror reflectance, τ is the receiver cover (if any) transmittance, α is the receiver absorptance, f is the fraction of the aperture not shaded by supports and absorber, γ is the intercept factor depending on mirror slope errors ψ_1 and the solar beam ψ_2 , and $F(\psi_3)$ is the tracking error factor where (ψ_3) is the angle between the solar direction and the aperture normal. The optical intercept factor for a paraboloid is given by (Ramsay et al. 1977)

$$\gamma(\psi_1, \psi_2) = 1 - \exp \left(-\frac{\pi D_r^2}{4\sigma^2} \right), \quad (3.120)$$

where D_r is the receiver diameter and σ^2 is the beam spread variance at the receiver. For a spherical segment receiver, σ^2 is given by (Duff and Lameiro 1974)

$$\sigma^2 = 2A_a \left(4\sigma_{\psi_1}^2 + \sigma_{\psi_2}^2 \right) (2 + \cos\phi)/3\phi\sin\phi, \quad (3.121)$$

where A_a is the aperture area, ϕ is the paraboloid rim half-angle, and σ_{ψ_1} and σ_{ψ_2} are the beam variances due to mirror surface errors and solar beam spread, respectively.

For a flat receiver with paraboloid optics, σ^2 is given by (Duff and Lameiro 1974)

$$\sigma^2 = 2A_a \left(4\sigma_{\psi_1}^2 + \sigma_{\psi_2}^2 \right) / \sin^2 \phi. \quad (3.122)$$

The concentration ratio of paraboloids can be determined easily from basic geometry. The aperture area is πR^2 , where R is the aperture radius and the area for a spherical receiver is $4\pi R_r^2$, where R_r is the spherical receiver radius. If the receiver is only a spherical segment, not a complete sphere, the receiver area to be used below is ΩR_r^2 , where Ω is the segment included solid angle, instead of $4\pi R_r^2$. The receiver radius for perfect optics is sized to collect all rays with the acceptance half-angle θ_{max} . Hence,

$$R_r = (R/\sin \phi)\sin \theta_{max}. \quad (3.123)$$

Therefore, the concentration CR is

$$CR = (\pi R^2) / [4\pi \times (R/\sin \phi)^2 \sin^2 \theta_{max}],$$

or

$$CR = \sin^2 \phi / (4\sin^2 \theta_{max}). \quad (3.124)$$

The small effect of absorber shading of the mirror is ignored. Its inclusion would reduce CR given by Equation 3.124. For $\theta_{max} = 1/4^\circ$ (the sun's half-angle), $CR \sim 13,000$ if $\phi = 90^\circ$. For $\theta_{max} = 1/2^\circ$, $CR \sim 3300$, and for $\theta_{max} = 1^\circ$, $CR \sim 800$. Note

that concentrations for this configuration are one-fourth the thermodynamic limit, which is $(\sin \theta_{\max})^{-2}$ for compound-curvature collectors. See Equation 3.89.

For a flat absorber, the concentration for perfect optics is

$$CR = \sin^2 \phi \cos^2 (\phi + \theta_{\max}) / \sin^2 \theta_{\max}, \quad (3.125)$$

where the small effect of mirror shading by the absorber is again ignored.

Example 3.4

Calculate the concentration ratio and diameter of a flat receiver for a 10-m-diameter paraboloid concentrator that is designed to accept 90% of the incident beam radiation. The rim half-angle is 90° and the mirror surface variance $\sigma_{\psi_1}^2$ is expected to be $(0.25^\circ)^2$. Assume that the standard deviation for the sun's disk is 0.125° .

Solution

From Equation 3.120,

$$\pi D_r^2 / 4\sigma^2 = -\ln(1 - 0.90) = 2.303,$$

and from Equation 3.122,

$$\begin{aligned} \sigma^2 &= 2A_a \left(4\sigma_{\psi_1}^2 + \sigma_{\psi_2}^2 \right) / \sin^2 \phi \\ &= 2 \times (\pi/4 \times 10^2) \cdot 4 \times (0.25)^2 + (0.125)^2 \cdot (\pi/180)^2 / \sin^2 90^\circ \\ &= 0.0127 \text{ m}^2 (\sigma = 11.3 \text{ cm}). \end{aligned}$$

Solving the first equation for D_r ,

$$D_r = [2.303 \times 4 \times \sigma^2 / \pi]^{1/2} = 0.193 \text{ m.}$$

The concentration ratio is

$$CR = A_a / A_r = \frac{\pi \times 10^2 / 4}{\pi (0.193)^2 / 4} = 2685.$$

Note that the effect of tracking error ψ_3 can be included in the intercept factor $\gamma(\psi_1, \psi_2)$ by defining an appropriate $\sigma_{\psi_3}^2$ and adding it to the slope and solar image variances in Equations 3.121 and 3.122.

The thermal losses from a paraboloid are quite small and primarily radiative. Since the absorber area is so small, it is generally not worthwhile to use any type of convection-suppressing cover. For example, consider the thermal losses from a planar absorber of $CR = 1500$ paraboloid with a receiver surface temperature of 600°C . For a cavity absorber ($\epsilon_{ir} \sim 1.0$), the radiation heat loss is approximately 20 W/m^2 aperture if the ambient temperature is 60°C . For a typical convection coefficient in light winds of $25 \text{ W/m}^2\text{ }^\circ\text{C}$, the convection loss is approximately 10 W/m^2

aperture. If the insolation is 900 W/m^2 and the optical efficiency is 65%, the total heat loss at 600°C represents less than 6% of the absorbed flux. Stated another way, the collector loss coefficient U_c at 600°C is only $0.064 \text{ W/m}^2\text{°C}$. The performance of high-concentration paraboloids is, therefore, much more sensitive to optical properties than to thermal losses.

Recent developments in paraboloidal concentrators include multifaceted mirror concentrators, single-faceted stretched-membrane mirror concentrators, and multifaceted stretched-membrane mirror concentrators. Figure 3.43 shows examples of such commercially developed paraboloidal concentrators.



(a)



(b)

FIGURE 3.43

Examples of commercially developed multifaceted and stretched-membrane paraboloidal concentrators: (a) multifaceted mirror, (b) stretched single membrane (Schlaich Bergermann & Partner, Germany).

3.7.2 Spherical Concentrators

A second type of compound-curvature collector uses spherical geometry instead of parabolic geometry. Figure 3.44c shows ray traces in a plane of symmetry for normal incidence (two-axis tracking) on a spherical concentrator. Spherical aberration is seen to be present and causes the reflected flux to be along a line instead of at a point as is the case for other compound-curvature mirrors. It is also clear that rays intercepted near the pivot end of

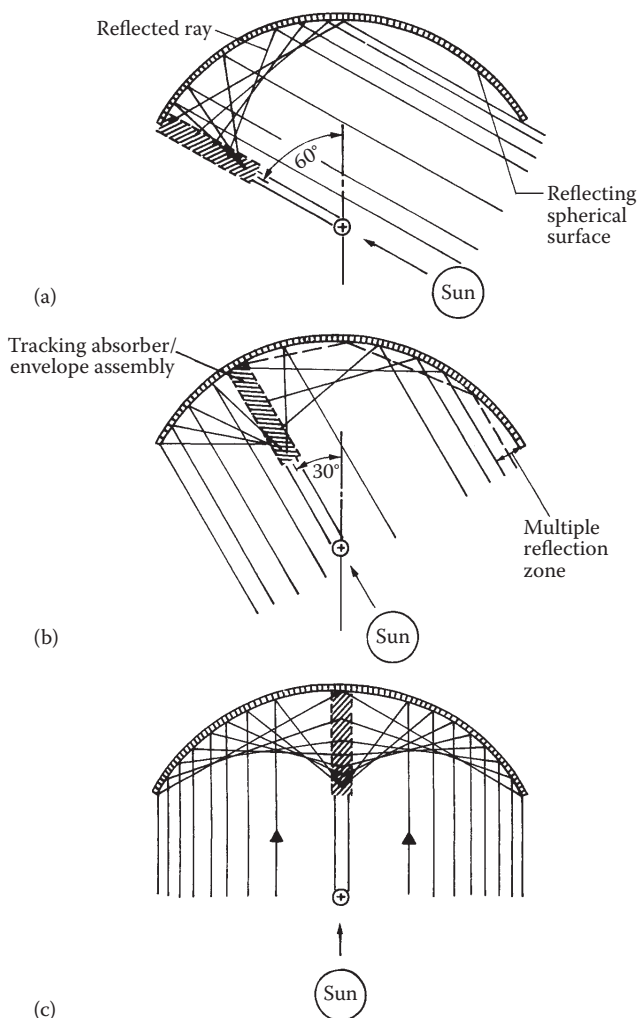


FIGURE 3.44

Ray traces for a fixed spherical concentrator for three incidence angles: (a) normal incidence for two-degree-of-freedom tracking of the mirror; (b and c) off-normal incidence for a fixed mirror and a moving absorber.

the absorber intercept the absorber at very large incidence angles. Therefore, an absorber envelope with very low reflectance or no envelope at all is used to avoid severe penalties to the optical efficiency.

The concentration ratio of a spherical concentrator can be calculated from the definition of CR:

$$CR = A_a / A_r = \pi R_o^2 \sin^2 \phi / \pi D_r L_r. \quad (3.126)$$

Taking the receiver length $L_r = R_o/2$,

$$CR = (2R_o / D_r) \sin^2 \phi. \quad (3.127)$$

If the absorber is a cylinder and is to intercept all singly reflected rays within the acceptance half-angle θ_{\max} ,

$$D_r = 2R_o \sin \theta_{\max}, \quad (3.128)$$

and

$$CR = \sin^2 \phi / \sin \theta_{\max}, \quad (3.129)$$

if the acceptance half-angle is $1/4^\circ$ for $\phi = 90^\circ$, $CR = 229$; for $\theta_{\max} = 1/2^\circ$, $CR = 115$ for perfect optics. It is obvious that the spherical concentrator cannot achieve concentration ratios approaching those of paraboloids owing to spherical aberration and hence this concentrator is much more sensitive to operating temperature than the point-focus type.

The efficiency of this concentrator is lower than that of other compound-curvature devices, because of smaller CR values; therefore, the unit cost of solar heat will be higher. One method of reducing the unit cost is to use the concentrator with a *fixed mirror*, thereby eliminating the expensive mirror tracking and structural components. This configuration is known as a stationary reflector tracking absorber (SRTA) concentrator. The collector is kept "in focus" by tracking only the absorber, aiming it directly at the sun's center. However, the effective aperture in this fixed mirror mode is reduced by the cosine of the incidence angle. Hence, the saving in cost by eliminating the reflector tracker is partly offset by reduced energy capture. If a value of rim half-angle $\phi = 60^\circ$ is used as shown in Figure 3.44 and if the fixed aperture faces the sun directly at noon, then the daylong cosine penalty will reduce the captured flux by approximately 17%. Of course, if the aperture does not directly face the sun at noon, the cosine loss will be larger.

3.7.3 Compound Parabolic Concentrator

A nonimaging concentrator concept called the compound parabolic concentrator (CPC) was developed by Winston (1974, 1975) and Rabl (1975, 1976a,b)

and described by Baranov and Melnikov (1966). The CPC can approach the thermodynamic limit of concentration discussed earlier; that is,

$$CR_{CPC} = CR_{max,2D} = 1/\sin \theta_{max}.$$

Figure 3.45 shows a schematic cross section of the original CPC concept. It is seen to be formed from two distinct parabolic segments, the foci of which are located at the opposing receiver surface end points. The axes of the parabolic segments are oriented away from the CPC axis by the acceptance angle θ_{accept} . The slope of the reflector surfaces at the aperture is parallel to the CPC optical axis. Figure 3.46 is a photograph of a CPC collector.

Different types of planar and tubular receivers have been proposed for CPCs. Of most interest in this book is the tubular-type receiver shown in Figure 3.47 since high-pressure heat-transfer fluid can flow through it.

3.7.4 Optical Analysis of CPC Collector

A number of the optical losses present in tracking collectors described above are negligible in CPC collectors because of their broad acceptance band and ability to use imprecise optical elements. Some of the optical loss mechanisms listed in Section 3.6.1 are reduced or nonexistent in CPCs.

The three optical parameters—mirror reflectance, cover transmittance, and absorber absorptance—are first-order effects for CPCs. Mirror reflectance

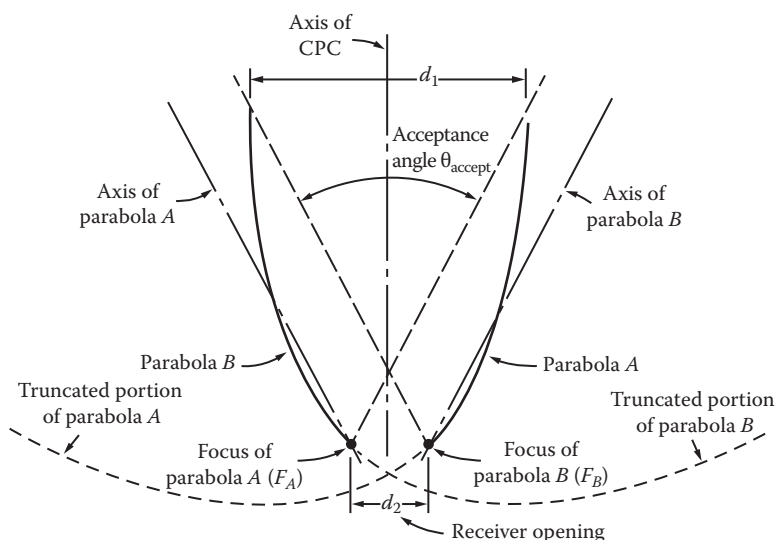
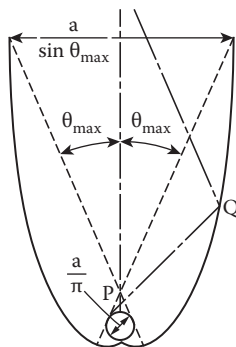


FIGURE 3.45

Schematic cross section of a CPC showing parabolic segments, aperture, and receiver.

**FIGURE 3.46**

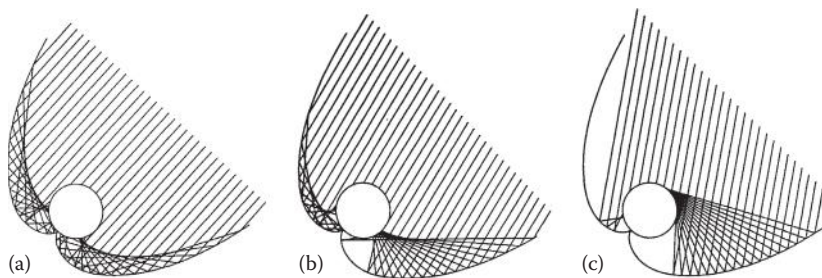
Commercial CPC collector module using an evacuated tubular receiver. (Courtesy of MHG Heating, UK.)

**FIGURE 3.47**

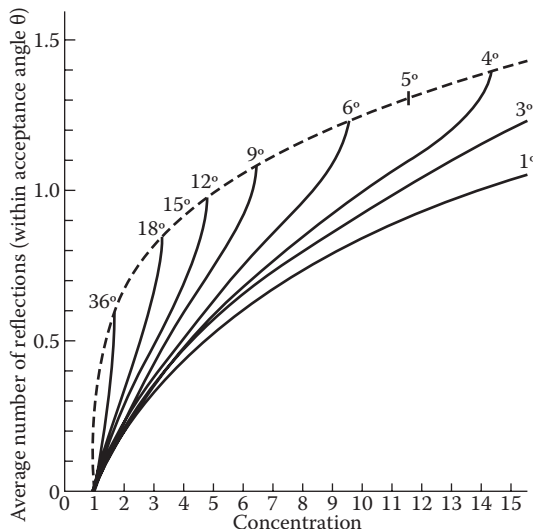
CPC collector concept with tubular receiver.

effects are slightly different for a CPC than for other line-focus reflectors since the CPC does not form a sharp image of the sun at the absorber. Figure 3.48 shows that some solar radiation incident near the aperture edges is reflected more than once on its way to the absorber. The effect of multiple reflectance can be simply accounted for in optical efficiency calculations, to lowest order, by using $\rho_m^{\bar{n}}$, where \bar{n} is the average number of reflections of all incident rays over the aperture. Some effect of incident angle on \bar{n} has been noted but Rabl (1976a) recommends the use of a constant \bar{n} for engineering purposes.

Figure 3.49 can be used to determine the average number of reflections \bar{n} for various concentration ratios CR for the basic CPC in Figure 3.45. For tubular receiver CPCs (Figure 3.47), \bar{n} should be increased by approximately 0.5 over the Figure 3.49 values. The dashed line in Figure 3.49 represents \bar{n} for a fully developed CPC. Since the upper half of the reflector for most CPCs is

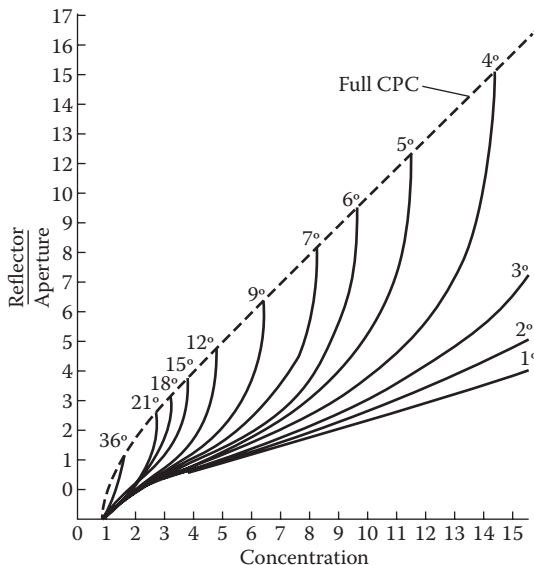
**FIGURE 3.48**

Ray trace diagrams of the tubular CPC collector at three values of incidence angle: (a) normal incidence, (b) intermediate, and (c) the limit of acceptance. (Courtesy of W. McIntire, Argonne National Laboratory.)

**FIGURE 3.49**

Average number of reflections for the basic CPC as a function of CR. The dashed line represents a full CPC. The number reflections for various truncations can be determined by using Figure 3.53 along with this figure. Values of acceptance angle are shown on the upper curve. (From Hsieh, C.K., *Sol. Energy* 27: 19, 1981.)

nearly parallel to the optical axis, it affords little concentration effect. In practice, the upper portion (approximately 40%–60% of the mirror) is normally eliminated to reduce CPC size and cost. Figure 3.50 shows the concentration achievable for various truncation amounts. This CR value and the corresponding value of acceptance angle then determine a point on the \bar{n} – CR map (Figure 3.49), and \bar{n} can be evaluated for any truncation. For careful designs, a ray trace procedure must be used to find \bar{n} and its dependence on incidence angle.

**FIGURE 3.50**

Effect of truncation on the basic CPC concentration ratio for various values of acceptance angle. (From Hsieh, C.K., *Sol. Energy* 27: 19, 1981.)

A final consideration in the optical analysis of the CPC family is the effect of partial acceptance of diffuse radiation. Equation 3.101 showed that at least $(CR)^{-1}$ of the incident diffuse flux reached the absorber. Since CPC collectors operate in the concentration range of 2 to 10 to capitalize on the corresponding reduced tracking requirement, from one-half to one-tenth of the incident diffuse radiation is accepted. This property of CPCs is conveniently included in the CPC optical efficiency by defining the intercept factor γ used for PTC analysis somewhat differently. If γ is defined as the fraction of total radiation accepted by a CPC, it can be expressed as

$$\gamma = [I_{b,c} + I_{d,c}/CR]/I_{tot,c} \quad (3.130)$$

where subscripts "b," "d," and "tot" refer to beam, diffuse, and total flux incident on the collector aperture, respectively.

The optical efficiency of a CPC can then be written as*

$$\eta_o = \rho_m^{\bar{n}} \tau_r \alpha_r \gamma. \quad (3.131)$$

* For the tubular receiver CPC, a small gap of width g is required between the mirror cusp and the absorber pipe to accommodate the absorber envelope. Some otherwise collectable rays escape the receiver at this point, reducing the optical efficiency by the factor $(1 - g/p_r)$, where p_r is the absorber perimeter. Other design details are given in Collares-Pereira and Rabl (1979).

γ depends on the characteristics of local solar flux and is not a purely geometric factor such as $\gamma(\psi_1, \psi_2)$. For the tubular CPC, $\bar{n} \sim 1.2$, $\rho_m \sim 0.85$, $\alpha_r \sim 0.95$, $\gamma \sim 0.95$, and $\tau_r \sim 0.90$. Therefore, $\eta_o \sim 0.67$. If an etched glass cover is used, $\eta_o \sim 0.71$. These values of optical efficiency are 7%–8% greater than those for a PTC device. Improved optical efficiency partially offsets the lower concentration and associated heat loss effect usually imposed on CPCs ($CR < 10$) in order to benefit from their reduced tracking requirements.

3.7.5 Thermal Performance of the CPC Collector

For a tubular receiver CPC, the same heat-loss analysis can be used as for a PTC collector with a tubular receiver. Some uncertainty in the convection heat loss from the tube to the environment exists, since the tube is in a partial enclosure and protected from the environment.

The thermal efficiency of a CPC (based on total beam and diffuse collector plane flux) is given by

$$\eta_c = \rho_m^{\bar{n}} \tau_r \alpha_r \gamma - U_c (T_r - T_a) / (I_c CR), \quad (3.132)$$

where U_c is based on the aperture area.

By analogy with the PTC analysis developed earlier for an evacuated receiver,

$$U_c = \epsilon_e \sigma (T_r^2 + T_a^2) (T_r + T_a) + (A_k / A_a) (1/R_k) (CR), \quad (3.133)$$

where R_k is the conduction heat-transfer resistance for all conduction paths of total effective area A_k . Hsieh (1981) and Hsieh and Mei (1983) presented a detailed thermal analysis of a CPC with an evacuated tubular selective coated receiver and the entire collector covered with a transparent cover. They proposed the following empirical equations for the heat-loss coefficient U_c .

$$\text{For } 29^\circ\text{C} \leq (T_r - T_a) \leq (137 + 0.0283T_a - 0.0000616T_a^2), \\ U_c = (0.18 + 16.95\epsilon_r)[0.212 + 0.00255T_a + (0.00186 + 0.000012T_a)(T_r - T_a)], \quad (3.134a)$$

$$\text{and for } (137 + 0.0283T_a - 0.0000616T_a^2) \leq (T_r - T_a) \leq 260^\circ\text{C}, \\ U_c = (0.168 + 17.16\epsilon_r)[0.086 + 0.00225T_a + (0.00278 + 0.000014T_a)(T_r - T_a)], \quad (3.134b)$$

where U_c is the collector loss coefficient (W/Km^2) of the absorber area, T_r is the receiver (absorber) temperature ($^\circ\text{C}$), T_a is the ambient temperature ($^\circ\text{C}$), and ϵ_r is the emissivity of the absorber surface.

These empirical equations are valid under the following conditions: $\epsilon_r = 0.05$ to 0.2, wind velocity $V = 0$ to 10 m/s, concentration $C = 1.5$ to 6; correspondingly, average number of reflections $\bar{n} = 0.55$ to 1.05, ambient temperature $T_a = -10^\circ\text{C}$ to 35°C , total radiation $I_t = 720$ to 1200 W/m^2 aperture area, diffuse-to-beam radiation ratio $I_d/I_b = 0.1$ to 0.5.

3.8 Central Receiver Collector

A central receiver collector consists of a large field of mirrors on the ground that track the sun in such a way that the reflected radiation is concentrated on a receiver/absorber on top of a tower. The mirrors are called *heliostats*. Central receivers can achieve temperatures of the order of 1000°C or even higher. Therefore, a central receiver concentrator is suitable for thermal electric power production in the range of 10–1000 MW. The concept of a central receiver solar thermal power has been known for a long time. Francia (1968) built a pilot model of a solar power tower plant in 1967 at the University of Genoa, Italy. Since the early 1970s, when the power tower concept was first proposed by Hildebrandt and Vant-Hull (1974), the central receiver technology has been actively developed in the United States. Since then, the technology has been pursued in Germany, Spain, Switzerland, France, Russia, Italy, and Japan (DeLaquil et al. 1993).

A central receiver collector consists of a heliostat field, a receiver/absorber, and the tracking controls for the heliostats. Since central receiver collectors are used to produce very high temperatures, which are used to produce thermal power, this topic is dealt in detail in Chapter 8.

3.9 Fresnel Reflectors and Lenses

If the smooth optical surface of a reflector or a lens can be broken into segments to achieve essentially the same concentration, the resulting concentrator is called the Fresnel concentrator. Figure 3.51 shows examples of a Fresnel mirror and a Fresnel lens. Use of Fresnel reflectors for large collectors reduces the wind load and simplifies manufacture. A Fresnel lens can achieve a concentration close to a corresponding plano convex lens with far less material and lower manufacturing costs. However, a disadvantage is that the facet edges become rounded in the manufacturing process, which makes the edges ineffective.

Off-normal incidence effects are present in a Fresnel device owing to the change in focal length with incidence angle.

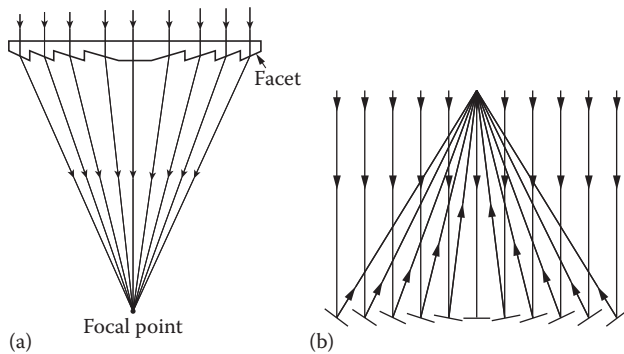


FIGURE 3.51
Fresnel concentrators: (a) lens, (b) mirror.

Figure 3.52 shows the focal point for normal and nonnormal incidence. Note that the effect of the shortened focal length is to cause the sun's image to appear wider at the nominal focal plane during off-normal periods. Figure 3.53 shows the decrease in focal length that occurs for various off-normal conditions (Collares-Pereira et al. 1977; Rabl 1978). It is seen that a $\pm 60^\circ$ excursion, which would be encountered for 8 h of collection at the equinoxes in an east–west axis alignment, would diminish the focal length by two-thirds. Hence, the Fresnel line-focus device with $CR > 10$ is restricted to a north–south orientation ($\pm 35^\circ$ excursion over a year) if the majority of daylight hours are to be collection hours.

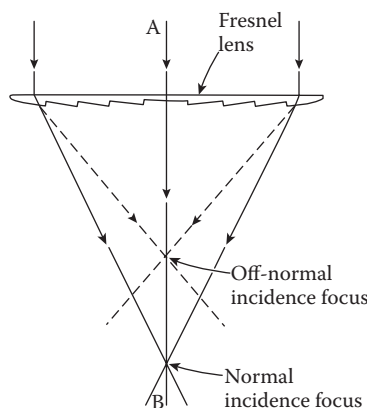
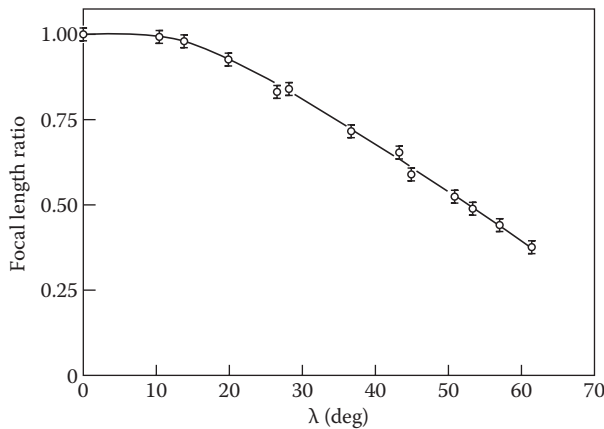


FIGURE 3.52
Line-focus Fresnel lens concentrator section showing nominal focus for normal incidence and shortened focal length at off-normal incidence.

**FIGURE 3.53**

Effect of off-normal incidence angle λ (measured in plane AB out of the plane of Figure 3.52) on apparent focal length of a line-focus Fresnel lens. The focal length ratio is the focal length at $\lambda \neq 0$ divided by the focal length at $\lambda = 0$ (i.e., normal incidence). (From Rabl, A., *Proc. Sol. Thermal Cone. Coll. Tech. Symp.*, B. Gupta, ed. Denver, CO, 1–42, 1978.)

3.10 Solar Concentrator Summary

Figure 3.54 contains a summary of all important optical properties of the common reflecting solar concentrators:

Concentration ratio, CR

Average number of reflections, \bar{n}

Capture parameter, γ

Beam spread variance, σ^2

The CR standard of comparison is the thermodynamic limit derived in Section 3.5.1. It is seen that all concentrators except the CPC family fall short of the ideal limit by a factor of 3 or more. For any meaningful concentration and rim half-angles $\phi > 45^\circ$, the SRTA is seen to fall short of the ideal limit by the greatest amount because of its focal aberration.

The optical parameter γ and its independent variable σ have been developed using analyses analogous to that used for the PTC collector. Duff and Lameiro (1974) have also derived expressions for σ for reflector systems with flat mirror segments instead of curved ones. They are slightly different in form from those in Figure 3.54 but are developed by using the same analysis method.

Collector parameter	Single curvature			Compound curvature		
	Nonimaging CPC family	Parabolic mirror	Cylindrical receiver	Spherical receiver	Paraboloidal mirror	Spherical mirror cylindrical receiver
CR/CR _{max} for perfect optics	1.0	$\frac{\sin \phi^a}{\pi}$	$\sin \phi \cos(\phi + \theta_{\max})$ $- \sin \theta_{\max}$	$\frac{\sin^2 \phi^a}{4}$	$\sin^2 \phi \cos^2 (\phi + \theta_{\max})$ $- \sin^2 \theta_{\max}$	$2 \sin^2 \phi \sin^2 \theta_{\max}$
\bar{n}	0.7–1.2	1.0	1.0	1.0	1.0	1.0
γ	$\frac{1}{1 + \sigma_\theta \cot \theta_{\max}}^b$	$\frac{1}{\sqrt{2\pi}\sigma} \int_{L_c/2}^{L_c/2} \exp\left[-\frac{1}{2} \left(\frac{y}{\sigma_y}\right)^2\right] dy$	#	$1 - e^{-\left(\frac{L_c/\sigma}{\sigma}\right)}$		(No closed-form expression)
σ^2	—	$\frac{A_a^2 \sigma_0^2 (2 + \cos \phi)}{12 \phi \sin \phi}$		$\frac{2 A_a^2 \sigma_0^2 (2 + \cos \phi)}{3 \phi \sin \phi}$	$\frac{2 A_a^2 \sigma_0^2}{\sin^2 \phi}$	(No closed-form expression)
L_c	$\frac{D_r}{2}$	$\frac{D_r}{2}$	$\frac{D_r}{2}$	$\frac{\pi D_r^2}{4}$	$\frac{\pi D_r^2}{4}$	$\frac{D_r}{2}$
A_a	Aperture width	Aperture width	Aperture width	Aperture area		

^a For Fresnel mirror arrangements or power towers, multiply expressions given by the ground cover fraction. It is usually on the order of 1/2.
^b Approximate expression for radiation incident near the limits of acceptance only; otherwise, $\delta = 1.0$.

$$\left\{ A_a^2 \left(4\sigma_{\psi_1}^2 + \sigma_{\psi_2}^2 \right) \left[\frac{-1}{3\sin^2 \phi \cos \phi} + \frac{2}{3\sin^3 \phi} + \frac{2}{\sin \phi} - \frac{\cos \phi}{3\sin \phi} - \frac{2\phi}{\sin \phi} + \frac{4\sin \phi}{3\cos \phi} - \ln \tan \left(\frac{\pi}{4} + \frac{\phi}{2} \right) + \ln \tan \left(\frac{\pi}{4} - \frac{\phi}{2} \right) \right] \right\}^{1/2}$$

Duff (1976) has given an alternative expression for ϕ^2 in which a different integration procedure was used.

FIGURE 3.54

Comparison of design parameters of solar concentrators. CR_{max} = thermodynamic limit to concentrations (see Equations 3.90 and 3.91); L_c = characteristic dimension of receiver; D_r = receiver diameter or width; θ_{\max} = acceptance angle; ϕ = mirror rim half-angle; $\sigma_0^2 = 4\sigma_{\psi_1}^2 + \sigma_{\psi_2}^2$; γ = optical capture factor; \bar{n} = average number of reflections. (Adapted from Duff, W.S., and G.F. Lameiro, A performance comparison method for solar concentrators, ASME Paper 74-WA/Sol-4, New York, 1974.)

Thermal properties of concentrators cannot be summarized conveniently since they are complex functions of surface properties, geometry, and conduction-convection suppression techniques. Each collector concept must be analyzed using the approach described in detail for the PTC.

Figure 3.55 summarizes the equations most often used for calculation of the incidence angles of beam radiation on the aperture of all common types of solar collectors. These equations are used to calculate daylong energy delivery of both concentrators and flat-plate collectors. A complete discussion of incidence angles is contained in Chapter 2.

In order to apply the method of Section 2.6.1 to find monthly averaged daily solar radiation on a tracking solar concentrator, the tilt factors in Equation 2.64 must be continuously changed owing to tracking. Collares-Pereira and Rabl have given expressions for various modes of tracking that can be used to calculate \bar{H}_c as

$$\bar{H}_c = \bar{r}_T - \bar{r}_d (\bar{D}_h / \bar{H}_h) \bar{H}_h. \quad (3.135)$$

Equations for \bar{r}_T and \bar{r}_d are given in Figure 3.56. The collection start (or stop) time, h_{coll} , used in Figure 3.56 represents the time measured from solar noon at which the collector starts (or stops) operating.

Orientation of collector	Incidence factor $\cos i$
Fixed, horizontal, plane surface	$\sin L \sin \delta_s + \cos \delta_s \cos h_s \cos L$
Fixed plane surface tilted so that it is normal to the solar beam at noon on the equinoxes	$\cos \delta_s \cos h_s$
Rotation of a plane surface about a horizontal east–west axis with a single daily adjustment permitted so that its surface normal coincides with the solar beam at noon every day of the year	$\sin^2 \delta_s + \cos^2 \delta_s \cos h_s$
Rotation of a plane surface about a horizontal east–west axis with continuous adjustment to obtain maximum energy incidence	$\sqrt{1 - \cos^2 \delta_s \sin^2 h_s}$
Rotation of a plane surface about a horizontal north–south axis with continuous adjustment to obtain maximum energy incidence	$[(\sin L \sin \delta_s + \cos L \cos \delta_s \cos h_s)^2 + \cos^2 \delta_s \sin^2 h_s]^{1/2}$
Rotation of a plane surface about an axis parallel to the earth's axis with continuous adjustment to obtain maximum energy incidence	$\cos \delta_s$
Rotation about two perpendicular axes with continuous adjustment to allow the surface normal to coincide with the solar beam at all times	1

FIGURE 3.55

Incidence angle factors for various orientations and motions of solar collectors. The incidence factor denotes the cosine of the angle between the surface normal and the solar beam.

Collector type	r_T^{abc}	r_d^d
Fixed aperture concentrators that do not view the foreground	$[cos(L - \beta)]/(d cos L) \{ -ah_{coll}cos h_{sr}(i = 90) + [a - b cos h_{sr}(i = 90) sin h_{coll} + (b/2)(sin h_{coll} cos h_{sr} + h_{coll})]$	$(sin h_{coll}/d) \{ [cos(L + \beta)/cos L] - [1/(CR)] \} + (h_{coll}/d) \{ [cos h_{sr}(\alpha = 0)/(CR)] - [cos(L + \beta)/cos h_{sr}(i = 90)] \}$
East–west axis tracking ^e	$\frac{1}{d} \int_0^{h_{coll}} \{[(a + b cos x)/cos L] \times \sqrt{\cos^2 x + \tan^2 \delta_s} dx$	$\frac{1}{d} \int_0^{h_{coll}} \{[1/cos L] \times \sqrt{\cos^2 x + \tan^2 \delta_s} - [1/(CR)] [\cos x - \cos h_{sr}(\alpha = 0)]\} dx$
Polar tracking	$(ah_{coll} + b sin h_{coll})/(d cos L)$	$(h_{coll}/d) \{[1/cos L] + [cos h_{sr}(\alpha = 0)/(CR)] - \sin h_{coll}/[d(CR)]\}$
Two-axis tracking	$(ah_{coll} + b sin h_{coll})/(d cos \delta_s cos L)$	$(h_{coll}/d) \{[1/cos \delta_s cos L] + [cos h_{sr}(\alpha = 0)/(CR)] - \sin h_{coll}/[d(CR)]\}$

^a $a = 0.409 + 0.5016 \sin[h_{sr}(\alpha = 0) - 60^\circ].$

^b $b = 0.6609 - 0.4767 \sin[h_{sr}(\alpha = 0) - 60^\circ].$

^c $d = \sin h_{sr}(\alpha = 0) - h_{sr}(\alpha = 0) \cos h_{sr}(\alpha = 0).$

^d CR is the collector concentration ratio.

^e Elliptic integral tables to evaluate terms of the form of $\int_0^h \sqrt{\cos^2 x + \tan^2 \delta_s} dx$ contained in r_T and r_d are given in the Appendix. Use the identity $\cos \delta_s = \sin(90^\circ - \delta_s)$ and multiply the integral by $\cos \delta_s$ a constant. For computer implementation, a numerical method can be used. For hand calculations, use Weddle's rule or Cote's formula.

FIGURE 3.56

Parameters r_T and r_d used to calculate monthly solar flux incident on various collector types. (From Collares-Pereira, M. and A. Rabl, *Sol. Energy* 23: 235–254, 1979.) (The collection hour angle value h_{coll} not used as the argument of trigonometric functions is expressed in radians. Note that the total interval $2 h_{coll}$ is assumed to be centered about solar noon.)

PROBLEMS

- Calculate the heat-removal factor for a collector having an overall heat-loss coefficient of $6 \text{ W/m}^2\text{K}$ and constructed of aluminum fins and tubes. Tube-to-tube centered distance is 15 cm; fin thickness is 0.05 cm; tube diameter is 1.2 cm; fluid tube heat-transfer coefficient is $1200 \text{ W/m}^2\text{K}$. The cover transmittance to solar radiation is 0.9 and is independent of direction. The solar absorptance of the absorber plate is 0.9, the collector is 1 m wide and 3 m long, and the water flow rate is 0.02 kg/s . The water temperature is 330 K.
- Calculate the efficiency of the collector described in Problem 1 on March 1 at a latitude of 40°N between 11 a.m. and 12 noon. Assume that the total horizontal insolation is 450 W/m^2 , the ambient temperature is 280 K, and the collector is facing south.
- Calculate the plate temperature in Example 3.2 at 10 a.m., if the absorbed insolation during the first 3 h is 0, 150, and 270 W/m^2 and the air temperature is 285 K.
- Calculate the overall heat-transfer coefficient, neglecting edge losses, for a collector with a double glass cover, with the following specifications:

Plate-to-cover spacing	3 cm
Plate emittance	0.9
Ambient temperature	275 K
Wind speed	3 m/s
Glass-to-glass spacing	3 cm
Glass emittance	5 cm
Back insulation thickness	5 cm
Back insulation thermal conductivity	$0.04 \text{ W/m}\cdot\text{K}$
Mean plate temperature	340 K
Collector tilt	45°

- The graph in Figure 3.20 gives the results of an ASHRAE standard performance test for a double-glazed flat-plate collector. If the transmittance for the glass is 0.90 and the absorptance of the surface of the collector plate is 0.92, determine the following:

The collector heat-removal factor F_R

The overall heat-loss conductance of the collector U_c in $\text{W/m}^2\text{K}$

The rate at which the collector can deliver useful energy in W/m^2 when the insolation incident on the collector per unit area is 600 W/m^2 , the ambient temperature is 5°C , and inlet water is at 15°C

The maximum flow rate through the collector, with cold water entering at a temperature of 15°C, that will give an outlet temperature of at least 60°C if this collector is to be used to supply heat to a hot-water tank. Area of the collector is 4 m².

6. Standard tests on a commercially available flat-plate collector gave a thermal efficiency of

$$\eta = 0.7512 - 0.138(T_{f,in} - T_a)/I_c$$

$$K_{ra} = 1 - 0.15(1/\cos(i) - 1)$$

where $(T_{f,in} - T_a)/I_c$ is in °C·m²/W.

Find the useful energy collected from this collector each hour and for the whole day in your city on September 15.

Assume that all the energy collected is transferred to water storage with no losses. Calculate the temperature of the storage for each hour of the day. Assume a reasonable ambient temperature profile for your city.

Given:

Collector area = 6 m²

Collector tilt = 30° (south facing in the Northern Hemisphere, north facing in the Southern Hemisphere)

Storage volume = 0.3 m³ (water)

Initial storage temperature = 30°C

7. What is the second law efficiency of a flat-plate collector operating at 70°C if the environmental temperature is 10°C and the collector efficiency is 50%? Compare with a single-curvature concentrator operating at 200°C and with a double-curvature concentrator operating at 2500°C, all with first law efficiencies of 50%.
8. Show that the plate efficiency F' for an air-cooled flat-plate collector is given by Equation 3.57.
9. The heat-removal factor F_R permits solar collector delivery to be written as a function of collector fluid *inlet* temperature T_f in Equation 3.48. Derive the expression for a factor analogous to F_R , relating collector energy delivery to fluid *outlet* temperature.
10. In nearly all practical situations, the argument of the exponential term in Equation 3.45 for F_R is quite small. Use this fact along with a Taylor's series expansion to derive an alternate equation for F_R . Determine the range where the alternate equation and Equation 3.45 agree to within 1%.
11. The stagnation temperature $T_{c,max}$ of a solar collector corresponds to the temperature at the zero efficiency point, that is, the no net

energy delivery point. Using Equation 3.76, calculate the stagnation temperature of a flat-plate collector with 75% optical efficiency and a U_c value of 4.5 W/m²K if the insolation is 900 W/m² and the ambient temperature is 20°C.

12. Calculate the stagnation temperature of the collector in Problem 12 if it were used with an optical booster of concentration ratio 2.0 having an optical efficiency of 70%.
13. What is the operating temperature for an evacuated-tube collector operating at 50% efficiency if the insolation is 800 W/m²? Use data from Figure 3.21.
14. A method of reducing heat loss from a flat-plate collector is to pull a partial vacuum in the dead air spaces between cover plates. What vacuum level is required to completely eliminate convection in a single cover flat-plate collector operating at 85°C and tilted at 45° if the cover plates are at 40°C and are spaced 2 cm apart? See Equation 3.57.
15. Derive an expression for the heat-loss conductance U_c for a flat-plate collector in which convection and conductance are completely eliminated in the air layers by use of a hard vacuum.
16. The effect of air flow rate in an air-cooled flat-plate collector appears in the heat-removal factor F_R (Equation 3.58). Calculate the effect of doubling the flow rate on the heat-removal factor for the collector analyzed in Example 3.3. What percentage increase in energy delivery would be achieved by doubling the fan size?
17. What are the maximum concentration ratios for trough concentrators with acceptance angles of 10°, 25°, and 36°?
18. What is the maximum achievable temperature of a double-curvature concentrator with a concentration ratio of 5000, a nonselective surface, and an 80% transmittance function?
19. Calculate the depth of a full CPC collector if the aperture is 1 m and CR = 5. Repeat for an aperture of 1 cm.
20. What is the reflectance loss in a 50% truncated CPC collector using silver mirrors if it has a 36° acceptance half-angle? What is the loss for an anodized aluminum reflector?
21. Compare the average number of reflections for a full and 50% truncated CPC if the acceptance half-angle is 9°.
22. How much concentration effect is lost by truncating a 7° half-angle CPC by 1/4, 1/3, and 1/2?
23. Explain how Figures 3.49 and 3.50 could be used to prepare a map showing the effect of truncation on average number of reflectors of a CPC collector. Sketch qualitatively what such a map would look like.

24. A parabolic trough 1 m wide and 10 m long with no end support plates is 30 cm deep and has a focal length of 20.83 cm. Calculate its optical efficiency at a 30° incidence angle for perfect optics and tracking if its reflector reflectance is 80%, $\tau\alpha$ product is 75%, and if the receiver supports shade 5% of the aperture.
 25. Calculate the maximum concentration ratio for a parabolic trough collector with a 50 cm aperture, which captures 92% of the incident radiation if the rim half-angle is 50° and the surface is accurate to 2 mrad in slope. What is the receiver diameter?
-

References

- Agarwal, V.K., and D.C. Larson. 1981. Calculation of the top loss coefficient of a flat plate collector. *Sol. Energy* 27: 69–71.
- Akhtar, N., and S.C. Mullick. 1999. Approximate method for computation of glass cover temperature and top heat-loss coefficient of solar collectors with single glazing. *Sol. Energy* 66: 349–354.
- Akhtar, N., and S.C. Mullick. 2007. Computation of glass cover temperatures and top heat loss coefficient of flat plate solar collectors with double glazing. *Energy* 32: 1067–1074.
- ASHRAE 93-2003. *Methods of Testing to Determine the Thermal Performance of Solar Collectors*. ASHRAE, Atlanta, GA.
- ASHRAE 96-1980. *Methods of Testing to Determine the Thermal Performance of Unglazed Solar Collectors*. ASHRAE, Atlanta, GA.
- Baranov, V.K., and G.K. Melnikov. 1966. Study of the illumination characteristics of hollow focons. *Sov. J. Opt. Technol.* 33: 408–411. Also 1975. Parabolocylindric reflecting unit and its properties. *Geliotekhnika* 11: 45–52.
- Beekley, D.C., and G.R. Mather. 1975. *Analysis and Experimental Tests of a High Performance, Evacuated Tube Collector*. Owens-Illinois, Toledo, OH.
- Bliss, R.W. 1959. The derivations of several plate efficiency factors useful in the design of flat-plate solar-heat collectors. *Sol. Energy* 3: 55.
- Collares-Pereira, M., and A. Rabl. 1979. Simple procedure for predicting long term average performance of nonconcentrating and of concentrating solar collectors. *Sol. Energy* 23: 235–254.
- Collares-Pereira, M., A. Rabl, and R. Winston. 1977. Lens mirror combinations with maximal concentration. Enrico Fermi Institute Rept. No. EFI 77–20. University of Chicago Press, Chicago.
- DeLaquil, III, P. et al. 1993. Solar thermal electric technology. In *Renewable Energy-Sources for Fuels and Electricity*, T. Johansson et al., eds. Island Press, Washington, DC, pp. 213–296.
- Duff, W.S. 1976. Optical and thermal performance of three line focus collectors. ASME Paper 76-WA/HT-15. ASME, New York.
- Duff, W.S., and G.F. Lameiro. 1974. A performance comparison method for solar concentrators. ASME Paper 74-WA/Sol-4. ASME, New York.

- Duffie, J.A., and W.A. Beckman. 1980. *Solar Energy Thermal Processes*. John Wiley & Sons, New York.
- Dushman, S. 1962. *Scientific Foundations of Vacuum Technology*, 2nd ed., J.M. Lafferty ed. John Wiley & Sons, New York.
- Emmett, W.L.R. 1911. Apparatus for utilizing solar heat. U.S. Patent 980, 505.
- EN 12975-2. 2006. *Thermal Solar Systems and Components—Solar Collectors—Part 2: Test Methods*. European Committee for Standardization, Brussels, Belgium.
- Francia, G. 1968. Pilot plants of solar steam generating stations. *Sol. Energy* 12: 51–64.
- Gaul, H.W., and A. Rabl. 1979. Incidence angle modifier and average optical efficiency of parabolic trough collectors. In *Sun II: Proceedings of the International Solar Energy Society, Silver Jubilee Congress*, Vol. 1, Atlanta, GA, May 1979, K.W. Boer, and B.H. Glenn, eds. Pergamon Press, New York, pp. 547–551.
- Gleckman, P., J. O'Gallagher, and R. Winston. 1989. Concentration of sunlight to solar surface levels using non-imaging optics. *Nature* 339: 198–200.
- Hildebrandt, A.F., and L.L. Vant-Hull. 1974. Tower top focus solar energy collector. *Mech. Eng.* 23(9): 23–27.
- Hottel, H.C., and A.F. Sarofim. 1967. *Radiative Transfer*. McGraw-Hill, New York.
- Hottel, H.C., and A. Whillier. 1958. Evaluation of flat-plate collector performance. *Trans. Conf. Use Sol. Energy* 2(Pt 1): 74.
- Hsieh, C.K. 1981. Thermal analysis of CPC collectors. *Sol. Energy* 27: 19.
- Hsieh, C.K., and F.M. Mei. 1983. Empirical equations for calculation of CPC collector loss coefficients. *Sol. Energy* 30: 487.
- Kennedy, C.E. 2002. Review of mid- to high-temperature solar selective absorber materials. Report NREL/TP-520-31267. National Renewable Energy Laboratory, Golden, CO.
- Klein, S.A. 1975. Calculation of flat-plate collector loss coefficients. *Sol. Energy* 17: 79–80.
- Klein, S.A., J.A. Duffie, and W.A. Beckman. 1974. Transient considerations of flat-plate solar collectors. *J. Eng. Power* 96A: 109–114.
- Kreith, F. 1975. Evaluation of focusing solar energy collectors. *ASTM Stand. News* 3: 30–36.
- Kreith, F., and J.F. Kreider. 2012. *Principles of Sustainable Energy*. CRC Press, Boca Raton, FL.
- Kutcher, C.F. 1996. Transpired solar collector systems: A major advance in solar heating. Paper presented at the *World Engineering Congress*, Atlanta, GA, November 6–8, 1996.
- Kutcher, C.F., and C.B. Christensen. 1992. Unglazed transpired solar collectors. In *Advances in Solar Energy*, Vol. 7, K. Böer, ed., pp. 283–307. American Solar Energy Society, Boulder, CO.
- Lippke, F. 1995. Simulation of the part-load behavior of a 30 MWe SEGS plant. Tech. Rep., SAND-95-1293. Sandia National Labs., Albuquerque, NM.
- Löf, G.O.G., and R.A. Tybout. 1972. Model for optimizing solar heating design. ASME Paper 72-WA/SOL-8. ASME, New York.
- Mahboub, C., and N. Maummi. 2012. Calculation of the glass cover temperature and the top heat loss coefficient for 60°C vee corrugated solar collectors with single glazing. *Sol. Energy* 86: 804–808.
- Malik, M.A.S., and F.H. Buelow. 1976a. Hydrodynamic and heat transfer characteristics of a heat air duct. In *Helio-technique and Development*, (COMPLES 1975), Vol. 2. Development Analysis Associates, Cambridge, MA, pp. 3–30.

- Malik, M.A.S., and F.H. Buelow. 1976b. Heat transfer in a solar heated air duct-a simplified analysis. In *Heliotherapy and Development*, (COMPLES 1975), Vol. 2. Development Analysis Associates, Cambridge, MA, pp. 31–37.
- Mullick, S.C., and S.K. Samdarshi. 1988. An improved technique for computing the top heat loss factor of flat-plate collector with a single glazing. *ASME J. Sol. Energy Eng.* 110: 262–267.
- Patnode, A.M. 2006. Simulation and performance evaluation of parabolic trough solar power plants. Master's thesis, University of Wisconsin-Madison, College of Engineering, Madison, WI.
- Rabl, A. 1975. Comparison of solar concentrators. *Sol. Energy* 18: 93–111.
- Rabl, A. 1976a. Optical and thermal properties of compound parabolic concentrators. *Sol. Energy* 18: 497. See also Rabl, A. 1977. Radiation through specular passages. *Int. J. Heat Mass Trans.* 20: 323.
- Rabl, A. 1976b. Ideal two dimensional concentrators for cylindrical absorbers. *Appl. Opt.* 15: 871.
- Rabl, A. 1978. In *Proc. Sol. Thermal Conc. Coll. Tech. Symp.*, B. Gupta, ed. Denver, CO, pp. 1–42. SERI, Golden, CO.
- Ramsay, J.W., B.P. Gupta, and G.R. Knowles. 1977. Experimental evaluation of a cylindrical parabolic solar collector. *J. Heat Transfer* 99: 163.
- Samdarshi, S.K., and S.C. Mullick. 1991. An analytical equation for top heat loss factor of a flat plate solar collector with double glazing. *ASME J. Sol. Energy Eng.* 113: 117–122.
- Speyer, F. 1965. Solar energy collection with evacuated tubes. *J. Eng. Power* 87: 270.
- Stuetzle, T. 2002. Automatic control of the 30 MWe SEGS VI parabolic trough plant. Master's thesis, University of Wisconsin-Madison, Madison, WI.
- Swinbank, W. 1963. Long wave radiation from clear skies. *Quart. J. Roy. Meteor. Soc.* 89(381): 339–348.
- Vasquez-Padilla, R. 2011. Simplified methodology for designing parabolic trough solar power plants. Ph.D. dissertation, University of South Florida, Tampa, FL.
- Welford, W.T. 1974. *Aberrations of the Symmetrical Optical System*. Academic Press, New York.
- Welford, W.T., and R. Winston. 1989. *High Collection Nonimaging Optics*. Academic Press, San Diego, CA.
- Winston, R. 1974. Solar concentrators of a novel design. *Sol. Energy* 16: 89–95. Includes references of early CPL work from 1966.
- Winston, R. 1975. Radiant energy collection. U.S. Patent 3,923,381.
- Zarza Moya, E. 2012. Parabolic trough concentrating solar power (CSP) systems, Chapter 7. In *Concentrating Solar Power Technology: Principles, Developments and Applications*, K. Lovegrove, and W. Stein, eds. Woodhead Publishing Lt., Cambridge, UK.

Suggested Reading

- Forristall, R. 2003. *Heat Transfer Analysis and Modeling of a Parabolic Trough Solar Receiver Implemented in Engineering Equation Solver*. National Renewable Energy Laboratory (NREL), Golden, CO.

4

Thermal Energy Storage and Transport

Energy storage becomes necessary whenever there is a mismatch between the energy available and the demand (ASHRAE 2011). Storage is especially important in solar energy applications because of the seasonal, diurnal, and intermittent nature of solar energy. Nature provides storage of solar energy in a number of ways, such as plant matter, also known as biomass, ocean thermal energy, and hydro-potential at high elevation by evaporation from water bodies and subsequent condensation (Jensen 1980). In fact, even fossil fuels are a stored form of solar energy because they are produced from biomass. Natural solar energy storage provides a longer-term buffer between supply and demand. Since solar energy availability varies by the time of the day and also by the time of the year (seasonal), and can have intermittency even during a day owing to clouds, energy storage systems can be short term or long term depending on the objective:

1. *Buffering* with the objective of overcoming cloudiness for short periods from a few minutes to a couple of hours.
2. *Delivery Period Displacement*, such as collection during the day for delivery during peak load period of evening hours.
3. *Delivery Period Extension* by storing enough during the day to have storage available for hours before sunrise and after sunset or even for longer times of non-sunshine hours of a day to a number of days.
4. *Seasonal Storage*, which would store heat during summer for usage during winter.

Energy can be stored as heat, electrochemical energy in batteries, mechanical energy in flywheels, or potential energy as pumped hydro or compressed air (Glendenning 1981). In this chapter, we will examine thermal energy storage (TES) in detail.

4.1 Thermal Energy Storage

TES in various solid and liquid media is used for solar water heating, space heating, and cooling as well as high-temperature applications such as solar thermal power (Garg et al. 1985). Important parameters in a storage system

include the *duration of storage*, *energy density* (or specific energy), and the *charging and discharging* (storage and retrieval) characteristics (Tomlinson and Kannberg 1990). The energy density is a critical factor for the size of a storage system (Swet 1987). The rate of charging and discharging depends on thermophysical properties such as thermal conductivity and design of the storage system (Beckman and Gilli 1984). The following sections describe the types of TES, materials, and storage system design.

4.2 Types of TES

Thermal energy can be stored as sensible heat, as latent heat, or as the heat of chemical reaction (thermochemical) (Jotshi and Goswami 1998).

4.2.1 Sensible Heat Storage

Sensible heat, Q , is stored in a material of mass m and specific heat c_p by raising the temperature of the storage material from T_1 to T_2 and is expressed by Equation 4.1:

$$\begin{aligned} Q &= \int_{T_1}^{T_2} mc_p dT \\ &= \int_{T_1}^{T_2} \rho V c_p dT, \end{aligned} \quad (4.1)$$

where ρ and V are density and volume of the storage material, respectively. For moderate temperature changes, such as for solar space and water heating systems, the density and specific heat may be considered constants (deWinter 1975). Therefore, $Q = \rho V c_p \Delta T$. Most common sensible heat storage materials are water, organic oils, rocks, ceramics, and molten salts (Yang and Garimella 2010). Some of these materials, along with their physical properties, are listed in Figure 4.1. Water has the highest specific heat value of 4190 J/kg·°C.

The most common medium for storing sensible heat for use with low- and medium-temperature solar systems is water. Water is cheap and abundant and has a number of particularly desirable properties. Table 4.1 lists the advantages and disadvantages of aqueous storage of thermal energy (Kreider 1979).

Water is the standard storage medium for solar heating and cooling systems for buildings today. For these systems, useful energy can be stored below the boiling point of water.

Storage medium	Temperature range, °C	Density (ρ), kg/m ³	Specific heat (C), J/kg K	Energy density (ρC) kWh/m ³ K	Thermal conductivity (W/m K)
Water	0–100	1000	4190	1.16	0.63 at 38°C
Water (10 bar)	0.180	881	4190	1.03	—
50-ethylene glycol-50-water	0–100	1075	3480	0.98	—
Dowtherm A® (Dow Chem. Co.)	12–260	867	2200	0.53	0.122 at 260°C
Therminol 66® (Monsanto Co.)	−9–343	750	2100	0.44	0.106 at 343°C
Draw salt (50NaNO ₃ -50KNO ₃) ^a	220–540	1733	1550	0.75	0.57
Molten salt (53KNO ₃ /40NaNO ₃ /7NaNO ₃) ^a	142–540	1680	1560	0.72	0.61
Liquid sodium	100–760	750	1260	0.26	67.5
Cast iron	mp. 1150–1300°C	7200	540	1.08	42.0
Taconite	—	3200	800	0.71	—
Aluminum	m.p. 660	2700	920	0.69	200
Fireclay	—	2100–2600	1000	0.65	1.0–1.5
Rock	—	1600	880	0.39	—

^a Composition in percent by weight.

Note: m.p. = melting point.

FIGURE 4.1

Physical properties of some sensible heat storage materials.

TABLE 4.1

Advantages and Disadvantages of Water as a Thermal Storage Medium

Advantages	Disadvantages
Abundant, low cost	High vapor pressure
Non-toxic	Difficult to stratify
Not combustible	Low surface tension, leaks easily
Excellent transport properties	Corrosive medium
High specific heat	Freezing and consequent destructive expansion
High density	Nonisothermal energy delivery
Good combined storage medium and working fluid	
Well-known corrosion control methodology	

4.2.2 Latent Heat Storage

Thermal energy can be stored as latent heat in a material that undergoes phase transformation at a temperature that is useful for the application. If a material with phase change temperature T_m is heated from T_1 to T_2 such that $T_1 < T_m < T_2$, the thermal energy Q stored in a mass m of the material is given by Equation 4.2:

$$Q = \int_{T_1}^{T_m} mc_p dT + m\lambda + \int_{T_m}^{T_2} mc_p dT, \quad (4.2)$$

where λ is the heat of phase transformation.

Four types of phase transformations useful for latent heat storage are as follows: solid \rightleftharpoons liquid, liquid \rightleftharpoons vapor, solid \rightleftharpoons vapor, and solid \rightleftharpoons solid. Since phase transformation is an isothermal process, thermal energy is stored and received at a fixed temperature known as the transition temperature. Some common phase change materials (PCMs) used for thermal storage are paraffin waxes, nonparaffins, inorganic salts (both anhydrous and hydrated), and eutectics of organic or inorganic compounds. For high-temperature storage, even metals may be used as PCMs. Table 4.2 lists some PCMs with their physical properties.

Most common PCMs used for solar energy storage undergo solid \rightleftharpoons liquid transformation. For such materials, the thermal energy stored may be written from Equation 4.2 as, approximately (Equation 4.3),

$$Q = m \bar{c}_{ps}(T_m - T_1) + \lambda + \bar{c}_{pl}(T_2 - T_m) , \quad (4.3)$$

where \bar{c}_{ps} and \bar{c}_{pl} are the average specific heats in the solid and liquid phases, respectively.

Example 4.1

A company is interested in 2 h of buffer storage for a 1.5 MW_{th} solar thermal power plant that operates between 285°C and 380°C. Estimate the amount of material that is needed if sodium nitrate, NaNO₃, is used as the latent heat storage medium.

Solution

The melting temperature, average solid and liquid specific heats, and the latent heat of sodium nitrate can be found from Table 4.2:

$$\bar{c}_{ps} = 1.27 \text{ kJ/kg}\cdot^\circ\text{C}$$

$$\bar{c}_{pl} = 1.64 \text{ kJ/kg}\cdot^\circ\text{C}$$

$$T_m = 307^\circ\text{C}$$

$$\lambda = 177 \text{ kJ/kg}$$

The energy that is required for 2 h of storage is

$$\begin{aligned} Q &= \text{number of hours of storage} \times \text{thermal power requirement} \\ &= 2 \text{ h} \times 1500 \text{ kW} = 3000 \text{ kWh} \\ &= 3000 \text{ kWh} \times \frac{3600 \text{ s}}{\text{h}} = 10.8 \times 10^6 \text{ kJ.} \end{aligned}$$

TABLE 4.2
Physical Properties of Latent Heat Storage Materials or PCMs

Storage Medium	Melting Point (°C)	Latent Heat (kJ/kg)	Specific Heat (kJ/kg·°C)		Density (kg/m ³)		Energy Density (kWh/m ³ ·K)	Thermal Conductivity (W/m·K)
			Solid	Liquid	Solid	Liquid		
<i>n</i> -Tetradecane	5.5	228	—	—	825	771	48	0.15
LiClO ₃ ·3H ₂ O	8.1	253	—	—	1720	1530	108	—
<i>n</i> -Octadecane	28	244	2.16	—	814	774	52.5	0.15
Na ₂ SO ₄ ·1OH ₂ O (Glauber's salt)	32.4	251	1.76	3.32	1460	1330	92.7	2.25
Na ₂ S ₂ O ₃ ·5H ₂ O	48	200	1.47	2.39	1730	1665	92.5	0.57
NaCH ₃ COO·3H ₂ O	58	180	1.9	2.5	1450	1280	64	0.5
Steric acid	70	203	—	2.35	941	347	48	0.1721
Ba(OH) ₂ ·8H ₂ O	78	301	0.67	1.26	2070	1937	162	0.6531
Mg(NO ₃) ₂ ·6H ₂ O	90	163	1.56	3.68	1636	1550	70	0.611
HDPE (cross-linked)	126	180	2.88	2.51	960	900	45	0.361
LiNO ₃	252	530	2.02	2.041	2310	1776	261	1.35
NaNO ₃	307	177	1.27	1.64	2260	1900	93	0.5
NaOH/NaCl/Na ₂ CO ₃ (77.2:16.2:6.6) ^b	318	290	—	—	—	—	—	—
LiCl/BaCl ₂ /KCl (54.2:6.4:39.4) ^b	320	170	—	—	—	—	—	—
KNO ₃	335	266	0.5	—	2110	1865	138	0.5
Zn/Mg (52:48) ^a	340	180	—	—	—	—	—	—
LiCl/KCl (58:42) ^b	348	170	—	—	—	—	—	—

(Continued)

TABLE 4.2 (CONTINUED)
Physical Properties of Latent Heat Storage Materials or PCMs

Storage Medium	Melting Point (°C)	Latent Heat (kJ/kg)	Specific Heat (kJ/kg/°C)			Density (kg/m ³)	Energy Density (kWh/m ³)	Thermal Conductivity (W/m·K)
			Solid	Liquid	Solid			
KOH	380	149.7	—	—	—	—	—	0.5
MgCl ₂ /KCl/NaCl (45:4:21:6:33) ^b	380	284	—	—	—	—	—	—
Zn/Al (96:4) ^a	381	138	—	—	—	—	—	—
LiCO ₃ /K ₂ CO ₃ /Na ₂ CO ₃ (32:35:33) ^a	397	277	1.34	1.76	2300	2140	165	—
Na ₂ CO ₃ /K ₂ CO ₃ /Li ₂ CO ₃ (37:35:31) ^a	397	275	1.67	1.63	2300	—	175	2.04
Al/Mg/Zn (59:35:6) ^a	443	310	—	—	—	—	—	—
NaCl/MgCl ₂ (48:52) ^a	450	430	0.92	1	2230	—	266	0.96
KCl/MgCl ₂ (36:64) ^a	470	388	0.84	0.96	2190	—	236	0.83
Na ₂ CO ₃ /Li ₂ CO ₃ (56:44) ^a	487	368	1.8	2.09	2320	—	237	2.11
NaCl/CaCl ₂ (33:67) ^a	500	281	0.84	1	2780	—	217	1.02
LiCO ₃ /K ₂ CO ₃ (35:65) ^a	505	345	1.68	1.63	2265	1960	1.88	—
LiBr	550	203	—	—	—	2528	142	—
LiF/NaF ₂ /MgF ₂ (46:44:10) ^a	632	858	1.4	—	2240	—	534	1.2
Al	660	398	—	—	—	2375	262	2.5
MgCl ₂	714	452	—	—	2140	1680	210	—

Note: 1 liquid.

^a Composition in percent by weight.

^b Composition in percent by mole.

By rearranging Equation 4.3, the mass requirement for 10.8×10^6 kJ of storage is

$$m = \frac{Q}{\bar{c}_{ps}(T_m - T_1) + \lambda + \bar{c}_{pl}(T_2 - T_m)}$$

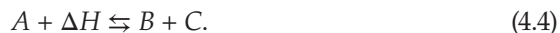
$$m = \frac{10.8 \times 10^6 \text{ kJ}}{1.27 \frac{\text{kJ}}{\text{kg} \cdot ^\circ\text{C}} (307^\circ\text{C} - 285^\circ\text{C}) + 177 \frac{\text{kJ}}{\text{kg}} + 1.64 \frac{\text{kJ}}{\text{kg} \cdot ^\circ\text{C}} (380^\circ\text{C} - 307^\circ\text{C})}$$

$$= 33,265.6 \text{ kg.}$$

Actual mass required will be more since some of the heat in the system can not be recovered economically and in a reasonable amount of time.

4.2.3 Thermochemical Energy Storage

Thermochemical energy can be stored as heat of reaction in reversible chemical reactions. In this mode of storage, the reaction in the forward direction is endothermic (storage of heat), while the reverse action is exothermic (release of heat). For example,



The amount of heat Q stored in a chemical reaction depends on the heat of reaction and the extent of conversion as given by Equation 4.5:

$$Q = a_r m \Delta H, \quad (4.5)$$

where a_r is fraction reacted, ΔH is the heat of reaction per unit mass, and m is mass.

Chemical reaction is generally a highly energetic process. Therefore, a large amount of heat can be stored in a small quantity of a material. Another advantage of thermochemical storage is that the products of reaction can be stored at room temperature and need not be insulated. For sensible and latent heat storage materials, insulation is very important. Examples of reactions include decomposition of metal hydrides, oxides, peroxides, ammoniated salts, carbonates, sulfur trioxide, and so on (Harrison and Pelanne 1977). Some useful chemical reactions are reported in Table 4.3.

TABLE 4.3
Properties of Thermochemical Storage Media

Compound	Temperature (°C)	Pressure (bar)	Reaction	ΔH (kJ/mol)	ΔH (kWh/m ³)
Manganese oxide	530	1	$\text{MnO}_2 + \Delta H \leftrightarrow 0.5\text{Mn}_2\text{O}_3 + 0.25\text{O}_2$	42	336
Calcium hydroxide	505	1	$\text{Ca}(\text{OH})_2 + \Delta H \leftrightarrow \text{CaO} + \text{H}_2\text{O}$	112	364
Calcium carbonate	896	1	$\text{CaCO}_3 + \Delta H \leftrightarrow \text{CaO} + \text{CO}_2$	167	113
Magnesium hydride	250–500	—	$\text{MgH}_2 + \Delta H \leftrightarrow \text{Mg} + \text{H}_2$	75	111
Ammonia	400–500	—	$\text{NH}_3 + \Delta H \leftrightarrow 1/2\text{N}_2 + 3/2\text{H}_2$	67	675
Methane/water	500–1000	—	$\text{CH}_4 + \text{H}_2\text{O} \leftrightarrow \text{CO} + 3\text{H}_2$	206	—
Magnesium oxide	250–400	—	$\text{MgO} + \text{H}_2\text{O} \leftrightarrow \text{Mg}(\text{OH})_2$	81	—
Iron carbonate	180	—	$\text{FeCO}_3 \leftrightarrow \text{FeO} + \text{CO}_2$	—	—
Methanolation-demethanolation	200–250	1–5	$\text{CH}_3\text{OH} \leftrightarrow \text{CO} + 2\text{H}_2$	98	—
Mg_2FeH_6	500	66	$\text{Mg}_2\text{FeH}_6 + \Delta H \leftrightarrow \text{Mg}_2\text{Fe} + 3\text{H}_2$	77.4	160
Magnesium carbonate	427–327	1	$\text{MgCO}_3 + \Delta H \leftrightarrow \text{MgO} + \text{CO}_2$	101.1	187
Sulfur trioxide	520–960	1	$\text{SO}_3 + \Delta H \leftrightarrow \text{SO}_2 + 1/2\text{O}_2$	99.6	280

4.3 Design of Storage System

Design of a storage system involves the selection of a storage material, design of containment, and heat exchangers for charging and discharging (Cole et al. 1980).

4.3.1 Selection of Storage Material

Selection of the storage material is the most important part of the design of a TES system. The selection depends on a number of factors. Below are some of those factors.

4.3.1.1 Solar Collection System

The solar collection system determines the temperature at which the storage material will be charged and the maximum rate of charge. Thermophysical properties of the storage material at this temperature are important in determining the suitability of the material. For example, flat plate liquid-type collectors may use water as the storage material, while air-type flat plate collectors for space heating may use a rock or pebble bed as the storage medium. If the storage material can be used as the heat-exchanger fluid in the collector, it avoids the need of a collector-to-storage heat exchanger. This criterion favors liquid storage materials. Water and glycol–water mixtures are the most common storage materials for flat plate and moderately concentrating collector systems. For parabolic trough concentrators, high-temperature oils are more appropriate. For higher-concentration and higher-temperature collectors such as central receiver tower, molten salts may be used.

Molten nitrate salt (50 wt% NaNO_3 /50 wt% KNO_3), also known as Draw salt, which has a melting point of 222°C, has been used as a storage and a heat-transfer fluid in an experiment in Albuquerque, New Mexico. It was the first commercial demonstration of generating power from storage (Delameter and Bergen 1986). Solar Two, a 10-MW solar thermal power demonstration project in Barstow, California, was also designed to use this molten salt to store solar energy (Chavez et al. 1995). Another molten nitrate salt is 40 wt% NaNO_2 /7 wt% NaNO_3 /53 wt% KNO_3 , known as HTS (heat-transfer salt) with a melting point of 142°C. This salt has been widely used in the chemical industry.

4.3.1.2 Application

The application determines the temperature at which the storage will be discharged and maximum rate of discharge. For hot water applications and moderate-temperature industrial process heat, water would be an obvious choice for heat storage. A PCM may be used if space considerations are very important.

For applications in heating and cooling of buildings, the containment of PCM can become an integral part of the building. It may be part of the ceiling, wall, or floor of the building and may serve a structural or a non-structural function. Tubes, trays, rods, panels, balls, canisters, and tiles containing PCMs have been studied in the 1970s and 1980s for space-heating applications (Rabl 1977). The PCMs used were mostly salt hydrates such as $\text{Na}_2\text{SO}_4 \cdot 10\text{H}_2\text{O}$ (Glauber's salt), $\text{Na}_2\text{S}_2\text{O}_3 \cdot 5\text{H}_2\text{O}$ (Hypo), $\text{NaCH}_3\text{COO} \cdot 3\text{H}_2\text{O}$, $\text{Na}_2\text{HPO}_4 \cdot 12\text{H}_2\text{O}$, $\text{Ba(OH)}_2 \cdot 8\text{H}_2\text{O}$, $\text{MgCl}_2 \cdot 6\text{H}_2\text{O}$, and $\text{Mg}(\text{NO}_3)_2 \cdot 6\text{H}_2\text{O}$. Paraffin mixtures have been used for thermal storage in wallboards.

4.3.1.3 Additional Considerations

Other considerations include space requirements, cost, long-term cycling stability, corrosivity, complexity of containment system, and complexity of heat-exchanger design for maximum rates of charge and discharge.

4.3.2 Design of Containment

Containment design is especially important for liquid and phase change storage materials. Water can be stored in any tank able to withstand the expected pressure. Some commonly used tanks for water storage include steel tanks with glass, epoxy or stone lining, fiberglass reinforced polymer, concrete with plastic liner, and wooden tanks.

Containment of PCMs can be problematic, since phase change is accompanied by a large change in volume and other thermophysical properties (Potter 1959). PCMs may be bulk stored in tanks or be micro- or macroencapsulated. Bulk storage requires special attention to the design of heat exchangers for charging and discharging. *Microencapsulation* involves very small particles of a PCM dispersed in a single phase matrix. It is usually considered a way of introducing high TES in building materials (Moses and Lane 1986). Some examples include PCMs encapsulated in concrete, floor tiles, and wallboard. The US Department of Energy sponsored the development of a composite wallboard by mixing up to 35% paraffin waxes in gypsum. The waxes contain *n*-octadecane as the main constituent with a melting point of 23°C and a heat of fusion of 184 kJ/kg.

Most of the successful developments to date have been made in *macroencapsulation* of PCMs. Capsules may be made out of plastics for low-temperature applications and metals for higher temperatures. They may be shaped as spherical balls, cylindrical rods, rectangular panels, or flexible pouches. Some of the materials used for macroencapsulation are listed in Table 4.4. Figure 4.2 shows some examples of commercially developed, macroencapsulated PCMs (Makansi 1994).

TABLE 4.4

Thermal Conductivity of Potential Containment Materials

Materials	Thermal Conductivity ^b	
	(W/m·K)	(Btu/h·ft·°F)
<i>Plastics^a</i>		
ABS	0.17–0.33	0.1–0.2
Acrylic	0.19–0.43	0.11–0.25
Polypropylene	0.12–0.17	0.07–0.1
Polyethylene (high density)	0.43–0.52	0.25–0.3
Polyethylene (medium density)	0.30–0.42	0.17–0.25
Polyethylene (low density)	0.30	0.17
Polyvinyl chloride	0.13	0.08
<i>Metals^c</i>		
Aluminum	237	137
Copper	401	232
Carbon steel (AISI 1095)	45	26

^a *Plastics, a Desk-top Data Bank*, 5th Ed., Book A, The International Plastics Selector, Inc., San Diego, CA, 1980.

^b As measured by ASTM C-177.

^c *CRC Handbook of Chemistry and Physics*, 88th Ed. 2007–2008.

**FIGURE 4.2**

Examples of commercially developed PCM capsules.

4.3.3 Heat-Exchanger Design

For liquid storage media, heat exchangers of the shell and tube type or submerged coil type are generally used for charging and discharging. These types of heat exchangers are described later in this chapter.

For solid storage media or macroencapsulated PCM, normally a packed bed type of storage configuration is designed. In this case, the heat is transferred to or from a heat-transfer fluid by flowing the heat-transfer fluid through the voids in the bed. Clark (1986) has reviewed research on heat transfer and pressure drop for flow through such storage systems. More recently, such systems have been reviewed for their applications in higher-temperature applications, such as CSP and industrial process heat (Karlekar and Desmond 1977; Kuravi et al. 2013).

4.3.3.1 Packed Bed Storage

Figure 4.3 shows a schematic of a packed bed storage system. Table 4.5 gives average void fractions for packed beds (Clark 1986). Packed bed storage systems are often designed by employing numerical models that rely on experimentally derived correlations. These models solve the relevant equations for a system such as the momentum and energy equations for the storage material and heat-transfer fluid. The results of the model can provide transient temperature and velocity data as well as performance characteristics such as efficiency and cyclic behavior.

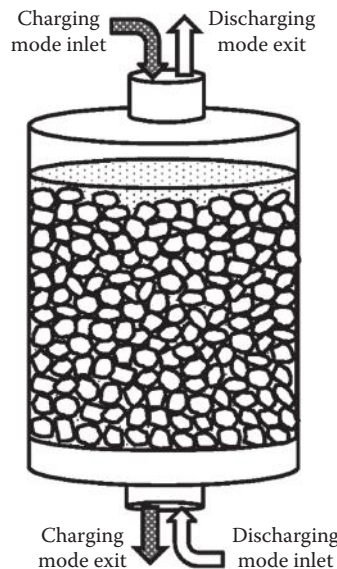


FIGURE 4.3
Schematic of a packed bed TES.

TABLE 4.5Representative Average Void Fractions, $\bar{\epsilon}$, for Packed Beds

Particle Type	Packing	Average Void Fraction
Sphere	Rhombohedral	0.26
Sphere	Tetragonal spheroidal	0.30
Sphere	Orthorhombic	0.40
Sphere	Cubic	0.48
Sphere	Random	0.36–0.43
Crushed rock	Granular	0.44–0.45
Sphere	Very loose, random	0.46–0.47
Sphere	Poured, random	0.37–0.39
Sphere	Close, random	0.36–0.38

Source: Adapted from Clark, J.A., Thermal design principles. In: *Solar Heat Storage: Latent Heat Materials*, Lane, G.A. (ed.), Chapter 5, CRC Press, pp. 185–223, 1986.

Recently, Sanduja et al. (2013) illustrated the use of a numerical model to design a sensible heat packed bed storage system for a solar thermal power plant. The model was validated with the numerical and experimental results presented by Hanchen et al. (2011) and Meier et al. (1991). They considered the storage system consisting of an axisymmetric tank with 1D plug flow assumption. The 1D assumption is valid when radial effects play a minor role in the velocity and temperature distribution of the bed and thus can be neglected. The unsteady governing energy equations for the storage material and heat-transfer fluid are, respectively:

Solid phase:

$$\rho_s c_s (1 - \varepsilon) \frac{\partial T_s}{\partial t} = h_v (T_f - T_s) + K_{\text{eff}} \frac{\partial^2 T_s}{\partial x^2} \quad (4.6)$$

Fluid phase:

$$\rho_f c_f \varepsilon \frac{\partial T_f}{\partial t} + c_f G \frac{\partial T_f}{\partial x} = h_v (T_s - T_f) + \frac{U_{\text{loss}} P}{A} (T_{\text{inf}} - T_f) \quad (4.7)$$

where K_{eff} is the effective thermal conductivity of the solid phase, h_v is the volumetric heat-transfer coefficient, ε is the porosity or void fraction of the packed bed, U_{loss} is the overall heat loss coefficient, A is the cross-sectional area of the bed, P is the perimeter of the tank (πD for a cylindrical tank of diameter D ; and $W \cdot D$ for a rectangular tank shown in Figure 4.3), T_{inf} is the ambient temperature, and c and ρ are the specific heat capacity and density

of the respective materials (Figure 4.4). G is defined as the superficial mass flow rate of HTF per unit bed cross-sectional area, or air mass flux:

$$G = \frac{\dot{m}}{A_{\text{bed}}} = \rho V = \rho \varepsilon v, \quad (4.8)$$

where \dot{m} is the mass flow rate of the heat-transfer fluid, V is the superficial velocity of the bed, and v is the interstitial particle velocity. The temperature of the storage material, T_s , and the temperature of fluid, T_f , are solved for with the numerical model.

They developed a numerical solution based on forward difference for temporal discretization and upwind difference for the first-order and central difference for the second-order space discretization. For guidance on numerical modeling, refer to Jaluria and Torrance (2003). The initial conditions are as follows:

Charging cycle:

$$T_f(t=0) = T_s(t=0) = T_{\text{initial}}. \quad (4.9)$$

Discharging cycle:

$$T_f(t=0) = T_f(t_{\text{end}}); \quad T_s(t=0) = T_s(t_{\text{end}}). \quad (4.10)$$

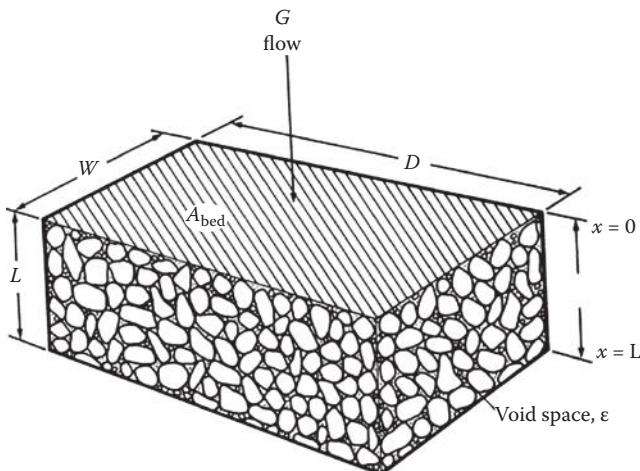


FIGURE 4.4

Representative element of the packed bed model. (Adapted from Clark, J.A., Thermal design principles, Chapter 5 in *Solar Heat Storage: Latent Heat Materials*, Lane, G.A. (ed.), CRC Press, pp. 185–223, 1986.)

The boundary conditions for the charging–discharging cycle are as follows:

$$\begin{aligned} T_f(x = 0) &= T_{\text{inlet}} \\ \frac{\partial T_f(x = H)}{\partial x} &= 0 \\ \frac{\partial T_s(x = 0)}{\partial x} &= \frac{\partial T_s(x = H)}{\partial x} = 0. \end{aligned} \quad (4.11)$$

Following validation, the model was used to predict the performance of a storage system under operating conditions that were specific to their application. The operating conditions are shown in Table 4.6. For a single-cycle analysis, the system is charged for 1 h, and for a multiple-cycle analysis, the system is continuously charged and discharged for 1 h each. Figure 4.5 shows the solid temperature distribution along the height of the bed for single and multiple cycles.

In the energy equations, the effective thermal conductivity, overall heat loss coefficient, and volumetric heat-transfer coefficient, h_v , are typically calculated from correlations that were experimentally developed. Various heat-transfer correlations are available in the literature that may be used to simulate the system temperature distribution. Sanduja et al. (2013) employed a heat-transfer coefficient developed by Coutier and Farber (1982):

$$h = \frac{700}{6(1 - \varepsilon)} G^{0.76} D_p^{0.24}, \quad (4.12)$$

TABLE 4.6

Input Parameters Used in the Model Simulations of Sanduja et al. (2013)

Parameter	Value
Charging inlet air temperature, T_c (K)	873
Discharging inlet air temperature, T_d (K)	383
Ambient temperature, T_{inf} (K)	293
Air mass flow rate, \dot{m} (kg/s)	0.568
Tank height (m)	4
Tank diameter (m)	1
Particle diameter (m)	0.009
ε , porosity	0.4
Overall heat loss coefficient, U (W/m ² ·K)	0.678
Particle density, ρ_s (kg/m ³)	3200
Particle specific heat, c_s (J/kg·K)	1158
Particle thermal conductivity, k_s (W/m·K)	6.14

where h is the particle surface heat-transfer coefficient and D_p is the equivalent diameter of the storage particle. The volumetric heat-transfer coefficient can be related to the surface heat-transfer coefficient, h , by Kim (1994):

$$h_v = h \frac{A_e}{V_e} , \quad (4.13)$$

where the ratio A_e/V_e represents the superficial particle surface area per unit bed volume. In Equation 4.13, it is important to find the active surface area of the elements and it is often difficult to predict this area for irregular shaped particles and irregular arrangement in a packed bed. For a bed of spheres or cylindrical particles with aspect ratio of unity, the volumetric heat-transfer coefficient is simply calculated using the following equation:

$$h_v = \frac{6(1-\varepsilon)}{D_p h} . \quad (4.14)$$

For a bed of randomly packed spheres, Clark (1986) recommends a correlation by Beasley and Clark (1984) for the heat-transfer coefficient h for air flow through the bed (Figure 4.4), valid for Reynolds numbers of 10–10,000.

$$\frac{hD_p}{k} = 2.0 + 1.354\text{Re}_o^{1/2}\text{Pr}^{1/3} + 0.0326\text{Re}_o\text{Pr}^{1/2}, \quad (4.15)$$

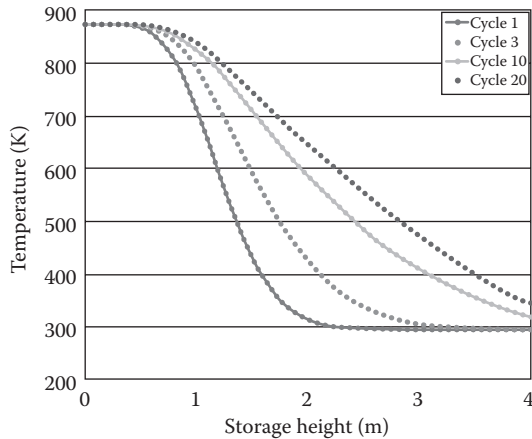
where Re_o and Pr are Reynolds and Prandtl numbers, respectively, as defined below:

$$\text{Re}_o = \frac{D_p G}{\mu}, \quad \text{Pr} = \frac{c_p}{k}. \quad (4.16)$$

D_p is the diameter of the storage particle and μ , c_p and k are the viscosity, specific heat, and thermal conductivity, respectively, of the heat-transfer fluid (air). This correlation may be used for low-temperature TES.

Kuravi et al. (2013) conducted an experimental study with a bed of solid bricks of *feelite* (an iron ore) arranged with channels for air flow (Figure 4.5) and found that the correlation shown in Equation 4.17 by Coutier and Farber (1982) with a modification proposed by Li and Ma (2011) for sphericity can predict the experimental results more accurately compared to other correlations. On the basis of this finding and their experimental study, they proposed the following correlation, which could be used for a packed bed system with channels for air flow:

$$h = \frac{1060}{6(1-\varepsilon)} G^{0.76} D_e^{0.24} \psi^{-0.56}. \quad (4.17)$$

**FIGURE 4.5**

Temperature distribution of the solid phase across the storage height (1.6 m) at the end of a single and multiple 1-h charge and discharge cycles. (Adapted from Sanduja, P. et al., Numerical analysis of a packed bed thermal storage system for concentrated solar power. *Energy Procedia, Proceedings of the ISES 2013 Solar World Congress*, 2013.)

The equivalent element diameter, D_e is given by the equation

$$D_e = \frac{6}{\pi} V_e^{(1/3)}, \quad (4.18)$$

where V_e is the volume of the element. The sphericity, ψ is given by

$$\psi = \frac{a_s}{a_e}, \quad (4.19)$$

where a_s is the surface area of a sphere having a volume equal to the material element and a_e is the surface area of the material element.

Similar to modeling of sensible heat storage systems, latent heat storage modeling requires a solution of the governing mass, momentum, and energy equations. Latent heat storage modeling is more complicated, however, because the interface between the two phases moves with time as latent heat is absorbed or released during the phase change process. An external heat-transfer coefficient is no longer sufficient since the assumption of a constant temperature distribution within the material is not accurate. To account for the additional thermal resistance during the phase change process within a spherical particle, Arkar and Medved (2005) employed an effective heat-transfer coefficient adopted from Jeffreson (1972):

$$h_{\text{eff}} = \frac{h}{1 + 0.2Bi}, \quad (4.20)$$

where h is the particle surface heat-transfer coefficient and Bi is the Biot number, a dimensionless number defined as

$$\text{Bi} = \frac{hD_p}{k_s}. \quad (4.21)$$

The effective heat-transfer coefficient replaces the surface heat-transfer coefficient in the energy equations. For additional details on various phase change modeling techniques, see Idelsohn (1994) and Voller (1996).

Example 4.2

A company is interested in designing a sensible heat storage system for a low-temperature waste heat application. Air is to be used as the heat-transfer fluid and crushed rock is to be used as the storage medium. A laboratory-scale system was first constructed and the experimental data were compared to the results of a numerical model that solves Equations 4.6 and 4.7 for the storage material and air temperatures. It was found that when the heat-transfer coefficient of Equation 4.15 was used, the model closely predicted the temperature distribution of the experimental packed bed. Following validation, the model is to be used to determine the optimum particle diameter for a large-scale system. The following table provides the design conditions of the large-scale system:

Design Parameter	Value
Tank height (m)	8
Tank diameter (m)	4
Mass flow rate (kg/s)	1.5
Particle diameters under consideration (m)	0.025, 0.035, 0.045
Charging air temperature (K)	373
Discharging air temperature (K)	301

Calculate the heat-transfer coefficient using Equation 4.15 for the particle diameter of 0.025 m. Air properties based on an average temperature of 648 K are assumed: $c_p = 1009 \text{ J/kg}\cdot\text{K}$, density = 1.049 kg/m^3 , $\mu = 2.081 \times 10^{-5} \text{ kg/m}\cdot\text{s}$, $k = 0.0292 \text{ W/m}\cdot\text{K}$.

Solution

To calculate h , the particle Reynolds number, Prandtl number, and air mass flux, G , must be calculated:

$$G = \frac{\dot{m}}{A_{\text{bed}}} = \frac{1.5 \text{ kg/s}}{\pi(4 \text{ m}^2)/4} = 0.1194 \text{ kg}/(\text{m}^2\text{s})$$

$$\text{Re}_o = \frac{D_p G}{\mu} = \frac{0.025 \text{ m} \times 0.1194 \text{ kg}/(\text{m}^2\text{s})}{2.081 \times 10^{-5} \text{ kg}/(\text{m} \cdot \text{s})} = 143.441$$

$$\text{Pr} = \frac{c_p}{k} = \frac{1009 \frac{\text{J}}{\text{kg} \cdot \text{K}} \times \frac{2.081 \times 10^{-5} \text{ kg}}{\text{m} \cdot \text{s}}}{0.0292 \frac{\text{W}}{\text{m} \cdot \text{K}}} = 0.7190.$$

Therefore, the particle surface heat-transfer coefficient is

$$\begin{aligned} h &= \frac{k}{D_p} \left(2.0 + 1.354 \text{Re}_o^{1/2} \text{Pr}^{1/3} + 0.0326 \text{Re}_o \text{Pr}^{1/2} \right) \\ &= \frac{0.0292 \frac{\text{W}}{\text{mK}}}{0.025 \text{ m}} \left(2.0 + 1.354(143.441)^{1/2}(0.719)^{1/3} + 0.0326(143.441)(0.719)^{1/2} \right) \\ &= 23.936 \frac{\text{W}}{\text{m}^2\text{K}}. \end{aligned}$$

The heat-transfer coefficient must be calculated for each particle diameter that is under investigation. Before solving the energy equations for the packed bed, the surface heat-transfer coefficient must be converted to the volumetric heat-transfer coefficient given in Equation 4.13.

4.3.3.2 Pressure Drop in a Packed Bed

To find the pressure drop in packed beds, the following equation developed by Ergun (1952) may be used:

$$\Delta p = f \frac{L}{D_p} \rho V^2 \frac{1-\varepsilon}{\varepsilon^3}, \quad (4.22)$$

where ε is the average void fraction (Table 4.5) and the friction factor f is given by

$$f = \frac{150(1-\varepsilon)}{\text{Re}_o} + 1.75. \quad (4.23)$$

Trahan et al. (2013) conducted an experimental study on pressure drop in a packed bed system and used the correlations of Ergun (1952), Eisfeld and

Schnitzlein (2001), and Singh et al. (2006) to determine the particle sphericity of crushed rock. They found that Ergun's equation showed the same power dependence of pressure drop on velocity in the Reynolds numbers range of 300 to 6000. Therefore, they proposed the following correlation for the pressure drop for nonspherical particles:

$$\frac{\Delta P}{L} = 150 \frac{(1-\varepsilon)^2}{\psi^2 \varepsilon^3} \frac{U}{D_e^2} + 1.75 \frac{1-\varepsilon}{\psi \varepsilon^3} \frac{\rho U^2}{D_e}, \quad (4.24)$$

where D_e is the equivalent diameter of the particles as defined in Equation 4.18.

Example 4.3

An estimate of the pressure drop of a packed bed is needed in order to determine the pumping energy and thus the pump size that is required to move fluid through a storage system. The company in Example 4.1 would like to encapsulate sodium nitrate in spherical capsules and place them in a random configuration in a storage tank that is 4 m tall. Air is used as the heat-transfer fluid and the diameter of the particles is 0.05 m. If the superficial bed velocity is 0.75 m/s, calculate the pressure drop of the packed bed. Assume an air density of 0.600 kg/m³ and a dynamic viscosity of 3.058×10^{-5} kg/m·s.

Solution

The sphericity is unity and the porosity of the bed can be determined from Table 4.5. Since the bed consists of spheres that are randomly poured in the tank, a porosity of 0.38 can be assumed. Equation 4.24 can then be used to calculate the pressure drop of the packed bed:

$$\begin{aligned} \frac{\Delta P}{L} &= 150 \frac{(1-\varepsilon)^2}{\varepsilon^3} \frac{U}{D_p^2} + 1.75 \frac{1-\varepsilon}{\varepsilon^3} \frac{\rho U^2}{D_p} \\ &= 150 \frac{(1-0.38)^2}{0.38^3} \frac{(3.058 \times 10^{-5} \text{ kg/m}\cdot\text{s}) \times 0.75 \frac{\text{m}}{\text{s}}}{(0.05 \text{ m})^2} \\ &\quad + 1.75 \frac{(1-0.38)}{(0.38)^3} \frac{(0.600 \text{ kg/m}^3) 0.75 \frac{\text{m}}{\text{s}}}{0.05 \text{ m}}^2 \\ \frac{\Delta P}{L} &= 9.64 + 133.47 = 143.11 \frac{\text{kg}}{\text{m}^2 \text{s}^2}. \end{aligned}$$

The height of the tank is 4 m; therefore, the estimated pressure drop is

$$\Delta P = 4 \text{ m} \times 143.11 \frac{\text{kg}}{\text{m}^2 \text{s}^2} = 572 \text{ Pa.}$$

4.3.3.3 Flow across Tube Banks

Figure 4.6 shows a schematic of flow across a tube bank. For flow of air across tube banks of 10 rows deep and Reynolds numbers from 2000 to 40,000, McAdams (1954) recommends a mean Nusselt number, Nu , as

$$\text{Nu} = \frac{hD_o}{k_f} = A \left(\frac{D_o G_{\max}}{f} \right)^{0.6} \text{Pr}_f^{1/3}, \quad (4.25)$$

where $A = 0.33$ for staggered tubes and 0.26 for in-line tubes. The subscript “f” indicates that the thermal property is to be determined at the film temperature or the average of the tube and the air temperatures. G_{\max} is defined as

$$G_{\max} = \frac{\dot{m}}{A_{\min}} \quad (4.26)$$

or the mass flow rate of air divided by the minimum free flow area (Singh et al. 2006).

For latent heat storage systems, sometimes a shell and tube arrangement is used such that the heat-transfer fluid flows through the tubes while the PCM

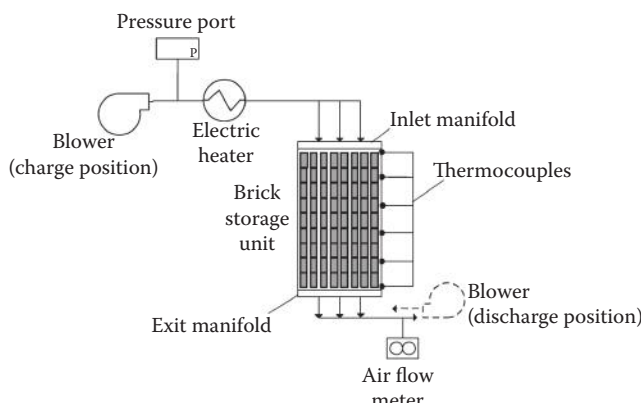


FIGURE 4.6

Schematic diagram of experimental sensible heat storage system. (From Kuravi, S. et al., *Progress in Energy and Combustion Science*, 39, 285–319, 2013.)

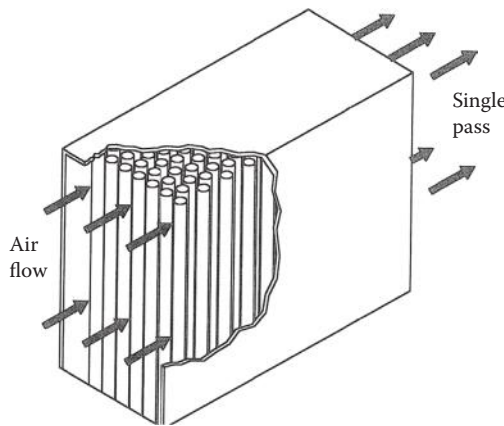


FIGURE 4.7
Schematic of a system with flow across tubes containing PCM.

fills the rest of the shell (Figure 4.7). For such systems, Zhang and Faghri (1996) suggest that the Nusselt number for flow within the tube is given by Edwards and Jensen (1994) as

$$\text{Nu} = \frac{0.023(l_c/D)^{0.2}}{1.32 - \frac{0.35l_c}{D}} \text{Re}^{0.8} \text{Pr}^{0.4}. \quad (4.27)$$

Pressure drop for flow through tubes is found from Equation 4.28, which is explained in detail in Section 4.4.

$$\Delta p = f \cdot 4(L/D) \cdot \frac{1}{2\rho} \bar{V}^2. \quad (4.28)$$

4.3.3.4 Performance of Packed Bed TES Systems

To evaluate the performance of a TES system, the charging and discharging efficiency can be calculated. The charging efficiency is based on the ratio of energy stored in the solid media to the energy input into the system and can be defined as

$$\eta_{\text{charging}} = \frac{E_{\text{stored}}}{E_{\text{Net Input}} + E_{\text{pump,charge}}}, \quad (4.29)$$

where E_{stored} accounts for the internal energy of the solid particles (Hanchen et al. 2011):

$$E_{\text{stored}} = \int_0^L \rho_{\text{solid}} c_{p,\text{solid}} A (T_{s(x)} - T_o) dx. \quad (4.30)$$

The temperature difference of the solid is calculated relative to a reference state, T_o , such as ambient temperature or the initial temperature of the bed.

The net energy input or removed from the system is calculated on the basis of the change of internal energy of the HTF and can be calculated as

$$E_{\text{input/output}} = \int_0^{t_{\text{end}}} \int_0^{T_{\text{HTF}}(t)} A \cdot G \cdot c_{p,\text{HTF}} dT dt, \quad (4.31)$$

where A is the cross-sectional area of the bed. The discharging efficiency is defined as

$$\eta_{\text{discharging}} = \frac{E_{\text{recovered/output}}}{E_{\text{stored}} + E_{\text{pump,discharge}}}. \quad (4.32)$$

The discharging efficiency is of particular interest since the design criteria of the TES system is based on the amount of energy that is needed during the discharging process. Yang and Garimella (2010) define the discharging efficiency with respect to a threshold value that characterizes the minimum temperature of HTF that exits the system. This value, Θ_o , is defined by the specific application, and any thermal energy that is delivered above the threshold temperature qualifies as useful energy. The dimensionless variable is given as

$$\Theta_o = \frac{T_o - T_c}{T_h - T_c}, \quad (4.33)$$

where T_h is the hot temperature of the HTF from the solar collector and T_c is the cold temperature of the HTF before entering the TES system during discharging. For example, if a value of 0.90 is chosen for Θ_o , T_h is 390°C and T_c is 285°C, then HTF exiting the TES system above 379.5°C during discharging is considered useful. Yang and Garimella (2010) defined the discharging efficiency as

$$\eta_{\text{discharging}} = \frac{\text{Energy retrieved with } \Theta > \Theta_o \text{ in a discharge half-cycle}}{\text{Energy delivered from the collector field in a charge half-cycle}} \quad (4.34)$$

and developed a correlation for discharging efficiency based on simulations that use molten salt as the HTF and $\Theta_o = 0.95$. The efficiency is a function of the Reynolds number, Re_o , and dimensionless tank height:

$$\eta = 1 - 0.1807 Re_o e^{0.1801} \frac{H}{100}^x, \quad (4.35)$$

where $x = 0.00234 Re_o^{-0.6151} + 0.00055 Re_o - 0.485$. This efficiency correlation can be used for Reynolds numbers between 1 and 50 and H between 10 and 800, where H is defined as

$$H = \frac{\text{tank height}}{\text{particle diameter}}. \quad (4.36)$$

The overall system efficiency is expressed as

$$\eta_{\text{overall}} = \eta_{\text{charging}} \cdot \eta_{\text{discharging}}. \quad (4.37)$$

Example 4.4

Calculate the discharging efficiency of a packed bed TES system that uses quartzite as the storage media and a molten salt mixture of 60 wt% $NaNO_3$ and 40 wt% KNO_3 as the HTF. The system must deliver energy to a central receiver power plant at a maximum temperature of $T_h = 600^\circ C$ and no less than $584^\circ C$ to prevent the turbine from shutting down. The temperature of the molten salt entering the bed during discharging is $285^\circ C$ and the superficial mass flow rate per unit area of the bed is $0.927 \text{ kg/s}\cdot\text{m}^2$. The height of the tank is 13 m and the equivalent particle diameter of the quartzite is 32.5 mm. The molten salt viscosity as a function of temperature (in $^\circ C$) is given as

$$\mu(\text{kg/m}\cdot\text{s}) = [22.714 - 0.12T + (2.281 \times 10^{-4})T^2 - (1.474 \times 10^{-7})T^3] \times 10^{-3}.$$

Solution

The viscosity of the molten salt can be calculated based on the average temperature of the bed ($T_{\text{ave}} = (285 + 600)/2 = 442.5^\circ C$):

$$\begin{aligned} &= [22.714 - 0.12(442.5^\circ C) + (2.281 \times 10^{-4})(442.5^\circ C)^2 - (1.474 \times 10^{-7})(442.5^\circ C)^3] \times 10^{-3} \\ &= 0.001506 \frac{\text{kg}}{\text{m}\cdot\text{s}}. \end{aligned}$$

The Reynolds number is then calculated as

$$\text{Re} = \frac{GD_p}{\mu} = \frac{(0.927 \text{ kg/m}^2\text{s})(0.0325 \text{ m})}{0.001506 \text{ kg/ms}} = 20.$$

In order to determine if Equation 4.8 can be used for the analysis, the threshold value and dimensionless tank height must be determined:

$$\Theta_o = \frac{T_o - T_c}{T_h - T_c} = \frac{584 - 285}{600 - 285} = 0.95$$

$$H = \frac{\text{tank height}}{\text{particle diameter}} = \frac{13 \text{ m}}{0.0325 \text{ m}} = 400.$$

Since the threshold value of the dimensionless temperature is 0.95, H lies between 10 and 800, and the Reynolds number falls between 1 and 50, Equation 4.8 may be used. To calculate the discharging efficiency, the value of x must be determined:

$$x = 0.00234(20^{-0.6151}) + 0.00055(20) - 0.485 = -0.4736.$$

Thus the discharging efficiency is

$$\eta = 1 - 0.1807 \text{Re}^{0.1801} \left(\frac{H}{100} \right)^x = 1 - 0.1807 (20^{0.1801}) \left(\frac{400}{100} \right)^{-0.4736} = 0.839 \times 100 = 83.9\%.$$

4.4 Energy Transport Subsystems

To transport solar heat from a solar collector to storage, and then to an end use, an energy transport subsystem is used. It consists of pipes, pumps, expansion tanks, valves of various types, and heat exchangers. Heat exchangers are treated in Section 4.4.4, and pipes and pumps, in this section. Valves and expansion tanks are standard items and are not described in detail.

4.4.1 Piping Systems

In most solar thermal processes considered in this book, standard circular pipes of steel, copper, aluminum, or special alloys are used to transport heat in the form of internal energy in the pumped fluid. Two parasitic losses occur in pipes—pressure drop and heat loss. Both losses are treated briefly herein.

4.4.2 Pressure Drop

Friction at the pipe walls, bends, valves, and so on results in flow resistance and pressure drop. To overcome the pressure drop, pumps are required. The sizing of pumps is a routine engineering exercise and is done by calculating two quantities, the friction factor at a given flow rate and the pipe length (Kent 1978). The friction factor f can be read from Figure 4.8 as a function of the Reynolds number and roughness ratio shown in Figure 4.9. The Darcy friction factor is defined as

$$f = \Delta p / \left(4(L/D) \frac{1}{2} \rho \bar{V}^2 \right), \quad (4.38)$$

where Δp is the pressure drop; D is the diameter; L is the pipe length including the equivalent length of smooth pipe for all fittings, expansions, and contractions; and \bar{V} is the space averaged velocity.

Churchill (1977) finds that the curves in Figure 4.10 can all be represented by one equation for the laminar, transition, and turbulent regimes:

$$f = 8[(8/\text{Re})^{1/2} + (A + B)^{-3/2}]^{1/12}, \quad (4.39)$$

where

$$A = -2.457 \ln \left(\frac{7}{\text{Re}} \right)^{0.9} + \frac{0.27 \epsilon}{D}^{16}; \quad B = \frac{37,530}{\text{Re}}^{16} \quad (4.40)$$

and ϵ is the average height of surface irregularities.

Pump motor horsepower P_p can be calculated using Equation 4.38 to be

$$P_p = f(L/D) \frac{1}{2} \rho A \bar{V}^3 / \eta_p \eta_m, \quad (4.41)$$

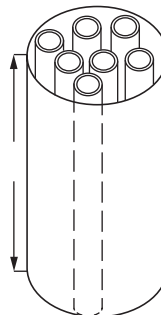


FIGURE 4.8

TES system with embedded tubes for increased heat-transfer area.

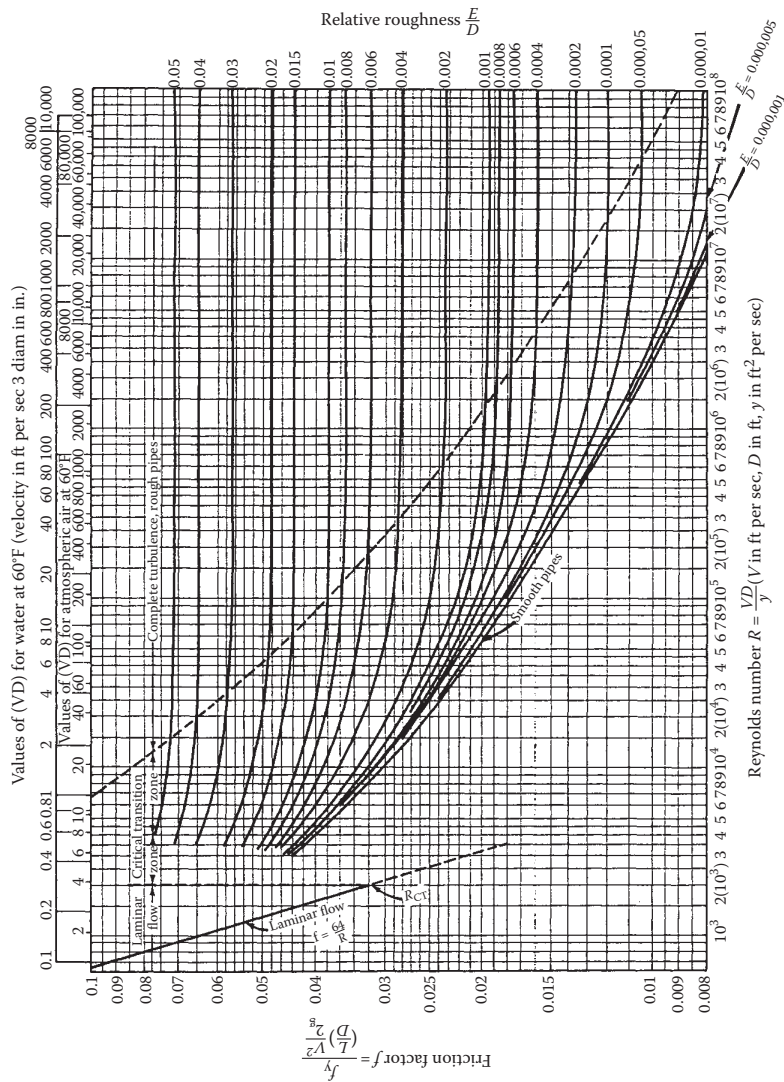
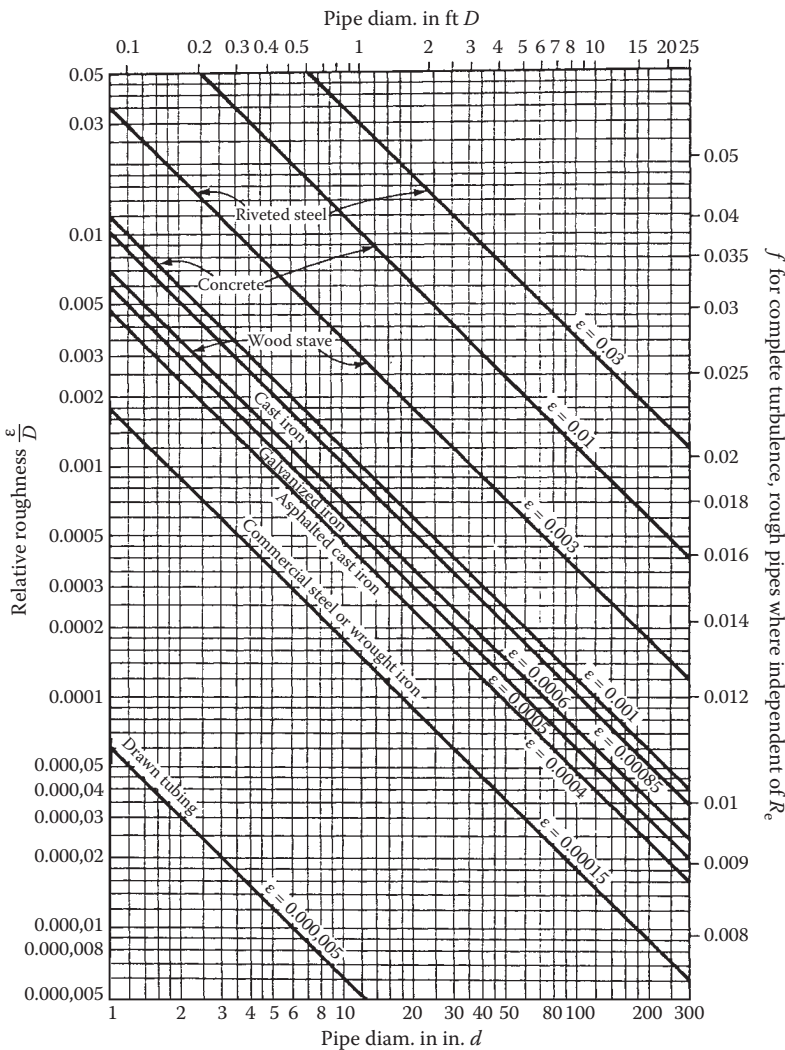


FIGURE 4.9
Friction factor for pipe flow as a function of Reynolds number and roughness ratio ϵ/D . (From Potter, P.J., *Power Plant Theory and Design*, Ronald Press, New York, 1959.)

**FIGURE 4.10**

Roughness ratio ϵ/D for various types of commercial pipe. (From Potter, P.J., *Power Plant Theory and Design*, Ronald Press, New York, 1959.)

where A is the flow area, η_p is the pump efficiency, η_m is the motor efficiency, and the average velocity \bar{V} is related to the volumetric flow as $\dot{Q} = \bar{A}\bar{V}$.

Although the fluid circuits in most parts of solar thermal systems are quite simple, the collector field is frequently connected in a complex series-parallel arrangement as dictated by trade-offs between piping costs, pump size, and fluid temperature rise. The flow in series-parallel arrays can be calculated using iterative techniques such as the Hardy-Cross method. However, for

preliminary design, a closed form solution has been developed for flow through arrays of solar collectors connected in parallel. For $j + 1$ identical collectors with the same flow rate connected in parallel with constant diameter D headers or manifolds, the array pressure drop (inlet header inlet port to outlet header outlet port) is given by

$$\Delta P = \frac{K_f \dot{m}^2}{6} [j(2j+1)(j+1)] \Delta p_{\text{coll}} \quad (4.42)$$

where Δp_{coll} is the collector pressure drop, \dot{m} is the mass flow rate per collector, and

$$K_f = 8 \bar{f} L / (\pi^2 \rho D^5). \quad (4.43)$$

The average friction factor, \bar{f} in the header is evaluated at one-half the total array flow, $(j+1)\dot{m}/2$, and the collectors are all connected into the manifold at a uniform distance L apart. It is noted that identical flow \dot{m} through each header does not occur automatically, but can be accomplished to within a few percent by requiring 90% or more of the total array pressure drop to occur across the collector; that is,

$$\Delta p_{\text{coll}} \geq 0.9 \Delta P. \quad (4.44)$$

In the design of piping systems, the absolute pressure must not be permitted to drop below the boiling point to avoid vapor lock, boiling, or pump cavitation. The critical design point is where the fluid is hottest and the pressure lowest—often at a circulating pump inlet port. Some common fluids used for high-temperature solar systems are shown in Table 4.7. The fluid manufacturer should be consulted for precise viscosity values to be used for system design. Typical values are in the range 0.2 to 5.0 c_p . Most are quite temperature sensitive.

4.4.3 Heat Loss

Parasitic heat losses from storage tanks, pipes, and pumps can be calculated from equations given in any heat-transfer text. For cylindrical insulation of thermal conductivity k , length L , inner diameter D , and thickness t for pipes and tanks,

$$q_{\text{cyl}} = \frac{2\pi k L}{\ln \frac{D+2t}{D}} (T_f - T_a), \quad (4.45)$$

TABLE 4.7
Properties of Liquid Heat-Transfer Media

Material	Composition	Density (kg/m ³)	Specific Heat (kJ/kg·°C)	Boiling Point (°C)	Manufacturer
Water		~1000	~4.2	~100	
Therminal VP-1	Diphenyl oxide 73.5% Biphenyl oxide 26.5 wt%	1060 (25°C)	2.18 (250°C)	257	Solutia Inc.
Dowtherm A	Diphenyl oxide 73.5% Biphenyl oxide 26.5 wt%	1056 (25°C)	2.23 (255°C)	257	Dow Chemical
Hitec	40% NaNO ₂ , 7% NaNO ₃ , 53% KNO ₃	1640 (300°C)	1.6 (300°C)	—	Coastal Chemical
Caloria HT-43	Hydrotreated heavy paraffinic 99%	880 (15.6°C)	2.1 (100°C)	293	Exxon Company
Diethylene glycol		1180 (20°C)	2.3 (25°C)	245	Dow Chemical
Tetraethylene glycol		1124 (20°C)	2.2 (25°C)	327	Dow Chemical
Xceltherm MK1	Diphenyl oxide 73% Biphenyl oxide 27%	1062 (25°C)	2.2 (260°C)	257	Radco
Dynalene MS-1	Potassium nitrate and sodium nitrate	1900 (300°C)	1.40 (300°C)	—	Dynalene
Syltherm XLT	Dimethyl polysiloxane	852 (25°C)	2.32 (280°C)	—	Dow Chemical

Source: Data collected from various manufacturers' brochures, MSDS, and online resources.

where T_f is the fluid temperature and T_a is the ambient temperature. For spherical storage tanks, the heat loss is

$$q_{\text{sph}} = \frac{\pi k D(D + 2t)}{t} (T_f - T_a). \quad (4.46)$$

In the above, it is assumed that the principal resistance to heat loss occurs in the insulation.

Although heat losses can be made arbitrarily small, the law of diminishing returns applies and a point is reached where added insulation costs more than the value of the extra heat retained. It can be shown that the optimum distribution of a given volume of insulation over all the components of a solar thermal system occurs when the surface heat flux is the same everywhere; note that this does not imply equal insulation thickness t (Harrison and Pelanne 1977).

For low-temperature applications such as heating, cooling, and domestic hot water, foam rubber or polyurethane foam insulation is normally used. For higher-temperature applications, the principal insulations include calcium silicate, mineral fiber, expanded silica (perlite), and fiberglass. Table 4.8 lists the properties of industrial-grade insulations useful in elevated temperature solar systems (Harrison and Pelanne 1977). Calcium silicate is a mixture of lime and silica reinforced with fibers and molded into shape. It has good compressive strength. Mineral fiber consists of rock and slag fibers bonded together and are useful up to 1200°F (650°C). The compressive strength is less than calcium silicate but is available in both rigid and flexible, shaped segments.

Perlite is expanded volcanic rock consisting of small air cells enclosed by a mineral structure. Additional binders are added to decrease moisture migration and to reduce shrinkage. Cellular glass is available in flexible bats or rigid boards and shaped sections. It has very low moisture absorption.

For very high temperatures, the selection of materials is quite limited. In addition to mineral fiber and calcium silicate noted above, ceramic fibers (to 1400°C), castable ceramic insulation (to 1600°C), Al_2O_3 or ZrO_2 fibers (to 1600°C), and carbon fibers (to 2000°C) are available. It is to be noted that these temperatures correspond to the refractory range of metals where service conditions are very severe.

An excellent summary of industrial insulation practice and design methods and economics analysis is contained in Harrison and Pelanne (1977).

4.4.4 Heat Exchangers

Heat exchangers are devices in which two fluid streams exchange thermal energy: one stream is heated while the other is cooled. There are a number of arrangements used to transfer heat from one fluid to another. The simplest

TABLE 4.8

Properties of Pipe Insulation for Elevated Temperatures

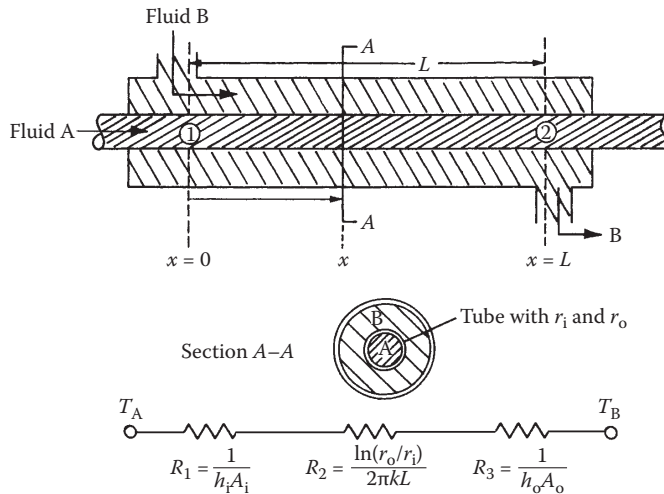
Insulation Type	Temperature Range (°F)	Conductivity k [Btu/(h) (ft²)(°F/in.)]	Density (lb/ft³)	Applications
Urethane foam	-300 to 300	0.11 to 0.14	1.6 to 3.0	Hot and cold piping
Cellular glass blocks	-350 to 500	0.20 to 0.75	7.0 to 9.5	Tanks and piping
Fiberglass blanket for wrapping	-120 to 550	0.15 to 0.54	0.60 to 3.0	Piping and pipe fittings
Fiberglass preformed shapes	-60 to 450	0.22 to 0.38	0.60 to 3.0	Hot and cold piping
Fiberglass mats	150 to 700	0.21 to 0.38	0.60 to 3.0	Piping and pipe fittings
Elastomeric preformed shapes and tape	-40 to 220	0.35 to 0.27	4.5 to 6.0	Piping and pipe fittings
Fiberglass with vapor barrier jacket	20 to 150	0.20 to 0.31	0.65 to 2.0	Refrigerant lines, dual-temperature lines, chilled-water lines, fuel-oil piping
Fiberglass without vapor barrier jacket	to 500	0.20 to 0.31	1.5 to 3.0	Hot piping
Cellular glass blocks and boards	70 to 900	0.20 to 0.75	7.0 to 9.5	Hot piping
Urethane foam blocks and boards	200 to 300	0.11 to 0.14	1.5 to 4.0	Hot piping
Mineral—fiber preformed shapes	to 1200	0.24 to 0.63	8.0 to 10.0	Hot piping
Mineral—fiber blankets	to 1400	0.26 to 5.60	8.0	Hot piping
Fiberglass field applied jacket for exposed lines	500 to 800	0.21 to 0.55	2.4 to 6.0	Hot piping
Mineral—wool blocks	850 to 1800	0.36 to 0.90	11.0 to 18.0	Hot piping
Calcium silicate blocks	1200 to 1800	0.33 to 0.72	10.0 to 14.0	Hot piping

Source: Harrison, M. and C. Pelanne, Cost effective thermal insulation, *Chem. Eng.*, 84, 62, 1977.

Note: 1 Btu/(h)(ft²)(°F/in.) = 1/12 Btu/h·ft·°F = 0.144 W/m·°C.

arrangement is the double-pipe heat exchanger shown in Figure 4.11. It will be discussed first.

In this system, fluid A flows inside a tube of inner radius r_i and the outer radius r_o . Fluid B flows in the annulus formed between the outer surface of the inner tube, A_o , and the inner surface of the outer tube. An overall heat-transfer coefficient U can be calculated from the thermal circuit shown in Figure 4.11. It may be based on any convenient area of the exchanger, but

**FIGURE 4.11**

Schematic diagram of a double-pipe heat exchanger in parallel flow.

usually the outside area $A_o = 2\pi r_o L$ of the inner tube is most convenient (Karlekar and Desmond 1977). Then,

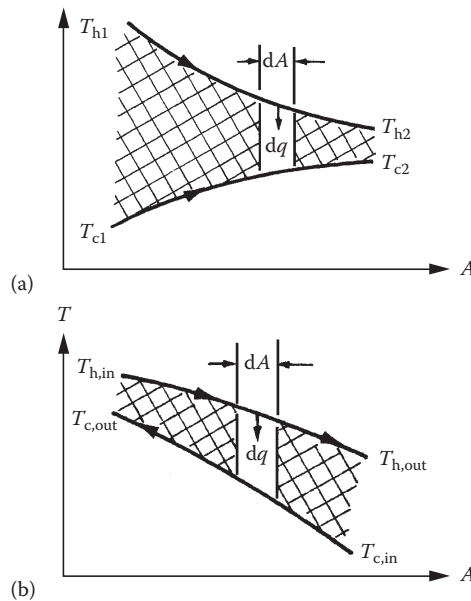
$$U_o A_o = \frac{1}{\frac{1}{h_i A_i} + \frac{\ln(r_o/r_i)}{2\pi k L} + \frac{1}{h_o A_o}}. \quad (4.47)$$

And at any cross section, the local rate of heat transfer across the tube is

$$dq = U_o dA_o (T_A - T_B) = U_o 2\pi r_o dx (T_A - T_B). \quad (4.48)$$

Simplifications in the evaluation of U_o are possible when one or two of the thermal resistances dominate. For example, the thermal resistance of the tube wall, R_2 in Figure 4.11, is often small compared to the convective resistances and sometimes one of the two convective resistances is negligible compared to the other.

The flow arrangement shown in Figure 4.9, where both fluids enter from the same end, is called parallel flow, and Figure 4.12a shows the temperature distribution for both fluid streams. If one of the two fluids were to enter at the other end and flow in the opposite direction, the flow arrangement would be *countercflow*. The temperature distribution for the latter case

**FIGURE 4.12**

(a) Parallel flow; (b) counterflow.

is shown in Figure 4.12b. If a counterflow arrangement is made very long, it approaches the thermodynamically most efficient possible heat-transfer condition. Figure 4.12 shows that the counterflow exchanger has the highest heat-transfer effectiveness and is therefore the preferred design for solar systems.

There are two basic methods for calculating the rate of heat transfer in a heat exchanger. One method employs a mean temperature difference between the two fluids in the exchanger ΔT_{mean} and then determines the rate of heat transfer from the relation (Karlekar and Desmond 1977)

$$q = UA\Delta T_{\text{mean}}. \quad (4.49)$$

This mean temperature difference is called the logarithmic mean temperature difference (LMTD). It can be evaluated directly only when the inlet and outlet temperatures of both fluid streams are specified. The use of the LMTD approach is explained in Karlekar and Desmond (1977). The other method is called the effectiveness-NTU method (ϵ -NTU). The ϵ -NTU method offers many advantages over the LMTD approach and will be discussed in the following.

First, we define the exchanger effectiveness ϵ :

$$\epsilon = \frac{\text{actual rate of heat transfer}}{\text{maximum possible rate of heat transfer}}. \quad (4.50)$$

The actual rate of heat transfer can be determined by calculating either the rate of internal energy loss of the hot fluid or the rate of internal energy gain of the cold fluid; that is,

$$\dot{q} = \dot{m}_h c_{p,h} (T_{h,in} - T_{h,out}) = \dot{m}_c c_{p,c} (T_{c,out} - T_{c,in}), \quad (4.51)$$

where the subscripts "h" and "c" denote the hot and cold fluid, respectively. The maximum rate of heat transfer possible for specified inlet fluid temperatures is attained when one of the two fluids undergoes the maximum temperature difference in the exchanger. This maximum temperature difference equals the difference in the entering temperatures for the hot and cold fluid. Which of the two fluids can undergo this maximum temperature change depends on the relative value of the product ($\dot{m}c_p$), the mass flow rate times the specific heat of the fluid at constant pressure, called the heat capacity rate \dot{C} . Since a thermodynamic energy balance requires that the energy given up by one fluid must be received by the other if there are no external heat losses, only the fluid with the smaller value of \dot{C} can undergo the maximum temperature change. Thus, the fluid that may undergo this maximum temperature change is the one that has the minimum value of the heat capacity rate; therefore, the maximum rate of heat transfer is

$$\dot{q}_{\max} = \dot{C}_{\min} (T_{h,in} - T_{c,in}), \quad (4.52)$$

where

$$\dot{C}_{\min} = (\dot{m}c_p)_{\min}.$$

The fluid with the minimum $\dot{m}c_p$ or \dot{C} value can be either the hot or the cold fluid. Using subscript "h" to designate the effectiveness when the hot fluid has the minimum \dot{C} and the subscript "c" when the cold fluid has the minimum \dot{C} value, we get

$$\varepsilon_{hx} = \frac{\dot{C}_h (T_{h,in} - T_{h,out})}{\dot{C}_h (T_{h,in} - T_{c,in})} = \frac{T_{h,in} - T_{h,out}}{T_{h,in} - T_{c,in}} \quad (4.53)$$

$$\varepsilon_{hx} = \frac{\dot{C}_c (T_{c,out} - T_{c,in})}{\dot{C}_c (T_{h,in} - T_{c,in})} = \frac{T_{c,out} - T_{c,in}}{T_{h,in} - T_{c,in}}, \quad (4.54)$$

where the subscripts "in" and "out" refer to the inlet and outlet of the fluid as shown in Figure 4.12.

Kays and London (1980) have calculated effectiveness values for many types of heat exchangers. They found that ε_{hx} can be expressed for a given

exchanger type as a function of two variables, the number of transfer units NTU,

$$\text{NTU} = UA_{\text{hx}} / (\dot{m}c_p)_{\text{min}} \quad (4.55)$$

and the capacitance ratio C ,

$$C = (\dot{m}c_p)_{\text{min}} / (\dot{m}c_p)_{\text{max}} = \dot{C}_{\text{min}} / \dot{C}_{\text{max}} \quad (4.56)$$

For boiling or condensation, $C = 0$.

Figure 4.13a through d shows effectiveness values for the common heat-exchanger types and Table 4.9 contains equations for calculating $\varepsilon_{\text{hx}}(\text{NTU}, C)$. For parallel flow and counterflow devices in which boiling or condensation occurs in one stream, $\varepsilon_{\text{hx}} = 1 - e^{-\text{NTU}}$. For the special case of $(\dot{m}c_p)_{\text{min}} = (\dot{m}c_p)_{\text{max}}$, a special effectiveness equation applies for counterflow heat exchangers.

$$\varepsilon_{\text{hx}} = \text{NTU} / (\text{NTU} + 1). \quad (4.57)$$

Figure 4.14 shows that the counterflow exchanger has the highest heat-transfer effectiveness and is therefore the preferred design for solar systems.

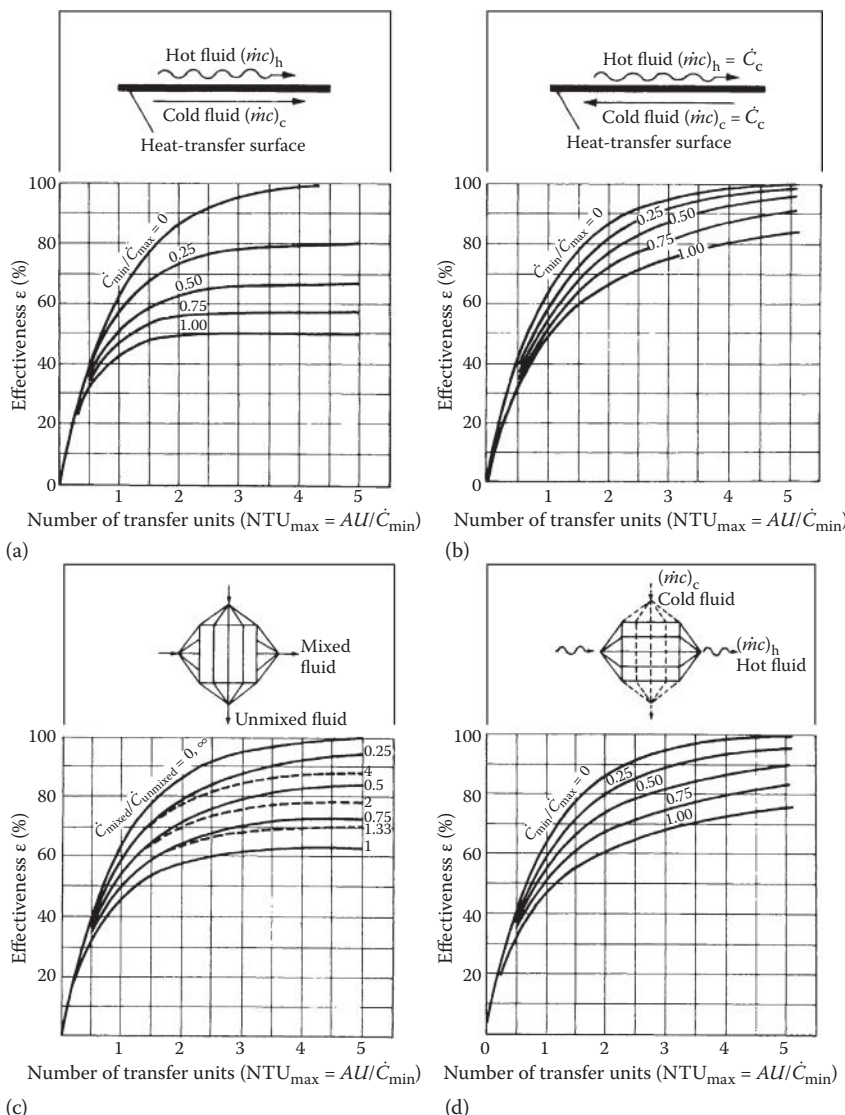
One of the most common uses of a heat exchanger is to isolate a fluid used in a solar collector field from the process fluid that conveys the heat energy to its end use as shown in Figure 4.15. If the required process inlet temperature is $T_{p,i}$, the collector outlet fluid must be at a temperature $T_{c,o}$ above $T_{p,i}$ because of the presence of the heat exchanger. Since collector efficiency decreases with increasing operating temperature, less energy is collected than if no heat exchanger were present. A heat-exchanger penalty factor F_{hx} , which can be applied to the linear collector model (Equation 3.46) developed earlier, has been calculated by deWinter (1975). Equation 3.46 can be rewritten in terms of the heat-exchanger inlet temperature (process return temperature) $T_{p,o}$ as

$$\eta_c = F_{\text{hx}} F_R [\eta_o - U_c (T_{p,o} - T_a) / I_c]. \quad (4.58)$$

The heat-exchanger factor is given by

$$F_{\text{hx}} = 1 + \frac{F_R U_c A_c}{(\dot{m}c_p)_c} \frac{(\dot{m}c_p)_c}{\varepsilon_{\text{hx}} (\dot{m}c_p)_{\text{min}}}^{-1}, \quad (4.59)$$

where c denotes collector properties and ε_{hx} is the heat-exchanger effectiveness. The collector loss coefficient U_c is evaluated at the mean collector operating temperature \bar{T}_c .

**FIGURE 4.13**

Heat-exchanger effectiveness as a function of NTU and C ; (a) parallel flow, (b) counterflow, (c) cross flow, one fluid mixed, and (d) cross flow, no mixing. (From Kays, W.M. and A.L. London, *Compact Heat-Exchangers*, McGraw-Hill, New York, 1980. Copyright 1964. With permission from McGraw-Hill Book Company.)

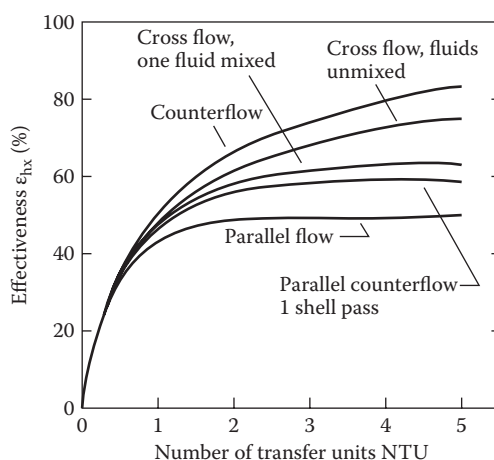
TABLE 4.9

Heat Exchanger Effectiveness Expressions

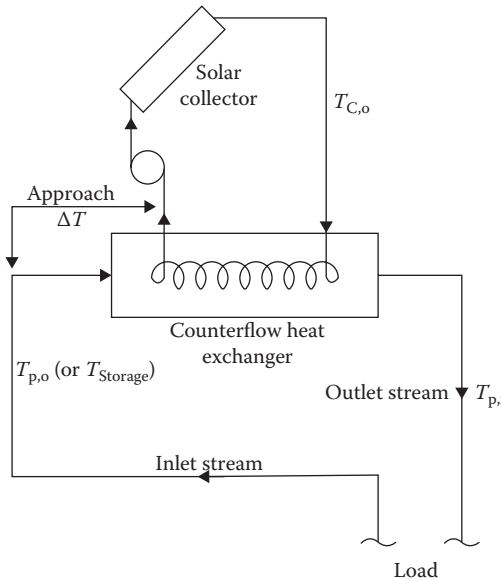
Flow Geometry	Relation
Double pipe; parallel flow	$\epsilon = \frac{1 - \exp[-N(1+C)]}{1+C}$
Counterflow	$\epsilon = \frac{1 - \exp[-N(1-C)]}{1 - C \exp[-N(1-C)]}$
Cross flow; both fluids unmixed	$\epsilon = 1 - \exp\{(C/n) [\exp(-NCn)-1]\}$ where $n = N^{-0.22}$
Both fluids mixed	$\epsilon = \frac{1}{1 - \exp(-N)} + \frac{C}{1 - \exp(-NC)} - \frac{1}{N}^{-1}$
C_{\max} mixed, C_{\min} unmixed	$\epsilon = (1/C)\{1 - \exp[C(e^{-N}-1)]\}$
C_{\max} unmixed, C_{\min} mixed	$\epsilon = 1 - \exp\{(1/C)[\exp(-NC) - 1]\}$
Shell and tube; one shell pass, 2, 4, 6 tube passes	$\epsilon = 2 \frac{1+C+(1+C^2)^{1/2}}{1+C-(1+C^2)^{1/2}} \frac{1+\exp -N(1+C^2)^{1/2}}{1-\exp -N(1+C^2)^{1/2}}^{-1}$

Source: Karlekar, B.V. and R.M. Desmond, *Engineering Heat Transfer*, West Publ., St. Paul, Minnesota, 1977.

Note: $N = NTU \equiv UA/\dot{C}_{\min}$, $C = \dot{C}_{\min}/\dot{C}_{\max}$.

**FIGURE 4.14**

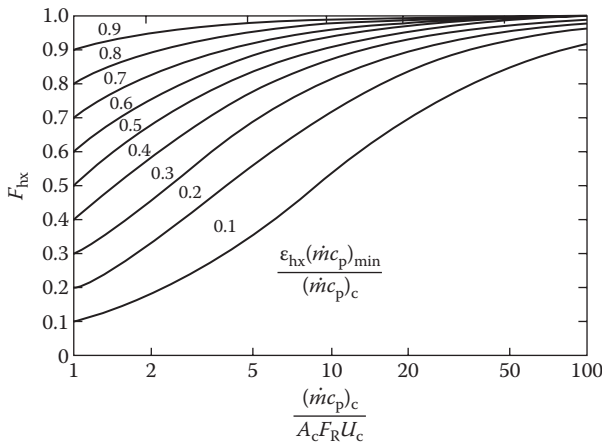
Heat-exchanger effectiveness as a function of NTU; effect of flow type for. (From Kays, W.M. and A.L. London, *Compact Heat-Exchangers*, McGraw-Hill, New York, 1980. Copyright 1964. With permission from McGraw-Hill Book Company.)

**FIGURE 4.15**

Use of a heat exchanger to isolate a collector from the thermal process.

Figure 4.16 shows F_{hx} for a range of operating conditions. Unless the collector flow is very low, $F_{hx} > 0.95$ for most high-performance collectors. For small $F_R U_C A_C / (\dot{m}c_p)_c$, F_{hx} is approximated closely by

$$F_{hx} = 1 - F_R U_C A_C \left\{ \frac{(\dot{m}c_p)_c - \varepsilon_{hx}(\dot{m}c_p)_{min}}{\varepsilon_{hx}(\dot{m}c_p)_{min}(\dot{m}c_p)_c} \right\}. \quad (4.60)$$

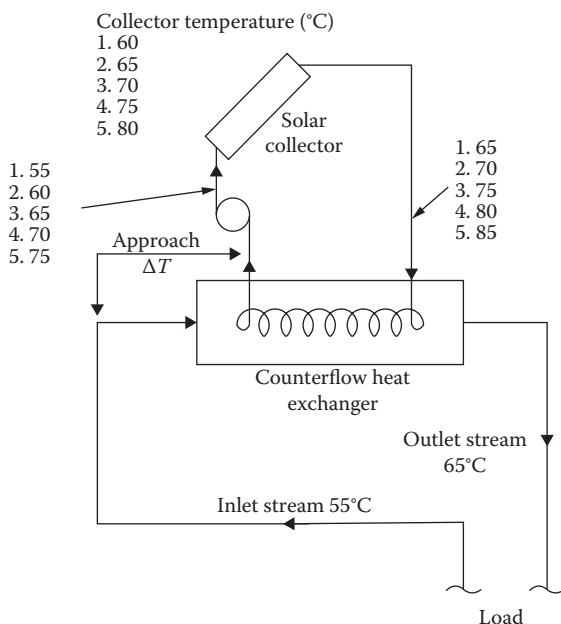
**FIGURE 4.16**

Heat-exchanger factor F_{hx} calculated from Equation 4.60.

Example 4.5

Calculate the efficiency at which the solar collector in Figure 4.17 operates in order to deliver energy to a working fluid at 65°C for several values of the approach temperature difference. The approach temperature is the difference between the incoming cool fluid and the exiting warm fluid at the heat exchanger (see Figure 4.17). The temperature rise through the heat exchanger is 10°C and is equal to the fluid temperature rise through the solar collector.

The collector has a $\tau\alpha$ product of 0.80 and loss coefficient U_c of 5 W/m²K. If the solar radiation normal to the collector surface is 500 W/m² and the ambient temperature T_a is 20°C, calculate the collector efficiency for the following five values of approach ΔT :



Case	Approach ΔT (°C)
1	0 (thermodynamic limit)
2	5
3	10
4	15
5	20

FIGURE 4.17

Fluid stream and solar collector temperatures for Example 4.5 (heat-exchanger problem).

Case	Approach ΔT (°C)
1	0 (thermodynamic limit)
2	5
3	10
4	15
5	20

Solution

Fluid stream temperatures are shown at several points for each case in Figure 4.17. The collector temperature T_c can be taken as the average of inlet and outlet fluid temperatures for purposes of the example as shown in the figure.

Collector efficiency can be calculated from the following equation (see Chapter 3):

$$\eta = \tau \alpha - U_c \frac{\Delta T}{I_c} ,$$

where

$$\Delta T = \bar{T}_c - T_a .$$

For the collector specified here,

$$\eta = 0.8 - 5 \frac{T}{I_c} \times 100\% .$$

The collector efficiency can be calculated in tabular form as shown in Table 4.10.

Note that the heat-exchanger design has a very strong effect on collector efficiency; for relatively small changes of approach temperature difference, efficiency, and therefore energy delivery, change significantly.

TABLE 4.10

Collector Efficiency Calculation for Example 4.5

Case	\bar{T}_c (°C)	ΔT (°C)	I_c (W/m ²)	$\Delta T/I_c$ (K·m ² /W)	η (%)
1	60	40	500	0.08	40
2	65	45	500	0.09	35
3	70	50	500	0.10	30
4	75	55	500	0.11	25
5	80	60	500	0.12	20

Example 4.6

Calculate the energy delivery penalty in a solar system caused by a required exchanger for values of effectiveness from 0.2 to 0.99. Compare the economic value of this energy penalty to the heat-exchanger cost if the annual amortized cost (see Section 1.4) of a heat exchanger per year is \$6/m²_{hx}. The economic value of the solar energy collection penalty is the value of nonsolar energy required to make up for the penalty resulting from the heat exchanger. The value of nonsolar, makeup energy is \$10/GJ for this example. System specifications are listed below. Water is the working fluid.

$$A_c = 100 \text{ m}^2$$

$$(\dot{m}c_p)_{\min} = (\dot{m}c_p)_{\max} = \frac{50 \text{ kg}}{\text{h} \cdot \text{m}_c^2} \times 4182 \frac{\text{J}}{\text{kg} \cdot \text{K}}$$

Energy delivery with no heat exchanger = 200 MJ/m_c²·year.

$$F_R U_c = 5 \text{ W/m}_c^2 \cdot {}^\circ\text{C} \left(= 5 \times 3600 \text{ J/h} \cdot \text{m}_c^2 \cdot {}^\circ\text{C} \right)$$

$$U_{hx} = 1400 \text{ W/m}_c^2 \cdot {}^\circ\text{C}$$

Solution

The heat-exchanger penalty factor F_{hx} with the above values substituted in Equation 4.59 is

$$F_{hx} = \frac{1}{1 + 0.0861 \frac{1}{\varepsilon_{hx}} - 1}.$$

Table 4.11 summarizes the thermal penalty from heat-exchanger use. Also shown is the heat-exchanger area required to provide a given effectiveness. The heat-exchanger area A_{hx} is evaluated by the use of Equation 4.55 and values of NTU required to provide a given effectiveness for counterflow heat exchangers from Table 4.11. The annual energy delivery Q_u in Table 4.12 is given by

$$Q_u = F_{hx} A_c (200) \text{ MJ/m}_c^2 \cdot \text{year}.$$

The solar energy penalty, which must be made up by the other fuels, is

$$Q_a = (1 - F_{hx}) A_c (200) \text{ MJ/m}_c^2 \cdot \text{year}.$$

TABLE 4.11

Counterflow Heat Exchanger Performance

NTU	ϵ_{hx} for Indicated Capacity Rate Ratios $(mc_p)_{min}/(mc_p)_{max}$							
	0	0.25	0.50	0.70	0.75	0.80	0.90	1.00
0	0	0	0	0	0	0	0	0
0.25	0.221	0.216	0.210	0.206	0.205	0.204	0.202	0.200
0.50	0.393	0.378	0.362	0.350	0.348	0.345	0.339	0.333
0.75	0.528	0.502	0.477	0.457	0.452	0.447	0.438	0.429
1.00	0.632	0.598	0.565	0.538	0.532	0.525	0.513	0.500
1.25	0.713	0.675	0.635	0.603	0.595	0.587	0.571	0.556
1.50	0.777	0.735	0.691	0.655	0.645	0.636	0.618	0.600
1.75	0.826	0.784	0.737	0.697	0.687	0.677	0.657	0.636
2.00	0.865	0.823	0.775	0.733	0.722	0.711	0.689	0.667
2.50	0.918	0.880	0.833	0.788	0.777	0.764	0.740	0.714
3.00	0.950	0.919	0.875	0.829	0.817	0.804	0.778	0.750
3.50	0.970	0.945	0.905	0.861	0.848	0.835	0.807	0.778
4.00	0.982	0.962	0.928	0.886	0.873	0.860	0.831	0.800
4.50	0.989	0.974	0.944	0.905	0.893	0.880	0.850	0.818
5.00	0.993	0.982	0.957	0.921	0.909	0.896	0.866	0.833
5.50	0.996	0.998	0.968	0.933	0.922	0.909	0.880	0.846
6.00			0.975	0.944		0.921	0.892	0.857
6.50			0.980	0.953		0.930	0.902	0.867
7.00			0.985	0.960		0.939	0.910	0.875
7.50			0.988	0.966		0.946	0.918	0.882
8.00			0.991	0.971		0.952	0.925	0.889
8.50			0.993	0.975		0.957	0.931	0.895
9.00			0.994	0.979		0.962	0.936	0.900
9.50			0.996	0.982		0.966	0.941	0.905
10.00			0.997	0.985		0.970	0.945	0.909
∞	1.000	1.000	1.000	1.000	1.000	1.000	1.000	1.000

Source: Kays, W.M. and A.L. London, *Compact Heat-Exchangers*, McGraw-Hill, New York, 1980. Copyright 1980 by McGraw-Hill Book Co. Used with permission of McGraw-Hill Book Co.

The economic value of the heat-exchanger energy penalty is

$$C_a = Q_a c_a,$$

where c_a is the cost of auxiliary energy in dollars per gigajoule. The host of heat-exchanger area C_{hx} is

$$C_{hx} = A_{hx} c_{hx},$$

where c_{hx} is the amortized cost per year of heat exchanger per unit in dollars per square meter per year (see Table 4.13).

TABLE 4.12

Thermal Performance Summary for Example 4.6

Effectiveness, ϵ_{hx}	Exchanger Penalty, F_{hx}	Energy Collection, Q_u (GJ/year)	NTU ^a	Exchanger Area, A_{hx} (m ²)
0.2	0.744	14.88	0.25	1.04
0.333	0.853	17.06	0.50	2.07
0.5	0.921	18.42	1.00	4.15
0.6	0.946	18.92	1.50	6.22
0.7	0.964	19.28	2.33	9.75
0.8	0.979	19.58	4.00	16.60
0.9	0.991	19.82	9.00	37.34
0.99	0.999	19.98	99.00	411.00
1.0 ^b	1.000 ^b	20.00 ^b	— ^c	0.00 ^b

^a Table 4.11 or Equation 4.57.^b Baseline.^c No exchanger baseline.**TABLE 4.13**

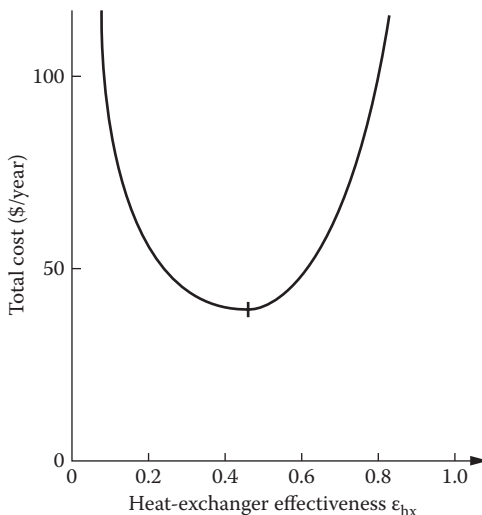
Economic Summary for Example 4.6

Effectiveness, ϵ_{hx}	Extra Nonsolar, Q_a (GJ/year)	Economic Value of Energy Penalty, C_a (\$/year)	Cost of Exchanger Area, C_{hx} (\$/year)	Total Cost ^a (\$/year)
0.2	5.12	51.20	6.24	57.44
0.333	2.94	29.40	12.42	41.82
0.5	1.58	15.80	24.90	40.70
0.6	1.08	10.80	37.32	48.12
0.7	0.72	7.20	58.50	65.70
0.8	0.42	4.20	99.60	103.80
0.9	0.18	1.80	224.04	225.85
0.99	0.02	0.20	2466.00	2466.20

^a $C_a + C_{hx}$.

The results of this example show that the cost of the extra exchanger area to provide increased effectiveness ϵ_{hx} rises rapidly. Since the heat-exchanger cost to provide the last few percent of solar energy delivery is high, the value of this energy is relatively small when compared with the additional exchanger cost. It is, therefore, not cost-effective to provide this energy. Likewise, small heat exchangers have a larger energy penalty, which has a correspondingly larger dollar value in replacement fuel. It is therefore cost-effective to add heat-exchanger area in order to recover a portion but not all of the solar energy required.

Figure 4.18 is a plot of the total extra cost required to provide a total demand of 20 GJ/year. This extra cost is required by the design stipulation that a heat exchanger be used. It is a cost above the basic solar and

**FIGURE 4.18**

Total cost of heat exchanger and nonsolar energy penalty for Example 4.6. Least-cost configuration has a heat-exchanger effectiveness of 0.46.

backup system costs. The least cost heat-exchanger configuration is for an effectiveness value of about 0.46. It is to be noted that this example considers only one component of the solar system. A complete system optimization requires making simultaneous trade-offs of many system components. This methodology is described later in this book. Note that the direct application of the F_{hx} factor to annual energy delivery instead of instantaneous delivery is correct only for the case of negligible loss from storage and no heat rejection by storage boiling or other means.

PROBLEMS

- On a clear day, the energy delivered by a solar system, Q_u , is approximately a sinusoidal function of time with a maximum, $Q_{u\max}$, near noon and a minimum at sunrise and sunset.
 - If this is a solar thermal system and thermal energy demand is a constant L_o , calculate the temperature history of storage for a day for the block system in Figure 4.19.
 - If this is a PV system with $Q_{u\max}$ from one solar panel at noon equal to 200 W_e and length of the day from sunrise to sunset as 10 h, how many solar panels would be needed to provide for a constant load of 1 kW_e for 24 h?
- A packed bed storage system consists of a bed of crushed rock. The average diameter of the particles is 35 mm, and the sphericity was

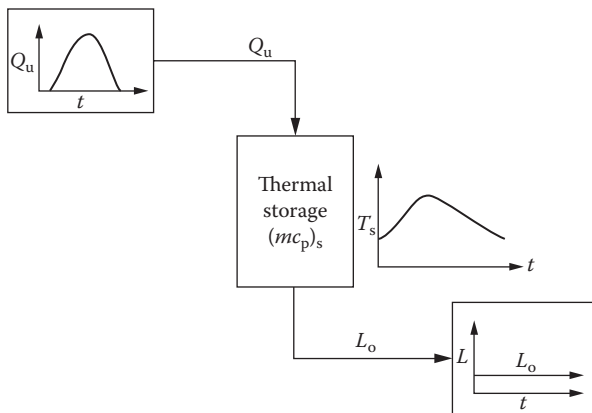
**FIGURE 4.19**

Figure for Problem 1.

determined to be 0.75. Air is used as the heat-transfer fluid and flows through the system with a superficial bed velocity of 0.90 m/s. Calculate the pressure drop per unit length, assuming the air density is 1.15 kg/m^3 and the air viscosity is $1.903 \times 10^{-5} \text{ kg/m}\cdot\text{s}$. How does this compare to the pressure drop when the particle diameter is 50 mm?

3. Compare the energy storage capability of sodium sulfate decahydrate (Glauber's salt) in a range from 30° to 60°C with that of water and rock in the same range. Also, compare the volumes of storage for the three media.
4. A 100-m^2 liquid solar collector (flat-plate type) is located 40 m from the building it serves. If the liquid pressure drop through the collector is 7 kPa, what is the total pressure drop in the collector fluid loop? What pipe size would you recommend for the collector loop? Why?

Assume:

1. Flow rate is 1.15 l/min per m^2 of collectors.
2. Pipe fittings add 20 equivalent m of pipe.
3. Fluid velocity in pipe is 1 m/s.
4. Actual pipe length is 2.5 times the distance of collector to building.
5. A cylindrical storage tank for the collector in Problem 2 is located in the basement of the dwelling it serves. If the basement temperature is 16°C and the storage tank is 70°C , what is the heat-loss rate from the tank? The tank is a cylinder with diameter equal to its height; it is insulated with a 15-cm-thick fiberglass batt.

6. How large should a water storage tank be if it is to supply the total daily heat load (1.5 GJ) of a building if the storage tank temperature may vary by 20°C ? Neglect parasitic transmission and conversion losses. If a 4-m³ carbon steel tank costs \$1000.00, what will this tank cost?
7. What is the pressure drop in 50 m of a 1-in pipe for fluid flowing at 0.4 m³/min?
8. If the fluid velocity in a pipe is to be kept below 4 ft/s, what pipe size should be used to flow 500 gal/min? What is the pressure drop in 500 ft of this pipe?
9. An array of twenty 40-ft² solar panels is connected in parallel. What is the pressure drop through the manifold if water is used at the rate of 0.03 gal/min ft² and the collectors are spaced 5 ft apart. Pipe with 1-in diameter is used.
10. A heat exchanger is used to isolate a collector loop from the storage loop in a solar-cooling system. Collector and storage fluid capacitance rates are $300 \text{ kJ/m}_c^2 \cdot \text{h} \cdot ^{\circ}\text{C}$ and the collector heat loss conductance is $5 \text{ kJ/kJ/m}_c^2 \cdot \text{h} \cdot ^{\circ}\text{C}$ with a heat removal factor $F_R = 0.9$. What is the energy delivery penalty from heat-exchanger use if the heat-exchanger effectiveness is 0.25, 0.5, and 0.9?
11. Water flowing at a rate of 70 kg/min is to be heated from 340 to 350 K in a counterflow double pipe heat exchanger by a 50% glycol solution that enters the heat exchanger at 360 K and exits at 345 K. If the overall heat-transfer coefficient is 300 W/m²·K, calculate the required heat-exchanger area.
12. A shell-and-tube heat exchanger with one shell pass and two tube passes, having an area of 4.5 m², is to be used to heat high-pressure water initially at 290 K with hot air initially at 400 K. If the exit water temperature is not to exceed 350 K, the air flow rate is 0.5 kg/s, and the overall heat-transfer coefficient is 300 W/m²·K, calculate the water flow rate.
13. A cross-flow fin-and-tube heat exchanger uses hot water to heat air from 290 to 300 K. Water enters the heat exchanger at 340 K and exits at 310 K. If the total heat-transfer rate is to be 300 kW and the average heat-transfer coefficient between the water and the air is 50 W/m²·K, calculate the area of the heat exchanger required and the mass rate of air flow through the exchanger.
14. A small steam condenser is to be designed to condense 0.8 kg/min steam at 80 kN/m² with cooling water at 290 K. If the exit temperature of the water is not to exceed 320 K, calculate the area required for a shell-and-tube heat exchanger with the steam making one shell pass and the water making two tube passes. The overall heat-transfer coefficient is 3000 W/m²·K.

References

- Arkar, C., and S. Medved. 2005. Influence of accuracy of thermal property data of a phase change material on the result of a numerical model of a packed bed latent heat storage with spheres. *Thermochim. Acta* 438: 192–201.
- ASHRAE. 2011. Thermal storage. In *ASHRAE Handbook, HVAC Application*. American Society of Heating, Refrigerating and Air-Conditioning Engineers, 1791 Tullie Circle, N.E., Atlanta, GA, p. 40.14.
- Beasley, D.E., and J.A. Clark. 1984. Transient response of a packed bed for thermal energy storage. *Int. J. Heat Mass Transfer* 27(9): 1659–1669.
- Beckman, G., and P.V. Gilli. 1984. *Topics in Energy—Thermal Energy Storage*. Springer-Verlag, New York.
- Chavez, J.M. et al. 1995. The solar two power tower project: A 10 MWe power plant. *Proceedings of the 1995 IECEC* 2: 469–475. ASME, New York.
- Churchill, S.W. 1977. Friction factor equation spans all fluid-flow regimens. *Chem. Eng.* 84(24): 91.
- Clark, J.A. 1986. Thermal design principles, Chapter 5. In *Solar Heat Storage: Latent Heat Materials*, G.A. Lane, ed. CRC Press, Boca Raton, FL, pp. 185–223.
- Cole, R.L. et al. 1980. *Design and Installation Manual for Thermal Energy Storage*, ANL-79-15, 2nd ed. Argonne National Lab., Argonne, IL.
- Coutier, J., and E. Farber. 1982. Two applications of a numerical approach of heat-transfer process within rock beds. *Sol. Energy* 29(6): 451–462.
- Delameter, W.R., and N.E. Bergen. 1986. Review of molten salt electric experiment: Solar central receiver project. SAND 86-8249. Sandia National Laboratory, Albuquerque, NM.
- deWinter, F. 1975. Heat exchanger penalties in double-loop solar water heating systems. *Sol. Energy* 17: 335.
- Edwards, D.P., and M.K. Jensen. 1994. Pressure drop and heat transfer predictions of turbulent flow in longitudinally finned tubes. *Adv. Enhanced Heat Transfer* 287: 17–23.
- Eisfeld, B., and K. Schnitzlein. 2001. The influence of confining walls on the pressure drop in packed beds. *Chem. Eng. Sci.* 56(14): 4321–4329.
- Ergun, S. 1952. Fluid flow through packed columns. *Chem. Eng. Prog.* 48: 89.
- Garg, H.P., S.C. Mullick, and A.K. Bhargava. 1985. *Solar Thermal Energy Storage*. D. Reidel, Boston.
- Glendenning, I. 1981. Advanced mechanical energy storage. In *Energy Storage and Transportation*, G. Beghe, ed. D. Reidel, Boston, pp. 50–52.
- Hanchen, M., S. Brückner, and A. Steinfeld. 2011. High-temperature thermal storage using a packed bed of rocks—Heat transfer analysis and experimental validation. *Appl. Therm. Eng.* 31: 1798–1806.
- Harrison, M., and C. Pelanne. 1977. Cost effective thermal insulation. *Chem. Eng.* 84: 62.
- Idelsohn, S.R., M.A. Storti, and L. Crivelli. 1994. Numerical methods in phase-change problems. *Arch. Computational Methods Eng.* 1: 49–74.
- Jaluria, Y., and K.E. Torrance. 2003. *Computational Heat Transfer*. Taylor & Francis Group, New York.
- Jeffreson, C.P. 1972. Prediction of breakthrough curves in packed beds: 1. Applicability of single parameter models. *AICHE J.* 18(2): 409–416.

- Jensen, J. 1980. *Energy Storage*. Newnes-Butterworth, Boston.
- Jotshi, C.K., and D.Y. Goswami. 1998. Energy storage. In *Mechanical Engineering Handbook*, F. Kreith, Editor-in-Chief. CRC Press, Boca Raton, FL, pp. 8–104.
- Karlekar, B.V., and R.M. Desmond. 1977. *Engineering Heat Transfer*. West Publ., St. Paul, MN.
- Kays, W.M., and A.L. London. 1980. *Compact Heat-Exchangers*. McGraw-Hill, New York.
- Kent, G.R. 1978. Preliminary pipeline sizing. *Chem. Eng.* 85: 199.
- Kim, L.V. 1994. Determination of the heat transfer coefficients in porous media. *J. Eng. Phys. Thermophys.* 65: 1168–1172.
- Kreider, J.F. 1979. *Medium and High Temperature Processes*. Academic Press, New York.
- Kuravi, S. et al. 2013. Thermal energy storage technologies and systems for concentrating solar power plants. *Prog. Energy Combust. Sci.* 39: 285–319.
- Li, L., and W. Ma. 2011. Experimental study on the effective particle diameter of a packed bed with non-spherical particles. *Transp. Porous Med.* 89: 35–48.
- Makansi, J. 1994. Energy storage reinforces competitive business practices. *Power* 138(9): 63.
- McAdams, W.H. 1954. *Heat Transmission*, 3rd ed. McGraw-Hill, New York.
- Meier, A., C. Winkler, and D. Wuillemin. 1991. Experiment for modeling high temperature rock bed storage. *Sol. Energy Mater.* 24: 255–264.
- Moses, P.J., and G.A. Lane. 1986. Encapsulation of PCMs. In *Solar Heat Storage: Latent Heat Materials*, Vol. II. G. A. Lane, Ed. CRC Press, Boca Raton, FL, pp. 93–152.
- Potter, P.J. 1959. *Power Plant Theory and Design*. Ronald Press, New York.
- Rabl, A. 1977. A note on the optics of glass tubes. *Sol. Energy* 19(2): 215.
- Sanduja, P. et al. 2013. Numerical analysis of a packed bed thermal storage system for concentrated solar power. *Energy Procedia, Proceedings of the ISES 2013 Solar World Congress*.
- Singh, R., R.P. Saini, and J.S. Saini. 2006. Nusselt number and friction factor correlations for packed bed solar energy storage system having large sized elements of different shapes. *Sol. Energy* 80(7): 760–771.
- Swet, C.J. 1987. Storage of thermal energy—Status and prospects. In *Progress in Solar Engineering*, D.Y. Goswami, ed. Hemisphere Publ., Washington, DC.
- Tomlinson, J.J., and L.F. Kannberg. 1990. Thermal energy storage. *Mech. Eng.* 9: 68–72.
- Trahan, J. et al. 2013. Evaluation of pressure drop and particle sphericity for an air-rock bed thermal energy storage system. *Energy Procedia, Proceedings of the 2013 ISES Solar World Congress*, Cancun, Mexico.
- Voller, V.R. 1996. An overview of numerical methods for solving phase change problems. In *Advances in Numerical Heat Transfer*, Vol. 1, Chapter 9. Taylor & Francis, London.
- Yang, Z., and S.V. Garimella. 2010. Thermal analysis of solar thermal energy storage in a molten-salt thermocline. *Sol. Energy* 84: 974–985.
- Zhang, Y., and A. Faghri. 1996. Heat transfer enhancement in latent heat thermal energy storage system by using the internally finned tube. *Int. J. Heat Mass Transfer* 39(15): 3165–3173.

5

Solar Heating Systems

For the well being and health ... the homesteads should be airy in summer and sunny in winter. A homestead promising these qualities would be longer than it is deep and the main front would face south.

Aristotle

The use of solar energy for heat production dates from antiquity. Historically, methods used for collecting and transferring solar heat were passive methods, that is, without active means such as pumps, fans, and heat exchangers. *Passive* solar heating methods utilize natural means such as radiation, natural convection, thermosyphon flow, and thermal properties of materials for collection and transfer of heat. *Active* solar heating methods, on the other hand, use pumps and fans to enhance the rate of fluid flow and heat transfer. Active methods for water heating, space heating, and industrial process heat (IPH) have been developed mainly in the last four decades. This chapter describes in detail the function and design of active systems for heating buildings and service water. Passive solar heating, cooling, and daylighting are covered in Chapter 7. Other applications, such as low-temperature solar heat for agriculture, agricultural drying, or aquaculture, can be analyzed with the principles set forth in this chapter and Chapters 3 and 4.

Energy for heating buildings and hot water consumes approximately one-quarter of the annual energy production in the United States. In many areas of the United States and the world, solar heating can compete economically with other types of fuel for heating, without even considering the environmental benefits.

5.1 Calculations of Heating and Hot-Water Loads in Buildings

Energy requirements for space heating or service water heating can be calculated from basic conservation of energy principles. For example, the heat required to maintain the interior of a building at a specific temperature is the total of all heat transmission losses from the structure and heat required to warm and humidify the air exchange with the environment by infiltration and ventilation.

Comfort in buildings has long been a subject of investigation by the American Society of Heating, Refrigerating and Air-Conditioning Engineers (ASHRAE). ASHRAE has developed extensive heat load calculation procedures embodied in the *ASHRAE Handbook of Fundamentals* (ASHRAE 2013). The most frequently used load calculation procedures will be summarized in this section; the reader is referred to the ASHRAE handbook for details.

Figure 5.1 shows the combinations of temperature and humidity that are required for human comfort. The shaded area is the standard US comfort level for sedentary persons. Many European countries have human comfort levels from 3°C to 7°C below US levels. If activity of a continuous nature

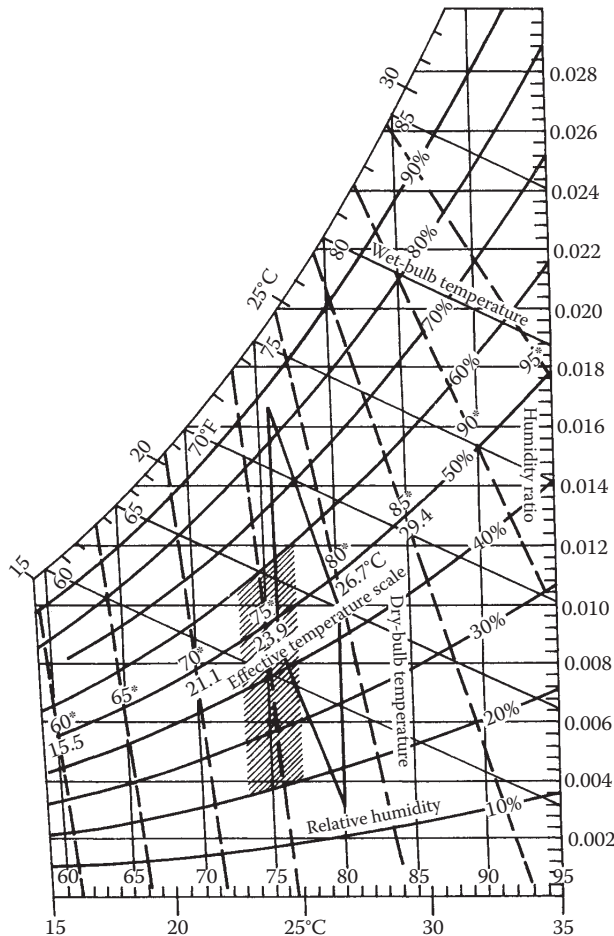


FIGURE 5.1
Heat-loss calculations for buildings.

is anticipated, the comfort zone lies to the left of the shaded area; if extra clothing is worn, the comfort zone is displaced similarly.

5.1.1 Calculation of Heat Loss

It is outside the scope of this book to describe the details of the heat load calculations for buildings. However, the method is described in brief in this section. For details, one should refer to the *ASHRAE Handbook of Fundamentals* (ASHRAE 2013) or some textbook on heating and air-conditioning. Table 5.1 lists the components of heat-loss calculations of a building.

Complete tables of thermal properties of building materials are given in Appendix 5. Appendix 5 also contains web addresses that list the average wind and design temperature data for many cities in the United States and the rest of the world.

Transmission heat losses through attics, unheated basements, and the like are buffered by the thermal resistance of the unheated space. For example, the temperature of an unheated attic lies between that of the heated space and that of the environment. As a result, the ceiling of a room below an attic is exposed to a smaller temperature difference and consequently would have lower heat loss than the same ceiling without the attic. The effective conductance of thermal buffer spaces can easily be calculated by forming an energy balance on such spaces.

The following example is an illustration of the heat-loss calculation method described in this section.

TABLE 5.1

Heating Load Calculations for Buildings

Heating Load Component	Equations 5.1 through 5.4	Descriptions/References
Walls, roof, ceilings, glass	$q = U \cdot A(T_i - T_o)$ (5.1)	T_i and T_o are inside and outside air temperature, respectively. U values of composite section are calculated from the thermal properties of components given in Appendix 5.
Basement floors and walls below ground level	$q_f = U_f A_f$ (5.2)	U_f has special units of W/m ² .
Concrete floors on ground	$q_{fe} = F_e P_e (T_i - T_o)$ (5.3)	F_e is the perimeter of the slab.
Infiltration and ventilation air	$q_{sensible} = Q \rho_a C p_a (T_i - T_o)$ or = $1200 * Q (T_i - T_o)$ watts $q_{latent} = Q \rho_a h_{fg} \Delta W$ or = $2808 * Q \Delta W$ watts (5.4)	Q is volume of air flow in m ³ /s. ρ_a and $C p_a$ are density and specific heat of air. h_{fg} is the latent heat of water at room temperature. ΔW is humidity ratio difference between inside and outside air.

* Assuming $\rho_a = 1.2 \text{ kg/m}^3$; $h_{fg} = 2340 \text{ J/kg}$, $C p_a = 1000 \text{ J/kg}\cdot^\circ\text{C}$.

Example 5.1

Calculate the heat load on a house for which the wall area is 200 m^2 , the floor area is 600 m^2 , the roof area is 690 m^2 , and the window area totals 100 m^2 . Inside wall height is 3 m. The construction of the wall and the roof is shown in Figure 5.2.

Solution

The thermal resistance of the wall shown in Figure 5.2 can be found by the electrical resistance analogy as

$$R_{\text{wa}} = R_{\text{outside air}} + R_{\text{wood siding}} + R_{\text{sheathing}} + R_{\text{comb}} + R_{\text{wall board}} + R_{\text{inside air}}$$

Combined thermal resistance for the studs and insulation (R_{comb}) is found as

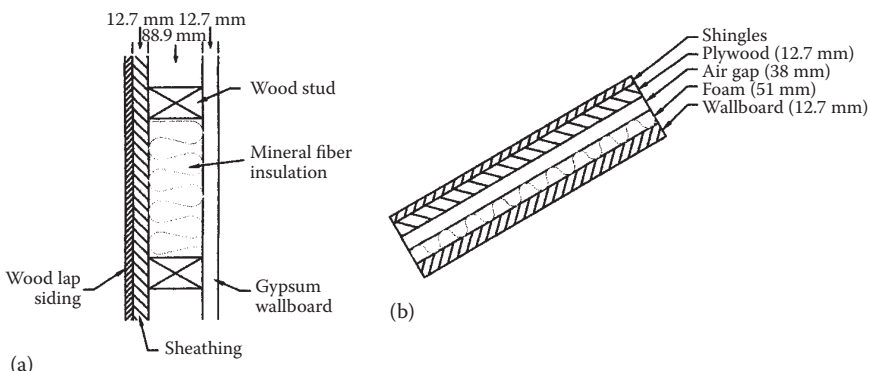
$$\frac{1}{R_{\text{comb}}} = \frac{A_{\text{stud}}}{R_{\text{stud}}} + \frac{A_{\text{insulation}}}{R_{\text{insulation}}} \frac{1}{A_{\text{stud}} + A_{\text{insulation}}}.$$

Assuming that the studs occupy 15% of the wall area,

$$\frac{1}{R_{\text{comb}}} = \frac{0.15}{0.77} + \frac{0.85}{1.94}$$

or

$$R_{\text{comb}} = 1.58 \frac{\text{m}^2 \cdot ^\circ\text{C}}{\text{W}}$$

**FIGURE 5.2**

Cross sections of the wall and the roof for Example 5.1. (a) Wall construction. (b) Roof construction.

Therefore, the wall thermal resistance, R_{wa} , can be found as

Element	Thermal Resistance (m ² ·°C/W)
Outside air (6.7 m/s wind)	0.030
Wood bevel lap siding	0.14
12.7 mm sheathing	0.23
88.9 mm combined wood stud and mineral fiber insulation	1.58
12.7 mm gypsum wallboard	0.079
Inside air (still)	0.12
$R_{wa} = 2.179$	

Therefore,

$$U_{wa} = \frac{1}{R_{wa}} = \frac{1}{2.179} = 0.46 \text{ W/m}^2 \cdot ^\circ\text{C.}$$

The heat loss through the windows depends on whether they are single or double glazed. In this example, single-glazed windows are installed, and a U factor equal to 4.7 W/m²·°C is used. (If double-glazed windows were installed, the U factor would be 2.4 W/m²·°C.)

The roof is constructed of 12.7 mm gypsum wallboard, 51 mm foam insulation board, 38 mm still air, 12.7 mm plywood, and asphalt shingles (wooden beams and roofing paper are neglected for the simplified calculations here). Therefore,

$$U_{rf} = \frac{1}{0.030 + 0.077 + 0.11 + 0.17 + 2.53 + 0.079 + 0.1} \\ \text{Outside Shingles Plywood Airgap Foam Wallboard Inside} \\ \text{air air} \\ = 0.32 \text{ W/m}^2 \cdot ^\circ\text{C}$$

If the respective areas and U factors are known, the rate of heat loss per hour for the walls, windows, and roof can be calculated.

$$\text{Walls: } q_{wa} = (200 \text{ m}^2) \times 0.46 \text{ W/m}^2 \cdot ^\circ\text{C} = 92 \text{ W/}^\circ\text{C}$$

$$\text{Windows: } q_{wi} = (100 \text{ m}^2) \times 0.47 \text{ W/m}^2 \cdot ^\circ\text{C} = 470 \text{ W/}^\circ\text{C}$$

$$\text{Roof: } q_{rf} = (690 \text{ m}^2) \times 0.32 \text{ W/m}^2 \cdot ^\circ\text{C} = 220 \text{ W/}^\circ\text{C}$$

$$\text{Total } q_{tr} = 782 \text{ W/}^\circ\text{C}$$

If double-glazed windows were used, the heat loss would be reduced to 552 W/°C.

The infiltration and ventilation rate Q for this building is assumed to be 0.5 ACH (air changes per hour). The sensible and latent heat loads of the infiltration air may be calculated using the equations given in Table 5.1. Therefore,

$$Q = 0.5 \times (600 \text{ m}^2 \times 3 \text{ m} \text{ (volume)}) = 900 \text{ m}^3/\text{h} = 0.25 \text{ m}^3/\text{s},$$

$$q_{\text{sensible}} = 0.25 \text{ m}^3/\text{s} \times (1.2 \text{ kg/m}^3)(1000 \text{ J/kg} \cdot ^\circ\text{C}) = 300 \text{ W}/^\circ\text{C}.$$

In residential buildings, humidification of the infiltration air is rarely done. Neglecting the latent heat, the total rate of heat loss q_{tot} is the sum of q_{sensible} and q_{tr} :

$$q_{\text{tot}} = (782 + 300) = 1082 \text{ W}/^\circ\text{C}.$$

This calculation is simplified for purposes of illustration. Heat losses through the slab surface and edges have been neglected, for example.

More refined methods of calculating energy requirements on buildings do not use the steady-state assumption used above (Klein et al. 1975). The thermal inertia of buildings may be expressly used as a load-leveling device. If so, the steady-state assumption is not met and the energy capacitance of the structure must be considered for accurate results. Many adobe structures in the US Southwest are built intentionally to use daytime sun absorbed by 1-ft-thick walls for nighttime heating, for example.

5.1.2 Internal Heat Sources in Buildings

Heat supplied to a building to offset energy losses is derived from both the heating system and internal heat sources. Table 5.2 lists the common sources of internal heat generation for residences. Commercial buildings such as hospitals, computer facilities, or supermarkets will have large internal gains specific to their function. Internal heat gains tend to offset heat losses from a building but will add to the cooling load of an air-conditioning system. The magnitude of the reduction in heating system operation will be described in Section 5.1.3.

5.1.3 Degree-Day Method

The preceding analysis of heat loss from buildings expresses the loss on a per-unit temperature difference basis (except for unexposed floor slabs). In order to calculate the peak load and total annual load for a building, appropriate design temperatures must be defined for each. The outdoor design temperature is usually defined statistically, such that the actual outdoor temperature will exceed the design temperature 97.5% or 99% of the time over a long period. The design temperature difference (ΔT) is then the interior building temperature minus the outdoor design temperature. The design ΔT is used for rating non-solar heating systems but is not useful for selection of solar systems, since solar systems rarely provide 100% of the energy demand of a building at peak conditions.

TABLE 5.2

Some Common Internal Sensible Heat Gains That Tend to Offset the Heating Requirements of Buildings

Type	Magnitude (W or J/s)
Incandescent lights	Total W
Fluorescent lights	Total W
Electric motors	$746 \times (\text{hp}/\text{efficiency})$
Natural gas stove	$8.28 \times \text{m}^3/\text{h}$
Appliances	Total W
A dog	50–90
People	
Sitting	70
Walking	75
Dancing	90
Working hard	170
Sunlight	$\text{Solar heat gain} \times \text{fenestration transmittance} \times \text{shading factor}^{\text{a}}$

Source: ASHRAE. *Handbook of Fundamentals*. ASHRAE, Atlanta, GA, 2013.

^a Shading factor is the amount of a window not in a shadow expressed as a decimal between 1.0 and 0.0.

A more useful index of heating energy demand is the total annual energy requirement for a building. This quantity is somewhat more difficult to calculate than the peak load. It requires knowledge of day-to-day variations in ambient temperature during the heating season and the corresponding building heat load for each day. Building heat loads vary with ambient temperatures as shown in Figure 5.3. The no-load temperature T_{nl} , above which no heat need be supplied to the building, is a few degrees below the required interior temperature T_i because of internal heat-generation effects.

The no-load temperature at which internal source generation q_i just balances transmission and infiltration losses can be determined from the energy balance

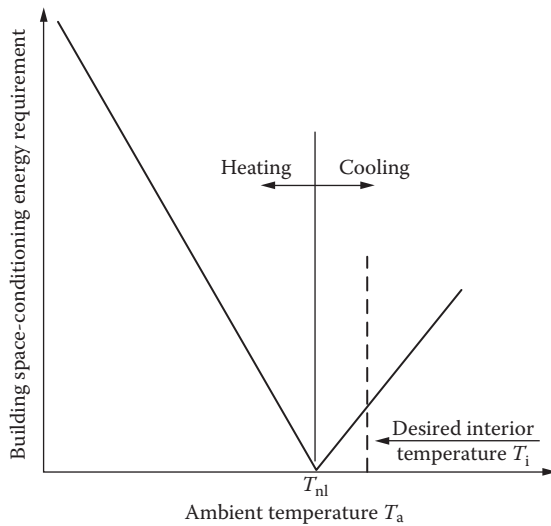
$$q_i = \overline{UA}(T_i - T_{nl}), \quad (5.5)$$

where \overline{UA} is the overall loss coefficient for the building (W/°C). Then,

$$T_{nl} = T_i - \frac{q_i}{\overline{UA}}. \quad (5.6)$$

The total annual heat load on the building, Q_T can be expressed as

$$Q_T = \int_{365 \text{ days}} \overline{UA}(T_{nl} - T_a)^+ dt, \quad (5.7)$$

**FIGURE 5.3**

Building load profile versus ambient temperature showing no-load temperature T_{nl} and desired interior temperature T_i .

in which all arguments of the integral are functions of time. The superscript “+” indicates that only positive values are considered. In practice, it is difficult to evaluate this integral; therefore, three simplifying assumptions are made:

1. \overline{UA} is independent of time.
2. T_{nl} is independent of time.
3. The integral can be expressed by the sum.

Thus,

$$\overline{UA} \sum_{n=1}^{365} (T_{nl} - \bar{T}_a)^+ \quad (5.8)$$

where n is the day number, and the daily average temperature \bar{T}_a can be approximated by $\frac{1}{2}(T_{a,\max} + T_{a,\min})$, in which $T_{a,\max}$ and $T_{a,\min}$ are the daily maximum and minimum temperatures, respectively.

The quantity $(T_{nl} - T_a)^+$ is called the *degree-day unit*. For example, if the average ambient temperature for a day is 5°C and the no-load temperature is 20°C, 15 degree C-days are said to exist for that day. However, if the ambient temperature is 20°C or higher, 0 degree-days exist, indicating 0 demand for

heating that day. Degree-day totals for monthly ($\Sigma_{\text{month}} (T_{\text{nl}} - T_a)^+$) and annual periods can be used directly in Equation 5.8 to calculate the monthly and annual heating energy requirements.

In the past, a single value of temperature has been used throughout the United States as a universal degree-day base, 65.0°F or 18.3°C.* This practice is now outdated, since many homeowners and commercial building operators have lowered their thermostat settings in response to increased heating fuel costs, thereby lowering T_{nl} . Likewise, warehouses and factories operate well below the 19°C level. Therefore, a more generalized database of degree-days to several bases (values of T_{nl}) has been created by the US National Weather Service (NWS).

A variable base degree-day method, which recognizes that T_{nl} may vary not only with location but also from building to building, is more accepted now (ASHRAE 2013). ASHRAE (2013) have listed heating degree days and cooling degree days for a number of worldwide locations.

Example 5.2

A building located in Denver, Colorado, has a heat-loss coefficient \overline{UA} of 1000 kJ/h·°C and internal heat sources of 4440 kJ/h. If the interior temperature is 20°C (68°F), what are the monthly and annual heating energy requirements? A gas furnace with 65% efficiency is used to heat the building.

Solution

In order to determine the monthly degree-day totals, the no-load temperature (degree-day basis) must be evaluated from Equation 5.6.

$$T_{\text{nl}} = 20 - \frac{4440}{1000} = 15.6^{\circ}\text{C} (60^{\circ}\text{F})$$

The monthly degree C-days for Denver are taken from the NWS and given in Table 5.3. The energy demand is calculated as

$$\text{Energy demand} = \overline{UA} \times 24 \frac{\text{h}}{\text{day}} \times \text{degree C-days}. \quad (5.9)$$

The monthly energy demand is given in Table 5.3.

* The degree-day base in SI units is defined as 19.0°C, not 18.3°C, which corresponds to 65.0°F. Therefore, precise conversion between the two systems is not possible by a simple multiplication by 5/9.

TABLE 5.3

Monthly and Annual Energy Demands for Example 5.2

Month	Degree C-days	Energy Demand ^a (GJ)
Jan	518	12.4
Feb	423	10.2
Mar	396	9.5
Apr	214	5.2
May	68	1.6
Jun	14	0.3
Jul	0	0
Aug	0	0
Sep	26	0.6
Oct	148	3.6
Nov	343	8.2
Dec	472	11.3
	2622	62.9

^a Energy demand equals $UA \times \text{degree C-days} \times 24 \text{ h/day}$.

The annual energy demand of 62.9 GJ is delivered by a 65% efficient device. Therefore,

$$\text{Average annual purchased energy} = \frac{62.9}{0.65} \text{ GJ} = 96.8 \text{ GJ}.$$

5.1.4 Service Hot-Water Load Calculation

Service hot-water loads can be calculated precisely with the knowledge of only a few variables. The data required for calculation of hot-water demand are as follows:

Water source temperature (T_s)

Water delivery temperature (T_d)

Volumetric demand rate (Q)

The energy requirement for service water heating q_{hw} is given by

$$q_{hw}(t) = \rho_w Q(t) c_{pw} [T_d - T_s(t)], \quad (5.10)$$

where ρ_w is the water density and c_{pw} is its specific heat. The demand rate, $Q(t)$, varies in general with time of day and time of year; likewise, the source temperature varies seasonally. Source temperature data are not compiled in

a single reference; local water authorities are the source of such temperature data.

Few generalized data exist with which to predict the demand rate Q . Table 5.4 indicates some typical usage rates for several common building types. Process water heating rates are peculiar to each process and can be ascertained by reference to process specifications.

Example 5.3

Calculate the monthly energy required to heat water for a family of four in Nashville, Tennessee. Monthly source temperatures for Nashville are shown in Table 5.5, and the water delivery temperature is 60°C (140°F).

Solution

For a family of four, the demand rate Q may be found using a demand recommended from Table 5.4:

$$Q = 4 \times 76 \text{ liters/day} = 0.30 \text{ m}^3/\text{day}.$$

The density of water can be taken as 1000 kg/m³, and the specific heat, as 4.18 kJ/kg·°C.

Monthly demands are given by

$$\begin{aligned} q_m &= (Q \times \text{days/month})(\rho_w c_{pw})[T_d - T_s(t)] \\ &= (0.30 \times \text{days/month})(1000 \times 4.18)[60 - T_s(t)]. \end{aligned}$$

The monthly energy demands calculated from the equation above with these data are tabulated in Table 5.5.

TABLE 5.4

Approximate Service Hot-Water Demand Rates

Usage Type	Demand per Person	
	Liters/day	Gallons/day
Retail store	2.8	0.75
Elementary school	5.7	1.5
Multifamily residence	76.0	20.0
Single-family residence	76.0	20.0
Office building	11.0	3.0

TABLE 5.5

Water Heating Energy Demands for Example 5.3

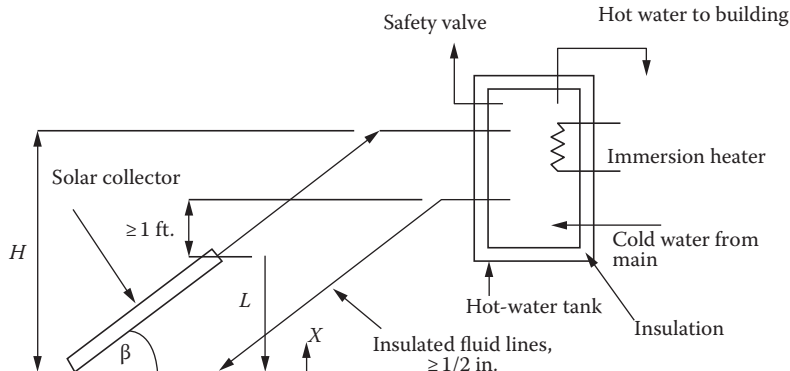
Month	Days/Month	Demand (m ³ /month)	Source Temperature (°C)	Energy Requirement (GJ/month)
Jan	31	9.3	8	2.0
Feb	28	8.4	8	1.8
Mar	31	9.3	12	1.9
Apr	30	9.0	19	1.5
May	31	9.3	17	1.7
Jun	30	9.0	21	1.5
Jul	31	9.3	22	1.5
Aug	31	9.3	24	1.4
Sep	30	9.0	24	1.4
Oct	31	9.3	22	1.5
Nov	30	9.0	14	1.7
Dec	31	9.3	12	1.9

5.2 Solar Water-Heating Systems

Solar water-heating systems represent the most common application of solar energy at the present time. Small systems are used for domestic hot-water applications while larger systems are used in IPH applications. There are basically two types of water-heating systems: *natural circulation* or passive solar system (thermosyphon) and *forced circulation* or active solar system. Natural circulation solar water heaters are simple in design and low cost. Their application is usually limited to nonfreezing climates, although they may also be designed with heat exchangers for mild freezing climates. Forced-circulation water heaters are used in freezing climates and for commercial and IPH.

5.2.1 Natural Circulation Systems

The natural tendency of a less dense fluid to rise above a denser fluid can be used in a simple solar water heater to cause fluid motion through a collector (Close 1962). The density difference is created within the solar collector where heat is added to the liquid. In the system shown in Figure 5.4, as water gets heated in the collector, it rises to the tank, and the cooler water from the tank moves to the bottom of the collector, setting up a natural circulation loop. It is also called a *thermosyphon loop*. Since this water heater does not use a pump, it is a passive water heater. For the thermosyphon to work, the storage tank must be located higher than the collector.

**FIGURE 5.4**

Schematic diagram of thermosyphon loop used in a natural circulation, service water-heating system. The flow pressure drop in the fluid loop must equal the buoyant force "pressure" $\int_0^L g\rho(x)dx - \rho_{stor}gL$, where $\rho(x)$ is the local collector fluid density and ρ_{stor} is the tank fluid density, assumed uniform.

The flow pressure drop in the fluid loop (ΔP_{FLOW}) must equal the buoyant force "pressure difference" ($\Delta P_{BUOYANT}$) caused by the differing densities in the hot and cold legs of the fluid loop:

$$\begin{aligned}\Delta P_{FLOW} &= \Delta P_{BUOYANT} \\ &= \rho_{stor}gH - \int_0^L \rho(x)g dx + \rho_{out}g(H-L) ,\end{aligned}\tag{5.11}$$

where H is the height of the legs and L is the height of the collector (see Figure 5.4), $\rho(x)$ is the local collector fluid density, ρ_{stor} is the tank fluid density, and ρ_{out} is the collector outlet fluid density; the latter two densities were assumed to be uniform. The flow pressure term ΔP_{FLOW} is related to the flow loop system head loss, which is in turn directly connected to friction and fitting losses and the loop flow rate:

$$\Delta P_{FLOW} = \oint_{LOOP} \rho d(h_L),\tag{5.12}$$

where $h_L = KV^2$, with K being the sum of the component loss velocity factors (see any fluid mechanics text) and V being the flow velocity.

Since the driving force in a thermosyphon system is only a small density difference and not a pump, larger-than-normal plumbing fixtures must be used to reduce pipe friction losses (Phillips and Cook 1975). In general,

one pipe size larger than normal used with a pump system is satisfactory. Figure 5.5 shows some passive water heaters.

Since the hot-water system loads vary little during a year, the angle of tilt is that equal to the latitude, that is, $\beta = L$. The temperature difference between the collector inlet water and the collector outlet water is usually 8°C - 11°C during the middle of a sunny day (Close 1962). After sunset, a thermosyphon system can reverse its flow direction and lose heat to the environment during the night. To avoid reverse flow, the top header of the absorber should be at least 30 cm below the cold leg fitting on the storage tank, as shown; otherwise, a check valve would be needed.

To provide heat during long cloudy periods, an electrical immersion heater can be used as a backup for the solar system. The immersion heater is located near the top of the tank to enhance stratification so that the heated fluid is at the required delivery temperature. Tank stratification is desirable in a thermosyphon to maintain flow rates as high as possible. Insulation must be applied over the entire tank surface to control heat loss.

Several features inherent in the thermosyphon design limit its utility. If it is to be operated in a freezing climate, a nonfreezing fluid must be used, which in turn requires a heat exchanger between collector and potable water storage. (If potable water is not required, the collector can be drained during cold periods instead.) Heat exchangers of either the shell-and-tube type or the immersion-coil type require higher flow rates for efficient operation than a thermosyphon can provide. Therefore, the thermosyphon is usually limited to nonfreezing climates. For mild freeze climates, a heat-exchanger

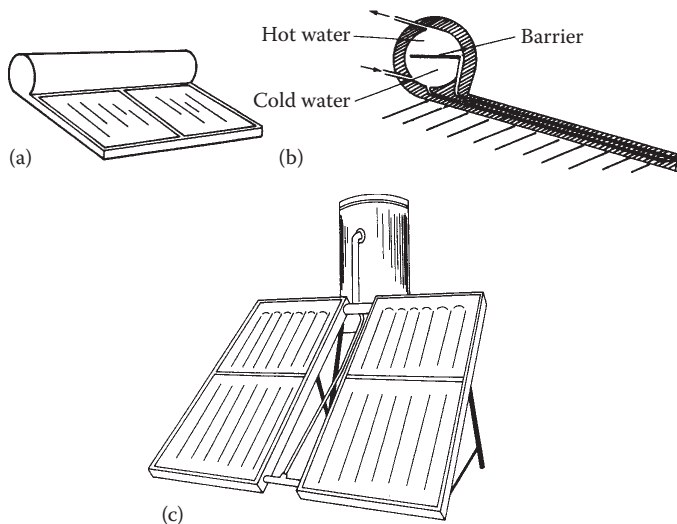


FIGURE 5.5

Passive solar water heaters: (a) compact model using combined collector and storage, (b) section view of the compact model, and (c) tank and collector assembly.

coil welded to the outer surface of the tank and filled with an antifreeze may work well.

Example 5.4

Determine the “pressure difference” available for a thermosyphon system with 1-m-high collector and 2-m-high legs. The water temperature input to the collector is 25°C and the collector output temperature is 35°C. If the overall system loss velocity factor (K) is 15.6, estimate the system flow velocity.

Solution

Equation 5.11 is used to calculate the pressure difference, with the water densities being found from the steam tables (see Appendix 3 and Tables 3.8 and 3.9).

$$\rho_{\text{stor}}(25^\circ\text{C}) = 997.009 \text{ kg/m}^3$$

$$\rho_{\text{stor}}(35^\circ\text{C}) = 994.036 \text{ kg/m}^3$$

$\rho_{\text{coll.ave.}}(30^\circ\text{C}) = 996.016 \text{ kg/m}^3$ (note: average collector temperature used in “integral”) and with $H = 2$ and $L = 1 \text{ m}$:

$$\begin{aligned}\Delta P_{\text{BUOYANT}} &= (997.009)9.81(2) - [(996.016)9.81(1) + (994.036)9.81(1)] \\ &= 38.9 \text{ N/m}^2(\text{pa}).\end{aligned}$$

The system flow velocity is estimated from the system K given, the pressure difference calculated above, taking the average density of the water around the loop (at 30°C) and substituting into Equation 5.12:

$$\Delta P_{\text{BUOYANT}} = (\rho_{\text{loop.ave.}})(h_L)_{\text{loop}} = (\rho_{\text{loop.ave.}})KV^2$$

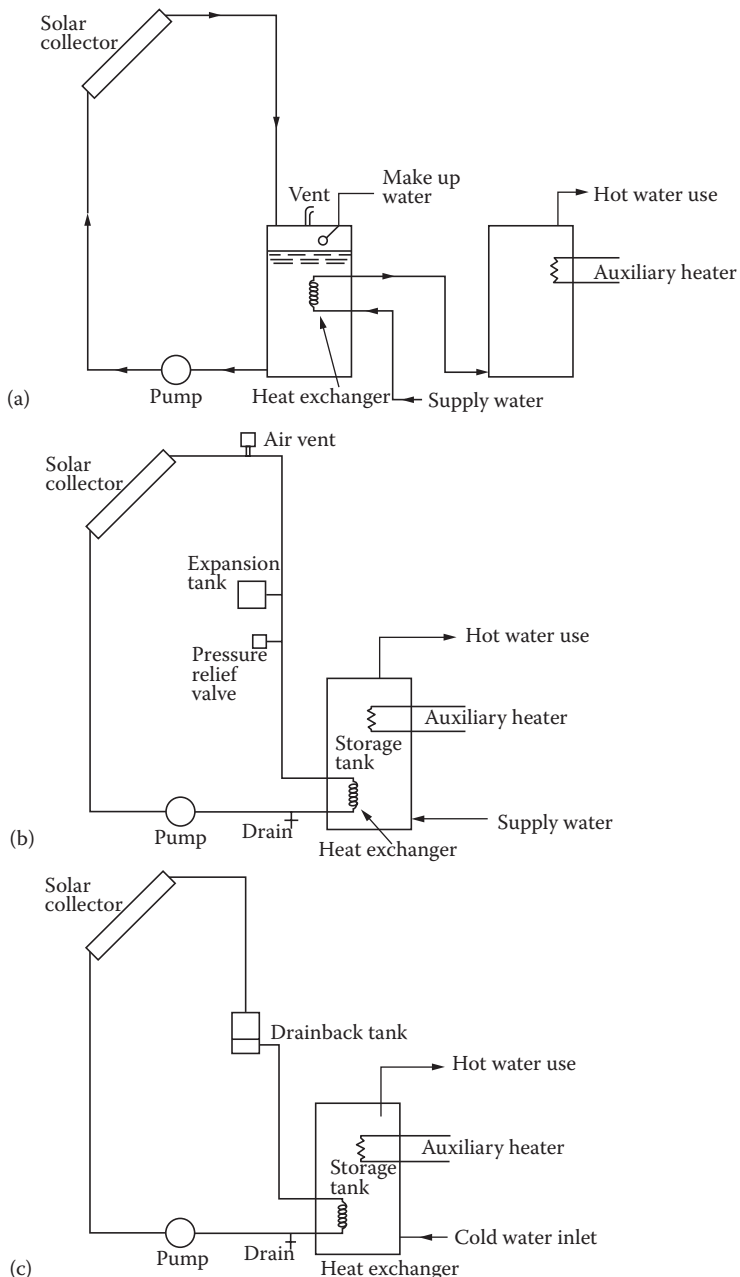
$$V^2 = 38.9/(996.016)(15.6)$$

$$V = 0.05 \text{ m/s.}$$

5.2.2 Forced-Circulation Systems

If a thermosyphon system cannot be used for climatic, structural, or architectural reasons, a forced-circulation system is required.

Figure 5.6 shows three configurations of forced-circulation systems: (1) open loop, (2) closed loop, and (3) closed loop with drainback. In an open loop system (Figure 5.6a), the solar loop is at atmospheric pressure; therefore, the collectors are empty when they are not providing useful heat. A disadvantage of this system is the high pumping power required to pump the water to the collectors every time the collectors become hot. This disadvantage is

**FIGURE 5.6**

Typical configurations of solar water-heating systems: (a) open loop system, (b) closed loop system, and (c) closed loop drainback system. (Adapted from Goswami, D.Y., *Alternative Energy in Agriculture*, Vol. 1, Boca Raton, FL, CRC Press, 1986.)

overcome in the pressurized closed loop system (Figure 5.6b) since the pump has to overcome only the resistance of the pipes. In this system, the solar loop remains filled with water under pressure.

In order to accommodate the thermal expansion of water from heating, a small (approximately 2-gallon capacity) expansion tank and a pressure relief valve are provided in the solar loop. Because water always stays in the collectors of this system, antifreeze (propylene glycol or ethylene glycol) is required for locations where freezing conditions can occur. During stagnation conditions (in summer), the temperature in the collector can become very high, causing the pressure in the loop to increase. This can cause leaks in the loop unless some fluid is allowed to escape through a pressure-release valve. Whether the result of leaks or of draining, air enters the loop causing the pumps to run dry. This disadvantage can be overcome in a closed loop drainback system that is not pressurized (Figure 5.6c). In this system, when the pump shuts off, the water in the collectors drains back into a small holding tank while the air in the holding tank goes up to fill the collectors. The holding tank can be located where freezing does not occur, but still at a high level to reduce pumping power. In all three configurations, a differential controller measures the temperature differential between the solar collector and the storage and turns the circulation pump on when the differential is more than a set limit (usually 5°C) and turns it off when the differential goes below a set limit (usually 2°C). Alternatively, a photovoltaic (PV) panel and a DC pump may be used. The PV panel will turn on the pump only when solar radiation is above a minimum level. Therefore, the differential controller and the temperature sensors may be eliminated.

5.3 Liquid-Based Solar Heating Systems for Buildings

The earliest active solar space-heating systems were constructed from enlarged water-heating components. Experiments beginning in 1938 at the Massachusetts Institute of Technology (MIT) showed that solar heating with liquid working fluids could be done without any major technical problems. The early MIT work formed the basis of many of the design techniques used today. Other experiments after World War II provided additional fundamental information on collector designs and storage operation for liquid-based heating systems. Figure 5.7 shows a modern solar-heated house in North Carolina.

Solar space-heating systems can be classified as active or passive depending on the method utilized for heat transfer. A system that uses pumps or blowers for fluid flow in order to transfer heat is called an active system. On the other hand, a system that utilizes natural phenomena for heat transfer is called a passive system. Examples of passive solar space-heating systems include direct gain, attached greenhouse, and storage wall (also called Trombe wall). Passive solar heating systems are described in Chapter 7. In

**FIGURE 5.7**

A picture of an active solar-heated house in North Carolina. (Picture courtesy of Jim Schmid, NREL.)

this section, configurations, design methods, and control strategies for active solar heating systems are described.

5.3.1 Physical Configurations of Active Solar Heating Systems

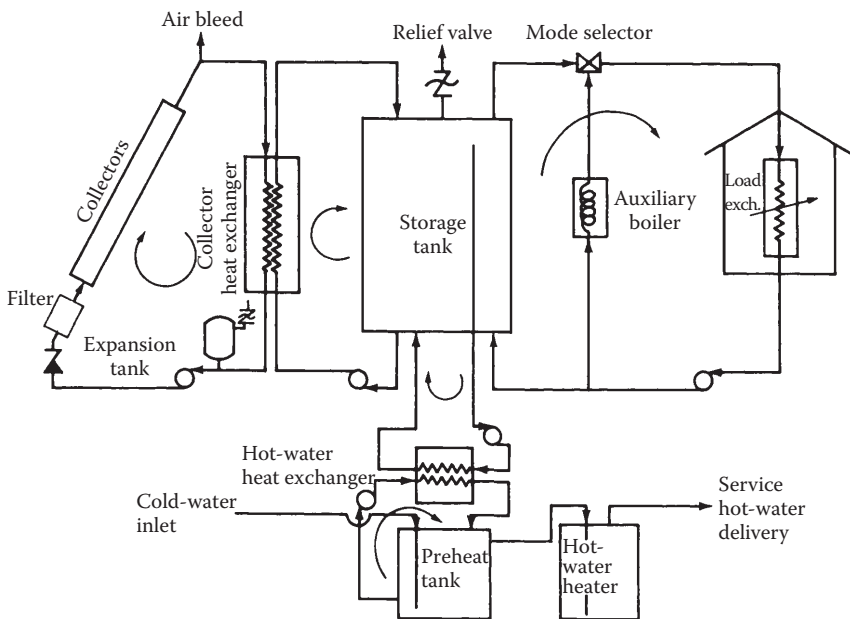
Figure 5.8 is a schematic diagram of a typical space-heating system. The system consists of three fluid loops—collector, storage, and load. In addition, most space-heating systems are integrated with a domestic water-heating system to improve the yearlong solar load factor.

Since space heating is a relatively low-temperature use of solar energy, a thermodynamic match of collector to task indicates that an efficient flat-plate collector or low-concentration solar collector is the thermal device of choice.

The collector fluid loop contains fluid manifolds, the collectors, the collector pump and heat exchanger, an expansion tank, and other subsidiary components. A collector heat exchanger and antifreeze in the collector loop are normally used in all solar space-heating systems, since the existence of a significant heating demand implies the existence of some subfreezing weather.

The storage loop contains the storage tank and pump as well as the tube side of the collector heat exchanger. To capitalize on whatever stratification may exist in the storage tank, fluid entering the collector heat exchanger is generally removed from the bottom of storage. This strategy ensures that the lowest temperature fluid available in the collector loop is introduced at the collector inlet for high efficiency.

The energy delivery-to-load loop contains the load device, baseboard heaters or fin-and-tube coils, and the backup system with a flow control (mode selector) valve.

**FIGURE 5.8**

Typical solar thermal system for space heating and hot-water heating showing fluid transport loops and pumps.

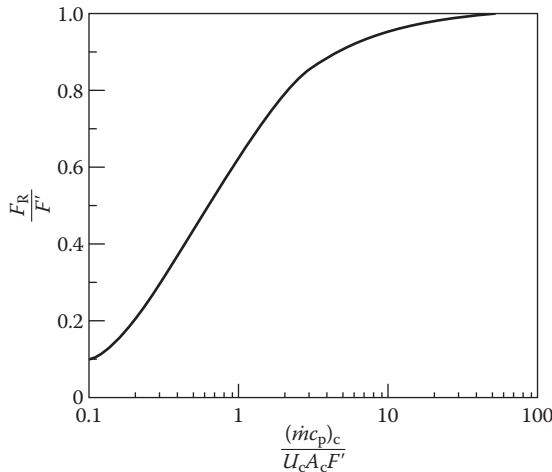
5.3.2 Solar Collector Orientation

The best solar collector orientation is such that the average solar incidence angle is smallest during the heating season. For tracking collectors, this objective is automatically realized. For fixed collectors in the Northern Hemisphere, the best orientation is due south (due north in the Southern Hemisphere), tilted up from the horizon at an angle of approximately 15° greater than the local latitude.

Although due south is the optimum azimuthal orientation for collectors in the Northern Hemisphere, variations of 20° east or west have little effect on annual energy delivery (Kreider and Kreith 1977). Off-south orientations greater than 20° may be required in some cases because of obstacles in the path of the sun. These effects may be analyzed using sun-path diagrams and shadow-angle protractors as described in Chapter 2.

5.3.3 Fluid Flow Rates

For the maximum energy collection in a solar collector, it is necessary that it operates as closely as possible to the lowest available temperature, which is the collector inlet temperature. Very high fluid flow rates are needed to maintain a collector-absorber surface nearly isothermal at the inlet temperature.

**FIGURE 5.9**

Effect of fluid flow rate on collector performance as measured by the heat-removal factor $F_R; F'$ is the plate efficiency factor (see Chapter 4).

Although high flows maximize energy collection, practical and economic constraints put an upper limit on useful flow rates. Very high flows require large pumps and excessive power consumption and lead to fluid conduit erosion.

Figure 5.9 shows the effect of mass flow rate on annual energy delivery from a solar system. It is seen that the law of diminishing returns applies and that flows beyond approximately $50 \text{ kg/h} \cdot \text{m}_c^2$ ($\sim 10 \text{ lb/h} \cdot \text{ft}_c^2$) have little marginal benefit for collectors with loss coefficients on the order of $6 \text{ W/m}_c^2 \cdot ^\circ\text{C}$ ($\sim 1 \text{ Btu/h} \cdot \text{ft}_c^2 \cdot ^\circ\text{F}$). In practice, liquid flows in the range of $50 - 75 \text{ kg/h} \cdot \text{m}_c^2$ ($10 - 15 \text{ lb/h} \cdot \text{ft}_c^2$) of water equivalent are the best compromise among collector heat-transfer coefficient, fluid pressure drop, and energy delivery. However, an infinitely large flow rate will deliver the most energy if pumping power is ignored for a nonstratified storage. If storage stratification is desired, lower flow rates must be used, since high flow destroys stratification.

In freezing climates, an antifreeze working fluid is recommended for collectors. Attempts to drain collectors fully for freeze protecting have usually been unsuccessful unless collector fluid conduits are very large and smooth and unless all piping is sloped to assure drainage. The potential damage risk from incomplete draining will usually dictate that additional investment in antifreeze be made.

5.3.4 Thermal Storage

Thermal storage tanks must be insulated to control heat loss, as described in Chapter 4. If a storage tank is located within a structure, any losses from

the tank tend to offset the active heating demands of the building. However, such storage loss is uncontrolled and may cause overheating in seasons with low heat loads. Some solar heating systems have used a ventilatable structure surrounding storage. This enclosure may be vented to the building interior in winter and to the environment in summer.

Safety concerns may cause storage to be located external to a building in some cases. Large volumes of hot water could be released to a building interior if a storage tank were to fail. Potential personal injury or property damage, which could result from an accident, must be assessed in siting storage tanks. Tank burial would seem to be the safest approach in some cases. Buried storage tanks must be sealed from ground moisture, insulated with waterproof insulation, and galvanically protected.

The amount of thermal storage used in a solar heating system is limited by the law of diminishing returns. Although larger storage results in larger annual energy delivery, the increase at the margin is small and hence not cost-effective. Seasonal storage is, therefore, usually uneconomical, although it can be realized in a technical sense. Experience has shown that liquid storage amounts of 50–75 kg H₂O/m² (10–15 lb/ft²) are the best compromise between storage tank cost and useful energy delivery. Klein (1976) has calculated the effect of storage size on annual energy delivery. The results of his study, shown in Figure 5.10, exhibit the expected diminishing returns to scale.

Since solar energy heating systems operate at temperatures relatively close to the temperatures of the spaces to be heated, storage must be capable of

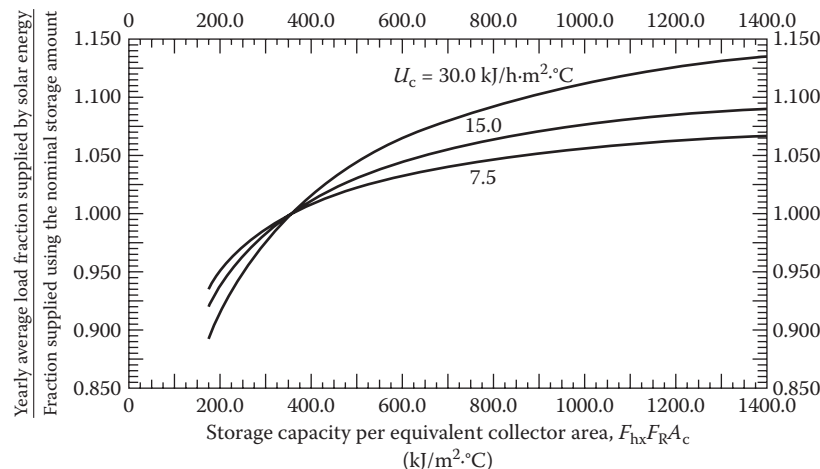


FIGURE 5.10

Effect of liquid storage capacity on liquid-based solar heating system energy delivery. (From Klein, S.A., A design procedure for solar heating systems, PhD dissertation, University of Wisconsin, Madison, WI, 1976.)

delivering and receiving thermal energy at relatively small temperature differences. The designer must consider the magnitude of these driving forces in sizing heat exchangers, pumps, and air-blowers. The designer must also consider the nonrecoverable heat losses from storage—even though storage temperatures are relatively low, surface areas of storage units may be large and heat losses therefore are appreciable.

Some investigators have proposed heating the storage medium with conventional fuels to maintain its temperature at useful levels during sunless periods. This approach has two major flaws:

1. If storage is heated with conventional fuels, it cannot be heated with solar energy when available; therefore, some collected solar energy cannot be used.
2. If storage is partially heated with conventional fuels, the collector inlet temperatures will be higher and efficiency will be lower than it would be if storage were not boosted. Therefore, the useful return on the solar system investment would be diminished.

In conclusion, it should be emphasized that storage heating with conventional fuels is uneconomical in any practical solar thermal system designed to date.

5.3.5 Other Mechanical Components

Other mechanical components in solar heating systems include pumps, heat exchangers, air bleed valves, pressure-release valves, and expansion tanks. Heat exchangers in solar systems are selected based on economic criteria described in Chapter 4. The best trade-off of energy delivery increase with increasing heat-exchanger size usually results from use of an exchanger with effectiveness in the range of 0.6–0.8. Counterflow heat exchangers are required for this level of effectiveness. A detailed example of heat-exchanger selection is contained in Chapter 4.

Achievement of the required effectiveness level may dictate fairly high flow rates in the storage tank side of the collector heat exchanger. Flows up to twice that in the collector side can improve exchanger performance significantly in many cases. Since the storage side loop is physically short and has a small pressure drop, increased flow in this loop increases pump energy requirements by a negligible amount. Typical solar heat-exchanger sizes range from 0.05 to 0.10 m² of heat-exchanger surface per square meter of net collector area.

In hydronic heating systems, it is essential that all air be pumped from the system. To facilitate this process, air bleed valves located at high points in a system are used. These are opened during system fill and later if air should collect. Air bleeds are required at points of low velocity in piping

systems where air may collect because the local fluid velocity is too low for entrainment.

5.3.6 Controls in Liquid Systems

Control strategies and hardware used in current solar system designs are quite simple and are similar in several respects to those used in conventional systems. The single fundamental difference lies in the requirement for differential temperature measurement instead of simple temperature sensing. In the space-heating system shown in Figure 5.8, two temperature signals determine which of three modes is used. The signals used are the collector-storage differential and room temperature. The collector-storage difference is sensed by two thermistors or thermocouples, the difference being determined by a solid-state comparator, which is a part of the control device. Room temperature is sensed by a conventional dual-contact thermostat.

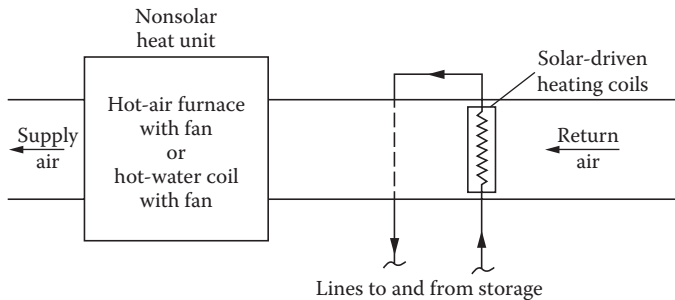
The control system operates as follows. If the first room thermostat contact closes, the mode selector valve and distribution pump are activated in an attempt to deliver the thermal demand from solar thermal storage. If room temperature continues to drop, indicating inadequate solar availability, the mode selector diverts flow through the backup system instead of the solar system, and the backup is activated until the load is satisfied.

The collector-storage control subsystem operates independently of the heating subsystem described above. If collector temperature, usually sensed by a thermistor thermally bonded to the absorber plate, exceeds the temperature in the bottom of the storage tank by 5°C – 10°C (9°F – 18°F), the collector pump and heat-exchanger pump (if present) are activated and continue to run until the collector and storage temperature are within approximately 1°C – 2°C (2°F – 4°F) of each other. At this point, it is no longer worthwhile to attempt to collect energy and the pumps are turned off. The collector-storage subsystem also has a high temperature cutout that turns the collector loop pump off when the storage temperature exceeds a set limit.

5.3.7 Load Devices in Liquid Solar Heating Systems

A heating load device transfers heat from the solar storage to the air in the space. Therefore, a liquid-to-air heat exchanger is sized on the basis of the energy demand of a building. Several generic types of load devices are in common use.

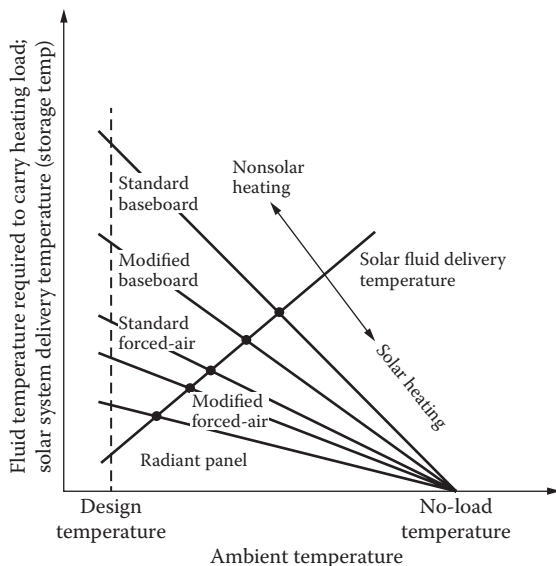
1. Forced-air systems—tube-and-fin coil located in the main distribution duct of a building or zone of a building (see Figure 5.11).
2. Baseboard convection systems—tube-and-fin coils located near the floor on external walls. These operate by natural convection from the convectors to the room air.

**FIGURE 5.11**

Forced-air heating system load device location upstream of nonsolar heat exchanger or furnace.

3. Heated floors or ceilings—water coils. These transfer heat to large thermal masses that in turn radiate or convect into the space. This heating method is usually called radiant heating.

Each load device requires fluid at a different temperature in order to operate under design load conditions as shown in Figure 5.12. Since baseboard heaters are small in heat-transfer area and rely on the relatively ineffectual

**FIGURE 5.12**

Heating load diagram for baseboard, forced-air, and radiant systems. Modified baseboard and forced-air systems are oversized in order to carry heating demands at lower temperature. Balance points are indicated by large dots at intersections.

mechanism of natural convection, they require the highest fluid temperature. Forced-air systems involve the more efficient forced-convection heat-transfer mode and, hence, are operable at lower fluid temperatures (see Figure 5.12). Radiant heating can use very large heat-transfer areas and is, therefore, operable at relatively low fluid temperatures.

In Figure 5.12 the intersection of the solar fluid temperature line and the load line for a specific configuration is called the *balance point*. At ambient temperatures below the balance point, solar energy cannot provide the entire demand, and some backup is required; above the balance point, solar capacity is sufficient to carry the entire load. Note that the load lines are specific to a given building. The solar fluid temperature line is not fixed for a building but depends on solar collector and storage size as well as local solar radiation levels. The line shown in Figure 5.12 is, therefore, an average line. The instantaneous solar line changes continuously in response to load and climatic forcing functions as described in Chapter 4.

It is possible to modify load devices to lower the balance point, as shown in Figure 5.12. For example, a forced-air tube-and-fin exchanger can be enlarged by adding one or more additional rows of tubes. This increased heat-transfer area will permit the same energy delivery at a lower fluid temperature. Figure 5.13 depicts the effect of forced-air load device size (heat-transfer

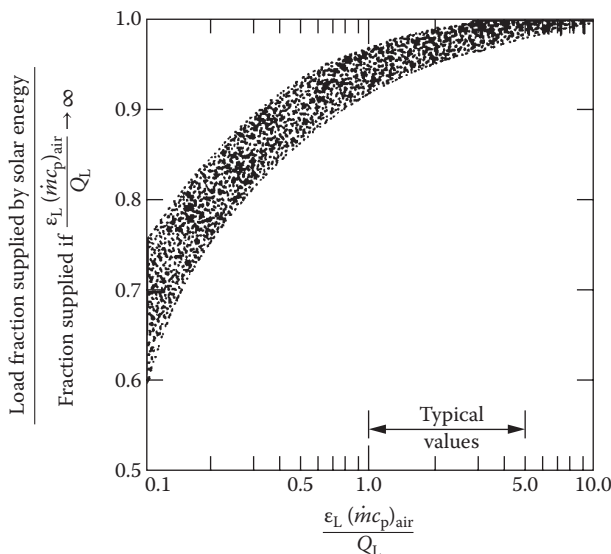


FIGURE 5.13

Effect of load device capacity for forced-air heating systems. Q_L is the building heat load expressed in units consistent with $(\dot{m}c_p)_{\text{air}}$. (From Klein, S.A., A design procedure for solar heating systems, PhD dissertation, University of Wisconsin, Madison, WI, 1976.)

effectiveness ε_L) on annual energy delivery. The law of diminishing returns is evident as increasing effectiveness returns progressively less energy. The effectiveness of a cross-flow heat exchanger of the type used in forced-air systems is calculated in Chapter 4 and shown in Figure 4.12.

5.4 Solar Air-Heating Systems

Air has been used as the working fluid in solar heating systems since World War II. Although demonstrated in fewer buildings than liquid systems, air systems have several advantages that can lead to their use in smaller installations in single-family and multifamily residences. In addition, air systems are well suited to crop drying and air preheating in certain processes.

Table 5.6 lists some of the advantages and disadvantages of air and liquid systems. Several of the disadvantages of an air system follow from the poor heat-transfer properties of air. Large space requirements for ducts preclude the use of air systems in large buildings because of space limitations. This is usually not a disadvantage in air systems used in residences. However, the

TABLE 5.6

Advantages and Disadvantages of Air and Liquid Space-Heating Systems

Advantages	Disadvantages
<i>Air Systems</i>	
No freezing problem	Space heating only
No internal corrosion problem with dry air	Large space requirements for ducts
Leaks of smaller consequence	Larger storage volume required for rocks
No heat exchanger between collector-storage and storage-building loops	Cannot store heat and heat building at the same time—major problem in low load seasons
No boiling or pressure problems	Low (ρc_p) product for air
Easy for do-it-yourselfers	
Simple and reliable	
<i>Liquid Systems</i>	
Higher transport energy density	Freezing problems
Better heat-transfer properties	Leakage problems
Water storage has higher energy density	Corrosion problem—water chemistry needs monitoring
Suitable for space heating and cooling	Heat exchanger required for collector-storage and storage-building loops
Small fluid conduits	Boiling and fluid expansion provisions required

thermal performance and costs for both systems are nearly identical if the air system does not have leaks.

In all air-based solar heating systems, a pebble-bed storage device is used. Although water offers a higher storage energy density than most solids, the difficulty of economically exchanging heat from an air stream to a liquid storage fluid stream precludes its use. Storage controls and operating parameters are described in detail in Section 5.4.1.

Flat-plate collectors are usually required for air-heating systems to provide sufficient area to transfer heat effectively from the absorber plate to the air stream. A flat-plate collector provides a good thermodynamic match for temperature demands in space-heating applications. Air-heating flat-plate collectors are described in Chapter 3.

5.4.1 Heating System Physical Configuration

In many ways, liquid-based and air-based solar systems are similar in operation. Figure 5.14 is a schematic diagram of a typical air-heating system.

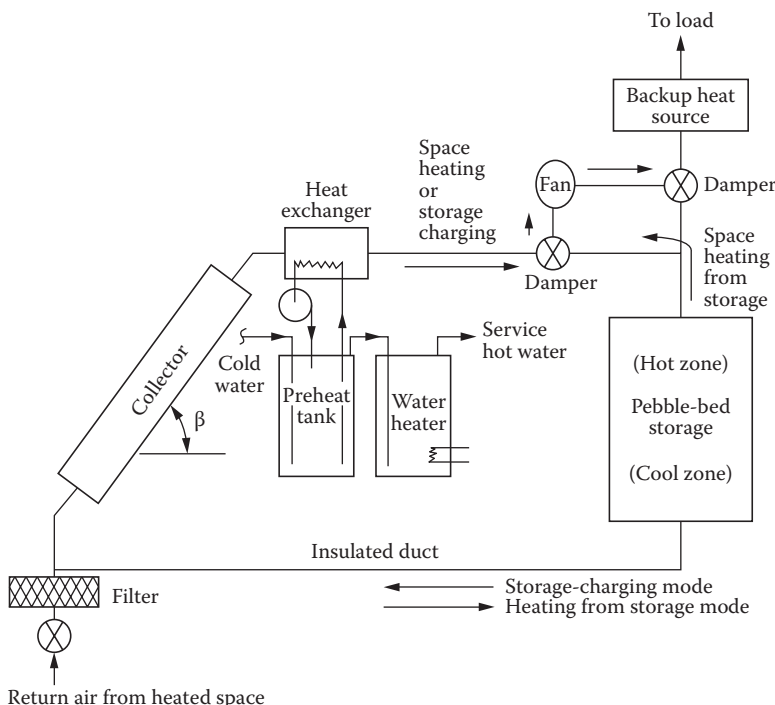


FIGURE 5.14

Typical air-based solar space-heating system showing directions of fluid flow and important components.

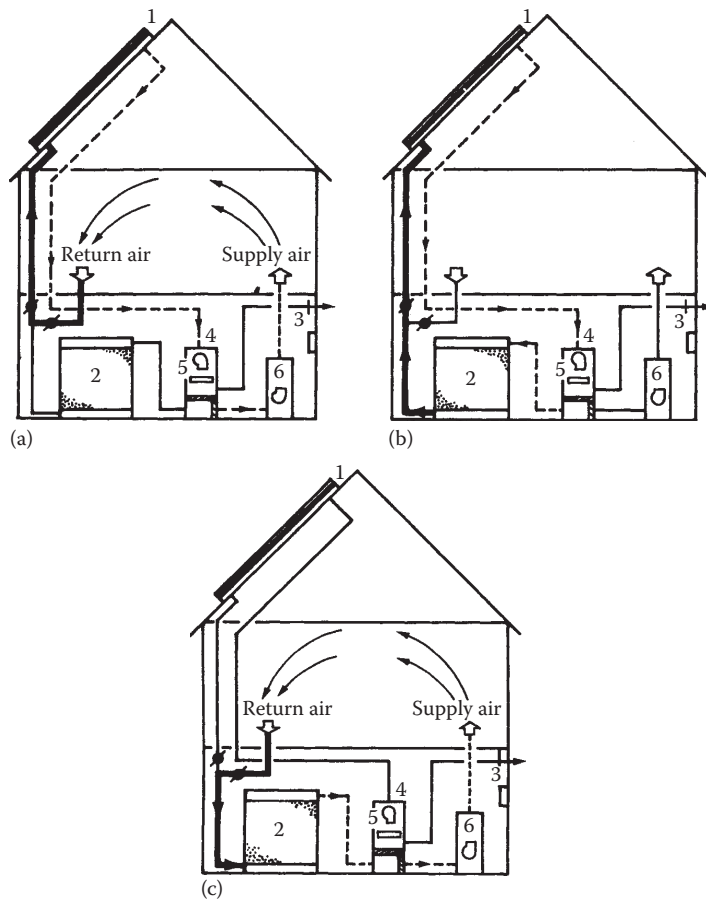
Similar flow regimes and collector orientations are used in both types of systems. The air system is simpler, however, since a collector heat exchanger and associated pumps, pipes, and expansion tanks are not present. The use of pebble-bed storage is advantageous because of the stratification that results. Stratification ensures a low inlet temperature to the collector; the collector inlet temperature is approximately the temperature of the cool zone of storage, which, in turn, is the building return air temperature ($\sim 15^\circ\text{C}$ – 20°C). Cool collector inlet temperatures are essential to efficient operation of an air system. Since stratification cannot be achieved with isothermal phase-change storage media, they are not suitable for use with air-based systems. Frequently, more dampers are required than shown in Figure 5.14 to prevent leakage and backflows through a cold collector via a leaky damper. Careful design of dampers and actuators is essential.

The collector-to-storage loop consists of insulated ducts, collector manifolds, and a hot-water preheat exchanger. These tube-and-fin exchangers provide some preheat to hot water if placed at the collector outlet to ensure their exposure to the hottest air available. Collector flow balancing is achieved by controlling the pressure drop through each collector and using equal duct lengths for each.

Figure 5.15 shows a hot-air system. During the storage-charging mode (Figure 5.15b), heated air flows through the rock bed at a low flow rate determined by the desired temperature rise in the collector, usually 10 – 15 liters/ $\text{s} \cdot \text{m}_c^2$. As progressively more heat is stored, the interface between the hot and cold regions of storage moves downward in the storage bin. The air returning to the collector is at the temperature of the cool region of storage.

During daytime heating on a sunny day (Figure 5.15a), air from the collector is diverted to the building instead of to storage. During sunny periods when no heating demand exists, storage is charged by warm air from the collector. During the nighttime or cloudy daytime heating modes, heat is removed from storage by a counterflow of air through the rock bed, as shown in Figure 5.15c. The outlet temperature from storage is close to the daytime collection (inlet) temperature, since the air being heated passes through the hottest zone of storage last. As progressively more heat is removed from storage, the interface between the hot and cold regions of storage moves upward.

The storage medium for air systems has typically been 25–50 mm diameter granite or river-bed rocks. An air filter is required between the heated space and storage to eliminate dust buildup in the gravel bed. Dust would reduce the heat-transfer coefficient to the rock pieces and increase the bed pressure drop. The recommended amount of storage to be used is roughly the same as for a liquid system—approximately 300 kg of rock per square meter of collector ($0.75 \text{ ft}^3/\text{ft}_c^2$, $0.25 \text{ m}^3/\text{m}_c^2$). Design information on the expected pressure drop through pebble-bed storage is contained in Chapter 4.

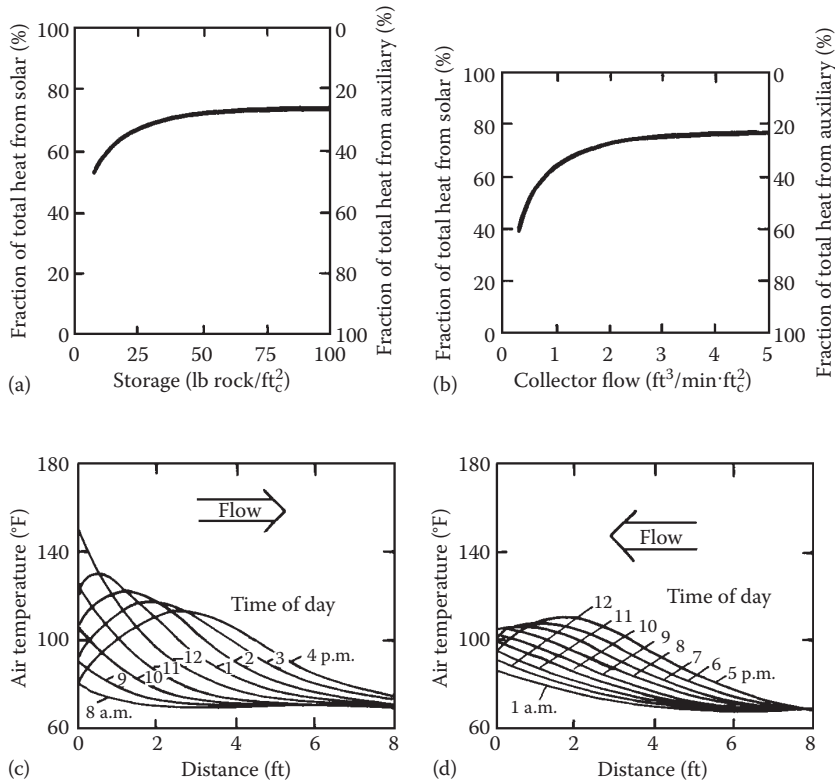
**FIGURE 5.15**

Schematic diagram of operating modes of solar air system: (a) space heating from collector; (b) storing solar heat, and (c) space heating from storage. The components are (1) collector, (2) storage, (3) control, (4) fan, (5) hot-water preheater (optional), and (6) backup heater. (Courtesy of the Solaron Corp.)

5.4.2 Collector Designs

Several air-heating collector designs are shown in Figure 3.7. However, relatively few performance data for such collectors have been published to provide designers with the information necessary to predict system performance and determine optimal system configurations reliably.

One of the early computer-aided design studies that does provide guidelines for the designer of air-collector systems was conducted by Balcomb et al. (1975, 1976). Figure 5.16 shows some of their practical results. Figure 5.16a depicts the variation of solar delivery with storage volume. It is clear that

**FIGURE 5.16**

Hot-air solar system operating parameters: (a) effect of storage size on annual energy delivery, (b) effect of collector air flow rate on annual energy delivery, (c) typical temperature distribution in rock bed during storage heating by solar energy, and (d) typical temperature distribution in rock bed during heat removal from storage. (Adapted from Balcomb, J.D. et al., *Solar Handbook for Los Alamos*, LASL, New Mexico, 1975; and Balcomb, J.D. et al., Design considerations of air-cooled collector/rock-bin storage solar heating systems, paper presented at the ISES Annual Meeting, Los Angeles, CA, 1975.)

storage volumes in excess of 60 lb rock/ft^2 (300 kg/m^2) improve the annual solar delivery by a negligible amount. Likewise, Figure 5.16b indicates that collector air flow rates greater than $15 \text{ liters/s} \cdot \text{m}^2$ increase delivery very little. Figure 5.16c and d show temperature profiles for a particular rock bed modeled for various times of day for both the storage-charging and storage-discharging modes. Any properly sized storage will have similar temperature distributions; the key property is that the outlet temperature from storage should be low to permit the inherently inefficient air collector to operate at as low a temperature as possible. The optimal geometric configuration of a storage bed is roughly cubical in order to minimize the air pressure drop.

5.4.3 Fluid Flow Rates

The flow rate through an air collector and storage loop is a compromise between pressure drop and energy transfer to the air stream. As shown in Figures 5.16 and 5.17, the effect of air capacitance rate $(\dot{m}c_p)_c$ can be significant. Apart from the beneficial effect of increased flow rate on the heat-removal factor F_R , which is usually quite low for air collectors (~ 0.6 – 0.7), increased flows tend to cause an offsetting decrease in storage bed stratification. Decreased stratification penalizes collector performance, since the collector inlet temperature is higher under these circumstances.

Nominal flow rates used in air collectors are approximately $10 \text{ liters}/\text{m}_c^2 \cdot \text{s}$ ($2 \text{ ft}^3/\text{min} \cdot \text{ft}_c^2$). This capacitance rate is well below that for liquid systems but is a compromise between the offsetting effects of stratification reduction and improved heat transfer from the absorber plate that would result from higher flow rates. This effect is not present in liquid systems, since storage stratification is generally of little consequence in liquid systems.

5.4.4 Other Mechanical Components

Air systems require fewer auxiliary components than liquid systems. Controls in air systems are similar in function to those in liquid systems and are not described in detail here. The controller operates one blower, one

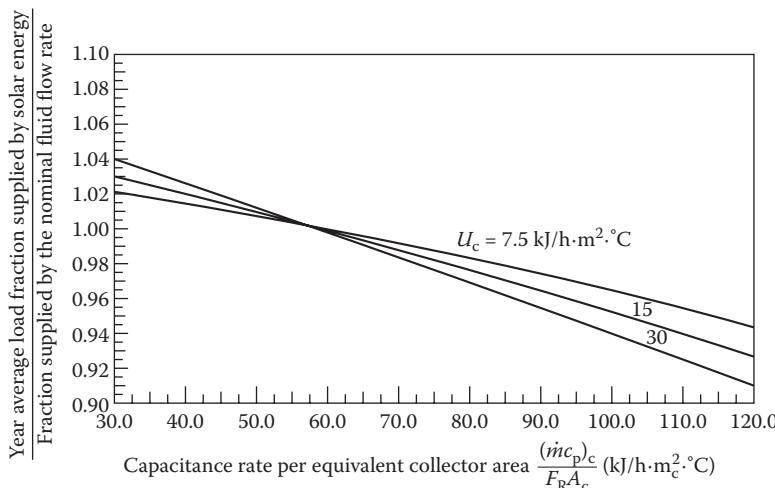


FIGURE 5.17

Effect of collector fluid flow rate on annual energy delivery in an air-based solar heating system. The effect of the collector loss coefficient U_c is also shown. The nominal fluid flow rate is $58 \text{ kg}/\text{m}_c^2 \cdot \text{°C} \cdot \text{h}$, based on the equivalent areas $F_R A_c (\dot{m}c_p)_{air}$. (Adapted from Klein, S.A., A design procedure for solar heating systems, PhD dissertation, University of Wisconsin, Madison, WI, 1976.)

pump (preheat), and two dampers, which are the analogs of valves in liquid systems. The dampers must seal tightly. For example, if the middle damper in Figure 5.15, controlling the air flow to the heated space, should leak, the fan could draw cold air from the nighttime collector through the damper to mix with warm air from storage. Such a leak could reduce the heating effect substantially.

Sizing of the blower and ducts in air systems can be done by conventional methods. Pressure-drop data for air ducts are presented in Appendix 4, in a convenient form for such calculations in Figure A4.4. In some cases, a two-speed blower is required in air systems if the system pressure drop in the collector-to-space heating mode is substantially different from the pressure drop through storage. Careful design can frequently avoid this problem, however.

5.4.5 Unglazed Transpired Wall System for Air Preheating

Ventilation air preheating systems using wall-mounted unglazed transpired solar air collectors are the only active solar air-heating systems that have found market acceptance in commercial and industrial buildings (Kutcher 1996). Such systems preheat the ventilation air in a once-through mode without any storage. Figure 5.18 shows a transpired wall system in which the air

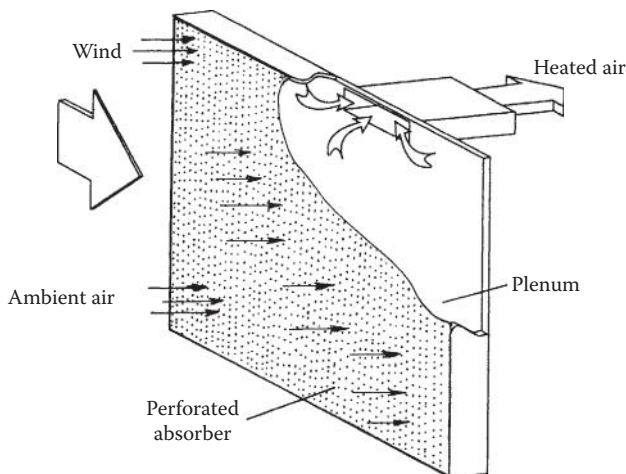


FIGURE 5.18

Unglazed transpired solar collector system for building ventilation preheat. Intake air is drawn by the building ventilation fan through the perforated absorber plate and up the plenum between the absorber and the south wall of the building. (Adapted from Kutcher, C.F. and C.B. Christensen. Unglazed transpired solar collectors. *Advances in Solar Energy*, K. Boer, ed., vol. 7, pp. 283–307, 1992.)

is drawn through a perforated absorber plate by the building ventilation fan. Kutcher and Christensen (1992) presented a thermal analysis of this system. From a heat balance on the transpired unglazed collector, the useful heat collected is

$$q_u = I_c A_c \alpha_s - U_c A_c (T_{\text{out}} - T_a). \quad (5.13)$$

The overall heat-loss coefficient U_c , which is attributed to radiative and convective losses, is given as

$$U_c = h_r / \varepsilon_{\text{hx}} + h_c \quad (5.14)$$

where ε_{hx} is absorber heat-exchanger effectiveness, h_r is a linearized radiative heat-transfer coefficient, and h_c is the convective heat-loss coefficient. The heat-exchanger effectiveness for air flowing through the absorber plate is defined as

$$\varepsilon_{\text{hx}} = \frac{T_{\text{out}} - T_a}{T_c - T_a}. \quad (5.15)$$

The forced convective heat-loss coefficient owing to a wind velocity of U_∞ is given as

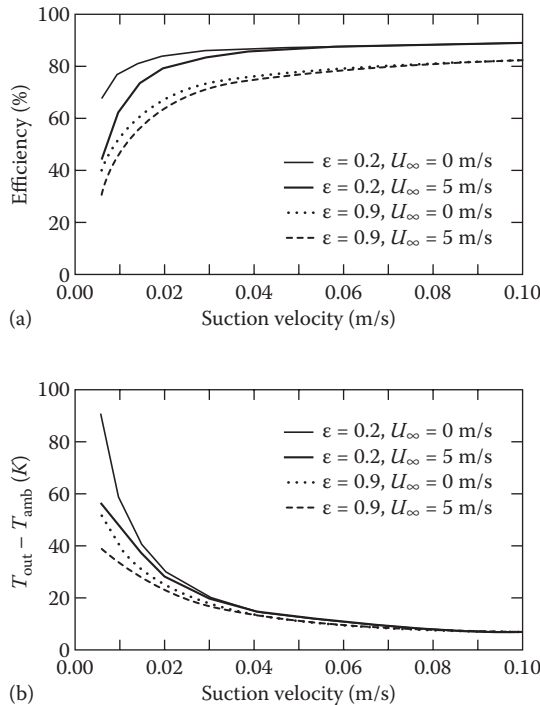
$$h_c = 0.82 \frac{U_\infty \nu c_p}{L v_0}, \quad (5.16)$$

where ν is the kinematic viscosity of air in m^2/s , c_p is the specific heat in $\text{J}/\text{kg}\cdot\text{K}$, v_0 is the section velocity, and L is the height of the collector.

Radiation heat loss occurs to both the sky and to the ground. Assuming the absorber is gray and diffuse with an emissivity ε_c , the radiative loss coefficient h_r is

$$h_r = \varepsilon_c \sigma \frac{\left(T_c^4 - F_{\text{cs}} T_{\text{sky}}^4 - F_{\text{cg}} T_{\text{gnd}}^4 \right)}{T_c - T_a}, \quad (5.17)$$

where F_{cs} and F_{cg} are the view factors between the collector and the sky and between the collector and the ground, respectively. For a vertical wall with infinite ground in front of it, both F_{cs} and F_{cg} will be 0.5 each. Using the above equations, Kutcher and Christensen (1992) showed that the predicted performance matches the measured performances well. Figure 5.19 shows their predicted thermal performances.

**FIGURE 5.19**

Predicted thermal performance of a vertical unglazed transpired solar collector as a function of suction velocity, absorber emissivity, and wind speed. Collector size = 3 m × 3 m, $T_{\text{amb}} = 10^\circ\text{C}$, $T_{\text{sky}} = T_{\text{amb}} - 15^\circ\text{C}$, $T_{\text{gnd}} = T_{\text{amb}}$, and $I_c = 700 \text{ W/m}^2$. (a) Efficiency versus suction velocity. (b) Suction air temperature rise versus suction velocity. (From Kutcher, C.F. and C.B. Christensen. Unglazed transpired solar collectors. *Advances in Solar Energy*, K. Boer, ed., vol. 7, pp. 283–307, 1992.)

5.5 Methods of Modeling and Design of Solar Heating Systems

Several methods of modeling and design of solar space and water heating have been developed including f -chart, TRNSYS, utilization, and SLR. The first three of these methods are described briefly in Sections 5.5.1 through 5.7. The SLR method is described in Chapter 7. Before design of a solar heating system can start, one must know the loads and the availability of solar radiation at the location. Estimation of solar radiation is described in Chapter 2 and estimation of the loads has been described briefly earlier in Chapter 5.

5.5.1 Design of a Liquid-Based Solar Heating System by f -Chart

Klein et al. (Beckman et al. 1977; Klein 1976; Klein et al. 1975, 1976a,b) developed a method of simplified prediction of the performance of a solar heating system

based on a large number of detailed simulations for various system configurations in various locations in the United States. The results from these simulations were then correlated with dimensionless parameters on charts that are general in form and usable anywhere. The charts are called *f*-charts, denoting a parameter f_s , the fraction of monthly load supplied by solar energy. The dimensionless groups used in the *f*-charts are derived from a nondimensionalization of the equations of governing energy flows; the groups therefore have a physical significance as described in the following. The *f*-chart method has been developed for standard solar heating and hot-water system configurations.

Schematic diagrams for standard solar heating systems based on liquid and air heat-transfer fluids are shown in Figures 5.8 and 5.14, respectively. Certain deviations from these configurations can be handled in the *f*-chart method. For example, the collector-to-storage heat exchanger in the liquid-based system may be eliminated. The domestic water heater in Figure 5.14 is shown as a two-tank system, which may be reconfigured as a one-tank system.

In the *f*-chart method, the fraction of load supplied by solar energy, f_s , is correlated with two dimensionless parameters, called the loss parameter P_L and the solar parameter P_s . Parameters P_L and P_s are defined as

$$P_L = \frac{A_c F_{hx} F_R U_c \Delta t (T_R - \bar{T}_a)}{L} \quad (5.18)$$

and

$$P_s = \frac{A_c F_{hx} F_R \bar{I}_c (\bar{\tau}\alpha)}{L}. \quad (5.19)$$

P_s and P_L are measures, respectively, of the long-term insolation gain by the collector and long-term thermal loss per unit load. The parameters in Equations 5.18 and 5.19 and in the *f*-chart are described in Table 5.7.

P_s may be rewritten as

$$P_s = \frac{A_c \bar{I}_c F_{hx} F_R (\bar{\tau}\alpha)_n}{L} \frac{(\bar{\tau}\alpha)}{(\tau\alpha)_n}. \quad (5.20)$$

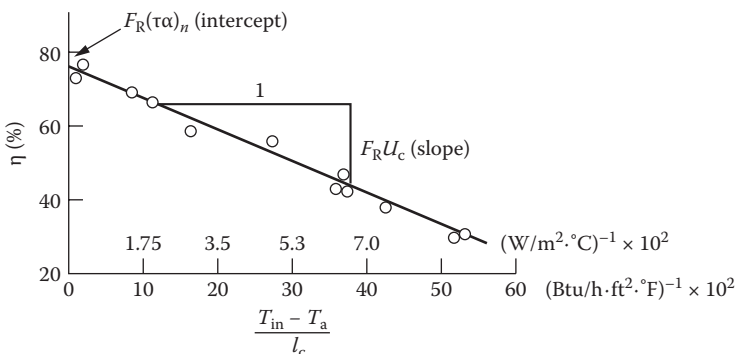
As shown in Chapter 3, $F_R U_c$ and $F_R(\tau\alpha)_n$ in the equations above can be determined directly from the slope and intercept of a collector efficiency curve plotted as shown in Figure 5.20. In addition, Klein suggests that the time-averaged value $F_R(\bar{\tau}\alpha)$ is related to the normal incidence value $F_R(\tau\alpha)_n$ as

$$\frac{F_R(\bar{\tau}\alpha)}{F_R(\tau\alpha)} = 0.95, \quad (5.21)$$

for a surface tilted within $\pm 20^\circ$ of the local latitude.

TABLE 5.7Definition of Parameters in *f*-Chart

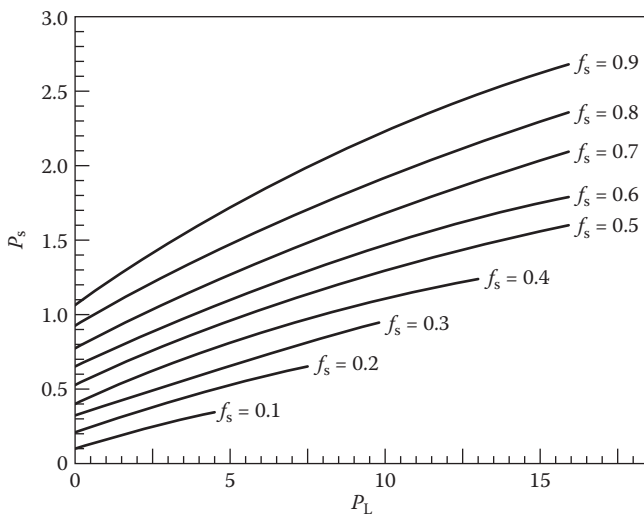
Parameter	Definition
A_c	Net collector aperture area (m^2)
f_s	The solar load fraction: fraction of monthly load carried by solar system
F_R	Collector heat-removal factor (see Equation 3.43)
F_{hx}	Collector loop heat-exchanger factor (see Equation 4.36) $F_{hx} = 1$ if no collector heat exchanger is used
\bar{I}_c	Total monthly collector-plane insolition ($\text{J}/\text{m}^2\cdot\text{month}$) (see Chapter 2)
L	Total monthly water-heating load (J/month) (see Example 5.3)
\bar{T}_a	Monthly average ambient temperature ($^\circ\text{C}$)
T_R	Reference temperature with a value of 100°C
U_c	Collector heat-loss coefficient ($\text{W}/\text{m}^2\cdot^\circ\text{C}$) (see Chapter 3)
Δt	Number of seconds per month (s/month)
$\bar{\tau}\alpha$	Monthly averaged collector transmittance-absorptance product

**FIGURE 5.20**

Typical flat-plate collector efficiency curve showing method of evaluating $F_R(\tau\alpha)_n$ and $F_R U_c$. (From Kreider, J.F. and F. Kreith, *Solar Heating and Cooling*, Hemisphere Publ. Corp., Washington, DC, revised 1st ed., 1977.)

Note that Figure 5.20 is a plot of efficiency versus collector *inlet* fluid temperature, as distinguished from *average* fluid temperature. Such curves are usually available from the collector manufacturers. Figure 5.21 shows the *f*-chart for a liquid-based solar heating and hot-water system. The results of the computer model used to generate the f_s curves in Figure 5.21 can also be expressed in the form of an empirical equation as (Klein et al. 1976a)

$$f_s = 1.029 P_s - 0.065 P_L - 0.245 P_s^2 + 0.0018 P_L^2 + 0.0215 P_s^3 \quad (5.22)$$

**FIGURE 5.21**

The f -chart for solar water-heating systems. (From Klein, S.A., A design procedure for solar heating systems, PhD dissertation, University of Wisconsin, Madison, WI, 1976.)

valid for the range

$$0 \leq P_s \leq 3.0; \quad 0 \leq P_L \leq 18.0; \quad \text{and} \quad 0 \leq f_s \leq 1.0.$$

It is further required that $P_s > P_L/12$ to ensure that the monthly insolation is above the useful threshold and that thermal losses are below an upper bound at which energy absorbed is equal to energy lost from the absorber plate.

The f -chart in Figure 5.21 is based on nominal values of collector flow rate, thermal storage mass, and load heat-exchanger effectiveness. It is possible to use the f -chart for other values of these important parameters if the loss parameter and a solar parameter are appropriately modified. Table 5.8 contains the nominal values used in generating the f -chart and the dimensionless groups that are used to modify the loss or the solar parameter for other system values. The f -chart in Figure 5.21 may be used for a water-heating-only system with the following modification for P_L :

$$P_L = \frac{F_{hx}R_cA_cU_c\Delta t(11.6 + 1.18T_{w,o} + 3.86T_{w,i} - 2.32\bar{T}_a)}{L}, \quad (5.23)$$

where $T_{w,i}$ and $T_{w,o}$ are water supply and delivery temperatures, respectively. Klein (1976) has prepared f -charts for air-based solar heating systems also as

TABLE 5.8

Nominal Values of Physical Parameters and Modifying Groups for *f*-Chart Use for Liquid-Based Systems

Parameter	Nominal Value	Modified Parameter ^a	
Flow rate ^b	0.0128 liters H ₂ O equivalent	$P_L = P_{L,nom} \frac{F_{hx} F_R}{(F_{hx} F_R)_{nom}}$	(5.24)
$\frac{(mc_p)_c}{A_c}$	$s \cdot m_c^2$	$P_s = P_{s,nom} \frac{F_{hx} F_R}{(F_{hx} F_R)_{nom}}$	(5.25)
Storage volume (water)			
$V_s = \frac{M}{\rho A_c}$	75 liters H ₂ O/m _c ²	$P_L = P_{L,nom} \frac{V_s^{-0.25}}{75}$	(5.26)
Load heat exchanger ^c			
$\frac{\varepsilon_L (mc_p)_{air}}{Q_L}$	2.0	$P_s = P_{s,nom} \quad 0.393 + 0.651 \exp -0.139 \frac{Q_L}{\varepsilon (mc_p)_{air}}$	(5.27)
		0.651 exp -0.139	

Note: The table was prepared from data and equations presented in Beckman et al. (1977) and Klein (1976).

^a Multiply basic definition of P_s and P_L in Equations 5.18 and 5.19 by a factor for nonnominal group values; $(F_{hx} F_R)_{nom}$ refers to values of $F_{hx} F_R$ at collector rating or test conditions.

^b In liquid systems, the correction for flow rate is small and can usually be ignored if variation is no more than 50% below the nominal value.

^c $(mc_p)_{min}$ is the minimum fluid capacitance rate, usually that of air for the load heat exchanger; Q_L is the heat load per unit temperature difference between inside and outside of the building.

shown in Figure 5.22. Loss and solar parameters P_L and P_s are identical to those for liquid systems and are defined in Equations 5.18 and 5.19. Since air systems do not use a collector-to-storage heat exchanger, the heat-exchanger factor is given by $F_{hx} = 1.0$.

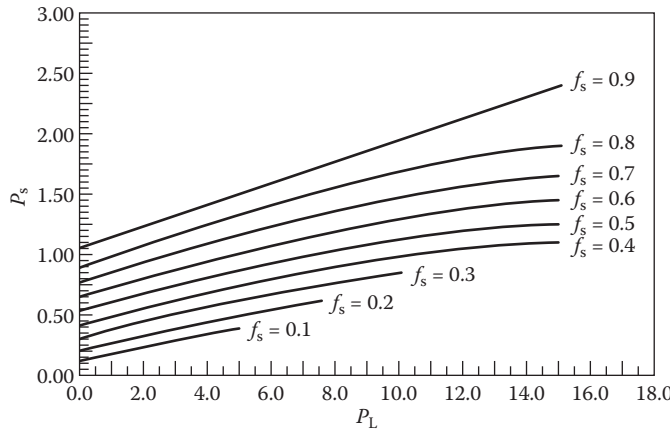
The data from which the *f*-chart was created can be expressed by an empirical equation as

$$f_s = 1.040 P_s - 0.065 P_L - 0.159 P_s^2 + 0.00187 P_L^2 - 0.0095 P_s^3 \quad (5.28)$$

valid for the following ranges:

$$0 \leq P_s \leq 3.0; \quad 0 \leq P_L \leq 18.0; \quad 0 \leq f_s \leq 1.0.$$

It is further required that $P_s > 0.07 P_L$ to ensure that the monthly insolation is above the useful threshold level and that thermal losses are below

**FIGURE 5.22**

The f -chart for air-based solar space-heating systems. (From Klein, S.A., A design procedure for solar heating systems, PhD dissertation, University of Wisconsin, Madison, WI, 1976.)

an upper bound at which energy absorbed is equal to energy lost from the absorber plate.

The f -chart for air systems is based on nominal values of air flow rate and storage capacity. Table 5.9 shows the nominal value of these two parameters and the dimensionless groups to be used to multiply the loss parameter to correct for flow rate or storage changes from the nominal value used to construct Figure 5.22.

TABLE 5.9

Factors for Storage Capacity and Air Flow Rate for f -Chart for Air-Based Systems

Parameter	Nominal Value ^a	Loss Parameter Multiplier
Storage capacity, V_s	$0.25 \text{ m}^3/\text{m}_c^2$	$\frac{0.25}{V_s}^{0.3}$
Fluid volumetric flow rate, Q_c	10.1 liters/s	$\frac{Q_c}{10.1}^{0.28}$

Sources: Adapted from Beckman, W.A. et al., *Solar Heating Design by the F-Chart Method*, John Wiley & Sons, New York, 1977; and Klein, S.A., A design procedure for solar heating systems, PhD dissertation, University of Wisconsin, Madison, WI, 1976.

^a Based on net collector area; fluid volume at standard atmosphere conditions.

Example 5.5

Calculate the annual heating energy delivery of a solar space-heating system using a double-glazed, flat-plate collector in Bismarck, North Dakota. The building and solar system specifications are given below.

Building Specifications

Location: 47°N latitude (see Appendix 2, Tables A2.2 and A2.3)

Space-heating load: 28,000 kJ/°C·day

Solar System Specifications

Collector loss coefficient: $F_R U_c = 4.44 \text{ W/m}^2 \cdot \text{K}$

Collector optical efficiency (average): $F_R (\overline{\tau\alpha}) = 0.70$

Collector tilt: $\beta = L + 15^\circ = 62^\circ$

Collector area: $A_c = 60 \text{ m}^2$

Collector fluid flow rate: $\dot{m}_c/A_c = 55 \text{ kg/h} \cdot \text{m}^2$

Collector fluid heat capacity: $c_{p_c} = 1.9 \text{ kJ}/^\circ\text{C} \cdot \text{kg}$ (antifreeze)

Storage capacity: 83 kg of $\text{H}_2\text{O}/\text{m}^2$

Storage fluid flow rate: $\dot{m}_s/A_c = 100 \text{ kg of H}_2\text{O/h} \cdot \text{m}^2$

Storage fluid heat capacity: $c_{p_s} = 4.187 \text{ kJ/kg} \cdot {}^\circ\text{C}$ (water)

Heat-exchanger effectiveness: 0.75

Load heat exchanger: $\epsilon_L (\dot{m} c_p)_{\text{air}}/Q_L = 2.0$

Climatic Data

Climatic data from the NWS are tabulated in Table 5.10.

Solution

The *f*-chart method is amenable to a step-by-step application. The following order is suggested:

TABLE 5.10

Climatic and Solar Data for Bismarck, North Dakota

Month	Average Ambient Temperature (°C)	Heating Degree C-days	Horizontal Solar Radiation (kJ/m ² ·day)
Jan	-13.2	978	6572
Feb	-10.3	801	10,465
Mar	-3.8	687	14,902
Apr	6.1	368	18,711
May	12.4	188	23,023
Jun	17.7	68	24,697
Jul	21.6	10	25,828
Aug	20.7	19	21,600
Sep	14.2	140	16,325
Oct	8.2	313	11,386
Nov	-1.7	601	6739
Dec	-9.1	851	5191

1. Calculate monthly collector-plane insolation for each month.
2. Calculate solar and loss parameters P_s and P_L (Equations 5.18 and 5.19) for each month and heat-exchanger penalty factor F_{hx} (Equation 4.36).
3. Evaluate f_s from the f -chart for each month.
4. Calculate total annual energy delivery from monthly totals.

Each of these steps is shown in Table 5.11.

The following are the calculations for the month of January. Results for the other months can be found similarly.

From Table A2.2 (by interpolation):

$$\bar{H}_{o,h} = 3048 \cdot \frac{\text{Wh}}{\text{m}^2 \cdot \text{day}} = 10,973 \frac{\text{kJ}}{\text{m}^2 \cdot \text{day}}.$$

From Table 5.10:

$$\bar{H}_h = 6572 \text{ kJ/m}^2 \cdot \text{day}.$$

Using Equation 2.54:

$$\bar{K}_T = \frac{\bar{H}_h}{\bar{H}_{o,h}} = 0.6.$$

TABLE 5.11

The f -Chart Summary for Example 5.5

Month	Collector-Plane Radiation (kJ/m ² ·day)	Monthly Energy Demand (GJ)	P_L	P_s	f_s
Jan	18,378	27.38	2.81	0.83	0.53
Feb	20,654	22.43	3.34	1.14	0.69
Mar	19,327	19.24	3.66	1.24	0.73
Apr	16,491	10.25	6.22	1.99	0.91
May	15,913	5.26	11.30	3.75	1.00
Jun	15,356	1.90	29.39	10.01	1.00
Jul	16,604	0.28	190.00	73.43	1.00
Aug	16,988	0.53	101.53	39.69	1.00
Sep	17,925	3.92	14.85	5.66	1.00
Oct	18,874	8.76	7.11	2.67	1.00
Nov	14,926	16.86	4.09	1.10	0.63
Dec	15,399	23.83	3.11	0.80	0.49
Annual	—	140.64	—	—	0.68

Note: $P_s > 3.0$ or $P_L > 18.0$ implies $f_s = 1.0$; no correction for storage size and flow rates is required.

By Equation 2.56:

$$\frac{\bar{D}_h}{H_h} = 0.775 + 0.347 \cdot h_{ss} - \frac{\pi}{2} - 0.505 + 0.0261 \cdot h_{ss} - \frac{\pi}{2} \cos(2\bar{K}_T - 1.8) = 0.2178$$

Therefore,

$$\begin{aligned}\bar{D}_h &= \frac{\bar{D}_h}{H_h} \times H_h = 0.2178 \times 6572 \text{ kJ/m}^2 \cdot \text{day} \\ &= 1431 \text{ kJ/m}^2 \cdot \text{day.}\end{aligned}$$

Using Equation 2.57:

$$\bar{B}_h = \bar{H}_h - \bar{D}_h = 5141 \frac{\text{kJ}}{\text{m}^2 \cdot \text{day.}}$$

From Equation 2.23, we can find

$$\delta_s = 23.45^\circ \sin[360(284 + 15)/365]^\circ = -21.27^\circ.$$

Using Equation 2.30:

$$\begin{aligned}h_{sr(\alpha=0)} &= -\cos^{-1}(-\tan L \cdot \tan \delta_s) \\ &= -\cos^{-1}[-\tan(47^\circ) \cdot \tan(-21.27^\circ)] \\ &= -65.3^\circ \text{ or } -1.14 \text{ rad.}\end{aligned}$$

Therefore, using Equation 2.60:

$$\begin{aligned}\bar{R}_b &= \frac{\cos(L - \beta) \cos \beta_s \sin h_{sr(\alpha=0)} + h_{sr} \sin(L - \beta) \sin \delta_s}{\cos L \cos \delta_s \sin h_{sr(\alpha=0)} + h_{sr(\alpha=0)} \sin L \sin \delta_s} \\ &= \frac{\cos(47^\circ - 62^\circ) \cos(-21.27^\circ) \sin(-65.3^\circ) - 1.14 \sin(47^\circ - 62^\circ) \sin(-21.27^\circ)}{\cos 47^\circ \cos(-21.27^\circ) \sin(-65.3^\circ) - 1.14 \sin 47^\circ \sin(-21.27^\circ)} \\ &= 3.36\end{aligned}$$

Using Equation 2.62:

$$\bar{R}_d = \cos^2(\beta/2) = \cos^2(62^\circ/2) = 0.7347.$$

Then, using Equation 2.64, neglecting reflection,

$$\begin{aligned}\bar{H}_c &= R_b \cdot \bar{B}_h + \bar{R}_d \cdot \bar{D}_h \\ &= 3.363 \times 5141 \text{ kJ/m}^2 \cdot \text{day} + 0.7347 \times 1431 \text{ kJ/m}^2 \cdot \text{day} \\ &= 18,341 \text{ kJ/m}^2 \cdot \text{day}.\end{aligned}$$

The monthly energy demand is

$$\begin{aligned}\text{Load} &= \overline{UA} \times {}^\circ\text{C days} \\ &= 28,000 \text{ kJ} \cdot {}^\circ\text{C} \times 978 {}^\circ\text{C day} \\ &= 27,384 \text{ GJ}.\end{aligned}$$

$$\begin{aligned}(\dot{m}c_p)_c &= (\dot{m}_c/A_c) \times A_c \times c_p \\ &= 55 \text{ kg/h} \cdot \text{m}^2 \times 60 \text{ m}^2 \times 1.9 \text{ kJ/kg} \cdot \text{K} \\ &= 6270 \text{ kJ/h} \cdot \text{K} \text{ or } 1742 \text{ W/K}\end{aligned}$$

$$\begin{aligned}(\dot{m}c_p)_s &= (\dot{m}_s/A_c) \times A_c \times c_{ps} \\ &= 100 \text{ kg/m}^2 \cdot \text{h} \times 60 \text{ m}^2 \times 4.187 \text{ kJ/kg} \cdot \text{K} \\ &= 25122 \text{ kJ/h} \cdot \text{K} \text{ or } 6978 \text{ W/K}\end{aligned}$$

$$(\dot{m}c_p)_{\min} = (\dot{m}c_p)_c.$$

Therefore, Equation 4.59 gives

$$\begin{aligned}F_{hx} &= \left\{ 1 + [F_R U_c A_c / (\dot{m}c_p)_c] [1/\epsilon_{hx} - 1] \right\}^{-1} \\ &= \left\{ 1 + 4.44 \text{ W/m}^2 \cdot \text{K} \times 60 \text{ m}^2 / 1742 \text{ W/K} [1/0.75 - 1] \right\}^{-1} \\ &= 0.951.\end{aligned}$$

Using Equation 5.18,

$$\begin{aligned}P_L &= \frac{A_c F_{hx} F_R U_c \Delta t (T_R - \bar{T}_a)}{\text{Load}} \\ &= \frac{60 \text{ m}^2 \times 0.951 \times 4.44 \frac{\text{W}}{\text{m}^2 \cdot \text{K}} \times (31 \times 24 \times 3600) \text{ s}}{27.384 \text{ GJ} \times (10^9 \text{ J}/1 \text{ GJ})} \\ &= 2.81.\end{aligned}$$

Using Equation 5.19,

$$\begin{aligned}
 P_s &= \frac{A_c F_{hx} F_R \bar{I}_c(\bar{\tau}_a)}{\text{Load}} \\
 &= \frac{60 \text{ m}^2 \times 0.951 \times 0.7 \times 18,341 \frac{\text{kJ}}{\text{m}^2 \cdot \text{day}} \times 31 \text{ days}}{27.384 \text{ GJ} \times \frac{10^6 \text{ kJ}}{1 \text{ GJ}}} \\
 &= 0.83.
 \end{aligned}$$

From Figure 5.21 or Equation 5.22,

$$f_s = 0.53.$$

Example 5.6

The cost of the solar heating system in Example 5.5 is \$25,000 and the building owner is allowed to take a 30% tax credit for this system. Find the payback period for the system in Example 5.5, if the backup system is a gas furnace with an efficiency of 95%. The average price of natural gas is \$1.20/therm. (Note: Since the density and heating value of natural gas vary depending on the source, natural gas is usually priced in terms of the heating value rather than volume or mass. In the United States, the unit used for natural gas is *therm*. A *therm* is 100,000 Btu, which is approximately equal to the heating value of 1000 ft³ of natural gas at standard conditions.)

Solution

The cost of the system = \$25,000

Tax credit = \$25,000 × 0.30 = \$7500

Effective cost of the system = \$25,000 – \$7500 = \$17,500

From Example 5.5, for January:

$$\text{Energy savings} = (\text{Energy demand})(f_s) = 27.38 \times 0.53 = 14.51 \text{ GJ}$$

$$\begin{aligned}
 \text{Natural gas savings} &= \text{Energy savings}/\eta_{\text{furnace}} = (14.51 \text{ GJ}/0.9) \\
 &\quad (1000 \text{ MJ/GJ}) (1 \text{ therm}/105.5 \text{ MJ}) \\
 &= 152.8 \text{ therms}.
 \end{aligned}$$

Table 5.12 gives the values for each month and for the whole year.

Assuming the life of the system to be approximately 20 years, the calculations are done for 25 years. It is assumed that the system performance will go down by approximately 0.25% per year, the price of

TABLE 5.12

Monthly and Yearly Natural Gas Savings Summary for Example 5.5

Month	Monthly Energy Demand (GJ)	f_s	Monthly Energy Savings (GJ)	Monthly Natural Gas Savings (therms)
Jan	27.38	0.53	14.51	152.8
Feb	22.43	0.69	15.48	163.0
Mar	19.24	0.73	14.05	147.9
Apr	10.25	0.91	9.33	98.2
May	5.26	1	5.26	55.4
Jun	1.9	1	1.90	20.0
Jul	0.28	1	0.28	2.9
Aug	0.53	1	0.53	5.6
Sep	3.92	1	3.92	41.3
Oct	8.76	1	8.76	92.3
Nov	16.86	0.63	10.62	111.9
Dec	23.83	0.49	11.68	123.0
Annual	140.64	0.68	96.31	1014.3

natural gas will go up by 5% per year, and the discount rate is 5%. The calculations are shown in Table 5.13.

For example, for the first year:

$$\text{Yearly savings} = (1014 \text{ therms})(\$1.2/\text{therm}) = \$1217$$

For the fifth year:

$$\text{Yearly natural gas savings} = (1014 \text{ therms})(0.9975)^{(5-1)} = 1004 \text{ therms}$$

$$\text{Price of natural gas} = (\$1.2)(1.05)^{(5-1)} = \$1.459/\text{therm}$$

$$\text{Savings for the year} = (1004 \text{ therms})(\$1.459/\text{therm}) = \$1465$$

$$\text{Present worth of savings} = \$1465/(1 + 0.05)^{(5-1)} = \$1205$$

According to Table 5.13, the payback period is 15 years.

Example 5.7

Find the payback period of the system in Example 5.6 if the backup system is an electric heat pump with the following information:

- The backup conventional system is an electric heat pump that operates on an average COP of 1.2 from November to March, and an average COP of 2.5 for the rest of the year.
- The effective price of electricity is \$0.15/kWh_e in the first year and is expected to increase at a rate of 5% per year.

TABLE 5.13

Energy Savings from the Solar Heating System Based on a Natural Gas Backup System

Year	Energy from Solar Heating System (GJ)	Natural Gas Savings (therms)	Natural Gas Price (\$/therm)	Annual Savings (\$)	Cumulative Annual Savings (\$)	PW Annual Savings (\$)	PW Cumulative Annual Savings (\$)
1	96.31	1014	1.2	1217	1217	1217	1217
2	96.07	1012	1.260	1275	2492	1214	2431
3	95.83	1009	1.323	1335	3827	1211	3642
4	95.59	1007	1.389	1398	5225	1208	4850
5	95.35	1004	1.459	1465	6690	1205	6055
6	95.11	1002	1.532	1534	8224	1202	7257
7	94.87	999	1.608	1607	9831	1199	8456
8	94.64	997	1.689	1683	11,514	1196	9652
9	94.40	994	1.773	1763	13,276	1193	10,845
10	94.16	992	1.862	1846	15,123	1190	12,035
11	93.93	989	1.955	1934	17,056	1187	13,222
12	93.69	987	2.052	2025	19,081	1184	14,406
13	93.46	984	2.155	2121	21,202	1181	15,587
14	93.23	982	2.263	2222	23,424	1178	16,766
15	92.99	979	2.376	2327	25,751	1175	17,941
16	92.76	977	2.495	2437	28,188	1172	19,113
17	92.53	974	2.619	2553	30,740	1169	20,282
18	92.30	972	2.750	2673	33,414	1166	21,449
19	92.07	970	2.888	2800	36,214	1163	22,612
20	91.84	967	3.032	2933	39,147	1161	23,773

Solution

Calculations for the first year:

$$\text{Savings for January} = 14.51 \text{ GJ}$$

Considering an average COP of 1.2 for January and conversion from GJ to kWh_e

$$\text{Monthly electric savings} = (14.51 \text{ GJ}/1.2)(1 \text{ kWh}_e/0.0036 \text{ GJ}) = 3359 \text{ kWh}_e$$

Calculations for the whole year are given in Table 5.14.

Calculations for the 20-year life of the system are shown in Table 5.15.

The payback period is 7 years.

TABLE 5.14

Monthly and Yearly Electric Savings Summary

Month	Monthly Energy Demand (GJ)	f_s	Monthly Energy Savings (GJ)	Monthly Electric Savings (kWh _e)
Jan	27.38	0.53	14.51	3359
Feb	22.43	0.69	15.48	3583
Mar	19.24	0.73	14.05	3251
Apr	10.25	0.91	9.33	1036
May	5.26	1	5.26	584
Jun	1.9	1	1.90	211
Jul	0.28	1	0.28	31
Aug	0.53	1	0.53	59
Sep	3.92	1	3.92	436
Oct	8.76	1	8.76	973
Nov	16.86	0.63	10.62	2459
Dec	23.83	0.49	11.68	2703
Annual	140.64	0.68	96.31	18,685

TABLE 5.15

Annual Savings from the Solar Heating System

Year	Energy from Solar Heating System (GJ)	Electricity Savings (kWh _e)	Electricity Tariff (\$/kWh _e)	Annual Savings (\$)	Cumulative Annual Savings (\$)	PW Annual Savings (\$)	PW Cumulative Annual Savings (\$)
1	96.31	18,685	0.15	2803	2803	2803	2803
2	96.07	18,638	0.158	2936	5738	2796	5598
3	95.83	18,592	0.165	3075	8813	2789	8387
4	95.59	18,545	0.174	3220	12,033	2782	11,169
5	95.35	18,499	0.182	3373	15,406	2775	13,944
6	95.11	18,453	0.191	3533	18,939	2768	16,712
7	94.87	18,406	0.201	3700	22,639	2761	19,473
8	94.64	18,360	0.211	3875	26,514	2754	22,227
9	94.40	18,315	0.222	4059	30,573	2747	24,974
10	94.16	18,269	0.233	4251	34,824	2740	27,714
11	93.93	18,223	0.244	4453	39,276	2733	30,448
12	93.69	18,178	0.257	4663	43,940	2727	33,174
13	93.46	18,132	0.269	4884	48,824	2720	35,894
14	93.23	18,087	0.283	5116	53,940	2713	38,607
15	92.99	18,042	0.297	5358	59,298	2706	41,313
16	92.76	17,996	0.312	5612	64,910	2699	44,013
17	92.53	17,951	0.327	5878	70,788	2693	46,706
18	92.30	17,907	0.344	6156	76,944	2686	49,392
19	92.07	17,862	0.361	6448	83,392	2679	52,071
20	91.84	17,817	0.379	6753	90,146	2673	54,743

5.6 Long-Term Performance of Solar Heating Systems

In order to assess the economic viability of any solar process, its cumulative energy delivery over its economic life (in years or decades) must be known. It is very difficult to calculate this number accurately since (1) solar systems and their energy delivery are subject to the vagaries of local microclimate, which can change on a time scale on the order of hours, and (2) future weather cannot be predicted at this level of detail. The standard approach used to estimate future performance of a solar system is to use a typical year of past weather data and assume that it will represent the future on the average, to engineering accuracy. Two common methods used to predict long-term performance of solar IPH (SIPH) systems are the utilizability method and the TRNSYS (Reddy 1987). These methods can also be used for the design of SIPH systems. Sections 5.6 and 5.7 describe both methods.

5.6.1 Critical Solar Intensity Ratio X

The instantaneous efficiency equation for many solar collectors has been shown to be of the form

$$\eta_c = F(\eta_o - U_c \Delta T^+ / I_c), (\eta_c > 0), \quad (5.29)$$

where ΔT^+ is the value of a collector to ambient temperature difference if positive and η_c is zero otherwise, and F is a heat-exchanger factor (F' , F_R), the expression for which depends on the definition of ΔT^+ . It is technically correct but not always economical to operate the solar collector system if $\eta_c > 0$. In practice, $\eta_c \geq \eta_{min} > 0$ is usually the system turn-on criterion since it is not worthwhile to operate collector loops for cases where η_c is very small.

Equation 5.29 can be used to determine the solar intensity level above which useful energy collection can take place. Solving Equation 5.29 for I_c ,

$$I_c \geq U_c \Delta T^+ / (\eta_o - \eta_{min}/F). \quad (5.30)$$

A dimensionless critical intensity ratio X is generally used and since $\eta_{min} \ll 1$ and F is close to 1, for convenience, the second term in the denominator above is dropped:

$$X \equiv U_c \Delta T^+ / \eta_o I_c \leq 1.0. \quad (5.31)$$

X is seen to be the ratio of collector heat loss to absorbed solar flux at $\eta_c = 0$, that is, at the no-net-energy-delivery condition. In many cases, the daily or monthly averaged daily critical intensity ratio X is of more interest and is defined as*

$$\bar{X} \equiv U_c \overline{\Delta T^+} \Delta t_c / \overline{\eta_o I_c}, \quad (5.32)$$

* Note that U_c can be defined to include pipe heat loss per collector array (Beckman 1978).

where $\bar{\eta}_o$ is the daily averaged optical efficiency and $\bar{\Delta T^+}$ is the daily mean temperature difference *during collection*. These can also be expressed as

$$\bar{\Delta T} = \frac{1}{\Delta t_c} \int_{t_o}^{t_o + \Delta t_c} (T_c - T_a) dt, \quad (5.33)$$

$$\bar{\eta}_o = \frac{\int_{t_o}^{t_o + \Delta t} \eta_o I_c dt}{\int_{t_o}^{t_o + \Delta t_c} I_c dt} \quad (5.34)$$

and

$$\bar{I}_c = \frac{1}{\Delta t_c} \int_{t_o}^{t_o + \Delta t_c} I_c dt. \quad (5.35)$$

The collector cut-in time t_o and cut-off time $t_o + \Delta t_c$ are described shortly. The time $t = [0, 24]$ h is related to the solar hour angle h_s by $t = (180 + h_s)/15$; Δt_c is the collection period in hours. In Equation 5.33, T_c can be collector surface, average fluid, inlet fluid, or outlet fluid temperature, depending upon the efficiency data basis.

5.6.2 Utilizability Method

Utilizability, ϕ , has been used to describe the fraction of solar flux absorbed by a collector, which is delivered to the working fluid. On a monthly time scale,

$$\bar{\phi} = \bar{Q}_u / F \bar{\eta}_o \bar{I}_c < 1.0, \quad (5.36)$$

where the overbars denote monthly average, \bar{Q}_u is the monthly averaged daily total useful energy delivery, and $\bar{\phi}$ is the fraction of the absorbed solar flux that is delivered to the fluid in a collector operating at a fixed temperature T_c . The $\bar{\phi}$ concept does not apply to a system composed of collectors, storage, and other components wherein the value of T_c varies continuously. The fixed temperature mode will occur if the collector is a boiler, if very high flow rates are used, if the fluid flow rate is modulated in response to flux variations to maintain a uniform T_c value, or if the collector provides only a minor fraction of the thermal demand. However, if the flow is modulated, note that the value of F (i.e., F' , F_R) may not remain constant to engineering accuracy.

When T_c is not constant in time as in the case of a collector coupled to storage, the $\bar{\phi}$ concept cannot be applied directly. However, for most concentrators for $CR > 10$, the value of U_c is small and the collector is relatively insensitive to a *small* range of operating temperatures. To check this assumption for a particular process, values of $\bar{\phi}$ at the extremes of the expected temperature excursion can be compared.

The value of $\bar{\phi}$ depends upon many system and climatic parameters. However, Collares-Pereira and Rabl (1979) have shown that only three are of first order—the clearness index \bar{K}_T (see Chapter 2), the critical intensity ratio \bar{X} (Equation 5.32), and the ratio r_d/r_T (see Chapter 2). The first is related to insolation statistics, the second to collector parameters and operating conditions, and the last to collector tracking and solar geometry.

Empirical expressions for $\bar{\phi}$ have been developed for several collector types (Collares-Pereira and Rabl 1979). For nontracking collectors,

$$\bar{\phi} = \exp \left\{ -\bar{X} - \left(0.337 - 1.76\bar{K}_T + 0.55r_d/r_T \right) \bar{X}^2 \right\} \quad (5.37)$$

for

$$\bar{\phi} > 0.4, \bar{K}_T = [0.3, 0.5], \text{ and } \bar{X} = [0, 1.2].$$

Also,

$$\bar{\phi} = 1 - \bar{X} + \left(0.50 - 0.67\bar{K}_T + 0.25r_d/r_T \right) \bar{X}^2 \quad (5.38)$$

for

$$\bar{\phi} > 0.4, \bar{K}_T = [0.5, 0.75], \text{ and } \bar{X} = [0, 1.2].$$

The $\bar{\phi}$ expression for tracking collectors ($CR > 10$) is

$$\bar{\phi} = 1.0 - (0.049 + 1.44\bar{K}_T)\bar{X} + 0.341\bar{K}_T\bar{X}^2 \quad (5.39)$$

for

$$\bar{\phi} > 0.4, \bar{K}_T = [0, 0.75], \text{ and } \bar{X} = [0, 1.2].$$

Also,

$$\bar{\phi} = 1.0 - \bar{X} \quad (5.40)$$

for $\bar{\phi} > 0.4$, $\bar{K}_T > 0.75$ (very sunny climate), and $\bar{X} = [0, 1.0]$ for any collector type.

Equations 5.37 through 5.40 were developed using curve-fitting techniques emphasizing large $\bar{\phi}$ values since this is the region of interest for most practical designs. Hence, they should be considered accurate to $\pm 5\%$ only for $\bar{\phi} > 0.4$. Empirical equations for utilizability were also given by Klein et al.; however, these equations were restricted to flat-plate collectors. Since SIPH systems may use concentrating solar collectors, equations given by Collares-Pereira and Rabl (1979) are used in this chapter.

5.6.3 Example Calculation

To illustrate the use of the long-term method, an example will be worked in stepwise fashion. The several steps used are as follows:

1. Evaluate \bar{K}_T from terrestrial \bar{H}_h data and extraterrestrial $\bar{H}_{o,h}$ data.
2. Calculate r_d/r_T for the concentration ratio and tracking mode for the collector.
3. Calculate the critical intensity ratio \bar{X} from Equation 5.32 using a long-term optical efficiency value $\bar{\eta}_o$ and monthly average collector-plane insolation.

$$\bar{I}_c = (r_T - r_d \bar{D}_h / \bar{H}_h) \bar{H}_h. \quad (5.41)$$

The collection time Δt_c may need to be determined in some cases for non-tracking, low-concentration collectors by an iterative method as described in Section 5.6.4.

Example 5.8

Find the energy delivery of a polar-mounted, parabolic trough collector operated for 8 h per day ($\Delta t_c = 8$) during March in Kabul, Afghanistan ($L = 34.5^\circ\text{N}$). The collector has an optical efficiency $\bar{\eta}_o$ of 60%, a heat-loss coefficient $U_c = 0.5 \text{ W/m}^2 \cdot ^\circ\text{C}$, CR = 20, and heat-removal factor $F_R = 0.95$. The collector is to be operated at 150°C . The mean, horizontal solar flux is $5.23 \text{ kWh/m}^2 \cdot \text{day}$ and the ambient temperature is 10°C .

Solution

Following the three-step procedure above, the clearness index is calculated:

$$\bar{H}_{o,h} = 8.22 \text{ kWh/m}^2 \cdot \text{day} \quad (\text{Table A2.1}) \quad \bar{K}_T = 5.23 / 8.22 = 0.64.$$

From Equation 2.52 and $h_{ss} = 90^\circ$ or $\pi/2$ radians

$$\bar{D}_h = 0.775 + 0.347(\pi/2 - \pi/2) - (0.505 + 0.0261(\pi/2 - \pi/2)) \cdot (\cos(2 \times 0.64 - 1.8))$$

$$\bar{H}_h = 0.34.$$

The geometric factors r_d and r_T are calculated from expressions in Table 3.13:

$$r_T = (ah_{coll} + b \sin h_{coll})/d \cos L,$$

$$r_d = (h_{coll}/d)(1/\cos L + \cos h_{sr}(\alpha = 0)/(CR)) - \sin h_{coll}/d(CR),$$

where

$$h_{coll} = (\Delta t_c/2) \times 15^\circ = 60^\circ = 1.047 \text{ rad.}$$

If the collection period is centered about solar noon,

$$h_{sr}(\alpha = 0) = 90^\circ = 1.571 \text{ rad, (for March 21)}$$

$$a = 0.409 + 0.5016 \sin 30^\circ = 0.66,$$

$$b = 0.6609 - 0.4767 \sin 30^\circ = 0.42,$$

$$d = \sin 90^\circ - 1.571 \cos 90^\circ = 1.0,$$

in which case

$$r_T = (0.66 \times 1.047 + 0.42 \times \sin 60^\circ)/1.0 \cos 34.5^\circ = 1.28,$$

$$r_d = (1.047/1.0)[1/\cos 34.5^\circ + \cos 90^\circ/20] - \sin 60^\circ/1.0 \times 20 = 1.31.$$

Finally, the critical intensity ratio is

$$\bar{X} = U_c \overline{\Delta T^+} \Delta t_c / \bar{\eta}_o \bar{I}_c,$$

and the collector-plane insolation \bar{I}_c from Equation 5.41 is

$$\bar{I}_c = (1.28 - 1.31 \times 0.34) \times 5.23 = 5.4 \text{ kWh/m}^2;$$

thus,

$$\bar{X} = 0.5 \times (150 - 10) \times 8 / 0.6 \times 5400 = 0.173.$$

The utilizability $\bar{\phi}$ from Equation 5.39 is

$$\bar{\phi} = 1.0 - (0.049 + 1.44 \times 0.64)(0.173) + 0.341 \times 0.64 \times (0.173)^2 = 0.84.$$

Finally, the useful energy is

$$Q_u = F_R \bar{\eta}_o \bar{I}_c \bar{\phi} = 0.95 \times 0.6 \times 5.4 \times 0.84 = 2.58 \text{ kWh/m}^2 \cdot \text{day}$$

for the month of March on the average.

5.6.4 Collection Period (Δt_c)

The collection period Δt_c can be dictated by either optical or thermal constraints. For example, with a fixed collector, the sun may pass beyond the acceptance limit or be blocked by another collector, and collection would then cease. Alternately, a high-efficiency solar-tracking concentrator operating at relatively low temperature might be able to collect from sunrise to sunset. A third scenario would be for a relatively low-concentration device operating at high temperature to cease to have a positive efficiency during daylight at the time that heat losses are equal to the absorbed flux. In this case, the cutoff time is dictated by thermal properties of the collector and the operating conditions.

Collares-Pereira and Rabl (1979) have suggested a simple procedure to find the proper value of Δt_c . Useful collection Q_c is calculated using the optical time limit first; that is, $\Delta t_c = 2 \min \{[h_{sr}(\alpha = 0), h_{sr}(i = 90)]/15\}$. Second, Q_u is calculated for a slightly shorter period, say, by one-half hour, than the optical limit. If this value of Q_u is larger than that for the first, optically limited case, the collection period is shorter than the optical limit. The period is then further reduced until the maximum Q_u is reached.

The above method assumes that collection time is symmetric about solar noon. This is almost never the case in practice since the heat collected for an hour or so in the morning is required to warm the fluid and other masses to operating temperature. A symmetric phenomenon does not occur in the afternoon. If the time constant of the thermal mass in the collector loop is known, the collection period may be assumed to begin at t_o , $\Delta t_c/2$ h (from above symmetric calculation) before noon decreased by two or three time constants. Another asymmetry can occur if solar flux is obstructed during low sun angle periods in winter. It is suggested that r_T and r_d from Table 3.13 under asymmetric collection conditions be calculated from

$$r_T = [r_T(h_{s,stop}) + r_T(h_{s,start})]/2 \quad (5.42)$$

$$r_d = [r_d(h_{s,stop}) + r_d(h_{s,start})]/2, \quad (5.43)$$

where the collection starting and stopping hour angles account for transients, shading, and so on, as described above:

$$h_{s,start} = 180 - 15t_o, \quad (5.44)$$

$$h_{s,stop} = 180 - 15(t_o + \Delta t_c). \quad (5.45)$$

Example 5.9

Calculations in Example 5.8 were based on $\Delta t_c = 8$ h. Repeat for 10 h to see the effect of collection time if a symmetric collection period about noon is used.

Solution

The values of r_T and r_d for $h_{\text{coll}} = 75^\circ = 1.31$ rad are

$$r_T = (0.66 \times 1.31 + 0.42 \times \sin 75^\circ) / 1.0 \cos 34.5^\circ = 1.98,$$

$$r_d = (1.31 / 1.0)(1 / \cos 34.5^\circ) - \sin 75^\circ / 20 = 1.54.$$

The collector-plane insolation is then

$$\bar{I}_c = (1.98 - 1.54 \times 0.34) \times 5.23 = 7.6 \text{ kWh/m}^2$$

and

$$\bar{X} = [0.5 \times (150 - 10) \times 10] / 0.6 \times 7600 = 0.154.$$

Then, $\bar{\phi}$ is 0.86 from Equation 5.39 and the useful energy delivery is 3.7 kWh/m²-day. Hence, it is worthwhile operating the collector for at least 10 h. The calculation can be repeated by the reader for an asymmetric case 4 h before noon and 6 h after to determine the effect of warm up.

5.6.5 Long-Term Performance of Collector Systems with Storage

Section 5.6.2 of this chapter described a method of predicting long-term performance of a solar collector operated at a temporally constant temperature. This situation is a good approximation of the operating conditions experienced by several types of generic thermal systems. Other systems, however, do not operate at constant temperature and the $\bar{\phi}$ method cannot be used. Although there is no simplified performance method now extant for varying temperature systems, Klein and Beckman (1979) have correlated some modeling results on collector-heat exchanger-storage subsystems coupled to a uniform, process-like load operating above some temperature T_{proc} . The method is called the $\bar{\phi}, f$ chart and is described below. Although the method was developed for flat-plate collectors and uses a different $\bar{\phi}$ calculation method than used above, it can be applied equally well to concentrators.

The calculation method requires first the determination of the utilizationability $\bar{\phi}$ from Equations 5.37 through 5.40. This represents the maximum energy deliverable to a load at T_{proc} . When storage is present and collected solar heat is greater than the demand, the temperature of storage, and hence

the collector inlet temperature, will rise. (The $\bar{\phi}, f$ method applies only to well-mixed, sensible heat storage with liquid heat-transfer fluids and storage media.) Hence, the monthly averaged, daily useful energy collected Q_u will be less than $F\bar{\eta}_o\bar{I}_c\bar{\phi}$, but storage may permit a greater fraction of the demand to be met by solar since the maximum amount of heat $F\bar{\eta}_o\bar{I}_c\bar{\phi}$ collectable may be more than can be used, depending on the demand amount. The $\bar{\phi}, f$ method can be employed to find Q_u in a system with storage.

The technical basis for the $\bar{\phi}, f$ method lies in the nondimensionalization of governing energy equations for a solar thermal system. Dimensionless groups, so identified, are used to correlate monthly thermal energy delivery-to-load for various systems simulated in various climates by an hourly time-scale computer model. The two dimensionless groups identified for use in the $\bar{\phi}, f$ method, in addition to $\bar{\phi}$ ($\bar{\phi}$ is defined in this context relative to the minimum temperature acceptable to the process T_{proc} , not relative to the collector temperature as in Section 5.6.2), are a solar parameter P_s , a measure of long-term solar gain by the collector receiver, and a collector heat-loss parameter P_L , a measure of long-term heat loss at a fixed collector-to-ambient temperature difference of 100°C. This 100°C value does not restrict the generality of the results, however. In equation form,

$$P_s = F_R \bar{\eta}_o \bar{I}_c A_c N_d / L, \quad (5.46)$$

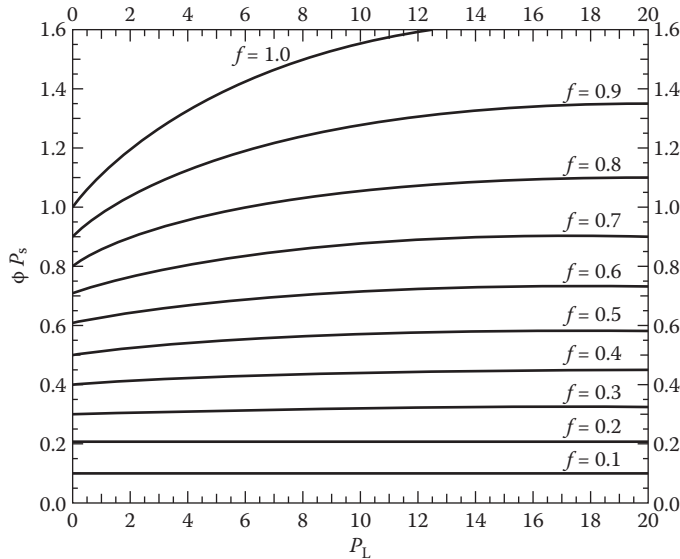
$$P_L = F_R U_c A_c N_h 100 / L, \quad (5.47)$$

in which F_R is given in Equations 3.44 and 3.46. L is the monthly thermal demand, and N_d and N_h are the number of days and hours in a month. The $\bar{\phi}, f$ chart predicts the monthly solar load fraction $f_s(\bar{\phi}, P_s, P_L) \equiv Q_u/L$ by an empirical equation (Klein and Beckman 1979)

$$f_s = \bar{\phi} P_s - a [e^{3.85 f_s} - 1] [1 - e^{-0.15 P_L}], \quad (5.48)$$

where $a = 0.015 \frac{Mc_p}{350A_c}^{-0.76}$, in which m is expressed in kg, c_p in kJ/kg·°C, and A_c in m².

Figure 5.23 is a $\bar{\phi}, f$ chart for a standard storage size of 350 kJ/°C·m² and is plotted with values of $\bar{\phi} P_s$ and P_L to give a monthly value of f_s . The calculation of $\bar{\phi} P_s$ and P_L is done once for each month of an average year, and the totals are added to give annual performance. Example 5.10 shows how the method is used. It is noted that $\bar{\phi} P_s$, the ordinate, is the ratio of maximum possible energy delivered by a collector operating at fixed T_{proc} , $(F\bar{\eta}_o\bar{I}_c\bar{\phi}A_c)$, to the monthly load L . At values of $f_s > 0.4$, the $\bar{\phi}, f$ curves are not independent of

**FIGURE 5.23**

The $\bar{\phi}, f$ chart used to calculate average, monthly solar fraction $f(f_s)$ of solar thermal systems.

X since at progressively higher load fractions, the average storage and collector temperatures are higher and collected solar heat per unit area is smaller because collector efficiency is lower at higher temperature.

This $\bar{\phi}, f$ chart is based upon several limiting assumptions that should be noted in interpreting f_s values:

1. The load L is distributed uniformly over the month between the hours of 6:00 and 18:00.
2. Standard storage amount is fixed at $350 \text{ kJ}/^\circ\text{C} \cdot \text{m}^2$ (approximately 2 gallons of $\text{H}_2\text{O}/\text{ft}^2$ or $84 \text{ l}/\text{m}^2$). For nonstandard storage, correction a (see Equation 5.48) is applied.
3. No energy is rejected from storage; therefore, the vessel is assumed to be designed for the peak temperature and pressure expected.
4. Storage is well mixed and no storage-to-load heat exchanger is used.
5. The load device uses solar heat at temperature-independent efficiency to meet the load L . Therefore, the load device cannot be a turbine, for example.
6. No parasitic heat losses from storage occur.

Some of these restrictions can be relaxed using work on the $\bar{\phi}, f$ method conducted by Klein and Beckman (1979). Users of the $\bar{\phi}$ methods must exercise caution in the proper choice of the $\bar{\phi}$ time scale. In the method presented

here, $\bar{\phi}$ and \bar{I}_c are calculated over the collection period Δt_c , not over all daylight hours. The method developed by Klein uses $\bar{\phi}$ and \bar{I}_c for all daylight hours. Although the Collares-Pereira $\bar{\phi}$ value can be used with the $\bar{\phi}, f$ chart, the two methods of finding $\bar{\phi}$ itself must not be confused.

Example 5.10

Repeat Example 5.8 from Section 5.6.3 for Kabul, Afghanistan, for a monthly averaged load of 260 kWh/day using a collector of 100 m^2 . From the previous example, recall that $F_R \bar{\eta}_o = 0.57$, $F_R U_c = 0.475 \text{ W/m}^2 \cdot ^\circ\text{C}$, $\bar{I}_c = 5.4 \text{ kWh/m}^2$, and $\bar{\phi} = 0.84$. What is the effect of storage on energy delivery per unit collector area?

Solution

First calculate P_s and P_L , then use the $\bar{\phi}, f$ chart to find the solar fraction.

$$P_s = F_R \bar{\eta}_o \bar{I}_c A_c N_d / L = 0.57 \times 5.4 \times 100 \times 31 / (260 \times 31) = 1.18,$$

$$P_L = F_R U_c A_c N_h 100 / L$$

$$= 0.475 \times 100 \times (31 \times 24) \times 100 / (260 \times 31 \times 1000) = 0.44.$$

The value of f_s from the chart with $P_L = 0.44$ and $\bar{\phi} P_s = 0.99$ is $f_s = 0.97$. Therefore, the energy delivery per unit area is $0.97 \times 260 / 100 = 2.52 \text{ kWh/m}^2 \cdot \text{day}$, nearly identical to the result using the $\bar{\phi}$ method. This is a result of the low value of U_c for the concentrator and its resulting insensitivity to temperature fluctuations above T_{proc} . The reader may repeat the calculations for a 200-m² collector with $U_c = 2.0 \text{ W/m}^2 \cdot ^\circ\text{C}$ to show that $\bar{\phi} = 0.43$, $P_L = 1.75$, $P_s = 2.37$, and $f_s = 0.85$. The energy delivery per unit area is then 1.11 kWh/m²·day compared with 1.32 kWh/m²·day predicted by the $\bar{\phi}$ method. Hence, the effect of storage is to reduce the unit energy delivery by 16% for the more lossy collector.

5.7 TRNSYS Computer Simulation Program

TRNSYS (Transient System Simulation) is a sequential-modular transient simulation program developed at the Solar Energy Laboratory of the University of Wisconsin (Klein et al. 1979). It is a widely used, detailed, design tool involving hourly simulations of a solar energy system over an entire year. The TRNSYS computer program contains FORTRAN subroutines of almost all the components that are necessary to build a solar energy system. The component models, which are either empirical or analytical, describe the component performance with algebraic or differential equations. A system

simulation model is created by interconnecting the models of individual components. The resulting set of simultaneous algebraic or differential equations is solved by TRNSYS. This public domain software is constantly being upgraded and is backed by technical support.

5.8 Solar Industrial Process Heat

IPH consumed over 15 EJ (10^{18} J) of energy in 1972 in the United States and this amount grew to 23 EJ by 1994. Although detailed industry specific numbers such as in Table 5.16 are not available for the present use, the total amount of IPH for the world grew to 1748 MTOE or 73 EJ according to the IEA 2010

TABLE 5.16

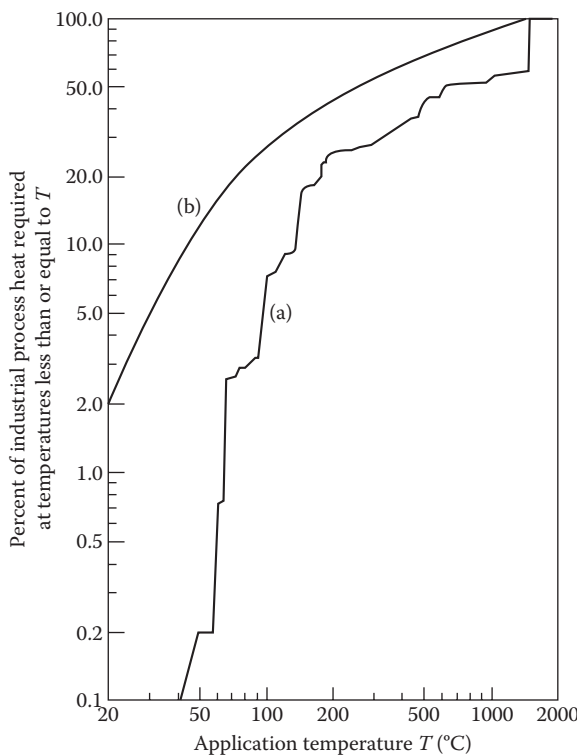
Summary of US Industrial Heat Usage by SIC Category for 1971 and 1994

SIC Group	Quantities in 10^{12} kJ	
	1971	1994
20. Food and kindred products	779	1254
21. Tobacco products	14	W
22. Textile mills	268	327
23. Apparel	22	W
24. Lumber and wood products	188	518
25. Furniture	37	73
26. Paper and allied products	2006	2812
27. Printing and publishing	16	118
28. Chemicals	2536	5621
29. Petroleum products	2576	6688
30. Rubber	158	303
31. Leather	19	W
32. Stone, clay and glass	1541	996
33. Primary metals	3468	2597
34. Fabricated metal products	295	387
35. Machinery	283	260
36. Electrical equipment	213	256
37. Transportation	310	383
38. Instruments	53	113
39. Miscellaneous	72	W
Subtotal	14,854	22,854

Source: Intertechology Corporation, Analysis of the economic potential of solar thermal energy to provide industrial process heat, ERDA Rep. No. COO/2829-1, 3 volumes, 1977.

Note: W, withheld to avoid disclosing data for individual establishments.

World Energy Outlook (IEA 2010). IEA projects the global IPH to grow to 2150 MTOE or 92 EJ by 2020. According to the latest studies (Taibi et al. 2012; Vajen et al. 2012), renewable energy could provide more than 20% of it. The economic outlook for industrial solar heat appears to be extremely favorable because process heat solar collectors could be used throughout the year and each system can be designed to fit the temperature level required for its specific applications, which is particularly important in the use of process heat. Table 5.16 shows the amount of heat used by selected industries in the United States. Majority of the heat is used in the mining, food, textiles, lumber, paper, chemicals, petroleum products, stone-clay-glass, and primary metals (Kreider 1979). The breakdown of industrial energy usage is as follows (Intertechology Corporation 1977): process steam, 41%; direct process heat, 28%; shaft drive, 19%; feedstock, 9%; and other, 3%. In addition to the quantity of heat, quality (i.e., temperature) is also very important to match the proper solar collection system to the application. Figure 5.24 shows the cumulative process heat use by temperature requirement (Intertechology Corporation 1977). It is seen that approximately 25% of the heat is used at

**FIGURE 5.24**

Distribution of US process heat use by required temperature level: (a) heat requirements; (b) IPH requirements plus preheat from 15°C.

temperatures below 100°C, which may be provided by flat-plate collectors, CPCs, or solar ponds, approximately 50% of the heat is used at temperatures below 260°C, and 60% is used below 370°C. Therefore, 50%–60% of all the US process heat could be delivered by parabolic trough collectors.

Since 50% of the IPH requirements that are below 260°C are provided by fossil fuels, it represents enormous waste of availability. Table 5.17 shows approximate second law efficiencies for IPH systems below 260°C assuming 80% first law efficiency for fossil fuel systems. Although the numbers in Table 5.17 are not precise, they do point out the potential to increase the efficiency of energy use by replacing the high-quality fossil fuels with SIPH. SIPH systems are quite simple and are based on the solar heating systems already discussed. The selection of the type of solar collectors depends on the process temperature requirements. Table 5.18 gives the temperature requirements and the type of solar collectors suitable for the process.

The material and type of storage depend on the temperature requirement, the design storage duration, the required energy density (space constraints), and the charging and discharging characteristics. These topics are discussed in detail in Chapter 4. The storage duration for SIPH systems is rarely more than 1 day since the solar systems are designed to displace part of the fossil fuel requirements. The size of storage must be evaluated based on a cost-benefit analysis. Land availability can be critical for SIPH for existing industries. However, in many cases, roofs of industrial buildings can be utilized for this purpose.

Since SIPH components and systems have already been described in Chapters 3 and 4 and this chapter, this section will give some examples of SIPH systems and a methodology for long-term performance prediction.

TABLE 5.17

Second Law Efficiencies for US Industrial Processes below 260°C (500°F)

Temperature	Fraction of US Process Heat (%)	Fossil Fuel (%) (η_2)	Solar (%) (η_2)
29.4°C (85°F)	10	<1	12
49°C (120°F)	5	6	52
65.6°C (150°F)	5	10	65
79.4°C (175°F)	5	13	71
98.9°C (210°F)	5	16	72
121.1°C (250°F)	5	20	77
148.9°C (300°F)	5	25	83
187.8°C (370°F)	5	30	85
237.8°C (460°F)	5	35	85
Total/averages	50	16	61

Source: Kreider, J.F., *Medium and High Temperature Solar Processes*, Academic Press, New York, 1979.

TABLE 5.18
IPH Applications and Types of Possible Solar Energy Systems

Industry/Process	Energy Form	Temperature (°C)	Shallow Ponds or Simple Air Heaters	Flat Plates	Fixed Compound Surfaces	Single-Tracking Troughs	Central Receivers
Aluminum							
Bayer process digestion	Steam	216				X	
Automobile and truck manufacturing							
Heating solutions	Steam (water) Air	49–82 21–29	X X				
Heating makeup air in paint booths							
Drying and baking	Air	163–218		X		X	
Concrete block and brick							
Curing product	Steam	74–177		X		X	
Gypsum							
Calcining	Air	160		X		X	
Curing plasterboard	Steam (air)	299		X		X	
Chemicals							
Borax, dissolving and thickening	Steam	82–99		X		X	
Borax, drying	Air	60–77	X		X		
Bromine, blowing brine/distillation	Steam	107				X	
Chlorine, brine heating							
Chlorine, caustic evaporation	Steam (water)	66–93		X		X	
Phosphoric acid, drying	Air	143–149 121				X	

(Continued)

TABLE 5.18 (CONTINUED)
IPH Applications and Types of Possible Solar Energy Systems

Industry/Process	Energy Form	Temperature (°C)	Shallow Ponds or Simple Air Heaters	Flat Plates	Fixed Compound Surfaces	Single-Tracking Troughs	Central Receivers
Phosphoric acid, evaporation	Steam	160		X	X		X
Potassium chloride, leaching	Steam	93		X	X	X	X
Potassium chloride, drying	Air	121					X
Sodium metal, salt purification	Steam	135		X			X
Sodium metal, drying	Steam (air)	116					X
Food							
Washing	Water	49–71		X	X		
Concentration	Steam (water)	38–43		X	X		
Cooking	Steam	121–188			X	X	
Drying	Steam (air)	121–232		X		X	
Glass							
Washing and rinsing	Water	71–93		X	X		
Laminating	Air	100–177			X	X	X
Drying glass fiber	Air	135–141			X	X	X
Decorating	Air	21–93		X			
Lumber							
Kiln drying	Air	66–99		X	X	X	
Glue preparation/plywood	Steam	99–177			X	X	
Hot pressing/fiberboard	Steam	199				X	X
Log conditioning	Water	82			X		
Mining (Frasch sulfur)	Presurized						
Extraction	Water	160–166				X	X

Paper and pulp		X						
Kraft pulping	Steam	182-188						
Kraft liquor evaporation	Steam	138-143	X	X				
Kraft bleaching	Steam	138-143	X	X				
Papermaking (drying)	Steam	177	X	X				
Plastics								
Initiation	Steam	121-146	X	X				
Steam distillation	Steam	146	X	X				
Flash separation	Steam	216	X	X				
Extrusion	Steam	146	X	X				
Drying	Steam	188	X	X				
Blending	Steam	121	X	X				
Synthetic rubber								
Initiation	Steam (water)	121	X	X				
Monomer recovery	Steam	121	X	X				
Drying	Steam (air)	121	X	X				
Steel								
Pickling	Steam	66-104	X	X				
Cleaning	Steam	82-93	X	X				
Textiles								
Washing	Water	71-82	X	X				
Preparation	Steam	49-113	X	X				
Mercerizing	Steam	21-99	X	X				
Drying	Steam	60-135	X	X				
Finishing	Steam	60-149	X	X				

Source: Kreider, J.F., *Medium and High Temperature Solar Processes*, Academic Press, New York, 1979.

5.9 Examples of SIPH Systems

Most of the IPH systems below 200°C require hot water, steam, or hot air. A typical low-temperature SIPH system is shown schematically in Figure 5.25. If the heat is needed in process air, water-to-air heat exchangers may be used or air heating collectors and rock storage may be used. Hot air is needed typically in agricultural drying, which may be provided by passive solar air heaters. If a large body of water is available, solar ponds may be used for low-temperature applications. Solar ponds are described later in this chapter.

A high-temperature SIPH system may be designed to use low-temperature, medium-temperature, and high-temperature collectors in stages in order to minimize the cost and maximize the efficiency. A schematic of such a system designed for textile dyeing process is shown in Figure 5.26.

5.9.1 SIPH for Textile Industries

The textile industry is one of the 10 largest energy-consuming industries. Of all the energy used in the textile industry, 60%–65% is used in wet processing, including dyeing, finishing, drying, and curing. The energy for wet processing is used as hot water and steam. The textile industry in the United States uses approximately 500 billion liters of water per day and approximately 25% of this water is used at an average temperature of 60°C. Tables 5.19 and 5.20 show typical calculations for determining energy consumption for jet dyeing (Wagner 1977) and tenter frame drying (Hebrank 1975), respectively, for 100% textured polyester circular knit fabric (Goswami and Langley 1987). In the analysis in Table 5.19, Wagner assumed 40% moisture content in the fabric. In carpet dyeing, moisture may be as much as 300% (Lowery et al. 1977). Drying involves the use of high-pressure (6 atm) steam so that the condensed water may be used for other processes. There are no known examples of SIPH for textile drying, but there are a number of examples of

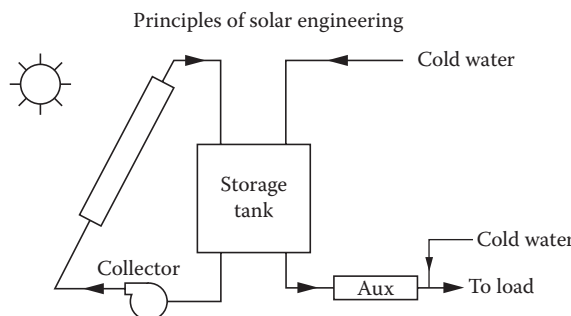
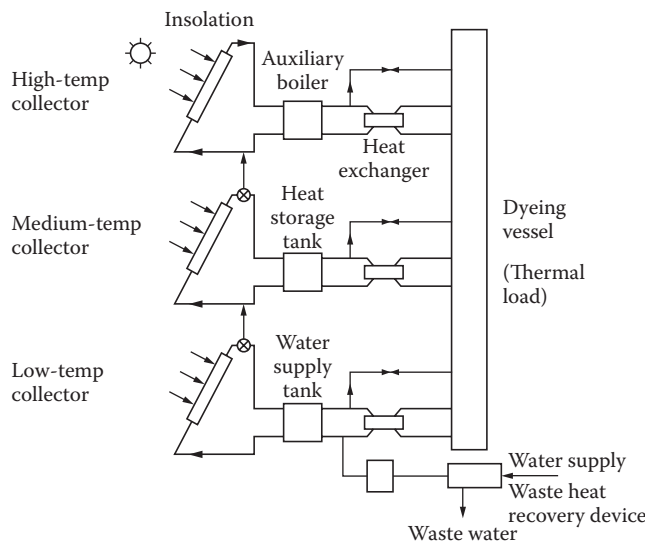


FIGURE 5.25

Schematic of a low-temperature SIPH system.

**FIGURE 5.26**

Schematic of a SIPH system for dyeing process.

TABLE 5.19Sample Calculations^a: Heat for Pressure Jet Dyeing

Scour	Energy Consumption GJ/100 kg Fabric
Heat bath, 21°C–60°C	163
Heat cloth, 21°C–60°C	9
Raise bath to 129°C	293
Raise cloth to 129°C	14
Replace heat loss from radiation	
During cycle 21°C–129°C	23
During dyeing at 129°C	65
Scour at 60°C	172
Total	739

Source: Goswami, B.C. and Langley, J., A Review of the Potential of Solar Energy in the Textile Industry, a chapter in *Progress in Solar Engineering*, Hemisphere Publishing Corporation, Washington, 1987; and Wagner, R., *Energy Conservation in Dyeing and Finishing, Textile Chemists and Colorists*, Vol. 9, p. 52, 1977.

^a Fabric load = 227 kg, bath ratio 10 of 1; cycle time = 2.75 h.

SIPH for textile dyeing. One of those is for a dyeing operation at the Riegel Textile Corp. plant in LaFrance, South Carolina (Goswami and Klett 1982; Goswami and Langley 1987). Figure 5.27 shows a schematic of the system.

The original system used evacuated tube collectors made by General Electric Corp. That system failed because of repeated tube breakage. Since

TABLE 5.20

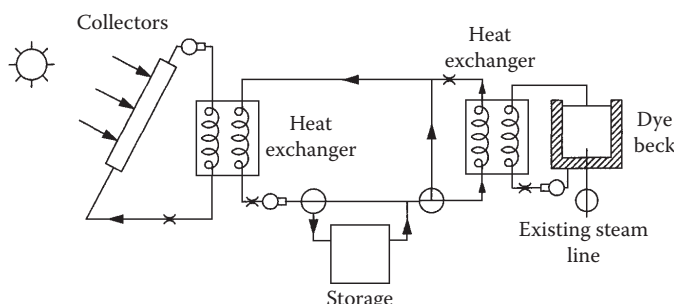
Energy Consumption during Tenter Frame Drying

Steps	Energy Requirements (MJ/100 kg H ₂ O)
Evaporate water	
$100 \text{ kg} \times 4.18 \text{ kJ/kg}\cdot\text{°C} (100\text{°C}-21\text{°C})$	33
Latent heat of vaporization	226
Raise steam temperature to 121°C	
$100 \text{ kg} \times 1.9 \text{ kJ/kg}\cdot\text{°C} (121\text{°C}-100\text{°C})$	4
Heat air (24 kg air/kg H ₂ O)	
$2400 \text{ kg} \times 1.015 \text{ kJ/kg}\cdot\text{°C} (121\text{°C}-21\text{°C})$	244
Heat fabric to 121°C	
$100 \text{ kg} \times 100/40 \times 2.08 \times (121\text{°C}-21\text{°C})$	52
Dryer run at 121°C	559
Dryer run at 149°C	647 (+15%)

Effect of Fabric Moisture Content on Tenter Frame Energy Demand

Steps	30%	80%
Evaporate water		
Raise temperature (21°C–100°C)	10.0	26.5
Latent heat of vaporization	67.7	180.5
Raise steam temperature to 121°C	1.4	3.5
Raise air to 121°C	73.3	195.2
Total	152.4	405.7

Source: Goswami, B.C. and Langley, J., A review of the potential of solar energy in the textile industry, a chapter in *Progress in Solar Engineering*, Hemisphere Publishing Corporation, Washington, DC, 1987; and Hebrank, W.H., *American Dyestuff Reporter*, Vol. 63, p. 34, April 1975.

**FIGURE 5.27**

Schematic of solar energy system at Riegel Textile Corporation plant at LaFrance, South Carolina.

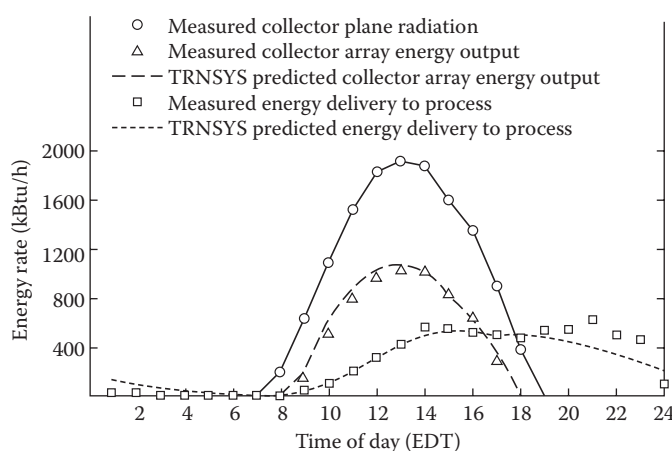
the dyeing process used water at a temperature of 70°C, the evacuated tube collectors were replaced with flat-plate collectors. The flat-plate collectors at this plant have copper absorbers and tubes painted flat black, low iron textured and tempered glass cover, and bronze-enamelled steel frames. The system has 621 m² of collector area.

The dyeing process at this plant is an atmospheric Dye Beck batch process at a maximum temperature of 90°C, which is also typical of the textile industry in the United States (Goswami and Langley 1987). The batch dyeing process involves heating of approximately 4500 liters of inlet water from 10°C–25°C to 90°C. The typical dye cycle is shown in Table 5.21. The refurbished SIPH system at Riegel Textile plant has been operating successfully. The system was simulated using the TRNSYS computer model (TRNSYS 1981). Figure 5.28 shows the actual performance of the system and that predicted by TRNSYS. According to the measured performance of the system from August 14 to October 8, 1983, the system operated with an efficiency of 46% (Goswami and Langley 1987).

TABLE 5.21

Typical Dye Beck Heat Requirements

Dye Process Operation	Temperature of Dye Beck (°C)	Time Interval of Cycle (h)	Percentage of Total Process Energy
Heat the initial load	16–32	0.5	7
Dyeing preparation	32–88	0.5	22
Dye period	88	7–9	68
Cool and reheat for dye fixation	32–43	1.0	3

**FIGURE 5.28**

Actual and predicted system operation, August 16, 1983.

5.9.2 SIPH System for Milk Processing

Food systems use approximately 17% of the US energy (Singh et al. 1986), almost 50% of which is for food processing as hot water (<100°C) or hot air. Proctor and Morse (1975) show that over 40% of the energy demand in the beverage industry in Australia was in the form of hot water between 60°C and 80°C. Considering the temperature and heat requirements of food processing, one would be tempted to conclude that SIPH would be ideal. However, many food processing requirements are seasonal, which may not be economical considering the present price of the conventional fuels unless the SIPH system can be used for the majority of the year. One application that is year-round is milk processing. Singh et al. (1986) simulated a SIPH system for milk processing in the United States using TRNSYS. The unit operations (and their respective temperatures) for this plant compatible with solar thermal energy are as follows:

1. Boiler feed make-up water (100°C)
2. Pasteurizer make-up water (21°C)
3. Case washer and rinsing (49°C)
4. Clean up (71°C)
5. High temperature short time clean up (79°C)
6. Bottle water (93°C)

They estimated that for a plant producing 170,000 kg/week of milk and 98,000 kg/week of orange juice, a total of 621.3 GJ (or 80%) of energy demand was compatible with solar energy in summer and 724.9 GJ (or 93%) of energy demand was compatible in winter. Simulating a solar system similar to the one in Figure 5.25, they found that a 4000 m² collector area could provide approximately 30%–35% solar fraction for the milk processing plant in Madison, Wisconsin; Fresno, California; or Charleston, South Carolina (Singh et al. 1986).

PROBLEMS

1. The no-load temperature of a building with internal heat sources is given by Equation 5.6. How would this equation be modified to account for heat losses through the surface of an unheated slab, the heat losses being independent of ambient temperature?
2. An unheated garage is placed on the north wall of a building to act as a thermal buffer zone. If the garage has roof area A_r , window area A_{wi} , door area A_d , and wall area A_{wa} , what is the effective U value for the north wall of the building if its area is A_n ? The garage floor is well insulated and has negligible heat loss. Express the effective

U value in terms of the *U* values and areas of the several garage surfaces.

3. What is the annual energy demand for a building in Denver, Colorado, if the peak heat load is 44 kJ/s based on a design temperature difference of 42°C? Internal heat sources are estimated to be 6 kJ/s and the design building interior temperature is 20°C.
4. What is the January solar load fraction for a water-heating system in Washington, DC, using 100 m² of solar collector if the water demand is 4 m³/day at 65°C with a source temperature of 12°C? No heat exchanger is used and the solar collector efficiency curve is given in Figure 5.20; the solar collector is tilted at an angle equal to the latitude.
5. Repeat Problem 4 for Albuquerque, New Mexico, in July if the water source temperature is 17°C.
6. Explain how the *f*-chart (Figure 5.21) can be used *graphically* to determine the solar load fraction for a range of collector sizes once the solar and loss parameters have been evaluated for only one system size. *Hint:* consider a straight line passing through the origin and the point (*P_s*, *P_L*).
7. The *f*-chart was generated using data for flat-plate collectors. What modifications would be necessary to use it for a compound parabolic concentrator collector? Describe the effect on each *f*-chart parameter in Table 5.7.
8. In an attempt to reduce cost, a solar designer has proposed replacing the shell-and-tube heat exchanger in Figure 5.8 with a tube coil immersed in the storage tank. The shell-and-tube heat exchanger originally specified had a surface area of 10 m² and a *U* value of 2000 W/m²·K to be used with a 100-m² solar collector. Using a Nusselt number correlation for free convection around a tube

$$\overline{\text{Nu}_D} = \frac{\overline{hD}}{k} = 0.53 (\text{Gr}_D \text{Pr})^{0.25}$$
 to estimate the *h* value of the submerged coil, find the length of a 12-mm-diameter copper pipe needed to achieve the same value of *UA* product as the shell-and-tube heat exchanger. What percentage of the storage tank volume would be consumed by this coil if 50 kg of water is used per square meter of collector? Use a storage water temperature of 60°C and a collector water outlet temperature of 70°C for the calculations.
9. If a solar system delivers 2500 MJ/m²·year with a water flow rate of 30 kg/m_c²·h and a plate efficiency factor *F'* = 0.93, how much energy will it deliver if the flow rate is doubled? Neglect the effect of flow rate on *F'*; the collector has a heat-loss conductance of 4 W/m²·°C.

10. How large (MJ/h) should a heat-rejection system be if it must dump the entire heat production of a 1000-m² solar collector array in Denver, Colorado, on August 21 if the collector is at 100°C and the ambient temperature is 35°C? Use solar collector data in Figure 5.20 and hourly solar radiation data in Appendix 2.
11. Use the *f*-chart to determine the amount of solar energy that can be delivered in Little Rock, Arkansas, in January for the following solar and building conditions:

Building

Load: 20 GJ/month

Latitude: 35°N

Solar System

Collector tilt: 55°, facing south

Area: 60 m²

Ambient temperature: 5°C

Collector efficiency curve: see Figure 5.20

No heat exchanger used

Nominal storage, flow rate, and load heat exchanger values used

12. Repeat Problem 11 if storage size is doubled and halved.
13. Repeat Problem 11 for an air-heating system for which $F_R U_c = 3.64 \text{ W/m}^2 \cdot \text{K}$ and $F_R(\tau\alpha)_n = 0.50$ (typical commercial values). Do air or liquid collectors deliver more energy per square meter in this case?
14. Repeat Problem 13 if collector fluid rate is doubled.
15. Using the data in Problem 11, calculate system performance for a horizontal and for a vertical collector. Assume Equation 5.22 applies to both cases.
16. Using the data in Problem 11, find the solar collector area and the size of the storage tank (assuming water storage) to provide f_s of 0.6 in January.
17. Calculate monthly energy requirements for hot-water supply for a residence in Tampa, Florida, with five occupants. Water source temperature, which is usually available from the city government, is presented in the table below and water delivery temperature is set to 60°C.
The building has a solar water-heating system consisting of two flat-plate collectors measuring 1.5 m × 2.5 m with the following performance characteristics, a 300-liter (~80 US gallons) water storage tank, and the associated controls:

$$F_R(\tau\alpha)_n = 0.75; F_R U_L = 0.13 \text{ W/m}^2 \cdot \text{K}; K_{\tau\alpha} = 1 - 0.15(1/\cos(i) - 1)$$

Using the *f*-chart method, find the total energy supplied by the solar energy system for the hot-water requirements.

Water Source Temperatures (°C)

Jan	Feb	Mar	Apr	May	Jun	Jul	Aug	Sep	Oct	Nov	Dec
16.5	18.5	20	23	26.5	29	30	30	29	25.5	20.5	18

18. The cost of the complete solar water-heating system described above is \$4000. The backup energy source is electricity with a tariff of \$0.14/kWh_e with an annual inflation rate for tariff of 4%.
- Find the payback period of the system assuming a discount rate of 5%. Assume that the system performance degrades at a rate of 0.3% per year.
 - Find the payback period, if the owner gets a rebate of \$1200 on this system.
 - If the owner finances the system with a 10-year loan from a bank at an interest rate of 4.5% per annum with equal monthly payments over the life of the loan, find the monthly payment. When does the monthly payment become less than the average monthly savings from the system?
 - Find the monthly payment due to the solar system only, if the system was included in the mortgage loan for the building at 5% for 25 years.
19. Using the following data for heating degree days for Little Rock, Arkansas, and the system described in Problem 11, find the monthly and yearly heating load provided by the solar heating system. If the cost of the system is \$25,000, find the payback period, given the following:
- The backup system is based on natural gas that costs \$1.20/therm and will increase at an average annual rate of 4%. Assume the discount rate to be 5%. How does the payback period change if the building owner gets a 30% tax credit for the solar energy system?
 - The backup system is electric heat pump that operates at an average COP of 1.3 during December to February and 2.5 during the rest of the heating season. Assume that the electricity tariff is \$0.15/kWh and will increase at an average annual rate of 4%. Assume the discount rate to be 5%.
 - If the homeowner can get financing from a bank at an annual interest rate of 5.5% for a 20-year loan, how will it affect the economics of the system?

Heating Degree C-Days for Little Rock, Arkansas (Base = 18.3°C)

Jan	Feb	Mar	Apr	May	June	July	Aug	Sept	Oct	Nov	Dec	Annual
403	300	204	78	11	0	0	0	7	66	211	372	1653

References

- ASHRAE. 2013. *Handbook of Fundamentals*. American Society of Heating, Refrigerating and Air Conditioning Engineers, Atlanta, GA.
- Balcomb, J.D. et al. 1975. *Solar Handbook for Los Alamos*. LASL, New Mexico; Balcomb, J.D. et al. 1975. Design considerations of air-cooled collector/rock-bin storage solar heating systems. Paper presented at the ISES Annual Meeting, Los Angeles, CA.
- Balcomb, J.D., and J.D. Hedstrom. 1976. Simulation analysis of passive solar heated buildings—Preliminary results. Los Alamos Rept. LA-UR-76-89; see also, under the same title, paper in *Sol. Energy* 19: 277–282, 1977.
- Beckman, W. 1978. Simulations of the performance of open cycle desiccant systems using solar energy. *Sol. Energy* 21: 531.
- Beckman, W.A., S.A. Klein, and J.A. Duffie. 1977. *Solar Heating Design by the F-Chart Method*. John Wiley & Sons, New York.
- Close, D.J. 1962. The performance of solar water heaters with natural circulation. *Sol. Energy* 6: 33.
- Collares-Pereira, M., and A. Rabl. 1979. Simple procedure for predicting long term average performance of nonconcentrating and of concentrating solar collectors. *Sol. Energy* 23: 235–253.
- Goswami, B.C., and J. Langley. 1987. A review of the potential of solar energy in the textile industry. In *Progress in Solar Engineering*, D.Y. Goswami, ed. Hemisphere Publishing Corporation, Washington, DC.
- Goswami, D.Y., and D.E. Klett. 1982. Solar industrial process heat for textile industries. Paper presented at the 1982 ASME, *Textile Industries Division Conference at Raleigh, NC*.
- Hebrank, W.H. 1975. Tenter frame drying. *Am. Dyestuff Rep.* 63: 34.
- IEA. *World Energy Outlook 2010*. International Energy Agency, Paris, France.
- Intertechnology Corporation. 1977. Analysis of the economic potential of solar thermal energy to provide industrial process heat, 3 Vols. ERDA Rep. No. COO/2829-1.
- Klein, S.A. 1976. A design procedure for solar heating systems. Ph.D. dissertation, University of Wisconsin, Madison, WI.
- Klein, S.A., and W.A. Beckman. 1977. General design method for closed loop solar energy systems, *Proc. 1977 ISES Meeting*.
- Klein, S.A., and W.A. Beckman. 1979. General design method for closed loop solar energy systems. *Sol. Energy* 22: 269.
- Klein, S.A., W.A. Beckman, and J.A. Duffie. 1976a. A design procedure for solar heating systems. *Sol. Energy* 18: 113.

- Klein, S.A., W.A. Beckman, and J.A. Duffie. 1976b. A design procedure for solar air heating systems. Paper presented at the 1976 ISES Conference, American Section, Winnipeg, Manitoba, August 15–20.
- Klein, S.A. et al. 1975. A method for simulation of solar processes and its application. *Sol. Energy* 17: 29–37.
- Klein, S.A. et al. 1979. TRNSYS—A transient system simulation. User's manual. Engineering Experiment Station Report 38-10. University of Wisconsin, Madison, WI.
- Kreider, J.F. 1979. *Medium and High Temperature Solar Processes*. Academic Press, New York.
- Kreider, J.F., and F. Kreith. 1977. *Solar Heating and Cooling*, revised 1st ed. Hemisphere Publ. Corp., Washington, DC.
- Kutcher, C.F. 1996. Transpired solar collector system: A major advance in solar heating. Paper presented at the *World Energy Engineering Congress*, Atlanta, GA, November 6–8.
- Kutcher, C.F., and C.B. Christensen. 1992. Unglazed transpired solar collectors. In *Advances in Solar Energy*, Vol. 7, K. Boer, ed. American Solar Energy Soc., Boulder, CO, pp. 283–307.
- Lowery, J.F. et al. 1977. Energy conservation in the textile industry. Technical Report of Department of Energy Project No. Ey-76S-05-5099. School of Textile Engineering, Georgia Institute of Technology, Atlanta, GA, p. 36. Report No. Ey-76-S-05-5099, 1978, 1979.
- Phillips, W.F., and R.D. Cook. 1975. Natural circulation from a flat plate collector to a hot liquid storage tank. ASME Paper 75-HT-53, ASME, NY.
- Proctor, D., and R.N. Morse. 1975. *Solar Energy for Australian Food Processing Industry*. CSIRO Solar Energy Studies, East Melbourne, Victoria, Australia.
- Reddy, T.A. 1987. *The Design and Sizing of Active Solar Thermal Systems*. Oxford University Press, Oxford.
- Singh, R.K., D.B. Lund, and E.H. Buelow. 1986. Compatibility of solar energy with food processing energy demands, Chapter 6. In *Alternative Energy in Agriculture*, Vol. I, D.Y. Goswami, ed. CRC Press, Boca Raton, FL.
- Taibi, E., D. Gielen, and M. Bazilian. 2012. The potential of renewable energy in industrial applications. *Renew. Sustain. Energy Rev.* 16: 735–774.
- TRNSYS. 1981. A transient simulation program, version 11.1. Engineering Experiment Station, Report 38. Solar Energy Laboratory, University of Wisconsin, Madison, WI.
- Vajen, K., C. Lauterbach, and B. Schmitt. 2012. Solar heat for industrial processes—Potential, technologies and applications. *Proceedings of the International Conference on Solar Energy for MENA Region (INCSOL)*, Amman, Jordan, October 22–23.
- Wagner, R. 1977. Energy conservation in dyeing and finishing. *Text. Chem. Color.* 9: 52.

6

Solar Cooling and Dehumidification

The real cycle you're working on is a cycle called yourself.

Robert Pirsig

6.1 Solar Space Cooling and Refrigeration

In some ways, solar energy is better suited to space cooling and refrigeration than to space heating, but this application of solar energy has not found much commercial success. The seasonal variation of solar energy is extremely well suited to the space-cooling requirements of buildings. The principal factors affecting the temperature in a building are the average quantity of radiation received and the environmental air temperature. Since the warmest seasons of the year correspond to periods of high insolation, solar energy is most available when comfort cooling is most needed. Moreover, as we have seen in Chapter 3, the efficiency of solar collectors increases with increasing insolation and increasing environmental temperature. Consequently, in the summer, the amount of energy delivered per unit surface area of collector can be larger than that in winter.

There are several approaches that can be taken to solar space cooling and refrigeration. Because of the limited operating experience with solar-cooling systems, their design must be based on basic principles and experience with conventional cooling systems. The material presented in this chapter will therefore stress the fundamental principles of operation of refrigeration cycles and combine them with special features of the components in a solar system.

The two principal methods of lowering air temperature for comfort cooling are refrigeration with actual removal of energy from the air or evaporation cooling of the air with adiabatic vaporization of moisture into it. Refrigeration systems can be used under any humidity condition of entering air, whereas evaporative cooling can be used only when the entering air has a comparatively low relative humidity.

The most widely used air-conditioning method employs a vapor-compression refrigeration cycle. Another method uses an absorption refrigeration cycle

similar to that of the gas refrigerator. The vapor-compression refrigeration cycle requires energy input into the compressor, which may be provided as electricity from a photovoltaic system or as mechanical energy from a solar-driven engine. Referring to Figure 6.1, the compressor raises the pressure of the refrigerant, which also increases its temperature. The compressed high-temperature refrigerant vapor then transfers its heat to the ambient environment in the condenser, where it condenses to a high-pressure liquid at a temperature close to (but higher than) the environmental temperature. The liquid refrigerant is then passed through the expansion valve where its pressure is suddenly reduced, resulting in a vapor–liquid mixture at a much lower temperature. The low-temperature refrigerant is then used to cool air or water in the evaporator where the liquid refrigerant evaporates by absorbing heat from the medium being cooled. The cycle is completed by the vapor returning to the compressor. If water is cooled by the evaporator, the device is usually called a chiller. The chilled water is then used to cool the air in the building.

In an absorption system, the refrigerant is evaporated or distilled from a less volatile liquid absorbent, the vapor is condensed in a water- or air-cooled condenser, and the resulting liquid is passed through a pressure-reducing valve to the cooling section of the unit. There, it chills the water as it evaporates, and the resulting vapor flows into a vessel, where it is reabsorbed in the stripped absorbing liquid and pumped back to the heated generator. The

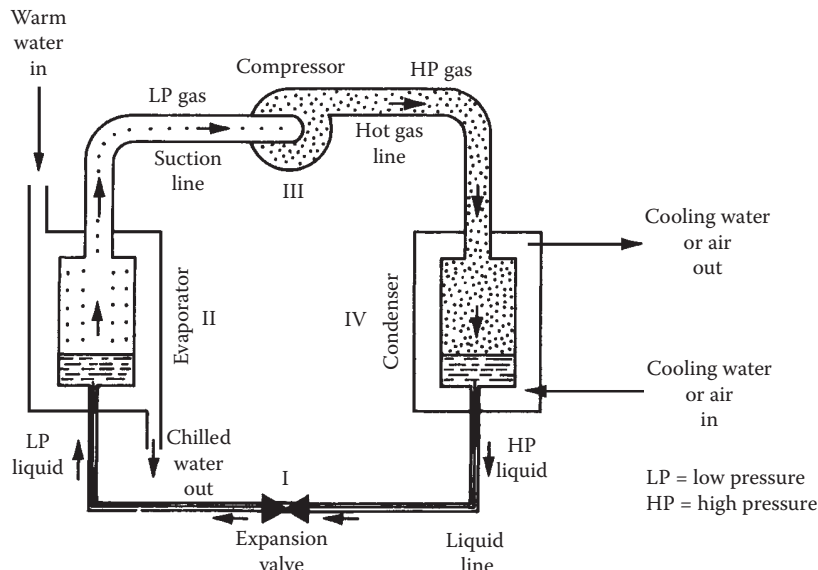
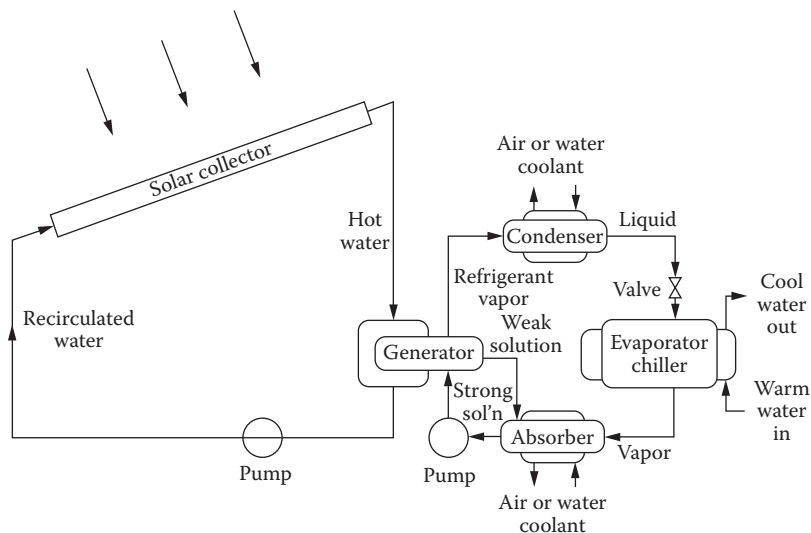


FIGURE 6.1

Schematic diagram illustrating the basic refrigeration vapor-compression cycle.

**FIGURE 6.2**

Schematic diagram of a solar-powered absorption refrigeration system.

heat required to evaporate the refrigerant in the generator can be supplied directly from solar energy as shown in Figure 6.2.

In humid climates, removal of moisture from the air represents a major portion of the air-conditioning load. In such climates, desiccant systems can be used for dehumidification, in which solar energy can provide most of the energy requirements. There are several passive space-cooling techniques, such as nocturnal cooling (night sky radiation), ground cooling, and underground air tunnels. These techniques are described in Chapter 7. The present chapter covers the active solar cooling techniques based on vapor-compression and vapor-absorption refrigeration cycles and desiccant humidification.

6.1.1 Cooling Requirements for Buildings

The cooling load of a building is the rate at which heat must be removed to maintain the air in a building at a given temperature and humidity. It is usually calculated on the basis of the peak load expected during the cooling season. For a given building, the cooling load depends primarily on

1. Inside and outside dry-bulb temperatures and relative humidities
2. Solar-radiation heat load and wind speed
3. Infiltration and ventilation
4. Internal heat sources

A method of calculating the cooling load is presented in detail in ASHRAE (2013).

The steps in calculating the cooling load of a building are as follows:

1. Specify the building characteristics: wall area, type of construction, and surface characteristics; roof area, type of construction, and surface characteristics; window area, setback, and glass type; and building location and orientation.
2. Specify the outside and inside wet- and dry-bulb temperatures.
3. Specify the solar heat load and wind speed.
4. Calculate building cooling load resulting from the following: heat transfer through windows; heat transfer through walls; heat transfer through roof; sensible and latent heat gains resulting from infiltration and ventilation; sensible and latent heat gains (water vapor) from internal sources, such as people, lights, cooking, and so on.

Equations 6.1 through 6.7 may be used to calculate the various cooling loads for a building. Cooling loads resulting from lights, building occupants, and so on may be estimated from ASHRAE (2013). For unshaded or partially shaded windows, the load is

$$\dot{Q}_{wi} = A_{wi} F_{sh} \bar{\tau}_{b,wi} I_{h,b} \frac{\cos i}{\sin \alpha} + \bar{\tau}_{d,wi} I_{h,d} \cos^2 \beta / 2 + \bar{\tau}_{r,wi} I_r + U_{wi} (T_{out} - T_{in}) . \quad (6.1)$$

$$I_r = \rho (I_{b,h} + I_{d,h}) \sin^2 (\beta / 2)$$

For shaded windows, the load (neglecting sky diffuse and reflected radiation) is

$$\dot{Q}_{wi,sh} = A_{wi,sh} U_{wi} (T_{out} - T_{in}). \quad (6.2)$$

For unshaded walls, the load is

$$\dot{Q}_{wa} = A_{wa} \bar{\alpha}_{s,wa} I_r + I_{h,d} \cos^2 \beta / 2 + I_{h,b} \frac{\cos i}{\sin \alpha} + U_{wa} (T_{out} - T_{in}) . \quad (6.3)$$

For shaded walls, the load (neglecting sky diffuse and reflected radiation) is

$$\dot{Q}_{wa,sh} = A_{wa,sh} [U_{wa} (T_{out} - T_{in})]. \quad (6.4)$$

For the roof, the load is

$$\dot{Q}_{rf} = A_{rf} \bar{\alpha}_{s,rf} I_r + I_{h,d} \cos^2 \beta / 2 + I_{h,b} \frac{\cos i}{\sin \alpha} + U_{rf} (T_{out} - T_{in}) . \quad (6.5)$$

Sensible cooling load owing to infiltration and ventilation is

$$\dot{Q}_i = \dot{m}_a(h_{out} - h_{in}) = \dot{m}_a C p_a (T_{out} - T_{in}). \quad (6.6)$$

Latent load owing to infiltration and ventilation is

$$\dot{Q}_w = \dot{m}_a (W_{out} - W_{in}) \lambda_w, \quad (6.7)$$

where

- \dot{Q}_{wi} = heat flow through unshaded windows of area A_{wi} ,
- $\dot{Q}_{wi,sh}$ = heat flow through shaded windows of area $A_{wi,sh}$,
- \dot{Q}_{wu} = heat flow through unshaded walls of area A_{wa} ,
- $\dot{Q}_{wu,sh}$ = heat flow through shaded walls of area $A_{wa,sh}$,
- \dot{Q}_{rf} = heat flow through roof of area A_{rf} ,
- \dot{Q}_i = heat load resulting from infiltration and ventilation,
- \dot{Q}_w = latent heat load,
- $I_{h,b}$ = beam component of insolation on horizontal surface,
- $I_{h,d}$ = diffuse component of insolation on horizontal surface,
- I_r = ground-reflected component of insolation,
- W_{out}, W_{in} = outside and inside humidity ratios,
- U_{wi}, U_{wa}, U_{rf} = overall heat-transfer coefficients for windows, walls, and roof, including radiation,
- \dot{m}_a = net infiltration and ventilation mass flow rate of dry air,
- $C p_a$ = specific heat of air (approximately 1.025 kJ/kg-K for moist air),
- T_{out} = outside dry-bulb temperature,
- T_{in} = indoor dry-bulb temperature,
- F_{sh} = shading factor (1.0 = unshaded, 0.0 = fully shaded),
- $\bar{\alpha}_{s,wa}$ = wall solar absorptance,
- $\bar{\alpha}_{s,rf}$ = roof solar absorptance,
- i = solar-incidence angle on walls, windows, and roof,
- h_{out}, h_{in} = outside and inside air enthalpy,
- α = solar-altitude angle,
- λ_w = latent heat of water vapor,
- ρ = ground reflectance,
- $\bar{\tau}_{b,wi}$ = window transmittance for beam (direct) insolation,
- $\bar{\tau}_{d,wi}$ = window transmittance for diffuse insolation, and
- $\bar{\tau}_{r,wi}$ = window transmittance for ground-reflected insolation.

Recent ASHRAE handbooks recommend the use of the CLTD (cooling load temperature difference) method. For more details of the method, one should refer to ASHRAE (2013).

Example 6.1

Determine the cooling load for a building in Phoenix, Arizona, with the specifications tabulated in Table 6.1.

TABLE 6.1

Building Specifications for Example 6.1

Factor	Description or Specification
Building characteristics	
Roof	
Type of roof	Flat, shaded
Area, $A_{rf,sh}$ (m^2)	240
Walls (painted white)	
Size, north and south	$3 \times 20 \text{ m}$ (two)
Size, east and west	$3 \times 12 \text{ m}$ (two)
Area, A_{wa} , north and south walls (m^2)	$60 - A_{wi} = 60 - 6 = 54 \text{ m}^2$ (two)
Area, A_{wa} , east and west walls (m^2)	$36 - A_{wi} = 36 - 6 = 30 \text{ m}^2$ (two)
Absorptance, $\bar{\alpha}_{s,wa}$ and $\bar{\alpha}_{s,rf}$, of white paint	0.12
Windows	
Size, north and south	$2 \times 1.5 \text{ m}$ (two)
Size, east and west	$2 \times 1.5 \text{ m}$ (two)
Shading factor, F_{sh}	0.20
Insolation transmittance	$\bar{\tau}_{b,wi} = 0.60; \bar{\tau}_{d,wi} = 0.81; \bar{\tau}_{r,wi} = 0.60$
Ground reflectance	0.2
Location and latitude	Phoenix, Arizona; 33°N
Date	August 1
Time and local-solar-hour angle, h_s	Noon; $h_s = 0$
Solar declination, δ_s (degree)	$17^\circ - 55'$
Wall surface tilt from horizontal, β	90°
Temperature, outside and inside ($^\circ\text{C}$)	$T_{out} = 38; T_{in} = 23$
Insolation, I (W/m^2)	$I_{h,b} = 200; I_{h,d} = 100; I_r = 70$
U factor for walls, windows, and roof	$U_{wa} = 0.19; U_{wi} = 1.09; U_{rf} = 0.061$
Infiltration ($\text{lbm dry air}/\text{h}$)	Neglect
Ventilation ($\text{lbm dry air}/\text{h}$)	Neglect
Internal loads	Neglect
Latent heat load, Q_w (%)	30% of wall sensible heat load

Solution

To determine the cooling load for the building just described, calculate the following factors in the order listed.

1. Incidence angle for the south wall i at solar noon can be written from Equations 2.44 and 2.28 as

$$\begin{aligned} \cos i &= \cos \beta \cos(L - \delta_s) + \sin \beta \sin(L - \delta_s) \\ &= 0.26. \end{aligned} \quad (6.8)$$

2. Solar altitude α at solar noon (from Equation 2.28)

$$\sin \alpha = \sin \delta_s \sin L + \cos \delta_s \cos L \cos h_s = \cos(L - \delta_s) = \cos 15^\circ = 0.966.$$

3. Insolation $I_{r,wa} = I_{r,wi} = 0.2(700 + 100)\sin^2(45^\circ) = 80 \text{ W/m}^2$

$$I_{r,rf} = 0.$$

4. South-facing window load (from Equation 6.1)

$$\begin{aligned} \dot{Q}_{wi} &= 2 \times 3 \quad 0.20 \times 0.6 \times 700 \frac{0.26}{0.966} + (0.81 \times 100 \cos^2(45^\circ)) + (0.60 \times 80) \\ &\quad + 1.09(38 - 23) \end{aligned} \Big\} = 765 \text{ W.}$$

5. Shaded-window load (from Equation 6.2)

$$\dot{Q}_{wi,sh} = (3 \times 6)[1.09(38 - 23)] = 295 \text{ W.}$$

6. South-facing wall load (from Equation 6.3)

$$\begin{aligned} \dot{Q}_{wa} &= (60 - 6) \quad 0.12 \quad 100 \cos^2(45^\circ) + 80 + 700 \frac{0.26}{0.966} + 0.19(38 - 23) \\ &= 2217 \text{ W.} \end{aligned}$$

7. Shaded-wall load (from Equation 6.4)

$$\dot{Q}_{wa,sh} = [(60 + 36 + 36) - (3 \times 6)] \times [0.19(38 - 23)] = 324 \text{ W.}$$

8. Roof load (from Equation 6.5)

$$\dot{Q}_{rf} = 240[\bar{\alpha}_{s,rf} \times 0 + 0.061(38 - 23)] = 220 \text{ W.}$$

9. Latent-heat load (30% of sensible wall load)

$$\dot{Q}_w = 0.3[(60 + 60 + 36 + 36) - (4 \times 60)][0.19(38 - 23)] = 144 \text{ W.}$$

10. Infiltration load

$$\dot{Q}_i = 0.$$

11. Total cooling load for the building described in the example

$$\begin{aligned} \dot{Q}_{tot} &= \dot{Q}_{wi} + \dot{Q}_{wi,sh} + \dot{Q}_{wa} + \dot{Q}_{wa,sh} + \dot{Q}_{rf} + \dot{Q}_w + \dot{Q}_i, \\ \dot{Q}_{tot} &= 3965 \text{ W.} \end{aligned}$$

6.1.2 Vapor-Compression Cycle

The principle of operation of a vapor-compression refrigeration cycle can be illustrated conveniently with the aid of a pressure–enthalpy diagram as shown in Figure 6.3. The ordinate is the pressure of the refrigerant in N/m² absolute, and the abscissa is its enthalpy in kJ/kg. The roman numerals in Figure 6.3 correspond to the physical locations in the schematic diagram of Figure 6.1.

Process I is a throttling process in which hot liquid refrigerant at the condensing pressure p_c passes through the expansion valve, where its pressure is reduced to the evaporator pressure p_e . This is an isenthalpic (constant enthalpy) process, in which the temperature of the refrigerant decreases. In this process, some vapor is produced and the state of the mixture of liquid refrigerant and vapor entering the evaporator is shown by point A. Since the expansion process is isenthalpic, the following relation holds:

$$h_{ve}f + h_{le}(1 - f) = h_{lc} \quad (6.9)$$

where f is the fraction of mass in vapor state, subscripts “v” and “l” refer to vapor and liquid states, respectively, and “c” and “e” refer to states corresponding to condenser and evaporator pressures, respectively. And,

$$f = \frac{h_{lc} - h_{le}}{h_{ve} - h_{le}}. \quad (6.10)$$

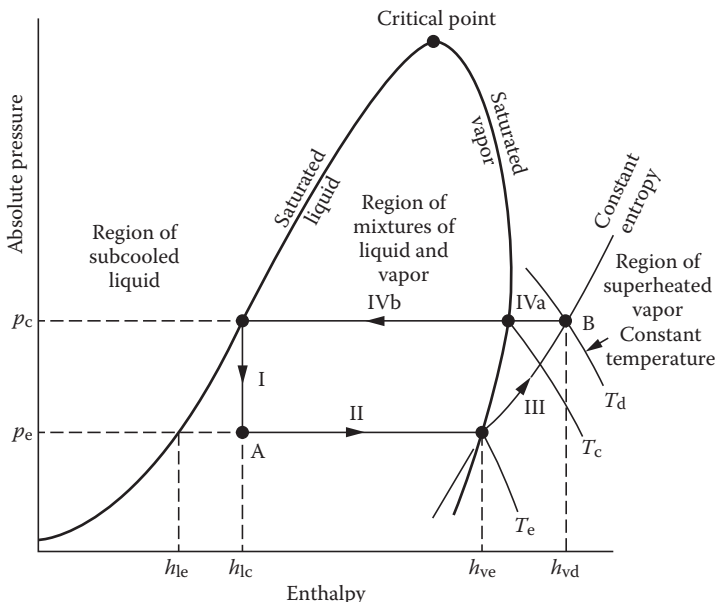


FIGURE 6.3
Simple refrigeration cycle on pressure–enthalpy diagram.

Process II represents the vaporization of the remaining liquid. This is the process during which heat is removed from the chiller. Thus, the specific refrigeration effect per kilogram of refrigerant q_r is

$$q_r = h_{ve} - h_{lc} \text{ in kJ/kg (Btu/lb).} \quad (6.11)$$

In the United States, it is still common practice to measure refrigeration in terms of *tons*. One ton is the amount of cooling produced if 1 ton of ice is melted over a period of 24 h. Since 1 ton = 907.2 kg and the latent heat of fusion of water is 334.9 kJ/kg,

$$1 \text{ ton} = \frac{(907.2 \text{ kg}) \times (334.9 \text{ kJ/kg})}{(24 \text{ h}) \times (3600 \text{ s/h})} = 3.516 \text{ kW} = 12,000 \text{ Btu/h.} \quad (6.12)$$

If the desired rate of refrigeration requires a heat-transfer rate of \dot{Q} , the rate of mass flow of refrigerant necessary \dot{m}_r is

$$\dot{m}_r = \frac{\dot{Q}_r}{(h_{ve} - h_{lc})}. \quad (6.13)$$

Process III in Figure 6.3 represents the compression of refrigerant from pressure p_e to p_c . The process requires work input from an external source, which may be obtained from a solar-driven expander turbine or a solar electrical system. In general, if the heated vapor leaving the compressor is at the condition represented by point B in Figure 6.3, the work of compression W_c is

$$W_c = \dot{m}_r(h_{vd} - h_{ve}). \quad (6.14)$$

In an idealized cycle analysis, the compression process is usually assumed to be isentropic.

Process IV represents the condensation of the refrigerant. Actually, sensible heat is first removed in subprocess IVa as the vapor is cooled at constant pressure from T_d to T_c and latent heat is removed at the condensation temperature T_c , corresponding to the saturation pressure p_c in the condenser. The heat-transfer rate in the condenser \dot{Q}_c is

$$\dot{Q}_c = \dot{m}_r(h_{vd} - h_{lc}). \quad (6.15)$$

This heat must be rejected into the environment, either to cooling water or to the atmosphere if no water is available.

The overall performance of a refrigeration machine is usually expressed as the ratio of the heat transferred in the evaporator \dot{Q}_r to the shaft work

supplied to the compressor. This ratio is called the *coefficient of performance* (COP), defined by

$$\text{COP} = \frac{\dot{Q}_c}{W_c} = \frac{h_{ve} - h_{lc}}{h_{vd} - h_{ve}}. \quad (6.16)$$

The highest coefficient of performance for any given evaporator and condenser temperatures would be obtained if the system were operating on a reversible Carnot cycle. Under these conditions,

$$\text{COP}(\text{Carnot}) = \frac{T_e}{T_d - T_e}. \quad (6.17)$$

However, frictional effects and irreversible heat losses reduce the COP of real cycles much below this maximum.

Example 6.2

Calculate the amount of shaft work to be supplied to a 1-ton (3.52-kW) refrigeration plant operation at evaporator and condenser temperatures of 273 K and 309 K, respectively, using Refrigerant 134a (R-134a) as the working fluid. The properties of R-134a are tabulated in Table 6.2. (More complete data are given in Appendix 6.) Also calculate the COP and the mass flow rate of the refrigerant.

Solution

From the property table, the enthalpies for process I are as follows:

$$\begin{aligned} \text{Saturated vapor at } 273 \text{ K} & \quad h_{ve} = 247.2 \text{ kJ/kg} \\ \text{Saturated liquid at } 309 \text{ K} & \quad h_{lc} = 100.3 \text{ kJ/kg} \\ \text{Saturated liquid at } 273 \text{ K} & \quad h_k = 50.0 \text{ kJ/kg} \end{aligned}$$

TABLE 6.2

Properties of R-134a for Example 6.2

Temperature (K)	Absolute Pressure (kPa)	Vapor-Specific Volume (m ³ /kg)	Liquid Enthalpy (kJ/kg)	Vapor Enthalpy (kJ/kg)	Vapor Entropy (kJ/kg·K)
<i>Saturated</i>					
273	292.8	0.0689	50.02	247.2	0.919
309	911.7	0.0223	100.25	266.4	0.9053
<i>Superheated</i>					
308.5	900	0.0226	—	266.18	0.9054
313	900	0.0233	—	271.3	0.9217
312.4	1000	0.0202	—	268.0	0.9043
313	1000	0.0203	—	268.7	0.9066

Therefore, from Equation 6.10,

$$f = \frac{100.3 - 50.0}{247.2 - 50.0} = 0.255.$$

The mass flow rate of refrigerant \dot{m}_r is obtained from Equation 6.13 and the enthalpies above, or

$$\dot{m}_r = \frac{3.52 \text{ kW}}{(247.2 - 100.3) \text{ kJ/kg}} = 0.024 \text{ kg/s.}$$

The specific shaft-work input required is

$$\frac{W_c}{\dot{m}_r} = h_{vd} - h_{ve}.$$

The entropy s_e of the saturated vapor entering the compressor at 273 K and 292.8 kPa is 0.919 kJ/kg-K. From the property table, superheated vapor at a pressure of 911.7 kPa has an entropy of 0.919 kJ/kg-K at a temperature of 313 K with an enthalpy of 270.8 kJ/kg. Thus, the energy input to the working fluid by the compressor is

$$W_c = 0.024(270.8 - 247.2) = 0.566 \text{ kW.}$$

Finally, the heat-transfer rate from the refrigerant to the sink, or cooling water in the condenser, is from Equation 6.15:

$$\dot{Q}_c = \dot{m}_r(h_{vd} - h_{lc}) = 0.024(270.8 - 100.3) = 4.09 \text{ kW.}$$

The COP of the thermodynamic cycle is

$$\text{COP} = \frac{247.2 - 100.3}{270.8 - 247.2} = 6.2,$$

whereas the Carnot COP is 273/36 or 7.6.

The above cycle has been idealized. In practice, the liquid entering the expansion valve is several degrees below the condensing temperature, while the vapor entering the compressor is several degrees above the evaporation temperature. In addition, pressure drops occur in the suction, discharge, and liquid pipelines, and the compression is not truly isentropic. Finally, the work required to drive the compressor is somewhat larger than W_c above, because of frictional losses. All of these factors must be taken into account in a realistic engineering design.

6.1.3 Absorption Air Conditioning

Absorption air conditioning is compatible with solar energy since a large fraction of the energy required is thermal energy at temperatures that currently available flat-plate collectors can provide.

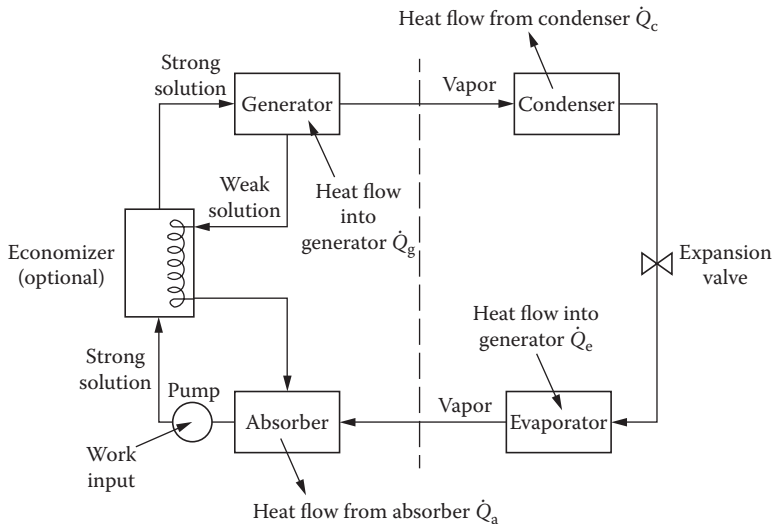
**FIGURE 6.4**

Diagram of heat and fluid flow of absorption air conditioner, with economizer. (From Kreider, J.F. and F. Kreith, *Solar Heating and Cooling*, Revised 1st Ed. Washington, DC: Hemisphere Publ. Corp., 1977.)

Solar absorption air conditioning has been the subject of investigation by a number of researchers (Chinnappa and Wijeyesundara 1992; Kochhar 1982; Macriss and Zawacki 1989; Manrique 1991; Siddiqui 1993; Thombloom and Nimmo 1996). Figure 6.4 shows a schematic of an absorption refrigeration system. Absorption refrigeration differs from vapor-compression air conditioning only in the method of compressing the refrigerant (left of the dashed line in Figure 6.4). In absorption air-conditioning systems, the pressurization is accomplished by first dissolving the refrigerant in a liquid (the absorbent) in the absorber section, then pumping the solution to a high pressure with an ordinary liquid pump. The low boiling refrigerant is then driven from solution by the addition of heat in the generator. By this means, the refrigerant vapor is compressed without the large input of high-grade shaft work that the vapor-compression air conditioning demands.

The effective performance of an absorption cycle depends on the two materials that comprise the refrigerant-absorbent pair. Desirable characteristics for the refrigerant-absorbent pair follow.

1. The absence of a solid-phase absorbent.
2. A refrigerant more volatile than the absorbent so that separation from the absorbent occurs easily in the generator.

3. An absorbent that has a strong affinity for the refrigerant under conditions in which absorption takes place.
4. A high degree of stability for long-term operations.
5. Nontoxic and nonflammable fluids for residential applications. This requirement is less critical in industrial refrigeration.
6. A refrigerant that has a large latent heat so that the circulation rate can be kept low.
7. A low fluid viscosity that improves heat and mass transfer and reduces pumping power.
8. Fluids that must not cause long-term environmental effects.

Lithium bromide–water ($\text{LiBr}-\text{H}_2\text{O}$) and ammonia–water ($\text{NH}_3-\text{H}_2\text{O}$) are the two pairs that meet most of the requirements. In the $\text{LiBr}-\text{H}_2\text{O}$ system, water is the refrigerant and LiBr is the absorber, while in the ammonia–water system, ammonia is the refrigerant and water is the absorber. Because the $\text{LiBr}-\text{H}_2\text{O}$ system has high volatility ratio, it can operate at lower pressures and, therefore, at the lower generator temperatures achievable by flat-plate collectors. A disadvantage of this system is that the pair tends to form solids. LiBr has a tendency to crystallize when air cooled, and the system cannot be operated at or below the freezing point of water. Therefore, the $\text{LiBr}-\text{H}_2\text{O}$ system is operated at evaporator temperatures of 5°C or higher. Using a mixture of LiBr with some other salt as the absorbent can overcome the crystallization problem. The ammonia–water system has the advantage that it can be operated down to very low temperatures. However, for temperatures much below 0°C , water vapor must be removed from ammonia as much as possible to prevent ice crystals from forming. This requires a rectifying column after the boiler. Also, ammonia is a safety Code Group B2 fluid (ASHRAE Standard 34-1992) which restricts its use indoors (ASHRAE 2013).

Other refrigerant–absorbent pairs include (Macriss and Zawacki 1989)

- Ammonia–salt
- Methylamine–salt
- Alcohol–salt
- Ammonia–organic solvent
- Sulfur dioxide–organic solvent
- Halogenated hydrocarbons–organic solvent
- Water–alkali nitrate
- Ammonia–water–salt

If the pump work is neglected, the COP of an absorption air conditioner can be calculated from Figure 6.4:

$$\text{COP} = \frac{\text{cooling effect}}{\text{heat input}} = \frac{\dot{Q}_c}{\dot{Q}_g}. \quad (6.18)$$

The COP values for absorption air conditioning range from 0.5 for a small, single-stage unit to 0.85 for a double-stage, steam-fired unit. These values are approximately 15% of the COP values that can be achieved by a vapor-compression air conditioner. It is difficult to directly compare the COP of an absorption air conditioner with that of a vapor-compression air conditioner because the efficiency of electric power generation or transmission is not included in the COP of the vapor-compression air conditioning. The following example illustrates the thermodynamics of a LiBr–H₂O absorption refrigeration system.

Example 6.3

A water–lithium bromide absorption refrigeration system such as that shown in Figure 6.5 is to be analyzed for the following requirements:

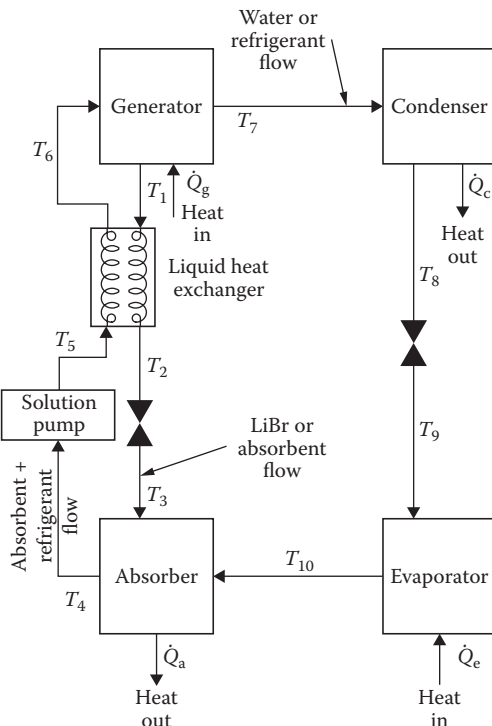


FIGURE 6.5

Lithium bromide–water, absorption refrigeration cycle (see Table 6.3). (From Kreider, J.F. and F. Kreith, *Solar Heating and Cooling*, Revised 1st Ed. Washington, DC: Hemisphere Publ. Corp., 1977.)

1. The machine is to provide 352 kW of refrigeration with an evaporator temperature of 5°C, an absorber outlet temperature of 32°C, and a condenser temperature of 43°C.
2. The approach at the low-temperature end of the liquid heat exchanger is to be 6°C.
3. The generator is heated by a flat-plate solar collector capable of providing a temperature level of 90°C.

Determine the COP, absorbent and refrigerant flow rates, and heat input.

Solution

For analytical evaluation of the LiBr–H₂O cycle, the following simplifying assumptions are made:

1. At those points in the cycle for which temperatures are specified, the refrigerant and absorbent phases are in equilibrium.
2. With the exception of pressure reductions across the expansion device between points 2 and 3 and points 8 and 9 in Figure 6.5, pressure reductions in the lines and heat exchangers are neglected.
3. Pressures at the evaporator and condenser are equal to the vapor pressure of the refrigerant, that is, water, as found in steam tables.
4. Enthalpies for LiBr–H₂O mixtures are given in Figure 6.6.

As a first step in solving the problem, set up a table (Table 6.3) of properties; for example, given

$$\begin{aligned}\text{Generator temperature} &= 90^\circ\text{C} = T_1 = T_7 \\ \text{Evaporator temperature} &= 5^\circ\text{C} = T_9 = T_{10} \\ \text{Condenser temperature} &= 43^\circ\text{C} = T_8 \\ \text{Absorber temperature} &= 32^\circ\text{C} = T_4 \\ \text{Neglecting the pump work, } T_5 &\approx T_4 = 32^\circ\text{C.}\end{aligned}$$

Since the approach at the low-temperature end of the heat exchanger is 6°C,

$$T_2 = T_5 + 6^\circ\text{C} = 38^\circ\text{C, and}$$

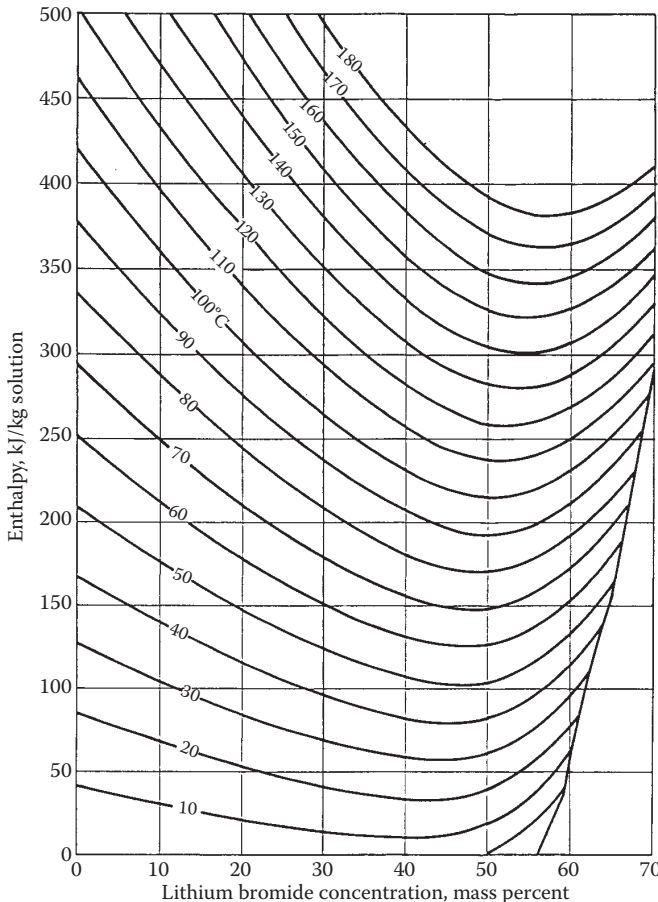
$$T_3 \simeq T_2 = 38^\circ\text{C.}$$

Since the fluid at conditions 7, 8, 9, and 10 is pure water, the properties can be found from the steam tables. Therefore,

$$P_7 = P_8 = \text{Saturation pressure of H}_2\text{O at } 43^\circ\text{C} = 8.65 \text{ kPa}$$

and

$$P_9 = P_{10} = \text{Saturation pressure of H}_2\text{O at } 5^\circ\text{C} = 0.872 \text{ kPa.}$$



Equations	Concentration range $40 < X < 70\%$ LiBr	Temperature range $15 < t < 165^\circ\text{C}$
$h = \sum_0^4 A_n X^n + t \sum_0^4 B_n X^n + t^2 \sum_0^4 C_n X^n$ in kJ/kg, where $t = {}^\circ\text{C}$ and $X = \% \text{LiBr}$		
$A_0 = -2024.33$	$B_0 = 18.2829$	$C_0 = -3.7008214 \text{ E-}2$
$A_1 = 163.309$	$B_1 = -1.1691757$	$C_1 = 2.8877666 \text{ E-}3$
$A_2 = -4.88161$	$B_2 = 3.248041 \text{ E-}2$	$C_2 = -8.1313015 \text{ E-}5$
$A_3 = 6.302948 \text{ E-}2$	$B_3 = -4.034184 \text{ E-}4$	$C_3 = 9.9116628 \text{ E-}7$
$A_4 = -2.913705 \text{ E-}4$	$B_4 = 1.8520569 \text{ E-}6$	$C_4 = -4.4441207 \text{ E-}9$

FIGURE 6.6
Enthalpy-concentration diagram for lithium–water bromide solutions.

Therefore,

$$P_1 = P_2 = P_5 = P_6 = P_7 = 8.65 \text{ kPa}$$

and

$$P_3 = P_4 = P_{10} = 0.872 \text{ kPa}.$$

TABLE 6.3

Thermodynamic Properties of Refrigerant and Absorbent for Figure 6.5

Condition No. in Figure 6.5	Temperature (°C)	Pressure (kPa)	LiBr Weight Fraction	Flow (kg/kg H ₂ O)	Enthalpy (kJ/kg)
1	90	8.65	0.605	7.07	215
2	38	8.65	0.605	7.07	110
3	38	0.872	0.605	7.07	110
4	32	0.872	0.53	8.07	70
5	32	8.65	0.53	8.07	70
6	74	8.65	0.53	8.07	162
7	90	8.65	0	1.0	2670
8	43	8.65	0	1.0	180
9	5	0.872	0	1.0	180
10	5	0.872	0	1.0	2510

Enthalpy,

$$h_9 = h_g = 180 \text{ kJ/kg} \text{ (Saturated liquid at } 43^\circ\text{C}),$$

$$h_{10} = 2510 \text{ kJ/kg} \text{ (Saturated vapor enthalpy at } 5^\circ\text{C}), \text{ and}$$

$$h_7 = 2670 \text{ kJ/kg} \text{ (Superheated vapor at } 8.65 \text{ kPa, } 90^\circ\text{C}).$$

For the LiBr–H₂O mixture, conditions 1 and 4 may be considered equilibrium saturation conditions, which may be found from Figures 6.6 and 6.7 as follows:

For

$$T_4 = 32^\circ\text{C} \text{ and } P_4 = 0.872 \text{ kPa}$$

$$X_s = 0.53, h_4 = 70 \text{ kJ/kg · Sol.}$$

Therefore,

$$h_5 \approx 70 \text{ kJ/kg · Sol.}$$

And for

$$T_1 = 90^\circ\text{C} \text{ and } P_1 = 8.65 \text{ kPa}, X_{ab} = 0.605, h_1 = 215 \text{ kJ/kg · Sol.,}$$

for

$$T_3 = 38^\circ\text{C}, X_3 = 0.605, h_3 = 110 \text{ kJ/kg · Sol.,}$$

$$h_2 = h_3 = 110 \text{ kJ/kg.}$$

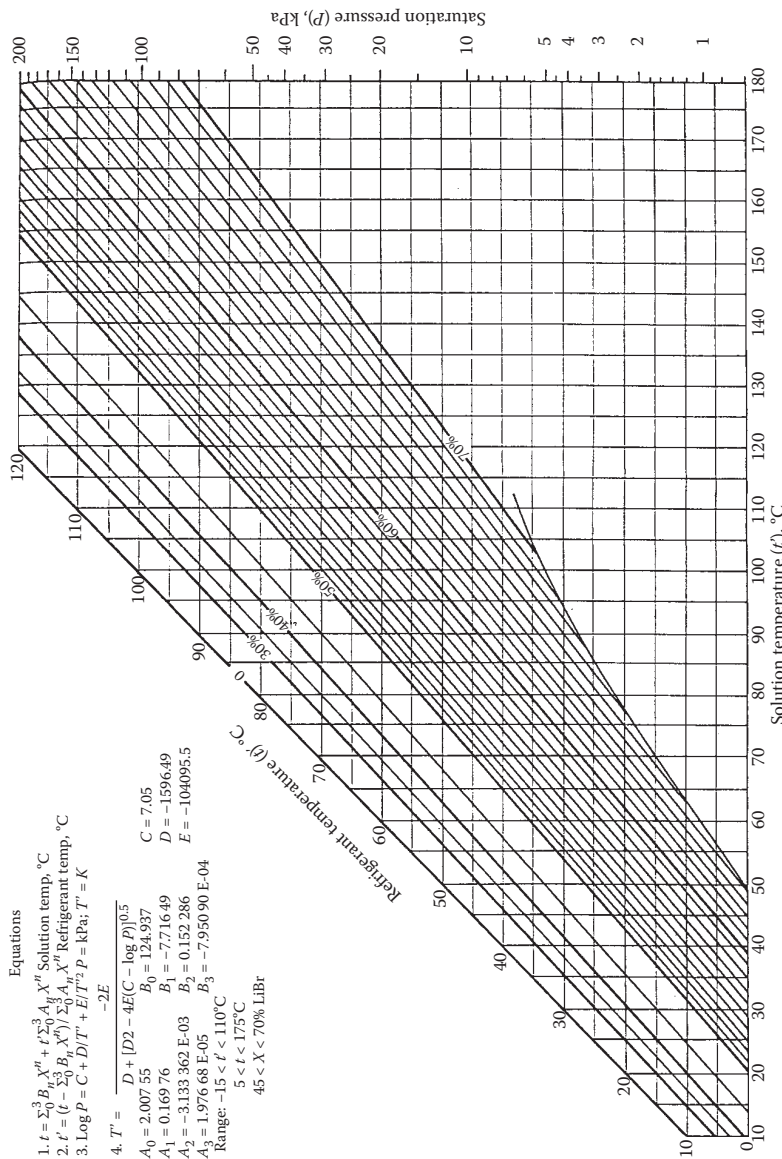


FIGURE 6.7
Equilibrium chart for lithium bromide–water solutions.

6.1.4 Mass Balance Equations

Relative flow rates for the absorbent (LiBr) and the refrigerant (H_2O) are obtained from material balances. A total material balance on the generator gives

$$\dot{m}_6 = \dot{m}_1 + \dot{m}_7,$$

while a LiBr balance gives

$$\dot{m}_6 X_s = \dot{m}_1 X_{ab},$$

where X_{ab} is the concentration of LiBr in absorbent solution and X_s is the concentration of LiBr in refrigerant-absorbent solution.

Substituting $(\dot{m}_1 + \dot{m}_7)$ for \dot{m}_6 gives

$$\dot{m}_1 X_s + \dot{m}_7 X_s = \dot{m}_1 X_{ab}.$$

Since the fluid entering the condenser is pure refrigerant, that is, water, \dot{m}_7 is the same as the flow rate of the refrigerant \dot{m}_r :

$$\frac{\dot{m}_1}{\dot{m}_7} = \frac{X_s}{X_{ab} - X_s} = \frac{\dot{m}_{ab}}{\dot{m}_r},$$

where \dot{m}_{ab} is the flow rate of absorbent and \dot{m}_r is the flow rate of refrigerant.

Substituting for X_s and X_{ab} from the table gives the ratio of absorbent-to-refrigerant flow rate:

$$\frac{\dot{m}_{ab}}{\dot{m}_r} = \frac{0.53}{0.605 - 0.53} = 7.07.$$

The ratio of the refrigerant-absorbent solution flow rate \dot{m}_s to the refrigerant solution flow rate \dot{m}_r is

$$\frac{\dot{m}_s}{\dot{m}_r} = \frac{\dot{m}_{ab} + \dot{m}_r}{\dot{m}_r} = 7.07 + 1 = 8.07.$$

Now, Table 6.3 is complete except for T_6 and h_6 , which may be found from an energy balance at the heat exchanger.

$$\dot{m}_s h_5 + \dot{m}_{ab} h_1 = \dot{m}_{ab} h_2 + \dot{m}_s h_6.$$

Hence,

$$h_6 = h_5 + \frac{\dot{m}_{ab}}{\dot{m}_s} (h_1 - h_2) = 70 + \frac{7.07}{8.07} [215 - 110] = 162 \text{ kJ/kg of solution.}$$

The temperature corresponding to this value of enthalpy and a LiBr mass fraction of 0.53 is found from Figure 6.6 to be 74°C.

The flow rate of refrigerant required to produce the desired 352 kW of refrigeration is

$$\dot{Q}_e = \dot{m}_r(h_{10} - h_9),$$

where \dot{Q}_e is the cooling effect produced by the refrigeration unit and

$$\dot{m}_r = \frac{352}{2510 - 180} = 0.15 \text{ kg/s.}$$

The flow rate of the absorbent is

$$\dot{m}_{ab} = \frac{\dot{m}_{ab}}{\dot{m}_r} \dot{m}_r = 7.07 \times 0.15 = 1.06 \text{ kg/s,}$$

while the flow rate of the solution is

$$\dot{m}_s = \dot{m}_{ab} + \dot{m}_r = 1.06 + 0.15 = 1.21 \text{ kg/s.}$$

The rate at which heat must be supplied to the generator \dot{Q}_g is obtained from the heat balance

$$\begin{aligned}\dot{Q}_g &= \dot{m}_r h_7 + \dot{m}_{ab} h_1 - \dot{m}_s h_6 \\ &= [(0.15 \times 2670) + (1.06 \times 215)] - (1.21 \times 162) \\ &= 432 \text{ kW.}\end{aligned}$$

This requirement, which determines the size of the solar collector, probably represents the maximum heat load that the collector unit must supply during the hottest part of the day.

The coefficient of performance COP is

$$\text{COP} = \frac{\dot{Q}_e}{\dot{Q}_g} = \frac{352}{432} = 0.81.$$

The rate of heat transfer in the other three heat-exchanger units—the liquid heat exchanger, the water condenser, and the absorber—is obtained from heat balances. For the liquid heat exchanger, this gives

$$\dot{Q}_{1-2} = \dot{m}_{ab}(h_1 - h_2) = 1.06[215 - 110] = 111 \text{ kW,}$$

where \dot{Q}_{1-2} is the rate of heat transferred from the absorbent stream to the refrigerant-absorbent stream. For the water condenser, the rate of heat transfer \dot{Q}_{7-8} rejected to the environment is

$$\dot{Q}_{7-8} = \dot{m}_r(h_7 - h_8) = 0.15(2670 - 180) = 374 \text{ kW.}$$

The rate of heat removal from the absorber can be calculated from an overall heat balance on this system:

$$\dot{Q}_a = \dot{Q}_{7-8} - \dot{Q}_g - \dot{Q}_e = 374 - 432 - 352 = -410 \text{ kW.}$$

Explicit procedures for the mechanical and thermal design as well as the sizing of the heat exchangers are presented in standard heat-transfer texts. In large commercial units, it may be possible to use higher concentrations of LiBr, operate at a higher absorber temperature, and thus save on heat-exchanger cost. In a solar-driven unit, this approach would require concentrator-type or high efficiency flat-plate solar collectors.

6.1.5 Ammonia–Water Refrigeration System

The main difference between an ammonia–water system and a water–lithium bromide system is that the ammonia–water system has a rectifier (also called dephlegmator) after the boiler to condense as much water vapor out of the mixture vapor as possible. Figure 6.8 shows a schematic of an $\text{NH}_3\text{-H}_2\text{O}$ absorption refrigeration system. Since ammonia has a much lower boiling point than water, a very high fraction of ammonia and a very small

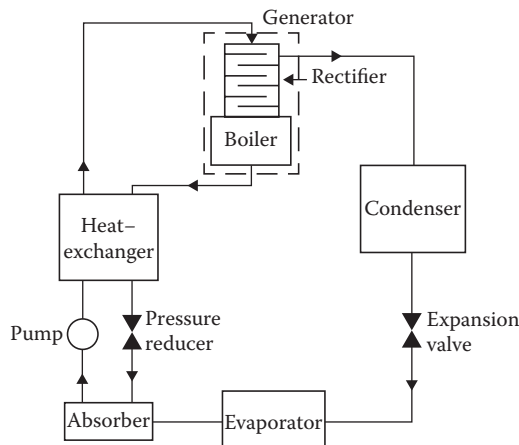


FIGURE 6.8
Schematic of an ammonia–water absorption refrigeration system.

fraction of water are boiled off in the boiler. The vapor is cooled, as it rises in the rectifier, by the countercurrent flow of the strong $\text{NH}_3\text{-H}_2\text{O}$ solution from the absorber; therefore, some moisture is condensed. The weak ammonia–water solution from the boiler goes through a pressure-reducing valve to the absorber, where it absorbs the ammonia vapor from the evaporator. The high-pressure, high-temperature ammonia from the rectifier is condensed by rejecting heat to the atmosphere. It may be further subcooled before expanding in a throttle valve. The low-pressure, low-temperature ammonia from the throttle valve provides refrigeration in the evaporator. The vapor from the evaporator is reunited with the weak ammonia solution in the absorber. Operating pressures are primarily controlled by the ambient air temperature for an air-cooled condenser, the evaporator temperature, and the concentration of the ammonia solution in the absorber. Thermodynamic analysis of an ammonia–water absorption cooling system will become clear from the following example.

Example 6.4

A 10.5 kW, gas-fired, ammonia–water absorption chiller is shown schematically in Figure 6.9. The chiller is operating with the following conditions:

Evaporator temperature: 2°C

Evaporator pressure: 4.7 bar

Condenser and generator pressure: 21.7 bar

Concentration of ammonia in refrigerant (X_r) = 0.985

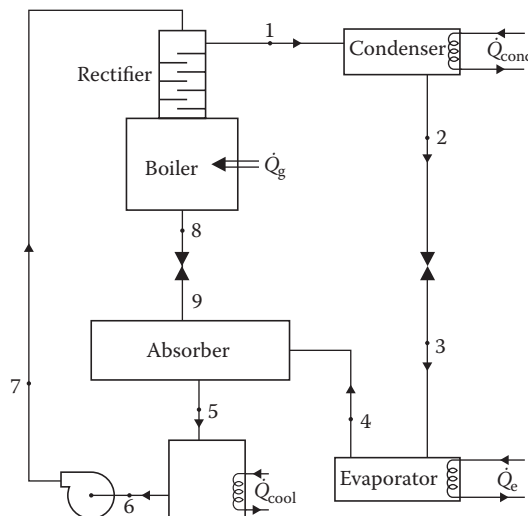


FIGURE 6.9

Schematic of a 10.5-kW, gas-fired, aqua–ammonia absorption chiller for Example 6.4.

Concentration of ammonia in strong solution (X_s) = 0.415
 Concentration of ammonia in weak solution (X_w) = 0.385

Find the mass flow rates, temperatures, and enthalpies at various points in the cycle, and find the COP of the cycle.

Solution

States are defined using Figure 6.10. Properties at all the points are summarized in Table 6.4 and they are calculated as follows.

State Point 2: Assume equilibrium saturated liquid condition

$$\begin{aligned} P_2 &= 21.7 \text{ bar}, & h_2 &= 250 \text{ kJ/kg}, \\ X_2 &= 0.985, & T_2 &= 54^\circ\text{C}. \end{aligned}$$

State Point 3: From an isenthalpic process at the valve,

$$h_3 = h_2 = 250 \text{ kJ/kg}.$$

State Point 4: Assume equilibrium saturated vapor condition,

$$\begin{aligned} P_4 &= 4.7 \text{ bar}, & h_4 &= 1425 \text{ kJ/kg}, \\ X_4 &= 0.985, & T_4 &= 2^\circ\text{C}. \end{aligned}$$

Energy balance at the evaporator,

$$\begin{aligned} \dot{Q}_e &= \dot{m}_r(h_4 - h_3) \\ \dot{m}_r &= \frac{\dot{Q}_e}{(h_4 - h_3)} = \frac{10.5 \text{ kW}}{(1425 - 250) \text{ kJ/kg}} = 0.01 \text{ kg/s}. \end{aligned}$$

Ammonia mass balance at the absorber,

$$\begin{aligned} \dot{m}_s X_s &= \dot{m}_r X_r + \dot{m}_w X_w, \text{ and } \dot{m}_w = \dot{m}_s - \dot{m}_r, \\ \dot{m}_s &= \dot{m}_r \frac{(X_r - X_w)}{(X_s - X_w)} = 0.01 \frac{(0.985 - 0.385)}{0.415 - 0.385} = 0.2 \text{ kg/s}, \\ \dot{m}_w &= \dot{m}_s - \dot{m}_r = 0.2 - 0.01 = 0.19 \text{ kg/s}. \end{aligned}$$

State Point 1: Assume equilibrium saturated vapor condition,

$$\begin{aligned} P_1 &= 21.7 \text{ bar}, & h_1 &= 1430 \text{ kJ/kg}, \\ X_1 &= 0.985, & T_1 &= 90^\circ\text{C}. \end{aligned}$$

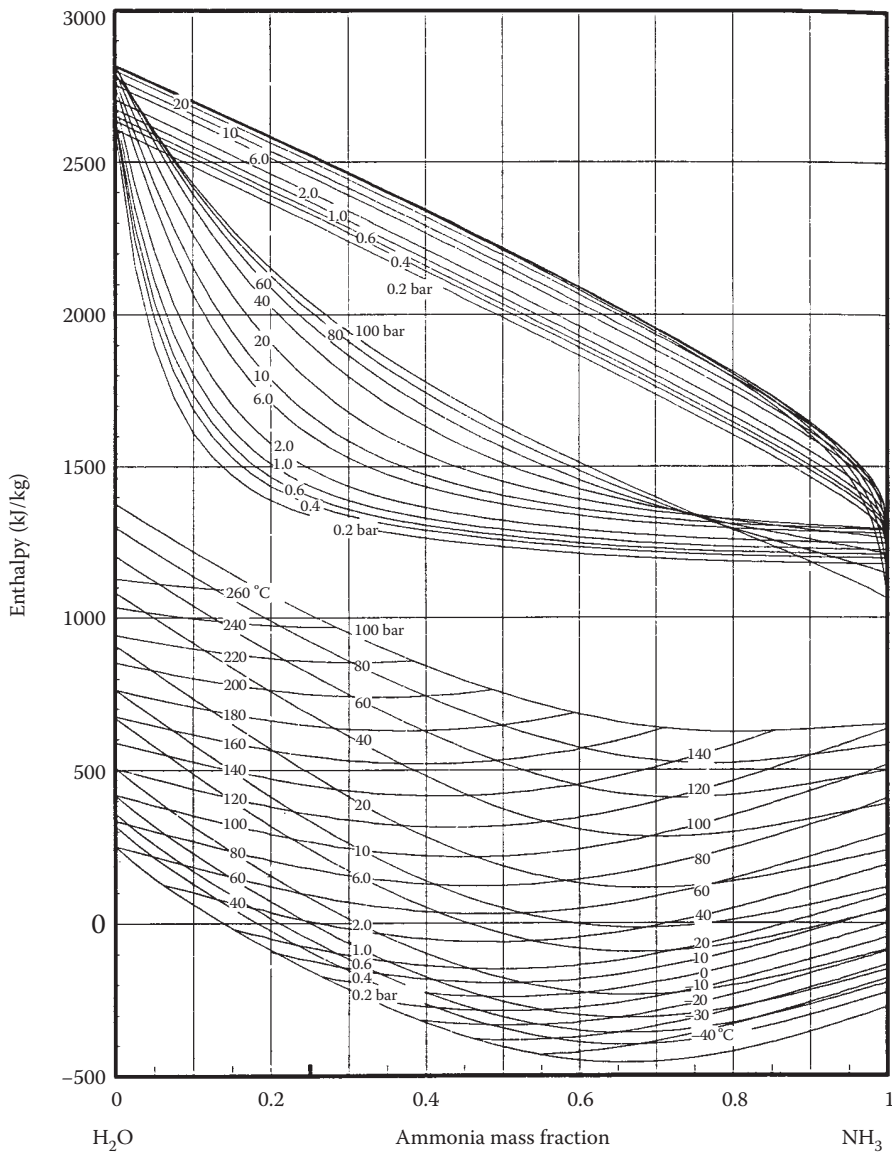


FIGURE 6.10
Enthalpy-concentration diagram for ammonia-water.

TABLE 6.4

Thermodynamic Properties of Ammonia–Water in Example 6.4

State Point	Pressure, P (bar)	Temperature, T (°C)	Enthalpy, h (kJ/kg)	Concentration, X (kg NH ₃ /kg mix)	Flow Rate, \dot{m} (kg/s)	Equilibrium Saturated Condition	Quality (\dot{m}_g/\dot{m}_r)
1	21.7	90	1430	0.985	0.01	✓	1
2	21.7	≈54	≈250	0.985	0.01	✓	0
3	4.7	2	250	0.985	0.01		
4	4.7	2	1265	0.985	0.01	✓	1
5	4.7	52	361	0.415	0.2		
6	4.7	52	0	0.415	0.2	✓	0
7	21.7	≈52	≈0	0.415	0.2		
8	21.7	120	305	0.385	0.19	✓	0
9	4.7	59	305	0.385	0.19		

State Point 6: Assume equilibrium saturated liquid condition,

$$P_6 = 4.7 \text{ bar}, \quad h_6 = 0 \text{ kJ/kg}, \\ X_6 = 0.415, \quad T_6 = 52^\circ\text{C}.$$

State Point 7: Neglecting the pump work,

$$P_7 = 21.7 \text{ bar}, \quad h_7 \approx h_6 = 0 \text{ kJ/kg}, \\ X_7 = 0.415, \quad T_7 \approx T_6 = 52^\circ\text{C}.$$

State Point 8: Assume equilibrium saturated liquid condition,

$$P_8 = 21.7 \text{ bar}, \quad h_8 = 305 \text{ kJ/kg}, \\ X_8 = 0.385, \quad T_8 = 120^\circ\text{C}.$$

Energy balance at the generator,

$$\dot{Q}_g = \dot{m}_r h_1 + \dot{m}_w h_8 - \dot{m}_s h_7 \\ \dot{Q}_g = 0.01 \times 1430 + 0.19 \times 305 - 0.2 \times 0 = 72.3 \text{ kW}.$$

Coefficient of performance,

$$\text{COP} = \frac{\dot{Q}_e}{\dot{Q}_g} = \frac{10.5 \text{ kW}}{72.3 \text{ kW}} = 0.15.$$

State Point 9: From an isoenthalpic process at the valve,

$$h_9 = h_8 = 305 \text{ kJ/kg.}$$

Energy balance at the absorber,

$$h_5 = \frac{\dot{m}_r h_4 + \dot{m}_w h_9}{\dot{m}_s} = \frac{0.01 \times 1425 + 0.19 \times 305}{0.2} = 361 \text{ kJ/kg.}$$

Example 6.5

It is proposed to convert the gas-fired chiller of Example 6.4 to a solar-based chiller. Propose the modifications and analyze the performance.

Solution

Assuming that we can use a flat-plate solar collector system to provide heat for the generator, which will operate at 75°C, the high pressure in the cycle would have to be reduced. Taking the high pressure to be 17 bar and following the procedure of Example 6.4, the properties are as in Table 6.5.

Note that the values of concentration in the cycle must change in order to obtain reasonable values of temperatures. For example, in order to achieve condensation (State 2) at a temperature above the ambient (we choose 40°C), the concentration at State 8 must be increased to 0.55. This will allow us to get ammonia vapor of concentration 0.99 at 70°C at State 1 (pressure 17 bars), which, in turn, will condense at 40°C. The concentration of 0.55 at State 8 is found by an iterative procedure.

$$\dot{Q}_g = 51.2 \text{ kW, and COP} = 0.205.$$

TABLE 6.5

Thermodynamic Properties of Ammonia–Water in Example 6.5

State Point	Pressure, P (bar)	Temperature, T (°C)	Enthalpy, H (kJ/kg)	Concentration, X (kg NH ₃ /kg mix)	Flow Rate, \dot{m} (kg/s)	Equilibrium Saturated Condition	Quality (\dot{m}_g/\dot{m}_r)
1	17	70	1400	0.99	0.0086	✓	1
2	17	≈40	≈180	0.99	0.0086	✓	0
3	4.7	2	180	0.99	0.0086		
4	4.7	2	1400	0.99	0.0086	✓	1
5	4.7	28	156	0.57	0.2		
6	4.7	28	-100	0.57	0.2	✓	0
7	17	≈28	≈-100	0.57	0.2		
8	17	75	100	0.55	0.1914	✓	0
9	4.7	25	100	0.55	0.1914		

6.2 Solar Desiccant Dehumidification

In hot and humid regions of the world experiencing significant latent cooling demand, solar energy may be used for dehumidification using liquid or solid desiccants. Rengarajan et al. (1989) compared a number of strategies for ventilation air conditioning for Miami, Florida, and found that a conventional vapor-compression system could not even meet the increased ventilation requirements of ASHRAE Standard 62-1989. By pretreating the ventilation air with a desiccant system, proper indoor humidity conditions could be maintained and significant electrical energy could be saved. A number of researchers have shown that a combination of a solar desiccant and a vapor-compression system can save from 15% to 80% of the electrical energy requirements in commercial applications, such as supermarkets (Meckler 1994, 1995, 1988; Meckler et al. 1993; Oberg and Goswami 1998a,b; Spears and Judge 1997; Thombloom and Nimmo 1994, 1995).

In a desiccant air-conditioning system, moisture is removed from the air by bringing it in contact with the desiccant and followed with sensible cooling of the air by a vapor-compression cooling system, vapor absorption cooling systems, or an evaporative cooling system. The driving force for the process is the water vapor pressure. When the vapor pressure in air is higher than that on the desiccant surface, moisture is transferred from the air to the desiccant until an equilibrium is reached (see Figure 6.11). In order to regenerate the desiccant for reuse, the desiccant is heated, which increases the water

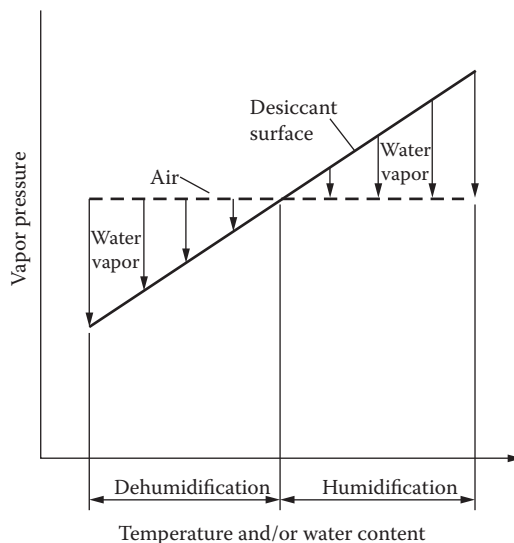


FIGURE 6.11

Vapor pressure versus temperature and water content for dessicant and air.

vapor pressure on its surface. If air with lower vapor pressure is brought in contact with this desiccant, the moisture passes from the desiccant to the air (Figure 6.11). Two types of desiccants are used: solids, such as silica gel and lithium chloride, or liquids, such as salt solutions and glycols.

6.2.1 Solid Desiccant Cooling System

The two solid desiccant materials that have been used in solar systems are silica gel and the molecular sieve, a selective absorber. Figure 6.12 shows the equilibrium absorption capacity of several substances. Note that the molecular sieve has the highest capacity up to 30% humidity, and silica gel is optimal between 30% and 75%—the typical humidity range for buildings.

Figure 6.13 is a schematic diagram of a desiccant cooling ventilation cycle (also known as Pennington cycle), which achieves both dehumidification and cooling. The desiccant bed is normally a rotary wheel of a honeycomb-type substrate impregnated with the desiccant. As the air passes through the rotating wheel, it is dehumidified while its temperature increases (processes 1 and 2) owing to the latent heat of condensation. Simultaneously, a hot air stream passes through the opposite side of the rotating wheel, which removes moisture from the wheel. The hot and dry air at state 2 is cooled in a heat-exchanger wheel to condition 3 and further cooled by evaporative cooling to condition 4. Air at condition 3 may be further cooled by vapor-compression or vapor-absorption systems instead of evaporative cooling. The return air from the conditioned space is cooled by evaporative cooling (processes 5 and 6), which in turn cools the heat-exchanger

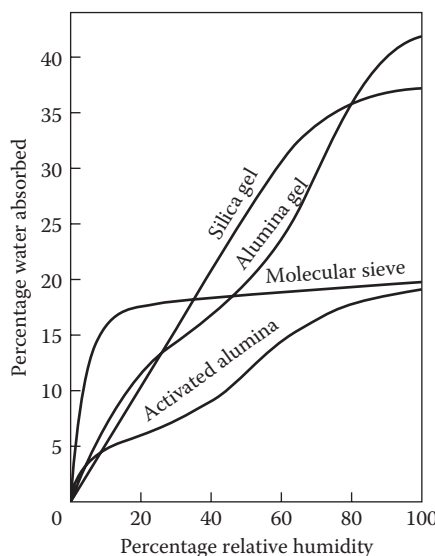
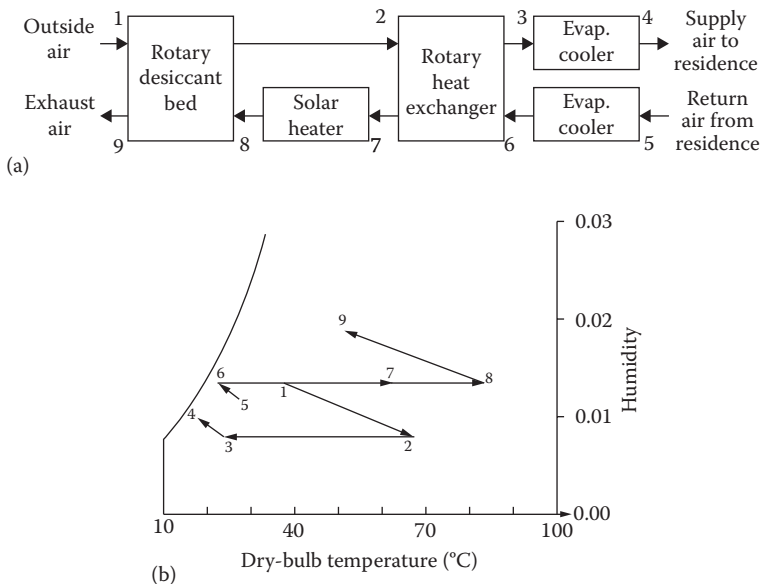


FIGURE 6.12
Equilibrium capacities of common water absorbents.

**FIGURE 6.13**

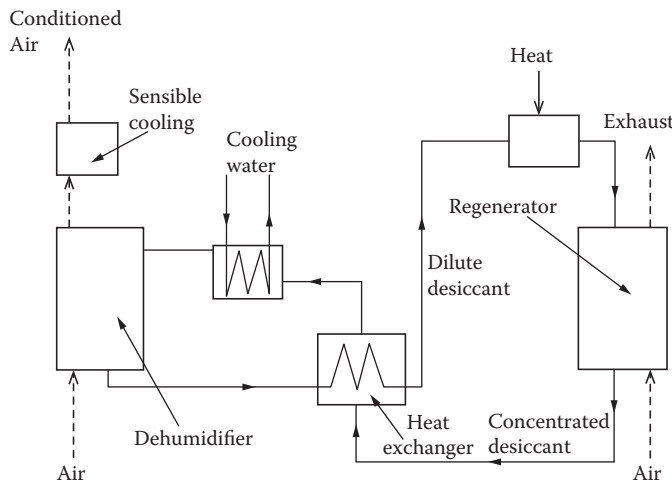
Schematic of a desiccant cooling ventilation cycle: (a) schematic of airflow, (b) process on a psychrometric chart.

wheel. This air is then heated to condition 7. Using solar heat, it is further heated to condition 8 before going through the desiccant wheel to regenerate the desiccant. A number of researchers have studied this cycle, or an innovative variation of it, and have found thermal COPs in the range of 0.5 to 2.58 (Pesaran et al. 1992).

6.2.2 Liquid Desiccant Cooling System

Liquid desiccants offer a number of advantages over solid desiccants. The ability to pump a liquid desiccant makes it possible to use solar energy for regeneration more efficiently. It also allows several small dehumidifiers to be connected to a single regeneration unit. Since a liquid desiccant does not require simultaneous regeneration, the liquid may be stored for later regeneration when solar heat is available. A major disadvantage is that the vapor pressure of the desiccant itself may be enough to cause some desiccant vapors to mix with the air. This disadvantage, however, may be overcome by proper choice of the desiccant material.

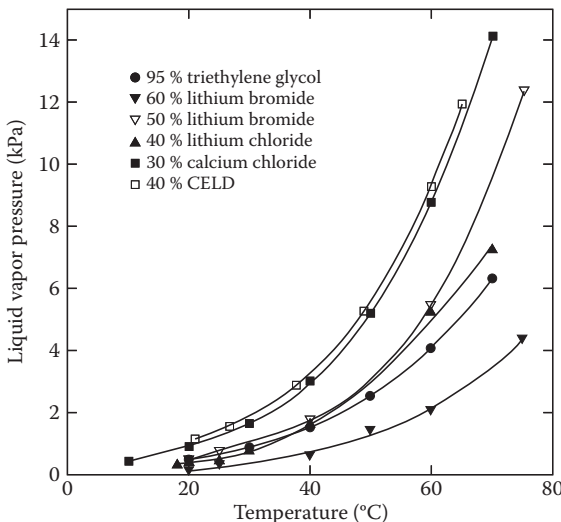
A schematic of a liquid desiccant system is shown in Figure 6.14. Air is brought in contact with concentrated desiccant in a countercurrent flow in a dehumidifier. The dehumidifier may be a spray column or packed bed. The packings provide a very large area for heat and mass transfer between the air and the desiccant. After dehumidification, the air is sensibly cooled before entering the conditioned space. The dilute desiccant exiting the dehumidifier

**FIGURE 6.14**

A conceptual liquid desiccant cooling system.

is regenerated by heating and exposing it to a countercurrent flow of a moisture scavenging air stream.

Liquid desiccants commonly used are aqueous solutions of lithium bromide, lithium chloride, calcium chloride, mixtures of these solutions, and triethylene glycol (TEG) (see Oberg and Goswami 1998b). Vapor pressures of these common desiccants are shown in Figure 6.15 as a function

**FIGURE 6.15**

Vapor pressures of liquid desiccants.

of concentration and temperature, based on a number of references (Dow Chemical Company 1992, 1996; Ertas et al. 1992; Zaytsev and Aseyev 1992). Other physical properties important in the selection of desiccant materials are listed in Table 6.6. Although salt solutions and TEG have similar vapor pressures, the salt solutions are corrosive and have higher surface tension. The disadvantage of TEG is that it requires higher pumping power because of higher viscosity.

Oberg and Goswami (1998b) have presented an in-depth review of liquid desiccant cooling systems. Based on an extensive numerical modeling and on experimental studies, they have presented correlations for the performance of a packed bed liquid desiccant dehumidifier and a regenerator.

The performance of a packed bed dehumidifier or a regenerator may be represented by a humidity effectiveness ϵ_y defined as the ratio of the actual change in humidity of the air to the maximum possible for the operating conditions (Chung 1989; Khan 1994; Ullah et al. 1988).

$$\epsilon_y = \frac{Y_{in} - Y_{out}}{Y_{in} - Y_{eq}}, \quad (6.19)$$

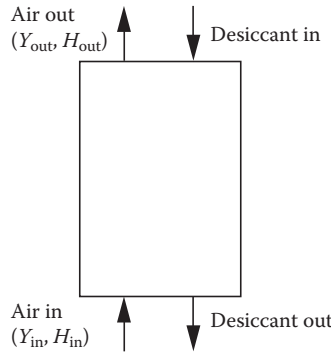
where Y_{in} and Y_{out} are the humidity ratios of the air inlet and outlet, respectively, and Y_{eq} is the humidity ratio in equilibrium with the desiccant solution at the local temperature and concentration (see Figure 6.16).

TABLE 6.6

Physical Properties of Liquid Desiccants at 25°C

Dessicant	Density, $\rho \cdot 10^{-3}$ (kg/nV)	Viscosity, $\mu \cdot 10^3$ (Ns/m ²)	Surface Tension, $\gamma \cdot 10^3$ (N/m)	Specific Heat, c_p (kJ/kg·°C)	Reference
95% by weight triethylene glycol	1.1	28	46	2.3	Kreider and Kreith (1977)
55% by weight lithium bromide	1.6	6	89	2.1	Kettleborough and Waugaman (1995) and Zaytsev and Aseyev (1992)
40% calcium chloride	1.4	7	93	2.5	Close (1965), Khan (1994), and Zaytsev and Aseyev (1992)
40% by weight lithium chloride	1.2	9	96	2.5	Zaytsev and Aseyev (1992)
40% by weight CELD	1.3	5	—	—	Löf and Tybout (1974)

Source: Oberg, V. and D.Y. Goswami, *Advances in Solar Energy*, ASES 12: 431–470, 1998.

**FIGURE 6.16**

Exchange of humidity and moisture between desiccant and air in the tower.

In addition to the humidity effectiveness, an enthalpy effectiveness ε_H is also used as a performance parameter (Kettleborough and Waugaman 1995; Khan 1994):

$$\varepsilon_H = \frac{H_{a,in} - H_{a,out}}{H_{a,in} - H_{a,eq}}, \quad (6.20)$$

where $H_{a,in}$, $H_{a,out}$, and $H_{a,eq}$ are the enthalpies of the air at the inlet and outlet, and in equilibrium with the desiccant, respectively. Oberg and Goswami (1998a) found the following correlation for ε_y and ε_H :

$$\varepsilon_y, \varepsilon_H = 1 - C_1 \left(\frac{L}{G} \right)^a \left(\frac{H_{a,in}}{H_{L,in}} \right)^b (aZ)^c, \quad (6.21)$$

where

$$a = k_1 \frac{\gamma_L}{\gamma_c} + m_1 \quad \text{and} \quad c = k_2 \frac{\gamma_L}{\gamma_c} + m_2.$$

Here, C_1 , b , k_1 , m_1 , and m_2 are constants listed in Table 6.7. L and G are the liquid and air mass flow rates, respectively; a is the packing surface area per unit volume for heat and mass transfer in m^2/m^3 ; Z is the tower height in

TABLE 6.7

Constants for Performance Correlations

	C_1	b	k_1	m_1	k_2	m_2
ε_y	48.345	-0.751	0.396	-1.573	0.033	-0.906
ε_H	3.766	-0.528	0.289	-1.116	-0.004	-0.365

meters; γ_L is the surface tension of the liquid desiccant; and γ_c is the critical surface tension for the packing material.

6.3 Summary

The techniques useful for active solar cooling, refrigeration, and dehumidification have been described in this chapter. The absorption method provides a suitable thermodynamic match of flat-plate collector to cooling machine because of the usability of low temperatures by the H_2O -LiBr and NH_3 - H_2O absorption methods.

Air dehumidification by desiccants and solar regeneration of desiccants is also a method whereby a large part of the cooling load can be met by solar energy. Both solid and liquid desiccants have been described.

PROBLEMS

1. The following table gives the characteristics of a building in Houston, Texas. Determine the cooling load for July 30 at solar noon. Any information regarding the load not given may be assumed or neglected.

Factor	Description or Specification
Roof	
Type	Flat, shaded
Area, $A_{rf,sh}$ (m^2)	250
U factor ($W/m^2 \cdot K$)	$U_{rf} = 0.35$
Walls	
Type	Vertical, painted white
Orientation, size ($m \times m$)	North, south, 3×10 ; east, west, 3×25
U factor ($W/m^2 \cdot K$)	$U_{wa} = 1.08$
Windows	
Orientation, area (m^2)	North, 8; south, 8; east, 20; west, 25
U factor ($W/m^2 \cdot K$)	$U_{wi} = 6.2$
Insolation transmittance	$\bar{\tau}_{b,wi} = 0.60$; $\bar{\tau}_{d,wi} = 0.80$; $\bar{\tau}_{r,wi} = 0.55$
Temperature	
Inside, outside ($^{\circ}C$)	$T_{in} = 24$; $T_{out} = 37$
Insolation	
Beam, diffuse, reflected (W/m^2)	$I_{h,b} = 580$; $I_{h,d} = 250$; $I_r = 200$

2. An air-conditioning system working in a vapor-compression cycle is used to manage the load for the building in Problem 1. If the high pressure and low pressure in the cycle are 915 and 290 kPa,

respectively, and the efficiency of the compressor is 90%, find the flow rate of R-134a used for the equipment and the COP of the cycle.

3. Consider the absorption refrigeration cycle, shown in the line diagram below, that uses lithium bromide as carrier and water as refrigerant to provide cooling. By using steam tables and the chart giving the properties of lithium bromide and water, calculate first:

- Heat removed from the absorber
- Heat removed from the condenser
- Heat added to the evaporator
- COP of the cycle

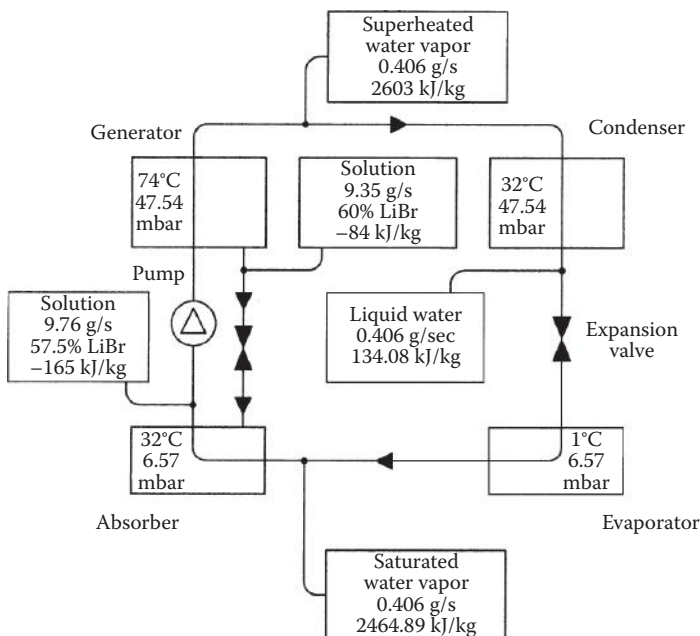
Then calculate, for a flat-plate collector with an $F_R(\tau\alpha)$ intercept of 0.81 and an $F_R U_c$ of 3 W/m²·K, the area required for operation in Arizona at noon in August for a 3-ton unit. Assume that the enthalpy of the water vapor leaving the evaporator can be approximated by the equation

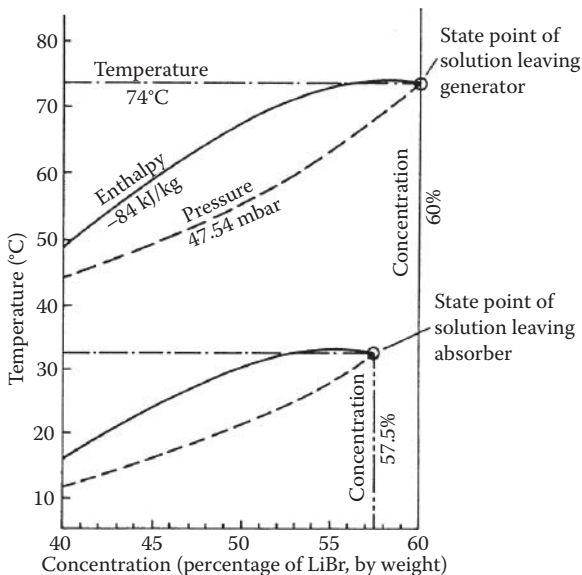
$$h_{ve} = 2463 + 1.9T_e \text{ kJ/kg}$$

and that the enthalpy of the liquid water is

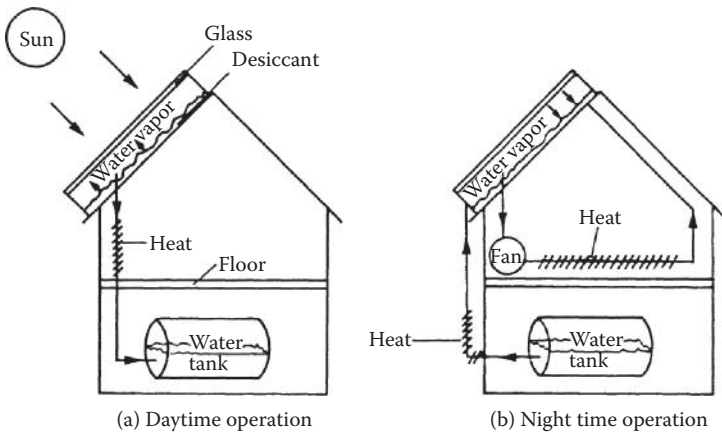
$$h_{le} = 4.2T_e \text{ kJ/kg},$$

where T_e is the temperature of the evaporator in °C. In the analysis, assume that evaporation occurs at 1°C and condensation occurs at 32°C.





4. Make a preliminary design for a solar-driven Rankine refrigeration machine to provide the temperature environment required below the surface of a 20×40 m ice skating rink that is to operate all year in the vicinity of Denver, Colorado. State all your assumptions.
5. An inventor has proposed a desiccant heat pump to augment the heat delivered by a solar collector, and a sketch of the system is shown below. The collector bottom is covered with a desiccant, such as silica gel or zeolite, that contains water, and during the day, the solar radiation heats up the desiccant bed and vaporizes a significant fraction of the water. The water vapor thus driven off passes through a heat exchanger in the building, and the vapor condenses with the release of heat into the building. At night, the liquid water stored in a tank passes through a heat exchanger outside the building where it absorbs heat and evaporates. The vapor produced then condenses in the desiccant at a temperature of 150°F, and air from the building is circulated between the building and collector to supply heat to the building at night. Comment on the feasibility of the system proposed and estimate the effective COP.



6. A 5-ton, ammonia–water refrigeration system as shown in Figure 6.9 was designed to work with solar energy. The low and high pressures are 3 and 15 bar, respectively. The concentrations are $X_r = 0.98$, $X_s = 0.6$, and $X_w = 0.58$, and the COP is expected to be 0.3. Determine the area and the required minimum temperature for a flat-plate solar collector system. Choose a site of interest to you.
 7. The table below shows data from a dehumidification process using aqueous solution of lithium chloride (LiCl) in a packed tower. The desiccant leaving the dehumidifier is passed through another packed tower for regeneration. For the regeneration process, it is known that the rate of evaporation of water as a function of the concentration X ($\text{kg}_{\text{LiCl}}/\text{kg}_{\text{sol}}$) and temperature, T (°C), of the desiccant is given by the following equation:

$$m_{\text{evap}} = (a_0 + a_1 T + a_2 T^2) + (b_0 + b_1 T + b_2 T^2)X + (c_0 + c_1 T + c_2 T^2)X^2 \text{ (g/s)},$$

where

$$\begin{aligned} a_0 &= 285,077, & b_0 &= -1,658,652, & c_0 &= 2,412,282, \\ a_1 &= -8992, & b_1 &= 52,326, & c_1 &= -76,112, \text{ and} \\ a_2 &= 70.88, & b_2 &= -412, & c_2 &= 600. \end{aligned}$$

Find the temperature to which a flat-plate collector must raise the temperature of the desiccant for the regeneration process. Assume that the flow rate of liquid desiccant in both processes (dehumidification and regeneration) is the same.

Variable	Air		Desiccant		Variable
	Inlet	Outlet	Inlet	Outlet	
Temp (°C)	30.4	32.6	30	33.1	Temp (°C)
RH (%)	66.7	36.7	35	—	Concent. (%)
Mass (kg/h)	260	—	850	—	Mass (kg/h)

References

- ASHRAE. 2013. *Handbook of Fundamentals*. American Society of Heating, Refrigerating and Air-Conditioning Engineers, Atlanta, GA.
- Chinnappa, J.C.V., and N.E. Wijeyesundara. 1992. Simulation of solar-powered ammonia-water integrated hybrid cooling system. *J. Sol. Energy Eng., Trans. ASME* 114: 125–127.
- Chung, T.-W. 1989. Predictions of the moisture removal efficiencies for packed-bed dehumidification systems. *Solar Engineering—1989, Proc. of the 11th Annual ASME Solar Energy Conf*, San Diego, CA, pp. 371–377.
- Close, D.J. 1965. Rock pile thermal storage for comfort air conditioning. *Mech. Chem. Eng. Trans. Inst. Eng. (Australia)* MC-1: 11.
- Dow Chemical Company. 1992. *A Guide to Glycols*. Dow Chemical Company, Midland, MI.
- Dow Chemical Company. 1996. *Calcium Chloride Handbook*. Dow Chemical Company, Midland, MI.
- Ertas, A., E.E. Anderson, and I. Kiris. 1992. Properties of a new liquid desiccant solution—Lithium chloride and calcium chloride mixture. *Sol. Energy* 49: 205–212.
- Kettleborough, C.F., and D.G. Waugaman. 1995. An alternative desiccant cooling cycle. *J. Sol. Energy Eng.* 117: 251–255.
- Khan, A.Y. 1994. Sensitivity analysis and component modeling of a packed-type liquid desiccant system at partial load operating conditions. *Int. J. Energy Res.* 18: 643–655.
- Kochhar, G.S. 1982. Optimum thermal performance of a flat plate solar collector driven ammonia-water absorption system. *Alternative Energy Sources 4 (Proceedings of the 4th Miami International Conference on Alternative Energy)*, Miami Beach, FL, USA, Vol. 8, pp. 333–343.
- Kreider, J.F., and F. Kreith. 1977. *Solar Heating and Cooling*, revised 1st ed. Hemisphere Publ. Corp, Washington, DC.
- Löf, G.O.G., and R.A. Tybout. 1974. Design and cost of optimal systems for residential heating and cooling by solar energy. *Sol. Energy* 16: 9.
- Macriss, R.A., and T.S. Zawacki. 1989. Absorption fluid data survey: 1989 update. Oak Ridge National Laboratory Report, Oak Ridge, TN, ORNL/Sub84-47989/4.
- Manrique, J.A. 1991. Thermal performance of ammonia-water refrigeration system. *Int. Comm., Heat Mass Transfer* 19(6): 779–789.
- Meckler, M. 1988. Off-peak desiccant cooling and cogeneration combine to maximize gas utilization. *ASHRAE Trans.* 94(Pt 1): 575–596.

- Meckler, M. 1994. Desiccant-assisted air conditioner improves IAQ and comfort. *Heating/Piping/Air Conditioning* 66(10): 75–84.
- Meckler, M. 1995. Desiccant outdoor air preconditioners maximize heat recovery ventilation potentials. *ASHRAE Trans.* 101(Pt 2): 992–1000.
- Meckler, M., Y.O. Parent, and A.A. Pesaran. 1993. Evaluation of dehumidifiers with polymeric desiccants. Gas Institute Report, Contract No. 5091-246-2247. Gas Research Institute, Chicago, IL.
- Oberg, V., and D.Y. Goswami. 1998a. Experimental study of heat and mass transfer in a packed bed liquid desiccant air dehumidifier. In *Solar Engineering*, J.H. Morehouse, and R.E. Hogan, eds., pp. 155–166.
- Oberg, V., and D.Y. Goswami. 1998b. A review of liquid desiccant cooling. In *Advances in Solar Energy*, K. Boer, ed., ASES, Boulder, CO, Vol. 12, pp. 431–470.
- Pesaran, A.A., T.R. Penney, and A.W. Czanderna. 1992. Desiccant cooling: State-of-the art assessment. NREL, Report No. NREL/TP-254-4147. National Renewable Laboratory, Golden, CO.
- Rengarajan, K., D.B. Shirley, III, and R.A. Raustad. 1989. Cost-effective HVAC technologies to meet ASHRAE Standard 62-1989 in hot and humid climates. *ASHRAE Trans.* (Pt 1): 166–182.
- Siddiqui, A.M. 1993. Optimum generator temperatures in four absorption cycles using different sources of energy. *Energy Convers. Mgmt.* 34(4): 251–266.
- Spears, J.W., and J. Judge. 1997. Gas-fired desiccant system for retail super center. *ASHRAE J.* 39: 65–69.
- Thombloom, M., and B. Nimmo. 1994. Modification of the absorption cycle for low generator firing temperatures. *Joint Solar Engineering Conf.*, ASME, American Solar Energy Society, Boulder, CO.
- Thombloom, M., and B. Nimmo. 1995. An economic analysis of a solar open cycle desiccant dehumidification system. *Solar Engineering—1995, Proc. of the 13th Annual ASME Conference*, Hawaii, Vol. 1, pp. 705–709.
- Thombloom, M., and B. Nimmo. 1996. Impact of design parameters on solar open cycle liquid desiccant regenerator performance. *SOLAR '96, Proc. of 1996 Annual Conf. of the American Solar Energy Society*, Asheville, NC, pp. 107–111.
- Ullah, M.R., C.F. Kettleborough, and P. Gandhidasan. 1988. Effectiveness of moisture removal for an adiabatic counterflow packed tower absorber operating with CaCl_2 -air contact system. *J. Sol. Energy Eng.* 110: 98–101.
- Zaytsev, I.O., and G.G. Aseyev. 1992. *Properties of Aqueous Solutions of Electrolytes*. CRC Press, Boca Raton, FL.

7

Passive Solar Heating, Cooling, and Daylighting

7.1 Introduction

Passive systems are defined, quite generally, as systems in which the thermal energy flow is by natural means: by conduction, radiation, and natural convection. Passive features increase the use of solar energy, ambient conditions, and earth and deep space to meet the heating, cooling, and lighting loads of buildings. For example, window placement can enhance solar gains to meet winter heating loads, provide daylighting, or do both. Using a solar chimney to draw air through a building directly or via an earth air tunnel is an example of passive cooling.

A *passive solar heating system* is one in which the sun's radiant energy is converted to heat upon absorption by the building. The absorbed heat can be transferred to thermal storage by natural means or used to directly heat the building. *Passive cooling systems* use natural energy flows to transfer heat to the environmental sinks: the ground, air, and sky (space).

A distinction is made between energy conservation techniques and passive solar measures. Energy conservation features are designed to reduce the heating and cooling energies required to thermally condition a building, for example, the use of insulation to reduce either heating or cooling loads or the use of window shading or window placement to reduce solar gains, reducing summer cooling loads.

If one of the major heat transfer paths employs a pump or fan to force flow of a heat transfer fluid, then the system is referred to as having an *active* component or subsystem. *Hybrid systems* use both passive and active energy flows. The use of the sun's radiant energy for the natural illumination of a building's interior spaces is called *daylighting*.

7.1.1 Current Applications and Costs

There are many examples of ancient buildings with passive heating, cooling, and daylighting. However, most building designs in the past century neglected passive features to provide a part of the energy needs of the

buildings. That began to change in the late last century as the cost of energy increased rapidly. A typical passive heating design in a favorable climate might supply up to one-third of a home's original load at a cost of 2–4¢/kWh energy saved. An appropriately designed daylighting system can supply lighting at a cost of 2.5–5¢/kWh (ASES [American Solar Energy Society] 1992).

The distinction between passive systems and energy conservation is not critical for economic calculations. An important consideration is the trade-off between the life-cycle costs of the energy saved (performance) and the initial investment and the operating and maintenance costs (cost). The other significant part of the economic trade-off involves determining the difference between the cost of construction of a passive building and that of a conventional building against which it is to be compared, that is, the "solar add-on cost."

Passive solar water heaters are described in Chapter 5. This chapter describes passive space heating and cooling systems and daylighting.

7.2 Passive Space Heating Systems

Passive heating systems contain the five basic components of all solar systems, as described in Chapters 4 and 5. Typical passive realizations of these components are as follows:

1. Collector—windows, walls, and floors
2. Storage—walls and floors, large interior masses (often these are integrated with the collector absorption function)
3. Distribution system—radiation, free convection, simple circulation fans
4. Controls—moveable window insulation, vents both to other inside spaces and to ambient
5. Backup system—any nonsolar heating system

The design of passive systems requires the strategic placement of windows, storage masses, and the occupied spaces themselves. The fundamental principles of solar radiation geometry and availability are instrumental in the proper location and sizing of the system's "collectors" (windows). Storage devices are usually more massive than those used in active systems and are frequently an integral part of the collection and distribution system.

7.2.1 Types of Passive Heating Systems

A commonly used method of cataloging the various passive system concepts is to distinguish three general categories: direct, indirect, and isolated gain.

Most of the physical configurations of passive heating systems are seen to fit within one of these three categories.

For direct gain systems (Figure 7.1), sunlight enters the heated space and is converted to heat at absorbing surfaces. This heat is then distributed throughout the space and to the various enclosing surfaces and room contents.

For indirect gain systems, sunlight is absorbed and stored by a mass interposed between the glazing and the conditioned space. The conditioned space is partially enclosed and bounded by this thermal storage mass; hence, a natural thermal coupling is achieved. Examples of the indirect approach are the thermal storage wall, the thermal storage roof, and the northerly room of an attached sunspace.

In the thermal storage wall (Figure 7.2a), sunlight penetrates the glazing and is absorbed and converted to heat at a wall surface interposed between the glazing and the heated space. The wall is usually masonry (Trombe wall) or containers filled with water (water wall), although it might contain phase-change material. The attached sunspace (Figure 7.2b) is actually a two-zone combination of direct gain and thermal storage wall. Sunlight enters and heats a direct gain southerly *sunspace* and a mass wall separating the northerly buffered space, which is heated indirectly. The *sunspace* is frequently used as a greenhouse, in which case the system is called an *attached greenhouse*. The thermal storage roof (Figure 7.2c) is similar to the thermal storage wall except that the interposed thermal storage mass is located on the building roof. A thermal storage roof using water for storage and movable insulation on the top was developed by Hay (Hay and Yellott 1969), which is also known as the *roof-pond* system.

The isolated gain category concept is an indirect system except that there is a distinct thermal separation (by means of either insulation or physical separation) between the thermal storage and the heated space. The convective

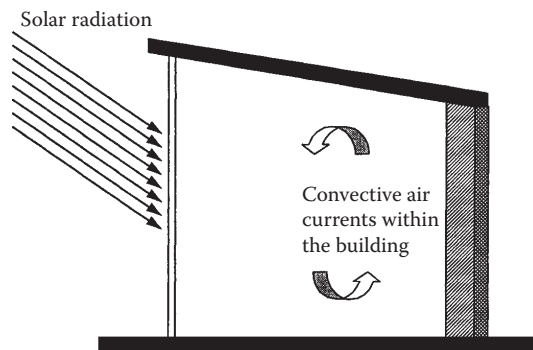
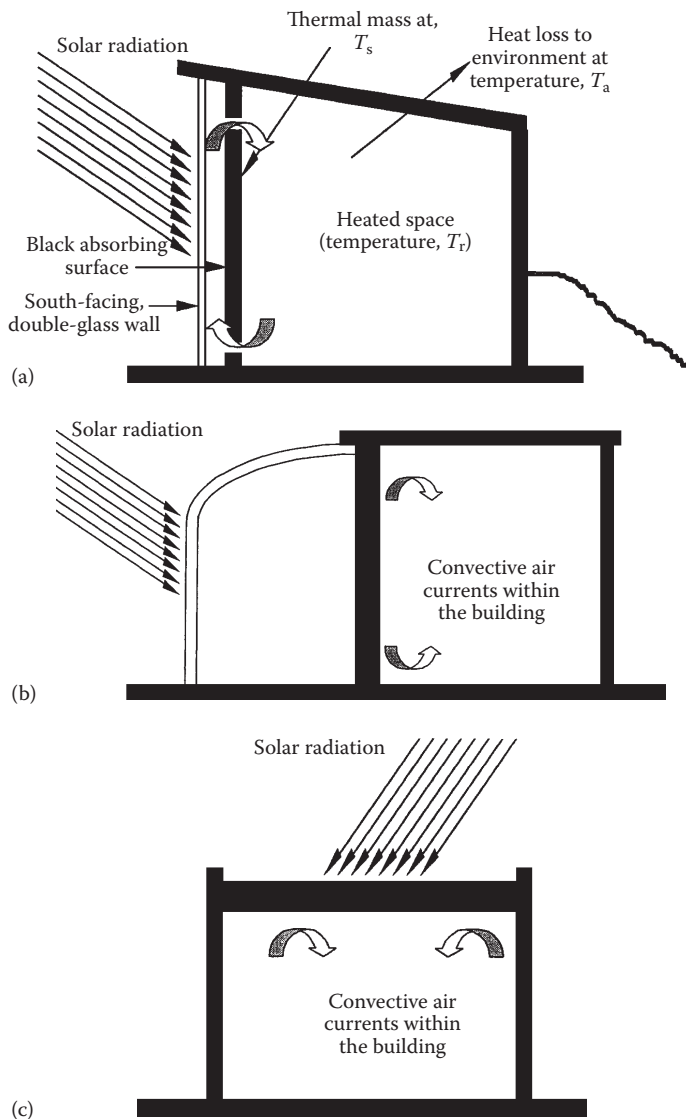


FIGURE 7.1
Concept of a direct gain passive heating system.

**FIGURE 7.2**

(a) Thermal storage wall. (b) Attached sunspace. (c) Thermal storage roof.

(thermosyphon) loop, as depicted in Figure 7.3, is in this category and is often used to heat domestic water. It is most akin to conventional active systems in that there is a separate collector and separate thermal storage. The thermal storage wall, thermal storage roof, and attached sunspace approaches can also be made into isolated systems by insulating between the thermal storage and the heated space.

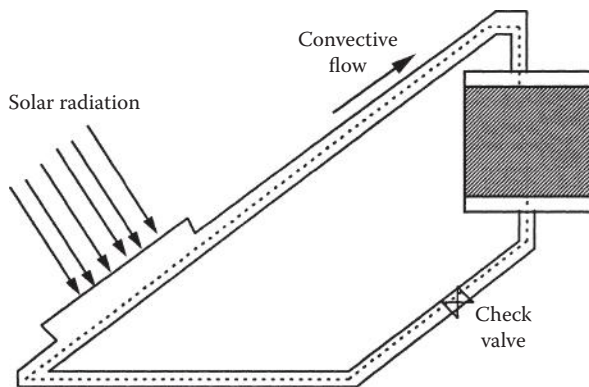


FIGURE 7.3
Convective loop.

7.2.2 Fundamental Concepts for Passive Heating Design

Figure 7.4 is an equivalent thermal circuit for the building illustrated in Figure 7.2a, the Trombe wall-type system. For the heat transfer analysis of the building, three temperature nodes can be identified—room temperature, storage wall temperature, and the ambient temperature. The circuit responds to climatic variables represented by a current injection I_s (solar radiation) and by the ambient temperature T_a . The storage temperature T_s and room temperature T_r are determined by current flows in the equivalent circuit. By using seasonal and annual climatic data, the performance of a passive structure can be simulated, and the results of many such simulations correlated to give the design approaches described in the following.

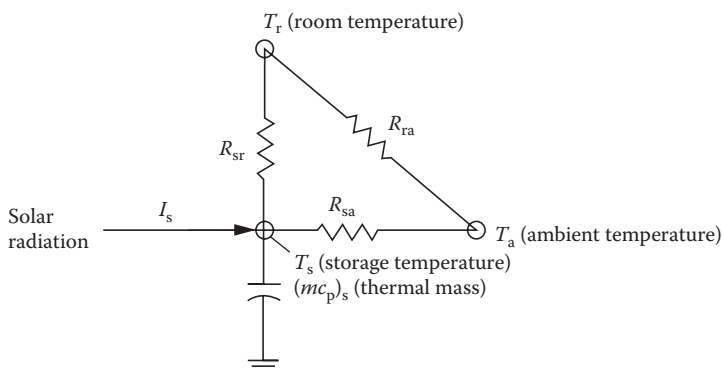


FIGURE 7.4
Equivalent thermal circuit for passively heated solar building in Figure 7.2a.

7.2.3 Generalized Passive Design Methods

Design of a passive heating system involves selection and sizing of the passive feature type(s), determination of thermal performance, and cost estimation. Ideally, a cost/performance optimization would be performed by the designer. Owner and architect ideas usually establish the passive feature type, with general size and cost estimation available. However, the thermal performance of a passive heating system has to be calculated.

There are several “levels” of methods that can be used to estimate the thermal performance of passive designs. First-level methods involve a rule of thumb or generalized calculation to get a starting estimate for size or annual performance. A second-level method involves climate, building, and passive system details, which allow annual performance determination, plus some sensitivity to passive system design changes. Third-level methods involve periodic calculations (hourly, monthly) of performance and permit more detailed variations of climatic, building, and passive solar system design parameters.

These three levels of design methods have a common basis in that they all are derived from correlations of a multitude of computer simulations of passive systems (PSDH [*Passive Solar Design Handbook*] 1980, 1984). As a result, a similar set of defined terms is used in many passive design approaches:

- A_p , solar projected area, m^2 (ft^2): The net south-facing passive solar glazing area projected onto a vertical plane.
- NLC, net building load coefficient, kJ/CDD (Btu/FDD): Net load of the nonsolar portion of the building per day per degree of indoor-outdoor temperature difference. The C-day and F-day terms refer to centigrade and Fahrenheit degree days, respectively.
- Q_{net} , net reference load, Wh (Btu): Heat loss from nonsolar portion of building is calculated by

$$Q_{\text{net}} = \text{NLC} \times (\text{no. of degree days}). \quad (7.1)$$

- LCR, load collector ratio, $\text{kJ}/\text{m}^2\cdot\text{C-day}$ ($\text{Btu}/\text{ft}^2\cdot\text{F-day}$): Ratio of NLC to A_p ,

$$\text{LCR} = \frac{\text{NLC}}{A_p}. \quad (7.2)$$

- SSF, solar savings fraction, is the fractional reduction in required auxiliary heating relative to net reference load,

$$\text{SSF} = 1 - \frac{Q_{\text{aux}}}{Q_{\text{net}}}. \quad (7.3)$$

Hence, using Equation 7.1,

$$\text{Auxiliary heat required, } Q_{\text{aux}} = (1 - \text{SSF}) \times \text{NLC} \times (\text{no. of degree days}). \quad (7.4)$$

The amount of auxiliary heat required is often a basis of comparison between possible solar designs as well as the basis for determining building energy operating costs. Thus, many of the passive design methods are based on determining SSF, NLC, and the number of degree days in order to calculate the auxiliary heat required for a particular passive system by using Equation 7.4.

7.2.4 First Level: Rule of Thumb

A first estimate or starting value is needed to begin the overall passive system design process. Rules of thumb have been developed to generate initial values for solar aperture size, storage size, SSF, auxiliary heat required, and other size and performance characteristics. The following rules of thumb are meant to be used with the defined terms presented previously.

7.2.4.1 Load

A rule of thumb used in conventional building design is that a design heating load of 120–160 kJ/C-day per m² of floor area (6–8 Btu/F-day·ft²) is considered an energy-conservative design. Reducing these nonsolar values by 20% to solarize the proposed south-facing solar wall gives rule-of-thumb NLC values per unit of floor area:

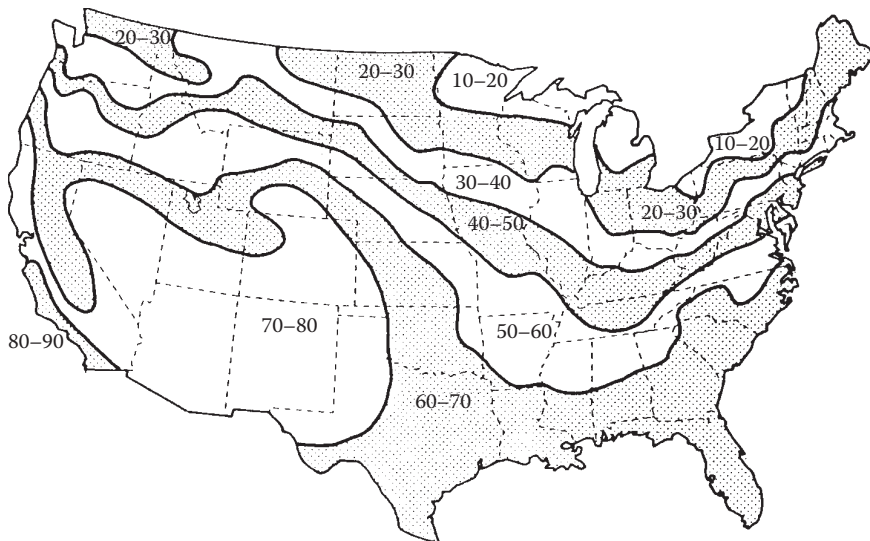
$$\frac{\text{NLC}}{\text{Floor area}} = 100 - 130 \text{ kJ/C-day} \cdot \text{m}^2 (4.8 - 6.4 \text{ Btu/F-day} \cdot \text{ft}^2). \quad (7.5)$$

7.2.4.2 Solar Savings Fraction

A method of getting starting-point values for the SSF is presented in Figure 7.5 (PSDH 1984). The map values represent optimum SSF in percentage for a particular set of conservation and passive solar costs for different climates across the United States. With the Q_{net} generated from the NLC rule of thumb above and the SSF read from the map, the Q_{aux} can be determined.

7.2.4.3 Load Collector Ratio

The A_p can be determined using the NLC from above, if the LCR is known. The rule of thumb associated with “good” values of LCR (Robbins 1986) differs depending on whether the design is for a “cold” or “warm” climate:

**FIGURE 7.5**

Starting-point values of SSF in percentage. (From PSDH, *Passive Solar Design Handbook*, Van Nostrand Reinhold Co., New York, 1984.)

$$\begin{aligned}
 \text{Good LCR} = & \quad \text{For cold climate: } 410 \text{ kJ/m}^2 \cdot \text{C-day} \quad (20 \text{ Btu/ft}^2 \cdot \text{F-day}) \\
 & \quad \text{For warm climate: } 610 \text{ kJ/m}^2 \cdot \text{C-day} \quad (30 \text{ Btu/ft}^2 \cdot \text{F-day})
 \end{aligned} \tag{7.6}$$

7.2.4.4 Storage

Rules of thumb for thermal mass storage relate storage material total heat capacity to the solar projected area (PSDH 1984). The use of the storage mass is to provide for heating on cloudy days and to regulate sunny day room air temperature swing. When the thermal mass directly absorbs the solar radiation, each square meter of the projected glazing area requires enough mass to store 613 kJ/C. If the storage material is not in direct sunlight, but heated from room air only, then four times as much mass is needed. In a room with a direct sunlight heated storage mass, the room air temperature swing will be approximately one-half the storage mass temperature swing. For room air heated storage, the air temperature swing is twice that of the storage mass.

A more location-dependent set of rules of thumb is presented in PSDH (1980). Comparing the results of that method to those of the method presented above, the two rules of thumb are seen to produce roughly similar answers. General system cost and performance information can be generated

with results from rule-of-thumb calculations, but a more detailed level of information is needed to determine design-ready passive system type (direct gain, thermal wall, sunspace), size, performance, and costs.

Example 7.1

A 200-m² residential building in Nashville, Tennessee, is designed to have an NLC of 20,000 kJ/°C-day. Using rule of thumb, find the projected passive area, SSF, and the auxiliary heat required.

Solution

Using the LCR for cold climate, the projected passive solar area can be found from Equation 7.2.

$$A_p = \frac{NLC}{LCR} = \frac{(20,000 \text{ kJ/C-day})}{410 \text{ kJ/m}^2 \cdot \text{C-day}} \\ = 48.8 \text{ m}^2$$

Figure 7.5 shows that Nashville, Tennessee, is at the border of 40%–50% and 50%–60% regions. Therefore, a value of 50% would be a good guess.

Table A7.2 gives 3696 F-days for Nashville, Tennessee, which is equivalent to 2053 C-days. Therefore, the auxiliary heat required, Q_{aux} , may be found from Equation 7.4:

$$Q_{aux} = (1 - 0.50)(20,000 \text{ kJ/C-day})(2053 \text{ C-days}) \\ = 20,530 \text{ MJ annually.}$$

7.2.5 Second Level: LCR Method

The LCR method is useful for making estimates of the annual performance of specific types of passive system(s) combinations. The LCR method was developed by calculating the annual SSF for 94 reference passive solar systems for 219 US and Canadian locations over a range of LCR values. Table A7.1 includes the description of these 94 reference systems for use both with the LCR method and with the solar load ratio (SLR) method described in the following. Tables were constructed for each city with LCR versus SSF listed for each of the 94 reference passive systems. (*Note:* The SLR method was used to make the LCR calculations, and this SLR method is described in Section 7.2.6 as the third-level method.) While the complete LCR tables (PSDH 1984) include 219 locations, Table A7.2 only includes six “representative” cities (Albuquerque, Boston, Madison, Medford, Nashville, and Santa

Maria), purely owing to space restrictions. The LCR method consists of the following:

1. Determine the building parameters:
 - a. Building load coefficient, NLC.
 - b. Solar projected area, A_p .
 - c. Load collector ratio, $LCR = NLC/A_p$.
2. Find the short designation of the reference system closest to the passive system design (Table A7.1).
3. Enter the LCR Tables (Table A7.2):
 - a. Find the city.
 - b. Find the reference system listing.
 - c. Determine annual SSF by interpolation using the LCR value from above.
 - d. Note the annual heating degree days (no. of degree of days).
4. Calculate the annual auxiliary heat required:

$$\text{Auxiliary heat required} = (1 - \text{SSF}) \times \text{NLC} \times (\text{no. of degree days}).$$

If more than one reference solar system is being used, then find the “aperture area weighted” SSF for the combination. Determine each individual reference system SSF using the total aperture area LCR, then take the “area weighted” average of the individual SSFs.

The LCR method allows no variation from the 94 reference passive designs. To treat off-reference designs, sensitivity curves have been produced that illustrate the effect on SSF of varying one or two design variables. These curves were produced for the six “representative” cities, chosen for their wide geographical and climatological ranges. Several of these SSF “sensitivity curves” are presented in Figure A7.1.

7.2.6 Third Level: SLR Method

The SLR method calculates monthly performance, and the terms and values used are monthly based. The method allows the use of specific location weather data and the 94 reference design passive systems (Table A7.1). In addition, the sensitivity curves (Figure A7.1) can again be used to define performance outside the reference design systems. The result of the SLR method is the determination of the monthly heating auxiliary energy required, which is then summed to give the annual requirement for auxiliary heating energy. Generally, the SLR method gives annual values within $\pm 3\%$ of detailed simulation results, but the monthly values may vary more (Duffie and Beckman 1991; PSDH 1984). Thus, the monthly SLR method is more “accurate” than the

rule-of-thumb methods and provides the designer with system performance on a month-by-month basis.

The SLR method uses equations and correlation parameters for each of the 94 reference systems combined with the insolation absorbed by the system, the monthly degree days, and the system's LCR to determine the monthly SSF. These correlation parameters are listed in Table A7.3 as A , B , C , D , R , G , H , and LCRs for each reference system (PSDH 1984). The correlation equations are as follows:

$$\text{SSF} = 1 - K(1 - F), \quad (7.7)$$

where

$$K = 1 + \frac{G}{\text{LCR}}, \quad (7.8)$$

$$F = \begin{cases} AX, & \text{when } X < R \\ B - C \exp(-DX), & \text{when } X > R, \end{cases} \quad (7.9)$$

$$X = \frac{S/\text{DD} - (\text{LCR}_s)H}{(\text{LCR})K}, \quad (7.10)$$

and X is called the generalized SLR. The DD term is the monthly number of degree-days. The term S is the monthly insolation absorbed by the system per unit of solar projected area. Monthly average daily insolation data on a vertical south-facing surface can be found or calculated using various sources (McQuiston and Parker 1994; PSDH 1984). The S term can be determined by multiplying by a transmission and an absorption factor and the number of days in the month. Absorption factors for all systems are close to 0.96 (McQuiston and Parker 1994), whereas the transmission is approximately 0.9 for single glazing, 0.8 for double glazing, and 0.7 for triple glazing.

Example 7.2

For a vented, 180-ft², double-glazed with night insulation, 12-in.-thick Trombe wall system (TWD4) in an NLC = 11,800 Btu/FDD house in Medford, Oregon, determine the auxiliary energy required in January.

Solution

Weather data for Medford, Oregon (PSDH 1984) yields for January ($N = 31$ days): daily vertical surface insolation = 565 Btu/ ft^2 and 880 FDD; thus, $S = (31)(565)(0.8)(0.96) = 13,452 \text{ Btu}/\text{ft}^2\text{-month}$.

$$\text{LCR} = \frac{\text{NLC}}{A_p} = \frac{11,800}{180} = 65.6 \text{ Btu/FDD ft}^2.$$

From Table A7.3 at TWD4: $A = 0$, $B = 1$, $C = 1.0606$, $D = 0.977$, $R = -9$, $G = 0$, $H = 0.85$, LCRs = 5.8 Btu/FDD ft^2 .

Substituting into Equation 7.8 gives

$$K = 1 + \frac{0}{65.6} = 1.$$

Equation 7.10 gives

$$X = \frac{13,452/880 - (5.8 \times 0.85)}{65.6 \times 1} = 0.16.$$

Equation 7.9 gives

$$F = 1 - 1.0606e^{-0.977 \times 0.16} = 0.09.$$

Equation 7.7 gives

$$\text{SSF} = 1 - 1(1 - 0.09) = 0.09.$$

The January auxiliary energy required can be calculated using Equation 7.4:

$$\begin{aligned} Q_{\text{aux}}(\text{January}) &= (1 - \text{SSF}) \times \text{NLC} \times (\text{no. of degree days}) \\ &= (1 - 0.09) \times 11,800 \times 880 \\ &= 9,450,000 \text{ Btu}. \end{aligned}$$

As mentioned, the use of sensitivity curves (PSDH 1984) as in Figure A7.1 will allow SSF to be determined for many off-reference system design conditions involving storage mass, number of glazings, and other more esoteric parameters. Also, the use of multiple passive system types within one building would be approached by calculating the SSF for each system type individually using a combined area LCR, and then a weighted area (aperture) average SSF would be determined for the building.

7.3 Passive Space Cooling Systems

Passive cooling systems are designed to use natural means to transfer heat from buildings, including convection/ventilation, evaporation, radiation, and conduction. However, the most important element in both passive and conventional cooling design is to prevent heat from entering the building in the first place. Cooling conservation techniques involve building surface colors, insulation, special window glazings, overhangs and orientation, and numerous other architectural/engineering features.

7.3.1 Controlling the Solar Input

Controlling the solar energy input to reduce the cooling load is usually considered a passive (vs. conservation) design concern because solar input may be needed for other purposes, such as daylighting throughout the year or heating during the winter. Basic architectural solar control is normally “designed in” via the shading of the solar windows, where direct radiation is desired for winter heating and needs to be excluded during the cooling season.

The shading control of the windows can be of various types and “controllability,” ranging from drapes and blinds, use of deciduous trees, to the commonly used overhangs and vertical louvers. A rule-of-thumb design for determining proper south-facing window overhang for both winter heating and summer shading is presented in Table 7.1. Technical details on calculating shading from various devices and orientations are found in ASHRAE (American Society of Heating, Refrigerating and Air-Conditioning Engineers) (2011) and Haggard et al. (2010).

7.3.2 Movement of Air

Air movement provides cooling comfort through convection and evaporation from human skin. ASHRAE places the comfort limit at 79°F (26°C) for an air velocity of 50 ft/min (0.25 m/s), 82°F for 160 ft/min, and 85°F for 200 ft/min. To determine whether or not comfort conditions can be obtained, a designer must calculate the volumetric flow rate, Q , which is passing through the occupied space. Using the cross-sectional area, A_x , of the space and the room air velocity, V_a , required, the flow is determined by

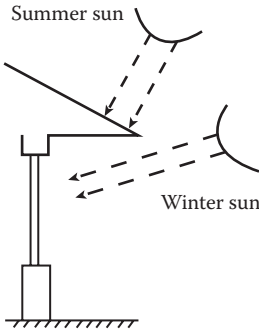
$$Q = A_x V_a. \quad (7.11)$$

The proper placement of windows, “narrow” building shape, and open landscaping can enhance natural wind flow to provide ventilation. The air flow rate through open windows for wind-driven ventilation is given by ASHRAE (2013):

$$Q = C_v V_w A_w, \quad (7.12)$$

TABLE 7.1

South-Facing Window Overhang Rule of Thumb

		Length of the Overhang = $\frac{\text{Window Height}}{F}$
(a) Overhang Factors		
North Latitude	F^a	(b) Roof Overhang Geometry
28	5.6–11.1	
32	4.0–6.3	
36	3.0–4.5	
40	2.5–3.4	
44	2.0–2.7	
48	1.7–2.2	
52	1.5–1.8	
56	1.3–1.5	

Properly sized overhangs shade out hot summer sun but allow winter sun (which is lower in the sky) to penetrate windows.

Source: Halacy, D.S., *Home Energy*, Rodale Press, Inc., Emmaus, PA, 1984.

^a Select a factor according to your latitude. High values provide complete shading at noon on June 21; lower values, until August 1.

where Q is the air flow rate (m^3/s), A_w is the free area of inlet opening (m^2), V_w is the wind velocity (m/s), and C_v is the effectiveness of opening = 0.5–0.6 for wind perpendicular to opening and 0.25–0.35 for wind diagonal to opening.

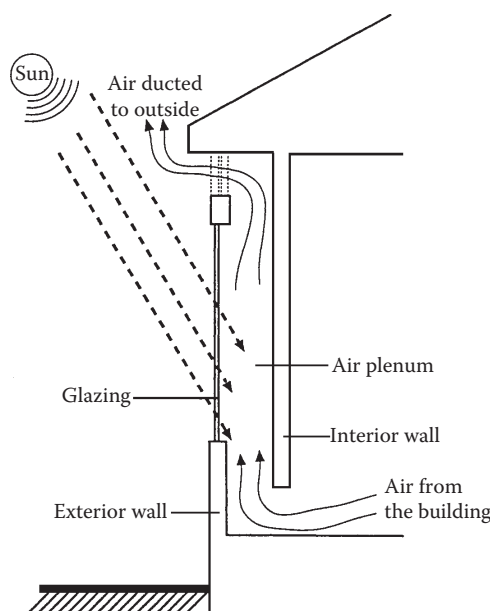
The stack effect can induce ventilation when warm air rises to the top of a structure and exhausts outside, while cooler outside air enters the structure to replace it. Figure 7.6 illustrates the solar chimney concept, which can easily be adapted to a thermal storage wall system.

The greatest stack-effect flow rate is produced by maximizing the stack height and the air temperature in the stack, as given by

$$Q = 0.116 A_j \sqrt{h(T_s - T_o)}, \quad (7.13)$$

where Q is the stack flow rate (m^3/s), A_j is the area of inlets or outlets (whichever is smaller) (m^2), h is the inlet-to-outlet height (m), T_s is the average temperature in stack ($^\circ\text{C}$), and T_o is the outdoor air temperature ($^\circ\text{C}$).

If inlet or outlet area is twice the other, the flow rate will increase by 25%, and by 35% if the areas' ratio is 3:1 or larger.

**FIGURE 7.6**

The stack-effect/solar chimney concept to induce convection/ventilation. (From PSDH, *Passive Solar Design Handbook*, Volume One: *Passive Solar Design Concepts*, DOE/CS-0127/1, March; Volume Two: *Passive Solar Design Analysis*, DOE/CS-0127/2, January. Washington, DC: U.S. Department of Energy, 1980.)

Example 7.3

A two-story (5 m) solar chimney is being designed to produce a flow of $0.25 \text{ m}^3/\text{s}$ through a space. The preliminary design features include a $25 \text{ cm} \times 1.5 \text{ m}$ inlet, a $50 \text{ cm} \times 1.5 \text{ m}$ outlet, and an estimated 35°C average stack temperature on a sunny 30°C day. Can this design produce the desired flow?

Solution

Substituting the design data into Equation 7.13,

$$\begin{aligned} Q &= 0.116(0.25 \times 1.5)[5(5)]^{1/2} \\ &= 0.2 \text{ m}^3/\text{s}. \end{aligned}$$

Since the outlet area is twice the inlet area, the 25% flow increase can be used:

$$Q = 0.2(1.25) = 0.25 \text{ m}^3/\text{s}. \quad (\text{Answer: Yes, the proper flow rate is obtained.})$$

7.3.3 Evaporative Cooling

When air with less than 100% relative humidity moves over a water surface, the evaporation of water causes both the air and the water to cool. The lowest temperature that can be reached by this direct evaporative cooling effect is the wet-bulb temperature of the air, which is directly related to the relative humidity, with lower wet-bulb temperature associated with lower relative humidity. Thus, dry air (low relative humidity) has a low wet-bulb temperature and will undergo a large temperature drop with evaporative cooling, while humid air (high relative humidity) can only be slightly cooled evaporatively. The wet-bulb temperature for various relative humidity and air temperature conditions can be found via the “psychrometric chart” available in most thermodynamic texts. Normally, an evaporative cooling process cools the air only part of the way down to the wet-bulb temperature. To get the maximum temperature decrease, it is necessary to have a large water surface area in contact with the air for a long time, and interior ponds and fountain sprays are often used to provide this air–water contact area.

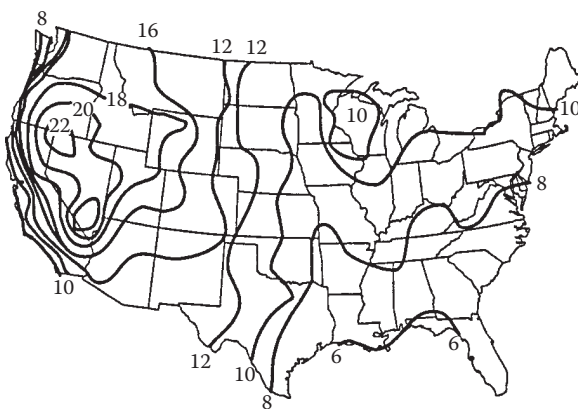
The use of water sprays and open ponds on roofs provides cooling primarily via evaporation. The hybrid system involving a fan and wetted mat, the “swamp cooler,” is by far the most widely used evaporative cooling technology. Direct, indirect, and combined evaporative cooling system design features are described in ASHRAE (2011, 2013).

7.3.4 Nocturnal and Radiative Cooling Systems

Another approach to passive convective/ventilative cooling involves using cooler night air to reduce the temperature of the building or a storage mass. Thus, the building/storage mass is prepared to accept part of the heat load during the hotter daytime. This type of convective system can also be combined with evaporative and radiative modes of heat transfer, utilizing air or water as the convective fluid. Work in Australia (Close et al. 1968) investigated rock storage beds that were chilled using evaporatively cooled night air. Room air was then circulated through the bed during the day to provide space cooling. The use of encapsulated roof ponds as a thermal cooling mass has been tried by several investigators (Hay and Yellott 1969; Marlatt et al. 1984) and is often linked with nighttime radiative cooling.

All warm objects emit thermal infrared radiation; the hotter the body, the more energy it emits. A passive cooling scheme is to use the cooler night sky as a sink for thermal radiation emitted by a warm storage mass, thus chilling the mass for cooling use the next day. The net radiative cooling rate, Q_r , for a horizontal unit surface (ASHRAE 2013) is

$$Q_r = \epsilon\sigma(T_{\text{body}}^4 - T_{\text{sky}}^4), \quad (7.14)$$

**FIGURE 7.7**

Average monthly sky temperature depression ($T_{\text{air}} - T_{\text{sky}}$) for July in Fahrenheit. (Adapted from Martin, M. and P. Berdahl, *Solar Energy*, 33(314): 321–336, 1984.)

where Q_r is the net radiative cooling rate, W/m^2 ($\text{Btu/h}\cdot\text{ft}^2$); ε is the surface emissivity fraction (usually 0.9 for water); $\sigma = 5.67 \times 10^{-8} \text{ W/m}^2\text{K}^4$ ($1.714 \times 20^{-9} \text{ Btu/h}\cdot\text{ft}^2\text{R}^4$); T_{body} is the warm body temperature, Kelvin (Rankine); and T_{sky} is the effective sky temperature, Kelvin (Rankine).

The monthly average air-sky temperature difference has been determined (Martin and Berdahl 1984) and Figure 7.7 presents these values for July (in Fahrenheit) for the United States.

Example 7.4

Estimate the overnight cooling possible for a 10-m², 30°C water thermal storage roof during July in Los Angeles.

Solution

Assume that the roof storage unit is black with $\varepsilon = 0.9$. From Figure 7.7, $T_{\text{air}} - T_{\text{sky}}$ is approximately 10°F for Los Angeles. From weather data for Los Angeles airport (ASHRAE 2013; Robbins 1986), the July average temperature is 20°C with a range of 8°C. Assuming night temperatures vary from the average (20°C) down to half the daily range (8 0/2°F), the average nighttime temperature is chosen as $20 - (1/2)(8/2) = 18^\circ\text{C}$. Hence, $T_{\text{sky}} = 18 - (10/1.8) = 12.5^\circ\text{C}$. From Equation 7.14,

$$\begin{aligned} Q_r &= 0.9(5.67 \times 10^{-8})[(273 + 30)^4 - (273 + 12.5)^4] \\ &= 91.1 \text{ W/m}^2. \end{aligned}$$

For a 10-h night and a 10-m² roof area,

$$\begin{aligned}\text{Total radiative cooling} &= 91.1 (10)(10) \\ &= 9110 \text{ Wh} = 9.11 \text{ kWh.}\end{aligned}$$

Note: This does not include the convective cooling possible, which can be approximated (at its maximum rate) for still air (Table A5.1) by

$$\begin{aligned}\text{Maximum total } Q_{\text{conv}} &= hA(T_{\text{roof}} - T_{\text{air}})(\text{Time}) \\ &= 5(129)(85 - 65)(10) \\ &= (1.63 \times 5.678)(10) (30 - 18)(10) \\ &= 11,110 \text{ Wh} = 11.1 \text{ kWh.}\end{aligned}$$

This is a maximum since the 30°C storage temperature will drop as it cools—which is also the case for the radiative cooling calculation. However, convection is seen to usually be the more dominant mode of nighttime cooling.

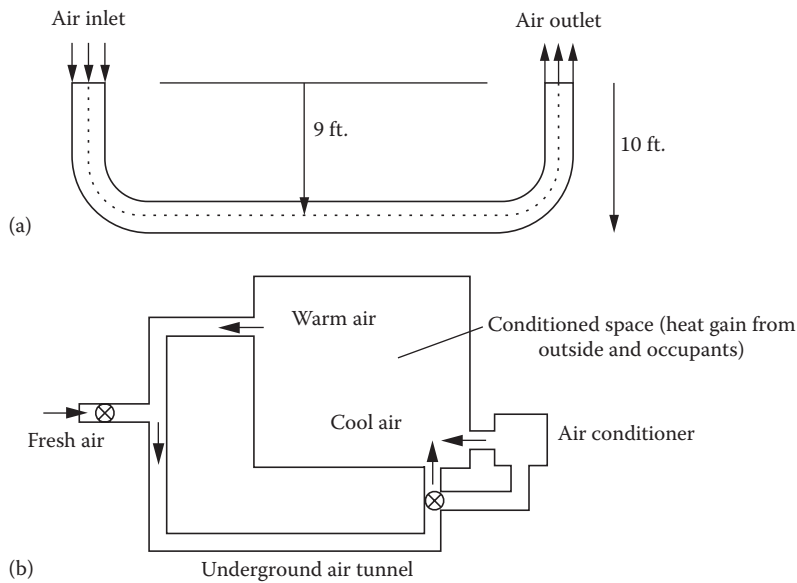
7.3.5 Earth Contact Cooling (or Heating)

Earth contact cooling or heating is a passive summer cooling and winter heating technique that utilizes underground soil as the heat sink or source. By installing a pipe underground and passing air through the pipe, the air will be cooled or warmed depending on the season. A schematic of an open loop system and that of a closed loop air-conditioning system are presented in Figure 7.8a and b, respectively (Goswami and Dhaliwal 1985).

The use of this technique can be traced back to 3000 BC when Iranian architects designed some buildings to be cooled by natural resources only. In the 19th century, Wilkinson (in USDA [US Department of Agriculture] 1960) designed a barn for 148 cows where a 500-ft-long underground passage was used for cooling during the summertime. Since that time, a number of experimental and analytical studies of this technique have continued to appear in the literature. Goswami and Dhaliwal (1985) have given a brief review of the literature, as well as presented an analytical solution to the problem of transient heat transfer between the air and the surrounding soil as the air is made to pass through a pipe buried underground. More recently, Krarti and Kreider (1996) have also presented an analytical model for heat transfer in an underground air tunnel.

7.3.5.1 Heat Transfer Analysis

The transient thermal analysis of the air and soil temperature fields (Goswami and Ileslamlou 1990) is conducted using finite elements with the convective heat transfer between the air and the pipe and using semi-infinite cylindrical

**FIGURE 7.8**

(a) Open loop underground air tunnel system. (b) Schematic of closed loop air-conditioning system using air tunnel.

conductive heat transfer to the soil from the pipe. It should be noted that the thermal resistance of the pipe (whether metal, plastic, or ceramic) is negligible relative to the surrounding soil.

7.3.5.1.1 Air and Pipe Heat Transfer

The pipe is divided into a large number of elements and a psychrometric energy balance written for each, depending on whether the air leaves the element (a) unsaturated or (b) saturated. Assuming that air with a flow rate, m , and temperature T_1 enters the element and leaves at a temperature T_2 :

- If the air leaves an element as unsaturated, the energy balance on the element is

$$mC_p(T_1 - T_2) = hA_p(T_{\text{air}} - T_{\text{pipe}}). \quad (7.15)$$

T_{air} can be taken as $(T_1 + T_2)/2$.

Substituting and simplifying, we get

$$T_2 = \frac{[(1 - U/2)T_1 + UT_{\text{pipe}}]}{(1 + U/2)}, \quad (7.16)$$

where U is defined as

$$U = \frac{A_p h}{m C_p}$$

- b. If the air leaving the element is saturated and the specific humidity at the entry and exit is W_1 and W_2 respectively, the energy balance is

$$mC_p T_1 + m(W_1 - W_2)H_{fg} = mC_p T_2 + hA_p(T_{\text{air}} - T_{\text{pipe}}). \quad (7.17)$$

Simplifying, we get

$$T_2 = \frac{1 - \frac{U}{2} T_1 + \frac{W_1 - W_2}{C_p} H_{fg} + U T_{\text{pipe}}}{(1 + U/2)}. \quad (7.18)$$

The convective heat transfer coefficient h in the preceding equations depends on Reynolds number, the shape, and roughness of the pipe. Using the exit temperature from the first element as the inlet temperature for the next element, the exit temperature for the element can be calculated in a similar way. Continuing this way from one element to the next, the temperature of air at the exit from the pipe can be calculated.

7.3.5.1.2 Soil Heat Transfer

The heat transfer from the pipe to the soil is analyzed by considering the heat flux at the internal radius of a semi-infinite cylinder formed by the soil around the pipe. For a small element, the problem can be formulated as

$$\frac{\partial^2 T(r, t)}{\partial r^2} + \frac{1}{r} \frac{\partial T(r, t)}{\partial r} = \frac{1}{\alpha} \frac{\partial T(r, t)}{\partial t}, \quad (7.19)$$

with initial and boundary conditions as

$$T(r, 0) = T_e \quad (7.20)$$

$$T(\infty, t) = T_e \quad (7.21)$$

$$-K \frac{\partial T}{\partial r}(r, t) = q'' , \quad (7.22)$$

where T_e is the bulk earth temperature and q'' is also given by the amount of heat transferred to the air from the pipe by convection; that is, $q'' = h(T_{\text{air}} - T_{\text{pipe}})$.

7.3.5.2 Soil Temperatures and Properties

Labs (1981) studied the earth temperatures in the United States. According to both of these studies, temperature swings in the soil during the year are damped with depth below the ground. There is also a phase lag between the soil temperature and the ambient air temperature, and this phase lag increases with depth below the surface. For example, the soil temperature for light dry soil at a depth of approximately 10 ft (3.05 m) varies by approximately $\pm 5^{\circ}\text{F}$ (2.8°C) from the mean temperature (approximately equal to mean annual air temperature) and has a phase lag of approximately 75 days behind ambient air temperature (Labs 1981).

The thermal properties of the soil are difficult to determine. The thermal conductivity and diffusivity both change with the moisture content of the soil itself, which is directly affected by the temperature of and heat flux from and to the buried pipe. Most researchers have found that using constant property values for soil taken from standard references gives reasonable predictive results (Goswami and Biseli 1994).

7.3.5.3 Generalized Results from Experiments

Figure 7.9 presents data from Goswami and Biseli (1994) for an open system, 100-ft-long, 12-in.-diameter pipe, buried 9 ft deep. The figure shows the relationship between pipe inlet-to-outlet temperature reduction ($T_{\text{in}} - T_{\text{out}}$) and the initial soil temperature with ambient air inlet conditions of 90°F and 55% relative humidity for various pipe flow rates.

Other relations from this same report that can be used with the Figure 7.9 data include the following: (1) the effect of increasing pipe/tunnel length on

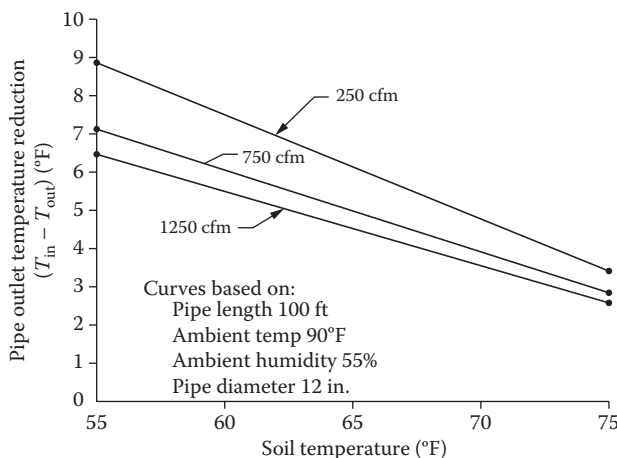


FIGURE 7.9

Air temperature drop through a 100-ft-long, 12-in.-diameter pipe buried 9 ft underground.

increasing the inlet-to-outlet air temperature difference is fairly linear up to 250 ft and (2) the effect of decreasing pipe diameter on lowering the outlet air temperature is slight and only marginally effective for pipes less than 12-in.-diameter.

Example 7.5

Provide the necessary 12-in.-diameter pipe length(s) that will deliver 1500 cfm of 75°F air if the ambient temperature is 85°F and the soil at 9 ft is 65°F.

Solution

From Figure 7.9, for 100 ft of pipe at 65°F soil temperature, the pipe temperature reduction is

$$\begin{aligned}T_{\text{in}} - T_{\text{out}} &= 6^\circ \text{ (at 250 cfm)} \\&= 5^\circ\text{F (at 750 cfm)} \\&= 4.5^\circ\text{F (at 1250 cfm).}\end{aligned}$$

Since the “length versus temperature reduction” is linear (see text above), the 10°F reduction required (85 down to 75) would be met by the 750 cfm case (5°F for 100 ft) if 200 ft of pipe is used. Then, two 12-in.-diameter pipes would be required to meet the 1500-cfm requirement.

Answer

Two 12-in.-diameter pipes, each 200 ft long. (*Note:* See what would be needed if the 250-cfm or the 1250-cfm cases had been chosen. Which of the three flow rate cases leads to the “cheapest” installation?)

7.4 Daylighting Design Fundamentals

Daylighting is the use of the sun’s radiant energy to illuminate the interior spaces in a building. In the last century, electric lighting was considered an alternative technology to daylighting. Today, the situation is reversed, primarily attributed to the economics of energy use and conservation. However, there are good physiological reasons for using daylight as an illuminant. The quality of daylight matches the human eye’s response, thus permitting lower light levels for task comfort, better color rendering, and clearer object discrimination (Robbins 1986).

7.4.1 Lighting Terms and Units

Measurement of lighting level is based on the “standard candle,” where the *lumen* (lm), the unit of *luminous flux* (ϕ), is defined as the rate of luminous energy passing through a 1-m² area located 1 m from the candle. Thus, a standard candle generates 4π lumens, which radiate away in all directions. The *illuminance* (E) on a surface is defined as the luminous flux on the surface divided by the surface area, $E = \phi/A$. Illuminance is measured in either *lux* (lx), as lumens per square meter, or *footcandles* (fc), as lumens per square foot.

Determination of the daylighting available at a given location in a building space at a given time is important to evaluate the reduction possible in electric lighting and the associated impact on heating and cooling loads. Daylight provides approximately 110 lm/W of solar radiation, fluorescent lamps provide approximately 75 lm/W of electrical input, and incandescent lamps provide approximately 20 lm/W; thus, daylighting generates only 1/2 to 1/5 the heating that equivalent electric lighting does, significantly reducing the building cooling load.

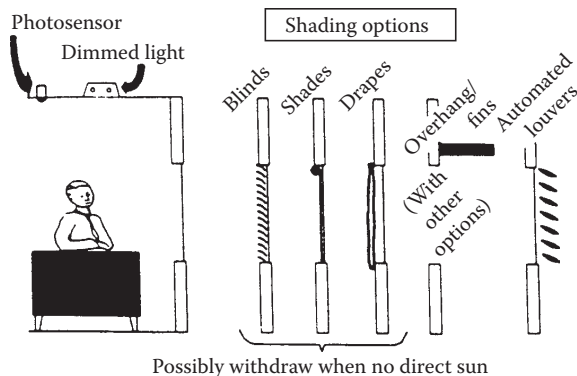
7.4.2 Economics of Daylighting

The economic benefit of daylighting is directly tied to the reduction in lighting electrical energy operating costs. Also, lower cooling system operating costs are possible because of the reduction in heating caused by the reduced electrical lighting load. The reduction in lighting and cooling system electrical power during peak demand periods could also beneficially affect demand charges.

The reduction of the design cooling load through the use of daylighting can also lead to the reduction of installed or first-cost cooling system dollars. Normally, economics dictate that an automatic lighting control system must take advantage of the reduced lighting/cooling effect, and the control system cost, minus any cooling system cost, savings should be expressed as a net first cost. A payback timer for the lighting control system (net or not) can be calculated from the ratio of first costs to yearly operating savings. In some cases, these paybacks for daylighting controls have been found to be in the range of 1 to 5 years for office building spaces (Rundquist 1991).

Controls, both aperture and lighting, directly affect the efficacy of the daylighting system. As shown in Figure 7.10, aperture controls can be architectural (overhangs, lightshelves, etc.) or window shading devices (blinds, automated louvers, etc.). The aperture controls generally moderate the sunlight entering the space to maximize or minimize solar thermal gain, permit the proper amount of light for visibility, and prevent glare and beam radiation onto the workplace. Photosensor control of electric lighting allows the dimming (or shutting off) of the lights in proportion to the amount of available daylighting luminance.

In most cases, using daylighting controls to increase the solar gain for daylighting purposes saves more in electrical lighting energy and in cooling

**FIGURE 7.10**

Daylighting system controls. (From Rundquist, R.A., *ASHRAE Journal* 11: 30–34, November, 1991.)

energy associated with the lighting than is incurred with the added solar gain (Rundquist 1991). In determining the annual energy savings from daylighting (ES_T), the annual lighting energy saved from daylighting (ES_L) is added with the reduction in cooling system energy (∇ES_C) and with the negative of the heating system energy increase (∇ES_H):

$$ES_T = ES_L + \nabla ES_C - \nabla ES_H. \quad (7.23)$$

A simple approach to estimating the heating and cooling energy changes associated with lighting energy reduction is to use the fraction of the year associated with the cooling or heating season (f_c, f_H) and the seasonal COP of the cooling or heating equipment. Thus, Equation 7.23 can be expressed as

$$\begin{aligned} ES_T &= ES_L + \frac{f_c ES_L}{COP_c} - \frac{f_c ES_L}{COP_H} \\ &= ES_L \left(1 + \frac{f_c}{COP_c} - \frac{f_H}{COP_H} \right). \end{aligned} \quad (7.24)$$

It should be noted that the increased solar gain attributed to daylighting has not been included here but would reduce summer savings and increase winter savings. If it is assumed that the increased wintertime daylighting solar gain approximately offsets the reduced lighting heat gain, then the last term in Equation 7.24 becomes negligible.

7.4.3 Daylighting Design Fundamentals

As mentioned, aperture controls such as blinds and drapes are used to moderate the amount of daylight entering the space, as are the architectural features of the building itself (glazing type, area, and orientation; overhangs and wing-walls; lightshelves; etc.). Dimming controls are used to adjust the electric light level on the basis of the quantity of the daylighting. With these two types of controls (aperture and lighting), the electric lighting and cooling energy use and demand, as well as cooling system size, can be reduced. However, the determination of the daylighting position and time *illuminance* value within the space is required before energy usage and demand reduction calculations can be made.

7.4.3.1 Architectural Features

Daylighting design approaches use both solar beam radiation (*sunlight*) and the diffuse radiation scattered by the atmosphere (*skylight*) as sources for interior lighting, with historical design emphasis being on utilizing skylight. Daylighting is provided through a variety of glazing features, which can be grouped as *sidelighting* (light entering via the side of the space) and *toplighting* (light entering from the ceiling area). Figure 7.11 illustrates several architectural forms producing sidelighting and toplighting. The dashed lines represent the illuminance distribution within the space. The calculation of work-plane illuminance depends on whether sidelighting or toplighting features are used, and the combined illuminance values are additive.

7.4.3.2 Daylighting Geometry

The solar illuminance on a vertical or horizontal window depends on the position of the sun relative to that window. In the method described here, the sun and sky illuminance values are determined using the sun's altitude angle (α) and the sun–window azimuth angle difference (a_{sw}). These angles need to be determined for the particular time of day, day of year, and window placement under investigation.

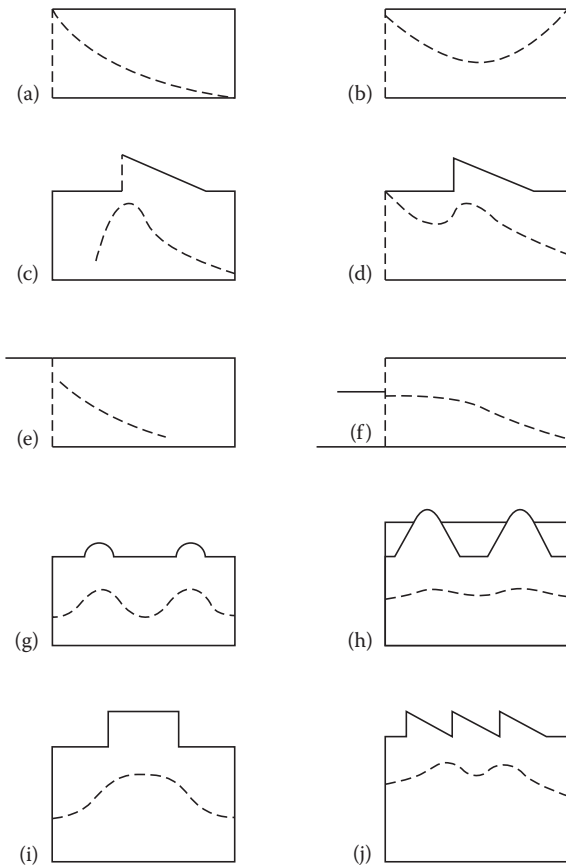
7.4.3.2.1 Solar Altitude Angle (α)

The solar altitude angle is the angle swept out by a person's arm when pointing to the horizon directly below the sun and then raising the arm to point at the sun. Equation 2.28 can be used to calculate solar altitude, α , as

$$\sin \alpha = \cos L \cos \delta_s \cos h_s + \sin L \sin \delta_s. \quad (2.28)$$

7.4.3.2.2 Sun–Window Azimuth Angle Difference (a_{sw})

The difference between the sun's azimuth and the window's azimuth needs to be calculated for vertical window illuminance. The window's azimuth

**FIGURE 7.11**

Example of sidelighting and toplighting architectural features (dashed lines represent illuminance distributions). (a) Unilateral. (b) Bilateral. (c) Clerestory. (d) Clerestory + unilateral. (e) Overhang. (f) Overhang + ground reflection. (g) Skylight. (h) Skylight + well. (i) Roof monitor. (j) Sawtooth. (Reprinted by permission from Macmillan Publishers Ltd. *Illumination Engineering—From Edison's Lamp to the Laser*, Murdoch, J.B., copyright 1985.)

angle, a_w , is determined by which way it faces, as measured from south (east of south is negative, westward is positive). The solar azimuth angle, a_s , is calculated using Equation 2.29:

$$\sin a_s = \cos \delta_s \sin h_s / \cos \alpha. \quad (2.29)$$

The sun–window azimuth angle difference, a_{sw} , is given by the absolute value of the difference between a_s and a_w :

$$a_{sw} = |a_s - a_w|. \quad (7.25)$$

7.4.4 Design Methods

To determine the annual lighting energy saved (ES_L), for the space under investigation, calculations using the lumen method described in the following should be performed on a monthly basis for both clear and overcast days. Monthly weather data for the site would then be used to prorate clear and overcast lighting energy demands each month. Subtracting the calculated daylighting illuminance from the design illuminance leaves the supplementary lighting needed, which determines the lighting energy required.

The approach in the following method is to calculate the sidelighting and the skylighting of the space separately and then combine the results. This procedure has been computerized and includes many details of controls, daylighting methods, weather, and heating and cooling load calculations. ASHRAE (2013) lists many of the methods and simulation techniques currently used with daylighting and its associated energy effects.

7.4.5 Lumen Method of Sidelighting (Vertical Windows)

The lumen method of sidelighting calculates interior horizontal illuminance at three points, as shown in Figure 7.12, at the 30-in. (0.76-m) work plane on the room-and-window centerline. A vertical window is assumed to extend from 36 in. (0.91-m) above the floor to the ceiling. The method accounts for both direct and ground-reflected sunlight and skylight; thus, both horizontal and vertical illuminances from sun and sky are needed. The steps in the lumen method of sidelighting are presented next.

The incident direct and ground-reflected window illuminances are normally calculated for both a cloudy and a clear day for representative days during the year (various months), as well as for clear or cloudy times during a given day.

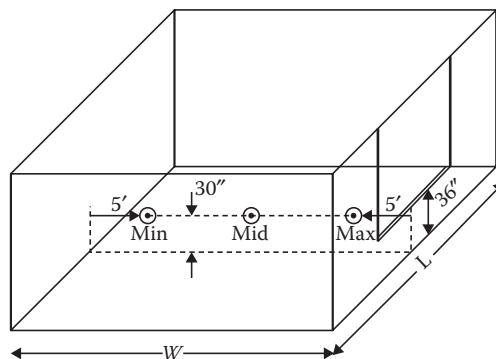


FIGURE 7.12

Location of illumination points within the room (along centerline of window) determined by the lumen method of sidelighting.

Thus, the interior illumination owing to sidelighting and skylighting can then be examined for effectiveness throughout the year.

Step 1: Incident direct sky and sun illuminances. The solar altitude and sun–window azimuth angle difference are calculated for the desired latitude, date, and time using Equations 2.28 and 7.25, respectively. Using these two angles, the total illuminance on the window (E_{sw}) can be determined by summing the direct sun illuminance (E_{uw}) and the direct sky illuminance (E_{kw}), each determined from the appropriate graph in Figure 7.13.

Step 2: Incident ground-reflected illuminance. The sun illuminance on the ground (E_{ug}) plus the overcast or clear sky illuminance (E_{kg}) on the ground make up the total horizontal illuminance on the ground surface (E_{sg}). A fraction of the ground surface illuminance is then considered diffusely reflected onto the vertical window surface (E_{gw}), where “gw” indicates from the ground to the window.

The horizontal ground illuminances can be determined using Figure 7.14, where the clear sky plus sun case and the overcast sky case are functions of solar altitude. The fractions of the ground illuminance diffusely reflected onto the window depend on the reflectivity (ρ) of the ground surface (see Table 7.2) and the window-to-ground surface geometry.

If the ground surface is considered uniformly reflective from the window outward to the horizon, then the illuminance on the window from ground reflection is

$$E_{gw} = \frac{\rho E_{sg}}{2}. \quad (7.26)$$

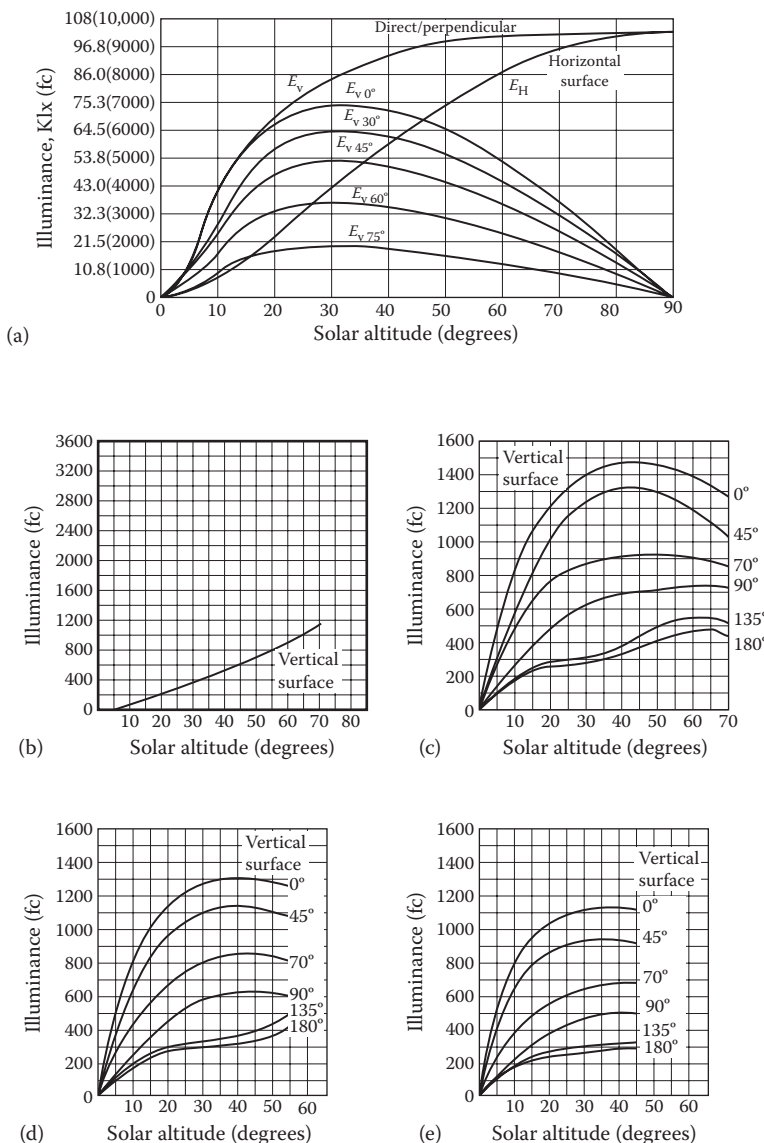
A more complicated ground-reflection case is illustrated in Figure 7.15, with multiple strips of differently reflecting ground being handled using the angles to the window, where a strip’s illuminance on a window is calculated:

$$E_{gw(\text{strip})} = \frac{\rho_{\text{strip}} E_{sg}}{2} (\cos \theta_1 - \cos \theta_2). \quad (7.27)$$

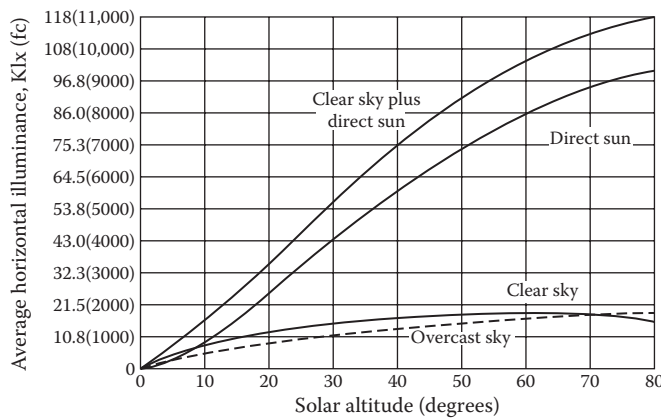
And the total reflected onto the window is the sum of the strip illuminances:

$$E_{gw} = \frac{E_{sg}}{2} [\rho_1(\cos \theta_0 - \cos \theta_1) + \rho_2(\cos \theta_1 - \cos \theta_2) + \dots + \rho_n(\cos \theta_{n-1} - \cos 90)]. \quad (7.28)$$

Step 3: Luminous flux entering space. The direct sky–sun and ground-reflected luminous fluxes entering the building are attenuated by the transmissivity of the window. Table 7.3 presents the transmittance fraction (τ) of several window glasses. The fluxes entering the space are calculated from

**FIGURE 7.13**

Vertical illuminance from (a) direct sunlight. (b) Overcast skylight. (c) Clear summer skylight. (d) Clear autumn/spring skylight. (e) Clear winter skylight, for various sun–window azimuth angle differences. (From IES, *Lighting Handbook, Applications Volume*, Illumination Engineering Society, New York, 1979.)

**FIGURE 7.14**

Horizontal illuminance for overcast sky, clear sky, direct sun, and clear sky plus direct sun. (Reprinted by permission from Macmillan Publishers Ltd. *Illumination Engineering—From Edison's Lamp to the Laser*, Murdoch, J.B., copyright 1985.)

the total sun-sky and the ground-reflected illuminances by using the area of the glass, A_w :

$$\begin{aligned}\phi_{sw} &= E_{sw} \tau A_w \\ \phi_{gw} &= E_{gw} \tau A_w.\end{aligned}\tag{7.29}$$

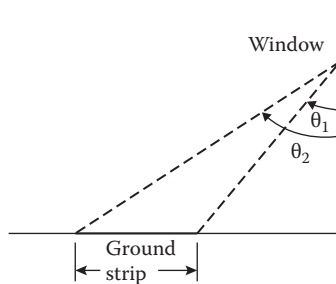
Step 4: Light loss factor. The light loss factor (K_m) accounts for the attenuation of luminous flux owing to dirt on the window (window dirt depreciation [WDD])

TABLE 7.2

Ground Reflectivities

Material	ρ (%)
Cement	27
Concrete	20–40
Asphalt	7–4
Earth	10
Grass	6–20
Vegetation	25
Snow	70
Red brick	30
Gravel	15
White paint	55–75

Source: Reprinted by permission from Macmillan Publishers Ltd. *Illumination Engineering—From Edison's Lamp to the Laser*, Murdoch, J.B., copyright 1985.

**FIGURE 7.15**

Geometry for ground strips. (Reprinted by permission from Macmillan Publishers Ltd. *Illumination Engineering—From Edison's Lamp to the Laser*, Murdoch, J.B., copyright 1985.)

TABLE 7.3

Glass Transmittances

Glass	Thickness (in.)	τ (%)
Clear	$\frac{1}{8}$	89
Clear	$\frac{3}{16}$	88
Clear	$\frac{1}{4}$	87
Clear	$\frac{5}{16}$	86
Gray	$\frac{1}{8}$	61
Gray	$\frac{3}{16}$	51
Gray	$\frac{1}{4}$	44
Gray	$\frac{5}{16}$	35
Bronze	$\frac{1}{8}$	68
Bronze	$\frac{3}{16}$	59
Bronze	$\frac{1}{4}$	52
Bronze	$\frac{5}{16}$	44
Thermopane	$\frac{1}{8}$	80
Thermopane	$\frac{3}{16}$	79
Thermopane	$\frac{1}{4}$	77

Source: Reprinted by permission from Macmillan Publishers Ltd. *Illumination Engineering—From Edison's Lamp to the Laser*, Murdoch, J.B., copyright 1985.

and on the room surfaces (room surface dirt depreciation [RSDD]). WDD depends on how often the window is cleaned, but a 6-month average for offices is 0.83 and that for factories is 0.71.

The RSDD is a more complex calculation involving time between cleanings, the direct–indirect flux distribution, and room proportions. However, for rooms cleaned regularly, RSDD is around 0.94, and for once-a-year-cleaned dirty rooms, the RSDD would be around 0.84.

The light loss factor is the product of the preceding two fractions:

$$K_m = (\text{WDD})(\text{RSDD}). \quad (7.30)$$

Step 5: Work-plane illuminances. As discussed earlier, Figure 7.12 illustrates the location of the work-plane illuminances determined with this lumen method of sidelighting. The three illuminances (max, mid, min) are determined using two coefficients of utilization, the C factor and the K factor. The C factor depends on room length, width, and wall reflectance. The K factor depends on ceiling–floor height, room width, and wall reflectance. Table 7.4 presents C and K values for the three cases of incoming fluxes: (a) sun plus clear sky, (b) overcast sky, and (c) ground reflected. Assumed ceiling and floor reflectances are given for this last case with no window controls (shades, blinds, overhangs, etc.). These further window control complexities can be found in IES (Illumination Engineering Society) (1987), LOF (Libbey–Owens–Ford Co.) (1976), and others. A reflectance of 70% represents light-colored walls, with 30% representing darker walls.

The work-plane max, mid, and min illuminance are each calculated by adding the sun–sky and ground-reflected illuminances, which are given by

$$\begin{aligned} E_{sp} &= \phi_{sw} C_s K_s K_m \\ E_{gp} &= \phi_{gw} C_g K_g K_m, \end{aligned} \quad (7.31)$$

where “sp” and “gp” refer to the sky-to-work-plane and ground-to-work-plane illuminances.

7.4.6 Lumen Method of Skylighting

The lumen method of skylighting calculates the average illuminance at the interior work plane provided by horizontal skylights mounted on the roof. The procedure for skylighting is generally the same as that described above for sidelighting. As with windows, the illuminance from both overcast sky and clear sky plus sun cases are determined for specific days in different seasons and for different times of the day, and a judgment is then made as to the number and size of skylights and any controls needed.

TABLE 7.4
 C and K Factors for No Window Controls for (a) Overcast Sky, (b) Clear Sky, and (c) Ground Illumination (Ceiling Reflectance, 80%;
 Floor Reflectance, 20%)

C: Coefficient of Utilization						K: Coefficient of Utilization							
Room Length	20 ft		30 ft		40 ft		Ceiling Height	8 ft		10 ft		12 ft	14 ft
	Wall Reflectance	70%	30%	70%	30%	70%		Wall Reflectance	70%	30%	70%	30%	
Room Width (ft)							Room Width (ft)						
<i>(a) Illumination by Overcast Sky</i>													
Max	20	0.0276	0.0251	0.0191	0.0173	0.0143	0.0137	Max	20	0.125	0.129	0.121	0.123
	30	0.0272	0.0248	0.0188	0.0172	0.0137	0.0131		30	0.122	0.131	0.122	0.121
	40	0.269	0.246	0.0182	0.0171	0.0133	0.0130		40	0.145	0.133	0.131	0.126
Mid	20	0.0159	0.0177	0.0101	0.0087	0.0081	0.0071	Mid	20	0.0908	0.0982	0.107	0.115
	30	0.0058	0.0050	0.0054	0.0040	0.0034	0.0033		30	0.156	0.102	0.0939	0.113
	40	0.0039	0.0027	0.0030	0.0023	0.0022	0.0019		40	0.106	0.0948	0.123	0.107
Min	20	0.0087	0.0053	0.0033	0.0043	0.0050	0.0037	Min	20	0.0908	0.102	0.0951	0.114
	30	0.0032	0.0019	0.0029	0.0017	0.0020	0.0014		30	0.0924	0.119	0.101	0.114
	40	0.0019	0.0009	0.0016	0.0009	0.0012	0.0008		40	0.111	0.0926	0.125	0.109
<i>(b) Illumination by Clear Sky</i>													
Max	20	0.0206	0.0173	0.0143	0.0123	0.0110	0.0098	Max	20	0.145	0.155	0.129	0.132
	30	0.0203	0.0173	0.0137	0.0120	0.0098	0.0092		30	0.141	0.149	0.125	0.130
	40	0.0200	0.0168	0.0131	0.0119	0.0096	0.0091		40	0.157	0.157	0.135	0.134

(Continued)

TABLE 7.4 (CONTINUED)

C and K Factors for No Window Controls for (a) Overcast Sky, (b) Clear Sky, and (c) Ground Illumination (Ceiling Reflectance, 80%; Floor Reflectance, 20%)

C: Coefficient of Utilization							K: Coefficient of Utilization																		
Room Length	20 ft			30 ft			40 ft			Ceiling Height			8 ft			10 ft			12 ft			14 ft			
	Wall Reflectance	70%			70%			70%			Wall Reflectance			70%			70%			70%			70%		
		Room Width (ft)	Room Width (ft)	Room Width (ft)	Room Width (ft)	Room Width (ft)	Room Width (ft)	Room Width (ft)	Room Width (ft)	Room Width (ft)	Room Width (ft)	Room Width (ft)	Room Width (ft)	Room Width (ft)	Room Width (ft)	Room Width (ft)	Room Width (ft)	Room Width (ft)	Room Width (ft)						
<i>(b) Illumination by Clear Sky</i>																									
Mid	20	0.0153	0.0104	0.0100	0.0079	0.0083	0.0067	Mid	20	0.110	0.128	0.116	0.126	0.111	0.111	0.103	0.108	0.111	0.111	0.111	0.111	0.111	0.111		
	30	0.0082	0.0054	0.0062	0.0043	0.0046	0.0037		30	0.106	0.125	0.110	0.129	0.111	0.111	0.112	0.120	0.111	0.111	0.111	0.111	0.111	0.111		
	40	0.0052	0.0032	0.0040	0.0028	0.0029	0.0023		40	0.117	0.118	0.122	0.118	0.111	0.111	0.123	0.122	0.111	0.111	0.111	0.111	0.111	0.116		
Min	20	0.0106	0.060	0.0079	0.0049	0.0067	0.0043	Min	20	0.105	0.129	0.112	0.130	0.111	0.111	0.111	0.116	0.111	0.111	0.111	0.111	0.111	0.116		
	30	0.0054	0.0028	0.0047	0.0023	0.0032	0.0021		30	0.0994	0.144	0.107	0.126	0.111	0.111	0.107	0.124	0.111	0.111	0.111	0.111	0.111	0.118		
	40	0.0031	0.0014	0.0027	0.0013	0.0021	0.0012		40	0.119	0.116	0.130	0.118	0.111	0.111	0.120	0.118	0.111	0.111	0.111	0.111	0.111	0.118		
<i>(c) Ground Illumination (Ceiling Reflectance, 80%; Floor Reflectance, 20%)</i>																									
Max	20	0.0147	0.0112	0.0102	0.0088	0.0081	0.0071	Max	20	0.124	0.206	0.140	0.135	0.111	0.111	0.0909	0.0859	0.111	0.111	0.111	0.111	0.111	0.111		
	30	0.0141	0.0012	0.0098	0.0088	0.0077	0.0070		30	0.182	0.188	0.140	0.143	0.111	0.111	0.0918	0.0878	0.111	0.111	0.111	0.111	0.111	0.111		
	40	0.0137	0.0112	0.0093	0.0086	0.0072	0.0069		40	0.124	0.182	0.140	0.142	0.111	0.111	0.0936	0.0879	0.111	0.111	0.111	0.111	0.111	0.111		
Mid	20	0.0128	0.0090	0.0094	0.0071	0.0073	0.0060	Mid	20	0.123	0.145	0.122	0.129	0.111	0.111	0.100	0.0945	0.111	0.111	0.111	0.111	0.111	0.105		
	30	0.0083	0.0057	0.0062	0.0048	0.0050	0.0041		30	0.0966	0.104	0.107	0.112	0.111	0.111	0.110	0.105	0.111	0.111	0.111	0.111	0.111	0.105		
	40	0.0055	0.0037	0.0044	0.0033	0.0042	0.0026		40	0.0790	0.0786	0.0999	0.106	0.111	0.111	0.118	0.118	0.111	0.111	0.111	0.111	0.111	0.118		
Min	20	0.0106	0.0071	0.0082	0.0054	0.0067	0.0044	Min	20	0.0994	0.108	0.110	0.114	0.111	0.111	0.107	0.104	0.111	0.111	0.111	0.111	0.111	0.116		
	30	0.0051	0.0026	0.0041	0.0023	0.0033	0.0021		30	0.0816	0.0822	0.0984	0.105	0.111	0.111	0.121	0.116	0.111	0.111	0.111	0.111	0.111	0.132		
	40	0.0029	0.0018	0.0026	0.0012	0.0022	0.0011		40	0.0700	0.0656	0.0946	0.0986	0.111	0.111	0.125	0.132	0.111	0.111	0.111	0.111	0.111	0.118		

Source: IES, *Lighting Handbook, Applications Volume*, Illumination Engineering Society, New York, 1987.

The procedure is presented in four steps: (1) finding the horizontal illuminance on the outside of the skylight, (2) calculating the effective transmittance through the skylight and its well, (3) figuring the interior space light loss factor and the utilization coefficient, and, finally, (4) calculating illuminance on the work plane.

Step 1: Horizontal sky and sun illuminances. The horizontal illuminance value for an overcast sky or a clear sky plus sun situation can be determined from Figure 7.14 knowing only the solar altitude (see Equation 2.28).

Step 2: Net skylight transmittance. The transmittance of the skylight is determined by the transmittance of the skylight cover(s), the reflective efficiency of the skylight well, the net-to-gross skylight area, and the transmittance of any light-control devices (lenses, louvers, etc.).

The transmittance for several flat-sheet plastic materials used in skylight domes is presented in Table 7.5. To get the effective dome transmittance (T_D) from the flat-plate transmittance (T_F) value (AAMA [Architectural Aluminum Manufacturers Association] 1977), use

$$T_D = 1.25T_F(1.18 - 0.416T_F). \quad (7.32)$$

If a double-domed skylight is used, then the single-dome transmittances are combined as follows (Pierson 1962):

$$T_D = \frac{T_{D_1}T_{D_2}}{T_{D_1} + T_{D_2} - T_{D_1}T_{D_2}}. \quad (7.33)$$

TABLE 7.5

Flat-Plate Plastic Material Transmittance for Skylights

Type	Thickness (in.)	Transmittance (%)
Transparent	$\frac{1}{8} - \frac{3}{16}$	92
Dense translucent	$\frac{1}{8}$	32
Dense translucent	$\frac{3}{16}$	24
Medium translucent	$\frac{1}{8}$	56
Medium translucent	$\frac{3}{16}$	52
Light translucent	$\frac{1}{8}$	72
Light translucent	$\frac{3}{16}$	68

Source: Reprinted by permission from Macmillan Publishers Ltd. *Illumination Engineering—From Edison's Lamp to the Laser*, Murdoch, J.B., copyright 1985.

If the diffuse and direct transmittances for solar radiation are available for the skylight glazing material, it is possible to follow this procedure and determine diffuse and direct dome transmittances separately. However, this difference is usually not a significant factor in the overall calculations.

The efficiency of the skylight well (N_w) is the fraction of the luminous flux from the dome that enters the room from the well. The well index (WI) is a geometric index (height, h ; length, l ; width, w) given by

$$\text{WI} = \frac{h(w+l)}{2wl}, \quad (7.34)$$

and WI is used with the well-wall reflectance value in Figure 7.16 to determine well efficiency, N_w .

With T_D and N_w determined, the net skylight transmittance for the skylight and well is given by

$$T_n = T_D N_w R_A T_C, \quad (7.35)$$

where R_A is the ratio of net to gross skylight areas and T_C is the transmittance of any light-controlling devices.

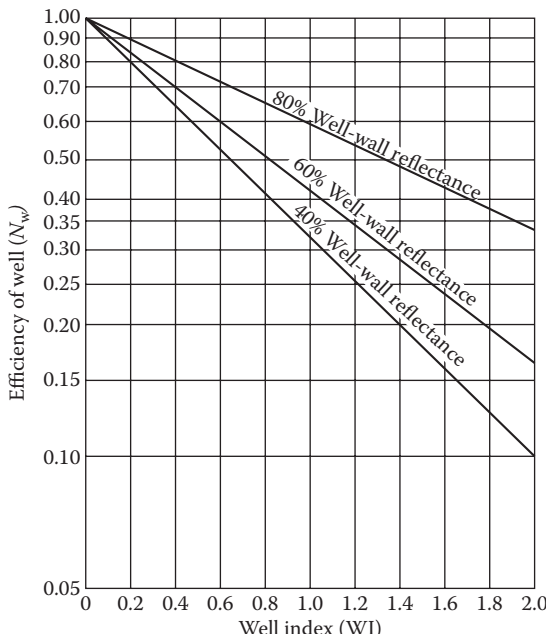


FIGURE 7.16

Efficiency of well versus well index. (From IES, *Lighting Handbook, Applications Volume*, Illumination Engineering Society, New York, 1987.)

Step 3: Light loss factor and utilization coefficient. The light loss factor (K_m) is again defined as the product of the RSDD and the skylight direct depreciation (SDD) fractions, similar to Equation 7.30. Following the reasoning for the sidelighting case, the RSDD value for clean rooms is around 0.94 and that for dirty rooms is 0.84. Without specific data indicating otherwise, the SDD fraction is often taken as 0.75 for office buildings and 0.65 for industrial areas.

The fraction of the luminous flux on the skylight that reaches the work plane (K_u) is the product of the net transmittance (T_n) and the room coefficient of utilization (RCU). Dietz et al. (1981) developed RCU equations for office and warehouse interiors with ceiling, wall, and floor reflectances of 75%, 50%, and 30%, and 50%, 30%, and 20%, respectively.

$$\text{RCU} = \frac{1}{1 + A(\text{RCR})^B}, \quad \text{if } \text{RCR} < 8, \quad (7.36)$$

where

$$A = 0.0288 \text{ and } B = 1.560 \text{ (offices)}$$

$$A = 0.0995 \text{ and } B = 1.087 \text{ (warehouses)}$$

and room cavity ratio (RCR) is given by

$$\text{RCR} = \frac{5h_c(l+w)}{lw}, \quad (7.37)$$

with h_c being the ceiling height above the work plane and l and w being room length and width, respectively.

The RCU is then multiplied by the previously determined T_n to give the fraction of the external luminous flux passing through the skylight and incident on the workplace:

$$K_u = T_n(\text{RCU}). \quad (7.38)$$

Step 4: Work-plane illuminance. The illuminance at the work plane (E_{TWP}) is given by

$$E_{\text{TWP}} = E_H \frac{A_T}{A_{\text{wp}}} K_u K_m, \quad (7.39)$$

where E_H is the horizontal overcast or clear sky plus sun illuminance from Step 1, A_T is total gross area of the skylights (number of skylights times

skylight gross area), and A_{WP} is the work-plane area (generally room length times width).

Note that in Equation 7.39, it is also possible to fix the E_{TWP} at some desired value and determine the skylight area required.

Rules of thumb for skylight placement for uniform illumination include 4%–8% of roof area and spacing less than 1 1/2 times ceiling-to-work-plane distance between skylights.

Example 7.6

Determine the work-plane clear sky plus sun illuminance for a 30' × 30' × 10' office with 75% ceiling, 50% wall, and 30% floor reflectance with four 4' × 4' double-domed skylights at 2 p.m. on January 15 at 32° latitude. The skylight well is 1' deep with 60% reflectance walls, and the outer and inner dome flat-plastic transmittances are 0.85 and 0.45, respectively. The net skylight area is 90%.

Solution

Follow the four steps in the lumen method for skylighting.

Step 1: Use Figure 7.14 with the solar altitude of 41.7° (calculated from Equation 2.28) for the clear sky plus sun curve to get horizontal illuminance:

$$E_H = 7400 \text{ fc.}$$

Step 2: Use Equation 7.32 to get domed transmittances from the flat-plate plastic transmittances given,

$$T_{D_1} = 1.25(0.85)[1.18 - 0.416(0.85)] = 0.89$$

$$T_{D_2} (T_F = 0.45) = 0.56,$$

and Equation 7.33 to get total dome transmittance from the individual dome transmittances:

$$T_D = \frac{(0.89)(0.56)}{(0.89) + (0.56) - (0.89)(0.56)} = 0.52.$$

To get well efficiency, use $WI = 0.25$ from Equation 7.34 with 60% wall reflectance in Figure 7.16 to give $N_w = 0.80$. With $R_A = 0.90$, use Equation 7.35 to calculate net transmittance:

$$T_n = (0.52)(0.80)(0.90)(1.0) = 0.37.$$

Step 3: The light loss factor is assumed to be from typical values: $K_m = (0.75)(0.94) = 0.70$. The room utilization coefficient is determined using Equations 7.36 and 7.37:

$$\text{RCR} = \frac{5(7.5)(30 + 30)}{(30)(30)} = 2.5$$

$$\text{RCU} = [1 + 0.0288(2.5)^{1.560}]^{-1} = 0.89$$

and Equation 7.38 yields $K_u = (0.37)(0.89) = 0.33$.

Step 4: The work-plane illuminance is calculated by substituting the above values into Equation 7.39:

$$E_{\text{TWP}} = 7400 \frac{4(16)2}{30(30)} 0.33(0.70) = 122 \text{ fc.}$$

7.5 Further Information

7.5.1 General Background Information

The most complete basic reference for passive system heating design is still the 1980 Los Alamos Lab's *Passive Solar Design Handbook*, all three parts of it. The *ASHRAE Handbook of Fundamentals* is a good general introduction to passive cooling techniques and calculations, with an emphasis on evaporative cooling. *Passive Solar Buildings* and *Passive Cooling*, both published by MIT Press, contain a large variety of techniques and details concerning passive system designs and economics. All the major building energy simulation codes (DOE-2, EnergyPlus, TRNSYS, TSB13, etc.) now include passive heating and cooling technologies.

The Illumination Engineering Society's *Lighting Handbook* presents the basis for and details of daylighting and artificial lighting design techniques. However, most texts on illumination present simplified format daylighting procedures. Currently used daylighting computer programs include various versions of *Lumen Micro*, *Lightscape*, and *Radiance*.

Solar Today magazine, published by the American Solar Energy Society (ASES), is a readily available source for current practice designs and economics, as well as a source for passive system equipment suppliers.

7.5.2 Technical Publication Information

Many of the current and archival passive solar technical papers are found from the conference proceedings and journals associated with the International Solar Energy Society, its affiliated ASES, the American Society of Mechanical Engineering, and ASHRAE. Also, many of the early passive solar practitioners

were architects and builders who published in their specific industry trade journals, as is still the case today. As an Internet search for passive solar articles today will reveal, there are several “new” energy/solar/sustainable technical journals that publish passive solar-related articles.

PROBLEMS

1. Explain how window placement in a building could be defined as (a) a passive solar feature, (b) an energy conservation technique, and (c) both of the above.
2. Write an equation for calculating the cost of savings life-cycle economics of a proposed passive solar system. Explain why it is important to be able to determine the auxiliary energy required for any given passive (or active) system design.
3. Referring to the thermal circuit diagram of Figure 7.4 for the thermal storage (Trombe) wall building, construct appropriate thermal circuits for (a) attached sunspace, (b) thermal storage, and (c) direct gain buildings.
4. Using rules of thumb for a 200-m² floor area Denver residence, determine (a) the auxiliary heating energy required, (b) the solar projected area, and (c) the concrete storage mass needed for a maximum 10°C daily temperature swing.
5. A 2000-ft² house in Boston is being designed with NLC = 12,000 Btu/F-day and 150 ft² of direct gain. The direct gain system includes double glazing, nighttime insulation, and 30 Btu/ft²°F thermal storage capacity. Using the LCR method, determine (a) the annual auxiliary heating energy needed by this design and (b) the storage mass and dimensions required.
6. Compare the annual SSF for 150 ft² of the following passive systems for the house in Problem 5: (a) direct gain (DGA3), (b) vented Trombe wall (TWD4), (c) unvented Trombe wall (TW14), (d) water wall (WWB4), and (e) sunspace (SSB4).
7. A design modification to the house in Problem 5 is desired. A 200-ft², vented, 12"-thick Trombe wall is to be added to the direct gain system. Assuming the same types of glazing and storage as described above, determine (a) the annual heating auxiliary energy needed and (b) the Trombe wall mass.
8. Using the SLR method, calculate the auxiliary energy required in March for a 2000-ft², NLC 12,000 Btu/F-day house in Boston with a 150-ft², night-insulated double-glazed direct gain system with 6-in.-thick storage floors of 45 Btu/ft²°F capacity.
9. Calculate the heating season auxiliary energy required for the Boston house in Problem 8.

10. Determine the length of the overhang needed to shade a south-facing 2-m-high window in Dallas, Texas (latitude $32^{\circ}51'$), to allow for both winter heating and summer shading.
11. A 10-mph wind is blowing directly into an open $3\text{ ft} \times 5\text{ ft}$ window, which is mounted in a room's 8-ft-high by 12-ft-wide wall. If the wind's temperature is 80°F , are the room's occupants thermally comfortable?
12. Design a stack-effect/solar chimney (vented Trombe wall) to produce an average velocity of 0.3 m/s within a 4-m-wide by 5-m-long by 3-m-high room. Justify your assumptions.
13. Estimate the overnight radiant cooling possible from an open, 30°C , 8-m-diameter water tank during July in Chicago. What would you expect for convective and evaporative cooling values?
14. Calculate the overnight cooling possible by radiation for a 10-m^2 water thermal storage roof with water as the storage medium, when the ambient air temperature decreases linearly from 20°C to 15°C during the first 5 h and then increases to 20°C in the next 5 h. The equivalent sky temperature is given by the following equation: Equivalent sky temperature, $T_{\text{sky}}(\text{K}) = T_{\text{air}}(\text{K}) \times e_{\text{sky}}^{0.25}$, where e_{sky} is the sky emissivity, given as $e_{\text{sky}} = 0.741 + 0.0062 \times (T_{\text{air}}(\text{C}) - 10)$.
Assume the initial temperature of storage water as 25°C and emissivity of the storage as 0.9.
15. For the buried pipe example (7.4) in Chapter 7, determine which of the three flow rate cases leads to the least expensive installation.
16. Using data from Figure 79, design a 9-ft-deep ground-pipe system for Dallas in June to deliver 1000 cfm at 75°F when the outside air temperature is 90°F .
17. A $30\text{ ft} \times 20\text{ ft}$ office space has a photosensor dimmer control working with installed lighting of 2 W/ft^2 . The required workplace illuminance is 60 fc and the available daylighting is calculated as 40 fc on the summer peak afternoon. Determine the payback period for the dimmer control system assuming the following: 1-1/2 ton cooling installed for 600 ft^2 at $\$2200/\text{ton}$, lighting control system cost at $\$/\text{ft}^2$, 30% reduction in annual lighting owing to daylighting, $\$0.10/\text{kWh}$ electricity cost, and cooling for 6 months at a $\text{COP}_c = 2.5$.
18. Determine the illuminances (sun, sky, and ground-reflected) on a vertical, south-facing window at solar noon at 36°N latitude on June 21 and December 21 for (a) a clear day and (b) an overcast day.
19. Determine the sidelighting workplace illuminances for a 20-ft-long, 15-ft-wide (deep), 8-ft-high light-colored room with a 15-ft-long by 5-ft-high window. Assume the direct sun plus clear sky illuminance is 3000 fc and the ground-reflected illuminance is 200 fc.
20. Determine the clear sky day and the cloudy day work-plane illuminances for a 30-ft-long, 30-ft-wide, 10-ft-high light-colored room. A

20-ft-long by 7-ft-high window with 1/4-in clear glass faces 10°E of south, the building is at 32°N latitude, and it is January 15 at 2 p.m. solar. The ground outside is covered by dead grass!

21. Determine the clear day and cloudy day illuminances on a horizontal skylight at noon on June 21 and December 21 in (a) Miami, (b) Los Angeles, (c) Denver, (d) Boston, and (e) Seattle.
 22. A 3 ft × 5 ft double-domed skylight has outer and inner flat-plate plastic transmittances of 0.8 and 0.7, respectively; a 2-ft-deep well with 80% reflectance walls; and a 90% net skylight area. Calculate the net transmittance of the skylight.
 23. Determine the number and roof placement of 10 ft × 4 ft skylights needed for a 50 ft × 50 ft × 10 ft high office when the horizontal illuminance is 6000 fc, the skylight has 45% net transmittance, and the required workplace illuminance is 100 fc.
 24. What would be the procedure for producing uniform workplace illumination when both sidelighting and skylighting are used simultaneously?
-

References

- AAMA. 1977. *Voluntary Standard Procedure for Calculating Skylight Annual Energy Balance*. Architectural Aluminum Manufacturers Association Publication 1602.1.1977, Chicago, IL.
- ASES. 1992. *Economics of Solar Energy Technologies*, R. Larson, F. Vignola, and R. West, eds. American Solar Energy Society.
- ASHRAE Handbook. 2011. *Heating, Ventilating, and Air-Conditioning Applications*. American Society of Heating, Refrigerating and Air-Conditioning Engineers, Atlanta, GA.
- ASHRAE Handbook. 2013. *Fundamentals*. American Society of Heating, Refrigerating and Air-Conditioning Engineers, Atlanta, GA.
- Close, D.J., R.V. Dunkle, and K.A. Robeson. 1968. Design and performance of a thermal storage air conditioning system. *Mech. Chem. Eng. Trans., Institute Eng. Australia* MC4: 45.
- Dietz, P. et al. 1981. A skylight energy balance analysis procedure. *J. Illum. Eng. Soc.* 11(1): 27–34.
- Duffie, J.A., and W.A. Beckman. 1991. *Solar Engineering of Thermal Processes*, 2nd ed. John Wiley and Sons, New York.
- Goswami, D.Y., and K.M. Biseli. 1994. Use of underground air tunnels for heating and cooling agricultural and residential buildings. Report EES-78. Florida Energy Extension Service, University of Florida, Gainesville, FL.
- Goswami, D.Y., and A.S. Dhaliwal. 1985. Heat transfer analysis in environmental control using and underground air tunnel. *J. Sol. Energy Eng.* 107: 141–145.

- Goswami, D.Y., and S. Ileslamlou. 1990. Performance analysis of a closed-loop climate control system using underground air tunnel. *J. Sol. Energy Eng.* 112: 76–81.
- Haggard, K., D. Bainbridge, and R. Aljilani. 2010. *Passive Solar Architecture Pocket Reference*, D.Y. Goswami, ed. International Solar Energy Society, Freiburg, Germany.
- Halacy, D.S. 1984. *Home Energy*. Rodale Press, Inc. Emmaus, PA.
- Hay, H., and J. Yellott. 1969. Natural air conditioning with roof ponds and movable insulation. *ASHRAE Trans.* 75(1): 165–177.
- IES. 1979. *Lighting Handbook, Applications Volume*. Illumination Engineering Society, New York.
- IES. 1987. *Lighting Handbook, Applications Volume*. Illumination Engineering Society, New York.
- Krarti, M., and J.F. Kreider. 1996. Analytical model for heat transfer in an underground air tunnel. *Energy Convers. Mgmt.* 37(10): 1561–1574.
- Labs, K. 1981. Regional analysis of ground and above ground climate. Report ORNAL/Sub-81/40451/1. Oak Ridge National Laboratory, Oak Ridge, TN.
- LOF. 1976. *How to Predict Interior Daylight Illumination*. Libbey–Owens–Ford Co., Toledo, OH.
- Marlatt, W., C. Murray, and S. Squire. 1984. Roof pond systems energy technology engineering center. Rockwell International Report No. ETEC 6.
- Martin, M., and P. Berdahl. 1984. Characteristics of infrared sky radiation in the United States. *Sol. Energy* 33(314): 321–336.
- McQuiston, P.C., and J.D. Parker. 1994. *Heating, Ventilating, and Air Conditioning*, 4th ed. Wiley, New York.
- Murdoch, J.B. 1985. *Illumination Engineering—From Edison's Lamp to the Laser*. Macmillan Publishing, New York.
- Pierson, O. 1962. *Acrylics for the Architectural Control of Solar Energy*. Rohm and Haas, Philadelphia, PA.
- PSDH. 1980. *Passive Solar Design Handbook, Volume One: Passive Solar Design Concepts*, DOE/CS-0127/1, March; *Volume Two: Passive Solar Design Analysis*, DOE/CS-0127/2, January. U.S. Department of Energy, Washington, DC.
- PSDH. 1984. *Passive Solar Design Handbook*. Van Nostrand Reinhold Co., New York.
- Robbins, C.L. 1986. *Daylighting: Design and Analysis*. Van Nostrand, New York.
- Rundquist, R.A. 1991. Daylighting controls: Orphan of HVAC design. *ASHRAE J.* 11: 30–34.
- USDA. 1960. *Power to Produce, 1960 Yearbook of Agriculture*. U.S. Department of Agriculture, Washington, DC.

Suggested Readings

- Kreith, F., and R. West. 2007. *CRC Handbook of Energy Efficiency and Renewable Energy*. CRC Press, Boca Raton, FL.
- Kusuda, T., and P.R. Achenbach. 1965. Earth temperature and thermal diffusivity at selected stations in the United States. *ASHRAE Trans.* 71(1): 965.

8

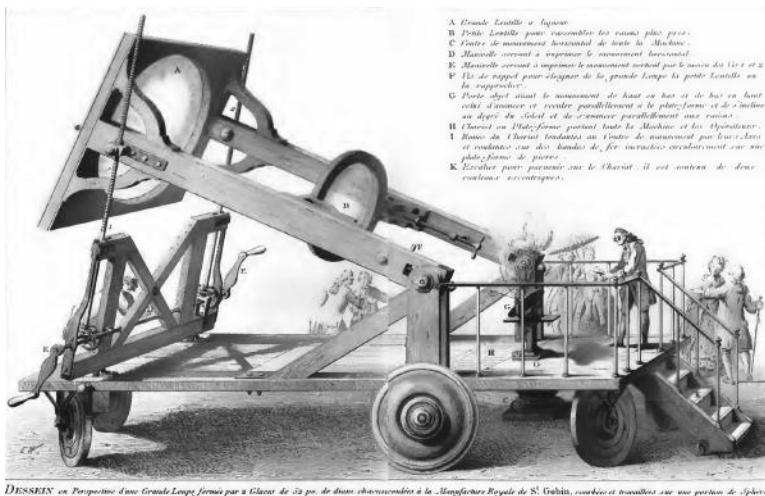
Solar Thermal Power

8.1 Historical Perspective

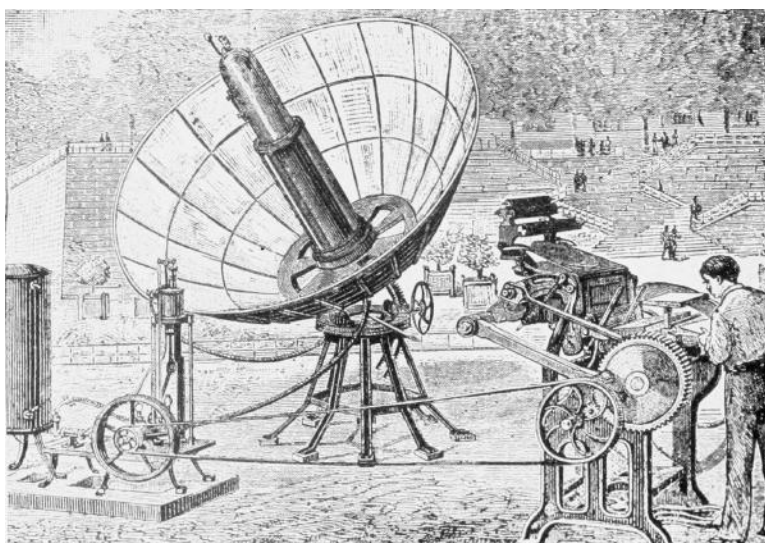
Attempts to harness the sun's energy for power production date back to at least 1774 (Trombe 1956) when the French chemist Lavoisier and the English scientist Joseph Priestley discovered oxygen and developed the theory of combustion by concentrating the rays of the sun on mercuric oxide in a test tube, collecting the gas produced with the aid of solar energy, and burning a candle in the gas. Also, during the same year, an impressive picture of Lavoisier was published in which he stands on a platform near the focus of a large glass lens and is carrying out other experiments with focused sunlight (see schematic, Figure 8.1).

A century later, in 1878, a small solar power plant was exhibited at the World's Fair in Paris (Figure 8.2). To drive this solar steam engine, sunlight was focused from a parabolic reflector onto a steam boiler located at its focus; this produced the steam that operated a small reciprocating steam engine that ran a printing press. In 1901, a 10-hp solar steam engine was operated by A.G. Eneas in Pasadena, California (Daniels 1964). It used a 700-ft² focusing collector the shape of a truncated cone as shown in Figure 8.3. Between 1907 and 1913, the American engineer F. Shuman developed solar-driven hydraulic pumps; in 1913, he built, jointly with C.V. Boys, a 50-hp solar engine for pumping irrigation water from the Nile near Cairo in Egypt (Figure 8.4). This device used long parabolic troughs that focused solar radiation onto a central pipe with a concentration ratio of 4.5:1.

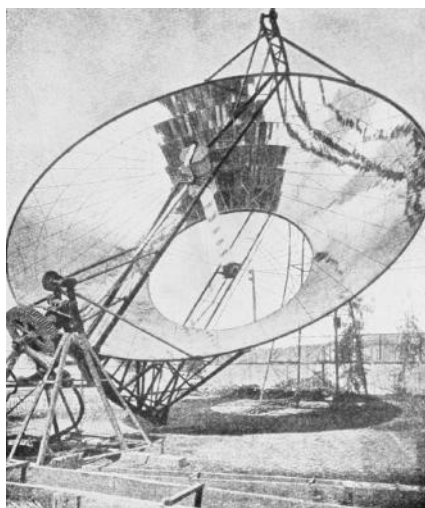
With the increasing availability of low-cost oil and natural gas, interest in solar energy for power production waned. Except for C.G. Abbott, who exhibited in 1936 a 1/2-hp solar-powered engine at an International Power Conference in Washington, D.C., and in 1938 in Florida, an improved, somewhat smaller version with a flash boiler, there was very little activity in the field of solar power between 1915 and 1950. Interest in solar power revived in 1949 when, at the centennial meeting of the American Association for the Advancement of Science in Washington, D.C., one session was devoted to future energy sources. At that time, the potentials as well as the economic problems of solar energy utilization were clearly presented by Daniels (1949).

**FIGURE 8.1**

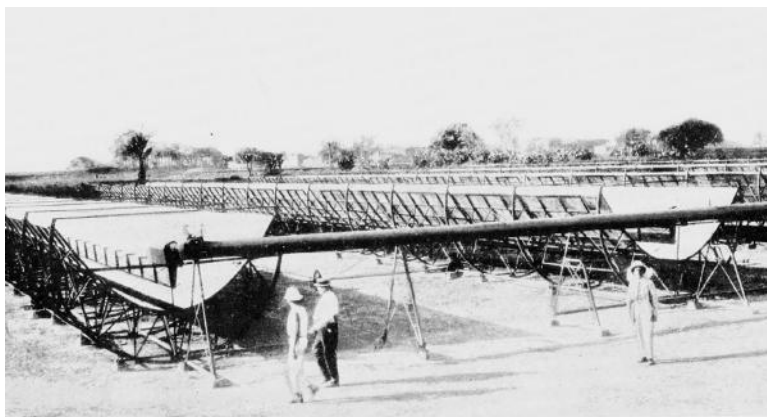
Solar furnace used by Lavoisier in 1774. (Courtesy of Bibliotheque Nationale de Paris. Lavoisier, Oeuvres, vol. 3.)

**FIGURE 8.2**

Parabolic collector powered a printing press at the 1878 Paris Exposition. (From Abbot, C.G., *The Sun and the Welfare of Man*, Washington, DC: Smithsonian Institution, 1929.)

**FIGURE 8.3**

Irrigation pumps were run by a solar-powered steam engine in Arizona in the early 1900s. The system consisted of an inverted cone that focused rays of the sun on the boiler. (From Abbot, C.G., *The Sun and the Welfare of Man*, Washington, DC: Smithsonian Institution, 1929.)

**FIGURE 8.4**

Solar irrigation pump (50 hp) operating in 1913 in Egypt. (From Abbot, C.G., *The Sun and the Welfare of Man*, Washington, DC: Smithsonian Institution, 1929.)

Some important conferences that considered solar power generation were held by UNESCO in 1954, the Association for Applied Solar Energy in 1955, the US National Academy of Sciences in 1961, and the United Nations in 1961. In addition, a research and development program supported by the National Aeronautics and Space Administration to build a solar electric power system capable of supplying electricity for the US space program was undertaken in the 1960s. However, widespread interest developed only after research funds

TABLE 8.1

Characteristics of CSP Systems

System	Peak Efficiency (%)	Annual Efficiency (%)	Annual Capacity Factor (%)
Parabolic trough/LFR	21	10–12 (d) 14–18 (p)	24 (d)
Power tower	30	14–25 (p)	25–70 (p)
Dish/engine	29	18–25 (p)	25 (p)

Source: Adapted from Romero-Alvarez, M. and E. Zarza, Concentrating solar thermal power, In *Energy Conversion*, D.Y. Goswami and F. Kreith (eds.), CRC Press, Boca Raton, FL, 2008.

Note: d, demonstrated; p, projected, based on pilot-scale testing.

became available for the development of earth-bound solar electric power and process heat after the oil embargo in 1973. Pace of development increased in the 1980s with the development of commercial parabolic trough collector (PTC)–based power plants SEGS I to SEGS IX totaling 354 MW_e capacity and the 1-MW_e Solar I central receiver tower demonstration plant in California. However, the progress stalled after that until a commercial 75-MW_e parabolic trough power plant started operating near Las Vegas, Nevada, in 2007. Since then, commercial and research activity in concentrated solar thermal power, also known as CSP, has increased tremendously in Europe, the United States, Asia, and Australia.

Currently, four different CSP technologies are in use based on the type of solar collection system: (1) PTC, (2) linear Fresnel reflector (LFR) system, (3) power tower or central receiver system (CRS), and (4) parabolic dish system. Of these, the PTC-based plants are the most in operation since 1985. The LFR system is in principle the same as the PTC except that the parabolic concentration is achieved via LFRs. CRS systems have the potential to achieve the highest efficiencies, which is why most of the present research activity in CSP is focused on CRS-based systems. Table 8.1 summarizes the characteristics of each solar technology.

8.2 Thermodynamic Power Cycles

There are two basic approaches to solar electric power generation. One is by photovoltaic process, a direct energy conversion, which is described in detail in Chapter 9. The other approach is to convert sunlight to heat at high temperatures and then heat to mechanical energy by a thermodynamic power cycle and, finally, convert the mechanical energy to electricity. This

indirect approach, called solar thermal power or CSP, is based on well-established principles of thermal power. A vast majority of electricity in the world is produced by thermal power conversion. Most of the thermal power production in the world is based on Rankine cycle and, to a smaller extent, Brayton cycle. Both of these are applicable to solar thermal power conversion, with Rankine cycle being the most popular. Normally, water is the working fluid for the Rankine cycle. However, for lower-temperature solar collection systems (70°C to approximately 300°C), organic fluids are used, in which case the cycle is commonly referred to as the organic Rankine cycle (ORC). When a Rankine cycle is operated under supercritical conditions of the working fluid, the cycle is usually referred to as the supercritical Rankine cycle (SRC). The Stirling cycle has also shown great potential, and solar thermal power systems based on this cycle are under development. More recently, researchers have been developing modifications of these cycles or entirely new cycles or combined cycles to increase the conversion efficiencies and to make them more applicable to the solar collection systems.

8.2.1 Rankine Cycle

Most of the existing thermal power plants are based on the Rankine cycle. The basic ideal Rankine cycle is shown in Figure 8.5, which also shows a temperature–entropy (T - s) diagram for steam as a working fluid. The ideal cycle consists of the following process:

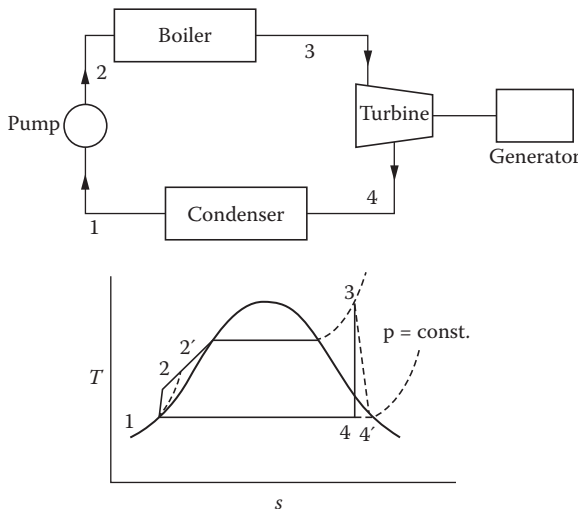


FIGURE 8.5
Basic Rankine power cycle.

Process

- 1–2 Saturated liquid from the condenser at state 1 is pumped to the boiler at state 2 isentropically.
- 2–3 Liquid is heated in the boiler at constant pressure. The temperature of the liquid rises until it becomes a saturated liquid. Further addition of heat vaporizes the liquid at constant temperature until all of the liquid turns into saturated vapor. Any additional heat superheats the working fluid to state 3.
- 3–4 Steam expands isentropically through a turbine to state 4.
- 4–1 Steam exiting the turbine is condensed at constant pressure until it returns to state 1 as saturated liquid.

In an actual Rankine cycle, the pumping and the turbine expansion processes are not ideal. The actual processes are 1–2' and 3–4', respectively. For the above cycle,

$$\text{Turbine efficiency } \eta_{\text{turbine}} = \frac{h_3 - h_4}{h_3 - h_4} \quad (8.1)$$

$$\text{Pump efficiency } \eta_{\text{pump}} = \frac{h_1 - h_2}{h_1 - h_2} \quad (8.2)$$

$$\text{Net work output} = (h_3 - h_4) - (h_{2'} - h_1) \quad (8.3)$$

$$\text{Heat input} = h_3 - h_{4'} \quad (8.4)$$

$$\text{Pump work} = h_2 - h_1 = \frac{v(P_2 - P_1)}{\eta_{\text{pump}}} \quad (8.5)$$

$$\text{Cycle efficiency} = \frac{\text{Net work output}}{\text{Heat input}} = \frac{(h_3 - h_4) - (h_{2'} - h_1)}{h_3 - h_2}, \quad (8.6)$$

where h represents enthalpy and v is the specific volume at state 1.

Example 8.1

In a simple steam Rankine cycle, steam exits the boiler at 7.0 MPa and 540°C. The condenser operates at 10 kPa and rejects heat to the atmosphere at 40°C. Find the Rankine cycle efficiency and compare it to

the Carnot cycle efficiency. Both pump and turbine operate at 85% efficiencies.

The cycle is shown in Figure 8.5.

The Rankine cycle efficiency:

$$\eta_R = \frac{(h_3 - h_4) - (h_2 - h_1)}{h_3 - h_2},$$

$$\eta_{\text{turbine}} = \frac{h_3 - h_4}{h_3 - h_2},$$

and

$$\eta_{\text{pump}} = \frac{h_2 - h_1}{h_2 - h_1} = \frac{v_1(P_2 - P_1)}{h_2 - h_1}.$$

The enthalpies at the state points are found as follows:

$$h_1 = h_f(10 \text{ kPa}) = 191.8 \text{ kJ/kg.}$$

Pump work from 1 to 2:

$$\begin{aligned} W_2 &= \frac{v_1(P_2 - P_1)}{\eta_{\text{pump}}} = h_2 - h_1 \\ h_2 &= h_1 + \frac{v_1(P_2 - P_1)}{\eta_{\text{pump}}} \\ &= 191.8 \text{ kJ/kg} + \frac{(0.00101 \text{ m}^3/\text{kg})(7000 - 10) \text{ kPa}}{0.85} \\ &= 200.1 \text{ kJ/kg} \\ h_3(540^\circ\text{C}, 7 \text{ MPa}) &= 3506.9 \text{ kJ/kg.} \end{aligned}$$

States 3 and 4 have the same entropy.
Therefore,

$$s_3 = 6.9193 \text{ kJ/kg}\cdot\text{K} = s_4.$$

Saturated vapor entropy at state 4 (10 kPa):

$$s_{4g} = 8.1502 \text{ kJ/kg}\cdot\text{K.}$$

Since s_4 is less than s_{4g} , 4 is a wet state:

$$s_4 = s_f + Xs_{fg} \text{ or } s_g - Ms_{fg},$$

where X is the vapor quality and M is the moisture.

$$M_4 = \frac{s_g - s_4}{s_{fg}} = \frac{8.1502 - 6.9193}{7.5009} = 0.1641 \text{ or } 16.41\%.$$

$$h_4 = h_g - M_4 h_{fg} = 2584.7 - 0.1641(2392.8) = 2192 \text{ kJ/kg.}$$

Therefore,

$$\begin{aligned} h_4 &= h_3 - \eta_{\text{turbine}}(h_3 - h_4) \\ &= 3507 - 0.85(3507 - 2192) = 2389 \text{ kJ/kg.} \end{aligned}$$

Actual moisture at the turbine exhaust:

$$h_{4'} = h_g - M_4 h_{fg}.$$

$$\begin{aligned} M_4 &= \frac{h_g - h_4}{h_{fg}} = \frac{2584.7 - 2389}{2391} \\ &0.0817 \text{ or } 8.17\%. \end{aligned}$$

$$\text{Net work} = (h_3 - h_4) - (h_2 - h_1) = 1109 \text{ kJ/kg.}$$

$$\eta = \frac{\text{Net work}}{h_3 - h_2} = \frac{1109}{3507 - 200} = 0.3354 \text{ or } 33.54\%.$$

$$\eta_{\text{Carnot}} = \frac{813K - 313K}{813K} = 0.615 \text{ or } 61.5\%.$$

Several improvements can be made to the basic Rankine cycle in order to improve the cycle efficiency. The efficiency of the Rankine cycle may be increased by increasing the pressure in the boiler. However, that will result in increased moisture in the steam exiting the turbine. In order to avoid this problem, the steam is expanded to an intermediate pressure and reheated in the boiler. The reheated steam is expanded in the turbine until the exhaust pressure is reached. Figure 8.6 shows the Rankine cycle with reheat.

The cycle efficiency of the Rankine cycle with reheat:

$$\eta = \frac{(h_3 - h_4) + (h_s - h_6) - (h_2 - h_1)}{(h_3 - h_2) + (h_5 - h_4)}. \quad (8.7)$$

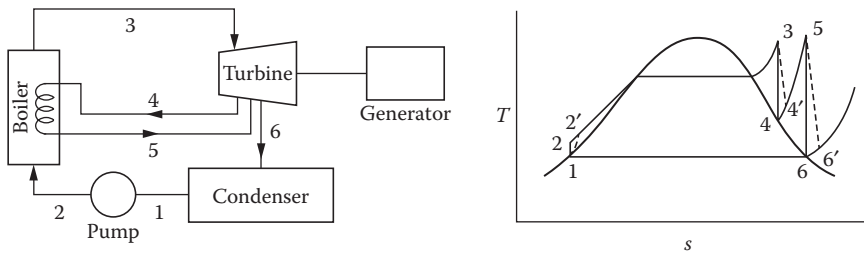


FIGURE 8.6
Rankine cycle with reheat.

Example 8.2

A reheat Rankine cycle uses steam as a working fluid. The steam leaves the boiler and enters the turbine at 5 MPa and 350°C, and it leaves the condenser as a saturated liquid. After expansion in the turbine to $P = 1.4$ MPa, the steam is reheated to 350°C and then expands in the low-pressure turbine to 20 kPa. If the efficiencies of the pump and turbine are 0.9 each, determine the cycle efficiency.

Solution

Point 3

$$P_3 = 5 \text{ MPa}, T_3 = 350^\circ\text{C}.$$

From steam tables,

$$h_3 = 3068 \text{ kJ/kg},$$

$$s_3 = 6.449 \text{ kJ/kg}\cdot\text{K}.$$

Point 4

$$s_4 = s_3 = 6.449 \text{ kJ/kg}\cdot\text{K}, P_4 = 1.4 \text{ MPa}.$$

From steam tables,

$$h_4 = 2781 \text{ kJ/kg}.$$

Using h_4 and turbine efficiency to find $h_{4'}$,

$$\eta_T = \frac{h_3 - h_4}{h_3 - h_{4'}},$$

$$h_{4'} = h_3 - \eta_T(h_3 - h_4) = 3082 - 0.9(3082 - 2781) = 2811.1 \text{ kJ/kg}.$$

Point 5

$$P_5 = 1.4 \text{ MPa}, T_5 = 350^\circ\text{C}.$$

From steam tables,

$$h_5 = 3149 \text{ kJ/kg},$$

$$s_5 = 7.136 \text{ kJ/kg}\cdot\text{K}.$$

Point 6

$$P_6 = 20 \text{ kPa},$$

$$s_6 = s_5 = 7.136 \text{ kJ/kg}\cdot\text{K}.$$

$$x = \frac{7.136 - 0.8319}{7.908 - 0.8319} = 0.89,$$

$$h_6 = h_f + xh_{fg} = 251.4 + 0.89(2610 - 251.4) = 2352.$$

Using the turbine efficiency to find h_6' ,

$$h_6' = h_5 - \eta_T(h_5 - h_6) = 3149 - 0.9(3149 - 2352) = 2432 \text{ kJ/kg}.$$

Point 1

$$P_1 = 20 \text{ kPa},$$

Saturated liquid:

$$v_1 = 0.001017 \text{ m}^3/\text{kg},$$

$$h_1 = 251.4 \text{ kJ/kg}.$$

Point 2

Pump work, 1 to 2,

$$w_2 = h_2 - h_1 = v(P_2 - P_1),$$

Pump efficiency,

$$\eta_p = \frac{h_2 - h_1}{h_2 - h_1},$$

$$h_2 - h_1 = \frac{h_2 - h_1}{\eta_p}.$$

But $h_2 - h_1 = v(P_2 - P_1)$,

$$h_2 - h_1 = \frac{v(P_2 - P_1)}{\eta_p} = \frac{0.001017(5000 - 20)}{0.9} = 5.6274,$$

and

$$h_2 = 257.03 \text{ kJ/kg.}$$

Computing the cycle efficiency,

$$\eta = \frac{(h_3 - h_4) + (h_5 - h_6) - (h_2 - h_1)}{(h_3 - h_2) + (h_5 - h_4)} = 0.3075 = 30.75\%.$$

Another improvement to the basic Rankine cycle is the regenerative cycle in which expanded steam is extracted at various points in the turbine and mixed with the condensed water to preheat it in the feedwater heaters. Figure 8.7 shows a schematic diagram and a $T-s$ diagram of a Rankine cycle with regeneration.

If a fraction f of the steam in the turbine is bled at state 5 to mix with the feedwater, the efficiency of the Rankine cycle with regeneration as shown in Figure 8.7 is

$$\eta = \frac{(h_5 - h_6) + (1-f)(h_6 - h_7) - (1-f)(h_2 - h_1) - (h_4 - h_3)}{h_5 - h_4}, \quad (8.8)$$

h_3 can be found from the energy balance

$$mh_3 = f mh_6 + (1-f)m h_2$$

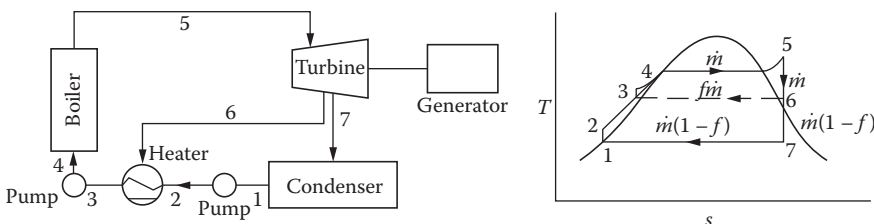


FIGURE 8.7
Rankine cycle with regeneration.

or

$$h_3 = f(h_6 - h_2) + h_2. \quad (8.9)$$

Example 8.3

A regenerative Rankine cycle uses steam as the working fluid. Steam leaves the boiler and enters the turbine at $P = 5 \text{ MPa}$, $T = 500^\circ\text{C}$. After expansion to 400 kPa, a part of the steam is extracted from the turbine for the purpose of heating the feedwater in the feedwater heater. The pressure in the feedwater heater is 400 kPa and the water leaving it is saturated liquid at 400 kPa. The steam that is not extracted expands to 10 kPa. Assuming the efficiencies of the turbine and the two pumps are 100% each, determine the fraction of the steam extracted to the feedwater heater (f) and the cycle efficiency (η).

Solution

Point 5

$$P_5 = 5 \text{ MPa}, T_5 = 500^\circ\text{C}$$

From the steam table, steam is superheated.

$$s_5 = 6.976 \text{ kJ/kg}\cdot\text{K},$$

$$h_5 = 3434 \text{ kJ/kg}.$$

Point 6

$$s_6 = s_5 = 6.976 \text{ kJ/kg}\cdot\text{K},$$

$$P_6 = 400 \text{ kPa}.$$

From the steam table, steam is superheated.

Using s_6 , we can interpolate for h_6 :

$$h_6 = 2773 \text{ kJ/kg}.$$

Point 7

$P_7 = 10 \text{ kPa}$. Again, $s_7 = s_5 = 6.976 \text{ kJ/kg}\cdot\text{K}$, mixture.

Computing,

$$x = \frac{6.976 - 0.6492}{8.1501 - 0.6492} = 0.84,$$

$$h_7 = h_f + xh_{fg} = 191.81 + 0.84(2392.8) = 2210 \text{ kJ/kg.}$$

Point 1

$$P_1 = 10 \text{ kPa.}$$

Saturated liquid,

$$h_1 = 191.81 \text{ kJ/kg.}$$

Point 2

$$P_2 = 400 \text{ kPa,}$$

$$h_2 - h_1 = v_1(P_2 - P_1) = 0.00101(400 - 10) = 0.3939 \text{ kJ/kg,}$$

$$h_2 = (191.81 + 0.3939) = 192.2 \text{ kJ/kg.}$$

Point 3

$$P = 400 \text{ kPa.}$$

Saturated liquid,

$$v_3 = 0.001084 \text{ m}^3/\text{kg,}$$

$$h_3 = 604.73 \text{ kJ/kg.}$$

Using the energy balance of feedwater heater, f may be computed as

$$\begin{aligned} h_3 &= fh_6 + (1-f)h_2 \\ f &= \frac{h_3 - h_2}{h_6 - h_2} = \frac{604.73 - 192.2}{2773 - 192.2} = 0.16. \end{aligned}$$

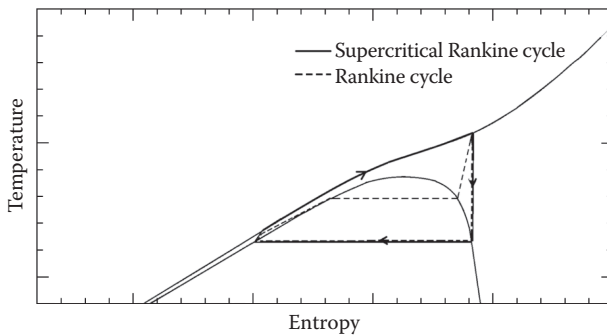
Point 4

$$w_{p2} = h_4 - h_3 = v_3(P_4 - P_3) = 0.001084(5000 - 400) = 4.9864 \text{ kJ/kg.}$$

$$h_4 = h_3 + 4.9864 = 609.72 \text{ kJ/kg.}$$

Efficiency (η) may be computed from Equation 8.8 as

$$\eta = \frac{(h_5 - h_6) - (1-f)(h_6 - h_7) - (1-f)(h_2 - h_1) - (h_4 - h_3)}{(h_5 - h_4)} = 0.399 = 39.9\%.$$

**FIGURE 8.8**

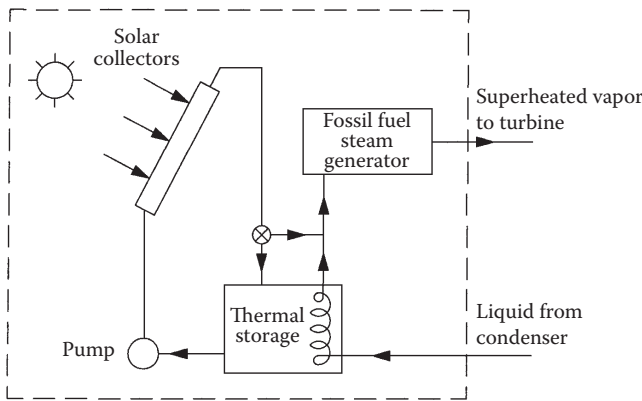
A supercritical Rankine cycle on a T - s diagram.

8.2.2 Supercritical Rankine Cycle

Conventional Rankine cycles work under subcritical conditions and generally use pure working fluids. Since a pure fluid boils at a constant temperature (Figure 8.8), it results in a mismatch with the temperature profile of the heat source. This mismatch results in higher losses in the heat exchange process, which can be reduced by the use of an SRC. In an SRC, shown in Figure 8.8, the working fluid is pressurized beyond its critical pressure and then heated isobarically directly to supercritical vapor phase. The supercritical vapor then expands in the turbine producing mechanical work. The turbine exhaust is then cooled to the liquid state in a condenser and the condensed fluid is pumped back to high pressure. A steam Rankine cycle can be operated under supercritical conditions; however, the critical pressure of steam is very high, which introduces corresponding material requirements, thus increasing the cost. On the other hand, organic fluids such as hydrocarbons and refrigerants have lower critical temperatures and pressures; therefore, they are being actively considered for SRC for low- and medium-temperature heat sources. These fluids give better efficiency in SRCs than the conventional ORC.

8.2.3 Components of a Rankine Power Plant

Major components of a Rankine power plant include boiler, turbine, condenser, pumps (condensate pump, feedwater booster, and boiler feed pump), and heat exchangers (open heaters and closed heaters). All of the components of a solar thermal power plant are the same as those in a conventional thermal power plant except the boiler. The boiler in a solar thermal power plant includes a solar collection system, a storage system, an auxiliary fuel heater and heat exchangers. Figure 8.9 shows a schematic representation of a solar boiler. The maximum temperature from the solar system depends on the type of solar collection system (PTCs, central receiver with heliostat field, parabolic dishes, etc.). Parabolic trough and parabolic dish collectors are described in detail in Chapter 3, while

**FIGURE 8.9**

Schematic of a solar boiler.

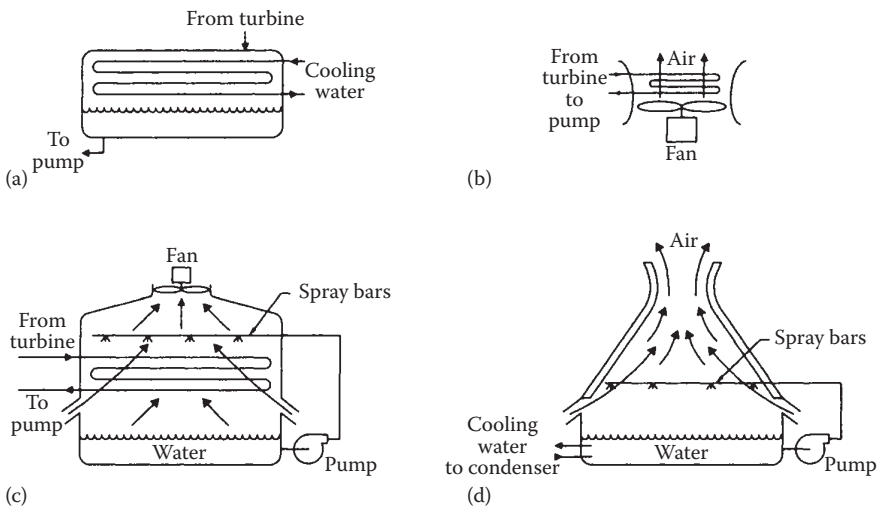
central receiver systems are described later in this chapter. If the temperature of the fluid from the solar system/storage is less than the required temperature for the turbine, an auxiliary fuel is used to boost the temperature. A fossil fuel or a biomass fuel may be used as the auxiliary fuel.

A condenser is a large heat exchanger that condenses the exhaust vapor from the turbine. Steam turbines employ surface-type condensers, mainly shell and tube heat exchangers operating under vacuum. The vacuum in the condenser reduces the exhaust pressure at the turbine blade exit to maximize the work in the turbine. The cooling water from either a large body of water such as a river or a lake, or from cooling tower, circulates through the condenser tubes. The cooling water is cooled in the cooling tower by evaporation. The air flow in the cooling tower is either natural draft (hyperbolic towers) or forced draft (see Figure 8.10). The condensate and feedwater pumps are motor-driven centrifugal pumps, while the boiler feed pumps may be motor- or turbine-driven centrifugal pumps.

Steam turbines and generators are described in detail in a number of books (Fitzgerald et al. 1971; Japikse and Nicholas 1994; Kreith and Goswami 2004; Salisbury 1950; Goswami and Kreith 2007) and will not be discussed here.

8.2.4 Choice of Working Fluid

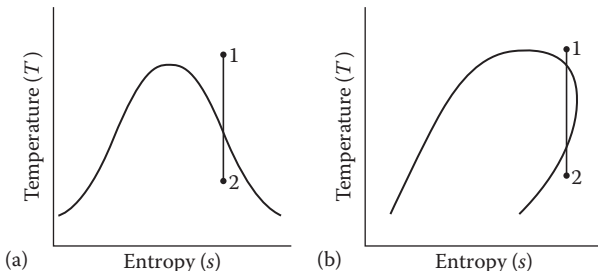
Working fluid in a solar Rankine cycle is chosen on the basis of the temperature from the solar collection system. The working fluid must be such that it optimizes the cycle efficiency based on the expected temperature from the source. Steam is the most common working fluid in a Rankine cycle. Its critical temperature and pressure are 374°C and 22.1 MPa, respectively. Therefore, it can be used for systems operating at fairly high temperatures. Systems employing parabolic trough, parabolic dish, or central receiver collection systems can use steam as a working fluid. Other major advantages of

**FIGURE 8.10**

Types of condenser or heat rejection used in Rankine cycle solar power systems: (a) tube-and-shell condenser, (b) dry cooling tower, (c) wet cooling tower, and (d) natural-draft cooling tower. (Stine, W.B. and R.W. Harrigan: *Solar Energy Fundamentals and Design: With Computer Applications*. 1985. Copyright Wiley-VCH Verlag GmbH & Co. KGaA. Reproduced with permission.)

steam are that it is nontoxic, environmentally safe, and inexpensive. Its major disadvantage is its low molecular weight, which requires very high turbine speeds in order to get high turbine efficiencies.

Steam is a wetting fluid; that is, as it is expanded in a turbine, once it reaches saturation, any further expansion increases the moisture content. In other words, steam becomes wetter as it expands as shown in Figure 8.11a. On the other hand, a fluid that has a T - s (temperature–entropy) diagram similar to that shown in Figure 8.11b is called a drying fluid. As seen from this figure, even though the working fluid passes through the two-phase region, it may exit the turbine as superheated. Normally, the turbine speed is so high that,

**FIGURE 8.11**

T - s characteristics of (a) wetting and (b) drying types of working fluids.

in such a case, there is no condensation in the turbine. Examples of drying fluids include hydrocarbons (toluene, methanol, isobutane, pentane, and hexane) and chlorofluorocarbons (CFCs such as R-11 and R-113). Since a drying fluid does not get wetter on expansion from a saturated vapor condition in an ideal or real process, it does not have to be superheated. Therefore, a Rankine cycle using a drying fluid may be more efficient than the cycle using a wetting fluid. In fact, a drying fluid may be heated above its critical point so that upon expansion, it may pass through the two-phase dome. Because of the T - s characteristics, the fluid may pass through the two-phase region and still exit from the turbine as superheated. These characteristics can be used to increase the resource effectiveness of a cycle by as much as 8% (Goswami et al. 1991). Chen et al. (2010) have given a comprehensive review of the potential working fluids for the Rankine cycle.

It has been mentioned that a working fluid can be classified as a dry, isotropic, or wet fluid depending on the slope of the saturation vapor curve on a T - s diagram (dT/ds) (Figure 8.12). Since the value of dT/ds leads to infinity for isentropic fluids, the inverse of the slope, (i.e., ds/dT) is used to express how "dry" or "wet" a fluid is. If we define $\xi = \frac{ds}{dT}$, the working fluid can be classified by the value of ξ ; that is, $\xi > 0$: a dry fluid (e.g., pentane), $\xi \approx 0$: an isentropic fluid (e.g., R11), and $\xi < 0$: a wet fluid (e.g., water). Figure 8.12 shows the three types of fluids in a T - s diagram.

Liu et al. (2004) derived an expression to compute ξ , which is

$$\xi = \frac{C_p}{T_H} - \frac{\frac{n \cdot T_{rH}}{1 - T_{rH}} + 1}{\Delta H_{H_2}} \quad (8.10)$$

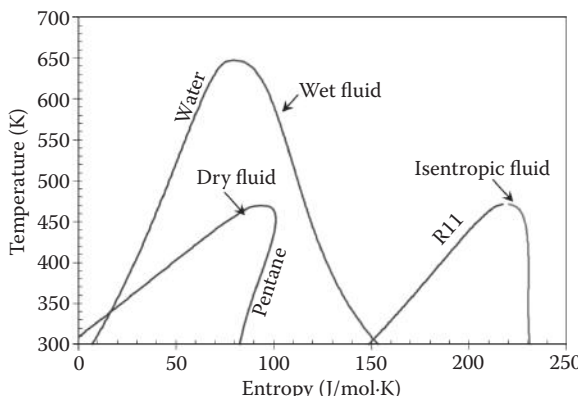


FIGURE 8.12

Three types of working fluids: dry, isentropic, and wet.

where ξ (ds/dT) denotes the inverse of the slope of saturated vapor curve on the $T-s$ diagram, n is suggested to be 0.375 or 0.38 (Poling et al. 2000), $T_{rH} = (T_H/T_C)$ denotes the reduced evaporation temperature, and ΔH_H is the enthalpy of vaporization.

Table 8.2 gives some characteristics of candidate working fluids for Rankine cycles (Chen et al. 2010) including their ξ values. Figure 8.13a and b show the ξ values of the fluids. Before selecting any of these fluids, one needs to look at their chemical stability under the conditions of operation and their environmental aspects, including the ozone depletion potential (ODP), the global warming potential (GWP), and the atmospheric lifetime. The ODP and GWP represent substance's potential to contribute to ozone degradation and global warming. Because of environmental concerns, some working fluids have been phased out, such as R-11, R-12, R-113, R-114, and R-115, while some others are being phased out in 2020 or 2030 (such as R-21, R-22, R-123, R-124, R-141b, and R-142b). Water is the most common working fluid for power plants based on solar energy, nuclear energy, and fossil fuels, while hydrocarbons and R134a and R245fa are commonly used for geothermal power. At present, CO_2 is being actively investigated as a working fluid in a supercritical cycle for high-temperature central receiver tower-based plants (Besarati and Goswami 2013). Chen et al. (2010) proposed using zeotropic mixtures of working fluids instead of pure fluids. They showed that using mixtures reduces the irreversibilities in a cycle, since the condensation process is not isothermal and there is no sharp pinch point during boiling, and improves the efficiency of conversion.

8.3 Design of Parabolic Trough-Based Power Plants

Design of a PTC-based CSP plant involves sizing and layout of the solar field, selection of the heat-transfer fluid (HTF), designing thermal energy storage (if any), design of the power block, and integration of the solar field with the power block and the control system. Vasquez-Padilla (2011) has presented a detailed methodology of the design of PTC-based CSP power plants. The following Sections 8.31 through 8.35 are based on Vasquez-Padilla (2011).

8.3.1 Sizing and Layout of the Solar Field

Details of a PTC and its performance parameters are described earlier in Chapter 3. Normally, PTC collectors are oriented N–S horizontally and they track the sun from E to W. Beam solar radiation per unit area of the tracking PTC is estimated for the selected location on the basis of the models described in Chapter 2. This is followed by a preliminary area of the solar

TABLE 8.2 Properties of Potential Working Fluids for Rankine Power Cycle

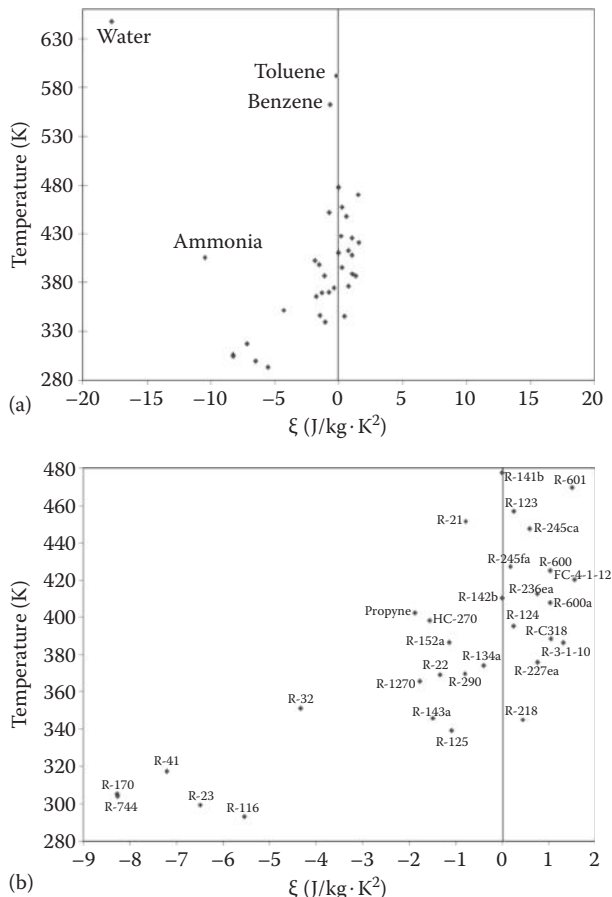
ASHRAE Number	Name	Molecular Weight	T _c (K)	P _c (MPa)	Vapor C _p (J/kg·K)	Latent heat L (kJ/kg)	ξ (J/kg·K ²)
R-21	Dichlorofluoromethane	102.92	451.48	5.18	339.85	216.17	-0.78
R-22	Chlorodifluoromethane	86.47	369.30	4.99	1069.13	158.46	-1.33
R-23 ^a	Trifluoromethane	70.01	299.29	4.83	3884.02	89.69	-6.49
R-32	Difluoromethane	52.02	351.26	5.78	2301.61	218.59	-4.33
R-41 ^a	Fluoromethane	34.03	317.28	5.90	3384.66	270.04	-7.20
R-116 ^a	Hexafluoroethane	138.01	293.03	3.05	4877.91	30.69	-5.54
R-123	2,2-Dichloro-1,1,1-trifluoroethane	152.93	456.83	3.66	738.51	161.82	0.26
R-124	2-Chloro-1,1,1,2-tetrafluoroethane	136.48	395.43	3.62	908.70	132.97	0.26
R-125	Pentafluoroethane	120.02	339.17	3.62	1643.89	81.49	-1.08
R-134a	1,1,1,2-Tetrafluoroethane	102.03	374.21	4.06	1211.51	155.42	-0.39
R-141b	1,1-Dichloro-1-fluoroethane	116.95	477.50	4.21	848.37	215.13	0.00
R-142b	1-Chloro-1,1-difluoroethane	100.50	410.26	4.06	1036.52	185.69	0.00
R-143a	1,1,1-Trifluoroethane	84.04	345.86	3.76	1913.97	124.81	-1.49
R-152a	1,1-Difluoroethane	66.05	386.4	4.52	1456.02	249.67	-1.14
R-170 ^a	Ethane	30.07	305.33	4.87	5264.72	223.43	-8.28
R-218	Octafluoropropane	188.02	345.02	2.64	1244.87	58.29	0.45
R-227ea	1,1,1,2,3,3-Heptafluoropropane	170.03	375.95	3.00	1013.00	97.14	0.76
R-236ea	1,1,1,2,3,3-Hexafluoropropane	152.04	412.44	3.50	973.69	142.98	0.76

TABLE 8.2 (CONTINUED)
Properties of Potential Working Fluids for Rankine Power Cycle

ASHRAE Number	Name	Molecular Weight	T _c (K)	P _c (MPa)	Vapor C _p (J/kg·K)	Latent heat L (kJ/kg)	ξ (J/kg·K ²)
R-245ca	1,1,2,2,3-Pentafluoropropane	134.05	447.57	3.93	1011.26	188.64	0.60
R-245fa	1,1,1,3,3-Pentafluoropropane	134.05	427.20	3.64	980.90	177.08	0.19
HC-270	Cyclopropane	42.08	398.30	5.58	1911.81	366.18	-1.54
R-290	Propane	44.10	369.83	4.25	2395.46	292.13	-0.79
R-C318	Octafluoroclobutane	200.03	388.38	2.78	896.82	93.95	1.05
R-3-10	Decafluorobutane	238.03	386.33	2.32	928.83	77.95	1.32
FC-4-1-12	Dodecafluoropentane	288.03	420.56	2.05	884.25	86.11	1.56
R-600	Butane	58.12	425.13	3.80	1965.59	336.82	1.03
R-600a	Isobutane	58.12	407.81	3.63	1981.42	303.44	1.03
R-601	Pentane	72.15	469.70	3.37	1824.12	349.00	1.51
R-717	Ammonia	17.03	405.40	11.33	3730.71	1064.38	-10.48
R-718	Water	18.00	647.10	22.06	1943.17	2391.79	-17.78
R-744 ^a	Carbon dioxide	44.01	304.13	7.38	3643.72	167.53	-8.27
R-1270	Propene	42.08	365.57	4.66	2387.36	284.34	-1.77
	Propyne	40.06	402.38	5.63	2100.54	431.61	-1.87
	Benzene	78.11	562.05	4.89	1146.72	418.22	-0.70
	Toluene	92.14	591.75	4.13	1223.90	399.52	-0.21
	Sodium						
	Potassium						
	Mercury						

Source: Chen H. et al., *Renewable and Sustainable Energy Reviews*, 14 (9), 3059–3067, 2010.

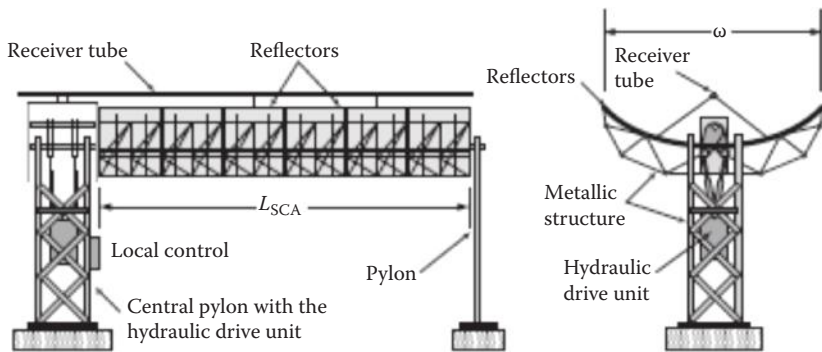
^a The critical temperature of the fluid is below 320 K, and the data are given based on 290 K.

**FIGURE 8.13**

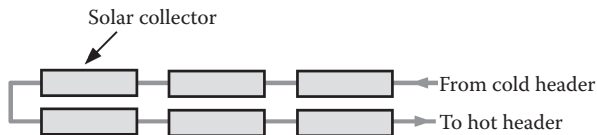
Distribution of the screened 35 working fluids in the $T-\xi$ chart: (a) all 35 fluids, (b) enlarged view of 31 fluids.

collectors determining for the design of the solar field. A solar field consists of a number of solar collector assemblies (SCAs) connected in a series parallel arrangement as described later. Each SCA consists of metallic support structure, parabolic mirrors, receiver/absorber tube, hydraulic drive unit, and pylon supports as shown in Figure 8.14. In order to reach the operational conditions of temperature, these SCAs are connected in series to form a solar collector loop. The number of SCAs in series, N , is calculated from the nominal design temperature rise, ΔT , in a loop and the temperature rise, ΔT_c , in an SCA.

$$N = \Delta T / \Delta T_c. \quad (8.11)$$

**FIGURE 8.14**

A solar collector assembly (SCA) for an LS-3 PTC. (Adapted from Romero-Alvarez, M. and E. Zarza, Concentrating solar thermal power, In *Energy Conversion*, D.Y. Goswami and F. Kreith (eds.), Boca Raton, FL: CRC Press, 2008.)

**FIGURE 8.15**

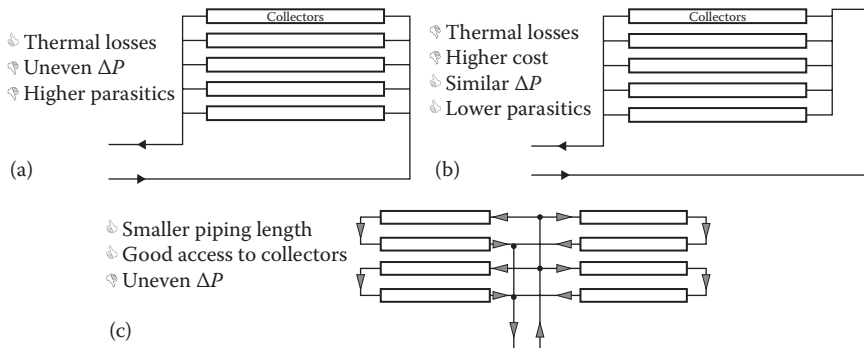
Schematic of a solar collector loop. (Adapted from Romero-Alvarez, M. and E. Zarza, Concentrating solar thermal power, In *Energy Conversion*, D.Y. Goswami and F. Kreith (eds.), Boca Raton, FL: CRC Press, 2008.)

Figure 8.15 shows a schematic of a solar collector loop.

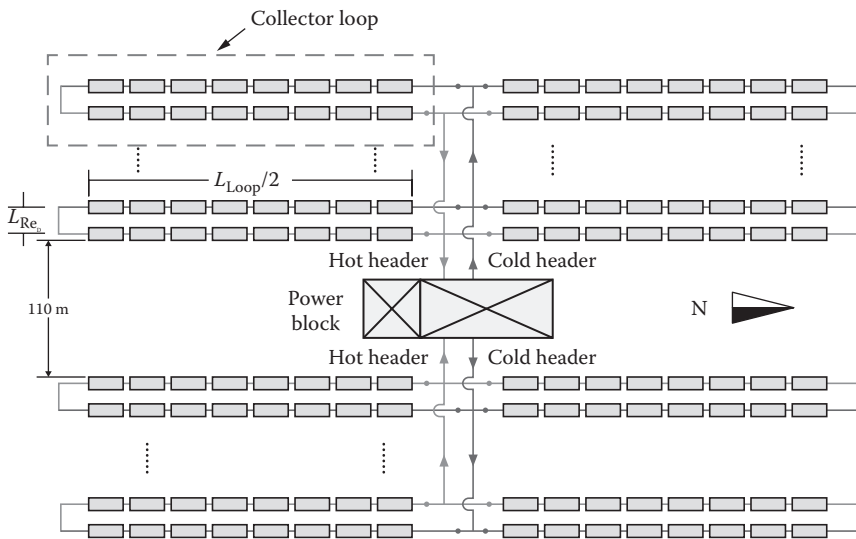
The number of parallel loops is then calculated from the thermal energy output from each loop and the total thermal energy needed from the total field. The parallel loops can be connected in three different ways as shown in Figure 8.16. The direct return layout has uneven pressure drops in each loop, therefore requiring flow-balancing valves. In contrast, the inverse return has similar pressure drops in all the loops; however, it requires longer pipe lengths. These two layouts are normally used in smaller industrial process heat applications, while much larger fields needed for CSP plants use a central feed and return. Therefore, the power block for the CSP plants is generally located in the center. The central feed can be an H-type or an I-type field layout as shown in Figures 8.17 and 8.18.

8.3.1.1 I Field Layout

As shown in Figure 8.17, the solar field is divided into two header pairs, with the power block located at the center of the field. Each collector loop consists of two rows connected in series, and the cold and hot headers run in the E-W direction. Because of uneven pressure drops in the loops, flow balancing valves are required.

**FIGURE 8.16**

Solar field layout loops. (a) Direct return. (b) Inverse return. (c) Central feed. (Adapted from Romero-Alvarez, M. and E. Zarza, Concentrating solar thermal power, In *Energy Conversion*, D.Y. Goswami and F. Kreith (eds.), Boca Raton, FL: CRC Press, 2008.)

**FIGURE 8.17**

I solar field layout. (Adapted from Vasquez-Padilla, R., Simplified methodology for designing parabolic through solar power plants. PhD dissertation, University of South Florida, Tampa, FL, 2011.)

8.3.1.2 H Field Layout

As shown in Figure 8.18, this field layout is divided into four header pairs, two on each side of the central power block. All four headers are in the E-W direction. In a solar collector loop, the SCAs may be connected by ball joints or flexible hoses to allow for independent rotation. Ball joints are preferred

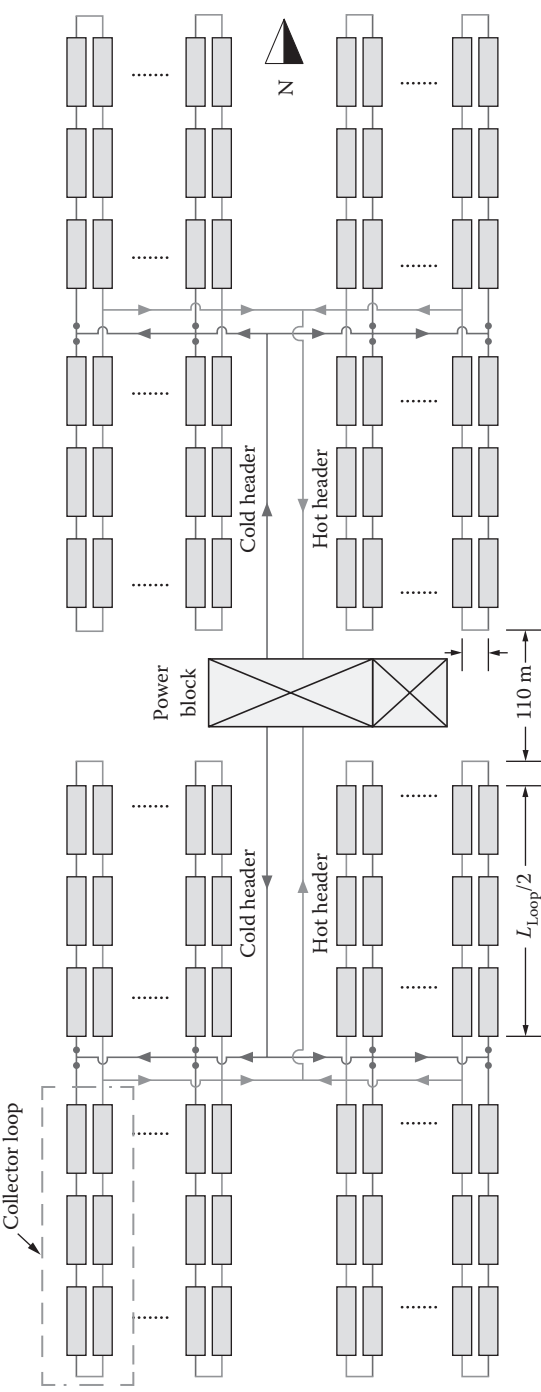


FIGURE 8.18
H solar field layout. (Adapted from Vasquez-Padilla, R., Simplified methodology for designing parabolic through solar power plants. PhD dissertation, University of South Florida, Tampa, FL, 2011.)

over flexible hoses because of their lower cost, reduced pressure drop, and reduced heat losses (Romero-Alvarez and Zarza 2008).

8.3.2 Pressure Drop in the Solar Field

The pressure drop in the solar field depends on the HTF mass flow rate, inner diameter of the pipes, and fittings (elbow, cross, reduction, expansion, valves, etc.). Initially, it is necessary to determine the optimum diameter for each section. According to Kelly and Kearney (2006), the optimum flow velocity is in the range of 2–4 m/s. For the pressure requirements, the required wall thickness of the pipe is calculated as (Megyesy 2004)

$$t_{\text{wall}} = \frac{(P_{\text{abs}} - P_{\text{atm}})D_0}{2S_y + 0.4(P_{\text{abs}} - P_{\text{atm}})}, \quad (8.12)$$

where P_{abs} is the absolute pressure of HTF in pounds per square inch (psi), P_{atm} is the atmospheric pressure in psi, D_0 is the outside diameter in inches, and S_y is the allowable stress in psi. Kelly and Kearney (2006) recommend three different pipe materials: ASTM A106, Grade B, Seamless Carbon Steel; ASTM A335 P9, Intermediate Alloy Steel; and ASTM TP347, Stainless Steel. The allowable stress for each material is shown in Table 8.3. The inner diameter and wall thickness for different pipe schedules and nominal diameters are shown in Appendix 4 (Figure A4.5).

Once the diameter is selected, the flow friction loss is calculated using the Darcy–Weisbach equation:

$$h_i = 2C_f \frac{L_i}{D_i} \frac{V_i^2}{g}, \quad (8.13)$$

where C_f is the friction coefficient (Fanning friction factor), L_i is the length of the pipe section in meters, and V_i is the flow velocity in meters per second. The friction coefficient can be calculated from the correlation given in Kakaç et al. (1987):

$$\frac{1}{\sqrt{C_f}} = 3.48 - 1.7372 \ln 2 \frac{\epsilon}{D_t} - \frac{16.2426}{\text{Re}_D} \ln A_2 \quad (8.14)$$

$$A_2 = \frac{(2\epsilon/D_t)^{1.1098}}{6.0983} + \frac{7.149}{\text{Re}_D}^{0.8981},$$

where Re_D is the Reynolds number and ϵ is the pipe roughness in meters. This correlation is valid for $4000 \leq \text{Re}_D \times 10^8$ and $2 \times 10^{-8} \leq \epsilon/a \leq 0.1$.

TABLE 8.3

Maximum Allowable Stress (ksi) for Different Materials

Temperature (°F)	Maximum Allowable Stress (ksi)		
	A106	TP347	A335
400	—	15.5	—
500	—	14.9	14.4
600	—	14.7	14.2
650	15	14.7	13.9
700	14.4	14.7	13.7
750	13.0	14.7	13.2
800	10.8	14.7	12.8
850	—	14.7	12.1
900	—	14.7	11.4
950	—	14.6	10.6
1000	—	14.0	7.4
1050	—	12.1	5.0
1100	—	9.1	3.3
1150	—	6.1	2.2
1200	—	4.4	1.5

Source: Adapted from ASME, ASME B31.1-2004, American National Standard, ASME Code for Pressure Piping, 2004.

The pressure drop in a section is given by

$$\Delta P_{Li} = \rho_i g h_i. \quad (8.15)$$

The additional pressure loss owing to the pipe fittings is accounted by calculating the equivalent pipe length for each fitting, L_f , as

$$L_f = K \frac{D_i}{2 C_f}. \quad (8.16)$$

The K factors for various fittings are given in Table 8.4. To calculate the total pressure drop, L_f is added to L_i before applying Equations 8.13 through 8.16.

The pressure drop through the solar field is calculated for the longest path traveled by the HTF. The HTF is circulated in a closed loop by using a variable speed pump (Turchi 2010). The pump power is the highest parasitic load in the solar plant and therefore a variable speed pump is used to reduce the power requirements when the solar field requires flow rates less than the nominal rate. The pumping power is calculated as

$$\dot{W}_{p,nom} = \rho_{HTF} T_{cold} g \Delta P_{total} \quad (8.17)$$

TABLE 8.4

K Values for Different Pipe Fittings Used in the Solar Field

Fitting	K
Gate valve	0.19
Globe valve	10.00
Check valve	2.50
Standard elbow	0.90
Medium elbow	0.75
Long elbow	0.60
Weldolet	1.80
Ball joint	4.73
Flexible hose	20.60

Source: Adapted from Kelly, B. and D. Kearney, Parabolic trough solar system piping model. Tech. Rep., National Renewable Laboratory, NREL/SR-550-40165, July, Golden, CO, 2006.

At different speeds, the pump law is used and the pump work is given by (Logan 1993)

$$\dot{W}_p = \dot{W}_{p,nom} \left(\frac{\dot{m}_{SF}}{\dot{m}_{SF,nom}} \right)^3, \quad (8.18)$$

where \dot{m}_{SF} is the actual HTF flow rate in the solar field and $\dot{m}_{SF,nom}$ is the nominal flow rate. Finally, the pumping power is calculated with the pump efficiency, which is affected by the flow rate through the pump.

$$\dot{W}_{p,actual} = \dot{W}_p / \eta_p. \quad (8.19)$$

All pipes are insulated and the heat losses from the pipes are calculated as explained in Chapter 4. During nights, the HTF flow is kept at approximately 20% of the nominal flow rate to keep the pipes and the solar collectors warm and avoid thermal shock. If the temperature of the HTF falls below the minimum allowable, auxiliary heaters heat the fluid.

8.3.3 Expansion Tank

An expansion tank is provided in the solar loop to account for expansion of the HTF as it heats up. It is normally installed at the highest point in the field close to the pump. The expansion tank is sized to be approximately 25% full at the cold conditions and approximately 75% full at normal operating conditions. The open space is filled with nitrogen at positive pressure to provide a nonreactive atmosphere and to keep the air and moisture from the atmosphere from entering the HTF loop.

8.3.4 Power Block

The power block commonly used in PTC-based CSP plants is a regenerative-reheat Rankine cycle as explained in Section 8.2.1 and Example 8.3. Figure 8.19 shows a schematic of a power block with a regenerative-reheat Rankine cycle configuration.

The HTF passes through three heat exchangers to heat the working fluid: preheater, boiler, and superheater. All of them are generally shell- and tube-type heat exchangers. The HTF flows through the tube side while the working fluid being heated flows through the shell side. The preheater heats the high-pressure working fluid to a saturated liquid condition, the boiler heats it to a saturated vapor condition while changing phase, and finally the superheater heats it to the high temperature of the cycle. The equations for sizing the heat exchangers and for calculating the exit temperatures of the two fluids based on the heat-exchanger effectiveness are given in Chapter 4.

There are normally two multistage turbines in the PTC power plants: high-pressure and low-pressure turbines. Reheat is normally applied between the high-pressure turbine and the low-pressure turbines. Closed feedwater heaters are used to heat the feedwater by extracting a small quantity of steam at various stages in the turbine. The closed feedwater heaters are shell- and tube-type heaters. Open feedwater heaters simply mix the extracted steam with the feedwater. The open feedwater heaters are also used as deaerators to remove any air and other dissolved gases from the working fluids.

8.3.5 Condenser

The condenser is a two-phase heat exchanger to condense the working fluid vapor from the turbine exhaust to saturated liquid. It is normally a shell- and tube-type heat exchanger where the cooling water flows through the tube while the steam flows through the shell side. The efficiency of the Rankine cycle depends on the condenser pressure, which should be designed to be as low as possible to obtain a condensing temperature that is as low as possible. Wet-bulb temperature of the ambient air is the minimum ambient temperature available to condense the working fluid. Normally, cooling towers are used to evaporate some of the cooling water to cool the water down to the wet-bulb temperature. However, this method uses a lot of water that cannot be recovered. Shortages of clean water around the globe require that the cooling water use be reduced to as small as possible. While fossil- or nuclear-based power plants can be located where the cooling water is available, solar power plants are often located in desert areas where cooling water may not be available.

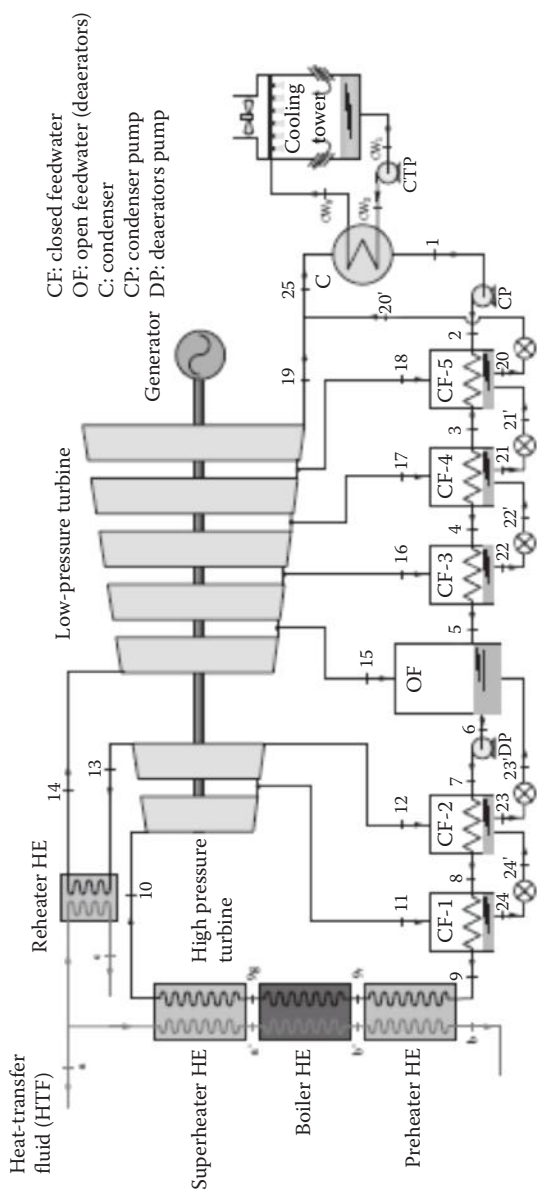


FIGURE 8.19
Schematic of a solar power block based on a regenerative-reheat Rankine cycle.

8.3.5.1 Air-Cooled Condensers

The air-cooled (also called dry-cooled) condensers become necessary for solar thermal power plants because of the scarcity of water where the solar radiation is the most attractive. There are many advantages of dry-cooled condensers:

- Reduced maintenance costs (no chemical additives or periodic cleaning required)
- Elimination of the cooling tower plume
- Reduction of condensation on the mirrors—no reduction in the optical efficiency of PTC
- Plant siting flexibility
- Emission of only warm and clean air reducing adverse environmental impact

On the other hand, the disadvantages of dry cooling are:

- Lower heat-transfer coefficients; therefore, larger heat exchanger area is needed.
- Greater fan power is required to achieve the same heat transfer.

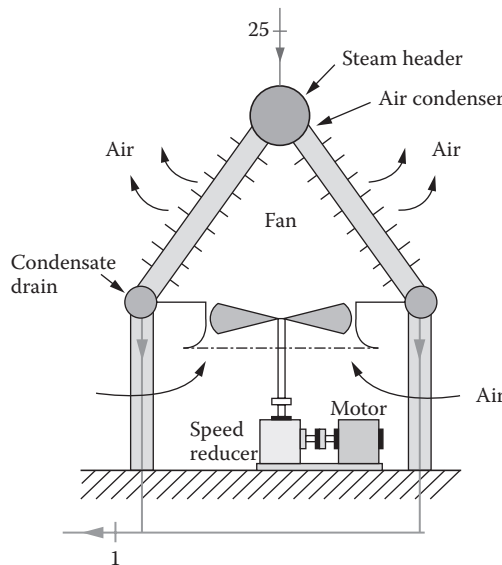


FIGURE 8.20

Configuration of an A frame air-cooled condenser. (Adapted from Kröger, D., *Air-Cooled Heat Exchangers and Cooling Towers: Thermal-Flow Performance Evaluation and Design*, Vol. 2. Pennwell Corp., Tulsa, OK, 2004.)

- Performance is strongly influenced by the ambient temperatures that change with the time of the day and the season.
- Lower power plant efficiency.

In dry-cooled condensers, the steam flows through finned coils over which the ambient air is blown. Figure 8.20 shows an A frame condenser in which the steam flows through the finned coils oriented at angles of 45°–60° to the horizontal. Figure 8.21 shows horizontal frame air-cooled condensers using forced flow and induced flow on the finned coil. Kröger (2004) gives detailed information about air-cooled condensers for power plants.

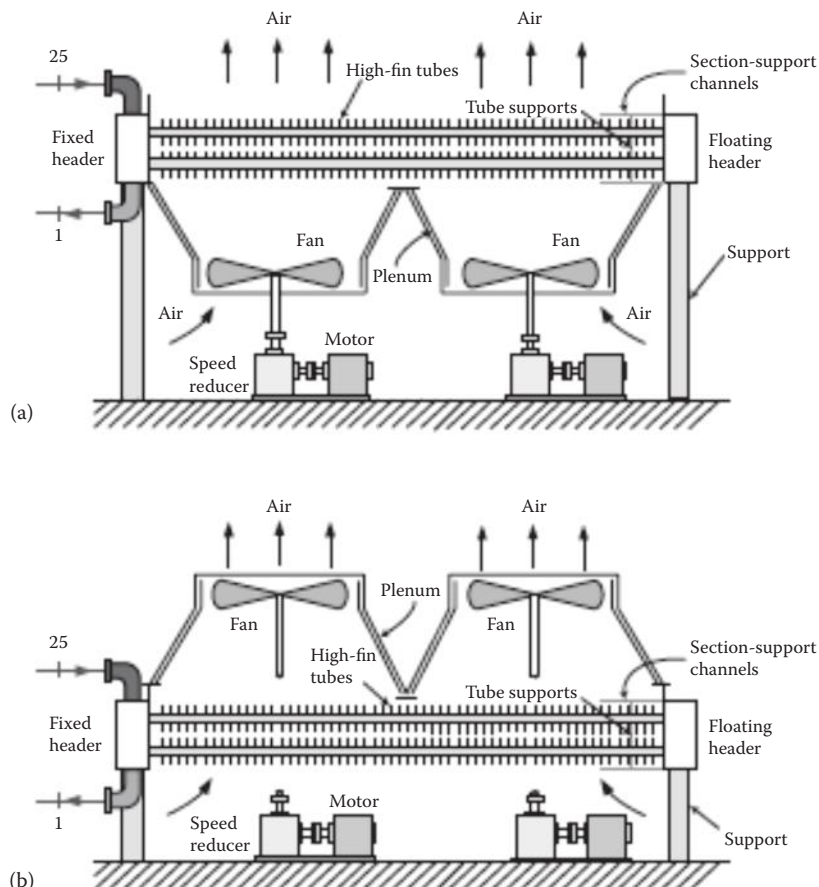


FIGURE 8.21

Configuration of horizontal frame air-cooled condenser: (a) forced flow; (b) induced flow. (Adapted from Serth, R.W., *Process Heat Transfer: Principles, Applications and Rules of Thumb*, Academic Press, 2007.)

8.4 Examples of PTC Solar Thermal Power Plants

There are successful examples of solar thermal power plants working on Rankine cycle and using parabolic troughs. An example of each type is given in the following.

Luz Corporation developed components and commercialized PTC-based solar thermal power by constructing a series of such power plants from 1984 to 1991. Starting with their first 14-MW_e Solar Electric Generating Station (SEGS I) in Southern California, they added a series of SEGS power plants with a total generating capacity of 354 MW_e. Figure 8.22 shows a schematic of the SEGS VIII and IX plants. Table 8.5 provides information about the solar field, power block, and other general information about SEGS I and SEGS IX plants. All of these plants use natural gas as the auxiliary fuel so that, on average, 75% of the energy is supplied from the sun and 25% is from natural gas. With power plant electrical conversion efficiencies of the order of 40% and solar field efficiencies of 40% to 50%, overall efficiencies for solar to electricity conversion of the order of 15% are being achieved in these plants. The cost of electricity from these plants has been decreased from approximately 30¢/kWh to less than 10¢/kWh. The SEGS plants have been operating successfully since 1990; however, the development of CSP plants stopped, mainly for policy reasons, until the construction and operation of the Nevada Solar One in 2007, a 64-MW nominal capacity PTC plant. Since then, a number of PTC power plants have been built or are under construction. Table 8.6 gives a list of the

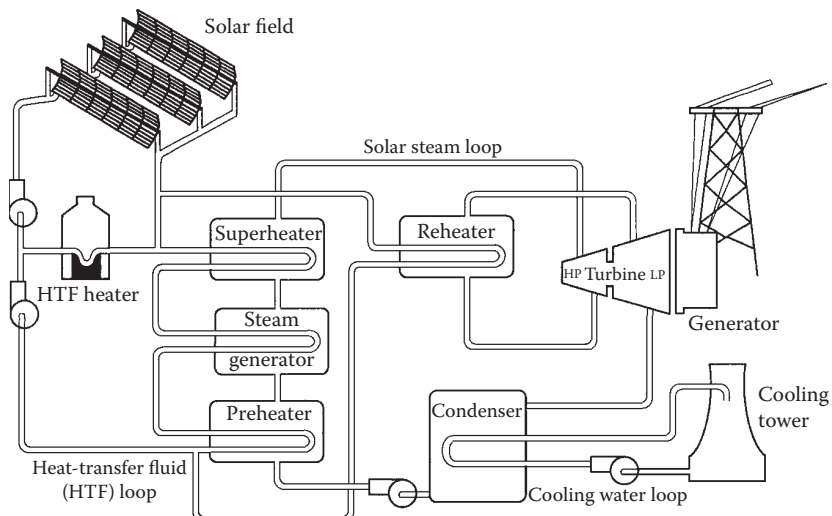


FIGURE 8.22

Flow of heat-transfer fluid through the SEGS VIII and IX plants. (Adapted from Fitzgerald, A.E. et al., *Electric Machinery*, 3rd ed., New York: McGraw-Hill, 1971.)

TABLE 8.5
Important Characteristics of SEGS I to SEGS IX Parabolic Trough Plants

	Units	I	II	III	IV	V	VI	VII	VIII	IX
<i>Power Block</i>										
Turbine-generator output	Gross MW _e	14.7	33	33	33	33	33	33	88	88
Output to utility	Net MW _e	13.8	30	30	30	30	30	30	80	80
<i>Turbine-Generator Set</i>										
Solar Steam Conditions										
Inlet pressure	Bar	35.3	27.2	43.5	43.5	43.5	100	100	100	100
Reheat pressure	Bar	0	0	0	0	0	17.2	17.2	17.2	17.2
Inlet temperature	°C	415	360	327	327	327	371	371	371	371
Reheat temperature	°C	na	na	na	na	na	371	371	371	371
Gas Mode Steam Conditions ^a										
Inlet pressure	Bar	0	105	105	105	105	100	100	100	100
Reheat pressure	Bar	0	0	0	0	0	17.2	17.2	17.2	17.2
Inlet temperature	°C	0	510	510	510	510	510	510	510	510
Reheat temperature	°C	na	na	na	na	na	371	371	371	371
<i>Electrical Conversion Efficiency</i>										
Solar mode ^b	%	31.5	29.4	30.6	30.6	30.6	37.5	37.5	37.6	37.6
Gas mode ^c	%	0	37.3	37.3	37.3	37.3	39.5	39.5	37.6	37.6
<i>Solar Field</i>										
Solar Collector Assemblies										
LS 1 (128 m ²)										

(Continued)

TABLE 8.5 (CONTINUED)
Important Characteristics of SEGS I to SEGS IX Parabolic Trough Plants

	Units	I	II	III	IV	V	VI	VII	VIII	IX
LS 2 (235 m ²)		560	536	0	0	0	0	0	0	0
LS 3 (545 m ²)		48	518	980	980	992	800	400	0	0
Number of mirror segments		0	0	0	0	32	0	184	852	888
Field aperture area	m ²	41,600	96,464	117,600	117,600	126,208	96,000	89,216	190,848	198,912
Field inlet temperature	°C	82,960	190,338	230,300	230,300	250,560	188,000	194,280	464,340	483,960
Field outlet temperature	°C	240	231	248	248	248	293	293	293	293
Annual thermal efficiency	%	307	321	349	349	349	390	390	390	390
Peak optical efficiency	%	35	43	43	43	43	42	43	53	50
System thermal losses	% of peak	71	71	73	73	73	76	76	80	80
		17	12	14	14	14	15	15	15	15
<i>Heat-Transfer Fluid</i>										
Type		Esso 500	VP-1							
Inventory	m ³	3213	416	403	403	461	416	416	1289	1289
Thermal storage capacity	MWh _t	110	0	0	0	0	0	0	0	0
<i>General</i>										
Annual power outlet	Net MWh/ year	30,100	80,500	91,311	91,311	99,182	90,850	92,646	252,842	256,125
Annual gas power use	10 ⁹ m ³ / year	4.76	9.46	9.63	9.63	10.53	8.1	8.1	24.8	25.2

^a Gas superheating contributes 18% of turbine inlet energy.

^b Generator gross electrical output divided by solar field thermal input.

^c Generator gross electrical output divided by thermal input from gas-fired boiler or HTF heater.

TABLE 8.6
PTC Solar Power Plants in Operation in 2012

Project Name	Country	Capacity (MW)	Power Block	HTF	Thermal Storage	Fossil Backup	Additional Description	Start Year
Andasol-1	Spain	50	STR	D/B/O	2-t-i-m, 7.5 h	HTF heater	η: 16%	2008
Andasol-2	Spain	50	STR	D/B/O	2-t-i-m, 7.5 h	HTF heater	η: 16%	2009
Andasol-3	Spain	50	STR	Thermal oil	2-t-i-m, 7.5 h	—	—	2011
Archimede	Italy	134.74	ISCC	Molten salt	2-t-d-m, 8 h	—	5 MW solar	2010
Arcosol-50	Spain	50	STR	D/B/O	2-t-i-m, 7.5 h	Natural gas	—	2011
Aste 1A	Spain	50	STR	Thermal oil	2-t-i-m, 8 h	HTF boiler	η: 15%	2012
Aste 1B	Spain	50	STR	Thermal oil	2-t-i-m, 8 h	HTF boiler	η: 15%	2012
Astexol II	Spain	50	STR	Thermal oil	2-t-i-m, 8 h	HTF boiler	η: 15%	2012
Cameo	United States	2 (solar)	STR	Food-grade mineral oil	None	—	Hybrid CSP/coal	2010
Extresol-1	Spain	50	STR	D/B/O	2-t-i-m, 7.5 h	HTF heater (12%)	η: 16%	2010
Extresol-2	Spain	50	STR	D/B/O	2-t-i-m, 7.5 h	HTF heater (12%)	η: 16%	2010
Helioenergy 1	Spain	50	STR	Thermal oil	None	HTF boiler	—	2011
Helioenergy 2	Spain	50	STR	Thermal oil	None	HTF boiler	—	2012
Helios I	Spain	50	STR	Thermal oil	None	—	—	2012
Holaniku	United States	2	STR	Xceltherm 600	2 h	—	η: 2%	2009
Ibersol Ciudad Real (Puertollano)	Spain	50	STR	D/B/O	—	HTF heater (gas fired)	—	2009
Hassi R'mel	Algeria	150	ISCC	Thermal oil	None	—	25 MW solar	2011
Kuraymat	Egypt	140	ISCC	Therminol VP-1	None	—	20 MW solar	2011
Morocco	Morocco	470	ISCC	Thermal oil	None	—	20 MW solar	2010

(Continued)

TABLE 8.6 (CONTINUED)
PTC Solar Power Plants in Operation in 2012

Project Name	Country	Capacity (MW)	Power Block	HTF	Thermal Storage	Fossil Backup	Additional Description	Start Year
La Dehesa	Spain	50	STR	D/DO	2-t-i-m, 7.5 h	HTF heater (12%)	η: 13.81%	2011
La Florida	Spain	50	STR	D/DO	2-t-i-m, 7.5 h	HTF heater (12%)	η: 13.81%	2010
Alvarado I	Spain	50	STR	D/BO	None	HTF heater (35 MWt)		2009
Lebrija 1	Spain	50	STR	VPI	None	HTF heater (12%)		2011
Majadas I	Spain	50	STR	D/BO	—	—		2010
Manchasol-1	Spain	50	STR	D/DO	2-t-i-m, 7.5 h	HTF heater (12%)	η: 16%	2011
Manchasol-2	Spain	50	STR	D/DO	2-t-i-m, 7.5 h	HTF heater (12%)	η: 16%	2011
Martin	United States	75	STR	Thermal oil	None	—		2010
Morón	Spain	50	STR	Thermal oil	None	HTF boiler		2012
Nevada Solar One	United States	75	STR	DOWTHERM A	0.5 h	—		2007
Palma del Río I	Spain	50	STR	D/BO	None	—		2011
Palma del Río II	Spain	50	STR	D/BO	None	—		2010
Saguaro	United States	1	ORC	Xceltherm 600	—	—	η: 7.5%-working fluid: <i>n</i> -pentane	2006
Solabén 3	Spain	50	STR	Thermal oil	None	HTF boiler		2012
Solacor 1	Spain	50	STR	Thermal oil	None	HTF boiler		2012
Solacor 2	Spain	50	STR	Thermal oil	None	HTF boiler		2012
SEGS I	United States	13.8	STR	Caloria	2-t-d-m, 3 h	None	Storage system was damaged by fire	1984

SEGS II	United States	30	STR	STR	None	Natural gas	Natural gas-fired superheater	1985
SEGS III	United States	30	STR	Thermolin	None	Natural gas	Natural gas-fired superheater	1985
SEGS IV	United States	30	STR	Thermolin	None	Natural gas	Natural gas-fired superheater	1989
SEGS V	United States	30	STR	Thermolin	None	Natural gas	Natural gas-fired superheater	1989
SEGS VI	United States	30	STR	Thermolin	None	Natural gas	Natural gas-fired superheater	1989
SEGS VII	United States	30	STR	Thermolin	None	Natural gas	Natural gas-fired superheater	1989
SEGS VIII	United States	80	STR	Thermolin	None	Natural gas	Natural gas-fired superheater	1989
SEGS IX	United States	80	STR	Thermolin	None	Natural gas	Natural gas-fired superheater	1990
Solnova 1	Spain	50	STR	Thermal oil	None	HTF boiler	HTF boiler	2009
Solnova 3	Spain	50	STR	Thermal oil	None	HTF boiler	HTF boiler	2009
Solnova 4	Spain	50	STR	Thermal oil	None	HTF boiler	HTF boiler	2009
Termesol 50	Spain	50	STR	D/DO	2-t-i-m, 7.5 h	Natural gas	Natural gas	2011
Thai Solar	Thailand	5	DSG	Water/steam	None	None	n: 12%	2012

Note: 2-t-d-m, 2 tank direct molten salt; 2-t-i-m, 2 tank indirect molten salt; DSG, direct steam generation; D/B O, diphenyl/biphenyl oxide; ISCC, integrated solar combined cycle; STR, steam Rankine cycle.

PTC-based CSP plants operating in the world and Table 8.7 gives a list of the PTC plants under construction. Table 8.8 shows the plants based on LFR.

The design of all CSP power plants is complex and is usually accomplished using computer modeling. Ho (2008) lists a number of computer programs available for the design of CSP plants, including TRNSYS, DELSOL,

TABLE 8.7

PTC Solar Power Plants under Construction

Project Name	Country	Capacity (MW)	Power Block	HTF	Thermal Storage	Fossil Backup Type	Start Year
Abengoa Mojave	United States	250	STR		None		2013
Agua Prieta II Arenales	Mexico Spain	478 50	ISCC STR	Thermal oil Thermal oil	None 2-t-i-m, 7 h	HTF heater	2013 2013
Borges Termosolar Casablanca	Spain	25 50	STR	Thermal oil	None	Biomass	2012
Enerstar (Villena)	Spain	50	STR	D/B O	2-t-i-m, 7.5 h	HTF heater (12%)	2013
Extresol-3 (EX-3)	Spain	50	STR	D/B O	2-t-i-m, 7.5 h	HTF heater (12%)	2012
Genesis Solar Energy Project	United States	250	STR	Theminol VP-1	None		2014
Godawari Solar Project	India	50	STR	Dowtherm	None		2013
Guzmán	Spain	50	STR	Thermal oil	None	HTF heater (12%)	2012
Helios II	Spain	50	STR	Thermal oil	None		2012
KaXu Solar one	South Africa	100	STR		2-t-i-m, 3 h		2014
La Africana	Spain	50	STR		2-t-i-m, 7.5 h		2012
NextEra Beacon	United States	250	STR		None		2014
Olivenza 1	Spain	50	STR	Thermal oil	None	HTF boiler	2012
Orellana	Spain	50	STR	Thermal oil	None		2012
Palen Solar Power Project	United States	500	STR		None		2014
Palmdale Hybrid Power Plant	United States	50	STR				2013

TABLE 8.8

Operational Fresnel Reflectors Power Plants

Project Name	Country	Capacity (MW)	Power Block	HTF	Thermal Storage	Start Year
Augustin Fresnel 1	France	0.25	STR	Water	Ruths tank, 0.25 h	2012
Kimberlina	United States	5	STR	Water	None	2008
Puerto Errado 1 (PE1)	Spain	1.4	STR	Water	Ruths tank, single-tank thermocline	2009
Puerto Errado 2 (PE2)	Spain	30	STR	Water	Ruths tank, single-tank thermocline, 0.5 h	2012

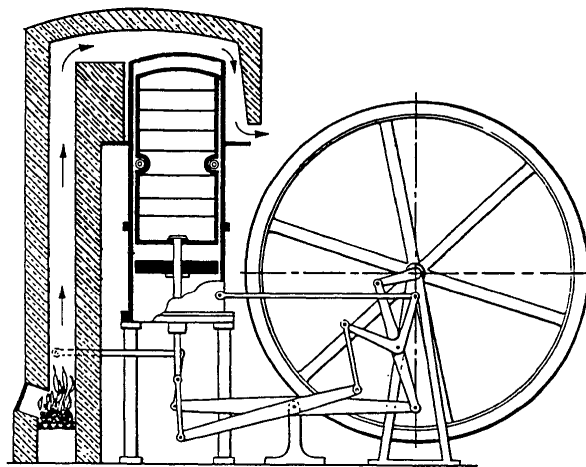
SAM, IPSEpro, DELSOL, GATECYCLE, SOLERGY, and HELIOS. Systems Advisor Model (SAM) was developed by NREL under contract with the US Department of Energy and is available for free.

8.5 Parabolic Dish Systems

Parabolic dishes, as explained in Chapter 3, can achieve very high concentration ratios and temperatures as high as 700°C. Therefore, CSP plants based on parabolic dishes can achieve very high thermodynamic efficiencies. One of the advantages of dish-based power plants is that they can be modular; that is, one dish could produce from approximately 10 kW_e to approximately 100 kW_e, which could be combined to give higher output. The Rankine cycle and the Stirling cycle are appropriate for dish systems. Since a Stirling cycle is one of the most efficient thermodynamic cycles, integration of the Stirling engine with a dish can be a very efficient solar power system. Even though a dish type of system has all of these advantages, somehow, these systems have not found commercial success. However, it is a matter of time before these systems will find commercial success. The dish systems, especially with a Stirling cycle, are described in detail in this chapter.

8.6 Stirling Cycle

The Stirling cycle has become very important in recent years because of its potential to operate at very high efficiency. In fact, theoretically, its efficiency is the same as the Carnot efficiency. It was proposed by Rev. Robert Stirling, a

**FIGURE 8.23**

The original patented Stirling engine of Rev. Robert Stirling.

Scottish minister, as a solar alternative to a steam engine (Figure 8.23). In the 1930s, Phillips Research Laboratory in Eindhoven, The Netherlands, developed the technology to commercialize it. More recently, interest in Stirling engines has increased with increased interest in solar and biomass energy sources (Stine and Diver 1994). The first solar application of a Stirling engine was conducted by John Ericsson, a Swedish engineer who spent a long and productive career in the United States. A Stirling cycle engine can use air as the working fluid; therefore, it is also called a hot air engine. Since it is an external combustion engine, it can use any fuel or concentrated sunlight. High-performance Stirling engines operate at very high temperatures, typically 600°C to 800°C, resulting in conversion efficiencies of 30% to 40% (Stine 2004). Stirling engines are being developed in small power capacities, typically 10 to 100 kW.

8.6.1 Thermodynamics of Stirling Cycle

Figure 8.24 shows thermodynamic diagrams of an ideal Stirling cycle. A gas is used as the working fluid. The cycle consists of two isothermal and two constant volume processes. The working gas is compressed isothermally (constant temperature) from state 1 to state 2. This process is accomplished by heat rejection at the low temperature of the cycle, T_L . It is then heated at constant volume to state 3. The gas is then expanded isothermally from 3 to 4. This process is accompanied by heat addition at the high temperature in the cycle, T_H . Finally, the gas is cooled at constant volume from temperature T_H to T_L (process 4–1). The hatched area under process 2–3 represents the heat addition to the working gas while raising its temperature from T_L to T_H .

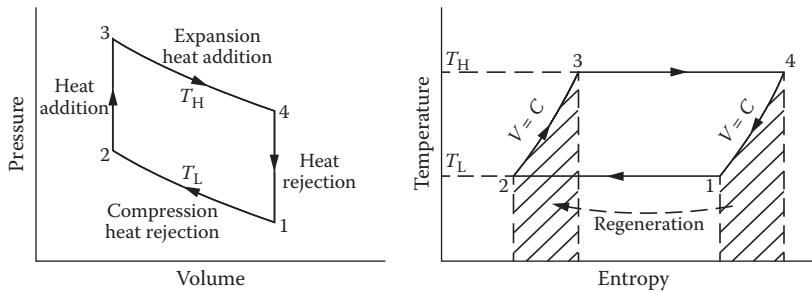


FIGURE 8.24
Thermodynamic diagrams of an ideal Stirling engine.

and the hatched area under process 4–1 represents heat rejection while the gas goes from T_H to T_L . The heat addition from 2 to 3 is equal to the heat rejection from 4 to 1, and they are between the same temperature limits:

$$Q_{2-3} = mC_v(T_H - T_L) \quad (8.20)$$

and

$$Q_{4-1} = mC_v(T_H - T_L). \quad (8.21)$$

Ideally, if the heat rejected in process 4–1 could be stored and transferred to the gas later in process 2–3 (perfect regeneration), the only external heat addition in the cycle would be in process 3–4:

$$Q_{3-4} = -W_{3-4} = \int_3^4 p dV = mRT_H \ln \frac{V_4}{V_3}. \quad (8.22)$$

The work input for compression from 1–2 is

$$\begin{aligned} W_{1-2} &= -\int_1^2 p dV = mRT_L \ln \frac{V_1}{V_2} \\ &= -mRT_L \ln \frac{V_2}{V_1} \end{aligned} \quad (8.23)$$

since

$$\frac{V_2}{V_1} = \frac{V_3}{V_4}.$$

The net work output is

$$mR \ln \frac{V_3}{V_4} (T_H - T_L). \quad (8.24)$$

Therefore, the cycle efficiency

$$\eta = \frac{\text{Net work out}}{\text{Heat input}} = \frac{T_H - T_L}{T_H}. \quad (8.25)$$

This efficiency, which is equal to the Carnot cycle efficiency, is based on the assumption that regeneration is perfect, which is not possible in practice. Therefore, the cycle efficiency would be lower than that indicated by the above equation. For a regeneration effectiveness e as defined below, the efficiency is given by (Stine and Harrigan 1985)

$$\eta = \frac{T_H - T_L}{T_H + [(1-e)/(k-1)][(T_H - T_L)/\ln(V_1/V_2)]}, \quad (8.26)$$

where $e = \frac{T_R - T_L}{T_H - T_L}$, T_R is the regenerator temperature, and $k = C_p/C_v$ for the gas.

For perfect regeneration ($e = 1$), the above expression reduces to the Carnot efficiency. It is also seen from the above equation that regeneration is not necessary for the cycle to work, because even for $e = 0$, the cycle efficiency is not zero.

Example 8.4

A Stirling engine with air as the working fluid operates at a source temperature of 400°C and a sink temperature of 80°C. The compression ratio is 5.

Assuming perfect regeneration, determine the following:

1. Expansion work
2. Heat input
3. Compression work
4. Efficiency of the machine

If the regenerator temperature is 230°C, determine the following:

5. Regenerator effectiveness
6. Efficiency of the machine
7. If the regeneration effectiveness is zero, what is the efficiency of the machine?

Solution

1. Expansion work per unit mass of the working fluid. Assuming air as an ideal gas,

$$w_{34} = - \int_3^4 P dv = RT_H \ln \frac{v_4}{v_3} = (0.287)(400 + 273) \ln 5 = -310.9 \text{ kJ/kg.}$$

The minus sign shows work output.

2. Heat input per unit mass of the working fluid:

$$q_{34} = w_{34} = 310.9 \text{ kJ/kg.}$$

3. Compression work per unit mass of the working fluid:

$$w_{12} = - \int_1^2 P dv = RT_L \ln \frac{v_2}{v_1} = -(0.287)(80 + 273) \ln \frac{1}{5} = 163.1 \text{ kJ/kg.}$$

4. Efficiency of the machine:

$$\eta = \frac{T_H - T_L}{T_H} = \frac{400 - 80}{(400 + 273)} = 0.475 = 47.5\%.$$

5. Regenerator effectiveness:

$$e = \frac{T_R - T_L}{T_H - T_L} = \frac{230 - 80}{400 - 80} = 0.469.$$

6. Efficiency of the machine:

$$\eta = \frac{T_H - T_L}{T_H + \frac{(1-e)(T_H - T_L)}{(k-1)\ln(v_1/v_2)}} = \frac{400 - 800}{(400 + 273) + \frac{(1-0)}{(1.4 - 1)} \frac{(400 - 80)}{\ln(5)}} = 0.341,$$

$$\eta = 34.1\%.$$

7. If the regeneration effectiveness is zero, the efficiency of the machine:

$$\eta = \frac{T_H - T_L}{T_H + \frac{(1-e)(T_H - T_L)}{(k-1)\ln(v_1/v_2)}} = \frac{400 - 800}{(400 + 273) + \frac{(1-0)}{(1.4 - 1)} \frac{(400 - 80)}{\ln(5)}} = 0.273,$$

$$\eta = 27.3\%.$$

In order to understand how the Stirling cycle shown in Figure 8.24 may be achieved, in practice, the simple arrangement and sequence of processes shown in Figure 8.25 is helpful. In the proposed arrangement, two cylinders with pistons are connected via a porous medium, which allows gas to pass through from one cylinder to the other. As the gas passes through the porous medium, it exchanges heat with the medium. The porous medium, therefore, serves as the regenerator. In practice, this arrangement can be realized in three ways as shown in Figure 8.26 (alpha, beta, and gamma types).

The choice of a working fluid for Stirling engine depends mainly on the thermal conductivity of the gas in order to achieve high heat-transfer rates. Air has traditionally been used as the working fluid. Since hydrogen has 40% higher thermal conductivity at 500°C, it is preferable over

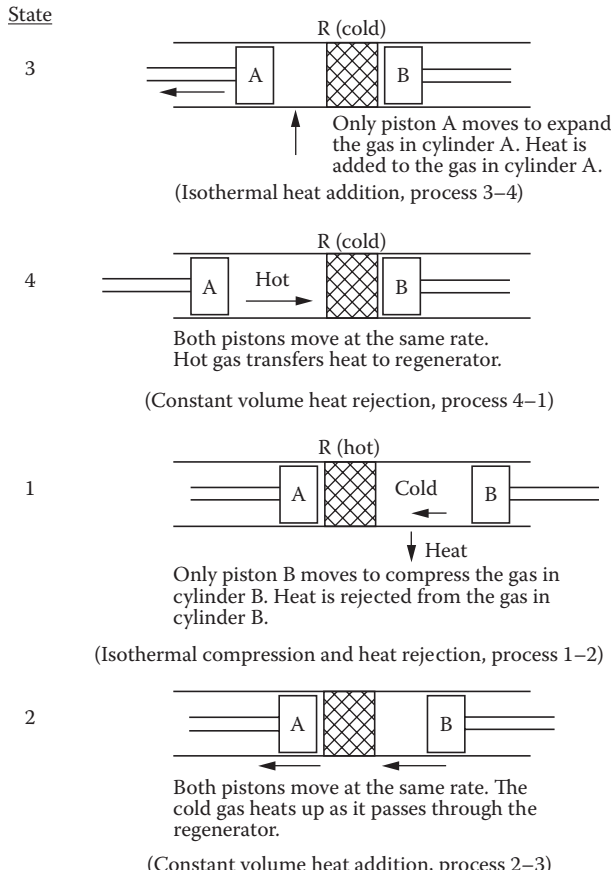
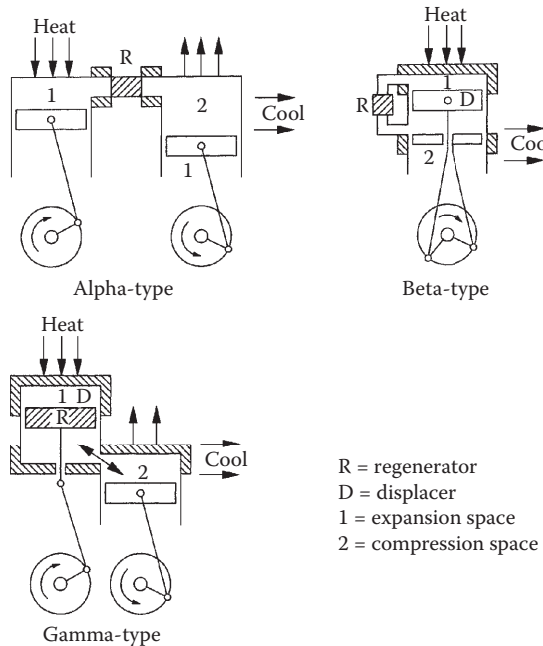


FIGURE 8.25

Stirling cycle states and processes with reference to Figure 8.24.

**FIGURE 8.26**

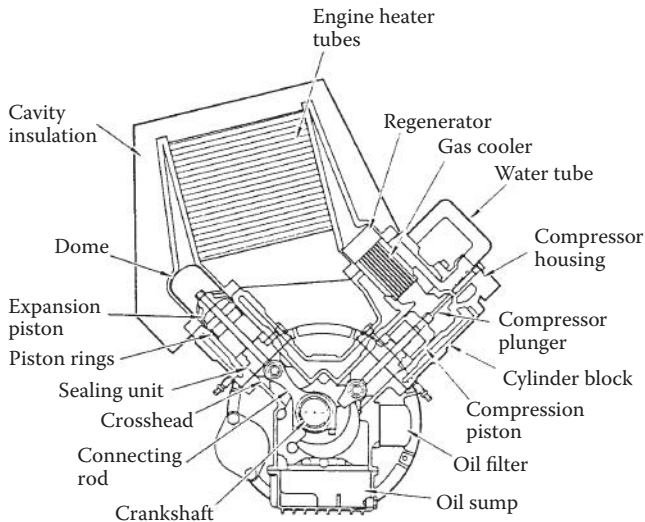
Three basic types of Stirling engine arrangements.

air. Helium has a higher ratio of specific heats (k), which lessens the impact of imperfect regeneration.

In the alpha configuration, there are two cylinders and pistons on either side of a regenerator. Heat is supplied to one cylinder and cooling is provided to the other. The pistons move at the same speed to provide constant volume processes. When all the gas has moved to one cylinder, the piston of that cylinder moves with the other remaining fixed to provide expansion or compression. Compression is done in the cold cylinder and expansion is done in the hot cylinder. The Stirling Power Systems V-160 engine (Figure 8.27) is based on an alpha configuration.

The beta configuration has a power piston and a displacer piston that divides the cylinder into hot and cold sections. The power piston is located on the cold side and compresses the gas when the gas is in the cold side and expands it when it is in the hot side. The original patent of Robert Stirling was based on beta configuration, as are free-piston engines.

The gamma configuration also uses a displacer and a power piston. In this case, the displacer is also the regenerator, which moves gas between the hot and cold ends. In this configuration, the power piston is in a separate cylinder.

**FIGURE 8.27**

Stirling Power Systems/Solo Kleinmotoren V-160 alpha-configuration Stirling engine. (Adapted from Stine, W.B., Stirling engines. In *The CRC Handbook of Mechanical Engineering*, D.Y. Goswami, ed., Boca Raton, FL: CRC Press, 2004.)

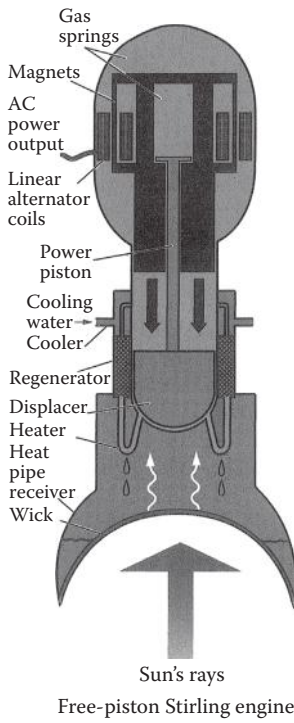
8.6.2 Piston/Displacer Drives

The power and displacer pistons are designed to move according to a simple harmonic motion to approximate the Stirling cycle. This is done by a crankshaft or a bouncing spring/mass second-order mechanical system (Stine 2004).

8.6.3 Kinematic or Free-Piston Engines

Stirling engines are designed as kinematic or free piston depending on how power is removed. In a kinematic engine, the power piston is connected to the output shaft by a connecting rod/crankshaft arrangement.

Free-piston arrangement is an innovative way to realize the Stirling cycle. In this arrangement, the power piston is not connected physically to an output shaft. The piston bounces between the working gas space and a spring (usually a gas spring). The displacer is also usually free to bounce. This configuration is called the Beale free-piston Stirling engine after its inventor, William Beale (Stine 2004). Since a free-piston Stirling engine has only two moving parts, it offers the potential of simplicity, low cost, and reliability. Moreover, if the power piston is made magnetic, it can generate current in the stationary conducting coil around the engine as it moves. This is the principle of the free-piston/linear alternator in which the output from the engine is electricity. Figure 8.28 shows a schematic of a free-piston Stirling engine with a linear alternator.

**FIGURE 8.28**

Basic components of a Beale free-piston Stirling converter incorporating a sodium heat pipe receiver for heating with concentrated solar energy.

8.6.4 Examples of Solar Stirling Power Systems

Stirling engines can provide very high efficiencies with high-concentration solar collectors. Since practical considerations limit the Stirling engines to small sizes (5 to 100 kW), a Stirling engine fixed at the focal point of a parabolic dish provides an optimum match. Therefore, all of the commercial developments to date have been in parabolic dish-Stirling engine combination. The differences in the commercial systems have been in the construction of the dish and the type of Stirling engine.

Advanco Corporation developed and tested a 25-kW_e dish Stirling system (called Vanguard I) in Rancho Mirage, California, in 1984 and achieved net conversion efficiency of approximately 30% (Gupta 1985). The system consisted of an 11-m-diameter parabolic dish with a concentration ratio of 2100 and a United Stirling Mark II engine operating at 800°C. Despite the technical success, the effort had to be abandoned by Advanco because of an exclusive agreement between McDonnell Douglas Corporation and United Stirling AB of Sweden.

McDonnell Douglas and United Stirling jointly developed a 25-kW_e dish Stirling system and tested it in California. The concentrator was

made from glass mirror facets on a structure to approximate a parabolic dish. Figure 8.29 shows a picture of the system. Tests showed the system efficiency to be in the same range as the Vanguard I system. McDonnell Douglas built six prototypes but decided to abandon the commercialization efforts.

In the 1990s, Cummins Power Generation and Stirling Technology Company developed a 25-kW_e free-piston, linear alternator engine. Cummins Power also developed a 5-kW_e dish Stirling power system for remote power applications with a view to mass produce the system (see Figure 8.30). The company, however, abandoned the effort in 1996.

Schlach Bergermann and Partner also developed a 7.7-kW_e dish Stirling power system using a V-160 two-cylinder Stirling engine developed by Stirling Power Systems and a stretched-membrane dish. Stirling engine development in Japan includes a 3-kW_e engine developed by Toshiba Corp. for residential heat pump applications and a 2.4-kW_e engine developed for space testing by Aisin Seiki Company (Kagawa et al. 1989; Proctor and Morse 1975).

Stirling Engine Systems, Inc. developed a Dish Stirling System and planned to build large-scale power plants with their 25-kW dishes (Figure 8.31). However, the company filed for bankruptcy in 2011. Its technology and

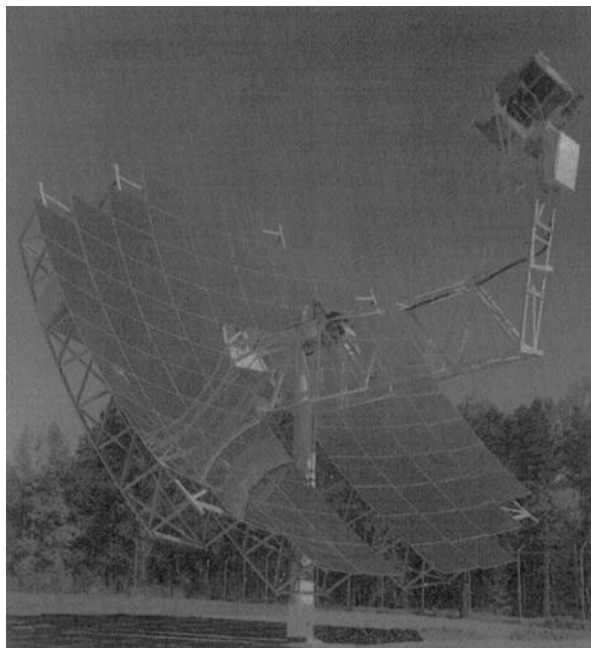


FIGURE 8.29

The McDonnell Douglas/United Stirling dish-Stirling 25 kW_e module.

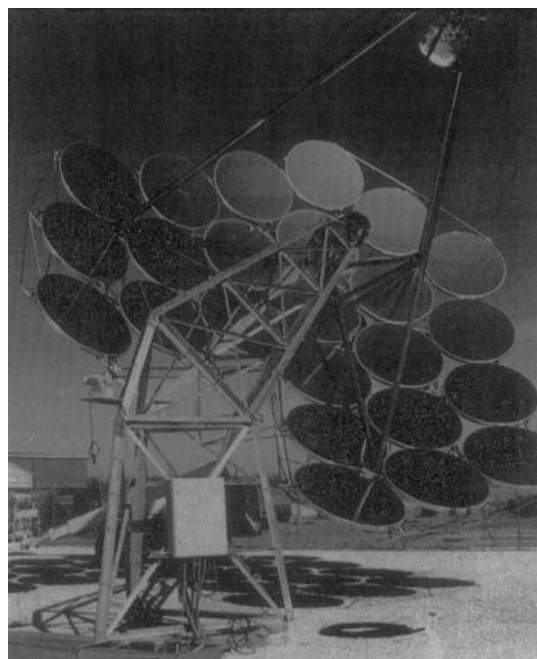


FIGURE 8.30

The Cummins Power Generation dish-Stirling engine power system.



FIGURE 8.31

A 25-kW_e dish Stirling system by Stirling Energy Systems, Inc., USA.

planned projects were bought by a British company, United Sun Systems International, headquartered in Gothenburg, Sweden, which plans to build large-scale plants in China in collaboration with its Chinese partners.

8.7 Central Receiver Tower Systems

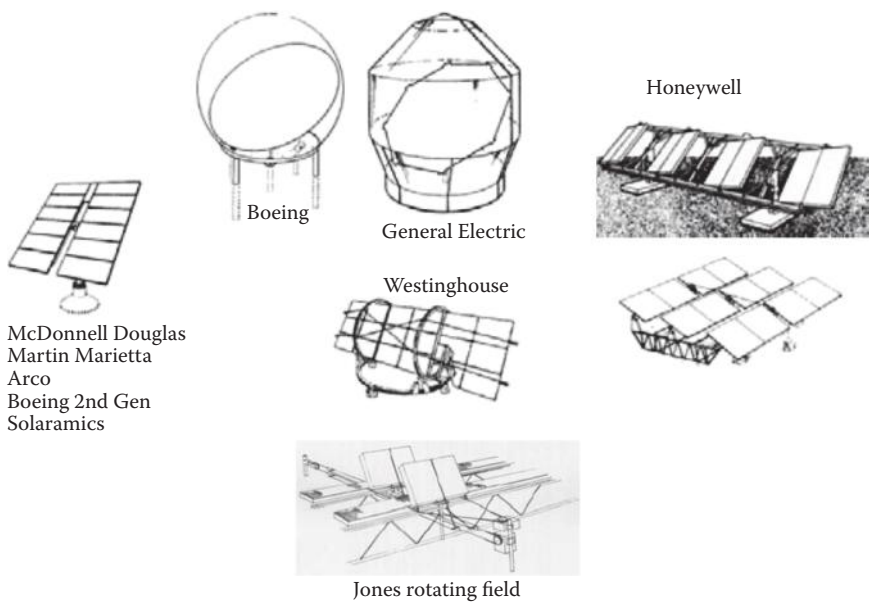
A central receiver collector consists of a large field of mirrors on the ground that track the sun in such a way that the reflected radiation is concentrated on a receiver/absorber on top of a tower. The mirrors are called *heliostats*. Central receivers can achieve temperatures of the order of 1000°C. Therefore, a central receiver concentrator is suitable for thermal electric power production in the range of 1–1000 MW. The concept of a central receiver solar thermal power, also known as *power tower*, has been known for a long time. Francia (1968) built a pilot model of a solar power tower plant in 1967 at the University of Genoa, Italy. Since the early 1970s, when the power tower concept was first proposed by Hildebrandt and Vant-Hull (1974), the central receiver technology has been actively developed in the United States. Since then, the technology has been pursued in Germany, Spain, Switzerland, France, Russia, Italy, and Japan (DeLaquil et al. 1993) and more recently in South Africa, India, and China.

A central receiver collector consists of a heliostat field, a receiver/absorber, and the tracking controls for the heliostats. Sections 8.7.1 and 8.7.2 briefly describe the heliostats and the receiver.

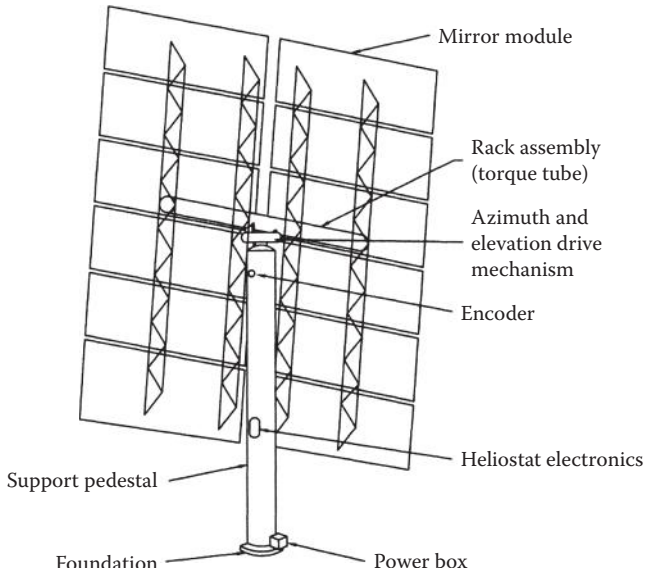
8.7.1 Heliostats

Developing cost-effective and optically efficient heliostats in the United States was initiated in the late 1970s. A number of designs were examined to be used in Solar One, the first 10-MW solar power tower plant in the Mojave Desert, which are shown in Figure 8.32. Five different concepts including seven different designs are shown in the figure: (1) pedestal mounted (left), (2) bubble-enclosed membrane (top), (3) ganged (right), (4) carousel (center), and (5) rotating field (bottom). Ultimately, the pedestal-mounted concept was found as the most cost-effective option and was selected for the Solar One plant in 1982 (Kolb et al. 2007).

Figure 8.33 shows the back side of a heliostat used at the Solar One plant. It consists of several mirror panels supported on a steel structure so that it forms a slightly concave mirror surface. The heliostat focal length is approximately equal to the distance of the heliostat from the receiver. Recent research and development of heliostats has been concentrated on using stretched-membrane reflectors in order to reduce the cost. A stretched-membrane heliostat consists of two polymer membranes stretched over a metal ring support

**FIGURE 8.32**

Heliostat designs developed in the United States between 1975 and 1982. (From Kolb, G.J. et al., Heliostat cost reduction study, Sandia Report, SAND2007-3293, June, Sandia National Lab., Albuquerque, NM, 2007.)

**FIGURE 8.33**

A heliostat consisting of glass mirrors supported on a structure (back view).

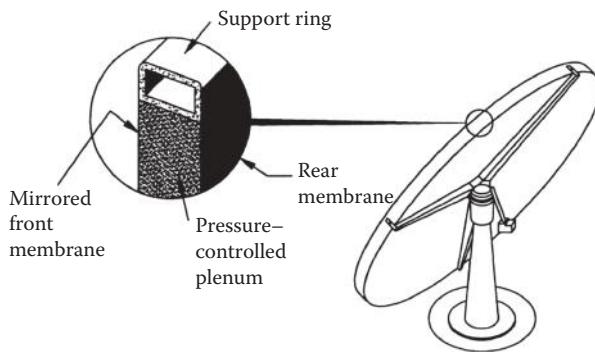


FIGURE 8.34

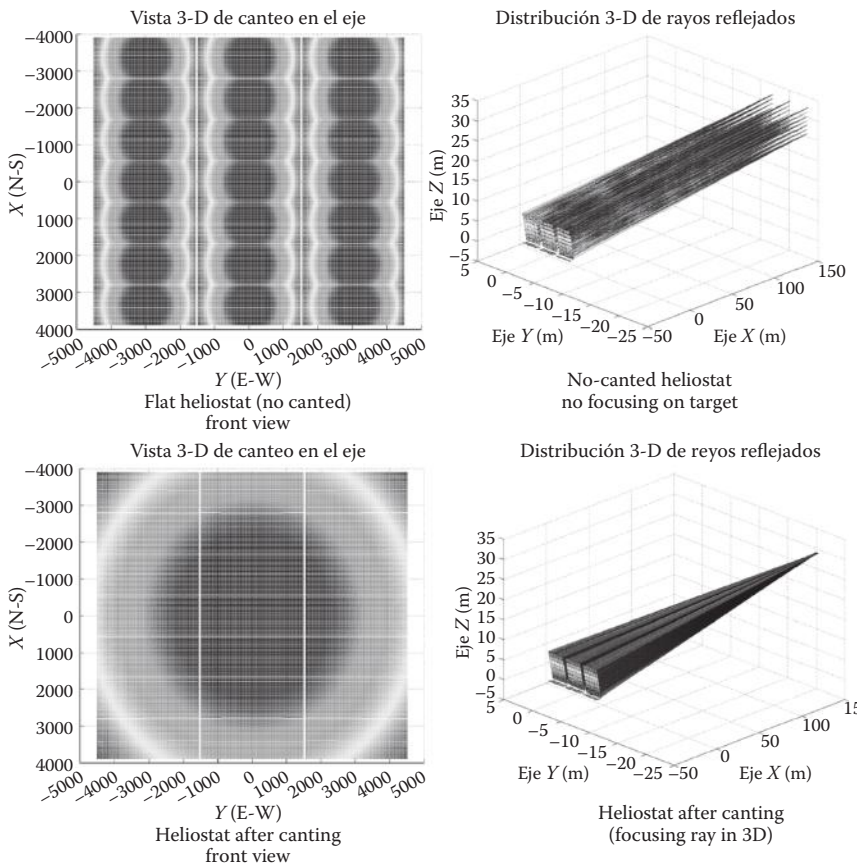
Stretched-membrane heliostat consists of two membranes, a mirror front one and supporting rear one, which are stretched across a support structure. Curvature of the heliostat is adjusted by changing the vacuum pressure of the space between the membranes. (Adapted from Colorado State University and Westinghouse Electric Corporation, *Solar Thermal Electric Power Systems*, 1974.)

structure. The front polymer is laminated with a silvered polymer reflector. The space between the two membranes is evacuated. The vacuum pressure is adjusted to achieve the desired focal length. Figure 8.34 shows a stretched-membrane heliostat developed by Science Applications International Corp. These heliostats have the potential to reduce the cost of the central receiver systems; however, the problems include uncertainties regarding their durability and lifetimes.

Another option for cost reduction is increasing the size of the heliostats. Therefore, the overall number of the required heliostats for power plant decreases, which consequently reduces other costs associated with each heliostat such as the drives. On the other hand, the performance of the heliostat might be affected by increasing the size. For example, mirror imperfections have higher impact on the reflected image when the heliostat is large. Moreover, the wind load is higher at a larger heliostat because of the larger surface area. A report by Sandia National Laboratory has predicted that the low-cost heliostats are most likely to be more than 150 m^2 (Kolb et al. 2007).

As can be seen from Figure 8.33, each heliostat consists of a number of mirrors (facets) that are mounted on a supporting structure. Mirror alignment or canting of the heliostats considerably influences the performance of the heliostat field. All the mirror modules of a heliostat have to be arranged in a specific orientation to achieve highly concentrated solar flux on the receiver surface. The effect of canting the facets is clearly shown in Figure 8.35.

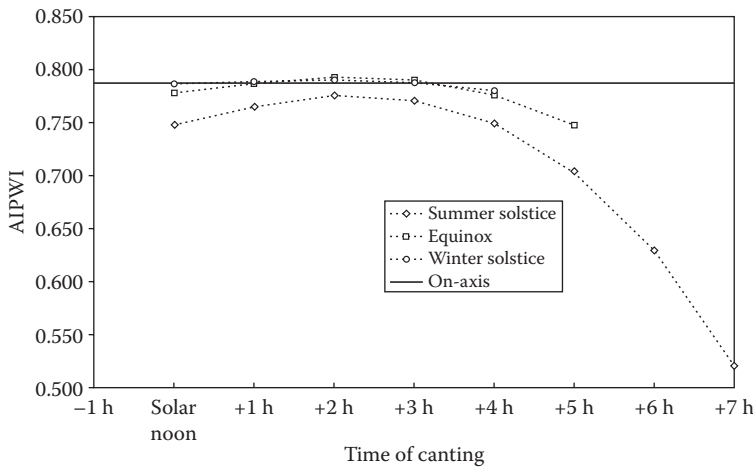
There are different on-axis and off-axis canting methods, which are extensively described in the literature (Buck and Teufel 2009; Jones 1996; Sproul et al. 2011; Landman and Gauché 2013). On-axis canting refers to the alignment adjustment when the heliostat center, target, and the sun all fall along a line. In this case, the facets are aligned to reflect the sun rays that are parallel to

**FIGURE 8.35**

Effect of canting facets in a glass metal heliostat. (From Jones, S.A., A comparison of on-axis and off-axis heliostat alignment strategies, Report SAND96-0566C, Sandia National Lab., Albuquerque, NM, 1996.)

the surface normal of the heliostat. On the other hand, in off-axis canting, the facets are aligned for a specific time in a specific day of the year. Therefore, both methods provide optimal performance only for specific times of the year. At other times of the year, the performance of the heliostat field is less than optimal.

Figure 8.36 compares the on-axis canting with off-axis canting for three different days of the year for a group of heliostats located at a certain location of the field. AIPWI represents the annual incident power weighted intercept, which is the fraction of the annual beam power reflected by the heliostats that is intercepted by the receiver surface (Jones 1996). As can be seen, on-axis canting leads to a uniform high-performance field. Although the off-axis canting performance could theoretically exceed that of on-axis, it

**FIGURE 8.36**

Effect of different canting methods on the annual performance of the heliostats. (From Jones, S.A., A comparison of on-axis and off-axis heliostat alignment strategies. Report SAND96-0566C. Sandia National Lab., Albuquerque, NM, 1996.)

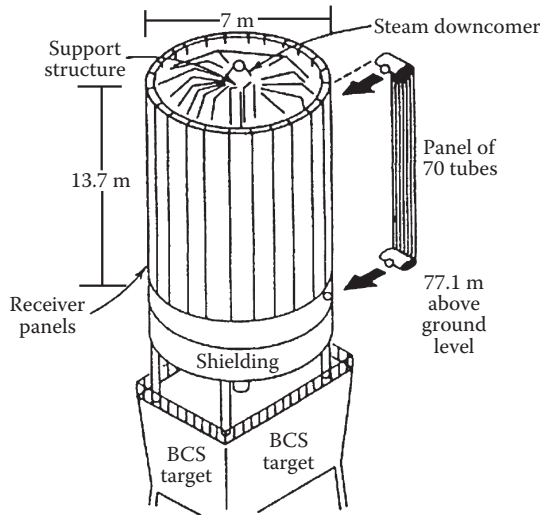
is very dependent on the time of day and varies at different seasons. It must be pointed out that the results in Figure 8.36 are based on a specific location on the field. Hence, one cannot conclude from this figure that performance on winter solstice is the best for all locations on the field. There is no single optimal approach for canting the heliostats and one needs to do a detailed performance analysis and consider the budget before selecting the canting method.

8.7.2 Receiver

Receivers are designed to accept and absorb very high solar flux and to transfer the heat to a fluid at a very high temperature. The HTF may be indirectly or directly irradiated depending on whether it is flowing through tubes irradiated by concentrated radiation or being directly exposed to solar radiation. External and cavity receivers are two types of indirectly irradiated receivers. Volumetric receivers are directly irradiated receivers.

8.7.2.1 External Receiver

External receivers consist of several panels of vertical tubes connected at the top and the bottom by the welded headers. The tubes are generally made of a stainless steel alloy. The panels are connected with each other to approximate a vertical cylinder. The number of tubes per panel, the number of panels, length of the tube, tube diameter, and receiver diameter are important

**FIGURE 8.37**

The receiver of the Solar One central receiver facility at Barstow, California. This is an external-type receiver.

parameters that need to be carefully determined. The Solar One central receiver facility used this type of receiver absorber as shown in Figure 8.37. It consists of 24 panels, each containing 70 tubes of 12.7 mm diameter. The tubes were made of Incoloy 800 and coated with high-absorptance black paint. The overall dimensions of the receiver were 7 m diameter and 13.7 m height.

The main drawback of external receivers is the heat loss from the high-temperature surface of the panels, which are exposed to the environment. Therefore, it is necessary to keep the area of the receiver as small as possible. On the other hand, the cylindrical shape of the receiver accommodates a heliostat field with 360° azimuth angle.

Heat loss from an external receiver can be approximated by

$$Q_{\text{loss}} = Q_{\text{loss rad}} + Q_{\text{loss conv}} + Q_{\text{loss ref}} \quad (8.27)$$

where $Q_{\text{loss rad}}$, $Q_{\text{loss conv}}$, and $Q_{\text{loss ref}}$ are losses due to radiation, convection, and reflection, respectively. The radiation loss can be calculated as

$$Q_{\text{loss rad}} = \varepsilon \sigma A (T_{\text{wall}}^4 - T_{\infty}^4), \quad (8.28)$$

where ε is the emissivity of the receiver surface, σ is the Stefan–Boltzmann constant, A is the receiver surface area, T_{wall} is the receiver surface temperature, and T_{∞} is the ambient temperature. The convective heat loss is the

combined loss by natural convection based on the temperature difference between the receiver surface and the ambient air, and forced convection due to wind at the receiver level. It can be found using a combined convective heat-transfer coefficient h_{mix} by

$$Q_{\text{loss conv}} = h_{\text{mix}} A (T_{\text{wall}} - T_{\infty}), \quad (8.29)$$

where h_{mix} can be estimated from (Siebers and Kraabel 1984)

$$h_{\text{mix}} = \left(h_{\text{forced}}^{3.2} + h_{\text{natural}}^{3.2} \right)^{\frac{1}{3.2}}. \quad (8.30)$$

The Nusselt numbers for natural and forced convection for smooth surfaces are given as

$$Nu_{\text{natural}} = \frac{h_{\text{natural}} H}{k} = 0.098 \text{ Gr}_H^{\frac{1}{3}} \left(\frac{T_{\text{wall}}}{T_{\infty}} \right)^{-0.14} \quad (8.31)$$

$$Nu_{\text{forced}} = \frac{h_{\text{forced}} D}{k} = 0.00239 \text{ Re}^{0.98} + 0.000945 \text{ Re}^{0.89}, \quad (8.32)$$

where H is the receiver height, D is the receiver diameter, and k is the thermal conductivity. Re and Gr are Reynolds and Grashof numbers respectively, which are given as

$$Re = \frac{VD}{\nu} \quad (8.33)$$

$$Gr = \frac{g\beta(T_{\text{wall}} - T_{\infty})H^3}{\nu^2}, \quad (8.34)$$

where ν is the kinematic viscosity and β is the bulk expansion coefficient, which can be approximated as $1/T$. The fluid properties are calculated at the film temperature, which is the average of the ambient and receiver surface temperatures. The correlation for the forced convection is valid for Reynolds numbers between 3.7×10^4 and 10^7 . The heat-transfer coefficients obtained from the above equations can be modified to account for the effect of surface roughness by multiplying by a $\frac{\pi}{2}$ factor.

Example 8.5

The following information is given for an external receiver. Determine the total heat loss and the receiver efficiency if the conduction heat loss is negligible.

- Receiver diameter (D) = 7 m
- Receiver height (H) = 13.7 m
- Ambient temperature (T_{∞}) = 20°C
- Receiver average surface temperature (T_{wall}) = 480°C
- Mean flux density at the receiver surface (q) = 200 $\frac{\text{kW}}{\text{m}^2}$
- Receiver surface absorptivity (α) = 0.95
- Mean wind velocity (V) = 8 m/s
- Thermal conductivity at 250°C = $42.17 \times 10^{-3} \frac{\text{W}}{\text{mK}}$
- Kinematic viscosity of air at 250°C = $41.90 \times 10^{-6} \frac{\text{m}^2}{\text{s}}$

Solution

$$\text{Receiver area } A = \pi \times 7 \times 13.7 = 301.28 \text{ m}^2$$

$$Q_{\text{in}} = q \times A = 200 \times 301.28 = 60.26 \text{ MW.}$$

$$Q_{\text{loss rad}} = \epsilon \sigma A (T_{\text{wall}}^4 - T_{\infty}^4) = 0.95 \times 5.67 \times 10^{-8} \times 301.28 \times (753^4 - 293^4) = 5.10 \text{ MW}$$

$$\text{Reflectivity } (\rho) = 1 - \alpha = 0.05.$$

$$Q_{\text{loss ref}} = \rho \times Q_{\text{in}} = 3.01 \text{ MW.}$$

$$T_f = \frac{T_{\text{wall}} + T_{\infty}}{2} = 523 \text{ K.}$$

At this temperature, the bulk expansion coefficient of air is equal to

$$\beta = \frac{1}{523} = 0.0019 \frac{1}{K}.$$

The dimensionless numbers are calculated as

$$\text{Re} = \frac{VD}{\nu} = \frac{8 \times 7}{41.90 \times 10^{-6}} = 1.336 \times 10^6,$$

$$\text{Gr} = \frac{g\beta(T_{\text{wall}} - T_{\infty})H^3}{v^2} = \frac{9.81 \times 0.0019 \times (480 - 20) \times 13.7^3}{(41.90 \times 10^{-6})^2} = 1.256 \times 10^{13}.$$

$$\begin{aligned} h_{\text{natural}} &= 0.098 \times \frac{k}{H} \times \text{Gr}_H^{\frac{1}{3}} \left(\frac{T_{\text{wall}}}{T_{\infty}} \right)^{-0.14} h_{\text{natural}} \\ &= 0.098 \times \frac{42.17 \times 10^{-3}}{13.7} \times (1.256 \times 10^{13})^{\frac{1}{3}} \times (2.57)^{-0.14} = 6.144 \frac{\text{W}}{\text{m}^2 \cdot \text{K}} \end{aligned}$$

$$h_{\text{natural rough}} = \frac{\pi}{2} h_{\text{natural}} = 9.651 \frac{\text{W}}{\text{m}^2 \cdot \text{K}}.$$

$$\begin{aligned} h_{\text{forced}} &= \frac{k}{D} (0.00239 \text{ Re}^{0.98} + 0.000945 \text{ Re}^{0.89}) = \frac{42.17 \times 10^{-3}}{7} \\ &\times (0.00239 \times (1.336 \times 10^6)^{0.98} + 0.000945 \times (1.336 \times 10^6)^{0.89}) = 16.119 \frac{\text{W}}{\text{m}^2 \cdot \text{K}} \end{aligned}$$

$$h_{\text{forced rough}} = \frac{\pi}{2} h_{\text{forced}} = 25.32 \frac{\text{W}}{\text{m}^2 \cdot \text{K}}.$$

$$h_{\text{mix}} = \left(h_{\text{forced}}^{3.2} + h_{\text{natural}}^{3.2} \right)^{\frac{1}{3.2}} = (23.32^{3.2} + 9.651^{3.2})^{\frac{1}{3.2}} = 23.744 \frac{\text{W}}{\text{m}^2 \cdot \text{K}}.$$

$$Q_{\text{loss conv}} = h_{\text{mix}} A (T_{\text{wall}} - T_{\infty}) = 23.744 \times 301.28 \times (480 - 20) = 3.29 \text{ MW}.$$

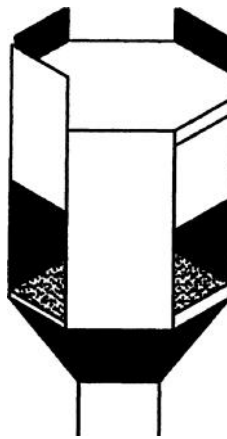
$$Q_{\text{loss}} = Q_{\text{loss rad}} + Q_{\text{loss ref}} + Q_{\text{loss conv}} = 5.10 + 3.01 + 3.29 = 11.4 \text{ MW}.$$

$$\eta = \frac{Q_{\text{in}} - Q_{\text{loss}}}{Q_{\text{in}}} = \frac{60.26 - 11.4}{60.26} = 0.81.$$

8.7.2.2 Cavity Receivers

A cavity receiver receives the concentrated flux inside a small insulated cavity in order to reduce the radiative and convective losses. Typical designs have an aperture area approximately one-third to one-half of the internal absorbing surface area. The acceptance angles range from 60° to 120°. There may be more than one cavity in a receiver, each receiving energy from a sector of the heliostat field (Batteson 1981). Figure 8.38 shows an example of a cavity receiver.

The optimal size of the cavity aperture is defined by a compromise between minimizing the thermal loss and maximizing the radiation capture. For an insulated cavity receiver with circular aperture, neglecting conduction,

**FIGURE 8.38**

A cavity-type receiver-type receiver design incorporating four apertures. It would operate in the 510°C–565°C temperature with steam, molten salt, or sodium. (From Battleson, K.W., Solar power tower design guide: Solar thermal central receiver power systems. A source of electricity and/or process heat, NASA STI/Recon Tech. Report N81, 31670, 1981.)

and convection losses, the absorption efficiency is given as (Steinfeld and Schubnell 1993)

$$\eta_{\text{absorption}} = \frac{\alpha_{\text{eff}} P_{\text{ap}} - \varepsilon_{\text{eff}} \pi r^2 \sigma T^4}{P_{\text{in}}} , \quad (8.35)$$

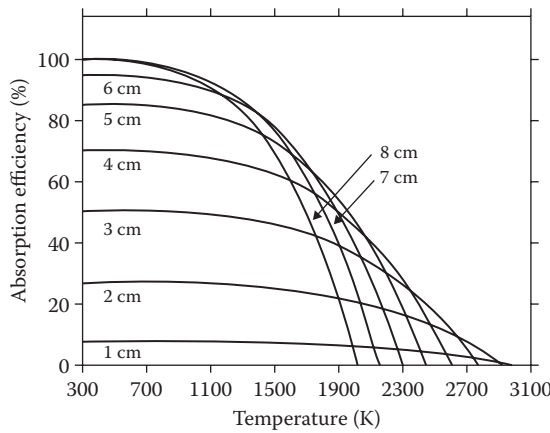
where P_{in} is the total power coming from the heliostat field, P_{app} is the power intercepted by the aperture, α_{eff} and ε_{eff} are the effective absorptance and emittance of the receiver, r is the radius of the circular aperture, σ is the Stefan–Boltzmann constant, and T is the nominal cavity temperature. The maximum cavity temperature can be obtained by setting the absorption efficiency equal to zero, which results in

$$T_{\text{max}} = \left(\frac{\alpha_{\text{eff}} I C}{\varepsilon_{\text{eff}} \sigma} \right)^{0.25} , \quad (8.36)$$

where I is the beam normal radiation and C is the concentration ratio, which is defined as

$$C = \frac{P_{\text{ap}}}{A_{\text{ap}} I} . \quad (8.37)$$

In order to capture solar energy at a reasonable efficiency, the operating temperature of the receiver should be significantly lower than the T_{max} value.

**FIGURE 8.39**

Absorption efficiency of a circular cavity receiver as a function of receiver temperature and aperture radius. (From Steinfeld, A. and M. Schubnell, *Solar Energy*, 50 (1), 19–25, 1993.)

Figure 8.39 depicts the variations of absorption efficiency versus receiver temperature and aperture size. At low temperatures where the radiation loss is negligible, the larger aperture has higher absorption efficiency as more power is intercepted. However, by increasing the temperature and consequently the radiation loss, the efficiency decreases with steeper slopes for larger apertures.

Similar to external receivers, the convective heat loss in cavity receivers is a combined effect of natural and forced convection. Siebers and Kraabel (1984) proposed using a mixed heat-transfer coefficient as the sum of the individual natural and forced heat-transfer coefficients. However, finding the coefficients is not straightforward and depends on the details of the receiver design, such as aperture area relative to that of the absorbing surfaces, tilt angle of the aperture, and wind velocities and directions (Winter et al. 1991). Kistler (1986) suggested the following equations that directly estimate the heat loss:

$$Q_{\text{loss conv}} = Q_{\text{forced}} + Q_{\text{natural}} \quad (8.38)$$

$$Q_{\text{forced}} = 7631 \frac{A_{\text{ap}}}{W_{\text{ap}}^{0.2}} \text{ Watts} \quad (8.39)$$

$$Q_{\text{natural}} = 5077 A_{\text{cav}} \text{ Watts} \quad (8.40)$$

where A_{ap} is the aperture area (m^2), W_{ap} is the aperture width (m), and A_{cav} is the total area inside of cavity (m^2).

8.7.2.3 Volumetric Receivers

Volumetric receivers usually use highly porous structures to absorb concentrated solar radiation substantially inside the structure rather than on the surface. While the HTF is passing through the porous media, it is heated by forced convection. In a good volumetric receiver, the temperature on the irradiated side of the absorber is lower than the outlet temperature, which tends to decrease the radiative losses at the inlet. This is the so-called volumetric effect (Ávila-Marín 2011). Figure 8.40 compares the temperature profiles of air as an HTF in a tube and a volumetric receiver. As can be seen, the temperature difference between the absorber surface and air vanishes in the middle of the volumetric receiver. On the other hand, the temperature of the outer surface of an external tube receiver is much higher than the air, which increases the heat loss. Moreover, the maximum flux that a tube receiver can sustain is significantly lower than a volumetric receiver.

A volumetric receiver may be open to the ambient or enclosed by a highly transparent window depending on the type of the HTF and the operating pressure. Open volumetric receivers are used to heat air at atmospheric pressure. The high-temperature air can be used to generate steam for steam power plants. The maximum operating temperature of a volumetric receiver is limited by the type of the material that is used to absorb solar radiation. With metal absorbers, air outlet temperatures between 800°C and 1000°C are achievable, while silicon-based ceramics are able to operate at higher temperatures. Figure 8.41 shows ceramic foams with different pore sizes and materials manufactured by Institut für Keramische Technologien und Sinterwerkstoffe (IKTS) in Dresden, Germany.

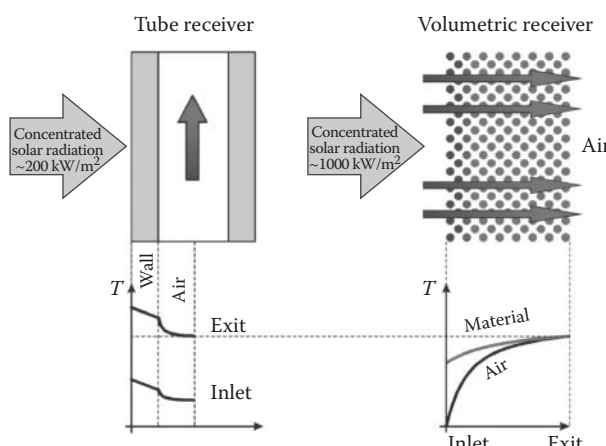
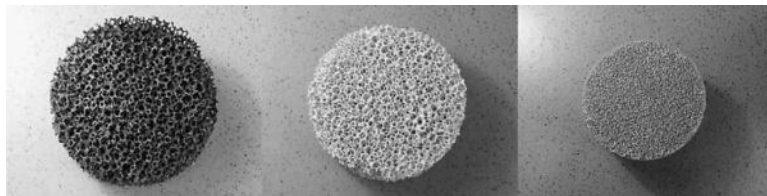


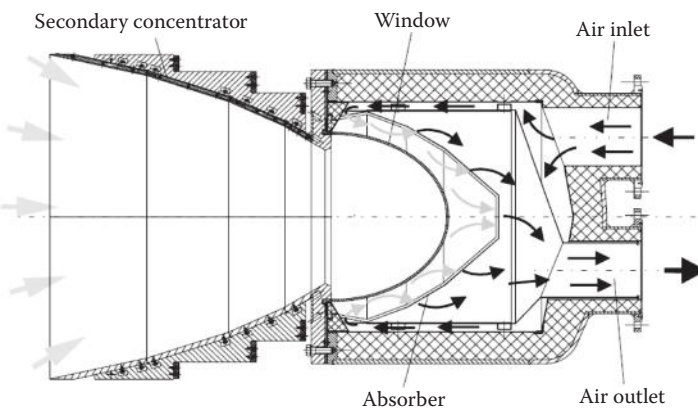
FIGURE 8.40

Comparison of a tube and a volumetric receiver. (From Fend, T., *Optica Applicata*, 11 (2), 271–284, 2010.)

**FIGURE 8.41**

Ceramic foams manufactured by IKTS. (From Fend, T. et al., *Energy*, 29 (5–6), 823–833, 2004.)

Volumetric receivers can be used to heat up the working fluid of a gas turbine. In this case, the receiver operates under elevated pressure and a window is used to separate the receiver cavity from the ambient air. Figure 8.42 shows a schematic of a pressurized volumetric receiver module called REFOS, which was installed in the CESA-1 solar tower test facility of the Plataforma Solar de Almería (PSA), Spain. A secondary concentrator is installed in front of the receiver to further concentrate the solar radiation. A domed quartz window is used to transmit the solar radiation. The pressurized air enters the plenum between the window and the absorber and is heated by passing through the absorber. Air exit temperatures up to 815°C and receiver efficiency in the range of 70% were achieved (Buck et al. 2002). The design of a window for a pressurized receiver is very challenging as it has to be highly transparent, yet strong and durable at high pressures and temperatures. Quartz windows (SiO_2) are widely used, which have a maximum operating temperature limit of 1000°C. A window made of fused silica was tested at the Weizmann Institute of Science in Israel, which successfully

**FIGURE 8.42**

REFOS volumetric receiver module. (From Buck, R. et al., *Journal of Solar Energy Engineering*, 124 (1), 2, 2002.)

**FIGURE 8.43**

Local melting in a honeycomb absorber. (From Karni, J. et al., *Journal of Solar Energy Engineering*, 120 (2), 85, 1998b.)

sustained an operating pressure and peak absorber temperature of 30 bar and 1700°C, respectively (Karni et al. 1998a).

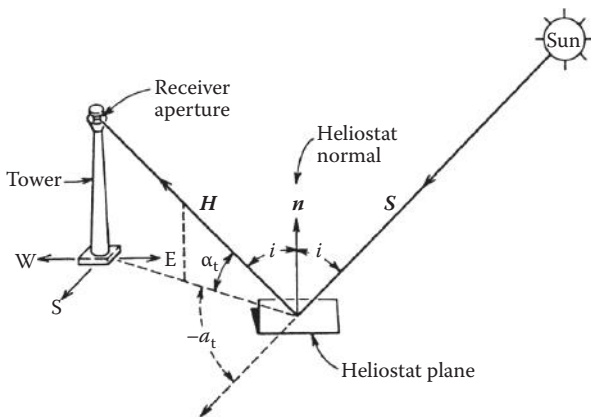
One of the main problems in the operation of the volumetric receivers is the relationship between local solar flux and the flow speed. High local solar flux increases the viscosity of air leading to a lower mass flow rate and, consequently, a higher material temperature. On the other hand, a low solar flux causes higher mass flow rate and lower material temperature. Therefore, it is possible for the material temperature to exceed the maximum allowable temperature at some points while the average air outlet temperature is still low. This may lead to local failures, such as melting or cracking (Becker et al. 2006). Local melting in a honeycomb absorber owing to high local temperature is shown in Figure 8.43.

A volumetric particle receiver is another type of directly irradiated receiver in which the HTF is seeded by small particles that act as absorbers. Carbon particles with sizes less than a micron have been suggested for absorbing solar energy (Fend 2010; Fend et al. 2004). If air is used as the HTF with carbon particles as the absorbers, carbon could be oxidized at the high temperatures in the receiver, which would provide additional heat to the fluid, although the additional heat is very small (Bertocchi et al. 2004). This type of receiver has a high surface-to-volume ratio, which minimizes the temperature difference between the absorber and the HTF. Moreover, a small-particle receiver can withstand higher fluxes and is immune to hotspots (Fend 2010; Fend et al. 2004).

8.7.3 Design of Heliostat Field

A detailed design of the heliostat field is beyond the scope of this book. However, some macroscale features are described here.

A heliostat is oriented in such a way that a solar ray incident on the heliostat is reflected toward the receiver as shown in Figure 8.44. In vector notation,

**FIGURE 8.44**

Sun-heliostat-tower geometry for calculating tracking requirements. Tower unit vector H altitude and azimuth angles are shown.

the angle between a heliostat to receiver vector H and the heliostat normal n is given by the scalar product

$$\cos i = \frac{\mathbf{n} \cdot \mathbf{H}}{|\mathbf{n}| |\mathbf{H}|}. \quad (8.41)$$

This equation, along with Equation 2.48, gives the incidence angle between a solar ray S and the heliostat normal n . The second equation relating the two heliostat rotation angles (surface tilt and azimuth angles) is the requirement that the incident ray S , heliostat normal n , and the reflected ray H all be coplanar; that is,

$$(\mathbf{S} \times \mathbf{n}) \cdot \mathbf{H} = 0. \quad (8.42)$$

Unit vectors S , n , and H are shown in Figure 8.44.

Using a Cartesian coordinate system in which (x,y,z) correspond to east, north, and vertical, the components of n , H , and S are

$$\begin{aligned} \mathbf{n} = & \begin{pmatrix} \cos \alpha_n \sin \alpha_t \\ -\cos \alpha_n \cos \alpha_t \\ \sin \alpha_n \end{pmatrix} \end{aligned} \quad (8.43)$$

$$\begin{aligned} \mathbf{H} = & \begin{pmatrix} \cos \alpha_t \sin \alpha_t \\ -\cos \alpha_t \cos \alpha_t \\ \sin \alpha_t \end{pmatrix} \end{aligned} \quad (8.44)$$

$$\begin{aligned} S = & \frac{\cos \alpha \sin a_s}{-\cos \alpha \cos a_s}, \\ & \sin \alpha \end{aligned} \quad (8.45)$$

where α and a_s are the solar altitude and azimuth angles, α_t and a_t are the altitude and azimuth angles of the reflected ray vector to the fixed tower shown in Figure 8.44, and α_n and a_n are the heliostat normal altitude and azimuth angles measured in the same way as α and a_s .

Optimal design of the heliostat field has been the subject of many studies because it typically accounts for approximately 50% of the total cost of the plant (Kolb et al. 2007) and 40% of energy losses (Sargent and Lundy LLC Consulting Group 2003). Several codes have been developed over the last few decades, which are well documented in Garcia et al. (2008). Different approaches are used in these codes to maximize the overall field efficiency, which is defined as

$$\eta_{\text{field}} = \eta_{\text{reflection}} \times \eta_{\text{cosine}} \times \eta_{\text{attenuation}} \times \eta_{\text{interception}} \times \eta_{\text{shading \& blocking}}, \quad (8.46)$$

where $\eta_{\text{reflection}}$ represents the reflectivity of the heliostats, η_{cosine} is the cosine factor, $\eta_{\text{attenuation}}$ is the atmospheric attenuation factor, $\eta_{\text{interception}}$ is the interception factor that accounts for the fraction of the reflected rays that hit the target, and $\eta_{\text{shading \& blocking}}$ is the shading and blocking factor.

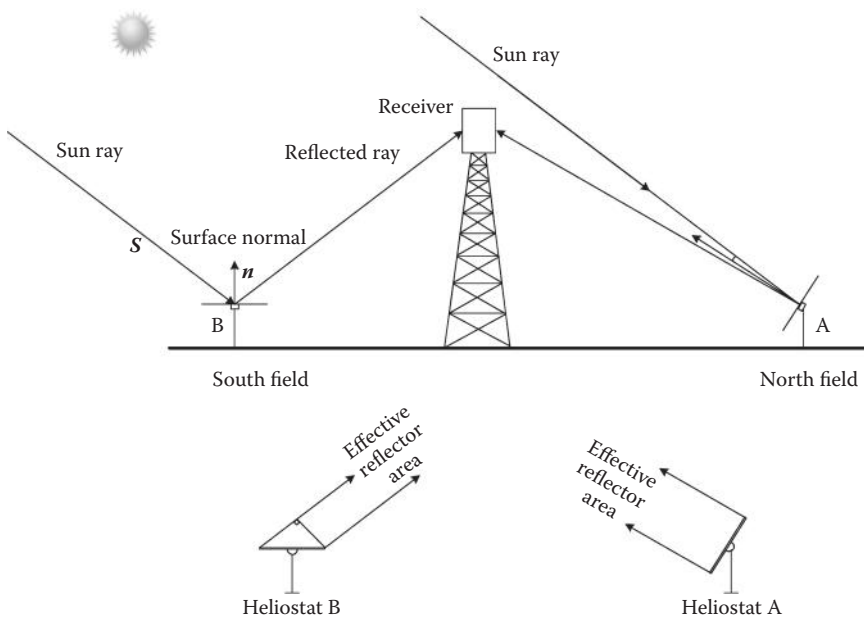
8.7.3.1 Reflection Factor ($\eta_{\text{reflection}}$)

A part of the incident radiation on a heliostat is absorbed by the surface. The fraction that is reflected depends on the absorptivity of the heliostat surface coating and the incidence angle.

8.7.3.2 Cosine Factor (η_{cosine})

This is the most significant loss in the heliostat field that is due to the angle between the incident solar beam and the surface normal (incidence angle). Therefore, it depends on both sun and heliostat positions. The reflected radiation from the heliostat is proportional to the cosine of this angle, which is why it is called the cosine effect. As shown in Figure 8.45, for a field located in the Northern Hemisphere, a heliostat situated in the south field has a higher incidence angle and, consequently, less effective reflector area and cosine factor. Knowing the sun ray vector S and surface normal n , the cosine factor is defined as

$$\eta_{\text{cosine}} = \frac{\mathbf{S} \cdot \mathbf{n}}{|\mathbf{S}| |\mathbf{n}|}. \quad (8.47)$$

**FIGURE 8.45**

The cosine effect for a heliostat field located at the Northern Hemisphere. (Stine, W.B. and R.W. Harrigan: *Solar Energy Fundamentals and Design: With Computer Applications*. 1985. Copyright Wiley-VCH Verlag GmbH & Co. KGaA. Reproduced with permission.)

8.7.3.3 Atmospheric Attenuation Factor ($\eta_{\text{attenuation}}$)

The reflected beam radiation from the surface of a heliostat may be scattered, depending on the distance between the heliostat and the receiver, ambient humidity, and particulate matter in the air. This atmospheric attenuation factor can be calculated by (Schmitz et al. 2006)

$$\eta_{\text{attenuation}} = 0.99321 - 0.000176 \times d + 1.97 \times 10^{-8} \times d^2 \quad (8.48)$$

for $d \leq 1000 \text{ m}$

$$\eta_{\text{attenuation}} = \exp(-0.0001106 \times d) \quad (8.49)$$

for $d > 1000 \text{ m}$,

where d is the distance between the heliostat surface and the receiver.

8.7.3.4 Interception Factor ($\eta_{\text{interception}}$)

A portion of the reflected image from the heliostat may fail to intercept the receiver aperture, which is the cumulative result of several factors such as tracking precision, shape of the sun, nonuniformity of mirror surface, and so

on. There are two general approaches to find the interception factor (spillage factor), that is, ray tracing method and analytical integration of the image shape produced by the mirror over the receiver domain. Two well-known analytical methods that are extensively used are the UNIZAR model from Universidad de Zaragoza (Collado et al. 1986; Collado and Turegano 1989) and the HFCAL model from the German Aerospace Center (Schwarzbözl et al. 2009). Collado (2010) compared the two models and concluded that both of them are appropriate tools while the HFCAL model is much simpler and slightly more accurate. In the HFCAL model, the flux density on the receiver aperture is given as (Collado 2010)

$$F(x, y) = \frac{P}{2\pi\sigma_{\text{tot}}^2} \exp - \frac{x^2 + y^2}{2\sigma_{\text{tot}}^2}, \quad (8.50)$$

where P is the total power reflected from an individual heliostat on the receiver plane and σ_{tot} is the total dispersion of the flux distribution. The total power is calculated as

$$P = I \times A_m \times \eta_{\text{cosine}} \times \eta_{\text{attenuation}} \times \eta_{\text{reflection}}, \quad (8.51)$$

where I is the direct solar radiation and A_m is the mirror surface area. The total dispersion can be calculated as

$$\sigma_{\text{tot}} = \frac{\sqrt{d^2 \left(\sigma_{\text{sun}}^2 + \sigma_{\text{ast}}^2 + \sigma_t^2 + (2\sigma_s)^2 \right)}}{\cos i}, \quad (8.52)$$

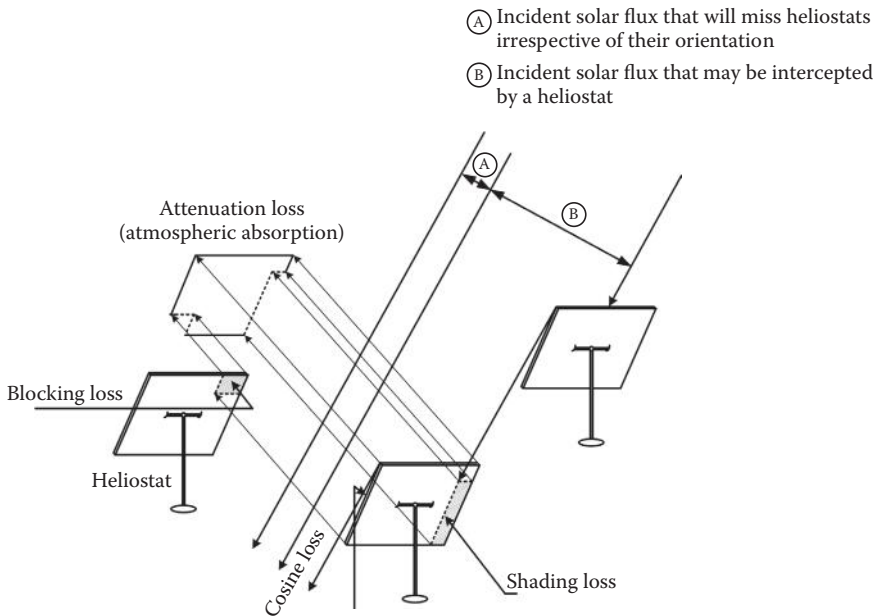
where σ_{sun} , σ_{ast} , σ_t , and σ_s are the standard deviations due to sun shape error, astigmatic effect, tracking error, and mirror slope error, respectively. Here, d represents the actual distance between the heliostat surface center and the aim point on the receiver while $\cos i$ is the cosine of the angle between the reflected central ray from the heliostat and the receiver surface normal.

The intercepted power is obtained by integrating the flux distribution along the receiver aperture. The interception factor can be obtained as

$$\eta_{\text{interception}} = \frac{1}{2\pi\sigma_{\text{tot}}^2} \iint_x_y \exp - \frac{x^2 + y^2}{2\sigma_{\text{tot}}^2} dy dx. \quad (8.53)$$

8.7.3.5 Shading and Blocking Factor ($\eta_{\text{shading \& blocking}}$)

The shading and blocking factor not only depends on the sun's position and the individual location of the analyzed heliostat but also is a function of the

**FIGURE 8.46**

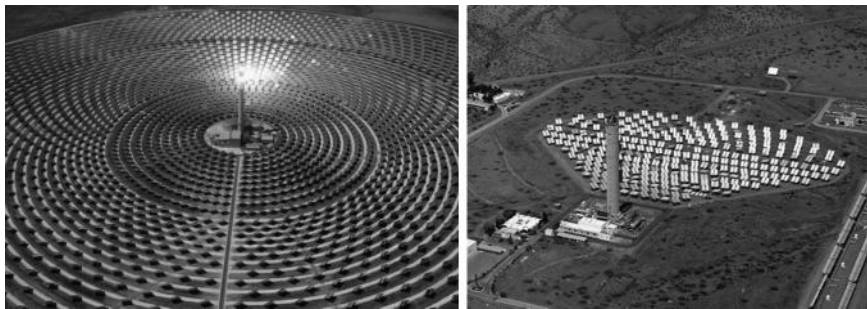
Shading and blocking losses in a heliostat field. (Stine, W.B. and R.W. Harrigan: *Solar Energy Fundamentals and Design: With Computer Applications*. 1985. Copyright Wiley-VCH Verlag GmbH & Co. KGaA. Reproduced with permission.)

location of the neighboring heliostats. Shading occurs when the incoming solar radiation is obstructed by a neighboring heliostat. On the other hand, blocking occurs when the reflected image from a heliostat is partially blocked by an adjacent heliostat from reaching the receiver (Figure 8.46). The shading and blocking factor of a heliostat is defined as the area not shaded or blocked divided by the total heliostat area.

The shading and blocking loss can be minimized by increasing the distance between the heliostats. On the other hand, increasing the size of the field leads to other consequences such as higher atmospheric attenuation and higher land costs. Therefore, an optimization study needs to be carried out to find the optimal field layout. A number of codes have been developed for this purpose, which are well documented in Garcia et al. (2008).

8.7.4 Field Layout

Heliostat field layout depends on the choice of the receiver. The north field layout (in the Northern Hemisphere) is commonly used for cavity receivers. The north field is more effective at a midday design point and consequently leads to a lower system cost. On the other hand, the surrounding field is used

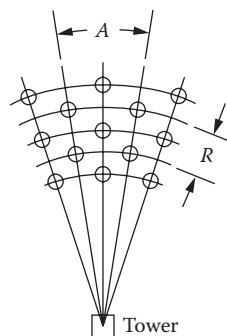
**FIGURE 8.47**

Aerial views of the plants Gemasolar (19.9 MW) and CESA-1 (1.2 MW) in Spain.

for cylindrical receivers, which allows the use of a smaller tower. In this case, the south field performs very well in the morning and evening while it is less effective at midday. Figure 8.47 shows a surrounding and a north field for the power plants in Spain.

The radial stagger layout (Lipps and Vant-Hull 1978) proposed by Lipps and Vant-Hull is commonly used for heliostat field design as it requires minimal computational effort and is well tested over time. There are two parameters that need to be optimally defined, that is, radial spacing R and azimuth spacing, which are depicted in Figure 8.48. The correlations for these parameters determined by curve fits to the optimized layouts are given for high reflectance heliostats in a large field as

$$R = h \left(1.44 \cot \alpha_t - 1.094 + 3.068\alpha_t - 1.1256\alpha_t^2 \right) \quad (8.54)$$

**FIGURE 8.48**

The radial stagger heliostat layout pattern developed by the University of Houston.

and

$$A = w \cdot 1.749 + 0.6396\alpha_t + \frac{0.2873}{\alpha_t - 0.04902} , \quad (8.55)$$

where h and w are the height and width of the heliostat and α_t is the tower altitude angle measured from the center of the front heliostat.

8.8 Central Receiver System (CRS) Design

The design of a CRS is complicated, involving the use of computer programs. There are many commercial computer programs that can be used to design the solar field and the receiver. The System Analyzer Model (SAM) is one of the programs that can be used for a preliminary design and economic analysis. Commercial computer models such as TRNSYS, GATECYCLE, and IPSEpro can be used to design the power block for a central receiver power plant.

The following example shows a preliminary design of the solar field of a CRS.

Example 8.6

A preliminary estimate of the power plant size can be helpful before performing a detailed system design. Provide a preliminary size of the solar field and the receiver for a 50-MW_e central receiver plant in Barstow, California, with a design point insolation of 950 W/m².

Solution

The method used here follows the approach proposed by Vant-Hull and Izgyon (2003) where the parameters are estimated from rules of thumb or prior experience. A solar multiple (SM) of 1.8 and an average receiver surface temperature of 700 K are considered. The calculation procedure is described step by step.

1. Receiver Design

The receiver thermal rating (RTR) can be found by knowing the power cycle efficiency (η_{cycle}), parasitics, and SM as

$$\begin{aligned} RTR &= \frac{SM \times (\text{Design point power} + \text{Parasitics})}{\eta_{cycle}} \\ &= \frac{1.8 \times (50 \text{ MW}_e + 5 \text{ MW}_e)}{0.4} = 248 \text{ MW}_{th}. \end{aligned}$$

It is assumed that the parasitics are 10% of the design point power and the cycle efficiency is 40%. Now, the receiver absorbing area (RAA) can be found from the average flux density. Typically, the average flux density is equal to allowable flux density $\times 0.53$. It is assumed that the allowable flux density is 0.825 MW/m². Therefore,

$$\text{RAA} = \frac{248}{0.825 \times 0.53} = 568 \text{ m}^2.$$

Receiver thermal losses (RTLs) can be found by the following correlation:

$$\text{RTL} = 30 \frac{\text{kW}}{\text{m}^2} \times \left(\frac{T}{800 \text{ K}} \right)^2 \times \text{RAA} = 30 \times \left(\frac{700}{800} \right)^2 \times 568 = 13 \text{ MW}_{\text{th}}.$$

Therefore, the total energy that needs to be provided by the field is $248 + 13 = 261 \text{ MW}_{\text{th}}$. However, absorptivity of the receiver surface as well as interception and atmospheric attenuation efficiencies need to be taken into account. Therefore, field rating (FR) is given as

$$\text{FR} = \frac{261}{\text{Absorptivity} \times \eta_{\text{int}} \times \eta_{\text{att}}} = \frac{261}{0.92 \times 0.98 \times 0.95} = 305 \text{ MW}_{\text{th}}.$$

2. Field Design

As previously described in Chapter 3, there are also other efficiency factors that need to be taken into consideration such as reflectivity, cosine factor, and shading and blocking efficiency. Assuming 99% availability, the field efficiency (FE) is obtained as

$$\text{FE} = \eta_{\text{ref}} \times \eta_{\text{cosine}} \times \eta_{\text{shading \& blocking}} \times \text{availability} = 0.88 \times 0.83 \times 0.92 \times 0.99 = 0.665.$$

Therefore, the reflector area (RA) is given as

$$\text{RA} = \frac{\text{FR}}{(\text{FE} \times \text{Insolation})} = \frac{305 \text{ MW}_{\text{th}}}{0.665 \times 950} = 483,000 \text{ m}^2.$$

The field area (FA) can be calculated by considering ground coverage (GC) and exclusion factor (EF), which accounts for the areas restricted for roads, power block, drainage, and so on.

$$\text{FA} = \frac{\text{RA}}{\text{GC} \times \text{EF}} = \frac{0.483 \text{ km}^2}{0.25 \times 0.97} = 1.99 \text{ km}^2.$$

The field radius to the north, east, and west for the surround field can be obtained by

$$R_{\text{surround}} = \frac{FA \times 1.25}{\pi}^{0.5}$$

Considering the reduced southern field, the radius of the south part of the field is given as

$$R_{\text{south}} = \frac{2}{3} \times R.$$

Moreover, the field radius for the north-only field is given as

$$R_{\text{north only}} = \frac{FA \times 2.25}{\pi}^{0.5}$$

Therefore,

$$R_{\text{surround}} = 0.89 \text{ km}$$

$$R_{\text{north only}} = 1.19 \text{ km.}$$

Tower focal height (HT) can be obtained by

$$HT = R \tan (8.8^\circ) = R \times 0.154.$$

HT is the distance from the plane of the reflector to the center of the receiver. In an optimized surround field, 8.8° is the typical elevation angle from the most distant heliostat. Therefore,

$$HT = 0.89 \times 0.154 = 137 \text{ m (surround field)}$$

$$HT = 1.19 \times 0.154 = 183 \text{ m (north field).}$$

8.9 Recent Developments in Solar Thermal Power Cycles

Solar thermal power technologies were successfully demonstrated in the 1980s, as noted in Section 8.4 in this chapter. In fact, SEGS thermal power plants built in the 1980s are still producing power commercially. With that

learning experience, a number of new CSP plants have been built or are under construction. However, the capital costs of \$2500–\$3500/kW for a solar power plant is still three to four times higher than the natural gas combustion turbines, and the plant efficiency of 12% to 14% has the potential to improve by as much as three times (Goswami 1998). This potential has drawn the interest of researchers to fundamental thermodynamic improvements in power cycles for solar energy.

8.9.1 Hybrid and Combined Cycles

The SEGS plants and the CPG dish/Stirling power plants were designed to use natural gas as a supplemental fuel. It has also been suggested that natural gas be used as a supplemental fuel for the CRS (Bohn et al. 1995). If the supplemental natural gas flows in the power system are large enough, it makes sense to use the natural gas in a combined-cycle mode. With the present-day technology of natural gas combustion turbines, a combined combustion turbine/steam Rankine cycle power plant can achieve a cycle efficiency as high as 58%. Figure 8.49 shows a schematic of a combined-cycle solar/natural gas power plant (Washam et al. 1993). In 2012, Florida Power & Light built a 75-MW parabolic trough-based solar thermal power plant

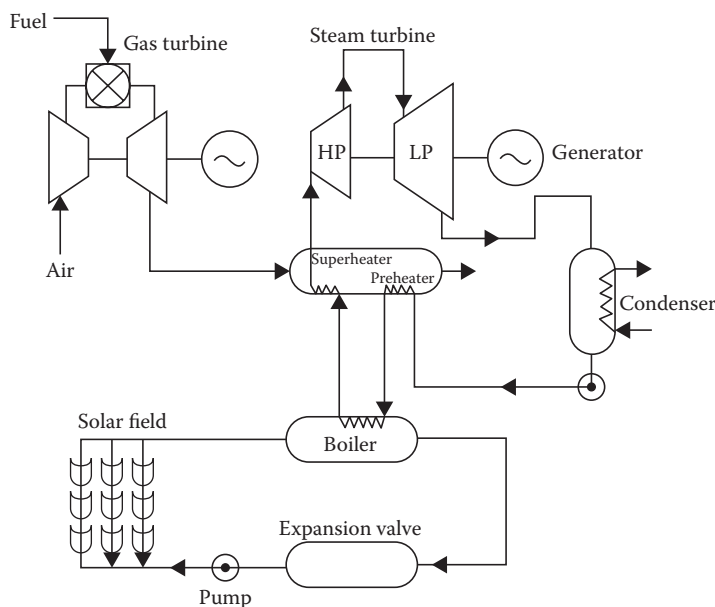


FIGURE 8.49

Concept of an integrated solar combination–cycle power system. (From Washam, B.M. et al., *Integrated Solar Combined Cycle Systems [ISCCS] Utilizing Solar Parabolic Trough Technology—Golden Opportunities for the '90s*, Diablo, CA: Spencer Management Associates, 1993.)

in Martin County as a preheater for a 1000-MW natural gas combined-cycle power plant. With the present cost of the commercially available, aeroderivative combustion turbines as low as \$500/kW, and the cost of a solar power plant being approximately \$2500–\$3000/kW, the capital costs of a combined-cycle solar/natural gas power plant could be as low as \$1000–\$2000/kW, depending on the natural gas fraction. This idea seems very attractive, especially where natural gas is to be used as a backup fuel anyway.

8.9.2 Kalina Cycle

Kalina (1984) proposed a novel bottoming cycle for a combined-cycle power plant that improves the overall performance of the cycle. This novel cycle, now known as the Kalina cycle, uses a mixture of ammonia and water as the working fluid for the bottoming cycle expansion turbine. Using a two-component working fluid and multipressure boiling, one can reduce heat transfer-related irreversibilities and therefore improve the resource effectiveness (Figure 8.50). Also, the ammonia–water mixture can be used as a working fluid for a lower-temperature (250°C) solar energy system employing lower-cost parabolic trough technology. According to Kalina and Tribus (1992), it is possible to improve the efficiency of the bottoming cycle by more than 45% over the steam Rankine cycle for a lower temperature resource ($\sim 250^{\circ}\text{C}$). Therefore, if the Kalina cycle is used for solar thermal power in place of the Rankine cycle, the capital cost could be reduced by at least 45% because of the higher efficiency and the possibility of using cheaper concentrating collectors owing to the lower temperature

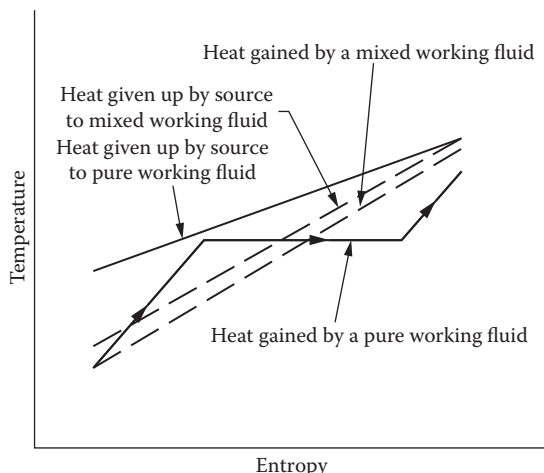


FIGURE 8.50
Heat transfer between a heat source and a working fluid.

requirement. These improvements may be enough to make solar thermal power economically competitive by itself and not a burden on natural gas for combined-cycle power plants. This offers an opportunity for research in solar thermal power utilizing the Kalina cycle.

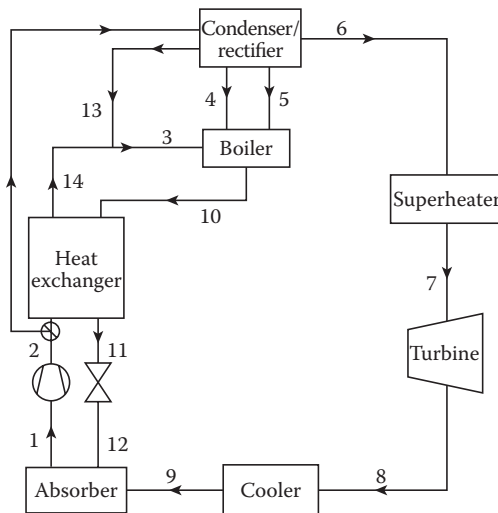
Although the use of mixed working fluids such as ammonia–water provides a big advantage in utilizing sensible heat sources in a boiler, they present a disadvantage in the condenser, since condensation must also take place with change in temperature. This disadvantage could be overcome if the normal condensation process is replaced by the absorption condensation process as proposed by Rogdakis and Antonopoulos (1991) and Kouremenos et al. (1994) as a modification of the Kalina cycle and, more recently, by Goswami (1995) as an ammonia-based combined power/cooling cycle.

8.9.3 Aqua–Ammonia Combined Power/Absorption Cycle

Kouremenos et al. (1994) showed an analysis of an aqua–ammonia power cycle that is similar to the Kalina cycle; however, it replaces the conventional condensation process of the aqua–ammonia mixture coming out of the low-pressure turbine with an absorption condensation process. They showed that with an ammonia concentration of 72.86% in the mixed working fluid in the turbine, cycle efficiencies of the order of 25%–45% could be achieved for a source temperature of 500°C and pressure ratios from 25 to 100.

8.9.4 Combined Power/Cooling Cycle

Goswami (1995) has proposed a new thermodynamic cycle that improves the cycle efficiency and, therefore, resource utilization by producing power and refrigeration in the same cycle. The new cycle, also known as the Goswami cycle, was developed to use ammonia as the working fluid in an innovative combination of an ammonia-based Rankine cycle and an ammonia–water absorption refrigeration cycle. The use of any mixture of fluids was later allowed provided that one is much more volatile than the other and the more volatile component could be condensed by absorption in the other. The ammonia–water mixture is an obvious example, but other examples include mixtures of hydrocarbons such as isobutane and heptane or pentane and decane. Figure 8.51 shows a schematic of the cycle. By boiling a mixture, for example, ammonia–water, this cycle reduces the irreversibilities associated with the heat transfer from a sensible heat source. Also, by expanding almost pure ammonia in the last-stage turbine, it allows the working fluid to go down to a much lower temperature, providing refrigeration. The working fluid is condensed by absorption in the water. The net effect lowers the sink temperature of the cycle. The cycle can use source temperatures as low as 100°C, thereby making it a useful power cycle for low-cost solar thermal collectors, geothermal resources, and waste heat from existing power plants.

**FIGURE 8.51**

A schematic diagram of the Goswami combined power/cooling cycle.

8.9.5 Supercritical CO₂ Power Cycle

Carbon dioxide, as a nontoxic, abundant, inexpensive, nonflammable, and highly stable compound with low critical properties, has been the subject of interest for many researchers to be used as a working fluid for thermodynamic power cycle for high-temperature solar fields such as a central receiver tower. Design of the first supercritical CO₂ (S-CO₂) cycle dates back to late 1960s when Feher (1967) and Angelino (1967, 1968) began their separate investigations on replacing the conventional working fluids with S-CO₂. However, the main problem about using CO₂ is the low critical temperature (30.98°C) that requires low-temperature cooling water, which is not available in many locations. This limitation led to studies on the CO₂ cycle in gas state only. It was reported by Angelino (1969) that compressing CO₂ around its critical point results in lower compression work and consequently higher cycle efficiency, which is mainly due to the reduction of the specific volume at critical condition. Since then, S-CO₂ power cycles have drawn attention for nuclear power generation in gas reactors (Dostal et al. 2006; Moisseytsev and Sienicki 2009).

On the other hand, there is a growing interest in deploying S-CO₂ in concentrated solar power plants owing to limitations of the current HTFs. Oil, molten salt, and steam are the common HTFs, which are used to absorb solar energy in the solar receiver. However, the maximum operating temperature of the oil is 400°C, which limits the overall performance of the plant. Although molten salt operates at higher temperatures (around 560°C), the high freezing point becomes a major challenge, which requires elaborate freeze protection systems. As the phase of the fluid changes in the receiver in direct steam

generation plants, complex control systems are required while the storage capacity is also limited (Turchi 2009). On the other hand, there is no maximum or minimum temperature limits for CO₂, and it is nontoxic, inexpensive, and nonflammable. Moreover, by employing an appropriate power cycle, it can be used as both heat transfer and working fluids, eliminating the need for a heat exchanger in between. It has been shown by Turchi et al. (2012) that the S-CO₂ Brayton cycle can achieve more than 50% efficiency under dry cooling conditions. The main advantages of the S-CO₂ Brayton cycle are its high efficiency, high power density, compactness, and low cost.

There are different S-CO₂ configurations, for example, recompression and partial cooling (Turchi et al. 2012), but all of them have been derived from the simple cycle that is shown in Figure 8.52. The CO₂ is pressurized in the

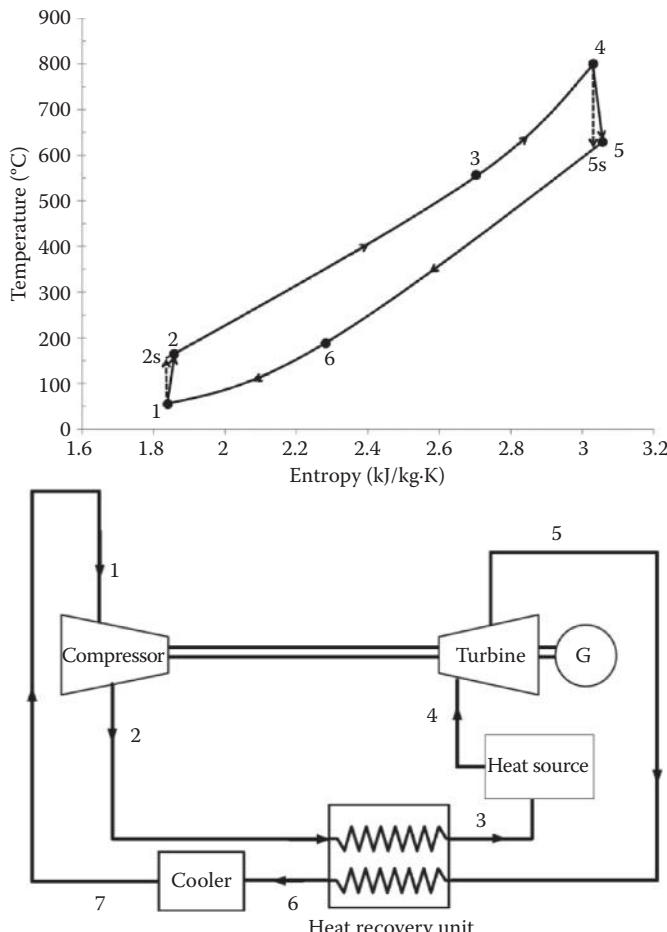


FIGURE 8.52
Basic S-CO₂ Brayton cycle.

compressor to above its critical pressure. The S-CO₂ is then heated by the heat source, for example, solar receiver, to the required turbine inlet temperature. After expansion in the turbine, the flow goes through the recuperator and transfers energy to the fluid exiting the compressor. The cycle is completed by cooling the working fluid in the cooler and rejecting heat to the cold sink. The cycle efficiency can be increased by dividing the compression into two stages and using an intercooler in between. Similarly, using two stages of expansion and a reheater can also increase the efficiency.

Example 8.7

In a closed-loop Brayton cycle (Figure 8.52), S-CO₂ enters the compressor at 7.5 MPa and exits at 25 MPa. The turbine inlet temperature is set at 750°C and the temperature of the fluid leaving the cooler is 32°C. The turbine and compressor efficiencies are 93% and 89%, respectively. If the heat exchanger effectiveness is 0.95, find the cycle efficiency assuming the pressure drop in the pipes is negligible and there is no heat loss to the environment.

Solution

Properties of S-CO₂ may be found from REFPROP database (Lemmon et al. 2002). Table A8.3 lists some of the properties needed for analyzing the S-CO₂ cycle.

State 1. Using the table of properties for S-CO₂ (Table A8.3) the enthalpy and entropy values can be found for 7.5 MPa by interpolation between 30°C and 40°C as:

$$P_1 = 7.5 \text{ MPa}, T_1 = 32^\circ\text{C} \rightarrow h_1 = 362.21 \text{ kJ/kg}, s_1 = 1.5310 \text{ kJ/kg}\cdot\text{K}$$

State 2. For an isentropic process between states 1 and 2s, and using Table A8.3:

$$P_2 = 25 \text{ MPa}, s_{2s} = s_1 = 1.5310 \text{ kJ/kg}\cdot\text{K} \rightarrow h_{2s} = 396.83 \text{ kJ/kg}$$

The enthalpy at state 2 can be determined using the compressor isentropic efficiency, η_c , as:

$$h_2 = h_1 + \frac{h_{2s} - h_1}{\eta_c} = 362.21 + \frac{396.83 - 362.21}{0.89} = 401.11 \text{ kJ/kg}$$

From Table A8.3, for the enthalpy, h_2 and pressure, $P_2 = 25$ MPa, by interpolation:

$$s_2 = 1.5426 \text{ kJ/kg}\cdot\text{K}$$

$$T_2 = 98.51^\circ\text{C}$$

State 4. The turbine inlet condition can be found from Table A8.3:
For

$$P_4 = 25 \text{ MPa}, T_4 = 750^\circ\text{C}$$

we find

$$h_4 = 1285.6 \text{ kJ/kg}, s_4 = 2.9691 \text{ kJ/kg}\cdot\text{K}.$$

State 5. For an isentropic expansion from 4 to 5s, using Table A8.3:

$$P_5 = 7.5 \text{ MPa}, s_{5s} = s_4 = 2.9691 \text{ kJ/kg}\cdot\text{K}, \text{ which gives } h_{5s} = 1067.6 \text{ kJ/kg}.$$

The enthalpy at state 5 can be determined using the turbine isentropic efficiency, η_t :

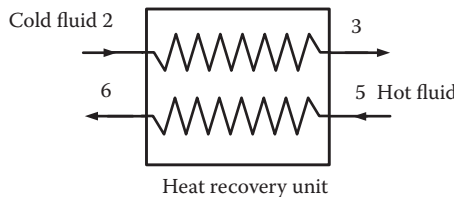
$$h_5 = h_4 - \eta_t(h_4 - h_{5s}) = 1285.6 - 0.93 \times (1285.6 - 1067.6) = 1082.86 \text{ kJ/kg}$$

From Table A8.3, for the enthalpy, h_5 and pressure, $P_5 = 7.5 \text{ MPa}$, by interpolation:

$$s_5 = 2.9871 \text{ kJ/kg}\cdot\text{K}$$

$$T_5 = 581.25^\circ\text{C}$$

Heat-Exchanger Calculation



The effectiveness of a heat exchanger is defined as the ratio between the actual heat transfer rate and the maximum possible heat transfer rate. The maximum heat transfer rate is determined from the fluid with the lower heat capacity, which undergoes the maximum possible temperature change. In order to find which fluid (cold or hot) has the lower heat capacity, we find the enthalpy change in the two fluids for the maximum possible temperature change (temperature difference between the inlets of the hot and cold fluids)

Cold fluid: h at $(T_5, P_3) = h_3$ at $(581.25^\circ\text{C}, 25 \text{ MPa}) = 1071.1 \text{ kJ/kg}$
Therefore, enthalpy change for cold fluid between 98.51°C and 581.25°C :

$$Q_{\max,\text{cold}} = h \text{ at } (T_5, P_3) - h_2 = 669.99 \text{ kJ/kg}.$$

Hot fluid: h at $(T_2, P_6) = h_6$ at $(98.51^\circ\text{C}, 7.5 \text{ MPa}) = 521.74 \text{ kJ/kg}$
Therefore, enthalpy change for cold fluid between 581.25°C and 98.51°C :

$$Q_{\max,\text{hot}} = h_5 - h \text{ at } (T_2, P_6) = 561.12 \text{ kJ/kg}.$$

Therefore, the hot fluid has lower heat capacity and $Q_{\max} = Q_{\max,\text{hot}} = 561.12 \text{ kJ/kg}$.

$$\text{The heat-exchanger effectiveness } = \frac{h_3 - h_2}{Q_{\max}} = \frac{h_5 - h_6}{Q_{\max}} = 0.95$$

$$h_3 = Q_{\max} \times 0.95 + h_2 = 934.17 \text{ kJ/kg}$$

$$h_6 = h_5 - Q_{\max} \times 0.95 = 1082.86 - 561.12 \times 0.95 = 549.79 \text{ kJ/kg}$$

Other properties can be found from Table A8.3.

State 3. $P_3 = 25 \text{ MPa}$, $h_3 = 934.17 \text{ kJ/kg}\cdot^\circ\text{C} \rightarrow T_3 = 471.91^\circ\text{C}$, $s_3 = 2.5686 \text{ kJ/kg}\cdot\text{K}$

State 6. $P_6 = 7.5 \text{ MPa}$, $h_6 = 521.74 \text{ kJ/kg}\cdot^\circ\text{C} \rightarrow T_6 = 120.84^\circ\text{C}$, $s_6 = 2.0934 \text{ kJ/kg}\cdot\text{K}$

The heat input to the cycle is:

$$Q_{\text{in}} = h_4 - h_3 = 351.43 \text{ kJ/kg.}$$

The work output from the turbine is:

$$W_t = h_4 - h_5 = 202.74 \text{ kJ/kg.}$$

The energy input to the compressor is:

$$W_c = h_2 - h_1 = 38.91 \text{ kJ/kg.}$$

The thermal efficiency is:

$$\eta_{\text{thermal}} = \frac{W_t - W_c}{Q_{\text{in}}} = 0.466.$$

8.10 Solar Distillation of Saline Water

Solar distillation for the production of potable water from saline water has been practiced for many years. A solar distillation plant, covering 4740 m² of land, was built in Las Salinas, Chile, in 1872, to provide fresh water from salt water for use at a nitrate mine (Talbert et al. 1970). Single-glass-covered flat-plate collectors with salt water flowing downward over slanting roofs were used to vaporize some of the water, which was then condensed on the air-cooled underside of the roof. This plant ran effectively for over 40 years and produced up to 23,000 liters of fresh water per day until the nitrate mine was exhausted.

Solar stills have been extensively studied and there are many different solar still configurations, as illustrated in Figure 8.53. Combining solar stills

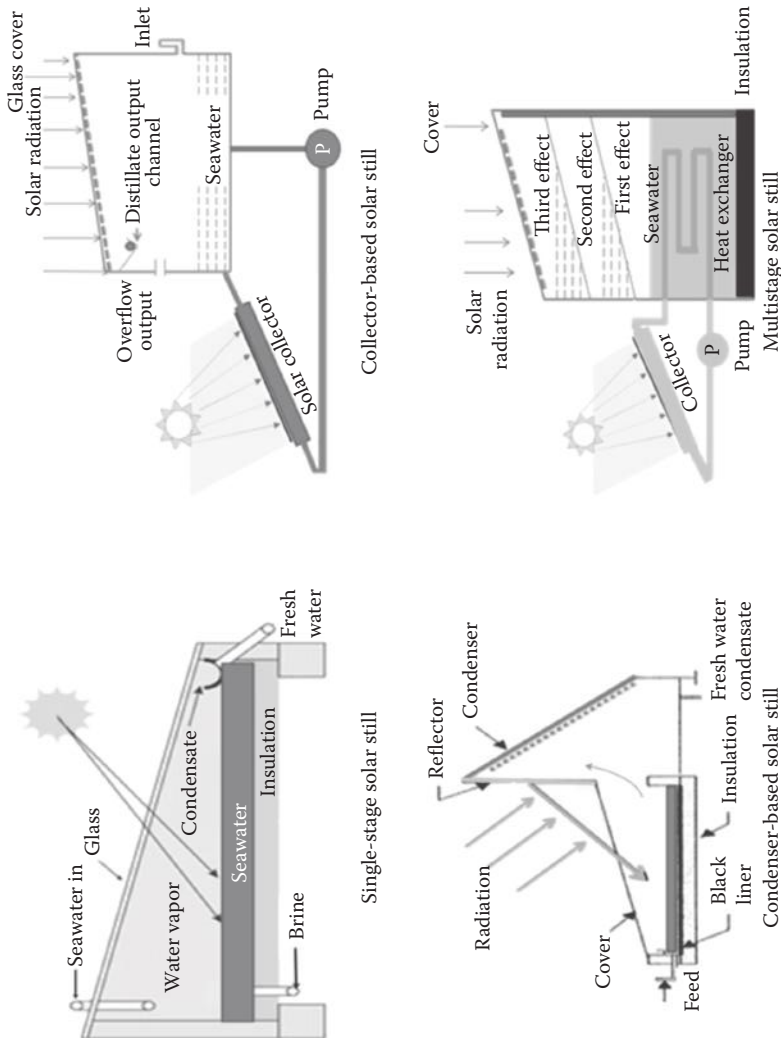


FIGURE 8.53
Different types of solar stills. (From Abutayeh, M. et al., Desalination: Water from water, In *Chapter 11: Solar Desalination*, J. Kucera (ed.), Scrivener/Wiley, Hoboken, NJ, 2014; Li, C. et al., *Renewable and Sustainable Energy Review*, 19, 136–163, 2013a.)

with flat-plate or concentrating solar collectors and integrating the passive vacuum method into solar stills provide different techniques to increase the feasibility of solar stills. Solar stills are relatively inexpensive and easy to maintain, which makes them a viable option for underdeveloped communities with good solar resource.

The stills used to date are called shallow basin-type stills and Figure 8.54 illustrates their method of operation. The still is irradiated by direct and diffuse solar radiation I_s as well as some infrared radiation I_i from the surroundings. The long-wavelength radiation is absorbed by the glass, but $\tau_{s,g}I_s$ of the solar radiation reaches the saline water; $\tau_{s,w}\tau_{s,g}I_s$ reaches the bottom of the trough where $\alpha_{s,t}\tau_{s,g}\tau_{s,w}I_s$ is absorbed per unit still area. A value of 0.8 has been suggested as a reasonable approximation for $\alpha_{s,t}\tau_{s,w}\tau_{s,g}$ if good glass, a blackened tray surface, and a 0.2-m-thick layer of water are used (Dunkle 1961). Typical shallow basin stills are 1.5 m wide, 2–25 m long, and approximately 0.2 m deep; the glass roof should have a slope of 10°–15°.

Of the energy absorbed at the bottom, one part $q_{k,s}$ is lost through the insulation by conduction, while the other part will be transferred to the saline water in the still tray above. Of the latter portion, some will heat the water, if the water temperature is less than the tray temperature, while the rest is transferred from the surface of the water by free convection, radiation, and evaporation to the underside of the glass cover. Some of this heat passes through the glass by conduction and is transferred from the outer surface of the glass cover by convection and radiation to the surrounding atmosphere. The thermal circuit for this system is shown in Figure 8.55.

To obtain the greatest yield, the rate of evaporation of water, which is proportional to q_e , should be as large as possible. An inspection of the thermal circuit shows that to achieve large values of q_e , $\tau_{s,g}\tau_{s,w}\alpha_{s,t}I_s$ should be as large as possible, while $q_{c,s}$, $q_{r,s}$, and $q_{k,s}$ should be as small as possible. To achieve these results, the transmittance of the glass cover and the absorptance of the tray surface must be large, and the bottom of the tray should be well

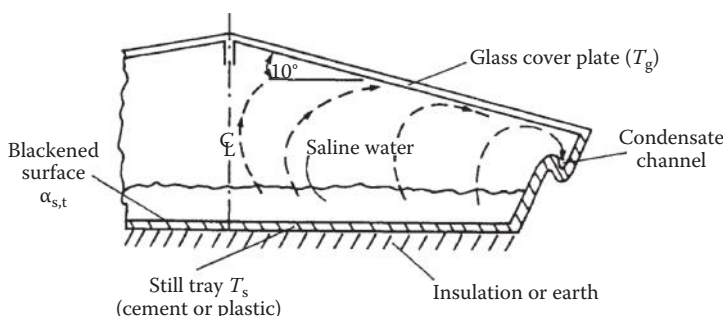


FIGURE 8.54

Sketch of shallow basic-type solar still.

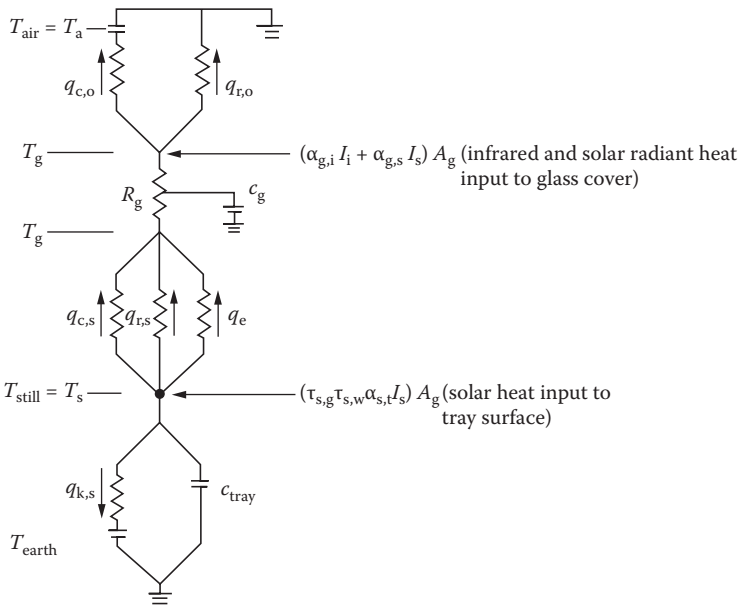


FIGURE 8.55
Thermal circuit for solar still.

insulated. Obviously, the amount of solar irradiation should be as large as possible.

In order to analyze the thermal performance, heat balances must be written for the glass cover and the tray, and the resulting equations must be solved simultaneously to obtain the tray and glass cover temperatures. The objective is to obtain the thermal efficiency, defined as the ratio of the energy used in evaporating saline water to the incident solar radiation.

If steady-state conditions prevail, the glass resistance R_g is neglected, and the water temperature is assumed equal to the tray temperature, a heat balance on the glass cover gives

$$q_e + q_{r,s} + q_{c,s} + \alpha_{g,i} I_i A_g + \alpha_{g,s} I_s A_g = q_{c,o} + q_{r,o}, \quad (8.56)$$

where

$q_{r,s}$ = rate of heat transfer by radiation from the water in the tray to the inner surface of the glass = $A \bar{h}_{r,s} (T_s - T_g)$,

$$\bar{h}_{r,s} = \sigma (T_s^2 + T_g^2) (T_s + T_g) / (1/\varepsilon_w + 1/\varepsilon_g - 1),$$

$q_{c,s}$ = rate of heat transfer by convection from water to the inner surface of the glass = $A \bar{h}_{r,s} (T_s - T_g)$,

$q_{c,o}$ = rate of convection heat loss from the glass to the ambient air = $A\bar{h}_{c,o}(T_g - T_a)$,

$q_{r,o}$ = rate of radiation heat loss from the glass = $A\bar{h}_{r,o}(T_g - T_a)$, and
 $\bar{h}_{r,o} \approx \epsilon_g \sigma (T_g^2 + T_a^2)(T_g + T_a)$.

Similarly, a heat balance on the saline water gives

$$\alpha_{s,t}\tau_{s,g}\tau_{s,w}I_s = q_k + q_{c,s} + q_{r,s} + q_e \quad (8.57)$$

In the enclosed space between the water surface and the glass cover, heat and mass transfer occur simultaneously as brine is evaporated, condenses on the lower surface of the cooler glass, and finally flows into the condensate channel. Since the glass cover is nearly horizontal, the correlations developed in Chapter 3 for free convection between parallel plates can be used to calculate the Nusselt number and heat-transfer coefficient. However, because heat and mass transfer occur simultaneously in the still, the buoyancy term in the Grashof number must be modified to take account of the density gradient resulting from composition as well as temperature. As shown in Battleson (1981), in horizontal enclosed air spaces in the range $3 \times 10^5 < \text{Gr}_L < 10^7$, the relationship

$$\text{Nu} = \frac{\bar{h}_c L}{k} = 0.075 \left(\frac{L^3 \rho^2 g \beta_T \Delta T}{2} \right)^{\frac{1}{3}} \quad (8.58)$$

can be used to calculate the heat-transfer coefficient if ΔT is considered an equivalent temperature difference between the water and the glass cover and includes the molecular weight difference resulting from the change in vapor concentration in evaluating the buoyancy. For an air–water system, $\Delta T'$ is given by Dunkle (1961) in English units.

$$\Delta T' = (T_s - T_g) + \frac{p_{w,s} - p_{w,g}}{39 - p_{w,s}} T_s \quad (8.59)$$

where $p_{w,s}$ is the partial pressure of water (in psia) at the temperature of the water surface T_s and $p_{w,g}$ is the vapor pressure of water in psia at the temperature of the glass cover T_g .

Since the size of the still does not affect the heat-transfer coefficient in the Grashof number range of interest, \bar{h}_c in Equation 8.58 can be approximated by evaluating all physical constants at an average still temperature or

$$h_c = 0.13 (T_s - T_g) + \frac{p_{w,s} - p_{w,g}}{39 - p_{w,s}} T_s^{\frac{1}{3}} \quad (8.60)$$

The rate of heat transfer by convection between the water and the glass is then

$$q_c = \bar{h}_c A_s (T_s - T_g), \quad (8.61)$$

and, using the analogy between heat and mass transfer, the rate of mass transfer q_m (in lb/h) is

$$q_m = 0.2 \bar{h}_c A_s (p_{w,s} - p_{w,g}). \quad (8.62)$$

The heat-transfer rate resulting from evaporation q_e (in Btu/h) equals the rate of mass transfer times h_{fg} , the latent heat of evaporation at T_g , or

$$q_e = 0.2 \bar{h}_c A_s (p_{w,s} - p_{w,g}) h_{fg}. \quad (8.63)$$

If the tray of the still is resting on the ground, the conduction loss is difficult to estimate because it depends on the conductivity of the earth, which varies considerably with moisture content. If the bottom of the tray is insulated and raised above the ground, the preferable arrangement, unless too expensive, the bottom heat loss is given by

$$q_k = U_b A_s (T_s - T_a), \quad (8.64)$$

where the bottom conductance U_b is composed of the tray insulation and the free convection elements in series and can be calculated by the methods given in Chapter 3.

Since $p_{w,s}$ and $p_{w,g}$ in Equations 8.59 and 8.60 are functions of T_s and T_g , respectively, Equations 8.56 and 8.57 can be solved simultaneously for T_s and T_g , provided I_s and all the physical properties are known. However, this approach is more complex than assuming a still temperature and solving for T_g and I_s .

Example 8.8

For a solar still operating at a brine temperature of 155°F (410 K) in ambient air at 76°F (298 K) with a bottom conductance $U_b = 0.3 \text{ Btu/h}\cdot\text{ft}^2\cdot^\circ\text{F}$ (1.7 W/m²°C), and $(1/\epsilon_g + 1/\epsilon_w - 1) = 0.9$, calculate the rates of heat transfer by convection q_c , radiation q_r , and conduction q_k , and the rate of evaporation per unit still area q_e . Then, calculate the still efficiency.

Solution

First, the temperature of the glass cover is calculated from Equation 8.56 (the partial pressure of water vapor was obtained from Keenan and Keys

1956). This temperature is found to be 135°F (390.5 K) and the various heat fluxes are shown below:

$$\begin{aligned} q_{c,s}/A_s & \text{ convection flux from brine} = 10 \text{ Btu/h}\cdot\text{ft}^2 (31.5 \text{ W/m}^2). \\ q_e/A_s & \text{ rate of evaporation per unit area} = 158 \text{ Btu/h}\cdot\text{ft}^2 (497 \text{ W/m}^2). \\ q_{r,s}/A_s & \text{ radiation flux from brine} = 28 \text{ Btu/h}\cdot\text{ft}^2 (88 \text{ W/m}^2). \\ q_{k,x}/A_s & \text{ conduction back loss flux} = 23 \text{ Btu/h}\cdot\text{ft}^2 (72 \text{ W/m}^2). \\ \alpha_{s,t} \tau_{s,g} \tau_{s,w} I_s & = 219 \text{ Btu/h}\cdot\text{ft}^2 (689 \text{ W/m}^2). \\ I_s & = 219/0.8274 \text{ Btu/h}\cdot\text{ft}^2 (863 \text{ W/m}^2). \end{aligned}$$

The thermal efficiency is then

$$\eta = \frac{q_e}{I_s} = \frac{158}{274} = 58\%.$$

A potentially important factor omitted in the preceding analysis is the effect of air leakage. It increases with increasing temperature and can also be accelerated by high wind. Leakage should be minimized for good performance.

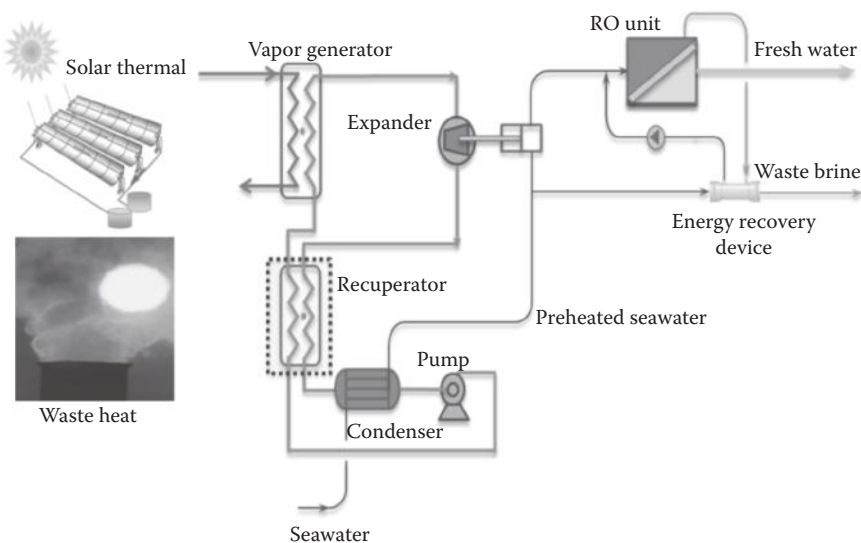
The maximum performance of a still is limited by the heat of vaporization of water and the solar insolation. Under favorable conditions with $I_s = 250 \text{ Btu/h}\cdot\text{ft}^2 (789 \text{ W/m}^2)$, $\eta_s = 40\%$, and $h_{fg} = 1000 \text{ Btu/lb (2326 kJ/kg)}$, 1 ft² of still can provide 0.1 lb of water per hour, or approximately 1 lb/day. Thus, approximately 10 ft² (1 m²) is required for a production rate of 1 gal/day (~3.8 L/day) and 27 ft² (~2.5 m²) of still would be required to produce 1000 gal/year (~3800 L/year).

8.10.1 Solar-Driven Reverse Osmosis

Osmosis is a natural phenomenon in which water passes through a membrane from a lower-concentration to a higher-concentration solution. The flow of water can be reversed if a pressure larger than the osmotic pressure is applied on the lower-concentration side. Reverse osmosis (RO) is the most common desalination process because of its superior energy efficiency compared to thermal desalination systems (Childs et al. 1999; Li et al. 2013a). However, RO uses mechanical energy/electricity as the energy source, which has to be generated by either PV arrays or solar heat engines.

PV-powered RO desalination is common in demonstration plants because of the modularity and scalability of both PV and RO systems (Alajlan and Smiai 1996; Alawaji et al. 1995; Hasnain and Alajlan 1998). Economic and reliability considerations are the main challenges to improving PV-powered RO desalination systems (Thomson and Infield 2005; Tzen et al. 2008). Solar thermal-assisted RO desalination is even further away from commercialization (Li et al. 2012).

However, the advantage of coupling a power cycle with RO is that seawater provides a heat sink for the power cycle condenser while it is being pre-heated to increase the RO membrane permeability leading to reduced power

**FIGURE 8.56**

Schematic of solar power cycle–driven RO system. (From Li, C. et al., *Applied Energy*, 102, 1071–1080, 2012; Li, C. et al., *Desalination*, 318, 107–117, 2013b.)

consumption and reduced thermal pollution (Li et al. 2013b). Furthermore, waste heat from a conventional power cycle could be used at night while solar energy is used during the day, so that the power cycle–RO system could provide consistent power and water, which are crucial for many remote areas, as shown in Figure 8.56.

Flat-plate, evacuated tube, or concentrating solar collectors may be used to heat the working fluid of the power cycle and a fraction of the mechanical energy generated by the power cycle could be used to drive the attached RO desalination system. The energy recovery device (ERD) recovers a part of the pressure head of the remaining brine to prepressurize the feedwater, which would otherwise be wasted.

8.10.2 RO Mathematical Model

The work required for the RO process with an ERD may be estimated by (Li et al. 2012)

$$W_{SWRO} = \frac{V_{\text{fresh}} * P_{\text{sea}}}{\eta_{\text{pump}}} + \Delta P * 1 + \frac{1}{\alpha} - 1 * (1 - \eta_{\text{ERD}}) , \quad (8.65)$$

where α is the seawater desalination system recovery ratio and ΔP is the overpressure above the osmotic pressure that drives the water flow through

the membrane. P_{sea} is the osmotic pressure given by the van't Hoff equation: $P_{\text{sea}} = cRT$, where c is the ionic molar concentration, R is the gas constant, and T is the absolute temperature. $\frac{P_{\text{sea}}}{1-\alpha}$ is the pressure used to overcome the concentrated brine osmotic pressure. The units of W , P , and V are kilojoules, kilopascals, cubic meters (or m^3/s if using flow rate), respectively; η_{pump} is the high-pressure pump efficiency, V_{fresh} is the fresh water volume, $\frac{V_{\text{fresh}}}{\alpha}$ is the total seawater pumped by the pump, and η_{ERD} is the efficiency of the ERD. The recovery rate ranges from 30% to 60% for RO.

Example 8.9

Consider a small RO desalination system driven by a series of solar collectors that provide heat. Preheated seawater is desalinated with a 50% recovery rate, which implies that 50% of the seawater turns to potable water and the rest is rejected into the sea. Assume that the organic working fluid of the power cycle is condensed at 37°C by the feed seawater that heats up from 25°C to 32°C .

Solution

The small RO system is simulated with the Dow Chemical Reverse Osmosis System Analysis (ROSA72). The simulated system is a single-stage RO system using 10 pressure vessels in each stage and seven elements in each vessel. Details of the small RO unit are not required to be understood but are available in Table 8.9. The feed seawater peak flow rate is 22.08 L/s and the Dow Chemical's FILMTEC SW30XHR-400i RO membrane is used. When the feed seawater temperature rises, the permeated total dissolved solids (TDS) of the RO increase. In this study, effluents with a TDS level higher than that of US average tap water TDS (approximately 350 mg/L) were not considered. The temperature correction factor (TCF) for the membrane is

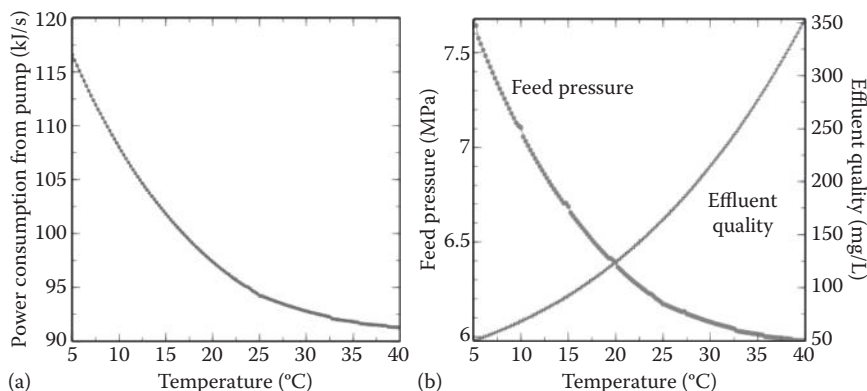
$$\text{TCF} = \text{EXP}[2640^* \frac{1}{298} - \frac{1}{T + 273.15}] ; \text{ when } T \geq 25^\circ\text{C} \quad (8.66)$$

$$\text{TCF} = \text{EXP}[3020^* \frac{1}{298} - \frac{1}{T + 273.15}] ; \text{ when } T \leq 25^\circ\text{C} \quad (8.67)$$

The energy consumption of the RO system with respect to the seawater temperature is shown in Figure 8.57a. The required RO pressure and effluent water quality are shown in Figure 8.57b. It can be seen that both the RO pressure and the energy consumption decrease when the seawater temperature increases, which is due to the increased flux through the membranes at higher temperatures. With the increased flux, the effluent

TABLE 8.9
Design Parameters of the RO Unit

Seawater TDS	35,240 mg/L
Water classification	Seawater (well/MF) SDI < 3
RO feedwater temperature	32°C
Seawater recovery	50.00%
Element type	SW30XHR-440i
Maximum operating pressure	8.3 MPa
Stage	1
Pressure vessels per stage	10
Elements per pressure vessel	7
Average flux	0.23 L/m ² ·min
Power consumption with ERD	92.356 kJ/s
Raw seawater flow to the system	22.08 L/s
Feed pressure	6.048 MPa
Total active area	2861 m ²
Concentrate pressure	5.96 MPa
Concentrate TDS	70,244.42 mg/L
High-pressure efficiency	0.8
Energy recovery device efficiency	0.9

**FIGURE 8.57**

(a) Power consumption of the designed RO versus seawater temperature; (b) RO system pressure and effluent TDS versus seawater temperature.

water quality decreases; nevertheless, the effluent TDS still meets the average US tap water quality. The changes in RO pressure and energy consumption are more dramatic at lower seawater temperatures, indicating the necessity of seawater preheating at low temperatures. Heated from 5°C to 32°C, the energy consumption is reduced by as much as 26.23%, while heated from 25°C to 32°C, the reduction is only 2.02%.

Note that with seawater preheated to 32°C, the RO system's pressure requirement is 6.048 MPa, the energy consumption is 8.365 kJ/L fresh water generated, and the effluent TDS is 238 mg/L. Both the RO fresh water and discharged brine are at 0.137 MPa.

8.11 Nonconvecting Solar Ponds

The nonconvecting solar pond is a horizontal-surfaced solar collector using the absorption of solar radiation at the bottom of a 1- or 2-m-deep body of water to generate low-temperature heat. Since heat storage is an integral part of ponds, they have promise in some parts of the world for continuous energy delivery to process or space-conditioning systems. Modern solar ponds were first studied scientifically in Israel by Tabor (1963, 1966). This section describes ponds in which a temperature substantially above ambient—by 50 K or more—may be achieved.

8.11.1 Introduction

When solar energy enters a pond, the infrared component is absorbed within a few centimeters, near the surface, since water is opaque to long-wave radiation. The visible and ultraviolet components of sunlight can penetrate clear water to a depth of several meters. These radiation components can be absorbed at the bottom of the pond by a dark-colored surface. The lowest layer of water is then the hottest and would tend to rise because of its relatively lower density if measures were not taken to prevent it.

In nonconvecting solar ponds, the water at the bottom is made heavier than that at the top by dissolving salt in the water as shown in Figure 8.58. The concentration of salt is decreased from bottom to top so that the natural

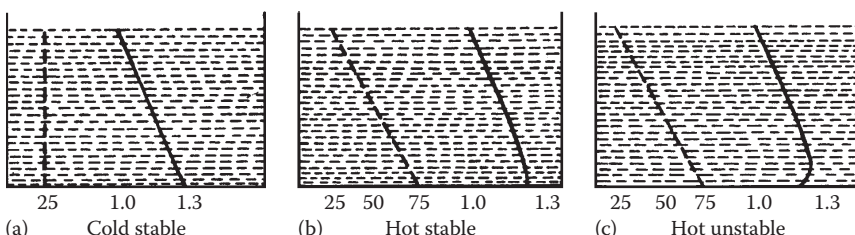
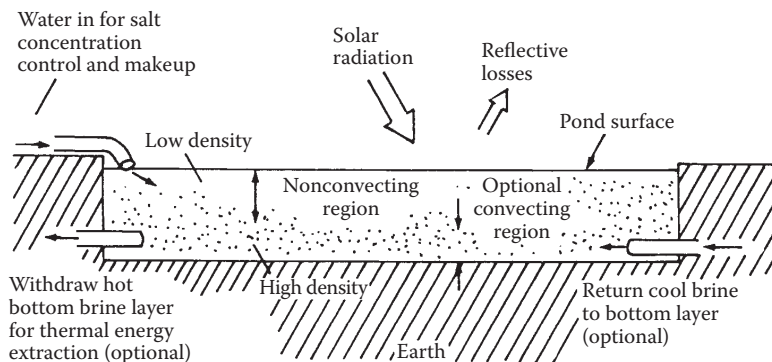


FIGURE 8.58

Density gradients in a solar pond. If the gradient is positive when cold (a), it becomes less positive when heated (b); if the lowest layers become too hot, the density profile may reverse (c) and the onset of convection will follow. Dashed lines represent temperature profiles and the solid lines represent density profiles (units are °C and g/cm^3).

**FIGURE 8.59**

Schematic diagram of a nonconvection solar pond showing conduits for heat withdrawal, surface washing, and an optional convecting zone near the bottom.

tendency of ponds to mix by the creation of convection currents is effectively eliminated if the density gradient is adequate.

Since stationary water is quite an effective insulator, it is possible for the lowest layers of a well-designed solar pond to boil. Boiling, of course, must be avoided, for it destroys the stable density gradient. Therefore, the design of a solar pond for heat generation must involve a mechanism for useful heat removal in sufficient quantity to avoid boiling (Figure 8.59).

Since solar ponds are usually envisioned to be on the order of hectares in size, a heat-exchanger pipe network using a separate working fluid is impractical. However, hydrodynamic principles predict that a layer of fluid could be removed slowly from the bottom of the pond without disturbing the main body of water. This is evidenced on a large scale by the ability of ocean currents—Gulf Stream, Benguela Current, and so on—to retain their identity over thousands of miles. The fluid in the removed layer of a pond is then passed through a heat exchanger for useful heat removal and returned to the bottom of the pond. Since the returned fluid is cooler than the extracted fluid, the required density gradient is maintained. In practice, the horizontal flows can disturb the hydrostatic equilibrium somewhat, depending on the Reynolds and Froude numbers, and a mixed layer can exist at the pond's bottom. In this layer, convection can occur, although it can be confined to a zone on the order of centimeters. Nielsen (1976) has described a pond in which a convective zone is an intentional feature of the design proposed for space heating.

Several practical difficulties arise during long-term use of solar ponds in the field. Since a salinity gradient exists, diffusion of salt from regions of high concentration to low concentration occurs naturally. Hence, the density gradient required for hydrostatic stability tends to destroy itself. This diffusion can amount to 60 tons/km²xd (Tabor 1966). To maintain the gradient, it is necessary to supply salt to the bottom of the pond and to wash the surface with a weak brine solution. The supply of salt to a pond is a major

maintenance cost for this type of solar collector. Tabor (1966) has suggested an idea whereby the bottom layer of a pond is decanted, partially evaporated, and returned to the pond bottom. Simultaneously, water is added to the top of the pond to replace that evaporated from the layer. As a result, the net flow of water is downward, and the *relative* flow (diffusion) of salt is upward. By proper matching of these rates, the salt can remain stationary in a fixed frame of reference.

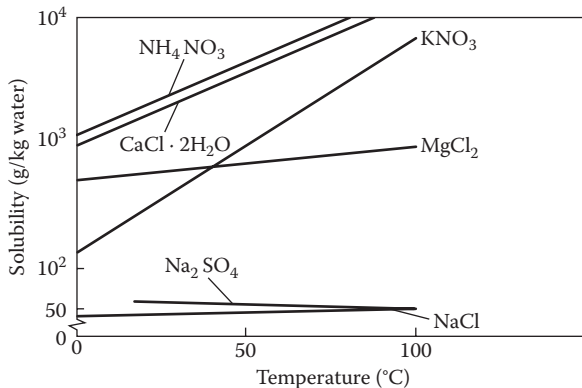
The replacement of water that evaporates naturally from the surface of a pond is a second practical consideration. If water is not replaced at the top, a local reversal of the stable salinity gradient will occur and a convective layer will form at the surface. This is to be avoided, since it destroys a part of the insulation effect of the stagnant pond. Nielsen (1976) proposed the use of a plastic cover over the pond to help maintain the proper gradient. Since reflection of solar radiation from plastic is greater than that for water (see Chapter 3), they also suggest maintaining a thin water layer over the plastic cover.

Other practical matters that must be considered are the effects of wind, waves, rain, and leaks on the pond gradient (halocline). Waves can destroy the halocline and therefore must be controlled. An economical and effective method for this task has yet to be developed. Very severe rainstorms and wind can destroy the surface gradient to a depth of 35–50 cm (Nogawa et al. 1989). A plastic cover could presumably avoid the problem if it could stay intact during severe storms. The problem of dirt in a pond depends on the location of the particles. Either on the surface or suspended within the pond, they reduce solar transmittance and must be removed by withdrawing, filtering, and replacing a layer of the pond. Dirt on the bottom can likewise be removed but may not cause a major problem if left in place. Leaves in a pond should be avoided, since they may float, may lose their color to the water, and may plug fluid circulation machinery and conduits. Algae growth in ponds should be readily controllable by chemical means.

A final feature of a solar pond determines its geographic limits. Since the ponds are horizontal and the sun is low in the sky north or south of the mid-latitudes in winter, ponds must be used near the equator if winter yields are not to be curtailed sharply. Other climatic effects in the tropic—monsoons or storms—must also be considered in finding the best sites for large-scale pond usage.

8.11.2 Solar Pond Stability Criteria

One of the principal costs of a solar pond is the dissolved salt required to establish a stable density gradient. For economical applications, it is essential that no more salt be used than necessary to assure hydrostatic stability. Figure 8.60 shows the solubility of several common salts in water as a function of temperature. Salts like NH_4 , NO_3 , or KNO_3 , whose solutions are as transparent as water, are best for solar ponds, since solubility increases significantly with temperature, thereby ensuring a significant density gradient.

**FIGURE 8.60**

Solubility of some common inorganic salts usable in solar ponds.

Salts such as Na₂SO₄ with the opposite solubility characteristic would not be suitable for ponds.

Weinberger (1964) has established the criteria for the hydrostatic and hydrodynamic stability of large solar ponds. To avoid convection, the fluid density must decrease upward from the bottom; that is,

$$\frac{d\rho}{dz} = \frac{\partial \rho}{\partial s} \frac{ds}{dz} + \frac{\partial \rho}{\partial T} \frac{dT}{dz} \geq 0, \quad (8.68)$$

where s is the salt concentration, ρ is the density, T is the temperature, and z is the vertical coordinate, increasing downward.

However, to avoid the growth of oscillatory motion, a stronger condition is required (Nielsen 1976):

$$\frac{v + K_s}{\rho} \frac{\partial \rho}{\partial s} \frac{ds}{dz} + \frac{v + K_T}{\rho} \frac{\partial \rho}{\partial T} \frac{dT}{dz} \geq 0, \quad (8.69)$$

where v , K_s , and K_T are momentum, salt, and thermal diffusivities, respectively. On the basis of this condition, a convective layer of thickness h will grow if (Nielsen 1976)

$$q_{\text{net}} > 0.89h(\rho c)\sqrt{\frac{K_T}{t}} - \frac{dT}{dz} - \frac{(v + K_s)}{(v + K_T)} \frac{(\partial \rho / \partial s)}{(\partial \rho / \partial T)} \frac{ds}{dz}, \quad (8.70)$$

where t is the time during which heat is absorbed at rate q_{net} in a region of heat capacity (ρc) per unit volume.

If the net heat rate is above that required for convective layer growth, the layer grows in thickness as (Leshuk et al. 1976)

$$h^2 = Cq_{\text{net}} + h^2 (t = 0), \quad (8.71)$$

where

$$C = \frac{2}{(\rho c)[(ds/dz)(\partial p/\partial s)/(\partial p/\partial T) + dT/dz]} . \quad (8.72)$$

If the heat rate q_{net} is less than the critical value from Equation 8.70, the convective layer may not decrease, as is the case in many other hydrodynamic phenomena. This is a result of the much greater numerical value of thermal diffusivity compared with salt diffusivity. Nielsen and Rabl (1976) have shown that the salinity gradient needed to stabilize a convective zone is about five times that required to maintain a stagnant zone. A density difference of 25% has successfully stabilized ponds in practice.

8.11.3 Thermal Performance of Solar Ponds

In a solar pond, solar radiation is partially reflected at the surface, partially absorbed in the water, and partially absorbed at the bottom. The absorption of solar energy by water does not follow a simple Bouguer's law since the absorption phenomena differ widely with wavelength. Table 8.10 is a summary of absorption of sunlight in water as a function of wavelength. Absorption in solutions of inorganic salts used in solar ponds is expected to be nearly the same.

The data from Table 8.10 are plotted in Figure 8.61. An adequate curve fit of these data is represented by the sum of several exponential terms. If $\tau(x)$ is the transmittance of water of depth x , it can be related to x by (Nielsen 1976)

$$\tau(x) = \sum_{i=1}^4 a_i e^{-b_i x}, \quad (8.73)$$

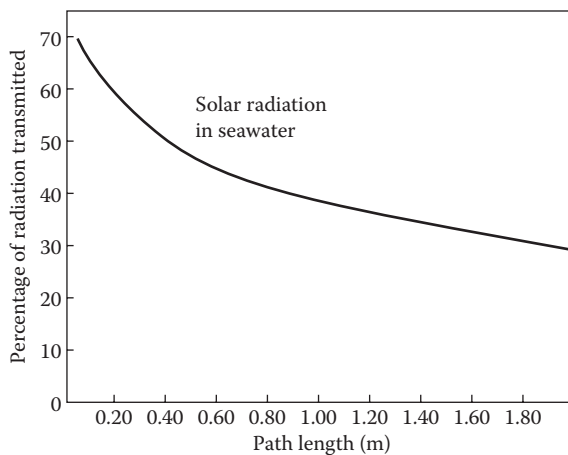
where the regression coefficients a_i and b_i are given in Table 8.11.

Equation 8.73 does not include the infrared spectrum ($\lambda > 1.2 \mu\text{m}$), since it is of no interest in solar pond analysis. As shown in Hipser and Roehm (1976),

TABLE 8.10
Spectral Absorption of Sunlight in Water

Wavelength (μm)	Layer Depth				
	0	1 cm	10 cm	1 m	10 m
0.2–0.6	23.7	23.7	23.6	22.9	17.2
0.6–0.9	36.0	35.3	36.0	12.9	0.9
0.9–1.2	17.9	12.3	0.8	0.0	0.0
1.2 and over	22.4	1.7	0.0	0.0	0.0
Total	100.0	73.0	54.9	35.8	18.1

Note: Numbers in the table show the percentage of sunlight in the wavelength band passing through water of the indicated thickness.

**FIGURE 8.61**

Transmittance of water to solar radiation as a function of the thickness of the water layer. See Table 8.10 for numerical values.

TABLE 8.11

Regression Coefficients a_i and b_i for
Transmittance of Solar Pond (Equation 8.73)

Wavelength (μm)	a_i	$b_i (\times 10^{-3} \text{ cm}^{-1})$
0.2–0.6	0.237	0.32
0.6–0.75	0.193	4.5
0.75–0.90	0.167	30.0
0.90–1.20	0.179	350.0

Reddy (1987), and Washam et al. (1993), a detailed analysis of heat transfer in a solar pond is very complex and must include effects of volumetric absorption, variation of density, and conductivity with salinity.

Figure 8.61 shows that approximately 30% of the incident radiation reaches the absorbing bottom surface of a 2-m solar pond. This represents the upper limit of collection efficiency of a pond. But since the bottom is an imperfect absorber and heat losses occur from the top and bottom surfaces, the thermal efficiency is an inadequate index of solar system viability; economics must be considered. Since solar ponds are presently not in commercial use, their economic analyses are not reliable. However, Rabl and Nielsen (1975) have predicted that solar ponds for building heating may be more economical than fuel oil heating in some areas. Styris et al. (1976) have analyzed solar ponds for process heat as well.

An additional consequence of the data shown in Figure 8.61 should be noted. The insulating effect of the nonconvecting layer in a solar pond increases linearly with depth. In most practical cases (Hipser and Roehm 1976; Reddy 1987; Washam et al. 1993), this insulating effect increases more rapidly than does the attenuation of sunlight because of increased depth. For

example, a 1-m-deep pond that can achieve a no-load temperature of 100°C could achieve a temperature of approximately 180°C if it were 2 m deep. Of course, brine costs increase with pond depth and pond depth should therefore be selected to match the task for which the heat is required.

PROBLEMS

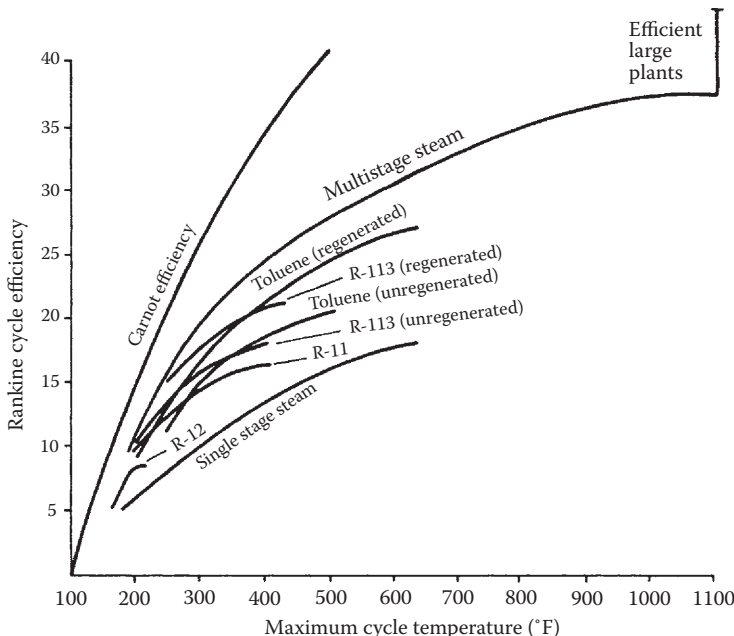
1. A reheat Rankine cycle uses steam as a working fluid. The steam leaves the condenser as saturated liquid. The steam leaves the boiler and enters the turbine at 5 MPa, 350°C. After expansion in the turbine to $P = 1.2$ MPa, the steam is reheated to 350°C and then expands in the low-pressure turbine to $P = 10$ kPa. If the efficiencies of the pump and turbine are 0.9, determine the following:
 - a. Work output from high-pressure turbine per unit mass of working fluid
 - b. Work output from low-pressure turbine per unit mass of working fluid
 - c. Work input to the pump per unit mass of working fluid
 - d. Heat added to the boiler
 - e. Quality of vapor at the exit of high-pressure turbine and low-pressure turbine
 - f. Cycle efficiency
2. A regenerative Rankine cycle uses steam as the working fluid. Steam leaves the boiler and enters the turbine at $P = 5$ MPa, $T = 500^\circ\text{C}$. After expansion to 400 kPa, a part of steam is extracted from the turbine for the purpose of heating the feedwater in the feedwater heater. The pressure in the feedwater heater is 400 kPa and the water leaving it is saturated liquid at 400 kPa. The steam not extracted expands to 10 kPa. Assuming the efficiencies of the turbine and two pumps are 90%, determine the following:
 - a. The fraction of steam extracted to the feedwater heater (f)
 - b. Heat added to the boiler per unit mass of working fluid
 - c. Work obtained from the turbine
 - d. Work for both pumps per unit mass of working fluid
 - e. The cycle efficiency (η)
3. Consider a Stirling cycle from Example 8.4 with imperfect regenerator ($T_R = 230^\circ\text{C}$). Assume ideal gas.
 - a. Compute the efficiency from

$$\eta = \frac{\text{work}_{\text{net}}}{\text{Heat}_{\text{input}}},$$

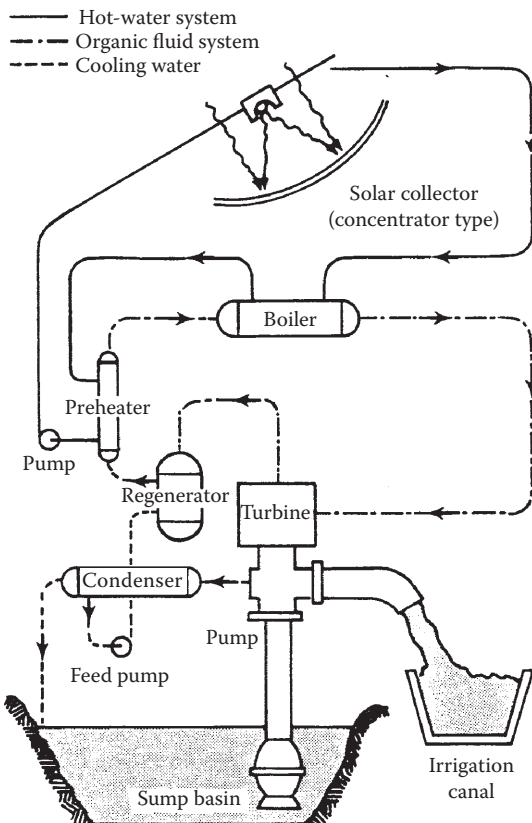
where $\text{Heat}_{\text{input}} = q_{34} + mC_v(T_H - T_R)$.

Verify that the efficiency you get is the same as the efficiency obtained by Equation 8.26.

- b. Start from the efficiency equation above. Derive the efficiency in Equation 8.26.
4. A solar electric engine operating between 5°C and 95°C has an efficiency equal to one-half the Carnot efficiency. This engine is to drive a 4-kW pump. If the collector has an efficiency of 50%, calculate the area needed for operation in Egypt where the insolation averages approximately 2800 kJ/m²×h during the day. State any additional assumptions.
5. The graph below shows the Rankine cycle efficiency as a function of maximum cycle temperature for different working fluids. Prepare a thermal analysis matching a line focusing collector, a paraboloid dish collector, and a CPC collector with a concentration ratio of 3:1 to a suitable working fluid in Washington, D.C., and Albuquerque, New Mexico. Comment on storage needs in both locations. Low-temperature organic and steam efficiencies were computed with the following assumptions: expander efficiency, 80%; pump efficiency, 50%; mechanical efficiency, 95%; condensing temperature, 95°F; regeneration efficiency, 80%; high side pressure loss, 5%; low side pressure loss, 8%.



6. The schematic diagram shown below for a solar-driven irrigation pump was developed by Battelle Memorial Institute and uses tracking PTCs. Solar energy is to heat the water in the collectors to 423 K, which then vaporizes an organic working fluid that powers the pump turbine. Calculate the surface area needed to power a 50-hp pump capable of delivering up to 38,000 L/min of water at noon in Albuquerque, New Mexico. (Answer: 510 m².)



7. Write a closed-form expression for the work output of a solar-powered heat engine if the energy delivery of the solar collector at high temperature is given approximately by the expression

$$q_u = (\tau\alpha)_{\text{eff}} I_c - \frac{\sigma\epsilon\bar{T}_f^4}{\text{CR}},$$

(convection and conduction losses are neglected), where \bar{T}_f is the average fluid temperature and CR is the concentration ratio. Two heat engines are to be evaluated:

a. Carnot cycle:

$$\text{Cycle efficiency } \eta_c = 1 - \frac{T_\infty}{T_f}$$

b. Brayton cycle:

$$\text{Cycle efficiency } \eta_B = 1 - \frac{C_B T_\infty}{T_f}, \quad C_B \geq 1,$$

where $C_B = (r_p)^{(k-1)/k}$ (r_p is the compressor pressure ratio and k is the specific heat ratio of the working fluid).

Write an equation with \bar{T}_f as the independent variable that, when solved, will specify the value of \bar{T}_f to be used for maximum work output as a function of concentration ratio, surface emittance and $(\tau\alpha)_{\text{eff}}$ product, insolation level, and C_B . Optional: solve the equation derived above for $CR = 100$, $\epsilon = 0.5$, and $(\tau\alpha)_{\text{eff}} = 0.70$, at an insolation level of 1 kW/m^2 . What is the efficiency of a solar-powered Carnot cycle and a Brayton cycle for which $C_B = 2$?

8. In a closed-loop S-CO₂ Brayton cycle, CO₂ enters the compressor at 8 MPa and exits at 20 MPa. The turbine inlet temperature is set at 700°C and the temperature of the fluid leaving the cooler is 35°C. The turbine and compressor efficiencies are 90%. If the heat exchanger effectiveness is 0.90, find the cycle efficiency assuming the pressure drop in the pipes is negligible and there is no heat loss to the environment.
9. An external receiver with the following information is used for a central receiver solar thermal power system. Determine the total heat loss and the receiver efficiency if the conduction heat loss is negligible.

Receiver diameter (D) = 5 m

Receiver height (H) = 12 m

Ambient temperature (T_∞) = 35°C

Receiver average surface temperature (T_{wall}) = 520°C

Mean flux density at the receiver surface $q = 300 \frac{\text{kW}}{\text{m}^2}$

Average receiver surface absorptivity (α) = 0.9

Average receiver emissivity (ϵ) = 0.9

Mean wind velocity (V) = 4 m/s

Thermal conductivity at 250°C = $42.363 \times 10^{-3} \frac{\text{W}}{\text{m}\cdot\text{K}}$

Kinematic viscosity at 250°C = $45.37 \times 10^{-6} \text{ m}^2/\text{s}$

10. The optical performance of a heliostat is evaluated in a solar power tower plant at PSA in Almeria, Spain (Lat. 37.43°N). The heliostat is 6.7 m wide and 6.8 m high. The target is a flat plate that is placed at $X = 0$ m, $Y = 0.74$ m, and $Z = 35.16$ m with respect to the origin of the coordinate system at the base of the tower (X pointing to East, Y to North, and Z to the zenith). The plate is 8 m wide and 7.2 m high. The test is performed at 12:53 p.m. on September 7. The coordinates of the heliostat with respect to the tower are as follows: $X = -50.60$ m, $Y = 155.44$ m, and $Z = 6.23$ m. If tracking error and astigmatic effect are negligible, sun shape error is 2.51 mrad, and mirror slope error is 1 mrad, find the optical efficiency of the heliostat. Reflectivity of the heliostat is 90%.
-

References

- Abutayeh, M. et al. 2014. Desalination: Water from water. In Chapter 11: *Solar Desalination*, Ed. J. Kucera. Scrivener/Wiley, Hoboken, NJ.
- Alajlan, S.A., and M.S. Smiai. 1996. Performance and development of PV—Plant for water pumping and desalination for remote area in Saudi Arabia. *Renew. Energy* 8(1–4): 441–446.
- Alawaji, S. et al. 1995. PV-powered water pumping and desalination plant for remote areas in Saudi Arabia. *Applied Energy* 52(2–3): 283–289.
- American Society of Mechanical Engineers (ASME). 2004. ASME B31.1-2004. American National Standard, ASME Code for Pressure Piping.
- Angelino, G. 1967. Perspectives for the liquid phase compression gas turbine. *J. Eng. Power Trans. ASME* 89: 229–237.
- Angelino, G. 1968. Carbon dioxide condensation cycles for power production. *J. Eng. Power* 90: 287–295.
- Angelino, G. 1969. Real gas effects in carbon dioxide cycles. ASME Paper No. 69-GT-103, ASME, New York.
- Ávila-Marín, A.L. 2011. Volumetric receivers in solar thermal power plants with central receiver system technology: A review. *Sol. Energy* 85(5): 891–910.
- Batteson, K.W. 1981. Solar power tower design guide: Solar thermal central receiver power systems. A source of electricity and/or process heat. NASA STI/Recon Tech. Report N81(1981): 31670.
- Becker, M. et al. 2006. Theoretical and numerical investigation of flow stability in porous materials applied as volumetric solar receivers. *Sol. Energy* 80(10): 1241–1248.
- Bertocchi, R., J. Karni, and A. Kribus. 2004. Experimental evaluation of a non-isothermal high temperature solar particle receiver. *Energy* 29(5–6): 687–700.
- Besarati, S.M., and D.Y. Goswami. 2013. Analysis of advanced supercritical carbon dioxide power cycles with a bottoming cycle for concentrating solar power applications. *J. Sol. Energy Eng., Trans. ASME* Vol. 136, No. 1. doi:10.1115/1.4025700.
- Bohn, M.S., T. Williams, and H.W. Price. 1995. Combined cycle power tower. Solar Engineering. ASME Solar Energy Conference. ASME, New York, pp. 597–606.
- Buck, R. et al. 2002. Solar-hybrid gas turbine-based power tower systems (REFOS). *J. Sol. Energy Eng.* 124(1): 2.

- Buck, R., and E. Teufel. 2009. Comparison and optimization of heliostat canting methods. *J. Sol. Energy Eng.* 131(1): 011001.
- Chen, H., D.Y. Goswami, and E. Stefanakos. 2010. A review of thermodynamic cycles and working fluids for the conversion of low grade heat. *Renew. Sustain. Energy Rev.* 14(9): 3059–3067.
- Childs, W.D. et al. 1999. VARI-RO solar-powered desalting technology. *Desalination* 125(1–3): 155–166.
- Collado, F.J. 2010. One-point fitting of the flux density produced by a heliostat. *Sol. Energy* 84: 673–684.
- Collado, F.J., A. Gomez, and J.A. Turegano. 1986. An analytic function for the flux density due to sunlight reflected from a heliostat. *Sol. Energy* 37(3): 215–234.
- Collado, F.J., and J.A. Turegano. 1989. Calculation of the annual thermal energy supplied by a defined heliostat at field. *Sol. Energy* 42(2): 149–165.
- Daniels, F. 1949. Solar energy. *Science* 109: 51–57.
- Daniels, F. 1964. *Direct Use of the Sun's Energy*. Yale University Press, New Haven, CT.
- DeLaquil, III, P. et al. 1993. Solar thermal electric technology. In *Renewable Energy-Sources for Fuels and Electricity*, Eds. T. Johansson et al. Island Press, Washington, DC, pp. 213–296.
- Dostal, V., P. Hejzlar, and M.J. Driscoll. 2006. The supercritical carbon dioxide power cycle: Comparison to other advanced power cycles. *Nucl. Technol.* 154(3): 283–301.
- Dunkle, R.V. 1961. Solar water distillation: The roof type still and a multiple effect diffusion still. *Proc. 1961 International Heat Transfer Conf.*, American Society of Mechanical Engineers, New York.
- Feher, E.G. 1967. Supercritical thermodynamic power cycle. *Proceeding of the IECEC*, Florida.
- Fend, T. 2010. High porosity materials as volumetric receivers for solar energetics. *Opt. Appl.* 11(2): 271–284.
- Fend, T. et al. 2004. Porous materials as open volumetric solar receivers: Experimental determination of thermophysical and heat transfer properties. *Energy* 29(5–6): 823–833.
- Fitzgerald, A.E., C.F. Kingsley, and A. Kusko. 1971. *Electric Machinery*, 3rd edition. McGraw-Hill, New York.
- Francia, G. 1968. Pilot plants of solar steam generating stations. *Sol. Energy* 12: 51–64.
- Garcia, P., A. Ferriere, and J.-J. Bezan. 2008. Codes for solar flux calculation dedicated to central receiver. *Sol. Energy* 82: 189–197.
- Goswami, D.Y. 1995. Solar thermal power: Status of technologies and opportunities for research. *Proc. of ASME Heat and Mass Transfer Conference*, Surathkal, India, December.
- Goswami, D.Y. 1998. Solar thermal power technology: Present status and ideas for the future. *Energy Sources* 20: 137–145.
- Goswami, D.Y., and F. Kreith (eds.). 2007. *Energy Conversion*. CRC Press, Boca Raton, FL.
- Goswami, D.Y., S. Hingorani, and G. Mines. 1991. A laser-based technique for particle sizing to study two-phase expansion in turbines. *J. Sol. Energy Eng., Trans ASME* 113(3): 211–218.
- Gupta, B.P. 1985. Status and progress in solar thermal research and technology. In *Progress in Solar Engineering*, Ed. D.Y. Goswami. Hemisphere Publishing Corporation, Washington, DC.

- Hasnain, S.M., and S.A. Alajlan. 1998. Coupling of PV-powered RO brackish water desalination plant with solar stills. *Desalination* 116(1): 57–64.
- Hildebrandt, A.F., and L.L. Vant-Hull. 1974. Tower top focus solar energy collector. *Mech. Eng.* 23(9): 23–27.
- Hipser, M.S., and R.F. Roehm. 1976. Heat transfer considerations of a non-convecting solar pond heat exchanger. ASME Paper 76-WA/Sol-4, ASME, New York.
- Ho, C. 2008. Software and codes for analysis of concentrating solar power technologies. SAND2008-8053. Sandia National Lab., Albuquerque, NM.
- Japikse, D., and C.B. Nicholas. 1994. *Introduction to Turbomachinery Concepts*. ETI, Norwich, VT.
- Jones, S.A. 1996. A comparison of on-axis and off-axis heliostat alignment strategies. Report SAND96-0566C. Sandia National Lab., Albuquerque, NM.
- Kagawa, N. et al. 1989. Mechanical analysis and durability for a 3KW Stirling engine. *Proc. of the 24th IECEC Conference*, Vol. 5, IEEE, NY, August 6–11, pp. 2369–2374.
- Kakaç, S., R.K. Shah, and W. Aung. 1987. *Handbook of Single-Phase Convective Heat Transfer*. John Wiley & Sons, New York.
- Kalina, A.I. 1984. Combined cycle system with novel bottoming cycle. *J. Eng. Gas Turbines Power* 106: 737–742.
- Kalina, A.I., and M. Tribus. 1992. Advances in Kalina cycle technology (1980–91), Part I: Development of a practical cycle, energy for the transition age. *Proc. of FLOWERS '92*, Nova Science Publishers, pp. 97–109.
- Karni, J. et al. 1998a. A high-pressure window for volumetric solar receivers. *J. Sol. Energy Eng.* 120(2): 101.
- Karni, J. et al. 1998b. The “porcupine”: A novel high-flux absorber for volumetric solar receivers. *J. Sol. Energy Eng.* 120(2): 85.
- Keenan, J.H., and F.G. Keys. 1956. *Thermodynamic Properties of Steam*. John Wiley & Sons, New York.
- Kelly, B., and D. Kearney. 2006. Parabolic trough solar system piping model. Tech. Rep., National Renewable Energy Laboratory, NREL/SR-550-40165, July, Golden, CO.
- Kistler, B.L. 1986. A user’s manual for DELSOL3: A computer code for calculating the optical performance and optimal system design for solar thermal central receiver plants. Sandia Report, SABD86-8018, Sandia National Lab., Albuquerque, NM.
- Kolb, G.J. et al. 2007. Heliostat cost reduction study. Sandia Report, SAND2007-3293, June, Sandia National Lab., Albuquerque, NM.
- Kouremenos, D.A., E.D. Rogdakis, and K.A. Antonopoulos. 1994. Cogeneration with combined gas and aqua-ammonia absorption cycles. In *Thermodynamics and the Design, Analysis, and Improvement of Energy Systems*, Vol. 33. American Society of Mechanical Engineers, Advanced Energy Systems Division (Publication) AES, ASME, New York, pp. 231–238.
- Kreith, F., and D.Y. Goswami (eds.). 2004. *The CRC Handbook of Mechanical Engineering*. CRC Press, Boca Raton, FL.
- Kröger, D. 2004. *Air-Cooled Heat Exchangers and Cooling Towers: Thermal-Flow Performance Evaluation and Design*, Vol. 2. Pennwell Corp., Tulsa, OK.
- Landman, W., and P. Gauché. 2013. Influence of canting mechanism and facet profile on heliostat field performance. *Energy Procedia* 49(2014): 126–135.
- Lemmon, E.W., M.O. McLinden, and M.L. Huber. 2002. NIST reference fluid thermodynamic and transport properties—REFPROP, NIST standard reference database 23. NIST, Boulder CO.

- Leshuk, J.P. et al. 1976. Solar pond stability experiments. In *Sharing the Sun*, Vol. 5. ISES, Winnipeg, pp. 188–202.
- Li, C. et al. 2012. Reverse osmosis desalination driven by low-temperature supercritical organic Rankine cycle. *Applied Energy* 102: 1071–1080.
- Li, C., Y. Goswami, and E. Stefanakos. 2013a. Solar-assisted seawater desalination: A review. *Renew. Sustain. Energy Rev.* 19: 136–163.
- Li, C. et al. 2013b. Performance investigation of concentrating solar collectors coupled with a transcritical organic Rankine cycle for power and seawater desalination co-generation. *Desalination* 318: 107–117.
- Lipps, F.W., and L.L. Vant-Hull. 1978. A cellwise method for the optimization of large central receiver systems. *Sol. Energy* 20: 505–516.
- Liu, B., K. Chien, and C. Wang. 2004. Effect of working fluids on organic Rankine cycle for waste heat recovery. *Energy* 29(8): 1207–1217.
- Logan, E. 1993. *Turbomachinery: Basic Theory and Applications*. CRC Press, Boca Raton, FL.
- Megyesy, E.F. 2004. *Pressure Vessel Handbook*, 13th edition. Pressure Vessel Publishing, Tulsa, OK.
- Moisseytsev, A., and J.J. Sienicki. 2009. Investigation of alternative layouts for the supercritical carbon dioxide Brayton cycle for a sodium-cooled fast reactor. *Nucl. Eng. Des.* 239(7): 1362–1371.
- Nielsen, C.E. 1976. Experience with a prototype solar pond for space heating. In *Sharing the Sun*, Vol. 5. ISES, Winnipeg, pp. 169–182.
- Nielsen, C.E., and A. Rabl. 1976. Salt requirement and stability of solar ponds. In *Sharing the Sun*, Vol. 5. ISES, Winnipeg, pp. 183–187.
- Nogawa, M. et al. 1989. Development of solar Stirling engine alternator for space experiments. *Proc. of the 24th IECEC Conference*, Vol. 5, IEEE, NY, August 6–11, pp. 2375–2378.
- Poling, B., J. Prausnitz, and J.O. Connell. 2000. *The Properties of Gases and Liquids*. McGraw-Hill.
- Proctor, D., and R.N. Morse. 1975. *Solar Energy for Australian Food Processing Industry*. CSIRO Solar Energy Studies, East Melbourne, Victoria, Australia.
- Rabl, A., and C.E. Nielsen. 1975. Solar ponds for space heating. *Sol. Energy* 17: 1–12.
- Reddy, T.A. 1987. *The Design and Sizing of Active Solar Thermal Systems*. Oxford University Press, Oxford.
- Rogdakis, E.D., and K.A. Antonopoulos. 1991. High efficiency NH₃/H₂O absorption power cycle. *Heat Recovery Syst. CHP* 11(4): 263–275.
- Romero-Alvarez, M., and E. Zarza. 2008. Concentrating solar thermal power. In *Energy Conversion*, Eds. D.Y. Goswami, and F. Kreith. CRC Press, Boca Raton, FL.
- Salisbury, J.K. 1950. *Steam Turbines and Their Cycles*. Robert K. Krieger Publishing, Malabar, FL. Reprint 1974.
- Sargent and Lundy LLC Consulting Group. 2003. Assessment of parabolic trough and power tower solar technology cost and performance forecasts. NREL/SR-550-34440, Golden, CO.
- Schmitz, M. et al. 2006. Assessment of the potential improvement due to multiple apertures in central receiver systems with secondary concentrators. *Sol. Energy* 80(1): 111–120.
- Schwarzbözl, P., M. Schmitz, and R. Pitz-Paal. 2009. Visual HFLCAL- A software tool for layout and optimization of heliostat fields. *SolarPACES*, 2009.
- Siebers, D.L., and J.S. Kraabel. 1984. Estimating convective energy losses from solar central receivers. SAND84-8717. Sandia National Laboratories, Livermore, CA.

- Sproul, E., K. Chavez, and J. Yellowhair. 2011. The development of the heliostat focusing and canting enhancement technique: An optical heliostat alignment tool for the national solar thermal test facility. *Proceedings of the ASME 2011, 5th International Conference on Energy Sustainability*, pp. 1–9.
- Steinfeld, A., and M. Schubnell. 1993. Optimum aperture size and operating temperature of a solar cavity-receiver. *Sol. Energy* 50(1): 19–25.
- Stine, W.B. 2004. Stirling engines. In *The CRC Handbook of Mechanical Engineering*, Eds. F. Kreith, and D.Y. Goswami. CRC Press, Boca Raton, FL.
- Stine, W.B., and R.E. Diver. 1994. A compendium of solar dish/Stirling technology. SAND93-7026. Sandia National Laboratory, Albuquerque, NM.
- Stine, W.B., and R.W. Harrigan. 1985. *Solar Energy Fundamentals and Design: With Computer Applications*. Wiley-Interscience, Hoboken, NJ.
- Styris, D.L. et al. 1976. The nonconvecting solar pond applied to building and process heating. *Sol. Energy* 18: 245–251.
- Tabor, H. 1963. Solar ponds. *Solar Energy* 7: 189–194.
- Tabor, H. 1966. Solar ponds. *Sci. J.* 21: 66–71.
- Talbert, S.G., J.A. Eibling, and G.O.G. Löf. 1970. Manual on solar distillation of saline water. Office of Saline Water, Research and Development Progress Rept. 546. U.S. Department of Interior, Washington, DC.
- Thomson, M., and D. Infield. 2005. Laboratory demonstration of a photovoltaic-powered seawater reverse-osmosis system without batteries. *Desalination* 183(1–3): 105–111.
- Trombe, F. 1956. High temperature furnaces. *Proc. World Symposium on Applied Solar Energy*, Phoenix, Arizona, 1955, Stanford Research Institute, Menlo Park, CA.
- Turchi, C.S. 2009. Supercritical CO₂ for application in concentrating solar power systems. *Proceedings of SCCO₂ Power Cycle Symposium, 2009*, no. Figure 1, pp. 1–5.
- Turchi, C. 2010. Parabolic trough reference plant for cost modeling with the Solar Advisor Model (SAM). Tech. Rep., National Renewable Energy Laboratory (NREL), Golden, CO.
- Turchi, C.S. et al. 2012. Thermodynamic study of advanced supercritical carbon dioxide power cycles for high performance concentrating solar power systems. *Proceedings of the ASME 2012, 6th International Conference on Energy Sustainability ES2012*.
- Tzen, E., D. Theofiloyianakos, and Z. Kologios. 2008. Autonomous reverse osmosis units driven by RE sources experiences and lessons learned. *Desalination* 221(1–3): 29–36.
- Vant-Hull, L.L., and M.E. Izgyon. 2003. Guideline to central receiver system heliostat field optimization. *Adv. Solar Energy* 15: 1–42.
- Vasquez-Padilla, R. 2011. Simplified methodology for designing parabolic trough solar power plants. PhD dissertation, University of South Florida, Tampa, FL.
- Washam, B.M. et al. 1993. *Integrated Solar Combined Cycle Systems (ISCCS) Utilizing Solar Parabolic Trough Technology—Golden Opportunities for the '90s*. Spencer Management Associates, Diablo, CA.
- Weinberger, H. 1964. The physics of the solar pond. *Sol. Energy* 8: 45–56.
- Winter, C.-J., R.L. Sizmann, and L.L. Vant-Hull. 1991. *Solar Power Plants: Fundamentals, Technology, Systems, Economics*. Springer, New York.

9

Photovoltaics

Photovoltaic (PV) conversion is the direct conversion of sunlight into electricity with no intervening heat engine. PV devices are solid state; therefore, they are rugged and simple in design and require very little maintenance. Perhaps the biggest advantage of solar PV devices is that they can be constructed as stand-alone systems to give outputs from microwatts to megawatts. That is why they have been used as the power sources for calculators, watches, water pumping, remote buildings, communications, satellites and space vehicles, and even megawatt-scale power plants. PV panels can be made to form components of a building skin, such as roof shingles and wall panels. With such a vast array of applications, the demand for photovoltaics is increasing every year. In 2012, global PV installations were approximately 32 GW with a cumulative global total of more than 100 GW.

In the early days of solar cells in the 1960s and 1970s, more energy was required to produce a cell than it could ever deliver during its lifetime (Nijs et al. 1997). Since then, dramatic improvements have taken place in the efficiencies and manufacturing methods. In 2008, the energy payback periods were reduced to approximately 2 to 5 years, depending on the location of use (http://en.wikipedia.org/wiki/File:SEPIC_Schematic.gif), while panel lifetimes were increased to more than 30 years. The costs of PV panels have come down to less than \$1.00 per peak watt by 2012.

Historically, the photoelectric effect was first noted by Becquerel in 1839 when light was incident on an electrode in an electrolyte solution (Angrist 1976). Adams and Day first observed the effect in solids in 1877 while working with selenium. Early work was done with selenium and copper oxide by pioneers such as Schottkey, Lange, and Grandahl. In 1954, researchers at RCA and Bell Laboratories reported achieving efficiencies of approximately 6% by using devices made of *p* and *n* types of semiconductors. The space race between the United States and the Soviet Union resulted in dramatic improvements in PV devices. Bube (1960) gives a review of the early developments in PV conversion.

9.1 Semiconductors

A basic understanding of the atomic structure is quite helpful in understanding the behavior of semiconductors and their use as PV energy conversion devices. Any fundamental book on physics or chemistry generally gives adequate background for basic understanding. Böer (1990) presents an in-depth treatment of a number of topics in semiconductor physics.

For any atom, the electrons arrange themselves in orbitals around the nucleus so as to result in the minimum amount of energy. Figure 9.1 shows the distribution of the electrons in various shells and subshells in light elements. In elements that have electrons in multiple shells, the innermost electrons have minimum energy and, therefore, require the maximum amount of externally imparted energy to overcome the attraction of the nucleus and become free. Electrons in the outermost band of subshells are the only ones that participate in the interaction of an atom with its neighboring atoms. If these electrons are very loosely attached to the atom, they may attach themselves with a neighboring atom to give that atom a negative charge, leaving the original atom as a positive charged ion. The positive and negatively charged ions become attached by the force of attraction of the charges, thus forming *ionic bonds*. If the electrons in the outermost band do not fill the band completely but are not loosely attached either, they arrange themselves so that neighboring atoms can share them to make the outermost bands full. The bonds thus formed between the neighboring atoms are called *covalent bonds*.

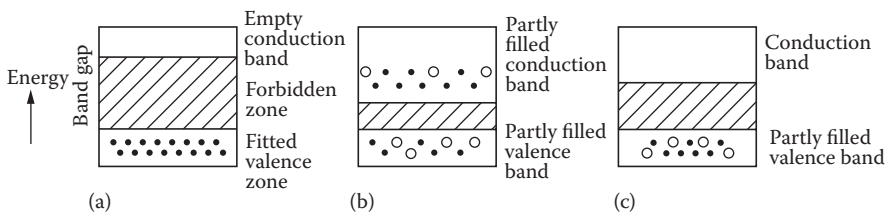
Since electrons in the outermost band of an atom determine how an atom will react or join with a neighboring atom, the outermost band is called the *valence band*. Some electrons in the valence band may be so energetic that they jump into a still higher band and are so far removed from the nucleus that a small amount of impressed force would cause them to move away from the atom. Such electrons are responsible for the conduction of heat and electricity, and this remote band is called a *conduction band*. The difference in the energy of an electron in the valence band and the innermost subshell of the conduction band is called the *band gap*, or the forbidden gap.

Materials whose valence bands are full have very high band gaps (>3 eV). Such materials are called *insulators*. Materials, on the other hand, that have relatively empty valence bands and may have some electrons in the conduction band are good *conductors*. Metals fall in this category. Materials with valence bands partly filled have intermediate band gaps (≤ 3 eV). Such materials are called *semiconductors* (Figure 9.2). Pure semiconductors are called *intrinsic semiconductors*, while semiconductors doped with very small amounts of impurities are called *extrinsic semiconductors*. If the dopant material has more electrons in the valence band than the semiconductor, the doped material is called an *n-type* of semiconductor. Such a material seems to have excess electrons available for conduction even though the material is

Principal quantum number n				1	2		3		4		5				
Azimuthal quantum number l				0	0	1	0	1	2	0	1				
Letter designation of state				1s	2s	2p	3s	3p	3d	4s	4p				
Z	Symbol	Element	V_i Volts												
1	H	Hydrogen	13.60	1											
2	He	Helium	24.58	2											
3	Li	Lithium	5.39	Helium core	1										
4	Be	Beryllium	9.32		2										
5	B	Boron	8.30		2	1									
6	C	Carbon	11.26		2	2									
7	N	Nitrogen	14.54		2	3									
8	O	Oxygen	13.61		2	4									
9	F	Fluorine	17.42		2	5									
10	Ne	Neon	21.56		2	6									
11	Na	Sodium	5.14				1								
12	Mg	Magnesium	7.64				2								
13	Al	Aluminum	5.98	Neon core			2	1							
14	Si	Silicon	8.15				2	2							
15	P	Phosphorus	10.55				2	3							
16	S	Sulfur	10.36				2	4							
17	Cl	Chlorine	13.01				2	5							
18	A	Argon	15.76				2	6							
19	K	Potassium	4.34						1						
20	Ca	Calcium	6.11						2						
21	Sc	Scandium	6.56						1	2					
22	Ti	Titanium	6.83						2	2					
23	V	Vanadium	6.74						3	2					
24	Cr	Chromium	6.76						5	1					
25	Mn	Manganese	7.43						5	2					
26	Fe	Iron	7.90						6	2					
27	Co	Cobalt	7.86	Argon core					7	2					
28	Ni	Nickel	7.63						8	2					
29	Cu	Copper	7.72						10	1					
30	Zn	Zinc	9.39						10	2					
31	Ga	Gallium	6.00						10	2	1				
32	Ge	Germanium	7.88						10	2	2				
33	As	Arsenic	9.81						10	2	3				
34	Se	Selenium	9.75						10	2	4				
35	Br	Bromine	11.84						10	2	5				
36	Kr	Krypton	14.00						10	2	6				

FIGURE 9.1

Electronic structure of atoms. (From Moore, C.E., *Atomic Energy Levels*, Vol. 2. Washington, D.C.: National Bureau of Standards Circular 467, 1952.)

**FIGURE 9.2**

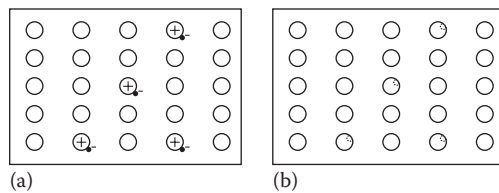
Electrical conduction is described in terms of allowed and forbidden energy bands. Band gap for insulators (a) is the highest, followed by semiconductors (c) and metals (b), respectively.

electronically neutral. For example, silicon has four electrons in the valence band. Atoms of pure silicon arrange themselves in such a way that, to form a stable structure, each atom shares two electrons with each neighboring atom with covalent bonds. If phosphorus, which has five valence electrons (one more than Si), is introduced as an impurity in silicon, the doped material seems to have excess electrons even though it is electrically neutral. Such a doped material is called *n*-type silicon. If, on the other hand, silicon is doped with boron, which has three valence electrons (one less than Si), there seems to be a positive hole (missing electrons) in the structure, even though the doped material is electrically neutral. Such material is called *p*-type silicon. Thus, *n*- and *p*-type semiconductors make it easier for the electrons and holes, respectively, to move in the semiconductors.

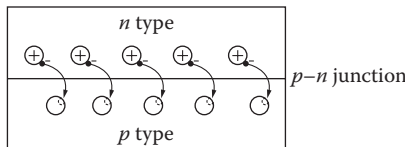
9.1.1 *p–n* Junction

As explained earlier, an *n*-type material has some impurity atoms with more electrons than the rest of the semiconductor atoms. If those excess electrons are removed, the impurity atoms will fit more uniformly in the structure formed by the main semiconductor atoms; however, the atoms will be left with positive charges. On the other hand, a *p*-type material has some impurity atoms with fewer electrons than the rest of the semiconductor atoms. Therefore, these atoms seem to have holes that could accommodate excess electrons even though the atoms are electrically neutral (Figure 9.3). If additional electrons could be brought to fill the holes, the impurity atoms would fit more uniformly in the structure formed by the main semiconductor atoms; however, the atoms will be negatively charged.

The above scenario occurs at the junction when a *p* and an *n* type of material are joined together as shown in Figure 9.4. As soon as the two materials are joined, “excess” electrons from the *n* layer jump to fill the “holes” in the *p* layer. Therefore, close to the junction, the material has positive charges on the *n* side and negative charges on the *p* side. The negative charges on the *p* side restrict the movement of additional electrons from the *n* side to the *p* side, while the movement of additional electrons from the *p* side to the

**FIGURE 9.3**

Representation of *n*- and *p*-type semiconductors: (a) *n* type showing “excess” electrons as dots; (b) *p* type showing “excess” positive holes as ☺.

**FIGURE 9.4**

“Excess” electrons from *n*-material jump to fill “excess” holes on the *p* side of a *p-n* junction, leaving the *n* side of the junction positively charged and the *p* side negatively charged.

n side is made easier because of the positive charges at the junction on the *n* side. This restriction makes the *p-n* junction behave like a diode. This diode character of a *p-n* junction is made use of in solar PV cells as explained in the following.

9.1.2 PV Effect

When a photon of light is absorbed by a valence electron of an atom, the energy of the electron is increased by the amount of energy of the photon. If the energy of the photon is equal to or more than the band gap of the semiconductor, the electron with excess energy will jump into the conduction band where it can move freely. If, however, the photon energy is less than the band gap, the electron will not have sufficient energy to jump into the conduction band. In this case, the excess energy of the electrons is converted to excess kinetic energy of the electrons, which manifests in increased temperature. If the absorbed photon had more energy than the band gap, the excess energy over the band gap simply increases the kinetic energy of the electron. It must be noted that a photon can free up only one electron even if the photon energy is a lot higher than the band gap. This fact is a big reason for the low conversion efficiency of PV devices. The key to using the PV effect for generating useful power is to channel the free electrons through an external resistance before they recombine with the holes. This is achieved with the help of the *p-n* junction.

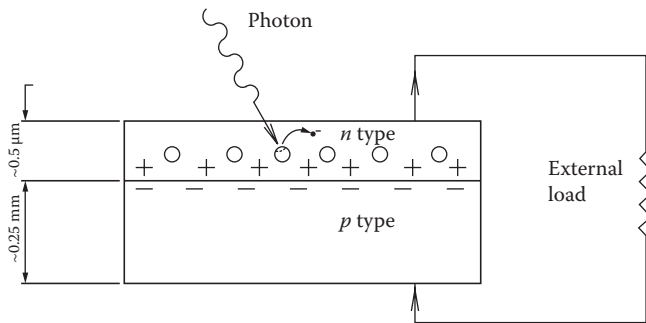


FIGURE 9.5
Schematic of a PV device.

Figure 9.5 shows a schematic of a PV device. As free electrons are generated in the *n* layer by the action of photons, they can pass through an external circuit, recombine with positive holes in the lateral direction, or move toward the *p* layer. The negative charges in the *p* layer at the *p-n* junction restrict their movement in that direction. If the *n* layer is made extremely thin, the movement of the electrons and, therefore, the probability of recombination within the *n* layer is greatly reduced unless the external circuit is open. If the external circuit is open, the electrons generated by the action of photons eventually recombine with the holes, resulting in an increase in the temperature of the device.

In a typical crystalline silicon cell, the *n* layer is approximately $0.5\text{ }\mu\text{m}$ thick and the *p* layer is approximately 0.25 mm thick. As explained in Chapter 2, energy contained in a photon E_p is given by

$$E_p = h\nu, \quad (9.1)$$

where h is Planck's constant ($6.625 \times 10^{-34}\text{ J}\cdot\text{s}$) and ν is the frequency that is related to the wavelength λ and the speed of light c as

$$\nu = \frac{c}{\lambda}.$$

Therefore,

$$E_p = hc/\lambda. \quad (9.2)$$

For silicon, which has a band gap of 1.11 eV , the following example shows that photons of solar radiation of wavelength $1.12\text{ }\mu\text{m}$ or less are useful in creating electron-hole pairs. This spectrum represents a major part of the solar radiation. Table 9.1 lists some candidate semiconductor materials for PV cells along with their band gaps.

TABLE 9.1

Energy Gap for Some Candidate Materials
for PV Cells

Material	Band Gap (eV)
Si	1.11
SiC	2.60
CdAs ₂	1.00
CdTe	1.44
CdSe	1.74
CdS	2.42
CdSnO ₄	2.90
GaAs	1.40
GaP	2.24
Cu ₂ S	1.80
CuO	2.00
Cu ₂ Se	1.40
CuInS ₂	1.50
CuInSe ₂	1.01
CuInTe ₂	0.90
InP	1.27
In ₂ Te ₃	1.20
In ₂ O ₃	2.80
Zn ₃ P ₂	1.60
ZnTe	2.20
ZnSe	2.60
AlP	2.43
AlSb	1.63
As ₂ Se ₃	1.60
Sb ₂ Se ₃	1.20
Ge	0.67
Se	1.60

Source: Garg, H.P. *Advances in Solar Energy Technology*, vol. 3, Dordrecht, Holland: D. Reidel Publishing Company, 1987.

Example 9.1

Calculate the wavelength of light capable of forming an electron–hole pair in silicon.

Solution

The band gap energy of silicon is 1.11 eV. From Equation 9.2, we can write

$$\lambda = \frac{hc}{E}$$

For $c = 3 \times 10^8 \text{ m/s}$, $h = 6.625 \times 10^{-34} \text{ J}\cdot\text{s}$, and $1 \text{ eV} = 1.6 \times 10^{-19} \text{ J}$, the above equation gives the required wavelength as

$$\lambda = \frac{(6.625 \times 10^{-34} \text{ J}\cdot\text{s})(3 \times 10^8 \text{ m/s})}{(1.11)(1.6 \times 10^{-19} \text{ J})} = 1.12 \text{ m.}$$

Example 9.2

A monochromatic red laser beam emitting 1 mW at a wavelength of 638 nm is incident on a silicon solar cell. Find the following:

- The number of photons per second incident on the cell
- The maximum possible efficiency of conversion of this laser beam to electricity

Solution

- The intensity of light in the laser beam (I_p) is equal to the energy of all the photons in it. If the number of photons is N_{ph} , then

$$I_p = N_{ph} \cdot E_p \quad (9.3)$$

$$1 \times 10^{-3} \text{ W} = N_{ph} \cdot E_p \quad (1 \text{ W} = 1 \text{ J/s})$$

$$E_p = hc/\lambda$$

$$= \frac{(6.625 \times 10^{-34} \text{ J}\cdot\text{s}) \cdot 3 \times 10^8 \text{ m/s}}{638 \times 10^{-9} \text{ m}}$$

$$= 3.12 \times 10^{-19} \text{ J}$$

$$\therefore N_{ph} = \frac{1 \times 10^{-3} \text{ J/s}}{3.12 \times 10^{-19} \text{ J}} = 3.21 \times 10^{15} \text{ photons/s.}$$

- Assuming that each photon is able to generate an electron, a total number of N_{ph} electrons will be generated. Therefore, the electrical output will be equal to $N_{ph} \cdot (\text{Band Gap})$. Therefore, the maximum possible efficiency is

$$\eta_{max} = \frac{(N_{ph}) \cdot (\text{B.G.})}{(N_{ph}) \cdot E_p} = \frac{\text{B.G.}}{E_p} \quad (9.4)$$

$$= \frac{1.11 \times 1.6 \times 10^{-19} \text{ J}}{3.12 \times 10^{-19} \text{ J}} = 0.569 \text{ or } 56.9\%.$$

From the above examples, it is clear that for a silicon solar cell, none of the photons of the sunlight over 1.12 μm wavelength will produce any electricity. However, photons of sunlight at a wavelength of 1.12 μm may be converted to electricity at a maximum efficiency of 100%, while photons at lower wavelengths will be converted at lower efficiencies. The overall maximum efficiency of a cell can be found by integrating the efficiency at each wavelength over the entire solar spectrum:

$$\eta = \frac{\int \eta_\lambda I_\lambda d\lambda}{\int I_\lambda d\lambda} \quad (9.5)$$

In addition, other factors such as probability of electron–hole recombination reduce the theoretical maximum achievable efficiency of a solar cell.

In 1961, William Shockley and Hans Queisser conducted a detailed analysis of the maximum possible solar cell efficiency based on possible electron–hole recombination. By assuming the solar spectrum as a smooth black-body spectrum at 6000 K, they plotted the efficiency limit of solar cells on the basis of the band gap (Shockley and Queisser 1961). When applied to a nonconcentrated real solar spectrum at AM1.5, the Shockley–Queisser (SQ) efficiency limit is shown in Figure 9.6. According to this figure, the maximum efficiency limit for a AM 1.5 solar spectrum (1000 W/m^2) at 25°C is 33.7% for a single p – n junction solar cell with a band gap of 1.34 eV. Figure 9.6 also shows the maximum efficiencies achieved so far for a few cells.

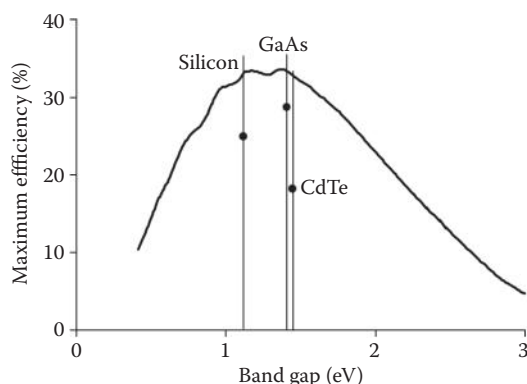


FIGURE 9.6

The maximum solar energy conversion efficiency as a function of the energy gap of the semiconductor calculated according to the SQ efficiency limit for a 1.5 AM solar spectrum (1000 W/m^2) at 25°C . Actual achieved efficiency of some of the materials is also shown. Actual efficiencies achieved as of 2012 are also given in Table 9.2.

The SQ limit can be exceeded by multi-junction cells, high-concentration sunlight, and other methods, which are still under research. On the basis of a theoretical analysis, the limit for a two-junction cell is 42%, and for a three-junction cell, it is 49%. For an infinite junction cell, the maximum limit is 68% (De Vos 1980). Other methods of exceeding the SQ limit include

TABLE 9.2

Confirmed Terrestrial Cell and Submodule Efficiencies Measured under the Global AM1.5 Spectrum (1000 W/m²) at 25°C

Classification	Efficiency (%)	Area (cm ²) ^a	V _{oc} (V)	J _{sc} (mA/cm ²)	FF (%)
<i>Silicon</i>					
Si (crystalline)	25.0 ± 0.5	4.00 (da)	0.706	42.7	82.8
Si (multicrystalline)	20.4 ± 0.5	1.002 (ap)	0.664	38.0	80.9
Si (thin-film transfer)	20.1 ± 0.4	242.6 (ap)	0.682	38.14	77.4
SI (thin-film submodule)	10.5 ± 0.3	94.0 (ap)	0.492	29.7	72.1
<i>III–V Cells</i>					
GaAs (thin film)	28.8 ± 0.9	0.9927 (ap)	1.122	29.68	86.5
GaAs (multicrystalline)	18.4 ± 0.5	4.011 (t)	0.994	23.2	79.7
InP (crystalline)	22.1 ± 0.7	4.02 (t)	0.878	29.5	85.4
<i>Thin-Film Chalcogenide</i>					
CIGS (cell)	19.6 ± 0.6	0.996 (ap)	0.713	34.8	79.2
CIGS (submodule)	17.4 ± 0.5	15.993 (da)	0.6815	33.84	75.5
CdTe (cell)	18.3 ± 0.5	1.005 (ap)	0.857	26.95	77.0
<i>Amorphous/Nanocrystalline Si</i>					
Si (amorphous)	10.1 ± 0.3	1.036 (ap)	0.886	16.75	67.8
Si (nanocrystalline)	10.1 ± 0.2	1.199 (ap)	0.539	24.4	76.6
<i>Photochemical</i>					
Dye sensitized	11.9 ± 0.4	1.005 (da)	0.744	22.47	71.2
Dye sensitized (submodule)	9.9 ± 0.4	17.11 (ap)	0.719	19.4	71.4
<i>Organic</i>					
Organic thin film	10.7 ± 0.3	1.013 (da)	0.872	17.75	68.9
Organic (submodule)	6.8 ± 0.2	395.9 (da)	0.798	13.50	62.8
<i>Multijunction Devices</i>					
InGaP/GaAs/InGaAs	37.7 ± 1.2	1.047 (ap)	3.014	14.57	86.0
<i>a</i> -Si/nc-Si/nc-Si (thin film) ^b	13.4 ± 0.4	1.006 (ap)	1.963	9.52	71.9
<i>a</i> -Si/nc-Si (thin-film cell)	12.3 ± 0.3	0.962 (ap)	1.365	12.93	69.4
<i>a</i> -Si/nc-Si (thin-film submodule)	11.7 ± 0.4	14.23 (ap)	5.462	2.99	71.3

Source: Adapted from Green, M.A. et al., *Prog. Photovolt: Res. Appl.*, 21, 1–11, 2013.

^a ap, aperture area; t, total area; da, designated illumination area.

^b nc-Si, nano-crystalline or microcrystalline silicon.

TABLE 9.3

Terrestrial Concentrator Cell Efficiencies Measured under ASTM G-173-03 Direct Beam AM1.5 Spectrum at a Cell Temperature of 25°C

Classification	Efficiency (%)	Area (cm ²) ^a	Intensity (suns)
<i>Single Cells</i>			
GaAs	29.1 ± 1.3	0.505 (da)	117
Si	27.6 ± 1.0	1.00 (da)	92
<i>Multijunction Cells (Monolithic)</i>			
GaInP/GaAs/GaInNAs	44.0 ± 3	0.3104 (ap)	942
InGaP/GaAs/InGaAs	43.5 ± 2.6	0.167 (da)	306
GaInP/GaInAs/Ge	41.6 ± 2.5	0.3174 (da)	364
<i>Submodule</i>			
GaInP/GaAs; GaInAsP/GaInAs	38.5 ± 1.9	0.202 (ap)	20
<i>Modules</i>			
Si	20.5 ± 0.8	1875 (ap)	79
Triple junction	33.5 ± 0.5	10,674.8 (ap)	N/A
<i>"Notable exceptions"</i>			
Si (large area)	21.7 ± 0.7	20.0 (da)	11

Source: Adapted from Green, M.A. et al., *Prog. Photovolt: Res. Appl.*, 21, 1–11, 2013.

^a ap, aperture area; t, total area; da, designated illumination area.

photon up-conversion (absorption of more than one photon of less energy than the band gap and emitting a photon of more energy than the band gap), hot electron capture, and photon down-conversion (capturing a photon of higher energy than the band gap and emitting more than one photon). Use of quantum dots is an example of research in this direction (Semonin 2011).

Table 9.2 gives the maximum efficiencies achieved by various solar cells around the world for global AM1.5 solar spectrum. Table 9.3 gives the maximum achieved efficiencies for concentrated solar radiation.

9.2 Analysis of PV Cells

This section presents an electrical analysis of PV cells, which will be useful in the design of PV devices for various applications. The physics leading to the expressions for the number density of electrons and holes in *n* and *p* materials at a temperature *T* will not be presented here. For such details, the reader is referred to books such as those by Angrist (1976) and Böer (1990). It would suffice to point out here that at the *p*-*n* junction, a current is generated, called the *junction current*. The junction current *J_j* is the net current owing to

the J_o from the p side to the n side (called the *dark current* or the *reverse saturation current*) and a *light-induced recombination current* J_r from the n side to the p side. On the basis of the temperature T , a certain number of electrons in the p material exist in the conduction band. These electrons can easily move to the n side to fill the holes created at the $p-n$ junction, generating a current J_o . Normally, the electrons occupying the conduction band owing to the temperature in the n material do not have enough potential energy to cross the $p-n$ junction to the p side. However, if a forward bias voltage V is applied, which in a PV cell is due to the action of the photons of light, some of the electrons thus generated have enough energy to cross over and recombine with the holes in the p region. This gives rise to a light-induced recombination current J_r , which is proportional to J_o , and is given by

$$J_r = J_o \exp(e_o V / kT), \quad (9.6)$$

where e_o is the charge of an electron = 1.602×10^{-19} coulombs or J/V and k is Boltzmann's constant = $1.381 \times 10^{-23} \text{ J/K}$.

The junction current J_j is the net current due to J_r and J_o .

$$\begin{aligned} J_j &= J_r - J_o \\ &= J_o [\exp(e_o V / kT) - 1]. \end{aligned} \quad (9.7)$$

Referring to Figure 9.7, it is clear that the current generated in the cell has two parallel paths, one through the junction and the other through the external resistance R_L . Figure 9.7 shows an equivalent circuit of a PV cell. It must be pointed out here that the current generated in a PV cell, including the junction current, is proportional to the area of the cell. Therefore, it

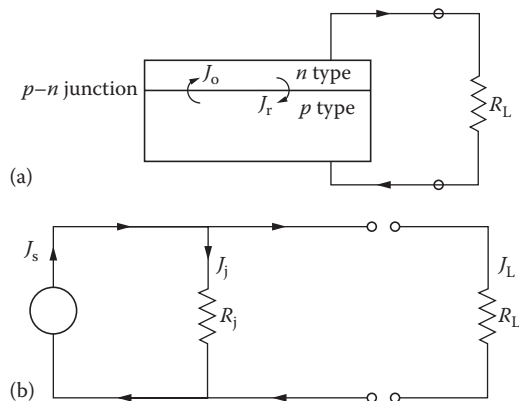


FIGURE 9.7
Equivalent circuit of a PV cell.

is appropriate to analyze in terms of the current density J (current per unit area) instead of the current I . The relationship between the two is

$$I = J \cdot A. \quad (9.8)$$

Referring to Figure 9.7, we can write

$$\begin{aligned} J_L &= J_s - J_j \\ &= J_s - J_o[\exp(e_o V/kT) - 1], \end{aligned} \quad (9.9)$$

where J_s is the *short-circuit current*.

For short circuit, $V = 0$ and $J_L = J_s$.

For open circuit, $J_L = 0$ and $V = V_{oc}$,

which gives

$$0 = J_s - J_o[\exp(e_o V_{oc}/kT) - 1], \quad (9.10)$$

or

$$V_{oc} = \frac{kT}{e_o} \ln \frac{J_s}{J_o} + 1.$$

Figure 9.8 shows a typical performance curve ($I-V$) of a solar cell. The power output is the product of the load current and voltage and is a function of the load resistance

$$\begin{aligned} P_L &= AJ_L V = I_L V \\ &= I_L^2 R_L, \end{aligned} \quad (9.11)$$

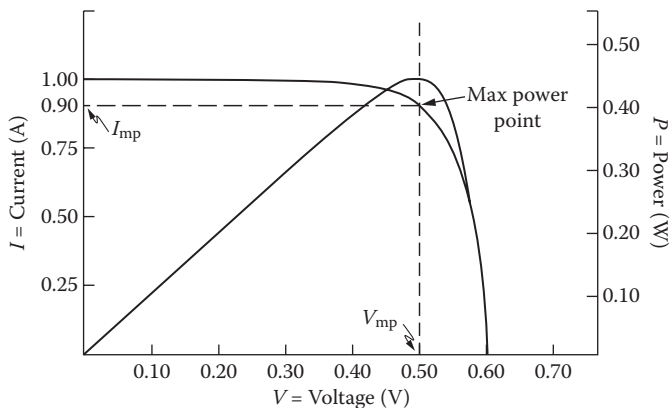
where A is the area of the cell.

The power output exhibits a maximum. To find the condition for the maximum power output (P_{max}), differentiate P_L with respect to V and equate it to zero:

$$\exp(e_o V_m/kT) \cdot 1 + \frac{e_o V_m}{kT} = 1 + \frac{J_s}{J_o}, \quad (9.12)$$

where V_m stands for voltage at maximum power. The current at max power condition $J_{L,m}$ and the maximum power P_{max} can be found from Equations 9.9 and 9.11, respectively.

$$J_{L,m} = J_s - J_o[\exp(e_o V_m/kT) - 1]. \quad (9.13)$$

**FIGURE 9.8**

Typical current, voltage, and power characteristics of a solar cell. (Adapted from Florida Solar Energy Center. Photovoltaic system design. FSEC-GP-31-86. Cocoa Beach, FL: Florida Solar Energy Center, 1991.)

Combining Equations 9.12 and 9.13, $J_{L,m}$ is found to be

$$J_{L,m} = \frac{e_o V_m / kT}{1 + (e_o V_m / kT)} (J_s + J_o) \quad (9.14)$$

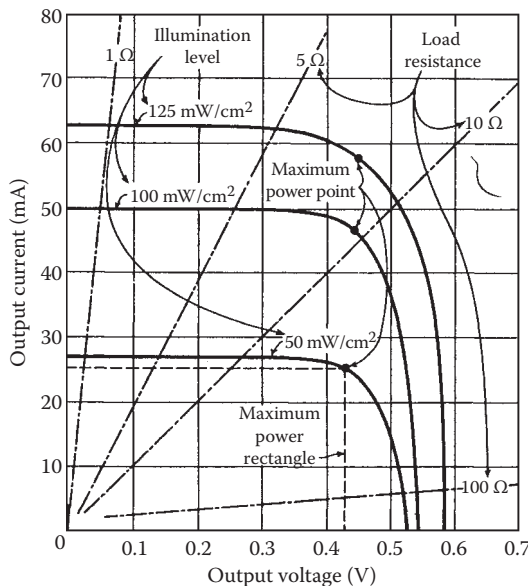
$$P_{\max} = \frac{e_o V_m^2 / kT}{1 + (e_o V_m / kT)} (J_s + J_o) \cdot A. \quad (9.15)$$

Figure 9.9 shows the effect of illumination intensity and the load resistance on the performance of a silicon cell. Temperature also affects the performance in such a way that the voltage and thus the power output decreases with increasing temperature.

Example 9.3

The dark current density for a silicon solar cell at 40°C is $1.8 \times 10^{-8} \text{ A/m}^2$ and the short-circuit current density is 200 A/m^2 . Calculate the following:

- Open circuit voltage
- Voltage at maximum power
- Current density at maximum power
- Maximum power
- Maximum efficiency
- The cell area required for an output of 25 W when exposed to a solar radiation of 900 W/m^2

**FIGURE 9.9**

Typical current–voltage characteristics of a silicon cell showing the effects of illumination level and load resistance.

Solution

Given:

$$J_o = 1.8 \times 10^{-8} \text{ A/m}^2$$

$$J_s = 200 \text{ A/m}^2,$$

and

$$T = 40^\circ\text{C} = 313 \text{ K.}$$

a. Using Equation 9.10,

$$V_{oc} = \frac{kT}{e_o} \ln \frac{J_s}{J_o} + 1 .$$

Since e_o/kT will be needed for other parts also, it can be evaluated separately as

$$e_o/kT = \frac{1.602 \times 10^{-19} \text{ J/V}}{(1.381 \times 10^{-23} \text{ J/K})(313 \text{ K})} = 37.06 \text{ V}^{-1}.$$

Therefore,

$$V_{oc} = \frac{1}{37.06} \ln \frac{200}{1.8 \times 10^{-8}} + 1 \\ = 0.624 \text{ V.}$$

b. Voltage at maximum power condition can be found from Equation 9.12 by an iterative or trial-and-error solution:

$$\exp(37.06 V_m)(1 + 37.06 V_m) = 1 + \frac{200}{1.8 \times 10^{-8}} \\ \text{or } V_m = 0.542 \text{ V.}$$

c. Current density at maximum power can be found from Equation 9.14:

$$J_{L,m} = \frac{e_o V_m / kT}{1 + (e_o V_m / kT)} (J_s + J_o) \\ = \frac{(37.06) \cdot (0.542)}{1 + (37.06) \cdot (0.542)} (200 + 1.8 \times 10^{-8}) \text{ A/m}^2 \\ = 190.5 \text{ A/m}^2.$$

d. $P_{max} = V_m \cdot J_m \cdot A$

$$\frac{P_{max}}{A} = (0.542 \text{ V}) \cdot (190.5 \text{ A/m}^2) \\ = 103.25 \text{ W/m}^2.$$

e. $\eta_{max} = \frac{103.25 \text{ W/m}^2}{900 \text{ W/m}^2} = 11.5\%.$

f. Cell area required:

$$A = \frac{P_{out}}{P_{max}/A} = \frac{25 \text{ W}}{103.25 \text{ W/m}^2} \\ = 24.2 \text{ cm}^2.$$

9.2.1 Efficiency of Solar Cells

Theoretical limitation on the efficiency of a solar cell can be calculated using Equation 9.5. These efficiency limitations and the practical efficiencies of some of the cells are shown in Figure 9.6. Some of the reasons for the actual efficiency being lower than the theoretical limitation are as follows:

1. Reflection of light from the surface of the cell. This can be minimized by antireflection (AR) coating. For example, AR coatings can reduce the reflection from a Si cell to 3% from more than 30% from an untreated cell.
2. Shading of the cell due to current collecting electrical contacts. This can be minimized by reducing the area of the contacts or making them transparent; however, both of these methods will increase the resistance of the cell to current flow.
3. Internal electrical resistance of the cell.
4. Recombination of electrons and holes before they can contribute to the current. This effect can be reduced in polycrystalline and amorphous cells by using hydrogen alloys.

9.2.2 Maximum Power Point Tracking

It is important to ensure that the solar cells in a system are operating at the “maximum power point (MPP)” as seen in Figures 9.8 and 9.9. There are several methods that can be used for maximum power point tracking (MPPT). They include simple methods (e.g., method of determining V_{mp} as equal to kV_{oc} or determining I_{mp} as equal to kI_{sc}) as well as more involved methods (perturb and observe [P&O], incremental conductance [IC], artificial neural networks, and fuzzy logic methods). Each method uses a DC–DC converter consisting of inductors and capacitors in a parallel circuit to measure the operating point of the cell and to change the output voltage to V_{mp} using a control algorithm. The parallel circuit consists of either a DC/DC single-ended primary inductor converter (SEPIC) or a buck–boost converter or a modification of these. Figure 9.10 shows a schematic of a SEPIC converter and Figure 9.11 shows a schematic of a buck–boost converter.

Although a detailed analysis of these converters is outside the scope of this book, opening and closing the switches allows the current to pass from the source through the inductor or from the capacitor to the load. The switching speed determines the output voltage seen by the load.

The differences in the MPPT methods consist of how the V_{mp} is determined. The simplest methods use a fixed constant “ k ” to determine it either from V_{oc} or I_{sc} . Both V_{oc} and I_{sc} change with insulation and the temperature of the cell

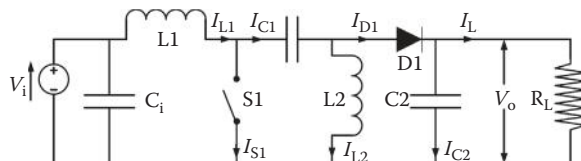
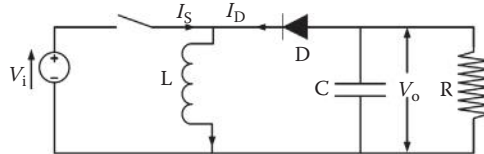


FIGURE 9.10

Schematic of a SEPIC DC/DC converter. (Adapted from http://en.wikipedia.org/wiki/File:SEPIC_Schematic.gif.)

**FIGURE 9.11**

Schematic of a buck-boost converter. (Adapted from http://en.wikipedia.org/wiki/File:Buckboost_conventions.svg.)

and therefore will not always give the best values of V_{mp} . The P&O method is much more accurate and more common in use. In a P&O algorithm, the output voltage is increased or decreased (perturbed) and the output power is compared with the power before perturbation. If the power increases ($dP/dV > 0$), then the voltage is increased more and vice versa. The method runs into problems if the insolation changes rapidly during a perturbation. IC is a similar method in which current I and voltage V are measured before and after a perturbation and dI/dV is compared with I/V .

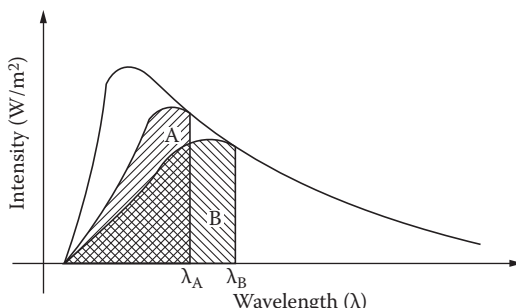
At MPP

$$(dI/dV + I/V) = 0.$$

If the MPP is to the right of the perturbed point, then $(dI/dV + I/V) > 0$ and vice versa.

9.2.3 Multijunction Solar Cells

The limits imposed on solar cells owing to band gap can be partially overcome by using multiple layers of solar cells stacked on top of each other, each layer with a band gap higher than the layer below it. For example (Figure 9.12), if the top layer is made from a cell of material A (band gap corresponding to λ_A), solar radiation with wavelengths less than λ_A would be absorbed to give an output equal to the hatched area A. The solar radiation with wavelength greater than λ_A would pass through A and be converted

**FIGURE 9.12**

Energy conversion from a two-layered stacked cell.

Band gap (eV)	Material	Deposition process	Thickness (nm)
	Glass		1.5–2.1 mm
	SnO_2 : F	Textured tin oxide	500–800
~1.95	P_1	$a\text{-Si}$: H; B	PECVD
~1.72	i_1	$a\text{-Si}$: H, H_2 diluted	PECVD
1.72	n_1	$\mu\text{c-Si}$: H; P	PECVD
~1.95	P_2	$a\text{-SiC}$: H; B	PECVD
~1.72	i_2	$a\text{-Si}$: H, H_2 diluted	PECVD
1.72	n_2	$\mu\text{c-Si}$: H; P	PECVD
~1.95	P_3	$a\text{-SiC}$: H; B	PECVD
~1.44	i_3	$a\text{-SiGe}$: H, H_2 diluted	PECVD
1.72	n_3	$\mu\text{c-Si}$: H; P	PECVD
	$ZnO:F$	Reactive magnetron sputtered or LPCVD	80–100
	Ag or Al	Sputtered	
		Polyurethane	

FIGURE 9.13

Typical triple-junction $a\text{-Si}$ cell structure. (From Crandall, R., and W. Luft. The future of amorphous silicon photovoltaic technology. NREL/TP-441-8019. Golden, CO: National Renewable Energy Laboratory, 1995.)

by the bottom layer cell B (band gap corresponding to λ_B) to give an output equal to the hatched area B. The total output and therefore the efficiency of this tandem cell would be higher than the output and the efficiency of each single cell individually. The efficiency would increase with the number of layers. For this concept to work, each layer must be as thin as possible, which puts a very difficult if not an insurmountable constraint on crystalline and polycrystalline cells to be made multijunction. As a result, this concept is being investigated mainly for thin-film amorphous solar cells.

At present, a triple-junction $a\text{-Si}$ solar cell is under development. This cell consists of layers of cells made from $a\text{-Si}_x\text{C}_y\text{H}$ (an amorphous silicon, carbon, and hydrogen alloy) with a band gap of 2.0 eV, $a\text{-Si:H}$ (an amorphous silicon and hydrogen alloy) with a band gap of 1.75 eV, and $a\text{-Si}_x\text{Ge}_y\text{H}$ (an amorphous silicon, germanium, and hydrogen alloy) with a band gap of 2.3 eV. The efficiency of a multijunction cell can be approximately 50% higher than a corresponding single cell. Figure 9.13 shows a conceptual device structure of a triple-junction $a\text{-Si}$ cell (Crandall and Luft 1995).

9.2.4 Thin-Film Solar Cells

Thin-film solar cells based on cadmium telluride (CdTe), copper indium gallium diselenide (CIGS), and gallium arsenide (GaAs) have been the most developed and have become commercially available in the last 10–15 years mainly

because of their potential highest efficiencies on the basis of their band gaps (see Table 9.1 and Figure 9.6). Among these, CdTe panels achieved the most commercial success because of their low cost of production. However, since 2010, silicon cells achieved the same cost reductions because of improved manufacturing technologies and high efficiencies. Multijunction GaAs cells have achieved efficiencies of 44% under concentrated sunlight (see Table 9.3). Achievement of high efficiencies under highly concentrated sunlight has given rise to a kind of PV device, known as concentrated PV or CPV. Figure 9.14 shows general schematics of CdTe and CIGS solar cells. Figure 9.15 shows a schematic of a triple-junction GaAs solar cell.

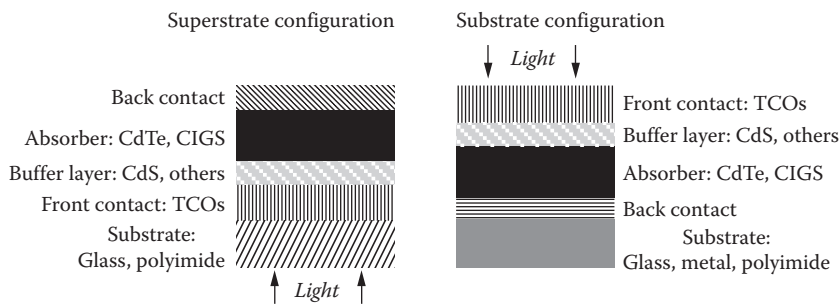


FIGURE 9.14

Schematic structure of a CdTe or a CIGS solar cell. (Adapted from Romeo, A.M. et al., *Prog. Photovolt: Res. Appl.*, 12, 93–111, 2004.)

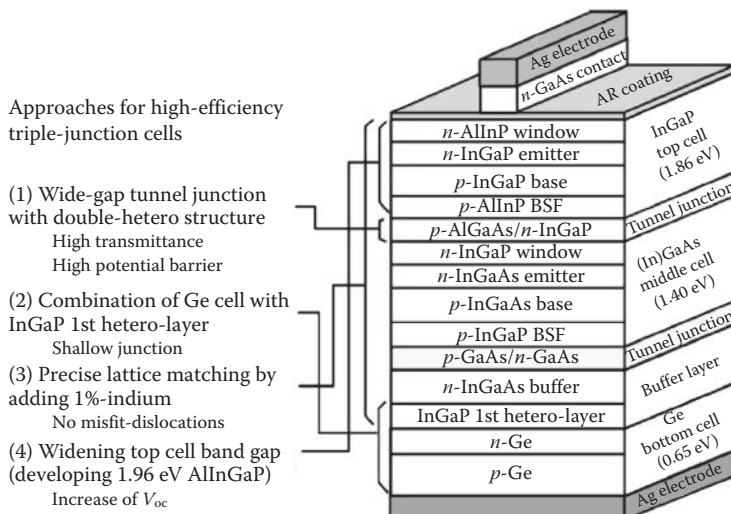


FIGURE 9.15

Schematic structure of a triple-junction GaAs solar cell. (Adapted from Yamaguchi, M. et al., *Solar Energy*, 79, 78–85, 2005.)

9.2.5 Dye-Sensitized Solar Cells and Polymer Solar Cells

Research over the last 30 years has resulted in the development of a new class of PV devices that are essentially photoelectrochemical cells and operate differently from the conventional *p-n* junction solar cells. Since they use cheap and abundant materials, the pace of research picked up after the publication of the seminal paper by O'Regan and Grätzel (1991). Since then, efficiencies greater than 12% have been reported (Grätzel 2009). Jena et al. (2012) and Hagfeldt et al. (2010) provide comprehensive reviews of the progress in this technology.

Figure 9.16 shows a schematic of a dye-sensitized solar cell (DSSC). The basic construction (Hagfeldt et al. 2010; Jena et al. 2012) of a DSSC consists of the following:

1. A photoanode consisting of a porous thick film ($\sim 10 \mu\text{m}$) of a wide-band semiconductor, such as TiO_2 (10–30 nm diameter) coated with a dye, which absorbs in the visible wavelength range. The film is deposited on a transparent conducting oxide (TCO) coated on a transparent glass substrate. The porosity of the TiO_2 film is around 50%.
2. An electrolyte, usually an organic solvent containing iodide/triiodide redox system.
3. A cathode consisting of a TCO coated on a glass substrate and containing a catalyst, such as platinum.
4. A sealant to seal the cell assembly.

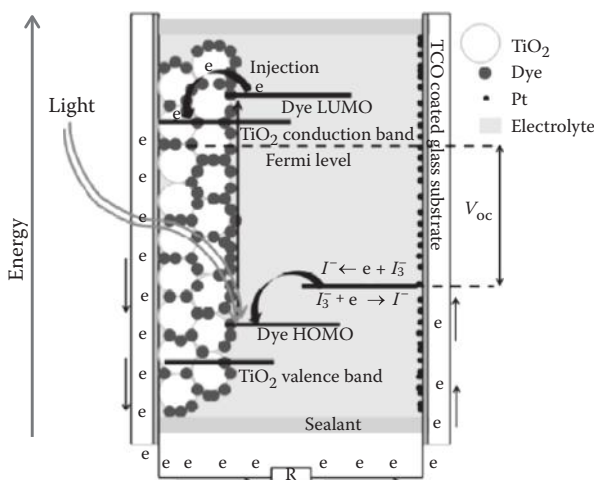


FIGURE 9.16

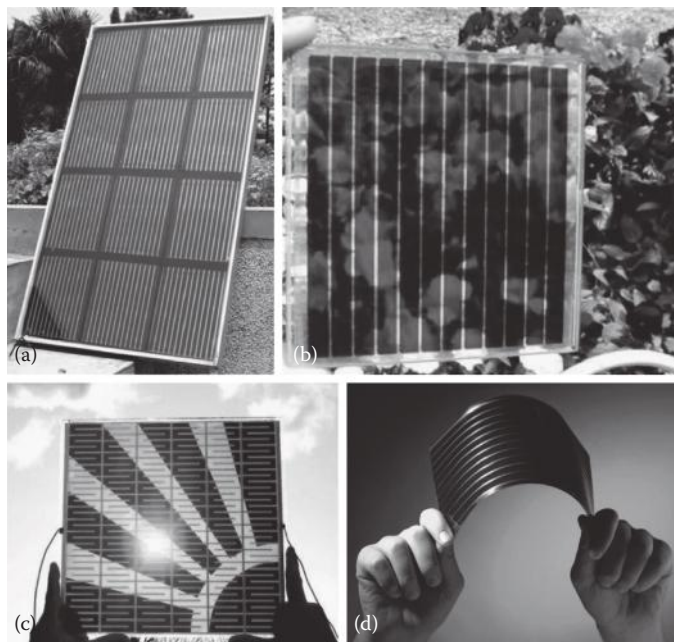
Schematic of a dye-sensitized solar cell. (Adapted from Jena, A. et al., *Transactions of the Indian Ceramic Society*, 71 (1), 1–16, 2012; Hagfeldt, A. et al., *Chem. Rev.* 110, 6595–6663, 2010.)

As the dye absorbs the visible light photons, with energy equal to or greater than the difference between its highest occupied molecular orbital (HOMO) and the lowest unoccupied molecular orbital (LUMO), the electrons from the ground state of the dye (S) get energized to an excited state (S^*), which is known as the photoexcitation of the dye. The energized electrons from the photoexcited dye are injected into the conduction band of TiO_2 . The dye in turn gets electrons from the electrolyte, thereby becoming electrically neutral. The excess electrons in the TiO_2 conduction band pass through the TCO to the external circuit returning through the cathode to the electrolyte. In the electrolyte, the I^- ions close to the dye transfer electrons to the dye, bringing it to the ground state and themselves being oxidized to I_3^- . The oxidized I_3^- ions diffuse a short distance ($>50\ \mu\text{m}$) to the cathode and get reduced to I^- with the injection of the electrons. The concentration of iodine (I_2) in the electrolyte is typically less than $1\ \mu\text{M}$. The transfer of electrons from the dye to the conduction band of TiO_2 is an extremely fast process (picoseconds); however, the speed of diffusion of electrons from TiO_2 to the anode depends on the crystallinity of TiO_2 . Higher crystallinity results in faster diffusion and therefore higher current density.

A number of dyes have been investigated for use as the photosensitizer (Hagfeldt et al. 2010). The classic dyes that have given the highest efficiencies are the ruthenium-based N3 dye that starts to absorb around 800 nm and the black N4 dye that starts to absorb around 900 nm.

9.2.5.1 Fabrication of DSSC

A number of inexpensive and established techniques may be used to fabricate DSSC cells and panels. These include screen printing, spray coating, doctor blading, and spin coating, among others. Since clear plastics could be used as substrates instead of glass, DSSCs could be made as flexible panels. A DSSC panel may be fabricated by thoroughly mixing nanoparticles of TiO_2 in water or an organic solvent, such as ethanol, and an organic binder, such as polyethylene glycol, making it into a paste that is then coated as a thick film on a TCO-coated transparent substrate, such as glass or a clear plastic. The film is then dried, followed by sintering at around 450°C to remove the organic binder and partially crystallize the TiO_2 to allow conduction of electrons through it. The film is then soaked in a dye for approximately 24 h to allow the dye molecules to cover and get adsorbed on the TiO_2 surface. A TCO- and catalyst-coated glass or clear plastic is then attached to it with a spacer around the edges to provide a uniform gap in between. The assembly is sealed around the sides with a hole to inject the iodine-containing electrolyte followed by sealing of the hole. Various groups around the world and commercial manufacturing companies have developed more sophisticated versions of the above simple method. Figure 9.17 shows some of the DSSCs made by various companies and research groups around the world. Latest research on DSSCs includes finding natural and organic dyes, which would

**FIGURE 9.17**

DSSC panels made by various companies and research groups. (a) Institute of Plasma Physics in Hefei, China; (b) Fraunhofer ISE, Germany; (c) Toyota Central R&D Laboratories., Inc. and Aisin Seiki Co., Ltd., Japan; (d) G24i Innovations Ltd., UK.

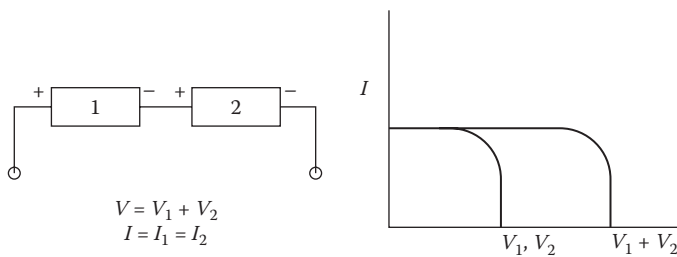
be much cheaper, solid and semisolid electrolytes, and improving the lifetimes of the cells.

9.2.6 Design of a PV System

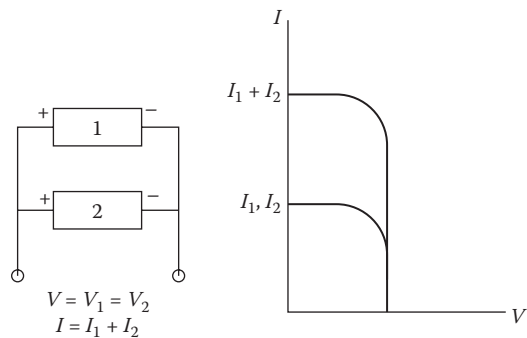
Solar cells may be connected in series, parallel, or both to obtain the required voltage and current. When similar cells or devices are connected in series, the output voltages and current are as shown in Figure 9.18. A parallel connection results in the addition of currents as shown in Figure 9.19. If the cells or devices 1 and 2 have dissimilar characteristics, the output characteristics will be as shown in Figure 9.20. Cells are connected to form modules, modules are connected to form panels, and panels are connected to form arrays. Principles shown in Figures 9.18 and 9.19 apply to all of these connections.

Example 9.4

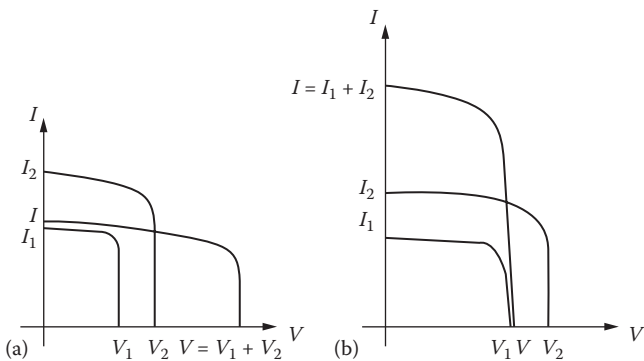
An application requires 300 W at 28 V. Design a PV panel using solar cells from Example 9.3 each with an area of 6 cm^2 .

**FIGURE 9.18**

Characteristics of two similar cells connected in series.

**FIGURE 9.19**

Characteristics of two similar cells connected in parallel.

**FIGURE 9.20**

Characteristics of two dissimilar cells connected in (a) series and (b) parallel.

Solution

Assuming that the cell will be operated at maximum power conditions, the voltage and current from each cell are

$$V_m = 0.542 \text{ V}, I_m = 190.5 \frac{\text{A}}{\text{m}^2} (6 \times 10^{-4} \text{ m}^2)$$

$$= 0.1143 \text{ A},$$

$$\text{Power/cell} = 0.542 \times 0.1143 = 0.062 \text{ W},$$

$$\text{Number of cells required} = \frac{300 \text{ W}}{0.062 \text{ W/cell}} = 4840,$$

$$\text{Number of cells in series} = \frac{\text{System voltage}}{\text{Voltage/cell}} = \frac{28 \text{ V}}{0.542 \text{ V}} = 52,$$

$$\text{Number of rows of 52 cells connected in parallel} = \frac{4840}{52} \approx 93.1.$$

Since the number of rows must be a whole number, we may increase the number to 94 rows, which will give a 303-W output (Figure 9.21).

A blocking diode is used in series with a module or an array to prevent the current from flowing backward, for example, from the battery to the cells under dark conditions. A bypass diode is used in parallel with a module in an array to bypass the module if it is shaded. A PV system may be connected to a DC or an AC load as shown in Figure 9.22.

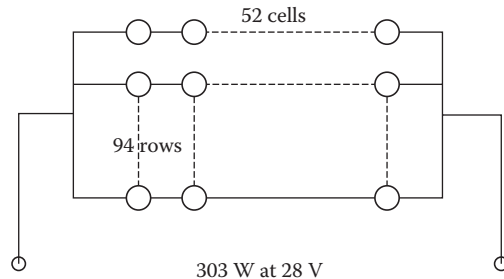


FIGURE 9.21

Connection of cells in rows and columns for Example 9.4.

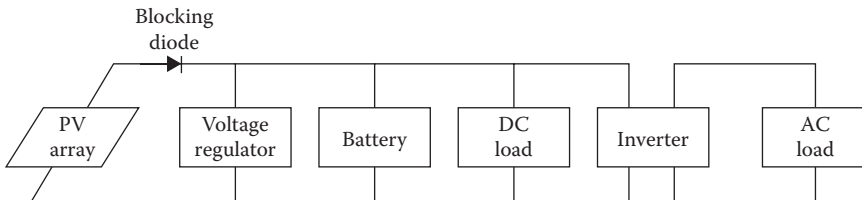


FIGURE 9.22

Schematic of a PV system.

9.3 Manufacture of Solar Cells and Panels

Manufacture of crystalline silicon solar cells is an outgrowth of the manufacturing methods used for microprocessors. A major difference is that silicon used in microprocessors is ultrapure, which is not needed for PV cells. Therefore, a major source of feedstock for silicon solar cells has been the waste material from the microelectronics industry. Solar cells are also manufactured as polycrystalline and thin films. The following are some of the common methods of manufacture of silicon solar cells.

9.3.1 Single-Crystal and Polycrystalline Cells

Single-crystal silicon cells are produced by a series of processes: (1) growing crystalline ingots of *p*-silicon, (2) slicing wafers from the ingots, (3) polishing and cleaning the surface, (4) doping with *n* material to form the *p–n* junction, (5) deposition of electrical contacts, (6) application of AR coating, and (7) encapsulation. Figure 9.23 illustrates the process.

The *Czochralski method* (Figure 9.24a) is the most common method of growing single-crystal ingots. A seed crystal is dipped in molten silicon doped with a *p*-material (boron) and drawn upward under tightly controlled conditions of linear and rotational speed and temperature. This process produces cylindrical ingots of typically 10 cm diameter, although ingots of 20 cm diameter and more than 1 m long can be produced for other applications. An alternative method is called the *float zone* method (Figure 9.24b). In this method, a polycrystalline ingot is placed on top of a seed crystal and the interface is melted by a heating coil around it. The ingot is moved linearly and rotationally, under controlled conditions. This process has the potential to reduce the cell cost.

Polycrystalline ingots are produced by casting silicon in a mold of preferred shape (rectangular) as shown in Figure 9.25. Molten silicon is cooled slowly in a mold along one direction in order to orient the crystal structures and grain boundaries in a preferred direction. In order to achieve efficiencies

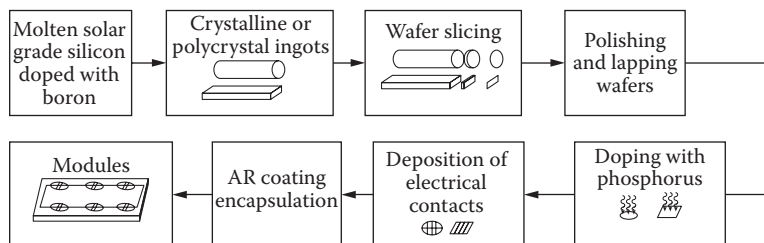


FIGURE 9.23

Series of processes for the manufacture of crystalline and polycrystalline cells.

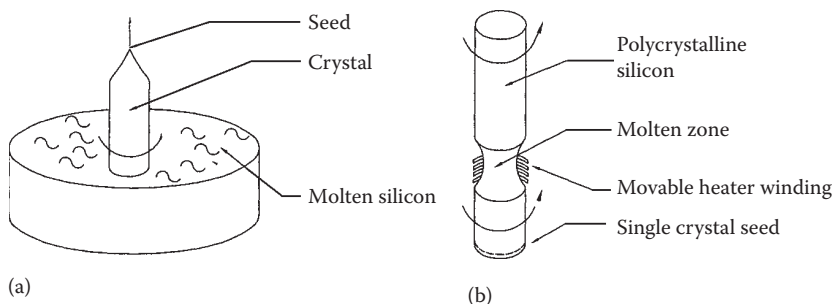


FIGURE 9.24
Crystalline silicon ingot production methods. (a) Czochralski method. (b) Float zone method.

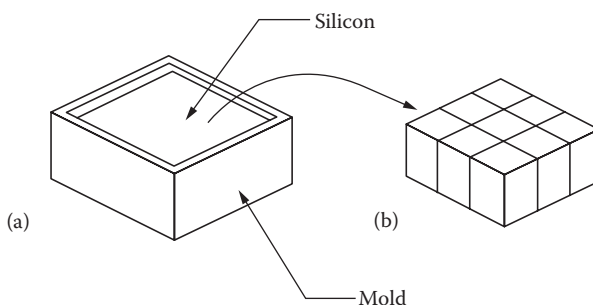


FIGURE 9.25
Polycrystalline ingot production: (a) mold, (b) ingots.

of greater than 10%, grain sizes greater than 0.5 mm are needed and the grain boundaries must be oriented perpendicular to the wafer. Ingots as large as 40 cm × 40 cm × 400 cm can be produced by this method.

Ingots are sliced into wafers by internal diameter saws or multiwire saws impregnated with diamond abrasive particles. Both of these methods result in high wastage of valuable crystalline silicon.

Alternative methods that reduce wastage are those that grow polycrystalline *thin films*. Some of the thin-film production methods include dendritic web growth (Figure 9.26), edge-defined film-fed growth (EFG) (Figure 9.27), ribbon against drop (RAD) method, supported web method, and ramp-assisted foil casting technique (RAFT) (Figure 9.28).

A *p-n* junction is formed in the cell by diffusing a small amount of *n* material (phosphorus) in the top layer of a *p*-silicon wafer. The most common method is diffusion of phosphorus in the vapor phase. In this case, the back side of the wafer must be covered to prevent the diffusion of vapors from that side. An alternate method is to deposit a solid layer of the dopant material on the top surfaces followed by high-temperature (800°C–900°C) diffusion.

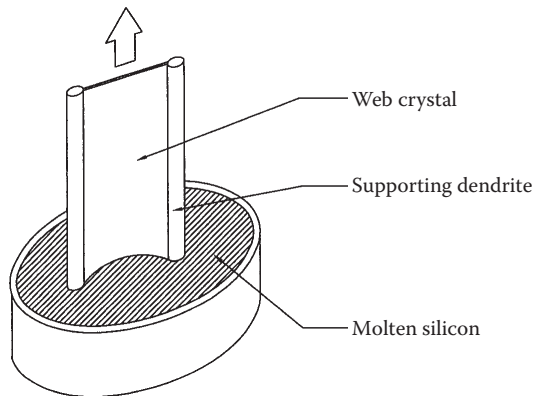


FIGURE 9.26
Thin-film production by dendritic web growth.

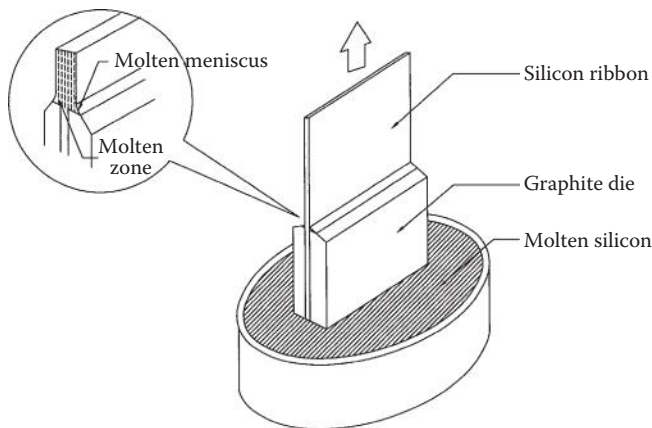


FIGURE 9.27
Thin-film production by edge-defined film-fed growth.

Electrical contacts are attached to the top surface of the cell in a grid pattern to cover no more than 10% of the cell surface and a solid metallic sheet is attached to the back surface. The front grid pattern is made by either vacuum metal vapor deposition through a mask or by screen printing. Figure 9.29 shows how cells are connected to form modules.

AR coatings of materials such as silicon dioxide (SiO_2), titanium dioxide (TiO_2), and tantalum pentoxide (Ta_2O_5) are deposited on the cell surface to reduce reflection from more than 30% for untreated Si to less than 3%. AR coatings are deposited by vacuum vapor deposition, sputtering, or chemical spraying. Finally, the cells are encapsulated in a transparent material to

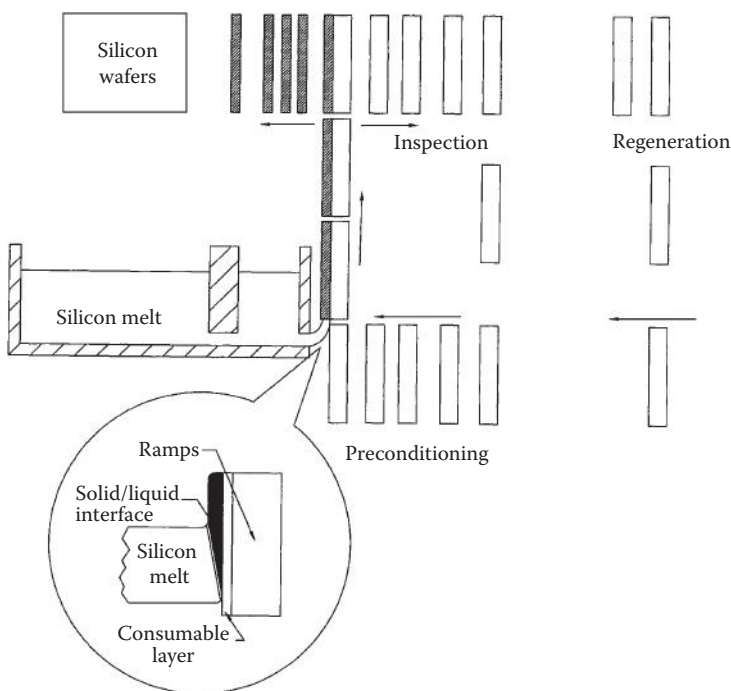


FIGURE 9.28
Schematic of RAFT processing.

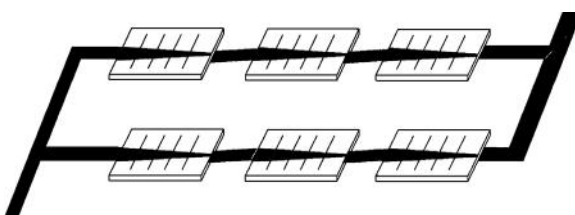
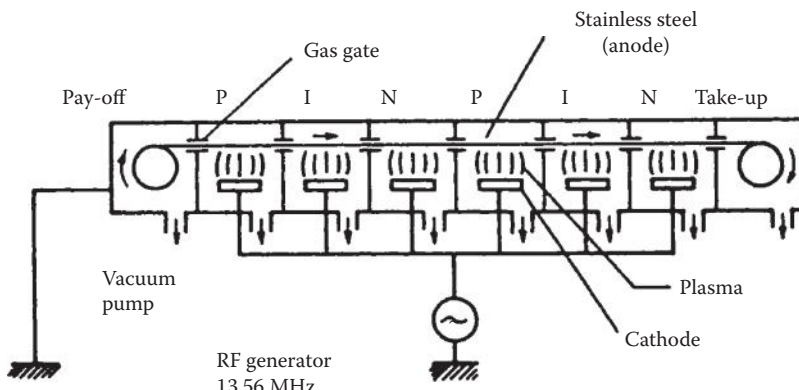


FIGURE 9.29
Assembly of solar cells to form a module.

protect them from the environment. Encapsulants usually consist of a layer of either polyvinyl butyryl or ethylene vinyl acetate and a top layer of low-iron glass.

9.3.2 Amorphous Silicon and Thin-Film Fabrication

Amorphous silicon (α -Si) cells are made as thin films of α -Si:H alloy doped with phosphorus and boron to make n and p layers, respectively. The atomic structure of an α -Si cell does not have any preferred orientation. The cells are manufactured by depositing a thin layer of α -Si on a substrate (glass,

**FIGURE 9.30**

A schematic diagram of a roll-to-roll plasma CVD machine. (From Lasnier, F. and T.G. Ang, *Photovoltaic Engineering Handbook*, New York: A. Hilger Publishing, 1990.)

metal, or plastic) from glow discharge, sputtering, or chemical vapor deposition (CVD) methods. The most common method is by an RF glow discharge decomposition of silane (SiH_4) on a substrate heated to a temperature of 200°C – 300°C . To produce *p*-silicon, diborane (B_2H_6) vapor is introduced with the silane vapor. Similarly, phosphene (PH_3) is used to produce *n*-silicon. The cell consists of an *n* layer, an intermediate undoped *a*-Si layer, and a *p* layer on a substrate. The cell thickness is approximately $1 \mu\text{m}$. The manufacturing process can be automated to produce rolls of solar cells from rolls of substrate. Figure 9.30 shows an example of roll-to-roll *a*-Si cell manufacturing equipment using a plasma CVD method. This machine can be used to make multifunction or tandem cells by introducing the appropriate materials at different points in the machine.

9.4 Design for Remote PV Applications

PV power may be ideal for a remote application requiring a few watts to hundreds of kilowatts of electrical power. Even where a conventional electrical grid is available, for some applications, where uninterruptible or emergency standby power is necessary, PV power would be appropriate. Some examples of remote PV applications include water pumping for potable water supply and irrigation, power for remote houses, street lighting, battery charging, telephone and radio communication relay stations, and weather stations. Examples of some other applications include electrical utility switching stations, peak electrical utility power where environmental quality is a concern, data acquisition systems, and speciality applications such as ventilation fans and vaccine refrigeration.

The design of a PV system is based on some basic considerations for the application.

1. Which is more important, the daily energy output or the power (average or peak)?
2. Is a backup energy source needed or available?
3. Is energy storage important? What type—battery, pumped water, and so on?
4. Is the power needed as AC or DC? What voltage?

There are three basic steps in the design of a PV system:

1. Estimation of load and load profile
2. Estimation of available solar radiation
3. Design of PV system, including area of PV panels, selection of other components, and electrical system schematic

Each of these steps will be explained in the following examples. These examples are based on the work of Post and Risser (1995) and Taylor and Kreider (1998).

9.4.1 Estimation of Loads and Load Profiles

Precise estimation of loads and their timings (load profile) are important for PV systems since the system is sized as the minimum required to satisfy the demand over a day. For example, if power is needed for five different appliances requiring 200, 300, 500, 1000, and 1500 W, respectively, so that only one appliance is on at any one time and each appliance is on for an average of 1 h a day, the PV system would be sized based on 1500 W peak power and 3500 watt hours (Wh) of daily energy requirement. The multiple loads on a PV system are intentionally staggered to use the smallest possible system, since the capital costs of a PV system are the most important as opposed to the energy costs in a conventional fuel-based system.

Example 9.5

Daily load calculations. How much energy per day is used by a remote weather station given the following load characteristics?

Load	Load Power (W)	Run Time (h/day)
Charge controller	2.0	8
Data gathering	4.0	3
Modem (standby)	1.5	22.5
Modem (send/receive)	30.0	1.5

Solution

$$\begin{aligned}\text{Daily energy} &= (2.0 \text{ W})(8 \text{ h}) + (4.0 \text{ W})(3 \text{ h}) + (1.5 \text{ W})(22.5 \text{ h}) \\ &\quad + (30 \text{ W})(2.5 \text{ h}) \\ &= 106.75 \text{ Wh.}\end{aligned}$$

Daily energy use is approximately 107 Wh/day.

Example 9.6

Load calculations. An owner of a remote cabin wants to install a PV power system. The loads in the home are described in the following. Assume that all lights and electronics are powered by AC. Find the daily and weekly peak and average energy use estimates. The system used is a 24-V DC system with an inverter.

Lights	Four, 23-W compact fluorescent bulbs	On at night for 5 h
Lights	Six 13-W compact fluorescent bulbs	2 h each (daytime)
Stereo	110 W (amplifier), 15 W (other)	On for 8 h per week
Water pump	55 W (3.75 amp start current)	Runs for 2 h per day
Computer	250 W (monitor included)	On for 1 1/2 h daily (weekend nights only)
Bathroom fan	40 W (3.5 amp start current)	On for 1 h per day
Microwave	550 W (AC)–1000 W surge	On for 30 min per day

Solution

Loads need to be broken down according to (1) run time, (2) peak power, (3) night or day use, and (4) AC or DC loads. The load profile is as follows:

Load Name Description	Power (W)		Run Time (h)		Energy (Wh)	
	Average	Peak	Day	Week	Day	Week
Lights (AC)	(4)(23)	(4)(23)	5.0	35	460	3220
Lights (AC)	(6)(13)	(6)(13)	2.0	14	156	1092
Stereo (AC)	(1)(110)	(1)(110)	—	8	—	880
Pump (DC)	(1)(55)	(3.75 A)(24 V)	2.0	14	110	770
Computer (AC)	(1)(250)	(1)(250)	1.5	3	—	750
Fan (DC)	(1)(40)	(3.5 A)(24 V)	1.0	7	40	280
Microwave (AC)	(1)(550)	(1)(1000)	0.5	3.5	275	1925

Average DC load: $[770 + 280]/7 = 150 \text{ Wh/day.}$

Average AC load: $[3220 + 1092 + 880 + 750 + 1925]/7 = 1124 \text{ Wh/day.}$

Peak DC load: $\max \{[(3.5)(24) + 55] :: [(3.75)(24) + 40]\} = 139 \text{ W.}^*$

Peak AC load: $(1000) + \max \{[(4)(23) :: (6)(13)] + 250 + 100\} = 1442 \text{ W.}^{\dagger}$

* It can be assumed that the pump and fan will not start precisely at the same instant.

[†] It is assumed that the night and day lighting loads will not be on simultaneously.

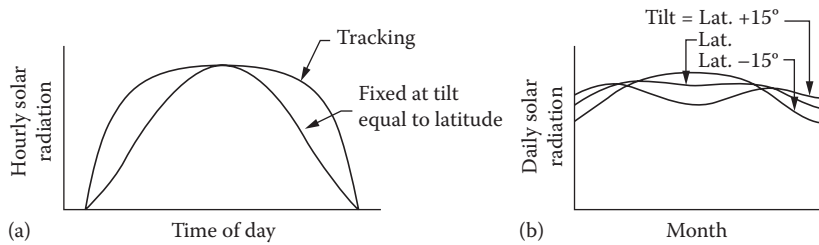


FIGURE 9.31
Solar radiation on panels at different tilt angles.

9.4.2 Estimation of Available Solar Radiation

Methods of estimation of available solar radiation are described in Chapter 2. If long-term measured solar radiation values are available at a location, Equations 2.56 through 2.65 can be used to estimate the average solar radiation per day. Otherwise, data for clear day can be used along with percent sunshine data (if available). For designing a PV system, a decision is made whether the PV panel will be operated as tracking the sun or will be fixed at a certain tilt and azimuth angle. For fixed panels, a tilt angle of latitude $+15^\circ$ works best for winter and latitude -15° works best for summer. To keep the panel fixed year round, an angle equal to the latitude provides the maximum yearly energy (see Figure 9.31).

9.4.3 PV System Sizing

If meeting the load at all times is not critical, PV systems are usually sized on the basis of the average values of energy and power needed, available solar radiation, and component efficiencies. This is known as the *heuristic approach*. It is important to note that a system designed by this approach will not give the best design but may provide a good start for a detailed design. A detailed design accounts for the changes in the efficiencies of the components depending on the load and the solar radiation availability and whether the system is operating in a PV-to-load, PV-to-storage, or storage-to-load mode.

Example 9.7

Heuristic approach to PV system sizing. A PV system using 50-W, 12-V panels with 6-V, 125 Ah batteries is needed to power a home in Farmington, New Mexico, with a daily load of 1700 Wh. System voltage is 24 V.

There is an average of 5 daylight hours in the winter. Specify the collector and storage values for the system using the heuristic approach.

Solution

Load = 1700 Wh/day.
 Daylight hours = 5 h/day.
 Average panel output = 50 W.

$$\text{Number of panels} = \frac{1700 \text{ Wh/day}}{(5 \text{ h/day})(50 \text{ W/panel})} = 6.8, \text{ round off to 7 panels.}$$

Since the system voltage is 24 V, but each panel produces only 12 V, an even number of panels will be needed. Therefore, the number of panels is equal to 8.

Farmington, New Mexico, is a very sunny location; thus, 3 days of storage is plenty. Assuming a battery efficiency of 75% and a maximum depth of discharge 70%,

$$\text{Storage} = (1700)(3)/(0.75 \times 0.7) = 9714 \text{ Wh}$$

$$\begin{aligned}\text{Number of batteries} &= (9714/\text{Wh})/(125 \text{ Ah} \times 6 \text{ V}) \\ &= 13 \text{ (rounded off to the next whole number).}\end{aligned}$$

Since the system voltage is 24 V, and each battery provides 6 V, the number of batteries is increased to 16. In a detailed design, the efficiencies of battery storage, inverter, and the balance of system (BOS) must be accounted for. The following example shows how these efficiencies increase the energy requirements of the PV panel.

Example 9.8

System operating efficiency. Using the cabin electrical system from Example 9.6, calculate the overall system efficiency for each operating mode possible for the system. Estimate the amount of energy required per day for the system. When load timing (day or night), assume half of the load runs during the day and half runs at night. The inverter used has an efficiency of 91%, the battery efficiency is 76%, and the distribution system efficiency is 96%.

Solution

From the example, the loads are as follows:

Average DC load: 150 Wh/day,
 Average AC load: 1124 Wh/day.

The various system efficiencies are as follows:

PV to load (DC):	0.96	(day, DC),
Battery to load (DC):	$(0.76)(0.96) = 0.73$	(night, DC),
PV to load (AC):	$(0.96)(0.91) = 0.874$	(day, AC),
Battery to load (AC):	$(0.76)(0.91)(0.96) = 0.664$	(night/AC).

Expected day and night loads are as follows:

$$\text{Day (DC): } (0.5)(110) + (0.5)(40) = 75 \text{ Wh/day},$$

$$\text{Night (DC): } (0.5)(110) + (0.5)(40) = 75 \text{ Wh/day},$$

$$\text{Day (AC): } (156) + (0.5)(880 + 750)/7 + (0.5)(275) = 409.9 \text{ Wh/day},$$

$$\text{Night (AC): } (460) + (0.5)(880 + 750)/7 + (0.5)(275) = 713.9 \text{ Wh/day}.$$

Without considering system efficiency, the daily energy requirement is

$$E_{\text{day}} = (150) + (1124) = 1274 \text{ Wh/day}.$$

The expected daily energy requirement is

$$E_{\text{day}} = (75)/(0.96) + (75)/(0.73) + (409.9)/(0.874) + (713.9)/(0.664)$$

$$E_{\text{day}} = 1725 \text{ Wh/day}$$

The actual energy requirement is 35% higher than simple calculation.

9.4.4 Water Pumping Applications

Water pumping for drinking water or irrigation at remote locations is an important application of PV. For a simple schematic shown in Figure 9.32, the power needed to pump water at a volumetric rate \dot{V} is given by $P = \rho \dot{V} g H / \eta_p$, where ρ is the density of water, g is the acceleration due to gravity, and η_p is the pump efficiency. The static head H_s is $(A + B)$. In case the water level is

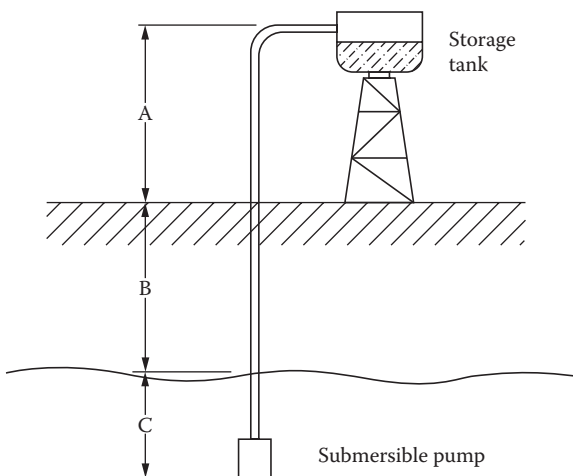


FIGURE 9.32

Water pumping using a submersible pump.

TABLE 9.4

Typical Range of Pump Performance Parameters

Head (m)	Pump Type	Wire-to-Water Efficiency (%)
0–5	Centrifugal	15–25
6–20	Centrifugal with jet	10–20
	Submersible	20–30
21–100	Submersible	30–45
	Jack pump	
>100	Jack pump	35–50

drawn down, the static head would be $(A + B + C)$. The pump must work against the total head H , which includes the dynamic head H_d also,

$$H_d = H_f + \frac{v^2}{2g},$$

where H_f is the frictional head loss in the pipe and the bends and v is the velocity of the water at the pipe outlet. The pump efficiency η_p is a function of the load (head and flowrate) and is available as a characteristic curve from the manufacturer. For general design purposes, typical values given in Table 9.4 may be used. The table lists two basic types of pumps, centrifugal and positive displacement. These pumps can be driven by AC or DC motors. DC motors are preferable for the PV applications, because they can be directly coupled to the PV array output. Centrifugal pumps with submersible motors are the optimum for PV applications because of their efficiency, reliability, and economy. However, for deep wells, jack pumps may be necessary. Jack pumps are the piston type of positive displacement pumps that move chunks of water with each stroke. They require very large currents; therefore, they are connected through batteries.

Example 9.9

A PV system is designed to pump water for livestock in the vicinity of El Paso, Texas. The following information is available:

Site:	Near El Paso, Texas 32°20'N, 106°40'W, 1670 m
Ambient temperature:	-5°C to 45°C
Water source:	Cased borehole 15 cm
Static head:	106 m
Maximum drawdown:	8 m
Water required:	8325 L/day, June to August

Solution

Since the required head is very high, a deep well jack pump with DC motor is needed. Assuming a friction factor of 0.05, the total head = 106 + 8 + (106) (0.05) = 122 m. We select a 75-V DC jack pump with an average efficiency of 0.45.

$$\begin{aligned}\text{Daily energy required} &= \rho \dot{V} g H / \eta_p \\ &= (8325 \text{ L/day}) \frac{1 \text{ kg}}{\text{L}} 9.81 \frac{\text{m}}{\text{s}^2} (122 \text{ m}) \frac{1}{0.45} \\ &= 22.14 \times 10^6 \text{ J/day} \\ &= 6150 \text{ Wh/day}\end{aligned}$$

Since the system will be used from June to August, a tilt angle of lat. -15° would be optimum. Daily solar radiation at El Paso for 1 axis tracking and a tilt angle of 17° is as follows:

June	11.51	$\text{kWh/m}^2\cdot\text{day}$
July	10.58	$\text{kWh/m}^2\cdot\text{day}$
August	10.02	$\text{kWh/m}^2\cdot\text{day}$

Since August has the minimum insolation, the panel area will be based on insolation for this month. We select PV panels with the following specifications (this information may be obtained from a manufacturer):

Voltage	$V_{oc} = 21.7 \text{ V}$	$V_m \text{ at } 25^\circ = 17.4 \text{ V}$
Current	$I_s = 3.5 \text{ A}$	$I_{L,m} = 3.1 \text{ A}$
Temperature correction factor for voltage = $1 - 0.0031 (T_c - T_{ref})$		

Assuming that the panels will operate at a maximum temperature of $45^\circ\text{C} + 15^\circ\text{C} = 60^\circ\text{C}$, the voltage at the highest expected temperature

$$\begin{aligned}&= 17.4 [1 - 0.0031 (60 - 25)] \\ &= 15.5 \text{ V} \\ \text{Voltage required} &= 75 \text{ V.}\end{aligned}$$

Therefore, the number of panels in series = $75/15.5 \approx 5$.

Power output/panel = $3.1 \text{ A} \times 15.5 \text{ V} = 48.05 \text{ W}$ at a standard insolation of 1000.

$$\begin{aligned}\text{Power output/panel/day} &= 48.05 \text{ W} \times \frac{10.02 \text{ kWh/m}^2 \cdot \text{day}}{1 \text{ kW/m}^2} \\ &= 481.5 \text{ Wh/day.}\end{aligned}$$

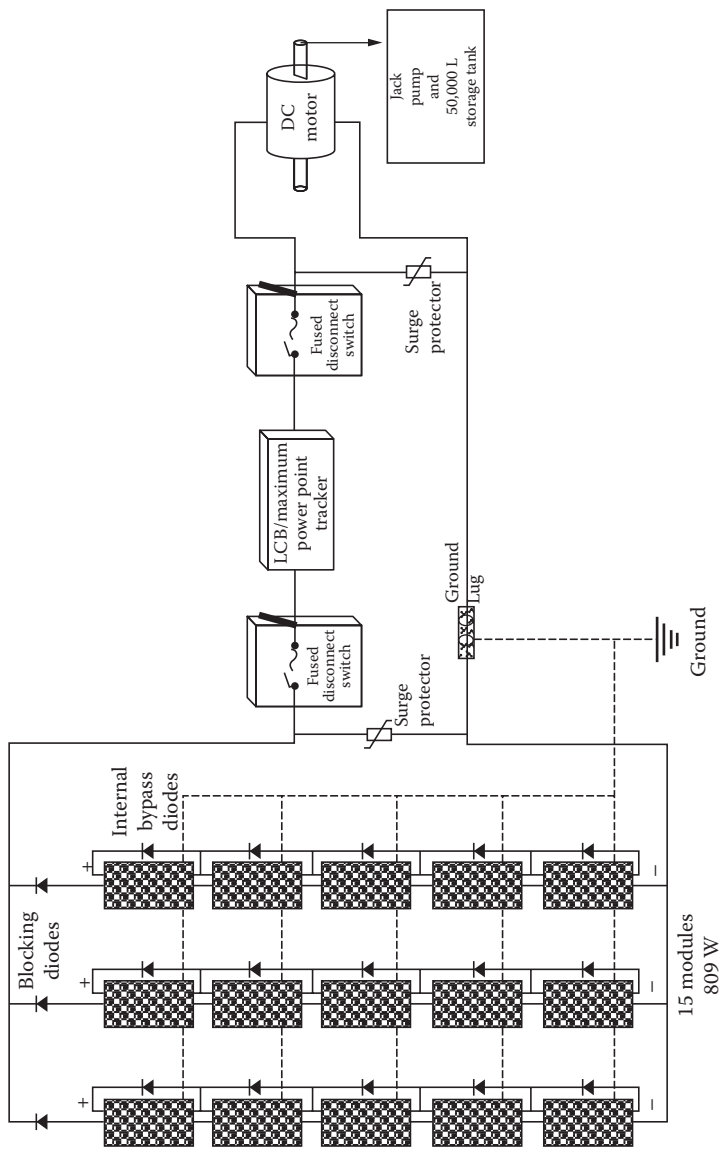


FIGURE 9.33
A system schematic for Example 9.9.

Assuming an overall efficiency of 90% owing to insolation times, wiring, and so on,

$$\text{Number of panels required} = \frac{6150 \text{ Wh/day}}{0.9 \times 481.5 \text{ Wh/day}} \approx 15$$

The array will consist of 3 parallel rows of 5 panels each in series.
As a check, the daily water pumping rate for August

$$\begin{aligned} &= \frac{15 \times 481.5 \times 0.9 \text{ Wh/day} \cdot 3600 \text{ s/h}}{9.81 \frac{\text{m}}{\text{s}^2} (1 \text{ kg/L})(122 \text{ m})} \times 0.45 \\ &= 8798 \text{ L/day} \end{aligned}$$

Therefore, the system will meet the requirement. A system schematic is shown in Figure 9.33.

PROBLEMS

1. Find the wavelength of radiation whose photons have energy equal to the band gap of GaAs.
2. What is the theoretical maximum efficiency of conversion if blue light of wavelength 0.45 μm is incident on a GaAs solar cell?
3. Find the theoretical maximum overall efficiency of GaAs solar cells in space.
4. The reverse saturation current I_o of a silicon cell at 40°C is 1.8×10^{-7} A/m^2 . The short-circuit current when exposed to sunlight is 5 A/m^2 . From this information, compute the following:
 - a. Open circuit voltage
 - b. Maximum power output of the cell
 - c. The number of $4 \text{ cm} \times 4 \text{ cm}$ cells needed to supply 100 W at 12 V. How must the cells be arranged? (Number of rows and number of panels in a row?)
5. At what efficiency is a PV array running if insolation on the collector is 650 W/m^2 , the total collector area is 10 m^2 , the voltage across the array is 50 V, and the current being delivered is 15 A?
6. If a PV array has a maximum power output of 10 W under an insolation level of 600 W/m^2 , what must the insolation be to achieve a power output of 17 W? Would you expect the open circuit voltage to increase or decrease? Would you expect the short-circuit current to increase or decrease?

7. A PV battery system has an end-to-end efficiency of 77%. The system is used to run an all-AC load that is run only at night. The charge controller efficiency is 96% and the inverter efficiency is 85%. How much energy will need to be gathered by the PV array if the load is 120 W running for 4 h per night?
8. If the average output of the PV system in Problem 7 is 200 W, the load is changed to run during the day, how much PV output energy is needed for the same load conditions? Assume that the battery bank is at 100% charge and that input efficiency is equal to output efficiency.
9. For the system in Problem 7, how many hours of sunlight are needed to ensure that the battery bank is at 100% charge at the end of the day assuming the same load?

Problems 10–14. The owner of a small cabin would like to convert her home to PV power. She has the following equipment and associated run times:

Household Equipment	Power (W)	Run Time, day (h)	Run Time, night (h)
Lighting (DC)	25	2	4
Stereo (AC)	40	3	2
Refrigerator (DC)	125	3 ^a	3 ^a
Water pump (DC)	400	1.5	0.5
Alarm clock (DC)	8	12	12
Computer (AC)	250	3	0
Printer	175	0.25	0
Outdoor safety lights	48	0	8
Answering machine (AC)	7	12	12
Coffee pot (AC)	1200	0.25	0

^a The refrigerator is assumed to run 25% of the time.

10.
 - a. What is the homeowner's daily energy requirement as measured from the load?
 - b. If she replaces her alarm clock with a wind-up clock, how much energy per day will she avoid using?
 - c. What would you suggest she do to cut back her daily load?
11. How many 50-W panels will the owner require assuming battery storage is 75% efficient and all loads are DC (no inverter)?
 - a. For a stationary system "seeing" 5 h of sunlight per day?
 - b. For a tracking system "seeing" 8 h of sunlight per day?

12. For the loads listed:
- What size inverter (peak watts) should she purchase?
 - If the inverter is 88% efficient, how much more daily energy is required from the PV array as compared to an all-DC system?
13. The homeowner decides to hire you to design a system for her. She has cut a deal with a local solar supplier for the following equipment. Specify the system and provide a line diagram showing system connection.

PV panels:	42 W, nominal 12 V
Batteries:	125 Ah, 6 V, end-to-end efficiency = 72%
Charge controller:	95% efficient, 12 V
Inverter:	90% efficient; sizes of 500, 1000, 2000, and 4000 W available; 12 V input

14. Through your connections, you have the following equipment available. Redesign the system.

PV panels:	51 W, nominal 12 V
Batteries:	200 Ah, 12 V, end-to-end efficiency = 78%
Charge controller:	97% efficient, 24 V
Inverter:	91% efficient; sizes of 500, 1200, 2500, and 5000 W available; 24 V input

15. A flashing beacon is mounted on a navigation buoy in the shipping channel at a port at 30°N latitude. The load consists of a single lamp operating 1.0 s on and 3.6 s off during the hours of darkness. Hours of darkness vary from 9.8 h in July to 13.0 h in December. The lamp draws 2 A at 12 V when lighted. A flasher controls the lamp and draws 0.22 A when the lamp is on. There is a surge current of 0.39 A each time the flasher turns on. This current flows approximately 1/10 of the time the flasher is on. The design has 14 days of battery capacity. Provision has to be made to disconnect the load if the battery voltage drops below 11 V.

The available module has a rated voltage of 17.2 V at 25°C (15 V at 55°C) and 2.3 A at 1 kW/m². The available battery has a rated capacity of 105 Ah at 12 V. Assume maximum depth of discharge 30%. Design the PV system.

16. Design a PV system for the following application: A refrigerator/freezer unit for vaccine storage in a remote island of Roatan, Honduras (16°N latitude, 86°W longitude, temperature range, 15°C–30°C).

Two compressors—one each for refrigerator and freezer.
Each compressor draws 5 A at 12 V.

Compressors remain on for	Summer	Winter
Refrigerator	9 h/day	5 h/day
Freezer	7 h/day	4 h/day

Design the PV system using the panels and the batteries described in Problem 15.

17. A village in Antigua (17°N , 61°W , 15°C – 30°C temperature range), West Indies, requires 20,000 liters of water per day for community water supply. Assuming a year-round average insolation of 8 kWh/ $\text{m}^2\text{-day}$, design the system using the following components:

PV panels:	Solarex panels 17.5 V and 3.6 A at 1000 W/ m^2 and 25°C
Pump:	Grundfos multistage pump input 105 V DC, 9 A, 30% efficiency

18. The energy required to produce the PV panels and BOS of a grid-connected PV system (GCPVS) was estimated to be (Perpinan et al. 2009) as follows:

Energy Required by the Main Components of Different GCPVS

Component	Double Axis		Horizontal N-S Axis		Fixed	
	(MJ _p /kW _p)	(%)	(MJ _p /kW _p)	(%)	(MJ _p /kW _p)	(%)
Module	41,819	69.54	41,819	78.67	41,819	81.99
Support structure	9329	15.51	6108	11.49	4459	8.74
Tracking mechanisms	248	0.41	58	0.11	0	0.00
Foundation (steel)	3371	5.61	1536	2.89	0	0.00
Foundation (concrete)	2445	4.07	1281	2.41	2352	4.61
Transport	1339	2.23	900	1.69	1037	2.03
Inverter	1.091	1.81	1091	2.05	1091	2.14
Wiring	497	0.83	364	0.68	248	0.49
Total	60,140	100	53,157	100	51,005	100

All the amounts are referred to a nominal PV power of 1 kW_p.

Estimate the energy payback time in years for this system operating in

- Tampa, Florida, USA
- Las Vegas, Nevada, USA
- Sydney, Australia
- Madrid, Spain
- New Delhi, India
- Beijing, China

19. Find the IRR of the following investment in a 15-MW_p PV system planned for Tampa, Florida (you may choose another location for which solar radiation data are available):

Total initial cost of the system: \$1.7 M/MW_p

Annual O&M costs: 2% of the initial costs

Equity investment: 30% of the initial costs

Debt financed by a bank: 70% of the initial costs at 10%/year

Annual reduction in performance: 0.2%/year

Electricity tariff for the plant: \$0.30/kWh_e for the first 20 years

Salvage value after 20 years: 20% of the initial costs

20. The investor in Problem 19 is able to get a preferential debt rate from a government-backed bank at a rate of 4%/year. What is the new IRR?

References

- Angrist, S.W. 1976. *Direct Energy Conversion*, 3rd ed. Allyn and Bacon, Inc., Boston.
- Böer, K.W. 1990. *Survey of Semiconductor Physics*. Van Nostrand Reinhold, New York.
- Bube, R.H. 1960. *Photoconductivity of Solids*. John Wiley & Sons, Inc., New York.
- Crandall, R., and W. Luft. 1995. The future of amorphous silicon photovoltaic technology. NREL/TP-441-8019. Golden, CO: National Renewable Energy Laboratory.
- De Vos, A. 1980. Detailed balance limit of the efficiency of tandem solar cells. *J. Phys. D: Appl. Phys.* 13(5): 839–846.
- Florida Solar Energy Center. 1991. Photovoltaic system design. FSEC-GP-31-86. Florida Solar Energy Center, Cocoa Beach, FL.
- Garg, H.P. 1987. *Advances in Solar Energy Technology*, Vol. 3. D. Reidel Publishing Company, Dordrecht, Holland.
- Grätzel, M. 2009. Recent advances in sensitized mesoscopic solar cells. *Acc. Chem. Res.* 42: 1788.
- Green, M.A. et al. 2013. Solar cell efficiency tables. *Prog. Photovolt.: Res. Appl.* 21: 1–11.
- Hagfeldt, A. et al. 2010. Dye sensitized solar cells. *Chem. Rev.* 110: 6595–6663.
- Jena, A. et al. 2012. Dye sensitized solar cells—A review. *Trans. Indian Ceram. Soc.* 71(1): 1–16.
- Lasnier, F., and T.G. Ang. 1990. *Photovoltaic Engineering Handbook*. A. Hilger Publishing, New York.
- Moore, C.E. 1952. *Atomic Energy Levels*, Vol. 2. National Bureau of Standards Circular 467, NIST, Gaithersburg, MD.
- Nijs, J. et al. 1997. Energy payback time of crystalline silicon solar modules, Chapter 6. In *Advances in Solar Energy*, Vol. 11, K.W. Böer, ed., ASES, Boulder, CO, pp. 291–327.

- O'Regan, B., and M. Grätzel. 1991. A low cost, high-efficiency solar cell based on dye-sensitized colloidal TiO_2 films. *Nature* 353: 737.
- Perpinan, O. et al. 2009. Energy payback time of grid connected PV systems: Comparison between tracking and fixed systems. *Prog. Photovolt.: Res. Appl.* 17: 137–147.
- Post, H.N., and V.V. Risser. 1995. *Stand-Alone Photovoltaic Systems—A Handbook of Recommended Design Practices*. Report SAND-87-7023. Sandia National Lab, Albuquerque, NM.
- Romeo, A.M. et al. 2004. Development of thin-film Cu(In,Ga)Se₂ and CdTe solar cells. *Prog. Photovolt.: Res. Appl.* 12: 93–111. doi: 10.1002/pip.527.
- Semonin, O.E. 2011. Peak external photocurrent quantum efficiency exceeding 100% via MEG in a quantum dot solar cell. *Science* 334: 1530–1533.
- Shockley, W., and H.J. Queisser. 1961. Detailed balance limit of efficiency of p–n junction solar cells. *J. Appl. Phys.* 32: 510–519.
- Taylor, M., and J. Kreider. 1998. *Solar Energy Applications*, 3rd ed. Univ. of Colorado Bookstore, Boulder, CO.
- Yamaguchi, M. et al. 2005. Multi-junction III–V solar cells: Current status and future potential. *Sol. Energy* 79: 78–85.

10

Solar Photochemical Applications

The use of solar energy for the production of food, fiber, and heat has been known to mankind for a long time. Research over the last five decades has also made it possible to produce mechanical and electrical power with solar energy. Although the potential of solar radiation for disinfection and environmental mitigation has been known for years, only recently has this technology been scientifically recognized and researched.

For anyone who has observed colors fading over long exposure to sunlight, certain materials deteriorating in the sunlight, or skin getting sunburned, it is not hard to imagine sunlight causing reactions that could be used beneficially to break up toxic chemicals. Older civilization considered it essential that human dwellings be designed to allow sunshine in. This may have been for disinfection or to keep the growth of microorganisms in check.

Research over the last three decades has not only confirmed the capability of sunlight for detoxification and disinfection but also accelerated the natural process by the use of catalysts. When sunlight is used to cause a chemical reaction by direct absorption, the process is called *photolysis*. If the objective is achieved by the use of catalysts, it is known as *photocatalysis*. Recent research has concentrated mainly on photocatalytic reactions for detoxification, disinfection, and production of hydrogen. Hydrogen energy systems, especially fuel cells, are being considered as a clean solution to transportation needs. Hydrogen can also provide solar energy storage that can be transported over long distances using pipelines and supertankers, and regionally in special containers via road and rail (Sherif et al. 1999, 2014).

10.1 Photocatalytic Reactions

The fundamentals of how photons affect molecules when absorbed have been described in Chapter 9. Basically, if a photon has more energy than the band gap of a material, it will free up an electron when absorbed. The band gap of a material represents the difference in the energy of the electrons in the valence band of the atom and the conduction band. As an electron moves up from the valence band to the conduction band and becomes free, it leaves a positive hole behind. The positive hole and the negative electron may recombine with the release of thermal energy, unless they interact with

neighboring atoms of other materials to cause chemical reactions. Such reactions are known as *photoreactions*, since they are initiated by photons. If the reaction involves atoms or molecules that act as catalysts, the reaction is known as *photocatalytic*. Sunlight may be used in both photolytic and photocatalytic reactions that could result in useful applications, such as the oxidation of toxic organic chemicals or production of hydrogen.

As noted in Chapter 9, the energy ϵ of a photon is

$$\epsilon = h\nu = \frac{hc}{\lambda}, \quad (10.1)$$

where h is Planck's constant ($6.625 \times 10^{-34} \text{ J}\cdot\text{s}$), ν is the frequency, λ is the wavelength, and c is the speed of light ($3 \times 10^8 \text{ m/s}$).

Titanium dioxide (TiO_2) has a band gap of 3.2 eV; therefore, the wavelength λ of a photon with energy equal to the band gap of TiO_2 is

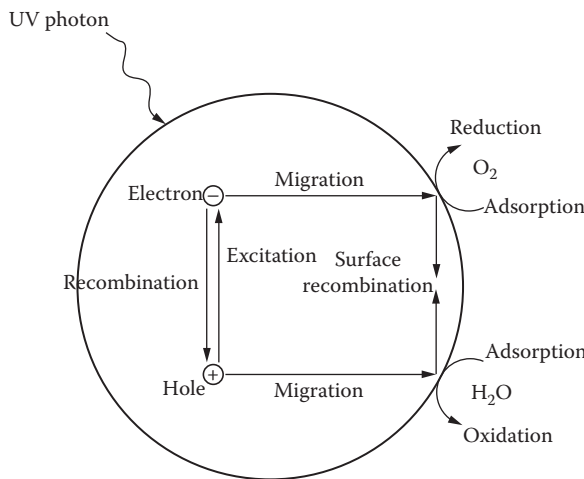
$$\begin{aligned} \lambda &= \frac{hc}{\epsilon} \\ &= \frac{(6.625 \times 10^{-34} \text{ J}\cdot\text{s}) \times (3 \times 10^8 \text{ m/s})}{3.2 \text{ eV}} \times \frac{1 \text{ eV}}{(1.6 \times 10^{-19} \text{ J})} \\ &= 0.388 \times 10^{-6} \text{ m or } 0.388 \text{ m or } 388 \text{ nm.} \end{aligned}$$

Therefore, a photon of sunlight with a wavelength of 388 nm or less (i.e., energy 3.2 eV or higher) will excite an electron from a valence band (vb) to a conduction band (cb) when absorbed, resulting in a free electron (e^-) and a positive hole (hole^+) (Bard 1979; Heller 1981).



The holes (hole^+) and the electrons (e^-) are both highly energetic and mobile. They may recombine and release heat or migrate to the surface. On the surface, they may react with adsorbed molecules of other species and cause a reduction or oxidation of that species.

Since recombination, in the bulk or near the surface, is the most common reaction, the *quantum yields* (molecules reacted/photons absorbed) of most photolytic reactions are low. Separation of the electron–hole pairs is aided by formation of a potential gradient near the surface of the semiconductor. This “space charge region” results from the different electrical potential of the solid semiconductor and the liquid phase of the ambient solution. For TiO_2 , this potential drives valance band holes toward the particle surface and conduction band electrons away from the surface. The electrons and holes at the surface become active sites for oxidation and reduction of adsorbed molecules, as illustrated in Figure 10.1.

**FIGURE 10.1**

Oxidation–reduction reaction occurring at the TiO_2 surface upon irradiation.

The positive holes cause oxidation of the surface-adsorbed species while the electrons cause reduction. Both reactions must take place in order to maintain electro-neutrality. Thus, if the objective is the oxidation of organics, the electrons must be consumed in a reduction reaction such as absorption by oxygen molecules to form superoxide, in order to keep the holes available for oxidation. On the other hand, if the objective is the reduction and recovery of metals, all other reducible species such as oxygen must be eliminated or kept away. The following equations (Bahnemann et al. 1991; Blake et al. 1991; Prairie et al. 1992) describe the oxidation and reduction reactions:



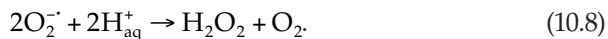
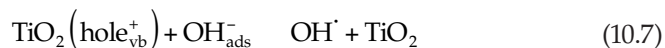
If the objective is oxidation of an organic pollutant, the electron is consumed by an adsorbed compound/molecule:



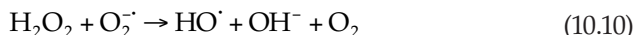
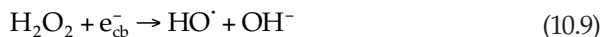
If a water molecule is adsorbed on the surface of TiO_2 , it may exist as hydroxyl and hydrogen ions.



The negatively charged hydroxyl ion adsorbed on the surface of TiO_2 gives up its negative charge (electron) to the positive hole to regenerate the neutral TiO_2 and it in turn becomes a neutral hydroxyl radical (OH^\cdot).



H_2O_2 may yield additional hydroxyl radicals by any of the following reactions:



The hydroxyl radical is a very potent oxidizing agent that can oxidize a pollutant organic molecule $\text{C}_l\text{H}_m\text{X}_n$ into CO_2 and H_2O , directly or through intermediate compounds as

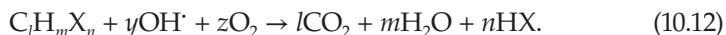


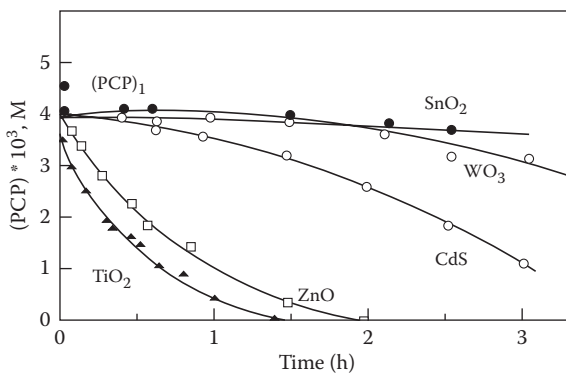
Table 10.1 shows the relative oxidation power of various species relative to that of chlorine. The oxidation power of the hydroxyl radical is ranked

TABLE 10.1

Oxidation Power for Various Species Relative to Chlorine

Species	Relative Oxidation Power
Fluorine	2.23
Hydroxyl radical	2.06
Atomic oxygen (singlet)	1.78
Hydrogen peroxide	1.31
Hydroxyl radical	1.25
Permanganate	1.24
Hypobromous acid	1.17
Chlorine dioxide	1.15
Hypochlorous acid	1.10
Chlorine	1.00
Bromine	0.80
Iodine	0.54

Source: Elizardo, K., Pollution Engineering, 106–109, 1991.

**FIGURE 10.2**

Photodegradation of pantachlorophenol (PCP) in the presence of various semiconductors. (From Barbeni, M. et al., *Chromosphere*, 14(2): 195–208, 1985.)

second among these known strong oxidizing agents. This demonstrates the hydroxyl radical's potential for oxidizing pollutants that normally are hard to destroy, like halogenated organics, surfactants, herbicides, and pesticides.

If the objective is to reduce and precipitate a metal from a metal compound, the electron is consumed by the metal compound as



Although the above photocatalytic reactions have been explained based on TiO_2 , almost all of the semiconductors may be used with varying degrees of usefulness. Figure 10.2 shows a comparison of some of the catalysts for photodegradation of a hazardous organic compound.

10.2 Solar Photocatalytic Detoxification

Solar photocatalytic detoxification refers to the destruction of hazardous pollutants from the environment by solar photocatalytic oxidation or reduction reactions. Solar detoxification has shown great promise for the treatment of groundwater, industrial wastewater, and contaminated air and soil. In recent years, the process has also shown great potential for disinfection of air and water, making possible a number of applications. Research studies on the photocatalytic oxidation process have been conducted over at least the last three decades (Blake 1994a). Blake (1994a) published a bibliography listing 660 publications, and even this long list is incomplete. He compiled a list of organic and inorganic compounds with references that shows over

300 compounds including approximately 100 on the US Environmental Protection Agency priority pollutant list that can be treated by the photocatalytic process. Blake (1994a) also lists 42 review articles including Blake et al. (1992), Kamat (1993), Legrini et al. (1993), Ollis et al. (1989a,b), and Venkatadri and Peters (1993) that cover various aspects of photocatalytic chemistry and technology.

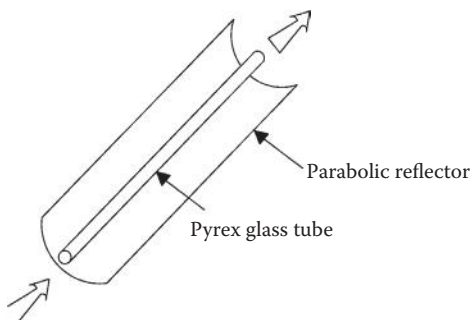
TiO₂ has been the most commonly used photocatalyst. The use of TiO₂ in water detoxification was first demonstrated by Carey et al. (1976). They showed that polychlorinated biphenyls were dechlorinated in aqueous suspensions of TiO₂. Other semiconductors have also been investigated as alternatives to TiO₂; however, TiO₂ has generally been shown to be the most active (Barbeni et al. 1985). Figure 10.2 shows a typical result from such a comparative study. Only ZnO has an activity similar to TiO₂. However, zinc oxides dissolve in acidic solutions, which make them inappropriate for technical applications. Titanium dioxide, on the other hand, is insoluble under most conditions, photostable, and nontoxic.

The energy needed to activate TiO₂ is 3.2 eV or more, which corresponds to near-ultraviolet (UV) radiation of a wavelength of 388 nm or less. As 4%–6% of sunlight reaching the earth's surface is characterized by these wavelengths, the sun can be used as the illumination source (Goswami et al. 1993). However, since UV radiation forms just 4%–6% of the usable solar spectrum, recent research has been aimed at improving the catalyst's performance by improving the reaction kinetics, increasing the useful wavelength range to utilize larger portions of the solar spectrum, developing appropriate reactors, and finding new engineering applications of the process for practical problems.

The following sections describe the engineering aspects of solar detoxification applications, including reactor design, modeling of kinetic reactions, system design, and industrial and commercial applications.

10.3 Solar Reactors

Designs of solar photocatalytic reactors have followed the well-known designs of solar thermal collectors including concentrating and nonconcentrating designs. The key differences are as follows: (1) the fluid to be treated must be exposed to UV solar radiation; therefore, the absorber must be transparent to UV solar radiation; and (2) no insulation is needed, since temperature does not play a role in the photoreaction. Therefore, the first engineering-scale outdoor reactor developed was a simple conversion of a parabolic trough solar thermal collector by replacing its absorber/glazing tube combination with a simple Pyrex glass tube through which contaminated water can flow (Figure 10.3).

**FIGURE 10.3**

Parabolic trough solar photocatalytic reactor.

Pacheco and Tyner (1990) used this reactor to treat water contaminated with trichloroethylene (TCE). The catalyst, TiO_2 powder, was mixed with contaminated water to form a slurry, which was passed through the Pyrex glass tube (reactor tube) located at the focal line of the parabolic trough. Since that time, a number of reactor concepts and designs have been advanced by researchers all over the world. Basically, all these reactors fall into the following categories:

- A. Reactor configuration
 - 1. Concentrating reactors
 - 2. Nonconcentrating reactors
- B. Catalyst deployment
 - 1. Fixed catalyst
 - 2. Slurry
 - 3. Neutral density large particles

10.3.1 Concentrator Reactors

As mentioned before, Pacheco and Tyner (1990) developed a simple modification of the parabolic trough solar thermal collector that worked successfully. They used this reactor in experiments with the catalyst deployed as a slurry. Since then, another configuration of this reactor has been developed and used by researchers at the Sandia National Laboratory (SNL) and at the National Renewable Energy Laboratory (NREL), in which the catalyst is fixed on a loosely woven fiberglass matrix that is inserted into the reactor tube. Both of these configurations have worked well. Parabolic concentrating type of reactors have been used for applications such as groundwater remediation (Mehos and Turchi 1993) and metal removal from water (Prairie et al. 1992).

A disadvantage of concentrating reactors is their inability to use diffuse solar radiation. For solar thermal applications, this limitation is not a major

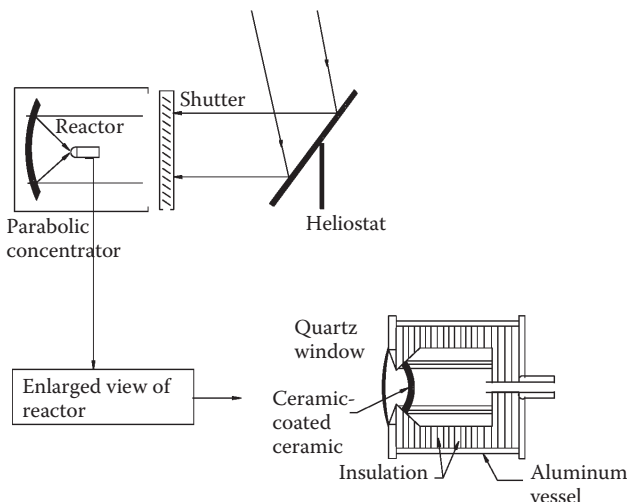
problem since diffuse radiation forms a small fraction of the total solar radiation. However, solar photocatalytic detoxification with TiO_2 as a catalyst uses only the UV portion of the solar radiation, approximately 4%–6% of the total spectrum. As much as 50% or more of the UV radiation can be diffuse, especially at locations with high humidity or during cloudy or partly cloudy periods. Therefore, concentrating reactors would be more useful at dry, high direct insolation locations. Another disadvantage of the concentrating reactors is low quantum efficiency (Bahnemann et al. 1991; Link and Turchi 1991), resulting in a reaction rate constant dependence on the intensity of UV radiation as

$$k \propto I^{1/2}. \quad (10.14)$$

These disadvantages tend to favor the use of nonconcentrating reactors. However, a big advantage of the concentrating reactors is that the reactor tube area is very small, which allows the use of high-quality UV transmitting materials, such as Pyrex glass, without increasing the cost too much, while also improving the lifetime of use of these reactors. Ultimately, the choice of these types of reactors or any other type will be based on the overall economics of the solar detoxification system. As explained later in this chapter, under certain conditions, the reactor capital cost may be a small portion of the overall costs, in which case the balance of the system costs, the catalyst costs, and the operation and maintenance costs dictate the economics of the solar detoxification process.

Other concentrating reactors that have been constructed and tested include very high concentration, high-temperature solar furnaces (Figure 10.4) and a heliostat concentration system with a vertical falling film reactor (Tyner et al. 1989). The high-concentration, high-temperature solar furnaces combine solar photolytic and thermal effects and have been demonstrated to work well for gas-phase detoxification as well as other applications.

The solar catalytic steam reforming furnace shown in Figure 10.4 uses a parabolic dish to concentrate the sunlight into a reactor through a quartz window, where it heats the reactor absorber to 700°C–1000°C. The toxic organic waste is destroyed by a steam reforming process over a rhodium catalyst supported by a porous ceramic absorber. A version of this direct catalytic absorption receiver reactor has been tested at the SNL solar furnace for engineering-scale experiments to demonstrate various steam reforming reactions including CO_2 /methane, steam/methane, steam/propanol, and steam/TCE (Skocypec and Hogan 1990). Another version of this system was built in Germany by a joint collaboration involving the SNL of the United States and the *Deutsche Forschungsanstalt für Luft- und Raumfahrt* (DLR) of Germany. A concentrating furnace has been built at NREL, which has been used for detoxification tests for various hazardous chemicals (Glatzmaier and Bohn 1993; Glatzmaier et al. 1990a,b). Although the high-concentration, high-temperature solar furnaces have worked well, the major impediment to their widespread use is the high capital cost.

**FIGURE 10.4**

Direct catalytic absorption steam reforming furnace. A furnace based on a similar concept was also built at NREL. (From Glatzmaier, G.C. et al., *J. Environ. Sci. Health A25(5)*: 571–581, 1990a; Glatzmaier, G.C. et al., *Solar Engineering 1990, Proceedings of the ASME International Solar Energy Conference*, pp. 153–158, 1990b.)

10.3.2 Nonconcentrating Reactors

Nonconcentrating reactors have a major advantage over concentrating reactors because they can utilize the diffuse part of solar UV radiation in addition to the beam part. While diffuse solar radiation forms only approximately 10%–15% of the total solar radiation over the whole solar spectrum, that is not the case for UV solar radiation. Since UV is not absorbed by water vapor, it can be as much as 50% of the total solar radiation at certain locations, especially locations with high atmospheric humidities (Saltiel et al. 1992). Moreover, the quantum efficiency of the photocatalytic process due to non-concentrated incident radiation is also higher than that due to a concentrated beam. In addition, nonconcentrating reactors have the potential to be simple in design and low in cost. A disadvantage of the nonconcentrating reactors is the requirement of a much larger reactor area (although the total solar aperture would be less) than the concentrating reactors. Researchers have proposed a number of different designs of nonconcentrating solar reactors. They are

1. Flat plate
2. Tubular
3. Falling film
4. Shallow solar pond

Researchers at the University of Florida have developed a number of non-concentrating solar reactors including trickle-down flat plate, pressurized flat plate, tubular (rigid and inflatable), free-falling film, and shallow solar pond.

10.3.3 Flat-Plate Reactors

Figure 10.5 shows a trickle-down flat-plate reactor with a thin film glazing (Wyness et al. 1994). This reactor consists of a back plate on which water trickles down from a spray bar at the top. A woven mesh (fiberglass) covers the back plate in order to damp out surface waves as the water trickles down and to even out the flow. This allows a thin even film of water to flow on the plate. A UV transparent glazing prevents any evaporation from the flow. This design allows contaminated water, mixed with the catalyst particles as a slurry, to be treated as the water trickles down when exposed to the sun. The reactor can be operated in a fixed catalyst configuration by replacing the plain woven mesh with a mesh with the catalyst fixed on it.

10.3.4 Tubular Reactors

Because of the weight of water, the glazing of the pressurized flat plate requires additional structural support. A simple concept of such a reactor is shown in Figure 10.6 (Goswami 1995). In this system, the contaminated water flows through the small channels between the lower and the upper headers. A variation of this concept is to substitute rigid transparent tubes in place of rectangular channels (Figure 10.7). Such tubular reactors were tested at the University of Florida to treat water contaminated by volatile organic compounds (Oberg et al. 1993). These reactors were also tested in the field

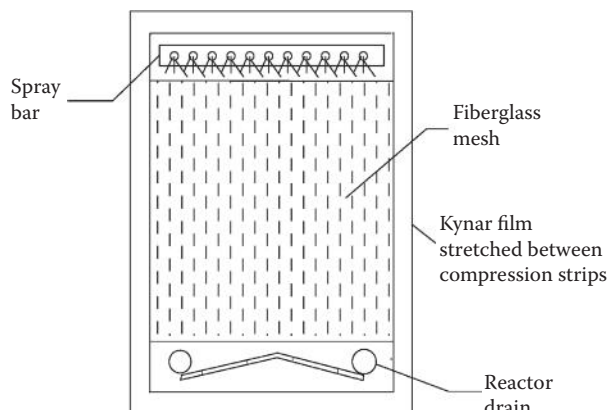
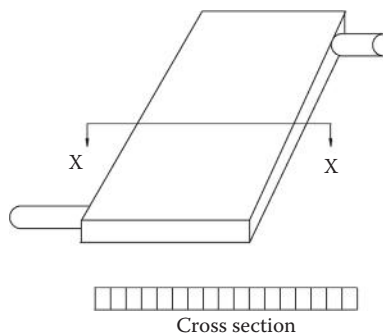
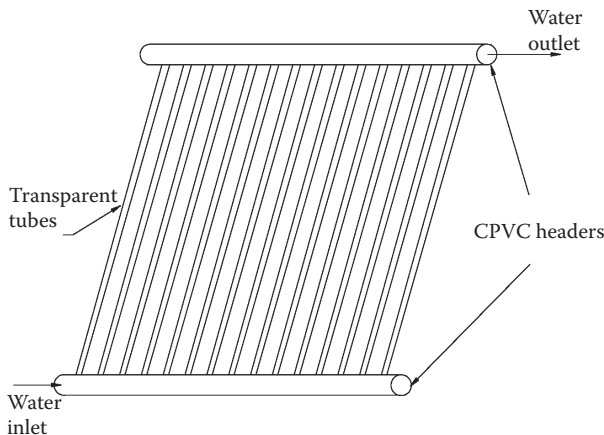


FIGURE 10.5

Trickle-down flat plate reactor. (From Wyness, P. et al., *J. Sol. Energy Eng.*, ASME 116(1): 2–7, 1994.)

**FIGURE 10.6**

Pressurized flat plate reactor. (From Goswami, D.Y., *Adv. Solar Energy* 13: 208, 1995.)

**FIGURE 10.7**

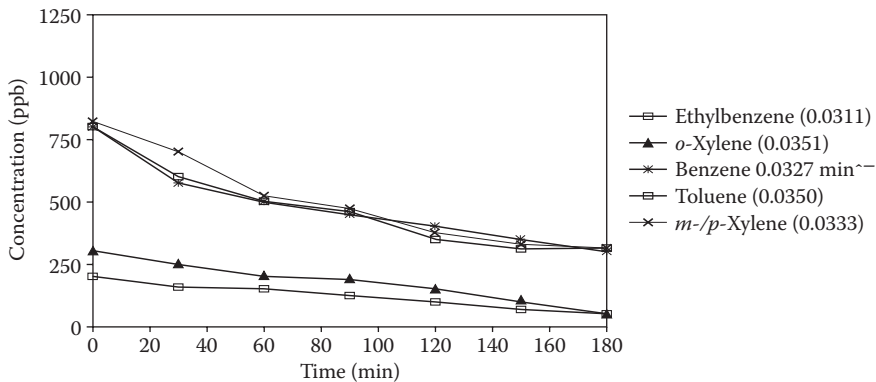
Flat plate reactor with rigid transparent tubes.

at Tyndall Air Force Base (TyAFB) to treat groundwater contaminated with fuel, oil, and lubricants (Goswami et al. 1993). Figure 10.8 shows the performance of this system.

A simple reactor concept consists of transparent inflatable tubes connected in parallel between two headers (Goswami 1995). As the water flows through the reactors under pressure, the tubes inflate. Large areas of this reactor can be rolled or folded into a small volume for portability and transported for on-site use.

10.3.5 Shallow Solar Ponds

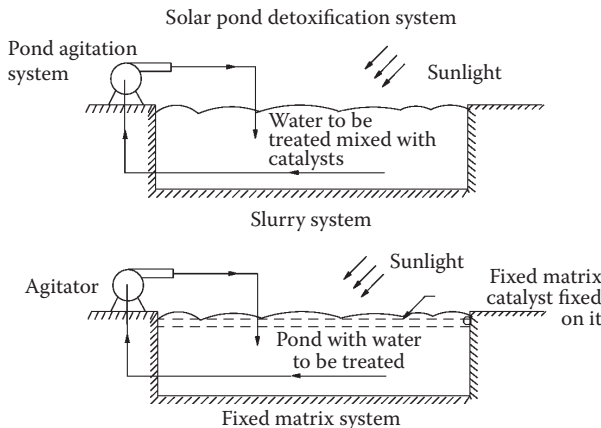
Shallow pond-type reactors, developed at the University of Florida, may be constructed on-site especially for industrial wastewater treatment (Bedford

**FIGURE 10.8**

Destruction of BTEX in groundwater at Tyndall AFB using nonconcentrating tubular reactors. (From Goswami, D.Y. et al., Solar photocatalytic treatment of groundwater at Tyndall AFB, field test results. *Solar* 1993, *Proceedings of the American Solar Energy Society Annual Conference*, pp. 235–239, 1993.)

et al. 1994). Since industries already use holding ponds for microbiological treatment of wastewater, shallow solar ponds can be used for the front end or the back end of a combined solar/microbiological treatment of wastewater. Therefore, these reactors would be ideal for wastewater treatment in industries such as pulp and paper, textiles, pharmaceuticals, and chemicals.

The reactor concept is simple, as shown in Figure 10.9. The reactor can be operated in a slurry or fixed catalyst configuration. If TiO_2 is used as a catalyst in a slurry configuration, it settles down to the bottom, if it is not continuously mixed. While the disadvantage of this configuration is that

**FIGURE 10.9**

Shallow solar pond reactors. (From Bedford, J. et al., *J. Sol. Energy Eng.*, ASME 116(1): 8–13, 1994.)

continuous mechanical mixing is needed, the advantage is that after the catalyst settles down, the treated water can be removed from the top without filtration. Bedford et al. (1994) tested shallow pond reactors in both slurry and fixed configuration, and various area-to-depth ratios, for treating contaminated water. The reactors worked extremely well under various insulation conditions (sunny, partly cloudy, and cloudy).

10.3.6 Falling Film

Some of the other nonconcentrating reactors developed include a vertically free-falling film reactor developed by Goswami (1995). The vertical film of this reactor is open to the atmosphere on both sides, which allows it to make maximum use of the diffuse atmospheric radiation. The integrity of the film is maintained by means of vertical strings appropriately spaced apart.

Finally, solar detoxification would work just as well, on-site, if the application involves treatment of large bodies of contaminated water, such as spills in lake, or the sea. Heller and Brock (1991) developed neutral density spheres coated with TiO_2 , which can be floated in large bodies of water to treat the contamination *in situ* in the presence of the sun (Heller et al. 1992).

10.4 Kinetic Models

An understanding of reaction rates and how the reaction rate is influenced by different parameters is important for the design and optimization of an industrial system. The rate of photolytic degradation depends on several factors including illumination intensity, catalyst type, oxygen concentration, pH, presence of inorganic ions, and the concentration of organic reactant. As is typical of many photo-assisted reactions, the effect of temperature is small. Figure 10.10 shows a typical change in pollutant concentration C with time t .

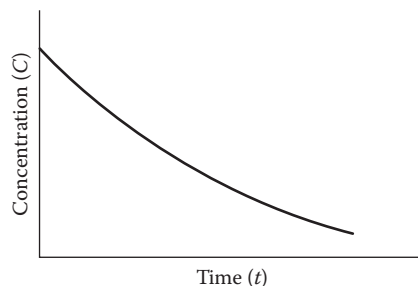


FIGURE 10.10

Typical concentration–time history.

The destruction rates of organics in photocatalytic oxidation have been modeled by different kinetic models. Langmuir–Hinshelwood (L–H) kinetics seems to describe many of the reactions fairly well.

The rate of destruction is given by

$$-\frac{dC}{dt} = \frac{K_1 K_2 C}{(1 + K_2 C)}. \quad (10.15)$$

In the ideal case for which the L–H model is derived, C is the bulk solute concentration, K_1 is the reaction rate constant, K_2 is the equilibrium adsorption constant, and t represents time. In the photocatalytic system, these definitions are less clear because of the importance of reactive radical species.

The L–H reaction rate constants are useful for comparing the reaction rate under different experimental conditions. Once the reaction constants K_1 and K_2 have been evaluated, the disappearance of reactant can be estimated if all other factors are held constant.

For low solute concentrations, C is almost equal to zero, which makes the denominator in the L–H expression equal to 1. This reduces the L–H expression to a pseudo-first-order expression:

$$-\frac{dC}{dt} = K_1 K_2 C = kC. \quad (10.16)$$

This equation has been shown to apply to many photocatalyzed reactions (Bahnemann et al. 1991). Industrial pollutant levels are typically on the order of parts per million (ppm), which are low enough for the reaction rate to follow pseudo-first-order kinetics.

For the design of a system, the reaction rate constant k can be determined from experimental data as described here. Figure 10.11 shows a simplified schematic of a batch-type solar photocatalytic detoxification facility. The

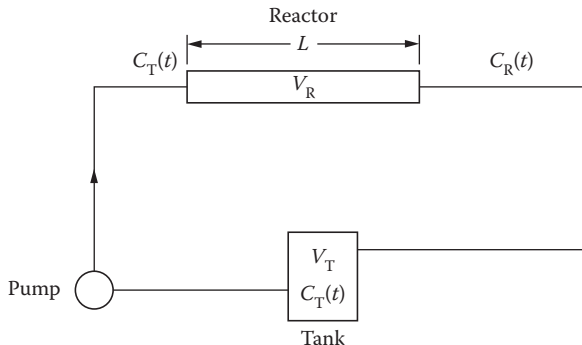


FIGURE 10.11

Simplified schematic diagram of a batch-type solar detoxification facility.

contaminated water is stored in a containment tank and pumped through a reactor, which is illuminated by the sun or another light source. The partially treated water coming out of the reactor is mixed with the water in the containment tank. The process continues until the mixed concentration in the containment tank reaches an acceptable level. Laboratory treatment studies normally employ such a facility to determine reaction rate constants that can be used in the design of treatment systems.

If the reaction rate constant is determined from Equation 10.15 or 10.16 by simply using the concentration–time history in the tank, the results would be in error, unless the tank volume (V_T) is negligible as compared to the reactor volume (V_R), which is usually not the case. Wolfrum and Turchi (1992) suggested that an apparent reaction rate constant k_{app} may be calculated using Equation 10.16 and the concentration–time history in the tank, from which actual reaction rate constants may be approximated by

$$k = k_{app} \frac{1 + \gamma}{\gamma}, \text{ where } \gamma = \frac{V_R}{V_T}. \quad (10.17)$$

From a rigorous analysis, Klausner et al. (1994) determined that the approximation given by Equation 10.17 gives reaction rate constants that are accurate to within 5% for

$$\frac{\gamma + 0.79}{\kappa^{0.62}} > 3.30, \text{ where } \kappa = \frac{V_R k}{Q} \quad (10.18)$$

and Q is the volume flow rate through the reactor, V_R is the volume of the reactor and V_T is the tank volume.

For $\kappa < 0.1$, Equation 10.16 is in error by less than 5%, regardless of γ .

Example 10.1

Assuming that pseudo-first-order kinetics can model the destruction of benzene as shown by the experimental concentration history data in Figure 10.8, determine the apparent and actual reaction rate constants if the reactor volume is 20 gal and the tank volume is 500 gal (neglect volume in pipes). If the solution flows at 30 gal/min, comment on the accuracy of the calculated actual reaction rate. What happens when the tank volume becomes much smaller than the reactor volume?

Solution

Using Equation 10.16,

$$\frac{-dC}{dt} = k_{app} C$$

$$\int_{c_i}^{c_f} \frac{dc}{C} = -k_{app} \int_0^{\Delta t} dt$$

$$k_{app} = \frac{\ln C_i/C_f}{\Delta t}.$$

From Figure 10.8 for benzene, $C_i = 800$ ppb, $C_f = 350$ ppb, and $\Delta t = 180$ min. Plugging into the above equation, we get

$$k_{app} = 0.00459 \text{ min}^{-1}.$$

From Equation 10.17,

$$k = k_{app} \frac{1 + \gamma}{\gamma} = k_{app} \frac{V_T}{V_R} + 1$$

or

$$k = 0.119 \text{ min}^{-1}.$$

Note that the actual reaction rate is faster than the apparent one, since no reaction occurs in the large tank where the concentration is measured.

From Equation 10.18,

$$\frac{\gamma + 0.79}{K^{0.62}} = \frac{\frac{V_R}{V_T} + 0.79}{\frac{V_R k}{Q}^{0.62}} = 3.99 > 3.30.$$

The inequality of Equation 10.18 holds, indicating that the actual reaction rate constant is accurate to within 5%.

As the tank volume decreases,

$$V_T \ll V_R \quad \text{or} \quad \gamma \gg 1;$$

with $\gamma \gg 1$, Equation 10.17 reduces to

$$k = k_{app}.$$

This indicates all the solution is in the reactor; hence, the reaction rate measured is the actual reaction rate.

It should be noted here that the reaction rate constant k determined herein is not the traditional rate constant used in reactor engineering. Because of the nature of the photocatalytic reaction, it is a function of external system parameters such as UV irradiation intensity, pH, catalyst loading, and possible degree of mixing in the fluid. It may also depend

on the geometry of the photoreactor. Of these parameters, the intensity of the solar UV radiation cannot be controlled; therefore, the experimentally determined reaction rate constant, k_o , must be adjusted for the actual UV intensity according to the following equations:

Concentrating reactors (Link and Turchi 1991):

$$\frac{k}{k_o} = a \left(\frac{I}{I_o} \right)^x, \quad (10.19)$$

where a is a constant given as A/V (Link and Turchi 1991) and x is an intensity-dependent exponent, which varies between 0.5 and 1. A value of 0.5 is recommended for x (Bahnemann et al. 1991).

Nonconcentrating tubular or channel-type reactors (Goswami et al. 1993):

$$\frac{k}{k_o} = a \left(\frac{I}{I_o} \right), \quad (10.20)$$

where $a = 0.88$ for 0.1% TiO_2 and 1.14 for 0.01% TiO_2 (Wyness et al. 1994).

Trickle-film flat-plate reactors (Wyness et al. 1994):

$$\frac{k}{k_o} = a \left(\frac{I}{I_o} \right) \frac{\delta_o}{\delta}. \quad (10.21)$$

Here, δ represents the film thickness and the value of a is 0.97 (Wyness et al. 1994). δ_o is the reference film thickness corresponding to k_o and I_o .

Shallow pond reactor (Bedford et al. 1994):

$$\frac{k}{k_o} = m \left(\frac{I(A/V)}{I_o(A/V)_o} \right)^n. \quad (10.22)$$

Values of m and n are given in Table 10.2 (Bedford et al. 1994).

It can be seen from the above equations that the liquid film thickness (δ) is an important parameter for a trickle bed reactor, while the ratio of the area to volume (A/V) is critical for the shallow ponds.

Example 10.2

Three reactors—a flat-plate, a parabolic trough concentrator, and a shallow solar pond—were tested for effectiveness in treating a water stream contaminated with 4CP. Using 0.1% TiO_2 solution, all three gave

TABLE 10.2

Empirical Constants m and n for Destruction of 4-Chlorophenol in a Shallow Pond Reactor

% TiO ₂	$C_o \times 10^{-4}$ (M)	m	n
0.01	1	0.28	0.50
0.1	1	0.66	0.70
0.3	1	0.95	1.00
0.01	4	0.52	0.44
0.1	4	0.95	0.65
0.3	4	1.23	0.66

Source: Bedford, J. et al., *Journal of Solar Energy Engineering*, ASME, 116 (1): 8–13, 1994.

a reaction rate constant k_o of 0.0172 min^{-1} for an incident UV radiation of 31 W/m^2 .

- Determine the reaction rate for a 0.1% TiO₂ solution of the contaminated water passing through each reactor experiencing a steady UV insolation of 43 W/m^2 .
- Determine the depth of a rectangular shallow pond reactor to give (a) the reaction rate found in part (i) and (b) double the reaction rate found in part (i).

Use the following reference values:

$$(A/V)_o = 19.7 \text{ m}^{-1} \text{ (for shallow pond reactor)}$$

$$a = 1.0 \text{ (for concentrating reactor).}$$

Solution

- From Equation 10.20, for a flat-plate reactor,

$$k = k_o a \frac{I}{I_o} = (0.0172 \text{ min}^{-1})(0.88) \frac{43 \text{ W/m}^2}{31 \text{ W/m}^2}$$

$$k = 0.021 \text{ min}^{-1}.$$

For a concentrating reactor, Equation 10.19 yields

$$k = k_o a \frac{I}{I_o}^x \quad \text{where } x = 0.5$$

$$k = (0.0172)(1.0)(43/31)^{0.5} = 0.0203 \text{ min}^{-1}.$$

For a shallow solar pond, Equation 10.22 yields

$$k = k_o \cdot m \cdot \frac{I(A/V)}{I_o(A/V)_o}^n.$$

For the same A/V ratio,

$$k = (0.0172)(0.66)(43/31)^{0.7} = 0.0143 \text{ min}^{-1}.$$

ii. For the same reaction rate constant, it was assumed that

$$(A/V) = (A/V_o) = 19.7 \text{ m}^{-1}.$$

For a rectangular pond, $V = A \cdot D$, where D is the depth of the pond,

$$\text{Therefore, } 1/D = 19.7 \text{ m}^{-1}$$

or

$$D = 0.051 \text{ m or } 5.1 \text{ cm.}$$

For double the reaction rate constant $k = 0.0143 \times 2 = 0.0286 \text{ min}^{-1}$ for the same insolation, from Equation 10.22,

$$\begin{aligned} (A/V) &= (A/V)_o \cdot (I_o/I)(k/mk_o)^{1/n} \\ &= (19.7 \text{ m}^{-1})(1)(2/0.66)^{1/0.7} \\ &= 96 \text{ m}^{-1} \end{aligned}$$

$$\text{Therefore, } D = 1/96 = 0.0104 \text{ m or } 1.04 \text{ cm.}$$

10.5 Useful Insolation

Photocatalytic detoxification using TiO_2 as catalyst requires photons of UV radiation with wavelength less than 388 nm. The extraterrestrial radiation supplied by the sun contains approximately 10% UV radiation when it first reaches the earth's atmosphere, which is reduced to approximately 4%–6% as the solar radiation travels to the surface (ground level). Typically, the maximum value of UV radiation is approximately 50 W/m^2 for a south-facing surface in the Northern Hemisphere or a north-facing surface in the Southern Hemisphere tilted at an angle equal to the latitude of the location. Typical solar radiation data available for most locations in the world represent the

insolation values for the entire spectrum. However, utilization of these data for modeling detoxification processes requires the estimation of the UV component. Riordan et al. (1990) developed correlations that related measured UV to measured total values. Based on their study, global horizontal and direct normal UV radiation can be calculated as

$$\frac{I_{uv,h}}{I_t} = 0.14315K_t^2 - 0.20445K_t + 0.135544 \quad (10.23)$$

$$\frac{I_{uv,b}}{I_{t,b}} = 0.0688e^{-0.575m} = 0.688 \exp \left(\frac{-0.575}{\sin \alpha} \right), \quad (10.24)$$

where K_t is the cloudiness index and m is the air mass. These correlations were based on limited measurements at only a few locations (Cape Canaveral, Florida; San Ramon, California; and Denver, Colorado) with an uncertainty greater than 20%.

The functional form of irradiance on the reactor aperture varies according to the reactor type. For a flat-plate reactor, UV irradiance can be calculated by using the following equation (Saltiel et al. 1992), which is a modified form of an equation given by Rabl (1981) for total solar radiation:

$$I_{uv} = I_{uv,b} K(i) \max\{\cos i, 0\} + 0.5K(i)[I_{uv,d}(1 + \cos \beta) + \rho_{uv,gr} I_{uv,h}(1 - \cos \beta)], \quad (10.25)$$

where i is the incident angle of the reactor aperture (calculated at the midpoint of each hour), $K(i)$ is the incident angle modifier, β is the reactor tilt, and $\rho_{uv,gr}$ is the UV reflectance of the ground. Ground reflectance values in the UV region are determined for various ground covers using a data fit developed by Green (1983). Ground cover may be assumed to be farmland, where reflectance is approximately 4%, unless covered by snow, where reflectance is approximately 29% (Green 1983). The incident angle modifier $K(i)$, defined as the ratio of the UV transmittance-absorbance product for the reactor at an angle i to the normal, is dependent on the materials used for reactors. Actual values of $K(i)$ for the reactor under consideration must be used whenever possible. In the absence of actual values, the following expression for a solar thermal collector may be used, although reactor receiver covers and the useful solar spectrum are generally not the same as those for solar thermal collectors.

$$K(i) = 1 - 0.10 \frac{1}{\cos i} - 1. \quad (10.26)$$

March et al. (1995) demonstrated the use of above-described reaction kinetic models and solar insolation models to simulate the performance of solar detoxification systems.

10.6 Catalyst Development

At present, TiO_2 in anatase form is the most common catalyst used in solar photocatalytic detoxification. As explained earlier, this limits the useful range of the solar spectrum to wavelengths of less than approximately 388 nm. Only approximately 4%–6% of the solar radiation is available in this wavelength range. Therefore, the catalyst improvement research is concentrated on

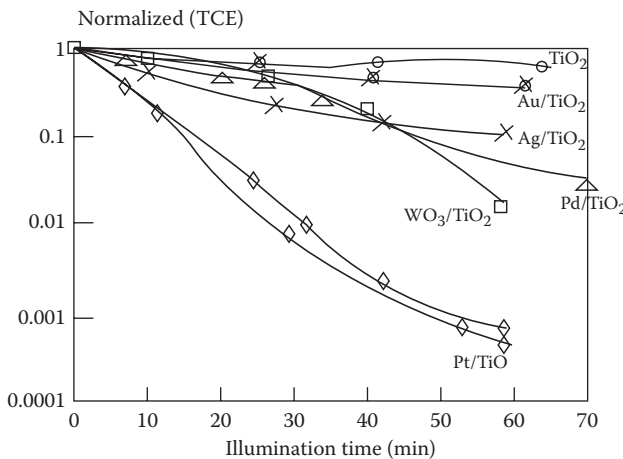
1. Physical and chemical modification of TiO_2 to improve the catalyst performance
2. Dye sensitization to increase the useful wavelength range of the solar radiation
3. Development of homogenous catalysts

Figure 10.12 shows the results of the comparative tests conducted on modified catalysts. It can be seen that several methods, by themselves or in combination, can be used to improve the performance of the TiO_2 catalyst.

According to Magrini et al. (1994), thermal treatment at 550°C–600°C can double the reaction rates. Manipulating the surface area and particle size can also improve the catalyst performance. Metallization of TiO_2 particles with Pt can improve the performance five times, while Pd, Ag, and WO_3 can improve it by factors of 2 to 3.*

Another improvement being investigated by researchers is the use of photosensitizer (dye) molecules on the surface of a semiconductor. In dye sensitization, a dye molecule absorbs visible light, gets excited to a higher energy state, and interacts with the semiconductor molecule (TiO_2), water, and oxygen to produce hydroxyl radicals. The result is an extension of the photoresponse of the semiconductor photocatalyst, making it capable of using a broader spectrum of solar radiation than the semiconductor alone (Dieckmann et al. 1994; Kamat 1993). Dye sensitization of TiO_2 photocatalyst has the potential to reduce the overall cost of treatment. Methylene blue and Rose Bengal have been the most common dyes investigated so far. The results have been inconclusive.

* For detailed data on the catalyst improvement research, see Crittendon et al. (1995), Linder et al. (1995), and Magrini et al. (1994, 1995).

**FIGURE 10.12**

Concentration vs. illumination time data for metallized TiO₂. The metal-containing catalyst contained 1–2 wt% metal, and the WO₃/TiO₂ contained 3 wt% WO₃. All reactions were conducted in a 0.51 circulating batch reactor with 0.05 wt% catalyst at 22°C, 25 ppm initial TCE, and illuminated with a 1000 W Xe source. (From Magrini, K.A. et al., *Solar Engineering* 1994. *Proceedings of the 1994 ASME International Solar Engineering Conference*, pp. 163–170, 1994.)

10.7 System Design Methodology

The effectiveness of solar detoxification systems has been demonstrated commercially (Goswami 1995). Goswami and Anheden (1994) have developed a methodology that can be used for the design of simple solar detoxification systems.

The procedure for designing a solar detoxification system requires the selection of the reactor, reactor operational mode (slurry or fixed matrix), reactor field configuration (series or parallel), treatment system mode (once through or batch), flow rate, pressure drop, pretreatment, catalyst and oxidant loading, pH control, and catalyst reuse system. For the treatment of groundwater or industrial wastewater, the following must be known or determined a priori:

1. Complete analysis of the water to be treated to determine pretreatments
2. Target chemicals and their initial and final desired concentrations
3. Amount of water to be treated daily

The following steps describe a design procedure:

A. Laboratory Treatment Study

A laboratory treatment study must be conducted to determine the following parameters for optimum treatment:

1. Reaction rate constant
2. Catalyst loading
3. Oxidant (H_2O_2 , O_3 , etc.) loading, if any
4. Required pH
5. Pre- and posttreatment

Indoor reactors, with simulated radiation similar to the expected solar radiation and reactor geometry similar to the chosen outdoor reactor, may be used for the laboratory treatment study.

Experiments are conducted to find the concentration–time history of the pollutant chemical under consideration from which the reaction rate constant k may be calculated as explained earlier. If more than one target chemical is present, reaction rate constants for all the chemicals must be determined. In this case, the lowest value of k should be used for the reactor design.

B. Treatment Facility Operational Mode

A solar detoxification facility may be operated in the following modes:

1. Batch mode (Figure 10.13a): In this mode, the effluent is stored in a tank and is continuously recirculated through the reactors until the desired destruction is achieved. Operation in this mode requires one or more storage tanks. If the desired destruction of the contaminated water is not achieved in a single day, the system is operated the following day until the desired destruction is obtained. Shallow solar ponds that combine reactor and storage fall in this category.

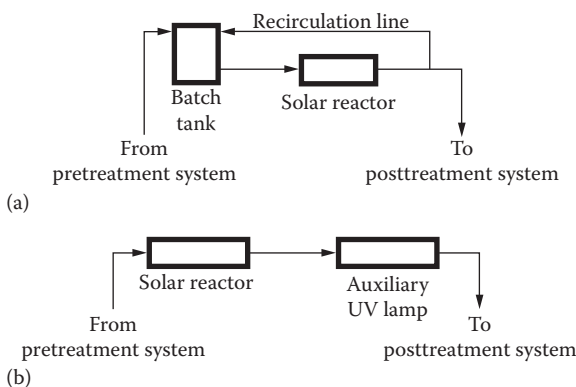


FIGURE 10.13

Schematics of treatment facility operational modes: (a) batch mode; (b) single pass mode. (From Blake, D.M. et al., Solar photocatalytic detoxification of water. In *Advances in Solar Energy*, Vol. 7, K.W. Boer, ed. American Solar Energy Society, Boulder, CO, pp. 167–210, 1992.)

2. Single-pass mode (once through) (Figure 10.13b): In this mode, the reactor area and the flow rates are designed such that the desired destruction is achieved in a single pass. The flow rates in this case are normally lower. The solar insolation varies throughout the day, and hence, the flow rate through the reactors should be varied with the intensity of the solar insolation. As the UV intensity decreases, the flow rate through the reactor should be decreased in order to maintain the same final concentration.

C. Residence Time

For the first-order reaction kinetics, the required residence time t is calculated by using Equation 10.16 as

$$\frac{C_f}{C_i} = e^{-kt} \quad (10.27)$$

or

$$t = \frac{\ln(C_i/C_f)}{k}, \quad (10.28)$$

where C_f is the final concentration of the contaminant, C_i is the initial concentration of the contaminant, and k is the rate constant (min^{-1}).

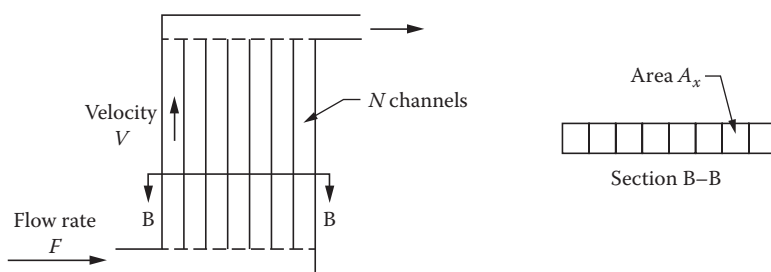
The rate constant k is obtained from k_o (which is the measured rate constant for the intensity I_o) by adjusting it for the actual intensity, I , according to Equations 10.19 through 10.22. Since the intensity I changes throughout the day, k would require continuous adjustment. An approximate and simplified value can be used by adjusting k_o for an average value of I for the useful part of the day.

The time needed for the detoxification of the wastewater depends on the desired amount of destruction of the contaminant. As can be seen from the above equation, the time increases exponentially for destruction approaching 100%.

D. Reactor Area

For a given amount of wastewater to be treated per day, q , an average useful time of operation per day, T , and the reactor geometry, the fluid velocity in the reactor can be calculated. For a reactor with N parallel tubes/channels that are connected between two headers, the flow velocity can be calculated as (Figure 10.14)

$$\text{Total flow rate } F = \frac{q}{T} \quad (10.29)$$

**FIGURE 10.14**

Flow through a reactor with N channels.

$$\text{Velocity in one channel } v = \frac{F}{(NA_x)}, \quad (10.30)$$

where A_x is the cross-sectional area of a channel.

From the required residence time t as calculated from Equation 10.28, the flow velocity v as calculated from Equation 10.30, and the length of one reactor L , the total number of reactors for a once-through system can be calculated as follows:

$$\text{Residence time for one reactor } t_r = \frac{L}{v}. \quad (10.31)$$

Total number of reactors = t/t_r (rounded off to the next integer number).

The following is given as an example of the reactor design using the experimental data from field tests conducted at TyAFB (Goswami et al. 1993).

Example 10.3

Using the experimental data for treatment of groundwater at TyAFB in Florida (Table 10.3), find (1) the residence time for 99.75% destruction of the contaminants and (2) the number of reactors required to treat 36,000 L of contaminated groundwater per day, using tubular reactors.

Each reactor is 2.44 m \times 1.83 m (nominal) and contains 132 tubes that are 2.44 m long and 6.4 mm in diameter. The volume capacity of each reactor is 25 L. Assume a yearly average UV radiation value of 28 W/m² for an average of 6 h each day.

TABLE 10.3

Experimental Parameters and Results for TyAFB Field Tests

Test No.	UV (W/m ²)	%	Rate Constants, K (min ⁻¹)						
			TiO ₂	pH	H ₂ O ₂	Benzene	Toluene	Ethylbenzene	<i>m</i> , <i>p</i> -Xylene
1	45.3	0.1	6	100	0.0327	0.0350	0.0311	0.0333	0.0351
2	47.7	0.05	6	100	0.0263	0.321	0.0304	0.0337	0.0309
3	47.2	0.1	5	100	0.364	0.364	0.364	0.364	0.364

Source: Goswami, D.Y. et al., Solar photocatalytic treatment of groundwater at Tyndall AFB, field test results, *Solar 1993, Proceedings of the American Solar Energy Society Annual Conference*, pp. 235–239, 1993.

Note: Test 3 consisted of city water spiked with BTEX.

Solution

From Table 10.3, the minimum *k* value is selected for the residence time and the design of the reactor. For example, for Test 1, the minimum *k* value is 0.0311 (min⁻¹). The solar UV intensity for this test data is 45.3 W/m². Since the *k* value depends on the UV intensity, it needs to be adjusted for the design UV intensity. In this case, we assume the design for yearly average conditions when the average UV intensity is 28 W/m². Thus, the adjusted *k* value is given by the following equation:

$$k = k_o \frac{I}{I_o} \quad (10.32)$$

or

$$k = 0.0311 \times \frac{28}{45.3} = 0.0192(\text{min}^{-1}). \quad (10.33)$$

Assuming first-order reaction kinetics, for a 99.75% destruction (*C_f/C_i* = 0.0025), the residence time can be found from Equation 10.28 as

$$t = \frac{\ln(C_i/C_f)}{k} \quad \text{or} \quad t = \frac{\ln(1/(0.0025))}{0.0192} = 312 \text{ min}$$

or

$$t = 312 \text{ min (approximately 5.2 h).}$$

The time that is needed for detoxification increases exponentially for destruction rates approaching 100%. For example, for the above kinetics, the residence time increases from 72.2 min for 75% destruction, to 156 min for 95% destruction, to 312 min for 99.75% destruction rate.

For a single-pass (once-through) system, number of reactors depends upon several parameters, such as the amount of material to be treated, residence time required, and the size and configuration of reactors. In this example, we have to treat 36,000 L of wastewater per day.

Assuming the length of a day as 6 h, the volume of water to be treated per minute would equal $36,000/(6 \times 60) = 100$ Lpm. Knowing the flow rate, we can now determine the residence time of wastewater in one reactor as follows:

$$\text{Total flow rate} = 100 \text{ Lpm}$$

$$\text{Flow in one tube} = 100/132 = 0.76 \text{ Lpm} = 760 \text{ cm}^3/\text{min}$$

$$\text{Cross-sectional area of one tube} = (\pi/4) d^2 = 0.32 \text{ cm}^2$$

Hence, velocity = $760/0.32 = 2375 \text{ cm/min} = 0.39 \text{ m/s}$ and residence time for one reactor = length of tube/velocity = $2.44 \text{ m}/0.39 \text{ m/s} = 6.26 \text{ s}$.

Therefore, the number of reactors required = total residence time/(residence time in one reactor) = $(5.2 \text{ h} \times 3600)/6.26 = 2990$ reactors.

The number of reactors strongly depends upon the reaction rate constant k . For example, the k value for the city water—spiked with the same amount of BTEX (benzene, toluene, ethylbenzene, and xylene) as found in the groundwater—was determined to be 0.361 in comparison to an average of 0.031 for the groundwater. The residence time required for the k value of 0.361 will be only 27 min, as compared to 5.2 h for a k value of 0.031. Following the above procedure in this case, the number of reactors required will be only 262 as compared to 2990 for the groundwater.

10.7.1 Catalyst Life

Catalyst life and the fraction of the catalyst useful after each run are important parameters in the process economics. Catalyst may be poisoned by contaminants and particles or washed away in the discharge water, reducing the catalyst's life and requiring additional catalysts for each run. Useful catalyst life can be estimated by conducting tests with actual contaminated water a number of times and determining the reduction in reaction rate constant each time. In the field tests conducted at TyAFB, Goswami et al. (1993) found that approximately 10% of the catalyst was lost in each run.

10.8 Gas-Phase Photocatalytic Detoxification

Since air contains approximately 21% oxygen and that contaminant levels are often in the range of 0.1 to 100 ppm, it follows that contaminated air has a great deal of excess oxidant available versus that needed for total oxidation

of impurities (Ollis 1994). Published literature shows that gas-phase photocatalytic oxidation can be used successfully to oxidize paraffins, olefins, and alcohol (Dibble and Raupp 1990); TCE (Anderson et al. 1993; Dibble and Raupp 1990; Nishida et al. 1993); *trans*-dichloroethylene (*trans*-DCE) and *cis*-dichloroethylene (*cis*-DCE) (Nimlos et al. 1993); toluene (Ibusuki and Takeuchi 1986); airborne nitroglycerin (Raissi and Muradov 1993); and 3-chlorosalicylic acid (Sabate et al. 1991; Tunesi and Anderson 1991).

10.8.1 Photoreactors

Many photoreactors have been successfully studied for liquid-phase photocatalysis, but reactor design information for gas-phase photocatalytic processes is scarce. There are two major differences between gas-phase systems and aqueous systems that affect the performance of the reactor. First, the concentration of oxygen in a gas-phase reactor, which is 20% by volume, provides a sufficient supply of electron acceptors. Second, the concentration of water vapor present in gas-phase reactors can vary considerably, unlike aqueous photoreactors in which water molecules are always the predominant species in contact with the catalyst (Anderson et al. 1993).

Because of intense commercial interest in using photocatalysis to clean indoor air and industrial emissions, very little information is available in the open literature on gas-phase reactors.

Figure 10.15 shows an off-gas photocatalytic treatment system based on a commercial system (Miller and Fox 1993; Turchi et al. 1994). This system is

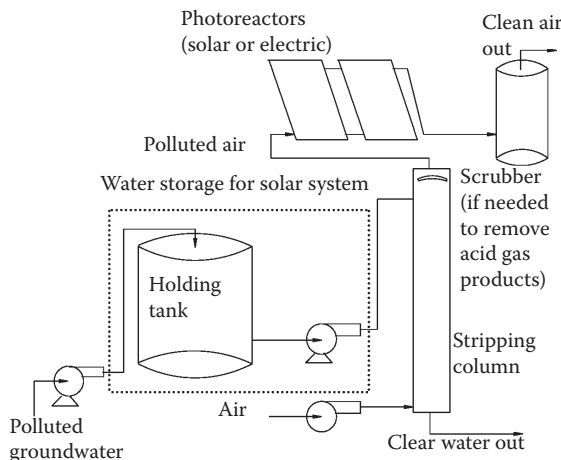


FIGURE 10.15

Schematic of an air stripper with photocatalytic off-gas treatment. (From Turchi, C.S. et al., Off-gas treatment by photocatalytic oxidation: Concepts and economics. *Proceedings of the First International Conference on Advanced Oxidation Technologies for Water and Air Remediation*, London, Ontario, Canada, Book of Abstracts, pp. 125–128, 1994.)

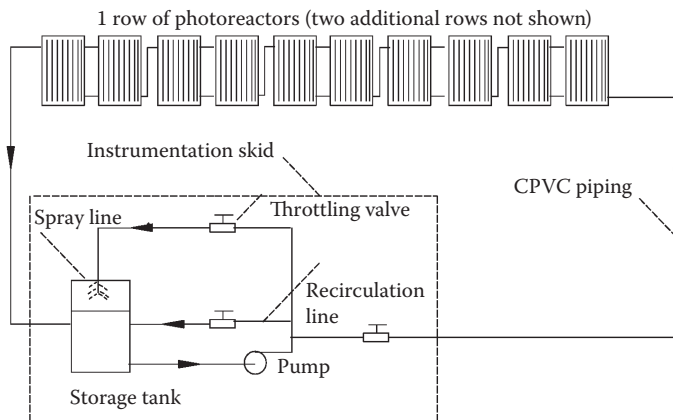
designed to transfer volatile contaminants from the groundwater to air in an air stripper tower. The contaminants transferred to air are then treated by solar radiation or UV lamps in photoreactors.

10.9 Commercial/Industrial Applications

Solar photocatalytic detoxification research to date has shown great potential for the application of this technology to treatment of groundwater and soils contaminated with toxic organic chemicals, as well as treatment of certain industrial wastewaters. Recent research also shows the potential of this technology for gas-phase detoxification and for disinfection of water and air. However, to date, there has been very little commercial/industrial use of this technology. Published literature shows only three engineering-scale applications for groundwater treatment in the United States and one industrial wastewater treatment in Spain. Field demonstrations of this technology for groundwater remediation took place at the Lawrence Livermore National Laboratory (LLNL) and TyAFB. Engineering-scale field experiments were conducted by NREL at LLNL to treat groundwater contaminated with TCE. The field system consisted of 158 m² of parabolic trough reactors, as described earlier, and used Degussa P25 TiO₂ particles as catalyst in a slurry flow configuration. With 0.1% TiO₂ concentration in the slurry, the TCE concentration was reduced from 200 ppb to less than 5 ppb. The field experiment is detailed in Blake (1994b).

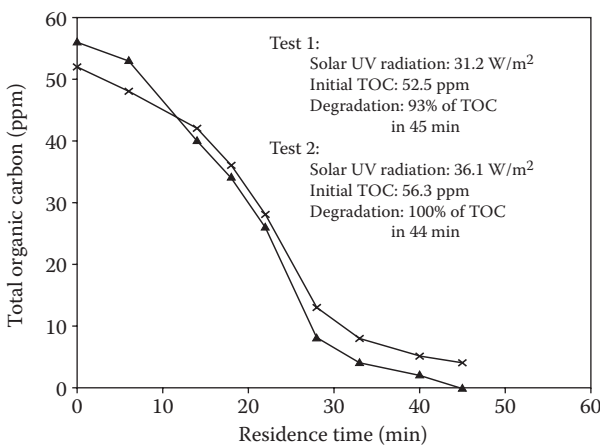
Engineering-scale demonstration of the nonconcentrating solar reactor technology was conducted at TyAFB in 1992 (Goswami et al. 1993). A "one-sun" solar detoxification facility was constructed to treat groundwater contaminated with fuel, oil, and lubricants leaking from the underground storage tanks. The contaminants of interest included BTEX, although there were other chemicals also present in the groundwater. The facility shown in Figure 10.16 consisted of three rows of five-each series connected 2.4 m × 3.1 m (nominal) photoreactors developed by the University of Florida and an equipment skid from NREL containing storage tanks and metering pumps for the addition of acid, base, H₂O₂, and TiO₂ to the contaminated water.

The field tests were successful in destroying the BTEX in the groundwater as seen from the results shown earlier in Figure 10.8. However, in a laboratory test using the same reactors in similar sunlight conditions and city water spiked with the same amounts of BTEX as in the groundwater, the reaction rates were an order of magnitude faster. These results suggest that a careful site treatability study and establishment of appropriate pretreatment methods are extremely important in the successful field deployment of solar photocatalytic processes.

**FIGURE 10.16**

Schematic diagram of solar groundwater treatment test facility at TyAFB.

Blanco and Malato (1994) have described an engineering-scale field demonstration of treatment of industrial wastewater from a resins factory containing organic contaminants such as phenols, fornol, phthalic acid, fumaric acid, maleic acid, glycols, xylene, toluene, methanol, butanol, and phenylethylene, amounting to 600 ppm TOC. They used 12 two-axis tracking parabolic troughs of total aperture area of 384 m², with borosilicate glass tube absorber reactors. One hundred milligrams per liter of TiO₂ was used as the catalyst and 0.007 molar concentration of sodium peroxydisulphate (Na₂S₂O₈) was used as an oxidizing additive. Figure 10.17

**FIGURE 10.17**

Treatment of industrial wastewater containing organic contaminants. (From Blanco, J., and S. Malato., Solar photocatalytic mineralization of real hazardous waste water at pre-industrial level. In *Solar Engineering 1994*, D.E. Klett, R.E. Hogan, and T. Tanaka, eds. pp. 103–109, 1994.)

shows 100% degradation of TOC in 44 min, amounting to 1.25 mg/L/min degradation rate of the mixed contaminants. On the basis of this rate, they estimated treatment costs of \$19.3/m³ of industrial wastewater treating 10 m³/day.

Other investigations of treatment of real industrial wastewater, although not to engineering scale, do show the potential of the solar treatment process where conventional treatment methods have been unsuccessful. Goswami and Anheden (1994) demonstrated the potential for solar photocatalytic oxidation for decolorization and COD reduction of wastewater from a 5-fluorouracil (a cancer drug) manufacturing plant. They showed that using 0.1% TiO₂ as the catalyst and 2400 ppm H₂O₂ as an oxidizing additive, the color of the wastewater is reduced by 80% in 1 h and the COD of the wastewater was reduced by 70% in 16 h. All of the conventional (nonsolar) treatments tried by the manufacturers for the reduction of color and COD failed (Anheden et al. 1995). Zaidi (1993) showed the potential of the solar photocatalytic technology to reduce color and COD of distillery wastewater pretreated by anaerobic microbiological methods. Figure 10.18 shows that both color and COD can be reduced successfully by the solar process where conventional methods have failed to work.

Both of the above studies report that the solar treatment works much better if the wastewater is first diluted with clean water to approximately 10%–20% of the initial concentration. Although this method increases the volume of water to be pumped, a continuous system can be designed by recirculating a fraction of the treated water for dilution.

In a laboratory study, Turchi et al. (1989) showed the potential of photocatalytic treatment of the wastewater from pulp and paper mills. Although no studies have been published on the potential use of the solar process for the cleanup of textile mill wastewater, preliminary studies indicate that the solar process can be very successful in treating textile plant wastewater, namely, dyehouse wastewater. Since many manufacturing plants, such as textiles, pulp and paper, and chemicals, are located in areas where a large part of the solar UV is diffuse and where large open areas with solar access are available, the shallow solar pond reactors may be used.

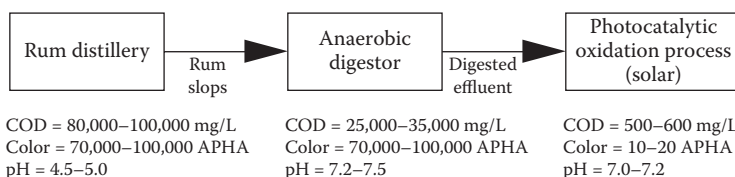


FIGURE 10.18

Treatment of distillery effluent by anaerobic digestion and post-treatment by solar photocatalytic oxidation process. (From Zaidi, A., Solar photocatalytic post-treatment of anaerobically digested distillery effluent. M.S. thesis, University of Florida, Gainesville, FL, 1993.)

10.10 Solar Disinfection of Water and Air

UV disinfection has been widely used in the past to destroy biological contaminants by using UV radiation from germicidal lamps primarily at 254 nm wavelength. Solar UV, which is primarily at 290–400 nm wavelength, is much less active as a germicide. However, a review of the literature has shown that photocatalytic disinfection has been demonstrated in Japan by Matsunaga (1985) and later by others (Ireland et al. 1993; Morioka et al. 1988; Nagame et al. 1989; Onoda et al. 1988). In a recent study, Block and Goswami (1995) have studied the antibacterial effect of solar photocatalytic reaction and the conditions that affect it. Their study showed that several common bacteria (*Serratia marcescens*, *Escherichia coli*, and *Streptococcus aureus*) were killed in just a few minutes on solar exposure in the presence of TiO_2 , whereas without TiO_2 , it took over an hour to destroy them (Figure 10.19). A concentration of 0.01% TiO_2 was most effective in killing bacteria and even 0.001% was quite effective. However, bactericidal activity went down at 0.1% and higher concentrations of TiO_2 .

Recently, some studies have appeared in the literature that report disinfection and deodorization of air (Goswami et al. 1995). Goswami et al. (1995) demonstrated the antibacterial effect of titanium dioxide in indoor air. They used a TiO_2 -coated fiberglass matrix reactor to kill *S. marcescens* bacteria in air. Recently, Dalrymple et al. (2010, 2011) conducted a detailed analysis of the disinfection mechanisms of photocatalytic oxidation and developed a model. Results indicated that the photocatalytic process can be a viable technique for controlling indoor air quality.

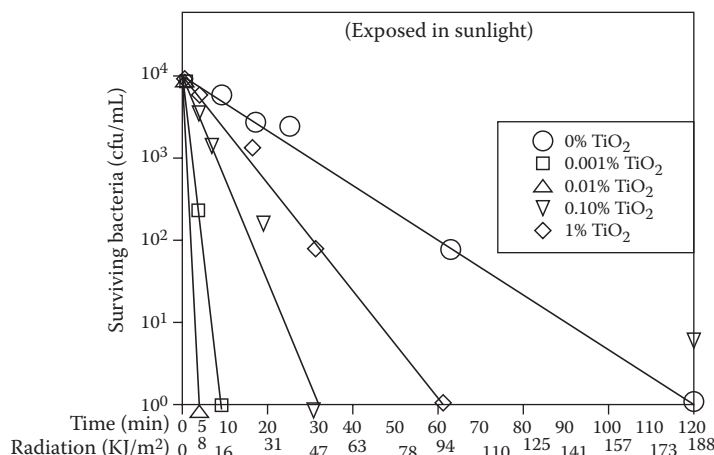


FIGURE 10.19

Effect of concentration of TiO_2 on survival of *Serratia marcescens* bacteria. (From Block, S.S., and D.Y. Goswami, Chemically enhanced sunlight for killing bacteria. *Solar Engineering, Proceedings of the ASME International Solar Energy Conference*, Hawaii, March, pp. 431–438, 1995.)

10.11 Summary

Solar photocatalytic detoxification and disinfection processes have shown great promise for the treatment of contaminated groundwater, industrial wastewater, air, and soil. Development of these processes has reached a point where the solar technology can be competitive with the conventional treatment methods. In some cases requiring decolorization and reduction of COD, the photocatalytic technology may be the only effective treatment technology. The next logical step is the commercial demonstration of the technology. Although only a few commercial demonstrations have been reported to date, it is expected and hoped that activity will pick up considerably in the future.

PROBLEMS

1.
 - i. A laboratory test with TiO_2 as the catalyst produced a concentration time plot of *o*-xylene destruction identical to that shown in Figure 10.8. The reactor used was of 40 gal while the storage tank contained 100 gal, with minimal volume in piping. Determine the reaction rate constant corrected for the finite volumes of the system.
 - ii. A single reactor is to be designed to decontaminate water with the same initial concentration of *o*-xylene as above to acceptable levels of 10 ppb. If the reaction rate is the same as found above, what is the required residence time for this process? What is the residence time for 99.9% destruction? 100% destruction?
 - iii. Each of 250 nonconcentrating channel-type reactors connected in series and parallel sets is composed of 140 channels 3 m long, 1 cm wide, and 3 cm deep. The system is designed to treat 1000 L of *o*-xylene-contaminated water per day. If the system operates for 7 h each day, what is average reaction rate constant? At what velocity does the solution flow? Use the residence time for destruction to acceptable levels of contaminant. Assume 90% destruction levels are achieved.
 - iv. A similar reactor tested with 35 W/m^2 insolation in a controlled indoor laboratory experiment yielded a reaction rate constant of 0.283 min^{-1} . What must be the insolation in the field trials based on these tests. A 0.01% TiO_2 catalyst solution is used? Can the field reactor site dictate which catalyst to use?
2. Discuss the effects of the following factors on the photocatalytic destruction of organic contaminants. How are the concentration–time histories of the contaminant affected?

- i. Illumination intensity
 - ii. Catalyst type
 - iii. Addition of inorganic and organic particles
 - iv. Dissolved oxygen concentration
 - v. pH of the solution
 - vi. Temperature
 - vii. Metallization of the catalyst
 - viii. Dye sensitization
-

References

- Anderson, M., S. Nishiida, and S. Cervera-March. 1993. Photodegradation of trichlorethylene in the gas phase using TiO₂ porous ceramic membrane. *Photocat. Purific. Water Air* 1: 405–420.
- Anheden, M., D.Y. Goswami, and G. Svedberg. 1995. Photocatalytic treatment of wastewater from 5-fluorouracil manufacturing. *Solar Engineering 1995, Proceedings of the 1995 ASME International Solar Energy Conference*.
- Bahnemann, D., D. Bockelmann, and R. Goslich. 1991. Mechanistic studies of water detoxification in illuminated TiO₂ suspensions. *Sol. Energy Mater.* 24: 564–583.
- Barbeni, M. et al. 1985. Photodegradation of pentachlorophenol catalyzed by semiconductor particles. *Chromosphere* 14(2): 195–208.
- Bard, A.J. 1979. Photoelectrochemistry and heterogeneous photocatalysis at semiconductors. *J. Photochem.* 10(1): 59–75.
- Bedford, J. et al. 1994. Performance of non-concentrating solar photocatalytic oxidation reactors, part II: Shallow pond configuration. *J. Sol. Energy Eng., ASME* 116(1): 8–13.
- Blake, D.M. 1994a. Bibliography of work on the photocatalytic removal of hazardous compounds from water and air. NREL Report #NREL/TP-430-6084. NTIS, Springfield, VA.
- Blake, D.M. 1994b. Solar processes for the destruction of hazardous chemicals, Chapter 10. In *Alternative Fuels and the Environment*, F.S. Sterrett, ed. Lewis Publishers, Boca Raton, FL.
- Blake, D.M. et al. 1991. Kinetic and mechanistic overview of TiO₂-photocatalyzed oxidation reactions in aqueous solution. *Sol. Energy Mater.* 24: 584–593.
- Blake, D.M., H.F. Link, and K. Eber. 1992. Solar photocatalytic detoxification of water. In *Advances in Solar Energy*, Vol. 7, K.W. Boer, ed. American Solar Energy Society, Boulder, CO, pp. 167–210.
- Blanco, J., and S. Malato. 1994. Solar photocatalytic mineralization of real hazardous waste water at pre-industrial level. In *Solar Engineering 1994*, D.E. Klett, R.E. Hogan, and T. Tanaka, eds. ASME, New York, pp. 103–109.
- Block, S.S., and D.Y. Goswami. 1995. Chemically enhanced sunlight for killing bacteria. *Solar Engineering, Proceedings of the ASME International Solar Energy Conference, Hawaii, March*, pp. 431–438.

- Carey, J.H., J. Lawrence, and H.M. Tosine. 1976. Photodechlorination of polychlorinated biphenyls in the presence of titanium dioxide in aqueous solution. *Bull. Environ. Contam. Toxicol.* 16(6): 697–701.
- Crittendon, J.C. et al. 1995. Destruction of organic compounds in water using fixed bed photocatalysts. *Solar Engineering 1995. Proceedings of the 1995 ASME International Solar Engineering Conference*, pp. 449–457.
- Dalrymple, O.K., E. Stefanakos, M.A. Trotz, and D.Y. Goswami. 2010. A review of the mechanisms and modeling of photocatalytic disinfection. *Appl. Catal. B: Environ.*, 98(1–2): 27–38.
- Dalrymple, O.K., W. Isaacs, E. Stefanakos, M.A. Trotz, and D.Y. Goswami. 2011. Lipid vesicles as model membranes in photocatalytic disinfection studies. *J. Photochem. Photobiol. A: Chemistry*, 221(1): 64–70.
- Dibble, L.A., and G.B. Raupp. 1990. Kinetics of the gas-solid heterogeneous photocatalytic oxidation of trichlorethylene by near UV illuminated titanium dioxide. *Catal. Lett.* 4: 345–354.
- Dieckmann, M.S., K.A. Gray, and R.G. Zepp. 1994. The sensitized photocatalysis of azo dyes in a solid system: A feasibility study. *Chemosphere* 28(4): 1021–1034.
- Elizardo, K. 1991. Fighting pollution with hydrogen peroxide. *Pollut. Eng.* 23: 106–109.
- Glatzmaier, G.C., and M.S. Bohn. 1993. Solar assisted combustion of 1,2 dichlorobenzene. *Proceedings of the AIChE/ASME National Heat Transfer Conference*, August.
- Glatzmaier, G.C., M.S. Mehos, and R.G. Nix. 1990a. Solar destruction of hazardous chemicals. *J. Environ. Sci. Health* A25(5): 571–581.
- Glatzmaier, G.C., M.S. Mehos, and R.G. Nix. 1990b. Solar destruction of hazardous chemicals. *Solar Engineering 1990, Proceedings of the ASME International Solar Energy Conference*, pp. 153–158.
- Goswami, D.Y. 1995. Engineering of solar photocatalytic detoxification and disinfection processes. *Adv. Solar Energy* 13: 208.
- Goswami, D.Y., and M. Anheden. 1994. Preliminary study of photocatalytic oxidation of wastewater from 5-fluorouracil manufacturing. Report #UFME/SEECL-9402. Solar Energy and Energy Conversion Laboratory, University of Florida, FL, February.
- Goswami, D.Y. et al. 1993. Solar photocatalytic treatment of groundwater at Tyndall AFB, field test results. *Solar 1993, Proceedings of the American Solar Energy Society Annual Conference*, pp. 235–239.
- Goswami, D.Y., D. Trivedi, and S.S. Block. 1995. Photocatalytic disinfection of indoor air. *Solar Engineering, Proceedings of the ASME International Solar Energy Conference*, Hawaii, March, pp. 421–430.
- Green, A.E.S. 1983. The penetration of ultraviolet radiation to the ground. *Phys. Plant* 58: 351.
- Heller, A. 1981. Conversion of sunlight into electrical power and photoassisted electrolysis of water in photoelectrochemical cells. *Acc. Chem. Res.* 14: 154–162.
- Heller, A., and J.R. Brock. 1991. Materials and methods for photocatalyzing oxidation of organic compounds in water. United States Patent 4,997,576, March 5.
- Heller, A. et al. 1992. Photoassisted oxidation of oil and organic spill on water. *Proceedings of the First International Conference on TiO₂ Photocatalytic Purification and Treatment of Water and Air*, London, Ontario, pp. 39–155.
- Ibusuki, T., and K. Takeuchi. 1986. Toluene oxidation on UV-irradiated titanium dioxide with and without O₂, NO₂ or H₂O at ambient temperature. *Atmos. Environ.* 20: 1711–1715.

- Ireland, J.S. et al. 1993. Inactivation of *Escherichia coli* by titanium dioxide photocatalytic oxidation. *Appl. Environ. Microbiol.* 59: 1668–1670.
- Kamat, P.V. 1993. Photochemistry on nonreactive and reactive (semiconductor) surfaces. *Chem. Rev.* 93: 267–300.
- Klausner, J.F. et al. 1994. On the accurate determination of reaction rate constants in batch-type solar photocatalytic oxidation facilities. *J. Sol. Energy Eng., ASME* 116(1): 19–24.
- Legrini, O., E. Oliveros, and A.M. Braun. 1993. Photochemical processes for water treatment. *Chem. Rev.* 93: 671–698.
- Linder, M. et al. 1995. Solar water detoxification: Novel TiO₂ powders as highly active photocatalysts. *Solar Engineering 1995. Proceedings of the ASME International Solar Engineering Conference*, pp. 399–408.
- Link, H., and C.S. Turchi. 1991. Cost and performance projections for solar water detoxification system. *Solar Engineering 1991. Proceedings of the ASME International Solar Energy Conference*, pp. 289–294.
- Magrini, K.A. et al. 1994. Improving catalyst performance for the solar based photocatalytic oxidation of organics. *Solar Engineering 1994. Proceedings of the 1994 ASME International Solar Engineering Conference*, pp. 163–170.
- Magrini, K.A., A. Watt, and B. Rinehart. 1995. Photocatalyst evaluation for solar based aqueous organic oxidation. *Solar Engineering 1995. Proceedings of the 1995 ASME International Solar Engineering Conference*, pp. 415–420.
- March, M., A. Martin, and C. Saltiel. 1995. Performance modelling of nonconcentrating solar detoxification systems. *Sol. Energy* 54(3): 143–151.
- Matsunaga, T. 1985. Sterilization with particulate photosemiconductor. *J. Antibact. Antifung. Agents* 13: 211–220.
- Mehos, M.S., and C.S. Turchi. 1993. Field testing solar photocatalytic detoxification on TCE-contaminated groundwater. *Environ. Prog.* 12: 194–199.
- Miller, R.A., and R. Fox. 1993. Treatment of organic contaminants in air by photocatalytic oxidation: A commercialization perspective. In *Photocatalytic Purification and Treatment of Water and Air*, D.F. Ollis, and H. El-Akabi, eds. Elsevier Publishers, pp. 573–578.
- Morioka, T. et al. 1988. Antibacterial action of powdered semiconductor on a Serotype g *Streptococcus mutans*. *Caries Res.* 22: 230–231.
- Nagame, S. et al. 1989. Antibacterial effect of the powdered semiconductor TiO₂ on the viability of oral microorganisms. *J. Dent. Res.* 68(Special Issue): 1696–1697.
- Nimlos, M. et al. 1993. Direct mass spectrometric studies of the destruction of hazardous wastes: Gas-phase photocatalytic oxidation of trichloroethylene over TiO₂. *Environ. Sci. Technol.* 27: 732–740.
- Nishida, S. et al. 1993. Photocatalytic degradation of trichlorethylene in the gas-phase using titanium dioxide pellets. *J. Photochem. Photobiol. A: Chem.* 70(1): 95–99.
- Oberg, V., D.Y. Goswami, and G. Svedberg. 1993. On photocatalytic detoxification of water containing volatile organic compounds. *Solar Engineering 1993. Proceedings of the ASME International Solar Engineering Conference*, pp. 147–153.
- Ollis, D.F. 1994. *Photoreactors for Purification and Decontamination of Air*. Department of Chemical Engineering, North Caroline State University, Raleigh, NC.
- Ollis, D.F., E. Pelizzetti, and N. Serpone. 1989a. Heterogeneous photocatalysis in the environment: Application to water purification. In *Photocatalysis Fundamentals and Applications*, N. Serpone, and E. Pelizzetti, eds. Wiley-Interscience, New York, pp. 603–637.

- Ollis, D.F., E. Pelizzetti, and N. Serpone. 1989b. Chapter 18. In *Photocatalysis Fundamentals and Applications*, N. Serpone, and E. Pelizzetti, eds. Wiley & Sons, New York.
- Onoda, K. et al. 1988. Photocatalytic bactericidal effect of powdered TiO₂ on *Streptococcus mutans*. *Denki Kagaku* 56(12): 1108–1109.
- Pacheco, J.E., and C.E. Tyner. 1990. Enhancement of processes for solar photocatalytic detoxification of water. *Solar Engineering 1990, Proceedings of the ASME Solar Energy Conference*, pp. 163–166.
- Prairie, M.R., J.E. Pacheco, and L.R. Evans. 1992. Solar detoxification of water containing chlorinated solvents and heavy metals via TiO₂ photocatalysis. *Solar Engineering 1992, Proceedings of the ASME International Solar Energy Conference*, Vol. 1, pp. 1–8.
- Rabl, A. 1981. Yearly average performance of the principal solar collector types. *Sol. Energy* 27: 215.
- Raiissi, A., and N. Muradov. 1993. Flow reactor studies of TiO₂ photocatalytic treatment of airborne nitroglycerin. *Photocat. Purific. Treat. Water Air* 1: 435–454.
- Riordan, C.J., R.L. Hustrom, and D.R. Myers. 1990. Influences of atmospheric conditions and air mass on the ratio of ultraviolet to total solar radiation. SERI Report SERI/TP-215-3895. NREL, Golden, Co.
- Sabate, J. et al. 1991. A kinetic study of the photocatalytic degradation of 3-chlorosalicylic acid over TiO₂ membranes supported on glass. *J. Catal.* 127: 167–177.
- Saltiel, C., A. Martin, and D.Y. Goswami. 1992. Performance analysis of solar water detoxification systems by detailed simulation. *ASME International Solar Energy Conference*, Maui, Hawaii.
- Sherif, S.A., F. Barbir, and T.N. Veziroglu. 1999. Hydrogen energy system. In *Wiley Encyclopedia of Electrical and Electronics Engineering*, J.G. Webster, ed. John Wiley & Sons, Inc., New York.
- Sherif, S.A., D.Y. Goswami, E.K. Stefanakos, and A. Steinfeld. 2014. *Handbook of Hydrogen Energy*. CRC Press, Boca Raton, FL.
- Skocypec, R.D., and R.E. Hogan. 1990. Investigation of a direct catalytic absorption reactor for hazardous waste destruction. *Solar Engineering 1990, Proceedings of the ASME International Solar Energy Conference*, pp. 167–173.
- Tunesi, S., and M. Anderson. 1991. Influence of chemisorption on the photodecomposition of salicylic acid and related compounds using suspended TiO₂ ceramic membranes. *J. Phys. Chem.* 95: 3399–3405.
- Turchi, C.S., L. Edmundson, and D.F. Ollis. 1989. Application of heterogeneous photocatalysis for the destruction of organic contaminants from a paper mill alkali extraction process. Presented at *TAPPI 5th International Symposium on Wood and Pulping Chemistry*, Raleigh, NC.
- Turchi, C.S., E.J. Wolfrum, and R.A. Miller. 1994. Off-gas treatment by photocatalytic oxidation: Concepts and economics. *Proceedings of the First International Conference on Advanced Oxidation Technologies for Water and Air Remediation*, London, Ontario, Canada, Book of Abstracts, pp. 125–128.
- Tyner, C.E. et al. 1989. Rapid destruction of organic chemicals in groundwater using sunlight. Paper presented at the *Hazardous Materials Management Conference/HASMAT CENTRAL*.
- Venkatadri, R., and R.W. Peters. 1993. Chemical oxidation technologies: Ultraviolet light/hydrogen peroxide, Fenton's reagent and titanium dioxide-assisted photocatalysis. *Hazard. Waste Hazard. Mater.* 10: 107–149.

- Wolfrum, E.J., and C.S. Turchi. 1992. Comments on "Reactor dynamics in the evaluation of photocatalytic oxidation kinetics." *J. Catal.* 136: 626–628.
- Wyness, P. et al. 1994. Performance of non-concentrating solar photocatalytic oxidation reactors. Part I: Flat plate configuration. *J. Sol. Energy Eng., ASME* 116(1): 2–7.
- Zaidi, A. 1993. Solar photocatalytic post-treatment of anaerobically digested distillery effluent. M.S. thesis, University of Florida, Gainesville, FL.

Appendix 1: International System of Units, Fundamental Constants, and Conversion Factors

The International System of Units (SI) is based on seven base units. Other derived units can be related to these base units through governing equations. The base units with the recommended symbols are listed in Table A1.1. Derived units of interest in solar engineering are given in Table A1.2.

Standard prefixes can be used in the SI system to designate multiples of the basic units and thereby conserve space. The standard prefixes are listed in Table A1.3.

Table A1.4 lists some physical constants that are frequently used in solar engineering, together with their values in the SI system of units.

Conversion factors between the SI and English systems for commonly used quantities are given in Table A1.5.

TABLE A1.1

The Seven SI Base Units

Quantity	Name of Unit	Symbol
Length	Meter	m
Mass	Kilogram	kg
Time	Second	s
Electric current	Ampere	A
Thermodynamic temperature	Kelvin	K
Luminous intensity	Candela	cd
Amount of a substance	Mole	mol

TABLE A1.2

SI Derived Units

Quantity	Name of Unit	Symbol
Acceleration	Meters per second squared	m/s^2
Area	Square meters	m^2
Density	Kilogram per cubic meter	kg/m^3
Dynamic viscosity	Newton-second per square meter	$\text{N}\cdot\text{s}/\text{m}^2$
Force	Newton (= $1 \text{ kg}\cdot\text{m}/\text{s}^2$)	N
Frequency	Hertz	Hz
Kinematic viscosity	Square meter per second	m^2/s
Plane angle	Radian	rad
Potential difference	Volt	V

(Continued)

TABLE A1.2 (CONTINUED)

SI Derived Units

Quantity	Name of Unit	Symbol
Power	Watt (= 1 J/s)	W
Pressure	Pascal (= 1 N/m ²)	Pa
Radiant intensity	Watts per steradian	W/sr
Solid angle	Steradian	sr
Specific heat	Joules per kilogram-Kelvin	J/kg·K
Thermal conductivity	Watts per meter-Kelvin	W/m·K
Velocity	Meters per second	m/s
Volume	Cubic meter	m ³
Work, energy, heat	Joule (= 1 N·m)	J

TABLE A1.3

English Prefixes

Multiplier	Symbol	Prefix	Multiplier	Symbol
10 ¹²	T	Tera	10 ³	M (thousand)
10 ⁹	G	Giga	10 ⁶	MM (million)
10 ⁶	m	Mega		
10 ³	k	Kilo		
10 ²	h	Hecto		
10 ¹	da	Deka		
10 ⁻¹	d	Deci		
10 ⁻²	c	Centi		
10 ⁻³	m	Milli		
10 ⁻⁶	μ	Micro		
10 ⁻⁹	n	Nano		
10 ⁻¹²	p	Pico		
10 ⁻¹⁵	f	Femto		
10 ⁻¹⁸	a	Atto		

TABLE A1.4

Physical Constants in SI Units

Quantity	Symbol	Value
Avogadro constant	N	6.022169 × 10 ²⁶ kmol ⁻¹
Boltzmann constant	k	1.380622 × 10 ⁻²³ J/K
First radiation constant	C ₁ = 2πhc ²	3.741844 × 10 ⁻¹⁶ W·m ²
Gas constant	R	8.31434 × 10 ³ J/kmol·K
Planck constant	h	6.626196 × 10 ⁻³⁴ J·s
Second radiation constant	C ₂ = hc/k	1.438833 × 10 ⁻² m·K
Speed of light in a vacuum	c	2.997925 × 10 ⁸ m/s
Stefan–Boltzmann constant	σ	5.66961 × 10 ⁻⁸ W/m ² ·K ⁴

TABLE A1.5

Conversion Factors

Physical Quantity	Symbol	Conversion Factor
Area	A	1 ft ² = 0.0929 m ² 1 acre = 43,560 ft ² = 4047 m ² 1 hectare = 10,000 m ² 1 square mile = 640 acres
Density	ρ	1 lb _m /ft ³ = 16.018 kg/m ³
Heat, energy, or work	Q or W	1 Btu = 1055.1 J 1 kWh = 3.6 MJ 1 Therm = 105.506 MJ 1 cal = 4.186 J 1 ft·lb _f = 1.3558 J
Force	F	1 lb _f = 4.448 N
Heat flow rate, refrigeration	q	1 Btu/h = 0.2931 W 1 ton (refrigeration) = 3.517 kW 1 Btu/s = 1055.1 W
Heat flux	q/A	1 Btu/h·ft ² = 3.1525 W/m ²
Heat-transfer coefficient	h	1 Btu/h·ft ² ·F = 5.678 W/m ² ·K
Length	L	1 ft = 0.3048 m 1 in = 2.54 cm 1 mi = 1.6093 km
Mass	m	1 lb _m = 0.4536 kg 1 ton = 2240 lb _m 1 tonne (metric) = 1000 kg
Mass flow rate	\dot{m}	1 lb _m /h = 0.000126 kg/s
Power	\dot{W}	1 hp = 745.7 W 1 kW = 3415 Btu/h 1 ft·lb _f /s = 1.3558 W 1 Btu/h = 0.293 W
Pressure	p	1 lb _f /in ² (psi) = 6894.8 Pa (N/m ²) 1 in. Hg = 3386 Pa
Radiation	I	1 atm = 101,325 Pa (N/m ²) = 14.696 psi 1 langley = 41,860 J/m ² 1 langley/min = 697.4 W/m ²
Specific heat capacity	c	1 Btu/lb _m ·°F = 4187 J/kg·K
Internal energy or enthalpy	e or h	1 Btu/lb _m = 2326.0 J/kg 1 cal/g = 4184 J/kg
Temperature	T	T(°R) = (9/5)T(K) T(°F) = [T(°C)](9/5) + 32 T(°F) = [T(K) - 273.15](9/5) + 32
Thermal conductivity	k	1 Btu/h·ft·°F = 1.731 W/m·K
Thermal resistance	R_{th}	1 h·°F/Btu = 1.8958 K/W

(Continued)

TABLE A1.5 (CONTINUED)

Conversion Factors

Physical Quantity	Symbol	Conversion Factor
Velocity	V	$1 \text{ ft/s} = 0.3048 \text{ m/s}$ $1 \text{ mi/h} = 0.44703 \text{ m/s}$
Viscosity, dynamic	μ	$1 \text{ lb}_m/\text{ft}\cdot\text{s} = 1.488 \text{ N}\cdot\text{s}/\text{m}^2$ $1 \text{ cP} = 0.00100 \text{ N}\cdot\text{s}/\text{m}^2$
Viscosity, kinematic	ν	$1 \text{ ft}^2/\text{s} = 0.09029 \text{ m}^2/\text{s}$ $1 \text{ ft}^2/\text{h} = 2.581 \times 10^{-5} \text{ m}^2/\text{s}$
Volume	V	$1 \text{ ft}^3 = 0.02832 \text{ m}^3 = 28.32 \text{ liters}$ $1 \text{ barrel} = 42 \text{ gal (U.S.)}$ $1 \text{ gal (U.S. liq.)} = 3.785 \text{ liters}$ $1 \text{ gal (U.K.)} = 4.546 \text{ liters}$
Volumetric flow rate	\dot{Q}	$1 \text{ ft}^3/\text{min (cfm)} = 0.000472 \text{ m}^3/\text{s}$ $1 \text{ gal/min (GPM)} = 0.0631 \text{ l/s}$

Appendix 2: Solar Radiation Data

DESCRIPTION OF METHOD*

To find the solar altitude and azimuth:

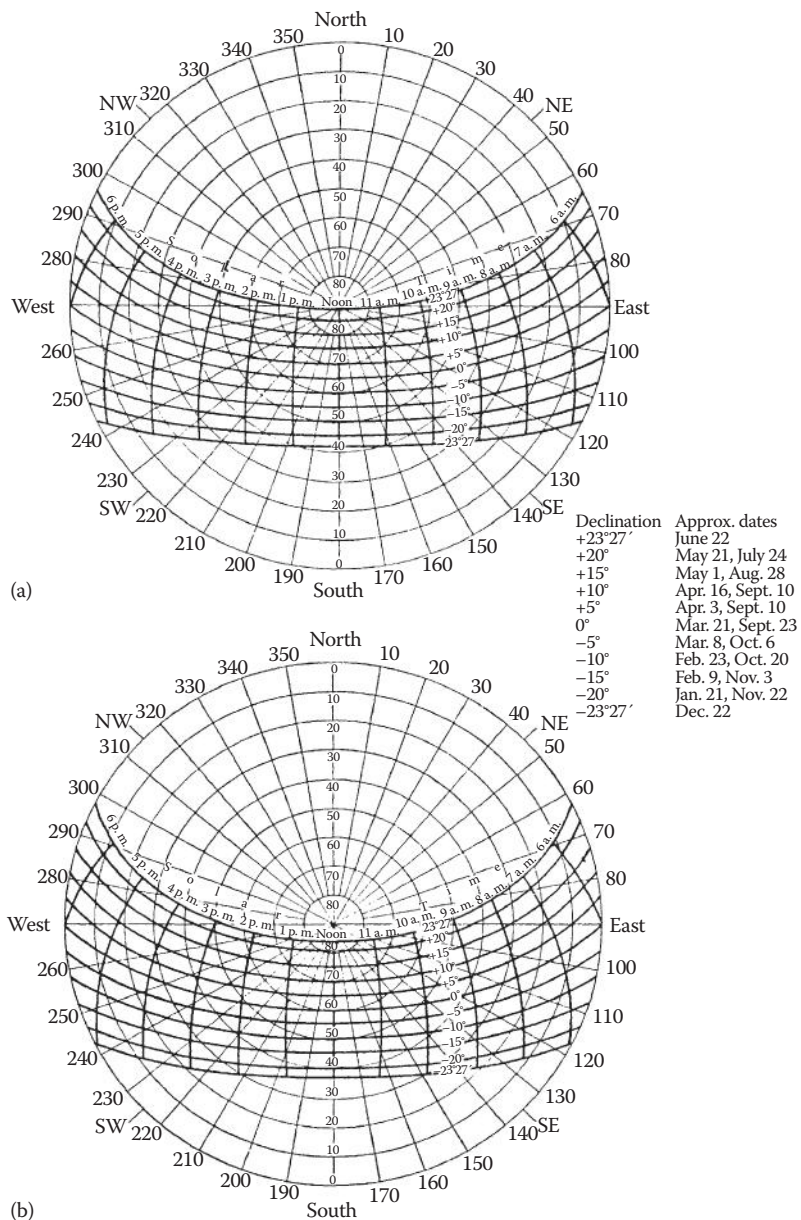
1. Select the chart or charts in Figure A2.1 that are appropriate to the latitude.
2. Find the solar declination δ corresponding to the date.
3. Determine the *true solar time* as follows:
 - a. To the *local standard time* (zone time), add 4' for each degree of longitude the station is east of the standard meridian or subtract 4' for each degree west of the standard meridian to get the *local mean solar time*.
 - b. To the *local mean solar time*, add algebraically the equation of time; the sum is the required *true solar time*.
4. Read the required altitude and azimuth at the point determined by the declination and the true solar time. Interpolate linearly between two charts for intermediate latitudes.

It should be emphasized that the solar altitude determined from these charts is the true geometric position of the center of the sun. At low solar elevations, terrestrial refraction may considerably alter the apparent position of the sun. Under average atmospheric refraction, the sun will appear on the horizon when it actually is approximately 34' below the horizon; the effect of refraction decreases rapidly with increasing solar elevation. Since sunset or sunrise is defined as the time when the upper limb of the sun appears on the horizon, and the semidiameter of the sun is 16', sunset or sunrise occurs under average atmospheric refraction when the sun is 50' below the horizon. In polar regions especially, unusual atmospheric refraction can make considerable variation in the time of sunset or sunrise.

The 90°N chart is included for interpolation purposes; the azimuths lose their directional significance at the pole.

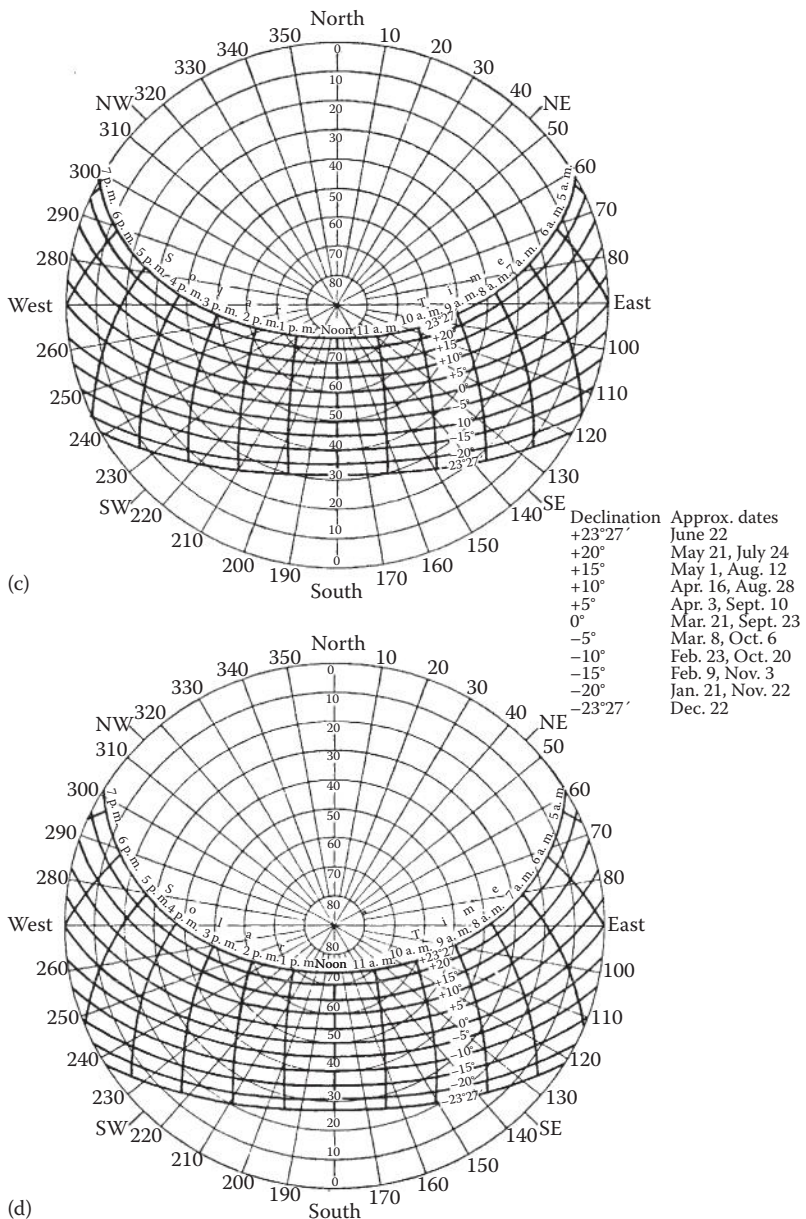
Altitude and azimuth in southern latitudes. To compute solar altitude and azimuth for southern latitudes, change the sign of the solar declination and proceed as above. The resulting azimuths will indicate angular distance from *south* (measured eastward) rather than from north.

* Description and charts in Figure A2.1 from *Smithsonian Meteorological Tables*, Smithsonian Institution, Washington, D.C.

**FIGURE A2.1**

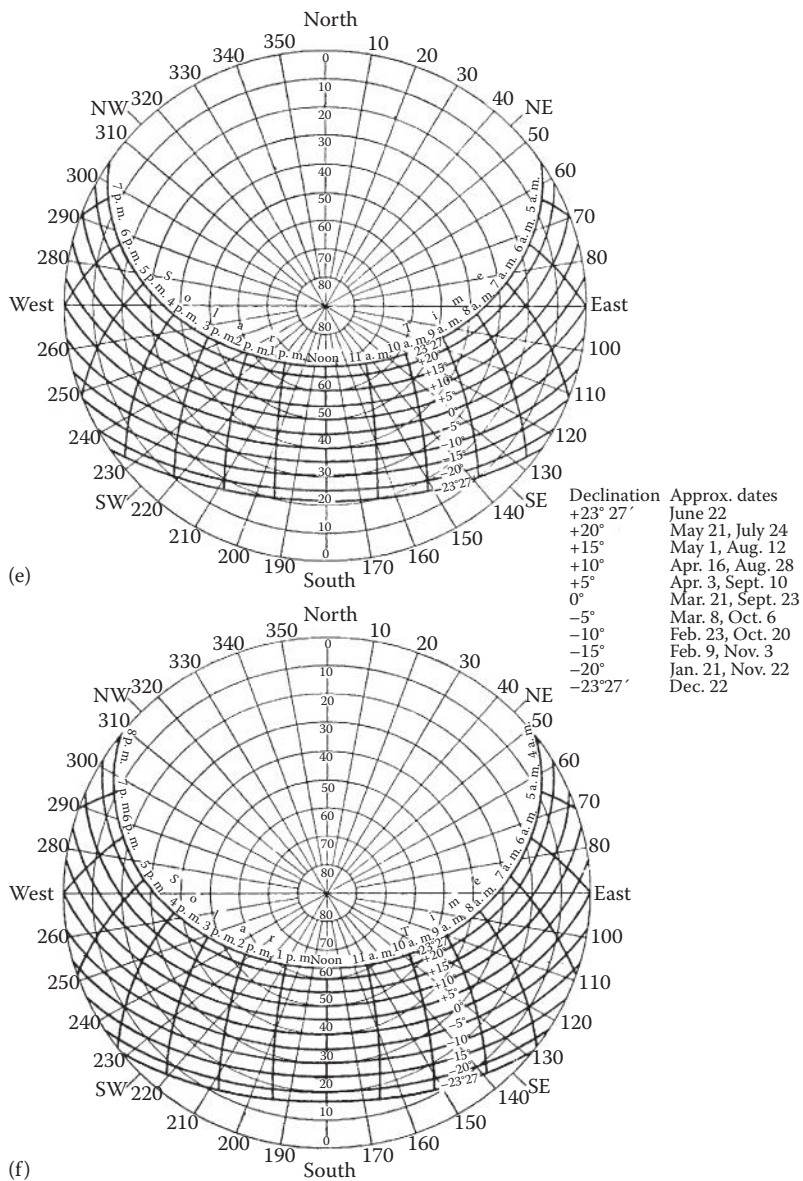
Meteorological charts for computing solar altitude and azimuth angles. (a) 25°N latitude; (b) 30°N latitude.

(Continued)

**FIGURE A2.1 (CONTINUED)**

Meteorological charts for computing solar altitude and azimuth angles. (c) 35°N latitude; (d) 40°N latitude.

(Continued)

**FIGURE A2.1 (CONTINUED)**

Description of method for calculating true solar time, together with accompanying meteorological charts, for computing solar altitude and azimuth angles. (e) 45°N latitude; (f) 50°N latitude.

TABLE A2.1
Monthly Averaged, Daily Extraterrestrial Insolation on a Horizontal Surface (Wh/m²)

Latitude (°)	Jan	Feb	Mar	Apr	May	Jun	Jul	Aug	Sep	Oct	Nov	Dec
-65	11,248	8502	5126	2199	570	96	286	1438	3903	7284	10,486	12,135
-60	11,398	9006	5897	3023	1237	596	871	2214	4713	7891	10,737	12,133
-55	11,589	9485	6628	3844	1986	1257	1575	3015	5490	8461	11,005	12,215
-50	11,765	9918	7310	4651	2774	1997	2337	3819	6227	8982	11,248	12,299
-45	11,901	10,295	7939	5431	3578	2779	3128	4611	6919	9445	11,445	12,350
-40	11,980	10,607	8508	6177	4380	3580	3929	5382	7559	9844	11,583	12,352
-35	11,995	10,848	9014	6881	5170	4385	4725	6121	8142	10,174	11,654	12,292
-30	11,940	11,016	9452	7538	5937	5182	5505	6823	8664	10,431	11,655	12,164
-25	11,811	11,107	9819	8141	6672	5959	6261	7479	9121	10,613	11,582	11,967
-20	11,608	11,120	10,111	8685	7368	6709	6984	8084	9509	10,718	11,433	11,697
-15	11,331	11,054	10,327	9166	8019	7423	7667	8634	9824	10,745	11,208	11,354
-10	10,980	10,909	10,465	9580	8618	8095	8304	9122	10,066	10,693	10,909	10,941
-5	10,556	10,686	10,524	9924	9161	8720	8888	9546	10,231	10,562	10,536	10,459
0	10,064	10,386	10,504	10,195	9642	9290	9416	9901	10,319	10,354	10,092	9911
5	9507	10,012	10,403	10,390	10,059	9803	9883	10,186	10,329	10,069	9581	9302
10	8888	9566	10,225	10,509	10,408	10,255	10,286	10,398	10,260	9711	9007	8635
15	8214	9053	9968	10,550	10,687	10,642	10,621	10,535	10,114	9281	8373	7918
20	7490	8475	9637	10,0514	10,895	10,962	10,888	10,597	9891	8784	7687	7155
25	6722	7839	9232	10,400	11,030	11,214	11,085	10,583	9594	8223	6953	6355
30	5919	7149	8758	10,211	11,092	11,399	11,213	10,495	9224	7603	6179	5525
35	5088	6412	8218	9948	11,084	11,518	11,272	10,334	8784	6929	5372	4675
40	4240	5635	7617	9614	11,008	11,573	11,266	10,103	8278	6208	4542	3816
45	3386	4826	6958	9211	10,869	11,572	11,199	9805	7710	5445	3700	2961
50	2541	3994	6248	8746	10,673	11,523	11,081	9445	7084	4649	2858	2127
55	1725	3150	5491	8224	10,432	11,443	10,925	9032	6406	3827	2033	1338
60	969	2309	4696	7653	10,166	11,365	10,756	8575	5682	2992	1251	633
65	334	1493	3869	7045	9915	11,366	10,631	8095	4917	2158	560	101

TABLE A2.2a
Worldwide Values of τ_b and τ_d for Solar Radiation Modeling

Position	Lat	Long	Jan	Feb	Mar	Apr	May	Jun	Jul	Aug	Sep	Oct	Nov	Dec	
<i>Argentina</i>															
Buenos Aires	34.57°S	58.42°W	τ_b	0.387	0.378	0.367	0.349	0.339	0.338	0.332	0.381	0.391	0.362	0.389	
			τ_d	2.329	2.377	2.438	2.474	2.455	2.412	2.448	2.196	2.176	2.369	2.298	
<i>Australia</i>															
Adelaide	34.95°S	138.53°E	τ_b	0.345	0.336	0.324	0.317	0.309	0.305	0.307	0.316	0.332	0.334	0.333	0.343
			τ_d	2.529	2.602	2.683	2.665	2.718	2.701	2.653	2.590	2.513	2.536	2.567	2.536
Brisbane	27.38°S	153.13°E	τ_b	0.391	0.380	0.368	0.352	0.339	0.324	0.322	0.330	0.355	0.379	0.384	0.383
			τ_d	2.435	2.515	2.542	2.589	2.644	2.658	2.670	2.608	2.486	2.387	2.398	2.446
Canberra	35.30°S	149.20°E	τ_b	0.363	0.340	0.326	0.313	0.299	0.291	0.292	0.297	0.315	0.318	0.334	0.342
			τ_d	2.403	2.559	2.606	2.638	2.730	2.747	2.702	2.678	2.582	2.609	2.520	2.519
Darwin	12.42°S	130.88°E	τ_b	0.410	0.411	0.401	0.368	0.369	0.364	0.359	0.375	0.418	0.451	0.458	0.434
			τ_d	2.446	2.445	2.491	2.717	2.610	2.581	2.607	2.492	2.294	2.171	2.149	2.291
Hobart	42.83°S	147.50°E	τ_b	0.361	0.359	0.340	0.334	0.322	0.319	0.323	0.325	0.340	0.339	0.345	0.353
			τ_d	2.415	2.445	2.533	2.515	2.554	2.504	2.484	2.511	2.443	2.491	2.461	2.440
Laverton	37.87°S	144.75°E	τ_b	0.374	0.353	0.339	0.327	0.311	0.312	0.309	0.316	0.333	0.336	0.342	0.364
			τ_d	2.360	2.499	2.555	2.573	2.698	2.611	2.630	2.589	2.510	2.514	2.497	2.390
Sydney	33.93°S	151.18°E	τ_b	0.401	0.388	0.359	0.340	0.323	0.316	0.314	0.322	0.346	0.351	0.374	0.386
			τ_d	2.301	2.368	2.516	2.577	2.671	2.635	2.627	2.572	2.475	2.479	2.373	2.355
<i>Austria</i>															
Wien	48.20°N	16.37°E	τ_b	0.326	0.363	0.435	0.473	0.469	0.491	0.509	0.479	0.418	0.398	0.351	0.331
			τ_d	2.280	2.072	1.876	1.810	1.876	1.861	1.827	1.919	2.089	2.084	2.236	2.291
Innsbruck	47.27°N	11.35°E	τ_b	0.306	0.367	0.423	0.427	0.454	0.456	0.461	0.443	0.413	0.366	0.345	0.319
			τ_d	2.268	1.923	1.799	1.836	1.867	1.950	1.973	2.043	2.078	2.178	2.131	2.226

(Continued)

TABLE A2.2a (CONTINUED)
 Worldwide Values of τ_b and τ_d for Solar Radiation Modeling

Position	Lat	Long	Jan	Feb	Mar	Apr	May	Jun	Jul	Aug	Sep	Oct	Nov	Dec
<i>Chile</i>														
Antofagasta	23.43°S	70.45°W	τ_b	0.390	0.399	0.372	0.326	0.315	0.312	0.318	0.320	0.326	0.331	0.359
La Serena	29.92°S	71.20°W	τ_d	2.269	2.239	2.376	2.633	2.653	2.593	2.595	2.614	2.567	2.545	2.399
China	39.93°N	116.28°E	τ_b	0.362	0.415	0.498	0.733	0.771	0.747	0.697	0.623	0.546	0.415	0.358
Beijing	39.93°N	113.33°E	τ_d	2.020	1.864	1.691	1.336	1.336	1.273	1.448	1.510	1.571	1.640	1.931
Guangzhou	23.17°N	113.33°E	τ_b	0.714	0.719	0.841	0.903	0.779	0.824	0.839	0.850	0.828	0.821	0.687
Harbin	45.75°N	126.77°E	τ_b	0.254	0.285	0.361	0.401	0.461	0.545	0.499	0.440	0.423	0.401	0.326
Kunming	25.02°N	102.68°E	τ_b	0.334	0.344	0.448	0.435	0.445	0.495	0.544	0.562	0.515	0.426	0.356
Lanzhou	36.05°N	103.88°N	τ_b	0.352	0.406	0.497	0.595	0.636	0.669	0.666	0.654	0.578	0.507	0.398
Shanghai	31.40°N	121.47°E	τ_b	0.741	0.818	0.931	0.961	0.996	1.006	0.882	0.784	0.758	0.807	0.797
Colombia	10.88°N	74.78°W	τ_b	0.416	0.470	0.581	0.576	0.506	0.488	0.486	0.475	0.472	0.455	0.439
Barranquilla	4.70°N	74.13°W	τ_d	2.291	2.071	1.748	1.776	1.991	2.055	2.064	2.118	2.136	2.195	2.237
Bogota	0.329	0.374	0.412	0.383	0.339	0.339	0.332	0.338	0.363	0.362	0.354	0.340	0.331	0.263

(Continued)

TABLE A2.2a (CONTINUED)
 Worldwide Values of τ_b and τ_d for Solar Radiation Modeling

Position	Lat	Long	Jan	Feb	Mar	Apr	May	Jun	Jul	Aug	Sep	Oct	Nov	Dec
<i>France</i>														
Agen	44.18°N	0.6°E	τ_b	0.313	0.342	0.383	0.402	0.434	0.469	0.457	0.447	0.393	0.369	0.336
Nice	43.65°N	7.20°E	τ_d	2.476	2.279	2.113	2.051	1.996	1.922	2.001	2.036	2.219	2.261	2.351
Paris	48.82°N	2.33°E	τ_b	0.343	0.387	0.421	0.447	0.469	0.495	0.476	0.479	0.438	0.427	0.376
			τ_d	2.181	2.100	2.003	1.950	1.948	1.903	1.999	1.985	2.093	2.048	2.324
<i>Germany</i>														
Bremen	53.05°N	8.80°E	τ_b	0.343	0.374	0.417	0.430	0.432	0.449	0.487	0.450	0.412	0.370	0.349
Hamburg	53.63°N	10.00°E	τ_d	2.229	2.088	1.957	1.948	1.987	1.967	1.869	1.991	2.094	2.217	2.165
Stuttgart	48.83°N	9.20°E	τ_b	0.355	0.361	0.406	0.431	0.420	0.428	0.479	0.451	0.408	0.366	0.356
Nuremberg	49.50°N	11.08°E	τ_d	2.280	2.141	1.989	1.940	2.030	2.043	1.892	1.983	2.105	2.229	2.218
			τ_b	0.322	0.373	0.413	0.408	0.428	0.442	0.449	0.433	0.398	0.369	0.337
			τ_d	2.309	2.040	1.961	2.025	2.004	1.998	2.004	2.061	2.145	2.203	2.289
<i>Great Britain</i>														
Belfast	54.65°N	6.22°W	τ_b	0.311	0.331	0.397	0.389	0.406	0.403	0.424	0.400	0.364	0.353	0.327
Jersey	49.22°N	2.20°W	τ_d	2.451	2.330	2.029	2.108	2.072	2.129	2.076	2.168	2.297	2.277	2.356
London	51.52°N	0.12°W	τ_b	0.342	0.365	0.403	0.407	0.427	0.423	0.428	0.416	0.387	0.383	0.346
			τ_d	0.334	0.345	0.412	0.409	0.437	0.452	0.471	0.443	0.397	0.373	0.348
			τ_b	2.270	2.239	1.974	2.009	1.951	1.942	1.912	2.001	2.142	2.171	2.222

(Continued)

TABLE A2.2a (CONTINUED)
Worldwide Values of τ_b and τ_d for Solar Radiation Modeling

Position	Lat	Long	Jan	Feb	Mar	Apr	May	Jun	Jul	Aug	Sep	Oct	Nov	Dec	
Nagpur	21.10°N	79.05°E	τ_b	0.491	0.490	0.533	0.549	0.610	0.710	0.771	0.650	0.572	0.498	0.480	
New Delhi	28.58°N	77.20°E	τ_d	1.841	1.854	1.765	1.754	1.652	1.506	1.419	1.607	1.766	1.920	1.913	1.948
<i>Iran</i>			τ_b	0.552	0.576	0.598	0.714	0.940	1.021	1.066	0.906	0.711	0.878	0.783	0.568
Abadan	30.37°N	48.25°E	τ_d	1.650	1.596	1.579	1.413	1.208	1.179	1.167	1.282	1.483	1.244	1.244	1.616
Anzali	37.47°N	49.47°E	τ_b	0.380	0.422	0.495	0.557	0.598	0.566	0.580	0.573	0.526	0.458	0.402	0.380
Esfahan	32.47°N	51.67°E	τ_d	0.331	0.350	0.424	0.633	0.741	0.725	0.771	0.683	0.600	0.446	0.381	0.337
Mashhad	36.27°N	59.63°E	τ_b	0.354	0.443	0.613	0.709	0.735	0.744	0.745	0.672	0.581	0.532	0.458	0.365
Shiraz	29.53°N	52.53°E	τ_d	0.330	0.395	0.449	0.596	0.653	0.658	0.731	0.771	0.661	0.483	0.433	0.385
Tabriz	38.08°N	46.28°E	τ_b	0.334	0.410	0.481	0.578	0.568	0.578	0.650	0.602	0.536	0.479	0.404	0.357
Tehran	35.68°N	51.32°E	τ_d	0.335	0.359	0.661	0.731	0.686	0.698	0.752	0.672	0.583	0.593	0.393	0.340
<i>Ireland</i>			τ_b	0.316	0.326	0.389	0.379	0.404	0.395	0.431	0.396	0.367	0.350	0.327	0.328
Dublin	53.43°N	6.25°W	τ_d	2.407	2.382	2.074	2.157	2.082	2.176	2.057	2.208	2.294	2.293	2.360	2.326

<i>Israel</i>	Tel Aviv	32.10°N	34.78°E	τ_b	0.404	0.451	0.547	0.650	0.696	0.455	0.496	0.507	0.477	0.475	0.447	0.445
<i>Italy</i>	Milan	45.43°N	9.28°E	τ_d	2.010	1.864	1.632	1.459	1.416	1.981	1.870	1.836	1.915	1.874	1.912	1.868
<i>Japan</i>	Rome	41.78°N	12.58°E	τ_b	0.340	0.395	0.499	0.561	0.579	0.578	0.515	0.495	0.504	0.495	0.392	0.338
	Fukuoka	33.58°N	130.38°E	τ_d	2.248	1.977	1.693	1.588	1.596	1.640	1.818	1.876	1.799	1.759	2.036	2.261
	Tokyo	35.68°N	139.77°E	τ_b	0.340	0.376	0.415	0.428	0.448	0.477	0.470	0.475	0.434	0.404	0.381	0.353
	Yonago	35.43°N	133.33°E	τ_d	2.292	2.113	1.989	1.992	1.980	1.924	1.975	1.963	2.070	2.122	2.127	2.226
<i>Kenya</i>	Mombasa	4.03°S	39.62°E	τ_b	0.423	0.422	0.421	0.388	0.405	0.424	0.433	0.419	0.422	0.411	0.399	0.407
	Nairobi	1.32°S	36.92°E	τ_d	2.294	2.283	2.326	2.564	2.430	2.263	2.221	2.296	2.297	2.360	2.443	2.399
<i>Lithuania</i>	Kaunas	54.88°N	23.88°E	τ_b	0.283	0.312	0.353	0.383	0.362	0.355	0.389	0.383	0.365	0.324	0.296	0.285
<i>Madagascar</i>	Antananarivo	18.80°S	47.48°E	τ_d	2.436	2.195	2.054	2.034	2.191	2.306	2.151	2.164	2.191	2.315	2.392	2.440

(Continued)

TABLE A2.2a (CONTINUED)
Worldwide Values of τ_b and τ_d for Solar Radiation Modeling

Position	Lat	Long	Jan	Feb	Mar	Apr	May	Jun	Jul	Aug	Sep	Oct	Nov	Dec
<i>Malaysia</i>														
Kuala Lumpur	3.12°N	101.55°E	τ_b	0.498	0.514	0.544	0.510	0.519	0.552	0.572	0.618	0.662	0.535	0.475
			τ_d	1.987	1.948	1.870	1.980	1.947	1.838	1.783	1.684	1.692	1.597	1.879
<i>Martinique</i>														
Le Lamentin	14.60°N	61.00°W	τ_b	0.383	0.386	0.409	0.438	0.501	0.589	0.567	0.491	0.456	0.417	0.401
			τ_d	2.447	2.439	2.339	2.231	1.999	1.749	1.803	2.061	2.213	2.213	2.466
<i>Mexico</i>														
Mexico City	19.43°N	99.13°W	τ_b	0.393	0.403	0.414	0.487	0.519	0.486	0.461	0.449	0.464	0.424	0.383
			τ_d	2.031	2.016	2.003	1.804	1.724	1.859	1.949	1.992	1.962	2.022	2.125
<i>Cancun</i>	21.03°N	86.87°W	τ_b	0.381	0.394	0.427	0.456	0.472	0.488	0.495	0.454	0.430	0.419	0.398
			τ_d	2.439	2.351	2.212	2.132	2.092	2.062	2.028	2.204	2.341	2.354	2.388
<i>Mongolia</i>														
Ulaanbaatar	47.92°N	106.87°E	τ_b	0.208	0.218	0.281	0.352	0.404	0.425	0.412	0.387	0.342	0.298	0.245
airport			τ_d	2.617	2.560	2.212	2.019	1.933	1.946	2.077	2.157	2.244	2.313	2.445
<i>Uliastai</i>	47.75°N	96.85°E	τ_b	0.198	0.205	0.244	0.325	0.381	0.406	0.409	0.382	0.332	0.298	0.238
			τ_d	2.553	2.513	2.318	2.044	1.948	1.966	2.017	2.079	2.203	2.159	2.383
<i>Morocco</i>														
Casablanca	33.57°N	7.67°W	τ_b	0.353	0.329	0.378	0.416	0.461	0.517	0.502	0.497	0.462	0.366	0.336
			τ_d	2.312	2.531	2.238	2.087	1.954	1.801	1.860	1.882	1.988	2.416	2.547
<i>Mozambique</i>														
Maputo	25.92°S	32.57°E	τ_b	0.406	0.401	0.393	0.378	0.353	0.349	0.355	0.412	0.443	0.465	0.423
			τ_d	2.330	2.364	2.381	2.388	2.480	2.441	2.415	2.151	2.075	2.027	2.210

(Continued)

TABLE A2.2a (CONTINUED)
 Worldwide Values of τ_b and τ_d for Solar Radiation Modeling

Position	Lat	Long	Jan	Feb	Mar	Apr	May	Jun	Jul	Aug	Sep	Oct	Nov	Dec	
<i>Pakistan</i>															
Karachi	24.90°N	67.13°E	τ_b	0.403	0.448	0.701	0.824	0.932	1.035	1.164	1.026	0.810	0.705	0.583	
			τ_d	2.089	1.918	1.399	1.269	1.191	1.142	1.094	1.167	1.326	1.416	1.580	
Islamabad	33.62°N	73.10°E	τ_b	0.337	0.400	0.449	0.688	0.735	0.920	0.974	0.912	0.630	0.433	0.384	0.348
<i>Peru</i>															
Lima	12.00°S	77.12°W	τ_b	0.603	0.610	0.601	0.546	0.484	0.457	0.446	0.507	0.586	0.611	0.612	0.638
			τ_d	1.715	1.710	1.734	1.862	2.042	2.117	2.150	1.953	1.760	1.705	1.676	1.633
<i>Poland</i>															
Warszawa	52.17°N	20.97°E	τ_b	0.348	0.380	0.455	0.471	0.457	0.467	0.506	0.454	0.428	0.393	0.363	0.340
			τ_d	2.191	2.002	1.787	1.815	1.906	1.925	1.819	1.994	2.026	2.096	2.163	2.262
Kolobrzeg	54.18°N	15.58°E	τ_b	0.363	0.373	0.415	0.429	0.429	0.425	0.454	0.441	0.411	0.387	0.378	0.362
<i>Portugal</i>															
Evora	38.57°N	7.90°W	τ_b	0.306	0.324	0.358	0.353	0.386	0.393	0.389	0.399	0.382	0.348	0.322	0.311
			τ_d	2.543	2.424	2.232	2.319	2.202	2.205	2.253	2.198	2.251	2.380	2.495	2.532
Lisbon	38.77°N	9.13°W	τ_b	0.327	0.349	0.390	0.371	0.404	0.411	0.404	0.413	0.399	0.372	0.345	0.334
			τ_d	2.425	2.312	2.124	2.274	2.163	2.163	2.207	2.172	2.215	2.297	2.381	2.410
<i>Romania</i>															
Bucuresti	44.48°N	26.12°E	τ_b	0.320	0.357	0.410	0.437	0.431	0.491	0.502	0.500	0.442	0.384	0.353	0.329
			τ_d	2.280	2.074	1.984	1.943	2.026	1.883	1.868	1.860	1.997	2.176	2.243	2.299
Constanta	44.22°N	28.65°E	τ_b	0.348	0.382	0.403	0.428	0.431	0.455	0.484	0.488	0.435	0.392	0.366	0.350
			τ_d	2.192	2.021	2.038	1.997	2.063	2.037	1.950	1.928	2.051	2.173	2.195	2.221

Galati	45.48°N	28.03°E	τ_b	0.315	0.344	0.383	0.419	0.412	0.458	0.484	0.486	0.426	0.370	0.344	0.317
			τ_d	2.340	2.163	2.088	2.004	2.105	1.993	1.924	1.908	2.052	2.240	2.273	2.381
<i>Russia</i>															
Aleksandrovskoe	60.43°N	77.87°E	τ_b	0.242	0.257	0.299	0.331	0.392	0.400	0.409	0.400	0.408	0.325	0.273	0.257
			τ_d	2.684	2.501	2.195	2.096	2.041	2.117	2.157	2.140	1.973	2.283	2.513	2.761
Moscow	55.83°N	37.62°E	τ_b	0.297	0.320	0.361	0.439	0.435	0.411	0.437	0.446	0.442	0.370	0.326	0.296
St. Petersburg	59.97°N	30.30°E	τ_b	0.294	0.304	0.326	0.403	0.390	0.395	0.413	0.408	0.378	0.341	0.328	0.319
Singapore			τ_d	2.491	2.349	2.209	1.968	2.118	2.194	2.146	2.143	2.186	2.278	2.330	2.597
Singapore	1.37°N	103.98°E	τ_b	0.500	0.507	0.523	0.486	0.485	0.494	0.508	0.571	0.610	0.678	0.515	0.489
			τ_d	1.983	1.967	1.930	2.072	2.076	2.030	1.984	1.810	1.722	1.577	1.952	2.028
<i>South Korea</i>															
Seoul	37.57°N	126.97°E	τ_b	0.409	0.483	0.571	0.631	0.712	0.789	0.682	0.560	0.503	0.479	0.441	0.387
			τ_d	1.844	1.669	1.529	1.476	1.397	1.343	1.526	1.771	1.845	1.808	1.861	1.982
<i>South Africa</i>															
Cape Town	33.97°S	18.60°E	τ_b	0.335	0.341	0.333	0.334	0.323	0.311	0.316	0.327	0.335	0.345	0.329	0.336
			τ_d	2.613	2.599	2.652	2.575	2.616	2.661	2.595	2.521	2.522	2.479	2.608	2.600
Port Elizabeth	33.98°S	25.62°E	τ_b	0.372	0.378	0.368	0.355	0.339	0.331	0.327	0.357	0.373	0.385	0.368	0.369
Pretoria	25.73°S	28.18°E	τ_b	0.379	0.381	0.378	0.350	0.308	0.307	0.295	0.352	0.374	0.396	0.361	0.364
			τ_d	2.279	2.272	2.242	2.308	2.526	2.445	2.563	2.221	2.190	2.138	2.331	2.338
<i>Spain</i>															
Barcelona	41.28°N	2.07°E	τ_b	0.333	0.364	0.402	0.421	0.467	0.505	0.511	0.492	0.449	0.404	0.361	0.337
			τ_d	2.394	2.221	2.075	2.041	1.934	1.863	1.862	1.927	2.030	2.137	2.266	2.364
Madrid	40.45°N	3.55°W	τ_b	0.307	0.329	0.376	0.372	0.424	0.457	0.446	0.453	0.408	0.368	0.328	0.318
			τ_d	2.446	2.306	2.075	2.140	1.976	1.895	1.933	1.906	2.048	2.189	2.357	2.378

(Continued)

TABLE A2.2a (CONTINUED)
Worldwide Values of τ_b and τ_d for Solar Radiation Modeling

Position	Lat	Long	Jan	Feb	Mar	Apr	May	Jun	Jul	Aug	Sep	Oct	Nov	Dec
<i>Sweden</i>														
Goteborg	57.72°N	12.00°E	τ_b	0.332	0.335	0.349	0.392	0.400	0.402	0.421	0.413	0.377	0.361	0.374
			τ_d	2.276	2.263	2.243	2.089	2.103	2.158	2.110	2.136	2.243	2.214	2.102
Stockholm	59.65°N	17.95°E	τ_b	0.307	0.313	0.337	0.384	0.388	0.390	0.395	0.393	0.361	0.354	0.349
			τ_d	2.403	2.323	2.247	2.094	2.126	2.199	2.220	2.214	2.295	2.203	2.226
<i>Switzerland</i>														
Geneva	46.25°N	6.13°E	τ_b	0.311	0.354	0.417	0.412	0.440	0.440	0.439	0.424	0.394	0.373	0.330
			τ_d	2.311	2.077	1.880	1.937	1.927	2.002	2.054	2.110	2.177	2.175	2.267
Zurich	47.48°N	8.53°E	τ_b	0.304	0.347	0.399	0.407	0.413	0.436	0.430	0.401	0.393	0.360	0.330
			τ_d	2.309	2.051	1.924	1.941	2.022	1.997	2.057	2.186	2.148	2.202	2.217
<i>Thailand</i>														
Bangkok	13.73°N	100.57°E	τ_b	0.612	0.762	0.827	0.666	0.612	0.619	0.629	0.585	0.612	0.653	0.566
			τ_d	1.654	1.429	1.366	1.598	1.701	1.684	1.663	1.764	1.700	1.605	1.762
<i>Trinidad and Tobago</i>														
Crown Point	11.15°N	60.83°W	τ_b	0.401	0.411	0.449	0.474	0.519	0.564	0.533	0.461	0.446	0.415	0.422
			τ_d	2.387	2.349	2.174	2.097	1.947	1.828	1.916	2.201	2.280	2.444	2.378

<i>Tunisia</i>	36.83°N	10.23°E	τ_b	0.360	0.406	0.436	0.490	0.510	0.515	0.545	0.541	0.505	0.466	0.406	0.384
Tunis			τ_d	2.214	2.013	1.934	1.803	1.794	1.815	1.731	1.764	1.847	1.905	2.052	2.097
<i>Ukraine</i>															
Kiev	50.40°N	30.57°E	τ_b	0.318	0.338	0.402	0.426	0.415	0.434	0.459	0.454	0.411	0.356	0.331	0.321
			τ_d	2.285	2.093	1.941	1.960	2.057	2.054	1.980	1.981	2.074	2.259	2.285	2.280
<i>Uzbekistan</i>															
Tashkent	41.27°N	69.27°E	τ_b	0.378	0.415	0.478	0.508	0.535	0.556	0.600	0.536	0.499	0.495	0.455	0.380
<i>Venezuela</i>															
Caracas	10.60°N	66.98°W	τ_b	0.395	0.413	0.472	0.539	0.528	0.525	0.505	0.457	0.444	0.432	0.427	0.409
			τ_d	2.418	2.341	2.079	1.877	1.913	1.925	1.995	2.201	2.273	2.317	2.320	2.372
<i>St. Antonio</i>	7.85°N	72.45°W	τ_b	0.443	0.510	0.671	0.641	0.501	0.484	0.485	0.492	0.483	0.484	0.471	0.449
			τ_d	2.227	1.981	1.601	1.654	2.021	2.080	2.085	2.071	2.114	2.095	2.124	2.199
<i>Zimbabwe</i>															
Harare	17.92°S	31.13°E	τ_b	0.350	0.360	0.351	0.316	0.297	0.302	0.312	0.346	0.397	0.400	0.364	0.362
			τ_d	2.532	2.434	2.447	2.656	2.716	2.613	2.544	2.341	2.113	2.138	2.347	2.412
<i>Masvingo</i>	20.07°S	30.87°E	τ_b	0.351	0.359	0.346	0.324	0.303	0.309	0.310	0.344	0.389	0.397	0.372	0.369
			τ_d	2.555	2.484	2.524	2.615	2.697	2.612	2.610	2.386	2.178	2.187	2.333	2.402

TABLE A2.2b Values of τ_b and τ_d for Solar Radiation Modeling for Sites in the United States

Position	Latitude	Longitude	Jan	Feb	Mar	Apr	May	Jun	Jul	Aug	Sep	Oct	Nov	Dec
Alabama Birmingham	33.56 N	86.75 W	τ_b 0.327	0.346	0.377	0.404	0.439	0.483	0.583	0.584	0.439	0.370	0.340	0.322
Montgomery	32.30 N	86.39 W	τ_b 0.332	0.352	0.382	0.399	0.438	0.490	0.573	0.581	0.441	0.372	0.344	0.328
Alaska Fairbanks	64.82 N	147.86 W	τ_b τ_d 0.186	0.250	0.251	0.281	0.350	0.380	0.387	0.403	0.309	0.269	0.226	0.171
Anchorage	61.18 N	149.99 W	τ_b τ_d 0.265	0.258	0.260	0.292	0.389	0.370	0.387	0.372	0.323	0.284	0.273	0.220
Nome	64.51 N	165.44 W	τ_b τ_d 0.195	0.240	0.241	0.286	0.387	0.369	0.408	0.455	0.318	0.292	0.232	0.183
St. Paul Island	57.16 N	170.22 W	τ_b τ_d 0.281	0.317	0.316	0.373	0.410	0.378	0.413	0.390	0.364	0.333	0.318	0.288
Yakutat	59.51 N	139.63 W	τ_b τ_d 0.266	0.280	0.280	0.333	0.397	0.389	0.371	0.370	0.333	0.307	0.279	0.282
Arizona Phoenix	33.44 N	111.99 W	τ_b τ_d 0.306	0.317	0.339	0.366	0.419	0.465	0.588	0.547	0.456	0.393	0.318	0.298
Tucson	32.13 N	110.96 W	τ_b τ_d 0.296	0.306	0.327	0.361	0.431	0.473	0.555	0.510	0.434	0.372	0.309	0.287
Arkansas Little Rock	34.75 N	92.23 W	τ_b τ_d 0.325	0.348	0.378	0.399	0.418	0.472	0.517	0.514	0.422	0.363	0.341	0.319
Adams Field			τ_b τ_d 0.457	2.319	2.218	2.175	2.183	2.028	1.901	1.895	2.205	2.386	2.410	2.503

Fort Smith	35.33 N	94.37 W	τ_b	0.320	0.339	0.361	0.387	0.420	0.465	0.490	0.482	0.416	0.359	0.336	0.314
<i>California</i>															
Bakersfield	35.43 N	119.06 W	τ_b	0.313	0.334	0.345	0.372	0.391	0.388	0.438	0.445	0.382	0.377	0.331	0.315
Fresno	36.78 N	119.72 W	τ_d	2.468	2.363	2.298	2.226	2.159	2.040	1.983	2.006	2.235	2.411	2.439	2.528
Long Beach	33.83 N	118.16 W	τ_b	0.304	0.323	0.337	0.371	0.388	0.378	0.428	0.428	0.379	0.370	0.328	0.310
Sacramento	38.51 N	121.49 W	τ_d	2.632	2.460	2.431	2.251	2.251	2.375	2.152	2.150	2.371	2.303	2.497	2.540
San Diego Lindbergh Field	32.74 N	117.17 W	τ_b	0.319	0.329	0.344	0.364	0.364	0.389	0.389	0.462	0.450	0.395	0.387	0.340
San Francisco	37.62 N	122.40 W	τ_d	2.583	2.518	2.458	2.351	2.272	2.301	2.159	2.214	2.401	2.360	2.536	2.601
Los Angeles	33.94 N	118.41 W	τ_b	0.326	0.334	0.362	0.368	0.368	0.353	0.371	0.365	0.352	0.335	0.320	0.318
Santa Maria Public Airport	34.92 N	120.47 W	τ_d	2.703	2.568	2.565	2.423	2.406	2.480	2.357	2.414	2.531	2.496	2.630	2.637
Colorado Springs	38.81 N	104.71 W	τ_b	0.247	0.269	0.292	0.343	0.370	0.391	0.408	0.387	0.328	0.297	0.261	0.244
Connecticut	41.94 N	72.68 W	τ_b	0.315	0.335	0.370	0.393	0.415	0.459	0.486	0.462	0.393	0.361	0.335	0.312
Hartford	2.350	2.235	2.130	2.119	2.105	2.003	1.943	2.020	2.271	2.315	2.358	2.438			

(Continued)

TABLE A2.2b (CONTINUED)
 Values of τ_b and τ_d for Solar Radiation Modeling for Sites in the United States

Position	Latitude	Longitude	Jan	Feb	Mar	Apr	May	Jun	Jul	Aug	Sep	Oct	Nov	Dec	
<i>Delaware</i>															
Wilmington	39.67 N	75.60 W	τ_b	0.319	0.358	0.428	0.423	0.493	0.567	0.567	0.419	0.373	0.352	0.317	
			τ_d	2.369	2.155	1.929	2.010	1.829	1.693	1.755	1.711	2.164	2.264	2.284	2.458
<i>Florida</i>															
Daytona Beach	29.18 N	81.06 W	τ_b	0.350	0.371	0.394	0.405	0.468	0.477	0.512	0.498	0.445	0.396	0.362	0.348
			τ_d	2.468	2.346	2.259	2.255	2.042	2.066	1.951	2.002	2.196	2.364	2.475	2.495
Jacksonville	30.49 N	81.69 W	τ_b	0.351	0.366	0.390	0.411	0.482	0.504	0.541	0.523	0.450	0.397	0.361	0.342
			τ_d	2.420	2.343	2.244	2.199	1.979	1.957	1.863	1.912	2.156	2.323	2.444	2.488
Tallahassee	30.39 N	84.35 W	τ_b	0.344	0.357	0.383	0.397	0.450	0.493	0.537	0.536	0.441	0.388	0.353	0.337
			τ_d	2.461	2.386	2.274	2.255	2.098	1.995	1.879	1.874	2.200	2.366	2.480	2.510
Miami	25.82 N	80.30 W	τ_b	0.368	0.388	0.418	0.433	0.501	0.520	0.528	0.505	0.473	0.425	0.389	0.370
			τ_d	2.439	2.306	2.190	2.160	1.945	1.929	1.905	1.987	2.095	2.257	2.362	2.400
Key West	24.55 N	81.75 W	τ_b	0.375	0.386	0.421	0.434	0.466	0.477	0.488	0.461	0.437	0.414	0.390	0.381
			τ_d	2.443	2.365	2.217	2.200	2.115	2.119	2.077	2.194	2.308	2.375	2.416	2.387
Tampa	27.96 N	82.54 W	τ_b	0.344	0.364	0.391	0.403	0.470	0.473	0.509	0.493	0.445	0.398	0.360	0.346
			τ_d	2.531	2.403	2.271	2.272	2.029	2.070	1.950	2.010	2.190	2.356	2.488	2.512
<i>Georgia</i>															
Athens	33.95 N	83.33 W	τ_b	0.320	0.341	0.375	0.390	0.438	0.492	0.539	0.570	0.426	0.371	0.336	0.317
			τ_d	2.507	2.371	2.215	2.199	2.062	1.934	1.828	1.734	2.177	2.331	2.454	2.550
Atlanta	33.64 N	84.43 W	τ_b	0.325	0.349	0.383	0.395	0.448	0.505	0.556	0.593	0.431	0.373	0.339	0.320
Columbus	32.52 N	84.94 W	τ_b	0.330	0.348	0.379	0.398	0.439	0.481	0.564	0.593	0.438	0.375	0.343	0.326
			τ_d	2.497	2.380	2.238	2.197	2.096	1.998	1.778	1.699	2.158	2.366	2.477	2.545

Macon	32.69 N	83.65 W	τ_b	0.328	0.348	0.381	0.395	0.442	0.481	0.549	0.595	0.434	0.377	0.341	0.324
Savannah	32.12 N	81.20 W	τ_d	2.498	2.367	2.220	2.200	2.078	1.995	1.812	1.686	2.172	2.345	2.481	2.548
Hawaii			τ_b	0.340	0.356	0.391	0.409	0.481	0.517	0.558	0.554	0.442	0.387	0.352	0.335
Honolulu	21.33 N	157.94 W	τ_d	2.461	2.353	2.199	2.173	1.956	1.899	1.811	1.811	2.173	2.338	2.456	2.506
Idaho			τ_b	0.332	0.350	0.370	0.401	0.391	0.385	0.385	0.382	0.371	0.373	0.359	0.346
Boise	43.57 N	116.22 W	τ_d	2.773	2.614	2.491	2.316	2.407	2.463	2.489	2.521	2.620	2.565	2.645	2.673
Illinois			τ_b	0.279	0.287	0.305	0.346	0.371	0.363	0.398	0.394	0.352	0.315	0.289	0.277
Chicago	41.99 N	87.91 W	τ_d	2.419	2.446	2.420	2.238	2.181	2.301	2.125	2.124	2.282	2.435	2.542	2.493
Rockford	39.85 N	89.68 W	τ_b	0.302	0.343	0.390	0.417	0.438	0.458	0.455	0.452	0.412	0.365	0.337	0.307
Springfield	39.85 N	89.68 W	τ_d	0.312	0.347	2.149	2.030	1.998	1.999	2.001	2.050	2.048	2.146	2.259	2.303
Indiana	39.71 N	86.27 W	τ_b	0.330	0.377	0.427	0.422	0.470	0.484	0.480	0.472	0.418	0.370	0.345	0.326
Iowa			τ_d	2.217	2.010	1.901	1.986	1.890	1.909	1.954	1.971	2.124	2.243	2.273	2.288
Mason City	43.16 N	93.33 W	τ_b	0.272	0.298	0.340	0.358	0.381	0.398	0.409	0.412	0.386	0.340	0.307	0.278
Waterloo	42.55 N	92.40 W	τ_b	0.286	0.331	2.491	2.243	2.191	2.234	2.227	2.241	2.210	2.171	2.209	2.329
			τ_d	2.381	2.082	0.417	0.371	0.380	0.400	0.417	0.427	0.430	0.394	0.347	0.325

(Continued)

TABLE A2.2b (CONTINUED)
 Values of τ_b and τ_d for Solar Radiation Modeling for Sites in the United States

Position	Latitude	Longitude	Jan	Feb	Mar	Apr	May	Jun	Jul	Aug	Sep	Oct	Nov	Dec
<i>Kansas</i>														
Dodge City	37.77 N	99.97 W	τ_b	0.273	0.301	0.328	0.356	0.384	0.422	0.419	0.414	0.370	0.326	0.289
Goodland	39.37 N	101.69 W	τ_d	2.618	2.374	2.305	2.226	2.187	2.086	2.142	2.165	2.294	2.409	2.577
<i>Kentucky</i>														
Lexington	38.04 N	84.61 W	τ_b	0.321	0.358	0.390	0.389	0.461	0.468	0.503	0.500	0.410	0.357	0.329
Louisville	38.18 N	85.73 W	τ_d	2.334	2.159	2.067	2.144	1.925	1.972	1.885	1.882	2.180	2.332	2.410
Standiford Field														
<i>Louisiana</i>														
New Orleans	29.99 N	90.25 W	τ_b	0.372	0.392	0.410	0.438	0.477	0.526	0.568	0.553	0.475	0.396	0.371
Lake Charles	30.13 N	93.23 W	τ_d	2.275	2.185	2.153	2.084	2.004	1.885	1.788	1.821	2.045	2.301	2.342
<i>Maine</i>														
Portland	43.64 N	70.30 W	τ_b	2.480	2.339	2.256	2.163	2.010	1.970	2.103	2.304	2.374	2.368	2.470
<i>Maryland</i>														
Baltimore	39.17 N	76.68 W	τ_b	0.319	0.353	0.411	0.417	0.474	0.546	0.552	0.580	0.421	0.370	0.342

Massachusetts													
Boston	42.36 N	71.01 W	τ_b	0.318	0.335	0.374	0.400	0.425	0.472	0.488	0.470	0.391	0.361
			τ_d	2.372	2.277	2.131	2.094	2.068	1.964	1.950	1.992	2.284	2.321
Michigan	42.22 N	83.35 W	τ_b	0.303	0.374	0.437	0.447	0.476	0.519	0.470	0.454	0.416	0.369
Detroit			τ_d	2.302	1.947	1.827	1.875	1.843	1.784	1.978	2.027	2.103	2.216
Lansing	42.78 N	84.58 W	τ_b	0.301	0.325	0.396	0.395	0.427	0.462	0.429	0.428	0.395	0.348
			τ_d	2.282	2.137	1.967	2.063	2.015	1.960	2.133	2.125	2.193	2.340
Minnesota	46.84 N	92.19 W	τ_b	0.249	0.263	0.302	0.338	0.363	0.382	0.398	0.387	0.362	0.316
Duluth			τ_d	2.728	2.559	2.353	2.284	2.276	2.279	2.218	2.265	2.316	2.474
Minneapolis	44.88 N	93.23 W	τ_b	0.263	0.282	0.356	0.374	0.393	0.409	0.416	0.411	0.385	0.337
Rochester	43.90 N	92.49 W	τ_b	0.268	0.287	0.361	0.364	0.381	0.398	0.404	0.401	0.377	0.334
			τ_d	2.490	2.297	2.041	2.178	2.208	2.224	2.226	2.225	2.254	2.361
Mississippi	32.32 N	90.08 W	τ_b	0.332	0.353	0.380	0.399	0.426	0.465	0.534	0.531	0.439	0.369
Jackson			τ_d	2.482	2.350	2.247	2.205	2.168	2.073	1.869	1.861	2.157	2.401
Missouri	38.82 N	92.22 W	τ_b	0.311	0.344	0.377	0.388	0.406	0.438	0.448	0.462	0.391	0.348
Columbia			τ_d	2.407	2.218	2.123	2.149	2.158	2.100	2.098	2.029	2.285	2.394
Kansas City	39.30 N	94.72 W	τ_b	0.303	0.349	0.393	0.395	0.405	0.427	0.438	0.448	0.387	0.345
Springfield	37.24 N	93.39 W	τ_b	0.304	0.337	0.357	0.374	0.404	0.434	0.448	0.452	0.389	0.342
St. Louis	38.75 N	90.37 W	τ_b	0.316	0.351	0.385	0.406	0.427	0.455	0.470	0.478	0.406	0.359

(Continued)

TABLE A2.2b (CONTINUED)
 Values of τ_b and τ_d for Solar Radiation Modeling for Sites in the United States

Position	Latitude	Longitude	Jan	Feb	Mar	Apr	May	Jun	Jul	Aug	Sep	Oct	Nov	Dec
<i>Montana</i>														
Helena	46.61 N	111.96 W	τ_b	0.253	0.252	0.296	0.341	0.370	0.375	0.380	0.416	0.362	0.299	0.269
			τ_d	2.529	2.583	2.310	2.177	2.149	2.222	2.232	2.044	2.215	2.505	2.568
Lewistown	47.05 N	109.47 W	τ_b	0.265	0.265	0.284	0.332	0.362	0.360	0.382	0.418	0.358	0.292	0.257
			τ_d	2.579	2.399	2.418	2.240	2.164	2.262	2.178	1.992	2.186	2.503	2.647
<i>Nebraska</i>														
Lincoln	40.83 N	96.76 W	τ_b	0.286	0.321	0.362	0.376	0.392	0.403	0.414	0.418	0.375	0.337	0.312
			τ_d	2.431	2.167	2.147	2.163	2.186	2.229	2.224	2.187	2.311	2.383	2.420
Omaha	41.31 N	95.90 W	τ_b	0.288	0.323	0.388	0.391	0.406	0.407	0.421	0.423	0.382	0.343	0.315
			τ_d	2.396	2.146	2.011	2.092	2.128	2.222	2.196	2.170	2.272	2.341	2.398
<i>Nevada</i>														
Elko	40.83 N	115.79 W	τ_b	0.249	0.278	0.306	0.332	0.358	0.373	0.446	0.431	0.358	0.319	0.275
			τ_d	2.489	2.292	2.282	2.230	2.177	2.165	1.888	1.919	2.195	2.315	2.524
Las Vegas	36.08 N	115.16 W	τ_b	0.314	0.333	0.355	0.382	0.404	0.412	0.550	0.560	0.407	0.380	0.317
			τ_d	2.386	2.277	2.211	2.099	2.062	2.059	1.674	1.654	2.084	2.096	2.388
Reno	39.48 N	119.77 W	τ_b	0.277	0.291	0.314	0.336	0.344	0.337	0.398	0.389	0.329	0.311	0.282
			τ_d	2.504	2.422	2.366	2.267	2.319	2.437	2.123	2.152	2.464	2.470	2.597
<i>New Hampshire</i>														
Concord	43.20 N	71.50 W	τ_b	0.292	0.319	0.351	0.382	0.412	0.439	0.459	0.441	0.383	0.350	0.323
			τ_d	2.506	2.284	2.175	2.136	2.090	2.059	2.014	2.072	2.289	2.346	2.416
<i>New Jersey</i>														
Atlantic City	39.46 N	74.46 W	τ_b	0.331	0.340	0.376	0.411	0.458	0.522	0.557	0.549	0.413	0.373	0.350
			τ_d	2.353	2.324	2.180	2.073	1.966	1.830	1.774	1.773	2.224	2.292	2.318

Newark	40.72 N	74.17 W	τ_b	0.327	0.366	0.406	0.431	0.464	0.526	0.528	0.516	0.413	0.376	0.352	0.323
New Mexico			τ_d	2.306	2.108	2.008	1.981	1.924	1.802	1.831	1.848	2.189	2.246	2.274	2.387
Albuquerque	35.04 N	106.62 W	τ_b	0.264	0.279	0.296	0.333	0.372	0.405	0.463	0.433	0.365	0.320	0.278	0.259
New York			τ_d	2.584	2.498	2.428	2.244	2.117	2.025	1.887	2.005	2.225	2.329	2.551	2.646
Albany	42.75 N	73.80 W	τ_b	0.308	0.332	0.388	0.392	0.407	0.457	0.490	0.456	0.400	0.362	0.338	0.309
Buffalo	42.94 N	78.74 W	τ_b	2.340	2.171	1.997	2.099	2.137	2.007	1.923	2.037	2.220	2.290	2.325	2.416
New York City	40.66 N	73.80 W	τ_b	0.331	0.362	0.401	0.439	0.476	0.534	0.541	0.527	0.418	0.362	0.332	0.306
Rochester	43.12 N	77.68 W	τ_b	0.307	0.323	0.373	0.404	0.413	0.469	0.463	0.440	0.401	0.362	0.336	0.308
North Carolina			τ_d	2.307	2.210	2.059	2.038	2.085	1.941	2.001	2.080	2.187	2.259	2.297	2.361
Charlotte	35.21 N	80.94 W	τ_b	0.318	0.338	0.373	0.411	0.435	0.488	0.557	0.567	0.421	0.359	0.331	0.314
Wilmington	34.27 N	77.91 W	τ_b	0.345	0.357	0.390	0.417	0.472	0.524	0.584	0.542	0.440	0.380	0.353	0.335
North Dakota			τ_d	2.384	2.325	2.181	2.113	1.973	1.869	1.738	1.841	2.163	2.345	2.414	2.462
Bismarck	46.77 N	100.75 W	τ_b	0.252	0.266	0.309	0.383	0.381	0.376	0.393	0.422	0.363	0.316	0.279	0.259
Fargo	46.93 N	96.81 W	τ_b	0.244	0.261	0.302	0.340	0.363	0.389	0.396	0.405	0.365	0.316	0.283	0.257
Ohio			τ_d	2.609	2.458	2.356	2.316	2.307	2.260	2.253	2.185	2.302	2.476	2.538	2.588
Cleveland	41.41 N	81.85 W	τ_b	0.308	0.368	0.435	0.427	0.464	0.488	0.471	0.455	0.413	0.364	0.338	0.313
			τ_d	2.337	2.023	1.852	1.960	1.897	1.886	1.988	2.035	2.147	2.269	2.295	2.339

(Continued)

TABLE A2.2b (CONTINUED)Values of τ_b and τ_d for Solar Radiation Modeling for Sites in the United States

Position	Latitude	Longitude	Jan	Feb	Mar	Apr	May	Jun	Jul	Aug	Sep	Oct	Nov	Dec	
Columbus	39.99 N	82.88 W	τ_b	0.329	0.359	0.419	0.405	0.469	0.487	0.484	0.482	0.410	0.364	0.343	0.320
			τ_d	2.200	2.087	1.928	2.057	1.887	1.898	1.943	1.931	2.166	2.271	2.285	2.330
Dayton	39.91 N	84.22 W	τ_b	0.338	0.376	0.436	0.427	0.498	0.490	0.478	0.475	0.409	0.367	0.349	0.328
			τ_d	2.122	1.988	1.858	1.959	1.790	1.879	1.955	1.944	2.150	2.234	2.234	2.253
Youngstown	41.25 N	80.67 W	τ_b	0.305	0.362	0.411	0.396	0.437	0.462	0.456	0.446	0.403	0.354	0.321	0.301
			τ_d	2.331	2.013	1.914	2.072	1.974	1.958	2.022	2.044	2.171	2.302	2.392	2.410
<i>Oklahoma</i>															
Oklahoma City	35.39 N	97.60 W	τ_b	0.305	0.324	0.339	0.361	0.401	0.430	0.426	0.431	0.393	0.345	0.317	0.300
			τ_d	2.478	2.389	2.371	2.310	2.211	2.157	2.214	2.179	2.298	2.430	2.484	2.524
<i>Oregon</i>															
Eugene	44.13 N	123.21 W	τ_b	0.299	0.311	0.324	0.356	0.362	0.355	0.357	0.352	0.346	0.329	0.317	0.303
			τ_d	2.742	2.624	2.565	2.366	2.397	2.515	2.559	2.603	2.576	2.606	2.635	2.668
Medford	42.39 N	122.87 W	τ_b	0.297	0.305	0.327	0.363	0.363	0.347	0.356	0.360	0.341	0.332	0.314	0.305
			τ_d	2.693	2.662	2.516	2.324	2.390	2.590	2.582	2.534	2.601	2.577	2.646	2.586
Portland	45.59 N	122.60 W	τ_b	0.296	0.309	0.324	0.356	0.371	0.368	0.364	0.358	0.349	0.330	0.315	0.298
			τ_d	2.719	2.600	2.507	2.328	2.316	2.401	2.503	2.549	2.529	2.558	2.591	2.687
<i>Pennsylvania</i>															
Philadelphia	39.87 N	75.23 W	τ_b	0.322	0.357	0.419	0.421	0.482	0.552	0.550	0.552	0.417	0.374	0.352	0.319
			τ_d	2.357	2.166	1.965	2.021	1.865	1.734	1.776	1.750	2.178	2.266	2.292	2.443
Pittsburgh	40.50 N	80.23 W	τ_b	0.307	0.336	0.386	0.379	0.440	0.474	0.479	0.473	0.401	0.352	0.319	0.305
			τ_d	2.357	2.184	2.037	2.159	1.963	1.913	1.937	1.936	2.175	2.307	2.420	2.417
<i>Rhode Island</i>															
Providence	41.72 N	71.43 W	τ_b	0.323	0.334	0.372	0.402	0.426	0.471	0.507	0.466	0.393	0.364	0.343	0.319
			τ_d	2.350	2.302	2.156	2.091	2.066	1.963	1.885	2.007	2.281	2.311	2.328	2.414

(Continued)

TABLE A2.2b (CONTINUED)
 Values of τ_b and τ_d for Solar Radiation Modeling for Sites in the United States

Position	Latitude	Longitude	Jan	Feb	Mar	Apr	May	Jun	Jul	Aug	Sep	Oct	Nov	Dec	
<i>Utah</i>															
Salt Lake City	40.79 N	111.97 W	τ_b	0.270	0.319	0.326	0.374	0.368	0.377	0.440	0.418	0.372	0.335	0.293	
<i>Vermont</i>			τ_d	2.426	2.115	2.197	2.039	2.184	2.199	1.968	2.037	2.185	2.259	2.394	0.270
Burlington	44.47 N	73.15 W	τ_b	0.282	0.307	0.374	0.380	0.394	0.419	0.459	0.421	0.391	0.354	0.330	2.445
<i>Virginia</i>			τ_d	2.468	2.245	1.994	2.095	2.163	2.130	2.002	2.151	2.227	2.291	2.316	0.292
Norfolk	36.90 N	76.19 W	τ_b	0.332	0.348	0.386	0.427	0.463	0.536	0.590	0.566	0.428	0.373	0.342	2.451
<i>Washington</i>			τ_d	2.401	2.323	2.158	2.038	1.967	1.804	1.703	1.747	2.176	2.330	2.422	0.326
Olympia	46.97 N	122.90 W	τ_b	0.295	0.300	0.328	0.349	0.377	0.373	0.364	0.359	0.345	0.328	0.310	0.297
<i>Seattle</i>			τ_d	2.686	2.652	2.437	2.346	2.263	2.367	2.492	2.536	2.558	2.548	2.607	2.645
Seattle	47.46 N	122.31 W	τ_b	0.289	0.290	0.325	0.351	0.377	0.370	0.362	0.352	0.343	0.323	0.302	0.289
<i>Yakima</i>			τ_d	2.641	2.681	2.392	2.292	2.224	2.361	2.489	2.561	2.539	2.534	2.618	2.633
Yakima	46.56 N	120.53 W	τ_b	0.278	0.288	0.326	0.391	0.419	0.416	0.395	0.397	0.373	0.342	0.310	0.284
			τ_d	2.571	2.584	2.319	2.040	2.005	2.104	2.249	2.227	2.277	2.345	2.454	2.517

TABLE A2.3a
Worldwide Global Horizontal Average Solar Radiation (MJ/m².day)

Position	Lat	Long	Jan	Feb	Mar	Apr	May	Jun	Jul	Aug	Sep	Oct	Nov	Dec
<i>Argentina</i>														
Buenos Aires	34.58°S	58.48°W	24.86	21.75	18.56	11.75	8.71	7.15	7.82	8.75	14.49	16.66	24.90	21.93
<i>Australia</i>														
Adelaide	34.93°S	138.52°E	20.99	17.50	20.15	18.27	17.98	—	18.81	19.64	20.11	20.88	20.57	20.72
Brisbane	27.43°S	153.08°E	25.36	22.22	13.25	16.61	12.23	11.52	9.70	15.10	17.61	19.89	—	—
Canberra	35.30°S	148.18°E	28.20	24.68	20.56	14.89	10.29	6.62	—	12.33	16.88	24.06	26.00	25.77
Darwin	12.47°S	130.83°E	26.92	23.40	18.13	13.62	9.30	7.89	9.41	11.15	14.85	18.87	23.43	22.34
Hobart	42.88°S	147.32°E	—	—	—	10.09	7.26	6.04	5.72	9.21	13.54	18.12	—	—
Laverton	37.85°S	114.08°E	22.96	20.42	15.59	13.40	7.48	6.10	6.54	10.43	13.24	18.76	—	—
Sydney	33.87°S	151.20°E	21.09	21.75	17.63	13.63	9.78	8.79	7.62	12.84	16.93	22.10	—	—
<i>Austria</i>														
Wien	48.20°N	16.57°E	3.54	7.10	8.05	14.72	16.79	20.87	19.89	17.27	12.55	8.45	3.51	2.82
Innsbruck	47.27°N	11.38°E	5.57	9.28	10.15	15.96	14.57	17.65	18.35	17.26	12.98	9.08	4.28	3.50
<i>Barbados</i>														
Husbands	13.15°N	59.62°W	19.11	20.23	—	21.80	19.84	20.86	21.55	22.14	—	—	18.30	16.56
<i>Belgium</i>														
Ostende	51.23°N	2.92°E	2.82	5.75	9.93	15.18	16.74	16.93	18.21	18.29	11.71	6.15	2.69	1.97
Melle	50.98°N	3.83°E	2.40	4.66	8.41	13.55	14.23	13.28	15.71	15.61	10.63	5.82	2.40	1.59
<i>Brunei</i>														
Brunei	4.98°N	114.93°E	19.46	20.12	22.71	20.54	19.74	18.31	19.38	20.08	20.83	17.51	17.39	18.12
<i>Bulgaria</i>														
Chirpan	42.20°N	25.33°E	6.72	6.79	8.54	13.27	17.25	17.39	19.85	14.61	12.53	8.52	5.08	5.09
Sofia	42.65°N	23.38°E	4.05	6.23	7.93	9.36	12.98	19.73	19.40	17.70	14.71	6.44	—	3.14

TABLE A2.3a (CONTINUED)
Worldwide Global Horizontal Average Solar Radiation (MJ/m²·day)

Position	Lat	Long	Jan	Feb	Mar	Apr	May	Jun	Jul	Aug	Sep	Oct	Nov	Dec
<i>Egypt</i>														
Cairo	30.08°N	31.28°E	10.06	12.96	18.49	23.04	21.91	26.07	25.16	23.09	21.01	—	11.74	9.85
Mersa Matruh	31.33°N	27.22°E	8.38	11.92	18.47	24.27	24.17	—	26.67	26.27	21.92	18.28	11.71	8.76
<i>Ethiopia</i>														
Addis Ababa	8.98°N	38.80°E	—	11.39	—	12.01	—	—	—	6.33	9.35	11.71	11.69	11.50
<i>Fiji</i>														
Nandi	17.75°S	177.45°E	20.82	20.65	20.25	18.81	15.68	14.18	15.08	16.71	19.37	20.11	21.78	25.09
Suva	48.05°S	178.57°E	20.37	17.74	16.22	13.82	10.81	12.48	11.40	—	—	18.49	19.96	20.99
<i>Finland</i>														
Helsinki	60.32°N	24.97°E	1.13	2.94	5.59	11.52	17.60	16.81	20.66	15.44	8.44	3.31	0.97	0.63
<i>France</i>														
Agen	44.18°N	0.60°E	4.83	7.40	10.69	17.12	19.25	20.42	21.63	20.64	15.56	8.41	5.09	5.01
Nice	43.65°N	7.20°E	6.83	—	11.37	17.79	20.74	24.10	24.85	24.86	15.04	10.99	7.08	6.73
Paris	48.97°N	2.45°E	2.62	5.08	7.21	12.90	14.84	13.04	15.54	16.30	10.17	5.61	3.14	2.20
<i>Germany</i>														
Bonn	50.70°N	7.15°E	2.94	5.82	8.01	14.27	15.67	14.41	18.57	17.80	11.70	6.15	3.42	1.90
Nuremberg	53.33°N	13.20°E	3.23	6.92	9.08	15.69	15.71	18.21	21.14	17.98	12.43	8.15	2.79	2.51
Bremen	53.05°N	8.80°E	2.36	4.93	8.53	14.52	14.94	14.52	19.40	15.02	10.48	6.27	2.80	1.66
Hamburg	53.63°N	10.00°E	1.97	3.96	7.59	12.32	14.11	12.69	19.00	14.11	10.29	6.45	2.33	1.43
Stuttgart	48.83°N	9.20°E	3.59	7.18	9.22	15.81	17.72	17.44	22.21	19.87	12.36	7.81	3.19	2.54
<i>Ghana</i>														
Bole	9.03°N	2.48°W	18.29	19.76	19.71	19.15	16.61	—	—	13.68	16.29	17.27	17.33	15.93
Accra	5.60°N	0.17°W	14.82	16.26	18.27	16.73	18.15	13.96	13.86	13.49	15.32	19.14	18.16	14.23
<i>Great Britain</i>														
Belfast	54.65°N	6.22°W	2.00	3.60	6.85	12.00	15.41	15.09	15.46	13.56	11.49	4.63	2.34	1.24

<i>Jersey</i>	49.22°N	2.20°W	2.76	5.65	9.51	14.98	18.51	17.83	18.14	18.62	12.98	6.16	3.26	2.83
<i>London</i>	51.52°N	0.12°W	2.24	3.87	7.40	12.01	12.38	13.24	16.59	16.23	12.59	5.67	2.87	1.97
<i>Greece</i>														
Athens	37.97°N	23.72°E	9.11	10.94	15.70	20.91	23.85	25.48	24.21	23.08	19.03	13.29	5.98	6.64
Sikiwna	37.98°N	22.73°E	7.60	8.16	11.99	21.06	22.62	24.32	23.56	21.73	17.30	11.75	9.45	6.35
<i>Guadeloupe</i>														
Le Raizet	16.27°N	61.52°W	14.88	18.10	20.55	19.69	20.26	20.65	20.24	18.47	17.79	13.49	14.38	
<i>Guyana</i>														
Cayenne	4.83°N	52.37°W	14.46	14.67	16.28	17.57	—	14.92	17.42	18.24	20.52	—	22.69	17.04
<i>Hong Kong</i>														
King's Park	22.32°N	114.17°E	12.34	7.39	6.94	9.50	11.38	13.60	16.70	17.06	15.91	16.52	14.19	10.09
<i>Hungary</i>														
Budapest	47.43°N	19.18°E	2.61	7.46	11.14	14.46	20.69	19.47	21.46	19.72	12.88	7.96	2.95	2.47
<i>Iceland</i>														
Reykjavík	64.13°N	21.90°W	0.52	2.02	6.25	11.77	13.07	14.58	16.83	11.35	9.70	3.18	1.00	0.65
<i>India</i>														
Mumbai	19.12°N	72.85°E	18.44	21.00	22.72	24.52	24.86	19.75	15.84	16.00	18.19	20.38	19.18	17.81
Calcutta	22.53°N	88.33°E	15.69	18.34	20.09	22.34	22.37	17.55	17.07	16.55	16.52	16.90	16.35	15.00
Chennai	13.00°N	80.18°E	19.09	22.71	25.14	24.88	23.89	—	18.22	19.68	19.81	16.41	14.76	15.79
Nagpur	21.10°N	79.05°E	18.08	21.01	22.25	24.08	24.79	19.84	15.58	15.47	17.66	20.10	18.98	17.33
New Delhi	28.58°N	77.20°E	14.62	18.25	20.15	23.40	23.80	19.16	20.20	19.89	20.08	19.74	16.95	14.22
<i>Ireland</i>														
Dublin	53.43°N	6.25°W	2.51	4.75	7.48	11.06	17.46	19.11	15.64	13.89	9.65	5.77	2.93	—
<i>Israel</i>														
Jerusalem	31.78°N	35.22°E	10.79	13.01	18.08	23.79	29.10	31.54	31.83	28.79	25.19	20.26	12.61	10.71
<i>Italy</i>														
Milan	45.43°N	9.28°E	—	6.48	10.09	13.17	17.55	16.32	18.60	16.86	11.64	5.40	3.52	2.41

(Continued)

TABLE A2.3a (CONTINUED)
 Worldwide Global Horizontal Average Solar Radiation (MJ/m².day)

Position	Lat	Long	Jan	Feb	Mar	Apr	May	Jun	Jul	Aug	Sep	Oct	Nov	Dec
Rome	41.80°N	12.55°E	—	9.75	13.38	15.82	18.89	22.27	21.53	16.08	8.27	6.41	4.49	
<i>Japan</i>														
Fukuoka	33.58°N	130.38°E	8.11	8.72	10.95	13.97	14.36	12.81	13.84	16.75	13.92	11.86	10.05	7.30
Tateno	36.05°N	140.13°E	9.06	12.17	11.00	15.78	16.52	15.26	—	—	—	9.60	8.55	8.26
Yonago	35.43°N	133.35°E	6.25	7.16	10.87	17.30	16.72	15.44	17.06	19.93	12.41	10.82	7.50	5.51
<i>Kenya</i>														
Mombasa	4.03°S	39.62°E	22.30	22.17	22.74	18.49	18.31	17.41	—	18.12	21.03	22.97	21.87	21.25
Nairobi	1.32°S	36.92°E	—	24.10	21.20	18.65	14.83	15.00	13.44	14.12	19.14	19.38	16.90	18.27
<i>Lithuania</i>														
Kaunas	54.88°N	23.88°E	1.89	4.43	7.40	12.97	18.88	18.74	21.41	15.79	10.40	5.64	1.80	1.10
<i>Madagascar</i>														
Antananarivo	18.80°S	47.48°E	15.94	13.18	13.07	11.53	9.25	8.21	9.32	—	—	16.43	15.19	15.62
<i>Malaysia</i>														
Kuala Lumpur	3.12°N	101.55°E	15.36	17.67	18.48	16.87	15.67	16.24	15.32	15.89	14.62	14.13	13.54	11.53
Penang	5.30°N	100.27°E	19.47	21.35	23.24	20.52	18.63	19.32	17.17	16.96	15.93	16.01	18.35	17.37
<i>Martinique</i>														
Le Lamentin	14.60°N	61.00°W	17.76	20.07	22.53	21.95	22.42	21.23	20.86	21.84	20.23	19.87	14.08	16.25
<i>Mexico</i>														
Chihuahua	28.63°N	106.08°W	14.80	—	—	26.94	26.28	24.01	24.22	20.25	19.55	10.57	15.79	
Orizabita	20.58°N	99.20°E	19.49	23.07	27.44	27.35	26.04	25.05	—	27.53	21.06	17.85	15.48	12.93
<i>Mongolia</i>														
Ulan Bator	47.93°N	106.98°E	6.28	9.22	14.34	18.18	20.50	19.34	16.34	16.65	14.08	11.36	7.19	5.35
Ulaanbaatar	47.75°N	96.85°E	6.43	10.71	14.83	20.32	23.86	20.46	21.66	17.81	15.97	10.92	7.32	5.08

<i>Morocco</i>	33.57°N	7.67°E	11.46	12.70	15.93	21.25	24.45	25.27	25.53	23.60	19.97	14.68	11.61	9.03
Casablanca														
<i>Mozambique</i>														
Maputo	25.97°S	32.60°E	26.35	23.16	19.33	20.54	16.33	14.17	—	—	—	22.55	25.48	26.19
<i>Netherlands</i>														
Maastricht	50.92°N	5.78°E	3.20	5.43	8.48	14.82	14.97	14.32	18.40	17.51	11.65	6.51	3.01	1.72
<i>New Caledonia</i>														
Koumac	20.57°S	164.28°E	24.89	21.15	16.96	18.98	15.67	14.55	15.75	17.62	22.48	15.83	27.53	26.91
<i>New Zealand</i>														
Wilmington	41.28°S	174.77°E	22.59	19.67	14.91	9.52	6.97	4.37	5.74	7.14	12.50	16.34	19.07	24.07
Christchurch	43.48°S	172.55°E	23.46	19.68	13.98	8.96	6.47	4.74	5.38	6.94	13.18	17.45	18.91	24.35
<i>Nigeria</i>														
Benin City	6.32°N	5.60°E	14.89	17.29	19.15	17.21	16.97	15.04	10.24	12.54	14.37	15.99	17.43	15.75
<i>Norway</i>														
Bergen	60.40°N	5.32°E	0.46	1.33	3.18	8.36	19.24	16.70	16.28	10.19	6.53	3.19	1.36	0.35
<i>Oman</i>														
Seeb	23.58°N	58.28°E	12.90	14.86	21.22	22.22	25.30	24.02	23.46	21.66	20.07	18.45	15.49	13.12
Salalah	17.03°N	54.08°E	16.52	16.92	18.49	20.65	21.46	16.92	8.52	11.41	17.14	18.62	16.42	—
<i>Pakistan</i>														
Karachi	24.90°N	67.13°E	13.84	—	—	19.69	20.31	16.62	—	—	—	—	12.94	11.07
Multan	30.20°N	71.43°E	12.29	15.86	18.33	22.35	22.57	21.65	20.31	20.44	20.57	15.91	12.68	10.00
Islamabad	33.62°N	73.10°E	10.38	12.42	16.98	22.65	—	25.49	20.64	18.91	14.20	15.30	10.64	8.30
<i>Peru</i>														
Puno	15.83°S	70.02°W	14.98	12.92	16.08	20.03	17.45	17.42	15.74	15.32	16.11	16.18	14.24	13.90
<i>Poland</i>														
Warszawa	52.28°N	20.97°E	1.73	3.83	7.81	10.53	19.22	17.11	20.18	15.00	10.65	4.95	2.39	1.68
Kolobrzeg	54.18°N	15.58°E	2.50	3.25	8.86	15.21	20.79	20.50	17.19	16.46	7.95	5.75	1.78	1.18

(Continued)

TABLE A2.3a (CONTINUED)

Worldwide Global Horizontal Average Solar Radiation (MJ/m²-day)

Position	Lat	Long	Jan	Feb	Mar	Apr	May	Jun	Jul	Aug	Sep	Oct	Nov	Dec
<i>Portugal</i>														
Evora	38.57°N	7.90°W	9.92	12.43	17.81	18.69	23.57	29.23	28.75	23.77	20.17	—	6.81	4.57
Lisbon	38.72°N	9.15°W	9.24	11.60	17.52	18.49	24.64	29.02	28.14	22.20	19.76	13.56	7.18	4.83
<i>Romania</i>														
Bucharest	44.50°N	26.13°E	7.05	10.22	12.04	16.53	18.97	22.16	23.19	—	17.17	9.55	4.82	—
Constanta	44.22°N	28.63°E	5.62	9.28	14.31	20.59	23.23	25.80	27.98	24.22	16.91	11.89	6.19	5.10
Galati	45.50°N	28.02°E	6.09	9.33	14.31	17.75	21.77	22.74	25.55	19.70	14.05	11.26	6.32	5.38
<i>Russia</i>														
Alexandrovsk	60.38°N	77.87°E	1.34	4.17	9.16	17.05	21.83	21.34	20.26	13.05	10.16	4.68	1.71	0.68
Moscow	55.75°N	37.57°E	1.45	3.96	8.09	11.69	18.86	18.12	17.51	14.17	10.92	4.03	2.28	1.29
St. Petersburg	59.97°N	30.30°E	1.03	3.11	4.88	12.24	20.59	21.55	20.43	13.27	7.83	2.93	1.16	0.59
Verkhoyansk	67.55°N	133.38°E	0.21	2.25	7.61	15.96	19.64	—	—	14.12	7.59	3.51	0.54	—
<i>St. Pierre and Miquelon</i>														
St. Pierre	46.77°N	56.17°W	4.43	6.61	12.50	17.57	18.55	17.84	19.95	16.46	12.76	8.15	3.69	3.33
<i>Singapore</i>														
Singapore	1.37°N	103.98°E	19.08	20.94	20.75	18.20	14.89	15.22	13.92	16.66	16.51	15.82	13.81	12.67
<i>South Korea</i>														
Seoul	37.57°N	126.97°E	6.24	9.40	10.34	13.98	16.35	17.49	10.65	12.94	11.87	10.35	6.47	5.14
<i>South Africa</i>														
Cape Town	33.98°S	18.60°E	27.47	25.57	—	15.81	11.44	9.08	8.35	13.76	17.30	22.16	26.37	27.68
Port Elizabeth	33.98°S	25.60°E	27.22	22.06	19.01	15.29	11.79	11.13	10.73	13.97	18.52	23.09	23.15	27.26
Pretoria	25.73°S	28.18°E	26.06	22.43	20.52	16.09	15.67	13.67	15.19	18.65	21.62	21.75	24.82	23.43
<i>Spain</i>														
Madrid	40.45°N	3.72°W	7.73	10.53	15.35	21.74	22.81	22.05	26.27	22.90	18.89	10.21	8.69	5.56

(Continued)

TABLE A2.3a (CONTINUED)
 Worldwide Global Horizontal Average Solar Radiation ($MJ/m^2\text{-day}$)

Position	Lat	Long	Jan	Feb	Mar	Apr	May	Jun	Jul	Aug	Sep	Oct	Nov	Dec
<i>Vietnam</i>														
Hanoi	21.03°N	105.85°E	5.99	7.48	8.73	13.58	19.10	21.26	19.85	19.78	20.67	14.78	12.44	13.21
<i>Yugoslavia</i>														
Beograd	44.78°N	20.53°E	4.92	6.27	10.64	14.74	20.95	22.80	22.09	20.27	15.57	11.24	6.77	4.99
Kopaonik	43.28°N	20.80°E	7.03	10.93	14.75	12.78	13.54	20.43	22.48	—	20.14	11.61	6.26	4.64
Portoroz	45.52°N	13.57°E	5.11	7.84	13.75	17.30	23.66	22.31	25.14	21.34	13.40	8.98	6.04	3.92
<i>Zambia</i>														
Lusaka	15.42°S	28.32°W	16.10	18.02	20.24	19.84	17.11	16.37	19.45	20.72	21.68	23.83	23.85	20.52
<i>Zimbabwe</i>														
Bulawayo	20.15°S	28.62°N	20.03	22.11	21.03	18.09	17.15	15.36	16.46	19.49	21.55	23.44	25.08	23.46
Harare	17.83°S	31.02°N	19.38	19.00	19.22	17.67	18.35	16.10	14.55	17.87	21.47	23.98	19.92	21.88

Source: Voeikov Main Geophysical Observatory, Russia (http://wrdc-mgo.nrel.gov/html/get_data-ap.html). Data for 872 locations are available from these sources in 68 countries. Source for Canadian data: Environment Canada (<http://www.ec.gc.ca/~envhome.html>).

TABLE A2.3b
Average Daily Solar Radiation on a Horizontal Surface in the United States (MJ/m²·day)

Position	Jan	Feb	Mar	Apr	May	June	July	Aug	Sep	Oct	Nov	Dec	Average
<i>Alabama</i>													
Birmingham	9.20	11.92	15.67	19.65	21.58	22.37	21.24	20.21	17.15	14.42	10.22	8.40	16.01
Montgomery	9.54	12.49	16.24	20.33	22.37	23.17	21.80	20.56	17.72	14.99	10.90	8.97	16.58
<i>Alaska</i>													
Fairbanks	0.62	2.77	8.31	14.66	17.98	19.65	16.92	12.36	7.02	3.20	1.01	0.23	8.74
Anchorage	1.02	3.41	8.18	13.06	15.90	17.72	16.69	12.72	8.06	3.97	1.48	0.56	8.63
Nome	0.51	2.95	8.29	15.22	18.97	19.65	16.69	11.81	7.72	3.63	0.99	0.09	8.86
St. Paul Island	1.82	4.32	8.52	12.72	14.08	14.42	12.83	10.33	7.84	4.54	2.16	1.25	7.95
Yakutat	1.36	3.63	7.72	12.61	14.76	15.79	14.99	12.15	7.95	3.97	1.82	0.86	8.18
<i>Arizona</i>													
Phoenix	11.58	15.33	19.87	25.44	28.85	30.09	27.37	25.44	21.92	17.60	12.95	10.56	20.56
Tucson	12.38	15.90	20.21	25.44	28.39	29.30	25.44	24.08	21.58	17.94	13.63	11.24	20.44
<i>Arkansas</i>													
Little Rock	9.09	11.81	15.56	19.19	21.80	23.51	23.17	21.35	17.26	14.08	9.77	8.06	16.24
Fort Smith	9.31	12.15	15.67	19.31	21.69	23.39	23.85	24.46	17.26	13.97	9.88	8.29	16.35
<i>California</i>													
Bakersfield	8.29	11.92	16.69	22.15	26.57	28.96	28.73	26.01	21.35	15.90	10.33	7.61	18.74
Fresno	7.61	11.58	16.81	22.49	27.14	29.07	28.96	25.89	21.12	15.56	9.65	6.70	18.62
Long Beach	9.99	12.95	17.03	21.60	23.17	24.19	26.12	24.08	19.31	14.99	11.24	9.31	17.83
Sacramento	6.93	10.68	15.56	21.24	25.89	28.28	28.62	25.32	20.56	14.54	8.63	6.25	17.72
San Diego	11.02	13.97	17.72	21.92	22.49	23.28	24.98	23.51	19.53	15.79	12.26	10.22	18.06
San Francisco	7.72	10.68	15.22	20.44	24.08	25.78	26.46	23.39	19.31	13.97	8.97	7.04	16.92
Los Angeles	10.11	13.06	17.26	21.80	23.05	23.74	25.67	23.51	18.97	14.99	11.36	9.31	17.72

(Continued)

TABLE A2.3b (CONTINUED)
Average Daily Solar Radiation on a Horizontal Surface in the United States (MJ/m²/day)

Position	Jan	Feb	Mar	Apr	May	June	July	Aug	Sep	Oct	Nov	Dec	Average
Santa Maria	10.22	13.29	17.49	22.26	25.10	26.57	26.91	24.42	20.10	15.67	11.47	9.54	18.62
<i>Colorado</i>													
Boulder	7.84	10.45	15.64	17.94	20.47	20.28	17.12	16.07	12.09	8.66	7.10	14.31	
Colorado Springs	9.09	12.15	16.13	20.33	22.26	24.98	23.96	21.69	18.51	14.42	9.99	8.18	16.81
<i>Connecticut</i>													
Hartford	6.70	9.65	13.17	16.69	19.53	21.24	21.12	18.51	14.76	10.68	6.59	5.45	13.74
<i>Delaware</i>													
Wilmington	7.27	10.22	13.97	17.60	20.33	22.49	21.80	19.65	15.79	11.81	7.84	6.25	14.65
<i>Florida</i>													
Daytona Beach	11.24	13.85	17.94	22.15	23.17	22.03	21.69	20.44	17.72	14.99	12.15	10.33	17.38
Jacksonville	10.45	13.17	17.03	21.12	22.03	21.58	21.01	19.42	16.69	14.20	11.47	9.65	16.47
Tallahassee	10.33	13.29	16.92	21.24	22.49	22.03	20.90	19.65	17.72	15.56	11.92	9.77	16.81
Miami	12.72	15.22	18.51	21.58	21.46	20.10	21.10	20.10	17.60	15.67	13.17	11.81	17.38
Key West	13.17	16.01	19.65	22.71	22.83	22.03	22.03	21.01	18.74	16.47	13.85	15.79	18.40
Tampa	11.58	14.42	18.17	22.26	23.05	21.92	20.90	19.65	17.60	16.01	12.83	11.02	17.49
<i>Georgia</i>													
Athens	9.43	12.38	16.01	20.21	22.03	22.83	21.80	20.21	17.26	14.42	10.45	8.40	16.29
Atlanta	9.31	12.26	16.13	20.33	22.37	23.17	22.15	20.56	17.49	14.54	10.56	8.52	16.43
Columbus	9.77	12.72	16.47	20.67	22.37	22.83	21.58	20.33	17.60	14.99	11.02	9.09	16.62
Macon	9.54	12.61	16.35	20.56	22.37	22.83	21.58	20.21	17.26	14.88	10.90	8.86	16.50
Savanna	9.99	12.72	16.81	21.01	22.37	22.60	21.80	19.76	16.92	14.65	11.13	9.20	16.58
<i>Hawaii</i>													
Honolulu	14.08	16.92	19.42	21.24	22.83	23.51	23.74	23.28	21.35	18.06	14.88	13.40	19.42

(Continued)

TABLE A2.3b (CONTINUED)
 Average Daily Solar Radiation on a Horizontal Surface in the United States (MJ/m²·day)

Position	Jan	Feb	Mar	Apr	May	June	July	Aug	Sep	Oct	Nov	Dec	Average
<i>Michigan</i>													
Detroit	5.91	8.86	12.38	16.47	20.33	22.37	21.92	18.97	14.76	10.11	6.13	4.66	13.63
Lansing	5.91	8.86	12.49	16.58	20.21	22.26	21.92	18.85	14.54	9.77	5.91	4.66	13.51
<i>Minnesota</i>													
Duluth	5.68	9.31	13.74	17.38	20.10	21.46	21.80	18.28	13.29	8.86	5.34	4.43	13.29
Minneapolis	6.36	9.77	13.51	16.92	20.56	22.49	22.83	19.42	14.65	9.99	6.13	4.88	13.97
Rochester	6.36	9.65	13.17	16.58	20.10	22.15	22.15	19.08	14.54	10.11	6.25	5.11	13.74
<i>Mississippi</i>													
Jackson	9.43	12.38	16.13	19.87	22.15	23.05	22.15	19.08	14.54	10.11	6.25	5.11	13.74
<i>Missouri</i>													
Columbia	8.06	10.90	14.31	18.62	21.58	23.62	23.85	21.12	16.69	12.72	8.29	6.70	15.56
Kansas City	7.95	10.68	14.08	18.28	21.24	23.28	23.62	20.78	16.58	12.72	8.40	6.70	15.44
Springfield	8.52	11.02	14.65	18.62	21.24	23.05	23.62	21.24	16.81	13.17	8.86	7.27	15.67
St. Louis	7.84	10.56	13.97	18.06	21.12	23.05	22.94	20.44	16.58	12.49	8.18	6.59	15.22
<i>Montana</i>													
Helena	5.22	8.29	12.61	17.15	20.67	23.28	25.21	21.24	15.79	10.45	6.02	4.43	14.20
Lewistown	5.22	8.40	12.72	17.15	20.33	23.05	24.53	20.78	15.10	10.22	5.91	4.32	13.97
<i>Nebraska</i>													
Omaha	7.50	10.33	13.97	18.06	21.24	2.40	23.51	20.56	16.01	11.81	7.61	6.13	15.10
Lincoln	7.33	10.10	13.65	16.22	19.26	21.21	22.15	18.87	15.44	11.54	7.76	6.20	14.16
<i>Nevada</i>													
Elko	7.61	10.56	14.42	18.85	22.71	25.67	26.69	23.62	19.31	13.63	8.29	6.70	16.58
Las Vegas	10.79	14.42	19.42	24.87	28.16	30.09	28.28	25.89	22.15	17.03	12.15	9.88	20.33
Reno	8.29	11.58	16.24	21.24	25.10	27.48	28.16	24.98	20.56	14.88	9.31	7.38	17.94

	New Hampshire	Concord	10.11	13.97	16.92	20.21	21.80	19.08	14.99	10.45	6.47	5.45	14.08
<i>New Jersey</i>													
Atlantic City	7.38	10.22	13.97	17.49	20.21	21.92	21.24	19.19	15.79	11.92	8.06	6.36	14.54
Newark	6.93	9.77	13.51	17.26	19.76	21.35	21.01	18.85	15.33	11.36	7.27	5.68	13.97
<i>New Mexico</i>													
Albuquerque	11.47	14.99	19.31	24.53	27.60	29.07	27.03	24.76	21.12	17.03	12.49	10.33	19.99
<i>New York</i>													
Albany	6.36	9.43	12.95	16.69	19.53	21.46	21.58	18.51	14.65	10.11	6.13	5.00	13.51
Buffalo	5.68	8.40	12.15	16.35	19.76	22.03	21.69	18.62	14.08	9.54	5.68	4.54	13.29
New York City	6.93	9.88	13.85	17.72	20.44	22.03	21.69	19.42	15.56	11.47	7.27	5.79	14.31
Rochester	5.68	8.52	12.26	16.58	19.87	21.92	21.69	18.51	14.20	9.54	5.68	4.54	13.29
<i>North Carolina</i>													
Charlotte	8.97	11.81	15.67	19.76	21.58	22.60	21.92	19.99	16.92	13.97	9.99	8.06	16.01
Wilmington	9.31	12.15	16.24	20.44	21.92	22.60	21.58	19.53	16.69	14.08	10.56	8.52	16.13
<i>North Dakota</i>													
Fargo	5.79	9.09	13.17	16.92	20.56	22.37	23.17	19.87	14.31	9.54	5.68	4.54	13.74
Bismarck	6.12	9.75	13.88	17.43	21.45	23.01	24.06	20.12	15.21	10.61	6.28	4.84	14.39
<i>Ohio</i>													
Cleveland	5.79	8.63	12.04	16.58	20.10	22.15	21.92	18.97	14.76	10.22	6.02	4.66	13.51
Columbus	6.47	9.09	12.49	16.58	19.76	21.58	21.12	18.97	15.44	11.24	6.81	5.34	13.74
Dayton	6.81	9.43	12.83	17.03	20.33	22.37	22.37	19.65	15.90	11.47	7.04	5.45	14.20
Youngstown	5.79	8.40	11.92	15.90	19.19	21.24	20.78	18.06	14.31	10.11	6.02	4.77	13.06
<i>Oklahoma</i>													
Oklahoma City	9.88	1.25	16.47	20.33	22.26	24.42	24.98	22.49	18.17	14.54	10.45	8.74	17.15
<i>Oregon</i>													
Eugene	4.54	7.04	11.24	15.79	19.99	22.37	24.19	21.01	15.90	9.65	5.11	3.75	13.40
Medford	5.34	8.52	13.17	18.62	23.39	26.23	27.82	23.96	18.62	11.92	6.02	4.43	15.67

(Continued)

TABLE A2.3b (CONTINUED)
 Average Daily Solar Radiation on a Horizontal Surface in the United States (MJ/m²/day)

Position	Jan	Feb	Mar	Apr	May	June	July	Aug	Sep	Oct	Nov	Dec	Average
Portland	4.20	6.70	10.68	15.10	18.97	21.24	22.60	19.53	14.88	9.20	4.88	3.52	12.61
<i>Pacific Islands</i>													
Guam	16.35	17.38	19.65	20.78	20.56	19.76	18.28	17.49	17.49	16.58	15.79	15.10	17.94
<i>Pennsylvania</i>													
Philadelphia	7.04	9.88	13.63	17.26	19.99	22.03	21.46	19.42	15.67	11.58	7.72	6.02	14.31
Pittsburgh	6.25	8.97	12.61	16.47	19.65	21.80	21.35	18.85	15.10	10.90	6.59	5.00	13.63
<i>Rhode Island</i>													
Providence	6.70	9.65	13.40	16.92	19.99	21.58	21.24	18.85	15.22	11.02	6.93	5.56	13.97
<i>South Carolina</i>													
Charleston	9.77	12.72	16.81	21.12	22.37	22.37	21.92	19.65	16.92	14.54	11.02	9.09	16.58
Greenville	9.20	12.04	15.90	19.99	21.58	22.60	21.58	19.87	16.81	14.08	10.22	8.18	16.01
<i>South Dakota</i>													
Pierre	6.47	9.54	13.85	17.94	21.46	24.08	24.42	21.46	16.35	11.24	7.04	5.45	14.99
Rapid City	6.70	9.88	14.20	18.28	21.46	24.19	24.42	21.80	16.92	11.81	7.50	5.79	15.33
<i>Tennessee</i>													
Memphis	8.86	11.58	15.22	19.42	22.03	23.85	23.39	21.46	17.38	14.20	9.65	7.84	16.24
Nashville	8.29	11.13	14.65	19.31	21.69	23.51	22.49	20.56	16.81	13.51	8.97	7.15	15.67
<i>Texas</i>													
Austin	10.68	13.63	17.03	19.53	21.24	23.74	24.42	22.83	18.85	15.67	11.92	9.99	17.49
Brownsville	10.33	13.17	16.47	19.08	20.78	22.83	23.28	21.58	18.62	16.13	12.38	9.88	17.03
El Paso	12.38	16.24	20.90	25.44	28.05	28.85	26.46	24.30	21.12	17.72	13.63	11.47	20.56
Houston	9.54	12.26	15.22	18.06	20.21	21.69	21.35	20.21	17.49	15.10	11.02	8.97	15.90
San Antonio	10.88	13.53	16.26	17.35	21.10	23.87	24.92	22.81	19.22	15.52	11.50	9.98	17.24

<i>Utah</i>	Salt Lake City	6.93	10.45	14.76	19.42	23.39	26.46	26.35	23.39	18.85	13.29	8.06	6.02	16.47
<i>Vermont</i>	Burlington	5.79	9.20	13.06	16.47	19.87	21.69	21.80	18.74	14.42	9.43	5.56	4.43	13.40
<i>Virginia</i>	Norfolk	8.06	10.90	14.65	18.51	20.78	22.15	21.12	19.42	16.13	12.49	9.09	7.27	15.10
<i>Richmond</i>	Richmond	8.06	10.90	14.76	18.62	20.90	22.49	21.58	19.53	16.24	12.61	8.97	7.15	15.22
<i>Washington</i>	Olympia	3.63	6.02	9.99	14.20	18.06	20.10	21.12	18.17	13.63	7.95	4.32	3.07	11.70
<i>Seattle</i>	Seattle	3.52	5.91	10.11	14.65	19.08	20.78	21.80	18.51	13.51	7.95	4.20	2.84	11.92
<i>Yakima</i>	Yakima	4.88	7.95	12.83	17.83	22.49	24.87	25.89	22.26	16.92	10.68	5.56	4.09	17.76
<i>West Virginia</i>	Charleston	7.04	9.65	13.40	17.15	20.21	21.69	20.90	18.97	15.56	11.81	7.72	6.02	14.20
<i>Elkins</i>	Elkins	6.93	9.43	12.83	16.35	19.08	20.56	19.99	18.06	14.88	11.13	7.27	5.79	13.51
<i>Wisconsin</i>	Green Bay	6.25	9.31	13.17	16.81	20.56	22.49	22.03	18.85	14.20	9.65	5.79	4.88	13.74
<i>Madison</i>	Madison	6.59	9.88	13.29	16.92	20.67	22.83	22.37	19.42	14.76	3.41	6.25	5.22	14.08
<i>Milwaukee</i>	Milwaukee	6.47	9.31	12.72	16.69	20.78	22.94	22.60	19.42	14.88	10.22	6.25	5.11	13.97
<i>Wyoming</i>	Rock Springs	7.61	10.90	15.10	19.42	23.17	26.01	25.78	22.94	18.62	13.40	8.40	6.70	16.58
<i>Sheridan</i>	Sheridan	6.47	9.77	13.97	17.94	20.90	23.85	24.64	21.69	16.47	11.24	7.15	5.56	14.99

Source: National Renewable Energy Laboratory, USA (<http://rredc.nrel.gov/solar>).

TABLE A2.4Regression Coefficients a and b for Page Model for Solar Radiation (Equation 2.52) for Worldwide Locations

Country	Station	Lat.	Alt. (m)	Climate (Khogali et al. 1983)	a	b	Ref.
Egypt	Bahiti	30.13°N	200	BWh	0.220	0.550	Ibrahim (1985)
	Cairo	30.08°N	112	BWh	0.140	0.610	Ibrahim (1985)
	Giza	30.05°N	19	BWh	0.230	0.540	Ibrahim (1985)
	Kharga Oasis	25.45°N	78	BWh	0.520	0.230	Ibrahim (1985)
	Mersa M.	31.33°N	20	BWh	0.170	0.590	Ibrahim (1985)
	Tahrir	30.65°N	16	BWh	0.290	0.460	Ibrahim (1985)
Ghana	Accra	5.33°N	~20	BS	0.290	0.470	Anane-Fenin (1986)
	Bole	9.02°N	~350	Aw	0.280	0.440	Anane-Fenin (1986)
	Ho	6.35°N	~300	Aw	0.210	0.460	Anane-Fenin (1986)
	Kumasi	6.41°N	~400	Aw	0.250	0.440	Anane-Fenin (1986)
	Saltpond	5.12°N	~50	BS	0.260	0.450	Anane-Fenin (1986)
	Takoradi	4.59°N	~20	BS	0.250	0.470	Anane-Fenin (1986)
	Tamale	9.25°N	~250	Aw	0.270	0.470	Anane-Fenin (1986)
	Wenchi	7.42°N	~300	Aw	0.280	0.360	Anane-Fenin (1986)
	Yendi	9.26°N	~300	Aw	0.320	0.410	Anane-Fenin (1986)
	Greece	38.63°N	60	Csa	0.240	0.520	Zabara (1986)
	Athens	37.97°N	~300	Csa	0.230	0.460	Zabara (1986)
	Chania	35.50°N	50	Csa	0.220	0.580	Zabara (1986)
	Kavala	40.93°N	150	Csa	0.250	0.460	Zabara (1986)
	Larissa	39.63°N	65	Csa	0.230	0.560	Zabara (1986)
	Mytilene	39.15°N	65	Csa	0.240	0.510	Zabara (1986)
	Rhodes	36.37°N	5	Csa	0.260	0.520	Zabara (1986)
	Hong Kong	Hong Kong	22.37°N	Caf	0.214	0.514	Leung (1980)
			~5				

India	Ahmedabad	22.37°N	55	Aw	0.302	0.464	Garg and Garg (1985)
	Bombay (Mumbai)	19.12°N	14	Aw	0.292	0.464	Garg and Garg (1985)
	Calcutta	22.65°N	6	Aw	0.327	0.399	Garg and Garg (1985)
	Goa	15.48°N	55	Am	0.279	0.514	Garg and Garg (1985)
	Jodhpur	26.30°N	224	BSh	0.309	0.439	Garg and Garg (1985)
	Madras	13.00°N	16	Aw	0.340	0.399	Garg and Garg (1985)
	Nagpur	21.10°N	310	Aw	0.293	0.460	Garg and Garg (1985)
	New Delhi	28.63°N	216	Caw	0.341	0.446	Garg and Garg (1985)
	Poona	18.53°N	559	Bs	0.330	0.453	Garg and Garg (1985)
	Trivandrum	8.48°N	64	Am	0.393	0.357	Garg and Garg (1985)
Italy	Vizagapatnam	17.72°N	3	Aw	0.286	0.467	Garg and Garg (1985)
	Alghero	40.63°N	40	Csa	0.118	0.765	Jain (1986)
	Amendola	41.53°N	56	Csa	0.212	0.635	Jain (1986)
	Ancona	43.63°N	105	Csa	0.197	0.679	Jain (1986)
	Balzano	46.47°N	241	Csa	0.192	0.719	Jain (1986)
	Bologna	44.53°N	49	Csa	0.216	0.639	Jain (1986)
	Brindisi	40.65°N	10	Csa	0.183	0.706	Jain (1986)
	Cagliari	39.25°N	18	Csa	0.175	0.679	Jain (1986)
	Cape Mele	43.95°N	221	Csa	0.129	0.779	Jain (1986)
	Cape Palinurus	40.02°N	185	Csa	0.213	0.604	Jain (1986)
Italy	Crotone	39.07°N	158	Csa	0.266	0.546	Jain (1986)
	Gela	37.09°N	33	Csa	0.105	0.851	Jain (1986)
	Genova	44.42°N	3	Csa	0.089	0.821	Jain (1986)
	M. Cimone	44.20°N	2137	H	0.104	0.755	Jain (1986)
	M. Terminillo	42.47°N	1875	H	0.246	0.482	Jain (1986)
	Messina	38.20°N	59	Csa	0.199	0.689	Jain (1986)

(Continued)

TABLE A2.4 (CONTINUED)Regression Coefficients *a* and *b* for Page Model for Solar Radiation (Equation 2.52) for Worldwide Locations

Country	Station	Lat.	Alt. (m)	Climate (Khogali et al. 1983)	<i>a</i>	<i>b</i>	Ref.
Milano	45.43°N	103	Csa	0.148	0.775	Jain (1986)	
Napoli	40.85°N	72	Csa	0.181	0.709	Jain (1986)	
Olbia	40.93°N	2	Csa	0.183	0.633	Jain (1986)	
Pantelleria	36.82°N	170	Csa	0.191	0.679	Jain (1986)	
Pescara	42.43°N	18	Csa	0.188	0.669	Jain (1986)	
Pianosa	42.58°N	27	Csa	0.143	0.771	Jain (1986)	
Pisa	43.67°N	1	Csa	0.205	0.614	Jain (1986)	
Roma	41.80°N	131	Csa	0.148	0.722	Jain (1986)	
Torino	45.18°N	282	Daf	0.161	0.780	Jain (1986)	
Trapani	37.92°N	14	Csa	0.204	0.662	Jain (1986)	
Trieste	45.65°N	20	Csa	0.157	0.701	Jain (1986)	
Udine	46.03°N	92	Csa	0.167	0.666	Jain (1986)	
Üstica	38.70°N	251	Csa	0.254	0.586	Jain (1986)	
Venezia	45.50°N	6	Csa	0.144	0.782	Jain (1986)	
Vigna Diwali	42.08°N	270	Csa	0.154	0.689	Jain (1986)	
Kota Bharu	6.17°N	5	Af	0.340	0.490	Chuah and Lee (1981)	
Kuala Lumpur	3.12°N	19	Af	0.340	0.490	Chuah and Lee (1981)	
Penang	5.33°N	35	Af	0.350	0.570	Chuah and Lee (1981)	
Enugu	6.47°N	137	Af	0.228	0.492	Eze and Ododo (1988)	
Makurdi	7.70°N	76	Aw	0.288	0.472	Eze and Ododo (1988)	
Nsukka	6.80°N	147	Af	0.217	0.490	Eze and Ododo (1988)	
Port Harcourt	4.85°N	6	Af	0.246	0.488	Eze and Ododo (1988)	
Lungi Free	8.61°N	25	Am	0.260	0.440	Massaquoi (1988)	
Abu Naama	12.73°N	445	BShw	0.433	0.271	Khogali (1983)	

Aroma	15.83°N	430	BWh	0.460	0.208	Khogali (1983)
Dongola	19.17°N	225	BWh	0.211	0.572	Khogali (1983)
El Fasher	13.63°N	773	BShw	0.361	0.366	Khogali (1983)
El Showak	14.22°N	380	BWh	0.325	0.423	Khogali (1983)
G. Ghawazat	11.47°N	480	Aw	0.350	0.353	Khogali (1983)
Hudeiba	17.57°N	350	BWh	0.208	0.544	Khogali (1983)
Jubo	4.87°N	460	Aw	0.402	0.234	Khogali (1983)
Kadugli	11.00°N	501	Aw	0.237	0.463	Khogali (1983)
Malakai	9.55°N	387	Aw	0.339	0.359	Khogali (1983)
Port Sudan	19.58°N	5	BWh	0.315	0.402	Khogali (1983)
Shambat	15.67°N	376	BWh	0.278	0.467	Khogali (1983)
Wadi Medani	14.38°N	405	BWh	0.357	0.374	Khogali (1983)
Zalingei	12.90°N	900	BShw	0.325	0.456	Khogali (1983)
Yemen	15.73°N	2100	H	0.331	0.385	Khogali et al. (1983)
El Khabar	14.38°N	2100	H	0.342	0.372	Khogali et al. (1983)
El Macca	13.25°N	10	BWh	0.358	0.346	Khogali et al. (1983)
Hodeidah	14.75°N	33	BWh	0.374	0.321	Khogali et al. (1983)
Sana	15.52°N	2210	BSh	0.347	0.364	Khogali et al. (1983)
Taiz	13.58°N	1400	H	0.364	0.335	Khogali et al. (1983)
Kasama	10.22°S	1384	Aw	0.268	0.454	Jain and Jain (1985)
Livingstone	17.82°S	986	Aw	0.187	0.613	Jain and Jain (1985)
Luangwa	13.27°S	570	Aw	0.253	0.588	Jain and Jain (1985)
Lusaka	15.32°S	1154	Aw	0.198	0.551	Jain and Jain (1985)
Mansa	11.10°S	1259	Aw	0.265	0.476	Jain and Jain (1985)
Mbala	8.37°S	1673	Aw	0.245	0.505	Jain and Jain (1985)
Mongu	15.25°S	1053	Aw	0.188	0.556	Jain and Jain (1985)
Ndolo	13.00°S	1270	Aw	0.288	0.386	Jain and Jain (1985)

Source: Data compiled from Akinoglu, B.G., A review of sunshine-based models used to estimate monthly average global solar radiation. *Renewable Energy*, 1 (3), 479–499, 1991.

TABLE A2.5Solar Collector Tilt Factor (\bar{R}_b) for South-Facing Collectors

Month	$L = 20^\circ$		$L = 30^\circ$		$L = 40^\circ$		$L = 50^\circ$	
	$\beta = 20^\circ$	$\beta = 40^\circ$	$\beta = 30^\circ$	$\beta = 50^\circ$	$\beta = 40^\circ$	$\beta = 60^\circ$	$\beta = 50^\circ$	$\beta = 70^\circ$
Jan	1.36	1.52	1.68	1.88	2.28	2.56	3.56	3.94
Feb	1.22	1.28	1.44	1.52	1.80	1.90	2.49	2.62
Mar	1.08	1.02	1.20	1.15	1.36	1.32	1.65	1.62
Apr	1.00	0.83	1.00	0.84	1.05	0.90	1.16	1.00
May	0.92	0.70	0.87	0.66	0.88	0.66	0.90	0.64
Jun	0.87	0.63	0.81	0.58	0.79	0.60	0.80	0.56
Jul	0.89	0.66	0.83	0.62	0.82	0.64	0.84	0.62
Aug	0.95	0.78	0.93	0.76	0.96	0.78	1.02	0.83
Sep	1.04	0.95	1.11	1.00	1.24	1.12	1.44	1.32
Oct	1.17	1.20	1.36	1.36	1.62	1.64	2.10	2.14
Nov	1.30	1.44	1.60	1.76	2.08	2.24	3.16	3.32
Dec	1.39	1.60	1.76	1.99	2.48	2.80	4.04	4.52

Source: Kreider, J.F. and F. Kreith, *Solar Heating and Cooling*, Revised 1st ed., Hemisphere Publ. Corp., 1977.

Note: The solar collector tilt factor is the ratio of monthly beam insolation on a tilted surface to monthly beam insolation on a horizontal surface. Here, β = collector tilt angle and L = collector latitude.

Date	Solar time		Solar position		Total insolation on surface (W/m ²)						
	a.m.	p.m.	Alt	Azm	Direct normal	Horiz.	South-facing surface angle with horizon				
Jan 21							14°	24°	34°	44°	90°
7	5	4.8	65.6	224	32	54	66	79	88	98	
8	4	16.9	58.3	753	262	347	397	432	457	400	
9	3	27.9	48.8	908	476	593	652	697	719	555	
10	2	37.2	36.1	971	643	775	845	889	905	652	
11	1	43.6	19.6	999	747	892	965	1005	1021	712	
12		46	0	1009	785	933	690	1046	1059	731	
		Surface daily totals					8718	5113	6254	6852	7250
Feb 21	7	5	9.3	74.6	498	110	139	154	167	177	145
	8	4	22.3	67.2	829	366	426	457	473	476	322
	9	3	34.4	57.6	939	589	671	709	725	719	444
	10	2	45.1	44.2	990	760	860	901	917	905	530
	11	1	53	25	1012	870	977	1021	1034	1018	583
	12		56	0	1021	908	1018	1062	1075	1056	602
	Surface daily totals					9569	6298	7174	7552	7678	7640
Mar 21	7	5	13.7	83.3	611	189	199	202	195	186	85
	8	4	27.2	76.8	842	444	473	479	470	448	202
	9	3	40.2	67.9	930	668	712	722	709	675	299
	10	2	52.3	54.8	974	838	898	908	892	851	378
	11	1	61.9	33.4	993	946	1015	1028	1009	961	426
	12		66	0	999	983	1053	1069	1050	999	441
	Surface daily totals					9702	7155	7653	7741	7603	7243
Apr 21	6	6	4.7	100.6	126	22	16	13	13	9	6
	7	5	18.3	94.9	640	262	243	221	195	161	32
	8	4	32	89	807	504	495	470	432	385	50
	9	3	45.6	81.9	883	716	716	693	649	586	145
	10	2	59	71.8	920	876	889	867	816	842	192
	11	1	71.1	51.6	939	977	996	974	924	848	233
	12		77.6	0	942	1012	1034	1012	961	883	249
Surface daily totals					9569	7735	7748	7483	7023	6354	1538
May 21	6	6	8	108.4	271	69	47	32	28	28	16
	7	5	21.2	103.2	640	309	268	230	186	139	38
	8	4	34.6	98.5	782	539	501	457	400	334	47
	9	3	48.3	93.6	848	734	706	662	599	520	50
	10	2	62	87.7	883	886	867	823	753	665	69
	11	2	75.5	76.9	901	980	968	924	851	756	107
	12		86	0	908	1015	999	958	886	788	117
Surface daily totals					9557	8057	7713	7205	6531	5674	769

FIGURE A2.2a

Solar position and insolation values for 24°N latitude.

(Continued)

Date	Solar time		Solar position		Total insolation on surface (W/m ²)							
	a.m.	p.m.	Alt	Azm	Direct Normal	Horiz.	South-facing surface angle with horizon					
							14°	24°	34°	44°	90°	
Jun 21	6	6	9.3	111.6	306	91	63	38	38	35	22	
	7	5	22.3	106.8	634	325	274	230	183	129	41	
	8	4	35.5	102.6	763	545	498	448	385	312	50	
	9	3	49	98.7	829	738	697	643	574	489	57	
	10	2	62.6	98	864	883	848	797	722	627	57	
	11	1	76.3	90.8	879	974	946	892	816	716	60	
	12		89.4	0	886	1005	977	927	848	744	69	
	Surface daily totals				9437	8113	7599	7029	6279	5358	643	
	Surface daily totals				9242	7962	7603	7092	6417	5566	775	
	Surface daily totals				9027	7590	7571	7300	6834	6172	1481	
Jul 21	6	6	8.2	109	255	72	50	35	32	28	19	
	7	5	21.4	103.8	615	309	268	230	186	139	41	
	8	4	34.8	99.2	753	533	495	451	394	328	50	
	9	3	48.4	94.5	823	728	697	652	589	507	57	
	10	2	62.1	89	857	876	851	807	741	649	66	
	11	1	75.7	79.2	876	968	952	905	835	741	101	
	12		86.6	0	883	999	983	939	867	772	113	
	Surface daily totals				9242	7962	7603	7092	6417	5566	775	
	Surface daily totals				9027	7590	7571	7300	6834	6172	1481	
	Surface daily totals				9027	7590	7571	7300	6834	6172	3127	
Aug 21	6	6	5	101.3	110	22	16	13	13	13	6	
	7	5	18.5	95.6	586	258	240	217	189	158	35	
	8	4	32.2	89.7	760	498	485	460	422	372	50	
	9	3	45.9	82.9	835	703	700	675	630	571	123	
	10	2	59.3	73	876	860	867	845	794	725	183	
	11	1	71.6	53.2	895	958	974	949	898	823	224	
	12		78.3	0	901	993	1009	987	933	857	236	
	Surface daily totals				9027	7590	7571	7300	6834	6172	1481	
	Surface daily totals				9027	7590	7571	7300	6834	6172	3127	
	Surface daily totals				9027	7590	7571	7300	6834	6172	3127	
Sep 21	7	5	13.7	83.8	545	180	189	189	186	177	82	
	8	4	27.2	76.8	782	429	454	460	451	429	195	
	9	3	40.2	67.9	876	646	687	697	684	649	293	
	10	2	52.3	54.8	920	813	867	876	860	823	366	
	11	1	61.9	33.4	942	917	980	993	974	930	413	
	12		66	0	949	952	1018	1031	1012	965	429	
	Surface daily totals				9027	6915	7382	7458	7319	6972	3127	
Oct 21	7	5	9.1	74.1	435	101	126	142	151	158	129	
	8	4	22	66.7	779	350	407	438	454	457	312	
	9	3	34.1	57.1	895	567	649	684	703	697	435	
	10	2	44.7	43.8	949	738	835	873	889	879	520	
	11	1	52.5	24.7	974	845	949	993	1005	990	574	
	12		55.5	0	980	879	990	1034	1046	1031	593	
	Surface daily totals				9040	6077	6928	7294	7451	7395	4545	

FIGURE A2.2a (CONTINUED)

Solar position and insolation values for 24°N latitude.

(Continued)

Date	Solar time		Solar position		Total insolation on surface (W/m ²)						
	a.m.	p.m.	Alt	Azm	Direct normal	Horiz.	South-facing surface angle with horizon				
Nov 21							14°	24°	34°	44°	90°
7	5	4.9	65.8	211	32	50	63	76	85	91	
8	4	17	58.4	794	258	340	388	426	448	391	
9	3	28	48.9	889	473	586	646	684	706	542	
10	2	37.3	36.3	955	640	769	835	876	892	643	
11	1	43.8	19.7	983	744	883	952	996	1009	700	
12		46.2	0	993	779	924	993	1034	1046	719	
		Surface daily totals					8529	5075	6184	6764	7149
Dec 21	7	5	3.2	62.6	95	9	22	28	35	38	44
	8	4	14.9	55.3	709	224	312	366	407	438	410
	9	3	25.5	46	886	432	555	624	675	703	580
	10	2	34.3	33.7	958	596	738	813	867	892	684
	11	1	40.4	18.2	990	697	851	930	983	1009	744
	12		42.6	0	999	731	889	971	1024	1046	766
	Surface daily totals					8271	4646	5838	6487	6947	7205

FIGURE A2.2a (CONTINUED)

Solar position and insolation values for 24°N latitude.

Date	Solar Time		Solar Position		Total Insolation on Surface (W/m ²)						
	a.m.	p.m.	Alt	Azm	Direct Normal	Horiz.	South-facing surface angle with horizon				
Jan 21							22°	32°	42°	52°	90°
7	5	1.4	65.2	3	0	0	0	0	3	9	
8	4	12.5	56.5	640	177	293	334	366	388	362	
9	3	22.5	46	848	372	552	608	649	668	571	
10	2	30.6	33.1	930	526	741	807	848	864	697	
11	1	36.1	17.5	965	624	860	930	971	983	772	
12		38	0	977	0	898	971	1012	1021	797	
		Surface daily totals					7748	4060	5797	6329	6676
Feb 21	7	5	7.1	73.5	381	69	107	117	126	132	120
	8	4	19	64.4	779	299	400	429	441	444	340
	9	3	29.9	53.4	908	507	649	684	700	693	498
	10	2	39.1	39.4	965	668	838	876	892	879	608
	11	1	45.6	21.4	993	769	958	999	1012	993	675
	12		48	0	999	804	996	1040	1053	1034	700
	Surface daily totals					9053	5434	6897	7250	7391	7319

FIGURE A2.2b

Solar position and insolation values for 32°N latitude.

(Continued)

Date	Solar time		Solar position		Total insolation on surface (W/m^2)						
	a.m.	p.m.	Alt	Azm	Direct normal	Horiz.	South-facing surface angle with horizon				
Mar 21							22°	32°	42°	52°	90°
7	5	12.7	81.9	583	170	189	189	186	177	101	
8	4	25.1	73	820	407	460	463	454	432	246	
9	3	36.8	62.1	914	611	700	706	693	659	375	
10	2	47.3	47.5	958	772	883	892	876	835	473	
11	1	55	26.8	980	873	999	1012	993	946	536	
12		58	0	987	905	1037	1050	1031	983	558	
		Surface daily totals					9494	6569	7495	7574	7432
Apr 21	6	6	61.1	99.9	208	44	28	19	19	16	9
	7	5	18.8	92.2	649	271	246	224	195	161	32
	8	4	31.5	84	804	498	492	466	429	378	110
	9	3	43.9	74.2	876	693	709	684	640	577	214
	10	2	55.7	60.3	914	842	879	857	807	738	299
	11	1	65.4	37.5	930	936	987	965	914	835	353
	12		69.6	0	936	968	1024	1002	949	870	372
Surface daily totals					9696	7533	7703	7426	6953	6285	2408
May 21	6	6	10.4	107.2	375	113	66	41	41	38	22
	7	5	22.8	100.1	665	337	277	236	189	139	41
	8	4	35.4	92.9	788	552	501	457	400	331	47
	9	3	48.1	74.7	848	734	703	659	593	514	104
	10	2	60.6	73.3	883	873	860	816	747	656	177
	11	2	72	51.9	898	961	961	914	845	842	227
	12		78	0	901	993	993	949	876	779	243
Surface daily totals					9809	8138	7735	7199	6506	5636	1478
Jun 21	6	6	12.2	110.2	413	142	82	50	47	44	28
	7	5	24.3	103.4	662	362	287	240	186	129	44
	8	4	36.9	96.8	775	567	501	451	385	312	50
	9	3	49.6	89.4	832	744	697	643	571	482	60
	10	2	62.2	79.7	864	879	845	791	716	621	129
	11	1	74.2	60.9	879	965	942	889	810	706	177
	12		81.5	0	883	993	974	920	842	738	189
Surface daily totals					9721	8302	7678	7042	6272	5327	1166
Jul 21	6	6	10.7	107.7	356	117	69	44	41	38	25
	7	5	23.1	100.6	640	337	274	236	189	139	44
	8	4	35.7	93.6	760	548	498	451	394	328	50
	9	3	48.4	85.5	823	728	693	646	583	501	98
	10	2	60.9	74.3	854	864	848	801	731	643	170
	11	1	72.4	53.3	873	952	946	898	8258	826	217
	12		78.6	0	879	980	977	933	860	763	233
Surface daily totals					9494	8063	7634	7092	6399	5529	1444

FIGURE A2.2b (CONTINUED)

Solar position and insolation values for 32°N latitude.

(Continued)

Date	Solar time		Solar position		Total insolation on surface (W/m ²)						
	a.m.	p.m.	Alt	Azm	Direct Normal	Horiz.	South-facing surface angle with horizon				
							22°	32°	42°	52°	90°
Aug 21	6	6	6.5	100.5	186	44	28	22	19	19	13
	7	5	19.1	92.8	599	268	243	217	189	158	38
	8	4	31.8	84.7	756	492	479	454	416	366	104
	9	3	44.3	75	829	681	693	668	621	561	205
	10	2	56.1	61.3	870	826	857	832	785	744	287
	11	1	66	38.4	889	920	961	939	886	810	337
	12		70.3	0	895	952	999	974	920	845	356
Surface daily totals					9147	7414	7527	7237	6758	6096	2320
Sep 21	7	5	12.7	81.9	514	161	177	177	173	164	95
	8	4	25.1	73	756	391	441	444	435	413	236
	9	3	36.8	62.1	857	593	671	678	665	634	359
	10	2	47.3	47.5	905	747	851	860	845	804	457
	11	1	55	26.8	927	845	965	974	955	911	517
	12		58	0	933	876	1002	1012	993	946	539
Surface daily totals					8851	6348	7212	7275	7136	6789	3864
Oct 21	7	5	6.8	73.1	312	60	91	101	107	113	101
	8	4	18.7	64	722	284	378	403	419	422	328
	9	3	29.5	53	860	489	624	656	671	668	482
	10	2	38.7	39.1	924	643	810	848	860	851	593
	11	1	45.1	21.1	952	744	927	968	980	965	659
	12		47.5	0	958	779	965	1009	1021	1002	684
Surface daily totals					8498	5213	6619	6960	7098	7035	5005
Nov 21	7	5	1.5	65.4	6	0	0	0	3	3	3
	8	4	12.7	56.6	618	173	287	328	356	375	350
	9	3	22.6	46.1	829	372	545	599	637	656	555
	10	2	30.8	33.2	911	523	734	794	835	851	684
	11	1	36.2	17.6	949	621	851	917	955	968	760
	12		38.2	0	958	652	889	958	996	1009	785
Surface daily totals					7584	4035	5724	6241	6569	6714	5491
Dec 21	8	4	10.3	53.8	555	129	243	284	318	340	337
	9	3	19.8	43.6	810	322	507	567	615	643	577
	10	2	27.6	31.2	908	473	697	769	816	842	712
	11	1	32.7	16.4	949	567	813	889	939	961	791
	12		34.6	0	958	599	854	930	980	1002	816
Surface daily totals					7401	3581	5371	5951	6354	6575	5513

FIGURE A2.2b (CONTINUED)

Solar position and insolation values for 32°N latitude.

Date	Solar time		Solar position		Total insolation on surface (W/m^2)						
	a.m.	p.m.	Alt	Azm	Direct normal	Horiz.	South-facing surface angle with horizon				
Jan 21							30°	40°	50°	60°	90°
8	4	8.1	55.3	448	88	205	233	255	268	265	
9	3	16.8	44	753	262	489	539	574	589	539	
10	2	23.8	30.9	864	400	66	747	785	801	703	
11	1	28.4	16	911	485	810	873	914	924	797	
12		30	0	927	517	851	917	955	965	829	
		Surface daily totals					6878	2988	5232	5705	6008
Feb 21	7	5	4.8	72.7	217	32	60	66	72	76	69
	8	4	15.4	62.2	706	230	359	385	397	400	337
	9	3	25	50.2	864	416	615	646	659	656	526
	10	2	32.8	35.9	930	561	807	842	854	842	662
	11	1	38.1	18.9	961	649	924	965	977	958	744
	12		40	0	971	681	965	1005	1018	999	772
Surface daily totals					8321	4457	6493	6815	6941	6859	5453
Mar 21	7	5	11.4	80.2	539	145	173	173	170	161	110
	8	4	22.5	69.6	788	359	441	444	435	413	281
	9	3	32.8	57.3	889	545	678	684	671	637	435
	10	2	41.6	41.9	936	687	860	870	854	813	555
	11	1	47.7	22.6	961	779	977	987	968	924	630
	12		50	0	968	810	1015	1028	1009	961	656
Surface daily totals					9191	5838	7275	7344	7199	6852	4678
Apr 21	6	6	7.4	98.9	281	63	35	25	22	22	13
	7	5	18.9	89.5	649	274	243	221	192	158	38
	8	4	30.3	79.3	794	479	482	457	419	369	167
	9	3	41.3	67.2	864	652	697	671	627	564	293
	10	2	51.2	51.4	901	788	867	842	794	722	397
	11	1	58.7	29.2	920	873	971	949	898	820	463
Surface daily totals					924	905	1009	987	933	854	485
May 21	Surface daily totals				9746	7168	7603	7313	6834	6165	3221
	5	7	1.9	114.7	3	0	0	0	0	0	0
	6	6	12.7	105.6	454	154	79	47	44	41	28
	7	5	24	96.6	681	675	281	240	189	139	41
	8	4	35.4	87.2	788	552	498	454	394	328	79
	9	3	46.8	76	842	716	697	649	586	504	189
Surface daily totals					873	842	851	804	734	646	281
	10	2	57.5	60.9	892	924	949	905	832	738	340
	11	1	66.2	37.1	895	949	983	936	864	766	359
	12		70	0	895	949	983	936	864	766	359
	Surface daily totals					9960	8044	7697	7136	6430	5548

FIGURE A2.2c

Solar position and insolation values for 40°N latitude.

(Continued)

Date	Solar time		Solar position		Total insolation on surface (W/m^2)						
	a.m.	p.m.	Alt	Azm	Direct normal	Horiz.	South-facing surface angle with horizon				
							30°	40°	50°	60°	90°
Jun 21	5	7	4.2	117.3	69	13	9	9	6	6	3
	6	6	14.8	108.4	489	189	95	57	54	50	32
	7	5	26	99.7	681	388	290	243	186	129	44
	8	4	37.4	90.7	775	574	501	448	381	306	50
	9	3	48.8	80.2	829	734	690	637	564	476	148
	10	2	59.8	65.8	857	857	838	782	706	611	233
	11	1	69.2	41.9	873	933	933	876	797	697	290
	12		73.5	0	879	958	965	911	829	725	309
	Surface daily totals				10,023	8346	7672	7010	6222	5264	1923
Jul 21	5	7	2.3	115.2	6	0	0	0	0	0	0
	6	6	13.1	106.1	435	158	82	54	47	44	28
	7	5	24.3	97.2	656	359	281	236	189	139	44
	8	4	35.8	87.8	760	548	495	448	391	322	76
	9	3	47.2	76.7	816	709	687	640	574	495	183
	10	2	57.9	61.7	848	835	838	791	722	630	271
	11	1	66.7	37.9	867	914	933	886	813	719	328
	12		70.6	0	870	939	968	920	848	750	350
	Surface daily totals				9651	7987	7593	7029	6323	5447	2213
Aug 21	6	6	7.9	99.5	255	66	38	28	25	22	16
	7	5	19.3	90.9	602	274	240	217	189	154	38
	8	4	30.7	79.9	747	473	473	444	407	356	158
	9	3	41.8	67.9	820	646	681	652	608	545	281
	10	2	51.7	52.1	857	775	842	816	769	697	378
	11	1	59.3	29.7	876	860	946	920	870	794	441
	12		62.3	0	883	889	980	955	905	826	463
	Surface daily totals				9191	7073	7420	7117	6632	5970	3083
Sep 21	7	5	11.4	80.2	470	136	161	161	154	148	101
	8	4	22.5	69.6	725	344	419	422	413	391	265
	9	3	32.8	57.3	829	526	649	656	640	608	416
	10	2	41.6	41.9	883	665	826	835	820	779	530
	11	1	47.7	22.6	905	753	939	949	930	886	605
	12		50	0	914	785	977	987	968	920	630
	Surface daily totals				8536	5636	6966	7023	6878	6537	4463
Oct 21	7	5	4.5	72.3	151	22	44	47	54	54	50
	8	4	15	61.9	643	214	334	356	369	372	315
	9	3	24.5	49.8	810	397	583	615	630	624	504
	10	2	32.4	35.6	883	536	772	810	823	810	640
	11	1	37.6	18.7	917	627	892	930	942	927	722
	12		39.5	0	927	656	930	971	983	965	750
	Surface daily totals				7735	4249	6184	6493	6613	6537	5213

FIGURE A2.2c (CONTINUED)

Solar position and insolation values for 40°N latitude.

(Continued)

Date	Solar time		Solar position		Total insolation on surface (W/m^2)						
	a.m.	p.m.	Alt	Azm	Direct normal	Horiz.	South-facing surface angle with horizon				
							30°	40°	50°	60°	90°
Nov 21	8	4	8.2	55.4	429	88	199	227	246	258	255
	9	3	17	44.1	731	258	479	526	561	577	526
	10	2	24	31	845	397	678	734	772	785	690
	11	1	28.6	16.1	892	482	801	860	898	908	782
	12		30.2	0	908	514	842	905	939	949	813
	Surface daily totals				6707	2969	5157	5604	5894	6014	5314
Dec 21	8	4	5.5	53	281	44	123	142	158	170	177
	9	3	14	41.9	684	205	426	479	517	539	514
	10	2	20	29.4	823	337	630	697	741	763	697
	11	1	25	15.2	883	422	753	826	870	892	794
	12		26.6	0	898	451	797	867	914	933	829
	Surface daily totals				6235	2465	4665	5150	5484	5661	5188

FIGURE A2.2c (CONTINUED)

Solar position and insolation values for 40°N latitude.

Date	Solar time		Solar position		Total insolation on surface (W/m^2)						
	a.m.	p.m.	Alt	Azm	Direct normal	Horiz.	South-facing surface angle with horizon				
							38°	48°	58°	68°	90°
Jan 21	8	4	3.5	54.6	117	13	54	60	66	69	69
	9	3	11	42.6	583	145	378	416	441	457	438
	10	2	16.9	29.4	753	262	599	649	681	693	649
	11	1	20.7	15.1	823	337	728	785	820	829	766
	12		22	0	842	362	772	832	867	876	804
	Surface daily totals				5390	1879	4287	4659	4886	4974	4659
Feb 21	7	5	2.4	72.2	38	3	9	13	13	13	13
	8	4	11.6	60.5	593	154	299	322	331	334	303
	9	3	19.7	47.7	791	315	561	589	602	599	526
	10	2	26.2	33.3	876	438	756	791	804	791	684
	11	1	30.5	17.2	914	520	876	914	927	908	779
	12		32	0	924	545	917	958	968	949	813
Surface daily totals				7344	3404	5926	6216	6380	6235	5421	

FIGURE A2.2d

Solar position and insolation values for 48°N latitude.

(Continued)

Date	Solar time		Solar position		Total insolation on surface (W/m^2)						
	a.m.	p.m.	Alt	Azm	Direct normal	Horiz.	South-facing surface angle with horizon				
Mar 21									38°	48°	58°
7	5	10	78.7	482	117	154	154	148	142	110	
8	4	19.5	66.8	744	303	413	416	407	385	303	
9	3	28.2	53.4	851	463	646	652	640	608	479	
10	2	35.4	37.8	905	589	829	838	823	782	615	
11	1	40.3	19.8	930	668	946	955	936	892	703	
12		42	0	939	693	983	993	974	927	731	
Apr 21	Surface daily totals				8763	4974	6960	7023	6878	6537	5144
	6	6	8.6	97.8	340	85	41	28	25	22	16
	7	5	18.6	86.7	646	268	240	217	186	151	66
	8	4	28.5	74.9	779	448	470	444	407	356	217
	9	3	37.8	61.2	845	602	681	656	611	548	362
	10	2	45.8	44.6	883	719	845	820	772	703	479
	11	1	51.5	24	901	794	949	927	876	801	558
May 21	12		53.6	0	908	820	987	961	911	832	583
	Surface daily totals				9696	6638	7432	7142	6663	5995	3978
	5	7	5.2	114.3	129	28	13	13	13	9	6
	6	6	14.7	103.7	416	192	85	50	47	41	32
	7	5	24.6	93	690	372	281	236	189	136	41
	8	4	34.7	81.6	782	539	492	448	388	318	142
	9	3	44.3	68.3	832	684	684	637	574	492	271
Jun 21	10	2	53	51.3	864	794	835	791	722	630	378
	11	1	59.5	28.6	785	864	933	886	813	719	444
	12		62	0	883	886	965	920	848	750	470
	Surface daily totals				11,108	7823	7622	7042	6336	5447	3095
	5	7	7.9	116.5	243	66	28	28	25	22	16
	6	6	17.2	106.2	542	233	104	60	57	50	38
	7	5	27	95.8	693	407	293	243	186	123	47
Jul 21	8	4	37.1	84.6	775	571	495	441	375	299	110
	9	3	46.9	71.6	823	709	681	624	552	463	233
	10	2	55.8	54.8	848	816	826	769	693	596	331
	11	1	62.7	31.2	864	883	917	860	782	681	397
	12		65.5	0	867	905	949	892	813	709	419
	Surface daily totals				10,439	8277	7628	6947	6146	5182	2755
	5	7	5.7	114.7	136	32	16	16	13	13	9
	6	6	15.2	104.1	492	195	88	57	50	47	35
	7	5	25.1	93.5	665	372	281	236	186	132	44
	8	4	35.1	82.1	756	539	485	441	381	312	136
	9	3	44.8	68.8	807	678	675	627	561	482	262
	10	2	53.5	51.9	838	788	823	775	706	615	366
	11	1	60.1	29	854	857	917	870	797	703	432
	12		62.6	0	857	879	949	901	829	731	454
Surface daily totals				9954	7798	7521	6934	6222	5339	3013	

FIGURE A2.2d (CONTINUED)

Solar position and insolation values for 48°N latitude.

(Continued)

Date	Solar time		Solar position		Total insolation on surface (W/m^2)									
	a.m.	p.m.	Alt	Azm	Direct normal	Horiz.	South-facing surface angle with horizon				38°	48°	58°	68°
Aug 21								38°	48°	58°	68°	90°		
6	6	9.1	98.3	312	88	44	32	28	25	19				
7	5	19.1	87.2	599	268	236	211	183	148	63				
8	4	29	75.4	731	444	457	432	394	344	205				
9	3	38.4	61.8	801	596	662	634	589	530	347				
10	2	46.4	45.1	838	709	820	794	747	675	460				
11	1	52.2	24.3	857	782	924	898	845	769	533				
12		54.3	0	864	807	958	933	879	804	558				
		Surface daily totals				9134	6575	7250	6934	6449	5787	3808		
Sep 21	7	5	10	78.7	413	110	139	139	136	126	98			
	8	4	19.5	66.8	678	290	391	391	381	362	284			
	9	3	28.2	53.4	791	448	618	621	608	577	451			
	10	2	35.4	37.8	848	571	791	801	782	744	583			
	11	1	40.3	19.8	876	646	905	911	895	848	668			
	12		42	0	883	671	942	952	933	886	697			
	Surface daily totals				8094	4797	6626	6676	6525	6197	4873			
Oct 21	7	5	2	71.9	13	0	3	3	3	3	3			
	8	4	11.2	60.2	426	139	271	287	299	299	274			
	9	3	19.3	47.4	734	296	526	555	567	561	495			
	10	2	25.7	33.1	826	419	719	753	763	753	652			
	11	1	30	17.1	864	495	838	873	886	870	747			
	12		31.5	0	876	523	879	917	927	908	779			
	Surface daily totals				6789	3221	5592	5863	5957	5882	5125			
Nov 21	8	4	3.6	54.7	113	16	54	60	66	69	69			
	9	3	11.2	42.7	564	145	369	407	432	444	426			
	10	2	17.1	29.5	734	262	586	637	668	678	634			
	11	1	20.9	15.1	804	337	716	772	804	813	845			
	12		22.2	0	823	362	760	816	851	857	788			
	Surface daily totals				5258	1879	4211	4564	4785	4867	4545			
	9		8	40.9	441	85	274	309	331	347	344			
Dec 21	10	2	13.6	28.2	675	199	517	567	605	621	599			
	11	1	17.3	14.4	763	271	652	712	753	769	728			
	12		18.6	0	788	296	700	760	801	820	769			
	Surface daily totals				4551	1406	3581	3940	4180	4299	4110			

FIGURE A2.2d (CONTINUED)

Solar position and insolation values for 48°N latitude.

Date	Solar time		Solar position		Total insolation on surface (W/m^2)							
	a.m.	p.m.	Alt	Azm	Direct normal	Horiz.	South-facing surface angle with horizon					
							46°	56°	66°	76°	90°	
Jan 21	9	3	5	41.8	246	35	158	173	186	189	189	
	10	2	9.9	28.5	536	123	426	460	485	492	482	
	11	1	12.9	14.5	652	183	577	621	649	656	634	
	12		14	0	684	205	624	675	700	709	684	
	Surface daily totals				3549	889	2944	3184	3335	3385	3291	
Feb 21	8	4	7.6	59.4	407	79	205	217	227	227	217	
	9	3	14.2	45.9	675	205	476	501	511	507	476	
	10	2	19.4	31.5	788	309	678	709	719	706	656	
	11	1	22.8	16.1	838	375	801	835	845	829	766	
	12		24	0	851	397	845	879	889	870	804	
Surface daily totals				6260	2332	5169	5409	5491	5409	5037		
Mar 21	7	5	8.3	77.5	403	88	126	126	123	117	101	
	8	4	16.2	64.4	678	236	375	378	369	350	306	
	9	3	23.3	50.3	797	372	605	608	596	567	485	
	10	2	29	34.9	857	476	785	791	775	738	646	
	11	1	32.7	17.9	889	542	898	908	889	845	744	
12				34	0	895	564	936	946	927	883	775
Surface daily totals				8151	3997	6512	6569	6430	6109	5358		
Apr 21	5	7	1.4	108.8	0	0	0	0	0	0	0	
	6	6	9.6	96.5	385	101	44	28	25	22	19	
	7	5	18	84.1	634	255	233	208	180	145	91	
	8	4	26.1	70.9	753	407	451	426	388	340	258	
	9	3	33.6	56.3	820	533	656	630	586	526	419	
10				29	857	634	816	791	744	675	548	
11				44.1	20.7	876	693	920	895	845	772	630
12				45.6	0	883	716	955	930	879	804	659
Surface daily totals				9532	5964	7193	6890	6424	5768	4596		
May 21	4	8	1.2	125.5	0	0	0	0	0	0	0	
	5	7	8.5	113.4	293	79	32	28	25	22	19	
	6	6	16.5	101.4	552	224	88	54	47	41	35	
	7	5	24.8	89.3	690	375	277	233	183	129	50	
	8	4	33.1	76.3	769	514	482	435	375	309	199	
9				40.9	61.6	816	634	668	621	555	476	344
10				47.6	44.2	845	728	816	769	700	611	460
11				52.3	23.4	860	785	908	864	791	700	536
12				54	0	867	804	942	895	823	728	561
Surface daily totals				10,528	7483	7483	6897	6184	5302	3839		

FIGURE A2.2e

Solar position and insolation values for 40°N latitude.

(Continued)

Date	Solar time		Solar position		Total insolation on surface (W/m^2)							
	a.m.	p.m.	Alt	Azm	Direct normal	Horiz.	South-facing surface angle with horizon					
Jun 21							46°	56°	66°	76°	90°	
4	8	4.2	127.2	66	13	6	6	6	6	3		
5	7	11.4	115.3	385	126	44	41	35	32	25		
6	6	19.3	103.6	583	271	107	60	54	47	38		
7	5	27.6	91.7	700	416	290	240	180	120	47		
8	4	35.9	78.8	766	552	485	432	366	290	173		
9	3	43.8	64.1	810	668	665	608	536	451	309		
10	2	50.7	46.4	835	756	804	750	675	580	419		
11	1	55.6	24.9	848	813	895	842	763	662	492		
12		57.5	0	854	832	927	870	791	690	517		
Surface daily totals				10,837	7962	7527	6827	6020	5062	3530		
Jul 21	4	8	1.7	125.8	0	0	0	0	0	0	0	
	5	7	9	113.7	287	85	35	32	28	25	19	
	6	6	17	101.9	533	227	95	57	142	44	38	
	7	5	25.3	89.7	668	375	277	233	328	129	47	
	8	4	33.6	76.7	747	514	476	429	504	303	192	
	9	3	41.4	62	794	634	656	608	545	463	334	
	10	2	48.2	44.6	823	725	801	753	684	596	448	
	11	1	52.9	23.7	835	782	892	845	772	681	520	
	12		54.6	0	842	801	924	876	804	709	545	
	Surface daily totals				10,212	7477	7382	6783	6071	5188	3738	
Aug 21	5	7	2	109.2	3	0	0	0	0	0	0	
	6	6	10.2	97	353	107	50	35	32	28	22	
	7	5	18.5	84.5	589	258	230	205	177	142	88	
	8	4	26.7	71.3	709	403	441	413	375	328	246	
	9	3	34.3	56.7	775	530	637	608	564	189	397	
	10	2	40.5	40	813	627	791	763	716	649	523	
	11	1	44.8	20.9	832	687	889	864	813	741	602	
	12		46.3	0	838	709	924	898	848	772	630	
	Surface daily totals				8983	5938	6991	6676	6197	5548	4388	
Sep 21	7	5	8.3	77.5	337	79	113	113	107	101	88	
	8	4	16.2	64.4	611	227	350	340	322	322	281	
	9	3	23.3	50.3	734	359	571	574	561	530	463	
	10	2	29	34.9	797	460	744	747	731	697	608	
	11	1	32.7	17.9	829	523	854	860	842	801	703	
	12		34	0	838	545	892	898	879	835	734	
	Surface daily totals				7464	3845	6146	6184	6046	5737	5024	
Oct 21	8	4	7.1	59.1	328	63	167	180	186	186	180	
	9	3	13.8	45.7	608	189	435	457	466	463	435	
	10	2	19	31.3	728	290	634	662	671	662	615	
	11	1	22.3	16	782	353	756	788	797	782	725	
	12		23.5	0	797	375	797	829	838	823	760	
	Surface daily totals				5686	2169	4778	4999	5081	5005	4665	

FIGURE A2.2e (CONTINUED)

Solar position and insolation values for 56°N latitude.

(Continued)

Date	Solar time		Solar position		Total insolation on surface (W/m^2)						
	a.m.	p.m.	Alt	Azm	Direct normal	Horiz.	South-facing surface angle with horizon				
Nov 21							46°	56°	66°	76°	90°
9	3	5.2	41.9	240	38	154	170	180	186	183	
10	2	10	28.5	520	123	416	422	470	479	466	
11	1	13.1	14.5	634	183	564	608	634	640	618	
12		14.2	0	665	205	611	659	684	690	665	
		Surface daily totals					3448	895	2881	1217	3253
Dec 21	9	3	1.9	40.5	16	0	9	13	13	13	13
	10	2	6.6	27.5	356	60	271	299	318	328	325
	11	1	9.5	13.9	523	117	444	485	514	526	517
	12		10.6	0	567	136	501	545	574	586	574
	Surface daily totals					2358	492	1954	2137	2257	2314

FIGURE A2.2e (CONTINUED)

Solar position and insolation values for 56°N latitude.

Date	Solar time		Solar position		Total insolation on surface (W/m^2)						
	a.m.	p.m.	Alt	Azm	Direct normal	Horiz.	South-facing surface angle with horizon				
Jan 21							54°	64°	74°	84°	90°
10	2	2.8	28.1	69	6	54	60	63	63	63	
11	1	5.2	14.1	255	38	227	243	252	255	255	
12		6	0	315	50	287	309	322	325	325	
Surface daily totals					965	142	845	914	952	965	958
Feb 21	8	4	3.4	58.7	110	13	54	60	60	60	60
	9	3	8.6	44.8	463	98	325	340	350	347	337
	10	2	12.6	30.3	627	173	536	561	571	561	545
	11	1	15.1	15.3	700	224	668	693	703	690	671
	12		16	0	719	243	709	741	747	731	712
Surface daily totals					4514	1261	3877	4053	4104	4041	3946
Mar 21	7	5	6.5	76.5	299	57	95	91	91	85	79
	8	4	20.7	62.6	583	170	318	322	312	296	281
	9	3	18.1	48.1	716	274	539	542	533	504	482
	10	2	22.3	32.7	785	353	716	722	706	671	640
	11	1	25.1	16.6	820	407	826	835	816	775	741
	12		26	0	829	422	864	873	854	813	775
Surface daily totals					7237	2938	5850	5894	5768	5472	5220

FIGURE A2.2f

Solar position and insolation values for 64°N latitude.

(Continued)

Date	Solar time		Solar position		Total insolation on surface (W/m^2)						
	a.m.	p.m.	Alt	Azm	Direct normal	Horiz.	South-facing surface angle with horizon				
Apr 21							54°	64°	74°	84°	90°
5	7	4	108.5	85	16	6	6	6	3	3	
6	6	10.4	95.1	419	117	47	28	25	22	19	
7	5	17	81.6	611	240	221	199	170	136	117	
8	4	23.3	67.5	719	353	429	403	366	322	287	
9	3	29	52.3	782	454	621	596	555	498	457	
10	2	33.5	36	820	533	775	753	706	640	593	
11	1	36.5	18.4	838	580	876	851	804	734	681	
12		37.6	0	845	599	911	886	838	766	709	
Surface daily totals				9399	5182	6859	6562	6102	5472	5024	
May 21	4	8	5.8	125.1	161	35	16	13	13	9	9
	5	7	11.6	112.1	416	132	41	35	32	28	25
	6	6	17.9	99.1	583	249	91	50	44	38	35
	7	5	24.5	85.7	687	369	271	227	177	123	88
	8	4	30.9	71.5	753	479	466	419	362	296	252
	9	3	36.8	56.1	794	574	643	599	536	457	403
	10	2	41.6	38.9	823	646	785	741	671	586	526
	11	1	44.9	20.1	835	690	876	832	763	671	608
	12		46	0	842	706	719	864	791	700	634
	Surface daily totals				10,937	7048	7297	6695	5982	5119	4526
Jun 21	3	9	4.2	139.4	66	13	6	6	6	3	
	4	8	9	126.4	293	85	32	28	25	22	19
	5	7	14.7	113.6	485	189	50	47	41	35	32
	6	6	21	100.8	611	303	107	60	54	44	41
	7	5	27.5	87.5	697	416	287	233	173	113	72
	8	4	34	73.3	753	523	473	419	353	277	230
	9	3	39.9	57.8	791	615	643	589	517	432	375
	10	2	44.9	40.4	813	684	779	725	649	558	495
	11	1	48.3	20.9	826	728	867	813	734	637	571
	12		49.5	0	829	741	895	842	763	665	596
Jul 21	Surface daily totals				11,505	7842	7382	6676	5869	4911	4274
	4	8	6.4	125.3	167	41	19	16	16	13	13
	5	7	12.1	112.4	403	139	44	41	35	32	28
	6	6	18.4	99.4	564	255	95	54	50	41	38
	7	5	25	86	665	372	271	227	177	120	88
	8	4	31.4	71.8	728	479	460	413	356	287	243
	9	3	37.3	56.3	772	574	634	586	523	444	391
	10	2	42.2	39.2	797	643	772	725	656	571	511
	11	1	45.4	20.2	810	687	860	813	744	652	589
	12		46.6	0	816	703	889	842	772	681	615
	Surface daily totals				10,629	7086	7187	6588	5875	5005	4413

FIGURE A2.2f (CONTINUED)

Solar position and insolation values for 64°N latitude.

(Continued)

Date	Solar time		Solar position		Total insolation on surface (W/m^2)						
	a.m.	p.m.	Alt	Azm	Direct normal	Horiz.	South-facing surface angle with horizon				
							54°	64°	74°	84°	90°
Aug 21	5	7	4.6	108.8	91	19	9	9	6	6	6
	6	6	11	95.5	388	123	50	35	32	25	22
	7	5	17.6	81.9	571	243	217	192	164	132	110
	8	4	23.9	67.8	675	356	416	388	353	306	274
	9	3	29.6	52.6	738	454	599	574	533	473	435
	10	2	34.2	36.2	775	530	747	722	678	611	564
	11	1	37.2	18.5	794	577	845	820	769	700	646
	12		38.3	0	801	593	876	851	804	731	678
Surface daily totals					8851	5188	6644	3177	5863	5239	4797
Sep 21	7	5	6.5	76.5	243	50	79	79	76	72	66
	8	4	12.7	72.6	514	161	290	290	284	268	255
	9	3	18.1	48.1	649	262	501	501	492	463	444
	10	2	22.3	32.7	722	340	668	671	659	624	596
	11	1	25.1	16.6	756	391	775	782	766	725	693
	12		26	0	769	407	813	820	801	760	725
	Surface daily totals					6537	2812	5440	5472	5346	5068
Oct 21	8	4	3	58.5	54	6	28	28	32	32	32
	9	3	8.1	44.6	385	82	271	287	293	290	284
	10	2	12.1	30.2	555	158	479	501	507	501	489
	11	1	14.6	15.2	634	205	608	634	640	630	615
	12		15.5	0	656	224	652	678	684	671	656
	Surface daily totals					3902	1128	3429	3581	3631	3574
Nov 21	10	2	3	28.1	72	9	57	63	66	66	66
	11	1	5.4	14.2	249	38	221	240	249	252	249
	12		6.2	0	306	54	281	303	315	318	315
	Surface daily totals					952	145	838	901	939	952
Dec 21	11	1	1.8	13.7	13	0	9	13	13	13	13
	12		2.6	0	50	6	44	47	50	54	54
	Surface daily totals					76	6	63	69	76	76

FIGURE A2.2f (CONTINUED)

Solar position and insolation values for 64°N latitude.

TABLE A2.6

Reflectivity Values for Characteristic Surfaces (Integrated over Solar Spectrum and Angle of Incidence)

Surface	Average Reflectivity
Snow (freshly fallen or with ice film)	0.75
Water surfaces (relatively large incidence angles)	0.07
Soils (clay, loam, etc.)	0.14
Earth roads	0.04
Coniferous forest (winter)	0.07
Forests in autumn, ripe field crops, plants	0.26
Weathered blacktop	0.10
Weathered concrete	0.22
Dead leaves	0.30
Dry grass	0.20
Green grass	0.26
Bituminous and gravel roof	0.13
Crushed rock surface	0.20
Building surfaces, dark (red brick, dark paints, etc.)	0.27
Building surfaces, light (light brick, light paints, etc.)	0.60

Source: Hunn, B.D. and D.O. Calafell, Determination of average ground reflectivity for solar collectors, *Sol. Energy*, 19, 87, 1977; see also List, R.J., *Smithsonian Meteorological Tables*, 6th ed., Smithsonian Institution Press, 442–443, 1949.

References

- Anane-Fenin, K. 1986. Estimating solar radiation in Ghana. *International Centre for Theoretical Physics*. Internal Report No. IC/86/68, Trieste, Italy.
- Chuah, D.G.S., and S.L. Lee. 1981. Solar radiation estimates in Malaysia. *Sol. Energy* 26: 33.
- Eze, A.E., and S.C. Ododo. 1988. Solar radiation prediction from sunshine in eastern Nigeria. *Energy Convers. Manage.* 28: 69.
- Ibrahim, S.M.A. 1985. Predicted and measured global solar radiation in Egypt. *Sol. Energy* 35: 185.
- Jain, P.C. 1986. Irradiation estimation for Italian localities. *Sol. Wind Technol.* 3: 323.
- Jain, S., and P.G. Jain. 1985. A comparison of the angstrom type correlations and the estimation of monthly average daily global irradiation. Internal Report, No. IC85-269, Trieste, Italy, International Centre for Theoretical Physics.
- Khogali, A. 1983. Star radiation over Sudan: Comparison of measured and predicted data. *Sol. Energy* 31: 45.
- Khogali, A. et al. 1983. Global and diffuse star irradiance in Yemen. *Sol. Energy* 31: 55.
- Leung, C.T. 1980. The fluctuation of solar irradiance in Hong Kong. *Sol. Energy* 25: 485.
- Massaquoi, J.G.M. 1988. Global solar radiation in Sierre Leone (West Africa). *Sol. Wind Technol.* 5: 281.
- Zabara, K. 1986. Estimation of the global solar radiation in Greece. *Sol. Wind Technol.* 3: 267.

Appendix 3: Supplementary Material for Chapter 3

TABLE A3.1

Properties of Dry Air at Atmospheric Pressures between 250 and 1000 K

T (K)	ρ (kg/m ³)	c_p (kJ/kg·K)	μ (kg/m·s × 10 ⁵)	ν (m ² /s × 10 ⁶)	k (W/m·K)	α (m ² /s × 10 ⁴)	Pr
250	1.4128	1.0053	1.488	9.49	0.02227	0.13161	0.722
300	1.1774	1.0057	1.983	15.68	0.02624	0.22160	0.708
350	0.9980	1.0090	2.075	20.76	0.03003	0.2983	0.697
400	0.8826	1.0140	2.286	25.90	0.03365	0.3760	0.689
450	0.7833	1.0207	2.484	28.86	0.03707	0.4222	0.683
500	0.7048	1.0295	2.671	37.90	0.04038	0.5564	0.680
550	0.6423	1.0392	2.848	44.34	0.04360	0.6532	0.680
600	0.5879	1.0551	3.018	51.34	0.04659	0.7512	0.680
650	0.5430	1.0635	3.177	58.51	0.04953	0.8578	0.682
700	0.5030	1.0752	3.332	66.25	0.05230	0.9672	0.684
750	0.4709	1.0856	3.481	73.91	0.05509	1.0774	0.686
800	0.4405	1.0978	3.625	82.29	0.05779	1.1951	0.689
850	0.4149	1.1095	3.765	90.75	0.06028	1.3097	0.692
900	0.3925	1.1212	3.899	99.3	0.06279	1.4271	0.696
950	0.3716	1.1321	4.023	108.2	0.06525	1.5510	0.699
1000	0.3524	1.1417	4.152	117.8	0.06752	1.6779	0.702

Source: Natl. Bureau Standards (U.S.) Circ. 564, 1955.

Note: K = absolute temperature, degrees Kelvin; $\nu = \mu/\rho$; ρ = density; c_p = specific heat capacity; $\alpha = c_p\rho/k$; μ = viscosity; k = thermal conductivity; Pr = Prandtl number, dimensionless. The values of μ , k , c_p , and Pr are not strongly pressure dependent and may be used over a fairly wide range of pressures.

TABLE A3.2

Properties of Water (Saturated Liquid) between 273 and 533 K

K	°F	°C	c_p (kJ/kg·°C)	ρ (kg/m ³)	μ (kg/m·s)	k (W/m·°C)	Pr	$g\beta\rho^2c_p$
								μk (m ⁻³ ·°C ⁻¹)
273	32	0	4.225	999.8	1.79×10^{-3}	0.566	13.25	
277.4	40	4.44	4.208	999.8	1.55	0.575	11.35	1.91×10^9
283	50	10	4.195	999.2	1.31	0.585	9.40	6.34×10^9
288.6	60	15.56	4.186	998.6	1.12	0.595	7.88	1.08×10^{10}
294.1	70	21.11	4.179	997.4	9.8×10^{-4}	0.604	6.78	1.46×10^{10}
299.7	80	26.67	4.179	995.8	8.6	0.614	5.85	1.91×10^{10}
302.2	90	32.22	4.174	994.9	7.65	0.623	5.12	2.48×10^{10}
310.8	100	37.78	4.174	993.0	6.82	0.630	4.53	3.3×10^{10}
316.3	110	43.33	4.174	990.6	6.16	0.637	4.04	4.19×10^{10}
322.9	120	48.89	4.174	988.8	5.62	0.644	3.64	4.89×10^{10}
327.4	130	54.44	4.179	985.7	5.13	0.649	3.30	5.66×10^{10}
333.0	140	60	4.179	983.3	4.71	0.654	3.01	6.48×10^{10}
338.6	150	65.55	4.183	980.3	4.3	0.659	2.73	7.62×10^{10}
342.1	160	71.11	4.186	977.3	4.01	0.665	2.53	8.84×10^{10}
349.7	170	76.67	4.191	973.7	3.72	0.668	2.33	9.85×10^{10}
355.2	180	82.22	4.195	970.2	3.47	0.673	2.16	1.09×10^{11}
360.8	190	87.78	4.199	966.7	3.27	0.675	2.03	
366.3	200	93.33	4.204	963.2	3.06	0.678	1.90	
377.4	220	104.4	4.216	955.1	2.67	0.684	1.66	
388.6	240	115.6	4.229	946.7	2.44	0.685	1.51	
399.7	260	126.7	4.250	937.2	2.19	0.685	1.36	
410.8	280	137.8	4.271	928.1	1.98	0.685	1.24	
421.9	300	148.9	4.296	918.0	1.86	0.684	1.17	
449.7	350	176.7	4.371	890.4	1.57	0.677	1.02	
477.4	400	204.4	4.467	859.4	1.36	0.665	1.00	
505.2	450	232.2	4.585	825.7	1.20	0.646	0.85	
533.0	500	260	4.731	785.2	1.07	0.616	0.83	

Source: Adapted from Brown, A.I. and S.M. Marco, *Introduction to Heat Transfer*, 3rd ed., McGraw-Hill Book Company, New York, 1958.

TABLE A3.3
Emittances and Absorptances of Materials

Substance	Short-Wave Absorptance	Long-Wave Emittance	$\frac{\alpha}{\epsilon}$
<i>Class I Substances: Absorptance-to-Emittance Ratios Less than 0.5</i>			
Magnesium carbonate, MgCO ₃	0.025–0.04	0.79	0.03–0.05
White plaster	0.07	0.91	0.08
Snow, fine particles, fresh	0.13	0.82	0.16
White paint, 0.017 in, on aluminum	0.20	0.91	0.22
Whitewash on galvanized iron	0.22	0.90	0.24
White paper	0.25–0.28	0.95	0.26–0.29
White enamel on iron	0.25–0.45	0.9	0.28–0.5
Ice, with sparse snow cover	0.31	0.96–0.97	0.32
Snow, ice granules	0.33	0.89	0.37
Aluminum oil base paint	0.45	0.90	0.50
White powdered sand	0.45	0.84	0.54
<i>Class II Substances: Absorptance-to-Emittance Ratios between 0.5 and 0.9</i>			
Asbestos felt	0.25	0.50	0.50
Green oil base paint	0.5	0.9	0.56
Bricks, red	0.55	0.92	0.60
Asbestos cement board, white	0.59	0.96	0.61
Marble, polished	0.5–0.6	0.9	0.61
Wood, planed oak	—	0.9	—
Rough concrete	0.60	0.97	0.62
Concrete	0.60	0.88	0.68
Grass, green, after rain	0.67	0.98	0.68
Grass, high and dry	0.67–0.69	0.9	0.76
Vegetable fields and shrubs, wilted	0.70	0.9	0.78
Oak leaves	0.71–0.78	0.91–0.95	0.78–0.82
Frozen soil	—	0.93–0.94	—
Desert surface	0.75	0.9	0.83
Common vegetable fields and shrubs	0.72–0.76	0.9	0.82
Ground, dry plowed	0.75–0.80	0.9	0.83–0.89
Oak woodland	0.82	0.9	0.91
Pine forest	0.86	0.9	0.96
Earth surface as a whole (land and sea, no clouds)	0.83	—	—

(Continued)

TABLE A3.3 (CONTINUED)

Emittances and Absorptances of Materials

Substance	Short-Wave Absorptance	Long-Wave Emittance	$\frac{\alpha}{\epsilon}$
<i>Class III Substances: Absorptance-to-Emittance Ratios between 0.8 and 1.0</i>			
Gray paint	0.75	0.95	0.79
Red oil base paint	0.74	0.90	0.82
Asbestos, slate	0.81	0.96	0.84
Asbestos, paper		0.93–0.96	—
Linoleum, red-brown	0.84	0.92	0.91
Dry sand	0.82	0.90	0.91
Green roll roofing	0.88	0.91–0.97	0.93
Slate, dark gray	0.89	—	—
Old gray rubber	—	0.86	—
Hard black rubber	—	0.90–0.95	—
Asphalt pavement	0.93	—	—
Black cupric oxide on copper	0.91	0.96	0.95
Bare moist ground	0.9	0.95	0.95
Wet sand	0.91	0.95	0.96
Water	0.94	0.95–0.96	0.98
Black tar paper	0.93	0.93	1.0
Black gloss paint	0.90	0.90	1.0
Small hole in large box, furnace, or enclosure	0.99	0.99	1.0
"Hohlraum," theoretically perfect black body	1.0	1.0	1.0
<i>Class IV Substances: Absorptance-to-Emittance Ratios Greater than 1.0</i>			
Black silk velvet	0.99	0.97	1.02
Alfalfa, dark green	0.97	0.95	1.02
Lampblack	0.98	0.95	1.03
Black paint, 0.017 in, on aluminum	0.94–0.98	0.88	1.07–1.11
Granite	0.55	0.44	1.25
Graphite	0.78	0.41	1.90
High ratios, but absorptances less than 0.80			
Dull brass, copper, lead	0.2–0.4	0.4–0.65	1.63–2.0
Galvanized sheet iron, oxidized	0.8	0.28	2.86
Galvanized iron, clean, new	0.65	0.13	5.0
Aluminum foil	0.15	0.05	3.00
Magnesium	0.3	0.07	4.3
Chromium	0.49	0.08	6.13
Polished zinc	0.46	0.02	23.0
Deposited silver (optical reflector) un tarnished	0.07	0.01	

TABLE A3.3 (CONTINUED)

Emittances and Absorptances of Materials

Substance	Short-Wave Absorptance	Long-Wave Emittance	$\frac{\alpha}{\epsilon}$
<i>Class V Substances: Selective Surfaces^a</i>			
Plated metals:			
Black sulfide on metal	0.92	0.10	9.2
Black cupric oxide on sheet aluminum	0.08–0.93	0.09–0.21	
Copper (5×10^{-5} cm thick) on nickel or silver-plated metal			
Cobalt oxide on platinum			
Cobalt oxide on polished nickel	0.93–0.94	0.24–0.40	3.9
Black nickel oxide on aluminum	0.85–0.93	0.06–0.1	14.5–15.5
Black chrome	0.87	0.09	9.8
Particulate coatings:			
Lamblack on metal			
Black iron oxide, 47 μm grain size, on aluminum			
Geometrically enhanced surfaces ^b :			
Optimally corrugated grays	0.89	0.77	1.2
Optimally corrugated selectives	0.95	0.16	5.9
Stainless-steel wire mesh	0.63–0.86	0.23–0.28	2.7–3.0
Copper, treated with NaClO_2 and NaOH	0.87	0.13	6.69

Source: Anderson, B., *Solar Energy*, McGraw-Hill Book Company, 1977. With permission.

^a Selective surfaces absorb most of the solar radiation between 0.3 and 1.9 μm and emit very little in the 5–15 μm range—the infrared.

^b For a discussion of how surface selectivity can be enhanced through surface geometry, see K.G.T. Hollands, Directional selectivity emittance and absorptance properties of vee corrugated specular surfaces, *J. Sol. Energy Sci. Eng.*, vol. 3, July 1963.

TABLE A3.4

Thermal Properties of Metals and Alloys

Material	<i>k</i> , Btu/(h)(ft)(°F)				<i>c</i> , Btu/(lb _m)(°F)	<i>ρ</i> , lb _m /ft ³	<i>α</i> , ft ² /h
	32°F	212°F	572°F	932°F			
Metals							
Aluminum	117	119	133	155	0.208	169	3.33
Bismuth	4.9	3.9	0.029	612	0.28
Copper, pure	224	218	212	207	0.091	558	4.42
Gold	169	170	0.030	1203	4.68
Iron, pure	35.8	36.6	0.104	491	0.70
Lead	20.1	19	18	...	0.030	705	0.95
Magnesium	91	92	0.232	109	3.60
Mercury	4.8	0.033	849	0.17
Nickel	34.5	34	32	...	0.103	555	0.60
Silver	242	238	0.056	655	6.6
Tin	36	34	0.054	456	1.46
Zinc	65	64	59	...	0.091	446	1.60
Alloys							
Admiralty metal	65	64					
Brass, 70% Cu, 30% Zn	56	60	66	...	0.092	532	1.14
Bronze, 75% Cu, 25% Sn	15	0.082	540	0.34
Cast iron							
Plain	33	31.8	27.7	24.8	0.11	474	0.63
Alloy	30	28.3	27	...	0.10	455	0.66
Constantan, 60% Cu, 40% Ni	12.4	12.8	0.10	557	0.22
18-8 Stainless steel,							
Type 304	8.0	9.4	10.9	12.4	0.11	488	0.15
Type 347	8.0	9.3	11.0	12.8	0.11	488	0.15
Steel, mild, 1%C	26.5	26	25	22	0.11	490	0.49

Source: Kreith, F., *Principles of Heat Transfer*, PWS Publishing Co., Boston, 1997.

Note: 1 Btu/h·ft·°F = 1.731 W/m·K.

1 Btu/lb_m·°F = 4187 J/kg·K.

1 lb_m/ft³ = 16.018 kg/m³.

1 ft²/h = 2.581 × 10⁻⁵ m²/s.

TABLE A3.5

Thermal Properties of Some Nonmetals

Material	Average Temperature, °F	k , Btu/(h) (ft)(°F)	c , Btu/(lb _m) (°F)	ρ , lb _m /ft ³	α , ft ² /h
Insulating materials					
Asbestos	32	0.087	0.25	36	~0.01
	392	0.12	...	36	~0.01
Cork	86	0.025	0.04	10	~0.006
Cotton, fabric	200	0.046			
Diatomaceous earth, powdered	100	0.030	0.21	14	~0.01
	300	0.036	...		
	600	0.046	...		
Molded pipe covering	400	0.051	...	26	
	1600	0.088	...		
Glass wool					
Fine	20	0.022	...		
	100	0.031	...	1.5	
	200	0.043	...		
Packed	20	0.016	...		
	100	0.022	...	6.0	
	200	0.029	...		
Hair felt	100	0.027	...	8.2	
Kaolin insulating brick	932	0.15	...	27	
	2102	0.26	...		
Kaolin insulating firebrick	392	0.05	...	19	
	1400	0.11	...		
85% magnesia	32	0.032	...	17	
	200	0.037	...	17	
Rock wool	20	0.017	...	8	
	200	0.030	...		
Rubber	32	0.087	0.48	75	0.0024
Building materials					
Brick					
Fire-clay	392	0.58	0.20	144	0.02
	1832	0.95			
Masonry	70	0.38	0.20	106	0.018
Zirconia	392	0.84	...	304	
	1832	1.13	...		
Chrome brick	392	0.82	...	246	
	1832	0.96	...		

(Continued)

TABLE A3.5 (CONTINUED)

Thermal Properties of Some Nonmetals

Material	Average Temperature, °F	k , Btu/(h) (ft)(°F)	c , Btu/(lb _m) (°F)	ρ , lb _m /ft ³	α , ft ² /h
Concrete					
Stone	~70	0.54	0.20	144	0.019
10% moisture	~70	0.70	...	140	~0.025
Glass, window	~70	~0.45	0.2	170	0.013
Limestone, dry	70	0.40	0.22	105	0.017
Sand					
Dry	68	0.20	...	95	
10% H ₂ O	68	0.60	...	100	
Building materials					
Soil					
Dry	70	~0.20	0.44	...	~0.01
Wet	70	~1.5	~0.03
Wood					
Oak ⊥ to grain	70	0.12	0.57	51	0.0041
Oak to grain	70	0.20	0.57	51	0.0069
Pine ⊥ to grain	70	0.06	0.67	31	0.0029
Pine to grain	70	0.14	0.67	31	0.0067
Ice	32	1.28	0.46	57	0.048

Source: Kreith, F. *Principles of Heat Transfer*, PWS Publishing Co., 1997.

TABLE A3.6
Thermal and Radiative Properties of Collector Cover Materials

Material Name	Index of Refraction (n)	τ (Solar) ^a (%)	τ (Solar) ^b (%)	τ (Infrared) ^c (%)	Expansion Coefficient (in/in. $^{\circ}$ F)	Temperature Limits (°F)	Weatherability (Comment)	Chemical Resistance (Comment)
Lexan (polycarbonate)	1.586 (D 542) ^d	125 mil 64.1 (± 0.8)	125 mil 72.6 (± 0.1)	125 mil 2.0 (est) ^e	3.75 (10^{-5}) (H 696)	250–270 service temperature	Good; 2 years exposure in Florida caused yellowing; 5 years caused 5% loss in τ	Good; comparable to acrylic
Plexiglas (acrylic)	1.49 (D 542)	125 mil 89.6 (± 0.3)	125 mil 79.6 (± 0.8)	125 mil 2.0 (est) ^f	3.9 (10^{-9}) at 60°F; 4.6 (10^{-9}) at 100°F	180–200 service temperature	Average to good; based on 20-year testing in Arizona, Florida, and Pennsylvania	Good to excellent; resists most acids and alkalis
Teflon F.E.P. (fluorocarbon)	1.343 (D 542)	5 mil 92.3 (± 0.2)	5 mil 89.8 (± 0.4)	5 mil 25.6 (± 0.5)	5.9 (10^{-5}) at 160°F; 9.0 (10^{-5}) at 212°F	400 continuous use; 475 short-term use	Good to excellent; based on 15-year exposure in Florida environment	Excellent; chemically inert
Tedlar PVF. (fluorocarbon)	1.46 (D 542)	4 mil 92.2 (± 0.1)	4 mil 88.3 (± 0.9)	4 mil 20.7 (± 0.2)	2.8 (10^{-5}) (D 696)	225 continuous use; 350 short-term use	Good to excellent; 10-year exposure in Florida with slight yellowing	Excellent; chemically inert
Mylar (polyester)	1.64–1.67 (D 542)	5 mil 86.9 (± 0.3)	5 mil 80.1 (± 0.1)	5 mil 17.8 (± 0.5)	0.94 (10^{-5}) (D 696–44)	300 continuous use; 400 short-term use	Poor; ultraviolet degradation great	Good to excellent; comparable to Tedlar

(Continued)

TABLE A3.6 (CONTINUED)
Thermal and Radiative Properties of Collector Cover Materials

Material Name	Index of Refraction (n)	τ (Solar) ^a (%)	τ (Solar) ^b (%)	τ (Infrared) ^c (%)	Expansion Coefficient (in/in. $^{\circ}$ F)	Temperature Limits (°F)	Weatherability (Comment)	Chemical Resistance (Comment)
Sunlite® (fiberglass)	1.54 (D 542)	25 mil (P) 86.5 (\pm 0.2)	25 mil (P) 75.4 (\pm 0.1)	25 mil (P) 7.6 (\pm 0.1)	1.4 (10^{-5}) (D 696)	200 continuous use causes 5% loss in τ	Fair to good; regular, 7-year solar life; premium, 20-year solar life	Good: inert to chemical atmospheres
Float glass (glass)	1.518 (D 542)	125 mil 84.3 (\pm 0.1)	125 mil 78.6 (\pm 0.2)	125 mil 2.0 (est) ^e	4.8 (10^{-5}) (D 696)	1350 softening point; 100 thermal shock	Excellent: time proved	Good to excellent: time proved
Temper glass (glass)	1.518 (D 542)	125 mil 84.3 (\pm 0.1)	125 mil 78.6 (\pm 0.2)	125 mil 2.0 (est) ^e	4.8 (10^{-5}) (D 696)	450–500 continuous use; 500–550 short-term use	Excellent: time proved	Good to excellent: time proved
Clear lime sheet glass (low iron oxide glass)	1.51 (D 542)	Insufficient data provided by ASG	125 mil 87.5 (\pm 0.5)	125 mil 2.0 (est)	5.0 (10^{-5}) (D 696)	400 for continuous operation	Excellent: time proved	Good to excellent: time proved

Clear lime temper glass (low iron oxide glass)	1.51 (D 542)	Insufficient data provided by ASG	125 mil 87.5 (± 0.5)	125 mil 2.0 (est)	5.0 (10^{-6}) (D 696)	400 for continuous operation	Excellent: time proved	Good to excellent: time proved
Sunadex white crystal glass (0.01% iron oxide glass)	1.50 (D 542)	Insufficient data provided by ASG	125 mil 91.5 (± 0.2)	125 mil 2.0 (est)	4.7 (10^{-6}) (D 696)	400 for continuous operation	Excellent: time proved	Good to excellent: time proved

Source: Abstracted from Ratzel, A.C. and R.B. Bannerot, Optimal Material Selection for Flat-Plate Solar Energy Collectors Utilizing Commercially Available Materials, presented at ASME-AICHE Natl. Heat Transfer Conf., 1976.

^a Compiled data based on ASTM Code E 424 Method B.

^b Numerical integration ($\sum \tau_{avg} F_{1,17-227}$) for $\lambda = 0.2\text{--}4.0 \mu\text{M}$.

^c Numerical integration ($\sum \tau_{avg} F_{1,17-227}$) for $\lambda = 3.0\text{--}50.0 \mu\text{M}$.

^d All numbers in parentheses refer to ASTM test codes.

^e Data not provided; estimate of 2% to be used for 125 mil samples.

^f Degrees differential to rupture $2 \times 2 \times \frac{1}{4}$ in samples. Glass specimens heated and then quenched in water bath at 70°F.

^g Sunlite premium data denoted by (P); Sunlite regular data denoted by (R).

TABLE A3.7
Saturated Steam and Water—SI Units

Temperature (K)	Pressure (MN/m ²)	Specific Volume (m ³ /kg)				Specific Internal Energy (kJ/kg)		Specific Enthalpy (kJ/kg)		Specific Entropy (kJ/kg·K)	
		<i>v_f</i>	<i>v_g</i>	<i>u_f</i>	<i>u_g</i>	<i>h_f</i>	<i>h_g</i>	<i>s_f</i>	<i>s_g</i>		
273.15	0.0006109	0.0010002	206.278	-0.030	2375.3	-0.02	2501.4	2501.3	-0.0001	9.1565	
273.16	0.0006113	0.0010002	206.136	0	2375.3	+0.01	2501.3	2501.4	0	9.1562	
278.15	0.0008721	0.0010001	147.120	+20.97	2382.3	20.98	2489.6	2510.6	+0.0761	9.0257	
280.13	0.0010000	0.0010002	129.208	29.30	2385.0	29.30	2484.9	2514.2	0.1059	8.975	
283.15	0.0012276	0.0010004	106.379	42.00	2389.2	42.01	2477.7	2519.8	0.1510	8.9008	
286.18	0.0015000	0.0010007	87.980	54.71	2393.3	54.71	2470.6	2525.3	0.1957	8.8279	
288.15	0.0017051	0.0010009	77.926	62.99	2396.1	62.99	2465.9	2528.9	0.2245	8.7814	
290.65	0.0020000	0.0010013	67.004	73.48	2399.5	73.48	2460.0	2533.5	0.2607	8.7737	
293.15	0.002339	0.0010018	57.791	83.95	2402.9	83.96	2454.1	2538.1	0.2966	8.6672	
297.23	0.0030000	0.0010027	45.665	101.04	2408.5	101.05	2444.5	2545.5	0.3545	8.5776	
298.15	0.003169	0.0010029	43.360	104.88	2409.8	104.89	2442.3	2547.2	0.3674	8.5580	
302.11	0.0040000	0.0010040	34.800	121.45	2415.2	121.46	2432.9	2554.4	0.4226	8.4746	
303.15	0.0042446	0.0010043	32.894	125.78	2416.6	125.79	2430.5	2556.3	0.4369	8.4533	
306.03	0.0050000	0.0010053	28.192	137.81	2420.5	137.82	2423.7	2561.5	0.4764	8.3951	
308.15	0.005628	0.0010060	25.216	146.67	2423.4	146.68	2418.6	2565.3	0.5053	8.3531	
309.31	0.0060000	0.0010064	23.739	151.53	2425.0	151.53	2415.9	2567.4	0.5210	8.3304	
312.15	0.0070000	0.0010074	20.530	163.39	2428.8	163.40	2409.1	2572.5	0.5592	8.2758	
313.15	0.007384	0.0010078	19.523	167.56	2430.1	167.57	2406.7	2574.3	0.5725	8.2570	
314.66	0.0080000	0.0010084	18.103	173.87	2432.2	173.88	2403.1	2577.0	0.5926	8.2287	
316.91	0.0090000	0.0010094	16.203	183.27	2435.2	183.29	2397.7	2581.0	0.6224	8.1872	

318.15	0.009593	0.0010099	15.258	188.44	2436.8	188.45	2394.8	2583.2	0.6387	8.1648
318.96	0.010000	0.0010102	14.674	191.82	2437.9	191.83	2392.8	2584.7	0.6493	8.1502
323.15	0.012349	0.0010121	12.032	209.32	2443.5	209.33	2382.7	2592.1	0.7038	8.0763
327.12	0.015000	0.0010141	10.022	225.92	2448.7	225.94	2373.1	2599.1	0.7549	8.0085
328.15	0.015758	0.0010146	9.568	230.21	2450.1	230.23	2370.7	2600.9	0.7679	7.9913
333.15	0.019940	0.0010172	7.671	251.11	2456.6	251.13	2358.5	2609.6	0.8312	7.9096
333.21	0.020000	0.0010172	7.649	251.38	2456.7	251.40	2358.3	2609.7	0.8320	7.9085
338.15	0.025030	0.0010199	6.197	272.02	2463.1	272.06	2346.2	2618.3	0.8935	7.8310
342.25	0.030000	0.0010223	5.229	289.20	2468.4	289.23	2336.1	2625.3	0.9439	7.7686
343.15	0.031190	0.0010228	5.042	292.95	2469.6	292.98	2333.8	2626.8	0.9549	7.7553
348.15	0.038580	0.0010259	4.131	313.90	2475.9	313.93	2221.4	2635.3	1.0155	7.6824
349.02	0.040000	0.0010265	3.993	317.53	2477.0	317.58	2319.2	2636.8	1.0259	7.6700
353.15	0.047390	0.0010291	3.407	334.86	2482.2	334.91	2308.8	2643.7	1.0753	7.6122
354.48	0.050000	0.0010300	3.240	340.44	2483.9	340.49	2305.4	2645.9	1.0910	7.5939
358.15	0.057830	0.0010325	2.828	355.84	2488.4	355.90	2296.0	2651.9	1.1343	7.5445
359.09	0.060000	0.0010331	2.732	359.79	2489.6	359.86	2293.6	2653.5	1.1453	7.5320
363.10	0.070000	0.0010360	2.365	376.63	2494.5	376.70	2283.3	2660.0	1.1919	7.4797
363.15	0.070140	0.0010360	2.361	376.85	2494.5	376.92	2283.2	2660.1	1.1925	7.4791
366.65	0.080000	0.0010386	2.087	391.58	2498.8	391.66	2274.1	2665.8	1.2329	7.4346
368.15	0.084550	0.0010397	1.9819	397.88	2500.6	397.96	2270.2	2668.1	1.2500	7.4159

Source: Bolz, R.E. and G.L. Tuve, eds., CRC Handbook of Tables for Applied Engineering Science, 2nd ed., Chemical Rubber Co., Cleveland, Ohio, 1973.

Note: Subscripts: "f" refers to a property of liquid in equilibrium with vapor; "g" refers to a property of vapor in equilibrium with liquid; "fg" refers to a change by evaporation.

TABLE A3.8
Superheated Steam—SI Units

Pressure (MN/m ²)		Temperature								
(Saturation Temperature)	50°C 323.15 K	100°C 373.15 K	150°C 423.15 K	200°C 473.15 K	300°C 573.15 K	400°C 673.15 K	500°C 773.15 K	700°C 973.15 K	1000°C 1273.15 K	1300°C 1573.15 K
0.001 (6.98°C) (280.13 K)	<i>v</i>	149.093	172.187	195.272	218.352	264.508	310.661	356.814	449.117	587.571
	<i>u</i>	2445.4	2516.4	2588.4	2661.6	2812.2	2969.0	3132.4	3479.6	4053.0
	<i>h</i>	2594.5	2688.6	2783.6	2880.0	3076.8	3279.7	3489.2	3928.7	4640.6
0.002 (17.50°C) (290.65 K)	<i>s</i>	9.2423	9.5129	9.7520	9.9671	10.3443	10.6705	10.9605	11.4655	12.1019
	<i>v</i>	74.524	86.081	97.628	109.170	132.251	155.329	178.405	224.558	293.785
	<i>u</i>	2445.2	2516.3	2588.3	2661.6	2812.2	2969.0	3132.4	3479.6	4053.0
0.004 (28.96°C) (302.11 K)	<i>h</i>	2594.3	2688.4	2793.6	2879.9	3076.7	3279.7	3489.2	3928.7	4640.6
	<i>s</i>	8.9219	9.1928	9.4320	9.6471	10.0243	10.3506	10.6406	11.1456	11.7820
	<i>v</i>	37.240	43.028	48.806	54.580	66.122	77.662	89.201	112.278	146.892
0.006 (36.16°C) (309.31 K)	<i>u</i>	2444.9	2516.1	2588.2	2661.5	2812.2	2969.0	3132.3	3479.6	4053.0
	<i>h</i>	2593.9	2688.2	2783.4	2879.8	3076.7	3279.6	3489.2	3928.7	4640.6
	<i>s</i>	8.6009	8.8724	9.1118	9.3271	9.7044	10.0307	10.3207	10.8257	11.4621
0.008 (41.51°C) (314.66 K)	<i>v</i>	24.812	28.676	32.532	36.383	44.079	51.774	59.467	74.852	97.928
	<i>u</i>	2444.6	2515.9	2588.1	2661.4	2812.2	2969.0	3132.3	3479.6	4053.0
	<i>h</i>	2593.4	2688.0	2783.3	2879.7	3076.6	3279.6	3489.1	3928.7	4640.6
0.008 (41.51°C) (314.66 K)	<i>s</i>	8.4128	8.6847	8.9244	9.1398	9.5172	9.8435	10.1336	10.6386	11.2750
	<i>v</i>	18.598	21.501	24.395	27.284	33.058	38.829	44.599	56.138	73.446
	<i>u</i>	2444.2	2515.7	2588.0	2661.4	2812.1	2969.0	3132.3	3479.6	4053.0
<i>h</i>	2593.0	2687.7	2783.1	2879.6	3076.6	3279.6	3489.1	3928.7	4640.6	5409.7
	<i>s</i>	8.5514	8.7914	9.0069	9.3844	9.7107	10.0008	10.5058	11.1422	11.6841

0.010 (45.81°C) (318.96 K)	<i>v</i>	14.869	17.196	19.512	21.825	26.445	31.063	35.679	44.911	58.757	72.602
	<i>u</i>	2443.9	2515.5	2587.9	2661.3	2812.1	2968.9	3132.3	3479.6	4053.0	4663.7
	<i>h</i>	2592.6	2687.5	2783.0	2879.5	3076.5	3279.6	3489.1	3928.7	4640.6	5409.7
0.020 (60.06°C) (333.21 K)	<i>s</i>	8.1749	8.4479	8.6882	8.9038	9.2813	9.6077	9.8978	10.4028	11.0393	11.5811
	<i>v</i>	7.412	8.585	9.748	10.907	13.219	15.529	17.838	22.455	29.378	36.301
	<i>u</i>	2442.2	2514.6	2587.3	2660.9	2811.9	2968.8	3132.2	3479.5	4053.0	4663.7
0.040 (75.87°C) (349.02 K)	<i>h</i>	2590.4	2686.2	2782.3	2879.1	3076.3	3279.4	3489.0	3928.6	4640.6	5409.7
	<i>s</i>	7.8498	8.1255	8.3669	8.5831	8.9611	9.2876	9.5778	10.0829	10.7193	11.2612
0.060 (85.94°C) (359.09 K)	<i>v</i>	3.683	4.279	4.866	5.448	6.606	7.763	8.918	11.227	14.689	18.151
	<i>u</i>	2438.8	2512.6	2586.2	2660.2	2811.5	2968.6	3132.1	3479.4	4052.9	4663.6
	<i>h</i>	2586.1	2683.8	2780.8	2878.1	3075.8	3279.1	3488.8	3928.5	4640.5	5409.6
0.080 (93.50°C) (366.65 K)	<i>s</i>	7.5192	7.8003	8.0444	8.2617	8.6406	8.9674	9.2577	9.7629	10.3994	10.9412
	<i>v</i>	2.440	2.844	3.238	3.628	4.402	5.174	5.944	7.484	9.792	12.100
	<i>u</i>	2435.3	2510.6	2585.1	2659.5	2811.2	2968.4	3131.9	3479.4	4052.9	4663.6
	<i>h</i>	2581.7	2681.3	2779.4	2877.2	3075.3	3278.8	3488.6	3928.4	4640.4	5409.6
0.100 (99.63°C) (372.78 K)	<i>s</i>	7.3212	7.6079	7.8546	8.0731	8.4528	8.7799	9.0704	9.5757	10.2122	10.7541
	<i>v</i>	1.8183	2.127	2.425	2.718	3.300	3.879	4.458	5.613	7.344	9.075
	<i>u</i>	2431.7	2508.7	2583.9	2658.8	2810.8	2968.1	3131.7	3479.3	4052.8	4663.5
	<i>h</i>	2577.2	2678.8	2777.9	2876.2	3074.8	3278.5	3488.3	3928.3	4640.4	5409.5
	<i>s</i>	7.1775	7.4698	7.7191	7.9388	8.3194	8.6468	8.9374	9.4428	10.0794	10.6213
	<i>v</i>	1.4450	1.6958	1.9364	2.172	2.639	3.103	3.565	4.490	5.875	7.260
	<i>u</i>	2428.2	2506.7	2582.8	2658.1	2810.4	2967.9	3131.6	3479.2	4052.8	4663.5
	<i>h</i>	2572.7	2676.2	2776.4	2875.3	3074.3	3278.2	3488.1	3928.2	4640.3	5409.5
	<i>s</i>	7.0633	7.3614	7.6134	7.8343	8.2158	8.5435	8.8342	9.3398	9.9764	10.5183

(Continued)

TABLE A3.8 (CONTINUED)
Superheated Steam—SI Units

Pressure (MN/m ²)		Temperature										
(Saturation Temperature)	50°C	100°C	150°C	200°C	300°C	400°C	500°C	700°C	1000°C	1273.15 K	1300°C	1573.15 K
0.200 (120.23°C) (393.38 K)	v	0.6969	0.8340	0.9596	1.0803	1.3162	1.5493	1.7814	2.244	2.937	3.630	
	u	2409.5	2496.3	2576.9	2654.4	2808.6	2966.7	3130.8	3478.8	4052.5	4683.2	
	h	2548.9	2663.1	2768.8	2870.5	3071.8	3276.6	3487.1	3927.6	4640.0	5409.3	
0.300 (133.55°C) (406.70 K)	s	6.6844	7.0135	7.2795	7.5066	7.8926	8.2218	8.5133	9.0194	9.6563	10.1982	
	v	0.4455	0.5461	0.6339	0.7163	0.8753	1.0315	1.1867	1.4957	1.9581	2.4201	
	u	2389.1	2485.4	2570.8	2650.7	2806.7	2965.6	3130.0	3478.4	4052.3	4683.0	
0.400 (143.63°C) (416.78 K)	h	2522.7	2649.2	2761.0	2865.6	3069.3	3275.0	3486.0	3927.1	4639.7	5409.0	
	s	6.4319	6.7965	7.0778	7.3115	7.7022	8.0330	8.3251	8.8319	9.4690	10.0110	
	v	0.3177	0.4017	0.4708	0.5342	0.6548	0.7726	0.8893	1.1215	1.4685	1.8151	
0.500 (151.86°C) (425.01 K)	u	2366.3	2473.8	2564.5	2646.8	2804.8	2964.4	3129.2	3477.9	4052.0	4682.8	
	h	2493.4	2634.5	2752.8	2860.5	3066.8	3273.4	3484.9	3926.5	4639.4	5408.8	
	s	6.2248	6.6319	6.9299	7.1706	7.5662	7.8985	8.1913	8.6987	9.3360	9.8780	
v	0.3146	0.3729	0.4249	0.5226	0.6173	0.7109	0.8969	1.1747	1.4521			
	u	2461.5	2557.9	2642.9	2802.9	2963.2	3128.4	3477.5	4051.8	4682.5		
	h	2618.7	2744.4	2855.4	3064.2	3271.9	3483.9	3925.9	4639.1	5408.6		
s	6.4945	6.8111	7.0592	7.4599	7.7938	8.0873	8.5952	9.2328	9.7749			

Source: Bolz, R.E. and G.I. Tuve, eds., *CRC Handbook of Tables for Applied Engineering Science*, 2nd ed., Chemical Rubber Co., Cleveland, Ohio, 1973.
Note: v = specific volume, m³/kg; u = specific internal energy, kJ/kg; h = specific enthalpy, kJ/kg; s = specific entropy, kJ/K·kg.

TABLE A3.9

Normal Distribution Function

$$F(z) = \frac{1}{\sqrt{2\pi}} \int_{-\infty}^z e^{-1/2t^2} dt$$

Appendix 4: Supplementary Material for Chapter 4

TABLE A4.1

Toxicological Properties of Common Glycols Used as Antifreeze in Solar Systems

	Single Oral LD ₅₀ Dose in Rats (ml/kg)	Repeated Oral Feeding in Rats Acceptable Level in Diet and Duration	Single Skin Penetration LD ₅₀ Dose in Rabbits (ml/kg)	Single Inhalation Concentrated Vapor (8 h) in Rats	Primary Skin Irritation in Rabbits	Eye Injury in Rabbits
Ethylene glycol	7.40 ^a	0.18 g/kg/day (30 days)	>20	Killed none of 6	None	None
Diethylene glycol	28.3	0.18 g/kg/day (30 days)	11.9	Killed none of 6	None	None
Triethylene glycol	28.2	0.83 g/kg/day (30 days)	>20	Killed none of 6	None	None
Tetraethylene glycol	28.9	1.88 g/kg/day (2 years)	>20	Killed none of 6	None	None
Propylene glycol	34.6	2.0 g/kg/day (2 years) ^b	>20	Killed none of 6	None	Trace
Dipropylene glycol	14.8	—	>20	Killed none of 6	None	Trace
Hexylene glycol	4.06	0.31 g/kg/day (90 days)	8.56	Killed none of 6	Trace	Minor
2-Ethyl-1,3-hexanediol	6.50	0.48 g/kg/day (90 days)	15.2	Killed none of 6	Trace	Moderate
1,5-Pentanediol	5.89 ^c	—	>20	Killed none of 6	None	Trace

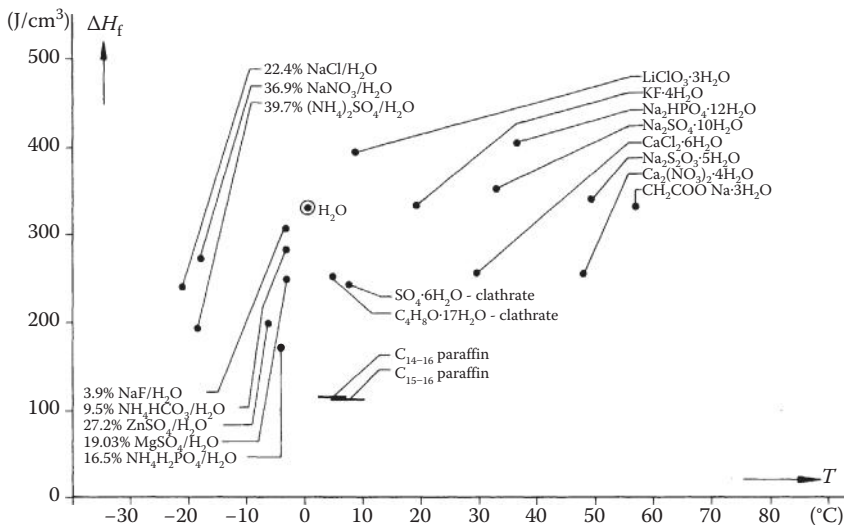
Source: Union Carbide, Glycols, F-41515A 7/71-12M, p. 68, 1971.

Note: The term LD₅₀ refers to that quantity of chemical that kills 50% of dosed animals within 14 days. For uniformity, dosage is expressed in grams or milliliters per kilogram of body weight. Single skin penetration refers to a 24-h covered skin contact with the liquid chemical. Single inhalation refers to the continuous breathing of a certain concentration of chemical for the stated period. Primary irritation refers to the skin response 24 h after application of 0.01-ml amounts to uncovered skin. Eye injury refers to surface damage produced by the liquid chemical.

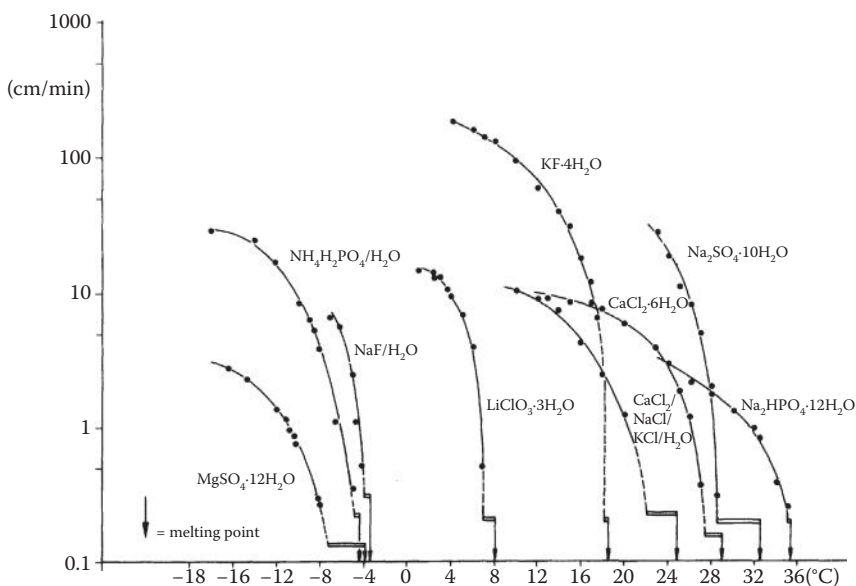
^a Single dose oral toxicity to humans is greater.

^b Dogs.

^c g/kg.

**FIGURE A4.1**

Enthalpy of fusion and phase change temperatures of low-temperature phase-change storage media. (From Schröder, J., Philips GmbH Forschungslaboratorium [Aachen] Report, 1977)

**FIGURE A4.2**

Rate of crystallization of several low-temperature hydrates and eutectics. Note that Na₂SO₄·10H₂O and CaCl₂/NaCl/KCl/H₂O have very inadequate rates without substantial supercooling. (From Schröder, J., Philips GmbH Forschungslaboratorium [Aachen] Report, 1977)

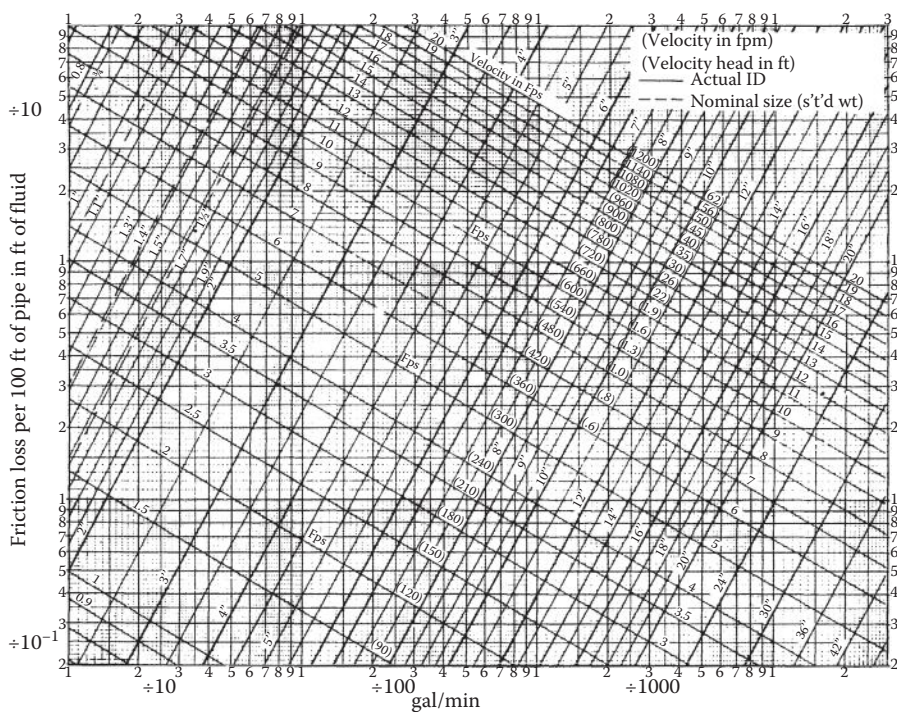
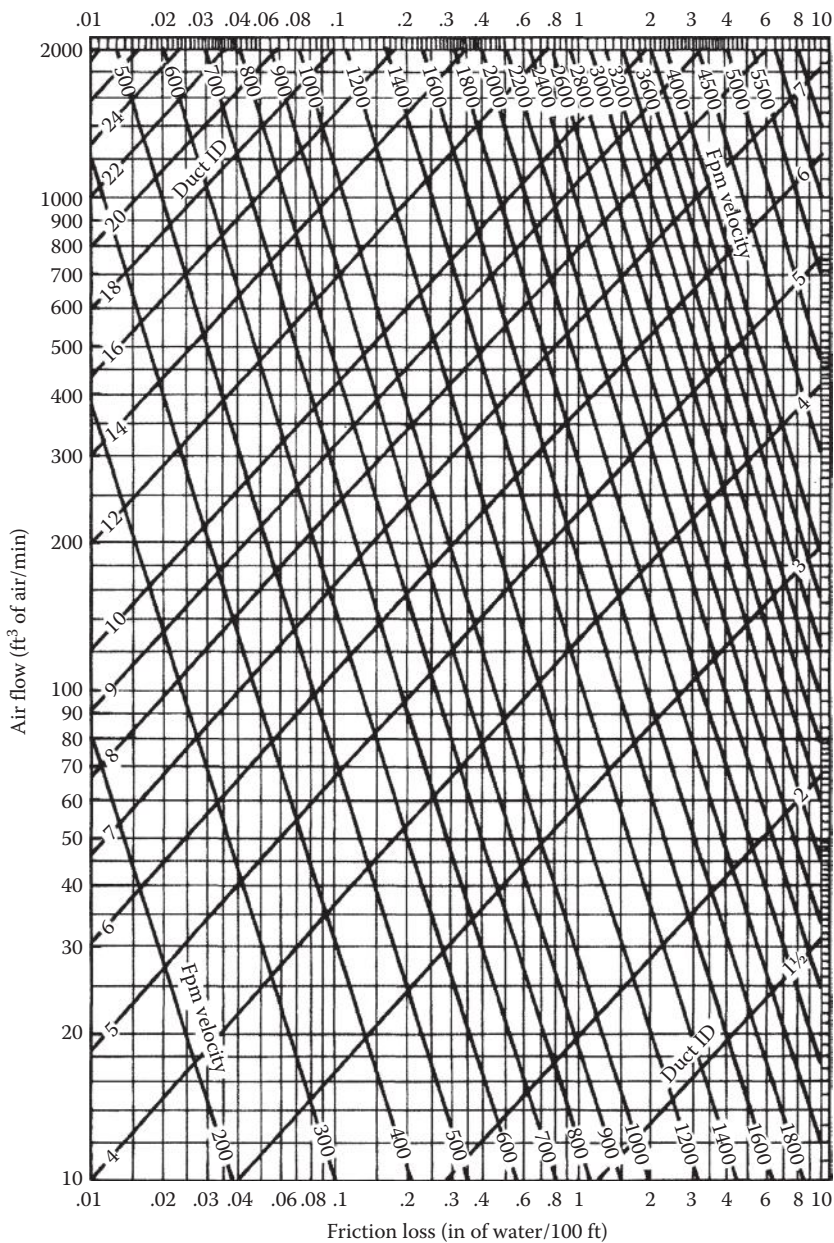
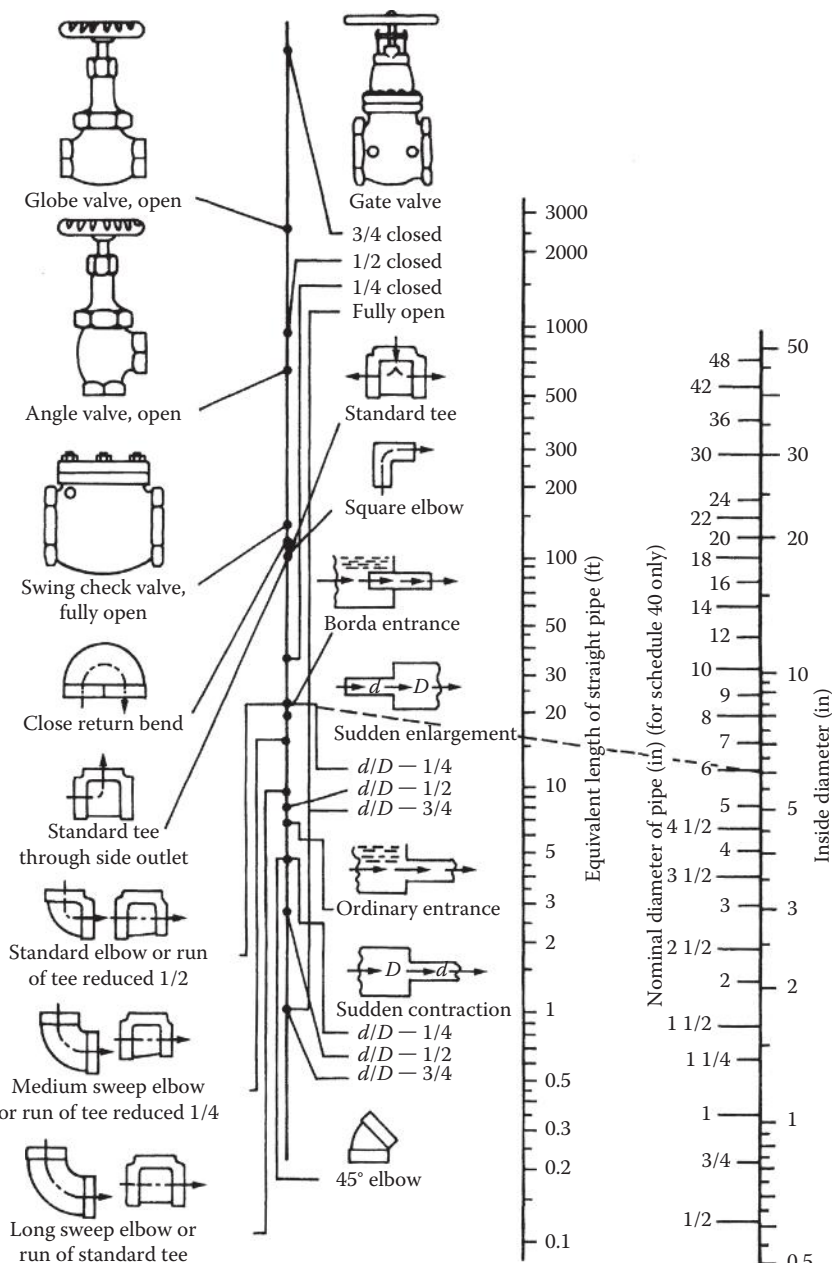


FIGURE A4.3

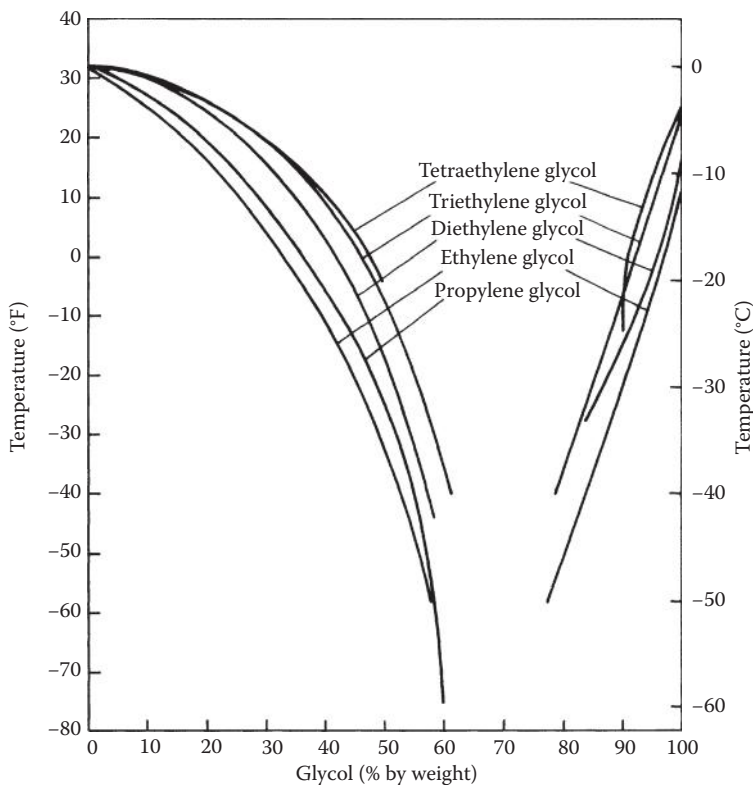
Pressure drop of water in turbulent flow for standard pipe sizes. (1 gal/min = 3.79×10^{-3} m³/min; 1 ft = 0.305 m; 1 in = 2.54 cm.) (From Potter, P.J., *Power Plant Theory and Design*, 2nd ed. Copyright © 1959. The Ronald Press Company, New York.)

**FIGURE A4.4**

Pressure drop of air flowing in ducts; velocities shown for circular ducts. ($1 \text{ in H}_2\text{O} = 249 \text{ N/m}^2$; $1 \text{ ft}^3 = 2.83 \times 10^{-2} \text{ m}^3$; $1 \text{ in} = 2.54 \text{ cm}$; $1 \text{ ft}^3 = 0.305 \text{ m}^3$) (From ASHRAE, *Handbook of Fundamentals*, American Society of Heating, Refrigerating, and Air Conditioning Engineers, New York, 1972.)

**FIGURE A4.5**

Equivalent lengths of pipe, standard pipe fittings. (1 ft = 0.305 m; 1 in = 2.54 cm.) For sudden enlargements and sudden contractions, the equivalent length is in feet of pipe of the smaller diameter d . Dashed line shows determination of equivalent length of a 6-in standard elbow. (From Crane Co., Flow of fluids, Technical Paper 410, 1957.)

**FIGURE A4.6**

Freezing-point depression of aqueous solutions of common glycol antifreezes. (From Union Carbide, Glycols, F-41515A 7/71-12M, p. 17, 1971.)

*Appendix 5: Supplementary
Material for Chapter 5*

TABLE A5.1
Conductance and Resistance Values for External Air Surfaces

Wind Condition		Type of Surface					
Position of Surface	Direction of Heat Flow	Foil		Aluminum-Coated Paper		Nonreflective Building Materials	
		Conductance $C, \text{Btu}/(\text{h})$ (ft^2) $(^\circ\text{F})$)	Resistance R, $I/\text{Btu}/(\text{h})$ (ft^2) $(^\circ\text{F})$)	Conductance $C, \text{Btu}/(\text{h})$ (ft^2) $(^\circ\text{F})$)	Resistance R, $I/\text{Btu}/(\text{h})$ (ft^2) $(^\circ\text{F})$)	Conductance $C, \text{Btu}/(\text{h})$ (ft^2) $(^\circ\text{F})$)	Resistance R, $I/\text{Btu}/(\text{h})$ (ft^2) $(^\circ\text{F})$)
<i>Still Air</i>							
Horizontal	Up	0.76	1.32	0.91	1.10	1.63	0.61
45° slope	Up	0.73	1.37	0.88	1.14	1.60	0.62
Vertical	Horizontal	0.59	1.70	0.74	1.35	1.46	0.68
45° slope	Down	0.45	2.22	0.60	1.67	1.32	0.76
Horizontal	Down	0.22	4.55	0.37	2.70	1.08	0.92
<i>7.5-mph Wind</i>							
Any position	Any direction (for summer calculations)	4.00	0.25
<i>15-mph Wind</i>							
Any position	Any direction (for winter calculations)	6.00	0.17

Source: Adapted from Johns-Mansville, Denver, Colorado.

TABLE A5.2
Conductance and Resistance Values for Internal Air Surfaces

		Type of Surface									
Position of Airspace	Direction of Heat Flow ^a	Thickness, in.	Temp. Cond.	Foil and Nonreflective Building Materials		Aluminum-Coated Paper and Nonreflective Building Materials		Both Surfaces Nonreflective Building Materials			
				Conductance $C, \text{Btu}/(\text{h})(\text{ft}^2)(^\circ\text{F})$	Resistance $R, \text{I}[\text{Btu}/(\text{h})(\text{ft}^2)(^\circ\text{F})]$	Conductance $C, \text{Btu}/(\text{h})(\text{ft}^2)(^\circ\text{F})$	Resistance $R, \text{I}[\text{Btu}/(\text{h})(\text{ft}^2)(^\circ\text{F})]$	Conductance $C, \text{Btu}/(\text{h})(\text{ft}^2)(^\circ\text{F})$	Resistance $R, \text{I}[\text{Btu}/(\text{h})(\text{ft}^2)(^\circ\text{F})]$		
				Up	3/4	W	0.45	2.23	0.59	1.71	1.15
45° slope	Up	3/4	S	0.44	2.26	0.61	1.63	1.32	0.76	0.76	0.76
		4	W	0.37	2.73	0.50	1.99	1.07	0.94	0.94	0.94
		4	S	0.36	2.75	0.53	1.87	1.24	0.80	0.80	0.80
	Horizontal	3/4	W	0.36	2.78	0.50	2.02	1.06	0.94	0.94	0.94
		3/4	S	0.36	2.81	0.53	1.90	1.24	0.81	0.81	0.81
		4	W	0.33	3.00	0.47	2.13	1.04	0.96	0.96	0.96
Vertical	Horizontal	4	S	0.33	3.00	0.51	1.98	1.21	0.82	0.82	0.82
		3/4	W	0.29	3.48	0.42	2.36	0.99	0.99	0.99	0.99
		3/4	S	0.31	3.28	0.48	2.10	1.19	0.84	0.84	0.84
	45° slope	4	W	0.29	3.45	0.43	2.34	0.99	0.99	0.99	0.99
		4	S	0.29	3.44	0.46	2.16	1.17	0.91	0.91	0.91
		3/4	W	0.28	3.57	0.42	2.40	0.98	1.02	1.02	1.02
Horizontal	Down	3/4	S	0.31	3.24	0.48	2.09	1.19	0.84	0.84	0.84
	Down	4	W	0.23	4.41	0.36	2.75	0.93	1.08	1.08	1.08
	Down	4	S	0.23	4.36	0.40	2.50	1.11	0.90	0.90	0.90
	Down	3/4	W	0.28	3.55	0.42	2.39	0.98	1.02	1.02	1.02

(Continued)

TABLE A5.2 (CONTINUED)
Conductance and Resistance Values for Internal Air Surfaces

Position of Airspace	Direction of Heat Flow ^a	Thickness, in.	Temp. Cond.	Type of Surface			
				Foil and Nonreflective Building Materials		Aluminum-Coated Paper and Nonreflective Building Materials	
				Conductance $C, \text{Btu}/(\text{ft}^2)\text{°F}$	Resistance $R, \text{h}/(\text{Btu}/(\text{ft}^2)\text{°F})$	Conductance $C, \text{Btu}/(\text{ft}^2)\text{°F}$	Resistance $R, \text{h}/(\text{Btu}/(\text{ft}^2)\text{°F})$
1 1/2	W	0.17	5.74	0.31	3.21	0.88	1.14
4	W	0.11	8.94	0.25	4.02	0.81	1.23
3/4	S	0.31	3.25	0.48	2.08	1.19	0.84
1 1/2	S	0.19	5.24	0.36	2.76	1.07	0.93
4	S	0.12	8.08	0.30	3.38	1.01	0.99

Source: Adapted from Johns-Manville, Denver, Colorado.

Note: W = winter; S = summer.

^a Heat flows from hot to cold. For ceiling instillation, the direction of heat flow would normally be "up" for winter and "down" for summer. In a floor the direction of heat flow would be "down" in winter and "up" in summer. Heat flow in walls would be in a horizontal direction.

TABLE A5.3

Conductance and Resistance Values for Exterior Siding Materials

Material	Description	Conductivity <i>k</i> , Btu/(h)(ft ²) (°F/in.)	Thickness, in.	Conductance <i>C</i> , Btu/(h) (ft ²)(°F)	Resistance <i>R</i> , l/[Btu/(h) (ft ²)(°F)]
Brick	Common	5.0	4	1.25	0.80
Brick	Face	9.0	4	2.27	0.44
Stucco		5.0	1	5.0	0.20
Asbestos cement shingles				4.76	0.21
Wood shingles	16–7 1/2-in. exposure			1.15	0.87
Wood shingles	Double 16–12 in. exposure			0.84	1.19
Wood shingles	Plus 5/16 in. insulated backerboard			0.71	1.40
Asbestos cement siding	1/4 in. lapped			4.76	0.21
Asphalt roll siding				6.50	0.15
Asphalt insulating siding			1/2	0.69	1.46
Wood	Drop siding, 1 × 8 in.			1.27	0.79
Wood	Bevel, 1/2 × 8 in. lapped			1.23	0.81
Wood	Bevel, 3/4 × 10 in. lapped			0.95	1.05
Wood	Plywood, 3/8 in. lapped			1.59	0.59
Hardboard	Medium density	0.73	1/4	2.94	0.34
	Tempered	1.00	1/4	4.00	0.25
Plywood lap siding			3/8	1.79	0.56
Plywood flat siding			3/8	2.33	0.43

Source: Adapted from Johns-Mansville, Denver, Colorado.

TABLE A5.4

Conductance and Resistance Values for Sheathing and Building Paper

Material	Description	Conductivity k , Btu/(h)(ft ²) (°F/in.)	Thickness, in.	Conductance C , Btu/(h) (ft ²)(°F)	Resistance R , l/[Btu/(h) (ft ²)(°F)]
Gypsum	...	1.11	3/8	3.10	0.32
			1/2	2.25	0.45
			5/8	1.75	0.57
Plywood	...	0.80	1/4	3.20	0.31
			3/8	2.13	0.47
			1/2	1.60	0.62
			5/8	1.28	0.78
			3/4	1.07	0.93
Nail-base sheathing	...	0.44	1/2	0.88	1.14
Wood sheathing	Fir or pine	0.80	3/4	1.06	0.94
Sheathing paper	Vapor- permeable			16.70	0.06
Vapor barrier	2 layers mopped 15-lb felt			8.35	0.12
	Plastic film			Negl.	Negl.

Source: Adapted from Johns-Mansville, Denver, Colorado.

TABLE A5.5
Conductance and Resistance Values for Masonry Materials

Material	Description	Conductivity <i>k</i> , Btu/(h) (ft ²)°F/in.)	Thickness, in.	Conductance <i>C</i> , Btu/(h) (ft ²)°F)	Resistance <i>R</i> , l/[Btu/(h) (ft ²)°F)]
Concrete blocks, three-oval core	Sand and gravel aggregate	...	4	1.40	0.71
			8	0.90	1.11
			12	0.78	1.28
	Cinder aggregate	...	4	0.90	1.11
			8	0.58	1.72
			12	0.53	1.89
	Lightweight aggregate	...	4	0.67	1.50
			8	0.50	2.00
			12	0.44	2.27
Hollow clay tile	1 cell deep	...	4	0.90	1.11
	2 cells deep	...	8	0.54	1.85
	3 cells deep	...	12	0.40	2.50
Gypsum partition tile	3 × 12 × 30 in. solid	...	3	0.79	1.26
	3 × 12 × 30 in. 4-cell	...	3	0.74	1.35
	4 × 12 × 30 in. 3-cell	...	4	0.60	1.67
Cement mortar		5.0	1	5.0	0.20
Stucco		5.0	1	5.0	0.20
Gypsum	Poured	1.66	1	1.66	0.60
	Precast	2.80	2	1.40	0.71
Concrete	Sand and gravel or stone	12.0	1	12.0	0.08
Lightweight concrete	Perlite or zonolite mixture				
	1:4 mix, 36 lb/ft ³	0.72–0.75	1	0.74	1.35
	1:5 mix, 30 lb/ft ³	0.61–0.72	1	0.67	1.49
	1:6 mix, 27 lb/ft ³	0.54–0.61	1	0.58	1.72
	1:8 mix, 22 lb/ft ³	0.47–0.54	1	0.51	1.96
Stone	...	12.5	1	12.5	0.08

Source: Adapted from Johns-Mansville, Denver, Colorado.

TABLE A5.6
Conductance and Resistance Values for Woods

Material	Description	Conductivity k , Btu/(h) (ft ²)(°F/in.)	Thickness, in.	Conductance C , Btu/(h) (ft ²)(°F)	Resistance R , I/[Btu/(h) (ft ²)(°F)]
Maple, oak, and similar hardwoods	45 lb/ft ³	1.10	3/4	1.47	0.68
Fir, pine, and similar softwoods	32 lb/ft ³	C.80	3/4	1.06	0.94
			1 1/2	0.53	1.89
			2 1/2	0.32	3.12
			3 1/2	0.23	4.35

Source: Adapted from Johns-Mansville, Denver, Colorado.

TABLE A5.7

Conductance and Resistance Values for Wall-Insulation Materials

Material	Description	Conductivity <i>k</i> , Btu/(h) (ft ²)(°F/in.)	Thickness, in.	Conductance <i>C</i> , Btu/(h) (ft ²)(°F)	Resistance <i>R</i> , l/[Btu/(h)] (ft ²)(°F)]
Fiber glass roof insulation	... Thickness includes membrane roofing on both sides	... 0.13	15/16	0.27	3.70
			1 1/16	0.24	4.17
			1 5/16	0.19	5.26
			1 5/8	0.15	6.67
			1 7/8	0.13	7.69
			2 1/4	0.11	9.09
Urethane roof insulation	Thickness includes membrane roofing on both sides	0.13	4/5	0.19	5.26
			1	0.15	6.67
			1 1/5	0.12	8.33
Styrofoam SM & TG	2.1 lb/ft ³	0.19	3/4	0.25	3.93
			1	0.19	5.26
			1 1/2	0.13	7.89
			2	0.95	10.52
Wood shredded	Cemented in preformed slabs	0.60	1	0.60	1.67
Insulating board	Building and service board, decorative ceiling panels	0.38	3/8	1.01	0.99
			1/2	0.76	1.32
			9/16	0.68	1.48
			3/4	0.51	1.98
Thermal, acoustical fiber glass	... 0.39 0.36 0.34	0.39	2 3/4	0.14	7.00
			4	0.09	11.00
			6 1/2	0.05	19.00
Corkboard	6.4 lb/ft ³	0.26	1	0.26	3.85
Expanded polystyrene	Extruded Molded beads	1.8 lb/ft ³ 1.0 lb/ft ³	0.25	1	0.25
			1	0.26	3.85
Urethane foam	1.9 lb/ft ³	0.17	3/4	0.23	4.41
			1 1/2	0.11	8.82
			2	0.09	11.76
Fiber glass perimeter insulation	1	0.23	4.30
Fiber glass form board	1 1/4	0.19	5.40
			1	0.25	4.00

Source: Adapted from Johns-Mansville, Denver, Colorado.

TABLE A5.8

Conductance and Resistance Values for Roofing Materials

Material	Description	Conductivity k , Btu/(h) (ft ²)°F/in.)	Thickness, in.	Conductance C , Btu/(h) (ft ²)°F)	Resistance R , l/[Btu/(h) (ft ²)°F)]
Asbestos cement shingles	120 lb/ft ³	4.76	0.21
Asphalt shingles	70 lb/ft ³	2.27	0.44
Wood shingles	1.06	0.94
Slate	1/2	20.0	0.05
Asphalt roll roofing	70 lb/ft ³	6.50	0.15
Built-up roofing	Smooth or gravel surface	...	3/8	3.00	0.33
Sheet metal	Negl.	Negl.

Source: Adapted from Johns-Mansville, Denver, Colorado.

TABLE A5.9

Conductance and Resistance Values for Flooring Materials

Material	Description	Conductivity k , Btu/(h) (ft ²)°F/in.)	Thickness, in.	Conductance C , Btu/(h) (ft ²)°F)	Resistance R , l/[Btu/(h) (ft ²)°F)]
Asphalt, vinyl, rubber, or linoleum tile	20.0	0.05
Cork tile	...	0.45	1/8	3.60	0.28
Terrazzo	...	12.5	1	12.50	0.08
Carpet and fibrous pad	0.48	2.08
Carpet and rubber pad	0.81	1.23
Plywood subfloor	...	0.80	5/8	1.28	0.78
Wood subfloor	...	0.80	3/4	1.06	0.94
Wood, hardwood finish	...	1.10	3/4	1.47	0.68

Source: Adapted from Johns-Mansville, Denver, Colorado.

TABLE A5.10

Conductance and Resistance Values for Interior Finishes

Material	Description	Conductivity k , Btu/(h) (ft ²)(°F/in.)	Thickness, in.	Conductance C , Btu/(h) (ft ²)(°F)	Resistance R , l/[Btu/(h) (ft ²)(°F)]
Gypsum board		1.11	3/8	3.10	0.32
			1/2	2.25	0.45
Cement plaster	Sand aggregate	5.0	1/2	10.00	0.10
			3/4	6.66	0.15
Gypsum plaster	Sand aggregate	5.6	1/2	11.10	0.09
			5/8	9.10	0.11
Gypsum plaster	Lightweight aggregate	1.6	1/2	3.12	0.32
			5/8	2.67	0.39
Gypsum plaster on Metal lath	Sand aggregate		3/4	7.70	0.13
Metal lath	Lightweight aggregate		3/4	2.13	0.47
Gypsum board, 3/8 in.	Sand aggregate		7/8	2.44	0.41
Insulating board		0.38	1/2	0.74	1.35
Plywood		0.80	3/8	2.13	0.47

Source: Adapted from Johns-Mansville, Denver, Colorado.

TABLE A5.11

Conductance and Resistance Values for Glass

Material	Description	Conductivity k , Btu/(h) (ft ²)(°F/in.)	Thickness, in.	Conductance $C (U)$, Btu/(h) (ft ²)(°F)	Resistance R (1/ U), l/[Btu/ (h)(ft ²)(°F)]
Single plate				1.13	0.88
Double plate	Air space, 3/16 in.	0.69	1.45
Storm windows	Air space, 1–4 in.	0.56	1.78
Solid-wood door	Actual thickness, 1 1/2 in.	0.49	2.04
Storm door, wood and glass	With wood and glass storm door	0.27	3.70
Storm door, metal and glass	With metal and glass storm door	0.33	3.00

Source: Adapted from Johns-Mansville, Denver, Colorado.

TABLE A5.12

Internet Sources of World Climatic Data

The following climatic data, useful for solar energy system design, are available for various locations in the countries listed below.

- *Temperature (Max., Min., Mean)*
- *Precipitation*
- *Wind Speed*
- *Dew Point (Mean)*
- *Pressure*

Additional information about national weather data for some countries is available from the internet. For websites, see the National Oceanic and Atmospheric Administration (NOAA) website [<http://www.ncdc.noaa.gov/cgi-bin/res40?page=climvisgsod.html>]

Additional data available for the United States from the National Oceanic and Atmospheric Administration (NOAA) [<http://www.ncdc.noaa.gov/ol/documentlibrary/hc/hcs.html>] include:

- *Heating Degree Days*
- *Cooling Degree Days*

Countries (Numbers in Parentheses Denote the Number of Sites for Which Data Are Available)

Africa

Algeria (55)	Angola (19)
Benin (6)	Botswana (17)
Bouvet Island (1)	Burkina Faso (11)
Burundi (2)	Cameroon (10)
Cape Verde (3)	Central African Republic (8)
Chad/Tchad (12)	Comoros (4)
Congo (14)	Cote D'Ivoire/Ivory Coast (12)
Democratic Republic of the Congo (73)	Djibouti (2)
Egypt (39)	Equatorial Guinea (2)
Eritrea (3)	Ethiopia (14)
Gabon (9)	Gambia (12)
Ghana (23)	Guinea (7)
Guinea-Bissau (4)	Kenya (11)
Lesotho (3)	Liberia (2)
Libyan Arab Jamahiriya (17)	Madagascar (9)
Madeira (2)	Malawi (7)
Mali (6)	Mauritania (6)
Morocco (24)	Mozambique (16)
Namibia (11)	Niger (7)
Nigeria (21)	Ocean Islands (12)
Rwanda (5)	Senegal (6)
Seychelles (5)	Sierra Leone (6)
Somalia (7)	South Africa (101)
Spain (Canary Islands) (7)	Sudan (8)
Swaziland (1)	Uganda (9)
Tunisia (17)	Togo (5)
United Republic of Tanzania (12)	Western Sahara (2)
Zambia (31)	Zimbabwe (27)

TABLE A5.12 (CONTINUED)

Internet Sources of World Climatic Data

Countries (Numbers in Parentheses Denote the Number of Sites for Which Data Are Available)

Asia

Afghanistan (17)	Bahrain (1)
Bangladesh (14)	Cambodia (9)
China (414)	North Korea (15)
Hong Kong (18)	India (540)
Iran (81)	Iraq (31)
Japan (315)	Kazakhstan (76)
Kuwait (19)	Kyrgyzstan (6)
Lao (19)	Macau (4)
Maldives (5)	Mongolia (38)
Myanmar (51)	Nepal (9)
Oman (12)	Pakistan (72)
Qatar (3)	South Korea (68)
Russian Federation (in Asia) (576)	Saudi Arabia (87)
Sri Lanka (26)	Tajikistan (9)
Thailand (73)	Turkmenistan (29)
United Arab Emirates (5)	Uzbekistan (36)
Vietnam (21)	Yemen (17)

Europe

Albania (8)	Armenia (36)
Austria (174)	Azerbaijan (72)
Belarus (23)	Belgium (19)
Bosnia and Herzegovina (10)	Bulgaria (34)
Croatia (47)	Cyprus (4)
Czech Republic (32)	Denmark (70)
Estonia (27)	Finland (49)
France (180)	Georgia (17)
Germany (306)	Gibraltar (2)
Greece (52)	Greenland (43)
Hungary (33)	Iceland (58)
Ireland (17)	Israel (8)
Italy (140)	Jordan (9)
Kazakhstan (Europe) (3)	Latvia (22)
Lebanon (6)	Lithuania (17)
Luxembourg (3)	Malta (1)
Netherlands (54)	Norway (198)
Poland (72)	Portugal (33)
Republic of Moldova (3)	Romania (42)
Russian Federation (in Europe) (342)	Slovakia (25)
Slovenia (23)	Spain (79)

(Continued)

TABLE A5.12 (CONTINUED)

Internet Sources of World Climatic Data

Countries (Numbers in Parentheses Denote the Number of Sites for Which Data Are Available)

Europe

Sweden (96)	Switzerland (70)
Syrian Arab Republic (35)	Macedonia (22)
Turkey (102)	Ukraine (117)
United Kingdom and No. Ireland (344)	Yugoslavia (47)

North and South America

Anguilla (1)	Antigua and Barbuda (2)
Argentina (90)	Bolivia (36)
Bahamas (7)	Barbados (2)
Belize (4)	Bermuda (1)
Brazil (342)	British Virgin Islands (1)
Canada (324)	Cayman Islands (2)
Chile (35)	Clipperton (1)
Columbia (54)	Costa Rica (5)
Cuba (69)	Curacao (3)
Dominica (18)	Ecuador (37)
El Salvador (6)	French Guyana (5)
Grenada (1)	Guatemala (7)
Guyana (8)	Haiti (6)
Honduras (7)	Islands (7)
Jamaica (4)	Martinique (2)
Mexico (89)	Paraguay (49)
Peru (54)	Suriname (7)
Uruguay (17)	Venezuela (33)
Nicaragua (13)	Panama (7)
Puerto Rico (5)	Saint Kitts (2)
Saint Lucia (2)	Saint Vincent (1)
St. Martin, St. Eustatius (5)	St. Pierre (1)
Trinidad and Tobago (2)	Turks and Caicos Islands (2)
United States of America (756)	Venezuela (1)

South-West Pacific

Australia (Additional Islands) (828)	Brunei (2)
Cook Islands (5)	Detached Islands (6)
East Timor/Timor Oriental (7)	Fiji (15)
French Polynesia (Austral Islands) (16)	Indonesia (198)
Islands (157)	Kiribati (6)
Malaysia (18)	Nauru (2)
New Caledonia (8)	New Zealand (126)
Niue (2)	Papua New Guinea (54)
Philippines (72)	Samoa and American Samoa (5)

TABLE A5.12 (CONTINUED)

Internet Sources of World Climatic Data

Countries (Numbers in Parentheses Denote the Number of Sites for Which Data Are Available)

South-West Pacific

Singapore (5)	Solomon Islands (7)
Southern Line Islands (3)	Tokelau (4)
Tonga (9)	Tuvalu (5)
Vanuatu (7)	

Appendix 6: Thermodynamic Data for Cooling Systems

TABLE A6.1a

Saturated Refrigerant-134a—Temperature Table

Temp., <i>T</i> °C	Press., <i>P</i> _{sat} MPa	Specific Volume, m ³ /kg		Enthalpy, kJ/kg			Entropy, kJ/(kg·K)	
		Sat. Liquid, <i>v</i> _f	Sat. Vapor, <i>v</i> _g	Sat. Liquid, <i>h</i> _f	Evap., <i>h</i> _{fg}	Sat. Vapor, <i>h</i> _g	Sat. Liquid, <i>s</i> _f	Sat. Vapor, <i>s</i> _g
-40	0.05164	0.0007055	0.3569	0.00	222.88	222.88	0.0000	0.9560
-36	0.06332	0.0007113	0.2947	4.73	220.67	225.40	0.0201	0.9506
-32	0.07704	0.0007172	0.2451	9.52	218.37	227.90	0.0401	0.9456
-28	0.09305	0.0007233	0.2052	14.37	216.01	230.38	0.0600	0.9411
-26	0.10199	0.0007265	0.1882	16.82	214.80	231.62	0.0699	0.9390
-24	0.11160	0.0007296	0.1728	19.29	213.57	232.85	0.0798	0.9370
-22	0.12192	0.0007328	0.1590	21.77	212.32	234.08	0.0897	0.9351
-20	0.13299	0.0007361	0.1464	24.26	211.05	235.31	0.0996	0.9332
-18	0.14483	0.0007395	0.1350	26.77	209.76	236.53	0.1094	0.9315
-16	0.15748	0.0007428	0.1247	29.30	208.45	237.74	0.1192	0.9298
-12	0.18540	0.0007498	0.1068	34.39	205.77	240.15	0.1388	0.9267
-8	0.21704	0.0007569	0.0919	39.54	203.00	242.54	0.1583	0.9239
-4	0.25274	0.0007644	0.0794	44.75	200.15	244.90	0.1777	0.9213
0	0.29282	0.0007721	0.0689	50.02	197.21	247.23	0.1970	0.9190
4	0.33765	0.0007801	0.0600	55.35	194.19	249.53	0.2162	0.9169
8	0.38756	0.0007884	0.0525	60.73	191.07	251.80	0.2354	0.9150
12	0.44294	0.0007971	0.0460	66.18	187.85	254.03	0.2545	0.9132
16	0.50416	0.0008062	0.0405	71.69	184.52	256.22	0.2735	0.9116
20	0.57160	0.0008157	0.0358	77.26	181.09	258.35	0.2924	0.9102
24	0.64566	0.0008257	0.0317	82.90	177.55	260.45	0.3113	0.9089
26	0.68530	0.0008309	0.0298	85.75	175.73	261.48	0.3208	0.9082
28	0.72675	0.0008362	0.0281	88.61	173.89	262.50	0.3302	0.9076
30	0.77006	0.0008417	0.0265	91.49	172.00	263.50	0.3396	0.9070
32	0.81528	0.0008473	0.0250	94.39	170.09	264.48	0.3490	0.9064
34	0.86247	0.0008530	0.0236	97.31	168.14	265.45	0.3584	0.9058

(Continued)

TABLE A6.1a (CONTINUED)

Saturated Refrigerant-134a—Temperature Table

Temp., $T^{\circ}\text{C}$	Press., P_{sat} MPa	Specific Volume, m^3/kg		Enthalpy, kJ/kg			Entropy, kJ/(kg·K)	
		Sat. Liquid, v_f	Sat. Vapor, v_g	Sat. Liquid, h_f	Evap., h_{fg}	Sat. Vapor, h_g	Sat. Liquid, s_f	Sat. Vapor, s_g
36	0.91168	0.0008590	0.0223	100.25	166.15	266.40	0.3678	0.9053
38	0.96298	0.0008651	0.0210	103.21	164.12	267.33	0.3772	0.9047
40	1.0164	0.0008714	0.0199	106.19	162.05	268.24	0.3866	0.9041
42	1.0720	0.0008780	0.0188	109.19	159.94	269.14	0.3960	0.9035
44	1.1299	0.0008847	0.0177	112.22	157.79	270.01	0.4054	0.9030
48	1.2526	0.0008989	0.0159	118.35	153.33	271.68	0.4243	0.9017
52	1.3851	0.0009142	0.0142	124.58	148.66	273.24	0.4432	0.9004
56	1.5278	0.0009308	0.0127	130.93	143.75	274.68	0.4622	0.8990
60	1.6813	0.0009488	0.0114	137.42	138.57	275.99	0.4814	0.8973
70	2.1162	0.0010027	0.0086	154.34	124.08	278.43	0.5302	0.8918
80	2.6324	0.0010766	0.0064	172.71	106.41	279.12	0.5814	0.8827
90	3.2435	0.0011949	0.0046	193.69	82.63	276.32	0.6380	0.8655
100	3.9742	0.0015443	0.0027	224.74	34.40	259.13	0.7196	0.8117

Source: Wilson, D.P. and R.S. Basu. Thermodynamic properties of a new stratospherically safe working fluid-refrigerant-134a. *ASHRAE Trans.* 94(2):2095–2118, 1988.

TABLE A6.1b

Saturated Refrigerant-134a—Pressure Table

Press., P (MPa)	Temp., T_{sat} ($^{\circ}\text{C}$)	Specific Volume, m^3/kg		Enthalpy, kJ/kg			Entropy, kJ/(kg·K)	
		Sat. Liquid, v_f	Sat. Vapor, v_g	Sat. Liquid, h_f	Evap., h_{fg}	Sat. Vapor, h_g	Sat. Liquid, s_f	Sat. Vapor, s_g
0.06	-37.07	0.0007097	0.3100	3.46	221.27	224.72	0.0147	0.9520
0.08	-31.21	0.0007184	0.2366	10.47	217.92	228.39	0.0440	0.9447
0.10	-26.43	0.0007258	0.1917	16.29	215.06	231.35	0.0678	0.9395
0.12	-22.36	0.0007323	0.1614	21.32	212.54	233.86	0.0879	0.9354
0.14	-18.80	0.0007381	0.1395	25.77	210.27	236.04	0.1055	0.9322
0.16	-15.62	0.0007435	0.1229	29.78	208.18	237.97	0.1211	0.9295
0.18	-12.73	0.0007485	0.1098	33.45	206.26	239.71	0.1352	0.9273
0.20	-10.09	0.0007532	0.0993	36.84	204.46	241.30	0.1481	0.9253
0.24	-5.37	0.0007618	0.0834	42.95	201.14	244.09	0.1710	0.9222
0.28	-1.23	0.0007697	0.0719	48.39	198.13	246.52	0.1911	0.9197

TABLE A6.1b (CONTINUED)

Saturated Refrigerant-134a—Pressure Table

Press., <i>P</i> (MPa)	Temp., <i>T</i> _{sat} (°C)	Specific Volume, m ³ /kg		Enthalpy, kJ/kg			Entropy, kJ/(kg·K)	
		Sat. Liquid, <i>v</i> _f	Sat. Vapor, <i>v</i> _g	Sat. Liquid, <i>h</i> _f	Evap., <i>h</i> _{fg}	Sat. Vapor, <i>h</i> _g	Sat. Liquid, <i>s</i> _f	Vapor, <i>s</i> _g
0.32	2.48	0.0007770	0.0632	53.31	195.35	248.66	0.2089	0.9177
0.36	5.84	0.0007839	0.0564	57.82	192.76	250.58	0.2251	0.9160
0.4	8.93	0.0007904	0.0509	62.00	190.32	252.32	0.2399	0.9145
0.5	15.74	0.0008056	0.0409	71.33	184.74	256.07	0.2723	0.9117
0.6	21.58	0.0008196	0.0341	79.48	179.71	259.19	0.2999	0.9097
0.7	26.72	0.0008328	0.0292	86.78	175.07	261.85	0.3242	0.9080
0.8	31.33	0.0008454	0.0255	93.42	170.73	264.15	0.3459	0.9066
0.9	35.53	0.0008576	0.0226	99.56	166.62	266.18	0.3656	0.9054
1.0	39.39	0.0008695	0.0202	105.29	162.68	267.97	0.3838	0.9043
1.2	46.32	0.0008928	0.0166	115.76	155.23	270.99	0.4164	0.9023
1.4	52.43	0.0009159	0.0140	125.26	148.14	273.40	0.4453	0.9003
1.6	57.92	0.0009392	0.0121	134.02	141.31	275.33	0.4714	0.8982
1.8	62.91	0.0009631	0.0105	142.22	134.60	276.83	0.4954	0.8959
2.0	67.49	0.0009878	0.0093	149.99	127.95	277.94	0.5178	0.8934
2.5	77.59	0.0010562	0.0069	168.12	111.06	279.17	0.5687	0.8854
3.0	86.22	0.0011416	0.0053	185.30	92.71	278.01	0.6156	0.8735

Source: Wilson, D. P. and R. S. Basu. Thermodynamic properties of a new stratospherically safe working fluid-refrigerant-134a. *ASHRAE Trans.* 94(2):2095–2118, 1988.

T (°C)	v (m ³ /kg)	h (kJ/kg)	s [kJ/(kg·K)]	$P = 0.10 \text{ MPa}$ ($T_{\text{sat}} = -26.43^\circ\text{C}$)		$P = 0.14 \text{ MPa}$ ($T_{\text{sat}} = -18.80^\circ\text{C}$)		$P = 0.14 \text{ MPa}$ ($T_{\text{sat}} = -18.80^\circ\text{C}$)	
Sat.	0.31003	224.72	0.9520	0.19170	231.35	0.9395	0.13945	236.04	0.9322
-20	0.33536	237.98	1.0062	0.19770	236.54	0.9602	0.14549	243.40	0.9606
-10	0.34992	245.96	1.0371	0.20686	244.70	0.9918	0.15219	251.86	0.9922
0	0.36433	254.10	1.0675	0.21587	252.99	1.0227	0.1531	0.15875	1.0230
10	0.37861	262.41	1.0973	0.22473	261.43	1.0531	0.16520	269.13	1.0532
20	0.39279	270.89	1.1267	0.23349	270.02	1.0829	0.17155	277.97	1.0828
30	0.40688	279.53	1.1557	0.24216	278.76	1.1122	0.17833	286.96	1.1120
40	0.42091	288.35	1.1844	0.25076	287.66	1.1411	0.18404	296.09	1.1407
50	0.43487	297.34	1.2126	0.25930	296.72	1.1696	0.19020	305.37	1.1690
60	0.44879	306.51	1.2405	0.26779	305.94	1.1977	0.19633	314.80	1.1969
70	0.46266	315.84	1.2681	0.27623	315.32	1.2254	0.20241	324.39	1.2244
80	0.47650	325.34	1.2954	0.28464	324.87	1.2528	0.20846	334.14	1.2516
90	0.49031	335.00	1.3224	0.29302	334.57	1.2799	0.21449	344.04	1.2785
100									
Sat.	0.10983	239.71	0.9273	0.09933	241.30	0.9253	0.08343	244.09	0.9222
-10	0.11135	242.06	0.9362	0.09938	241.38	0.9256	0.08574	248.89	0.9399
0	0.11678	250.69	0.9684	0.10438	250.10	0.9582	0.08993	257.84	0.9721
10	0.12207	259.41	0.9998	0.10922	258.89	0.9898	0.09339	266.85	1.0034
20	0.12723	268.23	1.0304	0.11394	267.78	1.0206	0.09794	275.95	1.0339
30	0.13230	277.17	1.0604	0.11856	276.77	1.0508	0.10181	285.16	1.0637
40	0.13730	286.24	1.0898	0.12311	285.88	1.0804	0.10562	294.47	1.0930
50	0.14222	295.45	1.1187	0.12758	295.12	1.1094			

FIGURE A6.1
Superheated refrigerant-134a.

(Continued)

$P = 0.28 \text{ MPa}$ ($T_{\text{sat}} = -1.23^\circ\text{C}$)							$P = 0.32 \text{ MPa}$ ($T_{\text{sat}} = -2.48^\circ\text{C}$)							$P = 0.40 \text{ MPa}$ ($T_{\text{sat}} = 8.93^\circ\text{C}$)											
Sat.	0.07193	246.52	0.9197	0.06322	248.66	0.9177	0.05089	252.32	0.9145																
0	0.07240	247.64	0.9238																						
10	0.07613	256.76	0.9566	0.06576	255.65	0.9427	0.05119	253.35	0.9182																
20	0.07972	265.91	0.9883	0.06901	264.95	0.9749	0.05397	262.96	0.9515																
30	0.08320	275.12	1.0192	0.07214	274.28	1.0062	0.05662	272.54	0.8937																
40	0.08660	284.42	1.0494	0.07518	283.67	1.0367	0.05917	282.14	1.0148																
50	0.08992	293.81	1.0789	0.07815	293.15	1.0665	0.06164	291.79	1.0452																
60	0.09319	303.32	1.1079	0.08106	302.72	1.0957	0.06405	301.51	1.0748																
70	0.09641	312.95	1.1364	0.08392	312.41	1.1243	0.06641	311.32	1.1038																
80	0.09960	322.71	1.1644	0.08674	322.22	1.1525	0.06873	321.23	1.1322																
90	0.10275	332.60	1.1920	0.08953	332.15	1.1802	0.07102	331.25	1.1602																
100	0.10587	342.62	1.2193	0.09229	342.21	1.1076	0.07327	341.38	1.1878																
110	0.10897	352.78	1.2461	0.09503	352.40	1.2345	0.07550	351.64	1.2149																
120	0.11205	363.08	1.2727	0.09774	362.73	1.2611	0.07771	362.03	1.2417																
130										0.07991	372.54	1.2681													
140										0.08208	383.18	1.2941													
$P = 0.50 \text{ MPa}$ ($T_{\text{sat}} = 15.74^\circ\text{C}$)							$P = 0.60 \text{ MPa}$ ($T_{\text{sat}} = 21.58^\circ\text{C}$)							$P = 0.70 \text{ MPa}$ ($T_{\text{sat}} = 26.72^\circ\text{C}$)											
Sat.	0.04086	256.07	0.9117	0.03408	259.19	0.9097	0.02918	261.85	0.9080																
20	0.04188	260.34	0.9264	0.03581	267.89	0.9388	0.02979	265.37	0.9197																
30	0.04416	270.28	0.9597																						

FIGURE A6.1 (CONTINUED)
Superheated refrigerant-134a.

(Continued)

T (°C)	ν (m ³ /kg)	h (kJ/kg)	s [kJ/(kg·K)]	$P = 0.50 \text{ MPa } (T_{\text{sat}} = 15.74^\circ\text{C})$		$P = 0.60 \text{ MPa } (T_{\text{sat}} = 21.58^\circ\text{C})$		$P = 0.70 \text{ MPa } (T_{\text{sat}} = 26.72^\circ\text{C})$	
40	0.04633	280.16	0.9918	0.03774	278.09	0.9719	0.03157	275.93	0.9539
50	0.04842	290.04	1.0229	0.03958	288.23	1.0037	0.03324	286.35	0.9867
60	0.05043	299.95	1.0531	0.04134	298.35	1.0346	0.03482	296.69	1.0182
70	0.05240	309.92	1.0825	0.04304	308.48	1.0645	0.03634	307.01	1.0487
80	0.05432	319.96	1.1114	0.04469	318.67	1.0938	0.03781	317.35	1.0784
90	0.05620	330.10	1.1397	0.04631	328.93	1.1225	0.03924	327.74	1.1074
100	0.05805	340.33	1.1675	0.04790	339.27	1.1505	0.04064	338.19	1.1358
110	0.05988	350.68	1.1949	0.04946	349.70	1.1781	0.04201	348.71	1.1637
120	0.06168	361.14	1.2218	0.05099	360.24	1.2053	0.04335	359.33	1.1910
130	0.06347	371.72	1.2484	0.05251	370.88	1.2320	0.04468	370.04	1.2179
140	0.06524	382.42	1.2746	0.05402	381.64	1.2584	0.04599	380.86	1.2444
150				0.05550	392.52	1.2844	0.04729	391.79	1.2706
160				0.05698	403.51	1.3100	0.04857	402.82	1.2963
$P = 0.80 \text{ MPa } (T_{\text{sat}} = 31.33^\circ\text{C})$				$P = 0.90 \text{ MPa } (T_{\text{sat}} = 35.53^\circ\text{C})$		$P = 1.00 \text{ MPa } (T_{\text{sat}} = 39.39^\circ\text{C})$		$P = 1.00 \text{ MPa } (T_{\text{sat}} = 39.39^\circ\text{C})$	
Sat.	0.02547	264.15	0.9066	0.02255	266.18	0.9054	0.02020	267.97	0.9043
40	0.02691	273.66	0.9374	0.02325	271.25	0.9217	0.02029	268.68	0.9066
50	0.02846	284.39	0.9711	0.02472	282.34	0.9566	0.02171	280.19	0.9428
60	0.02992	294.98	1.0034	0.02609	293.21	0.9897	0.02301	291.36	0.9768
70	0.03131	305.50	1.0345	0.02738	303.94	1.0214	0.02423	302.34	1.0093
80	0.03264	316.00	1.0647	0.02861	314.62	1.0521	0.02538	313.20	1.0405
90	0.03393	326.52	1.0940	0.02980	325.28	1.0819	0.02649	324.01	1.0707
100	0.03519	337.08	1.1227	0.03095	335.96	1.1109	0.02755	334.82	1.1000
110	0.03642	347.71	1.1508	0.03207	346.68	1.1392	0.02858	345.65	1.1286

FIGURE A6.1 (CONTINUED)
Superheated refrigerant-134a.

(Continued)

				$P = 1.20 \text{ MPa}$ ($T_{\text{sat}} = 46.32^\circ\text{C}$)	$P = 1.40 \text{ MPa}$ ($T_{\text{sat}} = 52.43^\circ\text{C}$)	$P = 1.60 \text{ MPa}$ ($T_{\text{sat}} = 57.92^\circ\text{C}$)
Sat.	0.01663	270.99	0.9023	0.01405	273.40	0.9003
50	0.01712	275.52	0.9164			
60	0.01835	287.44	0.9527	0.01495	283.10	0.9297
70	0.01947	298.96	0.9868	0.01603	295.31	0.9658
80	0.02051	310.24	1.0192	0.01701	307.10	0.9997
90	0.02150	321.39	1.0503	0.01792	318.63	1.0319
100	0.02244	332.47	1.0804	0.01878	330.32	1.0628
110	0.02335	343.52	1.1096	0.01960	341.32	1.0927
120	0.02423	354.58	1.1381	0.02039	352.59	1.1218
130	0.02508	365.68	1.1660	0.02115	363.86	1.1501
140	0.02592	376.83	1.1933	0.02189	375.15	1.1777
150	0.02674	388.04	1.2201	0.02262	386.49	1.2048
160	0.02754	399.33	1.2465	0.02333	397.89	1.2315
170	0.02834	410.70	1.2724	0.02403	409.36	1.2576
180	0.02912	422.16	1.2980	0.02472	420.90	1.2834
190				0.02541	432.53	1.3088
200				0.02608	444.24	1.3338

FIGURE A6.1 (CONTINUED)
Superheated refrigerant-134a. (From Wilson, D.P. and R.S. Basu. Thermodynamic properties of a new stratospherically safe working fluid-refrigerant-134a. *ASHRAE Trans.* 94(2):2095-2118, 1988.)

TABLE A6.2Properties of Ammonia, NH₃

<i>t</i>	<i>p</i>	Saturated					Degrees of Superheat			
		<i>v_g</i>	<i>h_f</i>	<i>h_g</i>	<i>s_f</i>	<i>s_g</i>	100°F		200°F	
							<i>h</i>	<i>s</i>	<i>h</i>	<i>s</i>
-70	3.94	61.65	-31.1	584.4	-0.0771	1.5026	635.6	1.6214	686.2	1.7151
-65	4.69	52.34	-26.0	586.6	-0.0642	1.4833	638.0	1.6058	688.7	1.6990
-60	5.55	44.73	-20.9	588.8	-0.0514	1.4747	640.3	1.5907	691.1	1.6834
-55	6.54	38.38	-15.7	591.0	-0.0381	1.4614	642.6	1.5761	693.6	1.6683
-50	7.67	33.08	-10.5	593.2	-0.0254	1.4487	644.9	1.5620	696.1	1.6537
-45	8.95	28.62	-5.3	595.4	-0.0128	1.4363	647.2	1.5484	698.6	1.6395
-40	10.41	24.86	0	597.6	0	1.4242	649.4	1.5353	701.0	1.6260
-35	12.05	21.68	5.3	599.5	0.0126	1.4120	651.7	1.5226	703.4	1.6129
-30	13.90	18.97	10.7	601.4	0.0250	1.4001	653.9	1.5103	705.9	1.6002
-25	15.98	16.66	16.0	603.2	0.0374	1.3886	656.1	1.4983	708.3	1.5878
-20	18.30	14.68	21.4	605.0	0.0497	1.3774	658.3	1.4868	710.8	1.5759
-15	20.88	12.97	26.7	606.7	0.0618	1.3664	660.5	1.4756	713.2	1.5644
-10	23.74	11.50	32.1	608.5	0.0738	1.3558	662.6	1.4647	715.5	1.5531
-5	26.92	10.23	37.5	610.1	0.0857	1.3454	664.7	1.4541	717.9	1.5423
0	30.42	9.116	42.9	611.8	0.0975	1.3352	666.8	1.4438	720.3	1.5317
5	34.27	8.150	48.3	613.3	0.1092	1.3253	668.9	1.4338	722.7	1.5214
10	38.51	7.304	53.8	614.9	0.1208	1.3157	670.9	1.4241	725.0	1.5115
15	43.14	6.562	59.2	616.3	0.1323	1.3062	672.9	1.4147	727.3	1.5018
20	48.21	5.910	64.7	617.8	0.1437	1.2969	675.0	1.4055	729.6	1.4924
25	53.73	5.334	70.2	619.1	0.1551	1.2879	677.0	1.3966	731.9	1.4833
30	59.74	4.825	75.7	620.5	0.1663	1.2790	678.9	1.3879	734.2	1.4744
35	66.26	4.373	81.2	621.7	0.1775	1.2704	680.8	1.3794	736.4	1.4658
40	73.32	3.971	86.8	623.0	0.1885	1.2618	682.7	1.3711	738.6	1.4575
45	80.96	3.614	92.3	624.1	0.1996	1.2535	684.5	1.3630	740.9	1.4493
50	89.19	3.294	97.9	625.2	0.2105	1.2453	686.4	1.3551	743.1	1.4413
55	98.06	3.008	103.5	626.3	0.2214	1.2373	688.2	1.3474	745.2	1.4335
60	107.6	2.751	109.2	627.3	0.2322	1.2294	689.9	1.3399	747.4	1.4260
65	117.8	2.520	114.8	628.2	0.2430	1.2216	691.6	1.3326	749.5	1.4186
70	128.8	2.312	120.5	629.1	0.2537	1.2140	693.3	1.3254	751.6	1.4114
75	140.5	2.125	126.2	629.9	0.2643	1.2065	694.9	1.3184	753.7	1.4044
80	153.0	1.955	132.0	630.7	0.2749	1.1991	696.6	1.3115	755.8	1.3976
85	166.4	1.801	137.8	631.4	0.2854	1.1918	698.1	1.3048	757.9	1.3909
90	180.6	1.661	143.5	632.0	0.2958	1.1846	699.7	1.2982	759.9	1.3843

TABLE A6.2 (CONTINUED)Properties of Ammonia, NH₃

<i>t</i>	<i>p</i>	Saturated					Degrees of Superheat			
		<i>v_g</i>	<i>h_f</i>	<i>h_g</i>	<i>s_f</i>	<i>s_g</i>	100°F		200°F	
							<i>h</i>	<i>s</i>	<i>h</i>	<i>s</i>
95	195.8	1.534	149.4	632.6	0.3062	1.1775	701.2	1.2918	761.8	1.3779
100	211.9	1.419	155.2	633.0	0.3166	1.1705	702.7	1.2855	763.8	1.3717
105	228.9	1.313	161.1	633.4	0.3269	1.1635	704.2	1.2793	765.7	1.3656
110	247.0	1.217	167.0	633.7	0.3372	1.1566	705.6	1.2732	767.6	1.3596
115	266.2	1.128	173.0	633.9	0.3474	1.1497	706.9	1.2672	769.5	1.3538
120	286.4	1.047	179.0	634.0	0.3576	1.1427	708.2	1.2613	771.3	1.3480
125	307.8	0.973	185.1	634.0	0.3679	1.1358	709.5	1.2555	773.1	1.3423

Note: *t*, °F; *p*, psia; *v_g*, ft³/lb; *h_f*, Btu/lb; *h_g*, Btu/lb; *s_f*, Btu/lb·°R; *s_g*, Btu/lb·°R; *h*, Btu/lb; *s*, Btu/lb·°R.

TABLE A6.3Psychrometric Table—SI Units; Properties of Moist Air at 101,325 N/m²

Temperature			Properties ^a						
°C	K	°F	<i>P_s</i>	<i>W_s</i>	<i>V_a</i>	<i>V_s</i>	<i>h_a</i>	<i>h_s</i>	<i>s_s</i>
-40	233.15	-40	12.838	0.00007925	0.65961	0.65968	-22.35	-22.16	-90.659
-30	243.15	-22	37.992	0.0002344	0.68808	0.68833	-12.29	-11.72	-46.732
-25	248.15	-13	63.248	0.0003903	0.70232	0.70275	-7.265	-6.306	-24.706
-20	253.15	-4	103.19	0.0006371	0.71649	0.71724	-2.236	-0.6653	-2.2194
-15	258.15	+5	165.18	0.001020	0.73072	0.73191	+2.794	5.318	21.189
-10	263.15	14	259.72	0.001606	0.74495	0.74683	7.823	11.81	46.104
-5	268.15	23	401.49	0.002485	0.75912	0.76218	12.85	19.04	73.365
0	273.15	32	610.80	0.003788	0.77336	0.77804	17.88	27.35	104.14
5	278.15	41	871.93	0.005421	0.78759	0.79440	22.91	36.52	137.39
10	283.15	50	1227.2	0.007658	0.80176	0.81163	27.94	47.23	175.54
15	288.15	59	1704.4	0.01069	0.81600	0.82998	32.97	59.97	220.22
20	293.15	68	2337.2	0.01475	0.83017	0.84983	38.00	75.42	273.32
25	298.15	77	3167.0	0.02016	0.84434	0.87162	43.03	94.38	337.39
30	303.15	86	4242.8	0.02731	0.85851	0.89609	48.07	117.8	415.65
35	308.15	95	5623.4	0.03673	0.87274	0.92406	53.10	147.3	512.17
40	313.15	104	7377.6	0.04911	0.86692	0.95665	58.14	184.5	532.31
45	318.15	113	9584.8	0.06536	0.90115	0.99535	63.17	232.0	783.06
50	323.15	122	12339	0.08678	0.91532	1.0423	68.21	293.1	975.27
55	328.15	131	15745	0.1152	0.92949	1.1007	73.25	372.9	1221.5
60	333.15	140	19925	0.1534	0.94372	1.1748	78.29	478.5	1543.5

(Continued)

TABLE A6.3 (CONTINUED)Psychrometric Table—SI Units; Properties of Moist Air at 101,325 N/m²

Temperature			Properties ^a						
°C	K	°F	P_s	W_s	V_a	V_s	h_a	h_s	s_s
65	338.15	149	25014	0.2055	0.95790	1.2721	83.33	621.4	1973.6
70	343.15	158	31167	0.2788	0.97207	1.4042	88.38	820.5	2564.8
75	348.15	167	38554	0.3858	0.98630	1.5924	93.42	1110	3412.8
80	353.15	176	47365	0.5519	1.0005	1.8791	98.47	1557	4710.9
85	358.15	185	57809	0.8363	1.0146	2.3632	103.5	2321	6892.6
90	363.15	194	70112	1.416	1.0288	3.3409	108.6	3876	11281

Source: Abstracted from Bolz, R.E. and G.L. Tuve, eds., *CRC Handbook of Tables for Applied Engineering Science*, 2nd ed., Chemical Rubber Co., Cleveland, Ohio, 1973.

Note: P_s = pressure of water vapor at saturation, N/m²; W_s = humidity ratio at saturation, mass of water vapor associated with unit mass of dry air; V_a = specific volume of dry air, m³/kg; V_s = specific volume of saturated mixture, m³/kg dry air; h_a = specific enthalpy of dry air, kJ/kg; h_s = specific enthalpy of saturated mixture, kJ/kg dry air; s_s = specific entropy of saturated mixture, J/K·kg dry air.

^a The P_s column gives the vapor pressure of pure water at temperature intervals of 5°C. For the latest data on vapor pressures at intervals of 0.1°C, from 0°C to 100°C, see Wexler, A. and L. Greenspan, Vapor pressure equation for water, *J. Res. Natl. Bur. Stand. Sect. A*, 75(3):213–229, May–June 1971. For very low barometric pressures and wet-bulb temperatures, the values of h_a here are somewhat low; for corrections, see the *Handbook of Fundamentals*, American Society of Heating, Refrigerating, and Air-Conditioning Engineers, 1972.

TABLE A6.4
Refrigerant Temperature ($t' = ^\circ\text{C}$) and Enthalpy ($h = \text{kJ/kg}$) of Lithium Bromide Solutions

Temp (t = °C)	Percent LiBr						
	0	10	20	30	40	45	50
20	<i>t'</i>	20	19.1	17.7	15.0	9.8	5.8
	<i>h</i>	84.0	67.4	52.6	40.4	33.5	38.9
30	<i>t'</i>	30.0	29.0	27.5	24.6	19.2	15.0
	<i>h</i>	125.8	103.3	84.0	68.6	58.3	56.8
40	<i>t'</i>	40.0	38.9	37.3	34.3	28.5	24.1
	<i>h</i>	167.6	139.5	115.8	96.0	82.5	79.7
50	<i>t'</i>	50.0	48.8	47.2	44.0	37.9	33.3
	<i>h</i>	209.3	175.2	147.0	123.4	106.7	102.6
60	<i>t'</i>	60.0	58.8	57.0	53.6	47.3	42.5
	<i>h</i>	251.1	211.7	179.1	151.4	131.7	125.8
70	<i>t'</i>	70.0	68.7	66.8	63.3	56.6	51.6
	<i>h</i>	293.0	247.7	210.5	178.8	155.7	148.9
80	<i>t'</i>	80.0	78.6	76.7	73.0	66.0	60.8
	<i>h</i>	334.9	287.8	243.6	207.3	181.0	172.8
90	<i>t'</i>	90.0	88.6	86.5	82.6	75.4	70.0
	<i>h</i>	376.9	321.1	275.6	235.4	206.1	195.8
100	<i>t'</i>	100.0	98.5	96.3	92.3	84.7	79.1
	<i>h</i>	419.0	357.6	307.9	263.8	231.0	219.9
110	<i>t'</i>	110.0	108.4	106.2	101.9	94.1	88.3
	<i>h</i>	461.3	394.3	340.1	292.4	255.9	243.3
120	<i>t'</i>	120.0 ^b	118.3 ^b	116.0 ^b	111.6	103.4	97.5

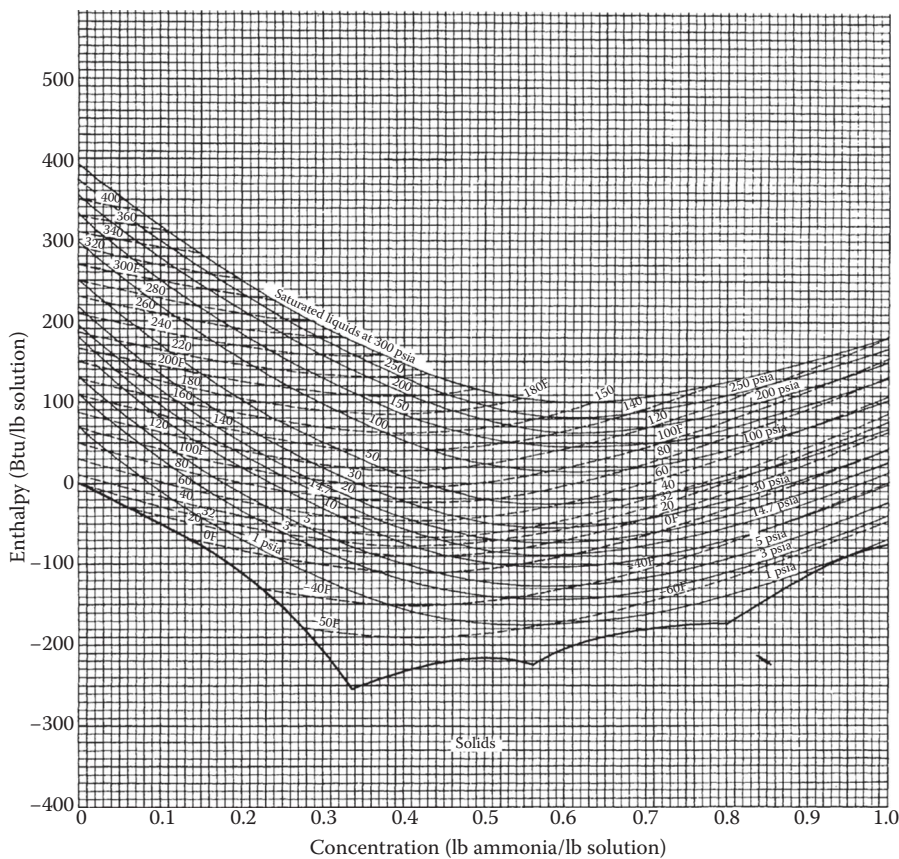
(Continued)

TABLE A6.4 (CONTINUED)
Refrigerant Temperature ($t' = {}^\circ\text{C}$) and Enthalpy ($h = \text{kJ/kg}$) of Lithium Bromide Solutions

Temp ($t = {}^\circ\text{C}$)	Percent LiBr											
	0	10	20	30	40	50	60					
130	h	503.7 ^b	431.0 ^b	372.5 ^b	320.9	281.0	267.0	259.0	260.0	270.2	289.5	313.4
	t'	130.0 ^b	128.3 ^b	125.8 ^b	121.3 ^b	112.8	106.7	92.8	88.7	78.4	67.1	55.0
140	h	546.5 ^b	468.4 ^b	404.5 ^b	349.6 ^b	306.2	290.7	281.0	280.4	289.1	306.9	330.2
	t'	140.0 ^b	138.2 ^b	135.7 ^b	130.9 ^b	122.2 ^b	115.8	107.1	97.4	87.0	75.3	62.7
150	h	589.1 ^b	505.6 ^b	437.8 ^b	377.9 ^b	331.3 ^b	314.2	303.2	301.1	308.1	324.7	346.9
	t'	150.0 ^b	148.1 ^b	145.5 ^b	140.6 ^b	131.5 ^b	125.0 ^b	116.1 ^b	106.2	95.5	83.5	70.3
160	h	632.2 ^b	542.7 ^b	470.5 ^b	406.8 ^b	356.6 ^b	337.8 ^b	325.5 ^b	321.6	327.3	342.7	363.6
	t'	160.0 ^b	158.1 ^b	155.3 ^b	150.3 ^b	140.9 ^b	134.2 ^b	125.0 ^b	115.0	104.1	91.8	78.9
170	h	675.6 ^b	580.8 ^b	503.1 ^b	435.4 ^b	381.9 ^b	361.2 ^b	347.7 ^b	342.2	346.1	360.3	380.1
	t'	170.0 ^b	168.0 ^b	165.2 ^b	159.9 ^b	150.3 ^b	143.3 ^b	134.0 ^b	123.7	112.7	100.0	85.7
180	h	719.2 ^b	618.9 ^b	536.1 ^b	464.3 ^b	406.8 ^b	384.9 ^b	369.9 ^b	362.9	365.4	378.3	396.0
	t'	180.0 ^b	177.9 ^b	175.0 ^b	169.6 ^b	159.6 ^b	152.5 ^b	142.9 ^b	132.5 ^b	121.2 ^b	108.2	93.3
h	h	763.2 ^b	657.1 ^b	569.4 ^b	493.4 ^b	432.1 ^b	408.8 ^b	392.1 ^b	383.4 ^b	384.3 ^b	395.8	411.3

^a Supersaturated solution.

^b Extensions of data above 115°C are well above the original data and should be used with care.

**FIGURE A6.2**

Thermodynamic properties of ammonia–water mixtures used for absorption air conditioning.

Appendix 7: Supplementary Material for Chapter 7

TABLE A7.1

Designations and Characteristics for 94 Reference Passive Systems

(a) Overall System Characteristics

<i>Masonry Properties</i>	
Thermal conductivity (<i>k</i>)	
Sunspace floor	0.5 Btu/h/ft/°F
All other masonry	1.0 Btu/h/ft/°F
Density (<i>Q</i>)	150 lb/ft ³
Specific heat (<i>c</i>)	0.2 Btu/lb/°F
Infrared emittance of normal surface	0.9
Infrared emittance of selective surface	0.1
<i>Solar Absorptances</i>	
Waterwall	1.0
Masonry, Trombe wall	1.0
Direct gain and sunspace	0.8
Sunspace: water containers	0.9
Lightweight common wall	0.7
Other lightweight surfaces	0.3
<i>Glazing Properties</i>	
Transmission characteristics	Diffuse
Orientation	Due south
Index of refraction	1.526
Extinction coefficient	0.5 inch ⁻¹
Thickness of each pane	1/8 inch
Gap between panes	1/2 inch
Infrared emittance	0.9
<i>Control Range</i>	
Room temperature	65°F to 75°F
Sunspace temperature	45°F to 95°F
Internal heat generation	0
<i>Thermocirculation Vents (When Used)</i>	
Vent area/projected area (sum of both upper and lower vents)	0.06
Height between vents	8 ft
Reverse flow	None

(Continued)

TABLE A7.1 (CONTINUED)

Designations and Characteristics for 94 Reference Passive Systems

<i>Nighttime Insulation (When Used)</i>						
Thermal resistance					R9	
In place, solar time					5:30 p.m. to 7:30 a.m.	
<i>Solar Radiation Assumptions</i>						
Shading					None	
Ground diffuse reflectance					0.3	
<i>(b) Direct-Gain (DG) System Types</i>						
Designation	Thermal Storage Capacity ^a (in Btu/ ft ² /°F)	Mass Thickness ^a (inches)	Mass-Area-to-Glazing-Area Ratio	No. of Glazings	Nighttime Insulation	
A1	30	2	6	2	No	
A2	30	2	6	3	No	
A3	30	2	6	2	Yes	
B1	45	6	3	2	No	
B2	45	6	3	3	No	
B3	45	6	3	2	Yes	
C1	60	4	6	2	No	
C2	60	4	6	3	No	
C3	60	4	6	2	Yes	
<i>(c) Vented Trombe-Wall (TW) System Types</i>						
Designation	Thermal Storage Capacity ^a (Btu/ft ² /°F)	Wall Thickness ^a (inches)	ρck (Btu ² /h/ ft ⁴ /°F ²)	No. of Glazings	Wall Surface	Nighttime Insulation
A1	15	6	30	2	Normal	No
A2	22.5	9	30	2	Normal	No
A3	30	12	30	2	Normal	No
A4	45	18	30	2	Normal	No
B1	15	6	15	2	Normal	No
B2	22.5	9	15	2	Normal	No
B3	30	12	15	2	Normal	No
B4	45	18	15	2	Normal	No
C1	15	6	7.5	2	Normal	No
C2	22.5	9	7.5	2	Normal	No

TABLE A7.1 (CONTINUED)

Designations and Characteristics for 94 Reference Passive Systems

(c) Vented Trombe-Wall (TW) System Types

Designation	Thermal Storage Capacity ^a (Btu/ft ² /°F)	Wall Thickness ^a (inches)	ρck (Btu ² /h/ ft ⁴ /°F ²)	No. of Glazings	Wall Surface	Nighttime Insulation
C3	30	12	7.5	2	Normal	No
C4	45	18	7.5	2	Normal	No
D1	30	12	30	1	Normal	No
D2	30	12	30	3	Normal	No
D3	30	12	30	1	Normal	Yes
D4	30	12	30	2	Normal	Yes
D5	30	12	30	3	Normal	Yes
E1	30	12	30	1	Selective	No
E2	30	12	30	2	Selective	No
E3	30	12	30	1	Selective	Yes
E4	30	12	30	2	Selective	Yes

(d) Unvented Trombe-Wall (TW) System Types

Designation	Thermal Storage Capacity ^a (Btu/ft ² /°F)	Wall Thickness ^a (inches)	ρck (Btu ² /h/ ft ⁴ /°F ²)	No. of Glazings	Wall Surface	Nighttime Insulation
F1	15	6	30	2	Normal	No
F2	22.5	9	30	2	Normal	No
F3	30	12	30	2	Normal	No
F4	45	18	30	2	Normal	No
G1	15	6	15	2	Normal	No
G2	22.5	9	15	2	Normal	No
G3	30	12	15	2	Normal	No
G4	45	18	15	2	Normal	No
H1	15	6	7.5	2	Normal	No
H2	22.5	9	7.5	2	Normal	No
H3	30	12	7.5	2	Normal	No
H4	45	18	7.5	2	Normal	No
I1	30	12	30	1	Normal	No
I2	30	12	30	3	Normal	No
I3	30	12	30	1	Normal	Yes
I4	30	12	30	2	Normal	Yes
I5	30	12	30	3	Normal	Yes
J1	30	12	30	1	Selective	No
J2	30	12	30	2	Selective	No

(Continued)

TABLE A7.1 (CONTINUED)

Designations and Characteristics for 94 Reference Passive Systems

(d) Unvented Trombe-Wall (TW) System Types

Designation	Thermal Storage Capacity ^a (Btu/ft ² /°F)	Wall Thickness ^a (inches)	ρck (Btu ² /h/ ft ⁴ /°F ²)	No. of Glazings	Wall Surface	Nighttime Insulation
J3	30	12	30	1	Selective	Yes
J4	30	12	30	2	Selective	Yes

(e) Waterwall (WW) System Types

Designation	Thermal Storage Capacity ^a (in Btu/ft ² /°F)	Wall Thickness (inches)	No. of Glazings	Wall Surface	Nighttime Insulation
A1	15.6	3	2	Normal	No
A2	31.2	6	2	Normal	No
A3	46.8	9	2	Normal	No
A4	62.4	12	2	Normal	No
A5	93.6	18	2	Normal	No
A6	124.8	24	2	Normal	No
B1	46.8	9	1	Normal	No
B2	46.8	9	3	Normal	No
B3	46.8	9	1	Normal	Yes
B4	46.8	9	2	Normal	Yes
B5	46.8	9	3	Normal	Yes
C1	46.8	9	1	Selective	No
C2	46.8	9	2	Selective	No
C3	46.8	9	1	Selective	Yes
C4	46.8	9	2	Selective	Yes

(f) Sunspace (SS) System Types

Designation	Type	Tilt (°)	Common Wall	End Walls	Nighttime Insulation
A1	Attached	50	Masonry	Opaque	No
A2	Attached	50	Masonry	Opaque	Yes
A3	Attached	50	Masonry	Glazed	No
A4	Attached	50	Masonry	Glazed	Yes
A5	Attached	50	Insulated	Opaque	No
A6	Attached	50	Insulated	Opaque	Yes
A7	Attached	50	Insulated	Glazed	No
A8	Attached	50	Insulated	Glazed	Yes
B1	Attached	90/30	Masonry	Opaque	No

TABLE A7.1 (CONTINUED)

Designations and Characteristics for 94 Reference Passive Systems

(f) *Sunspace (SS) System Types*

Designation	Type	Tilt (°)	Common Wall	End Walls	Nighttime Insulation
B2	Attached	90/30	Masonry	Opaque	Yes
B3	Attached	90/30	Masonry	Glazed	No
B4	Attached	90/30	Masonry	Glazed	Yes
B5	Attached	90/30	Insulated	Opaque	No
B6	Attached	90/30	Insulated	Opaque	Yes
B7	Attached	90/30	Insulated	Glazed	No
B8	Attached	90/30	Insulated	Glazed	Yes
C1	Semienclosed	90	Masonry	Common	No
C2	Semienclosed	90	Masonry	Common	Yes
C3	Semienclosed	90	Insulated	Common	No
C4	Semienclosed	90	Insulated	Common	Yes
D1	Semienclosed	50	Masonry	Common	No
D2	Semienclosed	50	Masonry	Common	Yes
D3	Semienclosed	50	Insulated	Common	No
D4	Semienclosed	50	Insulated	Common	Yes
E1	Semienclosed	90/30	Masonry	Common	No
E2	Semienclosed	90/30	Masonry	Common	Yes
E3	Semienclosed	90/30	Insulated	Common	No
E4	Semienclosed	90/30	Insulated	Common	Yes

Source: PSDH, *Passive Solar Design Handbook*, Van Nostrand Reinhold Co., New York, 1984.

^a The thermal storage capacity is per unit of projected area, or, equivalently, the quantity $\rho c k$. The wall thickness is listed only as an appropriate guide by assuming $\rho c = 30 \text{ Btu}/\text{ft}^3/\text{°F}$.

TABLE A7.2

LCR Tables for Six Representative Cities (Albuquerque, Boston, Madison, Medford, Nashville, and Santa Maria) LCR Units (Btu/ft²·F-day)

SSF	0.10	0.20	0.30	0.40	0.50	0.60	0.70	0.80	0.90
<i>Santa Maria, California</i>									
WW A1	1776	240	119	73	50	35	25	18	12
WW A2	617	259	154	103	74	54	39	28	19
WW A3	523	261	164	114	82	61	45	33	22
WW A4	482	260	169	119	87	65	48	35	24
WW A5	461	263	175	125	92	69	52	38	26
WW A6	447	263	177	128	95	72	54	40	27
WW B1	556	220	128	85	60	43	32	23	15
WW B2	462	256	168	119	88	66	49	36	25
WW B3	542	315	211	151	112	85	64	47	32
WW B4	455	283	197	144	109	83	63	47	32
WW B5	414	263	184	136	103	79	60	45	31
WW C1	569	330	221	159	118	89	67	49	33
WW C2	478	288	197	143	107	81	61	45	31
WW C3	483	318	228	170	130	100	77	57	40
WW C4	426	280	200	149	114	88	68	51	35
TW A1	1515	227	113	70	48	34	24	17	11
TW A2	625	234	134	89	63	46	33	24	16
TW A3	508	231	140	95	68	50	37	27	18
TW A4	431	217	137	95	69	51	38	28	19
TW B1	859	212	112	71	49	35	25	18	12
TW B2	502	209	124	83	59	43	32	23	15
TW B3	438	201	123	84	60	44	33	24	16
TW B4	400	184	112	76	55	40	30	22	14
TW C1	568	188	105	69	48	35	25	18	12
TW C2	435	178	105	70	50	36	27	19	13
TW C3	413	165	97	64	46	33	25	18	12
TW C4	426	146	82	54	38	27	20	14	10
TW D1	403	170	101	67	48	35	25	18	12
TW D2	488	242	152	105	76	57	42	31	21
TW D3	509	271	175	123	90	67	50	36	25
TW D4	464	266	177	127	94	71	53	39	27
TW D5	425	250	169	122	91	69	52	38	26
TW E1	581	309	199	140	102	76	57	42	28
TW E2	512	283	186	132	97	73	55	40	27
TW E3	537	328	225	164	123	94	71	53	36
TW E4	466	287	199	145	109	83	63	47	32
TW F1	713	198	107	68	47	34	25	18	12
TW F2	455	199	120	81	58	42	31	22	15

TABLE A7.2 (CONTINUED)

LCR Tables for Six Representative Cities (Albuquerque, Boston, Madison, Medford, Nashville, and Santa Maria) LCR Units (Btu/ft²·F-day)

SSF	0.10	0.20	0.30	0.40	0.50	0.60	0.70	0.80	0.90
<i>Santa Maria, California</i>									
TW F3	378	190	120	83	60	45	33	24	16
TW F4	311	169	110	77	57	42	32	23	16
TW G1	450	170	98	65	46	33	24	17	12
TW G2	331	163	102	70	51	38	28	20	14
TW G3	278	147	94	66	48	36	27	20	13
TW G4	222	120	78	55	40	30	22	16	11
TW H1	295	137	84	57	41	30	22	16	11
TW H2	226	118	75	52	38	28	21	15	10
TW H3	187	99	64	44	33	24	18	13	9
TW H4	143	75	48	33	24	18	14	10	7
TW I1	318	144	88	59	42	31	23	16	11
TW I2	377	203	132	93	68	51	38	28	19
TW I3	404	226	149	106	78	58	44	32	22
TW I4	387	230	156	113	84	64	48	36	24
TW I5	370	226	155	113	85	65	49	36	25
TW J1	483	271	179	127	94	71	53	39	26
TW J2	422	246	165	119	88	67	50	37	25
TW J3	446	283	199	146	111	85	65	48	33
TW J4	400	254	178	132	100	77	58	43	30
DG A1	392	188	117	79	55	38	26	16	7
DG A2	389	190	121	85	61	45	32	22	14
DG A3	443	220	142	102	77	58	44	31	19
DG B1	384	191	122	86	64	48	35	24	13
DG B2	394	196	127	91	69	53	40	29	19
DG B3	445	222	145	105	80	62	49	37	25
DG C1	451	225	146	104	78	61	47	34	21
DG C2	453	226	148	106	80	63	49	37	25
DG C3	509	254	167	121	92	73	58	45	31
SS A1	1171	396	220	142	98	69	49	34	22
SS A2	1028	468	283	190	135	98	71	50	33
SS A3	1174	380	209	133	91	64	45	31	20
SS A4	1077	481	289	193	136	98	71	50	32
SS A5	1896	400	204	127	86	60	42	29	18
SS A6	1030	468	283	190	135	97	71	50	32
SS A7	2199	359	178	109	72	50	35	24	15
SS A8	1089	478	285	190	133	96	69	48	31
SS B1	802	298	170	111	77	55	40	28	18
SS B2	785	366	224	152	108	79	57	41	27

(Continued)

TABLE A7.2 (CONTINUED)

LCR Tables for Six Representative Cities (Albuquerque, Boston, Madison, Medford, Nashville, and Santa Maria) LCR Units (Btu/ft²·F-day)

SSF	0.10	0.20	0.30	0.40	0.50	0.60	0.70	0.80	0.90
<i>Santa Maria, California</i>									3053 DD
SS B3	770	287	163	106	74	52	37	26	17
SS B4	790	368	224	152	108	78	57	40	26
SS B5	1022	271	144	91	62	44	31	22	14
SS B6	750	356	219	149	106	77	56	40	26
SS B7	937	242	127	80	54	38	27	19	12
SS B8	750	352	215	146	103	75	55	39	25
SS C1	481	232	144	99	71	52	39	28	19
SS C2	482	262	170	120	88	66	49	36	24
SS C3	487	185	107	71	50	36	27	19	13
SS C4	473	235	147	102	74	55	41	30	20
SS D1	1107	477	282	188	132	95	68	48	31
SS D2	928	511	332	232	169	125	92	66	43
SS D3	1353	449	248	160	110	78	56	39	25
SS D4	946	500	319	222	160	117	86	61	40
SS E1	838	378	227	153	108	78	56	40	26
SS E2	766	419	272	190	138	102	75	54	36
SS E3	973	322	178	115	79	56	40	28	18
SS E4	780	393	247	170	122	89	65	47	31
<i>Albuquerque, New Mexico</i>									4292 DD
WW A1	1052	130	62	38	25	18	13	9	6
WW A2	354	144	84	56	39	29	21	15	10
WW A3	300	146	90	62	45	33	24	18	12
WW A4	276	146	93	65	47	35	26	19	13
WW A5	264	148	97	69	50	38	28	21	14
WW A6	256	148	99	70	52	39	30	22	15
WW B1	293	111	63	41	28	20	15	11	7
WW B2	270	147	96	67	49	37	28	20	14
WW B3	314	179	119	84	62	47	35	26	18
WW B4	275	169	116	85	64	49	37	28	19
WW B5	252	159	110	81	61	47	36	27	19
WW C1	333	190	126	89	66	50	38	28	19
WW C2	287	171	115	83	62	47	36	27	18
WW C3	293	191	136	101	77	59	46	34	24
WW C4	264	172	122	91	69	54	41	31	22
TW A1	900	124	60	37	25	17	12	9	6
TW A2	361	130	73	48	33	24	18	13	8
TW A3	293	129	77	52	37	27	20	15	10

TABLE A7.2 (CONTINUED)

LCR Tables for Six Representative Cities (Albuquerque, Boston, Madison, Medford, Nashville, and Santa Maria) LCR Units (Btu/ft²·F-day)

SSF	0.10	0.20	0.30	0.40	0.50	0.60	0.70	0.80	0.90
<i>Albuquerque, New Mexico</i>									
TW A4	249	123	76	52	38	28	21	15	10
TW B1	502	117	60	38	26	18	13	9	6
TW B2	291	118	68	45	32	23	17	12	8
TW B3	254	114	68	46	33	24	18	13	9
TW B4	233	104	63	42	30	22	16	12	8
TW C1	332	106	58	37	26	19	14	10	6
TW C2	255	101	58	39	27	20	15	11	7
TW C3	243	94	54	36	25	18	13	10	7
TW C4	254	84	46	30	21	15	11	8	5
TW D1	213	86	50	33	23	17	12	9	6
TW D2	287	139	86	59	43	32	24	17	12
TW D3	294	153	97	68	49	37	27	20	14
TW D4	281	158	104	74	55	41	31	23	16
TW D5	260	151	101	73	54	41	31	23	16
TW E1	339	177	113	78	57	43	32	23	16
TW E2	308	168	109	77	56	42	32	23	16
TW E3	323	195	133	96	72	55	42	31	21
TW E4	287	175	120	88	66	50	38	28	20
TW F1	409	108	57	36	24	17	13	9	6
TW F2	260	110	65	43	31	22	17	12	8
TW F3	216	106	66	45	33	24	10	13	9
TW F4	178	95	61	42	31	23	17	13	9
TW G1	256	93	53	34	24	17	13	9	6
TW G2	189	91	56	38	27	20	15	11	7
TW G3	159	82	52	36	26	20	15	11	7
TW G4	128	68	43	30	22	16	12	9	6
TW H1	168	76	45	31	22	16	12	9	6
TW H2	130	66	41	29	21	15	11	8	6
TW H3	108	56	35	25	8	13	10	7	5
TW H4	83	42	27	19	13	10	7	5	4
TW I1	166	73	43	29	20	15	11	8	5
TW I2	221	117	75	52	30	28	21	16	11
TW I3	234	128	83	59	43	32	24	10	12
TW I4	234	137	92	66	49	37	28	21	14
TW I5	226	136	93	67	50	38	29	22	15
TW J1	282	156	102	72	53	40	30	22	15
TW J2	254	146	97	69	51	39	29	22	15
TW J3	269	169	118	86	65	50	38	29	20

(Continued)

TABLE A7.2 (CONTINUED)

LCR Tables for Six Representative Cities (Albuquerque, Boston, Madison, Medford, Nashville, and Santa Maria) LCR Units (Btu/ft²·F-day)

SSF	0.10	0.20	0.30	0.40	0.50	0.60	0.70	0.80	0.90
<i>Albuquerque, New Mexico</i>									
TW J4	247	155	106	80	60	46	35	26	18
DG A1	211	97	57	36	22	13	5	—	—
DG A2	227	107	67	46	32	23	16	10	5
DG A3	274	131	83	59	44	34	25	18	10
DG B1	210	97	60	42	30	21	13	6	—
DG B2	232	110	69	49	37	28	21	14	8
DG B3	277	134	85	61	47	37	28	21	14
DG C1	253	120	74	53	39	30	22	14	—
DG C2	271	130	82	59	45	35	26	19	12
DG C3	318	155	96	71	54	43	34	26	18
SS A1	591	187	101	64	44	31	22	16	10
SS A2	531	232	137	92	65	47	34	25	16
SS A3	566	170	90	56	38	27	19	13	8
SS A4	537	230	135	89	63	45	33	23	15
SS A5	980	187	92	56	37	26	18	13	8
SS A6	529	231	136	91	64	47	34	24	16
SS A7	1103	158	74	44	29	20	14	10	6
SS A8	540	226	131	87	61	44	32	23	15
SS B1	403	141	78	50	35	25	18	13	8
SS B2	412	186	111	75	53	39	28	20	14
SS B3	372	130	71	46	31	22	16	11	7
SS B4	403	181	106	72	51	37	27	20	13
SS B5	518	127	65	40	27	19	13	9	6
SS B6	390	179	106	73	52	38	28	20	13
SS B7	457	108	54	33	22	16	11	8	5
SS B8	379	171	102	69	49	35	26	19	12
SS C1	270	126	77	52	37	27	20	15	10
SS C2	282	150	97	68	49	37	28	20	14
SS C3	276	101	57	37	26	19	14	10	7
SS C4	277	135	83	57	41	31	23	17	11
SS D1	548	225	130	85	59	43	31	22	14
SS D2	474	253	162	113	82	61	45	33	22
SS D3	683	212	113	72	49	35	25	17	11
SS D4	484	248	156	107	77	57	42	30	20
SS E1	410	176	103	68	48	35	25	18	12
SS E2	390	208	133	92	67	50	37	27	18
SS E3	487	151	80	51	35	25	18	12	8
SS E4	400	195	120	82	59	43	32	23	15

TABLE A7.2 (CONTINUED)

LCR Tables for Six Representative Cities (Albuquerque, Boston, Madison, Medford, Nashville, and Santa Maria) LCR Units (Btu/ft²·F-day)

SSF	0.10	0.20	0.30	0.40	0.50	0.60	0.70	0.80	0.90
<i>Nashville, Tennessee</i>									3696 DD
WW A1	588	60	24	13	8	5	3	2	1
WW A2	192	70	38	23	15	11	7	5	3
WW A3	161	72	42	27	18	13	9	6	4
WW A4	148	72	43	29	20	14	10	7	5
WW A5	141	74	46	31	22	16	11	8	5
WW A6	137	74	47	32	22	16	12	8	5
WW B1	135	41	19	10	6	3	2	—	—
WW B2	152	78	48	33	23	17	12	9	6
WW B3	179	97	61	42	30	22	16	12	8
WW B4	164	97	65	46	34	25	19	14	9
WW B5	153	93	63	45	33	25	19	14	9
WW C1	193	105	67	46	33	24	18	13	8
WW C2	169	97	63	44	32	24	18	13	8
WW C3	181	115	79	58	43	33	25	18	12
WW C4	164	104	72	53	39	30	23	17	11
TW A1	509	59	25	13	8	5	3	2	1
TW A2	199	64	33	20	13	9	6	4	3
TW A3	160	65	36	23	15	11	8	5	3
TW A4	136	62	36	23	16	11	8	6	4
TW B1	282	57	26	15	9	6	4	3	2
TW B2	161	59	32	20	13	9	6	4	3
TW B3	141	58	32	21	14	10	7	5	3
TW B4	131	54	30	19	13	9	7	5	3
TW C1	188	53	27	16	10	7	5	3	2
TW C2	144	52	28	18	12	8	6	4	2
TW C3	139	49	27	17	11	8	5	4	2
TW C4	149	45	23	14	9	7	5	3	2
TW D1	99	33	16	9	5	3	2	1	—
TW D2	164	75	44	29	20	14	10	7	5
TW D3	167	82	49	33	23	17	12	8	5
TW D4	168	91	58	40	29	21	15	11	7
TW D5	160	89	58	40	29	22	16	12	8
TW E1	198	98	59	40	28	20	15	10	7
TW E2	182	95	59	40	29	21	15	11	7
TW E3	197	115	76	54	39	29	22	16	11
TW E4	178	105	70	50	37	27	20	15	10
TW F1	221	50	23	13	8	5	4	2	1
TW F2	139	53	29	18	12	8	6	4	2

(Continued)

TABLE A7.2 (CONTINUED)

LCR Tables for Six Representative Cities (Albuquerque, Boston, Madison, Medford, Nashville, and Santa Maria) LCR Units (Btu/ft²·F-day)

SSF	0.10	0.20	0.30	0.40	0.50	0.60	0.70	0.80	0.90
<i>Nashville, Tennessee</i>									
TW F3	116	52	30	19	13	9	7	5	3
TW F4	96	47	28	19	13	9	7	5	3
TW G1	137	44	22	13	9	6	4	3	2
TW G2	101	44	25	16	11	8	5	4	2
TW G3	86	41	24	16	11	8	6	4	2
TW G4	69	34	21	14	10	7	5	3	2
TW H1	89	36	20	13	8	6	4	3	2
TW H2	69	33	19	12	9	6	4	3	2
TW H3	59	28	17	11	8	5	4	3	2
TW H4	46	22	13	9	6	4	3	2	1
TW I1	74	26	13	7	4	2	1	—	—
TW I2	125	62	38	25	18	13	9	7	4
TW I3	133	69	43	29	20	15	11	8	5
TW I4	139	78	51	35	26	19	14	10	7
TW I5	137	80	53	37	27	20	15	11	7
TW J1	164	86	54	36	26	19	14	10	6
TW J2	150	82	53	36	26	19	14	10	7
TW J3	165	101	68	49	36	27	20	15	10
TW J4	153	93	63	46	34	25	19	14	10
DG A1	98	34	—	—	—	—	—	—	—
DG A2	130	55	31	19	11	6	—	—	—
DG A3	173	78	47	32	23	16	11	7	2
DG B1	100	36	17	—	—	—	—	—	—
DG B2	134	58	33	22	15	10	6	—	—
DG B3	177	81	49	33	24	18	14	10	6
DG C1	131	52	28	17	9	—	—	—	—
DG C2	161	71	42	28	20	14	10	6	—
DG C3	205	94	57	39	29	22	17	12	8
SS A1	351	100	50	29	19	13	9	6	4
SS A2	328	135	76	49	33	24	17	12	8
SS A3	330	87	41	24	15	10	6	4	2
SS A4	331	133	74	47	32	22	16	11	7
SS A5	595	98	43	24	15	10	7	4	2
SS A6	324	132	75	48	32	23	16	11	7
SS A7	668	79	32	17	10	6	4	2	1
SS A8	330	129	71	45	30	21	15	10	6
SS B1	236	74	38	23	15	10	7	5	3
SS B2	258	110	63	41	28	20	14	10	6

TABLE A7.2 (CONTINUED)

LCR Tables for Six Representative Cities (Albuquerque, Boston, Madison, Medford, Nashville, and Santa Maria) LCR Units (Btu/ft²·F-day)

SSF	0.10	0.20	0.30	0.40	0.50	0.60	0.70	0.80	0.90
<i>Nashville, Tennessee</i>									3696 DD
SS B3	212	65	32	19	12	8	5	3	2
SS B4	251	105	60	39	27	19	13	9	6
SS B5	307	65	30	17	10	7	4	3	2
SS B6	241	104	60	39	27	19	14	10	6
SS B7	264	52	23	12	7	5	3	2	—
SS B8	233	98	56	36	25	17	12	9	5
SS C1	141	60	33	21	14	10	7	5	3
SS C2	161	81	50	33	23	17	12	9	6
SS C3	149	48	25	15	10	7	4	3	2
SS C4	160	73	43	28	19	14	10	7	5
SS D1	317	119	64	39	26	18	13	8	5
SS D2	287	147	90	61	43	31	23	16	10
SS D3	405	113	55	33	21	14	10	6	4
SS D4	295	144	87	58	40	29	21	15	10
SS E1	229	89	48	29	19	13	9	6	4
SS E2	233	118	72	48	34	24	18	12	8
SS E3	283	77	37	22	14	9	6	4	2
SS E4	242	111	65	43	29	21	15	11	7
<i>Medford, Oregon</i>									4930 DD
WW A1	708	64	24	11	—	—	—	—	—
WW A2	212	73	38	22	13	7	3	—	—
WW A3	174	75	41	25	16	9	5	2	—
WW A4	158	74	43	27	17	11	6	3	1
WW A5	149	75	45	29	19	12	7	4	2
WW A6	144	75	46	30	20	13	8	4	2
WW B1	154	43	16	—	—	—	—	—	—
WW B2	162	80	48	31	21	14	9	6	3
WW B3	190	100	62	41	28	19	13	8	5
WW B4	171	99	65	45	32	23	16	11	7
WW B5	160	95	63	45	32	23	17	12	7
WW C1	205	108	67	45	31	21	15	10	6
WW C2	178	99	63	43	30	22	15	10	6
WW C3	189	117	80	57	42	31	23	16	10
WW C4	170	106	72	52	38	28	21	15	9
TW A1	607	63	25	12	5	—	—	—	—
TW A2	222	68	33	19	11	6	2	—	—
TW A3	175	67	36	21	13	8	4	2	—
TW A4	147	64	36	22	14	9	5	3	1

(Continued)

TABLE A7.2 (CONTINUED)

LCR Tables for Six Representative Cities (Albuquerque, Boston, Madison, Medford, Nashville, and Santa Maria) LCR Units (Btu/ft²·F-day)

SSF	0.10	0.20	0.30	0.40	0.50	0.60	0.70	0.80	0.90
<i>Medford, Oregon</i>									4930 DD
TW B1	327	61	27	14	7	3	—	—	—
TW B2	178	62	32	19	12	7	4	2	—
TW B3	154	60	33	20	12	8	4	2	1
TW B4	143	56	31	19	12	8	5	2	1
TW C1	212	56	27	15	9	5	2	—	—
TW C2	159	55	28	17	11	7	4	2	—
TW C3	154	52	27	16	10	6	4	2	1
TW C4	167	48	24	14	9	5	3	2	—
TW D1	112	34	14	—	—	—	—	—	—
TW D2	177	77	44	28	18	12	8	5	3
TW D3	180	85	50	32	21	14	9	6	3
TW D4	177	93	58	39	27	19	13	9	5
TW D5	168	92	58	40	28	20	14	10	6
TW E1	213	101	60	39	26	18	12	8	4
TW E2	194	98	59	39	27	19	13	9	5
TW E3	208	118	77	53	38	27	20	13	8
TW E4	186	108	71	49	36	26	19	13	8
TW F1	256	53	23	12	5	—	—	—	—
TW F2	153	56	29	17	10	5	2	—	—
TW F3	125	54	30	18	11	7	3	1	—
TW F4	102	48	28	18	11	7	4	2	1
TW G1	153	46	22	12	7	—	—	—	—
TW G2	109	46	25	15	9	5	3	1	—
TW G3	92	42	24	15	9	6	3	2	—
TW G4	74	35	20	13	8	5	3	2	—
TW H1	97	38	20	12	7	4	1	—	—
TW H2	75	34	19	12	7	5	3	1	—
TW H3	63	29	17	10	7	4	3	1	—
TW H4	49	23	13	8	5	3	2	1	—
TW I1	83	27	10	—	—	—	—	—	—
TW I2	133	64	38	24	16	11	7	4	2
TW I3	142	71	43	28	19	13	9	5	3
TW I4	146	80	51	35	25	17	12	8	5
TW I5	144	82	53	37	26	19	13	9	6
TW J1	175	89	54	36	24	17	11	7	4
TW J2	158	85	53	36	25	18	12	8	5
TW J3	173	103	69	48	35	26	18	13	8
TW J4	160	96	64	45	33	24	17	12	8

TABLE A7.2 (CONTINUED)

LCR Tables for Six Representative Cities (Albuquerque, Boston, Madison, Medford, Nashville, and Santa Maria) LCR Units (Btu/ft²·F-day)

SSF	0.10	0.20	0.30	0.40	0.50	0.60	0.70	0.80	0.90
<i>Medford, Oregon</i>									4930 DD
DG A1	110	35	—	—	—	—	—	—	—
DG A2	142	58	32	18	9	—	—	—	—
DG A3	187	82	48	32	22	15	9	5	—
DG B1	110	40	15	—	—	—	—	—	—
DG B2	146	61	35	21	13	7	—	—	—
DG B3	193	84	51	34	24	17	12	7	3
DG C1	144	57	29	13	—	—	—	—	—
DG C2	177	75	44	28	19	12	6	—	—
DG C3	224	98	60	41	29	21	14	10	5
SS A1	415	110	51	28	16	9	4	2	—
SS A2	372	146	79	48	31	21	14	8	5
SS A3	397	96	42	21	10	—	—	—	—
SS A4	379	144	76	46	29	19	12	7	4
SS A5	732	111	45	23	12	5	—	—	—
SS A6	368	143	77	47	30	20	13	8	4
SS A7	846	90	33	14	—	—	—	—	—
SS A8	379	140	73	44	27	17	11	6	3
SS B1	274	81	38	21	12	6	3	—	—
SS B2	288	117	65	40	26	18	12	7	4
SS B3	249	71	33	17	8	—	—	—	—
SS B4	282	113	62	38	25	16	11	7	4
SS B5	368	72	30	15	7	—	—	—	—
SS B6	269	111	62	30	25	17	11	7	4
SS B7	323	58	23	10	—	—	—	—	—
SS B8	262	106	57	35	23	15	9	6	3
SS C1	153	62	33	19	11	5	—	—	—
SS C2	172	83	50	32	22	15	10	6	3
SS C3	166	51	24	13	7	3	—	—	—
SS C4	173	76	43	27	18	12	8	5	3
SS D1	367	129	65	37	22	13	7	3	1
SS D2	318	156	92	60	40	27	18	12	7
SS D3	480	124	57	31	18	10	5	2	—
SS D4	328	153	89	57	38	26	17	11	6
SS E1	262	95	48	27	15	7	—	—	—
SS E2	257	124	73	47	31	21	14	9	5
SS E3	334	84	38	20	10	4	—	—	—
SS E4	269	118	67	42	27	18	12	7	4

(Continued)

TABLE A7.2 (CONTINUED)

LCR Tables for Six Representative Cities (Albuquerque, Boston, Madison, Medford, Nashville, and Santa Maria) LCR Units (Btu/ft²·F-day)

SSF	0.10	0.20	0.30	0.40	0.50	0.60	0.70	0.80	0.90
<i>Boston, Massachusetts</i>									5621 DD
WW A1	368	28	9	—	—	—	—	—	—
WW A2	119	41	20	12	7	5	3	2	—
WW A3	101	43	24	15	10	6	4	3	1
WW A4	93	44	26	16	11	7	5	3	2
WW A5	89	45	27	18	12	8	6	4	2
WW A6	87	46	28	19	13	9	6	4	3
WW B1	59	—	—	—	—	—	—	—	—
WW B2	103	52	31	21	15	10	7	5	3
WW B3	123	66	41	28	20	14	10	7	5
WW B4	118	70	46	33	24	18	13	9	6
WW B5	113	69	46	33	25	18	14	10	7
WW C1	135	72	46	31	22	16	12	8	5
WW C2	121	68	44	31	22	16	12	9	6
WW C3	136	86	60	44	33	25	19	14	9
WW C4	124	78	54	40	30	23	17	12	8
TW A1	324	30	11	4	—	—	—	—	—
TW A2	126	37	18	10	6	4	2	1	—
TW A3	102	39	21	13	8	5	3	2	1
TW A4	88	38	22	14	9	6	4	3	2
TW B1	180	32	13	7	4	2	—	—	—
TW B2	104	36	19	11	7	5	3	2	1
TW B3	92	36	19	12	8	5	3	2	1
TW B4	86	34	19	12	8	5	4	2	1
TW C1	122	32	15	9	5	3	2	1	—
TW C2	95	33	17	10	7	4	3	2	1
TW C3	93	31	16	10	6	4	3	2	1
TW C4	102	29	15	9	6	4	3	2	1
TW D1	45	—	—	—	—	—	—	—	—
TW D2	112	49	28	18	12	9	6	4	3
TW D3	113	54	32	21	15	10	7	5	3
TW D4	121	64	41	28	20	15	11	8	5
TW D5	118	66	42	30	21	16	12	8	6
TW E1	138	67	40	27	18	13	9	7	4
TW E2	130	66	41	28	20	14	10	7	5
TW E3	146	84	56	39	29	21	16	11	8
TW E4	133	78	52	37	27	20	15	11	7
TW F1	134	25	10	4	—	—	—	—	—
TW F2	86	30	16	9	5	3	2	1	—

TABLE A7.2 (CONTINUED)

LCR Tables for Six Representative Cities (Albuquerque, Boston, Madison, Medford, Nashville, and Santa Maria) LCR Units (Btu/ft²·F-day)

SSF	0.10	0.20	0.30	0.40	0.50	0.60	0.70	0.80	0.90
<i>Boston, Massachusetts</i>									
TW F3	72	31	17	11	7	4	3	2	1
TW F4	61	29	17	11	7	5	3	2	1
TW G1	83	24	11	6	3	2	—	—	—
TW G2	63	26	14	9	5	4	2	1	—
TW G3	54	25	14	9	6	4	3	2	1
TW G4	45	21	12	8	5	4	3	2	1
TW H1	54	21	11	6	4	2	1	—	—
TW H2	44	20	11	7	5	3	2	1	—
TW H3	38	17	10	6	4	3	2	1	—
TW H4	30	14	8	5	3	2	2	1	—
TW I1	30	—	—	—	—	—	—	—	—
TW I2	84	41	24	16	11	8	6	4	2
TW I3	91	46	28	19	13	9	7	5	3
TW I4	100	56	36	25	18	13	10	7	5
TW I5	101	58	38	27	20	15	11	8	5
TW J1	114	59	37	25	17	12	9	6	4
TW J2	107	58	37	25	18	13	10	7	4
TW J3	123	75	51	36	27	20	15	11	7
TW J4	115	70	47	34	25	19	14	10	7
DG A1	43	—	—	—	—	—	—	—	—
DG A2	85	34	18	9	—	—	—	—	—
DG A3	125	56	33	22	16	11	7	4	—
DG B1	44	—	—	—	—	—	—	—	—
DG B2	87	36	20	12	7	—	—	—	—
DG B3	129	58	35	24	17	13	9	6	3
DG C1	71	23	—	—	—	—	—	—	—
DG C2	109	47	27	17	12	8	4	—	—
DG C3	151	68	41	28	21	16	12	8	5
SS A1	230	61	29	16	10	6	4	2	1
SS A2	231	93	52	33	22	15	11	7	5
SS A3	205	48	20	10	4	—	—	—	—
SS A4	229	90	49	31	20	14	9	6	4
SS A5	389	58	23	11	6	3	—	—	—
SS A6	226	91	50	32	21	15	10	7	4
SS A7	420	40	12	—	—	—	—	—	—
SS A8	226	86	46	28	19	12	8	6	3
SS B1	151	44	21	12	7	4	2	1	—
SS B2	183	77	43	28	19	13	9	6	4

(Continued)

TABLE A7.2 (CONTINUED)

LCR Tables for Six Representative Cities (Albuquerque, Boston, Madison, Medford, Nashville, and Santa Maria) LCR Units (Btu/ft²·F-day)

SSF	0.10	0.20	0.30	0.40	0.50	0.60	0.70	0.80	0.90
<i>Boston, Massachusetts</i>									5621 DD
SS B3	129	36	16	8	3	—	—	—	—
SS B4	176	73	41	26	17	12	8	6	4
SS B5	193	36	15	7	3	—	—	—	—
SS B6	169	72	41	26	18	12	9	6	4
SS B7	157	25	7	—	—	—	—	—	—
SS B8	160	66	37	23	16	11	7	5	3
SS C1	84	33	17	10	6	4	2	1	—
SS C2	110	54	33	22	15	11	8	5	3
SS C3	91	26	12	7	4	2	—	—	—
SS C4	109	48	28	18	12	9	6	4	3
SS D1	206	73	38	22	14	9	5	3	2
SS D2	203	103	63	42	29	21	15	10	6
SS D3	264	69	32	18	10	6	4	2	1
SS D4	208	100	60	39	27	19	14	9	6
SS E1	140	51	25	14	8	4	2	—	—
SS E2	161	80	48	32	22	15	11	7	5
SS E3	177	44	19	10	5	2	—	—	—
SS E4	166	75	43	28	19	13	9	6	4
<i>Madison, Wisconsin</i>									7730 DD
WW A1	278	—	—	—	—	—	—	—	—
WW A2	91	27	12	—	—	—	—	—	—
WW A3	77	30	15	8	3	—	—	—	—
WW A4	72	32	17	10	5	—	—	—	—
WW A5	69	33	19	11	7	4	—	—	—
WW A6	67	34	19	12	7	4	2	—	—
WW B1	—	—	—	—	—	—	—	—	—
WW B2	84	41	24	15	10	7	5	3	2
WW B3	102	53	32	21	15	10	7	5	3
WW B4	101	59	39	27	19	14	10	7	5
WW B5	98	59	39	28	20	15	11	8	5
WW C1	113	59	37	25	17	12	8	6	3
WW C2	103	57	37	25	18	13	9	6	4
WW C3	119	75	51	37	28	21	15	11	7
WW C4	109	68	47	34	25	19	14	10	7
TW A1	249	16	—	—	—	—	—	—	—
TW A2	97	26	11	4	—	—	—	—	—
TW A3	79	28	13	7	3	—	—	—	—
TW A4	69	28	15	9	5	3	—	—	—

TABLE A7.2 (CONTINUED)

LCR Tables for Six Representative Cities (Albuquerque, Boston, Madison, Medford, Nashville, and Santa Maria) LCR Units (Btu/ft²·F-day)

SSF	0.10	0.20	0.30	0.40	0.50	0.60	0.70	0.80	0.90
<i>Madison, Wisconsin</i>									7730 DD
TW B1	139	20	5	—	—	—	—	—	—
TW B2	81	26	12	6	3	—	—	—	—
TW B3	72	27	13	7	4	2	—	—	—
TW B4	69	26	13	8	5	3	1	—	—
TW C1	96	23	10	4	—	—	—	—	—
TW C2	76	25	12	7	4	2	—	—	—
TW C3	75	24	12	7	4	2	1	—	—
TW C4	84	23	11	6	4	2	1	—	—
TW D1	—	—	—	—	—	—	—	—	—
TW D2	91	39	22	13	9	6	4	2	1
TW D3	93	43	25	16	10	7	5	3	1
TW D4	103	54	34	23	16	12	8	6	4
TW D5	102	56	36	25	18	13	10	7	4
TW E1	115	54	32	21	14	10	7	4	3
TW E2	110	55	34	22	16	11	8	5	3
TW E3	126	72	47	33	24	18	13	9	6
TW E4	116	68	45	32	23	17	13	9	6
TW F1	99	13	—	—	—	—	—	—	—
TW F2	65	20	8	—	—	—	—	—	—
TW F3	55	22	11	5	—	—	—	—	—
TW F4	47	21	11	7	4	2	—	—	—
TW G1	61	14	—	—	—	—	—	—	—
TW G2	47	18	8	4	—	—	—	—	—
TW G3	42	18	9	5	3	—	—	—	—
TW G4	35	16	9	5	3	2	—	—	—
TW H1	41	13	6	—	—	—	—	—	—
TW H2	34	14	7	4	2	—	—	—	—
TW H3	29	13	7	4	2	1	—	—	—
TW H4	24	10	6	3	2	1	—	—	—
TW I1	—	—	—	—	—	—	—	—	—
TW I2	68	32	18	12	8	5	3	2	1
TW I3	75	37	22	14	10	7	4	3	2
TW I4	85	47	30	21	15	11	8	5	3
TW I5	87	50	33	23	16	12	9	6	4
TW J1	95	48	29	19	13	9	6	4	3
TW J2	91	48	30	21	14	10	7	5	3
TW J3	106	65	43	31	23	17	12	9	6
TW J4	100	61	41	29	21	16	12	9	6

(Continued)

TABLE A7.2 (CONTINUED)

LCR Tables for Six Representative Cities (Albuquerque, Boston, Madison, Medford, Nashville, and Santa Maria) LCR Units (Btu/ft²·F-day)

SSF	0.10	0.20	0.30	0.40	0.50	0.60	0.70	0.80	0.90
<i>Madison, Wisconsin</i>									7730 DD
DG A1	—	—	—	—	—	—	—	—	—
DG A2	68	25	11	—	—	—	—	—	—
DG A3	109	47	28	18	12	8	5	—	—
DG B1	—	—	—	—	—	—	—	—	—
DG B2	70	27	14	6	—	—	—	—	—
DG B3	114	50	30	20	14	10	7	4	—
DG C1	47	—	—	—	—	—	—	—	—
DG C2	91	37	21	13	7	—	—	—	—
DG C3	133	59	35	24	17	13	9	6	3
SS A1	192	47	20	9	3	—	—	—	—
SS A2	200	78	42	26	17	12	8	5	3
SS A3	166	32	—	—	—	—	—	—	—
SS A4	197	74	39	23	15	10	6	4	2
SS A5	329	42	13	—	—	—	—	—	—
SS A6	195	75	40	25	16	11	7	5	3
SS A7	349	22	—	—	—	—	—	—	—
SS A8	192	69	36	21	13	8	5	3	2
SS B1	122	32	13	5	—	—	—	—	—
SS B2	158	64	36	22	15	10	7	5	3
SS B3	100	22	—	—	—	—	—	—	—
SS B4	150	60	33	29	13	9	6	4	2
SS B5	156	24	—	—	—	—	—	—	—
SS B6	145	59	33	20	13	9	6	4	2
SS B7	122	—	—	—	—	—	—	—	—
SS B8	136	54	29	18	11	7	5	3	2
SS C1	61	20	7	—	—	—	—	—	—
SS C2	90	43	25	16	11	7	5	3	2
SS C3	67	16	—	—	—	—	—	—	—
SS C4	90	38	22	13	9	6	4	2	1
SS D1	169	56	26	13	6	—	—	—	—
SS D2	175	86	51	34	23	16	11	7	5
SS D3	221	52	21	10	—	—	—	—	—
SS D4	179	84	49	32	21	15	10	7	4
SS E1	108	34	12	—	—	—	—	—	—
SS E2	135	65	38	24	16	11	7	5	3
SS E3	141	29	8	—	—	—	—	—	—
SS E4	140	61	34	21	14	9	6	4	2

Source: PSDH, *Passive Solar Design Handbook*, Van Nostrand Reinhold Co., New York, 1984.

TABLE A7.3

SLR Correlation Parameters for the 94 Reference Systems

Type	A	B	C	D	R	G	H	LCRs	STDV
WW A1	0.0000	1.0000	0.9172	0.4841	-9.0000	0.00	1.17	13.0	0.053
WW A2	0.0000	1.0000	0.9833	0.7603	-9.0000	0.00	0.92	13.0	0.046
WW A3	0.0000	1.0000	1.0171	0.8852	-9.0000	0.00	0.85	13.0	0.040
WW A4	0.0000	1.0000	1.0395	0.9569	-9.0000	0.00	0.81	13.0	0.037
WW A5	0.0000	1.0000	1.0604	1.0387	-9.0000	0.00	0.78	13.0	0.034
WW A6	0.0000	1.0000	1.0735	1.0827	-9.0000	0.00	0.76	13.0	0.033
WW B1	0.0000	1.0000	0.9754	0.5518	-9.0000	0.00	0.92	22.0	0.051
WW B2	0.0000	1.0000	1.0487	1.0851	-9.0000	0.00	0.78	9.2	0.036
WW B3	0.0000	1.0000	1.0673	1.0087	-9.0000	0.00	0.95	8.9	0.038
WW B4	0.0000	1.0000	1.1028	1.1811	-9.0000	0.00	0.74	5.8	0.034
WW B5	0.0000	1.0000	1.1146	1.2771	-9.0000	0.00	0.56	4.5	0.032
WW C1	0.0000	1.0000	1.0667	1.0437	-9.0000	0.00	0.62	12.0	0.038
WW C2	0.0000	1.0000	1.0846	1.1482	-9.0000	0.00	0.59	8.7	0.035
WW C3	0.0000	1.0000	1.1419	1.1756	-9.0000	0.00	0.28	5.5	0.033
WW C4	0.0000	1.0000	1.1401	1.2378	-9.0000	0.00	0.23	4.3	0.032
TW A1	0.0000	1.0000	0.9194	0.4601	-9.0000	0.00	1.11	13.0	0.048
TW A2	0.0000	1.0000	0.9680	0.6318	-9.0000	0.00	0.92	13.0	0.043
TW A3	0.0000	1.0000	0.9964	0.7123	-9.0000	0.00	0.85	13.0	0.038
TW A4	0.0000	1.0000	1.0190	0.7332	-9.0000	0.00	0.79	13.0	0.032
TW B1	0.0000	1.0000	0.9364	0.4777	-9.0000	0.00	1.01	13.0	0.045
TW B2	0.0000	1.0000	0.9821	0.6020	-9.0000	0.00	0.85	13.0	0.038
TW B3	0.0000	1.0000	0.9980	0.6191	-9.0000	0.00	0.80	13.0	0.033
TW B4	0.0000	1.0000	0.9981	0.5615	-9.0000	0.00	0.76	13.0	0.028
TW C1	0.0000	1.0000	0.9558	0.4709	-9.0000	0.00	0.89	13.0	0.039
TW C2	0.0000	1.0000	0.9788	0.4964	-9.0000	0.00	0.79	13.0	0.033
TW C3	0.0000	1.0000	0.9760	0.4519	-9.0000	0.00	0.76	13.0	0.029
TW C4	0.0000	1.0000	0.9588	0.3612	-9.0000	0.00	0.73	13.0	0.026
TW D1	0.0000	1.0000	0.9842	0.4418	-9.0000	0.00	0.89	22.0	0.040
TW D2	0.0000	1.0000	1.0150	0.8994	-9.0000	0.00	0.80	9.2	0.036
TW D3	0.0000	1.0000	1.0346	0.7810	-9.0000	0.00	1.08	8.9	0.036
TW D4	0.0000	1.0000	1.0606	0.9770	-9.0000	0.00	0.85	5.8	0.035
TW D5	0.0000	1.0000	1.0721	1.0718	-9.0000	0.00	0.61	4.5	0.033
TW E1	0.0000	1.0000	1.0345	0.8753	-9.0000	0.00	0.68	12.0	0.037
TW E2	0.0000	1.0000	1.0476	1.0050	-9.0000	0.00	0.66	8.7	0.035
TW E3	0.0000	1.0000	1.0919	1.0739	-9.0000	0.00	0.61	5.5	0.034
TW E4	0.0000	1.0000	1.0971	1.1429	-9.0000	0.00	0.47	4.3	0.033
TW F1	0.0000	1.0000	0.9430	0.4744	-9.0000	0.00	1.09	13.0	0.047
TW F2	0.0000	1.0000	0.9900	0.6053	-9.0000	0.00	0.93	13.0	0.041
TW F3	0.0000	1.0000	1.0189	0.6502	-9.0000	0.00	0.86	13.0	0.036
TW F4	0.0000	1.0000	1.0419	0.6258	-9.0000	0.00	0.80	13.0	0.032

(Continued)

TABLE A7.3 (CONTINUED)

SLR Correlation Parameters for the 94 Reference Systems

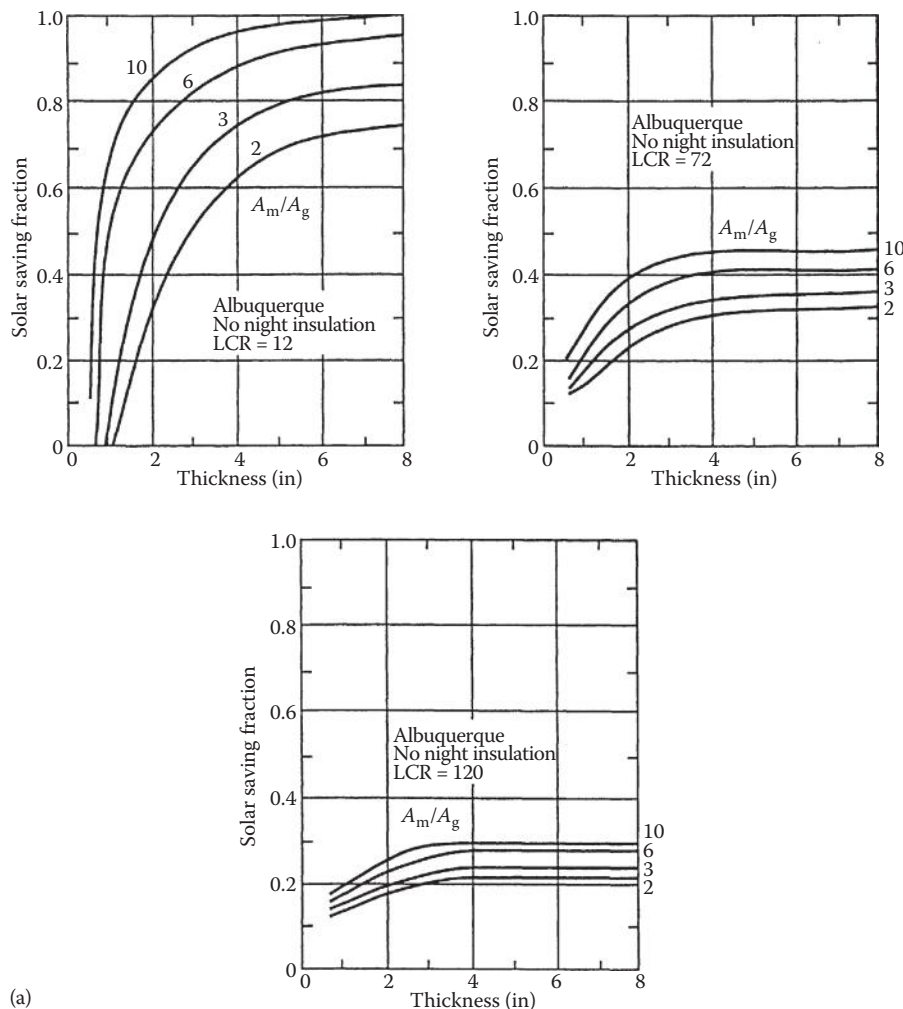
Type	A	B	C	D	R	G	H	LCRs	STDV
TW G1	0.0000	1.0000	0.9693	0.4714	-9.0000	0.00	1.01	13.0	0.042
TW G2	0.0000	1.0000	1.0133	0.5462	-9.0000	0.00	0.88	13.0	0.035
TW G3	0.0000	1.0000	1.0325	0.5269	-9.0000	0.00	0.82	13.0	0.031
TW G4	0.0000	1.0000	1.0401	0.4400	-9.0000	0.00	0.77	13.0	0.030
TW H1	0.0000	1.0000	1.0002	0.4356	-9.0000	0.00	0.93	13.0	0.034
TW H2	0.0000	1.0000	1.0280	0.4151	-9.0000	0.00	0.83	13.0	0.030
TW H3	0.0000	1.0000	1.0327	0.3522	-9.0000	0.00	0.78	13.0	0.029
TW H4	0.0000	1.0000	1.0287	0.2600	-9.0000	0.00	0.74	13.0	0.024
TW I1	0.0000	1.0000	0.9974	0.4036	-9.0000	0.00	0.91	22.0	0.038
TW I2	0.0000	1.0000	1.0386	0.8313	-9.0000	0.00	0.80	9.2	0.034
TW I3	0.0000	1.0000	1.0514	0.6886	-9.0000	0.00	1.01	8.9	0.034
TW I4	0.0000	1.0000	1.0781	0.8952	-9.0000	0.00	0.82	5.8	0.032
TW I5	0.0000	1.0000	1.0902	1.0284	-9.0000	0.00	0.65	4.5	0.032
TW J1	0.0000	1.0000	1.0537	0.8227	-9.0000	0.00	0.65	12.0	0.037
TW J2	0.0000	1.0000	1.0677	0.9312	-9.0000	0.00	0.62	8.7	0.035
TW J3	0.0000	1.0000	1.1153	0.9831	-9.0000	0.00	0.44	5.5	0.034
TW J4	0.0000	1.0000	1.1154	1.0607	-9.0000	0.00	0.38	4.3	0.033
DG A1	0.5650	1.0090	1.0440	0.7175	0.3931	9.36	0.00	0.0	0.046
DG A2	0.5906	1.0060	1.0650	0.8099	0.4681	5.28	0.00	0.0	0.039
DG A3	0.5442	0.9715	1.1300	0.9273	0.7068	2.64	0.00	0.0	0.036
DG B1	0.5739	0.9948	1.2510	1.0610	0.7905	9.60	0.00	0.0	0.042
DG B2	0.6180	1.0000	1.2760	1.1560	0.7528	5.52	0.00	0.0	0.035
DG B3	0.5601	0.9839	1.3520	1.1510	0.8879	2.38	0.00	0.0	0.032
DG C1	0.6344	0.9887	1.5270	1.4380	0.8632	9.60	0.00	0.0	0.039
DG C2	0.6763	0.9994	1.4000	1.3940	0.7604	5.28	0.00	0.0	0.033
DG C3	0.6182	0.9859	1.5660	1.4370	0.8990	2.40	0.00	0.0	0.031
SS A1	0.0000	1.0000	0.9587	0.4770	-9.0000	0.00	0.83	18.6	0.027
SS A2	0.0000	1.0000	0.9982	0.6614	-9.0000	0.00	0.77	10.4	0.026
SS A3	0.0000	1.0000	0.9552	0.4230	-9.0000	0.00	0.83	23.6	0.030
SS A4	0.0000	1.0000	0.9956	0.6277	-9.0000	0.00	0.80	12.4	0.026
SS A5	0.0000	1.0000	0.9300	0.4041	-9.0000	0.00	0.96	18.6	0.031
SS A6	0.0000	1.0000	0.9981	0.6660	-9.0000	0.00	0.86	10.4	0.028
SS A7	0.0000	1.0000	0.9219	0.3225	-9.0000	0.00	0.96	23.6	0.035
SS A8	0.0000	1.0000	0.9922	0.6173	-9.0000	0.00	0.90	12.4	0.028
SS B1	0.0000	1.0000	0.9683	0.4954	-9.0000	0.00	0.84	16.3	0.028
SS B2	0.0000	1.0000	1.0029	0.6802	-9.0000	0.00	0.74	8.5	0.026
SS B3	0.0000	1.0000	0.9689	0.4685	-9.0000	0.00	0.82	19.3	0.029
SS B4	0.0000	1.0000	1.0029	0.6641	-9.0000	0.00	0.76	9.7	0.026
SS B5	0.0000	1.0000	0.9408	0.3866	-9.0000	0.00	0.97	16.3	0.030
SS B6	0.0000	1.0000	1.0068	0.6778	-9.0000	0.00	0.84	8.5	0.028
SS B7	0.0000	1.0000	0.9395	0.3363	-9.0000	0.00	0.95	19.3	0.032

TABLE A7.3 (CONTINUED)

SLR Correlation Parameters for the 94 Reference Systems

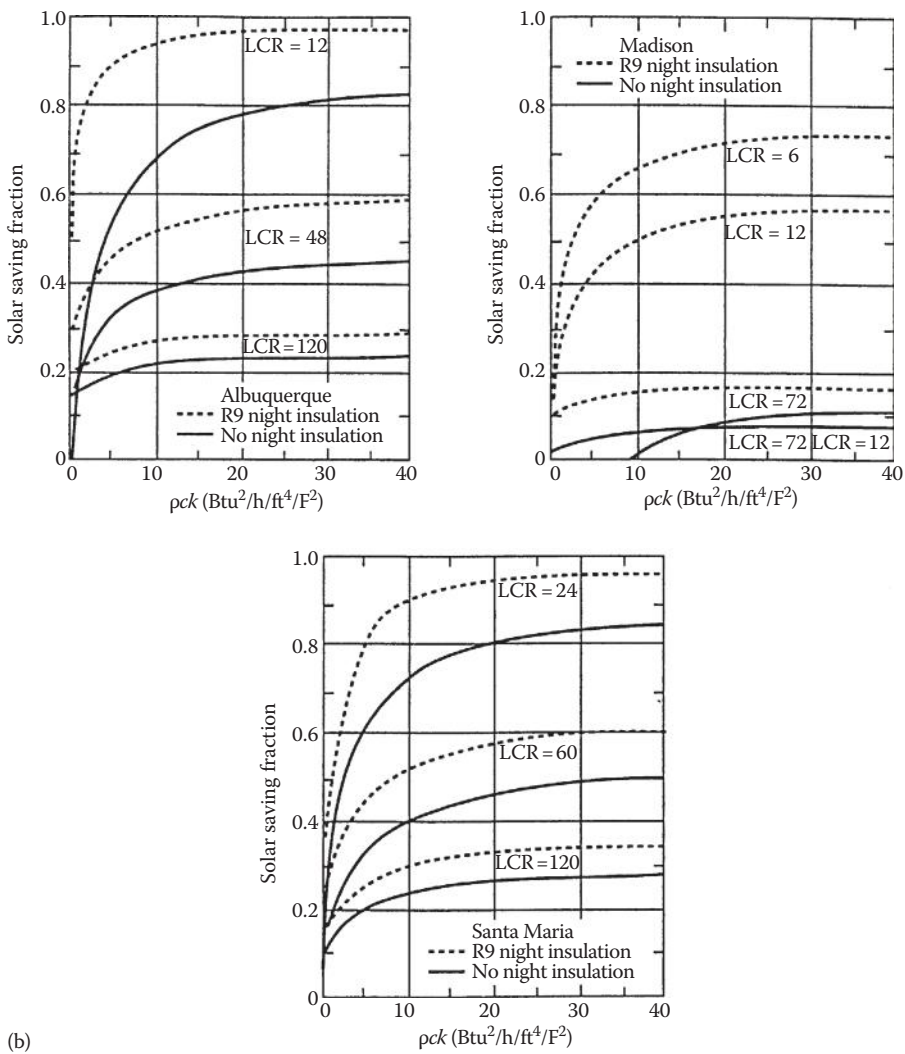
Type	A	B	C	D	R	G	H	LCRs	STDV
SS B8	0.0000	1.0000	1.0047	0.6469	-9.0000	0.00	0.87	9.7	0.027
SS C1	0.0000	1.0000	1.0087	0.7683	-9.0000	0.00	0.76	16.3	0.025
SS C2	0.0000	1.0000	1.0412	0.9281	-9.0000	0.00	0.78	10.0	0.027
SS C3	0.0000	1.0000	0.9699	0.5106	-9.0000	0.00	0.79	16.3	0.024
SS C4	0.0000	1.0000	1.0152	0.7523	-9.0000	0.00	0.81	10.0	0.025
SS D1	0.0000	1.0000	0.9889	0.6643	-9.0000	0.00	0.84	17.8	0.028
SS D2	0.0000	1.0000	1.0493	0.8753	-9.0000	0.00	0.70	9.9	0.028
SS D3	0.0000	1.0000	0.9570	0.5285	-9.0000	0.00	0.90	17.8	0.029
SS D4	0.0000	1.0000	1.0356	0.8142	-9.0000	0.00	0.73	9.9	0.028
SS E1	0.0000	1.0000	0.9968	0.7004	-9.0000	0.00	0.77	19.6	0.027
SS E2	0.0000	1.0000	1.0468	0.9054	-9.0000	0.00	0.76	10.8	0.027
SS E3	0.0000	1.0000	0.9565	0.4827	-9.0000	0.00	0.81	19.6	0.028
SS E4	0.0000	1.0000	1.0214	0.7694	-9.0000	0.00	0.79	10.8	0.027

Source: PSDH, *Passive Solar Design Handbook*, Van Nostrand Reinhold Co., New York, 1984.

**FIGURE A7.1**

(a) Storage wall: mass thickness sensitivity of SSF to off-reference conditions.

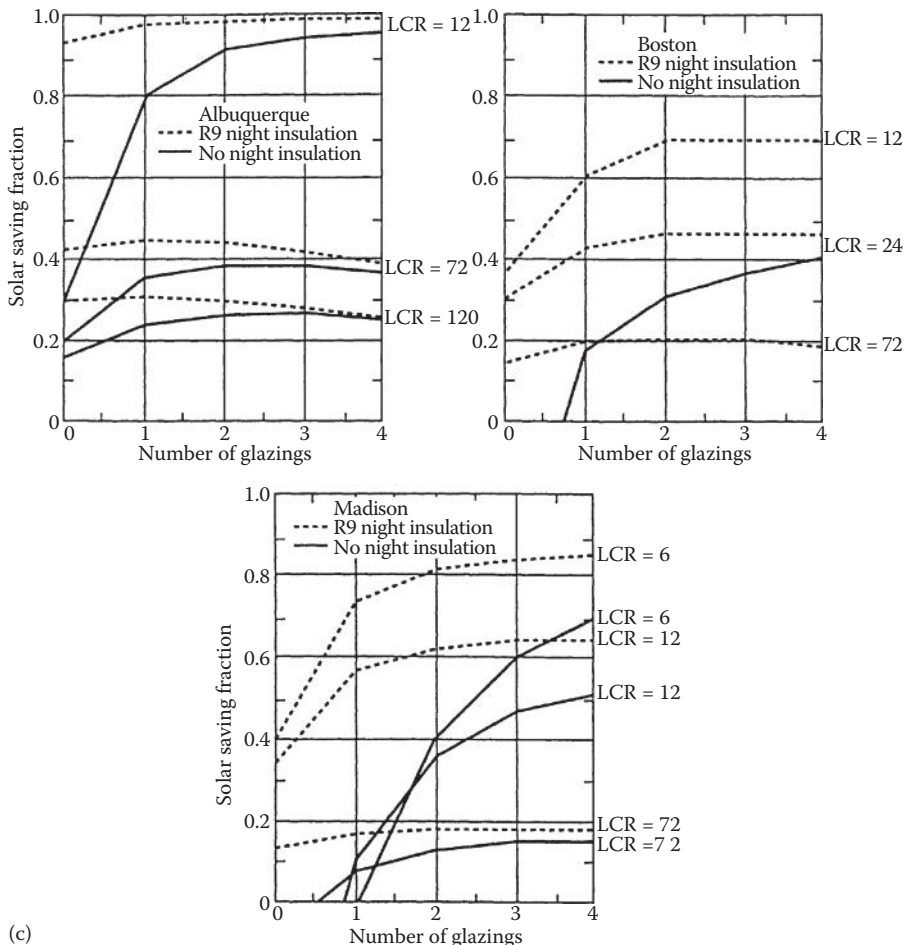
(Continued)



(b)

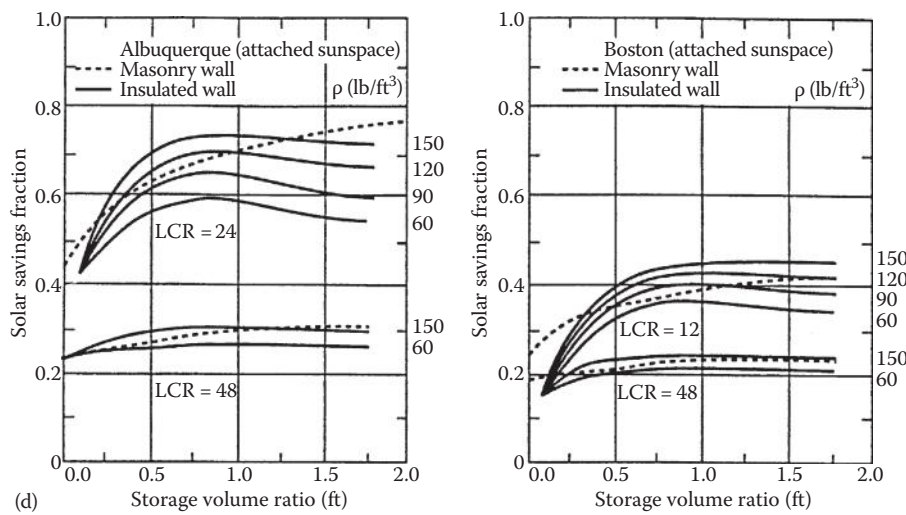
FIGURE A7.1 (CONTINUED)(b) Storage wall: pck product.

(Continued)

**FIGURE A7.1 (CONTINUED)**

(c) Storage wall: number of glazings.

(Continued)

**FIGURE A7.1 (CONTINUED)**

(d) Sunspace: storage volume to projected area ratio. (From PSDH, *Passive Solar Design Handbook*, Van Nostrand Reinhold Co., New York, 1984.)

Appendix 8: Supplementary Material for Chapter 8

TABLE A8.1a

Wall Thickness, in Millimeters, for Different Nominal Pipe Sizes
(Pipe Schedule A–G)

Nominal Pipe Size, in	Pipe Schedule						
	A	B	C	D	E	F	G
2.5	2.11	3.05	5.16	7.01	9.53	14.02	...
3	2.11	3.05	5.49	7.62	11.13	15.24	...
4	2.11	3.05	3.96	4.78	6.02	8.56	11.13
6	2.77	3.40	4.78	7.11	10.97	14.27	18.26
8	2.77	3.76	6.35	7.04	8.18	10.31	12.70
10	3.40	4.19	4.78	6.35	7.80	9.27	12.70
12	3.96	4.57	6.35	8.38	9.53	10.31	12.70
14	4.78	6.35	7.92	9.53	11.13	12.70	15.09
16	4.78	6.35	7.92	9.53	12.70	14.35	21.44
18	4.78	6.35	7.92	9.53	11.13	12.70	14.27
20	5.54	6.35	9.53	12.70	15.09	20.62	26.19
22	6.35	9.53	12.70	22.23	28.58	34.93	41.28
24	6.35	9.53	12.70	14.27	17.48	24.61	30.96
26	7.92	9.53	12.70
28	7.92	9.53	12.70	15.88
30	7.92	9.53	12.70	15.88
32	7.92	9.53	12.70	15.88	17.48
34	7.92	9.53	12.70	15.88	17.48
36	7.92	9.53	12.70	15.88	19.05
42	9.53	12.70	15.88	19.05
48	9.53	12.70	19.05	25.40
54	9.53	12.70	19.05	25.40
60	9.53	12.70	19.05	25.40
66	9.53	12.70	19.05	25.40
72	9.53	12.70	19.05	25.40

Source: Adapted from Kelly, B. and D. Kearney, Parabolic trough solar system piping model. Tech. Rep., National Renewable Laboratory, NREL/SR-550-40165, July, 2006.

TABLE A8.1b

Wall Thickness, in Millimeters, for Different Nominal Pipe Sizes
(Pipe Schedule H–M)

Nominal Pipe Size, in	Pipe Schedule					
	H	I	J	K	L	M
2.5
3
4	13.49	17.12
6	21.95
8	15.09	18.26	20.62	22.23	23.01	...
10	15.09	18.26	21.44	25.40	28.58	...
12	14.27	17.48	21.44	25.40	28.58	33.32
14	19.05	23.83	27.79	31.75	35.71	...
16	26.19	30.96	36.53	40.49
18	19.05	23.83	29.36	34.93	39.67	45.24
20	32.54	38.10	44.45	50.01
22	47.63	53.98
24	38.89	46.02	52.37	59.54
26
28
30
32
34
36
42
48
54
60
66
72

Source: Adapted from Kelly, B. and D. Kearney, Parabolic trough solar system piping model. Tech. Rep., National Renewable Laboratory, NREL/SR-550-40165, July, 2006.

TABLE A8.1c

Inside Diameter, in Millimeters, for Different Nominal Pipe Sizes
(Pipe Schedule A–G)

Nominal Pipe Size, in	Pipe Schedule						
	A	B	C	D	E	F	G
2.5	68.8	66.9	62.7	59.0	54.0	45.0	...
3	84.7	82.8	77.9	73.7	66.6	58.4	...
4	110.1	108.2	106.4	104.7	102.3	97.2	92.0
6	162.7	161.5	158.7	154.1	146.3	139.7	131.7
8	213.5	211.6	206.4	205.0	202.7	198.5	193.7
10	266.2	264.7	263.5	260.4	257.5	254.5	247.7
12	315.9	314.7	311.2	307.1	304.8	303.2	298.5
14	346.0	342.9	339.8	336.6	333.3	330.2	325.4
16	396.8	393.7	390.6	387.4	381.0	377.7	363.5
18	447.6	444.5	441.4	438.2	434.9	431.8	428.7
20	496.9	495.3	489.0	482.6	477.8	466.8	455.6
22	546.1	539.8	533.4	514.4	501.7	489.0	476.3
24	596.9	590.6	584.2	581.1	574.6	560.4	547.7
26	644.6	641.4	635.0
28	695.4	692.2	685.8	679.5
30	746.2	743.0	736.6	730.3
32	797.0	793.8	787.4	781.1	777.8
34	847.8	844.6	838.2	831.9	828.6
36	898.6	895.4	889.0	882.7	876.3
42	1047.8	1041.4	1035.1	1028.7
48	1200.2	1193.8	1181.1	1168.4
54	1352.6	1346.2	1333.5	1320.8
60	1505.0	1498.6	1485.9	1473.2
66	1657.4	1651.0	1638.3	1625.6
72	1809.8	1803.4	1790.7	1778.0

Source: Adapted from Kelly, B. and D. Kearney, Parabolic trough solar system piping model. Tech. Rep., National Renewable Laboratory, NREL/SR-550-40165, July, 2006.

TABLE A8.1d

Inside Diameter, in Millimeters, for Different Nominal Pipe Sizes (Pipe Schedule H–M)

Nominal Pipe Size, in	Pipe Schedule					
	H	I	J	K	L	M
2.5
3
4	87.3	80.1
6	124.4
8	188.9	182.5	177.8	174.6	173.1	...
10	242.9	236.5	230.2	222.3	215.9	...
12	295.3	288.9	281.0	273.1	266.7	257.2
14	317.5	307.9	300.0	292.1	284.2	...
16	354.0	344.5	333.3	325.4
18	419.1	409.5	398.5	387.4	377.9	366.7
20	442.9	431.8	419.1	408.0
22	463.6	450.9
24	531.8	517.6	504.9	490.5
26
28
30
32
34
36
42
48
54
60
66
72

Source: Adapted from Kelly, B. and D. Kearney, Parabolic trough solar system piping model. Tech. Rep., National Renewable Laboratory, NREL/SR-550-40165, July, 2006.

TABLE A8.2

Commercial Software and Codes for Solar Power Plant Design

Power Plant Type	Components	Software/Codes Used
Power tower	Optical design and performance of heliostat	ASAP [1], DELSOL [2], HELIOS, MIRVAL [3], SOLTRACE [4], Stress Analysis Codes such as ANSYS® [5] and CosmosWorks® [6], HFLCAL [7]
	Central receiver performance	FLUENT [8], Thermal Stress Analysis Codes such as ANSYS® [5] and CosmosWorks® [6]
	Heat transfer fluid transport, exchange, and storage	FLUENT [8], SAM [9], SOLERGY [10], TRNSYS [11]
	Power cycle	GATECYCLE [12], IPSEPRO [13], STEAM PRO [14], Epsilon [15]
	Total system performance	DELSOL [2], SAM [9], SOLERGY [10], TRNSYS [11]
Linear concentrator systems (troughs and linear reflectors)	Solar collectors	ASAP [1], CIRCE [16], FLUENT [8], SOLTRACE [17]
	Dish receiver	AAETES [18], FLUENT [8]
	Power cycle	GATECYCLE [12], IPSEPRO [13], STEAM PRO [14]
	Total system performance	SAM [9], SOLERGY [10], TRNSYS [11]
Dish engine systems	Dish solar collector	ASAP [1], CIRCE [16], SOLTRACE [17]
	Heat transfer fluid transport, exchange, and storage	FLUENT [8], SAM [9], SOLERGY [10], TRNSYS [11]
	Dish field system performance	Dish Field System Model [19] (an Excel-based model)

TABLE A8.3Properties of Supercritical CO₂ at Different Pressures and Temperatures

T (°C)	<i>h</i> (kJ/kg)	<i>s</i> (kJ/kg · K)	T (°C)	<i>h</i> (kJ/kg)	<i>s</i> (kJ/kg · K)
<i>Properties of Carbon Dioxide at P = 7.5 MPa</i>					
30	291.65	1.2994	420	891.33	2.7388
40	419.41	1.7169	430	902.97	2.7555
50	445.65	1.7994	440	914.65	2.772
60	465.04	1.8586	450	926.35	2.7883
70	481.57	1.9075	460	938.09	2.8044
80	496.51	1.9504	470	949.86	2.8204
90	510.44	1.9893	480	961.66	2.8361
100	523.67	2.0252	490	973.5	2.8517
110	536.41	2.0589	500	985.36	2.8672
120	548.77	2.0908	510	997.25	2.8825
130	560.85	2.1211	520	1009.2	2.8976
140	572.72	2.1502	530	1021.1	2.9126
150	584.42	2.1782	540	1033.1	2.9274
160	595.99	2.2052	550	1045.1	2.9421
170	607.46	2.2314	560	1057.2	2.9566
180	618.86	2.2568	570	1069.2	2.971
190	630.19	2.2816	580	1081.3	2.9853
200	641.48	2.3057	590	1093.5	2.9994
210	652.74	2.3292	600	1105.6	3.0134
220	663.98	2.3523	610	1117.8	3.0273
230	675.21	2.3748	620	1130	3.0411
240	686.43	2.3969	630	1142.3	3.0547
250	697.65	2.4185	640	1154.5	3.0682
260	708.87	2.4398	650	1166.8	3.0816
270	720.11	2.4607	660	1179.1	3.0949
280	731.35	2.4812	670	1191.5	3.108
290	742.62	2.5014	680	1203.9	3.1211
300	753.9	2.5212	690	1216.3	3.134
310	765.21	2.5408	700	1228.7	3.1468
320	776.53	2.56	710	1241.1	3.1596
330	787.89	2.579	720	1253.6	3.1722
340	799.26	2.5977	730	1266.1	3.1847
350	810.67	2.6162	740	1278.6	3.1971
360	822.1	2.6344	750	1291.1	3.2094
370	833.56	2.6523	760	1303.7	3.2216
380	845.06	2.6701	770	1316.3	3.2338
390	856.58	2.6876	780	1328.9	3.2458
400	868.13	2.7049	790	1341.5	3.2577
410	879.71	2.7219	800	1354.2	3.2696

TABLE A8.3 (CONTINUED)Properties of Supercritical CO₂ at Different Pressures and Temperatures

T (°C)	<i>h</i> (kJ/kg)	<i>s</i> (kJ/kg · K)	T (°C)	<i>h</i> (kJ/kg)	<i>s</i> (kJ/kg · K)
<i>Properties of Carbon Dioxide at P = 14 MPa</i>					
30	261.62	1.1727	420	882.44	2.608
40	288.21	1.259	430	894.41	2.6251
50	319.07	1.3559	440	906.4	2.642
60	355.38	1.4665	450	918.41	2.6588
70	392.61	1.5767	460	930.44	2.6753
80	423.79	1.6663	470	942.48	2.6916
90	449.04	1.7368	480	954.55	2.7077
100	470.38	1.7948	490	966.64	2.7237
110	489.21	1.8446	500	978.75	2.7394
120	506.35	1.8888	510	990.88	2.755
130	522.29	1.9288	520	1003	2.7704
140	537.37	1.9658	530	1015.2	2.7857
150	551.78	2.0003	540	1027.4	2.8008
160	565.69	2.0327	550	1039.6	2.8157
170	579.2	2.0636	560	1051.9	2.8305
180	592.39	2.093	570	1064.1	2.8452
190	605.32	2.1212	580	1076.4	2.8596
200	618.05	2.1484	590	1088.7	2.874
210	630.6	2.1747	600	1101.1	2.8882
220	643.02	2.2001	610	1113.4	2.9023
230	655.32	2.2248	620	1125.8	2.9162
240	667.53	2.2488	630	1138.2	2.93
250	679.66	2.2722	640	1150.6	2.9437
260	691.73	2.2951	650	1163.1	2.9573
270	703.74	2.3174	660	1175.6	2.9707
280	715.72	2.3393	670	1188.1	2.984
290	727.67	2.3607	680	1200.6	2.9972
300	739.59	2.3817	690	1213.1	3.0103
310	751.49	2.4023	700	1225.7	3.0233
320	763.39	2.4225	710	1238.2	3.0361
330	775.27	2.4424	720	1250.8	3.0489
340	787.15	2.4619	730	1263.4	3.0615
350	799.04	2.4811	740	1276.1	3.074
360	810.92	2.5	750	1288.7	3.0865
370	822.81	2.5187	760	1301.4	3.0988
380	834.71	2.537	770	1314.1	3.111
390	846.63	2.5551	780	1326.8	3.1232
400	858.55	2.573	790	1339.6	3.1352
410	870.49	2.5906	800	1352.3	3.1471

(Continued)

TABLE A8.3 (CONTINUED)Properties of Supercritical CO₂ at Different Pressures and Temperatures

T (°C)	<i>h</i> (kJ/kg)	<i>s</i> (kJ/kg · K)	T (°C)	<i>h</i> (kJ/kg)	<i>s</i> (kJ/kg · K)
<i>Properties of Carbon Dioxide at P = 20 MPa</i>					
30	255	1.128	420	875.03	2.5294
40	277.02	1.1994	430	887.28	2.5469
50	300.13	1.2721	440	899.54	2.5643
60	324.5	1.3463	450	911.8	2.5813
70	350.07	1.4219	460	924.08	2.5982
80	376.23	1.4971	470	936.36	2.6148
90	401.91	1.5688	480	948.66	2.6313
100	426.19	1.6348	490	960.97	2.6475
110	448.67	1.6942	500	973.29	2.6636
120	469.36	1.7475	510	985.63	2.6794
130	488.49	1.7956	520	997.98	2.6951
140	506.35	1.8394	530	1010.3	2.7106
150	523.19	1.8796	540	1022.7	2.7259
160	539.21	1.9171	550	1035.1	2.7411
170	554.57	1.9521	560	1047.5	2.756
180	569.39	1.9852	570	1060	2.7709
190	583.77	2.0166	580	1072.4	2.7856
200	597.79	2.0465	590	1084.9	2.8001
210	611.51	2.0752	600	1097.4	2.8145
220	624.98	2.1028	610	1109.9	2.8287
230	638.25	2.1295	620	1122.4	2.8428
240	651.34	2.1552	630	1135	2.8568
250	664.28	2.1802	640	1147.5	2.8706
260	677.09	2.2045	650	1160.1	2.8843
270	689.8	2.2281	660	1172.7	2.8979
280	702.42	2.2511	670	1185.3	2.9113
290	714.97	2.2736	680	1197.9	2.9247
300	727.45	2.2956	690	1210.6	2.9379
310	739.88	2.3171	700	1223.3	2.951
320	752.27	2.3381	710	1236	2.9639
330	764.62	2.3588	720	1248.7	2.9768
340	776.94	2.379	730	1261.4	2.9895
350	789.24	2.3989	740	1274.1	3.0022
360	801.52	2.4185	750	1286.9	3.0147
370	813.78	2.4377	760	1299.7	3.0271
380	826.04	2.4566	770	1312.5	3.0395
390	838.29	2.4752	780	1325.3	3.0517
400	850.54	2.4935	790	1338.1	3.0638
410	862.78	2.5116	800	1350.9	3.0758

TABLE A8.3 (CONTINUED)Properties of Supercritical CO₂ at Different Pressures and Temperatures

T (°C)	<i>h</i> (kJ/kg)	<i>s</i> (kJ/kg · K)	T (°C)	<i>h</i> (kJ/kg)	<i>s</i> (kJ/kg · K)
<i>Properties of Carbon Dioxide at P = 25 MPa</i>					
30	252.25	1.1007	420	869.47	2.4786
40	272.65	1.1669	430	881.93	2.4964
50	293.58	1.2327	440	894.4	2.514
60	315.07	1.2982	450	906.86	2.5314
70	337.11	1.3634	460	919.32	2.5485
80	359.57	1.4279	470	931.79	2.5654
90	382.13	1.4909	480	944.26	2.5821
100	404.4	1.5514	490	956.74	2.5985
110	426.04	1.6086	500	969.23	2.6148
120	446.8	1.6621	510	981.72	2.6308
130	466.6	1.7118	520	994.23	2.6467
140	485.42	1.758	530	1006.7	2.6624
150	503.34	1.8008	540	1019.3	2.6779
160	520.45	1.8408	550	1031.8	2.6932
170	536.86	1.8782	560	1044.4	2.7083
180	552.67	1.9135	570	1056.9	2.7233
190	567.98	1.947	580	1069.5	2.7382
200	582.87	1.9787	590	1082.1	2.7528
210	597.38	2.0091	600	1094.7	2.7674
220	611.59	2.0382	610	1107.3	2.7817
230	625.53	2.0662	620	1119.9	2.796
240	639.25	2.0932	630	1132.6	2.81
250	652.77	2.1193	640	1145.3	2.824
260	666.13	2.1446	650	1157.9	2.8378
270	679.35	2.1692	660	1170.6	2.8515
280	692.44	2.1931	670	1183.3	2.865
290	705.43	2.2163	680	1196.1	2.8784
300	718.33	2.239	690	1208.8	2.8917
310	731.16	2.2612	700	1221.6	2.9049
320	743.91	2.2829	710	1234.4	2.918
330	756.61	2.3041	720	1247.1	2.9309
340	769.26	2.3249	730	1260	2.9438
350	781.87	2.3453	740	1272.8	2.9565
360	794.45	2.3654	750	1285.6	2.9691

(Continued)

TABLE A8.3 (CONTINUED)Properties of Supercritical CO₂ at Different Pressures and Temperatures

T (°C)	<i>h</i> (kJ/kg)	<i>s</i> (kJ/kg·K)	T (°C)	<i>h</i> (kJ/kg)	<i>s</i> (kJ/kg·K)
<i>Properties of Carbon Dioxide at P = 25 MPa</i>					
370	807	2.385	760	1298.5	2.9816
380	819.52	2.4043	770	1311.3	2.994
390	832.03	2.4233	780	1324.2	3.0063
400	844.52	2.442	790	1337.1	3.0185
410	857	2.4604	800	1350	3.0306

Note: These properties were found from the REFPROP database from Lemmon, E.W., M.O. McLinden, and M.L. Huber, NIST reference fluid thermodynamic and transport properties—REFPROP, NIST Standard Reference Database 23. NIST, Boulder, CO, 2002. Additional properties may be found from the REFPROP database as needed.

References

1. <http://www.breault.com/software/asap.php>.
2. Kistler BL, A user's manual for DELSOL3: A computer code for calculating the optical performance and optimal system design for solar thermal central receiver plants, Sandia National Laboratories, Livermore, CA, 1987.
3. Leary PL, Hankins JD, User's guide for MIRVAL—A computer code for modeling the optical behavior of reflecting solar concentrators, Sandia National Laboratories, Livermore, CA, 1979.
4. http://www.nrel.gov/csp/troughnet/models_tools.html.
5. <http://www.ansys.com>.
6. <http://www.solidworks.com/sw/products/fea-cfd-simulation-software.htm>.
7. Schmitz M, Schwarzbozl P, Buck R, Pitz-Paal R, Assessment of the potential improvement due to multiple apertures in central receiver systems with secondary concentrators, *Solar Energy*, 80, 111–20, 2006.
8. <http://www.ansys.com/Products/Simulation+Technology/Fluid+Dynamics>.
9. <https://sam.nrel.gov>.
10. Stoddard MC, Faas SE, Chiang CJ, Dirks JA, SOLERGY—A computer code for calculating the annual energy from central receiver power plants, Sandia National Laboratories, Livermore, CA, 1987.
11. <http://sel.me.wisc.edu/trnsys>.
12. http://www.ge-energy.com/solutions/generation_solutions.jsp.
13. <http://www.simtechnology.com/IPSEpro/english/IPSEpro.php>.
14. http://www.thermoflow.com/ConvSteamCycle_STP.htm.
15. http://www.steag-systemtechnologies.com/ebsilon_professional+M5208_7573ab0.html.
16. Ratzel AC, Boughton BD, CIRCE.001: A computer code for analysis of point-focus concentrators with flat targets, Sandia National Laboratories, Albuquerque, 1987.

17. http://www.nrel.gov/csp/troughnet/models_tools.html.
18. Hogan J, R.E. AEETES—A solar reflux receiver thermal performance numerical model, *Proceedings of the 1992 ASME International Solar Energy Conference*, Maui, HI, 1992.
19. Igo J, Andraka CE, Solar dish field system model for spacing optimization, *Proceedings of the Energy Sustainability Conference*, Long Beach, CA, 2007.

Appendix 9: Economic Data Tables

TABLE A9.1

Capital-Recovery Factors

<i>n</i>	Annual Mortgage Interest Rate										
	7	7 1/2	8	8 1/2	9	9 1/2	10	10 1/2	11	11 1/2	12
1	1.070	1.075	1.080	1.085	1.090	1.095	1.100	1.105	1.110	1.115	1.120
2	0.553	0.557	0.561	0.565	0.568	0.572	0.576	0.580	0.584	0.588	0.592
3	0.381	0.385	0.388	0.392	0.395	0.399	0.402	0.406	0.409	0.413	0.416
4	0.295	0.299	0.302	0.305	0.309	0.312	0.315	0.319	0.322	0.326	0.329
5	0.244	0.247	0.250	0.254	0.257	0.260	0.264	0.267	0.271	0.274	0.277
6	0.210	0.213	0.216	0.220	0.223	0.226	0.230	0.233	0.236	0.240	0.243
7	0.186	0.189	0.192	0.195	0.199	0.202	0.205	0.209	0.212	0.216	0.219
8	0.167	0.171	0.174	0.177	0.181	0.184	0.187	0.191	0.194	0.198	0.201
9	0.153	0.157	0.160	0.163	0.167	0.170	0.174	0.177	0.181	0.184	0.188
10	0.142	0.146	0.149	0.152	0.156	0.159	0.163	0.166	0.170	0.173	0.177
11	0.133	0.137	0.140	0.143	0.147	0.150	0.154	0.158	0.161	0.165	0.168
12	0.126	0.129	0.133	0.136	0.140	0.143	0.147	0.150	0.154	0.158	0.161
13	0.120	0.123	0.127	0.130	0.134	0.137	0.141	0.144	0.148	0.152	0.156
14	0.114	0.118	0.121	0.125	0.128	0.132	0.136	0.139	0.143	0.147	0.151
15	0.110	0.113	0.117	0.120	0.124	0.128	0.131	0.135	0.139	0.143	0.147
16	0.106	0.109	0.113	0.117	0.120	0.124	0.128	0.132	0.136	0.139	0.143
17	0.102	0.106	0.110	0.113	0.117	0.121	0.125	0.129	0.132	0.136	0.140
18	0.099	0.103	0.107	0.110	0.114	0.118	0.122	0.126	0.130	0.134	0.138
19	0.097	0.100	0.104	0.108	0.112	0.116	0.120	0.124	0.128	0.132	0.136
20	0.094	0.098	0.102	0.106	0.110	0.113	0.117	0.121	0.126	0.130	0.134

Note: *n* is the mortgage term in years.

TABLE A9.2

Interest Fraction of Mortgage Payment

Years Left on Mortgage	Annual Mortgage Interest Rate										
	7	7 1/2	8	8 1/2	9	9 1/2	10	10 1/2	11	11 1/2	12
20	0.742	0.765	0.785	0.804	0.822	0.837	0.851	0.864	0.876	0.887	0.896
19	0.723	0.747	0.768	0.788	0.806	0.822	0.836	0.850	0.862	0.874	0.884
18	0.704	0.728	0.750	0.770	0.788	0.805	0.820	0.834	0.847	0.859	0.870
17	0.683	0.708	0.730	0.750	0.769	0.786	0.802	0.817	0.830	0.843	0.854
16	0.661	0.686	0.708	0.729	0.748	0.766	0.782	0.798	0.812	0.825	0.837
15	0.638	0.662	0.685	0.706	0.725	0.744	0.761	0.776	0.791	0.805	0.817
14	0.612	0.637	0.660	0.681	0.701	0.719	0.737	0.753	0.768	0.782	0.795
13	0.585	0.609	0.632	0.654	0.674	0.693	0.710	0.727	0.742	0.757	0.771
12	0.556	0.580	0.603	0.624	0.644	0.663	0.681	0.698	0.714	0.729	0.743
11	0.525	0.549	0.571	0.592	0.612	0.631	0.650	0.667	0.683	0.698	0.713
10	0.492	0.515	0.537	0.558	0.578	0.596	0.614	0.632	0.648	0.663	0.678
9	0.456	0.478	0.500	0.520	0.540	0.558	0.576	0.593	0.609	0.625	0.639
8	0.418	0.439	0.460	0.479	0.498	0.516	0.533	0.550	0.566	0.581	0.596
7	0.377	0.397	0.417	0.435	0.453	0.470	0.487	0.503	0.518	0.533	0.548
6	0.334	0.352	0.370	0.387	0.404	0.420	0.436	0.451	0.465	0.480	0.493
5	0.287	0.303	0.319	0.335	0.350	0.365	0.379	0.393	0.407	0.420	0.433
4	0.237	0.251	0.265	0.278	0.292	0.304	0.317	0.329	0.341	0.353	0.364
3	0.184	0.195	0.206	0.217	0.228	0.238	0.249	0.259	0.269	0.279	0.288
2	0.127	0.135	0.143	0.151	0.158	0.166	0.174	0.181	0.188	0.196	0.203
1	0.065	0.070	0.074	0.078	0.083	0.087	0.091	0.095	0.099	0.103	0.107

TABLE A9.3
Present-Worth Factors

Year	Discount Rate (%)													
	0	1	2	3	4	5	6	7	8	9	10	11	12	13
1	1.000	0.990	0.980	0.971	0.962	0.952	0.943	0.935	0.926	0.917	0.909	0.901	0.893	0.885
2	1.000	0.980	0.961	0.943	0.925	0.907	0.890	0.873	0.857	0.842	0.826	0.812	0.797	0.783
3	1.000	0.971	0.942	0.915	0.889	0.864	0.840	0.816	0.794	0.772	0.751	0.731	0.712	0.693
4	1.000	0.961	0.924	0.888	0.855	0.823	0.792	0.763	0.735	0.708	0.683	0.659	0.636	0.613
5	1.000	0.951	0.906	0.863	0.822	0.784	0.747	0.713	0.681	0.650	0.621	0.593	0.567	0.543
6	1.000	0.942	0.888	0.837	0.790	0.746	0.705	0.666	0.630	0.596	0.564	0.535	0.507	0.480
7	1.000	0.933	0.871	0.813	0.760	0.711	0.665	0.623	0.583	0.547	0.513	0.482	0.452	0.425
8	1.000	0.923	0.853	0.789	0.731	0.677	0.627	0.582	0.540	0.502	0.467	0.434	0.404	0.376
9	1.000	0.914	0.837	0.766	0.703	0.645	0.592	0.544	0.500	0.460	0.424	0.391	0.361	0.333
10	1.000	0.905	0.820	0.744	0.676	0.614	0.558	0.508	0.463	0.422	0.386	0.352	0.322	0.295
11	1.000	0.896	0.804	0.722	0.650	0.585	0.527	0.475	0.429	0.388	0.350	0.317	0.287	0.261
12	1.000	0.887	0.788	0.701	0.625	0.557	0.497	0.444	0.397	0.356	0.319	0.286	0.257	0.231
13	1.000	0.879	0.773	0.681	0.601	0.530	0.469	0.415	0.368	0.326	0.290	0.258	0.229	0.204
14	1.000	0.870	0.758	0.661	0.577	0.505	0.442	0.388	0.340	0.299	0.263	0.232	0.205	0.181
15	1.000	0.861	0.743	0.642	0.555	0.481	0.417	0.362	0.315	0.275	0.239	0.209	0.183	0.160
16	1.000	0.853	0.728	0.623	0.534	0.458	0.394	0.339	0.292	0.252	0.218	0.188	0.163	0.141
17	1.000	0.844	0.714	0.605	0.513	0.436	0.371	0.317	0.270	0.231	0.198	0.170	0.146	0.125
18	1.000	0.836	0.700	0.587	0.494	0.416	0.350	0.296	0.250	0.212	0.180	0.153	0.130	0.111
19	1.000	0.828	0.686	0.570	0.475	0.396	0.331	0.277	0.232	0.194	0.164	0.138	0.116	0.098
20	1.000	0.820	0.673	0.554	0.456	0.377	0.312	0.258	0.215	0.178	0.149	0.124	0.104	0.087

"The authors have done a nice job updating this edition of their classic textbook by enhancing the chapter on photovoltaics and by including more recent advances in solar thermal power technologies such as the supercritical Rankine cycle and the supercritical CO₂ power cycle."

—Dr. Kevin Anderson, Cal Poly Pomona, Mechanical Engineering, California, USA

"The organization of the book seems much better than the second edition... The present chapter eight is a great piece of work, which provides many details in solar thermal power design. To my best knowledge, no other textbook on solar engineering can compete with this book regarding this topic."

—Yuan Zheng, University of Wyoming, Laramie, USA

AN ENGINEERING-BASED SURVEY OF MODERN SOLAR ENERGY CONCEPTS AND PRACTICAL APPLICATIONS

Reflecting major developments in solar energy since the publication of the last edition, **Principles of Solar Engineering, Third Edition** follows the changes in energy policies that have led to the rapid growth of solar energy systems. This latest edition focuses on the fundamentals and the design of systems for various applications including building, heating and cooling, industrial process heat, electric power plants (including PV and CSP), and environmental systems.

WHAT'S NEW IN THE THIRD EDITION:

The revised edition introduces new topics that include organic and dye sensitized solar cells in the photovoltaics chapter, advanced thermodynamic power cycles such as supercritical CO₂ cycle and information on design software packages. The chapters on solar radiation and solar thermal collectors have been completely changed. Because of its increased importance, solar thermal power is covered in much more depth than in the previous edition.

The book contains increased coverage of high temperature thermal storage for CSP in the chapter for energy storage and transport. It changes many end-of-chapter problems, provides examples and problems for both northern and southern hemispheres and countries around the world, includes a solutions manual, and corrects all errors in the retained material. A significant change in the new edition is the addition of economic analysis in the first chapter, which includes a number of solved examples, and allows the students to analyze the applications in the later chapters from an economic stand point.

Principles of Solar Engineering, Third Edition addresses the need for solar resource assessment and highlights improvements and advancements involving photovoltaics and solar thermal technologies, grid power, and energy storage.



CRC Press

Taylor & Francis Group
an informa business

WWW.CRPCPRESS.COM

6000 Broken Sound Parkway, NW
Suite 300, Boca Raton, FL 33487
711 Third Avenue
New York, NY 10017
2 Park Square, Milton Park
Abingdon, Oxon OX14 4RN, UK

K16006

ISBN: 978-1-4665-6378-0
90000



9 781466 563780

SOLAR POWER DEMYSTIFIED

**THE BEGINNERS GUIDE TO SOLAR
POWER, ENERGY INDEPENDENCE
AND LOWER BILLS**



**By Lacho Pop, MSE
and Dimi Avram, MSE**

©2019 by Lachezar Popov and Digital Publishing Ltd

Published by Digital Publishing Ltd 2019

First Edition – published March 2015

Second Edition – published July 2016

Third Edition – published April 2019

All rights reserved.

No part of this e-book, in part or in full may be reproduced, redistributed or sold in any way without the written permission of the authors.

Disclaimer Notice

The authors of this e-book, named "**Solar Power Demystified: The Beginners Guide To Solar Power, Energy Independence And Lower Bills**", hereinafter referred to as the 'Book,' make no representation or warranties with respect to the accuracy, applicability, fitness or completeness of the contents of the Book. The information contained in the Book is strictly for educational purposes. Summaries, strategies, tips, and tricks are only recommendations by the authors, and the reading of the Book does not guarantee that readers' results will exactly match the authors' results.

The authors of the Book have made all reasonable efforts to provide current and accurate information for the readers of the Book, and the authors shall not be held liable for any unintentional errors or omissions that may be found.

The Book is not intended to replace or substitute any advice from a qualified technician, solar installer or any other professional or advisor, nor should it be construed as legal or professional advice, and the authors explicitly disclaim any responsibilities for such use.

The installation of solar power systems requires certain professional background qualification and certification for working with high voltages and currents dangerous to human life and for installing solar power systems and appliances. The reader should consult every step of your project or installation with a qualified solar professional, installer or technician and local authorities.

The authors shall in no event be held liable to any party for any direct, indirect, punitive, special, incidental or other consequential damages arising directly or indirectly from any use of this Book, which is provided on "as is, where is" basis, and without warranties.

The use of this Book, provided by Lachezar Popov and Digital Publishing Ltd should be based on the reader's own due diligence and the reader agrees that Digital Publishing Ltd shall not be liable for any success or failure.

This Book is ©copyrighted by Lachezar Popov and Digital Publishing Ltd and is protected under the applicable copyright laws and all other applicable intellectual property laws, with ALL RIGHTS RESERVED. No part of this book may be copied or changed, in any format, sold, or used in any way other, than what is outlined herein under any circumstances without explicit written permission from the authors.

About the Authors

Lacho Pop, Master of Science in Engineering, has more than 20 years of experience in market research, technological research and design, and implementation of various sophisticated electronic and telecommunication systems. His extensive experience helps him to present the complex world of solar energy in a manner that is both practical and easily understood by a broad audience. He authored and co-authored five books about solar power and its application for home, off-grid areas, and RVs. All the books were well received by the readers.

Dimi Avram, Master of Science in Engineering, has more than 15 years of experience in engineering of electrical and electronic equipment. He has specialized in testing electronic equipment and performing a techno-economic evaluation of various kinds of electric systems. His excellent presentation skills help him explain even the most complicated stuff to anybody interested. He authored and co-authored several books about solar power. All the books were well received by the readers.

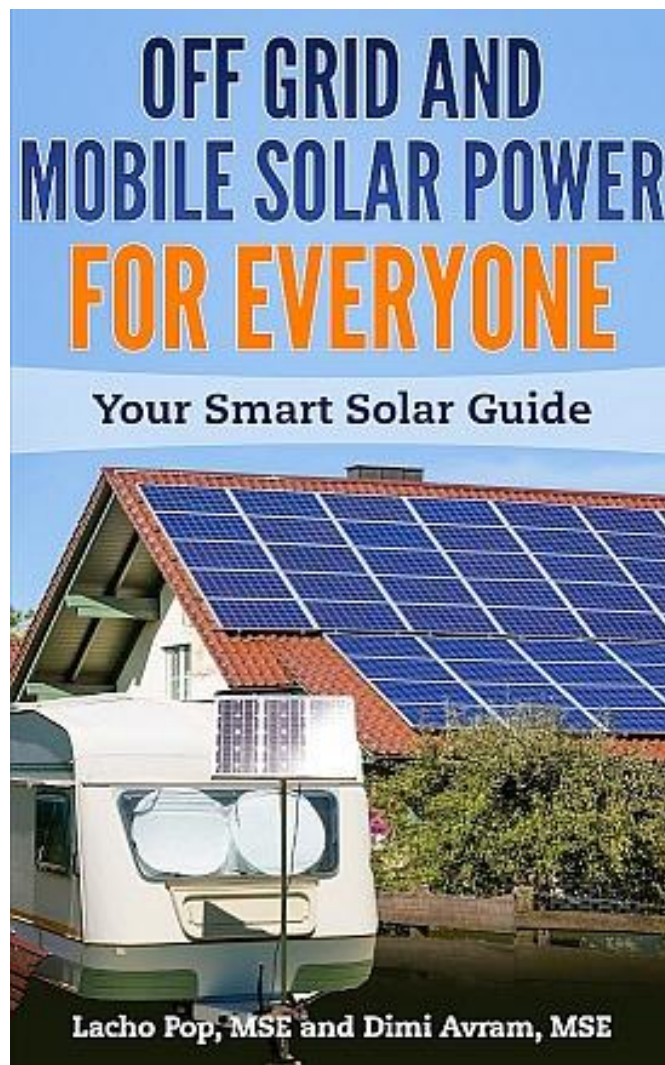
You can contact the authors by visiting the website:

solarpanelsvenue.com or by emailing them at

author@solarpanelsvenue.com

Also by the Authors:

Off Grid And Mobile Solar Power For Everyone: Your Smart Solar Guide [Kindle and Paperback Edition] **ASIN: B07B296DGQ**



Click on the link to get it NOW:

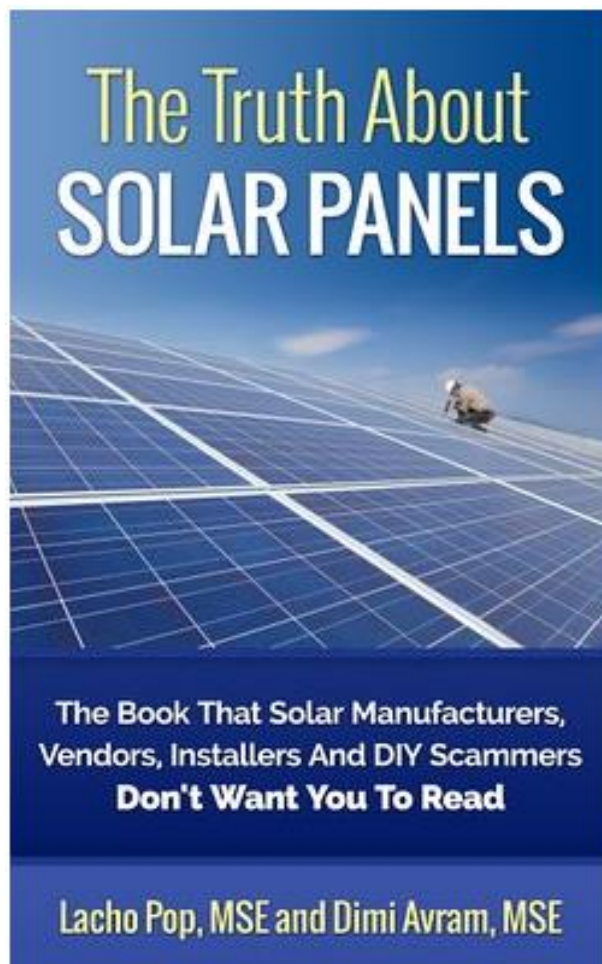
<https://www.amazon.com/Grid-Mobile-Solar-Power-Everyone-ebook/dp/B07B296DGQ/>

The Truth About Solar Panels: The Book That Solar Manufacturers, Vendors, Installers And DIY Scammers Don't Want You To Read [Kindle and Paperback Edition]

ASIN: B00Q95UZU0, ISBN: 978-6197258011

Click on the link to get it NOW:

<http://www.amazon.com/Truth-About-Solar-Panels-Manufacturers-ebook/dp/B00Q95UZU0/>



Click on the link to get it NOW:

<http://www.amazon.com/Truth-About-Solar-Panels-Manufacturers-ebook/dp/B00Q95UZU0/>

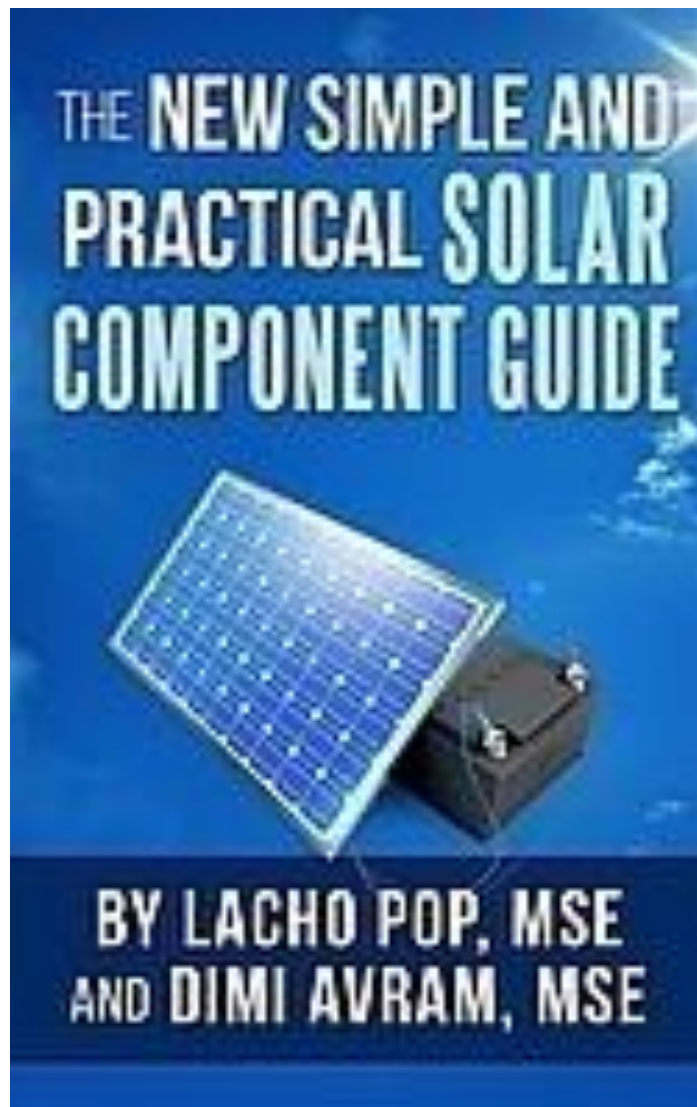
The New Simple And Practical Solar Component

Guide [Kindle Edition, Paperback, and Audio Edition]

ASIN: B07S9GPN4B

Click on the link to get it NOW on Amazon:

<https://www.amazon.com/Simple-Practical-Solar-Component-Guide-ebook/dp/B07S9GPN4B/>



Click on the link to get it NOW:

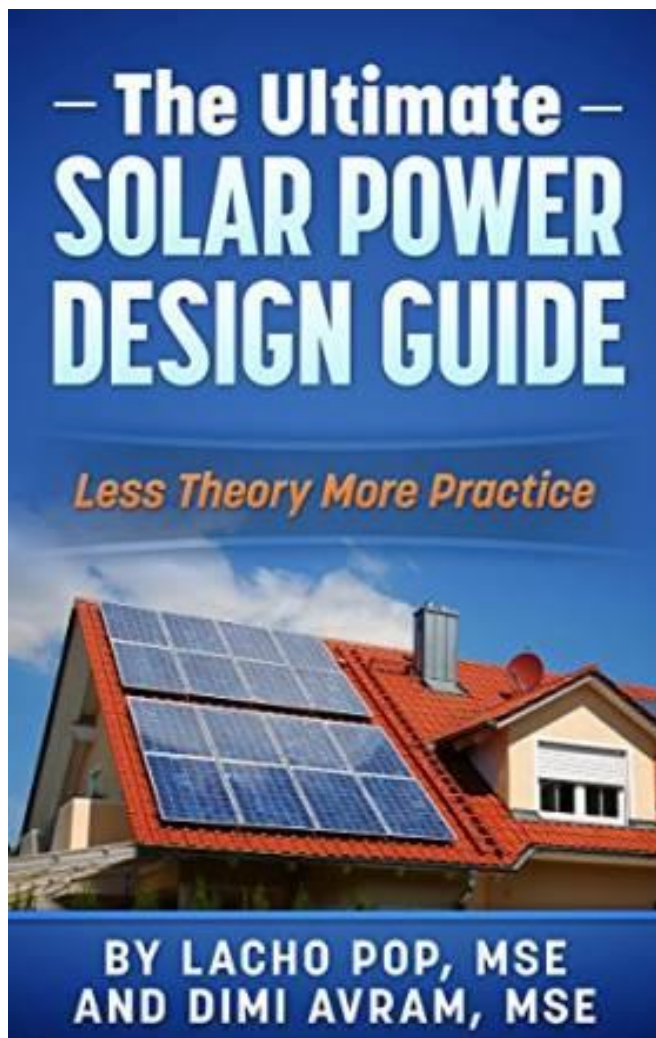
<https://www.amazon.com/Simple-Practical-Solar-Component-Guide-ebook/dp/B07S9GPN4B/>

The Ultimate Solar Power Design Guide: Less Theory More Practice [Kindle and Paperback Edition]

ASIN: B0102RCNOG, ISBN-13: 978-6197258042, ISBN-10: 6197258048

Click on the link to get it NOW:

<http://www.amazon.com/Ultimate-Solar-Power-Design-Guide-ebook/dp/B0102RCNOG/>



Click on the link to get it NOW:

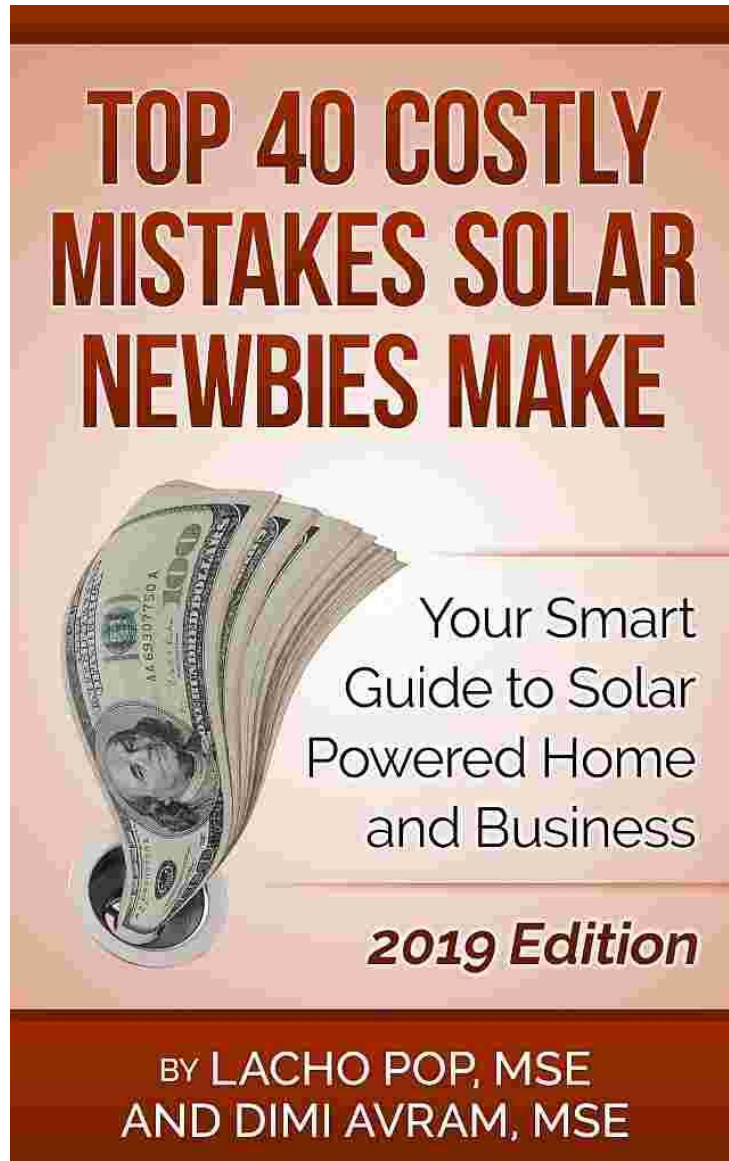
<http://www.amazon.com/Ultimate-Solar-Power-Design-Guide-ebook/dp/B0102RCNOG/>

Top 40 Costly Mistakes Solar Newbies Make: Your Smart Guide to Solar Powered Home and Business

2016 Edition [Kindle,Paperback, and Audio Edition], Kindle ASIN: B07QHLJTPZ, Paperback ISBN-13: 978-6197258073, Audio 2019 Edition ISBN 978-6197258080]

Click on the link to get it NOW:

<https://www.amazon.com/dp/B07QHLJTPZ>



Click on the link to get it NOW:

<https://www.amazon.com/dp/B07QHLJTPZ>

Table of contents

Photovoltaics in the world of renewable energy	13
Advantages of photovoltaics.....	16
Why are photovoltaics gaining worldwide popularity?	18
Why the cost of photovoltaics is decreasing	19
Drawbacks of photovoltaics	20
The main applications of solar power.....	21
Don't go solar before reading this!	22
Why energy efficiency comes first.....	26
How to improve the energy efficiency of your house or RV.....	26
The basics of photovoltaics and solar power system components	28
Solar power basics.....	28
Electricity basics	30
Solar (photovoltaic) panels	33
Solar panel types.....	33
Solar panel voltages.....	37
How to orientate in solar panel ratings?	39
Connecting solar panels.....	40
Mixing different solar panels.....	41
Which solar panels to select for your home solar system?	43
Which solar panels to select for your RV?	45
The risks of using secondhand or home-made panels	47
How many solar panels do you need?	50
Electricity and solar power basics summarized.....	51
Batteries.....	53
Why does a solar power system need a battery?	53
What are solar batteries and how do they work?	53
What kinds of batteries are used in solar power systems?	54
How to prolong the life of your lead-acid solar battery?	59
How many amp-hours of capacity do you need?	61
Charge controllers.....	63
Do you always need a charge controller?.....	64
Which charge controller is better?.....	66
Sizing and installing your charge controller	67
Inverters	69
Grid-tied solar inverters	69
Off-grid inverters.....	70
Selecting the inverter for your solar power system	71
Other solar system components	73
Why it is vital to select the right solar components.....	75
Solar electric systems	78
Grid-tied solar power systems	79
Grid-tied systems summarized	84
When do you need a grid-tied system?.....	85
Off-grid solar power systems	87

Off-grid systems summarized	91
Main applications of off-grid stand-alone PV systems.....	92
Limitations of off-grid stand-alone systems	93
When do you need an off-grid stand-alone system?	94
Hybrid systems	95
Additional power backup sources in hybrid systems	96
Benefits of hybrid power systems	99
When do you need a hybrid power system?	100
Which off-grid system to choose?	101
Mobile solar power systems	102
Differences between residential and mobile solar systems.....	103
Why it is important to size your solar system correctly	107
Solar site survey guide	109
Is your building or motorhome solar-ready?	109
How to assess your location for the solar resource?.....	110
Why the condition of your roof does matter	112
Roof-mounted or portable solar panels for your RV?	113
Should you tilt the solar panels on your RV?	114
How to perform a solar site survey?	116
What to do during a solar site survey?.....	118
Step 1: Assess any possible shading by nearby objects.....	118
Tips on how to avoid shading.....	119
Step 2: Determine your roof area.....	122
Step 3: Determine the orientation and tilt angle.....	122
Practical tips to determine the orientation and tilt angle.....	123
What if you select a tilt angle other than the latitude?	124
Reduce the solar-generated power in summer or winter?	125
Step 4: Choose a mounting method of the solar array.....	125
Photovoltaics in summary.....	128
Resources on the authors' website	129
Free Simple Solar Calculators	129
Free PWM Charge Controller Calculator	130

Photovoltaics in the world of renewable energy

Solar photovoltaic energy is the energy of the future. It can resolve a lot of the ecological and energy problems of the world.

The energy sources of our planet are running out. Petrol, gas, and coal are available in limited amounts. Utilization of such resources, however, harms the environment – gas emissions of greenhouse effect being the main reason for global warming.

Moreover, the energy consumption is increasing. Till 2030, a 50% increase in energy needs is expected. A possible limitation of electricity consumption would mean deteriorating of lifestyle. Therefore, existing without electrical energy is practically unthinkable.

Besides the problems related to limited amounts of energy resources and ecology issues, many people are experiencing the attitude of brutal negligence and shady pricing policy of local utilities and energy companies. Frequent power outages, continually changing and often incomprehensible tariffs, and pricing of electricity, oil, and natural gas are gradually becoming common. Also, it is proved that utilities have no short-term economic benefit to prevent infrequent large-scale power cuts and cascading failures in power grids. Naturally, they do little to none to improve customer satisfaction in that direction.

What is more, the uncertain geopolitical and ecological situation on the planet forces many people to embrace the idea of self-reliance and seek ways to become more energy independent even at any cost.

In this situation, renewable power sources are the only solution. Solar generators, wind generators, and biofuel products are by all means the Technology of the Future. Utilization of inexhaustible natural resources for energy production is a necessity standing in front of the whole of humanity.



Solar generators Wind generators Biofuel products

The sun is an inexhaustible source of energy and can meet the enormous energy demand.

A photovoltaic system located on your roof or near your home is not only going to decrease your dependency on any current and future energy providers but is also going to secure your energy needs.

Photovoltaics can power up reliably RVs, campers, boats thus improving the comfort of their owners.

The long lifecycle of photovoltaic components and the minimum maintenance required for solar systems makes photovoltaics the ideal investment offering users a minimal risk and steady income. Programs for supporting the renewable energy sources, e.g., high purchase prices of electricity and minimal guaranteed terms for buying up the electricity produced, are an additional source of generating profit.

Solar panels are successfully applied upon building façade design by adding modern hi-tech appearance. Photovoltaic

panels help contribute to the thermal isolation of buildings and save you expenses for façade tiling. With a solar panel façade, you don't need to repaint a building for at least 25 years!

A solar power system can reasonably increase the cost of your real estate. Such an increase is not only because your home becomes energy-secured, but also because the comfort of living is improved, especially in attics where a solar power installation can act as a conditioner in summer and as a heater in winter.

The need for renewable energy sources coincides with two phenomena – the increasing energy demands and the deposits of coal, oil, and gas, that are gradually running out.

Advantages of photovoltaics

For the user:

- A well-developed, proven, and reliable technology.
- No moving parts and little maintenance.
- No fuel needed for operation.
- An easy and quick mounting, especially grid-tied systems.
- Off-grid PV systems are capable of producing electricity anywhere in the world.
- Photovoltaic systems generate more energy than they consume – the energy invested in solar panels can be returned in 2 to 7 years, depending on the location and solar system type.
- Photovoltaics add value to the building where they are installed.
- Energy independence.
- Satisfaction from achieving more energy security and bringing family comfort during a power outage.

For the environment:

- PV systems help for reduction of carbon dioxide emissions, thus minimizing the greenhouse effect.
- PV systems reduce environmental pollution and do not cause any environmental risks – oil spills, nuclear disasters, global warming.

- PV save the scarce resources available in the bowels of the Earth.
- PV can be recycled – there are various technologies for recycling panels after they are worn out or damaged; solar cells, glass, aluminum frames can be either recycled or reused.

Why are photovoltaics gaining worldwide popularity?

- They stimulate sensible and economical energy use.
- They are a popular technology and advertise renewable energy successfully.
- They represent a fast-growing market everywhere in the world.
- The shining of the sun is more reliable and more predictable than the wind. Also, annual values of radiation are relatively constant per given area.
- The energy of the sun is uniformly distributed on the surface of the Earth.
- The solar power technology performs well both in countries located far from the equator and in tropical areas.
- Installation of photovoltaics fosters research and development of a technology of the future.
- Investing in solar power helps achieve energy efficiency and decrease the energy dependence from other countries.

Why the cost of photovoltaics is decreasing

The cost of solar power systems is decreasing, and their performance is increasing as a result of:

- Increased efficiency of PV cells and panels.
- Development of thin-film technologies.
- Further development of alternative coatings.
- Improved performance and higher production appliances for crystalline silicon solar cells and panels.
- Improved features and mass production of PV system components.

Drawbacks of photovoltaics

Photovoltaics do have their drawbacks:

- The overall initial cost of system buying and installation is still high.
- Compared to the efficiency of wind power generators, the efficiency of solar power systems is lower. In other words, the area needed to produce certain power is much larger if you use photovoltaics instead of wind generators.

However, the efficiency of solar panels is not as location-sensitive as in wind turbines. A solar power system can be deployed at almost any place. This is not valid for wind power, however, which is advantageous mostly in coastal areas and areas with relatively high wind speed. Also, thanks to the constantly decreasing prices of solar panels and other components of the solar panel system, solar power gradually becomes competitive with wind power.

- The sun is not always available as a source of energy. This means that for periods of 'sun outage' you need an additional system for electricity storage.

You can discover more about the disadvantages of solar power on author's blog here:

<https://solarpanelsvenue.com/disadvantages-of-solar-power/>

The main applications of solar power

Here are the main applications of PV systems:

- **Water pumping** for small-scale remote irrigation, stock watering, residential uses, remote villages.
- **Lighting** for residential needs, billboards, security, highway signs, streets and parking lots, pathways, recreational vehicles, remote villages and schools, marine navigational buoys.
- **Communications** by remote relay stations, emergency radios, orbiting satellites, cellular telephones.
- **Refrigeration** for medical and recreational uses.
- **Corrosion protection** for pipelines and docks, petroleum and water wells, underground tanks.
- **Utility grids.**
- **Household and RV appliances** – ventilation fans, swamp coolers, TV sets, blenders, stereos, etc.

Don't go solar before reading this!

- Solar-generated electricity is still more expensive than the electricity supplied from a utility grid unless you live in a remote area where connecting to a utility grid would cost you a fortune. PV systems make solar electricity more affordable than it was 20-30 years ago, but prices remain relatively high. Nevertheless, in the last few years, prices of solar photovoltaic panels have dropped 80% on average, and they are continuing to decrease.
- Photovoltaic systems are not recommended for heating. For heating, you should use a solar thermal system. Another option is propane or natural gas.
- High costs of PV systems are concentrated in a substantial initial investment. Often the biggest problem is to find initial funding. After you install your PV system, it is nice to feel independent from the utility grid or to see your monthly electricity bills going down. Buying a PV system is actually like paying your electricity bills in advance for years ahead, and the point is to avoid the essential burden of high initial costs. Thus, finding a suitable source of financing is essential.
- Solar electric systems only produce power when the sun is shining. Therefore, something should be done with the electricity produced – it should be either consumed right away, or exported to the grid (in grid-tied systems), or stored in a battery for later use (in off-grid systems).
- For people connected to the grid, usually the decision to purchase a photovoltaic system is based on cost-

saving – reducing their monthly bills by selling power to the utility. For people living in remote areas, far from any utility infrastructure, the decision to purchase a PV system is not determined by any cost-saving reasons but is a matter of securing a normal life instead.

Important:

If your home is already connected to the utility grid, COMPLETELY replacing the utility with a solar electric system might NOT be cost-effective.

However, offsetting **a part of** your electrical bills through a solar system can be the best way to save money on electricity.

The utility company's costs for producing electricity are always lower than yours because the utility spreads the costs of generating electricity among its customers.

For this reason, the price you pay for electricity is lower than the price you would pay to have electricity generated by your home solar system. You do pay for generating electricity because, although solar energy is free, PV equipment is not free.

Also, residential PV systems are usually not practical for powering large heating devices – heaters, large electric stoves, air conditioners, or electric clothes dryers.

For this reason, you have to solar-power just the most energy-efficient loads and search for reasonable alternatives for energy non-efficient ('power-hungry') devices.

Moreover, you should start by improving the energy efficiency of your home.

There are national or regional standards, like the National Electric Code (NEC) in the U.S., adopted to ensure safety in all systems that generate, store, transport, and consume electricity.

Your solar power vendor should follow such requirements so that the PV system would be approved by local electric code officials.

Thus, you can expect the price of your property to increase after installing the solar power system.

In many countries, it is required by law that all electrical equipment should be installed by a licensed electrician.

On the other hand, however, many local code officials do not have enough knowledge of PV systems. So even if you follow the rules of the adopted standards, you can have problems to prove to a code official that your solar system is a code-approved one.

It is recommended to contact local code officials and provide them with necessary explanations before you purchase and install a photovoltaic system.

A good plan is to invite them to inspect the installation process before the whole system is completed. This might help your system obtain the needed approval.

If you consider going solar, we highly recommend our book

'Top 40 Costly Mistakes Solar Newbies Make: Your Smart Guide to Solar Powered Home and Business.'

The book is available in audio, kindle and paperback format and is targeted to homeowners, RV, boat and business owners who make their first steps in solar power.

Its product identifiers are - Kindle ASIN: B01GGB7QP8,
Paperback ISBN-13: 978-6197258073, Audio 2019 Edition
ISBN 978-6197258080]

Click on the link to get it NOW:

<https://www.amazon.com/Costly-Mistakes-Solar-Newbies-Make-ebook/dp/B01GGB7QP8/>

Why energy efficiency comes first

If you are planning to buy a photovoltaic system, you should start with increasing the energy efficiency of your home or RV.

Achieving energy efficiency means reducing electrical consumption and your monthly electricity bills respectively.

Energy efficiency is vital simply because **saving energy is less expensive than producing energy**. By improving the energy efficiency, the cost of your photovoltaic system is going to be reduced.

You can reduce your electricity use in a variety of ways. You should, however, consider a specific approach and view your home as an energy system comprising various interrelated parts, with each part contributing to the overall efficiency.

How to improve the energy efficiency of your house or RV

- Replace incandescent light bulbs, where most of the energy used turns into heat rather than light, with compact fluorescent ones.
- Turn off all stand-by ('phantom') loads, such as DVDs, TV sets, and computers, while they are not in use.
- Upgrade your heating, ventilation, and air conditioning systems.
- Replace your old refrigerator and freezer with new, high-efficiency models (energy-efficient or propane ones).

- Replace high-consumption loads (high-wattage electric stoves, clothes dryers, water heaters, heating appliances) with their propane or natural gas alternative versions. Indeed, a solar thermal water heating system is a perfect option.
- Replace electrical air-conditioning appliances with evaporating cooling systems.
- Make internal isolation of your house.
- Utilize your large electrical loads (pool pumps, electrical mills) during off-peak hours.
- Install solar water heaters and summer shadings.
- Utilize devices with timers and other home automation systems.
- If you live in the U.S., when shopping for electrical appliances, look for devices labeled with Energy Star® label.

Important:

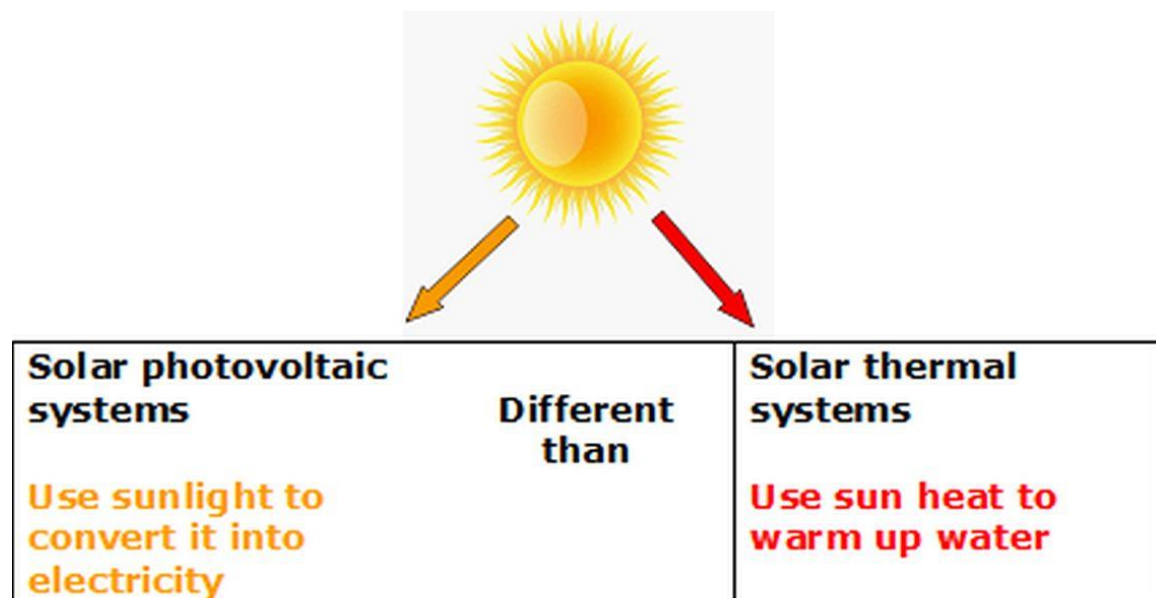
It is not recommended to power electrical heating appliances (dishwashers, washing machines, electrical boilers, tumble driers) by solar-generated electricity. These devices are known as 'power-hungry,' so solar-powering them is going to be very expensive. Therefore, you should find a proper energy-efficient alternative for every heating device.

The basics of photovoltaics and solar power system components

Solar power basics

A solar photovoltaic system converts sunlight into electricity (electrical energy).

In this book, the terms 'solar' and 'photovoltaic' are used interchangeably. However, 'solar' is also used for solar water-heating systems, which we are not going to discuss here.

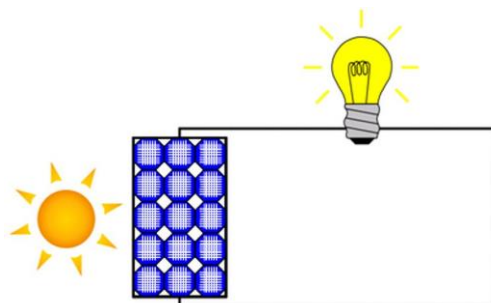


A photovoltaic (PV) system can generate a part of or all of your electricity demand.

A PV system can either reduce the amount of power you consume from your utility or replace the grid if you live far from any utility infrastructure.

The main component of a photovoltaic system is the photovoltaic solar panel. A solar panel consists of

connected solar cells. Solar panels are connected into solar arrays to achieve higher energy output.



Photovoltaic cells and panels are made of semiconductor material (silicon) capable of producing electricity when exposed to sunlight. Such ability is called 'photovoltaic effect.'

More energy is generated in sunny days, and less energy is generated in cloudy or rainy days, or when the photovoltaic array is shaded by obstructions (trees, buildings, etc.).

Solar panels generate DC electricity (explained further).

The solar-generated power generated can be:

- Used right away,
- Stored in a battery for later use, or
- Converted to AC power, and then either used by electrical appliances or exported to the utility grid.

Solar panels are designed for direct sunlight. Putting a glass between the sun and the panel results in charging the battery three times slower, even in the brightest part of the day (at noon, where the sun is the strongest), compared to when the panels are exposed to direct sunlight.

Electricity basics

Current is a flow of electrons, occurring as a result of a pressure called Voltage. Current is measured in Amperes or Amps (A), while voltage is measured in Volts (V).

On their way through, electrons encounter resistance which controls the current rate. Resistance is measured in Ohms (Ω) and is always related to losses, i.e., due to the resistance the current flow gets weaker. These losses are called 'voltage drops.'

When encounter resistance on its way, however, current is capable of performing work. It's this work that makes electrical appliances operate and serve us. The work performed by the current is called Power and is measured in Watts (W). Another unit of measuring power is kilowatt – 1 kilowatt is 1,000 Watts. Power is a multiple of voltage and current:

$$\mathbf{W = V \times I}$$

When the sun is shining, electrons in the solar panels produce voltage and current. This solar-generated current is flowing along wires to the devices and appliances in your home or RV and do some work. This work is the power generated by the solar panel when exposed to sunlight. Each solar panel has its voltage, current and watt ratings printed on its back label.

The work performed for some time is called Energy (E) and is measured in Watt-hours (Wh).

Energy can be either consumed or produced. It is a multiple of power and time, that is, how long this power is used or produced:

$$\mathbf{E = W \times T}$$

For example, a 100-watt solar panel produces 100 W of power. For 5 hours of peak sunlight (also known as 'peak sun hours' or PSH), such a panel produces 500 watt-hours (Wh) of energy.

The same goes for the power consumption estimation. For example, a 10W LED lamp operating for 3 hours daily, consumes 30Wh energy per day.

As a solar panel produces power, it's called a generator. Other types of generators are batteries and vehicle alternators. The devices and appliances in your home or RV consume energy.

Any device or appliance consuming electric power is called a 'load.'

Since $\mathbf{W} = \mathbf{V} \times \mathbf{I}$, then $\mathbf{I} = \mathbf{W}/\mathbf{V}$. Thus, you can obtain the current by dividing the watts by the volts. If you, however, divide the energy by the voltage, instead of the power by the voltage, you have:

$$\mathbf{C} = \mathbf{E}/\mathbf{V}$$

Where C is the energy in Amp-hours (Ah). Amp-hours are used to measure the capacity of a battery. This is the energy drawn or generated by a battery for some time.

For example, if the current rating of your 100-watt panel is 6 amps, for 5 hours you have $6 \text{ amps} \times 5 \text{ hours} = 30 \text{ amps-hours}$ generated. These 30 amps-hours are intended to recharge your battery from which you draw this electricity to power your appliances.

What is the difference between AC and DC electricity?

DC current only flows in a fixed, single direction, or 'forward.' AC current periodically changes its directions – sometimes it goes 'forwards,' but sometimes it goes 'backwards.'

AC electricity is what the local utility grid company provides to our homes is. The AC grid electricity voltage can be 120V or 220 volts. As you know, photovoltaic panels and batteries generate DC electricity. Most of the devices at our home, however, use AC electricity, and unfortunately, we like to use some of them also in our RV. To convert DC electricity into AC electricity, you need an inverter.

The shore power hookups available at most camping sites provide you with AC power. Thus you can power your appliances running on 120/220V AC (120/220V phone chargers, TV, laptops, stereos). To power your 12V DC appliances (lights, water pump, DC fridge), you need a power converter.

If you have a solar array, it usually generates 12V DC voltage. So, you can power your 12V DC appliances, while to power your 120/220V AC appliances you need an inverter (if you don't intend to use a diesel generator). It converts the 12V DC power into 120/220V AC power.

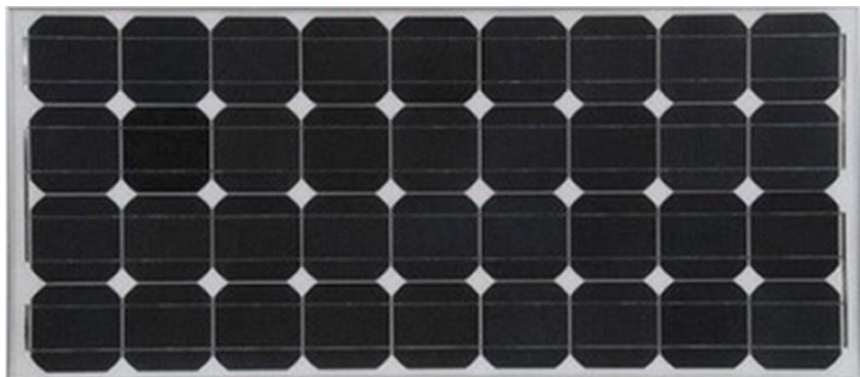
Solar (photovoltaic) panels

Solar panel types

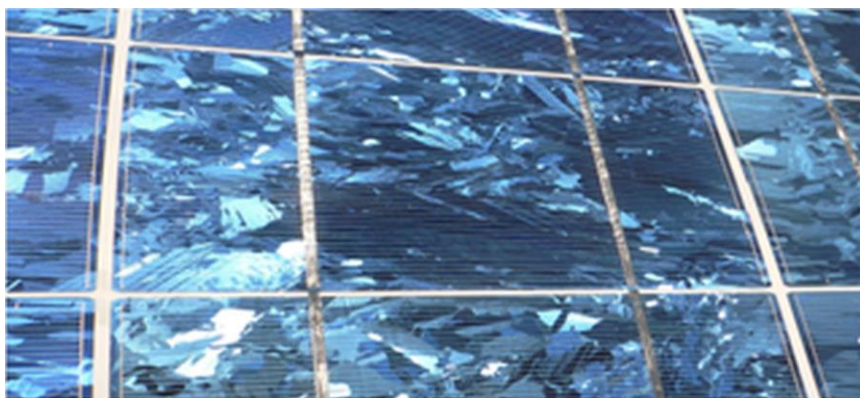
There are two main types of photovoltaic panels – crystalline and thin-film.

Crystalline panels can be monocrystalline or polycrystalline. A monocrystalline panel is manufactured by a single silicon crystal, while polycrystalline panels are produced by joining many small silicon crystals together. For this reason, these two panel types are very different in appearance, although the surface of both of them is covered with a glass layer.

Monocrystalline panels usually come in black color:



While polycrystalline ones come in bluish color:



Monocrystalline panels are the most efficient, but they are also the most expensive. ‘Efficiency’ of a panel is the power output provided per unit area of the panel. Thus, apart from their appearance, monocrystalline and polycrystalline panels differ also in their efficiency. For a mobile solar panel system, such a difference is not an issue. However, it cannot be neglected for residential solar systems of medium size, where lots of panels are connected in series and parallel (explained further).

Thin-film (amorphous) panels are made by amorphous silicon spread on a plastic surface.



Although thin-film panels had a much shorter lifespan in the past, they currently have a life expectancy similar to the crystalline solar panels. Thin-film panels are much cheaper than crystalline ones, but they are also much less efficient – as you usually need a twice larger area to produce the same amount of power by thin-film panels than by crystalline ones.

Solar panels can also be either flat or flexible. Flexible panels can be bent around the curves of your RV, caravan, camper, or boat. Also, they are lighter and more aerodynamic than flat panels, and more expensive. An RV with mounted flexible solar panels on the roof looks more aesthetically. Flat panels, however, are more durable than flexible panels and come with a more extended warranty (25 years of flat panels compared to 10 years of flexible ones). Moreover, flat panels are mounted on a surface in a manner that allows easy cooling underneath. Also, flat

panels can be tilted to match the optimal direction towards the sun. Unless aesthetics and improved aerodynamics are of the utmost importance for you, we recommend choosing flat panels for your RV, caravan, or camper.

Flat panels can be monocrystalline, polycrystalline, or thin-film. Flexible solar panels can only be thin-film ones. They are the best option for small mobile solar systems, where you need flexible, small-sized, and lightweight solar panels capable of withstanding physical wear and tear, such as RVs or boats. The more flexible the solar array, the less efficient will it be.

Due to their high reliability, crystalline panels typically come with a warranty of 25 years, which means that they can last much more. Depending on the manufacturing technology, materials used and whether flexible or rigid, thin-film solar panels have a wide range of warranty – from 5 up to 20 years.

Every solar panel has a nominal power rated in watts (W) or kilowatts (kW). Often, the nominal power of solar panels is denoted in ‘watts-peak’ (W_p) or ‘kilowatts-peak’ (kW_p). Here is a comparison between solar panel efficiency according to the area needed to install a solar array of 1 kW:

Solar cell material	Solar panel efficiency	Area need for 1 kW of solar-generated power
Monocrystalline silicon	13-16%	7 m ² (75 sq. feet)
Polycrystalline silicon	12-14%	8 m ² (86 sq. feet)
Amorphous silicon	6-7%	15 m ² (161 sq. feet)

Solar panels differ mostly in their:

- Type – monocrystalline, polycrystalline, thin-film

- Power output – between 10W and 300W
- Output voltage – 12V, 24V, 48V or 60V
- Size and weight – commonly 1.6 x 0.8 meters, or 5.25 x 2.62 feet.

The type and efficiency of the solar panels is not the only factor that determines the performance of your solar panel system. Buying the most efficient (and the most expensive) solar panels does not guarantee that your system will operate at maximum performance. Your target is to get the maximum amount of solar-generated electricity. Thus, your 'homework' is also to consider:

- **Shading** – by any obstacles: trees, buildings, lamp-posts or anything that could prevent the solar panels from getting the full sunlight.
- **Orientation** – this is a primary issue. If you, for example, live in the US, UK, Canada, Europe, or India, your panels should be facing South. If you live in Australia, New Zealand, or South Africa, your panels should be facing North.
- **Tilting** – it is the angle at which the sunbeams hit your panels. The tilt angle comprises two components – the slope of your roof and the tilt angle at which your panels are mounted.
- **Temperature** – in general, high temperatures are not recommended, although thin-film panels, unlike crystalline ones, are more tolerant to heat. High temperatures occur not only during a hot, sunny day but also when there is insufficient space left between the solar panels and your roof for cooling.

Solar panel voltages

The **nominal voltage** of a solar panel usually corresponds to the battery voltage for which the panel is designed. Nominal voltage is not the peak voltage of a solar panel. For example, a solar panel can have a nominal voltage of 12V, and its voltage at peak power can be 17-18V. Since a battery needs a voltage of 13.5-14V to be charged, obviously 12V are insufficient, but 17V is okay.

The **maximum power voltage (Vmp)** is the voltage at which a solar panel produces its maximum power under the standard test conditions (STC) (also known as 'maximum power point') while connected to a load. **Vmp** corresponds to the maximum power current (**Imp**) and is always higher than the panel's nominal voltage. A panel of 12V nominal voltage has a **Vmp** between 16V and 18V. **Vmp** and **Imp** are related to the total power and generated by a solar panel for a period of time. The multiple of **Vmp** and **Imp** is the solar panel peak power, sometimes denoted in watts-peak (Wp):

$$P \text{ (in Wp)} = V_{mp} \text{ (in V)} \times I_{mp} \text{ (in A)}$$

The **open circuit voltage (Voc)** is the voltage measured directly between the positive and the negative terminal of a solar panel with no loads connected. It is the highest voltage a solar panel can produce under certain conditions, that is, the lowest cell temperature. Under the same conditions, **Voc** is always greater than **Vmp**. It is not related to the performance of the solar system and is rather used when sizing some of the system components. The open circuit voltage is different from the maximum power voltage in that the solar panel is not connected to a load.

The **system voltage** is practically the same as the nominal voltage, but while the nominal voltage is used for solar panels, system voltage is used for batteries, charge controllers, and the solar system as a whole. There is a range of system voltages in solar power systems – 12V, 24V, 48V. Usually, most mobile photovoltaic systems on RV, caravans, campers, or boats have a system voltage of 12V.

For example, let's consider a solar power system of 12V system voltage. A solar panel of a 12V nominal voltage produces a higher voltage (about 18V), to charge a 12V battery bank. A battery voltage of 12V ranges from 10V to 14V, depending on the battery type and battery state of charge. The lowest voltage means a fully discharged battery, the highest voltage – a fully charged battery. Similarly, a 12V charge controller must provide the corresponding higher voltages allowing the battery bank to get charged.

If you use an inverter, the battery voltage should fall within the inverter's nominal DC input operating voltage window. However, the inverter's output AC ('mains') voltage must coincide with the standard AC voltage, which is 120V for the USA.

So, a 12V solar power system should comprise all these components with their generated voltage falling within these ranges.

For more info on how solar panels work, you can visit author's here:

<https://solarpanelsvenue.com/what-are-solar-panels-made-of-how-do-solar-panels-work/>

How to orientate in solar panel ratings?

The power output of a solar panel is rated by its 'peak power,' sometimes denoted in 'watts-peak' (W_p) rather than 'watts (W).' The peak power of the panel is a multiple of its peak current (the current of maximum performance **I_{mp}**) and peak voltage (the voltage of maximum performance **V_{mp}**).

The peak power of a solar panel is measured in a laboratory environment known as Standard Test Conditions (STC):

- 1,000 watts per square meter falling onto the Earth's surface,
- Temperature 25C (77F), and
- Atmospheric density 1.5.

Although manufacturers state the peak output power of their panels under the STC, these conditions are somewhat idealized and deviate from reality. The main reason for such a deviation is that solar panels typically operate at temperatures higher than 25C (77F), which inevitably reduces the solar-generated power. Eventually in 'real world conditions,' what you get as a peak power from a solar panel is as less as 80-85% of its peak power.

Thus, from a 100W solar panel, you get 80-85W even during the Peak Sun Hours of the day, that is, during the hours of maximum sunlight (which are around noon). What is more, on cloudy days what you get of such a panel would be even far below these 80-85W, for example, 10-20W.

Connecting solar panels

Solar panels are connected into solar arrays to increase the total solar-generated power.

Solar panels can be connected in series or parallel. In both connection modes, the total power of the solar array is a sum of the powers of the connected solar panels.

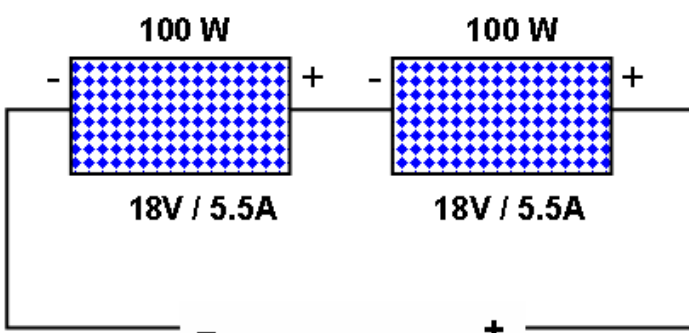
Series connection increases the voltage of the solar array while keeping the same current. In contrast, parallel connection increases the current of the solar array, while keeping the same voltage.

Series connection is preferred both in grid-tied and off-grid residential solar systems because it results in lower currents and hence, reduced cabling costs.

The parallel connection of solar panels is mainly used in mobile solar systems on RV, caravans, campers, or boats. Parallel connection increases the installed solar power while keeping the 12V battery voltage.

Example: Series and parallel connection of two 12V/100W (18V x 5.5A) solar panels

Series connection:

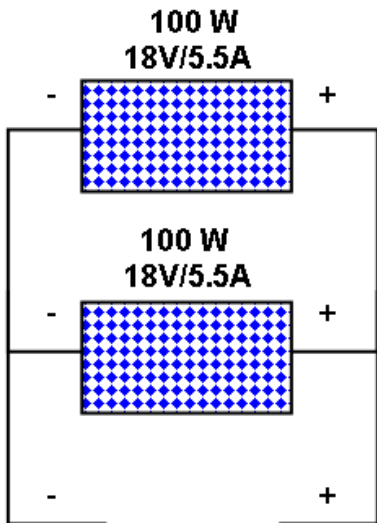


Total voltage: $2 \times 18V = 36V$

Total current: 5.5A

Total power: $36V \times 5.5A = 200W = 2 \times 100W$

Parallel connection:



Total voltage: 18V

Total current: $2 \times 5.5A = 11A$

Total power: $18V \times 11A = 200W = 2 \times 100W$

Please, have in mind that solar panels produce a voltage higher than the battery voltage. Otherwise, the battery cannot be charged. The typical voltage of a 12V solar panel is about 18V.

Mixing different solar panels

Mixing different solar panels can decrease the solar-generated power since the output power is limited by the most poorly performing panel in the array.

Generally, mixing different solar panels is not recommended. By following the below rules, however, you can mitigate the negative impact of such a mixing on the solar panel performance:

- In a series connection, the current passing through the solar panels is limited by the solar panel of the lowest rated current. Thus, if you have a panel of a

rated current lower than the current rating of the other panels, the total power of the whole string will go down.

- In a parallel connection, the solar panel with the lowest rated voltage determines the total voltage of the paralleled string. Thus, if you have a panel of a rated voltage lower than the voltage rating of the other panels, the total voltage of the whole string will go down. If you, however, add a new solar panel of a slightly higher rated voltage, only the performance of that new panel is going to degrade.

Important:

Avoid mixing different solar panels. If you, however, cannot avoid this, to mitigate the losses:

- In a series connection, only use new solar panels of rated current equal or slightly higher than the rated current of the other panels.
- In a parallel connection, only use solar panels of rated voltage equal or slightly higher than the rated voltage of the other panels.

To get more information on this topic, please visit author's site here:

<https://solarpanelsvenue.com/mixing-solar-panels/>

Which solar panels to select for your home solar system?

Monocrystalline solar panels are the most efficient ones. Their efficiency lies within the range of 12-25% with a typical value of 18%. Polycrystalline panels are similar to monocrystalline ones but they:

- Compared to monocrystalline panels, need a slightly larger area to produce the same amount of electricity,
- Cost less, and
- Are less efficient than monocrystalline solar panels of an efficiency range of 12-25% with a typical value of 15%. However, polycrystalline panels are less expensive than monocrystalline ones and are the most widely used solar panel type today.

Important:

Thin-film panels usually need a twice larger area to produce the same amount of electricity, compared to mono- and polycrystalline panels.

They are the least expensive type of PV panels with the following most common varieties:

- Cadmium Telluride (CdTe) thin-film panels.
- Copper Indium Gallium Selenide (CIGS) thin-film panels.
- Amorphous silicon (a-Si) thin-film panels.

Choosing thin-film panels would mean you have:

- ✓ **Minimum** budget, or

- ✓ **Quite a large** area to install the PV array.

Thus, unless you have the above combination, it does not seem quite reasonable to select solar panels of efficiency twice less as common.

For more information on different type of solar panels, you can check on our blog here:

<https://solarpanelsvenue.com/types-of-solar-panels-most-used-pv-solar-panels/>

To get more info about how to choose the best solar panels, you can visit us here:

<https://solarpanelsvenue.com/how-to-choose-the-best-solar-panels/>

Which solar panels to select for your RV?

The primary purpose of a mobile solar panel system is to charge your leisure battery when there is no shore power nearby. Thus, you might not need any mobile solar system at all, in case you drive your caravan just from an RV park to an RV park with shore power available.

Not all solar panels are created equal; neither are all of them suitable to install on the roof of an RV, camper, or boat.

The best portable solar panel systems for camping are made of monocrystalline cells. The so-called 'rigid monocrystalline panels' are the most durable and have the best warranty.

Cheaper portable solar systems are equipped with polycrystalline cells, but they also come with cheap frames and wiring and lower-grade charge controllers.

Thin-film (amorphous) solar panels are another option for portable solar kits. These panels, however, have a much lower efficiency than crystalline ones and much shorter warranty, because they can be broken easily (they do not have a glass surface) and are cheap to produce. Usually flexible and ultra-flexible thin-film panels are used for roof-mounting where they can match the curves of the caravan's surface. Thin-film panels perform better in hot weather. Their rippled surface, however, allow accumulation of dirt and dust which are not so easy to clean, and reportedly even small water pools that can damage the panel.

Portable solar kits are designed for smaller campers and RVs. They offer you more flexibility in deploying your solar array at a distance from your vehicle that has been

parked under the trees. Portable solar kits come with cables, stands, and even mounting tools. Initial costs of portable solar kits, however, are higher, compared to when you build the system on your own.

So, we recommend you to start with monocrystalline panels. If your calculations eventually boil down to a system that is too costly or too big, you could redesign it with polycrystalline panels instead.

For more info on how to choose the best solar panels for a caravan, camper, RV, or boat, you can visit us here:

<https://solarpanelsvenue.com/types-of-solar-panels-most-used-pv-solar-panels/solar-panels-for-rv/>

The risks of using secondhand or home-made panels

There are plenty of websites claiming it is possible to launch and run a home solar power system for as less as \$200-\$300. Moreover, you could find hundreds of websites offering you cheap secondhand panels or solar cells.



A half-built homemade solar panel, made from individual cells soldered together

Image by Victorgrigas at en.wikipedia.org used under Creative Commons CC0 1.0 Universal Public Domain Dedication license

Don't trust such websites! They provide you with wrong or misleading information!

Important:

Any credits and rebates you could apply for before the government institutions are NOT valid for home-built solar electric systems and their components!

What is more, launching a solar power system built of home-made panels could be a violation of local electric regulations. Thus, you might not be allowed even to install them, let alone operating them!

In many countries, it is illegal to export power to the grid by a solar system built of non-approved solar generation equipment.

Building a solar system for around \$200 is possible. Such a system, however, is going to be of low power output – around 100 Wp. Indeed, this is not enough to power an entire house.

Rather cheap solar panels, unless they are Chinese-made or home-made, are usually rejected by their manufacturers – either because they are physically damaged or because their characteristics differ from the stated ones. If you use such panels, it might be possible that neither of the stated values can be achieved during operation.

Important:

The high price of solar panels is related to the stringent and therefore expensive process of manufacturing.

Such a manufacturing process requires both expensive equipment to perform some special operations and stringent room conditions (with regards to room temperature, cleanliness, pressure).

The manufacturing process is so expensive because solar panels are designed not only to ensure maximum performance upon converting solar energy into electricity but also to withstand harsh weather conditions – cold, rain, snow, ice, and heat.

Using cheap panels to build a solar system is the same as plugging an electrical device you know nothing about into a live electrical network. What you should do is just pray not to see your house on fire!

Sources:

1. Boxwell, Michael. 2012. Solar Electricity Handbook, Greenstream Publishing, Amazon Kindle Edition
2. Pop, Lacho, Dimi Avram (2014-11-26). The Truth About Solar Panels: The Book That Solar Manufacturers, Vendors, Installers And DIY Scammers Don't Want You To Read The Truth About Solar Panels (Kindle Locations 483-490). Kindle Edition.

How many solar panels do you need?

Well, it depends on you want to start with. The number of panels you need depends on how much solar power you have to generate, and this power depends on how much energy you use every day. You can assess this through a load analysis which is the starting point of sizing your solar battery.

A good plan is to start with the maximum possible number of panels that can be mounted on your roof. Another case is to evaluate how many panels you need to provide a regular charge to your battery.

Important:

The total daily amount of solar-generated electricity is always related to the Peak Sun Hours (PSH) at your location. PSH is the number of hours a day during which a solar panel produces its rated voltage. PSH vary depending on the season and location.

PSH is not the same as available sunny hours. For example, in January the sun might be up for 7 hours every day, while the PSH might be as less as 2. In the calculations, you can use an averaged value for PSH you can obtain as an average PSH for all the months during which you are likely to need solar-generated power.

All these issues are explained in the section '**Why it is vital to size your system correctly**'. Read on!

Electricity and solar power basics summarized

Power (in W) = Current (in A) x Voltage (in V)

Energy (in Wh) = Power (in W) x Time (in h)

Battery capacity (in Ah) = Energy (in Wh) / Voltage (in V),

Where:

W – Watts

A – Amps

V – Volts

h – hours

Wh – Watt hours

Ah – Amp hours

Solar panels are rated in Watts. The solar generated electricity, however, is estimated in Watt-hours, since it's not power but energy.

Electrical devices and appliances (also known as 'loads') are rated in Watts.

Batteries are rated in amp-hours. If you need to recalculate the capacity of a battery in watt-hours, you should multiply the rated amp-hours **C** by the battery voltage **V**:

E (in Wh) = C (in Ah) x V (in V)

Important:

Do not mistake the nominal voltage of a solar panel with the open circuit voltage (**V_{oc}**). **V_{oc}** is always higher.

For a 12V solar panel, the nominal voltage is 12V, while the **V_{oc}** is 17-18V.

For a 24V solar panel, the nominal voltage is 24V, while the **V_{oc}** is 34-36V.

Typically, smaller solar panels are 12V, while larger are 24V. Also, lower-wattage solar panels (below 150 W_p) are usually 12V, while higher wattage panels (above 150 W_p) are usually 24V.

Each solar array can be further upgraded (expanded) with more solar panels. You should, however, consider the consequences of mixing different solar panels.

Parallel connection of solar panels is less tolerant to shade. Parallel connection, however, requires using thicker and larger wire. Such a wire is always harder to work with – it does not bend easily around corners and more laborious to crimp. It is also more expensive than thinner wire.

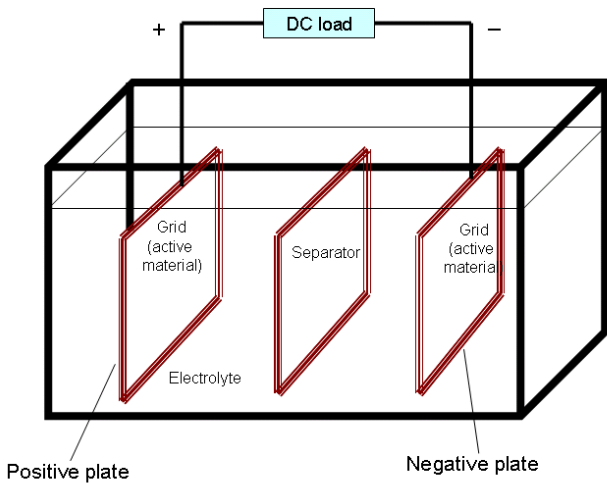
Batteries

Why does a solar power system need a battery?

When the sun is shining, solar panels are generating electricity but they cannot store it. On the other hand, you use many of your appliances not only in the daytime, but also at night or when it's cloudy. The most popular solution to this problem is to use batteries.

What are solar batteries and how do they work?

Batteries are electrochemical cells connected in series. An electrochemical cell converts chemical energy into electrical energy, so batteries generate electricity.



As you already know, batteries generate DC power, just like solar panels. Not all batteries, however, are capable of storing solar-generated electricity. Thus, not every battery can be used as a 'solar' one.

Starting (also known as 'cranking') lead-acid batteries are used to start engines, due to their capability of delivering

a high amount of power for a short time. They, however, show rather poor performance when used to store solar-generated electricity.

Unlike starting batteries, typical deep-cycle batteries (also known as 'domestic' or 'residential' ones) are capable of delivering a small amount of electricity over a long period.

Also, while starting batteries are immediately recharged after starting by the car alternator, deep-cycle batteries need to be recharged at a much slower rate. A 'deep cycle' means providing a fully charged battery to the solar panel system, discharge it down to the recommended 50% (for lead-acid batteries), and then fully recharge it.

Every deep-cycle battery has a rated number of charge/recharge cycles it can withstand before it has to be replaced. A deep-cycle lead-acid battery can withstand between 500 and 1,000 cycles, with a typical value 700-800 ones.

What kinds of batteries are used in solar power systems?

There are two main battery types used in solar panel systems today – lead-acid and lithium.

Lead-acid batteries come in a variety of configurations – flooded, gelled, and sealed AGM (Absorbed Glass Mat, also known as 'dry cells'). Although all these are based on the same chemistry, they differ in the construction of their plates.

Flooded lead-acid batteries have removable caps and need regular maintenance. Gelled and AGM batteries are

sealed, maintenance-free and are also known as 'valve-regulated lead-acid' (VRLA) batteries.

Starting automotive batteries (also known as SLI, for 'starting, lighting, ignition') are not recommended for solar panel systems. They are excellent for engine starters where very high current is needed within a short period. However, they are not 'deep-cycle' ones, since they are not intended for frequent and deep discharges. If used in an off-grid solar system, where typical discharges are down to 50%, an SLI battery is expected to fail after up to 100 charge/discharge cycles. Such a battery, however, can withstand thousands of cycles when used for providing instant power and not allowed to be discharged by more than 5%.

Here is how you can discover the state of charge by a 12V lead-acid battery by a voltmeter:

- A voltage reading of 12.6-12.65V – the battery is fully charged.
- A voltage reading of 12.2-12.25V – the battery is half-charged.
- A voltage reading below 12V – the battery is discharged.

A voltage of 12V or lower can damage the battery. A lead-acid battery should not be left discharged for more than a week since the sulfation of the electrodes becomes irreversible.

Every battery, even when left unused, is prone to self-discharge. The warmer the weather, the higher the rate of self-discharge.

A well-maintained lead-acid battery can stand up to 5 years and more.

There are two main types of lead-acid batteries – flooded (wet) and sealed.

Flooded batteries have a liquid electrolyte. They need to be vented during charging and require maintenance in terms of regularly adding distilled water to the cells. Wet lead-acid batteries are widely used in residential solar power systems. They are the least expensive and last 5-7 years if maintained properly. Wet batteries are offered in a wide range of sizes. As their electrolyte can easily be spilled in case of tipping over or fast moving, wet lead-acid batteries are not suitable for mobile solar applications.

Sealed lead-acid batteries do not have a liquid electrolyte. Sealed batteries are gel cell batteries and AGM batteries. Unlike wet batteries, the cells of sealed batteries cannot be accessed, so they do not need maintenance. Although they typically do not require venting, they still have vents to let the hydrogen escape when necessary.

In sealed lead-acid batteries (AGM and gel), the electrolyte is not in a liquid form, so the battery can be placed in any orientation without any hazard of spilling the electrolyte and causing damages. Sealed batteries last shorter than flooded batteries. Gel batteries are more expensive than AGM ones, but they are capable of withstanding low temperatures. Like AGM batteries, they do not require maintenance but are more intolerable to overcharging.

AGM batteries are an excellent choice for mobile solar panel systems since they are:

- Fully maintenance free.
- Safe – there is no hazard of spilling the electrolyte or breaking, or tipping the battery.

- Resistant to mechanical shocks and vibrations.
- Tolerant to freezing – temperatures below 4 degrees C/F or lower.
- Easy to mount and move.

Unlike flooded lead-acid batteries, AGM ones can be stored and operated in a place with poor ventilation. Another benefit is that they can be recharged by a standard automotive battery charger.

A 'lithium battery' is quite a common term. For solar panel systems, a 'lithium' battery means a 'lithium-iron-phosphate' battery. Lithium-ion batteries have a nominal voltage of 3.2V per cell. Lead-acid batteries, whether flooded, gelled or AGM, have a nominal voltage of 2.1V per cell. Thus, 4 lithium cells connected in series give a total voltage of 12.8V, while 6 lead-acid cells connected in series give a 12.6V.

Apart from a charge controller to monitor the voltage, a lithium battery also needs a battery monitor to track the current. Unlike lead-acid batteries, you cannot estimate the state of charge of a lithium battery only by its voltage.

Although much more expensive (5 times the cost of flooded batteries), lithium batteries have the following benefits:

- Fully maintenance-free.
- Can be stored and operated at any place.
- The most extended lifespan – up to 10,000 cycles.
- Tolerant to overheating.
- The safest – no caustic or poisonous electrolyte and no hazardous gasses vented.

- Can directly replace lead-acid batteries due to the similar charging voltages.
- Do not need to be fully charged before being discharged the next day. Also, lithium batteries do not need to get a full charge regularly.
- Can get fully charged within a much shorter time than lead-acid batteries.
- Can get a full discharge without any adverse consequences.

Lithium batteries need a Battery Management System (BMS) to track whether the individual battery cells do not over-discharge. The BMS ensures the safe operation of a lithium battery by monitoring and protecting the battery cells against overcurrent, overvoltage, or extreme temperatures.

If the voltage of a single cell of a lithium battery drops below 2.5V or rises above 4.2V, the cell will get damaged. The BMS system also balances the charge between the cells if one or more cells are fully charged (and there is a risk of overcharging them), while some other cells are not yet.

How to prolong the life of your lead-acid solar battery?

For residential solar power systems, flooded batteries are reported to be the best value for your money provided that you maintain and use them properly. 'Proper maintenance' means regularly charging them, adding distilled water (you should check the water level once per month), and keeping the terminals clean.

Here is in brief what reduces the lifespan of lead-acid solar batteries:

- Deep discharges down to more than 80% of the rated capacity. In contrast, discharging the battery down to as less as 30-40% will significantly prolong its lifespan.
- Regular overcharging causes the water in the electrolyte to evaporate and plates to get corroded.
- Regular undercharging leads to gradual plate sulfation. Thus part of the electrode becomes 'sulfuric' rather than lead, which decreases the available battery capacity.
- Adding anything else but distilled water to the electrolyte results in adverse chemical reactions preventing the normal battery operation.

Here is how you can have a lead-acid solar battery lasting more than 5 years:

- Always buy a new solar battery, never secondhand.
- Always keep the battery fully charged, even when it is not in use. Leaving your battery in a discharged state ('flat battery') quickly results in sulfation which is an irreversible process. When your RV is in the

garage, you should disconnect the battery and store it under room temperature.

- Never allow your lead-acid solar battery to drop below 50% state of charge. Every discharge down to more than 80% reduces the capacity and shortens the battery lifespan.
- Do not leave a solar battery on charge for a long time.
- Check the state of charge periodically by a multi-meter. Here is the relation between the battery voltage and state of charge:

State of Charge	12 Volt battery	Volts per Cell
Under charge	12.9-14.4	2.15-2.4
100%	12.7	2.12
90%	12.5	2.08
80%	12.42	2.07
70%	12.32	2.05
60%	12.20	2.03
50%	12.06	2.01
40%	11.9	1.98
30%	11.75	1.96
20%	11.58	1.93
10%	11.31	1.89
0	10.5	1.75

- Even low-consumption devices can drain your battery if left connected for a long time
- Faster discharges reduce solar battery capacity. For this reason, you should avoid running many devices simultaneously.
- A battery needs a charger providing charging current which is at least 1/10 of the battery capacity. So, a

100Ah battery should be charged with at least 10 amps charger.

- The self-discharge rate of any lead-acid battery is about 5% per month.
- Regarding solar batteries, you usually get for what you pay. The more expensive a solar battery, the longer its lifespan.

How many amp-hours of capacity do you need?

With too much capacity, there is a risk of not fully charging the solar battery, which leads to sulfation. With less capacity than needed, a battery of too small capacity will not be capable of using the full daily Peak Sun Hours (PSH) as it will get fully charged too fast and you might turn out to have invested a lot more in your solar array than needed.

For your RV, caravan, camper, or boat, a leisure battery of how many amp-hours to choose depends on how much electricity you use while camping. After selecting your leisure battery, you have to determine how many watts of solar panels you need to charge the battery. Then you have to select your charge controller and your inverter, should you need AC power. Finally, you should perform the necessary calculations about the wiring, connectors, and fuses.

What is more, with less solar-generated electricity the intended appliances in your household or RV will not be able to receive power for a long enough period.

Here we come to battery sizing. Sizing the battery in a solar panel system is essential. On the one hand, if a solar

battery is oversized, it might not be capable of being kept fully charged, which leads to plate sulfation. On the other hand, if a solar battery is undersized, it might not be able to power your devices and appliances long enough.

You can discover more about the batteries in our free definitive guide to solar batteries here:

<https://solarpanelsvenue.com/solar-batteries/>

Charge controllers

Your solar battery needs to be protected from the solar panels.

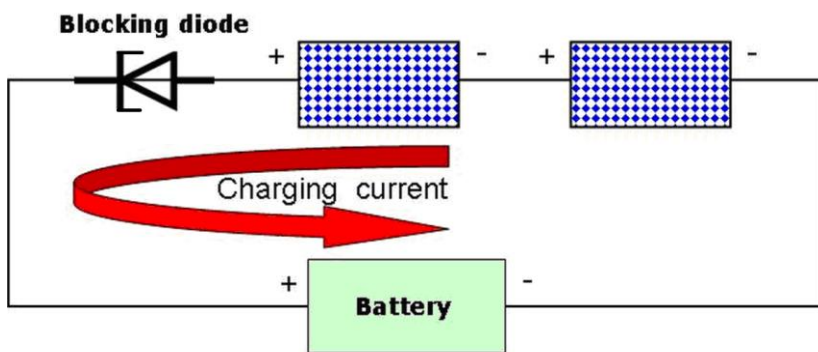
When you connect a battery directly to the solar array, you should consider the following risks:

- 1) If the solar-generated electricity is not regulated, the battery can get overcharged.
- 2) At night, when the sun is not shining, the electricity stored can flow back into the solar panels, and the battery can get discharged.

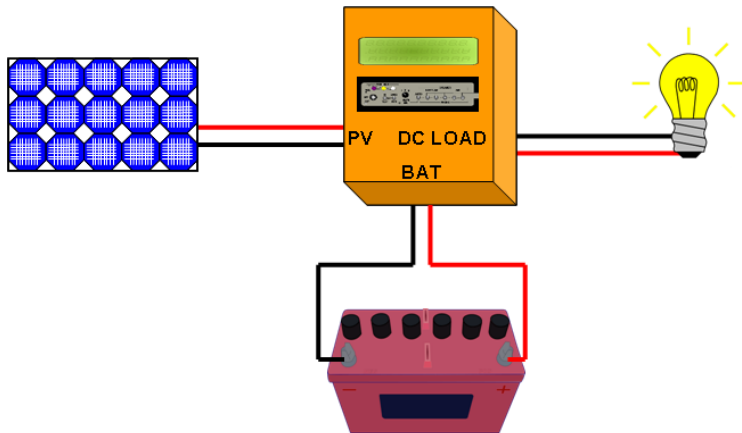
These two conditions can reduce battery lifespan dramatically.

To prevent 1) from happening, you need a charge regulator. It limits the current flowing from the panels to the battery in daytime down to a reasonable level.

To prevent 2) from happening, you need a blocking diode:



A charge controller is a device comprising both a regulator and blocking diodes to protect the battery from overcharging during the day and from discharging at night, and also to match the solar array's voltage to the battery voltage.



More sophisticated charge controllers are also capable of monitoring the battery voltage, thus making it operate at maximum performance.

Important:

Do you always need a charge controller?

If the total installed power of your solar array is less than 1/10 of the battery capacity, you do not need a charge controller. For example, for a battery of 100Ah, you don't need a charge controller if your installed solar power is less than 10Wp. Otherwise, you should install a charge controller to prevent the battery from overcharging and over-discharging.

Here is a summary of the charge controller's main features:

- Preventing the battery from getting overcharged by the solar panels.
- Preventing the current from returning from the battery to the panels.
- Preventing the battery from getting discharged by disconnecting the loads connected to the battery.

- Indicating whether any loads are connected to the battery.
- Indicating whether the solar array is connected.
- Improving battery performance and increasing system efficiency.

To cut a long story short, the charge controller is the battery manager of a solar panel system.

Here are some additional features of charge controllers:

- Indicate the incoming amps,
- Monitor battery temperature to prevent the battery from overheating, and
- Reduce the solar array total voltage down to the battery voltage – 6V, 12V, 24V, or 48V. The latter two are not typical for mobile solar systems.

There are two main types of charge controllers – Pulse Width Modulation (PWM) and Maximum Power Point Tracking (MPPT) ones. MPPT controllers perform much better than PWM ones, but they are also more expensive.

PWM charge controllers can be only used with lead-acid batteries. You can never use a PWM controller with a lithium battery as it requires a special battery management system (BMS) and a specific charge profile that cannot be provided by any PWM controller.

PWM controllers are only recommended for small solar power systems. With a PWM charge controller, the voltage of the solar array must be equal to the voltage of the battery bank. On the opposite, MPPT controllers are usually provided with a step-down feature enabling you to connect a 21V or 24V solar panel to a 12V battery.

The primary benefit of MPPT charge controllers is that they are capable of squeezing the maximum solar power from the solar array. This is possible because an MPPT controller operates at the most efficient combination of voltage and current, known as 'Maximum Power Point' (MPP). Squeezing the maximum possible solar-generated power means proving the maximum charging current to the battery.

An MPPT charge controller is an excellent solution in colder climates and when you regularly discharge your batteries. MPPT charge controllers are about 2.5 times more expensive than PWM ones.

Which charge controller is better?

Selecting the 'right' type of charge controller does not mean to decide which charge controller technology is better – PWM or MPPT. It means instead to estimate which type of these would be more suitable for your solar system. The idea is not only to avoid building a system that will not perform well but also save money on buying a costly device that you don't need.

Above all, however, you should remember never to use a charge controller that is not compatible with your battery type.

Sizing and installing your charge controller

If your charge controller is not sized correctly, this can result not only in drastically shortening the battery lifespan but also in damaging both the battery and the controller itself.

The main task when sizing the charge controller is to calculate the solar array's voltage and current and use the calculated values to select the matching model of a controller.

Above all, however, you should determine what type of controller would be optimal for your system. Thus you have neither to pay more than you need nor to buy a controller that can make your system underperform or even damage any of the other components.

When sizing the charge controller, a safety factor of 1.25 should be used. By this factor, the maximum input voltage and maximum input current of the controller are additionally increased by 25%, so that the controller would be able to meet some sporadic increases in voltage and current due to high temperature or light reflection.

The low-voltage disconnect (LVD) feature of the charge controller prevents the battery from over-discharging by disconnecting all the loads connected to it should the battery voltage falls below a certain level. Accordingly, the loads are to be reconnected to the battery when the latter reaches a certain high enough voltage. Most modern inverters and some electrical appliances (e.g., DC fridges) have a built-in LVD feature. If you use DC devices in your RV, your charge controller should be LVD-capable.

Here is how to install your charge controller:

- 1) Mount the controller.

- 2) Install the battery wires. Apart from observing the polarity, you should fuse the positive wire.
- 3) Set the battery type on the charge controller (Flooded lead-acid, AGM, Gelled, Li-Ion).
- 4) Connect the battery to the battery wires.
- 5) Connect the solar panel cables to the controller.
- 6) Connect the solar panels to the cables. If you are not sure about the correct polarity, use a voltmeter.

You can discover more about PWM and MPPT charge controllers in our free definitive guide to solar charge controllers here:

<https://solarpanelsvenue.com/mppt-and-pwm-charge-controllers-in-off-grid-solar-power-systems/>

Inverters

Grid-tied solar inverters

Every grid-tied system must have an inverter. A grid-tied inverter converts the DC voltage from the solar array into AC voltage that can be either used right away or exported to the utility grid. As a rule, grid-tied inverters without battery backup are highly efficient and straightforward to install.

A grid-tied inverter only operates when the utility is on. When the utility goes down, the grid-tied inverter turns off immediately.

Most grid-tied inverters are based on Maximum Power Point Tracking (MPPT) – a feature ‘squeezing’ the maximum possible power from the solar array.

The inverter is connected to the utility grid either directly or via the building’s electrical system. In a direct connection, the generated AC electricity is sent towards the utility grid. When the inverter is connected to the utility grid via the building’s system, the AC power generated by the PV system is first used by your appliances, and what remains unused, is directed to the utility grid.

A grid-tied inverter must strictly comply with the utility grid’s requirements and regulations. For example, grid-tied inverters must generate an AC voltage of a strictly sinusoidal form. One of the main features of a grid-tied inverter is that it stops operating in case of a grid failure. Thus technicians doing any repair works on utility network are prevented from getting an electric shock. This is called ‘anti-islanding protection.’

The solar inverter can be either an individual block located outside the solar array or physically integrated into the solar panels.

Since every grid-tied inverter stops working during the grid outage, you do not have any electricity during such an outage as well.

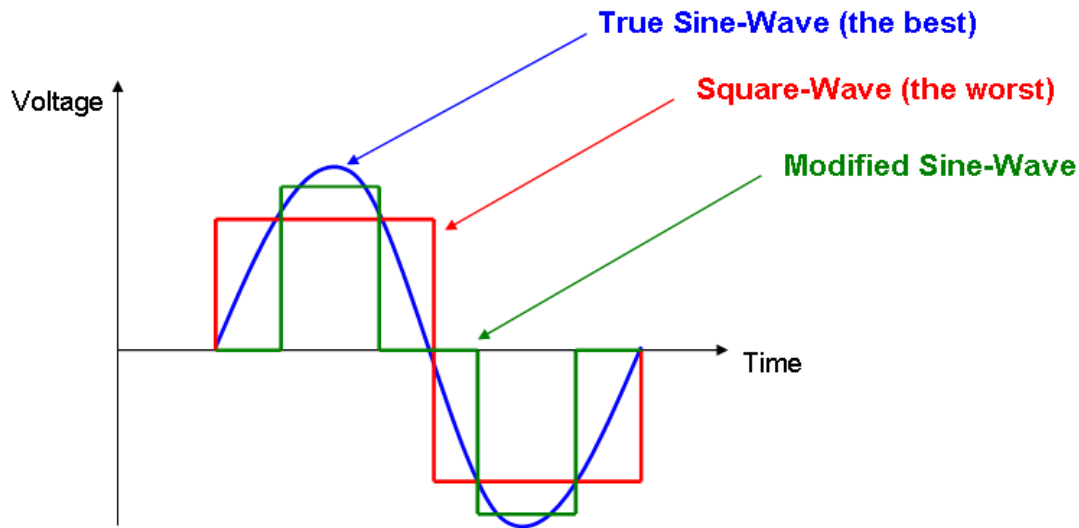
Off-grid inverters

Inverters in off-grid solar power systems differ from grid-tied inverters. An off-grid inverter takes DC power from the battery and converts it to AC power used by your AC appliances (such as TV, microwave oven, laptop, chargers, etc.).

An off-grid solar system might not contain an inverter if only DC loads are to be powered. Since off-grid systems are disconnected from the utility grid, off-grid inverters do not need to meet the utility grid requirements and regulations.

Grid-tied and off-grid photovoltaic systems use different kinds of inverters. Since inverters for off-grid systems are disconnected from the grid, they do not need anti-islanding protection.

There are three main types of off-grid inverters according to the form of the output AC voltage they produce – True Sine-Wave, Modified Sine-Wave, and Square-Wave ones. Square-wave inverters were the first to appear on the market. They, however, are not a good choice for most of your office and household appliances.



A True Sine-Wave inverter can produce AC voltage identical to the AC voltage supplied to your house outlets by the local electrical company.

A Modified Sine-Wave inverter produces an inferior quality waveform. It's not a clean and stable sinusoid but rather a stair-stepped AC signal. These inverters cost less than True Sine-Wave ones. The problem, however, is that some household appliances (such as TV and audio equipment, digital clocks, computers, and printers, as well as some distinctive brands of small devices like toothbrushes, razors, coffee-makers, etc.) do not operate with Modified Sine-Wave inverters.

Grid-tied inverters are always True Sine-Wave since they must strictly comply with the standard requirements defined for the frequency and waveform.

Selecting the inverter for your solar power system

The general rule for inverter selection is that the inverter wattage must be higher than the total watts of the appliances you run together.

If the inverter's output power is less than the total power of the devices you are trying to run, the inverter will turn off.

Important:

The inverter's rated wattage is only related to the appliances you are to use and NOT to the solar array's installed power.

However, the output AC current provided by the inverter at the maximum load, that is, all the appliances you use together, should match the discharging current rate of the battery, recommended by the battery manufacturer. Otherwise, the battery lifespan would be reduced severely.

You can find more information on how these two currents are related and how to select the battery by considering this, in our book:

Off Grid And Mobile Solar Power For Everyone: Your Smart Solar Guide [Kindle and Paperback Edition] ASIN: B07B296DGQ

<https://www.amazon.com/Grid-Mobile-Solar-Power-Everyone-ebook/dp/B07B296DGQ/>

Or, if you are an advanced solar enthusiast, we recommend you:

The Ultimate Solar Power Design Guide: Less Theory More Practice [Kindle and Paperback Edition]

<http://www.amazon.com/Ultimate-Solar-Power-Design-Guide-ebook/dp/B0102RCNOG/>

Other solar system components

Other solar system components, also known as 'Balance of System (BoS) equipment,' include all the mounting and wiring equipment necessary to integrate the solar system into the infrastructure of your house or motorhome. Such additional equipment includes array circuit wiring, fusing, inverter AC and DC disconnects, overcurrent protection and ground-fault protection.

As a rule, fuses, connectors, surge arrestors, and circuit breakers are mounted in one or more junction boxes that are usually located on the periphery of the solar panels and are designed to withstand environmental temperatures and ultraviolet radiation.

Utility meters are typical for grid-tied solar systems. Utility metering means selling the excess energy back to the local utility company usually at the same rate you are charged, while you are drawing energy from the utility.

Battery monitors are used in off-grid systems. They measure battery capacity and report how much energy is being used. Thus, you get informed whether the battery bank has enough capacity to sustain your needs.

Fuses are used to prevent too high currents flowing along other solar strings connected in parallel. The overcurrent protection is used to protect against voltages induced in the solar system internally. Such induced voltages caused by nearby lightning strikes can damage the solar equipment.

Surge protectors (arrestors) are used to direct the currents arising upon lightning strikes towards the ground since the photovoltaic array, blocking and bypass diodes,

and inverter need protection from high currents and voltages.

Disconnects are used for disconnecting the inverter, the loads, and the utility meter from the solar panels. The solar array cannot be switched off – it either produces power in the daytime when the sun is up or generates no power at night. Disconnects can be either DC or AC. A DC disconnect disconnects the link between the solar array and the inverter. AC disconnects are used to separate the household inverter and the loads connected to the solar generator from the utility grid.

Junction boxes, also known as '**combiner boxes**,' are used to connect the cables that will further be connected to the inverter, where a solar array comprises a couple of strings. Junction boxes are located on the back of the solar panels and are typically located on the roof. A combiner box should be provided with double insulation and should allow laying positive and negative cables separately. Often, junction boxes might not be needed at all – for example, if the solar array is built of just a couple of solar panels.

Cables are used to connect the individual components of a solar system. Cable is a wire put inside a conduit or a pipe for protection. There is DC cabling and AC cabling. DC cabling comprises the outdoor laid cables, and the wiring between the panels gathered in junction boxes, between the strings gathered in combiner boxes, and the connection to the inverter. AC cabling connects the inverter to the loads and the utility grid.

Why it is vital to select the right solar components

The battery is the heart of your solar panel system. Your solar project should start with evaluating how much energy you need daily. If you are not connected to any utility grid and the sunlight is not sufficient, the battery should provide you with enough electricity, so that you can run your appliances.

Thus, above all, you should start with estimating a battery of what kind and of what size you need. A battery of the wrong type can:

- Cost you too much,
- Have a too short lifespan, or
- Be a hazard for you and your family.

Also, an undersized battery will not be able to cover your electricity needs, while an oversized battery would mean a white elephant at home.

Next, you have to estimate how many solar panels you need to charge your battery. Above all, you have limited space and a limited budget. Your solar array should fit both of these. Next, the solar-generated power has to be enough to charge your battery. So, it's important what kind of solar panels you are going to choose so that the solar array should neither be oversized nor undersized. In all cases, the solar array size should match the battery size.

Also, you need a battery manager, that is, a charge controller. Choosing the wrong type and size of the charge controller will quickly damage the battery whose price can reach up to 60% of the price of the solar system!

Also, to power your AC appliances, you need an inverter. If you select an inverter of the wrong type and size, at best your devices are not going to operate. At worst, they can get damaged.

Finally, as you know, there is additional equipment, such as cables, fuses, and protectors. Selecting and sizing them is vital, as any miscalculation might result in the worst of all – damaging your solar system and setting your house or RV on fire.

In our book, '***The New Simple And Practical Solar Component Guide***' [available in Kindle, Paperback and Audio Edition], you can get all the info you need to select the components for your home or mobile solar power system properly.

You can find it here:

<http://www.amazon.com/Simple-Practical-Solar-Component-Guide-ebook/dp/B00TR7IJP0>

Also, our books '***Off Grid And Mobile Solar Power For Everyone: Your Smart Solar Guide***' [Kindle and Paperback Edition] and '***The Ultimate Solar Power Design Guide: Less Theory More Practice***' [Kindle and Paperback Edition] will reveal you how to size the components of your solar power system, residential or mobile, by yourself, fast and easy, thus ensuring both optimal performance and quick return of your investment.

The first book is for beginners to intermediate, while the second is targeted to advanced solar power users.

You can find them here:

Off Grid And Mobile Solar Power For Everyone: Your Smart Solar Guide [Kindle and Paperback Edition]
ASIN: B07B296DGQ

<https://www.amazon.com/Grid-Mobile-Solar-Power-Everyone-ebook/dp/B07B296DGQ/>

The Ultimate Solar Power Design Guide: Less Theory More Practice [Kindle and Paperback Edition]

<http://www.amazon.com/Ultimate-Solar-Power-Design-Guide-ebook/dp/B0102RCNOG/>

Also, selecting the solar system components goes hand in hand with system sizing.

A solar power system should be neither oversized nor undersized. An oversized system means a too big system you don't need. An undersized system cannot meet your daily energy needs. Both are a waste of time and money, and that might be the end of your solar project.

Read on to know how solar components are joined together in solar power systems!

Solar electric systems

There are two basic types of photovoltaic systems:

- Grid-tied
- Off-grid.

The main difference between these two types of PV systems is whether they are connected to the grid or not.

'The grid' is the distribution system used by public utility companies to deliver electricity to business and residential consumers. It includes the countrywide network of electrical towers, poles, and wires.

This network delivers electricity from coal burning, nuclear, or water-generated power plants to commercial buildings and residential houses.

Grid-tied solar power systems

Grid-tied (on-grid, grid-direct, grid-connected) photovoltaic systems:

- Produce electricity.
- Use electricity from the grid
- Export solar-generated electricity to the grid.

Important:

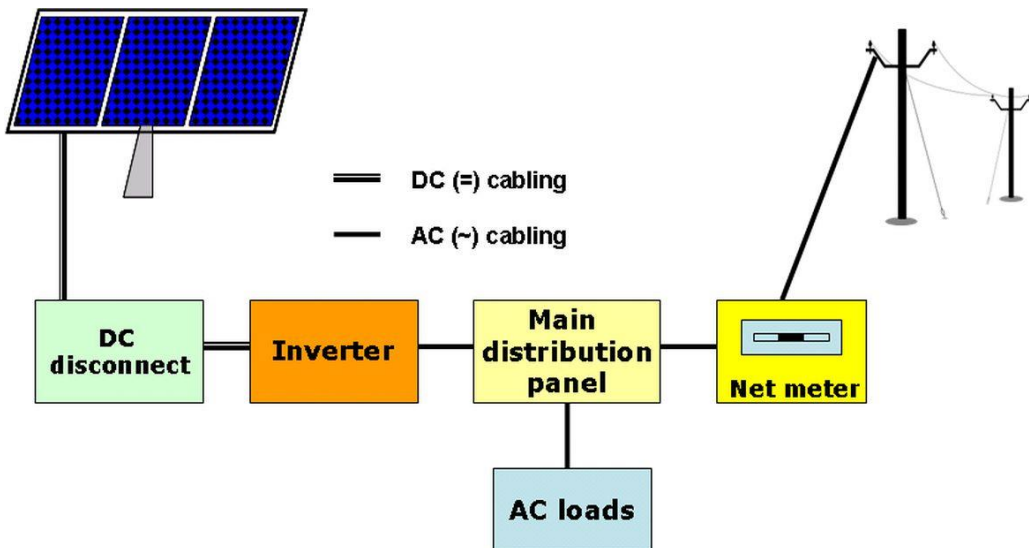
Grid-tied photovoltaic systems:

- Can be a source of significant saving from electricity bills.
- Satisfy user's own energy needs.
- Add value to the building.
- Protect the environment.
- Provide energy backup (for grid-tied systems with power backup).

Grid-tied systems can be designed with or without battery backup.

Grid-tied systems without battery backup are built in regions where power outages happen rarely.

Here are the main components of a grid-tied system without battery backup:



A simplified view of a grid-tied solar system without power backup

- Photovoltaic array - generates DC electricity from sunlight.
- DC disconnect – disconnects the solar array from the rest of the system.
- Inverter – converts DC electricity into AC electricity.
- Main distribution panel – the connection point between home electrical network and utility grid.
- AC loads – the devices operating on AC electricity.
- Net meter – measures the electricity imported from and exported to the utility grid.

During a power outage, every grid-tied solar system shuts down until the utility is up again. Thus technicians that might be doing certain repair works on the utility infrastructure are prevented from getting an electric shock.

Grid-tied systems with battery backup are preferred in areas where blackouts occur more often. Also, they are installed where power outage is not an option even for short periods – for example, hospitals or communications.

If you have a grid-tied system, you use the solar-generated electricity in the daytime, while the sun is shining. After the sun goes down, your home network automatically switches to using the electricity from the grid. Thus, you have to pay the utility for the electricity provided during night periods only.

You use electricity from the grid when electricity generated by your PV system does not fully cover your household electrical consumption.

Also, if your photovoltaic generator produces more electricity than you consume, the 'excess' of electrical energy is exported to the grid, for which you get paid.

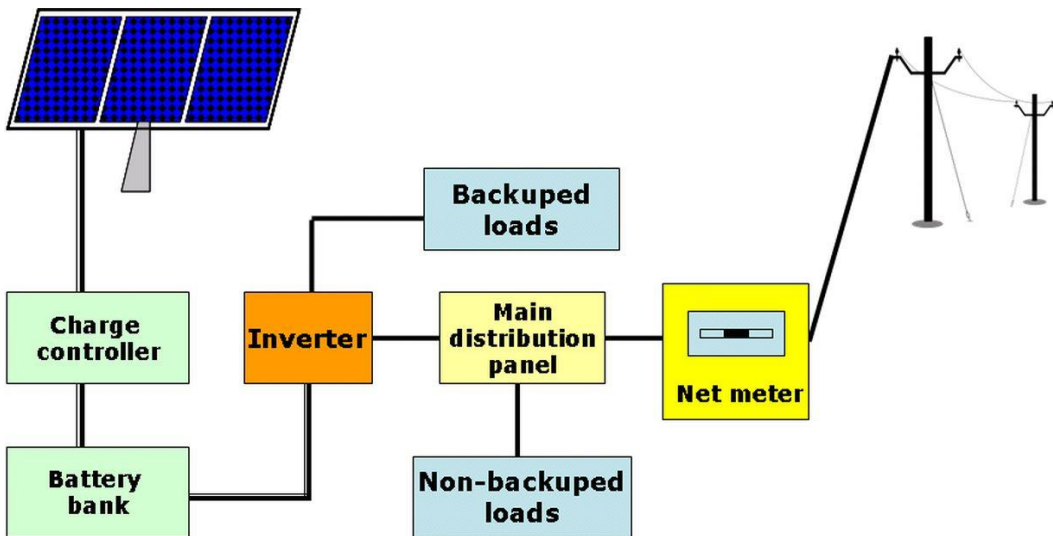
Grid-tied systems are less expensive and require less maintenance than off-grid systems.

A distinct disadvantage is that conventional grid-tied systems (without battery backup) shut down in case of a power outage. A grid-tied system with battery backup can avoid this.

Grid-tied photovoltaic systems with battery backup are similar to conventional grid-tied systems except in their ability to provide power backup for critical loads in the event of a grid power outage.

The solar array generates power while the sun is shining, thus reducing electrical consumption from the grid. If the solar-generated power is not enough to cover the user's needs, the excess electricity is provided by the utility. If the PV system generates more power than needed, the excess solar electricity is exported to the grid.

A grid-tied system with battery backup comprises the following components:



A simplified view of a grid-tied solar system with power backup

- Photovoltaic array – generates DC electricity from sunlight.
- Charge controller – regulates battery charging, thus increasing battery lifespan.
- Battery bank – stores the electricity generated by the PV array.
- Inverter – converts DC electricity into AC electricity.
- Main distribution panel – the connection point between home electrical network and utility grid.
- Backup loads – all the AC and DC devices provided with power backup.
- Non-backup loads – those electrical devices which are not provided with power backup.
- Net meter – measures the electricity imported from and exported to the utility grid.

The solar array charges the battery bank via a charge controller. The charge controller regulates the battery charging when the grid fails.

The DC electricity stored in the battery is converted to AC electricity by a battery-based inverter, and then it is delivered to the loads.

Such an inverter:

- Converts DC energy stored in the battery to AC power,
- Manages the battery charge via through an integrated charger, and
- Exports the surplus of energy to the grid thus preventing the battery bank from overcharging when the grid is available.

The inverter in a grid-tied system with battery backup is required by the standard to have 'anti-islanding protection.' Such protection ensures that the inverter is disconnected from the grid during the grid outages, while the solar system is powering only backup loads. During grid outage, backup loads are provided with power supply only until there is enough electricity stored in the battery bank.

Important:

The apparent advantage of grid-tied systems with battery backup is the ability to provide a backup power supply for critical loads.

The drawback, however, is increased costs for implementation and maintenance, as a result of adding a battery bank and charge controller.

The cost of the battery bank is usually within 20% to 50% of the overall system price. Batteries are to be replaced every 5 years and, for 'wet' lead-acid batteries, the electrolyte should be checked regularly.

Grid-tied systems summarized

	Grid-tied without battery backup	Grid-tied with battery backup
Similarities	Connection to utility grid (i.e. local electrical company)	
Advantages	- Less expensive - Do not require any maintenance	- Your building is not in outage if utility fails
Disadvantages	- Stop operating in case of a power outage if utility fails	- More expensive (more components to buy/install) - Require more maintenance (as a rule batteries need certain maintenance)

When do you need a grid-tied system?

Important:

A grid-tied photovoltaic system without power backup is a right solution for you...

...if you are connected to the grid...

...and also if:

- You want to reduce your monthly electricity bill.
- You wish to add value to your home.
- You want to avoid any future increases in the price of electricity.
- You need to increase your power security.
- You are passionate about renewable energy from photovoltaics.

Important:

A grid-tied photovoltaic system with power backup is the right solution for you if:

- You are a business owner who wants to ensure 24/7 backup and availability of the most critical business processes.
- You want to reduce your monthly electricity bill.
- You wish to add value to your home.
- You want to avoid any future increases in the price of electricity.
- You need to increase your power security.
- You are passionate about renewable energy from photovoltaics.

Sources:

1. Clean Energy Council, Australia. 2002. Grid-Connected PV Systems – System Design Guidelines for Accredited Designers, Issue 3 July 2007, November 2009 Update.
2. Clean Energy Council, Australia. 2008. Electricity from the Sun – Solar PV systems explained, 3rd Edition, June 2008

Off-grid solar power systems

Off-grid systems are not connected to a utility grid. They are preferred where getting connected to a utility infrastructure is too expensive.

Off-grid systems are more expensive than grid-tied systems because they have batteries.

There are two types of off-grid systems – stand-alone and hybrid.

Stand-alone systems are purely photovoltaic. They only rely on solar energy to generate power and are not backed by an additional power source.

Hybrid systems are modified stand-alone systems provided with an additional power generator operating by wind, combustive fuel, etc.

Important:

Here is what to remember above all on stand-alone systems:

- Having implemented power efficiency is of utmost importance.
- Stand-alone systems cannot provide you with unlimited access to electricity.
- Stand-alone systems can take advantage of DC loads (lighting, refrigeration, electronics).

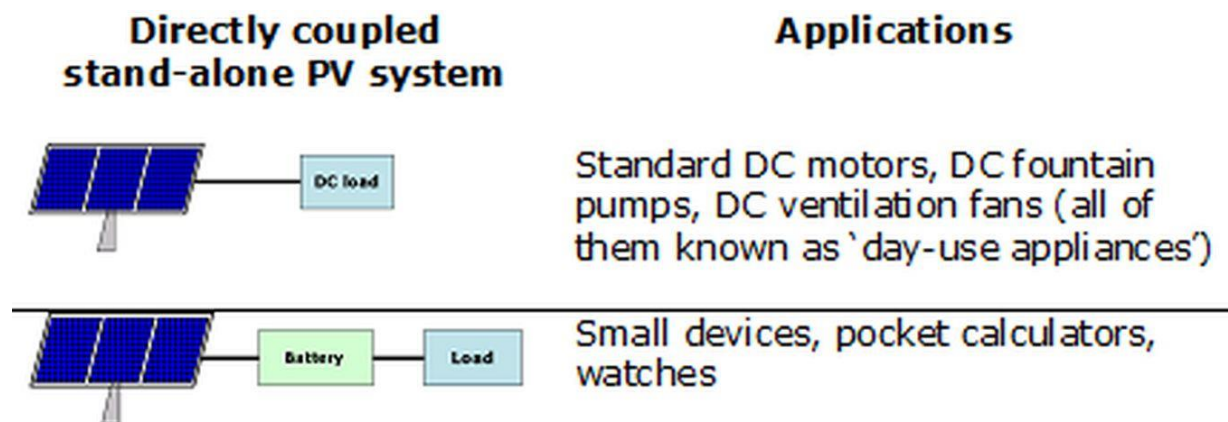
Stand-alone systems are typically supplied with battery storage because electricity is also needed when the sunlight is not enough – in the evening or at night, or during long periods of limited sunlight, such as in winter or on cloudy/rainy days.

If the daily electricity needs are too high, a PV system relying only on solar energy is not suitable. Otherwise, a too large and expensive battery bank is needed, making the purely photovoltaic option far from cost-effective.

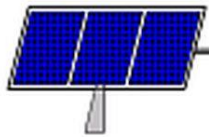
In such a situation, a hybrid off-grid system is a preferred solution. Hybrid systems have an additional power source supplementing the solar battery.

Directly coupled stand-alone PV systems are the simplest and the most used ones, as they:

- Only comprise a PV array, a battery (optional) and loads, and
- Are used in wide range of applications.



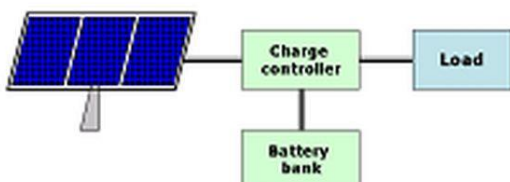
Here are some more configurations of stand-alone systems:



Inverter

AC load

Electricity is only needed while the sun is shining – cooling fans, pumping & irrigation equipment, some small devices (flashlights, clocks, shavers, etc.)



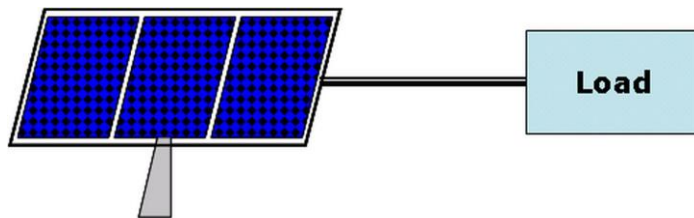
Charge controller

Battery bank

The system is provided with battery storage, usually combined with a charge controller, so that the electricity produced can be used later.

In a typical stand-alone system, the solar-generated electricity is used for charging batteries through a charge controller.

A charge controller, however, as well as the battery bank, might not be needed. An inverter might not be needed either. There are stand-alone solar systems where a DC load is connected directly to the solar array – like in pump stations, for example:



If you want your solar array to power AC loads, you need an inverter.

Inverters in stand-alone PV systems are different from inverters in grid-tied systems, although they do the same – convert DC into AC electricity.

Important:

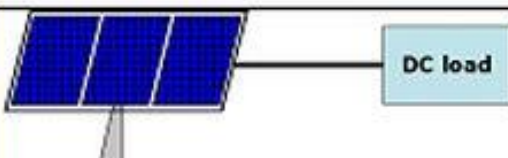
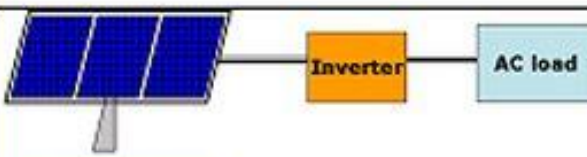
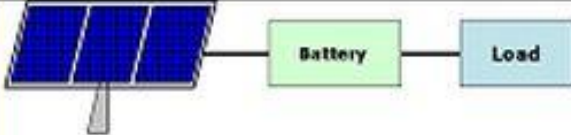
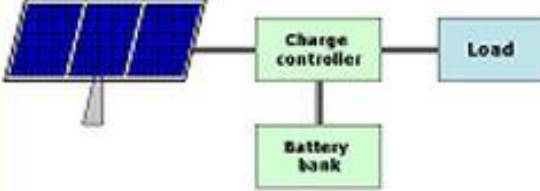
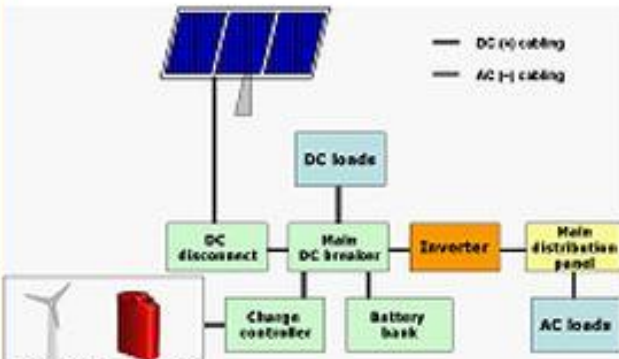
An off-grid inverter and a grid-tied inverter cannot be used interchangeably!

In stand-alone systems, it is vital that the solar-generated electricity should be enough to meet the energy needs of all the appliances powered by the PV system.

Stand-alone systems are usually built in rural areas where you have more options for installing solar panels. Usually, solar systems in rural areas are located on the ground rather than on the roof.

Stand-alone systems are supposed to perform well all the year round. In winter the sun is located lower in the sky and nearer the horizon than in summer. So in winter, the solar array orientation should be tilted at a higher angle which is easier to achieve with a solar array mounted on the ground rather than on a roof.

Off-grid systems summarized

Off-grid system subtype	Applications
	Standard DC motors, DC fountain pumps, DC ventilation fans (all of them known as 'day-use appliances')
	AC motors, AC pumps
	Small devices, pocket calculators, watches
	Mobile applications, telecommunications, medical cooling, bus-station lighting, small solar home systems
 <p>Legend: — DC (+) cabling — AC (+) cabling</p>	Hybrid systems: in houses, schools, hospitals located in remote areas, often in combination with additional power source – wind turbine or diesel generator.

Off-grid stand-alone photovoltaic systems:

- Are a reliable source of power.
- Are practically unlimited in size – a stand-alone system could serve a single device or a couple of buildings with a complex electrical network.
- Can be installed almost anywhere in the world.
- Can be less expensive than paying for getting connected to the utility grid, if the utility grid connection point is located miles away.
- Can provide electricity to the most household devices.

Main applications of off-grid stand-alone PV systems

- Small solar systems for household use in developing countries.
- Schools and hospitals in developing countries.
- Cooling for medical or veterinary use.
- Solar systems for remote homes or summer villas in well-developed countries.
- Power supply for telecommunication equipment.
- Water pumps.
- Street infrastructure equipment – street lamps, bus station dashboards, parking meters, etc.
- Recreational vehicles.
- Remote meteorological stations and airports.

Limitations of off-grid stand-alone systems

- Unless your building is located too far from the utility grid, replacing the utility grid with a stand-alone PV system is not cost-effective.
- Due to solar radiation variability, a PV system does not deliver a maximum performance all the year round. In winter, it is often more cost-effective to buy a hybrid system than spend a fortune on a battery bank and rely solely on solar-generated electricity.
- The solar-generated electricity can be stored in batteries for a limited period only.
- Making your home energy efficient is a must before buying a stand-alone system.
- For stand-alone residential systems, battery banks often need a separate, well-ventilated room, as well as certain maintenance activities.

Important:

When do you need an off-grid stand-alone system?

An off-grid stand-alone system is the right solution for you if you cannot get connected to the grid...

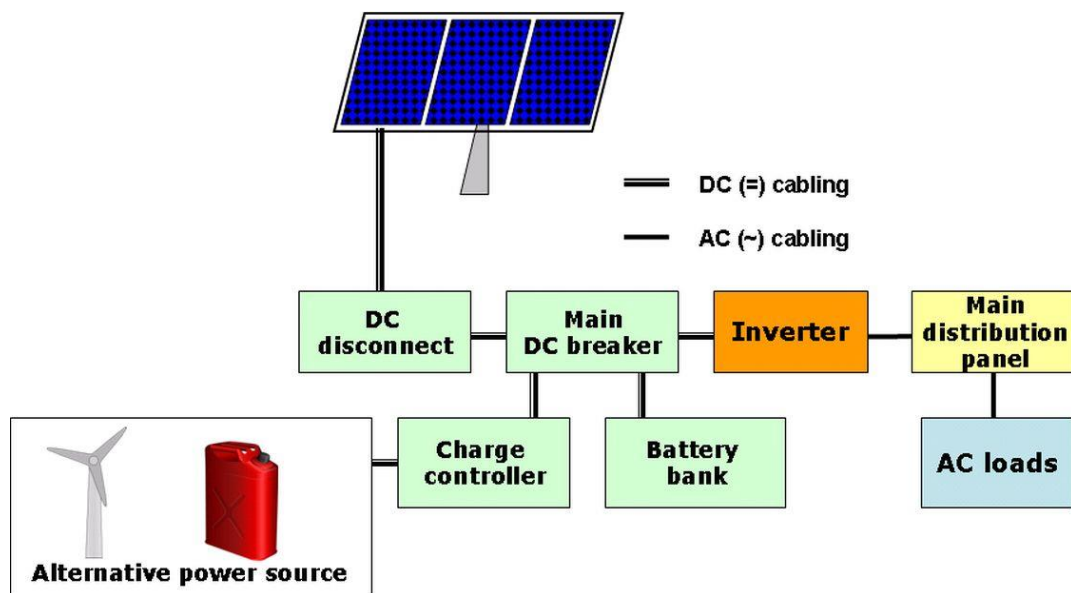
...and also if:

- You need electricity 24 hours a day.
- You are passionate about renewable energy from photovoltaics.
- You are not fond of combustible fuel generators based on diesel, propane, petrol, or natural gas.
- You do care about environmental pollution and want to preserve the Earth's fuel resources that are running out.

Hybrid systems

A backup power generator modifies a stand-alone system into a hybrid one.

A hybrid system is a combination of a photovoltaic generator and an alternative power generator – wind or fuel one. Such a generator charges the batteries upon lack of sunlight and is used either as a backup one or when the PV system alone cannot meet the specific energy needs.



Block picture of a hybrid system

In a hybrid system, the combustive fuel generator is a source of AC electricity. AC electricity is converted to DC electricity and then is stored in the battery bank.

The batteries are charged both by the PV array and by the generator. The available loads in the building draw power from the batteries.

Additional power backup sources in hybrid systems

You can do without a backup generator in a stand-alone system but at a higher cost – you have to oversize your system and choose a battery bank of a higher capacity.

Such a strategy, however, is highly impractical for two reasons:

- The initial costs of batteries are incredibly high.
- Such a system will work with maximum performance just a few months throughout the year (probably in winter), while in the rest of the time it is going to operate far below its maximum efficiency. The value of the electricity produced probably will be not enough to cover the expenses needed for the maintenance support of the battery bank.

The wind and fuel generators on the one hand, and photovoltaic generators, on the other hand, have rather few in common.

This implies the need for additional knowledge of different technologies, each one having its specifics. The minimum overlapping, however, means that the advantages of the other one can easily compensate the drawbacks of the first technology.

A wind generator appears as a suitable supplement to solar generator since in general windy periods very often coincide with periods of sunshine lacking – for example, when it's cloudy or at night.

Also, it is reported that a combination of a solar generator and a wind generator often makes the use of an additional fuel generator redundant.

Fuel generators are the most popular power backup generators. Their main advantages and disadvantages are listed below.

	Advantages	Disadvantages
Non-renewable fuel generators	<ul style="list-style-type: none">• Low initial expenses• Available on demand• Portable• Very popular	<ul style="list-style-type: none">• Relatively costly maintenance• Noise pollution• Air pollution• Low fuel to power conversion efficiency (maximum 25% but upon partial loading often goes below 10%)• A lot of the produced energy is dissipated in form of heat

Fuel generators and wind generators generate AC power. In a stand-alone system, the AC power produced by the fuel generator is used:

- By the existing AC loads, and
- By the battery charger to generate DC power used by the existing DC loads.

Important:

PV arrays and fuel generators do not produce the same kind of electricity.

PV generators are sources of DC power. In a stand-alone solar system, the DC power produced by the PV generator is used:

- By the existing DC loads

- For charging the battery bank.

Upon enough sunlight, the needed AC power is provided by the inverter converting the solar-generated DC power into AC power. If the sunlight is not sufficient, the needed AC power is provided by the fuel generator.

When compared to wind generators, fuel generators have some benefits:

- Quite an affordable price.
- Easy to launch.
- Highly portable.
- Operate independently on weather, at any time of the day.

In hybrid systems, fuel generators do not operate continuously but rather during sunless periods only.

So they have:

- More efficient use of fuel.
- A longer lifecycle.
- Lower maintenance costs.

Benefits of hybrid power systems

- **A cost-effective solution**, except for the remote spots with difficult access, where maintenance and fuel delivery can be quite expensive.
- **Low initial cost** – fuel generators have affordable prices. There is a great variety of models available at the market.
- **Increased reliability** – there is a simple rule “2 is more than 1”, which is applicable if there are two instead of one battery charging sources – a solar array and a generator.
- **Increased efficiency** – a fuel generator is used not only to charge the batteries but also to provide power to the loads operating simultaneously at a given moment. Thus, a generator could be turned on together with a large load consuming lots of power (for example, a dryer and washing machine). If such appliances are not used every day, this might be a preferred way to avoid supplying them with solar-generated power.

When do you need a hybrid power system?

Important:

A hybrid power system is recommended:

- If the daily consumption of electricity is more than 2.5 kWh.
- For regions with poor sunlight for long periods.

In these cases, a stand-alone solar system cannot meet your energy needs.

Sources:

1. Clean Energy Council, Australia. 2002. Grid-Connected PV Systems – System Design Guidelines for Accredited Designers, Issue 3 July 2007, November 2009 Update.
2. Clean Energy Council, Australia. 2008. Electricity from the Sun – Solar PV systems explained, 3rd Edition, June 2008.
3. Antony, Falk, Christian Durschner, Karl-Heinz Remmers. 2007. Photovoltaics for Professionals: Solar Electric Systems Marketing, Design and Installation, Routledge.
4. Mayfield, Ryan. 2010. Photovoltaic Design and Installation for Dummies, Wiley Publishing Inc.
5. MSE Pop, Lacho, Dimi Avram MSE (2015-02-17), The New Simple and Practical Solar Component Guide (Kindle Locations 1198-1199). Digital Publishing Ltd.

Which off-grid system to choose?

Important:

Whether to choose a stand-alone or a hybrid off-grid system depends on:

- Whether you use your building on a yearly or a seasonal basis.
- Whether the site is easily accessible or not.
- How much total daily you need.
- What kind of electrical applications you use – whether critical or not.

In a hybrid system, the alternative generator is usually a diesel, propane or gasoline one, and less commonly – wind generator.

As a rule, hybrid systems are recommended when daily energy needs exceed 2.5 kW.

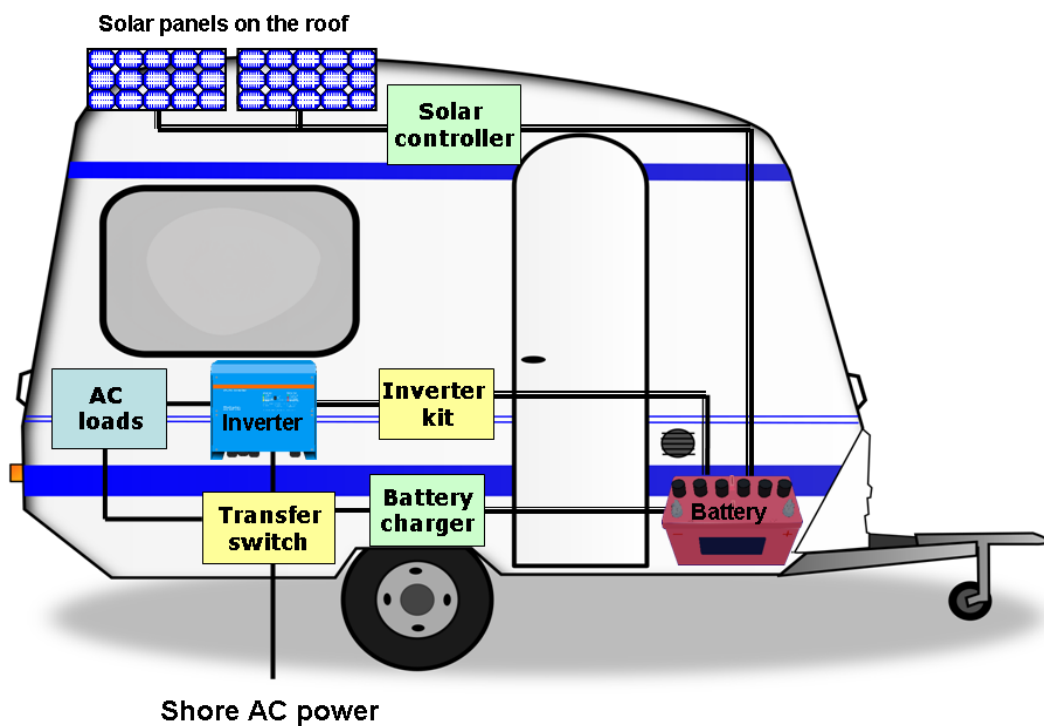
Also, a hybrid system is recommended when the available sunlight in your area is not enough to meet the desired Days of Autonomy (DoA) – the number of days where the battery is not expected to receive a sufficient charge from the solar panels. A higher DoA value always means a more expensive battery bank.

Mobile solar power systems

With solar power on your RV, you gain independence from any utility grid – you feel free to park wherever you want, and you don't care about finding shore power.

Mobile solar power systems are known for their lack of maintenance. In a residential photovoltaic system, you usually have a flooded lead-acid battery to maintain. In RVs and motorhomes, batteries are typically maintenance-free – AGM or lithium-ion ones. What is more, solar panels mounted on your caravan are easier to tilt and clean than panels on the roof of your house.

Mobile solar power systems are safe and reliable as long as they are sized and installed correctly. They usually operate at 12 V and up to 40 A.



Important:

Here are the most important benefits of using solar panels for camping and boondocking:

- Solar power is free (although solar power investment is not free).
- Solar power is everywhere you go.
- Solar power enables you to travel to sites with no power hookups available.
- Solar power allows you to save money on conventional power.
- Mobile solar power systems are maintenance-free, excluding the occasional solar panel cleaning. Also, no other activity is required, unless you need to replace your battery after 7-10 years or decide to add more panels to the system.
- Extends the life of your leisure battery.

Differences between residential and mobile solar systems

Photovoltaic systems installed on RVs, caravans, campers or boats do not differ much from typical off-grid residential systems regarding the components used – solar panels, charge controller, battery, inverter, cabling, breakers and fuses.

Mobile solar power systems, however, differ substantially from home off-grid photovoltaic system in the following:

- They have much less installed solar power as a result of the limited space of your RV, caravan, camper, or boat.
- The system voltage is most commonly 12V DC.

In residential photovoltaic systems, longer cable runs – between the solar array and the controller or between the battery and the inverter – are quite common. For the sake of reducing voltage drops and avoiding cables of larger gauge, home photovoltaic systems typically are based on a system voltage of 24V, 48V or higher. In RV and marine systems, a system voltage 12V DC is okay since distances are shorter, voltage drops are not so significant, and larger cable sizes are usually not needed. Also, 12 V DC is very convenient as a system voltage for RV and marine solar as many appliances operate directly on 12 V DC.

- Batteries are smaller – in weight, dimensions, and capacity – and typically sealed.

In mobile solar power systems, battery banks are smaller due to the typically lower daily consumption. What is more, flooded lead-acid batteries are rarely used. Instead, the most widely used battery types are sealed lead-acid (typically AGM, rarely gel ones) or lithium phosphate (also known as 'lithium-ion' or merely 'lithium') ones. In vehicles, wet lead-acid batteries are a safety hazard, while sealed batteries are much easier to handle, transport, and maintain. Sealed batteries can be turned upside down without the risk of spilling the electrolyte and are maintenance-free.

- In an RV solar panel system, it is possible to use high-power devices (such as air-conditioner, heaters, etc.) as long as the RV has been parked and connected to shore power. In residential solar panel

systems, high-power loads are generally excluded and replaced with their energy-efficient options.

In an off-grid system, using any high-power appliances with the purpose of air-conditioning or heating is not recommended from an energy efficiency point of view. Using large loads would require a costly battery bank which is expensive, needing a long time to get fully charged and tough to maintain.

- An RV or marine solar panel system typically includes an AC charging system to charge the battery when connected to shore power automatically.

As long as everything with the battery management system is okay, a leisure battery can be charged by several sources at the same time – a solar array, an external generator, and a shore power outlet.

- The solar charge controller can be designed to charge both the leisure battery (which is a deep-cycle one) and the vehicle starting battery.
- Marine solar systems (unlike RV solar ones) should be built with components resistant to the corrosive environment.

Often components for marine and RV solar systems are referred to the same way. Due to the highly corrosive salty air marine environment, marine solar components can be used in RV, while the opposite is often not possible. For this reason, solar components intended for use in marine PV systems are often denoted as 'marinized.'

Most devices and appliances used in RV or boats run on 12V DC. The size of the battery and the panels depend on how much electricity you need daily, which in turn is up to the appliances you plug in. Often it comes out that you

have neither enough room for a battery of specific capacity, nor sufficient space on your roof for the installed solar power you need. In such a case, you have to reduce your power usage.

Why it is important to size your solar system correctly

The size of the solar panel system you need depends on your daily electricity needs, the space available on the roof of your RV or boat, and your budget. Before making up your mind to invest in a mobile solar system, you should be in clear how you are going to use the daily generated solar power.

A wrongly sized photovoltaic system means either spending too much money on equipment you are not going to use fully or building a system that does not cover your daily energy needs and regularly runs out of power. In either of these cases, will have your money wasted and eventually fed up with solar power stuff.

In our books '**Off Grid And Mobile Solar Power For Everyone: Your Smart Solar Guide'** [Kindle and Paperback Edition] ASIN: B07B296DGQ

<https://www.amazon.com/Grid-Mobile-Solar-Power-Everyone-ebook/dp/B07B296DGQ/>

and

The Ultimate Solar Power Design Guide: Less Theory More Practice [Kindle and Paperback Edition]

<http://www.amazon.com/Ultimate-Solar-Power-Design-Guide-ebook/dp/B0102RCNOG/>

You are going to find all the details you need to build a solar power system matching your specific case. The first book is for beginners to intermediate, while the second is targeted to advanced solar power users.

Also, these books reveal to you how to size an optimal performing solar power system without exceeding your budget available. You'll find out how to expand your system quickly and how to maintain it. Also, you'll be provided with lots of tips and tricks, and you will find out how to avoid all the nasty moments you are likely to experience with an underperforming system, often meaning a loss of money.

Whichever source you decide to choose for sizing your solar system, what you should start with is evaluating your location, also known as 'solar site survey.'

Solar site survey guide

Is your building or motorhome solar-ready?

Even if your location has excellent solar potential, your building might not be fitted for a photovoltaic system.

Your building is prepared for installing a solar system if:

- You have already made it energy-efficient.
- Your roof or yard is unshaded, at least during the sunny hours of the day.
- Your roof has a Southern orientation if you live in the US, UK, Canada, or India, or, a Northern Orientation, if you live in South Africa, Australia or New Zealand.
- Your roof is in excellent condition.

How to assess your location for the solar resource?

The spot where you intend to install your solar array or park your RV should have:

- a) Clear and unobstructed access to the sun throughout the day (between 9 a.m. and 3 p.m.) and throughout the year.**

This means lack of any obstacles between the sunbeams and the solar panel surface – trees, chimneys, lamp-posts, buildings, etc.

- b) Preferably a South-facing roof, if you live in the USA, UK, India or Canada, or North-facing roof, if you live in Australia, New Zealand or South Africa**

An orientation towards True South (if you live in USA, UK, India, or Canada) or True North (if you live in Australia, New Zealand, or South Africa) is not mandatory.

A somehow Southeast or Southwest (for the Southern hemisphere Northeast or Northwest, respectively) facing roof is also acceptable.

A deviation within 20-30 degrees of the True South (or True North, respectively) results in a less than 10% degradation of solar array's performance, which is acceptable.

Important:

A pure Eastern or pure Western orientation is not recommended since as a rule, solar panels should be exposed to direct sunlight for at least 6 hours a day.

You should mind that installing a solar system on a roof facing East or West might result in **20% degradation of system performance**, which is a severe compromise!

The roof can be either sloped or flat. Flat roofs allow easier to implement the desired tilt angle of the panels, but a sloped roof will do as well.

c) Enough space for placing the solar panels

The area you need for your system depends mainly on:

- How much energy it is designed to produce.
- Types of PV panels you are going to install (monocrystalline, polycrystalline or thin-film).
- The size of the panels (to a lesser extent because, as a rule, solar panels do not differ much in size).

Important:

The less efficient panels you use, the larger the area you need for your solar array but also, the lower the costs.

Monocrystalline panels are the most efficient, while thin-film panels are the least efficient ones.

Why the condition of your roof does matter

A solar system can be installed on any roof. There are two options for installing the solar panels – either mounting them on the roof or replacing the roof tiles with solar panels.

As a rule, roofs with composition shingles are the easiest to work with, while those with a slate are the most difficult ones.

Here are the drawbacks of solar panels mounted on the roof:

- The panels must be removed upon performing any roof repair or replacement activity.
- Installation of brackets and racks can result in roof leaks.
- Roof warranty can be affected.
- The people to whom you are about to sell your house might find the solar panels of the roof unattractive.

However, the cost of roof-integrated installation is up to 40% more compared to roof-mounted installation.

If your roof is old and is to be replaced soon, to minimize any unnecessary costs, a smart idea is to replace it just while the solar system is being installed.

If you have a new roof, you should consult both your solar vendor and the roof repair company how the installation of a PV system will affect your roof warranty.

Solar panels can be placed on the ground as well, on a fixed or tracking mount.

Roof-mounted or portable solar panels for your RV?

When camping or boondocking, you can complement panels mounted on the roof of your RV with a portable solar kit.

Thus you can not only combine the pros of both approaches but also expand the capacity of your solar system by making it ready to meet any increase in your daily electricity needs.

In winter, a solar array mounted on the roof provides much less solar-generated electricity because in winter PSH decreases, and the sun is lower beyond the horizon than in summer. For this reason, it's more beneficial if in winter you have a portable (i.e., ground-mounted) solar panel that can be directly tilted towards the sun.

Also, if the installed power of the roof-mounted array is comparable to the capacity of the portable array, you are just free to choose where to set up camp without worrying about how much your system will underperform under shady trees on a bright, sunny day.

Should you tilt the solar panels on your RV?

Do you know that while a panel pointed directly at the sun is generating the maximum amount (100%) of electricity, such a panel is producing just 10% less electricity when tilted 25 degrees off the optimal angle?

For a mobile solar system, where we talk about just hundreds of watts, tilting and rotating solar panels is not worth the effort. 10% of the solar-generated electricity is not a significant loss.

Tilting the solar panels of your RV only makes sense during winter months when the sun is low over the horizon. In winter, solar panels tilted to 30 rather than 0 degrees results in more than 50% increase in the solar power output. In summer, the effect of tilting can be neglected since tilting would lead to an increase of as less as 10% in the solar-generated electricity. Mind, however, that tilting your panels at an angle for sure makes them more vulnerable to ripping off by the wind.

If mounted on the roof, your panels do not need to be tilted in summer since the sun is high in the sky. In winter, a tilt of 45 degrees towards the horizon is recommended to get the most irradiance from the sun which is low in the sky.

As to the azimuth – if you live in Europe, USA, India, or Canada, your solar array should be oriented towards South, i.e., the position of the sun at solar noon (the moment when half of the time has passed between the sunrise and sunset). If you live in Australia, New Zealand, South Africa, or South America, your solar panels should be oriented towards North.

Also, you don't need to install an automatic tilting or tracking mechanism for the solar panels on the roof of your RV. The profitability of such a mechanism is questionable, especially in the typical camping season. What is more, it compromises the reliability of your solar array, let alone the additional costs.

How to perform a solar site survey?

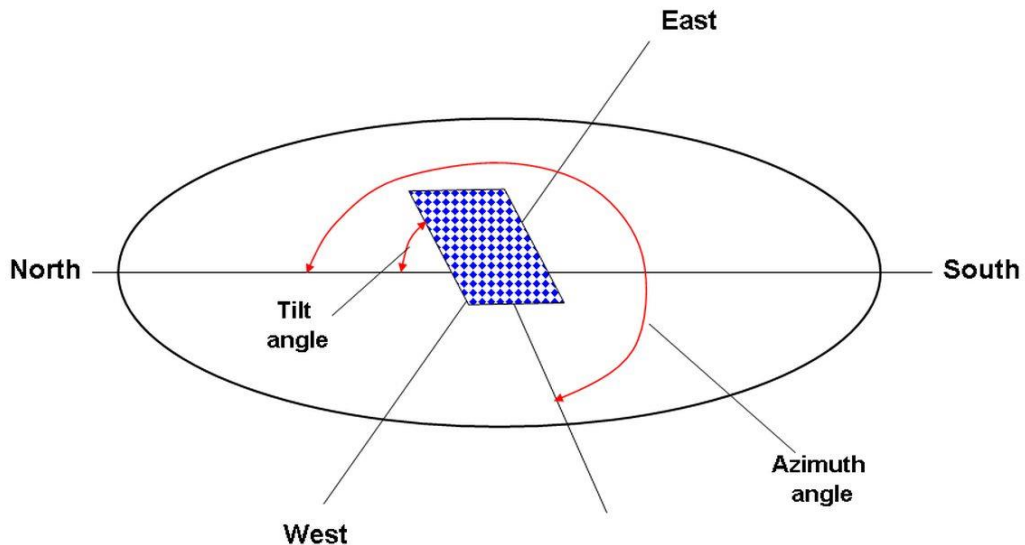
Performing a solar site survey is the starting point of launching every photovoltaic system.

Important:

When searching for an appropriate site for your solar panels, you should consider:

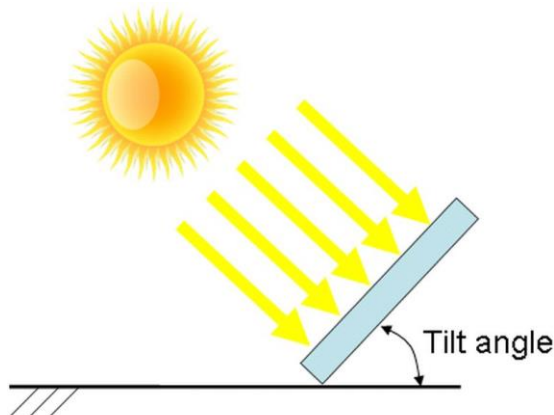
- The orientation towards the sun.
- Lack of any shading obstacles – during the whole day and throughout the whole year.
- Minimization of DC cable length between the solar panels and the charge controller (for off-grid systems) and between the solar panels and the inverter (for grid-tied systems).
- Aesthetics.
- Protection from theft and vandalism.
- Easy access for solar panel installation and maintenance.

To make better use of this guide, you should be familiar with some fundamental issues, such as azimuth and tilt angle:



Azimuth is the angle between the direction perpendicular to the array's surface and the True North.

Tilt (elevation) is the angle measured between a mounted PV panel and a horizontal ground surface:



Solar arrays are recommended to install on roofs facing True South (for North America – USA, Canada, Europe, or India) or True North – if you live in Australia, New Zealand, or South Africa.

Installation of panels on roofs facing North (or South – if you live in the Southern hemisphere) is **NOT** recommended.

What to do during a solar site survey?

Step 1: Assess any possible shading by nearby objects.

The PV array should be provided with clear and unobstructed access to sunlight between 9 a.m. and 3 p.m. every day, throughout the year.

Important:

Shading is not recommended, at least between 9:00 a.m. and 3:00 p.m. Even small shadows can affect the power output of the PV array severely.

To get the maximum of your survey, you should perform it during a bright and sunny day, preferably in summer, when trees have their full foliage mass.

During the site survey, you should be looking for the following obstacles:

- Buildings. Try to get some info on whether a new building is not being planned nearby, throwing shade to your site.
- Chimneys, power lines, poles, hedges, and neighboring roofs.
- Trees. If you're performing your site survey in winter, you should keep in mind that in summer trees look different than in winter.
- Hills and other earth obstacles – mind that in winter sun is much closer to the horizon than in summer.

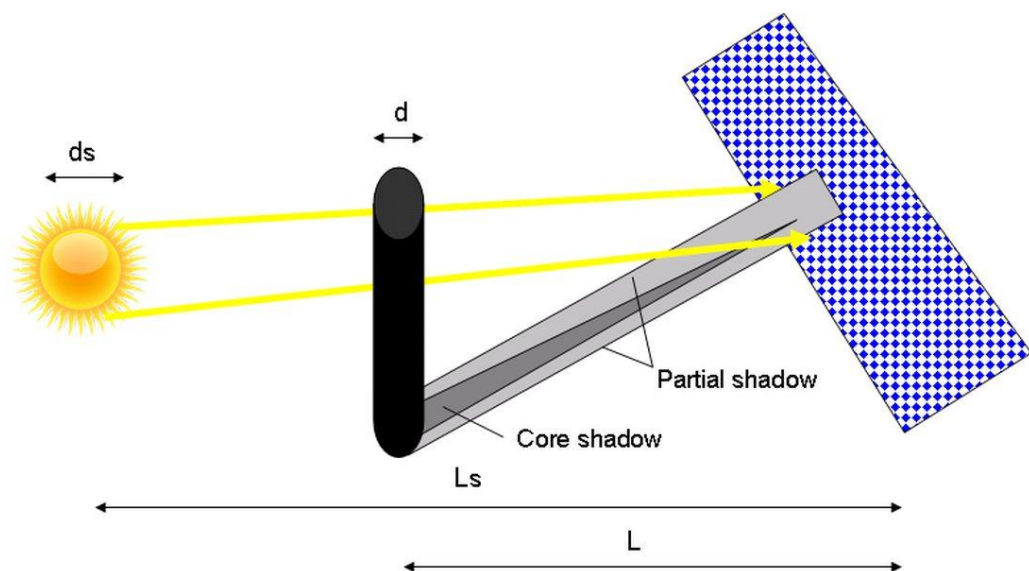
A site unshaded during a part of the day might be partially shaded during another part of the day.

Similarly, if a site is unshaded in summer, it might be shaded in winter, as in winter sun is lower than in summer (and close to the horizon) and casts longer shadows.

Important:

Tips on how to avoid shading

- Find out the optimum distance between a solar panel and a direct shading object:**



$$L = (L_s \times d) \div ds,$$

Where:

L is the optimum distance between a PV panel and a direct shading object, m

L_s is the distance from the Earth to Sun, km

d is the thickness of the shading object, m

ds is the diameter of the Sun, km

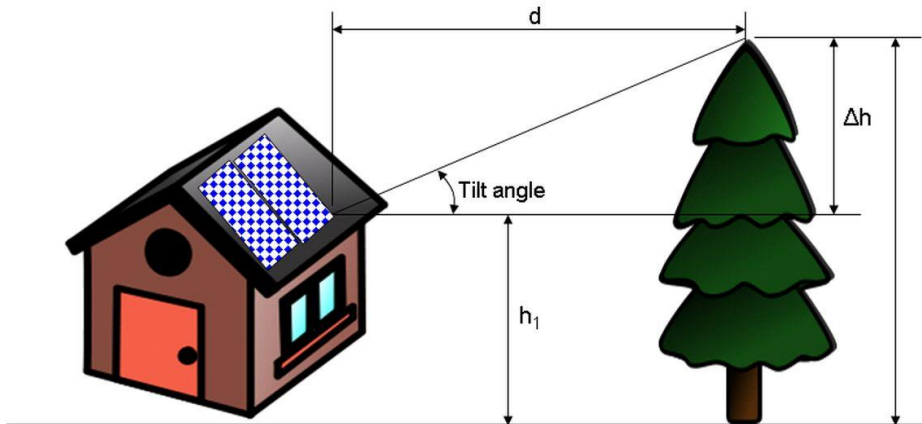
Since the distance from the Earth to the Sun is 150 million km, and the diameter of the Sun is 1.39 million km, the above formula could be simplified as follows:

$$L = 108 \times d,$$

Where **L** is in m and **d** is in m.

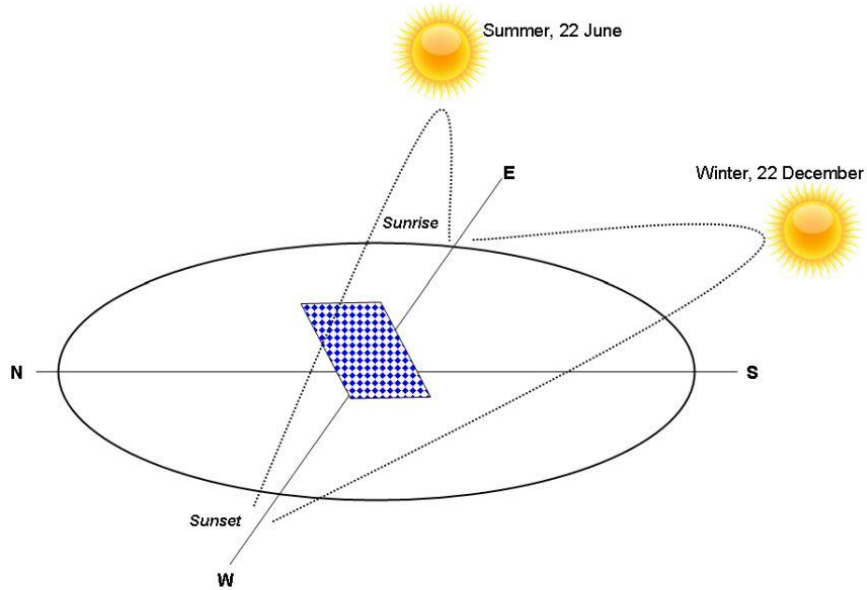
b) Find out the tilt angle to avoid shading of a nearby obstacle

Here is a practical formula for tilt calculation with regards to a shading obstacle in front of the solar panels.



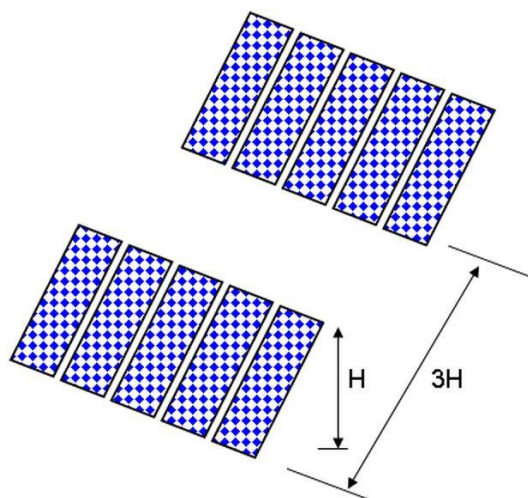
$$\text{Tilt angle} = \arctan [(h_2 - h_1)/d] = \arctan (\Delta h/d)$$

Regarding any cast-shading objects, it should be noted that in winter months the arc of the sun is the lowest over the horizon.



This means that while an object is not a shading obstacle in summer, it can cast a shadow in winter!

c) Placing the solar panels to avoid inter-row shading



To avoid inter-row shading, you should place two individual neighbor rows at a space that is at least 3 times the maximum height of a tilted row.

Step 2: Determine your roof area.

Usually, access space around the panels adds up to 20% to the solar panel area.

Important:

Don't try to use every last square inch on your roof to install a solar array because:

- The panels get challenging to install.
- The panels get hard to clean.
- Wind loading at the edge of the roof increases.
- From a regulatory point of view, you are likely to violate the provisions for providing available space for fire-fighters and other staff that might need to access the roof area.

Also, consider the dead spaces around the array. These are the spots that are either shaded or need to be provided between the panels to ensure good cooling.

Step 3: Determine the orientation and tilt angle.

In grid-tied systems, the orientation and tilt angle of the solar panels depend on the roof orientation and slope.

You can use a compass to check what direction your roof faces, and a spirit level to measure the angle of the roof from the horizontal.

If your site is located in the Northern hemisphere, you should look towards the South, East, and West. If your

location is in the Southern hemisphere, you should look towards North, East, and West. If you live near the equator, you should look towards East and West.

The ideal roof for mounting your PV array is a roof facing South if you live in the Northern hemisphere and facing North if you live in the Southern hemisphere.

Things, however, are not as crucial as appearing. You can get 90-95% of a PV panel's full power if it is located within 20 degrees of the sun's direction. This means 20 degrees to the East or the West from the full South.

Important:

Recommended limits for mounting PV array within:

Azimuth: ± 30 degrees East and West of due South (or due North)

Tilt angle: ± 15 degrees from the latitude

Practical tips to determine the orientation and tilt angle

Important:

A practical rule to find out the optimal orientation:

At solar noon (when the sun is highest above the horizon) place a straight object, such as a pencil or a ruler, perpendicularly to the surface of your PV panel.

If the panel is perpendicular to the sun, you'll see no shadow. Otherwise, the object will throw a shadow, and you have to make some adjustment to position the PV panel optimally.

Important:

Practical advice about determining the tilt angle:

- For maximizing the solar-generated power in summer, adjust the tilt of the array at the value of the latitude less 15 degrees.
- For maximizing the solar-generated power in winter, the optimal tilt angle is latitude plus 15 degrees.
- For maximizing the solar system performance for the maximum number of hours throughout the year, mount the PV array to a tilt angle equal to the latitude.

Important:

What if you select a tilt angle other than the latitude?

- If your PV array is tilted at an angle **lower** than the altitude, your system will produce the maximum power in summer but will underperform in winter. For grid-tied systems, this is not a critical issue – on the one hand, your house is connected to the grid, and on the other hand, there is less sun in winter anyway.
- On the opposite, if the solar array is tilted at an angle **higher** than the altitude, your system will produce the maximum power in winter but will underperform in summer.
- Of course, if it is technically feasible, you can choose to set one tilt angle in summer and another one in winter. This is recommended for off-grid systems

where the maximum performance is a target throughout the whole year.

Important:

Reduce the solar-generated power in summer or winter?

This depends on the solar system type.

If you have an off-grid (stand-alone) system, it's unlikely that you'd prefer less power output in winter, especially when it's cloudy, and there are less Peak Sun Hours (PSH) than in summer.

With an off-grid system it's normal to struggle for high power output both in summer and in winter to meet most of your daily energy needs.

If you have a grid-tied system, however, we would expect you not bother to seek for high solar performance in winter. First, you are connected to the grid, and your household power needs are satisfied anyway. Second, in winter it's often cloudy, and PSH is less than in summer.

Step 4: Choose a mounting method of the solar array.

There are the following types of solar panel mounting:

- Sloped roof mounting
- Flat roof/ground mounting
- Roof-integrated mounting

- Wall mounting.

Flat roof/ground mounting gives you the most freedom to optimize the position of the PV array according to the solar resource. There are four types of flat surface mounted racks:

Fixed racks:

- Fixed at one orientation facing due South.
- Slope (tilt angle) equal to the site latitude.

Manually adjustable racks:

- Allow changing the tilt angle.
- Usually, the tilt angle is changed at the beginning of every season.
- Result in a 12% power increase compared to fixed mount system.

Single axis tracking racks:

- Follow the sun from east to west every day.
- Require additional components and maintenance.
- Increase the power output by 25% compared to the fixed mount system.

Dual axis tracking racks:

- Continually orient the PV panels perpendicularly to the brightest part of the sky.

- Require additional components and maintenance.
- More common than single axis tracking racks.
- Increase the power output by more than 30% compared to the fixed mount system.

The other types of mounting give you less freedom since you are not able to orientate the solar array to receive the maximum irradiation. Remember, anyway, that the orientation of the solar panels is more important than the tilt.

Important:

Regarding the mounting constructions, mind that:

- Not every mounting construction is suitable for any panel, while certain kinds of panels are designed for a specific mounting method.
- It's a good plan to ask the supplier of the panels to install them on the roof.
- To ensure sufficient cooling of the panels, you should provide enough room beneath them.
- A design visa or a building permit might be required.
- All the necessary construction regulations must be complied with.

Photovoltaics in summary

- Solar photovoltaic systems use the sun's light rather than the sun's heat.
- You cannot benefit a solar power system unless you make your house energy-efficient.
- Photovoltaics deliver maximum performance and efficiency at a sufficient amount of direct sunlight, economical use of electricity, and improved energy efficiency.
- Solar irradiation depends on geographic location, roof orientation, slope, and shading.
- The two main types of solar electric systems are grid-tied and off-grid.
- Grid-tied systems are connected to the utility grid. They provide their owners with the opportunity to reduce their monthly electricity bill. Key components of such systems are the solar array and the inverter.
- Off-grid systems are an alternative to the utility grid in rural and remote areas. They are usually more complex and more expensive than grid-tied systems. Off-grid systems can be either stand-alone or hybrid ones. Key components of such systems are the solar array, the battery, and the charge controller.
- Small photovoltaic systems can be more cost-effective than larger solar systems and conventional electrical supply. Larger systems have high initial cost but low maintenance and operational costs.

Resources on the authors' website

Free Simple Solar Calculators

1. Free Simple Solar Panel Calculator and Solar Power Calculator

Calculate the size of your solar power system, whether off-grid or grid-tied. You will also find instructions on how to calculate the number of solar panels you needed. They are based on calculated values of the size of your system.

<http://solarpanelsvenue.com/free-solar-panel-calculator-solar-power-calculator/>

2. Free Simple Solar Cable Calculator

Determine the wire size based on DC power requirements and temperature influence:

<http://solarpanelsvenue.com/free-solar-cable-size-calculator/>

3. Free Solar Panel Output Calculator

You can use this calculator to estimate the solar energy a solar panel can produce daily based on the panel's rated power and solar energy available at your place. The results can be used to compare the performance of various solar panels available on the market. The simplicity of this calculator justifies 'the business case' accuracy. For example, you can get more accurate results if you use a calculator considering all electrical parameters of a solar panel and how they depend on temperature.

<http://solarpanelsvenue.com/solar-panel-output-calculator/>

Free PWM Charge Controller Calculator

Use this calculator to size your PWM charge controller based either on solar panels size or to estimate how many panels you can connect to your controller.

<http://solarpanelsvenue.com/pwm-solar-charge-controller-calculator/>

Stay tuned for more!

We constantly add new free calculators to our site. Check it out regularly.

Thank you very much for reading this book!

For updates about new releases, as well as exclusive promotions, visit the authors' website and sign up for the VIP mailing list at:

<http://solarpanelsvenue.com/authors.php>

We need your valuable feedback. If, by any chance, you are disappointed with our book, please let us know directly via our email:

authors@solarpanelsvenue.com.

We are going to work on your feedback and fix our mistakes in the updated version of the book.

Your voice does matter!

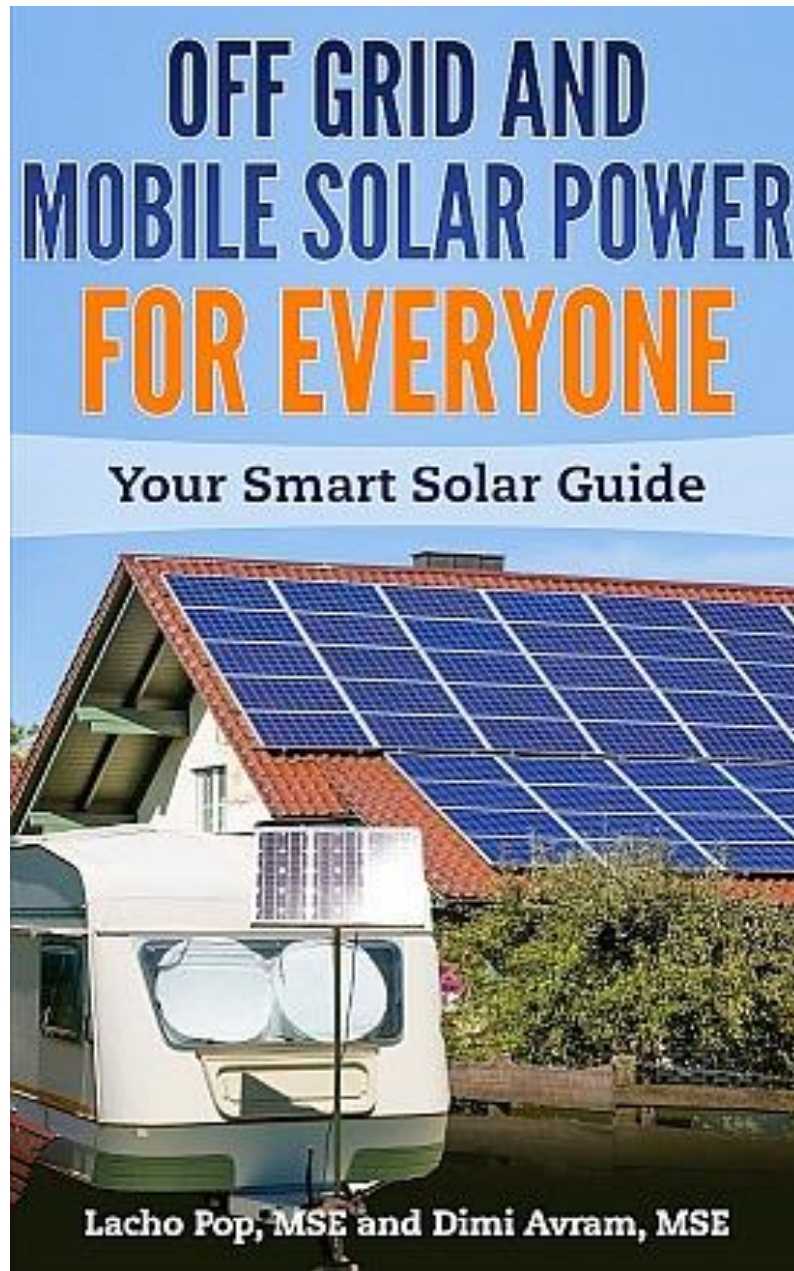
It helps the other readers to get oriented about the value of this book.

It helps us to improve the content of this book.

Thank you in advance for this gesture of goodwill.

Also by the Authors:

Off Grid And Mobile Solar Power For Everyone: Your Smart Solar Guide [Kindle and Paperback Edition] **ASIN: B07B296DGQ**



Click on the link to get it NOW:

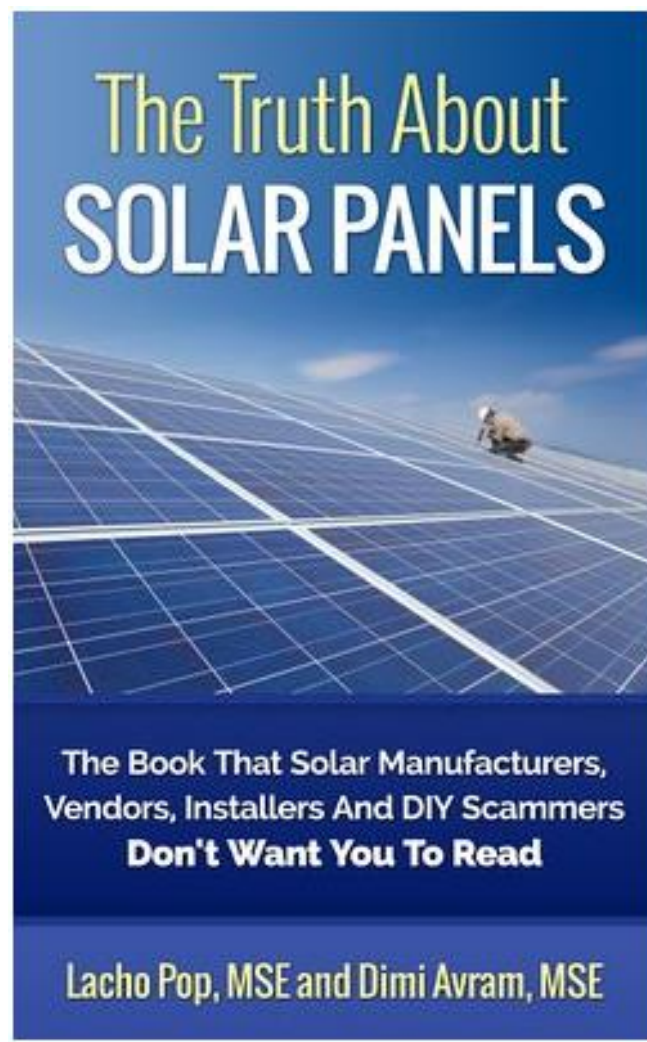
<https://www.amazon.com/Grid-Mobile-Solar-Power-Everyone-ebook/dp/B07B296DGQ/>

The Truth About Solar Panels: The Book That Solar Manufacturers, Vendors, Installers And DIY Scammers Don't Want You To Read [Kindle and Paperback Edition]

ASIN: B00Q95UZU0, ISBN: 978-6197258011

Click on the link to get it NOW:

<http://www.amazon.com/Truth-About-Solar-Panels-Manufacturers-ebook/dp/B00Q95UZU0/>



Click on the link to get it NOW:

<http://www.amazon.com/Truth-About-Solar-Panels-Manufacturers-ebook/dp/B00Q95UZU0/>

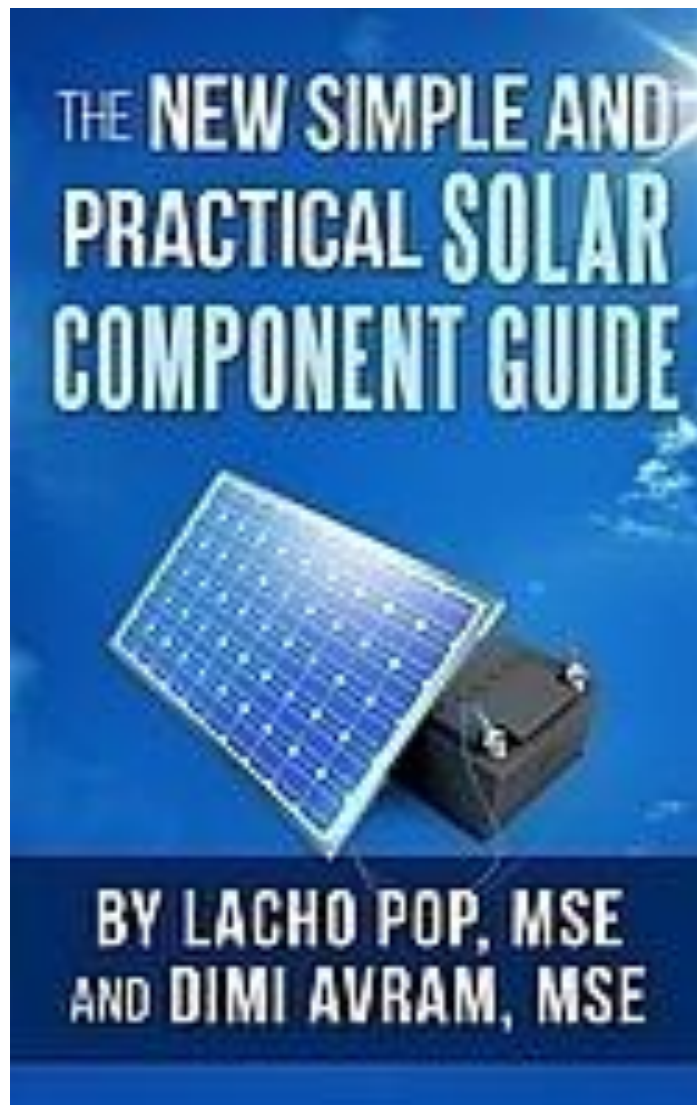
The New Simple And Practical Solar Component

Guide [Kindle Edition, Paperback, and Audio Edition]

ASIN: B07S9GPN4B

Click on the link to get it NOW on Amazon:

<https://www.amazon.com/Simple-Practical-Solar-Component-Guide-ebook/dp/B07S9GPN4B/>



Click on the link to get it NOW:

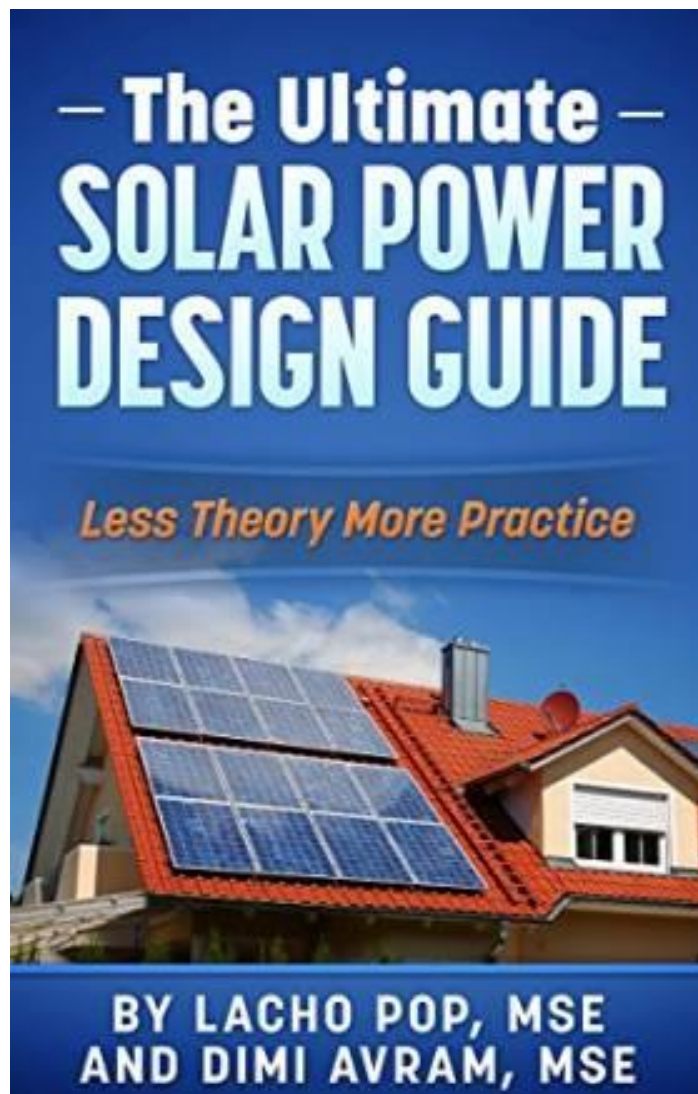
<https://www.amazon.com/Simple-Practical-Solar-Component-Guide-ebook/dp/B07S9GPN4B/>

The Ultimate Solar Power Design Guide: Less Theory More Practice [Kindle and Paperback Edition]

ASIN: B0102RCNOG, ISBN-13: 978-6197258042, ISBN-10: 6197258048

Click on the link to get it NOW:

<http://www.amazon.com/Ultimate-Solar-Power-Design-Guide-ebook/dp/B0102RCNOG/>



Click on the link to get it NOW:

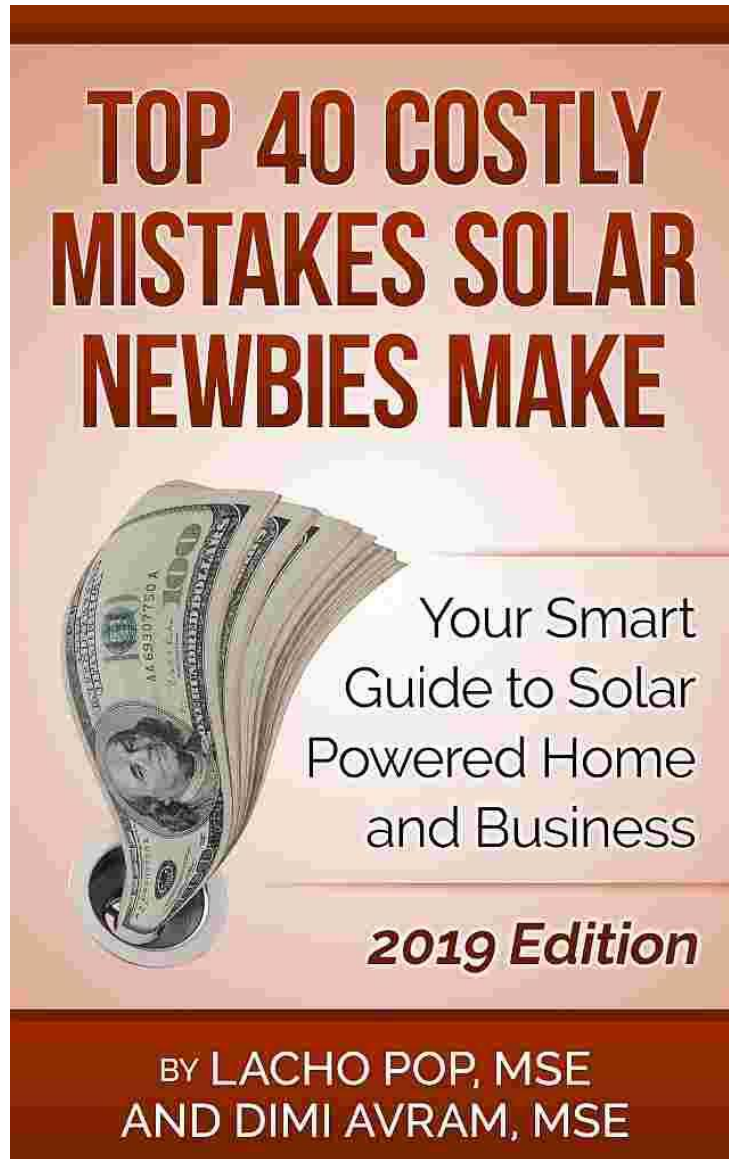
<http://www.amazon.com/Ultimate-Solar-Power-Design-Guide-ebook/dp/B0102RCNOG/>

Top 40 Costly Mistakes Solar Newbies Make: Your Smart Guide to Solar Powered Home and Business

2016 Edition [Kindle,Paperback, and Audio Edition], Kindle ASIN: B07QHLJTPZ, Paperback ISBN-13: 978-6197258073, Audio 2019 Edition ISBN 978-6197258080]

Click on the link to get it NOW:

<https://www.amazon.com/dp/B07QHLJTPZ>



Click on the link to get it NOW:

<https://www.amazon.com/dp/B07QHLJTPZ>